

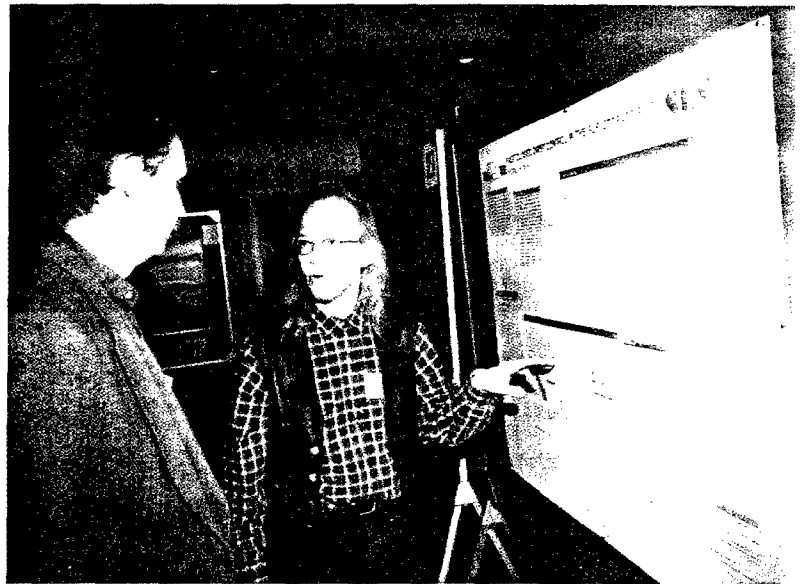
# PROCEEDINGS OF THE 1999 PARTICLE ACCELERATOR CONFERENCE

VOLUME 2 OF 5

PAGES 649 - 1476



BROOKHAVEN NATIONAL LABORATORY  
Brookhaven Science Associates





# REPORT DOCUMENTATION PAGE

Form Approved  
OMB No. 0704-0188

Public reporting burden for this collection of information is estimated to average 1 hour per response, including the time for reviewing instructions, searching existing data sources, gathering and maintaining the data needed, and completing and reviewing the collection of information. Send comments regarding this burden estimate or any other aspect of this collection of information, including suggestions for reducing this burden, to Washington Headquarters Services, Directorate for Information Operations and Reports, 1215 Jefferson Davis Highway, Suite 1204, Arlington, VA 22202-4302, and to the Office of Management and Budget, Paperwork Reduction Project (0704-0188), Washington, DC 20503.

1. AGENCY USE ONLY (Leave Blank)		2. REPORT DATE June 1999	3. REPORT TYPE AND DATES COVERED Final; March 27- April 2, 1999	
4. TITLE AND SUBTITLE Proceedings of the 1999 Particle Accelerator Conference Volumes 1 through 5			5. FUNDING NUMBERS G	
6. AUTHORS A. Luccio, W. MacKay - editors				
7. PERFORMING ORGANIZATION NAME(S) AND ADDRESS(ES) Brookhaven National Lab P.O. Box 500 Upton, NY 11973			8. PERFORMING ORGANIZATION REPORT NUMBER	
9. SPONSORING / MONITORING AGENCY NAME(S) AND ADDRESS(ES) U.S. DOE National Science Foundation Office of Naval Research			10. SPONSORING / MONITORING AGENCY REPORT NUMBER	
11. SUPPLEMENTARY NOTES				
12a. DISTRIBUTION / AVAILABILITY STATEMENT Available to public			12b. DISTRIBUTION CODE	
13. ABSTRACT (Maximum 200 words) Papers for the eighteenth biennial Particle Accelerator conference, an international forum on acceleator science and tehcnology held March 27-April 2, 1999 in New York City, organized by Brookhaven National Lab.				
14. SUBJECT TERMS			15. NUMBER OF PAGES 3779	
			16. PRICE CODE	
17. SECURITY CLASSIFICATION OF REPORT Unclassified	18. SECURITY CLASSIFICATION OF THIS PAGE Unclassified	19. SECURITY CLASSIFICATION OF ABSTRACT Unclassified	20. LIMITATION OF ABSTRACT UL	

NSN 7540-01-280-5500

Standard Form 298 (Rev. 2-89)  
Prescribed by ANSI Std. Z39-1  
298-102

20000229018



**BROOKHAVEN**  
NATIONAL LABORATORY

The  
American  
Physical  
Society

# Proceeding of the 1999 Particle Accelerator Conference

(Editors: A. Luccio, W. MacKay)

Volume 2 of 5

Pages 649 – 1476

**DISTRIBUTION STATEMENT A**  
Approved for Public Release  
Distribution Unlimited

Papers from the eighteenth biennial Particle Accelerator Conference, an international forum on accelerator science and technology held March 27 – April 2, 1999 in New York City, organized by Brookhaven National Laboratory. Sponsored by the Institute of Electrical and Electronics Engineers Nuclear and Plasma Sciences Society and the American Physical Society Division of Physics of Beams, and with support from the U.S. Department of Energy, the National Science Foundation, the Office of Naval Research, and Brookhaven Science Associates (BSA).

DTIC QUALITY INSPECTED 3

20000229 018

Proceedings of the  
1999 IEEE Particle Accelerator Conference

Abstracting is permitted with credit to the source. Libraries are permitted to photocopy, beyond the limits of U.S. Copyright law for private use of patrons, those articles in this volume that carry a code at the bottom of the first page, provided the per-copy fee indicated in the code is paid through the copyright Clearance Center, 222 Rosewood Drive, Danvers, MA 01923. For other copying, reprint, or republication permission, write to the IEEE Copyright Manager, IEEE Service Center, 445 Hoes Lane, P.O. Box 1331, Piscataway, NJ 08855-1331. All rights reserved. Copyright ©1999 by the Institute of Electrical and Electronics Engineers, Inc.

IEEE Catalog Number: 99CH36366  
Library of Congress Number: 88-647453

ISBN-Softbound: 0-7803-5573-3  
Casebound: 0-7803-5574-1  
Microfiche: 0-7803-5575-X  
CD-Rom: 0-7803-5576-8

Additional copies of this publication are available from:

IEEE Service Center  
445 Hoes Lane  
Piscataway, NJ 08854-4150, USA

1-800-678-IEEE (1-800-678-4333)  
1-732-981-1393  
1-732-981-9667 (FAX)  
e-mail: [customer.service@ieee.org](mailto:customer.service@ieee.org)

## **VOLUME 2: CONTENTS**

(A DETAILED TABLE CAN BE FOUND IN VOLUME 1)

**Volume 2: POSTER, pp. 649 – 1476**

<b>ACCELERATOR RING CONTROL SYSTEMS.....</b>	<b>649</b>
<b>ROOM TEMPERATURE RF .....</b>	<b>768</b>
<b>SUPERCONDUCTING RF .....</b>	<b>913</b>
<b>RF POWER SOURCES .....</b>	<b>998</b>
<b>FEEDBACK SYSTEMS.....</b>	<b>1061</b>
<b>BEAM INJECTION/EXTRACTION, TRANSPORT AND TARGETRY .....</b>	<b>1225</b>
<b>CRYOGENICS .....</b>	<b>1324</b>
<b>VACUUM TECHNOLOGY .....</b>	<b>1333</b>
<b>ALIGNMENT AND SURVEY .....</b>	<b>1378</b>
<b>SUBSYSTEMS, TECHNOLOGY AND COMPONENTS.....</b>	<b>1393</b>

# RESONANCE CONTROL COOLING SYSTEM FOR THE APT/LEDA CCDTL HOT MODEL \*

R. Floersch, G. Domer, N. Jett

AlliedSignal Federal Manufacturing & Technologies\*\*, Kansas City, Missouri 64141 USA

## Abstract

The Hot Model for the Coupled Cavity Drift Tube Linac (CCDTL) resonance control cooling system (RCCS) for the Low Energy Demonstration Accelerator (LEDA) [1] in support of the Accelerator Production of Tritium (APT) [2] is described. Two hydraulic control loops are described that control the frequency in the CCDTL Hot Model cavity. The two loops supply the required flow to the 32 channels. Control system schema is described to regulate resonant frequency during steady state operation.

## 1 THE HOT MODEL

The Hot Model was built to assess the design of the interface between single and dual gap cavities and is shown in Figure 1. Additionally, it will yield pressure drop and heat transfer information that will be useful for designing the LEDA CCDTL RCCS. The resonant frequency in the CCDTL Hot Model will be manipulated by independently changing the temperatures of the cavities and drift tubes to change their geometry which requires two hydraulic control loops.

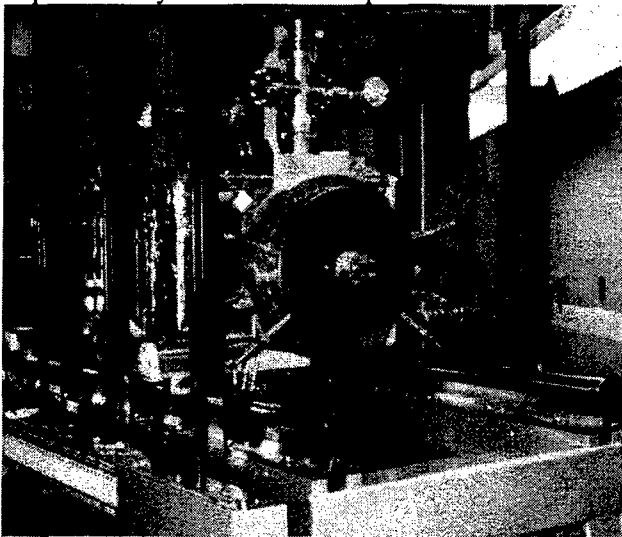


Figure 1 CCDTL Hot Model

## 2 COOLING SYSTEM

The resonance control cooling system is comprised of two independent hydraulic control loops, one drift tube and one end wall - equator.

\* Work supported by the US Department of Energy.

\*\* Operated for the US Department of Energy under Contract No. DE-ACO4-76-DP00613

## 2.1 Drift Tube Loop

The drift tube hydraulic control loop supplies controlled temperature coolant to the eight drift tube channel passages. Figure 2 illustrates the CCDTL Hot Model piping arrangement at the support stand. A total of 5.6 gallons per minute (GPM) of controlled temperature 60 °F water is required to dissipate approximately seven kilowatts of heat in these channels. The drift tube flows will be approximately 1 GPM in the single gap cavities and 0.6 GPM in the two gap cavities. Supply, return, and return bypass pipes distribute the controlled temperature water between the RCCS system (Figure 3) and the CCDTL Hot Model support stand (Figure 2).

Parallel piped flow metering valves are used to ensure the correct flow is supplied to each of the drift tube passages. Flow switches in each drift tube channel alarm when the flow drops too low.

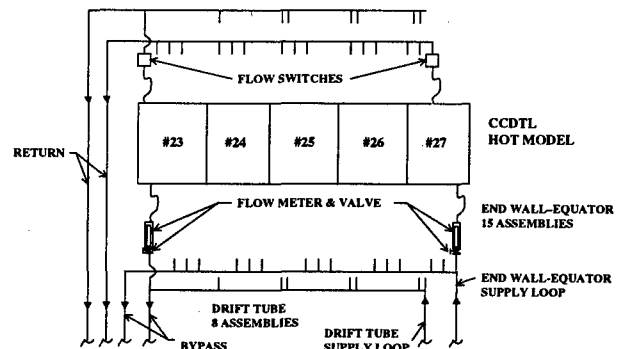


Figure 2 CCDTL Hot Model Piping Schematic

## 2.2 End Wall - Equator Loop

The end wall - equator loop is similar to the drift tube loop in that it supplies controlled temperature water to channel passages. A total of approximately 39 GPM of 75 °F controlled temperature water is required to dissipate approximately 29 kilowatts of heat in the channels. The flows in the 17 passages vary between 1.21 and 4.0 GPM among the end walls and equators.

Supply, return, and bypass piping; flow meters; and flow switches are similar to the drift tube loop.

## 2.3 Hydraulic Control Loop

Figure 3 illustrates the pump loop typical of both the drift tubes and end wall - equators. Each control loop uses a centrifugal pump to provide the driving energy. Pump flow is verified by flow meters in the suction piping of the pumping loop in combination with differential pressure

across each pump. Each pump was sized to provide excess flow (above that required to provide cooling) to support heat transfer experiments and to access the impact of flow excess or starvation on resonant frequency. In addition, excess flow is necessary to achieve a  $0.05^\circ\text{F}$  control sensitivity established as a design requirement.

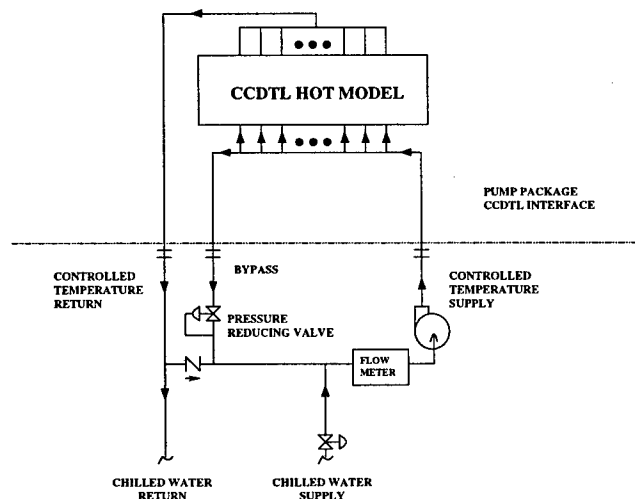


Figure 3 CCDTL Pump Loop - Typical

Pump flow is directed to a supply manifold where it is split to supply each of the drift tube channels. The excess flow passes through a pressure-reducing valve back to the pump suction. The pressure-reducing valve is set to match the resistance to flow through the drift tube channels. In the supply of each drift tube circuit, a flow indicator with metering valve is supplied to establish the desired flow. In the return of each drift tube circuit just prior to the return manifold is a flow switch to detect insufficient flow. The flow switches are monitored by the control system, which annunciates all flow alarms.

A pneumatic control valve effects control of the loop's temperature. The control valve allows a quantity of constant temperature  $50^\circ\text{F}$  water from the chilled water system to mix with the heated returning water from the drift tubes. Since the control loop is constant mass, an equal amount of heated water is returned to the chilled water system. The quantity of chilled water entering the loop is a function of the control valve's stem position and the differential-pressure in the chilled water system's supply and return legs. The pneumatic valves were purchased with linear flow characteristics and were sized relative to the loop flow rate to achieve a  $0.05^\circ\text{F}$  control sensitivity. Control sensitivity is defined as the change in loop temperature for the smallest change in valve stem position. A control algorithm (described in Section 3) manipulates the control valve.

Figure 4 shows the pump skid that houses the hydraulic control loops.

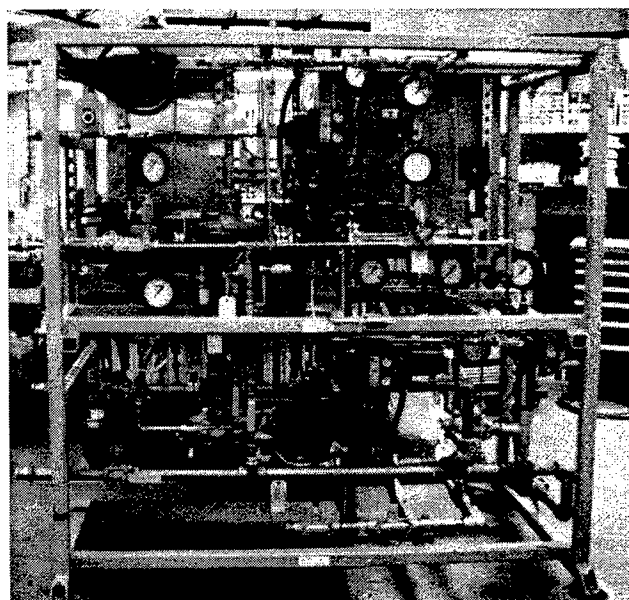


Figure 4 CCDTL Hot Model Pump Skid

### 3. CCDTL CONTROL SYSTEM

The CCDTL Hot Model RCCS provides continuous and discrete control of the cooling system. Operator interface screens are provided to change setup parameters for continuous control and to initiate discrete controls. Status screens are also provided to display information about the CCDTL Hot Model cooling system.

The RCCS is implemented using Experimental Physics and Control System (EPICS) based hardware and software. Figure 5 shows the network connections of the RCCS system.

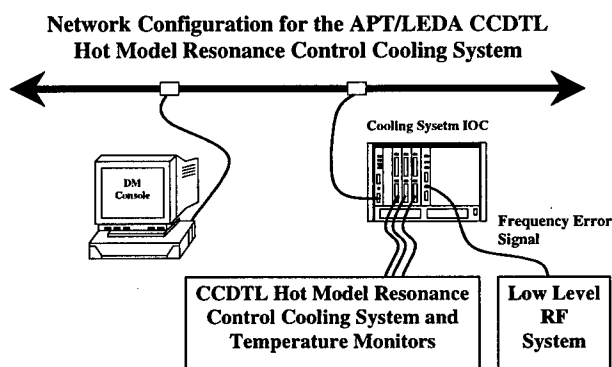


Figure 5 - Network Configuration

The RCCS software is constructed using EPICS State Notational Language (SNL) to track the condition of the system and to allow certain control actions to take place. Additional C functions contained in the SNL code are used to perform the control algorithms and file operations. Figure 6 shows the state diagram that represents the overall conditions of the RCCS.

The CCDTL Hot Model control system provides status screens that show temperatures of the water and cavities,

vacuum levels in the cavities, activation of the channel flow switches, conditions of the PID loops, and conditions of the RCCS pumping systems. Screens are also provided to configure the PID algorithms and operate the RCCS components in an OVERRIDE mode.

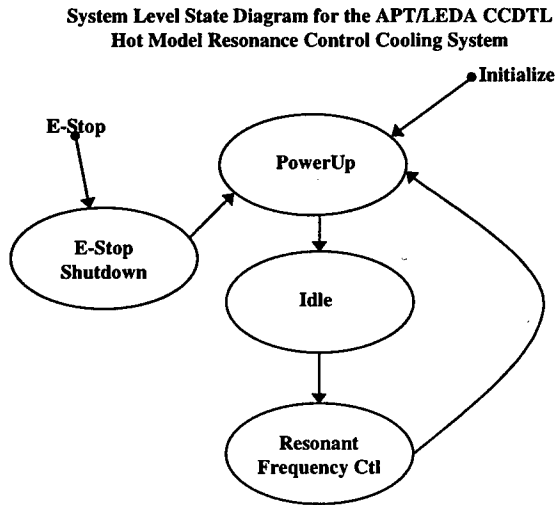


Figure 6 – System Level State Diagram

Resonant Frequency control (RFC) begins when the screen pushbutton pressed on the console system is detected and is the normal operating state of the RCCS. RFC regulates the resonant frequency of the CCDTL Hot Model using an independent single loop Proportional Integral Derivative (PID) control algorithm for each pump loop. The algorithms adjust the setting of the control valves based on the temperature of the water flowing to the Hot Model, the RF Power (calculated from the RF field signal), and the frequency error provided by the Low Level RF (LLRF) control system [3] (drift tube loop) or the change in length of the outer bodies (end wall - equator loop).

Figure 7 depicts the calculation of the error (e) supplied to the algorithms. From the figure,  $e_p$  represents the frequency error for the drift tube loop and the body lengths in the end wall - equator loop;  $x$  represents the RF field signal in the cavities. These 2 terms are combined to provide an adjustment to the temperature setpoint,  $T_{sp}$ .  $T_{cl}$  is the temperature of the water supplied to the Hot Model at the discharge of each pump and is used to calculate the actual temperature error. The differential of  $T_{cw}$  is used to anticipate the effects of a change in the chilled water temperature and apply it to the error. The error is supplied to the algorithm which makes valve adjustments that alter the temperature of the water flowing to the CCDTL Hot Model, thereby changing its frequency.

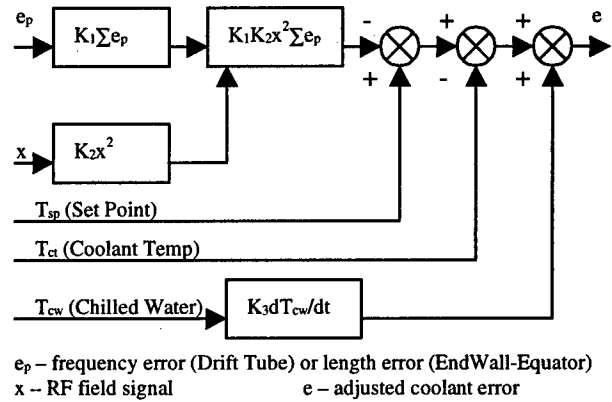


Figure 7 – Control Loop Setpoint Adjustment Schematic

The frequency error received via an analog signal from the LLRF system, ranges from 0 to 10V DC, where +0.5V represents -50KHz error and +9.5V represents +50KHz error. Any error reading outside the +0.5V to +9.5V range is considered an invalid signal.

The length measurements of the body will not be available for the CCDTL Hot Model. However, using the temperature readings of the bodies and a coefficient of expansion for the body materials we will be able to approximate the change in length.

RFC can only be halted and directed to make a transition to the proper state by the console system pushbuttons or an emergency stop condition.

The CCDTL Hot Model RCCS control system will be the basis for the design of the APT/LEDA CCDTL RCCS control system.

## 4. INSTALLATION STATUS

Installation of the RCCS CCDTL Hot Model and Cooling System Pump Package was completed in January 1999. Installation of the control system hardware and software was completed in February 1999. Final checkout and operation of the system will commence simultaneously with RF startup.

## 5. ACKNOWLEDGEMENTS

An immense amount of technical insight and installation assistance was provided by Rick Wood, Lloyd Young, and Paul Leslie, LANL.

## 6. REFERENCES

- [1] H. V. Smith, "Status Update for the Low-Energy Demonstration Accelerator (LEDA)."
- [2] G. Lawrence, "High Power Proton Linac for APT; Status of Design and Development."
- [3] A. Regan, et al., "LEDA LLRF Control System Performance: Model vs Measurement;" these proceedings.

## THE LEDA CONTROL SYSTEM\*

L. Dalesio, D. Kerstiens, P. McGehee<sup>#</sup>, M. Pieck, M. Stettler, R. Wright, LANL, Los Alamos, NM  
D. Moore, WSRC, Aiken, SC  
D. Floersch, Allied Signal, Kansas City, MO

### Abstract

The Accelerator Production of Tritium (APT) Low Energy Demonstration Accelerator (LEDA) is a CW linac comprised of a 75 KV, 110 mA H<sup>+</sup> injector, followed by an 8m long, 350 MHz, 6.7 MeV RFQ, a short beam transport section and a cooled beam dump. The control system is based upon the popular EPICS [1], [2] distributed control system toolkit. In addition to monitoring and control of the injector, vacuum systems, resonance control loops, high power radio-frequency system, beam control magnet power supplies and beam instrumentation, the control system performs overall timing and synchronisation and equipment protection functions. There are a total of 12 distributed Input-Output Controllers (IOCs) which are VME-, VXI- or PC-based. This paper reports on experience with the new PC-based IOCs, with interfaces to vendor-supplied Programmable Logic Controllers (PLCs), with a new archiver developed for this application; and discusses a number of lessons learned.

### 1 INTRODUCTION

Since the first beam through the 6.7 MeV RFQ on 16 March 1999, the LEDA control system has been successfully and safely supporting operations and commissioning.

The fundamental purpose of the LEDA Control System is to provide electronic and real-time software support for all LEDA subsystems and diagnostics. In addition to subsystem support it also implements key accelerator-wide services such as Fast Protect, Timing, and Networks.

Within the LEDA Control Room the control system maintains status and control operator interfaces and provides a suite of data handling facilities that encompass archival, display, and analysis.

Additionally, the control system is the foundation for the LEDA integration process as well as supporting the ongoing commissioning and testing.

### 2 EPICS

The LEDA Control System is based on the Experimental Physics and Industrial Control System (EPICS).

\*Work supported by the U. S. Department of Energy under contract W-7405-ENG-36.

<sup>#</sup>Email: peregrine@lanl.gov

EPICS is a toolkit for building distributed control systems that originated at Los Alamos, and is now developed jointly by a collaboration of over 100 institutions, including telescopes, detector collaborations, universities, etc. The EPICS collaboration grew by more than 20 sites during 1998. EPICS is licensed to two commercial suppliers, who have installed it in large industrial applications.

EPICS runs several accelerators of size comparable to planned APT facility. As an example, the control system for the Advanced Photon Source at Argonne National Laboratory spans 185 real-time IOCs.

LEDA makes use of recent EPICS developments including the most recent version of EPICS, the new standard Application Development Environment, a new data archiver, and PC-based IOCs.

### 3 LEDA CONTROL SYSTEM STRUCTURE

The control system exhibits a distributed hierarchical structure that at the time of initial beam commissioning is implemented across 12 IOCs.

The top-level of the hierarchy consists of four principal systems that cover the Supervisory Control, Machine Control, Diagnostics, and Safety and Protection functions.

#### 3.1 Supervisory Control

The advanced automation features of the LEDA Control System are implemented using two IOCs and several high-level workstation-based sequencing applications. The real-time IOCs that are involved in supervisory control are the System (or Run Permit) IOC that is responsible for operating mode definition and enforcement, and the Master Timer.

#### 3.2 Machine Control

The Machine Control principal system includes the traditional collection of moderately independent subsystems.

#### 3.3 Diagnostics

The Diagnostics principal system is implemented across 4 IOCs that provide the electronic interfaces and software support for the following suite of beam diagnostics: Phase and Energy measurements, AC Toroids, DC Toroids, Beam Position Monitors, Wire Scanners, Capacitive probes, and Video Cameras.



### 3.4 Safety and Protection

The hardware-based Safety and Protection principal system provides for the personnel safety and equipment protection. The Supervisory system includes the software interface required to determine the status of these critical components.

Personnel safety is insured by the Personnel Access Control System and Backbone Beam Enable services while equipment protection is handled by Fast Protect. All of these systems have the mitigating action of quickly turning off the accelerator beam at the injector.

### 3.5 List of LEDA IOCs

This table lists the IOCs operating in March 1999 as well as others that will be installed during the remainder of the year. Each IOC is identified by the bus architecture chosen: PC (ISA), VME, or VXI.

Subsystem	Now	Plan	Type
Supervisory	2	2	PC
Injector/ Low Energy Beam Transport	1	1	VME
RFQ and Windows Vacuum	1	1	VME
Resonance Cooling and Control	1	1	VME
Low Level Radio-Frequency	2	4	VXI
High Power Radio Frequency	4	5	PC
High Energy Beam Transport/ Beamstop	1	1	PC
CCDTL	0	1	VME
Diagnostics	0	4	VXI
<b>Total IOC Count</b>	<b>12</b>	<b>20</b>	

## 4 NETWORK DESIGN

The LEDA Control System communications service is built around a TCP/IP-based network and using EPICS Channel Access as the primary protocol. Access to the real-time controls network is limited by an Internet firewall that also divides the local network into three distinct sections.

### 4.1 Internet Firewall

The three major reasons that justified installation of an Internet firewall are that the LANL accelerator complex (TA-53) is one network; that there were limited available public IP address ranges; and that for machine protection issues we required isolation from all public networks.

Outside clients are tightly restricted and can access the interior controls network only via encrypted data channels such as the secure-shell (SSH) protocol. The firewall is transparent to certain inside clients.

### 4.2 Network Topology

With the Internet firewall installed three separate networks are created.

The interior and most restricted network is dedicated to controls traffic. The machines that exist here include the real-time IOCs, the operator consoles, and the file servers used by the control system.

Within the perimeter network reside the EPICS channel access proxy server and the LEDA HTML server. These hosts have access to the controls network and restrict access by external clients to two specific protocols - HTML and EPICS channel access.

The remainder of the TA-53, LANL, and the global Internet is considered as the public network.

## 5 NEW DEVELOPMENT TOOLS

### 5.1 EPICS R3.13.1

This is the latest and most advanced release of EPICS that is in use at several major operational facilities including Advanced Photon Source at Argonne National Laboratory.

### 5.2 LEDA Specific Development Tools

At Los Alamos National Laboratory a number of tools have been developed specifically for the APT/LEDA program for the purposes of configuration management, visualization, and the creation of EPICS real-time databases.

A collection of utilities has been created to aid developers in setting up new applications and keeping existing ones under configuration control.

IDL, the commercial visualization tool, has been integrated with the EPICS display manager to create more complex operator screens. This is one of the EPICS portable communications server applications that are described in the next sub-section.

The Microsoft Access relational database is now used together with the schematic capture utility CapFast from Phase Three Logic to create databases more quickly.

### 5.3 Portable Communications Server

Three new applications that are based on the new EPICS communications server have been built for use on LEDA. These include a fault logger, a camera interface, and an interface to IDL. Each of these has the ability to supply control system process variables that are accessible by other EPICS utilities.

The fault logger enables a networked display of current or logged faults from the high power radio-frequency system. This server resides on a UNIX-based operator console (OPI).

The second application is an interface between EPICS and a digital camera controlled by a vendor-provided Windows NT device driver.

On the OPI, there is a software library that mediates between EPICS data and widgets and IDL plotting and analysis routines. This allows IDL to provide information viewable by the EPICS display managers and other channel access clients.

#### 5.4 Data Archiver

A new archiver has been developed for EPICS-based control systems. The archiver is implemented as three programs – a channel archiver, a save-set archiver, and an graphical archive viewer.

The channel archiver deals with all standard data and array types. It can process up to 5000 channels/second on change, at a specified frequency, and on specified conditions, including demand.

Production of IOC warm reboot and set-point restore files is the purpose of the save-set archive tool.

Both channel and save-set archive files can be viewed by the distributed viewer (XARR) that also exports data in tab-delimited format for use by external programs such as Microsoft Excel.

### 6 PC IOCS

LEDA has deployed the first PC/VxWorks-based I/O Controllers. Each PC-based IOC is characterized by an Intel x86 CPU, ISA-bus architecture, and dual-bootable to both the VxWorks real-time operating system and Microsoft Windows 95. These PC IOCs have been deployed by the System (Run Permit), HPRF, Master Timer, and HEBT/Beamstop subsystems.

#### 6.1 Usage of PC IOCS

LEDA utilizes a mixture of VXI, VME and PC IOCs to meet diverse requirements.

VXI-bus IOCs are used for subsystems that have requirements for custom instrumentation.

When large numbers of I/O modules are required the traditional VME-bus IOC is the preferred choice.

However, PC IOCs have been proven to be a cost-effective solution for systems that either have limited I/O requirements or communicate with external devices such as Programmable Logic Controllers (PLCs).

### 7 CUSTOM PC BOARDS

Custom printed circuit boards have been developed for LEDA project. These provide specialized instrumentation support for the diagnostics, the low-level and high-power radio frequency systems, the injector, and the machine protection systems. The Industry Pack format is implemented when cross-platform use is required. Each custom board required its own device driver to be created, tested, and integrated with the subsystem EPICS applications.

### 8 EXTERNAL SYSTEMS

The integration of the LEDA control system required interfacing to subsystems provided by four external vendors. An assessment of the effectiveness of outsourcing these four subsystems is detailed in [3].

Subsystem	Vendor	Implementation
RFQ Resonance-Control Cooling	Allied Signal	VME IOC, EPICS
High-Power RF Transmitter	Continental Electronics	Allen-Bradley PLC-5/40
High-Power RF Power Supply	Maxwell Technologies	Allen-Bradley SLC 5/03
RFQ Vacuum	LLNL	Modicon PLC

### 9 SUMMARY

The control system for the Accelerator Production of Tritium program's Low Energy Demonstration Accelerator has been sufficiently developed to safe and reliable support of initial beam operations. The LEDA controls implementation has taken advantage of the most recent version of the EPICS toolkit and has created significant enhancements to the standard EPICS distribution including support for PC IOCs, a new data archiver, and several portable communications server applications.

Since LEDA is a test-bed for an accelerator that will be operated as an industrial or factory-like facility, the next steps in its control system evolution will focus on integration of the diverse machine control and diagnostic subsystems and on the maturation of the supervisory system.

### 10 ACKNOWLEDGEMENTS

The following individuals contributed to the design, fabrication, and support of the LEDA control system:

J. Booth, G. Cavasos, T. Cote, L. Day, D. Gurd, J. Hill, M. Jenkins, T. Jones, M. Harrington, B. Quintana, G. Salazar, M. Thuot, G. Vaughn, D. Warren, LANL.  
S. Hardage, Allied Signal.  
P. Gurd, J. Sage, General Atomic.  
S. Bolt, WSRC.

### 11 REFERENCES

- [1] The Success and the Future of EPICS, M. Thuot, et al., Proc. LINAC96 (Geneva, 26-30 Aug. 1996).
- [2] EPICS URL: <http://www.aps.anl.gov/asd/controls/epics/EpicsDocumentation/WWWPages/>
- [3] A Development and Integration Analysis of Commercial and In-House Control Subsystems, D. Moore and L. Dalesio, Proc. LINAC98 (Chicago, 23-28 Aug. 1998).

# VACUUM CONTROL SYSTEM FOR THE LOS ALAMOS LOW ENERGY DEMONSTRATION ACCELERATOR PROTON INJECTOR \*

Leo R. Dalesio, Debora M. Kerstiens, LANL, Los Alamos, N.M., Mitchell C. Richards #, WSRC, Aiken, S.C., Gilbert A. Salazar, Joseph D. Sherman, David S. Warren, Thomas Zaugg, LANL, Los Alamos, N.M.

## Abstract

A vacuum control system has been developed for use on the Los Alamos National Laboratory continuous wave (cw) Low Energy Demonstration Accelerator (LEDA) Proton Injector. This paper summarizes hardware and software implementation to satisfy the following design criteria: (1) performs as a standalone system – no direct access to CPU/memory components by computer control hardware during normal operations, (2) has local (chassis) and remote control (EPICS [1] & LabVIEW [2]) capabilities, (3) is electrically isolated and filtered from electrical transients created from injector high voltage spark-downs to ground, and (4) incorporates fast protect and fail safe components.

## 1. GENERAL OVERVIEW

The Los Alamos Low Energy Demonstration Accelerator (LEDA) project comprises a 75-keV proton injector, 6.7-MeV cw RFQ, a high-energy beam transport system, and a high power beam stop [3]. The injector vacuum chamber, pump, and gauge system is composed of three diagnostic boxes (DB), each supplied with a turbo pump (TP), scroll pump (SCP), turbo pump gate valve (TGV), two vacuum ion gauges (VGI), and three vacuum convectron gauges (VGC). There are also two beam line gate valves (BGV), BGV1 located between DB2 & DB3 and BGV2 located between DB3 and the radio frequency quadrupole (RFQ). Figure 1 is a drawing of the LEDA proton injector.

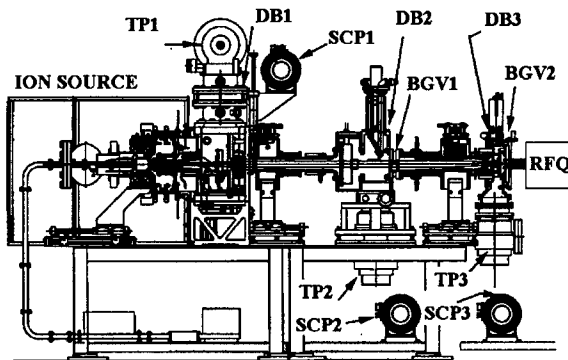


Figure 1. LEDA proton injector

Figure 2 is a typical hardware configuration for the diagnostic boxes.

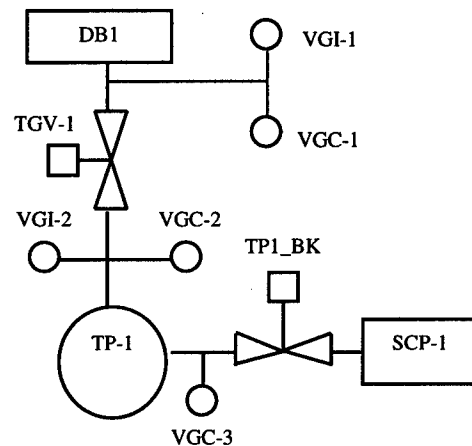


Figure 2. Typical vacuum hardware configuration for the diagnostic boxes.

The control system consists of one control chassis for each diagnostic box (e.g., Vacuum Pumping System #1 {VPS1} for DB1, etc.), six ion gauge controllers, three turbo pump controllers, three motor starters, three current sensing relays, two programmable logic controllers (PLCs), electrical noise filters, and associated cable/wiring. A more detailed description of the system is discussed in the sections below.

## 2. STANDALONE SYSTEM DESIGN

The LEDA vacuum control system operates as a standalone system. That is, all hardware components are local to the injector, hardwired together, network isolated, and fully functional – contains all interlocks and requires no inputs from remote computer control equipment during normal operations.

Figure 3 shows a block diagram of the system devices. There are two Modicon [4] Compact PLCs involved (i.e., the Injector PLC and the EPICS PLC). The EPICS PLC is for remote operation and will be discussed in the next section.

\* Work supported by the US Department of Energy  
# Email: mitch.richards@srs.gov

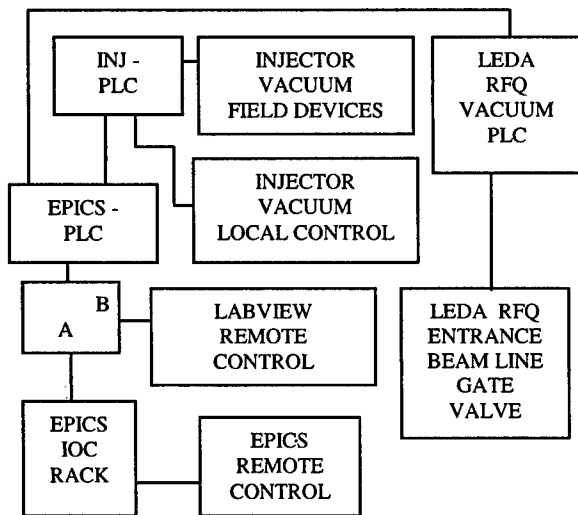


Figure 3. Block diagram of the LEDA Injector Vacuum Control System

The Injector PLC, however, processes all inputs and controls all outputs. There is no direct access to the PLC's CPU/memory components during normal operations. Thus, all signals are propagated through the associated input/output modules. A custom ladder logic program, containing all equipment interlocks, resides and runs (continuous loop) in the volatile memory of the CPU module. Of course, the program is lost during a power shutdown. There is, however, an Electrically Erasable Programmable Read Only (EEPROM) backup memory card installed in the CPU/memory module. Consequently, the ladder logic program is loaded and started shortly after power is resumed.

Control inputs are processed as requests. For example, if an operator desires to open TGV1 and presses the appropriate button on VPS1, the Injector PLC checks to see if all interlocks associated with TGV1 are enabled before opening the valve. Understandably, the PLC automatically shuts the valve, if during operations an associated interlock is disabled.

### 3. LOCAL & REMOTE CONTROL

Local control is achieved by using three operator interface chassis. Figure 4 shows the front panel of Vacuum Pumping System #2 (VPS2). Each chassis utilizes momentary push button switches and LED indicators. For example, if an operator wants to turn on turbo pump #2, he/she would press the button residing just under the TP2 indicator. If all interlocks are enabled, turbo pump #2 would turn on, verified by the illumination of the associated LED indicator. In short, the Vacuum PLC runs, as mentioned in section 2, a ladder logic program containing all the interlocks. Thus, the PLC makes the

decision on whether or not to carry out an operator's request to actuate a device. The interlock chain will be further discussed in section 5.

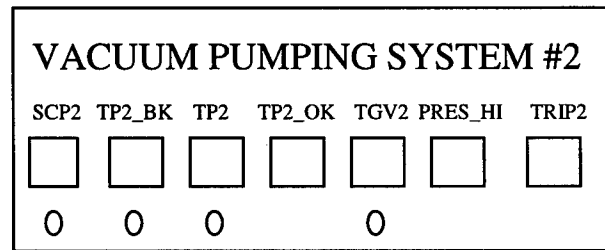


Figure 4. Front panel of VPS2

Remote control is achieved via the second Modicon PLC (i.e., EPICS PLC). It is called the EPICS PLC because it receives the remote operator requests via the EPICS network or a LabVIEW graphical interface. Basically, EPICS controls the LEDA injector vacuum control system by utilizing software screens, custom drivers, Input Output Controllers (IOCs), and two IOC modules. Those modules are a single board computer and a General Purpose Interface Bus (GPIB) card. The LabVIEW interface utilizes a personal computer, BusVIEW [5] (a Modbus [4] driver), serial port, GPIB board, and fiber optic cable & communication modules.

Associated with EPICS remote control, a single board computer is loaded with a custom driver. That driver writes and reads memory locations (coils) residing in the form of a ladder logic program loaded in the EPICS PLC CPU/memory module. The coils are associated with input and output modules. When EPICS writes a binary 1, for example, into the PLC memory location represented by an output coil, the associated output module signal changes to the "on" state. That output signal (from the EPICS PLC) is wired to an input module of the Injector PLC. Thus, the Injector PLC interprets the incoming signal as a request to actuate the associated field device.

An EPICS read command works in the opposite direction. The Injector PLC outputs a signal representative of the state of a field device. For example, if beam line gate valve #1 is open, the corresponding output signal is a binary 1. That binary one is wired to an input module associated with the EPICS PLC. The ladder logic program running in the EPICS PLC has software contacts representative of input module signals. That is, if input signal one is in the "on" state, the associated software contact is closed. That software contact is in series with a coil (memory location) that changes to the "on" state when the inline software contact is closed. Thus, the EPICS network reads the state of that coil to determine the status of the corresponding field device.

#### 4. ELECTRICAL ISOLATION AND FILTERING

The LEDA injector vacuum control system is exposed to electrical transients created from injector high voltage spark-downs to ground [6]. Electronic equipment is known to fail from these short but damaging occurrences. To eliminate the negative effect of these electrical transients, multiple power supplies, relay isolation, and passive filtering are used. Figure 5 shows the typical electrical isolation and filter configuration for TGV1.

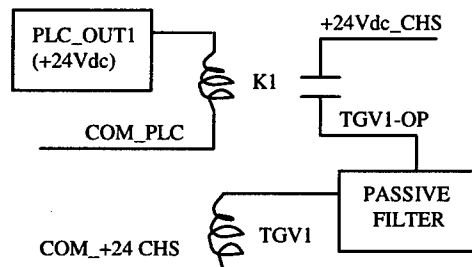


Figure 5. Electrical isolation and filter

Within each vacuum pumping system chassis, a power supply is mounted. The +24Vdc\_CHS is used to actuate vacuum pumps and valves, as well as read valve limit switches, corresponding to its associated diagnostic box. That is, the power supply in Vacuum Pumping System #1 controls and reads the field devices associated with DB1.

Mechanical relays are also used in each vacuum pumping system. They isolate the Injector PLC inputs and outputs (powered from the PLC supply) from the chassis supply driving the field devices. Consequently, the PLC supply voltage is better protected (since not distributed to the injector table) from the electrical transients produced from high voltage spark-downs.

Passive filters are used to protect equipment, as well. There are two stages. The first stage is a RC network. The second stage is a SEMIFILT [7] SP-H series distributed constant type noise filter, model SP333H.

#### 5. FAST PROTECT AND FAIL SAFE COMPONENTS

Fast protect and fail safe operation are achieved by microwave control, monitoring hardware, and protective ladder logic.

The microwave power system provides energy to the plasma chamber to stimulate proton beam production. Notwithstanding, if a beam line gate valve closes while the beam is on, damage is likely to occur. To protect the valves, a fast protect system is used. The fast protect

components consist of a magnetron pulser chassis, signal interface module, and valve control interface box. Basically, the valve control interface box monitors the status of the valve's out limit switch. When the valve is open, the out limit switch is closed – allowing the passage of a voltage to the signal interface module. The signal interface module receives the valve open signal and sends a microwave enable signal to the magnetron pulser. The magnetron pulser controls the power to the microwave producing magnetron tube. Thus, the valve is protected, since microwave power to the plasma chamber is extinguished within a few microseconds after a valve closure is initiated.

Fail safe operation is accomplished by system monitoring hardware and protective ladder logic. Since the most vulnerable parts (as well as very costly) are the pumps (i.e., turbo & scroll), monitoring hardware is installed. This hardware consists of flow meters, rotation relays, current-sensing relays, vacuum controllers, and overload devices. Interlocks from each of the devices are read by the Injector PLC and incorporated in the ladder logic program.

When a vacuum fault occurs, the turbo pumps are shut off and isolated – turbo gate and backing valves close. The scroll pumps (used for backing the turbos) continue to run, however, unless a current overload condition occurs. In either case, power is removed from the pumps, requiring fault correction and operator intervention before restart.

#### 6. CONCLUSION

The LEDA Injector vacuum control system is robust. It operates as a standalone system, provides local & remote control, is electrically isolated & filtered from high voltage spark-downs, and incorporates fast protect & fail safe components. In fact, the system has proven to be very reliable, with nearly a year of operation without failure.

#### 7. REFERENCES

- [1] Leo R. Dalesio, et. al., Nuclear Instruments & Methods in Physics Research A 352 (1994), 179-184.
- [2] LabVIEW®, trademark of National Instruments Corporation.
- [3] J. David Schneider, these conference proceedings.
- [4] Modicon®, Modbus®, trademarks of AEG Schneider Automation, Inc.
- [5] BusVIEW®, trademark of Soogatech Corporation.
- [6] Michael E. Thuot, these conference proceedings.
- [7] SEMIFILT®, trademark of SMI Electronic Devices America, Inc.

# FIRST EXPERIENCES WITH THE CONTROL SYSTEM FOR THE ACCELERATOR OF ANKA

H. Schieler\*, A. Weindl,

Forschungszentrum Karlsruhe, PEA, Postfach 3640, D-76021 Karlsruhe, Germany

B. Jeram, M. Juras, K. Kenda, I. Kriznar, B. Lesjak, K. Mele, T. Milharcic, M. Perko, M. Peternel,

U. Platise, M. Plesko, M. Smolej, R. Sabjan, G. Tkacik, I. Verstovsek, B. Zorko, K. Zagar,

J. Stefan Institute, Ljubljana, Slovenia

## Abstract

ANKA [1] is a 2.5 GeV synchrotron radiation light source being built in Karlsruhe, Germany. The control system for the accelerator is based on the three-tier standard model architecture. However, modern products based on standards in distributed objects and networking are applied in addition to low-cost hardware including PCs. We use the LonWorks field bus network with intelligent nodes and standard I/O modules to connect the individual devices directly to PCs that run device servers under Windows NT. Those PCs act as WWW servers for data transmission, application distribution and documentation retrieval. Applications in the control room run also on Windows NT hosts as WWW clients. However, they could run in any Web-browser on any platform, because all operator control is performed through a Web-browser with Java applets/applications. The communication with the control system data servers is done through CORBA. CORBA objects are wrapped in JavaBeans which are simply connected with commercial data-manipulation and visualization Beans into full-fledged applications or applets. First experiences with this control system during the operation of the ANKA microtron are presented.

## 1 INTRODUCTION

The control system (CS) of the accelerator is based on client and server PC's running under WinNT and the LonWorks field bus with intelligent nodes and standard I/O modules to connect the individual devices directly to the server PC's. These server PC's communicate via CORBA with client PC's in the control room. All operator control is performed through Java applets/applications.

The first real-world test of the system was on the 53 MeV microtron of ANKA during the period from October 98 to March 99, controlling its vacuum system and power supplies successfully.

\* Email: schieler@anka.fzk.de

## 2 CONTROL SYSTEM ARCHITECTURE

The control system architecture is planned to be as homogeneous as possible from the operator's point of view. The CS is designed to use existing intranet/internet infrastructure and web technologies such as HTML/HTTP, web browsers/servers with Java and CORBA/IOP. This decision was made because nowadays a large proportion of people are familiar with web browsers and because the WWW standards provide equal user interface to any information regardless of its type.

Technically, the control system follows the three-tier standard model architecture:

1. the field bus layer with devices;
2. the process control layer with accelerator objects;
3. the visualization layer with control GUIs.

Conceptually, it is composed of two layers, connected through the device servers:

1. the field bus layer with asynchronous event-driven data acquisition/control;
2. the object oriented layer with a model of devices where the client talks to devices as if they were there.

Following, an overview of the different layers is given. Further details can be obtained from [2],[3],[4],[5].

### 2.1 The Field Bus Layer

The LonWorks field bus is a powerful data acquisition and networking system that connects up to 32000 intelligent nodes with I/O modules directly to a PC that runs under Windows 98/NT. The PC interface is connected to all device interfaces through a twisted pair cable. On the Server PC, the LonWorks Network Service (LNS) management tool is used to register each node. LonWorks technology offers a complete network system in hardware and software in a single micro-controller (the Neuron chip) and eliminates any need for network programming. Many LonWorks boards are commercially available, however it is also relatively straightforward to interface own designs to the Neuron chip. After a careful

analysis of the ANKA CS I/O requirements, three I/O boards were designed that cover most cases:

- **Ariadne** is a serial interface board, which supports EIA-232, EIA-422 and EIA-485 standards at maximum baud-rate of 115kbps. It has 16k bytes long buffers on receive and transmit lines and an on-board power supply unit that can source current from 230 V AC line, unregulated 7-12 V DC and regulated 5 V DC.
- **Zeus** is a high precision I/O card with a 16-bit ADC and DAC, DAC trigger input, and optically isolated digital channels (8 inputs and 8 outputs). Four analog channels with a nominal sampling frequency of 1 kHz are multiplexed to the ADC, which is oversampled at 4 kHz to ensure 0.3 LSB precision. The DAC operates at a maximum rate of 10 kHz. An additional on-board peripheral micro-controller, specially designed to control booster and storage ring power supplies includes: a) function generator synchronized with DAC trigger input, b) 32 kb of memory to buffer DAC function and ADC data and c) peripheral self test.
- **Hera** is a digital I/O card with 24 inputs (50 mA), 8 in-/outputs (50 mA) and 8 outputs (solid state relays, 1 A). All I/O's are optically isolated. Two operating modes are provided for inputs and in-/outputs. There is also a 16-bit frequency counter with range of 0-100 kHz (absolute error 1.53 Hz).

The software written for the Neuron chips implements quite complex functions such as state machine and alarms, synchronous ramping in 0.1 millisecond steps and others. The communication to the PC is done by the device servers using the LCA (LonWorks Component Architecture) and LNS library through network variables and remote command invocation, which allows also network management. On top of this, additional functionality was written, such as a template compiler and a file transfer protocol, which loads all run-time constants at start-up from a centralized database. Thus, each constant that is used by the Neuron and the PC clients and servers is stored in one place only, which is the static database.

## 2.2 The Process Control Layer

Controlled devices are modeled as objects residing on device servers that run on the process control layer. The objects are exposed to remote clients through their interface only. The Accelerator Control Interface (ACI), a language independent collection of interfaces based on network distributed objects is using the CORBA standard. All common accelerator components such as power supplies, vacuum, RF, position and current monitors are defined by means of functions and parameters. The devices are described according to CORBA with the Interface Definition Language (IDL), which presents a language-independent way of defining

object interfaces. Each controlled parameter, called device property, is an object by itself, implementing atomic actions such as get/set, increment/decrement, etc. All constants related to a property such as min/max, name, description, etc. are obtained from the property directly by means of remote methods - no direct database access is necessary. Values of the properties are updated asynchronously by means of monitor objects. The ACI is meant to be a standardised interface so that applications and pieces of control systems can be hooked to it from either side. The ACI does not replace existing control system architectures and frameworks but rather tries to use their features in order to be as compatible as possible to those systems. CORBA automatically generates the appropriate communication libraries. There is no need to write other API libraries. CORBA is chosen for this reason and due to its platform and language independence. The need for speed and the necessity to communicate with external drivers require the servers to be written in C++.

The communication between clients and devices is completely asynchronous. Server's responses to client's requests are made via callbacks. There is also a possibility of using "repeated callbacks" - called monitors. The idea is that clients are able to register with servers about which data they require and how frequently it has to be obtained.

## 2.3 The Visualization Layer

Every operator's interaction with the control system goes through the control GUIs, written as Java applets/applications. These applications are build around the Java bean model. A Java bean is a component that can be manipulated in a visual builder environment; beans can be graphically arranged and connections between them established. The latter include, for example, event-to-method connections, where the event in one bean triggers the method in the other; property-to-method connections, where a change in property triggers the method; property-to-property connections and so on. Such environments enable the programmer to build an application without typing a single line of code.

Any accelerator application is composed of two types of beans:

- visual beans (GUI objects like buttons, gauges, charts, ...);
- accelerator beans (called Abeans; each Abean represents a real accelerator device).

An Abean encapsulates all remote calls from the client to a device server of the process control layer. Thus the network is invisible to the user of Abeans. Tasks of an Abean include opening the connection and performing the function calls on remote objects; report and manage all errors/exceptions/timeouts arising from network communication, provide handles for asynchronous messages, etc.

Visual beans are mostly commercial products. Therefore the work done in building a control panel for a device consists mostly of connecting the appropriate Abeans and commercial visual beans in a visual builder. The developing time is low, of the order of hours for a panel, or one or two days for a full-fledged application that instantiates and interconnects many Abeans - even of different devices.

### 3 THE CONTROL SYSTEM SETUP FOR THE ANKA MICROTRON

The microtron is the first part of the ANKA accelerator available. In fact, this is a less extensive setup for the CS than the complete storage ring will be, but it is the first real-world use of the CS and the first possibility to collect experience. The CS for the microtron consists of the following hardware and software components:

- Two PCs, a Client and a Server PC, both running under WinNT 4.0 with PII/266MHz CPUs and 128 MB of RAM, connected via TCP/IP.
- The Client PC runs all client GUIs, written as Java applets/applications. They are designed as tables, including all devices of one type (e.g.: all power supplies) or as panels, one for each single device.
- All device server C++ programs are running on the Server PC. For every kind of device type there is one server application, acting as software interface between client GUI and device, delivering values to clients and commands to devices.
- Server programs and client applications communicate using the CORBA implementation of Visibroker (Inprise).
- One LonWorks field bus interface card in the Server PC is connected to all I/O interfaces through one twisted pair cable. This is the field bus branch the device server programs use to communicate with the following I/O interfaces and their corresponding devices:
  - a) 5 Ariadne serial interfaces for power supplies,
  - b) 30 Zeus I/O boards for power supplies and vacuum gauges,
  - c) 2 Hera digital I/O boards for vacuum valves, - pumps and -pump power supplies.

### 4 FIRST EXPERIENCES

During the first test for the CS with the microtron setup, no principle problems occurred, and so it was possible to run the microtron successfully in this environment.

The field bus and device part implements most work, because all nodes must be registered and database values for every device have to be set. Once done, only device server executables and clients must be started for running the configured CS.

Control System GUIs are clearly designed with logical, mostly self-explaining functionality and

displays. Representing one single device, a panel shows virtually all necessary values and properties one may expect from the real device. Saving desktop place and preventing confusion, a table gives a comprehensive overview, listing all devices of one type and offering the possibility to control several devices at once.

Network communication raised no serious problems, neither the quantity of LonWorks nodes on the field bus branch, nor CORBA. Operators could work with clients, not caring about network details or problems.

Using Abeans in the Java Bean concept allows an easy extension of new client applications. Only Java knowledge is necessary, while client-server communication details are hidden in the Abeans. Connecting Abeans with beans using visual programming can deliver a lot of values and functionality. So much time is saved because of less code typing.

Fundamental changes/extensions in the software are sophisticated, because much knowledge is necessary to manage all layers of the CS.

The three different types of I/O interface boards are enough for running the microtron, but for future purposes additional interface types (e.g.: GPIB to TCP/IP converter) may be required.

PC requirements are high, because the CS needs a lot of resources. Each actual server or client application uses about 20 MB of RAM, some even more.

### 5 CONCLUSION

In general, the first real-world test of the Control System was successful. There were no principle problems controlling the microtrons vacuum system and power supplies, so that the commissioning of the microtron was possible in this environment.

Of course, the present microtron version of the CS software is not perfect, therefore some changes and extensions have to be made. The CS has to be optimized concerning performance and user-friendliness and the control of RF systems and the power supply ramping has to be added for further use in the booster synchrotron and the storage ring of the ANKA light source.

### 6 REFERENCES

- [1] D. Einfeld et al., "Status of the accelerator for the 2.7 GeV light source ANKA in Karlsruhe", Proc. PAC '99, New York, (1999)
- [2] M. Dach et al., "A Control System Based on Web, Java, CORBA, and Fieldbus Technologies", PCaPAC99 workshop, Tsukuba, (January 1999)
- [3] K. Kenda et al., "I/O Control with PC and Fieldbus", PCaPAC99 workshop, Tsukuba, (January 1999)
- [4] M. Plesko, "Implementing Distributed Controlled Objects with CORBA", PCaPAC99 workshop, Tsukuba, (January 1999)
- [5] G. Tkacik et al., "Java Beans of Accelerator Devices for Rapid Application Development", PCaPAC99 workshop, Tsukuba, (January 1999)



## A REVIEW OF OPTIONS FOR THE DIAMOND CONTROL SYSTEM

M.T. Heron, B.G. Martlew\*,

CLRC Daresbury Laboratory, Warrington, Cheshire, WA4 4AD, United Kingdom

### Abstract

DIAMOND is a new UK national light source project to replace the SRS at Daresbury. Many alternative control system designs and implementations exist that might be used as a model for the machine and beamline controls on DIAMOND. This paper surveys the recent developments in light source control systems and attempts to identify some of the main advantages and disadvantages of each alternative. Also, an attempt is made to assess the relative resource implications of each of the major options within the context of a modern light source project.

### 1 INTRODUCTION

DIAMOND is a design for a 3rd generation, 3Gev synchrotron light source based on a 20-cell DBA lattice of about 400m circumference. It uses a full energy booster synchrotron and linac for injection. The spectral output is optimised for high brightness up to 20keV from undulators and high flux up to 50keV from multipole wigglers. The project status is described in [1].

This paper presents the current view of the options for the DIAMOND control system. Many of the issues involved in selecting a model system will revolve around estimates of the required resources, the ease of development and ease of future expansion. The technical differences between competing options, although important, are unlikely to be the deciding factor. After all, the systems described here are all successful control systems and are all capable of meeting most, if not all, of the technical requirements presented in section 2 below.

### 2 CONTROL SYSTEM REQUIREMENTS

The final design model for the DIAMOND control system has not yet been selected, but several key requirements have already been identified that will help in deciding the most appropriate route to take.

The main requirements are:

- The ability to remotely operate and monitor accelerator systems at a rate sufficient to provide smooth, 'analogue-style' control. This implies update rates of 10 Hz or greater.
- Parameter archive and set facilities for post-mortem analysis of machine operations and for restoring the accelerator to a pre-determined mode.
- An easy to use, versatile Graphical User Interface (GUI). Ideally, this should be a GUI that is already familiar to the scientists and engineers working on the project to reduce the learning time.
- Tight integration with standard software packages. All control system data should be accessible directly from major desktop software packages such as spreadsheets, plotting packages, mathematical analysis tools, etc.
- Access to the control system via the web. As much information as possible should be presented via the web, including live control system displays, documentation, database access and, with appropriate security, limited control facilities.
- Use of a modular I/O system for plant interfacing.
- Use of standards. To reduce the resources required for the design and build phase of the project, as well as increasing future flexibility, maximum use should be made of readily available hardware and software solutions.
- Use of a standard solution for plant protection. A clearly defined strategy for handling plant status and interlocks needs to be included in the design.
- Comprehensive alarm system. This should be configurable to allow the operators and/or system specialists to tailor limits and trends, and to permit a wide variety of automatic fault reports to be generated.
- Storage of all important machine data in a relational database system (RDBMS). Development and overall management of both the control system in particular, and the entire project in general, will benefit from a comprehensive database containing all machine details and configuration data.
- A full set of support servers and services should be provided. These will include high performance file stores, compute servers, centralised printing and backup facilities, etc.
- Ease of expansion. Experience on the SRS has shown that a constant programme of development and expansion will take place throughout the operational life of the facility. The control system should be designed with this in mind.

\* Email: B.G.Martlew@dl.ac.uk

- The control system should exhibit a high degree of fault tolerance so that one isolated failure will not compromise operation of the entire light source.

### 3 REVIEW OF RECENT LIGHT SOURCE CONTROL SYSTEMS

Six recent projects have been selected to provide an indication of the current 'state-of-the-art' for light source control systems. The selection has been heavily biased towards European projects because the opportunities for close collaboration on control system design is likely to be greater here than for geographically more diverse laboratories. The APS has also been included in the list because of its major use of, and involvement with, the Experimental Physics and Industrial Control System (EPICS) collaboration, which is one of the main control system toolkits currently available.

#### 3.1 ANKA

The ANKA control system [2] makes much use of modern, distributed object techniques and web technology. Low-cost PCs running Windows NT are used as both operator consoles and as data collection servers. Device interfacing is via the LonWorks field-bus with intelligent nodes and standard I/O modules, again to keep hardware costs to a minimum. The data collection systems utilise TACO-style device servers and communicate with the rest of the control system through CORBA. All applications are being written as Java applets so that a standard web-browser can be used to provide a familiar working environment for the operators.

#### 3.2 APS

The APS control system [3] was one of the originating EPICS systems. It follows the classical standard model with Unix workstations as consoles connected over Ethernet and FDDI to VME crates with Motorola processor boards running VxWorks. It uses sub-nets of BitBus, GPIB and Allen Bradley 1771 to interface to the plant.

#### 3.3 BESSY II

The BESSY II control system [4] is based on the EPICS toolkit with HP workstations running Unix for the consoles.[4] These are connected using Ethernet and ATM to VME crates running VxWorks for the middle layer and in-house CAN-Bus modules as the third layer (the plant interface). Extensive use is made of CAN-bus as the principle interface to the plant. Some use of VME I/O is made at layer 2 for applications requiring high data volume and processing speed and hardware with EPICS support such as timing modules. Application development has used the Self-Describing Data Set (SDDS) toolkit and Tcl/Tk scripting. Oracle has been

selected as a RDBMS to store all configuration data and other associated information.

#### 3.4 ELETTRA

The ELETTRA control system [5] is, again, a three-layer structure with workstations running Unix as the consoles and two lower layers of VME crates running OS-9. The lower two layers are connected using MIL1553 bus and the upper two with Ethernet. The system makes extensive use of a RDBMS for storing parameter and machine settings.

#### 3.5 ESRF

The ESRF control system [6] is based on workstations running Unix and VME crates running OS-9, below which is an in-house field-bus connecting to G64 crates used for the majority of the plant interfacing. Intelligent subsystems are interfaced at the VME crate level.[6] This system has been further developed and is now packaged as the TACO toolkit.

#### 3.6 SLS

The SLS control system [7] is based on EPICS in a two-layer structure with PCs running Linux as consoles and VME crates with PPC processor boards running VxWorks for the plant interface. The majority of the plant is interfaced directly through digital and analogue connections, dispensing with the need for a field-bus layer. Applications are being developed in Java or Tcl/Tk to give an element of platform independence and will make use of an RDBMS. The CDEV interface has been implemented on top of the EPICS API to provide a more uniform and device oriented programming model.

## 4 MAJOR OPTIONS

#### 4.1 EPICS

The EPICS system [8] has been widely adopted throughout the accelerator community. It has been used as the primary software toolkit on several major light source control systems with great success. The majority of implementations use the traditional approach of VME/VXI-based I/O controllers and Motorola 68K CPUs running the VxWorks operating system and UNIX workstations as operator interfaces. However, a considerable amount of work has been done around the world to port some aspects of the EPICS software to other platforms such as PCs running Windows NT or Linux for consoles and PPC processors for IOCs. Although EPICS provides standard tools for display creation, archiving, alarm handling etc, many users have found these tools to be inadequate and developed in-house alternatives. The big success of EPICS is based on the definition of a standard IOC structure, together with

an extensive library of driver software for a wide range of I/O cards. The CDEV interface is often used in conjunction with EPICS to provide a more object oriented programming interface for application software. Many users of the system report a steep learning curve and the need for significant development resources, but this is balanced by the large installed base and proven ability of this approach.

#### 4.2 TACO/TANGO

The TACO control system, recently re-packaged and renamed as TANGO, is a development of the control system that was originally designed for the ESRF.[9] It is used extensively at the ESRF for both accelerator and beamline controls. It is also used to control the Hartebeesthoek radio telescope in South Africa and certain elements of the design have been adopted for the ANKA control system (see 3.1 above). The core of the design centres around object oriented device servers that communicate with higher levels via SUN ONC/RPC and XDR protocols. The original implementation used OS-9 on 68k CPUs for device servers and UNIX workstations for operator interfaces. More recently, TACO/TANGO has been ported to Linux, Windows NT, LynxOS and VxWorks although not all are fully supported. The core of TACO/TANGO doesn't provide as much functionality as EPICS, but it does benefit from the availability of ports to several alternative platforms.

#### 4.3 Commercial

There are several commercial products available that can be used to build a control system. Most of them, such as LabView, are intended for systems of limited size and do not scale well when used in a large, distributed arrangement typical with accelerator and light source control systems. To date there is only one serious commercial contender, Vsystem from Vista Controls Inc. [10] Vsystem is of a similar design to EPICS, but has all the advantages (and disadvantages) of commercial standard support and development. Vsystem has been on the market for several years and is more popular for small to medium scale control systems. It has yet to be adopted as the primary control system on any large-scale light source project.

#### 4.4 Other

A fourth alternative would be to adopt one of the less widely used control systems designs, develop the software currently being used on the SRS as Daresbury (based on the ISOLDE control system at CERN [11]) or to develop a new in-house design from scratch. The advantage of the home-brew approach is that the software can be very closely tailored to our exact needs. The disadvantage, however, is that this will inevitably lead to duplication of work already done at other

institutions, increased de-bugging and commissioning time and a lack of overall versatility.

### 5 CONCLUSIONS

It is possible to build a control system for a light source from any of the options presented. It is quite likely that the final choice will be influenced by some quite arbitrary factors: personal preference, experience with particular hardware platforms, operating systems and development tools. However, a dominating factor will be the level of available resources. It is clear that a lightweight system such as that currently used on the SRS would have a minimum resource requirement to a get a basic system up and running. It does this by deferring the implementation of some of the required functionality to a later date. Alternatively, a control system based on EPICS would include most of the functionality from day one and makes the job of the control system user much easier during machine commissioning and early operation. However, as a consequence, it is a more complex system and has a greater resource demand.

The TACO system occupies a middle ground. It can provide a sound basis for a successful control system with lesser resource requirements than for EPICS, but does lack some of the functionality and support.

While the use of a commercial system can reduce the required resource demand, it is not clear that these systems offer significantly more than the 'free' collaborative ventures such as EPICS and TACO.

### 6 REFERENCES

- [1] A.A. Chesworth, J.A. Clarke, G.S. Dobbins, D.J. Holder, H.L. Owen, M.W. Poole, S.L. Smith, V.P. Suller, A. Wolski, "DIAMOND: A UK National Light Source Project", these proceedings.
- [2] M. Plesko et al, "The Control System for the Accelerator of ANKA", Proc. EPAC98, Stockholm, June 1998.
- [3] M.J. Knott, W.P. McDowell, F.R. Lenkszus, M.R. Krammer, N.D. Arnold, R.T. Daly, G.R. Gunderson, B.K. Cha, M.D. Anderson, "The Advanced Photon Source Control System", Proc. PAC 91.
- [4] R. Muller et al, "Rapidly Installable High Performance Control System Facilitates BESSY II Commissioning", Proc. EPAC98, Stockholm, June 1998.
- [5] D. Bulfone, "Status and Prospects of the Elettra Control System", Nucl. Instr. and Meth. A 352 (1994), p63.
- [6] W.-D. Klotz, "The ESRF Control System; Status and Highlights", Proc. ICALEPCS91, Tsukuba, 1991.
- [7] [http://www1.psi.ch/www\\_sls\\_hn/controls/](http://www1.psi.ch/www_sls_hn/controls/)
- [8] <http://epics.aps.anl.gov/asd/controls/epics/EpicsDocumentation/WWPages/EpicsFrames.html>
- [9] A. Goetz et al, "TACO: An object oriented control system for PCs running Linux, Windows/NT, OS-9000 or LynxOS", Proc. PCaPAC96, DESY Hamburg, 1996.
- [10] <http://www.vista-control.com/>
- [11] J. Deloos, "Integrating the New Generation of ISOLDE Controls into a Multi-Platform Environment", Proc. PCaPAC96, DESY Hamburg, 1996.

## DESIGN OF THE CONTROL SYSTEM FOR THE 1.8-GEV THIRD-GENERATION SYNCHROTRON-RADIATION SOURCE AT TSRF

Noriichi KANAYA<sup>\*</sup>, Shoji SUZUKI<sup>†</sup>, Shigeru SATO<sup>†</sup> and Masahiro KATOH

Photon Factory

High Energy Accelerator Research Organization (KEK)

1-1, Oho, Tsukuba, 305-0801, Japan

<sup>\*</sup>) Department of Physics, Graduate School of Science, Tohoku University,  
Aobaku, Sendai, 980-8578, Japan

### ABSTRACT

A control system has been designed for the 1.8-GeV synchrotron-radiation source at Tohoku University Synchrotron Radiation Facility (TSRF), Sendai-city, Japan. TSRF is a third-generation synchrotron-radiation facility proposed at Tohoku University, Sendai, Japan. The control system comprises three physical layers: UNIX workstations, an FDDI (Fiber Distributed Data Interface) high-speed network, and VME modules. UNIX workstations are employed for the upper layer that provides process control and a user interface. The FDDI provides a 100-Mbps, token-passing, dual-ring LAN using a fiber-optic link suitable for reliably exchanging control data. On the bottom layer, there are VME crates with high performance CPUs that are interconnected to the magnets, RF, vacuum, beam-position monitors, wigglers/undulators, beamlines and related components of the storage ring for local process control. The design of the TSRF control system is discussed.

### 1 INTRODUCTION

TSRF (Tohoku-university Synchrotron Radiation Source Facility) is a new third-generation synchrotron-radiation source that is currently proposed at Tohoku University, Sendai, approximately 350km north of Tokyo, Japan. TSRF is planned to be constructed at the site of the Laboratory of Nuclear Science, Tohoku University, where a 300-MeV-Linac and a 1.2-GeV Stretcher Booster Ring are currently in operation for nuclear-physics experiments [1]. By taking advantage of the existing facility, TSRF employs the Stretcher Booster Ring as the injector for the TSRF storage ring. This can greatly reduce the construction cost for the TSRF synchrotron-radiation source.

TSRF is designed to provide VUV-SX synchrotron radiation to the experimental hall where VUV experiments, surface physics, soft x-ray lithography, microscopy and crystal structure analysis, will be simultaneously carried out.

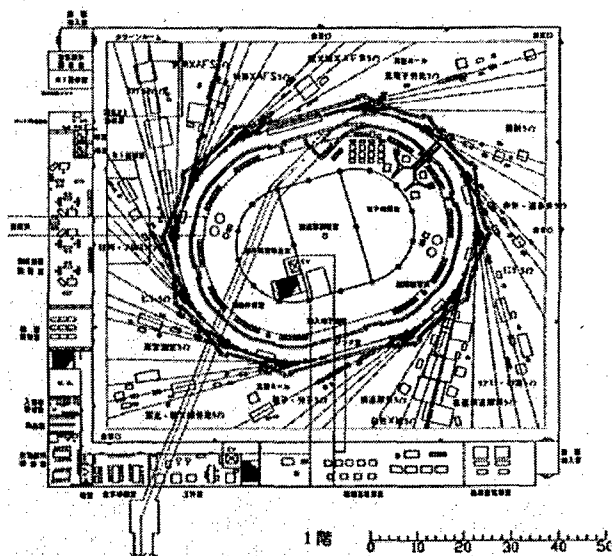


Fig.1 Plan view of the 1.8-GeV TSRF synchrotron-radiation storage ring at Tohoku University, Sendai, Japan

The high-power wiggler/undulator beam lines are simultaneously in operation, producing very intense synchrotron-radiation beams [2]. The high-power beam lines are distributed along the long circumference of the storage ring. TSRF has a 1.8-GeV storage ring with a DBA (double-bend-achromat) type, third-generation storage ring with emittance of 4.9nm rad, and a

<sup>\*</sup>Email: noriichi.kanaya@kek.jp

circumference of 244m. TSRF has more than ten wigglers/undulators, and thirty beamlines for soft X-ray and VUV experiments for research. Figure 1 shows a plan view of the TSRF facility, which includes the 1.2-GeV Stretcher Booster Ring.

The control system has been designed for the 1.8-GeV TSRF synchrotron-radiation source in order to operate the storage ring, providing stable synchrotron radiation to users at the experimental hall, and to improve the performance of the storage ring. In this paper, the design of the TSRF control system is discussed.

## 2 SYSTEM CONFIGURATION

The control system provides two major operating modes at the users' request: multi-bunch beam operation and single-bunch beam operation for time-resolved experiments. In addition, the control system allows an operator to provide both (1) automatic setup-and-go operation of the accelerator for users' experiments and (2) machine-study operation with remote control of the accelerator system in order to improve the accelerator performance and to study accelerator physics.

Figure 2 shows the hierarchy of the software system which comprises three layers based on a client-server model. On the top layer, there are Console Managers as clients for operator console management. At the bottom layer, there are Device Servers, which actually interface between the physical hardware devices and the servers at the upper layers. A Dispatcher is a server in the middle layer, which resides among Console Managers and Device Servers at the lowest level.

PCs are cost-effective equipment as operator consoles running at the top layer. Five PCs running under WindowsNT are utilized as console devices with a 20-inch bit-map color display, and a trackball used as a pointing device; they are also connected to the network. Under normal operation, two consoles are assigned to storage-ring control, and the other to the beam-transport-line, injection-pulse magnets, safety interlock system and the beamline control system. Man-machine interfaces, including graphics status displays, provide pull-down and pop-up menus, which are organized in a tree structure. Each branch menu is utilized to specify a device and its parameters. The Console Manager always depicts the present status of the accelerator complex.

There are five UNIX workstations at the middle layer for managing VME crates that are utilized for process control. Automatic operation is to setup, in principle, the parameters to devices, such as the bending magnets and families of quadrupole magnets, and then to initiate them. This can be carried out by invoking commands defined in a command file, whose file name is specified by an automatic instruction message solicited by an operator. The workstations automatically

carry out the following procedures: (1) Standby-for-beam-injection, (2) Beam-Injection, (3) Beam-Acceleration, (4) Re-injection (to set up parameters for injection of the beam after automatically initializing magnets), and (5) Shutdown.

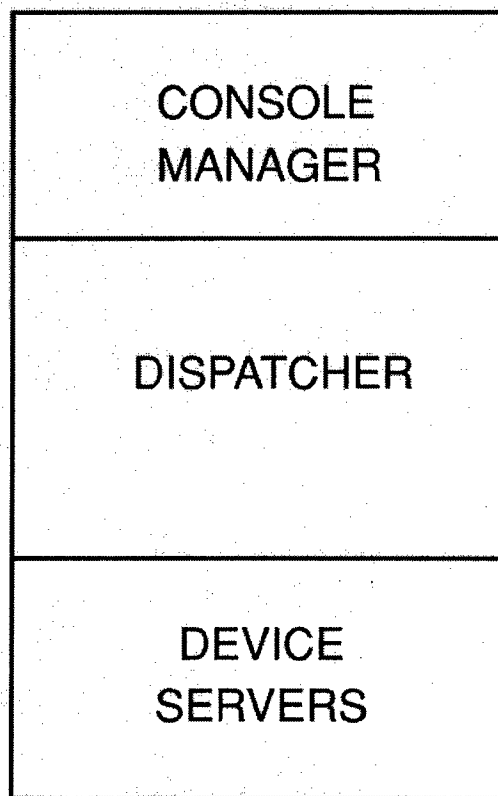


Fig. 2 Hierarchy of the software system

The UNIX workstations, VME crates and PCs are connected to the FDDI (Fiber Distributed Data Interface) high speed network as shown in Fig.3. The FDDI provides a 100-Mbps, token-passing, dual-ring LAN using a fiber-optic link suitable for exchanging control data reliably.

On the bottom layer, there are VME crates with high performance CPUs that are interconnected to the magnets, RF, vacuum, beam-position monitors, wigglers/undulators, beamlines and related components of the storage ring for local process control. VME modules in the crates carry out time-critical jobs for the accelerator components: during beam acceleration at the storage ring, a power supply for bending magnets of the storage ring, and power supplies for families of

quadrupole magnets are automatically synchronized in order to keep the betatron values constant.

There is a shared memory table in which all of the operational parameters of the accelerator complex are stored in the relevant data entries. The table is also mapped to the physical memory, which can be referenced by any application process. The purpose of the table is to allow all application processes to utilize the operational parameters as well as the present status of the accelerator complex necessary for their specific operation without directly accessing actual physical devices [3].

There is an on-line database system. The host collects all operational data and control data of the accelerator components. The operational and control data have been automatically stored in the database system to retrieve later specific combinations of behaviors of the accelerator components.

The storage ring has a number of components and sensors to be controlled, including vacuum valves, interlock devices, cooling water flow sensors, fast/slow vacuum sensors, pneumatic-pressure sensors, atmosphere sensors, open-request signals from the storage ring /the experimental hall, vacuum pressure gauges of the storage ring and the beam lines, valve driving units. These components are controlled and monitored by a computer of the control system.

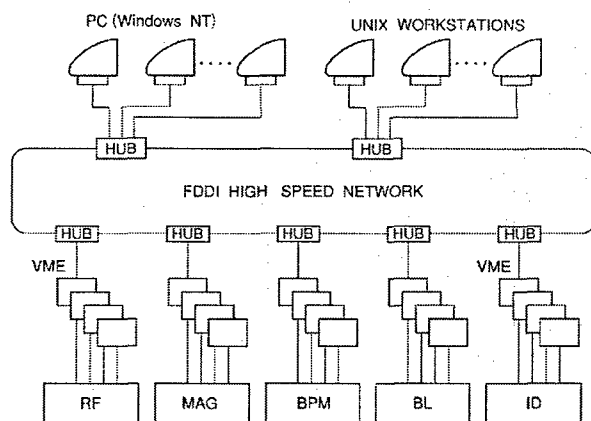


Fig.3 Configuration of the control system

### 3 CONCLUSION

The design of the control system is discussed for the 1.8-GeV third-generation synchrotron-radiation facility TSRF [4], Sendai-city, where a 300-MeV Linac and 1.2-GeV Stretcher Booster Ring are ready as the injector for the 1.8-GeV storage ring. The control system comprises three layers, and is composed of

workstations, VME crates and PCs, which are connected to the high-speed FDDI network. The control system provides automatic operation for users' experiments as well as machine-study operation to improve the accelerator performance and to study accelerator physics.

### 4 ACKNOWLEDGEMENTS

The authors wish to express their gratitude to Prof.J.Kasagi, Laboratory of Nuclear Science (LNS), Prof.M.Watanabe,. Research Institute of Scientific Measurements, Tohoku University for their valuable discussions, the staffs of LNS and all working group members of the project for their assistance and cooperation.

### 4 REFERENCES

- [1] M.Oyamada et al.,Proc. of 10th Symp. on Accel. Sci.Tech.p463,1995 (in Japanese).
- [2] M.Katoh, S.Sato, S.Suzuki and T.Yamakawa,"Lattice Design of the Synchrotron Radiation Source at Tohoku University," Proc. of the 5th European Particle Accelerator Conference,Spain,June,1996.
- [3] N.Kanaya, S.Asaoka and H.Maezawa, "A Generic Model for Monitoring Operational Parameters of Accelerators by Heterogeneous Multiprocesses at the Photon Factory", XIV Int'l Conf. on High Energy Accelerators, July, 1992, Hamburg, Germany.
- [4] <http://hera.kek.jp/>

# VACUUM-PUMP CONTROL SYSTEM USING PROGRAMMABLE LOGIC CONTROLLERS ON THE TCP/IP NETWORK FOR THE 2.5-GEV STORAGE RING

Noriichi KANAYA\*, Seiji ASAOKA and Hideki MAEZAWA

Photon Factory

High Energy Accelerator Research Organization (KEK)

1-1, Oho, Tsukuba, 305-0801, Japan

## Abstract

A vacuum-pump control system has been developed using programmable-logic controllers (PLC) for the 2.5-GeV storage ring at the Photon Factory, High Energy Accelerator Research Organization (KEK). There are sixty-six titanium-getter vacuum pumps at the storage ring. Evacuation of gases in the storage ring is done by controlling the current in the titanium filaments in the vacuum pump (max 50A). A PLC has a TCP/IP network port, 16-bit-digital output ports connected to sixteen solid-state relays (SSR) for current control. The PLC can simultaneously control up to sixteen pumps. These vacuum pumps are connected to SSRs which chop the AC current so as to control the current in the pumps. To operate the pumps, the pump current must have a trapezoidal-shaped current form. The PLC is configured so that the current in the pumps has a trapezoidal form associated with pre-heating, evacuation, and cooling-down phases of the pump. PLCs are connected to a personal computer (PC) through the network. The PC can automatically control the PLCs by sending a set of commands through the TCP/IP network. The commands specify the duration of the current form. Upon receiving a command from a PC running under WindowsNT through the network, the PLC generates pulse-trains through the digital output ports to trigger the SSRs in association with the operating phases. The design of the vacuum-pump control system is discussed.

## 1 INTRODUCTION

There are twenty-two synchrotron-radiation beam lines at the 2.5-GeV positron storage ring, Photon Factory at the High Energy Accelerator Research Organization (KEK). These beam lines feed synchrotron radiation to the experimental hall, where experiments, such as surface physics, x-ray lithography, microscopy and crystal

structure analysis, are simultaneously carried out. These beam lines are simultaneously in operation, providing intense synchrotron-radiation beams. The pressures in the storage ring and the beam lines are maintained at an ultra-high vacuum (UHV) of less than  $10^{-8}$  Pa so as to achieve a long beam lifetime, typically more than sixty hours. The beamline are controlled by the distributed control system [1].

There are sixty-six titanium-getter pumps for the rough evacuation of gases in the storage ring. The vacuum pumps are installed around the storage ring, and have to be periodically operated, depending upon the pressures in the storage ring. The evacuation of gases in the storage ring is done by controlling the current in the titanium filaments in the vacuum pump (max 50A). The control system for the titanium-getter pumps has been developed using Programmable Logic Controllers on the TCP/IP network at the Photon Factory.

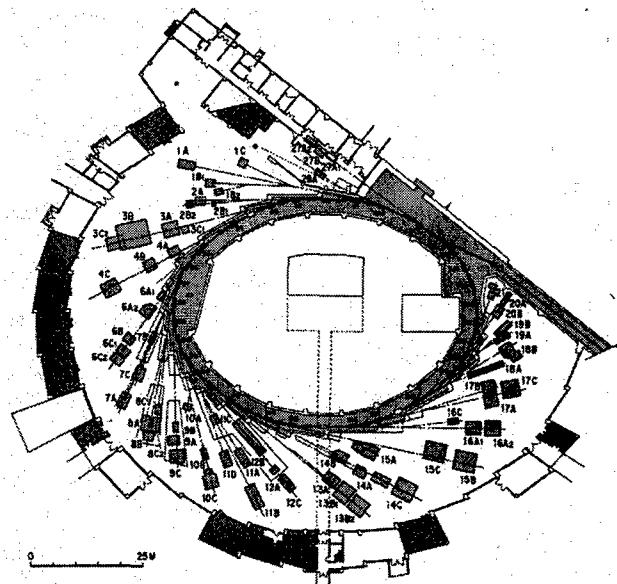


Fig.1 The 2.5-GeV storage ring and beamlines

\*Email: noriichi.kanaya@kek.jp

The titanium-getter pumps are installed at each beamline.

## 2 SYSTEM CONFIGURATION

Figure 2 shows the configuration of the system. A PLC has a 16-bit CPU (Intel 80386, 25MHz), a 2 MB DRAM, a TCP/IP network port and two sets of 16-bit-digital input/output ports connected to sixteen solid-state relays (SSR) for current control. The PLC can simultaneously control up to 16 pumps. These vacuum pumps are connected to the SSRs that chops the AC current so as to control the current in the pumps.

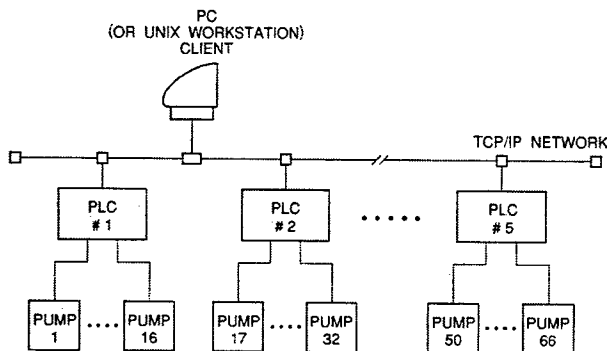
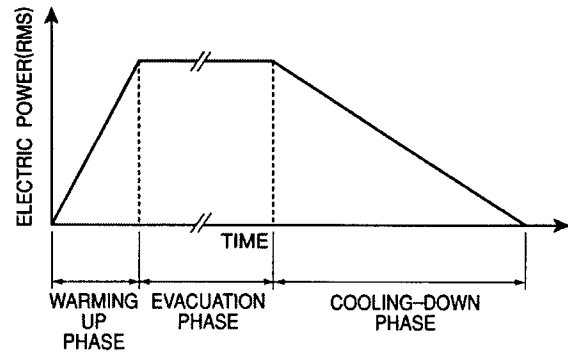


Fig.2 Configuration of the control system for titanium-getter pumps.

To operate the pumps, the pump current must have a trapezoidal shape as shown in Fig.3. The PLC is configured so that the current in the pumps has a trapezoidal form associated with the warming-up phase, evacuation phase, and cooling-down phase of the pump. Usually thyristors are employed to control the AC current for high-power devices, allowing us to linearly control the electric power in the power devices. However, thyristors can generate chopping noise when slicing the AC current to control the power for the power devices. In order to avoid such noise generated by chopping the high AC current, the PLC employs SSRs that can chop the AC current (50Hz) at the zero-crossing point, thus providing an arbitrary number of sinusoidal current waves to the filaments of the titanium-getter pump without much noise. The PLC controls the number of sinusoidal current wave forms ranging from 0 to 50 in a second for the titanium-getter pump. Thus, the PLC can control the average AC power consumed in the titanium-getter pump, thus ensuring a trapezoidal-shaped current.

The PLCs are connected to a personal computer (PC) through the network. The connection between the PC and the PLC is established using the TCP/IP socket mechanism. The PC is a client and the PLCs are servers. The PLC has only a simple connection mechanism i.e. the "socket mechanism" rather than Remote Procedure

Call (RPC) that supports rich client-server mechanism. Thus, communication between the PLCs (servers) and the PC (client) is established using the socket



mechanism.

Fig.3 Trapezoidal-shaped current (RMS) in the titanium-getter pump. The current in the pump must have a trapezoidal form associated with the warming-up phase, evacuation phase and cooling-down phase.

The PC can automatically control PLCs by sending a set of commands through the TCP/IP network. Control for the titanium-getter pumps is done by sending commands, for example, the execution command specifies the duration of the current form: the duration of warming-up phase, the duration of evacuation phase and the duration of cooling-down phase. The PLC listens to the TCP/IP port to receive a message or command from the PC through the network. Upon receiving a command from the PC running under WindowsNT through the network, the PLC generates pulse-trains through the digital output ports to trigger the SSRs in association with the operating phases, as shown in Fig.3. A command includes an ID number, which specifies the titanium-getter pump as well as the duration of the warming-up, evacuation, and cooling-down time in seconds. Upon receiving a command, the PLC initializes its timers associated with the command parameters, and starts triggering the gate of the SSR through the digital output port. Triggering the SSR chops the AC voltage that is fed to the titanium-getter pump, thus controlling the AC current in the filament of the titanium-getter pump. After setting up the timers, the PLC listens to the TCP/IP port again for the next command from the client.

In the case that the filament of the titanium-getter pump is burnt out, the PLC can automatically abort triggering the SSR. In order to avoid a high surge current when aborting, the PLC gradually reduces the number of triggering pulses for the SSR gate. This procedure can also be initiated by the PC by sending the abort command.

The man-machine interface on the PC was created using Java. Figure 4 shows a sample screen copy of the man-machine interface, which is in the development



phase. The operator can flash all titanium-getter pumps, or individually flash arbitrate combinations of the pumps by clicking the radio button on the screen. The functionality of the client on the PC will be ported to a UNIX workstation.

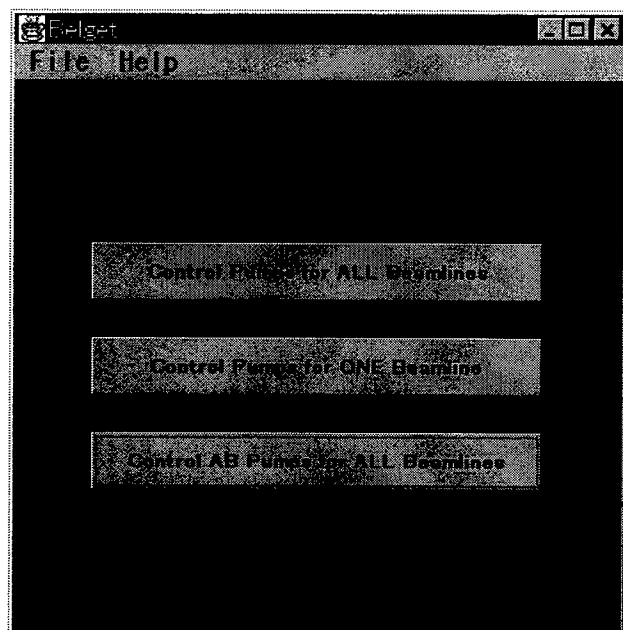


Fig.4 (a)

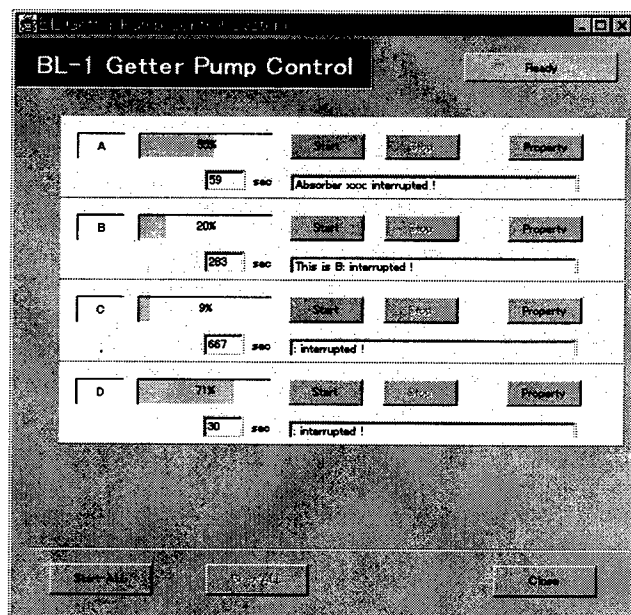


Fig.4 (b)

Fig.4 Sample screen copy of the man-machine interface of the client. (a) Main menu and (b) a sub-menu controlling four sets of titanium-getter pumps.

### 3 CONCLUSION

A vacuum-pump control system has been developed using programmable-logic controllers (PLC) for sixty-six titanium-getter vacuum pumps at the 2.5-GeV storage ring at the Photon Factory. The PLC has sixteen solid-state relays (SSR) that can control the AC current to control the current in the pumps. The PLCs and a PC are connected in development phase, and will be installed for all titanium-getter pumps.

### 4. ACKNOWLEDGEMENTS

The authors wish to express their gratitude to the staff of the Photon Factory Light Source Division for operating the beam lines and the storage ring.

### 5 REFERENCE

- [1] N.Kanaya, S.Sato, S.Asaoka, T.Koide and H.Maezawa, "Operational Experience with the Distributed Control System for Synchrotron Radiation Beam Lines at the Photon Factory", Particle Accelerators, Vol.29,pp.227-232,1990.

# LOCAL CONSOLE SYSTEM USING JAVA ON PERSONAL COMPUTERS FOR HIGH ENERGY ACCELERATORS

Noriichi KANAYA<sup>\*</sup>, Seiji ASAOKA and Hideki MAEZAWA

Photon Factory

High Energy Accelerator Research Organization (KEK)

1-1, Oho, Tsukuba, 305-0801, Japan

## Abstract

A Local Console System has been designed and implemented using Java for high-energy accelerators. The Local Console System provides information on accelerator control operation in order to control and monitor the high-energy accelerator components. The system was implemented on PC computers running under WindowsNT. The system allows operating the accelerator as well as diagnosing the accelerator at any place in the field through the network. The system provides functionality of consoles either in the control room or, if a failure occurs in the accelerator, in the vicinity of the faulty accelerator component. The system can greatly reduce the shutdown time caused by a malfunctioned accelerator component. The design and implementation of the system is described.

## 1 INTRODUCTON

There are twenty-two synchrotron-radiation beam lines at the 2.5-GeV positron storage ring, Photon Factory at the High Energy Accelerator Research Organization (KEK). These beam lines feed synchrotron radiation to the experimental hall where experiments, such as surface physics, x-ray lithography, microscopy and crystal structure analysis, are simultaneously carried out. These beam lines are simultaneously in operation, providing intense synchrotron-radiation beams. The pressures in the storage ring and the beam lines are maintained at an ultra-high vacuum (UHV) of less than  $10^{-8}$  Pa to achieve a long beam lifetime, typically of more than sixty hours.

Consoles in the control room for high-energy accelerators generally tend to be large, heavy displays, X-terminals and workstations. If there is a failure in the accelerator, it is useful to be able to locate any faulty component in the field, i.e., at the vicinity of the accelerator. Particularly, there are a number of users for a synchrotron radiation facility who use an intense photon beam for their experiment at the same time. Shutting down the accelerator caused by a malfunctioned device should be avoided as much as possible, even for a

half day. Thus, the Local Console System has been designed and implemented.

## 2 SYSTEM DESCRIPTION

Figure 1 shows the configuration of the Local Console System. The Local Console system comprises an applet on World-Wide-Web (WWW) browser, a proxy server on an SGI UNIX workstation, and the operation server running on the control computer VAX/VMS.

In addition to Java's capability, due to its tight network-security mechanism than CGI, the Java Applet was chosen as the implementation language for the system. Needless to say, the Local Console System can be utilized on any WWW browser on a PC running WindowsNT4.0 that supports Java Applet. Due to the security restrictions of the WWW browser, the Applet is not allowed to make a direct link to the control system on the VAX in this case, except for the host (i.e., the UNIX workstation) from which the Applet is loaded. Thus, the server works as a proxy server. The http server is always listening to a TCP/IP port, and accepts a request from a WWW browser.

When invoked, the WWW browser on the PC loads the Java class library of the Local Console System from the http server on the UNIX workstation through the network. Then, the WWW browser automatically initiates the Local Console System. After being invoked, the Local Console System establishes a connection with the proxy server on the UNIX workstation across the network. As shown in Fig.2, the operator can specify operation information of the accelerator components to be concerned. The Local Console System composes a request message associated with the operator's choice. The packet includes a list of components and time information to be concerned. Then, the Local Console sends the request message to the proxy server on the UNIX workstation using a socket communication, and waits for a reply from the proxy server. Upon receiving the request, the proxy server relays it to the server on the VAX/VMS, inquiring status information on the

---

<sup>\*</sup> Email:noriichi.kanaya@kek.jp

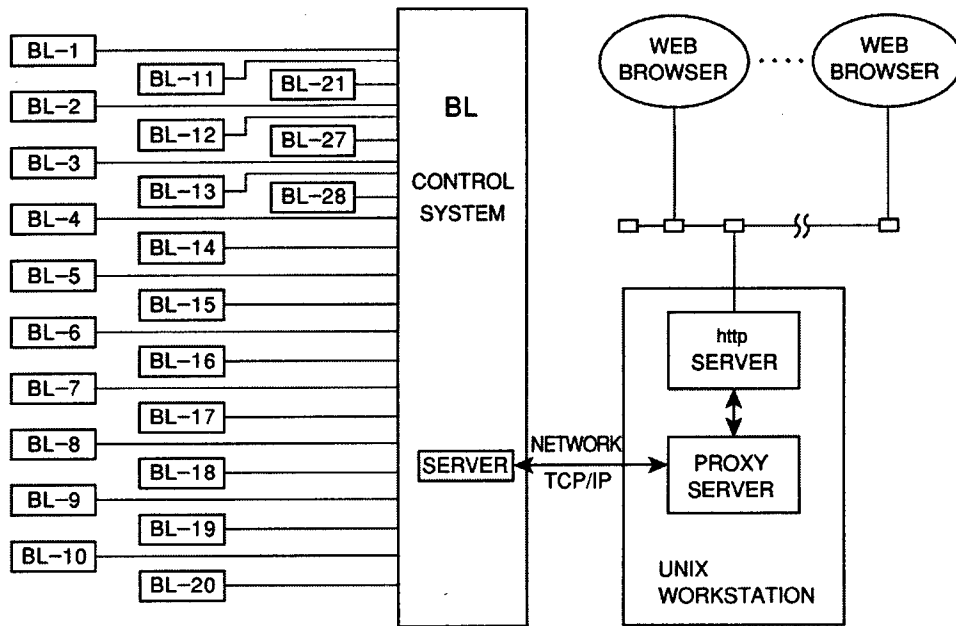


Fig1. Configuration of the Local Console System

accelerator components. After authenticating the contents of the request, the server at the VAX/VMS fetches operational information and control data from the control systems, for example, the control system for the synchrotron radiation beam lines [1][2].

The server replies to the proxy server by transmitting the operation information to the proxy server. The proxy server finally relays it to the Local Console System. The Local Console System can display the operational and control information on the WWW browser as the console screen. For security reasons, the proxy server accepts a request from PCs that have been registered to access.

The Local Console System also allows the operator to access the database on the control computer [3] in order to diagnose the accelerator when a failure occurs. Since a WWW browser on a lap-top computer can also invoke the Local Console System, it is possible to diagnose the accelerator at any place in the field through the network. The Local Console System provides functionality of consoles either in the control room or, if a failure occurs in the accelerator, the operator can diagnose the accelerator in the vicinity of the faulty accelerator component, making it possible to reduce shutdown time caused by the malfunctioned accelerator component.

Access to the database is carried out almost in the same way as normal access to the accelerator components, except for the role at the proxy server side. When the operator specifies operation information of the accelerator components to be concerned, the Local Console System composes a request message associated with the operator's choice. The packet includes a list of components and time information to be concerned. The Local Console System sends a request to the proxy server. The Local Console on the browser is waiting for the reply from the proxy server. Upon receiving a request, the server executes SQL statements to connect

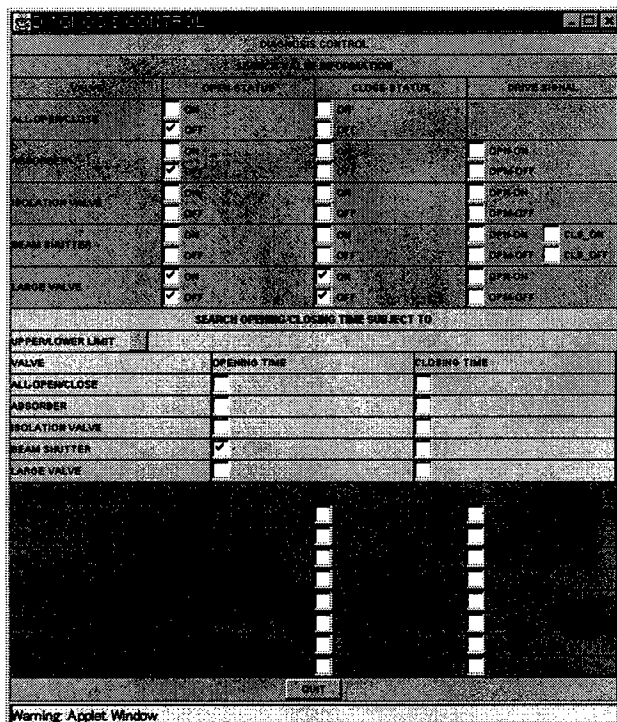


Fig. 2 A screen copy of the Local Console System.

the on-line Oracle database running on the VAX/VMS. The communication between the two servers is done through an SQL\*Net driver.

Once a connection is established, the server executes SELECT statements associated with the request submitted by the Local Console. After retrieving and collecting operational data of the accelerator components from the Database, the server transmits the operational information to the proxy server. After a completion message is sent back to the Local Console from the proxy server, it finally displays the operation information of the accelerator.

The Java environment is still evolving and growing rapidly. Since as of 1999 not all WWW browser supports Java RMI (Remote-Method-Invocation), we have implemented the Local Console using the Java Applet and the socket mechanism. This communication layer will be replaced by RMI. The VAX/VMS will be replaced by a UNIX workstation.

## 2 CONCLUSION

The Local Console System for accelerator components using Java Applet for high-energy accelerator components has been discussed. The system can obtain operational information of the accelerator components to allow inspecting the faulty accelerator component not only in the control room but also in the field.

## 3 ACKNOWLEDGEMENTS

The authors wish to express their gratitude to the staff of the Photon Factory Light Source Division for operating the beam lines and the storage ring.

## 4 REFERENCES

- [1] N.Kanaya, S.Sato, S.Asaoka, T.Koide and H.Maezawa, "Operational Experience with the Distributed Control System for Synchrotron Radiation Beam Lines at the Photon Factory", Particle Accelerators, Vol.29, pp.227-232, 1990.
- [2] N.Kanaya, S.Asaoka and H.Maezawa, "A Generic Model for Monitoring Operational Parameters of Accelerators by Heterogeneous Multiprocesses at the Photon Factory," Proc. of High Energy Accelerator Conference 1992, Hamburg, Germany, 1992.
- [3] N.Kanaya, S.Asaoka and H.Maezawa, "Operational Logging System Using the Database for the Synchrotron Radiation Beam Lines at the Photon Factory," Proc. of Particle Accelerator Conference 1997, Vancouver, Canada, Mar. 1997.

## THE CIS CONTROL SYSTEM AT IUCF\*

J.C. Collins<sup>†</sup>, Wm. Manwaring

IUCF, Bloomington, IN

### Abstract

CIS is the 200 MeV Cooler Injector Synchrotron now being commissioned at IUCF. This paper gives an outline of the entire control system, emphasizing its software aspects. While this is a modest project done with small budget and staff, it includes control of an ion source, an RFQ-Linac pre-injector, a synchrotron and associated beamlines. The hardware platform is based on VMEbus, using modules both purchased commercially and developed in-house, DEC Alpha workstations, X-Terminals and Vsystem software system. This paper discusses our hardware-software interfaces, experience with operator generated control screens, diagnostics displays using BPM and Harp beam sensors, magnet ramp calculation, modification and control, cycle-to-cycle ramp corrections and timing control.

### 1 INTRODUCTION

The Cooler Injector Synchrotron (CIS)[1] is a 200 MeV, 17m circumference machine now being commissioned at IUCF as an injector to our Cooler Ring. CIS itself is injected by a commercial RFQ-DTL and a simple duoplasmatron source. The duoplasmatron will soon be replaced by the CIS Polarized Ion Source (CPIOS)[2]. The control system for CIS and CPIOS evolved from that for the HIPIOS ion source[3], the latter representing a major shift in controls philosophy at IUCF from a totally (hardware and software) in-house built system to a commercially based one. (In fact, the Cooler control computer, its software and the timing system will be replaced later this year by the newer style computer and software to simplify operations. However, full hardware replacement does not seem cost effective at this time.)

One Compaq/DEC Alphastation 200-4/233 serves CIS. The computer communicates with an Allen-Bradley PLC via Ethernet for all on/off, binary status and interlock operations and with VMEbus via a commercial PCI-VME interface for analog, 1553, GPIB and serial control operations. CIS controls uses four 6U and 18 3U VME crates, at present. The computer and three 6U crates are connected in series via copper; the last 6U and all 3U crates are connected to this central group via optical fiber in a star topology. Everything with which the operator is to interact goes through the control computer. While we often use PCs to develop diagnostics, we always design

them for eventual integration with the VME system.

Vsystem[4] from Vista Controls provides the framework for building operator displays and control software. Most displays are created using the Vsystem GUI, although a few are windows generated directly by programs using Motif. All programs are written in C using the Vsystem API. The standard operator station is an X-terminal (or PC with suitable host software). To date, only one (of four) CIS operator stations has a pair of knobs for cost reasons. We have recently found a commercial solution, which, if it works, is inexpensive enough that a pair of knobs will become part of the "standard" station.

### 2 HARDWARE

The most interesting hardware in the CIS control system are the HiRel and sequencer modules, both designed and built at IUCF and described in detail elsewhere in these Proceedings[5]. In summary, the HiRel modules are DAC/ADC combinations which sacrifice speed for accuracy and isolate every signal. They were designed and built because commercial units could not meet the specifications of the CIS designers. The sequencers are limited purpose computers originally designed for ramping, for which we found no commercial alternative.

#### 2.1 Sequencer

The sequencer instruction set was designed to facilitate the generation of output voltages, signals (TTL levels and serial codes) and the reading of analog values at specified time intervals in a repetitive fashion, all for use in magnet ramping. In use, a program on the host control computer generates a sequencer program, downloads it and any necessary data and, perhaps, starts the sequencer program. For ramping, a sequencer is downloaded with ~20,000 DAC values and a program which outputs those values at timed intervals (typically, 30  $\mu$ sec) during the half-second long ramp. Sequencers also serve in the accelerator timing system and some high speed diagnostics readouts as described below.

#### 2.2 Timing System

The hardware timing system consists of one sequencer and four V102 modules designed at Brookhaven National Laboratory[6]. The sequencer is the master timer, sending trigger events to the V102s (perhaps multiple times in one timing cycle), sending start signals to the ramping sequencers, providing TTL output pulses and accepting TTL inputs for timing program control. The V102

\*Work supported by the National Science Foundation grant NSF PHY 96-02872 NUC RES and Indiana University.

<sup>†</sup>Email: [collins@iucf.indiana.edu](mailto:collins@iucf.indiana.edu)

modules assert TTL signals of programmable width at programmable delays relative to trigger events. Unlike the sequencer outputs, the V102 outputs are easily grouped together and associated with events. Also, their delay and width values can be changed on-the-fly, allowing users to tune timing in ways which are impractical using only sequencers.

### 3 SOFTWARE

Vsystem provides tools for display creation, data logging, status alarms and script-driven processes, all of which features we use but about which we shall say nothing here. The smallest unit of hardware access is the channel, which can have other uses as well. Channels are organized into databases. By adopting conventions for defining databases, channel names and reader/writer programs, operations people can name devices and generate displays in parallel with software development, speeding installation. This also helps give operations people a better understanding of the control system and allows them to make some changes themselves, helping keep the developers' blood pressure low. Although at one time there was a lot of talk at IUCF about personalizing operator displays, there has been no movement to actually do that after five years of use (for HIPIOS).

Problems of space and selection persuaded us to make this paper all text. Examples of all the display screens discussed herein may be found on the IUCF Web site[7].

#### 3.1 Knobs

Because IUCF operators used knobs in a particular fashion for 20 years, a Motif program was required to emulate that mode of operation. The program allows each of two knobs to be attached to DAC channels, the channels being organized into display pages defined in an ASCII file editable by operators. The program remembers and restores attachments as pages are changed, it can save and restore DAC values for all channels on a page and it supports "presets", predefined attachment selections to make standard tuning operations faster.

#### 3.2 Save/Compare/Restore

The operational data archival function is performed by a Motif program which performs the three functions in its name, using both disk files and the present machine state as data sources or sinks as appropriate. The data files are created with fixed length data items and no delimiters just so we are not tempted to edit DAC changes into archives.

#### 3.3 Timing

Access to timing hardware and generation of the timing sequencer program is done through a timing server program and timing channels. All event delays and timing parameters have their own channels in the timing

database. For operational purposes, we find it convenient to define two timing modes: one wherein beam is only injected into CIS and one which adds acceleration and extraction. When a request to start timing is made, the server program generates and downloads the sequencer program appropriate to the active mode and starts the timing sequencer. If timing mode or values are changed, the server stops the sequencer, creates and loads a new program and restarts the sequencer. The timing sequencer program can cause the sequencer to generate a VME interrupt at a defined point in the timing cycle; this is the end-of-ramp event referred to below. The program also uses bits set in a sequencer register by the host and sequencer TTL inputs to conditionally suppress source, ramp and/or extraction trigger events. This allows the operator to turn off CIS beam when it is not needed to fill the Cooler.

A Motif program provides the normal user interface to the server, although any program can access the server through the timing channels. For all time delays implemented in V102 modules, the user interface program supports direct manipulation of values via either keyboard or mouse buttons (for "no-look" tuning). Groups of outputs (e.g., ion source, RFQ/DTL) can be defined such that the delays of all group members can be moved with respect to all other delays while retaining relative delays within the group. Since updating time delays implemented in the sequencer is slow (create and download a new program), only keyboard input is supported for them. The program also supports temporary and archival storage of timing data.

#### 3.4 Ramp Calculation

This Motif program takes as input starting and ending beam energies (MeV), desired ramp duration  $\tau$ (msec) and ramp shape parameters  $P$ . Its output is seventeen 100-element ramp arrays of points equally spaced in time, one array for each ramping device. The 100-element length, a compromise between ramp accuracy and ease of modification of points by operators, came from experience on the Cooler and works quite nicely. Most ramps are functions of  $B_p(t)$  and are based upon a master  $B_p(t)$  curve, which can take various functional forms; at present we use  $B_p(t) \propto (\sin \pi t / 2\tau)^{**P}$ , where  $P=2$ . The dipole power supply requires both a current ramp, derived from  $B_p(t)$  and mapping data, and a feed-forward voltage ramp, based on  $V = iR + L(di/dt)$ , with empirical corrections for measured changes in  $L$  as a function of current. Ramps for quadrupoles, steerers and RF frequency are all derived from  $B_p(t)$ . The ramps for the RF cavity ferrite bias magnets are based on empirical data tables, with the user able to set the slope of the linear RF voltage ramp. Each ramp is stored in a Vista database array-channel, from where it can be graphed or accessed by other programs.

### 3.5 Ramp Modification

This is a Motif program that allows the operator to fine-tune ramps by modifying any of the 100 points of the ramp arrays generated by the calculation program. Modifications can be applied point-by-point or to each point in a specified interval and are entered as a percentage of the unaltered value in either case. The program also permits easy addition of a predefined ramp change to any of the four dipole trimcoils to position the beam properly near the end of the ramp for the extraction kick. A single command stops the ramp (via the timing server), loads all modified ramps and restarts the ramp. The RF Frequency ramp can be modified automatically via the BPM program described below. Those modifications are displayed by this program and are updated as the BPM program changes them.

### 3.6 Ramp Control Interface

This program acts as a server controlling the ramping sequencers. Its functions include

- Download the sequencer ramping programs; start and stop ramp execution.
- Read the 100-point ramp arrays, convert them, via interpolation, into ~20,000 DAC values, then download these values to sequencer RAM.
- Create the linear reset ramp and download it.
- Perform single write operations to a sequencer DAC when the corresponding channel value is changed, since a sequencer acts as the DAC and ADC for the power supply to which it is connected. Also, poll all sequencer ADCs, updating the corresponding channels (displays).

### 3.7 Beam Position and Ramp Correction

Pictures of the beam position during a ramp are obtained by attaching a 48-channel ADC multiplexer to a single sequencer and running a sequencer program that steps through the mux channels, reading and storing ADC values in RAM. During a ramp, each channel is sampled every two milliseconds. Upon receipt of an end-of-ramp event, a host program scans the sequencer RAM and extracts 200-point position (mm) and 200-point beam current (mA) arrays for each of four BPMs, writing these arrays to database channels for graphing and/or calculation. A single sample of BPM values during Fill or Flatop can be triggered by the timing system. This program can read these single values and update database channels for bar-graph display.

The host program can also correct the RF Frequency ramp in such a way as to flatten a chosen BPM position vs. time graph. The operator can choose to "flatten BPM-2 from 200 msec to 600 msec at -3mm offset from center", for example. In this case, to each RF frequency ramp value in the interval 200-600 msec after ramp start, the program applies a correction proportional to the

difference between the corresponding BPM-2 position and -3 mm and informs the Ramp Modification Program (see above) that a change was made. The modified ramp is then loaded. The present correction algorithm typically requires five or six iterations to achieve satisfactory results; more sophisticated algorithms are under test to achieve faster convergence and smoother RF ramps.

### 3.8 Harp Display

Three 48-wire (24 vertical, 24 horizontal) harps[8] are multiplexed to a commercial VME ADC module which includes FIFO RAM. A timing system trigger initiates sequential conversion and storage in the FIFO of the wire currents. Upon receipt of an end-of-ramp event, a host program reads the FIFO values into six 24-element database arrays. For each array, the program subtracts an array of background values, converts each resulting element into proper units and calculates a beam profile centroid and width (each array should contain one peak) and an equivalent Gaussian curve for visual comparison. A Vsystem tool displays three horizontal or vertical arrays in different colors on the same graph. The operator can use these displays to tune beam position and focus. Six additional harps will be included in the extraction beamline.

## 4 ACKNOWLEDGEMENTS

The authors would particularly like to acknowledge the efforts of all IUCF electronics technicians and operator Pete Goodwin for his work in generating control screens and maintaining databases.

## 5 REFERENCES

- [1] D.L. Friesel, "Performance of the IUCF Cooler Injector Synchrotron", these proceedings.
- [2] V.P.Derenchuk, et al., "Polarized Beam for the IUCF Cooler Injector Synchrotron", 7<sup>th</sup> Inter. Workshop on Polarized Gas Targets and Polarized Beams, Urbana, IL (1997).
- [3] J.C. Collins, et al., "The IUCF High Intensity Polarized Ion Source Control System", 13<sup>th</sup> Inter. Conf. On Cyclotrons and Their Applications, Vancouver (1992).
- [4] P.N. Clout, et al., "A Comparison of Vsystem and EPICS", ICALEPCS'97, Beijing, China (1997).
- [5] W. Hunt, "CIS Control Hardware at IUCF", these proceedings.
- [6] RHIC Report AD/RHIC/RD-16 (1993).
- [7] <http://www.iucf.indiana.edu/Facilities/Controls>.
- [8] M.Ball, et al., "Beam Diagnostics in the Indiana University Cooler Injector Synchrotron", 7<sup>th</sup> Workshop on Beam Instrumentation, Argonne, IL (1996).

# COOLER INJECTOR SYNCHROTRON CONTROL HARDWARE AT INDIANA UNIVERSITY CYCLOTRON FACILITY\*

W. A. Hunt\*, IUCF, Bloomington IN 47408

## Abstract

This paper describes the control hardware at IUCF for the newly commissioned 200 MeV CIS ring. A combination of "commercial off the shelf" and custom "in house" hardware makes up DAC, ADC, and timing control for this synchrotron. The focus of this paper is on the custom designed hardware.

## 1 INTRODUCTION

The control hardware designed and manufactured at IUCF meets strict specifications combined with self-calibration, self-diagnostic, I/O protection, and serviceability options not attainable commercially. The CIS control system is comprised of three primary subsystems, timing, ramping and non-ramping, all which interface with the host control computer via distributed VME buses. IUCF's custom ramping subsystem has two main components, Sequencers and Ramping Analog Heads, with a third, Timing/Frequency Heads, planned in the future. The 6U VME Sequencer is a timing computer and data sequencer that provides digital inputs and

outputs and a high speed fiber optic bi-directional data stream to a Analog Head. The Analog Head receives data from a Sequencer and converts the data to a single 18 bit DAC output channel and collects 16 bit ADC data returning it to the Sequencer. The timing subsystem consists of a master Sequencer which time synchronizes and triggers all the other Sequencers and Brookhaven V102 delay modules [1]. Together the Sequencers and the V102's provide all the digital timing input and output signals needed. IUCF's non-ramping system consists of custom 3U VME modules, which are low speed, high precision, 16 bit, 4 channel DAC's or ADC's. Both ramping and non-ramping analog sections employ optical data isolation for high noise rejection, very low drift voltage reference, extensive I/O protection, self-calibration, and self-diagnosis hardware for calibration or functional problems. All the IUCF modules have many front panel LED's indicating operational states, error conditions and histories. As well, all IUCF hardware can be "hot swapped" in and out of the VME crates for faster servicing. In total well over a hundred IUCF VME modules control the CIS ring. Commercial VMIC [2]

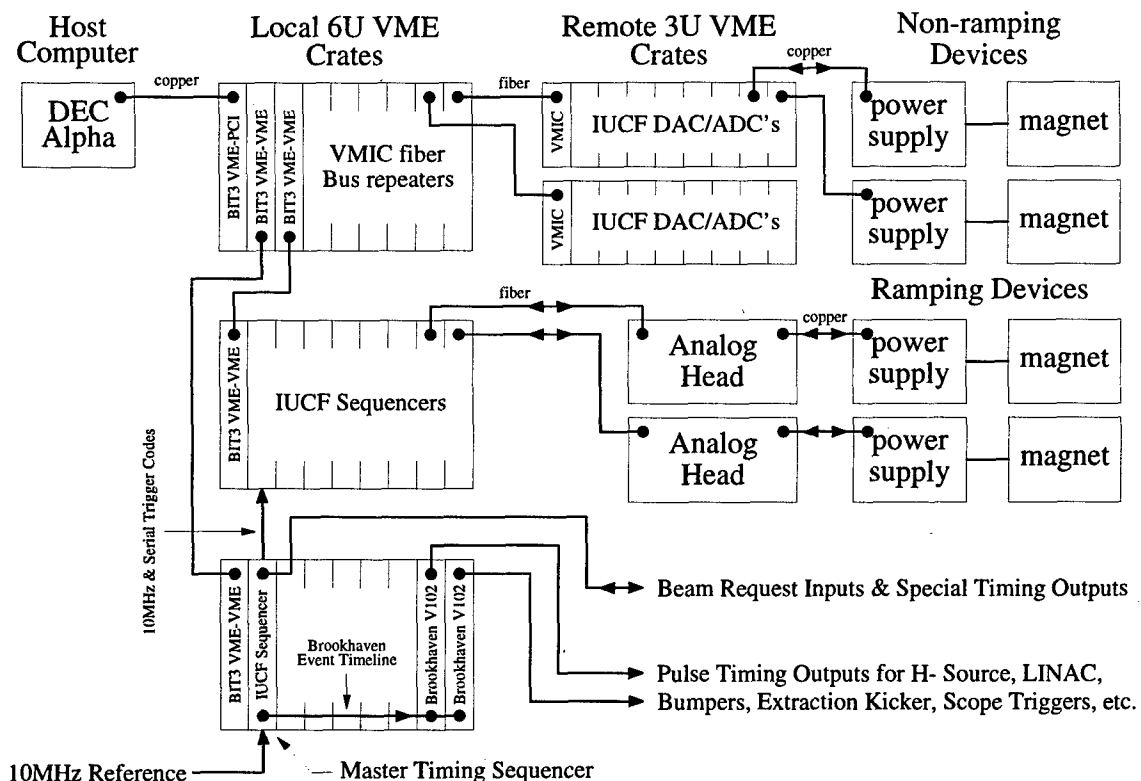


Figure 1: CIS Control System Overview

\* NSF PHY 96-02872 NUC RES

\* Email: willie@iucf.indiana.edu



fiber and BIT3 [3] wired VME bus repeaters fan out control to many VME crates from a single DEC Alpha desktop workstation. Figure 1 shows an approximate arrangement.

## 2 SEQUENCERS

IUCF Sequencers transmit and receive ramping data to IUCF Analog Heads over 10 megabyte/second glass fiber links. Each Sequencer provides 8 front panel digital ports, which can be individually configured to be 50 ohm series or parallel terminated inputs or outputs. Special I/O ports synchronize and exchange serial trigger codes to other Sequencers and provide phase locking of all Sequencer clocks. VME interrupt capability is also provided. The front panel of the Sequencer contains 24 tri-color LED's that provide a wealth of diagnostic and operational information.

The sequencer board contains a large multi-ported DRAM (Dynamic Random Access Memory) that is either 4, 8, 16, or 32 Megabytes depending on the SIMM installed. Its ports tie to the VME bus (A32; D32 D16 D8EO BLT UAT [4]), an on board FPGA (Actel A1240XL [5]) based hardware timing and data processor called the Sequencer Processing Unit (SPU), and a local bus that plugs into a daughter DSP card. From the VME bus the board appears as plain RAM memory, except for some reserved locations. The DSP port allows memory access just like the VME port.

Internally, the SPU reads instructions and data from this memory, processes it, transmits data out the fiber port to a remote head, and writes data received from the fiber port into this memory. The SPU can output digital data on the front panel, send serial codes to another Sequencer, interrupt the VME host, test digital inputs, test for serial codes coming from another Sequencer, and more. By design, SPU executes all instructions in exactly 1  $\mu$ s except for special delay instructions. These delay instructions execute in 1  $\mu$ s plus N times 100 nS or 1  $\mu$ s, or wait for an external event. In this way the SPU allows for totally flexible and precise timing of digital and analog control signals.

To use a sequencer, the host VME computer writes an instruction stream (I.E. download a binary program) into a block of memory locations, set the SPU's program counter, and start the SPU executing. The SPU then executes through this instruction stream which normally would send ramping data out the fiber interface to an Analog Head. The Analog Head acknowledges with an ADC sample which is sent back to the Sequencer and recorded in main memory. In this way, a diagnostic ramp of the supply output is available for inspection. Additionally, the SPU can write digital data out the front panel or to the digital outputs on the Analog Head. Also, a typical SPU program would wait at certain points for external triggering from the master timing Sequencer, so

that all analog ramps will be timed together as required to run the synchrotron.

## 3 GLASS FIBER LINK

Sequencers talk bi-directionally to the Analog Heads through a 10 megabyte/sec fiber link. 32 bit Sequencer data is broken into 4 bytes and serialized at 120 Mbaud using AMD TAXI transmitter (Am7968 [6]). The high-speed serial PECL data is converted to 1300 nm optical data using a Hewlett Packard HFBR5103 transceiver which allows for up to 2 Km transmission. At the Analog Head the same optical transceiver and the AMD TAXI receiver (Am7969) convert the optical data back to parallel bytes. Data from the Analog Head is sent back to the Sequencer in exactly the same way.

The AMD TAXI receiver and a local crystal PLL provide a local 10 MHz frequency reference that is phase locked to the driving Sequencer, which in turn is phase locked to the master timing Sequencer. In this way all remote data can be timed exactly to specific cycle of a master 10 MHz clock. Also, upon reception, parity bits and the data packet framing is checked for possible transmission errors. If an error does occur, the Analog Head requests the data be resent. Any data errors, signal strength loss, or phase lock problem shows up on front panel LED's and a history of these errors are kept.

## 4 RAMPING ANALOG HEADS

The Analog Head provides the interface between the Sequencer's ramping data stream and the power supply under control. This head is composed of fiber optic Interface card and an Analog card that slides in DIN 3U card cage, but does not use a backplane. The front panel has power, analog I/O, digital I/O, fiber, and backup connectors. The Interface card translates the incoming 10 megabyte/sec fiber data into a 32 bit word which is sent to the Analog card as parallel data over a 96 pin DIN connector that connect the 2 cards. Also, the Analog card sends a 32 bit response back.

This command word is used to control all operation of the Analog card. Control bits within this 32 bit word provide for large set of command instruction to the card. Primarily, 18 bits of this data is sent to the 18 bit DAC (Burr Brown DAC729KH [7]) which controls the connected power supply through the output channel. The 18 bit DAC is jumper selectable for 0 to 10 volt or -10 to 10 volt output. Normally, the card responds by taking a 16 bit ADC (Burr Brown ADS7805P [7]) value from one of three input channels and sending it back to the sequencer over the fiber. A different card command writes or reads 4 bits of digital I/O data.

Other commands allow for remote calibration, testing and re-calibration. This is accomplished by calibrating the 24 bit sigma-delta ADC (Analog Devices AD7712AN [8]) with an onboard ovenized 10 volt reference (Linear Technology LT1019 [9]), then using the 24 bit ADC to

measure the gain and offset of the 18 bit DAC. Finally, the octal trim DAC (AD8842) outputs are changed to re-calibrate the 18 bit DAC. In this way better than 1[ PPM/C temperature drift can be realized without having an ovenized DAC.

IUCF Analog Heads achieve outstanding analog noise rejection since they are individually fully isolated from ground and since they are normally located within a few feet of the power supply under control. Data isolation is provided by glass fiber and power isolation is provided by low capacitance, 120 VAC, linear power supplies.

The DAC output can detect an overload condition and reports this to front panel LED and to the hosting Sequencer. Transorb's and fuses protect all external

connections from severe abuse. Output relays provide quiet outputs while the Analog Head is powering up and also provide for active redundant switchover.

IUCF's ramping system allows for active redundant connections for critical applications in a primary/backup arrangement. If a primary ramping system should detect a fault and the primary Analog Head is plugged into an active and ready backup Analog Head then the primary can release control and let the backup take over. A large set of fault conditions are continuously tested by hardware and any detected fault condition will cause the switchover. Programming bits in control registers allows for masking of each fault individually.

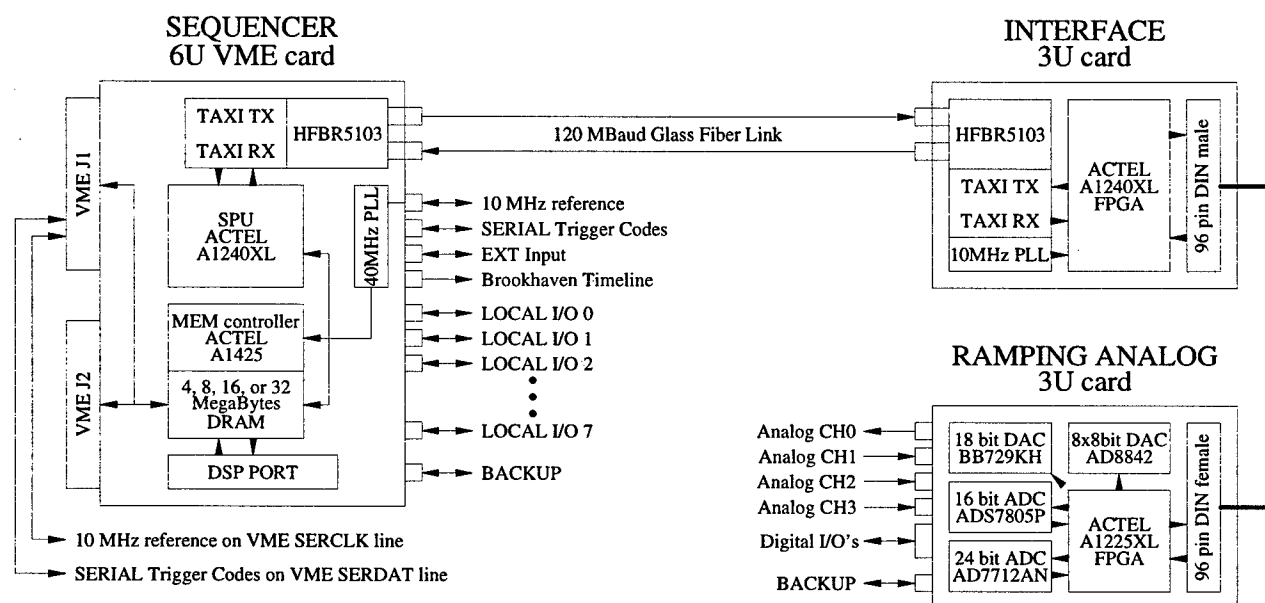


Figure 2: Ramping System Modules

## 5 NON-RAMPING DAC/ADC'S

IUCF's non-ramping DAC/ADC module provides four 16 bit, -10 to 10 volt, opto-isolated, individually switch selectable DAC or ADC channels, in a 3U VME package. The basic ADC works by digitally timing a voltage comparator's output whose inputs are connected to the an ultra linear ramp and the voltage to be sampled. The basic DAC is a digitally controlled integrator whose output ties to an ADC channel for feedback control. The ADC conversion's result steers the integrator up or down until the precise voltage is obtained. The main drawback is its very slow speed, but it is still more than fast enough for human controlled non-ramping devices. The main advantage is its absolute precision, and almost perfectly even DAC steps (DNL is much less than 1/16 bit). This gives the operator consistent power supply control, even when changing only one DAC step at a time.

This unique "in house" design achieves analog conversion has  $\pm 0.01$  percent absolute full-scale accuracy over the operating temperature range, with a

maximum of  $\pm 1$  bit zero error. This design accomplishes this by continuous self-calibration of the ultra linear ramp for positive full scale and zero. It tests positive, zero, and negative full scale for tolerance. Should the unit not meet specification, front panel LED's will show the fault and the host computer can also query for this condition. Each DAC output is checked for a 1.5 bit tolerance, which if not met will show a fault condition as well.

## 6 REFERENCES

- [1] <http://www.rhichome.bnl.gov/Hardware/timeline/eventsys.htm>
- [2] [http://www.vmic.com/products/chap8/hw\\_repeat\\_index.html](http://www.vmic.com/products/chap8/hw_repeat_index.html)
- [3] <http://www.bit3.com/>
- [4] ANSI/IEEE STD1014-1987 IEC821 AND 297
- [5] [http://www.actel.com/products/fpga\\_devices.html](http://www.actel.com/products/fpga_devices.html)
- [6] <http://www.amd.com/products/npd/techdocs/techdocs.html>
- [7] <http://www.burr-brown.com/products/products.html>
- [8] [http://www.analog.com/products/product\\_center.html](http://www.analog.com/products/product_center.html)
- [9] <http://www.linear-tech.com/prodinfo/>

# IMPROVEMENT OF VME CONTROL SYSTEM FOR VACUUM DEVICES AND MAGNET POWER SUPPLIES OF THE PLS STORAGE RING\*

I. C. Yoon<sup>#</sup>, J. W. Lee, T.-Y. Lee, and S. S. Chang  
Pohang Accelerator Laboratory, Pohang 790-784, Korea

## Abstract

In the Pohang Light Source storage ring, there are 12 VME systems, called VMMIU, in the local control sheds around the storage ring. The VMMIU's control and monitor vacuum devices, gate valves, LCW, Injection system, and magnet power supplies. All vacuum devices and magnet power supplies have local controllers. These controllers are connected to the VME system through RS422/RS232 serial communication. Now we are upgrading software and hardware of these VME systems to enhance device execution speed and communication reliability. In this paper, we describe control structure and scheme of both the current VME system and the upgraded one.

## 1 INTRODUCTION

The computer control system of the PLS storage ring has distributed control architecture, with three layers of hierarchy; operator interface computer (OIC) layer, subsystem control computer (SCC) layer, and machine interface unit (MIU) layer. The OIC layer is based on Sun Microsystems' SPARCstation with UNIX (SunOS 4.1.3) and X-terminals. The SCC acts as a data gateway between the OIC layer and the MIU layer. The MIU layer is directly interfaced to individual machine devices for low-level data acquisition and control. Both the SCC and MIU layer is based on VMEbus standard with OS-9 real-time operating system. Executable application software modules are downloaded from host computers at the system start-up time. There are 4 SCC's and 24 MIU's. The MIU's and host computers are linked through Ethernet (TCP/IP)[1].

The control system is now very stable and reliable enough to meet our control requirements. However, the control system is continuously being upgraded to accommodate additional control requirements. Recently we had a few additional control requirements. The first is U7 undulator, the first insertion device of PLS, which was installed at the storage ring in July 1997. It required

micron level control of the magnet gap, and also the development of VME application software for IDBPM (Insertion Device Beam Position Monitor) and operator interface software. Next some control requirements of the vacuum gauge controllers were upgraded to increase the vacuum monitoring speed. The third control system change came from the energy ramping of the storage ring. Even though the injection energy from linac is 2 GeV, the stored beam energy can be raised up to 2.5 GeV inside the storage ring. The energy ramping procedure needs fast and synchronized control of magnet power supplies. For this purpose, both hardware and software was changed. Finally the timing system was upgraded for the uniform fill pattern of the storage ring, which also needed hardware and software improvement.

## 2 SYSTEM CONFIGURATION AND HARDWARE

There are total 215 magnet power supplies in the storage ring. The magnet power supplies can be divided to unipolar power supplies and bipolar power supplies. Unipolar power supplies are used for bending, quadruple, sextuple, and septum magnets. Bipolar power supplies are used for vertical and horizontal corrector magnets. Each unit of unipolar power supplies has an RS422 serial communication port that is connected to VMMIU. On the other hand, each unit of (bipolar) corrector magnet power supplies has a digital type I/O port that is connected to the other machine interface called COMIU.

Vacuum system consists of 124 ion pumps, 36 penning ion gauges, 18 Bayart-Alpert ion gauges, 240 photon-stop temperature sensors, and 15 gate valves. These components have their own local controllers that are interfaced to VMMIU. Each of pumps and gauge controllers has an RS422/RS232 type serial communication port, while each of gate valve controllers has a relay type I/O port. The MIU is directly connected to individual devices and performs the low-level data acquisition. For the real time data acquisition and processes, we chose to use the VME system. Each MIU is a diskless ROM-based system. The ROM contains OS-9 real-time operation system, utility, user-define command, and other necessary application modules.

After the application software upgrade was

\*Work supported in part by the Korean Ministry of Science and Technology and the POSCO company.

<sup>#</sup>Email: jc0927@postech.ac.kr

accomplished in a separately prepared machine development system, the execution file is downloaded.

A summary of VME boards used for VMMIU's is shown in Table 1.

Table 1: Summary of VME boards used

Model	No.	Description
MVME147S-1	12	SBC, 25MHz, 4MB DRAM
BUS6522II	12	MIL-STD-1553B Interface
AVME9510-I	12	32 digital input/output, 16ADC
ESD-ASIO16	24	12xRS422, 4xRS232
IP-610	2	6U IP-Carrier Board
IP-Octal	2	Industry Pack, 8xRS422

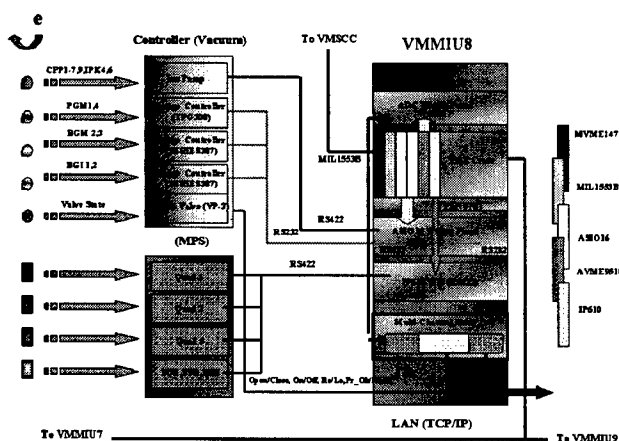


Figure 1: Structure of the VMMIU#8

### 3 SYSTEM UPGRADE

The computer control system for the remote operation of the U7 undulator is now under development. Development of the VME system for low-level position control and monitoring has been completed. Parker's INDEXER-500 controller was used for the step motor control, and Parker's AR-C absolute encoder was used for the position monitoring. For the motor driving, Parker's PK-130 model was used. A U7 test with local controllers was performed to obtain encoder reference data and to find the locations of the interlock limit switches. The VME control software for position control and monitoring consists of a position control routine and a position monitoring routine. The position control routine directly controls the INDEXER-500 step motor controller. This routine can handle three operator commands: start, normal stop, and emergency stop. The position monitoring routine directly controls the AR-C absolute encoder. This routine can monitor the absolute position of U7. The INDEXER-500 and AR-C are connected to the VME

system through an RS232C serial communication. Four limit switches are used for interlocking. If the undulator moves beyond these limit switches, motor driven pulses are immediately stopped. The developed VME control software was installed in the COMIU#7.

A related work is the development of the VME control system of the IDBPM. For this purpose, one VME ADC I/O board, Acromag's AVME9510-I, was installed in the COMIU#7. This ADC board receives 15 beam position analog signals (A, B, C, D, AGC, X, Y), two digital output signals (signal level check; TTL level), and four interlock state digital I/O signals, from BPM boards which measure beam positions at the insertion device. The VME control software and the operator interface software were developed, field installed, and the integration test was completed.

For the energy ramping control, two types of VME boards (IP-610, IP-Octal) were installed at the VMMIU#8 and #12 for the fast and efficient control of the magnet power supply currents. Also the appropriate VME control software was developed. The structure of the upgraded VMMIU#8 is shown in Figure 1. Present energy ramping control system has been redesigned and upgraded to reduce ramping time and ensure reliable operation. In a ramping process, the amplitudes of magnetic fields of storage ring magnets should be controlled synchronously for each energy ramping step in order to keep the same optics. This requires the synchronous control of current settings of tens of magnet power supplies distributed in the storage ring. New ramping control system took full advantage of the distributed three-layered PLS storage ring control system to reduce development time and cost. The VME's at the bottom layer, called VMMIU, calculate and control current setting values of magnet power supplies for each ramping step. The VME at an upper layer, called SCC (Subsystem Control Computer), generates synchronization signals for each ramping step. The MIL-1553B field bus, which is already installed for low-level data acquisition control, was used for the synchronization network through which the SCC sends synchronization signals to the lower MIU's. A graphical user interface based on Motif/X-Windows was developed for the operator control of energy ramping.

Some control requirements of the vacuum gauge controllers were changed to increase the vacuum monitoring speed. Four Bayard-Alpert ion gauge controllers were installed for insertion device. The 13 cold cathode vacuum gauge controllers have been replaced by Bayart-Alpert ion gauge controllers because of the bad signal caused by either data transmission errors or controller breakdowns. We have improved VME serial boards to resolve the data transmission error problem

from VME boards to device controllers. The block diagram of the improved serial VME boards is shown in Figure 2. The VMMIU's were upgraded and the VME control software was developed for these changes.

For the uniform fill pattern of the stored beam, the timing control VME system needs to know the stored beam current. One VME ADC I/O board was installed in the timing VME crate. This ADC board receives one analog signal from DCCT that measures the stored beam. The necessary VME software consists of two subroutines; a uniform fill pattern and an arbitrary fill pattern. The present operator interface software was also slightly modified to support the uniform fill pattern operation.

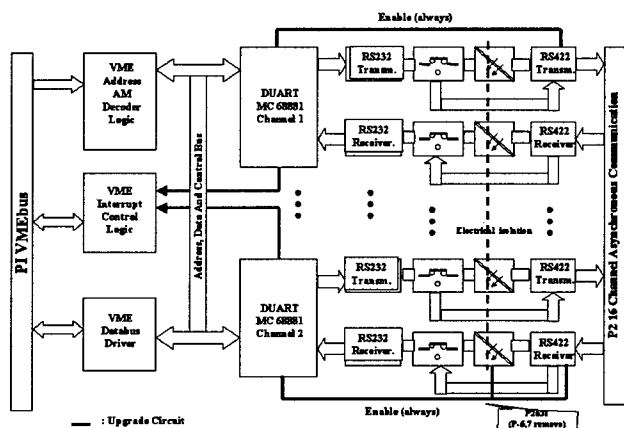


Figure 2: Block Diagram of the improved serial VME board

#### 4 SOFTWARE UPGRADE

We chose to use OS-9 68K, which is one of the most popular real-time operating systems for VMEbus. In parallel to the hardware structure, the software structure has also the three layer system. There are two important features in the control software; the client/server model to exchange the data between the OIC layer and the SCC layer, and the master/slave model to exchange data between the SCC layer and the MIU layer. The MIU software is basically divided as follows, device access software, application user software, diagnostic monitor software, communication software, and utility software.

Each MIU monitors and controls the software of the corresponding device. Hence, Failure of the application program may lead to the interruption of the related application programs and devices. In this case, the operator should immediately check up the VME computer system and resolve the problem. Moreover, the VME computer often needs to be tested in offline state to upgrade the system or modify the application programs. In order not to stop the running system, we used the dual

shared memory module. Shared memory module can provide safe process data, alarm data, and fail device data. The improved control software structure of the VMMIU is shown in Figure 3.

#### 5 Conclusion

We are upgrading and modifying the control system to accommodate new control requirements and to apply long-term operational experiences. We are preparing one more duplicated machine development system and operator computer system. This duplicated system will be used for research and development works in the normal operation. In case of main system failure, this system can be used as a backup. Now we have a plan to upgrade the operating system from OS-9 ver. 2.4 to ver. 3.0.3 that contains the Year 2000 Solution. Also, we have a plan to upgrade the control application programs to improve the monitoring refresh time interval of the vacuum pressure.

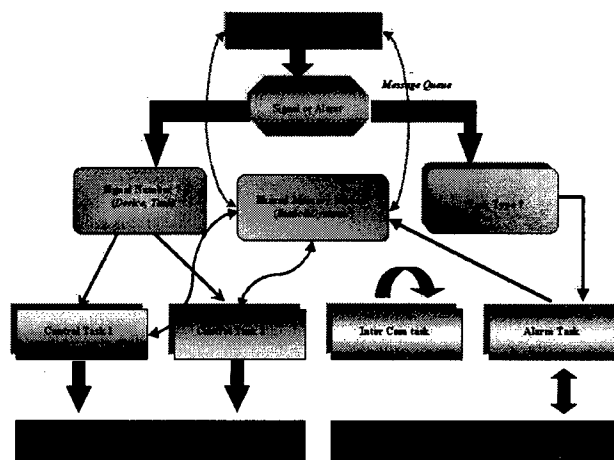


Figure 3: Structure of the upgraded control software

#### 6 REFERENCES

- [1] I.S.Ko, Jin W.Lee, Jong C. Yun, Eun H. Lee, and Byoung R. Park, "Computer Control System of PLS 2-GeV Storage Ring," *IEEE Trans. Nucl.* 45 (1998) 2012.

# PERFORMANCE OF THE REJUVENATED INJECTOR CONTROL SYSTEM IN SRRC

C. S. Chen, C. J. Wang, Jenny Chen, J. S. Chen, S. H. Lee, K. H. Hu, K. T. Hsu, K. K. Lin

Synchrotron Radiation Research Center

No 1, R&D Road VI, Hsinchu Science-Based Industrial Park, Hsinchu, Taiwan, R.O.C.

## Abstract

The original injector control system is a turnkey design and it was separated from the storage ring control system. It is not easy to maintain and install new devices. The control system of injector has been rejuvenated recently. There are two basic requirements for this plan, to provide more efficient and stable light source operation, and to reduce the maintenance resource need. Its implementation will also be helpful for improvement on reliability and control response time. Upgrade injector from 1.3 GeV to 1.5 GeV will be done before the end of 1999. The renewed injector control system will be able to provide improved environment for application program development and new devices installation. Automatic control operation for full energy injection will be implemented in SRRC.

## 1. INTRODUCTION

To simplify the system and provide upgrade options, injector control integration project has been launch in 1998 [1]. A homogeneous control system was put in operation from May 1999. It simplifies the operation of the accelerator and gets much more efficient in operation. Of course it reduces the injection time. SRRC will be an automatic operation machine. Topping-up mode test becomes possible in the new control environment. A series of application programs was built to support SRRC upgrade plans: full energy injector upgrade, new device installation and application program development. After the integration, not only the performances improved, but also it was provided data logging and archiving service.

## 2. NEW INJECTOR CONTROL SYSTEM ARCHITECTURE

Figure 1 show the new injector control system, VME crates replace the original Intel PC that run the iRMX III operating system, the VME crates are the local controller in the main control system. In order to save the time, manpower and cost, it keep the two main subsystems, PLC system and BITBUS system. New booster control system has software architecture same as the SRRC storage ring control system, to modify and develop the application program is much easily. A simply user

interface for the injector normal operation. New control system for SRRC booster is like a new life in the feature.

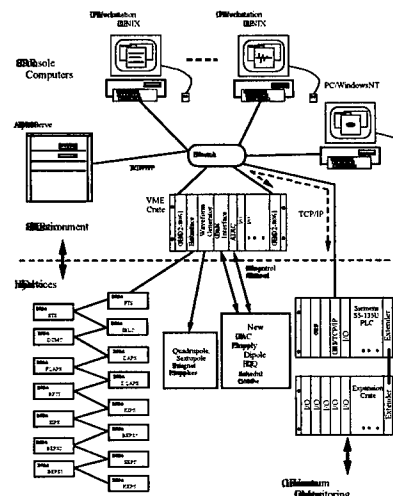


Figure 1. New injector control system configuration

## 3. STRATEGICS OF CONTROL INTEGRATION

Two local controller nodes were created for the integrated plan, one for PLC control interface, and another one for the master of the BITBUS network. These two nodes play a crucial role, as a protocol translator. Database format is fully same as the storage ring control system. An open and flexible control system just what we need, it has a grand advantage that is stable and easily maintains. An injector 1.5 GeV upgrade will finish before the end of this year. New booster control system provides the base requirement to support these activities.

The storage ring has been upgrade to 1.5 GeV operation in SRRC. Upgrade booster synchrotron from 1.3 GeV to 1.5 GeV to provide full-energy injection is under way. First, two cluster of power supply need to be replace, one is the dipole power supply of transport-line, and the other is the booster both DC and AC power supply. Second, in order to have enough safety margins and to avoid the insulation failure when operated at 1.5 GeV mode, a new septum magnet will be installed, and the extraction kicker must be increased 30% in field strength [2]. Third is the utilities, cooling water system and electricity capacity.

#### 4. HIGH LEVEL APPLICATION

It is not economically to modify the old injector control system and to build new application program to upgrade the function of injector control system. In the new environment, it provides data logging and archiving services. It is also easily to build a lattice file management for injector operation in the storage ring lattices file management. More application program will develop soon, some of these application is summary in following paragraphs.

In figure 2, a small size window shows the injector subsystem status. A serial of buttons was implemented for injector automatic operation. Beam current of the injector is displayed at the bottom in text and trend.

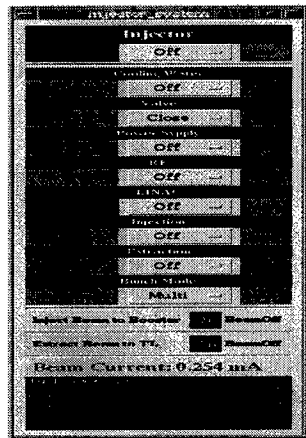


Figure 2. A user interface for the injector automatic operation

In figure 3., show graphical user interface of the linac system. A new environment for injector control and monitor is created by the control system integration in SRRS.

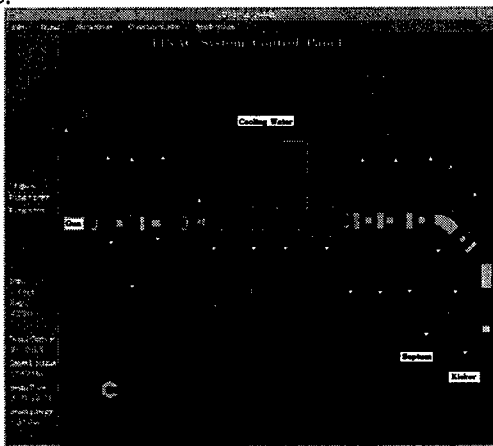


Figure 3. A graphical user interface for linac control

An application program was created for the new gun cathode high-voltage conditioning. In figure 4., it shows the procedure of anode high voltage processing.

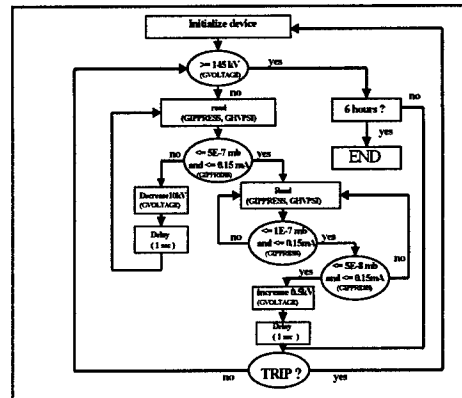
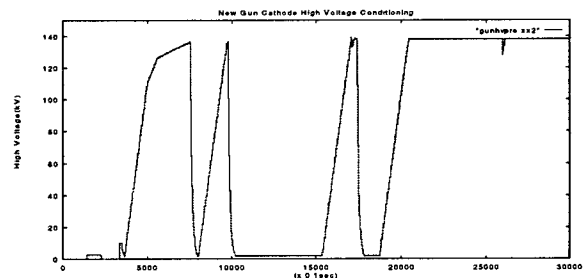
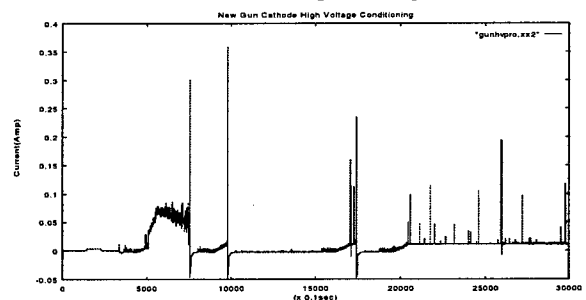


Figure 4. New gun cathode high-voltage conditioning

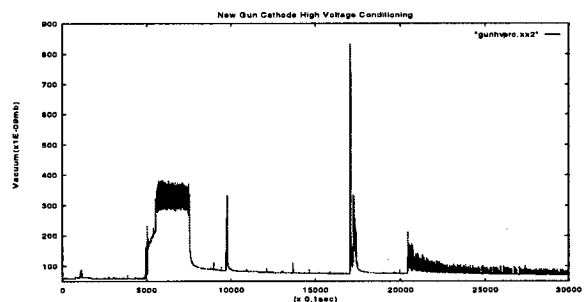
From the figure 5 (a, b, c), they show the conditioning process history. Because the application programs support, this time save a lot of time and manpower in this procedure.



(a) Anode High Voltage



(b) Cathode Emission Current



(c) Vacuum Pressure

Figure 5. A history for new gun cathode high-voltage conditioning

## 5. NEW FEATURE OF RENEWED CONTROL SYSTEM

In the new injector control system, it also has three layers structure. The second layer is VME crate; running real time operation system, it is local controller in new control environment, improved performance are in speed and reliability than the old booster control system. Its input and output channel update rate is about 4 times per second, this result that is acceptable for the new injector control system. Reproducibility is an important requirement for machine automatic operation. The first layer consists of a process computer and several console workstations, these keep all information relating to the controlled parameters and provides the graphic user interface for the machine operation. In the third layer, the new injector control system keeps the BITBUS network system and PLC system.

In order to accommodate 1.5 GeV upgrade, several of BITBUS nodes will be obsolete for new placed devices. Newly installed devices will connect to VME crate directly. New power supply control interfaces will build in the VME crate. As shown in figure 6., the design is similar with reference [3]. It provides amplitude reference to DC power supply and provides phase and amplitude regulated high spectral purity 10 Hz reference to AC power supplies in the new injector control system.

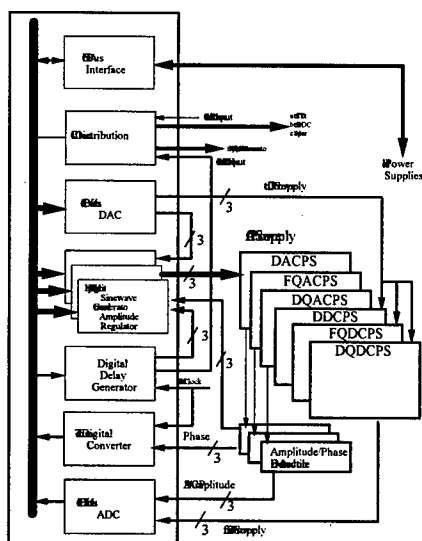


Figure 6. New power supply control interface

In the booster magnet system, each magnet group is powered from a White circuit. It operates on 10 Hz and provides a sine-wave current swinging. Both phase and amplitude of the AC power supply should be controlled. The task of the phase and amplitude regulation loop is to monitor and control the both phase and amplitude of current between the dipole, the defocusing quadrupole, and the focusing quadrupole. In order to improve the

phase regulation, a proper controller is need. A PID controller is used in the phase regulation loop now.

New Control system provide data archiving service. From the figure 7, Linac cooling water temperature regulating loop history. It is impossible to monitor the signal in the old control system environment.

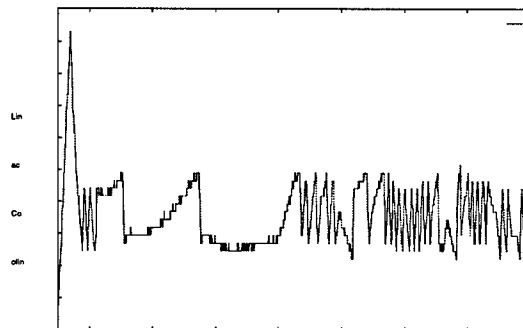


Figure 7: The temperature regulation in the linac cooling water unit

To improve the performance of the injector, several projects are ongoing, such as linac RF feedforward, close orbit measurements [4]. These will be put into operation soon.

## 6. CONCLUSIONS

A homogeneous control system is introduced by the new integrated injector control system plan. In order to reduce the budget, manpower and time need, the integration work keeps most of the field level devices. The new control system provides a basis for injector 1.5 GeV upgrade plans. It supports new devices installation and upgrade plans, and it also supports the application program development.

## 7. ACKNOWLEDGMENTS

The authors express thanks to the staff of the light source division and the instrument and development division for their cooperation in the 1.5 GeV upgrade project. The help from the administration staff is also appreciated

## REFERENCES

- [1] C. S. Chen, et al., "Control Integration for the Injector in SRRC" Proceedings of the 6th European Particle Accelerator Conference, Stockholm, 22-26 June 1998, p.1658.
- [2] J. P. Chiou, et al., "The Upgrade of SRRC Booster Extraction System", these proceeding.
- [3] K. Buerkmann, et al., "Performance of the White circuits of the BESSY II booster synchrotron", Proceedings of the 6th European Particle Accelerator Conference, Stockholm, 22-26 June 1998, p.2062.
- [4] K. H. Hu, et al., "Closed Orbit Measurement System for the Booster Synchrotron in SRRC", these proceeding.



# CONTROL ISSUES OF INSERTION DEVICES

Jenny Chen, C. S. Chen, C. J. Wang, C. H. Kuo, K. T. Hsu

Synchrotron Radiation Research Center  
No. 1 R&D Road VI, Hsinchu Science-Based Industrial Park, Hsinchu, Taiwan, R. O. C.

## Abstract

Insertion devices play crucial roles in new generation light source. Magnetic performance is the most important consideration factor during the design and construction phase. However, control performance is also an important issue from operation point of view. Motion control performance, residual filed compensation scheme and control response time for continue change in gap or phase during energy scan scenario is typical consideration to evaluate control performance of insertion devices. How to eliminate orbit excursion due to gap or phase change is also an important issue. Various methods have been used to address the problems. Detailed of these issues about insertion devices control will discuss in this report.

## 1 INTRODUCTION

Insertion devices (IDs) are souls in modern light source. Stringent requirements should be meet in IDs for new generation light source applications. Beside magnetic performance, control performance is equally important from operation point of view. Good control means that the design is balance on various issues. Motion control performance, residual filed compensation scheme, control response time for continues change gap or phase during energy scan scenario and protection mechanisms is typical consideration to evaluate control performance of insertion devices. Orbit issues are connected to magnetic performance directly. Orbit displacement when ID parameters change is unavoidable, especially in low energy storage ring. How to keep orbit fix is a big issue in the operation of storage ring in user mode.

## 2 CONTROL ELEMENTS OF INSERTION DEVICES CONTROL

Control element of various IDs is shown in Fig. 1. Motion control is the most important part of IDs control. Gap and phase are the control variables. Magnet gap can adjust fine as resolution of encoder in sub- $\mu\text{m}$  level by modern motion control technology. However, structure deformation due to strong magnet force is in the order of several tens  $\mu\text{m}$ . Gap calibration is needed to compensate the defect that is cause by deformation. Achieve good reproducible is very important in IDs mechanical design. Phase control is necessary in elliptically polarized IDs. Requirements of

motion control in phase axis are relax compare with gap, micron control resolution is enough and achieves easily. However, strong magnetic force challenges the design of mechanical supports and driver system.

Hierarchical protection mechanisms are used to protect IDs form over travel, taper and stall. Theses mechanisms are essential to prevent vacuum chamber and driver system from damage. Software limit is setting in firmware or control includes travel limit, stall, ...etc. Hardware protection devices include limit switches, tile sensors, hard limits, emergency stop buttons, hardwired logic, ...etc. More than three level protections in motion control loops is provided in IDs control.

For novel IDs to produce elliptically polarization light, some electromagnets or kickers are used to switch helicity dynamically. Special power supply is needed to provide fast switching in helicity. The power supplies are driven by waveform generator usually. Dynamic correction is needed to eliminate orbit transient cause by the residue filed error, local bump leakage, and eddy current effect of vacuum chamber.

Most demanded user allowed change limited ID parameters, such as gap or phase setting and stopping moves for the end-station. These operations need granted by control room operator.

Response time of desired operation is also crucial from experiments point of view. Synchronize the ID gap/phase operation with monochromator scan is needed by user. Helicity switching for mechanical phase switching undulator is also important in speed. Short switching time will benefit the experiments.

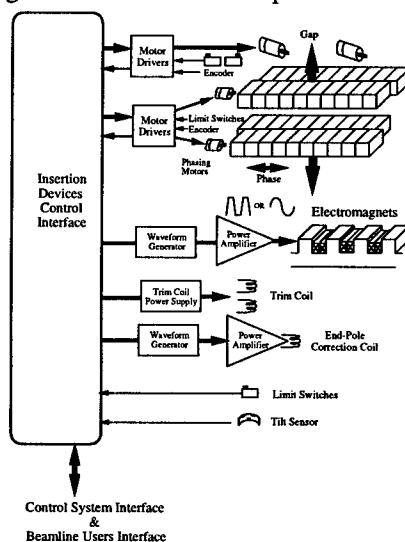


Figure 1: Control element of insertion devices.

### 3 ENGINEERING VIEW TO HANDLE BEAM DYNAMIC ISSUES IN INSERTION DEVICES CONTROL

There are many beam dynamic issues arise on IDs operation. These issues include dynamic aperture decrease due to reduced symmetry of the lattice by IDs, lifetime reduction cause by operation of IDs, tune changes due to gap change of insertion devices, orbit displacement, ...etc. Insertion devices control related items are summary in following.

Tune changes due to gap change of insertion devices is an issue. The operation of wiggler is fixed parameter operation. Tune shift can lift by appropriate setting of quadrupole by feed-forward techniques. However, tune change of undulator is small ( $< 0.01$ ) compare with wiggler ( $\sim 0.05$ ). Beam size as well as emittance change due to working point move is small for undulator with proper choice working point.

Imperfection in field integral will cause closed orbit displacement. The main interaction observed between the IDs and the stored electron beam is a small closed orbit displacement. The effect is small in X-ray ring and large in soft X-ray/VUV ring.

Orbit feed-forward is widely used to compensation the orbit displacement dependent on gap change. However, for exotic IDs, gap, and phase are two independent control variables, it is very difficult to use two-dimensional table for the operation of gap and phase at same time. Another possible is use orbit feedback to cope with orbit issues. Global orbit feedback eliminates large perturbation, while local feedback loop to steer photon beam on most stringent beamline.

Most severe effects in orbit control are in various novels IDs, such type IDs include various helical IDs [1][2] include EMW, EEW, APU, EPU, CPU, and some dynamic local bump system [3][4] to extract polarized light. Helicity switching rate in these systems is in 1 Hz - 100 Hz order or more. Special dynamic orbit compensation is necessary during operation.

### 4 USERS INTERFACE REQUIREMENTS

Insertion devices users have various requirements for variety experiments. Fixed gap experiment is the easy way for tradition experiments. Most demand user may need change gap and phase during one machine filling cycle or one data scans scenario. For fixed parameters experiment during one machine filled cycle, user may call machine operation set parameter after each filled. For most demand users, they may like set parameter by himself (herself).

For a homogeneous control system that is integrate control in machine and beamlines (e.g. EPICS [5], TACO/TANGO[6]). Users use same control environment as machine control in experiment station, user can integrated control function for their

experimental scan program. For heterogeneous control environment (SRRC) user can send their request to control server via local area network.

For electromagnet type devices, there are no movable mechanical parts. The control parameter is excitation current of coils. Excitation may static or dynamic dependent its applications. The user interface is same as mechanical driven wiggler and undulator. Synchronization signal should be provide to synchronized data acquisition system at beamline

Despite types of insertion devices, operators and users can monitor status and initiate actions from the control room or from computers located in offices or on beamlines. Security is maintained by the use of a process variable server that allocates control according to pre-defined access tables. The control system has been designed to enable users to control the ID on their own beamline simply an easily without involving facility operators.

### 5 INSERTION DEVICES CONTROL IN TLS

Taiwan Light Source (TLS) is a 1.5 GeV, 3rd generation storage ring. Four straight sections is available to accommodate four insertion devices. Major parameter of IDs is summarized in Table 1.

Name	W20	U5	U9	EPU5.6
Type	hybrid	hybrid	hybrid	pure
Length of magnetic period [cm]	20	5	9	5.6
Number of periods	13	76	48	66
Minimum magnetic gap [mm]	22.5	18	18	18
Vertical magnetic field [Tesla]	1.8	0.64	1.245	0.672
Horizontal magnetic field [Tesla]	—	—	—	0.453
Horizontal deflection parameter Kx	33	2.99	10.46	3.52
Vertical deflection parameter Ky	—	—	—	2.37
Maximum magnetic force [ton]	20	3	17	3.5
Photon energy [eV]	800-15000	60-1500	5-100	80-1400
Total length [m]	3.0	3.9	4.5	3.9
Installation	Dec. 1994	Mar. 1997	Apr. 1999	May 1999

Table 1: Insertion Devices of TLS (May 1999)

The EPU5.6 is developed in-house [7][8], while the other IDs were contacted to Danfysik and STI Optronics. IDs control in TLS is a heterogeneous system. Local controller of wiggler W20 is a PC/LabVIEW environment and connected to VME crate via IEEE-488 bus. The U5 local control software running in a PC running in MS-DOS, IEEE-488 bus is also used to connect to VME crate via IEEE-488 bus. The U9 and EPU5.6 control are compatible with SRRC control environment. The local controller based upon VME crate equip with PowerPC CPU running LynxOS. The U5 system can execute gap move request within a few seconds for mm range move. Control system overhead contributes about half of the elapse time for the operation. This is due to the slowly

operation in local controller through IEEE-488 interface. Overhead of the control system is almost negligible in EPU5.6 and U9 undulators. Current system is work but slightly complicates in maintenance. Cold start procedure is tedious in W20 and U5. Re-engineering of W20 and U5 control is under planning. The future system will share common hardware and common software as most as possible. Software of EPU5.6 is shown in Fig. 2. All ID control will have similar software structure in near future.

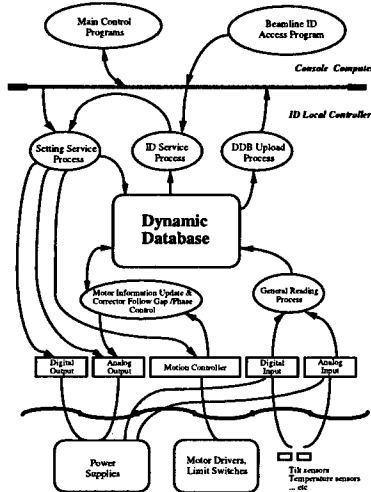


Figure 2: Structure of the EPU5.6 control software.

End-corrector set by a pre-defined value that is function of gap and stored on table are the standard residue filed compensation scheme. The controller has "Fixed" and "Follow" gap option to selected for residue field compensation. All IDs optical encoder is accessible via VME module directly. The update rate is 10Hz or 100 Hz depend on applications.

Beamline users interface have been designed, the user can send command to control server or VME crates directly to perform limited gap/phase setting and stopping. Status of IDs is always available for query in control system. Synchronized ID operation with monochromator in beamline is adequate for the response time point of view.

Beside end-corrector compensation scheme, orbit feed-forward is also used to compensation the orbit excursion. Efforts have been done on U5 and a 1m prototype EPU [9]. A few  $\mu\text{m}$  in RMS orbit displacement achieve. Eliminate orbit excursion during IDs motion by using orbit feedback that combines global and local is also available in TLS. A few  $\mu\text{m}$  RMS orbit displacement control is achievable during IDs motion either gap or phase change. Further improve in BPM performance and corrector control resolution should be done to improve orbit control performance.

EPBM is a dynamic local bump system to extract off-plane polarized light from bending magnet beamline. Functional block diagram of EPBM is shown in Fig. 3. Ideal local bump conditions are difficult to

achieve especially in dynamic operation due to local bump ratio error, eddy-current of vacuum chamber, difference response of magnet and power supplies. Dynamic orbit displacement occurs during EPBM operation is also eliminate by dynamic compensation scheme and orbit feedback system. The EPBM are expect work in frequency of 1 Hz - 100 Hz either trapezoidal or sine wave excitation soon.

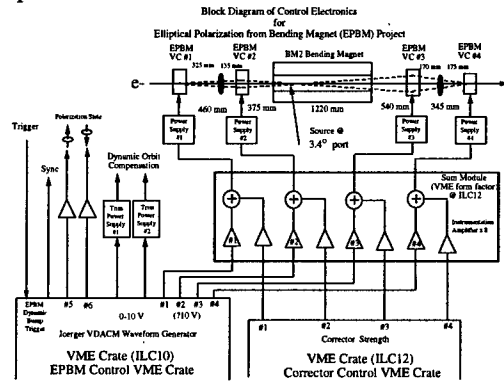


Figure 3: Function block diagram of EBPM dynamic bump system.

## 6 SUMMARY

In this report, discussion in various control issues of insertion devices. Control environment of IDs at TLS is also describe. Good control environment is important to mission critical IDs related experiments. Reliable in control and easily in maintenance is also equally important. Good control and supports are play a key role for the success of experiments that rely on insertion devices..

## 7 REFERENCES

- [1] Efim Gluskin, "APS Insertion devices: Recent Developments and Results", J. Synchrotron Rad. 5 (1988), pp.189-195.
- [2] J. Chavanne and P. Elleaume, "Insertion devices at the ESRF", Rev. Sci. Instrum. 66 (1995), p. 1868.
- [3] T. Bizen, et al., "Design of a local bump feedback system for a variably polarizing undulator", J. Synchrotron Rad. 5 (1998), pp. 465-467.
- [4] K. K. Lin, et al., "A dynamic local bump system for producing synchrotron radiation with an alternating elliptical polarization", J. Synchrotron Rad. 5 (1998), pp. 398-400.
- [5] <http://epics.aps.anl.gov/asd/controls/epics/EpicsDocumentation/WWWPages/EpicsFrames.html>.
- [6] A. Goetz, et al., "TACO: An Object Oriented Control System for Pcs running Linux, Windows/NT, OS-9000 or LynxOS", Proc. PCaPAC96, DESY Hamburg, 1996.
- [7] K. T. Pan, et al., "Control for Elliptically Polarizing Undulator at SRRC", Proceeding of the ICALEPCS '97, Beijing, November 3-7, 1997, p. 614.
- [8] K. T. Pan, et al., "The Control performance of Elliptically Polarizing Undulator at SRRC", Proceeding of the 6th European Particle Accelerator Conference EPAC-98, Stockholm, 22-26 June, 1998, p. 2231.
- [9] H. P. Chang, et al., "Modelling modulation and dynamic tuning of insertion devices at SRRC", Proceeding of the 5th European Particle Accelerator Conference EPAC-96, Barcelona, 10-14 June 1996, p. 694.

# Temperature Sensors and Controls for the Duke FEL Storage Ring

P.H. Morcombe, Y. Wu, Robert McGehee\*

Duke University, Free Electron Laser Laboratory, P.O. Box 90319, Durham, NC 27708

## Abstract

This paper describes a prototype system used for sensing and control functions associated with the Duke University 1 GeV electron storage ring. Low cost industrial control systems have been used. The system is capable of handling at least four hundred devices.

## 1. INTRODUCTION

The Duke storage ring uses deionized water to cool most of its high power devices. Initially, the water cooling systems gave very little trouble but over time the incidence of blocked cooling lines increased. Adding water filters improved the situation but did not entirely eliminate blockages. All critical items such as magnet coils are fitted with "Klixons" interlocked with the power supplies. While the Klixons prevent devices from being damaged through over heating, they also cause the stored electron beam to be lost without warning. As the blockage of the cooling system pipes is usually a gradual process, an early warning system capable of detecting partial blockages is highly desirable.

## 2. SYSTEM DESIGN

Given our very tight budget, approaches based on measuring the water flow directly were too expensive. Indirect approaches based on temperature measurement opened up a wide range of excellent low cost equipment and provided some side benefits.

The Dallas Semiconductors DS 1820 Digital Thermometer was chosen to perform the sensing task. This device measures temperature from  $-55$  to  $+125$  °C. The DS 1820 contains all the electronics needed to communicate over a Dallas Semiconductor MicroLAN. Each DS 1820 has its own unique address and converts temperatures into digital words that are transmitted over the MicroLAN under control of a server. The DS 1820 extracts the power it needs from the MicroLAN. The system configuration is shown in Fig. 1:

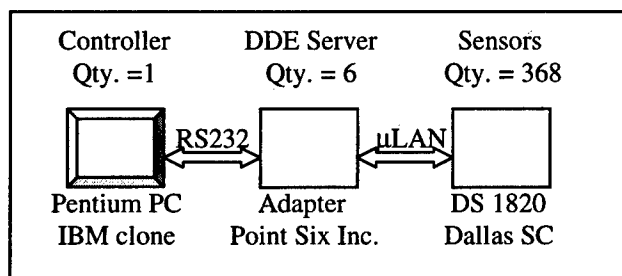


Fig 1. System configuration

The controller is a Pentium PC running under Windows 95. The data collection and display is handled by Excel 97 using DDE (Dynamic Data Exchange) to communicate with the six MicroLAN servers. The system programming consists of Excel macros written using Microsoft's VBA (Visual Basic for Applications) development tools and libraries.

Each MicroLAN server consists of a hardware adapter and software that runs on the PC. These items were provided by Point Six Inc. of Lexington, KY.

The system displays current temperature in bar chart form and logged data in line graph form. Devices that are over heating are collected in an alarm display. For easier viewing, the devices have been divided up into groups of 44, selected by means of pull down menus. It is also possible to customise the display by picking devices from a list. Anyone familiar with Microsoft Excel can learn to use the system in half an hour.

## 3. OPERATING EXPERIENCE

The system came into operation in mid August 1998 with 256 temperature sensors. The system worked well, so more devices were added:

Devices	Sensors
Quadrupole magnets	256
Dipole magnets	86
RF cavity	18
RF amplifier system	8
<b>TOTAL</b>	<b>368</b>

With 368 sensors, we are approaching the limit of the system as originally designed. However, improvements to the server hardware and software have the potential to increase the system capacity by a factor of five or more.

The system has enabled us to reduce the incidence of blockages to a very low level. A weekly review of temperatures is followed by preventative maintenance as necessary. The primary objective for installing the system has therefore been accomplished.

We are finding additional uses for low cost temperature sensing. For example, we are able to track power dissipation in our high power RF amplifier, its associated three port circulator and in all 17 water cooling loops on the ring accelerator cavity. We expect to be able to detect problems in these systems before catastrophic failure occurs.

\* Currently an undergraduate at Williams University

The use of shrink wrapped software essentially eliminated the need for professional programmers. This helped to speed up the system installation and subsequent system expansions. The cost of the entire system including the computer, adapters, cables, terminal blocks, sensors and software averaged \$24 per temperature sensor.

#### **4. CONCLUSIONS**

While the system is not suited to the high speed or high precision functions that our main EPICS control system performs, it has the potential to perform low speed sensing and control functions at a very low cost.

#### **5. ACKNOWLEDGEMENTS**

The authors thank all members of the Duke FEL Laboratory, especially Hank Goehring and Jim McDuff who installed the hardware and the DDE software links. The work was supported by the U.S. Office of Naval Research under Grant Number N00014-94-1-0818.

#### **6. REFERENCES**

- [1] Dallas Semiconductor, "Application notes #106 & #108", (1995)
- [2] Dallas Semiconductor, "Spec. DS 1820 Digital Thermometer", (1995)
- [3] Point Six Inc., "Spec. HA-4 Isolated Host Adapter", (1998)
- [4] Point Six Inc., "DDE server version 1.6h", (1998)

## **GPLS VME MODULE: A DIAGNOSTIC AND DISPLAY TOOL FOR NSLS MICRO SYSTEMS\***

S.Ramamoorthy, J.D.Smith, BNL, Upton, NY

### *Abstract*

The General Purpose Light Source VME module is an integral part of every front-end micro in the NSLS control system. The board incorporates features such as a video character generator, clock signals, time-of-day clock, a VME bus interrupter and general-purpose digital inputs and outputs. This module serves as a valuable diagnostic and real-time display tool for the micro development as well as for the final operational systems. This paper describes the functions provided by the board for the NSLS micro control monitor software.

### **1 INTRODUCTION**

The front-end computers that interface with the hardware in the NSLS control system [1] are VME-based microprocessor systems. The minimum requirements to configure a system are a CPU board with Ethernet controller (68k series: Motorola mvme162 or power PC series: Motorola mv1603, mv1604, mv230x are used at present), one megabyte battery-backed-up memory board and a General Purpose Light Source board (referred to as GPLS board). Additional boards are dictated by the specific hardware or equipment to be controlled and/or monitored. These systems are driven by real-time software known as the NSLS Control Monitor [2],[3]. This paper describes the hardware features of the GPLS board and how the software uses the various components.

### **2 HARDWARE DESCRIPTION**

The GPLS board in use since 1987, was originally developed by the NSLS controls and diagnostic groups to provide bus interrupter and ASCII video display functions. As some of the components used by the board have become obsolete, a new GPLS board has been redesigned by Apogee Lab Inc.[4], following the specifications from the NSLS controls group. The new board (Apogee Lab: Model number VME-TVI) provides new features such as a time code reader and generator and enhanced video functions. The board can be accessed through an extended (A32:D16/D08) or a standard (A24:D16/D08) address space of a VME-bus slave interface. The main components of the board are an interrupt generator, a video generator, a timer module and general-purpose inputs and outputs.

#### *2.1 Interrupt Generator*

The interrupt generator on the board is capable of generating four interrupts on the VME bus. The input pins for the TTL level signals are on the P2 connector. Each interrupt can be independently enabled or disabled by software. The trigger edge (rising or falling edge of the input signal) and the interrupt level are independently programmable for each interrupt. All the four interrupts can share the same level.

#### *2.2 Video Generator*

The video section of the board can generate ASCII video that can be displayed on a TV monitor. The board can accept an NTSC signal from an external source and overlay the text data onto the original signal. It uses Dual Ported RAM that permits simultaneous VME-bus access with video character generation. The RAM provides 4 video pages and three memory pages (4 Kbytes each) for general-purpose use. Page selection can be done using the slider switch at the front panel. The video memory can be read and written at any time but only the selected page will be displayed. The video hardware provides four screen formats (12 lines/16 char, 12 lines/20 char, 16 lines/32 char and 16 lines/44 char). It has four programmable color palettes. Each color palette can be set up to one of 64 color shades (e.g. A value 0 will set the color palette to black, 63 to white, 3 to red, 12 to green, 48 to blue and so on). Foreground or background color can be programmed on a character by character basis. The character generator PROM on the board can be programmed for user-definable fonts.

#### *2.3 Timer Module*

The time module provides three clock signals (1kHz, 4 kHz and 250Hz) on the P2 connector and a time code reader and generator. The time generator can be operated in two modes. In the standalone mode, one can load Time into the registers of the generator and start it by software. In the synchronized mode, an external signal (amplitude modulated 1 kHz IRIG-B carrier) is input through the P2 connector. If the IRIG-B input is lost or corrupted, the board will free wheel and continues to provide the Time. The Time-of-Day information can be read in three words with one microsecond resolution.

---

\*Work performed under the auspices of U.S. Dept. of Energy under the contact no: DE-AC02-98CH10886.

## 2.4 Digital I/O

The other general purpose components are 16-bit LEDs on the front panel, two banks of DIP switches, each consisting of 8 switches and 32 I/O lines for parallel TTL digital I/O (16 inputs and 16 outputs) on the P2 connector. More information on the board can be obtained from the user's manual supplied by Apogee Labs Inc.[5]. A transition module that will provide easy access to the various signals is also available from the same company.

## 3 SOFTWARE INTERFACE

The control monitor software uses VxWorks which is a commercial real-time operating system. The software consists of a set of system tasks, interrupt handlers, application specific modules and hardware drivers. The system software is standard for all micros and manages the system hardware (GPLS board, etc.), communications, command decoding, etc. It provides system timing, and uses real-time OS primitives to synchronize and coordinate the activities of other tasks. This module isolates all the kernel specifics and system hardware interfacing from application modules and provides services to them for real-time control.

### 3.1 Tasks and interrupt handlers

The system timing has a resolution of 2 milliseconds and it is derived from the 1 kHz clock on the GPLS board. The clock signal is connected to the first interrupt pin to generate the timer interrupt. The monitor provides a *wait* routine (equivalent to *sleep* call in Unix) to the application tasks. The tasks can set a wait time as low as 2 milliseconds. The task delay (*wait*) does not have to rely on the granularity of the time ticks provided by the real-time OS. A second interrupt is generated every 8 milliseconds by connecting the 250 Hz clock to the second interrupt pin. This interrupt is used both by system and application software to start data acquisition (e.g. reading of ADC boards) and to signal events to other tasks. The system provides interrupt handlers for 2 external signals (usually from external hardware or from another micro). The external signals are fed to the third and fourth interrupt pins via the transition card. The handlers call the appropriate module to service the interrupt. The levels of these interrupts can be changed by software based on the request from the application tasks.

The use of the GPLS board for generating timing, periodic interrupts and servicing external interrupts has made the software easily portable. Since the software does not use the CPU timers, there is no conflict with the real-time kernel timing. The software has been ported to different 68k series of CPU boards and Power PC boards and also from the RTUX real-time OS to VxWorks OS with minimum changes in the system module and absolutely no change in the application code.

## 3.2 Video Displays

The video feature of the GPLS board plays a very important role in the monitor software for micro development as well as for the final target systems. The simple **MEMORY WRITE** operation to generate an ASCII video display is very fast and can be used as a great debugging tool even in interrupt routines. The standard technique of using routines to send messages to a console (e.g. *logtask* in VxWorks) for diagnostic output is not sometimes suitable in interrupt or bus exception handlers. The system may crash even before the console output is initiated. Also programmers may have encountered cases where a software bug appears to have been removed by introducing the standard *printf* function for debugging. Since the console output is not synchronous with the code being executed, one can get a false indication of the bug location in the code when it crashes. The simple *memory write* on the video page exactly locates the problem area in the code.

The software multiplexes the first hardware page to 8 software pages. When hardware page 0 is selected, the software will display one of the eight pages. The software page for the display can be changed easily either by a push-button on a panel connected to the micro or by a remote command from any workstation in the control system network. Both system and application tasks generate displays for diagnostics and for continuous monitoring of device parameters (analog read backs and digital status). Error conditions can be highlighted in yellow and red colors. Figures 1 to 3 show some typical displays from the micros.

Since the board generates composite video (NTSC signal), one can monitor the displays on the local cable TV channels from anywhere in the lab. Some micros whose displays are crucial for operations have dedicated TV channels. Displays from other micros are routed through multiplexers to two general-purpose TV channels. The required display can be selected from any workstation. Since these displays are generated locally, the parameter updates are as fast as they are acquired and there is **zero loading** on the network.

The hardware page 1 is used by the system task to dump the stack registers and other pertinent information captured when a micro encounters bus errors. Before resetting the micro, one can get some information on the crash from the display. Pages 2 and 3 are used by applications to display the hardware initialization and other diagnostics.

### 3.3 Time stamping

The board extracts the time-of-day information from the amplitude-modulated 1 kHz IRIG-B carrier available from one of the outputs of a Spectracom NetCLOCK/2. This derives time from the atomic time standard at the National Institute of Standards and Technology via their WWVB

radio broadcast at 60 kHz. The system module reads the three timer-registers every 250 milliseconds, decodes the Time-of-Day information and makes it available to other tasks. In addition, the time registers can be used to time a code segment (with an accuracy of + or - 4 microseconds) and display the value on a video page. The time data is also used to time stamp data or an event such as an occurrence of an alarm.

### 3.4 Digital I/O interface

The 16 LEDs are used for diagnostic purposes. Each task sets up different LEDs. This provides a quick indication if a task gets into a loop. One LED is used to generate heartbeat signal by application tasks.

The DIP switches are used for setting up different configurations or modes of operation. One bank of switches is located on the board and is used to define configurations that cannot be accidentally altered. The front panel switches can be changed easily for the required mode of operation. As an example, one switch is assigned for controlling the parameter initialization during start-up. The micros save the parameters last set by the operators from a workstation, in the battery-backed-up memory. When the micro reboots following a "reset", "power-on" or "power-dip", it retrieves the battery-backed-up data for or the default values based on the switch setting. Another switch is used to inhibit the reporting of alarm messages.

The digital inputs and outputs are used by the applications for various purposes. One of the outputs is connected to the system **RESET** pin. Using a software command one can initiate a system RESET. The outputs have also been used to generate interrupts by software to other micros or external hardware.

## 4 CONCLUSIONS

The use of the GPLS board timers for system timing and interrupts by the software makes the porting of software to different VME-based CPU boards and to different real-time operating systems very easy. The video display serves as a great debugging tool during program development. The fast display of signal values and hardware status on TV without any load on the network are widely used for diagnostics and general monitoring by engineers, operators and physicists.

## 5 ACKNOWLEDGEMENT

The authors wish to thank Gary Frisbie for his technical support during the testing of the boards and to Dave Grebe of Apogee Lab for his constructive suggestions.

Radiation Monitor: 30 sec Data			
Area	mRem/hr	Area	mRem/hr
2-103	1.2	X13HUT	0.0
EFLOOR	0.6	XTUNNEL	0.0
UVWALK0	3.0	2-140A	0.6
2-112	0.0	2-148	1.8
U4IR	24.6	2-144	1.2
X04C	0.0	X21	0.0
2-123	0.3	X13	0.0
U05	5.3	X09	0.3
XTWALK0	0.0	X25	0.0
2-101NE	0.9	X01	0.3
24870 12:37:50 page 2			

Figure 1. Display of radiation levels.

XRAY RFI ALARM STATUS			
CAVPHR	37.4	KH	
CAVTEMP	+9.48	DEG	
INJPHASE	12.6	DEG	
ATPHASE	0.1	DEG	
TUNERPOS	4.38	V	
3 KH		125 KH	
ENDPHR	0.1	KH	76.3 KH
REVPUR	0.1	KH	2.8 KH
IFIL	98.7	A	220.7 A
EGRID	-55.8	V	-271.4 V
IGRID	-3.7	MA	0.8 MA
EPLATE	5.4	KV	15.6 KV
IPLATE	1.3	A	8.7 A
ESCRN	986.0	V	816.6 V
ISCRN	45.0	MA	73.1 MA

Figure 2. Display of XRF1 signals.

3/22/99		11:41:39	
----- VUV		OPS -----	
I= 401.5mA	DI=0.008		
U13 64.0	US 49.0		
LT= 6.0H	LT*I=2.40AH		
7 BUNCH	001111111		
800 MeV	4.06e-9t		
7.039	1165.884AH		
**BEAM AVAILABLE**			
NEXT FILL 1230 HRS			

Figure 3. Display of VUV ring Parameters.

## 6. REFERENCES

- [1] J.D.Smith, S.Ramamoorthy, Y.Tang, Nucl.Inst. and Meth.In Phys. Res, A32 (1994) 114.
- [2] S.Ramamoorthy, J.D.Smith, Proc.IEEE PAC 1993, 1849.
- [3] <http://www.nsls.bnl.gov/Systems/Controls>.
- [4] Apogee Lab Inc., Dickerson Rd, Unit3/4, North Wales, PA19454.
- [5] User's Manual for Time/Video/Interrupt Module Model VME-TVI.



## RHIC DATA CORRELATION METHODOLOGY\*

R. Michnoff<sup>\*</sup>, T. D'Ottavio, L. Hoff, W. MacKay, T. Satogata

Brookhaven National Laboratory

Upton, NY, USA 11973

### Abstract

A requirement for RHIC data plotting software and physics analysis is the correlation of data from all accelerator data gathering systems. Data correlation provides the capability for a user to request a plot of multiple data channels vs. time, and to make meaningful time-correlated data comparisons. The task of data correlation for RHIC requires careful consideration because data acquisition triggers are generated from various asynchronous sources including events from the RHIC Event Link, events from the two Beam Sync Links, and other unrelated clocks. In order to correlate data from asynchronous acquisition systems a common time reference is required. The RHIC data correlation methodology will allow all RHIC data to be converted to a common wall clock time, while still preserving native acquisition trigger information. A data correlation task force team, composed of the authors of this paper, has been formed to develop data correlation design details and provide guidelines for software developers. The overall data correlation methodology will be presented in this paper.

### 1 CONTROL SYSTEM ARCHITECTURE

The RHIC control system architecture consists of more than 100 VME based systems, each housing a front end computer (FEC) running the VxWorks operating system. The front end computers communicate to higher level workstations via an ethernet network. Software objects known as Accelerator Device Objects (ADO) [1] reside in the FEC and provide the interface between the local hardware and higher level workstations. Each ADO consists of a set of parameters where each parameter usually relates to a specific hardware operation, such as a configuration setting, a status value or a data set.

### 2 ACQUISITION TRIGGER SOURCES

Data acquired with synchronous or asynchronous trigger sources from ADOs on different FECs must be correlated for plotting and analysis at the workstation level.

Data acquisition systems for RHIC will typically be triggered using one of the following sources.

- a) Events on the RHIC Event Link (REL).
- b) Events on the Beam Sync Links (2).
- c) Triggers unrelated to the links.

The REL [2] is a 10 MHz serial link distributed throughout the accelerator complex. Accelerator-specific event codes are transmitted on the REL. Systems throughout the RHIC complex monitor the REL and perform system-specific actions when selected event codes are detected. General purpose periodic events used for data acquisition are transmitted at the following rates: 720 Hz, 60 Hz, 10 Hz, 1 Hz and 0.25 Hz. Data acquisition systems that use these events for triggering include the Beam Loss Monitor System (BLM) [3] and the Magnet Power Supply system.

Two Beam Sync Links [4] are used for RHIC, one for each collider ring. They are referred to as blue and yellow. Each Beam Sync Link is a 14 MHz serial link and transmits event codes similar to the REL. The carrier is synchronized to the RF frequency to allow bucket-specific triggering. The Beam Sync Link events are primarily used to trigger beam instrumentation systems. One important event on each Beam Sync Link is the revolution tick event. This event is transmitted when bucket 1 passes a known location in the ring. Instrumentation systems that use the Beam Sync Link events for bucket-specific triggering include the Beam Position Monitors, the Ionization Profile Monitor [5] and the Wall Current Monitor.

### 3 RTDL DISTRIBUTED TIME

Another serial link used in RHIC is the Real Time Data Link (RTDL) [6]. The purpose of RTDL is to distribute basic accelerator data to every FEC throughout the complex. RTDL data is sent on every REL 720 Hz event.

Wall clock time will be distributed on RTDL. Two 24-bit RTDL frames will be used to transmit 32 bits representing the number of seconds since Jan 1, 1970 (standard UNIX time) and 10 bits representing the number of 720 Hz ticks within each second.

A time generator module is currently being developed to produce the wall clock time. This module will reside in the RTDL system. A 720 Hz clock input from the main magnet power supply system is used to generate the 720 Hz, 60 Hz, 10 Hz, 1 Hz and 0.25 Hz events. The hardware triggers the 0.25 Hz event on an even 4 second boundary (when the least two significant bits of the number of seconds change to 00).

\*Work performed under the auspices of the U.S. Department of Energy.

\*Email: michnoff@bnl.gov

## 4 SYNC EVENT

The 0.25 Hz event code will be used as a synchronizing event (Sync Event) and is transmitted on the REL, the Blue Beam Sync Link, and the Yellow Beam Sync Link. Hardware modules use the Sync Event to perform such actions as resetting on-board timestamps, resetting scan counters, and copying data buffer pointers.

The period of time from one Sync Event to the next Sync Event is called a sync period.

## 5 TIME INFORMATION

The following time information has been defined to be associated with each data set. Not every item is necessarily delivered with each data set. Some items may be static and others may not be relevant for the specific data set. A data set may be an array of data, a single data value, an average, etc.

- a) Time associated with the data set. This consists of 3 components - TimeType, Time, and Index. TimeType is used to identify the meaning of Time and Index, as shown in table 1. Additional TimeTypes will be added as necessary. Sync time is the time of the sync period associated with the data set. This is expressed as the number of seconds since Jan 1, 1970 and is always evenly divisible by 4.

Table 1 - TimeType definitions

Time Type	Time	Index
1	Sync time	Beam sync blue turn ticks since last Sync Event
2	Sync time	Beam sync yellow turn ticks since last Sync Event
3	Sync time	720 Hz ticks since last Sync
4	Sync time	60 Hz ticks since last Sync
5	Sync time	10 Hz ticks since last Sync
6	Sync time	1 Hz ticks since last Sync
7	Sync time	Febbunch events since last Sync (febbunch occurs when bunch is extracted from AGS to RHIC)
8	Sync time	Trigger number since last Sync
9	Wall clock time (sec since Jan 1, 1970)	0

- b) Sample number associated with Time/Index. This is the element number in the data set that corresponds with Time/Index. This is typically used when the data set is an array, but may also be used to indicate that the time is associated with a specific element within an averaged data set.
- c) Time offset relative to Time/Index. This is used to correct for known delay times. For example, an acquisition trigger may be configured to be a delay from a specified REL code. Time/Index indicates the time that the event occurred and time offset is the configured delay time.
- d) Points per average. This is valid only when the data is an average of multiple samples.

- e) Time between samples.
- f) Selected bucket number.
- g) Bandwidth/Resolution of data acquisition hardware.
- h) Report frequency. This is the time interval at which data sets are sent to higher level workstations.
- i) Wall clock time translation information. In some cases additional information is required to convert the Time/Index to wall clock time. For example, the febbunch event may occur multiple times within an AGS cycle but is not a continuous periodic event. When Index is the febbunch event number, data from the event monitor is used to apply a time in microseconds since the Sync Event, to the febbunch event number.

## 6 EVENT MONITOR

A VME based event monitor module is used for each event link to provide a timestamp for selected event codes. The delivered data set is time, and is specified as the number of microseconds since the last Sync Event.

The event monitors provide information that is critical to applying a common wall clock time to all data. The Sync Event is transmitted on all three links at the same time (to within 12 microseconds). The microsecond timestamp counter for all event monitors is derived from the REL 10 MHz carrier to guarantee synchronous counting. Event timestamps are converted to a common wall clock time, thereby correlating data to within one RHIC revolution (approximately 12 microseconds).

The time information as described above will be provided with each event monitor data set. Time offset, points per average, time between samples, bucket selection, bandwidth/resolution, and wall clock translation information are not used for event monitor data.

## 7 ASSOCIATING TIME INFORMATION WITH DATA

Associating time information with a particular data set requires careful consideration. In order to provide ADO design flexibility, a data correlation design goal was to allow time information to reside in the same ADO as the data source or in an ADO different from the data source. Systems may be designed to correlate one set of time information to many data sets. The multiple association works as long as the order of data delivery can be guaranteed. For the RHIC control system, the order of data delivery can be guaranteed only for data sent from a single FEC. Therefore, for RHIC, the time information that changes on each data update must reside in the same FEC as the data source.

One option currently under consideration is to provide a database to associate time information items with each data ADO parameter. The database entry for each time information item may be the name of an ADO parameter or a static value. A static value may be used, for example

Table 2 - Example ADO parameter definitions

FEC name	ADO name	Parameter name	Description
BlmFec	BlmDataAdo1	dataArray1Hz	Array of 720 samples, delivered each second. This is data for 1 BLM channel.
BlmFec	BlmTimeAdo	syncTime1Hz	Sync time, delivered each second. Same for all 64 channels in same FEC.
BlmFec	BlmTimeAdo	index1Hz	Number of 720 Hz ticks since sync corresponding with first array element.
EvMonFec	EvMon720HzAdo	dataArray1Hz	Array of 720 times, delivered each second. This is time for each 720Hz event.
EvMonFec	EvMon720HzAdo	syncTime1Hz	Sync time, delivered each second.
EvMonFec	EvMon720HzAdo	index1Hz	Number of 720 Hz ticks since sync corresponding with first array element.

Table 3 - Example time information database entries

Database field	Loss Monitor channel ADO, parameter: BlmDataAdo1, dataArray1Hz	Event Monitor ADO, parameter: EvMon720Hz, dataArray1Hz
TimeType	3 (Sync time, 720 Hz ticks since Sync)	3 (Sync time, 720 Hz ticks since Sync)
Sync time ADO name, parameter name	BlmDataAdo1, syncTime1Hz	EvMon720HzAdo, syncTime1Hz
Index ADO name, parameter name	BlmDataAdo1, index1Hz	EvMon720HzAdo, index1Hz
Sample number assoc. with Time/Index	1	1
Time offset relative to Time/Index	0	Unused
Points per average	Unused	Unused
Time between samples	1389 microseconds (720 Hz)	Unused
Bucket selection	Unused	Unused
Report frequency	1 second	1 second
Wall clock time ADO name, parameter name	EvMon720HzAdo, dataArray1Hz	Unused

when the sample number associated with Time/Index is a constant.

The wall clock translation information item will typically point to a data source ADO parameter that resides in an ADO on a different front end computer. This will usually be an event monitor ADO, which returns time for selected event codes.

## 8 EXAMPLE

As an example, the process of applying wall clock time to an array of BLM channel data will be described. The BLM system acquires data on every REL 720 Hz event. For this example an array of 720 samples is delivered each second to higher level software.

Data from all the ADO parameters defined in table 2 are delivered once each second. The other time information shown in table 3 is not sent every second since it is static and can be retrieved directly from the database.

The correlation between dataArray1Hz, syncTime1Hz, and index1Hz delivered from the same FEC is accomplished simply by knowing the order of delivery.

syncTime1Hz and index1Hz are used to correlate the data array (BlmDataAdo1, dataArray1Hz) with the time array (Evmon720HzAdo, dataArray1Hz) to determine a wall clock time to the microsecond for each data sample.

Every system acquiring data on the REL 720 Hz event will use time data from EvMon720HzAdo. This guarantees that the microsecond timestamp for all data acquired on a given 720 Hz event will have the exact same timestamp to the microsecond.

Systems acquiring data using events from the Beam Sync Links will use the same mechanism as described

above to apply a wall clock timestamp. Once a wall clock timestamp has been applied, all data can be correlated.

Note that Sync Time and Index provide enough information to correlate data when acquisition triggers are on the same event. In these cases converting to wall clock time may not be necessary.

## 9 IMPLEMENTATION STATUS

Some software systems in RHIC are beginning to use data correlation mechanisms similar to the methodology described in this paper. However, significant implementation standards still need to be defined, and software development for data correlation will be continuing for many months.

## 10 REFERENCES

- [1] L.T. Hoff, J.F. Skelly, "Accelerator devices as persistent software objects", Proc. ICALEPCS 93, Berlin, Germany, 1993.
- [2] B. Oerter, C.R. Conkling, "Accelerator Timing at Brookhaven National Laboratory", Proc. 1995 Particle Accel. Conf., 1995.
- [3] R. Witkover, R. Michnoff, J. Geller, "RHIC Beam Loss Monitor System Initial Operation", these proceedings.
- [4] T. Kerner, C.R. Conkling, B. Oerter, "V123 Beam synchronous Encoder Module", these proceedings.
- [5] R. Connolly, P. Cameron, R. Michnoff, V. Radeka, T. Shea, R. Sikora, D. Stephani, S. Tepikian, N. Tsoupas, L. Woodworth, "The RHIC Ionization Beam Profile Monitor", these proceedings.
- [6] H. Hartmann, "The RHIC Real Time Data Link System", Proc. 1997 Particle Accel. Conf., 1997.
- [7] R. Michnoff, "The RHIC General Purpose Multiplexed Analog-to-Digital Converter System", Proc. 1995 Particle Accel. Conf., 1995.
- [8] H. Hartmann, T. Kerner, "RHIC Beam Synchronous Trigger Module", these proceedings.

# RHIC BEAM SYNCHRONOUS TRIGGER MODULE\*

H. Hartmann<sup>+</sup>, T. Kerner

Brookhaven National Laboratory, Upton, NY 11973

## Abstract

The RHIC Beam Synchronous Event System consists of centralized event encoders (one for each collider ring), which operate from the RF clock and the revolution clock provided by the RHIC RF system, and distributed embedded decoders. The Beam Synchronous Trigger Module (V124) is a general purpose 6U x 4HP, VMEbus controlled module that is compatible with the RHIC Beam Synchronous Event System and is designed to provide clocks and triggers for collider data acquisition systems and experiments. The V124 Module contains a separate memory (Bunch Fill Mask RAM) for each channel that is software configurable with the pattern of filled buckets (Bunch Fill Pattern) to permit bunch synchronous triggering/clocking. This module provides eight identical channels that can be configured independently or in pairs, and a buffered RF Clock output.

## 1 INTRODUCTION

The beam revolution time is approximately 12.78  $\mu$ s, or 78.196K revolutions/second. The number of RF Buckets (buckets) per revolution per ring is 360. From these data, a 28.15 MHz RF bucket frequency is derived. The Beam Synchronous Event System carrier tracks a varying 14.07 MHz RF clock derived from the RF bucket frequency [1].

The Revolution Clock Event is transmitted when Bucket #1 passes the RF Wall Current Monitor in the 4 o'clock sector. Transmission delays of events are equalized such that each event is received at all locations at the same time. The Revolution Clock Event is decoded and used for clocking the Bucket #1 Delay Counter. The Bucket #1 Delay Counter synchronizes the occurrence of the Revolution Clock Event with the occurrence of Bucket #1 passing by the particular hardware location. This allows the Bunch Fill Mask RAM to always reference the Bunch Fill Pattern to Bucket #1.

Beam Synchronous Event Codes are decoded by the Event Mask Ram to determine if a particular event is used for triggering. Events selected for triggering will be synchronized to the Revolution Clock before triggering a channel. The Beam Synchronous Clock will

be extracted from the input data stream so that the RF Clock (2x Beam Synchronous Clock) can be recovered. Recovery will be accomplished by phase locking to the Beam Synchronous Event System carrier and boosting the frequency by a factor of 2. Since only a fraction of RF buckets will contain beam (bunches), recovery of the RF Clock is mandatory for triggering on certain bunch fill patterns [2].

## 2 THEORY OF OPERATION

### 2.1 Phase Locked Loop

The fundamental purpose of the PLL (Phase Locked Loop) is to recover the RF Clock and reduce jitter from the bi-phase-mark modified Manchester serial data stream in the beam synchronous distribution system. The low jitter PLL output clock is then used to clock counters to provide accurate delays and is buffered for further distribution. Sub-nanosecond jitter is guaranteed by the use of an adaptive cable equalizer at the PLL input, and by the use of a differential loop filter design, low noise components, and careful component layout and PCB design. A digital frequency discriminator avoids harmonic lock-up on signal acquisition. An on-board crystal can be selected with a control signal to provide an output when no input signal is available. Prototype jitter was controlled to an RMSΔ of 32 ps over 17 hours with pseudo-random data over the maximum specified cable length.

### 2.2 Counters

Eight identical trigger channels are resident on each module. Each channel consists of four programmable, cascable counters: revolution, bucket, trigger and fine.

#### 2.2.1 Revolution Counter

The Revolution Counter is a 16-bit down counter which is loaded with the desired revolution number and whose clock input is the Revolution Clock. This counter can be enabled by:

- A VMEbus Command.
- A Beam Sync Event.
- An External Trigger.
- Paired Previous Channel Fine Delay Enable.

This counter can be reloaded and re-enabled by:

\*Work performed under the auspices of the U.S. Department of Energy.

<sup>+</sup> Email: [hartmann@bnl.gov](mailto:hartmann@bnl.gov)

- A Trigger Counter Terminal Count.
- A Bucket Counter Enable.
- Neither (one shot mode)

### 2.2.2 Bucket Counter

The Bucket Counter is a 10 bit down counter which is loaded with the desired bucket number for delayed triggering after enable and clocked by the recovered RF Clock. This counter can be enabled by:

- A VMEbus Command.
- A Beam Synchronous Event.
- The Revolution Counter Terminal Count.

This counter is reloaded and re-enabled by the Bucket Counter Terminal Count.

### 2.2.3 Trigger Counter

The Trigger Counter is a 32-bit down counter that is loaded with the desired number of triggers. This counter derives its' clock source from:

- The Bunch Fill Mask Ram Output.
- Bucket Counter Terminal Count.
- Paired Next Channel Bucket Counter Terminal Count.
- No Clock Input (No Halt).

This counter is enabled by the Fine Counter (Delay) Enable (Bucket Counter Enable). This counter is reloaded and re-enabled by the Trigger Counter Terminal Count.

### 2.2.4 Fine Counter

The Fine Counter (Delay) is a 16-bit delay which is implemented in two 8-bit silicon delay modules. Resolution is 500ps. The (counter) delay is adjustable from 20ns (latency) to 275ns. This (counter) delay is enabled by the Bucket Counter Enable and always disabled on the occurrence of the Trigger Counter Terminal Count. In addition, so that the Fine Counter (Delay) is enabled for only one revolution, the counter can be disabled on the occurrence of the delayed revolution clock. The clock source for this counter is:

- A Fixed Pulse Width (54ns) derived from the Bunch Fill Mask Ram Output.
- A Variable Pulse Width, programmable from 1 to 65536 RF Clocks (35ns to 2.29ms), derived from the Bunch Fill Mask Ram Output.
- A Variable Pulse Width, programmable from 1 to 65536 RF Clocks (35ns to 2.29ms), derived from the Bucket Counter Terminal Count.

### 2.3 Bunch Fill Mask RAM

Each channel contains 64 bytes (45 used) of RAM which can be loaded with a unique bunch fill pattern. The contents are shifted out a bit at a time at the RF Clock rate. Each bit corresponds to an RF bucket and determines whether that bucket will be used for triggering. The shifting is synchronized such that the sequence starts over at each occurrence of the delayed revolution clock.

### 2.4 Event Mask RAM

Beam Synchronous Event Codes are decoded and used as pointers into the Event Mask RAM to determine if that code will generate a channel trigger. Each module contains 256 bytes of SRAM that is configured with the channel-triggering pattern. Each bit in each memory location corresponds to a particular channel.

### 2.5 Timestamp

Each channel provides a 32-bit timestamp derived from the timestamp counter to allow data correlation [3] between data acquired from different systems in widely dispersed locations. The timestamp counter can be configured to count:

- Beam Synchronous Events.
- 1 $\mu$ s clocks derived from the RHIC Event System.

This counter is reset on the occurrence of a RHIC Beam Synchronous Event System SYNC Event. A timestamp (timestamp counter save) acquisition occurs on:

- A Beam Synchronous Event (software configurable).
- The First Trigger pulse of a series of pulses.
- The Trigger Counter terminal count.

The timestamp must be read before another timestamp counter save occurs or the contents will be overwritten.

## 3 TRIGGERING MODES

This module supports the following triggering modes:

- One or more pulses output every revolution, pulse width selectable, triggered after x number of revolution clocks. Rearm on Trigger Counter Terminal Count.
- One or more pulse output after x number of turns and y number of bunches. Rearm on Trigger Counter Terminal Count.
- One or more pulses output after specified event and y number of bunches. Rearm on Trigger Counter Terminal Count.
- Long Gate. Start is defined by channel 1 and Trigger Counter Terminal Count is defined by channel 2.

- One pulse output continuous for each bunch in bunch fill pattern not to exceed 9.37MHz. Pulse width is 54ns. No Trigger Counter Terminal Count.
- All above modes can be configured as one-shot mode. (No rearm on Trigger Counter Terminal Count).

## 4 VME INTERFACE

The V124 Module is a VMEbus slave. Status/ID registers (64 bytes), board configuration registers (16 bytes), channel configuration registers (256 bytes), Beam Synchronous Event Mask RAM (256 bytes), and Bunch Fill Pattern Mask RAM (64 bytes) are mapped to VME A16 space on jumper selectable 2K byte boundary (A15..A11). VME data transfers supported are D16 and D08(E0) only.

### 4.1 Interrupts

Interrupts are supported with a programmable interrupt vector and IRQ level. A nested interrupt structure is employed to service the following hardware interrupts:

- Timestamp Trigger Source.
- Beam Synchronous Event System SYNC Event.
- RHIC Event System Error.
- Beam Synchronous Event System Error.
- Channel Halt.

The RHIC Event System Error and Beam Synchronous Event System Error interrupts are change of status interrupts. Connection or removal of these inputs will cause an interrupt.

### 4.2 Shared Memory

The V124 shares access to the Beam Synchronous Event Mask RAM between the decoding requirement of the Beam Synchronous Event System interface and the VMEbus. Access to this area of memory by VMEbus requests is allowed only during idle periods of Event System decoding. Highest priority for access is always granted to channel triggering requirements.

Access to the Bunch Fill Pattern Mask RAM is also shared between loading the bunch fill shift register and the VMEbus. VMEbus reads and writes are only allowed during periods that the shift register is shifting out the bunch fill pattern. During loading of the shift register, VMEbus cycles are delayed. Highest priority is always granted to channel triggering requirements.

## 5 USER INTERFACE

### 5.1 Front Panel Connectors

The following twin axial inputs are provided:

- Beam Synchronous Event System (1)
- Event System (1)

The following 2-conductor LEMO Model EGG Series 0B connector inputs are provided:

- External Trigger Inputs (4)
- Trigger Outputs (8)
- RF Clock (buffered) Output

The Trigger Inputs, Trigger Outputs and RF Clock output are differential ECL levels.

### 5.2 Front Panel Indicators

- VME Select – indicates a VME bus access to an address within memory space.
- Beam Synchronous Event System – No Lock
- Event System – Carrier Active
- Trigger Active (8)

## 6 ACKNOWLEDGEMENTS

The authors would like to acknowledge the staff of the RHIC/AGS controls section who have contributed to the work on which this paper is based. Special thanks to R. Michnoff for his contributions during the conceptual stage, and to P. Pape and A. Watson for their work on the prototype.

## 7 REFERENCES

- [1] T. Kerner, C. R. Conkling, Jr., and B. Oerter, "V123 Beam Synchronous Encoder Module", these proceedings.
- [2] W. MacKay, "Considerations for Bunch Filling Patterns", Internal Note RHIC/AP/132, 29 Aug. 1997.
- [3] R. Michnoff, T. D'Ottavio, L. Hoff, W. MacKay, and T. Satogato, "RHIC Data Correlation Methodology", these proceedings.

## V123 BEAM SYNCHRONOUS ENCODER MODULE\*

T. Kerner<sup>†</sup>, C. R. Conkling Jr.<sup>‡</sup>, B. Oerter, BNL, Upton, NY

### Abstract

The V123 Synchronous Encoder Module transmits events to distributed trigger modules and embedded decoders around the RHIC rings where they are used to provide beam instrumentation triggers [1,2,3]. The RHIC beam synchronous event link hardware is mainly comprised of three VMEbus board designs, the central input modules (V201), and encoder modules (V123), and the distributed trigger modules (V124). Two beam synchronous links, one for each ring, are distributed via fiber optics and fanned out via twisted wire pair cables. The V123 synchronizes with the RF system clock derived from the beam bucket frequency and a revolution fiducial pulse. The RF system clock is used to create the beam synchronous event link carrier and events are synchronized with the rotation fiducial. A low jitter RF clock is later recovered from this carrier by phase lock loops in the trigger modules. Prioritized hardware and software triggers fill up to 15 beam event code transmission slots per revolution while tracking the ramping RF acceleration frequency and storage frequency. The revolution fiducial event is always the first event transmitted which is used to synchronize the firing of the abort kicker and to locate the first bucket for decoders distributed about the ring.

### 1 BEAM SYNCHRONOUS EVENT LINK SYSTEM ARCHITECTURE

The RHIC collider is composed of counter-rotating particle beams in two 3.8 km super-conducting rings which will be collided in four of the six interaction regions. There are two RHIC beam synchronous event encoding systems; one for each ring. Each beam synchronous event system is the same; therefore only one system will be described. Both RHIC beam synchronous event encoding systems are located in the 4 o'clock equipment house 1004A in a single VME chassis. Each beam synchronous event encoder system requires five VME chassis slots, one for the V123 master module, and four for the V201 input modules. The beam synchronous event link carrier tracks a varying 14.07 MHz RF clock, derived from half the RHIC injection and acceleration RF frequencies. A synchro-synthesizer board in an RF system chassis is the source of this RF clock. The beam synchronous event link is initiated as differential transformer coupled PECL, and connects to a 1 x 8 ECL

fan out module then to 6 fiber optic transmitters. The transmitters drive single mode 9/125  $\mu\text{m}$  fiber optic lines to 6 service buildings in a star configuration where they are passively split out to the 18 ring alcoves and 4 experimental halls. Each alcove has 2 beam synchronous fiber spools, one for each ring. Alcoves, and equipment houses have spools of fiber optic cable located at receiving locations to equalize the transmission delays. At an alcove, the fiber optic transmission is converted to differential ECL and fanned out by 1 x 8 ECL fan-outs to the V124 modules and embedded decoders in the beam position monitors. The output of the V124 modules may be used directly or fanned out by 1 x 8 fan out units with LEMO KLOC connectors where these signals are finally used by instrumentation triggers and experiments.

### 2 PURPOSE

The low jitter PLL [4] recovered clocks are intended to provide precise timing and synchronization information to instrumentation triggers and data acquisition systems used in experiments and for general beam bucket phasing purposes. Prioritized hardware and software triggered inputs can be output to any of 256 event codes after translation in a SRAM look-up table. There are a total of 15 event slots per revolution. The revolution event will have the highest priority and will always be output at the beginning of the revolution cycle. The event codes are decoded and used by devices such as extraction kickers, and as a reference for timing triggers and delayed timing triggers. Other beam synchronous events will be sent on an input prioritized basis, but can be delayed by the revolution event. Since the link is fanned out in a star configuration with equalized delays, an event will arrive simultaneously at all locations around the ring with nanosecond precision, and sub-nanosecond jitter. Programmable delays are provided by the V124 distributed trigger modules using the beam sync link recovered clock. Counters running on this clock will synchronize to the revolution event. The recovered low jitter distributed clock is the basis for the timing precision of the beam synchronous system. The passage of any and all bunches around the ring can be signaled precisely to sub-nanosecond resolution.

\* Work performed under the auspices of the U.S. Department of Energy.

<sup>†</sup> Email: kerner@bnl.gov

<sup>‡</sup> Deceased

### 3 SYSTEM OPERATIONAL REQUIREMENTS

The beam revolution time is approximately 12.78  $\mu$ s, or 78.196 k revolutions/second. The number of RF buckets per revolution is 360. From these data, a 28.15 MHz RF bucket frequency is derived. The beam synchronous event encoder requires a 2X clock to produce the bi-phase mark data stream. The beam synchronous encoder receives the RF 28.15 MHz clock and derives the 14.07 MHz beam synchronous event link. The RF system generates the 2X clock and revolution tick during RHIC operation. The revolution tick performs two functions: first it sets the phase of the beam synchronous event link bi-phase clock, and second it synchronizes the revolution tick event code. A 28.15 MHz crystal backup clock oscillator can provide an event link output when the RF clock and tick isn't available. A control register bit can control cancellation of automatic switching.

#### 3.1 Revolution Fiducial

The most important event transmitted by the V123 beam synchronous event encoder is the revolution fiducial. This fiducial is sent synchronously with the revolution tick provided by the RF system synchro synthesizer module. The revolution tick is derived from the first bucket passing the 4 o'clock RF wall current monitor. The revolution event always occupies the first event slot which is synchronized by the revolution tick. If the tick synchronization is removed or lost, the V123 counters will continue to send the revolution event every 360 cycles of the RF clock. Should the revolution tick not occur after 360 clock cycles or occur before or after this count an interrupt is generated and the synchronization loss error is flagged. A crystal backup clock oscillator may be used to provide a beam sync link carrier and revolution event code for testing purposes when no rf input signals are present.

#### 3.2 Beam Dump - Abort Kicker Timing

Prior to the revolution tick there are approximately 18 empty RF buckets. These empty buckets accommodate the abort kicker rise time, which is about 700 ns [5]. The abort kicker logic monitors the Beam Sync link for the rotation fiducial. All requests to abort the beam are synchronized to the rotation fiducial followed by an appropriate delay to properly time the kicker firing trigger

with the abort gap.

#### 3.3 Encoding

The beam synchronous event codes are transmitted using a serial modified Manchester code (bi-phase-mark). This modulation technique guarantees a signal level transition at each cell edge, rather than the cell center as is done in the true Manchester code (also bi-phase-mark). A "one" is defined as a level transition in the cell center, while no center transition is a "zero". There are 180 bi-phase cells per revolution, and 12 bi-phase cells per event transmission. This allows 15 event slots per revolution, of which 1 to all may be filled.

During idle periods, the beam synchronous event line contains continuous bi-phase-mark "ones" (14 MHz square wave) transmission, with a single revolution tick event once a revolution. Even parity is selected so that idle "ones" bi-phase cells always start with a positive, rising edge, transition at the V123 module output. A single beam synchronous event code transmission, which requires approximately 0.853 ms, is shown in figure 1.

### 4 V123 MODULE FEATURES

- FLEX® 10K [6] FPGA based design
- SRAM translation table
- Input error interrupts
- Change of status interrupts
- Re-synch error detection
- VME Interface
- VMEbus cycle stealing
- VMEID
- FIFO

#### 4.1 FLEX®10K FPGA based design

An Altera EPF10K10QC208-3 is used in this design because it has 3 EAB blocks that are used for SRAM, ROM, and FIFO without the need for external devices.

#### 4.2 SRAM translation table

The 256 x 8 SRAM table in the Altera FLEX10K EAB block acts as a trigger to event translation table. Any trigger can be mapped to any event code.

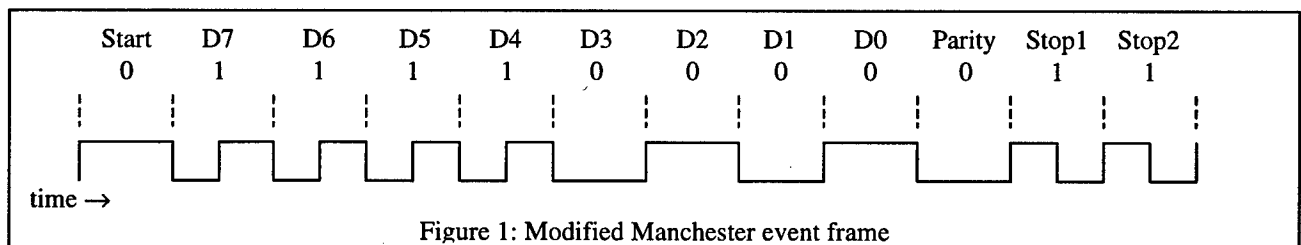


Figure 1: Modified Manchester event frame



### 4.3 Input error interrupts

If an event trigger code is received from the V201 input modules which is not one of the 63 allowed on this input, an out of range error interrupt is flagged.

### 4.4 Change of status interrupts

Two interrupts monitor the RF and beam tick inputs. If a signal is removed or reconnected an interrupt will be generated. The RF input is monitored for carrier. The beam tick input is monitored for phase relationship. Addition or deletion of this input will cause an interrupt.

### 4.5 Re-synch error detection

Any time a beam tick is received out of sequence, an error is flagged. This bit will not be set unless an error or discontinuity in the input signals is received.

### 4.6 VME Interface

The VME interface is A24, D08(OE). Interrupts are supported with a programmable interrupt vector and IRQ level. The SRAM lookup table, and all control and status registers are accessible through this interface. Each board occupies a 4K address block in the A24 space. The four V201 input modules occupy 64 addresses in sequential order from this base address, by having the V123 address decoder signal accessible on the dedicated P2 backplane.

### 4.7 VMEbus cycle stealing

The V123 shares access to its SRAM lookup table between the translation requirement of the output encoder and the VMEbus. If all transmission slots were filled, the translator would operate 100% of the time eventually causing a VME bus error to occur after a timeout. To ensure that the VMEbus is serviced with a full complement of trigger events from either the input triggers or batched through the FIFO, cycle stealing is employed. A portion of the encoder time which processes the framing start and stop bits need not access the SRAM, VMEbus read and write cycles are completed during this time.

### 4.8 VMEID

A 64-bit VMEID ASCII string is saved in the ROM implemented in one of the 3 EAB blocks in the Altera chip. This string is used by the front-end computer to identify the board in the VME chassis, and its revision. This information is checked at initialization.

### 4.9 FIFO

Software events are the lowest priority triggers. These events are processed last after other input triggers. A FIFO is necessary to preserve these events for the first available opening when no other triggers are active. The highest priority is the revolution event, followed by the

64 prioritized hardware triggers from the V201 followed by the events stored in FIFO. The FIFO may be used to batch events. An input filter prevents trigger values less than 64 from being written to the FIFO. This prevents the use of higher priority input trigger codes from being translated to lower priority FIFO events unless they are multiply mapped.

## 5 ACKNOWLEDGMENTS

The authors would like to acknowledge all the staff, of the RHIC/AGS controls section who have contributed to the work on which this paper is based. Special thanks to D. Barton, H. Hartmann, W. MacKay and the RF Systems Group, for their contributions.

## REFERENCES

- [1]R. Connolly, P. Cameron, R. Michnoff, V. Radeka, T. Shea, R. Sikora, D. Stephani, S. Tepikian, N. Tsoupas, and L. Woodworth, "The RHIC Ionization Beam Profile Monitor," these proceedings.
- [2]R. Michnoff, T. D'Ottavio, L. Hoff, W. MacKay, and T. Satogato, "RHIC Data Correlation Methodology," these proceedings.
- [3]RHIC Design Manual - RF Systems (WBS 1.7)  
[http://www.rhichome.bnl.gov/NT-share/rhicdm/00\\_toc1i.htm](http://www.rhichome.bnl.gov/NT-share/rhicdm/00_toc1i.htm)
- [4]H. Hartmann, and T. Kerner, "RHIC Beam Synchronous Trigger Module," these proceedings.
- [5]W. MacKay, "Considerations for Bunch Filling Patterns," Internal Note RHIC/AP-132, 29 Aug. 1997
- [6]FLEX is a registered trademark of Altera Corporation.

# THE RHIC INJECTION SYSTEM\*

W. Fischer,<sup>†</sup> J.W. Glenn, W.W. MacKay, V. Ptitsin, T.G. Robinson and N. Tsoupas,  
BNL, Upton, NY

## Abstract

The RHIC injection system has to transport beam from the AGS-to-RHIC transfer line onto the closed orbits of the RHIC Blue and Yellow rings. This task can be divided into three problems. First, the beam has to be injected into either ring. Second, once injected the beam needs to be transported around the ring for one turn. Third, the orbit must be closed and coherent beam oscillations around the closed orbit should be minimized. We describe our solutions for these problems and report on system tests conducted during the RHIC Sextant test performed in 1997. The system will be fully commissioned in 1999.

## 1 INTRODUCTION

Beam for the Relativistic Heavy Ion Collider (RHIC) is extracted from the Alternating Gradient Synchrotron (AGS), transported through the AGS-to-RHIC transfer line (AtR) and injected in either the Yellow or Blue ring of RHIC [1]. Fig. 1 shows the lattice through which the injected beam travels at the end of the transfer line and the beginning of the Yellow ring. We discuss here injection into the Yellow ring only; the Blue ring is mirror symmetric and in principle no different.

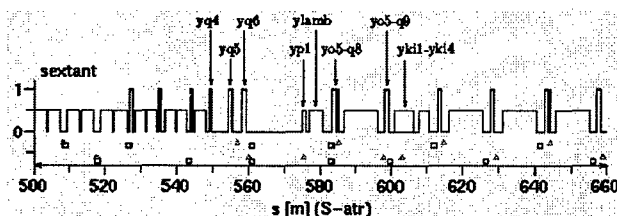


Figure 1: Lattice in the injection region. Shown is the end of the AtR and the beginning of the Yellow ring. Element names are the RHIC site wide names. Dipoles are of height 0.5, quadrupoles are of height 1. The upper (lower) squares show the locations of horizontal (vertical) beam position monitors, the triangles denote orbit correctors. The longitudinal s-position is taken from the beginning of the transfer line. The beam is in the ring after passing the septum magnet ylamb.

There are 6 quadrupoles at the end of the AtR, 3 of which are named in Fig. 1. They provide enough degrees of freedom to match the optical function at the end of the AtR to those at the beginning of the ring [2, 3]. The incoming beam lies in a plane 52 mm above the ring level and the

pitching magnet ypl bends the beam 3 mrad downwards. The septum magnet ylamb bends the beam 38 mrad horizontally and brings it in horizontal coincidence with the ring; it is seen as a drift by the circulating beam. The circulating and injected beams travel in the same beam pipe after passing ylamb. The injected beam then traverses vertically off center through the horizontally focusing quadrupole yo5-q8 (which thus acts as a dipole in the vertical plane), an arc bending magnet and the horizontally defocusing quadrupole yo5-q9 (which also acts as a dipole in the vertical plane). The incoming beam then experiences a vertical 1.86 mrad kick upwards which brings it onto the RHIC orbit.

Tab. 1 lists optical functions in the injection region. The relatively large vertical beta function in the injection kicker (the maximum in the arcs is 45 m) combined with the small inner beam pipe diameter (41.2 mm compared to 80 mm in the arcs) is a bottleneck for injection.

Table 1: Optical functions of Yellow ring injection region.

element	pos. [m]	$\beta_x$ [m]	$\beta_y$ [m]	$D_x$ [m]	$D_y$ [m]
ypl	575.93	22.86	25.32	-0.55	0.00
ylamb	580.83	38.22	14.50	-0.94	0.02
yo5-qf8	584.35	47.82	11.20	-1.08	0.03
yo5-qd9	599.18	11.18	47.82	-0.83	0.11
yki1	601.68	14.61	37.91	-1.00	0.10
yki2	603.13	17.28	32.79	-1.10	0.10
yki3	604.59	20.44	28.17	-1.20	0.09
yki4	606.04	24.08	24.04	-1.30	0.09

There are four injection kickers per ring, each 1.4 m long. They are described in detail in Ref. [4]. The kickers for the Yellow ring were commissioned during the RHIC Sextant test in 1996 [5]. After finding the correct timing, the kick strength has been measured. The optimal kicker voltage was found to be within 1% of the design value of 32 kV. The rise time was measured with beam and found to be below the design value of 95 ns. The kickers were also exercised in a multibunch injection mode with 4 bunches 100 ms apart.

## 2 INITIAL INJECTION

Filling patterns and bunch numbers for injection are stored in the electronic memory of a front end computer and can be changed via a graphical interface [6]. The injection process starts with an event requesting a new filling for either the Yellow or Blue ring. The rf system then orchestrates the synchronization and coggling so that the bunches in the AGS are transferred correctly into the buckets of

\* Work performed under the auspices of the US department of Energy

<sup>†</sup> Email: Wolfram.Fischer@bnl.gov

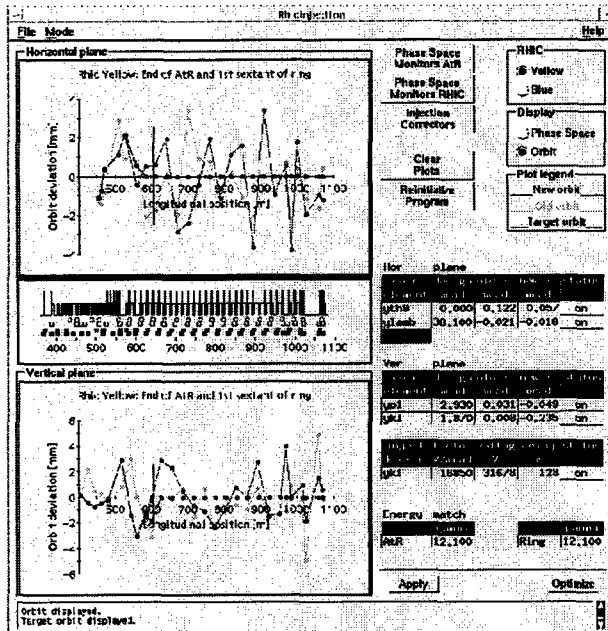


Figure 2: Graphical user interface for the injection tuning program showing the horizontal and vertical orbit and the lattice in the injection region. Active correctors and their settings are displayed.

RHIC. During the commissioning of RHIC the rf in the ring will be switched off before achieving circulation, however, since the revolution frequency of the beam is not yet known precisely. The rf system also generates pulses that are used to trigger the AGS extraction kicker and the RHIC injection kickers. The pulses are transported through dedicated fiber optic lines.

The injection tuning program guides the beam from the pitching magnet yp1 through the kicker magnets yk1 through yk4 (see Fig. 2 and Fig. 3). The program can show either the orbit in the injection region or position and angle of the beam at the end of the AtR and the beginning of the ring. In addition the lattice is depicted with dipoles, quadrupoles, beam position monitors and orbit correctors. The lattice and orbit plots zoom in concert. The phase space is reconstructed by orbit data from a pair of monitors in each plane in the AtR and RHIC. The used phase space monitors can be changed. One pair of correctors in each plane adjust the position and angle of the incoming beam in the middle of the injection kicker. Correctors too can be changed as shown in Fig. 3. However, in almost all cases the injection kickers will be one of the vertical correctors.

A table in the application shows the active correctors, their design value, last measured and target deviation from the design value and the status of their power supply. From the last measured orbit new deviations are computed to optimize the injection. New corrector deviations can also be given manually. The last two measured orbits and the target orbit are displayed.

The AtR magnet manager provides information about

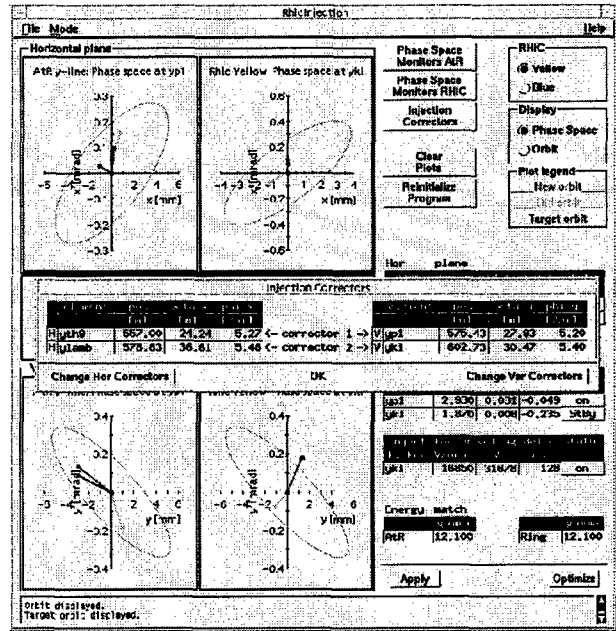


Figure 3: The injection tuning program showing the phase space at the end of the AtR and the beginning of the ring. An additional window is open in which different correctors can be chosen.

the particle species and the relativistic  $\gamma$  of the beam. With the measured kicker strength (in V/Tm), which is stored in and read from a database, the kicker voltage is computed and set.

The program also displays the settings for the relativistic  $\gamma$  of the beam that is used for the magnets in the transfer line and the ring.

### 3 FIRST TURN

After the beam has entered the ring it may be lost in the first turn and a correction is needed. In each of the RHIC rings there are 246 beam position monitors (BPMs) and 234 dipole correctors for both the horizontal and the vertical planes. The dipole correctors are part of corrector packages at almost each quadrupole magnet. BPMs are attached to a corrector-quadrupole or corrector-quadrupole-sextupole assembly and aligned relative to the quadrupole magnet center [8]. Interaction region BPMs are dual plane.

The first turn correction is performed by the Orbit Display and Correction application. This application uses the "sliding bumps" method [7] which can be applied to both, the orbit correction and the first turn correction. The ring correctors are organized into closed orbit bumps each of which contains 3 correctors (correctors are spaced close to  $\pi/2$  in the betatron phase). A change in the bump excitation only changes the orbit within the bump. The first turn correction is achieved by a consecutive one-by-one bump correction using the orbit data of the not yet lost beam. The correction proceeds until it reaches a region

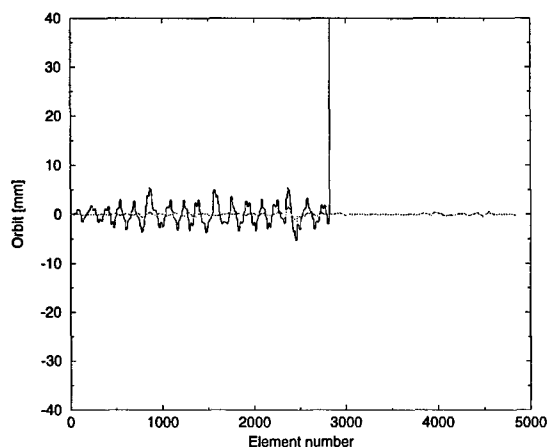


Figure 4: Simulated first turn orbit correction of RHIC, horizontal plane. One trace shows a particle with large oscillation that is eventually lost, the other trace shows a particle on a corrected orbit that completes the first turn.

where the beam has been lost or where the beam position exceeds some large value (1cm in our case). With several new bunches the point of loss can thus pushed forward until one turn is completed. Pushing the beam beyond the injection point establishes a closed orbit.

The first turn correction using sliding bumps has been tested on a model of RHIC using measured misalignment data [8]. The method not only provides the first turn correction but smoothes already the orbit in the ring. Fig. 4 and Fig. 5 show an example of such a simulation.

## 4 INJECTION OSCILLATIONS

Once a closed orbit is established, the revolution frequency of the beam can be measured with a wall current monitor and the rf frequency set accordingly [6]. The injection tuning program can then minimize the injection oscillations. This task in is principle no different from the initial injection except that the beam is not steered into the absolute orbit (as defined by zero orbit deviations in the BPMs) but into the closed orbit. Since the closed orbit is reached when the difference between the second turn orbit deviation and the first turn orbit deviation vanishes, this difference can be used as input in the algorithm used in the initial injection. The robustness of the application can be increased with fitting a sinusoidal function to the measured orbit oscillation in the first sextant instead of relying on two beam position monitors only. Not only is the signal averaged over many monitors, one can also reduce the dependence on a few BPMs. This method has been successfully applied at Fermilab's Tevatron [9].

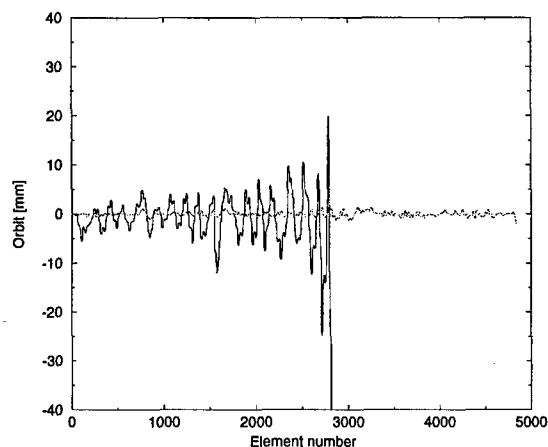


Figure 5: Simulated first turn orbit correction in RHIC, vertical plane.

## 5 SUMMARY

The RHIC injection system has been completed. Most of the hardware has been tested. Software tests were performed on realistic models of RHIC as well as during the Sextant test in 1996. The system is ready for full commissioning this year.

## 6 ACKNOWLEDGMENTS

We are thankful to all engineers, technicians and operators for their support in building and testing the injection system. We are thankful to M. Brennan and R. Bianco for discussion about the rf system.

## 7 REFERENCES

- [1] "The RHIC design manual" Revision of April 1998.
- [2] W.W. MacKay, "AGS to RHIC Transfer Line: Design and Commissioning", EPAC proceedings (1996).
- [3] N. Tsoupas et al., "Focusing and Matching Properties of the AtR Transfer Line", PAC proceedings (1997).
- [4] H. Hahn, J.E. Tuozzolo and N. Tsoupas, "The RHIC Injection Kicker", PAC proceedings (1997).
- [5] W. Fischer, H. Hahn, W.W. Mackay, T. Satogata, N. Tsoupas and W. Zhang, "Beam Injection into RHIC", PAC proceedings (1997).
- [6] M. Brennan and R. Bianco, private communication (1999).
- [7] S. Peggs, "Some Aspects of Machine Physics in the Cornell Electron Storage Ring", PhD thesis Cornell University (1981).
- [8] F. Pilat, M. Hemmer, S. Tepikian, D. Trbojevic, "Processing and analysis of the measured alignment errors for RHIC", these proceedings.
- [9] B. Joshel and G. Annala, private communication (1996).

## RAMP MANAGEMENT in RHIC \*

J. Kewisch, J. van Zeijts, S. Peggs, T. Satogata, BNL, Upton, NY

### Abstract

In RHIC, magnets and RF cavities are controlled by Wave Form Generators (WFGs), simple real time computers which generate the set points. The WFGs are programmed to change set points from one state to another in a synchronized way. Such transition is called a "Ramp" and consists of a sequence of "stepping stones" which contain the set point of every WFG controlled device at a point in time. An appropriate interpolation defines the set points between these stepping stones. This report describes the implementation of the ramp system. The user interface, tools to create and modify ramps, interaction with modeling tools and measurements and correction programs are discussed.

### 1 INTRODUCTION

As in all storage rings with energy ramping, magnet currents and RF parameters in RHIC must be ramped in a synchronized way. Because of RHIC's fast emittance growth at injection energies due to intrabeam scattering these ramps must be prepared before the rings are filled and executed as soon as the last bunch is injected. For that reason the control of magnets and RF is performed by WFGs.

Before a ramp can be loaded into the WFGs it must be specified. The input to this process comes from different sources. Initially, the specification comes from the design optics. Later, the operator may modify design parameters like tunes and chromaticities. An orbit correction procedure may supply new set points for the dipole correctors. Other correction procedures adjust the tunes, chromaticity, coupling, etc. All settings are not single values but functions of time and the change rate of the parameters is limited.

It is therefore necessary to provide an environment in which ramps can be created from a variety of sources.

### 2 ARCHITECTURE

The RHIC ramp system is shown in Figure 1. The central process is the "Ramp Manager" which is implemented as a CDEV[2] Generic Server[3]. The Ramp Manager provides an interface for various correction programs and for the "RAMP Editor". These Client applications are written using the CDEV Application Programming Interface (API) which gives a unified interface to accessing underlying services. The result is a "Ramp File" which is used by the "WFG Manager" to set up the WFGs. For each new ramp a new ramp file is created.

The ramp system allows also knobbing of parameters besides execution of programmed ramps. Similar to the ramp

manager, a "Knob Manager" creates a "Knob File" containing knob assignments and conversion constants.

The "WFG Manager" is used to download ramps and knob assignments into the WFGs. Monitoring and PLC control is performed by two "Magnet Managers", one for the Blue and one for the Yellow ring. Details are given in [1]. The AdoIf API is used to access the hardware.

Another service in this environment is the "Computational Modeling Engine" (CME) which is part of the RHIC/AGS Online Model Environment [4, 5]. The Ramp Manager provides the CME with a consistent set of magnet strength values. The CME provides optics parameters calculated from these values to correction programs and other applications.

### 3 STRUCTURE OF A RAMP FILE

A Ramp has to provide the set points of all magnets and RF devices as a function of time. This is implemented by defining "Step Stones", snap shots of all set points, and an appropriate interpolation between the Step Stones.

In the RHIC Ramp system a step stone is a data object which is independent of a ramp. It contains for each device a pair of strength parameters ("want" and "trim") which are independent of the beam energy: the deflection angle for dipoles, the inverse focal length for quadrupoles, etc. When the "want" parameter is fed to the CME service, it produces the "wanted" machine behavior. Because of machine imperfections, RHIC will display this behavior only if "trims" are added to the total strength value.

Step stones are referenced in ramps by the Stone name. A step stone can be used in multiple ramps and multiple times in one ramp. For example, the initial acceleration ramp references one step stone twice: at the start end the end of the ramp, since the device strength is independent of the energy. This allows storing the set points only once.

Since the set points of some devices change rarely and others often, step stones are split into six "pebbles": the BlueGlobal and YellowGlobal pebble contain the main dipole, quadrupoles, and multipole set points for the blue and yellow ring. The GreenGlobal pebble contains elements which are common to both rings. The RFGlobal pebble contains RF parameters. A step stone is therefore reduced to a reference to six pebbles. A pebble can be referenced in multiple step stones (Figure 2).

In between step stones cubic interpolation is used to calculate set points. However, the time is not used as independent variable, but a "pseudo time"  $P$ , which is a function of time. These power supplies are current regulated: a feedback system adjusts the voltage so that the requested current is maintained. By choosing a appropriate pseudo time

\* Work performed under the auspices of the US Department of Energy.

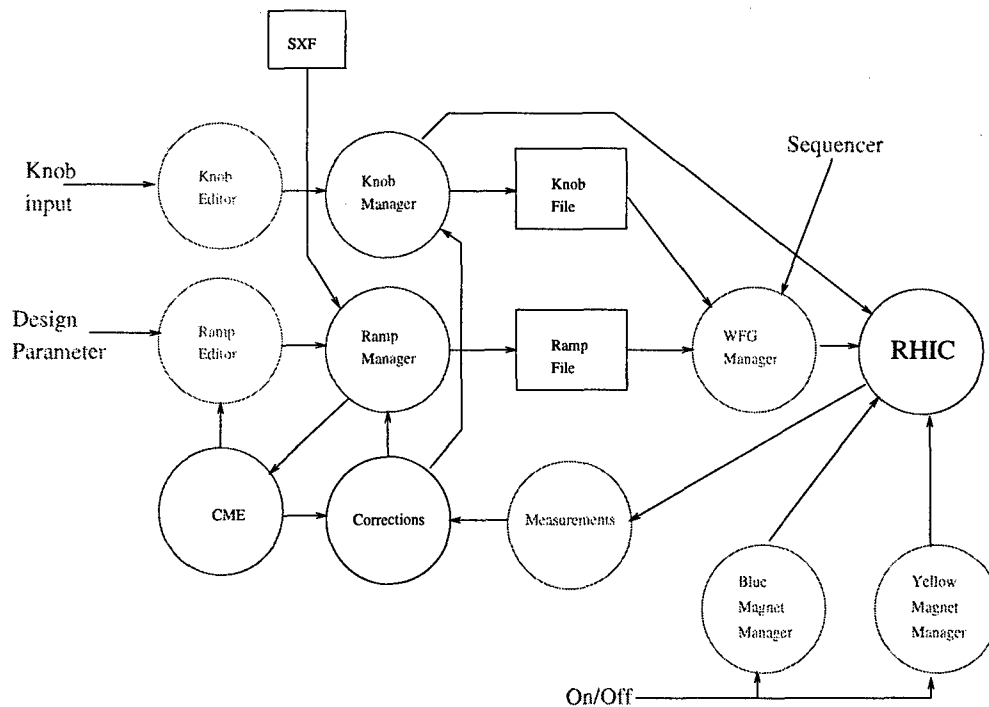


Figure 1: Software Configuration.

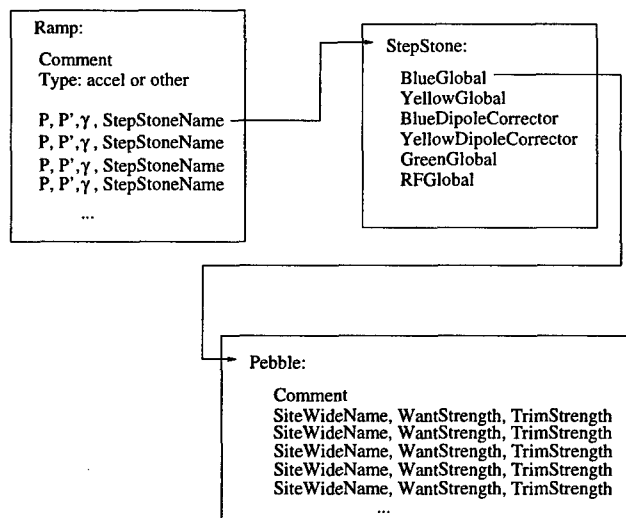


Figure 2: Ramp File structure.

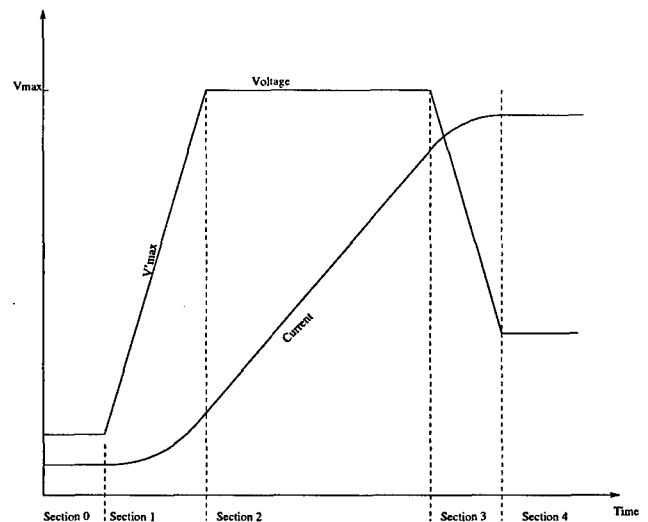


Figure 3: Current and voltage of a power supply during a ramp.

function regulation errors are avoided. We require that the voltage  $V = R \cdot I + L \cdot \dot{I}$  is a continuous function with a maximum value  $V_{max}$  and a maximum slope  $\dot{V}_{max}$ . The shortest ramp of a magnet current is shown in Figure 3. The pseudo time function is calculated so that for each magnet the maximum  $\dot{I}$  and  $\ddot{I}$  is not exceeded.

Ramps and step stones are addressed by unique names, under which they are available as "devices" in the CDEV interface, and multiple ramps and step stones are available simultaneously.

## 4 RAMP MANAGER INTERFACE

Messages are available to create, clone, and modify ramps and step stones. On demand, notification of changes are transmitted to interested clients by using the Generic Server callback mechanism. Applications using this interface include the RHIC Orbit Correction system, the RHIC injection system[6], and the ramping system editor GUI.

## 5 RAMP EDITOR

The user interface is implemented with the Tcl/Tk toolbox[7] which provides a flexible language for creating GUI applications. Windows for editing ramps and step stones are provided (see Fig. 4,5). the Ramp Editor allows changing high level parameters like tunes and chromaticities as well as set points. Step stones and pebbles can be copied from one ramp to another.

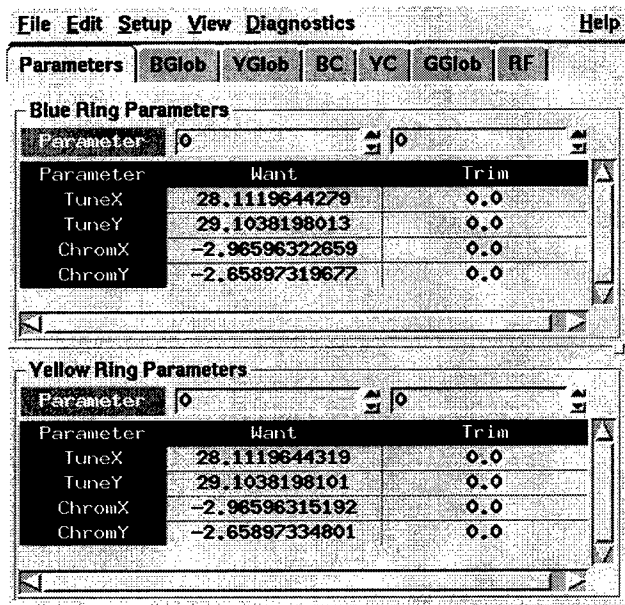


Figure 4: Step Stone parameter editing window.

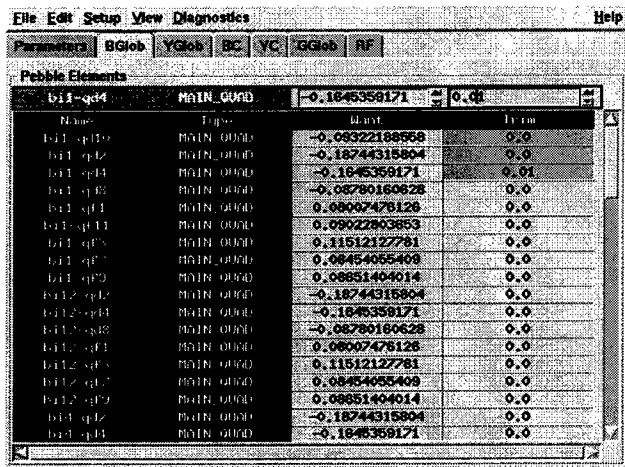


Figure 5: Pebble Magnet parameter editing window.

## 6 MODELING INTERFACE

A on-line model server can be synchronized with a given step stone; conversely a step stone can be created from the magnet values in the model. Model parameters such as tunes,  $\gamma_t$  and chromaticity are retrieved from the model

and presented in the GUI. The editor allows small changes to these parameters, which are performed by retrieving a sensitivity matrix from the model.

## 7 KNOB MANAGER

During the time a ramp is playing, magnet strength can be modified dynamically using the Real Time Data Link system. The WFG's can listen to a maximum of 2 different frames changing at a maximum rate of 720Hz. The frames available for this system are managed by the "Knob Manager" which allows creation, modification, and activation of knobs. They are described in high level terms like "tune x", etc. and the required coefficients relating a change in a set of magnets to these parameters are retrieved from the modeling server.

## 8 CONCLUSION

The RHIC ramp system provides an environment for creating ramps from multiple sources. Ramps are described using high level parameters. Besides programmed ramping the system allows knobbing of parameters during and after ramps.

## 9 REFERENCES

- [1] J. Kewisch, "Implementation of Ramp Control in RHIC", these proceedings.
- [2] J. Chen, G. Heyes, W. Akers, D. Wu, W. Watson, "CDEV: An Object -Oriented Class Library for Developing Device Control Application", Proceedings of ICALEPCS 1995.
- [3] W. Akers, "An Object-Oriented Framework for Client/Server Applications", Proceedings of ICALEPCS 1997.
- [4] T. Satogata, K. Brown, F. Pilat, A. Alai Tafti, S. Tepikian, J. van Zeijts, "The RHIC/AGS Online Model Environments: Design and Overview", these proceedings.
- [5] T. Satogata, F. Pilat, S. Tepikian, J. van Zeijts, "The RHIC/AGS Online Modeling Environments: Modeling RHIC", these proceedings.
- [6] W. Fischer, J.W. Glenn, W.W. Mackay, V. Ptitsin, T.G. Robinson, N. Tsoupas, "The RHIC Injection System", these proceedings.
- [7] <http://www.scripts.com/>

# IMPLEMENTATION OF RAMP CONTROL IN RHIC \*

Jörg Kewisch, BNL, USA

## Abstract

After the injection of beam into RHIC the beam energy is ramped from 10.8 GeV/u to 108 GeV/u and the beta function of the interaction points is reduced from 10 meters to 1 meter. The set points for magnet power supplies and RF cavities is changed during such ramps in concert. A system of Wave Form Generators (WFGs), interconnected by a Real Time Data Link (RTDL) and an Event Link is used to control these devices.

RHIC ramps use a two level system of WFGs: one transmits the beam energy and a "pseudo time" variable as functions of time via RTDL, the other calculates the device set points as functions of these RTDL variables. Energy scaling, saturation correction and the wiring of interaction region quadrupoles is performed on the second level.

This report describes the configuration and implementation of the software, firmware and hardware of the RHIC ramp system.

## 1 INTRODUCTION

The Relativistic Heavy Ion Collider (RHIC) consists of two intersecting storage rings. Using super-conducting magnets, RHIC will be able to collide ions from protons to gold. The existing AGS accelerator complex will be used as injector, supplying gold at 10.8 GeV/u and protons at 28.1 GeV. The beams are then accelerated in RHIC to 108 GeV/u and 249 GeV, respectively. All ion beams except protons will cross the transition energy during acceleration. At storage energy, the beta functions in the interaction points are reduced from 10 meters to 1 meter.

The RHIC ramp system, which brings the beams from injection to storage, controls the currents of the magnet power supplies including special jump power supplies for the transition crossing, cavity voltages and parameters for the RF phase and frequency feedback systems.

This system must fulfill the following requirements:

1) The system must be programmable to execute a complete ramp sequence on a start signal. This is especially important since the emittance of a gold ion beam grows rapidly at injection energies due to intra beam scattering. The complete sequence includes an acceleration ramp with transition crossing and the beta squeeze ramp. It is important that these ramps can be executed without delays once the machine is filled.

2) The system must allow tweaking of some components during and after the programmed ramps. Due to the large inductance of the super-conducting magnets the ramp speed is slow. A typical acceleration ramp takes 90 seconds. It is desirable that the operator has the ability to influ-

ence parameters like tunes, chromaticities and orbit bumps after a ramp is started. After the completion of a ramp the beam life time may be optimized by tweaking. Tweaking must be possible without major effort.

3) The system must support the easy control of magnet currents which are not supplied by a single power supply but are generated by a main power supply and several trim power supplies. The interaction region quadrupoles are wired this way in order to minimize the number of warm-cold feed-throughs.

4) The system must provide constant monitoring of magnet and RF parameters as well as a possibility for post mortem analysis after a magnet quench.

## 2 CONFIGURATION OF THE SYSTEM

The design of the RHIC controls hardware was inspired by the Fermilab control system. The general tool for the ramp control is the "Wave Form Generator" (WFG). The WFG is a VME module containing a computer based on the INTEL i960 CPU. Each WFG module has two fiber optics outputs which can be used in two ways: as the current reference for a power supply or as a source of the Real Time Data Link (RTDL).

RTDL [2] is one of two dedicated data lines around the ring. It transmits 256 "frames" with a update frequency of 720 Hz. Each frame contains a 24 bit integer number which can be generated by software, a WFG or any other device with a fiber optics output. The frames can be read by WFGs and used to determine the next output values.

The other data line is the event link [3]. This line provides 256 different start signals (events) to the hardware. This link is used to start ramps or change operation modes for WFGs, stop data collection into circular buffers after a quench, trigger the current jump of the  $\gamma_t$  quadrupoles and many other applications outside the ramp system.

The "Multiplexed Analog to Digital Converter" (MADC) [4] is used for monitoring the system. Each MADC module can monitor 64 signals and is programmable to scan one channel up to 50 kHz or all channels with a lower rate.

A PLC system allows switching power supplies on and off and reports error conditions of the power supply (regulation error, etc) and magnet (quench).

WFGs are programmed by specifying up to 15 "formulas". Events from the event link are used to switch from one formula to the next. Formulas may contain the following elements:

1. add, multiply and shift operations.
2. linear and cubic spline lookup in programmable tables.

\* Work performed under the auspices of the US Department of Energy.



3. Function of time:  $F(t)$  is given in a table with linear interpolation.
4. RTDL frames and programmable constants.

All operations are performed using 32-bit integers, floating point operations are not available. However, a “multiply and shift” operation with an intermediate 64-bit product is available.

The WFGs are used in a two level configuration (Figure 1): A pair of WFGs on the first level generate the beam rigidity  $B\rho$  and the “pseudo time”  $P$  as functions of time and distribute the value via RTDL.  $P$  is a function calculated to limit the second derivative of the magnet current  $\ddot{I}(t)$  when  $I(P)$  is a cubic function of  $P$ . In addition, RTDL is used to transmit the values of “knobs” used for tweaking.

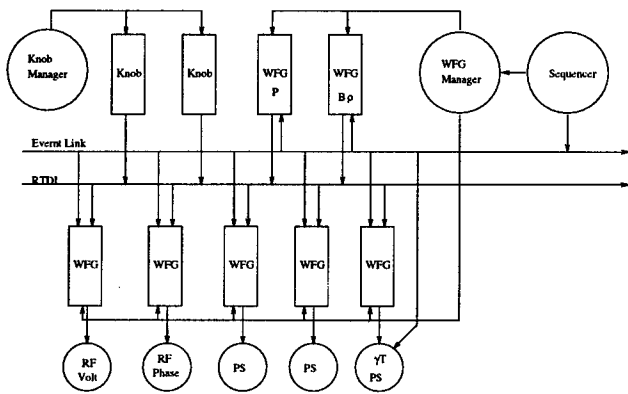


Figure 1: Two level WFG configuration using RTDL and Event link.

On the second level are WFGs which calculate magnet currents and RF parameters.

$$k = F_{ideal}(P) + F_{trim}(P) \quad (1)$$

$$+ [c_1 \cdot k_1 + c_2 \cdot k_2] \quad (2)$$

$$B = k \cdot B\rho \quad (3)$$

$$I_{magnet} = F_{fielddata}(B) \quad (4)$$

$k$  is the magnet strength (deflection angle for dipoles, inverse focal length for quadrupoles, etc.) which is the sum of the programmed strength given as functions <sup>1</sup> of  $P$  and optional knob values.  $k_1$  and  $k_2$  are RTDL knob frames,  $c_1$  and  $c_2$  are the conversion constants from knob value (i.e. tunes or orbit displacement) to magnet strength.

From the total value of  $k$  the magnetic field or gradient  $B$  is calculated and, using the measured field data, the magnet current  $I_{magnet}$ .

The thing left to do is to calculate the power supply current. Figure 2 shows the wiring of the interaction region quadrupoles. Each of the power supplies generates the difference of two magnet currents. Since the WFGs do not

communicate with each other<sup>2</sup>, this functionality was implemented in the power supply interface card (Figure 3).

The power supply interface card has two WFG inputs and calculates the difference value. Of course both signals must have the same scale factor which was chosen to be 1 mA per bit. The result is then multiplied, divided and shifted to produce a 16 bit number which maximum value corresponds to the maximum current of the power supply. A DAC converts this number into the reference voltages for the power supply.

Figure 3 shows also the signals monitored by the MADC: The reference current (set point), the measured current, the error current<sup>3</sup> and the voltage.<sup>4</sup> These signals are sampled with 60 Hz and stored in a circular buffer. Sampling is stopped by the “quench event” which is generated by the quench protection system. The data buffers are inspected for the post-mortem analysis before the system is restarted.

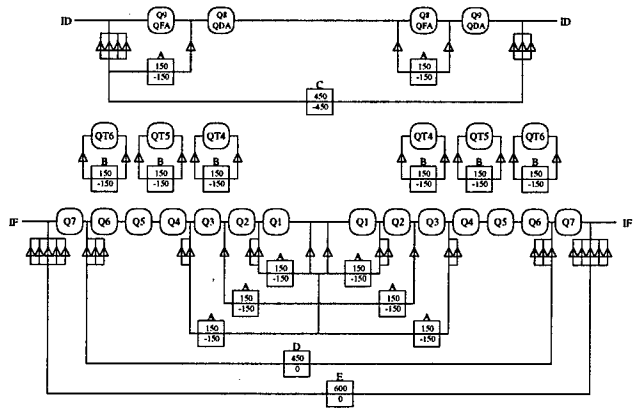


Figure 2: Power supply configuration for the IR quadrupoles.

### 3 SOFTWARE

WFGs, MADCs and PLCs are located in VME crates which are distributed around the ring. Each crate has a “Front End Computer” (FEC) which has a tcp/ip connection to the “Console Level Computers” (CLC). FECs allow access to WFGs, PLCs and MADCs through the “Accelerator Device Object” (ADO) software. ADOs provide a high level interface to accelerator devices and hide hardware details from the outside world. However, they control only a single device.

“Manager” programs run on the CLC level and provide the controls of logical groups of devices. The “WFG Manager” is the program that loads all ramp data into the WFGs. It can load several ramps using different formu-

<sup>2</sup>The current set points of the main power supplies are available as RTDL frames and are subtracted in the WFG.

<sup>3</sup>The error current is the difference of reference current and measured current, multiplied by 50 for better resolution.

<sup>4</sup>The main power supplies for dipoles and quadrupoles have additional signals for quench detection.

<sup>1</sup> $F_{ideal}(P)$  contains the settings for the ideal machine,  $F_{trim}(P)$  contains corrections

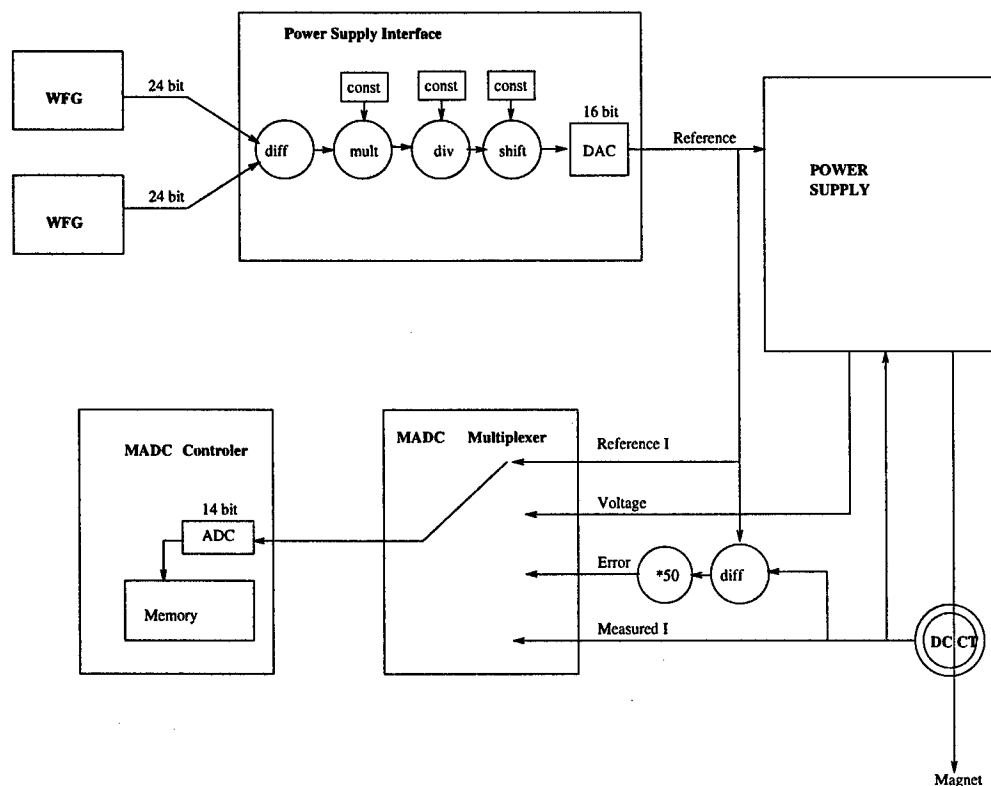


Figure 3: Control and monitoring of a power supply.

las and tables. Each ramp is connected to a specific event. The "Sequencer" is a scripting tool which is used to trigger these events and, ultimately, orchestrate to the whole injection-acceleration-storage cycle. More detail is given in [8].

## 4 CONCLUSION

The Ramp Control System for RHIC is build on powerful hardware which allows ramps to be programmed in advance and executed without operator intervention. However, tweaking of parameters during a ramp, which may take several minutes, is not excluded. This provides a valuable tool during commissioning.

The system is designed from the accelerator physicist point of view. Set points are integrated magnet strength and high level parameters and are converted into currents and voltages close to the hardware level. This allows encapsulation of hardware details and provides a simple interface for application programs.

The MADC system provides powerful post-mortem analysis.

## 5 REFERENCES

- [1] T. Clifford, V. Mane, S. Peggs, "RHIC Ramps: a proposal", RHIC/AP/16, December 1993.
- [2] H. Hartmann, "Specifications for the RHIC Real Time Data Link transmitter system", October 1993.
- [3] H. Hartmann, B. Oerter, S. Peggs, "RHIC Real Time Data Link System", October 1993.
- [4] R. Michnoff, "The RHIC General Purpose Multiplexed Analog to Digital Converter System", PAC 1995.
- [5] T. Kahn, "RHIC Power Supply Waveform Generator Board Application Notes", revised October 1994.
- [6] T. Kahn, "Power Supply Waveform Generator Programmer Manual", March 1995. October, 1994.
- [7] J. Kewisch, V. Mane, T. Clifford, H. Hartmann, T. Kahn, B. Oerter, S. Peggs, Model for RHIC Ramp Controls, EPAC 1996.
- [8] J. Kewisch, J. van Zeijts, S. Peggs, T. Satogata, "Ramp Management in RHIC", these proceedings.

## BEAM TRANSFER LINE TUNING AND STEERING BASED ON MINIMIZATION MODEL TOOLS\*

S. Assadi, F. Tecker<sup>†</sup>, M.-J. Yang,  
Fermi National Accelerator Laboratory, Batavia, IL

### Abstract

Accurate beam steering is crucial for transfers between different accelerators in the Fermilab accelerator complex.

During commissioning of the new 8-GeV beam transfer line from Fermilab Booster to Main Injector, we used a least square fit algorithm to achieve the desired beam line orbit. The program is based on the COCU orbit correction package used at CERN. The purpose and the need of this program is to keep the desired injection trajectories to the Fermilab Main Injector (FMI) constant and minimize the time required to tune the beam line. In addition, we performed a number of measurements to compare the optics of the line to the design values.

In this paper, we present the experience with the beam line steering in the 8-GeV line during commissioning and the results of detailed beam line studies.

### 1 INTRODUCTION

A new transfer line was built to transport 8.9 GeV protons from the Booster to the Fermilab Main Injector (FMI). The line is about 760 m long and is made from both permanent and conventional electromagnets [1]. The line was partly finished and tested in February 1997. After completion of the line, the final commissioning started in September 1998.

For regular operation, it is important to steer the beam through the line and into the Main Injector without losses, for which a good orbit is essential. This raises the need for a fast and convenient way to correct the trajectory to the desired reference.

### 2 ORBIT CORRECTION

The orbit correction that was implemented for the 8-GeV line is based on the MICADO algorithm [2]. It solves a system of linear equations

$$r = Ax + b \quad (1)$$

where  $b$  is the vector of the BPM measurements,  $x$  is the correction vector and  $A = (a_{ij})$  the beam response matrix

\* Work supported by the University Research Association Inc. under contract DE-AC02-76CH00300 with US Department of Energy

<sup>†</sup> Email: tecker@fnal.gov

to a set of corrector excitations. The algorithm iteratively minimizes the norm of the residual vector  $r$  using a least squares method. At each iteration, it finds the first best corrector excitation that yields the lowest residual r.m.s. BPM distortions. This corrector is appended to the corrector set, the residual distortion is reanalyzed and the next best corrector selected. The strengths of all correctors from previous iterations are recalculated. This is repeated for a number of correctors until the residual r.m.s. BPM distortions are as small as desired. The algorithm is fast and converges with a small number of corrector magnets.

Here, the MICADO algorithm is embedded in the orbit correction package COCU (Closed Orbit Correction Utilities) [3] which was developed at CERN. The package is capable of correcting the closed orbit, a trajectory in a circular accelerator or transfer line, and orbit or trajectory correction over a short range without affecting the rest of the machine. It also does calculation of bumps and simulation of the effects of correctors on the orbit. Calculations are based on the Twiss parameters which can be taken from simulations like MAD [4].

The COCU package had to be adapted for the use in the accelerator controls system at Fermilab. The existing code runs under HP-UX at CERN while the Fermilab controls system is based on VAX/VMS. Due to the complexity of the code it was decided not to port it to VMS but to run it under UNIX. The existing source could be compiled with minor changes under SunOS and Linux. An application program was written for the VAX control consoles. This program takes the beam position monitor (BPM) data and allows the selection of orbit correction type, plane to correct, number of correctors, etc. The BPM data and the correction commands are sent via TCP/IP to a server running on the UNIX side. The server program performs the data input to the COCU program, runs it and sends the predicted orbit and corrector excitations back to the console program. The console program shows the predicted orbit and corrector excitations and allows you to send the corrector excitations to the hardware.

The code is not particularly accelerator specific and can easily be extended to other transfer lines and circular machines. It will also be used for the transfer lines between Main Injector and Recycler and closed orbit correction in the Recycler Ring.

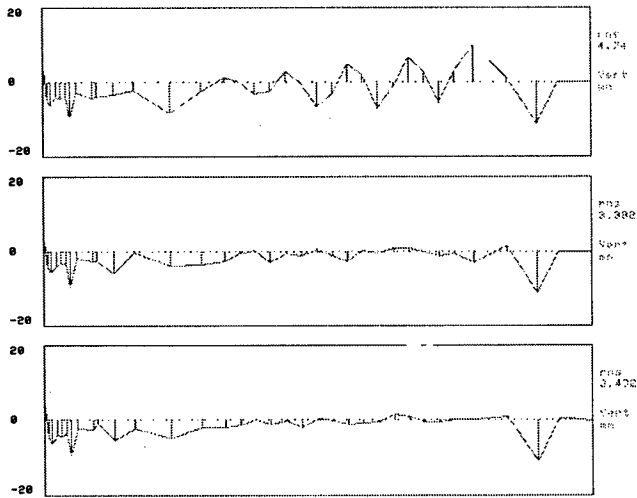


Figure 1: Vertical orbit data in millimeter as a function of the location. The upper graph shows the measured trajectory before correction. The center graph shows the predicted orbit for a short range correction where the injection trajectory into the Main Injector was kept constant. The lower graph shows the measured orbit after correction. It corresponds well to the predicted orbit.

During initial commissioning of the 8 GeV transfer line between Booster and Main Injector, the steering of the beam was done manually using 3-bumps to zero the orbit at the BPM locations. After implementation of the COCU package, it was tested and used.

The program successfully corrected the trajectory. It allowed a much faster, deterministic way of trajectory correction. An example of the measured, predicted and corrected orbit is shown in Fig. 1. The program has shown particularly useful to correct to a previous reference trajectory after changes in the Booster extraction orbit. It converges very fast, one iteration usually is sufficient. This indicates that the beam optics is close to the design optics.

Fig. 2 and Fig. 3 show examples of the corrected trajectory in the horizontal and vertical plane, respectively. The trajectory is well corrected to a few millimeter, except for the beginning of the beam line. The trajectory there results from Booster extraction orbit with no corrector magnets at upstream locations in the transfer line. This orbit excursion is not critical since it does not create beam loss. The transmission through the beam line obtained during the commissioning was 96-97%.

### 3 TRAJECTORY ANALYSIS

The effectiveness of the orbit correction strongly depends on the correspondence between the model and the actual machine. To verify the optics of the 8-GeV line, we studied the effect of single corrector excitations on the trajectory.

The COCU package has the feature to predict the effect of single corrector kicks on the BPM readings. This was used to calculate the deviation of the measured BPM data

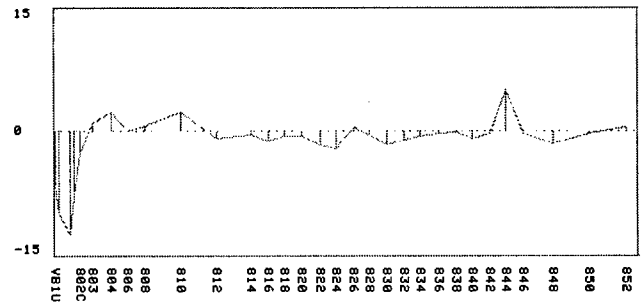


Figure 2: Horizontal BPM display in millimeter as a function of the BPM position. The orbit is well corrected except for the beginning of the beam line. The excursions there result from Booster extraction with no upstream corrector magnets in the transfer line. The apparent excursion at the 844 location results from a bad BPM reading.

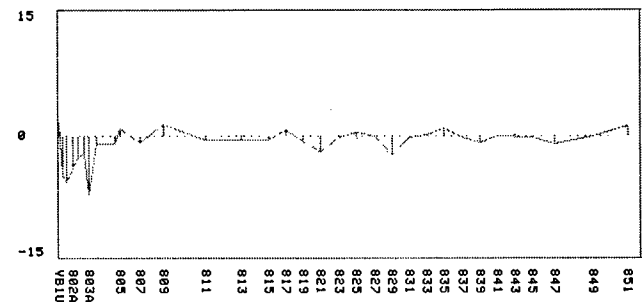


Figure 3: Vertical BPM display in millimeter as a function of the BPM position. The excursion at the upstream end cannot be corrected due to missing correctors.

from the expected trajectory for the design optics. A reference orbit was saved, a corrector magnet changed and the difference trajectory to the reference was recorded. The analysis of the difference orbit has the advantage that absolute BPM position errors do not influence the results. An example for the horizontal plane is shown in Fig. 4.

The graph shows that the difference trajectory from a kick at corrector HT802 corresponds to the theoretical expectation down to the BPM HP806. An oscillation is visible downstream of that location. An orbit correction with COCU was performed to find the origin of the kick and kick strength. The result shows that this oscillation can be corrected with one single kick at the 806 location, indicating an error in the quadrupole strength  $k_1$ . The gradient error  $\Delta k_1$  was estimated from the calculated correction kick  $\Delta\theta$  and the BPM reading  $x_{\text{BPM}}$  at this location as  $\Delta k_1 \cdot L = \Delta\theta / x_{\text{BPM}}$  where  $L$  is the length of the magnet.

The quadrupole strength was changed and the measurement was repeated. After final adjustment, the measured trajectories almost correspond to the theoretical design within the noise of the BPM system. Fig. 5 shows an example of a single horizontal kick trajectory after quadrupole adjustments.

A similar measurement for the vertical plane was performed by changing the strength of the Booster extraction

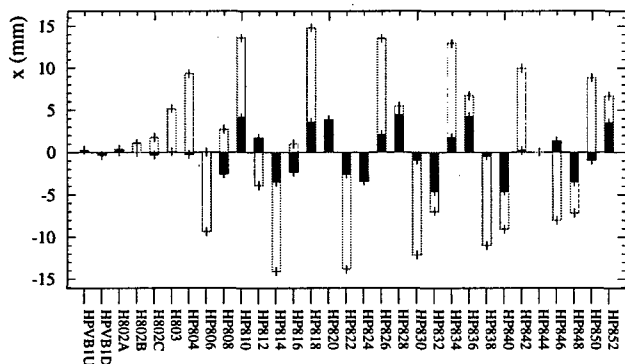


Figure 4: Horizontal BPM readings. The open data shows the measured trajectory difference for a single correction coil (HT802) excited. The filled data shows the difference between theoretical prediction and measured data. An oscillation starting from BPM HP808 is clearly visible.

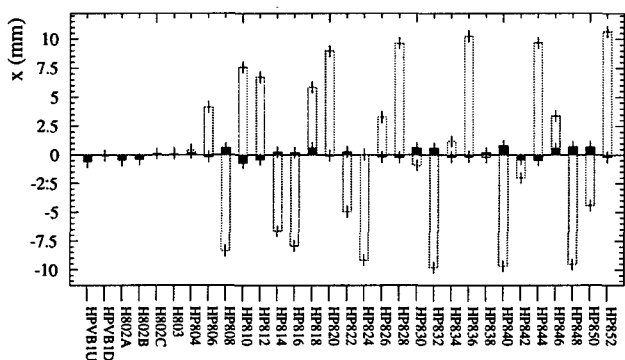


Figure 5: Horizontal BPM readings as in Fig. 4 after adjusting the quadrupole strength of Q806. The trajectory results from excitation of the single correction coil HT804. It corresponds well to the predicted trajectory for the quadrupole strengths as designed.

septum magnet (see Fig. 6). The results indicate that a few quadrupole magnets do not run at their design strength and have to be adjusted. The analysis will be repeated after adjustments made to the vertically focusing quadrupoles and also for kicks on the first corrector in the horizontal plane to diagnose the quadrupole strengths of the first magnets in the beam line. A more detailed analysis of the 8 GeV transfer line including lattice functions, dispersion, emittance propagation and matching to the Main Injector can be found in [5].

## 4 CONCLUSION

The COCU orbit correction package was successfully implemented at Fermilab and used during commissioning of the 8 GeV transfer line. The application program can easily reduce the time required to optimize the beam trajectory. It helped to achieve a transmission of 96-97% through the transfer line.

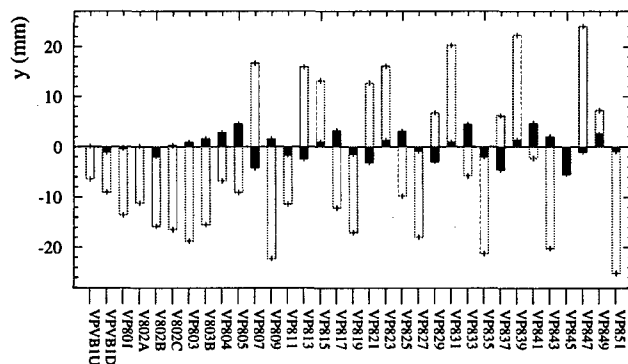


Figure 6: Vertical BPM readings. The trajectory results from a current change in the Booster extraction septum magnet MP02. Open data shows the measured data, the filled data shows the difference from the predicted trajectory for the design optics.

The COCU package was also used to compare the trajectory of orbit kicks to the design and helped to find quadrupole strength errors. The transfer line optics in the horizontal plane corresponds well to the design. A few gradient errors are still present in the vertical plane and will need further investigation.

## 5 ACKNOWLEDGEMENTS

We would like to thank Werner Herr who provided the source code for the COCU orbit correction package.

## 6 REFERENCES

- [1] John. A Johnstone, "Optics and Field Error Compensation in the FNAL Permanent Magnet 8.9 GeV/c Proton Transfer Line". In *Proceedings PAC'97*, Vancouver, (1997).
- [2] B. Autin and Y. Marti, "Closed Orbit Correction of A.G. Machines Using a Limited Number of Magnets", CERN ISR MA/73-17, (1973).
- [3] G. Crockford, Werner Herr, John Miles, V. Paris, and Rüdiger Schmidt, "COCU User Guide", (1995)
- [4] Hans Grote and F.C. Iselin, "The MAD Program", CERN SL/90-13 (AP), (1990).
- [5] S. Assadi, F. Tecker, M.-J. Yang, "The optics measurement and analysis of Femilab 8-GeV transfer line to Main Injector", these proceedings

# TUNE CONTROL IN THE FERMILAB MAIN INJECTOR

G. WU, B. C. BROWN,\* D. P. CAPISTA, R. H. FLORA, D. E. JOHNSON and K. S. MARTIN  
for the Main Injector Commissioning Team  
Fermi National Accelerator Laboratory † P.O. Box 500, Batavia, IL 60510

## Abstract

We describe methods used to measure and control tunes in the Fermilab Main Injector (MI). Emphasis is given to software implementation of the operator interface, to the front-end embedded computer system, and handling of hysteresis of main dipole and quadrupole magnets. Techniques are developed to permit control of tune of the Main Injector through several acceleration cycles: from 8.9 GeV/c to 120 GeV/c, from 8.9 GeV/c to 150 GeV/c, and from 150 GeV/c to 8.9 GeV/c. Systems which automate the complex interactions between tune measurement and the variety of ramping options are described. Some results of tune measurements and their comparison with the design model are presented.

## 1 INTRODUCTION

Many modes of operation are required of the Fermilab Main Injector[1] to permit the several tasks which it performs within the projected Fermilab physics program. Acceleration from 8.9 GeV/c to 150 GeV/c of both protons and antiprotons is required for injection into the superconducting Fermilab Tevatron. Acceleration of protons from 8.9 GeV/c to 120 GeV/c is required for production of antiprotons and for fixed target physics programs. The Fermilab Recycler ring will allow antiprotons which remain at the end of a proton-antiproton colliding beam run to be retained but this requires the Main Injector to decelerate beam from 150 GeV/c to 8.9 GeV/c. Software for current control in the main bending and focusing magnets must permit flexible and often changing mixtures of these ramping cycles.

The iron properties modify the linear relation between current and magnet strength expected for the electromagnetic dipoles and quadrupoles. Hysteresis differences at low fields and saturation at high fields are both important. Control of the bending and focusing magnets is based on their current so the resulting fields must be calculated from a model based on magnetic measurements. The field which results for a given magnet current will depend upon the previous history. It depends strongly on the most recent sign reversal in  $dI/dt$  and weakly on prior sign reversals. The cycle time for the 120 GeV/c cycles is an important parameter so adjustment of the minimum (reset) current, which will affect the resulting magnetic fields, is an important software design feature.

Design requirements to provide these features have been discussed in a previous paper[2]. This report updates that

work and describes the software implementation, some measured results and the status during the first months of Main Injector commissioning.

## 2 REQUIREMENTS AND HARDWARE

Following our previous work[2] we note that the momentum,  $p$ , is controlled by the magnetic field achieved in accordance with

$$p = \frac{e}{2\pi} \int_C B_y ds = e(B\rho) \quad (1)$$

where  $e$  is the elementary charge, and  $B_y$  is the vertical component of the magnetic field. This expression defines  $B\rho$  where  $\rho$  is a characteristic bending radius. We have  $p = (e/\theta_D)B_1L_{eff}$  for an MI 6-m dipole which bends by  $\theta_D = 2\pi/(301 \text{ } 1/3)$ . We can express the function which relates the tunes,  $\underline{\nu}$ , (horizontal and vertical) and the quadrupole strengths,  $\underline{k}_1$ , using a linear expansion about the operating point. Choosing to solve for the normalized quadrupole strengths we have  $\underline{k}_1 = \underline{Q}^{-1} \underline{\nu} + \underline{k}_{10}$ . Letting  $\underline{K} = \underline{Q}^{-1}$ , we express this more fully as

$$\begin{pmatrix} k_{1f} \\ k_{1d} \end{pmatrix} = \begin{pmatrix} K_{11} & K_{12} \\ K_{21} & K_{22} \end{pmatrix} \begin{pmatrix} \nu_x \\ \nu_y \end{pmatrix} + \begin{pmatrix} k_{01f} \\ k_{01d} \end{pmatrix}. \quad (2)$$

Using MAD[3], a lattice model calculation was performed on the design lattice MI19 at a variety of tunes. The results were fit to this form yielding

$$\begin{pmatrix} k_{1f} \\ k_{1d} \end{pmatrix} = \begin{pmatrix} 0.001022 & 0.000185 \\ -0.000196 & -0.001008 \end{pmatrix} \begin{pmatrix} \nu_x \\ \nu_y \end{pmatrix} + \begin{pmatrix} 0.008973 \\ -0.00901 \end{pmatrix}. \quad (3)$$

Note that since this quadrupole strength is normalized to  $B\rho$ , it already employs a relation between the dipole and quadrupole strengths. To improve tune control the quadrupole current is regulated with respect to the dipole current as described below. An analytic model for describing the magnetic field strength achieved for a specified magnetic current and current history is described in a companion paper[4].

The main dipoles and quadrupoles for the Main Injector are powered using a folded bus for the dipoles and two quadrupole buses with currents flowing in opposite directions. The power supply system[5] consists of 12 new dipole supplies and 6 quadrupole supplies moved from the Fermilab Main Ring.

Let us consider an operational cycle for the Main Injector. Beam will be injected into the machine with the magnets at a constant current chosen to provide the required momentum and tune properties. The magnet currents will

\*Email: bcbrown@fnal.gov

† Work supported by the U.S. Department of Energy under contract No. DE-AC02-76CHO3000.

then be ramped to match a specified momentum-time profile and a momentum-tune profile to the required peak current. The currents will then be ramped to a reset current below the injection current, to set the hysteretic fields and then the current will be returned to the injection level. A reset well below the injection field is required to minimize field variations due to variations in the reset current. The required precision increases exponentially as the reset current approaches the injection current. The desire to maximize the repetition rate of the machine encourages a high reset as does the natural limitations in regulating SCR supplies at a small fraction of their peak current.

The proposed physics program to be supported by the Main Injector will require the ability to flexibly mix a variety of ramp modes. Since a given ramp (say a 150 GeV Tevatron proton injection cycle) may follow any other ramp (say a 120 GeV  $\bar{p}$  production cycle), each must leave the magnets in a similar magnetic state such that history dependent differences are not important. Clearly all injection currents must be the same. The tool we have identified for restoring the magnetic state at the end of each different cycle (ready for 8 GeV injection) is a specific reset current appropriate to each specific cycle. No assurance exists that this will be sufficient. Main Injector commissioning has included a brief study of the field achieved for injection following 120 GeV or 150 GeV ramps. The observed differences in injection dipole field ( $4 \times 10^{-4}$ ) could be matched using changes in the reset current (from 358 A to 376.5 A). Based on the success of these studies and examination of special hysteresis studies of the measured magnetic field strength, we expect no serious problems in mixing different energy ramps.

### 3 SOFTWARE IMPLEMENTATION

Control of currents in the bending and focusing magnet circuits is performed by a control console program, I2, interacting with a real time controller, MECAR (Main injector Excitation Controller And Regulator)[6]. An operator uses I2 to define profiles of basic accelerator parameters such as momentum, tune and chromaticity as functions of time in a cycle. Different ramping modes are associated with specific clock reset events which are used to identify each ramp cycle. I2 converts the momentum and tune profiles to current profiles and sends them to MECAR.

From the momentum profile, I2 creates a profile of bending magnet (dipole) current vs. time using dipole properties of the lattice along with an analytic model of the history-dependent relation between the magnet current and the integrated field strength. The parameters for the model are extracted from fits[4] to magnet measurements. The profile of dipole current vs. time is calculated on a set of points whose time density is related to the current-time slope. This set of points is passed to MECAR.

The conversion from the tune profiles to quadrupole magnet current profiles is separated into two parts. The main contribution is calculated using a *calibration* table,

$C(I_b)$ , which contains a relation between tunes and the momentum and the current in the dipole and each quadrupole bus which can be determined directly from measurements. This relation is assumed the same for all ramp cycle types. It is prepared in I2 and made available to MECAR. The specified tune vs. momentum profile (*tune* table) is compared to the result of a linear interpolation in momentum and tune using the *calibration* table and the difference is found. The tune differences are converted to magnet strength differences using a sensitivity matrix  $Q^{-1}$  (see above) derived by fitting lattice calculations. The resulting quadrupole strength differences are converted to current changes,  $\delta(t)$ , using a model for quadrupole strength vs. current[4]. This calculation is also carried out on a sparse set of times chosen to match the requirements of the tune vs. momentum curve. Current difference curves for the horizontal and vertical focusing buses are passed to MECAR.

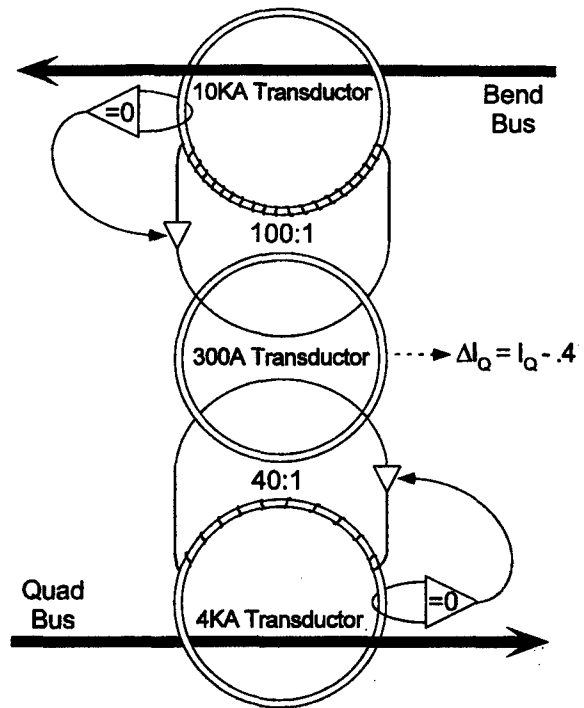


Figure 1: Schematic representation of a triple transductor for measuring the current in a quadrupole bus with respect to 40% of the dipole bus current.

MECAR reads the bend current vs. time points. A FIR filter is used to construct a gentle function, of bounded frequency, from the linear interpolation of these points to use as the dipole program function,  $I'_b(t)$ . MECAR regulates the dipole current,  $I_b(t)$  measured using the dipole transductor[7], to match the program function.

Measurement of the quadrupole current uses a triple transductor differencing system as shown in Figure 1 which measures the quadrupole current  $I_q(t)$  with respect to 40% of the bend current,  $\Delta I_q(t) = I_q(t) - .4I_b(t)$ . The desired

program signal  $\Delta I'_q(t)$  is created using inputs from the I2 program. The current difference curves  $\delta(t)$  are read and a FIR filter applied to a linear interpolation in time of these points. Employing the differential quad current program,  $\Delta I'_q(t) = C(I_b(t)) - .4I_b(t) + \delta(t)$ , MECAR regulates the current yielding:  $I_q(t) = C(I_b(t)) + \delta(t)$ .

#### 4 TUNE MEASUREMENT

Several tune measurement systems have been created and installed for the Main Injector, including previously described ones from the Fermilab Main Ring[8]. Commissioning of these systems is underway but not all yet provide convenient results in the Main Control Room so most of the measurements used employ the Turn-by-turn system (Console Application I42) which uses position measurements from the standard Main Injector beam position monitors. Transverse beam motion is excited with a pinger magnet whose time is varied to permit measurements at the required time. For most times, adjustments of the chromaticity are needed for coherent oscillations to be visible during a sufficient number of turns to allow a precise tune measurement.

#### 5 RESULTS

Initial values for the calibration table were created from the preliminary hysteresis models and design lattice properties. Efforts will continue to provide a seamless way to integrate upramp and downramp tune control. For now, we believe that we can provide a calibration table for downramp operation which we will use when deceleration is required. Separate understanding was obtained by using the magnet measurements and lattice properties directly and predicting the ratios of bus currents which control tune properties. These quantities provide guidance for understanding power supply control requirements but also give sensitive tuning parameters for machine commissioning.

In Figure 2, data directly from magnet measurements and from machine tune calibration are shown. Measurements of dipole IDA114-0 and quadrupole IQB310-1 were analyzed using design properties of the lattice and linear interpolation of measured strength to predict the required currents and current ratios (points labeled Magnet Measurements). To provide the calibration table, the tunes were measured and the requested tune modified until values near the design values of (26.425, 25.415) were achieved. Currents were measured in this condition. Ratios labeled MI Measurement are from this data. The general shape is in reasonable agreement but the actual values for the vertical quadrupole ratio will require further examination.

#### 6 SUMMARY

We have implemented a tune control scheme in the FMI using a real calibration table. Results of tune measurements have proved that the magnet model built upon the magnet measurement data works reasonably well. These efforts to

#### Current Ratios (Quad/Bend) for Main Injector

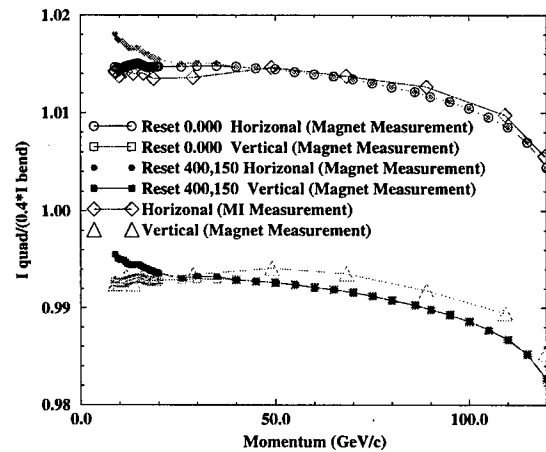


Figure 2: Ratios of quadrupole to dipole bus currents are shown as a function of momentum for the design tunes of ( $\nu_H = 26.425, \nu_V = 25.415$ )

describe the magnet performance continue in preparation for more complicated operation modes of the FMI.

#### 7 REFERENCES

- [1] The Fermilab Main Injector Technical Design Handbook. Fermilab, August 1994. Revised February 1997.
- [2] B.C. Brown *et al.* Design for Fermilab Main Injector Magnet Ramps Which Account for Hysteresis. In *Proceedings of the 1997 Particle Accelerator Conference, Vancouver, B.C., Canada, 12-16 May 1997*, page 3245. IEEE, 1998.
- [3] H. Grote and C. Iselin. The MAD Program Users Reference Guide. SL 90-13(AP), CERN, 1990.
- [4] B. C. Brown. Hysteresis Study Techniques and Results for Accelerator Magnets with Unipolar Current Excitation. This Conference (PAC99).
- [5] Steven Hays. A 5 Mega Watt Ramping Power Supply for the Fermilab Main Injector Dipole Bus. In *Conference Record of the 1993 IEEE Nuclear Science Symposium and Medical Imaging Conference*, page 390. IEEE, 1994.
- [6] R. Flora *et al.* MECAR (Main Ring Excitation Controller and Regulator): A Real Time Learning Regulator For The Fermilab Main Ring Or The Main Injector Synchrotron. In *Proceedings of the 1995 Particle Accelerator Conference and International Conference on High-Energy Accelerators*, page 2172. IEEE, Piscataway, N.J. 08855-1331, 1996.
- [7] S. Hays, D. Wolff, and H. Pfeffer. Power Supply Regulation Systems Installed in the Fermilab Accelerators. In *Conference Record of the 1991 IEEE Nuclear Science Symposium and Medical Imaging Conference*, page 957. IEEE, 1992.
- [8] D. Still, I. Kourbanis, and D. Capista. Tune Measurement Methods in the Fermilab Main Ring. In *Proceedings of the 1997 Particle Accelerator Conference*, page 2061. IEEE, Piscataway, N.J. 08855-1331, 1998.



# CHROMATICITY CONTROL IN THE FERMILAB MAIN INJECTOR

G. WU, C. M. BHAT, B. C. BROWN,\* and

D. E. JOHNSON for the Main Injector Commissioning Team, FNAL  
Fermi National Accelerator Laboratory† P.O. Box 500, Batavia, IL 60510

## Abstract

Chromaticity control in the Fermilab Main Injector will be important both in accelerating protons and antiprotons from 8 GeV to 150 GeV (or 120 GeV) and in decelerating recycled 150 GeV antiprotons to 8 GeV for storage in the Recycler Ring. The Main Injector has two families of sextupoles to control the chromaticity. In addition to the natural chromaticity, they must correct for sextupole fields from ramp-rate-dependent eddy currents in the dipole beam pipes and current-dependent sextupole fields in the dipole magnets. The horizontal sextupole family is required to operate in a bipolar mode below the transition energy of 20 GeV. We describe methods used to control chromaticities in the Fermilab Main Injector. Emphasis is given to the software implementation of the operator interface to the front-end ramp controllers. Results of chromaticity measurements and their comparison with the design model will be presented.

## 1 INTRODUCTION

Chromaticity control in the Fermilab Main Injector [1] is one of the important issues for the early design of the Main Injector. The Main Injector will be used to accelerate high intensity protons and anti-protons ( $\bar{p}$ ) from 8 GeV to 150 GeV for Tevatron injection and protons to 120 GeV for  $\bar{p}$  production and fixed target physics experiments and to decelerate the unused  $\bar{p}$ s from the Tevatron and store them in the Recycler Ring [2] at 8 GeV. The modes of operation for acceleration and the deceleration of the beams may be fundamentally different from one another because of the initial beam emittance and the hysteresis of the magnets of the FMI lattice. For example, longitudinal emittance of the 8 GeV beam at injection from the Fermilab Booster is expected to be  $\leq 0.1$  eV-sec, while, that for the anti-protons at 150 GeV from the Tevatron is expected to be 3-4 eV-sec.

## 2 REQUIREMENTS AND HARDWARE

The natural chromaticity of the FMI is about -33 units in both horizontal and vertical planes. The head-tail instability growth rate of the beam suggests that a chromaticity of about -5 units below transition energy and +5 units above transition is desired to keep stable beam in the Main Injector. Similar conclusions have been reached by particle tracking studies carried out at 8 GeV (injection energy) and at 120 GeV [1]. To avoid head-tail instability after

the transition energy of 20.49 GeV, the chromaticity must quickly jump to the new required value. To achieve the required chromaticity and control it through the acceleration/deceleration cycle, two families of 54 sextupole magnets [1],[3] are inserted in the FMI lattice. A model of chromaticity compensation in the presence of beam-pipe eddy current, dipole geometric and saturation sextupole fields have been developed [4] and subsequent improvements [5] have been made to include remnant fields of the sextupole magnets for different operating scenarios. Implementation of the fast ramps with  $\dot{\gamma} \approx 267 \text{ sec}^{-1}$  near transition, has resulted in dominance of the eddy current contribution to sextupole components at low momenta. Some of our early studies indicate that below transition the focusing set of sextupole magnets may have to run in bi-polar mode. Besides, it is extremely important that the sextupole magnet fields to be exactly identical at the end of each acceleration/ deceleration cycle for reproducibility of the beam behavior from cycle to cycle since any ramp may have been preceded by a variety of other possible ramps.

To drive the two families of sextupole magnets, new sextupole magnet power supplies which are capable of operating from -400 to 400 Amp have been built[6] and are used in the Main Injector chromaticity compensation scheme. These supplies are controlled using Fermilab C453 programmable ramp controllers housed in CAMAC. The output of the C453 is the sum of its three function generators which are 'clocked' by time,  $p$  and  $\dot{p}$  respectively.

## 3 SOFTWARE IMPLEMENTATION

Control of chromaticity  $\xi$  requires control of the magnet strength  $g$  thus the currents  $I$  of the two sextupole families. Their relationship in vector form were formulated [4][5][7] as follows

$$\underline{g} = \frac{p}{A} M^{-1} [\underline{\xi} - \underline{\xi}_0 - \underline{\varepsilon} \theta (b^{eddy} + b^{sat})] \quad (1)$$

$$b^{eddy} = \delta \frac{\dot{p}}{p} \quad (2)$$

$$b^{sat} = \sum a_n \frac{p^n}{A p^n} \quad (3)$$

where  $p$  is beam momentum in GeV/c,  $A$  relates momentum to magnetic rigidity,  $\xi_0$  natural chromaticity. The elements of the  $2 \times 2$  matrix  $M^{-1}$  and vector  $\underline{\varepsilon}$  are simulated for the FMI lattice.  $b^{eddy}$  is the normalized sextupole harmonics contributed by beam pipe eddy current,  $b^{sat}$  is the bending dipole contribution due to the static sextupole moment which is largely due to saturation fields.  $\delta$  is given

\* Email: bcbrown@fnal.gov

† Operated by Universities Research Association, Inc. under contract No. DE-AC02-76CH03000 with the U. S. Department of Energy

by calculation[8][9] confirmed by experiment[10][11], the  $a_n$  are fitted parameters of the dipole measurements,  $\rho$  is the design beam curvature radius in the dipoles and  $\theta$  is the bending angle of the dipole magnet.

Assuming that the sextupole strength is linear in the current, the above expression can be re-written in terms of currents  $I$  in the two sextupole circuits and in a form that separates contributions from  $p$  and  $\dot{p}$ .

$$I = \frac{1}{A\kappa} M^{-1} [(\xi - \xi_0)p - \theta \epsilon \sum a_n \frac{p^n}{A\rho^n} - \theta \delta \epsilon \dot{p}] \quad (4)$$

where  $\kappa$  is a conversion factor between integrated magnet strength and current. In principle  $\kappa$  represents a complicated conversion due to hysteresis and saturation effects of the sextupole magnets [7]. In the FMI commissioning  $\kappa$  is taken as a crude constant. When a variety of magnet ramp cycles are required the sextupole magnet excitation and excitation history have to be described in greater accuracy. But this will involve the same method being developed for the bending and focusing magnets [7].

## 4 MEASUREMENTS AND RESULTS

In the course of commissioning, both tunes and chromaticities are adjusted and measured repeatedly. Shown in Figure 1 are results of one set of systematic chromaticity measurements and the momentum ramp profile. Figure 2 shows data points plotted in coordinates of set and measured chromaticity values. The set values are the end results of efforts put into the whole scheme of chromaticity control - physics modeling, magnet measurements, software and hardware implementations. The fact that the data points are narrowly populated along a straight line with slope close to one satisfies us for the commissioning stage.

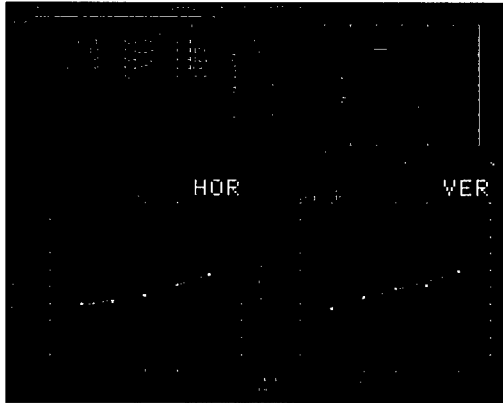


Figure 1: Horizontal and vertical chromaticity measurements for Main Injector at 70 GeV. The top right FMI ramp, bottom shows tune vs radial position: left  $\xi_H$  and right  $\xi_V$ .

## 5 SUMMARY

We have implemented a chromaticity compensation scheme (both hardware and software) in the Main Injector and have

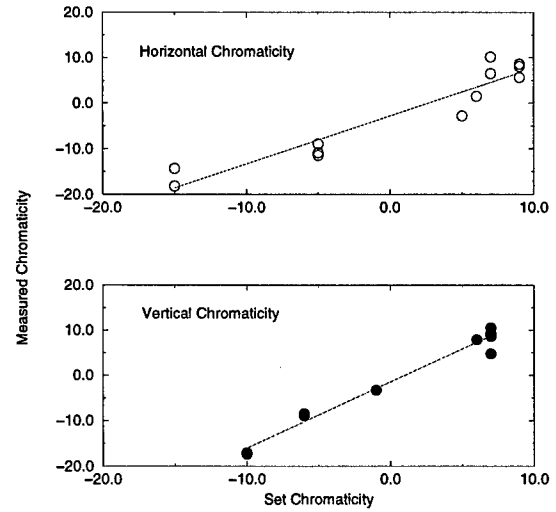


Figure 2: Comparison between measured and set horizontal and vertical chromaticities for the Main Injector in the energy range from 9 GeV to 110 GeV.

tested it during the 1998-1999 FMI commissioning runs. We have measured the chromaticities corresponding to the set values in an energy range of 9-110 GeV during the acceleration cycle. They are fairly in good agreement. Results of these studies will be used to control the chromaticities in the deceleration mode of the FMI.

Authors would like to thank Operation personnel for their help during these measurements.

## 6 REFERENCES

- [1] The Fermilab Main Injector Technical Design Handbook. Fermilab, August 1994. Revised February 1997.
- [2] G. Jackson. The Fermilab Recycler Ring Technical Design Report. TM 1991, Fermilab, November 1996.
- [3] D.J. Harding *et al.* Sextupole Magnets for the Fermilab Main Injector. In *Proceeding of the 1993 IEEE Particle Accelerator Conference*, page 2826. IEEE, 1993.
- [4] S.A. Bogacz. Chromaticity Compensation Scheme for the Main Injector. In *Proceeding of the 1993 IEEE Particle Accelerator Conference*, page 77. IEEE, 1993.
- [5] C.M. Bhat *et al.* The Main Injector Chromaticity Correction Sextupole Magnets: Measurements and Operating Schemes. In *Proceedings of the 1995 IEEE Particle Accelerator Conference, Dallas, May 1-5, 1995*, page 1334. IEEE, 1995.
- [6] Si Fang, George Krafczyk, Howie Pfeffer, and Dan Wolff. Four Quadrant 250KW Switching Power Supply for Fermilab Main Injector. This Conference (PAC99).
- [7] B.C. Brown *et al.* Design for Fermilab Main Injector Magnet Ramps Which Account for Hysteresis. In *Proceedings of the 1997 Particle Accelerator Conference, Vancouver, B.C., Canada, 12-16 May 1997*, page 3245. IEEE, 1998. Also available as FERMILAB-Conf-97/147.
- [8] S. D. Holmes. Eddy Current Effects in the Main Injector Beam Tubes. Main Injector Note MI-0013, Fermilab, April 1990.

- [9] Jean-Francois Ostiguy. Eddy Current Induced Multipoles in the Main Injector. Main Injector Note MI-0037, Fermilab, October 1990.
- [10] D. G. Walbridge *et al.* Measurements of Beam Pipe Eddy Current Effects in Main Injector Dipole Magnets. *Int. J. Mod. Phys. A (Proc. Suppl.)*, 2B:617, 1993. Proceeding of the XVth International Conference on High Energy Accelerators, Hamburg, July 20-24, 1992 also available as FERMILAB-Conf-92/220.
- [11] D. G. C. Walbridge *et al.* Field Errors Introduced by Eddy Currents in Fermilab Main Injector Magnets. In Shen Guo-liao Lin Liangzhen and Yan Luguang, editors, *Proceedings of 15th International Conference on Magnet Technology*, page 157. Science Press, Beijing, 1998. Also available as FERMILAB-Conf-97/342.

# OPTICS MEASUREMENT OF THE FERMILAB MAIN INJECTOR 8-GEV TRANSFER LINE<sup>†</sup>

S. Assadi, F. Tecker, M.J. Yang<sup>‡</sup>, FNAL, Batavia, IL

## Abstract

The new Fermilab 8-GeV transfer line for the Main Injector is now commissioned. Studies had been done to measure the optical characteristics of the beamline. In order to capture the state of the beamline as completely as possible all accelerator data, i.e. Beam Position Monitor, Multiwire Profile Monitor, magnet current, and other miscellaneous information, were read and saved. A recently developed beamline analysis program was used to collect data and to do the analysis. Orbit data was used to understand the beamline quadrupole strengths and to measure the dispersion function. The profile data was used to extract beam emittances and to estimate the initial lattice parameter of the beamline.

## 1. INTRODUCTION

The new 8-GeV transfer line from Booster to the Fermilab Main Injector is 764 meters long [1]. Conventional electro-magnets were used in the first section to match into a mid-section FODO lattice of permanent magnets. The final section uses conventional magnets to match the lattice into the Main Injector proper.

This write-up describes the measurements being done to document the properties of the transfer line and the beam emittances. Beam data was taken for the analysis of optics, dispersion function, and the beam emittances using the on-line beamline analysis program [2]. The data and the results of the analysis will be discussed. Both the design lattice as calculated by MAD [3] and the lattice as determined experimentally were used for the final analysis of emittances.

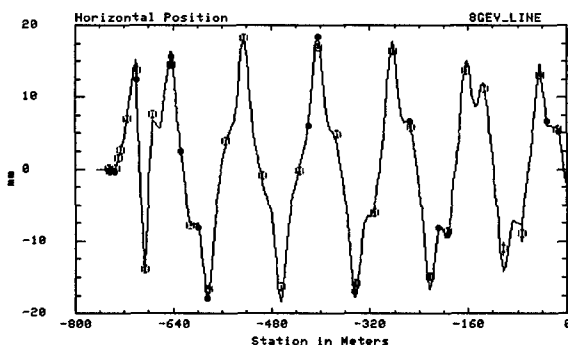


Figure 1. Horizontal plane difference orbit due to a kick from HT802 at 3 amps above nominal. The dots are data from MW profiles, the open circles are data from BPMs, and the solid line is the orbit calculation using matched quadrupole strengths. The beam is extracted from Fermilab Booster at -780 meter on the plot and at station of 0 is the injection point to the Main Injector.

## 2. DATA

There are 15 Multiwire Profile Monitors (MW) and over 50 Beam Position Monitors (BPM) in the 8-GeV transfer line. These multiwires are used to take data for one plane at a time. BPM data, profile data, magnet currents, the intensity monitor data, and other miscellaneous information are read through the Fermilab accelerator control system.

Reference beam data was taken with the machine at its nominal state at the beginning of each study period. The beam orbit data was taken with 1-bump kick applied at upstream of the beamline to excite position excursions. A data set consists of data with kicks at different strengths. Horizontal and vertical plane data were taken separately. An example of horizontal plane orbit is shown in Figure 1 and the vertical plane orbit is shown in Figure 2. The dispersion data was taken with beam momentum changed in steps of 0.08%. This was accomplished by changing RF frequency in the source Booster ring while keeping its magnet currents constant. All data sets taken have the MW profiles already included and no additional measurement is needed for lattice and emittance analysis.

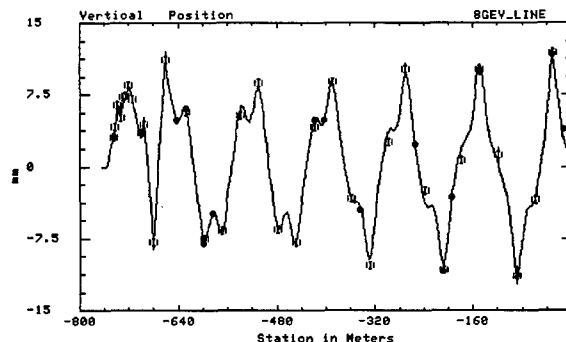


Figure 2. Vertical plane difference orbit data as caused by a kick at MP02. Dots are from MW profiles and open circles are from BPMs. The solid line represents the orbit calculation.

## 3. ANALYSIS

The goal of transfer line optics analysis is ultimately the matching of the lattice function into the down-stream machine, the Main Injector. The three types of analyses reported here were done to ensure that the optical characteristics were understood correctly.

The first step of analysis is to use 1-bump orbit data to diagnose the quadrupole magnet strengths. This analysis is independent of the beam source, the Fermilab Booster. The second is to compare the measured dispersion function with the calculation. This is used to verify that the bend strengths, the initial dispersion function, and the

<sup>†</sup> Work supported by the US Department of Energy under contract DE-AC02-76CH00300.

<sup>‡</sup> E-mail: YANG@FNAL.GOV

quadrupole strengths used in the calculation are consistent with the reality. The last is to use the beam profile width data to extract information on the beam emittance and the  $\sigma_p/p$ . For a transfer line the initial lattice functions directly affect lattice calculation everywhere. In the process of fitting for emittance the initial conditions were also varied such that the RMS error from the fitting process is minimized.

Given a set of initial lattice function the lattice function can be projected down the beamline and into the Main Injector. If needed, the changes in the transfer line magnet currents can also be estimated to improve the lattice matching.

## 4. RESULT

### 4.1 Orbits and quadrupoles

The orbit data used for analysis is actually the orbit difference from the reference orbit. In this way the issue of absolute accuracy of the position data is by-passed. During this analysis the strengths of the quadrupoles used in the calculation can be varied to find the best fit to a given set of orbit data. It is important that the fitted quadrupole strengths can be used in calculations to reproduce all other sets of orbit data, given the corresponding corrector kick strength and polarity.

In both examples shown, i.e. Figure 1 for horizontal plane and Figure 2 for the vertical plane, the fitted quadrupole strengths were used for orbit calculation. The positions from profile monitors in general are more accurate and exert more weight than those from BPM reading, which more susceptible to calibration errors.

The first quadrupole in the 8-GeV beamline starts with Q800, followed by Q801, Q802, and so on. The vertical orbit change was induced by the 1-bump kick using the Booster extraction septum magnet MP02. The first available 1-bump horizontal kick is from HT802, located where Q802 is. There was no information available for diagnosing Q800 and Q802 properly.

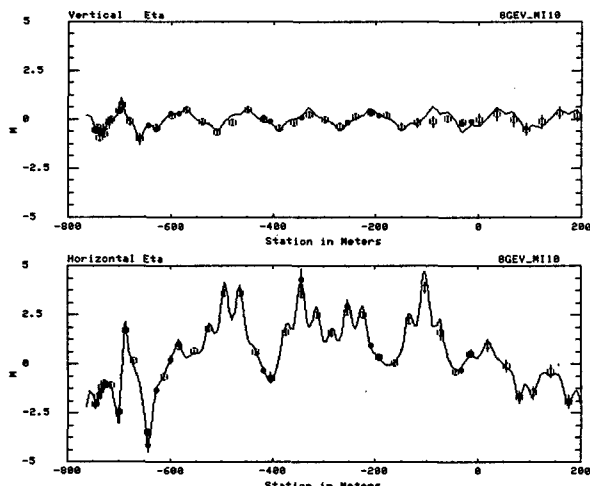


Figure 3. Measured MI 8-GeV transfer line dispersion function as compared with calculation. The horizontal plane data is at the bottom and the vertical plane at the top. Station 0.0 indicated the entrance to the Main Injector ring.

### 4.2 Dispersion function

The beamline dispersion function depends on the strengths of bending dipoles, the strengths of the quadrupoles, and the initial lattice function at the Booster extraction point. The horizontal and vertical plane dispersion function shown in Figure 3 were calculated using the designed dipole strengths and the quadrupole strengths as determined from the procedure above. The initial dispersion functions had to be modified in order for the calculation result to match the data. This modification is echoed in the emittance fitting procedure to be discussed next.

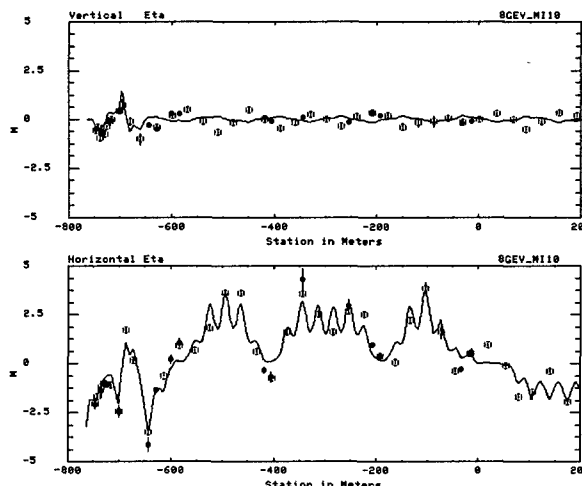


Figure 4. The dispersion function as designed for the 8-GeV transfer line is plotted against the same dispersion function data as was shown in Figure 3.

For the calculation of dispersion function there is very little differences between using the design lattice and using the lattice as determined from data. The single most significant factor is the initial dispersion used. Figure 4 plots the same dispersion function data as in Figure 3 but against the original 8-GeV transfer line design calculation. The difference is quite apparent.

### 4.3 Beam profile and emittance

The beta and dispersion functions at the profile monitor locations are needed to fit for the emittance. Different initial  $\beta$ ,  $\alpha$ ,  $\eta$ ,  $\eta'$  values result in different lattice function and, therefore, different fit result. The initial conditions that lead to smallest RMS error from the fitting algorithm is considered the optimized conditions.

Three scenarios were explored for the analysis of beam emittance and  $\sigma_p/p$ . The first is to use the design lattice and the design initial condition for calculation. The second is to use the design lattice but with a set of optimized initial conditions. The third is to use only experimentally determined quadrupole strengths and initial conditions.

Figure 5 shows the width sigma from profile data in solid green dots. The calculated sigma from the first scenario is shown in solid black line. The calculation from scenario 2 is overlaid in solid magenta. The calculation result of scenario 3 is shown separately in Figure 6.

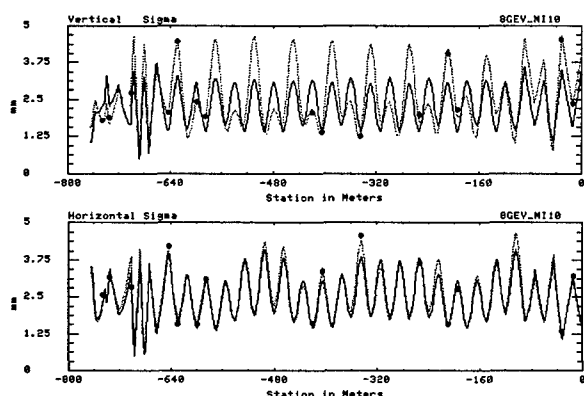


Figure 5. Plot of horizontal and vertical plane beam widths. Green dots are the data points from profile monitors. Solid lines are from calculation using design lattice and fitted emittance. The calculation using the design initial lattice function is shown in black and the calculation using optimized initial condition is shown in magenta.

#### 4.4 Lattice function

The first horizontal BPM after injection into the Main Injector is HP102. The projected horizontal lattice functions at this location were calculated using the second and third scenario mentioned above and listed in table 1. The calculation based on the first scenario is, by design, matched with the Main Injector design lattice and will not be listed. For vertical plane the first BPM is VP101 and the projected vertical lattice function is also listed in table 2.

From table 1, the horizontal plane calculation agrees fairly well among the two scenarios even with substantial differences in the initial lattice function. The difference in the vertical plane was appreciably larger. It should be mentioned that the lattice as was designed did not reproduce the vertical plane orbit data well. This may lead to additional systematic error. In either case substantial difference exist between projected lattice function and the expected Main Injector lattice function.

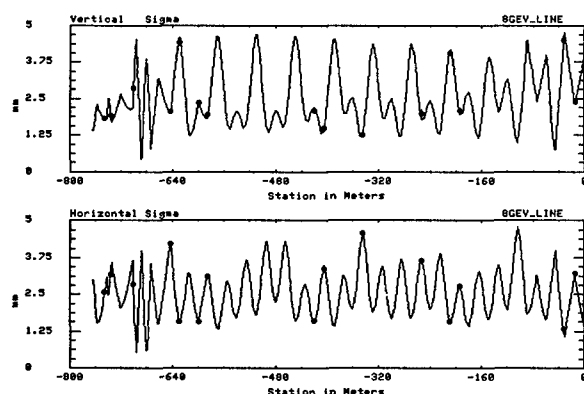


Figure 6. Same horizontal and vertical plane beam width sigma data as in Figure 5. The solid line shows the sigma as calculated using the adjusted quadrupole strength, optimized initial condition, and the fitted emittance.

The optimized initial lattice function is likely a result of the actual initial condition combined with the unknown

quadrupole errors at the beginning of the beamline. Beyond the first part of the beamline, and especially within the permanent magnet section, the quadrupole strengths are fairly well understood. From Figure 6 it is clear that the calculation fitted well with data within this part of the beamline and could still yield credible projection of the lattice function.

Table 1. Projected horizontal lattice function at the Main Injector HP102 location.

	MI/ring	MI8/design	MI8/fitted	Unit
$\beta$	54.830	63.27	60.42	M
$\alpha$	2.394	2.78	2.71	
$\eta$	0.081	0.89	0.99	M
$\eta'$	-0.001	-0.046	-0.05	

Table 2. Projected vertical lattice function at the Main Injector VP101 location.

	MI/ring	MI8/design	MI8/fitted	Unit
$\beta$	57.490	74.00	69.54	M
$\alpha$	2.468	3.94	3.80	
$\eta$	0.000	-0.47	-0.289	M
$\eta'$	0.000	0.044	-0.023	

## 5. CONCLUSION

The preliminary analysis indicates that the behavior of the MI8 beam line can be modeled quite well but not as was designed to be. The dispersion function is an indication that the bending dipoles behaved as designed. The data also showed that the permanent magnet portion of the beam line, starting from location 809 and up to 847, has worked as designed.

The horizontal plane optics appears to be quite close to the original design while the vertical plane optics may have deviated from it by some degree. The large lattice function deviations, as seen in the vertical plane, are due mostly to the initial conditions. In the case of dispersion function it was also found that the initial conditions were largely at fault.

Knowing the initial condition at the Booster extraction is very important for the proper operation of the 8-GeV transfer line. To do that the first part of the beamline needs to be well understood. More data will be taken in the future to establish the reproducibility of this analysis. The study of the Main Injector ring lattice function is also just starting and will likely take some time to mature. Adjustment will be made when the matching is verified one way or another.

## 6. REFERENCES

- [1] The Fermilab Main Injector Technical Design Handbook.
- [2] M.J. Yang, "A Beamline Analysis Program for Main Injector commissioning", Particle Accelerator conference, 1999.
- [3] Hans Groted and F.C. Iselin, *The MAD Program*, 1990, CERN SL/90-13 (AP)

# A BEAMLINE ANALYSIS PROGRAM FOR MAIN INJECTOR COMMISSIONING<sup>†</sup>

M.J. Yang<sup>‡</sup>, FNAL, Batavia, IL

## Abstract

From the start of Fermilab Main Injector commissioning in October of 1998 an on-line application program has been used to collect data from the accelerator control system. This is a comprehensive program that collects accelerator data, does modeling calculation, and performs analysis of the optical properties of the beamline. Data and calculation result are viewed with graphic display or text listing. This program is responsive and flexible. Interface is provided for modifying beamline setup, as well as importing from and exporting to MAD program.

## 1 INTRODUCTION

The accelerator modeling programs used for Fermilab Main Injector project, such as MAD [1] and TEAPOT [2], do not deal directly with actual data. This write-up describes an ACNET [3] console application program that fully integrated beamline setup, data acquisition, data storage, calculation, analysis, and display. It is responsive, requires minimum human intervention, and has sufficient flexibility. Extensive graphic displays are provided for viewing data and calculated result. Text listing is an alternative which also provides the means to e-mail data to user.

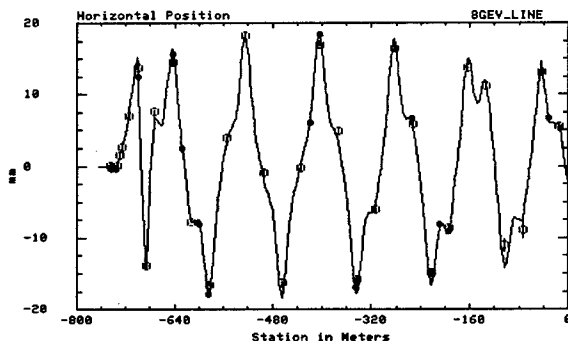


Figure 1. The horizontal plane orbit in the Main Injector 8-GeV transfer line. Circles are data from BPM and solid dots from the profile monitors. The connected line is the calculated orbit.

During the Main Injector commissioning this program has successfully demonstrated its ability to handle data and to provide calculation that reproduces data well [4] [5]. Figure 1 is an example of orbit data and calculation taken from the MI 8-GeV transfer line. Figure 2 shows one-bump data taken from the Main Injector ring at 8-GeV energy. Other data examples will be shown as each components of the program is described.

## 2 BEAM LINE SETUP

The program provides user the ability to edit devices and to configure beamline setup. New setup can be imported

from MAD program files. Existing setup can be exported in MAD input file format for calculation.

Beamline entities such as *Beamline*, *Segment*, *Element*, and *Devices* are used in the program. Figure 3 illustrates the relationships between these entities.

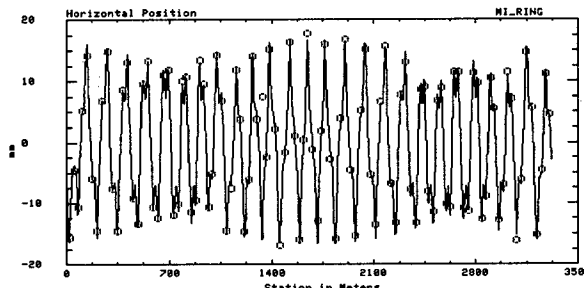


Figure 2. One-bump orbit data taken from the Main Injector. The circles are the BPM data and the connected line is the closed orbit calculation based on the design lattice.

### 2.1 Beamline devices

Two types of devices are used in the program. Physical devices are used in the actual beamline setup. Supplemental devices supply information for the physical devices to implement its functionality.

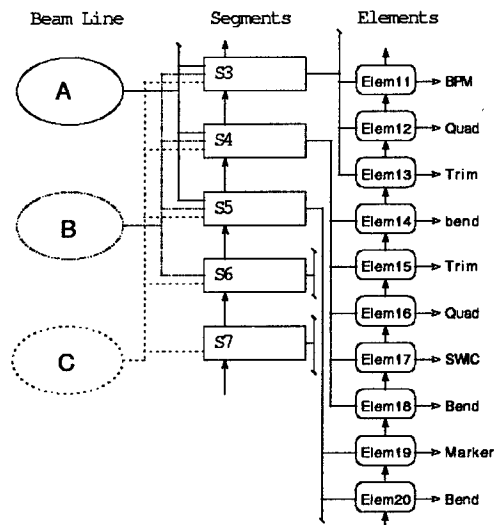


Figure 3. Example of beamline setup hierarchy used in the analysis program for calculation, display, and text listing. Beamline "B" includes exactly segments S3, S4, S5, and S6. "C" is all that plus S7. "A" has segments preceding S3 as well.

Physical devices are subdivided into three categories. Passive devices such as BPMs and Profile monitors keep beam data but do nothing to the beam. Active devices are dipoles, quadrupoles, lambertsons, and electrostatic septa. Others include *Aperture* device that is active only for phase space tracking and *Marker* that does nothing.

There are three kinds of supplemental devices. *Database* devices are used for data acquisition. Through refer-

<sup>†</sup> Work supported by the US Department of Energy under contract DE-AC02-76CH00300.

<sup>‡</sup> E-mail: YANG@FNAL.GOV

ence to the database device the beamline device gets its information. Changes to database devices are reflected by the calculation automatically. *Multipole* device provides integrated strengths in dipole, quadrupole, sextupole, and octupole field for active beamline devices. *Bump* device modifies database value to be referenced by other devices.

## 2.2 Elements

*Element* is the basic block in the calculation and is where data and calculation result are stored. Its function depends on its association to beamline device. *Elements* are sequentially ordered such that each points to its predecessor. An *element* belongs only to one segment.

## 2.3 Segments

*Segments* are also sequentially ordered. Each points to its own predecessor. It can be in multiple beamlines but only once in any one beamline. A valid *segment* contains a number of consecutive elements.

## 2.4 Beamlines

This is the entity on which all calculation, display, and listing are based. A valid beamline includes a number of consecutive segments.

# 3 DATA ACQUISITION

BPM and profile monitor data are needed for optics analysis. Magnet settings and readings are needed for lattice calculation. Other information such as intensity monitor data is also acquired to further document the state of the machine. All relevant data is acquired through the Fermilab accelerator control system with efficiency.

Multiple samples of the beamline at different states during a study of machine responses are supported. The data is analyzed on-line or saved for off-line analysis.

# 4 CALCULATION

Calculations are done for both the upstream and downstream of each beamline element, whenever database devices are modified. Fast response and minimum user intervention are important considerations in the program.

## 4.1 MAD compatibility

The calculation result of the program has been verified to be identical to that of the MAD program except in two cases. The first, MAD program retains the residual roll in its reference coordinate frame after skew dipole and that affects all down-stream elements. Secondly, appreciable difference exists in the calculation of twiss parameters when a skew quadrupole is included in the beamline.

## 4.2 Live

The program is designed such that the lattice calculation is updated using the acquired magnet current data. The recalculation starts the instant new data is loaded.

## 4.3 Lattice

Beam particle transport is the means of all calculation in this program. Execution starts with a chosen beamline, its segments, and to the elements. Element invokes the asso-

ciated device to do the actual transport. Twiss parameters, for example, are calculated by tracking four simultaneous beam particles of different initial conditions.

The program calculates transfer line orbit, closed orbit for synchrotron, twiss parameters, dispersion function, and others. The difference between calculation and the available data is updated along with the RMS deviation.

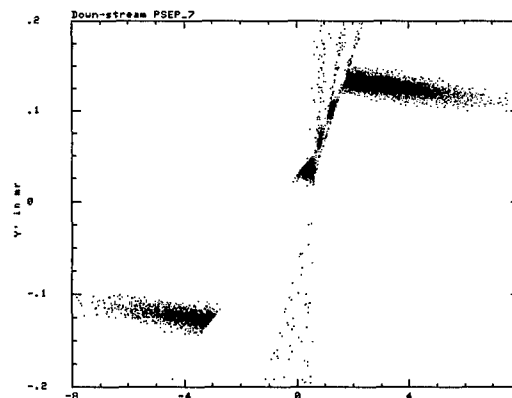


Figure 4. Vertical phase-space plot of result from tracking 10,000 beam particles in a 3-way split simulation.

## 4.4 Tracking

Phase space tracking simulates non-analytical effects due to devices such as electro-static beam splitting septum or aperture restrictions. Figure 4 shows the result of tracking 3-way split through seven septa, as are used in Fermilab Fixed-Target beamline. In this case the three downstream septa used for the second split were poorly aligned and the scattering of beam particles is evident. Figure 5 shows the would-be signal from a profile monitor.

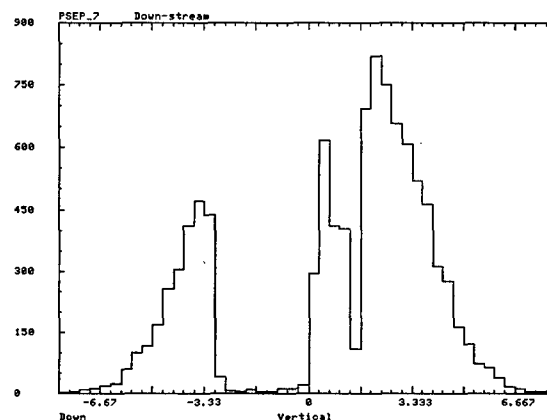


Figure 5. Histogram display here simulates the profile monitor response with tracking result as shown in Figure 4.

## 4.5 Site layout

Site layout calculates the invisible reference trajectory that is assumed in the beam particle transport. Only the dipole bend angles are used to calculate the 3-dimensional site coordinate for each beamline element.

# 5 ANALYSIS

The program provides user the ability to scan through data sets efficiently to identify potentially flawed data set. Analyses supported in the program are described here.



### 5.1 Quadrupole diagnostics

Quadrupole strengths affect the beta function and can be verified using the one-bump orbit data. Consistency between data and calculation is a necessary condition. If available data uniquely determines the quadrupole strengths a sufficient condition is also established. The consequence of having only necessary condition in the lattice analysis will be mentioned in Section 5.4.

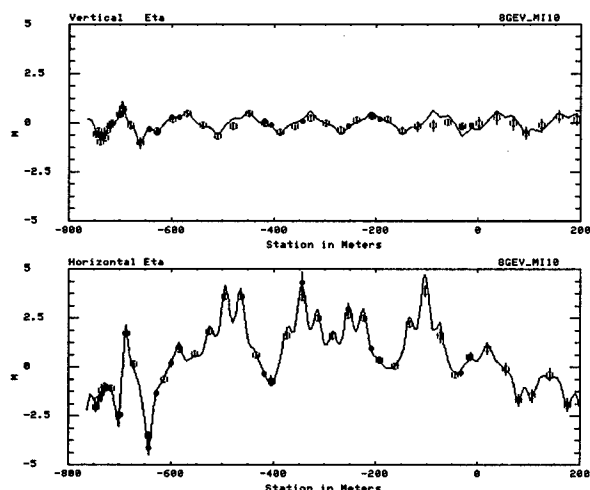


Figure 6. The dispersion function measurement data and the calculation using the optimized initial condition.

### 5.2 Dispersion function

The measurement of dispersion function requires only the knowledge of momentum error used and its accuracy. Figure 5 shows the dispersion function as measured from the new Main Injector 8-GeV transfer line. In a transfer line the initial condition, the bends, and the lattice all contribute to modifying the dispersion function.

### 5.3 Phase advance and beta function

This analysis applies only for the circular machine. In the first step, the BPM data is analyzed against the kick angle of the corrector to get the kick coefficient in "mm/mr". To do the phase analysis at least two data sets from different correctors are needed. Beta function can be calculated using only one data set. The phase advance used can be from data or from model calculation.

### 5.4 Emittance and lattice function

Beam profile width is used for the analysis of transfer line emittances. Given a set of initial twiss parameters and initial dispersion functions the program fits for the emittance and  $\sigma_p/p$ . Figure 7 plots the beam width sigma data from the 8-GeV transfer line and the calculation using fitted emittances and the optimized initial conditions.

This analysis has important implication on the projected lattice function at the end of the transfer line. As mentioned in Section 5.1, the quadrupoles affects the beta function at monitor locations and therefore the outcome. When the quadrupole strengths is not uniquely determined it is still possible that the fitted emittance is free of error. The optimized initial lattice parameters or the projected

lattice function, on the other hand, could be in doubt depending on the location of quadrupole uncertainty.

### 5.4 Miscellaneous

The program offers other analyses that may also be useful. Comparing orbit data against calculation can provide information for BPM calibration. Kick impact coefficient and data correlation can also be calculated.

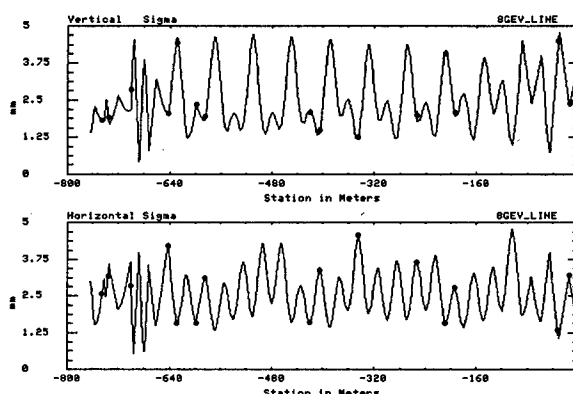


Figure 7. Result of fitting beam emittance to the sigma from profile data from the MI 8-GeV line, using the lattice which best matched the orbit data.

## 6 SUMMARY

The beamline analysis program as described above has performed well as a tool to study transverse beam optics. It is a stand along program with EXCEL like response. It runs on the VAX/VMS, the platform that runs the Fermilab accelerator control system. Its code is optimized to have flexible linkage and yet quick turn-around time for calculation. Features like individual magnet error handling already exist but yet to be explored.

Its ability to import from MAD program output is handy for starting a new setup that is identical to a known calculation. Its internal linkage, however, is vastly different and in order to achieve all the on-line capabilities further setup is required. The program is designed to work on most of the beamlines around Fermilab, with proper setup effort. The flexibility and many display features also make it well suited as an initial designing tool.

## 7 ACKNOWLEDGEMENTS

The author would like to thank G. Goderre for his valuable advises on lattice calculation and analysis.

## 8 REFERENCES

- [1] Hans Groted and F.C. Iselin. *The MAD Program*, 1990, CERN SL/90-13 (AP).
- [2] L. Schachinger and R. Talman, *Particle Accelerator* 22, 1987.
- [3] Accelerator Control NETwork, FNAL.
- [4] S. Assadi, F. Tecker, M.J. Yang, "Optics Measurement of the FNAL Main Injector 8-GeV Transfer Line", *Particle Accelerator conference*, 1999.
- [5] S. Assadi, C.S. Mishra, F. Tecker, M.J. Yang, "Lattice Function Main Injector at 8-GeV", *Particle Accelerator conference*, 1999.

# IS COMPREHENSIVE AND INTUITIVELY USABLE COMMISSIONING SOFTWARE FEASIBLE?

R. Bakker, T. Birke, R. Müller<sup>†</sup>, BESSY, Berlin, Germany

## Abstract

The commissioning period is challenging both for provider and user of accelerator operation software. With increasing knowledge of the specific accelerator new functionalities and methods become important. The variety of implemented features grows until certain standard procedures are settled and the programs can be simplified again for the all day tasks. It is not too difficult to provide the requested functionalities and certain handles for a graphical usage for expert users. For the general member of the commissioning crew, however, the GUI may consist of huge windows, context dependent presentations, hierarchically structured menu trees or compact screens dominated by (modifier) key and mouse click navigation. Understanding and usability of the programs tends to decrease with the increase of available features. By means of examples like the orbit display and control program the problem is outlined and some guidelines leading out of the dilemma are given.

## 1 GENERAL ORIENTATION

The fulfillment of the apparent requirements for a graphical user interface (GUI) on a windowing system is the easy part of the design for an accelerator man-machine interface. Windows should not be too large. This would often hide other relevant information. They should not be too small to be readable. Behaviour and appearance should be uniform and consistent. Conflicts, inconsistent or harmful usage has to be prevented by protection mechanisms within the code. Configuration of action elements (e.g. menus) should be determined by the actual program context.

In addition control software should obey some general rules that help to shuffle around the piles of windows. E.g. standardized head lines with a color coded title help to identify the scope of the application like accelerator part or device class involved. An 'About' button popping up author, version number and program status information helps to find the competent expert to get pointed support.

## 2 INFORMATION FINDING

The first obvious approach to give access to program functionalities would be an open arrangement of controllers on a flat screen. As the windows get overloaded or too big grouping of entries according to common area of functionality becomes necessary. This may be done by hierarchies of sub-windows or menu trees. Often the unifying root

entry is no more unique and meaningful. A not very precise search is required to find the desired function. One solution is to offer multiple ways to accept user entries simultaneously: menu, buttons on subwindows and keyboard shortcuts. The other way is to aim at very compact screens built from a few well designed and possibly multi-functional elements. A well designed example is the CERN wheel switch[1] (see Fig. 1).

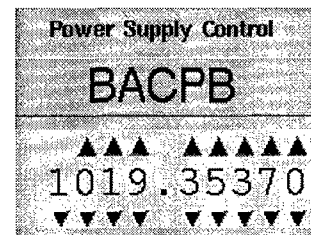


Figure 1: Wheel switch—example of a well designed widget

It can be operated in a secure way with mouse clicks, keyboard arrow keys and by entering the numeric value. The input field accepts only numerical digits. The accessible MIN/MAX values are apparent. Since it scales nicely it fits into most panel layouts.

The commercial XRT/graph[2] widget is another example. It supplies various convenient zooming, printing and data presentation options. The programming interface allows to install dedicated zooming grids, to attach pop-up labels to each data point, to (de)select points and to drag values.

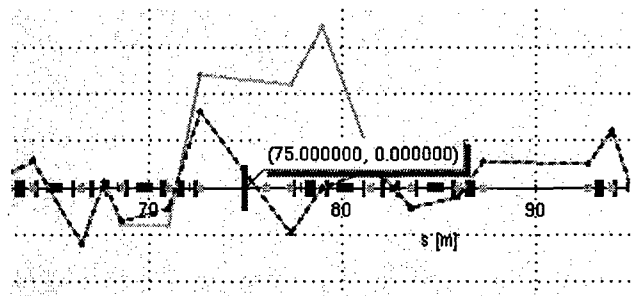


Figure 2: Clipping of a display showing the actually measured orbit data and the predicted effect of a 4-bump with angle and amplitude specified at 75.0 [m]

Fig. 2 gives an impression how it can be used to display the measured orbit and the predicted effect of a closed bump. The target position of the bump (long vertical bar) can be freely placed with arbitrary precision by zooming into the lattice and selecting the location with a mouse click. Experts like it, regular crew members are reluctant

\*Funded by the Bundesministerium für Bildung, Wissenschaft Forschung und Technologie and by the Land Berlin

<sup>†</sup> Email: mueller@bii.bessy.de

to memorize the corresponding mouse button bindings.

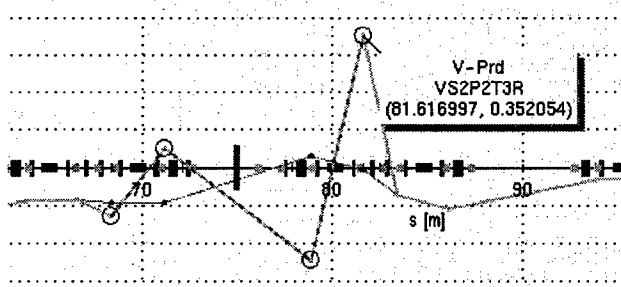


Figure 3: Clipping of a display showing the actual corrector set points and the new values the program would send to 4 power supplies to modify the orbit at 75.0 [m] as predicted in Fig. 2. The new set point of vertical corrector VS2P2T3R at 81.62 [m] will be 0.352054 [A].

Fig. 3 shows the corresponding corrector set point screen. The power supplies forming the closed 4-bump are selected by clicking into close vicinity of the desired element. As in the orbit screen device names, location and precise set points are accessible through pop-up labels.

During commissioning it frequently happens that newly released functionalities are hooked into the existing application tree as it is found to be adequate. After a time of experience or by adding other new features a better, cleaner and extendible structure becomes visible and the tree is adapted. Some users quickly accommodate to the new differing behaviour, others tend to feel lost and call for support.

### 3 BASIC PROGRAM UNDERSTANDING

Complexity and severity of actions caused by user request differ drastically. A mouse click may e.g. shuffle down a window and some pixels apart it may shut down a 1000 [A] power supply loosing valuable beam time. Conventional means to emphasize these differences are color coded 'dangerous' buttons, pop up confirmation windows, or blocked actions in inappropriate contexts.

However, there is a wide grey area where it seems to be impossible to give additional guidance. E.g. most users know that programs continue to run even if moved to another workspace or iconified. The majority would be annoyed if one would disallow iconification of a running correction algorithm to prevent it getting out of sight.

Where the perception of a certain action disagrees with reality the unrecognized misuse causes misleading problem descriptions and is a constant source of errors. An example is a user tuning the machine and saving several 'good' set points to the dedicated persistent memory fields[3] to be able to return to these values. For comparison with a reference he eventually reloads a snapshot file. As a specified behaviour all saved values are overwritten by values from the file. If the user is not aware of this sideeffect he notices an unexplainable modification of the data set he just worked on and reports an unreliable behaviour of the control system.

There is no self-explaining way of mapping commissioning progress into the system. E.g. during beam threading times the fluorescent screens are frequently needed and have to be freely and conveniently movable. As soon as beam based procedures prevail it is favourable to freeze the top level fluorescent screen drive buttons when reinjection is not possible. This prevents accidental beam loss. Of course on a lower layer the operator can force the screen to drive in. Without explicit explanation the user would notice a change and assume a malfunction. From his previous experience he would generally not be able to classify the new behaviour as a feature.

In another class of inappropriate understanding simple elementary assumptions about basic knowledge disagree. A programmer supplying a filter for the selection of device subsets takes the syntax of a regular expression for granted - which is unknown to a user not familiar with the underlying tools. The filter is then error-prone and of very limited use.

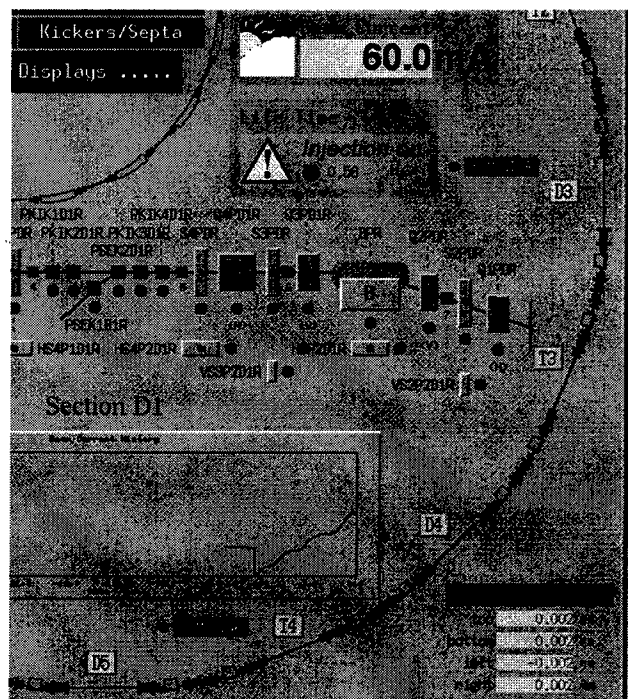


Figure 4: A complex synoptic view: action buttons, status information, related displays, performance summaries and active per-sector arrangements of the installed devices

For a power supply it is not acceptable if a new setpoint would require adjustment of internal regulator parameters until the required output current is delivered with the specified stability. This has to be already adjusted in the laboratory. Comparable tuning of the new accelerator requires beam under various conditions. Relevant parameters have to be identified and determined during commissioning. The meaning of necessary parameters require three levels of understanding. (1) basic elements: a user pushing a 'correct' button in an orbit control program has reasons to expect an action that results in an improved orbit. (2) program

intrinsic: information content of difference orbits comparing 'actual' and 'old' data is ambiguous if the knowledge is missing that 'old' denotes the orbit measured when a prediction/correction has been made or a 'Set Ref.' button has been pressed and 'actual' means the constantly updated one. (3) applied methods: to be able to set the cut off factor for the eigenvectors of a SVD correction procedure to a reasonable value one has to know in principle how the SVD algorithm works. During commissioning the number of adjustable parameters grows in level (2) and especially in (3). But as soon as the correction procedures are settled level (2) and (3) will collapse to a few action buttons and the rest disappears for the regular user.

## 4 USER DEPENDANT ABSTRACTION LEVEL

Synoptic views are a combination of navigation tool, documentation, aid to memory and fault detection facility (see Fig. 4). For the entry level user they are a kind of tutorial access to the control system. At a running facility synoptic views disappear. They are replaced by more efficient tools. Example is an alarm handler, which is a much faster, complete and selective fault detection tool than the human scanning of synoptic screens (see Fig. 5). But it is abstract, corresponds to a programmers view and does not meet the expectation of a running-in crew. At the beginning of commissioning a balanced compromise between pictorial and abstract tools is required.

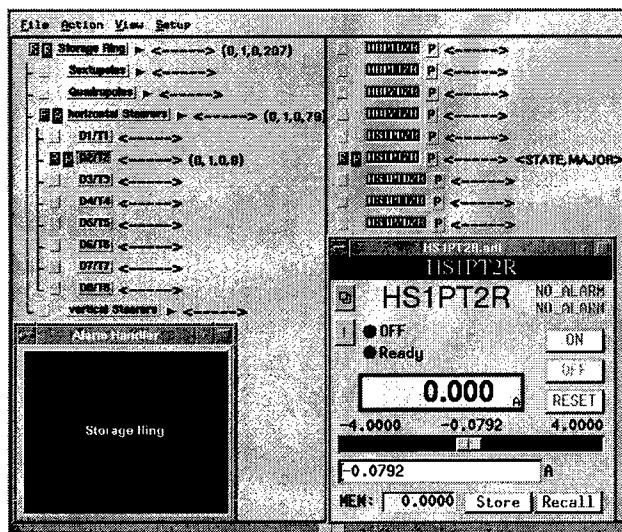


Figure 5: Alarm handler: the main button (lower left) starts blinking, clicking opens the tree leading to the faulty device(s), the 'P' button opens the device control panel suited to fix the problem.

An orbit measurement tool needs code for data handling, statistical evaluation, comprehensive display etc. A visual orbit correction tool needs most of this code too. In addition to the orbit data the corrector set points, conversion

factors, drive limits etc. have to be administered. With respect to management of all data orbit modifications by closed bumps and orbit flattening procedures are closely related orbit control tasks. Furthermore the described functionalities are very similar for any accelerator, especially for the different accelerator sections transfer line, synchrotron and storage ring. With respect to code re-usage and simultaneous development it is an efficient approach for a programmer to implement all functionalities named above within one generic program. The GUIs for the different accelerator sections and the corresponding specific functionalities are the remaining individualized code fragments that have to be adapted.

Typically operators have a different view. They have to concentrate on one task: orbit measurement *or* orbit correction *or* bump modifications. Additional elements superfluous for this task are disturbing, distracting, making an efficient usage of the program more difficult. It would be a considerable improvement to provide distinct GUIs for the elementary tasks measurement, correction and bump. They should contain only elements that are relevant for the specific context. In addition each of these instances should have a user mode with all default values set and hidden and an expert variant with full control of all parameters. Preference has to be given to a separate instantiation over an additional expert screen. Experienced users find additional navigation effort caused by expert level windows annoying. With the GUI server used at BESSY[4] these modifications would not be very complicated or hard to maintain - it simply has not been thought of.

## 5 SUMMARY

Complex software tasks like providing accelerator commissioning programs require a certain amount of teaching how the software is meant to be used. Providing concise manuals is mostly not sufficient. One has to allow for a learning time until a precise use of the tools is possible. Functionalities of effectivity-enhanced expert modes are appreciated later. Due to shortage in man power and a transient nature commissioning software can not compete with the streamlined and consistent graphical user interfaces of commercial packages. Further more the constantly ongoing software development under time pressure is accompanied by newly introduced bugs that did not show up during tests. This adds complexity to an already difficult situation.

## 6 REFERENCES

- [1] The wheel switch widget has been originally developed at CERN (Contact: [Franck.DiMaio@cern.ch](mailto:Franck.DiMaio@cern.ch)). Later other laboratories (ESRF, BESSY) contributed.
- [2] XRT/graph is a trademark of KL Group Inc., Toronto, Ontario
- [3] R. Bakker, T. Birke, B. Kuske, R. Lange, R. Müller, 'Experiences with Commissioning Software Tools at BESSY II Status', this conference (MOP31).
- [4] T. Birke, R. Lange, R. Müller, Proceedings of the 1995 ICALEPCS, Chicago, 1995, p.648

# SOFTWARE ENGINEERING PRACTICES FOR CONTROL SYSTEM RELIABILITY\*

S. K. Schaffner, K. S. White<sup>#</sup>

Thomas Jefferson National Accelerator Facility, Newport News, VA

## Abstract

This paper will discuss software engineering practices used to improve Control System reliability. We will begin with a brief discussion of the Software Engineering Institute's Capability Maturity Model (CMM) which is a framework for evaluating and improving key practices used to enhance software development and maintenance capabilities. The software engineering processes developed and used by the Controls Group at the Thomas Jefferson National Accelerator Facility (Jefferson Lab), using the Experimental Physics and Industrial Control System (EPICS) for accelerator control, are described. Examples are given of how our procedures have been used to minimize control system downtime and improve reliability. While our examples are primarily drawn from our experience with EPICS, these practices are equally applicable to any control system. Specific issues addressed include resource allocation, developing reliable software lifecycle processes and risk management.

## 1 INTRODUCTION

Jefferson Lab, a multi-use facility consisting of a Continuous Electron Beam Accelerator simultaneously serving three experimental halls and a Free Electron Laser outfitted with six user labs, is unique in its use of a single control system lab-wide. Both machines, along with their respective experimental areas and cryogenic facilities, use EPICS for their control and monitoring needs. EPICS is the result of a collaboration, which began in the early 1990's, between Los Alamos National Laboratory and the Advanced Photon Source at Argonne National Laboratory. Jefferson Lab is currently the second largest EPICS site in a collaboration that now encompasses over 100 laboratories and universities worldwide.

While EPICS continues to develop to include more capabilities, it is important to note that EPICS is a toolkit, providing development tools and runtime programs, to form the core of a complete control system based on the standard model.<sup>1]</sup> Known as an attractive alternative to the previously popular approach of custom coding all control system functions at each facility, EPICS embodies software sharing at its best. The functions provided by the collaboration represent the core requirements for most

modern control systems: control algorithm development and execution, data monitoring, storage, retrieval, and visualization, and network communication between front and back-end processors. Specific control algorithms, invariably different between sites, and some device drivers, must be implemented by each facility using EPICS development tools. These tools allow programmers to generate a combination of code and configuration files used to direct EPICS runtime programs. Using this approach, EPICS provides a well-tested core for a complete control system that behaves according to site-specific instructions.

Using code generated by other laboratories saves programming effort by eliminating the duplication of effort present when recreating commonly used functions at each site. Additionally, all sites benefit from the experience and expertise gained by others through their use of EPICS. The base code provided to the EPICS community benefits from more development effort and testing than could be achieved by a single site. However, using EPICS does not eliminate the need for software engineering and programming efforts at each site. The EPICS installation itself, specific control programs, and configuration data must be supported. Most often, this support includes software development, maintenance, and upgrade activities. While managing this body of collaborative and site specific software in a way that provides consistent, reliable controls for machine operations can be challenging, it is not substantially different than managing other software projects of similar size and complexity. Such management requires reliable processes suited to the needs of the project and staff.

While Jefferson Lab is operational, there are still many upgrades in progress and planned for the future that require modifications to existing control programs or the development of new code. Additionally, these upgrades must be accomplished during brief scheduled maintenance periods with limited time for testing. These project requirements mean we must be able to quickly install new software, perform tests and restore the operational machine. These needs have driven the development of an appropriate Applications Development Environment and corresponding software management processes.

\* Work supported by the U.S. Department of Energy, contract DE-AC05-84ER40150

<sup>#</sup> Email: karen@jlab.org

## 2 STANDARD PRACTICES

It is common for software organizations to develop their own internal standards and practices, but this effort can be streamlined by studying current best practices and incorporating this information in a way that is locally appropriate. Standard practices can provide proper guidelines, help prioritize the implementation of new processes, and be used as a checklist to ensure all necessary process areas are covered.

As the software industry grows and matures, much has been studied and written regarding software engineering practices. The most complete and definitive work on this topic, CMM, comes from Carnegie Mellon University's Software Engineering Institute (SEI).[2] This well documented model provides a framework for evaluating and improving key practices used to provide reliable software development and maintenance capabilities. Using a maturity based approach, CMM gives the software engineering community an effective and standardized means for modelling, measuring and defining software development processes. The model defines five levels of maturity, summarized in Table 1, and details the underlying principles and practices needed to improve process maturity and thus produce more robust, reliable, maintainable software systems. CMM recognizes that such improvements require ongoing effort and provides a framework to help organize and prioritize this effort. This model is very useful because the information is easily accessible and applicable regardless of the systems, projects, languages or techniques involved. The model allows software engineers to assess their systems to determine the current maturity level and the needed maturity level based on risk factors. Once this assessment has been done, process improvement can be introduced over a period of time, in parallel with project development. While it is ideal to have software processes defined and in use from the beginning of a project, in reality it seldom works this way. CMM allows processes to be added as the project grows and transitions from the development stage to an operational system.

Table 1:

Level	Characteristics	Focus Areas
1 Initial	Chaotic, few if any processes	None
2 Repeatable	Processes for management	Requirements Management Project Management
3 Defined	Processes for management and engineering	Training Process Definition Risk Management Project Performance
4 Quantified	Mechanisms to measure processes and quality	Quantitative Process Measurement Quantitative Quality Measurement
5 Optimized	Process optimization	Innovation and Improvement

Most typical software efforts in non-commercial, research oriented environments, like laboratories, begin at Maturity Level 1. Employing even a few of the CMM techniques can ensure that the project does not also end there. Left to their own devices, software engineers usually develop some processes resulting in varying levels of product quality. The challenge is getting all members of a software development group to adopt the same reliable practices. Adopting standard practices, like those described in CMM enables this to occur consistently and at the correct priority. In order to ensure success, it is important that the software development staff develop the actual process definitions. This ensures efficient processes without unnecessary overhead. The role of management is to specify the process goals and support the development and use of the resulting processes. Taking this approach usually results in maximum adherence to the processes and standards since the developers appreciate the benefits of the methods. Additionally, a properly designed and implemented development process will increase the efficiency of programmers by providing tools to execute redundant tasks, thus saving time and ensuring consistency, a key to reliability.

## 3 PROCESSES AND TOOLS

As with most projects, Jefferson Lab's control system development began as a chaotic effort. Over time, and without the benefit of CMM, the Controls Group naturally implemented processes designed to aid in the software development lifecycle. The group first began looking at the process of requirements management. This arose out of a need to organize the haphazard approach to system specification that produced few if any useful requirements documents. Requirements were received from many different customers, sometimes verbally, some requirements conflicted with others, and all were labelled high priority. Written requirements often did not exist or did not contain the kind of information needed to proceed with a project. To put order to this chaos, we developed a template for software requirements that was used to structure the information received and ensure that all necessary information was acquired. Additionally, for software that was to be used by multiple groups at the lab, meetings were scheduled with representatives from each group to aid in resolving conflicting requirements. Establishing this standard template quickly improved the requirements gathering process and ensured there was a documented baseline for each major subsystem. In order to continue to benefit, the documents must be updated when new features are requested. Although updates can be difficult to sustain, especially with frequent upgrade requests, they pay off during system maintenance and subsequent upgrade work.

Faced with a seemingly endless list of tasks and a fixed number of software engineers, we next focused on

methods for project planning, tracking and resource management. These issues were addressed by the development of a software task database to document requests, assign priorities and resources, and track progress. For larger projects, preliminary meetings are held to help determine the scope and complexity of the software effort to make advance planning easier. The group leader prioritizes requests based on lab-wide goals, customer input, and resource availability, and keeps the database information up to date. Another tool is employed by the software engineers to track changes to software as upgrades occur. This information is integrated into the configuration management system accessible via the World Wide Web and is also used to facilitate software quality assurance.

A number of tools and techniques have been developed to improve software quality and minimize controls system downtime. Software testing can be difficult due to the lack of adequate off-line facilities and limited machine test time. Before any software is installed in operations, a testplan is written documenting the application, software test procedure, and roll back information in case problems arise after beam operations commence. The testplan is reviewed and scheduled by a team leader. In addition to the application specific tests, machine maintenance periods are followed by a comprehensive control system quality assurance procedure. This ensures all controls computers, applications and communications are functioning correctly. The Controls Group also provides 24 hours on-call support for operations. The software on-call person is always available via pager and is trained to either solve problems that arise or to contact the system expert if needed. Even if software quality assurance led to error free operational code, control system on-call support would be needed to handle hardware failures and situations where new operational procedures introduce disruptive resource loading. It is interesting to note that the frequency of off-hours calls has been significantly reduced since the testplan process has been put in place and control system downtime has dropped as well.[3]

Another aspect of our software process involves configuration management. A source code structure has been adopted making it possible to introduce automated tools to create, version, and install operational software. These tools enable software developers to quickly load new code and roll back to previous versions, greatly enhancing reliability by insuring that all process steps have been consistently applied to each application. In addition to reliability improvements, such tools make the

developers' job easier by automating lengthy installation steps that were previously typed by hand.

## 4 CONCLUSION

At Jefferson Lab, the development and use of good software development processes has improved the quality of our software and reduced machine downtime due to control system problems. Because we inherited an unorganized development effort in progress, we have introduced new processes one at a time, phasing in supporting tools as time allowed. Our experience developing these processes and tools has led us to define the following list of characteristics of good software processes:

1. Processes are developed by those who will use them.
2. Processes are supported by management.
3. Processes take into account project and developer needs.
4. Processes make programmers' work easier, more efficient.
5. Processes produce repeatable, consistent results and automate repetitive steps.
6. Processes are documented and publicly available.

This list is useful to help design new processes and evaluate existing processes for possible improvements. We plan to continue developing and improving our processes using SEI guidelines such as the CMM framework. By standardizing our development approach and prioritizing work, we have been able to improve programmer productivity and reduce the level of stress and pressure on the group. The number of operational control system failures has been reduced along with the associated lost time. We have found the time invested in developing good processes has been well worth the effort, and believe that more improvements can be made.

## 5 REFERENCES

- [1] M. E. Thuot, L. R. Dalesio, "Controls System Architecture: The Standard and Non-Standard Models", Proceeding of the 1993 Particle Accelerator Conference", Washington D. C.
- [2] Mark C. Paulk, Charles V. Weber, Bill Curtis, "The Capability Maturity Model: Guidelines for improving the Software Process (SEI Series in Software Engineering), Addison-Wesley Publishing Company, June 1995.
- [3] K. S. White, H. Areti, O. Garza, "Control System Reliability at Jefferson Lab", ICALEPCS'97 Proceeding, Beijing, China.



# USING SERVERS TO ENHANCE CONTROL SYSTEM CAPABILITY\*

M. Bickley, B. A. Bowling<sup>#</sup>, D. A. Bryan<sup>+</sup>, J. van Zeijts<sup>\*</sup>, K. S. White, S. Witherspoon,  
Thomas Jefferson National Accelerator Facility, Newport News, VA

## Abstract

Many traditional control systems include a distributed collection of front end machines to control hardware. Back end tools are used to view, modify, and record the signals generated by these front end machines. Software servers, which are a middleware layer between the front and back ends, can improve a control system in several ways. Servers can enable on-line processing of raw data, and consolidation of functionality. In many cases data retrieved from the front end must be processed in order to convert the raw data into useful information. These calculations are often redundantly performed by different programs, frequently offline. Servers can monitor the raw data and rapidly perform calculations, producing new signals which can be treated like any other control system signal, and can be used by any back end application. Algorithms can be incorporated to actively modify signal values in the control system based upon changes of other signals, essentially producing feedback in a control system. Servers thus increase the flexibility of a control system. Lastly, servers running on inexpensive UNIX workstations can relay or cache frequently needed information, reducing the load on front end hardware by functioning as concentrators. Rather than many back end tools connecting directly to the front end machines, increasing the work load of these machines, they instead connect to the server. Servers like those discussed above have been used successfully at the Thomas Jefferson National Accelerator Facility to provide functionality such as beam steering, fault monitoring, storage of machine parameters, and on-line data processing. The authors discuss the potential uses of such servers, and share the results of work performed to date.

## 1 INTRODUCTION

The classic control system in use in many locations today consists of a collection of front end machines, distributed around a facility, largely in order to keep them close to the hardware they are controlling. These front end machines are interfaced directly to the hardware, and are responsible for maintaining variables associated with the hardware, as well as responding to queries about the state of or modifying settings for the hardware.

The users view the system from the point of view of the back end machines. These machines, often UNIX machines or PCs, run applications programs which modify the settings of hardware, display values from hardware, and monitor the control system's behavior.

Very frequently, the raw information obtained from the front end machines is not directly useful to the users, but needs to be processed in some way to make sense. Doing this in a back end program has the advantage of moving processing from the front end servers to the back end servers, which are generally less critical to the real-time control of the hardware, therefore reducing the overall load on the critical systems. This approach has several disadvantages, however.

One disadvantage is that if many programs need to look at some new value which is derived from several control system variables, each must calculate these new values independently. This increases the resource consumption on the back end servers, the chance of introducing errors into the system, and the development time for each new application that must support these new values. Additionally, these new derived values will generally not be directly available for archiving, viewing, or monitoring by traditional tools designed for direct monitoring of control system values.

## 2 MIDDLEWARE SERVERS

### 2.1 What is a middleware server?

The solution to these problems taken by the authors is to develop middleware servers. A middleware server is a program, a "software server", which obtains data from the front-end servers, calculates new values, and creates virtual control system variables for viewing by back end tools. The goal of the middleware server is for it to be virtually transparent to the user – the user should not be concerned with whether the variables are obtained directly from the front end machines or are virtual variables on a middleware server. In addition, the algorithms used to derive these new values are located in one point, and easily be modified without the need to modify the client programs.

### 2.2 Middleware servers at Jefferson Lab

At the Thomas Jefferson National Accelerator Facility (JLab), the front end machines are dedicated machines running WindRiver System's VxWorks, and EPICS, the Experimental Physics and Industrial Control System [1]. These systems monitor and control many aspects of the

\* This work was supported under U.S. D.O.E. contract #DE-AC05-84ER40150

<sup>#</sup> Now with Arrow Electronics, Baltimore MD

<sup>+</sup> Email: bryan@jlab.org

<sup>\*</sup> Now with BNL, Upton NY



machine, from magnets for beam optics, to beam position monitors, to cryogenics.

The back end tools at JLab are run on HP-UX UNIX machines, and consist of a mixture of the general purpose EPICS tools, such as viewers, archivers, and machine configuration save and restore tools, as well as in house developed applications. In addition, JLab uses a higher-level protocol called CDEV, for Common DEvice [2]. CDEV provides the advantage of making EPICS variables, and variables from other sources available to the user in such a way that they can be accessed with the same interface. Many of the existing tools for EPICS are being ported to CDEV, and much of the new development at JLab is based on CDEV.

CDEV is particularly well suited to developing servers, since a Generic Server engine is provided [3]. This is a simple software construct that can be used to rapidly develop middleware servers. It provides the framework for monitoring existing values from the control system, and for creating new attributes to be monitored by the back end servers. While enhancements to this framework are sometimes needed when developing an application, the developer is generally free to concentrate on developing the algorithm associated with processing the data, rather than being concerned with the framework and communications structure.

### 3 USES FOR SERVERS

There are many ways middleware can be used. As the authors continue to develop applications, more uses for these servers present themselves.

#### 3.1 Servers as online data sources

One of the primary areas in which servers are useful is in providing or storing information to the control system that would otherwise either not be available, or that might be stored in front end machines needlessly. The servers can be constructed to contain CDEV variables that can be read, set, or monitored by users. These values do not need to come from the front end servers, but can be standalone values. Virtually any arbitrary value, from the names of the current operations crew to theoretical machine parameters can then be used just as if they were control system values.

Additionally, these servers can be built with logic of their own. While still not manipulating the control system, they can be loaded with theoretical values for certain parameters, and calculate new values from these, perhaps using one or more control system values in the computation. Since such servers run on inexpensive UNIX workstations, the load of performing these calculations is moved off of the front end computers.

At JLab, our Model Server Artemis is an example of such a server [4]. Two instances of this application are used. Both are initially loaded with the theoretical optics for the machine. The second instance of the model is the

periodically updated with actual values for components from the machine. Based on these input values, transfer matrices, alpha and beta values etc. are calculated and made available to optics applications.

Additionally, information about the locations of signals (which front end server a particular channel resides on) is stored in such a server. This is used, along with modified versions of back end tools, to speed connection time when accessing control system channels [5].

#### 3.2 Servers as controllers

Another useful application of the server is as an actively controlling program. In this capacity, the server functions as a less deterministic feedback system. The server monitors a number of values related to certain parameters of the control system. Based upon these values, new parameters are calculated and loaded back into the machine. This can continue periodically. In addition, the server allows the controls for the algorithm, such as parameters, whether to apply changes or not, etc., to be made available as control system signals. This makes monitoring and controlling the behavior of the server simple.

At JLab, we use such servers for several beam control applications. Three servers fall into the category of "locks". These servers monitor parameters of the beam – position within the beampipe, energy, and current – and try to "lock" them to some predefined value [6]. This is accomplished by reading the current value of the parameter one wishes to lock, calculating new values for parameters that modify the desired parameter, and applying those changes to the control system. As an example, for beam position one would read the values of BPMs (Beam Position Monitors), determine where and by how much the beam is deviating from the ideal, and apply changes to steering magnets to return the beam to the optimal location. These servers perform these checks every 1 to 5 seconds, depending on the configuration of the accelerator.

#### 3.3 Servers as monitoring systems

Servers can also be used to provide online monitoring of values in the system for diagnostic purposes. Most control systems provide some mechanism for noticing if a single signal exceeds predefined limits and bringing this to the operators attention. Servers provide the benefit of monitoring multiple signals and inferring when a value is bad based upon its relationship with other signals.

The server can also monitor values from multiple signals, and calculate new values from these signals – a "value added" signal. As in the case of the online data sources, doing the processing at the server level saves CPU load on the front end servers, leaving them free to control hardware. It is also superior to calculating these in the client program if multiple clients need this combined information.

At JLab, this style of server is used for enhanced alarm servers, which monitor special parts of the machine and alert operators of trouble based on complex algorithms involving multiple signals. Additionally, this style of server is used in a program which calculates changes to the machines energy at a very low level, allowing interested parties to notice changes in the system.

Additionally, a new more generic form of this server is being explored. The proposed tool, called the Automator, is intended to allow for generic, user defined instances of such a server to be created and used [7]. The server could monitor for specific alarm conditions and, optionally, take predefined actions when such conditions occur.

### 3.4 Servers as caching devices/concentrators

Finally, servers can be used to cache or concentrate signals that are frequently accessed. By modifying the information flow so that the back end clients access the middleware server rather than the front end machine directly, the load on the front end machines is reduced, again freeing these machines for hardware control and processing. This type of server is often combined with some of the functionality of the monitoring servers mentioned above.

At JLab, we use a hybrid of this type of server and a monitoring server for BPM data. With many BPMs, and many applications interested in using them, we created a server to monitor this data. Multiple clients then connect to the middleware server, rather than connecting directly to the front end machine, which now has less connections to service.

Our server also provides several additional services. It monitors the status information provided by the BPMs and produces enhanced status information. It filters out transient failures in the BPMs, and attempts to ensure that different attributes of information about a given BPM are correlated in time. This ensures that the client sees an accurate picture of the machine status.

## 4 EXPERIENCE

The experience the authors have had with these servers has generally been positive. These servers seem to provide a reliable, simple way of implementing what would otherwise be very complex actions. There have been problems associated with these servers, as there are with all software applications, and perhaps a tendency to use the tool to try to solve all problems, but the concept seems to be very sound.

The authors have also found that these servers have practical limits to how large or how rapidly they can process information. Since these servers are monitoring values, and posting monitors to clients on changes, one must be careful not to overburden the code. One server developed on site attempted to process one hundred million events (changes in the control system that required modification to virtual variables) per day, or about 1000

events per second. The peak load during transient events (such as beam turning on or off) was much higher than 1000 events per second. This server exhibited occasional problems with coherence with the control system, particularly immediately following high event count peaks. The solution was to split this server into small servers, to reduce the high number of events handled.

Similarly, the active feed back programs, or locks, have a limit on how fast they can process. This is partially determined by the algorithm and the time needed to calculate a solution, but is also limited by the time needed to monitor the signals from the control system. For numerically intensive calculations a feedback loop of approximately 1Hz. seems to be a comfortable top speed for such servers, when running on a Hewlett Packard K-class machine.

## 5 CONCLUSION

In conclusion, these servers offer the developer a powerful tool for enhancing capability, often without the need to further burden front end servers or modify tested, working front end code. It is not a panacea for every control system problem, but when used properly is a powerful and effective way of addressing certain software problems.

## 6 REFERENCES

- [1] [http://www.aps.anl.gov/asd/controls/epics/EpicsDocumentation/EpicsGeneral/epics\\_overview.html](http://www.aps.anl.gov/asd/controls/epics/EpicsDocumentation/EpicsGeneral/epics_overview.html)
- [2] J. Chen, G. Heyes, W. Akers, D. Wu and W. Watson III, "CDEV: An Object-Oriented Class Library for Developing Device Control Applications", Proceedings of ICALEPCS 1995
- [3] W. Akers, "An Object-Oriented Framework for Client/Server Applications", Proceedings of ICALEPCS 1997
- [4] B. A. Bowling, W. Akers, H. Shoaee, W. Watson, J. van Zeijts, S. Witherspoon, "Evaluation of a Server Client Architecture for Accelerator Modeling and Simulation", Proceedings of CAP 1996
- [5] D. Jun, D. Bryan, W. Watson, "Centrally Managed Name Resolution Schemes for EPICS", Proceedings of ICALEPCS 1997
- [6] J. van Zeijts, et al., "Design And Implementation Of A Slow Orbit Control Package At Thomas Jefferson National Accelerator Facility", Proceedings of PAC 1997
- [7] D. Bryan, M. Bickley, K. White, "The Automator : Intelligent Control System Monitoring", these proceedings (1999)

# THE AUTOMATOR : INTELLIGENT CONTROL SYSTEM MONITORING\*

M. Bickley, D. A. Bryan<sup>\*</sup>, K. S. White,

Thomas Jefferson National Accelerator Facility, Newport News, VA

## Abstract

A large scale control system may contain several hundred thousand control points which must be monitored to ensure smooth operation. Knowledge of the current state of such a system is often implicit in the values of these points and operators must be cognizant of the state while making decisions. Repetitive operations requiring human intervention lead to fatigue, which can in turn lead to mistakes. The authors propose a tool called the Automator based on a middleware software server. This tool would provide a user configurable engine for monitoring control points. Based on the status of these control points, a specified action could be taken. The action could range from setting another control point, to triggering an alarm, to running an executable. Often the data presented by a system is meaningless without context information from other channels. Such a tool could be configured to present interpreted information based on values of other channels. Additionally, this tool could translate numerous values in a non friendly form (such as numbers, bits, or return codes) into meaningful strings of information. Multiple instances of this server could be run, allowing individuals or groups to configure their own Automators. The configuration of the tool will be file based. In the future these files could be generated by graphical design tools, allowing for rapid development of new configurations. In addition the server will be able to explicitly maintain information about the state of the control system. This state information can be used in decision making processes and shared with other applications. A conceptual frame work and software design for the tool are presented.

## 1 INTRODUCTION

Distributed and networked control systems have become very common for use in the control of large scale experimental systems, such as particle accelerators or telescopes, as well as for industrial control systems. As the scale of these control systems has increased, the number of parameters for controlling the system has increased as well. A large modern control system may have as many as a quarter million control parameters.

With such a large number of control parameters, determining the overall status of the control system or of

large subsystems has become difficult. This high-level view can be thought of as a "meta-parameter", a value which implicitly contains information obtained from many individual signals.

Users often must view tens or even hundreds of signals and infer the state of the machine from these values. Archiving information about these "meta-parameters" is difficult since one needs to archive the many individual signals and later post process the data to obtain these meta-parameters. This increases the volume of information that must be archived. Clearly it would be better to be able to dynamically monitor the individual values and create this "meta-parameter" as a single control system variable.

## 2 PRACTICAL CONSIDERATIONS

There are many ways to implement these meta-parameters, but some considerations could make them more useful. At an existing facility, there is most likely a large collection of tools in place to deal with existing control system parameters. These tools would include viewers, archivers, dynamic data analysis packages, etc. The tools are usually well tested and the operations crew is familiar with their use. This situation makes it desirable for the new meta-parameters be available to the control system using the same protocol as the existing signals. This approach allows for maximum code reuse.

Most facilities control hardware with a collection of front-end machines which monitor the hardware and make information about the hardware available to the control system as signals. The tools mentioned above run on back-end machines, often UNIX or PC based.

One approach to solving this problem would be to simply create a new signal on the front end server that contains the meta-parameters. This could be implemented via communication between front-end machines. In practice, this presents a number of problems. First, the front-end machines are usually responsible for critical operation of the hardware. As such, increasing the workload of these machines or modifying tested software is often undesirable. In addition, the meta-parameters that one is interested in may change frequently, perhaps even while the system is running. If these variables are placed directly on the front-end machines, modifying them could interfere with the operation of the control system.

Similarly, placing the processing of these meta-parameters in each client has drawbacks. Each client must be modified in order to use the new variables, and

\* This work was supported by U.S. D.O.E. contract #DE-AC05-84ER40150

\*Email: bryan@jlab.org

each must keep a separate copy of the logic needed to infer the meta-parameter from existing variables.

### 3 IMPLEMENTATION AS MIDDLEWARE

The authors have decided to implement the desired functionality using a middleware server [1]. Such a server is a piece of software which monitors signals from some source, in this case the front-end machines. These servers then produce new signals for the destination, such as the back-end machines. One can then treat these signals in the same way as the original signals. These new channels are often called virtual signals.

At the Thomas Jefferson National Accelerator Facility (JLab), there has been considerable positive experience with using such servers for various applications. Each server has been written individually as a separate program. The authors' proposal is for a general purpose, user configurable program for creation of these special meta-parameters.

JLab uses CDEV, or Common DEVICE, to communicate with the underlying EPICS control system. CDEV provides a generic server framework for allowing users to write such middleware servers. The Automator will be based on this CDEV Generic Server. [2,3,4]

### 4 DESIGN AND INTERFACE

The program provides the frame work to define a server for creation of new signals or to react to these new values. Users will configure the Automator by generating a configuration file. The configuration file contains information on the name of the server instance to be created and information about the interrelation of modules. These modules can perform a number of tasks. They can either monitor a variable in the system or produce a new signal to be used by client programs. They can process incoming signals. Finally, they can take an action such as executing a script. These modules are connected together to define the structure of an instance of an Automator, as shown in figure 1.

The user creates modules to monitor the desired signals and connects these to gates. Initially, the gates available will be simple, logic-based gates such as noting if a monitored value is within certain limits, logical "AND" gates, logical "OR" gates, and similarly simple structures. The user then connects the outputs of these gates to either a new signal to be monitored, an object which modifies a value in the control system or something which executes an action. By allowing for an arbitrary script to be executed, the tool can be used to automatically respond to problems in the control system.

Initially, the user will define the structure of an Automator instance by directly editing the configuration file. Eventually this process will be automated to allow a schematic capture tool to be used to create these files graphically.

The Automator will be implemented using C++ in such a way that the gates can be easily defined by users. The gates will be implemented as C++ objects. The user can create new ones by inheriting from the base object and defining the operation of the new gate. This will allow for more complicated, "intelligent" gates to be developed to handle site specific concerns. It is hoped that as the Automator is used at more sites, developers will share these modules, promoting software sharing and reducing development time for developers.

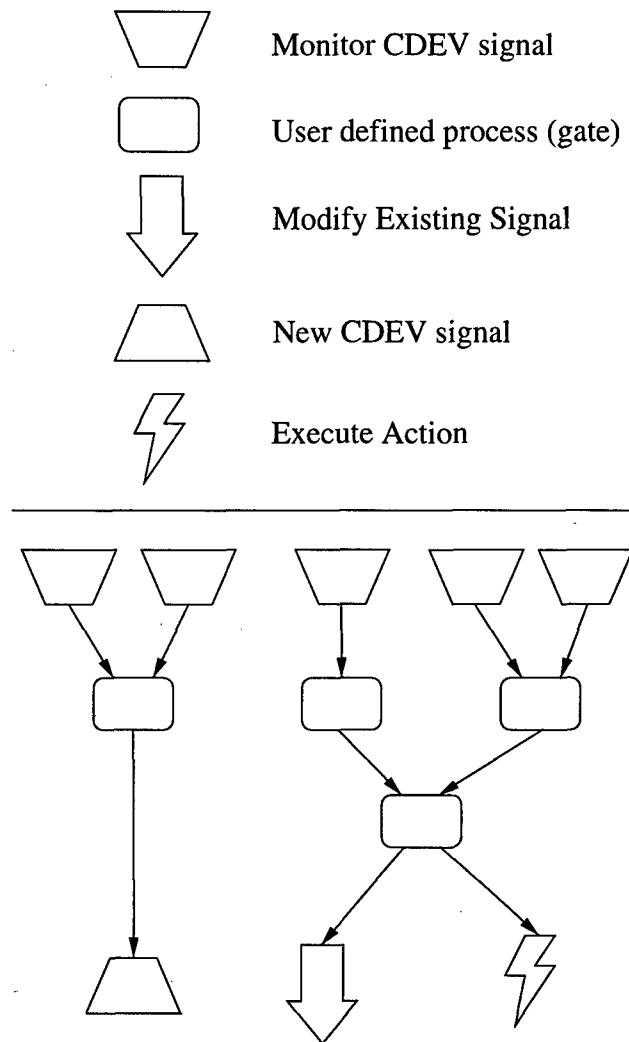


Figure 1 : Automator Configuration Layout

### 5 ADVANTAGES

#### 5.1 Operational Advantages

At a large facility, there are typically many simple but repetitive tasks that operators must perform manually. The tasks never seem to be pressing enough to warrant the development of a software tool to respond automatically. The Automator will allow rapid development of such responders.

Similarly, short term procedure changes and temporary workarounds can present problems that interfere with operations. These special instructions must be given to all personnel operating the machine and they must know the new limits or procedures to follow for a particular device. JLab's main accelerator is run twenty-four hours a day by three crews working on alternating seven day shifts. By automating such processing, the chance of instructions getting lost or distorted during crew changes is reduced.

Finally, such a tool allows software developers to capture some of the knowledge of a trained operator or technical specialist. If the operator's response to a certain condition is quantifiable it can be translated into an instance of the Automator. This response is then available even when the skilled operator is not.

### 5.2 Development Advantages

In addition to advantages to operators and all of the development advantages discussed above, the Automator provides a few more advantages. By controlling when and under what conditions certain tools are invoked, the developer can build complex tools from collections of small, tested, known good applications. The developer can also use the Automator to prototype servers (if they can be easily described by a collection of gates), and to monitor the control system for transient behavior that may lead to problems.

This design has several advantages over other tools designed to provide similar functionality. SDDS is a collection of scripts designed to be used together by piping the output of one script to another, providing some of the processing abilities of the Automator [5]. Because these scripts post-process data stored in SDDS files, they cannot provide the processed data to users dynamically. The Automator is a compiled program rather than a sequence of scripts connected using UNIX I/O, which should allow faster execution time. While there is some overlap the Automator is generally designed to provide simple but dynamic processing and response, while SDDS is intended to provide more complex offline processing.

Some of the automated response functionality can be provided by EPICS sequencer programs [6]. The fundamental difference between a sequencer instance and an Automator instance is the level in the control system where the response is taken. By running the Automator as a UNIX process access to common scripting languages for invoking responses is simplified. Additionally, changing a running instance of the Automator would be straightforward and would not interfere with the operation of the control system as modifying a sequence on a front end machine would. If one wishes to modify the action taken by the Automator in response to certain conditions one can substitute a new script in place of the old. Modifying logic for running

these scripts or producing new signals would require generating a new initialization script and restarting the Automator, but this could still be accomplished without interrupting the front end machine of the control system.

### 5.3 Diagnostic Advantages

Finally, by allowing for rapid development of tools to monitor the control system, individuals responsible for diagnosing problems with the system being controlled can easily develop one-off diagnostic tools. Since the tool can be configured to monitor signals constantly, noting and observing transient behavior is easier than with some other methods.

## 6 CONCLUSION

This tool is currently under development and a Beta version is expected in the next few months. The authors feel this will provide a powerful new tool to help in the operation of large scale control systems.

## 7 REFERENCES

- [1] M. Bickley, B. A. Bowling, D. Bryan, J. van Zeijts, K. White, S. Witherspoon, "Using Servers to Enhance Control System Capability", these proceedings (1999)
- [2] J. Chen, G. Heyes, W. Akers, D. Wu and W. Watson III, "CDEV: An Object-Oriented Class Library for Developing Device Control Applications", Proceedings of ICALEPCS 1995
- [3] [http://www.aps.anl.gov/asd/controls/epics/EpicsDocumentation/EpicsGeneral/epics\\_overview.html](http://www.aps.anl.gov/asd/controls/epics/EpicsDocumentation/EpicsGeneral/epics_overview.html)
- [4] W. Akers, "An Object-Oriented Framework for Client/Server Applications", Proceedings of ICALEPCS 1997
- [5] <http://www.aps.anl.gov/asd/oag/oagSoftware.html>
- [6] [http://www.aps.anl.gov/asd/controls/epics/EpicsDocumentation/ExtensionsManuals/Sequencer/snl\\_seq.ps](http://www.aps.anl.gov/asd/controls/epics/EpicsDocumentation/ExtensionsManuals/Sequencer/snl_seq.ps)

# SIMULTANEOUS MULTIPLE PASS STEERING AT JEFFERSON LAB\*

Y. Chao<sup>†</sup>, S. A. Bogacz, V. A. Lebedev

Thomas Jefferson National Accelerator Facility, Newport News, VA

## Abstract

The CEBAF recirculator at Jefferson Lab includes two linear accelerators, each 200 meters in length. Due to varying betatron phase advance for different recirculation passes, misalignment, and other steering effects, orbit correction in the CEBAF linacs presents a complicated problem defying pass-by-pass solutions. Utilization of information from the beam position measurements at all recirculation passes allows us not only to perform multi-pass steering minimizing beam displacements inside the linacs, but also to determine displacements of linac BPM's and focusing quadrupoles from an ideal axis. This paper describes a steering algorithm and presents the experience in multi-pass orbit correction.

## 1 THE PROBLEM

Jefferson Lab operates its CEBAF accelerator, with which it is often synonymous, as a nuclear physics research facility currently delivering CW electron beam to three fixed-target experiments with energy up to 5 GeV. CEBAF consists of injector, multi-pass linacs, recirculating arcs, beam separation (spreader) and recombination (recombiner) structures, and extraction lines to experiments. These are shown in Figure 1. The linacs

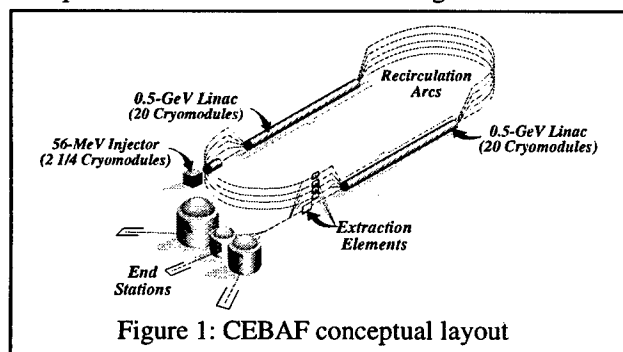


Figure 1: CEBAF conceptual layout

consist of FODO structures providing constant focal length for the first pass beam at 120 degrees betatron phase per period. Orbit correctors are active only at the focusing elements in each plane. This has proven effective in avoiding excessive correction for the first pass orbit.

In early 1998, despite successful steering to orbit within 1 mm in the first pass linacs, large and persistent orbit patterns in higher passes were seen to develop. In higher

passes orbit deviation could exceed 4 mm in the x plane in both linacs, while the typical operational requirement for absolute orbit was 1 mm. It was hypothesized that misaligned quadrupoles and BPM's, and other unaccounted disturbances to the beam were mainly responsible. Significant difference in betatron phase advances between different passes and absence of correctors exactly coinciding with all potential errors left higher pass orbits at the mercy of first pass corrections. This was exacerbated by unknown systematic offsets in the multi-pass BPM's [1] which monitor the orbit for all passes.

## 2 INTERPRETING THE ORBIT

An analysis on the multiple pass orbit was performed to interpret the observed anomaly. Table 1 gives a parameter count relevant to this analysis in the South Linac. The free parameters were unknown kicks and monitor offsets shared by all 5 passes, and injection errors distinct for each

Element	Per pass	Total
Orbit reading	27	135
Total constraints		135
Injection position	1	5
Injection angle	1	5
Unknown kick	27	27
Monitor error	27	27
Total free parameters		64

Table 1: Parameter counts

pass. The constraint came from the orbit readbacks at 27 linac BPM's for all 5 passes. An unknown kick was assigned to each quadrupole location, which was sufficient to represent the effect of all misalignment-related errors. The assumption that each monitor offset was the same for all passes was reaffirmed by the outcome of the analysis showing negligible pass-to-pass variation in the fit residual at all BPM's except one. This highly constrained system promised a redundancy important in ensuring the reliability of the analysis.

The analysis was done through least square fitting using the parameters and constraints of Table 1. All input data were generated by a machine snapshot program FOPT which, in addition to recording the orbit and magnet information at a given operating point, generated estimates of individual BPM resolution for the data set of interest. Input orbit data were weighted according to these estimates. A BPM known to display anomalous behavior was deleted from the input. Figure 2 shows the offset in quadrupoles and BPM's as calculated by the fit, where the fitted unknown kicks were converted to

\* Work supported by the U.S. Department of Energy, contract DE-AC05-84ER40150

<sup>†</sup>E-mail: chao@jlab.org

equivalent offsets of quadrupoles. The baseline in Figure 2 has been adjusted to minimize overall RMS of the quadrupole offsets. Error analysis was performed using

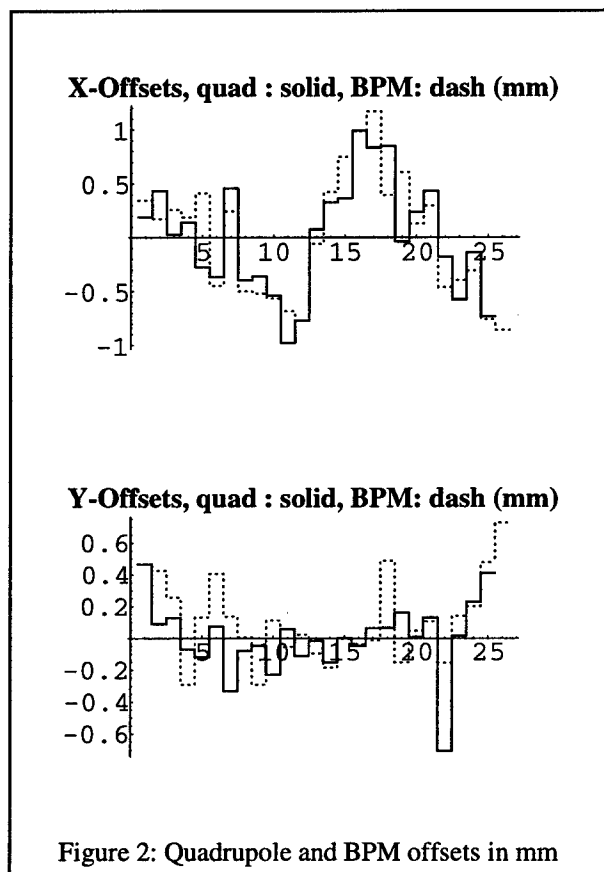


Figure 2: Quadrupole and BPM offsets in mm

the BPM resolution estimated by FOPT. The RMS errors on most of the fitted quadrupole and BPM offsets were on the order of 0.1-0.3 mm. The quadrupole next to the malfunctioning BPM displayed the largest RMS error in offset of 0.8 mm. The fit residuals at 135 locations were consistently below 0.2 mm in both planes, with the exception of the malfunctioning BPM displaying variable residuals from pass to pass with magnitudes of several millimeters. Figure 2 also demonstrates corroborating offset patterns between quadrupoles and BPM's, lending further credibility to the analysis<sup>\*</sup>. The persistent orbit in higher pass linacs was understood, after this analysis, as the cumulative effect of kicks caused by long range quadrupole offset pattern with respect to the ideal straight line<sup>†</sup>. This effect has been imperfectly cancelled in the first pass by correctors only in the focusing zones under the 120-degree optics. In higher passes the remnant of the first pass correction built up considerably over several zones due to much slower phase advance.

<sup>\*</sup> This also confirms the effort of beam-based BPM alignment with respect to the nearest quadrupole carried out at CEBAF.

<sup>†</sup> There is no independent confirmation as to whether this pattern reflects real distortion in the baseline, thus quadrupole offsets can also be viewed as representative of all unaccounted kicks.

### 3 MULTI-PASS STEERING

It was realized, after the above analysis, that using all the correctors inside the linac, which affects all passes differentially, as well as injection fixes from individual upstream recombiners, we could reduce the orbit in all passes significantly. Simulation of this process was encouraging. There was the option of whether to set the target of steering to the ideal straight line between the ends of the linac, or to set it to the centers of the working BPM's. The latter option was adopted in view of the possibility that the offset pattern of Figure 2 may indicate actual beam line distortion. In other words, apparent BPM centers may conform to the actual deformed baseline, and steering to an absolute straight line, instead of the apparent BPM centers, may in fact compromise aperture.

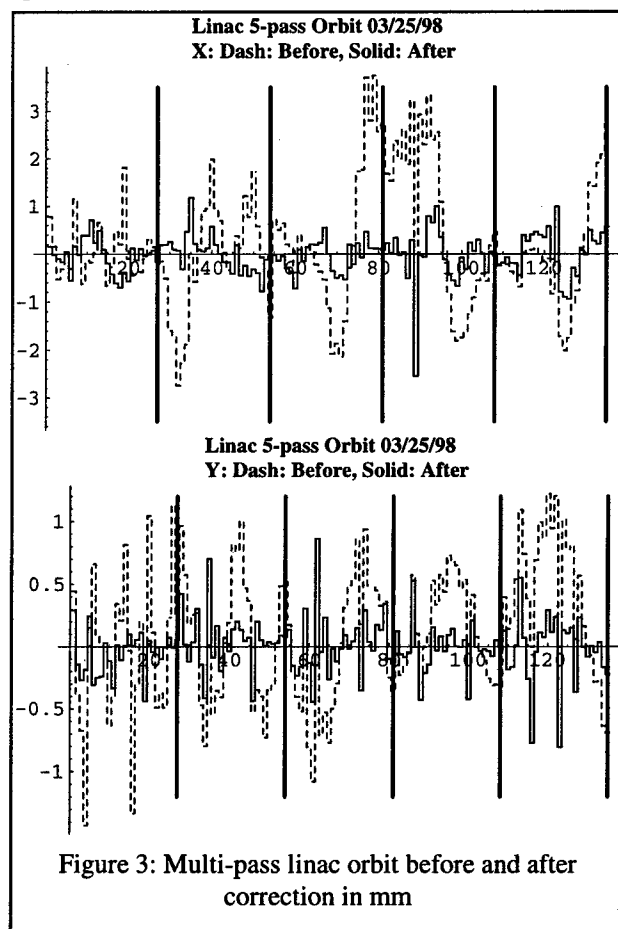


Figure 3: Multi-pass linac orbit before and after correction in mm

Corrector strengths needed for simultaneously steering all 5 passes in the South Linac were calculated using PROSAC, a locally developed steering algorithm with a strong emphasis on fully exploiting hard corrector limits while strictly conforming to them<sup>‡</sup>. This proved critical to multi-pass steering. This procedure was applied to the South Linac. The highly over-constrained nature of the

<sup>‡</sup> Expecting correctors reaching design limits, we did not use SVD-based steering with its intrinsically pathological limit-handling scheme.

problem forced several correctors to their limits as expected, but simultaneous orbit reduction was achieved. Figure 3 shows the BPM readings in mm before and after the correction, with all 5 pass orbits displayed in tandem for each plane. The solid line in x-plane is an order of magnitude smaller in RMS than the dashed line<sup>†</sup>. A total of 12 horizontal and 13 vertical correctors inside the South Linac and 10 correctors in each plane in the upstream recombiners were used to achieve this orbit reduction at 135 locations in each plane. Simulation also showed promise for multi-pass steering in the North Linac, where higher passes displayed persistent orbit similar in magnitude to the South Linac. However this was not implemented because orbit analysis indicated, at the time of test, that several BPM's displayed behavior anomalous enough to compromise the offset interpretation and the effectiveness of steering.

#### 4 CONCLUSION

We have successfully demonstrated simultaneous multi-pass steering in the CEBAF linac. Algorithm was developed to extract information on unknown kicks and monitor offsets, which were in turn translated into information on potential baseline misalignments. Multi-pass steering was done by an effective algorithm using common correctors in the linac and injection adjustments upstream. Implementation of this algorithm as a routine online program is included in the next phase of high level application plan at CEBAF.

#### REFERENCES

- [1]. T. Powers and S. Schafner, these proceedings.

---

<sup>†</sup> Some solid spikes correspond to malfunctioning BPM's.



## EPICS TOOLS ENHANCEMENTS AND TRANSPORTABILITY\*

M. Bickley, J. Chen, C. Larrieu<sup>†</sup>, Thomas Jefferson National Accelerator Facility, Newport News, VA

### Abstract

The Jefferson Laboratory electron accelerator is controlled by the *Experimental Physics and Industrial Control System* (EPICS), which was initially developed by the Los Alamos and Argonne National Laboratories, and which has since become an extensive collaboration among scientific institutions worldwide. In keeping with the spirit of cooperation and exchange fostered by the EPICS community, the Controls Software group at Jefferson Laboratory aims to produce portable software tools useful not only locally, but also at any EPICS site, and even at non-EPICS sites where feasible. To achieve this goal, the group practices several software engineering principles which have demonstrated success in producing sharable software. This paper first discusses those principles along with the practicalities involved in pursuing them, and then illustrates how they prevail within three different frameworks: the architecture and operating system (OS) portability provided by the EPICS environment, which assists in porting to other EPICS sites; the control system portability inherent in the Common Device (CDEV) abstraction layer, which facilitates porting to any supported control system; and the general system portability which follows from careful code design.

### 1 GENERAL CONSIDERATIONS

Because a control system is, by intent, uniquely customized to perform site-specific tasks, designing control system software for effective use at various unrelated sites might seem, at first, to require an amount of work disproportionate to the rewards such an endeavor might garner: not only must the programmer attempting do so solve the immediate problem which necessitates his application, but he must also devise some technique for dealing with the differences which arise among sites. Furthermore, he must decide how portable his application really can and should be before beginning to work on it.

Fortunately, these latter quandaries are substantially mitigated by the nature of the undertaking in question. It may be of a sort which is "algorithmically" portable from one site of a particular type, to another of the same type. Two particle accelerators, for example, might require software to measure and tune the phase of an RF cavity. While these sites may not use the same control system, the general solution to their common problem may be sufficiently parameterizable such that the same program could be used at both, if it were capable of controlling each system in the same generic way.

Another type of inherently portable application is the sort which provides basic facilities closely tied to the system being controlled. Examples include data acquisition, logging, and retrieval systems, human interfaces for monitoring and managing the underlying physical system, and utilities for measuring and analyzing the system in a user-specified manner. Such tools are fairly useful in a general sense across control systems and physical machines, so that for every site to design its own set seems tantamount to "reinventing the wheel". Ideally, the site-specific information should be configured via some localization method.

Of course, there are good and bad reasons for one site to avoid reusing software from another. In order to create a general purpose tool which another site will want to use, the designer must in some way address both. Among the former category are considerations arising from concern over efficiency and compatibility. Does the application make assumptions about the underlying system such that it works well in one situation but not in another? If it generates output data, will it do so in a format which other tools can read? Notorious among the bad reasons is reluctance arising from the well-known "not developed here" syndrome, a psychological phenomenon pervasive in the engineering world. It derives, perhaps, from the fear of becoming dependent upon the work of someone whose interests may not necessarily coincide with one's own.

This leads to a consideration of those factors which might induce a developer to produce code specifically designed only for local use. The benefit of such an approach is that it may allow for a tight integration among the tools in a local suite: if an application can make assumptions about the existence of other facilities, it can incorporate their features, providing users with multiple points of entry to the various system tools. Additionally, designing for a known system allows for faster development—because the programmer knows exactly the environment in which his application will run, he can avoid having to handle certain special exceptions which might arise from one site to another. Furthermore, a small user base will likely limit requirements and feature creep.

Note, however, that these assumptions about the environment imply that the benefits pertain only if the situation for which the application is written persists over time. What happens if something about it changes? What if one of the subsystems upon which the code depends is removed, or, more drastically, if the control system changes (not so preposterous: the CEBAF accelerator was switched from TACL[1] to EPICS during the commissioning of the machine in the mid '90s). The programmer can ameliorate the problems arising from such occurrences by designing his application to be portable from the outset. *Fundamentally,*

\* Work supported by the U.S. Department of Energy, contract DE-AC05-84ER40150

<sup>†</sup> Email: larrieu@jlab.org

*the principles pertinent to designing portable code are also those which lead to reliable, maintainable, and extensible code.*

While the primary mission of the controls software group at Jefferson Lab is to support the operation of the accelerator, we find that by designing our code to be portable, we are investing a small amount of additional time and effort in the initial development phase in order to facilitate future development work.

## 2 EXTENDING AN EPICS APPLICATION

The EPICS [2] system provides a fairly simple framework for developing control system client applications, by providing site-specific configuration files and a C/C++ application programming interface (API). All high-level interaction with the control system can be conducted through the channel access library, which is a set of routines for establishing connections to named parameters in the control system. Within this framework, the task of designing software for porting to other EPICS installations reduces to producing code based on UNIX portability standards to address the issue of OS and machine independence, and modularizing those portions which make use of site-specific subsystems.

One useful application which was originally written at APS, then subsequently enhanced and modularized at Jefferson Lab, is a real-time data plotting utility called StripTool. While the original version was designed specifically for EPICS, the revision produced by Jefferson Lab was designed with the intent that it be control system independent. Because its functionality was initially quite simple in concept (the user just supplies the name of a control system parameter whose value he wishes to see plotted), the process of compartmentalizing the platform-specific code was relatively straightforward: all functionality was broken out into modules, so that the data acquisition, data buffering, graphical presentation, user interface, and timing components all belonged in separate modules with very well defined interfaces.

The process of transporting StripTool from one EPICS system to another is trivial, because it capitalizes on the EPICS-supplied configuration files and compilation instructions ("makefiles"). The interested party can, for all intents and purposes, simply download the source code, run the EPICS build command to create the binary executable, and then run it. In order to port StripTool to another control system, however, the local programmer must supply a "plug-in" for the data acquisition module, which amounts to writing a minimal set of routines as specified in the *StripDAQ* file, and linking them into the compiled program. It took just a couple hours to implement a CDEV data acquisition module, following this procedure. Now, both the Channel Access and CDEV modules are included with the source code, and the proper one is linked depending upon the build environment.

After these initial enhancements, the natural progression

was to provide some support for viewing old data in addition to that which had been acquired through the real-time acquisition unit. Because StripTool only buffers the most recent data for some selectable time span, however, it requires some other facility from which to acquire the older data. In other words, providing such functionality introduces a dependency upon an auxiliary sub-system. Because a data logging and retrieval system is pretty much essential to any control system environment, several of the sites using StripTool have developed their own custom applications to serve this purpose. In order to accommodate all sites interested in incorporating this functionality into StripTool, another module, *StripHISTORY*, was defined. It describes a minimal set of routines specifying only those features of the system which StripTool requires. Regardless of how sophisticated a particular site's archiving service may be, StripTool just requires 3 functions in addition to an initialization routine: (1) "get data for parameter  $X$  over time range  $(t_0, t_1)$ ", (2) "exchange this data for a new time range", (3) "free this data". By implementing just these three routines as the "glue" between the application and a specific subsystem, a local programmer is able to hook his unique archiving service into StripTool with only a minimal amount of work, while still ensuring that the resulting code need not be merged back into a central repository. This last point is important, because it helps to preclude situations which lead to initially diverging, then redundant parallel work, brought about by small changes in code from one site to another which never synchronize.

This technique is, in some sense, a "reverse black box" (it's also the model used for operating system device drivers), in that the application defines an empty plug-in mechanism, which can be filled by site programmers to translate an application's requests for auxiliary services into a protocol which the underlying subsystem can understand. However, if a site does not wish to use the specific feature, it need take no special action. This approach allows for integrating system tools by defining the interfaces between them in simple terms. A concomitant benefit of this approach is that, as the subsystems become more integrated, the interfaces will necessarily become more detailed, leading to better documented code.

## 3 THE CDEV ABSTRACTION LAYER

The Common Device API (CDEV) is an abstraction layer developed at Jefferson Laboratory[3], which allows the various subsystems of a control system to be addressed in a generic and consistent manner. It has been used to integrate multiple control systems, as well as to incorporate client-side applications into the control system.

An application designed specifically for CDEV must adhere to conventional portability standards to remain portable across platforms, and becomes entirely dependent upon being run in a special environment, which the local programmer must build, install, and configure. While this process may not seem easier than simply writing some

small amount of "plug-in" code, it does present the benefit that the requisite work represents a one-time investment, whereas having to write small bits of code for lots of applications can become wearisome, particularly when those bits are intended to perform the same task!

An EPICS Channel Access component has been written which allows CDEV applications to talk to Channel Access without directly relying upon the EPICS code. This has the effect of moving the control system dependency away from the user application and into the intermediary layer. Several EPICS utilities, like the alarm handler and medm have been modified to use CDEV in lieu of Channel Access, allowing them to be used in conjunction with non-EPICS control systems.

The controls software group at Jefferson Lab have also developed several new utilities. Zplot is a motif application that plots device attribute values against their coordinates along an accelerator. Xtract, the "X-windows Tool for Recording And Correlating Things" allows the user to change the system in a highly configurable manner, measuring various parameters along the way, resulting in data describing a discrete function of the stepped parameters. In this regard it is a general purpose experimentation program.

#### 4 PORTABILITY THROUGH OBJECT-ORIENTED DESIGN

One of the greatest benefits of object oriented programming language like C++ is that it provides support for designing abstraction into an application. In designing a new application, the desired end product can be conceptualized as a virtual machine, comprised of distinct parts. The programmer's task is to forge actual software constructs (*Classes*, in C++ OO terminology) from these general specifications. The interesting thing about this process, is that it leads to a natural separation between the conceptual nature of the components and their corresponding implementation.

At Jefferson Lab, we use the EPICS archiver to log tens of thousands of control system parameters continuously, producing massive amounts of data which are subsequently compressed and cataloged in a locally developed database. Of course, once the data is nicely organized, one requires some mechanism by which to retrieve it: a program to facilitate browsing through the archived data, and converting it into a useful format. Because such a tool would be generally useful to other sites, and because we anticipated that our archiving system will change as we phase in new subsystems, we decided to develop a portable system based upon OO design principles.

The resulting tool (XARR: the Xwindows ARchive Retriever), as used at Jefferson Lab, is comprised of 3 layers. At the top is the graphical interface, which is implemented in C++, using the Motif widget set. Beneath this is the database layer which catalogues the available data. At the lowest level is an I/O library for reading and writing data from and to the storage medium. Because the two bottom layers are primarily specific to Jefferson Lab's stor-

age system, while the top layer is not, the interface between them is implemented as a set of three abstract object types, corresponding conceptually to the components describing a general purpose data retrieval machine and the items it would require to perform its task: a DataSource, a DataHandle, and a DataBuffer. The DataSource enumerates the objects stored in the archive, provides lookup and search capability, and retrieves data. The DataHandle conceptually represents a way to identify some unique parameter in the archive. The DataBuffer encapsulates the data for a particular DataHandle over some time range, and provides methods for iterating over the contained data points.

The programmer interested in building XARR for use with some other archive must create three C++ classes derived from those named above, overriding the default behavior with site-specific details. When the application is compiled, the appropriate class definitions are included in the main startup routine.

#### 5 CONCLUSIONS

While the ultimate goal in portability is to eliminate as much site-specific "tweaking" as possible, this often proves unattainable without also decreasing the efficiency or usefulness of an application. The most useful sort of portability within an open-source environment is the kind that allows local programmers at various sites to acquire code which they can easily modify to suit their own needs. Fortunately, this naturally follows from good design and coding principles. As illustrated above, by designing code modularly, those portions which require modification from site to site are isolated and readily found by the local programmers. If the code is also well documented, then the local programmer may more easily and confidently supply the necessary site-specific modifications, helping to relieve the "not developed here" syndrome. Because the local code is isolated in distinct modules, the process of upgrading to new versions of the software reduces to plugging in those site-specific modules to the new source code. While all these good things benefit the recipients of the "free" work, they also benefit the original developer and his site by providing software which is easily maintainable, extensible, and likely to remain useful through system changes.

#### 6 REFERENCES

- [1] K. S. White, H. Shoaee, W. A. Watson, M. Wise, "The Migration of the CEBAF Accelerator Control System from TACL to EPICS", *CEBAF Controls System Review*, 1994, Newport News, VA.
- [2] Leo R. Dalesio, et. al., "The Experimental Physics and Industrial Control System Architecture: Past, Present, and Future", *International Conference on Accelerator and Large Experimental Physics Control Systems*, Oct. 1993.
- [3] J. Chen, G. Heyes, W. Akers, D. Wu and W. Watson III, "CDEV: An Object-Oriented Class Library for Developing Device Control Applications", *Proceedings of ICALEPCS 1995*, p 97.

## NEW FEATURES IN MEDM\*

K. Evans, Jr.†

Argonne National Laboratory, Argonne, IL

### Abstract

MEDM, which is derived from Motif Editor and Display Manager, is the primary graphical interface to the EPICS control system. This paper describes new features that have been added to MEDM in the last two years. These features include new editing capabilities, a PV Info dialog box, a means of specifying limits and precision, a new implementation of the Cartesian Plot, new features for several objects, new capability for the Related Display, help, a user-configurable Execute Menu, reconfigured start-up options, and availability for Windows 95/98/NT. Over one hundred bugs have been fixed, and the program is quite stable and in extensive use.

### 1 INTRODUCTION

MEDM is an X-Windows, Motif program that displays objects, such as meters, sliders, menus, and plots. These objects are used to read and set parameters in a control system. In addition to supervising these objects and interacting with the control system, MEDM is also a drawing package that provides the means of laying them out in screens, also called displays. A significant control system can have thousands of screens, each with as many as hundreds of objects.

MEDM has been developed primarily at the Advanced Photon Source at Argonne National Laboratory starting around 1990. It is arguably the principal graphical interface to EPICS [1] and now works with CDEV [2] and other control systems as well. In the last two years MEDM has been made more robust and a number of features have been added. It is the purpose of this paper to describe some of these new features. Additional information on MEDM, which is an extensive program with many other features than those described here, may be obtained from the MEDM Reference Manual [3].

### 2 NEW EDITING FEATURES

Since MEDM is used to design the many screens that operators and engineers use to control a system, it is essential that it be a full-fledged, convenient, and robust drawing tool. To that end, many features commonly found in other drawing packages have been added to MEDM. The top-level menu to access these capabilities is shown in Fig. 1. The foremost of these editing features

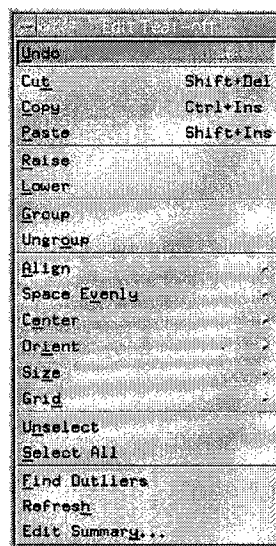


Figure 1: Edit-Mode Menu.

is the ability to Undo and Redo. The basic operations of cut, copy, paste, group, and ungroup were already in MEDM. There are now ways to align, space evenly, center, flip, rotate, and size selected objects or groups of objects. An example of flip and rotate is shown in Fig. 2. There is also now a grid and snap-to-grid option. Additional keystroke combinations have been added to control moving, resizing, and selecting objects. It is now possible to change the colors of all grouped objects simultaneously.

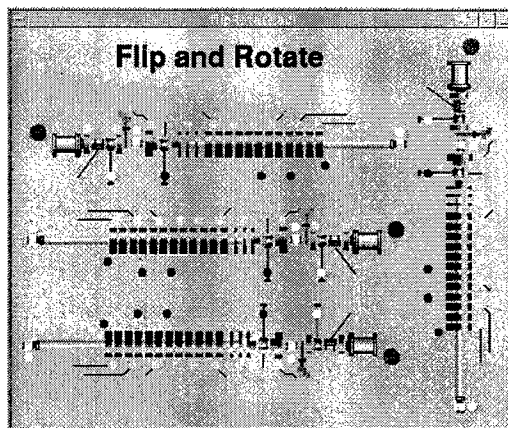


Figure 2: Flip and rotate options. The items shown were designed with the MEDM drawing tools.

### 3 PV INFO

The PV Info dialog box, shown in Fig. 3, gives extended information about the control parameters (known as process variables in EPICS) associated with an object. This information has proven very useful, particularly in tracking down problems.

\*Work supported by the U. S. Department of Energy, Office of Basic Energy Sciences, under Contract No. W-31-109-ENG-38.

† Email: evans@aps.anl.gov

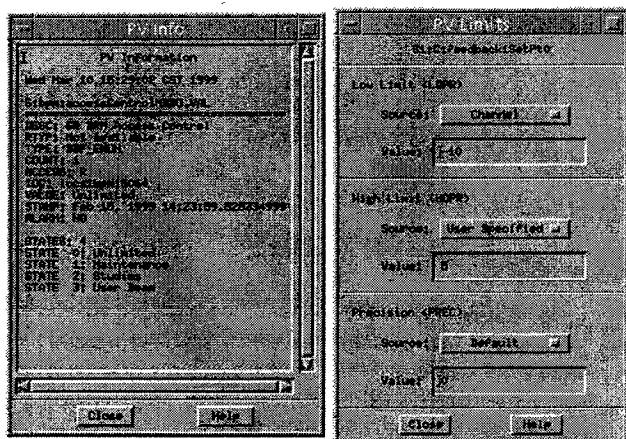


Figure 3: PV Info and PV Limits Dialog boxes.

#### 4 LIMIT AND PRECISION INFORMATION

A shortcoming of MEDM was that the limits of MEDM objects such as the Meter, Slider, Bar, and Scale were set by data stored with the process variable. This meant it could not be different for different users, nor easily adjusted. A similar situation existed with the number of figures after the decimal point, or precision, for text objects. The limits and precision defaults can now be set by the screen designer. The user can choose either to get the values from the process variable as before, use the designer's defaults, or set his own values, perhaps for fine or coarse tuning. The PV Limits dialog box for doing this is shown in Fig. 3.

#### 5 CARTESIAN PLOT

The Cartesian Plot is the most complicated object in MEDM and one of the most useful. An example is shown in Fig. 4. In the past it was implemented with the commercial product XRT/Graph [4]. The Cartesian Plot logic has been rewritten to make it more generic so it may be used with other plot packages. In particular, the public-

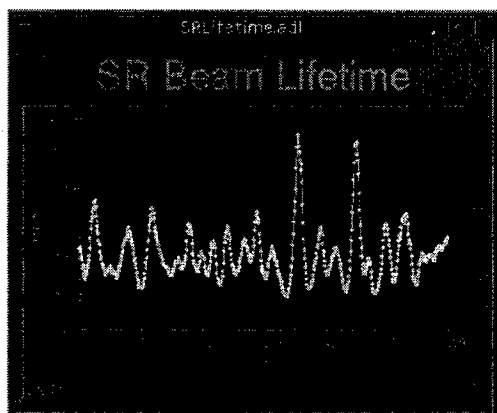


Figure 4: Cartesian Plot using SciPlot.

domain SciPlot [5] widget has been enhanced and adapted to MEDM. It is used for the Windows version of MEDM, where XRT/Graph is not available, and provides a free alternative on other platforms.

#### 6 NEW FEATURES FOR OTHER OBJECTS

All objects have been made to have consistent shadows using the Motif look and feel and to have consistent sizes between EDIT and EXECUTE mode. The Bar object now has a "no-decorations" attribute that allows it to be used to make bar graphs as in Fig. 5.

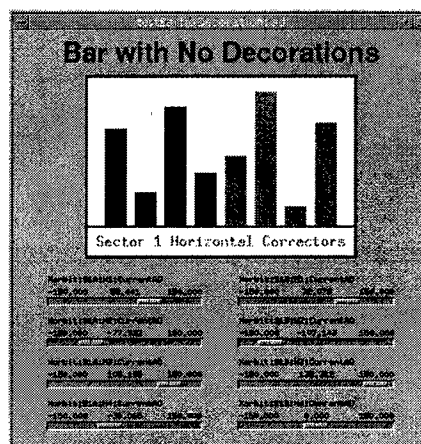


Figure 5: Bar object used to make a bar graph.

#### 7 RELATED DISPLAY

The Related Display, shown in Fig. 6, is an MEDM object used to bring up other screens. Formerly, it presented a menu of choices. Now, if there is only one item, it behaves like a button and just brings up the screen. If there is a single button, the graphics and label text are placed in the center of the label rather than left justified, so the user will be aware the action will happen immediately. Further, the designer can specify whether a new screen replaces the old screen, and the user can also decide

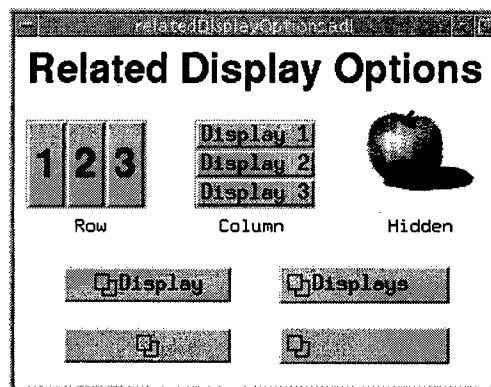


Figure 6: Some Related Display options.

whether to replace any screen or not. This capability allows drill-down screen hierarchies and screens that change to fit the conditions. Screens have also been implemented with "More" and "Less" buttons to display varying amounts of information. The Related Display can be a "hidden button" so that if it is placed under a graphic, clicking on the graphic brings up the new screen. Some of the options are shown in Fig. 6. These capabilities give the designer a chance to be creative.

## 8 HELP

Formerly there was little or no help available for MEDM. Now there is an extensive reference manual [3] that can be formatted as text for printing or as HTML for the Internet. Both context-sensitive and menu-driven help are implemented through Netscape [6], which can be controlled from MEDM. There is also bubble help that pops up over tool icons.

## 9 EXECUTE MENU

There is now a configurable menu in EXECUTE mode that appears as part of the popup menu obtained by right clicking on the background of a display. This menu can be used to conveniently call other programs. There are special characters that insert the name of the screen definition file (called ADL file) for the current screen or insert a process variable name from an object into the command to be executed.

For example, the following environment variable:

```
MEDM_EXEC_LIST=Probe;probe &P &:  
ADL File;echo &A:PV Name(s);echo &P
```

results in the menu shown in Fig. 7. These particular menu items implement (1) calling another program, Probe, for a process variable associated with an object, (2) echoing the name of the ADL file, and (3) echoing the process variable names associated with an object. See the manual [3] for the syntax and other details.

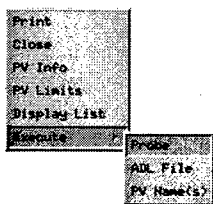


Figure 7: Execute-Mode Menu with customizable Execute Menu. PV Info and PV Limits are also selected via the Execute-Mode Menu.

## 10 STARTUP OPTIONS

MEDM allows new executions of MEDM to attach to an existing one to provide efficiency and prevent a proliferation of MEDMs. Formerly this was the default; however, the mechanism by which this is done is complicated and

often misunderstood, leading to problems with ownership and access permissions in particular. The default is now to not engage this mechanism, making life simpler for the casual user and leaving the more complicated operation to places like control rooms, where knowledgeable people are available and where it is more relevant.

## 11 WINDOWS 95/98/NT SUPPORT

MEDM now runs on Windows. It is available as a self-extracting, InstallShield [7] executable that also includes other EPICS extensions, such as Probe and Namecapture [1]. The Windows version of MEDM uses the Sciplot [5] widget for its Cartesian Plot. A Windows version is, of course, useful for people who use PCs rather than UNIX. It is also useful for people who connect to the control system via a modem from home or from a laptop. When MEDM is running locally, only the control-system data need to go over the phone line. When connected to a remote workstation, the X-Windows information has to be transmitted as well. The PC version is being used regularly and is stable. It requires Hummingbird Exceed [8] as an X server.

## ACKNOWLEDGEMENTS

Jie Chen of the Thomas Jefferson National Accelerator Facility did the adaptation of MEDM for CDEV. Jie was also responsible for the initial implementation of SciPlot. The author is indebted to many people for testing and feedback on MEDM, but to Frank Lenkszus, Ned Arnold, and Nick Dimonte in particular. The author is also grateful to Janet Anderson for continuing help with the EPICS build system, which she has had a large part in developing.

## REFERENCES

- [1] <http://www.aps.anl.gov/asd/controls/epics/EpicsDocumentation> has extensive information on all parts of EPICS as well as links to both the HTML and Postscript versions of the MEDM Reference Manual.
- [2] <http://www.jlab.org/cdev>.
- [3] <http://www.aps.anl.gov/asd/controls/epics/EpicsDocumentation/ExtensionsManuals/MEDM/MEDM.html>.
- [4] XRT/Graph is a product of the KL Group Inc., Toronto, Ontario, Canada.
- [5] <http://www.ae.utexas.edu/~rwmcm/SciPlot.html>.
- [6] Netscape is a product of Netscape Communications Corporation, Mountain View, CA.
- [7] InstallShield is a product of InstallShield Software Corp., Schaumburg, IL.
- [8] Exceed is a product of Hummingbird Communications Ltd., North York, Ontario, Canada.

# JEFFERSON LAB PLOTTING TOOLKIT FOR ACCELERATOR CONTROLS\*

J. Chen, M. Keesee, C. Larrieu, G. Lei\*\*

Thomas Jefferson National Accelerator Facility, Newport News, VA

## Abstract

Experimental physics generates numerous data sets that scientists analyze using plots, graphs, etc. The Jefferson Lab Plotting Toolkit, JPT, a graphical user interface toolkit, was developed at Jefferson Lab to do data plotting. JPT provides data structures for sets of data, analyzes the range of the data, calculates the reasonable maximum, minimum and scale of axes, sets line styles and marker styles, plots curves and fills areas.

## 1 INTRODUCTION

The Continuous Electron Beam Accelerator Facility at Jefferson Lab provides high current electron beams of up to 4 GeV energy to three experimental halls. The machine consists of two superconducting linear accelerators connected together with 9 arcs. An injector system provides polarized and unpolarized electrons from two different sources. The Jefferson Lab Control System, which is built on the Experimental Physics and Industrial Control System (EPICS), is a distributed system using a client-server architecture. The system consists of two computing levels. The first level is composed of Unix workstations and X-terminals that execute a wide variety of system applications and high level applications. The second level is composed of single board computers, EPICS software and the corresponding device control applications. [1]

One of the high level applications, called lute, analyzes and displays data from the Jefferson Lab wire scanners. The lute data analysis program relied on a commercial software package for its graphics. This package contains many more features than that are required by the few applications at Jefferson Lab that use it. So, when the controls group decided not to support the license for the commercial software for HP-UX 10.XX and higher systems, another solution was needed. The plotting toolkit, JPT, was developed to accomplish the analysis, calculation, scaling, and display of data for lute. Emphasis was placed on developing JPT to replace the functionality of the commercial package while keeping the source codes that use it unchanged.

\*Work supported by the U.S. Department of Energy, contract DE-AC05-84ER40150

\*\*Email: leige@jlab.org

\*On leave from the Institute of High Energy of Physics, Chinese Academy of Sciences

## 2 DESCRIPTION OF LUTE

Lute is a high level application that is used for data reduction and analysis for wire scanner data. Due to the geometry of the wires in relation to the beam, the wire scanners at Jefferson Lab provide scanned profiles representing the horizontal, x/y coupling, and vertical beam sizes. See figure 1. The wire scanner data is used for beam emittance measurement, beam matching, beam halo determination, beam energy spread measurement, and absolute beam energy measurement.

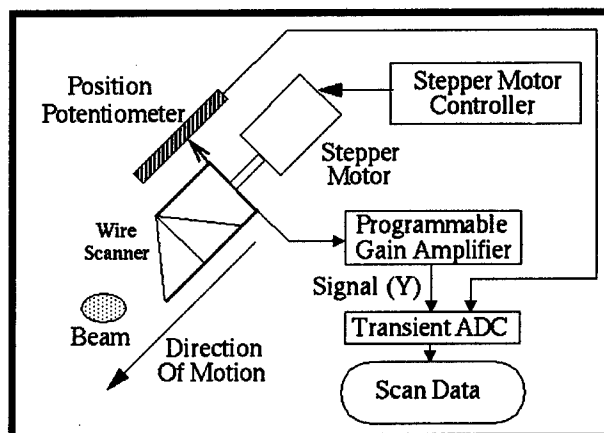


Figure 1. Jefferson Lab wire scanner

The lute application displays the wire scanner data graphically. See figure 2. The entire scan, beam signal

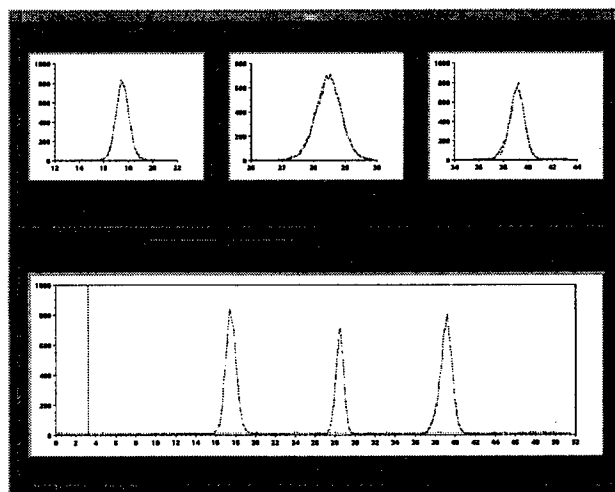


Figure 2. Display of Lute



versus position in mm, is displayed in a large graph across the bottom of the interface, and the 3 distinct peaks (one from each wire) are displayed in 3 graphs at the top of the interface. Several calculations are also performed on the data for each peak and the results displayed on the lute interface. These include sigma, position, RMS and centroid calculations. The graphical displays and calculations assist the operators and accelerator physicists in determining beam characteristics.

### 3 JEFFERSON LAB PLOTTING TOOLKIT

The Jefferson Lab Plotting Toolkit (JPT) provides a graph widget that displays data graphically in a window and can interact with users. The graph widget can be used just like other X Toolkit and Motif widgets such as buttons, labels and menus. It has resources that determine how the graph will look and behave. Writing programs using JPT is similar to writing any other kind of X Toolkit and Motif program [2][3].

JPT has resources that allow control of:

- Graph data to be plotted, on one or more plots.
- Graph type (plot and area). A Plot graph draws each set as connected points of data. An Area graph draws each set as connected points of data, filled in below the points.
- Data styles: line colors and patterns; fill colors and patterns; line thickness; point style, size and color. How a data value looks when it is displayed depends on the data style that has been defined for the data values.
- Strings, position, color and font for the title.
- Strings, position, color and font for the legend.
- Graph color, font and border style.
- Axis label font; label string; color for axis and its label, tick marks and tick labels.
- Axis and data minimum and maximum, numbering and ticking increments, grid increments, origins.
- Placement of axes, annotation, origins.
- Control of user-interaction with the widget using callback resources.
- Markers and Text Areas.

JPT also provides several procedures and methods which

- Allocate and load data objects containing the numbers to be displayed;
- Attach the data to the axes;
- Create, attach, detach, destroy text object;
- Map data from pixel values to floating point values in a graph;
- Convert a floating point value to an X Toolkit parameter *ArgVal*

### 3.1 Implementation

JPT was developed based on the AthenaTools Plotter Widget Set (AtPlotter for short) [4]. 114 new resources were added into the original AtPlotterWidget to develop the JptPlotterWidget. Axes and plots were created inside the methods of the JptPlotterWidget and connected to the data to be displayed. Procedures were added to create data objects for plotting, to read data from files into data objects, and to attach the data object to the plotter to create plots. Data types for some of the resources were changed also. Text objects with multiple strings, foreground color, background color, font, border style etc. were created. The algorithm for calculating the tick-mark interval was improved for more accurate output of the plotting. This prevents plots that are too small, and axis tick-mark labels that are too crowded.

### 3.2 Make Data

JPT accepts data in two ways:

- Array data, which has successive integers as the common horizontal values (X values), and sets of floating point numbers, corresponding to each X value, for the vertical values (Y values)
- General data, each set of data has pairs of X-Y values.

When JPT begins to draw a graph, it uses the data values located in the data structure pointed to by the *XtJptData* resource. Data to be displayed can originate from diverse sources: Unix files, databases, real-time data feeds, or unrelated processes running on other machines.

If the data resides in a Unix file (and it does not need to be changed or updated in real time), there are two options to consider. The first option is to massage the data so that the file conforms to syntax understood by *JptDataCreateFromFile()*. This procedure will allocate the data object, load it with data from a named file, and return a handle to the data. Another approach is to allocate a data object using *JptDataCreate()*, and populate it with data by reading the data file (perhaps using *fgets()* or *fscanf()*). When the data object is loaded, the graph can be created and the *XtJptData* resource set to the *JptDataHandle* that references it.

Data that changes in real-time, and graphs that need to be updated in real-time, require more careful coding. The X Toolkit Intrinsics provides functions that can be used to trigger application callback routines to deal with real-time events.

### 3.3 Axis Controls

JPT detects the minimum and maximum value of the data object and determines the extent of the axes based on the minimum and maximum data values, the origin, and the numbering increment. By default, JPT displays all data in the data object. The minimum and maximum resources can be set by applications if a particular part of the data set needs to be displayed.



The increment between tick marks and sub-tick marks on the axis is calculated by the JPT inner algorithm. The increment can also be controlled by setting the resources in the application. There are also resources to specify whether to draw grid lines, which grid line style to use, etc.

The axes are optionally labelled and the labels can be horizontal or vertical.

### 3.4 Fonts and Colors

JPT has resources to set colors for the widget, graph, axis, title and legend. JPT supports the specification of colors for the window background and foreground, as well as for the lines, fill patterns and points that represent data in the graph itself. Colors are specified using a string containing the color name, which should appear in the X Window Server's color database. On Unix systems, this is normally the file `/usr/lib/X11/rgb.txt` [5].

JPT can choose default colors for the application, so simple applications need not concern themselves with color specification. The default foreground and background color for the widget is black and white. The graph, axes, title and legend take the widget's foreground and background color as default.

A font may be specified for the title, the legend areas and for the axes annotation. JPT can use any font supported by the X Server. JPT accepts the font id to set the font for axis labels, title strings and legend strings. If the font is invalid, the "fixed" font will be used instead.

### 3.5 Calculate Data Scope

JPT is capable of analyzing the scope of the data to be displayed, getting a reasonable representation of the maximum, minimum, tick and sub-tick intervals on the axes. Consider an example with a real maximum value of the data for the Y-axis of 10.03, and the minimum value of 68.96, with the length of the Y-axis of about 200 pixels. It is ugly and difficult to set the ticks in the toolkit to draw the Y-axis with 10.03 as the lowest point and 68.96 as the highest point. It is better to use 10.00 as the lowest point and 70.00 as the highest point. Therefore, the algorithm that is used calculates and rounds four times to get a reasonable presentation.

### 3.6 Text Method

A text area is an independent rectangular region drawn over the graphed data. A data structure is provided for the programmers to define the attributes of the text area including text strings, text position, string adjustment, border style, foreground color, background color and font.

A text area can be attached to the graph in one of four ways:

- To a pixel location on the window
- To graph data X- and Y-value
- To a data point (set, point index), or

- Above or below a data point (set, point index, Y-value)

An application can use a text object to highlight special points on the graph, or as a more general-purpose label. There are methods to create, attach, detach and destroy text area. Any number of text areas can be attached to a graph, dynamically created, updated and destroyed.

### 3.7 Wrapper

We created a wrapper file that defines macros to map existing widget, class, resources and functions to the corresponding parts of JPT. Therefore the current applications need not change anything. They just need to re-link to the JPT library to get new executable codes that have a very similar output to what they had before.

## 4 CONCLUSION

JPT provides a graph widget that can be used like other widgets in the X Toolkit and OSF/Motif. It has many of the features scientific and business users need in a graph that will be embedded in another program. It is easy to use for creating X-Y plots for scientific-style graphics with an unlimited number of plots on each graph. The axes can be logarithmic or linear. It is also easy to access application data.

Figure 2 shows the display of lute using JPT.

## 5 ACKNOWLEDGMENT

Many thanks should be given to Valerie Bookwalter who helped us maintain the computing environment.

## 6 REFERENCES

- [1] Karen S. White, Hari Areti, Omar Garza, "Control System Reliability at Jefferson Lab", ICALEPCS'97 Proceedings
- [2] Adrian Nye, Tim O'Reilly, "X Toolkit Intrinsics Programming Manual", O'Reilly & Associates, Inc.
- [3] Paul M. Ferguson & David Brennan, "Motif Reference Manual", O'Reilly & Associates, Inc.
- [4] <http://lune.csc.liv.ac.uk/hppd/hpux/X11/Toolkits/plotter-6.0p17>
- [5] Adrian Nye, "Xlib Programming Manual for Version 11", O'Reilly & Associates, Inc.

# FORINJECTOR VEPP-5 KLYSTRON GALLERY CONTROL SYSTEM

A.N. Aleshaev, I.V. Belousov, I.E. Borunov, R.G. Gromov, K.V. Gubin, A.A. Nikiforov  
BINP, Novosibirsk, Russia

## 1 INTRODUCTION

VEPP-5 forinjector klystron gallery (KG) is a large electrophysical installation that includes main part of forinjector RF-system: RF-power supply, synchrosystem, klystron units. This paper presents the control system (CS) of it. CS is based on the "standard" 3-level model [1].

Details of its realization reflects KG functional requirements and experience accumulated in BINP, as well as financial and technical abilities.

## 2 BASIC PROBLEMS, REQUIREMENTS AND STRUCTURE OF CONTROL SYSTEM

As the control object, the klystron gallery consists of 6 logically independent subsystems:

- 4 klystron posts (klystron amplifier with modulator and power supply);
- system of RF-power and synchronization;
- system of RF-phase and amplitude monitoring.

Operating condition of whole installation is pulsed with repetition rate up to 50 pps.

Each subsystem includes a large number of input/output channels. Some of the channels require the service at every impulse, some of them are "oscilloscopic" in principal. CS hardware is based on CAMAC standard, each subsystem needs 1-2 crate for supply.

Particularities of installation are:

- high level of interference;
- logical independence of subsystems;
- operating condition are static.

CS problems are:

- control and monitoring supply for each input/output channel during 1-2 operation cycles are required;
- it is necessary to receive the whole KG condition data at least for 2-3 operation cycles;
- maintenance of log file;
- ability for organization of local control console to debug a subsystem;

- interaction with CS of other VEPP-5 installations.

To solve these problems and to take into account the installation features:

- each subsystem has a corresponding hard and software unit
- field electronics are concentrated near the corresponding subsystem
- extern connections of subsystems are minimized, only impulse or numerical channels are used
- main stream of information is concentrated on the second level, where control of the field electronics (level 3) and primary data processing are performing.

The first CS level (servers and consoles) is connected with the second level (based on the intellectual crate controllers (ICC)) by Ethernet link with specially developed in INP protocols (like UDP) on this top. CS structure is presented in fig. 1:

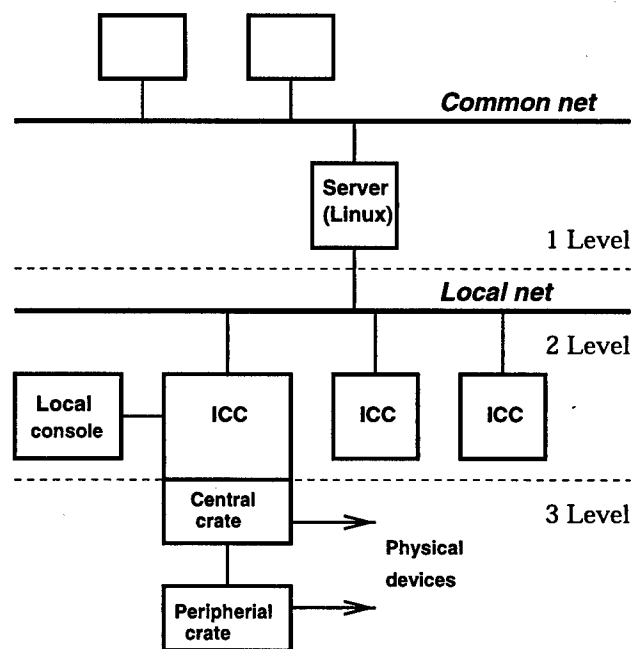


Figure 1: Control system hardware structure.

- each ICC supplies personal subsystem

- central computer (Server) runs as file server and channel of connection with each ICC
- control programs (operators console, dynamic data base at al.) work in the Server
- high level clients can access Server only
- local control console is organized on the basis of the proper ICC.

### 3 HARDWARE

As ICC we use Odrenok that is widespread in INP. To connect CAMAC and Ethernet, the special CAMAC-Ethernet adapter was developed. Pentium-166 with OS Linux is used as Server. ICC Odrenok has a ICL 1900 instruction set, added by the commands for CAMAC bus processes and vector operations. Odrenok provides the data transfer through CAMAC bus with the speed up to 1 Mbyte/sec. The speed and the reaction time on the interruption (about 15 mks) may be well used for design of the effective CS. The moderate requirements for exchange speed between subsystems and Server (average data stream is close to 10 kbyte/sec) make Ethernet protocol suitable for the ICC connection. Besides, the use of Ethernet doesn't requires the specialized drivers and interfaces in Server. CAMAC-Ethernet adapter used in our workstations provides the speed of the data exchange up to 400 kbyte/sec. It is sufficient for real-time network design.

### 4 MID-LEVEL SOFTWARE

The basis of a mid-level software is the specialized operation system ODOS for ICC Odrenok designed in INP [2]. It is multi-task OS with reaction time on the external events 1 ms approximately. ODOS supports a lot of special abilities for real-time control:

- timing of programs with step 100ms and 1s
- synchronization of the programs with LAM signals from CAMAC modules
- synchronization of the programs with signals from interruption register (CAMAC module where external pulse signals are registered with repetition rate up to 1 kHz)
- mechanism of interprogram and interprocessor communication

For interaction with other computers (for example high level) a special protocols based on Ethernet were developed. We can not install the whole TCP/IP (even UDP) due to Odrenok features. But our protocols are sufficiently complete and can be translated into TCP/IP in power servers. These protocols supplies:

- booting and starting of ODOS

- loading of programs during operation
- information exchange between any network processes
- terminal connection with high-level consoles
- transfer of directives from other computers
- access to filesystem.

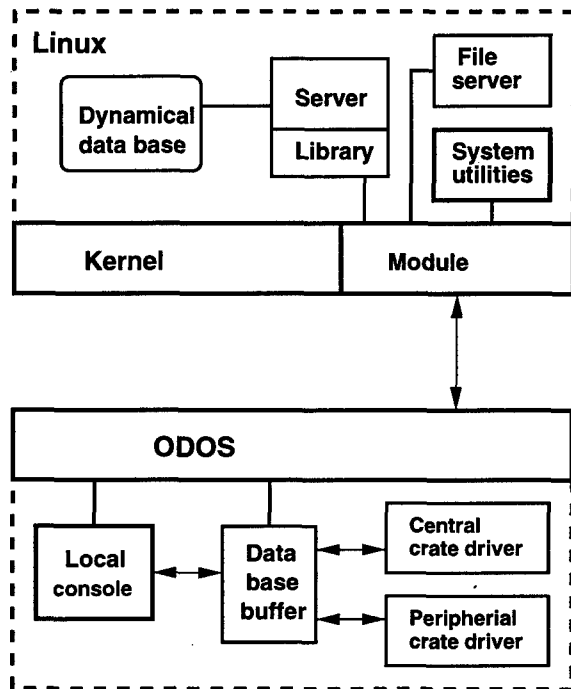


Figure 2: Control system software structure.

Protocols provide sufficiently high protection from deformations and losses of data, and guarantee the speed of exchange up to 200 kbyte/sec between two workstations. This OS is developed with the framework of the VEPP-4 and VEPP-2M control system modernization [3]. ICC drives CAMAC modules, collects and performs primary data analysis. ICC software typically consists of 4 programs (fig. 2):

- driver for central crate with ICC and CAMAC devices, necessary service at every cycle of installation operation
- driver for peripheral crate with non-intellectual controller
- "buffer" - fragment of distributed data base - where accumulation an primary data analysis, and communication between Server and local control console are performing
- local console for organizations of an operative debugging near the devices.

Drivers are synchronized by means of LAM signals with CAMAC devices, and by ODOS interruption system with other programs. Data and "command" flags exchange are organized through "buffer" only. Data preparation and transfer to Server (or to local console) as well as the system reconfiguration appears by Server (local console) request only.

## 5 SERVER SOFTWARE

ODOS protocols use Ethernet packets of non-standard type. Therefore the Server requires input/output facilities for these packets. Support of the work with these packets is integrated into OS Linux as one of the protocols supported by kernel. This method allows to operate with ODOS packets using standard UNIX facilities. It is realized by loaded module supporting primary functions for transfer, receiving and stand by of this packets by standard socket interface and formalized as a client libraries and utilities. For normal interaction between ICC and Server, and for convenient user operation we also need the following minimum of the special software (fig. 2):

- file server for booting ICC through local network and maintenance of ODOS file system
- terminal console ICC client
- client library where main network functions for ODOS protocols are supported.

Client software consists of control and visualizations programs as well as data base for description of whole installation [4]. Client programs compose the high level of CS and realize next functions:

- form of the control commands from operator to level 2 software
- form of request for receiving data of system condition, settings and measurements
- data visualizations and store

Data base consists of number of text files, where full description of the installation is stored. Special compiler translates data to binary dynamics data base for ICC. Server and ICC use the same data base text files, but binary data bases are different since the ICC and Server has different hardware platforms.

## 6 PRESENT STATUS

In present the working versions of loaded module, client libraries and utilities are completed and tested. Direct speed of the packets exchange between Server and ICC is up to 350 kbyte/sec (fig. 3) with maximum packet size of 1200 bytes. The Server operation with three concurrent ICC reduces the speed of exchange for not more than 10%. ICC application software and current version of Server software are tested. CS for the first subsystem is completed.

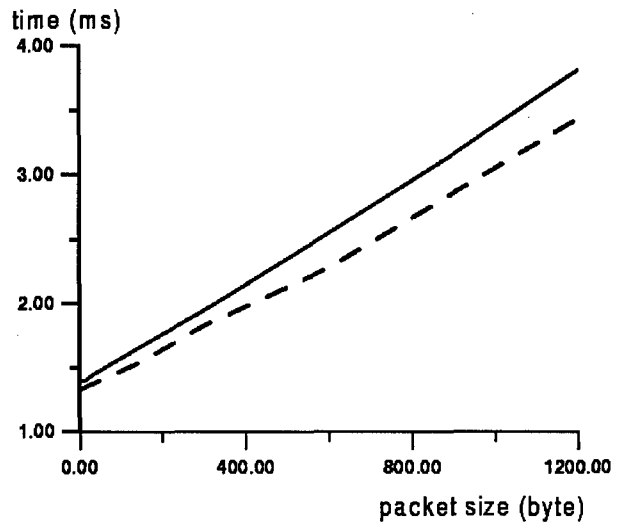


Figure 3: Dependencies of the packet exchange time versus packet size: solid line – between Server and single ICC, dashed line – between Server and 3 ICC simultaneously.

## 7 REFERENCES

- [1] Gotz at al. *Experience with a standard model'91 based control system at the ESRF*, Proc. ICALEPCS'93 (Berlin) NIM 352A (1994) p. 22-27
- [2] A.N. Aleshaev, Preprint INP 89-67, Novosibirsk 1989 (in Russian)
- [3] A.N. Aleshaev at al. *VEPP-4 control system upgrade*. Proc. ICALEPCS'97 (Beijing) p. 34-36
- [4] D.Yu. Bolkhovityanov at al. *The project of a control system software for a VEPP-5 complex*, Preprint INP 98-53, Novosibirsk 1998 (in Russian)

# MONITORING OF THE ELECTRON BEAM POSITION IN INDUSTRIAL LINACS

V.N.Boriskin\*, A.N.Savchenko, V.I.Tatanov.

National Science Center, Kharkov Institute of Physics and Technology (NSC KIPT), Ukraine

## Abstract

Recently the technological linear electron accelerators with the energy up to 10 and 25 MeV and the pulse current up to 1A have been developed and put into operation in the "Accelerator" R&D Production Establishment of the National Science Center, Kharkov Institute of Physics and Technology [1]. The zone of the technological object irradiation by the accelerated electrons is created by the magnetic scanning system. Wide-aperture (50 x 200mm) magneto-induction position monitor has been designed to control the electron beam position. Signals from the monitor are used in the accelerator control system.

## 1 THE OUTPUT BEAM SCANNING AND FORMING

The technoloical object irradiation zone is formed by the magnetic scanning system [2] presented by the laminated electromagnet with spatially homogeneous field and normal boundaries on the beam input and output. The magnet is excited by the generator of the two-polar sawtooth current. The scanning system provides the required value and uniformity of the scanning as well as the measurement and operative control of the electron beam energy characteristics.

Table 1: Parameter specifications

Parameter	Value
The electron energy	$\Delta = 8-25$ MeV
The beam diameter at the inlet of the scanning device	$\varnothing \approx 1$ cm ( $r_0 = z_0 = \pm 0.5$ cm)
The input beam angular divergence	$r'_0 = z'_0 \approx 5 \cdot 10^{-3}$ radn
Energy dispersion	$\Delta E / E \approx \pm 5 \cdot 10^{-2}$
The maximum angle of the beam scanning	$\varphi = \pm 20^\circ$
The effective length of the magnet field	$L_n \approx 16.3$ cm
The scanning frequency (controlled)	$f = 1...3$ Hz

\*E-mail: boriskin@nik.kharkov.ua

The electron beam is injected to the atmosphere through a thin titanium foil. The swing of the beam track in the foil plane is about 12 cm in the scanning regime. The basic characteristics of the accelerator beam and the irradiation zone, which determine the type and construction of the scanner, are presented in the following Table 1. Uniformity of the irradiation of the longitudinal object surfaces behind an output scanner window as well as characteristics of the accelerator natural initial beam is determined mainly by the configuration and quality of the magnetic field of scanning magnet, and also by the time characteristics and the form of the sawtooth exciting current. Fig. 1 shows schematically the scanning zone from the accelerating section outlet to the output window with real boundaries of the edge field on the inlet and outlet of the scanner magnet clearance.

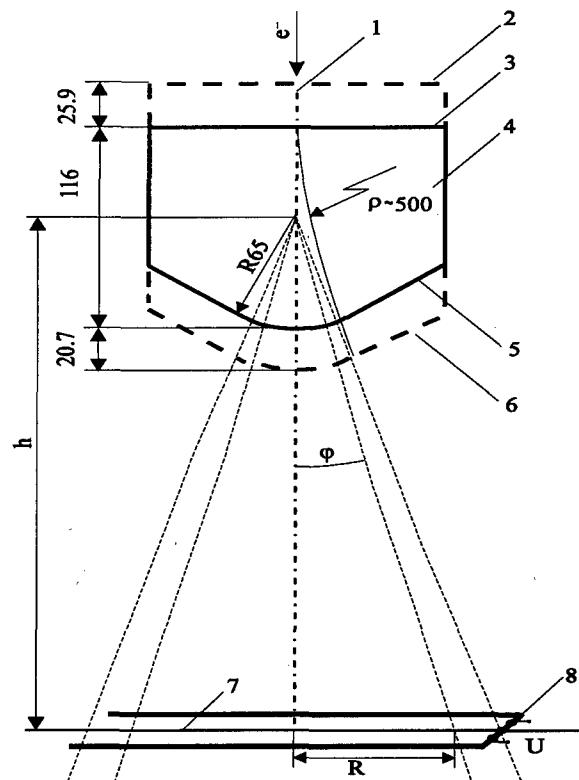


Fig. 1. The zone of beam scanning and output: 1- the accelerator axis; 2 and 6- the effective field boundaries on the inlet and outlet of the scanning magnet; 3 and 5 -the magnet boundaries (by iron); 7- the beam energy and location control plane; 8- position induction monitor.

## 2 OUTPUT BEAM POSITION MONITOR

Induction single-coordinate monitor to determine the position of the electron beam center is placed at the accelerator output in the atmosphere at 40 mm from the separating foil (Fig.2). The monitor aperture is 50x200 mm. The ferrite core cross-section is 10x20 mm. A number of winding coils is 30. Amplitude of the signal excited in the winding by the pulse electron beam  $I_p$  is directly proportional to  $I_p$  and inversely proportional to the distance  $Y$  to the winding:

$$Y = aU/I_p + b.$$

The coefficients were determined during the bench testing when a rectangular current pulse of duration 4 mcsec was advanced along a thin long conductor (fig.2). Obtained dependence in the current working range ( $I_p=0.7A$ ,  $t_p=4$  mcsec) is presented in Fig.3.

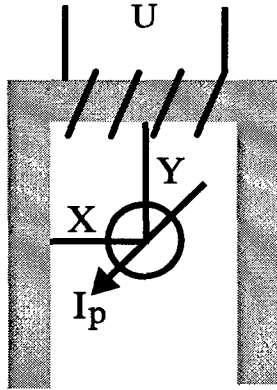


Fig. 2.The induction monitor scheme.

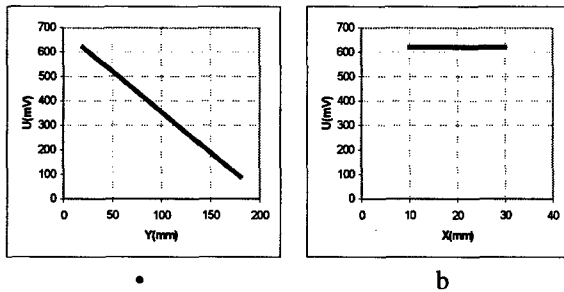


Fig.3. Amplitude  $U$  versus coordinate  $Y$  (•) and coordinate  $X$  (b).

The slope of the monitor characteristic is 3,4 mV/mm. After the placement of the monitor at the accelerator output the coefficients are defined more accurately by using the photometric method. At that the beam position is exposed on the glass located at the monitor aperture.

## 3 AUTOMATIC CONTROL SYSTEM

The special control system has also been developed [3] for controlling the electron beam current, energy and position as well as the control of parameters and defense of the accelerating and scanning systems from the damage caused by the beam; blocking of the modulator and klystron amplifier in the case of the intolerable operation regimes; current control in the magnetic system feeder; regulation of the phase and power of the HF signals in the injecting system; the radiation dose control and control of the target devices. The program & technical complex consists of PC equipped with CAMAC crate or measuring channels in PC standard, synchronization unit, microprocessor-operated complexes to monitor the klystron amplifier operation, the thermostating system, and the target equipment. The measuring devices provide receiving the signal from the analog pulse probes with the 50 or 100 nsec discreteness by two or four switched channels simultaneously. The information about the accelerator system state and the electron beam parameters is displayed on the local unit terminals and on the color graphics display in the form of the triple-screen control panel (Fig.4). The operator can monitor the work of the accelerator from the PC keyboard and from the local control panels. Program units can provide the single-shot or repeated control of system parameters or give out operating commands. Simultaneously the parameters of several systems can be controlled and only one of them can be regulated. One of the system modules provides the simultaneous measurement of the values of the signals from the winding of the expanded electron beam location probe and the scanning magnet excitation current (Fig.4).

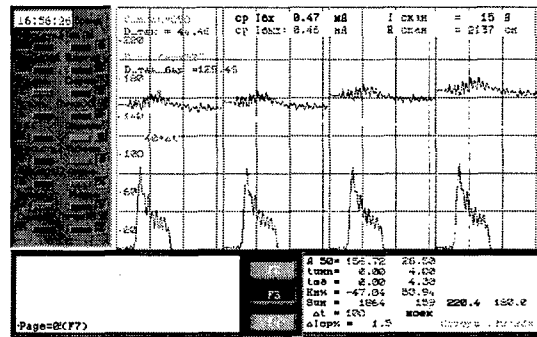


Fig.4. Videogram of the process of the electron beam energy control.

By the results of the measurements of several scanning cycles maximum  $Y_{max}$  and minimum  $Y_{min}$  values of the electron beam center deviation are calculated and the value  $2R = Y_{max} - Y_{min}$  is determined.

#### 4 THE OPERATIVE CONTROL OF THE ELECTRON ENERGY

It was shown [4] that the electromagnet of the output device can be used for the operative control of the electron energy. The proposed technique is based on the relationship between the total energy of the charged particle  $E_n$  and the magnetic field  $H\rho$ :

$$H\rho = \frac{1}{ec} \sqrt{E_n^2 - E_0^2},$$

where  $c$  - is the light speed,  $e$  and  $E_0$  0.5 MeV- are the electron charge and rest energy, respectively,  $\rho$  - is the radius of the particle trajectory in the magnetic field with intensity  $H$ . The following expression for the kinetic energy of the electron can be obtained by a simple transformation of (1) taking into account dimensions and units of measurement:

$$E_k = \sqrt{E_0^2 + (3 \cdot 10^{-4} H\rho)^2} - E_0,$$

where  $E_k$  is counted in MeV,  $\rho$  in cm. One can see that to measure the  $E_k$  value it is enough to determine two values: the intensity of the deflecting magnetic field  $H$  and the radius of the electron turn in this field  $\rho$ . However, while working with an accelerated beam the direct measurement of the specified characteristics, especially  $\rho$ , is very difficult. That is why the technique is based on the measurement of the linear and angular parameters - the effective length of the deflecting magnetic field  $L_n$  (taking into account the scattered fields on the inlet and outlet of the magnet), and the geometry of the scanning zone (Fig. 1). These parameters are measured in advance and do not change their values during the experiment. The excitation current force of the scanning electromagnet is obtained from the curve of magnetization  $H = f(I)$ . Noticing that for the small angles of the beam deflection ( $\varphi \leq 20^\circ$ ) the following relationship is valid

$$\rho = \frac{L_n}{\sin \varphi},$$

we arrive at the practical formula for  $E_k$ :

$$E_k = \sqrt{E_0^2 + \frac{k^2 I^2}{\sin^2 \varphi}} - E_0,$$

where  $k$  is the constant accounting the relationship between  $H$ ,  $I$  and  $L_n$  for a specific magnet and is determined by bench testing. From Fig. 1 one can see that if the value of the electron beam deflection from the axis ( $R$ ) on the plane located at distance  $h$  from the magnet is found by using any appropriate method and the value  $I$  is known, the most expectable value of  $E_k$  can be obtained. In this case

$$\varphi = \arctg(R/h)$$

The monitor described above enables to evaluate the current value  $R$  with an error of about 3%. The amplitude of the electromagnet excitation current  $I$  is determined at the same time, and then the value  $E_k$  is calculated. The videogram of the process of the electron beam energy control is shown in Fig.5.

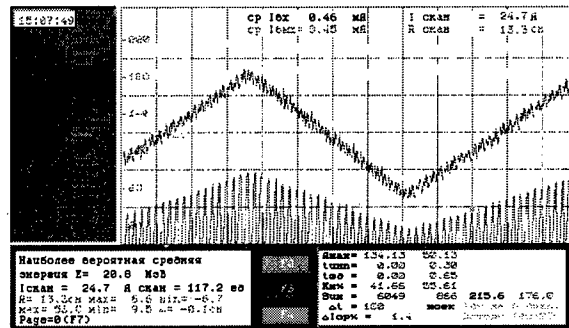


Fig.5. Videogram of the process of the electron beam energy control.

The evaluation of value  $R$  and the electron energy is performed without a denormalization of the accelerator working regime and takes about 2 sec.

#### 5 REFERENCES

- [1] A.N.Dovbnya et al. Electron Linacs Based Radiation Facilities of Ukrainian National Science Center "KIPT / Bulletin of the American Physical Society, May 1997, V.42, No.3, p.1391."
- [2] A.N.Dovbnya, et al. , "The Output Beam Scanning and Forming in the Multipurpose Electron Accelerators of KIPT", VANT, Series: Nucleic Physics, 1997, vol 1(28). p. 114-121.
- [3] V.N.Boriskin et al. Control system for a linear resonance accelerator of intense electron beams / Nucl. Instr. and Meth. in Phys. Res A 352 (1994) 61-62.
- [4] V.N.Boriskin, A.E.Tolstoy, V.L.Uvarov et al., "Automatic Control of the Electron Energy in the Technological Linear Electron Accelerators", Digest of the XIV Meeting on the Accelerated Particles, Protvino, Russia, 1994, vol.2, pp.97-98

## A SYSTEM FOR PROVIDING HIGH QUALITY TRIGGERS TO EXPERIMENTAL AREAS.\*

M.P. Fahmie<sup>#</sup>

Lawrence Berkeley National Laboratory, University of California  
1 Cyclotron Road, Berkeley, CA 94720 USA

### Abstract

Many researchers require a high resolution trigger to synchronize their data gathering electronics with the arrival of a synchrotron radiation pulse at their target. At the Advanced Light Source (ALS), this requirement was initially satisfied in a case by case manner by running Heliac cables from the Accelerator Timing System[1] to the various experiment locations. This approach was less than ideal due to poor risetimes, cost and difficulty of running Heliac cables, and the inconvenience of fixed timing. A new system has been installed at ALS that provides the researcher with a high quality, adjustable delay fiducial trigger, and a low level sample of the Accelerator RF (499.66 Mhz). The Ring Orbit Clock (1.523 Mhz) is distributed from the Accelerator Timing System to the various experiment locations using inexpensive twisted pair cable, where it is processed by a Phase Locked Loop Multiplier and High Speed Logic to integrate out noise/jitter and to produce the desired signals. Local drivers provide the researcher with sharp edged robust triggers.

### 1. INTRODUCTION

High resolution timing signals degrade as they are transported from their source to the timing user. Both high frequency losses and dispersion effects take their toll in the sharpness and accuracy of the product. These effects can be minimized by using higher grade transmission lines, but these lines are both expensive and awkward to handle. Noise, resulting in apparent jitter, is added by ground loop and inductive mechanism to further degrade the signal. Since ALS houses about 6000 square meters of experimental floor, a means of wide distribution, without excessive cost, was needed.

### 2. CONCEPT

Since ALS timing is strictly periodic, a solution that employs a low resolution fiducial that is processed in the user-end equipment to improve its quality is acceptable.

Clearly, a signal can be distributed at much lower cost if significant degradation can be tolerated, this is the basis of my solution.

Instead of distributing the accelerator RF signal (499.66 Mhz), I use its 328<sup>th</sup> subharmonic, the Storage Ring Orbit Clock (SROC), at 1.523 Mhz. This moderately low frequency can easily be distributed over inexpensive twisted pair cable and general purpose fiber optic links.

This signal, along with any phase and amplitude noise that it may have acquired in the course of distribution, is used as a reference signal to a Phase Locked Loop[2,3] (PLL) frequency multiplier that reproduces the desired 499.66 Mhz clock. If the PLL loop filter bandwidth is sufficiently narrow, then the noise integrates out and the quality of the output is primarily dependent on the quality of the PLL Voltage Controlled Oscillator (VCO).

### 3. DESIGN CONSIDERATIONS

Since low jitter is a primary goal, some effort was put into selection of the VCO. Oscillator jitter is a strong function of the loaded Q of the oscillator resonator[4], so an oscillator employing a high Q resonator was desirable. Since Quartz resonators typically possess Q's a thousand times those typical of LC oscillators, several crystal controlled VCO's (VCXO) were evaluated. A small module from Raltron Inc.[5] was chosen for its low jitter and comparatively low cost.

Although long term stability is controlled by the reference signal, temperature variations in an early prototype produced large phase offsets. These offsets were traced to the temperature sensitivity of the threshold voltage in the digital logic and its effect on the relatively slow risetime of the reference signal, later versions utilize the fully differential features of the ECL logic family to eliminate this phase error.

The loop bandwidth is set at 10 Hz in order to use as much of the short term stability of the VCXO as possible. Such narrow bandwidths can make it difficult to achieve initial phase lock if a simple phase comparator is used. A fairly new dual mode comparator is now available from

\* This work was supported by the Director, Office of Energy Research, Office of Basic Energy Sciences, of the U.S. Department of Energy under Contract No. DE-AC03-76SF00098.  
<sup>#</sup> mpfahmie@lbl.gov



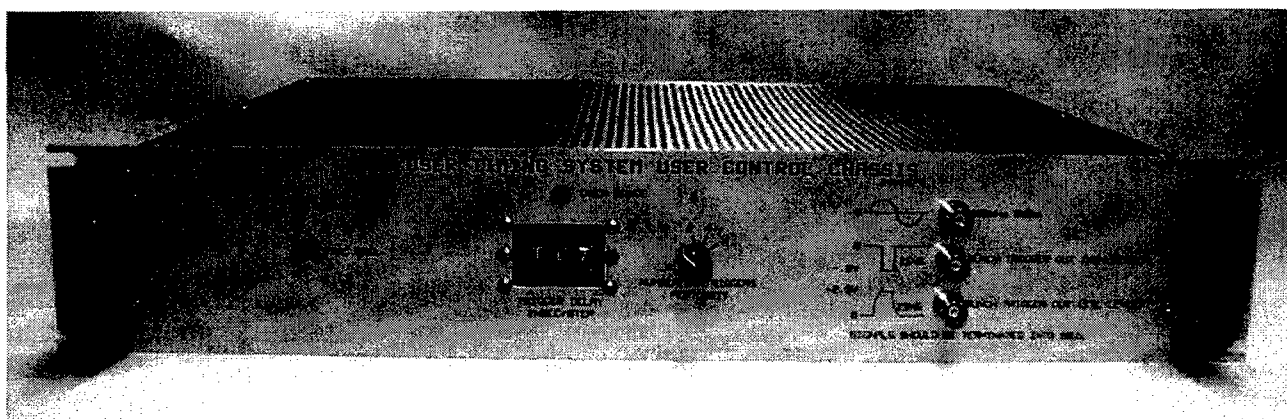


Figure 1

Analog Devices (AD9901) that begins the lock sequence in the frequency comparator mode and automatically becomes a phase comparator after frequency lock has occurred.

This manufacturer has solved a deadband problem that existed in phase/frequency comparators of other designs. An additional feature of the Analog Devices device is its fully differential input and output structure. This allows us to use differential techniques throughout the phase detector and loop amplifier to minimize baseline errors in the analog circuitry.

#### 4. FEATURES

The User Timing Chassis provides two output signals; the accelerator RF frequency (499.66 Mhz.) and a user configurable trigger. The user can select 1,2,4, or 8 evenly spaced triggers per storage ring revolution, and he may position these triggers anywhere in the accelerator period in precision steps of one beam bucket.

The trigger is simultaneously available in TTL, Differential ECL, and NIM. The NIM output features 500 picosecond rise/fall time. All output drivers are designed to drive 50 ohm loads, but are also series terminated to minimize reflections when driving a mismatched load.

Distribution of the reference signal to the various User Timing Chassis around the accelerator is simplified since the only signal that is distributed is a relatively low frequency (1.523 MHz.). The PLL effectively cleanses it of any noise it may have acquired in transit and inexpensive twisted pair wiring is all that is necessary.

#### 5. PERFORMANCE

The output of the User Timing Chassis has been compared with a highly filtered signal from the ALS Master Oscillator to evaluate the phase jitter of the regenerated RF signal. The reference signal was routed across the accelerator through cable trays and used a combination of fiber optic and RS-422 twisted pair transmission. A Tektronics CSA-803 Communications analyzer was used to create a jitter histogram. The analyzer's statistical functions indicate that the RMS jitter measured ~16 picoseconds.

#### 6. ACKNOWLEDGMENTS

The author would like to acknowledge the assistance of Allen Geyer, Moises Balagot, and Ronald Gervasoni of LBNL in the construction, debug, and deployment of this system.

#### 7. REFERENCES

- [1] M. Fahmie, "Design of the Advanced Light Source Timing System," Proceedings of the 1993 IEEE Particle Accelerator Conference, Washington DC, p. 1869
- [2] Motorola Inc., "Phased Locked Loop Design Articles", AR-254
- [3] F. Walls, S. Stein, "Servo Techniques in Oscillators and Measurement Systems", National Bureau of Standards Technical Note 692
- [4] J. Jespersen, J. Fitz-Randolph, National Bureau of Standards Monograph 155, p. 31-40
- [5] Raltron part number VH7126A, Raltron Inc., Miami, FL.

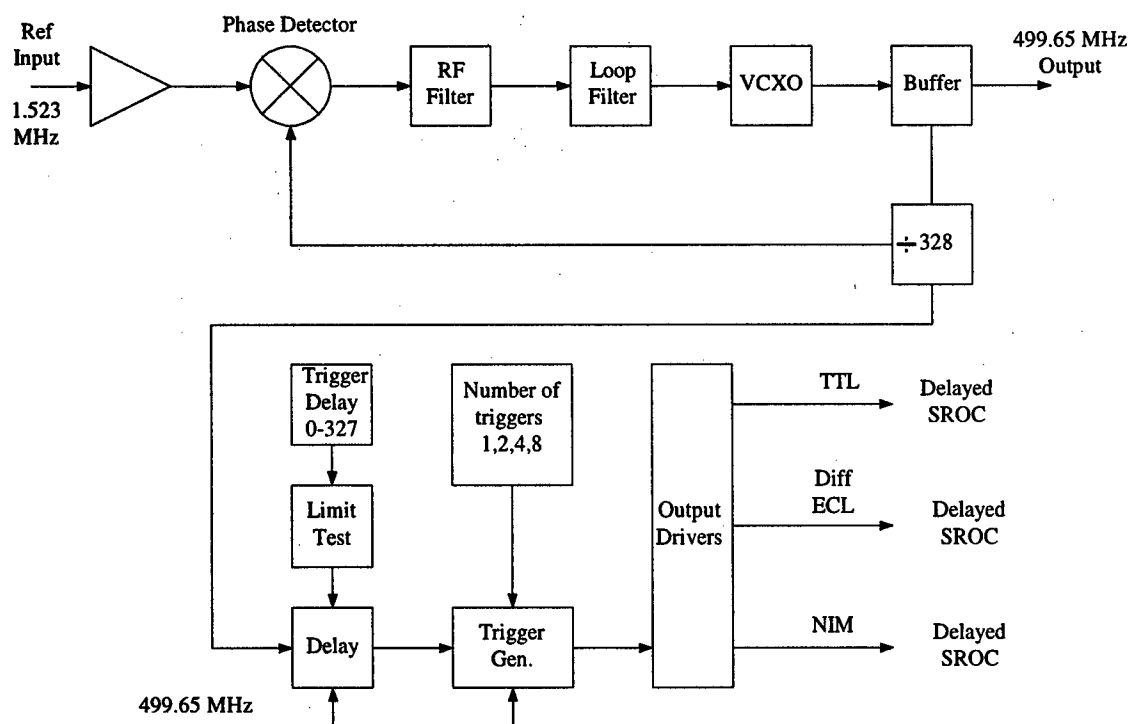


Figure 2 - Block Diagram

# A TUNING PROCEDURE FOR A RACETRACK MICROTRON

W.H.C. Theuws<sup>1</sup>, F.F. de Wit<sup>1</sup>, S.R. Weijers<sup>2</sup>, M. Weiss<sup>2</sup>, J.I.M. Botman<sup>1</sup>, A.F.J. Hammen<sup>1</sup>,

<sup>1</sup>Eindhoven University of Technology, Cyclotron Laboratory,

P.O. Box 513, NL-5600MB Eindhoven, The Netherlands.

<sup>2</sup>Eindhoven University of Technology, Systems and Control Group,

P.O. Box 513, NL-5600MB Eindhoven, The Netherlands.

## Abstract

The electron-optical system of the Eindhoven RTM has been designed and constructed with non-stringent alignment and machining tolerances in the order of 0.1–1 mm and 0.1–1 mrad. The alignment and machining errors that are present can and must be counteracted with slightly different settings of the seventeen adjustable parameters (i.e. the excitation currents of the two end magnets and of twelve correction magnets (one at every turn), the beam energy and phase at injection, and the energy gain per turn), otherwise the beam will not be accelerated properly. All the errors are unknown and consequently their effects are unknown. Therefore, twenty-five beam-position monitors (BPMs) have been installed in the RTM (two for each turn and one at the extraction point) in order to measure the effects of the errors on the electron beam. The responses of the beam-positions at the BPMs with varying values of the RTM parameters have been studied. Based on these studies a tuning procedure is proposed and its usability and performance has been investigated with numerical simulations of the accelerator.

## 1 TUNING PROCEDURE

The approach for the Eindhoven racetrack microtron [1] is that all alignment and machining tolerances have been chosen such that these can be achieved without extraordinary measures (no difficult and expensive machining procedures and alignment procedures). The main bending magnets have been produced of ordinary steel with a constant gap for each sector, such that the field inhomogeneity is in the order of 1 % [2]. No expensive measures have been taken to decrease this inhomogeneity [3][4].

For the Eindhoven racetrack microtron it has been shown by Webers [2] that if the misalignments are within their (relatively large) tolerances there is always a solution for the adjustable machine parameters such that the isochronism deviations as well as the closed-orbit deviations are sufficiently small.

The seventeen adjustable parameters that can be used for tuning are listed in table 1. From the basic microtron equations [1] it can be seen that either  $E_{inj}$ ,  $E_r$ , or  $B_r$  can be

fixed, and the others should be adapted to it. For the Eindhoven racetrack microtron it has been chosen to fix the injection energy of the beam  $E_{inj}$ . Hence, sixteen adjustable parameters are left to counteract all the errors. Furthermore, twenty-five BPMs (two for each orbit and one at the extraction point) are used to find the optimal settings of the seventeen adjustable parameters.

Table 1 : The seventeen adjustable parameters of the Eindhoven racetrack microtron (the variable  $\delta B$  is defined as the half of the magnetic-field difference between the right and the left main bending magnet).

Adjustable parameter	Notation	Unit
Kinetic energy at injection	$E_{inj}$	MeV
Amplitude of the cavity potential	$E_{cav}$	MeV
Injection phase	$\phi$	deg
Mean field of bending magnets	$B$	T
Field difference of bending magnets	$\delta B$	T
Excitation of $n^{th}$ correction magnet	$B_{c,n}$	Gauss

The approach for the optimisation of the adjustable parameters is based on a brute-force method combined with a linear feed-back mechanism for the closed-orbit errors. Those parameters that influence the beam more than once, i.e.  $B$ ,  $\delta B$ ,  $E_{cav}$ ,  $\phi$ , will be tuned using a brute-force method, and those parameters that influence the beam once only, i.e. the correction magnets  $B_{c,1}$  through  $B_{c,12}$  will be tuned using a linear feed-back mechanism.

From figure 1, where  $B$ ,  $\delta B$ ,  $E_{cav}$ , and  $\phi$  are varied over typical initial errors, it has been decided that  $B$  will be varied over 5 steps from -1 % to +1 %,  $\delta B$  over 3 steps from -1 % to +1 %,  $E_{cav}$  over 5 steps from -1 % to +1 %, and  $\phi$  over 5 steps from -10 to +10 degrees. In total this gives  $5 \times 3 \times 5 \times 5 = 375$  grid points in the four-dimensional  $B - \delta B - E_{cav} - \phi$  space. At each grid point it is tried to guide the beam through the racetrack microtron by means of the twelve correction magnets.

For the tuning of the twelve correction magnets a linear feed-back mechanism is applied. For this purpose the beam-position monitors BPM<sub>1</sub>, BPM<sub>2</sub>, BPM<sub>3</sub>, ..., BPM<sub>25</sub> are used. The responses of the correction dipoles on the beam positions at these twelve monitors have been determined by means of the numerical simulation

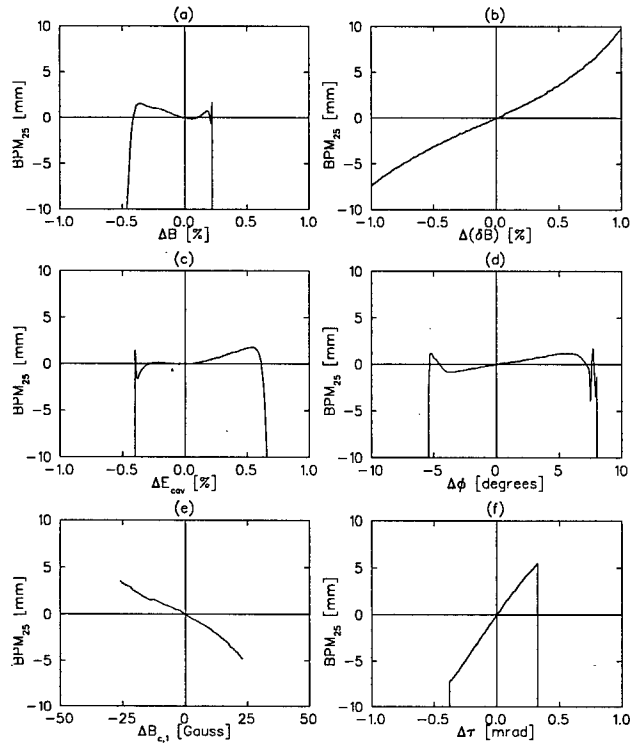


Figure 1 : The responses on the beam-position monitor at the extraction point of the Eindhoven racetrack microtron,  $BPM_{25}$ , as a function of variations in  $B$  (a),  $\delta B$  (b),  $E_{cav}$  (c),  $\phi$  (d),  $B_{c,1}$  (e), and the tilt angle  $\tau$  (f), respectively.

program of the racetrack microtron, and these are used for the feedback control.

Most of the 375 grid points will not result in proper acceleration of the electron beam up to the extraction point. Consequently, in many cases the beam positions will be corrected well up to a certain orbit (this means that the beam-position deviations will be small up to a certain orbit), and in the next orbit the beam will not arrive at all. This is due to too high isochronism deviations. The control mechanism at this grid point has to be stopped.

## 2 TEST OF THE TUNING PROCEDURE

The tuning mechanism as described in the previous section has been tested using a numerical simulation program of the Eindhoven racetrack microtron. Many parameters of the racetrack microtron have been given all kinds of typical random Gaussian errors. The standard deviations of the microtron parameters are listed in table 2. Then the tuning mechanism has been applied. For each individual grid point in the four-dimensional  $B - \delta B - E_{cav} - \phi$  space the maximum number of iterations has been set to 50. The result of one typical case is shown in figure 2. In this figure the last orbit where the beam is still measurable after the optimisation procedure of the

Table 2: The standard deviations for the microtron parameters as have been used for the test calculations.

Microtron Parameter	Standard deviation
Main magnetic fields	0.3 %
Cavity potential	0.3 %
Beam phase at injection	3.0 degrees
Kick of the correction magnets	0.3 mrad
Magnet positions	0.1 mm
Magnet angles	0.3 mrad

correction magnets is shown as a function of  $B$ ,  $\delta B$ ,  $E_{cav}$  and  $\phi$  (these four parameters have been varied, with regular steps over the intervals shown in figure 1). There are two cases where the beam is extracted:  $\Delta E_{cav}=1\%$ ,  $\Delta\phi=0$  degrees,  $\Delta B=0.5\%$ , and  $\Delta(\delta B)=-1\%$  or  $\Delta(\delta B)=0\%$ . The estimated beam-current efficiency, i.e. the ratio of the extracted beam current and the injected beam current of the racetrack microtron, is 0.66 and 0.64, respectively. These are both acceptable. For the optimum the response on  $BPM_{25}$  has been calculated as a function of parameters  $B$ ,  $\delta B$ ,  $E_{cav}$  and  $\phi$  (similar as in figure 1), and the results are shown in figure 3. The response plots are similar as those shown in figure 1.

This test has been applied many times for microtrons which all had different values for the alignment errors, machine errors, and initial parameter deviations. In all cases the problem has been solved. This means that there

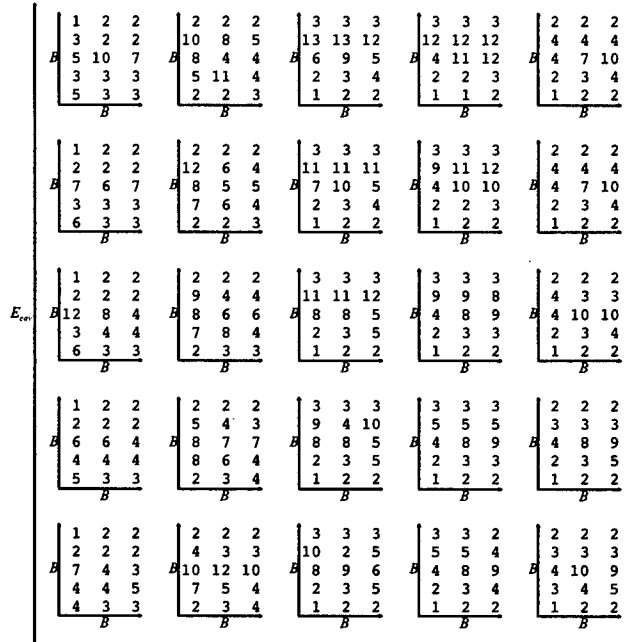


Figure 2 : The last orbit where the beam is still present after optimisation of the correction magnets as a function of  $B$  (-1.0, -0.5, 0.0, 0.5, 1.0 %),  $\delta B$  (-1.0, 0.0, 1.0 %),  $E_{cav}$  (-1.0, -0.5, 0.0, 0.5, 1.0 %) and  $\phi$  (-10, -5, 0, 5 10 degrees).

has always been at least one grid point for which a solution has been found such that the beam reaches the extraction point with a reasonable amount of beam current. The mean number of total iteration steps appeared to be  $(2710 \pm 90)$ . The average of the total efficiency of the Eindhoven racetrack microtron, i.e. the percentage of the injected beam current that will be extracted eventually, appeared to be  $(68 \pm 2)\%$ .

Assume that about 3 seconds are needed between two iteration steps, mainly used for the re-adjustment of the correction magnets. In total, this means that about 2.3 hours are needed for the whole procedure, which is certainly acceptable. This time can be made shorter (if necessary) by making the tuning procedure more efficient in terms of the stopping criteria. In some cases it must be possible to terminate the control efforts for a certain grid point in an earlier stage. Furthermore, if the microtron has been operated several times, the starting values of the adjustable microtron parameters can be chosen better, and consequently the tuning procedure can become much quicker.

### 3 CONCLUDING REMARKS

The Eindhoven racetrack microtron has been designed without extremely-stringent requirements on machining and alignment. Therefore, a tuning mechanism has been

designed which optimises the adjustable parameters that influence the electron beam in each orbit by means of a brute-force method. The adjustable parameters that influence the beam only once are optimised by means of a linear feed-back mechanism that uses the measured beam positions in the drift space. This method has been tested. An optimum has been found in all tested cases with an average efficiency of  $(68 \pm 2)\%$  and an average number of iteration steps of  $(2710 \pm 90)$ .

### 4 REFERENCES

- [1] W.H.C. Theuws, J.I.M. Botman, H.L. Hagedoorn, *The Eindhoven linac-racetrack microtron combination*, Nucl. Instr. and Meth. B 139 (1998) 522-526.
- [2] G.A. Webers, *Design of an electron-optical system for a 75 MeV race-track microtron*, Ph.D. Thesis, Eindhoven University of Technology (1994).
- [3] H. Herminghaus, K.H. Kaiser, U. Ludwig, Beam optics and magnet technology of the microtron in Mainz, Nucl. Instr. and Meth. 187 (1981) 103-107.
- [4] L.R.P. Kassab, P. Gouffon, The use of correction coils in end magnets of accelerators, Proc. Part. Acc. Conf. Vancouver (1997) 3239-3241.

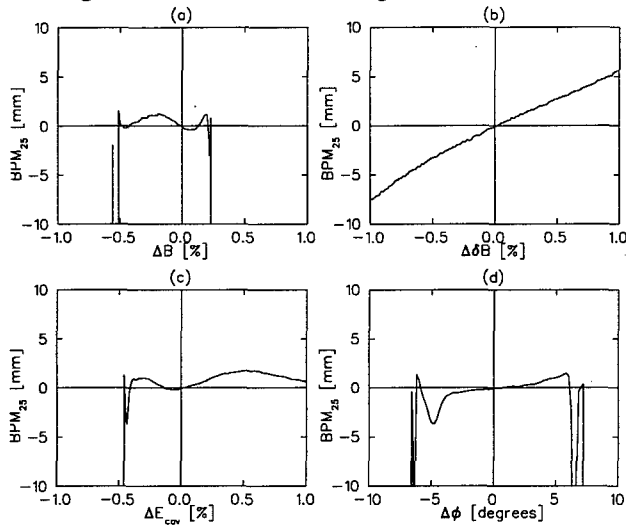


Figure 3: The responses on BPM25 as a function of variations in  $B$  (a),  $\delta B$  (b),  $E_{cav}$  (c), and  $\phi$  (d), respectively. These calculations have been performed for the optimal setting as it has been found in the example.

# OPTIMISATION OF THE CURRENT RAMP FOR THE LHC

P. Burla <sup>\*</sup>, Q. King, J.G. Pett  
CERN, Geneva, Switzerland

## Abstract

The field quality of the main magnets in the LHC will be, in part, dependent upon the shape of the magnetic field as a function of time. A theoretical optimisation of this function has been carried-out with the aim of minimising the dynamic errors [3]. This work resulted in the definition of a current ramp function composed of mathematically defined, smoothly joining segments. A prototype digital controller based on a DSP has been developed and built [4]. In this equipment the current ramp is computed from the segment equations in real time. The user need only supply the characteristic parameters for the segments in order to define the ramp. In this paper, the effect of the ramp function on the error terms is discussed and the corresponding segment equations are given. The prototype implementation is described and actual results are shown.

## 1 BACKGROUND

For the LHC, the shape of the dipole current acceleration ramp as a function of time will have a profound effect on the performance of the accelerator. In particular, the start of the ramp, just above injection energy will be critical due to the phenomenon known as "snap back".

Field errors in the LHC superconducting magnets have been studied extensively over the last few years [1] [2]. Non-linear field imperfections due to the ramping rate can be reduced to an acceptable level only by employing a smooth and gradually increasing transition to the linear ramp. The choice of this curve must also try to minimise the overall ramp time.

## 2 DYNAMIC ERROR SOURCES (AND POSSIBLE REMEDIES)

### 2.1 Magnetisation decay and "Snap-back"

The LHC superconducting magnets are characterised by a significant drift in the magnetic field when the current is constant (e.g. on the injection plateau). At the restart of the ramp (for beam acceleration) the field bounces back abruptly, reaching the original value at the start of the injection plateau after an increase in current of about 30 A.

This effect, called "snap-back", has a magnitude approximately independent of the ramp-rate. However, it occurs over a very small current increment and it can

be shown [1] that the time duration of this effect is inversely proportional to the ramp rate (Fig 1).

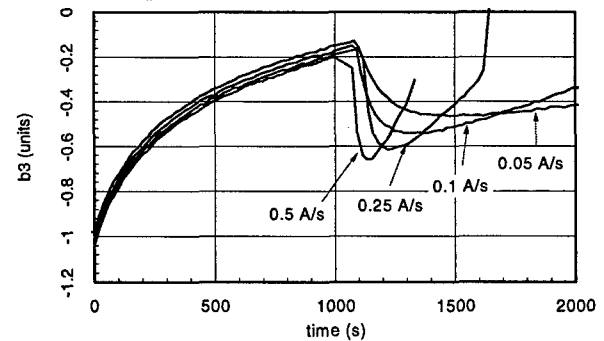


Figure 1: Snap-back observed in a dipole prototype at different ramp-rates after the injection plateau. Units are  $10^{-4}$  of the main field, at 10 mm. reference radius.

The magnitudes of the field harmonics can be reduced by ramping very slowly, which would also give time for a feedback correction scheme to work. Of course, remaining at a very slow rate would result in excessive overall ramp times. The obvious remedy is to employ a gradually increasing ramp rate, such that "snap-back" occurs at a low rate, but the nominal maximum linear ramp rate is attained as early as possible.

Small, independently controlled corrector magnets will be needed to maintain the beam variables within the pre-specified tolerances, especially during the "snap back" phase. Control signals for the corrector circuits will be derived by real-time feedback algorithms

### 2.2 Inter-strand eddy currents

In a superconducting magnet, eddy currents develop in the loops formed by the twisted strands inside the superconducting cable. These currents, induced during ramping, produce field distortions having a magnitude proportional to the ramp-rate and inversely proportional to the inter-strand resistance. The relative value of ramp induced field harmonics for a constant ramp rate:

$$b_n = C_n \cdot \frac{\dot{B}}{B}$$

which is greatest at low field near injection. The effect of these imperfections is to distort the linear optics and cause a reduction of the dynamic aperture. The design of LHC sets limits on these harmonics and therefore directly determines the allowable ramp rate as a function of current. Any choice of ramp function must respect these limits while minimising the overall ramp time.

<sup>\*</sup> Email: Paolo.Burla@cern.ch

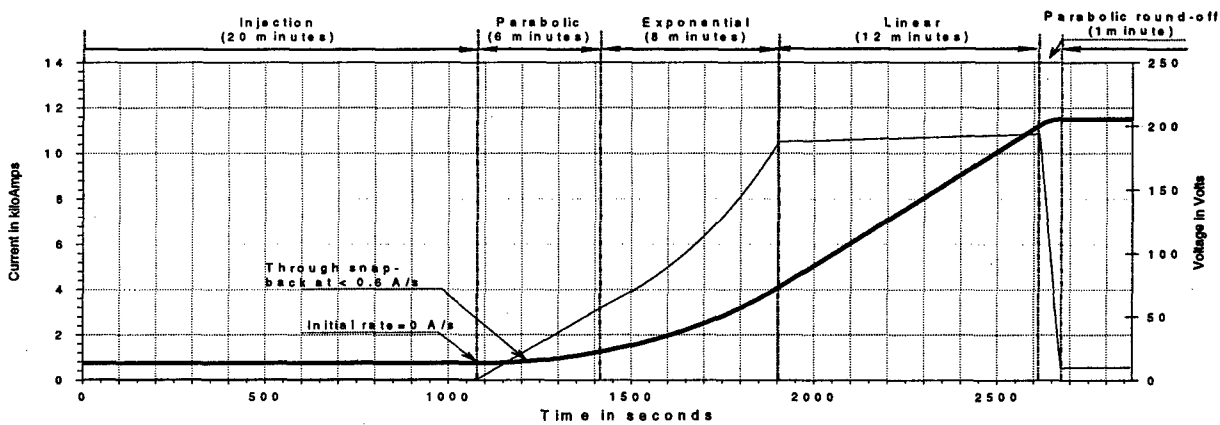


Figure 2: Current and voltage functions for the "Beam-in" part of the LHC cycle

### 3 POWER CONVERTER SYSTEM DESIGN CONSIDERATIONS

Each of the LHC power converters, along with its inductive magnet load, is a closed-loop device that has a limited bandwidth and a limited output voltage. Due to these considerations, the rates of change of current are limited, as well as the dynamic accuracy of the output current with respect to the value demanded. Step changes of both voltage and current cannot be produced by such a system and economic limits must also be imposed on the maximum output voltage required. This implies that an optimum choice of ramp rate must include these considerations and also that no discontinuities in ramp rate can be allowed. Furthermore, the desire to incorporate on-line magnetic and beam feedback at a suitable rate adds a further set of limits.

In view of the above, the design of the reference generation and regulation system in each power converter must also be optimised to ensure that no additional sources of discontinuities, overshoots or following errors are significant. In order to address these issues, a digital approach has been adopted [4]. These methods can generate smooth ramping functions as opposed to the traditional straight line segment method, and can ensure that resolution, overshoot and following errors will be less than one part per million of the maximum current.

### 4 DEFINITION OF THE RAMP SEGMENTS

The optimised LHC acceleration ramp that is proposed has been divided into four segments which are joined to the constant, injection and flat-top regions. This ramp is shown in Fig. 2. At the end of the flat-top another region comprised of six segments brings the field down to injection value. These latter segments along with 'degaussing' and pre-injection porches are

not the subject of this paper and will not be mentioned further. Each of the segments has been chosen such that the criteria outlined above are met and in addition are joined together such that no discontinuity occurs. This optimisation process is essentially iterative and the rates chosen are determined largely from field harmonic results obtained during testing of prototype LHC dipoles. However, care has been taken to ensure that all power converter specifications of maximum output voltage and slew rate etc. are adequate to allow the needed corrections to take place well within the performance limits of each converter.

The first segment has a **parabolic function**:

$I = I_{inj} \cdot (1 + \alpha \cdot t^2)$  from injection current to the end of the segment. The rate of acceleration for this segment is presently constant at  $9 \cdot 10^{-3} \text{ A/s}^2$  (that is  $\sim 0.75 \text{ ppm/s}^2$ ) which gives a total time to traverse the "snap back" region of approximately 67 seconds, thus allowing corrections to be applied.

The second segment follows an **exponential function**:

$I = I_0 \cdot e^{\beta \cdot t}$ . The reason to change to an exponential is that the magnitude of sextupole ( $b_3$ ) and other terms is bound to a constant value as long as such a function is applied. This would also reduce the ramp time by one minute.

The third segment is **linear** and corresponds to the design rate of 10A/s. This segment continues to just before the flat top is reached.

The fourth segment is also a **parabolic** function, but which now decelerates to zero. The deceleration rate is chosen here to ensure that no power converter limit is exceeded, and in particular that absolutely no overshoot of the current can occur. All segments join together at the same acceleration rate to ensure no discontinuities.

The entire acceleration curve can therefore be defined by the mathematical expressions for each segment and by the desired and permitted rates of change. From a given injection current, just four numbers need to be input to the digital function generator to produce the

entire LHC acceleration current ramp. The ramp is started with a synchronising pulse and every millisecond the function generator evaluates the ramp equations to determine the precise current required. The ramp algorithm determines precisely the points of transfer from one function to the next, such that no abrupt change of rate occurs. The digital regulation system employed in the prototype power converter control equipment then ensures that the actual current is accurate to approximately 1ppm of full-scale current.

## 5 PRELIMINARY RESULTS

The prototype digital controller was programmed in C to generate an LHC ramp based on the segment equations described above. The controller period is 1ms. Figure 3 shows the measurement of the current in a 10m superconducting dipole during a short LHC ramp.

The current was limited to 5kA, however, all the segments are included.

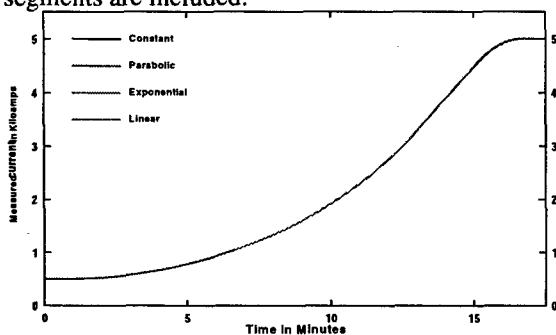


Figure 3: Measured current ramp to 5kA on 10m dipole.

Figure 4 shows an expanded view of the beginning of the ramp where it can be seen that the resolution and errors are less than 1ppm.

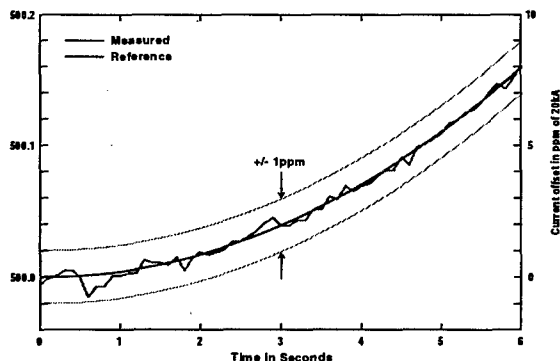


Figure 4: Detail of the start of ramp from figure 3.

## 6 CONCLUSIONS

An optimised shape for the LHC acceleration ramp has been developed, based on the constraints of field quality, time minimisation and practical power converter limits as well as on-line feedback considerations. This complex curve has been implemented in a prototype power converter system

and has shown that the expected result can be obtained. The fact that this curve is mathematically defined considerably simplifies implementation and subsequent magnetic testing methods. Magnetic measurements will now proceed in order to further prove and refine the ramp function.

## REFERENCES

- [1] L.Bottura, A.Faus-Golfe, L.Walckiers, R.Wolf, "Field Quality of the Main Dipole Magnets for the LHC Accelerator" (CERN LHC Project Report 17, June 1994)
- [2] A. Faus-Golfe, "Minimization of the ramp-induced non-linear field imperfections in LHC" (CERN SL/AP LHC Project Note 9, May 1995)
- [3] L.Bottura, P.Burla, R. Wolf, "LHC Main Dipole proposed baseline current ramping"(CERN LHC Project Report 172, March 1998)
- [4] I. Barnett, D. Hundzinger, Q. King, J.G.Pett. "Developments in the High Precision Control of Magnet Currents for LHC" contribution to this conference.



## GPS PRECISION TIMING AT CERN

Beetham C.G., Ribes J-B.

### Abstract

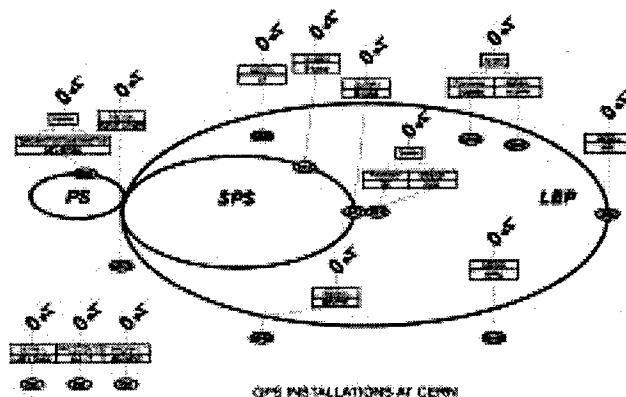
For the past decade, the Global Positioning System (GPS) has been used to provide precise time, frequency and position co-ordinates world-wide. Recently, equipment has become available specialising in providing extremely accurate timing information, referenced to Universal Time Co-ordinates (UTC). This feature has been used at CERN to provide time of day information for systems that have been installed in the Proton Synchrotron (PS), Super Proton Synchrotron (SPS) and the Large Electron Positron (LEP) machines. The different systems are described as well as the planned developments, particularly with respect to optical transmission and the Inter-Range Instrumentation Group IRIG-B standard, for future use in the Large Hadron Collider (LHC).

### 1 INTRODUCTION

The Global Positioning System (GPS) is claimed to be the most accurate system for worldwide distribution of precise time, frequency and position ever deployed. Each of the 24 operational satellites, plus spares, carry an ensemble of on-board atomic clocks which are controlled and maintained by the US military from their control base in Colorado Springs. Monitor stations in Hawaii, Kwajalein, Ascension Is. and Diego Garcia ensure a worldwide absolute time reference, with respect to UTC, from 3 to 100 ns. depending upon technique and the good will of the US military.

The "Interface Control Document" (Letter of Intent) was signed in 1982 by six leading US firms and the "NAVSTAR USER'S OVERVIEW" was published in 1986, [1]. The system was officially declared operational in 1995. While the NAVSTAR GPS system was financed by the US most equipment sold is now for recreational use which explains the significant price reductions over the recent years. Also, the system was originally conceived for its extreme precision in position, it is only recently that affordable equipment has become available to provide the accurate time facility.

This note summarises the majority of installed operational GPS systems at CERN. To avoid duplication, identical hardware has been used for all the installations. The equipment choice was influenced more by widespread usage of the VME standard at CERN than price performance factors.



### 2 SYSTEMS

#### 2.1 Beam Dump Trigger

The initial LEP Beam Dump Triggering system was installed during the 1993 shutdown. The system enables physicists to dump the beam whenever they consider that their detectors are being damaged by beam induced radiation. This is achieved by a hardwired connection from each of the four experiments, plus the control room, to the beam dump equipment located at LEP point 5. Each connection consists of a constant current loop with an electronic switch located within each experiment. Whenever the switch is activated, either manually or by the user's circuitry, the current loop is opened which causes the beam dump kicker to be fired, thus dumping the beam.

However, during the 1993/1994 runs a few physicists complained that the beam was not being dumped until several milliseconds after they had activated their switch, thus causing expensive damage to their detectors. In order to clarify this situation it was decided to install a GPS monitoring system.

A GPS receiver is installed wherever there is a switch and also at the beam dump. When a switch is activated the time of day, to the nearest microsecond, (with a resolution of 300 nanoseconds), is "frozen" by the receiver. At LEP point 5, a signal that is derived from the actual high voltage pulse, that fires the beam dump kicker, is used to "freeze" the time in the GPS receiver located there. After the beam has been dumped the control system reads and also "unfreezes" the GPS receivers concerned and displays the values via the alarm system. Since the system became operational there has not been a single complaint about the beam being dumped late.

## 2.2 Time of day source for Master Timing Generators (MTG's)

The MTG's are used to generate millisecond based machine timing for the PS, SPS and LEP machines. The original PC based systems used a "Computime" instrument made by Patek Philippe of Geneva. This unit receives 77.5kHz radio signals from Mainflingen, Germany, and then passes them on to the MTG by means of an RS-232 port. This resulted in a time accuracy of  $\pm 10$  milliseconds.

When it was decided to upgrade the control system by replacing the PC based 386/486 systems running XENIX with VME platforms using LynxOS operating systems, it was logical to replace the Patek Philippe with VME GPS. The time of day information is now transferred via the VME backplane with an accuracy of less than two microseconds.

## 2.3 Cosmics

Besides monitoring the results of  $e^+e^-$  collisions in LEP, the four experiments are also excellent devices for detecting cosmic particles. For many years physicists have been exploiting this feature, either interleaved with daily LEP operations or else during the start-up periods. Then they have access to the detectors without the background noise of LEP.

This CosmoLep project requires the synchronisation of the individual observations from the four experiments. This will be achieved by tagging data with the GPS time. Each experiment will have a "time of day" generator synchronised to the GPS receivers located in each pit. The project may be extended to include other European and possibly worldwide, laboratories.

## 2.4 Bunch length Interlocks

High intensity short bunches excite higher order modes in LEP. This causes overheating, exceeding the capabilities of the cryogenic system, resulting in equipment damage. It is proposed to install an instrument that will continuously monitor the bunch length and intensity of the beam on a turn-by-turn basis. If the set threshold is exceeded then the beam will be dumped, via the triggering system and tagged by GPS.

## 2.5 ATM Tests

ATM (Asynchronous Transfer Mode) networking technology is being evaluated for its use in transporting data in the future Large Hadron Collider (LHC). In order to gain experience with ATM, it is being used in a feedback loop for control of betatron tunes in the SPS. The two principle elements of the Q-loop are a transverse damper, used to excite the beam, situated in building BA2 and the focussing and de-focussing quadrupole magnets powered from building BA3. Correction data is calculated

from beam response observed in BA2 and sent over an ATM link to the power converter in BA3.

The data is transmitted using a standard 53 byte ATM cell. Immediately before transmitting the cell the time of day is read from the GPS receiver, located in BA2, and included in the cell. When the cell is received in BA3 a local GPS receiver is read. The difference between the two times, minus the time it takes to read out a GPS receiver, is used to calculate the latency of the system.

## 2.6 RF Interlocks

The RF interlock system monitors up to 24 different parameters, i.e. temperature, water flow, vacuum etc. These parameters are then multiplexed down to a single entity that controls a switch. Each switch is included in series with a RF current loop circuit, which follows the LEP circumference, and any switch that is opened breaks the current loop. This action activates the "freeze" register in the GPS receiver located at LEP point 4 (ALEPH) and dumps the beam. The control system then interrogates the GPS module and informs the alarm system who was responsible for the dump.

For the high intensity 1999 run a duplicate system has been installed in LEP point 6 (OPAL).

## 2.7 WorldFIP

WorldFIP [2] is a fieldbus network protocol designed to provide links between low level sensors and actuators and the bus controllers, VME, PC etc. One of its principle characteristics is that it is deterministic. This feature will be utilised to control the 1700 magnet power converters that will be required for LHC [3].

Although the WorldFIP macro-cycles are deterministic, they are referenced to an internal oscillator contained in each bus controller. Whilst this is acceptable for most industrial applications the inherent "drift" of each oscillator exceeds the LHC requirements.

To overcome this problem, it is intended to externally synchronise the WorldFIP macro-cycles to the GPS system. A test system is currently being assembled to evaluate if this proposal is feasible. The aim being to synchronise the entire 1700 LHC magnet power converters to the GPS.

## 2.8 Lab Tests

The lab systems are used for both hardware and software developments. These tests resulted in the choice of the active antenna and the type of cable to be used, in addition to the in-line amplifier and the splitters. The lab has direct optical links, both single-mode and multimode, to the control room where one can branch into the main CERNwide optical transmission infrastructure. The accurate map reference co-ordinates of the lab plus all the GPS installations were provided by CERN's survey group

[4]. This was done to verify the correct operation of the GPS equipment.

### 3 EQUIPMENT

#### 3.1 Receiver

The choice of the GPS receiver was dictated by the operation of the LEP Beam Dump Triggering system. There were two essential requirements, the unit must be compatible with the existing SL control system and it had to have an externally triggered hardware "freeze" register. The chosen module, TrueTime Model GPS-VME, fully conforms to these requirements.

The specifications of the module can be found at [www.trutime.com](http://www.trutime.com)

#### 3.2 Active Antenna

The antenna used is NovAtel Model 521. It is environmentally sealed for protection against rain, ice and lightning strikes. For extra durability it is housed in a waterproof "Teflon" structure which protects the TNC connector as well as the antenna.

Full specifications are available at [www.novatel.ca](http://www.novatel.ca)

#### 3.3 Cable

Low-loss coaxial cable type CERN CK50.

#### 3.4 Ancillaries

4 way splitter, SCHWAIGER type VTF 7844; 5-2250 MHz. 2 way splitter, Radio Materiel type VTF 7842; 5-2300MHz. In-line amplifier, Axing type SVS 2-00; 12-26dB, 450-2400MHz.

### 4 DEVELOPMENTS

#### 4.1 Optical

For operation of the LHC magnet power converters, there is a requirement to transmit time of day timing information, referenced to the GPS standard, to each of the LHC alcoves. At the moment GPS referenced timing is only available in the experimental pits. The distance from the pits to the alcoves is approximately 1000m.

Tests have been carried out using single-mode optical fibres in conjunction with FOXCOM optical transmitter receivers, series 7000 [5]. It has been demonstrated that the GPS antenna L1 frequency at 1.575GHz, can be transmitted over a distance of 1762m. This is more than adequate to transmit the antenna signals to each alcove. However, this solution is expensive, the transmitter receiver units cost over 5000 dollars a pair. A cheaper alternative may be possible with the use of IRIG-B.

Also being evaluated is the transmission of the current MTG type timing over multimode fibres, using FOXCOM type 105 transmitter/receiver units. These

modules are far less expensive than singlemode equipment and transmission tests of up to 10Km have been successful.

#### 4.2 IRIG-B

The task of standardising instrumentation timing systems was assigned to the Tele-Communications Working Group (TCWG) of the Inter-Range Instrumentation Group (IRIG) in 1956. The standard defines the characteristics of six serial time codes presently used by U.S Government agencies and private industry [6].

The GPS receivers used at CERN generate a 1kHz amplitude modulated IRIG-B coded signal synchronised to the GPS time. This will be connected to the module VME-SG2, also made by TrueTime. This is a time of day generator, either free running or synchronised by an IRIG-B input signal. The manufacturers claim an accuracy of 1 microsecond, this will be evaluated with respect to the GPS receiver time whilst using an interconnecting cable of 1km. This will be done in conjunction with the WorldFIP jitter tests. This scenario may result in a simple inexpensive method of providing GPS synchronised timing in the alcoves for the LHC era.

### 5 CONCLUSIONS

At CERN, all the GPS systems are used to provide sub-microsecond time of day information. Since the original 1993 project, the LEP Beam Dump Triggering System, GPS has been integrated into many different systems. This trend will certainly continue.

For LHC operation greater use of GPS is foreseen. The quench protection system alone will generate over 4000 possible inputs to the beam dump trigger system. In order to perform meaningful post mortem analysis, all systems will have to be time stamped. Due to the uniform distribution of the major systems throughout the LHC complex, it will be essential to use GPS as the source of the time reference.

### 6 ACKNOWLEDGEMENTS

To Robin Lauckner for his support, i.e. funding, of the project plus his assistance in testing the equipment.

### REFERENCES

- [1] GPS NAVSTAR YEE-82-009B
- [2] European Standard WorldFIP EN50170
- [3] Developments in the High Precision Control of Magnet Currents for LHC. I.Barnett, D.Hundzinger, Q. King, J.G.Pett. This conference
- [4] Système Tridimensionnel de Coordonnées Utilise Au CERN. J. Gervaise, M.Mayoud, E.Menant. Copyright CERN 1976
- [5] FOXCOM, Website [WWW.foxcom.com](http://WWW.foxcom.com)
- [6] IRIG Serial Time Code Formats. IRIG Standard 200-98, May 1998

# A LOW-COST, NIST-TRACEABLE, HIGH PERFORMANCE DIELECTRIC RESONATOR MASTER OSCILLATOR\*

L.R. Doolittle, C. Hovater, L. Merminga, J. Musson\*, M. Wissmann  
Thomas Jefferson National Accelerator Facility, Newport News, VA

## Abstract

The current CEBAF Master Oscillator (MO) uses a quartz-based 10 MHz reference to synthesize 70 MHz and 499 MHz, which are then distributed to each of the klystron galleries on site. Due to the specialised nature of CEBAF's MO requirements, it has been determined that an in-house design and fabrication would provide a cost-effective alternative to purchasing or modifying vendor equipment. A Global Positioning System (GPS) disciplined, Direct Digital Synthesis (DDS) based MO is proposed which incorporates low-cost consumer RF components, designed for cellular communications. A 499 MHz Dielectric Resonant Oscillator (DRO) Voltage Controlled Oscillator (VCO) is phase-locked to a GPS-disciplined 10 MHz reference, and micro-tuned via a DDS, in an effort to achieve the lowest phase noise possible.

## 1 INTRODUCTION

The Thomas Jefferson National Accelerator Facility (Jefferson Lab) consists of a 5.5 GeV nuclear physics accelerator (CEBAF) and a 500 watt IR Free Electron Laser (FEL). Both machines have placed tight requirements on their beam parameters, most notably energy spread. Future beam requirements for accelerators used in nuclear physics and as UV FEL drivers will demand stringent timing requirements for the RF MO. In the case of the nuclear physics accelerator, the timing jitter (induced by phase noise) contributes to the overall energy spread of the electron beam[1]. Similarly, in the FEL, the laser cavity performance is affected by the timing jitter between successive light pulses and electron bunches [2]. Typically, accelerator designers have taken a rather easy, but expensive, approach and purchased high-end full-featured frequency synthesizers, most notably from Hewlett Packard. This paper serves as a survey of the many cost-effective oscillator options available to the RF engineer. The paper is divided into three sections; the first is a brief discussion of phase noise / timing jitter, the second is a comparison of four types of resonator-oscillators: crystal, SAW, DRO, and CRO. An attempt is made to simulate the performance with the application of a 2nd-order phase-lock loop (PLL). The paper concludes with a discussion on technology and cost, and a proposed RF MO.

\*Work supported by the Department of Energy, contract DE-AC05-84ER40150.

\* email: musson@jlab.org

## 2 OSCILLATOR EVALUATION

Precision oscillators are characterized in both the time and frequency domains. Timing jitter is the relative measure of stability from cycle-to-cycle, over a prescribed interval. The common method for reporting stability, as prescribed by the IEEE, involves averaging differences in consecutive sample pairs (a two-sample variance AVAR), and is known as the Allan Variance [3]. Although small Allan Variance values for long intervals are regarded as good clocks, accelerator applications require a high stability for the brief time a particle is in orbit within the machine.

Jitter is the composite of a large sum of Fourier fractional frequency, or phase, fluctuations about the carrier frequency. In the frequency domain, this is phase noise, and is defined by the IEEE to be the total noise power in a 1 Hz bandwidth, divided by the total carrier power (including sidebands), as measured at a carrier-offset frequency,  $f$ :

$$S_{\phi}(f) = \Delta\Phi(f) * BW^{-1}, \text{ Radians}^2 / \text{Hz}$$

Typically, only one sideband is presented, and the units are logarithmic:

$$L(f) = 10 * \log ( \frac{1}{2} * S_{\phi}(f) ), \text{ dBc} / \text{Hz}$$

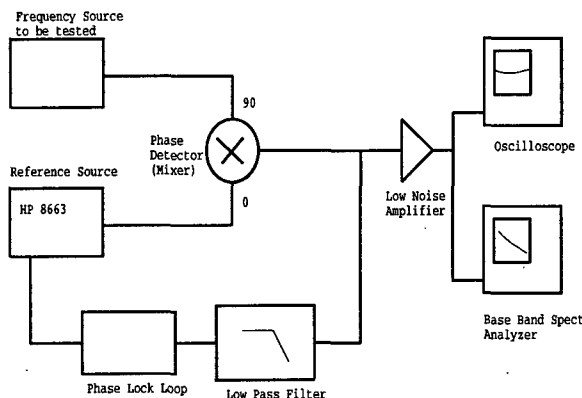
The 1 Hz measurement bandwidth allows a universal comparison to be performed, while the  $L(f)$  eliminates restrictions on the values for  $f$ . Unnecessary phase noise redistributes carrier energy into the sidebands, where power is wasted. This effect can be quite considerable, as in the case of the Jefferson Lab UV FEL RF control system, which powers the high-Q ( $10^7$ ) superconducting RF cavities. The UV FEL specification requires a 1497 MHz phase noise envelope of  $2.6 \times 10^{-10} / f$  [2].

Measurement of phase noise is accomplished by either an autocorrelation, or a cross-correlation with a known, low-noise reference oscillator. The technique employed to measure phase noise at Jefferson Lab is shown in Figure 1. An ultra-low phase noise Hewlett Packard HP 8663 synthesized microwave signal source was used as a standard, to which the unit under test (UUT) was loosely phase-locked. After the two oscillators are multiplied together, the baseband signal is applied to an FFT spectrum analyzer for analysis. A dBV/Hz readout with a correction for detector gain was used to determine the  $L(f)$  in dBc/Hz.

SIGINT, a numerical method used to transform the phase noise spectrum into a time-domain description of frequency stability, was developed at NIST, which allows

the designer to accurately predict oscillator performance [4].

**Figure 1.** Phase noise test fixture.



### 3 RESONATOR OPTIONS

#### 3.1 Crystal Oscillator

Historically, quartz-crystal resonators have been used to construct high-stability oscillators which exhibit good phase noise, particularly close to the carrier. In addition, recent availability of Global Positioning Satellite (GPS) technology permits easy phase-lock capability, with NIST traceability [5]. Their frequency use is restricted to the 1-20 MHz range, with 5 MHz being the optimum frequency for phase noise performance [6]. Frequency multiplication is required above these ranges. Although phase noise is a non-linear phenomenon, scaling to other carrier frequencies is possible if integrated phase noise values of less than 0.2 Radians are obtained [7]. A naïve scaling can then be applied:

$$L(f)_{v_2} = L(f)_{v_1} + 20 * \log(v_2/v_1)$$

To move from a carrier frequency of 5 MHz to a frequency of 499 MHz, the entire  $L(f)$  spectrum is scaled by 34 dB. Although the close-in performance is retained, an ultimate high-frequency limit of -130 dBc/Hz is reached for Fourier frequencies above 1kHz. For this reason, it is desirable to use the close-in behavior of quartz as a synthesizer reference, but appeal to other resonators which might exhibit better high-frequency characteristics.

#### 3.2 Surface Acoustic Wave

The Surface Acoustic Wave (SAW) oscillator is well suited for the 500 MHz - 1GHz portion of the RF spectrum, due mainly to its small size. The SAW device tested at Jefferson Lab was an off-the-shelf component sampled by a vendor. A free-running center frequency of 500 MHz was measured. The tuning port was terminated in 50 Ohms to minimize frequency drift. The SAW

possessed a high resistance to microphonics, short of tapping directly on the enclosure.

#### 3.3 Dielectric Resonant Oscillator

Dielectric Resonant Oscillators (DRO) have become popular as potential low-noise microwave sources. They serve to provide high-Q resonators, of relatively small size. Phase noise performance is suggested to be optimized for the 1-2 GHz range.

A DRO was fabricated at TJNAF, primarily in accordance with Loboda et al. and technical briefs from the dielectric supplier [8]. Two software models were employed to determine cavity dimensions and coupling schemes. Copper was chosen, due to its superior RF characteristics.

Raw measurements produced Q and insertion loss (IL) values of 10,000 and -4 dB. Minimal attempts were made to optimize cavity coupling. Final values for loaded-Q and IL, to be used in the test DRO oscillator were 15,000 and -10 dB, respectively.

A transmission type of oscillator was assembled using the high-Q cavity, a low-noise amplifier, and a coaxial transmission line of appropriate electrical length to sustain oscillation.

Phase noise performance was carefully measured by acoustically isolating the cavity from surroundings, minimizing susceptibility of environmental effects. Microphonics were prevalent, adding to the close-in phase noise.

##### 3.3.1 Frequency Divider for DRO

A 499 MHz DRO presents a cavity structure too large for most practical applications, so a tradeoff of 1497MHz was employed. A divider scheme is required to arrive at the 499 MHz operating frequency.

Prescalers are susceptible to additional phase noise, mostly from amplitude fluctuations. A Miller divider, first proposed in 1939, employed a regenerative feedback approach to achieve a divide by (N+1) output. Recently, NIST engineers have applied the Miller circuit to microwave oscillators, appearing in Figure 5, and achieving exceptional PM performance [9]. Since the overall divide ratio is N+1, a divide-by-two scheme requires no multiplier, improving reliability. This configuration was selected for its simplicity, in order to determine feasibility.

After the measurement, a full phase-locked-loop (PLL) was induced, in order to evaluate in-situ performance. No attempt was made to optimize the loop filter, other than to achieve stability.

The measured SAW, divided DRO phase noise, locked DRO and UV FEL specification, scaled for 499 MHz, are all summarized in Figure 2. The test fixture appears to have an ultimate noise floor at ~ -130 dBc, providing a worst-case performance bound. Despite that, the trends of

each of the oscillators is evident. Loboda, et al. Have demonstrated 1.5 GHz DRO phase noise performance of  $-130$  dBc at 1kHz, further supporting their use[8].

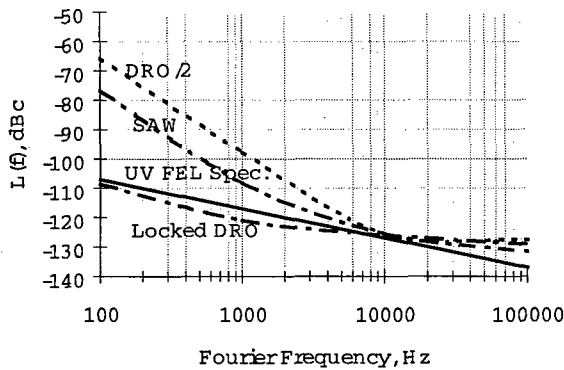


**Figure 2.** Phase noise summary of SAW and DRO oscillators

### 3.4 Coaxial Resonator

Another trend in the communications industry is the use of coaxial resonant oscillators (CRO), which employ a  $\frac{1}{4}$ -wave coaxial dielectric structure as a feedback element. They are commonly used at UHF frequencies, and have typical Q values of less than 1000. Therefore low phase-noise performance is difficult to achieve, without the use of loop filters of high-order ( $>5$ ). These filters permit the designer to tailor resultant phase noise by optimizing poles and zeros within the control loop, but often present an enigmatic design challenge.

## 4 CONCLUSION

Of the four options explored, the most attractive appears to be the DRO oscillator. Although the SAW exhibited excellent noise, along with immunity to microphonics, its cost per unit is quite high. At the time of this manuscript, a typical price for an off-the-shelf SAW, for standard frequency dies, was  $\sim \$2000$ . Custom frequencies incur an additional engineering-setup charge which could be as high as  $\$8000$ . Conversely, the DRO material is relatively inexpensive ( $\sim \$30$  per puck) in small quantities. Additional cost would exist for optimizing puck dimensions for a specific frequency, with the remaining cost embedded in cavity fabrication. Despite the susceptibility of the cavity to microphonics, little was required to eliminate with the use of a PLL. Additionally, the proliferation of software tools for DRO applications made cavity designs particularly easy. Popularity of these devices surely rests on having these design tools available.

The unit cost for CRO elements is by far the least expensive ( $\$1.00$  / unit), and the same software as was used in the DRO design is applicable to CROs. Given the

requirement for complex loop filters to minimize phase noise, the CRO would not be the first choice for a precision UHF oscillator. However, software simulation packages such as MatLab or Elanix would certainly reduce design time.

The use of a crystal-only arrangement would demand that a  $\sim 5$ -10 MHz oscillator be multiplied to the necessary frequency, achieving an ultimate phase noise floor of  $\sim -130$  dBc, not achieving Jefferson Lab specifications.

Finally, a system diagram of a proposed low-cost Master Oscillator, exhibiting high stability, low phase noise, Global Positioning Satellite (GPS) reference, and limited frequency agility is demonstrated in figure 3. Estimated cost for such a system is less than  $\$10,000$ .

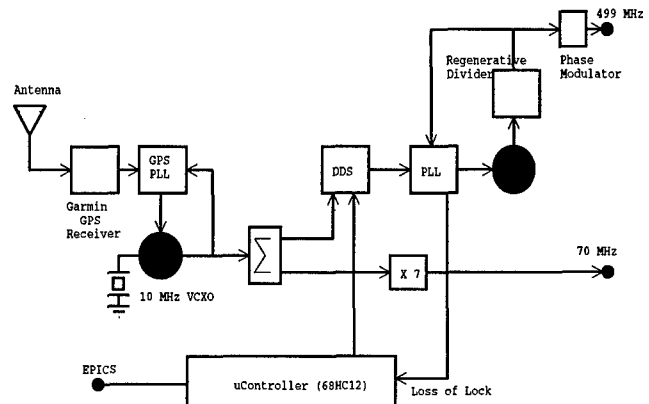


**Figure 3.** Proposed Master Oscillator

## 6 REFERENCES

- [1]G. Krafft, J. Bisognano, and R. Miller "Revised Energy Spread Estimate," CEBAF Tech note CEBAF-TN-0050, May, 1987
- [2] *Free Electron Lasers for Industry*, Vol. 2, UV Demo Conceptual Design, Laser Processing Consortium, TJNAF, Newport News, VA, May, 1995
- [3]*Characterization of Clocks and Oscillators*, NIST Technical Note 1337, NIST, Boulder, CO March, 1990
- [4]F.L. Walls, J. Gary, A. O'Gallagher, R. Sweet, and L. Sweet, "Time Domain Frequency Stability Calculated from the Frequency Domain Description," SIGINT Software package description, NIST, Boulder, CO. Sept. 1991
- [5]B. Shera, "A GPS-Based Frequency Standard," QST Magazine, American Radio Relay League, July, 1998
- [6]U. L. Rhode, J. Whitaker, and T.T.N. Bucher, *Communications Receivers*, 2<sup>nd</sup> ed., McGraw-Hill, New York, 1997
- [7]L.W. Couch II, *Digital and Analog Communication Systems*, 3<sup>rd</sup> ed., Macmillan Publishing, New York 1990
- [8]M.J. Loboda, T. Parker, and G. Montross, "Frequency Stability of L-Band, Two-Port Dielectric Resonator Oscillators," *IEEE Trans. Microwave Theory Tech.*, vol. MTT-35, pp. 1334-1338, Dec. 1987
- [9]E.S. Ferre-Pikal and F.L. Walls, "Low PM Noise Regenerative Dividers," *Proc. 1997 IEEE Freq. Symp.*, pp. 478.484

## Low Current, Long Beam Pulse with SLED

F.-J. Decker, Z. D. Farkas, M.G. Minty

Stanford Linear Accelerator Center, SLAC\*, CA 94309, USA

### Abstract

The 3 km long linac at the Stanford Linear Accelerator Center (SLAC) is used for fixed target experiments such as E-155, with energies up to 50 GeV. The SLAC Energy Development (SLED) system increase the maximum no-load energy by a factor of 1.6, but it also causes a varying beam energy curve. To provide a long pulse or bunch train for the experiment the energy profile has to be flat. Besides more sophisticated methods such as varying the phase of two klystrons feeding one structure section as proposed in the NLC design, we describe the method used for E-155 in spring of 1997. The desired low charged beam didn't have any significant beam loading, but by inserting a  $180^\circ$  phase notch during the SLED pulse, a beam pulse of up to 500 ns was achieved. The energy range without compensation would have been 15%, while with compensation the energy spread was reduced to about 0.15%. The phase notch was achieved by triggering a pair of two additional  $180^\circ$  phase switches about half a structure fill-time after the SLED pulse was triggered. Simulations are compared with the experimental result.

### 1 INTRODUCTION

In a complementary paper [1] the current was varied to achieve a low energy spread. In this paper we treat currents that are so low that their self induced beam voltage is negligible, say, less than 0.1 % of the no-load voltage.

For a 460 ns pulse, the beam impedance of the SLAC linac is  $30.5 \text{ G}\Omega$  hence a current of 1 mA, corresponding to a charge of  $2.9 \cdot 10^9$  particles, has a self-induced voltage of only 0.1% of 32 GV, the operating voltage of E-155x experiment. The charge required by E-155x is somewhat less than  $2.9 \cdot 10^9$ . The SLAC linac has nearly the required energy without SLED, but with SLED the operating beam energy is attained with fewer klystrons.

Thus, we have to manipulate the SLED output (the rf input to the accelerator sections), to achieve a nearly constant no-load voltage for up to 500 ns. We can do this by varying the SLED output amplitude, but this is difficult. We achieve the same effect by inserting a  $180^\circ$  phase notch during the SLED pulse in a fraction of sectors. The number of sectors notched,  $n_{sn}$  out of the total number of sectors with rf,  $n_{st}$  determines the effective depth of the notch, hence the slope of the no-load beam voltage.

Thus, at a given beam voltage and beam current pulse width, we can reduce the current amplitude from a maximum to zero.

### 2 SIMULATIONS

When after the normal SLED  $180^\circ$  phase switch, another pair of these switches is generated, a notch will appear in the SLED rf output. Figure 1 shows the relative SLED output with and without this notch. The notch begins 280 ns after the phase flip at the beginning of the SLED pulse and lasts for 400 ns. With this notch the energy is not wasted, but stored again in the SLED cavity, so the output is higher at the end.

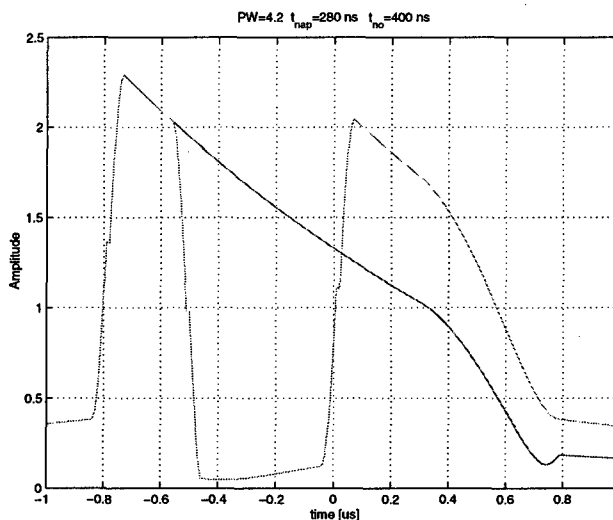


Fig. 1: Relative rf amplitude after the SLED cavity. The relative SLED output with and without a notch is shown as a function of time. With the notch the energy is not wasted but stored again in the SLED cavity, therefore the notched pulse is higher at the end.

Figure 2 shows the relative SLED gain, which is the rf output integrated over the accelerator structure. When the output has a notch, the relative SLED gain (which is also the relative beam voltage) falls sharply and can be used to compensate the rising slope of the SLED gain curve without notch. With 6 out of 16 sectors notched the gain is nearly flat. Fig. 3 shows the beam voltage and energy spread for the mixed sectors. The maximum beam voltage with  $n_{st} = 16$  is 38.5 GV. The charge is  $1.6 \cdot 10^9$  and the current is only 0.56 mA.

\*Work supported by Department of Energy contract DE-AC03-76SF00515.

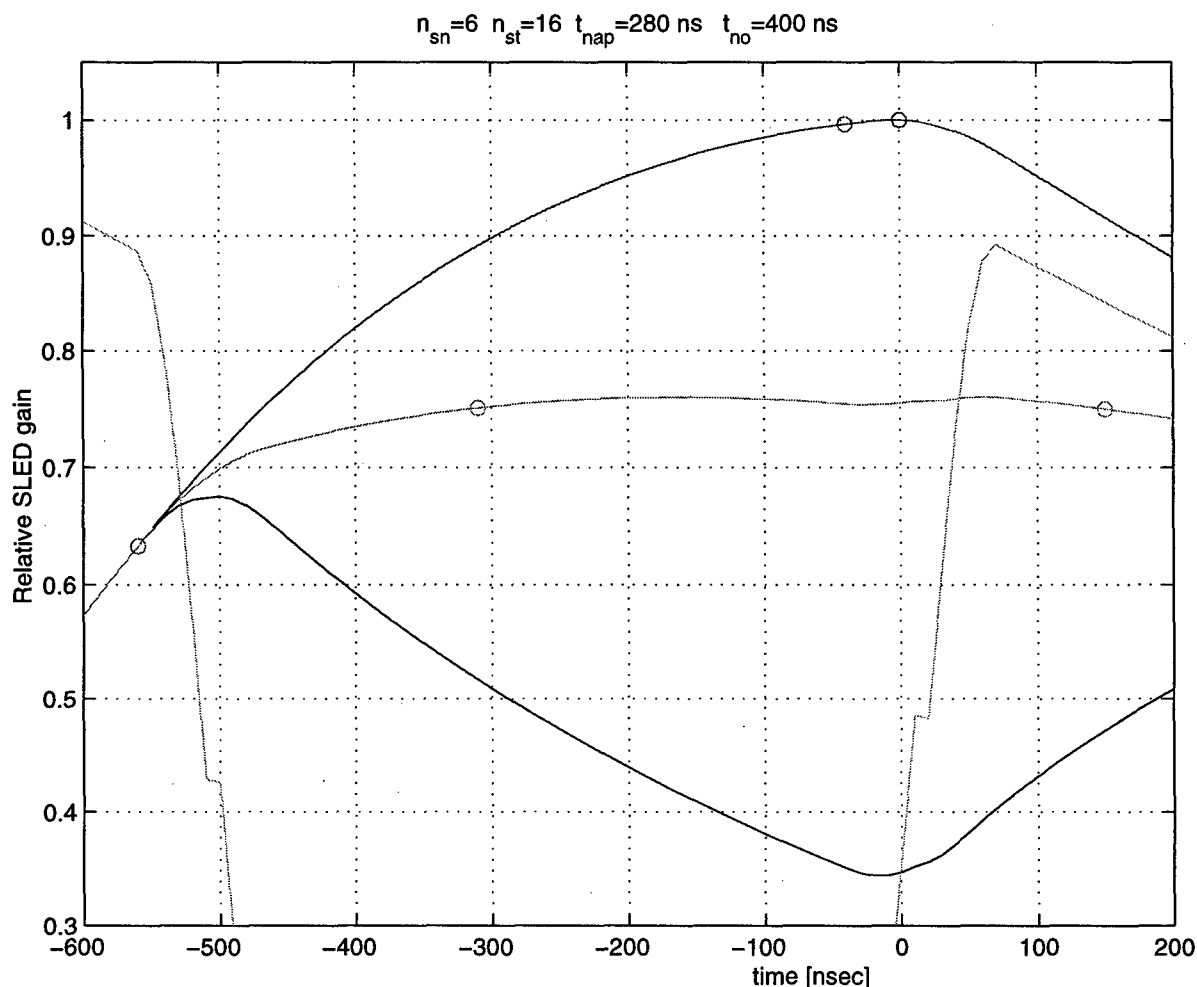


Fig. 2: SLED energy curve.

The relative SLED output (top) and with a 450 ns long notch (bottom) changes by about 30% over 500 ns, but with 6 out of 16 sectors notched (middle) the average variation is reduced.

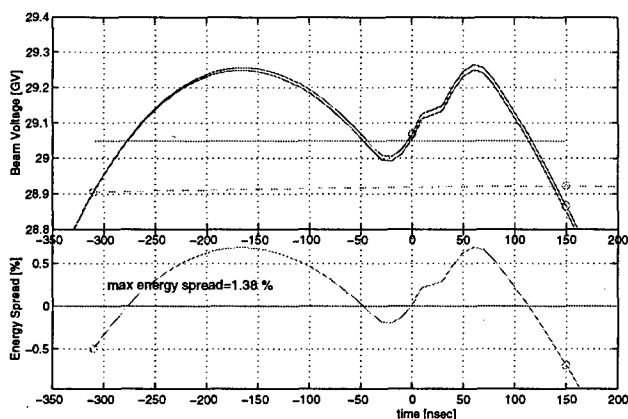


Fig. 3: No-load, loaded voltage and energy spread. In simulations with 6 out of 16 sectors notched the energy variation along the pulse can be reduced to  $\pm 0.5\%$ .

### 3 EXPERIMENTAL RESULTS

The E-155 experiment and now in spring of 1999 its extension E-155x can use beam pulses up to 500 ns length. Creating this pulse had some longitudinal and transverse challenges.

#### 3.1 Energy Spread

The full energy spread due to the rising part before the peak of the SLED output energy curve is about 30% (Fig. 2). The compensation with a one-size notch gives about 1.2% (full width, Fig. 3). To get this further down, especially the two high energy peaks, we had to use different size notches with different timing and/or a double-notch consisting of two additional 130 ns long phase flips (see Fig.4).



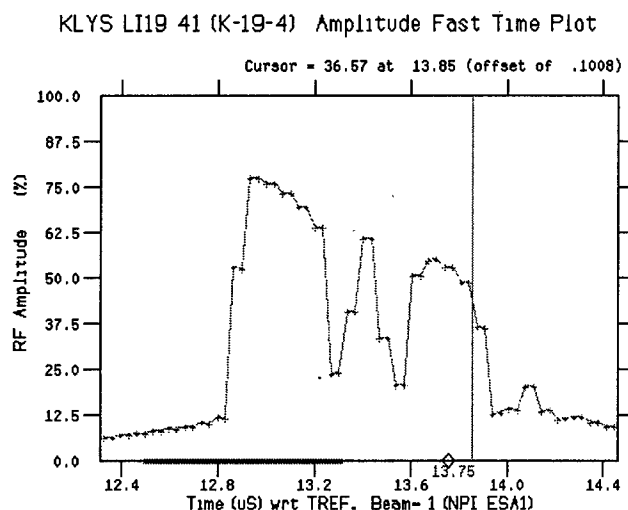


Fig. 4: Measured RF amplitude with a double notch. By having some sectors with a double notch or a shorter pulse length, the energy spread can be minimized further.

This reduced the energy spread over the 450 ns long pulse to about  $\pm 0.1\%$  which is better than the single bunch energy spread of 0.15% rms. The measurement of Fig. 5 was obtained using the synchrotron light at a dispersive location, which was digitized by a gated camera with a 70 ns gate width. The overall energy spread of the pulse is about 0.15% with some small lower energy tails in the front and the back. Shorting the pulse could eliminate these, but since the experiment accepts a whole energy range of  $\pm 0.4\%$  the whole pulse was used.

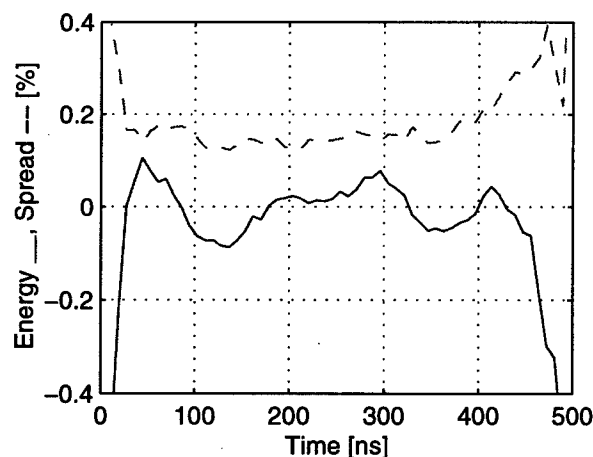


Fig. 5: Energy and energy spread along pulse.

### 3.2 Transverse Dynamic

Since the compensation of the energy spread is global over 30 different sectors and not a local cancellation, the beam would have a huge energy spread mainly in the early part of the accelerator. This was initially observed when increasing the pulse length from 300 to 500 ns, that part of the beam got lost near the first 100 to 200 m. An explanation is that in the first two sectors (= 200 m) there is no notch and therefore a 30% energy spread, which could not pass through the betatron focussing lattice. This was improved to 10% by putting the beam centered over the peak. A fine-adjustment was the use of a short notch in Sector 1, creating a local M-shaped energy distribution. All these have helped to get the full transmission of the whole pulse, but some parts of the beam have still a different betatron match. This is visible on a screen, where the different parts of the pulse have up to a factor of two different spot sizes.

## 4 SUMMARY

Notching the SLED output or, in other words, using SLEDF (for a Flat SLED energy "curve") has made it possible to increase the pulse length from about 100 ns to 500 ns with an energy spread of 0.15%.

## 5 ACKNOWLEDGEMENT

Special thanks go to Jerry Yocky and Howard Smith from the Operations Group for setting up the gated camera.

## 5 REFERENCES

- [1] F.-J. Decker, Z.D. Farkas, J. Turner, *High Current, Long Beam Pulse with SLED*, PAC99, New York, March 1999.

# High Current, Long Beam Pulse with SLED

F. J. Decker, Z. D. Farkas, J. Turner

Stanford Linear Accelerator Center, SLAC, CA94309, USA

## Abstract

A proposed, high charge, fixed target experiment (E-158) is planned to run with the highest possible energies available at the Stanford Linear Accelerator Center (SLAC), at 45 and 48 GeV. The charge is up to  $6 \cdot 10^{11}$  particles in a 370 ns long beam pulse. The SLAC Energy Development (SLED) rf system generates an increasing no-load beam energy, with a linearly decreasing slope. We show how to obtain a current variation that tracks the no-load voltage, resulting in zero energy spread. We discuss the results of a lower energy experiment that verifies the predicted charge and current at the energies required for E-158.

## 1 INTRODUCTION

In steady state the no-load and current induced voltages are constant, hence their difference, the loaded voltage, is also, constant. With SLED, the no-load or rf-generator voltage,  $V_g(t)$  and the current induced voltage  $V_b(t)$ , vary with time and do not reach steady state.

Let  $t_i$  be the time when the beam starts,  $t_e$  when the beam ends,  $V_i$  the no-load voltage at  $t_i$ , and  $V_{gb}$  the no-load voltage during the beam pulse minus  $V_i$ . Thus,

$$V_i = V_g(t_i), \quad V_{gb}(t - t_i) = V_g(t - t_i) - V_i.$$

Reset the starting time to zero by replacing  $t - t_i$  by  $t$ . To minimize energy spread,  $V_b(t)$ , should track  $V_{gb}(t)$  as closely as possible. To accomplish this we can vary the rf into the accelerator section, or the current or both. Let the no-load voltage at the end of the beam pulse minus the no-load voltage at the beginning of the beam pulse be  $V_d = V_g(t_e) - V_g(t_i)$ .

Define the optimum current,  $I_o$ , as the current that at the end of a beam pulse of duration  $T_b$ , induces a voltage  $V_b(T_b)$ , equal to  $V_d$ . The loaded voltage as a function of time is  $V_L(t) = V_i + V_{gb}(t) - V_b(t)$ . Define the loaded voltage  $V_L$  as the median of  $V_L(t)$  and the energy spread  $dv/v = (V_L(t) - V_L)/V_L$ . With the optimum current there will be, in general, an unacceptable energy spread. We will show that for any variation of  $V_{gb}(t)$ , we can vary the current so that  $V_b(t)$  tracks  $V_{gb}(t)$  exactly.

The steady state no-load voltage without SLED

$$V_{gs} = \sqrt{Z_g N_{gs} P_s}, \quad Z_g = \eta_s s T_f N_{gs} L_s.$$

$N_{gs}$  is the number of sections with rf,  $P_s$  is the rf power into the section,  $\eta_s$  is the section efficiency,  $s$  ( $\omega r/Q$ ) is

the elastance/m,  $T_f$  is the fill time and  $L_s$  is the section length. Using the given SLAC parameters, [?, page 117] we obtain for a typical klystron

$$Z_{gk} = \frac{V_k^2}{P_k} = 400 \text{ M}\Omega, \quad V_k = 20\sqrt{P_k}.$$

For the linac  $V_{gs} = \sqrt{\eta_s s T_f N_{gs} P_s N_{gs} L_s}$ .

The shape of  $V_g(t)$  is determined by the SLED cavities. Let  $S_g(t)$  be the SLED gain as a function of time, let  $S_{gm}$  be its maximum value and let  $V_{gm}$  be the maximum SLEDed voltage. Then, the SLEDed voltage as a function of time

$$V_g(t) = S_g(t) V_{gs} = \frac{S_g(t)}{S_{gm}} V_{gm}.$$

The SLEDed voltage used in this note is based on an experimentally obtained curve.

## 2 OPTIMUM AND ZERO ENERGY SPREAD CURRENTS

For a step function current,  $i_b$ , passing through an accelerator of length  $L_b = N_{bs} L_s$ , the current induced voltage as a function of time  $t$  starting at beam injection, is

$$V_b(t) = i_b R_b(t), \quad R_b(t) = \eta_b(t) s T_f L_b / 4.$$

For the constant gradient SLAC sections, using  $t_p = t/T_f$ ,

$$\begin{aligned} \eta_b(t) &= \frac{1 - e^{-2\tau t_p} - t_p 2\tau e^{-2\tau}}{\tau(1 - e^{-2\tau})} & 0 \leq t_p \leq 1 \\ &= \eta_{bs} = \frac{1 - e^{-2\tau} - 2\tau e^{-2\tau}}{\tau(1 - e^{-2\tau})} & t_p \geq 1 \end{aligned}$$

The difference of the no-load voltage between the end and the beginning of the beam pulse is

$$V_d = S_{gd} V_{gs}, \quad S_{gd} = S_g(t_e) - S_g(t_i).$$

The beam induced voltage at the end of the beam pulse for a step current

$$V_{bm} = i_b \eta_b(T_b) s T_f L_b / 4.$$

Equate  $V_d$  to  $V_{bm}$ , solve for  $i_b$  and obtain

$$I_o = \frac{4 S_{gd}(T_b)}{\eta_b(T_b)} \sqrt{\frac{\eta_s P_s}{s T_f L_s}} \times \frac{N_{gs}}{N_{bs}}. \quad (1)$$

In terms of measurable parameters  $I_o = V_d / R_b(T_b)$ .

We, now, calculate the current variation that yields a specified self induced beam voltage, in this case,  $V_{gb}(t)$ . Let  $n = 1, 2, 3 \dots N_i$ , where  $N_i$  is the number of injected currents. The interval between current injections is  $\Delta t = T_b / (N_i - 1)$ . Let the time when the  $n$ th current is injected  $t_n = (n - 1) \times \Delta t$ . The beam induced voltage at time  $t_{n+1}$  is the voltage due to the current injected at time  $t_n$  plus the voltage due to the  $n - 1$  previously injected currents. Using  $V_b(t_n) = V_{gb}(t_n)$  we obtain the injected currents at each point  $n$ :

$$\begin{aligned} V_{gb}(1) &= 0 \\ V_{gb}(2) &= i_{b1} R_b(\Delta t) \\ i_{b1} &= V_{gb}(2) / R_b(\Delta t) \\ V_{gb}(3) &= i_2 R_b(\Delta t) + i_1 R_b(2\Delta t) \\ i_2 &= \frac{V_{gb}(3) - i_1 R_b(2\Delta t)}{R_b(\Delta t)} \\ V_{gb}(4) &= i_3 R_b(\Delta t) + i_1 R_b(3\Delta t) + i_2 R_b(2\Delta t) \\ i_3 &= \frac{V_{gb}(4) - [i_1 R_b(3\Delta t) + i_2 R_b(2\Delta t)]}{R_b(\Delta t)} \end{aligned}$$

For  $n > 1$

$$V_{gb}(n+1) = i_n R_b(\Delta t) + V_p(n+1),$$

$$V_p(n+1) = \sum_{p=1}^{n-1} i_p R_b([n+1-p]\Delta t).$$

$$i_n = \frac{V_{gb}(n+1) - V_p(n+1)}{R_b(\Delta t)}.$$

$$i_b(n) = \sum_{j=1}^n i_j.$$

We can increase the number of injected currents and, consequently, decrease  $\Delta t$  and obtain a continuous total current waveform where, during the beam pulse,  $V_b(t)$  tracks  $V_{gb}(t)$  exactly, resulting in zero energy spread. The zero energy spread average current is about the same as the optimum current. The injected currents are either positive or negative, the the total current is positive as long as  $V_{gb}$  does not decrease precipitously.

### 3 PREDICTED BEAM CURRENTS AND BEAM ENERGIES

The no-load voltage,  $V_g(t)$ , is plotted in Fig. 1, as a function of time. We used the previously measured beam energy of the SLEDed linac of 53.7 GeV. Also plotted are the current induced and loaded voltages and the energy spread for a 300 ns optimum current pulse starting when the no-load voltage is 46 GV and ending 50 ns before the maximum no-load voltage is reached. The charge is  $6.0 \cdot 10^{11}$  particles per pulse about the charge required for E-158. The zero energy spread current for a beam pulse starting the same time as the optimum current pulse but ending 50 ns

after the maximum no-load has been reached and its self induced voltage (dot-dash) are also plotted in Fig. 1. Note that it tracks the no-load voltage. This increases the charge to  $6.8 \cdot 10^{11}$  particles per pulse. During the first part of the zero energy spread beam pulse, the current is linearly decreasing, because the slope of the no-load beam energy is linearly decreasing. This, in turn, is because the SLED output that provides the accelerator rf input is, also, nearly linearly decreasing.

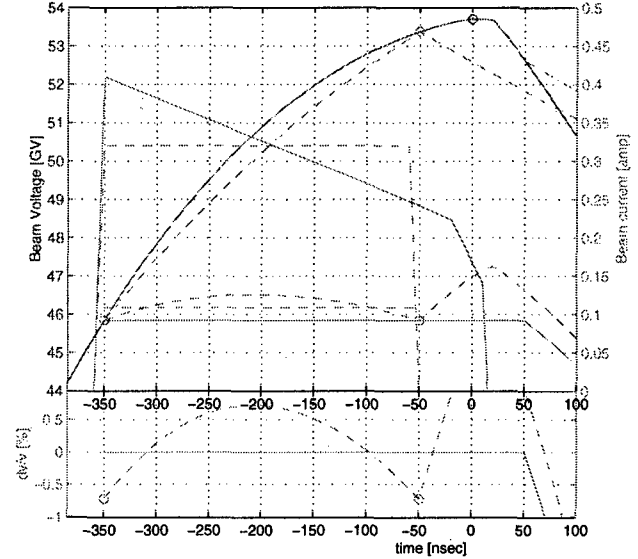


Figure 1: No-load voltage,  $V_g(t)$ , current induced and loaded voltages,  $V_b(t)$  and  $V_l(t)$ , and the energy spread,  $dv/v$ , for a 300 ns optimum (dash) and zero energy spread current pulses, left axis; optimum (dash) and zero energy spread currents, right axis. All as a function of time.

The charge per pulse and electrons per pulse are, respectively,

$$q_p = \int_0^{T_b} i_{bt} dt, \quad e_p^- = 10^{10} \times \frac{q_p(\text{nC})}{1.6}.$$

The beam energy and beam power per pulse and the beam average power are, respectively,

$$U_b = q_p V_i, \quad P_b = U_b / T_b, \quad P_{ba} = U_b \times f_{pr}.$$

Here,  $f_{pr}$  is the pulse repetition frequency. The loaded beam energy and the number of electrons per pulse are plotted in Fig. 2 (top) as a function of beam pulse width. The beam average power at  $f_{pr} = 120\text{Hz}$ , and pulse power are also plotted in Fig. 2 (bottom). Their maximum values of 1.6 MW and 22 GW, respectively, are reached at a beam pulse width of about 600 ns.

### 4 EXPERIMENTAL DATA FOR E-158

Two test experiments for E-158 were performed. One, with 1 sector rf and 1 sector beam had a measured energy of 1.2 GeV and with a sloped beam pulse of 350 ns had a

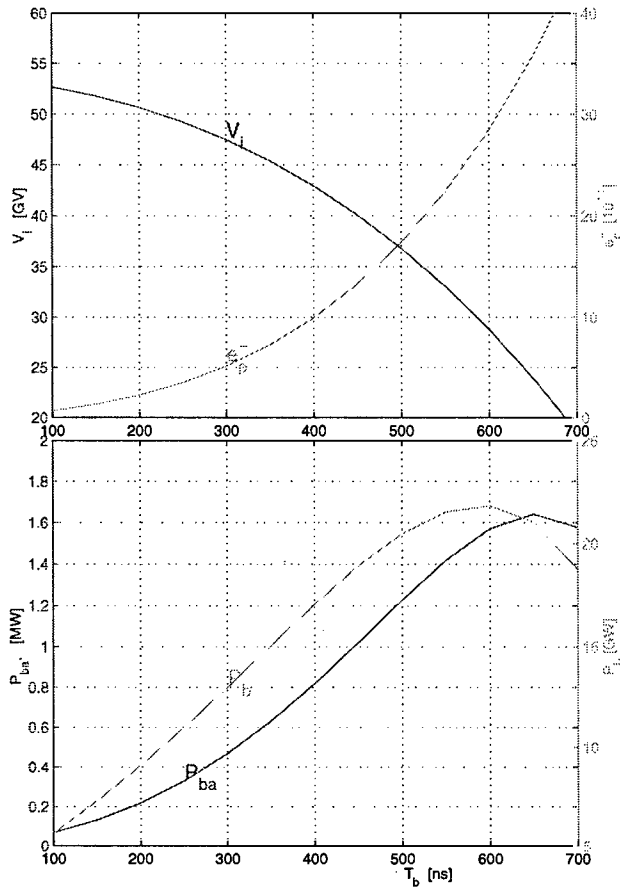


Figure 2: Loaded beam energy and number of electrons per pulse (top), beam average power at 120 pulses per second and beam power per pulse (bottom). All as a function of beam pulse width.

measured charge of  $7 \cdot 10^{11}$  particles. Two, with 20 sectors and 30 sector beam the measured energy at the end of 30 sectors was 29 GeV and the charge was  $4.5 \cdot 10^{11}$  particles. The ratio of the two charges was 1.56 as predicted by eq. 1. An energy spread of about 0.25% was achieved. A small low energy tail could be reduced by a fast phase adjustment of the S-band buncher and capture klystron, but was barely necessary.

#### 4.1 Transverse Jitter

The interesting observation was in the transverse plane. The beam position monitors, which integrate over the pulse, should indicate a beam offset by a rising or falling linear slope. A curved slope was observed with an increased jitter at the end of the pulse (see Fig. 3). The curved slope can be explained by a tilted beam pulse and the jitter by the transverse wake fields or dispersion. This tail jitter is correlated with the charge intensity and was up to 2 mm for a 10% charge change at the end of the linac. This could be reduced by a factor of five with one corrector making a betatron oscillation to minimize the rms jitter down to about 10% of the beam size.

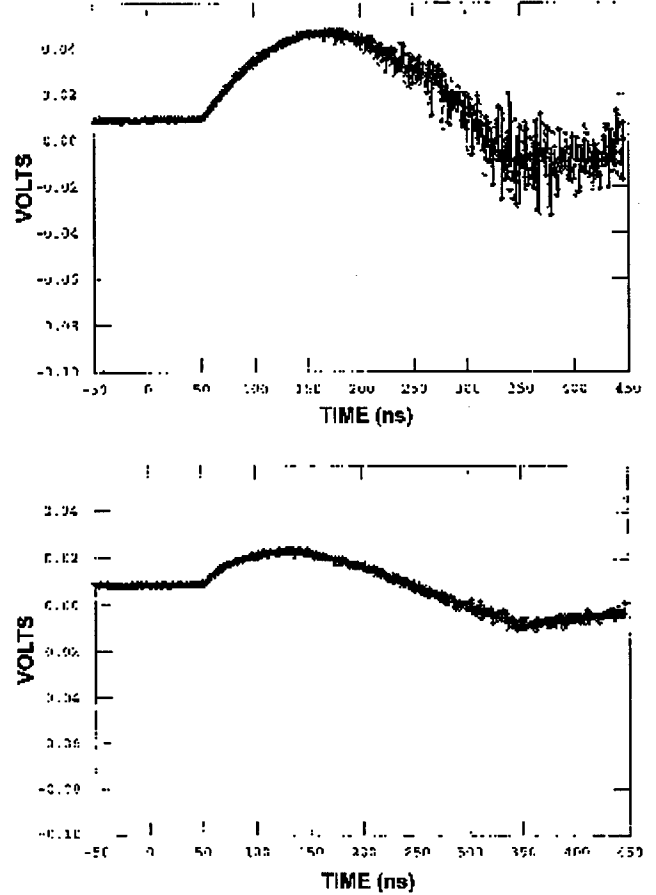


Figure 3: The beam position monitor signal (volts, 1 volt=70  $\mu$ m) for a 300 ns beam pulse with a jittery tail, (top) which can be reduced by steering the beam (bottom).

## 5 REFERENCES

- [1] R. Neal ed., "The Stanford Two-Mile Accelerator" Benjamin 1968.

# FABRICATION OF DDS-3, AN 11.4 GHz DAMPED-DETUNED STRUCTURE

J. Klingmann, J. Elmer, M. Mugge, K. van Bibber, LLNL, Livermore, CA 94550 USA

K. Asano\*, Y. Funahashi, Y. Higashi, T. Higo, N. Hitomi, T. Suzuki, T. Takatomi, N. Toge, Y. Watanabe, KEK, Tsukuba, Ibaraki 305, Japan

C. Adolphsen, H. Hoag, R. Jones, N. Kroll, R. Miller, C. Pearson, R. Pope, J. Rifkin, R. Ruth, J. Wang, SLAC, Stanford, CA 94309 USA

## Abstract

A 1.8 m X-band Damped-Detuned Structure (DDS-3) has been fabricated and characterized as part of the structure development program towards a TeV-scale  $e^+e^-$  linear collider. In this joint venture, the copper cells were precision-fabricated by LLNL, diffusion-bonded into a monolithic structure by KEK, and the structure completed and tested by SLAC. The overall process constitutes a baseline for future high-volume structure manufacture.

## 1 INTRODUCTION

The US-Japan technical baseline for a TeV-scale  $e^+e^-$  linear collider builds upon a 1.8 m long X-band accelerator structure for the main linacs. These structures are of the Damped-Detuned type, whereby the cell dimensions are varied continuously along the length in such a way to maintain a uniform  $2\pi/3$  phase advance in the accelerating mode at 11.424 GHz, but distribute the first dipole mode frequencies according to a broad, smooth function centered around 15 GHz. Furthermore, the dipole modes excited by off-axis bunches are effectively coupled out to damping manifolds, where their energy propagates to terminations at either end. In this way, the long-range dipole wakefields may be suppressed. The basic DDS concepts are discussed in [1], and an overall summary of the R&D on Detuned and Damped-Detuned Structures is found in [2]. This paper will focus mainly on the production of the 206 different copper cells. The stacking and two-step bonding of these cells into the DDS-3 structure is described in detail in [3]. The actual wakefields of DDS-3 as measured in the SLAC ASSET facility is reported in [4]. A cross section of the DDS-3 structure is shown in Figure 1.

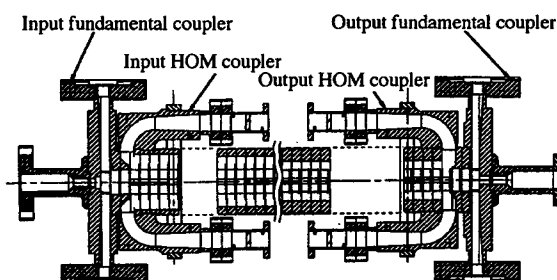


Figure 1: Cross section of the DDS 3 structure.

## 2 CELL FABRICATION

A schematic of the DDS-3 cell is shown with an isometric rendering in Figure 2. Five dimensions are specified on the drawing, 'A', 'B', 't', 'H', and 'L', which vary over the length of the structure. Table 1 shows the dimensions of three cells along the structure to indicate the magnitudes of the variations. All dimensions are specified at 20 °C.

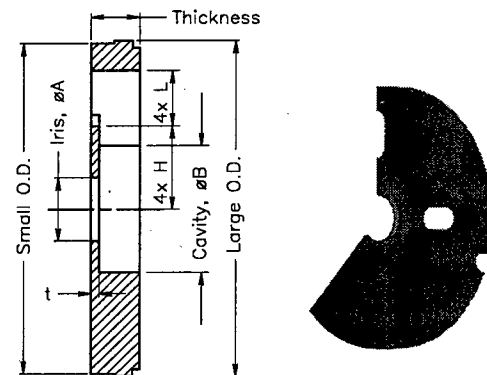


Figure 2: Cross-section and rendering of the DDS-3 cell.

### 2.1 Tolerance Requirements

The axisymmetric features of the DDS-3 cells have tolerances in the 0.5 to 1.0 micrometer range and surface finish requirements of less than 500 Å  $R_a$ . The primary and secondary datums of the design are the flat face on the non-cavity side of the cell and the outside diameter of the cell, respectively. Two relationships are critical to maintain for proper performance. The first is parallelism of the two bonding surfaces to 0.5 micrometer over the diameter to prevent a variable "walk" in the straightness of the structure. The second is 1 micrometer concentricity of the cavity and iris to the outside diameter, the radial reference during assembly. The HOM port dimensions have tolerances in size and position in the 20-micrometer range.

Table 1: DDS-3 Cell Parameters

Cell No.	A (mm)	B (mm)	t (mm)	H (mm)	L (mm)
3	11.175	22.311	1.056	11.053	14.668
103	9.593	21.527	1.459	10.514	11.997
201	8.186	20.853	1.876	10.300	8.804

\*Now at Akita National College of Technology.

## 2.2 Fabrication Procedure

Disks were first saw-cut from annealed high-purity copper (UNS C10100) barstock, and the axisymmetric features turned to leave overstock material of 20 to 25 micrometers. The slot features that constitute the higher order mode (HOM) manifolds were then milled out to their final finished surface. At this point, the part was annealed in  $10^{-6}$  Torr vacuum at 500 °C for one hour, to remove residual compressive stresses left in the surface from the roughing operations. This was necessary to prevent shape changes as material is removed during finishing.

The finishing operation was completed on a Precitech T-base diamond-turning lathe. This lathe has an air-bearing spindle, oil hydrostatic slideway bearings, and Zerodur glass scales with resolution of 8.4 nanometers. Of course, machine accuracy is significantly poorer, largely due to thermal errors. Single crystal diamond tools with a 0.25-millimeter radius and the rake set to 0 degrees were used for finishing. The usual procedure was to finish the non-cavity side of the part first, holding the part with a collet on the larger outside diameter (see Figure 2). This step resulted in precision finished surfaces on the smaller outside diameter, one flat surface, and half of the iris. In the second step, the part was fixtured with a vacuum chuck on the side turned flat in the first operation and with a close-fitting (0 to 0.5 micrometers clearance) ring around the smaller outside diameter. The vacuum chuck, collet, and a part are shown in Figure 3.

This method can yield very accurate parts because it allows the datum (larger outside diameter), cavity, and half of the iris to be cut in a single setup. Non-concentricities of these features should only result from the machine spindle errors which are quite small. The only feature that could be significantly non-concentric is the half of the iris that is cut during the first operation. Additionally, because the second set of axial surfaces is cut when the part is located on a machined-in-place vacuum chuck, parallelism should also be very good. About half the parts were finished with only two setups; the other half required successive operations.

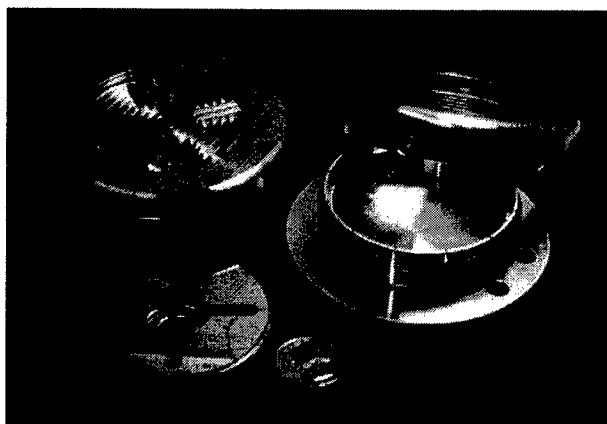


Figure 3: DDS-3 cell with diamond-turning fixtures.

Quality control was challenging due to the very small tolerances. Our strategy was to derive most of our accuracy from the metrology loop on the turning machine. For axial dimensions, the vacuum chuck was cut as a reference surface and, with intimate contact between this surface and the part, faces could be cut accurately. The vacuum chuck was designed to minimize contact area and thus particulate contaminants were not likely to compromise cell axial location. For diameters, a part that could be measured accurately was first cut. The difference between the measured and programmed diameters on this part contained thermal expansion and tool-spindle relationship errors. The machine that turned the DDS-3 parts did not have good temperature control and the temperature of the part had to be estimated to correct for the thermal error. After applying this correction, the remaining error in the test part was due to the tool not being registered to the spindle centerline. This error causes inside and outside diameter size errors that are equal in magnitude but opposite in sign. By contrast, thermal errors are proportional to the radius of the feature and are of the same sign. These references, the axial face cut and a test part diameter, must be set each time that a new tool is installed on the machine. With the precision machine metrology found on diamond-turning lathes, this strategy can result in more accurate dimensions throughout the part than can be measured by other means.

## 2.3 Metrology

Sufficiently accurate metrology was one of the major shortcomings in cell fabrication. The only features that could be measured to the accuracy of the specifications on the drawing were the cell flatness and outside diameters. Being a fast and inexpensive procedure, flatness was measured frequently with a Zygo Mark IV interferometer. Typical cell interferograms are shown in Figure 4; most cells were flat to less than 0.4 micrometers over the bonding surface. A 'bookshelving' error, where the individual cell axes are not parallel with the structure axis, was noted during post-assembly tests. It is unlikely that non-parallelism in the cells would yield the character of the error seen in the data. Furthermore, the parallelism for each cell was measured at KEK prior to assembly and all were less than 2 micrometers parallel (across the diameter) with the average value and standard deviation being 0.45- and 0.44-micrometers, respectively.

The only dimension that was measured in a somewhat in-process manner was the outside diameter, which was also the setup diameter for the quality control on the machine. LLNL has the capability to measure outside diameters in this size range with accuracy to 0.125-micrometers, NIST-traceable. At that level of accuracy however, the measurement is not fast enough to be very useful in an in-process sense. Thus only a limited number were measured, these data shown in Figure 5. The outside diameters of more parts were checked with a

comparison gauge that compares the diameter to an artifact part; repeatability of this instrument was in the 0.125-micrometer range.

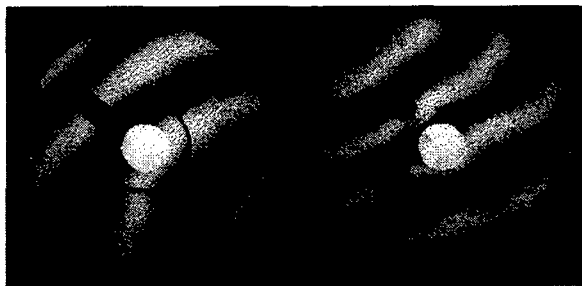


Figure 4: Interferogram showing better than 0.3-micrometer flatness on each side of cell #178.

Independently verifying the other critical axisymmetric cell features to a higher precision than can be made on the diamond-turning lathe is difficult; we relied heavily on the quality control process described in the previous section. For large-volume production, the emphasis will be on microwave qualification, both single-cell and full-structure, more closely related to actual performance. Functional tests that were performed included single-cell and bead-perturbation microwave tests and the ASSET wakefield characterization [2,4].

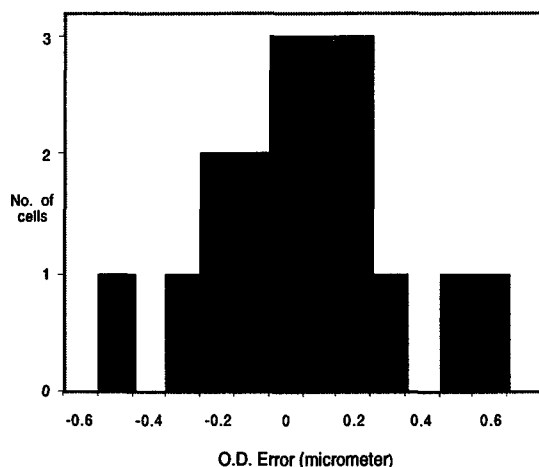


Figure 5: Cell O.D. error distribution.

### 3 CONCLUSIONS & FUTURE WORK

The purpose of this prototype was to gain practical experience in building structures to guide the manufacturing strategy. Future structures will incorporate a new electromagnetic design, the Round Damped-Detuned Structure (RDDS) [5,6], that will significantly improve machine efficiency. However, lessons learned in DDS-3 will carry over completely to the new design.

Our initial assumption had been that the production of a structure was a precision engineering problem, requiring machines that could fabricate cells with absolute accuracy in all dimensions. While ultimately successful, the difficulty of this task was greatly underestimated. Two

important conclusions resulted from this project. First, large-volume structure manufacturing can not require machining with high absolute (sub-micrometer) accuracy. On the other hand, we are optimistic that the right strategy will be to require only that the machining is highly reproducible and the error in absolute dimensions will be driven to zero by feedback from accurate functional metrology in the production line. Second, the tolerances for DDS-3 were specified as 'top-hat' distributions, but it is now thought that this is overly restrictive. As structures are ensembles of a large number of cells, tolerances could be specified in terms of a mean error within a well-behaved error distribution. This should result in a much more relaxed machining procedure; in fact it may be essential for mass production. How this would actually be implemented has not yet been considered in detail.

One further outcome from this work has been to examine the possibility of making the cells with interlocking features (see Fig. 6). Such a design should be much more amenable to robotic assembly, as well as eliminate 'bookshelving' of cells within the structure. Tooling and cells are being fabricated for a test of this idea in a sub-section prototype.

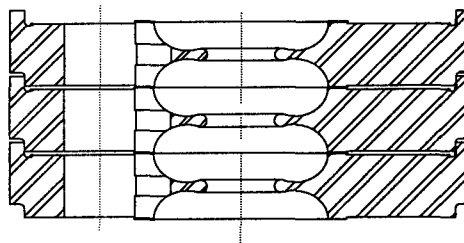


Figure 6: An interlocking cell with RDDS cavities.

### 4 ACKNOWLEDGEMENTS

We would like to acknowledge the contributions of our colleagues at the Oak Ridge National Laboratory, Joe Cunningham and Art Miller, and at LLNL, Anthony Demiris, Blaine Beith, Don Bennett, and Larry Wagner.

This work was supported in part by the Japan-U.S. Collaboration Program in High Energy Physics Research, and the U.S. Department of Energy under Contract Nos. DE-AC03-76SF00515 (SLAC), and W-7405-ENG-48 (LLNL).

### 5 REFERENCES

- [1] N. Kroll, Proc. PAC'97, SLAC-PUB-7541.
- [2] J.W. Wang et al., paper FRA18, PAC'99.
- [3] T. Higo et al., paper FRA16, PAC'99.
- [4] C. Adolphsen et al., paper FRA40, PAC'99.
- [5] R.M. Jones et al., paper FRA37, PAC'99.
- [6] Z. Li et al., paper FRA41, PAC'99.

# A HIGH THERMAL CONDUCTIVITY WAVEGUIDE WINDOW FOR USE IN A FREE ELECTRON LASER\*

T. Schultheiss\*\*\*, V. Christina\*\*, M. Cole\*\*, J. Rathke\*\*

NORTHROP GRUMMAN CORP, Bethpage, NY.

T. Elliott, V. Nguyen, L. Phillips, J. Preble, JEFFERSON LAB, Newport News, Va.

## Abstract

A high thermal conductivity waveguide window with a goal of propagating greater than 100 kW average power operating at 1500 Mhz has been designed, analyzed and tested. The favorable material properties of Beryllia (BeO) make this possible. The window is brazed to a soft copper frame and then the frame is brazed to a KOVAR flange, providing the vacuum seal. RF analysis combined with thermal/structural analysis shows the benefits of the material. The KOVAR flange with a CTE, coefficient of thermal expansion, that matches that of BeO enables a strong braze joint. RF testing to 35 kW has been successful. This design can be expanded to applications with lower frequencies and higher average power, i.e., larger windows

## 1 INTRODUCTION

The Free Electron Laser Facility being developed at Jefferson Lab requires much higher RF power throughput than is needed for their main facility. Much of the accelerator technology for the free electron laser is taken from the main facility which uses a two window design. The window design for the FEL consists of a room temperature warm window and a 2K cold window like the main facility. The warm window design from the main facility does not work at the power levels required for the FEL, therefore, Jefferson Lab initiated the development of a warm window using the cold window design as a baseline. In a corroborating effort, Northrop Grumman began developing a backup warm window design to enable greater than 100 kW average power operating at 1500 Mhz. The design was developed as a direct replacement in the FEL warm window location.

## 2 MECHANICAL DESIGN

The design evolved as a backup warm window that would fit in the TJNAF envelope. Preliminary analysis between alumina and beryllia windows showed that for standard grade material the high thermal conductivity of beryllia, shown in Table 1, resulted in low thermal gradients, and therefore low thermal stress within the window.

Table 1: Comparison of Thermal Conductivity's at 25C

Material	W/mK
Copper	380
Beryllia	300
Alumina	20

To match the thermal expansion of beryllia, KOVAR was chosen as the flange material, minimizing thermal stresses in the beryllia during the braze cycle [1]. A thin OFHC copper frame, .010 inches thick, between the beryllia window and the relatively stiff flange was added for strain relief and for its high thermal conductivity. Figure 1, shows a solid model of the window, the copper frame, and the KOVAR flange, which was copper plated.

The preferred BeO window geometry was an 'off the shelf' flat piece of Thermalox 995, .100 inches thick, from Brush Wellman. The thickness was chosen to keep the stress due to pressure low while using a stock size of standard grade material, ensuring repeatable material properties. Presently there is no multipacting coating on the window.

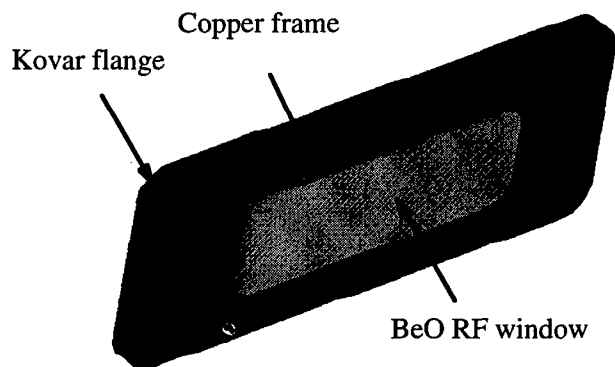


Figure 1: BeO RF Window, Flange and Frame

## 3 RF DESIGN

RF analysis was used to determine the S parameters for the structure and to optimize the structure within the requirements set by the envelope and mechanical design. Table 2 compares the electrical properties of BeO with other standard grade candidate materials.

\* Work supported by CRADA between NGC and Thomas Jefferson National Accelerator Facility SURA 95-S003 CRADA

\*\* Present address, Advanced Energy Systems Inc., Medford NY.



Table 2: Comparison of Electrical Properties

Material	Dielectric Const (1MHz)	Loss Tangent
Beryllia (Thermalox 995)	6.7	.0003
AlN	9.0-10.0	
Alumina	9.0	.0003

To optimize the structure with a .100 inch thick BeO window, metal 'wings' forming an iris were added to the flanges. These iris 'wings' are shown in figure 2. RF results showed wings were needed on both sides of the window.

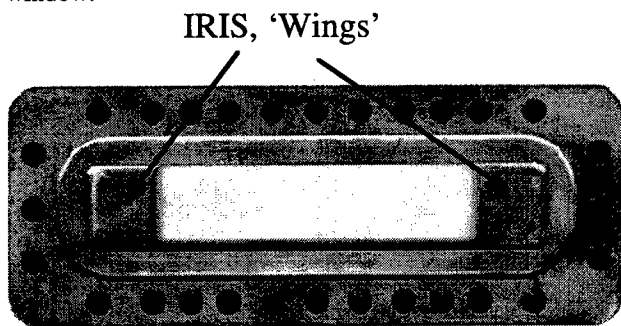


Figure 2: RF window and Iris ('wings') and flange

The following MAFIA RF analysis results were obtained for a wing width of .750", and a wing thickness of .100", Table 3.

Table 3: S Parameter Results

S11 amplitude	S11 phase	S21 amplitude	S21 phase
.0066	87.30	.99956	-2.740

After this configuration was selected, the power deposited into the ceramic and the fields in the waveguide were calculated. Contours of the heat deposited in the window are shown in figure 3 after scaling to a loss tangent of .0003 and 100 kW of through power.

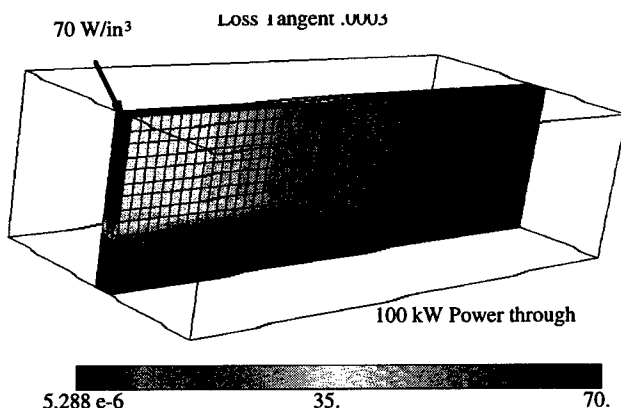


Figure 3: Heat loss contours determined by MAFIA

## 4 THERMAL ANALYSIS

The power loss distribution calculated in MAFIA was then mapped into an ANSYS finite element model. This model was used to determine thermal gradients and stresses in the window. Figure 4 shows the resulting temperature contours in the window, the frame, and the flange. On the edge of the flange a boundary temperature of 20C was set. The results show very small gradients in the window and a temperature rise of 29C between the window and the flange edge.

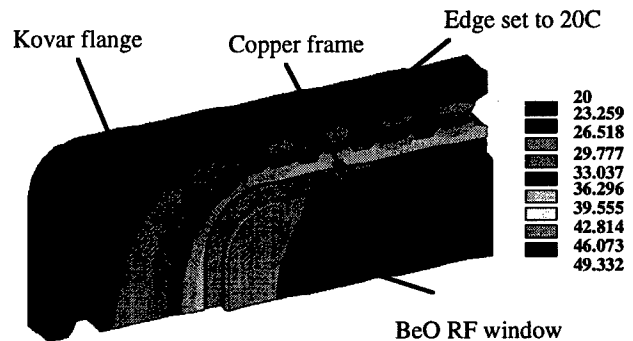


Figure 4: Temperature contours from ANSYS

## 5 STRUCTURAL ANALYSIS

Structural analysis was completed using the temperature contour data shown in figure 4. Symmetry conditions were applied to the two cut boundaries of the model and it was held perpendicular to the window face allowing the window and flange to expand freely. Stress results are shown in figure 5 for the assembly, they do not include pressure loads. Von Mises stresses are given here which show that the copper frame attached to the window and flange is the most highly stressed component.

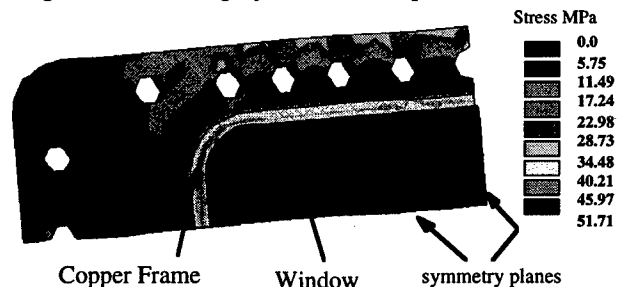


Figure 5: Von Mises contours of the window assembly

Though not indicated here, the stress in the frame is primarily compressive. The thermal stress in the copper could be mitigated by minimizing the thermal gradients in the flange. Figure 6 shows the stresses that develop in the BeO window. The high thermal conductivity of the ceramic results in low thermal stresses.

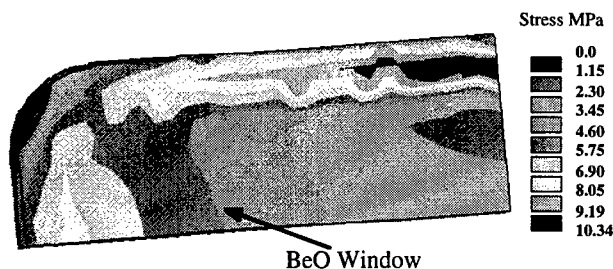


Figure 6: Von Mises stress of the BeO window

## 6 RF TESTS

Thomas Jefferson National Accelerator Facility (TJNAF) provided the facility and manpower to test the window. Figure 7 shows the layout of the high power test. The space between the PN001 JLAB window and the BeO test window was evacuated by a 160 l/s Vac-Ion pump while the waveguide between the BeO window and the load was at atmospheric pressure. The window flanges were water cooled. The baseline pressure prior to testing was  $1.4 \times 10^{-9}$  torr. Temperatures at different locations of the waveguide and window flanges were monitored by thermocouples. Temperature of the BeO ceramic was measured by an infrared thermometer through a viewing port on the waveguide elbow. The waveguide between the two windows was equipped with a pick-up probe to monitor the electron current. A vacuum interlock and an arc detector interlock were used to prevent a catastrophic destruction of the ceramic. During the test, the incident and reflected powers, the vacuum pressure, the electron current, the temperature of the BeO ceramic and the temperatures of the window flanges were continuously monitored and recorded.

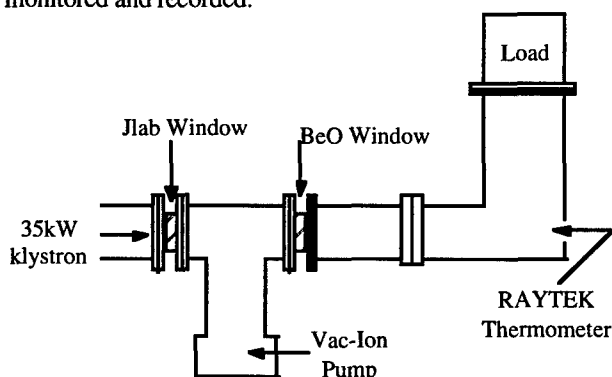


Figure 7: RF window test set up

Prior to applying high CW power, the windows were first submitted to high pulsed power (pulse length .01 ms - .1 ms, with a repetition rate of 100 Hz). Table 4 shows the temperature rise of the BeO ceramic as the power is increased. The temperature of the ceramic at zero power was 28C. The vacuum pressure increased to  $9.4 \times 10^{-8}$  torr at 35 kW and no electron current was detected.

Table 4: Temperature Rise In BeO Ceramic

Power (kW)	BeO Temp C	T(BeO)-27.7 $\Delta T$ C
0	27.7	0
5.04	35	7.3
10.1	40.8	13.1
15.1	45.7	18
20.2	51.2	23.5
25.2	58.2	30.5
35	70.9	43.2

The temperature rise between the coolant and the BeO window was much higher than expected. This could be from high losses in the braze material, which was not included in the model.

## 7 CONCLUSIONS

Analysis shows that for the expected power loss in the window the goal of 100 kW of through power at 1500 Mhz is achievable. The high thermal conductivity of BeO results in low thermal gradients within the ceramic. Modifications to the design which would include coolant nearer the ceramic would ensure lower ceramic temperatures. Modifying or eliminating the braze process is expected to decrease the heat loss and therefore decrease the thermal gradients within the assembly. BeO as an RF window material shows promise based on the analysis and tests to date.

## 8 REFERENCES

- [1] T. Schultheiss, et al., "Design, Analysis and Testing of a High Thermal Conductivity Waveguide Window for use in a Free Electron Laser"; XIX International Linac Conference, Chicago, Illinois, August 23-28, 1998; MO4078.
- [2] E. Chojnacki, et al., "Design Of A High Average-Power Waveguide Window"; Proceedings of the Particle Accelerator Conference, 1997, Vancouver, Canada.
- [3] M. Neubauer, et al., "High-Power RF Window and Coupler Development for the PEP-II B Factory"; Presented at 16th IEEE PAC 95 Conference and International Conference on High Energy Accelerators, Dallas, Texas, May 1-5, 1995.
- [4] D. Proch, et al., "Measurement of Multipacting Currents of Metal Surfaces in RF Fields"; Proceedings at the 16th IEEE PAC 95 Conference and International Conference on High Energy Accelerators, Dallas, Texas, May 1-5, 1995; pp 1776-1778.
- [5] Conversations with Brush Wellman.

# LARGE DIAMETER REDUCED FIELD TE<sub>01</sub> TRAVELING WAVE WINDOW FOR X-BAND

W. R. Fowkes, R. S. Callin, E. N. Jongewaard, S. G. Tantawi  
Stanford Linear Accelerator Center, Stanford University, Stanford, CA 94309 USA

## Abstract

A single overmoded sized window is being considered for use on the SLAC 75 MW X-Band Klystron. The 65 mm diameter window operates in the circular TE<sub>01</sub> mode in the reduced field, traveling wave configuration. Double step transitions were designed using MLEGO modematching program to suppress conversion to TE<sub>02</sub>. This compact design has a maximum peak rf electric field of 3.4 MV/meter at 75 MW. Design details and high power test results are reported.

## 1 INTRODUCTION

The high power window presently used on all of the SLAC X-band klystrons has been reported on previously [1]. It is usually referred to as a TE<sub>01</sub> reduced field traveling wave window. A pair of symmetrically located inductive irises are used to set up a standing wave in the regions between each iris and each 47 mm diameter ceramic window surface. This results in "forcing" a lower impedance at the window surface that exactly matches the characteristic impedance inside the ceramic thereby causing a pure traveling wave condition inside the ceramic. This design has been tested successfully to over 100 MW in a traveling wave resonator (TWR) and has been serving as a single output window on the 50 MW XL-4 series klystrons. This design however, is considered marginal at this power level.

The new 75 MW periodic permanent magnet (PPM) focussed klystron presently uses a pair of the windows described above, each passing 37.5 MW. Four TE<sub>10</sub>/TE<sub>01</sub> mode transducers are presently required—an expensive luxury due to the cost of the mode transducers.

## 2 SINGLE WINDOW REQUIREMENT

A single window alternative has been sought that will safely handle the full 75 MW. The 47 mm TW window described above is considered to be very reliable up to a peak power level of about 40 MW where the peak rf electric field at the window is 3.4 MV/meter. Using this electric field level as a design criterion for a single 75 MW window, an increase in diameter to 65 mm would be required. This assumes of course that TE<sub>01</sub> mode purity is maintained and the reduced field TW scheme is used. A problem that must be addressed in all all overmoded diameter circular windows is mode conversion.

TE<sub>11</sub> windows are susceptible to conversion to TM<sub>11</sub>, TE<sub>12</sub> and TM<sub>12</sub> in the transitions (tapered or stepped) going from single moded to overmoded diameters. TE<sub>01</sub> windows are not as vulnerable to mode conversion with increases in diameter providing the mode converter has launched TE<sub>01</sub> with good purity. Gradual tapers maintain TE<sub>01</sub> mode purity but are not usually very compact. Stepped transitions to larger diameters are normally susceptible to conversion to higher order TE<sub>0n</sub> modes unless special attention is given to the step design.

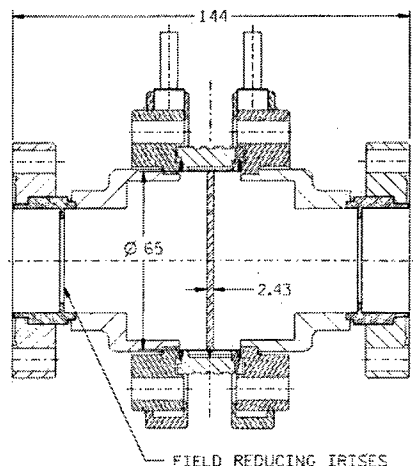


Figure 1. Compact overmoded 65 mm diameter TE<sub>01</sub> window. Field reduction is accomplished by a combination of the 2-stage steps and irises. The double step is optimized to cancel TE<sub>02</sub> that is created at each individual step.

## 3 NEW TE<sub>01</sub> TW WINDOW CONFIGURATION

Here we describe a compact 65 mm diameter TE<sub>01</sub> TW window that is virtually free of higher order modes. The maximum electric field at the surface of this window at 75 MW is about the same as exists at for the previously described window at 40 MW; 3.4 MV/meter. The TE<sub>01</sub> mode is created in 38 mm diameter circular waveguide using the recently designed compact wrap-around mode transducer [2] shown in Fig 5. We are presently testing this window in the Traveling Wave Resonator and expect to reach a peak power level of 150 MW. At this writing power testing has been progressed towards higher levels

Work supported by Department of Energy Contract DE-AC03-76SF00515

The peak power achieved thus far is 100 MW.

The input and output ports for this window design are 38 mm in diameter. The transitions from 38 mm to 65 mm are two-stage steps designed using MLEGO© which sets

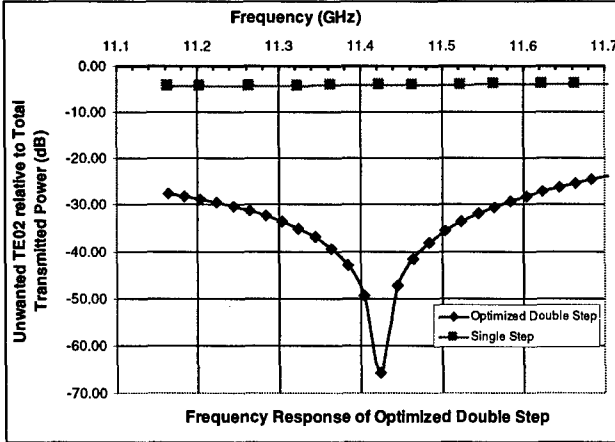


Figure 2. The above graph compares the conversion as a function of frequency of TE<sub>01</sub> to unwanted TE<sub>02</sub> for two types of stepped transitions; an optimized double-step and an abrupt single-step. The input and output diameters are 38mm and 65mm respectively.

up the cancellation of the TE<sub>02</sub> mode excited at each step stage [3]. If one were to use a single sudden step in diameter from 38 mm to 65 mm, the resulting mode conversion is the following: S<sub>21</sub> of 0.78 for TE<sub>01</sub> and 0.62 for TE<sub>02</sub> with only pure TE<sub>01</sub> exciting the smaller diameter port. By going to a two-step design, the length and diameter of the intermediate step is optimized to null out the natural conversion to TE<sub>02</sub>. The optimum intermediate diameter is 58.14 mm with a length of 19.48 mm. The residual S<sub>21</sub> for TE<sub>02</sub> drops to 0.00051. The effectiveness of this optimized step is shown in the graph in Fig. 2. It is compared with a single abrupt step as a function of frequency. The unwanted conversion from TE<sub>01</sub> to TE<sub>02</sub> is minimized for the operating frequency of 11.424 GHz.

All this is accomplished at the expense of a residual TE<sub>01</sub> mismatch S<sub>11</sub> of 0.167 in the 38 mm port. This residual mismatch, however, can be used to advantage in combination with an additional iris to set up the standing wave that is necessary to force the electric field down at the surface of the ceramic. The result is a pure traveling wave inside the ceramic.

It can be shown that the optimum VSWR needed to produce the TW condition within the ceramic is

$$\sigma_{opt} = \frac{Z_0}{Z_g} = \frac{\lambda_g}{\lambda_g'} \quad (1)$$

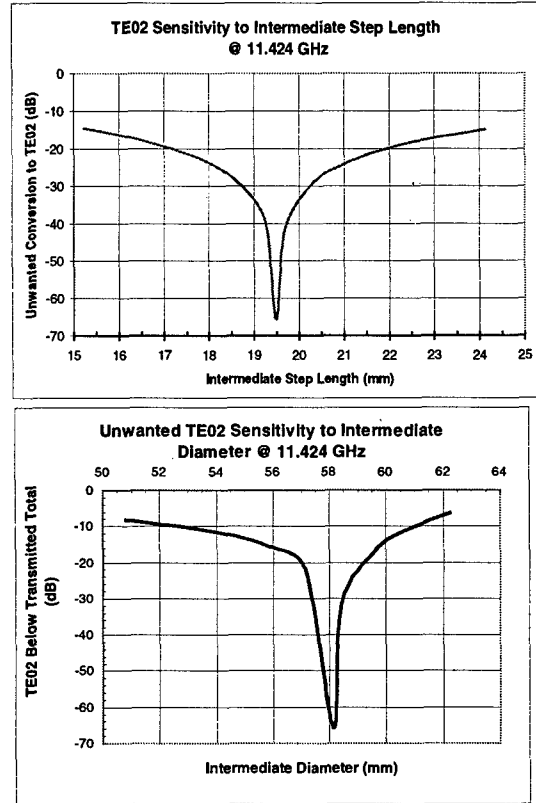
and the total normalized iris susceptance that would give  $\sigma_{opt}$  is given by

$$\left| \frac{B}{Y_0} \right| = \frac{\lambda_g - \lambda_g'}{\sqrt{\lambda_g \lambda_g'}} = 1.3476 \quad (2)$$

where  $\lambda_g$  and  $\lambda_g'$  are the guide wavelengths in the large diameter outside and inside the ceramic window respectively[1]. The double-step reflection of 0.167 corresponds to a normalized susceptance of 0.3388. The difference is made up with symmetrical inductive irises each having a normalized susceptance of

$$\left| \frac{B}{Y_0} \right| = 1.3476 - 0.3388 = 1.0088 \quad (3)$$

located properly so that the stored energy between the iris and the 2-stage step is minimum. It is important that the irises be located in the smaller (38.1 mm) port since an inductive iris will convert to TE<sub>02</sub> in the larger (65 mm) port.



Figures 4a and 4b. The Double step from 38.1 mm to 65 mm has been optimized to nearly cancel any conversion to TE<sub>02</sub> occurring at each step at the operating frequency of 11.424 GHz. This was accomplished using the mode matching code MLEGO. The variable parameters are the length and diameter of the intermediate step. The above graphs show the theoretical sensitivity of the conversion to unwanted TE<sub>02</sub> to each of these parameters while the other is kept constant at the optimum value.

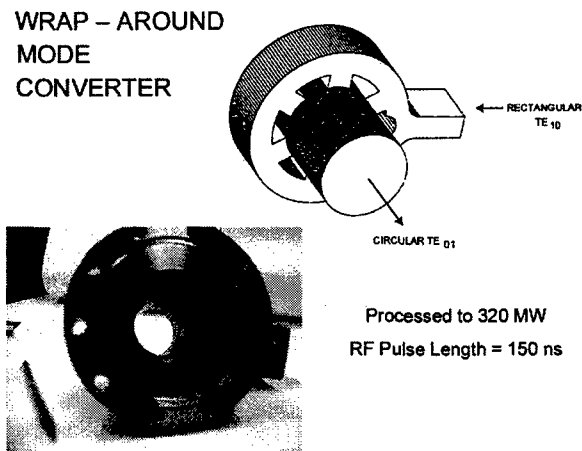


Figure 4. The new compact Wrap-around  $TE_{10}/TE_{01}$  mode transducer that is used to launch a high purity  $TE_{01}$  mode in 38 mm circular waveguide. It has lower electric field and higher mode purity than the original "Flower Petal" mode transducer design.

#### REFERENCES

- [1] W. R. Fowkes, R. S. Callin, S. G. Tantawi, and E. L. Wright, "Reduced Field  $TE_{01}$  X-Band Traveling Wave Window", Proceedings of 1995 Particle Accelerator Conference, Dallas, May 1995 pp 1587-9.
- [2] S. G. Tantawi, "The Wrap-around Converter: A compact  $TE_{10}/TE_{01}$  Mode Transducer" (to be published).
- [3] MLEGO© A mode matching code, Copyright S. G. Tantawi.

# SPECTRAL ANALYSIS OF BREAKDOWN AT OR NEAR RF WINDOWS\*

D. L. Borovina<sup>#</sup>, J. M. Gahl, UNM, Albuquerque, NM

D. Rees, LANL, Los Alamos, NM

## Abstract

The University of New Mexico (UNM) klystron test stand can generate microwave pulses up to 2-ms long with a frequency of 850 MHz and a peak power of 1.26 MW. For these experiments, the klystron output was used to simulate field breakdown near or on the surface of RF vacuum windows. RF-driven discharges were initiated in vacuum waveguide sections between copper electrodes. Data were gathered for discharges in the gap between the electrodes and for discharges between the electrodes and across the surface of the ceramic alumina. The generated optical signals were captured through three different windows (sapphire, crystal quartz, and NaCl) using different photo-multiplying tubes (PMTs). Issues addressed include a partial analysis of the spectra from metal/metal and metal/ceramic arcs and an investigation of arc precursor emission. The results of these preliminary tests will be used to optimize selection of optical components in arc detection systems.

## 1 INTRODUCTION

RF window failure in particle accelerators is an issue of great concern. Arc detection systems utilizing photo-multiplying tubes (PMTs) are commonly used to observe and possibly avoid this process. This work seeks to characterize the response of PMTs to RF-driven metal/metal and metal/ceramic arcs through a variety of arc detector window materials. We intend to characterize these arc detection systems with regard to their intensity, duration, and promptness of response.

## 2 EXPERIMENTAL LAYOUT

### 2.1 Microwave Generation

Extensive work was conducted on the construction of a high power, Klystron-based, microwave test stand at the University of New Mexico. This test stand was built to investigate RF windows, waveguide components, and new diagnostics that will predict or detect quickly window or waveguide breakdown. The test stand was used to characterize RF-load film resistors for the Low Energy Demonstration Accelerator (LEDA) at Los Alamos with the results reported separately at this meeting [1].

\*Work supported by the U. S. Department of Energy under Contract No. DE-FG04-97AL77993.

<sup>#</sup> Email: dlborovina@aol.com

The test facility depends heavily on equipment transferred to the University of New Mexico from Los Alamos National Laboratory (LANL) and DOE and is housed in a 2500 square foot high-bay facility on UNM's south campus.

A water cooling system as well as an oil storage and transfer system has been installed in the high bay. A screen room has been constructed to house diagnostic equipment. An Allen Bradley rack controls a modulator which is driven by a Universal Voltronix power supply. This arrangement, shown in Figure 1, was designed for a high-power, 850-MHz TH2138 Klystron tube, which drives the test stand with pulses up to 2-ms long and a peak power of 1.26 MW.

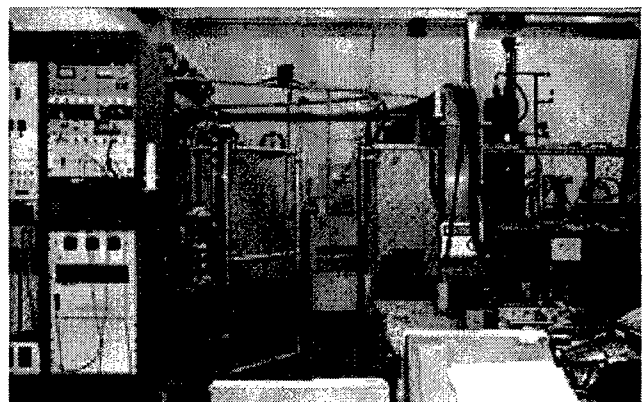


Figure 1: The University of New Mexico klystron test stand.

### 2.2 Microwave Breakdown Experiments

For these experiments, the test stand's output was used to simulate field breakdown near or on the surface of RF vacuum windows. RF driven discharges were initiated in vacuum waveguide sections between copper electrodes. Breakdown was achieved with a RF drive power of two to three hundred kilowatts. An isolator was utilized to protect the klystron from the RF reflected by the arcs generated.

Data were gathered for discharges struck in the vacuum gap between the electrodes (metal/metal arcs) and for discharges between the electrodes and across the surface of the ceramic alumina (metal/ceramic arcs). The generated optical signals were captured through three different detector window materials (sapphire, crystal quartz, and NaCl) using photo-multiplying tubes that had different spectral responses.

Two Hamamatsu 38-mm-diameter PMTs were used [2]. The 6199 type is a general purpose PMT that has a spectral response of 300 – 650 nm, covering most of the visible range and the near ultra violet. The typical rise time of the tube is 2.8 ns with an electron transit time of 40 ns. The second photo-multiplying tube used was the 7102 type with a spectral response of 400 – 1200 nm, covering the visible range and the near infrared. The typical rise time of the tube is 2.2 ns with average electron transit time of 37 ns.

The three different window materials have a flat spectral transmission characteristic over the spectral response of both tubes. The different window materials were used to see their potential effect on the magnitude of light transmission to both of the PMTs. The quartz window was approximately 3.3-mm thick, the sapphire window 1.1-mm thick, and the NaCl window was approximately 4.3-mm thick.

Data were taken under all possible combinations. Both PMTs viewed metal/metal and metal/ceramic discharges through all three window types. Of course experimental conditions such as gap separation and electrode configuration were kept as constant as possible. RF power levels of 200 – 300 kW were required to drive RF breakdown between the electrodes. At these power levels, electrodes were regularly degraded and required adjustment. Due in part to the concern that large amounts of RF energy were being reflected back at the protection isolator and the klystron, data acquisition was limited for this preliminary study to roughly 100 discharge events.

### 3 EXPERIMENTAL RESULTS

No significant variation in magnitude of signal was observed though the various window types. Nor did the two different PMTs show a variation in duration of light emitted. The most interesting effect we observed was a difference in the promptness of the response of the two PMTs.

When viewing metal/ceramic arcs, the 7102 type PMT (with a spectral response into the infrared) detected light on average approximately 18  $\mu$ s earlier than the 6199 type PMT. Figure 2 shows the reflected RF power from a metal/ceramic arc with the corresponding response of the 7102 PMT. Figure 3 shows the reflected RF power from a metal/ceramic arc with the corresponding response of the 6199 PMT.

The effect was not as significant for metal/metal arcs but still seemed to exist. When viewing metal/metal arcs, the 7102 type PMT detected light on average approximately 6  $\mu$ s earlier than the 6199 type photo-multiplying tube.

As described earlier from the manufacture's data sheets, electrical differences in the two tubes should only account for response variations on the order of a few nanoseconds.

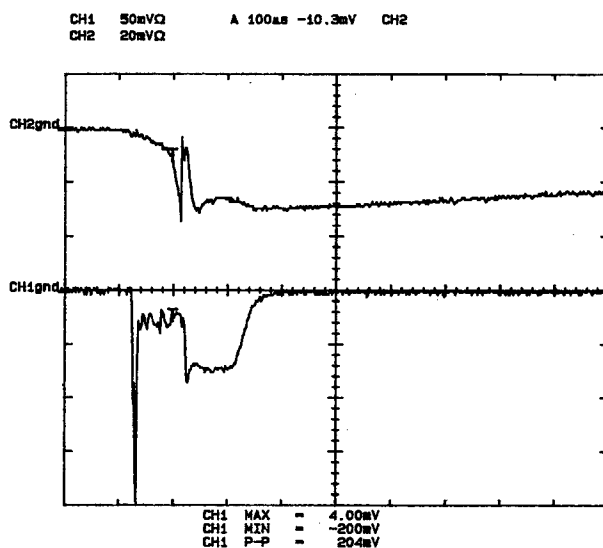


Figure 2: Reflected RF power from a metal/ceramic arc with the corresponding response of the 7102 PMT (100  $\mu$ s/div).

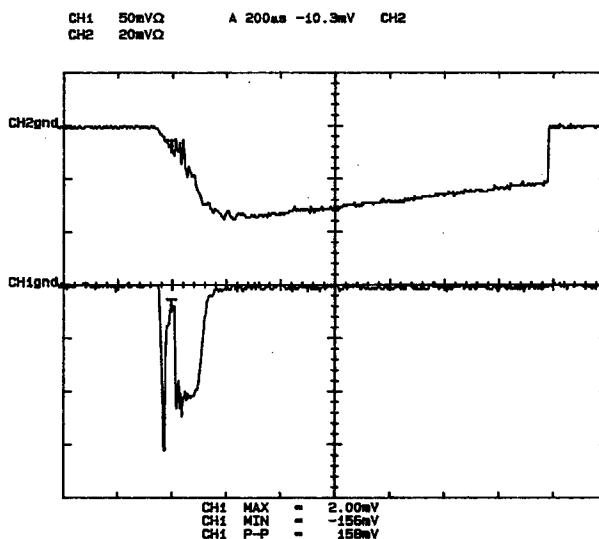


Figure 3: Reflected RF power from a metal/ceramic arc with the corresponding response of the 6199 PMT (200  $\mu$ s/div).

### 4 CONCLUSIONS

A variety of conclusions and recommendations for future investigations can be drawn from the results of this preliminary study, namely:

1. Infrared radiation may be emitted from RF window arcs, particularly metal/ceramic arcs, earlier than visible radiation.
2. To insure the most prompt response to a window arc, detection systems should be able to detect infrared radiation.

3. A more comprehensive spectroscopic study of metal/metal and metal/ceramic arcs may lead to the ability of arc detection systems to delineate such breakdowns.

### **5 ACKNOWLEDGEMENTS**

We acknowledge and thank Lee Terry of UNM for his help in experimental preparations and high-voltage safety precautions.

### **6 REFERENCES**

- [1] D. L. Borovina, J. M. Gahl, S. Humphries, Jr., D. Rees, L. Toole, "Experimental and Analytic Studies of an RF Load Resistor", presented at the Particle Accelerator Conference PAC'99, New York, April 1999.
- [2] Photomultiplier Tubes, Catalog No. TPMO 0002E04, Hamamatsu Corporation, Bridgewater, N.J., August 1995.



# MULTIPACTING STUDY OF THE RF WINDOW AT THE ADVANCED PHOTON SOURCE\*

J.J. Song\*, Argonne National Laboratory, IL

## Abstract

Multipacting current can cause breakdowns in high power rf components such as input couplers, waveguide windows, and higher-order mode (HOM) dampers. To understand and prevent the loss of a ceramic window or an input coupler in the Advanced Photon Source (APS) storage ring rf cavity, the multipacting phenomenon is being investigated experimentally. This paper begins with a description of simple model, presents a hardware design, and concludes with measurement of multipacting. Multipacting is explored in conjunction with conditioning the cavities and interaction with the stored beam.

## 1 INTRODUCTION

The APS at Argonne National Laboratory is fully operational at 7-GeV with a beam current up to 100 mA producing various types of x-ray radiation. Since energy is lost due to synchrotron radiation, the storage ring (SR) rf system typically provides about 9.6 MeV/turn at 100 mA. The SR rf system consists of four sectors, each consisting of four single-cell cavities (4x4). The four rf sectors are powered by two 1-MW klystrons for 100-mA operation.

However, several ceramic windows have been damaged during full operation of the SR rf system. The main symptoms are higher temperature, beam loss due to pressure bursts, and arcing. The inspection revealed a copper coating inside the ceramic windows as well as vacuum leaks due to cracks and/or pinholes on the windows. To prevent further loss of a ceramic window/input coupler in the APS SR rf cavity, an experimental study of the multipacting phenomena on the cavity has been prepared.

## 2 MULTIPACTING

Multipacting is a well-known phenomenon frequently observed in rf systems such as rf cavities, HOM absorbers, and klystrons. When an rf field exists across a gap, an electron from one surface is accelerated toward the other surface. Upon impact, another electron may be released due to secondary electron emission. The secondary emission coefficient  $\delta$  depends on the electron impact energy  $E_i$  and properties of the surface material. If the secondary emission coefficient of the surface is high enough ( $\delta > 1$ ) and the emitted electrons can be accelerated with a resonant field, this process can continue and lead to multipacting.

There has been a substantial investigation regarding this subject by others. Most of these concentrate on a simple 1-D model simulation or an experimental measurement with planar electrodes. R.A. Kirhek et al. [1] introduces a simple model as shown in Figure 1. In this model, the multipacting current due to the planer structure is added to the ordinary LRC circuit of the rf cavity in the typical representation. He addresses issues such as the multipacting saturation level, the multipacting mechanism, and the evolution of multipacting. On the other hand, D. Proch et al. [2] presents a systematic measurement of the rf multipacting current. The multipacting current between two planar electrodes of a specially designed 500-MHz coaxial resonator was measured. Various measurements were made by changing the surface material and condition of the electrodes.

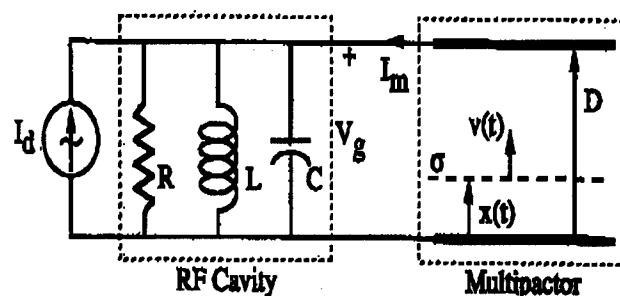


Figure 1: A simple model for interaction of multipacting with an rf cavity. The LRC circuit represents the rf cavity, loading by multipacting current  $I_m$ .

Multipacting is clearly undesirable. It results in the dissipation of large amounts of power and thereby generates destructive thermal-stress gradients. Furthermore, the power loss may occur in localized regions, leading to increased outgassing or evaporation of the material. Ultimately, the multipactor loading may become so great that the desired rf gap voltage cannot be reached or may cause significant reflection.

Unfortunately, few elements have low secondary emission characteristics. Moreover, many of these are unsuitable for vacuum and/or rf applications. Of particular interest to coupler windows for the APS SR rf cavity are the secondary emission coefficients of alumina and copper, which are  $\delta_{\max} = 2$  to 9 and 1.3, respectively. To reduce the multipacting phenomenon, the rf windows at APS have been coated with titanium, using a simple deposition system before conditioning and operation [3].

\* Work supported by U.S. Department of Energy, Office of Basic Energy Sciences under Contract No. W-31-109-ENG-38.

\* Email: jsong@aps.anl.gov

### 3 MEASUREMENT SETUP

A prototype electron detector system (e-detector) was built, bench-tested, and connected to the APS SR rf cavity near the ceramic window to measure the secondary electron emission (SEE) current. This device is similar to the e-detector initially developed at DESY [2].

The ceramic window allows for rf power to be transmitted from the WR2300 waveguide to the 352-MHz single-cell cavity through an H-loop-type input coupler as shown in Figure 2. The field patterns are transformed from  $TE_{11}$  mode in the waveguide to  $TM_{010}$  mode in the cavity. While the electromagnetic field is transmitted through a coaxial input coupler, the field configuration appears to be a TEM type. The e-probe of the detector was embedded at the bottom of the input coupler near the window.

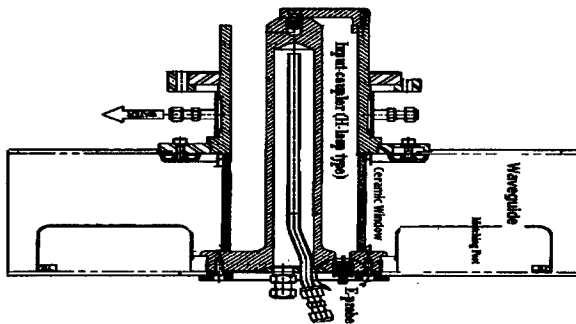


Figure 2: The ceramic window, where the rf power transmits through input coupler, showing the e-probe at the bottom near the window.

The electronic block diagram of the e-detector is shown in Figure 3. The rf lowpass filter is used to prevent interference with the 352-MHz and any other HOM frequencies. The incoming signal is obtained while applying the 30-V bias voltage in the circuit. An instrumentation amplifier amplifies the incoming signal, and then the current is converted to a voltage. The voltage signal passes through a buffer integrated circuit and finally reads into another amplifier circuit that sends the output to "signal out" or compares with the trip setting.

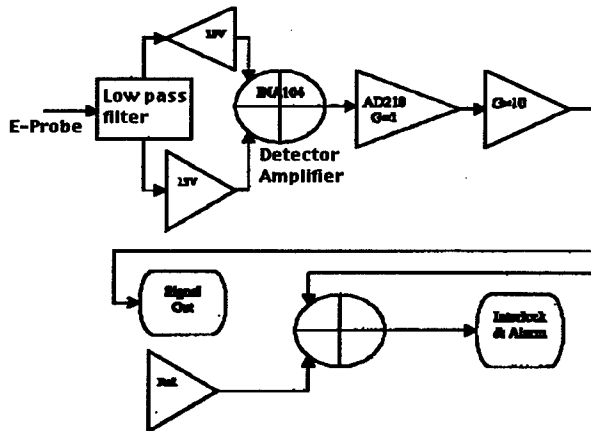


Figure 3: The block diagram of the e-detector board.

The signal output is read on a Sun workstation after it has been routed through an Alan Bradley circuit with EPICS codes. An output signal will be sent to the safety interlocks, once a reasonable trip point is determined.

### 4 INITIAL MEASUREMENT

#### 4.1 X-ray-induced Multipacting

The most troublesome area due to multipacting was located in sector 36 cavity #2 (S36 C2). In the past three years of operation, the input coupler/ceramic window was replaced three times. E-detectors designed at APS were installed on the sector 36 cavities (one per cavity). A SEE current was measured during rf conditioning as well as during injection and stored beam. Although there was no signal from any of the e-detectors during the rf-conditioning, the e-detector recorded 6 volts from cavity #2 with stored beam at 100 mA, as shown in Figure 4.

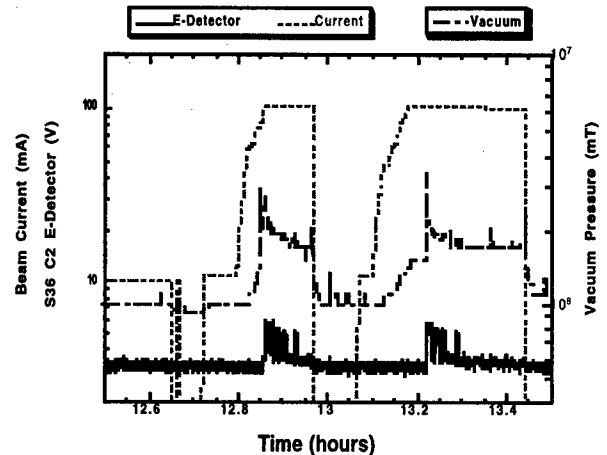


Figure 4: E-detector signal at sector 36 cavity #2; the stored beam current and vacuum pressure are also shown.

As shown, the vacuum pressure follows the e-detector signal. However, the SEE current appears to be too high. Later, it was found this was due to the synchrotron radiation from the upstream bending magnet (S35BM-B) hitting the waveguide, where the ceramic window was located in this particular cavity (see Figure 5).

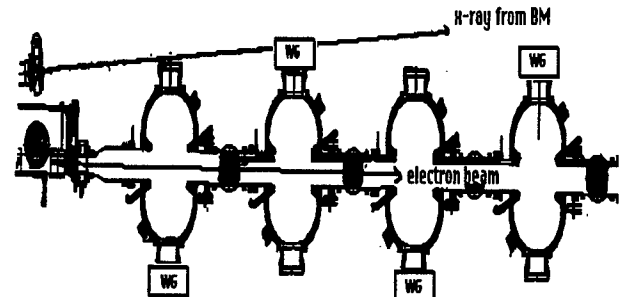


Figure 5: The layout of the sector 36 cavities, where the cavity #2 waveguide is in the line of sight of the x-ray trajectory from the upstream bending magnet.

It appeared that the end absorber (copper block) at the end of the antechamber was not thick enough to block the x-rays completely. After the transmitted x-ray dose was measured, more lead blocks were added (8 inches or 200 mm total) to prevent the x-ray from penetrating the ceramic. The corresponding x-ray dose calculation, shown in Figure 6, shows that 8 inches of lead shielding was required to block the x-rays.

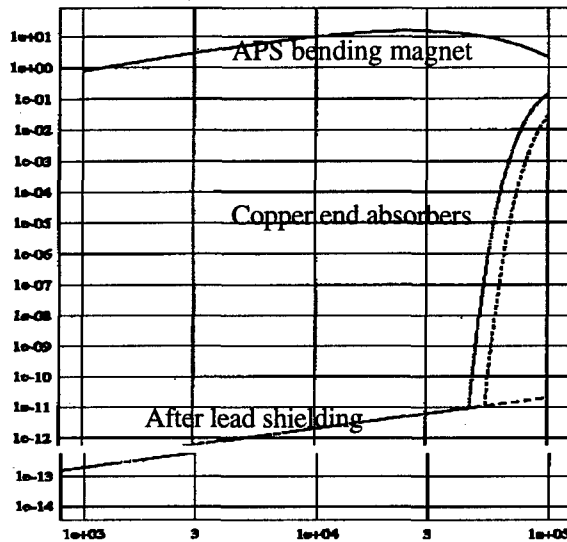


Figure 6: Calculation of transmitted x-ray energy from the APS bending magnet, shown with and without the lead shielding.

#### 4.2 Beam-induced Multipacting

After the lead shielding was installed and the input coupler was replaced, the measurement continued. A typical result with a 100-mA beam is shown in Figure 7. The top line represents the stored beam current. The e-detector signal from the S36 C2 cavity appears to be a step-like pulse. The pulsed signal from the #2 cavity e-detector repeats at about 80 seconds and stays at maximum value for 20 seconds. The signal due to the multipacting current is a series of short pulses on the order of nanoseconds. The pulse period was confirmed later in separate measurements with a fast sampling scope. This time scale is comparable with a gap of a few cm and an operating rf frequency of 352 MHz. The bottom of the step-like pulse from S36 C2 is overlapped with the S36 C1 cavity e-detector signal, which is basically zero volts (noise signal in the middle of the graph).

The pulse width appears to be longer and higher as beam current and/or rf power increases in the cavity. In fact, when the beam current later reached more than 95 mA, the signal saturated. Also shown is the vacuum pressure in the cavity (shown at the bottom of the graph). The pressure change is very small, which indicates local outgassing in the cavity. This is consistent with the SEE current from the e-detector. The ceramic temperature, taken from the upstream and downstream ceramic windows with infrared cameras, increases after the electron is bombarded on the surface (zigzag curves as shown).

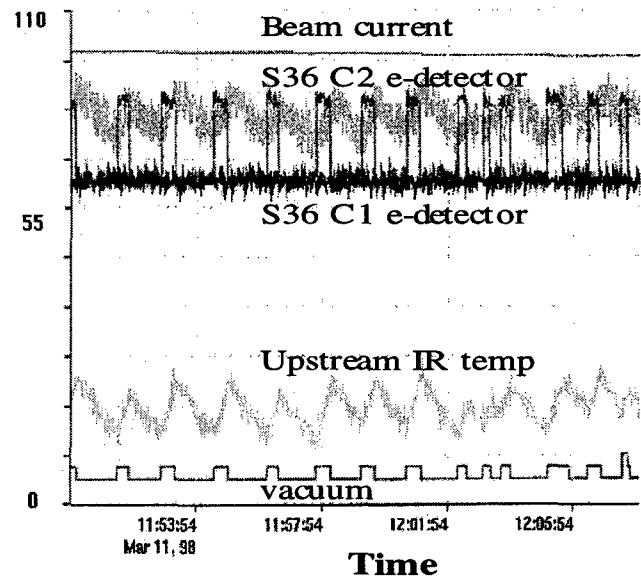


Figure 7: Electron detector signal from the newly replaced cavity. Also shown are vacuum pressure and ceramic temperature.

#### 4.3 Progress and Further Works

- The prototype e-detector was tested, installed, and shown to respond to the multipacting current under various conditions.
- Recently, more emphasis is given to determine the SEE current using a multipacting simulation code developed by the University of Helsinki [4].
- More systematic measurements will be made during rf conditioning once construction of the rf test-bed (the independent 350-MHz rf conditioning system) has been completed.

### 5 ACKNOWLEDGMENTS

The author would like to thank D. Proch at DESY for use of their e-detector design in early development stage. Many thanks also go to the students, especially W. Dower and W. Wu, for their technical assistance.

### 6 REFERENCES

- [1] R.A. Kishek et al., "Steady state multipactor and dependence on material properties," *Phys. Plasmas*, V4 (3), 863 (1988).
- [2] D. Proch et al., "Measurement of multipacting currents of metal surfaces in rf fields," *Proc. of the 1995 Particle Accelerator Conference*, 1776 (1996).
- [3] K. Primdahl et al., "Reduction of multipactor in rf ceramic windows using a simple titanium-vapor deposition system," *Proc. of the 1995 Particle Accelerator Conference*, 1687 (1996).
- [4] E. Somersalo et al., "Computational methods for analyzing electron multipacting in rf structures," *Particle Accelerators*, V59, 107 (1998).

# MULTI-MODE OPERATION OF THE ACCELERATOR RF CAVITY.

Daniel Wisnivesky<sup>#</sup>, LNLs and IFGW Unicamp, Campinas, Brazil

## Abstract

In this paper we discuss a new mode of operation and design criteria of the RF cavity of a circular accelerator. It is shown that, for a specified energy aperture, a room temperature RF cavity can operate with a significant reduction in wall heat dissipation if, together with the fundamental mode, high order modes of a properly design cavity are simultaneously excited.

## 1 INTRODUCTION

Room temperature RF cavities used in circular accelerators are low efficient components. A large fraction of the RF power delivered to the cavity is dissipated in the cavity walls, while, in some cases, a relatively small part is effectively used to accelerate the beam. In a synchrotron accelerator the efficiency is typically of the order of 50%. In general, several tens of kW are transformed into heat on the cavity walls in order to get the energy aperture and accelerating field needed. To control cavity detuning and to avoid undesirable high order mode (HOM) resonances, the cavity temperature is required to stay constant, which in general implies a large cooling system. As a consequence, the RF cavity design results in a compromise among conflicting requirements: ultra high vacuum, high heat dissipation, high electric fields and precise temperature and frequency control. It is clear that much could be gained if the system would be able to operate with a substantial reduction of the heat load in the cavity.

The spectrum of HOM is another aspect that deserves careful attention in the design and operation of the RF cavity. Special effort is devoted to either provide for methods that would damp the Q of the HOM, or temperature control the resonant frequencies so as to avoid undesirable coincidences with the revolution frequency or any of its multiples. In general, HOM are seen as an inconvenient consequence of the discrete spectrum of the system.

In this paper we want to discuss a different mode of operation of the RF cavity: multi-mode excitation. The cavity is designed to resonate at specifically chosen frequencies. In this cavity, several HOM modes are simultaneously excited and carefully combined in such a way that they provide for the necessary longitudinal acceleration of the beam and the required energy aperture

with a significantly reduction of the total power dissipated in walls.

An available growing number of high frequency, high power amplifiers, together with a large experience in the design of complex cavities makes it tenable to discuss multi-mode excitation as a practical possibility.

## 2 EFFECTIVE FIELD AND ENERGY APERTURE OF HOM

We consider a cavity that is simultaneously excited with different transverse magnetic modes. The longitudinal component of the TM<sub>0np</sub> mode electric field along the axis of the cavity is given by the equation:

$$E = E_{np} \cos\left(\frac{p\pi z}{d}\right) \sin\left(\frac{2\pi t}{T_p}\right) \quad (1)$$

where  $f_p = 1/T_p$  is the frequency of the mode. The time needed for a particle to transverse the cavity is

$$T_0 = d / \beta_0 c.$$

with  $d$ , the axial length of the cavity.

The effective electric field sensed by a charged particle going through the cavity is given by the expression

$$E_{eff} = \frac{E_{np}}{d} \int_{z(-\frac{T_0}{2}+t)}^{z(\frac{T_0}{2}+t)} \cos\left(\frac{p\pi z}{d}\right) \sin\left(\frac{2\pi t}{T_p}\right) dz \quad (2)$$

computed along the particle trajectory,  $z = \beta_0 ct$ .

Evaluation of equation (2) results in an expression for the effective E field of the form:

$$E_{eff} = E_{np} \left[ \frac{\sin\left(\frac{\pi T_0}{T_p} - p\frac{\pi}{2}\right) \sin\left(\frac{2\pi}{T_p} - \frac{p\pi}{T_0}\right)t}{\left(\frac{2\pi T_0}{T_p} - p\pi\right)} + \frac{\sin\left(\frac{\pi T_0}{T_p} + p\frac{\pi}{2}\right) \sin\left(\frac{2\pi}{T_p} + \frac{p\pi}{T_0}\right)t}{\left(\frac{2\pi T_0}{T_p} + p\pi\right)} \right] \quad (3)$$

In general, neither one of the oscillatory terms in equation (3) will be coherent with the fundamental mode. Nevertheless, by proper design of the cavity, it is possible for the frequency of each TM<sub>0np</sub> mode to satisfy the relationship:

$$\frac{2}{T_p} - \frac{p}{T_0} = \frac{2}{T} \quad (4)$$

where  $f = 1/T$  is the frequency of the fundamental mode. In that case, the effective field contribution of TM<sub>0np</sub> is

<sup>#</sup> Email: daniel@lnls.br

$$E_{eff} = \frac{E_{np}}{2} \frac{\sin\left(\pi \frac{T_0}{T}\right)}{\pi \frac{T_0}{T}} \left[ \sin \frac{2\pi t}{T} + (-1)^p \frac{1}{\left(1 + \frac{pT}{T_0}\right)} \sin \left(1 + \frac{pT}{T_0}\right) \frac{2\pi t}{T} \right] \quad (5)$$

with a corresponding mode frequency given by

$$f_p = f + p/2T_0 \quad (6)$$

Equation (5) indicates that, for  $p > 0$ , the  $TM_{0np}$  mode has 2 contributions to the effective E field:

- an electric field with the same frequency as the fundamental mode and  $1/2$  its effective amplitude,
- a component with a larger frequency  $f_{equiv}^p = f + p/2T_0$ , and an amplitude reduced by a factor  $T_0/(T_0 + pT)$ .

The corresponding contribution to the energy acceptance [1] can be obtained, for large over voltage from the integral

$$A_p = \int_0^{T/2} E_{eff}(t) dt$$

which reduces to

$$A_p = E_{np} \frac{\sin\left(\pi \frac{T_0}{T}\right)}{\pi \frac{T_0}{T}} \frac{T}{\pi} \left[ \frac{1}{2} + \frac{(-1)^p}{4} \frac{1 + \cos\left(\frac{pT}{T_0}\right)}{\left(1 + \frac{pT}{T_0}\right)^2} \right] \quad (7)$$

The first term in equation (7) shows that all  $p$ -modes make an equal contribution to the energy aperture of  $1/2$  the value of the contribution of the fundamental mode. The second term, corresponding to the higher frequency excitation of the cavity, adds or subtracts a small correction to the value of the energy acceptance. We will neglect this contribution in the following discussion.

If several modes are simultaneously excited, the electric field of each one could be smaller than the amplitude of the field in case of single mode excitation. This indicates that, multi-mode excitation of the cavity makes possible to reduce the total power dissipation while keeping the same energy aperture. Something similar to what occurs when several cavities are used in substitution of a single cavity. If we assume that the cavity is excited with  $s$  modes with frequencies  $f_p = f + p/2T$  and amplitudes  $E_p$  ( $p=0,1,\dots,s$ ), the energy acceptance is proportional to

$$E_{acc} \approx E_0 + \frac{1}{2} E_1 + \dots + \frac{1}{2} E_s$$

and the power dissipation is proportional to

$$P \approx \frac{E_0^2}{R_0} + \frac{E_1^2}{R_1} + \dots + \frac{E_s^2}{R_s}$$

where  $R_0, R_1, \dots, R_s$  are the corresponding shunt impedance.

Minimum power in the cavity is obtained if:

$$\begin{aligned} E_1 &= \frac{R_1}{2R_0} E_0 \\ &\dots \\ E_s &= \frac{R_s}{2R_0} E_0 \end{aligned} \quad (8)$$

In this case, for the same energy acceptance, the power dissipated in the cavity in the multi mode case is given, in terms of the corresponding power dissipation for a single mode, by the equation

$$P = \frac{1}{1 + \frac{R_1}{4R_0} + \dots + \frac{R_s}{4R_0}} P_0 \quad (9)$$

We can make an estimate of the multi-mode power in the cavity if we take the case when all shunt impedance are approximately equal. Table I gives the multi-mode power dissipated in the cavity in terms of the single mode power, considering different number of modes. It also shows the fraction of the total power in the cavity delivered by each generator.

Number of modes in the cavity	Total multi-mode power (P) relative to single mode power	Relat. power in mode f <sub>0</sub> P <sub>0</sub> /P	Relat. power in mode f <sub>1</sub> P <sub>1</sub> /P	Relat. power in mode f <sub>2</sub> P <sub>2</sub> /P	Relat. power in mode f <sub>3</sub> P <sub>3</sub> /P
1	100%	1	-	-	-
2	80%	0.8	0.2	-	-
3	66%	0.66	0.16	0.16	-
4	57%	0.57	0.14	0.14	0.14

Table I: multi-mode power relative to single mode power for different numbers of modes in the cavity.

### 3 DISCUSSION OF A CAVITY DESIGN

As an example, we have discussed the design of a simple cavity for 2 modes operation. The main design parameters are:

Number of modes: 2 ( $s=1$ ).

Fundamental mode: TM<sub>010</sub>

Frequency: 300 MHz.

Cavity length  $d$ : 500 mm.

Second mode: TM<sub>011</sub>

Frequency: 600 MHz, in agreement with equation (6)

The simulation was made using Superfish [2] and adjusting the cavity shape so as to obtain a large  $Q$  and shunt impedance for each mode. Figure 1 shows the general boundary of the cavity

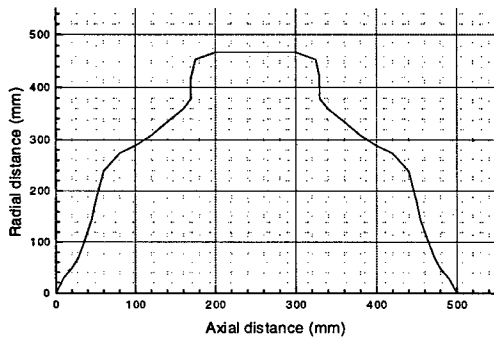


Figure 1. General picture of the 300/600 MHz cavity

The main results obtained by Superfish are summed up in table II.

Cavity mode	Frequency	Shunt Impedance	$Q$
TM <sub>010</sub>	300 MHz	14 M $\Omega$	45,000
TM <sub>011</sub>	600 MHz	11.5 M $\Omega$	60,800

Table II: Superfish parameters for the modes TM<sub>010</sub> and TM<sub>011</sub>.

As a working example we can compute the power requirements of this cavity when 2 modes are excited as compared to the single mode operation.

According to equation (9), for every 10 kW dissipated in the 300 MHz resonance in single mode operation we get:

	Power dissipated in 300 MHz	Power dissipated in 600 MHz
For every 10 kW single mode dissipation	5.7 kW	2.6 kW

Table III: Power dissipation in the modes TM<sub>010</sub> and TM<sub>011</sub>.

If the cavity is adjusted to have in addition a TM<sub>0n2</sub> resonance at 900 MHz we get (assuming similar shunt impedance for TM<sub>011</sub> and TM<sub>012</sub>) a power dissipation distributed in each one of the 3 modes according to table IV, for every 10 kW single mode dissipation:

	Power dissipated in 300 MHz	Power dissipated in 600 MHz	Power dissipated in 900 MHz
For every 10 kW	5.0 kW	1.1 kW	1.1 kW

Table IV: Power dissipation distributed in 3 modes.

### 4 CONCLUSIONS

We have discussed the power dissipation in the accelerator RF cavity when several resonant modes are excited. We have shown that, with an adequate design of the cavity, these modes make a significant contribution to the energy aperture of the ring. Thus, the amplitude of each mode and the power dissipation are smaller than in the normal single-mode excitation of the cavity. The reduction in power dissipation increases with the number of modes. The effect is similar to the one produced by augmenting the number of cavities in the ring: the field amplitude in each cavity is smaller and the total power is reduced. In the present case, no additional cavities are required. Instead a more complex multi frequency transmitter is involved. The growing number of high frequency, high power transmitters available in recent years makes multi-mode operation of the accelerator RF system a practical possibility.

### 5 REFERENCES

- [1]/ M. Sands. The physics of electron storage rings. Int. Sch. of Physics "Enrico Fermi" Academic Press 1971, p 342.
- [2]/ Superfish Code. PC version distributed by LAACG. Laacg.lanl.gov

# DEVELOPMENT OF A NEW HIGH POWER CAVITY FOR THE 590 MeV RING CYCLOTRON AT PSI

H. Fitze\*, M. Bopp, H. Frei, PSI, Switzerland

## Abstract

The cavity development is done in two steps: The design concept is first verified with a fully operational model cavity and then, based on this experience, a 1:1 scale prototype cavity is constructed and fabricated. Right now we are in between the two steps. This paper presents the proposed layout for the new full scale cavity and summarises the results gained with the model cavity. Special emphasis is given on the transient behaviour of the tuning system under large load changes.

## 1 INTRODUCTION

The main cyclotron at PSI [1] routinely accelerates with four 50 MHz RF cavities a 1.5 mA beam up to 590 MeV. Each cavity dissipates 300 kW of RF power and generates a peak voltage of 730 kV. To allow the acceleration of even higher currents this voltage has to be increased. Due to limitations in the cooling system and the tuning range of the cavity [2] this requires a new design. It was decided at PSI to build a new cavity, which can produce stable accelerating voltages of up to 1 MV and dissipate 500 kW of RF power [1]. Such a cavity would also serve as a prototype for the driver cyclotron of an energy amplifier or transmutation machine [3].

## 2 CAVITY LAYOUT

Table 1 lists the main parameters of the new cavity in comparison with the existing one.

Table 1: Cavity parameters

	EXISTING CAVITY	NEW CAVITY
Frequency	50.6 MHz	50.6 MHz
Shunt Impedance	1 M $\Omega$	1.8 M $\Omega$
unloaded Q	30000	48000
Dissipated Power CW	300 kW	500 kW
Accelerating Voltage	730 kV	1 MV
RF-Wall Material	Al	Cu
Mech. support structure	cast Al	stainless steel

Figures 1 and 2 depict the proposed layout for the 1:1 scale prototype (for the results with the 1:3 model see section 3).

This new design will allow:

- an operation with an accelerating voltage of up to 1 MV, or with the "standard" voltage of 730 kV but decreased energy consumption.
- the cavity to stay tuned all the time. (e.g. when the input power trips due to a spark in the cavity.)

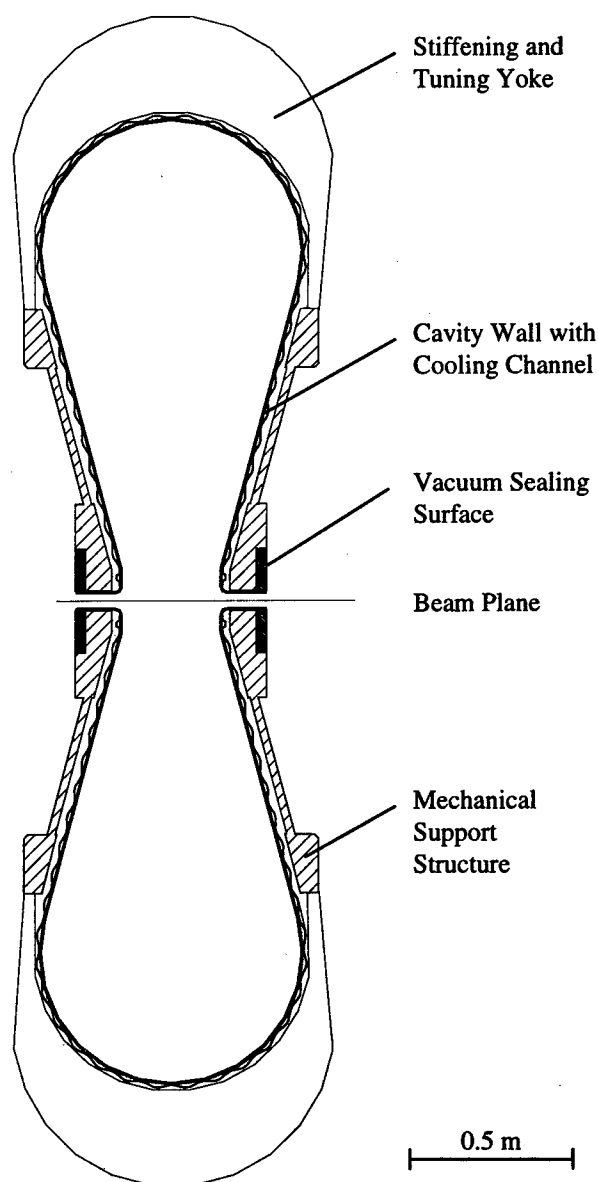


Figure 1: Cross section of the proposed 1:1 scale cavity

\*Email: Hansruedi.Fitze@psi.ch

The main features of the cavity layout are listed below:

- The cavity wall consists of an inner liner of a 6 mm copper sheet, directly electron-beam welded onto a corrugated stainless steel sheet, forming the outer shell. The large number of channels generated hereby provide a very efficient water cooling of the entire cavity surface with very small thermal gradients. To facilitate the welding process, the copper sheets have to be as thin as possible.
- The shape of the cavity is optimised for a maximum shunt impedance with the constraint that the whole structure has to fit into an existing sector of the ring cyclotron.
- The end sections of the cavity serve to connect to the water feed lines and to distribute the cooling water into the individual channels. Integrated into the end sections are the ports for the vacuum pump and the RF-window.
- To prevent the structure from collapsing under atmospheric pressure, a solid and stable stainless steel frame is built around it. This support structure is constructed such that it can be separated from the cavity shell at any time. It also provides the necessary vacuum flange connections in the beam plane and a good sealing surface because it's built from stainless steel.
- The tuning system is integrated into the support structure and consists of a fast and a slow system (see section 3.2).

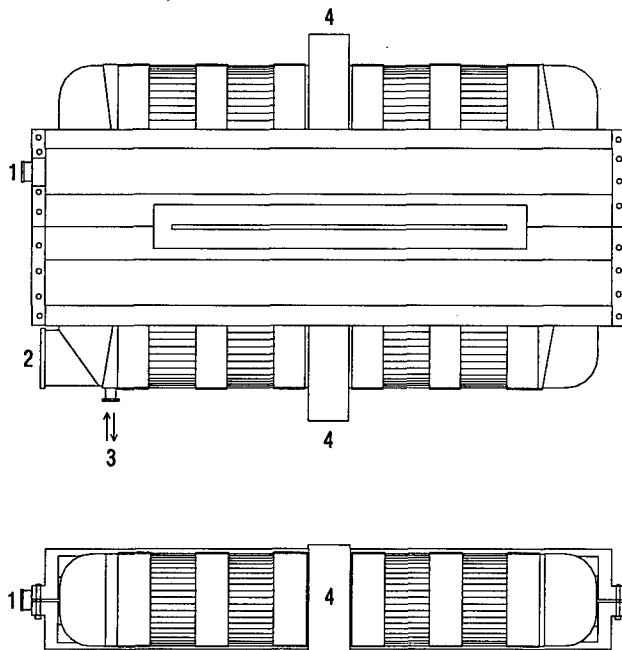


Figure 2: Side and top view of the proposed 1:1 scale cavity.

- 1: opening for the RF coupling loop  
 2: vacuum pumping port  
 3: cooling water inlet/outlet  
 4: stiffening and tuning yoke

### 3 MODEL CAVITY

To be able to study all aspects of such a high power cavity, we have built a model on a 1:3 scale and which is able to dissipate at least 100 kW of RF power (see Figure 3). The scale factor of 1:3 comes from the fact that we have a high power amplifier available operating at 150 MHz.

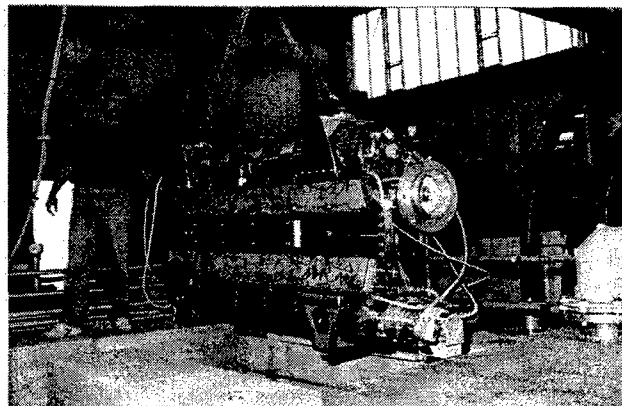


Figure 3: 150 MHz 1:3 scale model cavity before installation in the testing vault.

The model allows us to

- Experiment with new design ideas.
- Test fabrication techniques.
- Study the tuning behaviour in the case of large load changes.
- Validate simulation models which are necessary to predict the behaviour of the full scale cavity.

#### 3.1 Cold tests

Using this design concept, copper and stainless steel have to be joined together. After having had great difficulties with these welds we can now maintain a vacuum pressure better than  $10^{-5}$  mbar in the cavity.

Table 2: RF parameters of the evacuated 1:3 scale cavity

	calculated	measured <sup>1)</sup>
Frequency in MHz	151.834	148.951
unloaded Q	27550	24750
Shunt Impedance in MΩ	1.084	1.064 <sup>2)</sup>

<sup>1)</sup> without the stiffening yokes

<sup>2)</sup> measured in air

The difference between calculated and measured values in table 2 is mainly due to the larger than expected mechanical deformations caused by the atmospheric pressure, and due to the fact that the cavity shape had to be slightly deformed in order to fit into the mechanical support structure.

Up to now we did not try to get closer to the nominal frequency, because the bandwidth of the amplifier chain is large enough to drive the cavity. Since we have to 'hit' the



exact resonance frequency with the full scale cavity, the model contains an adjusting mechanism, with which enables us to do so.

### 3.2 Power tests

When feeding RF power to the cavity for the first time, virtually no multipacting could be observed and the incident power could be increased almost instantaneously to the limit of the amplifier chain (80 kW CW).

We could show that the foreseen tuning system based on thermal expansion and acting on the support structure neither could provide the necessary tuning range nor the required speed.

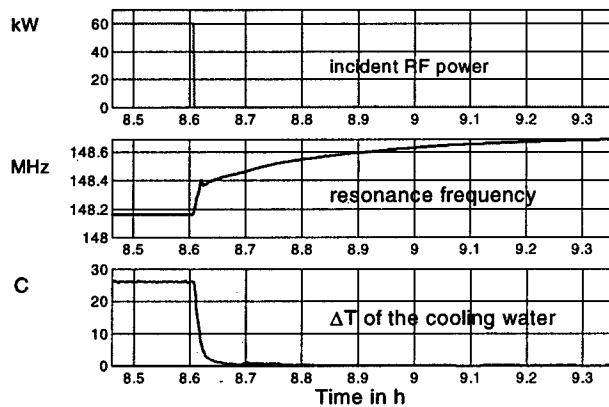


Figure 4: Cavity response to a step in RF input power. The oscillator is following the resonance frequency of the cavity with the tuning system switched off.

The second trace in figure 4 shows that the resonance frequency of the cavity changes roughly by 0.5 MHz when the incident RF power goes from 60 kW to zero. About half of this large detuning is caused by an unwanted residual thermal coupling between the cavity wall and the mechanical support structure. We believe that we can remove it to a large extent by changing the layout of the cooling channels around the beam plane.

The resonance frequency can, as finite element calculations (see figure 5) and experiments [4] show, be changed over more than 1 MHz by intentionally heating (or cooling) part of the mechanical support structure. This effect allows to compensate for the slow drift.

To cope with the fast changes of the resonance frequency, we will build into the stiffening yokes a hydraulic adjusting mechanism which is at least an order of magnitude faster than the slow system.

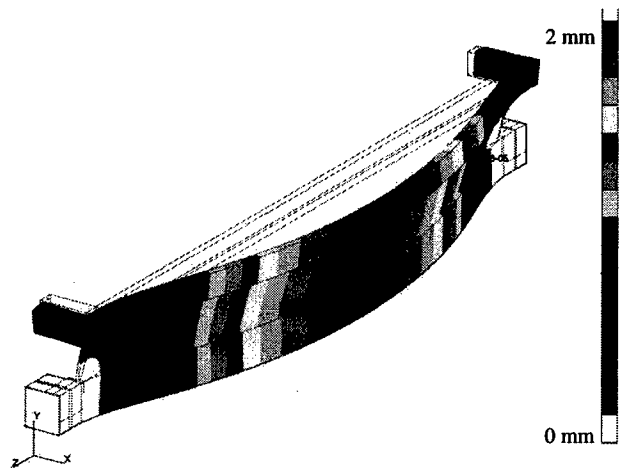


Figure 5: Deformation of the mechanical support structure due to thermal expansion.

The temperature of the upper rod is raised by 60°C above the rest of the support structure. This deformation would yield in a change of the resonance frequency of 1.4 MHz.

## 4 THE NEXT STEPS

To come up with a working full scale cavity, we are planning the following steps:

1. Already under way are tests of the tuning system on the model cavity.
2. Learn how to reproducibly join copper and stainless steel.
3. Mechanically design and fabricate the prototype cavity together with a partner in industry
4. Test the prototype cavity in our 1 MW testing installation, which is now being set up.

## 5 REFERENCES

- [1] U. Schryber et al., "High Power Operation of the PSI Accelerators", Proc. 14<sup>th</sup> Int. Conf. on Cyclotrons and their Applications, Cape Town (RSA), Oct.1995
- [2] P.K. Sigg et al., "High Beam Power RF-Systems for Cyclotrons", Proc. 14<sup>th</sup> Int. Conf. on Cyclotrons and their Applications, Cape Town (RSA), Oct.1995
- [3] Th. Stammach et al., Proc. 2nd Int. Conf. on Accelerator Driven Transmutation Technologies and Applications, Kalmar (Sweden), June 1995
- [4] L. Stingelin, "Etude d'un système thermique pour le contrôle de la fréquence de résonance de la nouvelle cavité au PSI". PSI internal report, 1998.

# THE FIRST BEAM ACCELERATION TEST USING HIGH GRADIENT CAVITY AT HIMAC

R. Muramatsu\*, M. Fujieda, Y. Mori, H. Nakayama, C. Ohmori, Y. Sato, A. Takagi, T. Uesugi, M. Yamamoto, M. Yoshii, KEK-Tanashi, Tokyo 188-8501, Japan  
M. Kanazawa, K. Noda, NIRS, Chiba 263-8555, Japan

## Abstract

The first beam acceleration test using a High Gradient Cavity (HGC) loaded with Magnetic Alloy (MA) cores has been carried out at the HIMAC (Heavy Ion Medical Accelerator in Chiba). Acceleration of heavy ions, which required a wide frequency sweep from 1 MHz to 8 MHz, was successfully carried out without resonant frequency tuning.

## 1 INTRODUCTION

The HGC loaded with MA cores has been developed[1] for the JHF (Japan Hadron Facility) proton synchrotrons. The maximum voltage of 20 kV has been obtained by the cavity of 40 cm in length. The cavity was driven by a push-pull amplifier using two 150 kW tetrodes. The frequency sweeping from 1 to 5 MHz has been achieved without any tuning circuit because of its broadband characteristics of the MA-loaded cavity[2].

The cavity has been installed in the HIMAC[3] for the beam acceleration to examine the characteristics of the broad-band system. Two major changes has been carried out for both cavity and amplifier. One is to reduce the number of cores to increase the resonant frequency of the cavity. Another is to replace the amplifier. A push-pull amplifier with two 30 kW tetrodes was newly employed, which covered the required rf frequency range of 1–8 MHz for accelerating heavy ions.

The beam acceleration of He, C, Ne and Si ions was successfully carried out and the results are reported in this paper. The fundamental rf and higher harmonics could be driven by the cavity simultaneously because the cavity has a broad impedance, which covers these frequencies. Further improvement of the acceleration efficiency is expected by adding the higher harmonics[4].

## 2 PERFORMANCE OF HGC

Parameters of the cavity are listed in Table 1.

The cavity loads four MA cores and the total shunt impedance is about 400  $\Omega$ . Since the MA core has a very low-Q value, the gap voltage can be obtained over a wide range of frequency without tuning system. In this cavity, a half of the peak impedance is guaranteed in the frequency from 1 to 8 MHz. The wide-band push-pull amplifier has two tetrodes and each tube is connected to each side of the accelerating gap through the capacitors [5]. Figure 1 shows the cavity impedance measured at the accelerating gap.

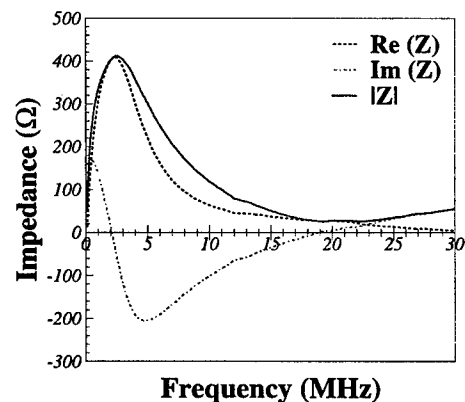


Figure 1: The measured impedance of HGC.

The maximum gap voltage of 4 kV was achieved at the frequency range from 2 to 3 MHz, and the voltage of more than 3 kV was achieved at the frequency range from 1 to 6 MHz. The gap voltage of 2 kV was obtained up to the frequency of 8 MHz because the gain of driver amplifier was gradually dropped when the frequency increased.

Table 1: Parameters of the HGC installed in HIMAC.

Length	40 cm
Freq. Range	1 ~ 8 MHz
Gap Voltage	Max. 4 kV
Shunt Impedance	400 $\Omega$ @ 2 MHz (4 cores loaded)
Q value	0.6
Amplifier	60 kW push-pull, 4CW30,000A $\times$ 2

\* E-mail: ryosaku@tanashi.kek.jp

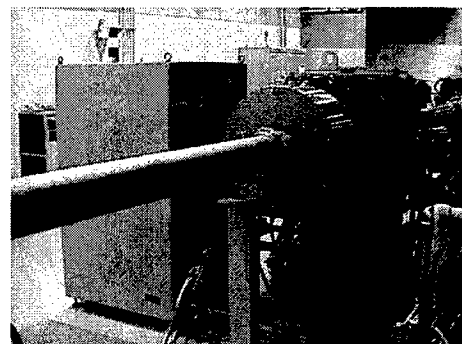


Figure 2: The HGC installed in HIMAC.

Figure 2 shows the prototype of the HGC installed in HIMAC synchrotron.

### 3 EXPERIMENT

The beam acceleration test was carried out up to the flat top energy of 230 MeV/u (frequency range: 1.045–5.527 MHz) for He, C and Ne, and that of 800 MeV/u for Si (frequency range: 1.045–7.8 MHz). Some parameters of the beam are listed in Table 2.

Table 2: Parameters of the HIMAC synchrotron.

Injection Energy	6 MeV/u
Momentum Spread at Injection	$\pm 0.1\%$
Revolution Frequency at Injection	261.3 kHz
Harmonic Number	4
Intensity at Injection	$1.0 \times 10^{10}$ ppp
Repetition	0.3 Hz
Ramping Time	1 s

Because the particles are injected into the synchrotron as a coasting beam, the adiabatic capture process was employed to increase the capture efficiency. The input signal to the amplifier was adjusted to keep the gap voltage constant because of the frequency dependence of the cavity impedance. Setup of the amplitude modulation of the gap voltage is shown in Fig. 3. In this experiment the modulation signal was programmed beforehand because no feedback loop was necessary.

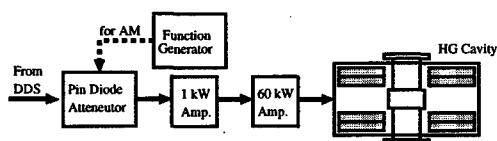


Figure 3: Setup of amplitude modulation.

Figure 4 shows the measured gap voltage. The upper and lower side in Fig. 4 is the input signal and the flattened gap voltage respectively. This shows that the gap voltage of 3 kV was achieved during whole cycle.

With this system, the beam was adiabatically captured at injection by increasing the rf voltage gradually during 10 ms, which is relatively slow compared with the synchrotron oscillation period of about 1 ms.

The beams of He, C and Ne ions were successfully accelerated up to the energy of 230 MeV/u. About 50 % of the beam was accelerated up to the flat top. The beam current was measured by DC Current Transformer (DCCT) as shown in Fig. 5.

For Si ions, the beam was accelerated up to 800 MeV/u, which was the maximum attainable energy of this ring.

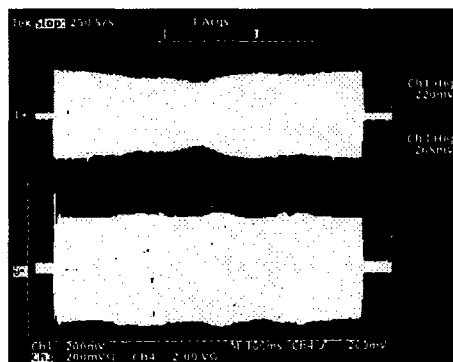


Figure 4: The measured envelope of the gap voltage for Ne beam acceleration (1.0–5.5 MHz). The rf turned on during 800 ms.

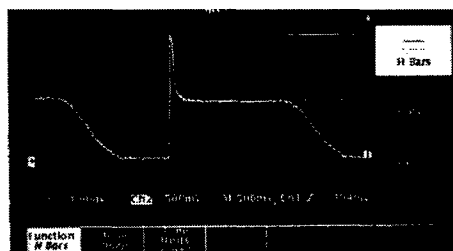


Figure 5: The beam current measured by DCCT. The beam was extracted at the flat top.

### 4 SUMMARY

The first beam acceleration test with HGC was successfully carried out at HIMAC. The accelerating voltage of 3 kV over the frequency range from 1 MHz to 6 MHz was obtained by a small 60 kW push-pull amplifier without frequency tuning. The beams of He, C, Ne and Si ions were successfully accelerated with the efficiency of more than 50 %.

### 5 ACKNOWLEDGMENT

We would like to thank the members of HIMAC and AEC for operation of HIMAC.

### 6 REFERENCES

- [1] Y. Mori *et al.*, 'A New Type of RF Cavity for High Intensity Proton Synchrotron using High Permeability Magnetic Alloy', p.299–p.301, Proc. of EPAC98, 1998.
- [2] C. Ohmori *et al.*, 'High Field Gradient Cavity loaded with Magnetic Alloys for Synchrotrons', in this conference.
- [3] S. Yamada, 'Commissioning and performance of the HIMAC Medical Accelerator', p.9–p.13, Proc. of PAC95, 1995.
- [4] M. Yamamoto *et al.*, 'Multi-Harmonic Acceleration with High Gradient MA Cavity at HIMAC', in this conference.
- [5] Y. Sato *et al.*, 'Wide-Band Push-Pull Amplifier for High Gradient Cavity', in this conference.

# THE NEXT LINEAR COLLIDER DAMPING RING RF SYSTEM\*

J.N. Corlett<sup>#</sup>, D. Li, R.A. Rimmer, G. Koehler, J. Rasson,  
LBNL, Berkeley, CA

P. Corredoura, M. Minty, C. Ng, T.O. Raubenheimer, M.C. Ross, H. Schwarz, R.C. Tighe,  
SLAC, Stanford, CA

M. Franks, LLNL, Livermore, CA

## Abstract

We report progress on the design of the RF systems for the Next Linear Collider (NLC) Damping Rings [1]. The 714MHz RF system is a critical component of the damping ring complex, and must provide flexible operation with high-power systems generating 1.5 MV in the main damping rings and 2 MV in the positron pre-damping ring. Average beam currents are approximately 750 mA, and bunch trains are rapidly injected and extracted. A cavity design incorporating higher-order-mode (HOM) damping schemes to minimize beam impedance and maximize current thresholds for coupled-bunch instabilities will be presented. Cavity construction techniques are designed to reduce costs while providing a reliable system with excellent performance. Descriptions of feedback systems requirements will be presented, with particular attention to the klystron bandwidth requirement for feedback against transient beam loading. Flexible low-level controls and feedback loops will be described.

## 1 OUTLINE OF DAMPING RING RF PARAMETERS

The design of the NLC damping rings is described elsewhere [1], here we present the parameters most relevant to the choices of RF systems designs. Table 1 lists parameters for the pre-damping ring and the main damping rings.

Synchrotron radiation loss in the main rings is dominated by the damping wiggler, and requires approximately 600 kW of RF power, and an additional 125 kW is needed to provide the peak voltage. We have chosen to base our design on a 1 MW klystron to allow adequate overhead for operation of feedback and feedforward systems.

Based on recent experience from PEP-II B-factory RF systems, we propose to use conventional copper cavity design and similar technology for the NLC damping rings. To obtain the required voltage, with a reasonable dissipated power density in the cavity, three cavities will be used in the main damping rings and four in the positron pre-damping ring.

The RF systems design is driven mostly by the large beam current. The beam is arranged in bunch trains with

substantial gaps to allow for the rise and fall of injection and extraction kickers. The large current can result in rapid growth of single-bunch and coupled-bunch instabilities, and the RF cavities may be a dominant part of the impedance driving these instabilities. Transients in the RF voltage waveform experienced by bunches along a train may result in phase errors in the extracted beam, which propagate into energy errors in the bunch compressors following the damping rings.

Table 1: NLC Damping Rings Parameters

	Pre-damping ring	Main damping rings
Energy (GeV)	1.9 – 2.1	1.9 – 2.1
Circumference (m)	214	297
Bunch spacing (ns)	2.8	2.8
Fill pattern	2 trains 95 bunches 2 gaps 100 ns	3 trains 95 bunches 3 gaps 68 ns
Damping time (ms)	< 5.21	< 5.21
$N_{\text{max}}/\text{bunch}$	$1.9 \times 10^{10}$	$1.6 \times 10^{10}$
Current (mA)	800	750
Injected emittance X/Y (m-rad) (normalized) (edge)	$< 9 \times 10^{-2}$	$< 150 \times 10^{-6}$ (rms)
Extracted emittance X/Y (m-rad) (rms, normalized)	$< 1 \times 10^{-4}$	$< 3 \times 10^{-6}$ / $0.03 \times 10^{-6}$
RF voltage (MV)	2	1.5
Momentum compaction	0.0051	0.00066
Energy spread (%)	0.09	0.09
Bunch length (mm)	8.4	3.8

A flexible low-level system including various feedback and feedforward loops, controls, and protection interlocks will be provided. The system will be designed to provide cavity voltage and beam phase control, minimize the effects of transient beam loading, and to provide ease of monitoring of RF systems performance with a minimum of complexity.

\* Work supported by the U.S. Department of Energy under Contract Nos. DE-AC0376SF00098 (LBNL), DE-AC03-76SF00515 (SLAC), W 7405-ENG-48 (LLNL).

<sup>#</sup> email jncorlett@lbl.gov

To avoid coupled-bunch instabilities driven by the cavities where possible, and allow control of residual oscillations by coupled-bunch feedback systems, we propose to damp the cavity higher-order-modes (HOM's) using waveguides attached to the cavity in a manner similar to that used in the PEP-II B-factory cavities [2].

Table 2: NLC Main Damping Rings RF Parameters

RF Frequency	714 MHz
Harmonic Number	708
$U_{s.r.}$	750 keV/turn
$U_{HOM's}$	5.6 keV/turn
$U_{parasitic}$	36 keV/turn
VRF	1.5 MV
Cavity Wall Dissipation	42 kW/cavity
Klystron Power	1 MW
Shunt Impedance	3.0 M $\Omega$ /cavity
Unloaded Q	25500
Coupling Factor	5.8
Synchronous Phase Angle	32°
Synchrotron Frequency	6.9 kHz
Energy acceptance	$\pm 1.8\%$

## 2 HIGH POWER SYSTEMS

Figure 1 shows a schematic of the RF system layout for the main damping rings, a similar layout is proposed for the positron pre-damping ring but with an additional cavity and modified power split to feed four cavities.

A single klystron, protected from reverse power by a high-power circulator, feeds a 2:1 waveguide hybrid power divider. The greater part of the power is further split in a waveguide magic-T (which provides additional isolation and protection for the klystron), and then feeds two cavities in the ring. The third cavity is fed from the low power arm of the power divider.

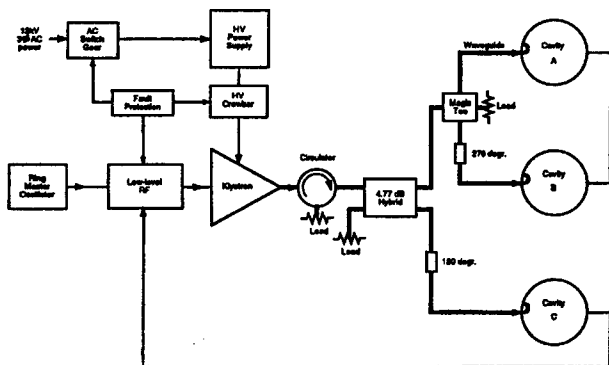


Figure 1: Main damping rings RF systems layout

A 2 MW high-voltage power supply with SCR voltage control and solid-state crowbar based on the successful PEP-II design is proposed. Voltage ripple on the power supply will be filtered to 0.1% or less.

Klystron bandwidth of up to 10 MHz is presently being considered, to allow feedforward control of cavity voltage and phase during the bunch train gap transient. The increase in bandwidth results in a high perveance and reduces the efficiency of the klystron.

A network of WR1500 waveguide connects the high-power components, with the circulator, hybrid, and magic-T splitters terminated in 1 MW waveguide loads. Cavities are placed in the beamline 4.75 wavelengths apart, to direct common mode reflected power into the loads, and fine adjustment of the phase between cavities is obtained with the use of waveguide bellows.

## 3 LOW-LEVEL SYSTEMS

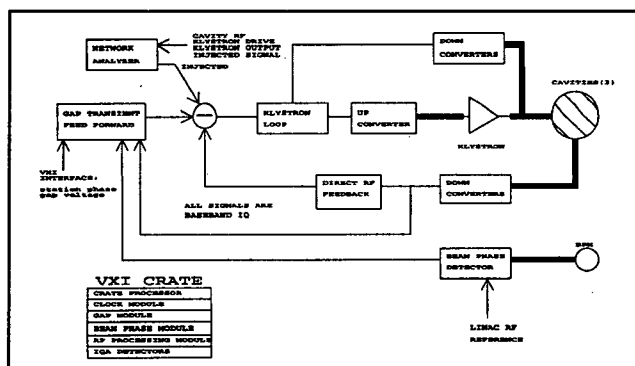


Figure 2: Block diagram of low-level RF systems

A modular LLRF system is planned based in the PEP-II system [3]. The RF hardware will reside in a single VXI crate and interface to a family of commercial programmable logic controller (PLC) modules to handle slow interlocks and tuner stepper motor control. The pulsed aspect of the ring operation will be supported by connecting several machine timing system triggers to VXI interrupts, allowing software to launch any time critical tasks related to injection, store or extraction.

Many RF vectors throughout the system will be monitored with digital IQ detectors. The bandwidth of each channel will need to be sufficient to detect the desired signal in the pulsed environment of the damping ring. Diode based analog detectors will provide hardwired RF interlocks with programmable trip levels and response times.

The system will perform the following functions:

1. Station voltage and phase control with software feedback loops.
2. Interlock functions by a combination of fast RF hardware and PLC protection.
3. Tuner control in the pulsed environment via triggered software loops.

4. Direct RF feedback will be implemented in baseboard electronics.
  5. A baseboard network analyzer similar to the PEP-II design will be included.
  6. Precise measurement and control of the mean bunch phase for next train to be extracted by a dedicated detection module with a DSP.
  7. Feed forward damping of the cavity phase (gap) transient caused by the empty buckets with an adaptive algorithm driving a wideband klystron.
- The gap transient is a critical parameter since it effects the energy spread in the main linacs. Early results from simulations show that a 4.5 degree transient can be reduced to  $\pm 0.05$  degrees with a klystron bandwidth of 10 MHz. Other options to deal with the gap transient issue are being investigated. One method is to change the frequency of the RF system such that the bunches will be properly spaced for injection in to the linac. This approach introduces additional constraints to the timing scheme. Another possibility is to reduce beam loading transients by use of a low R/Q cavity or a high stored energy device.

#### 4 RF CAVITY DESIGN

An extensive R&D program has been initiated to develop a high-power spectrally pure cavity for the NLC damping rings. We propose a copper structure, with HOM damping accomplished by three waveguide loads attached to the cavity shell. Lossy dielectric materials in the waveguides absorb the higher-order-mode power. Input power is coupled to the cavity from the WR1500 waveguide through a ridged iris aperture.

To reduce the broadband transverse impedance, the beampipe aperture at the cavity is increased from the nominal 1.6 cm diameter by a factor of approximately two. Tapers connect the larger cavity aperture to the adjacent vacuum chamber at the ends of the RF section; the larger diameter is continued between the cavities. This allows a reduction in transverse loss factor while maintaining a high shunt impedance for the fundamental mode.

Over 200 modes are expected to be trapped below the beampipe cut-off frequency (the highest dipole mode cut-off frequency is 5.9 GHz), and the damping waveguides must de-Q each of these modes by approximately two orders of magnitude to reduce coupled-bunch growth rates below the radiation damping rate. In addition, the strength of any modes trapped between cavities and between a cavity and taper must be ensured to be below a threshold which may induce coupled-bunch motion. So far our studies have not shown trapped modes outside the cavities which are not strongly coupled to fields within the cavities, which are damped by the waveguides on the cavities. We will continue to search for such modes.

We propose to achieve such broadband damping by use of double-ridged waveguides, with absorptive material placed

along the length of the guide to provide a good match to the waveguide modes and power density commensurate with the heat flow through tiles brazed to a water cooled copper plate.

The maximum dissipated power density in cavities scaled from PEP-II design is  $72 \text{ Wcm}^{-2}$ , comparable with the PEP-II operating power density of up to  $67 \text{ Wcm}^{-2}$ . We have designed ridged waveguide apertures to reduce the associated heating from RF currents crowding at the waveguide coupling apertures in the cavity. The intersecting surfaces are designed with large radii to decrease power density. Figure 3 shows a three-dimensional design drawing for a half-cavity shell with short damping waveguides attached. To reduce manufacturing costs we propose to form the blended radii on the cavity apertures using a plunge electric-discharge method.

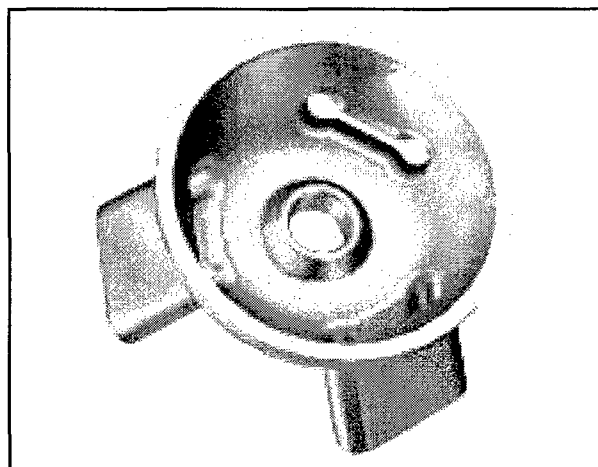


Figure 3: 3-D engineering sketch of half-cavity showing ridged damping waveguides, beampipe, and nose cones.

Cooling of the cavity will be accomplished by water flow through channels cut in the outer wall of the cavity shell and covered with an electroplated copper layer [4].

Other design considerations for the cavity may be found in [5].

#### 5 REFERENCES

- [1] "The Next Linear Collider Damping Ring Complex", M.C. Ross et al., this conference
- [2] "RF System Research and Development for the PEP-II B Factory", R.A. Rimmer, Nucl. Instr. & Methods B 99 (1995) 717-720
- [3] P. Corredoura et al, "Low Level System Design for the PEP-II B Factory", Particle Accelerator Conference, Dallas, 1995
- [4] "Fabrication Processes for the PEP-II RF Cavities", R.M. Franks et al., Proc PAC 97, Vancouver BC, 12-16 May, 1997
- [5] "Design Considerations for a Second Generation HOM-Damped RF Cavity", R. A.Rimmer, D. Li, this conference

# MECHANICAL DESIGN AND FABRICATION PROCESSES FOR THE ALS THIRD-HARMONIC CAVITIES<sup>\*,†</sup>

R.M. Franks<sup>#</sup>, K. Hernandez, D. Otting, LLNL, PO Box 808 Livermore, CA 94551, USA  
T. Henderson, D. Plate, R.A. Rimmer, LBNL, 1 Cyclotron Road, Berkeley, CA 94720, USA

## Abstract

It is planned to install five third-harmonic (1.5 GHz) RF Cavities in May/June 1999 as an upgrade to the Advanced Light Source (ALS) at Lawrence Berkeley National Laboratory (LBNL) [1]. This paper presents mechanical design features, our experiences in using electronic design models to expedite the manufacturing process, and the fabrication processes employed to produce these cavities for the ALS. We discuss some of the "lessons learned" from the PEP-II RF Cavity design and fabrication, and outline the improvements incorporated in the new design. We also report observations from our current effort.

## 1 INTRODUCTION

A minimal risk design and build cycle, to be accomplished in approximately 12 months, was desired for the ALS cavity upgrade. Upon investigation it was determined that the primary engineering, design, and fabrication issues involved in producing a third-harmonic cavity for ALS were very similar to those resolved during the Lawrence Livermore National Laboratory (LLNL) production of the PEP-II cavity [2]. It was decided to build upon this existing body of knowledge and incorporate lessons learned during PEP-II in order to achieve this goal [3].

## 2 MECHANICAL DESIGN

The design of the harmonic cavities employs many technologies developed for the PEP-II RF cavities, however, to mitigate design, schedule, and fabrication risk we sought to minimize the number of piece parts, processes, and 5-axis machining operations. The design focused on making the cavity body a spherical shape rather than the more conventional toroidal cavity shape. This allowed the port bodies to be lathe turned as integral parts of the cavity body rather than being fabricated separately and electron beam welded (EBW) to the cavity. We wanted to incorporate an end cap into the main cavity body to eliminate one piece-part and an EBW operation. Additionally, to augment our use of conventional paper drawings, we desired to use the three-dimensional electronic design model as a fabrication tool to define tool path geometry.

<sup>\*</sup>This work was supported by the US Department of Energy under contracts W-7405-ENG-48 (LLNL) DE-AC03-76SF00098 (LBNL). <sup>†</sup><http://kevlar.llnl.gov/3hrf/3hrf.htm>  
<sup>#</sup>Email: franks1@llnl.gov

## 2.1 Design Reality

The thickest plate readily available in UNS10100 class 2 OFE copper [4] was determined to be 4.5 inch (114 mm) stock. This influenced the design since we could not include an end cap within this constraint; this drove the need for two end caps that are joined to the center body by EBW during the manufacturing sequence. Line of sight requirements for EBW resulted in shortening the beam ports and providing spool pieces to be joined after the end caps are EBW to the cavity body (Figure 1). While custom forged blanks would have enabled us to design an integral end cap, the long lead-time for forging was a prime factor in our decision to use the plate material.

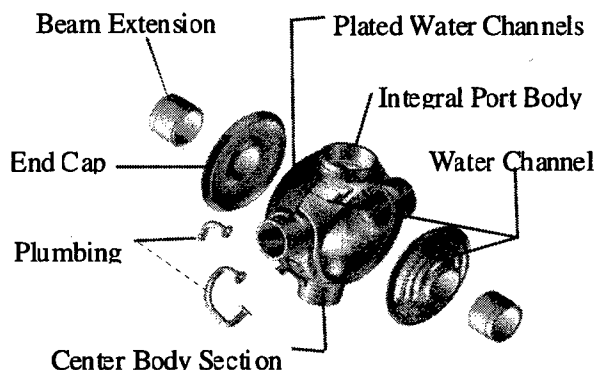


Figure 1: An exploded view (flanges omitted) of the ALS third-harmonic cavity showing integral equatorial port bodies, end caps, beam tube extensions, and plumbing.

## 2.2 Design Model as a Manufacturing Tool

The LBNL design team used Solid Designer (HP) CAD software to model the cavity, while LLNL's manufacturing operation used Pro-Engineer (Parametric) CAM software to generate cutting path data for the NC machinery. By using IGES file format we were able to transfer information between the sites, however, while we could measure features and make tool programs we could not change any features in the model on the manufacturing system. This proved a bit cumbersome since, when several small design changes were needed, we had to replicate the entire translation, transfer, and verification sequence before manufacturing could access the modifications. Additionally, the complexity of defining water channel geometry in the manner we desired tended to overwhelm the file transfer mechanism and we had to

produce the channel geometry in a Pro-Engineer model to generate the desired tool path programs.

### 3 FABRICATION

As the components progressed through the fabrication sequence the nomenclature evolved, the center body section was joined to one end cap and became the cavity body; after finishing the RF surface, tuning, and joining the final end cap, the cavity body became the RF cavity.

The center body, including the four round equatorial ports, was machined from a solid copper billet. The elimination of many joints and additional components outweighs the complexity introduced to the process by making the ports integral to the cavity body. The end caps, two per cavity, are machined from plate stock and remain identical parts for most of the fabrication process.

#### 3.1 Center Body Section

The center body fabrication began with 4.5-inch (114 mm) thick by 11 inches (279 mm) square OFE Copper plates weighing approximately 155 pounds (70 kg) each. Initial work included rough boring a 3-inch (76.2 mm) diameter hole through the blank and squaring the rough sawn sides. Additionally, 1-1/2 inch (38 mm) diameter holes were drilled at the four port positions spaced 90° about the periphery of the body.

Accurate positioning and indexing of the blank throughout the entire fabrication process was deemed necessary; therefore, extra care was taken from the outset to establish consistency between blanks. With this in mind the central bore was machined to a diameter of 4.000 inches (101.6 mm) with a tolerance of  $\pm 0.0005$  inch (.013 mm.) One face was also machined perpendicular to the bore at this time.

A horizontal CNC milling machine was used to remove the bulk of the excess material. Its CNC rotary table enabled accurate positioning of the body prior to making a  $\pm 0.0005$  inch (.013 mm) bore in each port. These "identically" sized bores served as alignment points for the creation of datum features during the next operation.

Each cavity body was indexed four times to turn the port body and a segment of the spherical outer radius. Since close tolerances were maintained during the initial steps we were able to hold indicator runout to  $\pm 0.0015$  inch (.04 mm) for each of the four indexed positions. We also counterbalanced the lathe fixture to minimize spindle vibrations due to the asymmetry of the fixture.

A horizontal CNC milling machine with a CNC rotary table was employed to cut the serpentine water channel into the copper body. The continuous channel is about 58 inches (1.47 m) long. These channels are about 3/8 inch wide x 3/8 inch deep (10 mm x 10 mm) with a 3/32 inch (2.4 mm) radius in the corners. A fully radiused channel would require a "ball" mill cutter that has zero cutting speed at its center point. The copper resists cutting freely

under this condition, therefore we chose to have a flat-bottomed channel with the small corner radii.

To eliminate 5-axis milling the sidewalls of the body channels were designed to be perpendicular to the beam axis rather than normal to the outer surface. This reduced programming and machining costs as well as minimizing the technical risk due to a less complex setup and program. Shallow counterbores were cut at the channel inlet and outlet points to locate the water fitting stubs that were plated into position during the water channel covering.

The RF surface was machined, leaving .080 inch (2 mm) to be removed during the final machining stage, and the port bores were finished to within .01 inch (.25 mm).

#### 3.2 End Caps

Two end caps, one designated "body end cap" the other "tuning end cap", were required. All end caps were machined with .080 inch (2 mm) to be removed at a later point in the fabrication process. A 39-inch (1-m) long cooling channel was cut into each end cap. At this point all surfaces of the tuning end cap were finished, except the nose radius, to enable a fine adjustment of the cavity's frequency during the tuning sequence.

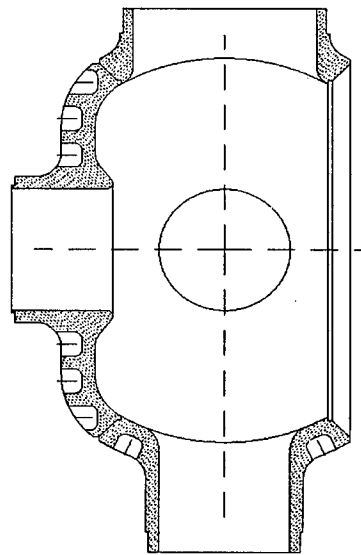


Figure 2: View of the cavity body configuration at time of inner and port blend radii finishing.

#### The 3.3 Cavity Body

The body end cap was joined to the body center section by EBW. We employed a structural weld from the outside, then placed a sealing weld from the inside to overlap the root of the external structural weld [5]. This process assured that trapped volumes and porosity were minimized and also eliminated weld joint gaps, providing a fully cleanable cavity.

The inner contour of the cavity body was then turned through the remaining opening to a surface finish of 24  $\mu$ inch (.6  $\mu$ m) Ra or better (Figure 2). This eliminated



surface irregularities left by the welding process and enabled us to locate the attached beam nose at a nominal position. Machining of the blend radii between the RF surface and the port bores, as well as final sizing of the bores, was completed.

The cavity's in-process frequency was determined by clamping temporary flanges to the ports, installing dummy tuners, and placing the tuning end cap in position. This allowed calculation of the amount to be removed from the tuning end cap nose to achieve the desired frequency. Once the frequency is correct, and verified, the end cap is EBW in place using the welding procedure detailed earlier. The frequency is once again verified as the last step in the tuning process.

### 3.4 RF Cavity

Plating wax was poured into the cooling channels and finished to be flush with the outer contour of the cavity. The wax surface was made conductive by burnishing silver powder into it and then processing through an activating sequence. A jacket of plated copper, approximately .2 inch (5 mm) thick, was grown over all of the channels. We chose to use a brightened copper, which deposits more rapidly and more uniformly than the pure copper used previously. By using the brightened copper plating we have eliminated the intermediate turning stage required with the pure copper jacket used on the PEP-II cavities.

As this copper is not weldable with conventional techniques the design calls for joining six stainless steel water fitting stubs to the cavity using the plating. The protrusion of the stubs render machining of the outer surface impractical, therefore we needed to understand the plating process prior to introducing a production cavity into the process. We built an aluminum mandrel to mock up the outer features of the cavity to refine the design and placement of masking, and optimize the plating parameters. Through this effort we identified an area between the water fittings and the beam ports needing an auxiliary anode to assure the plating thickness matches the rest of the cavity, thereby avoiding a potentially thin spot in the plating at one of the higher heat load areas.

The smaller harmonic cavity (one-third the PEP-II size) also presented a concern that the wax would fall out of the water channel grooves when the cavity was turned over to wax the opposite side. We performed the waxing process on the aluminum mandrel and determined that, while our concern was valid, there was not a problem.

Once plating was completed the wax was melted and flushed out of channels. Small holes were drilled through the plating into the wax placed over the EBW joints and the wax flushed out to create a water-to-vacuum air guard. After fittings and jumper tubes were TIG welded to the water stubs the passages were hydrostatically tested to 150 psi (1 MPa).

Flange locating features were cut at the four port bodies and the two beam ports. This reduced the risk that the flanges would be out of square to the beam axis, a concern

as we join the cavities together with rigid spool pieces. There is a bellows between the last cavity (in a string of five) and the mating vacuum chamber. The flanges, standard stainless steel circular knife-edge seals, with copper inserts, were then attached by EBW.

The final process cleans and lightly etches the inside of the cavity using a mild chromic acid bright dip followed by rinsing in clean DI water. This process is designed to remove any residue that condenses on the inside wall from the EBW process as well as any contaminants that may have been inadvertently introduced during the fabrication process. Historically, this cleaning and etching process has improved internal cavity surfaces to 16  $\mu$ inch (0.4 $\mu$ m) Ra or better. The cavity was then blown dry with nitrogen, blanked off and backfilled with dry nitrogen at atmospheric pressure for shipping.

## 4 CONCLUSIONS

Our use of design models for manufacturing generated small discomforts yet these were greatly offset by the avenue of communication opened between the design and manufacturing organizations. Also, programmers and machinists were able to manipulate the model on the CAD screen to see what the "other side" of the part actually looked like, rather than having to try and visualize it from two-dimensional paper drawings.

Including the ports as integral parts of the cavity body proved to require more care in fixture design and machining efforts than initially estimated. We would chose this path again as our PEP-II experience showed that the myriad parts and fixtures needed to fabricate and weld these ports present a far greater expense and yields more technical risk.

We placed the water channel stubs too closely together and too near the beam port bodies for the plating to be the same as the remainder of the cavity. A supplemental anode was used to cause the copper to preferentially plate in the problem areas. We expect that by providing at least a 1-inch (25.4-mm) gap between features we could alleviate this problem.

## 5 ACKNOWLEDGMENTS

The authors thank the many designers, machinists, physicists, and technicians for their personal commitment and technical excellence in producing the ALS Third-Harmonic RF Cavities.

## 6 REFERENCES

- [1] R. Rimmer et. al., "A Third-Harmonic RF Cavity for the Advanced Light Source", Proc. EPAC 98, Stockholm, Sweden
- [2] R.M. Franks, et. al., "Fabrication Processes for the PEP-II RF Cavities", Proc. PAC 97, Vancouver, B.C., Canada
- [3] R. Rimmer et. al., "Notes from the RF cavity production close-out meeting, LLNL, 11/13/97", PEP-II EE note 97.07
- [4] "Standard Specification for Oxygen Free Copper in Wrought Forms for Electron Devices", ASTM designation F68-82.
- [5] R.M. Franks, et. al. "Electron Beam Welding of Thick Cross-Section Copper with Minimal Porosity," Proc. 1997 AWS Convention, Los Angeles, American Welding Society, Miami, Florida, 1997, pp. 184-85, UCRL-JC-125896 Ext Abs

# INTERLOCK AND CONTROL FOR THE RF SYSTEM OF THE ANKA STORAGE RING

D. Einfeld, F. Pérez<sup>\*,\*\*</sup>, S. Voigt, ANKA, Forschungszentrum Karlsruhe, Germany  
M. Humpert, Bonn University, Germany

## Abstract

The RF system for the ANKA storage ring has two plants, each plant consists of one 250 kW transmitter at 500 MHz feeding two cavities, with all the peripherals [1]. It has three levels of control: the machine control, the transmitter control and interlock, and the fast interlock. Each one with different response times: 1 sec, 20 msec and 10  $\mu$ sec, respectively. The first is based on Java language for NT-Windows and LonWorks, the second on an industrial PLC system and the third is hardware electronic. The machine control, controls the whole RF system, but any instruction referred to the transmitter is filtered by the PLC system that executes the action, or not, depending on the status of the interlocks. The fast interlock is running in parallel and shut down the system when a major fault occurs, independent of the others. In this paper we will present the two interlock systems, the general control system of ANKA has already been widely presented elsewhere [2].

## 1 INTRODUCTION

During the present year the storage ring ANKA is being constructed at the Forschungszentrum Karlsruhe. It will be completely assembled after summer and the commissioning should start in October of this year [3].

To run ANKA, at 2.5 GeV and 400 mA beam current, two RF plants, each one with two cavities powered by a single 250 kW klystron, will be installed [1]. To assure the safe operation of the RF plants a proper control and interlock system should be implemented. At ANKA we have chosen to use an industrial PLC standard, the SPS system from the company BOSCH, for the control and the slow interlock (20 ms). This system will control the RF plant, from the HV power supply up to the interlock signals from the cavities, switching off the plant when any fault occurs. It does not include the low level electronics for the control of the cavities: amplitude, phase and tuning loops. These electronics are provided by Sincrotrone Trieste together with the cavities.

On the other hand, a hardware interlock system will run in parallel for the major faults, acting on a PIN diode switch to shut down the plant in a few microseconds.

## 2 RF PLANT

In figure 1 an scheme of the RF plant with the components and the control structure is shown.

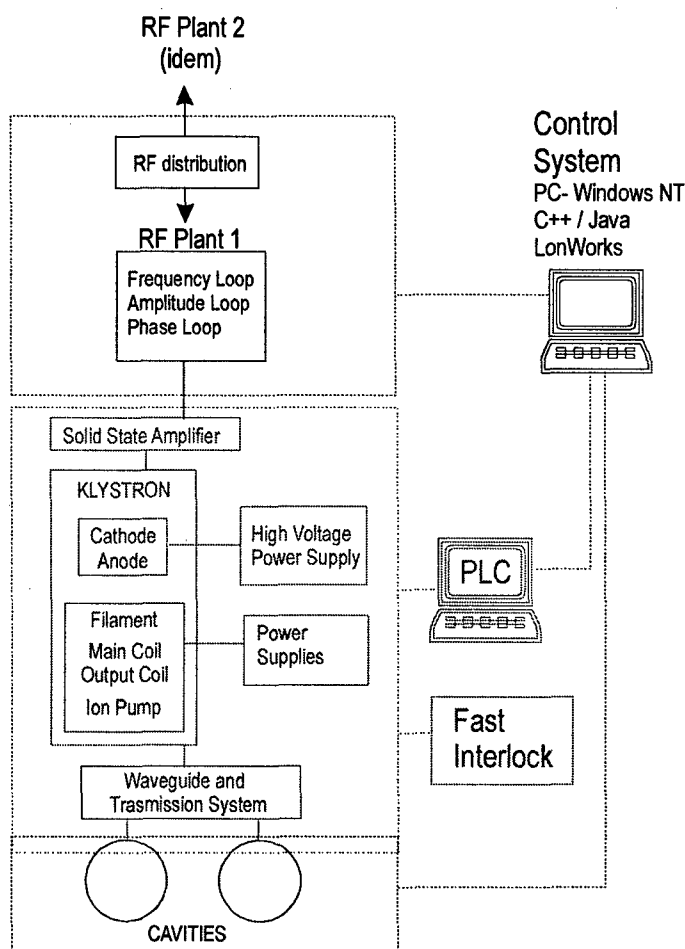


Figure 1: Scheme of the control of the RF system.

The PLC system controls all the components related with the transmitter (pre-amplifier, klystron, HV power supply, small power supplies, ...) and the signals from the waveguide system and the cavities related to the interlock and safety.

The machine control system takes care of the rest of the RF components and controls the transmitter through the PLC system.

\*On leave from LSB-IFAE, Barcelona, Spain

\*\* Email: perez@anka.fzk.de

### 3 CONTROL AND SLOW INTERLOCK

The PLC, or local control, is composed of the hardware boards and two software programs, one that processes the signals and executes the appropriate actions, installed in the PLC-CPU; and a second used to visualise this control process.

#### 3.1 Hardware

Different kind of boards are used [4]:

- The CPU ZE200, contains the code that analyse the signals and acts to switch off the RF system.
- The boards to read and write analogue and digital signals, E-ANA, A-ANA, E-24V and A-24V.
- The board for world-wide communication: RS232, Profibus or Ethernet.

They are located in a rack close to the RF plant and they manage more than one hundred signals.

#### 3.2 Software

The process code is mainly a read-out loop with an execution time of around 20 ms. The code compares the incoming signals with the reference ones and in case of mismatch executes the correspondent action:

- Switch off the RF drive
- Switch off the high voltage power supply
- Switch off the complete system

A second code used to visualise the control process has been developed. The aim of this code is to provide a user friendly interface to identify quickly the status of the RF plant and the source of failure, when a fault occurs. The generation of alarms is done automatically.

Figure 2 shows one of the interface panels. The configuration of one of the RF plants is schematically represented: one klystron feeding two cavities through the waveguide system which includes a circulator and a magic tee. The RF power, forward and reflected, at the different points where the directive couplers are located is displayed also in this panel.

The box in the upper side at the centre allows the user:

- Switch On/Off the auxiliaries: small power supplies and other peripheral components.
- Switch On/Off the high voltage power supply and set its operating voltage level.
- Switch On/Off the RF drive.
- Reset the interlocks

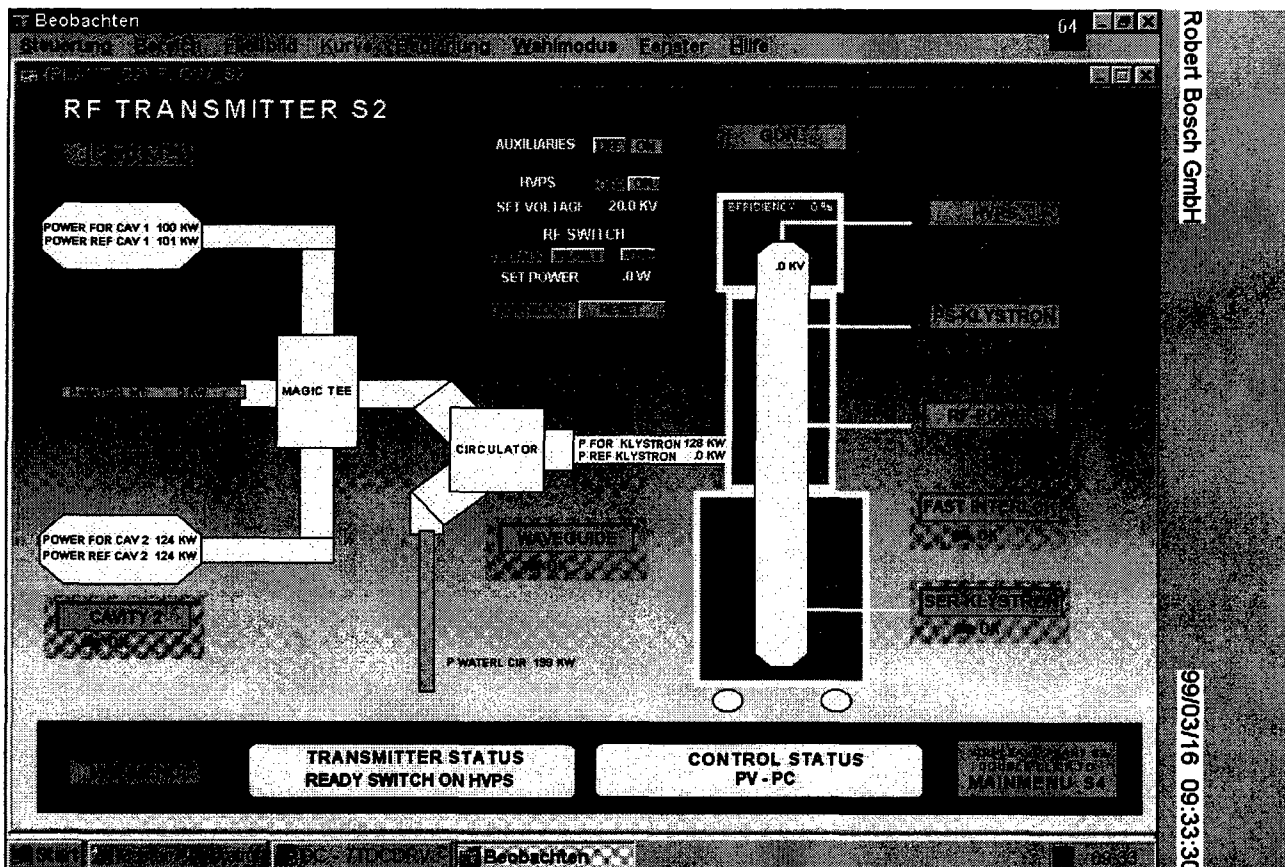


Figure 2: Control panel interface of one of the RF plants

The different interlock signals are grouped in nine groups:

- Ser-klystron: water and air cooling signals
- Gun: gun current and voltage.
- HVPS: high voltage PS interlocks.
- PS-klystron: PS for the coils and vacuum pump.
- RF power: interlock related to excess of RF power.
- Waveguide: cooling and arc detector signals.
- Cavity 1: interlocks of the cavity 1.
- Cavity 2: interlocks of the cavity 2.
- Fast interlock

The nine small boxes with a virtual LED identify the source of the interlock when a fault occurs (red), or show a correct performance (green). Clicking on one of these boxes another panel opens showing the list of interlock signals and its status: correct (green) or fault (red).

#### 4 FAST INTERLOCK

In parallel to the control provided by the SPS system, we need a hardware interlock to switch off the system in microseconds when a major fault occurs, i.e. faults that can damage the klystron, the circulator or/and the cavity's window. Figure 3 shows the signals that are included in this fast interlock system

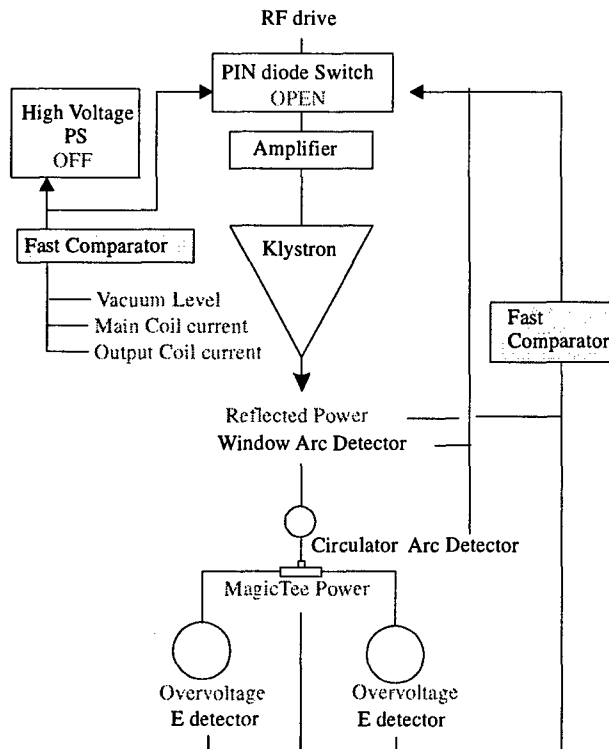


Figure 3: Signals for the fast interlock.

In figure 4 the basic scheme of the fast interlock is shown. The analogue signals are sent to a fast comparator

board which compares the signal level to a pre-set value, when the level is over this pre-set value gives a signal to open:

- the PIN diode switch when the fault occurs in the high power RF line; or,
- both, the PIN diode and the HVPS switches, when the fault occurs into the klystron.

The digital alarms from the arc detectors are sent directly to the PIN diode switch. The status of these alarms are accessible from the control panels.

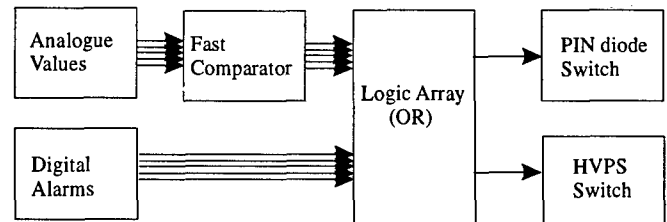


Figure 4: Scheme of the fast interlock.

We will also implement in this fast interlock an electron detector, i.e. an antenna in the cavity's body that, together with an electronic board [5], should be able to detect the flow of electrons just before any sparking occurs inside the cavity. We expect that despite the antenna will located in the cavity's body, it will also help us to protect, in the same way, the cavity's window [6].

#### 5 CONCLUSIONS

The two interlock systems are finished and ready to be tested at ANKA before its implementation on the RF system.

#### 6 REFERENCES

- [1] D.Einfeld, F.Pérez, S.Voigt, A.Fabris, C.Pasotti, M.Svandrik, "Status of the RF System for the ANKA Storage Ring", these proceedings.
- [2] B.Jeram, M.Juras, K.Kenda, G.Mavric, M.Peternelj, U.Platisse, M.Plesko, R.Sabjan, M.Smolej, G.Tkacik, H.Schieler, "First Experiences with the Control System for the accelerator of ANKA", these proceedings.
- [3] D.Einfeld, S.Hermle, E.Huttel, A.Kruessel, M.Lange, F.Perez, M.Pont, U.Ristau, R.Rossmannith, H.Schieler, S.Voigt, R.Walther, A.Weindl, M.Plesko, "Status of the accelerator for the 2.5 GeV light source ANKA in Karlsruhe", these proceedings.
- [4] Speicherprogrammierbare Steuerungen, BOSCH Katalog.
- [5] Following the DESY design.
- [6] M.Ebert, DESY, private communication.

## STATUS OF THE RF SYSTEM FOR THE ANKA STORAGE RING

D. Einfeld, F. Pérez<sup>+,\*\*</sup>, S. Voigt, ANKA, Forschungszentrum Karlsruhe, Germany  
A. Fabris, C. Pasotti, M. Svandrik, Sincrotrone Trieste, Italy

### Abstract

The RF system for the ANKA storage ring has two plants, each plant consists of one 250 kW transmitter at 500 MHz feeding two cavities, with all the peripherals. The different components, namely the high voltage power supply, the klystron, the waveguide system and the cavities, are now under construction and test. The HV power supply is provided by Jäger (Germany), and is been built on site. The first klystron, from the company EEV (England), has been assembled at the factory and the next two are under way. The components of the waveguide system have been already delivered by the firm Dielectric (USA), except the circulator that has been built by AFT (Germany). The factory acceptance tests of the cavities, together with the low level electronic systems, consisting of a frequency loop for each cavity and an amplitude and phase loop for each RF plant, have started at the end of 98 and, following the foreseen schedule, will be concluded in July 99 at Sincrotrone Trieste (Italy).

### 1 INTRODUCTION

During the present year the storage ring ANKA is being constructed at the Forschungszentrum Karlsruhe. It will be completely assembled after summer and the commissioning should start in October of this year [1].

The ANKA storage ring is designed to run at an energy of 2.5 GeV and at a maximum beam current of 400 mA.

Two RF plants, each one with two cavities powered by a single 250 kW klystron, will be installed. Figure 1 shows a 3D view of one of these plants and in table 1 the main parameters are listed.

At the moment, most of the components are in the latest stage of construction and some of them have been already tested at the factory. The waveguide system has been delivered two weeks ago and the rest of components will arrive within the next four months.

<sup>+</sup> On leave from LSB-IFAE, Barcelona, Spain

<sup>\*\*</sup> Email: perez@anka.fzk.de

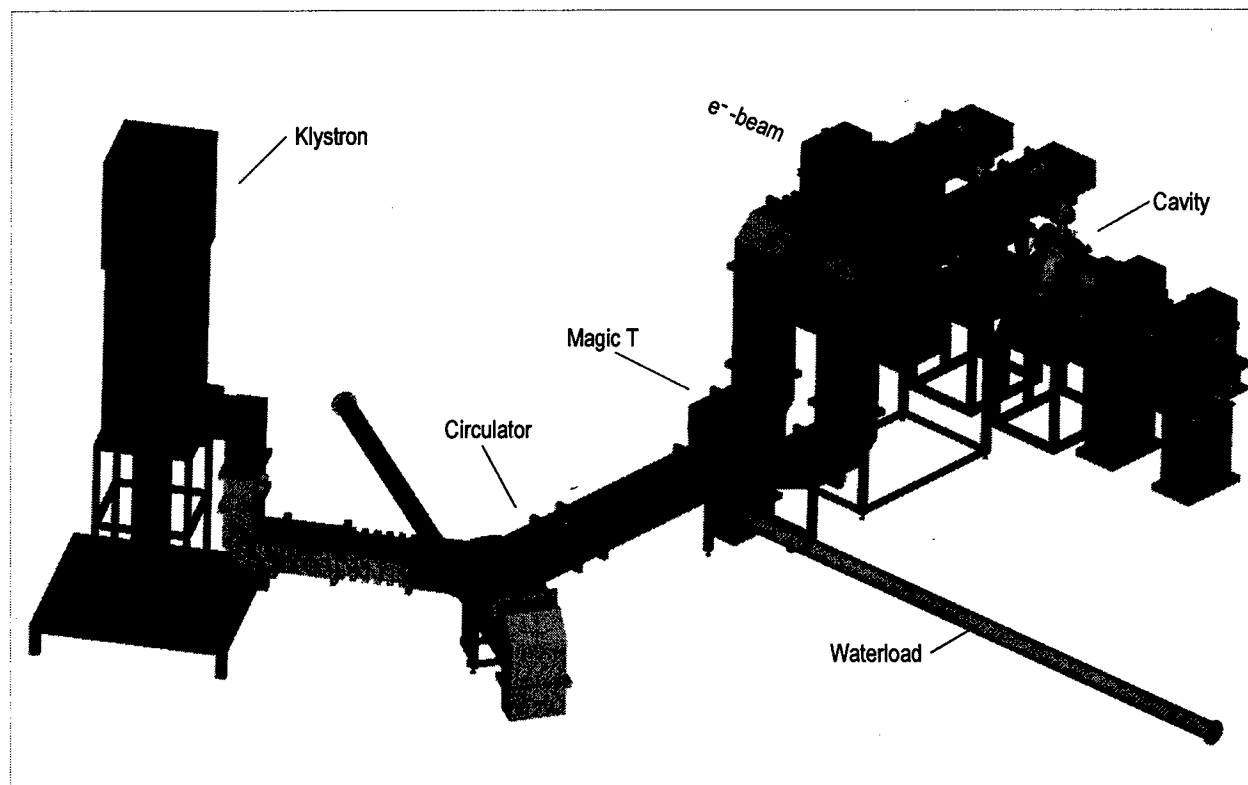


Figure 1: 3D view of one RF plant

Table 1: Main RF parameters

Parameter	Value
Beam Energy	2.5 GeV
Energy Loss per Turn	662 keV
Beam Current (maximum)	400 mA
Harmonic Number	184
Revolution Frequency	2.72 MHz
RF Frequency	499.65 MHz
Momentum Compaction Factor	0.0081
Energy Spread	0.09 %
Total RF voltage	2 MV
Overvoltage Factor	3
Energy Acceptance	1.5 %
Synchrotron Frequency	36 kHz
Synchronous Phase	160.7 °
Bunch Length	9.8 mm
Number of Cavities	4

## 2 CAVITIES

The cavities together with the low level electronics - phase, amplitude and tuning loops- are provided by Sincrotrone Trieste, Italy.

### 2.1 Cavity Parameters

The two first cavities are ready and their main parameters have been measured. Table 2 compares the measured values with the target ones.

Table 2. Cavity parameters

Parameter	Target	Measured	
		Cav 1	Cav 2
Resonant frequency, MHz	499.65	499.64	499.65
Quality factor	40000	38900	41000
R/Q	175	174	174
Shunt Impedance, M $\Omega$	3.3	3.3	3.5
Max Coupling Coefficient	3.5	3.3	3.6

The lower quality factor of the first cavity is due to a contamination of the cavity's surface by the filler material used during the fabrication procedure. The problem has been fixed and solved as can be seen by the higher quality factor of the second cavity. The next two cavities are expected to have parameters similar to those of the second one.

The HOMs of both cavities have been already characterised. The results are presented in a separate paper in this conference [2]

### 2.2 High Power Test

Two different power tests have been performed with the first cavity:

- Forward power test: 8 hours of continuously running at 52 kW CW with the cavity on tune, figure 2.
- Reflected power test: ½ hour of continuously running at 52 kW CW with the cavity out of tune. This test is done mainly to test the input coupler.

Both tests have been successfully passed at the power stand test of Sincrotrone Trieste, figure 3.

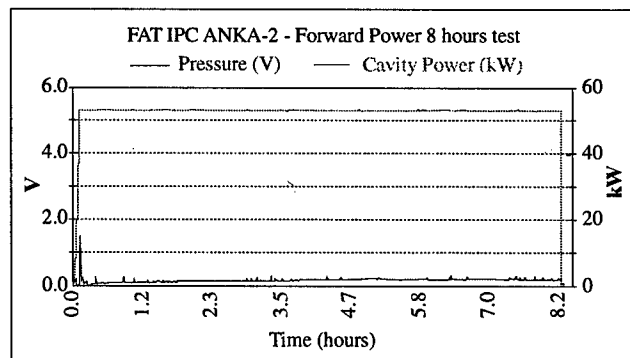


Figure 2. 8 hours power test without vacuum trips

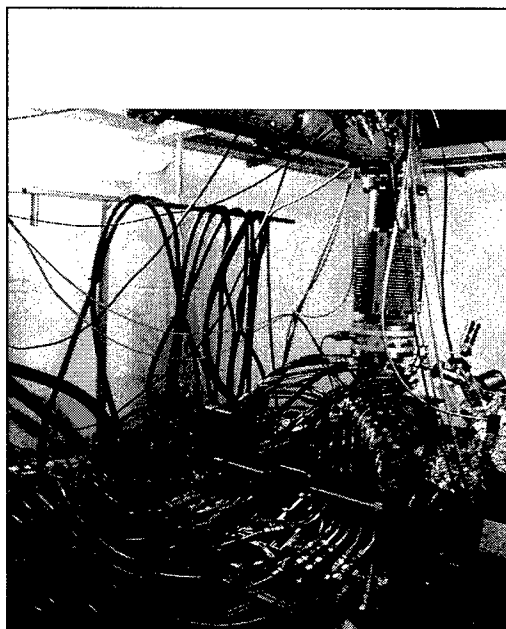


Figure 3. Cavity at the power stand during the power test

The power test of the second cavity will be done at the beginning of April, the third at the end of Mai and the last one at the beginning of July.

## 3 LOW LEVEL ELECTRONICS

The low level electronics for the ANKA RF system will be composed of four frequency loops (one for each cavity), two amplitude and two phase loops (one for each RF plant) plus all the ancillary equipments for the phasing of the two plants and the interlock electronics [3]. The design of the low level electronics has taken into account the different operating conditions of ANKA, where the beam is injected at 500 MeV and ramped in the ring to the final 2.5 GeV energy. Amplitude and phase of the cavity

gap voltages must be kept constant during the different status of machine operation (injection, ramping and beam storage), considering that all the low level electronics loops interact with each other and are coupled via the beam.

From the construction point of view, the low level electronics has been designed in a modular way which eases maintenance and troubleshooting. All the low level electronics for the ANKA RF system will be hosted in six racks, three for each plant.

The first frequency loop has been tested together with the first cavity, satisfying the required specifications. Table 3 compares the target and measured parameters.

Table 3. Frequency loop parameters

Parameter	Target	Measured
Speed (nominal), Hz/sec	700	704
Speed (maximum), Hz/sec	1000	1040
Op. Loop 3 dB bandwidth, Hz	200	210
100 Hz option		
Sensitivity of the loop, Hz	100	75-100
Open loop dc gain, dB	> 36	41
500 Hz option		
Sensitivity of the loop, Hz	500	450
Open loop dc gain, dB	> 23	28

The second frequency loop, the first amplitude and phase loops and ancillary equipments will be tested at the beginning of next April, together with the second storage ring cavity. Therefore at this stage all the low level electronics for one of the two storage ring plants will be completed. The low level electronics for the second plant is now under assembly. Each component has been acquired and individually tested. The acceptance test of the low level electronics for the second RF plant is planned in parallel with the factory acceptance tests of the third and fourth storage ring cavities.

#### 4 TRANSMITTER

The transmitter will be assembled at ANKA and it is formed by a 250 kW klystron, a 470 kVA high voltage power supply, a PLC system for its control and interlock, and the ancillaries components to complete it: power supplies, sensors, etc.

The klystrons are produced by EEV, at England. The tube of the first klystron has been already assembled and is now under vacuum conditioning. Three klystrons will be delivered, two for operation of the machine and one as a spare. The main parameters are listed in table 4.

Table 4. Main parameters of the klystron

Parameter	Value
Operating frequency	499.65 MHz
RF output power	> 250 kW
Efficiency	> 62.5 %

The high voltage power supply is at the moment being assembled at ANKA by the company JÄGER, from Germany. Its main parameters are listed in table 5.

Table 5. Main parameters of the HV power supply

Parameter	Value
Voltage	-20 to -52 kV
Current	9 A
Stability	$\pm 0.5$ %
Ripple, peak at peak	< 0.4 %
Maximum stored energy	20 Ws

For the control and interlock of the transmitter we have chosen to use an industrial PLC standard from the company BOSCH. This is separately presented in this conference [4].

The rest of the components, power supplies for the focusing coils and the gun of the klystron, sensors and connectors, etc are already in house.

The assembly of the first transmitter will start at the end of April, when all the components will be delivered, and during May it will be brought into operation.

#### 5 WAVEGUIDE SYSTEM

The waveguide system has been designed to feed two cavities with only one klystron. A circulator to isolate the klystron and a magic tee to split the power in two are the main components (figure 1).

The distance from the centre of one cavity to the other one is 900 mm, i.e. one and a half the wavelength of the 500 MHz RF voltage. For that reason the power input loop of one cavity will be rotated 180° with respect the position of the loop at the other cavity, in that way the bunches will see the correct phase. The difference in phase between the two arms of the magic tee has been measured at Dielectric and it is less than 1°. It has to be noted that no phase shifter has been foreseen, so that we rely on the symmetry and the proper performance of the components.

#### 6 SUMMARY

The first RF plant with two cavities will be ready in June and the second plant in August.

#### 7 REFERENCES

- [1] D.Einfeld, S.Hermle, E.Huttel, A.Krussel, M.Lange, F.Pérez, M.Pont, U.Ristau, R.Rossmann, H.Schieler, S.Voigt, R.Walther, A.Weindl, M.Plesko, "Status of the accelerator for the 2.5 GeV light source ANKA in Karlsruhe", these proceedings.
- [2] A.Fabris, C.Pasotti, M.Svandrik, "Characterization of the ANKA RF Cavities HOMs for Coupled Bunch Instability Calculations", these proceedings.
- [3] A.Fabris, C.Pasotti, M.Svandrik, D.Einfeld, F.Pérez, S.Voigt, "Low level RF System for the ANKA Storage Ring", EPAC 98, p1761.
- [4] D.Einfeld, F.Pérez, S.Voigt, M.Humpert, "Interlock and Control for the RF System of the ANKA Storage Ring", these proceedings.

# Design of an On-Axis Coupled Planar MM-Wave Structure

R. Apel and H. Henke

Technische Universität Berlin, EN-2 Einsteinufer 17, D-10587 Berlin, Germany

## Abstract

The paper presents the design of an on-axis coupled structure which is planar double-sided and suited for fabrication with deep X-ray lithography. It is a standing wave structure with an operating frequency of 91.392 GHz and is designed for the  $\pi$ -mode. End cells and input power coupler are matched numerically by means of the code *GdfidL*. The main RF parameters are also determined numerically. Reflection and bead pull measurements with a scaled-up model at 10 GHz are presented.

## 1 INTRODUCTION

Very high frequency accelerating structures will explore new parameter ranges and new applications. Among other things, a very attractive feature and a potential breakthrough concept is an 'integrated' accelerator module, i.e. the manufacturing of accelerating structures, power sources and focusing elements with one technology and on a common support. The avenue to realize this vision is X-ray lithography (LIGA). It meets the requirements in fabrication precision, 1 micrometer tolerances and about 0.1 micrometer surface roughness, and it allows for nearly arbitrarily complicated structures as long as they stay planar.

That is where the skill of the design engineer is challenged: to develop and build planar structures and components.

Based on the concept of a doubled-sided, open muffin-tin structure [1] we have been working on different devices [2]. Since we believe that a constant impedance structure is easier to build and that a standing-wave (SW) structure with equal power dissipation facilitates cooling and operation we had at first designed a side-coupled SW muffin-tin [3]. However, the RF parameters, especially bandwidth and attenuation, were not very satisfactory. Therefore in the present paper, we present an on-axis coupled double-periodic muffin-tin with a larger aperture, lower attenuation and large bandwidth.

## 2 STRUCTURE GEOMETRY AND RF PARAMETERS

Since the RF power dissipation increases with the square root of the frequency and since additional losses due to surface roughness are inevitable, high frequency structures have high losses. Therefore, an adequate cooling and temperature control system may impose a constant-gradient operation. But a constant-gradient structure is not a straight

forward solution for a fully planar geometry. On the other hand, SW structures have a constant gradient but a lower shunt impedance. The only exception is zero- or  $\pi$ -mode operation, where the group velocity is small, the structure is sensitive to fabrication errors and only a few cells can be coupled. The apparent solution to this dead end are double-periodic structures which are confluent and have high shunt impedance and group velocities. The first solution we had was a side-coupled structure [3]. Although the paper design and a scaled-up model behave reasonably well, we were not completely satisfied with the group velocity and a distorted Brillouin diagram due to the direct coupling between main cells. Therefore, we started the design of an on-axis coupled structure, Figure 1.

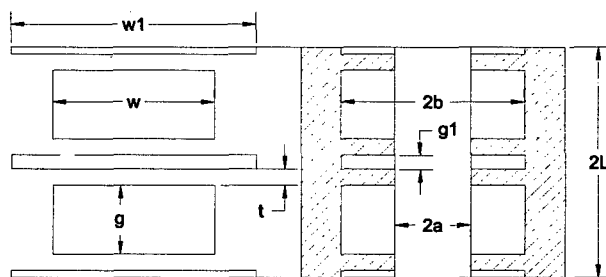


Figure 1: Topview and cross section of an on-axis coupled muffin-tin:  $g = 0.980$ ,  $w = 2.231$ ,  $t = 0.230$ ,  $w1 = 3.374$ ,  $g1 = 0.200$ ,  $2a = 1.050$ ,  $2b = 2.540$  (in mm)

The iris thickness and the gap of the coupling cells were fixed to  $t = 0.23 \text{ mm}$  and  $g1 = 0.20 \text{ mm}$ , respectively. The period length follows from the  $\pi$ -mode operation as

$$L = \pi / \beta = \lambda / 2 = 1.64 \text{ mm}.$$

The beam aperture is in principle a free parameter and influences bandwidth, shunt impedance and wakefields. As a trade-off we chose

$$2a / \lambda = 0.32 \Rightarrow 2a = 1.05 \text{ mm}.$$

The other dimensions were calculated with *GdfidL* [4] and are shown in Figure 1. The resulting RF parameters are given in Table 1. As a comparison the Table shows also the parameters of the side-coupled structure (SCS) and of a single-periodic muffin-tin (SPMT). As can be seen, the on-axis coupled structure (OACS) has the largest bandwidth, highest group velocity and lowest attenuation. An estimate of the number of cells which can be coupled together gives

$$\frac{\omega}{Q_0} < \text{mode spacing} = \frac{\pi B}{4 N} \text{ or } N < 136.$$



Symbol	OACS	SCS	SPMT	Unit
$f$	91.392	91.392	91.392	$GHz$
$r/Q_0$	58	53.8	81.6	$k\Omega/m$
$\tau$	155	166	200	$M\Omega/m$
$Q_0$	2680	3090	2490	
$\alpha$	3.6	8.6	4.1	$1/m$
$v_g/c_0$	0.10	0.036	0.094	
$B$	11.9	7.8	9.3	$GHz$
$B'$	0.13	0.085	0.102	

 Table 1: RF parameters for  $2a = 1.05\text{ mm}$ 

Then assuming a central feeding point and an attenuation parameter  $\tau = \alpha l = 0.18$  an overall structure length  $l$  of  $10\text{ cm}$  comprising 60 main cells seems to be a good design goal. The large bandwidth and the resulting high group velocity together with the point of confluence can be seen in the beautifully symmetric Brillouin diagram, Figure 2.

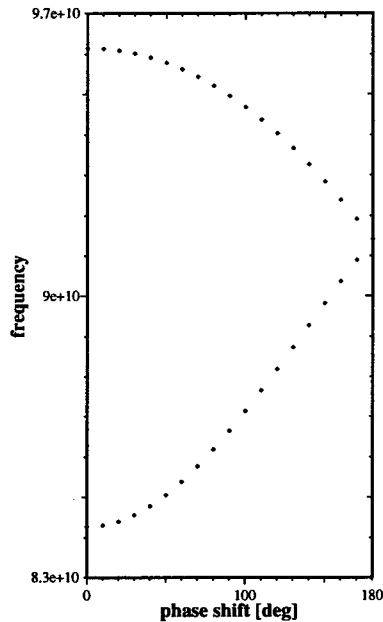


Figure 2: Brillouin diagram for OACS

### 3 FULL STRUCTURE WITH END CELLS AND COUPLER

Special care has to be taken to get a flat  $\pi$ -mode distribution. This requires a detuning of the end cells which was done with *GdfidL* and is shown in Figure 3.

For the power coupler we have chosen a straight forward solution for the time being. The feeding line couples to the mid-cell via the side-wall, Figure 3. Since we did not want a cut in the coupling iris for fabrication reasons and the coupling was undercritical we added a double  $\lambda/4$  stub-line for the match. We also had to add a  $\lambda/4$  transmission-line transformer and special matching elements in the side-wall in order to taper and match the groove-guide to the rectan-

gular guide. The resulting match of the whole structure was found with the time-domain option of *GdfidL* and is given in Figure 4. The losses were simulated by a lossy dielectric filling.

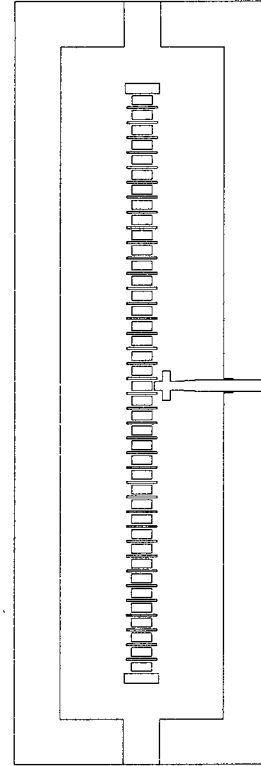
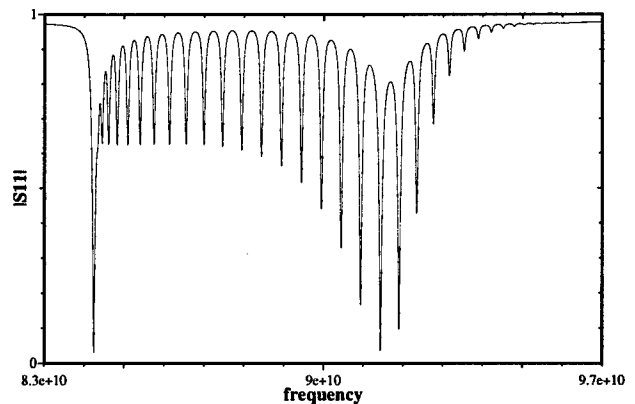


Figure 3: Full structure with feeding line, coupler and detuned end cells


 Figure 4: Simulated magnitude of  $S_{11}$  of the full structure.

### 4 SCALED-UP MODEL AND PROTOTYPE

In order to verify the design we build an Al-model scaled to  $10.2\text{ GHz}$  with seven main cells, see Figure 5. Reflection measurement and bead pull measurement of the  $\pi$ -mode were done with a network analyzer (HP 8722C), Figures 6

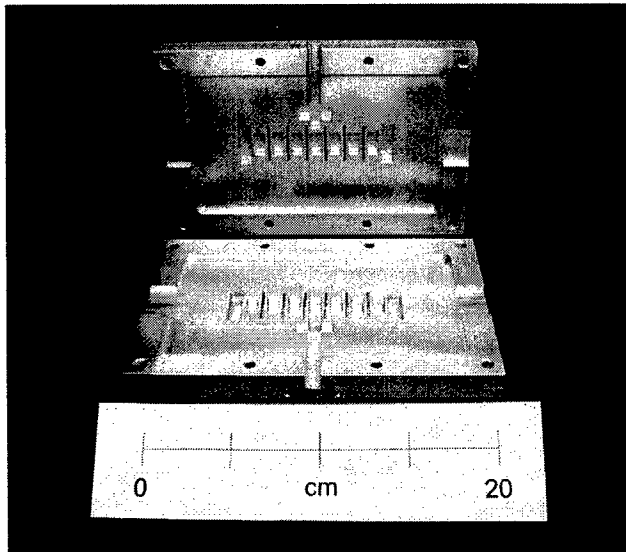


Figure 5: Scaled-up model

and 7. The measured frequency response is in principal in good agreement with the simulation. Only one thing still requires improvement. If we compare the *GdfidL* simulation to the measured reflection coefficient, we have only four measured resonances instead of six resonances in the simulation, see Figure 6. One reason for this may be tolerances during the fabrication process.

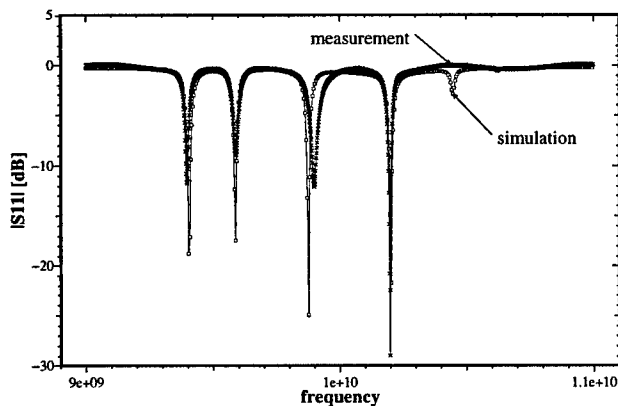


Figure 6: Reflection coefficient for the scaled-up model

Finally, bead pull measurement of the  $\pi$ -mode has been performed. The bead was made by silver painting on a pure cotton fiber. Figure 7 shows the reflection coefficient of the  $\pi$ -mode in resonant condition. One can see the seven main cells with resonant fields and a clear  $\pi$ -mode field distribution along the beam axis. Since the feeding line couples to the mid-cell, the field distribution is nearly symmetrical w. r. t. this cell and the field decays slightly to the structure ends. Due to the good results of the scaled-up model we have built a first LIGA mask for a 91 GHz structure with 39 main cells, the end cells, the coupler and the transformers. The department of precision and micro technology at the TU-Berlin has started to build up the electroplating.

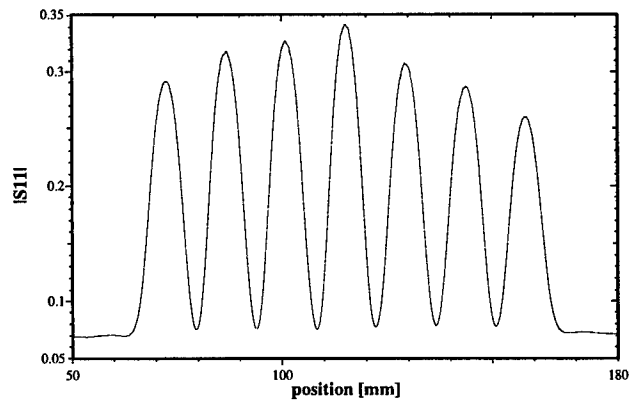


Figure 7: Bead pull measurement for the scaled-up model

## 5 CONCLUSION

The concept of an on-axis coupled, double-periodic muffin-tin shows very attractive features for a very high frequency SW-structure. It has an exceptional wide bandwidth and high group velocity and is therefore insensitive to fabrication errors. The shunt impedance is reduced only about 25 % as compared to the single-periodic,  $2\pi/3$ -mode structure. The relatively low attenuation allows for coupling a large number of cells. About 60 cells should be possible and would give a 10 cm long structure at 91 GHz. This corresponds just to a 4 inch wafer for a LIGA mask and yields a sound attenuation parameter  $\alpha l = 0.18$ . A model scaled-up to 10.2 GHz has been manufactured. Measurements have verified the design parameters well. Therefore a first LIGA mask for a 91 GHz structure with 39 main cells has been made and electroplating of the structure is under process.

## 6 ACKNOWLEDGEMENT

All the LIGA related work on the prototype is and will be in collaboration with the department of precision and micro technology at the TU-Berlin, H. Lehr and M. Schmidt.

## 7 REFERENCES

- [1] H. Henke, Y.W. Kang and R.L. Kustom, "A mm-wave RF Structure for Relativistic Electron Acceleration", Argonne National Laboratory, internal report ANL/APS/MMW-1, 1993.
- [2] H. Henke, R. Merte, A. Nassiri, J. Song, Y.W. Kang and R.L. Kustom, "Millimeter-Wave RF Structure", Proceedings of the XVIII International Linear Accelerator Conference, CERN, Geneva, internal report 96-07, 15 Nov. 1996, Vol. II, pp524.
- [3] W. Bruns, H. Henke and R. Merte, "Design of a 94 GHz Accelerating Structure", Proceedings of the 5th European Accelerator Conference, Barcelona, June 1996.
- [4] W. Bruns, "GdfidL: A finite difference program for arbitrarily small perturbations in rectangular geometries", IEEE Trans. Magn. Vol. 32, No. 3 May 1996.

# Development And Test Of A Planar R-band Accelerating Structure\*

R. Merte, H. Henke, M. Peikert

Technische Universität Berlin, EN-2, Einsteinufer 17, D-10587 Berlin, Germany

D. Yu

Duly Research Inc., CA, USA

## Abstract

Planar accelerating structures, so called muffin tins, are of great interest for new accelerating techniques which are operating at high frequencies. At present the upper frequency limit for high power sources is 29.9855 GHz available at CERN. Therefore a new design of a planar traveling wave constant impedance accelerating structure is presented. A fully engineered 37-cell prototype with an operating frequency of 29.9855 GHz, which is designed for the  $2\pi/3$ -mode, was fabricated by CNC milling technology. The design includes a power coupler, a cavity geometry optimized to compensate the effect of transverse forces, vacuum flanges and beam pipe flanges. Shown are the frequency scan of transmission and reflection measurements compared to numerical simulations with GdfidL [1]. Further, a non resonant bead pull measurement was made to determine and verify the fundamental modes of the structure. The cavity is planned to be powered at the CLIC test stand at CERN.

## 1 INTRODUCTION

Planar structures are very different as compared to round structures. The accelerating mode excites transverse forces which depend on the longitudinal and transverse position. The excitation of higher order modes is expected to be much weaker in the vertical plane, and the surface quality and the shaping of the irises are different. This will affect the power handling compatibility and the beam dynamics. Therefore and because planar structures have never been used to accelerate particles, it was decided to build a fully engineered cavity and to test it under real conditions at the highest possible frequency.

In a collaboration with the CLIC team at CERN it is planned to make the experiments at the CLIC test facility this summer. If possible two experiments are planned. First, the planar structure shall be powered by the drive beam and generate RF power in the multi MW regime. In a second experiment the planar structure shall be fed from the CLIC transfer structure and powered by a test beam.

The planar structure is a 37-cell,  $2\pi/3$ -mode traveling muffin-tin operating at 29.9855 GHz. The depth and width of the cavities were chosen such that the transverse forces have equal magnitude while the sign is opposite. Such a

design allows for the compensation of the forces by rotating every other structure by  $90^\circ$  around the longitudinal axis, resulting in a weak focusing effect.

The design of the structure [2], the machining of a model scaled up to 10 GHz and measurements at 10 GHz [4] as well as 29.9855 GHz, were performed at the TU-Berlin. Two prototypes were machined by industry, the flanges provided by CERN. One prototype was brazed at the HMI, Berlin, the other will be brazed at CERN.

## 2 GEOMETRY OF THE STRUCTURE AND RF PARAMETERS

The structure is a traveling wave, constant impedance structure at 29.986 GHz [2]. From the wavelength of  $\lambda = 9.997$  mm follows a period length of  $p = 3.332$  mm for the  $2\pi/3$ -mode. The iris thickness has been fixed to  $t = 0.7$  mm. The length of one cavity in beam direction, the gap, results therefore to  $g = p - t = 2.632$  mm. The aperture  $2a$ , the width  $w$  and the depth  $2b$  of the cavity are the parameters which adjust the mentioned  $F_x = F_y$  property and the frequency. The aperture for the beam influences bandwidth, shunt impedance, wakefields and transverse forces. Thus a parameter analysis of these general cavity dimensions was necessary. The best results have been found for an aperture to wavelength ratio of  $a/\lambda = 0.18$ , resulting in  $2a = 3.6$  mm. The frequency was adjusted by the cavity width and depth of  $w = 6.688$  mm and  $2b = 8.4$  mm, respectively. Figure 1 shows a planar cavity in different views.

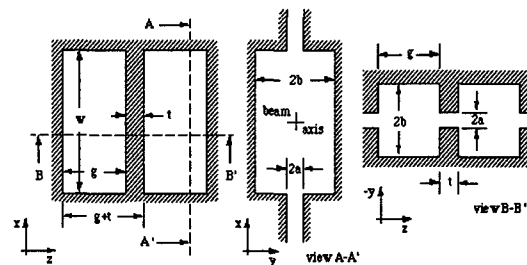


Figure 1. Typical cavity, a) top view, b) cross section and c) longitudinal cut.

The basic RF parameters are determined numerically with GdfidL [1] and listed in table 1. For the determination of the maximum length  $L_{max}$  of the structure we used an attenuation parameter of  $\tau = \alpha l = 0.8$ , resulting in a

\* Work supported by DOE SBIR grant DE-FG03-96ER82213

maximal number of cells of  $N_{max} = 375$ . A test model should have a small number of cells, but it should be large enough to present a measurable impedance. We chose 37 cells for the prototype.

$$\begin{aligned} r/Q_0 &= 22,62 \text{ k}\Omega/\text{m} \\ Q_0 &= 4420, r = 100 \text{ M}\Omega/\text{m} \\ v_g/c_0 &= 11,2\% \\ \alpha &= 0,64 \text{ m}^{-1} \\ \rightarrow \tau = 0.8 &\Rightarrow L_{max} = 1,25 \text{ m} \Rightarrow N_{max} = 375 \end{aligned}$$

Table 1. RF parameters of a  $F_x = F_y$  cavity.

### 3 MECHANICAL DESIGN

A 37-cell accelerating section has been modeled, consisting of 35 accelerating cells with  $F_x = F_y$  property and terminated with two coupling cells. The input and output couplers are matched with a cut iris. The power couplers are planar and the input and output ports are from one side. The matching procedure has been done in the time domain with GdfidL [1].

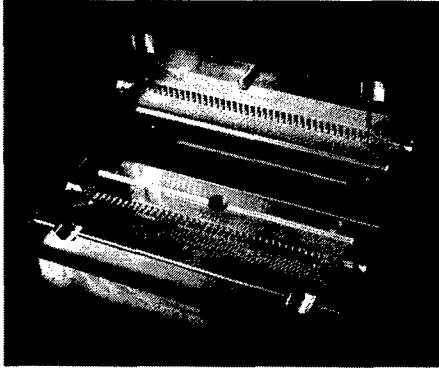


Figure 2. Manufactured 37-cell structure.

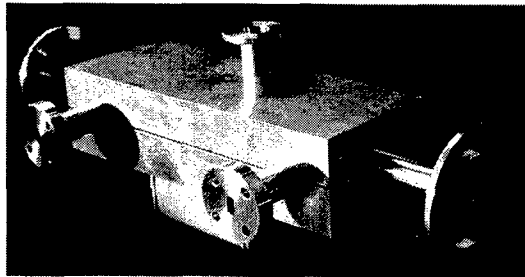


Figure 3. Manufactured structure with RF-, beam pipe- and vacuum-flanges.

The structure was produced by CNC milling technology with an accuracy of 0.004 mm. The machining by inline milling has the disadvantage that cavity corners are rounded with the radius of the milling cutter. The rounded corners cause a frequency shift and detune the match, as recently

seen in measurements of X-band models [3], [4]. In order to take account of these effects all simulations are made with rounded corners.

The structure is fully engineered for a high power experiment in vacuum. The design includes ports for vacuum, RF and beam pipe. Figure 2 shows a picture of the manufactured structure and figure 3 the mounted structure with RF-, beam pipe- and vacuum-flanges, ready for brazing. Thermal control for cooling and tuning is also planned. Cooling tubes will be glued on the top and the bottom of the structure.

### 4 MEASUREMENT

The main interest was to see how the  $S_{11}$  and  $S_{21}$  parameters of the numerical simulation compare to the measurement, as well as in the field patterns of the fundamental modes.

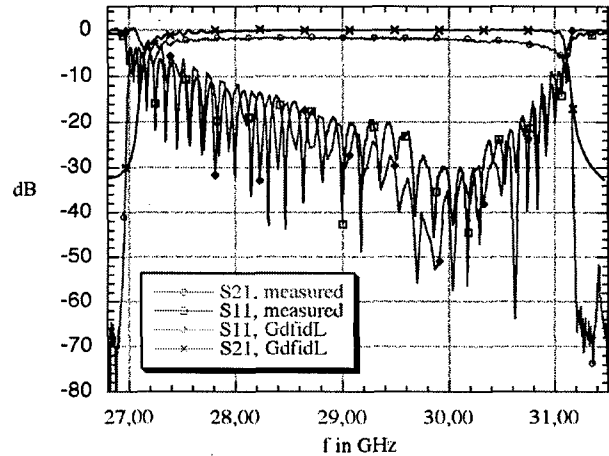


Figure 4. Comparison of the unperturbed measurement with the GdfidL simulation.

#### 4.1 Frequency scan

The measurements were made with a Hewlett Packard HP-8722C vector network analyzer (NWA), working in the frequency range from 50 MHz up to 40 GHz. The first step was a full 2-port calibration in the frequency range from 28.8 GHz up to 31.5 GHz using a HP-11644A waveguide calibration kit. A second measurement was made with the fiber inside the structure, but no bead. The fiber is a perturbation by itself and causes a frequency shift. Table 2 gives an overview of the measured frequencies compared to the data obtained with GdfidL [1]. The relation between the  $S_{11}$  chart and the dispersion chart is given by:

$$\#-mode = \frac{\pi(i-1)}{N-1}, \quad (1)$$

where  $N$  is the number of cells (37) and  $i$  is the number of the peak  $i = 1 \dots 37$ .

The mentioned rounded corners lead to the further problem that the numerical simulation needs a huge amount

of RAM and time. Therefore the 37-cell GdfidL simulation was terminated before the steady state was reached. Figure 4 shows a comparison of the  $S_{11}$  and  $S_{21}$  parameters of the measured unperturbed 37-cell structure with the terminated simulation. You can see a good quantitative agreement concerning the bandwidth and the match for the  $2\pi/3$ -mode, but also unexpected high losses in transmission.

peak NO	target mode	unperturbed $f_{up}$ [GHz]	perturbed $f_p$ [GHz]	GdfidL $f$ [GHz]
13	$\pi/3$	28.302	28.086	—
19	$\pi/2$	29.162	28.954	—
25	$2\pi/3$	30.012	29.985	29.986

Table 2. Some frequencies in the fundamental pass band.

#### 4.2 Bead Pull Measurement

A standard traveling wave bead pull measurement was performed. In order to keep the perturbation of the fiber small, a very thin pure silk fiber with 0.2 mm of diameter was used. The bead itself was made by painting the fiber over a length of 0.5 mm with liquid silver.

The measurements were made in an uncalibrated mode of the NWA. A first measurement, with fiber inside but bead outside the structure, takes the unperturbed reflection  $\Gamma_{up}$ . The next run with the bead pulled through the structure measures the perturbed reflection  $\Gamma_p(z)$ . The corrected data  $\Gamma_{cor}$ , results from:

$$\Gamma_{cor}(z) = \Gamma_p(z) - \Gamma_{up}(z) = c|E(z)|^2 e^{-j2\Phi(z)}. \quad (2)$$

The characteristics of the bead, such as material, shape and volume, represented by the constant  $c$  in eq. (2), were not determined. Therefore, no unit is assigned to the electric field in figure 5.

All measurements were made with a bead on the beam trajectory (no transverse off sets). Figures 5 – 6 show one result of the non resonant bead pull measurement. The  $2\pi/3$ -mode has been found at 30.130 GHz. The magnitude of the electric field follows from eq. (2) to:

$$C * |E(z)| = \sqrt{|\Gamma_p(z) - \Gamma_{up}(z)|} = \sqrt{|\Gamma_{cor}(z)|} \quad (3)$$

and is presented in figure 5, where the abscissa indicates the number of mesh points and represents the  $z$  direction. A polar chart of  $\Gamma_{cor}(z)$  with phase information is presented in figure 6. There one may find a good agreement between the phase advances per cell and the factor 2 in eq. (2). The presented structure is not an infinite periodic structure and terminated with coupling cells. These coupling cells have a decreased volume compared to the inner cavities and an aperture for the power input and output. Therefore the  $Q$ -value is different and the resonant frequency is detuned. This mismatch causes an error in the phase advance per cell and in

the field magnitude. The attenuation of the modes is also clearly visible.

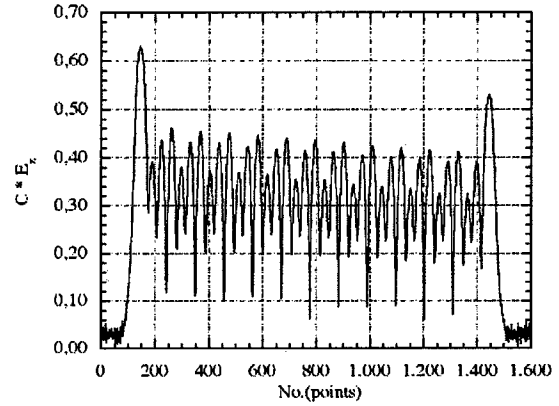


Figure 5. Magnitude of the  $2\pi/3$ -mode at 30.13 GHz, determined with bead pull.

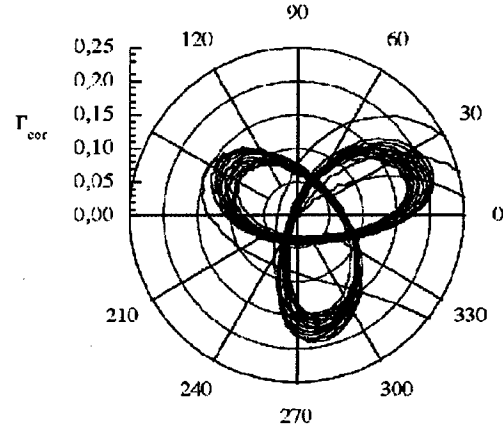


Figure 6. Polar chart of the  $2\pi/3$ -mode at 30.13 GHz, determined with bead pull.

## 5 ACKNOWLEDGMENT

The authors would like to thank the CLIC team for the ideal and material support of the project.

## 6 REFERENCES

- [1] W. Bruns, *GdfidL: A finite difference program for arbitrarily small perturbations in rectangular geometries*, IEEE Trans. Magn. Vol. 32, No. 3 May 1996.
- [2] R. Merte, *Design of a new R-band 7-cell cold test model RBAND-002*, TET Note 98/15, Inst. f. Theoretische Elektrotechnik, TU-Berlin.
- [3] R. Merte, *Influence of rounded corners seen in X-band RF measurements*, TET Note 99/01, Inst. f. Theoretische Elektrotechnik, TU-Berlin.
- [4] R. Merte, *Realization and RF measurement of a scaled 37-cell X-band model of the new R-band structure RBAND-003 E2*, TET Note 99/02, Inst. f. Theoretische Elektrotechnik, TU-Berlin.

## DESIGN, FABRICATION AND RF MEASUREMENT OF A W-BAND ACCELERATING STRUCTURE

R. Merte, H. Henke, R. Apel

Technische Universität Berlin, EN-2, Einsteinufer 17, D-10587 Berlin, Germany

### Abstract

The paper presents a design of a W-band planar accelerating structure (muffin tin) [1]. The structure is a  $2\pi/3$ -mode traveling wave, constant impedance structure with an operating frequency of 91.392 GHz. The design includes a new power coupler and a cavity geometry optimized for high shunt impedance. A 7-cell cold test prototype has been fabricated by wire electro discharge machining. Measurements were performed with a scalar network analyzer for both S-parameters and bead pull measurements. The RF parameters and measured results are presented and compared with the numerical results obtained by GdfidL [3] simulations.

### 1 INTRODUCTION

Very high frequency accelerating structures find more and more interest. They have the potential for very high gradient application due to a higher breakdown field and a better pulsed heating behavior. But they can also be a perfect match to particular applications such as medical accelerators. Or, they may even be a must as in space applications. On the other hand, very high frequencies, say above 60 to 80 GHz, require planar geometries for fabrication reasons. While planar geometries and the necessary technologies have to be developed, this avenue may lead to completely new concepts as for instance integrated modules, where the accelerating structure, the power sources and the focusing elements are produced on a common support.

Modern micro fabrication has developed, at least, two technologies which meet the requirements for accelerating structures: wire electro-discharge-machining (WEDM) and X-ray lithography (LIGA). Both technologies allow fabrication tolerances in the micrometer or even submicrometer range and surface roughness in the order of 0.1 micrometer, and they have relative advantages and disadvantages. For WEDM the structure must be constructed in layers and brazed or diffusion bonded together and the process is not well suited for mass production. LIGA is first of all expensive since it requires an X-ray mask which typically must be manufactured in several steps, a synchrotron radiation beam line for a many-hour exposure and facilities for developing and electroforming. It should, however, be much cheaper when producing large numbers because molding can be used. WEDM is intensely pursued at SLAC [4]. In Berlin our main focus will be on LIGA which is already

available at BESSY I and where a full production line is going to be build up at BESSY II. Nevertheless, our first structure was WEDM'ed, partly for financial reasons but also because we could profit from the experience SLAC has made and use the same manufacturer.

### 2 MECHANICAL DESIGN AND FABRICATION

The first design for the structure design was presented in [2]. The prototype is a 7-cell structure suited for wire EDM. Therefore special limitations were taken into account.

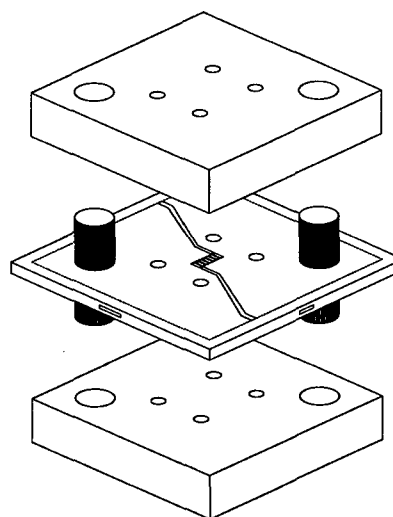


Figure 1. Explosion view of the cold test model.

Figure 1 shows the explosion view of the cold test model. The top and the bottom plates have the function of a mechanical support and represent the plates of the cavity's ground. The middle sheet is the structure with cavity section, beam pipe, pumping slots, input/output coupler plus detoured wave guides, integrated taper and holes for screws and alignment pins. The power couplers are planar and input and output are from both sides, left and right. The dashed line indicates a sacrificial region, which has been cut away after mounting the structure together. It serves the stabilization during machining. The thickness of this sheet is  $2b = 2.54$  mm. The design allows two different kinds of bead pull measurements: the conventional longitudinal pull through the beam pipe and a pull with a transverse dielectric fiber, positioned and moved in the pumping slots. The

connected WR-10 flange is as large as half the structure and overlaps the pumping slots which are needed for the transverse fiber bead pull measurement. Therefore it was necessary to detour the wave guide from the input and output coupling cells to the exterior boundary of the structure. Further the gap size of the first and last cells  $g_1 = 0.864$  mm, are smaller than the size of a WR-10 wave guide  $w_g = 1.27$  mm, so that tapering in this direction was necessary. The transition from the coupling cells to the outer WR-10 flange via the integrated taper is smooth and optimized for minimal reflection.

Figure 2 shows a typical planar cavity in different views. The iris thickness has been fixed to  $t = 0.23$  mm. The length of one cavity in beam direction, the gap, results from the condition that we chose the  $2\pi/3$ -mode with  $g = \lambda/3 - t = 0.864$  mm. The aperture for the beam influences bandwidth, shunt impedance and wakefields. A relatively large aperture to wavelength ratio of  $a/\lambda = 0.16$  was chosen, which results in an aperture of  $2a = 1.05$  mm. The width of the inner cavities which adjust the frequency is  $w = 2.363$  mm. The depth is  $2b = 2.54$  mm which is the size of the standard WR-10 wave guide and, therefore, does not require tapering in this direction.

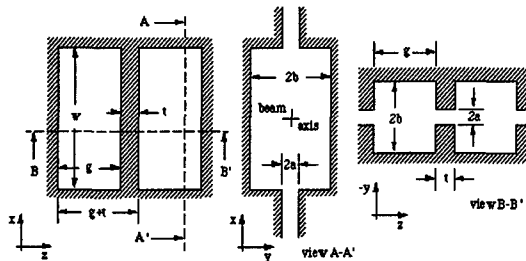


Figure 2. Typical cavity, a) top view, b) cross section and c) longitudinal cut.

The input and output couplers of the prototype have been matched with a cut coupling iris. The terminating coupling cells have a width of  $w_1 = 1.89$  mm and the coupling iris has an aperture of  $a_1 = 0.79$  mm. A disadvantage is the different depth  $a_1$  in case of a fabrication with LIGA.

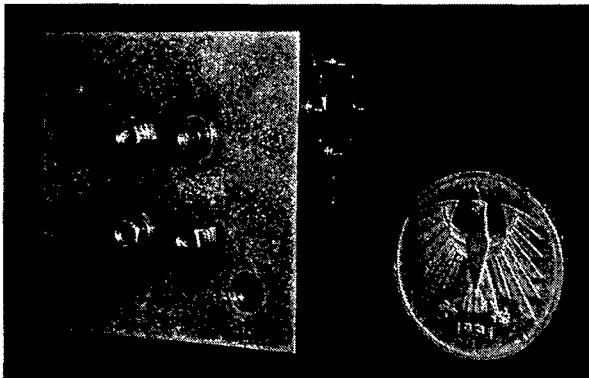


Figure 3. Prototype with RF-flange and bolts.

Figure 3 shows the final structure bolted together, which was fabricated by Ron Witherspoon, Inc., Campbell, California.

### 3 RF DESIGN AND NUMERICAL SIMULATION

As mentioned above the cold test model is a traveling wave constant impedance structure. It is designed for the  $2\pi/3$ -mode. The operating frequency is 91.392 GHz, 32 times the SLAC frequency (2.856 GHz), and corresponds to a wavelength of  $\lambda = 3.283$  mm. The period length  $p$  follows therefore with  $p = \lambda/3 = 1.094$  mm. The basic RF parameters are determined numerically with our code GdfidL [3] and listed in table 1. The cavity geometry is designed for an optimized shunt impedance. For the determination of the maximum length  $L_{max}$  of the structure, we used a  $\tau$  of 0.8 ( $\tau = \alpha l$ ), resulting in a maximal number of accelerating cells of  $N_{max} = 178$ .

$$\begin{aligned} r/Q_0 &= 81.6 \text{ k}\Omega/\text{m} \\ Q_0 &= 2490, r = 200 \text{ M}\Omega/\text{m} \\ v_g/c_0 &= 9.4\% \\ \alpha &= 4.1 \text{ m}^{-1} \end{aligned}$$

$$\rightarrow \tau = 0.8 \Rightarrow L_{max} = 19.5 \text{ cm} \Rightarrow N_{max} = 178$$

Table 1: Basic RF parameters.

The results of the numerical simulation in the time domain of the entire structure of the reflection and transmission coefficient, computed with GdfidL, are shown in figure 4.

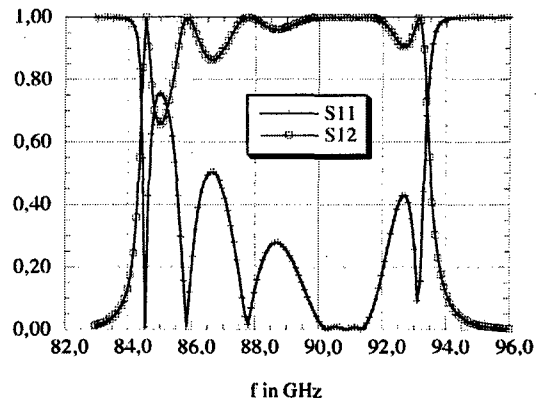


Figure 4. Reflection and transmission coefficient, GdfidL [3] simulation.

### 4 RF-MEASUREMENT

In the following a relatively cheap possibility to make transmission and reflection measurements as well as bead pull

measurement with a scalar measurement system in the W-band (75 – 110 GHz), are shown. Figure 5 shows the block diagram of the scalar measurement system for transmission and reflection measurements and figure 6 the set up for bead pull measurements.

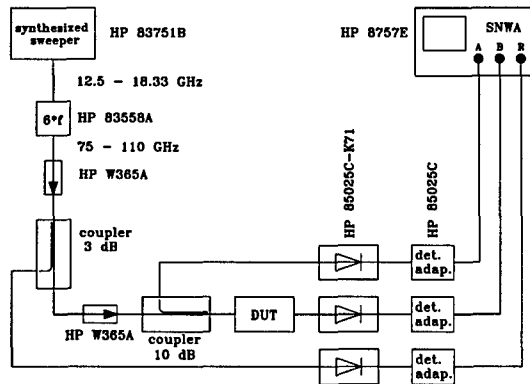


Figure 5. Block diagram for S11 and S12 measurements.

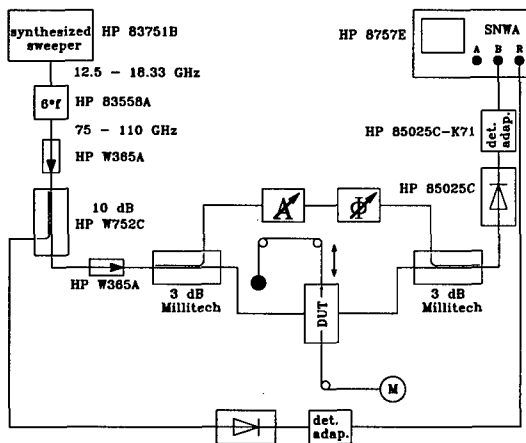


Figure 6. Block diagram for bead pull measurements.

The results of the transmission and reflection measurement are presented in figure 7. The measured frequency response is in good qualitative agreement with the numerical simulation. The measured 4 dB loss in transmission is not yet understood. We believe that it has something to do with the surface roughness and the bad contact between the irises and the cavity. For bead pull measurements a nylon fiber with a diameter of ca. 0.05 mm and a knot as a bead was threaded through the beam pipe. The bead was pulled along the seven cells in longitudinal direction and the perturbed transmission coefficient at the input port was measured. The constant  $c$  in equation (1) depends on the shape of the knot and the input power level and is not determined at this time. Therefore, no unit is assigned to the field in figure 8. Figure 8 shows the result of the measured amplitude of the  $2\pi/3$ -mode at 91.392 GHz, determined with bead pull.

$$\Gamma_p(z) = c|E(z)|e^{-j\Phi(z)} \quad (1)$$

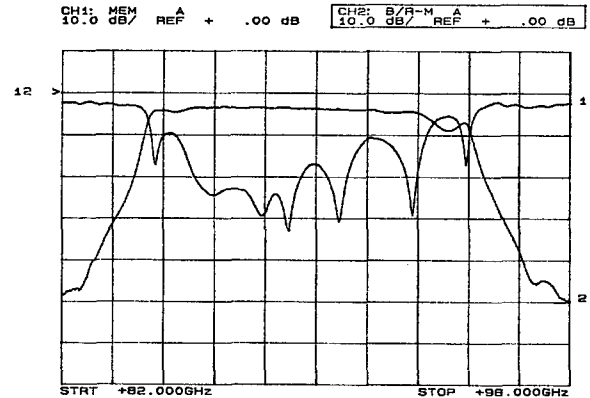


Figure 7. Reflection and transmission coefficient, measurement.

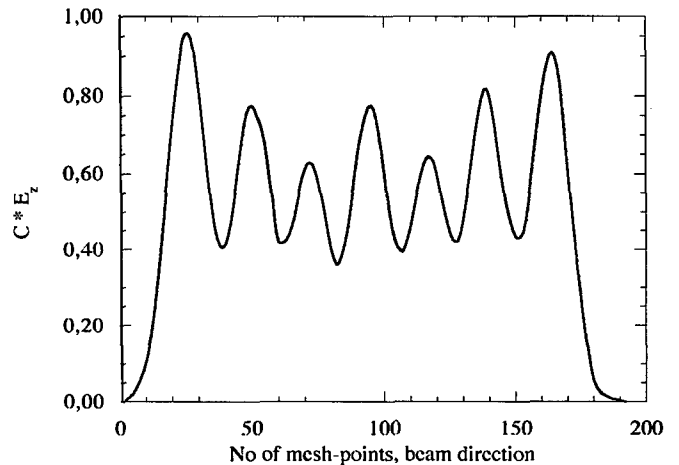


Figure 8. Field distribution measured with bead pull.

## 5 ACKNOWLEDGMENT

Part of the work was done at SLAC by one of the authors (R. Merte). We would like to thank the SLAC staff for their generous help and support.

## 6 REFERENCES

- [1] H. Henke, Y.W. Kang and R.L. Kustom, *A mm-wave RF Structure for Relativistic Electron Acceleration*, Argonne National Laboratory, internal report ANL/APS/MMW-1, 1993.
- [2] R. Merte, *First Design of a W-Band Muffin Tin, Cold Test Model*, Internal Note, Inst. f. Theoretische Elektrotechnik, TU-Berlin.
- [3] W. Bruns, *GdfidL: A finite difference program for arbitrarily small perturbations in rectangular geometries*, IEEE Trans. Magn. Vol. 32, No. 3 May 1996.
- [4] P.J. Chou, R.H. Siemann, et. al., *The Fabrication of Millimeter-Wavelength Accelerating Structures*, SLAC-PUP-7339, November 1996.



# RF LOADS FOR THE CLIC MULTIBUNCH STRUCTURE

M. Luong, I. Wilson, W. Wuensch, CERN, 1211 Geneva 23, Switzerland

## Abstract

The CLIC multibunch accelerating structure, called the TDS (Tapered Damped Structure), relies on heavy damping of higher-order modes [1]. Each cell of the structure is damped by its own set of four individually-terminated waveguides. A compact, low-cost and large-bandwidth terminating load with a reflection coefficient below 0.05 has been developed for this application. The load consists of a silicon carbide pyramid centered in a tapered waveguide. The design process, including the technique used to measure complex permittivity, is described. Measurements made on scaled prototypes are presented.

## 1. INTRODUCTION

Beam dynamics simulations of the CLIC main linac have shown that in order to preserve small emittances a substantial transverse wakefield suppression is required in accelerating structures. The required suppression is achieved in the TDS design by strong damping and moderate detuning.

Each cell of the TDS is damped by its own set of four waveguides which produce a quality factor of about 16 for the lowest transverse passband. The cutoff frequency of the waveguides (33.5 GHz) is chosen to lie above the accelerating frequency (29.985 GHz) but below the transverse mode spectrum (starting from about 36 GHz). The waveguide acts as a high-pass filter - higher order modes are damped while the accelerating mode is not.

Each damping waveguide is individually terminated by an absorbing load - a reflection coefficient less than 0.05 over a large bandwidth (extending to near the waveguide cutoff frequency) is required for effective damping. The terminating load must also satisfy a number of technical constraints - it must be compact, mechanically simple, brazeable, ultra-high vacuum compatible, radiation resistant and inexpensive. A load that fulfills these design criteria has been developed. The design process and the performance of a scaled prototype load are presented here.

## 2. SILICON CARBIDE AND THE MEASUREMENT OF PERMITTIVITY

The RF design of the termination depends strongly on the permittivity of the absorbing element. Following the example of other accelerator applications, SiC has been chosen as the absorbing material. SiC satisfies the technical constraints listed above and is widely-available,

low-cost and used in diverse industrial applications. There is, however, little published data on the high frequency permittivity of SiC and no specific data available from individual suppliers. In order to validate the choice of SiC and then to design the load, a simple technique to measure permittivity has been developed.

The technique involves measuring the complex reflection coefficient from a small slab of the material under test. The permittivity is obtained by comparing the measured reflection coefficient to the reflection coefficient computed on the same geometry but with an estimated permittivity. An increasingly accurate estimate of complex permittivity is obtained through iterative optimization.

A typical setup used to produce experimental reflection coefficient data for SiC is shown in Fig. 1 and data was taken at other frequencies using similar setups. The shape of the slab is not important but its dimensions must be accurately measured for setup of the computer simulation. The experimental setup has no contacts between the SiC and the copper except where the back plane of the SiC is glued with epoxy to the waveguide short circuit. The contact does not influence the reflection coefficient since the fields are already attenuated by the SiC. The complex reflection coefficient,  $\Gamma_m$ , is measured in the usual way using an HP8510B network analyzer. Reflection data for two different thickness SiC slabs are shown in Figs. 2 and 3. The  $S_{11}$ -port calibration provides an accuracy better than 0.01 for the amplitude and 0.5 degrees for the phase of the reflection coefficient.

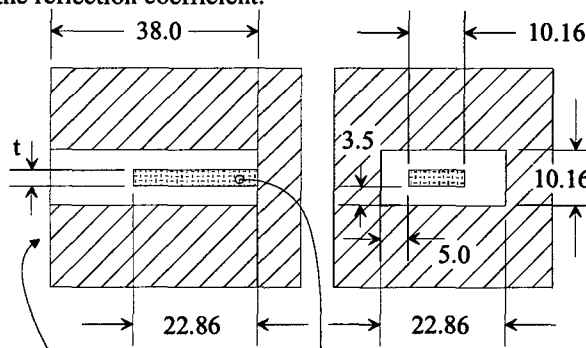


Figure 1: X-band experimental setup (dimensions in mm).  
Reference plane Dissipative material (SiC)

The notation for complex relative permittivity that will be used is the one based on a real relative dielectric constant,  $\epsilon'$ , and a loss tangent,  $\tan \delta$ .

$$\epsilon = \epsilon' + i\epsilon'' = \epsilon'(1 + i \tan \delta) \quad (1)$$

It is assumed that SiC has relative permeability,  $\mu=1$ .

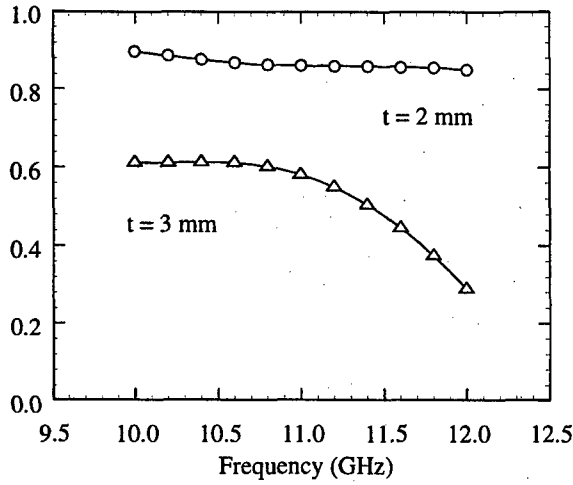


Figure 2: Amplitudes of measured reflection coefficients.

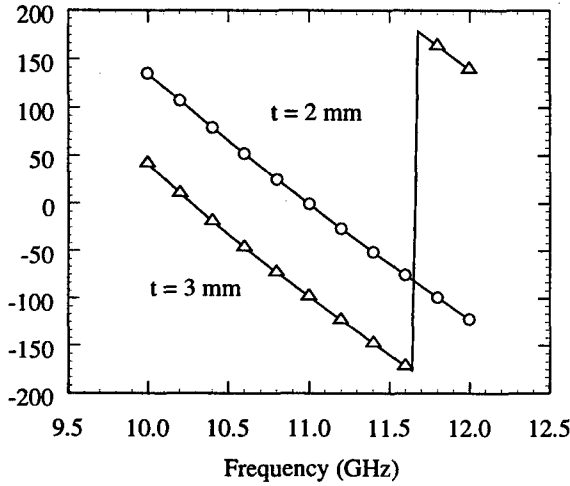


Figure 3: Phases of measured reflection coefficients.

The reflection coefficients were computed using the program HFSS [2]. An initial reflection coefficient is computed for each frequency using a starting value of  $\epsilon$ . A new  $\epsilon$  estimate at each frequency is found by minimizing the error between measured and computed reflection coefficients using the Newton algorithm. This algorithm converges quickly as long as the seed values are not too far from the solution. The two equations to be minimized are:

$$\begin{aligned} a(\epsilon', \tan \delta) &= \text{real}\{\Gamma_c(\epsilon', \tan \delta) - \Gamma_m\} = 0, \\ b(\epsilon', \tan \delta) &= \text{imag}\{\Gamma_c(\epsilon', \tan \delta) - \Gamma_m\} = 0. \end{aligned} \quad (2)$$

The Newton algorithm gives incremental steps,  $d\epsilon'$  and  $d\tan \delta$ , between iterations of,

$$\begin{bmatrix} \frac{\partial a(\epsilon'_n, \tan \delta_n)}{\partial \epsilon'} & \frac{\partial a(\epsilon'_n, \tan \delta_n)}{\partial \tan \delta} \\ \frac{\partial b(\epsilon'_n, \tan \delta_n)}{\partial \epsilon'} & \frac{\partial b(\epsilon'_n, \tan \delta_n)}{\partial \tan \delta} \end{bmatrix} \begin{bmatrix} d\epsilon' \\ d\tan \delta \end{bmatrix} = - \begin{bmatrix} a(\epsilon'_n, \tan \delta_n) \\ b(\epsilon'_n, \tan \delta_n) \end{bmatrix}. \quad (3)$$

Partial derivatives are obtained by numerical approximation:

$$\frac{\partial F(x_i, \dots)}{\partial x_i} \cong \frac{F(x_i + h, \dots) - F(x_i, \dots)}{h}, \quad (4)$$

where  $h = 0.05x_i$  is a practical value. The algorithm is implemented in a C routine in which HFSS is called as a subroutine with input parameters  $\epsilon'$  and  $\tan \delta$ . The algorithm is stopped once  $a(\epsilon', \Delta)$  and  $b(\epsilon', \Delta)$  are less than 0.01. With seed values of 20 and 0.2 for  $\epsilon'$  and  $\tan \delta$  respectively, the algorithm converges within four passes.

An accurate value of permittivity requires a judicious compromise in the size of the SiC sample. The sample must be large enough to absorb a significant amount of energy but must also be small enough that the reflection is not dominated by the reflection from the front of the sample. Nonetheless the technique is insensitive to sample geometry. Raw and analyzed X-band measurements for samples 2 and 3 mm thick are shown in Figs. 2 to 5. Despite the large changes in raw reflection coefficients, the estimation technique converges on values of permittivity that agree to within 5%.

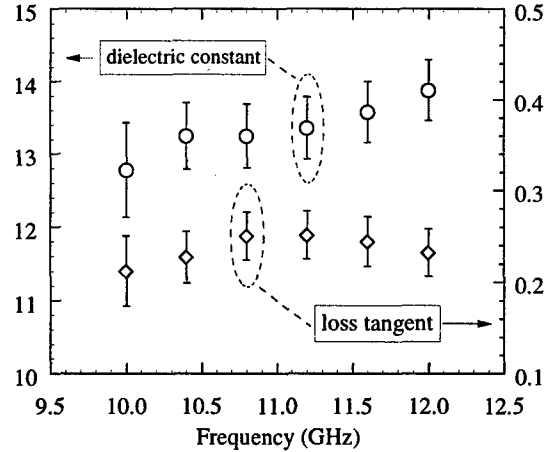


Figure 4: Permittivity values extracted from data from a 2 mm thick SiC sample.

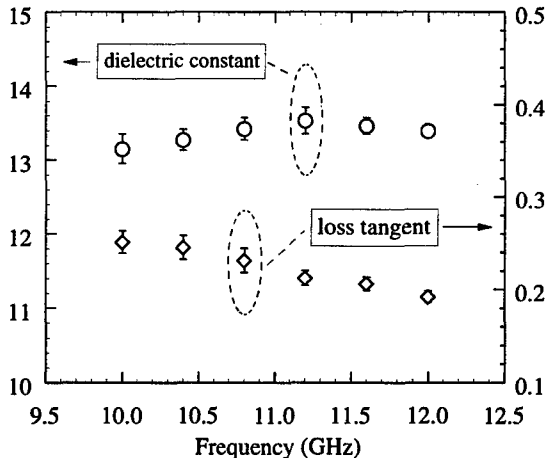


Figure 5: Permittivity values extracted from data from a 3 mm thick SiC sample.

### 3. PERMITTIVITY OF SiC

SiC-100, manufactured by Ceramiques et Composites, has been chosen for use in TDS prototype studies. SiC-100 has a high density  $> 3.1 \text{ g/cm}^3$ . A compilation of complex permittivity data taken over a number of frequencies is shown in Figure 6.

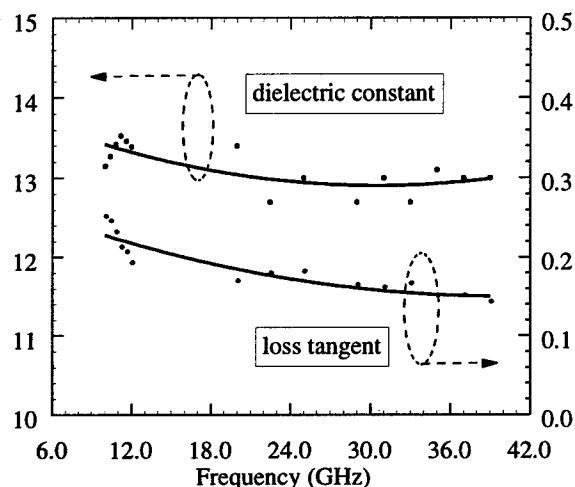


Figure 6: Complex permittivity of SiC-100.

### 4. DESIGN OF THE LOAD

The main requirements for the load: a reflection coefficient better than 0.05 for frequencies beyond 1.05 times the cutoff frequency of the damping waveguide and as good a performance as possible close to the cutoff. The load should be as short as possible and must have a simple form because many millions must be manufactured for CLIC. With the permittivity determined it was possible to use the program HFSS to compare various design principles and also to determine final dimensions.

The performance away from cutoff is easily achieved using a pyramidal tapered load. Near cutoff however, the relative impedance mismatch caused by the SiC rises quickly. Load designs based on three ideas were pursued to decrease the mismatch near cutoff. In the first, the width of the guide is tapered out before introducing the load material - thus moving the cutoff mismatch of the SiC away from the passband of the waveguide. Such a load has a low reflection coefficient but is quite long. In the second, a pair of pyramids are placed along the sides of the waveguide in the zone where the waveguide is tapering out. Impedance variations are reduced by smoothing the effective width changes of the guide. The load has a good reflection coefficient and is short but each load requires two pieces of SiC. In the third design, the waveguide is tapered in at the same time the SiC tapers out. The impedance change caused by the SiC is compensated by the impedance change of the narrowing guide. The third solution gives the best compromise of simplicity, size and performance and was thus chosen.

The load for the 30 GHz TDS has not yet been designed because of the limited frequency range of the available network analyzer. A factor 3.5 scaled prototype has been made in preparation for a planned test of a scaled TDS structure in ASSET. The measured performance of the load is shown in figure 8. It should be noted that some care must be used to extract  $S_{11}$  near the cutoff of the waveguide - a calibration with a reference plane inside the damping waveguide can be made using a pair of tapers and straight section of damping waveguide.

The agreement between expected and measured performances is excellent. The only differences are where the return loss is above 30 dB. In addition this load achieves all the required RF performance objectives.

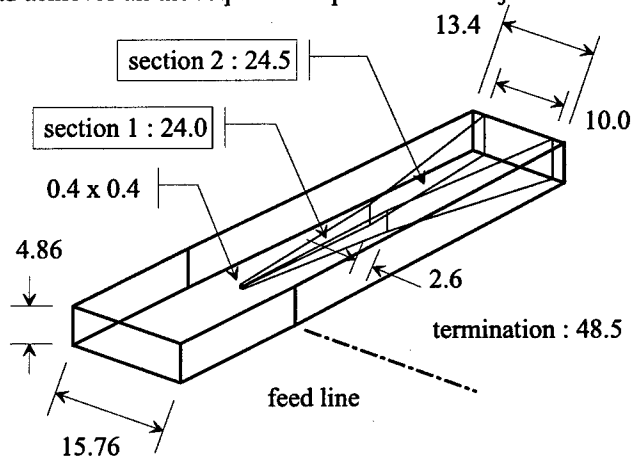


Figure 7: Load design .

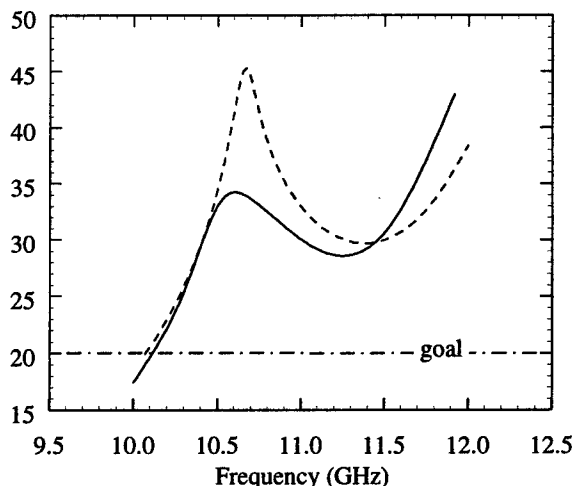


Figure 8: Measured (solid) and computed (dashed) load return loss as a function of frequency (in dB).

### 5 REFERENCES

- [1] M. Dehler, I. Wilson, W. Wuensch, 'A Tapered Damped Accelerating Structure for CLIC', LINAC98, Chicago, August 1998.
- [2] HFSS, 'High Frequency Structure Simulator', Ansoft and Hewlett Packard Co.'s.

## EXPERIMENTAL DESIGN TO STUDY RF PULSED HEATING\*

D. P. Pritzkau<sup>†</sup>, G. Bowden, A. Menegat, R. H. Siemann

Stanford Linear Accelerator Center, Stanford University, California 94309

### Abstract

An experiment to study the effects of RF pulsed heating on copper has been developed at SLAC. The experiment consists of two circularly cylindrical cavities operating in the  $TE_{011}$  mode at a resonant frequency of 11.424 GHz. These cavities are connected by a magic tee and driven by a 50 MW X-band klystron. Each cavity receives an input pulse of 20 MW with a pulse length of 1.5  $\mu$ s. This input corresponds to a maximum temperature rise of 350 K on the copper surface. The details of the experimental setup will be described.

### 1 INTRODUCTION

RF pulsed heating results from local Joule heating on a metal surface due to surface magnetic fields created from pulsed RF. Lateral stresses are induced in the material since the metal cannot expand fast enough. Cyclic stress results from the pulsing of RF and can lead to metal fatigue if the stress amplitude is larger than the elastic limit for the material. This effect represents high power limitations of metals like copper and may determine feasible accelerator structures at short wavelengths. For more information on pulsed heating please refer to the references [1], [2], [3].

### 2 EXPERIMENTAL SETUP

Due to the availability of 50 MW X-band klystrons at SLAC, we designed a circular cylindrical resonant cavity to be operated in the  $TE_{011}$  mode at 11.424 GHz to study the effects of pulsed heating on OFE copper. Two such cavities are used in conjunction with an asymmetric magic tee in order to protect the klystron from reflected power. The cavity design presented in this paper is a revised version compared to the design presented in ref. [1].

#### 2.1 Cavity Design

We chose the  $TE_{011}$  mode to be the operating mode for several reasons. In order to accommodate multiple experiments without having to machine additional cavities, we require the endcaps to be removable. The  $TE_{011}$  mode does not require current to flow between the endcaps and the cylindrical sidewall of the cavity, thus the endcaps may be inserted or removed without the need for

physical contact. This mode only has azimuthal electric fields, so no perpendicular electric fields exist on the metal surface. This property reduces the likelihood of breakdown and field emission from interfering with our study of pulsed heating. Removable endcaps also facilitate study of surface damage using optical and electron microscopes. One such cavity is shown in Figure 1 with one of the endcaps in the foreground.

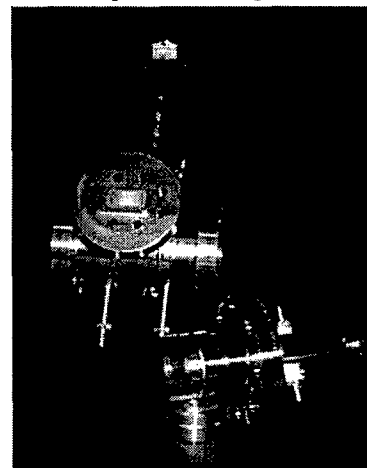


Figure 1: Picture of test cavity with one of the endcaps in the foreground.

Since it is our desire to reuse the cylindrical sidewall, the dimensions of the cavity were chosen to maximize the power dissipation on the endcaps while minimizing it on the sidewall. The cavities have diameters of 4.415 cm and axial lengths of 1.9 cm. Although the surface of the cylindrical sidewall will also heat up, a general property of cyclic metal fatigue is that the lifetime of the material depends exponentially on the stress amplitude [4]. Hence, many experiments can be performed with the same cavities before they become unusable.

The mode is excited through a circular aperture with a WR-90 waveguide coupler mounted on the sidewall of the cavity with the waveguide's long dimension parallel with the axis of the cavity. The coupling is accomplished with a circular aperture designed with a coupling coefficient  $\beta=1.28$  assuming a 10% degradation of the theoretical  $Q$  of 21890 due to machining. The coupling was chosen to maximize the heating in the cavity taking the fill time of the mode into account. Since the long dimension of the waveguide is longer than the length of the cavity, the sidewall and the endcaps are made longer than necessary to create the cavity in order to mount the waveguide.

For easy placement of the endcaps into the cavity a 0.1 mm gap exists between the outer radius of the endcap and

\*Work supported by Department of Energy contract DE-AC03-76SF00515

<sup>†</sup>Email: pritzkau@slac.stanford.edu

the inner radius of the cavity. This gap is rather long due to the problem with the size of the waveguide coupler. A RF spring gasket from BalSeal<sup>®</sup> is used to shunt this gap to prevent other spurious modes from being excited. A groove of 1.0 mm by 1.0 mm also exists on the outer radius of the endcap to remove the degeneracy of the operating mode with the  $TM_{111}$  mode. According to 2D simulations using MAFIA [5], the resonant frequency of the  $TM_{111}$  mode is reduced over 100 MHz and other modes are at least 400 MHz away. The unloaded Q's of all of these modes are at least 10000.

The endcaps are mounted on bellows to facilitate tuning of the cavity using differential screws. The endcaps were made even longer to also allow vacuum pumping behind the RF spring gaskets in addition to the pumping that will occur through the coupling aperture. Water channels were cut in the back of the endcap to allow cooling of the average heating that occurs from multiple RF pulses. Water-cooling is also implemented for the cylindrical sidewall as well.

## 2.2 Diagnostic Setup

Damage to the metal due to surface fatigue will manifest itself in degradation of the unloaded Q of the cavity. We wish to measure this degradation as well as the local pulsed temperature rise of the surface while high power is applied to the cavity. Exciting and measuring the properties of a low-power steady-state  $TE_{012}$  mode in the cavity allows us to perform such a measurement.

The  $TE_{012}$  mode is excited through a circular aperture by a waveguide coupler with a width of a WR-42 waveguide and a height of a WR-62 waveguide. Including the effects of the coupling aperture the resonant frequency of this mode is 17.811 GHz. The so-called diagnostic coupler is mounted similarly to the fundamental mode coupler except it is placed one-fourth of the cavity length away from the center where the maximum of the magnetic field for the  $TE_{012}$  mode occurs. The width of the diagnostic coupler is tapered to the width of a WR-62 waveguide after a length of 10 cm to allow the use of available vacuum windows. The diagnostic coupler is cutoff to the fundamental mode frequency of 11.424 GHz. After 10 cm, this signal is attenuated by over 150 dB to ensure no damage occurs to the diagnostic equipment.

The  $TE_{012}$  mode is designed to be critically coupled assuming a 10% degradation in the theoretical Q of 21906. As with the fundamental mode, MAFIA was used to model the endcap groove and radial gap in the cavity. The resonant frequency of the degenerate  $TM_{112}$  mode is reduced by 200 MHz and all other spurious modes are at least 150 MHz away. The unloaded Q's of all these modes are at least 8000.

The measurement of the pulsed temperature rise will be performed as follows. Before the application of a high-power RF pulse, the  $TE_{012}$  mode will be set up in steady state using a frequency generator. The surface of the

cavity will heat up as high power is applied. Since the resistivity of the surface of the metal will increase with temperature, the unloaded Q of the mode will decrease. This Q degradation will result in a change of coupling over the time of a RF pulse causing a change in the reflected power seen from the diagnostic port. The phase of the reflected signal will also change because of the change in resonant frequency due to thermal expansions and a changing Q. The local temperature rise of the surface of the cavity can be inferred from the knowledge of the amplitude and phase of the reflected power over time and the variation of the surface magnetic field.

The diagnostic apparatus used to perform these measurements is shown in Figure 2. A quadrature IF mixer is used to measure the amplitude and phase of the reflected signal over time. A RF switch is also utilized to allow the measurement of Q between RF pulses when the effects of pulsed heating have disappeared. This measurement allows us to determine when the Q gets permanently degraded from surface fatigue. Not shown in Figure 2 is the ability to use an event-counter to count the number of RF pulses applied to the cavity and bin them by power level. The counter will allow us to determine the number of RF cycles it takes to cause a certain amount of Q degradation.

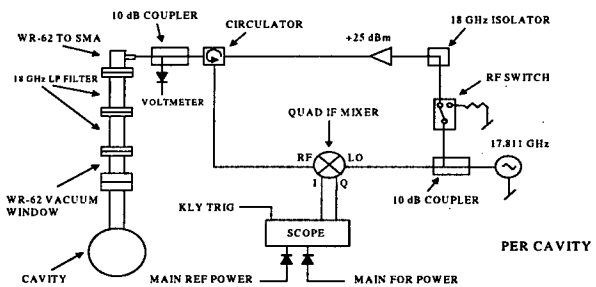


Figure 2: Diagram of diagnostic setup

## 3 COLD-TEST RESULTS

Some problems have arisen during the cold-test phase of the experiment. Broadband resonances are noticed while measuring the reflected signal of the  $TE_{012}$  mode. A representative spectrum is shown in Figure 3. These broadband resonances change the apparent coupling to the  $TE_{012}$  mode as well as its unloaded Q. Accurate values for these quantities cannot be determined at the time of this writing.

There are two possible explanations for these problems. One is the coupling aperture for the fundamental mode greatly affects the coupling of the diagnostic coupler to the  $TE_{012}$  mode and perhaps introduces spurious modes. High transmission (-7 dB) is measured from the diagnostic coupler to the fundamental mode coupler and it is known that the signal propagates in the fundamental  $TE_{10}$  mode in the WR-90 waveguide at 17.8 GHz.

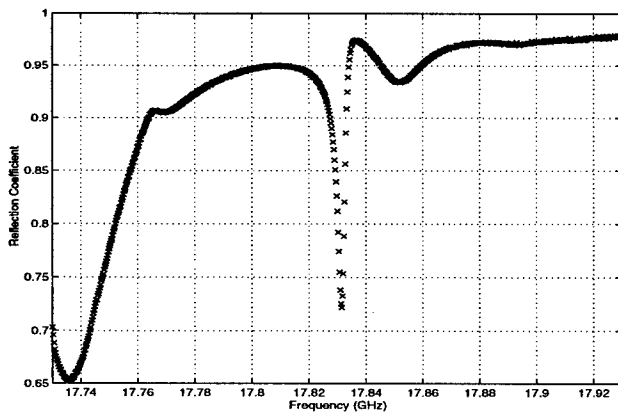


Figure 3: Frequency spectrum of  $TE_{012}$  mode. Resonant frequency is approximately 17.83 GHz.

Another possibility to consider are the effects of the RF spring gaskets used to shunt the gap between the endcaps and the cylindrical sidewall. The data show that the  $TE_{011}$  and  $TE_{012}$  modes are sensitive to the placement and type of springs used. It should be noted that most of the material behind the RF spring gaskets is stainless steel.

A plunger with copper tape was used to short the fundamental coupling aperture from the waveguide side while measurements were taken of the reflected signal from the diagnostic coupler. One such spectrum is shown in Figure 4. It can be seen from this figure that the coupling to the  $TE_{012}$  mode is greatly affected by some broadband resonance. This spectrum suggests that power is leaking through the spring gaskets and being dissipated in the stainless steel. It is also seen that when the springs are removed the transmission from the diagnostic coupler to the fundamental coupler is reduced from -7 dB to -14 dB. This suggests much power loss behind the endcaps to the stainless steel.

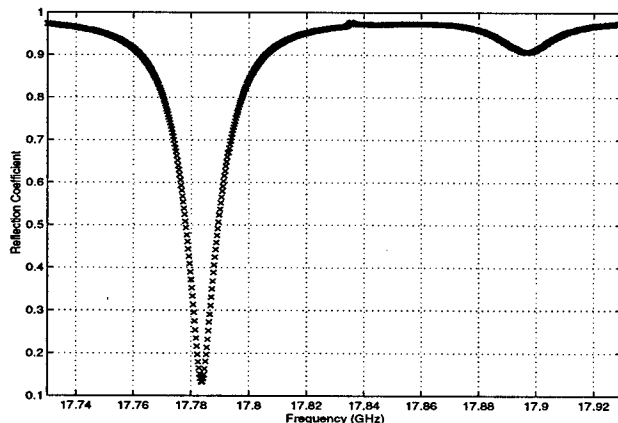


Figure 4: Frequency spectrum of  $TE_{012}$  mode with plunger inserted. The  $TE_{012}$  mode is washed away by the broadband resonance.

The effect of the springs is better characterized by looking at the  $TE_{011}$  mode. There are fewer modes nearby to the  $TE_{011}$  mode and the diagnostic coupling aperture does not affect this mode. The unloaded  $Q$  of the  $TE_{011}$

mode is measured while varying the wire diameter, compression, and material of the springs. The results are given in Table 1. In one case shown in the table, one particular type of spring was inserted into the cavity twice and the unloaded  $Q$  changed by over 1000. These results suggest that the  $TE_{011}$  and  $TE_{012}$  modes are highly sensitive to the presence of the springs. The springs are known to become less effective at higher frequencies, which may help explain the behavior seen at the diagnostic frequency.

In the present design the springs are housed in rectangular grooves on the endcaps. There are plans to perhaps modify the groove shape to improve contact with the springs as well as to determine the best type of spring to use. There are also plans to modify an older cavity [1] to isolate the effect of the apertures on one another from the effect due to the springs. In this way, the problem will be isolated and a solution sought.

Material	Wire Diam (.001 in.)	Compression Ratio (%)	$Q_0$
No Spring	N/A	N/A	10465
SS	6.0	22	11940
1 SS/1 SS- Au plated	6.0	32	20154
SS	4.5	32	17931
BeCu	4.5	32	17491
BeCu	4.5	32	18505

Table 1: Table of values for unloaded  $Q$  for various spring configurations. SS=Stainless Steel 302, BeCu=Beryllium Copper. External  $Q \approx 13000$ .

## 4 CONCLUSION

An experimental design to study RF pulsed heating has been presented. Cold-test results show some problems with the initial design. There are plans to fully characterize and isolate the effects of these problems and to design a solution. In the meantime, a high-power test will be conducted; although, accurate data cannot be collected from the diagnostic  $TE_{012}$  mode.

## 5 REFERENCES

- [1] D. P. Pritzkau, A. Menegat, R. H. Siemann, T. G. Lee, D. U. L. Yu, "Experimental Study of Pulsed Heating of Electromagnetic Cavities", Proceedings of the 1997 Particle Accelerator Conference, 1998, pp. 3036-3038
- [2] D. P. Pritzkau, G. B. Bowden, A. Menegat, R. H. Siemann, "Possible High Power Limitations From RF Pulsed Heating", 1998, SLAC-PUB-8013
- [3] O. A. Nezhevenko, "On the Limitations of Accelerating Gradient In Linear Colliders Due to the Pulse Heating", Proceedings of the 1997 Particle Accelerator Conference, 1998, pp. 3013-3014
- [4] A. Weroniński and T. Hejwowski, *Thermal Fatigue of Metals*, New York: Marcel Dekker, Inc., 1991, p.164
- [5] MAFIA User Guide Version 4.00, CST GmbH, Darmstadt, Germany

# Calculation of the Transverse Wake Function of a Highly Damped Periodic Structure

W. Wuensch, CERN, 1211 Geneva 23, Switzerland

## Abstract

Higher order wakefields in the CLIC multibunch accelerating structure (called the TDS, Tapered Damped Structure) are suppressed through a combination of heavy damping and moderate detuning. A new approach to computing the transverse wake function of such a highly damped periodic structure is presented. The driving bunch produces fields that travel with the propagation characteristics (given by the frequency dependent complex wave number) of the damped periodic waveguide. The fields in the structure are calculated by integrating the propagated waves excited by the Fourier decomposed driving bunch. Strong damping produces a propagated wave integral that converges within a few cells. Computational and experimental techniques to obtain wave numbers are described.

## 1 INTRODUCTION

Higher order wakefields in the CLIC multibunch accelerating structure are suppressed through a combination of heavy damping by waveguides and moderate detuning. The techniques needed to compute the transverse wake function of a damped structure such as the TDS have been developed and include an uncoupled circuit model, a coupled double-band circuit model and MAFIA time domain computations [1,2,3]. The transverse wake functions of the TDS computed using these techniques agree very well and confirm that the structure achieves the required performance. None of the techniques, however, give a simple and intuitive understanding of the physics underlying the interaction between a relativistic beam and a heavily damped periodic structure. An attempt to clarify this has resulted in the formulation of a new method to determine the transverse wake.

This new method, named the "wave number" method, derives the wake directly from the propagation characteristics of fields inside a periodic structure and from the coupling of the fields to a small current slice. The derivation is made in the frequency domain, giving the transverse kick spectrum, and the time domain wake function is found by taking the Fourier transform. The propagation characteristics and coupling can be obtained simply from either measurement or computation.

The wave number method naturally takes into account such effects as the cutoff frequency of damping waveguides and imperfect waveguide terminations. The

concept of synchronism, confusing in the presence of heavy damping, emerges naturally from the derivation. The wake can be calculated over an arbitrary frequency band so higher passbands can be included without any reformulation as is necessary in a circuit model.

## 2 DERIVATION OF THE KICK SPECTRUM

The derivation of the transverse kick spectrum is made in the following steps: First the bunch driving the wake is Fourier decomposed into a steady state current distribution. Next the waves radiated by this current distribution are described and propagation is included. An integral is then made which sums the fields that propagate to a point in the structure from all other points in the structure. These fields give the kick spectrum.

A very short driving bunch that travels to the right (towards +z) at the speed of light and which crosses  $z = 0$  at  $t = 0$  is described by the delta function current,

$$I(z, t) = \delta(z - ct) \quad (1)$$

The Fourier transform of this driving current is simply,

$$I(z, \omega) = \int_{-\infty}^{\infty} \delta(z - ct) e^{i\omega t} dt \\ = e^{iz \frac{\omega}{c}} \quad (2)$$

This represents a flat spectrum of currents, each frequency with a spatial variation given by the wave number  $k_{beam} = \omega/c$ .

Every differential slice of current acts as a small antenna launching fields that travel to the right and left inside the waveguide. The coupling of the current slice to the fields is a function of frequency, since the field pattern of a mode changes with frequency, and is represented by the term  $A(\omega)$ . The phase of the radiated wave is determined by the phase of the current slice. The phasors of the waves radiated by the current distribution at the position they are radiated are consequently,

$$A(\omega) e^{iz \frac{\omega}{c}} \quad (3)$$

Depending on the direction, the waves then propagate according to the wave number,

$$\begin{array}{ll} e^{ik(\omega)z} & \text{to the right} \\ e^{-ik(\omega)z} & \text{to the left} \end{array} \quad (4)$$

A schematic picture of the fields that fall on the origin which have been radiated from reference distances  $-z_0$  and  $z_0$  is shown in Figure 1.

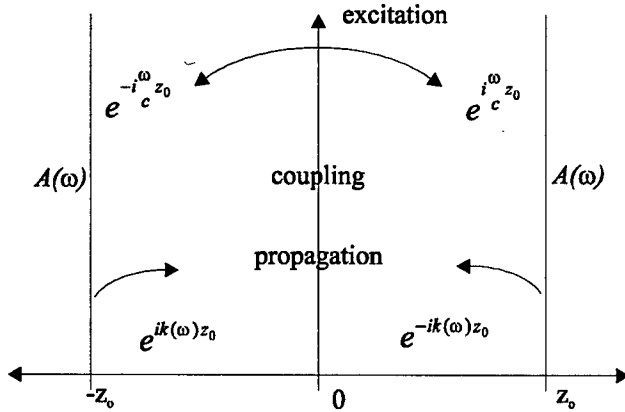


Figure 1: Schematic picture of the excitation and propagation of waves inside the waveguide.

The phasors of the wave radiated from the positions  $\pm z_0$  and arriving at the origin are found by multiplying the phasor of the excitation by that of the propagation. The waves travelling to the right from  $-z_0$  are given by,

$$e^{-i\frac{\omega}{c}z_0} A(\omega) e^{ik(\omega)(z+z_0)} = e^{-i\frac{\omega}{c}z_0} A(\omega) e^{ik(\omega)z_0} \quad (5)$$

The waves travelling to the left from  $z_0$  are,

$$e^{i\frac{\omega}{c}z_0} A(\omega) e^{-ik(\omega)(z-z_0)} = e^{i\frac{\omega}{c}z_0} A(\omega) e^{ik(\omega)z_0} \quad (6)$$

The total field at the origin is the integral of the phasors radiated from all distances,

$$\begin{aligned} E(\omega) &= A(\omega) \int_0^\infty \left( e^{i(k(\omega)-\frac{\omega}{c})z_0} + e^{i(k(\omega)+\frac{\omega}{c})z_0} \right) dz_0 \\ &= A(\omega) \left[ \frac{e^{i(k(\omega)-\frac{\omega}{c})z_0}}{i(k(\omega)-\frac{\omega}{c})} + \frac{e^{i(k(\omega)+\frac{\omega}{c})z_0}}{i(k(\omega)+\frac{\omega}{c})} \right]_0^\infty \quad (7) \end{aligned}$$

If there are any losses,  $k(\omega)$  is complex and the integral converges,

$$\begin{aligned} E(\omega) &= iA(\omega) \left( \frac{1}{k(\omega)-\frac{\omega}{c}} + \frac{1}{k(\omega)+\frac{\omega}{c}} \right) \\ &= \frac{2ik(\omega)A(\omega)}{k^2(\omega)-\left(\frac{\omega}{c}\right)^2} \quad (8) \end{aligned}$$

The kick on the beam is derived from the field by multiplying by the same factor  $A(\omega)$  as the coupling of the current to the field and is given by,

$$\text{Kick}(\omega) = \frac{2ik(\omega)A^2(\omega)}{k^2(\omega)-\left(\frac{\omega}{c}\right)^2} \quad (9)$$

Equation 8. shows that the kick spectrum, and consequently the transverse wake function, is a remarkably simple function of only a wave number spectrum and a normalized frequency dependant coupling. Equation 8. is referred to as the 'propagated wave integral'.

### 3 INTERPRETATION OF THE DERIVATION

A number of physical effects emerge from the derivation. Synchronism between the relativistic beam and the structure's phase velocity is evident in equation (8). A low loss mode has a wave number that is predominantly real and there is a strong peak in the spectrum  $E(\omega)$  for the frequency where the real part of  $k(\omega)$  is equal to  $\omega/c$ . The peak occurs in the integral of the fields generated behind the exciting bunch (left hand term in equation 7), because the radiated waves from behind the bunch add constructively over large distances. A narrow peak dominates the kick spectrum and results in a strong wake at the synchronous frequency.

In a damped structure, the imaginary part of  $k(\omega)$  is larger compared to the real part so the denominator in equation (8) does not become small when the real part equals  $\omega/c$ . The kick spectrum is broadened, resulting in the expected decay when the Fourier transform is taken.

From another perspective, fields in a damped structure are attenuated with distance causing a suppression of the constructive addition of fields over long distances that otherwise leads to a sharply peaked wake spectrum. The interaction between beam and structure occurs only over distances of the order of the attenuation length. This emerges in equation (7), where the integral converges more quickly for increasing losses. A convenient side effect is that short models can be used for computations and measurements on heavily damped structures.

The derivation given in section 2 has implicitly assumed that the interaction with the mode is dominated by interaction with the lowest space harmonic. A higher space harmonic can be considered separately, and the kick spectrum added to that of the lowest space harmonic. All space harmonics of course have the same value of complex wave number.



## 4 PRINCIPLES OF MEASUREMENT AND COMPUTATION

The derivation of the kick spectrum has shown that the wakefield behavior of a structure can be computed from a simple function of only  $k(\omega)$  and  $A(\omega)$ . These two terms are readily determined for a particular structure geometry using both measurement and computer modeling. Both measurement and computer modeling are simplified by including a conducting azimuthal symmetry plane: dipole modes are supported and monopolar modes are not. Measurement will be considered first.

The most conceptually simple measurement of  $k(\omega)$  in a periodic structure can be made by measuring the transmission through two lengths of guide that differ by one structure period (with period length  $l$ ). The change in transmission directly gives  $e^{ik(\omega)l}$ . Good accuracy requires a good match between the periodic structure and the measuring waveguide. The damping inherent to a high loss structure like the TDS can be used to eliminate multiple reflections and the measurement can be made on a relatively short section of line with large reflections into and out of the periodic line.

$A(\omega)$  can be measured in an experimental setup using small loop antennas because an offset beam excites dipole modes with the same sensitivity to field configuration, and consequently frequency variation, as a small loop antenna. An offset beam excites dipole modes equivalently to two beams traveling in opposite directions and offset in opposite directions. A pair of offset beams can be decomposed into a series of infinitesimal current loops. Currents flowing between the beams cancel in adjacent loops. A schematic representation of this is shown in Figure 2. These current loops have the same topology and thus the same field pattern sensitivity as a loop antenna.

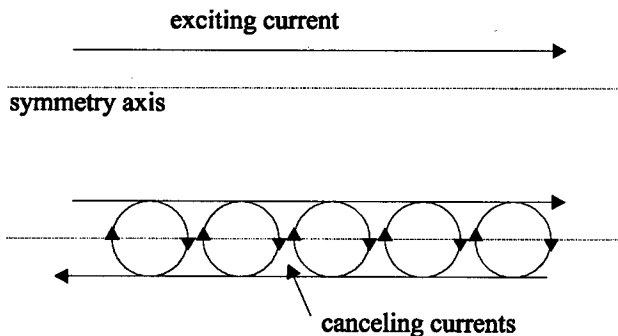


Figure 2: Equivalence between the driving beam and a decomposition in current loops.

$A(\omega)$  and  $k(\omega)$  can be simultaneously extracted from a short model shown schematically in Figure 3. The model has a conducting azimuthal symmetry plane and a pair of

small half loops mounted on the end of a coaxial cable. The measurement consists of comparing the transmission across one cell,  $T_1$ , to the transmission across two cells,  $T_2$ .

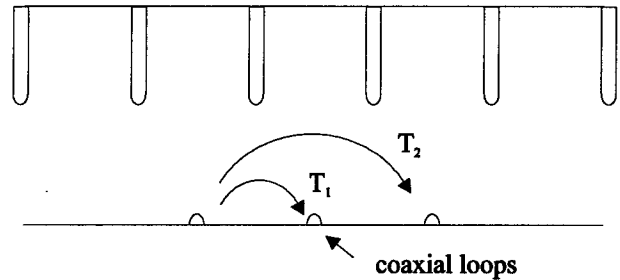


Figure 3: Schematic view for the measurement of  $A(\omega)$  and  $k(\omega)$ .

The two transmission coefficient can be expressed in terms of  $A(\omega)$  and  $k(\omega)$ ,

$$\begin{aligned} T_1 &= A^2(\omega) e^{ik(\omega)l} \\ T_2 &= A^2(\omega) e^{i2k(\omega)l} \end{aligned} \quad (10)$$

Thus,

$$\begin{aligned} A^2(\omega) &= \frac{T_1^2}{T_2} \\ k(\omega) &= \frac{1}{il} \ln \left( \frac{T_2}{T_1} \right) \end{aligned} \quad (11)$$

This measurement is in principle possible with any periodic structure although the ends of a low-loss structure must be well matched to avoid creating standing waves. The ends of a highly-damped structure are effectively matched by the internal attenuation over a sufficient length. The loops must be small compared to about a quarter of the free space wavelength at the frequency of measurement.

The measurement techniques presented above are also easily transferable to computer programs, such as HFSS, that are able to compute scattering matrices. In this way the intermediate results in the computation of a transverse wake function can be compared directly to the results from simple experiments.

## REFERENCES

- [1] M. Dehler, "Modelling a 30 GHz Waveguide Loaded Detuned Structure for the Compact Linear Collider (CLIC)", CERN PS/RF/Note 98-09.
- [2] M. Dehler, I. Wilson, W. Wuensch, "A Tapered Damped Accelerating Structure for CLIC", Proc. LINAC 98, Chicago, August 1998.
- [3] M. Dehler, I. Wilson, W. Wuensch, "CLIC Waveguide Damped Accelerating Structure Studies", Proc. Linac 96, Geneva, August 1998.

# PHOTONIC BAND GAP ACCELERATOR CAVITY DESIGN AT 90 GHz\*

N. Kroll<sup>†</sup>, S. Schultz<sup>‡</sup>, and D. R. Smith<sup>‡</sup>, D. C. Vier<sup>§</sup>

## Abstract

In previous work we have proposed utilizing Photonic Band Gap (PBG) structures as a new class of high-energy, high-intensity accelerator cavities. We have completed extensive MAFIA numerical calculations of multicell PBG structures, with each cell consisting of a square array of metal cylinders terminated by conducting sheets and surrounded by microwave absorber on the periphery. We find that our PBG structure has good higher order mode suppression, superior pumping properties, and potential fabrication advantages when compared to conventional cavity designs. These advantages scale favorably with increasing frequency, leading us to propose use of a PBG accelerator structure at W-band (91.392 GHz).

## I INTRODUCTION

We have previously proposed that a new type of microwave resonator, the Photonic Band Gap (PBG) cavity, may be useful as a novel high energy accelerator structure [1]. Briefly, the PBG cavity structure consists of a 2D periodic lattice of metal cylindrical scatterers, which are bound between a pair of metal plates. Removing a cylinder from the center of the lattice forms a defect site, where a highly localized electro-magnetic accelerating "defect" mode can exist over a wide range of lattice parameters.

When the frequency of the "defect" mode lies within the bandgap of the PBG structure the energy density decays exponentially in all directions from the defect site. This rate of energy decay can be very large, typically two orders of magnitude per lattice constant. At room temperature, with  $Q$  values corresponding to a copper construction, a  $7 \times 7$  lattice of cylinders easily suffices to prevent any significant energy loss of the fundamental in the radial direction.

In high energy accelerators Higher Order Modes (HOMs) such as dipole modes, can be excited by off-axis electrons and other perturbations. In a usual pillbox cavity these HOMs, unless specially damped (e. g. by damped detuning), have  $Q$  values comparable to the fundamental mode, and can generate a long-lived wakefield that will seriously degrade the next electrons in a traveling bunch.

The PBG cavity structure is novel in that the fundamental resonant mode can be strongly localized, with high  $Q$  and arbitrarily low leakage, while all other HOMs in the system can be very strongly damped. The way that this can be achieved for a PBG system, is to have the metal plates and cylinders surrounded by a very lossy absorbing material strategically placed around the periphery of the finite PBG lattice. It then becomes possible to have a suitably high  $Q$  for the fundamental mode, and simultaneously have all HOMs strongly damped. This condition can occur in a PBG system by a proper choice of parameters causing the HOMs to occur in "pass bands", and hence readily propagate to the periphery, where they may be absorbed. In contrast, the fundamental mode is highly localized within the center of the structure, and since there is no significant field amplitude at the periphery it is essentially undamped.

We have previously described the results of wakefield calculations for single PBG cavities without a beam iris [2]. In this paper we present results of extensive numerical calculations for an iris-coupled periodic PBG cavity structure. An iris in each metal plate, centered on the defect position axis, provides the coupling between successive cells, and as usual is the path of the pulsed electron beam [3]. We utilize MAFIA, a commercial finite-difference electromagnetic analysis program, to perform both frequency- and time-domain studies. We have concentrated on simulating the  $Q$  and loss-factors associated with the HOMs of the metal PBG cavity as a function of absorber geometry, and estimating the wakefield associated with the iris coupled chain of PBG cavities.

## II HOM AND WAKEFIELD STUDIES IN THE FREQUENCY-DOMAIN

Our main goal was to perform a complete calculation of the wakefield for a multicell PBG structure and to thoroughly test the hypothesis that all HOMs could be effectively damped by the peripheral absorber. To facilitate the wakefield calculation, we model our PBG cell as one of an infinitely periodic set of identically coupled cavities. We choose the height of our cell (34.99 mm, including plate thickness) to set the frequency of the fundamental accelerating mode at 2.856 GHz, with  $2\pi/3$  phase advance across the cell. The post diameter is 16.09 mm, the lattice spacing is 42.9 mm, the thickness of the plates is 6.0268 mm, and the beam iris radius is 18 mm. In Figure 1 we present the dispersion curves for the first seventeen (of the 160 actually calculated) dipole modes in the metal PBG cavity.

\*Work supported by the U.S. Department of Energy under Contract Nos. DOE-DEFG-03-93ER40793 and DOE-DEFG-0393ER40759

<sup>‡</sup>Department of Physics, University of California, San Diego, 9500 Gilman Drive, La Jolla, CA 92093-0319

<sup>§</sup>Stanford Linear Accelerator Center, Stanford University Stanford, CA 94309

\* Email: [dvier@ucsd.edu](mailto:dvier@ucsd.edu)

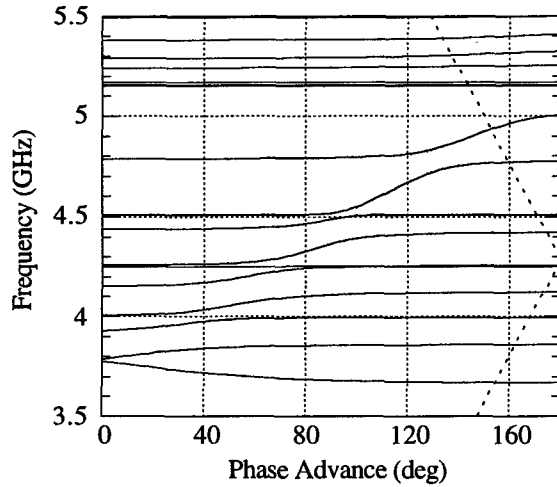


Figure 1. Dispersion curves for the first 17 dipole mode bands of our 7x7 PBG cavity as calculated by MAFIA. The intersection of each curve with the  $v=c$  line (dashed) gives the synchronous phase and frequency for which each dipole mode kick-factor is calculated.

We are only concerned with modes whose frequency coincides with the synchronous frequency, since these may produce unwanted beam deflection if their kick-factor is large enough.

From the dispersion curves we determine the synchronous phase and frequency for each of the 160 calculated modes and then calculate the kick-factor for each of these synchronous modes. The resulting transverse wake potential can then be calculated from the formula:

$$\text{Wake Potential}(t) = 2 \sum_{n=1}^N V(\omega_n) \sin(\omega_n t) \quad (1)$$

where  $V$  is the kick-factor,  $\omega_n$  is the frequency of the  $n$ th dipole mode, and  $t$  is the time step.

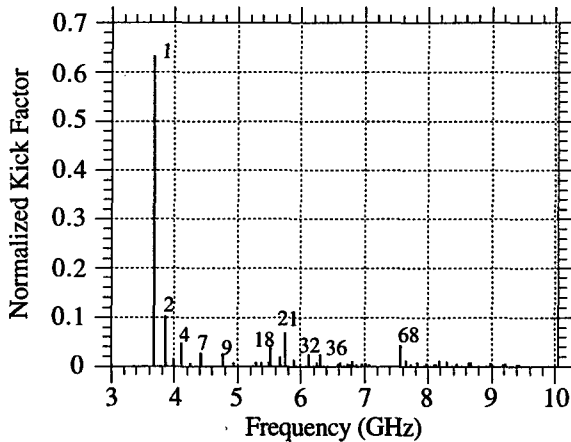


Figure 2. The synchronous kick-factors for the first 160 dipole modes (0-10 GHz). The ten modes with the largest kick-factors are labeled with their respective mode number.

In Figure 2 the kick-factors,  $V(\omega_n)$ , normalized to the kick-factor of the first dipole mode of the equivalent pill-box cavity are shown for the lowest 160 synchronous modes. Most of the synchronous modes have negligible kick-factor, and we find that the wake potential calculated from the ten modes with the largest kick-factor (labeled in Figure 2 with their corresponding mode number) is nearly identical to that calculated using all 160 modes. The wake potential is found to be about half of that calculated for a pill-box cavity over the same frequency range (0-10 GHz).

The most troublesome PBG dipole mode we found is the first (lowest) dipole mode. It has the largest contribution to the wake potential and is also found to be quasi-localized. All other synchronous PBG dipole modes with significant kick-factors were found to be highly extended in space. To obtain some idea of the effect of the beam iris parameters on this dipole mode, we calculated the kick-factor as a function of the beam iris radius (0-30 mm) for both the lowest PBG and lowest pill-box dipole modes. The PBG mode was found to always have a lower kick-factor than the pill-box mode. The results also indicate that, with a beam iris radius of 18 mm, our current PBG design is not optimal from the standpoint of minimizing the first dipole mode kick-factor. They suggest that improvement may be achieved for applications that can withstand a significant alteration in the beam iris radius. We have also determined that the effect of the beam iris thickness on the kick-factor of the first PBG dipole mode is minor.

### III DAMPED WAKEFIELD STUDIES IN THE TIME-DOMAIN

Of primary interest is the behavior of the metal PBG cavity when absorber is introduced around the structure. As the first PBG dipole mode is the only quasi-localized dipole HOM with a significant kick-factor, we expended serious effort in designing an absorber configuration that would significantly damp this mode without affecting the  $Q$  of the fundamental mode. The three dimensional cone absorber configuration shown in Figure 3 was found to give optimal damping of the first PBG dipole mode, while minimizing the damping of the fundamental mode. The absorber dielectric parameters are  $\epsilon=27$  and  $\tan(\delta)=0.23$ , typical of the absorber material used at SLAC.

Utilizing MAFIA in the time-domain, the  $Q$  values for the ten dipole modes with largest kick-factors (Figure 2) were calculated in the presence of the absorber configuration shown in Figure 3. These dipole HOMs, including the first dipole mode, were all determined to have  $Q$  values of  $\sim 100$  or less, whereas the fundamental mode  $Q$  was only reduced by a few percent (from 11,950 to 11,540). We note that the calculated  $Q$  values of the dipole HOMs are only approximate, as the MAFIA time-domain solver does not usually allow us to perform time-domain simulations at the correct synchronous phases of each mode.

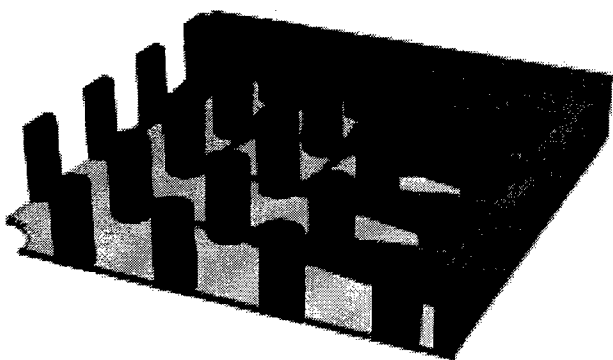


Figure 3. The absorber configuration found to be optimal for damping the lowest dipole HOM.

From the calculated dipole HOM  $Q$  values, we can compute a reasonable simulation of the wake potential for the PBG cavity in the presence of absorber by adding a  $Q$  time-dependence for each mode into the wake potential formula:

$$\text{Wake Potential}(t) = 2 \sum_{n=1}^N V(\omega_n) \sin(\omega_n t) e^{\frac{-\omega_n t}{2Q}} \quad (2)$$

In Figure 4 we plot the envelope of Eq. 2, the wake envelope function, for the ten damped PBG dipole modes with the largest kick-factor.

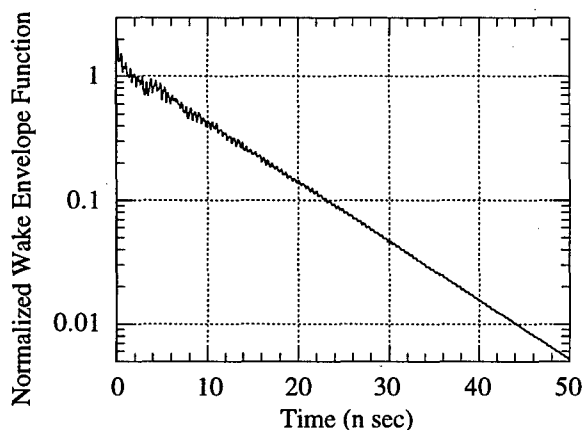


Figure 4. The calculated wake envelope function, with damping, for the ten dipole modes having the largest kick-factors. Note the semi-log scaling.

The longitudinal wake potential is also of interest for accelerator design, and we have utilized the same procedure as for the transverse wake potential (over the frequency range from 0-8 GHz). The simulation revealed that three monopole HOMs had a significant synchronous longitudinal kick-factor. Two are readily damped by the absorber configuration of Figure 3. However, the third monopole HOM (synchronous frequency=5.87 GHz) exhibited a degree of localization much greater than that of any of the dipole HOMs studied previously. This mode had been discovered in our earlier work, and is associated

with a pseudo-PBG in the pass bands. For this undesired monopole HOM, we found it possible to perturb the inner cylinder configuration positions, such that its localization is significantly reduced (making the mode more easily damped), while the fundamental mode suffers only a minor perturbation.

In fact, the fundamental mode is extremely robust with respect to deviations of the innermost posts from a perfect lattice. Frequency deviations of the fundamental are of course expected, but can always be compensated for by appropriate changes in the lattice constant. What is most important is that there are no significant perturbations of the field patterns and degree of localization of the fundamental mode. This field pattern stability is due to the fundamental frequency occurring deep within a large PBG, where slight perturbations only act to increase or decrease the mode localization in a minor way. A given perturbation can however have a drastic impact on HOMs in the pass bands, effectively moving them from pseudo-localized to extended in space.

## IV FUTURE WORK

The modes for the intrinsic PBG structure (i.e., without absorber) scale with frequency in the same manner as a pill-box cavity, or any other metal structure. Thus, all of the field properties, localization, etc. apply equally to a reduced size 1/32 structure whose fundamental mode is at 91.392 GHz. The characteristic physical dimensions (in mm) at 91.392 GHz are: plate spacing 1.093 mm, plate thickness 0.189 mm, post diameter 0.504 mm, and lattice constant 1.344 mm. We believe that the fabrication of a multicell PBG structure based on components with these dimensions is practical, and should require only well-established NC and EDM machining techniques. The relatively open design of the PBG structure should allow for adequate pumping properties, as well as simplifying the tuning of multicell PBG structures operating at 91.392 GHz. A multicell test structure is under development.

## V REFERENCES

- [1] D. R. Smith, Derun Li, D. C. Vier, N. Kroll, S. Schultz, "Recent progress on photonic band gap accelerator cavities", Proceedings of the seventh workshop on advanced accelerator concepts, Lake Tahoe, CA, October (1996)
- [2] Derun Li, N. Kroll, D. R. Smith, S. Schultz, "Wake-field studies on photonic band gap accelerator cavities", Proceedings of the seventh workshop on advanced accelerator concepts, Lake Tahoe, CA, October (1996)
- [3] N. Kroll, D. Smith, S. Schultz, "Photonic band-gap structures: a new approach to accelerator cavities", Third Advanced Accelerator Concepts Workshop, Port Jefferson, New York., June 1992.

# PHOTONIC BANDGAP STRUCTURE BASED ACCELERATING CELL

M.A.Shapiro, W.J.Brown, and R.J.Temkin, Plasma Science and Fusion Center,  
Massachusetts Institute of Technology, Cambridge MA 02139

## Abstract

We present detailed calculations of photonic bandgap (PBG) accelerating cavities including estimation of the important effects of an input coupler. The PBG structures consist of a triangular lattice of metal rods containing a single defect on axis. The operating frequency is selected to be 17.1 GHz. The accelerating mode is a quasi-TM<sub>010</sub> mode localized near the defect. We analyzed the excitation of the cell using a rectangular waveguide with aperture coupling. Both the design of the PBG cell and the design of the input coupling were varied in order to optimize the design. Results are compared with a conventional TM<sub>010</sub> cavity design. Ohmic loss is found to be comparable for the different cavity designs. The results indicate that the PBG cavity can have the following advantages relative to a conventional cavity: rarified spectrum of modes; oversized dimensions; and simplified input coupling with no frequency shift.

## 1 INTRODUCTION

Photonic bandgap structures (photonic crystals) [1] have recently found a number of applications at the frequencies from microwave to optical [2]. A 2-D photonic bandgap structure based accelerating cell was proposed by S.Schulz et al. at PAC'93 [3]. The cavities made of metal and dielectric rods with a single defect were analyzed, and the defect mode was observed in a cold test in X-band [4-6].

PBG based accelerating cells may be attractive at higher frequencies (17 GHz and up to 90 GHz) since the cavity is oversized. Therefore, the following features can be employed: (a) oversized quasi-optical waveguides can be utilized because conventional rectangular waveguides have large Ohmic losses at these frequencies; (b) the operating mode is localized near the defect whereas higher order, higher frequency modes fill the entire volume of the cavity and, therefore, they can be damped or removed.

The MIT experimental facility operating at 17 GHz includes a 1-1/2-cell photoinjector RF gun [7], the Haimson Research Corporation (HRC) 36 MeV linear accelerator [8] and HRC 20 MW relativistic klystron. This report is devoted to the design a 17 GHz PBG structure based accelerating cell. This cell may be accommodated and experimentally investigated at MIT.

The design we present includes calculations of the frequency, transverse field distribution, and Ohmic Q-factor of the defect mode as well as analysis of coupling into the defect mode using a rectangular waveguide.

## 2 PBG CAVITY MODE

### 2.1 Frequency and Field Distribution

We use a triangular lattice of metal rods with a defect to form a PBG cavity (Fig1). Since a finite number of circular rows of rods is required to localize the defect mode, we utilize only 3 rows of rods. The rods are of a finite length and placed between two metal planes parallel to the plane of the drawing (Fig.1). The operating mode is a quasi-TM<sub>010</sub> mode. Therefore, the electric field is parallel to the rods, and the magnetic field is in the plane of the drawing.

We use SUPERFISH code [9] to examine two PBG cavities. The parameters of the cavities are shown in Table 1. Figure 1 plots the lines of constant electric field in Cavity #1. It is seen that the mode is localized near the defect and slightly penetrates to the space between the 2<sup>nd</sup> and 3<sup>rd</sup> rows. The results of the resonance frequency calculation are shown in Table 1.

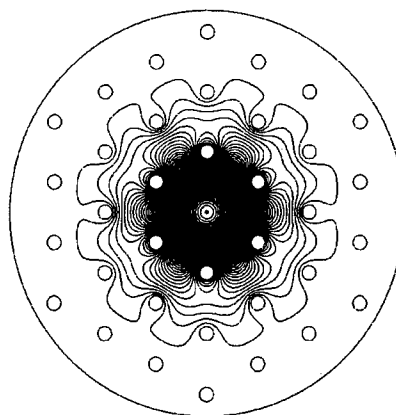


Fig.1. Electric field in Cavity #1.

### 2.2 Ohmic Losses and Shunt Impedance

The Ohmic Q-factor of the cavity is expressed as follows:

$$Q_{ohm} = d_{sk}^{-1} \left( 1/R_{eff} + 1/L_{||} \right)^{-1}$$

where the skin-layer depth  $d_{sk}=0.5 \mu m$  at 17 GHz,  $L_{||}$  is the axial length, and an effective radius of the mode,  $R_{eff}$ , is

$$R_{eff} = 2 \int_{S_{\perp}} H^2 ds_{\perp} \left( \oint_{l_i} H^2 dl \right)^{-1}$$

where the magnetic field  $H$  is integrated over the cavity cross-section  $S_{\perp}$  and over all contours  $l_i$  of the rods.

SUPERFISH output gives the stored energy per unit of axial length:

$$W = \frac{\mu_0}{2} \int_{S_{\perp}} H^2 ds_{\perp}$$

where  $\mu_0 = 4\pi \cdot 10^{-7}$  H/m. The contour integral can be determined using the SUPERFISH data. Note that  $R_{eff}$  is equal to the cavity radius  $R$  for a conventional pill-box cavity. A specific shunt impedance is expressed as follows:

$$r_{cy} = \frac{E_{max}^2}{\omega W} Q_{ohm}$$

Table 1.

	PBG Cavity #1		PBG Cavity #2	Pill-Box Cavity
Lattice vector $b$ (cm)	0.64		0.774	
Rod radius $a$ (cm)	0.076		0.175	
Cavity radius (cm)	2.2		2.9	0.657
Frequency (GHz)	17.172		17.099	17.466
Length $L_z$ (cm)	0.45		0.45	0.45
Effective radius $R_{eff}$ (cm)	0.388		0.57	0.657
Ohmic Q-factor $Q_{ohm}$	4200		5000	5300
Shunt impedance $r_{cy}$ (MΩ/cm)	2.1		2.5	2.9
Coupling scheme	Fig.2	Fig.3	Fig.4	Fig.5
External Q-factor $Q_{ext}$	9000	2400	9000	5500
Coupling hole length (cm)				0.2
Coupling hole width (cm)				0.37
Coupling frequency (GHz)	17.171		17.098	17.166
Maximum magnetic field ratio $H_{max}/E_{max}$	1.3		0.95	0.94

where  $E_{max}$  is the axial electric field. The results of calculation of the effective radii, Ohmic Q-factors, and shunt impedances are shown in Table 1 for two PBG cavities and a pill-box cavity.

### 2.3 External Losses

We analyze the coupling to the PBG cavity from the WR62 rectangular waveguide (the width of the wide wall is  $a_{wg} = 1.575$  cm). Figure 2 shows the coupling scheme. We excite the cavity from the left waveguide, and the right waveguide is utilized to symmetrize the cavity.

We calculate external losses (an external Q-factor) in two steps using SUPERFISH: (1) determine the resonance frequency of the cavity including the waveguides with the magnetic walls placed on the ends (Fig.2); (2) at this frequency, simulate one cycle of propagation using the initial sinusoidal electric field distribution at the left-side magnetic wall. The ratio of the electric fields,  $E_{max}$  at the axis and  $E_{wg}$  at the left-side wall, gives the external Q-factor:

$$Q_{ext} = \left( \frac{E_{max}}{E_{wg}} \right)^2 \frac{16\omega W Z_{wg}}{E_{max}^2 a_{wg}}$$

where  $Z_{wg} = 455 \Omega$  is the waveguide impedance.

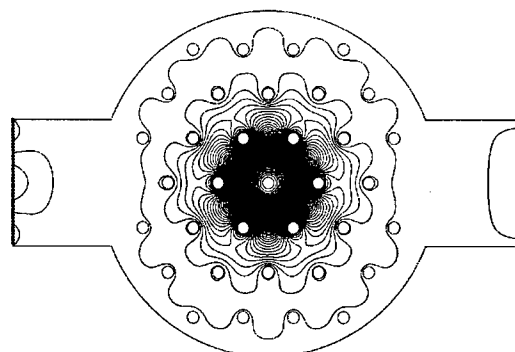


Fig. 2. Cavity #1, coupling scheme A.

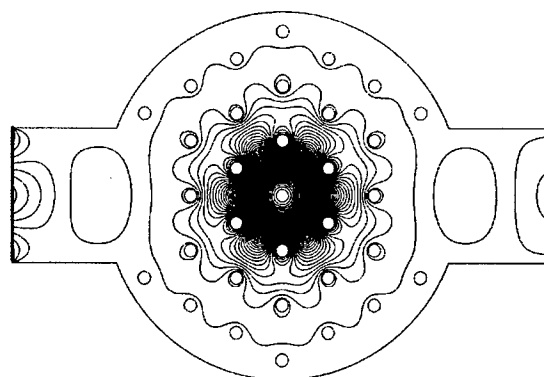


Fig. 3. Cavity #1, coupling scheme B.

We treat two schemes of coupling into Cavity #1: (A) 1 rod from the 3<sup>rd</sup> row, from both sides, is removed (Fig.2); (B) 2 rods from both sides are removed, and the orientation of the cavity is rotated 90° (Fig.3). To couple into Cavity #2, we remove 1 rod of the 3<sup>rd</sup> row and 1 rod of the 2<sup>nd</sup> row from both sides (Fig.4). The calculated external Q-factors are shown in Table 1. On the example of Cavity #1, we indicate a great difference in external Q-factors between the coupling schemes A and B.

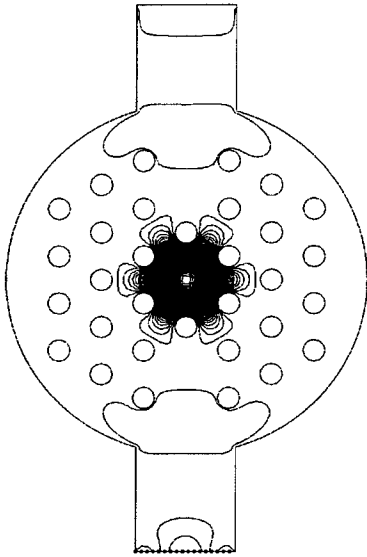


Fig.4. Cavity #2.

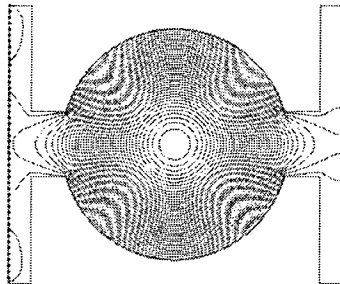


Fig.5. Pill-box cavity.

The pill-box cavity (Fig.5) excitation through the coupling hole is simulated for comparison. The cavity and the coupling hole dimensions are shown in Table 1. Note the relatively small size of the conventional cavity in Fig.5. A critical coupling to the pill-box cavity is obtained since  $Q_{\text{ohm}} \approx Q_{\text{ext}}$ . Optimization on the rod diameter of the PBG cavities is required to reach the critical coupling.

The important feature indicated in the PBG cavity is that there is no frequency shift caused by coupling, whereas there is a significant coupling frequency shift

in the pill-box cavity (Table 1). This effect is a result of distributed coupling in a PBG cavity. Since the 1<sup>st</sup> row of rods is not disturbed, the PBG cavity field does not vary due to coupling.

#### 2.4 Rod Surface Current

A critical issue is the rod surface current which infers heating while high RF power is coupled into the cavity. The rod surface magnetic field distribution has been calculated, and the maximum magnetic field characterized by its ratio to the axial electric field. This ratio multiplied by  $Z_0 = 377 \Omega$  is shown in Table 1. For the pill-box cavity, we indicate that this ratio reaches its maximum at the coupling hole edge. For the PBG cavity, it is at the inner surface of the rods of the 1<sup>st</sup> row. The results (Table 1) demonstrate that, for Cavity #1, the maximum surface magnetic field is about 40% larger than that for both the pill-box cavity and Cavity #2.

### 3 CONCLUSIONS

Two examples of 17 GHz PBG accelerating cavities are examined, the resonance frequencies and Q-factors are calculated, and schemes of coupling are designed. We found that coupling into a PBG cavity can be controlled by removing the rods from the 3<sup>rd</sup> row of the lattice. We demonstrated the effect of no frequency shift caused by the coupling, which is a great advantage of PBG cavities. We also demonstrated that the heating of rods in PBG cavities, caused by the magnetic field increase near the rod, is of about the same order of the heating in a coupling-hole unit of a conventional cavity.

### 4 REFERENCES

- [1] E.Yablonovitch and T.J.Gmitter, 'Photonic Band Structure: The Face-Centered Cubic Case', Phys. Rev. Lett., 1989, Vol. 63, p. 1950.
- [2] J.D.Joannopoulos, R.D.Meade, and J.N.Winn, 'Photonic Crystals: Molding the Flow of Light', Princeton Univ. Press, 1995.
- [3] S.Schulz, D.R.Smith, and N.Kroll, 'Photonic Band Gap Resonators for High Energy Accelerators', Proc. of 1993 Particle Accelerator Conference, IEEE, p. 2559.
- [4] D.R.Smith, N.Kroll, and S.Schulz, 'Studies of a Metal Photonic Bandgap Cavity', Advanced Accelerator Concepts, AIP Conf. Proc. 335, 1995, p. 761.
- [5] D.R.Smith et al., 'Recent Progress on Photonic Band Gap Accelerator Cavities', Advanced Accelerator Concepts, AIP Conf. Proc. 398, 1997, p. 518.
- [6] D.R.Smith et al., 'Photonic Band Structure and Defects in One and Two Dimensions', JOSA-B, 1993, Vol.10, p. 314.
- [7] S.Trotz et al., 'Experimental Operation of a 17 GHz Photocathode RF Gun', Proc. of 1997 Particle Accelerator Conference, IEEE, p. 2690.
- [8] J.Haimson et al., 'A Fully Demountable 550 kV Electron Gun for Low Emittance Beam Experiments with a 17 GHz Linac', Proc. of 1997 Particle Accelerator Conference, IEEE, p. 2808.
- [9] J.H.Billen and L.M.Young, 'POISSON/SUPERFISH', LA-UR-96-1834, LANL.

# HIGH POWER MITER-BEND FOR THE NEXT LINEAR COLLIDER

M.A.Shapiro and R.J.Temkin, Plasma Science and Fusion Center,  
Massachusetts Institute of Technology, Cambridge MA 02139

## Abstract

In the design of the Next Linear Collider (NLC), it may be necessary to transmit very high power levels (hundreds of megawatts) of microwave radiation over distances of tens of meters. The microwave transmission system will require the use of oversized waveguides and higher order modes in order to either avoid breakdown or to optimize the microwave system properties. We have studied one critical component of the proposed waveguide transmission system, namely a miter-bend for the  $TE_{01}$  mode capable of transmitting over 600 MW of power at 11.424 GHz. The miter-bend is a quasi-optical 90-degree bend. The design is based on previous, successful designs of miter-bends for high average power gyrotrons at frequencies of 35 GHz and above. The design consists of a profiled mirror and two oversized rippled-wall mode converters optimized to provide less than 0.1 dB operating mode losses.

## 1 INTRODUCTION

In the NLC Test Accelerator built at SLAC, the pulse compressor SLED-II producing 200 MW, 250 ns, 11.424 GHz pulses has been designed and successfully tested [1]. This pulse compressor contains the following microwave components capable of handling 60 MW pulses: circular waveguides operating at the  $TE_{01}$  mode, a magic tee, and a flower-petal  $TE_{10}$  to  $TE_{01}$  mode transducer [2]. To make a 90-degree bend of the circular waveguide  $TE_{01}$  mode transmission line, two flower-petal transducers and the rectangular waveguide bend are used. To operate at high powers, a bend of a ridged circular waveguide of a 4 cm diameter has been proposed [3]. However, such a design cannot be used with a 12 cm diameter waveguide because of sufficient conversion of the  $TE_{01}$  mode into spurious modes and, as a result, breakdowns.

The Delay Line Distribution System (DLDS) as a pulse compressor for NLC is under design at SLAC to enhance the peak power up to 600 MW [4]. We propose a quasi-optical miter-bend which can be used with a 12.7 cm circular waveguide in DLDS. This design is based on the developments of miter-bends for the 35 GHz  $TE_{01}$  mode circular waveguides [5], and for the 110 GHz  $HE_{11}$  mode corrugated waveguides [6] employed to transmit to long distances the radiation of high power gyrotrons.

## 2 MITER-BEND DESCRIPTION

In the quasi-optical miter-bend, we employ two circular waveguide sections cut under the angle of  $45^\circ$  and placed such that the waveguide axes form an angle of  $90^\circ$ . These waveguides are optically connected using a mirror (Fig.1). The waveguide wall goes all the way to the mirror. This eliminates diffraction expansion of the mode in the direction perpendicular to Fig.1. The mirror is profiled to compensate for the diffraction in the plane of Fig.1.

An unusual feature of the proposed miter-bend is that the operating mode is a mixture of waveguide modes. It is known that the diffraction of the  $TE_{01}$  mode at an open end of the waveguide is small compared to that of the other modes since the electric field is zero at the wall. Nevertheless, the mixture of the  $TE_{01}$  and  $TE_{02}$  modes forms not only the zero field but the derivative of the electric field equal to zero at the junction of the waveguide and the mirror. This allows to reduce diffraction [5,6]. By this reason, we introduce two periodic rippled-wall waveguides (mode converters) converting the  $TE_{01}$  mode into the optimum mixture of the  $TE_{01}$  and  $TE_{02}$  modes (Fig1.).

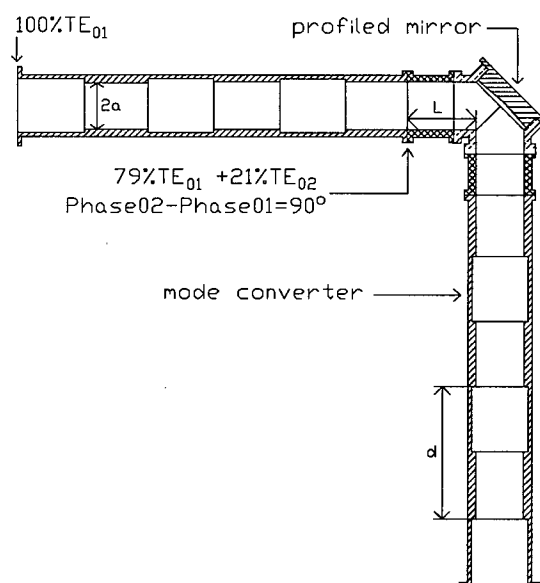


Fig.1. Miter-bend schematic.



### 3 MITER-BEND DESIGN

We design the miter-bend for the waveguide of the radius  $a=6.35$  cm, which is oversized at the frequency of 11.424 GHz. Therefore, a quasi-optical approach, valid if  $ka \gg 1$  ( $k$  is a wavenumber), can be employed for calculations. Within this approximation, the mirror is represented as a thin phase corrector. The equivalent quasi-optical schematic includes the waveguide cut by two  $45^\circ$  planes and the phase corrector placed as shown in Fig.2.

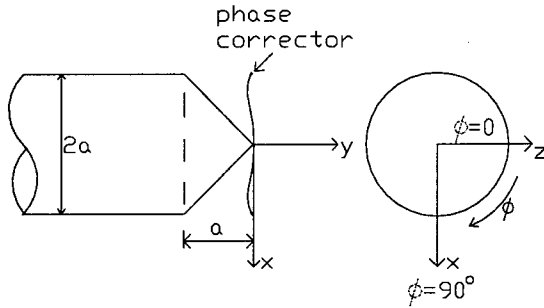


Fig.2. Quasi-optical schematic.

#### 3.1 Diffraction Losses

The procedure of numerical calculation is the following. We take an initial field distribution as a superposition of the  $TE_{01}$  and  $TE_{02}$  modes and propagate it through the gap of the length of  $a$  to the plane of the phase corrector. In the direction  $\phi=0$  (Fig.2) at the corrector, the incident electric field is the waveguide field distribution over radius  $r$ :

$$E_{\phi=0}^{inc} = \sum_{n=1,2} \frac{A_{0n}}{\sqrt{R_{0n}}} \frac{J_1(X_{0n}r/a)}{aJ_0(X_{0n})} \exp(-jkR_{0n}a)$$

where  $A_{01}$  and  $A_{02}$  are amplitudes of the  $TE_{01}$  and  $TE_{02}$  modes,  $X_{01}=3.832$ ,  $X_{02}=7.016$ , and

$$R_{0n} = \sqrt{1 - (X_{0n}/ka)^2}$$

In the perpendicular direction  $\phi=90^\circ$  (Fig.2), the incident electric field distribution varies due to the diffraction and is expressed as follows [6]:

$$E_{\phi=90}^{inc} = \sum_{n=1,2} \frac{A_{0n}}{\sqrt{R_{0n}}} X_{0n} \times \int_0^\infty \frac{\gamma J_1(\gamma a) J_1(\gamma r)}{(\gamma a)^2 - X_{0n}^2} \exp(-j\sqrt{k^2 - \gamma^2}a) d\gamma$$

To calculate the diffraction losses we represent the latter field distribution as a mode series of the waveguide of the radius  $a$ , propagate it back at the distance of  $a$  using the same integral transformation, and again express the result as a superposition of the  $TE_{0n}$  modes. The relationship between the initial amplitudes  $A^{ini}$  and the receiving amplitudes  $A^{rec}$  gives the efficiency of the miter-bend:

$$\eta = \frac{1}{2} + \frac{1}{2} \frac{|A_{01}^{rec}|^2 + |A_{02}^{rec}|^2}{|A_{01}^{ini}|^2 + |A_{02}^{ini}|^2}$$

Here we use the fact that a half area of the gap is covered by the waveguide wall (Fig.2), so the diffraction losses are twice smaller than those for the uncovered gap.

#### 3.2 Mode Converter

We specify the amplitudes  $A_{01}$  of  $TE_{01}$  mode and  $A_{02}$  of  $TE_{02}$  mode to minimize the diffraction at the mirror aperture. A smaller diffraction at the mirror can be obtained if  $(d/dr)E^{inc}=0$  at the  $r=a$ , at the corrector (Fig.2). This gives the amplitude ratio  $A_{02}/A_{01} = -(R_{02}/R_{01})^{1/2} X_{01}/X_{02} = -0.51$  at the corrector, and  $A_{02}/A_{01} = 0.51 \exp(j\alpha)$  at the distance of  $a$  from the mirror, where  $\alpha = \pi - k(R_{01} - R_{02})a = 110^\circ$ .

This amplitude ratio corresponds to 79% of power in the  $TE_{01}$  mode and 21% of power in the  $TE_{02}$  mode. To convert the pure  $TE_{01}$  mode into this mixture, the periodic waveguide section (Fig.1) of the following geometry can be used: period  $d = 2\pi / (k(R_{01} - R_{02})) = 32.6$  cm, total length  $Md$ , where  $M \geq 3$  is the number of periods, the step of the waveguide radius is

$$\varepsilon = \frac{a}{M} \frac{X_{02}^2 - X_{01}^2}{X_{01}X_{02}} \frac{\sqrt{R_{01}R_{02}}}{R_{01} + R_{02}} \frac{\arctan 0.51}{\pi}$$

Thus, for  $M=3$ ,  $\varepsilon=0.2$  cm.

The phase of the  $TE_{02}$  mode is of  $90^\circ$  ahead of the phase of the  $TE_{01}$  mode at the output of the mode converter. Therefore, to get these modes in phase at the mirror, we insert a waveguide section such that the length between the mode converter and the mirror is  $L=0.75d$  (Fig.1).

#### 3.3 Mirror Profile and Efficiency

The incident electric field at the corrector can be written in coordinates  $(x, z)$  of Fig.2 as follows:

$$E^{inc}(x, z) = \frac{1}{2} (E_{\phi=0}^{inc} + E_{\phi=90}^{inc}) + \frac{1}{2} (E_{\phi=0}^{inc} - E_{\phi=90}^{inc}) \cos\left(2 \arctan \frac{x}{z}\right)$$

To calculate the mirror profile we determine the phase distribution of this field:

$$\Phi^{inc}(x, z) = \arg(E^{inc})$$

We represent the mirror surface in the coordinates  $(x, y)$ , connecting to the surface. Since the mirror is tilted by  $45^\circ$ , the relationship between the coordinates  $(x, y)$  and  $(x, z)$  is  $y = z / \cos 45^\circ$  and  $x = z \cos 45^\circ$ . Therefore, the profile of the mirror, to conjugate the phase, is the following:

$$y_s = \Delta(x_s, z) = -2\cos 45^\circ \Phi^{inc}(x_s \cos 45^\circ, z)/k$$

For the mode amplitude ratio of 0.51 and the mode phase shift  $\alpha=110^\circ$  determined in Sec.3.2, the numerically calculated efficiency of the miter-bend is  $\eta=0.983$ , which corresponds to less than 0.1 dB diffraction losses. The 3D mirror profile is depicted in Fig.3. The mirror is almost cylindrical because there is no diffraction in  $z$ -direction (Fig.2), plus the phase shift between the modes is specified to provide a flat phase front in  $z$ -direction at the mirror. A correction in  $x$ -direction is needed, and the optimum profile is plotted in Fig.4.

The simulations indicated that the efficiency varies from 0.984 to 0.980 while the ratio of mode amplitudes  $A_{0z}/A_{01}$  varies from 0.4 to 0.6 and the phase shift  $\alpha=110^\circ$  remains the same. In this case, the mirror profile is cylindrical, and the losses are only due to the diffraction at the waveguide aperture.

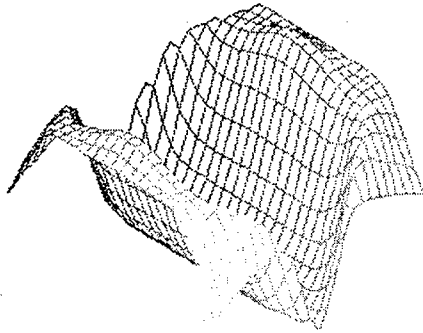


Fig.3. 3D profile of the mirror (off scale).

The efficiency can be raised up to 0.993 using optimization by  $\alpha$ . Varying  $\alpha$ , we minimize the diffraction at the waveguide aperture as well as at the mirror. However, there is a parasitic polarization conversion due to scattering at a non-cylindrical mirror. This effect has not been taken into account by the quasi-optical approach. The estimation indicates that the polarization losses are about 0.013, which brings the efficiency down to 0.98.

#### 4 CONCLUSIONS

We design a quasi-optical miter-bend for DLDS. It is capable to handle high peak power microwave pulses because highly oversized waveguides are utilized. Such a design cannot be employed with a small diameter (4 cm) waveguide, smooth bends are preferable for that.

The efficiency of the miter-bend meets the DLDS requirements. Less than 0.1 dB losses are obtained in the calculations. The mirror can be made mechanically steerable to reach maximum efficiency in a cold test. The length  $L$  of the straight waveguide section can be optimized in a cold test as well. The mode converter is designed as a periodic waveguide of the length of 3 periods, and the corrugation is rectangular.

The mode converter can be modified to employ a sinusoidal corrugation. The length of the mode converter can be lowered, though the corrugation profile should be optimized for that.

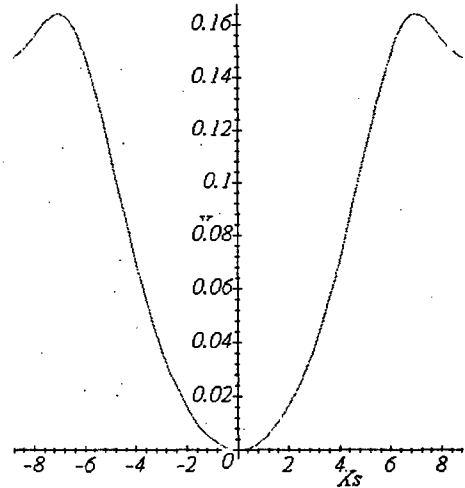


Fig.4. Mirror cut in  $x$ -direction (dimensions in cm).

#### 5 ACKNOWLEDGMENTS

We are thankful to Dr. Sami Tantawi for useful discussions. This research was supported by US Department of Energy, High Energy Physics.

#### 6 REFERENCES

- [1] S.G.Tantawi et al., 'The Next Linear Collider Test Accelerator's RF Pulse Compressors and Transmission Systems', Proc. of 1997 Particle Accelerator Conference, IEEE, p.3192.
- [2] S.G.Tantawi, K.Ko, and N.Kroll, 'Numerical Design and Analysis of a Compact TE10 to TE01 Mode Transducer', Conference on Computational Accelerator Physics, Los Alamos, NM, 1993, AIP Conference Proceedings 297, p.99.
- [3] C.Nantista, N.M.Kroll, and E.M.Nelson, 'Design of a 90° Overmoded Waveguide Bend', Proc. of 1993 Particle Accelerator Conference, IEEE, p.983.
- [4] S.G.Tantawi et al., 'A Multi-Moded RF Delay Line Distribution System for the Next Linear Collider', Proc. of 1998 European Particle Accelerator Conference, p.305.
- [5] M.A.Shapiro and S.N.Vlasov, 'Study of Combined Transmission Line for High Power Wave Generated by a Gyrotron in the Millimetre Wavelength Range', International Journal of Electronics, 1992, Vol.72, p.1127.
- [6] J.L.Doane and C.P.Moeller, 'HE11 Mitre Bends and Gaps in a Circular Corrugated Waveguide', International Journal of Electronics, 1994, vol.77, p.489.

# A 35 MHZ SPIRAL RE-BUNCHER CAVITY FOR THE TRIUMF ISAC FACILITY

A. K. Mitra and R. L. Poirier, TRIUMF, 4004 Wesbrook Mall, Vancouver, B.C., Canada.

## Abstract

A full-scale prototype of a 35 MHz re-buncher cavity was built for the ISAC project at TRIUMF. The re-buncher will be operated in cw mode to maintain the beam intensity and quality. Due to the longitudinal space limitation in the beam line, a compact spiral structure was constructed and investigated to determine its parameters. Natural frequencies and vibration amplitudes were measured. Vibration amplitudes of the spiral structure with 10 liter per minute water flow are two orders of magnitude lower than the allowable values. Measurements also show that the shunt impedance of the structure is 370 k $\Omega$  with a Q of 2740 at a resonant frequency of 39.5 MHz. MAFIA simulation predicts the resonant frequency, Q and shunt impedance to be 39.8 MHz, 5520 and 686 k $\Omega$  respectively. Due to poor rf contacts of the prototype cavity, measured Q is much less than that predicted by MAFIA, however, R/Q values of the prototype and simulation are 135 and 124 respectively. Construction details and final dimensions of the spiral for 35 MHz will also be presented.

## 1 INTRODUCTION

A radioactive ion beam facility is currently being built at TRIUMF. The linear accelerator complex consists of an RFQ [1] operating at 35 MHz and a DTL [2] operating at 105 MHz. In order to match the longitudinal beam characteristics between the RFQ and the DTL, a re-buncher cavity operating at 35 MHz has been specified in Table 1. A 20 cm space restriction in the longitudinal direction and moderate voltage requirements on the drift tube, led to the choice of a spiral cavity [3], after studying other design options [4]. The structure is a two and a half turn spiral mounted in a circular tank. The spiral is shorted to the tank at the root and the drift tube is mounted on the other end at the center of the spiral. The design takes into account the mounting of quadrupole magnets on both sides of the re-buncher and a diagnostic box attached to the up stream end of the cavity. MAFIA was used to determine the desired resonant frequency and the frequency sensitivity of the various mechanical dimensions. One of the major concerns for this type of cavity is the mechanical stability during operation. A prototype cavity was fabricated to investigate the mechanical properties of such a spiral. One of the main advantages of the spiral structure is its self-supporting feature and does not require an insulator. Vibrations amplitudes of the spiral structure, with 10 liters /min water flow, were measured to be two orders of magnitude lower than the allowable values.

Table 1: Parameters of the MEBT re-buncher

Description	Value
Resonant frequency, f	35.0 MHz
Velocity ( $=\beta c$ )	0.018%
Accelerating voltage, V	30 kV/gap
Beam aperture, diameter	20.0 mm
Length of cavity, $\beta\lambda$	154.3 mm
Voltage stability	$\pm 1\%$
Phase stability	$\pm 0.3\%$
Tuning range	$\pm 2\%$
Maximum longitudinal length	200 mm
Vibration amplitude	$\pm 0.1$ mm
Operation	cw

## 2 DESIGN

### 2.1 Spiral

3D MAFIA was used to simulate the spiral and obtain the desired resonant frequency with optimum shunt impedance. It was found that a ratio of 2.0 between the width of the spiral in the xy plane to the pitch of the spiral gave optimum shunt impedance. The ratio of the tank depth to the depth of the spiral in the z-axis (beam axis) also affects the shunt impedance. Although a higher ratio gives higher shunt impedance, the spiral depth was chosen to be 3 cm to provide better mechanical stability. The variation of resonant frequency and shunt impedance with depth of the spiral is shown in figure 1.

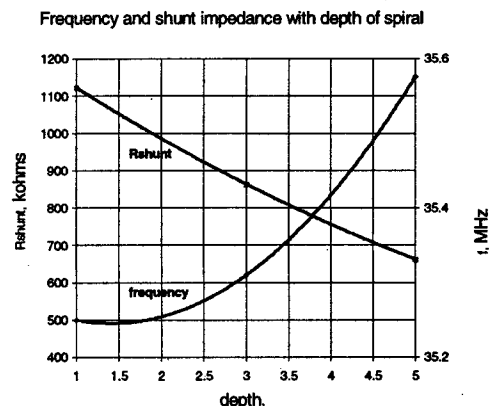


Figure 1: Graph of Rshunt and frequency Vs depth of spiral in z-axis

The spiral is housed in a 91.4 cm diameter tank. Although the optimum diameter is 96.5 cm, to reduce cost of fabrication a 91.4 cm diameter was chosen in order to make it the same diameter as DTL tank #1. Table 2 gives dimensions of the spiral and the tank. Figure 2 shows the electric field strength plot obtained from 3D MAFIA.

Assuming only 75% of theoretical Q, the power required to produce 30 kV on the drift tube, is 900 watts. About 30 % will be dissipated in the end covers where the power density is 0.05 watts/cm<sup>2</sup>. Hence, these covers are not cooled. Also, about a 20 cm length of the spiral from the drift tube mounting need not be cooled. A water flow of 6 liters/minute will be adequate to remove the heat from the rest of the spiral.

Table 2: Dimensions of the spiral and rf parameters.

Description	Value
Tank diameter	91.44 cm
Tank length external(cover to cover)	20.0 cm
Tank length internal	14.92 cm
Spiral depth (beam direction)	3.0 cm
Spiral width (x-y plane)	5.0 cm
Spiral leg radius	4.7 cm
Resonant frequency	35.4 MHz
Q	5200
R	675 k $\Omega$
R/Q	129 $\Omega$
Power required for tube voltage of 30 kV(at 75% Q)	900 watts

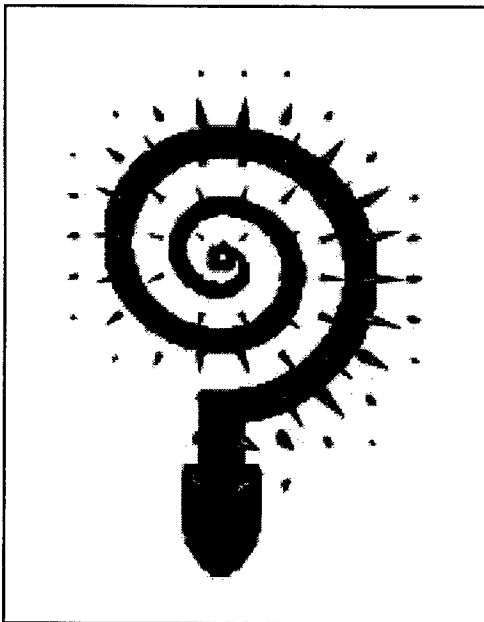


Figure 2: 3D MAFIA plot of H field

## 2.2 Frequency tuning

One of the major concerns is to design the re-buncher cavity such that the resonant frequency of the fabricated

structure is within 1% of 35 MHz. The spiral will be made by CNC machining and hence it will not be possible to change any of the spiral dimensions after fabrication, with the exception of the spiral (root) support. The drift tube will be fabricated separately and attached to the spiral. MAFIA simulations were used to obtain the resonant frequency of 35 MHz + 1% since it is easier to lower the resonant frequency by an external capacitive tuner. The sensitivity of the spiral leg and the drift tube dimensions are listed in Table 3. The spiral cross section near the root is 5 cm X 3 cm. A circular cylinder is envisaged here where the diameter and the length can be adjusted to get the desired frequency. Also, the drift tube diameter and the gap between the drift tube and the nose cone can be adjusted for a fine frequency change. A 14 cm X 10 cm capacitive tuning plate can lower the frequency by 0.34% (120 KHz/cm) when the distance between the plate and the outer section of the spiral is changed from 5 cm to 1.5 cm.

Table 3. Sensitivity of the spiral leg and the drift tube

Description	Lower Value	Upper Value	Frequency Change
Spiral leg radius for spiral leg length of 10.4 cm	4.0 cm	6.0 cm	470 KHz/cm
Spiral leg length for spiral leg radius of 4.7 cm	5.4 cm	10.4 cm	100 KHz/cm
Drift tube outer diameter	2.25 cm	2.5 cm	160 KHz/cm
Gap between drift tube and nose cone	3.6 cm	4.6 cm	160 KHz/cm

## 2.3 Coupling Loop

Power will be coupled to this cavity by a coupling loop, which will be located near the root of the spiral. A loop area of 100 cm square is adequate to provide 50  $\Omega$  matching. Couplers of this kind employing tubular ceramic windows, have already being designed and developed at TRIUMF.

## 3 SPIRAL PROTOTYPE

A full-scale prototype was constructed mainly to measure natural frequencies of vibrations and vibration amplitudes with and without water cooling in the spiral. Also, the resonant frequency and the shunt impedance were measured on the prototype. The photograph of the prototype spiral, housed in a rectangular box is shown in figure 3.

The prototype spiral was made of 1/8" thick copper strip. In the center portion of the spiral, the cross section is a

hollow square (3 cm by 3 cm); in the outer portion of the spiral, the cross section is a hollow rectangle (5 cm by 3 cm). The two and half turn spiral is supported at the base by a cylinder. Inlet and outlet for water cooling are provided at the base of the structure. Cooling water enters the structure through a hollow 1/2" copper tube and flows



Figure 3: Photograph of the prototype spiral.

around the hollow body of the spiral before leaving [4]. A Fast Fourier Transform (FFT) analyzer and two accelerometers were used to measure the vibrations of the spiral structure. The natural frequency of the structure was measured by applying an impulse to the spiral when it is filled with water. The vibration amplitude was measured at the drift tube with cooling water running in the spiral. Although, a flow of 6 liters/minute will be adequate to remove the heat dissipated in the spiral, the above tests were conducted with a flow of 10 liters/minute and are shown in Table 4. The vibrations measured up to 200 Hz were much lower than the allowable amplitude of vibration of 20 micron. This limit is from the voltage and the phase stability criteria (see Table 1) of the structure.

Table 4: Vibration measurement with 10 liter/minute water flow.

Axis	Frequency of vibration	Amplitude
x	5 Hz	0.6 $\mu\text{m}$
y	6.5 Hz	0.5 $\mu\text{m}$
z	8.5 Hz	1.7 $\mu\text{m}$
z	60 Hz	0.7 $\mu\text{m}$
x	96 Hz	0.5 $\mu\text{m}$

The power dissipated per unit length of the spiral has been calculated with MAFIA. A spiral length of 20 cm from the drift tube end, has a dissipation of 1 watt/cm and need not be cooled. Figure 4 shows the power dissipated along the spiral and the maximum heat is a few cm away from the junction of the leg and the spiral.

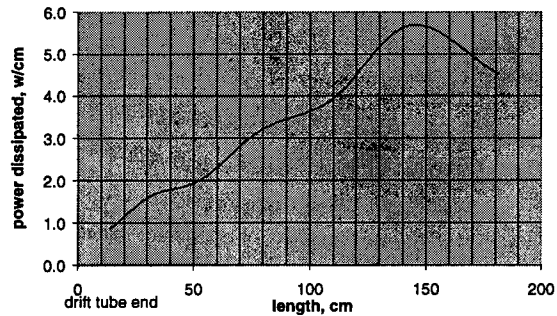


Figure 4: Computed power dissipated in the spiral.

## 4 DISCUSSION

The prototype cavity was built mainly to study the mechanical properties of such a structure. Although the final cavity for the MEBT re-buncher employs a different cooling option and fabrication technique, the mechanical stability should be comparable to the prototype. The cooling pipes are continuous and are soldered to pre-machined grooves on the spiral body. This removes any chance of water leak inside the cavity. The pipes are taken out from the bottom of the tank through rf and vacuum seals. The detail design is in progress with rf power test scheduled to take place by end of this year.

## 5 ACKNOWLEDGMENTS

The authors would like to thank Peter Harmer for providing technical assistance, Alan Wilson for detail drawing and Anson Chan for constructing and measuring the mechanical properties of the spiral. We also wish to thank Guy Stanford for many helpful discussions in the detail design of the MEBT buncher.

## 6 REFERENCES

- [1] R.L. Poirier, et al, "RF Tests on the Initial 2.8 Section of the 8m long ISAC RFQ at TRIUMF", LINAC98, Chicago, USA.
- [2] R.E Laxdal, "The Separated Function Drift Tube Linac for ISAC", TRIUMF Design Note, TRI-DN-ISAC (Feb. 7. 1997)
- [3] J. Hauser, H. Klein and A. Schempp, "Properties of Spiral Loaded Cavities", Proc. Europ. Part. Acc. Conf., Rome, Italy, June 7-11, 1988.
- [4] D.Li, J. Corlett and A.K. Mitra, "A 35 MHz Re-buncher RF Cavity for ISAC at TRIUMF", EPAC 98, Sixth European Particle Accelerator Conference, Stockholm, Sweden, 22-26 June 1998
- [5] A.K. Mitra and A. Chan, "Design Considerations and Measurements of a 35 MHz Spiral Re-buncher Cavity", TRIUMF Design Note, TRI-DN-98-16 (August 1998)

# EXPERIENCE ON THE HIGH-POWER SiC MICROWAVE DUMMY-LOAD USING SiC ABSORBER

H. Matsumoto, KEK; Y. Iino, C. Fujiwara, Z. Kabeya, T. Onda; Mitsubishi Heavy Industries Ltd., Japan

## Abstract

A new type microwave dummy-load using Silicon Carbide (SiC) ceramic, which has an indirect water cooling structure, was successfully operated with up to 50-MW of rf power at a 1- $\mu$ s pulse width and 50-pps repetition rate in the S-band frequency. The input VSWR obtained was less than 1:1.1 at the maximum rf power. The vacuum pressure in the rf-load raised from the base pressure of  $1 \times 10^{-6}$  Pa with no rf power to  $2 \times 10^{-6}$  Pa at the maximum rf-power; and there was found to be no special out gassing from the SiC-ceramics.

## 1 INTRODUCTION

Our first microwave dummy-load using SiC-ceramic was originally developed for an S-band 2.5-GeV electron linac at KEK in 1980, and has been used for 17 years without trouble. The old model SiC-dummy-load used a direct water cooling method, because there was no brazing method available due to the big difference in thermal expansion coefficients of SiC and Oxygen-Free-Copper.

The upgraded version of the S-band dummy-load using brazed rod-shaped SiC pieces for the high peak power microwave absorber was developed in 1993 during the course of R&D for the e-e Japan Linear Collider (JLC). It will be used for the more than 10,000 dummy-loads in the rf system for 500 GeV C.M. version accelerator [1]. Because of the large numbers, increased reliability and cost reduction become very important design considerations. Therefore, I decided to use an indirect water cooling method instead of the previous direct cooling. In 1995 at KEK, the resulting design was tested up to a maximum input rf power of 50 MW, 1  $\mu$ sec pulse width and 50 pps repetition rate.

The new type SiC-dummy-loads have already been in use on the KEKB 8 GeV electron linac (250 pieces) since 1998 [2, 3]; a photograph is shown in Figure1.

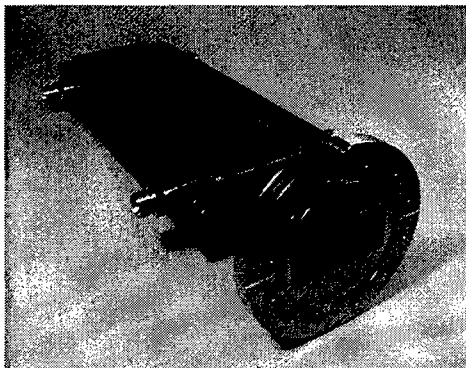


Figure 1: Indirect water cooling type SiC-dummy-load for the KEKB 8 GeV electron linac.

The SiC-ceramic rods are brazed along both narrow

inner walls of the rectangular wave-guide; the overall length is less than 45-cm. Two water channels are welded to both narrow outer walls of the wave-guide.

The final design targets for the dummy-load for the JLC are listed in Table 1.

Table 1: Target specifications of the SiC-dummy-load for the 500-GeV C.M. version of JLC.

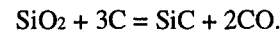
	Achieved	Final goal	
Frequency (MHz)	2856	2856 <sup>1)</sup>	5712 <sup>2)</sup>
Peak input rf power (MW)	50	50	50
RF pulse width ( $\mu$ sec)	1.0	1.0	0.5
RF pulse repetition rate (pps)	50	150	150
Physical length (m)	< 1.0	< 1.0	< 1.0

Note: 1) pre-injector. 2) main linac. Common specifications: in vacuum, indirect water-cooling and within the 1:1.1 of VSWR.

This paper will describe the basic characteristics of the SiC-ceramic and the high power experimental test results.

## 2 BASIC CHARACTERISTICS OF THE SiC CERAMIC

SiC powders can crystallize into either  $\alpha$ - or  $\beta$ -forms. I choose the  $\beta$ -crystallization SiC powder to reduce the variation in microwave loss-tangent after the sintering process. The  $\beta$ -crystallized SiC, which has a good uniformity of powder size is produced by a chemical reaction between silicon-dioxide ( $\text{SiO}_2$ ) and carbon-black (3C) powder at a temperature range of 1500 to 1800  $^{\circ}\text{C}$  in an inert gas atmosphere. The reaction can be expressed as



SiC-ceramic is then made from the SiC power by sintered in a vacuum furnace at a 2100  $^{\circ}\text{C}$  temperature [4]. The basic characteristics of the SiC-ceramic are listed in table 2.

Table: 2 Basic characteristics of the SiC-ceramic.

Density ( $\text{g}/\text{cm}^3$ )	3.14	
Hardness (Knoop, $\text{kgf}/\text{mm}^2$ )	2900	at RT <sup>1)</sup>
Thermal conductivity ( $\text{cal}/\text{cm}\cdot\text{sec}\cdot^{\circ}\text{C}$ )	0.19	at RT <sup>1)</sup>
	0.14	at 600 $^{\circ}\text{C}$
Thermal expansion coefficient ( $^{\circ}\text{C}^{-1}$ )	$4.6 \times 10^{-6}$	RT <sup>1)</sup> to 1200 $^{\circ}\text{C}$
Oxidation weight gain ( $\text{mg}/\text{cm}^2$ )	0.015	at 1200 $^{\circ}\text{C}$ for 24 hours
DC Resistivity ( $\Omega\cdot\text{cm}$ )	$5 \times 10^5$	at RT <sup>1)</sup>
	$7 \times 10^{-1}$	at 800 $^{\circ}\text{C}$
Dielectric constant	30~35	0.5 to 20 GHz <sup>2)</sup>
Loss tangent	0.3~0.5	0.5 to 20 GHz <sup>2)</sup>

Note: 1) RT: Room Temperature, 2) The measured frequency range is limited by the network analyzer.

Figures 2 and 3 show the variations in dielectric constant and loss tangent of some SiC-ceramic samples, for the KEKB dummy-load. This result shows that the variation of both parameters (dielectric constant and loss) are dependent on amount of sintering binders, since the binder is evaporated from the SiC-ceramic during the second sintering process.

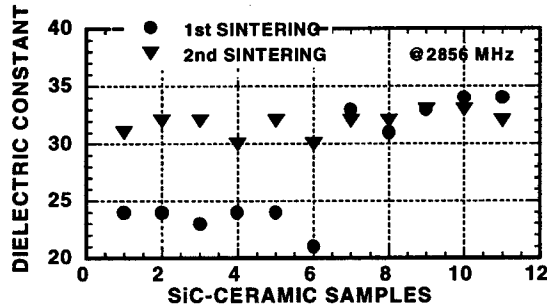


Figure 2: Variations of the dielectric constant of SiC-ceramic samples after one and two sintering cycles.

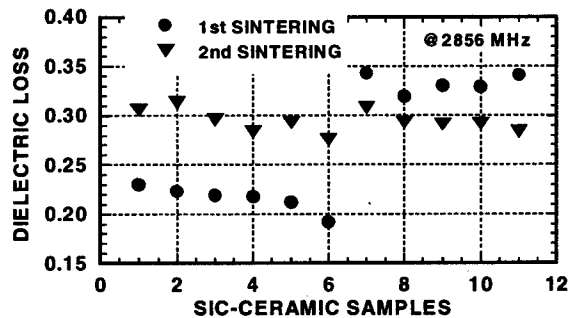


Figure 3: Variations of the dielectric loss of SiC-ceramic samples after one and two sintering cycles.

### 3 DUMMY-LOAD DESIGN

An important design consideration is that the structure be as simple as possible; this includes the shape of SiC-ceramic absorber, housing and cooling structures. I decided to use a conventional S-band rectangular waveguide for the housing, with a 7.21-cm x 3.4-cm cross section and a 5-mm wall thickness. Simple rod shaped SiC-ceramics each 2-cm in diameter were chosen for the microwave absorbers; they are brazed to the inner wall on the narrow side of the wave-guide as shown in Figure 4 [5].



Figure 4: Cut-away view of the SiC-dummy-load. The SiC-ceramic absorbers brazed on the narrow wall (3.4-cm) of the conventional S-band rectangular wave-guide are black in color. All the SiC-ceramic absorbers have the same 2-cm diameter.

The design arrives at a compromise to obtain an input VSWR of less than 1:1.1 while keeping the temperature rise at the top of each SiC-ceramic rod below 30 °C; both at the maximum operation condition (2.5-kW average power). The input VSWR was minimized by adjusting the spacing between the SiC-ceramic rods using a simple quarter-wave impedance matching method as shown in Figure 5. It was still necessary to experimentally tune the SiC positions to minimize the input VSWR of below 1:1.1. Figure 6 shows typical characteristics of the reflection coefficient (S11) as a function of the distance between SiC-ceramic rods.

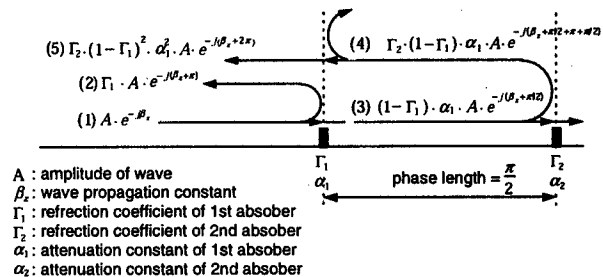


Figure 5: Principle of quarter-wave impedance matching method for locating the SiC-ceramic absorbers. The second reflection wave between SiC-ceramic rods is ignored because the amplitude is already very small.

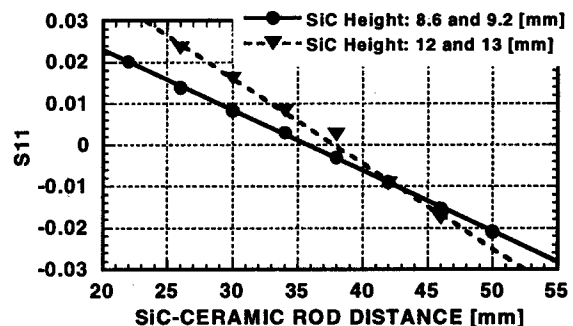


Figure 6: Variation of the reflection coefficient (S11) as a function of the distance between SiC-ceramic rods. The zero cross point in S11 appears roughly a quarter-wave length at 2856-MHz. Position sensitivity on the SiC-ceramic height is due to superimposition of the large reflection vectors.

We calculated the temperature rise between bottom and top of the SiC-ceramic absorbers using steady state thermal conducting theory based on an attenuation curve along the axis of the dummy-load and the measured rf power loss per cubic centimeter of ceramic absorber.

Figure 7 shows the first high-power model S-band dummy-load. A total of 28 SiC-ceramic rods are brazed to the narrow walls of the rectangular wave-guide housing. Two water channels attach to both narrow walls and the typical flow rate for the cooling water is 20 liters per minute. In this case, the maximum temperature raise at each top of the SiC-ceramic rod is below 30 °C at 2.5-kW average rf power. In actual operation, the inlet water temperature is around 30 °C, so that the absorber rod temperature will be increased to close to 60 °C. Good frequency response was obtained in low power measurements as shown in Figure 8.

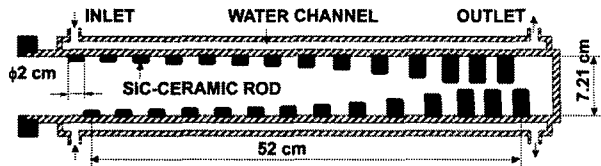


Figure 7: End and Side cut-away views of the SiC-dummy-load. The SiC-ceramic absorbers are the black objects brazed on the narrow side (3.4-cm) of the conventional S-band rectangular wave-guide. All SiC-ceramic absorbers have the same 2-cm diameter.

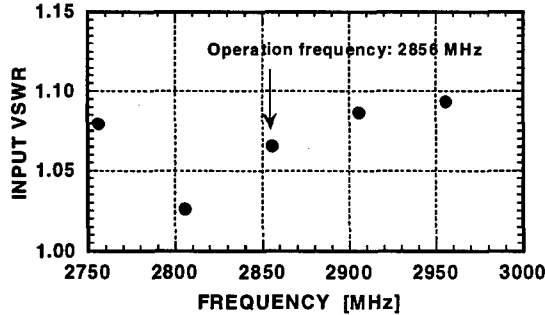


Figure 8: Over-all frequency response of a high power SiC-ceramic dummy-load measured at low power level.

## 4 EXPERIMENTAL RESULTS

Figure 9 shows the high power test stand for the dummy-load. It is comprised of an S-band 80-MW klystron system, connecting wave-guide system and vacuum pumping system. The base vacuum pressure of  $1 \times 10^{-6}$  Pa was achieved by an ion-pump. A cold cathode gauge (CCG) was used in the vacuum interlock system during rf test.

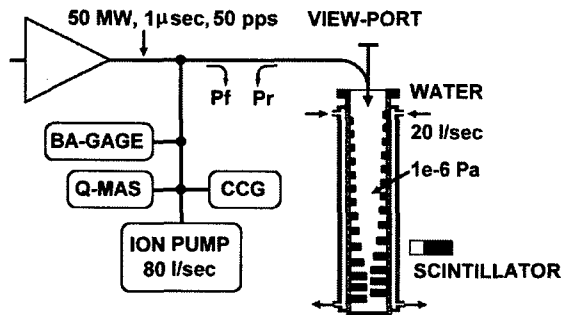


Figure 9: High power test stand of SiC-ceramic dummy-load.

The high power operation was carried out while monitoring the vacuum pressure, x-ray signal and rf power levels at various points in the system. The forward rf power from the klystron and reflected rf power from the SiC-dummy-load were measured with two Beth-hole couplers. The x-ray signal as measured by a scintillator was used to monitor discharge breakdown in the dummy-load. A viewing port was also used to observe visual conditions, such as frequent discharging.

After a total operation time of 100 hours, the input rf power was increased to 50-MW with a 1 μsec pulse width and 50-pps repetition rate as shown in Figure 10. As can be seen, the reflected rf power is only 98-kW, which corresponds to an input VSWR of around 1:1.1 at the maximum operating specification for this model [6].

Further there was no breakdown signal from the scintillator. At this time, the vacuum pressure of  $2 \times 10^{-6}$  Pa was achieved during rf power turn on.

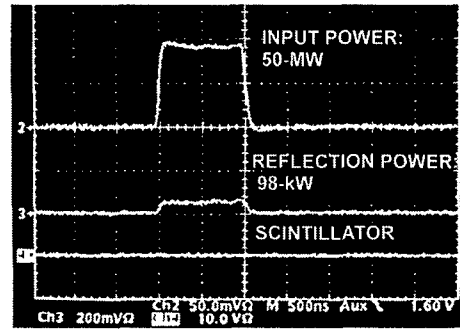


Figure 10: A typical waveforms of the SiC-dummy-load high power test 50-MW, 1-μsec and 50-pps.

The temperature sensitivity of the SiC-ceramic absorber was studied by measuring the input VSWR as a function of cooling water flow rate as shown in Figure 11. It is clear that the SiC-ceramic absorber is not sensitive to its temperature of operation.

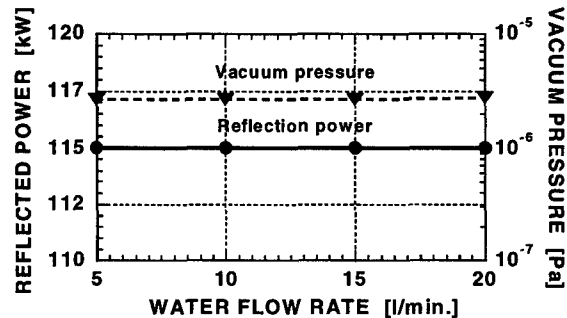


Figure 11: Temperature sensitivity check of the SiC-ceramic type high power dummy-load at 2856-MHz.

## 5 CONCLUSIONS

We have confirmed the design and operation of a new type high power dummy-load using SiC-ceramic absorber. The load is improved in using an indirect cooling method to increase reliability. The first model was successfully operated at 50-MW of rf power (1-μsec and 50-pps for a 25-kW average power). Thus, we may conclude that this SiC-ceramic dummy-load can provide the same reliability as the conventional metal type load.

## 6 REFERENCE

- [1] H. Matsumoto, "Application of the SiC-ceramic for Microwave Absorber" (in Japanese), Proc. of the Linac Meeting in Japan, 1983.
- [2] JLC group, "JLC-1", KEK Report 92-16, December, 1992.
- [3] Y. Igarashi, S. Yamaguchi and A. Enomoto, "Development of a Dummy-load", KEK Report, 98-12.
- [4] R. Enomoto, "SiC powders for the Sintering material", internal report (in Japanese) of IBIDEN Co., Ltd., 1982.
- [5] S. Morita and H. Matsumoto, "Development of the S-band High Power RF load" (in Japanese), Proc. of the Linac Meeting in Japan, 1995.
- [6] W. H. Hwang et al., "High Power rf performance Test of an Improved Load", Proc. of International APAC98, Japan, 1998



# BEAMLINE RF LOAD DEVELOPMENT AT CORNELL\*

E. Chojnacki<sup>†</sup>, Cornell University, Ithaca, NY  
W. J. Alton, Ferrite Components Inc., Hudson, NH

## Abstract

Details of design and fabrication of a beamline RF load suited to accommodate SRF cavities are presented. Bonding an RF absorber to a heat sink is the key aspect of the load. Production loads have been effectively tested to 10.8 kW and operated *in situ* up to 3 kW.

## 1 INTRODUCTION

Many new and proposed accelerator facilities are forging frontiers in beam intensity. The degree of intensity is relative to each type of accelerator (circular, linear, CW, pulsed) and the applications range from high energy physics with diminishing event cross sections to brighter and shorter wavelength light sources to nuclear transmutation drivers. One consequence of high beam intensity is increased excitation of destructive higher-order RF modes (HOM's) in the accelerating structure. RF feedback can damp these instabilities to a certain extent, but aggressive resistive damping is required to avoid inordinate feedback power levels.

The superconducting RF (SRF) program at Cornell has long anticipated the need for ever-increasing beam intensity [1]. The large aperture, low-impedance, and high  $Q$  of SRF cavities are ideally suited to intense beams. Modest tailoring of the beampipe near an SRF cavity iris allows all HOM modes to leak out of the cavity and propagate down the beampipe. It was thus natural to place HOM RF loads directly on the beampipe in close proximity to the SRF cavity [2]. The current Cornell HOM load design has been effectively tested up to 10.8 kW per load, with two loads typically associated with each cavity [3]. SRF cavities requiring less aggressive HOM damping utilize a coaxial antenna coupled to the beampipe.

Fabrication of beamline HOM loads can be challenging, the most difficult task being bonding RF absorbing material to a heat sink. For this reason, the Cornell design evolved to modular panels containing the RF absorbing element. The panels are individually prepared, tested, then installed into a beampipe as shown in Fig. 1. Described below are materials, processes, and tests required to fabricate an HOM load developed over several years at Cornell with numerous instances of outside consultation.

## 2 RF ABSORBER

The close proximity of the load to the accelerating cavity places numerous demands on the load, particularly the RF absorber, as stipulated in Ref. [2]. Among commonly known RF absorbing materials, two that satisfy beamline requirements are unbiased ferrites, such as nickel-zinc, and

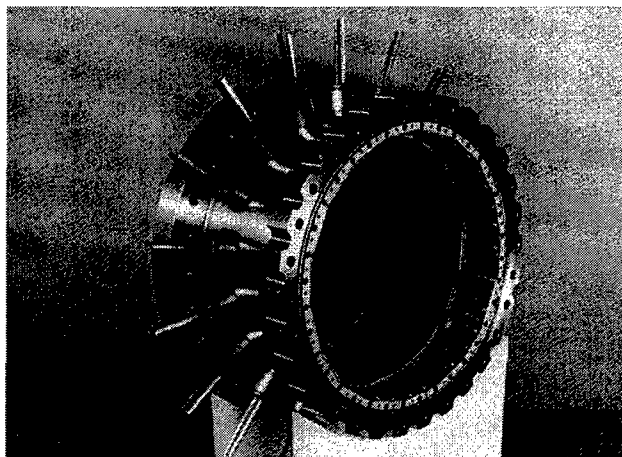


Figure 1. A Cornell HOM load.

lossy dielectrics, such as silicon carbide. Ferrites have the advantage of complex permeability  $\mu$  as well as complex permittivity  $\epsilon$ . Complex  $\mu$  is necessary since the absorber located on the wall must have strong interaction with the magnetic field characteristic of most HOM's.

A ferrite satisfying beamline requirements and having an absorption frequency range covering the CESR III SRF cavity HOM spectrum is identified in Ref. [4], although other manufacturers of similarly acceptable ferrites exist. Complex  $\mu$  and  $\epsilon$  of such materials have been determined by thorough measurement [5].

## 3 BONDING AND HEAT SINK

Heat generated by RF in the ferrite must have a high-conductance thermal path to a sink. Thus the ferrite must have a high-conductance bond to a cooled, good thermal conductor.

### 3.1 Soldering

Bonds based on adhesives satisfy neither ultra-high vacuum nor thermal conductivity requirements, and simple mechanical clamping has insufficient thermal conductivity. One of the best bonds from a thermal conductance point of view is to apply a metal plating to the ferrite and solder it to a water-cooled metal substrate. Unfortunately, therein lies a problem fundamental to ceramic bonding: the ferrite's coefficient of thermal expansion is about half that of copper or other solderable metals, causing the ferrite to readily fracture during the soldering thermal cycle or when heated by RF in service. Further, soldering must be performed fluxless to preserve the porous ferrite's ultra-high vacuum integrity.

Successful solder bonds can indeed be accomplished between plated ferrite and copper if the copper is thoroughly annealed (>800°C in a vacuum furnace) prior

\* Work supported by NSF and DOE STTR Grant No. DE-FG02-96ER86049.

<sup>†</sup> Email: epc1@cornell.edu

to soldering, conferring it a very low mechanical yield point. However, the "dead-soft" copper *must not be work hardened*, in even the slightest fashion, forever thereafter. Otherwise, the induced mechanical stress in the copper will fracture the ferrite the first time it is heated.

### 3.2 Elkonite

Obviously, a heat sink material with thermal expansion coefficient similar to ferrite avoids these thermal expansion problems. The material must also be solderable and preferably have a low mechanical yield point to forgive slight differences in thermal expansion or work hardening. The only candidate found to date is a material called Elkonite [6]. Elkonite is made by sintering tungsten to a specified porosity, then filling the refractory metal with molten copper to form a nearly fully dense, vacuum-tight body. The final coefficient of thermal expansion is approximately the volume average of the composites, the available ratio 58% W and 42% Cu nearly matching ferrite's nominal  $9 \times 10^{-6} / ^\circ\text{C}$ . Beside thermal expansion matching, Elkonite is rugged and much more tolerant than Cu to rough handling. In its delivered form, Elkonite does not wet as well to solder as pure Cu, thus it is electroplated with 0.001" of Cu onto its surface. This layer of Cu being very thin and fully annealed (from the braze step described in Section 3.4) does not negate Elkonite's desirable properties. The electroplater should be aware that Elkonite is sintered and the plating operation must not allow it to disintegrate in the acid solution [7].

### 3.3 Ferrite Tile Geometry

Once bonded, a ferrite tile heated by RF is mechanically stressed so as to convex the exposed face, also known as a "crowning". The peak mechanical stress familiarly occurs near corners of rectangular tiles, and ferrite fractures experienced with Cu heat sinks predominantly originated in corners. Peak stress is minimal in a *circular* ferrite tile and is reduced by rounding the corners of a rectangular tile. The smaller the diameter of a circular tile, the lower the accumulated thermo-mechanical stress, and the higher the allowable absorbed RF power density. A lower limit in tile diameter is set by having to prepare and solder more tiles to obtain a desired surface area, especially given the typical 75% yield of successful solder bonds as discussed in Sections 4.1 and 5.

### 3.4 Coolant Interface

The next link in the heat-sink circuit is coolant. For the modular load shown in Fig. 1, cooling water flows in a copper tube brazed to the face of the Elkonite opposite the ferrites. Naturally, the difference in thermal expansion between Cu and Elkonite warps the Elkonite during the high temperature braze as well as the low temperature ferrite solder. Thus, the brazing and soldering fixtures must incorporate rigid clamping of the Elkonite to minimize warping. The cooling tube braze is performed in a vacuum furnace, using Cusil as filler with a 780°C eutectic liquidus, typically heated to 820°C with a 10 minute soak at temperature. After the braze, the assembly is tamped onto a flat surface to restore Elkonite flatness prior to ferrite soldering. The sintered W and annealed Cu

easily yield, yet do not causing work-hardening problems encountered with pure Cu.

## 4 FERRITE PROCESSING

Ferrite tiles are typically cleaned with alkaline solution by the manufacturer, and upon delivery ultrasonically cleaned in methanol baths, 6 cycles of 15 minutes each with changing of the methanol between cycles. Tests showed that after the 3rd ultrasound bath, no more particulate leaves the ferrite of Ref. [4]. The ferrites are then fired in air with 100°C/hr ramp up to 900°C, 2 hr soak at 900°C, and 100°C/hr ramp down. Air firing reduces later vacuum outgassing and is reputed to help homogenize the ferrite.

### 4.1 Plating

The ferrites are next plated with a solderable material. Since nickel is a primary constituent of ferrite, it was reasoned that sputtered Ni would have good adhesion. A problem with this plating has been spots of complete "scavenging" off the ferrite by the molten solder. In Cornell HOM load production, about 25% of ferrite solders exhibit scavenging problems. The thicker the plating the less scavenging is observed, but sputtering is a slow process and too thick a plating builds surface tension that may shear the ferrite. Nickel-vanadium can be sputtered at a higher rate than pure Ni, thus to date Cornell production has targeted 25000 Å of Ni-V.

A promising alternate plating is a layered approach whereby 300 Å of titanium is first sputtered, then a 2000 Å graded layer of Ti and Cu (requiring two sputter guns), then 5000 Å of pure Cu, ending with a gold flash to inhibit oxidation [8]. The reasoning behind this plating is that Ti adheres very strongly to the ferrite, the Ti-Cu composite retains Cu from scavenging, then the Cu wets well to solder though some may be scavenged. There have not been statistically significant tests of the Ti-Cu graded plating to date, but a few samples have soldered well.

### 4.2 Soldering

From thermal stress considerations, ferrite soldering is performed at as low a temperature as possible while providing a safety margin from solder melting during HOM load operation. The majority of Cornell soldering has used 90% Sn / 10% Ag filler having a 221°C solidus and 295°C liquidus. The 0.004" Sn-Ag foils are sandwiched between the ferrite and Elkonite, then heated to 370°C in a vacuum furnace with several intermediate soaks and a 10 minute soak at temperature. Generous spacing among fixtures prevents shadowing of radiative heat transfer, providing uniform fixture temperatures. There is no gas backfilling of the furnace, the slow cool (>8 hrs) allowing the solder to noticeably crystallize, with loose flakes later removed by wire brushing. Tests with argon and nitrogen gas backfilling after the heat cycle have yielded very poor bonds, with nearly all the Ni-V plating being scavenged and the ferrite readily falling off. Perhaps the gas backfill enables such a good bond to Ni-V that the plating is completely cleaved off the ferrite, and vacuum cooling with crystallization simply yields numerous

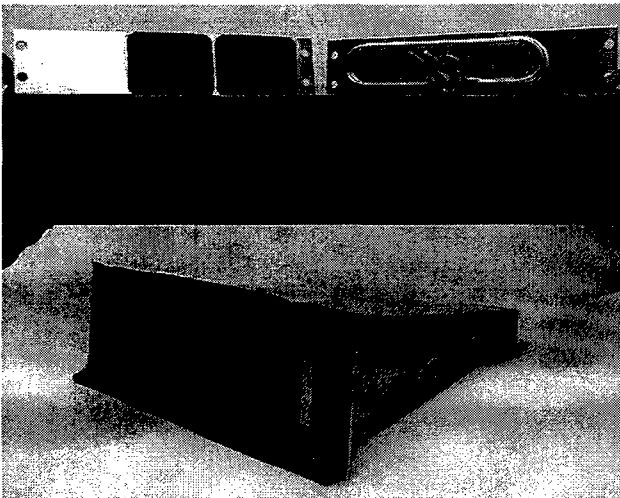


Figure 2. HOM load individual panel test setup.

islands of adhesion. Details of such chemistry and mechanics remain to be studied.

An alternate solder filler is 80% Au / 20% Sn with a 280°C eutectic liquidus. Au-Sn wets better than Sn-Ag, although the foil is less malleable at the outset. There have not been statistically significant tests of the Au-Sn filler to date, and among a few samples one case had a poor bond. Thus, the added expense of Au remains to be justified.

## 5 RF TESTS

Individual panels of Elkonite with bonded ferrite are tested in an RF setup pictured in Fig. 2. The panels are mounted on a broad wall of WR-284 waveguide, fed by up to 1 kW CW at 2450 MHz by a magnetron, with a sliding short downstream to adjust the standing wave along the ferrite. Water flows through the cooling tube at 0.6 GPM. The panels are viewed with an infra-red camera through a hole in the opposite wall of the waveguide, covered by a screen and RF evanescent cone, also shown in Fig. 2. Areas of poor solder bond are evident by heating in excess of the standing wave pattern as seen by the IR camera, an example of which is shown in Fig. 3. Thermal transients at turn-on and turn-off of RF are also excellent diagnostics, areas of even slightly poor solder bond showing thermal lag.

The RF power in the test is typically limited to 600 W, corresponding to an average power absorption density of 15.5 W/cm<sup>2</sup> on each of two 5.08 cm × 3.81 cm × 0.32 cm ferrite tiles. The RF standing wave pattern scanned over the ferrite raises regions up to twice this power density, but such inhomogeneous heating probably also occurs in service [9]. With 18 such assemblies per load, the assembled unit is effectively tested up to 10.8 kW average HOM power, and two loads are connected to each SRF cavity [3]. The upper limit in absorbed power density for a few test assemblies has been 25 W/cm<sup>2</sup>, at which point the ferrite cracked. This power density could be raised by use of circular tiles with small diameter and a broader cooling tube attachment. As

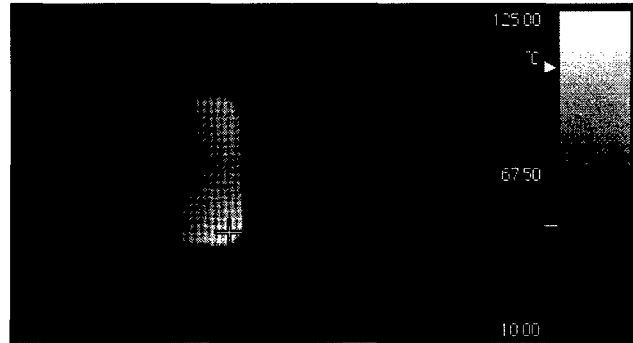


Figure 3. Infra-red image from the test setup exhibiting a hot area due to poor solder bond. The grid pattern is due to the screen covering the waveguide hole.

mentioned in Section 4.1, 25% of the panels are rejected due to "hot spots", later diagnosed as scavenged plating.

## 6 FINAL ASSEMBLY

Elkonite/ferrite panels that pass the RF test are inserted into a stainless steel beamline housing as shown in Fig. 1. The panels are tightly fastened with screws to provide good electrical grounding to accommodate beam image wall currents. Direct interaction of beam fields with the ferrite has been demonstrated to be negligible [10]. Brazed fittings that incorporate the cooling tubes for each assembly are then welded into the steel housing to provide a vacuum-tight enclosure. The finished unit is rinsed with methanol, the screws temporarily loosened, and the unit vacuum baked at 150°C for several days. After baking, the room temperature vacuum bottoms out at  $<10^{-9}$  T. Upon HOM load attachment to the SRF cavity beamline, the panel screws are re-tightened. Performance of six such prepared loads has been quite satisfactory, dissipating up to 3 kW per load to date [3].

## 7 REFERENCES

- [1] M. Tigner, "Imperatives for Future High Energy Accelerators", *AIP Conf Proc* 279, *Advanced Accelerator Concepts* (Port Jefferson, NY, 1992), p. 1.
- [2] D. Moffat, et. al., "Design and Fabrication of a Ferrite-lined HOM Load for CESR-B", *Proc. 1993 Part. Accel. Conf.* (Washington, DC, 1993), p. 977.
- [3] S. Belomestnykh, et. al., "Commissioning of the Superconducting RF Cavities for the CESR Luminosity Upgrade", *these proceedings*.
- [4] C-48, Countis Industries, Carson City, NV, (775) 882-6123.
- [5] W. Hartung, et. al., "Measurements of the Microwave Properties of Some Absorbing Materials", *Proc. Workshop on Microwave-Absorbing Materials for Accelerators* (Newport News, VA, 1993), p. 162.
- [6] 10W3 Elkonite, CMW Inc., Indianapolis, IN, (317) 634-8884.
- [7] Anoplate Corp., Syracuse, NY, (315) 471-6143.
- [8] JP Argana Contract Services, Caledonia, NY, (716) 538-4682.
- [9] B. Vakoc, "HOM Spectra and Dissipated Power Density Profiles for the SRF Cavity with a Ferrite HOM Load", *Cornell LNS Report SRF 950811-11* (1995).
- [10] W. Hartung, et. al., "Measurement of the Interaction between a Beam and a Beam Line Higher-Order Mode Absorber in a Storage Ring", *Proc. 1995 Part. Accel. Conf.* (Dallas, TX, 1995), p.3294.

# A NON-RESONANT RF CAVITY LOADED WITH AMORPHOUS ALLOY FOR PROTON CANCER THERAPY

Y. Makita<sup>#</sup>, H. Harada, T. Nagayama, H. Tsuchidate, C. Tsukishima, and K. Yoshida

Mitsubishi Electric Corporation

8-1-1 Tsukaguchi-Honmachi, Amagasaki, Hyogo 661-8661, Japan

## Abstract

A non-resonant rf cavity loaded with amorphous alloy cores has been designed and tested. The cavity has a re-entrant structure loaded with 8 amorphous alloy toroidal core and its characteristic impedance is designed as 450  $\Omega$ . The rf power is fed by 1 kW solid state amplifier using a step-up transformer with 1:9 impedance ratio. In the high power test, an accelerating gap voltage of more than 900 V was measured with input power of 1 kW in the frequency range of 1 to 10 MHz. The voltage standing wave ratio (VSWR) was less than 2.0. The results prove that the cavity may be used successfully within a compact proton synchrotron for a cancer therapy facility.

## 1 INTRODUCTION

Cancer is the leading cause of death. In fact, more than one in four die of cancer at present in Japan. Use of the proton beam in cancer therapy is a promising mode of treatment because of its ability to selectively destroy cancer cells while causing minimum damage to the surrounding healthy tissues. At present, research in proton and ion beam cancer treatment is being pursued at several institutions in Japan.

At Mitsubishi Electric, we have been developing a cancer treatment facility based on the proton synchrotron. It is required that such a system be easily operated without the assistance of accelerator experts. Low cost and compactness are also important features for widespread use in the hospital environment.

Because of such considerations, a non-resonant cavity [1] is the natural choice for the accelerating system since the need for a tuning element is eliminated, leading to a substantial reduction in the system complexity. The performance of such a cavity is determined to a large degree by the choice of the core which loads the gap. We chose an amorphous material having a large magnetic permeability, high saturation flux density and a high Curie temperature in order to attain a high gap voltage and stability against the heat load.

We have constructed such a cavity and performed high-power tests to measure its properties such as the impedance, accelerating voltage and temperature rise during operation. In this paper, we discuss the design features of this cavity along with the results of these measurements.

<sup>#</sup>Email: yo@wel.crl.melco.co.jp

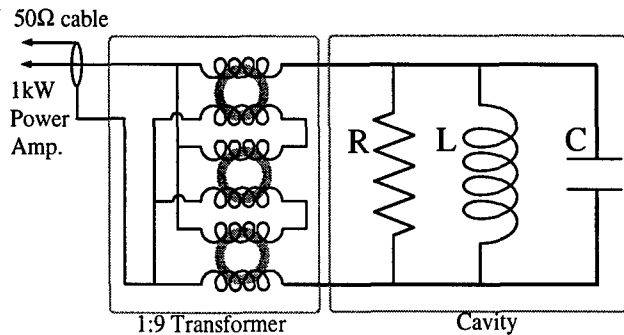


Figure 1 The circuit diagram of the RF system

## 2 RF CAVITY

Figure 1 is a circuit diagram of the RF system including the RF cavity, the power amplifier and the transformer. The cavity is described as a parallel resonant circuit with impedance  $Z_{cav}$  given by the following equations;

$$\frac{1}{Z_{cav}} = \frac{1}{R} + \frac{1}{j\omega L} + j\omega C \quad (1)$$

where,

$$R = \frac{|\mu|^2}{\mu'} \omega L_0, \quad L = \frac{|\mu|^2}{\mu''} L_0, \quad C = C_g$$

$$\mu = \mu' - j\mu''$$

$\mu'$  = the real part of the complex permeability

$\mu''$  = the imaginary part of the complex permeability

$L_0$  = the inductance of the cavity with no core

$C_g$  = the capacitance of the cavity

To design a non-resonant cavity, it is desirable to keep the absolute value of the complex impedance flat in the operating frequency range. This is accomplished by using the magnetic property of the core material above the Snoek's limit. i.e. in this region both the real and imaginary parts of the magnetic permeability falls inversely with frequency, hence the first two terms in equation (1) becomes independent of frequency. Furthermore, a high value of permeability is also preferred from the point of view of power economy.

In the past, the ferrite core has been commonly chosen as the loading material [2]. However, by selecting an amorphous material it is possible to obtain a higher permeability and at the same time a higher saturation flux density and a higher Curie temperature. Thus the amorphous core is suited in fabricating a more compact cavity.

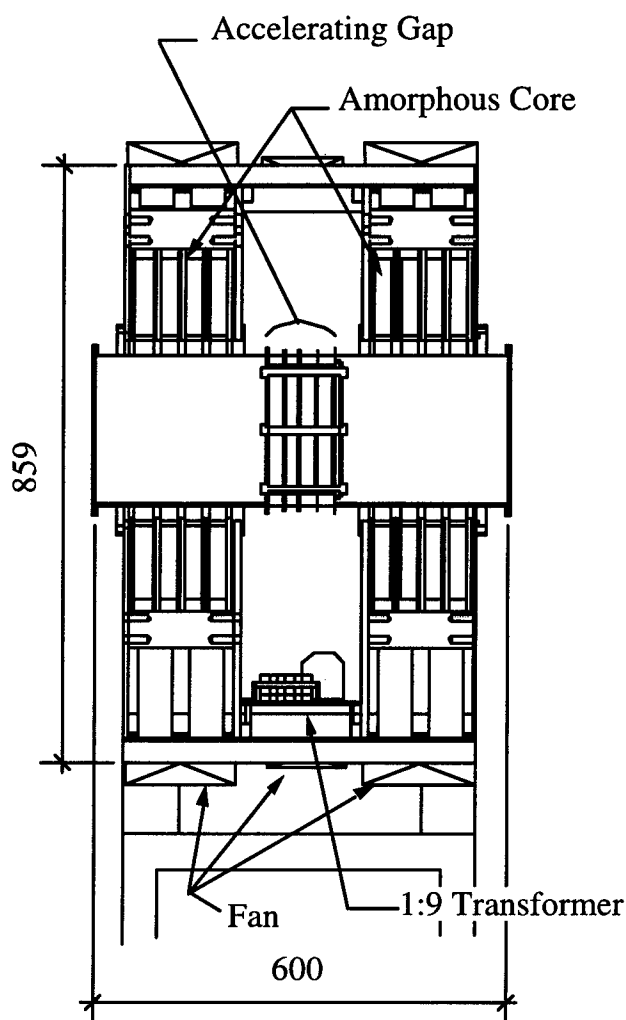


Figure 2 The schematic diagram of the RF cavity

The schematic diagram of the cavity is shown in Figure 2. The cavity has a single accelerating gap in the middle, consisting of two quarter-wavelength coaxial resonators each loaded with four amorphous cores. The design parameters of the cavity are summarized in Table 1.

Since the amplifier has a driving impedance of  $50 \Omega$ , a step-up transformer with a 1:9 impedance ratio was used to match to the cavity impedance [3].

Table 1 Design specifications of the cavity

operation frequency	1 - 10 MHz
cavity impedance	450 $\Omega$
accelerating voltage	900 V
disipated power	1 kW
cavity dimension	H:830
[mm]	L:600
	W:700
duct dimension	$\phi$ : 216
[mm]	L:600
amorphous core	$\phi$ in: 270
[mm]	$\phi$ out:487
	t:25.5
number of cores	8

### 3 MEASUREMENTS

The fabricated cavity was not intended for testing under vacuum. Hence MC Nylon was used as the accelerating gap, rather than ceramic. The gap length was made variable but kept at 92 mm for all measurements described here. The total cavity length was required to be 600 mm or less by the circumference of the synchrotron.

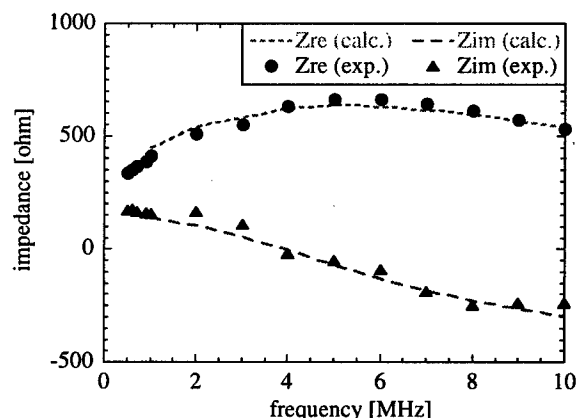


Figure 3 The complex impedance of the cavity

The complex impedance of the cavity was measured with a network analyzer. The result is given in Figure 3. The data are compared to a calculation using lumped circuit approximation. A good agreement is obtained between measured and calculated results in all cases.

To confirm that the transformer works properly, the impedance was measured with a  $450 \Omega$  resistor load connected to the transformer. The results are shown in Figure 4.

A high-power test was performed using a 1 kW solid-state amplifier. For the measurement, high voltage probes were directly attached to both sides of the gap. An accelerating gap voltage of more than 900 V was obtained in the frequency range of 1 to 10 MHz as shown in Figure 5. A good agreement is obtained between measured and calculated results.

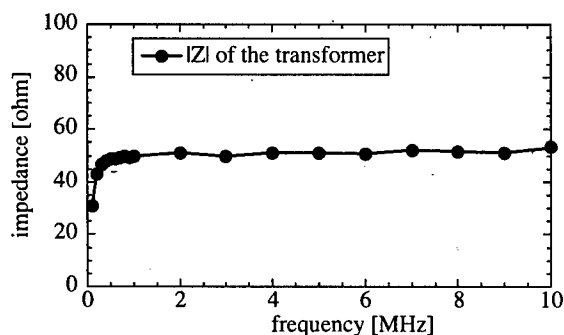


Figure 4 The impedance of the transformer

VSWR was measured with a power meter during the high-power test. The frequency dependence of the VSWR is given in Figure 5. The measured VSWR was lower than 1.9 throughout the frequency range, which corresponds to less than 10 % reflected power from the cavity.

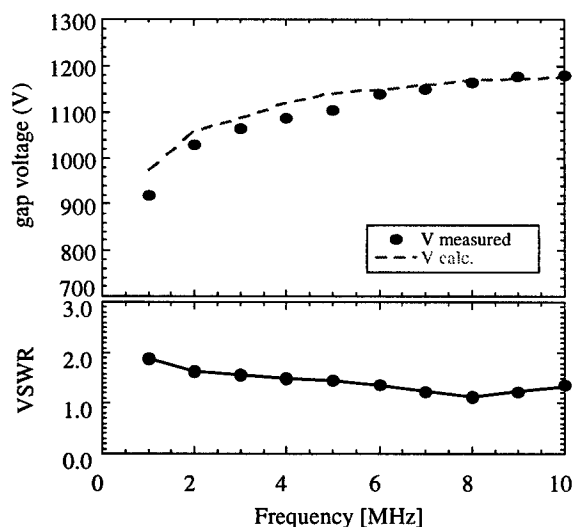


Figure 5 The accelerating voltage and VSWR of the cavity

A heat-up test was also performed. The temperature was monitored with thermocouples attached to the surface of the amorphous core of the cavity and to the ferrite core of the impedance matching transformer during a high-power operation which lasted for one hour. The measured data are shown in Figure 6. Due to forced air cooling with 8 fans for the amorphous cores and 4 small fans for the ferrite cores, the temperature increases were as small as 14 deg C and 10 deg C respectively.

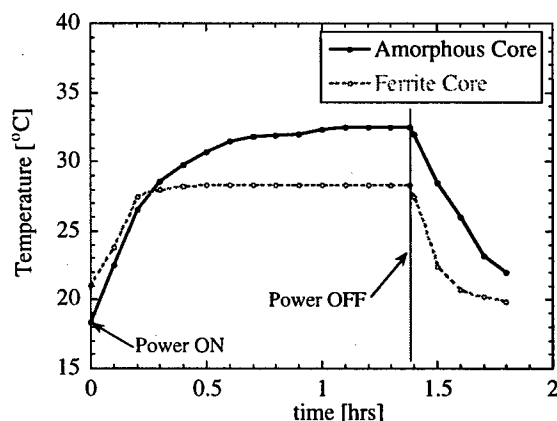


Figure 6 The temperature of amorphous core of the cavity and ferrite core of the transformer

## 4 CONCLUSION

A non-resonant cavity loaded with amorphous cores has been fabricated and tested. An accelerating gap voltage of more than 900 V was measured with a 1 kW amplifier in the frequency range of 1 to 10 MHz. The reflected power from the cavity was confirmed to be less than 10 % for a measured VSWR of less than 1.9. The temperature rise was observed to be less than 15 deg C at the surface of the amorphous and ferrite cores, indicating that magnetic saturation in the core material will not be a problem.

## 5 ACKNOWLEDGEMENT

The authors are grateful to Eiji Ezura and Shigeshi Ninomiya of KEK for the valuable advice they provided in carrying out this project.

## 6 REFERENCES

- [1] K. Muto et al., "Ferrite Loaded Untuned RF Cavity for Synchrotron", Proc. of the 1989 Particle Accelerator Conference.
- [2] T. Nagayama, "A Prototype Non-Resonant RF Cavity for a Medical Synchrotron", Proc. of Multi-GeV High-Performance Accelerators and Related Technology, p.230, Osaka, March 1997.
- [3] S. Ninomiya, "Conceptual Design of a Non-Resonant Accelerating System for Low-Energy Proton and Heavy-Ion Accelerators", KEK Report, 92-2, April 1999

# BROADBAND SYNCHROTRON CAVITY FOR COSY WITH MINIMUM SIZE BASED ON VITROPERM

M. Böhnke, F.-J. Etzkorn, R. Maier, U. Rindfleisch, A. Schnase\*, H. Stockhorst,  
Forschungszentrum Jülich GmbH, IKP, D-52425 Jülich

## Abstract

A cavity design that deviates from conventional rules of RF engineering is presented. Preliminary studies in collaboration with SATURNE [1] and TERA [2] were carried out to employ the amorphous material VitroVac for a cavity with reduced size. The idea to use a nano-crystalline material instead of an amorphous one was stimulated by KEK where metglass is applied [3]. The analysis led to the magnetic material VitroPerm 500F, resulting in a reduced cavity size as compared to the existing one. Now, new space becomes available in COSY for additional equipment used for a polarized proton beam.

The cavity is optimized for operation at the Cooler Synchrotron COSY [4]. The frequency ranges from 400 kHz to 2 MHz without any tuning device. No gap-capacitors and no cooling discs are necessary. The VitroPerm is directly water cooled. Together with the fundamental higher harmonics (2nd or 4th), adjusted in real time in amplitude and phase, can be applied to bunch or to accelerate with non-sinusoidal voltages [5].

## 1 MOTIVATION OF MATERIALS DIFFERENT FROM FERRITE

The ferrite-filled cavity being in operation at COSY is about 2.1 m long and occupies space in one of the telescopes that will be needed for a (partial)-snake to optimize acceleration of polarized protons. The ferrite cavity has to be tuned to the actual revolution frequency and only works with sinusoidal voltages. In collaboration with SATURNE we worked on a shorter cavity (1.4 m) filled with the amorphous material VitroVac 6025F. This cavity operates from 0.2 to 8 MHz and allows the application of higher harmonics together with the fundamental frequency. With such a cavity we have performed rf-gymnastics without beam to show the feasibility of the cavity for applications like:

- improved capture of injected beam
- acceleration at different harmonics
- $\gamma$ -transition crossing
- stochastic cooling of bunched beams
- high power shaped noise for stochastic extraction in seconds.

However, a significantly shorter design is possible by filling another cavity with the high permeability material

VitroPerm 500F, shown in figure 1. The total length is about 780 mm, where 212 mm account for the vacuum gap. The 6 VitroPerm toroids per side are placed directly in water, avoiding the use of cooling plates. The broadband nature of this cavity eliminates tuning loops and allows the application of higher harmonics and noise. The impedance will be high enough to reach a maximum rf-amplitude of 5 kV (2.5 kV for each half of the structure) with an rf-power of less than 50 kW. The disadvantages are related to the water bath: A protection against corrosion is needed, the cavity has to be protected against too high water pressure, and the purity of the water is important.

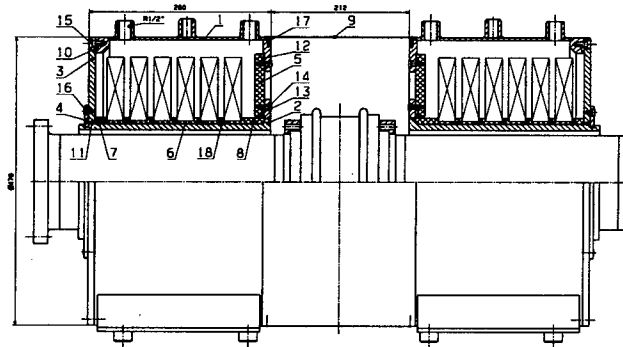


Figure 1: Layout of the broadband cavity

### 1.1 Technical details of figure 1

The housing (1) of 470 mm diameter is made of 5 mm stainless steel to stand the water pressure. The inner structure (2) is separated from the beam pipe to allow modifications without breaking the vacuum. The VitroPerm toroids are mounted on POM (DELIN®-acetyl-resin)-carriers (6) which reduces the capacitance to ground and enables high voltage operation. Circular windows (5), oriented to the gap serve as barrier between water and the air-filled outer area of the gap. The flow of the cooling water will be from bottom to top. We expect 25 kW to be dissipated per side, resulting in a water flow of about 20 l/min.

### 1.2 Measurements with samples

We compared small toroids of VitroVac and VitroPerm. The size and the initial permeability at DC are listed in table 1. The value for the toroids foreseen is estimated.

\* email: A.Schnase@fz-juelich.de

Table 1: Sample specifications

	VitroVac 6025F	VitroPerm W531-51	VitroPerm W468-51	foreseen in cavity estimate ()
sample	A		B	
$\phi_i$ / mm	35	50	76	200
$\phi_a$ / mm	72	80	102	400
h / mm	25	20	25	25
L / nH	3.336	1.739	1.361	(3.2)
$\mu_r$ at DC	90000	30000	80000	80000
L/mH at DC	0.300	0.052	0.109	(0.25)

Low level impedance measurements were carried out with a network analyser HP 8751A. Figure 2a shows the impedance as a function of frequency for one VitroVac toroid (sample A) connected with a one-turn loop. This sample was tested at higher rf-power to reach temperatures of 100 °C in water. The coupling loop was driven by an ENI-A500 amplifier. The rf-power resulting in an amplitude of 200 V is displayed in figure 2b. We observed no substantial change in impedance as temperature rises. Therefore we expect a good safety margin in operation between 20 to 50 °C.

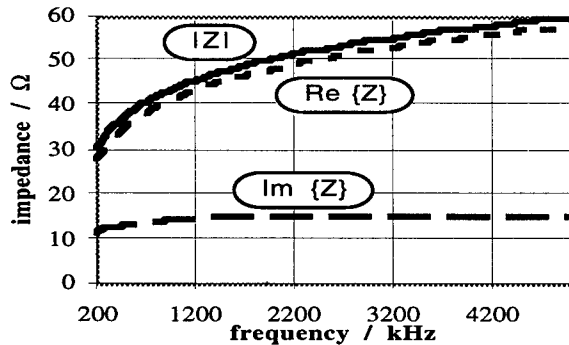


Figure 2a: Impedance measurement of VitroVac sample A

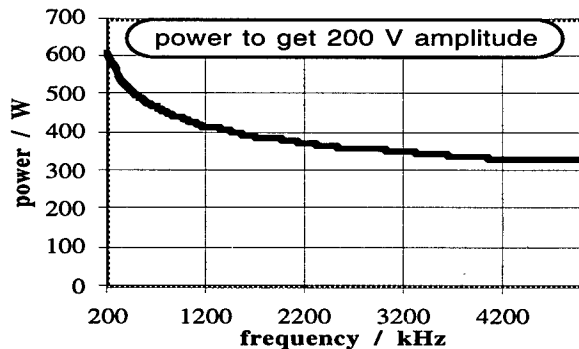


Figure 2b: Power measurement of VitroVac sample A.

In figure 3 the impedance of a combination of 4 VitroPerm sample toroids B in a test structure is plotted. The arrangement of 6 toroids per side in the final cavity guarantees the heat transfer to the cooling water and results in a higher impedance. The scaled result is sufficient for 2.5 kV amplitude. The estimated power per side is displayed in figure 4.

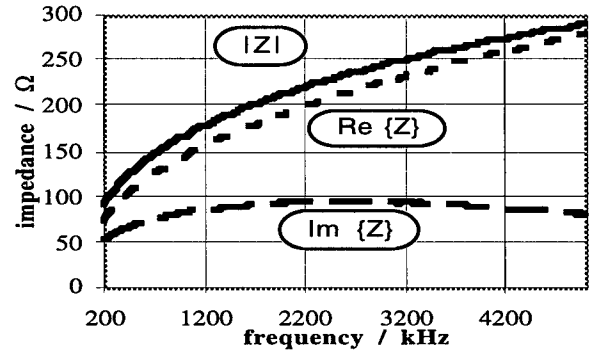


Figure 3: Impedance measurement with four samples B.

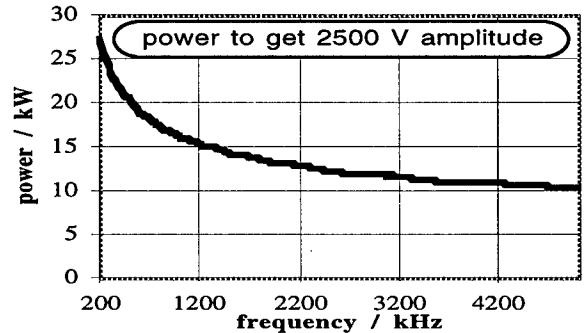


Figure 4: Estimated power from impedance measurement.

### 1.3 Application of higher harmonics

The suitability of the cavity for higher harmonics is proven by a setup where a signal composed of a fundamental at 500 kHz and two harmonics drives an amplifier AR 15A250 directly connected to the test-structure with four toroids. The broadband behavior is clearly visible in figure 5: the upper trace is the pre-distorted generator signal and the lower trace the voltage at the structure measured with a 1:10 probe.

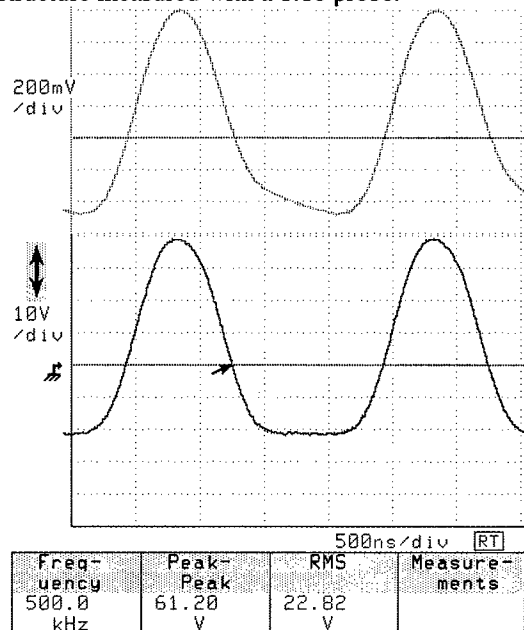


Figure 5: Waveform with a flat top, power ≈ 4W.



## 2 SIGNAL GENERATION

A dedicated synthesizer [6] generates the higher harmonics for the measurement of the behavior of the VitroPerm in time domain. It has been upgraded to perform a synchronous sweep with the nonlinear frequency ramp of COSY while preserving the shape of the waveform. The Fourier components are controlled in real time. Figure 6 depicts the structure of signal generation. The hardware is installed in 2 VME-crates. One of the crates contains a communication CPU and 7 DSP boards which generate the digital set values of the different harmonics as a function of time. The amplitude is controlled with a DAC that drives an analog multiplier. The frequency word is fed to a numerical oscillator (NCO) that generates the clock  $16 \cdot f_{\text{rev}}$  for the Lookup-tables, the 16 bit complex multipliers and the DAC, where  $f_{\text{rev}}$  varies between 0.4 MHz to 1.6 MHz. The amplitudes of the higher harmonics are much lower than the fundamental. Therefore the signal of the DACs is fed to attenuators, to keep the signal-to-noise ratio of 12...14 bit, which results in -70dBc when measured.

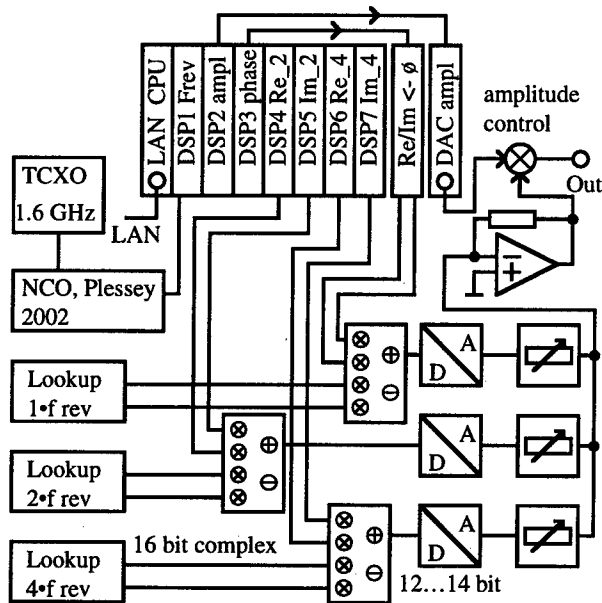


Figure 6: Layout of agile signal synthesis

## 3 INSTALLATION PROCEDURE

The preparation of the installation of the cavity is on its way. In the end of June 99 we expect to have the structure and the material available. We will test the cavity performance at low level and stress the structure to find out the influence of water pressure. We will find out, if the impedance, influenced by the capacitance of the water - some 100 pF - is high enough, or if we have to rearrange the position of the cores inside the water tank.

Due to the compact size and small weight of the cavity and the material, the setup is mobile. We therefore plan to

perform first power measurements at the test bed of the VitroVac cavity at CERN. When we know the power requirements (50...100 kVA), we will install the tube amplifier in the „eye“ of the COSY-ring. The anode power supply will be specified to minimize operational cost. In the mean time we use the anode power supply of the existing tube amplifier to feed the amplifier of the broadband structure. If the new cavity performs as expected, we install it in the target telescope in a way that allows to switch between the ferrite cavity and the higher harmonic cavity in reasonable time. A Klöckner-Möller SPS will control the power supplies and check for error and fault conditions. The locations of the existing ferrite cavity and the new one in COSY are sketched in figure 7.

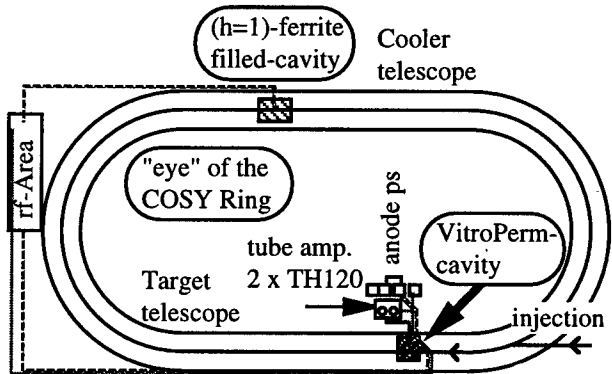


Figure 7: Locations of the rf-systems in the COSY-ring.

## 4 OUTLOOK

An interesting question will be the connection of the amplifier to the cavity gap. Depending on the installation, a distance of 3 to 7 m has to be bridged with an coaxial air filled transmission line of 200  $\Omega$  impedance.

With both cavities operational this year, we have new opportunities in modifying the longitudinal phase-space. We will find out, if the cavity will perform as expected to replace the existing one, which then acts as a backup.

## 5 REFERENCES

- [1] P. Ausset et. al. „A Broad-Band (0.2 - 8 MHz) Multiple-Harmonic VITROVAC®-Filled Acceleration Structure“, EPAC94, Berlin
- [2] A. Schnase et. al. „Higher Harmonic (VitroVac) Cavity: Measurement results with the Prototype“, IKP Annual report 1997, Forschungszentrum Jülich GmbH
- [3] Y. Mori et al. „A new type of RF cavity for high intensity proton synchrotron using high permeability magnetic alloy“, EPAC98, Stockholm
- [4] H. Stockhorst et. al. „The Performance Of COSY“, EPAC 98, Stockholm
- [5] H. Stockhorst „Longitudinal Beam Dynamics in a Multiple Harmonic RF-System“, IKP Annual report 1994, Forschungszentrum Jülich GmbH
- [6] F.-J. Etzkorn et. al. „Towards a cavity for higher harmonics“, IKP Annual report 1994, Forschungszentrum Jülich GmbH

# MEASUREMENT AND SIMULATION RESULTS OF Ti COATED MICROWAVE ABSORBER

Ding Sun and David McGinnis

Fermi National Accelerator Laboratory\*, Batavia, IL 60510

## Abstract

Microwave absorbers are coated with resistive thin films. S parameters are measured before and after coating. The measured data are used to check the simulation results of software HFSS which are in good agreement with the measurement results.

## 1 INTRODUCTION

At Fermi lab anti-proton cooling system, ferrite materials are to be put on walls of beam lines to absorb unwanted microwave signals. A layer of resistive coating can change the distribution of electromagnetic fields and affect attenuation of the signals. In order to study such effect, microwave absorbers (Ni-Zn ferrite) were coated with titanium thin film and put into a waveguide (see Figure 1.) S parameters were measured before and after coating.

The combination of thin layers of ferrite material with large variation of magnetic loss tangent and resistive surface boundary composes a challenge to the simulation software used for designing microwave system. Therefore measurement results have been used to check the simulation results from commercial software HFSS (High Frequency Structure Simulator.) These results can also be used to confirm the correctness of permittivity and permeability parameters measured by us.

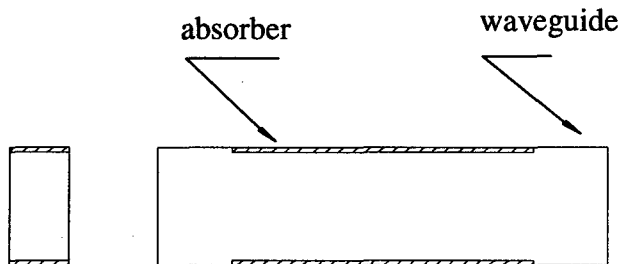


Figure 1. Configuration of absorbers and a waveguide

## 2 SAMPLE DESCRIPTION

Nickel-Zinc ferrite samples (TT2-111 from Trans-Tech Inc.) were cut into rectangular shape (0.795 in x 1.98 in). Sixteen pieces were grounded to 0.065 inch thick and

eight pieces were grounded to 0.125 inch thick. Samples were divided into 6 groups. Half of these samples (group 4 - 6) were sputtered with Ti at Fermilab, and half of them (group 1 - 3) were sputtered with Ti at Thin Film Technology Inc., California. Samples in each group (4 pieces with same thickness) were coated together. The goal of the coating was to achieve surface resistance of 210 - 270  $\Omega$ /square. The thickness of Ti thin film coated at Fermilab (Group 4 - 6) is 137A°-141A°. The corresponding surface resistance is 210 -260  $\Omega$ /square. The thickness of Ti thin film coated at Thin Film Technology Inc. (Group 1 - 3) is ~216A°. The corresponding surface resistance is 216 -252  $\Omega$ /square. These parameters are listed in Table 1.

Table 1: Surface resistance of coated absorbers

Group #	Thickness of Absorber	Thickness of Ti film	Surface Resistance $\Omega$ /square
1	0.065"	216 A°	230-240
2	0.065"	216 A°	216-252
3	0.125"	216 A°	230-240
4	0.065"	137 A°	240-260
5	0.065"	141 A°	210-230
6	0.125"	141 A°	210-230

Since the coating is very thin, the resistivity of these films is sensitive to the parameters of sputtering process such as purity and mixture of gas, sputtering rate and kinetic energy of the sputtered target particles. This can be seen in samples made by both Fermilab and Thin Film Technology Inc. This fact can also contribute to the thickness difference of Ti films made at Fermilab and Thin Film Technology Inc. However, thickness difference of ~80 A° does not matter since the surface resistance is the only factor to be considered.

In order to see the stability of these thin films, surface resistance was measured immediately after coating and re-measured 7-10 days later. There was no significant change.

Permittivity, permeability and loss tangent of TT2-111 material and other ferrite materials were measured at Fermilab. To measure these parameters, a ferrite material was machined into a rectangular slab (1.59" x 0.795") to fit into a section of WR-159 waveguide (area of the cross section is 1.59" x 0.795".) Cables and coax-waveguide

\* Operated by the Universities Research Association under contract with the U. S. Department of Energy

adaptors were calibrated using TRL (Thru-Reflect-Line) method. The S parameters were measured using a network analyzer (HP 8510.) The real and imaginary part of permittivity and permeability were deduced from measured  $S_{11}$  and  $S_{21}$  parameters with a computer program [1][2]. These parameters are listed in Table 2 and used in simulation discussed later.

Table 2: Permittivity/permeability of absorber

Freq. (GHz)	$\epsilon_r$	Loss tangent (E)	$\mu_r$	Loss Tangent (M)
5.0	12.83	0.025	0.0155	137.2
5.2	12.83	0.027	0.0322	63.25
5.4	12.83	0.027	0.0547	35.66
5.6	12.87	0.027	0.0797	23.24
5.8	12.89	0.027	0.0906	19.59
6.0	12.92	0.029	0.1058	15.95
6.2	12.95	0.031	0.1187	13.47
6.4	12.92	0.033	0.1281	11.96
6.6	12.92	0.030	0.1288	11.29
6.8	12.93	0.031	0.1328	10.54
7.0	12.92	0.031	0.1361	10.05

### 3 MEASUREMENT RESULTS

S parameters were measured before and after resistive coating using a 6" long waveguide (WR159) and a network analyzer (HP8510.) Four pieces of absorbers (a group) were measured each time. Absorbers were put inside of the waveguide (against inner surfaces of two narrow sides of the waveguide, two pieces of samples on each side, see Figure 1.) The measured S parameters of un-coated absorbers with same thickness of 0.065" are very close to each other: deviation of  $S_{21}$  from mean value of group 1,2,4 and 5 (listed in Table 1) is less than 3%. After coating with Ti thin film, each group of absorbers was measured again. The measured S parameters of coated absorbers with same thickness are still close to each other, though the deviation of  $S_{21}$  from mean value of the 4 groups increased to less than 5% which was due to the variation of surface resistance.

Since the results are close to each other, only two groups' results are presented here. Shown in Figure 2 and 3 are the measured  $S_{21}$  and  $S_{11}$  parameters for group 1 (samples with thickness of 0.065 inch.) Shown in Figure 4 and 5 are the measured  $S_{21}$  and  $S_{11}$  parameters for group 3 (samples with thickness of 0.125 inch.) All results show that attenuation of microwave signals was decreased after resistive coating. The decreases of attenuation depended on the thickness of samples: the thicker samples' attenuation decreased more since thicker samples occupied more space where the electric field was stronger.

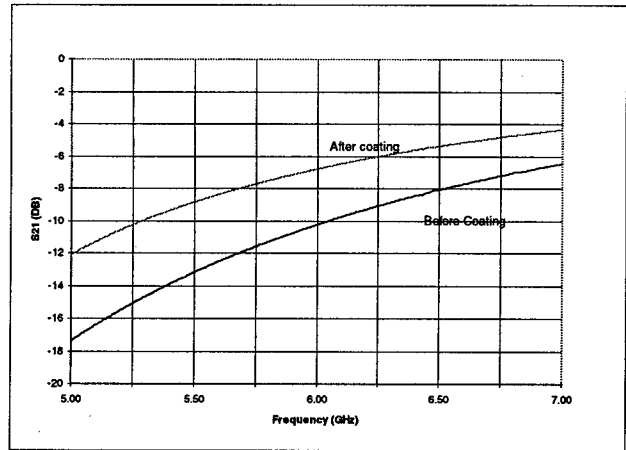


Figure 2.  $S_{21}$  of group 1 (sample thickness: 0.065")

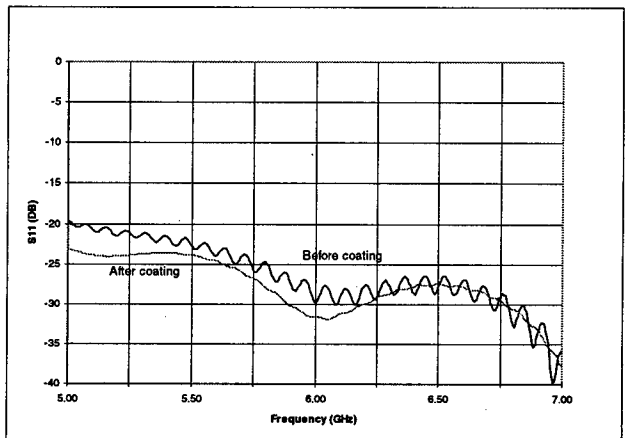


Figure 3.  $S_{11}$  of group 1 (sample thickness: 0.065")

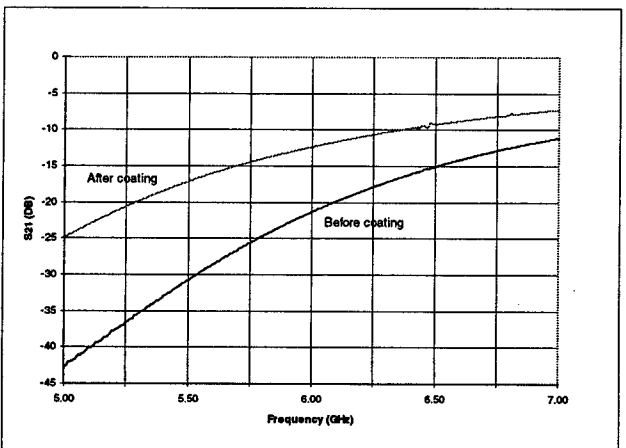


Figure 4.  $S_{21}$  of group 6 (sample thickness: 0.125")

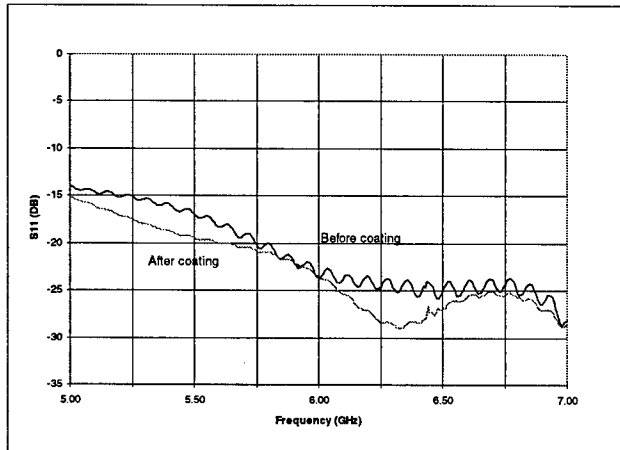


Figure 5.  $S_{11}$  of group 6 (sample thickness: 0.125")

#### 4 SIMULATION RESULTS

Commercial software HFSS is extensively used for designing microwave components at Fermi lab. In order to check the capability of this software dealing with complex permittivity and permeability, large loss tangent, resistive surface boundary conditions and relatively large geometry ratio between different materials (area of the cross section of WR159 waveguide is 1.59"x0.795" while the thickness of the absorbers is 0.065"), simulations were performed using software HFSS from Ansoft corporation (v.6 beta.) In simulations, thickness of absorbers was 0.065 inch and surface resistance was 235 ohm/square. Therefore the simulation results should be compared with the measured results of group 1. Since HFSS does not have the capability to change permittivity and permeability with frequencies during a simulation, simulations were performed at 11 single frequencies. At each frequency, permittivity, permeability and loss tangent were set to the measured value listed in Table 2. In this way the software is more accurately evaluated since the meshes are refined at the same frequency and the permittivity/permeability parameters are the true value at that frequency. The convergence criterion of simulation was set to 0.001 for  $\Delta S$ . Shown in Figure 6 and 7 are simulation results. As a comparison, the measured data are also plotted ( $S_{11}$  data of "Before coating" has been smoothed out at each frequency by averaging adjacent 20 points.) These figures show that the simulation results are in excellent agreement with the measured data.

This result also indirectly prove that the measured complex permittivity and permeability parameters (used in simulation) are reliable. (Since the real part of permeability of such ferrite can be close to zero, extra care has to be taken during the measurements and data extraction of these E-M parameters. Therefore an extra prove of those data is always a good practice.)

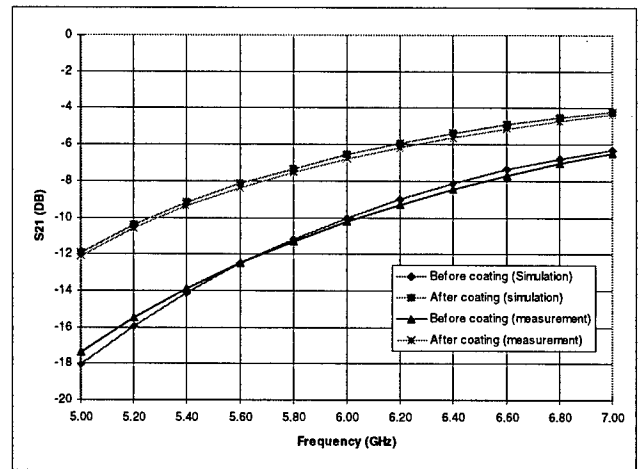


Figure 6.  $S_{21}$  of Group 1 (simulation and measurement)

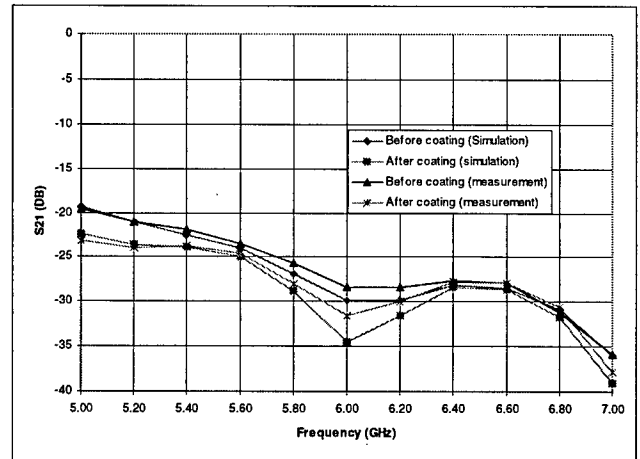


Figure 7.  $S_{11}$  of Group 1 (simulation and measurement)

#### 5 ACKNOWLEDGEMENT

We thank Eileen Hahn for her technical support and titanium thin film sputtering.

#### 6 REFERENCES

- [1] David McGinnis, Fermilab PBAR NOTE No. 594
- [2] Ding Sun, Fermilab PBAR NOTE No. 599

# MAGNETIC ALLOY LOADED RF CAVITY FOR BARRIER BUCKET EXPERIMENT AT THE AGS\*

M. Fujieda<sup>†</sup>, Y. Iwashita and A. Noda, Kyoto University, Gokanoshio, Uji 611, JAPAN

Y. Mori, C. Ohmori and Y. Sato<sup>‡</sup>, KEK-Tanashi, 3-2-1 Midori-cho, Tanashi 188, JAPAN

M. Yoshii, KEK, 1-1 Oho, Tsukuba 305, JAPAN

M. Blaskiewicz, J. M. Brennan, T. Roser, K. S. Smith, R. Spitz and A. Zaltsmann,  
BNL, Upton, NY 11973, USA

## Abstract

A magnetic alloy(MA) loaded cavity which was developed by KEK was used for the barrier bucket experiment at the AGS. The MA loaded cavity could generate a single sine-wave of 40kV with less RF power than a ferrite loaded cavity because of its broad-band impedance. In order to reduce the voltage induce by beam, the feedforward system was applied and the beam loading was compensated. With the barrier bucket scheme, five bunches were transferred successfully. Total of  $3 \times 10^{13}$  protons were accumulated without beam loss. They were re-bunched by the accelerating cavities and accelerated.

## 1 INTRODUCTION

A Magnetic Alloy(MA) loaded cavity[1, 2] has been developed. The cavity was installed in the AGS for the barrier bucket experiment. It was the first experiment for the MA loaded cavity to be tested in synchrotron. The beam loading and the method to cure it were important issues. The cavity and the RF amplifier worked stably. The beam loading compensation system was established.

The barrier bucket experiments[3, 4] were performed to increase the intensity at the AGS. Two barrier cavities were used to generate a fixed barrier and moving one. Both cavities generated a single sine-wave of 40kV at the repetition rate of 351kHz. The former is the MA loaded cavity, the latter is a ferrite loaded cavity modified by BNL. This paper describes the MA loaded cavity and the barrier bucket experiment.

## 2 BARRIER CAVITY

### 2.1 MA Loaded Cavity

The peak current to generate a single sine-wave for a LCR circuit on resonance is represented as follows,

$$I_{peak} = \frac{V}{R}(1 + Q).$$

If the impedance is given, the system with lower Q value can generate a barrier voltage with less RF power. The KEK barrier cavity is loaded with MA cores, FINEMET. The cores have large inductance and low Q value. A push-pull amplifier is suitable to drive an MA loaded cavity be-

cause the waveform of the drive signal is bipolar.

The impedance seen by beam is  $3.6k\Omega$  and the Q value is 0.6. Accordingly the MA loaded cavity has large R/Q as  $6k\Omega$ . The voltage induced by high intensity beam is not negligible and a compensation is necessary for the cavity.

The cavity has 4 gaps and it generates a barrier voltage of 10kV per gap. Two 30kW tetrodes are used for the RF power amplifier[5]. A 2kW solid-state amplifier is employed for the drive amplifier. An arbitrary function is applied for the drive signal. Figure 1 shows the barrier voltage and the RF bucket.

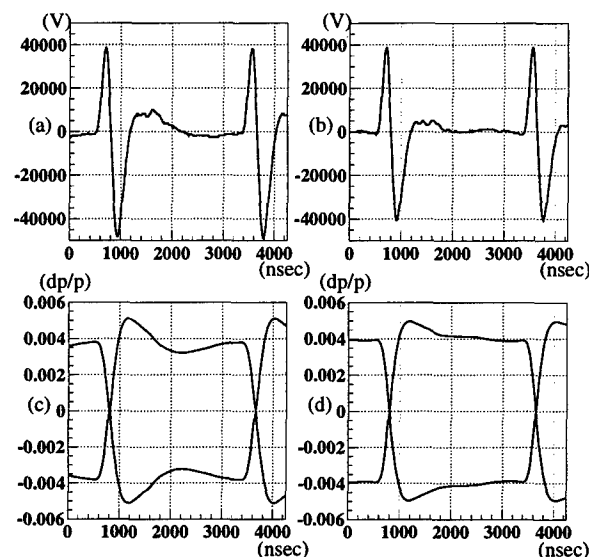


Figure 1: The gap voltage(a),(b) and the RF bucket(c),(d). The waveform(a) was used in the experiment. The waveform(b) was improved to achieve a flatter RF bucket(d) by a drive signal modification and the overshoot is expected to disappear by mixing several harmonics.

### 2.2 Feedforward System

If the beam signal is fed to the broad-band RF amplifier, the beam induced voltage can be canceled[6]. The feedforward[7] scheme was applied for the compensation of the beam loading. The frequency responses of the beam monitor, cables and the grid circuit of the amplifier are important because the Q value is low and R/Q is large. The cavity is suitable for the feedforward scheme, because all parameters are stable against the temperature rise or the beam loading. It is easy to add a compensation signal, because the time response of the cavity to the signal is fast.

\* Work supported by Department of Energy

<sup>†</sup> Email: miho@tanashi.kek.jp

<sup>‡</sup> also : Japan Steel Works Co. Ltd.

Figure 2 shows the schematic feedforward system. The beam signal was picked up by the wall current monitor. The signal was split into three because of the frequency dependence of the grid circuit and the cable used for delay. Then they were filtered by three types of the filters: low-pass( $h=1$ ), band-pass( $h=2$ ) and high-pass( $h\geq 3$ ) filters. The phase and amplitude of each Fourier component of the gap voltage were adjusted independently. The signal was delayed for one revolution period after the beam passed the cavity. It was because the feedforward path was longer than the beam traveling time from the monitor to the cavity.

The induced voltages per gap with or without the feedforward are shown in Figure 3. It can be seen that the amplitude of the induced voltage decreases to 1/9 effectively. The system worked stably.

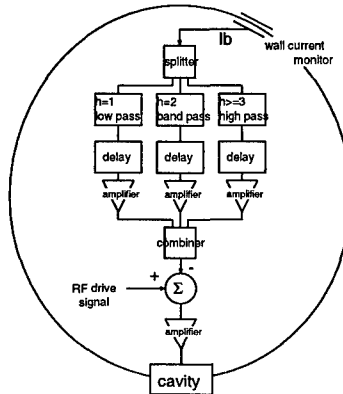


Figure 2: The feedforward system. The revolution frequency is 351kHz.

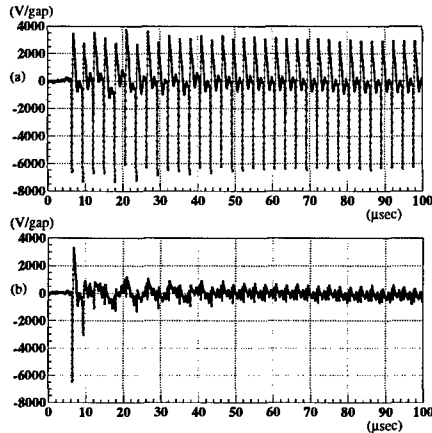


Figure 3: The induced voltages per gap without(a) or with(b) feedforward. The horizontal axis is time. The vertical one is voltage per gap. The beam intensity was  $8.2 \times 10^{12}$  protons per bunch and one bunch was circulating.

### 3 BARRIER BUCKET

#### 3.1 RF Gymnastics

The barrier cavity has to play two important roles during injection with barrier bucket. The first barrier create a flat RF potential in the longitudinal phase space to keep the beam gap. The second one performs RF gymnastics to accept and accumulate the injected beam. The BNL and KEK

cavities took parts of the former and latter, respectively.

One of the barriers is moved to expand the injected beam. This debunch method with using barriers is called as "adiabatic debunch". After debunching, the moving barrier is turned off. It is turned on again at the same phase as the fixed barrier and moved to make the space for next injection. The next bunch is injected into the longitudinal space. Then it debunched adiabatically by the moving barrier, while the stored beam is compressed. The moving barrier is turned off when their momentum spreads become equal. Thus the stored beam and the injected one merge. If those processes are repeated adiabatically, the total emittance of bunches is conserved and beam can be injected as much as the limit of the longitudinal acceptance.

The RF gymnastics were optimized not to cause beam loss and leakage from RF bucket. Figure 4 shows the gymnastics of barriers in case of transfers of five bunches.

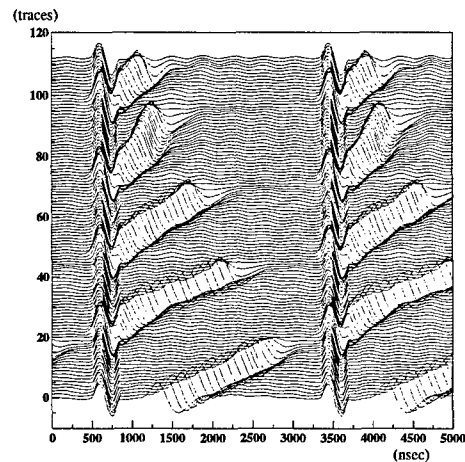


Figure 4: The mountain range plot of the barrier voltages. The interval of the traces is 5.8msec.

#### 3.2 Adiabatic Debunch

The sweep speed of a barrier should be slow enough to satisfy the adiabatic condition to conserve the emittance. The time for sweep, however, is limited by the AGS Booster cycle of 150msec

The adiabatic condition was studied measuring the momentum spread by Schottky signal, to determine the longitudinal emittance. The measurement was done varying the barrier speed with one transfer. The initial phase gap between two cavities was  $77^\circ$  which was wider about 3 times than the bunch width. The phase gap was spread to  $315^\circ$ . The result is shown in Table 1.

In case of the sweep time longer than 100msec, the minimum momentum spread was achieved. The results agree with the fact that if the barrier is swept as slow as 10 times of the debunching time, the momentum spread after debunch is minimized. The longitudinal emittance grew 2~3 times. It has been considered to be mainly due to the longitudinal mismatch. The potential distortion also seems to relate with it.

Table 1: The momentum spread by "adiabatic debunch".

sweep time (msec)	momentum spread(%)	
	$(\frac{dp}{p})_0=0.30\%$	$(\frac{dp}{p})_0=0.44\%$
0	0.30	0.44
25	0.24	
50	0.16	
100	0.13	0.11
150	0.13	
300	0.12	

### 3.3 Spacing

The initial RF bucket should be matched with the bunch width not to cause the longitudinal mismatch. On the other hand, it should be wide enough to avoid that the injection kicker disturbs the circulating beam. The initial phase gap between the barriers was optimized observing beam loss. There was no beam loss by the kicker when the phase gap was wider than 770nsec, which was consistent with the kicker pulse width. However this phase gap width was much wider than the typical bunch width of 200nsec, which should have degraded the emittance. Actually when the phase gap was narrow, smaller emittance was achieved.

### 3.4 Re-bunch and Acceleration

Total of  $3 \times 10^{13}$  protons were accumulated successfully. The beam intensity of the first bunch was  $6.4 \times 10^{12}$  protons per bunch. After five bunches were transferred, the gaps of the barrier cavities were shorted and the accumulated beam debunched freely. The beam was re-captured by the accelerating cavities of the harmonic number of 6, which voltage was ramped up linearly. After the re-capture it was accelerated. There was a beam loss at the gamma jump because of the large longitudinal emittance. The emittance after re-bunching by harmonics of 6 was 5.5~7.0 eV s per bunch, which grew about 3 times. During the re-bunching and the acceleration, no emittance growth nor beam loss was observed. Figure 5 shows the accumulation of 5 bunches and re-bunching.

## 4 CONCLUSION

An MA loaded cavity has been developed for the barrier bucket experiment. It can generate a single sine-wave of 40kV by the 60kW RF amplifier. The feedforward system to compensate the induced voltage worked successfully. The cavity was suited to barrier bucket due to its operational flexibility.

The barrier bucket experiment has been accomplished with both the MA loaded cavity and the modified AGS RF cavity. The RF gymnastics with the two barrier cavities was established and worked well. The five bunches were transferred. Total of  $3 \times 10^{13}$  protons were accumulated without beam loss. Then they were re-bunched and accelerated by the accelerating cavities even though the longitudinal emittance grew.

Following reasons are considered to produce the emittance growth.

- Longitudinal mismatch
- Potential distortion
- Snap off of the barrier by the high Q cavity

The first one seems be major reason. The improvement of the injection kicker will be helpful to decrease the emittance growth caused by the longitudinal mismatch. A special barrier gymnastics also enables to reduce the mismatch. The KEK barrier distorted the RF potential with its overshoot in the waveform. The overshoot has almost disappeared by mixing several harmonics for the drive signal[8] and this scheme can be applied to the cavity. The feedback or feedforward system will help to cancel the induced voltage at the BNL barrier cavity. Amplitude modulation of the BNL cavity will also reduce emittance growth.

## 5 ACKNOWLEDGMENT

We would like to thank all members of AGS and KEK-Tanashi RF group for their great helps.

## 6 REFERENCES

- [1] Y. Mori et al., Proc. of EPAC 98, p1796, Stockholm, (1998).
- [2] M. Fujieda et al., Proc. of APAC 98, Tsukuba, (1998).
- [3] M. Blaskiewicz et al., in this conference.
- [4] M. Blaskiewicz and J. M. Brennan, Proc. of EPAC 96, p2373, Barcelona, (1996).
- [5] Y. Sato et al., Proc. of APAC 98, Tsukuba, (1998).
- [6] Y. Hashimoto et al., Proc. of EPAC 98, p1770, Stockholm, (1998).
- [7] P. Barratt et al., Proc. of EPAC 90, p949, Nice, (1990).
- [8] C. Ohmori et al., in this conference.

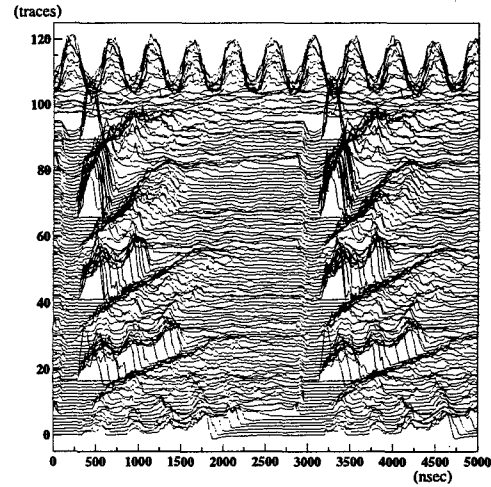


Figure 5: The mountain range plot of the wall current monitor. The interval of their traces is 5.8msec.

# BEAM LOADING EFFECTS ON HIGH GRADIENT MA-LOADED CAVITY

M. Yamamoto\*, M. Fujieda, Y. Hashimoto, Y. Mori, R. Muramatsu,  
C. Ohmori, Y. Sato, A. Takagi, T. Uesugi, M. Yoshii KEK-Tanashi, Japan

## Abstract

We studied the beam loading effects on the High Gradient Cavity(HGC) loaded with Magnetic Alloy(MA) by multi-particle tracking simulation. The Q-Value of the cavity is variable from 0.6 to more than 10. From the view point of multi-bunch effect, it was found that either very high Q-value or low Q-value was preferable to suppress the periodic transient beam loading. The experimental results of the beam loading compensation using an electron beam are also described.

## 1 INTRODUCTION

We have developed a HGC loaded with MA and achieved the high accelerating field gradient of 50 kV/m [1]. The HGC has some advantages such as the variable Q-value, high stability at the large rf amplitude and realizing low total impedance. Because of these merits, the aspects on the beam loadings are different from that of ordinary ferrite-loaded cavity especially on the transient effect and bucket distortion.

So far, small  $R/Q$  of the cavity, that is, increasing the Q-value has been preferred to cure the transient beam loading effect. However the particle tracking simulation shows that the transient effect becomes only a single bunch problem in the low-Q cavity, while it is a multi-bunch effect in the high-Q one. For the HGC, there are two choices to suppress the transient effect because the Q-value of the MA can be changed using radial cut core [2].

On the single bunch effect, the beam-induced voltage is composed of both fundamental frequency and higher harmonics in the low-Q cavity although the high-Q cavity has only fundamental component. However the higher harmonics can be quickly controlled in the low-Q cavity because of the broad-band impedance. In order to study the beam loading effect, an electron-gun and one-path beam line were prepared. Then, the beam-induced voltages up to 3rd higher harmonics were significantly compensated by the beam signal feedback method.

## 2 PERIODIC TRANSIENT BEAM LOADING

In the previous paper [3], the results of the particle tracking simulation under the periodic transient beam loading were shown, and it was found that very low-Q or very high-Q were preferable to avoid the periodic transient beam

loading. It is seemed that the transient effect is most severe around  $Q \sim h/2$ . It is understood qualitatively that when the cavity damping time is near the revolution frequency, that is,  $2Q/h\omega_{rev} \sim 1/\omega_{rev}$ , then the difference of the wake field on each bunch will be largest. It means  $Q \sim h/2$ .

The simulation results under the periodic transient beam loading were shown in [3], where 8 of 17 buckets were occupied by the bunch and the others were empty. Simulations for 4 bunches in the 10 buckets and 2 bunches in the 5 buckets were newly performed in the same ring parameters except the harmonic number. Number of the particle per bunch is same in all Q value,  $1.25 \times 10^{13}$ , and cavity shunt impedance is 6 k $\Omega$ .

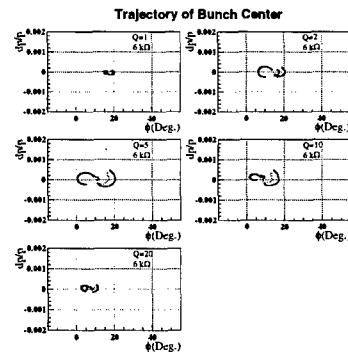


Figure 1: Trajectory of the bunch center in the longitudinal phase space (harmonic number 10, 4 bunches).

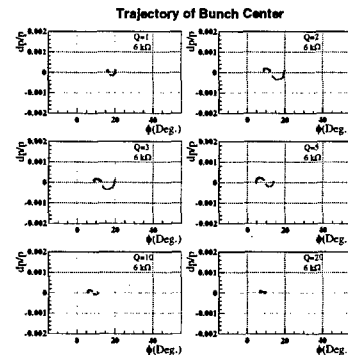


Figure 2: Trajectory of the bunch center in the longitudinal phase space (harmonic number 5, 2 bunches).

In Fig. 1 and 2, each line shows a trajectory of a bunch center in the longitudinal phase space. Vertical axis and horizontal axis are momentum difference and the phase

\* E-mail: masanobu@tanashi.kek.jp



measured from the nominal synchronous particle, respectively.

Each bunch is oscillated apart from a locked phase of the  $\Delta\phi$ -feedback by the transient effect. In case of  $h = 10$ , increasing  $Q$  up to 5, the oscillation of each bunch center becomes larger. And increasing  $Q$  further, the oscillation becomes smaller again. In the same manner, the oscillation becomes smaller around  $Q = 2 \sim 3$  in case of  $h = 5$ .

In the longitudinal motions of multi-bunches including the energy loss by the wake field, the arrival time of  $m$ -th bunch on the cavity,  $\tau_m$ , is expressed by the perturbative theory as;

$$\tau_m = \tilde{\tau}_m + \tau_m \quad (1)$$

where  $\tau_m$  and  $\tilde{\tau}_m$  are a perturbation and an equilibrium part, respectively. For the equilibrium part,  $\tilde{\tau}_m$  is defined that the energy gain of the bunch by the cavity gap voltage is equal to the energy loss by the wake field;

$$eV_0 \sin(\omega_{rf}\tilde{\tau}_m) = \sum W(t), \quad (2)$$

where  $W(t)$  is the wake function, and the summation is performed for the past turns and all bunches. In the periodic transient beam loading,  $\tilde{\tau}_m$  becomes different value on each bunch.

In order to calculate  $\tilde{\tau}_m$  simply even under the periodic transient beam loading condition, the assumption which the wake field affects only one turn is employed, and resonant type impedance is assumed. Figure 3 shows the calculation result of Eq. (2) in the case of 2 bunches  $m = 0, 1$  filled in the 4 buckets.

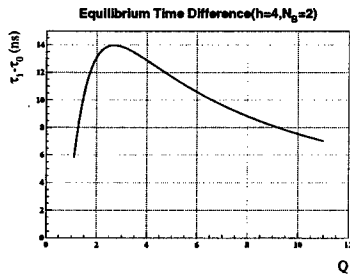


Figure 3: Difference of the equilibrium time  $\tilde{\tau}_m$  in the case of 2 bunches in the 4 buckets.

The difference between the equilibrium time  $\tilde{\tau}_0$  and  $\tilde{\tau}_1$  is largest around  $Q \sim 2.5$ , and it is near the suggestion by the simulation,  $Q \sim h/2$ .

### 3 THE EXPERIMENT OF BEAM LOADING COMPENSATION

In order to investigate the beam loading effects on the HGC, the beam test using electron has been performed. The detail of the electron gun and its setup are described in [4]. In the low- $Q$  cavity, since the bucket distortion by the higher harmonics of the beam-induced voltage is severe problem, the beam loading compensation by the beam signal feedback has been considered.

The beam signal picked up by a Fast Current Transformer is attenuated and delayed by cable line arbitrary, then fed into the cavity through amplifiers. When the attenuation and delay can be optimized, it is expected that the wake voltage is compensated clearly.

The simple scheme of the beam loading compensation was already demonstrated using the electron beam, where the beam signal was simply returned to the amplifier, and it was effective for compensating the one component of the beam-induced voltage [3]. In order to compensate the higher harmonics of the beam-induced voltage as well, the beam signal was separated into each harmonic and the adjustment were done for them, then each signal were combined and fed into the cavity. The setup of the filtering the beam signal is shown in Fig. 4. In this experiment, up to the 3rd higher harmonics of the beam signal were returned to the cavity.

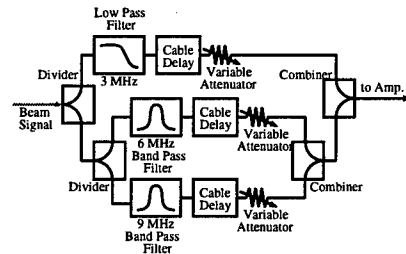


Figure 4: The setup of filtering the beam signal.

The measured voltage of the cavity gap without compensation and with compensation are shown in Fig. 5-(a) and -(b), respectively, and frequency spectrum is shown in Fig. 6, white bar is the spectrum without compensation, and black one is the spectrum with compensation. In this Fourier analysis, ten bunches were counted by a period. As clearly seen in Fig. 6, the fundamental component of the gap voltage became about one hundredth. The second and the third higher harmonic also became one tenth and one fourth, respectively.

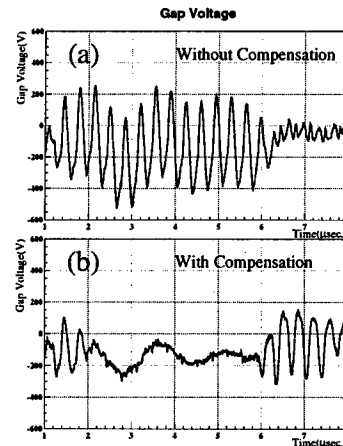


Figure 5: The measured gap voltage with compensation and without compensation.

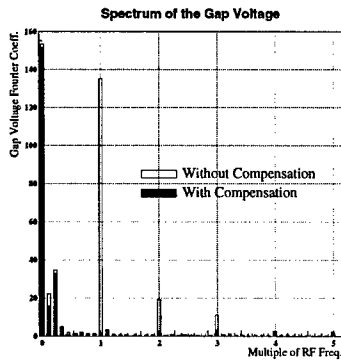


Figure 6: The spectrum of the gap voltage.

In order to study the transient effect, the beam which has some missing bunches is prepared. the test will be done by the variable-Q HGC.

#### 4 SUMMARY

Beam loading effects on HGC were investigated, especially for the periodic transient beam loading. From the results of particle tracking simulation and analytic calculation, it was found that the Q-value around a half of a harmonic number should be avoided.

The experiment of the beam loading compensation by the beam signal feedback were done with filtering the beam signal, then three harmonics of the beam-induced voltage were clearly compensated.

#### 5 REFERENCES

- [1] C. Ohmori *et al.*, 'High Field-Gradient Cavities Loaded with Magnetic Alloys for Synchrotrons, in this conf., 1999
- [2] Y. Mori *et al.*, 'A New Type of RF Cavity for High Intensity Proton Synchrotron using High Permeability Magnetic Alloy', p299-p301, Proc. of EPAC98, 1998
- [3] M. Yamamoto *et al.*, 'Beam Loading Effects in JHF Synchrotron', Proc. of APAC98, p399-402, 1998
- [4] Y. Hashimoto *et al.*, 'Beam Loading Experiment with Short Bunched Electron Beams for New Type of Accelerating RF System of High Intensity Proton Synchrotron, Proc. of EPAC98, p1770-1772, 1998

# MULTI-HARMONIC ACCELERATION WITH HIGH GRADIENT MA CAVITY AT HIMAC

M. Yamamoto\*, M. Fujieda, Y. Mori, R. Muramatsu, C. Ohmori, Y. Sato, A. Takagi, T. Uesugi and M. Yoshii KEK-Tanashi, Japan; M. Kanazawa and K. Noda NIRS, Chiba, Japan

## Abstract

A high field gradient cavity(HGC) which has been developed for high intensity proton synchrotrons is suitable to generate multi-harmonic voltage on the accelerating gap because of the broad band impedance of the cavity. In this paper, the experimental results on the dual harmonic rf, saw-tooth rf, and bunch compression by barrier bucket are described.

Some beam parameters are shown in Table 2.

Particle	${}^4\text{He}^{2+}$
Number of Particle at Injection	$1.4 \times 10^{14}$ ppp(Typical)
Injection Energy	6 MeV/u
Momentum Spread at Injection	$\pm 0.1\%$
Revolution Frequency	261.3 kHz

Table 2: Parameters of the beam.

## 1 INTRODUCTION

We have developed a prototype HGC loaded with Magnetic Alloy(MA) for synchrotrons. We have succeeded to achieve the field gradient of 50 kV/m [1], because of high stability of the MA core under the large rf magnetic field.

Another advantage of the HGC is that it is a broad-band cavity. High accelerating voltage over the wide frequency range can be obtained without the tuning system. In such a wide band system, some different frequencies can be generated simultaneously on the gap. The bunch shape can be manipulated by the higher harmonics, it leads to suppressing the space charge effects. The HGC has been installed in Heavy Ion Medical Accelerator in Chiba(HIMAC) for the beam experiments.

## 2 EXPERIMENT

Parameters of the cavity are listed in Table 1. Using the cavity, the beam acceleration has been successfully carried out [2].

Freq. Range	1 ~ 8 MHz
Gap Voltage	Max. 4 kV
Shunt Impedance	400 $\Omega$ @ 2 MHz (4 cores loaded)
Q value	0.6
Amplifier	push-pull, 60 kW, 4CW30,000A $\times$ 2
Length	40 cm

Table 1: Parameters of the HGC installed in HIMAC.

The experiment with the higher harmonics were demonstrated on the flat base(no acceleration). The control system of the higher harmonics for the acceleration is under designing.

\* E-mail: masanobu@tanashi.kek.jp

### 2.1 Dual Harmonics Mixing

The beam capture experiment by dual harmonic rf has been carried out. Usually, the experiments with dual harmonic rf need another cavity for the higher harmonics [3, 4]. In this experiment, only HGC has been used. The second higher harmonic was mixed with fundamental rf and the dual harmonic voltage on the gap was obtained. The gap voltage  $V_{\text{gap}}$  and the potential  $U$  are written as;

$$V_{\text{gap}}(\phi) = V_1 \sin \phi + V_2 \sin 2(\phi - \phi_s) \quad (1)$$

$$U(\phi) = \int_{\phi_s}^{\phi} (V_{\text{gap}}(\phi) - V_1 \sin \phi_s) d\phi \\ = -V_1 \{(\cos \phi - \cos \phi_s) + (\phi - \phi_s) \sin \phi_s\} \\ + \frac{1}{2} V_2 [\cos \{2(\phi - \phi_s) - 1\}], \quad (2)$$

where  $V_1$  and  $V_2$  are the amplitude of the voltage for the fundamental rf and the 2nd higher harmonic one, respectively and  $\phi_s$  is a synchronous phase and  $\phi_s = 0$  for the flat base. The voltage and the potential well in case of  $V_1 = 1$  kV and  $V_2 = 500$  V are shown in Fig. 1.

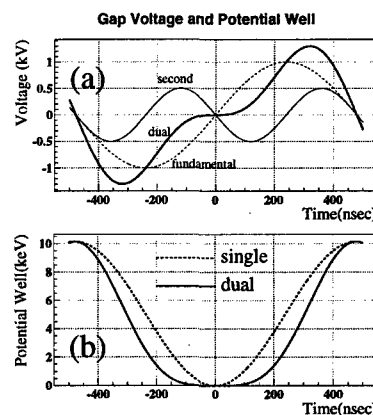


Figure 1: The gap voltage and the potential well for the dual harmonics.

The bottom of the potential well in case of the dual harmonic rf(solid line) becomes more flat than that of the single rf (dotted line) as shown in Fig. 1-(b). Since a bunch shape is related to the shape of the potential well, it is expected that the bunch is flattened and lengthened in case of the dual harmonic rf. It leads to alleviating the space charge effects.

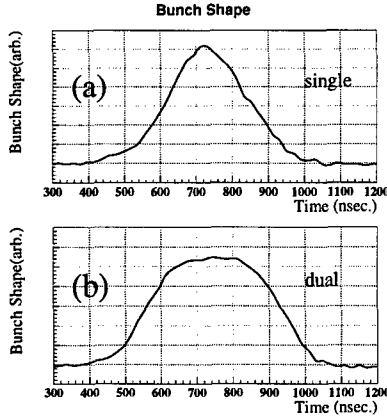


Figure 2: Experimental results of bunch lengthening by mixing the 2nd higher harmonic rf.

The bunch shape measured by an electro-static beam monitor is shown in Fig. 2. Figure 2-(a) and -(b) are the shapes for the single and dual rf, respectively. As seen clearly, the bunch shape became flat by the dual harmonic rf, then the bunching factor of 0.28 for the single rf was increased to 0.4 by the 2nd harmonic. From Eq. (2), the bunching factor for the beam with momentum spread of  $\pm 0.1\%$  can be calculated numerically, and they are 0.27 for the single rf and 0.4 for the dual harmonic rf. It has good agreement with the experimental results.

## 2.2 Saw-tooth RF

In the case of single rf frequency, non-linearity appears for the particles which have large amplitude in the longitudinal phase space. On the other hand, if complete saw-tooth voltage like  $V_{\text{gap}} = \frac{V_0}{\pi} \phi$  ( $-\pi < \phi < \pi$ ) (solid line in Fig. 3) is applied to the rf acceleration, then linear rf bucket will be obtained, and it is useful to investigate non-linear effects by comparing with the sinusoidal one.

The saw-tooth voltage is expressed as the Fourier series;

$$V_{\text{gap}} = \frac{2V_0}{\pi} \sum_{n=1}^{\infty} \frac{1}{n} \sin n\phi, \quad (3)$$

where  $V_0$  is the amplitude of the saw-tooth voltage. We have produced pseudo saw-tooth voltage by combining up to the 3rd higher harmonics in Eq. (3).

The measured gap voltages in case of the pseudo saw-tooth rf(bold line) and the sinusoidal rf(dotted line) are shown in Fig. 3-(a). The amplitude of the sinusoidal rf is adjusted as the gradient at  $\phi = 0$  is equal to the gradient of pseudo saw-tooth one. Because the saw-tooth voltage

makes a potential well to be a complete parabolic shape, the bunch shape in the the saw-tooth rf will become more parabolic than that of the sinusoidal one. Figure 3-(b) shows that the bunch shapes for the saw-tooth rf(solid line) and the sinusoidal rf(dotted line).

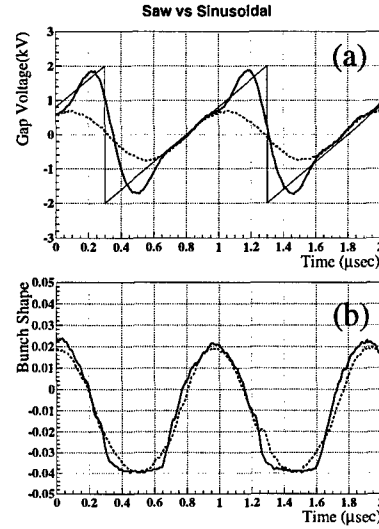


Figure 3: The measured gap voltage and the bunch shape in saw-tooth rf.

We assume the amplitude of the synchrotron motion is small to obtain the equation of the synchrotron frequency for the sinusoidal voltage;

$$\omega_s = \sqrt{\frac{heV\omega_{\text{rev}}^2|\eta|\cos\phi_s}{2\pi\beta^2E_0}}, \quad (4)$$

where  $h$  is harmonic number,  $e$  is unit electric charge,  $\omega_{\text{rev}}$  is revolution frequency,  $\eta$  is slippage factor,  $\beta = v/c$ ,  $E_0$  is total energy of the particle. However, if the beam emittance occupies the large area of the rf bucket, then the measured synchrotron frequency tends to deviate from Eq. (4) and become smaller value [5]. On the other hand, the synchrotron frequency at large amplitude of the synchrotron motion is as same that at small one for the saw-tooth rf. The measured synchrotron frequency should be consistent with Eq. (4). Actually, the measured synchrotron frequency of 1.03 kHz had good agreement with calculated one of 1.08 kHz for the saw-tooth rf, although the measured one was 0.75 kHz for the sinusoidal rf.

## 2.3 Barrier Bucket

Barrier bucket is a scheme to manipulate the bunch length by moving a single sinusoidal voltage [6]. It is mostly used to store more beam in the ring [7]. Conversely, it is possible to make coasting beam into one high density bunch by the barrier bucket, then it is profitable to produce high peak current for the study of the wake field.

In this experiment, the barrier voltage was 2 kV, which corresponded to the bucket height of  $\pm 0.4\%$  with respect to the momentum spread. The bunch of  $3.8 \mu\text{sec}$  length was

compressed into  $1.4 \mu\text{sec}$  by the barrier bucket gymnastics spending 100 msec to conserve the longitudinal beam emittance.

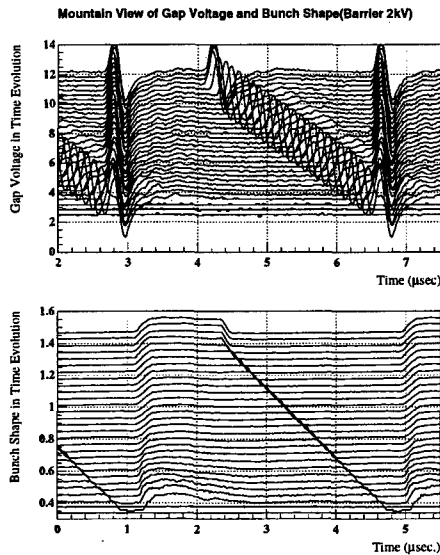


Figure 4: Bunch compression by the barrier bucket operation.

Figure 4 shows the experimental result, the upper side shows the barrier voltage gymnastics and the lower side shows the bunch shape in the mountain range view. The interval of the trace is 4 ms. The compression was performed for the beam of  $7 \times 10^{10}$  ppp. Since a half of the beam was lost, the peak current was not so high that the beam induced voltage has not been observed.

### 3 SUMMARY

The experiments of the multi-harmonic rf have been succeeded by a HGC due to its broad band impedance. Although the beam was lost, the bunch shape could be manipulated.

### 4 ACKNOWLEDGEMENT

We would like to thank AEC staffs for their careful operation of HIMAC. We would like to thank to K. Sato and S. Ninomiya for their valuable suggestions and comments.

### 5 REFERENCES

- [1] Y. Mori *et al.*, 'A New Type of RF Cavity for High Intensity Proton Synchrotron using High Permeability Magnetic Alloy', Proc. of EPAC98, p299-p301, 1998
- [2] R. Muramatsu *et al.*, 'The First Beam Acceleration Test using High Gradient Cavity at HIMAC, in this conf., 1999
- [3] P. Bramham *et al.*, IEEE Trans. Nucl. Sci. NS-24, No.3, p.1490(1977)
- [4] J.M. Baillod *et al.*, IEEE Trans. Nucl. Sci. NS-30, No.4, p.3499(1983)
- [5] K. Koba, Longitudinal Impedance Tuner using High Permeability Material, in this conf., 1999
- [6] J.E.Griffin *et al.*, IEEE Trans. Nucl. Sci. NS-30, No.4, p.3502(1983)
- [7] M. Fujieda *et al.*, 'Magnetic Alloy Loaded RF Cavity for Barrier Bucket Experiment at AGS', in this conf., 1999

# OPERATIONAL EXPERIENCE WITH THE DAΦNE RADIO-FREQUENCY SYSTEMS

R. Boni, A. Gallo, F. Marcellini and G. Vignola

INFN, Laboratori Nazionali di Frascati, P.O. Box 13, 00044 Frascati (Rome), Italy

## Abstract

The RF systems of the Frascati double ring ( $e^+/e^-$ ) Φ-Factory DAΦNE are fully operative since the autumn 1997. The RF complex consists of one 73.65 MHz system for the damping ring and one 368.26 MHz system per each ring. The accelerating cavities are room-temperature single cell copper resonators, broadband loaded by waveguides to reduce the impedances of their High Order Modes and, consequently, the coupled-bunch instability growth rates.

The main operational features of the DAΦNE radiofrequency systems are reported in this article, including the performances observed under heavy beam loading conditions.

## 1 INTRODUCTION

The commissioning of DAΦNE, the 510 MeV double ring  $e^+/e^-$  Φ-Factory [1], is in its final stage at the Frascati laboratories of the INFN. A maximum of 120 electron-positron bunches can be stored in each ring. Being DAΦNE a multibunch machine, intense R&D was dedicated to design the RF cavities since they can cause coupled bunch instabilities because of undamped high order modes (HOM) [2].

The DAΦNE injector is a full energy system composed by a Linac [3] and a damping ring (DR) [4]. Herein, the operational experience with the DAΦNE RF systems, together with some remarks about their behavior under high current, multibunch operation, are reported. The Main Ring (MR) RF frequency is 368.26 MHz while the DR one is 73.652 MHz, i.e. the MR frequency divided by 5.

## 2 DAMPING RING RF SYSTEM

The aim of the DAΦNE DR is to reduce the beam energy spread and emittance before injection in the MR. The  $e^+/e^-$  beams are accelerated to 510 MeV with a 2856 MHz linear accelerator, injected at 50 pps in one DR bucket and extracted at 1 pps for transportation to the MR. The DR cavity is a single ended copper coaxial resonator with an internal profile designed to minimize the probability of resonant discharge (multipacting) [5]. The cavity is fed by a 50 kW tetrode amplifier through a 6-1/8" coaxial line. The cavity shunt impedance is  $\approx 1.6 \text{ M}\Omega$ , and the required accelerating voltage for the operation is in the 150-200 kV range.

A ferrite circulator protects the tube from reflected power bursts due to transient beam loading caused by the

continuous 50 Hz injection/1 Hz extraction process during the injection sequence into the MRs. To prevent continuous activity of the plunger gear, the tuning servo-loop is usually kept off during the injection sequence. The circulator also allows to set safely a large Robinson detuning.

In the initial DR commissioning phase, longitudinal instabilities have been occasionally observed. Two cavity HOMs were found to lay very close to unstable synchrotron sidebands of the revolution harmonics and might be responsible for such instabilities. Anyway, after a small correction to the RF frequency to synchronize the DR to the MRs and a small change of the cavity temperature set point, longitudinal instabilities have not been observed anymore. So far, no significant faults or incorrect function of the whole RF system have occurred.

## 3 MAIN RINGS RF SYSTEMS

### 3.1 The Damped Cavities

The most relevant parameters of the MR DAΦNE RF systems are reported in Table 1.

Table 1: Main ring cavity parameters

$f_{RF}$	Resonant frequency	368.26 MHz
$V_c$	Accelerating voltage	250 kV
$Q_0$	Unloaded quality factor	33,000
$R_{sh}$	Shunt impedance	2 $\text{M}\Omega$
$P_c$	Power loss	16 kW
$\beta$	Input coupling factor	2.5
$P_k$	Non saturated klystron RF power	150 kW
$I_b$	Max beam current	5 Amps
$E_t$	Beam energy loss per turn	$\approx 15 \text{ keV}$
$P_{HOM}$	HOM power	$\approx 3 \text{ kW}$
$\Delta f_{bl}$	Max. beam loading detuning	$\approx -500 \text{ kHz}$

The cavities are room-temperature single cell resonators, designed with the aim to reduce at the most their contribution to the ring broadband and narrowband impedances. The cavities have rounded profiles and are connected to the ring pipe with long tapered tubes to reduce the longitudinal and transverse HOM R/Q's and the loss factor. Further damping of HOM shunt impedances is obtained by connecting to the cavity 3 rectangular waveguides (wg), with cut-off at 500 MHz, which couple

out the parasitic mode energy in the TE<sub>10</sub> mode. The coupled waves are transformed into standard 7/8" coaxial TEM waves by means of broadband transitions [6]. The HOM energy is then dissipated on external 50  $\Omega$  commercial attenuators via wideband ceramic feedthroughs. Each attenuator output is connected through a cable to the accelerator control area, where the waveguide outcoming signals can be analyzed. Damping is more effective on monopoles because they couple better to the rectangular waveguide apertures. Two additional wg's with 1.2 GHz cut-off are placed on the tapers with a 90° relative position. They can couple those HOMs that mainly resonate in the tapers. The longitudinal HOMs have been measured up to 3 GHz on bench with the wire technique, and the results are shown in Fig. 1. The upper plot is obtained with all the waveguides terminated on 50  $\Omega$  loads.

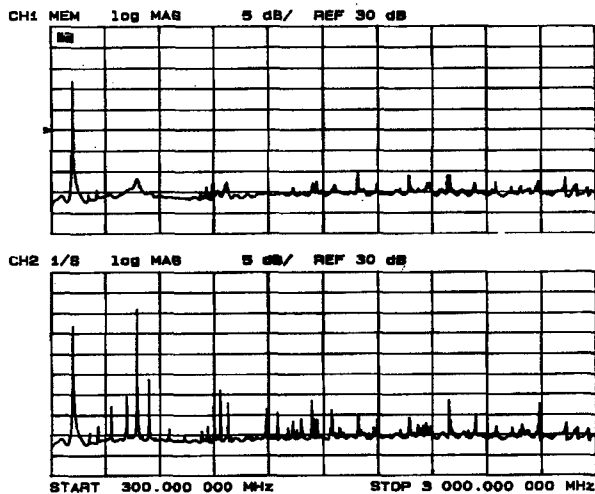


Figure 1: Cavity spectrum with the waveguides loaded with 50  $\Omega$  (up) and shorted (down).

Table 2: HOM cavity impedances measured with the wire technique.

F[MHz]	Q	Z <sub>  </sub> [ $\Omega$ ]	F[MHz]	Q	Z <sub>  </sub> [ $\Omega$ ]
672.5	40	110	1086.4	1650	66
728.0	47	149	1138.0	5120	300
862.8	4470	58	1142.9	1060	147
1047.0	2680	75	1172.9	510	226
1065.3	2080	94	1181.0	336	310
1074.5	340	95	1297.2	860	110

Figure 1 gives a glance of the successful HOM damping. The sole undamped line (the first one in the upper plot) represents the cavity fundamental mode. However, the wire technique perturbs significantly the mode frequencies and the unloaded quality factors, so that the measurement results have to be taken with some caution. The measured values are listed in Table 2.

It has been estimated [7] that, even being heavily damped, the RF cavity HOM's can drive longitudinal coupled bunch mode instability with rise times faster than

500  $\mu$ s at the maximum machine current, calling for an efficient operation of the dedicated bunch-by-bunch feedback system [8] in order to keep the beam stable.

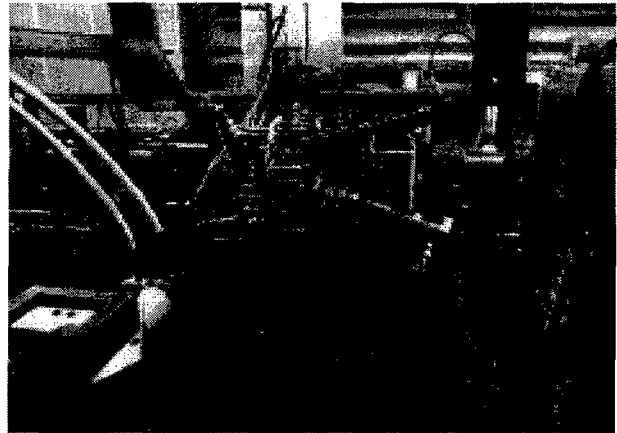


Figure 2: The RF cavity installed in the positron ring.

### 3.2 The RF System Assembly

A view of the positron ring cavity installed on the machine is given in Fig. 2. The cables connecting the wg's to the dummy loads are visible in the picture. Each cavity is connected to a 150 kW/cw klystron through a 3 port ferrite circulator. Such high power is needed for the full current operation.

The RF power couplers are similar to those of the LEP normal-conducting cavities and they are basically waveguide to coaxial transitions, ending with loops through a vacuum tight ceramic window which is air-water cooled and monitored with an infrared probe for temperature check. Moreover, a fast interlock turns off the power if excessive reverse to forward cavity power ratio occurs and in case of a steep cavity pressure increase. This avoids stress of the RF windows in case of sudden beam losses or arcs. One window has cracked in January '98 because of a human error and caused 2 weeks of machine shut down. So far, this window crack and a tuning plunger seizing were the only significant faults during the DAΦNE RF system operation.

Intense beam loading is foreseen at full beam current. To increase the threshold of the 2<sup>nd</sup> Robinson limit, an RF feedback system has been developed and tested in the cavity test hall [9]. The final implementation of the RF feedbacks will be made as soon as we approach the full design beam current.

The low power RF control electronics includes servo loops to regulate the cavity tuning, level and phase. The RF phase stability directly impacts on that of the longitudinal position of the interaction point, as well as on the injection efficiency. In the DAΦNE MRs a long term RF phase stability within few tens of ps has been measured.

The operation of the main ring radiofrequency has been very reliable so far; also, the performances of the whole system were fully satisfactory.

## 4 THE FAST RF PHASE JUMP

During the first machine shifts dedicated to the luminosity tune-up, the performances were limited by injection saturation when injecting in the collision mode [1]. On the other hand, schemes of transverse beam separation (horizontal or vertical) did not work satisfactorily, due to the lack of synchronism in the variation of the fields in the corrector magnets.

In order to get over these limitations we adopted a "fast RF phase jump" technique. This consists in injecting the beams with an adequate longitudinal separation and put them suddenly in collision by fast changing the RF phase of one of the two beams.

The RF phase jump is obtained by a fast electronic delay line acting on the RF reference signal entering the positron cavity control electronics and driven by pulses of a suitable amplitude and rise time.

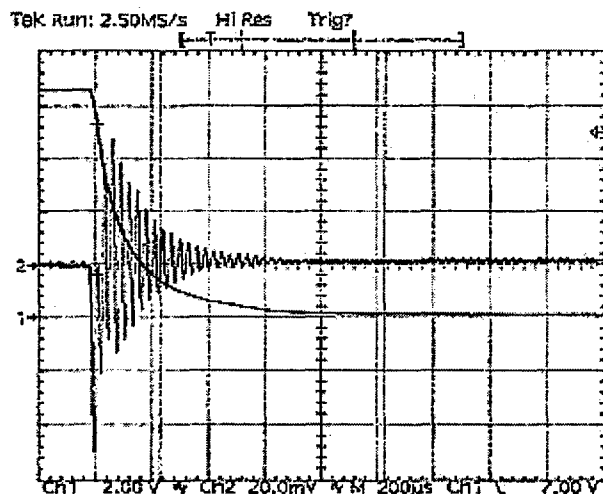


Figure 3: Driving signal (CH1,  $\approx 3$  rad/div vert. scale) and detected synchrotron oscillation (CH2,  $\approx 58$  mrad/div vert. scale) during a  $4\pi$  rad. RF phase jump.

The driving signal ( $\approx 600 \mu\text{s}$  long) together with the induced synchrotron oscillation around the moving synchronous phase for a two-buckets ( $4\pi$  radians) RF phase jump are reported in Figure 3. The derivative of the phase pulse is a modulation of the RF frequency. This transient frequency modulation puts temporarily the beam on external (internal) orbits and is responsible for the increasing (decreasing) bunch delay.

The phase jump is basically a barycentric longitudinal motion of the beam, and therefore the synchrotron oscillation damping is dominated by the Robinson effect. The envelope decay shown in Fig. 3 gives a Robinson damping time of  $\approx 120 \mu\text{s}$  (@ 25 mA of beam current in 1 bunch), in a fairly good agreement with the expected value. The Robinson damping is beneficial for the fast RF jump technique since it reduces the amplitude of the oscillations as well as the transient duration.

## 5 SOME REMARKS ON HIGH CURRENT OPERATION

The maximum achieved current during the DAΦNE commissioning is  $\approx 550$  mA in 30 bunches in both  $e^-$  and  $e^+$  rings. Some longitudinal and transverse coupled-bunch instabilities have been observed in the  $e^-$  and  $e^+$  ring respectively [10], but none of them could be clearly attributed to the cavity HOMs. On the contrary, in spite of the strong Robinson damping, we occasionally observed longitudinal barycentric oscillations of the beam at high current. They were due to excessive wide band response of the RF amplitude and phase loops, an effect known in literature [11]. Once the gain and the bandwidth of the servo loops have been reduced, no more barycentric instabilities have been observed.

The performances of the RF systems under high beam loading were quite satisfactory, since no special operation difficulties have been observed. However, the 550 mA current value is still far from the 2<sup>nd</sup> Robinson limit threshold, and the implementation of the fast RF feedback system remain necessary to approach the ultimate current value.

## ACKNOWLEDGMENTS

The authors warmly thank the technical staff of the DAΦNE RF group for the invaluable support to the management and the operation of the RF system.

## REFERENCES

- [1] S. Guiducci and the DAΦNE Team, DAΦNE Operating Experience, invited paper, these Proceedings.
- [2] S. Bartalucci et al., Analysis of Methods for Controlling Multibunch Instabilities in DAΦNE, Particle Accelerator, Vol. 48, N° 4 (1995), pp. 213.
- [3] R. Boni et al., DAΦNE Linac Operational Performances, Proc. of EPAC '98, Stockholm, June '98, p. 764.
- [4] M.E. Biagini et al., Performances and Operation of the DAΦNE Accumulator, Proc. of EPAC '98, Stockholm, June '98, p. 415.
- [5] R. Boni and B. Spataro, The Multipacting-Free RF Cavity of the DAΦNE Accumulator, DAΦNE Tech. Note, RF-19, 1996.
- [6] R. Boni et al., A Broadband waveguide to coaxial transition for High Order Mode damping in particle accelerators RF cavities, Particle Accelerators, vol. 45 (4), p. 195, 1994.
- [7] M. Zobov et al., Collective effects and Impedance Study for the DAΦNE Phi-Factory, DAΦNE Techn. Note, LNF-95/041(P), 1995.
- [8] M. Serio et al., Multibunch Instabilities & Cures, Proc. of EPAC '96, Sitges, June '96, p. 148.
- [9] R. Boni et al., Experimental test of the DAΦNE RF Feedback System, Proc. of EPAC '96, Sitges, June '96, p. 1878.
- [10] A. Drago et al., Single and Multibunch Beam Dynamics in the DAΦNE Main Rings, these Proc.
- [11] D. Boussard, Design of a ring RF system, CERN 92-03, vol. II, p. 474.



# WIDEBAND RF SYSTEM FOR THE FERMILAB RECYCLER RING\*

J. E. Dey and D. W. Wildman, Fermilab, Batavia, IL

## Abstract

A broadband RF system has been built for the new Fermilab Recycler Ring. It is designed to both bunch and capture beam during transfers and create multiple, moveable RF barrier buckets for azimuthal control of the stored antiproton beam. Beam will be bunched and captured using bursts of four RF cycles at 2.5 MHz. To maximize bucket area, the multiple barrier buckets will be generated by pairs of 2000 V bipolar square pulses (1 to 2  $\mu$ s in duration). The high level portion of the system consists of four 50  $\Omega$  ferrite loaded cavities, each driven by a 3.5 kW broadband (10 kHz - 100 MHz) solid-state amplifier.

## 1 INTRODUCTION

The Fermilab Recycler Ring [1] is an 8 GeV/c antiproton storage ring, utilizing permanent magnets, located directly above the new Fermilab Main Injector. The Recycler will perform multiple functions in the Tevatron colliding beams program. Cooled antiprotons from the Accumulator will be periodically injected and stored in the Recycler. When the desired antiproton current is reached, four bunches of antiprotons will be formed in adjacent 2.5 MHz RF buckets and be extracted from the Recycler into the Main Injector. The Main Injector will then accelerate these bunches to 150 GeV/c and inject them into the Tevatron collider. This process will be repeated 9 times until a total of 36 bunches are circulating in the Tevatron.

After the luminosity of the Tevatron collider has decreased due to beam emittance growth, the proton and antiproton beams will be decelerated back down to 150 GeV/c, the protons will be scraped away, and the remaining antiproton bunches will be transferred, in groups of four, back into the Main Injector. Once in the Main Injector, the four bunches will be further decelerated to 8 GeV/c and injected into the Recycler to be cooled and reused in the collider. This process will be repeated a total of 9 times until all of the antiprotons that were initially in the Tevatron are transferred back into the Recycler.

## 2 RF SYSTEM REQUIREMENTS

At any given time, the Recycler ring may contain cooled beam, hot recycled beam from the Tevatron, beam being injected from the Accumulator, or beam being transferred either into or out of the Main Injector. During these processes, the various beam segments must be separated from each other azimuthally around the ring.

In addition, newly injected beam has to be captured, debunched, and combined with the beam from earlier transfers. For transfers into the Main Injector, a fraction of the cooled beam has to be isolated and then bunched in 2.5 MHz RF buckets. To accommodate all of these beam manipulations, a wideband RF system capable of generating three independent sets of barrier [2] RF buckets has been constructed. To maximize the barrier bucket area for a given azimuthal extent, the barrier buckets are formed by two bipolar rectangular pulses of adjustable width and amplitude. To generate the 2.5 MHz buckets needed during transfers, the RF system will also produce a train of four RF cycles at 2.5 MHz between two of the bipolar barrier buckets.

For a rectangular barrier bucket, formed by two pulses of width T and amplitude  $\pm V_0$ , the bucket half height is given by:

$$\Delta E_{1/2} = \sqrt{\frac{T}{T_0} \frac{2\beta^2}{\eta} e V_0 E_0} \quad (1)$$

where  $E_0$  is the beam energy,  $\eta$  is the momentum compaction factor, and  $T_0$  is the revolution period. If the two rectangular barrier pulses of width T are allowed to touch, the resulting bucket area A is

$$A = \frac{8}{3} \Delta E_{1/2} T \quad (2)$$

To ensure that there is sufficient bucket area available to capture and confine the hot recycled beam from the Tevatron, the RF system must be capable of generating 1 to 2  $\mu$ s wide rectangular bipolar pulses with a peak voltage of 2 kV. Lee and Ng [3] have shown that the dynamics of a pair of these barrier pulses depend only on the total voltage integral of the barrier pulses and is independent of the actual RF waveform. This important fact relaxes many of the hardware requirements since the two halves of the barrier pulse pairs need not have equal amplitudes, be symmetric, or even have similar shapes.

## 3 HARDWARE

The high level RF system consists of four 50  $\Omega$  cavities, each driven individually by an Amplifier Research model 3500A100 broadband solid-state amplifier. Each amplifier, operating in the push-pull mode, can supply a minimum of 3500 watts output power over the frequency range of 10 kHz to 100 MHz. The amplifiers, located in the MI-60 service building, are connected to the cavities in the tunnel by 20 m of 7/8" Andrew LDF5-50 coaxial line.

\*Operated by the Universities Research Association, Inc. under contract with the U.S. Department of Energy.

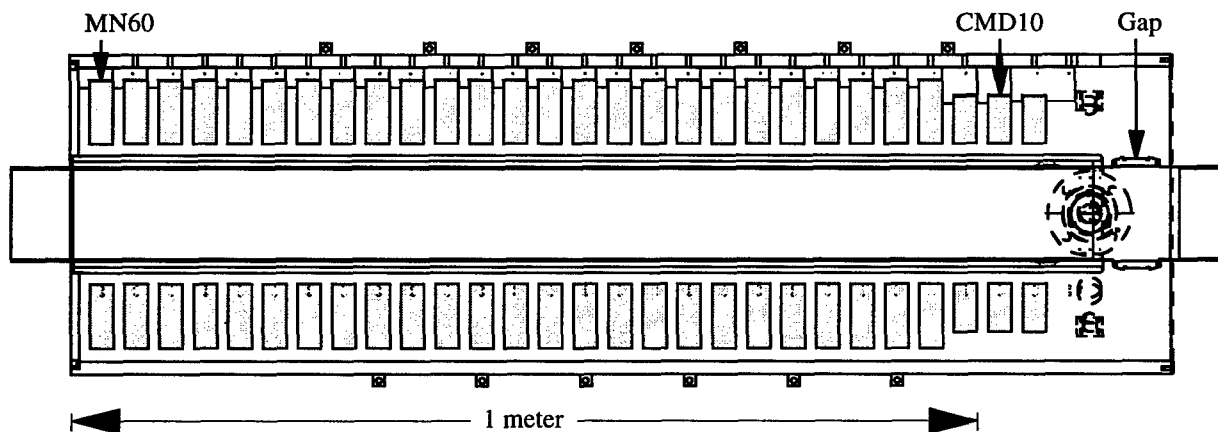


Figure 1: Schematic drawing of Recycler Wideband RF Cavity

A schematic drawing of the wideband cavity is shown in Figure 1. It consists of a water-cooled outer aluminum shell, an aluminum inner conductor, and a 4" diameter stainless steel beam pipe with a 1" ceramic gap which is electrically connected to the cavity with beryllium-copper finger stock. A thin copper end plate completes the electrical connection between the beam pipe and outer cavity shell. The beam pipe is thermally isolated from the cavity and is wrapped with heating tapes to allow the vacuum system to be baked out after installation. The cavity is filled with twenty-five, 11.5"OD x 6"ID x 1" thick Mn-Zn ferrite cores (Ceramic Magnetics MN60) and three, 10"OD x 6"ID x 1" thick Ni-Zn ferrite cores (Ceramic Magnetics CMD10). The ferrite cores are air-cooled, spaced by 0.5", and supported by Kapton spacer blocks. A 10 kW, water-cooled, RF load; modified with a 60 ohm resistor, is connected directly across the cavity gap. This resistor in parallel with the stack of ferrites results in an input impedance of approximately 50 ohms over the frequency range of 100 kHz to 20 MHz. Both the input drive and the 60  $\Omega$  resistor are connected to the inner conductor at the gap by 1" wide x 4" long flat copper straps. The voltage developed across the gap is monitored by two 1000/1 resistive voltage dividers.

The low level RF drive signal is derived from eight, DSP controlled, arbitrary waveform generators synchronized to the machine revolution frequency of 89.8 kHz [4]. A feedforward circuit is used to compensate for the droop induced by the ac coupled high power amplifier and the low frequency response of the RF cavity. The feedforward circuit utilizes an AD830 high speed video difference amplifier and a passive network that models the amplifier/cavity response to produce the modified drive signal. The modified low level signal is then amplified by a 2kHz – 500 MHz amplifier (Mini-Circuits ZHL-6A), divided by resistive splitters, and then distributed with the proper delays to the four 3500 watt amplifiers.

Photographs of a wideband amplifier and cavity are shown in Figures 2 and 3. In Figure 2, four identical air cooled RF modules, which are combined to form its 3.5 kW output, are visible in the rear view. Figure 3

is a photograph of the cavity, taken in the laboratory, showing the outer shell aluminum cooling coils, the 60  $\Omega$  RF load, and the copper end plate connecting to the protruding beam pipe.

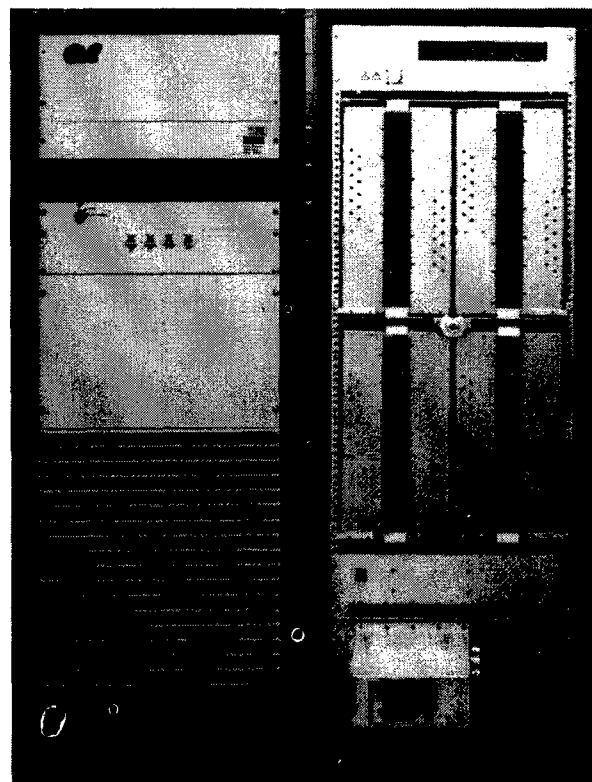


Figure 2: Front and Rear views of Amplifier Research model 3500A100.

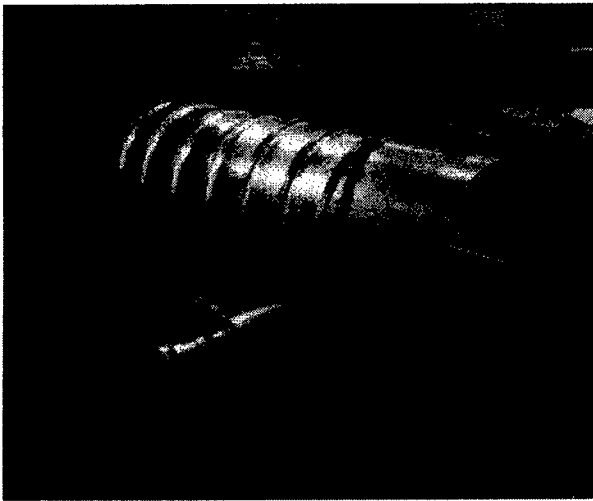


Figure 3: Wideband Cavity.

## 4 RESULTS

A network analyzer plot, from 50 kHz to 20 MHz, of the real and imaginary parts of the wideband cavity input impedance is shown in Figure 4. This impedance represents the load seen by the high power RF amplifier. The upper trace shows the real impedance on a 2  $\Omega$ /div scale centered around 52  $\Omega$ . The lower trace is the imaginary component centered at 0  $\Omega$  with a 5  $\Omega$ /div scale. At low frequencies the cavity looks inductive. It is slightly capacitive between 0.5 and 4 MHz and then becomes inductive over the remaining frequency range.

Figure 5 shows the output signal from one of the four Recycler RF cavity gap monitors averaged over 16 machine revolutions. The data were taken without any beam in the machine with a final amplifier average power output of 2560 watts. Three sets of rectangular barrier pulses with different amplitudes and durations are shown along with four cycles of 2.5 MHz for beam capture. The peak gap voltage is approximately  $\pm 500$  volts. With all four RF systems operating, a combined total accelerating gap voltage of more than  $\pm 2$  kV will be available. Tests of the new RF system with beam are scheduled for late spring.

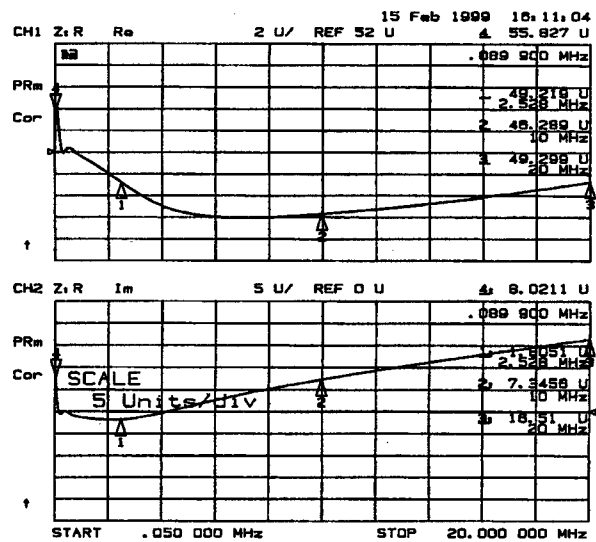


Figure 4: Input Impedance of Wideband Cavity.

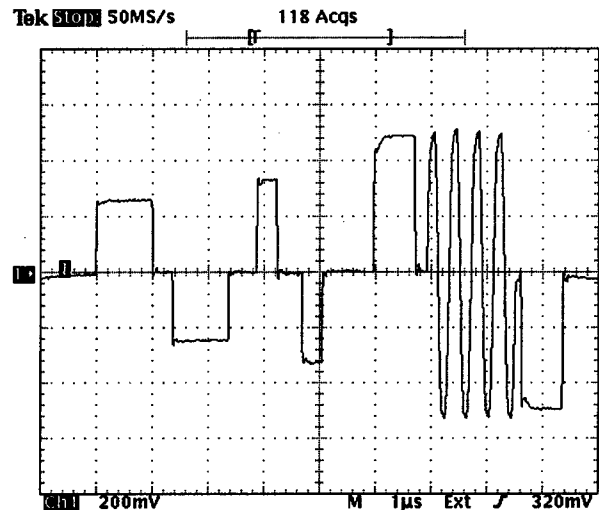


Figure 5: Gap voltage monitor output (1000V/V).

## 5 REFERENCES

- [1] Fermilab Recycler Ring Technical Design Report, Fermilab (1996)
- [2] J.E. Griffin, C. Ankenbrandt, J.A. MacLachlan, and A. Moretti, "Isolated Bucket RF Systems in the Fermilab Antiproton Facility", IEEE Trans. Nuc. Sci. NS-30, 3502 (1983)
- [3] S.Y. Lee and K.Y. Ng, "Particle dynamics in storage rings with barrier rf systems", Phys. Rev. E55, 5992 (1997)
- [4] B. Chase, A. Mason, and K. Meisner, "Current DSP Applications in Accelerator Instrumentation and RF", Proceedings of the 1997 Int. Conference on Accelerator and large Experimental Physics Control Systems, Beijing, China (1997)

# FINEMET VERSUS FERRITE — PROS AND CONS

K.Y. Ng and Z.B. Qian, FNAL\*, Batavia, IL 60510

## Abstract

There is a new magnetic alloy called Finemet which has very constant  $\mu'_p Q f$  up to  $\sim 2$  kG and is very stable at high magnet flux density and temperature. It may be a good candidate for high-gradient rf cavities. However, it has a rather low quality factor and is therefore very lossy. We compare the pros and cons of Finemet versus the common ferrite, when used in low-energy accelerating cavities, insertion for space-charge compensation, and barrier cavities.

## 1 INTRODUCTION

Ferrite has been used extensively in rf cavities for particle accelerators that require tuning. Some ferrite used can operate up to more than 100 MHz but the saturation magnetic flux intensity is often limited to 100~200 G. Recently, there is a met-glass-like material called Finemet developed in Japan [1] that can hold up to 2 kG of magnetic flux intensity (Fig. 1). Ferrite is ceramic in nature and is manufactured by baking in an oven. Therefore, large ferrite cores are difficult to produce. On the other hand, Finemet is in the form of a tape which can be wound into a core over 1 m in diameter, making very high magnetic flux possible. For this reason, Finemet may open up a new way to the construction of high gradient acceleration cavities. However, there are also shortcomings. Its relative permeability  $\mu'_p$  starts to drop at a much lower frequency,  $\sim 2$  MHz, and the quality factor is low,  $Q \sim 1$ , although they can be boosted to  $\sim 8$  MHz and  $Q \sim 12$  by cutting the cores and leaving an air gap between the two semicircular halves. This implies that Finemet is more lossy with larger power consumption. Fortunately, Finemet has a Curie temperature  $\sim 600^\circ\text{C}$  while that for ferrite is only 100 to  $200^\circ\text{C}$ , meaning that heat dissipation will be more efficient. The manageable power dissipation [1] is believed to be around  $10\text{ W/cm}^3$ . Thus, the limitations Finemet are power dissipation and high frequency, while that of ferrite is high magnetic flux density. In this note, we compare the use of Finemet and ferrite in three respects: accelerating cavities, space-charge compensating insertions, and rf barriers for multiple-turn injection. The proposed fu-

ture Fermilab low-energy booster and the Brookhaven AGS will be used in the application.

## 2 ACCELERATING CAVITIES

The future Fermilab booster consists of two rings [2]. The low-energy ring has a circumference of 158.0676 m (1/3 of present booster), cycles at 15 Hz, and accelerates 4 proton bunches,  $N_b = 2.5 \times 10^{13}$  protons each, from kinetic energy 1 GeV to 3 GeV. The 10 accelerating cavities have a rf frequency span of 6.638 to 7.368 MHz, and require a total peak voltage of  $\sim 190$  kV, or  $\sim 20$  kV each. For such a small ring, small cavities are preferred, making high-field Finemet very appealing. The FT3M Finemet cores considered here have inner and outer radii 10 and 50 cm, respectively, while the Philips 4M2 ferrite cores have inner and outer radii 10 and 25 cm. Both cores have a thickness of 2.54 cm. The Finemet cores are cut with an air separation of 4.6 cm so that the quality factor can be boosted to  $Q = 11.4$  [1]. The details are listed in Table 1. If there were only one core, the flux density would be  $B_{rf} = V_{rf}/(\omega_{rf} A_f)$ . To limit dissipation to below the manageable  $10\text{ W/cm}^3$ , at least 2 Finemet cores are required per cavity. Allowing  $\sim 2.54$  cm separation between cores for air cooling, the length of a cavity can be made as short as  $\sim 13$  cm. However, the power loss is 324 kW per cavity. On the other hand, if ferrite is used, to satisfy its flux density limitation, we need 11 cores with a total cavity length  $\sim 28$  cm. Here core spacing is not required because the total power loss for the whole cavity is only 10.2 kW. Although longitudinal space is saved in the Finemet cavities, power loss will be 31.8 times larger, totaling 3.24 MW for 10 cavities. Assuming the acceleration of  $1 \times 10^{14}$  particles takes place in 1/30 of a second, the average

Table 1: Properties of a Finemet and a ferrite cavity.

	Finemet	Ferrite
Inner radius $r_i$	10.00	10.00 cm
Outer radius $r_o$	50.00	25.00 cm
Core width $t$	2.54	2.54 cm
Flux area $A_f = (r_o - r_i)t$	101.60	38.1 cm <sup>2</sup>
Core volume $V_c = \pi(r_o^2 - r_i^2)t$	19155	4189 cm <sup>3</sup>
Rf frequency $f_{rf}$	7.37	7.37 MHz
Quality factor $Q$	11.4	45
$\mu'_p Q f$ at $f_{rf}$	6.00	61.0 GHz
Permeability ( $\mathcal{R}e$ ) $\mu'_p$	71.43	184.0
Permeability ( $\mathcal{I}m$ ) $\mu''_p = Q\mu'_p$	814.33	8279
Inductance $L$	0.5840	0.8654 $\mu\text{H}$
Resistance $R = Q\omega_{rf}L$	308.2	1784 $\Omega$
Capacitance $C = 1/(\omega_{rf}^2 L)$	798.9	544.9 pF
Accelerating voltage $V_{rf}$	20	20 kV
Total flux density if one core $B_{rf}$	425.2	1134 G
Suitable flux density per core	250	100 G
Number of cores required $N$	2	11
Power per core $P_1$	162.2	0.926 kW
Power for $N$ cores $P = NP_1$	324.4	10.19 kW
Power per volume $P_1/V_c$	8.47	0.221 W/cm <sup>3</sup>

\* Operated by the Universities Research Association, under contract with the US Department of Energy.

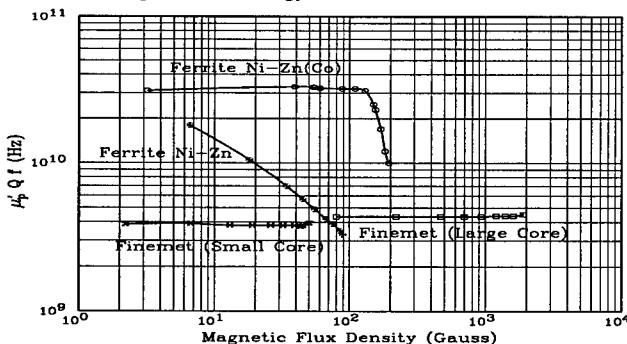


Figure 1: Plots showing the  $\mu'_p Q f$  properties of ferrite and Finemet as a function of magnetic flux density.

power delivered to the particles is only 0.96 MW. Of course, more Finemet cores can be used to reduce the power dissipation, but its advantage of accommodating high flux density will be lost. However, Finemet cavities do have other merits. Because of the low quality factor, no tuning may be necessary during the whole acceleration cycle, and the cavity may be able to encompass several higher harmonics. In fact, a multiple-harmonic cavity had been built using similar material but in amorphous form called Vitrovac [4].

Each bunch carries a charge of  $q = 4.0 \mu\text{C}$ . On passage of a cavity, some amount of negative charge will be deposited at the upstream end of the gap. An equal amount of positive charge will accumulate at the downstream end. For a Gaussian bunch, the transient beam-loading gap voltage at a time  $t$  after the bunch center passes the cavity gap is

$$V_t = \frac{q\omega_r R}{2Q \cos\phi} \text{Re} e^{j\phi - t^2/(2\sigma_\tau^2)} w \left[ \frac{\sigma_\tau \omega_r e^{j\phi}}{\sqrt{2}} - \frac{j t}{\sqrt{2}\sigma_\tau} \right], \quad (1)$$

where  $w$  is the complex error function,  $\sin\phi = 1/(2Q)$ ,  $R$  the total resistance of all the cores in series. When the rms bunch length  $\sigma_\tau \rightarrow 0$ , this becomes  $q/C$ ,  $C$  being the total capacitance of all the cores in series. With  $\sigma_\tau = 12.63 \text{ ns}$ ,  $V_t$  reaches the maxima of 5.30 and 44.6 kV, respectively, for the Finemet and ferrite cavities when  $t \approx 0.85\sigma_\tau$ . This is understandable because there are many more ferrite cores than Finemet cores in a cavity. Since  $V_t$  are not negligible with respect to the designed gap voltage, compensations must be made at the gap through feed-forward [3]. If the Finemet cores do not have the 4.6 cm gap, one will have  $\mu'_p Q f = 3.7 \text{ GHz}$  and  $Q = 1$  instead. Now 3 cores have to be used. The power dissipation increases to only 351 kW, but the maximum beam-loading voltage to 34.8 kV.

The inductance of Finemet is very sensitive to the longitudinal bias field, as is illustrated in Fig. 2. This is a merit in the sense that the inductance can be changed easily. However, this can also be a disadvantage that the precision of inductance control will be much worse than ferrite.

### 3 SPACE-CHARGE COMPENSATION

A high-intensity and low-energy bunch experiences a large longitudinal space-charge force. A particle at time advance  $\tau$  from the bunch center sees, for each turn, a space-charge voltage  $V_{\text{sph}} = -\omega_0^{-1} (d\rho/d\tau) |Z_{||}/n|_{\text{sph}}$ , where  $\rho(\tau)$  is the linear density of the bunch and  $\omega_0$  the angular frequency of the ring. The space-charge impedance per harmonic is  $Z_{||}/n = -jZ_0 [1 + 2 \ln(b/a)] / (2\beta\gamma^2)$ , where  $\beta$  and  $\gamma$  are the Lorentz factors,  $Z_0 \approx 377 \Omega$ ,  $a$  and  $b$  the radii of the beam and the beam pipe. In order to keep the beam particles bunched, extra rf voltage will be required. One way to cancel this space-charge impedance is to add an inductive insertion in the vacuum chamber [5]. Such an attempt [6] had been performed at the Los Alamos PSR, where 60 Toshiba  $\text{M}_4\text{C}_{21}\text{A}$  ferrite cores were inserted intending to cancel about 2/3 of the space-charge force. Wire windings on the outside were used to provide perpendicular biasing so that the relative permeability of the ferrite could be controlled. With the ferrite insertion, it was found that only about 2/3 of the usual rf voltage would be required to keep

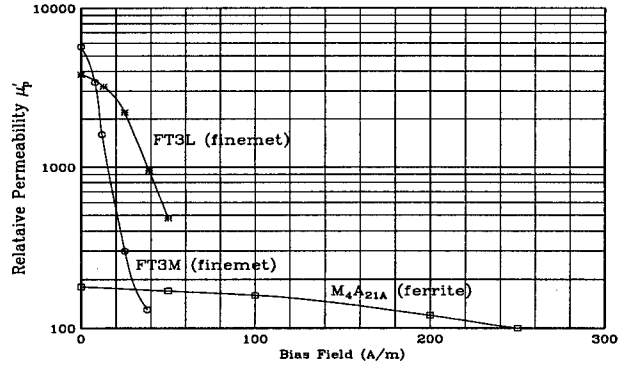


Figure 2: Sensitivity to bias field for Finemet and ferrite.

the bunch stable. When the solenoidal current was turned on, the bunch was found lengthened. Thus the ferrite insertion did actually cancel part of the space-charge force. Another similar experiment had been performed at the KEK Proton Synchrotron with 8 Finemet cores [7]. The incoherent quadrupole synchrotron frequency was measured as a function of beam intensity. The slope of the frequency was reduced by half. The result is consistent with a partial cancellation of the space-charge impedance.

Here, we would like to apply the inductor insertion to the Fermilab low-energy booster ring, with bunches having half widths  $\hat{\tau} = \sqrt{5}\sigma_\tau = 28.25 \text{ ns}$ . The space-charge impedance per harmonic is about  $-j89.5 \Omega$ . Unlike the accelerating cavities, the bunch current will dump energy into the insertion at all frequencies. To estimate this energy, assume a simple model consisting of an ideal inductance  $L$  and an ideal resistor  $R$  in parallel, which gives

$$Z(\omega) = j\omega L \frac{1 - j\omega/\omega_r}{1 + \omega^2/\omega_r^2} \propto j\omega(\mu'_s - j\mu''_s), \quad \omega_r = \frac{R}{L}, \quad (2)$$

so that the series  $\mu'_s$  is relatively constant at low frequencies and rolls off near  $\omega_r$ , while  $\mu''_s$  increases as  $\omega$  at low frequencies and resonates at  $\omega_r$ . The corresponding longitudinal wake potential is  $W(t) = R [\delta(t) - \omega_r e^{-\omega_r t}]$ , and the energy the particle lost to the inductor in one passage is

$$\mathcal{E} = \frac{3e^2 N_b}{2} \left[ \frac{\tau}{\omega \hat{\tau}^3} + \frac{1}{\omega_r \omega_0} \right] \left| \frac{Z_{||}}{n} \right|_{\text{ind}}, \quad (3)$$

where a parabolic bunch distribution has been assumed. The first term is the linear force from the inductive impedance  $Z_{||}/n|_{\text{ind}} = j\omega_0 L$ , which is supposed to cancel the space-charge force, leaving behind the second term, which is the actual energy lost to the insertion. Thus for  $n_b = 4$  bunches the total power lost to the insertion becomes

$$P = \frac{3en_b N_b^2}{4\pi\omega_r \hat{\tau}^3} \left| \frac{Z_{||}}{n} \right|_{\text{ind}}. \quad (4)$$

If ferrite having a resonant frequency  $\omega_r/(2\pi) = 60 \text{ MHz}$  is used, the power lost to the insertion amounts to 0.16 MW. Assuming the ferrite cores in Table I,  $\sim 34$  cores will be required for space-charge cancellation. On the other hand, if Finemet having a resonant frequency 6 MHz is used, the loss becomes 1.6 MW. According to Table 1, 15 Finemet cores are required. The heat dissipation will be  $5.6 \text{ W/cm}^3$ . However, not much longitudinal space is gained by using Finemet but much more energy has to be injected to counteract the power loss. If uncut Finemet core with  $Q = 1$

is used, the resonant frequency is  $\sim 1$  MHz and the power loss will be increased 6-fold. Here, the merits of high  $\mu'_p$  for Finemet can hardly be utilized, because that will lead to a lower  $Q$  and lower  $\omega_r$ , thus increasing the power loss.

Using the same calculation, the power loss to the ferrite cores in the Los Alamos experiment is only 0.82 kW even when the resonant frequency is only 30 MHz. This is because the power loss is inversely proportional to the cubic power of the bunch length. At the Los Alamos PSR, the half bunch length was  $\tau \sim 133.6$  ns, which is 4.73 times longer. Also, there were only  $2.5 \times 10^{13}$  particles in the PSR.

#### 4 RF BARRIERS

Rf barriers are designed in the Fermilab Recycler ring to confine the antiproton beam bunch and shape the bunch distribution waiting for the next collider refill. Rf barriers are also planned to be used in the Brookhaven AGS and the Japan Hadron Project for multiple injections. For the latter, tens of kV are required and a barrier cavity is necessary. We model the cavity by a parallel  $RLC$  circuit. When the switch is closed, the current generator delivers a current  $I(t) = I_0 \theta(t)$ . The cavity gap will respond with a voltage

$$V(t) = \theta(t) \frac{I_0 R}{Q} e^{-\alpha t} \sin \bar{\omega} t, \quad (5)$$

where  $\omega_r = (LC)^{-1/2}$  is the angular resonant frequency,  $\alpha = \omega_r/(2Q)$ ,  $\bar{\omega} = \sqrt{\omega_r^2 - \alpha^2}$ , and  $Q = R/(\omega_r L)$  the quality factor. If the current is turned off at  $t = 2\pi/\bar{\omega}$ , or another current pulse of opposite sign is turned on at that time, the cavity gap voltage will vanish due to cancellation, providing that the degradation  $\exp(-2\pi/\sqrt{4Q^2 - 1})$  is not too excessive. A cycle of sinusoidal gap voltage is generated with peak voltage  $V_0 \approx I_0 R/Q$ . Thus, a large  $Q$  will require a large current pulse. But a small  $Q$  will lead to incomplete cancellation of the sinusoidal rf wave after the current pulse.

Consider a rf barrier at barrier frequency  $f_b = \omega_b/(2\pi) = 2$  MHz and barrier voltage  $V_b = 40$  kV in the AGS. This implies a barrier length of  $0.5 \mu s$ , while the AGS circumference at 1.5 GeV injection kinetic energy is  $2.917 \mu s$ . Again we use the large FT3M Finemet cores with a cut of 4.6 cm and the 4M2 ferrite listed in Table 1. The properties of such a Finemet or ferrite barrier cavity are listed in Table 2. In order to keep the power loss of Finemet below  $10 \text{ W/cm}^3$ , we have to use at least 6 cores with an average flux density of 522 G. If ferrite is used, the average flux density has to be limited to 100 G, requiring 84 cores. The Finemet cavity will take up only  $\sim 33$  cm while the ferrite cavity  $\sim 214$  cm. However, the power dissipation in the Finemet is 95.6 times larger than the ferrite. Since the barrier wave is only present for  $0.5 \mu s$ , the average power dissipation  $P_{av}$  is about 148 kW for the Finemet and 1.55 kW for the ferrite, much less than those computed in the rf cavities in Section 1. Finemet may therefore be a good choice in building a barrier cavity if space limitation is a serious problem.

For an AGS bunch with  $6.0 \times 10^{12}$  protons and  $\sigma_r = 60$  ns, the transient beam-loading voltages computed using Eq. (1) have maxima 0.20 and 4.5 kV, respectively, for the Finemet

Table 2: Properties of a Finemet and a ferrite barrier cavity.

	Finemet	Ferrite
Barrier frequency $f_b$	2.00	2.00 MHz
Quality factor $Q$	24	110
$\mu'_p Q f$ at $f_b = 2$ MHz	3.00	36.0 GHz
Permeability ( $Re$ ) $\mu'_p$	62.5	163
Permeability ( $Im$ ) $\mu''_p = Q\mu'_p$	1500	18000
Inductance $L$	0.511	0.762 $\mu H$
Resistance $R = Q\omega_b L$	154	1053 $\Omega$
Capacitance $C = 1/(\omega_b^2 L)$	12400	8314 pF
Barrier voltage $V_b$	40	40 kV
Total flux density if one core $B_{Tf}$	3133	8355 G
Suitable flux density per core	522	100 G
Number of cores required $N$	6	84
Peak power per core $P_1$	144.2	0.1077 kW
Pk power for $N$ cores $P = NP_1$	865.2	9.046 kW
Average power for $N$ cores $P_{av}$	148.3	1.55 kW
Av power per volume $P_{av}/(NV_c)$	7.53	0.026 $\text{W/cm}^3$

and ferrite barrier cavities. If required, they should be compensated by feed-forward. If uncut Finemet cores are used,  $\mu'_p Q f = 2$  GHz and  $Q = 1$ . One requires 7 cores so that the loss is still below  $10 \text{ W/cm}^3$ . The total average power dissipation increases to only 191 kW, but the maximum transient beam-loading voltage jumps to 2.2 kV.

#### 5 CONCLUSION

It is clear that longitudinal space will be saved and transient beam loading will be smaller when Finemet is used instead of ferrite, especially in acceleration and barrier cavities. However, this gain arrives at the expense of much larger power dissipations. The obvious reason comes from the fact the Finemet has much lower resonant frequencies and lower  $Q$ 's than ferrite. Therefore when longitudinal space is limited, especially for very small low-energy rings, Finemet cavities may be a solution. It is possible that Finemet will become very valuable in other applications at sub-MHz frequencies when high magnetic flux densities are required.

The authors wish to thank Dr. J. Griffin for discussions.

#### 6 REFERENCES

- [1] Y. Mori, KEK Tanashi, private communication. Y. Tanabe, "Evaluation of Magnetic Alloy(MA)s for JHF rf Cavity", talk given at Mini Workshop, Tanashi, Japan, Feb. 23-25, 1998.
- [2] C. Ankenbrandt, private communication.
- [3] J.E. Griffin, "RF System Considerations for a Muon Collider Proton Driver Synchrotrons", Fermilab report FN-669, 1998.
- [4] P. Ausset, G. Charreau, F.J. Etzkorn, C. Fougeron, H. Meuth, S. Papureanu, and A. Schnase, "A High-Power Multiple-Harmonic Acceleration System for Proton- and Heavy-Ion Synchrotrons", PAC 95, May 1-5, 1995, Dallas, p.1781.
- [5] A.M. Sessler and V.G. Vaccaro, "Passive Compensation of Longitudinal Space Charge Effects in Circular Accelerators: the Helical Insert", CERN, ISR Div. 68-1, 1968.
- [6] J.E. Griffin, K.Y. Ng, Z.B. Qian, and D. Wildman, "Experimental Study of Passive Compensation of Space Charge Potential Well Distortion at the Los Alamos National Laboratory Proton Storage Ring", Fermilab FN-661, 1998.
- [7] K. Koba, S. Machida, and Y. Mori, KEK Note, 1997.

# DESIGN AND COLD MODEL TEST OF KOMAC CCDTL\*

Y.S. Cho<sup>#</sup>, J.M. Han, H.E Ahn, B.H. Choi

Korea Atomic Energy Research Institute, P.O.Box 105, Taejon, Korea 305-600

## Abstract

For the first phase of the KOMAC (Korea Multi-purpose Accelerator Complex) project, a CCDTL (Coupled Cavity Drift Tube Linac) which accelerates a 20mA cw proton beam from 3 MeV to 20 MeV is designed. An Al cold model is fabricated to check the design, the tuning method, and the coupling coefficients. To check the engineering design, a Cu cold model is fabricated. The design and the test results will be presented.

## 1 INTRODUCTION

The KOMAC CCDTL has been designed to accelerate a 20 mA cw proton/H- beam from a 350MHz, 3MeV cw RFQ and to inject the 100MeV beam to a 700 MHz, final energy 1GeV cw superconducting linac. The CCDTL is a coupled cavity drift tube linac (CCDTL) structure [1, 2] which allows the focusing magnets to remain outside the vacuum system and does not require permanent magnets that are susceptible to radiation damage due to the high average beam current. The CCDTL structure is less efficient than a conventional DTL, but relatively easier to fabricate and operate.

## 2 KOMAC CCDTL DESIGN

### 2.1 RF Structure

The 700MHz frequency, which is the same frequency of the superconducting linac, can be used for the CCDTL due to the ample space for the quadrupoles. The design parameters of the CCDTL cavity are shown in Table 1. These values, except for the aperture, are conservative for fabrication and cw operation.

Table 1: Design Parameters of the CCDTL cavity

- Frequency : 700MHz
- Space for Quadrupole : >8cm
- Real Estate E : <1MV/m
- Surface E : <0.9 Kilpatrick
- Synchronous Phase : -60 ~ -30 degree
- Focusing : 8  $\beta\lambda$  FODO
- Aperture : Acceptance > 2 transverse emit.

The aperture of the CCDTL can be determined by iterative calculations of the shunt impedance and the beam trajectory for the optimisation. A larger aperture decreases the shunt impedance, but increases the ratio of aperture to beam size (less beam loss). The optimised aperture of the CCDTL is shown in Fig. 1. The transition energy for the number of gaps per focusing period is determined by the space for the quadrupole magnet.

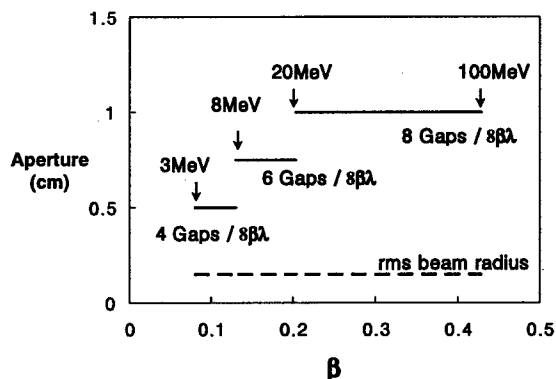


Figure 1: Aperture of the CCDTL and Beam Size

The cavity shapes are determined by SUPERFISH code. Fig. 2 shows the plot of the effective shunt impedance for the cavity and the real estate effective shunt impedance versus particle velocity. In spite of the small aperture, the effective shunt impedance is small in the first part of the CCDTL. This is not serious problem because this part works as a buncher and a matching section.

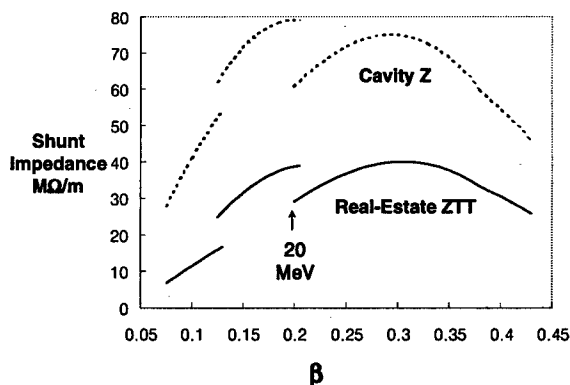


Figure 2: Shunt Impedance versus particle velocity for the CCDTL Cavity

\*Work supported by the Korea Ministry of Science and Technology

<sup>#</sup> Email: choys@nanum.kaeri.re.kr

## 2.2 Beam Dynamics

Beam dynamics for the KOMAC CCDTL are performed using the PARMILA code. For longitudinal matching with 350MHz RFQ, the synchronous phases and the amplitudes of the first part of the CCDTL are adjusted [3].

The beam trajectory and the emittance in the CCDTL are shown in Fig. 3 and 4 with the beam from the RFQ (longitudinal emittance: 0.4 pi degree MeV, transverse rms emittance: 0.32 pi mm mrad) with 100,000 particles. The GL of EMQ is 2.6 T, and the length of poles is 6 cm. The phase and amplitude of the first part for matching is given to obtain the smallest emittance growth. In the final simulation, there is virtually no growth in transverse emittance, and no more than 20% growth in longitudinal emittance, which is not critical.

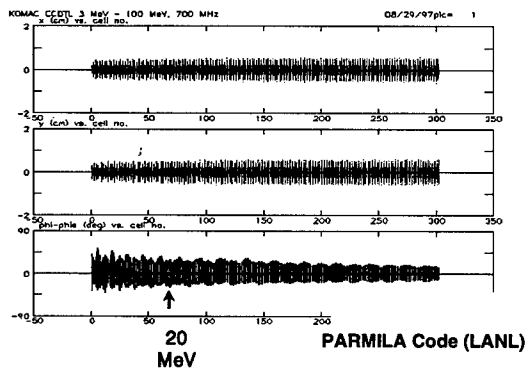


Figure 3: Beam trajectory in the CCDTL

To estimate the tolerances of the CCDTL structure, an error analysis has been done with PARMILA code. With the error in Table 2, which is achievable, the beam envelop calculated with PARMILA code does not grow more than 20%, as shown in Fig. 5.

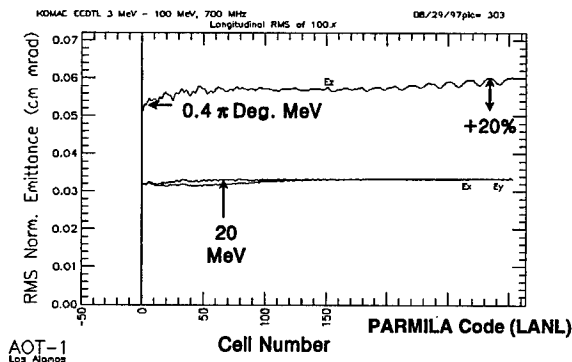


Figure 4: Emittance Profile in the CCDTL

Table 2: Tolerances of the CCDTL

- Field Amplitude : 1%
- Field Gradient : 1%
- Phase : 1 Degree
- Quadrupole displacement : 0.05mm
- Quadrupole rotation : 1 Degree
- Quadrupole strength (GL) : 1%

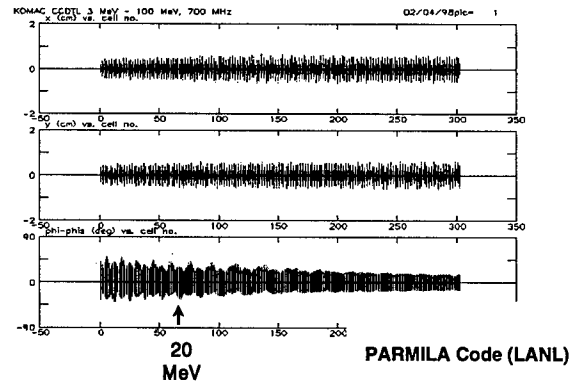


Figure 5: Beam trajectory with the errors in the CCDTL structure

## 2.3 Mechanical Design

To evaluate the manufacturing tolerances of the CCDTL cavity, the perturbation analysis of coupled resonators is used [4]. The tolerance of the cavity frequency is 100kHz, and the coupling coefficient is 0.02 with a tolerance of 1%.

The coupling coefficient between the accelerating cavity and the coupling cavity has been calculated by using the frequency shift between modes, which can be calculated with MAFIA code as shown in Fig. 6. Also, the machining tolerance for the coupling coefficient is 0.1mm, which can be calculated by MAFIA code.

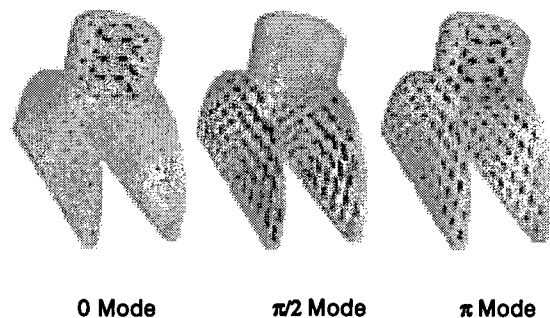


Figure 6: Modes of CCDTL

From this analysis, it has been found that there is no critical problem in fabricating the KOMAC CCDTL



cavities. The technology for conventional CCL, which is well established, can be used in fabrication, tuning, installation, alignment, and operation. For the cooling of CCDTL cavities, the water-cooling channel has been designed and analyzed by ANSYS code as shown in Fig. 7 [5]. The frequency shift due to the thermal expansion is 50kHz. The coolant water velocity is 3 m/s, and the bulk temperature increase of the coolant water is less than 5 K.

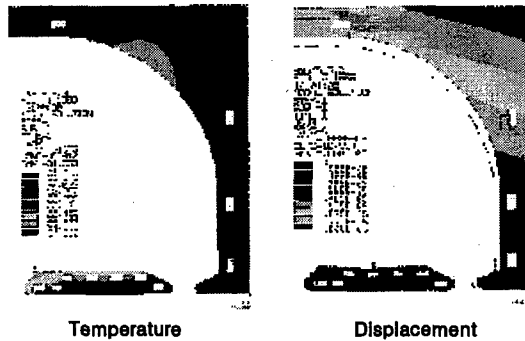


Figure 7: Thermal Analysis of CCDTL Cavity

#### 2.4 Cold Model

The CCDTL cold models are fabricated to check the design, the tuning method, and the coupling coefficients and to check the engineering design. The Al cold model for design check is shown in Fig. 8. The test with this cold model is under study. The Cu cold model for fabrication check is shown in Fig. 9. The measured Q value of the cavity without brazing is 87% of the SUPERFISH calculated Q. The super-drilled coolant path is well fabricated, and this type cooling method will be used for the CCDTL construction. The brazing test will be performed.

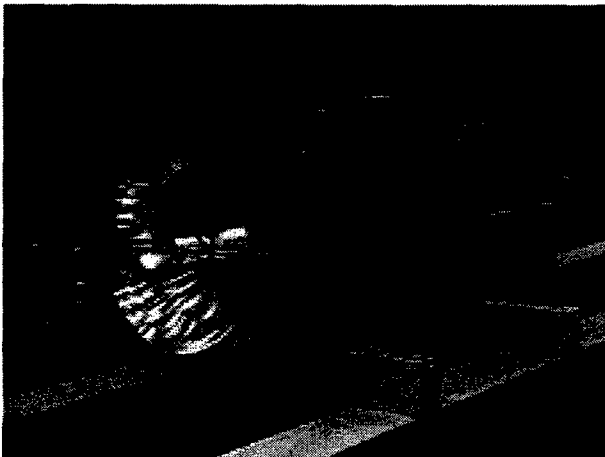


Figure 8: KOMAC CCDTL Cold Model at 20MeV

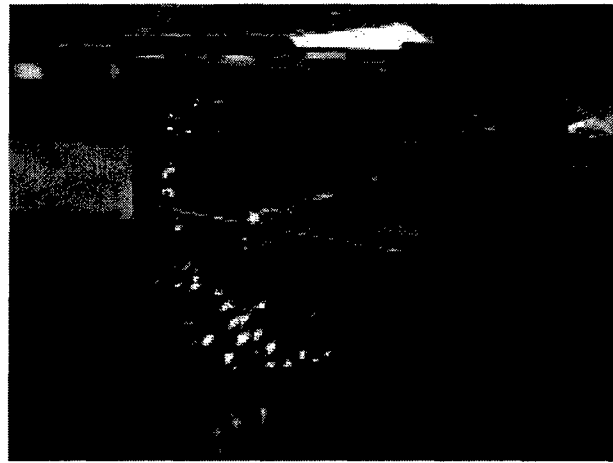


Figure 9: KOMAC CCDTL Cold Model at 20MeV

### 3 SUMMARY

The design of KOMAC CCDTL is summarised in Table 3. The cold models are fabricated and the test is being performed. This model test will improve the KOMAC CCDTL design.

Table 3: Summary of KOMAC CCDTL

Energy (MeV)	3~20	20~100
Current (mA)	20mA	
Structure	CCDTL	
Focusing	8 $\beta\lambda$ FODO	
Gaps per Focusing Period	4 & 6	8
Length (m)	29.8	94.2
# of EMQ	130	173
# of cavity modules	10	32
$P_{\text{cav}}/P_{\text{total}}$ (MW)	1.15/1.49	3.43/5.03

### 5 REFERENCES

- [1] J.H.Billen, F.L.Krawczyk, R.L.Wood, and L.M.Young, 'New RF Structure for Intermediate-Velocity Particles', Proceedings Of the 1994 International Linac Conference, Vol. 1, p. 341.
- [2] 'National Spallation Neutron Source, Conceptual Design Report', the NSNS Collaboration, May 1997.
- [3] S.Nath, J.H.Billen, J.E.Stovall, H.Takeda, and L.M. Young, 'Front-end Physics Design of APT Linac', Proceedings of the 1997 Particle Accelerator Conference.
- [4] D.E.Nagle, E.A.Knopp, and B.C.Knapp, 'A Coupled Resonator Model for Standing Wave Accelerator Tanks', Rev. Sci. Instr. 38, 1583 (1967).
- [5] R.L.Wood, W.L.Clark, F.Martinez, and F.E. Sigler, 'Thermal/Structural Design and Fabrication Development of High Power CCDTL and CCL Structures', Proceedings of the 1997 Particle Accelerator Conference.

# NEXT NEAREST COUPLING FROM ANALYTICAL EXPRESSIONS FOR THE APT LINAC\*

Paul Greninger<sup>#</sup>

General Atomics, San Diego, CA

## Abstract

In order to design any accelerator one should know three constants,  $\Delta f$ ,  $k$  and  $kk$ . The  $\Delta f$  determines the no-slot cavity frequency i.e., the cavity frequency will drop with the introduction of coupling slots. Constant  $k$  determines the coupling between on-axis cavity to cavity. Constant  $kk$  determines the next nearest coupling from on-axis cavity to cavity. In a Couple Cavity Drift Tube Linac the quantity  $kk$  is minuscule. However in a Coupled Cavity Linac [1] because of the close proximity of the coupling cavity slots the quantity  $kk$  or next nearest becomes significant. Recent work at Los Alamos National Laboratory has employed a perturbation technique by J. Gao [2]. Good values of  $k$  are obtained from analytical expressions. With less success the quantity  $\Delta f$  can be calculated. It is the purpose of this paper to extend this type of analysis to include  $kk$  in a CCL. The approach will be to calculate the dipole induced in the slot by the field in the accelerating cavities. Next calculate an interaction energy between the two dipoles and finally employ Slater perturbation [3]. The calculated value of  $kk$  is approximately 0.002, a reasonable number compared to experimental data from the LAMPF [4] accelerator at LANL.

## 1 INTRODUCTION

The motivation for the present paper is to calculate the frequency of coupled cavity structures, rather than measure them. Presently, there is work being performed at Los Alamos National Laboratory in the design of CCDTL [1] for the Accelerator Production of Tritium project. Good values of nearest coupling are obtained by a perturbation technique [2], which involves fields from Superfish models of the on-axis cavity, and the coupling cavity. These fields are entered into analytical expressions, which yield the coupling constant, and the  $\Delta f$ , due to slots. The Superfish cavity frequency is tuned beyond the nominal frequency such that when the slots are introduced the end result is the coupled cavity structure that will resonate at 700 MHz. The unperturbed cavity dimensions, along with the slots are iterated until a self-consistent solution exists at the nominal cavity

frequency. It is the goal of the present paper to extend this work to the design of the CCL, where next nearest coupling is significant, and affects the mode spectrum. The next nearest neighbor coupling constant presented here is based upon a theoretical calculation. Cold models are presently being built for experimental verification. Next nearest neighbor coupling can then be estimated from the mode frequencies and program DISPER [5].

## 2 APPROACH TO COUPLING

J. Gao has published a paper calculating nearest neighbor coupling from analytical expressions [2]. On-axis cavity coupling is calculated from Superfish models of the on-axis cavity and the coupling cavity. The fields in these models set up a pair of interacting electric and magnetic dipoles in the coupling slots. The energy of a self-induced dipole of one cavity interacting with the fields from another cavity is related to the energy term in the Slater perturbation formula. Analytical expressions for the dipole moments set up in elliptical slots came from an earlier paper by Hans Bethe [6]. We will extend the present technique to calculate next nearest neighbor coupling.

## 3 FORMULAS

Because the slots are only in a region of high magnetic flux, we concern ourselves solely with the magnetic dipole term. We shall calculate the coupling from one on-axis cavity to another on-axis cavity. Some coupling may occur through the drift tubes. This can be calculated with Superfish and we found this term negligible.

The magnetic field intensity of a dipole can be expressed as [7]

$$H = \frac{1}{4\pi} \frac{3n(n \cdot m) - m}{|x|^3} \quad (\text{m.k.s.}) \quad (1)$$

Where  $m$  is the magnetic dipole moment, and  $n$  is the unit vector in the  $x$  direction. The interaction energy between dipoles can be derived by summing the effect of magnetic dipole 1 in the field of 2, and conversely dipole 2 in the field of 1. The one-half coefficient in front of the parenthesis in (2) for time averaging.

\*supported by D.O.E. under the A.P.T. program.

<sup>#</sup>Email: grenin@gat.com

$$\Delta W = \frac{1}{2} \left( \frac{\mu_0}{2} m_1 \cdot H_2 + \frac{\mu_0}{2} m_2 \cdot H_1 \right) \quad (2)$$

Employing the notation,

$$\Delta W = \Delta W_{1,2} + \Delta W_{2,1} \quad (3)$$

the quantity  $\Delta W_{1,2}$  is formed by substituting the value of dipole 1 into the  $H$  field of 2.

$$\Delta W_{1,2} = \frac{\mu_0}{16\pi} \frac{m_1 \cdot (3n(n \cdot m_2) - m_2)}{|x|^3} \quad (4)$$

Performing the vector algebra and expressing the total energy

$$\Delta W = \frac{\mu_0}{16\pi} \left( \frac{3(n \cdot m_1)(n \cdot m_2) - m_1 \cdot m_2}{|x|^3} \right) + \Delta W_{2,1} \quad (5)$$

The  $H$  field and the induced dipole orientation for the  $\pi/2$  mode are shown in Fig. 1. Our notation will be AC = Accelerating Cavity, CC = Coupling Cavity.

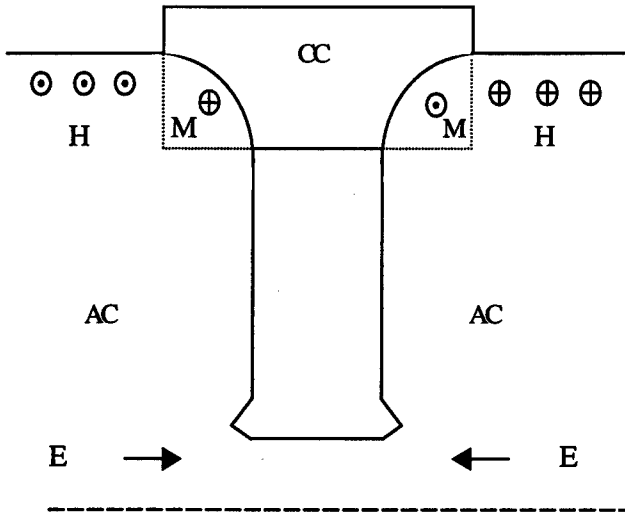


Figure 1: Diagram for Two Coupled Cavities in the  $\pi/2$  Mode.

From the J. Gao paper the value of  $m$  is listed as:

$$m_1 = \frac{\pi \left( \frac{l_1}{2} \right)^3 e_0^2}{3(K(e_0) + E(e_0))} H_1 \quad (6)$$

Where  $e_0^2 = 1 - (l/w)^2$ ,  $l$  is the length of the slot,  $w$  is the width of the slot,  $K(e_0)$  and  $E(e_0)$  are elliptical integrals, and  $H_1$  is the unperturbed field in the AC. A diagram of a slot is listed below.

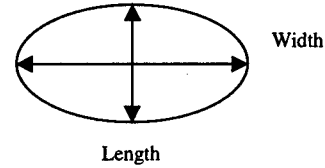


Figure 2. Diagram for Slot Geometry.

The unit normal,  $n$ , from one slot to another is perpendicular to the  $H$  in the slots, therefore the quantity  $n \cdot m$  vanishes.

To calculate  $kk$  look at the mode separation of two AC cavities in the 0 and the  $\pi$  mode. Assume next nearest coupling only. Then in Fig. 1 without the presence of the coupling cavity, the two on-axis cavities behave as if they are in the  $\pi$  mode. From Slater Perturbation the frequency of a perturbed mode can be written as

$$\omega_{\text{mode}}^2 = \omega^2 \left( 1 + \frac{2}{U} \Delta W \right) \quad (7)$$

For the  $\pi$  mode the  $m$ 's are anti-parallel therefore

$$\omega_{\pi}^2 = \omega^2 \left( 1 + \frac{\mu_0}{4\pi} \frac{m_1 \cdot m_2}{U|x|^3} \right) \quad (8)$$

For the zero mode, the  $m$ 's have the same direction.

$$\omega_0^2 = \omega^2 \left( 1 - \frac{\mu_0}{4\pi} \frac{m_1 \cdot m_2}{U|x|^3} \right) \quad (9)$$

From a Talyor expansion one can show

$$2\omega\Delta\omega = \omega_\pi^2 - \omega_0^2, \quad (10)$$

substituting,

$$\Delta\omega = \omega \frac{\mu_0}{4\pi} \frac{m_1 \cdot m_2}{U|x|^3} \quad (11)$$

Finally, with

$$kk = \frac{\Delta\omega}{\omega}, \quad (12)$$

$$kk = \frac{\mu_0}{4\pi} \left( \frac{\pi \left( \frac{l}{2} \right)^3 e_0^2}{3(K(e_0) + E(e_0))} \right)^2 \frac{H_{ac}^2}{|x|^3 U_{ac}}. \quad (13)$$

In analogous fashion, a CC to CC term can also be calculated. This term tends to be less because the coupling cavities are usually staggered off the axis of symmetry, and their slots further apart.

If more cells are added a bi-periodic structure can be formed. The addition of more cells distances us from half-cell end boundary conditions. These end cells do not have the proper boundary conditions to fully reveal next nearest coupling. With all on-axis cavities tuned to one frequency  $\omega_1$ , and all coupling cells tuned to another frequency  $\omega_2$ , the  $\pi/2$  modes are related by the formula [8]:

$$\omega_{\pi/2}^2 = \frac{\omega_1^2}{1 - kk_{ac}} \quad (14)$$

$$\omega_0^2 = \frac{\omega_2^2}{1 - kk_{cc}} \quad (15)$$

The difference between the two modes is the stop band. In a well tuned accelerator the  $\pi/2$  mode for the CC cells is not present because there is no stored energy in them.

## 4 RESULTS

Presently we are calculating a value of 0.00188 for an on-axis cavity with  $\beta=0.42277$  in our CCL. This number is in line with the final tuning data for the Los Alamos LAMPF accelerator [4] where for  $k=0.05$ ,  $kk$  is in the range 0.001 to 0.005.

## 5 CONCLUSION

Reasonable values of the next nearest neighbor coupling coefficient can be calculated approximating the slots as magnetic dipoles and applying the Gao theory. Our value of next nearest neighbor coupling falls within the range 0.001 to 0.005 for values stated in the literature for a CCL with 5% coupling.

## 6 REFERENCES

References:

- [1] Thomas Wangler, *RF Linear Accelerators*. New York: Wiley, 1998, pg. 103
- [2] J. Gao, "Analytical Formulas for the Resonant Frequency Changes due to Opening Apertures on the Cavity Walls," *Nuclear Instruments & Methods in Physics Research*. A311 (1992) 437-443
- [3] John C. Slater, *Microwave Electronics*. New York: Van Nostrand, p. 81
- [4] LAMPF 805-MHz Accelerator Structure Tuning and its Relation to Fabrication and Installation. LA- 7915-MS informal report.
- [5] Computer Program "Disper", written by James Billen, of Los Alamos National Laboratory.
- [6] H.A. Bethe, *Phys. Rev* 66 (1944) 163.
- [7] J. D. Jackson, *Classical Electrodynamics*, New York: Wiley, 1<sup>st</sup> Ed., p. 147
- [8] D.E. Nagle, E.A. Knapp, and B. C. Knapp, "Coupled Resonators Model for Standing Wave Accelerator Tanks," *Review of Scientific Instruments*, Vol. 38, Number 11, Nov. 1967

# HIGH POWER RF CONDITIONING OF THE LEDA RFQ\*

L. M. YOUNG, D. E. REES, L. J. RYBARCYK, and K. A. CUMMINGS,

Los Alamos National Laboratory, Los Alamos, NM, 87545

## Abstract

We are preparing the radio frequency quadrupole (RFQ) for the Low Energy Demonstration Accelerator (LEDA) [1] to accelerate beam. The LEDA RFQ accelerates a 100-mA CW proton beam from 75 keV to 6.7 MeV. We will report our experience with high-power RF conditioning the RFQ, first with one klystron and then with two klystrons. The RFQ will dissipate 1.2 megawatts of RF power at design fields. This 350-MHz CW RFQ [2] has peak fields on the vane tips of 33 MV/m. The average power dissipation is 13 watts/cm<sup>2</sup> on the outer walls of the RFQ near the high energy end. The power from each klystron is split 4 ways to lower the stress on the RF windows. Each klystron can produce 1.3 megawatts of RF power.

## 1 INTRODUCTION

The LEDA RFQ consists of four 2-meter-long RFQs resonantly coupled together to form an 8-meter-long structure. These sections are labeled A, B, C, and D starting from the low-energy end. RF drive ports are located in the B, C and D sections. The RF power is coupled into the RFQ through half-height WR2300 waveguide and a section of tapered ridge-loaded waveguide to a coupling iris. The tapered waveguide has the dimensions of the half-height WR2300 waveguide at one end and tapers to only 7 inches wide at the iris of the RFQ as shown in Figure 1. The gap between the ridges of the ridge-loaded waveguide slowly increases as the cross section increases in size toward the half-height WR2300 waveguide.

RF conditioning of the LEDA RFQ started on November 19, 1998. At that time one klystron was connected through a network of waveguide splitters to the four window-waveguide assemblies that feed RF power to

section B of the RFQ. The four RF drive ports in section C were filled with water-cooled plugs. The four RF drive ports in section D had the lower part of the waveguide taper with the coupling iris installed. A shorting plate affixed to each tapered waveguide positioned the short at  $\lambda_g/4$  from the iris where  $\lambda_g$  is the wavelength of the 350 MHz RF in the waveguide. This arrangement makes each section of waveguide anti-resonant, which results in no net power flow into these waveguides.

## 2 INITIAL CONDITIONING

After the initial demonstration, High Power RF (HPRF) conditioning began in earnest about 9 AM on 11/20/98. For the first hour of conditioning, the RF power level was set at 3 to 5 kW. Multipacting occurred in the vacuum waveguides, most likely near the iris where the gap between the tapered waveguides is slightly larger than the 1/16-inch gap at the iris. This gap increases slowly with distance from the iris. The evidence for this multipacting is the low power level at which the multipacting occurred and the increase in the pressure in the RFQ and the vacuum waveguides. This multipacting disappeared after about an hour and the RF power level was relatively quickly increased to 10 kW as the pressure in the RFQ and waveguides permitted. At the 10 kW power level, the first radiation survey was performed, and as expected, nothing above background was detected outside the accelerator tunnel exclusion area. Radiation surveys were performed at 10, 30, 50, and 70 kW power levels; nothing above background was detected.

The pressure in the vacuum waveguides paced the rate at which we could increase the RF power. A vacuum interlock system used the pressure readings from ion gauges on the RFQ vacuum manifold and on each of the vacuum waveguides to turn off the RF power whenever one of them indicated poor vacuum. The vacuum interlock

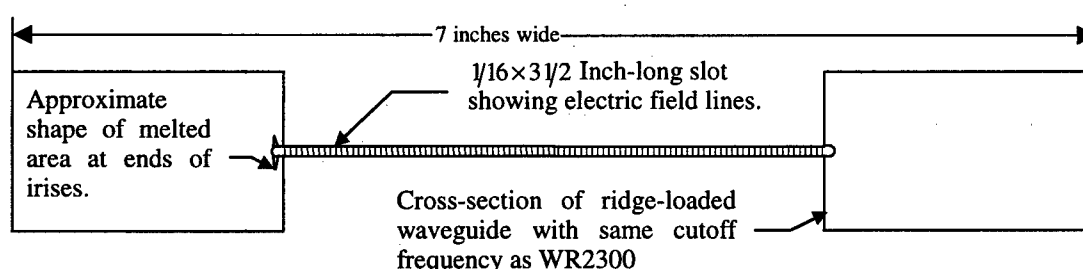


Figure 1 Cross section of ridge-loaded waveguide and dimensions of iris. The iris is a slot 3.5 inches long with a ~1/16-inch diameter hole at each end.

\*Work supported by the US Department of Energy.

thresholds on the RFQ and waveguide were set at  $2 \times 10^{-6}$  and  $5 \times 10^{-6}$  Torr, respectively. On the waveguides this interlock protects the windows from damage that could result from RF power being present under poor vacuum conditions.

The "Blanking Box" (formerly used to protect the CRITS RFQ [3]) was used during the conditioning process to protect the RFQ from internal arcs. This circuit interrupts the drive to the klystrons for 200  $\mu$ s whenever the reflected power exceeds a specified level.

By midnight November 23<sup>rd</sup>, a forward power level of 100 kW had been reached with waveguide vacuum on quadrant 2 at  $5 \times 10^{-6}$  Torr. The pressure in this vacuum waveguide had limited the rate of progress all evening. Various processing schemes were tried, e.g. no amplitude modulation (AM), processing with up to 100% AM (sine wave) and processing with an AM consisting of 100 Hz, 1-2 ms long pulses on top of an 85-90 kW CW background. None of these methods seemed to help increase the sustainable RF power level. This stage of the conditioning process proceeded rather slowly.

### 3 MULTIPACTING

We believe that multipacting in the tapered section of the waveguide caused the slow progress in conditioning the RFQ. At low RF power levels the multipacting occurs close to the iris where the gap is slightly greater than  $1/16^{\text{th}}$  inch. As the RF power increases, the position where multipacting can occur moves up the taper toward the WR2300 waveguide. At the halfway point in the tapered section the gap is 2.9 cm and simple multipacting theory indicates that multipacting can occur with the RF power equal to 68 kW with VSWR=1. This theory indicates that this power level is about the limit for the simple half cycle multipacting. However, it will occur at higher power levels when the VSWR>1 and the waveguide is over coupled to the RFQ.

Our current plan to mitigate the multipacting problem reduces the number of RF waveguide feeds by a factor of two. We will use one klystron on section B and only feed quadrants 3 and 4. On section D we will use two klystrons, each feeding two quadrants. Our original plan used one klystron per section to drive sections B, C, and D with each klystron driving 4 quadrants. Currently with two klystrons attached to the RFQ we must drive the RFQ with at least 800 kW to be above the power level where multipacting is a problem. If we stayed with our original plan, the multipacting would occur at up to 1.2 MW with 3 klystrons. This power is our design power level without beam. By halving the number of waveguide feeds, we will be above the multipacting level at 600kW.

### 4 HIGH POWER CONDITIONING

Conditioning with high power RF pulses began on November 24<sup>th</sup>. By setting the peak RF power to > 400 kW and limiting the pulse length to 67  $\mu$ s we were able to break through the multipacting in the waveguides. Initially, the pulse length was limited to 67  $\mu$ s when the Blanking Box, which was tripping on the fast RF turn-on,

was disabled. Later we modified the Blanking Box to ignore these turn-on transients. We were able to increase the power level to 600 kW with 67- $\mu$ s pulses and 33  $\mu$ s between pulses on this day.

The next day the peak power was raised to 958 kW at 12% duty factor. On both of these two days the conditioning was paced by vacuum in the RFQ. At the high peak power levels the waveguides were not multipacting and the vacuum remained good in the waveguides.

### 5 WINDOWS INSTALLED ON D-SECTION.

The four D-section windows were installed during the first week in December. Because we were not ready to connect a second klystron to the RFQ and the length of the vacuum waveguide and window was effectively  $\lambda_g$ , we installed a piece of  $\lambda_g/4$  waveguide and a short to make each waveguide coupled to section D anti-resonant again. The following week was spent on RF conditioning the vacuum waveguide on section D. Even though there was no klystron connected to the D-section waveguide, the RFQ transmits RF power into the waveguide. This power reflects off the short creating a standing wave in the waveguide. Because of the standing wave multipacting can occur in the tapered waveguide section. By the end of the second week in December the RFQ and waveguides could be operated at power levels up to 100 kW CW from the klystron driving section B. On December 16<sup>th</sup>, the RF power was then increased above the multipacting band to operating levels of 800 kW CW and up to 900 kW peak with a pulsing format.

### 6 TWO KLYSTRON OPERATION

A second klystron was connected to the D-section waveguide network December 17<sup>th</sup>. Continued operation required phase control of the second klystron with respect to the first klystron. By December 24<sup>th</sup>, the RFQ was conditioned to about 1.08 MW average power in a pulsed format with about 1.1-1.2 MW peak.

### 7 IRIS MELTING

The conditioning process resumed on January 5<sup>th</sup> with further operation at 1 MW CW power levels in the RFQ. On January 7<sup>th</sup> a valve was discovered in the closed position preventing cooling from flowing in the vane-tip cooling channels in section C. Although no damage to the RFQ occurred as a result of this lack of cooling, the fields at the D1 waveguide irises were about 10 % higher than normal. Subsequently, when the RFQ was conditioned with the proper level of cooling in section C, 1.2 MW of net RF power in the RFQ was achieved.

However, the reflected power on the D-section waveguide network was now about 10% instead of the 2% observed on December 24<sup>th</sup>. Also, the frequency of the RFQ was 80 kHz lower than previously measured. In the process of looking for the cause of the high-reflected power we removed the window on quadrant 3 of section D and discovered that some melting had occurred at both ends of the iris as shown on Figure 1. Further

investigation revealed that waveguide iris in quadrant 2 of section D also showed evidence of melting. None of the B-section irises or quadrant 1 and 4 irises of section D displayed any evidence of melting. The RF field strength in section B is 10% lower than section D. Also, the field strength in quadrants 2 and 3 were slightly higher than in quadrant 1 and 4 of section D.

A MAFIA calculation on a simplified model of the iris showed the current at the ends of the iris slot was enhanced a factor of 10 over the RFQ wall current. The copper iris plate was only 1/16 inch thick at this point. This localized heating coupled with the increase in surface resistance at elevated temperatures was enough to melt the ends of the iris slots when the RFQ was operated CW at close to the design fields. The model results also showed that by increasing the thickness of the iris plate to 3/8 inch, the size of the hole at the end of the slot doubles for the same coupling. This change will reduce the enhancement of the wall currents from a factor of 10 to only 2.5. We will replace the present 1/16-inch-thick iris plates with iris plates that are 3/8-inch thick.

## 8 RETUNING

The RFQ was retuned in January because the drop in frequency of 80 kHz (caused by the iris melting) was believed to have resulted in a change in the field distribution. A bead perturbation measurement confirmed that the field distribution had changed a small amount. By adjusting the length of only 21 of the 128 tuners we restored the fields to within 1% of the original tune [4] performed before the waveguide coupling irises were installed.

## 9 CONDITIONING AND BEAM

During the final conditioning from January 27 to March 15, 1999 we restricted the RF power dissipated in the RFQ to 1.2 MW or less. This restriction required conditioning the RFQ with a pulsed format whenever we raised the RF fields above the design value. During this period we integrated the low-level RF (LLRF), the HPRF, and the water cooling system to reliably maintain the RF fields in the RFQ. The LLRF system sends a frequency error signal to the RFQ's water cooling system. This resonance control cooling system (RCCS) adjusts the temperature of the water cooling the outer walls of the RFQ to maintain the resonant frequency of the RFQ at 350 MHz. The cooling system also supplies 50° F water to cooling channels near the vane tips.

By March 15<sup>th</sup> the RFQ would run for long periods of time with 1.1 MW average power. On March 16<sup>th</sup>, a 6-mA beam pulsed at 5 Hz and 300  $\mu$ s duration was injected into the RFQ for the first time. We pulsed the RF in the RFQ to ~1.2 MW at 500 Hz and 90% duty factor. The RF pulses were 1.8 milliseconds long. Without steering the beam and with the initial settings of the focusing solenoids in the injector beam line, 4 mA of beam at 6.7 MeV was obtained that first day [5]. By March 19<sup>th</sup> we had increased the injected current to 10 mA with ~100% transmission.

## ACKNOWLEDGEMENTS

We would like to thank Frank Krawczyk for performing the MAFIA calculations to help resolve the iris-melting problem. In addition to the large number of people at LANL, we would also like to acknowledge other institutions participating in the LEDA project including LLNL and TECH-SOURCE (vacuum system), and AlliedSignal (RCCS).

## REFERENCES

- [1] H. V. Smith, Jr. and J. D. Schneider, Status Update on the Low-Energy Demonstration Accelerator (LEDA)," Proc. 1998 LINAC Conf. [Chicago, 24-28 August 1998] (in press).
- [2] D. Schrage *et al.*, "CW RFQ Fabrication and Engineering," Proc. 1998 LINAC Conf. [Chicago, 24-28 August 1998] (in press).
- [3] G. M. Arbique *et al.*, "Beam Parameter Measurements on the CW RFQ-1 Accelerator," Proc. 1992 LINAC Conf. (AECL-10728, November, 1992) 55-57.
- [4] L. M. Young and L. Rybaryk, "Tuning the LEDA RFQ 6.7 MeV Accelerator," Proc. 1998 LINAC Conf. [Chicago, 24-28 August 1998] (in press).
- [5] K. F. Johnson *et al.*, "Commissioning of the Low-Energy Demonstration Accelerator (LEDA) Radio-Frequency Quadrupole (RFQ)," this Conf.

## THE SNS RFQ PROTOTYPE MODULE\*

A. Ratti<sup>#</sup>, R. Gough, M. Hoff, R. Keller, K. Kennedy, R MacGill, J. Staples,  
S. Virostek, R. Yourd

Lawrence Berkeley National Laboratory, Berkeley, CA, USA

### Abstract

The RFQ included in the Front End [1] injector for the Spallation Neutron Source (SNS) operates at 402.5 MHz, with a maximum  $H^-$  input current of 70 mA at a 6% duty factor. It is 3.72 m long and consists of four equally long modules. A brazed copper structure has been chosen due to the high power, high duty factor operation. The 1 MW peak r.f. power is coupled into the structure via eight ports, two per module. Quadrupole mode stabilization is obtained with a set of  $\pi$ -mode stabilizing loops. The conceptual design has been completed, and a single, full size prototype RFQ module has been designed and is under construction to test the fabrication processes and r.f. performance. It will be operated at full r.f. power in order to test its cooling scheme, dual temperature water tuning, mode stabilization and beam acceptance. The detailed design, assembly processes, thermal analyses and a status report for the prototype module are presented.

## 1 INTRODUCTION

The preparation for construction of the SNS RFQ, scheduled for completion by the second half of the year 2001, has begun. An initial step is the fabrication of a single, 93 cm long prototype module. This unit will test and validate all construction techniques, as well as the r.f., vacuum, cooling and tuning performance of the cavity. This paper outlines several details of the design and analysis of the prototype RFQ cavity. In particular, the module-to-module joining and sealing technique, the cavity penetration designs (r.f. ports, vacuum ports, r.f. tuners) and the thermal static and transient response analyses will be described. A schematic view of the prototype module is shown in Figure 1.

## 2 CONCEPTUAL DESIGN

The SNS RFQ [2] is a high power, high duty factor accelerator designed to capture, accelerate and transport up to 70 mA of  $H^-$  beam at a 6% duty factor, with a 60 Hz repetition rate. A four vane configuration has been chosen which will use  $\pi$ -mode stabilizer loops to achieve quadrupole-dipole mode separation [3].

\* Work sponsored by the Director, Office of Energy Research, of the U.S. Department of Energy, under Contract No. DE-AC03-6SF00098.

<sup>#</sup> Email: aratti@lbl.gov

The RFQ operates at 402.5 MHz and will require up to 1 MW of r.f. power to provide the 83 kV vane-to-vane voltage (corresponding to a 1.85 Kilpatrick peak field). The power will be fed into the cavity through 8 coupling ports equally distributed along the RFQ. Most of the power is required to compensate for cavity wall losses with only about 17% of the total power transferred to the beam.

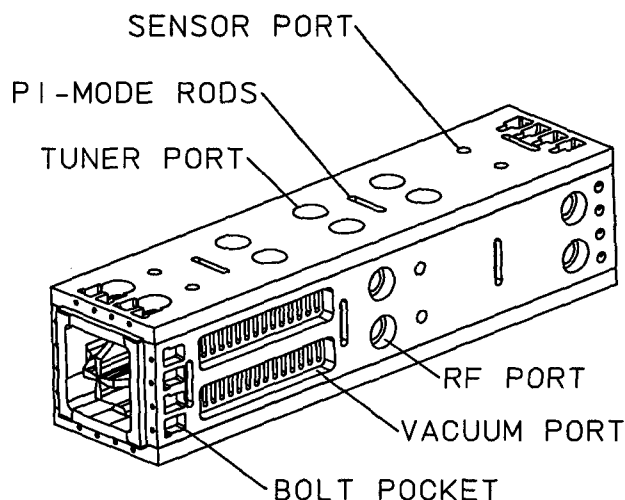


Figure 1: Schematic view of prototype RFQ module

The full RFQ consists of four 93 cm long modules and is constructed of a combination of GlidCop AL-15 and C10100 oxygen free copper (OFE). These materials have been chosen to take advantage of the structural strength of GlidCop and the superior brazing characteristics of OFE copper. The GlidCop is attached to the outer surfaces of the OFE by a braze which is kept completely outside of the vacuum shell. All penetration (r.f. ports, tuners, vacuum ports) vacuum seals are recessed beyond the outer layer of GlidCop and applied directly to the OFE. In order to maintain the very tight tip-to-tip vane tolerances ( $\pm 0.001$  inches) during the final, four vane brazing cycle, a zero-thickness brazing process has been selected. With this technique, the two copper surfaces are brought into direct contact, and the brazing alloy is fed to the adjacent surfaces by means of capillary action. The cavity wall heat is removed by a dual temperature water cooling system, which has been chosen to allow fine tuning of the structure in operation as well as during the initial r.f. power transient after start-up.



### 3 DESIGN AND FABRICATION DETAILS

The RFQ cavities are constructed of OFE copper with an outer layer of GlidCop. The GlidCop plates are machined flat, and rough openings for the vacuum, tuner, r.f. feed and sensing loop ports are added. A rough vane profile is machined on one side of the OFE copper, and 5 mm by 5 mm cavity wall cooling channels are milled into the opposite side. The vane cooling channels are formed by cutting a 6 mm wide by 50 mm deep slot into the back surface of the OFE with a slitting saw. An appropriate filler piece of copper is brazed into place to complete the vane cooling channel. The filler includes squirt tubes at the ends to ensure sufficient cooling where the vanes are cut back at the entrance and exit of the RFQ. The details of the filler piece and squirt tube are shown in Figure 2. Next, the GlidCop is brazed to the OFE using a gold/copper foil to provide a structural connection and to cover the milled cooling channels. This braze is completely outside of the cavity vacuum. Since the cooling channels do not penetrate the ends of the modules, there are no water-to-vacuum joints in the system.

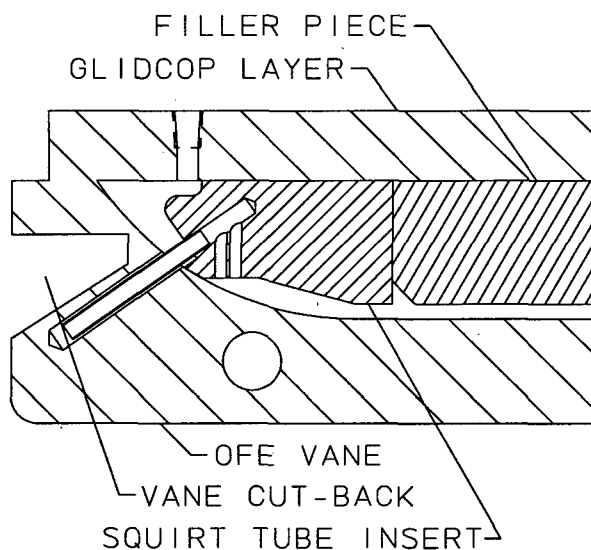


Figure 2: Vane cooling channel and squirt tube details

After brazing, the final vane and cavity profiles are machined into the OFE work piece using custom-made form cutters and end mills. A tolerance of less than  $\pm 0.001$  inches between the quadrant mating surfaces and the vane tips is maintained during this process. The final braze of the four vane quadrants consists of a 'zero-thickness' vacuum braze using Cusil wire. This method allows the RFQ modules to be assembled and the cavity frequency measured prior to the completion of the final braze to allow for adjustments, if necessary. Grooves are machined into the mating surfaces to allow insertion of the braze wire which melts and flows via capillary action

between the preloaded contact areas. The OFE copper  $\pi$ -mode stabilizer rods will also be inserted and brazed into position during this step. The rods are constructed from hollow tubing to allow for active cooling.

The module-to-module r.f. connection will be accomplished by means of a 3 mm wide, 250  $\mu$ m high raised surface machined into the module ends around the periphery of the cavity. This sealing surface is backed up by a canted coil spring which will absorb any r.f. that leaks past the primary seal. Outside of the canted spring is an O-ring which provides the vacuum seal. The load on these seals will be provided by bolts which are recessed into the outer layer of GlidCop by means of bolt pockets and barrel nuts (refer to Figure 1).

The numerous penetrations into the RFQ cavities also require both r.f. and vacuum sealing. The vacuum, tuner, r.f. feed and sensing pick-up ports have sealing surfaces which are recessed beyond the GlidCop and into the OFE in order to keep the GC/OFE joint out of the vacuum. The vacuum ports consist of slotted holes penetrating the OFE copper of the RFQ cavity. The slots are designed to maximize gas conductance while preventing r.f. leakage into the pumps. An O-ring will provide the vacuum sealing for these ports. The tuner, r.f. feed and sensing pick-up ports will use a 250  $\mu$ m thick tin gasket to provide both r.f. and vacuum sealing against the OFE. The tuner ports will use a large snap ring embedded in the GlidCop along with a loading disk to transfer the sealing forces to the RFQ body. This is shown schematically in Figure 3.

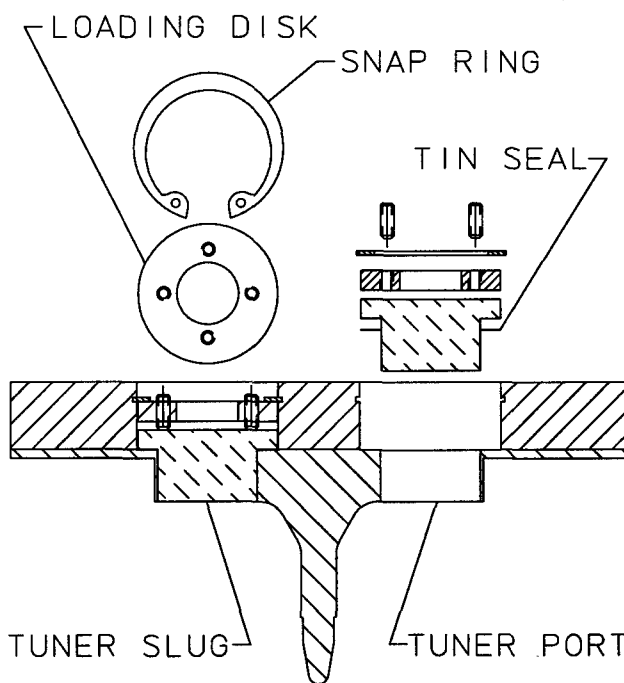


Figure 3: RFQ vane section view showing tuner details

## 4 THERMAL ANALYSES

A thermal model of the RFQ has been created with ANSYS consisting of a 3-D slice of one quadrant of the RFQ cross section. The surface nodes on either side of the slice are constrained to remain coplanar such that the longitudinal stresses are appropriately calculated while allowing for overall thermal growth in the z-direction. This could not be achieved with 2-D plane strain elements which would over-constrain the model longitudinally and result in artificially high z-component compressive stresses. The loads and constraints applied to the model include cavity wall heat from the r.f., vacuum pressure on the cavity walls, convective heat transfer and water pressure on the cooling passage walls and boundary conditions imposed by symmetry constraints.

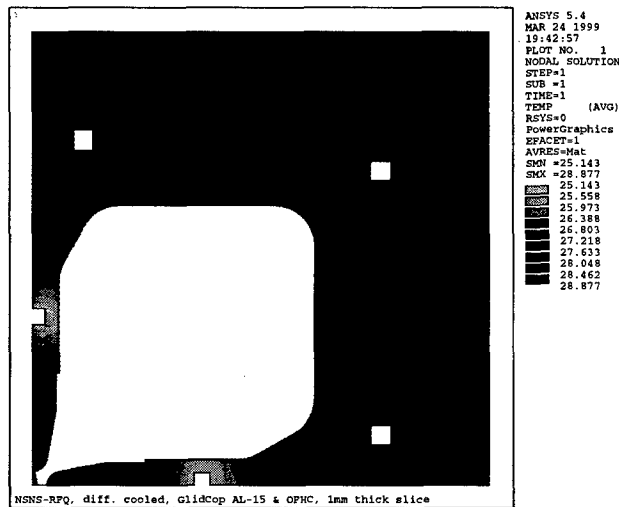


Figure 4: Predicted RFQ cavity wall temperature profile

With 18°C water in the vane channels and 24°C water in the cavity walls, the resulting temperature profile ranges between 25 and 29°C as shown in Figure 4. The highest stresses occur around the cooling channels and are in the range of 800 to 900 psi. In order to predict the frequency shift of the RFQ cavity due to thermal loading, a model was developed which combines the ANSYS displacement results with SUPERFISH calculations of frequency sensitivity. It was determined that the RFQ frequency can be shifted by -33.2 kHz for every 1°C rise in the vane cooling water temperature. This sensitivity to vane water temperature will be used to fine tune the RFQ frequency during operation.

The calculations described above were based on the nominal input temperatures of the vane and wall cooling water. However, as the water flows from the input to outlet end of one RFQ module, its temperature will rise as it absorbs heat. The vane water temperature rises by 3.7°C and the wall water by 1.6°C, thus creating a

different cross section temperature profile at the end of the RFQ module. The calculated frequency error due to the higher water temperatures is -80 kHz. This error will be corrected by adjusting the position of the fixed slug tuners along the length of the RFQ modules.

A series of transient analyses were performed using the same FEA model to determine the frequency performance of the system during turn on of the r.f. power. With 18°C water in the vanes and 24°C water in the walls and no heat on the cavities, the frequency of the system is 216 kHz higher than the nominal 402.5 MHz. To correct this situation, the vane water is initially run at about 23.7°C and immediately switched to 18°C as the r.f. power is turned on. However, since the system responds faster to the wall heat than to the change in coolant temperature, a peak frequency error of -90 kHz occurs about 20 seconds after the r.f. turn-on, with the nominal frequency being achieved after 4 minutes. To minimize the frequency error, the r.f. is initially applied at 70% of full power and ramped up to 100% over the next 150 seconds, resulting in a maximum error of less than 15 kHz.

## 5 STATUS

Most of the manufacturing steps have been successfully tested in small samples and models, including vane profile, modulation cutting and module-to-module r.f. and vacuum sealing. The machining of the material of the prototype module has started. Testing of this unit is expected to begin this fall.

## 6 ACKNOWLEDGMENTS

The authors would like to acknowledge the continuous support received from Dale Schrage and the design team of the LEDA RFQ at LANL [4]. The inspired leadership of Bill Appleton and the ORNL project office is also acknowledged.

## 7 REFERENCES

- [1] Keller, et al., "The SNS Front End Systems", Int. Topical meeting AccApp '98, Nuclear Applications of Accelerator Technology, Gatlinburg, 1998
- [2] Ratti, et al., 'Conceptual Design of the SNS RFQ', LINAC98, Chicago, IL, August 1998
- [3] Ueno, et al., "Beam Test of the Pre-Injector and the 3-MeV H<sup>-</sup> RFQ with a New Field Stabilizer PISL", LINAC96, August 1996, Geneva, CH
- [4] Schrage, et al., 'CW RFQ Fabrication and Engineering', LINAC98, Chicago, IL, August 1998

# IHEP 2K-RFQ CAVITY STUDY

E. Zaplatine\*,  
Forschungszentrum Juelich, Germany

## Abstract

The abandon of a constant RF voltage on the accelerating periods of the structure with spatial periodic RFQ focusing critically extends the range of the applicability, but complicates the tuning. The tuning procedure of the required increasing voltage on the accelerating periods along the accelerator, partition of this voltage between accelerating and focusing gaps are described in the paper. Some features of the tuning are discussed.

## 1 INTRODUCTION

An accelerating complex of IHEP (Institute of High Energy Physics, Protvino) includes a linac with a final energy of 30 MeV (URAL)[1]. This is a first and up to now the only accelerator in the world on such energy with the initial and main parts built on the base of the radio-frequency quadrupoles. The complete project is developed in IHEP. The machine comission has been made in 1977 and since 1983 it is in a full operation.

In two initial parts of the accelerator a well-known and wide used RFQ structure with modulated along cavity length electrodes is used.

The way of forming of an accelerating voltage component using the voltage on quadrupole electrodes does not allow to create the required accelerating gain. The particles during their motion along the homogenous quadrupole interact only on the certain parts with an electric RF field where the field is close to its amplitude value. Those parts of the quadrupole where the interaction with field is weak could be removed. The quadrupole channel becomes space-periodical but nearly with the same focus rigidity. The required longitudinal accelerating field component is created in the parts where the quadrupole is removed.

Based on this idea the RF field space-periodic focusing is used in the main part of an accelerator. The acceleration and focusing are accomplished in the "double gap" formed by three electrodes of a special shape (Fig. 1). One of the electrodes, "intermediate", is under zero potential. Two others, "main", are fixed to the cuts of H-cavity. The focusing field component is created in the space between "horns", fixed on the backs of neighboring electrodes. The electrodes are installed in two chamber H-cavity (2K-Cavity) schematically shown on Fig. 2.

## 2 2K CAVITY TUNE

The main disadvantage of an RFQ accelerating structure on the base of H-cavity is an accelerating gain decrease,

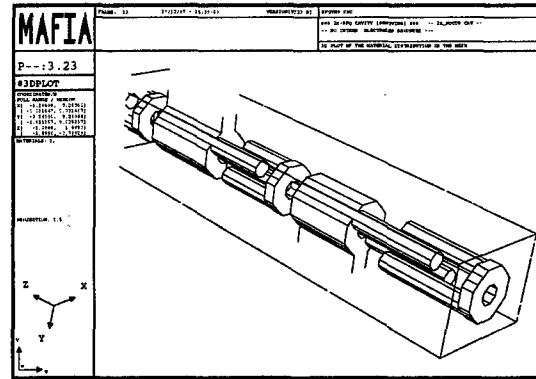


Figure 1: Electrodes at the Beginning of Cavity.

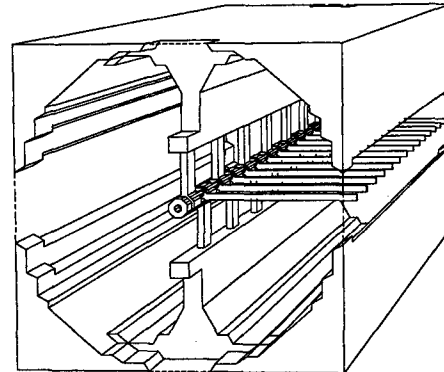


Figure 2: 2K-RFQ Cavity Geometry.

which limits an application of such structure. The reason of such decrease lies in the choosen voltage distribution on electrodes – voltages on accelerating  $U_{acc}$  and quadrupole  $U_{quad}$  gaps are equal.

During a such structure tuning a condition  $U_{acc} = U_{quad}$  is accomplished by equalization of capacitances of accelerating  $C_{acc}$  and quadrupole  $C_{quad}$  gaps by means of special elements. An absence of currents along intermediate electrodes is a moment of an equalization of gap capacitances.

This disadvantage can be eliminated by  $U_{acc} = U_{quad}$  condition violation. In[2] it is shown that the accelerating voltage grow along the cavity while the quadrupole voltage kept constant reasonably increases a such structure application. For such idea realization a two-chamber (2K) cavity can be used.

A changeable voltage ratio on accelerating periods leads to a more complicate structure tuning procedure. The volatge ratio corresponds to the capacitance gap ratio –

$$\frac{U_{acc}}{U_{quad}} = \frac{C_{quad}}{C_{acc}} \quad (1)$$

\* On leave from the Joint Institute of Nuclear Research, Dubna.

And in the case of an absence of a current along an intermediate electrode –

$$\frac{\int_{S_{acc}} H_{acc} ds}{\int_{S_{quad}} H_{quad} ds} = \frac{C_{quad}}{C_{acc}} \quad (2)$$

Thus, in the considered case the task of rf tuning is to provide the required voltage ratio by means of accomplishment of a certain ratio between  $C_{quad}$  and  $C_{acc}$  at the intermediate electrode current absence. This can be achieved by a choice of intermediate electrode ground connector position corresponding to  $S_{acc}/S_{quad}$  ratio.

### 3 3D CAVITY SIMULATION

To simulate this cavity structure 3D MAFIA codes have been used[3].

The main characteristics which differ an accelerating structure built on H-wave from other cavities is a small cross-section (less than  $\lambda/2$ ) and a complicate boundary configuration. Such cavity is excited on the wave, which is similar to H-wave of a regular waveguide with the same cross-section. At the moment the most developed H-cavity is a basic cavity of a linear accelerator-injector for the Serpukhov Booster Synchrotron. An application of two-chamber 2K-cavity should result in a higher quality value than in H-cavity, a higher shunt impedance and to increase the energy range where the RFQ cavity use is more effective to compare with other accelerating structures.

During a numerical simulation the maximal number of mesh points that we used is under 1 million. The total cavity length is 2176 mm, cavity diameter is 540 mm, the electrode and aperture radius is 5 mm. The smallest mesh size is 3.3 mm. For the proper simulation of electrode structure we concentrated most of the mesh in a central region. The real electrodes should be rounded at their ends. To avoid an electrode tip radius simulation electrode lengths have been reduced by 1/3 of radius. As soon as the purpose of the work was to investigate the behaviour of a field distribution depending on intermediate electrode positions this simplifies requirements on overall accuracy of calculations.

Fig. 3 shows the electric field distribution along cavity when all intermediate electrodes are grounded like on Fig. 2. The inductance of the cavity walls is shunted by the inductances of intermediate electrode connectors and current flows only along few first these connectors.

To fulfill a condition (2) the connectors have been placed under a certain angles (Fig. 4). As soon as electrodes in end regions disturb a magnetic field flux the connectors close to end regions placed slightly under different angles. The electric and magnetic field distributions for this case are presented on Fig. 5. The behavior of an electric field distribution along cavity axes is defined mainly by the difference in the type of end region electrodes - "horns" at the beginning of cavity and "gap" at its end (Fig. 1). If to remove "horns" at the beginning the electric field distribution changes into sinusoidal. Here big picks are the field

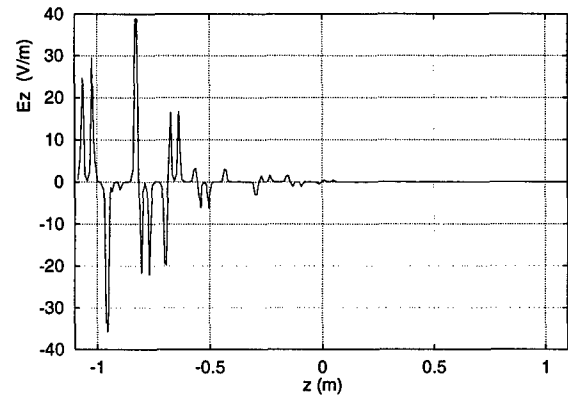


Figure 3: Electric Field Distribution for Grounded Intermediate Electrodes at the Same Side.

in "gaps" and two in series small picks after every big are fields between "horns" and drift tubes.

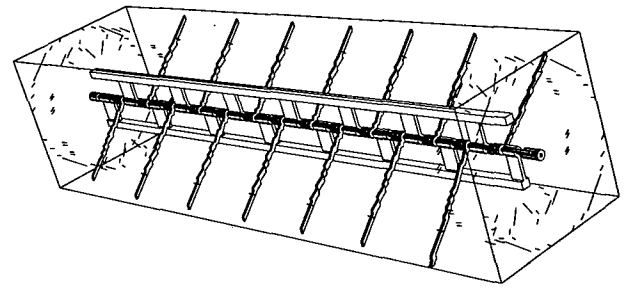


Figure 4: "No Current" Position of Intermediate Electrodes.

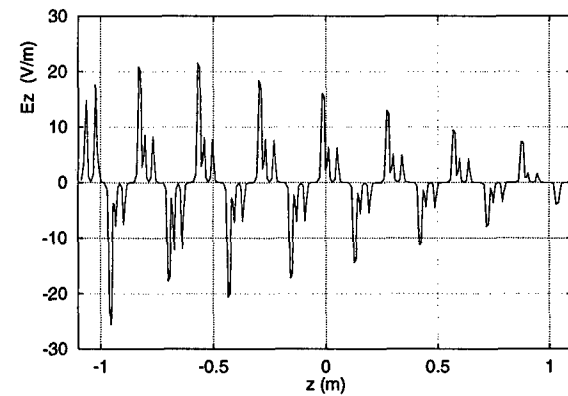


Figure 5: Electric Field Distribution for "No Current" Position of Intermediate Electrodes.

The required accelerating voltage grow along the cavity can be achieved by a structure cross section size change (Figs. 6- 7).

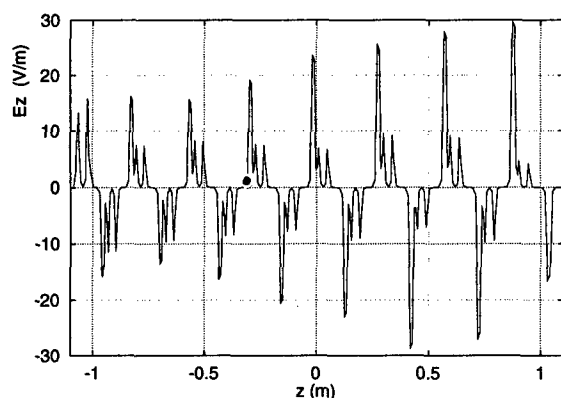


Figure 6: Electric Field Distribution Along Cone Cavity.

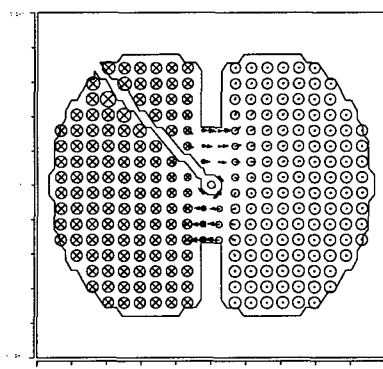


Figure 7: Magnetic Field Distribution Across Cavity.

For a fine cavity frequency tune an inductive plunger without sliding spring contacts has been proposed. The plunger design allows to work without heating of inner components of plunger housing[4]. It can be installed in end regions as well as in the middle of cavity. Fig. 8 shows the results of plunger simulations. A plunger diameter is 140 mm. In our case the plunger is installed in the minimum of the magnetic field of second harmonic.

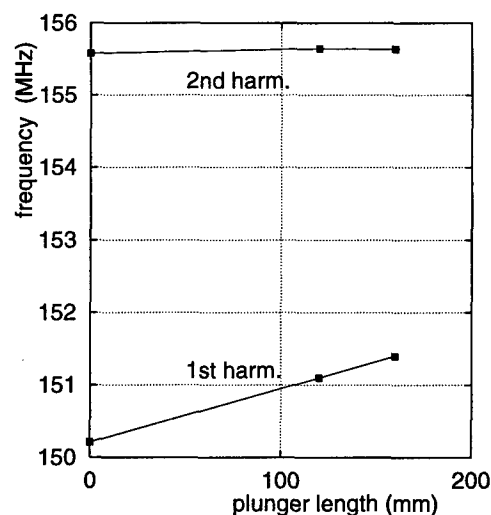


Figure 8: Cavity Frequency Dependence on Plunger Length.

#### 4 ACKNOWLEDGMENTS

The author would like to thank Prof. V. A. Tepljakov and Dr. V. B. Stepanov for the permanent interest to this work and helpfull discussions.

#### 5 REFERENCES

- [1] V.A.Tepljakov, in "Pribory i Technika Experimenta", 1964, No.6, p.24.
- [2] A.B. Barsukov, IHEP Preprint 90-4; 90-7. Protvino, 1990.
- [3] T. Weiland, "Solving Maxwell's equations in 3D and 2D by means of MAFIA", Proc. of the Conf. on Computer Codes and the Linear Accelerator Community, LA-11857-C, (1990).
- [4] Yu. Senichev et al., "Solving the Problem of heating of RF contacts in Cavity Tuners", Proc. of PAC'97, Vancouver.

# DESIGN AND TESTING OF THE ISAC RFQ CONTROL SYSTEM

M. Lavery, K. Fong, S. Fang  
TRIUMF, 4004 Wesbrook Mall Vancouver, BC

## Abstract

A Digital Signal Processor-based control system has been designed and tested for use with the ISAC RFQ accelerator. This system uses a direct digital synthesizer and phase-locked loop to generate the 35MHz nominal cavity frequency. One DSP provides both in-phase and quadrature control for the system. A second DSP operates the cavity tuning mechanism. A reference signal with digital controlled phase shift is output for use in the upstream cavity in the beam path, an 11.66 MHz prebuncher. The system incorporates spark and high Voltage Standing Wave Ratio detection and protection. It also includes operator-controlled hardware limiting, and visual feedback of operating conditions. The complete system including low-level RF components is housed in a VXI rack. Turn-key operation is achieved via a supervisory control, which consists of a Windows-based server. This server broadcasts system status using User Datagrams, and listens on control commands via TCP. Network-aware database objects interpret these messages to provide control and display of the system operating parameters.

## 1 INTRODUCTION

This paper outlines the design and describes some of the test results for the ISAC RFQ control system. The design of the frequency source for the RFQ was detailed in an earlier paper [1]. This system shares several elements in common with an earlier predecessor, the ISAC pre-buncher [2]. It differs largely because of the significantly different drive requirements of these two systems. The buncher's requirement was for a relatively low power (hundreds of watts) sawtooth drive waveform into a resistive load. The RFQ, on the other hand, is a high Q (~7000) resonant system with a maximum drive level of 70 kW at a voltage of 80 kV. This increases the requirements for frequency tuning, maximum drive limiting, spark detection, and response time.

The RFQ control system also provides a phase adjustable reference frequency to the pre-buncher.

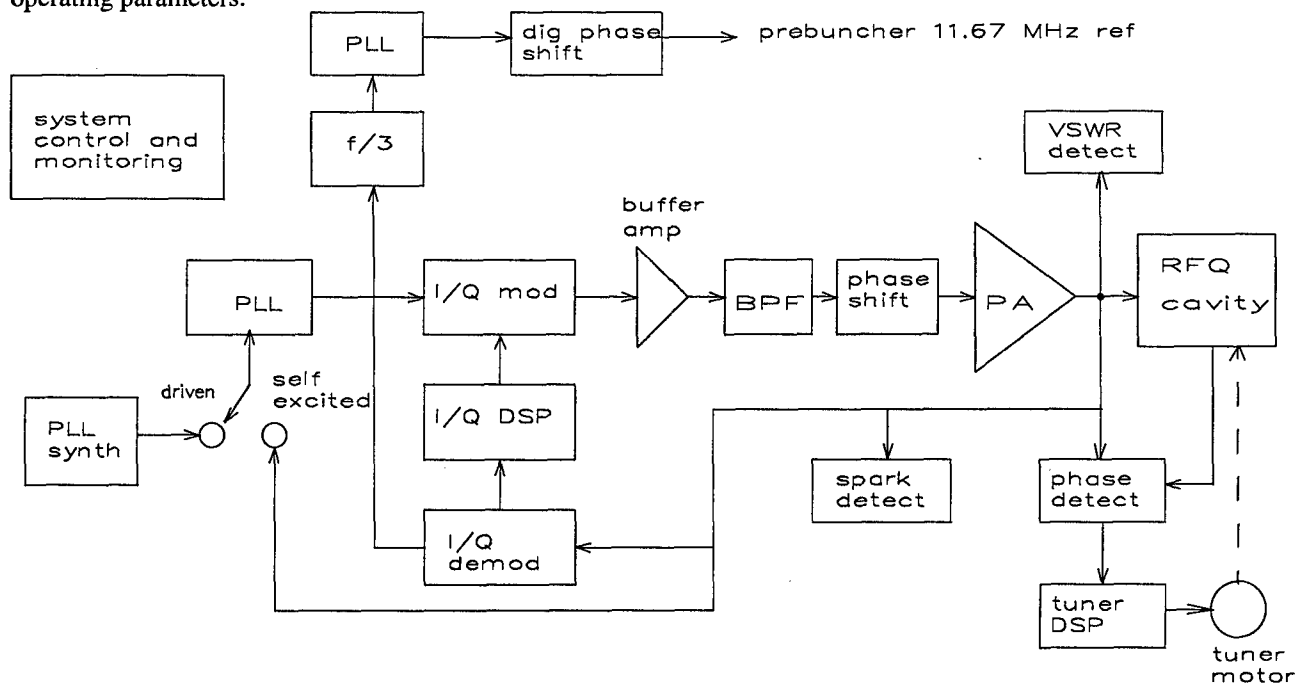


Figure 1 - System Block Diagram

## 2 SYSTEM BLOCK DIAGRAM

A block diagram of the RFQ control system is given in Figure 1. This system has two operating modes - either driven from a digital synthesizer, or self-excited via feedback from the cavity. The latter mode is used during warm-up to alleviate the problem of a continually changing cavity resonant frequency. Once the RFQ has reached its operating temperature, operation is normally switched to driven to improve frequency stability and phase noise. A phase-lock loop is used after the switch. The loop filter prevents any phase jump during switching. It also provides an excitation frequency in the self-excited mode before the cavity voltage is high enough for self-sustained oscillation. Conventional I/Q modulator and demodulator modules, together with the I/Q DSP, provide the basic control loop. A high VSWR detection circuit and spark detector provide protection to the power amplifier and cavity in the event of fault conditions.

A phase detector provides the input to the tuner DSP. The amplified tuner DSP output drives a servomotor to provide the cavity tuning. As mentioned previously, the RFQ reference frequency is divided by three and fed to a PLL to produce a reference for the preceding stage in the beamline, the prebuncher. A programmable phase shifter is also provided for this signal.

## 3 I/Q DSP FIRMWARE

When the RFQ control system is initially set up, the loop phase is adjusted to minimize crosstalk between the I and Q channels. The DSP can then implement two independent PID loops to regulate the two channels. The basic PID algorithm was derived from the continuous time equation as follows:

Time Domain:

$$m(t) = K \left[ e(t) + \frac{1}{T_i} \int e(t) dt + T_d \frac{d}{dt} e(t) \right]$$

Laplace Transform Frequency Domain:

$$Y(s) = X(s) \cdot K \left( 1 + \frac{1}{T_i s} + T_d s \right)$$

Applying bilinear Z transform:

$$s \Rightarrow \frac{z+1}{z-1}$$

$$y(z) = x(z) \cdot \left\{ \frac{k_1 + k_2 z^{-1} + k_3 z^{-2}}{z^{-1} - 1} \right\}$$

Several implementations of this equation are possible. The one which proved most efficient to implement using this DSP (Motorola 56002) is the following:

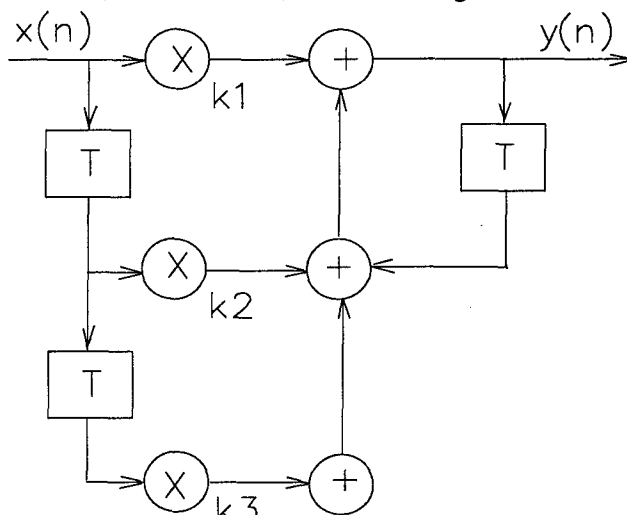


Figure 2 - PID Implementation

This is achieved by this discrete time DSP calculation:

$$y(n) = y(n-1) + k_1 x(n) + k_2 x(n-1) + k_3 x(n-2)$$

This equation requires three instructions to implement on the DSP. Input, output, and overhead add three more instruction cycles for a total of six for the basic algorithm. At the 64 MHz clock rate used, this would yield a sampling frequency in excess of 5 MHz for a single PID controller. Since the system bandwidth is limited by the high Q cavity to about 5 KHz, this far exceeds the minimum desired rate of about ten times the Nyquist frequency. To make better use of this capacity, it was decided to implement both I and Q control on the same DSP.

Also, several other features were added to the basic control firmware. The built in DSP hardware limiting is used to provide symmetrical bipolar limiting of the control output signals. This is achieved relatively simply by alternately adding and subtracting an offset value to the output. If the output is within the limiting window, it is unchanged. If not, it is limited to a fixed positive or negative value.

The DSP also reports back its open or closed loop status, as well as the value of the error signals for the two loops. A large part of the DSP dynamic range is used to reduce line frequency power supply ripple. When the system was first tested, this resulted in large variations in output power when switching to open loop mode. Previous practice had been to freeze the last close-loop output values when switching to open loop operation. To reduce this variation, a 60 Hz cutoff low pass filter was added to the DSP firmware to average the output drive and give consistent levels when switching to open loop.

The firmware also provides for a pulsed mode of operation with a fixed 10% duty cycle, and amplitude control only. This mode is used to test the step response of the system and allow for quick optimization of the PID loop parameters.

The output of the high VSWR detector is returned to the DSP as a stream of interrupts. The first interrupt opens the control loop and reduces the output drive by a predetermined amount. Successive interrupts continue to reduce the output drive until the reflected power is brought down to a tolerable level. At that point, the VSWR detector ceases to interrupt the DSP, the problem can be corrected, and normal operation can be restored.

#### 4 RFQ TUNER DSP FIRMWARE

For the RFQ tuner the required control bandwidth is in the fractional Hz range. To achieve this, the DSP sampling rate was reduced to 100 Hz. Since only one dimensional control is required, only the I channel is used. The coefficients are adjusted so that the control is basically proportional, with both the integral and derivative modes effectively disabled. Since the control output corresponds to tuning motor drive, while the feedback is the cavity phase, the integral function is an inherent part of the system.

#### 5 CONTROL SOFTWARE

An embedded PC located in Slot 0 of the VXI mainframe provides supervisory control to the regulating feedback loops. This includes switching the RF on or off, selecting the PID coefficients for the feedback loops, and selecting the maximum allowable drives and the regulating amplitudes and phases. It also enables the regulating loop, as well as monitoring the loops' status and voltages at various locations. The remaining task it performs is to provide communications to a central control system for remote operation. The supervisory code is a Windows-based application program written to provide interfaces among the hardware modules, and between the hardware and the local/remote operators. The multi-tasking control software is written in C++, using Borland's Object Window Library.

The supervisor is connected to the overall control system via a private ethernet. Using Winsock 1.1, the system provides two sockets for communications, one as an User Datagram Packets (UDP) server and the other as a Transmission Control Protocol (TCP) server. UDP is chosen for commands and status that are frequently adjusted such as voltage, phase setpoints, and readbacks. TCP, which is a more reliable and positive connection protocol, is used for commands that are infrequently changed, such as switching the RF to a particular operating mode.

### 6 TEST RESULTS

The system was commissioned without any major problems, other than the length of time required to condition a new cavity. Several refinements were added during the testing phase, one of which - adding a line frequency filter to the open loop hold value - has already been mentioned. A sample spectrum of the system in operation is shown in Figure 3.

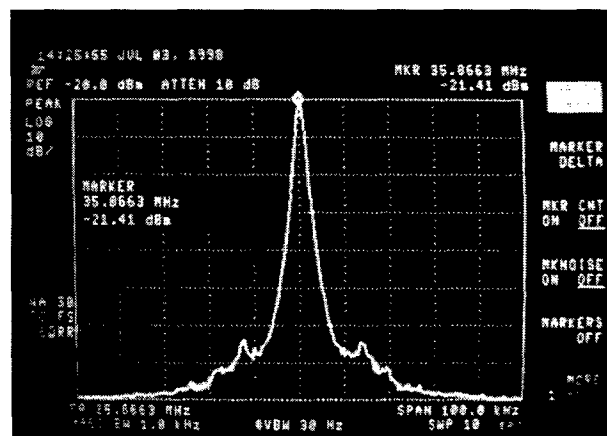


Figure 3 - Close-loop Spectrum

As may be seen, the sidebands are suppressed by a minimum of 65 db, which is approaching the noise floor of the system.

Also during this period, the spark and VSWR detection were optimized to meet the needs of this system. A photo of the spark detector in operation is shown in Figure 4. The logic was ultimately set to ignore sparks of under 80 usec. duration.

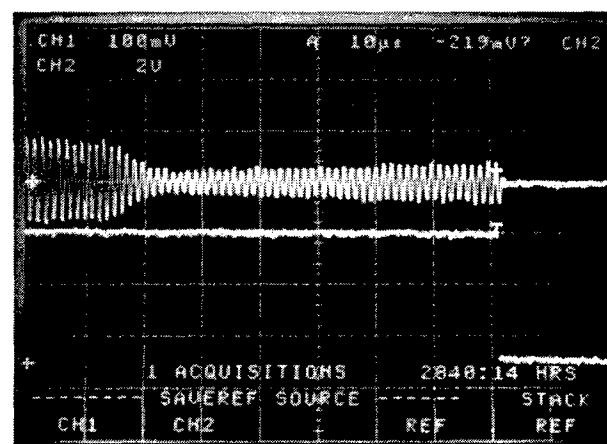


Figure 4 - Spark Detector Operation

### 8 REFERENCES

- [1] K. Fong, S. Fang, and M. Laverty, "Frequency Source for the ISAC RFQ", Linear Accelerator Conference, Chicago, August 1998.
- [2] M. Laverty, K. Fong, S. Fang, "A DSP-based Control System for the ISAC Pre-Buncher", Proceedings of the International Conference on Accelerator and Large Experimental Physics Control Systems, Beijing, November 1997, pp. 263-5.



# HIGH POWER TEST OF THE ISAC TRIPLE GAP BUNCHER OPERATING IN CW MODE

Y. V. Bylinsky, A. I. Kvasha, A. A. Menshov, P. N. Ostroumov, V. V. Paramonov, INR RAS  
G. Dutto, R. E. Laxdal, A. K. Mitra, R. L. Poirer, TRIUMF

## Abstract

A separated function, variable energy, drift tube linac (DTL) operating in cw mode at 105 MHz is being built for the ISAC radioactive beam facility at TRIUMF. Included in the design are three buncher cavities installed in the first, second and third drift spaces between the five IH tanks. The main requirements of the bunchers are: cw mode, high effective voltage (up to 0.32 MV), large velocity acceptance (1.8-4.1%). The first DTL buncher has been developed at INR and is being tested at TRIUMF. It is a triple gap split-ring rf structure operating at 105 MHz. Signal level measurements give a Q-value of 4300 which is 74% of MAFIA simulation predictions and a resonant frequency within 0.6% of the calculated value. With cooling water flow of 20 l/min the mechanical vibrations were measured to be of the order of 1  $\mu$ m. Although the design parameters are 56 kV gap voltage and 8 kW nominal power, we demonstrated 85 kV and 16 kW respectively with stable operation.

## 1 INTRODUCTION

Buncher is designed as a triple gap split-ring rf structure operating at 105 MHz in cw mode. Buncher specifications are given in Table 1 and described in details elsewhere [1]. The effective voltage  $V_{eff}$  is quoted for the particle design velocity.

Table 1: Summary of parameter specifications for triple gap Split-ring buncher

Frequency	$f$	105 MHz
Particle design velocity	$\beta_0$	0.023
Effective voltage	$V_{eff}$	190 kV
Drift tube voltage	$V_i$	56 kV

Detailed study based on the MAFIA 3-D simulations has been performed in order to meet buncher specifications [2]. A series of various measurements has been conducted at TRIUMF to ensure a stable and reliable device operation. Basing on these results two other DTL bunchers will be designed and manufactured in a year from now.

## 2 MECHANICAL DESCRIPTION

A general view of the buncher structure is shown in Figure 1. Buncher basic dimensions are presented in Table 2.

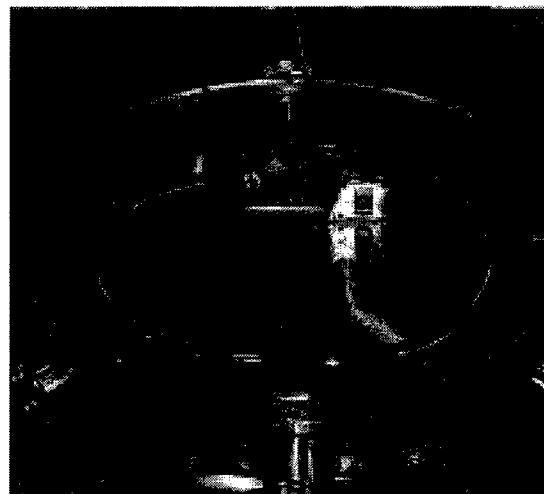


Figure 1: General view of the Split-ring buncher.

Table 2: Split-ring buncher basic dimensions

Tank diameter	[mm]	550
Tank length	[mm]	98
Ring bending curvature radius	[mm]	175
Ring tube diameter	[mm]	25
Aperture diameter	[mm]	14
Drift tube diameter	[mm]	30

Split-ring is made of copper tube. 2 half rings, which carry the drift tubes, are mounted on a supporting leg. Rings are declined in beam direction in order to bring ring tips right at the corresponding drift tube centres. Half-rings contain straight cylindrical extensions at the bottom and 2 short cones on top to support the drift tubes. Straight cylindrical part and cones serve for the coarse frequency tuning. The rings are water cooled.

A capacitive frequency tuner is dedicated for fine tune of the buncher fundamental frequency and to operate as an executive body in the frequency feedback loop of the rf control system. It is a cooper plate with 55 mm in diameter, supported by the rod. An automatic mechanical actuator allows 40 mm movement, brining the plate to the drift tubes as close as 10 mm. Tuner is not cooled.

Buncher is fed through a coupling loop, attached to a standard transmission line (3.125"). A ceramic tube serves as an rf vacuum window. Window area is cooled, while the loop itself is not.

Both cooper buncher body and stainless steel lid are water cooled.

### 3 RF SIGNAL LEVEL TEST

First frequency measurement gave 600 kHz offset from the MAFIA prediction. The coarse frequency tuning was done by means of ring length correction. A bead-pull measurement allowed reconstruction of the electric field distribution along the beam axis as well as shunt impedance evaluation. Figure 2 shows experimental points in comparison with SUPERFISH simulated data for the accelerating field distribution.

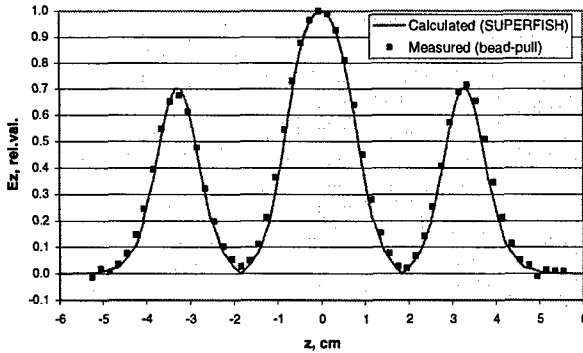


Figure 2: Accelerating field distribution.

The most general rf parameters are presented in Table 3 in comparison with figures obtained from MAFIA simulations.

Table 3: Buncher general rf parameters.

Parameter	Calc.	Meas.
Design velocity, $\beta_0$	2.3%	-
Operating frequency, MHz	104.6	105.2
Frequency tuning range, kHz	900	1200
Nearest mode frequency, MHz	102.7	103.5
Q-factor	5800	4300
Shunt impedance $R_s^*$ , M $\Omega$	9.16	6.15
$R_s^*/Q$ , $\Omega$	1580	1430
Maximum surface field, MV/m	13.2	-
Nominal power, kW	5.5	~ 8.1

$$R_s^* = V^2/P, V=4V_1, V_1 - \text{peak voltage across first accelerating gap, } P - \text{dissipated rf power.}$$

A delicate study has been performed in order to determine buncher mechanical stability. Basically, the Split-ring structure can be considered as two identical curved cantilever beams, fixed at one end and free to vibrate at the other. Ring mechanical oscillations have been measured with a dynamic signal analyzer (HP #35665A) and two accelerometers attached to the drift tube. Table 4 presents measurement results for the most sensitive direction (lateral axis). Here induced oscillations were caused by the water flow of 20 l/min. Measurements show that vibration amplitude is much below the drift tube displacement tolerance of 0.2 mm.

Table 4: Split-ring mechanical vibration parameters in the lateral direction.

Frequency	MHz	11	36	39	96	107
Amplitude	$\mu\text{m}$	1	1	1	0.1	0.1

### 4 HIGH POWER TEST RESULTS

A 105 MHz amplifier with output power up to 20 kW was used as a buncher rf power supply. A flexible stable phase coaxial line with air insulation served as an rf transmitting line. A high power phase shifter (trombone) was implemented to rf feeding line in order to remove waveguide parasitic modes from the fundamental frequency.

High power rf test was preceded with delicate vacuum test and conditioning. Surface outgassing was forced with bake out at 50°-60° C. Following 10 hours of vacuum conditioning a base pressure of  $2 \cdot 10^{-7}$  Torr was achieved.

A low level (<100 W) rf conditioning was one of the longest stages (~7 hours) on the way to the buncher nominal power. It was accompanied with electron multipactor discharge and intense outgassing. Following voltage rise was restricted by high voltage discharges which were initiated when vacuum dropped to  $\sim 2 \cdot 10^{-6}$  Torr. Nominal voltage was obtained in 6 hours with intermediate half-power conditioning for 26 hours during weekend. Rf conditioning was performed in cw mode because pulsed mode eventually appears to be ineffective. Long-term conditioning has brought a significant vacuum improvement: from  $\sim 1 \cdot 10^{-6}$  Torr to  $\sim 3 \cdot 10^{-7}$  Torr at the full power. And although the design parameters are 56 kV gap voltage and ~8 kW nominal power, we eventually achieved 85 kV and 16 kW respectively with stable operation. After conditioning it took couple of hours to put buncher under full power after short term vacuum brake and ~15 minutes from standby mode. The longest continuous run at nominal voltage lasted for 80 hours. Taking into account a number of various runs from 5 to 20 hours duration, the buncher operated stable for ~250 hours in total.

Rf conditioning has left multipactor discharge traces on the cavity and endplate walls in a small area around the leg. But finally buncher operated without multipactoring in the voltage range from 10% to the highest level.

Figure 3 demonstrates typical dependencies of rf power and residual gas pressure upon the drift tube voltage. Vacuum drop at low rf voltage level vanished after the buncher rf conditioning.

In order to double check the voltage level, achieved in the buncher, a calibration of the drift tube voltage has been performed. It was based on the measurement of the energy of the x-rays, produced with free electrons accelerated in the buncher electric field. Measurement showed very good agreement with pickup loop data, based on the shunt impedance figure.

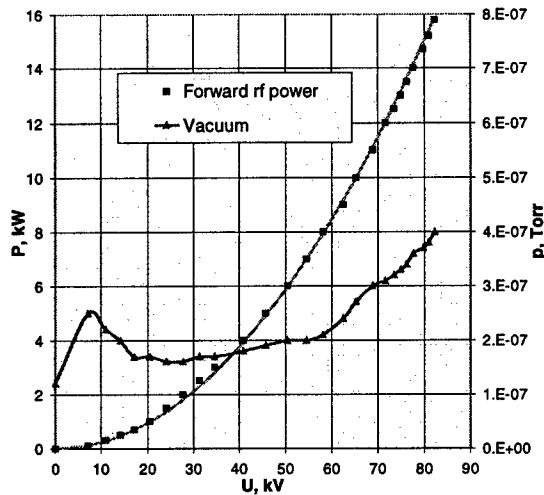


Figure 3: Rf power and vacuum vs drift tube voltage.

Measurements of the operating frequency dependence upon rf power showed frequency increasing with Split-ring heating (see Figure 4, curve 2), while opposite tendency (see Figure 4, curve 1) has been observed with rf off and structure heating by the water passing through the buncher cooling channels.

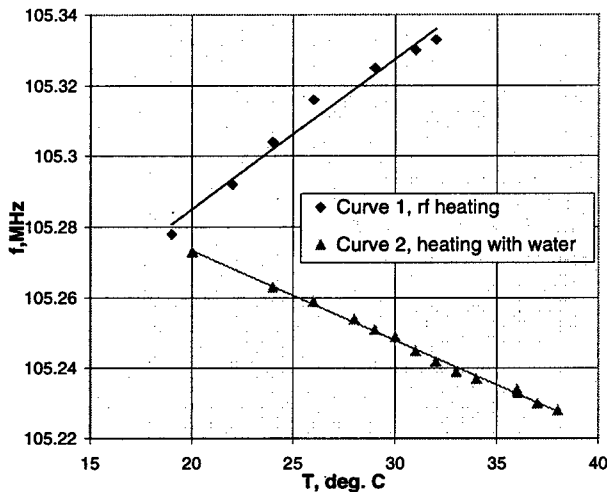


Figure 4: Buncher frequency vs Split-ring temperature.

This unexpected frequency behaviour can be explained with non-uniform thermal load due to rf losses in the Split-ring structure. It can cause a deformation of the ring. MAFIA simulations confirm this phenomena of the frequency increasing assuming small movement of the rings along beam direction. In fact ring deformation take place in the buncher. Thus drift tube transverse movement due to rf thermal load of the ring was measured using a telescope on targets installed in the drift tubes. Initially drift tube displacement from the beam axis reached 580  $\mu\text{m}$  for nominal rf power. Then it was reduced to 230  $\mu\text{m}$  with increasing of the cooling water flow in the Split-ring

from 13 to 35 l/min. Another reduction of the drift tubes movement by factor 2 was achieved by reversing the water flow direction to cool the hottest ring area first.

High surface electric fields, up to 13 MV/m, initiate electron emission. Those electrons accelerated in the electric field knock to the cavity walls and other elements of structure producing x-rays. Radiation field measurement at the buncher surface showed level over 1000 mS/h for the full rf power. Thus additional lead shielding has been implemented to allow acceptable working conditions at the test stand.

Charged particle current produced and accelerated in the buncher was detected in the diagnostics box, which is attached to the buncher. Field emission is considered to be the nature of this current. Observed current is bunched at the fundamental frequency with an intensity of tens of  $\mu\text{A}$  for the nominal buncher setting. This current is intense enough to overwhelm signals from the desired beam of ions and even harm the delicate beam diagnostic devices. Special measures should be foreseen to avoid this problem.

During the high power tests both: tuner and coupling loop demonstrated very reliable performance in the whole working range without any indication of sparks or multipactoring.

## 5 CONCLUSION

The 105 MHz Split-ring buncher showed stable and reliable rf performance under full power (8 kW) and much higher (up to 16 kW). No multipactor discharge has been observed in the specified voltage region.

Split-ring structure design appears to be rather stable against mechanical vibrations. Measured vibration amplitude of  $\sim 1 \mu\text{m}$  is two orders lower than tolerated value. However considerable movement of the drift tubes ( $\sim 500 \mu\text{m}$ ) due to rf thermal load of the ring has been observed. It could be reduced below tolerance of 200  $\mu\text{m}$  with more effective cooling.

Essential x-ray field was measured around the buncher especially over the nominal voltage. It is caused by the electrons, produced in the buncher volume due to field emission and accelerated in the electrical field. Bunched electron current of tens of  $\mu\text{A}$  was measured on the beam axis at the buncher entrance. This could be a grate concern for the DTL bunchers #2 end #3 as their voltage specification is much higher then for the first one.

## 6 REFERENCES

- [1] R. Laxdal, The Separated Function Drift Tube Linac for ISAC, TRI-DN-97-4, TRIUMF Design Note, April 1997.
- [2] Y. Bylinsky et al., A Triple Gap Resonator Design for the Separated Function DTL at TRIUMF, Proc. Of the PAC-97, Vancouver, May 1997, pp. 1135-1137.

# A High Power RF Coupler Design for Muon Cooling RF Cavities \*

J. Corlett, Derun Li<sup>†</sup>, R. Rimmer, LBNL, Berkeley, CA 94720  
 N. Holtkamp, A. Moretti, FNAL, Batavia, IL 60510  
 H. Kirk, BNL, Upton, NY 11973-5000

## Abstract

We present a high power RF coupler design for an interleaved  $\frac{\pi}{2}$  805 MHz standing wave accelerating structure proposed for an muon cooling experiment at FNAL. The coupler, in its simplest form, is a rectangular waveguide directly connected to an accelerating cell through an open slot on the cavity side-wall or end-plates. Two of such couplers are needed to feed the interleaved cavities. Current high power RF test requires the coupler to be at critical coupling. Numerical simulations on the coupler designs using MAFIA will be presented.

## 1 INTRODUCTION

One of the most critical issues towards the feasibility of building an  $\mu^+ - \mu^-$  collider is how to effectively cool the six-dimensional emittance of the muon beams down by a factor of  $10^5$  to  $10^6$ . Substantial progress has been made recently on the cooling studies both theoretically and experimentally. Among many possible cooling schemes, ionization cooling has been chosen to be a candidate to cool the  $\mu$  beams at early stage. A muon cooling collaboration, headed by FNAL, was established a few years ago to concentrate on the ionization cooling studies [1]. An experiment to demonstrate ionization cooling was proposed and has been developed since 1997. The cooling channel consists of about 20 cooling sections and each section has a 1.3 meters long linac and two absorbers surrounded by a super-conducting solenoid. A highest possible gradient accelerating structure is required to compensate the longitudinal beam energy losses in each section. An  $\frac{\pi}{2}$  interleaved structure has been developed between LBNL, FNAL, BNL and University of Mississippi [2, 3], and will be employed for this purpose. The structure closely resembles a pill-box cavity, but has the conventional beam irises covered by thin beryllium foils to enhance the on-axis accelerating fields. This brings the ratio of the surface field to accelerating field to one while for conventional structures it is typically between 2 to 5. The structure may be cooled down to liquid nitrogen temperature to further reduce the RF power losses on cavity wall which increases the shunt impedance by nearly another factor of two. Table 1 lists the relevant RF parameters of the cavity.

A three-cell low power test model, as shown in Figure 1, has been built and is currently under test at LBNL. A high power test on the structure will be conducted at FNAL

Table 1: RF parameters of the  $\frac{\pi}{2}$  interleaved cavity

Frequency (MHz)	805
Speed of muon ( $\beta = v/c$ )	0.87
Shunt impedance ( $ZT^2$ ) (M $\Omega$ /m)	36.2
Average gradient (MV/m)	34
Peak power (MW/m)	32
Quality factor $Q_0$	18,700
Cell length (cm)	8.1
Beryllium thickness/radius (mm)	0.127/80

after learning all the necessary information from the test model. A 5 Tesla super-conducting solenoid has also been designed and built at LBNL, and will be installed at FNAL for the high power test to study the performance of the structure under strong magnetic fields.

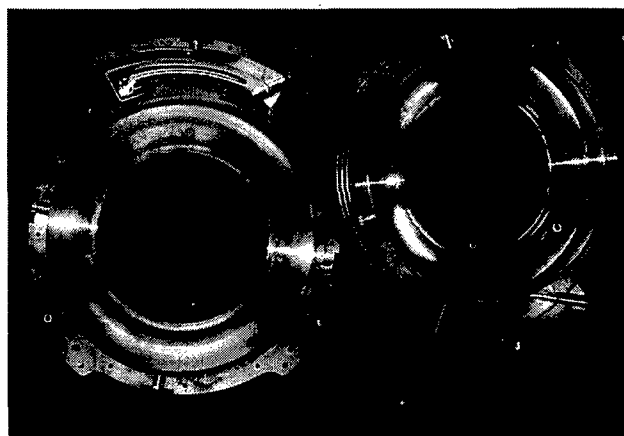


Figure 1: The three-cell copper test model of the  $\frac{\pi}{2}$  interleaved RF structure. The open irises will be covered by two beryllium windows of 127  $\mu$ m of thickness and 16 cm of diameter.

## 2 THE COUPLER

The coupler, in its simplest form is a rectangular open slot either on the side wall or on the end-plate of the cavity and connected directly to a waveguide. For the high power test, the RF power has to be coupled through the end-plate since there will be no access available to the side wall once the super-conducting solenoid is in place. The rectangular open slot has been chosen to have a cross section of 12 cm  $\times$  2 cm. The coupler and waveguide need to be fitted within the bore size of the super-conducting solenoid of 440 cm of

\* This Research Work is supported by the Director, Office of Energy Research, Office of High Energy and Nuclear Physics, High Energy Physics Division, of the U.S. Department of Energy, under Contract No. DE-AC03-76SF00098

<sup>†</sup> Email: DLi@lbl.gov

ID, and leave a clear passage for the  $\mu$  beams at region of  $R \leq 8$  cm, and transition to a standard WR975 waveguide. Critical coupling is required at resonant frequency of 805 MHz.

## 2.1 The Simulation Model

MAFIA (T3 module) time domain simulations were used to determine the coupling between the coupler and the cavity. A simplified 3D model was used to simulate the *coupler + cavity* system. The model consists of a pill-box cavity with one of the end-plates having a rectangular open slot coupled to a WR975 waveguide, shown in Figure 2. The area of the slot was kept unchanged while the depth of the slot was varied to adjust the coupling strength. The radius of the cavity was tuned to get the resonant frequency of 805 MHz. It is worth pointing out that only one single pill-box cell is needed to simulate the coupling of the system if each accelerating cell is identical, the coupling constant for the multi-cell case is then determined by,

$$\beta_c(N) = N\beta_c(1) = N \frac{Q_0}{Q_{\text{ext}}}, \quad Q_{\text{ext}} = \omega \frac{U}{P_{\text{ext}}}, \quad (1)$$

where  $\beta_c(1)$ ,  $\beta_c(N)$  are coupling constants for single and  $N$  cells;  $U$  is the stored energy in the single cavity;  $\omega$  is the angular resonant frequency and  $P_{\text{ext}}$  is the power loss to a matched load;  $N$  is the number of total cells. For the three-cell interleaved  $\frac{\pi}{2}$  structure (only two accelerating cells) we design  $\beta_c(1) = 2$  with the one cell model.

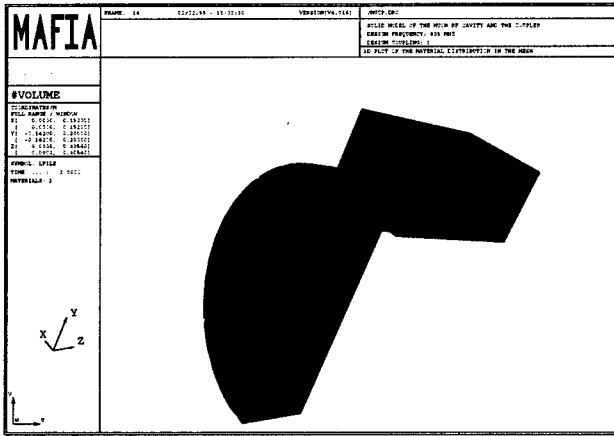


Figure 2: A 3D solid MAFIA model used for the coupling simulations

## 2.2 Simulation Procedures

The waveguide boundary condition at the waveguide port was used, the electro-magnetic field in the cavity was excited by a broad band dipole pulse with its frequency centered around 805 MHz (fundamental  $TM_{010}$  mode). To simulate the waveguide boundary conditions a two-dimension frequency domain run is necessary in order to obtain the propagation modes in the waveguide. These waveguide modes are loaded into the waveguide port when

the time domain simulation starts. To avoid exciting unwanted higher order modes, a filament (a line dipole) was defined on the axis with a length of about half the cavity gap and its polarization pointed to  $z$ . The band-width of the pulse was chosen to be wide enough (short pulse), but not too wide to drive the nearest higher order modes. For a high  $Q$  cavity, the induced *em* fields will be dominated by the fundamental mode quickly once the excitation pulse is gone. The power loss from the *cavity + coupler* system (perfect conductor was assumed) is the one exiting from the waveguide port, namely  $P_{\text{ext}}$ . The *em* fields in the cavity are then oscillating at its natural resonant frequency, and its amplitude (either  $E$  or  $B$  field) exponentially decays with a time constant of  $\tau_{\text{ext}}$  given by,

$$\tau_{\text{ext}} = \frac{2Q_{\text{ext}}}{\omega} = \frac{2U}{P_{\text{ext}}}. \quad (2)$$

For a weakly coupled system ( $\beta_c < 1$ ),  $\tau_{\text{ext}}$  could be as long as  $10^4$  times of one RF period. Measuring  $\tau_{\text{ext}}$  of the *em* amplitudes from a short time domain simulation, for instance 100 RF periods, becomes difficult and inaccurate. Nevertheless, the induced time varying *em* fields in the cavity does provide enough information to allow for an accurate measurement of the resonant frequency of the system. The resonant frequency can simply be calculated by counting the time of the last 10-20 RF periods. The time step of the simulations is of the order of  $10^{-12}$  to  $10^{-13}$  seconds, which gives at least one order of magnitude better accuracy of the frequency than the one obtained from FFT when approximately total 100 RF periods ( $\sim 10^{-7}$  seconds) are used. Two methods (we call *energy and decay methods*) have been used for  $Q_{\text{ext}}$  calculation. These methods have been discussed in detail in [4]. At most two MAFIA time domain runs are needed for each configuration. Both  $Q_0$  and  $Q_{\text{ext}}$  can be calculated from the time domain simulation results. After obtaining the resonant frequency  $\omega$  (discussed above), we excite the system with a  $\sin(\omega t)$  line dipole. The *em* fields in the cavity should build up coherently. The fields are recorded at a few carefully chosen time steps during the simulation, and used later in the MAFIA post-processor (P3) to re-construct quasi-time harmonic *em* fields. Taking the advantage of many built-in functions in P3, both  $Q_0$  and  $Q_{\text{ext}}$  can be readily calculated [4]. This method (*energy method*) works very well for high  $Q$  systems with weak coupling where the decay method becomes impractical because a long time record is needed. For a strongly coupled system, both methods work equally well, but the decay method is more efficient if only  $Q_{\text{ext}}$  is measured. To save cpu time, typically 50 ~ 80 RF periods are long enough for each simulation. A model with about 11,000 mesh points takes approximately 20 minutes of cpu time on an Ultra 60 Unix Sun-Workstation.

It is important to point out that when using the *energy* method, the continuous dipole excitation fields contribute to both the stored energy in the cavity and  $P_{\text{ext}}$ . In general one should wait until the *em* fields of the cavity mode dominate before recording the fields where the contribu-

tions from the dipole become negligible. However, for a strongly coupled system (or a complex system), the time that it takes for the cavity mode to dominate could be quite long, this contribution can not be neglected in a short time-domain run. However the dipole fields can be subtracted in the post-processor because their contributions are steady over the time. By recording the fields at two time steps,  $Q_0$  and  $Q_{\text{ext}}$  can be computed by,

$$Q_0 = \omega \frac{U(t_2) - U(t_1)}{P_w(t_2) - P_w(t_1)}; \quad Q_{\text{ext}} = \omega \frac{U(t_2) - U(t_1)}{P_{\text{ext}}(t_2) - P_{\text{ext}}(t_1)}, \quad (3)$$

where  $U(t_i)$ ,  $P_w(t_i)$  and  $P_{\text{ext}}(t_i)$  are stored energy in the cavity, power loss on cavity wall and power loss in the matched load at time  $t_i$ , respectively. Equation 3, in fact, can be used even at times when the dipole contributions become negligible. Another alternative solution is to compute for longer time (more cpu time of course!) until the dipole fields becomes negligible. The  $Q_0$  and  $Q_{\text{ext}}$  are simply given by,

$$Q_0 \approx \omega \frac{U(t_i)}{P_w(t_i)}; \quad Q_{\text{ext}} \approx \omega \frac{U(t_i)}{P_{\text{ext}}(t_i)}. \quad (4)$$

Calculations of  $U(t_i)$ ,  $P_w(t_i)$  and  $P_{\text{ext}}(t_i)$  using time-domain simulation results are also presented in details in [4].

### 2.3 Simulation Results

Based on the methods discussed above, MAFIA simulations were performed on the model shown in Figure 2. As an example for the *energy* method, Figure 3 shows a snap shot of electric fields in the *cavity + coupler* system driven by a continuous line dipole resonating at  $\omega$ . The fundamental  $\text{TM}_{010}$  mode is clearly dominant in the system. Fields at the coupling slot can barely be seen. Figure 4 gives a

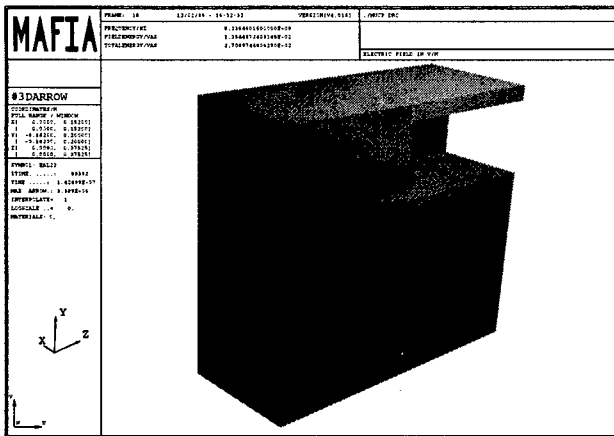
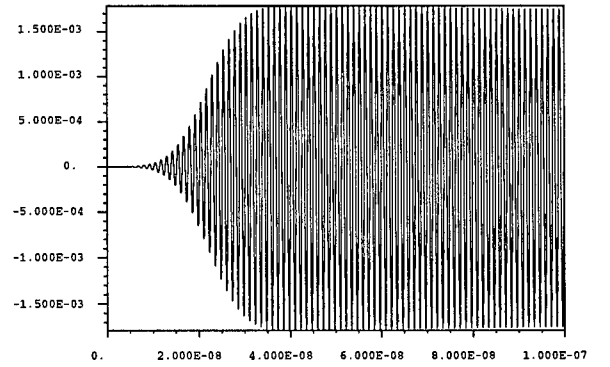


Figure 3: A snap shot of electric fields in the cavity and the coupler

time record of a magnetic component of  $B_x(t)$  monitored at a large radius. It is apparent that the field is oscillating at a single mode, namely the fundamental mode, after the excitation pulse. In this example, the  $Q$  is fairly high and

the expected exponential decay can hardly be observed at this time scale. Nevertheless zooming into the last 10-20 RF periods, the resonant frequency of the system can be measured.



CST

Figure 4: Magnetic field  $B_x(t)$  recorded as a function of time

For a strongly coupled system, the *em* fields exhibit an exponential decay pattern (it looks like a linear pattern if time record is less than  $\tau_{\text{ext}}$ ). Calculation of  $Q_{\text{ext}}$  is straight forward, and given by,

$$Q_{\text{ext}} = -\left(\frac{\omega}{2}\right) \frac{t_2 - t_1}{\ln B_x(t_2) - \ln B_x(t_1)}, \quad (5)$$

where  $B_x(t_i)$  is the  $B_x$  measured at  $t_i$ .

### 3 CONCLUSION

The coupler has been designed using the MAFIA time domain simulations. The coupling slot dimension was determined to be 12 cm  $\times$  2 cm  $\times$  8 cm (width  $\times$  height  $\times$  depth) to give critical coupling ( $\beta_c(1) = 2$ ) at the frequency of 805 MHz for a three-cell  $\frac{\pi}{2}$  interleaved structure. The MAFIA time domain simulations and the methods we developed have been proved to be a powerful tool our coupler designs, and can be easily applied to other similar applications.

### 4 REFERENCES

- [1] R. Palmer, A. Tollestrup and A. Sessler, "New Directions for High Energy Physics", Snowmass, CO, (1996); "Status of Muon Collider Research and Development and Future Plans", Fermilab-PUB-98/179
- [2] W.C. Turner, A. Moretti, J.N. Corlett, D. Li, H. Kirk, R. Palmer, Y. Zhao, "RF System Concepts for a Muon Cooling Experiment", EPAC'98, Stockholm, (1998);
- [3] A. Moretti, J.N. Corlett, D. Li, W.C. Turner, H. Kirk, R. Palmer, Y. Zhao, " $\frac{\pi}{2}$  Interleaved Cavity Developments for Muon Collider Cooling Experiment", LINAC'1998, Chicago, IL, (1998)
- [4] Derun Li, R. Rimmer, S. Kosta, "Calculations of External Coupling to a Single Cell RF Cavity", LINAC'1998, Chicago, IL, (1998)

# HOM SUPPRESSION OF THE CAVITIES WITH PLUGGER TUNER BY THE TEMPERATURE TUNING

M. Kwon, H. J. Park, and I. S. Park

PAL/POSTECH, San-31 Hyoja-Dong, Pohang 790-784, Korea

## Abstract

New storage ring cavity temperature system was successfully operated for the Pohang Light Source (PLS) and increased the stable maximum beam current up to 200 mA. The storage ring cavity for PLS has the plunger-type tuner which is controlled by the phase feedback loop to always tune the resonant frequency. Optimum temperature windows for the PLS cavities were obtained by intensive but tiresome measurements. The measured results is compared to the calculation based on the relations expressed as a function of the tuner position.

## 1 INTRODUCTION

Temperature tuning of the storage ring cavities has been used effectively for shifting the dangerous cavity HOMs at the Elettra[1, 2] and couple of other third generation light sources. At the Pohang Light Source (PLS) a new temperature control system[3] for the cooling water of the cavities was installed and has been actively used for suppressing amplitudes of HOMs. A clear difference of the PLS cavities from the Elettra is the tuning mechanism; the plunger-type tuner. Effects of the temperature change on the HOM frequency shift should consider the plunger movement controlled by the resonant frequency feedback circuit. This makes the analysis cumbersome. At Photon Factory an elaborate length adjustment of a fixed block was used in stead of the temperature tuning[4].

Here a systematic approach to temperature tuning of RF cavities with plungers is presented in the following sections and a comparison with the initial operation results will be given.

## 2 DERIVATION

The parameter, Critical Temperature, defined as the cavity temperature for which the frequency of the HOM exactly overlaps the frequency of the coupled bunch mode[2] is adopted here for a systematic analysis. According to the definition of the critical temperature, the operating temperature of the cavities should not be near the critical temperature, where the coupling is at maximum.

There are several parameters to shift HOM frequency at the cavities. Cavity volume changes caused by thermal expansion, by change in the dissipating power or by change in beam loading are typical. Change in rf

frequency obviously shift HOM frequency. In cavities with plunger-type tuner all these changes affect tuner position since a phase loop always tune the cavity to the proper rf frequency by adjusting the tuner position. The change in tuner position can be written as

$$\Delta l_{total} = \Delta l_{thermal} + \Delta l_{beam\ loading} \dots$$

It should be noted that each term in the RHS does not couple to each other. The frequency shift of HOM becomes

$$\Delta f_{HOM} = -\left(\frac{f_{HOM}}{f_{rf}}\right)\left(\frac{df_{rf}}{dl}\right)\Delta l_{thermal} + \left(\frac{df_{HOM}}{dl}\right)\Delta l_{total}$$

The first term in the RHS represents the HOM frequency shift due to the thermal expansion and the second term is caused by the tuner position adjustment[4]. Note that different  $\Delta l$  is used for each term.

Now we describe  $\Delta l$  as a known parameters. For thermal expansion, it is known as[4]

$$\Delta f = -\alpha \cdot \Delta T \cdot f$$

where  $\alpha$  is the thermal expansion coefficient of copper. Since tuner always moves to tune to the resonant frequency, the rf frequency shift can be written as Therefore

$$\Delta f_{rf} = -\left(\frac{df_{rf}}{dl}\right)\Delta l_{thermal}$$

In a similar fashion the tuner position change due to the

$$\Delta l_{thermal} = \frac{\alpha f_{rf}}{df_{rf}/dl} \cdot \Delta T.$$

beam loading can be obtained as

where all the parameters are represented with the conventional notations. Now the HOM frequency shift

$$\Delta l_{beam\ loading} = \frac{R_s f_{rf} \cos \psi_s}{\theta(1 + \beta)V_c} \frac{1}{df_{rf}/dl} \Delta I_b,$$

can be expressed as a function of the temperature change as well as the beam loading. These two are major factors shifting frequency by changing the tuner position accordingly. The frequency shift of HOM can be written in terms of these two parameters,  $\Delta T$  and  $\Delta I$ , as follows.

$$\Delta f_{HOM} = (\alpha \Delta T) \left[ -f_{HOM} + f_{rf} \frac{df_{HOM}/dl}{df_{rf}/dl} \right] + \frac{R_s \cos \psi_s}{Q(1+\beta)V_c} f_{rf} \frac{df_{HOM}/dl}{df_{rf}/dl} \Delta I_b.$$

Here the accelerating voltage is defined as  $V_c \cos \Psi_s$ .  $\Delta T$  and  $\Delta I$  are the variations from the preset reference points and other parameters should have values at the reference point. By equating this to the condition for invoking a multi-bunch instability mode, the critical temperature can be calculated as

$$T_c = \frac{1}{\alpha} \left[ -\frac{R_s \cos \psi_s}{Q(1+\beta)V_c} \frac{\delta_{HOM}}{\delta_{rf}} f_{rf} \Delta I_b + (f_{l,n} - f_{HOM}^0) \right] / \left( \frac{\delta_{HOM}}{\delta_{rf}} f_{rf} - f_{HOM}^0 \right) + T_0,$$

where  $\delta$  is the derivative of frequency change with respect to the tuner position and the superscript zero means the values at the reference temperature,  $T_0$ . Since all rf parameters could only be measured at cases without beam, the reference point for the beam current is set to zero and for the temperature set to 30°C. The growth rate of a longitudinal coupled bunch mode instability for a beam current  $I_b$  stored in  $M$  uniformly filled and spaced bunches and for a high Q cavity HOMs can be approximated by [2],

$$\frac{1}{\tau_{||}} = \frac{\eta I_b}{4\pi Q_s (E/e)} \omega_{l,n} \Re(Z_{||}(\omega_{l,n})) e^{-(\omega_{l,n} \sigma_t)^2},$$

where,

$$\omega_{l,n} = \frac{(lM + n + Q_s) f_{rf} / h}{[\alpha(T - T_0)] \left[ -f_{HOM}^0 + f_{rf} \frac{\delta_{HOM}}{\delta_{rf}} \right] + \frac{R_s \cos \psi_s}{Q(1+\beta)V_c} f_{rf} \frac{\delta_{HOM}}{\delta_{rf}} \Delta I_b + f_{HOM}^0},$$

$$Z_l(\omega_{l,n}) = \frac{\left( \frac{R}{Q} \right)_{HOM} Q_{HOM}}{1 + iQ_{HOM} \left( \frac{\omega_{l,n}}{\omega_{HOM}} - \frac{\omega_{HOM}}{\omega_{l,n}} \right)}.$$

### 3 APPLICATION TO THE PLS CAVITIES

To apply the above analysis to PLS cavities, necessary parameters were measured in situ. Since it is impossible to measure frequencies with rf power on, measured values without rf power should be converted to the reference values, which are extrapolated by considering the effects of rf power-on at temperature  $T_0$  without beam current. Before going further three points should be examined for checking the usefulness of this analysis. First it should be checked whether the total tuner position movement is just a summation of contributions from each factor. Second check whether the tuner position is linearly proportional to the temperature and beam current. Third the effect of balance mismatch of the beam loading

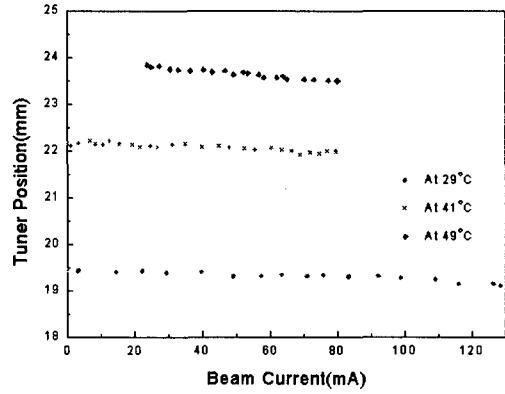


Figure 1. Tuner position as a function of beam current at three different cavity temperatures which shows that the thermal expansion and beam loading independently contribute to the total displacement.

between cavities should be checked. Checking the first point, tuner position was measured as a function of the amount of beam current stored and the cavity temperature as shown in Fig. 1. In the figure, the slope of the tuner position as the stored current increases does not change at different temperatures. This clearly represents that two factors (thermal and beam loading) are decoupled as assumed. The slope is also linearly fitted, which means that the second point is satisfied for the beam loading factor, whereas the effect of the thermal expansion was already tested in the Ref [5]. Testing third point requires a bit more speculation. Relations between  $\Delta I$  and  $\Delta I$  are for

the case with the optimum tuning, i.e.  $\psi_s$  is the tuning angle for the case of the minimum reflected power. If there is any balance mismatch, then  $\psi_s$  is not optimum any longer. In this case, relations between  $\Delta I$  and  $\psi_s$  are very important. If the balance between cavities changes,

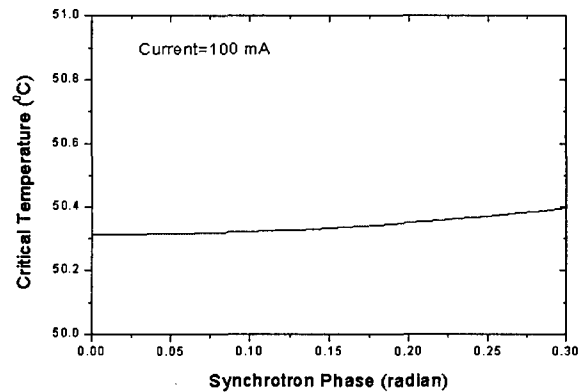


Figure 2. Change of the critical temperature as a function of the tuning angle. Large change in tuning angle due to the unbalanced beam loading between stations does not affect much on the critical temperature calculations.



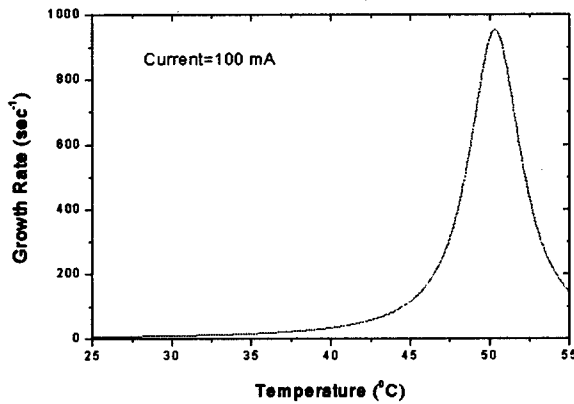


Figure 3. Growth rate calculated for TM011 mode of #2 cavity.

$\psi$ , changes, too. Thus sensitivity should be analyzed. Figure 2 shows the change in critical temperature as a function of tuning angle for a typical case. The critical temperature does not change much for a relatively large change in tuning angle.

Back to the main subject, parameters required to calculate the critical temperature and the growth rate were measured and recalculated. Let us take TM011 mode of the second cavity as an example. The HOM frequency is 757.857 MHz at 30°C. The derivative  $\delta_{\text{HOM}}$  was measured of -59.19 kHz/mm. For  $\Delta I$  is 100 mA, the critical temperature is calculated as 50.86°C. Since the critical temperature has a current dependence, it changes from 52°C to 45°C as the current increases from zero to 200 mA, respectively. The growth rate can be also calculated as shown in Fig. 3. By comparing the growth rate with the natural damping time the threshold current can be determined for this mode at certain temperature. Though not seen in the Figure, the threshold current at the critical temperature is about 60 mA, which agrees quite well with the experimental observations. Also this growth rate decreases above 160 mA since the plunger tuner position continuously moves out as the current increases, which shifts the HOM frequency towards a favorable region again.

Since the critical temperature changes as the beam current does so, the calculated growth rate at the critical temperature for a given current is always the largest. Therefore the growth rate at a fixed temperature is normally smaller at any current except the current at which the fixed temperature equals to the critical temperature. This is shown in Fig. 4. When T is below 40°C, the growth rate for this mode is lower than the natural damping rate up to 200 mA.

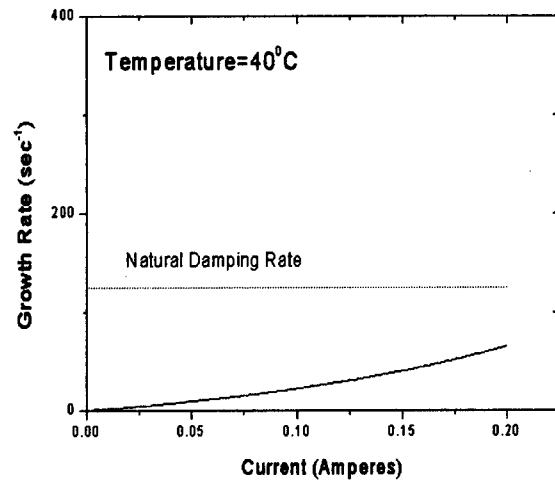


Figure 4. Threshold current for the second cavity at 40°C temperature.

As an another example, we take same mode at the cavity 1. Unlike the previous one, this mode does not have a dependence of the tuner position on the frequency, i.e.  $\delta_{\text{HOM}}=0$ . Even though tuner does not perturb this mode, the thermal expansion of the cavity body can shift the mode frequency. This fact clearly show the difference between cavities with and without plunger-type tuners in response to a thermal disturbance. The calculation in this case also shows similar characteristics. From this analysis, the optimal operating temperature can be determined after overlapping all the contributions from all HOMs. In PLS the temperature tuning improved the stable operation current up to 200 mA. Above that current, a strong transverse instability appeared to limit the maximum stored current. The active feedback system will be installed in PLS, but the temperature tuning can still provide flexible and useful operating modes such as operation with longer lifetime. The system also contribute very much to reduce the power requirement of the feedback system by decreasing HOM impedances substantially even at higher beam current.

## REFERENCES

- [1] M. Svandrlik, et al., 'The cure of Multibunch Instabilities in Elettra,' in PAC95 Proceedings, Dallas, 1995.
- [2] M. Svandrlik, et al., 'Improved Methods of Measuring and Curing Multibunch Instabilities in Elettra,' in EPAC96 Proceedings, Sitges, 1996.
- [3] I. S. Park, et al., 'Operation Results of Upgraded Cooling Water System for the Storage Ring RF Cavities in PLS,' in APAC98 Proceedings, Tsukuba, 1998..
- [4] H. Kobayakawa, et al., 'Suppression of Beam Instabilities Induced by Accelerating Cavities,' Rev. Sci. Instrum. 60 (1989) 1732 .

# DISK-TYPE INPUT COUPLER WITH A HOM DAMPER FOR THE PLS STORAGE RING CAVITY

J. S. Yang, I. S. Park, and M. Kwon

PAL/POSTECH, San-31 Hyoja-Dong, Pohang 790-784, Korea

## Abstract

A disk-type input coupler for the Pohang Light Source (PLS) storage ring cavity was fabricated and tested up to 60 kW. A coaxial adapter is required for this system which should have an exit for the loop coupling tubes. Since this input coupler can extract HOMs better than the cylinder-type one out of the cavity, a specially designed HOM absorber was implemented in the design of the adapter. A characteristic of the system is simulated by the HFSS code. The result of the simulation and a preliminary measurement will be presented.

## 1 INTRODUCTION

For PLS RF cavities loop couplers with cylindrical ceramic window have been used. These couplers have one drawback; the output port, WR-1500 waveguide does not match to the transmission line, which is a coaxial type. Therefore interface requires a coax-to-waveguide transition which wastes small amount of RF power and makes whole system little bit complicated to handle. This motivated us to design a new disk-type coupler with coaxial port out[1]. A 3D MAFIA modeling shows good performance and low power test proved that point. It also shows a good HOM extraction characteristics which led us to develop a outside HOM absorber. A high power test and the design work for the filter of the HOM absorber will be covered in the following sections.

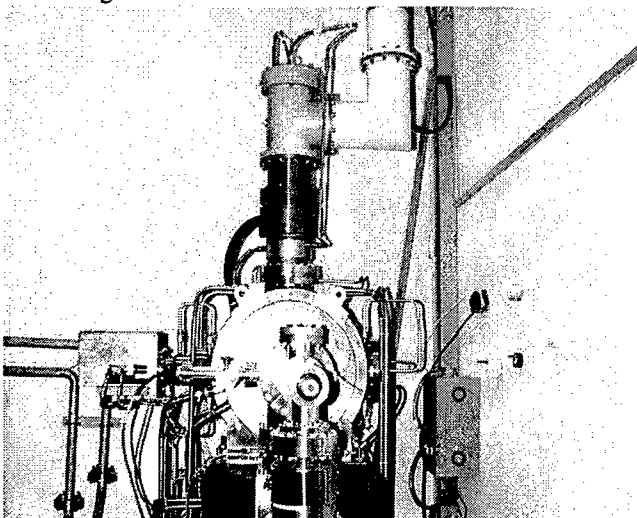


Figure 1. Prototype input coupler installed for the high power test.

## 2 HIGH POWER TEST OF THE PROTOTYPE INPUT COUPLER

The high power test stand (HPTS) in PLS consists of a 60 kW cw klystron amplifier, a circulator, low level control system and a spare cavity. Inside cavity the ceramic window region is monitored by a CCD camera and the reflected power, vacuum pressure and the arc signal are connected to the interlock circuit to trip off the input rf power when signal exceed the preset limits. All data for the forward and reflected power, vacuum pressure, temperatures on various points along with monitoring signal of the klystron amplifier are taken, stored and processed for display. A PC with a GPIB interface and HP DAQ modules control and monitor the whole system.

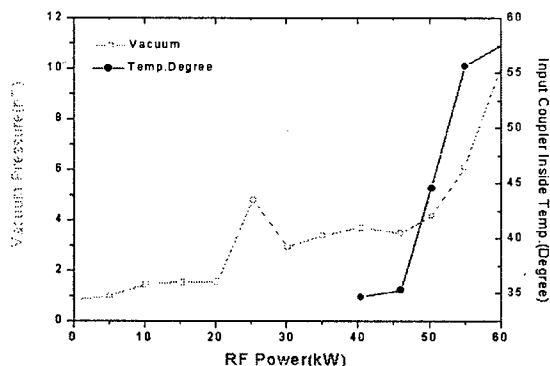


Figure 2. Changes in vacuum pressure and the temperature of the inside wall of the inner conductor during the aging of the prototype input coupler.

The high power test went through as normal. In low power region multipactoring occurred often but decreased as aging process went on. The reflected power was kept very low proving good VSWR as expected in the previous low power test. Above 40 kW of input power occasional arcs appeared followed by a vacuum pressure burst to 0.01mT range. The number of occurrence decreased substantially in two days of operations. This means that the arc may not be caused by a structural problems. A qualitative improvement of the surface treatment may be required.

A thermocouple attached to the inner wall of the center conductor shows a rapid increase of the temperature above 50 kW of power applied whereas the vacuum

pressure gradually increased to a nano-Torr level (Figure 2).

### 3 HOM DAMPER

During the low power measurements, it was observed that in the prototype coupler more HOMs was coupled out compared to the previously used disk-type coupler. This is shown in Fig. 3. The spectra were measured from a loop probe placed inside cavity. For the prototype coupler less modes are visible, meaning that more HOMs are coupled outside through the disk window. To absorbed these HOMs not to turn back to the cavity, an absorber should be provided. The quarter wavelength reflection plate of the T-adapter is the best place to use if a proper way is found to filter out HOMs only. The fundamental mode should be reflected fully at this plate for minimum power loss.

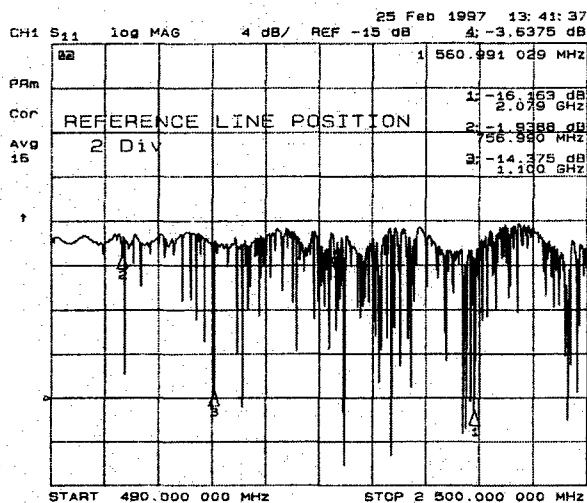


Figure 3(a). HOM spectrum for cylindrical-type window coupler.

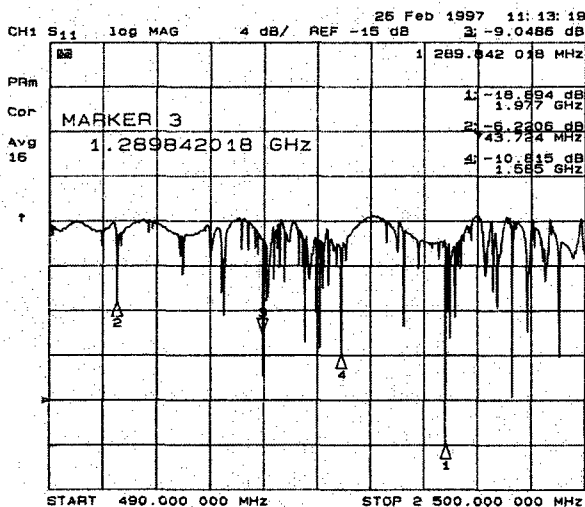


Figure 3(b). HOM spectrum for disk-type window coupler.

In the preliminary study, a simple stub-type filter was investigated. The rejection characteristics of the single

stub design was reported to show poor rejection characteristics[3]. Here multi-stub design were tested initially. Simulation with the HFSS shows filter characteristics. As in Fig. 4, the initial results show that the design still need more fundamental mode rejection ratio and less attenuation in the pass-band. Optimization and study for other type of filters such as the Chebyshev-type one[2] should be pursued.

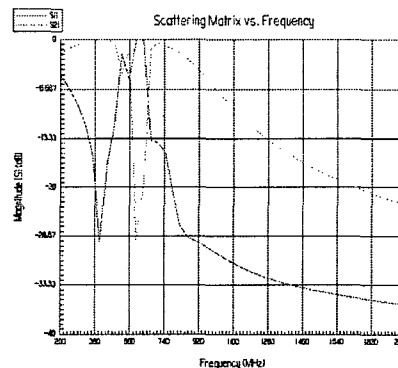
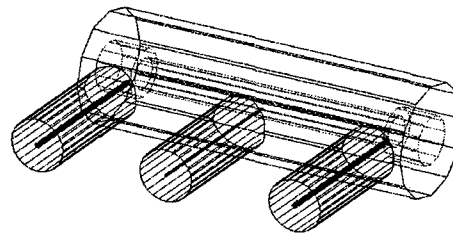


Figure 4. A model of the stub-type high pass filter simulated by the HFSS. Bottom graph shows S11 and S12 of the model filter.

For the dampers, matched load will be used. Detail design study of the damper just begins. Design, low power model and high power model development will be paralld with the T-adapter fabrication. The whole system will be tested and characterized in late this year.

### REFERENCES

- [1] I. S. Park, et al., 'Development of a Disk-Type Cavity Input Coupler,' in APAC98 Proceedings, Tsukuba, 1998.
- [2] Y. W. Kang, et al., 'Coaxial Higher-Order Mode Damper Employing a High Pass Filter,' in PAC97 Proceedings, Vancouver, 1997.
- [3] P. Matthews, et al., 'Storage Ring Cavity Higher-Order Mode Dampers for the Advanced Photon Source,' in PAC95 Proceedings, Dallas, 1995.

# Design of a HOM Coupler for a Damped Cavity at the Photon Factory Storage Ring

M. Izawa, S. Sakanaka, T. Takahashi<sup>\*</sup>, Photon Factory, KEK, Ibaraki, 305-0801, Japan  
T. Koseki, Y. Kamiya, ISSP, University of Tokyo, Tokyo 188-8501,

## Abstract

We designed a higher order mode (HOM) coupler with a rod-type antenna to reduce HOM's impedances of trapped modes in a damped cavity. The antenna is followed by a standard coaxial line. A tapered silicon-carbide (SiC) load is fixed at the end of the coaxial line. The HOM coupler is attached to an opening for the fixed tuner which is used to detune the resonance frequencies of trapped modes to avoid the coupled-bunch instabilities. The shape of the SiC load and the insulator for the inner conductor of the coaxial line is optimized so that an input SWR is as small as possible by using the computer code HFSS [1]. The input SWR was obtained to be less than 1.7 over the wide frequency range between 0.7 to 1.4 GHz. The low power measurement showed this type of HOM coupler sufficiently damped the HOM's in the cavity. The fabrication of the high power model based on this design is in progress.

## 1 INTRODUCTION

We have developed a damped structure RF cavity for a high brilliance configuration of Photon Factory (PF) storage ring [2] and a VSX project of the University of Tokyo [3]. The four damped cavities have been operating in the PF ring since 1997 [4]. The damped cavity has a large diameter beam duct. HOMs whose frequencies are above the cut-off frequency of the beam duct propagate out from the cavity to the beam duct, and the HOMs are damped by the SiC absorber which is placed inside wall of the beam duct. The several HOMs, with frequencies lower than the cut-off, still remain in the cavity with high Q values and have the possibility of introducing coupled-bunch instabilities. These HOMs frequencies are detuned so as not to introduce any coupled bunch instabilities using two fixed tuners of the cavity in the PF storage ring. For a ring with a larger circumference such as the VSX ring, the frequency detuning becomes less effective, because of its low revolution frequency. We have developed HOM coupler [5~7] with a rod antenna to reduce Q values of the trapped HOMs. We fabricated low-power models of the HOM coupler and measured the RF characteristics of the trapped modes. The results of the measurement showed that the HOM coupler could

sufficiently reduce the Q-values of six out of nine dangerous HOMs without influence on the Q-value of the accelerating mode [8].

## 2 DESIGN CONCEPT OF THE HOM COUPLER

The dangerous trapped HOMs are TM011, TM020, TM021, TE111, TM110 and TM111 mode. These HOM's frequencies are distributed from 0.7 to 1.4 GHz. Figure 1 shows a schematic cross-sectional view of the cavity with the HOM coupler. The rod antenna of the HOM coupler is located in the center of the cylindrical wall of the cavity. Therefore the HOM coupler strongly couples with TM011, TE111, TM021, and TM111 mode, and does not couple with the fundamental mode. The input reflection coefficient of the HOM coupler should be small enough over the wide frequency range between 0.7 to 1.4 GHz. We set a design goal to achieve an input VSWR of less than 1.7 (10% power reflection) in the frequency range.

As for the load, we chose SiC (CERASIC-B, Toshiba Ceramics co. Ltd), which is the same material as that used in the beam duct, since it has the high loss-tangent in the wide frequency range, the high thermal conductivity and the low outgassing rate, and is working well as the HOM absorber of the damped cavity in the PF ring [9~11].

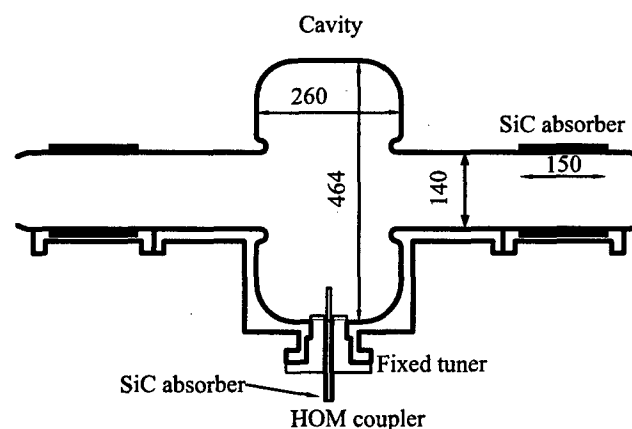


Figure 1. Cross-sectional view of the cavity with the HOM coupler.

<sup>\*</sup>Email: takeshi.takahashi@kek.jp

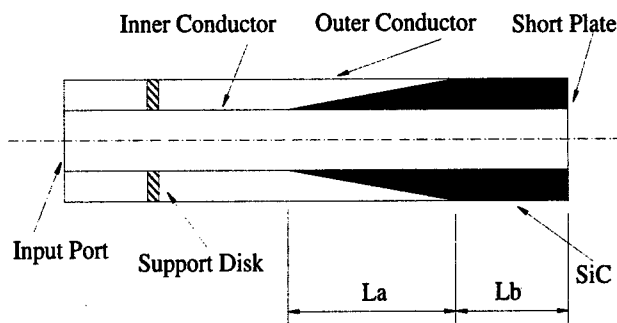
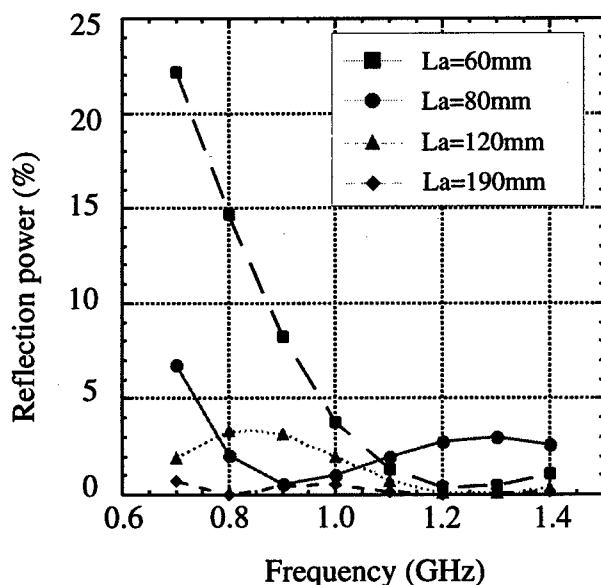


Figure 2. A simulation model of the HOM load.

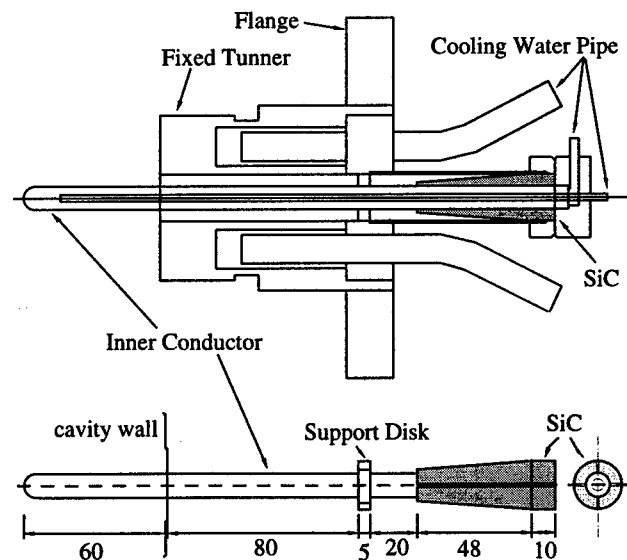
### 3 DESIGN OF THE HOM ABSORBER

The small size HOM coupler is preferable to avoid the interference with other ring components such as synchrotron radiation beam line. To satisfy this requirement, we designed the structure of the HOM coupler by using the computer simulation codes HFSS. Figure 2 shows an example of the simulation model. We set the basic design of the HOM coupler as follows. The diameters of the inner and outer conductors are 10mm and 20mm, respectively. The inner conductor is supported by a support disk and the SiC absorber which is fixed between the outer and inner conductors at the end of the coaxial line. The end of the coaxial line is shorted by metal (short plate) to seal vacuum. The SiC absorber is made in the shape of a taper to reduce reflections. We calculated reflection characteristics of the taper of the SiC. Figure 3 shows the reflection characteristics versus frequency on the taper section length ( $L_a$ ) of the SiC without support disk.


 Figure 3. Reflection characteristics of SiC absorber on some taper lengths  $L_a = 60, 80, 120$  and  $190$  mm.

The calculation conditions are as follows. Straight section length ( $L_b$ ) of SiC absorber is 80mm that is long enough to absorb incident power completely. The reflections from the short plate can be ignored. We assumed that the dielectric constants of the SiC are a permittivity  $\epsilon' = 25$  and  $\tan\delta = 1.4$ , which are the approximate values of the beam duct SiC. The longer the taper length ( $L_a$ ), the lower reflection coefficient is obtained as expected. As seen in Fig. 3, the reflection power of the taper section of the SiC become lower than 10% at a taper length  $L_a$  of 80mm. Then we adopted the taper length  $L_a$  of 80mm, and cut the thin part (below 2mm in thickness) of the taper, since a thin SiC is fragile. Figure 4 shows our final design. The taper length ( $L_a$ ) is 48mm and the minimum thickness of the SiC absorber is 2mm. The straight section length ( $L_b = 10$ mm) of the SiC absorber is not long enough to completely absorb incident power. However, the straight section length ( $L_b$ ) and the distance between the support disk and the SiC absorber were adjusted, so that the reflection waves from the support disk, the SiC absorber, and the short plate (the end of the SiC absorber), cancel each other. The SiC absorber is divided into four pieces since they are easily brazed to the inner conductor. The inner and outer conductors have cooling water channels. The SiC is cooled via the inner conductor. The support disk is located at 80mm distant from the cavity wall, where an electromagnetic field strength of the fundamental mode is weak enough.

The influence of the support disk on the reflection characteristics is very important in our design. Figure 5 shows the frequency dependence of the reflection power on three different types of support disk materials, alumina ceramics (permittivity  $\epsilon' = 10$ ), macor ( $\epsilon' = 6$ ) and teflon ( $\epsilon' = 2$ ). As seen in Fig. 5, the reflection power is lower than 7% in the frequency range 0.7 - 1.4 GHz for three support disk materials.


 DETAILS OF INNER CONDUCTOR AND SIC ABSORBER  
 Figure 4. The final design of the HOM absorber.

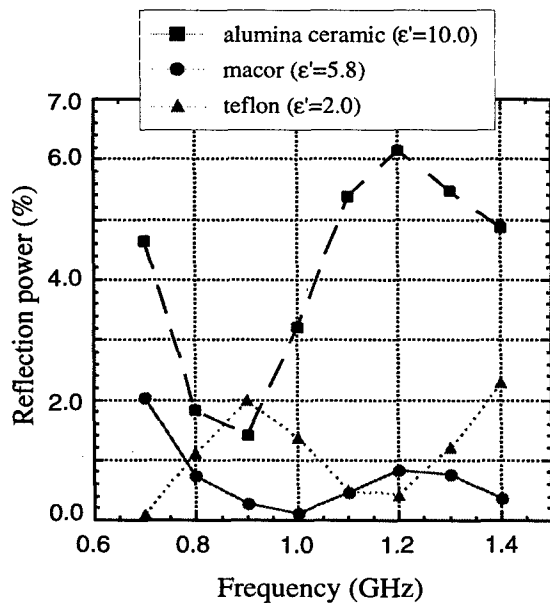


Figure 5. Reflection characteristics of our final design of the HOM coupler, for three different types of the support disk materials alumina ceramics ( $\epsilon'=10$ ), macor ( $\epsilon'=5$ ) and teflon ( $\epsilon'=2$ ).

We adopted the macor as the support disk material since the reflection coefficients become below 2%.

The reflection characteristics are affected also by the dielectric constant of SiC which changes easily depending on the fabrication condition. Figure 6 shows the effect of the dielectric constants of the SiC on the reflection characteristics.

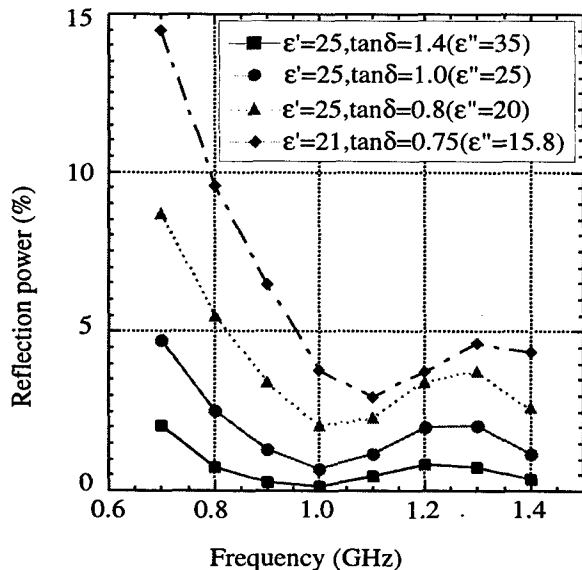


Figure 6. Reflection characteristics of our final design of the HOM coupler, for some different dielectric constants of the SiC.

The required permittivity is about  $\epsilon'' = \sim 20$  to satisfy our design goal as shown in Fig. 6. We fabricated SiC samples to verify the process of manufacturing the SiC absorber and measured the complex dielectric constant. The measured values were  $\epsilon' = 20 \sim 21$ ,  $\tan\delta = \sim 1.0$  ( $\epsilon'' = \sim 20$ ) at 1 GHz. These dielectric constants are barely acceptable to achieve our design goal. The SiC absorber of our final design is being manufactured in Toshiba corporation.

## 4 CONCLUSION

The HOM coupler with a SiC absorber was designed by the use of the computer code HFSS. The VSWR of the HOM coupler could be less than 1.7 (10 % power reflection) in frequency range 0.7 - 1.4 GHz. The dielectric constants of the SiC samples were found to be barely acceptable. The HOM coupler will be tested at the PF ring.

## 5 ACKNOWLEDGMENTS

We would like to thank Yasunao Takeuchi for valuable discussions and offering useful data of SiC properties. And we also acknowledge their valuable advises to K. Satoh and other members of Toshiba corporation. We would like to thank Dir. M. Kobayashi for his encouragement.

## 6 REFERENCES

- [1] Hewlett-Packard Company.
- [2] M. Izawa, T. Koseki, et al., "Installation of new damped cavities at the Photon Factory storage ring", *Journal of Synchrotron Radiation* (1998). 5, 369-371
- [3] H. Takaki, et al., "A Lattice for the Future Project of VUV and Soft X-Ray High-Bright Light Source", 1997 PAC, Vancouver, May 12-16 1997
- [4] M. Kato, et al., "Reconstruction for the brilliance-upgrading project of the Photon Factory storage ring", *Journal of Synchrotron Radiation* (1998). 5, 366-368
- [5] M. Izawa, et al., "Higher-Order-Mode Damping Coupler for Beam Instability Suppression", *Japanese Journal of Applied Physics*, Vol. 26, No. 10, October, 1987, pp. 1733-1739
- [6] R. Sundelin, M. Billing, R. Kaplan, J. Kirchgessner, R. Meller, D. Morse, L. Phillips, D. Rice, J. Seeman and E. von Borstel: *IEEE Trans. Nucl. Sci.* NS-28 (1981) 2844
- [7] Y. Yamazaki, K. Takata and S. Tokumoto: *IEEE Trans. Nucl. Sci.* NS-28 (1981) 2915
- [8] Y. Kamiya, et al., "HOM Coupler for the Damped Cavity of High Brilliance SR Source", 6th
- [9] S. Sakanaka, et al., "Development of a Broadband HOM Load for the 714-MHz HOM-Damped Cavity", 1997 PAC, Vancouver, May 12-16 1997
- [10] Y. Takeuchi, et al., "HOM Absorber for the ARES Cavity", 1997 PAC, Vancouver, May 12-16 1997
- [11] M. Izawa, et al., "Operation of new rf Damped Cavity at the Photon Factory storage ring", APAC98, KEK, Tsukuba, Japan, , March 23-27 1998

# DESIGN CONSIDERATIONS FOR A SECOND GENERATION HOM-DAMPED RF CAVITY\*

R. A. Rimmer<sup>†</sup>, D. Li, LBNL, 1 Cyclotron Road, Berkeley, CA 94720, USA

## Abstract

The first generation of strongly HOM-damped RF cavities are now being operated with beam in accelerators with good success. We briefly review these designs and consider some factors in the design of a second generation HOM damped copper RF cavity suitable for use in high current storage rings such as linear collider damping rings, light sources and high luminosity colliders. We consider the problem of broad-band coupling to the higher-order modes (HOMs) and describe how straightforward modifications to the traditional cavity shape can lead to significant simplification of the mechanical design and reduction in cost. We also consider the problem of broad-band HOM damping in a multi-cell cavity.

## 1 INTRODUCTION

The development of machines with high average current in many bunches has focused attention on the need to reduce the impedance of the higher order modes (HOMs) of the RF cavities. At low to moderate current the HOMs may be detuned to safe frequencies, often by adjustment of the cavity temperature, or the beam motion may be controlled by feedback systems of modest power. At high current the HOM impedances must be reduced at source to keep the beam stable or allow containment by feedback systems of reasonable power. Several machines are currently operating or being commissioned to operate in this regime where broad-band damping of a large number of HOMs is required, including the PEP-II and KEK-B meson factories [1], the DAPHNE  $\Phi$  factory and CESR-B. Many proposed fourth generation light sources, upgrades to third generation light sources, linear collider damping rings and other high intensity machines will also fall into this regime.

## 2 OVERVIEW OF CURRENT DESIGNS

All of the "factory" type machines mentioned above employ single-cell type cavities with strong broad-band HOM damping, although they employ a variety of technical solutions to achieve similar results. PEP-II and DAPHNE use room temperature copper cavities with the addition of rectangular HOM damping waveguides and broad-band loads. The PEP-II cavities typically operate at about 850 kV and 103 kW of wall dissipation [2]. The HOM openings are limited in size and strategically placed

to maximize coupling to the worst HOMs. Figure 1 shows the calculated longitudinal impedance spectrum of the PEP-II cavity, which agrees well with measurements and beam-signal observations. The three HOM loads are designed to dissipate up to 10 kW each and the window is designed to transmit up to 500 kW. The PEP-II high-energy ring has operated at its design value of 750 mA [2] while the low energy rings has achieved 1.2 A of its 2 A goal in a short time [3].

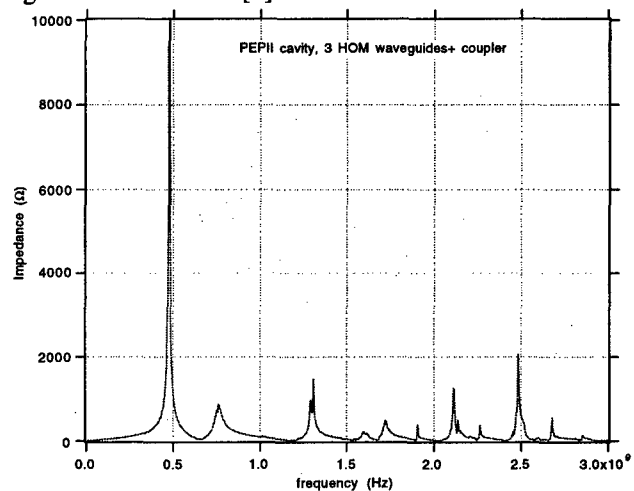


Figure 1. Calculated longitudinal impedance spectrum of PEP-II cavity (MAFIA T3 simulation).

The DAPHNE cavity [3] is a bell-shaped design with a lower shunt impedance, reflecting the modest voltage requirements and priority of low transverse impedance. It uses wide-band ridged-waveguide to coaxial transitions, coaxial feedthroughs and external loads. Two sizes of couplers cover the range of frequencies in the cavity and tapers. The feedthroughs and loads can comfortably handle the approximately 1 kW per load of beam-induced power.

CESR-B uses a single-cell superconducting cavity design with large beam pipes to propagate the HOMs to external loads [4]. The inherently low R/Q of this shape and the strong coupling to the loads results in very small residual impedances, while the shunt impedance for the fundamental mode is very high [5].

KEK-B has developed a similar superconducting design for the high energy ring, but will also employ room temperature cavities which have a combination of waveguide and beam-pipe dampers and an external energy storage cavity to reduce detuning for beam loading compensation. The KEK-B rings are currently being commissioned [6].

Future machines such as the linear collider damping rings will require HOM damped cavities that are as good or better than these existing designs.

\*This work was supported by the U.S. Department of Energy under contracts DE-AC03-76SF00098.

<sup>†</sup> Email: RARimmer@lbl.gov

### 3 DESIGN IMPROVEMENTS

#### 3.1 Cavity profiles

The PEP-II cavity uses the traditional re-entrant "nosecone" type profile that has been shown to give the highest shunt impedance for copper cavities. Most cavities of this type have a toroidal profile for the body of the cavity which means that the transition blend or fillet of all ports entering the body is a complex surface that must be made by a process such as multi-axis milling. For the PEP-II cavity with its many equatorial ports, see figure 2, this was a significant expense.

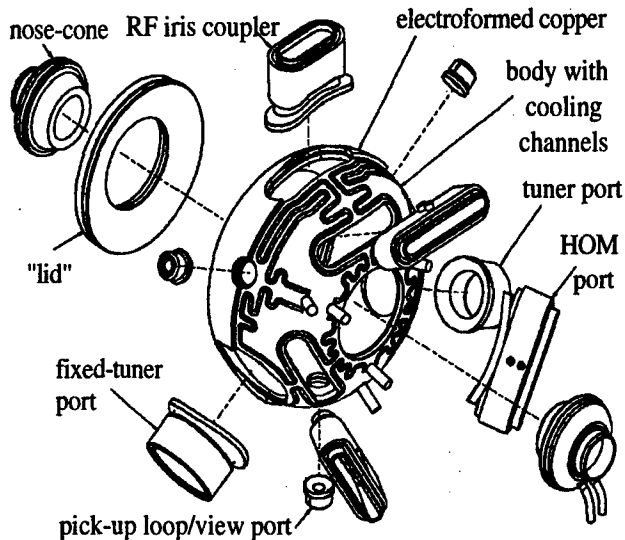


Figure 2. Assembly of PEP-II cavity showing body cooling channels on one half (exposed), equatorial and HOM port inserts, nose-cones and "lid" section.

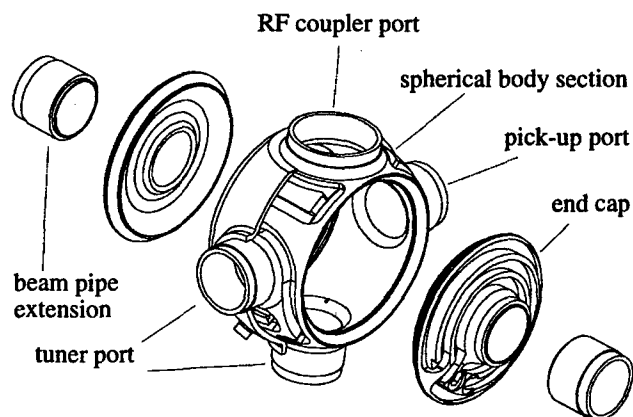


Figure 3 Assembly view of ALS Landau cavity

For the ALS 1.5 GHz Landau cavities which were recently designed by LBNL [7] and built by LLNL [8], a different shape was used, see figure 3, in which the center part of the cavity was spherical. This allowed all of the port blends to be turned on a lathe. The ports were

actually integral to the body and the center section was all machined from a single piece of copper. This greatly simplified the fabrication process and reduced cost and technical risk compared to the PEP-II design. A similar fabrication scheme is being considered for the NLC damping ring cavities, see figure 4.

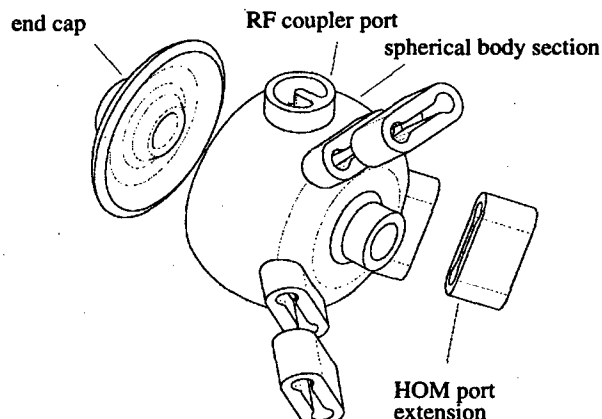


Figure 4. Possible NLC damping ring cavity assembly

#### 3.2 HOM waveguides

For the PEP-II cavity simple rectangular waveguides were used, see figure 5a. The width of the waveguide was considered too great to enter the cavity directly so a smaller racetrack shaped iris was used between the cavity and the waveguide. This required additional parts and machining operations. The HOM waveguide opening causes a strong current concentration at the ends of the slot which results in the highest power density and stresses in the cavity and requires a carefully optimized cooling channel layout [9].

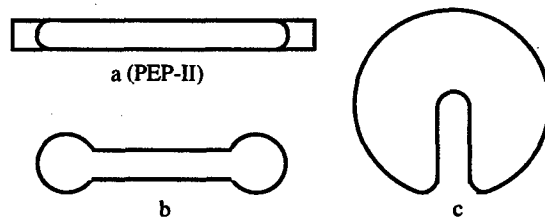


Figure 5. HOM waveguide cross sections with the same cut-off frequency, a: PEP-II rectangular guide, b: compact ridged guide, c: circular ridged guide

The peak power density is strongly dependent on the radius at the end of the slot and the radius of the fillet between the waveguide and the cavity wall. Figure 5b shows a more compact ridged guide cross section with the same cut-off frequency, which does not require an iris. This shape is being evaluated for the NLC damping ring RF cavity. Figure 5c shows a circular ridged waveguide that could be used on the mid-plane of the cavity as a HOM damping aperture or main coupler. The single sided ridge breaks the symmetry of the aperture which may be useful in coupling to HOMs that have no magnetic field on the mid-plane (the PEP-II cavity used an offset slot to



gain useful extra damping of some modes). The circular section lends itself to the use of circular flanges which may improve reliability over the rectangular type used for PEP-II. With wire EDM techniques it is straightforward to make smooth transitions between these various profiles or to a broad-band load or coaxial feedthrough. A plunge-EDM technique is being evaluated to cut the port profiles and blend radii into the cavity body, which may simplify the manufacturing.

#### 4 MULTI-CELL CAVITIES

Multi-cell cavities have the advantage that they offer very high shunt impedance but unfortunately they also have a large number of potentially harmful HOMs, some of which may not be well damped by couplers at the ends of the cavities. Adding damping waveguides to each cell would solve this problem but would lead to an ungainly structure. The problem may lie in the cell to cell coupling schemes often used for these structures. Beam iris coupling, figure 6a, is poor at transmitting many HOMs along the structure. Magnetic coupling via pairs of kidney-shaped slots between cells, figure 6b, is commonly employed in linacs and multi-cell cavities, but in this case some or all of the dipole modes will not be propagated through long structures. The simple expedient of using three equally spaced slots between cells, see figure 6c, will allow the dipole modes to propagate through the structure without introducing any dipole or quadrupole components into the accelerating mode. This coupling method is currently being investigated for short multi-cell structures, and appears promising. Figure 7 shows a preliminary calculation of the longitudinal impedance spectrum of a 3-cell HOM-damped structure, there are more HOMs visible than the single cell but even without optimization the total impedance does not appear to be worse than three single cells of the same profile and no modes appear to be completely trapped in the structure. The size of the coupling slots determines the frequency difference between the various versions of the fundamental mode ( $0, \pi, \pi/2$  etc.), which may allow them to be tuned to safe frequencies. The impedance of modes other than the accelerating mode will also be reduced by the transit-time factor.

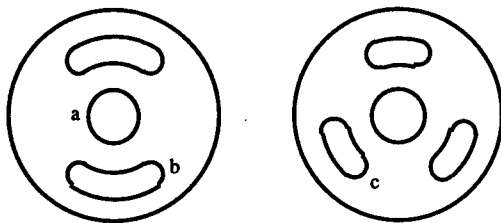


Figure 6. Coupling slot configurations. a: beam iris, b: dual kidney slots, c: triple kidney slots

#### 5 CONCLUSIONS

HOM damped structures have been proven to be effective in reducing instabilities in high current storage rings. Changing the cavity body shape from toroidal to partly spherical may allow simpler fabrication with no penalty in shunt impedance. Modified HOM damping apertures may eliminate the iris feature, simplifying the design, and may use larger radii at the ends of the slots to reduce the RF surface current concentration, lowering the temperature and reducing stresses. HOM damping in multi-cell cavities may be practical and effective and will be studied further.

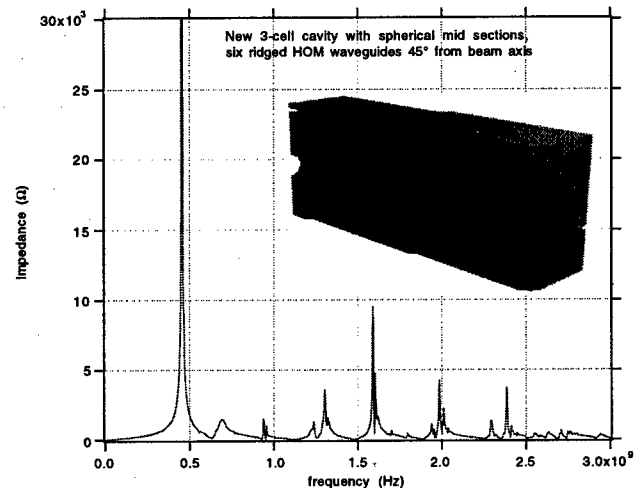


Figure 7. Calculated impedance spectrum of 3-cell cavity with 3 HOM waveguides at each end and three kidney slots between cells (MAFIA T3 simulation).

#### REFERENCES

- [1] John T. Seeman, "Commissioning Results of B-Factories", these proceedings.
- [2] R. A. Rimmer et. al., "Commissioning of the PEP-II High-Power RF Systems", EPAC 98, Stockholm, Sweden, June 1998, pp 1805-7, SLAC-PUB-7852.
- [3] A. Gallo et. al. "Operational Experience with the DAFNE Radio-frequency Systems", these proceedings.
- [4] S. Belomestnykh et. al. "Commissioning of the Superconducting RF Cavities for the CESR Luminosity Upgrade", these proceedings.
- [5] H. Padamsee et. al. "RF Superconductivity for Accelerators", Ch. 20, pp 440-446, Wiley, 1998.
- [6] K. Akai et. al. "Commissioning of the KEKB RF System", these proceedings.
- [7] R. A. Rimmer et. al., "A Third-Harmonic RF cavity for the Advanced Light Source", EPAC 98, Stockholm, Sweden, pp 1808-10.
- [8] R.M. Franks et. al., "Mechanical Design and Fabrication Processes for the ALS Third-Harmonic Cavities", these proceedings.
- [9] R. Rimmer, et. al., "High-power RF Cavity R&D for the PEP-II B Factory", Proc. EPAC 94, June 27-July 1 1994, London, pp 2101-3, LBL-34960, PEP-II EE note 3-94.

# A NOVEL RACETRACK MICROTRON ACCELERATING STRUCTURE\*

D.V. Kostin<sup>#\*</sup>, V.I. Shvedunov<sup>†</sup>, N.P. Sobenin<sup>#</sup>, and W.P. Trower  
World Physics Technologies, Blacksburg VA

## Abstract

We have designed, constructed, and evaluated a Rectangular Cavities Biperiodic Structure prototype for our compact 70 MeV pulsed RaceTrack Microtron [1]. We present here the design details and test measurements.

## 1 INTRODUCTION

Our mobile 70 MeV RTM requires a narrow accelerating structure to allow 1<sup>st</sup> orbit electrons to bypass the structure. We solved this problem by using a rectangular accelerating structure with rectangular vertically extended beam slots. This structure also produces high frequency horizontal focusing, which we use to simplify the RTM construction and operation [1,2].

## 2 STRUCTURE CALCULATION

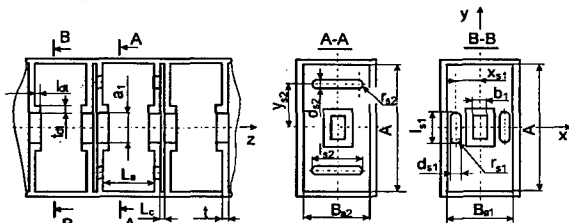


Figure 1: Rectangular cavities biperiodic structure

We found the RCBS structure dimensions with optimal electrodynamics characteristics, seen in Fig. 1, using analytical and numerical calculations as well as computer simulations [3]. We calculated a seven cell section, seen in Fig. 2, whose first cell is for  $\beta=0.67$ . In Table 1 we present the structure dimensions where the first and last end cells are listed separately. In Fig. 3 we show the calculated RCBS dispersion characteristics. Figure 4 contains the calculated on-axis longitudinal electrical field.

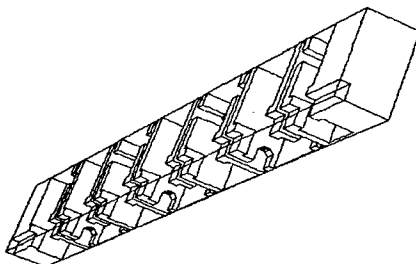


Figure 2: Seven cell RCBS section

\*Work supported in part by NSF DMI-9704039

<sup>†</sup>Permanent address: Electrical Engineering Department, Moscow Engineering Physics Institute, Moscow, Russia

<sup>#</sup>Email: wptinc@naxs.net

<sup>#</sup>Permanent address: Institute of Nuclear Physics, Moscow State University, Moscow, Russia

Table 1: RCBS dimensions (in mm)

Main Cells		End Cells	
$D=\lambda_w/2$	52.5		
A	110.0	$A[1]/A[7]$	110.0/110.0
$B_{a1}$	54.9	$B_{a1}[1]/B_{a1}[7]$	52.98/55.76
$B_{a2}$	55.3		
$B_c$	52.5		
$L_a$	38.0	$L[1]$	20.68
$L_c$	3.5		
T	5.5		
$A_1$	20.0		
$B_1$	10.0		
$l_{dt}$	4.4		
$t_{dt}$	5.0		
$x_{s1}$	20.0		
$l_{s1}$	32.1	$l_{s1}[1]/l_{s1}[7]$	51.70/37.36
$d_{s1}$	8.0		
$y_{s2}$	45.0		
$l_{s2}$	38.2		
$d_{s2}$	8.0		

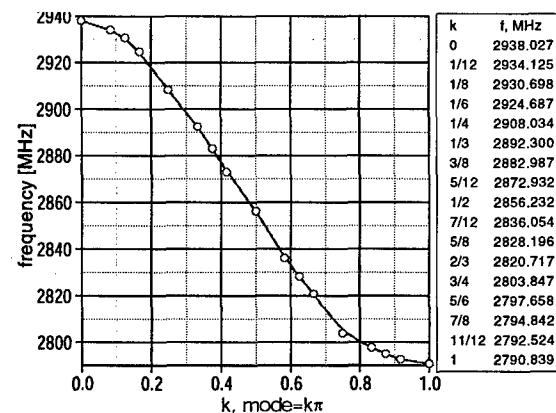


Figure 3: Seven cell RCBS section dispersion characteristics

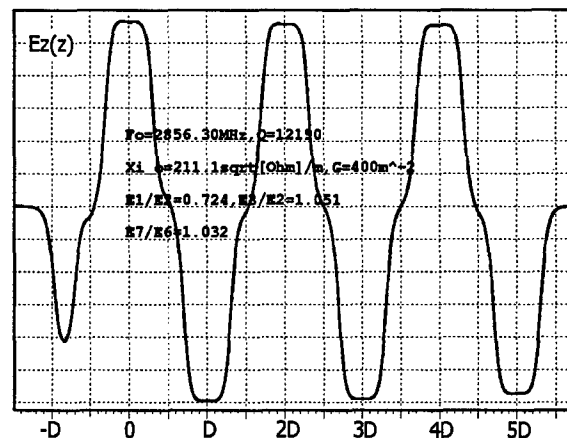


Figure 4: Seven cell RCBS section  $E_z(0,0,z)$

### 3 STRUCTURE TUNING

Our manufactured seven accelerating and six coupling cell section geometry was adjusted to obtain the operating frequency in various resonant setups, each with a different number of RCBS periods. We then tuned the end cells to obtain the required accelerating field distribution at the operating frequency by adjusting the end cell coupling slot lengths and narrow wall dimensions,  $B_{a1}[i]$ ,  $i=1$  and 7. Next we tuned the coupler cell frequency by decreasing its narrow wall dimension by 0.6mm ( $B_{A,CPL}=54.3\text{mm}$ ). We chose the coupling window width for the  $72\times 34\text{mm}^2$  feeding waveguide using its analytical dependence on the normalized impedance, seen in Fig. 5 [4]. To support a 0.7A total beam current from all orbits, we matched the coupler using a coupling coefficient of  $\sim 3.5$  [4]. An approximate analytical formula gave a window width of 31.7mm, which we made 28mm and increased to 28.8mm during tuning.

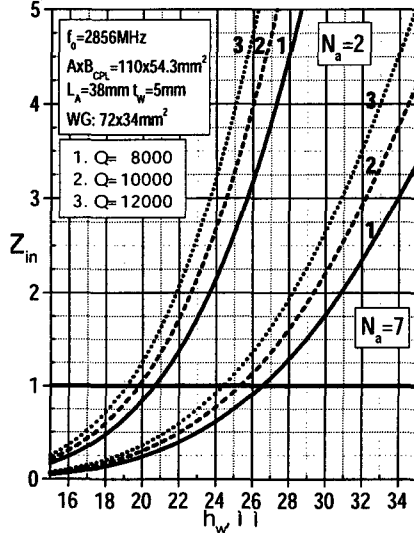


Figure 5: Coupler impedance with window width

### 4 STRUCTURE MEASUREMENTS

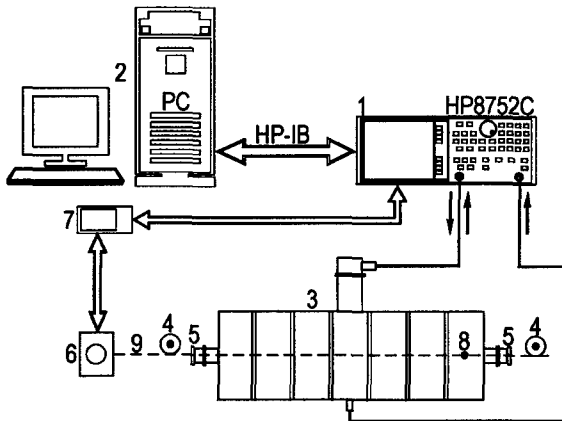


Figure 6: Measurement setup

We measured the section electrodynamics characteristics using the setup shown in Fig. 6, which consisted of (1) a

network analyzer, (2) a personal computer, and a mechanical assembly. This assembly included (3) the structure, (4) a bead pulling system with (5) pulleys, (6) thread directors inserted into drift tubes, and (7) a stepper motor/controller. The stepper motor, used to drive the (8) ceramic bead attached to (9) a nylon thread, was controlled by the computer through the network analyzer.

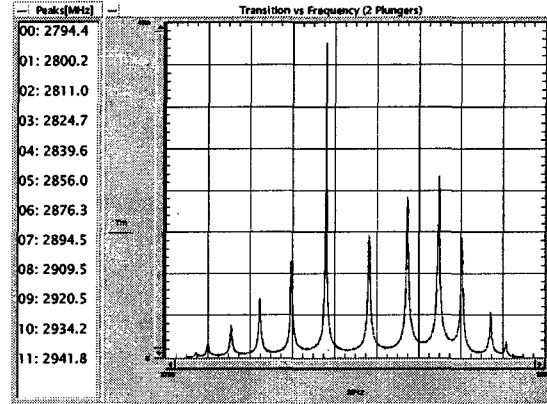


Figure 7: RF modes spectra measurements

After tuning and matching the coupler with the structure, we obtained the  $\pi/2$  mode operating frequency of  $f_0=(2856\pm 0.1)\text{MHz}$  at  $20^\circ\text{C}$  in agreement with the calculated value. We realized the lowest passband  $E_{11}$  resonance frequencies, seen in Fig. 7, using both reflection (standing wave ratio) and transition ( $K_{tr}$ ) coefficient measurements, with two different field exciting and pick-off points, through a waveguide adapter connected to the coupler and through a metal plunger inserted into the drift tube.

After matching the coupler with the rectangular waveguide, the structure coupling coefficient was 3.0. Using a small 5mm diameter metal rod mounted near the narrow rectangular waveguide wall, we obtained the 1.0 standing wave ratio used in field measurements. We also measured the Q-factor.

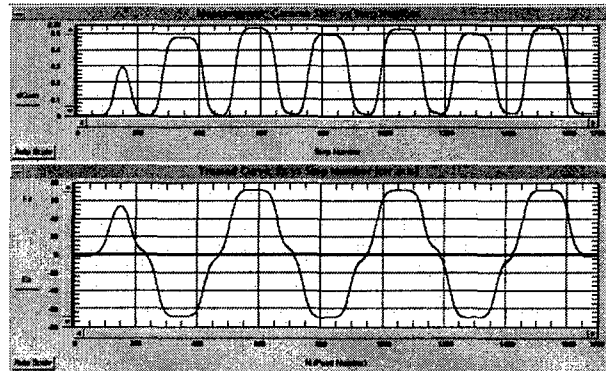


Figure 8: Seven cell  $E_z(0,0,z)$  measured distribution

We measured the field distribution and effective shunt impedance using the bead-pull method with a 6mm long, 0.6mm diameter dielectric cylinder as the perturbing bead. The bead form factor, measured in the  $E_{010}$  cylindrical

resonator mode, was  $8.849 \times 10^{-20} \text{ m}^2 \text{ c} / \Omega \text{ m}$ . We made these field distribution measurements, seen in Fig. 8, in two ways. In the first we obtained the shunt impedance by measuring, with the network analyzer, the induced frequency shift as the bead moved along the structure axis. From  $\xi(z) = E_z(z) / \sqrt{PQ} = \sqrt{\Delta f / (2\pi K_r^E f_0^2)}$ , where  $E_z(z)$  is the on-axis longitudinal electric field,  $P$  is RF power, and  $Q$  is the Q-factor,  $\xi_0 = E_{z0} / \sqrt{PQ}$  was obtained by integrating over the regular part of the field distribution curve and its first harmonic amplitude for  $\xi(z)$ .

In the second more accurate method, we measured the reflection coefficient,  $\Gamma$ , at a fixed frequency to obtain the longitudinal electrical field gradient. Here the electric field at the bead position is proportional to  $\sqrt{\Delta \Gamma}$ , and we calculated the focusing gradient,  $G_x = 2(I(x)/I_0 - 1) / x^2$  (or y-axis).  $I_0$  is the integral of  $\sqrt{\Delta \Gamma(z)}$  over the regular part of the on-axis field data and  $I(x)$  is this measurement off-axis by a distance  $x$ . The measured adjacent cell electrical field amplitude ratios were found to be  $E_1/E_2=0.78$ ,  $E_3/E_2=1.06$ , and  $E_7/E_6=1.04$ .

The effective shunt impedance to Q-factor ratio was obtained from  $r_{\text{sh,eff}}/Q = \xi_0^2 L/2$ , where  $L$  is the regular structure length. The test section is not a regular structure so we used an indirect effective shunt impedance measurement. We found  $\xi_0$  and related it to the effective shunt impedance by  $r_{\text{sh,eff}}/Q \sim \xi_0^2$ . We then obtained the full section shunt impedance to Q factor,  $R/Q$ , by integrating  $\xi(z)$  over the full section length. The structure electrodynamic characteristics results are seen in Table 2.

Table 2: Structure Electrodynamic Characteristics

Characteristic	Measured	Calculated
$f_0$ (MHz)	2,856±0.1	2,856.0
$k_c$ (%)	5.1	5.1
$Q$	10,800±200	12,400
$\xi_0$ ( $\sqrt{\Omega}$ /m)	205±5	211
$r_{\text{sh,eff}}/Q$ (k $\Omega$ /m)	3.3±0.3	3.65
$r_{\text{sh,eff}}$ (M $\Omega$ /m)	37±3	45
$R/Q$ (k $\Omega$ )	1.25±0.02	1.23
$G_x$ (m $^{-2}$ )	500±100	410
$G_y$ (m $^{-2}$ )	-300±100	-410

## 5 CONCLUSIONS

The RCBS for our compact 70 MeV pulsed RTM has measured EDC in good agreement with those we calculated. Our RCBS, which operates in the  $\pi/2$  mode at 2,856 MHz with a Q of 11,000, has a ~40 M $\Omega$ /m effective shunt impedance and a ~400m $^{-2}$  focusing gradient.

## 6 REFERENCES

- [1] E.A. Knapp, A.W. Saunders, V.I. Shvedunov, N.P. Sobenin and W.P. Trower, "A Mobile Racetrack Microtron", Nucl. Instrum. Meth. B139 (1998) 517.
- [2] D.V. Kostin, V.N. Melekhin, V.I. Shvedunov, N.P. Sobenin, and W.P. Trower, "High Frequency Focusing-Accelerating Structures", in *Applications of Accelerators in Research and Industry*, J.L. Dugan, and I.L. Morgan, eds. (AIP Press, Woodbury, 1997) vol. CP392, p.1135.
- [3] R. Klatt, F. Krawczyk, W.R. Novender, C. Palm, and T. Weiland, "A Three Dimensional Electromagnetic CAD System for Magnets, RF Structures and Transient Wake-Field Calculations", in *Proc. 1986 Linear Accelerator Conf.*, SLAC-303 (1986) p.276.
- [4] N.P. Sobenin and B.V. Zverev, *Electrodynamic Characteristics of Accelerating Cavities*, (Energoatomizdat, Moscow, 1993) 220pp. (in Russian).

## RF PULSED TESTS ON 3GHZ NIOBIUM CAVITIES

J. Le Duff, C. Thomas\*, G. Bienvenu, H. Sun† LAL, Orsay, France  
M. Fouaidy, IPN, Orsay, France, R. Parodi, INFN, Genova, Italy

### Abstract

The achievable limiting RF field for S-Band and L-Band superconducting cavities is still an open question today. Previous studies on Sn and In have shown that a surface magnetic field  $B_s$  higher than the thermodynamical critical field  $B_c$  might be reached. The ultimate limiting field is then the superheating field  $B_{sh}$  ( $B_{sh} = 240$  mT or  $E_{acc} = 60$  MV/m for Nb at  $T = 0$  K). However, the maximum accelerating field observed so far is in the range  $E_{acc} = 37$ -40 MV/m for the best 1.3 GHz Nb cavities. A dedicated facility (NEPAL Supra Test Facility) is currently used at LAL for measuring  $B_{sh}$  on bulk Nb 3 GHz cavities supplied by INFN-Genova. High power pulses (4.5  $\mu$ s, up to 5 MW) are used to reach  $B_{sh}$  before cavity thermal breakdown occurs. A method for analyzing the response of a SRF cavity when subjected to pulsed high RF power was developed and the corresponding numerical simulation results were validated by comparison to experimental data. This technique is successfully applied to detect  $E_{acc}$  and  $B_{sh}$  at which the cavity magnetic breakdown occurs. Magnetic penetration depth ( $\lambda$ ) measurements were also performed with a low RF level test bed and the corresponding data analyzed then compared to theoretical predictions.

## 1 INTRODUCTION

The maximum achieved accelerating fields in SRF cavities are usually limited by field emission and thermal breakdown. These two limits have been pushed back thanks to improvements of niobium purity, cavity preparation, assembling and conditioning techniques. In principle, a theoretical limit of the surface field higher than  $B_c$  (i.e  $B_c = 200$  mT or 50MV/m accelerating field  $E_{acc}$  for TESLA shape bulk niobium (Nb) cavities at  $T = 0$  K) is expected in CW mode of operation. Previous RF measurements performed on indium and tin samples and the corresponding theoretical estimation have shown that  $B_s \geq B_c$  might be reached [1]. Moreover, the fundamental limit  $B_{sh}$  of bulk Nb is now close to being reached [2]. Due to lack of sufficient experimental data on  $B_{sh}$  for Nb, it is important to measure this parameter precisely.

## 2 SUPERHEATING FIELD AND PENETRATION DEPTH

In this section, we briefly summarize the useful relationships dealing with the predictions of  $B_{sh}$  and  $\lambda$  according to different theories.

\* Email: cthomas@lal.in2p3.fr

† visitor, IHEP, Beijing, PRC

### 2.1 Superheating Field

For Type-II superconductors such as niobium, subjected to an external magnetic field  $B_a$  (static or slowly varying), the Meissner effect persists up to the first critical field,  $B_{c1}$ . For  $B_a$  lying between  $B_{c1}$  and  $B_{c2}$ , normal conducting areas are nucleated : this thermodynamic state is called the mixed state. Beyond  $B_{c2}$ , superconductivity is completely destroyed. Moreover, in the case of non-zero  $B_a$ , the transition from superconducting to normal conducting state is of first order. In this case, superheating is possible and a magnetic field ( $B_{sh}$ ) higher than the critical field  $B_{c1}$  could then be sustained by the superconducting material. The superheating field  $B_{sh}$  is related to the critical thermodynamic field  $B_c$ . According to Ginzburg-Landau (GL) theory [3], we distinguish two kinds of superconductors depending on the value of the material's GL parameter  $\kappa_{GL} = \frac{\lambda_{GL}}{\xi_{GL}}$  where  $\xi_{GL}$  is the GL coherence length:

For type I superconductors,  $B_{sh} \approx \frac{0.89}{\sqrt{\kappa_{GL}}} B_c$ .

For type II,  $B_{sh} \approx 0.75 B_c$ .

Note that niobium, which is a type II superconductor but with a peculiar behaviour due to a  $\kappa$  value close to the critical value  $\kappa_{GL}^{Nb} \simeq \kappa_{GL}^c = \frac{1}{\sqrt{2}}$ , we have :

$$B_{sh} = 1.2 * B_c \quad (1)$$

### 2.2 Penetration depth

The London magnetic penetration depth  $\lambda_L(0)$  at absolute zero is given, according to the well-known phenomenological London theory, by  $\lambda_L(0) = \sqrt{\frac{m}{\mu_0 n_s e^2}}$  where  $m$ ,  $e$  are respectively the mass and charge of the electron and  $n_s$  is the density per unit volume of super electrons at  $T = 0$  K. The temperature dependence of the cooper pair density, introduced in the two fluid model by Gorter-Casimir (GC), results in an empirical temperature-dependent London penetration depth :  $\lambda_{GC}(t) = \lambda_{L0} \frac{1}{\sqrt{1-t^4}}$ , where  $t$  is the reduced temperature ( $t = T/T_c$ ) with reference to the material critical temperature  $T_c$ . This expression was derived in the London limit where  $\xi_0 \gg \lambda$  and is not valid in the neighbourhood of  $T_c$  (i.e  $t$  close to 1) [4]. Ginzburg and Landau [3] showed that the penetration depth depends on the material purity, or equivalently the electron mean free path, leading to the following asymptotic expressions :

- for "clean" superconductors ( $l \gg \xi_0$ )

$$\lambda_{GL}(t) = \frac{\lambda_L(0)}{\sqrt{2(1-t)}} \quad (2)$$

- for "dirty" superconductors ( $l \ll \xi_0$ )

$$\lambda_{GL}(t) = \frac{\lambda_L(0)}{\sqrt{2}} \sqrt{\frac{\xi_0}{1.33l}} \frac{1}{\sqrt{(1-t)}} \quad (3)$$

where  $\xi_0$  is the BCS coherence length and  $l$  the mean free path of a normal electron. Note that measuring the magnetic penetration depth allow us to determine  $l$  and to obtain the RRR of our cavity in-situ. Direct RRR measurements on cavities [5] will be used to cross-check the first results. Moreover, we plan to measure both  $B_{sh}$  and  $\lambda$  (Eq. 3) before and after cavity heat treatment with Ti gettering (i.e material purification), hence we will be able to check the validity of the relationship given by Eq. 1 (i.e.  $B_{sh}$  doesn't depend on  $\kappa_{GL}$ ).

### 3 METHOD OF $B_{SH}$ MEASUREMENT

In most case, the maximum accelerating field is limited, in DC or long RF pulsed mode (1 – 10ms) by cavity thermal breakdown. To circumvent this problem, we use RF pulses of duration  $\tau_p = 1 - 4.5\mu s$  which are much shorter than the characteristic time needed for cavity thermal breakdown or quench induced by anomalous RF losses to occur ( $\approx 100\mu s$  [6]). In order to achieve a good transfer efficiency between the RF source and the cavity, a strong external coupling is needed (i.e  $Q_{ext} = 5.10^4$ ). As long as the cavity is in the superconducting state ( $Q_0(4.2K) \approx 7.10^7$ ), the cavity decay time  $\tau = \frac{Q_L}{\omega}$ , where  $Q_L$  is the loaded quality factor, is dominated by the external coupling (i.e  $\tau \approx \frac{Q_{ext}}{\omega}$ ). When a thermal or magnetic breakdown occurs,  $Q_0$  jumps instantaneously to  $10^6 - 10^5$  and consequently  $\tau$  decreases. The transmitted power integral  $U_t = \int A \exp -\frac{t}{\tau} dt$ , which is proportional to the incident power integral  $U_i$ , when the cavity is in the superconducting state, shows a deviation from the linear behaviour when the cavity quenches (i.e transition to the normal state) as illustrated in Fig. 1. The point, where such a deviation (eq. jump of  $U_t$ ) is initiated and referred to as "B" in this figure, corresponds exactly to the quench field. Note that other methods of quench field measurements are not appropriate to our test stand [7].

### 4 EXPERIMENTAL APPARATUS AND PRELIMINARY RESULTS

In order to reach a high accelerating field, we use a 3 GHz-35 MW klystron with a maximum pulse length of  $4.5\mu s$ . The experimental set-up block diagram is shown in Fig. 2. Data acquisition of all the experimental parameters and processing (RF signal integration) is performed using a dedicated Labview<sup>TM</sup> program.

Experimental runs were performed and the corresponding preliminary results are displayed in Fig. 3. The shape of the experimental curve is close to the expected simulation results (see Fig. 1). More precisely, we clearly observe a linear part of  $U_t$  versus  $U_i$  up to a critical value of  $U_i$  ( $U_i^c \approx 1.4 - 1.5$  J). Moreover as expected, at this value  $U_t$  decreases sharply (cavity magnetic breakdown) when  $U_i$  is slightly increased, reaching a plateau at  $U_t \approx 0.6\mu J$  for  $U_i \geq 1.5$  J. Note that a precise value of the maximum  $E_{acc}$  and hence  $B_s$  at which the cavity magnetic breakdown occurs could not be deduced from these results at the time

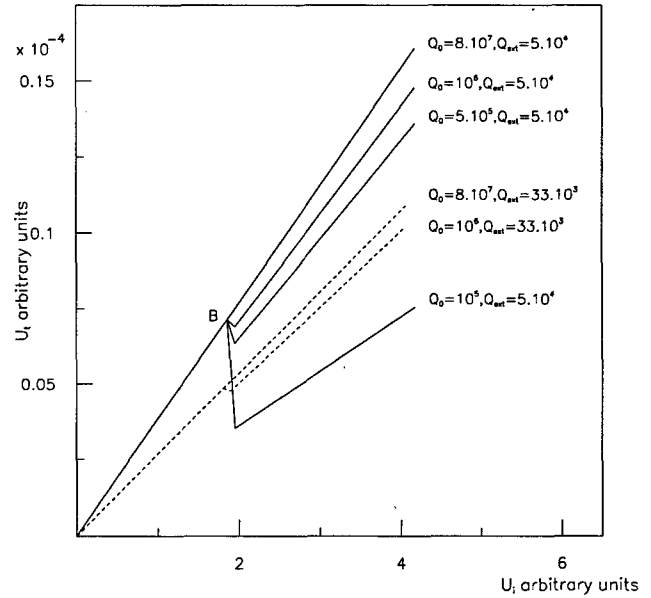


Figure 1: Simulation of the variation of the transmitted power integral versus the incident power integral.

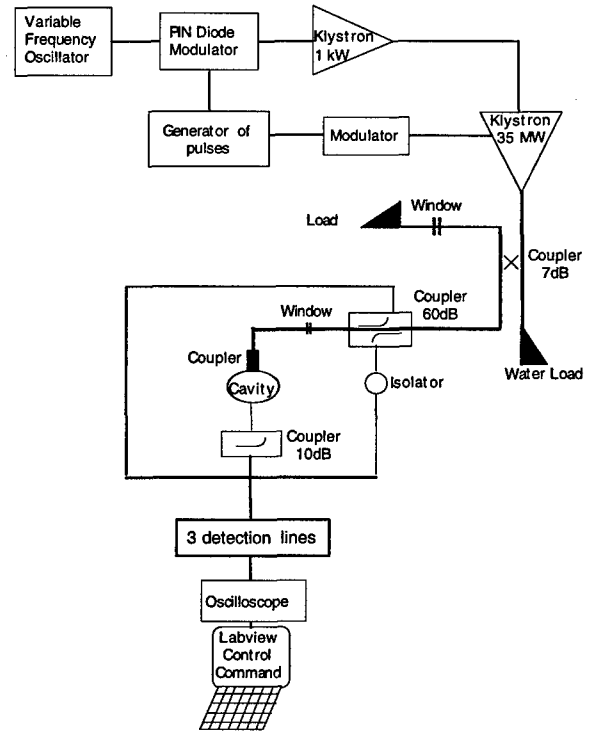


Figure 2: Schematic of experimental set-up

being because of some calibration uncertainties.

### 5 MAGNETIC PENETRATION DEPTH : METHOD AND RESULTS

The cavity resonant frequency is influenced by the magnetic penetration depth which is a temperature dependent parameter. More precisely, the reactive component of the cavity surface impedance  $X$  is related to the resonant fre-

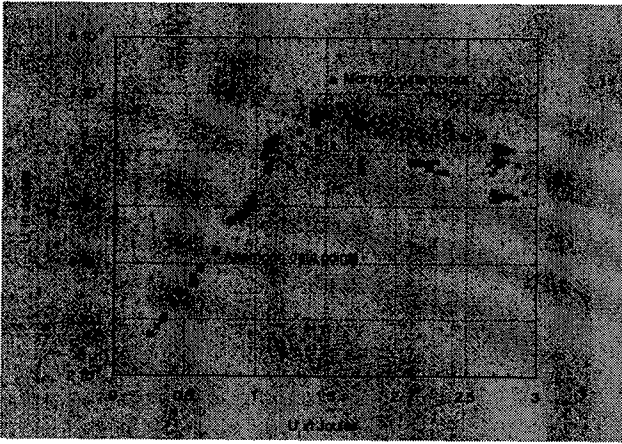


Figure 3: Integral of transmitted power versus integral of incident power (performed at  $T = 4.2$  K on cavity CAT2)

quency  $f$  by the formula :  $X = 2G \frac{(f-f_0)}{f_0}$  where  $G$  is the geometric factor and  $f_0$  is the frequency of an ideal cavity (perfectly conducting). Moreover,  $X$  is proportional to the frequency and magnetic penetration depth ( $X = 2\pi f \mu_0 \lambda$ ). Consequently, starting at an initial temperature  $T_0 = 4.2$  K and recording the cavity frequency shift due to temperature variation, we can easily deduce the corresponding  $\Delta\lambda$  :

$$\Delta\lambda(T) = \lambda(T) - \lambda(T_0) = \frac{G}{\pi\mu_0} \frac{\Delta f}{f(T_0)^2} \quad (4)$$

This procedure was used and the corresponding data (160 data points) analysed and compared (Fig. 4) to the theoretical relationships of GL (Eq. 3) or GC. These results clearly show that GL theory fits the data better than the GC theory : the corresponding mean standard deviation are respectively 23.1nm and 22.2nm for GC and GL theories. Note that the two fitting parameters are very sensitive to the Nb critical temperature  $T_c$  ( $T_c$  was ajusted by trial and error in the range : 9.1 K-9.4 K), and the optimum value was 9.3 K. This figure is close to published data ( $T_c = 9.3$  K) [8]. The measured  $\lambda_{GL}(4.2K) = 33$ nm is in good agreement with previous results [9] leading to a mean free path  $l = 670$  Å and hence a Residual Resistivity Ratio RRR = 10. The estimated RRR obtained from Nb impurities contents (O, C, N) [10] is 40. The apparent discrepancy between the RRR deduced from  $\lambda_{GL}$  and the estimated one could be explained by RRR decrease near the Nb surface [11]. Finally, the corresponding experimental GL parameter is  $\kappa_{GL}^{exp} = 1.1$  which is close to  $\kappa_{GL}^e$ .

## 6 ACKNOWLEDGEMENTS

We would like to thank J.N.Cayla for his technical support, G.Arnaud, Ph.Dufresne and M.Roch for their assistance concerning vacuum and cryogenics as well as the IPN Superconducting cavity group and S.Buhler for their helpful advice. A special thank to B.Mouton for his friendly help.

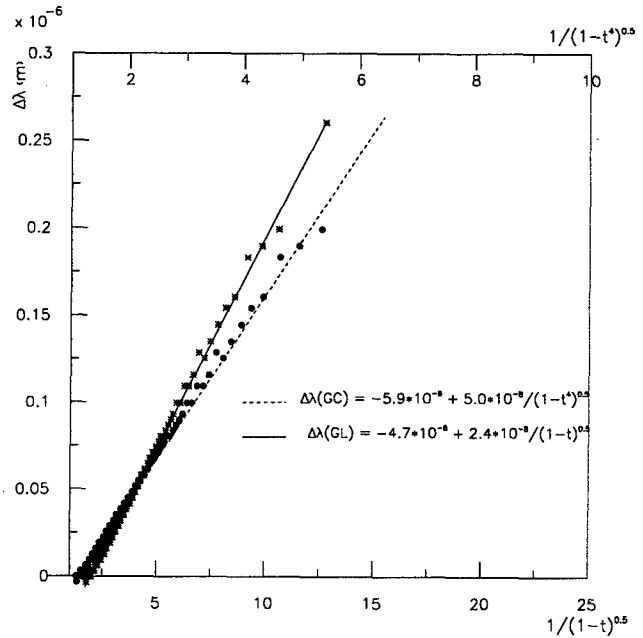


Figure 4: Effect of temperature on the relative magnetic penetration depth for  $T_c = 9.3$  K [8] for cavity GEN1 ( $\chi_{GL}^2 = 1.58$  and  $\chi_{GC}^2 = 21.08$  respectively)

## 7 REFERENCES

- [1] T.Yogi, G.J.Dick, J.E.Mercereau, Phys. Rev. Letters 39, (1977), pp826-829
- [2] E.Kako et al. "Improvement of cavity performance by electropolishing in the 1.3GHz Nb superconducting cavities", this conference
- [3] V.L.Ginzburg and L.D.Landau, JETP 20 (1950), p1064.
- [4] J.Bardeen, L.N.Cooper, J.R.Schrieffer, Phys.Rev. 108 (1957), pp1175-1204.
- [5] H.Safa et al., "RRR Mapping of SRF cavities by a magnetometric method", Proc. of 8<sup>th</sup> SRF Workshop, Abano Terme, (1997).
- [6] T. Junquera et al., "Thermal stability analysis of superconducting RF cavities", Advances in Cryogenic Eng., Vol 43.
- [7] T.Hays, H.Padamsee, "Measuring the RF critical fields of Pb, Nb, Nb<sub>3</sub>Sn", SRF 980804-06, LNS, Cornell Univ..
- [8] M Cyrot and Davor Pavuna, "Introduction to superconductivity and High-Tc Materials", (1992), p113.
- [9] B.Bonin, "Materials for superconducting cavities", CERN96-03, p194.
- [10] M.Fouaidy, Private communication.
- [11] C.Antoine et al., "Nuclear Microprobe studies of impurities segregation in Niobium used for radiofrequency cavities", Proc. of 8<sup>th</sup> SRF Workshop, Abano Terme, (1997).

# COAXIAL DISC WINDOWS FOR A HIGH POWER SUPERCONDUCTING CAVITY INPUT COUPLER

S. Chel, M. Desmons, C. Travier, CEA/DSM/DAPNIA/SEA Saclay  
T. Garvey, P. Lepercq, R. Panvier, CNRS/IN2P3/LAL Orsay

## Abstract

A  $\lambda/2$  coaxial L-band window has been tested up to 1 MW (1 ms pulses), both at room temperature and at 80 K. Dielectric losses were measured. A travelling wave window with lower dielectric losses has been fabricated.

## 1 INTRODUCTION

In the framework of the TESLA collaboration, Saclay and Orsay are designing an alternate input power coupler. The aim is to develop a simplified version of the present TTF coupler, in order to reduce the cost. The way to achieve this simplification is to consider a fixed (non tunable) and rigid (non flexible) coupler. As part of this effort, a coupler test stand including a 80 K cryostat was constructed [1], and several coupler parts were designed and tested. This paper presents the experimental results concerning a  $\lambda/2$  disc window. It also describes the design of a travelling wave (TW) disc window.

## 2 $\lambda/2$ DISC COAXIAL WINDOW

The simplest coaxial window one can imagine is a ceramic disc brazed inside the 50  $\Omega$  coaxial pipe. In order to be self-matched, the ceramic should be half a wavelength thick. Using WESGO Al300 alumina which has a permittivity  $\epsilon_r = 9$  at the designed frequency of 1.3 GHz (as given by the vendor), the window was designed with the parameters given on table 1. The inner conductor is made of copper, while the outer conductor is made of kovar, an alloy which has a linear thermal expansion coefficient very close to that of the ceramic and is therefore often used in ceramic/metal assemblies. The kovar piece is then TIG welded to the stainless steel copper coated outer conductor as shown in fig. 1. The ceramic is coated with a thin layer of TiN. This window was fabricated by SICN [2].

The main advantages of this type of window are its relative simplicity, its robustness, the absence of electric field perpendicular to the ceramic surface which is favorable for avoiding multipactor, and the ease with which the window can be cleaned prior to its assembly on the cavity. The potential drawbacks are the high electric field at the braze location and the high dielectric losses due to the large volume of ceramic used.

## 3 WINDOW TEST CONDITIONS

The window was mounted on the test stand presented in reference [1]. It is inserted on the test line between a door-

Table 1: Windows characteristics

Characteristics		
	$\lambda/2$	TW
Inner diameter (mm)	26.8	75.6
Outer diameter (mm)	61.6	142.2
Ceramic thickness (mm)	38.4	10
Performances		
Bandwidth (MHz) ( $S_{11} < 0.1$ )	80	80
Ratio between max field at brazing and max field in coax	1	0.2
Avg. dielectric losses (W) at 1 MW (TESLA pulse)	44	6.5

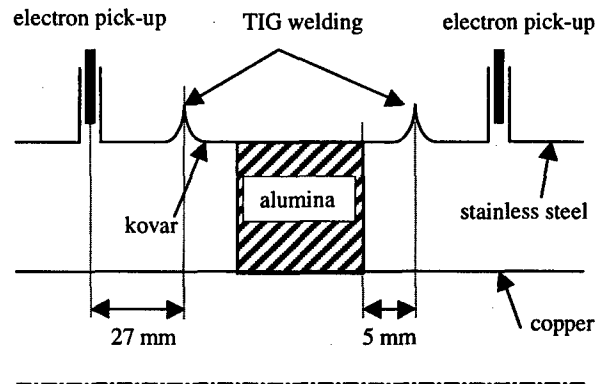


Figure 1:  $\lambda/2$  disc coaxial window

knob type and an antenna type waveguide to coax transition as shown schematically on fig. 2. The diagnostics used are 2 electrons pick-ups located on both sides of the window and 2 photomultipliers located as shown on fig. 2.

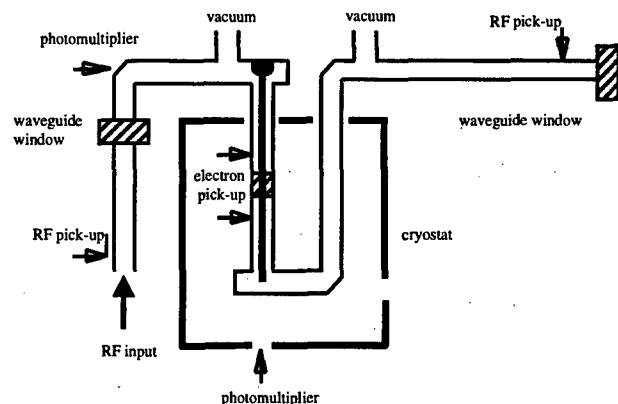


Figure 2: Coupler test stand



The present capability of the power source allows tests at a peak power of 1 MW, for pulses of 800  $\mu$ s and a repetition rate of 0.1 Hz. The system runs continuously and all signals (RF power, vacuum, electrons, light, temperatures) are recorded for each pulse. This  $\lambda/2$  window was tested for almost 5 months between August 1998 and January 1999, this period corresponding to 990,983 pulses. For each pulse, 80 parameters are recorded, so that the total amount of data represents 1.3 Gbytes. Since the analysis of such a huge amount of data cannot be made with standard spreadsheet softwares, PAW [3] is used.

The window was tested under all possible conditions: at room temperature and at liquid nitrogen temperature, with standing and travelling wave rf input, with vacuum on both side and with atmospheric pressure on one side. The result of all these tests are presented in the next sections.

#### 4 TEST UNDER STANDING WAVE CONDITIONS

By using a short-circuit at the end of the line, one can operate the test stand under standing wave conditions thus simulating what is happening during the filling of the cavity. The initial conditioning of the window was done under these standing wave conditions. It took nearly 30,000 pulses to reach the 1 MW level. At that point, while the system was processing at 1 MW, an incident occurred that exhibited large electron, light and vacuum signals, downstream of the window. Unfortunately, the software interlock that would normally reduce the input power in such case didn't work. As this event happened at the beginning of the week-end, the system ran for the whole week-end at 1 MW. Due to large electron emission at or near the downstream side of the window, the power was fully reflected at this location. After that unfortunate event, it took more than 300,000 pulses to recondition the window up to 1 MW. Once conditioned, we cannot observe any systematic and significant electron or light signal at any power level. At a very erratic rate, one can see some electron signal when the electric field is maximum at the window surface, especially on the side that was potentially damaged by the event described above. To illustrate this behaviour, fig. 3 shows that, while running at 1 MW, some strong electron signal can be seen. After a few tens of pulses these signals are processed away. The figure shows that these multipacting events are seen on the vacuum recording, on the light signal and on the temperature indicator located on the outer conductor in the vicinity of the window. However, all these signals do not allow one to know precisely if the emission is occurring exactly at the window surface (brazing location) or somewhat further in the conductor and especially at the kovar/stainless steel weld that is only 5 mm downstream. The behaviour of the window under standing wave conditions is exactly the same both at room temperature and at 80 K.

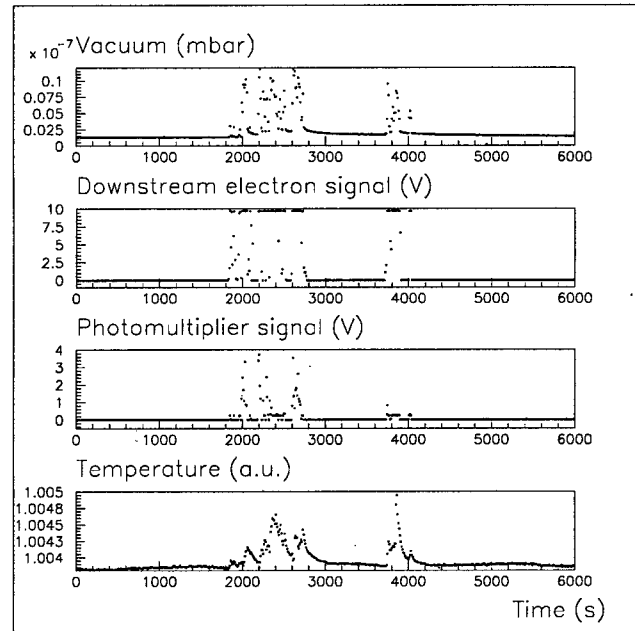


Figure 3: An example of multipactor behaviour at 1 MW (standing wave conditions)

#### 5 TEST UNDER TRAVELLING WAVE CONDITIONS

Under travelling wave operation, one can observe electron activity on both sides of the window. However as shown on fig. 4, the signal is much stronger and the power range is wider on the damaged side. Fig. 4 also shows that this multipactor can be processed: after 180,000 pulses, signal was strongly diminished on the downstream damaged side and completely disappeared on the upstream side. We didn't wait long enough to see, if it would also disappear on the downstream side. Here again, the behaviour is similar at room temperature and at 80 K.

#### 6 DIELECTRIC LOSSES IN THE WINDOW

Since the window is thermally connected to the liquid nitrogen cooled shield, the total heat load it produces is of major concern. In the case of the  $\lambda/2$  window, the main part of the heat load is due to the dielectric losses. By choosing properly the distance between the superconducting cavity and the window itself, the dissipation at LN2 temperature can be reduced. For the complete TESLA pulse (filling time of 530  $\mu$ s and beam time of 800  $\mu$ s), the dissipated power  $P_{diss}$  in the dielectric is evaluated to be:  $8.79 * \tan \delta * \text{Average incident power with a distance} = (2N+1)\lambda/4$  and  $5.83 * \tan \delta * \text{Average incident power with a distance} = N\lambda/2$ . In the standing wave case and for a distance corresponding to  $(2N+1)\lambda/4$ , we measured a dissipation corresponding to 1.1% of the average input power, from which we infer that  $\tan \delta = 5.8 * 10^{-4}$ .

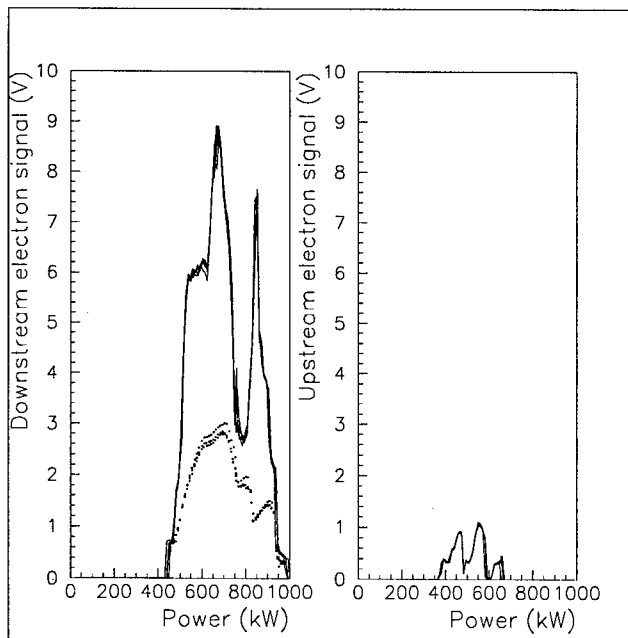


Figure 4: Multipactor as a function of power for TW operation, upstream and downstream sides: at some time (line) and 180,000 pulses later (dots).

## 7 TRAVELLING WAVE WINDOW

In order to reduce the dielectric losses in the ceramic, one can use a thinner ceramic and/or reduce the electric field inside the ceramic. With a thin ceramic, the matching is achieved by adding some inductive or capacitive components on the coax on both side of the ceramic. The simplest solution is to use some bumps on the coaxial inner conductor as proposed in reference [4]. Here, we are trying to find a design where the ceramic would be completely shielded from the electrons coming from the cavity to avoid the potential problems seen, for example, at CEBAF [5]. The advantages of the window, shown on fig. 5, are a low field inside ceramic and therefore low losses, a low field at the brazing location, no field components perpendicular to the ceramic surface, no direct exposure of the ceramic to cavity electrons, while the main drawback are its relative complexity, its large diameter, and the difficulty to clean it. Two windows that are now ready to be tested, were fabricated by SICN [2]: one where titanium is used for the outer conductor brazed on the ceramic and the other for which copper is used. In both cases, the inner conductor is made of plain copper.

## 8 CONCLUSION

In this paper we present the results of the high power tests made on the coaxial  $\lambda/2$  window that we designed and fabricated. The first results are encouraging. Though a failure of the control system at the beginning of the conditioning led to a metallic coating of one side of the window (the precise nature of this coating is under investigation), it was later on capable of sustaining 1 MW of peak power, both

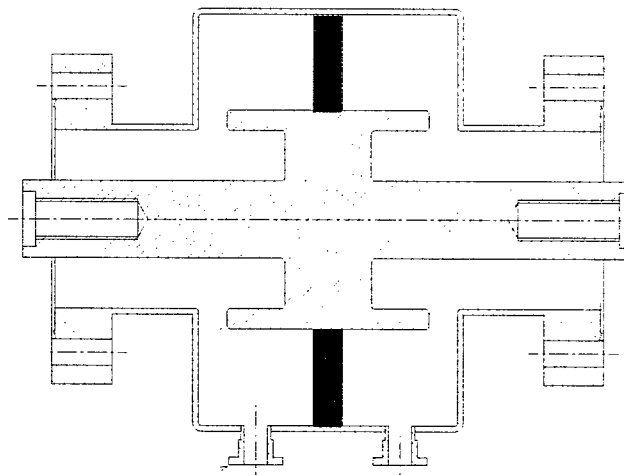


Figure 5: Travelling wave window

under travelling and standing wave operation, both at room temperature and at 80 K, and both under vacuum and atmospheric pressure. Up to 400 kW, the window works without any signs of electron activity. Between 500 kW and 1 MW, the travelling wave operation reveals some electron activity that we cannot attribute with certainty to the window. It will be necessary to test a second, identical, window that was fabricated to confirm these results. It will then be necessary to fabricate a new window with a slightly different design (replace kovar by titanium or copper, and replace the TIG welding by electron beam welding) to see whether it is possible to eliminate electron activity over the full power range.

The dielectric losses were measured and proved to be too high for operation at the TESLA repetition rate and peak power needed for the superstructures [6]. To improve this situation, it would be necessary to use ceramics with a higher purity. These ceramics exist but the brazing to metal is more difficult. Another solution is to use the travelling wave window that was presented in this paper, and which will soon be tested.

## 9 ACKNOWLEDGEMENTS

We would like to thank all the people at IN2P3 and DAPNIA involved in this work for the design, construction and operation of the test stand, especially F. Blot, D. Braud, P. Dufresne, A. Hamdi, M. Kalmykow.

## 10 REFERENCES

- [1] S. Chel et al., EPAC98, p. 1882.
- [2] SICN, BP 1, 38113, Veuvey-Voroize, France.
- [3] PAW, CERN Program Library Long Writeup Q121, 1995.
- [4] X. Hanus, A. Mosnier, Proc. of the 7<sup>th</sup> Workshop on RF superconductivity, Gif sur Yvette, October 17-20, 1995, p. 701.
- [5] T. Powers, P. Kneisel, *ibid*, p. 713.
- [6] M. Ferrario, J. Sekutowicz, EPAC98, p. 1876.

# AN ALTERNATIVE SCHEME FOR STIFFENING SRF CAVITIES BY PLASMA SPRAYING

S.Bousson, M.Fouaidy, H.Gassot, T.Junquera, J.Lesrel, IPN Orsay, France

J.L Borne, J.Marini, LAL Orsay

C.Antoine, J.P.Charrier, H.Safa, DSM/DAPNIA/SEA CEA Saclay

## Abstract

Stiffening of bulk niobium SRF cavities is mandatory for reducing the frequency shift induced by Lorentz forces at high accelerating gradients. Experimental and computational data previously reported show that with the actual scheme (i.e. EB welded stiffening rings) the frequency shift of TESLA 9 cells SRF cavities is higher than the cavity bandwidth above  $E_{acc}=28$  MV/m. We propose a new stiffening method, using a Plasma Sprayed Copper Layer (PSCL) onto bulk niobium cavities. As compared to the actual technique, this method offers several advantages (simplicity, reliability...). The first experimental data obtained with monocell cavities produced by this method demonstrate the efficiency of cavities stiffening with plasma spraying. Thermal and mechanical properties measured on niobium samples with a PSCL are also presented. These data will allow us choose the plasma spraying process suitable for achieving the best cavities performances.

## 1 INTRODUCTION

Recent results obtained with 9-cells TESLA cavities point out a new problem for cavity stiffening. The actual EB welded stiffening rings are no more efficient for accelerating field above 28 MV/m, Lorentz forces detuning becoming too important as compared to the cavity bandwidth. As cavities recently reached 33 MV/m [1], stiffening is already a problem and a solution has to be found. A new stiffening method is proposed, based on the coating of bulk Nb cavities by a plasma sprayed copper layer. The coating must be efficient for accelerating fields up to 40 MV/m, which is the ultimate TESLA goal. Thanks to its good thermal conductivity, copper was the best material candidate to avoid cavity performances degradation. Mechanical characteristics of the copper coating could be close to bulk material with a suitable spraying process. As the Young modulus decreases strongly with the porosity, we have to find a spraying process which allows the lowest possible porosity (a few percent). Bond strength and achievable thickness are also very important issues. These properties are essential for choosing the more suitable spraying process.

## 2 THERMAL SPRAYING TECHNIQUES

The different thermal spraying methods can be divided into 3 different kinds [2].

### a) Plasma spraying.

The principle is to create a plasma by an electric arc discharge initiated in a gas (usually Ar/H<sub>2</sub>). The copper powder is injected in the high temperature plasma and the molten particles are sprayed out of the plasma gun. Depending on the spraying environment, different techniques were developed: under air (Atmospheric Plasma Spaying, APS), under inert gas (Controlled Atmosphere Plasma Spraying, CAPS), and under vacuum (Vacuum Plasma Spraying, VPS).

### b) Combustion flame spraying.

The flame spraying (FS) principle is to use the chemical energy of combustion of fuel gas in oxygen to heat up the powder. If the oxygen is at a high pressure, the method is called High Velocity Oxy-Fuel Spraying (HVOF), and when an explosive mixture of oxygen and acetylene is used to post accelerate with the detonation (1-15 detonations per second), it is called Detonation-Gun Spraying (DGS).

### c) Arc Spraying (AS).

Consumable electrodes made by two wires of the coating material are molten by arc heating, and the produced droplet is propelled by compressed gas. Some coating mechanical properties are summarised in Table 1.

Table 1: Main coating properties.

Method	porosity	bond strength	Comments
APS	medium	high	
VPS	low	high	no oxidation
CAPS	medium	high	no oxidation
FS	high	low	
DGS	low	high	pulsed
HVOF	low	high	
AS	high	low	

The first cavities were copper coated using the industrial APS method, and we are now working in a close collaboration with Ecole Nationale Supérieure des Mines de Paris to improve this technique (lower porosity, higher bond strength without bonding layer). Moreover the HVOF and VPS methods are investigated with help of Institut Polytechnique de Sevenans (LERMPS, France).

### 3 RF TESTS ON Nb/Cu CAVITIES

In order to study the feasibility of the new fabrication method, we performed RF tests on a 1.3 GHz monocell cavity before and after the copper coating. Initially, the cavity was 2.5 mm thick, made from RRR 200 Nb sheets, and then stiffened with a 2.5 mm thick copper layer. The coating was made by a "rough APS", a not optimised process, with the use of an intermediate  $\approx 0.2$  mm thick bonding layer (bronze/aluminium alloy) between niobium and copper. The two resulting  $Q_0$  vs  $E_{acc}$  curves (Fig.1) show only a slight reduction of the maximum attainable field (quench), while the  $Q_0$  level is almost not decreased.

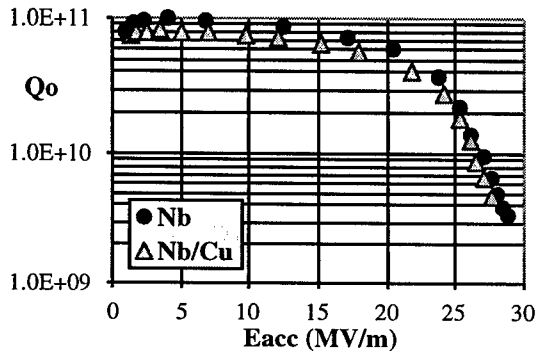


Fig. 1:  $Q_0$  vs  $E_{acc}$  curves before and after copper coating on a 1.3 GHz monocell cavity (C1 02) @ 1.7 K.

During these experiments, the cavity frequency shift induced by Lorentz forces was measured. As theoretically expected, the frequency shift due to Lorentz forces depends quadratically on the accelerating field:  $\Delta f = K \cdot E_{acc}^2$ , where  $K$  is a constant. On the Fig. 2, the 35 % decrease of the slope of  $\Delta f$  vs  $E_{acc}^2$  curve (Nb vs Nb with APS Cu coating) gives the stiffening efficiency of the APS copper coating.

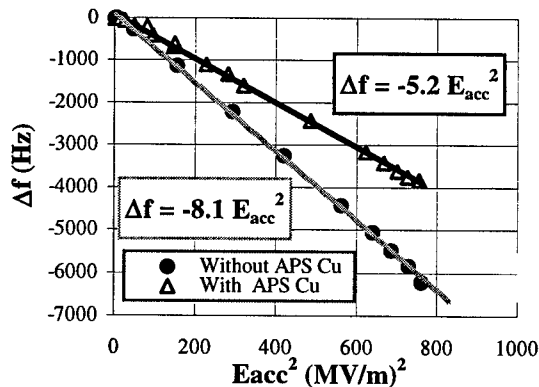


Fig 2 :  $\Delta f$  vs  $E_{acc}^2$  with and without APS Cu.

To carry on the study of the new stiffening method, five 3 GHz cavities were fabricated from RRR 40 Nb sheets of 0.5 mm thickness [3]. The copper deposition process was first tested on the cavity #3, and then two more cavities

(#4 and #5) were RF tested before and after Cu coating by the "rough APS" method. The results summarised in Table 2 show that the cavity performances are almost not modified by the APS Cu coating. Cavities #1 and #2 were tested before stiffening and reached high accelerating fields despite the poor Nb quality ( $E_{acc} = 24.5$  MV/m for cavity #2). A study of several PS methods are currently in progress on samples in order to define the best stiffening method that will be tested on cavity #1 and #2.

Table 2: 3 GHz cavity tests @ 1.8 K.

Cavity number	$E_{acc}$ max before Cu deposition	$E_{acc}$ max with Cu
# 1	12.5 MV/m	to be tested
# 2	24.5 MV/m	to be tested
# 3	not tested	10 MV/m
# 4	16.5 MV/m	16.5 MV/m
# 5	14.5 MV/m	13.5 MV/m

### 4 THERMAL INVESTIGATIONS

The stiffening coating adds a supplementary thermal resistance  $\Delta R_g$  on the overall thermal resistance ( $R_g$ )  $R_g = R_c + R_k + \Delta R_g$ , with  $R_c$  the conductivity term for the niobium and  $R_k$  the Kapitza resistance term (Kapitza resistance is nearly the same for Nb and Cu). Thermal simulations were performed to determine the  $\Delta R_g$  threshold above which the cavity thermal behaviour could be modified (either by a maximum accelerating field decrease or by an effect on the  $Q_0$  level). Both defect free case and defect case were studied. On the figure 4 is plotted the defect free case theoretical  $Q_0$  vs  $E_{acc}$  for bulk Nb ( $\Delta R_g = 0$ ). We have then calculated the  $Q_0$  vs  $E_{acc}$  curves for an increase  $\Delta R_g$  of the overall thermal resistance, which is arbitrarily taken as equal to  $R_k$  and  $3 R_k$ . These two runs simulates a possible increase of  $R_g$  due to the copper coating.

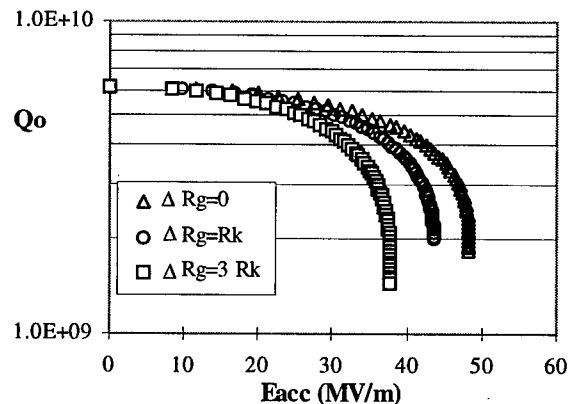


Fig. 4 : Simulation of  $Q_0$  vs  $E_{acc}$  (defect free case) at  $T=2$  K @ 1.3 GHz with RRR=200 and 2.5mm thick.

The results clearly show that if  $\Delta R_g = R_k$  ( $\approx 1.4 \cdot 10^{-4}$  W.m<sup>2</sup>/K @ 2 K), the TESLA goal ( $E_{acc} = 40$  MV/m)

could be achieved, whereas if  $\Delta R_g = 3 R_k$ , this goal is not reached. The defect case study leads to the same conclusion, so a threshold on the coating thermal resistance was determined for achieving the stiffening without drawbacks at 40 MV/m.

In order to measure  $\Delta R_g$  due to the copper layer on our cavities, Nb samples were coated by the same "rough APS" process.  $\Delta R_g$  is obtained from the overall thermal resistance difference between a Nb sample and a Cu coated Nb sample [3]. At 1.8 K,  $\Delta R_g$  was found to be  $6.4 \cdot 10^{-4} \text{ Km}^2/\text{W}$  (about 4 times  $R_k$ ). In this result, the effect of the bonding layer (0.2 mm thick bronze/aluminium alloy) was suspected to dominate the thermal resistance, so another Nb sample coated with only the alloy coating was also measured. The result was the same ( $\Delta R_g = 6.2 \cdot 10^{-4} \text{ Km}^2/\text{W}$ ) clearly indicating the very low thermal conductivity of the bonding layer.

## 5 MECHANICAL SIMULATIONS

Numerical simulations have been performed to study the effect of different stiffening schemes using an additional copper layer on a TESLA 9-cells cavity detuning. The basics of the model are to consider a bimetal Nb/Cu cavity (see Fig. 5), each material considered as bulk material perfectly bonded to each other [3].



Fig.5 : Stiffened bimetal Nb/Cu cavity.

This ideal case was used to model different stiffening options, with homogeneous or non-homogeneous (thicker coating at the iris) copper layer, and Lorentz forces detuning @  $E_{acc} = 40 \text{ MV/m}$  was computed for TESLA 9-cells cavities. The results are reported in Table 3. They show that with the actual stiffening scheme (2.5 mm Nb thickness and EB welded stiffening rings), the frequency shift is twice the cavity bandwidth (434 Hz for  $Q_{ext} = 3 \cdot 10^6$ ). Thanks to a non-homogeneous copper coating (2 mm thick layer and 20 mm at the iris), a frequency shift @ 40 MV/m within the cavity bandwidth was obtained.

Table 3: Computed frequency shift for TESLA cavities at  $E_{acc} = 40 \text{ MV/m}$  for different stiffening schemes.

Configuration	$\Delta f$
niobium 2.5 mm unstiffened	-2135Hz
Nb 2.5 mm + EB welded stiffening rings	-863 Hz
Nb 2.5 mm + Cu coating 2 mm	-883 Hz
Nb 2.5 mm + Cu coating 2 mm + iris stiffening (h=20mm)	-358 Hz

The Young modulus of the coating used with the 3 GHz cavity prototypes was estimated to 27 GPa from a simple experiment which consists in measuring the coated cavity deformation versus the applied axial force and comparison with a model calculation. Using this value,

simulations on 9-cells TESLA cavities give a  $\Delta f$  of 616 Hz at 40 MV/m (non-homogeneous scheme), a value higher than the cavity bandwidth, but still an improvement as compared to the 863 Hz obtained with the actual EB welded stiffening rings. Simulations also show that this coating is efficient for accelerating fields up to 33 MV/m. Different theoretical approaches modelled the effect of the porosity on the Young modulus. As the bulk copper Young modulus is 130 GPa, the estimated value (27 GPa) is in the range of expected values of APS coating with porosity lying between 15% and 30%. Mechanical model calculations show that to achieved an effective stiffening at 40 MV/m, it is necessary to have a coating Young modulus of 95 GPa, which corresponds to a porosity of a few percent.

## 6 CONCLUSION AND FUTURE

A new fabrication method for SRF cavities is presented. The principle is to stiffen niobium cavities with a copper layer deposited by thermal spraying. Comparison of RF performances obtained with the first cavities tested before and after copper deposition showed that the maximum accelerating field was not affected, while a stiffening effect was measured. These results demonstrate the interest of the method. But this "rough APS" copper coating is efficient only for  $E_{acc} < 33 \text{ MV/m}$ . Mechanical simulations have proved that porosity have to be less than a few percent. Thermal measurements showed that for this coating at 40 MV/m, the cavity thermal stability should not be affected if the bonding layer is removed. This first study pointed out the important parameters involved in the cavity stiffening. Now, a new program has just started to investigate other spraying process (VPS, HVOF, and a more controlled APS), more suited to our application. After measurements of mechanical and thermal properties on samples, 3 GHz and 1.3 GHz cavities will be fabricated from 1 mm thick Nb sheets of RRR 130 and then stiffened with the copper layer.

## 7 ACKNOWLEDGMENTS

The authors would like to thank M.Boloré, A.Caruelle, J.Y.Gasser, N.Hamoudi, A.Le Goff, J.C.Le Scornet, J.P.Poupeau, for their technical assistance and helpful discussions. They would like also to thank C.Coddet, C.Verdy (LERMPS) and V.Guipont, M.Jeandin (Ecole des Mines) for collaborating on plasma spraying.

## 8 REFERENCES

- [1] W.D.Möller "The performance of the 1.3 GHz superconducting RF cavities in the first module of the T.T.F linac" linac98, Chicago (1998).
- [2] Lech Pawlowski " The Science and Engineering of Thermal Spray Coating " J.Wiley & sons.
- [3] M.Fouaidy et al. And reference here cited, " A New Fabrication and Stiffening Method of SRF Cavities " EPAC'98, Stockholm,(1998).

# EVIDENCE FOR A STRONGLY COUPLED DIPOLE MODE WITH INSUFFICIENT DAMPING IN TTF FIRST ACCELERATING MODULE

S. Fartoukh, M. Jablonka, J. M. Joly, M. Lalot, C. Magne, O. Napoly, CEA/Saclay, France  
M. Bernard, LAL/Orsay, France,  
N. Baboi, S. Schreiber, S. Simrock, H. Weise, DESY/Hamburg, Germany

## Abstract

A beam experiment has been conducted on the first accelerating module of the TESLA Test Facility (TTF) to investigate transverse higher order modes (HOM) in the superconducting cavities. By injecting the beam with a transverse offset and by modulating the intensity of the 216 MHz bunch train with a tunable frequency in the 0-108 MHz range, transverse HOMs can be excited resonantly. On a resonance the outgoing bunch orbits, measured with a broadband BPM, are transversely modulated at the same frequency. A dipole mode at about 2585 MHz, belonging to the third passband of the TESLA cavities, has been excited and observed in this way, with unexpected low damping in 2 out of the 8 cavities of the module.

## 1 AIM OF THE EXPERIMENT

The transport of very low emittance beams along the TESLA linac requires transverse higher order mode damping at a level defined in [1]. HOM couplers mounted on the beam tubes of the TESLA 9-cell superconducting cavities, have been designed to achieve damping with  $Q$  factors of the order of  $10^4$  to  $10^5$ , depending on the mode coupling impedance, especially for the first two dipole passbands. Modes from higher passbands, supposedly above cutoff, are expected to propagate and therefore to couple efficiently to the HOM couplers except for few so-called "trapped" modes whose energy is concentrated in the central cells of the cavity. Of the experiments proposed at the TTF to verify with beam that the HOM damping is adequate and to detect unwanted trapped modes, the one reported here, described in [2], consists of excitation of higher order modes with the sidebands of the bunch train  $f_b = 216$  MHz harmonics generated by modulation of the bunch charge with a variable frequency  $F$  in the range of 0 to 108 MHz. If the beam is injected off axis in the accelerating module, these sidebands build up in the Fourier transform of beam dipole moment and a resonant transverse instability can develop when one of the sidebands and one transverse HOM frequency coincide, i.e.  $nf_b \pm F = f_{HOM}$ . Hence, at the cavity exit, the transverse position of the beam is modulated at the frequency  $F$  with in phase and out of phase components.

A broadband BPM can be used to detect these oscillations.

## 2 EXPERIMENTAL SETUP

The first accelerating module of TTF includes eight 9-cell superconducting cavities at 1.3 GHz RF frequency. HOM couplers are located on both sides of each cavity to extract the power lost by the beam at high current. During the experiment, the thermoionic gun delivered up to 8 mA of beam current at a pulse duration of 600  $\mu$ s with bunch frequency of 216.7 MHz. The additional experimental set-up includes the following devices:

- A tuneable voltage modulator at the cathode of the gun, providing the required charge modulation along the bunch train, with a modulation amplitude nearly up to 100 % of the nominal 37 pC bunch charge.
- A 'dog-leg' magnet (half a chicane) in front of the accelerating module providing a steady horizontal offset, in the range from 0 to 20 mm.
- A broadband cavity BPM [3] to measure individual positions of the bunches located about 10 m downstream of the accelerating module exit.

Entering the module, beam energy was about 9 MeV. The gradients of the eight cavities in the module were set to a minimum value of 2 MV/m in order to maximise the sensitivity of the beam to HOM deflections. With such energy settings and quadrupole magnets off, the BPM is at a focal point for parallel trajectories entering the module. This makes it easier to measure HOM kicks in the cavities.

## 3 OBSERVATION OF THE 2585 MHz HOM

As discussed in [2], all HOMs can be excited by sidebands of the beam harmonics, at frequencies  $nf_b \pm F$ , by scanning the charge modulation frequency  $F$  through half a Brillouin zone  $[0, f_b/2]$ . Dipole modes are in principle excited by injecting the beam off-axis in the cavities. By doing so, a beam instability was observed on the broadband BPM for  $F = 15.022$  MHz with a short beam pulse of 35  $\mu$ s and 5 mA current, and a large injection offset of about 20 mm. The beam pulse length could be increased to up to 500  $\mu$ s while remaining on the HOM resonance. Fig.1 shows the comparison of the BPM envelope signals with charge modulation off or on for a 400  $\mu$ s long beam pulse. With modulation off, the

broadband BPM integrates a high but constant 100 mV level of beam induced noise, although the beam is steered through its centre. This is due to the rejection of the *sum* signal into the *difference* signal BPM antennas. While the modulation is on, the beam offset reaches a maximum of about 10 mm but, due to the excessive noise no quantitative measurement could be made. A damped oscillatory behaviour of the envelope signal is visible in Fig.1 with a period of about 125  $\mu$ s, on top of the constant envelope of the beam oscillations reached at the steady state. This behaviour was later explained, and reproduced by simulations, by the fact that the modulation frequency was off HOM-resonance by about 8 kHz (1/125  $\mu$ s). The resonant oscillations then reach a steady state after some damped overshooting. Simulations predict that for a perfectly on-resonance excitation, the oscillations reach the aperture limit within the 35  $\mu$ s short pulse: this agrees with the observed veto from the beam loss protection system occurring at every attempt to fine tune the modulation frequency towards lower values of  $F$ .

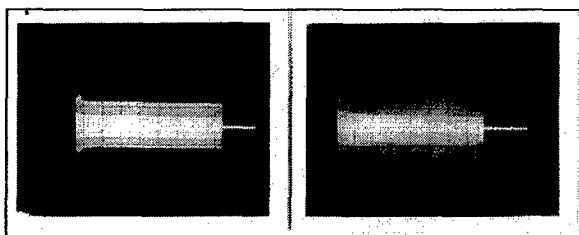


Figure 1: BPM signal on oscilloscope for 400  $\mu$ s beam pulse without (left) and with (right) charge modulation

#### 4 HOM RF CHARACTERISATION

The beam experiment revealed the existence of a HOM with a frequency  $f_{\text{HOM}} = n f_b \pm (15.022 \text{ MHz} - 8 \text{ kHz})$  in the accelerating module. While detuning cavities #1 and #2 had no effect on the beam instability, detuning cavity #3 by about  $\pm 16 \text{ kHz}$  in the fundamental mode did suppress the instability. It was then possible to measure and identify the mode at the HOM coupler outputs of cavity #3 (cavity S10 in Table 1) with a spectrum analyser. The frequency domain signal around the 12<sup>th</sup> beam harmonics at 2.6 GHz in Fig.2 shows a beam modulation side-band peak enhanced by the HOM resonance on the low side of this harmonics. The same signal, when analysed in time domain in Fig.3, shows the 35  $\mu$ s beam-pulse cavity loading, followed by the relaxation of the field amplitude with a characteristic time  $\tau = 110 \mu$ s. The dipolar nature of the mode was demonstrated by checking the perfect linear dependance of the height of the amplitude maximum with the offset of the beam entering the module, over a range from 0 to 20 mm.

The resonant modes of cavity #3 were studied over a wider range of frequencies while the beam was turned off. As shown by Fig.4, the measured HOM is the highest frequency mode of the 3<sup>rd</sup> dipole passband. Its frequency is:

$$f_{\text{HOM}} = 2584.986 \text{ MHz} \pm 1 \text{ kHz}.$$

The damping factor is then given by :

$$Q = \frac{2\pi f_{\text{HOM}} W}{P_d} = \frac{2\pi f_{\text{HOM}} \tau}{2} \approx 9 \times 10^5$$

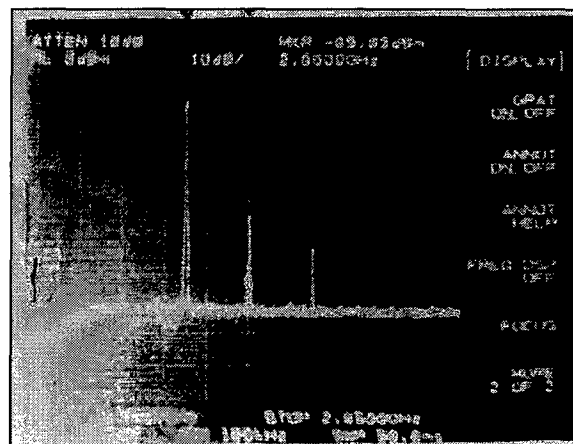


Fig.2 Sidebands around the 2.6 GHz beam harmonics

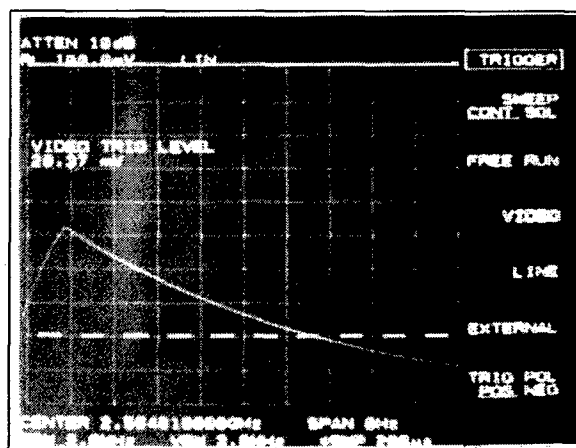


Fig.3 Time domain signal from HOM pickup on the 2585 MHz mode

An URMEL [4] calculation of the 3<sup>rd</sup> passband of the TESLA cavity was performed in parallel [5] showing that the highest frequency mode of this passband has indeed a large beam coupling impedance

$$\frac{1}{a^2} \left( \frac{R}{Q} \right) \approx 15 \Omega / \text{cm}^2.$$

It is foreseen to compare this prediction with a quantitative measurement of the beam displacement

using a BPM with an improved resolution in a future experiment.

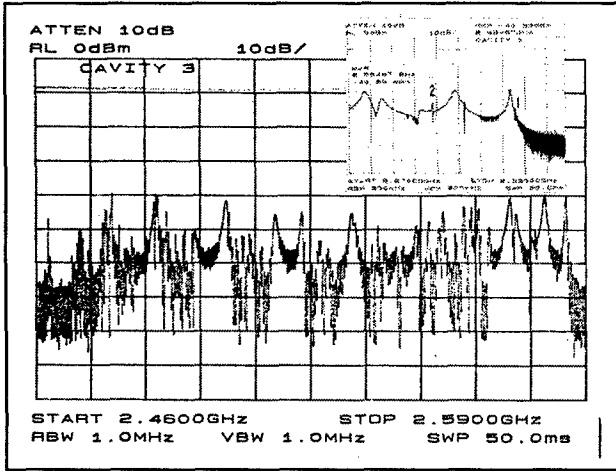


Fig.4: Third dipole passband of cavity #3. The high frequency edge of this passband is zoomed, showing the 2585 MHz (1) and 2577.5 MHz (2) very sharp modes discussed in the text.

## 5 OTHER MEASURED MODES

Three other modes have been excited and observed with the intensity modulated beam. The HOM excitation signal, taken either from the HOM coupler outputs or from the BPM itself, was analysed with a spectrum analyser, like in the previous section.

- 2586 MHz mode in cavity #6: a close inspection of the last mode of third dipole passband of the eight cavities (cf. Table 1) showed, in cavity #6 (S11), the same excitation curve as the one shown in Fig.3 with a time decay constant of  $\tau = 8 \mu\text{s}$ . It corresponds to a quality factor  $Q = 6.5 \times 10^4$ . No measurable excitation could be observed in other cavities.
- 2577.5 MHz mode in cavity #3: this mode also belongs to the 3<sup>rd</sup> dipole passband, as can be seen in Fig.4. Its coupling impedance [5] is also large, about  $9 \Omega/\text{cm}^2$ . Its excitation curve gave  $\tau = 22 \mu\text{s}$  which corresponds to  $Q = 1.8 \times 10^5$ .
- 1876 MHz mode in cavity #3: this well-known TM110 mode of the first dipole passband has a high coupling impedance of about  $9 \Omega/\text{cm}^2$ . In cavity #3, and for one polarisation, it appears to be less efficiently damped than in the other cavities [6] with a measured  $\tau = 20 \mu\text{s}$ , corresponding to  $Q = 1.2 \times 10^5$ . This damping is at the limit of the TESLA tolerances [1].

Table 1: Cavities of TTF Module #1

Name	HOM coupler type	3 <sup>rd</sup> dipole passband
D3	fixed	2458 – 2548 MHz
S8	dismountable	2458 – 2576 MHz
S10	dismountable	2471 – 2585 MHz
D1	fixed	2464 – 2562 MHz
D2	fixed	2462 – 2560 MHz
S11	dismountable	2480 – 2586 MHz
D4	fixed	2456 – 2556 MHz
S7	dismountable	2472 – 2576 MHz

## 6 CONCLUSION

A higher order 2585 MHz dipole mode has been observed and excited with beam with low damping,  $Q = 9 \times 10^5$  in cavity #3 and  $Q = 6.5 \times 10^4$  in cavity #6, in two out of eight cavities of the first TTF cryomodule. Identifying this mode with the highest mode of the third dipole passband leads to quite a high transverse coupling parameter  $1/a^2(R/Q_{\perp}) \approx 15 \Omega/\text{cm}^2$ . This is notably above the TESLA tolerance for the preservation of the vertical emittance in the linac. The origin of the insufficient damping of this mode and of its non-systematic character is not yet understood. A localised HOM coupler defect is of course one possibility. The large cavity-to-cavity spread in HOM frequencies, with highest and similar frequencies in cavities #3 and #6, may also be a clue. This observation is currently being completed by RF and beam measurements at the cold module. On the other hand, in order to complete the search of dangerous HOMs, it is foreseen to equip the new TTF photo-injector with a pockell-cell device which allows to modulate the charge of a 54 MHz bunch train.

## 7 REFERENCES

- [1] "TESLA Conceptual Design Report", R. Brinkmann, G. Materlick, J. Rossbach and A. Wagner Editors, DESY 1997-048, (1997)
- [2] "A New Method to Detect the High Impedance Dipole Modes of TESLA Cavities", S. Fartoukh, CEA/Saclay preprint, DAPNIA/SEA-98-18, (1998)
- [3] "High Resolution BPM for Future Colliders", C. Magne, M. Juillard, M. Lalot, A. Mosnier, B. Phung, Y. Lussignol and R. Bossart, LINAC98 Conf., Chicago, (1998)
- [4] "On the computation of resonant modes in cylindrically symmetric cavities", T. Weiland, NIM 216 (1983).
- [5] We thank S. Chel for doing this calculation while the experiment was going on.
- [6] G. Krepis, unpublished.



# LIGHT EMISSION PHENOMENA IN SUPERCONDUCTING NIOBIUM CAVITIES\*

J. R. Delayen , J. Mammoser#

Thomas Jefferson National Accelerator Facility  
Newport News, Virginia 23606

## Abstract

During the investigation of field emission limitations of superconducting niobium cavities, a CCD camera [1] was inserted at the end of the beam pipe on a single-cell 1500 MHz cavity. When operating the cavity in field emission, glowing filaments of light were observed trapped by RF fields in closed-orbit trajectories. These filaments were traveling at frequencies much lower than the oscillating RF fields and formed various patterns of light for up to several seconds. This experiment was then repeated on a production CEBAF five-cell cavity with similar results. Events from both experiments were captured on video tape and are presented in this paper along with a discussion of the possible origin of these types of light patterns and the plans to further investigate the phenomena.

## 1 BACKGROUND

During the investigation into sources of field emission on single-cell cavities, a CCD camera assembly was added below the cavity, which was being tested as part of a series of single-cell tests. The camera assembly [2] consisted of an inexpensive, miniature CCD camera, in a copper tube filled with epoxy. This assembly was mounted in a stainless outer tube sealed at each end with stainless blanks. The cavity end of the tube contained a sapphire view port to isolate the camera assembly from the inner cavity surfaces and the other end contained ceramic feedthrus for instrumentation.

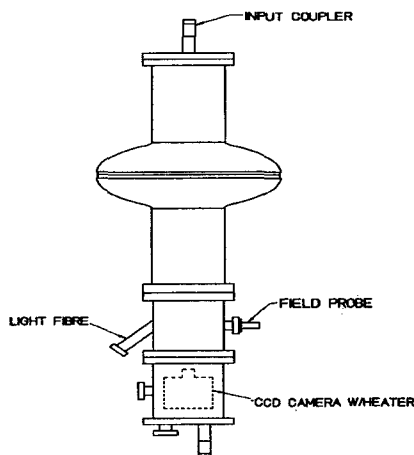


Figure 1. Experimental Setup for Single-Cell Cavity.

A vacuum was maintained around the camera to reduce the overall heat leak of the system and an additional heater and temperature diode were used to keep the camera operational during the cryogenic testing of the cavity. The heater was adjusted to keep the camera at 295K throughout the testing. The placement of the camera allowed for the complete viewing of input coupler, beam tubes and cell irises ( Figure 1).

## 2 SINGLE-CELL TEST RESULTS

During the testing of the cavity #HP, three classes of glowing filaments were observed: 1) regular-shaped closed (Figure 2a), 2) irregular-shaped closed (Figure 2b) and 3) open (Figure 2c). These filaments were located mostly in the center of the beam axis, between the irises. The closed and open filaments were repeatedly observed during the 1-2 hours of testing and some of the patterns lasted for several seconds. The closed filaments changed plane of rotation frequently during the few seconds and varied in size from 3 cm in diameter to larger than 7 cm in diameter (the diameter of the cavity beamtube). During both closed and open observations, filaments generated reflections on the beamtube and irises (Figure 2c) From the video tape, consecutive frames were analyzed to determine the frequency of oscillation and the velocity for the closed and open patterns of light. The closed filaments' frequency of oscillation was about a few tens of hertz; the open filaments had a velocity of a few meters per second.

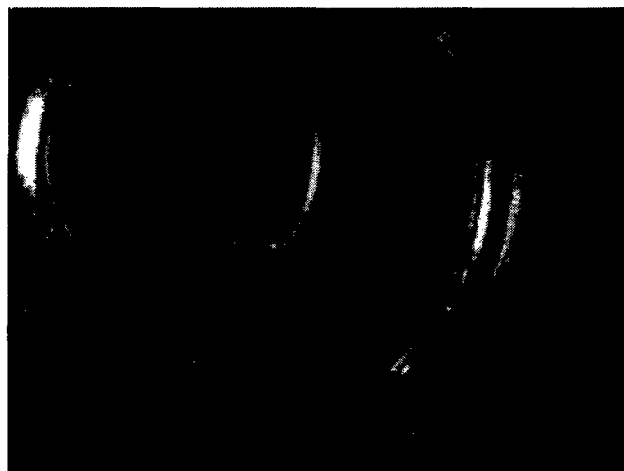


Figure 2a. Single-Cell Closed Filaments.

# Email: mammosse@jlab.org

This work was supported by the U.S. Department of Energy under contract DE-AC05-84ER40150

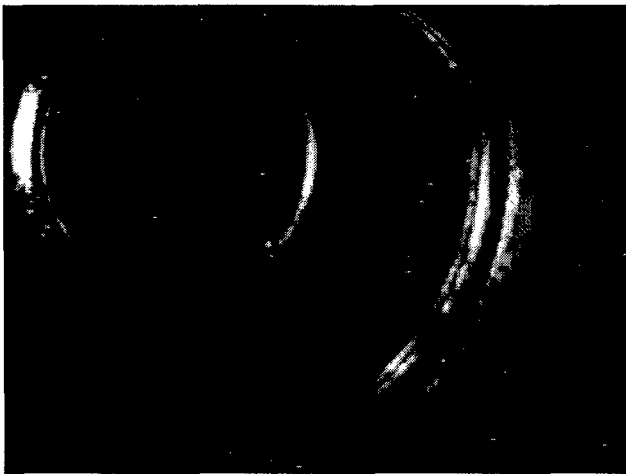


Figure 2b. Single-Cell Irregular-Shaped Closed Filaments.

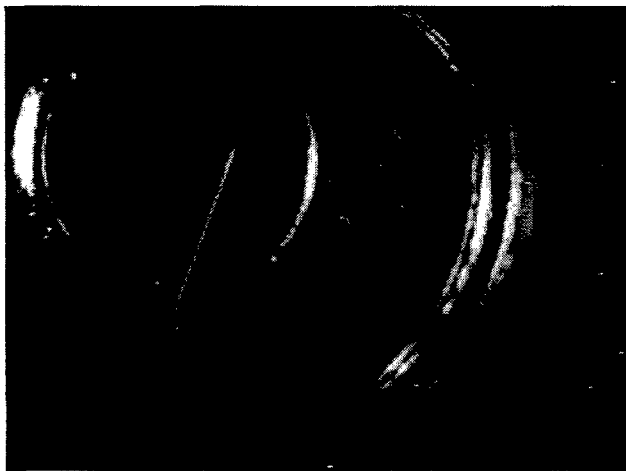


Figure 2c. Single-Cell Open Filaments with Reflection on Beamtube Wall.

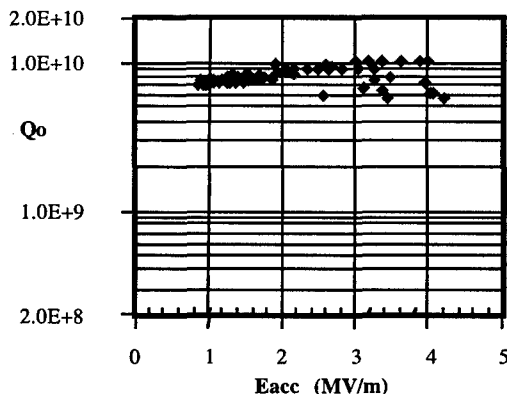


Figure 3. Single-Cell Vertical Test Results.

The single cell cavity started at a  $Q$ -value of  $7 \times 10^9$  and processed to  $10^{10}$  with no radiation present at the dewar top plate. Cavity gradients during these filament events were between 2-4 MV/m. Figure 3 shows the vertical test results for the single-cell cavity. The RF testing was stopped at 4 MV/m to protect the camera from over exposure to radiation (local to the camera) and to prevent arcing and glowing of the sapphire window. To

investigate this phenomena further, a five-cell cavity was assembled with the same camera and slightly different hardware (Figure 4).

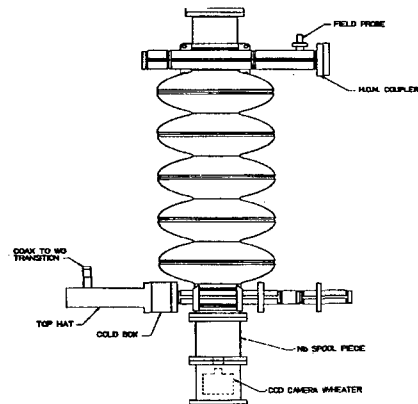


Figure 4. Five-Cell Experimental Test Setup.

### 3 FIVE-CELL TEST RESULTS

A standard CEBAF five-cell cavity including cold RF window, coax to waveguide transition and field sampling probe were used for the test. The goal was to look for similar types of events that were seen in the single cell and capture them on video tape to make comparisons. The cavity was powered up to low field ( $\approx 2$  MV/m) and was increased slowly by an automated RF testing program while data was being taken. At fields around 3 MV/m glowing point sources showed at several iris locations but with no radiation present at the camera.

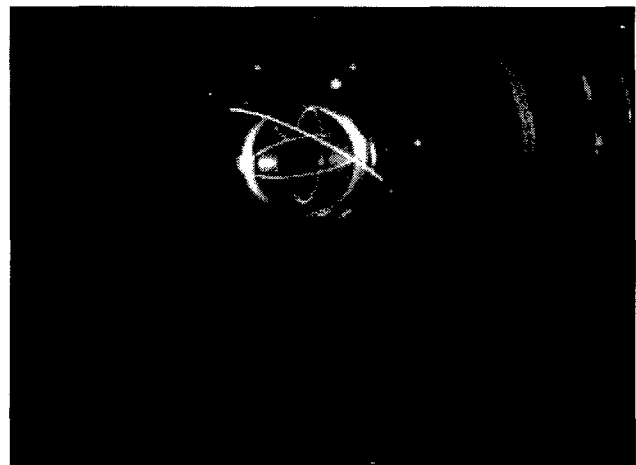


Figure 5a. Closed Filaments in the Five-Cell Cavity.

At approximately 4.4 MV/m several closed filaments occurred at the center cell of the cavity, at the same time and lasted for several seconds. The glowing point sources at the irises and the multiple closed filaments are present in Figure 5. As with the single-cell cavity test the five-cell generated closed filaments following a flash of light. These filaments, however, only appeared one time during

the five cell cavity test, just at the start of field emission as represented with "A" in Figure 6. Following this event the cavity Q-value decreased with increasing gradient until point "1". Then with a flash of light the Q-value went up to point "2". At this time the gradient was lowered to 2.5 MV/m and a new run was started. This second run showed no events and the Q value at the higher level. A review of the video tape showed that a single glowing point source was removed in conjunction with the increasing Q-value.

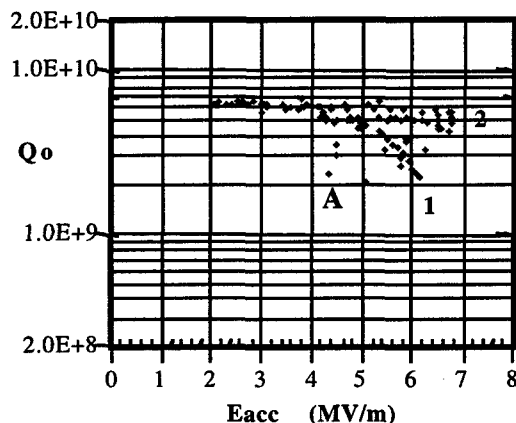


Figure 6. Five-Cell Vertical Test Results.

#### 4 DISCUSSION

Filaments of three types were observed and captured on video tape during the 2K testing of both a single-cell and five-cell 1500 MHz cavity. Filament types identified were closed regular, closed irregular and open. The nature, sources and conditions for such events to occur are currently being investigated.

One possible explanation for such events is that the light filaments are plasma in nature. In experiments done in 1958, P. L. Kapitza found that rings of thin filaments (plasma) could be generated in spherical resonators of  $H_{01}$  and  $E_{01}$  type [3,4]. The resonators were filled with helium and other gases such as argon, carbon dioxide, and air; and resonated around 1.5 GHz. Kapitza found that, in helium, the filaments were generated in the region of maximum electric field at pressures from several cm of Hg to several atmospheres. Discharges in Kapitza's apparatus lasted a few seconds, had a high degree of stability and floated in the resonator without altering the filament discharge. Filaments generated in helium were bright, easily "ignited" and were thinner with higher purity helium. Kapitza also discovered that the impurities in the helium gas such as hydrogen at the 1% level played an important role in generating the filaments at lower pressures. Besides these similarities, our experiment is fundamentally different from Kapitza's in that the residual pressure in our resonator is much lower than his. The filaments we observed also were thin and very well defined, apparently in contradiction to those described by Kapitza, which were thicker and more diffuse.

It is also conceivable that these filaments are due to charged particles generated by field emission and trapped in the RF fields. The particles could be heated on the cavity surface and projected toward its center, where, in the case of the closed orbits, they are trapped by the RF fields. The glow could be due to light emission generated from the interaction with field emission, or by ionization of the residual helium gas. It is not apparent, however, how the fields of a  $TM_{01}$  mode can produce the closed trajectories that were observed.

Luminous spots and tracts have also been observed in room temperature cavities which were deliberately contaminated with metallic and dielectric particles [5].

#### 5 FURTHER INVESTIGATION PLANS

The plans to investigate this phenomena will be aimed at determining what is the nature of the filaments and central force to generate such light patterns. The testing will continue with single-cell cavities under typical vertical test conditions to gain additional information aimed at deeper investigation of these phenomena. The following is a list of some of the types of data that will be collected in additional tests and the test setup modifications necessary to generate them:

1. Light spectrum from closed and open filament events by piping light out of the dewar.
2. The relationship to input power changes and the shape of the closed filament. This requires no changes to the test setup.
3. Increasing the image resolution by increasing the shutter speed of the camera. This can be accomplished by removing the camera from the dewar through the use of mirrors and upgrading the camera.
4. Obtain a second view point by adding a second camera in the test setup.
5. Collect vacuum data from a Residual Gas Analyzer during testing.

#### 6 REFERENCES

- [1] Edmund Scientific Co., Industrial Optics Division, Catalog: 609-573-6250, pp. 177., Model #H53004.
- [2] P. Kneisel, "Understanding and Improvements of Limitations through Application of Cryogenic Instrumentation", Proceedings from the CEC/ICMC-97, (1997).
- [3] P. L. Kapitza, "Free Plasma Filament in a High Frequency Field at High Pressure", Soviet Physics JEPT, Vol. 30, No. 6, pp. 973-1224, (1970).
- [4] P. L. Kapitza and S. I. Filimonov, "Apparatus for Production of a Free Plasma Filament. Determination of the Current and Resistance of the Filament", Soviet Physics JEPT, Vol. 34, No. 3, pp. 542-553, (1971).
- [5] T. Junquera et. al., "Study of Luminous Spots Observed on Metallic Surfaces Subjected to High RF Fields", Proc. PAC95.

# FREQUENCY TUNING OF THE CEBAF UPGRADE CAVITIES\*

J.R. Delaven, L. Doolittle, E. Feldl, V. Nguyen<sup>#</sup>, and W. Sachleben,  
Thomas Jefferson National Accelerator Facility, Newport News, VA

## Abstract

Long-term plans for CEBAF at Jefferson Lab call for achieving 12 GeV in the middle of the next decade and 24 GeV after 2010. In support of these plans, an Upgrade Cryomodule capable of providing more than twice the voltage of the existing ones is under development. One requirement is to operate the superconducting cavities, which are 40% longer than existing ones, at 2.5 times the original design gradient with the same amount of rf power. This puts stringent requirements on the accuracy of the frequency tuner: range of 400 kHz and resolution of 1 Hz. A new tuner design to meet these requirements is under development. This system avoids problem areas of previous designs by holding to the principles of not placing moving parts in the vacuum and / or low temperature space, and of having all drive components readily accessible for maintenance and replacement without cryomodule warm up.

## 1 INTRODUCTION

In a superconducting accelerator, the frequency tuners perform several functions: bring the cavities on resonance after installation and cooldown, detune the cavities that are not operating, and track the changes in frequency due to Lorentz detuning, pressure, and temperature fluctuations. For the CEBAF Upgrade Cryomodule [1], the band width will be small ( $\sim 75$  Hz), the Lorentz detuning large ( $\sim 500$  Hz), and we want to track the frequency accurately ( $\sim 2$  Hz) in order to minimize the rf power requirements.

The cost of removing a cryomodule from the accelerator tunnel for disassembly and repair is considerable. Add the beam time lost and the interruption of experiments and it is then quite obvious that the operating reliability of the tuner is of great importance. The cavity tuner is a mechanism with obvious potential for failure, since it continuously adjusts the length of the cavity to keep it in tune to the operating frequency of the accelerator

## 2 TUNER REQUIREMENTS

The cavities in the CEBAF Upgrade Cryomodule will differ from the existing ones in several respects: they will be 40% larger (7-cell instead of 5-cell) and have a design gradient of 12.1 MV/m instead of 5 MV/m.

In spite of having an energy content 7 times larger at design field, we have adopted as a goal only a modest increase of the rf power per cavity from 5.5 to 6 kW.

As shown in Figure 1, in order to operate at 12.5 MV/m with a circulating current of 400  $\mu$ A, the total amount of detuning, both static (average frequency offset) and dynamic (microphonics) must not exceed 25 Hz. This would give sufficient margin for rf control and allow for errors in the external coupling. For this reason, the frequency tuner will be required to achieve a frequency resolution of 1 Hz. Because the needed resolution is much less than the Lorentz detuning ( $\sim 500$  Hz) and the sensitivity to pressure fluctuations ( $\sim 100$  Hz/torr), the cavity frequency may need to be adjusted frequently without impact on operation. It is unlikely that a pure mechanical tuner, similar to the one in use at CEBAF, would fulfill the requirements because of the associated vibration, deadband, backlash, and non-monotonicity.

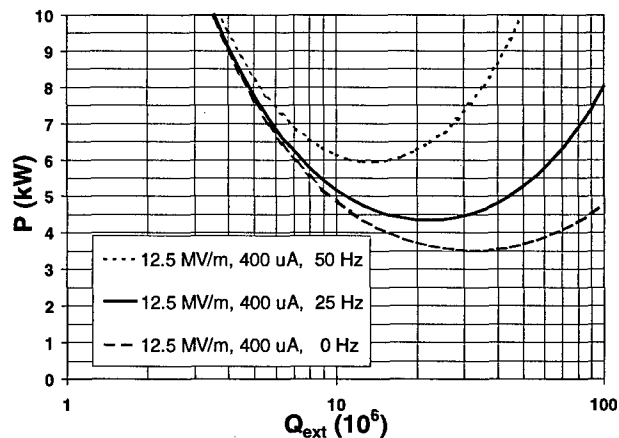


Fig. 1: Required rf power vs external  $Q$  at the design gradient of 12.5 MV/m, design current of 400  $\mu$ A and maximum detuning of 0, 25 and 50 Hz.

On the other hand, the tuning range must be adequate ( $\pm 200$  kHz) to compensate for variability in manufacturing, chemical processing, and cooldown; and to allow for substantial detuning of cavities that are not operating.

In order to satisfy these requirements, the tuning system has been divided into two parts: a coarse tuner with a range of  $\pm 200$  kHz and resolution of 100 Hz, that is expected to be used infrequently, and a fine tuner with a range of  $\pm 1$  kHz and resolution of 1 Hz that will be used during normal operation.

\* Work supported by the U.S. Department of Energy under contract DE-AC05-84-ER40150.

<sup>#</sup> Email: [nguyen@jlab.org](mailto:nguyen@jlab.org)

### 3 TUNER DESCRIPTION

The fine tuner makes use of piezoelectric actuators to avoid the friction on mechanical components that would otherwise adversely affect the resolution and the life expectancy of the mechanism. The fine tuner can therefore be used for continuous small corrections to the cavity frequency, over its range of  $\pm 1$  kHz. The coarse tune adjustment of  $\pm 200$  kHz is actuated by a stepping motor through a harmonic drive reducer and a ball screw. Both systems are external to the vacuum enclosure, and are at ambient temperature and therefore accessible for maintenance and repair. The tuning motion of either drive system is brought into the cryostat through two thin-wall concentric tubes (Items 1 & 2, Fig. 2), both moving axially and relative to one another. From that linear motion feedthrough, all other tuning motion is generated using metal flex joints only. The tubes are connected respectively to the upper and lower arms (Item 3 & 4, Fig. 2) of a scissors type jack and in this way the motion of the tubes translates into a linear stroke parallel to the cavity center line.

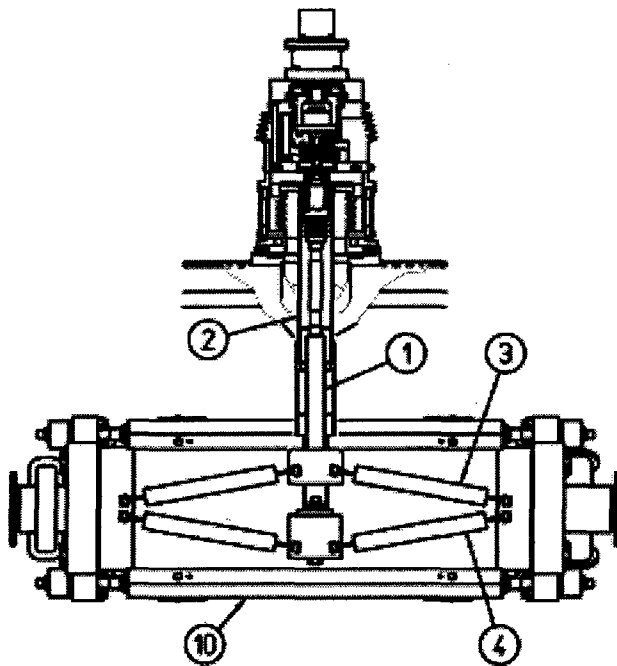


Fig. 2: Scissors Type Jack

The niobium cavity (Item 5, Fig. 3) has two reinforcing and attachment rings (Item 6, Fig. 3), one on each end of the seven-cell array, with each having a wedge-shaped groove machined into its outside surface for positive

attachment points. There is a split-ring clamp (Item 7, Fig. 3) engaging each of these that is used to mount the tuner. Titanium flex inserts (Item 8, Fig. 3) connect the split rings to two pivot plates (Item 9, Fig. 3), one on each end of the cavity. At the midpoint of these plates, two compression bars (Item 10, Fig. 1), extend from one plate parallel to the cavity center line to the other plate, providing fulcrum points for both pivot plates. Titanium flex inserts again are used at the connecting points of this arrangement. The other end of these pivot plates are fastened to the above described scissors type jacks, again using flex inserts, to complete the power train of the system.

The cavities are manufactured 1.5 mm shorter than their in-tune length, so that the tuner components are in tension at all times, to provide a backlash free tuning range. The fine tuning actuators are three piezoelectric post type units (Item 11, Fig. 4), located between the upper and lower mounting plates (Item 12 & 13, Fig. 4). They are spaced uniformly around the ball screw nut (Item 14, Fig. 4) and work in compression only. They are low voltage units (150 VDC) with a stroke of 50  $\mu\text{m}$ .

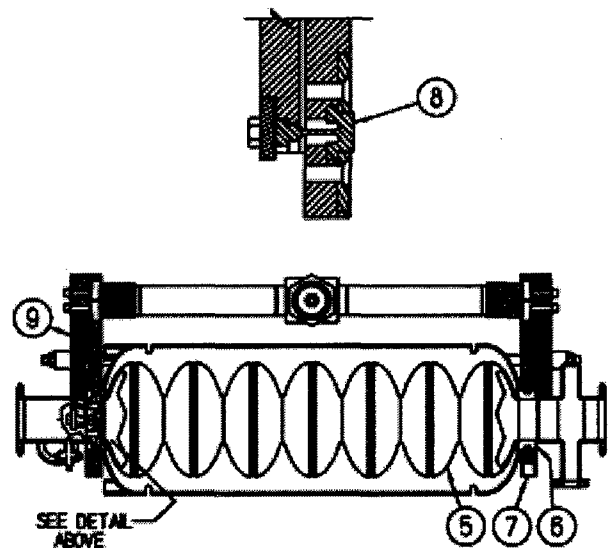


Fig. 3: Pivot Plate Arrangement

The scissors jack, pivot plates and split rings are machined from 6AL/4V titanium, which has similar coefficient of thermal expansion to niobium. The thrust tubes are made of type 304 stainless steel, and have thin wall areas to minimize thermal conduction to the cavities.

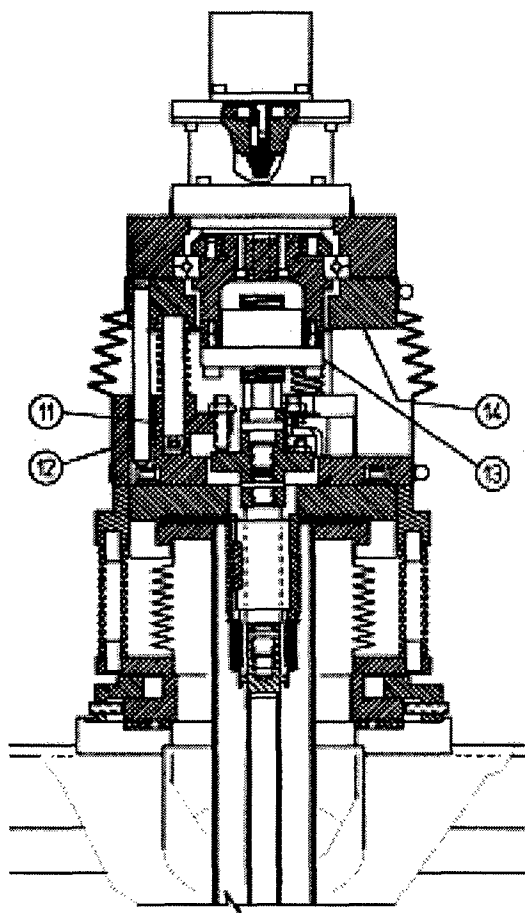


Fig. 4: Drive Assembly

#### 4 CONCLUSIONS

A Horizontal Test Bed is being constructed to perform demonstration tests on different key components for the Energy Upgrade Cryomodule (tuner, coupler, and cavity). A prototype of the tuner is under construction and testing in this Horizontal Test Bed is scheduled to begin in July of this year.

#### 5 ACKNOWLEDGEMENTS

We would like to thank the members of the Upgrade Cryomodule Development team for their helpful discussions.

#### 6 REFERENCES

- [1] J.R. Delayen "Upgrade of the CEBAF Acceleration System" these proceedings

# A MAGNETOSTRICTIVE TUNING MECHANISM FOR SRF CAVITIES<sup>1</sup>

Chad Joshi<sup>2</sup> and Bruce Bent, Energen, Inc., Billerica, MA

Michael Drury, Joseph Preble, Viet Nguyen, Jefferson Laboratory, Newport News, VA

## Abstract

Energen, Inc. has designed, built and demonstrated a fine tuning mechanism for superconducting radio frequency (SRF) cavities used in particle accelerators. This tuner is based on giant magnetostrictive materials being developed by Energen, Inc. Magnetostrictors elongate when exposed to a small magnetic field. This extension is reversible and repeatable enabling a wide range of applications. The magnetostrictive tuner was specifically designed to meet the requirements of the Thomas Jefferson National Accelerator Facility in Newport News, VA. The tuner consists of a high force linear actuator that elongates the cavity along its axis thereby changing its resonant frequency. It is installed in the dead leg of the existing mechanical tuner. This mechanism has a motion range that provides a tuning range of up to 6400 Hz. Preliminary tests at Jefferson Laboratory demonstrated cavity tuning capability.

this system, like any other mechanical assembly, has backlash. In addition to the elastic behavior of the components, split shaft couplers are used for the rotating feedthrough to allow for thermal contraction during cooldown. This split assembly adds to the inherent backlash of the system.

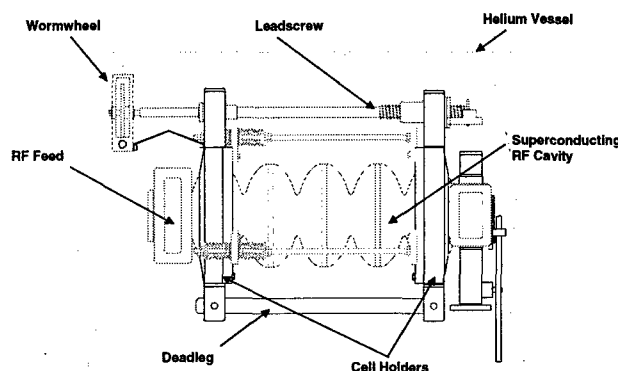


Figure 1: The CEBAF superconducting RF cavity showing its mechanical tuner.

## 1 INTRODUCTION

The Jefferson Laboratory of Newport News, VA operates the largest continuous beam electron accelerator in the world. Approximately 344 superconducting RF cavities operate at a resonant frequency of 1497 MHz to accelerate the electrons as they pass through each cavity. To obtain a homogeneous and continuous electron beam, these cavities are designed to exacting geometric tolerances. However, small imperfections in their manufacture and the large dimensional change that occurs as a result of cooling from room temperature to 1.8 K necessitates active compensation for the cavity length during the actual operation of the accelerator in order to match the resonance frequencies of multiple SRF cavities used in any accelerator.

## 2 SRF CAVITY TUNING

SRF cavity tuning is accomplished by physically elongating or compressing the cavity along its axis. Jefferson Laboratory uses a mechanical system as shown in Figure 1. The system uses a stepper motor at room temperature to drive a wormwheel gear reduction connected to a ball screw shaft. As the shaft turns, the two cell holders are squeezed together compressing the cavity and changing its resonant frequency. This mechanical system is relatively simple in concept, however, it is difficult to use for accurate cavity tuning. In operation,

## 3 MAGNETOSTRICTIVE MATERIALS

Magnetostrictive materials belong to a class of materials known as "smart materials". Magnetostriction arises from a reorientation of the atomic magnetic moments. In ferromagnetic materials, an applied magnetic field causes rotation of the magnetization towards the field direction within domains and/or motion of the domain walls to increase the size of the domains with magnetization vectors close in direction to the applied field. When the magnetization is completely aligned, saturation occurs and no further magnetostriction can be produced by increasing the applied magnetic field. Magnetostriction only occurs in a material at temperatures below the Curie temperature. The amount of magnetostriction at saturation is the most fundamental measure of a magnetostrictive material. Table 1 shows a compilation of some materials and the maximum strain they exhibit at saturation. Note that the materials exhibiting the highest magnetostrictive strain have Curie temperatures below room temperature. These materials show great promise for cryogenic actuator applications such as the SRF cavity tuners.

Magnetostrictive materials for cryogenic applications are not commercially available. Energen, Inc. has worked with the Ames Laboratory's Materials Preparation Center

<sup>1</sup> Supported by the Nuclear Physics Division of the U. S. Dept. of Energy through the SBIR Program

<sup>2</sup> E-mail: chad@EnergenInc.com

to obtain samples of the materials for testing and building prototype devices.

Several alloys from the  $Tb_{1-x}Dy_xZn$  family of materials were fabricated as follows. Appropriate quantities of the elemental constituents were alloyed together in a sealed tantalum crucible. The crucible was then held just below the melting temperatures to promote crystal growth. Once cooled, the crucible was removed and the resulting ingot was machined into rods for testing purposes. For testing the magnetostriction, samples of each alloy were cut into 2 mm diameter rods of lengths varying from 20 to 30 mm.

Table 1: Saturation strain and Curie temperatures of selected materials [1].

Material	Saturation Strain ( $\times 10^{-6}$ )	Curie Temperature (K)
Ni	-50	630
Fe	-14	1040
SmFe <sub>2</sub>	-2340	690
Fe <sub>3</sub> O <sub>4</sub>	60	860
DyFe <sub>2</sub>	650	630
TbFe <sub>2</sub>	2630	700
Tb <sub>0.3</sub> Dy <sub>0.7</sub> Fe <sub>1.9</sub> (Terfenol-D)	1600-2400	650
Tb <sub>0.6</sub> Dy <sub>0.4</sub> @ 77 K	6300	210
Tb <sub>0.5</sub> Zn <sub>0.5</sub>	5500	180
Tb <sub>1-x</sub> Dy <sub>x</sub> Zn	5000	200

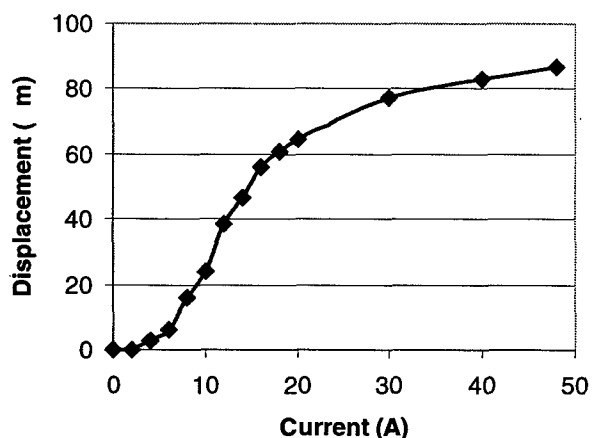


Figure 2: Magnetostriction of a TbDyZn alloy at 4.2 K shows high saturation strain.

Measurements of magnetostriction were made at 77 K and at 4.2 K. The data for 77 K are very reproducible and agree with data from the literature [2]. Figure 2 shows the measurements on one sample of the TbDyZn alloy at 4.2 K. These data are believed to be the first direct measurement of magnetostriction in this material system at 4.2 K and indicate that the high saturation strain remains at these low temperatures.

## 4 TUNER DESIGN

Energen, Inc. designed a magnetostrictive tuner based on these materials that replaces the deadleg of the existing mechanical tuner. This tuner was designed to provide fine tuning capability in parallel with the existing tuner. The mechanical tuner would be used for coarse tuning of the resonant frequency and then the magnetostrictive tuner would be used for fine tuning.

Figure 3 shows the magnetostrictive dead leg. Because of limitations in the size of magnetostrictor rods currently available, the magnetostrictor consists of six 0.5 inch disks of equal thickness on a 1.108" bolt circle. They are surrounded by a NbTi coil and compressed between two ferromagnetic end pieces that connect to the dead leg. The coil has 20 turns of superconductor with a critical current of 325 A at 4.2 K, 5.0 T. The ferromagnetic end pieces serve to focus the magnetic flux from the coil onto the magnetostrictor. The peak field in the end pieces and in the magnetostrictor is less than 1.6 tesla.

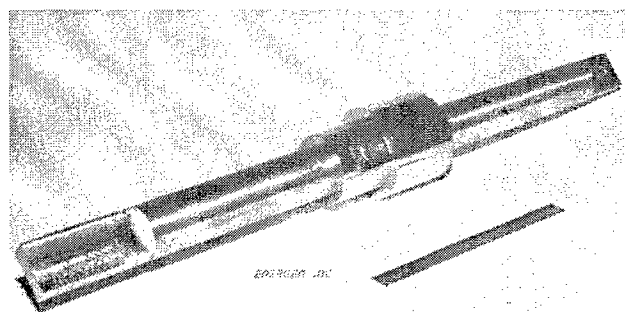


Figure 3: Magnetostrictive SRF cavity tuner designed by Energen, Inc.

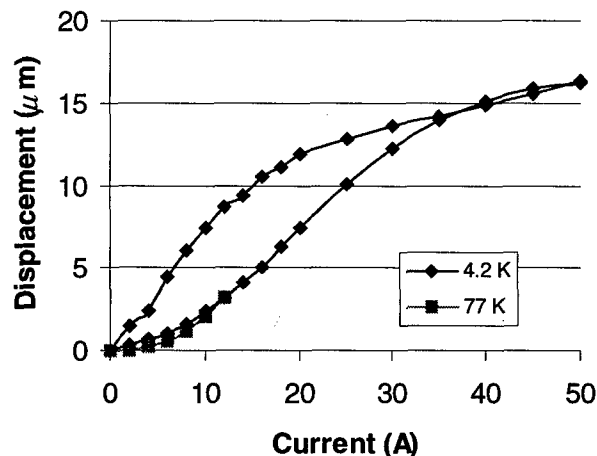


Figure 4: Measurement of dead leg tuner motion.



## 5 TUNER PERFORMANCE

The tuner was tested at Energen's facility at 77 K and at 4.2 K. At 77 K, the current in the coil was limited to 15 A to prevent potential damage to the coil and actuator from overheating. Figure 4 shows the results of tests at 77 K and 4.2 K.

Figure 4 indicates a total stroke of 16 microns is available for tuning the SRF cavity. Based on the known characteristics of the Jefferson Laboratory SRF cavities, this corresponds to a tuning bandwidth of 6400Hz - greater than the design goal by a factor of three.

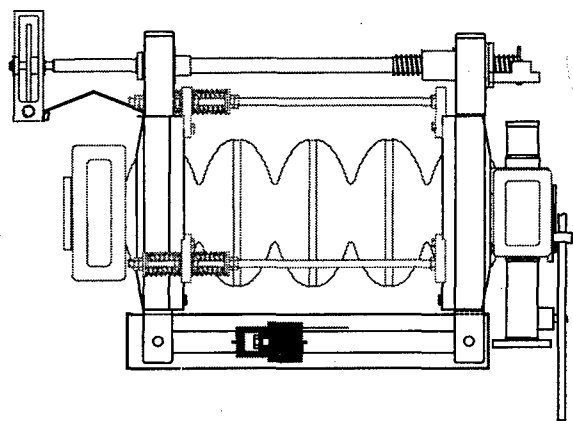


Figure 5: The magnetostrictive tuner was installed in place of the dead leg of the mechanical tuner.

It is clear that there is some hysteresis in these measurements. The source of this hysteresis is the anisotropic magnetic properties of the material and can be reduced by properly adjusting the chemistry of the material.

At Jefferson Laboratory, the tuner was installed on a SRF cavity as shown in Figure 5. In operation, a combination superconducting and mu-metal shield would be used to prevent the magnetic field from the magnetostrictive tuner from affecting the performance of the cavity.

The cavity was inserted vertically in a dewar and cooled in liquid Helium to approximately 2 Kelvin. A network analyzer (Hewlett Packard 8753) was used to drive the cavity and measure the cavity's operating frequency ( $f_o$ ). An RF frequency preamp was used to boost the signal from the cavity field probe before returning to the analyzer. A Sorenson programmable power supply capable of 45 A was used as the current source for the tuner. A 50 Amp shunt was installed in the return leg of the circuit between tuner and power supply. The shunt was calibrated for 1 mV / A. A 5 1/2 digit HP multimeter was used to measure the shunt voltage. The apparatus was controlled with a laptop PC running Labview. The laptop used a GPIB card to talk to the network analyzer

and the multimeter. A National Instruments analog box was attached to the parallel port. This gave an Analog output with which we could control the current source. The resolution of the current drive under this setup was about a 1/2 A. The resolution of the network analyzer was about 10 Hz.

In the first two tests, the maximum current for the tuner was 30 A. While the pressure in the helium vessel was constant during each test, there is a slight variation over a longer period of time. This pressure affects the tuning of the cavities. During the third test, when the current was increased to 50 A, a large change in pressure from 21 torr to 12 torr occurred during the test. There was likely a shift in frequency because of the pressure change exacerbating the hysteresis that is evident in the data.

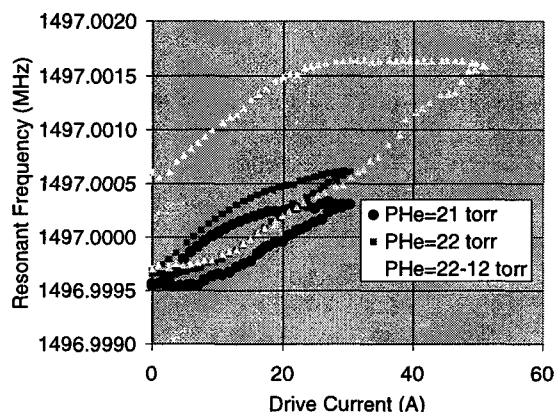


Figure 6: Tuner tests on a SRF cavity.

## 6 CONCLUSION

Energen, Inc. has designed, built and demonstrated a fine tuning mechanism for superconducting radio frequency (SRF) cavities used in particle accelerators. The tuner is designed specifically for the Jefferson Laboratory and operates in parallel with an existing mechanical tuning system that uses a wormwheel and ball screw assembly. The magnetostrictive tuner has demonstrated the desired 2000 Hz of tuning bandwidth and can be actively controlled during the operation of the SRF cavity. Further refinements should increase this tuning range providing an alternative tuning system to traditional mechanical tuner.

## 7 REFERENCES

- [1] *Magnetostrictive Materials*, K. B. Hathaway and A. E. Clark, MRS Bulletin, Vol. XVIII, No. 4, April 1993.
- [2] A. E. Clark, *High Power Magnetostrictive Materials from Cryogenic Temperatures to 250 C*, Materials Research Society Fall Meeting, Boston, MA, November 28-30, 1994.

## CRYOMODULE DEVELOPMENT FOR THE CEBAF UPGRADE\*

J.R. Delayen, L.R. Doolittle, E. Feldl, J. Hogan, J. Mammosser, V. Nguyen, H.L. Phillips,  
J. Preble<sup>#</sup>, W.J. Schneider, D.X. Wang, and M. Wiseman

Thomas Jefferson National Accelerator Facility, Newport News Virginia 23606 USA

### *Abstract*

Long term plans for CEBAF at Jefferson Lab call for achieving 12 GeV in the middle of the next decade and 24 GeV after 2010. In support of those plans, an Upgrade Cryomodule capable of providing more than three times the voltage of the original CEBAF cryomodule specification within the same length is under development. Development activities have been focused on critical areas thought to have maximum impact on the overall design. These have included the cavity structure, rf power coupling, cavity suspension, alignment, cavity tuning, and beamline interface. It has been found that all design and development areas are tightly coupled and can not be developed independently. Substantial progress has been made toward an integrated design for the Jefferson Lab Upgraded Cryomodule.

## 1 CRYOMODULE REQUIREMENTS

### *1.1 Tunnel Layout*

The CEBAF energy upgrade to 12 and then 24 GeV will be accomplished within the existing accelerator tunnel. The 12 GeV upgrade will be accomplished using an additional pass through one of the two linacs for a total of five and one half passes or eleven transits of a linac [1]. Currently each of the linacs has five module positions that were left empty during CEBAF construction. These ten positions will be filled with upgrade cryomodules along with the replacement of six existing cryomodules in the linacs and the two injector cryomodules.

### *1.2 Cavity*

In order for the CEBAF accelerator to reach 12 and 24 GeV the upgrade cryomodules will be required to supply an average energy gain of 68 MeV [2]. This will be accomplished with an increase in both the operating gradient and the active length of the cryomodule. An increase in active length from 4 to 5.6 meters must be accomplished within the same footprint as the existing CEBAF cryomodules. The increased active length and an average operating accelerating gradient of 12.5 MV/m

provides the required energy gain from a cryomodule. In order to operate at these gradients without exceeding the planned 2 Kelvin refrigeration capacity the quality factor of the cavities must be maintained at  $6.5 \times 10^9$  at operating gradients.

### *1.3 Fundamental Power Coupling*

The upgrade cryomodule will be operated with the existing 5 kW RF power sources. The fundamental power coupler (FPC) is designed to use a minimum of RF power for gradient and phase control [3]. The nominal fundamental power coupler  $Q_{ext}$  is  $2.1 \times 10^7$  [4][5]. An additional requirement for the coupler is an insensitivity to mechanical deformation of 0.0013 meters axially and 0.050 radians angularly. This is required to support cavity to cavity alignment in the cavity string.

### *1.3 Beamline Interface*

The beamline between cavities became crowded as efforts to maximise the active length of the cryomodule progressed. The decision was made to remove all bellows between cavities allowing for an additional two cells or 0.20 meters active length per cavity. The beamline outside the helium vessel contains the Higher Order Mode (HOM) coupler ports, fundamental power coupler, field probe port, and frequency tuner attachment.

### *1.4 Helium Vessel*

The helium vessel encloses the cavity cells only, minimising the liquid helium inventory in the cryomodule. This is a change from the existing CEBAF design that encloses the FPC and the HOM coupler ports. The vessel design uses titanium construction with two titanium bellows at the outer diameter.

### *1.4 Tuning*

The new tuning system design includes a coarse and fine tuning actuator. This is a change from the existing CEBAF design that has a single tuning actuator. The requirement for the fine tuning results from the limited RF power available and resulting requirement to minimise the RF power used for gradient and phase control. A control resolution of 1 Hz with a range of 1 kHz is required for the fine tuner and a resolution of 200 Hz with a range of 400 kHz is required for the coarse tuner [6]. The range of the fine tuner is sufficient to handle the normal operating

\* Work supported by the U.S. Department of Energy under contract DE-AC05-84-ER40150.

# Email: preble@jlab.org

requirements which are typically within 100 Hz while the coarse tuner is used to tune the cavities after cooldown when additional range is required.

### 1.5 Cavity Suspension and Alignment

The cavity alignment requirements are unchanged from the original CEBAF requirements [7][8]. This requires the cavities to be aligned relative to the nominal beam trajectory with a root mean-square angular precision of 0.002 radians. To accomplish this a space frame will be constructed around the completed cavity string that will allow individual cavities to be final aligned in the "as installed" support configuration.

### 1.6 Requirements Summary

Many of the requirements for the upgrade cryomodule are very similar to the original CEBAF cryomodule. This results from maintaining the existing cryomodule footprint. Differences in the cryomodule are primarily driven by the increased energy gain, improvements in fabrication techniques, and changes in beam requirements. Table 1 lists the major differences in the upgrade cryomodule.

Table 1: Cryomodule Comparison

Parameter	CEBAF	Upgrade
Voltage <sub>2</sub>	20 MV	68 MV
E <sub>acc</sub> Average	5 MV/m	12.5 MV/m
Q <sub>0</sub> @ E <sub>acc</sub>	2.4×10 <sup>9</sup>	6.5×10 <sup>9</sup>
RF Windows	2	1
FPC Coupling	λ/2 stub on stub	λ/4 stub
Q <sub>ext</sub> FPC	6.6×10 <sup>6</sup>	2.2×10 <sup>7</sup>
HOM Coupling	Waveguide	Coaxial
B.L. Bellows	5	2
Vac. Valves	10	4
Freq. Tuner	Single	Dual-Coarse/Fine
Cryounits (CU)	4	1
Cavities/CU	2	8
2 K RF Heat	45 watts	140 watts
50 K RF Heat	40 Watts	120 watts

## 2 DESIGN STATUS

### 2.1 Cavity

The cavity assembly has seven cells using the CEBAF cell designs for interior and end cells. The cells are assembled with an end collar that provides the interface to the helium vessel, beamline, and tuner attachment. The cavity design is complete at this time. A major difference from the CEBAF design is the use of a single eight cavity hermetic

sealed string replacing the four two cavity strings used in the original CEBAF design.

### 2.2 Fundamental Power Coupler

The fundamental power coupler is a waveguide design and has been designed and tested using a copper model. The coupler uses a λ/4 stub geometry providing two significant benefits, the first is the minimisation of steering kicks resulting from the coupler electric fields and the second is the insensitivity to minor mechanical deformations in the coupler. The first is important to reduce the effects on the beam quality in the accelerator while the second allows for using the coupler for small cavity alignment adjustments. The copper coupler model has been used to determine final dimensions and demonstrate the required tolerance to mechanical deformations. The waveguide section that provides the thermal transition between the cavity and vacuum vessel has a common vacuum with the cavity and is sealed with a warm ceramic window. The waveguide incorporates a S bend which allows for the grouping of waveguides in pairs prior to penetrating the vacuum vessel and removes the warm ceramic window from the line of sight of the beam line.

### 2.3 Beamline

The beamline is the area outside the helium vessel and includes the FPC, HOM coupler ports, field probe, beamline flanges, and tuner attachment points. Noticeably missing between the cavities are any bellows or vacuum valves. To allow for no bellows in the beamline the beamline flanges and FPC must provide the adjustment required to maintain cavity alignment. The beamline flanges allow for an angular deflection by utilising a design that thins the material interior to the sealing surface. Deformation of the membrane results in the required angular deflection. The FPC provides additional axial and angular deflection where the beamline tube intersects the waveguide box. The combination of these allows for a dogleg displacement in the beamline.

### 2.4 Helium Vessel

The helium vessel is one of the major changes from the CEBAF design. The vessel has been reduced from a 0.61 to a 0.25 meter diameter. This is made possible by moving the RF couplers outside of the helium vessel. The vessel material is titanium to match the thermal properties of the cavities and eliminate differential thermal contraction difficulties. Two titanium bellows are incorporated into the vessel which allow for the remaining differential thermal contraction and tuning requirements.

### 2.5 Cavity Frequency Tuning

The tuner design is complete and being fabricated at this time. The design incorporates a single mechanism acted on by two actuators, one providing coarse and the other

fine tuning adjustments. The coarse adjustment is accomplished using the same stepper motor used in the CEBAF design while the fine tuning is done using three piezo-electric actuators acting in parallel. Both actuators are mounted outside the insulating vacuum providing easy access to them at all times. The cold portion of the tuner is made of titanium matching the thermal properties of the cavities and eliminating differential contraction issues. The cold assembly has no friction generating parts and uses all flex joints to accomplish the required movement.

### 2.6 Support and Alignment

A warm space frame using support rods configured in a double paired cross pattern at each end supports each cavity in the cavity string. The space frame is supported inside the vacuum vessel at the quarter points, each being between the second and third cavity from the end. The frame is made up of a series of hoop rings installed perpendicular to the beam axis down the length of the cavity string and connected by axial support members. The frame is assembled around the string along with the tuner assemblies starting from one end and progressing to the other. When the space frame is completed magnetic shielding, thermal shielding, and associated components will be added to the structure. When complete the space frame will be wheeled into the vacuum vessel and locked into position.

### 2.7 Vacuum Vessel

The vacuum vessel is designed as a single pipe running the length of the cavity string. Four horizontal penetrations allow for bringing the waveguides and instrumentation out of the vacuum vessel. Eight smaller penetrations on the top of the cryostat allow for the tuner interface.

### 2.8 Testing

The upgrade cryomodule includes new design concepts for several components. A testing program has been designed to validate these concepts early on, providing confidence for the continuing design effort. A facility is under construction to provide a means to test various components. An important feature of this facility is the ability to quickly install, test, and remove components allowing for multiple tests in a short period of time. This facility, the Horizontal Test Bed (HTB), is being fabricated by modifying an early CEBAF prototype cryounit and will allow for the testing of two cavities with prototype components attached. Its commissioning is planned for May and the first test with prototype components is scheduled for June of this year.

### 2.9 Design Integration

The design of the cryomodule includes many closely interacting components. An attempt has been made to

optimise critical high impact systems as a whole with regard to these interactions. This has necessitated a number of iterations in design as one component design evolves and impact on others is evaluated and considered. The beamline area has been the focus of considerable effort to date. This area includes all the rf coupling, the tuner attachment, and cavity support and alignment. The important issues include space, performance, fabrication, and processing considerations.

## 3 SUMMARY

The design of a upgrade cryomodule to support the energy upgrade of the CEBAF accelerator is underway. The design effort has focused on the least understood components of the cryomodule. These areas include the cavity and beamline, cavity string design, fundamental power coupling, cavity frequency tuning, and cavity string support and alignment. These efforts are not independent and require a series of iterations in order to look for a system optimisation. A test program is planned to allow for early and easy testing of prototype components allowing for effective development. The higher risk designs are scheduled to be tested in an integrated test by October of this year.

## 4 ACKNOWLEDGEMENTS

The work reported here has been accomplished by the Jefferson Lab Accelerator Development Department and Mechanical Engineering group.

- [1] D.R. Douglas, R.C. York, and J. Kewisch, "Optical Design of the CEBAF Beam Transport System" Proc. 1989 IEEE Part. Accel. Conf., Chicago, IL, March, 1989.
- [2] J.R. Delayen "Upgrade of the CEBAF Acceleration System", these proceedings
- [3] Lawrence R. Doolittle, D.X. Wang, "RF Control Studies For Moderate Beamline Coupling Between SRF Cavities", Proceedings of the LINAC Conference 1998
- [4] Lawrence R. Doolittle, "Strategies for Waveguide Coupling For SRF Cavities", Proceedings of the LINAC Conference 1998
- [5] J.R. Delayen et al., "An RF Input Coupler System for the CEBAF Upgrade", these proceedings
- [6] J.R. Delayen et al., "Frequency Tuning of the CEBAF Upgrade Cavities", these proceedings
- [7] J.J. Bisognano, D.R. Douglas, and B.C. Yunn "Alignment Tolerances for CEBAF Accelerating Cavities", CEBAF-TN-91-081, 15 October 1991
- [8] D.R. Douglas and J. Preble, "Alignment Tolerance for 7-Cell SRF Cavity", JLAB-TN-98-022, 22 May 1998

# SUPERCONDUCTING CAVITY DEVELOPMENT FOR THE CEBAF UPGRADE\*

I. E. Campisi, J. R. Delayen<sup>#</sup>, L. R. Doolittle, P. Kneisel, J. Mammoser, L. Phillips,  
Thomas Jefferson National Accelerator Facility, Newport News, VA

## Abstract

Long-term plans for CEBAF at Jefferson Lab call for achieving 12 GeV in the middle of the next decade and 24 GeV after 2010. In support of these plans, an Upgrade Cryomodule, capable of providing more than twice the operating voltage of the existing CEBAF modules within the same length, is being developed. In particular, this requires the development of superconducting cavities capable of consistently operating at gradients above 12 MV/m and  $Q \sim 10^{10}$ . We have engaged in a complete review of all the processes and procedures involved in the fabrication and assembly of cavities, and are modifying our chemical processing, cleaning, and assembly facilities. While we have retained the cell shape of existing CEBAF cavities, the new superconducting structure will be substantially different in several respects, such as the higher-order-modes damping and the fundamental power coupling systems. Design features and experimental results will be presented.

## 1 INTRODUCTION

CEBAF's long-term institutional plan calls for an energy upgrade to 12 GeV in the middle of the next decade, and to 24 GeV after 2010. While the details of the upgrade path are still being developed, a top-level parameter list has been generated which guides the selection between the various options [1]. The Upgrade Cryomodule is the key component of the upgrade of the acceleration system. Its design is also somewhat insensitive to the details of the upgrade option that is ultimately chosen, once the top-level parameters have been defined, and it can be viewed as a building block that can be applied to a large number of upgrade paths. For these reasons, most of the development efforts in support of the upgrade are directed toward the development and demonstration of prototype Upgrade Cryomodules.

In order to increase the voltage that is provided by a cryomodule within a given length, one can either increase the gradient at which the cavities are operating, or increase the effective accelerating length, or both. While it may be argued that maximizing the accelerating length is the approach that presents the least technological risk, for cw accelerators such as CEBAF, maximizing the

length instead of the gradient has the added advantage of lowering the dynamic load on the refrigeration system.

For this reason, it was decided early that the Upgrade Cryomodule would still include 8 cavities, but that these would be 7-cell cavities (70 cm) instead of the present 5-cell (50 cm). The baseline option calls for these cavities to provide a minimum voltage of 8.75 MV with a maximum power dissipation of 17.5 W at 2K, *i.e.* their  $Q$  must be at least  $6.5 \times 10^9$  at 12.5 MV/m. Thus the greatest challenge is not so much in achieving a high gradient but in maintaining a high  $Q$  at high gradient. Given the constraint imposed by the available refrigeration (17.5W per cavity), cw operation at 15 MV/m would be practical only if the  $Q$  at that field were at least  $10^{10}$ .

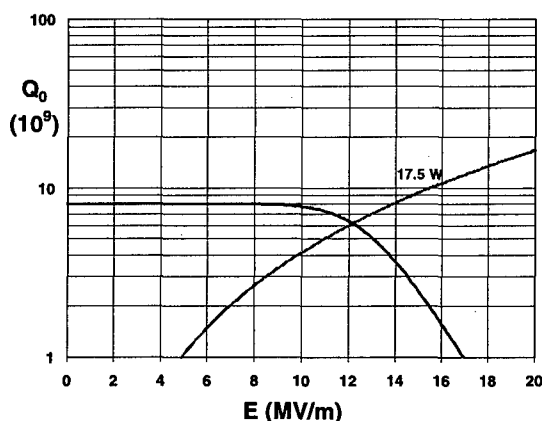


Figure 1: Design  $Q$ -curve for the Upgrade 7-cell cavity, with line of constant 17.5 W power dissipation

## 2 CAVITY DESIGN

### 2.1 Cell Geometry

While the CEBAF cavity cell design could be improved, the potential benefits do not seem critically important, and the first 7-cell cavity prototype has been built using the existing cell geometry.

The existing cell shape is characterized by ratios  $E_p/E_{acc}$  of 2.6 and  $H_p/E_{acc}$  of 47 Oe/(MV/m). Designs with lower ratios exist; however, as was mentioned before, the greatest challenge is not so much high gradient as low power dissipation. In that respect, the shunt impedance of the existing design compares well with that of others. Another attractive feature of the existing cell design is the

\*Supported by US DOE Contract No. DE-AC05-84ER40150.

<sup>#</sup> delayen@jlab.org

relatively high cell-to-cell coupling coefficient (3.3%), which reduces the sensitivity of the field profile to the lack of dimensional uniformity and mechanical stability as the number of cells is increased. A redesign of the cells is still an option, although a low priority one.

## 2.2 Intercavity Beamline

The topology of the Energy Upgrade cryomodule places a full complement of couplers between each pair of adjacent cavities. The mechanical design of this region has proved a challenge. The required functionality includes: a Fundamental Power Coupler (FPC), 2 Coaxial Higher-Order-Mode (HOM) dampers, a field probe, tuner, connections to the LHe vessel, and a demountable joint.

One of the concerns raised in the desire for longer accelerating length within the same overall footprint of the module (increasing fill factor) is that the separation between cavities is small enough to lead to undesirable amounts of crosstalk. This was explored at some length [2] and found not to be a problem. For very short separations, half-integral wavelength separations ( $\lambda/2$ , or  $\lambda$ ) are needed to keep the real power flow small.  $\lambda/2$  spacing is much too short to place couplers in the intercavity space and places severe demands on the demountable joint.  $\lambda$  spacing has some attractive features, and some attempts were made to design the needed functionality into this space. No solutions were found that appeared practical to assemble.

For separations larger than  $\lambda$ , the crosstalk between adjacent cavities is small enough not to require a "magic" choice of distance. At the current design value of 30 cm ( $1.5 \lambda$ ), the power flow between cavities under nominal conditions is negligible.

## 2.3 Fundamental Power Coupler

Experience with waveguide couplers in the CEBAF design was generally positive. Waveguide couplers can be made relatively flexible and forgiving of displacements along the beamline. Heat loads are easily controlled, and there are no tight manufacturing tolerances.

One unpleasant feature of the original waveguide coupler was a large transverse beam kick. This characteristic originated from its synchrotron heritage, where the damping of the  $4\pi/5$   $TM_{010}$  mode was important for beam stability. In the present (relatively) low-current linac application, this is not an issue, and the coupler itself could be adjusted for near zero transverse kick [3].

The remaining displeasure with our existing coupler system centered on the windows, in particular the location of the cold window close to the beamline. We have settled on a revised topology [4] that has a single warm ceramic window (shielded from line-of-sight interaction with the cold cavity) that is not required to pass HOMs. This does place more stringent demands on the waveguide thermal transition. It must be installed nearly free of particulates, and with low outgassing characteristics.

## 2.4 Higher-Order-Mode Couplers

Among the modifications implemented in the cavities for the CEBAF Energy Upgrade is the HOM damping scheme. In the original CEBAF design a healthy safety factor against multipass beam breakup was included. The  $Q$ 's of the relevant dipole modes were maintained at the  $10^3$ - $10^4$  level in order to guarantee two orders of magnitude margin in the threshold current for instability.

To re-evaluate the requirements for HOM damping in CEBAF, a program of measurements, simulations and experiments is being implemented. Measurements of HOMs in the accelerator and FEL have shown that self-polarization of the coupler can enhance the  $Q$  of some modes to levels as high as  $5 \times 10^7$ . Even with these high  $Q$ 's the machine is stable against BBU for the nominal current. Therefore we expect that, for the Energy Upgrade, even higher  $Q_{ext}$  would be acceptable because the average current in the accelerator will be lower, and the injection energy and the overall energy of CEBAF will be higher. We estimate that the requirements on the  $Q_{ext}$  of dipole modes could be relaxed by about two orders of magnitude, up to  $10^5$ - $10^6$  from  $10^3$ - $10^4$ .

At present, the baseline design includes a tuned filter HOM damping scheme following the TESLA-Saclay design [5], which is compatible with the integrated helium vessel used for the Upgrade cavities.

The possibility of eliminating entirely specialized HOM absorbers is also under investigation. A program of studies of HOMs is being implemented, which will help in clarifying the true HOM limitations at CEBAF and in the FEL.

## 3 FACILITIES AND PROCEDURES

In order to meet the design specification of high gradients and low losses with tighter distribution in performance, and mechanical changes to the cavity and cryostat design, we concluded that an upgrade of the facilities and the assembly procedures used for the fabrication of CEBAF cryomodules was needed. The goal was to increase the control over process and assembly variables. The production run of CEBAF cryomodules (1990-1994) generated a broad distribution of acceptable operating gradients between 4 and 14 MV/m. The most predominant limitation in individual cavity performance is field emission and field-emission-related RF window arcing, mainly due to surface contamination from process and hardware particulates. Our review has led to an assembly procedure that will pre-qualify the 7-cell cavities by vertical testing of the 7-cell assembly prior to addition of beam tube couplers. After qualification, the couplers and helium vessel will be added and the cavity will be prepared for final assembly of an 8-cavity string. The final string assembly will then be completed in the Class 100 production cleanroom. To reduce particulates and to narrow the individual cavity performances in the final

string, production semiconductor-style chemistry and high-pressure rinsing (HPR) cabinets have been installed in the cleanroom. The chemistry and the HPR cabinets are self-contained, PLC-controlled and menu-driven. In addition to these cabinets, a part-cleaning cabinet and a final ozone-rinsing cabinet are currently being designed as part of the final string assembly procedures. During the commissioning of these new facilities, procedures will be adjusted as necessary to reduce exposure of internal cavity surfaces to particulates generated by assembly in order to meet the new module performance specifications.

#### 4 PROTOTYPE 7-CELL CAVITY

A 7-cell cavity was built from existing half-cells and dumbbells remaining from the CEBAF cavity production phase. Particular care was taken in the preparation of the dumbbells prior to joining them by electron beam welding: each dumbbell was carefully inspected and mechanically ground, removing all visible surface imperfections such as indentations or scratches. Subsequently, the dumbbells were degreased and chemically polished for 1 - 2 min, partially removing the surface damage layer. The equatorial welds were done from the outside with standard welding parameters, but only one dumbbell was added at a time starting from one end half-cell and each weld was thoroughly inspected. If necessary, some mechanical grinding of the welds was done with subsequent degreasing and slight chemical polishing. Prior to completing the equatorial welds, beam pipe assemblies were welded to the end half-cells.



Figure 2: Prototype 7-cell cavity

The cavity had a  $\pi$ -mode frequency of 1494.45 MHz with a field-nonuniformity of 16 % (in  $E^2$ ). After pretuning the  $\pi$ -mode to 1494.6 MHz and a field flatness of 5%, the cavity was chemically prepolished 3 times for 2.5 min; the acid temperature did not rise above 25 °C. The total frequency shift was about -500 kHz, corresponding to a material removal of approximately 90  $\mu\text{m}$ , assuming a uniform material removal over the entire cavity surface.

For the final surface preparation, the cavity was degreased for 1 hour in a caustic solution with ultrasonic agitation. After pure water rinsing, buffered chemical polishing was done, removing an additional 75  $\mu\text{m}$ .

Thorough rinsing was followed by high-pressure ultrapure water rinsing for more than 90 min.

In the clean room the cavity was rinsed twice with reagent grade methanol. Immediately after assembly, the cavity was attached to the vertical test stand and evacuated by a turbo pump for typically 15 min. When a pressure of less than  $5 \times 10^{-6}$  torr was reached at the turbo pump, the cavity vacuum system was transferred to the ion pump on the test stand. Fast cooldown of the cavity to 4.2K took place in approximately 1 hour; during pump-down to 2K the temperature dependence of the surface resistance was measured. A residual surface resistance of 7.8 n $\Omega$  corresponding to a  $Q_{\text{res}}$  of  $3.5 \times 10^{11}$  was measured.

At 2K the cavity gradient was initially limited to 16.3 MV/m by a breakdown, which seemed to be initiated by field emission. After He-processing the quench limit improved to 17.5 MV/m at a Q-value of  $6.2 \times 10^9$ . During the pump-down of the helium bath from 4.2K to 2K a pressure sensitivity of 99 Hz/torr was measured.

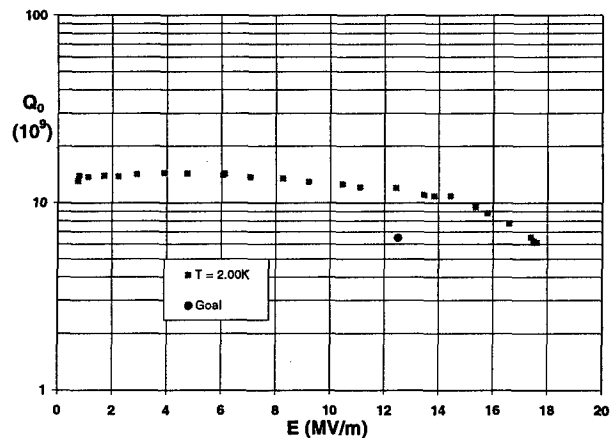


Figure 3: Results of the test of the first 7-cell prototype.

#### ACKNOWLEDGEMENTS

We would like to acknowledge the contributions of J. Brawley and L. Turlington to the fabrication of the prototype 7-cell cavity.

#### REFERENCES

- [1] J. R. Delayen, "Upgrade of the CEBAF Acceleration System", these Proceedings.
- [2] L. R. Doolittle, D. X. Wang, "RF Control Studies for Moderate Beamline Coupling between SRF Cavities", Proceedings of LINAC98.
- [3] L. R. Doolittle, "Strategies for Waveguide Coupling for SRF Cavities", Proceedings of LINAC98.
- [4] J. R. Delayen *et al.*, "An RF Input Coupler System for the CEBAF Upgrade Cryomodule", these Proceedings.
- [5] J. Sekutowicz, 6<sup>th</sup> Workshop on RF Superconductivity, p. 426, October 1993, CEBAF, Newport News, VA.

# OPERATIONAL OPTIMIZATION OF LARGE-SCALE SRF ACCELERATORS\*

J. R. Delayen, L. R. Doolittle<sup>†</sup>, C. E. Reece

Thomas Jefferson National Accelerator Facility, Newport News, Virginia 23606 USA

## Abstract

Unlike other types of accelerator subsystems, because of the flexibility in setting the gradient in each cavity, an SRF linac has many operational degrees of freedom. The overall linac has an operational envelope (beam voltage and current) that depends on acceptable reliability, cryogenic capacity, and RF power budget. For economic and end-user physics reasons, one typically wants to run as close to the edge of the operational envelope as possible. With about 160 cavities in each of the CEBAF linacs, we have been forced to treat this problem in a very general way, and satisfy other non-fundamental needs as energy lock and rapid recovery from failures. We present a description of the relevant diverse constraints and the solution developed for CEBAF.

## 1 GOALS

We seek a method for choosing the accelerating voltage for a large set of cavities, such that the behavior of the set as a whole is optimized. The aggregation of cavities has exactly four properties that we care about: the total voltage delivered to the beam, the amount of beam current it can carry while maintaining voltage regulation, the amount of cryogenic losses, and the frequency of trips. The optimization could, in general, be based on any restrictions and figures of merit that depend on these four quantities. In practice, the simplest arrangement is satisfactory, where individual parameters can be fixed, constrained, or floating.

## 2 PRELIMINARIES

Table 1: notation

$V$	Cavity voltage
$I$	Beam current
$W$	RF power
$R_c$	coupling impedance, $Q_L(R/Q)$
$R_d$	dissipation impedance, $Q_0(R/Q)$
$\delta$	Detune angle, radians

Table 1 shows the notation used. The operating voltage of the SRF cavities at CEBAF is constrained by four very specific limitations:[1, 2]

\* Work supported by the U.S. DOE Contract # DE-AC05-84ER40150

<sup>†</sup> Email: ldoolitt@jlab.org

### 2.1 Hard limit

During commissioning, a safe upper bound for operation is determined. This may be a safe margin below a quench, or the point at which X-ray fluxes are deemed dangerous for long term operation of equipment near the cavity. If nothing else, it is the highest field achieved during commissioning, since there is no positive evidence showing safe operation above that point.

### 2.2 RF Power budget

Given a long series of assumptions about the cavity and its RF system, it is straightforward to compute the amount of RF power required to run the cavity at any specified gradient and beam current. Given a value for available RF power (at which there is still adequate gain for feedback), and the overall linac beam current, an upper limit on the each cavities voltage can be computed. This expression is postponed until later in the paper.

### 2.3 Trip limit

Given trip rate as a function of voltage (assumed to be well known)  $R(V)$ , the formal condition of balance is that all cavities limited by this phenomenon have the same value of  $\partial R/\partial V$ . This means that shifting a Volt of beam energy gain from one of these cavities to another will not change the total machine trip rate.

### 2.4 Cryogenic capacity limit

Given cryogenic dissipation as a function of voltage (assumed to be well known)  $C(V)$ , the formal condition of balance is that all cavities limited by this phenomenon have the same value of  $\partial C/\partial V$ . This means that shifting a Volt of beam energy gain from one of these cavities to another will not change the total machine cryogenic dissipation. This limit has not yet been an issue at CEBAF, but will soon become one as the energy is pushed to 6 GeV and beyond. The cryogenic limit will become severe in the planned energy upgrade.

## 3 SYNTHESIS

Given a complete description of each cavities capabilities, and the three global constructive parameters  $I$ ,  $\partial R/\partial V$ , and  $\partial C/\partial V$ , a setpoint voltage for each cavity can be computed, which is the lowest of the four limits. This set of



cavity voltages represents one possible complete and balanced accelerator configuration.

These three constructive parameters completely span the space of rational configurations, so choosing a setup involves a search in these three dimensions, a great improvement over the 160 cavities in each linac at CEBAF. Of course, CEBAF's users and operators can not be expected to choose  $\partial R/\partial V$  and  $\partial C/\partial V$  by themselves to give the desired linac energy, stable cryogenic operation, and tolerable trip rate. Software has to be constructed to aid them in that search. That magic word "search" implies the ability to compute derivatives, so that the process can converge rapidly.

The expression for the power needed for a given voltage, current, and detune angle is

$$W = \frac{1}{4R_c} |(1 + j\delta)V + R_c I|^2$$

The expression can be inverted to find the cavity voltage limit due to available RF power

$$V = \frac{1}{1 + \delta^2} \left[ \sqrt{4WR_c(1 + \delta^2) - I^2 R_c^2 \delta^2} - IR_c \right]$$

In this case  $I$  is considered the globally tunable parameter.

$$\frac{\partial V}{\partial I} = -\frac{R_c}{1 + \delta^2} \left[ \frac{IR_c \delta^2}{\sqrt{4WR_c(1 + \delta^2) - I^2 R_c^2 \delta^2}} + 1 \right]$$

This technique works as long as one can construct a unique cavity voltage limit from  $t_R = \partial R/\partial V$  (this can be thought of as a "tune parameter"), and the function  $V(t_R)$  for each cavity is non-pathological, so that small changes in  $t_R$  can be used to make small changes in total linac energy. The implementation to date assumes

$$R(V) = e^{a+bV},$$

where  $a$  and  $b$  empirically parameterize observed trip rates. From this we derive

$$V(t_R) = \frac{1}{b} \left[ \ln \frac{t_R}{b} - a \right]$$

$$\frac{\partial V}{\partial t_R} = \frac{1}{bt_R}$$

$$\frac{\partial R}{\partial V} = be^{a+bV}.$$

This technique also requires that one can construct a unique cavity voltage limit from  $t_C = \partial C/\partial V$  (this can be thought of as another "tune parameter"), and the function  $V(t_C)$  for each cavity is non-pathological, so that small changes in  $t_C$  can be used to make small changes in total linac energy. The implementation to date assumes

$$C(V) = \frac{V^2}{R_d},$$

where  $Q_0$  is measured at the time of cavity commissioning. From this we derive

$$V(t_C) = \frac{1}{2} t_C R_d$$

$$\frac{\partial V}{\partial t_C} = \frac{1}{2} R_d$$

$$\frac{\partial C}{\partial V} = \frac{2V}{R_d}.$$

Each of the above expressions is written in the single cavity form. The voltage  $V$  actually selected for a cavity is the lowest of  $V(I)$ ,  $V(t_R)$  and  $V(t_C)$ . The overall ensemble  $R$  and  $C$  are clearly summations of the individual cavity amounts, where the actual cavity voltage is used for each cavity. The ensemble derivatives  $\partial V/\partial I$ ,  $\partial V/\partial t_R$ , and  $\partial V/\partial t_C$  need some care—a cavity only contributes to the sum corresponding to its limit.

## 4 SPACE EXPLORATION

As mentioned earlier, a rational ensemble setup is based constructively on the values of the three tune parameters,  $I$ ,  $t_R$ , and  $t_C$ . Four "result" terms are  $V$ ,  $I$ ,  $R$ , and  $C$ . One expects that any three of these may be specified, and the fourth solved for (along with the tune parameters, and therefore the exact setup). While in general a set of non-linear equations can be quite pathological, or at least have multiple solutions, the monotonic relations we have chosen between, e.g.,  $t_R$ ,  $R$ , and  $V$  make it very generally true that solutions, when they exist, are unique. It is, of course, true that asking to solve for unreasonable values of the "result" terms will give a null answer.

The current implementation allows searches for any three given values of  $V$ ,  $I$ ,  $R$ , and  $C$ . One can also directly provide  $I$ ,  $t_R$ , and  $t_C$ .

## 5 GRITTY DETAILS

Other functionality than the pure theory has to be accreted to the core before the lab has a usable software tool:

- Acquisition and control of all the input
- Operator override of specific troublesome cavities
- Computation and setting of the quadrupoles (sensitive to the energy profile down the linac)
- Smooth changes to the cavity gradient (don't overrun the tuners or the module heaters)
- Operator interface

The implementation of all these requirements was purposefully quite modular. The inner math program has no user interface or control system dependence; those features are implemented as separate programs, with simple data streams and handoff rules between them.

A fringe benefit of this modularity is that the (debugged, ready-to-run) inner math program is available for scans of parameter space. A total of 67 lines of sh and perl suffice

to generate figures 1 through 4 by repeatedly invoking the math program to do the actual calculations.

These figures show that the nominal relationship between voltage and cryogenic load ( $C \propto V^2$ ) breaks down when the machine operates near its voltage or RF power maximum. Similar slices can be taken for other combinations of beam current, trip rate, beam energy, and cryogenic losses.

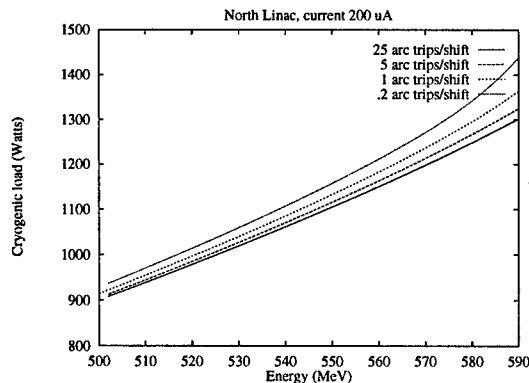


Figure 1: Variation with energy of the Cryogenic Load generated by CEBAF's North Linac, with RF headroom to sustain 200  $\mu$ A beam loading and various trip rates.

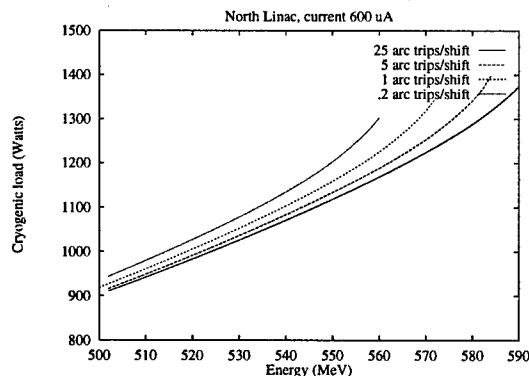


Figure 2: Variation with energy of the Cryogenic Load generated by CEBAF's North Linac, with RF headroom to sustain 600  $\mu$ A beam loading and various trip rates.

## 6 CONCLUSIONS

It is interesting to note that no single phenomena even represents a majority limitation in the machine under our current high energy setups (5.5 GeV, 600  $\mu$ A). This could be construed as a sign of several poorly controlled manufacturing steps (such as the wide range of cavity voltages showing onset of field emission). It can also be argued that this is a natural consequence of efficient design where most subsystems are not overdesigned[3] (such as with the sizing of the cryogenic refrigerator).

This pattern of large, complex systems, bounded by a complex envelope, is likely to recur in the accelerator com-

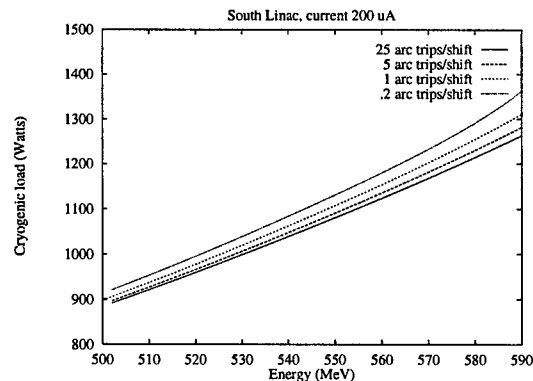


Figure 3: Variation with energy of the Cryogenic Load generated by CEBAF's South Linac, with RF headroom to sustain 200  $\mu$ A beam loading and various trip rates.

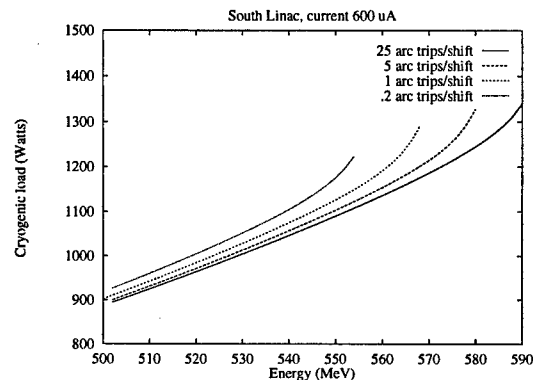


Figure 4: Variation with energy of the Cryogenic Load generated by CEBAF's South Linac, with RF headroom to sustain 600  $\mu$ A beam loading and various trip rates.

munity. Modern trends of careful design and simulation, applied to large, costly projects, will tend to create situations where many phenomena interact in the final operation of the device. Work such as this can make an important contribution to actually achieving performance at the edge of the predicted envelope.

While more complex models would improve the realism of the simulated performance, the dominant source of error at the moment seems to be our inability to accurately measure some of the parameters of the simple model. One lesson to the designers and builders of large scale systems, therefore, is the necessity of embedding adequate in-situ measurement capability.

## 7 REFERENCES

- [1] C.E. Reece et al., "Performance Experience with the CEBAF SRF Cavities," Proceedings of PAC 1995, p. 1512.
- [2] J. R. Delaysen et al., "Analysis of Performance Limitations of Superconducting Cavities," Proceedings of LINAC 1998.
- [3] Henry Petroski, "To Engineer is Human," Random House, New York, 1992 and "The Deacon's Masterpiece," by Oliver Wendell Holmes, referenced and copied therein.

## DEVELOPMENT OF SEAMLESS NIOBIUM CAVITIES FOR ACCELERATOR APPLICATIONS\*

P. Kneisel<sup>†</sup>, Jefferson Lab, Newport News, Va 23606

V. Palmieri, Istituto Nazionale di Fisica Nucleare, Laboratori Nazionali di Legnaro, Italy

### Abstract

Superconducting niobium cavities for application in particle accelerators are usually fabricated by standard techniques such as forming of subcomponents by deep drawing and joining by electron beam welding. Even though these techniques are being used successfully in many larger-scale accelerator projects and improvements in accelerating gradients have been achieved over the last several years, there are often still problems with making defect-free electron beam welds. In addition, the manufacturing costs for such devices are significant and a drastic reduction in production costs is a necessary condition for future very large scale applications in, e.g., linear colliders.

Seamless cavities made by spinning from a single sheet of material will dramatically reduce the fabrication costs and eliminate any problems associated with electron beam welding.

The fabrication technique for seamless niobium cavities has been developed over the last few years at INFN LNL and several prototype single-cells of different material thickness and purity have been manufactured as well as a 5-cell cavity. Results from tests on these cavities after application of surface treatment techniques, such as buffered chemical polishing, "barrel polishing" and high temperature heat treatments, are discussed in this contribution. Q-values as high as  $10^{11}$  and accelerating gradients up to  $E_{acc} \approx 30$  MV/m have been measured.

### 1 INTRODUCTION

Superconducting radio-frequency (SRF) technology has been applied successfully in the last decade in several large-scale particle accelerator projects around the world such as TRISTAN, LEP, HERA and CEBAF. Future applications in B-factories, proton accelerators, linear colliders for electrons/positrons or muons and in higher-power free electron lasers are being pursued seriously in various laboratories. The reasons for this continued interest in SRF technology are elimination of limiting phenomena and application of improved processing and handling techniques resulting in better cavity performances. However, future projects, which involve

hundreds or thousands of meters of superconducting structure, demand a significant simplification of procedures to achieve even better performance than has been required for the presently operating accelerators. One of such simplifications could be a replacement of the typical cavity fabrication technique of electron-beam-welding precision-machined niobium parts into an accelerating cavity by the fabrication technique of seamless cavities. In the following sections we will describe the technical approach pursued for several years at INFN LNL and will report on the encouraging cavity performances achieved after various processing steps mainly performed at Jefferson Lab.

### 2 CAVITY FABRICATION

The idea of manufacturing seamless cavities is not new, because this technology offers several potential benefits:

- elimination of electron beam welds
- streamlining of Quality Assurance (QA) procedures
- significant reduction in manufacturing cost
- reduction of necessary infrastructure for mass production because of "speedy" manufacturing

Several attempts have been made in the past to form cavities without welding either by hydroforming [1,2] or by explosion forming. Hydroforming was only successful for copper as the base material and needed two intermediate annealing steps; it failed when niobium was used, mainly because of structural non-uniformity of the niobium tubes. Despite these earlier setbacks, groups at DESY [3] and at Saclay [4] are pursuing this technology—backed by computer modelling—with initial encouraging results. Both laboratories succeeded in bulging monocell resonators, and accelerating gradients around  $E_{acc} \approx 20$  MV/m were reached.

Initial tests on explosive formation of cavity shapes showed also discouraging results due to the inevitability of intermediate annealing steps. Therefore the work at INFN LNL concentrated on developing the well-known spinning technique for manufacturing of seamless niobium cavities.

The process developed at INFN LNL involves basically two steps: in the first step a tube is formed from a sheet of material either by spinning it onto a frustum-shaped mandrel of proper dimensions or, more recently, by deep drawing a tube with a diameter equal to the diameter of the cavity equator; in the second step the tube is then spun onto a demountable die of the true shape of the cavity, which is either made of precision machined nylon or

Supported jointly by the U.S. DOE under contract number DE-AC05-84ER40150 and by INFN Special Project on New Technology for Electron Acceleration

\*E-mail: kneisel@jlab.org

stainless steel. When the spinning process is completed—it takes typically one hour to spin a single-cell cavity and the better part of a day to spin a 5-cell cavity—the mandrel is extracted by collapsing the “keyed” elements of it. The main advantage of this process lies in the possibility of avoiding intermediate annealing and even multicell cavities can be cold formed straightforwardly from a planar disc. More details can be found in ref. [5-7].

Figure 1 is a snap shot of the incomplete cavity during the spinning. Figure 2 is a collection of single and 5-cell cavities tested during this investigation.

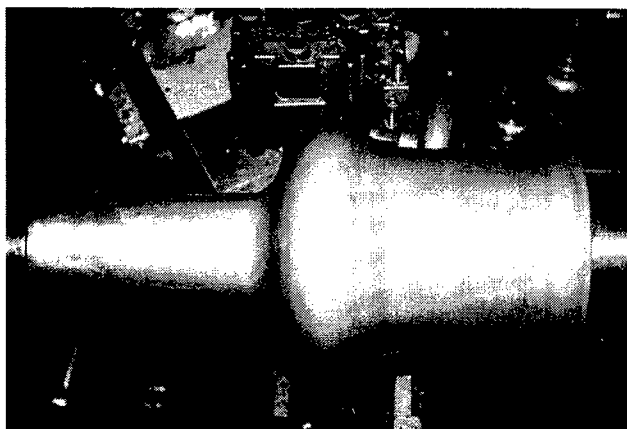


Figure 1: Spinning of a single-cell cavity, example Cu

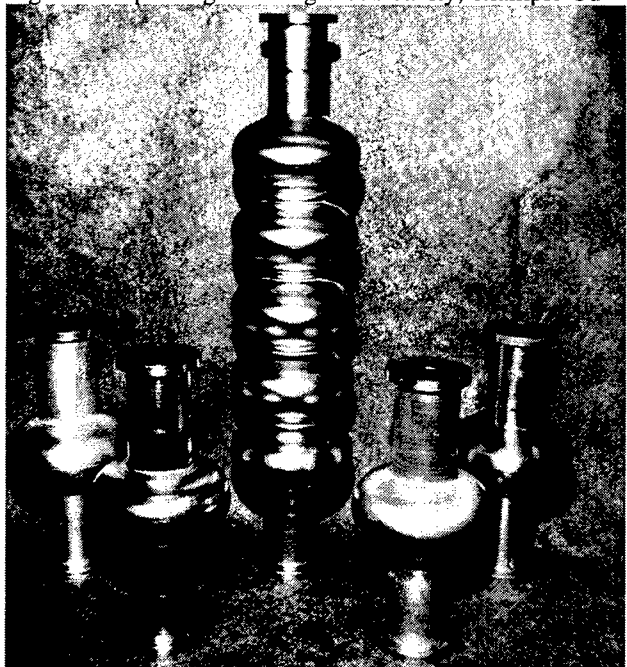


Figure 2: Selection of spun cavities used in this investigation

In total six single-cell cavities and one 5-cell cavity were tested during the course of this investigation. Cavities P1, P2, P5 and P6 were spun from high-purity niobium ( $RRR \geq 250$ ), whereas cavities P3 and P4 were made from reactor-grade niobium. The first 5-cell cavity P5-1 was again manufactured from high-purity niobium. Cavity P1 was originally fabricated for CERN and tested there. A few

tests were performed at Jefferson Lab afterwards after mechanical grinding.

### 3 RESULTS AND DISCUSSION

After the spinning was completed at INFN LNL, beam pipe sections and flanges were electron beam welded to the cavities at Jefferson Lab [8].

Subsequently, standard processing procedures such as buffered chemical polishing (bcp) followed by high pressure ultrapure water rinsing for up to 2 hrs and clean room assembly were applied. In the case of cavity P2, which was the first cavity sent to Jefferson Lab for investigation, a series of small subsequent material removal steps were carried out in order to study the effect of the removal of the surface damage layer on cavity performance as measured by the  $Q_0$  vs.  $E_{acc}$  at 2K. The results of these tests are shown in figure 3. As can be seen, a continuous improvement of  $E_{acc}$  is achieved by etching away more and more material from the surface, indicating that the spinning process introduces a rather deep damage layer in the material. The steep decrease of the Q-value beyond a certain field is not caused by the onset of field emission loading. This field is shifted towards higher values with deeper material removal. The additional resistance represented by this Q-degradation is, in most cases, proportional to  $E_{acc}^n$  with  $4 \leq n \leq 8$  and is not understood.

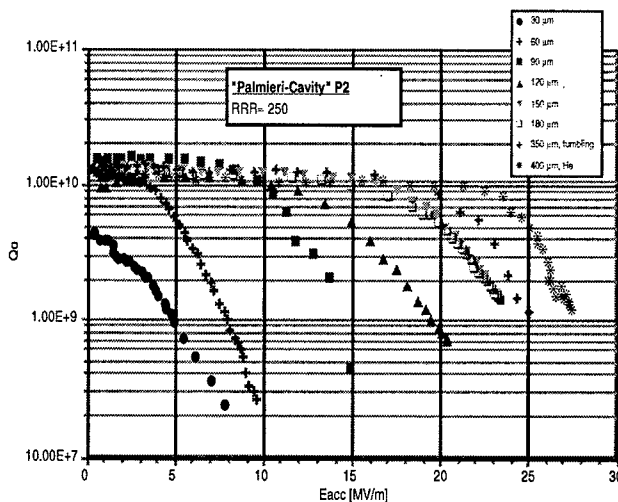


Figure 3: Dependence of cavity performance on removal of surface layer; data from single-cell cavity P2 (He = Helium processing)

In figure 4 the final performance of cavity P5 is plotted; the cavity “quenched” at  $E_{acc} \approx 33$  MV/m.

However we noted that the spinning process left a large amount of narrow cracks in the material at the irises near the beam pipes as shown in figure 5. Mechanical removal of these cracks by either grinding with an abrasive or by “barrel polishing” [BP] [9] seemed to significantly reduce the severe Q-drop at high fields.

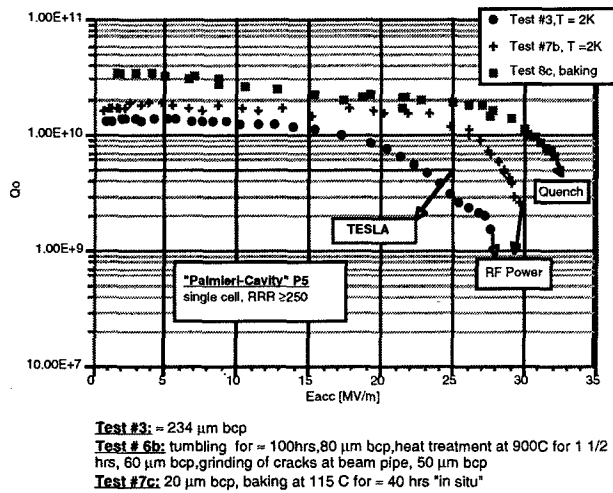


Figure 4: Best Performance of Cavity P5

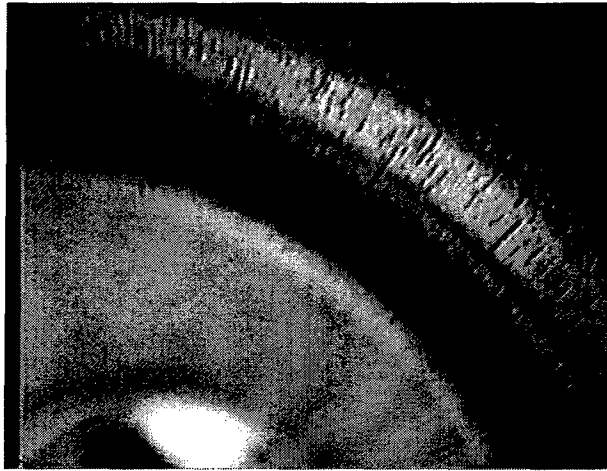


Figure 5: Cracks in the niobium located at the beam pipe iris.

The best performances of all the tested cavities are listed in Table 1; in several cases a heat treatment was applied either for hydrogen degassing and stress relieving purposes ( $T \approx 800\text{--}900\text{ C}$ ) or for post-purification in order to increase the thermal conductivity ( $T \geq 1200\text{ C}$ ) of the material. No major improvements beyond the effect of material removal were seen, however. In several cases also surprisingly low residual resistances in the order of 2 - 3  $\text{n}\Omega$  were measured corresponding to Q-values  $\geq 10^{11}$ . The 5-cell cavity P5-1 initially was limited by a quench at  $E_{\text{acc}} \approx 11.5\text{ MV/m}$  in the  $\pi$ -mode and from measurement of the other pass-band modes it was concluded that the defect most likely was located in one of the end-cells. By analyzing the results of the measurements of the other pass-band modes it also became clear that the three inner cells of the 5-cell cavity were performing much better than the end-cells; the center cell quenched at about 25 MV/m and the two neighboring cells sustained at least a field of 17 MV/m. An attempt to improve the cavity performance by mechanical grinding of the end-cells has not been successful yet and further work is needed.

Table 1: Best Results Achieved with the Seamless Cavities (RG = reactor grade, RRR= high purity, HT=heating, BP= barrel polishing)

CAV	Nb	$Q_{\text{res}}$ [ $10^{10}$ ]	$E_{\text{acc}}$ [MV/m]	Comments
P1	RRR	0.3	25	40 $\mu\text{m}$ grinding, insufficient bcp
P2	RRR	>9	28	400 $\mu\text{m}$ bcp, BP, HT $\approx$ 1200 C
P3	RG	>10	16.5	200 $\mu\text{m}$ bcp, BP HT $\approx$ 1300 C, 100 $\mu\text{m}$ bcp
P4	RG	>10	15	BP, 100 $\mu\text{m}$ bcp HT $\approx$ 1200 C 250 $\mu\text{m}$ bcp
P5	RRR	>10	33	230 $\mu\text{m}$ bcp, BP HT $\approx$ 900 C 280 $\mu\text{m}$ bcp
P6	RRR			low Q, needs work
P5-1	RRR	>7	11.5	120 $\mu\text{m}$ bcp end cells need work

## 4 SUMMARY

This investigation has shown that the fabrication of seamless cavities with its potential benefits of lower cost at high performance levels is feasible. Future work has to concentrate on eliminating some of the observed drawbacks such as the cracks in the material, the rather large amount of material removal necessary for good performance, non-uniformity in material thickness, and, for multi-cell cavities, the need for a stringent control of tolerances to maintain good electric field flatness. Cavity P6 was manufactured from a deep drawn tube and a significant reduction in material defects and much improved material uniformity were observed. This seems to be the right direction for future work. In addition it seems quite prudent that the skillful manual spinning process so far applied for the fabrication of these cavities needs to be transferred to mass production equipment.

## 5 REFERENCES

- [1] C. Hauviller, Proc. 1989 IEEE Part. Acc. Conf, p.484, Chicago (1989)
- [2] J. Kirchgessner, Proc. 3rd Workshop on RF Superconductivity, Report ANL-PHY-88-1, p. 533ff, Argonne (1988)
- [3] W. Singer et al.; private communication
- [4] C. Antoine; private communication
- [5] V. Palmieri; invited talk this conference
- [6] V. Palmieri et al.; Nucl. Instr. & Meth. A342(1994), 353-356
- [7] V. Palmieri et al.; Proc. 6th Workshop on RF Superconductivity, CEBAF(1993), p. 857ff, Newport News, VA
- [8] EBW done by J. Brawley, Jefferson Lab
- [9] T. Higuchi, K. Saito et al.; Proc. 7th Workshop on RF Superconductivity, p.723ff, Saclay (1995)

# THE LHC SUPERCONDUCTING CAVITIES

D. Boussard\*, E. Chiaveri, E. Haebe, H.P. Kindermann,  
R. Losito, S. Marque, V. Rödel and M. Stirbet†, CERN, Geneva, Switzerland

## Abstract

The LHC RF system, which must handle high intensity (0.5 A d.c.) beams, makes use of superconducting single-cell cavities, best suited to minimizing the effects of periodic transient beam loading. There will be eight cavities per beam, each capable of delivering 2 MV (5 MV/m accelerating field) at 400 MHz. The cavities themselves are now being manufactured by industry, using niobium-on-copper technology which gives full satisfaction at LEP. A cavity unit includes a helium tank (4.5 K operating temperature) built around a cavity cell, RF and HOM couplers and a mechanical tuner, all housed in a modular cryostat. Four-unit modules are ultimately foreseen for the LHC (two per beam), while at present a prototype version with two complete units is being extensively tested. In addition to a detailed description of the cavity and its ancillary equipment, the first test results of the prototype will be reported.

## 1 INTRODUCTION

Cavities having a large stored energy (low  $R/Q$ , high voltage) are best suited for the LHC to minimize the effects of transient beam loading due to the long gaps (up to 3  $\mu$ s) in the high intensity (0.56 A) proton beams [1]. This leads naturally to single-cell superconducting (SC) cavities with large beam tubes very similar to those designed for the high current  $e^+e^-$  factories. There will be eight 400 MHz cavities per beam, grouped by four in each of two cryomodules. Each cavity is connected inside a cryomodule to its neighbours by large diameter ( $\varnothing = 300$  mm) beam tubes and (unshielded) bellows. The operating voltage of the cavities (2 MV during storage, i.e. 5 MV/m) is quite low by to-day's standards, but gives ample margin to boost the LHC RF voltage and reduce bunch length in the future, if necessary.

A variable coupler will equip the LHC cavities in order to give maximum flexibility for the various modes of operation of the cavities during injection, ramping and storage. The cryomodules are located on either side of a long straight section (point 4) where the distance between the two beams has been increased from 195 mm to 420 mm. Additional room-temperature 200 MHz cavities will be installed in the LHC for optimum capture of beams having a large emittance ( $\sim 1$  eV.s).

## 2 CAVITY MANUFACTURE

The cavity technology is similar to that used successfully on a large scale for LEP2 [2]; it is based on niobium film on copper cavities operating at 4.5 K and on a modular cryostat with easy lateral access. Bare cavities are produced by spinning and electron-beam welding and are coated with a thin (1 to 2  $\mu$ m) thickness) film of niobium by magnetron sputtering. The series production of 21 bare cavities is now being carried out by industry; seven cavities have already been accepted at CERN. Their typical performance is displayed in Figure 1 together with the acceptance curve. The copper wall thickness results from a compromise between tuning force and mechanical stability against buckling. With a thickness of 2.8 to 3 mm, the cavity axial spring constant is about 20 kN/mm.

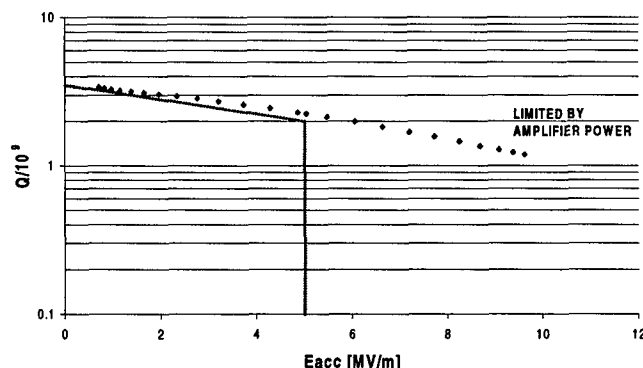


Figure 1: Typical cavity performance and acceptance curve

The helium tank of each cavity is made of 2 mm thick stainless steel. Its cross-section is cylindrical around the cavity cell and octagonal at the location of the ports. The four helium tanks within a cryomodule are interconnected at the liquid and gas levels in such a way that a common helium feed and a common gas return are sufficient (Figure 2). Individual safety exhaust pipes with rupture disks are, however, provided for each cavity. As in LEP, each cavity cradle is suspended inside the cryostat to allow for contraction during cooldown. The longitudinal fixed point corresponds to the main coupler position to avoid stresses on the double-walled tube. Neither a magnetic shield nor a heat shield is necessary. The measured static losses of the prototype cryomodule (having only two cavities, no couplers and no second beam tube) amount to about 25 W.

\* Daniel.Boussard@cern.ch

† On leave from Institute of Atomic Physics, Bucharest, Romania

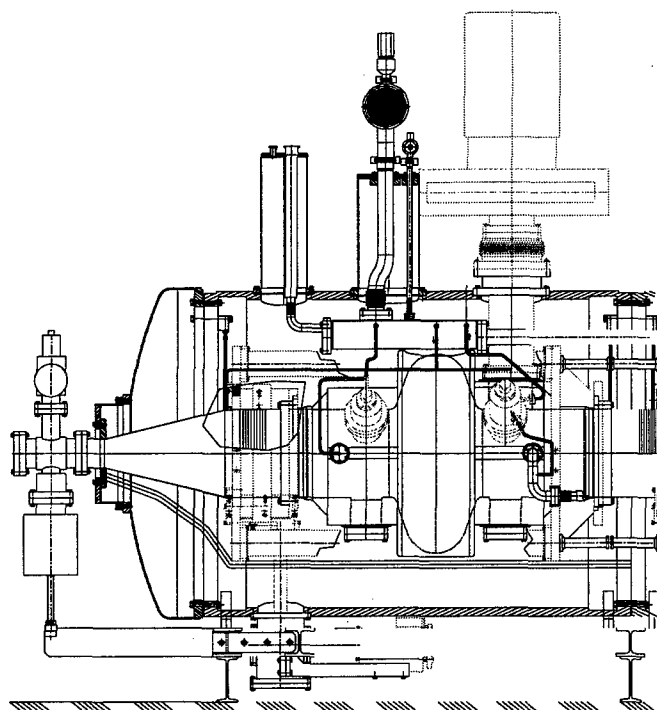


Figure 2: Partial view of the prototype cryomodule with two cavities (a series cryomodule has four cavities)

A modular construction was adopted for the vacuum tanks of the cryomodule (Figure 2). Each tank is a stainless steel cylinder, without any welds, with large lateral openings to permit easy access to the cavity. The four cavities are connected together with the wide bellows in a clean room; this assembly is then rolled inside the complete vacuum tank. The main couplers are mounted last, again in a clean room. It is also possible to disassemble and reinstall a single cavity in the middle of a cryomodule, without moving its neighbours. The second beam tube (cold) is attached to the side of the cavity cradle.

### 3 TUNER

Contrary to the case of LEP cavities [2], the LHC cavity tuner is purely mechanical in order to provide the large tuning range at full speed required to compensate beam loading. The cavity cradle, with its two thick end plates joined by four columns forms a rigid assembly, free of harmful resonances, which can take the strong tuning forces ( $\sim 20$  kN) without excessive deformation. The cavity end plate and the cradle end plate are pulled together via thin (0.75 mm) stainless-steel blades and torsion shafts with long lever arms (Figure 3). This arrangement provides a lever action (ratio 14:1) without sliding parts or backlash. The internal stresses (290 Mpa) inside the blades stay below the elastic limit. The axial force and movement at the extremities of the two lever arms, inside the cold cradle, are transferred to the outside via two thin-

walled stainless-steel cylinders acting as counter-rotating torsion shafts. The latter are driven by stainless steel cables ( $\varnothing = 3$  mm) providing again a transmission without friction or backlash.

Furthermore, this system allows displacement of the cradle during cooldown and provides a low heat conductance. A slightly different version of this tuner

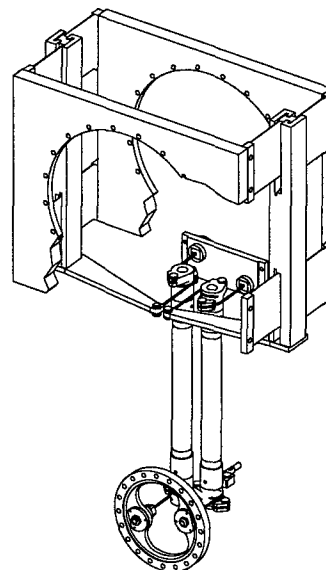


Figure 3: Tuner mechanism

was successfully tested on the prototype cryomodule; the achieved tuning range and speed (limited by the stepping motor) were 180 kHz and 9 kHz/s respectively. The resolution is too small to be measurable.

### 4 POWER COUPLER

The LHC variable coupler is an upgraded version of the LEP2 fixed coupler [2][3] (Figure 4). An open-ended  $75 \Omega$  coaxial line is coupling to the cavity. The outer conductor (not represented in Figure 4) is made of copper-plated stainless-steel (double-walled) and cooled with 4.5 K helium gas, while the inner conductor (antenna) is a copper tube cooled by forced air. A cylindrical ceramic window, with massive copper rings brazed on its edges is placed in the waveguide-to-coaxial transformer. A reduced height waveguide provides directly the matching to the coaxial line, avoiding the usual "doorknob". In order to suppress multipactor during operation, a d.c. bias of 3 kV is applied to the antenna, isolated from ground with a coaxial capacitor mounted in the waveguide. Air cooling is provided on the window and other critical elements of the coupler. A vacuum gauge and an electron pick-up antenna are located close to the window.

The antenna is moved (60 mm stroke) by making use of bellows about  $\lambda/4$  long. A low impedance ( $7\Omega$ )  $\lambda/4$  line transformer brings the current in the bellows to low enough values, not requiring copper plating of this stainless steel part. The displacement of the antenna is guided by a (motor driven) high precision device.

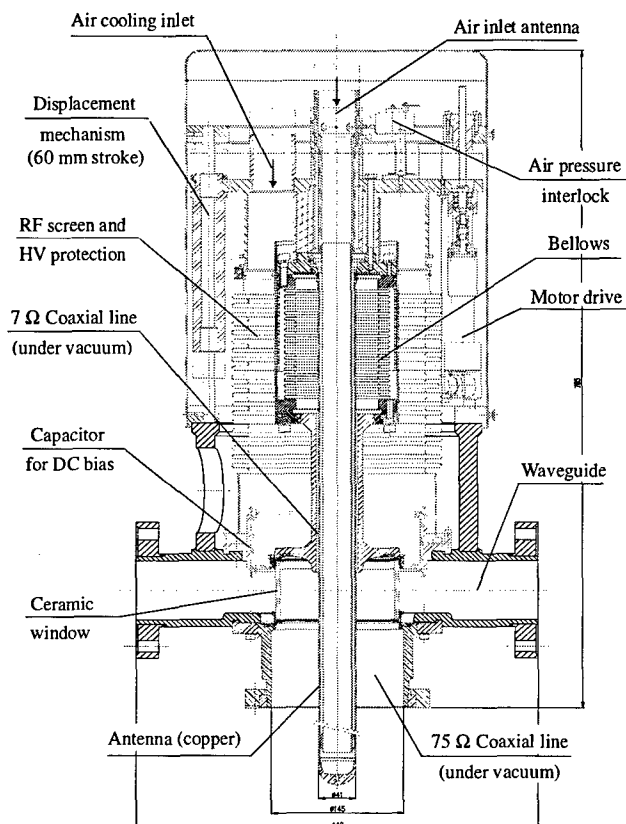


Figure 4: The LHC variable coupler

Two prototype LHC couplers have been manufactured, assembled and vacuum-tested. Technical problems occurred during electron-beam welding of the ceramic window to the copper body and during titanium coating of the vacuum side of the ceramic, resulting in the breaking of some ceramic windows. Solutions to avoid these failures have been found. We also suffered from the bad quality of the OFE copper material used for the copper body, which developed vacuum leaks after baking out at 200°C for 24 h. In the future forged OFE copper will be used.

High-power RF tests at room temperature were done with two couplers, mounted horizontally on a 400 MHz copper test cavity. One coupler is connected to a 500 kW 400 MHz klystron [4], via a circulator, the second to either a 1 MW load or to a mobile short circuit. In travelling-wave mode, and with a pressure limit of  $2 \times 10^{-7}$  mbar, the RF power could be ramped between 15 and 500 kW, crossing several multipactor levels, for which d.c. bias was effective. Below 15 kW multipactor occurred inside the  $7\Omega$   $\lambda/4$  line, with no electrons picked up on the antenna and no influence of

d.c. bias. (An additional bias on the  $\lambda/4$  line is being considered.) The maximum power could be sustained for long periods (400 kW for 150 hours, 500 kW for 50 hours) with no sign of damage inside the coupler.

At full reflection, any phase and any coupling the coupler sustains a 500 kW forward power (2 MW equivalent power) provided it is pulsed (50 ms on, duty cycle 10%) to avoid local overheating.

## 5 HOM COUPLERS

During the design of the LHC cavity its higher order mode (HOM) characteristics were carefully studied [5]. Due to the large iris diameter and a cell length smaller than  $\lambda/2$ , only two of the HOMs do not propagate into the intercell beam tubes. These are the two dipole modes  $TE_{111}$  and  $TM_{110}$  which also have the highest coupling impedance of all transverse modes. Clearly for damping them beam tube couplers near the cells are needed. These are of a doubly resonant type and tuned to provide equal shunt impedances  $(R/Q) \cdot Q$  of about 1.5 k $\Omega$  for the two modes with one coupler mounted for each polarization.

In addition two broadband couplers are installed per cell. Derived from LEP design they can each carry a HOM power of 800 W. They have response peaks near the frequencies of the high  $(R/Q)$  mode  $TM_{011}$  (770 MHz) and the trapped mode [5]  $TM_{012}$  (1240 MHz) respectively. On a model cavity external  $Q$ s of 500 have been measured for these modes ensuring that even if mode excitation by the LHC beam is resonant the RF power coupled out will not exceed 500 W.

## 6 ACKNOWLEDGEMENTS

The authors wish to thank the many persons who contributed efficiently to the design, construction and tests of the LHC cavities and their ancillary equipment.

## 7 REFERENCES

- [1] "The Large Hadron Collider — Conceptual Design", CERN/AC/95-05 LHC
- [2] LEP Design Report, Vol. III, LEP2, CERN/AC/96-01 (LEP2)
- [3] H.P. Kindermann, E. Haebe, M. Stirbet, V. Vescherevitch, "Status of RF Couplers for SC Cavities at CERN", EPAC, Sitges 1996
- [4] H. Frischholz, W.R. Fowkes, C. Pearson, "Design and Construction of a 500 kW CW, 400 MHz Klystron to be used as RF Power Source for LHC/RF Component Tests", PAC, Vancouver 1997.
- [5] E. Haebe, V. Rödel, F. Gerick, Z.T. Zhao, "The Higher-Order Mode Dampers of the 400 MHz SC LHC Cavities", CERN-SL-98-008 RF



## TECHNICAL DEVELOPMENTS ON REDUCED- $\beta$ SUPERCONDUCTING CAVITIES AT CERN

O. Aberle, D. Boussard, S. Calatroni, E. Chiaveri, E. Haebel, R. Hanni, R. Losito, S. Marque, J. Tückmantel, CERN, 1211 Geneva 23, Switzerland

### Abstract

Several authors proposed the construction of superconducting proton linacs using the LEP2 cavities once LEP will be decommissioned. However only a fraction (about half) of these cavities can be used as they are for the high-energy part ( $\beta \sim 1$ ) of such a linac, the low energy part requiring the development of accelerating structures optimized for lower values of the particle velocity.

At CERN an R&D programme on reduced- $\beta$  single-cell cavities started in 1996 in order to study and explore the limits of the technology successfully used for the production of LEP2 cavities (copper cavities niobium-plated using the magnetron sputtering technique). Four different geometries were extensively investigated, each representing part of a multicell structure optimized for particles having  $\beta=0.48$ ,  $\beta=0.625$ ,  $\beta=0.66$  and  $\beta=0.8$  respectively. The results were encouraging for the last two types and therefore a new phase of R&D aimed at the production of multicell cavities for  $\beta=0.66$  and  $\beta=0.8$  was started. The goal is to demonstrate simultaneously the feasibility of such cavities and the possibility of producing them by low-cost modification of LEP cavities.

In the paper, after a brief review of the results obtained on the single-cell cavities, we shall present in more detail the procedure for the transformation of the LEP cavities, which should allow a realistic estimate of the costs of such operation.

### 1 INTRODUCTION

In 1996 an R&D programme has been launched at CERN to study the feasibility of reduced-beta niobium/copper superconducting cavities. The motivation of this work resides in the various proposals for high-intensity proton linacs to be used for different purposes (e.g. for the drive beam of an energy amplifier, transmutation of radioactive waste, for neutron and muon sources, for FEL applications etc.) [1-3]. The 352 MHz superconducting RF system successfully working in LEP has been considered for a reconversion, after LEP decommissioning in year 2000, into the medium  $\beta$  ( $0.5 \div 0.8$ ) and high  $\beta$  ( $\sim 1$ ) part of some of these linacs. One reason for that is of course economical, but there are also other important points in favor of this option:

- the reliability of the system has already been demonstrated during operation in LEP, where only about 10% of the downtime was due to faults of the RF system.
- the large aperture of the irises (over 200 mm), which is made possible by the choice of the frequency of operation (352 MHz), should prevent the activation of the cavities by the beam halo.

Each LEP "module" is made up of 4 cavities and delivers in average 40 MV to the beam (hopefully 47 MV in 2000). Considering the variation of the transit time factor from cavity to cavity due to the acceleration along a linac, a superconducting machine going from  $\sim 240$  MeV up to  $\sim 2$  GeV would need between 50 and 80 of such modules, with several stages optimized for growing betas. LEP cavities, which are designed for  $\beta=1$ , have a reasonable efficiency (R/Q) only starting from  $\sim 1$  GeV,  $\beta \sim 0.9$  (which corresponds anyway to a half of the linac).

Our research has shown that for values of  $\beta$  ranging from 0.66 up to 0.8 the reconversion of LEP cavities into reduced  $\beta$  niobium/copper cavities is feasible, and can be very interesting from the economical point of view. For lower values of  $\beta$  (0.48, 0.625) on the contrary the RF performances of the cavities produced with the niobium/copper technology are not so satisfactory, so the interest of modifying LEP cavities into  $\beta \sim 0.5$  cavities is low.

We will present in detail the results of the RF measurements and the procedure we used to transform one 4-cell existing LEP cavity into a 5-cell  $\beta=0.8$  cavity fully equipped, and the real costs of such an operation.

### 2 RESULTS OF SINGLE-CELL CAVITIES

Since August 1996 four different types of single-cell copper cavities niobium-plated using the magnetron sputtering technique were produced at CERN:  $\beta=0.48$ ,  $\beta=0.625$ ,  $\beta=0.66$  and  $\beta=0.8$ . The best performances obtained for each type are shown in fig. 1 and 2. A typical performance of a LEP cavity is shown as well in fig. 1.

The Q(Eacc) curve for the  $\beta=0.8$  cavity fits the expectations (calculated by scaling with the geometry factor the analogous LEP cavity curve). For the others the results are lower than the scaling, showing a degradation of the niobium film quality. This is probably due to the low impact angle of the niobium atoms on the surface of the cavity during the sputtering process for these

geometries (for more details see [4]). In spite of that, we believe that it is reasonable to use at least the  $\beta=0.66$  cavity if one limits the average accelerating field to 3 MV/m.

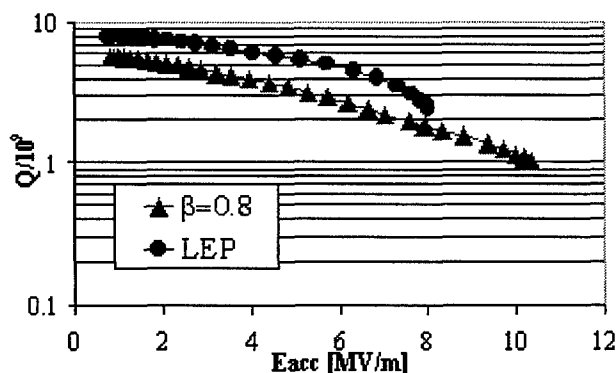


Figure 1: Results for a 4-cell LEP cavity and a single-cell  $\beta=0.8$  cavity (all limited by amplifier power)

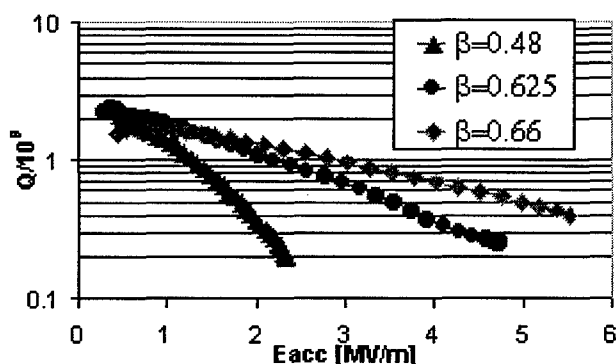


Figure 2: Results for  $\beta=0.48$ ,  $\beta=0.625$ ,  $\beta=0.66$  single-cell cavities (all limited by amplifier power)

### 3 THE 5-CELL $\beta=0.8$ CAVITY.

The length of a cell is related to the  $\beta$  for which it is optimized. Since  $5 \times 0.8 \times \lambda/2 = 4 \times 1 \times \lambda/2$ , a 5-cell  $\beta=0.8$  will have exactly the same length than a 4-cell  $\beta=1$ .

This consideration is the basis for a low cost transformation of a LEP cavity. In fact as the lengths are the same, we can re-use almost all the ancillary equipment:

- the thermal tuners, which provide coarse tuning and have a range of at least  $\pm 25$  KHz;
- the magnetostrictive tuners, which provide fine and fast tuning and have a range of  $\pm 1$  KHz;
- the two "cut-offs", which are the part of the cavity connecting the two end cells to the beam pipe (see fig. 4). These are the most expensive mechanical parts of the whole copper cavity, because all the flanges for the different couplers have to be welded on them;
- some parts of liquid helium circuit;

- the vacuum tank, which provides the thermal insulation between the helium tank and the atmosphere at 300K;
- the main coupler and the Higher Order Modes (HOM) couplers, after some minor modifications to adjust the coupling factors.

In practice we need to build only the 5 copper cells and the helium tank.

The necessary steps for the transformation are the following:

- dismantling the cavity from its vacuum tank ;
- chemical etching of the niobium layer on the whole cavity, to clean the cut-offs;
- cutting the helium tank and the copper cavity at the cut-off level;
- production of the new copper cells;
- welding of the cells to the old cut-offs;
- coating a new niobium layer;
- welding the new Helium tank;
- remounting the cavity in the old vacuum tank.

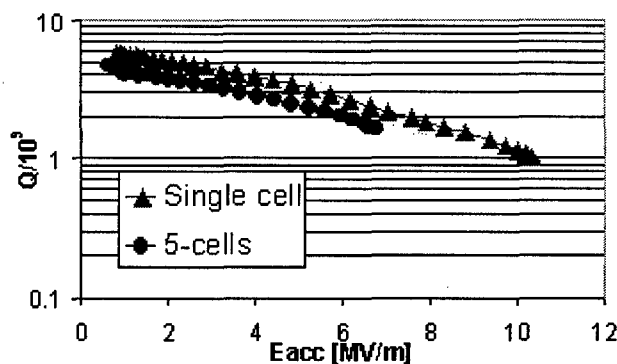


Figure 3: Comparison of the results for the single-cell and the 5-cell  $\beta=0.8$  (all limited by amplifier power).

We performed all these steps on an old LEP spare cavity. The cut-offs were laser-cut from the stainless steel He tank, to insure a good surface quality for the subsequent welding. The 4 cells were separated by plasma cutting. We built a helium tank much simpler (and cheaper) than the LEP one which should result in a slightly bigger consumption of liquid He. All the other operations are quite standard.

We measured the bare reconstructed cavity (without He tank) and the result is reported in fig. 3. It is interesting to note that the degradation of the performance from the single-cell to the 5-cell cavity is less than 25%. We are limited only by the power of the amplifier.

Some photos of the transformation process are shown in fig. 4-5. We are presently mounting the cavity into the vacuum tank and we will measure it before summer '99.

The cost of the whole operation amounts to approximately 20% of the price of one new LEP cavity.



Figure 4: Laser cutting the He tank at the good dimension. The cutoff is visible inside the tank.

#### 4 FUTURE DEVELOPMENTS.

Since  $6 \times 0.66 \times \lambda/2 = 4 \times 1 \times \lambda/2$  one can envisage a low cost modification of a LEP cavity into a  $\beta=0.66$  6-cell cavity. We showed that for a single-cell this geometry gives acceptable performances up to 3 MV/m, but the scaling of this performance to 6-cell should be demonstrated by an experiment that will be done only if a real interest in that will arise. Some measurements would also be necessary on the main couplers and HOM couplers to determine the modifications needed to get the good coupling factors.

#### 5 A TENTATIVE SCHEME FOR A LINAC.

A possible solution for a superconducting proton linac using the cavities described above (to be confirmed by beam dynamics simulations) could consist of three sections,  $\beta=0.66$ ,  $\beta=0.8$ ,  $\beta=1$ . The injection energy could be around 240 MeV ( $\beta \sim 0.6$ ). To reach 2 GeV one would need around 56 6-cell cavities  $\beta=0.66$ , 78 5-cell cavities  $\beta=0.8$  and 140 LEP cavities. The price to be paid for the cavities (including main and HOM couplers and the cold tests) of such a linac would be less than 10% of the price paid for the LEP energy upgrade.

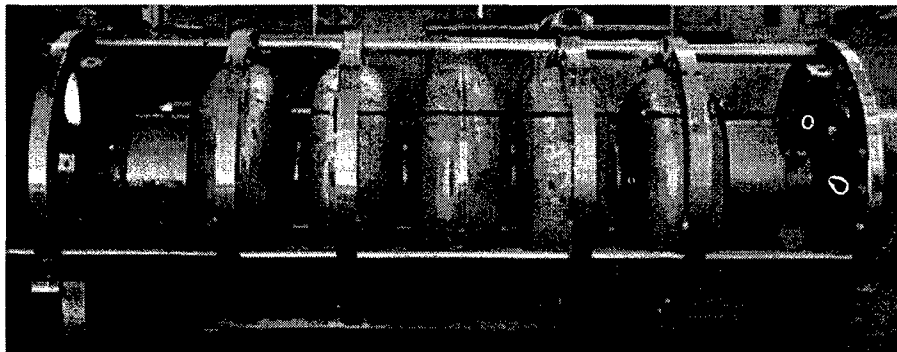


Figure 5: The 5-cell cavity ready to be electron beam welded on the cut-offs using an internal gun.

#### 6 CONCLUSIONS

We have shown the results of the measurements of single and multi-cell reduced-beta cavities produced at CERN with the niobium sputtered on copper technology used for LEP2 cavities.

We believe that the minimum value of  $\beta$  for which one can obtain reasonable performances for this kind of cavities is around  $\beta=0.66$ . Because of simple geometrical considerations,  $\beta=0.8$  and  $\beta=0.66$  multi-cell cavities can fit a vacuum tank of a LEP  $\beta=1$  cavity, leading to a low cost recycling of the LEP2 RF accelerating system.

We built a 5-cell  $\beta=0.8$  cavity by modifying a LEP cavity at  $\sim 20\%$  of the cost of a new LEP cavity. This estimate includes: cavity and ancillary equipment modification, manpower cost and low temperature tests.

About the same price would be spent to modify a LEP cavity into a 6-cell  $\beta=0.66$  cavity.

A linac using  $\beta=0.66$ ,  $\beta=0.8$  and  $\beta=1$  cavities could accelerate particles from 240 MeV up to 2 GeV.

#### 7 ACKNOWLEDGEMENTS

We are indebted to all of our technicians, without their work this development would not have been possible. We are grateful as well to our colleagues of EST/SM group for chemical treatment and in particular H. Neupert for niobium coating.

#### REFERENCES

- [1] D. Boussard et alii, "Preliminary parameters of a Proton Linac using the LEP 2 RF System when decommissioned", CERN/SL-RF Technical Note 96-04.
- [2] C. Rubbia, J.A. Rubio, "A tentative programme towards a full scale energy amplifier", CERN/LHC 96-11.
- [3] R. Garoby, M. Vretenar, "Proposal for a 2 GeV Linac Injector for the CERN PS", PS/RF/Note 96-27.
- [4] C. Pagani et alii, "A high Current Linac with 352 MHz SC Cavities", Proceedings of the 1996 Linac Conference.
- [5] R. Losito, "Design of a  $\beta=0.66$  monocell cavity", CERN SL-Note-98-008 (RF).

# STATUS OF THE NIOBIUM RESONATOR CONSTRUCTION PROJECT FOR THE NEW DELHI BOOSTER LINAC

P.N.Potukuchi\* and S.Ghosh\*

Nuclear Science Centre, Aruna Asaf Ali Marg, New Delhi 110067, India

and

K.W.Shepard

Physics Division, Argonne National Laboratory, 9700 S. Cass Ave, Argonne, IL 60439, USA

## Abstract

This paper reports the construction of niobium superconducting quarter wave resonant cavities for a booster linac for the 15 UD Pelletron accelerator at the Nuclear Science Centre. The resonators have been developed, and are being constructed, in collaboration with Argonne National Laboratory. Construction of the first batch of ten resonators started in May '97 and is expected to be completed by June '99. The incremental cost is expected to be about \$36K per cavity. Status and details of construction, and results of the first cold test are presented.

## 1. INTRODUCTION

A superconducting linear accelerator booster for the existing 15 UD tandem Pelletron accelerator [1], at the Nuclear Science Centre, is presently being constructed in collaboration with Argonne National Laboratory (ANL). A prototype quarter wave resonator (QWR) was designed, fabricated and tested successfully at ANL [2]. The linac will eventually consist of three cryostat modules each containing eight QWRs [3]. A total of twenty seven cavities, including one for the superbuncher and two for the rebuncher, will be needed for the linac. Construction of the first batch of ten resonators is presently nearing completion at ANL [4].

Figure 1 shows a schematic diagram of the 97 MHz quarter wave resonator optimised for a particle velocity  $\beta$  ( $=v/c$ ) = 0.08. Details of the cavity design have been presented elsewhere [5].

## 2. PRODUCTION DETAILS

The entire production is being carried out with commercial vendors in USA and India [6,7,8], unlike the prototype development project which was done in-house at ANL. Before the production started the technology of fabricating niobium resonators was transferred to the vendors. Considerable time and effort went into training vendors to perform the machining and sheet metal work

on niobium. Similarly, a major effort went into developing electron beam welding parameters for welding different thickness of niobium [9]. The electron beam welder is a five-axis CNC machine with movable gun and tilt, and a large vacuum chamber. The machine is equipped with a three head stock rotary fixture with matching tail stocks. To increase productivity, the entire weld fixturing was designed to perform multiple welds in a single pump down.

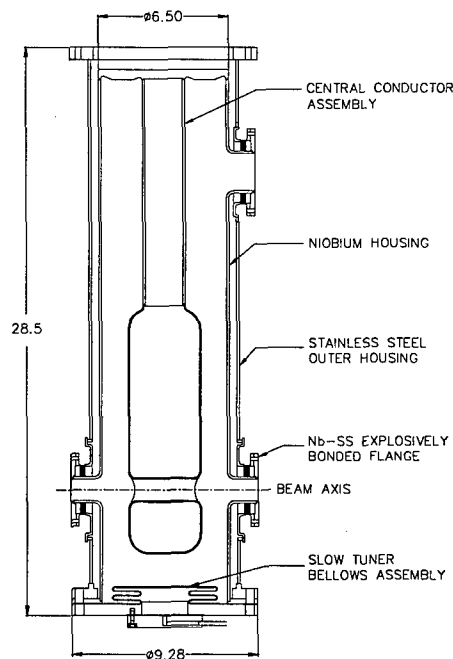


Figure 1: Schematic diagram of the 97 MHz quarter wave coaxial-line cavity. Dimensions are in inches.

The contract for the first batch of production calls for fabricating ten resonators. Because of higher productivity from the electron beam welder, than anticipated, we will produce twelve complete resonators and most of the parts for two more. The entire fabrication effort has been done in several major groups of tasks [4].

\* Currently at the Physics Division, Argonne National Laboratory, 9700 S. Cass Ave, Argonne, IL 60439, USA

### 3. PRESENT STATUS

At the time of writing this paper all the major sub-assemblies of the resonators, except the slow tuner bellows, have been fabricated. This represents about 85% of the total machining & sheet metal work, and about 66% of the total electron beam welding work for the project. Figures 2 and 3 show the bare niobium housings and the central conductor assemblies respectively.

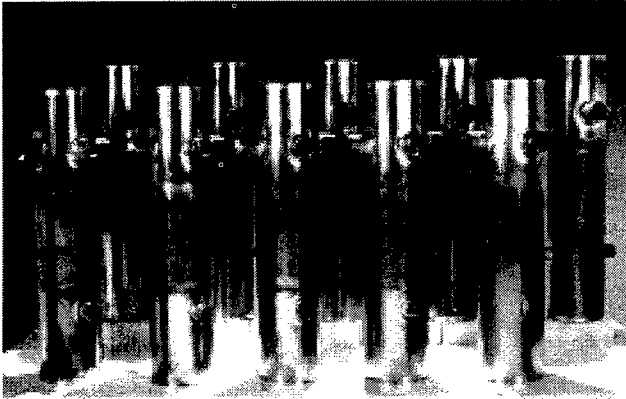


Figure 2: Niobium housings with the beam & coupling ports.

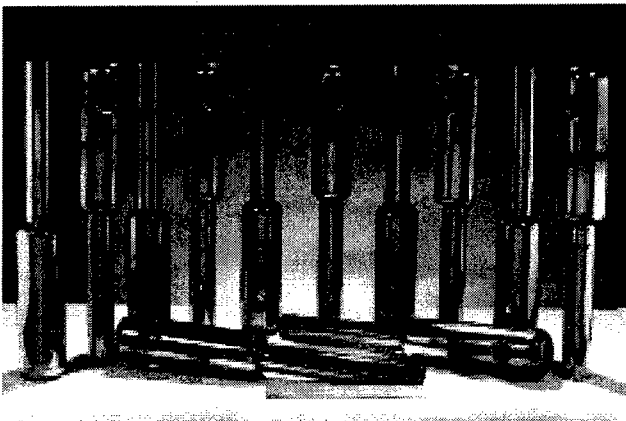


Figure 3: Niobium central conductor assemblies.

We have completed fabricating two resonators, which are being tested. Figure 4 shows the first two resonators complete with the stainless steel jackets. The remainder are 70% complete, they have been tuned to frequency and the central conductor assemblies are being prepared for welding to the top flange. The slow tuner fabrication work will start shortly.

### 4. COLD TEST RESULTS

The first resonator was recently tested (without the slow tuner bellows) at 4.5 K and performed as shown in figure 5. The minimum performance goal of 3 MV/m with 4 watts of rf input power has been exceeded. The magnetic

shielding in the test cryostat has been found to be inadequate, and the higher rf losses in the cavity are thought to be from trapped magnetic flux from earth's magnetic field. Magnetic shielding is now being put around the test cryostat.

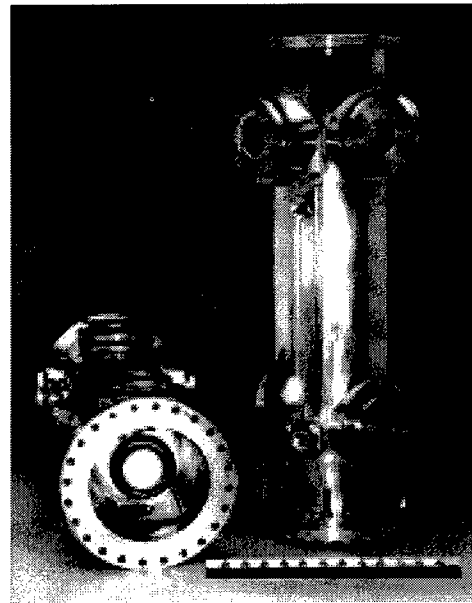


Figure 4: First two resonators complete with the stainless steel outer housings.

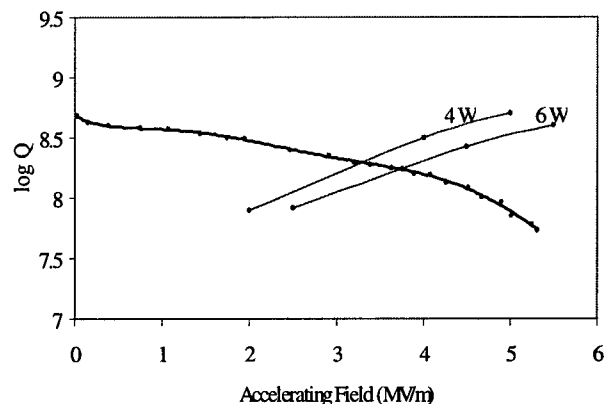


Figure 5: Resonator Q as a function of accelerating gradient at 4.5 K

### 5. COSTS AND EFFORT

Figure 6 shows the niobium material, fabrication and electron beam welding cost for the project. Several points should be noted:

- We are building twelve complete resonators and most of the parts for two more. We consider the effort to be equivalent to building thirteen resonators.
- The costs indicated represent the incremental costs and do not include the cost of the tooling. Most of the tooling made during the prototype resonator

development project has been used. However, additional tooling was made as felt needed.

- c) The fabrication cost indicates the machining and sheet metal work on the niobium parts of the resonators. In addition to this cost, approximately 750 hours of effort was involved in fabricating the stainless steel parts at the vendor in reference 8.
- d) The cost of fabrication is about \$60/hr, and the cost of electron beam welding is \$200/hr.

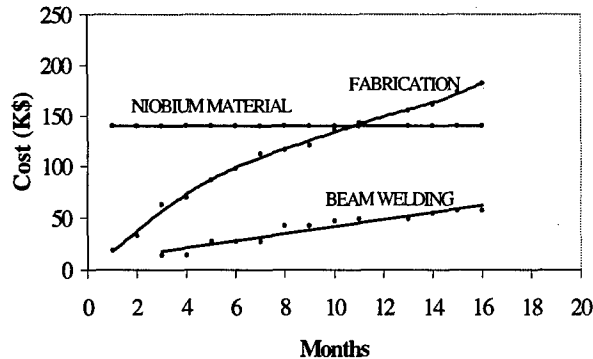


Figure 6: Production costs as a function of time. The entire work is expected to be completed before the end of the twentieth month.

- e) The electropolishing and heat treatment of the niobium parts is being performed in-house at ANL. The resonator tests are also performed at ANL.

## 6. CONCLUSIONS

Production of the first batch of resonators for the New Delhi linac is nearing completion. Major sub-assemblies of all the resonators have been fabricated and the entire production work is expected to be completed by June '99. Two cavities have been completed initially and the first resonator has performed above the nominal design goal. The incremental projected cost will be \$36K per cavity.

## ACKNOWLEDGEMENTS

The authors would like to thank Mr. Radwan Mourad and Mr. Tadeusz Hejna of Sciaky Inc., Mr. Edward Bonnema and Mr. Lester Dudek of Meyer Tool & Mfg., Inc., and the staff of Don Bosco Technical Institute, for their help during this work. The authors would like to thank Mr. Mark Kedzie for his help and suggestions during the electron beam welding of the resonator parts. Thanks are due to Mr. Rajeev Mehta and Dr. Amit Roy for getting the stainless steel work, and the transition flange machining, done at New Delhi. The authors acknowledge the continuing support of Prof. G.K.Mehta, Dr. Jerry Nolen and Dr. Walter Henning during the project.

This work is performed at Argonne National Laboratory, and is funded by the Nuclear Science Centre, New Delhi by the University Grants Commission of the Government of India.

## REFERENCES

- [1] D.Kanjilal et al., Nucl. Instr. and Meth. **A328** (1993), p97
- [2] K.W.Shepard, A.Roy and P.N.Potukuchi, Proc. of the 1997 Particle Accelerator Conference, May 12-16, 1997, Vancouver, BC, Canada, p3072
- [3] A.Roy et al. to be published in the Proc. of the 8<sup>th</sup> International Conference on Heavy Ion Accelerator Technology, October 5-9, 1998, Argonne, IL, USA
- [4] P.N.Potukuchi, S.Ghosh and K.W.Shepard, to be published in the Proc. of the 8<sup>th</sup> International Conference on Heavy Ion Accelerator Technology, October 5-9, 1998, Argonne, IL, USA
- [5] K.W.Shepard, A.Roy and P.N.Potukuchi, Proc. of the 1993 Particle Accelerator, May 17-20, 1993, Washington, DC, p1045
- [6] Meyer Tool & Mfg., Inc., 4601 Southwest Hwy., Oak Lawn, IL 60453, USA
- [7] Sciaky Inc., 4915 W. 67<sup>th</sup> street, Chicago, IL 60638, USA
- [8] Don Bosco Technical Institute, Okhla Road, Jamia Nagar, New Delhi, 110025, India
- [9] Mark Kedzie, ATLAS, Argonne National Laboratory, Private Communication

## PROTOTYPE 350 MHZ NIOBIUM SPOKE-LOADED CAVITIES

K. W. Shepard, M. Kedzie, ANL, Argonne, IL

J. R. Delayen, J. Mammosser, C. Pillar, JLAB, Newport News, VA

### Abstract

This paper reports the development of 350 MHz superconducting cavities of a spoke-loaded geometry [1], intended for the velocity range  $0.2 < v/c < 0.6$ . Two prototype single-cell cavities have been designed, one optimised for velocity  $v/c = 0.4$ , and the other for  $v/c = 0.29$ . Construction of the prototype niobium cavities is nearly complete. Details of the design and construction will be discussed, along with the results of cold tests

### 1 INTRODUCTION

The Argonne Physics Division several years ago put forward a concept for an ISOL-type exotic beam facility using a proton/light-ion linac to drive a spallation source for radioactive ions [1,2,3]. As initially proposed, the driver linac would be a normally-conducting, fixed velocity profile, 220 MV linac which could provide beams of protons or light ions at a output energy of 100 MeV per nucleon with a total beam power of 100 kW

A normal-conducting linac would have several limitations. The velocity profile would need to be fixed in order to maximise shunt impedance. Consequently, for the lighter ions, particularly protons, the linac would have to be operated at substantially less than maximum gradient. Also, operation would be pulsed, with a duty factor of at most a few percent which could cause transient heating problems in the spallation target and also make voltage stability of the ion source problematic.

These limitations would be overcome by making the driver linac superconducting [4]. Then, the linac could be formed of short independently-phased cavities. The resulting broadly variable velocity profile would greatly enhance performance, for example, nearly doubling the maximum proton energy.

The cw operation possible with a superconducting linac would be advantageous in several respects. The reduction in peak beam current would reduce space charge and enable increased beam current, allowing, for example, the driving of several targets simultaneously. Also, the injector ion sources would be simplified.

We must note, however, that little development work has been done on superconducting cavities for the required velocity range  $0.2 < \beta < 0.6$  [5].

Cavities currently under development for  $\beta > 0.6$  are foreshortened versions of the  $\beta = 1$ , multi-cell elliptical cavities used for accelerating electrons [6]. The present application, however, deals with energies below 200 MeV/A, and appropriate cavities would require excessive foreshortening. To obtain a reasonable

accelerating voltage, particularly in the single or double cell structures needed to obtain broad velocity acceptance, would require cavity diameters approaching a meter. Construction, handling, and cryostat design would all be rendered difficult. Also, the mechanical stability of such large, highly foreshortened cavities would be at best marginal.

A more promising geometry is the spoke resonator, which has been successfully prototyped in the form of an 855 MHz, single-cell niobium cavity [7,8]. For the linac contemplated here, a substantially lower frequency, say in the range 300-400 MHz, is desirable. Lower frequency would provide increased voltage, larger beam aperture, and higher operating temperature. Since this frequency range is more than an octave lower than tested to date, further prototyping is required.

In what follows, we discuss parameter choices and construction of two prototype cavities [9]. Preliminary test results are also discussed.

### 2 CAVITY DESIGN AND CONSTRUCTION

Principal parameters for the two prototype cavities are shown in Table 1. To minimise time and cost, the two prototype cavities were designed to require no sheet-metal forming dies. Also, cavities were formed for two different velocities by changing only the cavity length and spoke diameter. For use in a linac, the frequencies of

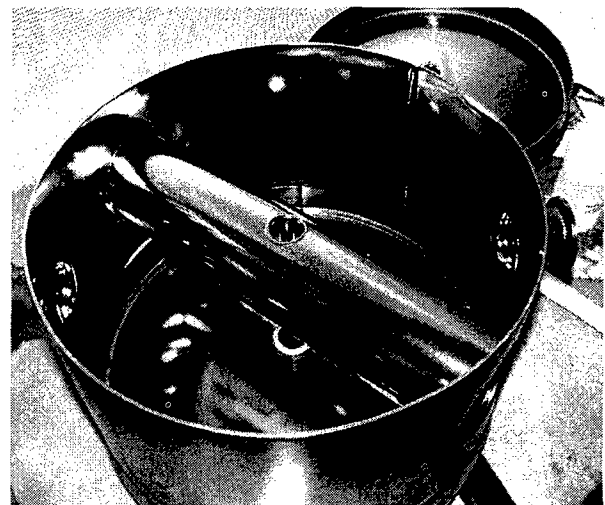


Figure 1: Prototype niobium spoke cavity for  $\beta = 0.4$  prior to welding on the end bulkhead. The outer diameter of the 350 MHz cavity is 44 cm.

Table 1: Parameters for the prototype cavities

Parameter	$\beta = 0.4$	$\beta = 0.3$
Active length	22.2 cm	17.7
Frequency	349 MHz	338
Geometric Factor $QR_s$	72	75
*RF Energy	85 mjoule	51
*E peak surface	4.0 MV/m	4.2
*B peak surface	107	91

\*Referenced to an accelerating field of 1 MV/m

the two cavities would need to be matched. But for purposes of evaluating prototype resonator performance, the slightly lower frequency that results from using the same tooling for both cavities is of no consequence

The cavity housings are formed from 1/8 inch sheet, and the central spoke of 1/16 inch sheet niobium. The 17 inch diameter bulkheads at either end are dished inwards by 1.3 inches to reduce cavity deformation under external pressure. To further enhance mechanical stability, a series of support ribs are welded to the exterior of the end bulkheads. The two coupling ports provide access for vacuum and rf coupling, and also for chemical processing, rinsing, and cleaning.

### 3 EXPERIMENTAL RESULTS AND CONCLUSIONS

Construction of both prototype cavities has recently been completed. The critical niobium surfaces of both cavities were heavily electropolished, approximately 150 microns, just prior to the final closure weld being made. After the final weld, both cavities were chemically polished to remove 50 microns of material and then rinsed with a high-pressure water spray.

Very preliminary results from initial cold tests of the  $\beta$

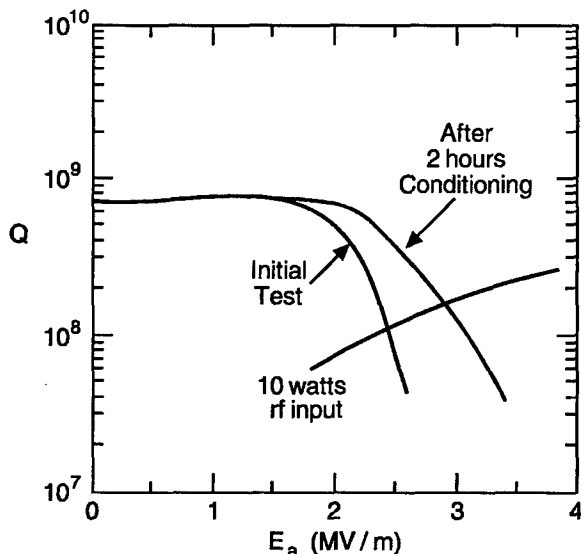


Figure 2: Preliminary results of initial tests at 4.5 K of the  $\beta = 0.4$  prototype 350 MHz niobium spoke

= 0.4 cavity are shown in Fig. 2. The  $Q$  observed at 4.5 K is characteristic of a surface resistance  $R_s$  of 100 n $\Omega$ , within a factor of two of the BCS surface resistance for niobium at this frequency and temperature.

On initial cooldown, the cavity exhibited multipacting starting at low field levels, a few tenths of a MV/m, and extending continuously to the highest field levels so far reached, 3.5 MV/m. This level may be limited by the amount of rf power, 100 watts, currently available for pulse conditioning of the multipacting barriers.

Mechanical stability of the  $\beta = 0.4$  cavity seems adequate. Ambient mechanical noise was observed to cause rf eigenfrequency jitter on the order of a few tens of Hz peak to peak. It should be noted that these observations were made while the test cryostat system was connected into the continuously circulating helium refrigeration loop cooling the ATLAS linac, so that the test conditions realistically simulate a linac environment.

Further tests are scheduled for both the  $\beta = 0.4$  and the  $\beta = 0.3$  cavities. Increased rf power will be available for conditioning of multipacting barriers.

### 4 ACKNOWLEDGEMENTS

The authors wish to acknowledge John Brawley of JLAB, who suggested techniques for several critical electron beam welds, and also Don Henley of Argonne's TD Division, who performed numerical analysis of the mechanical properties of the cavities.

This work was supported by the U. S. Department of Energy, Nuclear Physics Division, under contract number W-31-109-ENG-38.

### 5 REFERENCES

- [1] "Proceedings of the Accelerated Radioactive Beams Workshop", September 5-7, 1985, Parksville, Canada, eds. L. Buchmann and J. M. D'Auria, TRIUMF report TR-85-1.
- [2] J. A. Nolen, in the "Proceedings of the 1996 Linear Accelerator Conference", August 26-30, 1996, Geneva, Switzerland, 32 (1997).
- [3] "Concept for an Advanced Exotic Beam Facility", a working paper, Physics Division, Argonne National Laboratory, February, 1995.
- [4] K. W. Shepard, et al., in Proc. of the 8th Workshop on RF Superconductivity, October 6-10, 1997, Padua, Italy (to be published in Particle Accelerators).
- [5] K. W. Shepard, Nuclear Instruments and Methods A382, 125 (1996).
- [6] K. C. D. Chan, et al., in the Proc. of the 1998 Linear Accelerator Conference, August 23-28, 1998, Chicago, Illinois, (in press).
- [7] J. R. Delayen, W. L. Kennedy, and C. T. Roche, in Proc. 1992 Linear Acc. Conf., August 24-28, 1992, Ottawa, Canada, AECL-10728, 695 (1992).
- [8] J. R. Delayen, et al., in Proc. 1993 Particle Acc. Conference, May 17-20, 1993, Washington D. C., IEEE93CH3279-7, 1715 (1993).
- [9] K. W. Shepard, et al., in Proc. 1998 Linear Accelerator Conference, August 23-28, 1998, Chicago, Illinois (in press).



# A SUPERCONDUCTING ACCELERATING TEST MODULE FOR THE EUROPEAN SPALLATION NEUTRON SOURCE

W. Diete, B. Griep, M. Peiniger, P. vom Stein, H. Vogel,  
ACCEL Instruments GmbH, Bergisch Gladbach, Germany  
B. Bräutigam, Forschungszentrum Jülich, Germany

## Abstract

In 1993 a multinational study group started to evaluate the feasibility for a next generation pulsed European Spallation Neutron Source (ESS) [1]. The beam is specified to have an average power of 5 MW at the target point with a repetition rate of 50 Hz. The final energy of the accelerated negative Hydrogen ions is 1334 MeV. The high energy part of the accelerator will consist of 168 5-cell cavities arranged in 7 groups in the beta range from 0.37 to 0.91. For the high beta cavities a superconducting option is planned [2].

A first superconducting accelerating module was designed and is currently under construction at ACCEL Instruments. The objective is to study the performance of the cavity and the cryomodule. The completed module will be delivered ready for cryogenic RF testing at

Forschungszentrum Jülich (FZJ) in the summer of this year.

At present the cryogenic and rf supply for the test area is installed at FZJ. Besides the measurement of the cavity performance it is planned to study the influence of microphonics on the cavity and the rf stabilisation in pulsed mode operation. In a second step the rf equipment for high power coupler tests will be installed.

## 1 THE CAVITY

The module is equipped with a 500 MHz 5-cell cavity. The cell shape is optimised for a relative particle velocity of  $\beta=0.75$ . The mechanical stability of the cavity was analysed by finite element calculations. The lowest eigenfrequency is well above 50 Hz.

For the manufacturing of the cavity high purity niobium sheet material is used. The Residual Resistivity Ratio

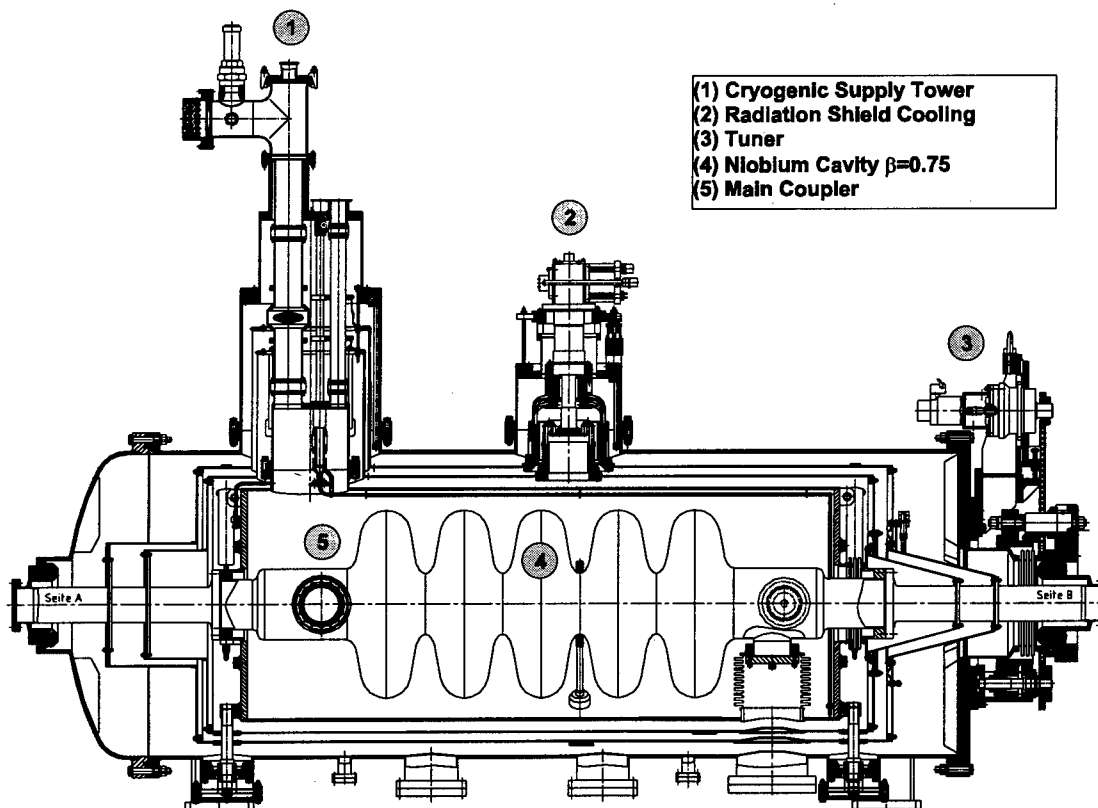


Fig 1: Overview of the Cryomodule

(RRR) is about 300. The individual half cells are formed by deep drawing from the niobium sheets. The half cells are joined together by electron beam welding. All chemical preparation and assembly steps of the cavity are done at ACCEL facilities. The performance sensitive steps of the assembly will be carried out within a class 100 clean room.

### 3 REFERENCES

- [1] The ESS Technical Study Volume III, ESS-96-53-M
- [2] Conceptual Design of the SC High Energy Linear H-Accelerator for the ESS, ESS-96-60-L
- [3] M. Shibata, "Superconducting Rf Activities at JAERI", In Proc. of the 6th Workshop on Rf Superconductivity, Newport News, p. 124-130, 1993

Table 1: Cavity Parameters

$f_0$ [MHz]	500
beta factor	0.75
Geometry factor [ $\Omega$ ]	207
$E_{\text{peak}}/E_{\text{acc}}$	2.6
$H_{\text{peak}}/E_{\text{acc}}$ [mT/(MV/m)]	5.6
$ZT^2/Q$ [ $\Omega/\text{m}$ ]	272
Tuning range [KHz]	600

## 2 THE CRYOMODULE

The cryostat (fig. 1) is based on ACCEL's design for the low loss cryomodules for the JAERI FEL Linac [3]. The two radiation shields are cooled by a Gifford Mc Mahon type refrigerator at the temperature levels of 20 K and 80 K. The static heat losses at 4.2 K temperature level are designed to be well below 3 Watt.

The tuner drive is mounted outside the cryostat. This simplifies the maintenance and increases the reliability of the tuning system. The tuning forces are transferred to the cavity by the beam tubes.

Table 2: Calculated Heat Load of the Cryomodule

	Heat Load at Temperature (Watt)		
	4.2 K	20 K	80 K
beam tube A	0.08	1.62	5.83
beam tube B	0.08	1.62	4.94
main coupler	0.74	3.90	5.69
GF-UP support	0.003	0.06	0.23
radiation 80 K shield			5.20
radiation 20 K shield		0.32	
radiation LHe tank	0.1		
supply tower	0.07	0.65	3.40
rf cable	0.42	1.65	1.70
sum	1.48	9.85	26.98

# DESIGN STUDY FOR SC PROTON LINAC ACCELERATING CAVITIES.

E. Zaplatine\*, W. Braeutigam, S. Martin,  
Forschungszentrum Juelich, Germany

## Abstract

A 70-1334 MeV superconducting proton linac is under consideration as a possible version for the high energy part of European Spallation Source accelerator. In this paper we describe two alternative options of an accelerating structure (500 MHz) for this machine. First is the 5-cell elliptical cavities designed for the  $\beta=0.4-0.9$ . The second type is a spoke cavity extended to multigap design ( $\beta=0.3-0.5$ ). Results of numerical simulations are compared with low level experimental data. A full scale SC elliptical cavity prototype is under construction in collaboration with ACCEL.

## 1 INTRODUCTION

In some recently launched projects[1]-[3] for high intensity proton beam acceleration the possibility to use superconducting cavities is under investigation. For this purpose a well established "elliptical" (Fig. 1)  $\beta=1$  cavity shape is adapted for much slower proton beams with  $\beta$  range from 0.4 to 0.9. At the same time from mechanical calculations such type cavity use for  $\beta$  lower than 0.5 is accomplished with a need of serious mechanical structure stiffeners. As a possible alternative a so called spoke cavity[4] is under consideration. During past year, at Forschungszentrum Juelich, we have been looking at the possibility to use SC cavities in European Spallation Source project (ESS)[5].

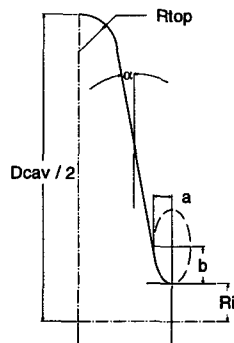


Figure 1: Elliptical Cavity Geometry (1/4 of cell is shown)

## 2 ELLIPTICAL CAVITY

Usually, an elliptical cavity design is a compromise between various geometric parameters which should define a most optimal cavity shape in terms of an accelerator purpose. Within a SC proton linac design there is a need of grouping of cavities with different  $\beta = v/c$  values.

\* On leave from the Joint Institute of Nuclear Research, Dubna.

It means that the process of cavity designs for SC linac becomes time consuming. Here we present some basics which can help to obtain rather fast the main cavity parameters and which we used for ESS project. A further cavity optimization can be made afterwards but we believe that an improvement will be within 5%.

The main advantage of any SC cavity is a possibility of high accelerating electric field maintenance ( $E_{acc}$ ). There are two characteristics which limit in principle an achievable value of  $E_{acc}$ . They are the peak surface electric field ( $E_{pk}$ ) and the peak surface magnetic field ( $H_{pk}$ ).  $H_{pk}$  is important because a superconductor will quench above the critical magnetic field.  $E_{pk}$  is important because of the danger of field emission in high electric field regions. All these mean that to maximize the accelerating field first of all it is therefore important during a cavity design to minimize the ratios of peak fields to the accelerating field. There are some more figures of merit to compare different designs such as power dissipation  $P_c$ , a quality factor  $Q$  and shunt impedance  $R_{sh}$ . But these parameters are not so crucial to the cavity design and may be varied in some limits without any sufficient harm for a system in whole. Here we should mention also such figure like the cavity aperture (bore radius in elliptical cavity design  $R_i$ ). This characteristic is obtained in conjunction with beam dynamic calculations and is defined as a first. The choice of  $R_i$  limits  $E_{pk}$  (Fig. 2) and  $H_{pk}$ , defines cell-to-cell coupling in multicell cavity, influences the shunt impedance value and field flatness.

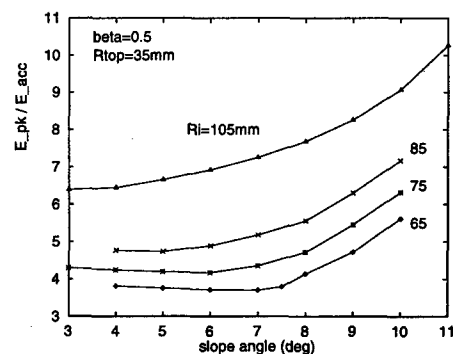


Figure 2: Maximum Electric Surface Field to Accelerating Field Ratio vs. Slope Angle  $\alpha$

We start an elliptical cavity design with  $R_i$  definition. Now, as to concern the cavity shape design itself there are some geometric characteristics (dome radius  $R_{top}$ , slope angle  $\alpha$ , ellipse axis) which should be defined for a most optimal cavity shape in terms of mentioned above RF parameters. And as a next step of design we made  $E_{pk}/E_{acc}$  and  $H_{pk}/E_{acc}$  investigations on slope angle  $\alpha$  value. The

reason of this is that an optimal value of  $\alpha$  could be define unique if to consider dependences of  $E_{pk}/E_{acc}$  (a cavity frequency 500 MHz) (Fig. 3). From these grafs one may make a decision about a cavity shape. These calculations have been done by means of 2D cavity simulation code SUPERFISH[6]. The ellips parameters have been defined by program automatically to satisfy the fixed cell length  $\beta\lambda/2$ . After this set of simulations the choice of  $R_i$  should be checked. Fig. 4 shows dependences of the cavity coupling on iris radius for the chosen above optimal in terms of  $\alpha$  points.

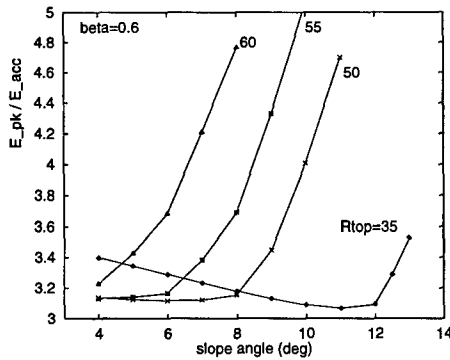


Figure 3: Maximum Electric Surface Field to Accelerating Field Ratio vs. Cavity Slope Angle  $\alpha$

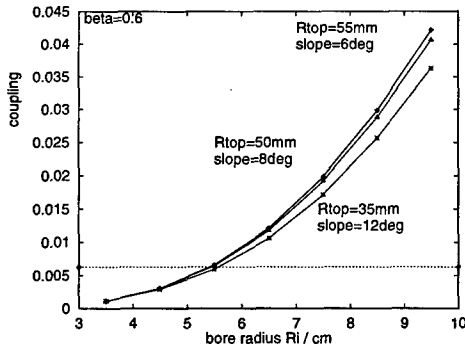


Figure 4: Cavity Coupling vs. Iris Radius

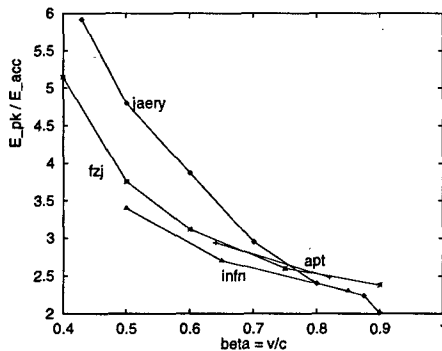


Figure 5: Maximum Electric Surface Field to Accelerating Field Ratio

The results of our calculations are presented on Fig. 5

along with results from other calculations[1]-[3]. These results reffer to the projects with quite different basic purposes and parameters (pulsed and cw, different final energies and RF frequencies), but all sets are for the same aperture ( $R_i=65$  mm for FZJ).

Table 1 lists the main parameters of elliptical cavity designs for different  $\beta$  values. Here we kept coupling approximately constant for all  $\beta$ 's.

Table 1: Some Parameters to Compare Elliptical Cavities with Different  $\beta = v/c$

$\beta$	0.4	0.5	0.6	0.75	0.9
aperture $R_i$ (cm)	4.5	5.0	5.5	6.0	6.5
dome $R_{top}$ (cm)	2.5	3.5	4.5	6.5	8.5
slope $\alpha$ (deg)	6	7.5	10	12	14
cell-length (cm)	12	0.15	0.18	0.225	0.27
transit time factor	.775	.772	.768	.764	.762
coupling (%)	0.53	0.57	0.66	0.66	0.62
$E_{pk}/E_{acc}$	3.52	3.13	2.88	2.56	2.31
$H_{pk}/E_{acc}$ (Gs/(MV/m))	83.8	73.9	67.5	59.8	54.9
$R_s * Q_0$ (Ohm)	103	132	161	203	238
$R_{sh}/Q_0$ (Ohm/m)	387	474	541	650	730
$Q_0 * 10^{-10}$	0.83	1.06	1.29	1.62	1.90

### 3 SPOKE CAVITY

As an alternative to the elliptical cavity for small  $\beta$ 's a spoke cavity is under consideration (Fig. 6). This one cell cavity has been built and tested at high fields at Argonne National Lab. The advantages of such type cavity before elliptical ones are smaller dimensions and higher mechanical rigidity. An accelerating  $\pi$ -mode electrical field is similar to the elliptical cavity accelerating mode but magnetic peak field on surface is defined by spoke diameter. To provide the calculations of  $E_{pk}/E_{acc}$  on the cavity surface the spokes have been made round (Fig. 7). There is an optimum of  $E_{pk}/E_{acc}$  depending on the spoke length (Fig. 8) which explains by co-dimensions of an accelerating gap and a space between the spoke and a cavity wall.

Table 2 lists some parameters for multycell spoke cavities.

An experimental stand and normal conducting 5-cell cross bar spoke cavity model have been built. First measurements show a good agreement with numerical simulations. On Fig. 10 a first result of an electric field profile measurement along a model axis is presented.

### 4 ACKNOWLEDGMENTS

The authors would like to thank Dr. Yu. Senichev for helpful discussions, K. Sobota, A. Richert and R. Stassen for the construction of an experimental stand and the measurement help.

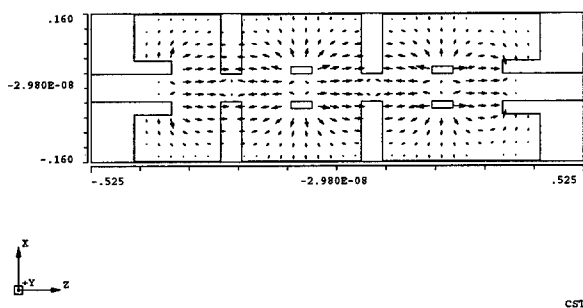


Figure 6: Spoke Cross Bar Cavity Geometry

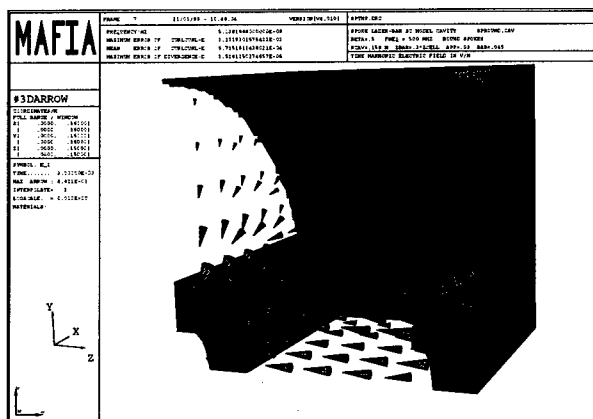


Figure 7: Electric Field in Spoke Lader Cavity (1/4 of cell is shown)

## 5 REFERENCES

- [1] N. Ito et al., "Development of a Superconducting Cavity for the High Intensity Proton LINAC in JAERI", Proceedings of the XVIII Int. Linear Acc. Conf., Geneva, 1996, p.671.
- [2] F. L. Krawczyk et al., "Superconducting Cavities for the APT Accelerator", Proceedings of the 1997 Particle Acc. Conf., p. 2914.
- [3] D. Barni et al. "SC Beta Graded Cavity Design for a Proposed 350 MHz LINAC for Waste Transmutation and Energy Production", EPAC'98, Stockholm, p.1870 (1998).
- [4] J. R. Delayen et al., "Design and Test of a Superconducting Structure for High-Velocity Ions", LINAC'92, Ottawa, 1992.
- [5] W. Braeutigam et al., this proceeding.
- [6] J. H. Billen and L. M. Young, "POISSON/SUPERFISH on

Table 2: Some Parameters to Compare Spoke Cavities with Different  $\beta = v/c$

$\beta$	0.3	0.4	0.5
cell-length (cm)	9	12	15
acc. gap (cm)	4.5	7.8	10
transit time factor	0.805	0.783	0.770
$E_{pk}/E_{acc}$	4.48	3.53	3.27
$R_s * Q_0$ (Ohm)	68.7	86.7	95.4

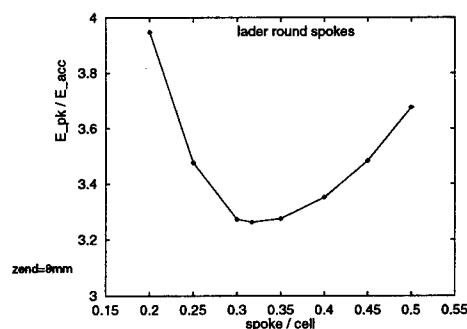


Figure 8: Maximum Electric Surface Field to Accelerating Field Ratio vs. Spoke Length

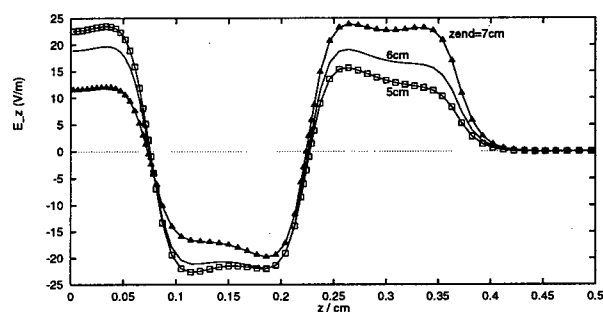


Figure 9: Electric Field Distribution in Spoke 5-Cell Lader Cavity Depending on End Region Tune

PC Compatibles", Proceedings of the 1993 Particle Acc. Conf., Vol. 2, p. 790.

- [7] M. Bartsch et al. "Solution of Maxwell's Equations", Computer Physics Comm., 72, 22-39 (1992).

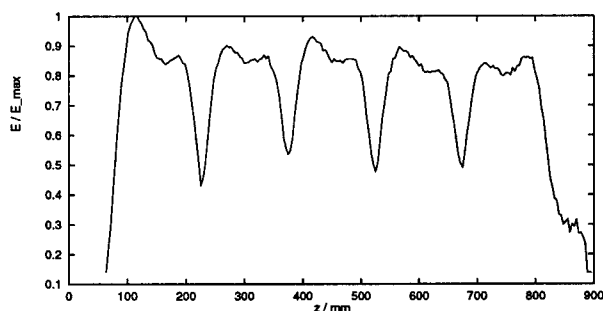


Figure 10: Electric Field Distribution in 5-Cell Cross Bar Spoke Cavity Experimental Model

## DISSIMILAR METAL JOINTS FOR THE APT SUPERCONDUCTING CAVITY'S CRYOGENIC PLUMBING SYSTEM

M.J. Cola, M.B. Lyons, D.F. Teter and R.C. Gentzlinger\*

Materials Science & Technology—Metallurgy

\*Engineering Science and Applications—Design Engineering

Los Alamos National Laboratory, Los Alamos New Mexico, 87545

### Abstract

Titanium (Ti) is the material of choice for the helium (He) vessel surrounding the accelerator for the accelerator production of tritium (APT) superconducting cavities. The Ti helium vessel must be joined to a stainless steel (SS) cryogenic plumbing system in the cryomodule. In addition, a niobium (Nb) to SS joint must be developed that can replace a braze connection currently used to attach the stainless-steel Conflat flange to the Nb beam tube of the cavity. Inertia friction welding (IFRW) was chosen to ensure that sound joints were formed for both applications. IFRW is typically well suited for joining dissimilar metals. However, even this process has its limitations, particularly when the base metals are not physically or metallurgically compatible. Such incompatibilities can lead to the formation of brittle intermetallics at the interface; consequently, mechanical properties suffer. To remedy this, interlayer materials are used that are both structurally and microstructurally compatible with both base metals. The interlayer metal, while ideally at least as strong as the weakest base metal, is kept thin so that constraint effects will raise its apparent yield strength to match that of the base-metal yield strength. With this in mind, the main objective for the current study was to develop tube-to-tube parameters for joining 316L SS to Nb, and to commercially pure Ti using a Nb interlayer.

In the present study, welding parameters were developed and this paper highlights the salient microstructural features associated with the interface regions between the base metals and the interlayer metal, and reports on the mechanical properties of various joint combinations. To accomplish this, specimens were metallurgically prepared from as-welded and tested joints, and analyzed using light, scanning electron and transmission electron microscopy.

### 1. INTRODUCTION

Dissimilar metal joining Ti to other metals has met with limited success; brittle weldments result [1-7]. In response to this problem, an interlayer material was used by several researchers as a means of achieving sound, high-integrity joints between dissimilar metals [6,7]. Sassani and Neelam evaluated the feasibility of interlayer metals for joining incompatible base metals; less than optimal joint strengths were achieved [6].

A similar approach was attempted by Kou during friction welding trials using Alloy 718, Ti 6Al-2Sn-4Zr-2Mo and Ti 6Al-4V base metals [7]. Kou extended the concept of an interlayer to include two interlayer metals compatible with each other and their respective base metals. Results indicated an average as-welded joint strength of approximately 345 MPa, and PWHT strengths as high as 497 MPa. Finally, Kuo reports that a consistent relationship between weld strength and failure location remained illusive.

The present study investigated the metallurgical characteristics and mechanical properties of Nb to SS IFR welds, and Ti to SS IFR welds made with a Nb interlayer.

### 2. EXPERIMENTAL APPROACH

#### 2.1 Material Preparation

The commercially available Ti and SS used in this study were in the form of 2-mm wall by 25-mm diameter tubes. A 25-mm diameter bar of Nb was the interlayer material. Prior to IFR welding, the tubes were sectioned into 75-mm lengths and the faying surfaces machined while bathed in alcohol. Additionally, the machining of the Nb bar provided a tubular geometry for joining to the SS and subsequently to the Ti. The Nb wall thickness was thicker (3.2-mm) than the tube's walls (2 mm) to provide for greater forging action during the welding cycle.

#### 2.2 Friction Welding

IFR welds were produced using an MTI Model 90B inertia friction welding system. Two separate welds were made to achieve the final three-metal joint. First, SS was joined to Nb followed by a Nb to Ti weld. Separate parameters were developed for each weld joint. Since previous researchers work with Ti and SS did not employ an interlayer material, starting parameters were chosen because they were thought to be close to the optimum. Emphasis for this phase was on achieving weld joints capable of bending through 90 degrees. Once suitable starting parameters were developed, welds were made at various levels of rotational speed (60 to 188 m/min) and axial force (89 to 268 MPa) while maintaining a constant moment of inertia ( $0.16 \text{ kg-m}^2$ ). After welding and prior to testing, each weld joint was He leak checked achieving a minimum leak rate of  $1 \times 10^{-10} \text{ atm.-cc/s}$ .

### 2.3 Weld Characterization

Visual examination was performed for weld axial displacement and flash. Disks about 3 mm in diameter were sectioned transverse, from the interlayer region of the Ti/Nb/SS welds. Thin foils were examined in a Philips CM30 analytical-electron microscope operated at 300 kV. Line scans across the Nb/SS interface region were performed using a VG HB601 scanning transmission electron microscope (STEM) operated at 100 kV and equipped with a Link ISIS EDS system.

Knoop microhardness testing (200-g load) was performed across the weld region at the axial centerline. Machining of full-scale tensile specimens removed weld flash and obtained a reduced-diameter of 24-mm over a gage length of 75-mm. In accordance with ASTM E8, testing was at an extension rate of 0.635 mm/min, and performed at 294 K and 77 K. Following mechanical testing, selected fracture surfaces were characterized using scanning electron microscopy.

## 3. RESULTS AND DISCUSSION

### 3.1 Macro and Microscopic Analysis

An as-welded Ti/Nb/SS IFR weld is shown in Figure 1. Consistent with the appreciably lower elevated-temperature strength of Ti relative to the Nb, these welds exhibited preferential flash formation in the Ti. A macrograph of an axially sectioned Nb/SS weld specimen is shown in Figure 2. Flash formation was predominately in the Nb. As expected, the axial displacement increased with an increase in axial force from 1 mm to 6 mm.

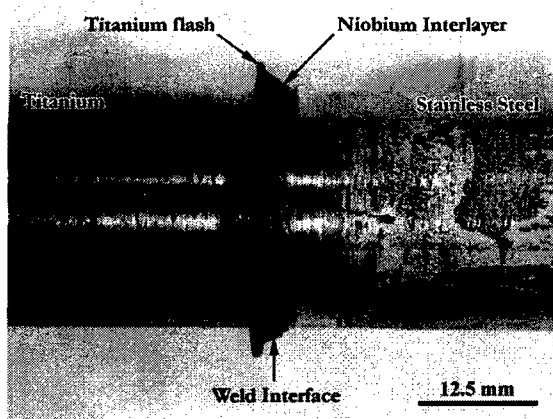


Figure 1. Photograph of as-welded Ti/Nb/SS joint.

### 3.2 TEM and STEM Analysis

A TEM micrograph of the as-welded 316L SS/Nb interface reveals a continuous interaction layer (Figure 3). Convergent beam electron diffraction patterns show that the interaction layer has a structure based on the  $\text{NbFe}_2$   $\text{C14}$  Laves phase. STEM line scans for Cr, Fe and Nb indicate a uniform distribution of these elements across the interaction layer (Figure 4). The sharp 316L

SS/Nb $\text{Fe}_2$  interface indicates Fe and Cr diffusion into the Nb, while the diffuse Nb $\text{Fe}_2$ /Nb interface suggests there was no Nb diffusion into the 316L SS.

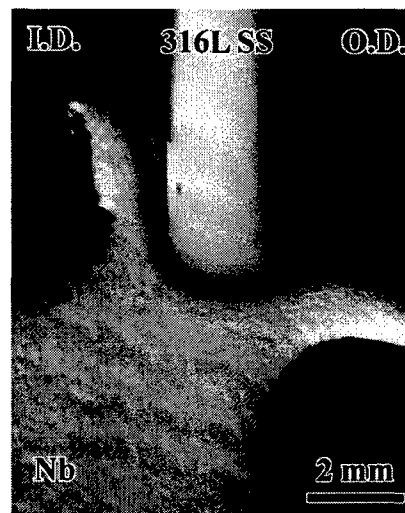


Figure 2. Macrograph of Nb/SS IFR weld. Notice the preferential flash formation in the Nb.

### 3.3 Hardness Testing

Knoop hardness traverses for each joint combination are shown in Figure 5. For the 316L SS/Nb weld, a slight hardness increase was observed near the weld interface in both metals. The increased hardness was attributed to cold worked metal near the interface resulting from deformation during the IFR weld process. KHN hardness measurements across the interlayer region of the Ti/Nb/SS weld also exhibited increased hardness near the interface because the cold worked metal was not extruded during the weld cycle. Additionally, the reduced hardness across the Nb interlayer of the Ti/Nb/SS weld versus the Nb/SS weld appears to result from annealing effects provided by the Ti/Nb weld thermal cycle.

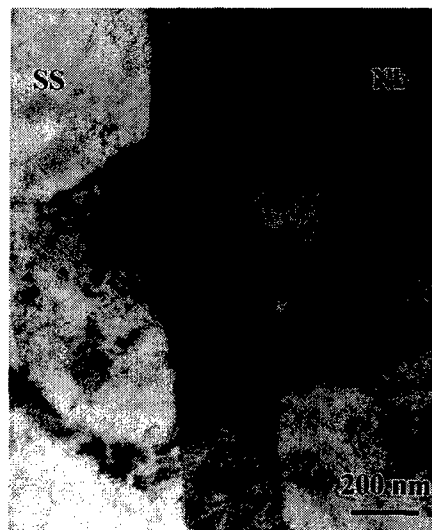


Figure 3. TEM micrograph of 316L SS/Nb interface.

### 3.4 Tensile Testing

Room temperature uniaxial tensile test results ranged from 338 to 527 MPa. Failure occurred in both the Ti base metal and through the interlayer metal. Specimens failing through the interlayer exhibited considerable reduction in area in the Ti base metal away from the interface. Since there was no noticeable reduction in area in the SS, it appears to have constrained the Nb interlayer thus transferring strain/stress to the Ti, hence, the joint's tensile strength was appreciably higher than would be expected from a tensile test of a monolithic Nb tube.

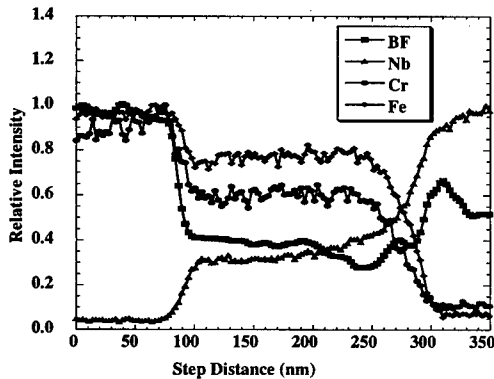


Figure 4. STEM line scans across the interaction layer. BF represents bright field image.

### 3.5 Fracture Analysis

An SEM fractograph of a Ti/Nb/SS weld tensile test specimen that failed through the interlayer region is shown in Figure 6. Microscopically, the fracture surface exhibited two fracture surface topographies. At some locations, a relatively flat smooth surface was exhibited. Tear ridges separated regions of flat, nearly featureless fracture and regions of microvoids. The microvoids had nucleated in the soft Nb interlayer.

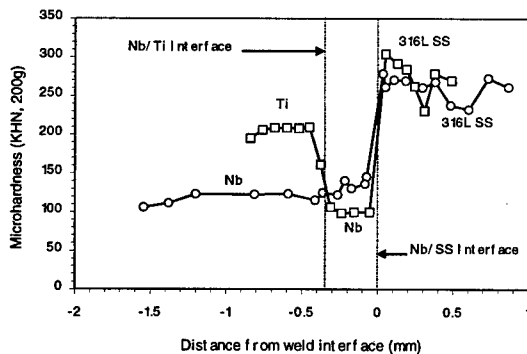


Figure 5. Microhardness traverses across weld joints.

## 4. CONCLUSIONS

From the results of light and analytical electron microscopy, and mechanical property evaluations, the following conclusions can be drawn:

1. Using conventional IFR welding techniques, 316L SS was successfully joined to Nb and to commercially pure Ti using an interlayer of Nb;
2. The inherent solid-state nature and rapid thermal cycle afforded by IFR welding restricted base-metal interdiffusion, however, STEM results revealed a thin (200-nm) intermetallic phase of Nb(Fe,Cr)<sub>2</sub> between the 316L SS base metal and Nb interlayer;
3. STEM results also revealed a uniform distribution of Fe, Cr and Nb across the NbFe<sub>2</sub> Laves-type interaction layer;
4. The favorable results permit use of Ti/316L SS joints and Nb/316L SS joints in a superconducting cavity and cryomodule chosen as a candidate for the Department of Energy's accelerator production of tritium program.

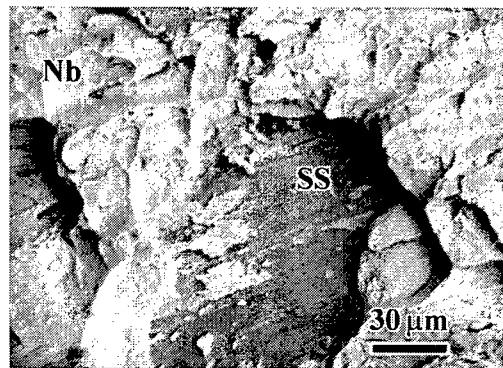


Figure 6. Fractograph of Ti/Nb/SS IFR weld. Fracture was through the Nb interlayer region.

## 5. ACKNOWLEDGEMENTS

This research was funded under DOE contract no. W-7406-ENG-36. The authors wish to thank Ms. Ann Kelly and Ms. Pallas Papin for their experimental assistance.

## 6. REFERENCES

1. Akizuki, S. *et al*, "Welding between titanium and mild steel", *Titanium and Zirconium* 10 (9) 31-36 (1962)
2. Akizuki, S. *et al*, "Welding between titanium and steel", *Titanium and Zirconium* 10 (9) 8-14 (1962)
3. Futamata, M. and Fuji, A., "Friction welding of titanium and SUS 304L austenitic stainless steel", *Welding Int'l*, 4 (10) 768-774 (1990)
4. Fuji, A. *et al*, "Improving tensile strength and bend ductility of titanium/AISI 304L stainless steel friction welds", *MS&T* 3 (8) 219-235 (1992)
5. Fuji, A., *et al*, "Improved mechanical properties in dissimilar Ti-AISI 304L joints", *J.Mat.Sc.* 31 819-827 (1996)
6. Sassani, F. and Neelam, J.R., "Friction welding of incompatible materials", *WJ*, 11 264s-270s (1988)
7. Kou, M., "Dissimilar friction welding of titanium alloys to Alloy 718", PhD Dissertation, The Ohio State University, (1993)



## DESIGN, ANALYSIS, AND FABRICATION OF THE APT CAVITIES\*

S. Atencio, B. Campbell, K. Chan, A. Cimabue, W. Clark, G. Ellis, R. Gentzlinger<sup>#</sup>, H. Haagenstad, D. Hammon, W. B. Haynes, J. P. Kelley, F. Krawczyk, M. Manzo, F. Martinez, H. Martinez, J. McClellan, J. Mitchell, R. Mitchell, D.I. Montoya, D.R. Montoya, J. Moss, S. Quintana, A. Rendon, B. Rusnak, D. Schrage, F. Smith, M. Trujillo, LANL, Los Alamos, NM  
J. Kuzminski, General Atomics, Los Alamos, NM

### Abstract

The design for the superconducting cavities of the high-energy accelerator for the Accelerator Production of Tritium (APT) project has been extensively changed in the last two years. The original accelerator design incorporated 0.48 and 0.71 beta cavities with stiffeners, and a stainless-steel helium vessel. Today, the accelerator uses unstiffened 0.64 and 0.82 beta cavities, and a titanium helium vessel. This paper discusses the design process, including the supporting analyses, prototype cavities built, and the decisions made to support the current design. The design of the integrated cavity-helium vessel is presented. Future plans and testing for design validation are also discussed.

### 1. INTRODUCTION

The original APT machine proposed in the fall of 1995 included a room-temperature accelerator. A team was created to investigate the viability of using a superconducting accelerator for the high-energy end. A candidate design was developed [1] using two different ( $\beta=0.48$  and  $0.71$ ) cavities for beam energies between 100 MeV to 1200 MeV. The cavities were designed with a three-degree and five-degree wall slopes, respectively, which maximized the radio frequency (RF) performance while still allowing the acid to drain during chemical polishing. A stainless-steel liquid-helium containment vessel surrounding the cavity was incorporated into the design. Since there was little performance and manufacturing experience with low beta elliptical superconducting RF structures, a program to build four prototype single-cell cavities was undertaken. The cavities were manufactured at Los Alamos. The multi-cell cavities would be manufactured by US and European companies. The cavities would then be tested in the RF-structures laboratory at Los Alamos to see if a low-beta cavity could meet the program performance requirements.

During fabrication of the cavities, the accelerator architecture was revised to include three different beta cavities. The beta of the  $\beta=0.71$  cavity was reduced to  $\beta=0.64$  and a beta of 0.82 was added. The energy range of the superconducting high-energy accelerator was now

100 MeV to 1700 MeV. The fabrication of the  $\beta=0.71$  cavity was stopped and the tooling was shelved. A  $\beta=0.64$  single-cell cavity was designed and fabricated.

The test results of the cavities were encouraging [2], but the fabrication costs were high. Modifications to the design, for enhancing the mechanical strength/stiffness while trading off RF performance, were undertaken. A compromise was reached, where the predicted RF performance [3] of the  $\beta=0.64$  cavity was slightly reduced ( $\sim 4\%$  in field level due to increased  $B_{peak}$ ); the  $\beta=0.82$  cavity performance under these criteria was affected by  $<1\%$ , while the mechanical design became much simpler and easier to manufacture. The  $\beta=0.48$  cavity was dropped from the accelerator architecture and the  $\beta=0.64$  and  $\beta=0.82$  cavities were redesigned. The energy range of the superconducting high-energy accelerator was now 240 MeV to 1700 MeV. The helium vessel material was changed from stainless steel to titanium. With a slight reduction in the predicted cavity performance for the new  $\beta=0.64$  design (with the new wall slope), and with the program schedule having the delivery of the 5-cell cavities on the critical path, a single-cell cavity-test program was not undertaken.

### 2. CAVITY DESIGN & FABRICATION

#### 2.1 Original Cavity Design

The original goal for the high-energy superconducting accelerator was to use off-the-shelf technology. No research and development was to be utilized in creating the accelerator design. Some engineering development would be required because, unlike an electron accelerator of  $\beta=1.00$ ,  $\beta<1.00$  cavities were needed. The APT cavity manufacturing plan was to use pure niobium sheet (RRR 250) and either press or spin it into the elliptical shape commonly used in electron accelerators. Other methods, such as niobium sputtering on copper, were considered too risky and therefore were not investigated. To maintain a reasonable accelerator length, two power couplers per cavity approach was adopted.

The three-degree to seven-degree wall slope resulting from the original design maximized performance and still

\* Work supported by DOE under contract No. DE-AC04-96AL89607.

<sup>#</sup> Email: gentzlinger@lanl.gov

allowed the chemicals to drain from the cavity after polishing.

The five-degree slope of the  $\beta=0.64$  cavity wall did not provide adequate stiffness or strength [4]. The applied pressures during the cool-down of the cavity would cause excessive yielding in the cavity. A  $\beta=1.00$  cavity has more curvature and a smaller conical section than a  $\beta=0.64$  cavity, which is more efficient at supporting the applied pressures. The conical section of the  $\beta=0.64$  cavity is almost a flat plate when a five-degree slope is used.

The walls of the 0.48 and 0.64 beta cavities would yield significantly without any reinforcement. The original cavity design had cylindrical stiffeners between the cavity cells and a conical stiffener at each end of the cavity. The stiffeners are perforated with large diameter holes to allow the liquid helium to reach the cavity wall. The stiffeners allow the first mechanical resonant frequency of the cavity to be above the desired 100 Hz. A stainless-steel helium vessel was installed over the niobium cavity. With the conical stiffeners covering up the beamtubes, the only place to fasten the vessel was the beamtube flanges. The five ports, (two RF power input couplers, two higher order mode couplers (HOM), and one RF pick-up) had to penetrate the helium vessel. Bellows were incorporated at the flange of each port to allow for the differential thermal contraction between the niobium cavity and the stainless-steel helium vessel.

The prototype stiffened, single-cell cavity was expensive and time consuming to fabricate. The APT machine would have been too expensive to fabricate if this cavity approach was adopted for the high-energy accelerator.

## 2.2 Second Generation Cavity

The second approach was to redesign the cavity with a revised cone angle to increase the stiffness. The more the cone angle could be increased (three to five to 10 degrees), the lower the resulting stresses would be. Increasing the angle too much would reduce the radius at the equator, raising the possibility of multipacting. A compromise of 10 degrees was adopted for both the 0.64 and 0.82 beta cavities. This slope allowed the stresses to be below the room temperature yield stress of 7,000 psi without the additional stiffeners. The 2.2 atm applied pressure from the cryogenic system during cool-down gave the smallest margin between the yield strength and the calculated state of stress in the cavity. The 2.2 atm is higher than what was originally used. The 3.0 atm at cryogenic temperature is not a problem with yield strength, since the yield increases by a factor of 10 at low temperature. Fracture toughness may be an issue at low temperatures and is being investigated. The cavity could still withstand the pressures without the additional stiffeners. However, the thickness had to be increased to 4.0 and 3.5 mm for the 0.64 and 0.82 beta cavities,

respectively. The increased thickness added cost to the cavity fabrication, but it was less than adding the cost of the stiffeners.

With removal of the stiffeners, the five cavity ports could now be external to the helium vessel. To achieve this, the vessel would be attached to the beamtube. The original stainless-steel vessel design had a welded joint between the helium vessel and the port flanges. If the cavity ports were to be outside the helium vessel, a method of attaching the vessel to the niobium beamtube would have to be developed. Stainless steel could be attached to the niobium beamtubes by using a niobium (82% gold and 18% nickel) braze. The braze works quite well (the method is used for attaching the stainless-steel conflat™ flanges to the niobium beamtubes), giving at least a 4000 psi shear stress capability.

Titanium is soluble in niobium and these metals can be electron-beam welded together. This approach ensures super fluid helium will not leak from the helium vessel. Titanium also has a coefficient of thermal expansion similar to that of niobium. This reduces the thermal stresses during cool down and reduces the requirement on the tuning range of the tuner. Titanium will not have any residual magnetic fields in the welds, therefore, it will not decrease the quality factor (Q) of the cavity, thereby increasing the load on the cryogenic system.

The original requirement of having the lowest mechanical resonant frequency of 100Hz could not be achieved with the current cavity design. It was decided that the microphonics issue would be resolved by evaluating the response of the cavity to the input power spectrum density of the APT plant or an equivalent. If the cavity's response was unacceptable, the cavity could be mechanically coupled to the helium vessel. This would be cheaper than adding stiffeners to the cavity. Coupling of the cavity to the helium vessel can be explained by reviewing the design of the helium vessel.

The original helium vessel had a tear-drop shape and was made from unalloyed grade 2 titanium. This allowed the vessel to encompass the cavity and have a minimal amount of liquid-helium storage. The bulkheads on each end of the vessel were machined from plates of titanium. The tuner end bulkhead had a flexure integrally machined into it. This gave compliance to the head, allowing the cavity to be tuned. The other end bulkhead had triangular stiffeners welded between it and the niobium beamtubes to reduce the stresses at the interface. The 2.2 atm design condition caused the almost flat section of the tear-drop shape to have unacceptable stresses. Stiffeners were needed in this region to lower the stresses to an acceptable level. Support rods were added internally to the vessel to strengthen and stiffen the two bulkheads to react the tuning loads. After the tuning range of the cavity tuner was increased to incorporate a 500 kHz cool-down uncertainty (the  $\beta=0.64$  cavity has a tuning sensitivity of 319Hz/micron), the flexure design was scrapped. Then, after reviewing cleanliness issues and ideas of how best to

couple the cavity to the vessel, the helium vessel was redesigned.

### 2.3 Final Cavity Design

The new and final helium vessel design (Figure 1) incorporates a vessel within a vessel concept and is made out of unalloyed grade 2 (yield strength of 40 Ksi) titanium. The inner vessel provides the strength and stiffness to support the cavity and its tuner. The outer vessel provides the storage volume for the liquid helium. The tuner is supported off of one bulkhead of the inner vessel, having its loads transmitted down the vessel to the far bulkhead and then to its attached adjustable struts. The struts provide a load path for the tuning loads to return back to the cavity. This design provides a stiff path to react tuning loads against. The compliance of the second bulkhead would be too great if the struts were omitted, which causes the tuner to deflect the helium vessel instead of the cavity.

An edge-welded titanium bellows was added between the bulkhead and the niobium beamtubes on each end of the cavity. The bellows on one end allows the cavity beamtube to move relative to the helium vessel during the actuation of the tuner. The other bellows has two purposes. First, it minimizes the impact the manufacturing tolerances will have on the cavity's tuning range. The envelope for the bellows is quite limited due to the proximity of the cavity ports to the end half-cell, therefore, the stroke will be small. If the helium vessel and the cavity had significant variations from their desired design lengths, the range of the bellows would be significantly reduced. The second bellows allows the adjustable struts to relocate the vessel relative to the cavity. Second, the purpose of the second bellows is to decouple the cavity from the helium vessel. The cavity will be supported at one end by the power couplers. A statically indeterminate structure would arise if the cavity were welded directly to the independently supported helium vessel. This could be a significant problem during cool-down. The bellows will allow the cavity to move relative to the helium vessel. In the future, the second bellows may be eliminated if it is found unnecessary during cavity testing.

The inner vessel is perforated to allow the liquid helium to stay in contact with the cavity. The holes are located in-between the cavity cells. Complete rings are located at each of the five cells. Bumpers or spacers could be added at these locations to support the cavity if microphonics becomes an issue. The cavity will go through some significant testing to determine if bumpers or supports will be required. Note: if the bellows were located on the outside diameter of the inner vessel, the cavity could not be supported off the vessel.

The outer helium vessel provides the storage volume of the liquid helium. The vessel holds approximately 125 liters of liquid helium for the  $\beta=0.64$  cavity. The vessel

requires a titanium-to-stainless-steel transition [5] joint to go between the titanium vessel and the stainless-steel conflats<sup>TM</sup> flanges. Preliminary trials of this joint were successful using inertial welding between the two materials.

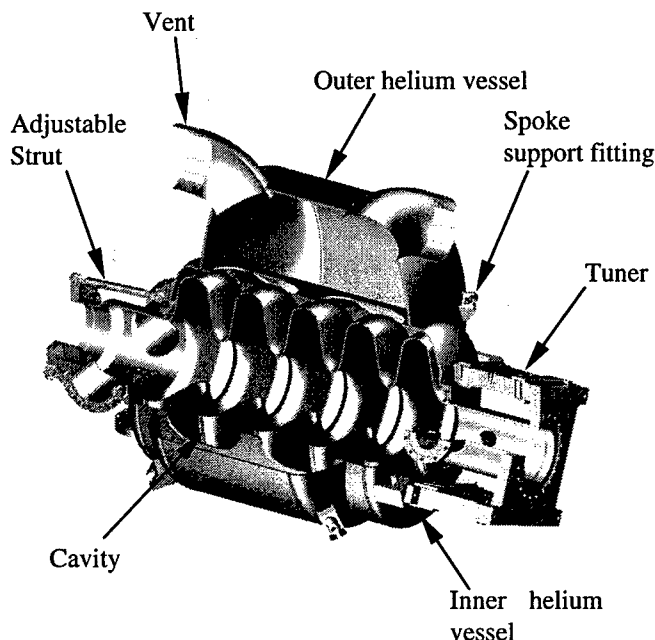


Figure 1: The current  $\beta=0.64$  cavity and helium vessel

### 3. ADDITIONAL WORK

The designs of the cavity and helium vessel were presented to the Los Alamos Pressure Vessel Review Committee during the fall of 1998. The committee is responsible for reviewing the engineering and operations of cryogenic and pressure vessel systems. Their approval is required before any operations can begin. The designs of both components would be accepted as long as the design passed a fracture toughness analysis. This analysis could not begin without some fracture toughness data being generated. A contract was placed at the High Magnetic Lab at Florida State University to develop fracture toughness data for niobium and unalloyed grade 2 titanium. This data should be available by June of 1999.

### 4. REFERENCES

- [1] K.C. Dominic Chan et al., LANL Memo: LA-UR-95-4045
- [2] W.B. Haynes et al., LANL Memo: LA-UR-98-682
- [3] F. Krawczyk et al., LANL Memo: LA-UR-97-1700
- [4] D. Schrage & E. Swensen, LANL Memo: AOT-1:95-180
- [5] M. Cola et al., "Inertia Friction Welded Joints between a Titanium Vessel and a Stainless Steel Cryogenic Plumbing System for the APT", for PAC '99", New York City, (Mar 99)

## FABRICATION OF A PROTOTYPE MEDIUM-BETA, 700 MHz APT SUPERCONDUCTING RF CAVITY WITH INDUSTRY \*

J. Kuzminski,<sup>#</sup> General Atomics, San Diego, CA

K.C.D. Chan, R. Gentzlinger, F. Smith LANL Los Alamos National Laboratory, NM

### Abstract

We have designed and fabricated a prototype  $\beta = 0.64$ , 700 MHz, 5-cell superconducting cavity in support of the Engineering Development and Demonstration (ED&D) effort for the Accelerator Production of Tritium (APT) project. The design incorporates all of the features of the production cavities. To develop future potential U.S. suppliers for the production cavities, a technology transfer program was initiated. In the first phase of the program the U.S. suppliers are using LANL supplied tooling, expertise, and niobium to fabricate the same prototype cavity. This paper addresses our experience in the fabrication of the ED&D cavity. It also describes interactions with various industries involved in the fabrication of other cavity components.

### 1 INTRODUCTION

An extensive ED&D effort is underway at Los Alamos National Laboratory (LANL) in support of the Preliminary and Final Design of the APT project. One of the goals of ED&D is to demonstrate performance of superconducting RF (SCRF) cavities to be used in the high-intensity proton linac, to assess difficulties in manufacturing large number of such cavities, and to optimize the final design. General Atomics (GA), selected by DOE as a partner to the prime industrial contractor for the APT project, is actively involved in ED&D program as a member of the SCRF team, serving as a liaison between LANL and industry.

### 2 ED&D CAVITY DESIGN

The design of ED&D medium- $\beta$  SCRF cavity is described in detail in a paper submitted by to this conference [1]. The cavity is made from high-purity bulk niobium (Nb) of RRR > 250. Each cavity has a system of two tuners that allow cavity tuning at the operating temperature of 2.15 K. In addition, special bulkhead-bellow assemblies are provided to support the LHe vessel. A computer generated 3D view of the cavity is depicted in Fig 1. A detailed statement of work (SOW) and manufacturing drawings based on this design, were made available to potential cavity manufacturers.

\*Work supported by DOE under contract No. DE-AC04-96AL89607.

<sup>#</sup> Email: jozef.kuzminski@gat.com

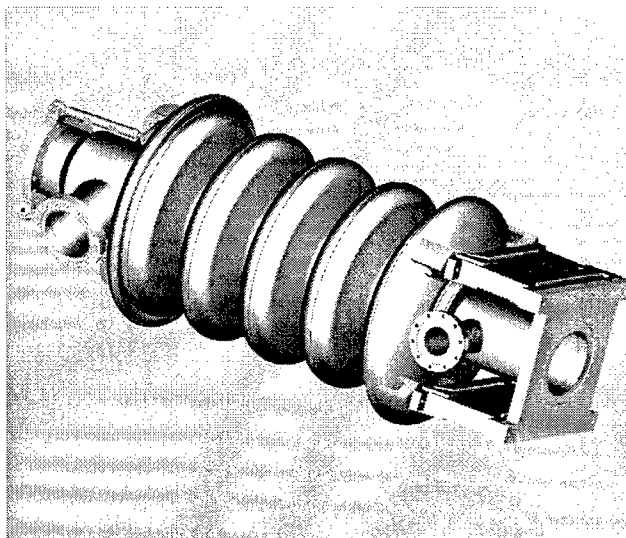


Figure 1. Computer generated layout of the medium- $\beta$  SCRF cavity. Two tuners are visible on the right-side. Ports for power coupler are located on the left-side.

In addition, in August, 1998, the LANL SCRF team completed fabrication of the first five-cell, medium- $\beta$  cavity prototype. The valuable experience gained during this exercise is being transferred to industry.

### 3 MANUFACTURING OF THE CAVITY

Over the past twenty years, a great wealth of experience in manufacturing superconducting cavities has been accumulated at various laboratories and some industries around the world [2]. Most of this experience is related to fabrication of SCRF cavities for electron accelerators. However, little experience exists in fabrication of medium- $\beta$  SCRF cavities for proton accelerators. The present scale of accelerator projects such as APT requires delivery of several hundred SCRF cavities. For such large projects to succeed, industrial participation is mandatory. Therefore, from the beginning of the ED&D program, industry has been included in the process of manufacturing prototype cavities. This process was structured in the following way:

- Identify qualified suppliers of high-quality Nb material for cavity manufacturing
- Identify qualified suppliers of special subassemblies (such as Titanium (Ti) bulkheads-bellows subassemblies and tuners )

- Acquire the world's best SCRF cavity for the ED&D program through a competitive bid process, open to all qualified manufacturers.
- Transfer this technology to U.S. industry

### 3.1 Nb Material

The quality of Nb sheet for SCRF cavity fabrication is one of the most important factors in determining the final performance of the cavity. Therefore, a special material specification was developed that defined impurity levels, material and electrical properties including RRR value, and provided requirements for finished Nb sheets. Today, industry is able to deliver high-quality material with  $RRR > 250$  that satisfies such stringent requirements. Three qualified suppliers of Nb sheets were identified. Each supplier has implemented a Quality Assurance QA program approved by the purchaser to ensure the quality of supplier materials. In addition, the RRR measurements were performed on supplied samples by the independent certified laboratory to validate the Nb sheets.

### 3.2 Special Titanium Bulkhead-Bellow Subassemblies

The ED&D SCRF cavity design calls for Ti vessel to contain LHe. The choice of Ti was made for the following reasons:

- Coefficient of thermal expansion (CTE) for Ti is almost the same as for Nb
- Electron-beam (EB) weldability of Ti to Nb
- Immunity of Ti to residual magnetic field



Figure 2. Special titanium bulkhead-bellow subassembly manufactured by industry.

Because of the limited space between the power coupler flange and the end cell, special edge-welded bellows were designed and fabricated by industry. One of the requirements was that the bellows integrity would survive 15,000 full-strokes cycles (assumed lifetime) at operating temperature of 2.15 K. Recent tests performed at Thomas

Jefferson National Accelerator Facility at 77 K showed that bellows survived up to 75,000 full cycles.

### 3.3 Cavity Half-Cell Formation

Deep drawing is frequently used method for half-cell fabrication. This process however is mainly used in large-scale production because of the high cost of forming dies. For a limited series of cavity prototypes, spinning or hydroforming is a more preferred method. In addition, experience shows that the final geometry of half-cells formed by spinning may be better controlled. One of the manufacturers of the cavity prototype built under this program chose spinning as the method of half-cell formation. The tolerances in the geometry of the half-cell were met. This method of half-cell formation is relatively inexpensive and rather fast, but requires a constant QA control to ensure proper final geometry. Alternatively, another manufacturer used hydroforming as a method of half-cell formation. Here again, a constant QA control of formation process is required.

### 3.4 Stainless Steel- Niobium joints

The ED&D design calls for Conflat™ flanges to connect the SCRF cavity to the other components. All flanges are made from 304 stainless steel. Since welding of Nb to stainless steel is impossible, brazed joints were developed to join the Conflat™ flanges to Nb tubes. LANL developed a brazing procedure that uses a NIOBOR™ layer (82% Au+18% Ni). Another manufacturer used a proprietary procedure. Figure 4 shows a brazed, large tuner stainless-steel Conflat™ flange brazed to a Nb beam tube.

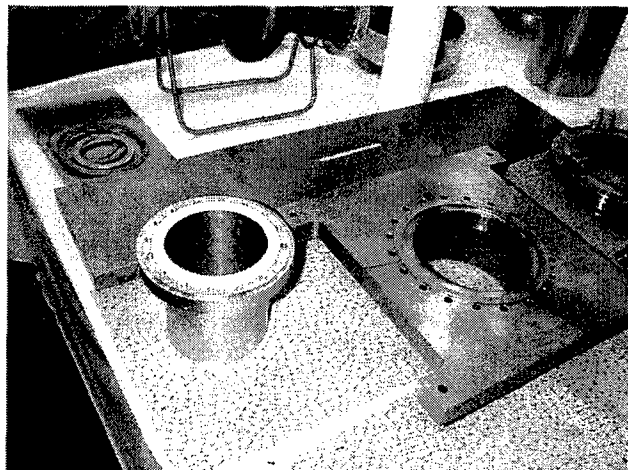


Figure 3. Conflat™ 304 stainless-steel flanges brazed to Nb tubes. The large square flange is a tuner flange; the round one is a power coupler flange.

Once the brazing of the stainless-steel Conflat™ flanges to Nb tubes was performed, the manufacturers were requested to test the parts for possible leaks according to

the following procedure: the parts were thermally cycled between 77 K (liquid nitrogen boiling temperature) and 373 K (water boiling temperature), then tested for possible leaks. This operation was performed three times for each brazed joint.

#### 4 TECHNOLOGY TRANSFER PROGRAM

Within the U.S. industry, there is presently little experience in manufacturing a large number of Nb SCRF cavities. Therefore, a special technology transfer program was initiated. For this program, one qualified company with previous experience in fabrication of accelerator components was selected. Company personnel was invited

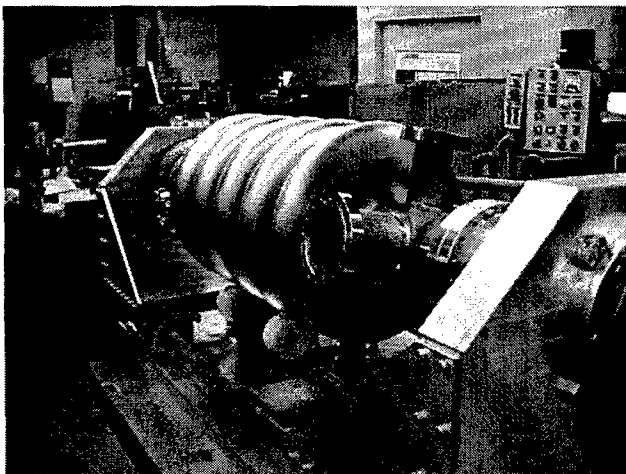


Figure 4. ED&D SCRF cavity prototype fabricated by the U.S. industry

to LANL to witness all steps of fabrication of the LANL cavity prototype, including half-cell formation, buffered chemical polishing, and electron-beam (EB) welding. During their visits, an exchange of information occurred that allowed the potential manufacturer to prepare a realistic manufacturing plan. All manufacturing drawings were supplied with essential fabrication tooling including rotatory welding fixture. After the contract was awarded for the manufacture of a SCRF cavity prototype, members of the SCRF team regularly visited the manufacturer's plants to provide advice on various manufacturing steps, witnessed the progress, and shared experiences. These visits were followed by periodic teleconferences to assess difficulties that might occur, in the process of cavity fabrication, and to ensure the compliance of the final product to SOW requirement. Fig. 4 shows a cavity prototype fabricated through this collaborative effort. The experience gained during this technology transfer program was judged positive by both parties. It suggests that U.S. industry is capable of delivering SCRF cavities for a large accelerator program like APT.

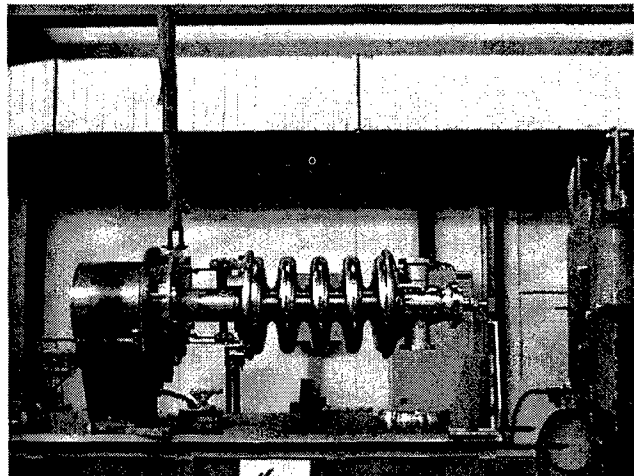


Figure 5. ED&D SCRF cavity mounted for the final EB welding.

#### 5 CONCLUSIONS

Two medium- $\beta$  SCRF cavities were successfully fabricated by industry in the frame of the ED&D program. One cavity, shown in Fig. 5, is the first of four to be manufactured by industry under contract with APT according to the LANL design that incorporates all of the features of the production cavities. These cavities are equipped with the bulkhead-bellow assemblies and dummy tuners. The cavities will be soon cold tested at LANL to determine the accelerating gradient and unloaded quality factor  $Q_0$ . The two best will be selected for use in the assembly of the first APT cryomodule. In addition, a SCRF cavity prototype has been manufactured by U.S. industry in the spirit of technology transfer, using LANL-supplied tooling and expertise. That cavity does not include bulkhead-bellow assemblies or a dummy tuner. The preliminary tests show that the frequency of this cavity and the field flatness meet the requirements of the ED&D program.

#### 6 REFERENCES

- [1] R. Gentzlinger, et al. Design, Analysis, and Fabrication of the APT Cavities (Paper No. MOP 127 submitted to this conference.)
- [2] Proceedings of the International Workshops on RF Superconductivity. (Seven published volumes)

# APT CRYOMODULE ASSEMBLY PROCESS AND MOCKUP MODEL\*

B. Campbell, K.C.D. Chan, E. Newman<sup>\*</sup>, and R. Valicenti  
Los Alamos National Laboratory

## Abstract

The cryomodule for the APT  $\beta=0.64$  high energy accelerator incorporates either two or three RF cavities, two sets of magnetic shields, one active heat shield, multi-layer insulation blankets, cryogenic plumbing for the shields and cavities, power couplers, cavity spokes and cavity frequency tuners. Maintaining cavity cleanliness is the most important aspect of the cryomodule assembly. The clean assembly of the cryomodule is done in a class 100 clean room. The final assembly, such as tungsten inert gas welding used to join the cryogenic plumbing, is done in a controlled environment. To address the assembly issues early in the design process, a full-scale mock-up of the entire cryomodule was fabricated. In this paper we will also describe the assembly process, and illustrate how the mock-up facilitated the procedures.

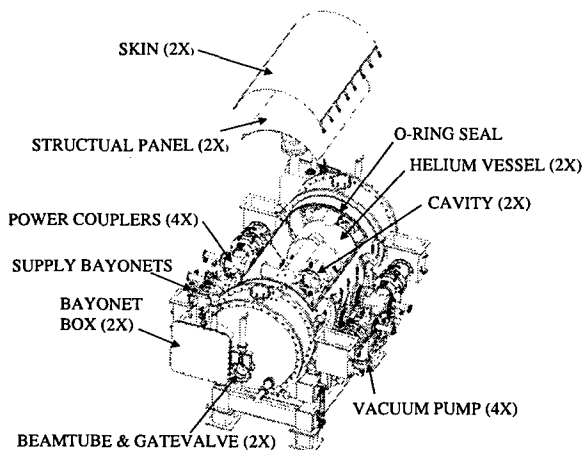


Figure 1: The  $\beta=0.64$ , two cavity, ED&D cryomodule.

## 1 INTRODUCTION

When the design of the superconducting accelerator was initiated for the APT program, the cryomodule stood out as one of the important building blocks. Failure or success of the accelerator depends on how well the cryomodule performs. It is the centrepiece, where all of the components are integrated together. The program made a decision to build a mock-up of the cryomodule before the real one would be fabricated. This mock-up would allow the designers and engineers to review their designs in a full-scale model before they were implemented later.

The six requirements for this mock-up are: 1) it will represent the actual dimensions with enough detail to

effectively represent the final product. 2) it will be constructed out of various materials, which are selected for ease of manufacturing and minimal cost. 3) it is a living piece of equipment, it should be capable of being revised quickly and easily. 4) it could be used, as a tool for doing planned performance experiments that otherwise couldn't be tested until the real article was built (i.e. measuring the magnetic field at the cavity). 5) the mock-up should be capable of being substituted for the real thing for fit checks and component evaluation. 6) its appearance should be satisfactory, it will be the only thing the program will have to show for a long period of time. The  $\beta=0.64$  ED&D cryomodule design is shown in Figure 1. The mock-up was modelled around this design.

## 2 CRYOMODULE/MOCK-UP DESIGN

This section will give a brief description of the current cryomodule design shown in Figure 1 and how that design is modelled in the mock-up assembly Figure 2.

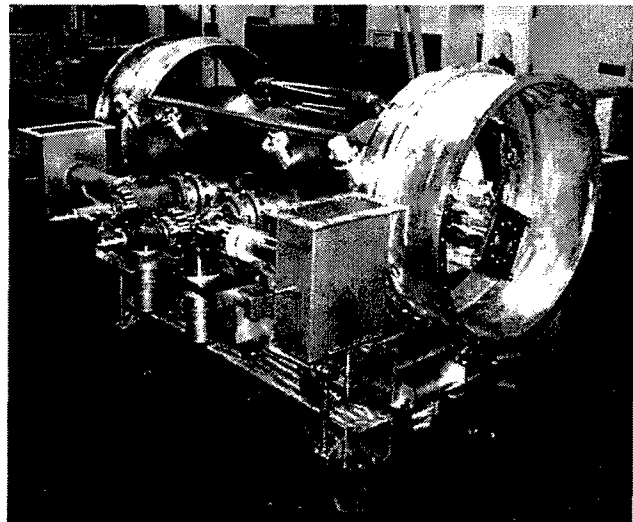


Figure 2: The  $\beta=0.64$ , two cavity, cryomodule mock-up.

### 2.1 Vacuum Tank

This vacuum tank uses the same design approach as was used in the CERN-LEP "wrap-up" cryomodule [1],[2]. The approach maximises accessibility to the cryomodule. The CERN-LEP wrap-up design has one fixed stave on which all of the penetrations to the cryomodule are mounted. The stave is welded at each end to the vacuum vessel end bulkheads. The vessel is sealed to the atmosphere using an elastomer o-ring. Removable staves are added around the circumference of the vessel to keep the thin cover from collapsing. A thin stainless steel cover is wrapped around the vessel covering the o-ring.

\* Work supported by the US Department of Energy.

\* Email: enewman@lanl.gov



Buckles, with one end mounted to the cover and the other to the stave, are tightened causing the cover to compress the o-ring. This design has worked very well. There is a maximum amount of accessibility to the cavities inside when the removable staves are removed. APT adopted this approach because of the accessibility to the cavities and the success CERN has had with the design.

There are some differences between the CERN and LANL design approaches. The CERN cryomodule has one power coupler per cavity where APT will have two. The CERN power coupler penetrates the upper quadrant of the cryomodule through the only permanent stave. The two APT couplers are on opposite sides of the cavity and are on the horizontal plane. This requires the APT vessel to have 2 permanent staves. The thin stainless steel cover is split into two pieces, one on top as shown in figure 1, and one on the bottom. Two separate o-ring grooves will be machined into the vessel.

The APT cryomodule vacuum tank will have a top opening which will be approximately 120° of the circular annulus. A similar large opening will be in the bottom. This provides for excellent access for assembly and laminar airflow in the clean room. This is shown in Figure 1 where the structural panel and vacuum skin are raised above and the magnetic, heat shields and the multi-layer insulation are removed. This design also provides for easy cleaning of the vacuum tank before it is moved into the clean room.

The main vacuum vessel of the mock-up was fabricated out of 6061 aluminium and maintains the same material thickness and sizes as the actual design, which is 310 stainless-steel plate. It is barely tack welded together for structural integrity, and therefore is not intended to be vacuum leak tight. This represents the overall design, including the vacuum sealing techniques used on the large top and bottom openings.

## 2.2 Support Stand

The support stand is fabricated out of 8" square 6061 aluminium tubing with 0.18" wall thickness. The overall dimensions are the same as the real stand, but unlike the final design as the total weight of the mock-up is approximately 3,000 pounds compared to the approximate 10,000-pound weight of the real cryomodule. The mounting legs have been replaced with heavy-duty casters for ease of movement.

## 2.3 Cavity and Helium Vessel

The APT 5-cell,  $\beta=0.64$  cavity is fabricated from RRR (Residual Resistivity Ratio) 250 niobium for the cavity cells and RRR 40 niobium tubing for everything else [3]. The two ends of the cavity as well as on all of the ports protruding from the beamtubes have stainless-steel conflat® flanges brazed to them. A titanium liquid helium vessel encloses the cavity to provide the 2.15 K environment the cavity will operate in. Each cavity

assembly is supported with eight diagonal spokes from the vacuum vessel wall. The mock-up cavity assemblies are constructed out of a combination of aluminium and wood. This assembly only represents the outer contour of the helium vessel and cavity including the tuner mechanism. The eight diagonal spokes are included and are mocked-up using brass threaded rod

## 2.4 Power Coupler

The APT power couplers are designed to deliver a maximum of 250 kW per coupler to the cavity [4]. There are 2 couplers per cavity. A WR1500 waveguide section is transitioned to a coax line. There will be two coaxial windows in the line to make the air to vacuum transition. The coax line will go through a right angle transition into the power coupler. The power coupler is a coaxial line with the outer conductor fabricated from copper plated stainless steel. The inner conductor is fabricated from oxygen free copper. The assembly is supported from the cryomodule using a flexure, which constrains the unit in five degrees of freedom. The transverse direction is left to permit contraction during cool down.

The mock-up power coupler outer conductors are modelled from acrylic tubing. One station is clear to view the internal components. All vacuum flanges are commercially available ConFlat type knife-edge seals. The gate valves and turbo pumps are of wood.

## 3 ASSEMBLY PROCEDURE

The assembly procedure for the cryomodule is complex and important. Having the mock-up greatly visualises this entire process and allows for testing and developing these procedures. The superconducting cavity is extremely sensitive to dust and any type of contamination on its interior surface. Therefore the assembly of the cavity and its components must be done in a very clean environment. A class-100 clean room will be used to do the assembly. To minimise the number of components to be brought into the clean room, the assembly is divided into two phases. The first phase, the clean assembly, includes the components that have to be assembled in order to seal the cavity. Once sealed, contaminants cannot enter the cavity. The cavity can then be moved outside the clean room into phase 2 the final assembly. The remainder of the equipment would then be installed without concern of contaminating the cavity.

### 3.1 Clean Assembly

The assembly in the clean room would consist of the vacuum tank, 2 cavity/helium vessel assemblies, 4 power coupler assemblies, 4 HOM couplers, 2 rf pick-up probes, an inter-cavity spool piece, 16 spokes, 2 gate valves and all of the assembly hardware. This assembly has been demonstrated on the mock-up. The mock-up clearly shows that it is impossible to approach the vacuum tank from either side. The location of the power couplers in



the APT design blocks the access to the center of the cryomodule. The mock-up shows the necessity of a tool to support the vacuum vessel and also provides access from underneath.

### 3.2 Final Assembly

The final assembly of two of magnetic shields, one active heat shield, multi-layer insulation blankets, extensive cryogenic plumbing, and remaining components are then installed outside the clean room. The power couplers do not allow access to the cryomodule during this process. A rotating fixture was developed so the cryomodule can be rotated 90° to allow access to the center Figure 3.

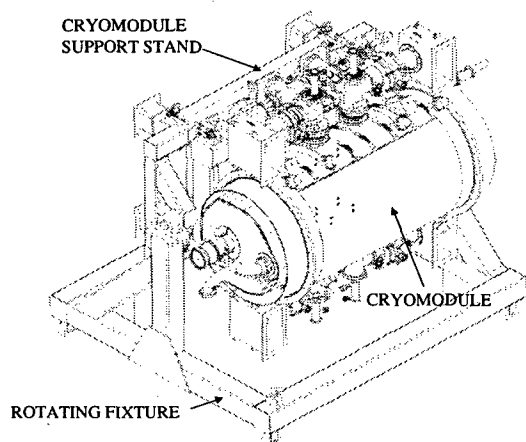


Figure 3: Rotating assembly fixture.

## 4 SIX MOCK-UP REQUIREMENTS

### 4.1 Representation of the final product

The components of the mock-up assembly were designed after reviewing the actual drawings and layouts. Where it was critical to have the actual size of the component, the mock-up component would have the same dimensional tolerances. In other areas where the dimensions weren't so critical, off-the-shelf components were used. Material selection was very important.

### 4.2 Material Selection:

The materials for the mock-up components were selected to facilitate the manufacturing process and minimise cost, but still provide an accurate model where required. Wood was used as the fabrication material in many places. It is cheap and easy to work with, it is easy to modify and it doesn't have any residual magnetic fields.

No magnetic materials were incorporated into the mock-up. The stainless-steel conflat® flanges were the only potential source of magnetic fields in the actual cavity design. The same flanges were used in the mock-up. This should create an accurate assessment of the magnetic fields exposed to the cavity.

### 4.3 Easy to Modify:

The design of the mock-up allowed it to be modified easily. Since many of the components are made from wood and other cheap easy to work with materials, modifications are easy to do.

### 4.4 Experimental Tool

The mock-up will be used to evaluate the effectiveness of the magnetic shielding. This way the magnetic shielding can be evaluated for sufficiency before the cryomodule is fabricated.

### 4.5 Component Evaluation

The mock-up can give the designer and engineer time to reflect on the design. In one instance, after reviewing the cavity support system, a potential virtual leak was discovered. The gas trapped in the capsule over the spoke adjustment mechanism had no way to be evacuated.

Also the mock-up could be used to fabricate components in parallel. The thermal and magnetic shields could be fit checked on the mock-up prior to being installed in the cryomodule. The MLI thermal blankets could be trimmed using the mock-up and then installed in the cryomodule.

### 4.6 Appearance

The mock-up was available for show and tell session's two years before the actual cryomodule will be delivered. Everything in the cryomodule has been painted and looks clean and neat. It has been used as a prop to describe the concept of the superconducting accelerator.

## 5 CONCLUSION

One never appreciates the value of a mock-up until after it has been built. It is a very useful and cheap tool for evaluating ideas and designs. It is also very useful as a tool to aid others to visualise the concepts being proposed by the designers and engineers.

It helps prevent schedule delays due to redesign by highlighting shortfalls early in the fabrication cycle.

## REFERENCES

- [1] B.M. Campbell, "Design Status of the Cryomodules for the APT Linac", Padoua Italy, (Oct 1998)
- [2] B.M. Campbell, "Engineering Design of the APT Cryomodules", for LINAC"98", Chicago, (1998)
- [3] R. Gentzlinger, "Design, Analysis, and Fabrication of the APT Cavities", for PAC"99", New York City, (Mar 1999)
- [4] R. E. Lujan, "Development of the SCRF Power Coupler for the APT Accelerator", for PAC"99", New York City, (Mar 1999)

# SUPERCONDUCTING RF LAB FACILITY UPGRADES AT LOS ALAMOS\*

D. J. Katonak<sup>#</sup>, B. Rusnak, LANL, Los Alamos, NM

## 1 ABSTRACT

Research and testing of multi-cell superconducting cavities demands extensive contamination control resources to achieve high-cavity fields. Facility upgrades at Los Alamos National Laboratory (LANL) included the modernization of test equipment, expanding and modernizing cleanroom facilities, improving safety, and expanding the high-pressure rinse cleaning process equipment. Each upgrade was integrated into the facility to enable users to assemble prototype cryomodules. The scope of the upgrades, the new installed capability, and budget and schedule for certain aspects of the project are discussed in this paper.

## 2 INTRODUCTION

Previous research at LANL focused on single-cell superconducting cavities at 805-MHz to 3-GHz. These cavities required minimal assembly and testing space. Testing larger 700-MHz multi-cell cavities, with the associated higher x-ray emissions, required the expansion of our current laboratory resources. We needed to increase floor space, reduce radiation exposure, and improve the procedure for handling the cavity test assembly.

## 3 PROJECT SCOPE

Facility upgrades for this project included the expansion of the 800 ft<sup>2</sup> class-100 cleanroom to approximately 2600 ft<sup>2</sup>. This will accommodate processing and assembly of longer 5-cell 700-MHz cavities as well as scheduled cryomodule construction, utilizing up to four helium vessels. Outside the cleanroom, work on the cavity test area included adding x-ray shielding to the test area to better contain radiation. A mezzanine was added to support the cavity test structures for assembly.

### 3.1 Test Area

The Superconducting RF (SCRF) Lab, originally designed for the lower radiation levels resulting from single-cell cavity tests, needed additional shielding in the cryostat area for multi-cell cavity tests. Our goal was to contain the higher radiation levels expected from testing larger cavities, making personnel exposure consistent with

ALARA (As Low As Reasonably Achievable), a LANL policy. This prompted the design and development of a hydraulically operated shielding system. Since the cavity test structure is sunk below floor level, the majority of the x-rays are emitted vertically; the shielding was designed to accommodate this geometry. The type and quantity of material needed was determined through analysis. Typically, higher density materials provide more effective shielding. Due to its lower density and space constraint in the SCRF Lab, concrete was eliminated. Lead was also eliminated due to LANL's safety concerns with lead. The material chosen was steel. The goal was to keep the emissions below 100 mrem/hr measured at a 30 cm distance at full field level from the source. Analysis determined 8 inches of steel in the top, 2 inches on three sides, with 3 inches on the side closest to the test console, where personnel will be regularly stationed, would suffice. The shielding shown in Fig. 1, is moved over the

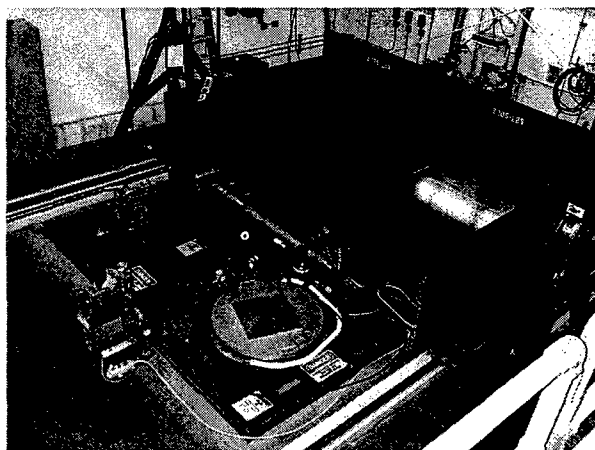


Figure 1: Shielding system at LANL's SCRF Lab

test area by two hydraulic cylinders during energized testing.

To facilitate the handling of the cavity test assembly, a mezzanine was constructed as shown in Fig. 2. The mezzanine improves accessibility to the insert assembly, improving serviceability and eliminating top-heavy wheeled carts that were previously utilized.

\* Work supported by the US Department of Energy

<sup>#</sup> Email: katonak@lanl.gov



Figure 2: Mezzanine for cavity test assembly

### 3.1 Cleanroom

The old cleanroom, originally designed for single cell testing, needed more cleanroom floor space. In preparation for cleanroom installation, additional electrical circuits were needed, and we wanted to bring the building electrical up to code. The old electrical system routed circuits from panels to multiple rooms throughout the facility. During the upgrade, many of these circuits were rerouted such that each room would have its own panel. Panels and circuits were added, and existing circuits were rerouted. One panel was dedicated specifically to the cleanroom and its associated electrical. This approach reduced confusion and made for an easier cleanroom installation.

A great deal of work went into defining a cleanroom that would meet our needs. The floorplan, as shown in Fig. 3, was determined by cryomodule size, available floorspace, and our intended cleaning process. First we defined our space requirements by considering cavity and cryomodule size. We could neither infringe on the space of other tenants, nor could we add-on to the existing building. We planned to clean each piece of hardware in successively cleaner areas. Next we defined our cleaning process which included ultrapure water, compressed air to drive high pressure pumps, and ultrapure nitrogen for drying.

We began researching cleanroom contractors, to find one that could meet our needs. Clean Air Technology (CAT) was able to provide a modular cleanroom that would accommodate our unusual building geometry. CAT provided the cleanroom, a local general contractor provided the electrical, mechanical, fire protection and

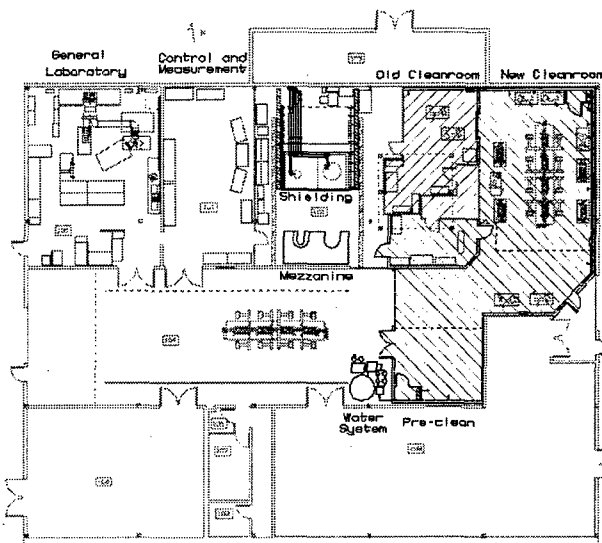


Figure 3: Current floorplan layout showing cleanroom, shielding, mezzanine and ultrapure water system

ultrapure water system work. While this approach supported the end goal, in retrospect, it would have been helpful to utilize a general contractor with experience in cleanroom installation. For example, on one occasion concrete was cut and removed generating dust during the assembly of the cleanroom, temporarily compromising cleanliness. A more experienced general contractor familiar with cleanroom installations understands the importance of cleanliness, and would plan tasks to maximize contamination control integrity. Constant oversight by an individual knowledgeable of the users needs and possessing the authority to make on-site decisions was critical to timely project completion. Issues related to project coordination and design arose frequently and most were dealt with on-site which helped maintain the momentum of the project.

### 3.2 Water System

A new larger capacity ultrapure water system was needed to clean the increased volume of the multi-cell cavities. Polyvinylidene fluoride (PVDF) piping was used in much of the system as well as to supply the cleanroom with ultrapure water for cleaning. The system is capable of delivering 2000 gallons per day of ultrapure water with the following water quality:

Residue	0.1 ppm
Total Oxidizable Carbon	5 ppb
Silica, dissolved	1 ppb
Particles/liter	500 counts

Water quality specification was based on ASTM grade E-2.

## 4 THEORY OF OPERATION

The facility improvements were designed to be used in concert with the goal of reliably achieving specified gradient at Q in cavities installed in a cryomodule. The

installed cleanroom and ultrapure water system are used to rinse cavities after buffered chemical polishing (BCP) and to clean cavities by spraying them with ultrapure water at high pressure. The cavities would then be sealed and transported and affixed to cavity testing inserts that are suspended on the mezzanine. Cavity vertical testing would be done to determine if the cavities made the specified field at Q and to evaluate the limiting mechanism. The installed radiation shielding over the vertical test cryostats is required for reducing personnel exposure to the higher x-ray levels that are produced from the multi-cell superconducting cavities during field emission.

The tested cavity would then be taken back into the clean room where the cavity exterior is cleaned with high-pressure ultrapure water. The assembly procedure for the Accelerator Production of Tritium (APT) cryomodule necessitates all components assembled together in the cleanroom, e.g., cavities, power couplers, flanges, and cryomodule support structures, be thoroughly cleaned with high-pressure ultrapure water. This step is needed to minimize possible contamination during cryomodule assembly that could degrade cavity performance.

## 5 COST AND SCHEDULE

One person was assigned to project controls, scheduling and budgeting. Schedules and budgets were updated on a biweekly basis, tracking progress and spending. Budget figures are presented in Table 1 for our project.

### Cleanroom

Cleanroom construction and installation	\$0.7M
Demolition, building mods, engineering, design, inspection, project management	\$1.0M
Total Project Cost	\$1.7M

### Shielding and Mezzanine

Shielding construction and installation	\$100K
Mezzanine construction and installation	\$ 15K
Demolition, electrical, mechanical	\$ 65K
Total Project Cost	\$180K

Table 1: Budget for SCRF Lab Facility Upgrade

The project was originally scheduled for January-October '98, however delays extended the schedule into December '98. This schedule reflects all facets of the project, initial concept development, assembling a project team, forming the design team, soliciting contractors, project construction, and inspection. Some schedule slip can be attributed to difficulties in scheduling outages for electrical and fire protection systems. Outages had to be coordinated with other tenants in the building and those being fed power from our facility.

## 6 CONCLUSION

LANL now has a cleanroom totaling 2600 ft<sup>2</sup>. The pre-assembly areas are class-1000 environments while the main assembly area is a class-100 environment, a photo is shown in Fig. 4. The facility upgrades project gives



Figure 4: Inside cleanroom at Superconducting RF Lab

LANL a greatly increased capability for testing superconducting cavities. We now have the ability to clean and test 700 MHz multi-cell cavities, and can construct cryomodules inside a class-100 cleanroom.

The shielding system allows cavity testing at higher field levels while reducing worker exposure to radiation, complying with ALARA policy. Adding a mezzanine reduced manual labor and provided easier access to the cavity test assemblies. It provided a stable platform from which to work and eliminated ladder usage.

## 7 ACKNOWLEDGEMENT

The authors would like to thank the personnel of PM (Project Management) Division and BUS-5 (Business Operations, Procurement) group at LANL who graciously contributed and made this project a success.

## DEVELOPMENT OF THE SCRF POWER COUPLER FOR THE APT ACCELERATOR

Eric N. Schmierer, Richard E. Lujan, Brian Rusnak, Brian Smith, W. B. Haynes, Cort Gautier, J. A. Waynert, Frank Krawczyk, Los Alamos National Laboratory, Los Alamos, NM, Jack Gioia, General Atomics, Los Alamos, NM

### Abstract

The team responsible for the design of the Accelerator Production of Tritium (APT) superconducting (SC) radio frequency (RF) power coupler has developed two 700-MHz, helium gas-cooled power couplers. One has a fixed inner conductor and the other has an adjustable inner conductor (gamma prototype and alpha prototype). The power couplers will be performance tested in the near future. This paper discusses the mechanical design and fabrication techniques employed in the development of each power coupler. This includes material selection, copper coating, assembly sequences, and metal joining procedures, as well as the engineering analyses performed to determine the dynamic response of the inner conductors due to environmental excitations. A bellows is used in both prototype inner conductors in the area near the ceramic RF window, to compensate for thermal expansion and mechanical tolerance build-up. In addition, a bellows is used near the tip of the inner conductor of the alpha prototype for tuning the power coupler after it is installed on the accelerator. Extensive analytical work has been performed to determine the static loads transmitted by the bellows due to thermally induced expansion on the inner conductor and on the RF window. This paper also discusses this analysis, as well as the mechanical analysis performed to determine the final geometric shape of the bellows. Finally, a discussion of the electromagnetic analysis used to optimize the performance of the power couplers is included.

### 1 INTRODUCTION

The superconducting portion of the 1100 MeV APT accelerator will have numerous five-cell cavities. Each cavity will require two power couplers, which will transmit up to 420 kW of continuous RF power at a 700 MHz frequency. RF power is transmitted to the accelerator from a klystron via WR 1500 waveguide at atmospheric pressure. A waveguide-to-coaxial conductor transition will be located near the RF cavity. Accelerator vacuum will be maintained through the coaxial conductor by a planar coaxial ceramic window located in the coaxial conductor portion of the window assembly. Figure 1 shows a cutaway view of a power coupler and a vacuum window assembly on a cryomodule.

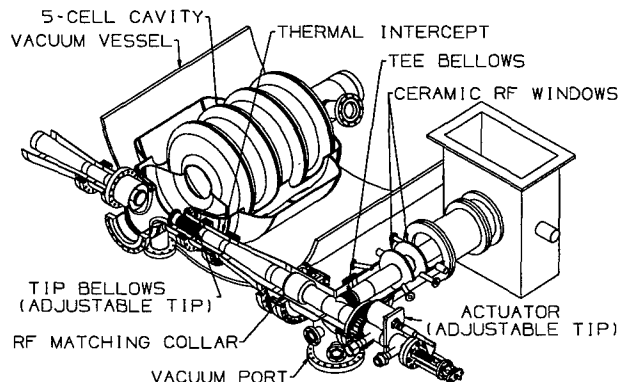


Figure 1: Power Coupler, Window, Cryomodule Assembly

### 2 RF ANALYSIS

The 420 kW RF power is delivered to each five-cell cavity by two power couplers. To ensure a reliable long-term operation for this plant-type facility, an attempt was made to create a power coupler design using features and components suggested by recent experience gained at other accelerator laboratories. These features include planar coaxial windows (a standard in high-power klystrons), coaxial couplers (successfully operated at high-power, e.g., at DESY [1]), positioning of the RF windows outside the line-of-sight of the proton beam, an additional vacuum-pump port in the quarter wave stub region for a good vacuum at the windows (recent experience at KEK [2]), and provisions for a simple cooling scheme of the center conductor. These were integrated into a new power coupler design. To achieve this design, extensive three-dimensional electromagnetic modeling has been done with the MAFIA electromagnetic simulator [3]. The modeling procedure started with the design of separate components and benchmarking the simulations by building and measuring some of these components [4]. Then a fully integrated study was performed with interaction with RF window fabricators.

The simulations investigated several variations of sub-components (various quarter-wave stubs and matching devices), and multiple iterations with mechanical and thermal evaluations. The thermal evaluation of the RF power deposited onto the inner and outer conductor was derived from the three-dimensional RF simulations. Figure 2 shows the MAFIA analytical model of the quarter wave stub.

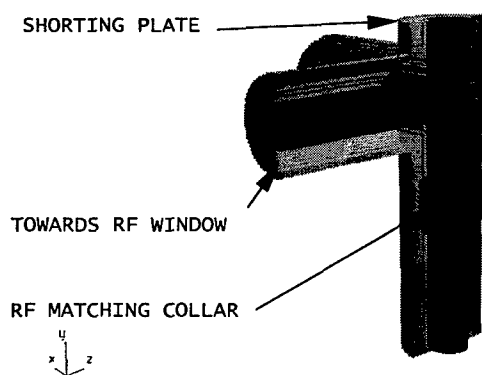


Figure 2: MAFIA Analytical Model

### 3 THERMAL ANALYSIS

A 200-node, axisymmetric model using the finite difference approximation was made to describe the inner and outer conductors. The model includes grey body; diffuse; infra-red radiation exchange; conduction through stainless steel, copper, and niobium; RF heating (travelling or standing wave power distributions); and convection cooling of the inner and outer conductors.

Detailed results for the inner and outer conductors have been published [5]. The inner conductor is found to be adequately cooled for both travelling and standing waves by using 300 K helium at 1.2 atmospheres pressure, flowing at 3 g/s through a 3-mm annular space formed by a stainless-steel sleeve within the copper inner conductor.

The outer conductor cooling approaches considered distributed counter-flow and localized thermal intercepts. The selected cooling scheme was the result of an extensive trade-study which considered: integration of the power coupler cooling into the cryomodule; impact on the cryoplant and distribution system; room temperature refrigeration input power; and manufacturability, maintainability, and reliability issues. The selected configuration is a double point thermal intercept where the low temperature thermal intercept inlet fluid is 4.6 K, 12-bar helium. After exiting the low temperature intercept, the supercritical helium is used to intercept heat loads from the beam tube, thermal shield, and structural supports. It is then circulated through the power-coupler high-temperature intercept. The fluid is returned to the cryoplant at about 30 K.

### 4 MECHANICAL DESIGN

The WR 1500 waveguide-to-coaxial conductor transition is of the tee-bar type and it is water or air cooled. The transition is integrated into the RF window assembly. The coolant(s) is also circulated inside the inner conductor section of the RF window assembly to the interface with the power coupler. Cooling air is also circulated between the ceramic windows. The coaxial conductor is nominally 6.125 in. diameter from the tee-bar location through the

ceramic window and the quarter-wave stub, to an area that is approximately 17.25 in. from the shorting plate. At this location, the coaxial conductor tapers down to nominally 4.06-in. diameter through a distance of 8.44 in. The coaxial conductor remains this size through the interface of the power coupler with the five-cell cavity. The inner conductor is supported at the shorting plate and is cantilevered through a distance of approximately 36.43 in. The center of the RF matching collar is located 11.87 in. away from the shorting plate. A nominal 2.60-in. diameter bellows is used at the intersection of the two coaxial conductors, which comprise the quarter-wave stub geometry. The adjustable inner conductor has a nominal 1.71-in. diameter bellows located near its tip. The RF window assembly connects to the inner conductor at a re-entrant receiver located at the interface. The conductive material for the inner conductor is oxygen-free electronic grade copper, ASTM F68-93 class 2 or better. The material for the receiver and both bellows is beryllium copper, B194 alloy 25. The 300-K helium is delivered to the intake plenum located at the rear of the inner conductor. Inside the plenum, the flow is orificed and split so that some of the coolant is circulated through a stainless-steel liner towards the tip. The coolant is returned through the annular space formed by the outside of the stainless-steel liner and the inside of the copper tube. The beryllium copper receiver and bellows in the quarter-wave stub region are cooled with the coolant flowing through a small supply tube that provides helium directly onto the bottom of the receiver and flows down the inside of the bellows. Figure 3 shows the inner conductor coolant flow path.

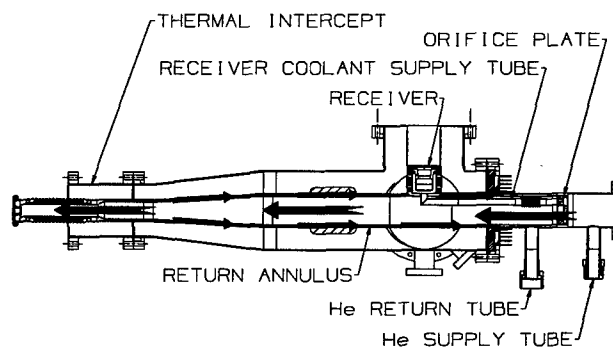


Figure 3: He Coolant Flow Path

All copper-to-copper joining for the inner conductor is specified as e-beam welding. To expedite fabrication, however, tungsten-inert gas (TIG) welding with appropriate final machining was approved. All copper-to-stainless steel joints are furnace brazed. The outer conductor material is stainless steel type 304, whose conductive surfaces are electroplated with copper per specification APT-CG-RFPC-001. The double point thermal intercept is integrated with the outer conductor as a flanged spool piece. Metal seal flanges are used at all

RF/vacuum connections with modified copper gaskets to enhance RF integrity. A vacuum pumping port is located in the vicinity of the quarter wave stub. The RF analysis indicates that the geometry of the port is such that an RF grill is not needed at this location.

Using COSMOS/M Ver. 2.0 linear dynamic module, a finite-element model was developed and fundamental modes of vibration calculated for the inner conductor. The first four were 39.7 Hz, 55.9 Hz, 180.5 Hz, and 187.4 Hz for the tip of the gamma power coupler. For the tip of the alpha power coupler, they were 29.96 Hz, 35.71 Hz, 101.6 Hz, and 206.4 Hz, with an assumed damping coefficient of 0.01. The harmonic analysis of the tip resulted in a Q of 40. The first source of excitation directly attached to the alpha power coupler is the 250 l/s vacuum pump. The specified displacement of the vacuum pump applied to the shorting plate resulted in a RMS displacement of the tip of  $1.6 \times 10^{-5}$  m. Using a random vibration excitation previously obtained from another accelerator facility, the RMS displacement of the tip was  $3 \times 10^{-6}$  m.

The force required to make the RF joint at the interface with the RF window assembly was large enough to warrant mechanical testing. Two receivers were tested to 4200 lbs., resulting in no detectable yielding of the receiver material.

## 5 BELLOWS DEVELOPMENT

The inner conductor is constrained by the ceramic vacuum windows and the shorting plate located on the quarter-wave stub. The tee-bellows must accommodate thermally induced expansion and any misalignments of the assembly when docking the vacuum window assembly to the power coupler, so the ceramic windows must react any forces transmitted by the bellows. Maximum allowable forces on the ceramic windows of 3-lb. axial force and 10-lb. lateral force were set as design goals. Based on anticipated thermally induced expansion and installation compression, spring rates of 150 lb./in. maximum axial and 1000 lb./in. maximum lateral are required of the bellows. This assumes no mechanical assembly preloads. The tip bellows allows adjustment of the inner conductor tip. The tip-bellows spring rate was specified at 150 lbs./in. maximum axial, with a compression of 0 in. to 0.6 in.

Bellows convolution shape was determined from RF analysis and was optimized for fabrication and spring rate requirements. Three materials were pursued. They are Be-Cu, electro-formed Cu, and Cu-plated stainless steel. Be-Cu was the primary choice because of its superior mechanical properties. An electro-formed copper bellows was the second choice. Type II electro-formed copper has a better yield strength than OFE Cu but is still susceptible to work hardening, and there are issues with outgassing, weldability, and consistency in the bellows convolution

thickness. Other electro-form alloys and configurations were considered but were not pursued. Cu plated stainless steel would add the process of brazing Cu end-rings for welding to the assembly and would add the issues associated with the plating process. It is unknown whether thermal and mechanical cycling, high power RF, or electron-beam welding would degrade the plating, create Ni flashing interference, or affect the plating adhesion.

## 6 CONCLUSION

The engineering and experimental effort has yielded a power coupler design that analysis indicates has a power transmission of better than -40dB at or around the 700-MHz operation frequency. Figure 4 shows the broad band transmission/reflection curve of the power coupler taken from electromagnetic simulations. Fabrication of three gamma prototype power couplers has been completed, and they are scheduled to be tested on the Room Temperature Test Bed [6] in the near future.

S11/S21

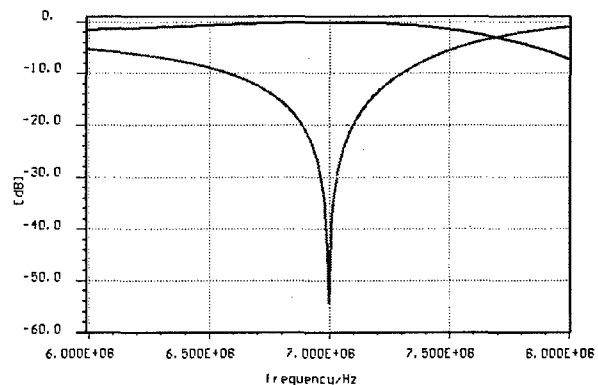


Figure 4: Transmission/Reflection Curve

## 7 REFERENCES

- [1] B. Dwersteg, DESY, "Progress of TTF High Power Input Coupler Design at DESY," Proceedings of the 8th RF Superconductivity workshop, Abano Terme, Italy, (1997).
- [2] S. Mitsunobu, KEK, "High Power Input Coupler and Windows," Proceedings of the 8th RF Superconductivity workshop, Abano Terme, Italy, (1997).
- [3] The MAFIA Collaboration, "User Guide," CST GmbH, Darmstadt, Germany.
- [4] Frank Krawczyk, LANL, "Electromagnetic Modeling of Cavities and Power Couplers for SC High-Current Proton Accelerators," Invited Talk at the APS Spring Meeting, Columbus, Ohio, (1998).
- [5] J.A. Waynert, F.C. Prenger, "A Thermal Analysis and Optimization of the APT 210 kW Power Coupler," Proceedings of LINAC98, Aug. 1998, Chicago, IL.
- [6] J. Gioia, General Atomics et.al, "A Room Temperature Test Bed for Evaluating 700-MHz RF Windows and Power Couplers for the Superconducting Portion of the APT Accelerator," Proceedings of PAC' 99, New York, NY, (1999).

# COMMISSIONING OF THE SUPERCONDUCTING RF CAVITIES FOR THE CESR LUMINOSITY UPGRADE\*

S. Belomestnykh<sup>#</sup>, P. Barnes, E. Chojnacki, R. Ehrlich, R. Geng<sup>+</sup>, D. Hartill, R. Kaplan, J. Knobloch, E. Nordberg, H. Padamsee, S. Peck, P. Quigley, J. Reilley, D. Rubin, J. Sears, V. Veshcherevich, Laboratory of Nuclear Studies, Cornell University, Ithaca, NY 14853, U.S.A.

## Abstract

The new superconducting RF system consisting of four single-cell cavity modules is an important part of the CESR Luminosity Upgrade. We describe the commissioning of the first three accelerating modules. This includes *in situ* testing and conditioning, pulsed power and beam processing of RF windows, commissioning of various cryogenic feedback loops, measuring cavity spacing and phasing with beam, and high-current operation.

## 1 INTRODUCTION

Since 1997 the new superconducting RF (SRF) system for the CESR Luminosity Upgrade [1, 2] is in the stage of installation and commissioning of cavities one by one. This allows the collider to continue its high energy physics operation with short shutdowns for cavity installations. As it was described in Ref. [1], there are two RF straight sections in CESR, East one and West one, each hosting two single-cell cavity cryomodules. Correspondingly, cavities are called E1 and E2, W1 and W2. Each cavity pair is fed by RF power from one klystron via WR1800 waveguide and an RF power splitter (magic T or hybrid) and by cryogen liquids via a station cryogen distribution box.

The first of four cavities, E2, was the first superconducting HOM damped cavity in the world installed for a long-term operation. Initially, its performance with beam was limited by multipacting in the ceramic window and waveguide region of cavity RF coupler [3] in travelling wave regime. This limitation was eventually overcome after using several techniques of *in situ* processing, and after several cavity warm ups to room temperature. Obtained experience and understanding of the nature of limitations allowed us to introduce several important modifications to the cryomodule design and preparation procedures. After that, installation of the second module, E1, in October'98 and its subsequent commissioning was significantly easier. W1 cavity is installed in CESR during February-March'99 shutdown, and is being commissioned. W2 cryomodule is being assembled and is scheduled for installation in summer.

\*Work supported by the National Science Foundation.

<sup>#</sup>Email: sab@lns62.lns.cornell.edu

<sup>+</sup>On leave from the IHIP, Peking University, Beijing 100871, PRC.

## 2 ACCELERATING MODULE PREPARATION AND TESTS

Prior to assembly of the superconducting cavity into a horizontal cryostat [4], all major components, such as cryostat, cavity, RF window, and HOM loads, are subjected to acceptance tests. The cryostats are tested at liquid nitrogen temperature with dummy cavity inserts. Upon receiving from a manufacturer, all Nb cavities are tested in a vertical cryostat [5]. The cavity preparation procedure includes chemical etching by 1:1:2 BCP acid mix with the acid temperature below 15°C, then high-pressure rinsing and drying in a class 10 clean room. All high vacuum components are assembled and leak checked in the clean room, then vacuum baked. RF windows are processed in pairs in standing wave mode to 125 kW and in travelling wave mode up to 450 kW CW [3]. After assembly is complete, a cryomodule (Figure 1) must pass a final high power acceptance test. In different tests our four cavities reached maximum accelerating gradients of 12 MV/m, 10 MV/m, 11 MV/m, 7.8 MV/m.

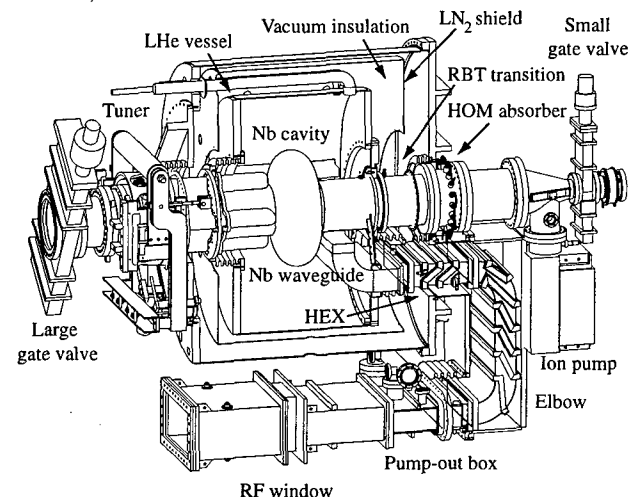


Figure 1: The CESR B-cell cryomodule.

## 3 CONTROLS AND DATA ACQUISITION

Each cryostat has several cryogenic feedback loops. Most important of them are: cryostat liquid helium level, helium bath pressure, and waveguide heat exchanger (HEX) gas flow loops. PID controllers are used in all feedback loops. The station cryogen distribution box



contains the supply and return control valves, which are used to regulate the level and bath pressure correspondingly. The helium level is kept constant within  $\pm 1\%$ , and the pressure is kept constant within  $\pm 0.02$  psi. The waveguide HEX is a short section of vacuum waveguide cooled by cold helium gas borrowed from the cryostat (Figure 1). A feedback loop keeps HEX gas flow constant by regulating a gas flow valve installed in the HEX return line.

In addition to incorporating SRF into the CESR data acquisition system, a new graphics display system, based on the "little language" GDL (Graphics Display Language) developed by S. Peck, is used to show data from the database on an X-terminal [6]. The GDL provides such features to display signals and parameters as labelled schematics, strip charts, meters, and tables. These features allow easy access to data and straight forward interface between users and sensors.

## 4 OPERATING EXPERIENCE WITH THE FIRST CAVITY

### 4.1 Installation and commissioning

E2 SRF cavity was installed into CESR storage ring in September '97 in place of one of the 5-cell normal-conducting (NRF) copper cavities. At first, E2 cavity operated at a field of 6.3 MV/m. Later the field was raised to 7 MV/m.

The cryomodules have gate valves on both ends. Therefore, we connect them to the machine vacuum chamber under vacuum and they do not require reprocessing from scratch. The base pressure in the cold cryomodule without RF is 3 to  $5 \times 10^{-10}$  Torr at the taper and RF window. The pressure rise with RF and beam is about one order of magnitude by the end of a three month CESR running period. After the first cool down, as the beam current increased in CESR, hard vacuum trips occurred in the cavity window region at currents around 230 mA. The vacuum trips occurred when the power in travelling wave, i.e. forward power minus reflected power, was 90 kW. This was a repeatable limit at different beam currents due to gas evolution in the input window/coupler region. We associated those vacuum trips with multipacting in the RF coupler region.

### 4.2 RF coupler in situ processing

To increase the power delivered to beam we explored several processing techniques. RF processing without beam and off cavity resonance with powers up to 160 kW CW had essentially no effect on the travelling wave vacuum trip limit.

It is a well known approach to suppress multipacting in coaxial RF windows by applying DC bias *electric* field on the inner conductor. This external field disturbs trajectories of electrons and changes resonant conditions of multipacting. Depending on strength and direction of

the external field, the multipacting can be either suppressed or enhanced. In the case of a rectangular waveguide it is easier to achieve the same goal by using DC *magnetic* field instead. We used 10 Gauss transverse magnetic field of permanent magnets. This enhanced multipacting in the RF window region and allowed us to "clean" the surface of the ceramics and adjacent waveguide without beam. Later, calculations [7] confirmed that a transverse magnetic field enhances both intensity and bandwidth of multipacting zones. This technique advanced travelling wave limit to 110 kW.

Quite often, especially in case of "weak" multipacting, it is possible to use "beam processing". The beam injection is stopped as soon as window vacuum activity is detected and started again as soon as vacuum is improved. Alternatively, the RF phase between two RF stations can be adjusted to increase or decrease power to the SRF cavity. However, the beam is frequently lost during beam processing, making it slow and inefficient. We use it mainly as a way to check RF power limit after processing with other techniques.

The greatest success so far has been achieved when processing without beam by increasing power in the pulsed mode on or close to cavity resonance. Such processing allows us to process the coupler region in the travelling wave mode. Because the SRF cavity is heavily overcoupled without beam, the emitted power at RF shut-off is four times higher than the incident power. This creates the travelling wave mode for a very short time though. Changing the frequency around resonance shifts the standing wave pattern in the waveguide, and processes its different regions. Above 90-100 kW forward power, the cavity quenches and becomes close to matched load. At this and higher powers we disable the quench detector and allow the cavity to sit in quench state for entire duration of pulse, typically 10 ms at 10% duty cycle. By pulse processing to 150 kW, the beam power could gradually be raised to 140 kW and beam current to 350 mA. At this power level we observed for a first time dependence of the RF power on the cavity field: transmitted power is higher when there is bigger standing wave component. Computer simulations [7] confirmed that travelling to standing wave mixing ratio affects multipacting bands.

### 4.3 Operating experience

Alongside with normal vacuum actions (multipacting), which we were able to process, other, very fast, vacuum events were observed. Those events were accompanied by temperature rise on the HEX and huge spikes of hydrogen on RGA. We attributed this effect to releasing cryopumped hydrogen due to RF heating of the HEX surface and following arc. The number of fast vacuum trips was increasing with time and eventually they limited maximum RF power through the coupler. Analysis of the residual gas evolution [8] during cavity warm up showed that during 3 months of operation cold surfaces accumulated up to 7 equivalent monolayers of

hydrogen. RGA spectra showed different gas species. Most pronounced among them are hydrogen, carbon monoxide, and water vapour.

After warming up the cavity to room temperature and baking the window *in situ* to 110°C during scheduled CESR shutdown, the beam power delivered began to rise steadily and reached 180 kW. After about 2 months in operation, the ability of the cavity to deliver RF power began to deteriorate again due to the fast vacuum trips.

Operating experience obtained with the first SRF cavity allowed us to introduce several changes in cryomodule design and preparation procedure: i) to improve pumping speed near the RF window [9], we redesigned its pumping layout; ii) to lower heat deposition to the HEX wall due to RF losses and to improve cooling, we increased thickness of copper plating from 6.4  $\mu\text{m}$  to 25  $\mu\text{m}$  and increased helium gas flow through the HEX by a factor of three; iii) we rounded sharp corners in the vacuum waveguide; iv) baking temperature for RF window ceramics was increased from 110°C to 150°C, following suggestion in [10]; v) all high vacuum components, including copper plated ones, are now thoroughly vacuum baked. We did not bake all of the copper plated parts before, being afraid to damage plating.

## 5 HIGH BEAM CURRENT OPERATION

The second SRF cavity, E1, was installed in the machine in October'99. Its commissioning went very smoothly and we were soon able to reach and exceed 200 kW power delivered to beam by one cavity. Operating with two SRF cavities proved to be easier and more stable than with one SRF and one NRF cavity in the same pair. The history of RF power delivered to beam by the SRF cavities is shown in Figure 2. We must note that the RF coupler vacuum trips were the main limiting factor for the beam current increase only in the beginning of E2 cavity operation. Lately, as CESR reached total beam current in excess of 500 mA, a longitudinal dipole coupled bunch instability and overheating of some vacuum chamber components became the major limitations [11, 12].

To keep beam loading the same for both cavities, RF voltage equal for electron and positron beams and maintain interaction point in the center of the detector, it is necessary to carefully position cavities along the beam axis and adjust their waveguide feed lengths. This is especially important at high beam currents. The procedure of deducing errors in relative cavity spacing and phasing from RF forward and reflected power measurements with and without beam was developed by D. Morse at CESR (see appendix A in [13]). We use this procedure to verify installation and make fine adjustments when necessary.

One of the most important features of a CESR B-cell cavity is its low beam coupling impedance due to strong HOM damping [14]. Installation of the E2 and E1 SRF cavities increased beam current thresholds of a longitudinal dipole coupled bunch instability in CESR, though the total HOM impedance of the ring is still

dominated by remaining NRF cavities [15]. Beam-induced HOM power is dissipated in two ferrite-lined beam pipe absorbers [16, 17]. The maximum extracted E2 cavity HOM power was about 5.7 kW at 510 mA total current in two beams of nine three-bunch trains each. According to calculations [18] two tapers provide a significant portion of the cryomodule loss factor. Therefore, there are no tapers between E1 and E2 cavities.

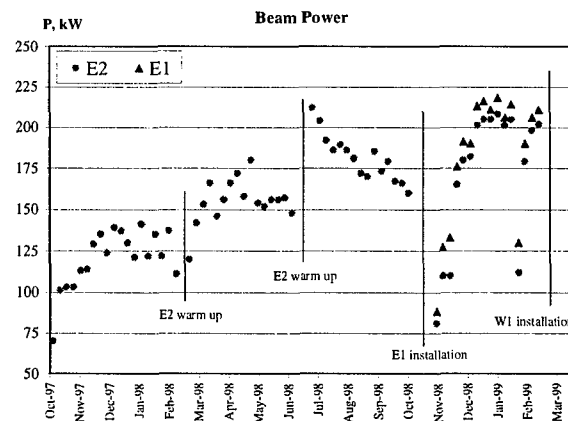


Figure 2: RF power delivered to beam by SRF cavities.

## 6 CONCLUSIONS

Three superconducting cavity modules are installed in CESR so far. Two of them have been successfully commissioned and are in operation. The third module is being commissioned now. The SRF cavities provided very safe and reliable operation with high beam currents up to 550 mA and allowed CESR to establish a new peak luminosity record of  $8 \times 10^{32} \text{ cm}^{-2} \text{ s}^{-1}$  as well as several integrated luminosity records. The fourth cryomodule is being assembled and is scheduled for installation in summer'99. Complete installation of all four HOM damped cavities will reduce ring broad band impedance by 48% and will provide stable operation of CESR with many bunches at high beam currents.

## 7 REFERENCES

- [1] S. Belomestnykh, et al., *Proc. 5th EPAC*, Vol. 3, pp. 2100-2103.
- [2] S. Belomestnykh, et al., *Proc. 1997 PAC*, Vol. 3, pp. 3075-3077.
- [3] E. Chojnacki, et al., *Part. Accel.*, **61**, pp. [309-319]/45-55 (1998).
- [4] J. Kirchgessner, et al., *Proc. 7th SRF Workshop*, Vol. 1, pp. 35-37.
- [5] D. Moffat, et al., *Proc. 1993 PAC*, Vol. 2, pp. 763-765.
- [6] R. Geng and S. Peck, Cornell LNS Report SRF/D980407-01.
- [7] R. L. Geng and H. Padamsee, *THAL5, these proceedings*.
- [8] R. L. Geng and H. Padamsee, MOP136, *these proceedings*.
- [9] R. L. Geng and P. Barnes, Cornell LNS Report SRF980227-02.
- [10] M. Neubauer, et al., *Proc. 5th EPAC*, Vol. 3, pp. 2059-2061.
- [11] D. L. Rubin, *Proc. 6th EPAC*, Stockholm, 1998.
- [12] A. Temnykh, *Proc. XVIII ICHEA*, Dubna, 1998.
- [13] S. Belomestnykh, et al., Cornell LNS Report SRF961217-04.
- [14] H. Padamsee, et al., *Part. Accel.*, **40**, pp. 17-41 (1992).
- [15] M. G. Billing and S. Belomestnykh, TUA18, *these proceedings*.
- [16] S. Belomestnykh, et al., *Proc. 1995 PAC*, Vol. 5, pp. 3394-3396.
- [17] E. Chojnacki, W. J. Alton, MOP77, *these proceedings*.
- [18] S. Belomestnykh, W. Hartung, Report SRF960202-01 (1996).

# CONDENSATION/ADSORPTION AND EVACUATION OF RESIDUAL GASES IN THE SRF SYSTEM FOR THE CESR LUMINOSITY UPGRADE\*

R.L. Geng<sup>††</sup>, H. Padamsee, Laboratory of Nuclear Studies, Cornell Univ., Ithaca, NY14853

## Abstract

Condensed/adsorbed gases can enhance field emission in superconducting cavities and deteriorate the input coupler performance in a superconducting RF system. It is therefore important to understand condensation/adsorption of residual gases in such a system. In this paper, we present some related results for the first two superconducting cavities installed in the CESR for luminosity upgrade. The total amount of adsorbed gases for different working periods are compared. Gas species are analyzed. A Monte-Carlo computer code is used to simulate the gas condensation/adsorption profile along the waveguide. The warm-up desorption curve is extracted, which might help us to understand the interaction between gas molecules and substrates. The pumping speed of the window pump-out box was evaluated by using the same code and was compared with the speed due to cryo-pumping. New designs of the pump-out box were explored to improve its pumping speed.

## 1 INTRODUCTION

Condensed/adsorbed gases can enhance field emission in superconducting cavities[1] and deteriorate the input coupler performance in a superconducting RF (SRF) system[2]. For SRF cavities installed in a routinely running accelerator, like B-cells for the CESR luminosity upgrade[3], the desorption and condensation/adsorption of residual gases are of great importance to the cavity performance, especially when high RF power and high beam current are involved. Possible gas sources in such a system include the ceramic window, beam line components nearby, and HOM absorbers. Gas molecules can be desorbed from surfaces of gas sources through different processes: heating of the ceramic window by RF power, heating of HOM absorbers by HOM power, bombarding of the waveguide and ceramic surfaces by multipacting electrons. The desorbed gases are finally condensed/adsorbed on the cold surfaces of the system, if not properly evacuated.

The implementation of SRF cavities (Fig. 1) for the CESR luminosity upgrade started from October 1997[4]. Till now, two cavities, referred to as E2 and E1, have been installed. During the commissioning period, it was found that the input coupler benefited a lot from room temperature warming-up cycles[5], during the course of which significant amount of gases evolved from the system. It was believed that gases condensed/adsorbed on the waveguide surface enhanced the secondary emission coefficient (SEC). As a result, more multipacting bands be-

came active[6] to cause RF trips. By warming up the cavity, most adsorbates were released, giving a "clean" surface with a lower SEC. Accordingly, the multipacting problem was alleviated.

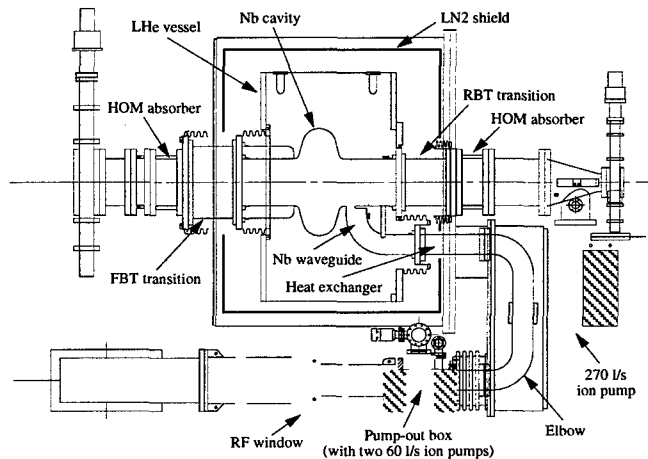


Figure 1: The SRF cavity for the CESR luminosity upgrade

It is always desirable to keep the gas load to the system as low as possible. This can be achieved by following ways. 1) Reducing gas content of gas sources, e. g. baking the window prior to the cavity cooling down. 2) Improving the pumping speed of the evacuating system.

## 2 GAS EVOLUTION BY WARMING-UP

During the cavity warming-up, ion pumps were used for evacuation with pressures monitored with cold cathode gauges installed near the pump ports. Fig 2 shows a typical pressure curve during a warming-up event. Total amount

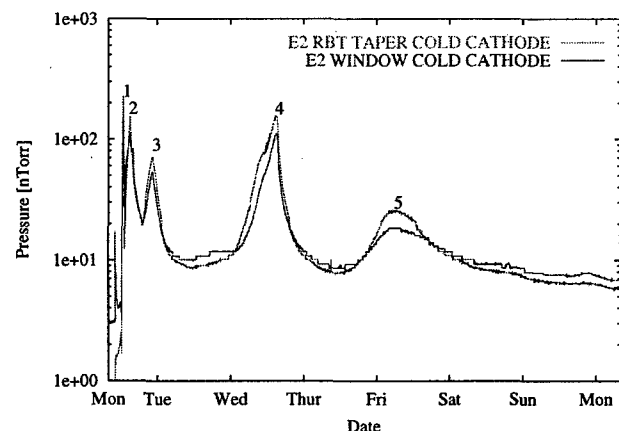


Figure 2: Pressures during the warming-up (E2, Jun.98)

\* Work supported by the National Science Foundation.

<sup>†</sup> on leave from IHIP, Peking University, Beijing 100871, PRC.

<sup>††</sup> Email: rg58@cornell.edu

of evolved gases during warming-up was obtained by pressure integration. Table 1 shows results for the E2 and E1

Table 1: Gas evolution during the warming-up

Cavity	Warm Up @	Gas evolution [torr-Liter]	Gas Layers [ $H_2$ eq.]
E2	Feb. 98	14.68	7.03
E2	Jun. 98	5.51	2.64
E2	Oct. 98	9.25	4.43
E2	Feb. 99	14.30	6.84
E1	Feb. 99	8.62	4.12

Table 2: Integrated  $P_b$  and  $I_b$  between CESR down

Cavity	Warm Up @	Total cold time [day]	$\int P_b dt$ [MW-hr]	$\int I_b dt$ [A-hr]
E2	Feb. 98	120	138	440
E2	Jun. 98	99	160	470
E2	Oct. 98	90	184	490
E2	Feb. 99	95	213	593
E1	Feb. 99	95	232	593

cavities in different warming-up events. Note that the layer number of gases is given in that of an equivalent amount of  $H_2$  over an area of  $3.3 \text{ m}^2$ , the total surface area of cold components, including the cavity, the cold He gas cooled heat exchanger (HEX), and the  $LN_2$  cooled RBT/GBT transitions and waveguide elbow.

Table 2 shows the total time that the cavity was cold, the integrated RF power delivered to the beam ( $P_b$ ) and integrated CESR current ( $I_b$ ) over the period between the current warming-up and previous CESR down. The first warming-up of the E2 in Feb. 98 gave roughly 7 layers of equivalent  $H_2$  with only a 138 MW-hr integrated beam power delivered in the past four months. After the first warming-up, we were able to deliver more beam power. We found the more integrated beam power in the past four months, the more gas evolution during the succeeding warming-up. However, the gas evolution seems not directly correlated with the cold time, neither with the integrated current. The first warming-up of the E1 in Feb. 99 gave only 4 layers of equivalent  $H_2$  with a 232 MW-hr integrated beam power delivered in the past four months. In Comparison, the E1 has a much abated gas load and better performance upon the first warming-up. It was believed that the baking of the E1 window prior to the installation helped a lot in reducing the gas load.

### 3 GAS SPECIES

In Fig. 2, one can see several distinct pressure peaks. This is suggestive that different gas species are desorbed over the warming-up period. Fig. 3 shows the desorption curves, the cavity pressure as a function of the cavity temperature. All desorption curves, both for the E2 and E1, show pressure peaks at the same cavity temperatures. (Note that

peaks between  $100^\circ\text{K}$  and  $120^\circ\text{K}$  are due to the turning off of the  $LN_2$  supply.)

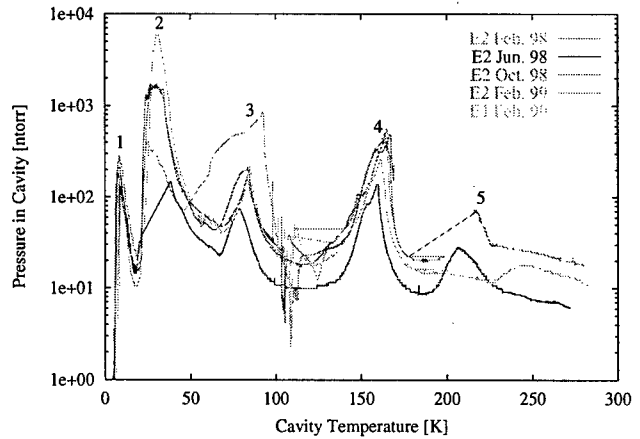


Figure 3: Warming-up desorption curves of cavities

RGA Spectrums, recorded during warming-up, indicates that residual gas species are mainly  $H_2$ ,  $H_2O$ , and  $CO/N_2$ , along with small amount of  $CO_2$ ,  $O_2$ , He and Ne. It is also indicated that different species prevail in different desorption peaks as shown in Table 3. For reference, temperatures of the cavity, the cold end of the HEX and the cold end of the elbow are also listed in the table. The exceptionally high amplitude of the third peak for the E2 warming-up in Feb. 98 suggests that excessive  $CO_2$  and  $CO/N_2$  were adsorbed between the installation and the first warming-up of the E2 cavity.

Table 3: Prevailing gas species and nominal temperatures of the cavity, the HEX cold end, and the elbow cold end at the time of desorption peaks

Peak #	Gas species	Cavity [ $^\circ\text{K}$ ]	HEX [ $^\circ\text{K}$ ]	Elbow [ $^\circ\text{K}$ ]
1	$H_2$ , He	9	22	85
2	$CO/N_2, H_2, O_2, Ne$	27	35	92
3	$CO_2, CO/N_2$	83	92	130
4	$H_2, H_2O, CO/N_2$	163	165	190
5	$H_2, H_2O$	230	220	240

### 4 WHERE DO GASES LODGE

Among all possible gas sources, special attention was paid to the ceramic window, from which most gas load was suspected to come. If not properly evacuated, those gases would condense/adsorb on cold surfaces of the waveguide, or even enter the cell of the cavity through the tongue.

When the cavity is at  $4.2^\circ\text{K}$ , measurements show that the elbow temperature ranges from  $180^\circ\text{K}$  (warm end) to  $80^\circ\text{K}$  (cold end) and the HEX temperature ranges from  $45^\circ\text{K}$  (warm end) to  $10^\circ\text{K}$  (cold end). Below  $120^\circ\text{K}$ ,  $H_2O$  vapor pressure is many orders of magnitude lower

than  $1 \times 10^{-9}$  torr[7]. This means that virtually all the residual  $H_2O$  would condense on the surface of the waveguide elbow, most likely that of the section from the middle to the cold end. By the same token,  $CO_2$ ,  $CO/N_2$  and  $O_2$  would condense on the surface of the HEX.

A Monte-Carlo simulation code, MOLFLOW[8], was used to estimate the condensation profile of  $CO_2$ ,  $CO/N_2$  and  $O_2$  along the HEX. A unity sticking coefficient ( $s$ ), regardless the condensation thickness[7], was used for these species. The results suggested that 90% of these gases would condense on the HEX surface with an exponential distribution. Only 10% of them might enter the Nb waveguide of the cavity.

The residual  $H_2$  is the hardest to condense ( $H_2$  vapor pressure is higher than  $1 \times 10^{-6}$  torr even at 4.2 °K). However, there are possibilities for the  $H_2$  to be adsorbed by a 4.2 °K Nb[9] and a 10 °K copper plated stainless steel[10][11]. Fig. 4 shows the simulation result on the

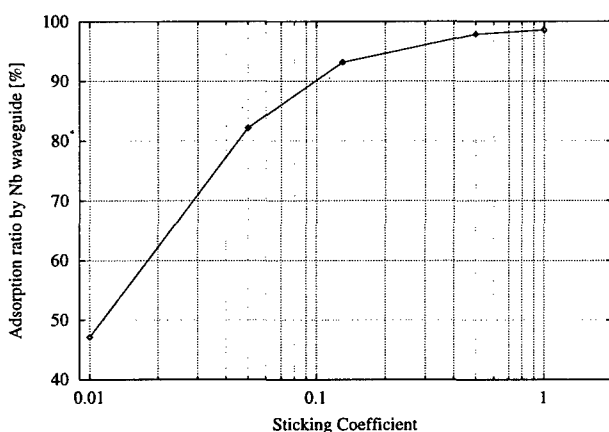


Figure 4: Ratio of the  $H_2$  adsorbed by the Nb waveguide to that enters the cell of the cavity as a function of  $s$

ratio of the  $H_2$  adsorbed on the Nb waveguide to that enters the cell of the cavity. Experimental data[12] show that the  $s$  of  $H_2$  on a clean Nb surface at 77 °K is 0.2 and decreases quickly with  $H_2$  uptake, reaching 0.05 after 3 mono-layers of adsorption. This suggests that more than 80% of the initial  $H_2$  gas load from the ceramic would adsorb on the surface of the Nb waveguide. The other 20% might be able to enter the cell of the cavity through the coupler tongue. With more  $H_2$  gas load, there are more chances for the  $H_2$  to enter the cell of the cavity.

According to the previous analysis, it is quite likely that the HEX and the top half of the elbow are well coated with condensable gases, like  $CO_2$ ,  $CO/N_2$  and  $H_2O$ . Those pre-coated condensates usually provide effective cryo-sorption of the  $H_2$ [7], which means that the chance of the  $H_2$  entering the cell could be much lower than 20%. In Table 3, it is shown that the  $H_2$  presents nearly in all the desorption peaks. This is a direct indication that part of the  $H_2$  is adsorbed on surfaces of the HEX and the elbow in mixing with condensable gases.

## 5 EVACUATING RESIDUAL GASES

A powerful evacuation system is always desirable to compete effectively with the cryo-pumping due to cold surfaces.

The estimated cryo-pumping speed is 600 l/s with respect to the gas load from the ceramic. MOLFLOW simulations show that the E2 pump-out box gives only a 30 l/s net pumping speed. Modifications on the E1 pump-out box were pursued. The net pumping speed was improved to 60 l/s.

To compete with the cryo-pumping, further improvement on the pump-out box is favorable. A suggested configuration, consisting of 250 shower drain holes, 120 mm ID elbows and 500 l/s pumps, will give a 320 l/s net pumping speed, which is hopefully able to compete with the 600 l/s cryo-pumping.

## 6 CONCLUSIONS

Gas evolution during warming-up of the CESR SRF cavities was evaluated. A few equivalent mono-layers of  $H_2$  were adsorbed on cold surfaces, even after several warming-ups. There seems to be a correlation between the integrated beam power and the gas evolution during the succeeding warming-up. Residual gas species were found mainly  $H_2$ ,  $H_2O$ , and  $CO/N_2$ . They condensed/adsorbed selectively on surfaces of different sections. The initial  $H_2$  was most likely adsorbed on the Nb waveguide surface. With heavier  $H_2$  gas load,  $H_2$  molecules could enter the cell of the cavity and adsorb on the cell surface. The current pumping speed of the pump-out box is much lower than that due to cryo-pumping. Further modifications on the pump-out box is necessary to compete with the cryo-pumping.

## 7 REFERENCES

- [1] Q.S. Shu et al., *IEEE Trans. Magn.* 25, 1868(1989).
- [2] E. Haeberl et al., *Proc. 7th workshop on RF superconductivity* (Gif sur Yvette, France, 1995), p.707.
- [3] H. Padamsee et al., *Proc. PAC91*, (San Francisco, 1991), p. 786.
- [4] S. Belomestnykh, these proceedings.
- [5] H. Padamsee, *Proc. EPAC98* (Stockholm, Sweden, 1998).
- [6] R.L. Geng and H.S. Padamsee, *these proceedings*.
- [7] R.A. Haefer, *Cryopumping: theory and practice*, Clarendon Press, Oxford, 1989.
- [8] R. Kersevan, MOLFLOW, a 3-D Monte-Carlo program, available from the author, now at ESRF, Grenoble, France; a C version has been developed at Laboratory of Nuclear Studies, Cornell University, available from N. Mistry.
- [9] M.G. Rao, P. Kneisel and J. Susta, *Cryogenics*, 34, 377(1994).
- [10] S. Anderson et al., *Phys. Rev.*, B40(12), 8146(1989).
- [11] E. Wallen, *J. Vac. Sci. Technol.*, A14(5), 2916(1996).
- [12] S.M. Ko and L.D. Schmidt, *Surf. Sci.*, 42(2), 508(1974).

# RF SYSTEM FOR THE SLS BOOSTER AND STORAGE RING

M.E. Busse-Grawitz, P. Marchand, W. Tron, Paul Scherrer Institute, CH 5232 Villigen PSI

## Abstract

The RF system which was adopted for the SLS (Swiss Light Source) initial phase [1] is based on the use of conventional, already well-proven equipment. In the storage ring (SR), it consists of four 500 MHz plants, each comprising a normal conducting (nc) single-cell cavity of the ELETTRA type, powered with a 180 kW CW klystron amplifier via a WR1800 waveguide line. In spite of the lower power requirement, one similar plant will be used for the booster with the intention of standardizing. Although the use of superconducting (sc) cavities has been ruled out as a starting solution, combining idle (no external RF source) sc cavities with the initial nc system is regarded as a possible way of further improving the beam lifetime in the SR when operating at very high brightness [2].

## 1 MAIN DESIGN PARAMETERS

The basic parameters of the SR which were determining for the design of the RF system are listed in Table 1. At the nominal energy of 2.4 GeV and beam current of 0.4 A, the radiation power to be restored by the RF system is 240 kW. A peak accelerating voltage of 2.4 MV (at 500 MHz) is needed to achieve the energy acceptance of  $\pm 3.5\%$ .

Table 1 : Basic SR parameters

Circumference L [m]	288.
Revolution frequency, $f_0$ [MHz]	1.04
Energy, E [GeV]	2.4
Radiation loss / turn, $\Delta U$ [MeV]	0.6
Beam current, $I_b$ [A]	0.4
Beam power loss, $P_b$ [kW]	240.
Momentum compaction, $\alpha$	7. E-4
Momentum spread, $\sigma_p$ [%]	0.09
Longitudinal damping time $\tau_s$ [ms]	4.5
Transverse damping time, $\tau_{x,y}$ [ms]	9.
RF frequency, $f_{RF}$ [MHz]	499.652
Harmonic number, $h = f_{RF} / f_0$	480
RF voltage, $V_{RF}$ [MV]	2.4
RF acceptance, $\epsilon_{RF}$ [%]	$\pm 3.5$
Bunch length, $\sigma_s$ [mm]	4.
Synchrotron frequency, $f_s$ [kHz]	7.5
Synchronous phase, $\phi_s$ [degree]	14.5

## 2 RF CAVITY ASSEMBLY

Four nc single-cell cavities of the ELETTRA type [3] with a shunt impedance of 3.4 M $\Omega$  and a quality factor of 40000 will provide the required RF voltage and power in the SR. The parameter values in Table 2 show that, using

four such cavities, the RF system has the potential for achieving the SLS requirement with a cavity input power ( $P_i / \text{cav}$ ) lower than 150 kW. Besides, would one of the four cavities be out of use, the operation at full beam current is still possible with an RF voltage of about 2 MV. The four cavities will be accommodated in pairs in two of the dispersion free, low  $\beta$ , 4 m long straight sections of the SR.

The input coupler must be capable to feed into the cavity a CW RF power of at least 150 kW (forward) and also to handle the full reflection. It will be similar to those operating in ELETTRA which are of the coaxial type, terminated by a coupling loop. Although the operating power at ELETTRA does not exceed 65 kW, the same coupler has successfully been tested up to 330 kW [4] and therefore should be capable to fulfil the SLS requirement. The coupling coefficient shall be adjustable within a range of 1 to 3.3 in order to match different beam loading conditions.

The cooling system consists of water flowing through pipes which are brazed on the cavity outer surface and must be able to remove up to 65 kW of power dissipation into the cavity wall ( $P_d / \text{cav}$ ). In addition, it shall be possible - thanks to the cooling system - to set the cavity operating temperature at any value within  $60 \pm 25$  °C with a stability of  $\pm 0.05$  °C. This is achieved by properly isolating the cavity and by re-circulating the cooling water through an appropriate heat exchanger water station (cooling rack) dedicated to each cavity. Controlling the cavity temperature - and therefore the HOM frequencies in a way to avoid resonance excitations by the beam - should allow to prevent coupled bunch instabilities [1,5].

A plunger tuner provides an additional degree of freedom in tuning the fundamental and HOM's.

The tuning of the fundamental frequency for variable beam loading - with different operating temperatures and plunger positions - will be performed by means of a mechanical system driven with a stepping motor which will change the cavity length (longitudinal squeezing or stretching), within the range of elastic deformation. In operation, the cavities will be automatically tuned by a regulation loop (see section 4).

Table 2 : RF operating parameters with 4 and 3/4 cav.

( $\beta_m$ ,  $\Delta f_m$  : optimum coupling factor and detuning)

$I_b$ [A]	$V_{RF}$ [MV]	$P_d / \text{cav}$ [kW]	$P_b / \text{cav}$ [kW]	$P_i / \text{cav}$ [kW]	$\beta_m$	$\Delta f_m$ [kHz]	nb of cav.
0.4	2.6	60.	60.	120.	2.0	26.	4
0.4	2.0	65.	80.	145.	2.2	24.	3

### 3 RF AMPLIFIER AND FEEDER LINE

Each cavity will be individually powered with a CW klystron amplifier capable to deliver more than 180 kW (efficiency > 60 %). The klystrons will be provided by EEV Ltd, the DC power supplies for the cathode and auxiliaries (anode modulation, cathode heating, focal coils, ion pump) by THOMCAST AG.

The DC power supply for the cathode is a Pulse Step Modulator (PSM), a technology currently used for broadcast transmitters [6]. Designed for 46 kV - 7.5 A, this PSM essentially consists of 68 power modules which are connected in series and supplied through their own secondary winding from two transformers. The two transformers are shifted in phase, resulting in a 12-pulse loading of the mains with a 6-pulse rectification in the module chain. Each one of the 68 modules represents an autonomous voltage source ( $U_s \approx 800$  V) which may be switched on/off individually by means of fast IGBT switches operating up to 14 kHz. The switching sequence and pulse duration is generated and supervised by the PSM control system such that the thermal loading of all modules is distributed equally. The switching frequency can be suppressed at the output of the module chain, by means of a low pass filter.

The main PSM features (efficiency, regulation speed and accuracy, compatibility with large variation of the load impedance) are well suited for our purpose. Moreover, the modular concept with high redundancy (up to four defective modules without performance degradation) makes it very reliable, easy to maintain and there is no need for HV crowbars.

The RF power delivered by the klystron is fed into the cavity input coupler via a WR1800 waveguide line including monitoring directional couplers as well as a circulator to isolate the klystron from the variable (beam-loaded) cavity impedance. All these waveguide components are commercially available. The four RF plants of the SR are arranged in pairs in two diagonally opposite RF stations. Figure 1 shows a layout of one of them.

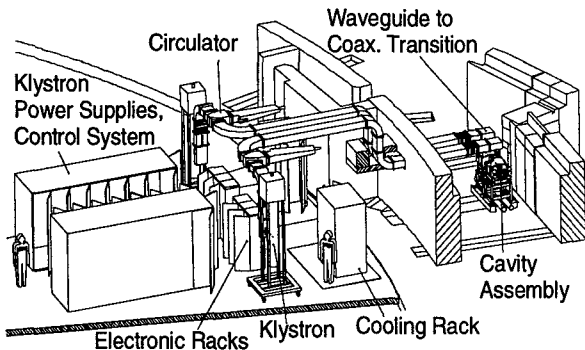


Figure 1 : Layout of one of the two SR RF stations

### 4 LOW LEVEL ELECTRONIC SYSTEM

The low level electronic system comprising standard frequency, amplitude and phase regulation loops as well as the amplifier drive chain and the RF signal measurement channels will be supplied by Sincrotrone Trieste. It will be based on the system operating in ELETTRA with minor modifications for the SLS purpose as described below. A simplified block diagram is shown in Figure 2.

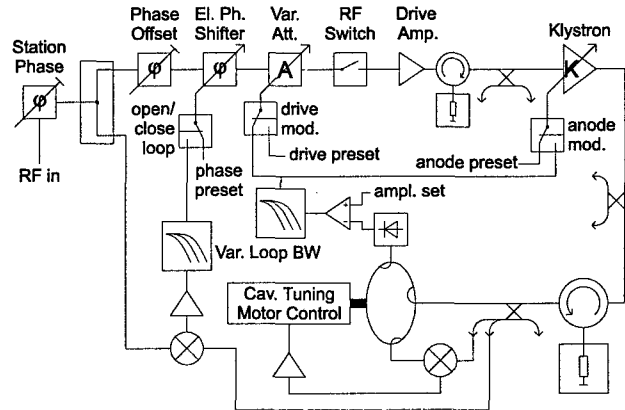


Figure 2 : Low level electronic system

The frequency regulation loop has a tuning range of  $\pm 200$  kHz which corresponds to a change in cavity length of  $\pm 0.2$  mm (within the limit of elastic deformation). This allows to handle cavity temperature variations of about  $\pm 20$  °C with a sufficient margin for the compensation of the largest beam loading effect which is around 25 kHz (see Table 2). The maximum tuning speed of 1 kHz/s is fast enough for injecting the full beam in less than 30 s and the sensitivity of the loop (adjustable between  $\pm 100$  Hz and  $\pm 1$  kHz) will be experimentally optimised such that to avoid undue wear of the tuner.

The amplitude loop whose 3 dB bandwidth is adjustable up to 5 kHz regulates the cavity accelerating voltage with a stability better than 1 % by controlling the drive power. The option for modulating the klystron anode voltage - instead of the drive power - is implemented as an alternative scheme of amplitude regulation.

The phase loop compensates for the phase changes (up to  $\pm 30$  °) in the amplification chain with variable power. It also has a 3 dB bandwidth adjustable up to 5 kHz and must ensure a phase stability of  $\pm 0.5$  °.

The bandwidth of both the phase and amplitude loops will be experimentally optimized to provide enough damping while remaining insensitive to the synchrotron frequency.

In the drive chain the signal from the 500 MHz master oscillator, after being split, phase and amplitude regulated, is amplified with a 50 W solid state amplifier. A fast RF switch at the input of the chain can remove within less than 5  $\mu$ s the driving RF signal under certain conditions (beam dump, klystron/cavity interlocks).

## 5 RF CONTROL SYSTEM

The RF control system will be produced in collaboration between THOMCAST and PSI. A block diagram is shown in Figure 3.

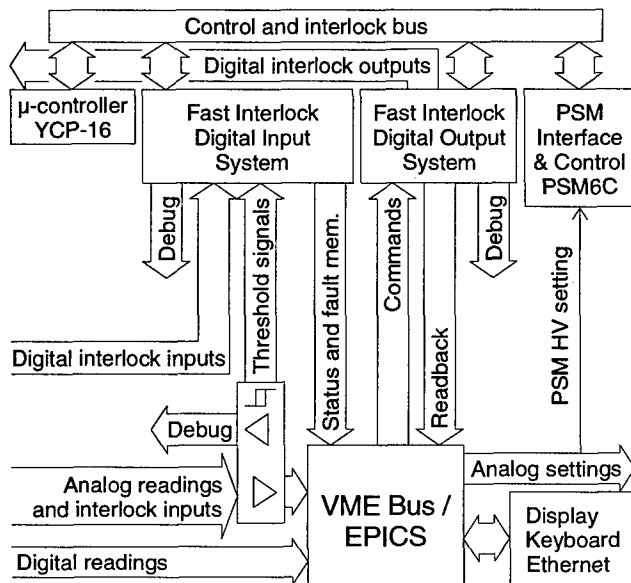


Figure 3 : Block diagram of the RF control system

The top level controller consists of a VME-bus crate operating under VxWorks and EPICS with an associated keypad and visual display. This constitutes the operator-machine interface.

The control of the PSM is ensured by the PSM6C unit, a THOMCAST standard control and interface system which communicates with the PSM modules via fibre optic links.

The interlock protection system consists of a fast microcontroller (YCP16 from THOMCAST) and digital input/output printed circuit boards with field programmable logic devices. The interlock state machine which controls the start-up and switch-off sequences of the various RF equipment parts is realised in YCP16 and each digital interlock input/ output signal has its own logic programmed locally. In this logic, it is programmed under which condition the input has to cause a fallback of the state machine and the output (action) is processed as a function of the actual state and commands from EPICS. The analog interlock inputs are converted into digital inputs by means of comparators with adjustable thresholds. For each interlock input, three memories are used which store the first fault event, the status of all the signals at that time and the sequence of the faults occurring afterwards (up to 9 events). The fault event and status information is available in EPICS and also indicated on the front panel of the printed circuit boards by means of two-colour LED's.

The different sub-units communicate via the control and interlock bus. Fibre optical links are used for all signals at high potential and the other input/ output signals are galvanically isolated by means of opto-couplers or

isolating amplifiers. The relevant analog and digital signals are also available on a connector panel for debugging purposes.

This system will be integrated in the SLS central control system - also based on VME and EPICS - for remote operation from the control room; nevertheless, it shall allow a stand-alone operation of each RF plant (independently of the SLS central system).

## 6 BOOSTER RF SYSTEM

A single cavity can provide the maximum RF voltage of 0.5 MV required for the booster. With the beam current of 12 mA, the cavity input power of 40 kW is significantly less than in the SR. However, with the intention of standardising we decided to use one 500 MHz plant similar to those of the SR. The major difference is that the RF voltage shall be cycled at 3 Hz by varying the reference voltage of the amplitude regulation loop as a function of the magnet field program. Contrary to the SR, the coupled bunch instabilities should not be an issue and therefore the cooling rack for the temperature control of the HOM frequencies is not needed.

## 7 POSSIBLE FURTHER UPGRADING

The RF system described before - although quite conventional and while operating at relatively conservative performance levels - should be capable to achieve the SLS nominal requirements.

The use of sc cavities has been ruled out as a starting solution. However, for improving the beam lifetime in the SR when operating at very high brightness, the initial nc system could be further complemented with idle (beam-driven) sc cavities. Within this scheme, the nc system provides the power to the beam and the sc system only contributes to the potential well. Two possible applications of such a system were considered: either doubling the fundamental RF voltage with one 500 MHz sc cavity, or lengthening the bunches - by a factor of about four - with one (possibly two) third harmonic sc cavity(ies) [2]. Computer simulations indicated that the latter option would be more efficient for our purpose [7] and this is therefore the approach presently investigated.

## 8 REFERENCES

- [1] P. Marchand, PSI Note SLS-TME-TA-1998-0011.
- [2] P. Marchand, PSI Note SLS-TME-TA-1998-0012 and these Proc.
- [3] M. Svandrlik et al EPAC98, p. 1817 - 1819, 1998.
- [4] M. Svandrlik, private communication.
- [5] M. Svandrlik et al, PAC97, p. 1735 - 1737, 1997.
- [6] THOMCAST AG, TSM6 - E.PM5, Sept. 1996.
- [7] M. Boege et al, these Proceedings



# POSSIBLE UPGRADING OF THE SLS RF SYSTEM FOR IMPROVING THE BEAM LIFETIME

P. Marchand, Paul Scherrer Institute, CH 5232 Villigen PSI

## Abstract

The RF system which was adopted for the SLS (Swiss Light Source) initial phase [1] is based on the choice of conventional, already well-proven equipment. The use of superconducting (sc) cavities has been ruled out as a starting solution. However, for improving the beam lifetime in the storage ring (SR) when operating at very high brightness, the initial normal conducting (nc) system could be further complemented with idle (only-beam-driven) sc cavities. Within that scheme, two different approaches have been investigated: either doubling the fundamental RF voltage using one 500 MHz sc cavity, or lengthening the bunches with one (possibly two) third harmonic sc cavity(ies) [2,3]. These upgrading options are discussed here.

## 1 INTRODUCTION

The RF system which was adopted for the SLS starting phase is described in more details in [1]. For the SR, it consists of four 500 MHz plants, each comprising a nc single cell cavity of the ELETTRA type, powered with a 180 kW CW klystron amplifier via a WR1800 waveguide line. The main characteristics of this system as well as the basic parameters of the SR are listed in Table 1.

Circumference, L [m]	288.
Revolution frequency, $f_0$ [MHz]	1.04
Energy, E [GeV]	2.4
Radiation loss / turn, $\Delta U$ [MeV]	0.6
Beam current, $I_b$ [A]	0.4
Beam power loss, $P_b$ [kW]	240.
Momentum compaction, $\alpha$	7. E-4
Momentum spread, $\sigma_p$ [%]	0.09
Longitudinal damping time $\tau_s$ [ms]	4.5
Transverse damping time, $\tau_{x,y}$ [ms]	9.
RF frequency, $f_{RF}$ [MHz]	499.652
Harmonic number, $h = f_{RF} / f_0$	480
Total RF voltage, $V_{RF}$ [MV]	2.4
Number of cavities, $n_{cav}$	4
Cavity shunt impedance, $R_s$ [M $\Omega$ ] [[M $\Omega$	3.4
Cavity quality factor, $Q_0$	40000
Cavity wall dissipation, $P_d$ [kW]	60.
Cavity input power $P_t$ [kW]	120.
Number of klystron amplifiers, $n_k$	4
Max. klystron power, $P_k$ [kW]	180.
Synchronous phase, $\phi_s$ [degree]	14.5
RF acceptance, $\epsilon_{RF}$ [%]	$\pm 3.5$
Bunch length, $\sigma_s$ [mm]	4.
Synchrotron frequency, $f_s$ [kHz]	7.5

Table 1: Main SR and RF parameters

In order to further improve the beam lifetime - which is dominated by Touschek scattering - in the SR when operating at very high brightness, the RF system described before could be upgraded following two different approaches: either increasing the energy acceptance by doubling the 500 MHz voltage or lengthening the bunches using a 3<sup>rd</sup> harmonic system. Both schemes would be advantageously realized in complementing the initial nc system with idle (only-beam-driven) sc cavities.

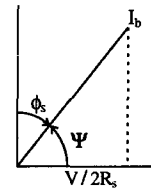
## 2 THE HYBRID "POWERED NC AND IDLE SC" RF SYSTEM

The basic idea is to separate the functions of the two RF systems in order to optimize their respective performance: the nc system supplies the power for restoring the losses per turn; the beam-driven sc system only contributes to the potential well [4].

### 2.1 Beam induced voltage in an idle cavity

The power lost by the beam passing through an idle cavity is:  $P_b = V I_b \cos \psi = -V I_b \sin \phi_s = V^2 / (2 R_s)$ ;

$V = 2 R_s I_b \cos \psi$ , is the cavity voltage induced by the beam,  $\psi$  is the cavity tuning angle defined as :  $\tan \psi = 2 Q_0 \delta f / f_r$  where  $\delta f = h f_0 - f_r$  is the cavity frequency detuning;  $\phi_s = \psi - \pi / 2$  is the synchronous phase.



If the cavity is detuned sufficiently far from resonance ( $\delta f \gg f_r / Q_0$ ), one gets:

$$\psi \approx \pi / 2, \phi_s \approx 0, P_b \approx 0 \text{ and } V \approx I_b (R/Q) f_r / \delta f.$$

A sc cavity with its very high  $Q_0$  is the ideal component for making use of the induced voltage while keeping the beam energy losses at negligible level: assuming a typical  $R/Q$  value of 50  $\Omega$  and the SLS nominal beam current ( $I_b = 0.4$  A), one finds that 2.6 MV are induced when the cavity is detuned by about 4 kHz at 500 MHz. This amount of detuning which corresponds to several thousands of the cavity bandwidth well fulfills the required condition,  $\delta f \gg f_r / Q_0$  and it remains much smaller than the revolution frequency. The induced voltage could be easily maintained even at extremely low current by controlling the detuning, still within the previous limits. The beam power deposited into the sc cavity, equal to the wall dissipation ( $\sim 50$  W), is negligible as compared to the radiation losses.

During the injection, the RF voltage in the sc cavity builds up with the current and the induced transients always remain quite tolerable. Note that, during the injection, the detuning of the sc cavity is a "free" parameter that can be set "at will". In the storage regime

the RF voltage of the sc cavity is controllable in closed loop via its frequency tuning system.

All the above considerations remain valid for a higher harmonic cavity.

## 2.2 Increase of the energy acceptance using a 500 MHz idle sc cavity

If one combines the previously described 500 MHz nc system with an idle sc cavity of same frequency and voltage ( $V_{sc} = V_{nc} = 2.6$  MV), one gets for the overall RF voltage an amplitude of 5.2 MV and a synchronous phase,  $\phi_s$  of  $6.5^\circ$ . As compared to the initial situation with only the nc system, this corresponds to an enhancement factor of 1.6 in terms of *RF energy acceptance* (from 3.7 % up to 5.8 %). Concurrently, since the sc cavity is detuned such as to produce additional focusing, the bunches are shortened by a factor of 1.4. Taking into account both effects, the Touschek life time could theoretically be improved by a factor of about 3. With the introduction of mini-gap undulators, the actual efficiency of this method could finally be limited below the previous expectation by the *lattice energy acceptance*; computer simulations are in progress to estimate its effective value [3].

On the other hand, for the operation modes where the lifetime is less critical, the sc cavity would permit to save a significant amount of the power dissipated in the nc cavities by operating them at reduced voltage and larger synchronous phase.

Concerning the Robinson's criterions for the stability of synchrotron oscillations, the presence of the idle sc cavity is beneficial since it reinforces the oscillation damping strength while keeping the instability current threshold unchanged [2,4].

## 2.3 Lengthening of the bunches using a 3<sup>rd</sup> harmonic idle sc cavity

An alternative method of improving the beam lifetime consists in producing longer bunches with less density. Again, this could be advantageously realized using a hybrid system as described before but with a higher harmonic cavity detuned in the other direction (defocusing case). Figure 1 shows the RF voltages (nc, sc and nc+sc) versus phase, as well as the corresponding computed RF buckets and bunch profiles, in the SLS case with a 3<sup>rd</sup> harmonic (1.5 GHz) idle sc cavity. The beam induced voltage of about 0.8 MV, required to have a quasi zero slope over the phase domain covered by the bunch, is obtained with a detuning of 36 kHz (for  $R/Q \approx 50 \Omega$  and  $I_b = 0.4$  A, as before). One finds that the bunches are lengthened by a factor of about 4 ( $\sigma_z \approx 4 \cdot \sigma_{z0} \approx 15$  mm) while the energy acceptance is nearly unaffected as compared to the single nc system. Consequently, the Touschek lifetime should be also improved by a factor of about 4. Note that, with the introduction of mini-gap undulators, the actual lifetime begins to be affected by gas scattering effects [3].

Concerning the Robinson stability, the condition is more delicate than in the focusing case since the harmonic sc cavity is now detuned such that it contributes to anti-damping. The computation of the oscillation growth (or damping) rates [2] showed that the stability condition is largely fulfilled with full stored beam current since the sc cavity is then detuned far from the first satellites of the synchrotron frequency. If one wants to maintain the same voltage at reduced beam current, instabilities could theoretically occur ( $\sim 100$  mA) when exciting a satellite of the synchrotron frequency exactly in resonance. On the other hand, this is easily avoidable: changing the frequency of the sc cavity - which naturally has an extremely narrow bandwidth - by a fraction of a kHz should be sufficient to re-establish stable conditions without affecting too much the operating parameters. Using two cavities instead of a single one (see next section) should permit to extend the operating beam current range down to a few tens of mA.

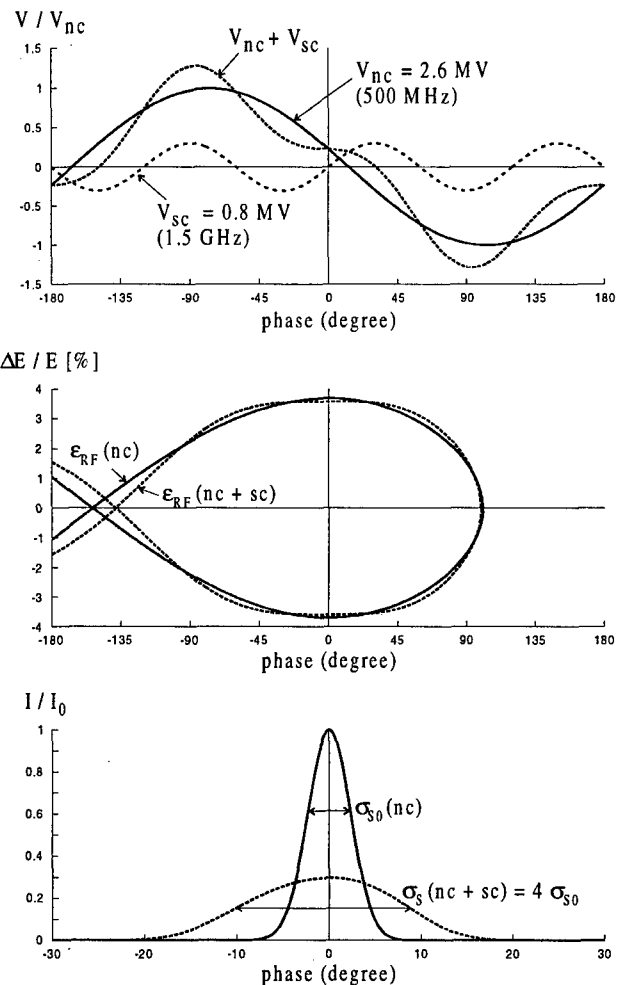


**Figure. 1 :** Normalized RF voltages (nc, sc, nc+sc) vs phase, RF buckets and bunch profiles (nc, nc+sc) for  $V_{nc} = 2.6$  MV,  $V_{sc} = 0.8$  MV and  $f_{sc} = 3 \cdot f_{nc} = 1.5$  GHz.

### 3 DISCUSSION OF THE UPGRADING ALTERNATIVES

The previous results indicate that, in order to improve the beam lifetime of the SLS, the bunch lengthening technique is more efficient than increasing the fundamental RF voltage. With the former solution, an enhancement of the beam Touschek lifetime by about a factor 4 is anticipated. Moreover, one can expect a significant amount of Landau damping - due to the nonlinearity of the RF waveform - which should help in fighting the coupled bunch instabilities. Another benefit is that the resulting decrease in peak current should raise the threshold for single bunch instabilities. Note also that the harmonic cavity could easily be detuned in the other direction, shortening the bunches by a factor of about 1.5, if wished.

Different possible versions of harmonic systems were considered and compared. This is summarized in Table 2 which shows typical operating parameters for an idle sc system using one or two cavities and for a nc alternative.

	idle sc system		idle nc system
$f_r$ [GHz]	1.5		1.5
$n_{cav}$	1	2	10
$R_s * n_{cav}$ [ $\Omega$ ]	10 E9	40 E9	10 E6
$Q_o$	2 E8	4 E8	1.5 E4
$V$ [MV]	0.85	0.85	0.85
$E$ [MV/m]	8.5	4.25	0.85
$P_d$ [W]	40	10	36 000 *
$I_b$ [A]	0.4	0.4	0.4
$\phi_s$ [degree]	$\sim 0$	$\sim 0$	6
$\delta f$ [kHz]	35.5	71	470
$\epsilon_{RF}$ [%]	$\pm 3.65$		$\pm 3.45$
$\sigma_z$ [mm]	15		15
$f_s$ [kHz]	2.2		2.2

**Table 2 :** nc and sc versions of a 3<sup>rd</sup> harmonic idle RF system for bunch lengthening (\* power to be restored by the 500 MHz system:  $\Delta\phi_s \approx 2^\circ$ ).

Although the required level of performance is fully compatible with the use of a single sc cavity, adding a second one presents significant advantages:

- lower accelerating gradient and cryogenic losses for the same total voltage;
- higher voltage capability;
- extension of the operating beam current range down to lower values (doubled detuning for the same voltage and current);
- possibility of applying the two-cavity HOM damping technique developed for SOLEIL (at 350 MHz) [5].

The SOLEIL design consists of a pair of sc cavities with the HOM damped by means of coaxial couplers, located on the tube in between the two cavities. Following this approach, the space requirement and investment cost

should remain quite comparable with equivalent systems based on a single cavity [6].

Idle harmonic nc cavities are being operated (or planned) in other laboratories [7,8]. For our purpose, this solution would require about ten cavities in order to keep at a reasonable level ( $\sim 40$  kW) the power to be restored by the main RF system and ensure the stability within a range  $100 \text{ mA} < I_b < 400 \text{ mA}$  [2]. Moreover, making this system "invisible for the beam" would require an unpractical amount of detuning.

All the above considerations led us to favor the idle sc version based on the SOLEIL two-cavity design, "scaled down to 1.5 GHz".

### 4 CONCLUSIONS

In order to further improve the beam lifetime in the SLS SR when operating at very high brightness, two approaches have been considered: either increasing the energy acceptance by doubling the 500 MHz voltage or lengthening the bunches using a 3<sup>rd</sup> harmonic system. Both schemes could be advantageously realized by complementing the initial nc system with idle (only-beam-driven) sc cavities. Such a *hybrid "powered nc and idle sc" system* appeared to be particularly flexible and easy to control; moreover, the difficulties related to the transmission of large power through the sc cavities with the associated technological and operational problems are naturally eliminated.

Computer simulations indicated that the bunch lengthening option would be more efficient, improving the beam Touschek lifetime by a factor of about four. This is the approach presently investigated and amongst the possible variants of such a system, the favored one is an idle sc version based on the SOLEIL two-cavity design, "scaled down to 1.5 GHz". This solution is well suited to provide the necessary damping of the parasitic HOM impedances and moreover should lead to a quite good compromise in terms of reliability, flexibility, space requirement as well as investment and operational costs.

### 5 REFERENCES

- [1] P. Marchand, Note SLS-TME-TA 1998-0011 and these Proc.
- [2] P. Marchand, Note SLS-TME-TA 1998-0012.
- [3] M. Boege et al, these Proceedings.
- [4] P. Marchand, Particle. Accelerator, 1992, Vol. 36, pp. 205-222.
- [5] A. Mosnier et al, EPAC98, p. 1864, 1998.
- [6] H. Padamsee, EPAC98, p. 185, 1998.
- [7] A. Anderson et al, EPAC98, p. 273, 1998.
- [8] R.A. Rimmer et al, EPAC98, p. 1808, 1998.

# BEAM TEST OF A SUPERCONDUCTING CAVITY FOR THE FERMILAB HIGH-BRIGHTNESS ELECTRON PHOTO-INJECTOR

W. Hartung, J.-P. Carneiro,\* M. Champion, H. Edwards, J. Fuerst, K. Koepke, M. Kuchnir  
Fermi National Accelerator Laboratory,† P. O. Box 500, Batavia, Illinois 60510 USA

## 1 INTRODUCTION

An electron photo-injector facility has been constructed at Fermilab for the purpose of providing a 14–18 MeV electron beam with high charge per bunch (8 nC), short bunch length (1 mm RMS), and small transverse emittance [1]. The facility was used to commission a second-generation photo-cathode RF gun for the TeSLA Test Facility (TTF) Linac at DESY [2, 3]; in the future, the Fermilab electron beam will be used for R & D in bunch length compression, beam diagnostics, and new acceleration techniques. Acceleration beyond 4 MeV is provided by a 9-cell superconducting cavity (see Figure 1). The cavity also provides a longitudinal position-momentum correlation for subsequent bunch length compression. We report on the RF tests and a first beam test of this cavity.

## 2 SYSTEM DESCRIPTION

### 2.1 Cavity

The accelerating cavity is a 9-cell superconducting Nb structure of the TeSLA Test Facility (TTF) type. The shape is optimised for a smaller ratio of surface electric field to accelerating gradient and larger iris diameter for better propagation of higher-order modes (HOM's); RF parameters are given in Table 1. The cavity and He tank were built by industry for TTF. The cavity is one of a batch with low quench field, attributed to contamination in the welds at the equator.

### 2.2 Couplers and Tuner

The input coupler was developed for TTF by Fermilab [4]. It is designed for 200 kW of peak power for normal operation (1.3 ms pulses, 10 Hz repetition rate), as well as 1 MW of peak power in short pulses for high peak power pulsed processing (HP<sup>4</sup>). The coupling strength can be varied over an external  $Q$  range from  $1 \cdot 10^6$  to  $9 \cdot 10^6$ . This coupling range is appropriate for heavy beam loading; in the absence of a beam, the cavity is highly over-coupled.

The coaxial HOM couplers were designed at DESY [5]. They provide strong coupling to the non-propagating HOM's and have a notch filter to inhibit damping of the accelerating mode. The 2 couplers are about 90° apart azimuthally, one on each beam tube, in order to couple to both polarisations of the dipole HOM's. There is also an antenna on one of the beam tubes to monitor the field level in the cavity.

The TTF cold tuner was designed at Saclay [6]. It changes the resonant frequency of the cavity by changing

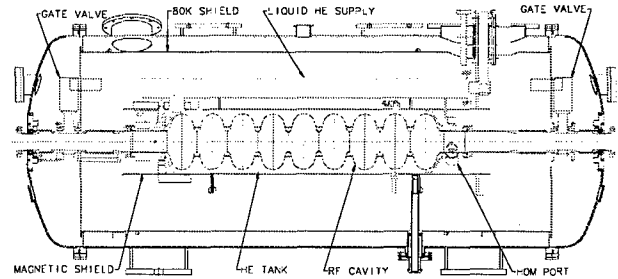


Figure 1. Side view of the cavity and cryostat for Fermilab.

Table 1. Cavity parameters [2, 3]. In the following,  $E_a$  is accelerating gradient,  $E_p$  and  $B_p$  are the peak electric and magnetic field on the surface of the cavity, respectively, and  $R_s$  is the shunt impedance (linac definition).

Mode	$TM_{010}\pi$
Resonant frequency $f$	1.3 GHz
Cell-to-cell coupling	2.0 %
$E_p/E_a$	2
$cB_p/E_a$	1.3
$R_s/Q$ per cell	114 $\Omega$
$df/dL$	315 kHz/mm
Cavity active length $L$	1036 mm
Aperture	70 mm
Operating temperature	1.8 K

the overall length of the cavity, which is done by winching on the beam tube relative to the helium tank. It provides a tuning range of about  $\pm 400$  kHz.

### 2.3 Helium Tank, Cryostat, and Cryogenics

The titanium helium tank is electron-beam welded directly to the Nb cavity. It is intended to minimise the volume of liquid helium in the cryostat. The cryostat is nominally identical to the TTF capture cavity cryostat designed and built at Orsay [7], albeit with some differences, for example, in the cavity support rods and their attachment to the helium tank, as well as the presence of a 5 K radiation shield. The vacuum vessel was built by industry.

Cryogenics are supplied from dewars of liquid He and liquid N<sub>2</sub>. Roots blower pumps are used to pump down to 1.8 K. The pressure and liquid level in the He tank are regulated by control loops which actuate variable flow valves on the supply and exhaust lines.

### 2.4 Beam Tube

The beam tube inside the cryostat was redesigned for use at Fermilab (see Figure 1). A larger aperture (59 mm diameter or more) is maintained through it, in contrast to the 35 mm aperture through the original Orsay cryostat. The Fermi-

\*Visitor from Université d'Orsay, France.

†Operated by the Universities Research Association under contract with the U. S. Department of Energy.

lab scheme incorporates 2 gate valves inside the cryostat, which take the place of demountable valves outside the Orsay cryostat. The gate valves are always open when the cavity is cold.

### 2.5 Drive RF

High peak power RF drive is required due to the strong input coupling. At the design beam current, the power goes into accelerating the beam; in the absence of beam loading, the power is reflected by the coupler. The pulsed RF power is provided by a klystron and modulator with an RF pulse length of up to 2 ms, peak power  $\sim 150$  kW, and variable repetition rate.

The RF control system was developed for TTF [8]. It incorporates digital control of the amplitude and phase of the RF field. The monitor probe signal is used for feedback. The klystron drive RF is controlled by a vector modulator.

## 3 PREPARATION AND INSTALLATION

### 3.1 Cavity Preparation at DESY

A total of  $135 \mu\text{m}$  was chemically etched off the inside surface of the cavity. The cavity was fired in vacuum at  $800^\circ\text{C}$  before the final etch to inoculate it against the "Q virus" associated with hydrides on the RF surface. The last preparation step was a high-pressure water rinse to eliminate particulates from the RF surface. Vertical RF tests were done before the He tank was installed; a horizontal test was done in the CHECHIA test cryostat after the He tank was welded on. After the CHECHIA test, the cavity was bled up with clean Ar gas and sent (in its He tank) to Fermilab.

### 3.2 Cavity Installation at Fermilab

At Fermilab, the cavity was leak-checked and installed in its cryostat. During the process, critical operations were carried out in a small mobile Class 100 clean room. An effort was made to maintain laminar flow in the vacuum system when pumping down and bleeding up the cavity. Precautions were taken to ensure cleanliness of beam line components downstream (all the way to the beam dumps) and upstream (up to and including the RF gun) of the cavity. Using hand-held particle counters, we confirmed that valves and flanges are a major source of particulate contamination.

## 4 CRYO AND RF MEASUREMENTS

### 4.1 RF Tests at DESY

In the best vertical test at DESY, the cavity quenched at  $E_a = 13 \text{ MeV/m}$  in CW; the  $Q$  exceeded  $10^{10}$  below the quench level [2].

In the horizontal test in the CHECHIA cryostat, the field was limited by cryo capacity. The attainable fields under different conditions are summarised in Table 2. The cryo losses as a function of  $E_a$  were measured (the  $Q$  cannot be measured with RF after the input coupler is installed, due to the strong input coupling), as shown in Figure 2. The power was deduced from the flow rate of He gas into the vacuum pumps.

Table 2. Maximum field values at 1 Hz repetition rate.

RF test in CHECHIA			
Fill Time [ $\mu\text{s}$ ]	Flat Top Duration [ $\mu\text{s}$ ]	Forward Power for Fill [kW]	Max $E_a$ [MeV/m]
500	800	$\sim 100$	18.8
1100	0	150	26.5
200	0	1000	27.4

RF tests at Fermilab			
Fill Time [ $\mu\text{s}$ ]	Flat Top Duration [ $\mu\text{s}$ ]	Max $E_a$ [MeV/m]	Cryo
500	800	17.4	overloaded
		15.3	okay
800	0	25.7	overloaded
600	0	22.5	okay

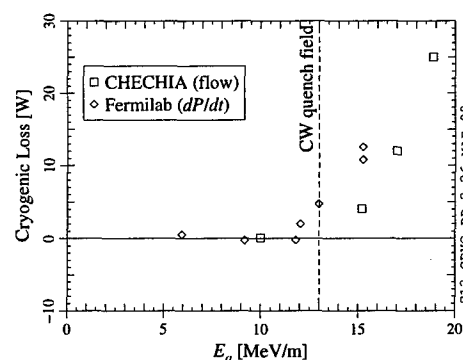


Figure 2. Cryogenic loss measurements with  $500 \mu\text{s}$  fill time and  $800 \mu\text{s}$  flat top at 1 Hz.

### 4.2 Cryo Measurements at Fermilab

The static heat leak into the He tank at 4.2 K was measured via the rate of decrease in liquid level with the supply valve closed:  $3.6 \text{ W} \pm 0.3 \text{ W}$ , which is equivalent to 5.8 litres/hour of He consumption. This is larger than values measured at Orsay for the TTF cryostat ( $2.3 \text{ W}$  at 4.2 K,  $3.2 \text{ W}$  at 1.8 K), but still tolerable. The static He consumption of the cryo system at 1.8 K is typically 25 to 30 litres/hour. This high consumption is believed to be due to a significant heat leak in the transfer lines and inefficient operation of the JT heat exchanger (optimised for 100 to 200 W) at low flow rates. The capacity of the system is limited by the vacuum pumps. Static fluctuations in the bath pressure are typically  $\pm 1.3 \text{ mbar}$ ; the time scale is about 6 minutes.

### 4.3 RF Tests at Fermilab

The field level in the cavity is determined from the monitor probe signal after measuring the strength of the coupling between the cavity and the probe. Iteration was required to obtain a reliable coupling calibration. Our present value ( $Q_{ext} = 2.2 \cdot 10^{10}$ ) is somewhat different from what was measured in CHECHIA at DESY ( $Q_{ext} = 1.5 \cdot 10^{10}$ ).

As was the case at DESY, the cavity field in tests at Fer-

milab was limited by the cryo capacity. The attainable field levels are given in Table 2. Measurements of the cryo losses vs.  $E_a$  were repeated. The method was to close the supply and exhaust valves and measure the rate of pressure increase in the He tank, as done at the accelerator facility formerly known as CEBAF [9]. The rate of pressure rise was calibrated with a resistance heater in the bath. Our main difficulties with this measurement were in getting reliable and repeatable operation of cold valves; our technique is not yet very satisfactory. Our preliminary results are compared to the measurements at DESY in Figure 2.

With feedback on, the typical fluctuations in the amplitude and phase during the flat top portion of the RF pulse are  $\pm 1\%$  and  $\pm 0.5^\circ$ , respectively. Figure 3 shows a detail of the amplitude and phase of the monitor probe signal during the flat top. We measured the change in resonant frequency with bath pressure to be about 28 Hz/mbar. This is 1.4 times larger than predicted [3], but the feedback can still compensate for the pressure fluctuations.

## 5 FIRST BEAM TESTS

So far, we have operated the cavity with beam only long enough for beam energy measurements with a spectrometer. Measurements were done with the RF gun for TTF (in October 1998, just before the gun was shipped to DESY) and the RF gun for the Fermilab photo-injector (in March 1999).

The phase of the gun relative to the laser pulse was chosen to maximise the photo-current at the exit of the gun. The phase of the 9-cell cavity was then varied relative to the gun phase to maximise the beam energy as measured with the spectrometer. Results are given in Table 3. The agreement between the spectrometer measurement of the beam energy and the beam energy expected based on RF measurements for the gun and 9-cell is reasonable, given the uncertainties in both measurements.

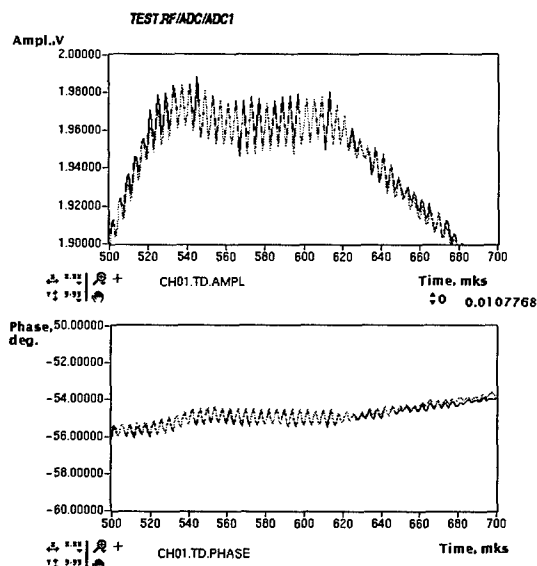


Figure 3. Detail of the amplitude and phase of the transmitted power during a 100  $\mu$ s flat top, with feedback on.

Table 3. Beam energy measurements.

Conditions	Oct 1998	Mar 1999
Fill time	500 $\mu$ s	
Flat top	$\sim 200 \mu$ s	100 $\mu$ s
Bunches per train	1	70
Charge per bunch		$\sim 0.25$ nC
Rep rate	1 Hz	
<b>RF Results</b>	<b>Total Energy</b>	
From Gun	4.3 MeV	4.3 MeV
From 9-cell	15.0 MeV	8.1 MeV
Total from RF	19.3 MeV	12.4 MeV
<b>Spectrometer</b>	<b>Total Energy</b>	
Dark current	19.9 MeV	
Photo-current	18.5 MeV	13.7 MeV

## 6 CONCLUSION

A TTF superconducting cavity has been installed and operated at Fermilab without severe degradation in its RF performance. We have accelerated beam with the RF gun and the superconducting cavity. The measured beam energy in the first beam tests is consistent with RF power measurements. Future plans for the machine, after it has been understood and optimised, include longitudinal compression with a chicane and experiments in fast diagnostics, plasma wake field acceleration, and channelling acceleration.

## ACKNOWLEDGEMENTS

We thank our colleagues at Fermilab and in the TTF collaboration for contributing to this project, especially S. Buhler, E. R. Colby, P. L. Colestock, J. Crandall, A. C. Crawford, D. A. Edwards, R. J. Florian, S. Goloborodko, G. Johnson, M. Julliard, T. Junquera, T. W. Koeth, M. J. Kucera, R. Lange, A. Matheisen, W.-D. Möller, W. V. Muranyi, J. R. Noonan, M. J. Pekeler, H. Pfeffer, P. S. Prieto, D. Reschke, J. K. Santucci, T. Schilcher, S. N. Simrock, W. Soyars, J. G. Spencer, L. K. Spentzouris, J. J. Urban, M. M. White, D. A. Wolff, and K. Zapfe-Düren.

## REFERENCES

- [1] J.-P. Carneiro *et al.*, "First Results of the Fermilab High-Brightness RF Photo-Injector," these proceedings.
- [2] M. Pekeler, "Experience with Superconducting Cavity Operation in the TeSLA Test Facility" these proceedings.
- [3] D. A. Edwards, Editor, "TeSLA Test Facility Linac—Design Report," TeSLA 95-01, DESY (March 1995).
- [4] M. Champion, in *Proceedings of the 6th Workshop on RF Superconductivity*, CEBAF, 1994, p. 406–425.
- [5] Jacek Sekutowicz, *ibid.*, p. 426–439.
- [6] Ph. Leconte *et al.*, TeSLA 93-29, DESY (June 1993).
- [7] S. Buhler *et al.*, in *Proceedings of the Seventh Workshop on RF Superconductivity*, CEA/Saclay 96 080/1, 1996, p. 689–693.
- [8] S. N. Simrock *et al.*, in *Proceedings of the Fifth European Particle Accelerator Conference*, 1996, p. 1863–1871.
- [9] M. Drury *et al.*, in *Proceedings of the 1993 Particle Accelerator Conference*, p. 841–843.

# SUPERCONDUCTING RF CAVITY R&D FOR A SEPARATED KAON BEAM AT FERMILAB

Reported by T. W. Koeth, Rutgers University

## Abstract

Fermilab is considering the implementation of a high flux pure kaon beam in order to study rare  $K^\pm$  decays and to produce  $K_0$  beams for  $K_L$ - $K_S$  interference experiments. The 22-25 GeV/c kaon beam is produced using an RF cavity beam separator scheme which rejects most of the more numerous pions and protons emitted from the production target. With a beam spill time of 1 sec out of 3 sec, superconducting cavities are preferred for providing the required transverse deflection. Although the separator scheme is not a new idea, the technology involved with this program will push the envelope of RF superconductivity technology. Cavities operating at 3.9 GHz in the TM110  $\pi$  mode are under evaluation. An R&D program to construct and test these cavities has been initiated. A goal of 5MV/m deflection has been chosen. Description of the superconducting RF R&D program and status will be given.

## 1 INTRODUCTION

The new Fermilab Main Injector will produce intense extracted proton beams of 120 GeV/c momentum for fixed target experiments. Design intensity is  $3 \times 10^{13}$  per pulse at a 3 sec cycle time with a 1 sec extracted spill duration. A fraction of the beam ( $5 \times 10^{12}$ ) would be used to provide secondaries for a 22 – 25 GeV/c beam line with a yield of up to  $\approx 2 \times 10^8$  kaons to the high energy physics experiments.

The kaons would be “separated” from the other secondaries (primarily pions and protons) by RF cavities operating in a transverse deflection mode (TM110,  $\pi$ ). The long spill time and 1/3 duty factor require that superconducting resonators be used. RF separated beams have been around for a long time[1] and a version using superconducting cavities was implemented at CERN in the 70’s[2].

The separated beam principal is as follows. The primary proton beam strikes a thick target, and the emerging hadrons pass through a momentum selection stage, which in this case is a chicane. The particles then are primarily a mix of protons, pions, and kaons of the same momentum but with differing speeds. Speed selection is accomplished by two RF stations that are designed to provide transverse deflection. The distance between the stations, resonator frequency, and the relative phase of the RF are selected so that kaons will be transmitted to the users, while pions and protons will be rejected. The transverse optics between the two RF stations is set to provide  $\pm I$ . Thus the deflection of the beam particles emerging from the second RF station will depend on: the phase at which the particles enter the first station, the relative phase of the two stations, the RF frequency ( $f$ ), the distance between the stations ( $L$ ), and

the speed of the particles ( $\beta$ ) relative to  $c$ . It is possible to choose a particular  $fL$  product such that for a specific  $\beta$ , a “closed” beam bump is produced so that there is no resultant deflection after the second station independent of the particle arrival phase at the first RF station. Particles of other velocities will arrive at a different time at the second station so the resultant bump will not be closed and they will have a net deflection dependent upon their arrival phase relative to the first station. Thus if the RF deflection takes place all in one plane (h or v), the result will be that one particle species will have no resultant kick whereas others will be swept into a fan. If circular polarized RF deflection is used (say by each station having horizontal and vertical deflection 90 degrees out of phase) then one species again has no deflection and other species will exit in a cone about this central trajectory. The cone angle will be dependent on the relative  $\beta$  of these other species.

For deflection in one plane, kaons are produced in a fan and the unwanted protons and pions are directed straight ahead into a stopper plug. In the case of conical deflection, the station to station RF phase is chosen so kaons are undeflected and the protons-pions would be stopped in a collimator with a hole.

Because of the relatively short charged kaon life time, 12 ns in its rest frame, it is desirable to keep the beam line short. At energies of interest the pion speed is very close to light and the difference in time delay from the first station to the second between the pion and a K or p can be written

$$\Delta t = (\Phi/2\pi)/f = L/(2c\gamma^2)$$

or

$$fL = 2c\gamma^2(\Phi/2\pi),$$

where  $\Phi$  is the relative RF phase delay.

If a frequency-distance product,  $fL$ , is selected so the the proton arrives at the second station  $2\pi$  after the pion the the kaon will be at a phase delay of about  $\pi/2$ . This is a result of the circumstance that the mass of the kaon is about half that of the proton. We have chosen an RF frequency of 3.9GHz as the upper limit to be acceptable from the point of surface resistivity, thermal conductivity and experience with superconducting cavities. This leads to a station to station distance of 107 m for a 25 GeV/c kaon beam. The overall beam line is of order 350 m.

The desired energy range of 22–25 GeV/c can be accommodated in a one plane deflection situation by interposition of another deflection station between the two mentioned above. For two plane deflection, the two stations are sufficient. At this writing, it is not necessary to select between these alternatives.

## 2 R&D PROGRAM

This material is extracted from the design study for the superconducting aspects of an RF separated kaon beam at Fermilab[3]. The parameters and specifications chosen for the purpose of a point design are listed in Tab. 1. Definitions and field patterns may be found in the design study, or in Padamsee *et al*[4] in their discussion of crab cavity development at CESR.

Table 1: Provisional parameters for initiation of the R&D program and for the point design outlined in this report

frequency	3.9 GHz
mode	$\pi$ , TM110
equator diameter	94 mm
iris diameter	30 mm
cell length	38.4 mm
cells per meter	26
cells per cavity	13
$(R/Q)'$	55 ohm/cell
$(r/Q)'$	1430 ohm/m
$V_{trans}$ @ 0.1 T	5.7 MV/m
$E_{peak}$	22 MV/m
$B_{peak}$	0.100 T
U (stored energy)	0.92 J/m
coupling factor	0.051
$G_1 = Q \times R_{sur}$	236 ohms
$R_{sur}$ @ 2K, $T_c/T=4.6$	$1.04 \times 10^{-7} \Omega$
$Q$ @ $R_{sur}$	$2.2 \times 10^9$
Power dissipated @ 5.7MV/m, 2K	10 watts/m
System Requirements for 60 MV/m total kick	
Total cryogenic power	95 watts @ 1.8K
	230 watts @ 2K
$Q_L$ (loaded Q)	$6 \times 10^7$
RF power @ 5.7 MV/m	380 watts/m
RF power including factor of 2 for regulation	760 watts/m
Total RF power	8 kilowatts

A 3.9 GHz structure operating in  $\pi$ -mode and scaled from the TESLA shape has been adopted in order to initiate the R&D program. The cavity shape is shown in Fig. 1. Fig. 2 illustrates a 13 cell cavity in a helium vessel, and Fig. 3 shows a concept for a cryomodule containing two cavities.

The 13 cell cavity has 1/2 meter active length, and an overall length of 0.7 m. The length has been selected in order to limit the number of cells per structure to what is expected to be a manageable number for tuning, field flatness, and mode frequency separation. The equator and iris diameters are 94.4 mm and 30 mm respectively. The cavity would be polarized either by deforming a finished azimuthally symmetric cavity, or by using slightly elliptical dies.

There are two beam pipe flanges and four coupler flanges

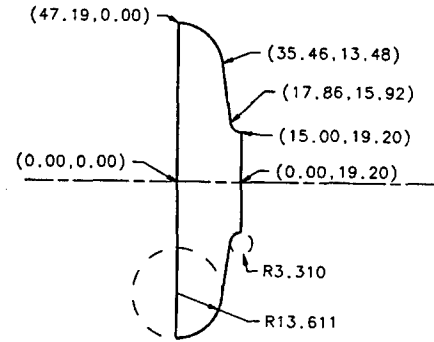


Figure 1: Half-cell

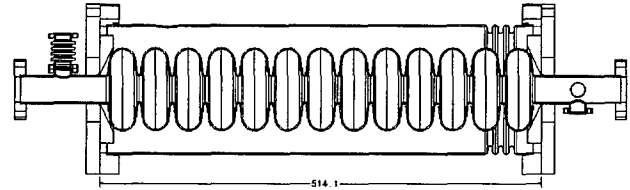


Figure 2: Conceptual drawing of cavity in demountable helium vessel.

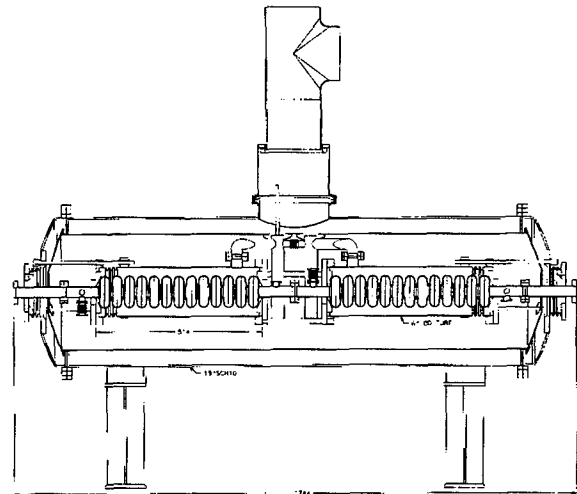


Figure 3: Cryostat module with two cavities.



which must seal the cavity vacuum. One of the coupler flanges would be for the input RF power. The others are for monitor and (fundamental or HOM) power extraction. Beam pipe and coupler flanges are of a size comparable with CF35 and mini-conflat respectively.

The flange arrangement shown in Fig. 2 would allow for a demountable helium vessel. End flanges of NbTi would be welded on the cavity end pipes. The rest of the vessel would consist of end caps and a cylindrical spool of titanium preferably (or of 316L, 316LN stainless). As shown this arrangement would allow for easy testing of different length cavities and a bellows section would accommodate tuning adjustment and thermal contraction. The vacuum seals here could be helico-flex as they are not associated with the cavity surface. Those associated with the cavity would be solid aluminum rings as in the TESLA Test Facility.

The  $\pi$ -mode has been selected, at least for the initial study. Other cavity modes such as  $\pi/2$  or  $2\pi/3$  have been suggested because of their more favorable location on the dispersion curve and consequently their lower sensitivity to tuning and frequency errors, and the possibility of longer structures with more cells which clearly would be an advantage. Further work will need to be done to justify the choice of cavity mode. However the greatest experience lies with the  $\pi$ -mode and it minimizes the number of cells per meter and consequently the number of welds. Some investigation of cavity shape has been made. Perhaps more investigation is necessary; however multipacting is probably the key criterion and actual test results are needed.

The choice of operating gradient or transverse kick of 5.7 MV/m per meter has been made by requiring that the maximum surface  $B$  field on the cavity (near the iris) not exceed 0.1 Tesla. This can be compared with a peak of 0.105 Tesla at 25 MV/m for the TESLA 1.3 GHz accelerating mode cavities. (The theoretical limit is  $\approx 0.2 - 0.24$  T.) It is interesting to note that TESLA cavity gradients are not only limited by  $B$  field quenches but also by field emission. In the transverse mode it may be possible to reach higher peak  $B$  because of the reduced ratio of peak electric to peak magnetic field. It will be interesting to compare maximum gradient limitations in transverse and accelerating modes. At this stage, the figure of 5.7 perhaps is better characterized as a goal rather than a choice.

In order to size the cryosystem which might be needed for the separators we have assumed a budget of about 20 watts/m and 10 meters of RF. Also we have assumed an operating duty factor of one second in three ( $DF=1/3$ ) and an overall contingency of a factor of 3, so that these two terms cancel resulting in a cryosystem size requirement of  $\approx 200$  watt. We realize that this requirement has a somewhat arbitrary justification. Also we note that if higher gradients can be achieved the RF losses will increase.

The RF power requirement depends on the loaded  $Q$ ; our present choice of  $Q_L$  is  $6 \times 10^7$  - a factor of 20-40 less than  $Q_0$ . This would lead to an RF power requirement of 400 watts/m, or total power of 4 kW. 200-400 watts is

well within the range of TWT's though other sources may be more economical. The bandwidth ( $f/Q$ ) at this  $Q_L$  is only 50 Hz, which may present a problem in terms of microphonics and RF phase/amplitude control. Lower  $Q_L$ 's will need more RF power on resonance but may actually use less if microphonics and resonance frequency control lead to an  $f_0$  spread larger than the bandwidth. We note that Darmstadt operates with a  $Q_L$  of  $3 \times 10^7$  at 3 GHz.

### 3 STATUS AND OUTLOOK

One and two cell resonators of copper and niobium have been fabricated using deep-drawing. The copper models were used for verification of URMEL predictions; the niobium cells are currently being used for ebeam welding studies.

A goal of this first year of the R&D activity is cold testing of one and two cell niobium models. For this purpose, some of the necessary infrastructure is in place (e.g., clean rooms, ultra-pure water); a high pressure rinsing system is undergoing assembly as is a vertical test dewar. The principal facilities not available on-site are ebeam welding and a high temperature oven; industrial or other-laboratory sources will be used. Concurrently, design of 5 cell models and 13 cell prototypes is underway.

Although this effort was undertaken within the context of the fixed target program for the Fermilab Main Injector, there are other potential applications for high-duty factor resonators operating in a deflecting mode. Use as a crab cavity has already been cited above[4]. For the separated beam, a range of frequency choices is possible; the particular figure of 3.9GHz was motivated by the convenience for cavity tests with beam in the 1.3GHz photoinjector laboratory at Fermilab. Deflecting cavities may also be used as beam splitters and bunch pickers. For instance, a 3.25GHz deflection station would kick alternate bunches from a 1.3GHz linac into different beamlines.

### 4 REFERENCES

- [1] H. Hahn and H. Halama, *Rev. Sci. Instr.*, **36**, 1094 (1965)
- [2] A. Citron, G. Dammertz, M. Grundner, L. Husson, R. Lehm, and H. Lengeler, "The Karlsruhe-CERN RF Separator", Kernforschungszentrum Karlsruhe, Institut für Kernphysik Primary Report IK-Nr. 316/78 (unpublished) 1978
- [3] R. N. Coleman, J. E. Dey, D. A. Edwards, H. T. Edwards, M. H. Foley, J. D. Fuerst, W. H. Hartung, J. Doornbos, T. R. Kobilarcik, K. P. O. Koepke, T. W. Koeth, M. Kuchnir, M. S. McAshan, Y. Terechkin, G. B. Thomson, H. B. White, "An RF Separated Kaon Beam from the Main Injector: Superconducting Aspects", Fermilab Technical Memorandum TM-2060, October 19, 1998
- [4] H. Padamsee, P. Barnes, C. Chen, J. Kirchgessner, D. Moffat, D. Rubin, Y. Samed, J. Sears, and Q. Shu, *Proc. IEEE Particle Accelerator Conference*, San Francisco, May 1991, p. 2426

# COMMISSIONING THE UPGRADED RF BUNCHER AT THE LANSCE PROTON STORAGE RING\*

J. Lyles, A. Browman, R. Kustom†, Los Alamos National Laboratory  
Los Alamos, New Mexico 87545 USA

## Abstract

The 2.8 Megahertz (MHz) cathode-follower RF amplifier system and ferrite-loaded gap assembly for the Proton Storage Ring (PSR) were improved as part of the Los Alamos Neutron Science Center (LANSCE) upgrade for a Short Pulse Spallation Source (SPSS) [1]. The commissioning of PSR commenced in July of 1998. The performance of the cathode-follower amplifier system and gap was measured with as much as five microcoulombs ( $\mu\text{C}$ ) of circulating beam, approximately forty Amperes of peak current before extraction. The output impedance of the cathode follower was estimated to be approximately eleven Ohms. This was calculated from beam-induced voltage on the gap with the amplifier operating class A (full conduction of plate current), with RF drive off. Measurements showed the perturbation of the gap voltage with beam loading to be minimal. The improved RF system handled the beam loading well. A new phase feedback control system corrected for three degrees of phase shift from unloaded to fully loaded beam conditions, with 18 kV of peak RF voltage across the gap. The amplitude feedback controller made 300 volts of correction for droop, also minimal because of the low output impedance at the gap. Beam instability at PSR with higher current was controlled, as expected, with higher voltage [2]. Analysis of these and other measurements are presented.

## 1 RF BUNCHER REQUIREMENTS

The PSR is a fast-cycling high current ring designed to accumulate beam over a macropulse from the LANSCE linac, with multi-turn injection. Stacking these protons over approximately 2100 turns allows very high charge densities to be stored. A single-turn extracted pulse (250 ns) of high current drives the new SPSS target, to produce neutrons of the desired characteristics. In January of 1999 LANSCE achieved  $3.1 \times 10^{13}$  at 20 Hz, with an average current of 100 microamperes ( $\mu\text{A}$ ), a 43 percent increase over 1998 operation. The SPSS end goal is to double this current, to 200  $\mu\text{A}$ .

The PSR uses a RF buncher system to control longitudinal beam distribution. The improved RF buncher is described in a companion paper [1] in these proceedings.

## 1.1 Increasing Bunching Factor

This project raised the buncher gap voltage to 18 kV peak at 2.8 MHz (exactly 2.79513), and designed the amplifiers to also be usable at  $h=2$ , or 5.6 MHz. Continuing to raise the 2.8 MHz bunching voltage alone would eventually result in excess space charge tune shift. It would be better for the peak charge density to be accumulated in a long flat bunch to allow higher beam current in the ring. The application of a second harmonic voltage of the proper phase can increase bunching factor from 0.35 to 0.5, creating this flat bunch. Figure 1 shows the PSR current during optimal bunching for a single frequency  $h = 1$  system.

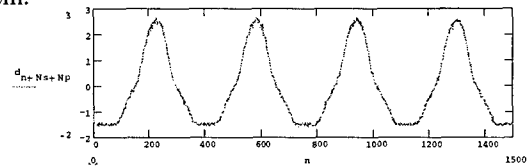


Figure 1. PSR beam current for four bunches, 2.8 MHz

## 1.2 PSR Instability Threshold

The PSR has operated just below a fast transverse instability, which has been studied and described [3]. It becomes evident when the beam intensity exceeds about  $2 \times 10^{13}$  ppp. The buncher RF voltage has demonstrated a strong coupling to the instability threshold level. Because of this, it was expected that increasing the RF voltage would give more latitude for future increases in beam current. This will eventually be limited by space charge factors. At 200  $\mu\text{A}$ , the goal for PSR is  $4.2 \times 10^{13}$  ppp at 30 Hz.

## 2 TEST RESULTS OF RF BUNCHER

### 2.1 High Power RF

The improved buncher delivered 18 kV peak to the gap in July of 1998. We also operated the new intermediate power amplifier (IPA) at  $h = 2$ , to demonstrate that it was capable of tuning to 5.6 MHz, at full output. Initially the IPA was operated into dummy load for 5% duty factor, purchased from the Ohm-Weve® Company. It simulated the  $2 \times 500$  Ohm input resistors plus the capacitive reactances of the grids of the final power amplifier (FPA).

We operated with 5% duty factor with pulses up to 2.2 ms wide, and rep rates to 30 Hz with 1.7 ms. The IPA output pi-networks were easily tuned under power. A fast

\* Work supported by the US Department of Energy

† Visiting from Argonne National Laboratory

digitizing oscilloscope (TDS 784D) connected to a pair of internal Jennings capacitive voltage dividers allowed for simple adjustment for 180 degrees between the two IPA output feeders. The value of internal amplifier diagnostics was quickly proven.

## 2.2 Low Level RF Control

The amplitude and phase controls were tested without beam. The improved lower threshold of the amplitude feedback control (AGC) is 500 Volts, whereas it had been difficult to set the level below 2 kV. Open loop phase skew of the amplifier was measured while the amplitude was ramped at the input. Across the full range of usable output, about 20 degrees of phase change was measured, in the same direction for both tetrodes.

The IPA was coupled to the FPA with the new interconnections, and the same measurements were made (except for 5.6 MHz) while driving the beam gap. The ferrite bias was set for 2.8 MHz resonance. A pair of calibrated LANL voltage dividers is mounted within the cavity, and these signals normally provide feedback to the low level RF controls. The differential signal is combined. The RF voltage in figures 3 - 6 were measured this way.

## 3 TEST RESULTS WITH BEAM IN PSR

In September of 1998, beam was provided to commission the upgraded buncher. The low level RF now provides error signals for the amplitude channel and the new phase controller. These signals were monitored while beam was injected. All tests were performed at very low duty factor. Figure 2 shows the errors as 2.5  $\mu\text{C}$  of charge is stored. The envelope store mode was used, with 20 pulses (several minutes). The amplitude controller has a correction of about 600 V pk-pk before extraction, and for droop from the power supplies. The phase controller has one degree of error across the ramp.

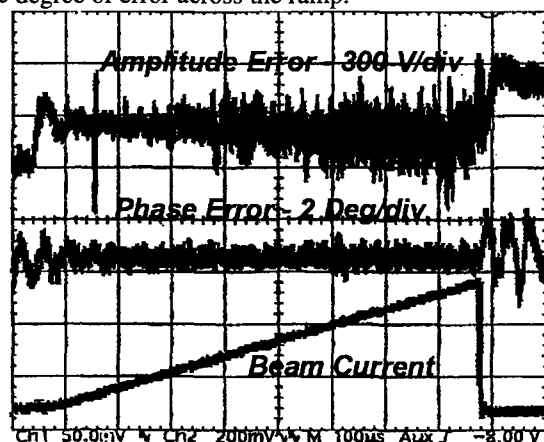


Figure 2. Amplitude and Phase Errors

### 3.1 FPA Output Impedance Verification

This test involved measuring a single cycle of gap voltage near the peak of the ramp, once with beam, and then at the same time period without beam. These were subtracted in

the digitizer memory, creating the residual voltage in figure 3. This is 1.3% ripple due to the beam current in the gap. This change is too rapid for the AGC to compensate, but it is damped by the low output impedance.

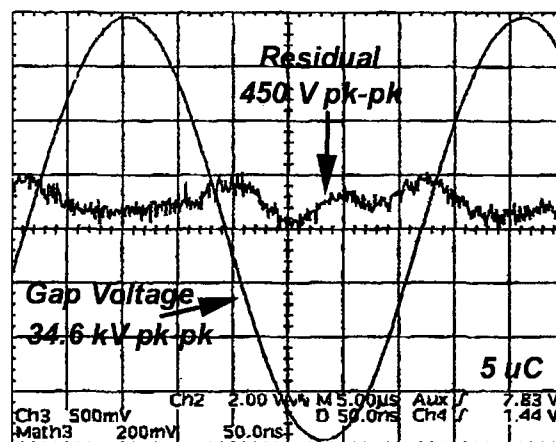


Figure 3. Change in Gap Voltage Due to Beam

Another experiment measured the induced voltage at the gap, when the beam is coasting. The RF drive was off, but the cathode followers were in conduction at 45 Amperes quiescent plate current. The top trace in figure 4 is the induced voltage across the gap, and the bottom trace is the beam current. At extraction, the voltage decays. The voltage was about 11 Volts peak, and the triangular beam current was about 1 Ampere. This gives an estimate of 11 Ohms for  $R_0$  across the gap from the cathode followers.

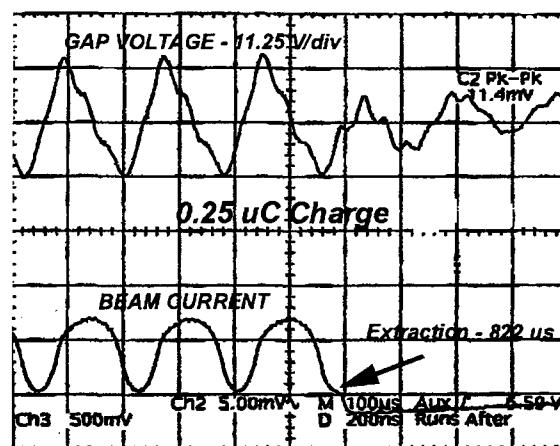


Figure 4. Induced Gap Voltage from Coasting Beam

### 3.2 Ferrite Coupling Loop Tests

In this experiment, the "figure-eight" coupling loop in the cavity is tested with a worst-case scenario. One amplifier is completely shut off, while observing the gap voltage waveform for distortion. This was performed at low buncher voltage, to prevent damage to the termination networks on the ends of loops. This arrangement is described in the companion paper on the buncher improvements. The buncher was set for 3.4 kV peak at 2.8 MHz. Without beam, one cathode follower was put in

cutoff with the control grid bias supply. There was no visible change in the gap voltage.

The same test was performed with  $0.25 \mu\text{C}$  of charge. Figure 5 shows the before and after waveforms, with the beam current superimposed below the voltage trace. Beam was extracted during the interval being digitized. No discernable change in the sinewave was noted, either from beam extraction or from the shutdown of one triode.

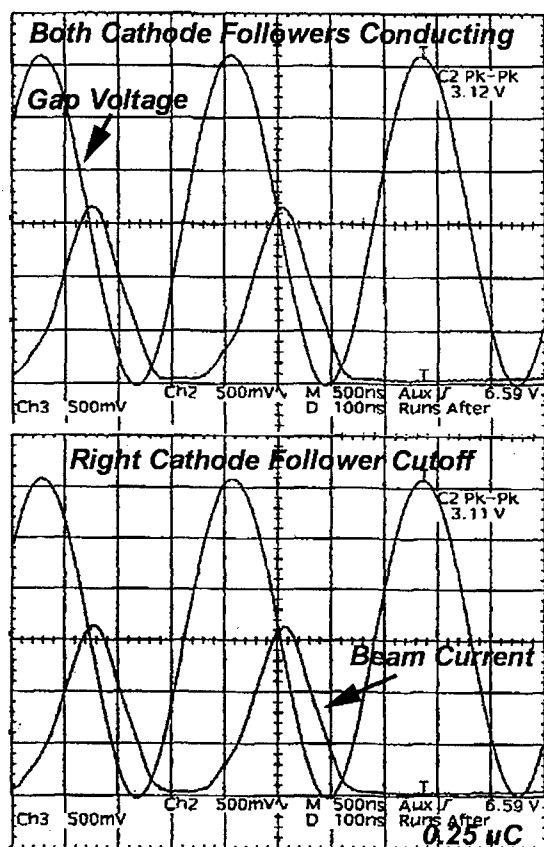


Figure 5. Effect of RF Coupling Loop

It is important to note that this was done with  $0.25 \mu\text{C}$  of charge to prevent damage. We would not have been able to do this at 18 kV, at full PSR current. At 20 times this amount of charge, it is expected that the loss of one amplifier should be noticeable, as the peak image current is forced through the cathode followers.

### 3.3 Tests of Added Second Harmonic Voltage

This experiment occurred in December of 1998. It required temporary modifications be made to the buncher, in a rapid timeframe. Because of this, the work was done with available components, and the RF duty factor was kept low to prevent damage to the amplifiers and gap. Despite this precaution, several grid resistors were destroyed in the FPA, before we began monitoring the peak dissipation in them. Modeling of the circuit with Spice showed that there would be asymmetry in the cathode currents, and that the phase of 5.6 MHz would have to be carefully monitored to prevent inadvertent peak voltages.

The pi-networks were removed from the IPA, and other modifications were made to eliminate stray resonances in the output, since the high gain tetrodes were now broadbanded. A case in point was the removal of half of the tetrode screen bypass capacitors, when it was discovered that they contributed to a 17 MHz resonance. The ferrite was tuned in-between 2.8 and 5.6 MHz, clearly not optimal but manageable with the RF amplifiers.

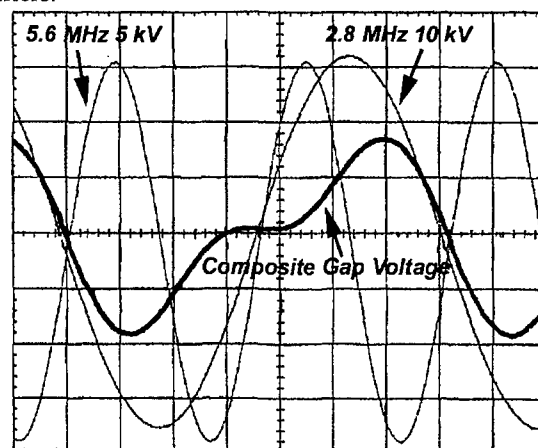


Figure 6. Dual Frequency RF Buncher Voltages

In figure 6, we see the two individual voltages and the composite voltage. This was the highest level of dual frequency operation that was tested. The improved bunching factor was observed in the beam current in PSR, as expected. Figure 7 shows four flat-topped bunches.

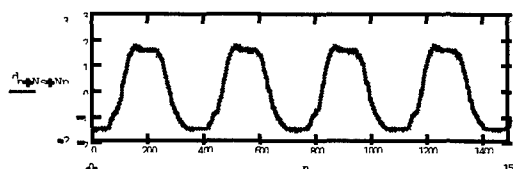


Figure 7. Improved Bunching with Dual Frequency Buncher

## 4 CONCLUSION

The cathode follower RF buncher system at PSR is very robust with high stored beam current. Without the need for high level feedback or turn-to-turn feedforward control it has excellent output regulation. Two harmonics were amplified and the results were favorable for increased charge density. Future plans can be made, based on these experimental results.

## 5 REFERENCES

- [1] J. Lyles, J. Davis, "Improvements to the Cathode-Follower RF Amplifier System for the LANSCE Protons Storage Ring Buncher", Proceedings of 1999 Particle Accelerator Conference, New York, NY.
- [2] R. Macek, et al. "Overview of Progress on the Improvement Projects for the LANSCE Accelerator and Target Facilities", Proceedings of 1997 Particle Accelerator Conference, Vancouver, BC.
- [3] M. Plum, et al. "Recent Experimental Evidence For the Los Alamos Proton Storage Ring Beam Instability", Proceedings of 1997 Particle Accelerator Conference, Vancouver, BC.

# IMPROVEMENTS TO THE CATHODE-FOLLOWER RF AMPLIFIER SYSTEM FOR THE LANSCE PROTON STORAGE RING BUNCHER\*

J. Lyles, J. Davis, Los Alamos National Laboratory,  
Los Alamos, New Mexico 87545 USA

## Abstract

Los Alamos Neutron Science Center (LANSCE) is upgrading the Proton Storage Ring (PSR) for the Short Pulse Spallation Source, to deliver 200 microamperes ( $\mu\text{A}$ ) of beam current to a new target assembly [1]. Previous operation had been limited to 70  $\mu\text{A}$ , partly as a consequence of the peak radiofrequency (RF) voltage available from the  $h=1$  buncher. After an extensive series of performance tests in 1996, an upgrade was proposed to the 2.8 Megahertz (MHz) cathode-follower RF amplifier system and the ferrite-loaded gap assembly. A new intermediate power amplifier (IPA) was designed and installed at the ring, to eliminate a troublesome oscillation which occurred when the final power amplifier (FPA) was operated in class A. This also increased the drive to the FPA to raise the gap voltage. The cathode-follower FPA was modified to accept the direct connection of a pair of short transmission line feeders from the IPA. The beam gap was replaced with one having larger ceramic insulating sleeves in a simplified mechanical configuration. A new RF coupling loop/ferrite bias conductor was designed to tightly couple the two halves of the ferrite-loaded resonant circuit connected to the gap, to improve waveform symmetry and to reduce the effects of gain differences in the amplifiers. Improvements were made to the amplitude feedback controller and a phase controller was designed and installed. Changes to the utility systems, the controls, and the power supplies completed this upgrade in 1998. A description of the circuit modeling and the hardware changes in the equipment will be presented. As demonstrated, the upgraded RF buncher has delivered the specified performance at LANSCE [2].

## 1 ORIGINAL RF BUNCHER

The PSR utilizes a RF barrier system to control longitudinal beam distribution. The 90.2 meter circumference ring has a rotational frequency of 2.79513 MHz, hereafter referred to as 2.8 MHz. With a bunch length of 250 nanoseconds (ns), there is a 107 ns longitudinal space kept clear to allow for beam extraction. The original  $h=1$  RF system has been providing up to 13 kilovolts (kV) of 2.8 MHz voltage at the buncher gap.

### 1.1 Motivation to Upgrade Buncher

A series of performance measurements were made to determine shortcomings of the original RF buncher, which could be problematic when the average beam

current is increased to 200  $\mu\text{A}$ . The RF voltage in the present gap would need to be as high as 18 kV at 2.8 MHz. Another goal was to configure the system to allow a second harmonic at 5.6 MHz, to improve the bunching factor without reaching a space charge limit in PSR. A plan was developed to upgrade the original buncher and build a second system with the ability to operate at the fundamental or at  $h=2$  [3].

### 1.2 Buncher Gap

The buncher gap is a 1 cm break in the PSR beam pipe, which is insulated with an outer alumina cylinder. The RF structure consists of a pair of opposing horizontal stubs approximately 79 cm long. These beam pipes are grounded at the far ends to the enclosure shell, and open-circuited at the center, where the insulator bridges the structure. Twenty water-cooled Philips type 4H ferrite toroids are stacked on each pipe to raise the inductance, and foreshorten the resonator. Direct current is routed through a bias winding to tune resonance to 2.8 MHz. This circuit has 16  $\mu\text{H}$  of inductance, and 200 pf of capacitance at the gap, where 150 pf is provided with three fixed vacuum capacitors. At resonance it provides a 5000 Ohm load to the FPA. The fixed capacitors are usable to 80 MHz, and pass the higher frequency Fourier components of the image current.

### 1.3 Final Power Amplifier

The PSR may store peak beam currents as high as 35 Amperes ( $\geq 200$  ns bunch,  $6.25 \times 10^{13}$  protons), so it is imperative to maintain a very low longitudinal impedance,  $|Z| < 20$  Ohms. Shunting the gap with a low resistance was impractical due to the power required. Active feedback around the final amplifier is a standard approach for many circular machines. The PSR buncher uses a cathode-follower (common-anode) FPA. For a cathode-follower using a triode with a high amplification factor, the low frequency output impedance can be estimated as:

$$R_o \approx \frac{1}{g_m} \text{ . This low output impedance loads the resonant}$$

gap, and provides a path for the image current through the power triodes. A pair of industrial triodes (EEV part number BW1643J2, formerly Amperex 8918) rated for 240 kW plate dissipation are used in a push pull arrangement, with the cathodes feeding both sides of the gap with short wide straps. They are mounted under the beamline. The transconductance ( $g_m$ ) at our operating

\* Work supported by the US Department of Energy

point is 0.23 mhos for these power tubes. The low frequency output resistance is calculated to be less than 10 Ohms, across the two cathodes. It is higher at the gap, due to the strap lengths and skin effect. This arrangement has worked successfully since 1984, and is used in the upgraded system as well [4].

It is known that a cathode-follower operating with a tuned grid circuit in the high frequency range can be unsatisfactory, due to possible oscillation in the Colpitts arrangement when the cathode load is capacitive [5,6]. At PSR this is overcome with a 25 Ohm water-cooled resistance in series with the grid of each triode, making a net positive input resistance. Cathode followers have less than unity voltage gain:

$$A = \frac{g_m R_k}{1 + g_m R_k}, \text{ where } R_k \text{ is } 1/2 \text{ of the resonant load for}$$

the push-pull situation, or 2500 Ohms for each triode. The calculated gain is 0.99, but in hardware it is about 0.93, because of the series-connected stability resistor at each grid, and circuit drops and losses.

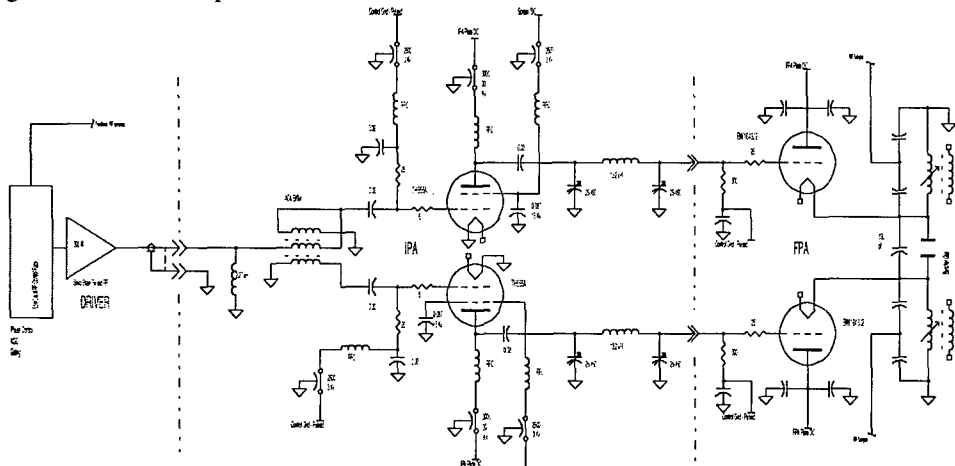


Figure 1. Simplified Schematic of Improved Buncher

### 1.4 Intermediate Power Amplifier

The original system used two cascaded amplifiers for two stages of voltage amplification. One amplifier used two 4CW25,000A tetrodes, which drove another amplifier with four of the same tubes, near the limit of their voltage rating. They were located in the equipment building above the PSR, interconnected with a pair of Heliac<sup>®</sup> coaxial cables. These were both fed and terminated in high voltage RF transformers, which then drove the FPA grids. The long cables between stages had reflections responsible for a line resonance at 7 MHz, which caused an oscillation in the cathode followers when biased into class A at high quiescent current. Hence, they were operated in class AB, occasionally reaching cutoff and saturation during peak excursions. This hindered the ability to raise buncher voltage and maintain low output impedance. The ferrite cavity lacked RF coupling

between halves, so the followers acted as independent amplifiers for each half of the total gap voltage.

## 2 UPGRADED RF BUNCHER

### 2.1 New Intermediate Power Amplifier

The replacement IPA is sized to provide all of the voltage gain with 19.5 kV peak output voltage to drive the FPA to provide 18 kV at the gap. Tetrodes are optimal for voltage gain and stage isolation. The parasitic oscillation was eliminated closely coupling a new IPA to the FPA, with the series grid resistors. This is schematically shown in figure 1. A pair of TH555A tetrodes from Thomson Electron Tubes, rated for 250 kW plate dissipation, are used in the IPA, operating 180 degrees out of phase. Because we intended to operate them in class A, the manufacturer recommended a ring of lossy ferrites around the circumference of the screen to plate ceramic, to suppress higher order UHF modes. We saw no evidence of UHF energy with this socket. Figure 2a shows the interior of one half of the IPA. The left side of the

enclosure houses a duplicate amplifier.

For the IPA stage, we used a 500 Ohm plate loadline so that 20 Amperes of RF current will give us 10 kV peak. Each tube swings 20 kV peak to peak. A 500 Ohm water-cooled shunt resistor loads the grid of each cathode-follower. A pi-network ( $Q = 8$ ) absorbs the capacitive reactance of each TH555A plate and the input capacitance of each cathode-follower. This low

pass filter provides two tunable elements for compensation of any phase shift in each amplifier. An electric clutch arrangement was designed to mechanically lock the capacitors on each half of the IPA together, to hold the 180 degree phase offset while tuning a single knob for best performance. The TH555A input capacitance is shunted with a 25 Ohm resistor, and the pair of these is driven out of phase by a Ruthroff 1:1 balun on a 4C4 ferrite core. Tuning is broadly accomplished with a shunt inductor at the input, reflected through the balun, placing resonance at about 4 MHz, and presenting a reasonable match at both 2.8 and 5.6 MHz for drive from a solid state amplifier. This allowed for testing at dual frequencies later.

The output power in this stage is 100 kW peak per tube, with 5% duty factor. The quiescent plate current during the bias pulse is 40 Amperes DC per tetrode, in class A. Drive requirements are provided by a single ENI A300 linear amplifier, rated at 300 Watts. IPA stage power gain is approximately 27 dB.

## 2.2 RF Interconnection

The front of the FPA cabinet was modified to accept a pair of shielded "feeders" connected to the grid resistors. They physically resemble 108 Ohm air insulated coaxial line. The outer conductor is a 7.69 cm diameter flexible section made from a Myatt corrugated line, with the inner being a 1.27 cm diameter solid brass rod. At the FPA end, the rod has a gold-plated tip which mates with a high reliability receptacle, made by Hypertronics Corp. A funnel-shaped insulator guides the pin into the hole for

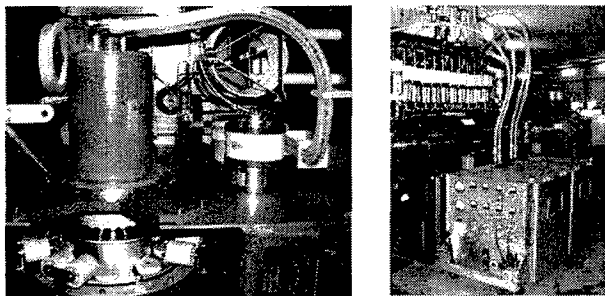


Figure 2a and 2b. Interior of IPA, and System Installation

blind alignment. The line was optimized to minimize inception of 60 Hz AC corona, having a maximum gradient of 8.8 kV/cm at the buncher peak voltage. Figure 2b shows the installed IPA along with the FPA and cavity.

## 2.3 Final Power Amplifier Operating Point

The maximum current in each FPA triode for class A operation is chosen to handle half the peak beam current plus losses. The quiescent current is 40 Amperes, with the same plate voltage as the IPA, 15 kV DC. Bias pulsing is used to keep the DC current under 3 Amperes. Cavity losses are less than 2 kW at 5% duty factor.

## 2.4 New Gap, Bias and Coupling Loop

The original gap had a pneumatic-actuated shorting sleeve on one side. It was no longer used, and was a source of unwanted stray capacitance to ground on that side only. Further inspection found the shorting sleeve inside the beam pipe in poor condition, with burned wiping contacts due to arcing. This mechanism was removed and replaced with a symmetric gap structure for electrical balance.

The original biasing system for the ferrite was a pair of parallel copper loops for DC, with RF bypassing capacitors to ground. DC was shunt fed through a large RF choke inductor external to the cavity. There was conducted RF leakage into the power cables. With the upgrade, the bias loops were converted to a "figure-eight" arrangement with RF coupling and DC on the same busswork. Figure 3 shows the arrangement. Since the loops are now in series, the DC current is half the old value for resonance at 2.8 MHz, allowing the same power supply to push resonance as high as 5 MHz for testing. There is very little residual RF at the bias feed point, with this balanced hookup. A small common-mode ferrite

choke is used as an RFI filter, encompassing both DC conductors to prevent saturation. The RF coupling capacitors at the ends are de-Q'd with a low inductance resistor of 0.1 Ohms, composed of 100 individual carbon resistors in parallel on copper plates. These loops tightly couple the halves of the cavity in push-pull. Modeling and testing demonstrated improved output compliance. The bussbars are free of stray resonances to 30 MHz.

## 2.5 Low Level RF Feedback Control

The amplitude of the RF buncher is ramped with injection. A feedback control system is driven from a differential gap voltage sample. In the upgraded system, the loop bandwidth was significantly increased and an integral gain term was incorporated. An active detector was designed to control at a lower gap voltage, about 500 volts versus 2 kV for the original controller. The original system had no phase control. With the addition of the tuned IPA, a phase feedback loop was designed. Using a log amp as a limiter, a double balanced mixer is used to derive a phase signal, and a steerable phase modulator is controlled. This reduced open loop phase slew during the amplitude ramp from 18 to 9 degrees, as well as locking the phase to a reference. Beam effects on the buncher will be discussed in the companion paper [2].

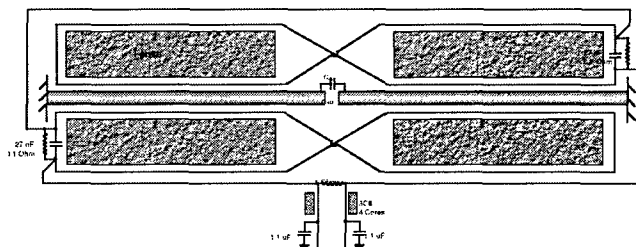


Figure 3. Figure-Eight Coupling and DC Bias Bussbars

## 3 REFERENCES

- [1] R. Macek, et al. "Overview of Progress on the Improvement Projects for the LANSCE Accelerator and Target Facilities", Proceedings of 1997 Particle Accelerator Conference, Vancouver, BC.
- [2] J. Lyles, A. Browman, R. Kustom, "Commissioning of The Upgraded RF Buncher at the LANSCE Proton Storage Ring", Proceedings of 1999 Particle Accelerator Conference, New York, NY.
- [3] J. Lyles, A. Browman, J. Doss, "RF Buncher Upgrade for SPSS Enhancement Project", PSR Tech Note 97-004.
- [4] T. Hardek, "A Low Impedance, 2.8 MHz, Pulsed Bunching System for the Los Alamos Proton Storage Ring", Sixteenth Power Modulator Symposium, Arlington, VA. June 18-20, 1984.
- [5] S. Giordano, M. Puglisi, "A Cathode Follower Power Amplifier", IEEE Transactions on Nuclear Science, Vol. NS-30, No. 4, August, 1983.
- [6] F. Clapp, "Some Aspects of Cathode-Follower Design at Radio Frequencies", Proceedings of the I.R.E., Waves and Electrons Section, August 1949.

# ELECTRON GUN BEAM EXTRACTION WITH MOSFETS

F. Niell, Fermilab, Batavia, IL

## Abstract

Electron beams with an energy range of 10keV at 2A requiring intensity modulation with bandwidth from 50kHz 7.5MHz pose an interesting problem to the RF designer. Driving the extraction electrode of an electron gun can be a challenge with these requirements. The straight forward approach is the construction of a vacuum tube, single ended amplifier capable of delivering the anode voltage to the extraction electrode of the gun. However, vacuum tubes of this size and power are becoming increasingly expensive, and as the technology dies, the reliability of new components comes into question. The logical alternative is the implementation of solid state electronics. However, the 7.5MHz 7kV requirements pose a problem, as the solid state high voltage, high current technology does not exist in a single package. A new system of driving the extraction electrode of a Pierce type gun was developed using MOSFETs. Arranged in ultra-reliable "bricks" of series-parallel arrays, the MOSFETs allow for highly efficient amplification-mode operation. Amplitude linearity to 0.1% is achieved. The proposed system, capable of producing 7kV at 25kW will be implemented in the Electron Compressor experiment at Fermilab.

## 1 INTRODUCTION

The Fermilab Tevatron collider has several constraints on its luminosity and intensity. One of the limits on luminosity is the beam-beam interaction. The space charge of one beam creates an electromagnetic lens for the other beam in a collider (and vice versa), and thus, perturbations arise in both beams. This limit is caused by a bunch-to-bunch tune spread introduced by the lensing effect. This tune spread is one cause of the wide distribution of tunes and higher-order lattice resonances seen on the Tev beam footprint.

There have been several suggested methods for beam-beam compensation, but one that shows some promise is the linear electron lens. A beam of electrons, traveling in the opposite direction of the antiproton beam is used to compensate for the beam-beam effect. The amount of electromagnetic lensing a "stiff" beam of antiprotons feels interacting with a weak beam of electrons is determined by the current density of the electron beam. Thus, a properly modulated beam of low energy, high intensity electrons could compensate for the beam-beam interaction.

The Electron Compressor experiment is a collaboration set up to determine the feasibility of a Tevatron electron lens for the Tev 2 run [1].

## 2 ELECTRON COMPRESSOR

The Electron Compressor is a linear electron beam of roughly 3A in a solenoidal magnetic field of 4kG [2]. The electron beam comes from a high perveance Pierce type electron gun.

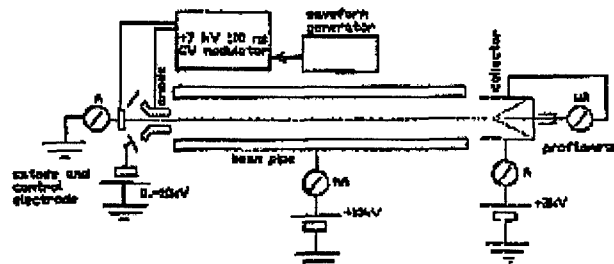


Figure 1: Electrical scheme of the "electron lens" [2].

The Pierce gun has an extraction electrode, with which the current density of the beam may be controlled. The extraction electrode allows the electrons from the cathode region to escape the field from the control electrode, and be pulled into the accelerating field supplied by the anode. The extraction electrode itself has a funnel shape [2, contains more detailed device information]. This geometry gives the extraction electrode a capacitance to ground of approximately 72pF.

Modulation of the electron beam current density at the bunch spacing of the Tevatron, as planned in the Tev 2 run, of 132ns makes the extraction electrode look like 300 Ohms due to the. The geometry of the structure requires about 7kV peak to turn the beam on. This translates to 25kW RMS power. The predicted waveform necessary to drive the extraction electrode to compensate the beam-beam effect have been calculated (see Fig.2).

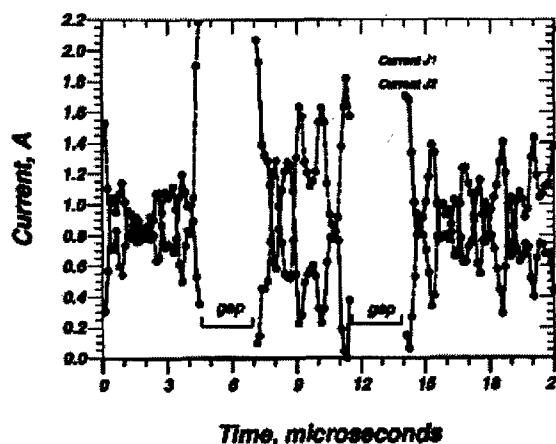


Figure 2: Predicted waveform of modulated current density. Beam currents for 2 lenses are shown. J1, J2 are the two waveforms of interest [1]



FFT shows that there are components of this waveform that range from 50kHz to 7.5MHz. Thus, a modulator capable of supplying 25kW peak into a 72pF capacitive load with bandwidth from 50kHz to 7.5Mhz is needed.

### 3 MODULATOR DEVELOPMENT

Traditionally, there existed only one way to provide this type of power for particle accelerator technology applications. Vacuum tubes, such as the EIMAC 4CW25000B tube, would be perfectly suited to this purpose. However, due to the costly nature of tubes, the declining product support, and poor reliability and uniformity of tubes available on today's market, the author chose to pursue a new approach.

A means for replacing conventional tube technology with new transistor technology was sought. Transistors are not easily used in the high power, high voltage, high frequency domain. Since commercially available transistors typically have a voltage limit of 1kV, several transistors are needed to operate in series to properly share the load.

Drawing on traditional cascade architecture for tubes [3], and modern transistor technology [4], a hybrid architecture was born. MOSFETs lend themselves to RF amplification well, as their power/volume ratio is high, but have a very low impedance gate. The author began with a simple Class A amplifier, utilizing the new DEI 102N20 MOSFET [5] (see Fig.3).

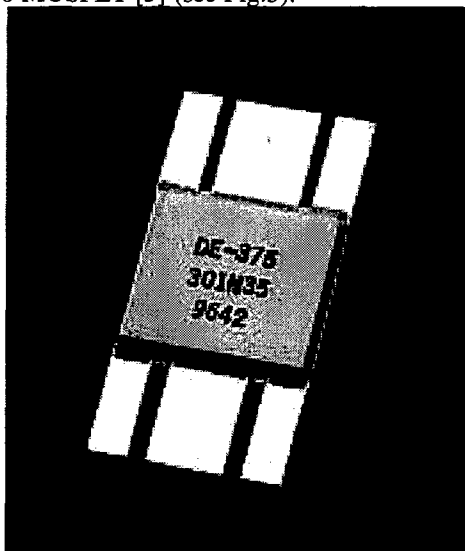


Figure 3: The DEI DE series MOSFETs offer 375W at 1kV, in a package that lends itself to higher frequency operation for that power level than existing 0.5" flange type MOSFETs [5]

The major difficulty with cascading MOSFET amplifiers is the requirements of the devices themselves. Each device has a linear range of roughly 75mV, and a gate voltage of 3.25V. This is a technical hurdle because the drive circuitry for each MOSFET in series must be

isolated to the voltage that the cascaded MOSFETs are sitting at.

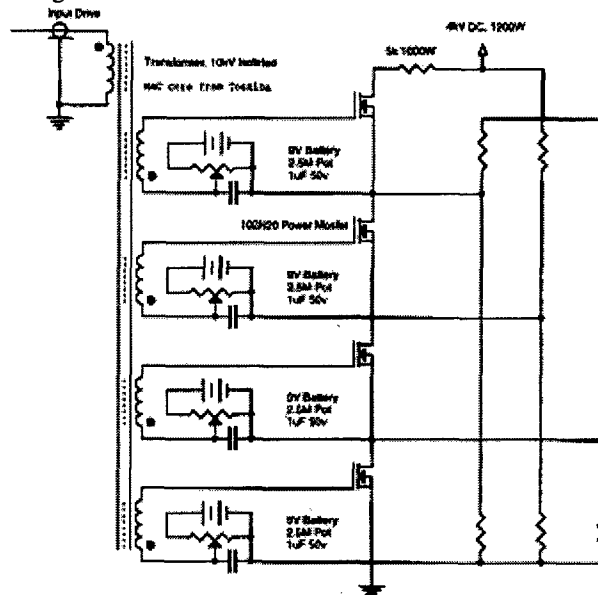


Figure 4: Circuit diagram for a "brick" of MOSFETs

Two options presented themselves. I could stand off the DC high voltage on each MOSFET with a capacitor, and thus capacitively couple the gate to the RF source. Or, I could use a wide band isolation transformer to stand off the high voltage. Since the devices must be mounted on a large water cooled heat sink, they must be electrically insulated to the voltage the cascaded MOSFET sees. This requires Kapton insulation, and creates a capacitor in series with the gate circuit to ground (due to the device geometry). This, in effect dumps the gate drive power into the space between the MOSFET and the heatsink, instead into the gate. As such, capacitive coupling was not an option.

*Circuit description* (see Fig.4)

An isolation transformer was constructed using an M4C Toshiba core, and RG-213 center conductor for high voltage insulation.

The gate bias supplies must be isolated to at least 10kV (maximum voltage of the modulator with safety margin), and be able to supply only a few nA. In order to supply a DC bias to the AC signal, a 1uF cap was used to act as a low Z shunt for the AC signal. Thus, the 9Volt battery, parallel with the potentiometer across the cap provides the variable gate bias. This DC offset is added to the AC signal through one of the secondaries on the transformer. The summed bias and drive signal are sent to the gate of the MOSFET.

Also, since when the MOSFETs are all turned off (no drive signal), the situation could arise that one MOSFET would potentially see more than 1kV if they are not all biased properly. Thus, an external voltage divider network was made to ensure that each MOSFET would only see 1kV drain to source.

Cooling is achieved by mounting the MOSFETs on a 5x5" square block of 1" thick copper magnet buss bar, with a cooling channel in the middle. Four MOSFETs can be mounted on the heat sink safely, and thus the resulting four MOSFET assembly is referred to as a "brick." The four MOSFETs in series are able to modulate voltages up to 4kV, and handle up to 1200W.

The series load resistance is a simple series parallel combination of 8 10kOhm, 225W resistors to make 5kOhm, 1600W resistor.

## 4 PERFORMANCE

The modulator currently operates over its specified bandwidth, however the power as a function of frequency is not linear, as claimed in the abstract. Recent results have shown that the claim in the abstract is not true. The bandwidth, in fact, follows the general form of a resistance in parallel with a series RC circuit. This implies that much of the frequency dependence of the modulator is due to the reactive nature of the load. A non-reactive load made of water cooled conductive ceramic resistors will be constructed in the next few weeks, and is expected to linearize the output greatly. The reactive nature of the load also current limits the output greatly, and as such, only 2.25kVpp is possible at this point. It is expected that the new load will allow the brick currently under test to modulate the entire 4kV (see Fig. 5).

Once the entire voltage dynamic range is achieved, several more bricks will be made. They will be arranged in series-parallel arrays to build up the current and voltage necessary for the full implementation of the device. Most likely, there will be two bricks in series (vertical stacks), and seven or eight in parallel (horizontal stacks) creating a matrix of devices, with probably 64 devices. The finished matrix should handle 24kW conservatively.

## 5 CONCLUSIONS

The bandwidth linearity is a small problem compared to the overall proof of capability of the series MOSFET circuit architecture. The peak-to-peak output is more than 2.2 times the maximum operating voltage of a single MOSFET, and thus they are truly operating in series as linear amplifiers. As a stopgap measure, a tetrode tube amplifier was constructed [2]. Implementation of the solid state modulator is expected in Jun. '99. Since the MOSFETs are a relatively new technology as compared to vacuum tubes, it seems that the more reliable, cheaper technology is long overdue as a replacement for comparable vacuum tube technology. It is hoped that this research will help initiate the shift from vacuum tube reliance to solid state for high voltage, high power RF electronics.

## 5 REFERENCES

- [1] V. Shiltsev, *et.al.*, "Compensation of Beam-Beam Effects in the Tevatron with Electron Beams", FNAL-Pub-98/260 (1998)
- [2] V. Shiltsev, *et.al.*, "Prototype "Electron Lens" Set-up for the Tevatron Beam-Beam Compensation", these proceedings
- [3] E. Ginzton, *et.al.*, "Distributed Amplification", Proceedings of the IRE, (1948)
- [4] Intech, "PA5K-30LC Hardware Technical Manual MN161786", Lambda RF Systems (1994)
- [5] <http://dirnrg.com/Products/specs/deseries.htm>

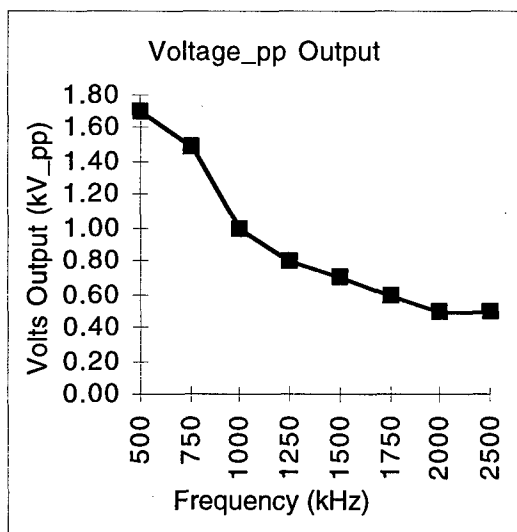


Figure 5: Modulator output in Volts peak to peak with a sinusoidal input wave, plotted as a function of frequency

# WIDE-BAND PUSH-PULL AMPLIFIER FOR HIGH GRADIENT CAVITY

Y. Sato, M. Fujieda, Y. Mori, H. Nakayama, C. Ohmori, R. Muramatsu,  
T. Uesugi, M. Yamamoto, M. Toda, A. Takagi and M. Yoshi, KEK;  
Y. Taniguchi, Denki Kogyo Co.; K. OHTA, Ohta Electronics Co.

## Abstract

A high gradient cavity(HGC) using high permeability magnetic alloy (MA) cores has been developed at KEK for the JHF(Japan Hadron Facility) proton synchrotrons. In this paper, we describe two types of push-pull amplifiers to drive the cavity, which were constructed for verifying the cavity performance. An accelerating voltage of 20kV across the gap of the HGC was generated by the high power push-pull amplifier. This is equivalent to high gradient field of 50kV/m. The other amplifier and the cavity were prepared for accelerating heavy ions at the HIMAC(Heavy Ion Medical Accelerator in Chiba). For this purpose, it is necessary to sweep the frequency over the wide range from 1MHz to 8MHz.

## 1 INTRODUCTION

In order to generate a high field gradient with HGC using MA-cores, a high power push-pull type of rf amplifier which uses two 150kW class tetrodes (4CW150,000E) was constructed. The HGC with MA has the following two remarkable features: (1)the ability to generate high gradient field up to 50kV/m and (2)broad band impedance over the frequency range of 5MHz. The characteristics of the HGC with MA have been reported [1, 2, 3, 4]. We have built in the medium power push-pull amplifier using two 30kW class tetrodes (4CW30,000A) for acceleration of heavy ions at HIMAC.

## 2 PUSH-PULL AMPLIFIER

A schematic view for the RF system including the cavity and the amplifier is shown in Figure 1. The push-pull amplifier in class-B operation has the following two features: (1)The high rf output voltage close to dc plate voltage can be obtained. That is, the plate dissipation is less than that of an amplifier in class-A operation. (2)The output voltage will be less distorted even if a tuning circuit is not utilized for the load cavity. This is because the even harmonics introduced by nonlinearity of the dynamic-tube characteristics are eliminated at the output by a push-pull connection.

### 2.1 300kW Push-pull Amplifier

Concerning the tube performance of the push-pull amplifier using two tetrodes 4CW150,000E, the measured and

calculated specifications are presented in Table 1.

Parameter	Measured value	Calculated value
DC plate voltage $V_p$	15kV	15kV
DC idling current $I_{po}$	2.9A	1.0A
DC plate current $I_p$	3.71~6.84A	5.94A
DC screen voltage $V_{g2}$	1550V	1500V
DC screen current $I_{g2}$	not measured	466mA
DC grid voltage $V_{g1}$	-390V	-390V
DC grid current $I_{g1}$	65~87mA	44mA
Driving grid voltage $E_g$	602V	602V
Fundamental plate curr. $I_{p1}$	—	25.7A
Peak plate voltage $E_{pm}$	14kVp	14kVp
Peak plate current $I_{pm}$	not measured	85A
Plate input power $W_i$	55.7~102.6kW	89.1kW
Plate output power $W_o$	—	59.0kW
Plate dissipation $W_l$	55.4kW(max.)	30.1kW
Voltage at gap end $V_{gap}$	-14kVp, +7.2kVp	±14kVp
Accelerating voltage $V_{acc}$	±16kVp	—

Table 1: Tube performance of the 300kW push-pull amplifier.

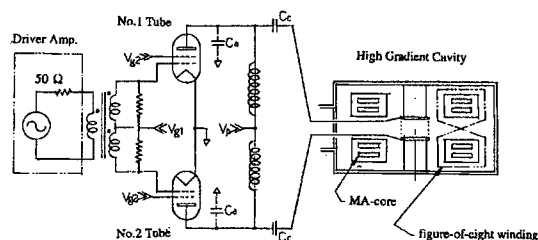


Figure 1: Schematic view for the RF system.

The measured values were taken when the amplifier was operated at 20% duty factor in burst mode sweeping the frequency from 2MHz to 3.4MHz with repetition rate of 2Hz. The calculated values were derived from the operating line on the constant-current curves for the tube by reading the instantaneous values of plate, screen, and grid current during the negative half cycle of the plate voltage swing. In order to compare the measured values to the calculated ones, the calculated values for  $I_p$ ,  $I_{g2}$ ,  $I_{g1}$ ,  $W_i$ ,  $W_o$  and  $W_l$  are adjusted to 20% duty factor operation. The measured value of idling current  $I_{po}$  was higher than the calculated value. This means that the amplifier was in class AB<sub>2</sub> operation mode, where the conduction angle of plate current was more than 180° and grid current was flowing. Thus the measured plate dissipation  $W_l$  was rather higher than the calculated one.

Since the MA-loaded HGC has a low- $Q$  ( $< 1$ ) value and the cavity is directly connected to the plate of the amplifier via a low impedance capacitor ( $C_c$ ) as shown in Figure 1, the plate voltage swing would substantially depend on the cavity impedance. The cavity impedance can be estimated by dividing the peak plate voltage by the peak plate current:  $E_{pm}/I_{pm} = 165\Omega$ . This would be consistent with the cavity impedance of approx.  $178\Omega$  at 2.3MHz which was measured from the plate by a network analyzer.

Since the rf plate current at a positive rf half cycle is nearly zero, the power delivered by one tube is about a half of  $W_o$ , which is given by  $W_o = E_{pm} \cdot I_{p1}/2$ . Thus the power  $W_o$  is almost the output power delivered by two tubes. Using the values of  $E_{pm}$  and  $I_{p1}$  presented in Table 1, the power  $W_o$  becomes 295kW in cw mode operation. Taking account of rather high dc screen current  $I_{g2}$  in Table 1, we should be careful that the screen dissipation can not exceed the normal rating of the tube. It would be pointed out that the excessive driving power at the control grid should be avoided because it may allow instantaneous plate voltage drop lower than the dc screen voltage, resulting in abnormal screen dissipation. In addition, if the dc plate voltage can be raised, it may contribute not only to decrease screen dissipation but to reduce the distortion of the accelerating voltage waveform, which may be introduced by plate current saturation.

## 2.2 60kW Push-Pull Amplifier

The MA-loaded HGC and the 60kW push-pull amplifier with two tetrodes 4CW30,000A were installed at HIMAC. In order to accelerate heavy ions at HIMAC, it is necessary to sweep the frequency over the wide range from 1MHz to 8MHz. The accelerating rf voltage depends not only on the characteristics of the shunt impedance, but also the gain-frequency characteristics of the amplifier. With respect to the 60kW push-pull amplifier, a maximum gain drop at the grid input circuit was 4.6dB at the frequency range from 1MHz to 8MHz. Thus proper voltage control was employed to obtain the constant rf voltage [3, 5, 6].

## 3 EQUIVALENT CIRCUIT AND COUPLING METHOD

### 3.1 Equivalent Circuit for the RF system

The impedance seen from the tube was measured by a network analyzer. It includes both impedance of the cavity and the plate circuit of the amplifier. The Figure 2 shows the measured impedance where the fundamental resonance was stayed at 2.3MHz, on the other hand, series resonance was at 14.8MHz and parallel resonance was at 21.5MHz, respectively. The impedance is almost equal to the shunt impedance  $Z_s$  corresponding to one-half of the cavity at low frequency region below 5MHz, even though two-halves of the cavity are coupled each other with the capacitance  $C_g$  for the accelerating gap. This would be justified by a comparison:  $|1/\omega C_g| \gg |Z_s|$ , where  $|1/\omega C_g| \cong$

$3.8k\Omega$ ;  $|Z_s| \leq 178\Omega$  around the frequency of 2.3MHz. The value of  $Z_s$  can be estimated by the parameters  $L_p$ ,  $C_p$  and  $R_p$  of the equivalent circuit shown in Figure 3. The shunt resistance  $R_p$  at fundamental resonance is  $178\Omega$  as above-mentioned. On the other hand, the impedance seen from the both ends of the gap is almost twice the  $R_p$  which is reported by the referenced paper [3]. It would be explained as the impedance quite corresponds to that of two-halves of the cavity.

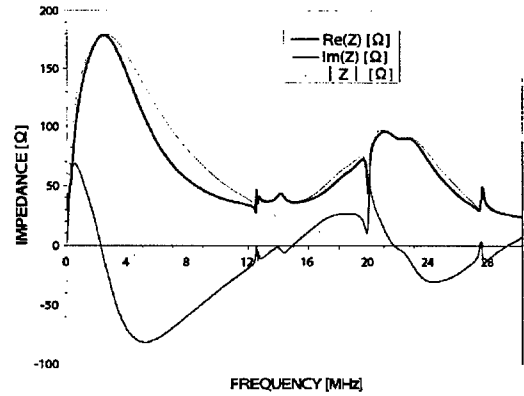


Figure 2: Impedance characteristics seen from the plate of one tube.

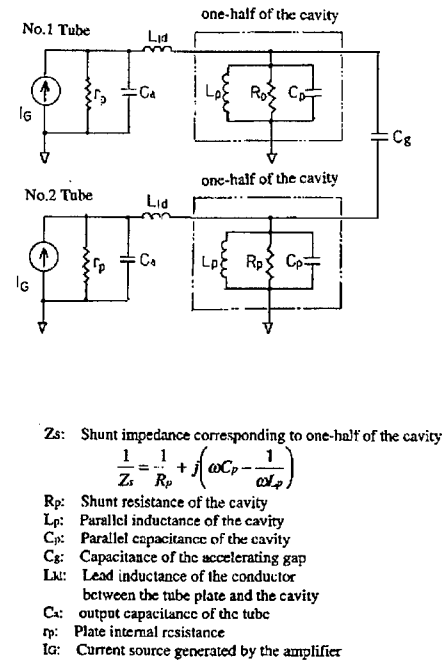


Figure 3: Equivalent circuit for the RF system.

### 3.2 Coupling Method with Figure-of-Eight Winding

By means of coupling two-halves of the cavity with a figure-of-eight winding looped through each other, the RF cavity is intrinsically capable of operating in a push pull mode [7]. Due to this coupling a load impedance seen

from the plate substantially becomes one half of the shunt impedance  $Z_s$ . The figure-of-eight winding works as a transformer as shown in Figure 5. The characteristics of load impedance for the cavity with this coupling is also represented in Figure 4. The load impedance which is one half of the  $Z_s$  may cause a plate dissipation to increase, because it may deteriorate the matching condition of the impedance between the plate and the cavity.

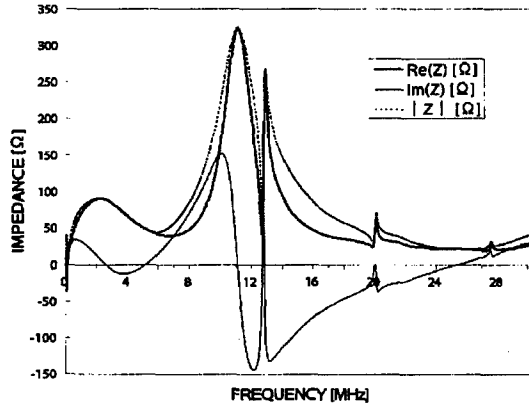


Figure 4: Impedance characteristics of the cavity seen from the plate of one tube; Two halves of each cavity are looped with a figure-of-eight winding.

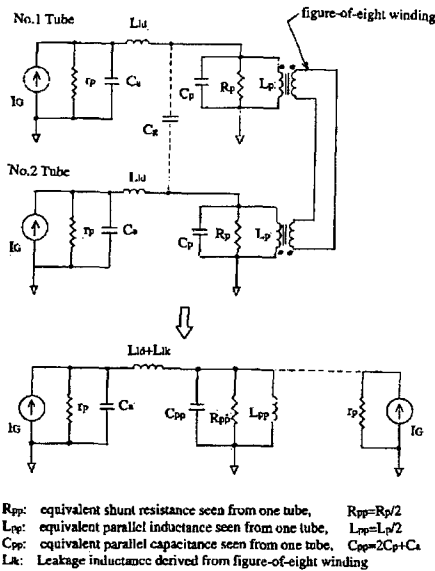
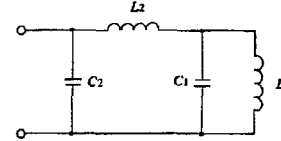


Figure 5: Equivalent circuit for two-halves of the cavity coupled with a figure-of-eight winding.

A parasitic resonance at the frequency around 11MHz can cause harmful distortion to the accelerating voltage. The circuit with this coupling can be simplified as a reactance circuit shown in Figure 6. Applying a same reactance function described in the previous paper [8], parallel resonant frequency  $f_h$  will be given by the following equation.

$$f_h = 1/2\pi \sqrt{L_2 \left( \frac{C_1 C_2}{C_1 + C_2} \right)}$$

In the equation,  $L_2$  comprises leakage inductance  $L_{lk}$  and lead inductance  $L_{ld}$ ,  $C_2$  is the tube capacitance and  $C_1$  is the sum of the tube capacitance and total capacitance for two-halves of the cavity. Assuming parameters as shown in Figure 6,  $f_h$  is calculated to be about 13.5MHz, which is not so large different from the measured value of 11.0MHz. The figure-of-eight winding intrinsically introduces a parasitic resonance and allows its frequency lower. We did not adopt the figure-of-eight winding.



$$C_1 = C_{pp} = 179 \text{ pF}, \quad C_2 = C_a = 43 \text{ pF}, \\ L_1 = L_{pp} = 5 \mu\text{H}, \quad L_2 = 2(L_{ld} + L_k) = 4 \mu\text{H}$$

(The values of above parameters for the cavity are estimated at 10MHz.)

$jX(\omega)$ : reactance function seen from one-port terminal of the reactance circuit

$$jX(\omega) = \frac{j\omega \left( \frac{L_2 + L_1}{C_1 C_2 L_2} - \omega^2 \right)}{\omega^4 - \omega^2 \left( \frac{1}{C_1 L_1} + \frac{1}{C_2 L_2} \right) + \frac{1}{C_1 L_1 C_2 L_2}}$$

Figure 6: Reactance circuit.

## 4 CONCLUSION

A push-pull amplifiers using two tetrodes 4CW150,000E has delivered the output power of 295kW in cw mode to generate an accelerating voltage of about 16kV in the HGC. The maximum voltage of 20kV was achieved at a small duty factor operation. Another amplifier using two tetrodes 4CW30,000A has generated an rf voltage of about 4kV at 3MHz when sweeping the frequency from 1MHz to 8MHz. Further investigation and development to improve the gain-frequency characteristics of grid input circuit are going to be carried out.

We have investigated a figure-of-eight winding coupling. We found that the impedance seen from the tube drops to a quarter of the total cavity shunt impedance and a parasitic resonance is inevitably introduced.

## 5 REFERENCES

- [1] Y. Mori *et al.*, Proc. of EPAC98, p1796, Stockholm,(1998)
- [2] Y. Mori *et al.*; "A new type of rf cavity for high intensity proton synchrotron", Proc. of Symp. On ACC. Sci. and Tech., Nishiharima, Japan, 1997
- [3] C. Ohmori *et al.*, in this conference
- [4] M. Fujieda *et al.*, Proc. of f APAC98, Tukuba,(1998)
- [5] M. Yamamoto *et al.*, in this conference
- [6] R. Muramatsu *et al.*, in this conference
- [7] M. Meth *et al.*; "PUSH PULL OPERATION OF THE RF CAVITY", Booster Tec. Note No.84, B.N.L., 1987
- [8] Y. Sato *et al.*, Proc. of APAC98, Tukuba,(1998)

# OPERATIONAL EXPERIENCE WITH TWO TYPES OF 2 MW HVDC POWER SUPPLIES ON LEDA.\*

J. Bradley III, D. Rees, R. Przeklasa, Los Alamos National Laboratory, New Mexico;  
R. Jaitly, G. Schofield, Maxwell Technologies;  
M. Scott, Continental Electronics

## Abstract

The high voltage DC power supplies are predicted to be the most expensive component of the accelerator at the Accelerator Production of Tritium (APT) plant. Two different types of candidate HV power supplies are being tested on the Low Energy Demonstration Accelerator (LEDA) at Los Alamos National Laboratory. The first type uses SCRs in a twelve pulse topology with a spark gap crowbar. The second type uses IGBTs in a Solid State Modulator topology without a crowbar. While both topologies have been proven in existing high voltage applications, both systems contain new features to improve performance and reliability that have advanced the state of the art in HVDC power supply design. LEDA is being used demonstrate the benefits of these features for the APT plant and evaluate their impact on power supply reliability, serviceability and cost. We present detailed measurements of total power supply efficiency and the effect each topology has on the power factor and harmonic input currents drawn from the local power distribution system in addition to operational performance with other accelerator systems.

## 1 INTRODUCTION

The requirements, construction and performance of the SCR controlled center tapped High Voltage Power Supply (HVPS) are compared to the requirements, construction and performance of the Insulated Gate Bipolar Transistor (IGBT) controlled Solid State Modulator (SSM) style HVPS.

## 2 COMPARISON OF REQUIREMENTS

### 2.1 Performance Requirements

Table 1 shows how the performance requirements for the two types of HVPS systems are similar but not identical. The IGBT controlled HVPS specifications were fixed significantly later than the SCR controlled HVPS specifications. The efficiency, power factor, output voltage regulation and ripple requirements were made more restrictive because the IGBT controlled HVPS topology made tighter requirements more feasible. In this time it was also determined that the allowable energy dissipated in a klystron arc could be increased from 20 to 40 Joules.

The efficiency of the SCR controlled HVPS was specified at full output power. This is not a typical operating point for the klystrons so the efficiency of the IGBT controlled HVPS was specified to be  $\geq 97\%$  when

operating at -95 kV at 17 to 21 amps,  $\geq 96\%$  when operating between -80 kV and -95 kV at 12 to 21 amps, and  $\geq 95\%$  when operating between -60 kV and -80 kV at 10 to 21 amps.

The SCR controlled HVPS input voltage was limited to 1500 V by Los Alamos' decision to use only one SCR per leg in the SCR controller bridge. The IGBT controlled HVPS's input voltage was specified to be 4160 V due to safety constraints at the LEDA facility. The number of input phases was reduced to three to minimize facility cost.

Input current harmonics are a concern because specific harmonics can excite resonances in the power distribution system. For this reason smaller harmonic currents are desirable. The requirements on the input current harmonics for both supplies were determined by IEEE Std 519-1992.

Table 1: HVPS Requirements

Requirement	SCR	IGBT
Output Voltage	0-95 kV	0-95 kV
Output Current	0-21 A	0-21 A
Voltage Regulation	$\pm 770$	$\pm 400$ V
Voltage Ripple	$< 1540 V_{pp}$	$< 1100 V_{pp}$
Load Arc Energy.	$\leq 20$ J	$\leq 40$ J
pf at full power	$\geq 0.93$	$\geq 0.98$
efficiency at full power	$\geq 95\%$	$\geq 97\%$
Input Voltage	1500V $\pm 5\%$	4160V $\pm 5\%$
Input phases	6	3
Input current Harmonics	IEEE Std. 519-1992	

### 2.2 Environmental Requirements

Both power supply types were required to operate in the expected environmental conditions at the Savanna River Site and the environmental conditions at Los Alamos. All components located indoors were required to function over an ambient temperature range of 10°C to 32°C and a humidity range of up to 85% non-condensing. All outdoor components were required to operate over an ambient temperature range of -30°C to 41°C and a humidity range of up to 95% non-condensing. The power supply was required to function at an altitude of up to 2438 m to allow it to be tested at Los Alamos.

### 2.3 Reliability, Maintenance and Safety Requirements

The Mean Time Between Failure (MTBF) goal for the power supplies was 25,000 hours. This goal was driven by the combination of the MTBF for all other components in each RF system and the number of high power RF systems that are required in the APT plant.

\* Work supported by US Department of Energy.

Serviceability was given consideration from the beginning of the power supply design. The goal for the Mean Time To Repair of the supply for all but the most major repairs was one hour or less to reduce the cost of maintaining the APT accelerator.

Kirk® Key locks on the power supplies were required to integrate with the existing Kirk® Key lock system used at the LEDA accelerator. The power supplies were also required to meet all safety requirements at Los Alamos National Laboratory including the requirement that debugging the low level power supply control circuits could be done without exposure to voltages in excess of 24 V.

### 3 COMPARISON OF CONSTRUCTION

#### 3.1 SCR Controlled Center Tapped Power Supply

The SCR controlled HVPS's were built by Maxwell Laboratories. These supplies utilize an SCR bridge which regulates the current through the center tapped transformer primaries to control the secondary output voltage as shown in Fig. 1. Center point control allows the output voltage filter inductance to be placed across the SCR bridge on the low voltage side of the transformer, which reduces the filter inductor operating voltage. An SCR placed across the inductor is used to dissipate the energy stored within the filter inductor in the event of a klystron arc.

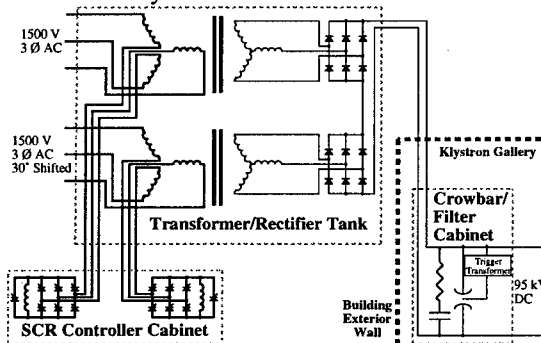


Figure 1: Voltage is controlled by SCR bridges located in the centers of the transformer primaries.

Two sources of 1500 V, 3-phase power are supplied by the unit-substation. One set of 3 phase power is offset by 30° with respect to the other set to produce 12-pulse rectification from two 6-pulse rectifiers whose outputs are wired in series.

The Transformer/Rectifier and SCR controller sub-units are located adjacent to the unit substation, while the Crowbar/Filter sub-unit is located inside the accelerator building adjacent to the klystron. In the event of a klystron arc, the crowbar circuit protects the klystron from stored energy in the filter capacitor and from any power supply follow-through energy.

#### 3.2 IGBT Controlled SSM Style Power Supply

The second power supply type that has been built for LEDA is the IGBT controlled SSM style power supply made by Continental Electronics. The power supply design is based on the Solid State Modulators that are

currently produced for AM radio service. Figure 2 shows how these supplies utilize 96 separate rectifying modules wired in series to produce high voltage. Each module is connected to a unique isolated 3-phase secondary on one of the four transformers as shown in Fig. 3. The relative phase differences between the sets of 3-phase secondaries on each of the four transformers are arranged to achieve 24-pulse rectification at the output.

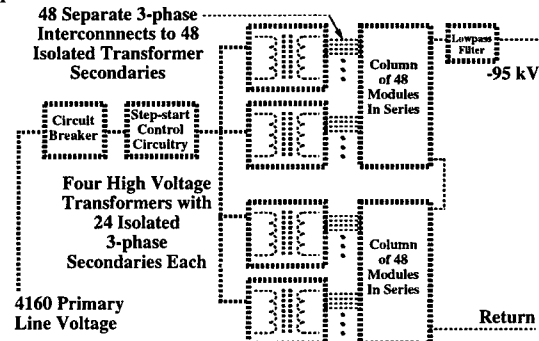


Figure 2: Two transformers serve each power column.

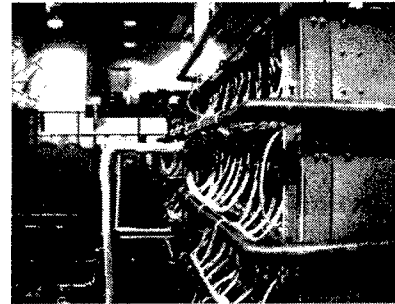


Figure 3: Each module in a power column is connected to one of 96 isolated secondaries.

An IGBT is used on each module for current control as shown in Fig. 4, eliminating the need for a crowbar. A diode allows current produced by other modules to pass through when the IGBT is turned off. The control system cycles through the array of modules to evenly load each module in the system. Each module contains independent control circuitry to monitor the module output and inhibit the three SCRs in the six pulse bridge in the event that the IGBT fails closed. Failed modules are bypassed by the control system to provide graceful degradation of operation. If more than five modules have failed, then the maximum voltage the supply can produce under the condition of 5% input voltage droop is reduced by roughly 1 kV per failed module after the first five.

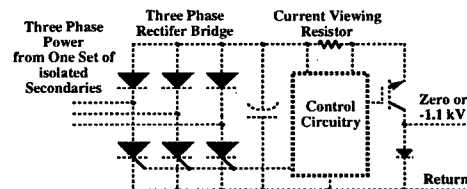


Figure 4: Each module contains a six pulse rectifier.

The power supply is contained within a 6.5 by 5.5 m fenced enclosure. Each module is built on a removable circuit card. The circuit cards are arranged in the two power columns in four rows of twelve. This

arrangement allows cooling air to be blown up the columns and across each module. The columns support corona rings on each row to grade the electric field as the potential increases toward the top of the column. The backplanes of the power columns contain connections to the 96 isolated 3-phase secondaries on each of the four transformers as shown in Figure 3. The backplanes also contain the shorting mechanisms which insure that all modules are discharged when the fenced enclosure is opened.

## 4 COMPARISON OF PERFORMANCE

### 4.1 Installation and Facility Requirements

The practical issues involving power supply installation and facility requirements become significant when over a hundred power supplies are to be installed in a short period of time. All the components in the IGBT controlled HVPS are located in one indoor location which covers 36 square meters. The SCR controlled HVPS has a smaller indoor footprint because the largest of the three major sub-units is located outdoors. The cost of the larger indoor area required by the IGBT controlled power supply must be compared to the cost of making and maintaining the interconnections between the sub-units of the SCR controlled HVPS.

### 4.2 Output Parameters

Both power supplies performed within their requirements for voltage regulation, ripple and load arc energy. The measured values are shown in Table 2.

Table 2: Measured Output Values

Measured Value	SCR	IGBT
Voltage Regulation	$\pm 500$ V	$\pm 400$ V
Voltage Ripple	$< 500$ V <sub>pp</sub>	$< 350$ V <sub>pp</sub>
Load Arc energy	3 J	$< 10$ J

### 4.3 Power Factor and Efficiency

Efficiency measurements were calculated by taking the output power, as measured by output voltage and current, divided by the primary input power as measured by the facility power distribution diagnostics. Input power for controls and cooling was not factored into this calculation.

The power factor and efficiency of the SCR controlled HVPS were measured at a typical operating point of 88.3 kV and 18.06 A. This point is determined by the klystron operating parameters and the amount of RF power required by the accelerator. At this output power level the power factor was 0.97 and the efficiency was 94%.

Arcing in the LEDA 2 MW HV resistive test load limited the voltage at which the power factor and efficiency of the IGBT controlled HVPS could be reliably measured at this time. At 50 kV output voltage and 10.6 A of output current the power factor was 0.95 and the efficiency was 95.2%. The power factor and efficiency are expected to improve at higher output power levels as the transformer excitation current and power become a smaller fraction of the total input current and power.

### 4.4 Input Current Harmonics

The measured harmonic components of the primary input current are shown in Table 3. The SCR controlled HVPS input currents were measured at an output current and voltage of 18 A at 88 kV. The IGBT controlled HVPS currents were measured at an output current and voltage of 10 A at 50 kV.

Table 3: Input Currents at Harmonics of 60 Hz

Harmonic Current Frequency	SCR (% of fund)	IGBT (% of fund)
180 Hz	1.3	6.6
300 Hz	4.4	2.1
420 Hz	5.2	1.6
540 Hz	0.7	0.1
660 Hz	7.7	9.3
780 Hz	9.2	7.7
900 Hz	0.6	0.3

The operation of the IGBT controlled HVPS at roughly half of its typical operating voltage may have caused input harmonic currents were a larger percentage of the fundamental than would be expected in normal operation. With only half of the power modules turned on, it is possible that at any given time only two transformers drew most of the power. This would produce uncanceled input harmonic currents at 660 and 780 Hz.

### 4.5 Operational Performance

Four SCR controlled HVPS's have been installed and are in use in the LEDA project. The SCR controlled HVPS's have been successfully operated in all weather conditions at Los Alamos and have fully protected the klystrons from damage in more than 100 klystron arcs. No arcing or corona damage has been observed in the 95 kV enclosures or components. Initial installation and startup problems included the replacement of the trigger circuit capacitors due to a manufacturing defect, the redesign of the open circuit voltage control network to reduce the network's operating temperature and the repair of fiber optic connections damaged by nearby construction work.

The first IGBT controlled HVPS has been installed and is presently being tested with the LEDA 2 MW HV resistive test load. It will be connected to LEDA's second 700 MHz klystron at the conclusion of these tests.

## 5 CONCLUSIONS

The tests that have been conducted indicate that the performance of the two types of power supplies is similar. Arcing within the LEDA 2 MW HV resistive test load limited the performance measurements that could be taken on the IGBT controlled HVPS. Demonstration of the predicted increased efficiency and lowered harmonic currents of the IGBT controlled HVPS will require testing at higher power levels. These tests are scheduled to be conducted in April, 1999.

The SCR controlled HVPS's have proven to be very reliable. The IGBT controlled HVPS's do not yet have sufficient operating hours to evaluate their reliability.



## A UNIVERSAL MULTI-MODE FILAMENT REGULATOR FOR HARD TUBES

Roy Church, Alan Stevens, Rutherford Appleton Laboratory, Chilton, Didcot, Oxon, UK.

### ABSTRACT

High power RF triodes used to power the injector linac cavities on the ISIS spallation neutron source at RAL tended to fail prematurely through low emission. The implication of this was a tube temperature problem. The tube manufacturer was consulted and in parallel a review instigated of the heater control system.

A direct relationship between applied power and filament temperature exists and the Richardson-Dushman equation shows that for a small increase in filament temperature, a significant increase in the availability of electron emission occurs. The resulting increased depletion of filament carburization shortens the lifetime of the tube. Development and installation of a universal filament management system to replace obsolete equipment and simultaneously improve the operational stability has resulted in significantly extended tube service life. Reductions in capital costs and the ability to predict RF tube life has become possible, promoting the establishment of an effective tube replacement strategy. Actual filament lifetime data, accumulated over several years, is presented.

### 1. INTRODUCTION

In the late 1980's tube lifetime was a concern and after consultation with Thomson, modifications were introduced to assist in the transfer of heat from inside the tube to the external cooling arrangements. The need to improve equipment performance and tube lifetime provided the impetus behind the development of a universal filament regulator allowing all high power RF tubes at ISIS to be driven from one standard unit. Information gained from various sources<sup>3,4,5</sup> suggested that a tight filament voltage control system could increase heater lifetimes by 100%. Elsewhere<sup>1</sup> the idea of stabilising thoriated tungsten filament power rather than voltage seemed sensible. A Filament Regulator was designed and built to allow closed loop control of filament voltage, current or power. One unit was capable of stabilising, to better than 1%, any of the 4 different high power RF tubes used at ISIS. The Filament Regulator has been in use for ~ 6000 hours per year since ~ 1990, but, because of the resultant increase in tube lifetimes, it is only recently that the relevant statistics have become meaningful. This paper concentrates on the Thomson TH116 tubes used as the final drives for the ISIS linac cavities.

### 2. FILAMENTS

Factors affecting the TH116 triode lifetimes were high internal temperatures and the use of step-change filament supplies.

Statistics produced by Thomson<sup>4</sup> based on French TV station transmitter tubes, showed that a small percentage increase in filament voltage reduced a tube's expected life from a minimum of 8,657 hours down to 3,500 hours. Ziegler<sup>3</sup> made reference to the possibilities of extended tube life by controlling filament temperature.

Thoriated tungsten filaments are made by adding 1 or 2 per cent thorium oxide ThO<sub>2</sub> to the tungsten before it is sintered and drawn into shape. After drawing, the filament is heated in a hydrocarbon vapour atmosphere converting the surface layer to tungsten carbide.

Langmuir<sup>2</sup> discovered that, through evaporation, the end of useful filament life occurred when this layer became depleted. Work done elsewhere<sup>1</sup> suggested that a carburized filament would, at 2000°K, provide a possible tube lifetime of 35,000 hours. Because tungsten carbide has a higher resistance than thoriated tungsten, a filament with a 25% carburized cross-section has an increased hot filament resistance of approximately 15% (cold resistance by 30%).

By monitoring filament voltage and current, the characteristic resistance curve may be plotted over a tubes lifetime. From the initial resistance value observed, the tube is considered near or at the end of its life when the hot filament resistance is down 15%.

Depletion of the carburised layer, results in a fall in filament resistance and, with a constant voltage across it, current increases. Increased power demand results in a rise in filament temperature. It is argued, therefore, that a power management system be employed.

The Richardson-Dushman<sup>5</sup> equation

$$I_s = AT^2 e^{-\phi_0/kT}$$

where  $I_s$  = filament emission current density,

$A = 60.2$  a constant for pure metal

$T$  is absolute temperature,

$\phi_0$  filament work function, for thoriated tungsten 2.55

$k$  is Boltzmann's constant ( $0.863 \times 10^{-4}$  V/°K)

(1 amp =  $0.624 \times 10^{19}$  electrons/sec)

permits evaluation of electron emission for various filament temperatures.

So for an increase in filament temperature say from 2000°K to 2100°K due to RF heating, or over driving the filament, then the following figures are obtained: -

At 2000°K,  $I_s = 92.3 \text{ amps/cm}^2$   
Or  $5.76 \times 10^{20} \text{ electrons/sec}$

At 2020°K,  $I_s = 109.6 \text{ amps/cm}^2$   
Or  $6.84 \times 10^{20} \text{ electrons/sec}$

i.e. ~ 20% increase in electron emission and a significant reduction in filament life due to the higher temperatures.

### 3. FILAMENT REGULATOR

#### 3.1 Specification

The requirement was for a regulator, of simple design, capable of voltage, current or power control. To rationalise spares, the unit should be able to be configured to drive any one of 4 different types of high power RF tube at ISIS. Soft start, hard off, overcurrent interlocks and the ability to monitor all relevant voltages, currents and powers for each tube were incorporated.

#### 3.2 The System

The Filament Regulator System comprises a Filament Regulator module, SCR Trigger module and an SCR module. Fig. 1 shows a schematic of the system.

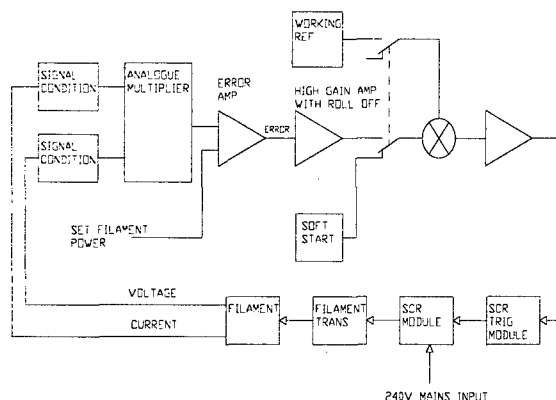


Figure 1. Schematic diagram of Filament Regulator

#### 3.3 Filament Regulator

Samples of filament voltage and current waveforms are filtered and scaled, converted to dc, multiplied together and compared to a reference. The resulting error voltage is passed to a high gain amplifier with roll-off

and summed with a switchable arrangement of a 'working level' reference and a ramp generator. The latter provides a soft start for filament run-up. When power in the filament reaches that set by the reference level, the ramp input is switched out and replaced by a dc level and the error signal voltage.

#### 3.4 SCR Trigger Module & SRC Module

A zero to 5V dc output level is compared to a stable ac derived reference ramp to produce a variable width pulse. This is used to gate an asynchronous pulse train and drives a pair of FET switched pulse transformers. Proprietary SCR trigger modules available at the time provided an unreliable zero crossing start and therefore an 'in-house' design was used.

Mains power is switched by a solid state relay, via isolator and applied to an inverse parallel pair of phase angle controlled thyristors. The trigger pulse train drives the appropriate phase controlled thyristor, a typical waveform is shown in Fig. 2. At stabilization, the filament voltage is shown in Fig. 3.

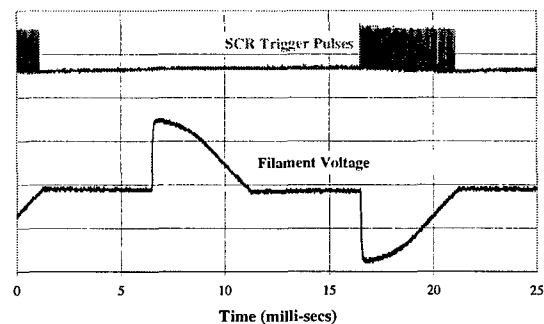


Fig. 2 SCR Trigger pulses Filament Voltage (shown during run up)

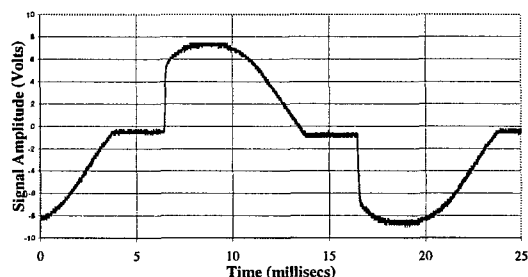


Figure 3. Filament Voltage (shown stabilized)

### 4. DATA

The data contained in Table 1 was recorded over the period October 1986 to the present day. Bracketed numbers in the tube serial no. column indicate various incarnations of the TH116 in a bid to overcome lifetime problems. Type (3) became the standard.

Figure 4 gives complete lifetime curves of hot filament voltage and resistance for TH116 tube serial no. AR1 with measurements taken on a monthly basis. Upward variations in filament voltage were due to operator adjustments. The resistance curve shows a high rate of carbon loss over the first 1000 hours with some degree of linearity thereafter.

Tube S/N	Hours	Failure Mode
<b>RF System 1 (10MeV)</b>		
W3 (1)	3,331	Low emission
Z2 (1)	2,828	Low emission
AB2 (2)	5,755	Low emission
AH2 (2)	5,020	Low emission
AJ6 (3)	5,140	Low emission
AL1 (3)	23,456	Low emission (Filament Regulator installed 6.10.90)
AR1 (3)	25,927	Low emission
AR2 (3)	7,968	In Service at Present
<b>RF System 2 (20MeV)</b>		
AF4 (2)	4,227	Low Emission
AF3 (2)	678	Undocumented Failure
AJ4 (3)	5,499	Low Emission
AK1 (4)	730	Glass cracked (Filament Regulator installed 26.4.89)
AK4 (3)	8,575	Spark Damage
AM1 (3)	12,549	Low Emission
AR4 (3)	27,836	Low Emission
AP3 (3)	11,272	In Service at Present
<b>RF System 3 (20MeV)</b>		
AF1 (5)	5,348	Low Emission
AJ5 (3)	4,166	Not failed. Returned to Thomson for Inspection
AF5 (2)	3,794	Low Emission
AF3 (2)	4,842	Low Emission
AK2 (3)	8,486	Low Emission (Filament Regulator installed 22.5.90)
AM3 (3)	10,775	Low Emission
AN5 (3)	19,467	Low Emission
AK5 (3)	14,691	Low Emission
AW1 (3)	5,879	In Service at Present
<b>RF System 4 (20MeV)</b>		
AA4 (2)	3,567	Low Emission
AE3 (2)	2,831	Filament o/c
AF1 (5)	5,348	Low Emission
AJ3 (4)	11,130	Low Emission (Filament Regulator installed 24.8.90)
AL2 (3)	12,517	Low Emission
AM5 (3)	9,132	Suspect tube
AQ3 (3)	19,437	Low Emission
AQ1 (3)	14,170	In Service at Present

Table 1. ISIS Linac - TH116 History

It should be noted that even though RF system 1 is a low dissipation system, tube life prior to incorporation of tube modifications and power stabilisation was similar to that of high dissipation systems.

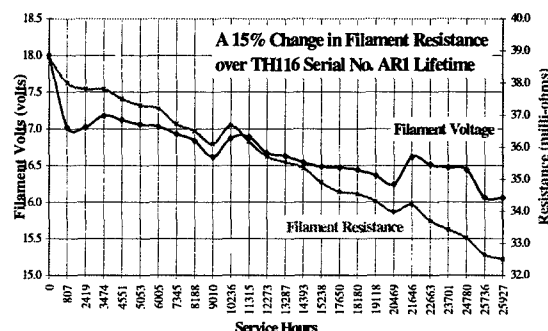


Figure 4. TH116 Serial No. AR1 Filament Voltage & Resistance Curves over its Entire Lifetime

## 5. CONCLUSIONS

The 15% change in hot filament resistance has proved to be the yardstick for 'end of life' predictions and allows for tube changes within maintenance schedules. It is essential, therefore, that filament data is recorded at the time of new tube installation and throughout its life to enable the characteristic resistance to be plotted.

From the historical data shown, it is clear that, for ISIS, the change from a 'window' operated voltage regulator system to that of power control of the TH116 filament has had a marked beneficial effect on tube lifetimes. An estimated saving of the order £60k per annum, based on average lifetimes prior to installation, compared with the most recent whole-life filament data, are made.

## 6. REFERENCES

1. High Power Transmitting Valves With Thoriated Filaments For Use In Broadcasting, Walker H S, IEE, Paper No. 3200E, March 1960.
2. The Electron Emission from Thoriated Tungsten Filaments, Langmuir I, Physical Review, 1923, 22, p.357
3. Design and Operational Characteristics of Thoriated Tungsten Filaments in High Power Valves, Ziegler, Proceedings I.R.E.E Australia, August 1964.
4. Transmitter Tubes: The Tetrode, James Wood, International Broadcasting, Jan/Feb 1988
5. Handbook of Electron Tube and Vacuum Technology, Fred Rosebury, Addison Wesley, 1965

## EXPERIMENTAL DEMONSTRATION OF HIGH POWER MILLIMETER WAVE GYRO-AMPLIFIERS\*

M. Blank, J. Calame, B. Danly<sup>#</sup>, B. Levush, J. Choi<sup>+</sup>, NRL, Washington DC

M. Garven, University of Maryland, College Park, MD

K. Nguyen, KN Research, Silver Spring, MD, D. Pershing, MRC, Newington, VA

**Abstract** The Naval Research Laboratory is currently investigating gyro-amplifiers as high power, broadband sources for millimeter wave radars. A three-cavity Ka-band gyroklystron achieved 225 kW peak output power with 0.82% bandwidth. At W-band, several multi-cavity gyro-amplifiers have been experimentally demonstrated. A four-cavity gyroklystron amplifier has achieved 84 kW peak output power at 34% efficiency with 370 MHz bandwidth. A five-cavity gyroklystron demonstrated 72 kW peak output power with 410 MHz bandwidth and 50 dB saturated gain. For applications requiring greater bandwidth, gyrotwystron amplifiers are also under study. A four section W-band gyrotwystron demonstrated 50 kW peak output power at 925 MHz bandwidth.

### 1 KA-BAND GYROKLYSTRON EXPERIMENTS

In the three-cavity Ka-band gyroklystron amplifier experiment an electron beam of up to 12 A is produced from a thermionic, double anode magnetron injection gun by applying voltages of 65-75 kV. The magnetic field at the cathode can be varied with the gun coils to control the beam velocity ratio,  $\alpha$  ( $v_{\perp}/v_z$ ). The beam is adiabatically compressed as it enters the region of high magnetic field (approx. 13 kG) generated by the 14 coil superconducting magnet. The three cavities of the gyroklystron circuit are positioned in the region of constant magnetic field. Each cavity operates in the  $TE_{011}$  cylindrical waveguide mode. Drive power is directed into a passive  $TE_{411}$  coaxial resonator which surrounds the  $TE_{011}$  input cavity. Power is coupled to the circular-electric mode inside the inner cavity by four axial slots placed every 90 degrees in azimuth. The measured cold resonant frequency of the input cavity is 34.89 GHz and the loaded  $Q_L$  is 188 (primarily diffractive due to the coupling slots). The intermediate (buncher) cavity employs an annular ring of lossy ceramic against the upstream endwall to provide the desired cold-test  $Q_L$  of 194 and a resonant frequency of 34.62 GHz. The downstream end of the output cavity employs an outward radial step and a nonlinear uptaper to achieve a cold-test  $Q_L$  of 175 and a resonant frequency of 34.83 GHz. The frequency upshift due to the presence of

the electron beam is approximately 70 MHz. The drift tubes between cavities are loaded with lossy ceramic rings to suppress instabilities. A 3.81 cm, half-wavelength thick BeO disk positioned immediately after the pumping manifold functions as the output window. The experiment employed two different diagnostic systems for measuring output power. The main diagnostic was an anechoic chamber joined to the output waveguide which had an absolute accuracy of 8% and a relative accuracy of 0.25%. A high-average power calorimeter with 5% absolute accuracy was also used to confirm the higher power measurements.

Systematic studies were performed over a wide range of operating voltages, currents, magnetic fields, and drive frequencies. A peak power of 225 kW at 34.90 GHz, with a -3 dB bandwidth of 0.82%, a saturated gain of 30 dB, and an efficiency of 31% was obtained. These values were measured with a beam voltage of 70.2 kV, a current of 10 A, a magnetic field of 13.1 kG and a pulse width of 2  $\mu$ s. The beam velocity ratio  $\alpha$  was determined to be  $1.27 \pm 0.05$  using a capacitive probe placed just upstream of the input cavity. Additional enhancements in bandwidth were achieved with magnetic field adjustments and changes in beam voltage and current, at the expense of output power. For example, raising the voltage to 73.10 kV and the nominal magnetic field to 13.40 kG produced a -3 dB bandwidth of 0.94% but with a lower peak output power of 200 kW (shown in Fig. 1). The beam current was 10 A, and the efficiency was 27.5% for this case. Detailed studies of how the bandwidth varies with operating parameters, along with comparisons to theory is summarised in [1]. In general, the measured bandwidth of the three-cavity device is 2.0-2.7 times as large as that obtained from the previous two-cavity gyroklystron experiment [2].

### 2 W-BAND GYRO-AMPLIFIER EXPERIMENTS

Several  $TE_{011}$  mode W-band gyro-amplifiers operating near the fundamental cyclotron frequency have been built and tested. Each circuit consists of four or five interaction sections separated by drift sections cutoff to the operating mode. For each circuit, a coaxial drive

\* Work supported by ONR.

<sup>#</sup> Email: danly@nrl.navy.mil

<sup>+</sup> Current Address: Kwangwoon University, Seoul, South Korea.

cavity, similar to that described above for the Ka-band experiment, was used. The input cavity parameters were determined through theoretical modeling with HFSS, a finite element code that computes field distributions and S-parameters for passive 3D structures.

As in the case of the Ka-band buncher cavity, the desired Q values (100-200) of the intermediate cavities are achieved by ohmically loading the cavities with rings of lossy ceramic placed at one end of each cavity. In the output sections, where no ceramic loading is used, power is diffractively coupled through a 5 degree linear uptaper to the collector radius. For each circuit, the parameters of the intermediate cavities and the output cavities/sections were determined through cold test measurements. A 2 kW peak power, mechanically tunable Extended Interaction Oscillator was used to supply the drive power. The tests were typically performed with 2  $\mu$  sec pulses at 250 Hz for 0.05% duty. The measured results for five recently demonstrated W-band gyro-amplifier circuits are shown in Table 1.

TABLE 1. Measured performance of NRL W-band gyro-amplifiers.

Circuit	Peak Power (kW)	Efficiency (%)	BW (MHz)	Gain (dB)
WGKL1	67	28	460	29
WGKL2	60	25	640	27
WGKL3	84	34	370	42
WGKL4	72	27	410	50
WGTWY	50	18	925	30

Results from the WGKL1 circuit [3], which was used to benchmark the design tools, and WGKL2 [4] have been previously reported. The WGKL3 circuit was designed to demonstrate high peak output power and efficiency at moderate bandwidths. The efficiency and peak output power as functions of drive frequency for a 56 kV, 4.4 A electron beam are shown in Fig. 2. In the figure, experimental data points are indicated by the filled circles and the predictions of theory are shown by the solid line. The measured results are in good agreement with theoretical predictions. Also shown on Fig. 2 are the resonant frequencies and Q's for each cavity, determined by modeling (cavity 1) and cold test (cavities 2-4). The high efficiency is achieved through the combination of the high Q output cavity and the minimized stagger tuning of the intermediate cavities about the resonant frequency of the output cavity.

The five cavity WGKL4 circuit was designed to demonstrate large gain, as well as high power and efficiency. A peak saturated output power of 72 kW was produced for a 54 kV, 5 A electron beam with 1 W drive power, corresponding to 50 dB saturated gain. In the

experiment, the drive power was measured at the output of the EIO driver and the losses in the drive line and input cavity were not taken into account.

In the four section WGTWY1 circuit, the output cavity was replaced by a travelling wave section to maximise the bandwidth of the device. Figure 3 shows the measured and theoretically predicted peak output power and efficiency versus drive frequency for a 57 kV, 5 A electron beam. As shown in Fig.2, the measured FWHM bandwidth was 925 MHz and the peak output power was 50 kW, corresponding to a power-bandwidth product of 46.25 kW-GHz. This power-bandwidth product represents a significant increase over the power-bandwidth product of the gyrokystron amplifiers (see Table 1). The measured data and predictions of non-linear theory are in good agreement. The cavity and output section parameters are also indicated on the plot. The traveling wave output section has a measured Q of 70, which is 15% below the minimum diffractive Q.

### 3 SUMMARY

Several multi-cavity Ka-band and W-band gyro-amplifiers have been experimentally demonstrated at the Naval Research Laboratory. Each circuit was designed to optimize certain aspects of performance such as output power, bandwidth, or gain. A three-cavity, Ka-band gyrokystron amplifier has demonstrated a peak output power of 225 kW at 34.90 GHz, with a -3 dB bandwidth of 0.82%, 30 dB saturated gain and 31% efficiency. A four-cavity gyrokystron amplifier has achieved 84 kW peak output power at 34% efficiency with 370 MHz bandwidth. A five-cavity gyrokystron demonstrated 72 kW peak output power with 400 MHz bandwidth and 48 dB saturated gain. A four section W-band gyrotwyston demonstrated 50 kW peak output power at 925 MHz bandwidth. The measured results were found to be in good agreement with theoretical performance predictions.

### 4 REFERENCES

- [1] J.P. Calame *et al.* Physics Plasmas, **6**, 285, 1998
- [2] J. J. Choi *et al.* IEEE Trans. Plasma Sci., **26**, 416, 1998.
- [3] M. Blank *et al.*, Phys. Rev. Lett., **79**, 4485, 1997.
- [4] M. Blank *et al.*, IEEE Trans. Plasma .Sci., **26**, 409, 1998

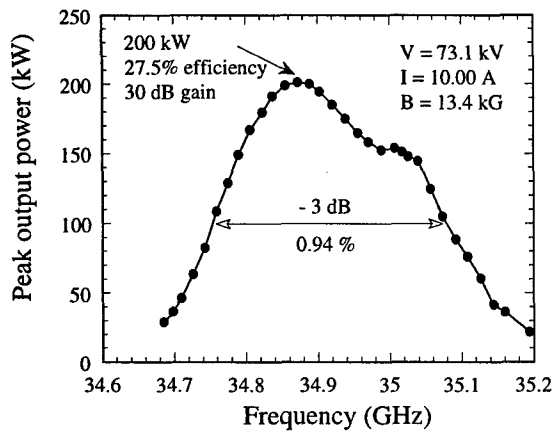


Fig. 1 Experimental frequency response of 3 cavity Ka-band circuit at 13.4 kG

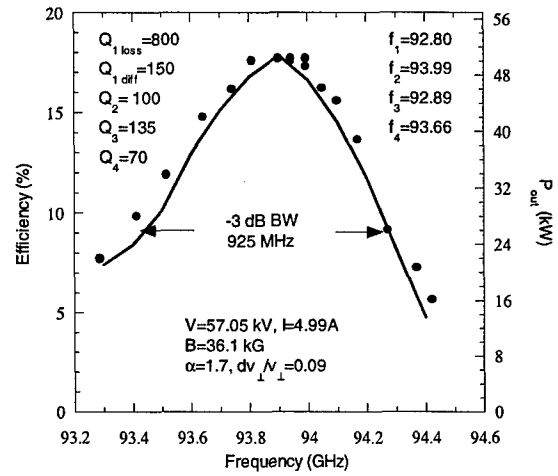


Fig 3. Measured (filled circles) and theoretical (solid line) peak output power and efficiency versus drive frequency for the WGTWY circuit

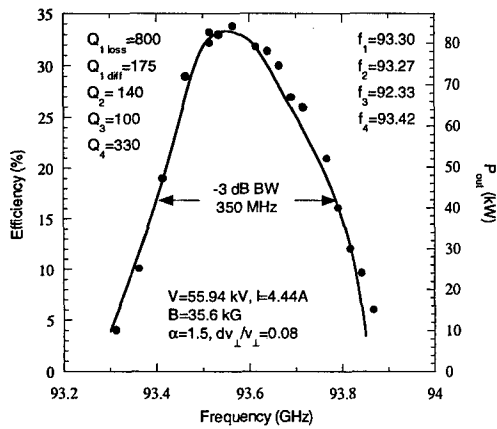


Fig 2. Measured (filled circles) and theoretical (solid line) peak output power and efficiency versus drive frequency for the WGKL3 circuit

# AN ANALOG RF GAP VOLTAGE REGULATION SYSTEM FOR THE ADVANCED PHOTON SOURCE STORAGE RING\*

D. Horan<sup>#</sup> and E. Cherbak

Argonne National Laboratory, 9700 South Cass Avenue, Argonne, IL 60439 U.S.A.

## Abstract

An analog rf gap voltage regulation system has been designed and built at Argonne National Laboratory to maintain constant total storage ring rf gap voltage, independent of beam loading and cavity tuning effects. The design uses feedback control of the klystron mod-anode voltage to vary the amount of rf power fed to the storage ring cavities. The system consists of two independent feedback loops, each regulating the combined rf gap voltages of eight storage ring cavities by varying the output power of either one or two rf stations, depending on the mode of operation. It provides full operator control and permissive logic to permit feedback control of the rf system output power only if proper conditions are met. The feedback system uses envelope-detected cavity field probe outputs as the feedback signal. Two different methods of combining the individual field probe signals were used to generate a relative DC level representing one-half of the total storage ring rf voltage, an envelope-detected vector sum of the field probe rf signals, and the DC sum of individual field probe envelope detector outputs. The merits of both methods are discussed. The klystron high-voltage power supply (HVPS) units are fitted with an analog interface for external control of the mod-anode voltage level, using a four-quadrant analog multiplier to modulate the HVPS mod-anode voltage regulator set-point in response to feedback system commands.

## 1 APS GAP VOLTAGE CONTROL REQUIREMENTS

The APS utilizes a 7-GeV storage ring to generate synchrotron light for material research. The ring is designed to store 300 mA and has been operated routinely at 102 mA maximum current to date. The storage ring uses 16 single-cell cavities, arranged in groups of four at discrete sectors, to generate 9.4 megavolts of total rf gap voltage. Four 1-MW rf stations are used to supply power to the cavities, and a waveguide switching/combining system allows operation of the storage ring with any two or more of the four rf stations simultaneously.

Because the maximum beam loading in the storage ring cavities will represent a coupling coefficient of approximately 4, the amount of rf power required to maintain 9.4 megavolts of total rf gap voltage varies widely depending on the amount of stored current [1].

\* Work supported by U.S. Department of Energy, Office of Basic Energy Sciences, under Contract No. W-31-109-ENG-38.

<sup>#</sup> Email: horan@aps.anl.gov

The present method used to regulate total storage ring gap voltage is a "control law" software program, utilizing two separate software amplitude control loops. This system has worked well, but it can only sample the cavity field probe powers and make adjustments to the rf system output power at a rate no faster than 1 Hz. This slow data acquisition and transmission rate has caused delays in reducing the output power of the rf stations, resulting in rf system trips. The trips occur when the storage ring beam is suddenly dumped or lost, resulting in an instantaneous increase in the rf power dissipation of the rf cavities by an amount equal to the beam loading effect. This sudden increase in power can degrade cavity vacuum and cause damage to cavity components such as tuners and couplers. The analog automatic gain control (AGC) system was developed to provide fast and accurate control of the rf system power output as a function of stored beam current intensity.

## 2 ANALOG REGULATION SYSTEM OVERVIEW

The analog gap voltage regulation system is a true DC-coupled feedback system for maintaining constant rf gap voltage amplitude in the APS storage ring cavities (see Fig. 1). The system consists of two identical and independent amplitude-control feedback loops. Each loop regulates the combined gap voltage of eight storage ring cavities (a sector-pair) by making real-time adjustments of the rf power into the cavities in response to cavity beam-loading effects. This maintains agreement between the combined envelope-detected field-probe powers and an operator-selected gap-voltage setpoint.

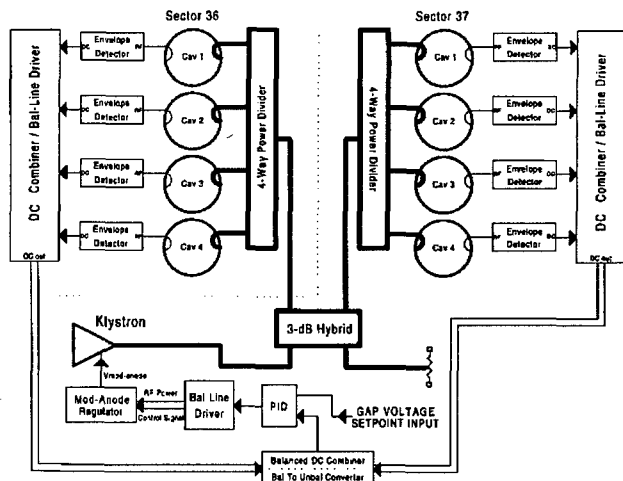


Figure 1: Analog rf gap voltage regulation system

At every sector, each of the four cavity field probes drives a dedicated envelope detector, the DC output of which is then converted from single-ended to balanced output by an active line converter. The balanced outputs of all four balanced converters are then combined at each sector using a passive resistor network. This DC sum is sent to another DC-combiner chassis that sums the two sector-pair DC outputs together and generates a DC signal directly proportional to the combined field probe power in eight cavities. This signal is converted to single-ended topology and applied to the input of a VXI-based PID controller, which allows for remote control of proportional, integral, and differential (PID) gain in the feedback loop, plus remote loop setpoint adjustment. The PID controller output is then converted from single-ended to a pair of equal-amplitude balanced outputs, which are then each sent via single-pair cable to the external mod-anode voltage control input of the two rf stations that can drive the sector-pair of cavities. This signal controls the rf system output power by increasing or decreasing the operator-selected klystron mod-anode voltage regulator setpoint value.

The AGC feedback system also includes control logic that permits feedback control of the rf system output powers under conditional constraints. Each rf station has a logic control chassis that allows feedback to be engaged on the rf station only if all of the following conditions are met:

- system operator consciously selects gap voltage feedback operation,
- the collector-dissipation interlock is set [2],
- the particular rf system output is switched into the ring,
- a minimum of seven out of the eight cavities in the sector-pair are in tune, and
- the klystron has a sufficient level of rf drive.

If any of these conditions are not met, a situation is defined where feedback control of the rf system output power either is not desired or not possible. The control logic chassis will then disable the AGC feedback control within 6 ms. This reaction time has proven fast enough to prevent klystron outgassing caused by sudden large increases in beam current when the AGC loop is suddenly opened.

### 3 RF SYSTEM POWER OUTPUT CONTROL

The AGC feedback system uses a four-quadrant analog multiplier [3] on an interface card to externally control the klystron mod-anode voltage (see Fig. 2). The DC control signal from the AGC feedback system is used as a value by which to multiply the operator-selected mod-anode regulator setpoint voltage, thus providing the ability to increase and decrease the klystron beam current in response to the feedback system commands. The external mod-anode control card converts the balanced-

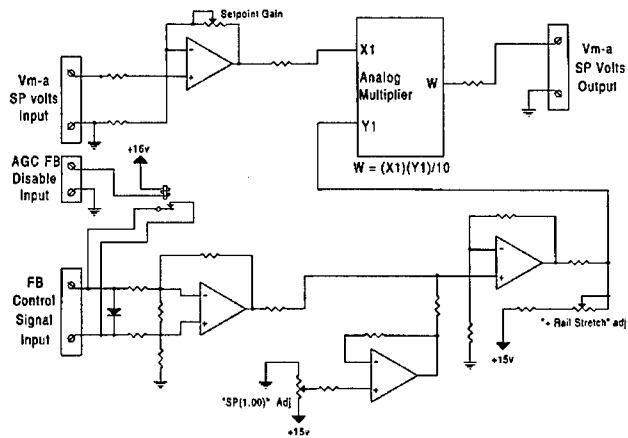


Figure 2: External mod-anode control interface

line feedback control signal to single-ended, and also diode-clips the feedback control signal in the negative direction so that the analog multiplier cannot generate a mod-anode setpoint voltage significantly lower than the operator-selected setpoint value. It provides DC offset controls to optimize the available range of the setpoint multiplication to a maximum of 1.5, which will result in approximately 4 dB of klystron rf output power control range. The use of an analog multiplier for this function has two discrete advantages, (1) the AGC feedback system can never increase the klystron mod-anode voltage by more than approx. 1.5, and (2) the operator still has control of the baseline value for mod-anode setpoint. The feedback is disabled on the external control card by a fast reed relay that shorts the analog feedback control signal input when the feedback logic control chassis detects an operating condition that is not compatible with engaged feedback. The Experimental Physics Industrial Control System (EPICS) [4] remote-control screens have been developed to allow for remote operator control and monitoring of the feedback control logic chassis and system DC operating points from all operating locations.

### 4 FEEDBACK SYSTEM PERFORMANCE

Two methods of generating the analog feedback system input signal were tested to determine which would perform best for this application. One method used the vector-sum of eight field probe rf signals (see Fig. 3), which was then envelope-detected to develop a DC voltage proportional to the amplitude of the combined field probe rf signals. The other method used the DC-sum of eight individual field-probe envelope detector outputs (see Fig. 1). The performance of both analog feedback system methods was measured. During these tests, eight storage ring cavities were under analog-feedback gap voltage control, while the other eight cavities were regulated using the traditional software control law gap-voltage regulation system.



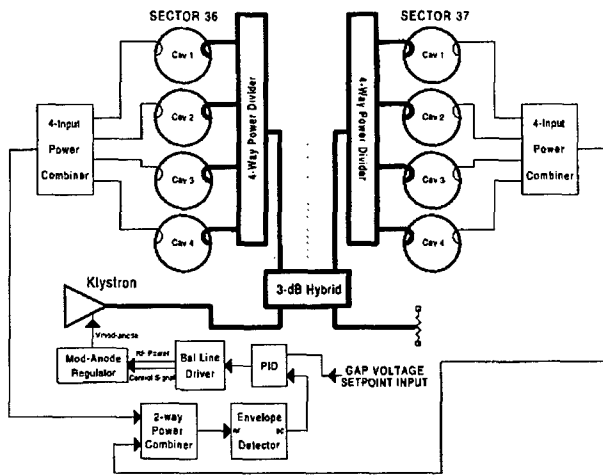


Figure 3: Rf vector-sum feedback input signal generation

It was found that using the vector-sum of eight field-probe rf signals as the feedback system input resulted in very poor gap voltage regulation in response to beam loading. At a stored current of 100 mA, the combined gap voltage of the eight cavities under analog control had sagged approximately 14% from injection-power levels.

This poor regulation was caused by phase-to-amplitude cross-modulation of the field probe rf signals when they were combined in the rf regime. Because each of the storage ring cavities and their associated tuner control systems react differently to cavity beam loading effects, a vector-sum of individual cavity field probe signals will always contain an amplitude distortion generated by the differential phase shifts of the individual signals. This amplitude distortion affects the gap voltage regulation by allowing the beam to unevenly load the cavities without causing a corresponding reduction in the vector-sum field-probe signal applied to the gap voltage feedback system input. Phase-to-amplitude cross-modulation of the combined field-probe signals creates an artificial increase in total field probe signal level; therefore the feedback system does not call for more rf power to combat the beam loading effects, and the gap voltage sags as more beam is stored.

Using the DC-sum of individual field-probe envelope detector outputs as the feedback system input produced much better gap voltage regulation. By combining DC signals proportional to the amplitude of the individual cavity field probe powers, differential phase errors between the cavity field probe rf signals are ignored; the resulting signal is a very sensitive indicator of the combined cavity Q reduction caused by beam loading. It allowed the feedback system to accurately detect beam loading and increase the rf power to the cavities in order to maintain 9.4-MV total gap voltage, with no detectable sag from injection to 102 mA stored current.

Closed-loop frequency response measurements on the AGC feedback system were performed (see Fig. 4). The

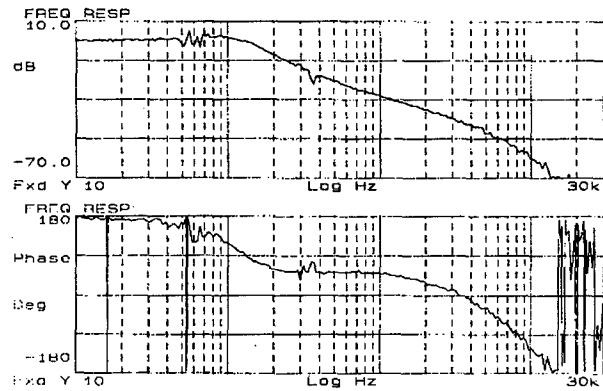


Figure 4: AGC system closed-loop response test

rapid roll-off of the loop frequency response above approximately 150 Hz is caused by the limited operating bandwidth of the mod-anode regulator.

## 5 CONCLUSION

The analog gap voltage regulation system has been successful in providing good storage ring gap voltage regulation in response to beam loading effects up to 102 mA stored beam. This system will reduce the number of klystron and cavity-related vacuum trips due to overpower events when beam is lost or dumped. Closed-loop frequency response tests indicate that the loop operates in a stable region and has adequate bandwidth for the application. This system will be fully installed at APS by April of 1999.

## 6 ACKNOWLEDGMENTS

The authors would like to acknowledge Mike Phelan and Bill Yoder for their efforts in constructing and installing the feedback system hardware on schedule to meet studies deadlines.

## 7 REFERENCES

- [1] Jin Wook Cho, Yoon Kang, "Measurement of Input Coupler Matching of a Loaded Storage Ring Single-Cell Cavity," Advanced Photon Source Light Source Note LS-247, August 14, 1995.
- [2] The "collector interlock" is an interlock system that will limit klystron beam power if the rf output of the klystron falls below a preset minimum for longer than 0.5 second.
- [3] Analog Devices Engineering Staff, Nonlinear Circuits Handbook, Analog Devices, Inc., pp. 203-227 (1976).
- [4] <http://www.aps.anl.gov/asd/controls/epics/EpicsDocumentation>

## 352-MHZ KLYSTRON PERFORMANCE AT THE ADVANCED PHOTON SOURCE\*

D. Horan<sup>#</sup>, G. Pile, A. Cours

Argonne National Laboratory, 9700 South Cass Avenue, Argonne, IL 60439 U.S.A.

### Abstract

The general performance of the Advanced Photon Source (APS) 352-MHz/1-MW continuous wave (CW) klystrons is discussed. The original seven-klystron inventory at the Advanced Photon Source has been in operation since 1995 with good results. Five tubes are presently in accelerator operation, with two tubes as spares. The overall performance of the tubes has been very good. Two tubes were removed from service due to intolerable operational problems: one suffered collector heat damage and was subsequently rebuilt and placed back in service; the other developed a suspected high-voltage (HV) leakage path between the mod-anode terminal and body. One tube has a history of high 3rd to 5th harmonic power production and is presently kept as a spare. Several of the tubes have experienced damage to the oil-tank HV connectors due to over-tightening of the bayonet clamps, and one tube had high leakage current in an ion pump that gave a false indication of bad vacuum.

### 1 SERVICE HISTORY

Five 1-MW rf stations are used at APS to produce the required rf power, one for the 7-GeV booster synchrotron and four to drive the storage ring. Each of these rf stations uses a super-power, high-efficiency CW klystron capable of 1300 kW maximum rf output at 351.93 MHz (see Fig. 1). As of January 26, 1999, the original inventory of seven Thomson TH2089A 352-MHz klystrons have logged more than 83,000 hours of operation with very good performance (see Table 1), contributing to rf system availability as high as 99%. Two of the original seven klystrons developed operational problems that prevented them from being used. One of these klystrons was rebuilt at the factory and subsequently returned to service. The other klystron is presently in storage awaiting further diagnostic tests. At this time, the inventory includes one well-conditioned klystron in storage that is available as a spare.

Typical operating conditions for the APS 352-MHz klystrons vary depending on their application. The booster synchrotron uses one klystron to produce a ramped rf envelope, ramping from 7 kW to 350 kW peak in 250 ms, at a 2-Hz rate, developing an average rf power of approximately 125 kW. It is

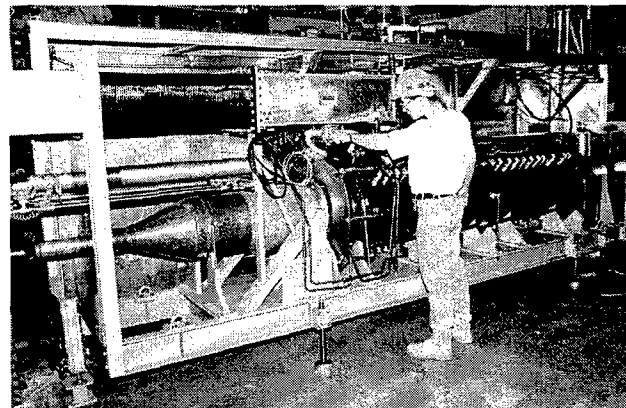


Figure 1: APS klystron installation

operated in class-A with a cathode voltage of 68 kV and 11.15 A of beam current. Once injection into the storage ring is completed, the booster synchrotron rf system is placed in a "hot standby" state, where rf drive is removed and the beam current is reduced to 3 A. The booster synchrotron rf station then remains in standby until the storage ring is refilled, resulting in nominal rf power operation approximately 20% of the time.

Table 1: APS 352-MHz klystron data

KLYSTRON	SERVICE/STATUS	OPERATING HOURS (as of 1/26/99)
#023	Collector damage; rebuilt as #041	2,804
#024	Booster synchrotron	22,874
#026	Storage ring, RF4	12,531
#029	High harmonic output; in spares storage	4,949
#030	HV leakage problem in gun; awaiting further tests	9,374
#033	Storage ring, RF1	14,609
#036	Storage ring, RF2	13,885
#041	Storage ring, RF3	5,163

Storage ring service requires the klystrons to operate in CW mode at higher power levels. At this time, the maximum storage ring current during normal operation is 102 mA. This requires a minimum of two klystrons driving the ring. The remaining two klystrons are typically kept in "hot-standby" mode, which is diode operation at a cathode voltage of 85 kV and 4 A of beam current. A waveguide switching system allows for rapid switching to a spare rf station in the event of a failure. Each of the two klystrons driving the ring operate at a

\*Work supported by U.S. Department of Energy, Office of Basic Energy Sciences, under contract No. W-31-109-ENG-38.  
# Email: horan@aps.anl.gov

maximum rf output power of approximately 650 kW with 102 mA of stored beam. When driving the ring, the storage ring klystrons operate in class-A at a cathode voltage of 88 kV, with beam current ranging between 11 A to 15.5 A, depending on the amount of stored current. Unless equipment problems preclude, main/standby status between the four storage ring rf stations is typically switched on a weekly basis to equalize the operating time on the stations, resulting in a duty cycle of approximately 50%.

In both booster synchrotron and storage ring service, the APS klystrons are operating well below their design maximums, both in terms of rf output and collector dissipation. This has enhanced APS operational reliability, suggesting that loading power systems at approximately 70% of their design limits is a pragmatic approach to improving overall reliability.

## 2 COLLECTOR HEAT DAMAGE

On October 16, 1995, klystron #023 suffered a catastrophic failure during operation into the storage ring. At the time of the failure, the tube was operating at 80 kV/14 A, with approximately 250 kW rf output. The first and only sign of trouble was a HVPS trip on klystron ion-pump overcurrent, which fired the HVPS crowbar and shut down the klystron magnet and filament supplies. Subsequent investigation confirmed that both ion pump supplies indicated a current in excess of 10 mA. It was also determined that the filament was shorted. At this point, the decision was made to ship the klystron back to the Thomson factory for failure analysis and repair.

After further examination at the factory, it was discovered that cooling water had entered the evacuated region of the tube through a hole in the collector wall. Subsequent examination revealed several small areas on the interior surface of the collector where the spent electron beam had melted the copper, and one area where the local heating was sufficient to cause penetration of the collector wall, allowing water to enter the tube. Due to the extensive heat damage to the collector and contamination of the klystron rf structures caused by the water in the vacuum areas, the klystron was basically stripped down to its chassis and totally rebuilt. It was subsequently returned to service at APS.

After extensive investigation, the root cause of this failure was narrowed down to two possibilities: (1) A local obstruction to water flow on the exterior collector surface, which created a localized hot spot on the interior surface of the collector. This theory is reinforced by the fact that a small amount of stainless steel shavings, sufficient in size to possibly cause a small local disruption in water flow at the collector surface, were found inside the collector boiler when it was disassembled at the factory. It was assumed that the shavings were cuttings produced by pipe threading processes during facility

construction that were in the cooling water flow and became trapped in the narrow water passages of the collector. (2) Collector outgassing caused spent beam to be ion-focused to a small area, locally exceeding the dissipation capability of the collector and creating an avalanche condition that rapidly increased temperatures high enough to melt copper. Such failure scenarios involving local heating seem plausible based on the fact that all klystron interlock systems were found to be functioning normally immediately after the tube failure, but such localized heating would not be detected by measuring return water temperature.

## 3 EXCESSIVE HARMONIC POWER PRODUCTION

Klystron #029 was removed from storage ring service on 12/8/96 at 4,949 hours due excessive harmonic output that was damaging the rf system harmonic damper loads. Coaxial cables connecting the harmonic damper loads to the waveguide damper probes became very hot during tube operation, indicating the presence of power at higher harmonics. Subsequent signal samples from the harmonic probes indicated higher harmonic levels relative to levels produced by other klystrons operating in the same socket. Changes were made in waveguide length between the klystron output and circulator input in an attempt to reduce the amount of harmonic power developed, but this had no effect. All other aspects of the tube operation were normal, with no sidebands or other instabilities noted. This tube is presently in spares storage, awaiting further testing.

## 4 SIDEBAND GENERATION

High-efficiency klystrons can become unstable and generate unwanted sideband energy under certain conditions. These sidebands can be at levels as high as -20 dBc and can also move about in frequency relative to the carrier. This allows them to pass through the storage ring cavity bandwidth and modulate the storage ring beam.

Klystron #030 is the only APS klystron that has been proven to generate sidebands (see Fig. 2), which began to

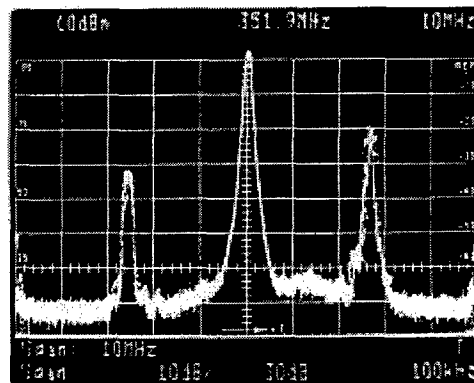


Figure 2: Klystron sidebands

appear at approximately 5,000 hours of operation. Two cavity tunings were performed to eliminate the problem, but ultimately it was determined that the klystron must operate at a minimum cathode voltage of 92 kV to be free of sidebands. This klystron had other operational problems (see the next section) that may be related to the tendency to produce sidebands.

## 5 GUN HIGH VOLTAGE LEAKAGE

At approximately 4500 hours of operation, klystron #030 developed a substantial DC leakage condition between the mod-anode and tube body. High reverse mod-anode currents (5 mA at  $V_{\text{mod-anode}} = 40\text{kV}$ , electron current flowing into klystron) were the first indication of the problem. The leakage path allowed klystron beam current to flow without any mod-anode bias applied to the tube (see Fig. 3). Subsequent gun leakage current tests indicate that this leakage condition has a very nonlinear voltage-current relationship, suggesting a field-emission discharge point somewhere in the gun. However, the klystron vacuum does not degrade when this leakage becomes measurable. This klystron is in storage until it can be HV-conditioned in an attempt to characterize and eliminate the leakage path.

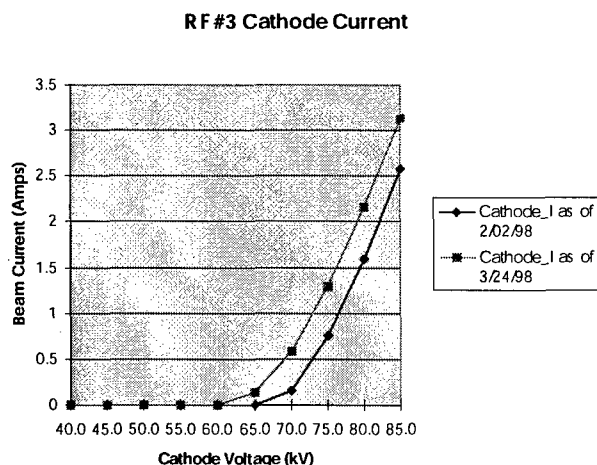


Figure 3: Effect of gun leakage

## 6 VACUUM PROBLEMS

Klystron #033 has exhibited symptoms of a slow vacuum leak. If left off without any ion pumping for longer than two hours, the tube vacuum will degrade, requiring ion pumping for approximately 30 minutes to recover sufficiently for HV operation. The tube also exhibits nonlinear rf gain characteristics between 38 and 40 watts of drive power, suggesting a possible multipactor condition at the input cavity. It is not clear if these two conditions are related. During normal operation, the tube vacuum always returns to normal, with ion pump readings in the area of  $0.5 \mu\text{A}$ . This klystron also has had two

instances of false poor vacuum caused by dirty insulators on the ion pump high-voltage connectors. The ceramic insulators in the ion pumps were cleaned, and the ion pump current returned to normal values.

## 7 BROKEN HIGH-VOLTAGE CONNECTORS

Several of the APS klystrons have experienced oil tank leaks due to cracked or broken high-voltage connectors. The damage to the connectors was caused by over-adjusting the bayonet clamp force of the connector when the mating plug was inserted. As a result, more attention is paid to connector insertion and use, which has reduced this type of failure to a minimum.

## 8 DIRTY RF WINDOWS

On June 14, 1998, klystron #033 suddenly began experiencing window arc detector trips while in storage ring service. Inspection of the output flange and window revealed evidence of arcing from center to outside conductor of the coaxial line between the output cavity window and the waveguide transition. The surface of the ceramic window was found to be very dirty. It was later determined that the arc detector trips began happening concurrent with the start of interior concrete block construction activity in the vicinity of this klystron. This work generated a very fine airborne dust that got past the klystron window air filtration system and resulted in a film of fine dirt particles on the klystron window.

The output waveguide of the klystron was removed, and the ceramic window was cleaned using a sandblast procedure with #60 grit at 6 psi. The tube was re-assembled and tested at full power with no further arc trips.

## 9 CONCLUSION

In general, the performance of the APS 352-MHz klystrons has been very good, with very few klystron-related problems interrupting accelerator beam time. Knowledge gained during the first four years of operation has improved our ability to identify potential problems and situations before they result in significant downtime. The long-term effects of low-power diode "standby" operation on the klystrons are still being studied to determine if this mode of operation is detrimental to the klystrons.

## 10 ACKNOWLEDGMENTS

I would like to thank Don Voss, Mike Douell, Ernie Cherbak, and Mike Phelan for their assistance in maintenance of the APS 352-MHz klystrons.

# RECOMMISSIONING OF THE RF SYSTEM AFTER THE SRS UPGRADE

J. Counsell, D. M. Dykes, P. E. Gibbins, P. A. McIntosh, A. J. Moss, CLRC Daresbury Laboratory, Warrington, UK, WA4 4AD

## Abstract

The SRS has been upgraded with the installation of two high-field multipole wiggler (MPW) insertion devices. The four RF cavities have been relocated to enable the MPW's to be installed in the appropriate straights. As a consequence, the whole of the high power RF system, including the essential services, has been reconfigured. The changes to the system and the recommissioning details are presented.

## 1 INTRODUCTION

Two high-field multipole wiggler (MPW) insertion devices (ID) have been installed in the SRS. They will provide users with a higher brightness photon source in the 5 to 20keV region, a level which is currently not available on the SRS. Details of this project were first presented at EPAC'96 in Sitges [1]. The necessary changes for the storage ring layout were also presented, highlighting particularly the changes in the RF waveguide system [2].

To facilitate the installation of two 2T MPW IDs in the SRS storage ring, a scheme was devised which moved the RF cavities to free up two straights enabling not only the installation of the IDs, but also provided enough room for the associated beamlines.

Opportunity was taken during the machine shutdown to rationalise the RF controls and cavity cooling water system, to improve operational efficiency. As the shutdown was only 3 months (October to December 1998), a limited rationalisation was achievable. The installation programme, including the MPW vacuum vessels, other vacuum components and the cavity moves as well as all the RF system changes had to be completed before Christmas to allow the pumping down of the vacuum envelope over the Christmas period.

This paper reviews the relocation of the RF cavities, details some of the modifications that were made to the RF controls and the cavity cooling system, to enable a more efficient mode of operation on the SRS. Recommissioning of the RF system after the MPW installation is also discussed.

## 2 THE RF SYSTEM IMPLICATION

By installing these two new devices in the SRS storage ring, obviously additional RF power was required to replace the additional energy lost due to synchrotron radiation. Calculations of the increased RF power both to the beam and in the cavity are shown in Table 1.

Table 1. RF Parameters

Parameter	Pre upgrade	Post upgrade
$I_h$ (mA)	250	250
RF frequency (MHz)	499.71	499.71
Loss/turn (keV)	302	322
Overvoltage	4	4
Total cavity power (kW)	50.6	57.6
Beam power (kW)	75.5	80.5
Source power (kW)	138.6	152

The current EEV klystron is rated at 250kW and so the additional total RF power required can easily be accommodated using the present power source.

## 3 STORAGE RING LAYOUT MODIFICATIONS

The SRS is a 16-cell machine, with typically 1 metre available in each straight for the installation of non lattice elements. The RF cavities occupy four straights, four more straights are utilised by various injection elements, and the SRS already has three installed IDs. This leaves five straights that can be used for various diagnostics and the installation of the new MPW's. Table 2 shows how the straight allocation has evolved to accommodate the new IDs. Those items shown in *italic* are devices, which cannot be moved from their present straight location.

Table 2. SRS Straight Allocation

Straight	Pre upgrade	Post upgrade
1	<i>Septum</i>	<i>Septum</i>
2	<i>Kicker 1</i>	<i>Kicker 1</i>
3	<i>Kicker 2</i>	<i>Kicker 2</i>
4	Cavity 1	TCM/Diag Strip
5	<i>Undulator</i>	<i>Undulator</i>
6	Cavity 2	MPW 1
7	Current Monitor	Cavity 1
8	Cavity 3/Octupole	Cavity 2
9	<i>SC Wiggler 1</i>	<i>SC Wiggler 1</i>
10	Cavity 4	Free
11	Diagnostic Strip	Cavity 3
12	Octupole	Cavity 4
13	<i>Collimator</i>	<i>Collimator/Tune Meas</i>
14	Tune Measuring	MPW 2
15	<i>Kicker 3</i>	<i>Kicker 3</i>
16	<i>SC Wiggler 2</i>	<i>SC Wiggler 2</i>

The old and new RF system configurations are compared in Figure 1.

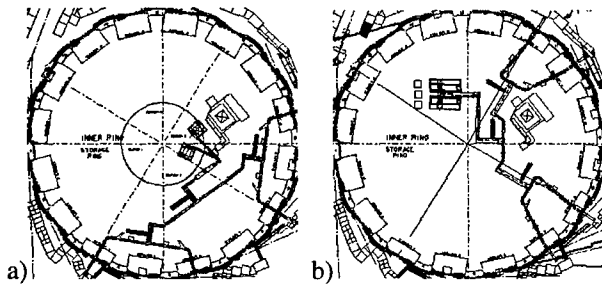


Figure 1. a) Pre-upgrade and b) Post-upgrade Evolution of RF Cavity Layout.

Figure 2 shows the physical layout of the new RF waveguide system on the SRS. The klystron isolator is now at ground level, rather than at a height of 4m.

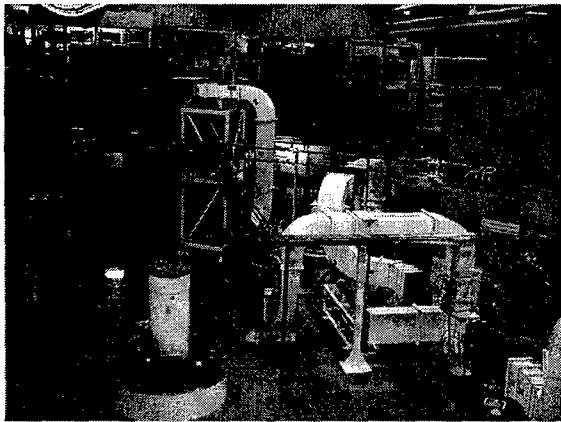


Figure 2. New RF System Layout.

#### 4 RF CONTROLS IMPROVEMENTS

A single EEV klystron is used to feed, via a waveguide feeder system, all four RF cavities. Prior to the upgrade shutdown, if it was necessary to change to the spare klystron, which was possibly from a different manufacturer, all the associated control systems also had to be either changed or re-calibrated, which entailed a lengthy change over process, typically 1 days work.

##### 4.1 Rapid Klystron Changeover.

Taking advantage of the RF cavity relocation, the control system was redesigned to enable two klystrons to be controlled through the same control system, by a simple means of changing over control interfaces. Both klystrons would have a permanent waveguide feed to the RF cavities, via a MEGA WR1800 SPDT manual waveguide switch (see Figure 3).

The utilisation of such a system means that the spare klystron would be available for conditioning within 1 hour.

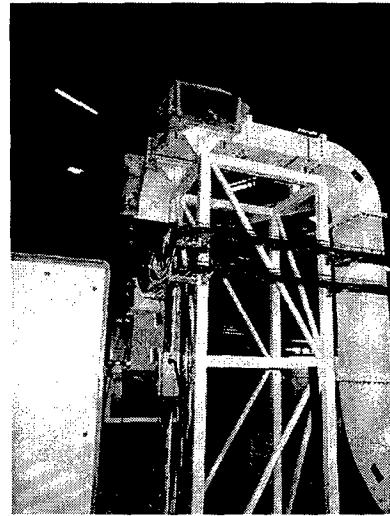


Figure 3. Klystron with Waveguide Switch in Position.

##### 4.2 Cavity Temperature Control

The cavity water control systems have been improved to allow for a more efficient system operation and a more precise cavity temperature control. Before the shutdown, both the cold and the hot water were piped from a remote water plant room to the cavity mixer valve local to the cavity, now all the water circuits have been placed local to the RF cavities. This has allowed the main inlet pump to be de-rated from 4.45 to 3.34kW, and approximately 60m of pipe-work has been removed, minimising the inefficiencies in the cooling system in transporting temperature stable water over unnecessarily long distances. A saving in operational running costs of ~£8k/year is anticipated. Figure 4 shows a photo of the cavity water control circuit, incorporating the heat exchanger and mixer valves.

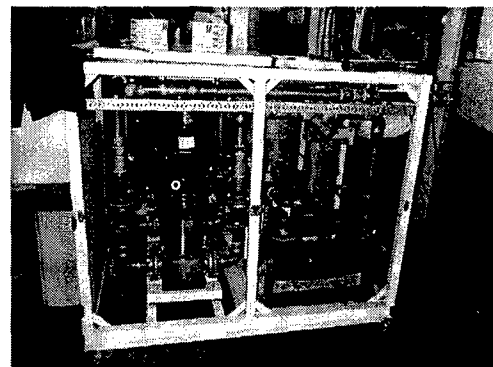


Figure 4. Cavity Water Control Station.

#### 5 RECOMMISSIONING THE RF SYSTEM

The RF system was scheduled to be relocated and commissioned, ready for first beam operation by 21<sup>st</sup> December 1998. This meant that all the RF control and water systems had to be operational, and also that the cavity and waveguide phase relationships were correct.

### 5.1 Cavity Coupling

The cavity coupling on the SRS cavities is set by a fixed matcher assembly, located in the feeder waveguide, which is in parallel with the cavity impedance, when viewed from the RF driving source. This matcher unit was converted from a motor driven device to a manual system and by adjustment of this match position, a coupling factor  $\beta$ , approaching 3 could be set for each cavity. Under beam loading conditions, this enables the cavity to operate with a minimum amount of RF reverse power, whilst sustaining the required accelerating voltage.

### 5.2 Cavity Phase

The cavity repositioning in the storage ring has altered the path length between each cavity, but the phase relationship has remained the same (see Table 3).

Table 3. Cavity Gap and Phase Relationships.

From	Previous Gap ( $\lambda$ )	New Gap ( $\lambda$ )	Gap ( $^\circ$ )	To
Cavity 1	19.75	9.75	-90	Cavity 2
Cavity 2	20.25	20.25	+90	Cavity 3
Cavity 3	19.75	9.75	-90	Cavity 4

To confirm this phase relationship between each cavity is a difficult process to achieve without being able to use the electron beam as an ultimate diagnostic, and so the phases were re-set as close to the cavity as possible. This meant that there was a small section of waveguide beyond the calibration set point, which would need fine-tuning once beam could be injected into the storage ring.

### 5.3 Cavity Vacuum Conditioning

There was a period of several weeks when the cavities were at atmospheric pressure, but stored in clean conditions. As soon as was practical the cavities were installed in their new locations and pumped down. Before Christmas the cavity pressures were better than  $1 \times 10^{-8}$  torr, and cavity conditioning could begin. The conditioning period was much shorter than anticipated. There were no signs of multipactor, no burst of x-radiation and only minor vacuum pressure excursions. Conditioning of all cavities took only 2 – 3 hours.

### 5.4 Beam Commissioning

Attempts at first injection into the re-configured storage ring began on 4<sup>th</sup> January 1999, and within the first week, accumulation was achieved and beam ramped to 2GeV. The only change needed to the RF system was a change in the klystron drive phase.

On the 25<sup>th</sup> January routine operation of the SRS restarted, with no further changes to the RF system. In a later beam studies shift, in March, the phase of one cavity

was changed by  $\sim 3^\circ$ . Evidence of longitudinal phase instability is still apparent under normal user beam conditions, highlighted by strong synchrotron side bands around each orbit harmonic (see Figure 5). Some further 'fine tuning' will take place in the Easter shutdown.

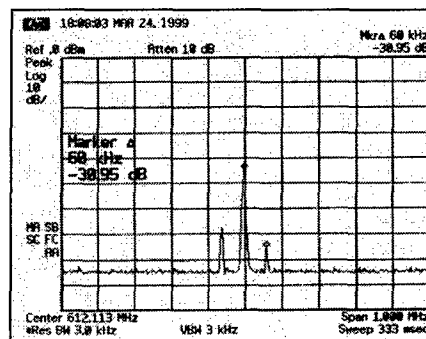


Figure 5. Synchrotron Side-bands at 2GeV

### 5.5 Induced Cavity Higher Order Modes (HOMs).

The commissioning time for the storage ring was short, and operations resumed with a poor beam lifetime, because of relatively high vacuum pressure, of only a few hours at the 100mA level. This has made it difficult to assess the effect of HOM's. The cavity temperatures have been set to their previous values, and the storage ring current has been limited to 250mA, so no HOM's should be present. As the vacuum pressure falls and any damping effect from ions reduces, instability effects will be investigated.

## 6 SUMMARY

The RF system was completely reconfigured during the 3-month upgrade shutdown. This involved moving the 4 accelerating cavities to new locations, new waveguide layout, new cavity water cooling system, and new RF control system. The commissioning time was shorter than envisaged, with the vacuum conditioning taking only a few hours. The RF system was set up by RF measurements, and no changes were needed to the system before routine SRS operation restarted.

## 7 ACKNOWLEDGEMENTS

The author would like to thank Colin Brown and Andrew Goulden for their efforts in completing the RF system relocation in such a short period of time.

## 8 REFERENCES

- [1] J.A. Clarke and M.W. Poole, "Upgrading the Daresbury SRS with Additional Insertion Devices and its Implications for the Storage Ring Layout", Proc. 5<sup>th</sup> Euro. Part. Accel. Conf., Sitges, June 1996, p623.
- [2] D.M. Dykes, "RF System Changes Associated with the SRS Upgrade", Proc. 5<sup>th</sup> Euro. Part. Accel. Conf., Sitges, June 1996, p1946.

# THE DESIGN, CONSTRUCTION AND PERFORMANCE OF THE 53 MHZ RF CAVITIES FOR THE NSLS X-RAY RING

J. Keane, P. Mortazavi, M. Thomas, N. Towne, M. Woodle  
Brookhaven National Laboratory, Upton, NY 11973-5000

## Abstract

Four single cell rf cavities currently provide the required energy to the x-ray ring beam. Mechanical deficiencies and limitations of these early cavities necessitated their replacement with newly designed units. The selection of forged OFHC copper, replacement of traditional Conflat flanges with integrally machined Marmon type flanges, use of commercial spring loaded metal seals for both vacuum and rf purposes and an enhanced thermal cooling system are among the new design features. Ancillary components such as the input couplers and HOM antennae have also been redesigned utilizing a thermally conductivity ceramic material. The design characteristics and performance will be reviewed.

## 1 INTRODUCTION

The National Synchrotron Light Source (NSLS) consisting of a linac, three transfer lines, a booster and two storage rings (uv and x-ray), has been in operation since early 1980. A total of four 52.887 MHz rf cavities currently provide rf power to the x-ray ring, which operates at current limits of 350mA at 2.584GeV or 254mA at 2.8GeV. The NSLS has upgraded all components to withstand the thermal load associated with increased operating currents of 500mA at 2.5GeV, 438mA at 2.584GeV or 318mA at 2.8GeV. The additional rf power required would increase  $I^2R$  losses beyond the design limits of the existing cavities. The original cavity bodies were constructed of copper clad steel. The choice of this material has presented considerable heat transfer difficulties since the water cooling tubes were attached to the external steel surfaces resulting in inefficient thermal conduction. Other significant problems were poor internal surface quality, existence of water to vacuum joints and difficulties in tuning. These difficulties along with new operating conditions have necessitated replacement of these cavities with a new design.

## 2 NEW DESIGN

A basic goal of the new design was to have a uniform material throughout the rf cavity. Other requirements such as increased reliability by eliminating water to vacuum joints, better temperature control, an easier tuning mechanism, elimination of stainless steel Conflat flanges and considerably fewer external welds and braze joints, have also been implemented. The relatively large physical size, about one meter in diameter by 0.8 meter long,

created an engineering challenge to accommodate all these goals.

The design concept was centered on minimizing the number of subassemblies. To accomplish this, the entire cavity was designed mainly from four forged pieces, Fig. 1.

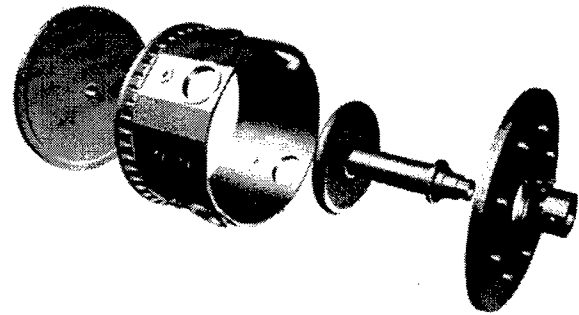


Fig. 1. RF Cavity, Basic Design Concept

The cylinder section, which contains most of the peripheral port flanges, was forged to achieve adequate hardness at the integrally machined port sealing surfaces. The use of conventional Conflat flanges were ruled out due to both incompatibility with rf and the difficulties in joining them to the base copper material. A combination of Marmon type flanges integrally machined into the main forging and a stock seal/clamp mechanism from the Helicoflex company, was proven acceptable. This flange/seal design requires a sealing surface with a minimum hardness of 30 - Rockwell "B". The measured hardness after forging was >40 RB. Electron Beam Welding (EBW) was used as the only joining technique in order to preserve the hardness and prevent grain enlargement. The thermal loads extracted from the SUPERFISH computer program were used to optimize the cooling channel configuration on the structure. Finite element analyses were carried out on the cooling channels to determine the temperature rise and the thermal/pressure deformations. A water flow velocity of 8 Ft/sec yields a film coefficient of 4 Watts/ in<sup>2</sup>-°C. An annealed, copper-jacketed seal of approximately 1 meter diameter x 8 mm cross section, furnishes rf contact as well as a vacuum seal for the front cover. This has a sufficient seal deflection range for initial frequency tuning, Fig.2



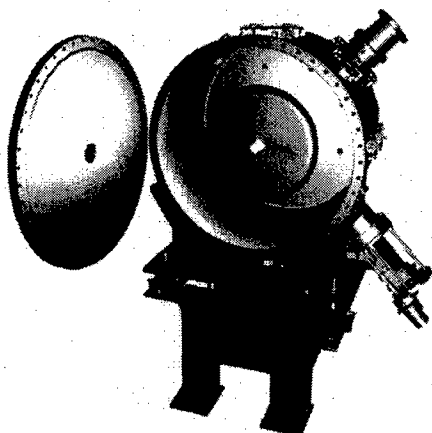


Fig. 2. 52.887 MHz RF Cavity Assembly

To accommodate higher RF power transfer to the cavity and beam, a new, water-cooled, 6" coaxial power input loop/vacuum window was designed, built, tested and installed into the new cavity. Two windows were built, one using an aluminum oxide ( $\text{Al}_2\text{O}_3$ ) ceramic, the other, a beryllium oxide ( $\text{BeO}$ ) ceramic. The window body is OF copper and is directly brazed to the ceramic. The loop itself is made from a copper bar in which the cooling channels were gun-drilled to meet within the copper so that no water to vacuum joint exists. In this way the cooling water is very effective in cooling the center conductor. This is brazed to the loop close to the ceramic, insuring minimum heating. The ceramic itself coated with approximately 20 Å of titanium nitride for charge leakage and to reduce multipactoring, Fig. 3.

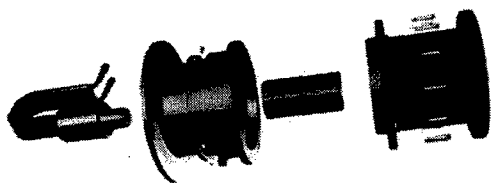


Fig. 3. Coaxial Power Window, Basic Design Concept.

Using the copper cavity with both loops installed, one as the input loop, 3x over-coupled, the other as a 50Ω loaded output loop, 2x over-coupled, rf power at 150 kW-cw was passed through the windows for 10 hours with no noticeable heating or arcing. The  $\text{Al}_2\text{O}_3$  window has successfully been in operation in the x-ray ring for the past ten months.

### 3 RF TESTING

After the cavity was received,  $Q_0$  was measured at 18000. The input loop was installed, the cavity evacuated to  $10^{-9}$

Torr, and the center electrode heated to 40°C with a closed-loop water system. The center electrode temperature coefficient was measured to be -2.13kHz/°C; the gap sensitivity is 2.2 kHz per mil. Cavity power was then introduced. Several regions of multipactoring were found and recorded. High power was applied to 50 kW within the first eight hours of testing and was increased to 65 kW after several hours for RF conditioning. The overall temperature stability remained within a few tenths of a degree, steady state. The multipactoring regions were conditioned out after 24 hours of operation.

To compensate for reactive beam loading and cooling water temperature variation, a motor driven shorted-loop tuner is used, Fig. 4.

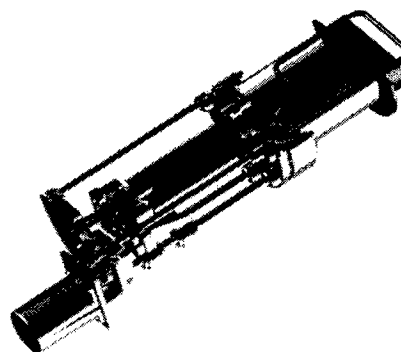


Fig. 4. Shorted Loop Tuner Assembly

By inserting the water-cooled shorted loop into the cavity, the center frequency will be increased. The advantage of shorted loop over plunger tuner is the fact that the high cavity current no longer passes through a sliding contact. However, the small displacement current due to interception of electric field that travels down the loop shaft is returned to the ground through a sliding contact located in the loop assembly.

Seven antennae are inserted into various ports in the cavity for higher order mode damping. Since modes deviate with cavity perturbations, modes were measured throughout the tuner range and the dampers adjusted to insure adequate suppression at all tuner positions. The cavity has been installed into the x-ray ring and successfully operated for the past ten months. Since some of the damping antennae are quite long and intercept many kilowatts of the fundamental field, a high pass filter was designed and installed on them.

Collectively, the damping antennae intercept more than 10 kW of the fundamental field when terminated into 50-ohm loads. To reduce this RF power loss, four of these antennae are fitted with high-pass filters (HPFs) with a cutoff at the first significant higher-order mode (HOM) frequency of 270 MHz, Fig. 5.

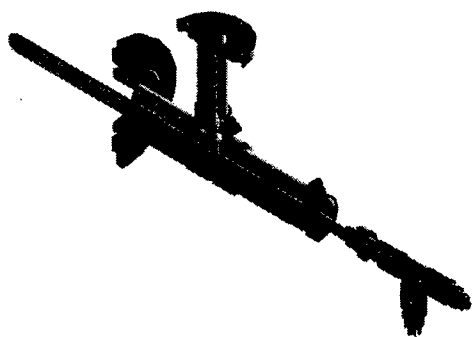


Fig. 5 High Pass Filter Assembly

These HPFs are mounted close to the cavity. One filter is a four-element HPF of the type used on the main cavity of the VUV ring with a fundamental rejection of >60 db. This antenna and HPF is located near the center-electrode E-field region and needs no provision for water cooling of the antenna. Three antennae of significant length are located in the shorting wall of the cavity and are heated by rf currents generated by the large magnetic field present there. These antennae dissipate up to 300 watts and are therefore fitted with three-element HPFs designed to pass cooling water through a shorted stub which also acts as the first inductive element of the filter (see Figure 5). Water is supplied through a spit tube and returns coaxially through the center conductor. A coaxial capacitor and a shunt inductor complete the three-element HPF and carry away the HOM power from a tap on the shorted stub. These HPFs have a fundamental rejection of >40 db. The antennae have been in operation for more than ten months.

#### 4 CONCLUSION

The replacements of NSLS x-ray ring RF cavities are being implemented with newly designed peripherals. ACCEL Instruments in Germany has built the first two RF cavities, Fig. 6.

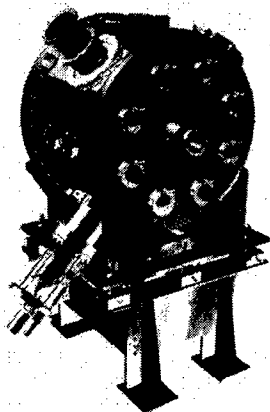


Fig. 6. 52.887 MHz RF Cavity Assembly

The first unit was tested and installed with newly designed ancillary components. The RF, vacuum and temperature stability and control performance have been well within design goals. The repeatability and reliability

of the Marmon type flanges using Helicoflex seals have been found mainly to depend on the seal quality control. The second rf cavity is scheduled to be installed during the NSLS 1999 winter shutdown.

#### 5 ACKNOWLEDGEMENTS

The authors Would like to thank the NSLS support personnel, particularly, R. D'Alsace, R. Freudenberg, N. Guglielmino, J. Newburgh, G. Ramirez, T. Rodrigues, S. Pjerov and J. Vaughan for their excellent technical efforts.

#### 6 REFERENCES

- [1] P. Mortazavi, M. Thomas, "A Design Upgrade of the Rf Cavity and its Power Window for High Current Operation of the NSLS X-Ray Storage Ring", Proc. 1995 Part. Acc. Conf. Vol. 3 pp. 1768-1769.
- [2] M. Thomas, R. Biscardi, W. Broom, S. Buda, R. D'Alsace, S. Hanna, J. Keane, P. Mortazavi, G. Ramirez, J. Wang, "NSLS X-Ray System Rf System Upgrade", Proc. 1993 Par. Acc. Conf., Vol. 2, pp. 1419-1420

# SLOW FEEDBACK LOOPS FOR A LANDAU CAVITY WITH HIGH BEAM LOADING

N. Towne\*, National Synchrotron Light Source  
Brookhaven National Laboratory, Bldg. 725B, Upton, NY 11973-5000†

## Abstract

Equilibrium bunch shapes for bunches stretched with a higher-harmonic cavity are sensitive functions of beam and RF parameters. This paper gives results of calculations of equilibrium bunch shapes as a function of Landau-cavity phase, the relationship between the stretched-beam phase and slow feedback controls for the cavity is described, and a control system capable of stretching, compressing, controlling the cavity phase arbitrarily (within the limits of the power amplifier), and operating without beam for use in the NSLS Vacuum-Ultraviolet (VUV) ring is presented. The last is compared with the existing RF controls for the VUV-ring harmonic cavity [1].

## 1 INTRODUCTION

The sensitivity of the bunch shapes to the RF-system parameters of a Landau cavity has important implications to the RF controls for the cavity. Small shifts in the bunch's potential well shift the bunch centroid by an exaggerated amount through changes in the equilibrium bunch distribution. In particular, shifts in the phase of the harmonic cavity voltage have an amplified effect on the beam phase. There is negative feedback, when there is beam loading, resulting from the movement of the bunch centroid. This is described in section 2.

The original control system for the powered harmonic cavity, the one that is in use now [1], has worked remarkably well with very high beam loading. There are three loops—the tuning loop, a loop that levels the forward power on the transmission line, and a loop that levels the cavity field by controlling the phase of the forward power. The tuning loop controls the phase of the cavity field relative to the forward wave on the transmission line [2]. The crossed level and phase loops work well with substantial beam loading because of the large detuning of the cavity. (By crossed loops is meant that the phase detector in one loop drives the attenuator and the level detector drives the phase shifter in the drive to the amplifier.) The shortcoming of the existing system is that it is not able to vary the phase of the cavity over a sufficiently wide range due to the polar nature of the RF modulators and the fact that the cavity tuning is controlled through the incident RF wave on the transmission line. For this reason bunch shapes are not optimal.

\* Email: townen@bnl.gov

† Work performed under the auspices of the U.S. Department of Energy, under contract DE-AC02-76CH00016.

Section 3 contains a description of a proposed RF control system capable of stretching, compressing, controlling the cavity phase arbitrarily (within the limits of the power amplifier in high beam loading), and operating without beam. In that section it is assumed that the main-cavity field is fixed and that the harmonic-cavity loops are slow compared to the coherent frequencies: coherent instabilities [3] (aside from the equilibrium-phase instability) are not considered. Machine parameters are given in table 1.

Table 1: Values of VUV ring, cavity parameters, and symbols.

Beam energy	$E_0$	800 MeV
Energy loss per turn	$U_0$	20.4 keV
Momentum compaction	$\alpha$	0.0245
Revolution frequency	$\omega_0/2\pi$	5.8763 MHz
RF peak voltages	$V_1/V_2$	80/20 kV
RF harmonic numbers	$h_1/h_2$	9/36

## 2 BUNCH SHAPES

This section considers the sensitivity of stretched bunch shapes to cavity phase. Due to the use of a near- $\phi^4$  potential, bunch shapes [4] are sensitive functions of the harmonic cavity field—in particular the phase—when the bunches are optimally stretched. This occurs because the equilibrium distribution sloshes in the shallow potential well. Furthermore, the shifts of the beam phase and the cavity phase are of opposite signs. To see this, if the harmonic-cavity phase is shifted so that the harmonic-cavity voltage lags a small amount, the total voltage is shifted downward locally. This shift moves the synchronous phase forward in time to where the main cavity, having a lower frequency, brings the waveform up. In this way the new synchronous phase leads the original synchronous phase. The amount by which it leads is large compared to the original phase shift since the RF waveform is locally flat. The degree to which the bunch centroid moves depends on the intrinsic energy spread. In figure 1 is shown calculated bunches shapes for the VUV ring when optimally stretched and when the cavity phase has been shifted by  $-2^\circ$ . The bunch phase is shifted by the factor  $-4.5$  times the cavity-phase shift.

This phase shift of the beam in response to a perturbation of the cavity phase, through beam loading, provides negative feedback from the beam to the cavity field. This negative feedback is a mechanism by which perturbations of the cavity phase are suppressed. This is to say, e.g., that

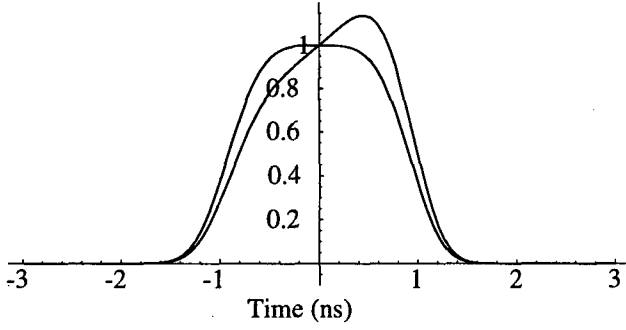


Figure 1: Calculated bunches shapes for the VUV ring when optimally stretched and when the cavity phase has been shifted by  $-2^\circ$ . In the second case the beam phase has shifted  $+9^\circ$  at the harmonic-cavity frequency.

a perturbation of the generator current affecting the phase of the total current is largely cancelled by the shift in the beam's contribution to the total current in the cavity. An estimate of the degree to which this cancellation occurs, in the limit that  $|I_g| \ll |I_b|$  and  $I_g$  is approximately orthogonal to  $I_T$ , goes as follows. One expresses the perturbation in the phase of the cavity voltage  $\delta\Psi_V$  as

$$\delta\Psi_V = \delta\Psi_{I_T} \quad (1)$$

$$\approx \delta\Psi_{I_b} + \delta\Psi_{V0} \quad (2)$$

$$\approx G\delta\Psi_v + \delta\Psi_{V0}, \quad (3)$$

where  $G$  is the phase multiplication factor obtained from figure 1 ( $-4.5$ ) and  $\delta\Psi_{V0}$  is a shift in the phase of the cavity field that would be present in the absence of a shift in the beam phase. Solving this last equation for  $\delta\Psi_V$ , we have

$$\delta\Psi_V \approx \frac{1}{1-G} \times \Psi_{V0}. \quad (4)$$

In summary, the shift in the bunch centroid due to perturbations influencing the harmonic-cavity phase reduces such perturbations by the factor  $1/(1-G)$ .

A consequence of this result is that much larger swings of amplifier power are required to vary the cavity phase a given amount than if there were no shift in the beam phase. In fact, one would like that the forward-wave amplitude on the transmission line be able to pass through zero to different quadrants of the forward-wave plane. This is inconsistent with features of the existing control system.

Therefore, conclusions to be carried to the next section are that:

- control of the cavity tuning using the difference between phases of the cavity and the forward wave on the transmission line is not adequate and
- a vector modulator must be used in place of a phase shifter/attenuator combination for the control of the drive to the power amplifier.

Both conclusions are necessitated by the fact that the forward-wave amplitude must be able to go through zero.

### 3 HARMONIC CAVITY CONTROLS

In this section is discussed the proposed control system for the harmonic cavity. Several major functions the system is required to perform are:

- stretched-bunch operation,
- compressed-bunch operation,
- passive operation for injection, and
- off-line or low-current operation.

In stretched-bunch mode the control system must be able to control the cavity phase over a substantial range. This range is limited by the RF power available.

In figure 2 is shown the complete configuration for the control system proposed here. In the figure a complex-phase modulator (CPM) is used to control the drive to the amplifier. The reason for this, as discussed in section 2, is that control through cartesian coordinates is more appropriate for this problem where the forward-wave amplitude  $a$  on the transmission line may be required to go near zero and into different quadrants of the complex- $a$  plane.

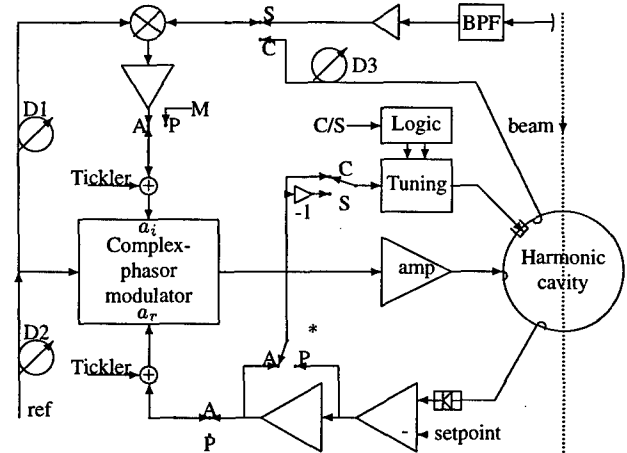


Figure 2: Configuration for the harmonic-cavity control system. The labels 'A' and 'P' represent switch positions for active and passive operating modes respectively and 'S' and 'C' represent switch positions for stretched and compressed operating modes. The ticker inputs are intended for diagnostic use only. The active/passive switch marked with the asterisk selects a lower loop gain for the passive mode.

For the level regulation of the cavity ordinary envelop detection is used to sense the cavity voltage and provide feedback to  $a_r$  (the real part of  $a$ ; the nominal beam phase provides the phase reference so that  $a_r$  is in-phase with the beam while  $a_i$  is in quadrature with the beam); phase detection is through a mixer and the phase of the beam is used to generate the phase error instead of the phase of the cavity. There are two reasons for doing this. The first is that the bunch-phase factor  $G$  provides additional gain compensating the  $1/(1-G)$  factor of equation 4. The second is that the beam phase is the quantity that needs to be regulated; it is the most appropriate diagnostic for maintaining optimal bunch stretching.

Cavity detuning is handled differently than in the usual method of detuning for beam-loading compensation [5] where the tuning error signal is derived from the phase between the cavity field and the forward wave on the transmission line  $V/a$ . The latter method is not applicable here because it is required that tuning control operate when the forward wave is zero. To resolve this problem the tuning block of figure 2 is required to move the cavity resonant frequency upwards for a given sign of  $a_r$  and limit the detuning to the high side of the RF frequency. In this way the modulation amplitude  $a_r$  is kept at zero, even when  $a_i$  is small.

When using the harmonic cavity to compress the bunch, the phase of the cavity is reversed so that the slope of the RF wave at the phase of the bunch is increased. This is in contrast to the stretched-bunch mode where the harmonic cavity cancels the slope in the RF wave generated by the main cavity. There are two main differences in the low-level controls between these two modes. The first is that the cavity phase is used as feedback instead of the beam phase because the gain advantage of beam feedback in stretched operation is not present in compressed operation. The other difference is that the tuning control is required to move the resonant frequency in the opposite direction—to the low side of the RF frequency—and to confine it there. The  $-1$ -gain and tuning-logic blocks of figure 2 make this happen.

In passive operation the RF amplifier and CPM are switched off and the cavity driven by beam alone. In this configuration the tuning servo loop, which is used during active operation, may be used to level the RF field in the cavity by detuning the cavity sufficiently, when there is sufficient beam current, to provide the correct field in the cavity. The starred active/passive switch of figure 2 adjusts the gain of the loop appropriately. Tuning control is as described for powered (active) operation. Passive operation is used during injection. Alternatively, one can dispense with this loop altogether by using fixed detuning.

The transition from passive to active operation occurs as follows. After the ring is filled and ramped and the harmonic-cavity control systems is switched to active, there is a jump in the operating point of the CPM that brings the cavity phase to the optimum for stretching (when stretching). In this state  $a_i$  jumps to a new value and  $a_r$  becomes nonzero. In response to the latter condition the cavity tuning shifts to bring  $a_r$  to zero. When this is completed the CPM is at its normal active operating levels.

Off-line operation with cavity voltage leveled is not accommodated explicitly in figure 2 and is accomplished by fixing the detuning of the cavity. The level-regulating loop controlling  $a_r$  provides the drive to the CPM. Open-loop operation requires opening the level-regulating loop and applying a bias to terminal M or one of the 'tickler' inputs.

## 4 CONCLUSIONS

This control system described here, intended to be slow compared to the coherent motion, provides passive and ac-

tive operation for both stretched and compressed modes. Arbitrary cavity phases can be maintained, within the limit of available RF power, and cavity tuning does not require use of the forward wave on the transmission line. Beam phase has the best potential for maintaining optimal bunching and is used for phase-loop feedback in stretched mode; in compressed mode the cavity phase is used. The cross-coupled amplitude and phase control loops present in the existing control system are retained.

Perturbations of the cavity phase are reduced by negative feedback provided by the beam sloshing in a flat potential well. The implications of this fact on the cavity control system are explored.

The control system described here is far from optimal in the context of what the formalism of optimal-control theory offers to the control of RF systems [6]. Optimal control theory requires, when there is beam loading, that a realistic model of the beam be available or nonsensical results are obtained. Unfortunately, theoretical models of the behavior of stretched beams are not available and one must rely on the use of empirically constructed models. Development of such empirical models is a challenge and is a longer-term prospect at NSLS.

## 5 REFERENCES

- [1] R. Biscardi, S. L. Kramer, and G. Ramirez, Nucl. Instrum. Methods A 366 (1995), p. 26-30.
- [2] F. Pedersen, IEEE Trans. Nuc. Sci., Vol. NS-32 No. 5, p. 2138 (1985).
- [3] S. Krinsky and J. M. Wang, *Particle Accelerators* Vol. 17, p. 109. (1985)
- [4] M. Sands, SLAC Report No. SLAC-0121 (UC, Santa Cruz), Nov 1970.
- [5] W. Broom, J. M. Wang, BNL Report 62789 (1996).
- [6] D. Boussard and E. Onillon, CERN Report No. CERN SL/93-09 (RES), (1993).

# THE MM-WAVE SHEET BEAM KLYSTRON: PERFORMANCE AT DIFFERENT VOLTAGES

S. Solyga, M. Schmolke and H. Henke\*

Technische Universität Berlin, EN2, Einsteinufer 17, D-10587 Berlin, Germany

## Abstract

The aim of our work is the design of a simple and light, small and cheap mm-wave source with moderate power. Our choice has been a 25kV PPM-focused sheet beam klystron (SBK). However, the efficiency predicted for such a device is very poor: A low beam voltage means small coupling coefficients and a sheet beam profile means a gun with one-dimensional compression only resulting in a low current density. Thus, the performance can be improved by either splitting the wide beam into several round beams with higher current density, or by raising the beam voltage. In this paper the performance of a 25, 50 and 100kV mm-wave SBK is investigated. Simulation results for the electron guns and the cavity resonators are presented and an overview on the predicted electrical parameters is given.

## 1 INTRODUCTION

The concept of a low voltage sheet beam implies several advantages which led to our choice of a 25kV PPM focused SBK: A low voltage drastically reduces the requirements of x-ray shielding and power supply while a flat beam is well adapted for modern microfabricational techniques where a planar geometry is necessary. The moderate level of current density permits focusing using a light periodic permanent magnet structure.

Unfortunately, opposed to the advantages inherent in a low voltage sheet beam concept is the drawback of a low efficiency resulting from a low current density and a small shunt impedance value. A low beam velocity degrades the shunt impedance for two reasons: the transit angle as well as the transverse dependence of the impedance is increased. The best possible efficiency within reach for a 25kV PPM focused SBK was predicted to be approximately 10% (without making use of a depressed collector). A way to improve this situation is going to higher voltages. Within the present study simulations have been performed to examine what gain in klystron performance may be achieved by raising the beam voltage. Due to the high aspect ratio of the beam (25:1), a twodimensional treatment yields good approximation results and is used throughout this paper.

\* henke@TU-Berlin.DE

## 2 ELECTRON GUN SIMULATIONS

Basis for the electron guns considered here is a design of a 25kV electron gun providing a sheet beam of  $400\text{ }\mu\text{m}$  thickness and current of  $1.9\text{ A/cm}$  at a cathode loading of less than  $5\text{ A/cm}^2$ , [1]. The implemented modulation anode allows nearly powerless beam switching for pulsed operation while keeping the costs for the power supply at a moderate level. Together with the anode it forms an electrostatic lense thus heavily increasing the compression up to a ratio of 10:1. Keeping the number of electrodes included small and their shapes as simple as possible is expected to reduce the manufacturing costs.

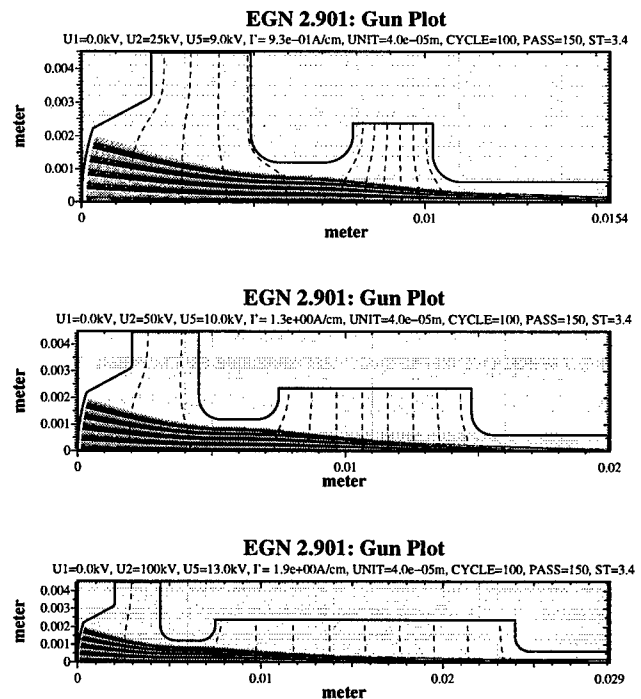


Figure 1: Vertical cut of 25kV, 50kV and 100kV electron gun

Starting with an anode voltage  $V_0$  of 25kV its value was increased in two steps to 50kV and 100kV. One way would have been simply scaling all the voltages leading to a modanode voltage of 36kV in case of 100kV applied to the anode. Since we prefer a low modanode voltage switching the beam we did not further follow this idea. The minimum electrode spacing  $d_{min}$  between modulation anode and anode necessary to avoid electrical breakdown

was determined using Kilpatrick's criterion [2] and a relationship given by Staprans [3] as a guideline which reads in the worst case (D.C. operation and beam switched off)  $d_{min} = (V_0/3 \cdot 10^6)^{1.25}$  with  $d_{min}$  and  $V_0$  taken in MKS units leading to 2.5mm, 6.0mm and 14.2 mm spacing for 25kV, 50kV and 100kV anode voltage, respectively.

In order to keep the already achieved beam shape and compression ratio nearly unchanged while varying the anode voltage, the voltage and position of the modulation anode was carefully adapted. This was accomplished performing simulations using the electron optics code EGUN. Figure 1 shows a vertical cut of the three guns under investigation together with the according electron trajectories and equipotentials. The obtained results apparently exhibit that the beam thickness of 0.4mm can be maintained while the beam current increases to 2.6 A/cm in case of the 50kV beam and to 3.8 A/cm for the 100kV beam. The corresponding modanode voltages required are 10kV and 13kV only and the cathode loading amounts to 7 A/cm<sup>2</sup> and 10.2 A/cm<sup>2</sup> respectively.

### 3 CAVITY RESONATORS

The resonator cavities are considered to consist of a certain number of identical simple muffin tin cells, see fig. 2. For each beam voltage, the gap width  $g$  has been optimized for maximum shunt impedance at  $y = 0$  by means of the code GdfidL [4] with the frequency fixed to 91.392GHz.

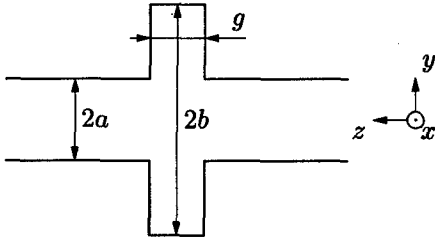


Figure 2: Two-dimensional single cell resonator

At 25kV, the optimum gap width is  $g = 0.4$ mm and the shunt impedance is 520Ωcm. For synchronous operation, a cell distance of 1mm, 0.75mm and 0.5mm is required for  $2\pi$ -,  $3\pi/2$ - and  $\pi$ -mode, respectively. Correspondingly, within  $\lambda_q/16 \approx 5$ mm 5, 7 and 9 cells can be placed, yielding a total shunt impedance of 2.6kΩcm, 3.6kΩcm and 4.7kΩcm, respectively.

At 50kV, the optimum gap width is  $g = 0.55$ mm with 2.3kΩcm shunt impedance. The cell distances are 1.35mm, 1.02mm and 0.68mm for  $2\pi$ -,  $3\pi/2$ - and  $\pi$ -mode, respectively. Again, assuming a maximum structure length of  $\lambda_q/16 \approx 7.5$ mm, 5, 7 and 11 cells should be realistic, yielding a shunt impedance of 13, 18 and 25kΩcm, respectively.

Finally at 100kV, the gap should be 0.75mm wide and the shunt impedance predicted for a single cell is 6.5kΩcm. For  $2\pi$ -,  $3\pi/2$ - and  $\pi$ -mode, the cell spacing must be 1.8, 1.35 and 0.9mm, respectively. Within  $\lambda_q/16 \approx 12$ mm,

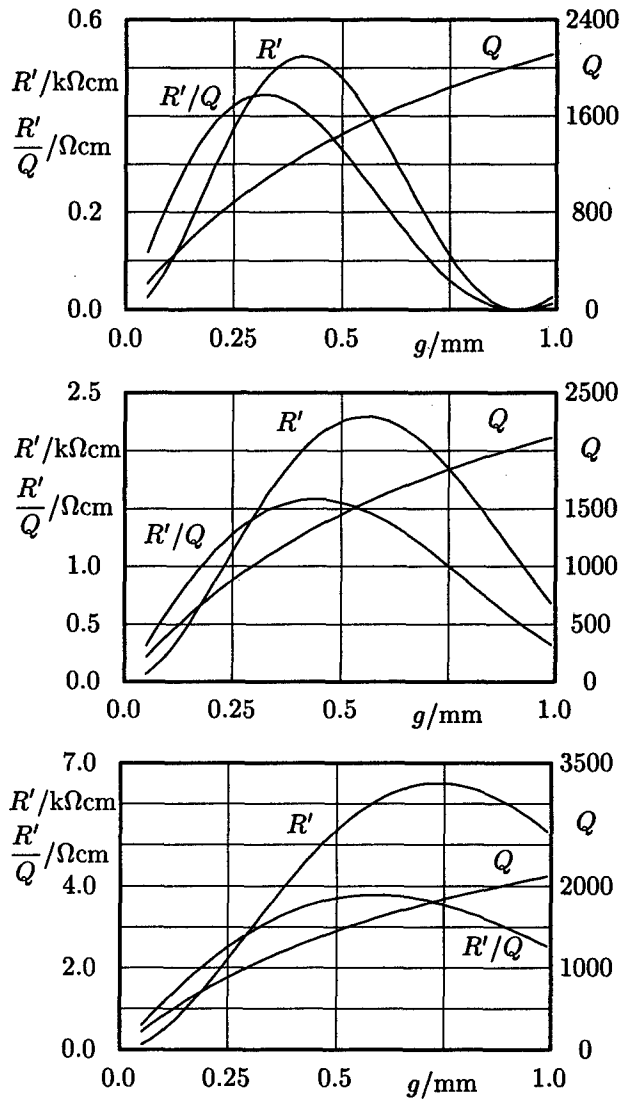


Figure 3: Parameters of the cavity from fig. 2 for 25, 50 and 100kV beam voltage

6, 9 and 12 cells may be placed, and the total impedance would be 39, 58 and 78kΩcm.

### 4 PREDICTED EFFICIENCIES

As shown in [5], the d.c. to r.f. conversion efficiency takes its maximum

$$\eta = \begin{cases} \frac{m^2 R}{8 R_0} & \text{for } mR \leq 2R_0 \\ \frac{m}{2} - \frac{R_0}{2R} & \text{for } mR \geq 2R_0 \end{cases}$$

at an external load of

$$Q_{ext} = \begin{cases} Q & \text{for } mR \leq 2R_0 \\ Q/(mR/R_0 - 1) & \text{for } mR \geq 2R_0 \end{cases}$$

where the lower lines refer to saturation drive. Here,  $m$  is the current modulation,  $R_0$  the beam resistance,  $R$  the

unloaded shunt impedance,  $Q$  the unloaded and  $Q_{ext}$  the external quality factor of the resonator.

For all voltages, maximum shunt impedance is achieved at  $\pi$ -mode, and the predicted efficiencies are 11% at 25kV, 41% at 50kV and 63% at 100kV. - Saturation drive is possible only at the the higher beam voltages. - The external quality factors required are 1260, 1430 and 490, respectively. Here, a current modulation of 1.6 has been assumed.

## 5 REFERENCES

[1] S. Solyga and H. Henke, "Two-Dimensional Design of a Low Voltage mm-Wave Sheet Beam Klystron", ITG-Conference:

Displays and Vacuum Electronics, Garmisch-Patenkirchen, Germany, April 29-30, 1998.

[2] W.D. Kilpatrick, "Criterion of vacuum sparking designed to include both RF and DC", Review of Scientific Instruments, vol. 28, no. 10, October 1957, pp.824-826.

[3] A. Staprans, "Electron gun breakdown", 1985 High-Voltage Workshop, Monterey, CA, Feb. 1985.

[4] W. Bruns, "GdfidL: A Finite Difference Program for Arbitrarily Small Perturbations in Rectangular Geometries" IEEE Trans. on Magn., vol. 32, no. 3, 1453-1456, May 1996

[5] S. Solyga, H. Henke and W. Bruns, "Output Cavity Studies for a Low Voltage mm-Wave Sheet Beam Klystron", Proceedings of the 6th European Particle Accelerator Conference, June 22-26, 1998

Table 1: Parameter values according to 25kV, 50kV and 100kV beam voltage, respectively

section	parameter	symbol	25kV	50kV	100kV	unit
main	frequency	$f$	91.392			GHz
	D.C. input	$P_0$	47.5	130	380	kW
	rf output	$P$	5.2	53	240	kW
	efficiency ( $I_{rf}/I_0 = 1.6$ )	$\eta$	11	41	63	%
	duty cycle		1:100			1
	pulse width		1			ms
beam	voltage	$V_0$	25	50	100	kV
	current	$I_0$	1.9	2.6	3.8	A
	beam width	$w$	10			mm
	beam height	$h$	0.4			mm
	current density	$J_0$	47.5	65.0	95.0	A/cm <sup>2</sup>
	perveance per square	$K_{\square}$	19	9.3	4.81	nP
	resistance	$R_0$	13.2	19.2	26.3	k $\Omega$
	velocity	$v_0$	0.302	0.413	0.548	c
	charge density	$\rho_0$	$5.2 \cdot 10^{-3}$	$5.2 \cdot 10^{-3}$	$5.8 \cdot 10^{-3}$	C/m <sup>3</sup>
	plasma frequency	$\omega_p$	10.2	10.2	10.7	GHz
	reduced plasma frequency	$\omega_q$	7.6	6.6	5.8	GHz
	reduced plasma wavelength	$\lambda_q$	75	118	178	mm
gun	mod. anode voltage	$V_m$	9	10	13	kV
	cathode width	$w_c$	10			mm
	cathode height	$h_c$	4.0			mm
	cathode loading	$J_c$	5.0	7.0	10.3	A/cm <sup>2</sup>
	beam compression		10:1			1
focusing	period length	$L_f$	8.0			mm
	half-aperture	$a_f$	0.6			mm
	magnet thickness	$t_f$	2.0			mm
	field amplitude	$B_0$	60	53	47	mT
	pole tip field	$\bar{B}$	110	94	84	mT
	magnetization	$M$	87	75	67	kA/m
cavities	half-aperture	$a$	0.30			mm
	half-depth	$b$	0.92	0.90	0.89	mm
	gap length	$g$	0.40	0.55	0.75	mm
	shunt resistance p. cell	$R$	0.52	2.29	6.51	k $\Omega$
	R/Q ratio p. cell	$R/Q$	0.42	1.48	3.52	$\Omega$
	unloaded quality factor	$Q$	1260	1545	1850	1
	external quality factor	$Q_{ext}$	1260	1430	490	1
	number of cells ( $\pi$ -mode)	$N$	9	11	12	1



# THE S-BAND TRANSMITTER DESIGN FOR THE INSTITUTE OF ACCELERATING SYSTEMS AND APPLICATIONS RACETRACK MICROTRON

A. Hawkins, W. North, C. Wolcott, A. Zolfaghari, MIT-Bates;  
D. P. Economou, D. Baltadoros, A. V. Filippas, A. Karabarounis,  
N. Papanicolas, E. Stiliaris, N.Uzunoglou, IASA-Greece;

## Abstract

A high-power CW (continuous-wave) source, at 2380 MHz, for the IASA (Institute of Accelerating Systems and Applications), (Athens, Greece), Microtron (see Table 1.) is based on the CPI (Communications and Power Industries) type VKS-8270 multi-cavity klystron. The high-level DC power conditioning for the klystron uses an existing high-voltage transformer-rectifier (HVPS) and variable-voltage transformer (VVT), designed to operate from 60 Hz power, whereas the local power is at 50 Hz. Other features include a new electronic crowbar system and high-speed primary-power disconnect.

## 1 INTRODUCTION

To transplant the Microtron RF source to its new venue, making use of its iron-cored components, adjustments are made for the use of 50 Hz primary power instead of 60Hz. In addition, a more effective electronic crowbar and surge-current limiting, for protection in the event of a klystron gun arc, is provided. A simplified schematic of the system is shown in Figure 1.

Table 1: The main characteristics of the IASA Cascade RaceTrack Microtron.

	Injector	RTM I	RTM II
Injection Energy [MeV]		6.5	41
Gain per Turn [MeV]		1.32	8
Number of Recirculations		26	25
Max Output Energy [MeV]	6.5	41	240
Max Current [uA]	600	100	100
Incremental Number v		1	1
Magnets Field [Tesla]		0.22	1.34
Spacing [m]	8.8	3.25	8.7
RF Power Consump. [kW]	117	29	168

## 2 Effect of 50 Hz Line Frequency

The VVT and the HVPS were designed to operate from 13.8 kV, 3-phase, 60 Hz power. With 50 Hz power the voltage must be reduced by a factor of 50/60 for the volt-time integrals to be the same to avoid iron-core saturation. The maximum line voltage is thus 11.5 kV. The local power is at 20 kV L-L, which must be stepped down to 11.5 kV. This is done with a "bucking"

transformer, T1, whose primaries are across the 20 kV and whose 8.5 kV secondaries are in series-opposition with the 20 kV line, yielding 11.5 kV L-L with only 74% of the kVA rating of a 20kV/11.5kV transformer.

## 3 AC to DC Converter

### 3.1 Variable-Voltage Transformer (VVT)

The VVT is of dry construction, air cooled, and housed in an enclosure 8.8' x 7.5' x 9.1', weighing 15,000 pounds. At its simplest, the VVT, T2, is a linear-format version of a variable autotransformer. The advantage of linear is increased contact surface area. The disadvantage is increased leakage inductance of the magnetic circuit. The VVT circumvents leakage inductance by means of a transformer with a multiple-tapped secondary winding. The multiple taps are connected to points along the linear winding, short-circuiting the leakage reactance. The E-70381 VVT is far more complicated than just three ganged variable transformers however. Each phase has two linear commutating windings and a transformer whose primary winding bridges the incoming line and which has dual secondary windings, each with 14 taps. There are two sets of dual brushes on each commutating winding, one at each end, motor driven in opposite directions. The brushes are connected to the primary of each phase of a "buck-boost" output transformer. One side of each secondary winding is connected to a tap on the input transformer secondary, which establishes the mid-point of the adjustment range. With the brushes opposite each other, the primary voltage is zero and the output is the midpoint voltage. As the brushes are driven away from each other in one direction, the primary voltage increases in the "buck" direction reducing the output. When driven in the opposite direction, the primary voltage increases in the "boost" direction increasing the output. With 13.8 kV, 60 Hz input, the minimum voltage is 6.2 kV, and the maximum, no-load, is 14.1 kV, 28% buck and boost. With the 11.5 kV, 50 Hz input the corresponding values are 5.2 and 11.75 kV.

### 3.2 High-Voltage AC-DC Converter (HVPS)

The E-18645 HVPS is oil-insulated, self-cooled, housed in a steel tank 5.25' x 7.1' x 8.8', and weighs 28,600 pounds.

The HVPS, PS1, has a step-up transformer with a single 3-phase delta primary and two secondary windings, one delta and the other wye, having identical line-line voltages. A three-phase, full-wave rectifier (six-pulse) is connected to each set of windings, and the rectifier outputs are connected in series-aiding. There is an inherent 30-degree phase difference between the outputs of the delta and wye windings, which interleaves the conduction intervals of the 6-pulse rectifiers, producing a 12-pulse output with 30-degree conduction intervals. The first theoretical ripple component is the 12<sup>th</sup> harmonic, or 600 Hz, having a no-load amplitude of 2/143 of the DC component. The average output is 0.9886 times the peak AC input and the peak-valley ratio is 0.97. Line voltage amplitude imbalance, however, produces ripple components at 2, 4 and 6 times the line frequency. Load current produces phase-phase commutation delays in the rectification process because of AC source inductive reactance, primarily leakage reactance. Because of these imperfections an internal ripple filter comprising a 7.5 H

voltage across which is proportional to klystron beam current.

## 4 Protection for the Klystron

The klystron, V1, is prone to breakdown between cathode and body, which short-circuits the DC input. The threats to the klystron are the energy and charge stored in the capacitance and the charge transport produced by short-circuit current before the switchgear disconnects the input line.

### 4.1 Capacitive Stored Energy and Charge

The energy and charge stored in the 4.3 uF capacitor at 54 kV are 6.3 kJ and 0.23 Coulomb. The fundamental protection against stored energy is current-limiting resistance in series with the klystron cathode. It is optimally effective if it limits current to 1000 A or less.

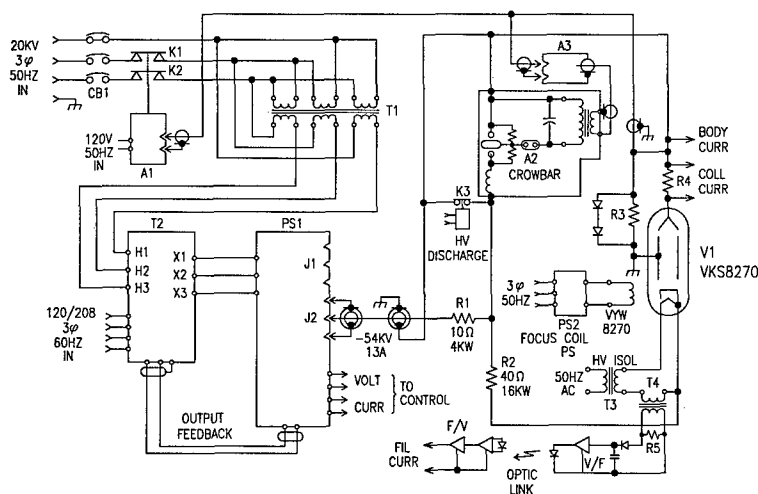


Figure 1: A simplified schematic of the IASA transmitter

series inductor and a shunt capacitor of 3 uF is used.

With 13.8 kV, 60 Hz, the combination of VVT and HVPS produces an output variable from -33 kVDC to -65 kVDC, at 16.5 ADC. With 11.5 kV, 50 Hz input, the output range is -27.5 kVDC to -54 kVDC. In order for the filter to have the same ripple-reduction at 50 Hz as at 60 Hz the shunt capacitance is increased by the square of 60/50, or 1.44, to 4.3 uF.

An internal 65 Megohm resistor is connected to the HV terminal of the transformer-rectifier. At the low end of the resistor is a current meter and an 8.2 kOhm fixed and 5 kOhm variable resistance, in series with the low-voltage return. The voltage across the resistors is fed to the control input of the VVT, for voltage regulation. The current meter output is proportional to output voltage. In series with the low-voltage return to the rectifier is a high-speed current-overload relay and a 20 A. meter shunt, the

At this current vacuum arcs are stable and have voltage drop of 20 Volts or less. This calls for approximately 50 Ohms series resistance. Following an arc, all but 20 V of the capacitor voltage will be across the series resistor. Most of the 6.3 kJ is dissipated in the resistor. With the VKS-8270 operated at 54 kV beam voltage, and corresponding beam current of 11.4 A the resistor voltage drop is 570 V, reducing actual klystron beam voltage to 53.4 kV.

### 4.2 Short-Circuit Power Supply Current

The second component of charge transport is short-circuit power supply current, limited by the series reactance on the AC side of the rectifier, measured to be a total of 10%. The rated output current is 16.5 A. The short-circuit current will be 165 A. Opening within 1/2 cycle, 10

milliseconds at 50 Hz, the charge transport, with half-sinusoidal waveform, is 1 Coulomb.

#### 4.3 Klystron Arc Energy and Discharge "Action"

With no protection other than series resistance and  $\frac{1}{2}$ -cycle primary interrupt, the energy dissipated in an arc, assuming constant arc drop of 20V, is  $20 \text{ V} \times \text{charge transport} = 20 \text{ V} \times 1.23 \text{ C} = 24.6 \text{ J}$ . Also of importance is the "action" or the time integral of the square of the discharge current, which determines the temperature-rise of a conductor passing the current. The component due to stored energy is  $6.3 \text{ kJ}/50 \text{ Ohms} = 126 \text{ Amp-squared-seconds}$ . The component due to  $\frac{1}{2}$ -cycle follow current of 165 A peak is  $136 \text{ Amp-squared-seconds}$ . The total of 262 Amp-squared-seconds is slightly more than the 207 required to fuse an AWG #30 copper wire. This is often the criterion of efficacy of a protection system.

#### 4.4 Series Resistor Characteristics

The resistor must hold off at least 54 kV, dissipating an average power of 6.5 kW, during normal operation, and a total impulse energy of 6.3 kJ, due to stored energy and 6.8 kJ due to short-circuit power-supply current without exceeding a peak temperature of  $375^\circ\text{C}$ . Resistors of the edge-wound type are custom-designed by Milwaukee Resistor Corp to have sufficient surface area and resistive mass to do this, using special high-mass/Ohm resistive alloys. A total of ten 5-Ohm, 2-kW resistors are used.

#### 4.5 Electronic Crowbar

It is considered prudent to additionally protect the klystron by means of an electronically-triggered low impedance, such as another arc, shunting the high-voltage isolated by a portion of the series resistance. In this case a mid-plane-triggered air-insulated spark gap, of the "infinite-voltage-range" type, A2 is used. It is triggered by the output of the crowbar driver, A3, which is stepped-up to a 200 kV open-circuit pulse by a pulse transformer and applied to the midplane electrode through a sharpening spark gap. The spacings between the midplane electrode and the upper and lower main electrodes are biased so that the trigger arc will be to the electrode having the inductor in series with it, which prevents the arc from short-circuiting the trigger source, allowing the gap between midplane and the other electrode to ionize as well, without the need for external high voltage between main electrodes, hence "infinite voltage range". The 50 Ohm series resistor is divided into two segments, one of 10 Ohms, R1, and one of 40 Ohms, R2. The high-side of the crowbar is connected to their intersection. The 40 Ohms in series with the klystron is much higher in impedance than the fired crowbar, assuring that most of charge is diverted from the klystron. The maximum peak current through the crowbar is  $54 \text{ kV}/10 \text{ Ohms} = 5400 \text{ A}$ . Having a crowbar means that the 10-Ohm segment in

series with the crowbar must meet all of the impulse criteria described in 4.4, since the crowbar protects the remaining 40 Ohms as well as the klystron.

#### 4.6 High-Speed Mains Disconnect

The 20 kV circuit breaker, shown as CB1, has an opening time of 3-5 line cycles, which is too long. At 20 kV line voltage, solid-state SCR-based relays are impractical. Vacuum relays, however, with close-spaced contacts, can achieve opening times as short as 2 milliseconds, or  $\frac{1}{5}$  cycle, giving  $\frac{1}{2}$ -cycle clearing time, assuming the post-opening arc extinguishes at the current zero crossing. Only two such relays, Ross Engineering HBF-51-NC, K1 and K2, are required, with normally-closed contacts. They are driven open by the output of an SCR-switched stored-energy driver, type HCB, A1.

### 5 Klystron RF Amplifier

The VKS-8270 multi-cavity CW klystron amplifier has coaxial RF input, waveguide RF output, electromagnet beam focussing, and liquid cooling. Filament power is from a high-voltage isolation transformer, T3. Filament current is monitored by series transformer, T4, developing voltage across R5, which is rectified, converted to a train of optic pulses with frequency proportional to voltage, and converted back to voltage, at ground level. Focus coil excitation is from PS2. Voltages proportional to body and collector current are developed across R3 and R4. R3 is shunted by high-surge-current diodes to conduct the current resulting from a gun arc. The voltage drop is clamped to 7 V, which is the fault input to the crowbar driver and the stored-energy driver, which have 5 V input thresholds.

Klystron tests, at 2380 MHz, with beam voltage of 65 kVDC and current of 15.1 A showed power output of 490 kW with 1 Watt RF input. With 50 Hz primary power, however, the DC beam voltage available is only 54 kV. Beam current drops as the  $\frac{3}{2}$  power of voltage and beam power by the  $\frac{5}{2}$  power. RF output drops even faster than the cube of beam voltage because it is proportional to the square of the fundamental-frequency RF current traversing the output gap, which, at best, diminishes as the cube of beam voltage. As beam voltage is reduced, the spacing between RF cavities is no longer optimum because the beam velocity is lower and bunching effectiveness is diminished, reducing further the RF component of current. The peak RF voltage across the output gap falls more rapidly than beam voltage. Some of the loss in RF power can be regained by means of a properly positioned iris in the output waveguide to effect an increase in the RF impedance reflected into the RF output gap of the klystron, restoring the match between RF impedance and electron-beam impedance, which varies as the  $\frac{1}{2}$  power of beam voltage.

# DESIGN OF FOUR-CAVITY HIGH POWER GYROKLYSTRON AMPLIFIER\*

I. Yovchev<sup>#+</sup>, W. Lawson, M. Castle, G. Nusinovich, V. Granatstein, and M. Reiser,  
University of Maryland, College Park, MD 20742, USA

## Abstract

In order to develop a high power Ku-band gyroklystron amplifier with high gain and efficiency for driving future linear colliders, a theoretical design of a four-cavity coaxial 17.1 GHz gyroklystron amplifier has been carried out. The X-band input cavity operates at  $TE_{011}$  mode while the remaining three cavities (buncher, penultimate and output) operate at  $TE_{021}$  mode, doubling the frequency of the input signal. The simulations show that both a very high efficiency of 45.6 % and a gain of 71 dB can be realized using a 500 kV, 700 A electron beam with a perpendicular-to-parallel velocity ratio of 1.5 and a parallel velocity spread of 6.4 %.

## 1 INTRODUCTION

Relativistic klystrons, gyroklystrons, magnicons and free-electron lasers are considered as the most promising candidates for driving future linear colliders. For TEV-scale linear colliders it is desirable to increase the electric field gradients which can be attained by increasing the radiation frequency. In recent experiments with a three cavity 1-1-1 coaxial gyroklystron carried out at the University of Maryland very high peak microwave powers of 75-85 MW at 8.6 GHz frequency were obtained [1]. The sequence 1-1-1 means that all three cavities, input, buncher and output, operate at the fundamental electron cyclotron frequency, so 1 is the cyclotron resonance harmonic number. To increase the frequency, the output cavity can be designed for operation at the second harmonic.

In previous computer simulations two-cavity and three-cavity frequency doubling gyroklystrons were studied (1-2 and 1-2-2 circuits) [2]. It was shown that introducing a second harmonic buncher cavity into a two-cavity 1-2 circuit (in this way a 1-2-2 circuit can be obtained) may increase the efficiency from 30 % to 41 % and gain from 26 dB to 49 dB; these results were obtained for a 500 kV, 700 A electron beam with a perpendicular-to-parallel velocity ratio (pitch-ratio)  $\alpha$  of 1.508 and a parallel velocity spread of 6.4 %.

To improve the device performance further we have undertaken a design of a four-cavity circuit, using the same beam parameters.

## 2 RESULTS FROM A POINT-GAP MODEL OF A FOUR-CAVITY GYROKLYSTRON

There exist at least four possible schemes of a four-cavity gyroklystron in which the input cavity operates at the fundamental and the output cavity – at the second cyclotron harmonic: 1-1-1-2, 1-1-2-2, 1-2-1-2 and 1-2-2-2. Here we may also add the scheme 1-2-4-2 where the third cavity resonates at the fourth harmonic frequency.

The design of each of these possible circuits requires a large consumption of computer time. In order to save this time we have first used a point-gap model (PGM) of the gyroklystron [3] to qualitatively estimate the performance of the five schemes. The PGM implies that the cavities lengths are much shorter than the drift spaces, thus electrons' energy is modulated in each cavity and this modulation causes electron phase bunching in drift regions. The three-cavity gyroklystron PGM developed in [3] was generalized for a four-cavity gyroklystron. The corresponding maximum efficiencies for the five schemes are given in Table 1. These values characterize the efficiency of electron bunching only but not the overall efficiency of the device. It is seen that the 1-2-2-2 circuit is the most efficient. Therefore detailed computer simulations were performed for this circuit.

Table 1: Maximum efficiencies calculated in the framework of PGM for 5 different circuits.

Circuit	Efficiency (%)
1-1-1-2	60.0
1-1-2-2	51.0
1-2-1-2	66.5
1-2-2-2	76.0
1-2-4-2	54.3

## 3 DESIGN OF 1-2-2-2 CIRCUIT

Our 1-2-2-2 circuit was based on the previously optimized 1-2-2 design [2]. The modification was done by inserting before the output cavity a second buncher (or penultimate) cavity with the same dimensions as the first buncher cavity. The geometry of the four-cavity

\*Work supported by the Department of Energy, Contract DE-FG02-94ER40855.

# Email: igy@glue.umd.edu

+On leave from the Dept. of Physics, University of Chemical Technology and Metallurgy, Sofia, Bulgaria.

system is shown in Fig.1 and dimensions are tabulated in Table 2.

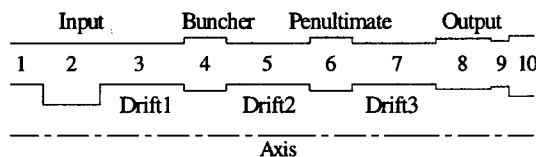


Figure 1: Geometry of the four-cavity 1-2-2-2 circuit

The operating modes are the  $TE_{011}$  mode for the input cavity and  $TE_{021}$  mode for the remaining three cavities. For operation in the 17.1 GHz frequency range, based on previous studies of a 1-2-2 design, the resonant frequencies of the input, buncher, penultimate and output cavities calculated by the scattering matrix code COAX [4,5] are 8.567 GHz, 17.136 GHz, 17.136 GHz and 17.063 GHz, respectively.

The large-signal code GYCOAX [6] was used for optimization of parameters to get maximum efficiency and gain. In the case of a four-cavity gyrokystron it means a search in a 7-dimensional parameter space: 4 amplitudes ( $a_1$ ,  $a_2$ ,  $a_3$  and  $a_4$ ) and three relative phases ( $\phi_2$ ,  $\phi_3$  and  $\phi_4$ ) of the fields in each cavity – the phase  $\phi_1$  in the input cavity can be set to 0 without loss of generality.

Table 2: Dimensions of the four-cavity 1-2-2-2 circuit

Cavity or Section	No.	Inner Radius (cm)	Outer Radius (cm)	Length (cm)
Inlet	1	1.825	3.325	5.000
Input	2	1.100	3.325	2.286
Drift 1	3	1.825	3.325	3.328
Buncher	4	1.610	3.520	1.691
Drift 2	5	1.825	3.325	3.328
Penultimate	6	1.610	3.520	1.691
Drift 3	7	1.825	3.325	3.328
Output	8	1.620	3.520	1.712
Output	9	1.760	3.360	0.693
Outlet	10	1.400	3.550	5.000

Exploration of such a multidimensional space is almost hopeless without certain optimization procedure. For this reason a subroutine which varies all  $a$ 's and  $\phi$ 's according to the Hooke-Jeeves method [7] and looks for the maximum efficiency was written and successfully embedded into the code GYCOAX. A further improvement of the optimization procedure was made by incorporating in the subroutine additional 3 parameters  $I_1$ ,  $I_2$  and  $I_3$ , which correspond to the currents in three sets

of coils creating the guide magnetic field. Thus, the parametric space becomes 10-dimensional. In this way, however, we merge into one optimization procedure two previously separate procedures: first, optimization of the  $a$ 's and  $\phi$ 's and second, optimization of the guide magnetic field.

The improved large-signal code was first applied to the configuration, presented in Fig. 1 where all drift spaces have the same length – 3.328 cm (see also Table 2). Both very high efficiency of 43.2 % and gain of 71 dB were calculated (compare with 41.1 % and 49 dB for the three-cavity 1-2-2 gyrokystron design [2]).

Additional simulations were performed to further increase the efficiency by: 1) optimizing the drift space lengths and 2) stagger tuning (ST) [8,9] of the last two cavities.

At the first step, there exists an experimental setup constraint: the distance between the input cavity exit and the output cavity entrance have to be kept constant. For that reason, only the buncher and the penultimate cavities were moved. The results are presented in Table 3. In its first two rows 0 means that the cavity is in the same position as in Fig. 1, while +1 or -1 means that the corresponding cavity is displaced by 1 cm on the right or on the left, respectively. The efficiency for each configuration is given in the last row. The best result is obtained when the buncher cavity position is unchanged while the penultimate cavity is displaced 1 cm on the right (see fifth column in Table 3). For all five considered cases the gain is approximately 71 dB.

Table 3: Displacements of the buncher and penultimate cavities in cm and corresponding efficiencies

Displacement of the Buncher cavity	0	+1	-1	0	0
Displacement of the Penultimate cavity	0	0	0	+1	-1
Efficiency (%)	43.2	43.0	40.7	44.2	43.4

At the second step, ST was applied to the penultimate and the output cavities for the case of the highest efficiency at the previous step. The results are shown in Table 4. By small changes in their dimensions, the penultimate and the output cavities resonant frequencies were slightly modified. This leads to an essential efficiency increase – from 44.2 % before ST to 45.6 % after ST.

Table 4: Cold-cavity frequencies (in GHz) and efficiency without and with stagger tuning.

	Penultimate cavity	Output Cavity	Efficiency (%)
Without ST	17.136	17.063	44.2
With ST	17.070	17.086	45.6

The study of the stability of operation performed by using the code QPB [10] shows that the input, the buncher and the penultimate cavities are stable. However, the starting currents (approximately 600 A) for the output cavity operating  $TE_{021}$  mode and parasitic  $TE_{131}$  mode are lower than the beam current of 700 A, i.e. the output cavity is not zero-drive stable. Zero-drive stability of the output cavity was demonstrated at  $\alpha = 1.4$ . The efficiency decrease to 43.1 % for this  $\alpha$ -value but is still very high. Since the pitch-ratio can be varied experimentally between approximately 1.0 and 1.5 the dependence of the efficiency on  $\alpha$  is also studied (see Fig. 2). It is evident that the efficiency differs by a factor of about 2 for the end values of the examined  $\alpha$ -range.

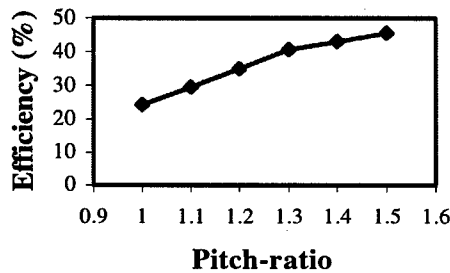


Figure 2: Efficiency dependence on pitch-ratio

#### 4 CONCLUSION

A four-cavity coaxial gyrokystron amplifier design for the 17.1 GHz frequency range was presented in this paper. The simulations were performed for a circuit in which the input cavity operates at the fundamental frequency, while the buncher, penultimate and output cavities operate at the second harmonic of the cyclotron frequency (1-2-2-2 circuit). Calculations based on the point-gap model show that this is the most efficient scheme among the schemes with input and output cavities operating at first and second harmonic, respectively.

In order to accelerate the finding of the optimum device parameters with respect to the efficiency and gain a subroutine using the Hooke-Jeeves optimization method was embedded into the large-signal code GYCOAX. Additional optimization of the drift spaces and stagger tuning of the last two cavities were carried out. The simulations predict both very high efficiency and gain of 45.6 % and 71 dB, respectively, for the 1-2-2-2 gyrokystron, using an electron beam with 500 kV voltage, 700 A current, perpendicular-to-parallel velocity ratio of 1.5 and parallel velocity spread of 6.4 %. Even if we restrict ourselves to a zero-drive stability of the output cavity (at  $\alpha \leq 1.4$ ) the efficiency of the studied four-cavity gyrokystron decreases slightly to 43.1 % but

it could deliver output microwave power of up to 150 MW.

#### 5 REFERENCES

- [1] W. Lawson, J. Cheng, J. Calame, M. Castle, B. Hogan, V. Granatstein, M. Reiser, and G. Saraph, "High-Power Operation of a Three-Cavity X-Band Coaxial Gyrokystron", *Phys. Rev. Lett.*, vol. 81, No. 14, pp. 3030-3033 (1998)
- [2] G. Saraph, W. Lawson, M. Castle, J. Cheng, J. Calame, and G. Nusinovich, "100-150 MW Designs of Two- and Three-Cavity Gyrokystron Amplifiers Operating at the Fundamental and Second Harmonics in X- and Ku-Bands", *IEEE Trans. Plasma Sci.*, vol. 24, No. 3, pp. 671-677 (1996)
- [3] G. Nusinovich, G. Saraph, and V. Granatstein, "Scaling Law for Ballistic Bunching in Multicavity Harmonic Gyrokystrons", *Phys. Rev. Lett.*, vol. 78, No. 9, pp. 1815-1818 (1997)
- [4] J. Neilson, P. Latham, M. Caplan, and W. Lawson, "Determination of the Resonant Frequencies in a Complex Cavity Using the Scattering Matrix Formulation", *IEEE Trans. Microwave Theory Tech.*, vol. 37, No. 8, pp. 1165-1170 (1989)
- [5] W. Lawson and P. Latham, "The Scattering Matrix Formulation for Overmoded Coaxial Cavities", *IEEE Trans. Microwave Theory Tech.*, vol. 40, No. 10, pp. 1973-1977 (1992)
- [6] P. Latham, W. Lawson, and V. Irwin, "The Design of a 100 MW, Ku-Band Second Harmonic Gyrokystron Experiment", *IEEE Trans. Plasma Sci.*, vol. 22, No. 5, pp. 804-817 (1994)
- [7] B. Bunday in "Basic Optimisation Methods", E. Arnold Publ. Ltd., London (1984), Translated into Russian, pp. 37-42.
- [8] G. Nusinovich, B. Danly, and B. Levush, "Gain and Bandwidth in Stagger-Tuned Gyrokystrons", *Phys. Plasmas*, vol. 4, No. 2, pp. 469-478 (1997)
- [9] M. Blank, B. Danly, and B. Levush, "Circuit Design of a Wideband W-Band Gyrokystron Amplifier for Radar Applications", *IEEE Trans. Plasma Sci.*, vol. 26, No. 3, pp. 426-432 (1998)
- [10] P. Latham, S. Miller, and C. Striffler, "Use of Lie Transforms to Generalize Madey's Theorem for Computing the Gain in Microwave Devices", *Phys. Rev. A*, vol. 45, No. 2, pp. 1197-1206 (1992)

# THE DESIGN OF SHEET-BEAM ELECTRON-GUN FOR HIGH-POWER MICROWAVE SOURCES\*

S. K. Wong<sup>†</sup>, J. S. Kim, J. D. Goldberg, D. H. Edgell, and W. L. Spence,  
FARTECH, Inc., San Diego, CA

## Abstract

A set of software tools based on Pierce theory and the Cutler-Hines approach for thermal velocity effects have been developed for the design of sheet-beam electron guns. The tools yield parameters for rudimentary gun geometry, which are further refined using the 2-D particle-in-cell code EGUN. Candidate designs for guns suitable for applications to high-power, high-frequency microwave sources have been obtained. The results indicate good potential for the use of sheet-beams to generate microwaves applicable to future accelerators.

## 1 INTRODUCTION

High power microwave sources in the 30 to 100 GHz range are needed to power the next generation of linear accelerators and colliders. Several recent proposals for the generation of high power microwaves make use of sheet electron beams. The inherent advantage of these beams, with a typical width-to-height ratio of 10, is the reduced space charge effect for a given beam current. In comparison with round beams, past design work of sheet beams is quite scanty, particularly in the relativistic, high-current density, cases now being considered. This paper describes efforts to design such beams. A two-pronged approach is taken. Preliminary designs with rudimentary geometry of electrodes are first made using the Pierce method, supplemented by the effects of thermal velocity. Although the basis of these methods are well-known, substantial developmental work has been gone through to carry out the formulation and to produce a computer code for design purposes. Detailed designs are then performed by particle simulation using the 2-D code EGUN.

## 2 PRELIMINARY DESIGN

### 2.1 Pierce Method

A preliminary design of sheet-beam electron guns can be made using an approach pioneered by Pierce[1]. The rudimentary gun geometry consists of a cathode in the form of a circular arc of half-angle  $\alpha$ , an anode with a slit to let the beam through, and an exit plane at equal potential to the anode. The electron flow and the potential

distribution between the cathode and the anode are approximated by those of the space-charge-limited diode with concentric cylindrical electrodes. The anode slit acts as a diverging lens. Beyond the anode, the beam moves under the influence of its own space charge. The paraxial approximation is taken throughout. The treatment is fully relativistic.

For a given geometry, the beam current and the electron paths depend only on the anode potential, which is characterized by the relativistic energy factor  $\gamma = 1 + eV/mc^2$  of the beam. The electron paths beyond the anode are self-similar and parabolic. They either cross the mid-plane or achieve a minimum deviation at some location beyond the anode. The only geometry parameter which controls such behaviors is  $\kappa$ , defined as  $d/a$  where  $d$  is the anode-cathode separation and  $a$  is the radius of curvature of the cathode. This factor is always less than unity. When it is too small, the beam diverges from the mid-plane upon emerging from the anode. When it is too large, the beam crosses the mid-plane. It would appear that the optimum design is to choose  $\kappa$  so that the minimum beam thickness is zero, and let the actual beam thickness be determined from considerations of thermal effects. Indeed, such an approach has been undertaken in the past[2]. However, a new calculation of thermal effects reveals that this approach is far from optimal.

### 2.2 Thermal Velocity Effects

The effects of transverse velocity spread of electrons originating from the cathode can be investigated using the method of Cutler and Hines[3]. This entails computing the perturbed orbits from the cold beam paths. It gives rise to an expression for the deviation from the cold path for a warm path of a given transverse velocity at the cathode. The expression diverges at the location where the cold beam crosses the mid-plane, a result at variance from those of earlier calculations[4] quoted by Reference [3]. The divergence is traceable to the fact that, in the region between the anode and the exit plane, the deviation  $y$  from the mid-plane satisfies the linear equation

$$\frac{d^2y}{dz^2} = \frac{K}{s(z)}y \quad (1)$$

where  $K$  is a constant and  $s(z)$  is the envelope of the cold beam, which is a quadratic function. As a result, all paths

\* Work supported by the U.S. DOE-SBIR Grant Number DE-FG03-98ER82575

<sup>†</sup> Email: [skwong@far-tech.com](mailto:skwong@far-tech.com)

except those with zero initial transverse velocity approaches infinity at the location where  $s(z)$  vanishes. Therefore, designs for which the cold beam crosses or touches the mid-plane are to be avoided as the thermal spread would be large. The location of the exit plane can still be chosen to be where the thickness of the cold beam is the smallest.

For a given temperature  $T$  of the cathode, the current density profile at the exit plane is found to be

$$dI = \frac{I}{4s_m} \left[ \operatorname{erf}\left(\frac{y+s_m}{\sigma_{th}}\right) - \operatorname{erf}\left(\frac{y-s_m}{\sigma_{th}}\right) \right] dy \quad (2)$$

where  $S_m$  is the minimum half-thickness of the cold beam, and  $\sigma_{th}$  equals  $f(\kappa, \gamma) d\sqrt{kT/eV}$  for some function  $f$  involving integrals that can be computed numerically. The thickness  $t_{95}$  containing 95% of the beam current can be found from Eq.(2).

### 2.3 Design Optimization

A MATLAB based computer program has been created to make optimum designs. The program accepts as inputs the beam energy, the current per unit width, the current density at the cathode, and the temperature of the cathode. It completely determines the rudimentary geometry by minimizing  $t_{95}$ . The code has been partially validated against sheet-beam design calculations and experimental measurements performed in the past[2].

As an example, consider a 140kV and 15A sheet-beam with a width of 0.8cm, which is a candidate for applications to future W-band accelerators. Taking the current density at the cathode to be 5A/cm<sup>2</sup>, and the temperature to be 1473K, the optimum design has the following parameters:

$$d = 3.3\text{cm} \quad a = 5.0\text{cm} \quad \alpha = 21.3^\circ \quad \ell = 12.5\text{cm} \\ t_{95} = 0.18\text{cm}$$

Here  $\ell$  is the distance between the cathode and the exit. The areal compression based on  $t_{95}$  is 21. The cold beam thickness in this case is 0.09cm. The beam thickness at the anode is 1.28cm. The electric field at the anode is 93 kV/cm, well within the break-down limit.

### 2.4 Brillouin Field

An external magnetic field in the direction of the beam near the exit is required to prevent the beam from diverging. For round beam, this is the well-known Brillouin field. A similar derivation based on the conservation of canonical angular moment and the cancellation of the space-charge force by the pinching

effect of the self magnetic field and the Lorentz force from the imposed field can be performed for sheet-beams. This gives rise to the following expression for the required field:

$$B^2 = \left(\frac{m}{e}\right)^{3/2} \frac{1}{\sqrt{V}} \frac{1}{\sqrt{1+\gamma}} \frac{I}{w t} \quad (3)$$

where  $I/w$  is the beam current per unit width and  $t$  is the beam thickness. Although the choice of guide field is immaterial in the Pierce approach, it is needed in detailed designs where electron orbits are obtained with realistic electrode geometry. Note that the scaling of  $B$  with beam thickness is favorable with the sheet beam in comparison with the round beam (i.e.  $B \propto r^{-1}$  for round beam).

## 3 DETAILED DESIGN

Detailed designs can be made using specialized or general purposed particle motion simulation codes. These codes determine the trajectories of a large number of electrons emitted from the cathode self-consistently with the electric and magnetic fields, thereby obtaining the current of the beam once the electrode arrangement is specified. Besides improving on the accuracy of the Pierce method, the codes also allow detailed designs of electrode geometry so that optimization can be performed in a large parameter space. The 2-D gun design code EGUN has been used for the purpose. Output from the preliminary design code can be used as guidance for preparing input to EGUN.

A detailed design for a gun with similar parameters as the sample design in section 2.3 has been made. The electrode geometry and the paths of electrons are shown in Fig.1. This gun delivers a 140kV beam with 10.7A/cm and a thickness  $t_{95}$  equal to 0.36cm. Other parameters are

$$a = 5\text{cm} \quad \alpha = 20^\circ \quad d = 4.5\text{cm} \quad \ell = 13.9\text{cm} \quad (4)$$

The angle between the focusing electrode and the cathode arc is chosen to be 65.5°. In addition, the maximum electric field is 94.4kV/cm and the cathode current density is 3.1A/cm<sup>2</sup>. It is seen that with the exception of the beam thickness, there is reasonable agreement with the preliminary design.

Smaller beam thicknesses can be achieved by rescaling. For example, rescaling the geometry of (4) above, down by a factor of 2, reduces estimated beam thickness to 1.8 mm and increases current density to 21.4 A/cm. In this case, the maximum E field increases to 189 kV/cm which is still within acceptable limits.

In the numerical calculations, the paths of electrons are not self-similar as in Pierce's theory. The paths and the beam envelope depend on the choice of the magnetic field. Some amount of midplane crossing is unavoidable if the



field is close to or exceeds the Brillouin field. The beam envelope also tends to oscillate, with amplitudes and periods that depend on the value of the field chosen. The paths in Fig.1 correspond to the choice  $B=300\text{G}$ , below the Brillouin field of  $536\text{G}$ . Design for a higher power beam at  $400\text{kV}$  and  $78\text{A/cm}$  have also been made, with a thickness equal to  $0.2\text{cm}$ .

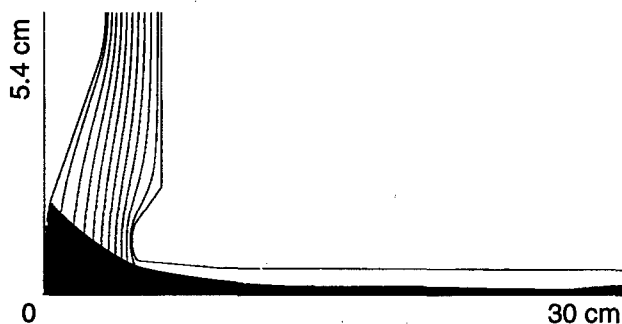


Figure 1: Electrode geometry and electron paths for a  $140\text{kV}$  sheet-beam electron gun according to EGUN.

With higher external magnetic fields the beam waist were found to be reduced as shown in Eq. (3). With higher magnetic field, however, the beam tends to cross the midplane as seen in Fig. 2. The crossing occurs more frequently as  $B$  increases.

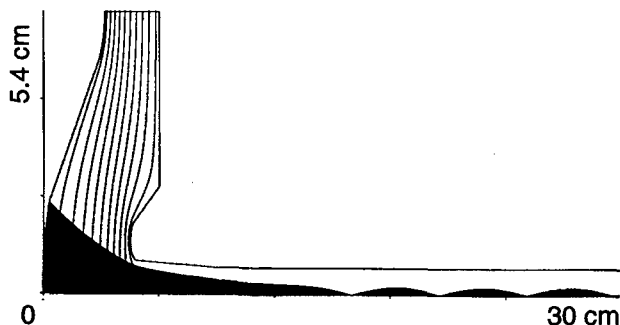


Figure 2: Electrode geometry and electron paths for a  $140\text{kV}$  sheet-beam electron gun with  $1000\text{G}$  magnetic field according to EGUN.

#### 4 SCALING STUDIES

In an effort to map out the possible parameter range of sheet-beams, scaling studies have been performed using the software which implements the Pierce method with thermal velocity effects. Three parameters are considered: beam voltage ( $70\text{-}280\text{kV}$ ), current per unit width ( $10\text{-}40\text{A/cm}$ ), and cathode loading ( $2.5\text{-}10\text{A/cm}^2$ ). Each is varied while keeping the others fixed at values corresponding to a reference design, which is chosen to be the one discussed in earlier sections. The main results are:

- compression ratio in the range 15 to 40 is achievable
- beam thickness of  $0.1$  to  $0.25\text{ cm}$  can be obtained

- increasing the current per unit width causes the beam to thicken
- Increasing the voltage has the same effect, but to a lesser extent
- increasing the cathode loading is very effective in reducing the beam thickness

#### 5 CONCLUSIONS

Developmental work carried out in the implementation of Pierce theory for the design of sheet-beams and Cutler-Hines approach for the effects of thermal velocity leads to software tools suitable for preliminary design work and scaling studies. New results have also been obtained.

The combination of such software tools and a 2-D particle simulation code proves to be an effective way of designing sheet-beams. Designs have been obtained for beams suitable for the generation of high-power, high-frequency microwaves. Based on point designs and scaling studies, sheet-beams should have good potential for application in future accelerator technology. Future work should include 3-D effects such as edge control, and more detailed characterization of beam qualities.

#### 6 REFERENCES

- [1] J.R. Pierce, *Theory and Design of Electron Beams*, D. Van Nostrand Co. (1954)
- [2] N.B. Kramer and E.G. Todd, Design of Hollow and Strip Beam Guns, *IEEE Transaction of Electron Devices*, Nov 63 p394 (1963)
- [3] C.C. Cutler and M.E. Hines, Thermal Velocity Effects in Electron Guns, *Proc. I.R.E.*, vol. 43, p307 (1955)
- [4] L.E. Bakhrakh and V.G. Medoks, Effect of Thermal Velocities on Blurring of Electron Beams, *Radio Engineering and Electron Physics*, vol.1, p107 (1962); C.B. Crumly, Thermal Velocity Effects on Two-dimensional Electron Beams, Stanford Electronics Lab., Rept. No. 457-2 February (1958)

# OPERATION OF A THREE CAVITY SECOND HARMONIC COAXIAL GYROKLYSTRON\*\*

M. Castle, I. Yovchev, W. Lawson, B. Hogan, V.L. Granatstein, and M. Reiser,  
Institute for Plasma Research, University of Maryland, College Park, MD 20742

## Abstract

At the University of Maryland, we have been developing gyroklystrons for advanced electron-positron linear collider applications. We have recently achieved over 80 MW of peak power at 8.6 GHz with a three-cavity first harmonic gyroklystron [2]. The interaction was observed between a 470 kV, 500 A annular, rotating beam and a sequence of  $TE_{011}$  coaxial cavities. The efficiency was about 32% and the gain was about 30 dB. We are currently testing a three-cavity tube that is designed to produce over 100 MW of power at 17.14 GHz with an efficiency of 40%. The input cavity is the same  $TE_{011}$  cavity used in the first harmonic experiment, but the buncher and output cavities are  $TE_{021}$  cavities that operate at twice the cyclotron frequency. In this paper we will describe the design of the circuit and detail the hot test results. Finally, we will also describe the designs of tubes that are capable of higher gain and higher rep-rate operation.

## 1 INTRODUCTION

Various types of microwave power sources are currently under serious investigation as accelerants of particle beams in linear colliders. At the University of Maryland, we have been investigating the prospects and potential of using gyro-amplifiers as drivers for particle beams in a linear accelerator. [1] The main thrust of this work has been geared towards development of the gyroklystron. This device uses discrete cavities along a linear path where the beam-field interaction takes place as in a klystron, while utilizing the helically spiralling electron beam profile typically found in small orbit gyrotrons. The beam-field interaction occurs when the cyclotron frequency of the beam is close to the group velocity of the electromagnetic waves. By employing this mechanism, overmoded cavities may be utilized and higher frequencies of operation may be achieved without decreasing tube radius unduly. Indeed, the gyroklystron has shown the potential to achieve much higher powers at high frequencies (>30 GHz) than that of the conventional linear-beam tubes. Past results achieved at Maryland include 32 MW of power at 19.7 GHz with a 28% efficiency. This circuit employed was used in the

second harmonic mode of operation, had cylindrical geometry, and a smooth-walled output cavity.

Two years ago, a new 100 MW test bed was completed and operated. Coaxial geometry was instituted to reduce mode densities. Because of this geometry, the cavities could be made with abrupt radial transitions, which are beneficial for their ease of manufacture and ease of modification. Tight control over resonant frequency and Q values can be obtained. Two fundamental circuits were tested and results culminated in about 80 MW of power at 8.6 GHz for 1.7  $\mu$ sec at 32 % efficiency. [2] Now testing is underway on a second harmonic three-cavity circuit. The results to date will be reported. Analysis of the limitations and problems encountered will be discussed. An account of the theoretical redesign of the output cavity will be given in section 3. Current efforts for this second harmonic experiment will also be described.

Theoretical efforts on designs for tubes to be made in the future are being performed. These tubes will be made to be compatible with a linear accelerator. Slight modifications to the existing second harmonic system that should improve performance and enable high rep rate operation have been designed. Cold testing has been partially completed for these upgrades.

## 2 SECOND HARMONIC TUBE 'SH1'

The first second harmonic tube to be put on the system in an attempt to create a 100 MW of power was called SH1. Testing on this tube has been completed.

Table 1: System Parameters

Output Frequency (GHz)	17.110
Input Frequency (GHz)	$TE_{02}$
Simulated SH1 efficiency	41%
Pulse Length ( $\mu$ sec)	$\sim 1$
Modulator Voltage (kV)	460
Beam Current (Amps)	500
Ave. Magnetic Field (kG)	5.3
Input Cavity Q	$68 \pm 7$
Buncher Cavity Q	$390 \pm 10$
Output Cavity Q	$320 \pm 10$

\*Work supported by the U.S. Department of Energy

## 2.1 Experimental Results

Tube SH1 was never able to achieve repeatable amplifier performance. Cathode voltages were usually kept in the 400-470 kV range. Currents were variable, but generally were in the 350-500 A range. The tube was generally quite stable and only small bands of parameter space yielded microwaves. Various magnetic fields detuning and slope combinations and drive power frequencies were attempted to produce amplification to no avail.

## 2.2 Analysis of Tube Limitations

The design of this tube was predicated on the ability to achieve up to 800 A from the electron beam. A 'safe' value of 720 A was chosen as the nominal design point. This was an attempt to balance both the quest for high power and the need for stability. The maximum current attained during the testing was 530 A. Subsequent large signal code analysis determined that the predicted efficiency at this current was approximately 2%. This value was not achieved because of lower alpha values than those simulated (simulation  $\alpha=1.5$ ) from pressure problems and low beam currents. To increase current, most likely a new emitter must be installed. This is a likely possibility for the summer.

## 3 THEORETICAL REDESIGN

A redesign of the output cavity for the lower current values was undertaken for expediency. A value of 540 A was chosen as the nominal value. Instead of increasing the Q, the cavity was increased in length. Designs with 10, 20 and 30% increases were tried. The 30 % increase was the most efficient and made to be zero drive stable. Previously, the length to wavelength ratio,  $L/\lambda$ , in the cavity had been 0.98, with this new design the value was 1.24. Figure 1 indicates the circuit efficiency with changing values of velocity pitch ratio.

A maximum efficiency of 39.2% is predicted at  $\alpha = 1.5$ . Figure 2 shows the threshold of oscillation in terms of beam currents as a function of the magnetic field. The operating point of 540 amps is indicated by the horizontal line. As indicated, this tube is theoretically zero-drive stable to all modes, which the previous design was not quite, but had relied on some non-linear suppression of the modes due to bunched beam and magnetic field tapering. Both efficiency and stability simulations were carried out assuming that the axial velocity spread was 6.4%.

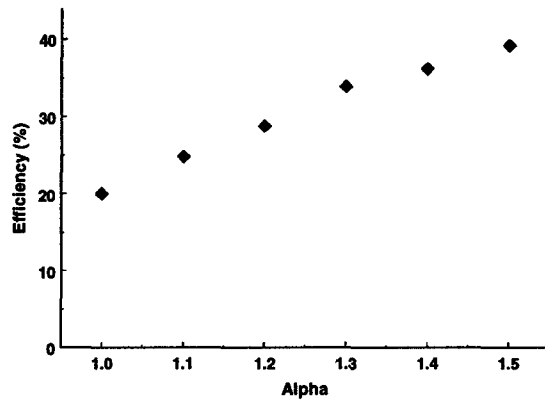


Figure 1: Dependence of efficiency on velocity pitch ratio

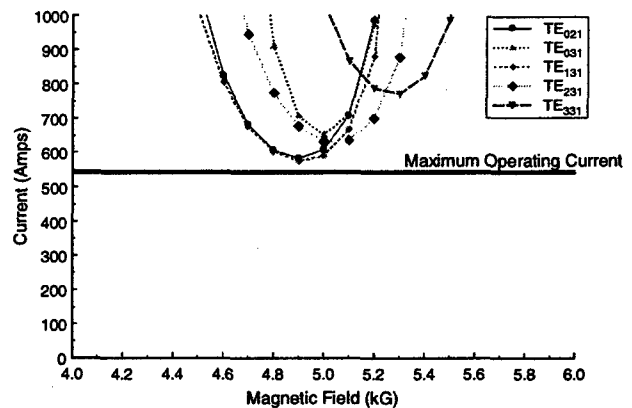


Figure 2: Start oscillation current for main mode competitors

## 4 ACCELERATOR COMPATIBLE DESIGNS

In an effort to make the gyrokystron more compatible with an accelerator, modifications to the system have been started.

### 4.1 Dual-Cavity Input Coupler

In order to more effectively couple input power to the system, a coupler which features two concentric coaxial cavities has been designed using Hewlett-Packard's HFSS. An outer coaxial cavity receives the input signal and resonates in the  $TE_{411}$  mode. Slots on the inner wall of this cavity couple field through to the inner coaxial cavity, which resonates in the  $TE_{011}$  mode. Cold testing

has verified the design. The resonant frequency and  $Q$  of this inner cavity were measured in the cold test to be 8.570 GHz and 73.

#### 4.2 Radial Extracting Output Cavity

One of the biggest limitations for the present system is the limitation on firing repetition rate. Because this system was mounted horizontally, small tungsten pins are required to hold up the inner conductor of the coaxial circuit. Designs have been completed on HFSS and cold testing is currently underway. The design features the same output cavity as in the second harmonic system except for eight slots cut into the inner conductor wall. These slots couple the power from the  $TE_{021}$  mode in the cavity to the  $TE_{01}$  mode in coaxial waveguide inside. The main benefit is that the inner conductor of the system can be supported from the downstream end because of this extraction method, eliminating the need for the small support pins and freeing up the modulator to increase the repetition rate. In addition, stability may be increased due to the elimination of travelling wave interactions in the post-cavity regions. Finally, conversion from  $TE_{01}$  to other modes is more readily done than from  $TE_{02}$ .

### 5 CURRENT AND FUTURE WORK

Cold testing of the redesigned output cavity has been completed. It finalized the dimensions for the output cavity, only a slight change of radius on the inner conductor being necessary to make the resonant frequency 17.11 GHz and the  $Q = 320$ . The vacuum compatible version of the cavity is now being built and Tube SH2 will be installed and evacuated immediately thereafter. Hot testing of this tube will be complete by summer. Assimilation of the accelerator compatible design will be a focus of the project and should run in parallel with an emitter change in summer. Soon, investigations into the performance of a four-cavity 35 GHz design will be undertaken.

### 6 REFERENCES

- [1] V.L. Granatstein and W. Lawson, "Gyro-Amplifiers as Candidate RF Drivers for TeV Linear Colliders", *IEEE Trans. Plas. Sci.*, Vol.24, (1996)
- [2] W. Lawson, et. al., "High-Power Operation of a Three-Cavity X-Band Coaxial Gyroklystron", *Phys. Rev. Lett.*, vol. 81 n.14 (1998)

## X-BAND MAGNICON AMPLIFIER

O. A. Nezhevenko, V. P. Yakovlev, J. L. Hirshfield, and E. V. Kozyrev<sup>\*</sup>  
Omega-P Inc., 345 Whitney Avenue, New Haven, CT 06511

S.H. Gold and A.W. Fliflet  
Beam Physics Branch, Plasma Physics Division,  
Naval Research Laboratory, Washington, DC 20375-5346

A.K. Kinkead  
Sachs/Freeman Associates, Inc., Landover, MD 20785

R.B. True and R.J. Hansen  
Litton Systems, Inc., Electron Devices Division, San Carlos, CA 94070

### 1 INTRODUCTION

The magnicon is a RF power source with circular beam deflection [1] invented in the 1980's at Budker INP. The first magnicon with the power of 2.6 MW and efficiency of 73% at 915 MHz was built and tested in the pulse of 30  $\mu$ sec in 1985 [2]. The second magnicon was developed as a prototype RF source for a linear collider. In order to achieve power of more than 50 MW at 7 GHz, the tube was built as a frequency doubling amplifier. The following parameters finally were achieved in 1998: power of 55 MW, efficiency of 56% and the gain of 72 dB in a pulse of 1.1  $\mu$ sec [3]. The X-band (11.424 GHz) magnicon [4,5] is being developed jointly by Omega-P, Inc. and NRL as a potential high efficiency RF source for the Next Linear Collider (NLC) project. As for the 7 GHz device, this 11.424 GHz magnicon is a frequency doubling amplifier. The design has been optimized for the parameters of a 500 kV, 210 A, 1  $\mu$ sec modulator with the repetition rate of 10 Hz. This modulator was built for NRL by Titan Beta for a previous project. In this paper, we present a progress report on 11.424 GHz magnicon as well as the results of the gun tests and the beam envelope measurements.

### 2 MAGNICON DESIGN

Fig. 1 shows schematic of the 11.424 GHz magnicon. The tube consists of an electron gun, 6.5 kGs solenoid, RF circuit and collector, insulated from the ground. The 500 kV, 210 A (0.59 microperv) diode gun is designed to obtain the beam area compression of 2500:1 and the beam diameter in the magnet of about 1.5 mm [6]. The complete RF circuit has six 5.712 GHz  $TM_{110}$  deflection cavities (a drive cavity, three gain cavities and two penultimate cavities), followed by an 11.424 GHz  $TM_{210}$  output cavity. The gain and penultimate cavities have inductive measuring probes. In contrast to [3] the two penultimate cavities are not coupled in order to eliminate possible instability [7]. To extract RF power there are

two output apertures at the downstream end of the output cavity, separated by 135°, and ending in WR-90 waveguide.

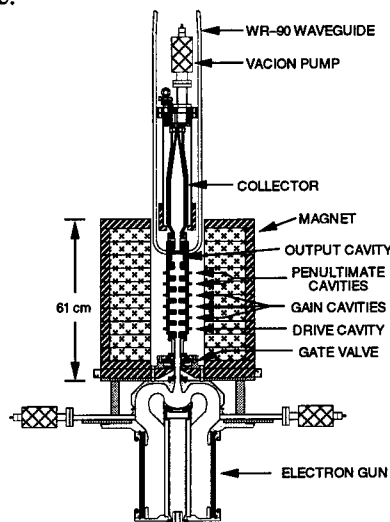


Fig.1 The magnicon schematic.

Special wall perturbations (similar to [3]) to restore quadrupole symmetry are employed. The tube does not have output windows and WR-90 waveguides are connected to the SLAC-type vacuum loads directly. The gun, RF circuit and collector are bakable up to 400° C. The gun is supplied with the gate valve (bakable also) in order to protect the cathode while changing experimental setups: the gun tests, the beam measurements, the tests of the complete tube, etc.. The magnicon design parameters are given in the Table 1. Beam dynamics simulations in the magnicon in both time-dependent and steady-state regimes were performed using computer code [8]. The physical model includes: realistic RF fields in the cavities and DC magnetic fields, finite beam size and multiple reflection of electrons from the collector surface. The code SLANS2 [9] was used for RF field calculations, the codes DEMEOS [10] and SUPERSAM [11] were used for the gun optimization, and the code SAM [12] was

<sup>\*</sup> Permanent address: Budker INP, Novosibirsk 630090, Russia

used for calculation of DC magnetic field and fields in the gun. The optimization of the tube was done taking into account possible instabilities and excitation of different parasitic modes in the cavities.

Table 1

Frequency	11.424	GHz
Power	66	MW
Efficiency	63	%
Pulse duration	1	$\mu$ s
Repetition rate	10	Hz
Gain	62	dB
Drive frequency	5.712	GHz
Drive power	40	W
Beam voltage	500	kV
Beam current	210	A
Microperveance	0.59	
Beam diameter in the magnet	1.5	mm
Beam area compression	2500:1	

The simulations of the beam dynamics in the magnicon were done neglecting space charge effects, which should be small according to estimates. Besides, experiments [3] show excellent agreement with the simulation results even for higher microperveance of 0.88.

### 3 THE GUN TESTS

The electron gun [6] was designed jointly by Omega-P and Litton Electron Devices, and fabricated by Litton. A 75-mm diameter, 30°-half-angle dispenser cathode was used, with a maximum cathode loading of  $\sim 5$  A/cm<sup>2</sup>. The maximum focus-electrode gradient is  $< 190$  kV/cm, which should allow pulse length greater than 3  $\mu$ sec. A unique feature of the gun is use of an electrically isolated focus electrode biased negatively with respect to the cathode [13]. This serves to reduce beam halo and helps to overcome the effect of gun tolerances [6]. The electron gun underwent initial high voltage tests in June 1998. It was immediately determined that the gun microperveance exceeds 1. This meant that the anode-cathode (A-K) gap was substantially smaller than the design value. An assembly error in the gun fabrication was discovered. The gun was cut open and rewelded with an additional spacer to correct the A-K gap back to its design value. However, measurements made on the repaired gun still show excessive current, corresponding to a microperveance of  $\sim 0.64$ . This higher perveance is attributed to more cathode and focusing electrode expansion, than was accounted for during fabrication, based on expansion measurements that were carried out after  $\sim 0.5$  hours of heater operation. The final perveance value (see Fig. 2) is reached after 2-2.5 hours of heater operation. This error in A-K gap leads to a beam optics change, mismatching with magnetic field and beam diameter increase. In order to correct this effect and to make the beam diameter close to its design value, the

magnetic field profile was changed by means of an iron corrector plate in the magnet (see Fig.3).

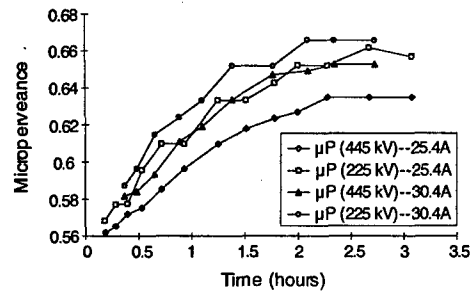


Fig. 2 Perveance vs time for different beam voltage and heater current

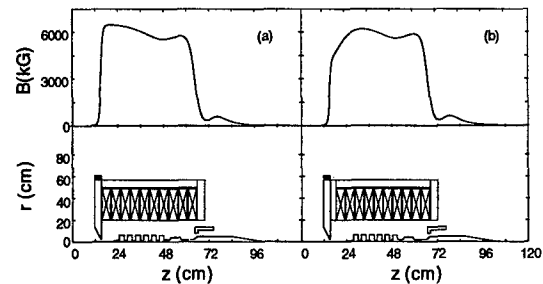


Fig. 3. Original magnetic field profile (a), and magnetic field profile with corrector plate (b).

### 4 THE BEAM MEASUREMENTS

In order to characterize and optimize the electron beam, a high-vacuum bakable beam analyzer was designed and built. It is similar to one reported in [14]. Schematic of the analyzer is shown in Fig. 4. The location of the beam edges is determined by using a set of 8 mm-wide graphite apertures (Fig. 4) that are translated laterally until they

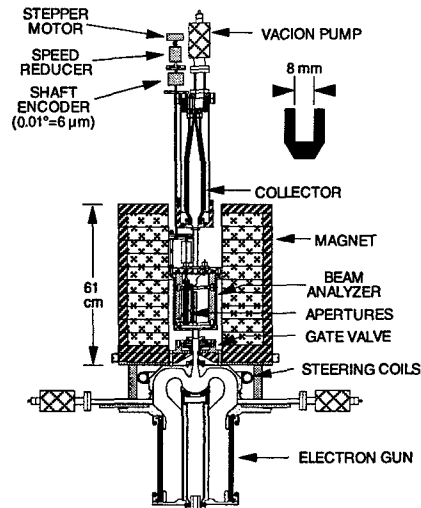


Fig. 4 Beam analyzer

just begin to collect current from the edge of the beam. The analyzer has a rotating cylinder with 12 equally-spaced angular positions. Ten of these positions are used to position graphite apertures at 10-mm intervals along

the axis of the device. The remaining two angular positions support 100-mm-long graphite tubes with 4-mm and 8-mm inner diameters, that can be used to measure total beam interception. In order to measure intercepted current, the rotating cylinder is electrically isolated from the ground. The cylinder is rotated by a stepper-motor. The angular position is measured to  $0.1^\circ$  accuracy using an absolute shaft encoder, corresponding to a displacement of  $\sim 60 \mu\text{m}$ . The beam measurements show that minimal achieved transverse beam size exceeds the design value. Measured beam envelopes for optimal case are shown in the Fig. 5. One can see that the beam is not axially symmetric. The current density on the one side of the beam rises rapidly, while on the other side the current density is more gradual.

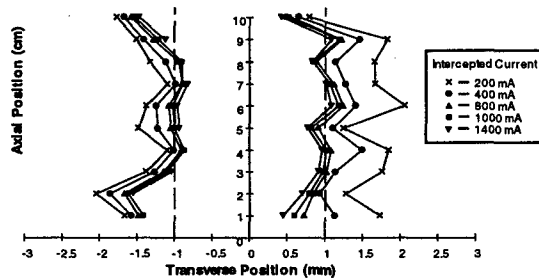


Fig. 5 The measured beam envelopes.

This minimum beam size was achieved for negative focus electrode biasing of 100 V. In the Fig. 6 the beam size dependence on the focus bias voltage is shown. Measurements show an apparent misalignment between cathode and focus electrode: large beam diameter; asymmetric beam edges; increased focus electrode biasing makes this worse; steering coils (Fig. 4) make only small improvements.

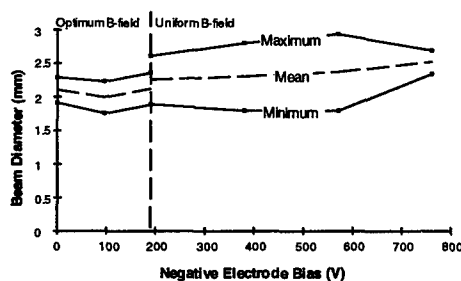


Fig. 6 Beam size vs focus electrode bias.

Additional evidence of this transverse misalignment is shown by measurement of the beam centroid position (Fig. 7). One may see an increase of the beam centroid displacement off the axis when bias voltage is increased.

## 5 SUMMARY

At present the magnicon gun is conditioned and tested up to a voltage of 480 kV, which is considered as an adequate level for reliable operation of the modulator. The measurements of the beam size have been completed. Due to gun manufacturing errors, the transverse beam

size is  $\sim 2.3 \text{ mm}$  instead of design value of  $1.5 \text{ mm}$ . The beam area compression remains high (1100:1) and current density exceeds  $6 \text{ kA/cm}^2$ . The measured increase in beam size leads to some decrease in efficiency. Newly calculated magnicon design parameters for the measured beam are presented in Table 2.

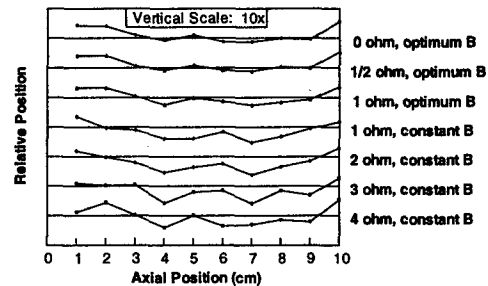


Fig. 7 Beam centroid at 1 A intercepted current. Negative bias voltage equals to  $\sim 200 \text{ V/Ohm}$ .

Table 2

Power	56	MW
Efficiency	55	%
Gain	59	dB
Beam voltage	480	kV
Beam current	210	A

The RF structure fabricated at Budker INP (Novosibirsk) has been delivered and is being prepared for high power tests. It is expected that high power conditioning of the magnicon tube will begin in April, 1999.

## 6 ACKNOWLEDGMENTS

This research was supported by the US DoE SBIR contract DEFG002-95-ER-82045, and DoE and ONR under Interagency Agreement DE-AI02-94ER40861. We are grateful to Dr. G. Caryotakis of SLAC for the contribution of several high-power microwave output components for magnicon.

## REFERENCES

- [1] O.A. Nezhevenko, *IEEE Tr. Plasma Sci.*, **22**, p.756, 1994.
- [2] M.M. Karlner, et al., *NIM*, vol. A269, pp. 459-473, 1988.
- [3] E.V. Kozyrev, et al., *Proc. EPAC 98*, pp. 1897-1899, 1998.
- [4] S.H. Gold, et al., *Phys. Plasmas*, **4**, p. 1900, 1997.
- [5] S.H. Gold, et al., *Proc. PAC 97*, pp. 3153-3155, 1997.
- [6] V.P. Yakovlev, et al., *Proc. PAC 97*, pp. 3186-3188, 1997.
- [7] O.A. Nezhevenko and V.P. Yakovlev, to be published.
- [8] V.P. Yakovlev, et al., *Proc. PAC 95*, pp. 1569-1571, 1995.
- [9] D.G. Myakishev, et al., *Proc. PAC 95*, pp. 2348-2350, 1995.
- [10] R.B. True, "Electron Beam Formation, Focusing and Collection in Microwave Tubes," Academic Press, v.1, p.497, 1995.
- [11] D.G. Myakishev, et al., *Int. J. Mod. Phys.*, **2**, pp. 915-917, 1993.
- [12] M.A. Tiunov, et al., *Proc. 13<sup>th</sup> Int. Conf. High Energy Acc.*, p.387, 1987.
- [13] R.B. True, et al., *IEEE Microwave Power Tube Conf.*, Monterey, CA, May 1996.
- [14] Y.V. Baryshev, et al., *NIM*, vol. A340, pp. 241-258, 1994.

# MULTI-MEGAWATT W-BAND RF SOURCE BASED ON GYROHARMONIC CONVERSION AT THE EIGHTH HARMONIC\*

Changbiao Wang<sup>1</sup>, J. L. Hirshfield<sup>1,2</sup>, and O. A. Nezhevenko<sup>2</sup>

<sup>1</sup>Physics Department, Yale University, New Haven, Connecticut 06520-1820

<sup>2</sup>Omega-P, Inc., 202008 Yale Station, New Haven, Connecticut 06520

## Abstract

A new version of an eighth-harmonic converter is analysed, which consists of a  $TE_{111}$ -mode cavity and an adjacent  $TE_{81}$ -mode cylindrical waveguide. Driven by 40 MW of rf power at 11.424 GHz, a 500 kV, 60.5 A Brillouin beam is accelerated in the cavity and generates up to 13 MW of output power at 91.392 GHz.

## 1 INTRODUCTION

Gyroharmonic conversion as a process for efficient production of high-power radiation has been discussed in a number of publications [1-6] and various approaches have been proposed. In one approach [1], low frequency rf drive power is used to accelerate an electron beam using the  $TE_{11}$  mode in a cylindrical waveguide by means of cyclotron autoresonance acceleration (CARA). The beam then passes through a transition region into a converter section, where it can selectively emit coherent radiation at a harmonic of the drive frequency. To allow the accelerated beam from CARA to fulfill the synchronous and grazing conditions in the converter section, the magnetic field in the transition region is tapered up. The operating harmonic index is specified by proper choice of converter circuit parameters and magnetic field profile. One deficiency in this approach is degradation in beam quality when the beam passes through the transition region where trapping in the strong rf fields is absent.

Another approach to gyroharmonic conversion is co-generation [5,6], which exploits a near-degeneracy for cylindrical waveguide, where nearly equal phase and group velocities prevail for the  $TE_{11}$  mode at frequency  $\omega$  and the  $TE_{72}$  mode at frequency  $7\omega$ . As a result, gyroresonant interactions in the two modes require essentially the same resonant magnetic field profile. Thus efficient transfer of rf energy from the fundamental to the seventh-harmonic can occur in the self-same structure. The harmonic index is selected by the synchronous interaction mechanism itself, instead of through the circuit parameters. The near-degeneracy in cylindrical waveguide referred to above does not exist for an eighth-harmonic  $TE$ -mode interaction.

A new approach to eighth-gyroharmonic conversion is described here. Here the CARA drive section uses a  $TE_{111}$ -mode cavity and the converter section uses a  $TE_{81}$  waveguide where the  $TE_{11}$  mode is cutoff and the resonance with the eighth-harmonic is maintained by a proper choice of waveguide radius. Accordingly, no

transition region is required between the CARA section and the converter section. A cavity is shorter than a waveguide would be for similar beam and rf parameters, and does not require a terminating absorber; both features help in preserving good beam quality.

In this paper, we present preliminary simulation results for the eighth-harmonic converter.

## 2 BASIC PRINCIPLES

Conditions for sustaining resonance for a beam at the end of CARA and the beginning of eighth-harmonic converter section are given by

$$\omega = \frac{\Omega_1}{\gamma_1} + k_{z1}c\beta_{z1}, \text{ and } 8\omega = \frac{8\Omega_2}{\gamma_2} + k_{z2}c\beta_{z2}, \quad (1)$$

where the electron gyrofrequency is  $\Omega = eB_0/m$  with  $e$  the electron charge in magnitude,  $m$  the rest mass, and  $B_0$  the axial magnetic field,  $k_z$  is the axial wavenumber, and the relativistic energy factor is  $\gamma = (1 - \beta_{\perp}^2 - \beta_z^2)^{-1/2}$  with  $\beta_{\perp}$  and  $\beta_z$  the transverse and axial velocities normalized to the vacuum light speed  $c$ . The parameters with subscript 1 are for the end of CARA and 2 for the beginning of converter section. Since the eighth-harmonic output section is directly adjacent to the CARA cavity, the continuity of magnetic field, particle energies, and velocities (that is,  $\Omega_1 = \Omega_2$ ,  $\gamma_1 = \gamma_2$ , and  $\beta_{z1} = \beta_{z2}$ ) requires  $8k_{z1} = k_{z2}$ . From dispersion equations for  $TE_{111}$  and  $TE_{81}$  modes, we obtain

$$\frac{R_2}{R_1} = \frac{j'_{81}}{8j'_{11}} = 0.65498, \quad (2)$$

where  $R_1$  and  $R_2$  are, respectively, the  $TE_{111}$ -cavity radius and  $TE_{81}$ -waveguide radius, and  $j'_{11} = 1.84118$  and  $j'_{81} = 9.64742$  are the Bessel function roots. It can be noted that an equation similar to the above, but for the  $TE_{72}$  mode at frequency  $7\omega$  could be nearly satisfied with  $R_1 = R_2$ , since  $j'_{72}/7 = 1.84748$ ; this fact is responsible for the near-degeneracy mentioned previously that can make seventh-harmonic co-generation in the CARA waveguide an efficient process.

Eq. (2) insures that a beam exiting the  $TE_{111}$ -mode cavity at frequency  $\omega$  remains resonant with the  $TE_{81}$  mode at frequency  $8\omega$ . According to selection rules for axisymmetric beams [2],  $TE_{11}$  mode at the fundamental is the most competitive to the  $TE_{81}$  mode in the converter section. It can be shown that a proper choice of the cavity radius  $R_1$  insures that the  $TE_{11}$  mode at the fundamental (or the  $TE_{72}$  mode at the seventh harmonic) is cutoff. If the fundamental frequency  $f_1$  is 11.424 GHz

\* The work was supported by the U. S. Department of Energy, Divisions of High Energy Physics and Advanced Energy Projects.



( $\lambda_1 = 2.626$  cm), and the eighth-harmonic frequency  $f_8$  is 91.392 GHz ( $\lambda_8 = 0.328$  cm). Taking the cavity radius  $R_1 = 0.798$  cm, from Eq. (2) we have the converter section radius  $R_2 = 0.522$  cm. The cutoff wavelengths of  $TE_{11}$  mode at  $f_1$  and  $TE_{81}$  mode at  $f_8$  are, respectively, 1.783 cm and 0.340 cm, which means that  $TE_{81}$  is a propagating mode while  $TE_{11}$  is cutoff.

### 3 SIMULATION RESULTS

A preliminary simulation study has been performed for this harmonic converter configuration. The design parameters are chosen to accommodate as initial conditions at the CARA entrance a Brillouin beam. The beam radius  $r_b$ , beam current  $I$ , guide magnetic field  $B_0$ , and beam energy factor  $\gamma_0$  are related by [7]

$$r_b = \frac{1}{B_0} \left[ \frac{2m}{\pi \epsilon_0 e c} \frac{I}{(\gamma_0^2 - 1)^{1/2}} \right]^{1/2} \quad (3)$$

For the example that was analyzed, a 500 keV, 60.5 A Brillouin beam with a radius of 0.35 mm is injected along the axis of a  $TE_{111}$  CARA cavity with a radius of 0.798 cm and a length of 4.95 cm. The cavity resonates at 11.424 GHz and is driven with a power of 40 MW; the unloaded cavity quality factor  $Q_0$  is 5000. The  $TE_{81}$ -mode output waveguide has a radius of 0.522 cm and a length of 3.0 cm, following which a gentle up-taper in wall radius accompanies a linear down-taper to zero in guide magnetic field, allowing the beam to be collected on the wall. The simulation parameters are given in Table I.

Table I: Parameters in simulation

Beam energy	500 keV
Beam current	60.5 A
Beam radius	0.35 mm
Input rf power	40 MW
Drive frequency	11.424 GHz
$TE_{111}$ cavity radius $R_1$	0.798 cm
Cavity length $L$	4.95 cm
Unloaded cavity quality factor $Q_0$	5000
Loaded cavity quality factor $Q_L$	100
$TE_{81}$ waveguide radius $R_2$	0.522 cm
$TE_{81}$ waveguide length	3 cm
Final collector radius	0.6 cm
Collector length	10 cm

Fig. 1 shows the rf structure outline and orbits of 8 sample particles in the  $r-z$  plane, and Fig. 2 shows the relativistic energy factors for the particles. In the CARA section (from  $z=0$  to 4.95 cm), the electrons are accelerated and their energies are increased. In the output section including the  $TE_{81}$  waveguide and collector (from  $z=4.95$  to 17.95 cm), the electrons lose energy to  $TE_{81}$  mode at the eighth harmonic and then the wall intercepts all the electrons, because the axial magnetic field is linearly reduced to zero between  $z=7.95$  and 17.95 cm.

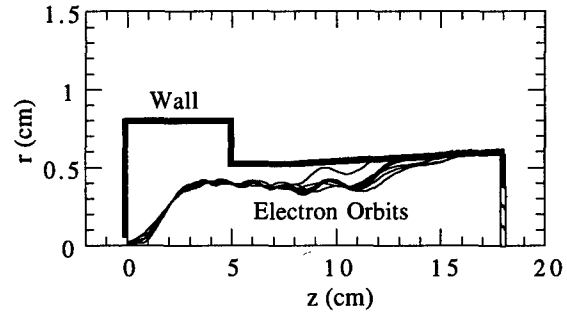


Figure 1: Wall profile for CARA cavity, output waveguide and tapered collector, and orbits throughout device for 8 sample electrons of 512 taken in simulation, including those orbits with extreme excursions.

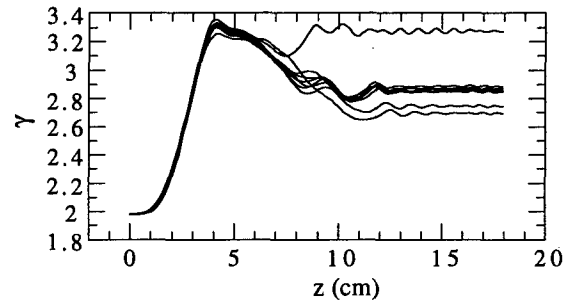


Figure 2: Energy factors for the 8 electrons in Fig. 1.

Fig. 3 shows the rf power levels and axial magnetic field profile along the full 17.95-cm length of the device. With a power of 40 MW at 11.424 GHz, the beam is accelerated initially from 500 keV to 1.15 MeV at the end of the cavity; this corresponds to an acceleration efficiency of 98% and an loaded cavity quality factor of 100; the magnetic field varies from 6.2 to 12.5 kG. In the output section, the eighth-harmonic rf power at 91.392 GHz is gradually increased and then reaches a maximum of 14.9 MW at  $z=11$  cm. Because of wall loss after about  $z=13$  cm where no net energy exchange takes place, the power is slightly reduced with a final output power of 13.1 MW. The magnetic field is resonantly decreased from 11.6 kG ( $z=4.95$  cm) to 10.3 kG ( $z=7.95$  cm), and then linearly to zero ( $z=17.95$  cm).

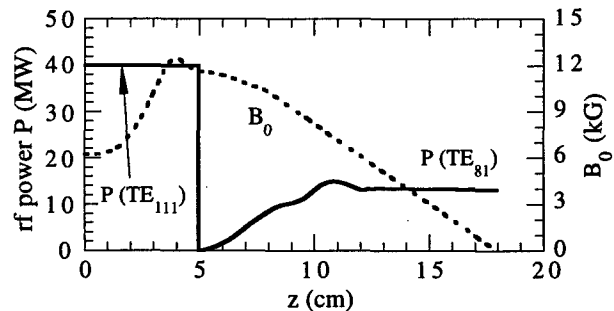


Figure 3: rf power levels in CARA and in output section (solid line), and magnetic field profile (dashed line).

Peak field strengths and ohmic power loss in the structure have been computed as well, and have been found to be well below the accepted levels for carefully built high power structures at X-band and W-band [8]. Results of these computations are shown in Figs. 4 and 5.

Fig. 4 shows the dependence of peak radial rf field strength at the walls in CARA and output section on axial distance. The maximum electric field in the CARA is 0.326 MV/cm and 0.266 MV/cm in the output section, well below the accepted breakdown limits for copper with 1–2  $\mu$  sec pulses [9].

Fig. 5 shows the dependence of peak wall loss power  $P_{\text{wall}}$  and power density  $dP/dA$  on axial distance  $z$  for the output waveguide. Note that for a duty cycle less than  $10^{-3}$ , the maximum average power density to be dissipated at the walls of the output waveguide would be less than 30 W/cm<sup>2</sup>. The cavity must dissipate an average power of 800 W at this duty cycle.

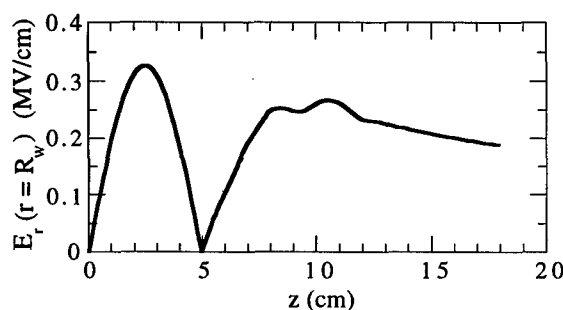


Figure 4: Peak radial rf field strength at the walls in CARA and in the output waveguide.

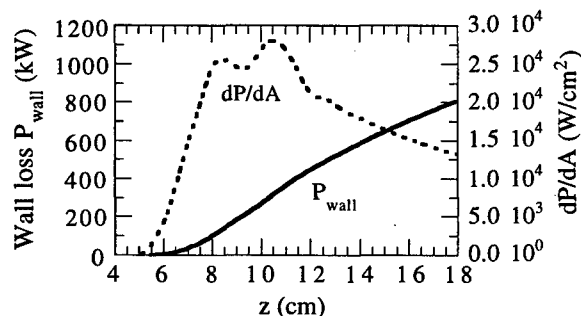


Figure 5: Cumulative peak power (solid line) and power density to be dissipated on the walls of the output waveguide (dashed line).

#### 4 REMARKS

By simulation, we have analyzed an eighth-harmonic converter which uses a  $TE_{111}$ -mode cavity as the drive section and a  $TE_{81}$ -waveguide as the output section, without any required transition region. With an input power of 40 MW at 11.424 GHz and a 0.35-mm radius, 500-kV, 60.5-A Brillouin beam, a net output power of 13 MW at 91.392 GHz is obtained. As beam current and beam radius increase, the efficiency for eighth-harmonic

conversion falls, although the absolute magnitude of output power can increase; likewise, an increase in rf drive power level can be tolerated at higher current, thereby also making higher output power possible.

Mode competition which is not taken into account in the simulation can occur in an overmoded rf structure as used in such a harmonic converter. In the CARA cavity, co-generation of seventh-harmonic power could arise, should it turn out that one of the  $TE_{72m}$  modes of the cavity were to resonate at 79.968 GHz. For a perfect cylinder with  $R_1 = 0.798$  cm,  $L = 4.95$  cm, probably the most dangerous (i. e., nearest) eigenmode is the  $TE_{727}$ , whose eigenfrequency is 80.222 GHz. But if the loaded  $Q$  for the  $TE_{727}$  mode is much larger than  $80.222/(80.222 - 79.968) = 158$ , it should be possible to avoid excitation of the seventh harmonic because of detuning. Mode competition might also pose a problem in the output waveguide, since the  $TE_{61}$  and  $TE_{71}$  modes are not cutoff at the sixth and seventh harmonics. In the extreme, it is possible to operate with a cavity in place of the output waveguide, in order to discriminate against frequencies other than the design frequency of 91.392 GHz. In a preliminary simulation for a  $TE_{811}$ -mode output cavity, whose ohmic  $Q$  for copper cannot be higher than about 5000, and for the beam parameters and 40 MW-11.424 GHz drive level used in Figs. 1-5, a power of 12.06 MW is obtained. But 4.28 MW of this is dissipated in wall losses in the output cavity where  $Q_L = 1774$ ; so the net output is 7.78 MW. These considerations suggest that strategies to avoid serious mode competition, and to operate insofar as possible without undue ohmic wall losses, will probably be the major challenges for further investigations.

#### 5 REFERENCES

- [1] J. L. Hirshfield, C. Wang, and A. K. Ganguly, *IEEE Trans. Plasma Sci.* **PS-24**, 825 (1996).
- [2] A. K. Ganguly and J. L. Hirshfield, *Phys. Rev. E* **47**, 4364 (1993).
- [3] A. J. Balcum, D. B. McDermott, K. C. Leou, F. V. Hartmann, and N. C. Luhmann, Jr., *IEEE Trans. Plasma Sci.*, **PS-22**, 913 (1994).
- [4] H. R. Jory and A. W. Trivelpiece, *J. Appl. Phys.* **39**, 3053 (1968).
- [5] C. Wang, J. L. Hirshfield, and A. K. Ganguly, *Phys. Rev. Lett.* **77**, 3819 (1996).
- [6] J. L. Hirshfield, C. Wang, and A. K. Ganguly, *IEEE Trans. Plasma Sci.*, **PS-26**, 567 (1998).
- [7] M. Reiser, *Theory and Design of Charged Particle Beams* (Wiley, New York, 1994).
- [8] J. W. Wang and G. A. Loew, *SLAC-PUB-7684*, Stanford University (1997).
- [9] D. G. Myakishev, M. A. Tiunov, and V. P. Yakovlev, *Int. J. Mod. Phys. A*, 915 (1993).

## FEL-OSCILLATOR FOR FEEDING OF HIGH-GRADIENT ACCELERATING STRUCTURE\*

C.A.Goldenberg, A.A.Kaminsky, A.K.Kaminsky<sup>#</sup>, S.N.Sedykh, A.P.Sergeev, JINR, Dubna, Russia  
N.S.Ginzburg, N.Yu.Peskov, IAP, Nizhny Novgorod, Russia

### Abstract

Millimeter-wave FEL-oscillator is one of a possible source of RF power for accelerating structures of future linear colliders with high energy gain. JINR-IAP collaboration develops a high-efficiency single-mode FEL-oscillator with a Bragg resonator and reversed guide field. Output power of 48 MW at the frequency of 30.6 GHz with spectrum width 0.25% was registered in recent experiments using induction linac LIU-3000 (0.8 MeV, 200 A, 200 ns).

In this paper we discuss technical solutions for providing of:

- frequency stability with accuracy better than 0.3%;
- precise frequency coincidence of the oscillator and the accelerating structure;
- RF power transportation from the oscillator to the structure.

### 1 INTRODUCTION

Our group studies possible applications of millimeter-wave free-electron laser (FEL) in oscillator configuration as a source of RF-power for high-gradient accelerating structures of two-beam accelerators [1]. The main features of developed oscillator are Bragg resonator and regime with reversed guide field [2], when cyclotron rotation of the beam electrons and their rotation imposed by helical wiggler have opposite directions. Using the electron beam of an induction linac LIU-3000 (0.8 MeV, 200 A, 200 ns) the highest FEL-oscillator's efficiency of 26% was achieved at a frequency of 31 GHz, while the output power was about 35 MW [2,3]. The radiation frequency and spectrum width in a single-mode regime ( $\Delta\lambda / \lambda \leq 0.25\%$ ) are very close to the values required in CLIC project [4]. But some important problems must be solved to create FEL-oscillator usable for such application.

Traditional Bragg resonator [5] consists of two mirrors separated by a smooth waveguide. You can easily have the interaction length large enough for operating of the oscillator. The quality factor of the resonator can be varied both by mirror lengths and by the distance between them.

The resonator has a set of longitudinal eigenmodes with integer number of half-waves between the mirrors and frequencies inside the reflectivity band of the mirrors. The frequency difference between the modes is about 0.5%, so fixing one of them by proper choice of the operating regime is rather difficult taking into account inevitable jitter of beam energy and pulsed wiggler field.

Another problem in experimental realization of accelerating structure feeding is the precise frequency matching between the FEL-oscillator and the structure. Typical Q-factor of the structure is 300, so the value of 0.3% is an upper limit for admissible frequency mismatch. Central frequency of Bragg resonator is determined by the mirror corrugation period (typically one-half of wavelength), hence required precision of the mirror period can be estimated as 0.1% of 5 mm, i.e. 5 mkm. This size tolerance is rather hard to realize. Besides the frequency variation due to the beam loading of the waveguide can break the matching. We think that the best solution of the problem is to provide a possibility of the precise tuning of the FEL-oscillator's radiation frequency.

Residual pressure in the accelerating section must be much lower than in typical induction linac. It forced us to use output windows, differential vacuum systems etc.

Technical solutions of mentioned problems are discussed in this paper.

### 2 RADIATION FREQUENCY STABILIZATION

There exists another type of Bragg resonator also proposed in [5]. It consists of two mirrors of lengths  $L_1$  and  $L_2$  with corrugation phase shift between them. Such resonator has only one mode inside the reflection band of the mirrors (central) and two symmetrical modes just outside the reflection band (side modes). Traditionally this type of the resonator seemed to have insufficient quality factor due to the small volume occupied by the RF field. But the proper choice of the mirrors coupling coefficient allowed us to design a resonator with the optimal Q-factor.

Dynamics of the oscillation build-up in the FEL with a two-mirror Bragg resonator with the corrugation phase shift was studied numerically. Time domain analysis taking into consideration the dispersion properties of the Bragg reflectors was used [6]. It allows us to investigate both the transient process and the stationary regime.

\*Work is supported by grants 97-02-16643 and 97-02-17379 of Russian Foundation for Basic Research.

<sup>#</sup> Email: alikk@sunse.jinr.ru

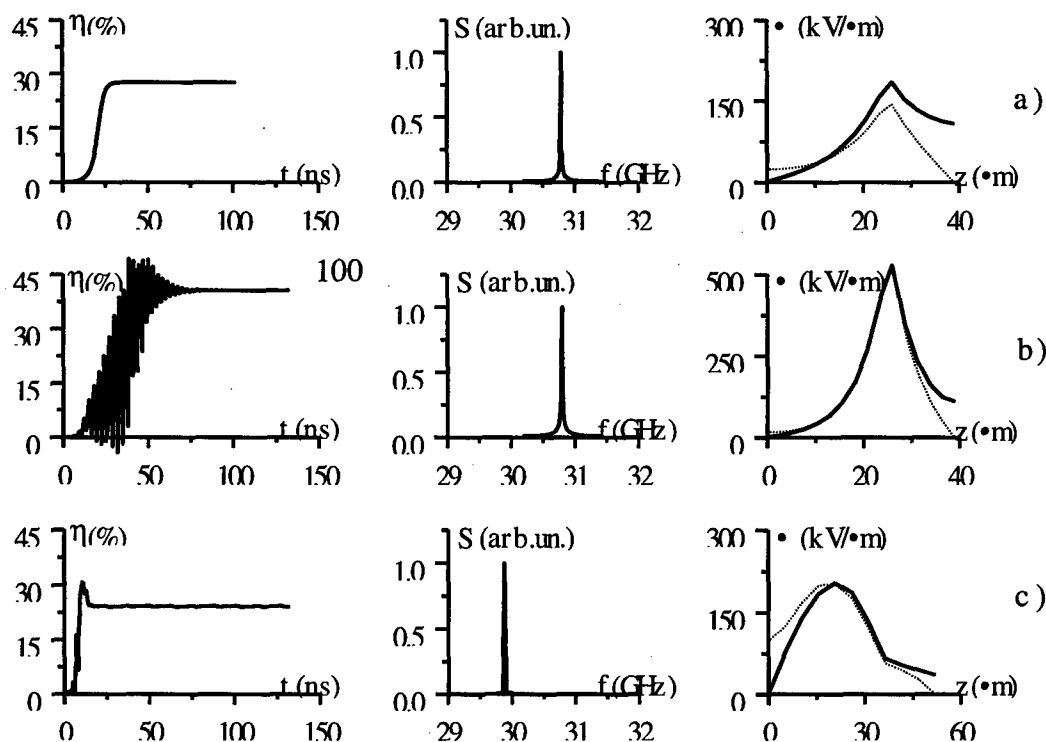


Figure 1. Numerical simulation of the oscillators with the two-mirror Bragg resonator:

Efficiency  $\eta$  versus time, radiation spectrum  $S$  and electric field  $E$  distribution versus length (forward wave - solid line, backward wave - dashed line). Resonator's quality factor grows from a) to c). Fig. c) represents one of the possible operating modes.

Figure 1 presents some results of the simulation. When the Q-factor of the resonator is high enough for central mode but insufficient for side modes, the single-mode oscillation exists both in the transient regime and in the stationary regime at all the possible values of the synchronism detuning (a). If the Q-factor is large enough for the central mode and side modes too, the beating of several modes occurs in transient stage. In stationary regime the nonlinear mode competition results in the single-mode operation. The short effective interaction length (the RF field is high only near the mirrors junction) results in low sensitivity of the FEL-oscillator to the initial electron energy spread, so the oscillator efficiency can be very high (b). For too big Q-factor it is possible to operate at the central mode as well as at one of the side modes depending on the synchronism condition, but the oscillator efficiency decreases (c).

Experimental investigation of the two-mirror resonator in the optimal configuration allowed us to increase the FEL efficiency up to 35% in the single-mode regime [7].

### 3 PRECISE RADIATION FREQUENCY TUNING

Precise frequency tuning of a FEL with the two-mirror Bragg resonator may be based on the fact that the Bragg resonator eigen-frequency changes as we change the distance between the mirrors. Indeed, resonance takes

place when the phase gain of a wave travelling from one mirror to another and back is equal  $2\pi n$ . But unlike "usual" mirrors the phase of a wave reflected from a Bragg mirror also depends on frequency. Let us take a Bragg resonator with the length of a smooth waveguide between the mirrors varying from zero to the corrugation period. Obviously, because each of the mirrors has many periods of corrugation, we can neglect the short section of the smooth waveguide, so changing of the length of the smooth waveguide is equivalent to the changing of corrugation phase of one mirror. At phase shift equal to zero and  $2\pi$  the resonator spectrum must be the same and coincide with the spectrum of a regular Bragg waveguide [5] (fig. 2a).

There are two resonance frequencies outside the reflection band symmetrical to the exact Bragg frequency (29.9 GHz in this figure). Distance between the two "side" frequencies is close to the reflection bandwidth and depends on the depth of the mirror corrugation. When the phase shift increases, the spectrum becomes asymmetric, and the upper "side" eigen-frequency moves inside the reflection band (fig. 2b). At the  $\pi$  shift of phase we have again a well-known type of resonator [5]: the eigen-frequency coincides with the exact Bragg frequency (fig. 2c). Then the eigen-frequency moves to the lower border of the reflection band (fig. 2d). Thus the tuning range is restricted by the reflection bandwidth, for the typical

### Spectra for some phase shifts

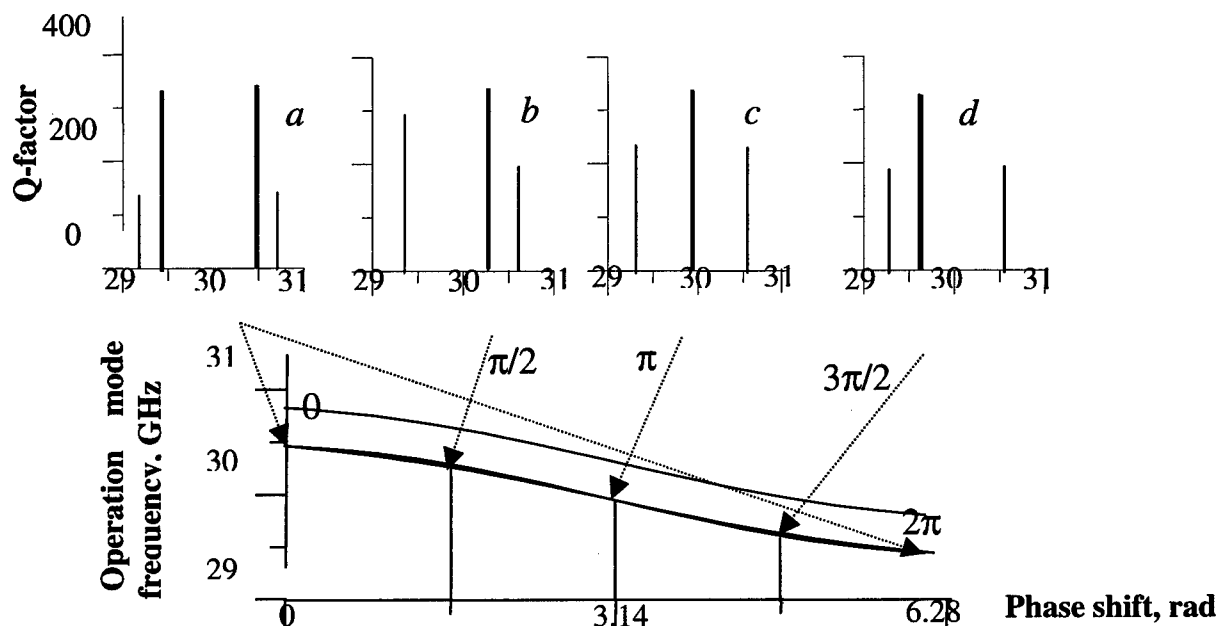


Figure 2. Spectra for some phase shifts for case 3 ( $L_1=28$ ,  $L_2=12$  cm) and operation frequency of tunable Bragg resonators versus shift of corrugation phase for some lengths of mirrors (cm): 1)  $L_1=20$ ,  $L_2=20$ , 2)  $L_1=25$ ,  $L_2=15$ , 3)  $L_1=28$ ,  $L_2=12$ , 4)  $L_1=30$ ,  $L_2=10$ . Period of corrugation = 0.565 cm, waveguide radius = 1.05 cm, corrugation = 0.11/cm, modes H<sub>-F</sub>.

mirrors used in our experiments it is about 0.5 – 1 GHz which equals to (2-3)% of the operation frequency (30 GHz).

## 4 EXPERIMENTAL SETUP

Principal advantage of the FEL is the oversized waveguide in the interaction region. It allows us to use output horn and output window as large as needed for the prevention of the window breakdown. The installation includes also the mode converter of the output radiation and separated vacuum systems for induction linac and high-gradient accelerating structure. This experiment is planned to be performed at the LIU-3000. In recent experiments on the FEL-oscillator the output power of 48 MW at the frequency of 31 GHz with spectrum width 0.25% was registered [7].

## 5 CONCLUSION

Using the two-mirror Bragg resonator with tunable phase shift between mirrors makes it possible to tune output radiation frequency of the FEL-oscillator with accuracy better than 0.3% while the radiation spectrum width do not exceeds 0.3%. The radiation spectrum can be controlled by tunable narrow-band frequency filters using similar resonator with the Q-factor more than 2000. Due to the oversized waveguide the output windows can be as large as needed for preventing the RF-breakdown. So modified FEL-oscillator can be the suitable RF-source for testing the high-gradient accelerating structure at the

frequency about 30 GHz and the output power up to 50 MW.

## 6 REFERENCES

- [1]. G.G. Denisov, V.L. Bratman, A.K. Krasnykh et al., "Problems of autobunching and phase stability for the TBA-driver: calculations and design for a modeling experiment" - Nuclear Instrum. and Meth., A358 (1995) 528-531.
- [2]. A.K. Kaminsky, A.A. Kaminsky, V.P. Sarantsev et al., "High efficiency FEL-oscillator with Bragg Resonator operated in the reversed guide field regime." - Nuclear Instrum. and Meth., A375 (1996) 215-218.
- [3]. N.S. Ginzburg, A.K. Kaminsky, A.A. Kaminsky et al., "Experimental observation of mode competition and single-mode operation in JINR-IAP millimeter-wave FEM oscillator". - Nuclear Instrum. and Meth., A407 (1998) 167-171.
- [4]. CLIC, a 0.5 to 5 TeV e<sup>+</sup>/e<sup>-</sup> Compact Linear Collider CERN/PS/98-009 (LP), Jean-Pierre Delahaye for the CLIC Study Team: 6th European Particle Accelerator Conference (EPAC 98), 22-26.06.98, Stockholm, Sweden and XVII International Conference on High Energy Accelerators, 7-12.09.98, Dubna, Russia
- [5]. V.L. Bratman, G.G. Denisov, N.S. Ginzburg and M.I. Petelin, "FEL's with Bragg reflection resonators: autoresonance masers versus ubitrons". - IEEE J. of Quant. Electr., 1993, vol. QE-19 282-295.
- [6]. N.S. Ginzburg, A.S. Sergeev, N.Yu. Peskov et al., "Mode competition and control in free-electron lasers with one and two dimensional Bragg resonators." - Nuclear Instrum. and Meth., A375 (1996) 202-206.
- [7]. A.V. Elzhov, N.S. Ginzburg\*, I.N. Ivanov et al. "Recent experiments on free-electron maser for two-beam accelerators" - Presented at XVII International Conference on High Energy Accelerators, Dubna, September 7-12, 1998, report c20p.

## STUDY OF RF COMPONENTS FOR JLC 2x2 DLDS

J.Q. Wang, Y.H. Chin, S. Kazakov<sup>†</sup>, S. Yamaguchi and H. Tsutsui  
KEK, 1-1 Oho, Tsukuba-shi, Ibaraki-ken, 305-0801, Japan

### Abstract

We have studied a multi-mode Delay Line Distribution System (DLDS)[1][2] as the RF power distribution system from klystrons to RF structures for linear colliders. In particular, a 2x2 DLDS has been proposed and studied at KEK for Japan Linear Collider(JLC). It has been proved that the 2x2 DLDS is simple, but has good transmission efficiency. We have designed RF components of a basic unit of a DLDS using the High Frequency Structure Simulator (HFSS) code[3]. They include the TE<sub>01</sub> extractor, the TE<sub>11</sub> to TE<sub>01</sub> converter, and the TE<sub>11</sub> to TE<sub>12</sub> converter for TE<sub>12</sub> mode. HFSS calculation of the system, which consists of TE<sub>01</sub> extractor and TE<sub>11</sub> to TE<sub>01</sub> converter, shows that the transmission efficiency of each mode is better than 95%. The components, as well as the system are being studied experimentally. A low power test model for the mode stability experiment in 55m long wave guide in DLDS is also being developed..

### 1 INTRODUCTION

The Delay Line Distribution System (DLDS) invented by KEK has been considered for the compression and distribution of the RF power from klystrons to accelerator structures in the proposed projects of linear colliders, such as the Japan Linear Collider (JLC)[4] and Next Linear Collider (NLC)[5]. In DLDS, the long pulse of combined klystron output is subdivided into a train of shorter pulses and each subpulse is delivered to accelerating structures through a delay line distribution system. This system utilizes the delay of the electron beam in the accelerator structure of the linear collider to reduce the length of the waveguide assembly. A conceptual improvement is proposed by SLAC to further reduce the length of waveguide system by multiplexing several low-loss RF modes in a same waveguide. Thus, the subpulse in the distribution waveguide are carried by different waveguide modes so that they can be extracted at designated locations according to their mode patterns. Based on the SLAC multi-mode DLDS, a 2x2 DLDS [6] is proposed in KEK for JLC. The advantage of 2x2 DLDS is that it's simple and easy to be expended to accommodate combinations of more klystrons, and also it has good transmission efficiency.

In this paper the design of the main RF components of a basic unit of 2x2 DLDS is presented. The main

components include the mode launcher, the TE<sub>01</sub> extractor, and the TE<sub>11</sub> to TE<sub>01</sub> mode converter. A basic system of DLDS that consists of TE<sub>01</sub> mode extractor and the TE<sub>11</sub> to TE<sub>01</sub> mode converter is also studied. For long distance transmission, the low loss TE<sub>12</sub> mode is preferred, so a TE<sub>11</sub> to TE<sub>12</sub> mode converter and the low choked flange needed for connecting between waveguide is also designed. The High Frequency Structure Simulator (HFSS) code, which evaluates in frequency domain with 3D finite element method, is used for design and study.

### 2 BASIC UNIT OF 2x2 DLDS

A test unit is proposed and studied to verify the principle of multi-mode 2x2 DLDS. It includes the mode launcher, the TE<sub>01</sub> extractor and the TE<sub>11</sub> to TE<sub>01</sub> converter. Fig. 1 is the schematic layout of the unit.

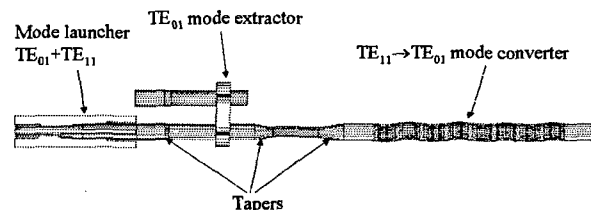


Figure 1: Schematic layout of 2x2 DLDS unit.

#### 2.1 TE<sub>01</sub>-TE<sub>11</sub> Multi-mode Launcher

The TE<sub>01</sub>-TE<sub>11</sub> multi-mode launcher converts the power from four rectangular waveguide feeds to separate modes i.e. TE<sub>01</sub> and TE<sub>11</sub> modes, in a multi-moded circular guide through coupling slots. Here, we adopt the same design as that proposed by Zenghai Li, et al [7].

The original design is modeled with MAFIA [8], so HFSS is used to check the performance of the same geometry as the MAFIA model. But the result got by HFSS is not so good as that predicted by MAFIA: though the power transmission efficiency from the rectangular waveguide to circular waveguide for TE<sub>01</sub> mode in the can be 97.4%, the efficiency for TE<sub>11</sub> mode is only about 90%. We think that the deviation may be caused by the different mesh method between MAFIA and HFSS. By perturbation study [9], we found that it's possible to improve the HFSS result either by increasing the length of the coupling slot on the circular waveguide for 0.35mm or

<sup>†</sup> On leave from Branch of Institute of Nuclear Physics, Protvino, Russia.

adjusting both short positions in the rectangular and circular waveguide for 0.35mm from the original MAFIA geometry. Then the requirement for high efficiency and low surface field can be satisfied [10]. This suggests that the prototype of the launcher should have the short position tunable. Present measurement has confirmed the above feature of the mode launcher.

## 2.2 $TE_{01}$ Mode Extractor

The design  $TE_{01}$  extractor is based on the so call wrap-around converter [2]. When  $TE_{01}$  and  $TE_{11}$  modes pass through the extractor, the  $TE_{01}$  is extracted into another parallel waveguide, while the  $TE_{11}$  mode is not affected. The circular waveguide is tapered down to cutoff the  $TE_{01}$  mode while allowing the  $TE_{11}$  to go through, and the parallel one was shorted at one end to control the direction of  $TE_{01}$  mode transmission. Fig. 2 is the HFSS solid model. The rectangular waveguide is warped around the circular waveguide as shown. There are 6 coupling holes spaced  $60^\circ$  apart in the azimuthal direction around the circular wave guide. The size of the coupling hole is the same as the cross section of the rectangular waveguide. The distance between the center of every two holes is near the wavelength of the  $TE_{10}$  mode in the rectangular waveguide, so that the azimuthal resonant coupling between the two waveguides can be achieved. Thus the  $TE_{01}$  mode in the circular waveguide can be extracted efficiently into the wrap-around rectangular waveguide. Due to reciprocity, the extracted power in the rectangular waveguide can be converted back to  $TE_{01}$  mode in the parallel circular waveguide. The symmetry of the structure prevents the  $TE_{11}$  mode in the circular waveguide being affected.

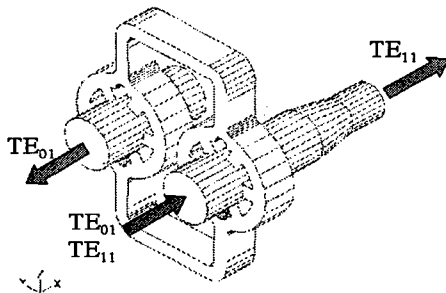


Figure 2: Solid model of  $TE_{01}$  mode extractor.

The geometrical structure is optimized with HFSS [10]. Simulation of present design shows that about 99.4% of the power of  $TE_{01}$  mode can be extracted, 97.2% of  $TE_{11}$  mode goes through without perturbation, while 2.3% converted to  $TM_{01}$  mode. The peak electric surface field at 600MW is around 80MV/m, which locates in the bifurcation area in the rectangular waveguide. Improvement of the design aiming to decrease the peak electric field at high power, and increase the transparency to  $TE_{11}$  mode is underway.

## 2.3 $TE_{11}$ to $TE_{01}$ Mode Converter

In DLDS, the  $TE_{11}$  mode has to be converted back to  $TE_{01}$  mode so that it can be extracted efficiently. The "Serpentine" style structure is adopted [11]. The radius of the circular waveguide keeps constant, but the axis of the propagation is deformed as a sinusoidal. The diameter of the waveguide is 20mm, the amplitude of the sinusoidal deformation is 2.33m, and the one periodical length is 80.4mm. The conversion efficiency can be better than 99.5% when four periods cascaded together. Here, We reproduced the SLAC design [12]. A novel idea has been proposed which can simplify the manufacture, that to cut the waveguide slantingly and then weld them in a right way, as shown in Fig. 3. With the slant angle chosen properly, the  $TE_{11}$  to  $TE_{01}$  conversion efficiency can be better than 99%. That can be a hopeful candidate in 2x2 DLDS scheme. A primary design has been confirmed by HFSS. Efforts are still continuing for further improvement in the performance.

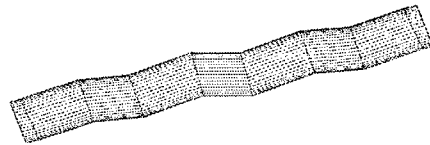


Figure 3: Solid model of  $TE_{11}$  to  $TE_{01}$  mode converter.

## 2.4 Simulation of Test Unit

Due to the computer memory limit, we only simulate the performance of the system consisting of the  $TE_{01}$  extractor, the  $TE_{11}$  to  $TE_{01}$  converter, and the tapers between them. Fig. 4 shows the electric filed pattern propagating in the system.



(a)  $TE_{01}$  mode input from left.



(b)  $TE_{11}$  mode input from left.

Figure 4: Electrical field patterns in the test unit.

The power of  $TE_{01}$  mode is extracted to a parallel waveguide with efficiency better than 96% as shown in Fig. 4(a), while the power of  $TE_{01}$  mode goes through the extractor directly and then is converted to again to  $TE_{01}$  as shown in Fig. 4(b). The transmission efficiency is better than 95%. With the wall loss taken into account, it's expected that the transmission efficiency in DLDS can be better than 90%. All the above components are being manufactured. The low power test will be done soon.

### 3 MODE STABILITY EXPERIMENT

In order to reduce the resistive loss in long distance transmission, the low loss  $TE_{12}$  mode is considered in the circular waveguide. The experiment to test the stability of  $TE_{12}$  mode propagating for long distance i.e. its sensitivity to all kinds of perturbations is being planned. The main purpose is to measure the purity of  $TE_{12}$  mode in a 55m long waveguide whose diameter is 4.75 inches. The experiment needs a  $TE_{11}$  launcher, a  $TE_{11}$ - $TE_{12}$  converter, and the flange to connect waveguides.

#### 3.1 $TE_{11}$ Mode launcher

$TE_{11}$  mode in circular waveguide can be converted from  $TE_{10}$  mode in rectangular waveguide. The converter, whose main part is the smooth taper from the  $22.86 \times 10.16$ mm rectangular waveguide to the  $\phi 50.2$ mm circular waveguide, is designed by HFSS. The conversion efficiency is better than 99.2%.

#### 3.2 $TE_{11}$ to $TE_{12}$ Mode Converter

The structure with rippled diameters [13] has adopted. The radius of the waveguide varies longitudinally as sinusoidal wave. To avoid the conversion between  $TE_{01}$  and  $TE_{02}$ , the diameter of the waveguide is chosen to vary from 50.2mm to 57.8mm. Nine ripples are needed. Optimization is done on the periodic length of one ripple. We found that when the periodic length is 64mm, the converter has the highest efficiency. The whole structure is modeled with HFSS, it's confirmed that more than 99.6% of the power of  $TE_{11}$  mode will be converted to  $TE_{12}$  mode after it goes through the converter.

#### 3.3 Choke flange

The 55 meters long waveguide is composed of 11 5-meter long sections, so choke flanges are needed to connect them in order to avoid the possible distortion to the transmission of  $TE_{12}$  mode. The geometry of the flange is proposed and designed by S. Tantawi. We used HFSS to verify its performance and tolerance to the manufacture errors. The transmission efficiency of  $TE_{12}$  mode is better than 99.9%, and the tolerance is acceptable to manufacture. The solid model of flange used in HFSS is shown as Fig 5.

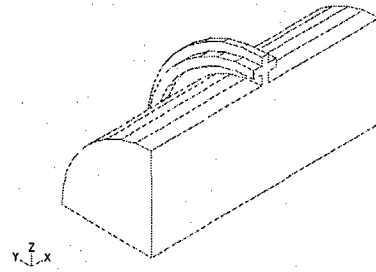


Figure 5: 1/4 solid model of the choke flange.

### 4 CONCLUSION

The main components have been designed using HFSS code. According to HFSS result, the power transmission efficiency in the components can at least meet the requirement of DLDS at low power, so the DLDS principle can work. A low power test facility is being setup in KEK, and the components are being manufactured. The performance of the components as well as the principle of the DLDS will be tested experimentally in near future. Meantime, the experiment to study the mode stability after long distance microwave transmission in DLDS is being developed. Improvement on the design of components of DLDS for high power test, or practical use is continuing.

### 5 ACKNOWLEDGEMENT

The author would like to thank Dr. S.G. Tantawi, Dr. Zenghai Li for their kind help. The author, J.Q. Wang, is invited by the Japan Society for the Promotion of Science (JSPS) under the postdoctoral fellowship program.

### 6 REFERENCES

- [1] H. Mizuno and Y. Otake, "A New RF Power Distribution System for X Band Linac Equivalent to an RF Pulse Compression Scheme of Factor 2<sup>n</sup>", LINAC94 Proceedings.
- [2] S.G. Tantawi, et al., "A Multi-Moded RF Delay Line Distribution System for the Next Linear Collider (NLC)", EPAC98
- [3] HP High-Frequency Structure Simulator 5.0 User's Reference, Sept, 1997, Hewlett-packard.
- [4] JLC Design Study Group, "JLC Design Study", KEK Report 97-1, 1997.
- [5] The NLC Design Group, "Zeroth-order Design Report for the Next Linear Collider, SLAC Report 474, 1996.
- [6] Y.H. Chin et al, LCC-005, <http://lcdev.kek.jp/JLC/ISG/ISG2.html>.
- [7] Zenghai Li, et al., "Mode Launcher Design for the Multi-moded DLDS", *ibid*.
- [8] MAFIA User's Guide Version 3.20, CST GmbH, Darmstadt, Germany.
- [9] Zenghai Li, private communication.
- [10] J.Q. Wang et al, "Design of 2x2 DLDS RF components for JLC", ICAP'98, Monterey, Sept. 1998.
- [11] Eric Giguet et al, IEEE Trans. On Microwave Theory and Tech. , Vol. 46, No.1, Jan. 1998, p. 1-9.
- [12] S. Tantawi, private communication.
- [13] K. Eppley, et al., "A Four port Launcher for a Multimode DLDS Power Delivery System", EPAC98



## RESPONSE OF THE RF POWER SYSTEM TO OFF-NORMAL CONDITIONS ON APT\*

M. McCarthy\*\*, T. Overett, J. Tooker, General Atomics, San Diego, CA  
M. Lynch, D. Rees, A. Regan, T. Wangler, LANL, Los Alamos, NM

### Abstract

The Accelerator Production of Tritium (APT) plant utilizes a 1700 MeV linear accelerator. The accelerating potential for the 100 mA proton beam is provided by up to (depending on production requirements) 244 one MW klystrons. Control of amplitude and phase at each coupling port provides optimum beam parameters. However, when a fault occurs or operation is required at reduced beam currents ('off-normal conditions'), the Radio Frequency (RF) system must compensate to maintain the cavity field. This paper will describe the projected off-normal conditions and the response of the RF system to accommodate these conditions and minimize downtime.

### 1 INTRODUCTION

There are three distinct sections of the linac with respect to RF power coupling [1]. These are: 1) the Radio Frequency Quadrupole (RFQ), which immediately follows the injector and serves primarily to bunch the beam (6.7MeV). 2) The Coupled Cavity Drift Tube Linac (CCDTL) and Coupled Cavity Linac (CCL) modules, which accelerate the beam in normal conducting (NC) cavities up to 211 MeV. There are eleven of these type modules. Except for the first module, which has only one klystron driving it, the other ten have between three and seven klystrons driving them. The term 'supermodule' has been given to a module with synchronous multiple klystron drives. 3) The cryomodule section, which uses superconducting (SC) cavities, accelerates the beam up to 1700MeV. Under normal operating conditions with 100 mA of beam, the RF power is well matched to the linac cavities and little power is reflected back through the waveguides. However, before achieving normal operating conditions, the cavities must be brought up to full RF accelerating field strength with no beam present. All klystrons are ramped up to their design operating power of 80-90% of maximum. To ameliorate AC power draw on the utility grid, the klystrons are brought up gradually in groups. Because of the nature of accelerator operations, the RF Power Distribution System must have loads sized to handle reflected power under no-beam conditions continuously. With no beam the RFQ reflects 4% (VSWR=1.5) of the incident RF power and similarly, the CCDTL/CCL (VSWR=4) reflects 36%. The

superconducting modules have low loss, very high Q cavities that, without a beam to absorb the incident RF, reflect nearly all power back through the waveguides.

The length of time during linac commissioning or restart conditions that the cavities are sans beam can not be dictated by the RF System. The RF System must be able to absorb this reflected power continuously. Under no-beam conditions most of the reflected RF power travels back to the circulator load in the RFQ and NC sections. This occurs because the reciprocal nature of the waveguide power splitters. It is also a result of the relative reflected phase at the splitter arms being equal to the incident phase. In all of the NC linac sections, the cavities are driven in-phase; thus the reflected power is also in phase. However, in the SC section, the reflected power (~1 MW) is absorbed in both the circulator load and in local splitter loads. The power in each is a function of the phase difference between the cavities in the SC module [2]. The sum of the power dissipated in the loads and dissipated in the linac cavities must equal the incident power from the klystrons.

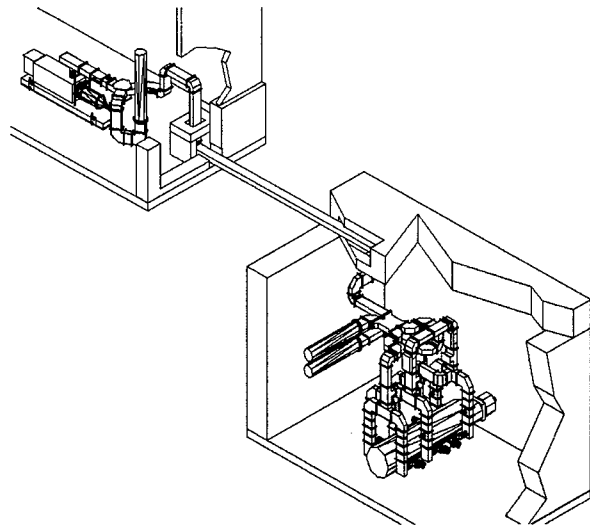


Figure 1: Typical RF power distribution from the klystron gallery to the linac tunnel.

In Figure 1, a pair of cylindrical high power RF water-cooled loads can be seen in the tunnel and one in the klystron gallery. These loads share the total reflected power.

\* Work supported by DOE contract DE-AC04-96AL89607.

\*\* mccartm@gat.com

## 2 OFF-NORMAL DETECTION

Before considering the response to various off normal conditions, the conditions themselves and their method of detection must be defined. Other than commissioning and re-start operations, all other off-normal conditions are the result of a system fault. Typical faults include RF arcs at the waveguide windows or cavities, window failures, RF System failures, high voltage power supply (HVPS) faults and beam loss resulting from injector, vacuum or other malfunctions.

### 2.1 RF Diagnostics

To detect an unexpected off-normal condition, the RF System has several diagnostics which run under the control of a low-level RF (LLRF) sub-system [3]. These diagnostics follow:

1)Fiber-optic (FO) lines are placed near the RF windows at the accelerating structure and in vacuum waveguide to view the flash from an arc. The FO lines carry light pulses back to optical detectors in racks on the mezzanine of the klystron gallery.

2)RF directional couplers are integrated in the waveguide transmission system near the cavity couplers and near the RF splitter loads. These couplers detect forward and reflected RF power levels. The signals are carried back to the mezzanine by standard coax cables for processing by the RF diagnostic system.

3)Air and surface temperature Resistance Temperature Devices (RTD's) or thermocouples. These devices will measure the outer surface of the window frame and the temperature of the cooling air that blows across the RF vacuum windows. These are excellent predictors of impending window failure. Cables are routed back to the klystron gallery to the RF diagnostic system.

### 2.2 Low Level RF

The LLRF system controls many functions, primarily the level of RF fields in the accelerating cavities. The LLRF controls the amplitude and phase of the klystrons by monitoring pick-ups from the linac and directional coupler feedback and reference signals running the length of the linac. It communicates with the Integrated Control System (ICS) to provide the status of the RF Systems to plant operations. The LLRF can issue a fast command to the injector in the event of a fault to terminate beam operations. It also interfaces with the RF diagnostics to evaluate a fault. The LLRF operates one RF power control function in response to a fault and that is the interruption of the RF drive to the klystron. The LLRF evaluates the fault and interrupts the drive for an appropriate amount of time. During the time the drive is off, all of the klystron power is dumped into the klystron's collector. The klystrons have been specified to withstand this power continuously. This feature is essential to the external AC utility grid [4] which would be seriously

affected by 244 MW (worst case) suddenly turning off and on.

## 3 SYSTEM SCENARIOS & RESPONSES

The following are off-normal operating modes and fault conditions and the corresponding RF Power and LLRF responses:

**Start up scenario:** All klystrons are brought up to full CW power (<1 hr.) Reflected power is absorbed in RF loads. The beam duty factor is set very low (< 5 Hz, 100-200  $\mu$ sec) and the steering, focusing, RF phase and amplitudes are optimized. The beam current is then increased to 100 mA at low duty and the phasing is rechecked. Once the accelerator is commissioned the duty factor is brought to CW at 100mA. At this point most of the RF power is absorbed in the linac cavities and beam and little is absorbed in the RF loads. [5]

**Klystron power supply trip (crowbar).** Action: The corresponding klystron shuts down. Beam is turned off to prevent beam spill, which would result from improper accelerating potentials in the cavities. If the klystron is part of a group that drives a supermodule, then all of the klystrons driving the supermodule are shut down to prevent RF induced power from coupling from the cavity to the waveguide. The power supply is reset and the klystron(s) brought back on line. The beam is restarted.

**Waveguide or cavity arc.** Action: The window arc detector sees the arc or the directional coupler of the waveguide associated with the arc detects high reflected power. The LLRF system shuts down the associated klystron(s) (<10  $\mu$ s). The LLRF also sends a signal to the injector to shut down the beam. The LLRF system can be programmed as to the time to restart the klystron drive after an arc and the number of arcs to permit before shutting down the klystron. The klystron is brought back up (~30  $\mu$ sec) and the beam is restored. If the arc reoccurs and the RF is off for more than 500 ms, the RFQ and NC structures will lose resonance. The LLRF system will go into a frequency agile mode and restore the structures to resonance. If the klystron is part of a group that drives a supermodule, then the RF drive to all the klystrons driving the supermodule are shut down to prevent RF induced power from coupling from the cavity to the waveguide and possibly maintaining an arc. The LLRF system restarts the klystron(s) after a predetermined time (~150 ms).

**RF System Failure:** Action: Any RF System failure will interrupt the RF drive to the klystron. The LLRF system shuts down the beam. If the klystron is part of a group that drives a supermodule, then all of the klystrons driving the supermodule are shut down to prevent RF induced power from coupling from the cavity to the waveguide. A waveguide switch is thrown (~5 sec) on the failed system which causes the waveguide to present a 'short' to the cavity aperture. Therefore effectively no cavity power is lost. This switch will be located before the waveguide splits to the couplers and will function for

all four couplers simultaneously. If an RF vacuum valve is employed, we will gain the option to operate with one of the two coupler-pairs with an increase in availability. The beam is restarted and the NC cavity structures retuned. If the klystron was part of a supermodule, the remaining klystrons on that module are brought up at full power to compensate for the lost klystron. If the failed klystron drives a superconducting (SC) module, that cavity is de-tuned (~1 min.) and the linac is returned to service. The succeeding SC modules are phase adjusted to compensate for the lost module. The medium beta and high beta SC modules are divided into four sections. The linac can lose a module in each of these sections and still meet operational requirements. The failed RF station can then be repaired while the linac continues to operate.

**Window Failure:** Thermal or arc sensors indicate impending window failure. Actions: For NC linac: shut down klystron and beam. Close waveguide switch. Restart beam. For SC linac: shut down klystron, detune cavity and restart beam.

**Vacuum System failures, Injector failures, diagnostic failures, etc.:** Failures in these categories may mean

beam downtime in excess of 10 minutes for repair or while redundant systems are implemented. If the failure is judged to be in excess of 2-3 hours, RF Systems may be shut down to conserve power. There are many other possible failure modes. These will be identified and categorized as to the appropriate response. For the RF Power Distribution System, all failure modes need only be categorized into whether they cause a beam interruption and for how long. Table 1 summarizes the off-normal conditions, response, and expected downtime [6].

## 4 CONCLUSION

The RF system responds to off-normal conditions both passively (waveguide loads) and actively (LLRF control of klystron drive). It does so in a manner, which minimizes damage and downtime. The exact response and timing to a particular fault will be refined empirically as experience with this particular accelerator is acquired.

Table 1 The APT RF Power Distribution System under Off-Normal conditions.

Off Normal Condition	RF System Response	Time	LLRF Response	Other Actions	Down time
Start-up scenario	Full power to cavities (no beam)	Hours-days	Monitor phase of beam pulses.		NA
Klystron power supply trip (Crowbar).	Shut down klystron, reset PS, Turn on klystron		Shut down beam, bring up beam after cavities filled.		5 min.
Klystron Waveguide Arc or Cavity Arc	Shut down klystron, Turn on klystron	150 ms	Detect arc. Kill beam. Interrupt klystron drive.		150 ms
Klystron Failure	Shut down klystrons, close waveguide switch.	10 $\mu$ sec	Detect failure. Shut down beam,	Other klystrons in supermodule shut down	30 min.
Impending Window Failure	Shut down associated klystron, close WG switch	5 sec.	Detect thermal aberration or arc.	Other klystrons in supermodule shut down	5 sec.
Leaking Window	Shut down klystron, close WG switch	5 sec.	Shut down beam, close gate valve,	Actuate air and vacuum valves.	5min.-24 hrs.

## 5 REFERENCES

- [1] Overview of the APT RF Power Distribution System, M. McCarthy, et al., LINAC'98.
- [2] Based on cavity phase relationships provided by T. Wangler, LANL, April 8, 1998.
- [3] LEDA LLRF Control System Performance: Model and Operational Experience, A. Regan, et al., PAC'99 Conference.
- [4] Linear Accelerator Impact Study; K. Clark, et al., Sept., 1996, South Carolina Electric & Gas.
- [5] Development of a Commissioning Plan for the APT Linac, M. Schulze, et al., PAC'99 Conference.
- [6] M. Lynch, Analysis of Options for Spare RF Systems for CCDTL-1, LANL memo# LANSCE-5-98-010 Rev 0, Feb. 25, 1998.

# LEDA LLRF Control System Performance: Model and Operational Experience\*

A.H. REGAN, S.I. KWON, Y.M. WANG, Los Alamos National Laboratory, Los Alamos, NM  
C.D. ZIOMEK, ZTEC-Inc, Albuquerque, NM

## Abstract

In modern industrial control, a relay experiment can be used for auto-tuning a PI controller. It gives the ultimate frequency and ultimate gain of the open loop system. Based on the ultimate gain and the ultimate frequency, the PI control parameters, the proportional gain, and the integration time, are determined. A relay experiment can be used to determine the sensitivity of a closed loop system against external disturbances. This paper addresses a method to estimate the sensitivity represented by the gain margin of a closed loop low-level RF (LLRF) control system based on the Matlab/Simulink model of the Low Energy Demonstration Accelerator (LEDA) RFQ. This paper will discuss some of the modeling performed and our operational experience to date.

## 1 INTRODUCTION

This paper discusses a method to measure the amplitude margin of the LLRF control system. The method is based on a relay experiment. Basically a relay experiment uses a square wave as the disturbance input, rather than a sine wave. Because the Fourier transform of a square wave contains a multitude of frequencies, rather than a single one, it is a more efficient way of evaluating the performance of the system. It gives the ultimate frequency and ultimate gain of the open loop system. Based on the ultimate gain and the ultimate frequency, PID controller parameters, i.e., the proportional gain  $K_p$ , the integration time  $T_i$  and the derivative time  $T_d$  are determined [1]. (Design of a similar controller is covered in [6]). LEDA operational experience is also discussed.

## 2 PREDICTED AMPLITUDE MARGINS OF LLRF CONTROL SYSTEM

The relay experiment is also applicable as part of the identification process of the ultimate gain  $K_{cr}$  and the ultimate frequency  $f_{cr}$ , calculated from the stable limit cycles. Based on the measured ultimate gain and ultimate frequency, we can estimate the amplitude margin of the closed loop system. Let  $G_f(i\omega)$  be the loop transfer function of the closed loop system. The ultimate frequency  $f_{cr}$  is the frequency where the phase of the closed loop transfer function  $G_f(i\omega)$  is

$\arg G_f(i2\pi f_{cr}) = -\pi$ . The ultimate gain,  $K_{cr}$  is the amplitude of the loop transfer function at the ultimate frequency  $f_{cr}$ . Then the amplitude margin of the closed loop system is given by

$$A_m = \frac{1}{|G_f(i2\pi f_{cr})|}$$

$$= K_{cr} = \frac{4M}{\pi a}$$

where  $M$  is the amplitude of the ideal relay and  $a$  is the limit cycle amplitude.

Figure 1 shows the Matlab set-up of the relay experiment for analyzing the LLRF control system.

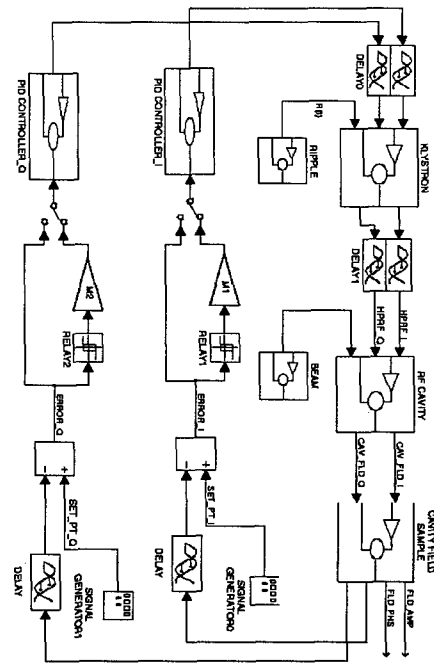


Figure 1. Relay Experiment Model.

Matlab was used to predict the amplitude margin of this model for a given square wave amplitude. Different  $M$  values were used for the In-phase loop, and Quadrature loop. The test results are given below for  $M1=0.035$  (in-phase) and  $M2=0.045$  (quadrature).

\* Work supported by the US Department of Energy.

Table 1. Ultimate frequencies and amplitude margins

$T_{cr}^I$	3.997 $\mu$ s	$T_{cr}^Q$	4.024 $\mu$ s
$f_{crI}$	250.2 kHz	$f_{crQ}$	248.5 kHz
$aI$	0.164	$aQ$	0.029
$A_m^I$	2.712	$A_m^Q$	1.967

$A_m^I$  and  $A_m^Q$  are the amplitude margins of the loop transfer functions  $G_I'(s) = C_I(s)G_I(s)$  and  $G_I^Q(s) = C_Q(s)G_Q(s)$  [1], respectively, where  $G_I'(s)$  represents the transfer function from LLRF\_I to FLD\_I and  $G_I^Q(s)$  represents the transfer function from LLRF\_Q to FLD\_Q. Amplitude margins typically vary from 2.0 to 5.0 [1].

### 3 LEDA OPERATIONS

The LLRF control system has gone through much development and system integration on the LEDA facility these past few months. In addition to providing open loop and closed loop continuous wave (CW) in-phase and quadrature (I/Q) field control performance, it also operates in a pulsed mode. Also, cavity field amplitude-only control is included as a means of conditioning the RFQ. In order to condition the LEDA RFQ, it is necessary to operate in a controlled amplitude-modulated scenario, where a higher RF pulse amplitude on top of a lower DC level is injected into the cavity. Because the RFQ drifts in frequency with the amount of RF power in it, this control must be able to operate at frequencies other than just 350.000 MHz.

#### 3.1 Implementation

As reported previously, the implementation of the LEDA LLRF control system is five LANL-designed VXibus modules [2]. The Field Control Module has two parallel circuitry paths for control: a digital portion (centered around a digital signal processor (DSP)), and an analog portion. Operational requirements for field Amplitude Control are met through the use of the DSP portion only. We measure the in-phase and quadrature portion of the cavity field in the RFQ, calculate the square of its magnitude, and compare this to the square of the setpoints. This method eases the computational time required to perform square roots in the DSP (via a lengthy Taylor series expansion).

#### 3.2 Field Control

The Field Control Module is setup to run in six independent modes as defined by the operator: CW Open Loop, CW Amplitude Control, CW I/Q Control, and their Pulsed counterparts. These are used for Calibration, Conditioning, Turn-on, and Normal Operations. The

following figure indicates the differences in the cavity field for each mode, and what is being controlled.

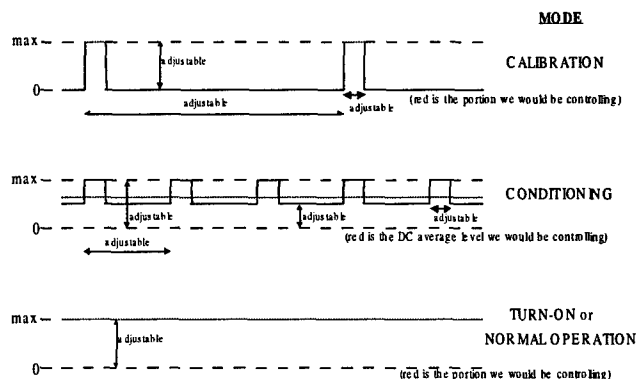


Figure 2. Modes of Operation

Field Amplitude Control is implemented in the FCM in such a way as to provide a broader system response at the expense of the bandwidth of field I/Q control, since the system must operate at whatever frequency the RFQ resonates, typically  $\pm 250$  kHz around 350 MHz. These two control schemes are implemented quite differently and hence, system response differs dramatically. Initially, we intended to have many different digital decimating filter (DDF) coefficient sets to accommodate different system responses. For example, in order to achieve field control at the wide 350 MHz  $\pm 250$  kHz frequencies, we slowed the on-board (DDF) coefficients to a set that had 250 kHz bandwidth, 1  $\mu$ s data rate thereby providing amplitude control only at low bandwidth ( $\sim 10$  Hz). When we implement full I/Q control, the DDF coefficient set was to have a 25 kHz bandwidth, 16  $\mu$ s data rate thereby providing full I/Q control at the full bandwidth ( $\sim 10$  kHz). During LEDA operations, however, we have found that the short time required to switch modes causes a brief transient in klystron drive which in turn trips reflected power monitors and hence, turns things off. Therefore we have changed this operation philosophy to performing Amplitude only, and full I/Q control both at the 25  $\mu$ s data rate, such that the closed loop bandwidth will be on the order of 10-15 kHz.

#### 3.3 Resonance Control

At the same time cavity field Amplitude Control is performed, the LLRF system monitors and tracks the resonance frequency of the cavity [3]. In order to raise the power into the cavity correctly without creating a lot of high reflected power faults, we have found it necessary to start at a low power level, at low duty cycle, allow the resonance control module to find the resonance frequency of the cavity (typically 350.250 MHz) and bring that resonance frequency in to around 350.000 MHz. The cooling water system chills the RFQ such that its resonant frequency swings from 350.350 MHz without RF power to 349.800 MHz with RF power. This implies that the

frequency agile mode of the Resonance Control Module must be able to track and maintain the cavity's resonance condition throughout this range. It does so by calculating the error of the transmitted equation given below

$$\text{Im}(Y_C) = 0.2 [I_T \cdot Q_F - I_F \cdot Q_T] / [(I_F + I_R)^2 + (Q_F + Q_R)^2]$$

where  $Y_C$  is the cavity admittance,  $I_F$  and  $Q_F$  are the in-phase and quadrature components of the forward signal, and  $I_T$  and  $Q_T$  are the in-phase and quadrature components of the transmitted signal in the cavity, and keeping it zero through a proportional integral algorithm. Reference 4 discusses this thoroughly. Implementing this function on the actual RFQ has not been trivial.

Because the frequency shifting is implemented digitally, there is a discrete 90° phase shift which occurs between the positive and negative side of 350.000 MHz. This phase reversal is enough to cause a high reflected power spike which momentarily trips off the klystron. In order to minimize the occurrence of this phase jump, we have implemented a programmable "deadband zone" around 350.000 MHz. Now as the module tracks the RFQ resonant frequency in towards 350.000 MHz from the

outer "RFQ off-resonance" extremes, it enters a frequency deadband where it automatically switches to the 350.000 MHz master oscillator and allows just the water control system [5] to keep the RFQ on resonance. Should the RFQ drift out of this region, we then automatically switch back to frequency tracking. To minimize the number of phase jumps, we have also built in some hysteresis into this deadband zone such that we switch into it at  $\pm 0.5$  kHz, but do not switch out of it until  $\pm 8$  kHz.

### 3.4 Software

The software control of the LLRF system can be performed with either LabVIEW or EPICS. Both have been implemented. A typical EPICS field control operating screen is shown below. Note that it provides displays of both the analog and digital history buffers, allowing the user to debug the performance of both sets of control circuitry. Because Amplitude control is performed with the digital portion of the Field Control Module only, the digital history buffer is the only one of real interest. The display below shows the various control parameters which identify the mode and all of its setpoints for field control.

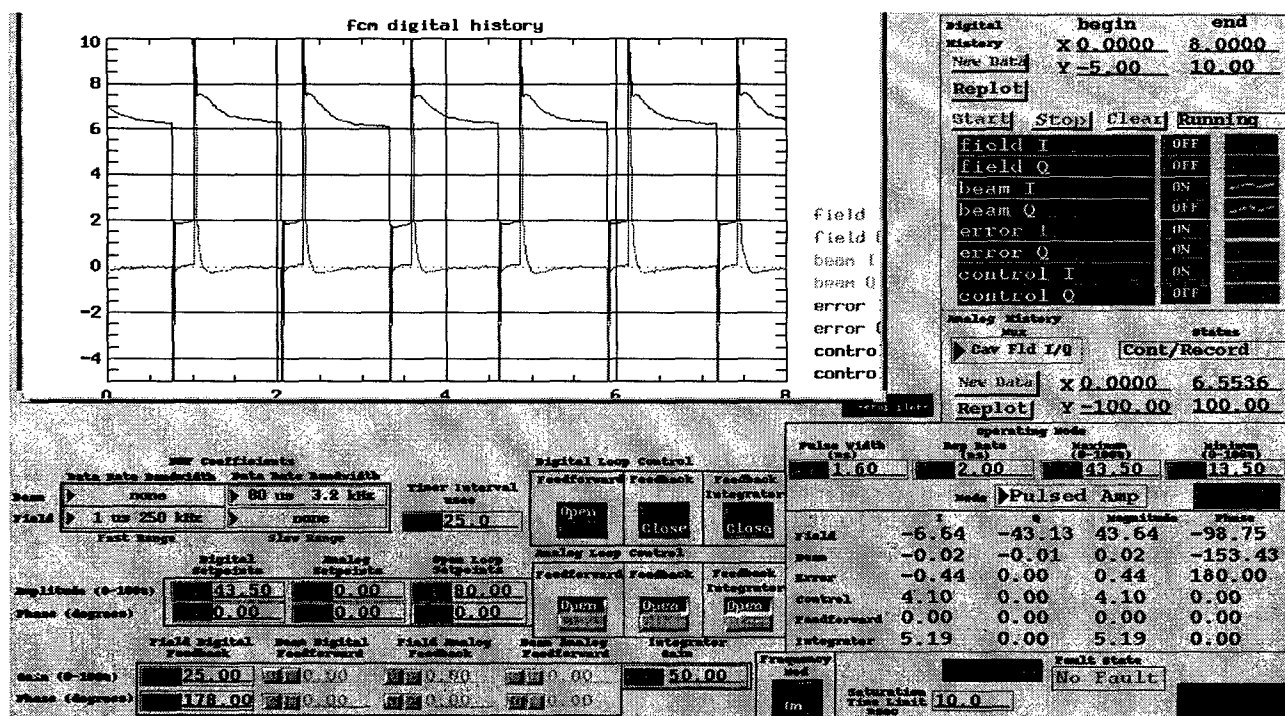


Figure 3. Field Control display

## 4. REFERENCES

- 1- K. J. Astrom and T. Hagglund, *PID controllers: theory, design, and tuning*, 2nd edn. Instrument Society of America, 1995, Research Triangle Park, NC.
- 2- Regan, A., et al, "APT LLRF Control System Functionality and Architecture," *Proceedings of Linear Accelerator Conference 1996*, Geneva, Switzerland, August 1996, pp. 225-227.
- 3- Wang, Y.M., and Regan, A.H. "Algorithms and Implementations of APT Resonant Control System," PAC97.
- 4- Ziomek, C.D. et al, "I/Q Resonance Control Algorithms," Tech Note AOT-5-TN:008, LANL LANSCE-5, 3/4/97.
- 5- Floersch, R. et al. "Resonance Control Cooling System for the APT/ LEDA CCDTL Hot Model," MOP-1 these Proceedings.
- 6- Kwon, S. et al "SNS LLRF Control System model Design," These Proceedings.

# SNS LLRF CONTROL SYSTEM MODEL DESIGN

Sung-il Kwon, Yi-Ming Wang, Amy Regan, LANL, Los Alamos, NM

**Abstract-** This paper addresses part of the design of the LLRF control system for the Spallation Neutron Source. Based on the Matlab/Simulink model of the Klystron and Cavity, considered as a two input two output (TITO) system, we design a PID controller which achieves the tracking of the set point reference. The PID controller design method modifies a relay-feedback-based PID auto-tuner for a single input single output (SISO) system. The original modeling was developed for the Low Energy Demonstration Accelerator and has been modified for the SNS. The advantage of this method is that the only system information required for tuning the PID controller gains is the oscillation gain (critical gain) and the oscillation frequency (critical frequency) from the relay-feedback control of the open loop system. From the oscillation gain (critical gain), we obtain the proportional gain, and from the oscillation frequency (critical frequency), we obtain the integration time and the derivative time by applying some algebraic rules.

## 1 INTRODUCTION

The low level RF(LLRF) control system for Spallation Neutron Source(SNS) is being designed at Los Alamos National Laboratory. The primary function of LLRF control system for SNS is to control RF fields in the accelerating cavity and maintain field stability within  $\pm 1\%$  peak to peak amplitude error and  $1^\circ$  peak to peak phase error.

This paper addresses the problem of the LLRF control system for SNS. As an extension of the case of LEDA, we propose a PID controller. PID controller is the most popular controller for interacting multi-input multi-output systems in industries[1]. The main reason for this is its relatively simple structure which is easy to implement. In the case of actuator or sensor failure, it is relatively easy to stabilize manually. Despite the wide popularity of PID control, the number of applicable tuning methods is extremely limited. In this paper, we use auto-tuning of PID controller, which is a full extension of single-relay auto-tuner to the two input two output system[4]. The system assumptions are that first, the system is open-loop stable, second, the system has the low-pass characteristics. The klystron-cavity system meets this require-

ments.

## 2 KLYSTRON AND CAVITY MODEL

The klystron is the most commonly used linear accelerator RF power source. The klystron used in SNS has two inputs, LLRF\_I and LLRF\_Q and two output HPRF\_I and HPRF\_Q. Let  $u_k = [LLRF\_I \ LLRF\_Q]^T$  and let  $y_k = [HPRF\_I \ HPRF\_Q]^T$ . The klystron in SNS is modelled as

$$\dot{x}_k = A_k x_k + B_k u_k \quad (1)$$

$$y_k = h(x_k, R(t)) \quad (2)$$

where  $A_k \in R^{2 \times 2}$ ,  $B_k \in R^{2 \times 2}$ ,  $x_k \in R^2$ .  $h(x_k, R(t)) \in C^2$  is a continuous, nonlinear function vector of state  $x_k$  and the high voltage power supply(HVPS) ripple  $R(t)$ . The details of the klystron model is given in [6].

The RF cavity can be expressed in the state space form.

$$\dot{x}_c = A_c x_c + B_{c1} u_{c1} + B_{c2} u_{c2} \quad (3)$$

$$y_c = C_c x_c \quad (4)$$

where  $u_{c1} = [HPRF\_I \ HPRF\_Q]^T$ ,  $u_{c2} = [BEAM\_I \ BEAM\_Q]^T$ ,  $y_c = [CAV\_FLD\_I \ CAV\_FLD\_Q]^T$ ,  $A_c \in R^{2 \times 2}$ ,  $B_{c1} \in R^{2 \times 2}$ ,  $B_{c2} \in R^{2 \times 2}$ ,  $C_c \in R^{2 \times 2}$ , and  $x_c \in R^2$ . From the perspective of cavity, beam can be treated as an external disturbance for control purpose. Also, FLD\_I and FLD\_Q of sensor system are given by

$$\begin{bmatrix} FLD\_I \\ FLD\_Q \end{bmatrix} = FA \cdot \begin{bmatrix} \cos(GD) & -\sin(GD) \\ \sin(GD) & \cos(GD) \end{bmatrix} y_c \quad (5)$$

where  $FA$  is an attenuation parameter and  $GD$  is the phase offset of the open loop system. Series connection of the klystron and the cavity yields stable two input two output(TITO) nonlinear system.

## 3 LLRF CONTROL SYSTEM

Consider a TITO system whose transfer function matrix  $P(s)$  is given by

$$P(s) = \begin{bmatrix} P_{11}(s) & P_{12}(s) \\ P_{21}(s) & P_{22}(s) \end{bmatrix} \quad (6)$$

The control matrix  $C(s)$  is given by

$$C(s) = \begin{bmatrix} C_1(s) & 0 \\ 0 & C_2(s) \end{bmatrix} \quad (7)$$

where  $C_i, i = 1, 2$  are

$$C_i(s) = K_p^i \left( 1 + \frac{1}{sT_{Ii}} + \frac{sN_i}{s + \frac{N_i}{T_{Di}}} \right) \quad (8)$$

and PID controller parameters  $K_p^i, T_{Ii}^i, T_{Di}^i, N_i, i = 1, 2$  are tuned by applying relay experiments.

Figure 1 shows the auto-tuning system for LLRF control system. STEAD1 and STEAD2 and two constant inputs are used for obtaining the steady state gain  $P(0)$ . RELAY1 and RELAY2 are used for obtaining the critical gains and the critical frequencies.

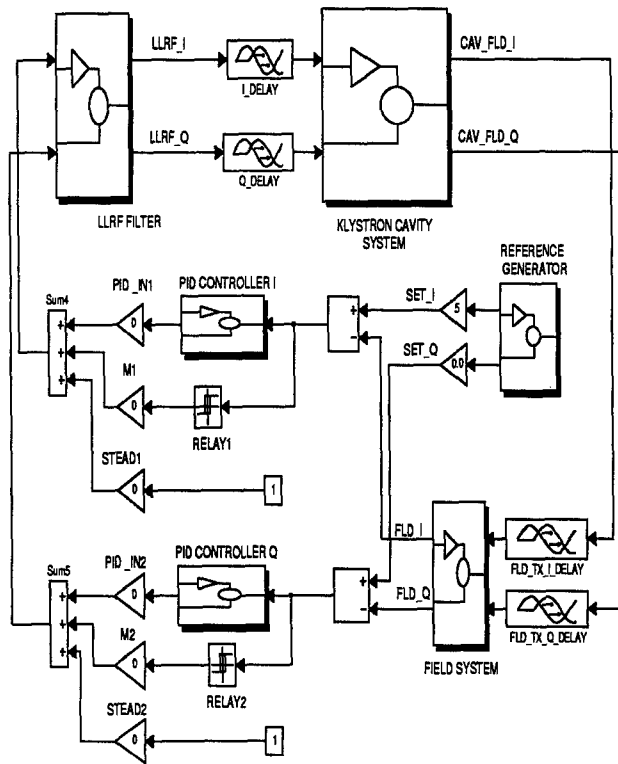


Figure 1. TITO LLRF decentralized relay system

In order to obtain the steady state gain  $P(0)$ , we disconnect unspecified PID controllers, two relays, RELAY1 and RELAY2. First, set the amplifier gain STEAD1 and reset amplifier gain STEAD2 and measure data FLD\_I and FLD\_Q. Second, set the amplifier gain STEAD2 and reset amplifier gain STEAD1 and measure data FLD\_I and FLD\_Q. From output data, we obtain the steady state gain  $P(0)$  given by

$$P(0) = \begin{bmatrix} \overline{FLD_I^1} & \overline{FLD_I^2} \\ \overline{FLD_Q^1} & \overline{FLD_Q^2} \end{bmatrix} \quad (9)$$

where the superscripts indicate the simulation number and *overline* represents the steady state values of the outputs.

The next stage of simulations is obtaining the critical points of the system. In order to get the critical points, first, reset the amplifier gains STEAD1 and STEAD2 and connect RELAY1 and RELAY2. When the magnitudes of the relays are varying, the identified critical points move along the stability limits.

When the general describing function assumptions[3] are met, a good approximation of a critical point is given by

$$K_{icr} = \frac{4M_i}{\pi a_i} \quad (10)$$

$$w_{icr} = \frac{2\pi}{T_{icr}}, \quad i = 1, 2. \quad (11)$$

where  $M_i$  is the amplitude of the ideal relay and  $a_i$  is the limit cycle amplitude. The critical frequency  $w_{icr}$  is calculated from the limit cycle time period which is determined by measuring the time between zero-crossings and the amplitude of oscillation is determined by measuring peak-to-peak value.

Then the desired critical point weighting  $C_d$  which is defined by  $C_d = K_{2cr}|P_{22}(0)|/K_{1cr}|P_{11}(0)|$  between direct channels is given by

$$\frac{M_1}{M_2} = \frac{1}{C_d} \frac{a_1}{a_2} \left| \frac{P_{22}(0)}{P_{11}(0)} \right|. \quad (12)$$

The final stage is to tune the PID controller gains based on the critical points. A simple way is to choose a proportional gain with a rule

$$K_p^i = \frac{K_{icr}}{A_m^i}, \quad i = 1, 2 \quad (13)$$

where  $A_m^i, i = 1, 2$  are the desired amplitude margins. In order to determine the integration time and the derivative time, we introduce a design parameter  $\alpha_i, i = 1, 2$ . Based on  $\alpha_i$ , we set  $T_{Ii}^i, T_{Di}^i, i = 1, 2$  as

$$T_{Ii}^i = \alpha_i \frac{\pi}{w_{icr}}, \quad (14)$$

$$T_{Di}^i = \frac{1}{w_{icr}^2 T_{Ii}^i}, \quad i = 1, 2. \quad (15)$$

Varying  $\alpha_i, i = 1, 2$  within bounded sets, we can obtain  $T_{Ii}^i$  and  $T_{Di}^i, i = 1, 2$ .

## 4 $H_\infty$ CONTROL

PID controllers yields good performance and robustness when the system perturbation is small. However, real world is different. It is apparent that the real klystron-cavity system has unmodelled dynamics, disturbances, sensor noises, electrical circuitry noises, which must be included in the model. For disturbances, we consider beam noise in beam system and high voltage power supply(HVPS) ripple in the klystron. Simulations[2] show that the effect of HVPS



ripple is much more significant. For modelling uncertainties, we have to consider the ripple in frequency response and beam loading effect of the multi-pole klystron, and also we have to consider other modes in multi-cavities. These disturbances and model uncertainties affect the performance and stability of LLRF control system. When the uncertainties and the disturbances are small, then simple PID controllers with good stability margin can guarantee stability and performance of the LLRF control system. However, the real situation is not so positive. Simulation shows that 3% HVPS ripple degrades the LLRF control system performance significantly (phase error is serious). A remedy for this is an approach of  $H_\infty$  controller. Modelling uncertainties, disturbances, noises, and desired performance specifications are characterized by weighting filters. Weighting filters are augmented to the nominal klystron-cavity system, which yields a generalized system. Then, we design a  $H_\infty$  controller for the generalized system and is implemented for the real klystron-cavity system. We know that klystron is a nonlinear system and so the klystron-cavity system is nonlinear. This is mainly due to power saturation curve of the klystron. In order to capture the nonlinearity, a set of  $H_\infty$  controllers are designed for each operating point and the scheduled controller is applied to the nonlinear klystron-cavity system. This is so called gain scheduling. When the operation range is small, then we can design one (robust)  $H_\infty$  controller and apply the controller to the nonlinear klystron-cavity system. We design a  $H_\infty$  controller having the property of gain scheduling, construct LLRF control system, and compare its performance with PID controller designed in previous sections. We assume that beam noise, sensor noise, and model uncertainty are ignorable and investigate HVPS ripple rejection (reduction). Figure 2 shows the LLRF control system with  $H_\infty$  gain scheduling controller[2] and Figure 3 shows simulation results of open loop system, LLRF control system with PID controller, and with  $H_\infty$  gain scheduling controller.

## 5 REFERENCES

- [1] K. J. Astrom and T. Hagglund, *PID controllers: theory, design, and tuning*, 2nd edn. Instrument Society of America, 1995, Research Triangle Park, NC.
- [2] Sung-II Kwon, "Velocity Algorithm based on  $H_\infty$  control for SN," *preprint*, LANSCE-5, RF Technology Group, LANL, 1999.
- [3] I. J. Nagrath and M. Gopal, *Control systems engineering*, 2nd edition, John Wiley and Sons, Inc., New York, 1982.
- [4] Z. J. Palmor, Y. Halevi, and N. Krasney, "Automatic tuning of decentralized PID controllers for TITO processes," *Automatica*, vol. 31, pp. 1001-1010, 1995.
- [5] J. G. Ziegler and N. B. Nichols, "Optimum settings for automatic controllers," *Trans. ASME*, Vol. 64, pp. 759-768, 1942.

- [6] C. Ziomek and A. Regan, "Simplification of Matrixx Model: Preliminary LLRF System Design" *Technical Note*, AOT-5-TN:001, RF Technology Group, AOT Division, LANL, 1996.

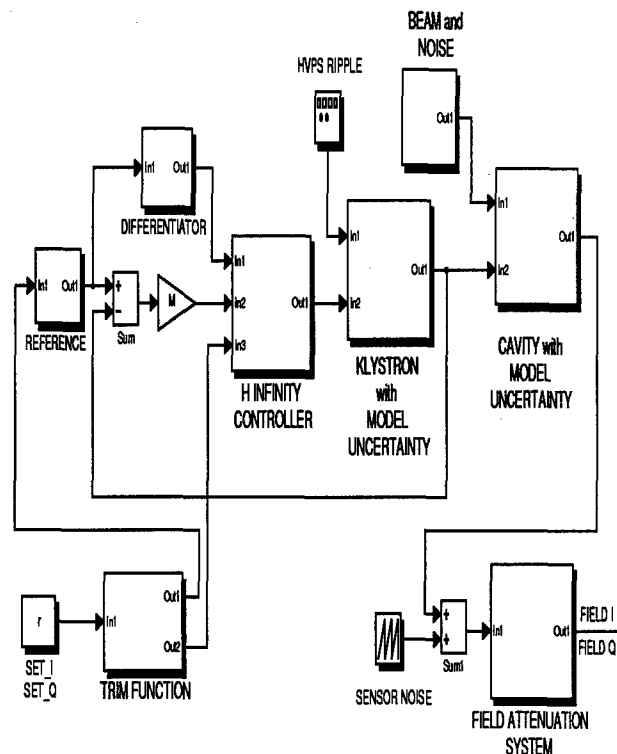


Figure 2. LLRF control system with gain scheduled  $H_\infty$  Controller.

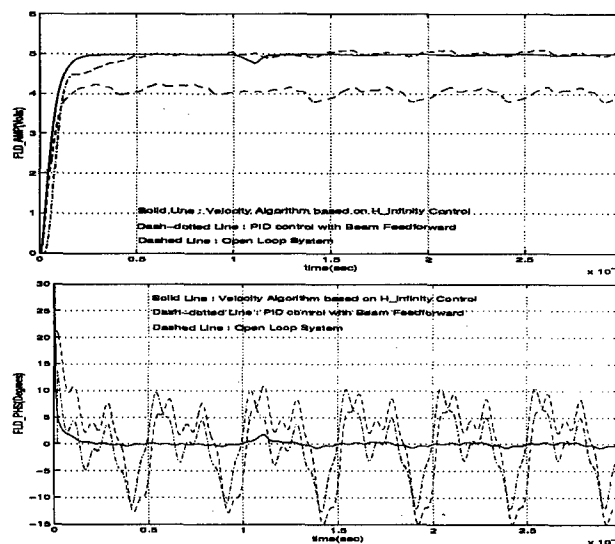


Figure 3. PID and  $H_\infty$  Control System Responses with 3.0% HVPS ripple. Phase shift in klystron due to HVPS ripple is assumed to be  $11.5^\circ$ .

# DIGITAL LLRF CONTROL SYSTEM DESIGN AND IMPLEMENTATION FOR APT SUPERCONDUCTING CAVITIES\*

Yi-Ming Wang, Amy Regan, and Sung-Il Kwon, LANL, Los Alamos, NM  
Chris Ziomek, ZTEK, Albuquerque, NM

## Abstract

With a rapid development of the digital signal processor in recent years, a full digital control system for the superconducting section of APT is designed and implemented by using TI's C6x processor. A digital control system is first modeled and simulated using Matlab/Simulink. Simulation results confirmed the feasibility and flexibility of the digital control system for LLRF feedback system. Due to flexibility of DSP, different control algorithms will be implemented and compared in the system. Particular attention will be paid to the inherent pipeline delay problem associated with a digital control system and its effect and limitation on the overall system performance.

## 1 INTRODUCTION

The advance of digital signal processors and high performance digital data acquisition and conversion devices in the last few years makes it possible to have a full digital LLRF control system design for superconducting cavity of APT due partly to the narrow bandwidth of a high Q cavity. The advantages of the digital system over the analog one include flexibility and versatility provided by digital signal processor. Due to enormous computational power of DSP, it becomes feasible to implement sophisticated control and digital filter algorithms[1]. However, on the other hand, its drawback is added time delay in data conversions and computations associated with digital systems.

The digital control system implemented in the LLRF includes a digital I/Q demodulation circuit, DSP, and D/A converter. In the digital I/Q demodulation circuit, 50MHz IF signal is sampled by a fast 40MHz A/D converter which generates a data string of I, Q, -I, -Q, .... The output of the A/D is fed into a PLD, which separates I and Q components of the data string and applies adequate sign swap. The digital I and Q signals are sent to two digital decimate filters (DDF) whose outputs are digital I/Q with an update rate up to 1MHz. The DSP reads the decimated I/Q signals from DDF and processes with a chosen control algorithm. The output of the DSP is sent to a D/A converter, and the output of the D/A converter is directed to the amplifier control module of the LLRF system. The total time delay through the digital control system, which

includes A/D converter pipeline delay, I/Q decomposition and digital decimate filter delay, DSP I/O time delay, DSP processing delay, and D/A pipeline delay, is in the order of 2-5 $\mu$ s. The time constant of a high Q superconducting cavities is typically in the order of 500-1000 $\mu$ s. Therefore, the phase margin reduced by the digital control system is only at maximum about 3-5 degree which is a very good trade off for the advantages of the digital control system over analog one.

## 2 LLRF SYSTEM

The basic requirements of the LLRF control system for superconducting cavity is specified in terms of amplitude and phase stability of the cavity field in the superconducting cavity. In our case, the control requirements are 1% of amplitude error and 1° of phase error for the cavity field. These requirements are for entire accelerator RF systems, therefore, the individual RF system needs tighter control margin than that. On top of these, the LLRF system must be reliable and robust.

The overall LLRF system for APT's superconducting system is given in Reference [3]. The RF operating frequency is 700MHz. Here we have one LLRF control system for multiple superconducting cavities driving by one klystron. The amplitude and phase control of the cavity field is accomplished by control I/Q components of the klystron driving signal. The multiple cavity fields are vector-summed before fed to the LLRF control system. The RF signals are converted to an IF frequency of 50MHz and sampled at 40MHz sampling rate. The DSP processes the incoming data and sends the corrected I/Q signals to the klystron. In order to reduce the effect of the beam noise on the cavity field, a digital feed forward control is implemented.

In the centre of the digital control system is a TI's TMS320C6201 digital signal processor, which performs maximum of 1,600MIPS with a 200MHz internal clock. An Analog Devices' AD9042, whose maximum sampling rate is 41MSPS with 12bits accuracy, is selected for A/D converter. An additional DSP may be required to perform supervising and communicating with VXibus system. A digital decimate filter (HSPS43220 from Harris) is used between ADC and DSP to synchronise I/O data and to perform additional digital filtering functions. The decimation filter also provides additional enhancement on the signal accuracy and dynamic range.

\* Work is supported by the Department of Energy.

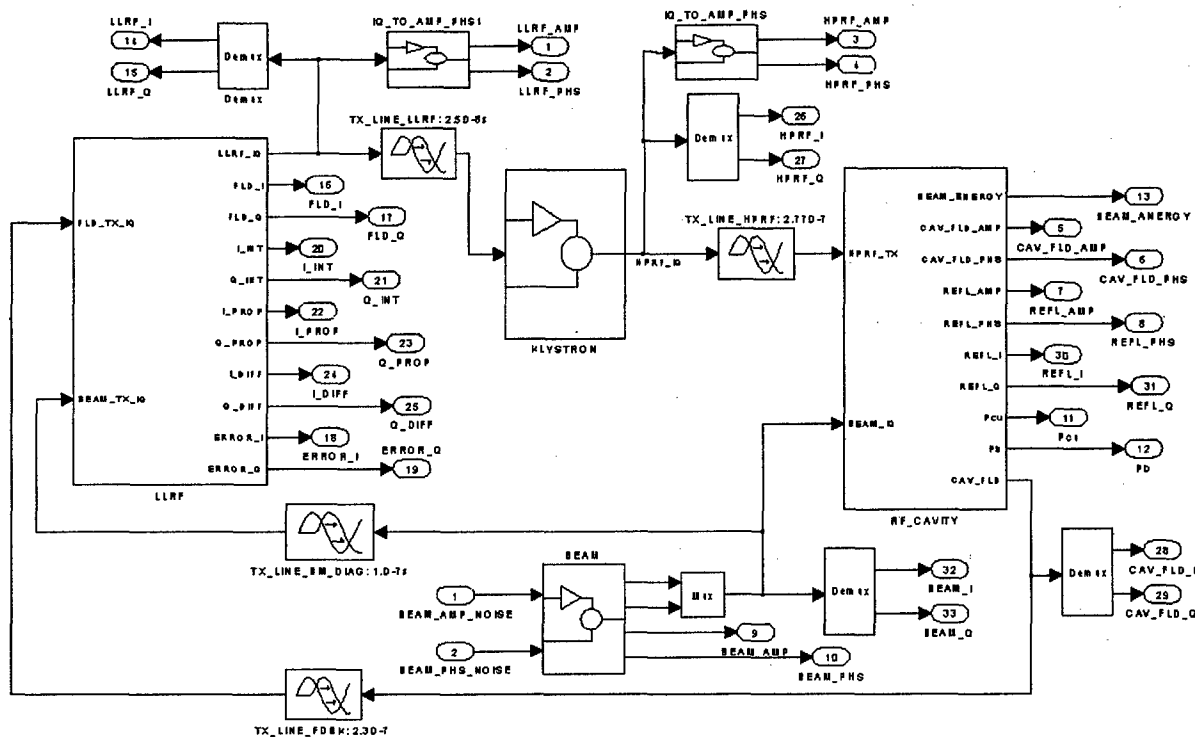


Figure 1. LLRF model

For example, for a digital loop bandwidth of 5kHz, the data should be processed at a rate of 50 KSPS. The filtering rate reduction from 20 MSPS to 50 KSPS provides a 52 dB improvement in the signal accuracy and dynamic range. The system clock from the backplane is 40MHz with a 10MHz synchronise clock. Both A/D and D/A converters are operated at 40MHz clock. Two DDFs are driven by a 20MHz clock generated by I/Q decomposition PLD. The data I/O of the DSP is also uses 40MHz clock. The internal clock of the DSP is 200MHz by multiplying 5 of the system clock. Total processing time will be in the order of 200ns to 1 $\mu$ s, which includes both I/O time and data processing time, depending on the complexity of the control algorithms. A cable delay is about 700ns. Data conversion of the A/D converter is 75ns with 40MHz clock. The time delay over the digital decimate filter is about 40ns when the DDF is operated at 1MHz output rate with filtered bandwidth of 250kHz. D/A conversion time delay is only 25ns. Summing the above together, the total time delay of the digital control system is about 2 $\mu$ s to 3 $\mu$ s which is significantly lower compared to 500 $\mu$ s time constant of the superconducting cavities. Notice that the phase shift caused by the time delay of the digital control system is about 3 degrees at 2 kHz.

### 3 MODEL SIMULATIONS

A Matlab/Simulink model is developed to simulate the system response and perform the stability analysis of the control system. Simulink, a companion program to Matlab, is an interactive system for simulating nonlinear dynamic systems. It can work with linear, nonlinear, continuous-time, discrete-time, multivariable, and multirate system. It is extremely useful for us in both system level and board level design. It helps us to verify system designs and performance, optimise control parameters, perform stability analyses. This model has been applied and proven on a number of LLRF control system designs. The overall model is given in the block diagram form by Figure 1. In this model, only LLRF sub-model is a discrete subsystem, all others are continuous system.

First, in order to verify the time delay effect of the digital control system over the system performance and stability, we simulated both the original system and the system with an added time delay contributed by the digital control system. The result is given in Figure 2 which reveals that the added time delay dose not give a significant effect on overall system performance due to a dominant pole at a lower frequency contributed by the

superconducting cavities. A simple PID controller is used in the above simulation. PID gains are chosen by using the Nonlinear Control Design Blockset to have a desired performance of the cavity field. The klystron is operated at 80% from the maximum power in the saturation curve.

HVPS ripple is evaluated for white noise to determine the worst-case frequencies. For a 1% ripple at 2 kHz caused a 3.0% peak-to-peak amplitude error and a  $1.6^\circ$  peak-to-peak phase error. This indicates a need for local feedback loop around the klystron to correct for HVPS ripple in the superconducting cavities.

An  $H^\infty$  controller is implemented around the klystron to reduce the ripple effect from HVPS. The  $H^\infty$  controller includes an estimator and a PI controller. The control gains are determined by an optimal control algorithm. The simulation results together with the original data without the local control loop are given in Figure 3. The ripple noise is reduced significantly by introduce a local feedback loop around the klystron. In this section, Lorenz-force detuning is not included due to its limited effect on the cw beam operation.

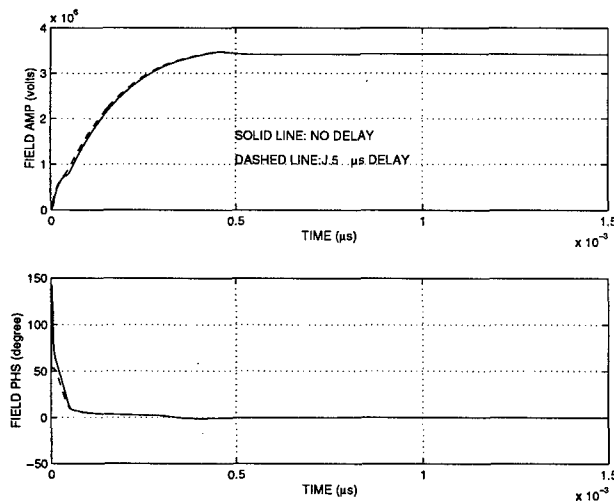


Figure 2. Cavity field response

The effect of the microphonic noise is modelled by a low frequency sinusoidal noise in the superconducting cavities. With a relatively higher gains for PID controller below 150 Hz, we can expect that the microphonic noise could be suppressed effectively with the global PID control loop. The simulation results confirmed the effectiveness of the digital control system on reducing the microphonic noise in the superconducting cavities.

The effect of the beam noise on the cavity field is also analysed using the Matlab/Simulink model of the LLRF control system. The cavity field response of the beam noise is first simulated with a normal digital PID controller without beam feed forward. The low closed-loop bandwidth of the superconducting system places less stringent demands upon the beam forward. Beam forward signals are only required with signal bandwidths of around

10 kHz. With manual gain adjustment, the beam forward is able to reduce the error caused by 1% beam amplitude noise and 1 degree beam phase noise at 2 kHz from 0.40%/0.11° to 0.01%/0.02. This demonstrated that beam forward is both necessary and could be easily implemented for the superconducting system[2].

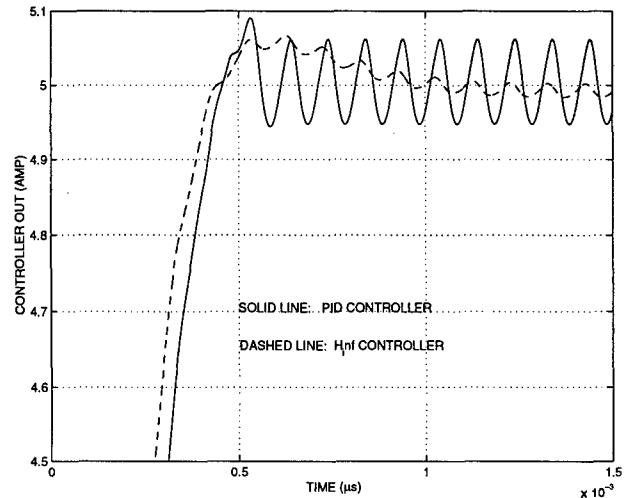


Figure 3. Cavity field with a local control loop.

## 4 CONCLUSIONS

A digital control system design has been developed for the superconducting cavities of APT. Application of the fast TI's C6x DSP together with the high speed and high performance devices for data conversion makes the implementation of the hardware design both feasible and reliable. The simulation results reveal that the time delay associated with the digital control system is acceptable and has no significant effect over phase margin and stability of the overall superconducting system. With the help of beam feed forward and local fast response control loop around the klystron, the cavity field of the superconducting system can be controlled in the range of the design requirements. Further investigation is required to compare the hardware and system performance with the simulated results given in this paper. The comparison between the simulations and experiment data will be conducted as soon as data is available.

## 5 REFERENCES

- [1] Simrock, S. N., I. Altmann, K. Rehlich, and T. Schilcher, *Design of the digital RF control system for the TESLA test facility*, PAC'95, 1995.
- [2] Ziomek, C. and A. Regan, *Superconducting system model*, Private communication, 1996.
- [3] Regan, A., S. I. Kwon, Y.M. Wang, and C. Ziomek, *LEDA LLRF control system performance: model versus measurement*, these proceedings.

# A PERIODICALLY-SWITCHED ODE MODEL FOR N-BUNCH BEAMLOADING IN A STORAGE RING\*

C. Schwartz, A. Nassiri

Argonne National Laboratory, 9700 S. Cass Avenue, Argonne, IL 60439 U.S.A.

## Abstract

A new baseband formulation of the coupled cavity/longitudinal-bunch ODEs is derived. Assuming linearity, a model of the form  $\dot{x}(t) = A(t)x(t) + B(t)u(t)$  arises, where  $A(t)$  and  $B(t)$  are piecewise constant, and periodic with the revolution period  $T_o$ . Such models, known in the control community as (periodic) switched systems, have known (in)stability criteria and control theoretic properties, which can be useful in the analysis and control of multiple bunch beamloading.

## 1 BASEBAND FORMULATION

The term beamloading is to imply here the dynamical interaction between a given cavity resonance and the  $N$ -bunches' longitudinal dynamics. Resonance implies band-limitedness (BL), and a standard tool for the analysis of bandlimited signals and systems (ODEs) is the IQ formalism [1]. The formalism has been applied to beamloading, especially w.r.t. the cavity ODE in [2], [3].

In the way of review and to establish notation: The Fourier transform of the resonance  $Z(j\omega)$ , of order  $M$  in  $j\omega$ , is assumed to be (effectively) zero for  $\omega$  outside its band. Denote the positive part of the band by  $\Omega$ . Then using some carrier frequency  $\omega_c \in \Omega$ , the impulse response kernel of  $Z(j\omega)$  is

$$z(t) = z_I(t) \cos \omega_c t - z_Q(t) \sin \omega_c t. \quad (1)$$

The utility of the IQ formalism lies in the fact that we need only consider the complex envelope, defined as  $\tilde{z}(t) = z_I(t) + jz_Q(t)$ , whose Fourier transform  $\tilde{Z}(j\omega)$  is also of order  $M$  in  $j\omega$ . In particular, the cavity output signal  $v(t)$  to an (AM/PM) sinusoid  $f(t)$  is obtained via  $\tilde{v}(t) = \tilde{f}(t) * \tilde{z}(t)$ .

### 1.1 Bunch Train Signal

Use of the IQ formalism presupposes AM/PM signals of the form (1). It is now shown that the beam current, modeled here as an impulse train, is seen by the resonance approximately as an AM/PM signal about the carrier  $\omega_c$ .

The width of  $\Omega$  determines the minimum number of bunches that need be considered in a time domain analysis; arbitrary gaps in the beam current may make this determination difficult. Here, the number of representative bunches  $N$  is assumed known, chosen through modal analysis or made safely large.

\* Work supported by U.S. Department of Energy, Office of Basic Energy Sciences, under Contract No. W-31-109-ENG-38.

Define  $N_o$  as the number of bunch current "segments": each  $n$ th beam current segment is of duration  $T_b = T_o/N_o$  and has a charge  $q_n, n = 1, \dots, N_o$ .  $q_n$  may be identically zero if and only if the segment represents a gap; if there are no gaps  $N = N_o$ . Henceforth the word bunch shall mean bunch segment.

Let  $\tau_{n,p}$  denote the  $n$ th bunch's deviation in arrival time at the cavity from the nominal, for the  $p$ th arrival. Of course if  $q_n = 0$  then  $\tau_{n,p}$  is devoid of physical meaning; otherwise it is governed by the synchrotron ODE. However, the cavity sees the beam current as a signal, and that is the perspective of this section.

The time-infinite beam current is written, using Wilson's phasor convention [4], as

$$i(t) = - \sum_{n=1}^{N_o} q_n \sum_{p=-\infty}^{\infty} \delta \left( t - \left[ p + \frac{n-1}{N_o} \right] T_o - \tau_{n,p} \right) \quad (2)$$

but, as proven in section 1.2, the following Proposition applies:

**Proposition** The beam current (2) is seen by an  $\Omega$ -BL resonance approximately as

$$i(t) \approx -q(t) \frac{2}{T_b} [\cos \omega_c t + \omega_c \tau(t) \sin \omega_c t]. \quad (3)$$

In (3),  $q(t) = q(t + T_o)$  is a continuous-time interpolation (CTI) of  $q_n, n = 1, \dots, N_o$ , and  $\tau(t)$  is a CTI of  $\tau_{n,p}, \forall n, p$ , as depicted in Figures 1-2 and defined in the next section. Note that  $\tau(t)$  is of use only in discussing the beam current as a signal; when addressing the system aspect (section 1.3 and on),  $\tau(t)$  will be abandoned.

### 1.2 Proof of the Proposition

The Proposition is proved in three steps: interpolation, Taylor series approximation, and application of some Fourier properties.

**Interpolation** [1] The signals  $q(t)$  and  $\tau(t)$  are formally constructed via the interpolation kernel  $S_{T_1}(t) = u(t + T_1/2) - u(t - T_1/2)$ , where  $T_1$  is some period, and  $u(t) = 1$  for  $t \geq 0$ , and is zero otherwise. Define  $\bar{q}_k = q_{-1+k \bmod N_o}$ . Then formally,

$$q(t) = \sum_{k=-\infty}^{\infty} \bar{q}_k S_{T_b}(t - kT_b), \quad (4)$$

$$\tau(t) = \sum_{p=-\infty}^{\infty} \sum_{n=1}^{N_o} \tau_{n,p} S_{T_b} \left( t - \frac{n-1}{N_o} T_o - pT_b \right). \quad (5)$$

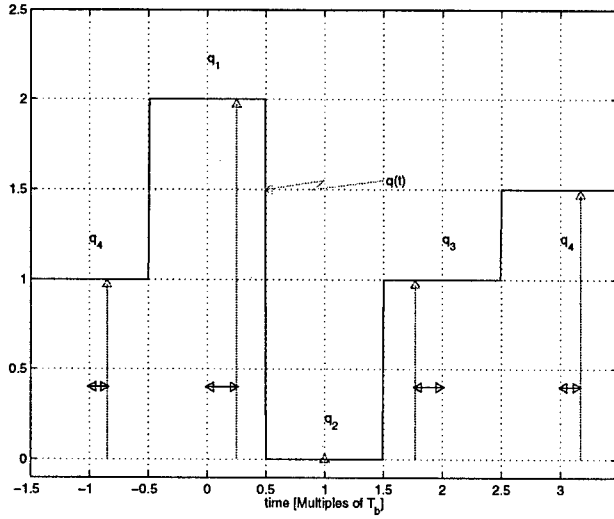


Figure 1:  $i(t)$  and  $q(t)$  for a case where  $N_o = 4, N = 3$  (ordinate units are arbitrary).  $q(t)$  is the “envelope” of  $i(t)$ . The horizontal arrows indicate arrival time deviations and are interpolated sequentially into  $\tau(t)$ .

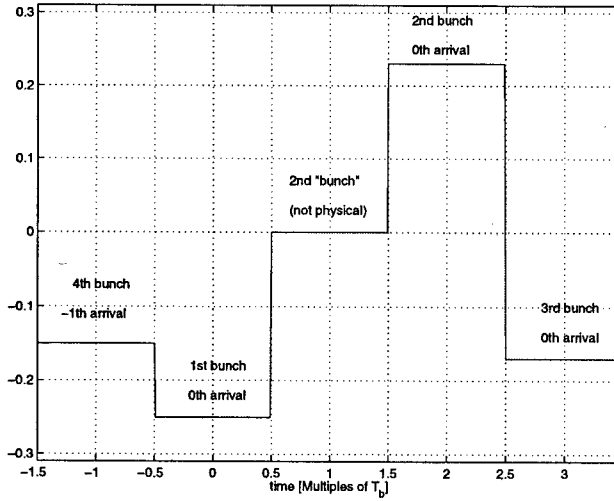


Figure 2:  $\tau(t)$  as interpolated from the  $\tau_{n,p}$  of  $i(t)$  of Figure 1.

Since  $y(t)\delta(t-a) = y(a)\delta(t-a)$ , (2) can be rewritten as

$$i(t) = -q(t) \sum_{k=-\infty}^{\infty} \delta(t - kT_b - \tau(t)). \quad (6)$$

**Taylor Series Approximation** Assuming that  $|\tau(t)|$  of (6) is small for all  $t$ , then the bilinear (first two) terms of the signal's Taylor series expansion approximate the signal [5]. Hence, the RHS of (6) can be rewritten as

$$i(t) \approx -q(t) \sum_{k=-\infty}^{\infty} [\delta(t - kT_b) - \tau(t)\delta'(t - kT_b)]. \quad (7)$$

**Fourier Analysis** Via Fourier series it is known that  $\sum \delta(t - nT_1) = 2/T_1 \sum \cos n\omega_1 t$ , where the sum is for

$n$  over the set of all integers. Applying the transform identity  $\dot{y}(t) \leftrightarrow j\omega Y(\omega)$  yields that  $\sum \delta(t - nT_1) = -2\omega_1/T_1 \sum n \sin n\omega_1 t$ . Thus the RHS of (7) can be written as

$$q(t) \frac{2}{T_b} \left[ \sum_{p=0}^{\infty} \cos p\omega_b t + \tau(t)\omega_b \sum_{p=0}^{\infty} p \sin p\omega_b t \right]. \quad (8)$$

Finally, aside from the considerations mentioned in section 1.1 regarding the choice of  $N$  and hence  $N_o$ , here a further imposition on  $N_o$  is introduced:  $N_o$  is chosen s.t.  $k_o\omega_b \in \Omega$  for one and only one integer  $k_o$ . Choose the carrier frequency according to  $\omega_c = k_o\omega_b$ . Thus by design, no harmonics of  $\omega_b$  fall in the band  $\Omega$ , and it can be shown (e.g., via convolution) that the  $\Omega$ -BL resonance sees only the harmonic  $p = k_o$  of (8), concluding the Proof.

**Remark** The derivation of (3) does not impose any assumptions on the bunch longitudinal motion other than it is of small amplitude, cf. the traditional derivations using modal analysis and Bessel functions [6]. In addition, it allows for gaps in the bunch train.

### 1.3 Beamloading ODEs

It is convenient henceforth to use deviation from nominal values for all variables. Then the cavity portion of the overall beamloading system at baseband can be written as

$$\begin{aligned} \tilde{\Delta}v(t) &= \tilde{z}(t) * [\Delta i_I(t) + j\Delta i_Q(t)] \\ &= \tilde{z}(t) * 2 \left[ \frac{q(t)}{T_b} - I_o + j \frac{\omega_c q(t)\tau(t)}{T_b} \right] \\ &\equiv \Delta v_{II} - \Delta v_{QQ} + j[\Delta v_{IQ} + \Delta v_{QI}], \end{aligned} \quad (9)$$

where  $I_o$  is the DC beam current.

From the perspective of the cavity resonance  $\tau(t)$  is a signal, but in truth it is determined over time by  $N$  synchrotron ODEs. These are incorporated in the overall system by now abandoning the variable  $\tau(t)$ , and instead working with the new continuous *state* variables  $\tau_m(t), m = 1, \dots, N$ , which represent each  $m$ th bunch's arrival time deviation from nominal. The relationship between  $\tau_m(t)$  and (9) will be evident in the following development.

From the perspective of the  $m$ th bunch, the cavity voltage represents a forcing function that is nonzero only during the time intervals  $\mathbf{T}_m$ , during which the bunch couples to, i.e., passes through, the cavity. For example, bunch No. 1 of Figure 1 passes through the cavity during the intervals

$$\mathbf{T}_1 = \bigcup_{p=-\infty}^{\infty} \left[ pT_o - \frac{T_b}{2}, pT_o + \frac{T_b}{2} \right). \quad (10)$$

Otherwise, i.e.,  $\forall t \in \mathbf{T}_m^c$ , where  $\cdot^c$  denotes set complement, the bunch is not coupled to the cavity. The set of all time intervals that correspond to gaps is  $\mathbf{T}_o = \cap \mathbf{T}_m^c$ .

Defining  $\phi_m(t) = \omega_c \tau_m(t)$ , the *linearized* synchrotron ODE can thus be written as

$$\ddot{\phi}_m + 2\alpha\dot{\phi}_m + \omega_s^2\phi_m = \begin{cases} f_c(t) & t \in \mathbf{T}_m \\ 0 & t \in \mathbf{T}_m^c \end{cases}, \quad (11)$$

where  $\alpha$  is the inverse damping time, and  $\omega_s$  is the synchrotron frequency. It can be shown that given linearization, the RHS forcing function is given by  $f_c(t) = \frac{\omega_s^2}{V_c \sin \phi_s} [\Delta v_{II}(t) - \Delta v_{QQ}(t)]$ , where  $V_c$  is the peak cavity voltage, and  $\phi_s$  is the synchronous phase.

**Remark**  $\Delta v_{II}(t)$  is a function of  $q(t)$ , and hence is not a state but a stationary forcing function, not governed by an ODE. Therefore it does not have any bearing on (linearized) stability, see e.g., [7], Theorem 12.6. Thus, the quadrature impulse response of the cavity resonance  $z_Q(t)$  and not  $z_I(t)$  determines linearized beamloading stability, aside from the beam ODEs. Compare the argument proposed in [3] to prove this. Note also that the result is particularly transparent here after having used the phasor reference plane of [4].

## 2 SWITCHED SYSTEM FORMULATION

By merging the cavity (9) and beam (11) system formulations developed above, one arrives at a single ODE of the form  $\dot{x}(t) = A(t)x(t) + B(t)\Delta v_{II}(t)$ : The  $M$  cavity states  $\Delta v_{QQ}^{M-1}(t), \dots, \Delta v_{QQ}(t)$  and the two bunch states  $\phi'_m(t), \phi_m(t)$  for each of the  $N$  bunches are ordered in the column vector  $x$ , where the superscript now denotes derivative order. Thus  $x$  has  $2N + M$  elements. The ODE coefficients are corresponding elements of  $A(t)$  and  $B(t)$ . More specifically, the resulting overall system is of the form

$$\dot{x}(t) = \begin{cases} A_m x(t) + B_m \Delta v_{II}(t) & t \in T_m \\ A_o x(t) & t \in T_o \end{cases} \quad (12)$$

The top part of the RHS conveys that while the  $m$ th bunch passes through the cavity, the beam current [quadrature modulated by the state  $\phi_m(t)$ ] perturbs the cavity. Meanwhile the bunch is perturbed by the cavity state  $\Delta v_{QQ}(t)$ , and by the forcing function  $\Delta v_{II}(t)$ . During the periods corresponding to gaps (bottom of RHS), the cavity and bunches are uncoupled. Thus,  $A_o$  is a  $(2N+M)$  by  $(2N+M)$  block diagonal matrix, and  $A_m$  contains the same block diagonal elements as well as off diagonal coupling terms.  $B_m$  is  $(N+M)$  by 1, and contains only a single nonzero element.

## 3 APPLICATIONS

Given an initial condition  $x_o$ , say at  $t = 0$ , then (12) represents an initial value problem,  $\dot{x}(t) = A(t)x(t)$ ,  $x(0) = x_o$ . Two properties of the system readily lend themselves to application of ODE system theory, see e.g., [7]. First,  $A(t)$  is piecewise constant, or a switched system, which means that the state transition matrix  $\Phi(t, 0)$  for any  $t$  can be computed as the product of matrix exponentials. For example, in the case of Figure 1, starting at  $t = 0$ , the state at  $3.5T_b$  is given by  $e^{T_b A_3} e^{T_b A_2} e^{T_b A_o} e^{0.5T_b A_1} x_o$ . Thus, using the state transition matrix, the state  $x(t)$  for any  $t$  can be computed, see [8].

Second, since  $A(t)$  is  $T_o$  periodic, Floquet Theory can be applied to assess (in)stability:

**Theorem [Floquet]** *The system (12) is stable (unstable) if and only if the magnitudes of the eigenvalues of  $\Phi(T_o, 0)$  are s.t. all are less than unity (at least one is greater than unity).*

A particularly useful application of this criterion is the identification of the cavity higher mode(s) that cause coupled bunch instabilities in a partially filled storage ring [9]: For each cavity mode, a new  $\omega_c$  is determined, and then the eigenvalues of the corresponding  $\Phi(T_o, 0)$  are checked for stability.

A final application (but originally the motivating application) is beamloading control. The authors of [10] note that the now classic optimal state space control theory does not readily apply to multiple bunch beamloading. The switched system formulation, along with some recent control-theoretic results relating to the control of such systems [11], are therefore of particular interest and are currently under study.

## 4 ACKNOWLEDGEMENTS

The authors are most grateful to Dr. K. Harkay for her generous and able assistance with physics issues. Dr. A. H. Haddad, Dever Professor in ECE at Northwestern University, has also greatly assisted in his capacity as Doctoral Advisor to C.S. Finally, the financial support of the Accelerator Systems Division of APS is gratefully acknowledged.

## 5 REFERENCES

- [1] A. Papoulis, *Signal Analysis*, McGraw Hill, (1977).
- [2] S. J. Jachim and B. R. Cheo, "Dynamic Interactions Between RF Sources and LINAC Cavities with Beam Loading," *IEEE Trans. Electron Devices*, October 1991.
- [3] S. Y. Zhang and W. T. Weng, "A New Formulation of Longitudinal Coherent Instabilities," *Proc. 1993 PAC*, (1993).
- [4] P. B. Wilson, "High Energy Electron Linacs: Applications to Storage Ring RF Systems and Linear Colliders," SLAC-2884, (1982).
- [5] A. Papoulis, "Error Analysis in Sampling Theory," *Proc. IEEE*, 54(7), July 1966.
- [6] A. Hofmann, "Beam Instabilities," *CAS-CERN Accelerator School Fifth Advanced Physics Course*, CERN (1993).
- [7] W. J. Rugh, *Linear System Theory*, Prentice Hall, (1996).
- [8] K. L. F. Bane et al., "Compensating the Unequal Bunch Spacing in the NLC Damping Rings," *Proc. Fifth EPAC*, (1996).
- [9] K. Harkay et al., "Compensation of Longitudinal Coupled-Bunch Instability in the APS Storage Ring," *Proc. PAC-97*, pp. 1575, (1997).
- [10] D. Boussard and E. Onillon, "Application of the methods of optimum control theory to the rf system of a circular accelerator," CERN SL 93-09 RFS, 1993.
- [11] J. Ezzine and A. H. Haddad, "Controllability and Observability of Hybrid Systems," *Intl. J. of Control*, 49(6), pp. 2045-2055, June 1989.

# STATUS OF LONGITUDINAL FEEDBACK SYSTEM FOR THE PLS STORAGE RING\*

Yujong Kim, J. Y. Huang, M. Kwon, I. S. Ko<sup>†</sup>, *PAL, POSTECH, Pohang 790-784, Korea*

## Abstract

Originally, the Pohang Light Source (PLS) storage ring was designed to store the beam current up to 400 mA. But owing to the interactions between the HOMs of RF cavities and bunched beams which make the coupled bunch mode instabilities (CBMIs) such as dipole, quadrupole, and sextupole modes, the beam current can be stored up to 200 mA. So, to cure those CBMIs, a longitudinal feedback system (LFS) using parallel digital signal processors is necessary. After having considered the developing cost and the period, it was decided to install the LFS with electronics fabricated by SLAC and a pickup and a kicker designed by the PLS. At present, one aluminum kicker with 4 input/output ports and a nose cone is fabricated for the PLS longitudinal feedback system. With this LFS, it is possible to find the best operating condition for the temperatures of RF cavities and various fill patterns. The programmable LFS is useful for various beam diagnostics as well as for the cure of the CBMIs. Thus, it is also possible to measure the growth and damping rates of the instabilities, the HOM frequencies of RF cavities which generate the CBMIs, bunch-by-bunch current, bunch-by-bunch synchronous phase, and the longitudinal aliased impedances seen by the beam at revolution harmonics.

## 1 INTRODUCTION

To store the beam current up to 400 mA at 2.0 GeV and 250 mA at 2.5 GeV, the fourth RF cavity with 60 kW CW klystron amplifier was added in the PLS storage ring in 1996. But owing to HOMs of RF cavities that make the CBMIs, the stored beam current of the PLS storage ring is about 120 mA at 2.0 GeV. By analyzing the reverse signal of RF cavities and the sidebands of the BPM spectrum, it is found that the most dangerous HOMs of RF cavities are longitudinal  $TM_{011}$  (758 MHz) and  $TM_{013}$  (1707 MHz). To shift the frequencies of two dangerous HOMs, the cooling water temperature control system for the RF cavities was installed during 1997 Summer maintenance period. With the temperature control system, the stored beam current was increased from 120 mA to 200 mA. This means that all dangerous HOMs of the RF cavities can not be damped or avoided by the cooling system. Therefore, an active feedback system for curing the CBMIs is necessary for the PLS storage ring. There various types of LFS running at several accelerators such as PEP-II (SLAC), ALS (LBL), DAΦNE (LNF), KEKB (KEK), etc. In terms of the origin of impedance that generates

the CBMIs, the feedback system can be classified into two kinds; the time domain system and the frequency domain system. The dangerous transverse or longitudinal HOMs of accelerating RF cavities can be cured by the time domain, bunch-by-bunch feedback system. The dangerous longitudinal fundamental mode of accelerating RF cavities and the dangerous transverse resistive wall impedance due to the beam pipe can be cured by the frequency domain feedback system. In case of the time domain feedback system, no pre-knowledge of the dangerous coupled modes is required while the pre-knowledge is required for the frequency domain feedback system. The LFS which have been developed by the collaboration of SLAC, LBL, LNF laboratories is a time domain, bunch-by-bunch feedback system which uses the programmable digital signal processing processors (DSPs). The typical LFS consists of a phase error pickup, digital signal processing units, and a kicker. For the PLS storage ring, one pickup which have already been installed for beam diagnostic purpose will be used as the phase error pickup, and one cavity which have been fabricated by the PLS and domestic manufacturer will be used as the LFS kicker. After having considered the developing cost and period, it is decided that the digital signal processing unit is purchased from SLAC [1].

## 2 LFS FOR THE PLS

The digital signal processing unit for the PLS LFS as shown in Fig. 1 consists of a system oscillator and a DSP farm with a VXI and two VME crates. A VXI controller, a timing module, a front end module, a down sampler module, a hold buffer module, and a back end module are housed in a VXI crate, and a VME controller, five DSP board modules, an interface module are housed in a VME crates.

### 2.1 Phase Error Detection

The longitudinal phase error detection is performed by a reserved BPM. The signals from the BPM are combined and then fed into the stripline comb generator where a coherent tone burst from the BPM signals is generated by a periodic microwave coupler circuit at six harmonic of RF frequency (3000 MHz). The phase error detection is performed by the double balanced mixer (DBM) where the signal from the comb generator is compared with 3000 MHz ( $6 \times f_{RF}$ ) signal from the master oscillator phased locked to the ring. It is possible to obtain a phase processing range of  $\pm 15^\circ$  at the  $f_{RF}$  with a resolution better than  $0.5^\circ$  by choosing the  $6 \times f_{RF}$  as an operating frequency. A low pass filter is used to reduce the noise of DBM output.

\* Work supported by POSCO and MOST, Korea.

<sup>†</sup> Email : isko@postech.ac.kr



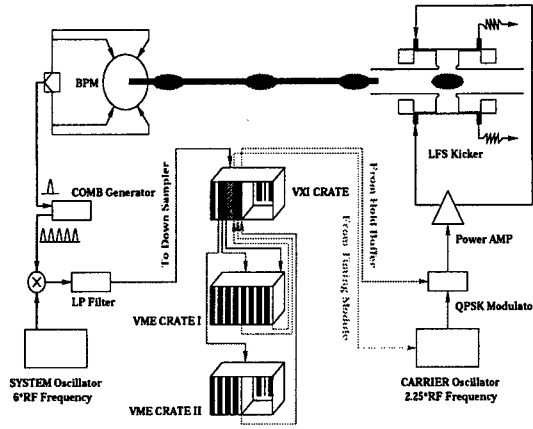


Figure 1: Block diagram of LFS for the PLS

Table 1: Parameters for the PLS LFS

Parameters	Value
RF frequency $f_{RF}$	500.082 MHz
Revolution frequency $f_o$	1.06855 MHz
Synchrotron frequency $f_s$	11.72 kHz
Ratio of $f_o/f_s$	90
Tap No of FIR algorithm $N$	$\geq 6$
Down sampling factor $d$	$\leq 15$
Bunch spacing for full filling	2 ns

## 2.2 Down Sampling

The detected phase error signals are digitized by an eight bit ADC converter at the bunch crossing rate (2 ns for fully filled buckets). To perform the longitudinal feedback, correction outputs must be calculated for every bunches and every turns in parallel, which means that a large number of DSPs will be needed. From the fact that the revolution frequency  $f_o$  of the PLS storage ring is ninety times greater than the synchrotron frequency  $f_s$  as summarized in Table 1, the calculating process can apply the Nyquist sampling theorem which states that it is possible to recover a signal from its samples if the signal is band-limited and the samples are taken at least at twice the highest frequency existing in the signal. Especially, in case of the sinusoid signal, it is possible to recover its amplitude and phase by taking only four samples per period. But, since the phase error oscillation (synchrotron oscillation) is not a perfect sinusoidal signal, six is selected as the number of taking samples per one synchrotron period for safety. In case of the PLS storage ring, taking six samples during one synchrotron period means that only the phase error values of every fifteenth turns will be used to calculate the correction output and the others (the phase error values from the first to the fourteenth turns) will be rejected in calculating the output. This process is called the down sampling whose the down sampling factor  $d$  is  $90/6 = 15$ . With this down sampling, the correction output can be calculated by sixty DSPs in parallel.

## 2.3 DSP Farm and FIR Algorithms

The DSP farm for the PLS LFS consists of two VME crates (three VME backplanes) and one VXI crate. The VME crates are fitted with VSB backplanes. The VME buses are used as the data buses while the VSB buses are used as the control paths. One VME crate has two VME backplanes where one Motorola MVME166 control processor and five DSP boards are housed. Each DSP board contains four 80 MHz AT&T 1610 DSPs. Each DSP chip has a 16 kB dual port memory (DPM) that can be accessible by the DSP and MVME166 control processor. The VXI crate having good electromagnetic shielding properties contains a National Instruments VXIcpu-030 control processor. After the longitudinal phase errors are detected and down sampled, the feedback correction output can be calculated by sixty DSPs in parallel which are housed at the fifteen DSP boards ( $4 \times 15 = 60$ ) in three VME backplanes. To calculate the correction output, the DSPs use the  $N$ -taps finite impulse response (FIR) algorithm which is given by

$$y(t_n) = \sum_{k=0}^{N-1} h(k) \cdot \phi(t_{n-k}) \quad (1)$$

$$h(k) = 2^{G_s} \cdot G \cdot \sin(2\pi[k/N] + \varphi) \quad (2)$$

where  $y(t_n)$  is the present correction output of the FIR filter,  $h(k)$  is the programmable coefficient of the filter,  $\phi(t_{n-k})$  is the phase error of previous turn as an input of the filter,  $G_s$  is the post multiply-accumulate shift gain of the filter, and  $G$  and  $\varphi$  are the gain and the phase of filter which can be used to choose the coefficient of FIR filter on EPICS operator interface.  $G = 0$  means that feedback is off. In case of tap number  $N = 6$ , six sampled phase errors ( $\phi(t_n) \sim \phi(t_{n-5})$ ) in one synchrotron period will be used to calculate a correction output  $y(t_n)$ . Therefore, DSPs will calculate one kicking output per every fifteen turns for a bunch. For 468 bunches, this calculation is performed by sixty DSPs in parallel according to lookup tables of the down sampler module.

## 2.4 Hold Buffer

The calculated correction outputs are sent to hold buffer with gigabit serial links. The hold buffer is a memory where the most recent kicking values are stored. Because of the down sampling, the most recent kicking values must be used to kick each bunch until a new kicking output is calculated by the DSPs. The output of the hold buffer drives a fast DAC converting at bunch crossing frequency and generates an analog signal which will be gone through the QPSK modulator, then be sent to the power amplifier.

## 2.5 QPSK Modulator

The central frequency of the LFS kicker can be given by

$$f_c = (p + 1/4) \cdot f_{RF} \quad (3)$$

or

$$f_c = (p + 3/4) \cdot f_{RF} \quad (4)$$

where  $p$  is any integer. When  $p = 2$ ,  $f_{RF} = 500$  MHz, and fully filled buckets, the central frequency  $f_c$  is given as 1125 MHz or 1375 MHz.  $f_c = 1125$  MHz (1375 MHz) means that the electromagnetic fields in the LFS kicker is changed 2.25 (2.75) times faster than the bunch crossing frequency (500 MHz). Therefore, to synchronize the electromagnetic fields in the LFS kicker with the bunch crossing, a phase shift must be needed at the bunch crossing frequency. For the  $f_c = 1125$  MHz (1375 MHz),  $-\pi/2$  ( $+\pi/2$ ) phase shift of the carrier oscillator will be needed to synchronize the kicking timing against the turning bunches. This process is called the quad phase shift key (QPSK) which enhances the kicking efficiency of the LFS kicker. The QPSKed signal is modulated in amplitude by the output signal of the hold buffer.

## 2.6 Power Amplifier and LFS Kicker

The selected power amplifier for the LFS kicker is a solid state type model AS0820-250R from MILMEGA. Its operation frequency range is 800 MHz  $\sim$  2000 MHz and the maximum output is 250 W. Its frequency response is tuned to operate two frequency ranges (for  $p = 2$ , 1000 MHz  $\sim$  1250 MHz and for  $p = 3$ , 1500 MHz  $\sim$  1750 MHz) with its best performance. This wide bandwidth and the frequency response tuning of the power amplifier make the upgrade of the LFS kicker easily. One aluminum single-ridged waveguide-overloaded cavity has been fabricated and tested to use it as a longitudinal bunch-by-bunch LFS kicker for the PLS storage ring. It has 4 input/output ports to obtain wide bandwidth ( $\geq 250$  MHz) and a nose cone is attached to increase the shunt impedance. Its measured bandwidth is about 344.4 MHz and its the maximum value of the shunt impedance is about 470  $\Omega$ . The phase error oscillation having phase deviation less than 10 mrad can be damped within 1 ms by this kicker without any amplifier saturation. By attaching the single ridge to a general waveguide and then adjusting the geometry, the frequencies of all dangerous HOMs can be increased higher than the cutoff frequency of the beam pipe ( $\sim 2295$  MHz) [2]. Therefore, the kicker is free from the dangerous HOMs which generate the CBMIs. The distribution of E field in the kicker which is an output of 3D HFSS code is shown in Fig. 2. Later, the kicker will be upgraded to improve the kicking efficiency by increasing the central frequency up to 1625 MHz.

## 2.7 EPICS Operator Interface

For the PLS LFS, the Experimental Physics and Industrial Control System (EPICS) is used for the control operator interface (OPI). The OPI has already been ported in a Sun sparc workstation. The setting of FIR algorithm, the diagnostic of LFS hardwares and data acquisition can be performed with the OPI.

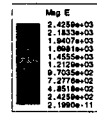


Figure 2: The distribution of E field in the LFS kicker

## 2.8 Data Acquisition with LFS

The feedback data is recorded in the dual port memory. With a code (gd\_post), MATLAB compatible data file (gd.mat) can be obtained. With the MATLAB programmed codes, it is possible to obtain useful information such as the growth and damping rates of the instabilities, the HOM frequencies of RF cavities which generate the CBMIs, bunch-by-bunch current, bunch-by-bunch synchronous phase, and the longitudinal aliased impedances seen by the beam at revolution harmonics.

## 3 CURRENT STATUS

The pickup for the phase error detection has been installed and the power amplifier, the circulators, and all cables for the PLS LFS are ready. The LFS kicker has been fabricated and measured its properties. The kicker will be installed to the PLS storage ring in April 1999. If the electronics of the LFS is completed and delivered from SLAC, it will be possible for PLS to find the best operating condition for the temperatures of RF cavities and various fill patterns as well as damping the dangerous HOMs generating CBMIs. Also, the much narrower and higher intensity spectrum of U7 undulator can be obtained.

## 4 ACKNOWLEDGMENTS

The authors thank Dr. J. Fox, Dr. S. Prabhakar, D. Teytelman, A. Young, and W. Ross of SLAC and G. Stover of LBL for their endless help and kindness. The authors also thank Dr. T. Y. Lee, Dr. M. H. Cho, Dr. K. B. Lee, and Dr. W. Namkung of PAL for their cheer.

## 5 REFERENCES

- [1] G. Oxoby et al, "Bunch-by-Bunch Longitudinal Feedback System for PEP-II," Proc. of the Fourth European Particle Accelerator Conference, (London, U. K., June 1994), 2660 (1995).
- [2] Yujong Kim, M. Kwon, and I. S. Ko, "Design of Longitudinal Feedback System Kicker for the PLS Storage Ring," In these proceedings.

# DESIGN OF LONGITUDINAL FEEDBACK SYSTEM KICKER FOR THE PLS STORAGE RING\*

Yujong Kim, M. Kwon, I. S. Park, I. S. Ko<sup>†</sup>, PAL, POSTECH, Pohang 790-784, Korea

## Abstract

The higher order modes (HOMs) of RF cavities at the Pohang Light Source (PLS) storage ring cause longitudinal coupled bunch mode instabilities (CBMIs). To cure these instabilities, a longitudinal feedback system (LFS) is introduced. As a key component of the LFS, there is a single-ridged waveguide-overloaded cavity as a longitudinal bunch-by-bunch LFS kicker for the PLS storage ring. To damp any coupled bunch modes, the bandwidth of this kicker should be wider than 250 MHz. Also, the higher shunt impedance of the kicker is selected to use lower power amplifier. One aluminum kicker is fabricated and the bandwidth, HOMs, and shunt impedance of the kicker are measured with a network analyzer. This kicker has several different features from LFS kicker for DAΦNE. First of all, there are 4 input/output ports to obtain a wider bandwidth. Secondly, there is a nose cone to obtain higher shunt impedance. Finally, the symmetric frequency response of the shunt impedance around central frequency is provided. According to the simulation result done by HFSS code, high shunt impedance of 620  $\Omega$  (transit time factor considered value) and the wide bandwidth of 255 MHz are obtained. These are compared with the measured result.

## 1 INTRODUCTION

The PLS is the 3rd generation synchrotron light source. Originally, the PLS storage ring is designed to store the beam current up to 400 mA at 2 GeV and 250 mA at 2.5 GeV. By adding one RF cavity in 1996, there are four RF cavities with 60 kW CW klystron amplifier operating at the PLS storage ring to store the desired beam current [1]. But owing to HOMs of RF cavities that make the CBMIs such as dipole, quadrupole, sextupole modes, the current of PLS storage ring is possible up to 200 mA at 2.0 GeV without CBMI. By analyzing the reverse signal of RF cavities and the sidebands of the BPM spectrum, it is found that the most dangerous HOMs of RF cavities are longitudinal  $TM_{011}$  (758 MHz) and  $TM_{013}$  (1707 MHz) modes. To avoid these HOMs, the precession temperature control system for the RF cavities has been installed during 1997 Summer maintenance period. This system can regulate the cooling water to better than 0.2°C. With this system, the stored beam current without CBMIs has been increased from 120 mA to 200 mA. It means that the cooling system is not enough to avoid such dangerous HOMs fully. So, an active feedback system for CBMIs is necessary for the PLS. The typical LFS consists of a signal pickup, digital signal pro-

cessing units, and a kicker. There are various types of LFS developed at several accelerator laboratories such as SLAC, LBL, Frascati, KEK, etc. In the PLS case, it is decided that the digital signal processing unit is purchased from SLAC and the kicker is fabricated by the PLS and domestic manufacturer. By considering these design, the PLS has decided to design the kicker following DAΦNE design [2] that is a single-ridged waveguide-overloaded cavity with HFSS and SUPERFISH codes.

## 2 DESIGN OF LFS KICKER

There are many things to be considered in order to design the LFS kicker for the PLS storage ring such as kicker length, working central frequency, bandwidth, shunt impedance, kicker filling time, contents of HOMs, kicker input power or kicker amplifier power. The LFS kicker will be installed at the straight section for RF cavities where there is a space of 42 cm reserved for future fifth cavity. Thus, the kicker length is determined to be 42 cm. According to CBMI theory, coupled bunch modes are characterized by a definite phase relation between the oscillations from one bunch to the next. Since all CBMIs are located within the frequency range of  $p \cdot f_{RF} \sim (p + 1/2) \cdot f_{RF}$  where  $p$  is any integer, the minimum bandwidth of kicker to cure all CBMIs is  $f_{RF}/2$ , and the central frequency of the kicker  $f_c$  is the average of the frequency range,  $(p + 1/4) \cdot f_{RF}$ . Next is the selection of central frequency which is determined by choosing an integer  $p$ . By considering commercially available amplifiers and the operating frequency of PLS RF system of 500 MHz, the possible choice of  $p$  for the PLS LFS is either 2 or 3, which corresponds the central frequency of 1125 MHz or 1625 MHz, respectively, and  $p = 2$  is selected. The selected RF amplifier is a solid state type model AS0820-250R from MILMEGA. Its operation frequency range is 800 MHz  $\sim$  2000 MHz and maximum output is 250 W. Even though the PLS LFS is designed to operate at  $p = 2$  mode with bandwidth of 250 MHz and the central frequency of 1125 MHz, this amplifier will also be used at  $p = 3$  mode in the future for more efficient kicking with lower RF power. Because the maximum power of amplifier is limited, the amplitude of the correction kick will be saturated easily in damping the phase oscillation with very high amplitude (i.e., very fast instability growth rate). One way to lower the required power of the amplifier in damping the CBMIs is to design the kicker with high shunt impedance. Since the RF frequency of the PLS storage ring is 500 MHz and the harmonic number is 468, the bunch spacing in fully filled case is 2 nsec. To perform the bunch-by-bunch kicking properly, the filling time of LFS kicker must be shorter than 2

\* Work supported by POSCO and MOST, Korea.

<sup>†</sup> Email : isko@postech.ac.kr



Table 2: PLS LFS kicker dimensions

Parameter	Dimension [mm or °]
Inner cavity radius $R_1$	67.5
Outer cavity radius $R_2$	101.5
Port base radius $R_3$	95.1
Cavity gap $d$	74.0
Gap between cones $d_1$	64.0
Barrier angle $\alpha$	24.0
Port base angle $\beta$	16.9
Back cavity size $b$	35.8
Port base gap $g$	6.4
Ridge length $\delta$	50.2
Ridge distance $p$	87.2
Back cavity distance $e$	123.0
Port round radius $m$	2.0
Port base round $h$	1.0

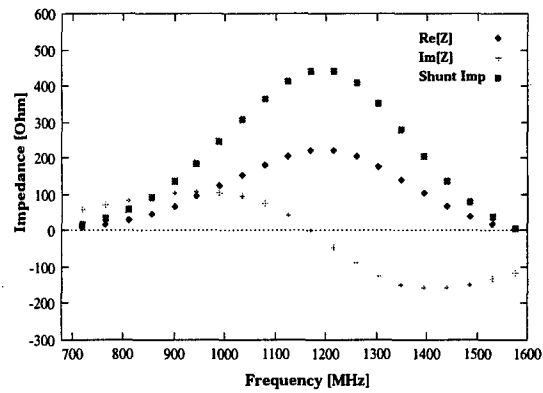
Table 3: HOMs of the kicker

Mode	$f$ [MHz]	$R/Q$ [ $\Omega$ ]	$Q$ factor
TM <sub>010</sub>	1130.5	49.0	21557.2
TM <sub>011</sub>	2322.4	17.5	26524.4
TE <sub>211</sub>	2503.0	17.3	40126.6
TM <sub>111</sub> (TE <sub>011</sub> )	2749.4	5.6	44380.9
TM <sub>211</sub>	3130.0	20.5	44898.5

of  $R/Q$ , it is important to increase the value of  $R/Q$  for higher shunt impedance, which depends on the geometry of pill-box. Therefore, it is possible to increase this value by change the geometry of the pill-box with help of SUPERFISH simulation. From the facts that the radius of beam chamber is fixed as 50 mm and that the central frequency of the kicker  $f_c$  depends on the radius of outer cavity  $R_2$ , only the gap size  $d$  can be adjustable to increase  $R/Q$ . Since the transit time factor  $T$  and  $R/Q$  are increased as the gap size  $d$  is decreased, the shunt impedance (the transit time factor considered) will be increased by attaching a nose cone between a gap of pill-box cavity. The final pill-box cavity with nose cone attached has 255 MHz of bandwidth and 1130.5 MHz of central frequency which is near 1125 MHz. The final dimensions of the PLS LFS kicker are summarized in Table 2.

### 3.3 Global performance of the kicker

Investigation into the dangerous HOMs of the nose cone attached cavity is performed with the SUPERFISH and the result is summarized in Table 3. Frequencies of all dangerous HOMs are higher than the cutoff frequency of beam pipe ( $\sim 2295$  MHz). By considering the fact that the single-ridge of the waveguide widens the frequency separations between the HOMs, their frequencies are increased further beyond 2295 MHz. Therefore, they do not generate any undesirable CBMIs within the cutoff frequency of vacuum chamber. Thus, the kicker is free of dangerous HOMs. With 3D HFSS, the maximum value of gap voltage is 35.25


 Figure 2: Measured  $R_s$  and its frequency response

V for 1 W input power and its maximum shunt impedance is about 620  $\Omega$  (transit time factor considered). The central frequency of the shunt impedance is about 1131 MHz that is only 6 MHz higher than the desired value of 1125 MHz.

## 4 CURRENT STATUS

With the LFS kicker design as described above, an aluminum kicker was fabricated by local manufacturer. After cleaning and assembly work was done, a series of performance test were followed with WILTRON 360B network analyzer. Measured central frequency and the bandwidth are 1115.6 MHz, and 344.4 MHz, respectively. The frequency response of the shunt impedance is shown in Fig. 2 with its maximum value of about 470  $\Omega$ . The  $R/Q$  of measured HOMs within the cutoff frequency is lower than 3.3. So, they will not generate any dangerous CBMIs to the beam. This kicker will be installed to the PLS storage ring in April 1999 [3].

## 5 ACKNOWLEDGMENTS

The authors thank Dr. M. Tobiyama of KEK, Dr. D. H. Han of Kyungpook Univ., J. S. Yang, M. K. Park, Dr. J. Y. Huang, Dr. T. Y. Lee, Dr. M. H. Cho, and Dr. W. Namkung of PAL for their endless help and cheer.

## 6 REFERENCES

- [1] M. Kwon et al, "The PLS RF System Upgrade Activities," Proc. of the First Asian Particle Accelerator Conference, (Tsukuba, Japan, March 1998), 749 (1999).
- [2] R. Boni et al, "A Waveguide Overloaded Cavity as Longitudinal Kicker for the DAΦNE Bunch-by-Bunch Feedback System," Particle Accelerator, **52**, 95 (1996).
- [3] Yujong Kim, J. Y. Huang, M. Kwon, and I. S. Ko, "Status of Longitudinal Feedback System for the PLS Storage Ring," In these proceedings.

# IMPLEMENTATION OF MAGNETIC MEASUREMENTS, ERRORS, AND THEIR CONSEQUENCE IN AN OPTIMIZED FERMILAB 8-GEV TRANSFER LINE<sup>†</sup>

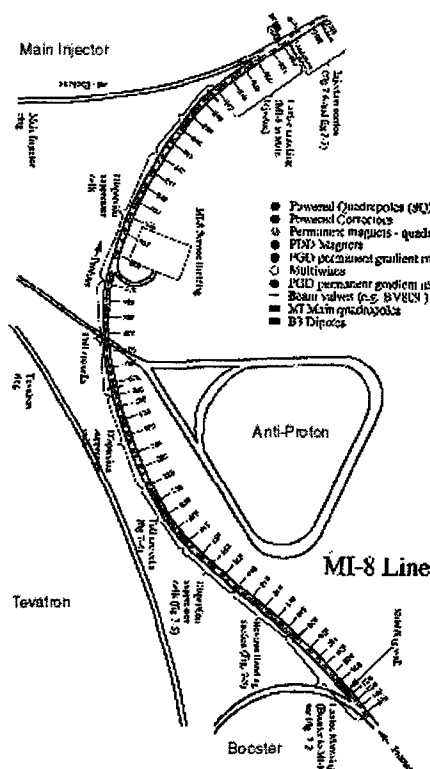
S. Assadi, J. Johnstone, P. Martin, F. Tecker, M. J. Yang, Fermi National Accelerator Laboratory, Batavia, IL.

## Abstract

The purpose of the newly constructed 8 GeV transfer line is to provide a reliable interconnection of the Booster and the Main Injector. This transfer line is constructed from the combination of the Permanent and Electro-magnets. We present data obtained during the commissioning along with our experience of combined function permanent magnets, DC operation of the electro-magnets and optics model vs. measurement of the beamline is also presented.

## 1. INTRODUCTION

The new 8 GeV line differs in concepts from a conventional transfer lines implemented at Fermilab. The line consists of two matching sections, one to Booster and the other to the Main Injector are built from tunable electromagnet quadrupoles. However, the long repetitive FODO cells are made from permanent dipoles, gradient magnets, and quadrupoles [Fig.1].



The layout of the beamline and site coordinate with respect to other accelerators are shown. The vertical extraction from Booster is facilitated by a pulsed septum in the straight section L3 with an angle of 2.77 degrees. In this paper, the origin is the middle of the L3. A vertical dipole (VBC1) levels the trajectory ~.50 meter above the Booster elevation followed by 6.54° horizontal bend. There are 2 vertical doglegs afterward to bring the beam to the Booster elevation without impacting civil constructions.

The motivation for employing permanent magnets in the line was to acquire the manufacturing and operation experience necessary to ensure the success of the 8 GeV Recycling Ring. Important questions such as the temperature dependence, field quality and exposure to radiation of the permanent magnets resulted in commissioning and operation of the first section (station M833). Using the C++ online model, we learned that 9 PQP's in the reversed bend section from M810-M814 were weaker by ~15% that were replaced promptly. We also concluded that permanent vertical bend magnets at the beginning of the line need to be replaced due to aperture limitations and correctors needed to control the orbit throughout the beamline.

## 2. MEASUREMENTS AND ANALYSIS

There are over 50 Beam Position Monitors (BPMs), 40 Beam Loss Monitor (BLMs), 15 multi-wires and 2 toroids to measure the intensities at the entrance and exit of the transfer line. Fermilab control system provides magnetic currents, the power supply readbacks, distributed tunnel temperature and so on.

We first calibrated the quadrupole transfer constant by using 3-bump measurements. Fig. 2 presents the closure of 3-bump Q808-Q810-Q812 constructed using dipole trims. The closure confirms the power supply calibration and it is a useful tool for calibrating the quadrupole fields. The trajectory closure is sensitive, to first order only to the middle quadrupole's field as the phase advance is the same between the quads. Three-bumps are also used to center the beam through the quadrupoles and dynamic aperture is measured. The Booster matching section has ten SQ series quadrupoles. SQ's were originally designed for the Antiproton Source.

Lattice functions for the 8 GeV line is measured by single

<sup>†</sup>Work supported by the US Department of Energy under contract DE-AC02-76CH00300.

kick method. A reference nominal beam data is subtracted from a one-bumped orbit. Results are compared with the model. In Fig. 3, horizontal and vertical measured BPM orbit is compared with the model.

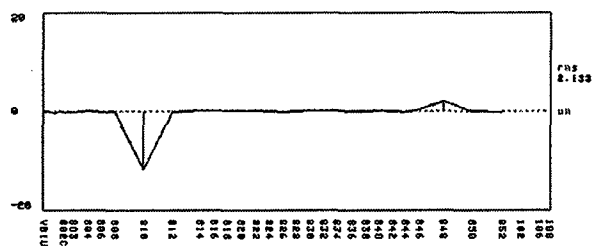


Fig. 2) The closure of 3-bumps confirms the PS calibration and the middle quadrupole field.

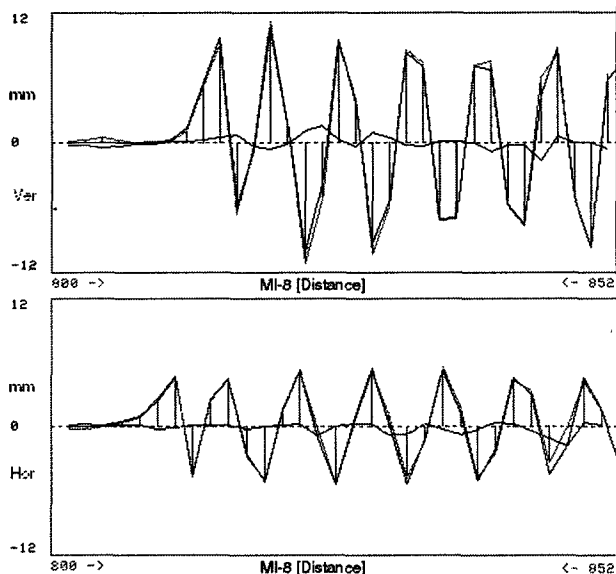
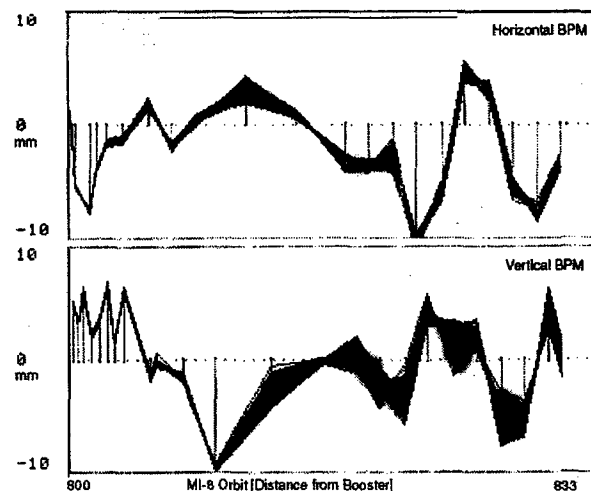


Fig.3) Vertical (Top), Horizontal (bottom) BPM difference orbit shown. Green line is the measurement, red is produced by the C++ online model and the error is shown in blue.

We should point out that the magnitude of the error in the horizontal plane has systematically increased. This error which is proportional to the phase advance error is partly due to the alignment of the combined permanent function magnets, partly due to running slight mismatch that initially were not detected due to BPM resolution during 3-bump quad field calibration.

Due to economic reasons, a number of decisions had to be made during the construction of the MI-8. We shared the power supplies among the electromagnets. Table 1 Lists the arrangements. We also cut cost by operating the electromagnets as DC powered devices. We have been concerned about shared power supplies among the quads coupled by shunts and DC operation of the quads. Fig. 4

shows the operation of the phase one of the MI-8 line.



Fi.4) over-plot of 120 consecutive BPM orbits show substantial orbit deviation as beam propagates toward the Main Injector. The injection from the Booster is shown to be stable.

Reproducibility, high efficiency and emittance preservation has been our top priority during the commissioning of the MI-8 beam line. Understanding the orbit variation shown above is the subject of the remainder of this paper.

Q800-Q804-Q805	One power supply
Q801-Q808-Q809	One power supply
Q802-Q806-Q807	One power supply
Q803	One power supply

Table 1. Shows the arrangement of the PS and shunts.

We had previously observed that the Beamline orbit could change dramatically as temporarily one of the shunt currents were varied and brought back to the nominal value. The anomalous latency effect could last for minutes although the current readbacks were returned to normal. We performed a systematic study of Q809. The quadrupole current is driven off a bulk supply minus the shunt circuit current. To enhance the effect from Q809, a positive or a negative 3-bumps with and without the large shunt setting change around the Q809 was set up. After the shunt setting was restored to its nominal value, we recorded the orbit at approximately one minute interval. Table 2. Shows the conditions and Figure 5 presents the results. We analyzed the data for the change in Q809 current required to close the 3-bump orbit ( the 3-bumps using trims VT807,VT809, and VT811 was originally closed). All trim magnet reading and settings had

previously calibrated and verified to be reproducible.

Frame 1 to 3	Nominal setting
Frame 4 & 5	Negative 3-bump
Frame 6 & 7	Positive 3-bump
Frame 8 & 9	+3-bump + 46 Amps on shunt (reduced quad current)
Frame 10 & 11	Negative 3-bump
Frame 12 to 27	Shunt is set back to nominal value.

Table 2 presents the quad 809 shunt current setting condition. Figure five shows that the orbit variation is independent of the sign of the three bump through the

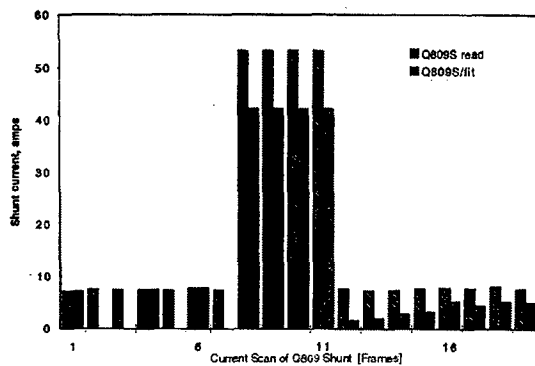


Fig.5) The calculated shunt current from frame 12 on are consistent with observed orbit changes over time.

Q809 and the reported shunt current is incompatible with the actual Q809 field. The shunt current regulation is under investigation.

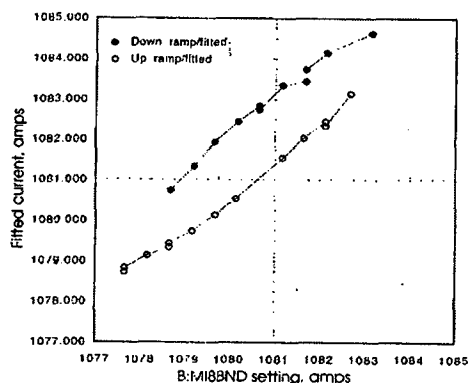


Fig. 6) The magnetic hysteresis effect is known.

Another restriction on the operational reproducibility of the MI-8 line is the DC operation of the powered magnets and the turn-on procedure. Figure 6 shows the well known magnetic hysteresis effect of the Bend magnet. Figure 6 shows the bulk power supply MI8BND which powers four magnets has to have a designated turn-on procedure. By not accounting the hysteresis effect, the error could be as large as 2-amp error or 12mm orbit deviation at the Main Injector entrance. We have also established the underlying reason correlating the orbit variation are related to leaking RF

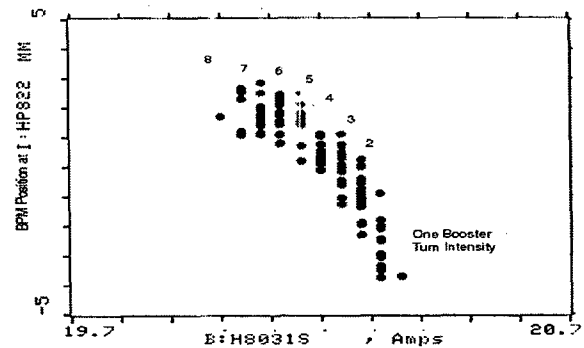


Fig.7) Beam position variation with intensity is due to shunts current being affected.

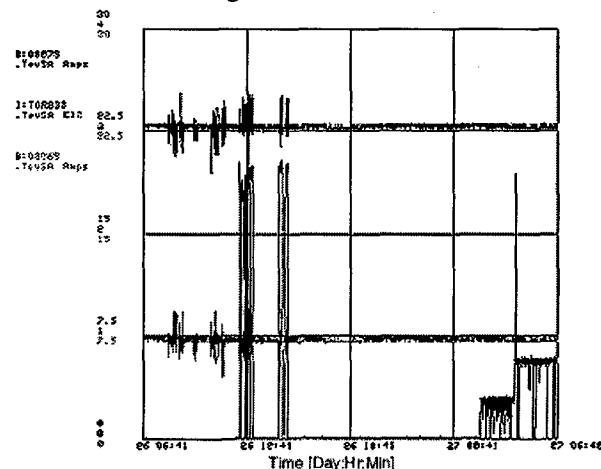


Fig. 8) During high intensity operations, shunts are affected and results in the observed orbit variation.

from the Booster affecting the shunts electronics.

### 3. CONCLUSION

We have an excellent understanding of the MI-8 optics and the permanent magnet section of the beamline has performed per design. Orbit variation is well correlated to be due to RF from the Booster affecting the electronics and are being repaired. Turn-on procedure is essential for the reproducibility and ~97% beam transfer efficiency is achieved.



# MEASUREMENT OF LONGITUDINAL MODE MIXING IN THE FERMILAB LARGE HADRON ACCELERATORS<sup>†</sup>

S. Assadi, W. Blokland, A. Hahn, M. J. Yang, Fermi National Accelerator Laboratory, Batavia, IL.

## Abstract

Fermilab High Energy Physics research program for RUN-II requires rapid generation of antiprotons and high intensity protons. We had previously observed longitudinal mode mixing in the Main Ring and Tevatron at intensities desirable for the RUN-II. We incorporated high-speed digitizer (RTD-720) and (LeCroy 9384CM) to measure the time domain, and further spectral analyses were performed to measure the mode couplings. We have refined our measurement analysis in conjunction with higher digitization to pursue higher mode couplings. Data during the commissioning of the newly constructed Main Injector will be compared to previously obtained data.

## 1. INTRODUCTION

The Main Injector Sampled Bunch Display pickup (wide-bandwidth resistive wall monitor) is used to measure the longitudinal time evolution of the beam. Three different data acquisition systems are used for this paper; 1) fast 4 Gs/s LeCroy 9384 Oscilloscope and a LabVIEW analysis program, 2) Two Gs/sec RTD-720 digitizer with 1024 segment-able memory in conjunction with the Fermilab control system, 3) Five Gs/sec dual-channel TVS-645 digitizer with a proprietary Tektronix snapshot capture PC-based data acquisition software.

Longitudinal bunched beam modes and their interaction with the beam were first described by Sacherer in 1973. For  $M$  equidistant bunches, there are  $M$  coupled bunch modes characterized by  $n$  waves  $0 \leq n \leq M-1$  around the storage ring. The theory of longitudinal bunched beam contain radial and within-bunch modes. Due to lack of high resolution pickups, DSP's and possibility of Landau damping of the higher order modes, only the lowest radial and azimuthal modes are observed. The interaction among charged particles and their surrounding environment, such as RF cavities, kickers and bellows can drive the beam unstable resulting in unwanted longitudinal coherent beam oscillations. These oscillations will cause the eventual growth in longitudinal emittance. The beam acceleration throughout the cycle is a result of two fields: one is externally controlled by the RF cavities and the other comes from the wake fields generated by the frontal bunches. This wake field is clearly intensity dependent. As the bunch intensity increases, the wake potential produced by the frontal

bunches need to be considered in the particle equation of motion. The RF cavities installed in the newly constructed Fermilab Main Injector, were a part of the decommissioned Main Ring. This paper addresses the search, observation and measurements of the coupled bunch modes in the Main Injector at 8 GeV. Modeling and the cure of the longitudinal mode coupling is left out.

## 2. EXPERIMENTAL RESULTS

The purpose of the rapidly cycled Main Injector is to provide high intensity beams to different experimental areas within a supercycle (a repetitive cycle that could include beam transmission for antiproton production, 120 GeV fixed target, collider run injection and so on). The complex supercycles could require holding beam in the Main Injector for power supply reconfiguration. We have

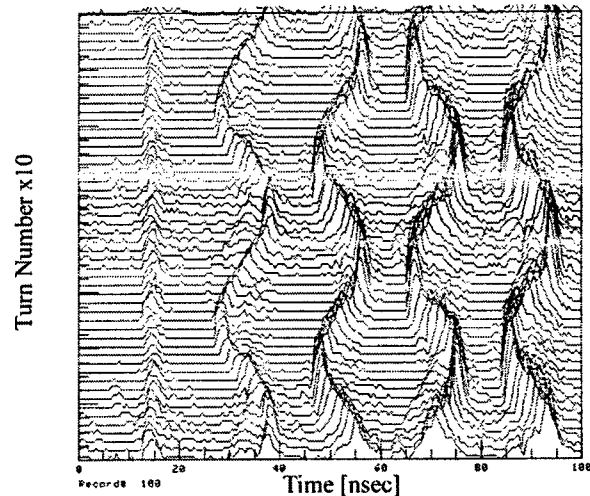


Fig.1) Each trace shows 5 consecutive bunches starting from bunch one (leading bunch). Every 10 turn is shown.

observed (Fig. 1) coupled bunch modes in Tevatron few seconds after injection.

Each trace in the above figure is triggered externally based on a count down of the RF and recorded by the segment-able memory RTD720 for 10240 consecutive turns. Every 10 turns is registered to enhance the synchrotron oscillation observation. We have injected 11 bunches into 11 consecutive buckets and leaving the remainder of the ring empty. we observe that leading

<sup>†</sup>Work supported by the US Department of Energy under contract DE-AC02-76CH00300.

bunch does not go under any oscillation and the wake field generated by the bunches decays prior to the return of the first bunch. We also observe that the wake field is additive as expected by the theory. We also observe the longitudinal bunch length of the 5<sup>th</sup> bunch has drastically increased.

Figure 2 shows that during the high intensity

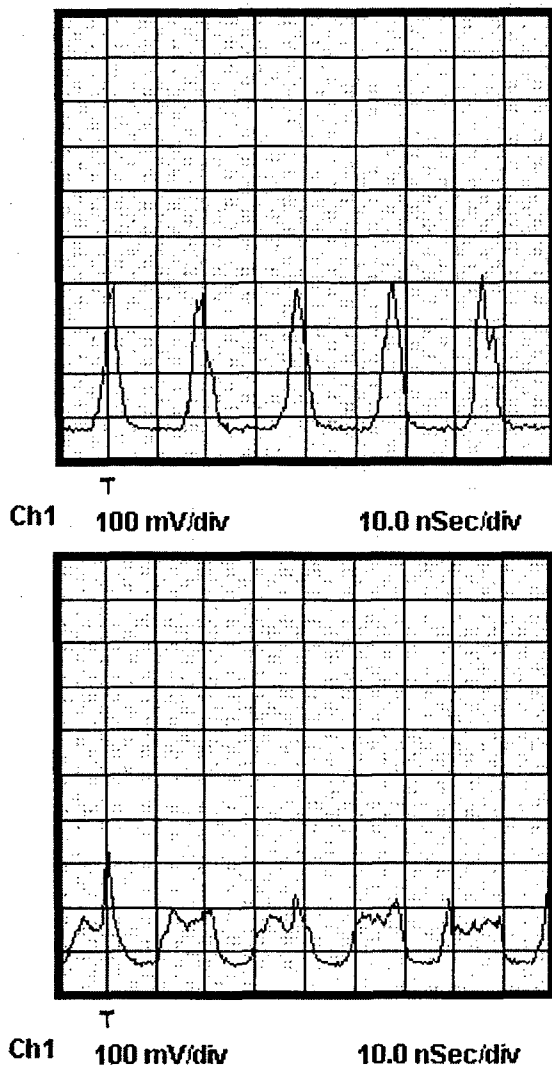


Figure 2) The above trace shows 5 bunches of a 40 bunch injected immediately after injection and the lower figure shows the same bunches after 3 second.

commissioning of the Main Injector an increase in the bunch length as we kept the beam for periods up to 10 second at 8 GeV.

In the Main Injector, the wake field for the higher order cavity modes can reach several kV for a beam with  $3E12$  particles per bunch while the peak fundamental RF

voltage at 8 GeV is 1.1MV per turn. The above observation lead us to seek the reason for the above behavior. Figure 3 and 4 show that as the intensity increases by filling the MI with beam, some bunches undergo oscillation and their bunch length increases. We can cures the instability by changing the injection synchronous phase. We note that bunch intensity can

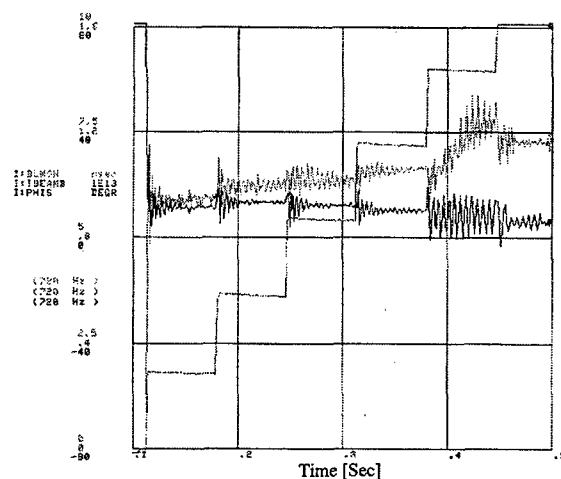


Figure 3) The above figure shows that 5<sup>th</sup> and 6<sup>th</sup> batch exhibit oscillations much larger than the 1<sup>st</sup> to 4<sup>th</sup> and their bunch length increases.

vary during the operation of the MI and continues synchronous phase manipulations is not favorable. A successful longitudinal feedback system is installed by McGinnis et. al.

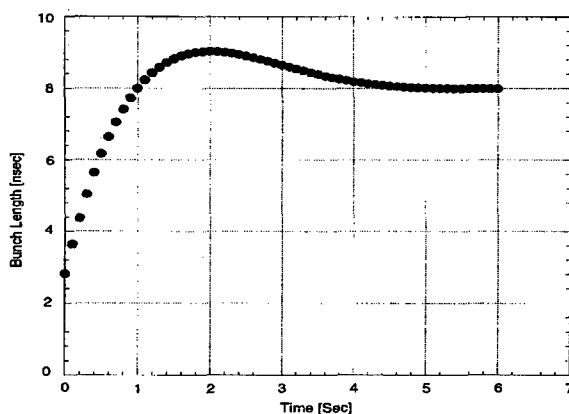


Figure 4) Bunch length grows at 8 GeV from 2.8 nsec at injection to greater than 8 nsec after 2 seconds.

Time evolution of one bunches at 8 GeV is measured

†Work supported by the US Department of Energy under contract DE-AC02-76CH00300.

and shown below. We observe that the decrease in the bunch length after 2 seconds is correlated with beam loss rather than cooling.

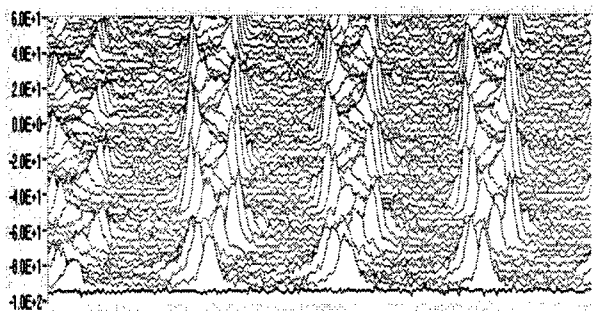


Figure 5) At 8 GeV, an equivalent to the synchronous phase to stabilize the oscillation in figure 3 is added to generate the phase error and measure the coupled bunch mode prior to dilution.

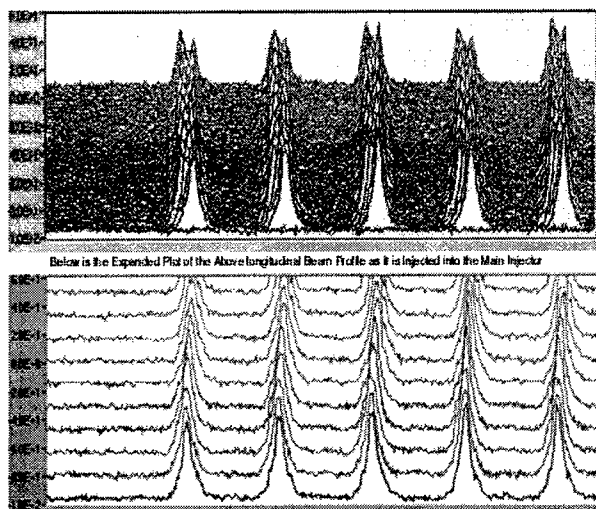


Figure 6) Time evolution of longitudinal motion. The first trace of the above figure is prior to the injection and followed by plots of every 13 turns.

The remainder of this paper tries to pursue the characteristics of the bunch lengthening and how one can reduce or eliminate that.

The resulting time series data gathered in figure 7) is broken up to 1000 realizations. Each realization contains data from every 15 turns of each bunch which are then Fourier transformed. The phase shift  $\Delta\phi$  of the perturbing bunch motion with respect to a reference bunch is  $2\pi n/M$ . We then infer the wake field mode structure by calculating the wavenumbers  $k_n = \Delta\phi_n / \Delta x$ .

### 3. CONCLUSION

†Work supported by the US Department of Energy under contract DE-AC02-76CH00300.

Although we have just recently started to commission the Main Injector, we have achieved intensities to the highest

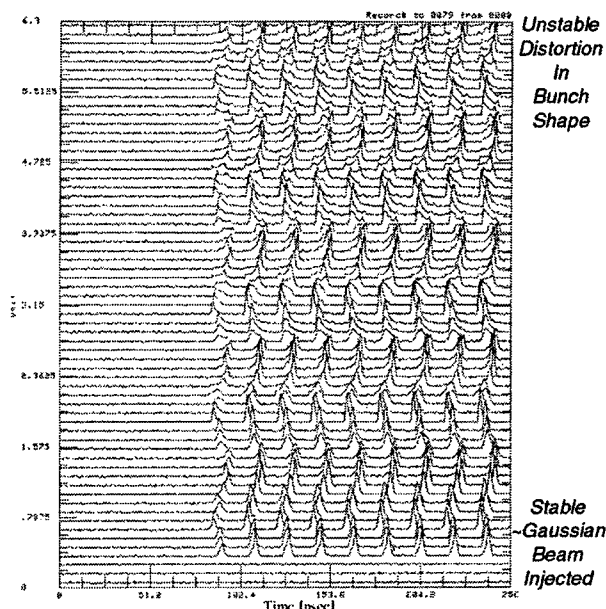


Figure 7) Waterfall plot of Main Injector beam vs turn number. We observe that all bunches oscillate and the bunch shape distorts as time progresses.

intensities of the Main Ring but we have only observed the lowest longitudinal mode. Unlike the Tevatron or the Main Ring, the Main Injector does not exhibit higher longitudinal coupled bunch modes although the same particle flux density is present.

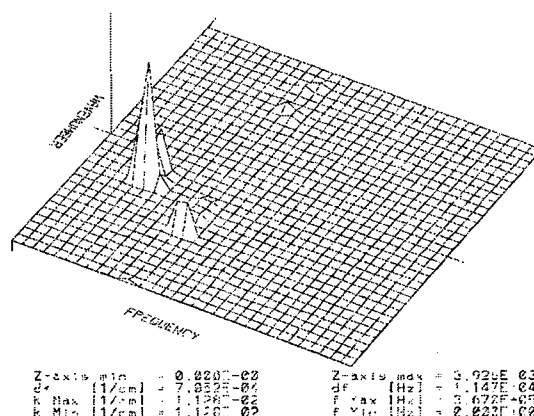


Figure 8) Measured Peak is associated with dipole oscillation between adjacent bunches

# Envelope Instabilities in Electron Cooling

A. Burov and S. Nagaitsev  
*Fermi National Accelerator Laboratory*  
*P.O. Box 500, Batavia, Illinois 60510*

## Abstract

The envelope instabilities are considered as factors responsible for the observed limitations for a current of cooled particles.

## 1 OBSERVATIONS

Electron cooling is proved to be a way to increase a phase space density of heavy particles. However, its possibilities and limits are not completely studied. One of the unclear phenomena is the limit on the cooled beam intensity observed at several cooling facilities [1, 2, 3, 4]. The main features of the phenomenon experimentally studied in the IUCF cooler [1] are listed below.

1. Under the continuous stripping injection of protons in the cooler, the accumulated proton current was limited by a certain value independent on the injected current. The rate of the current increase was seen to be constant until just below the limiting current where the rate sharply dropped to zero. The phenomenon can be described as the beam lifetime being a highly nonlinear function of the beam intensity, see Fig. 1.
2. The operations with the bunched proton beam showed that the peak proton current, not the average one, is limited.
3. The beam current decreased smoothly between injection cycles, thus suggesting the beam scraping is not of concern.
4. The size of the cooled beam at the limit current was found to be very small, the rms radius  $a_c = 0.5$  mm, which is deeply inside the electron beam with the radius  $a_e = 1.2$  cm. The space charge tune shift in the cooled beam was found to be high and approximately constant during the accumulation,  $\Delta Q \simeq 0.2$  [5].
5. The beam halo significantly increased near the accumulation threshold, see Fig. 2 [6].
6. Attempts to dilute the transverse emittance of the cooled beam by means of the applied transverse broad band noise resulted only in the decrease of the accumulated current [6].
7. Coherent transverse signals were not observed.

For the present moment, there is no satisfactory explanation of these facts. It is not clear, why instead of the gradual emittance growth proportionally to the peak current (to keep the tune shift constant), the life time of the protons sharply drops and the accumulation stops.

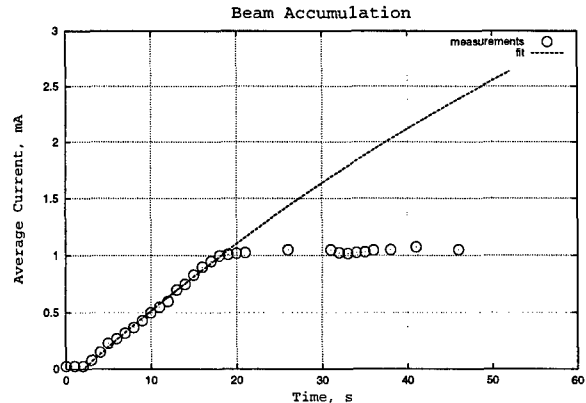


Figure 1: Accumulated current  $I$  as a function of time  $t$  during stripping injection with cooling accumulation (IUCF). Dots are the measurements, line is a fit  $I \propto 1 - \exp(-t/\tau_0)$  for the lifetime  $\tau_0 = 100$  s.

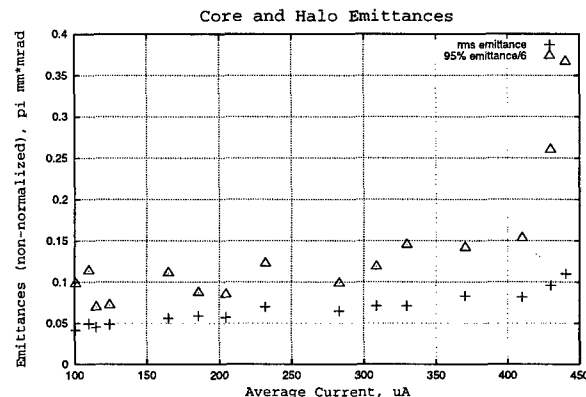


Figure 2: Beam core and halo measurements during the accumulation of bunched beam (IUCF). The upper set of points is 1/6 of 95% emittance, and the lower set is rms emittance. If the transverse distribution were Gaussian, both sets would be equal.

An attempt was made to explain these facts by a microwave electron-proton instability [4]. However, Ref [7, 8] found that the coherent electron-proton interaction introduces a stabilization in the proton beam motion under normal conditions.

The main hypothesis of this paper is that it is the envelope instability of the cooled beam which might be a reason for the described phenomenon.

## 2 ENVELOPE INSTABILITIES

Due to the periodic modulation of the focusing force, there is a possibility of parametric excitation of the beam second-order (quadrupole) modes, resulting in the envelope instabilities [9, 10]. The instability takes place when the space charge of the beam shifts frequency of one or both quadrupole modes to the parametrical resonance with the focusing structure. It means that the mode frequency referred to the structure frequency reaches half of an integer,  $n/2$ , which approximately corresponds to the quarter of integer,  $n/4$ , in terms of the single particle tune.

The structure period of a storage ring is, generally, the total circumference. Taking this into account, it can be concluded that a threshold of the envelope instability in the storage ring is reached when the space charge shift brings one of the betatron tunes to a quarter of an integer which sets the limit on the space charge tune shift  $|\Delta\nu| < 0.25$ .

Strictly speaking, the envelope instabilities can be avoided for any space charge, if the storage ring is constructed from identical or almost identical cells. Such a storage ring has to obey the limit  $\Delta\nu < N_c/4$  which would be valid for any space charge if the number of cells  $N_c$  is high enough,  $N_c > 4\nu$ . Due to the ring curvature, there is a minimal periodicity to satisfy this requirement. A storage ring of such a kind was suggested for experiments aimed to reach a crystalline state of a stored ion beam [11], the minimal periodicity was found to be  $N_c = 8$ .

Apart from this special case, the restriction on the envelope instability coincides with the conventionally accepted single-particle limit on the space charge tune shift,  $|\Delta\nu| < 0.25$  [12].

The numerous simulations show that if the beam is unstable initially, the coherent oscillations start to grow so that after a few structure periods the beam emittance is diluted enough to be in the stable area.

Situation would be different, were the beam under the cooling. Cooling would not allow the beam just permanently stay in the stable area: it would continue to shrink the emittance and lead the beam again to the instability threshold.

## 3 COLD BEAM AS A SOURCE OF NOISE

Thus, the electron cooling and the envelope instability can be considered to be in a dynamic equilibrium resulted in keeping the cooled beam at the threshold of the instability. The electric field of the oscillating beam core acts on the

outer, hot protons. The perturbation of the proton transverse energy is mainly contributed by such betatron phases when it passes the oscillating beam close enough, at impact parameters less or about the beam radius  $a_c$ . For a proton with an amplitude  $a \gg a_c$ , this happens in average once per time interval

$$\Delta t \simeq a/a_c \omega_b^{-1} \gg \omega_b^{-1},$$

where  $\omega_b = \nu\omega_0$  is the betatron frequency,  $\omega_0$  is the revolution frequency. Every time when the proton passes near the oscillating core, its angles are changed (increased or decreased) by about

$$\Delta\theta \simeq \frac{2\rho_p r_p c}{\beta\gamma^3 a_c} \frac{\tilde{a}_c}{a_c} \omega_b \tilde{\tau}^2, \quad (1)$$

where  $\rho_p$  is the proton beam linear density,  $r_p$  is the proton classical radius,  $c$  is the speed of light,  $\beta$  and  $\gamma$  are the relativistic factors,

$$\tilde{\tau} \simeq a_c/a\omega_b^{-1}$$

is a time of the interaction,  $\tilde{a}_c/a_c \simeq 1$  is the relative amplitude of the beam size oscillations responsible for the considered interaction. The quadratic dependence on the interaction time,  $\Delta\theta \propto \omega_b \tilde{\tau}^2$ , is related to the fact that the change of the proton transverse energy is caused by the free oscillations of the beam core, which contributes  $\propto \omega_b \tilde{\tau}$ . The constant field changes the momentum components, but not the total energy.

The main hypothesis of the presented model is that this energy change of the hot proton can be considered as random. In other words, it is assumed that the oscillating fields of the beam seen by the proton when it passes the core, are completely unrelated to the fields seen on the previous pass. This assumption looks acceptable due to the following factors:

- A correlation time for oscillations of a system near its instability threshold is typically not more than several periods of the oscillations.
- The longitudinal correlations of the envelope oscillations extend not longer than for the core radius. Due to the longitudinal velocity of the proton, every pass it sees the core at various longitudinal coordinates where the fields are not correlated.
- Finally, this assumption of random interactions can be modified: it could be assumed that the correlation time is by a certain factor  $f_r$  higher than the average time between consequent interactions. However, the calculations show that the resulted dependence on this factor is very weak, it enters as  $\propto f_r^{2/7}$ .

Thus, the interactions of the remote proton with the oscillating beam core are considered as independent inelastic scatterings causing a diffusion of the proton energy. The proton angle changes due to the simultaneous action of this diffusion with the coefficient

$$D = (\Delta\theta)^2/\Delta t = \frac{4\rho_p^2 r_p^2 a_c^3 c^2}{\omega_b a^5 \beta^2 \gamma^6} \quad (2)$$

and the electron cooling with the rate

$$\lambda = \frac{4\pi n_e r_e r_p L_C \eta c}{\theta^3 \beta^3 \gamma^5} \quad (3)$$

where  $n_e$  is the electron beam density,  $r_e, r_p$  are the electron and proton classical radii,  $L_C$  is the Coulomb logarithm and  $\eta$  is the cooling length related to the ring circumference,  $\theta = a\omega_b/(\beta c)$  is a proton angle amplitude.

Evolution of the proton distribution  $f(\theta)$  under an influence of the cooling and diffusion is described by the Fokker-Plank equation:

$$\frac{\partial f}{\partial t} = \frac{\partial}{\partial \theta} \left( -\lambda \theta f + \frac{D}{2} \frac{\partial f}{\partial \theta} \right). \quad (4)$$

This determines an equilibrium distribution:

$$f(\theta) = f_0 \exp \left( -2 \int_0^\theta \frac{\lambda(\theta') \theta' d\theta'}{D(\theta')} \right) \quad (5)$$

with  $f_0 \simeq 1/\theta_c$ , where  $\theta_c = a_c \omega_b/(\beta c)$  is the angle amplitude of the core particles. Assuming the aperture limit  $\theta = \theta_a = a_m \omega_b/(\beta c)$ , the life time  $\tau$  follows from (4), (5):

$$\tau^{-1} \simeq \lambda_a \theta_a \exp \left( -2 \int_0^{\theta_a} \frac{\lambda(\theta) \theta d\theta}{D(\theta)} \right), \quad \lambda_a = \lambda(\theta_a). \quad (6)$$

The lifetime (6) contains current-dependent terms in the exponent, so it is highly nonlinear function of the beam intensity.

Assuming a finite storage time  $\tau_s = d \ln N/dt$ , and taking into account the dependencies (2), (3) the intensity limitation follows:

$$\frac{\lambda_a \theta_a^2}{2D_a} = L_a, \quad L_a = \ln(\lambda_a \tau_s a_m/a_c), \quad D_a = D(\theta_a). \quad (7)$$

Then, the proton beam linear density  $\rho_p$  and its radius  $a_c$  determine the space charge tune shift

$$\Delta\nu = \frac{\rho_p r_p R^2}{2\nu \beta^2 \gamma^3 a_c^2} \quad (8)$$

where  $R$  is the storage ring average radius. The threshold condition (7) can be resolved for the proton beam peak current  $I_p = \rho_p e \beta c$  and presented in the following form:

$$I_p = e c \beta \gamma^{11/7} a_m^{8/7} \left( \frac{\pi n_e \eta L_C r_e}{2 L_a r_p} \right)^{2/7} \left( \frac{2\nu \Delta\nu \beta^2}{r_p R^2} \right)^{3/7}. \quad (9)$$

The obtained threshold (9) can be calculated for the parameters of the IUCF cooler. The aperture logarithm  $L_a$  (7) calculated with  $a_m = 1.5$  cm,  $a_c = 0.5$  mm,  $\lambda_a = 0.3$  s<sup>-1</sup>,  $\tau_s = 18$  s, comes out  $L_a = 6$ . Substituting  $I_e = \rho_e e \beta c = 400$  mA,  $a_e = 1.2$  cm,  $\beta = 0.3$ ,  $L_C = 3$ ,  $\eta = 0.03$ ,  $\nu = 4$ ,  $\Delta\nu = 0.25$ ,  $R = 15$  m, it gives  $I_p = 6$  mA, in an agreement with the observations [1]. Assuming the same aperture limitations and electron current, approximately same numbers ( $\pm 50\%$ ) comes out for the proton threshold current in CELSIUS and Kr<sup>34+</sup> current in SIS.

So we may conclude about an agreement between this model and the observations.

## 4 HOW TO INCREASE THIS THRESHOLD

A slight misalignment  $\psi$  introduced in both transverse directions between the electron and proton beam could increase the threshold. In this case the protons with smaller angles cannot be accumulated, this phase space area is unstable for the single particle motion (the so-called monochromatic instability). The angle provided in both transverse planes should be higher than the threshold beam angles  $\theta_c$  but smaller than the angle at the injection  $\theta_i$ :

$$\theta_c < \psi_{x,y} < \theta_i. \quad (10)$$

The higher is the misalignment, the higher is both the threshold current and the temperature of the accumulated protons.

An improvement with the similar restrictions (10) could be reached by means of the electron cooler with a hollow cathode [1, 13].

## 5 REFERENCES

- [1] T. Ellison et al., "Cooled Beam Intensity Limits in the IUCF Cooler", in *Proc. of Workshop on Beam Cooling and Related Topics, Montreux, Oct. 1993*, CERN 94-03, p. 377.
- [2] D. Reistad et al., "Measurements of Electron Cooling and 'Electron Heating' at CELSIUS", *ibid*, p. 183.
- [3] M. Steck et al., "Commissioning of the Electron Cooling Device in SIS", in *Proc. EPAC'98*, Stockholm, p. 550.
- [4] V. Parkhomchuk, "Limitation of Ion Beam Intensity in Electron Cooling Systems", in *Proc. HEACC'98*, Dubna, Russia.
- [5] S. Nagaitsev et al., *NIM A*, **391**, p.32 (1997).
- [6] S. Nagaitsev, PhD Thesis, Indiana University, 1995.
- [7] A. Burov, *Part. Accel.*, **57**, 131 (1997).
- [8] D. Pestrikov, *NIM A*, **412**, p.283 (1998).
- [9] I Hofmann, L. J. Laslett, L. Smith and I. Haber, *Part. Accel.*, **13**, 145 (1983).
- [10] J. Struckmeier and M. Reiser, *Part. Accel.*, **14**, 227 (1984).
- [11] L. Tecchio et al. "CRYSTAL Ring, Feasibility Study", LNL-INFN Rep., Legnaro, Italy (1996).
- [12] M. Reiser, *Theory and Design of Charged Particle Beams*, J. Wiley & Sons Inc., 1994.
- [13] A. Sharapa, A. Shemyakin, *NIM A* **336** p.6 (1993).

# COGGING IN THE FERMILAB BOOSTER\*

D. Herrup, FNAL, Batavia, IL<sup>†</sup>

## Abstract

The Fermilab Booster is a rapid-cycling synchrotron which accelerates 84 bunches of protons from 401 MeV to 8 GeV for injection into the Fermilab Main Injector. The entire circumference, ie., all RF buckets, of the Booster is filled. At extraction, a kicker deflects the beam into the extraction channel. The kicker risetime is long enough so that several of the bunches do not receive the full kick and are deflected instead into Booster magnets, creating radioactive components in the tunnel and radiation at ground level outside. At future Booster intensities and repetition rates, the radiation levels will be unacceptably high. One way of reducing these losses is to create a "notch" of several consecutive unfilled RF buckets. If the beam can be accelerated while tracking and controlling the position of the notch so that the unfilled buckets are aligned with the rising edge of the extraction kicker, losses will be eliminated. We have studied this process and developed an algorithm to count and control RF cycles during the Booster ramp and move ("cog") the notch longitudinally so that it is aligned with the kicker at extraction time. We will describe the relevant parts of the Booster hardware, measurements we have made to understand what controls the total number of RF cycles during a Booster ramp, and the algorithm we intend to use for cogging during the Booster cycle.

## 1 BOOSTER PARAMETERS

When the Fermilab Main Injector is in full operation, the Booster must deliver its batch of 84 bunches to a specified RF bucket in the Main Injector. In addition, the notch in the beam must be located at the Booster kickers when they fire. In order to move the notch to the proper location, we must be able to predict the total number of RF cycles in a Booster pulse to within a multiple of 84, the Booster harmonic number. Cogging is done by adding a radial offset to the beam, changing the revolution frequency, to add or subtract the necessary number of RF cycles. This technique has been used routinely at Fermilab in the Main Ring and Tevatron but in these accelerators cogging is done at flattop, ie., at a time when the RF frequency is constant. Cogging in the Booster is more complicated because there is no flattop. In addition, the shape of the Booster ramp (number of RF cycles) changes from pulse to pulse in ways which we do not completely understand.

The Booster design ramp is a 15 Hz. sinusoidal ramp in which the gradient magnets ramp at a "15 Hz." rate determined from the power line frequency. In principle, this

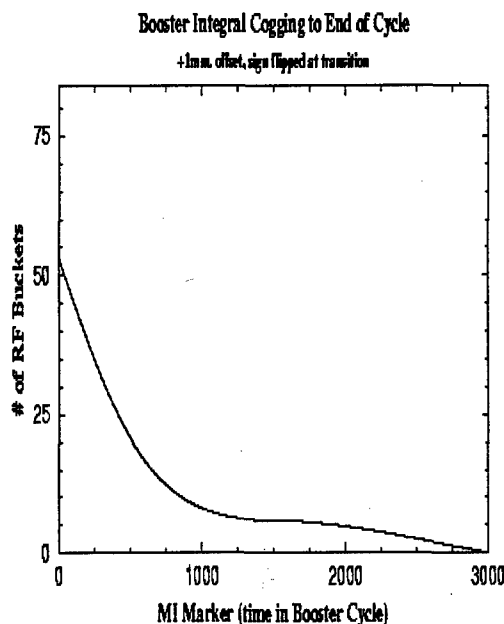


Figure 1: Integral cogging for a 1 mm. radial offset. The horizontal axis is in Main Injector marker units. There are roughly 3000 Main Injector revolutions in a single Booster pulse.

enables us to calculate the RF ramp exactly. However, the power line frequency is not exactly 60 Hz. but fluctuates by  $\pm 30$  mHz. A 30 mHz. difference in the line frequency causes a change of about 80 RF cycles from the ideal ramp. One could try to correct for variations in the line frequency by measuring the instantaneous frequency and calculating the change in the ramp, but it is not clear that the calculations could be done in real time. Changes in the radial position of a few mms. over the pulse also effect the number of RF cycles by roughly the same amount. Finally, there may be synchronization differences between the start of the magnet ramp and the start of the RF ramp, adding or subtracting hundreds of RF cycles to a pulse.

The Booster harmonic number is 84 so moving the notch to an arbitrary location at extraction requires cogging by  $\pm 42$  RF buckets. Fig. 1 is a plot of the number of RF buckets cogged for a 1 mm. radial offset whose sign is reversed at transition. The horizontal axis is in Main Injector Marker units where 1 unit represents about 11  $\mu$ sec., the Main Injector revolution time. Several important features are apparent from this plot. It is "easiest" to cog from about MI markers 200 to 800 (about 2 msec. to 8 msec. in time) in the cycle when the number of buckets cogged/radial offset is maximum. Conversely, the amount of cogging that can be done at the end of the cycle is very small. Of course, there is also

\* Work supported in part by the Department of Energy.

<sup>†</sup> Email: herrup@fnal.gov

a large period around transition (17 msec.) in which no cogging can occur. This information has already been applied [1] to do a simple form of cogging to try to align the notch with the kickers. In the rest of this paper I will describe a cogging algorithm which will attempt to do feedback during the cycle to align the gap with the kickers while minimizing the radial offset.

## 2 COGGING ALGORITHMS

The variations from Booster pulse to pulse mentioned earlier make it impossible to calculate the ramp from first principles. Instead, we must look for a set of measurements that can be performed during the cycle which will let us calculate the number of RF cycles. Two pieces of hardware are used to perform the measurements [1]: the Main Injector revolution marker and a module which will count the number of Booster RF cycles between consecutive Main Injector markers. These devices make it possible for us to calculate the number of RF cycles throughout the pulse in real time.

The algorithm I have found that seems to predict the location of the notch at extraction uses the RF cycles data acquired continuously throughout the pulse to make better and better predictions for the extraction location. We divide the Booster pulse into segments 100 Main Injector turns in length and count the number of RF cycles during each segment. Starting after receipt of the 500th Main Injector marker, we do a linear, 2 parameter fit of the form

$$TRF_i = a_i + b_i \sum_{j=0}^{j=i} RF_j$$

where  $TRF_i$  is the total number of RF cycles in the Booster pulse that one predicts based on measurements up to and including segment  $i$ . The slope ( $b_i$ ) and offset ( $a_i$ ) are different for each segment and have been determined from fits to complete Booster pulses. The 20 Booster pulses used for the comparison were chosen at random and are representative of the overall pulse to pulse variation in the total number of RF cycles. Application of this algorithm results in the data in Fig. 2 which shows the standard deviation between the predicted number of pulses at extraction and the measured number. By the midpoint of the cycle we can predict the extraction location to better than 2 RF buckets, and by the end of the cycle the standard deviation is less than 0.5 RF buckets.

I should make several comments about Fig. 2. We have found that there is very little predictive power contained in the information in the first 5 msec (500 MI markers) of the Booster cycle. This is the period during which the RF frequency changes most rapidly. Also, the radial loop turns on during this period, and we have observed large excursions in the horizontal closed orbit caused by the radial loop, and this certainly will effect the number of RF cycles at that

instant without necessarily changing any other parts of the ramp. The plateau from segment 12 to 20 corresponds to transition, in which no cogging occurs. This is the same plateau that occurs in Fig. 2 between MI markers 1200 and 2000.

From these data, we can sketch a more detailed version of the cogging algorithm. No cogging is done until 5 msec. after injection. Between 5 and 12 msec, the predictions for the extraction location improve to under 1 RF bucket, and we can set the radial offset at the end of each 100 MI-marker segment to align the notch with the kickers to a precision of about 1 RF bucket. The maximum radial offset needed will be less than 3 mm., comfortably within the Booster aperture. For the rest of the cycle until extraction, we can continue this "feedback" process every 100 MI markers, but since the predicted extraction location is now accurate to within 1 RF bucket, only very small radial offsets will be needed.

This algorithm requires only a small number of calculations (summing RF cycles and performing the multiplications needed to predict the total number of RF cycles in a pulse) and can easily be done in the DSP which runs the low level RF system [1] and which can control the radial offset.

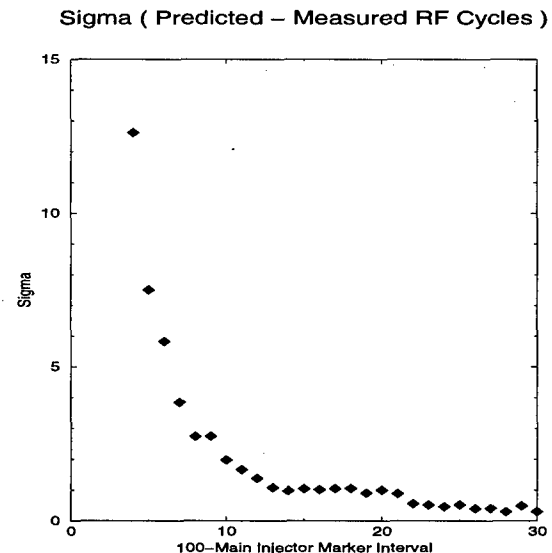


Figure 2: Integral cogging for a 1 mm. radial offset. The horizontal axis is in Main Injector marker units. There are roughly 3000 Main Injector revolutions in a single Booster pulse so extraction occurs at about MI marker 3000.

## 3 CONCLUSIONS

I have outlined an algorithm which I believe will allow the notch in the Booster beam to be aligned with the kickers at extraction, thereby eliminating extraction losses which occur in a completely filled ring. The algorithm develops a cogging trajectory which tries to use as small a radial off-



set as possible by improving the estimate of the extraction location of the notch throughout the pulse.

Considerably more work must be done before we shall have a working cogging system. There are, of course, the hardware issues associated with creating the notch and ensuring that instrumentation will work properly [1]. We shall repeat these measurements and try to refine the algorithm in small ways and to re-determine the constants. Finally, the algorithm must be coded in the low level RF DSP and diagnostics developed.

#### **4 ACKNOWLEDGEMENTS**

Thanks to Bob Webber for suggesting this problem and Bill Pellico for developing the hardware.

#### **5 REFERENCES**

- [1] William A. Pellico and Robert C. Webber, RF Cogging in the FNAL Booster Accelerator, proceedings of this conference.

# WIDE BAND FREE SPACE TRANSMISSION LINK UTILIZING A MODULATED INFRARED LASER

Ralph J. Pasquinelli, Fermilab\*, Batavia, IL

## Abstract

For years, Fermilab has utilized wide bandwidth transmission links for stochastic cooling feed back systems.<sup>1,2,3</sup> Stochastic cooling requires the feed back signal arrive at the kicker in time synchrony with the beam on the same turn. While coaxial cables suffice at lower microwave frequencies, their high loss and dispersion make them unsuitable at higher frequencies. Coaxial cables up to 125 meters in length have been utilized in the Antiproton Source. With the advent of the Recycler ring, (600-900 meters in diameter) coaxial cables have unacceptable losses. Stochastic cooling will be utilized in the Recycler to maintain a small beam emittance and momentum spread. A new means of transmitting the signal across the ring is necessary. While optical fibers have very low loss and excellent bandwidth characteristics, their propagation velocity is too slow to meet the beam on the other side of the ring. A modulated infrared laser is expanded from single mode fiber (utilizing telescopes) and transmitted in an evacuated pipe across the ring. The system will be described with preliminary results presented.

## 1 ACCUMULATOR SYSTEM

The first free space light link to be constructed at Fermilab was for the core transverse cooling systems in the Accumulator. These systems operate between 4-8 GHz with cable lengths approaching 100 meters. The insertion loss on half-inch coax is 18 dB to 28 dB for this length and frequency range. In addition, up to 360 degrees of phase dispersion is experienced, requiring a specialized phase equalizer.

These optical links provide flat amplitude and phase response for broadband microwave links. Typical response is plus minus 1 dB and 10 degrees phase flatness for the bandwidths mentioned. This comes at the expense of an overall insertion loss approaching 35 dB.

A means of transmitting the signal in free space is required to meet the timing needs of stochastic cooling. An optical setup consisting of a fiber to graded index (GRIN) lens and a twenty-time telescope expander is utilized to enlarge the nine-micron diameter laser beam to approximately one-centimeter diameter. At

this size, the beam can propagate with minimal increase in spot size for the 76 meters of the accumulator test. A similar telescope is used on the receiving end to focus the 1310 nanometer beam onto a Hamamatsu fast photo diode.<sup>4</sup> This photo diode not only has a response beyond 8 GHz, but also a large active area of 200 microns square. This large active area allows building a system that is relatively insensitive to random laser beam motion. (Earlier tests utilized a GRIN lens on the receiving end that required motion feedback.)

Because timing stability is critical to stochastic cooling performance, the transmission medium must have a stable propagation velocity. The velocity of light in a medium is inversely proportional to the index of refraction of the medium. In addition, the defocusing caused by changes in the index of refraction could cause the laser beam position to vary as a function of time. Anyone who has experienced "heat ripple" in a parking lot on a hot day has observed this phenomena. The only way to preserve the five picosecond timing tolerance is to transmit the laser through a vacuum.

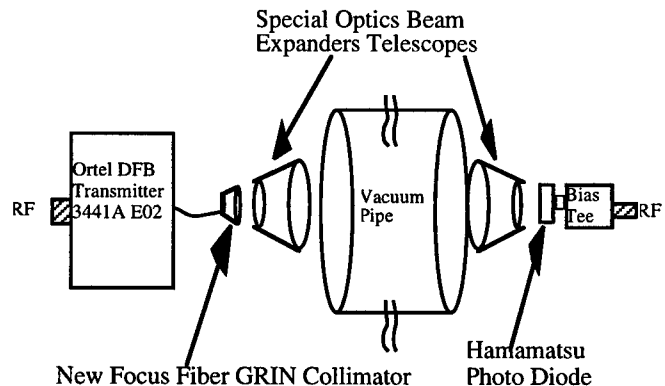


Figure 1. Optical link hardware configuration.

A twenty-inch diameter steel pipe was buried across a cord of the Accumulator ring to provide the light path for the laser beam. A Roots blower vacuum pump is utilized to reach a vacuum of approximately one Torr. Quartz vacuum windows provide the seal between the telescopes and the vacuum pipe. Figure 1 is a schematic of the test setup.

\*Operated by Universities Research Association for the Department of Energy

## 2 RECYCLER SYSTEM

The Recycler Ring is the new antiproton depository storage ring that is being commissioned at Fermilab.<sup>5</sup> This ring is fabricated with permanent magnets and is housed in the same enclosure with the Main Injector. Although electron cooling is planned for the future, stochastic cooling will be utilized initially. The size of the Recycler is approximately 3.3 kilometers in circumference. As with all stochastic cooling, feedback must be applied on the same turn of the beam for optimum performance. In the Recycler, this means a chord across the ring approaches 600 meters.

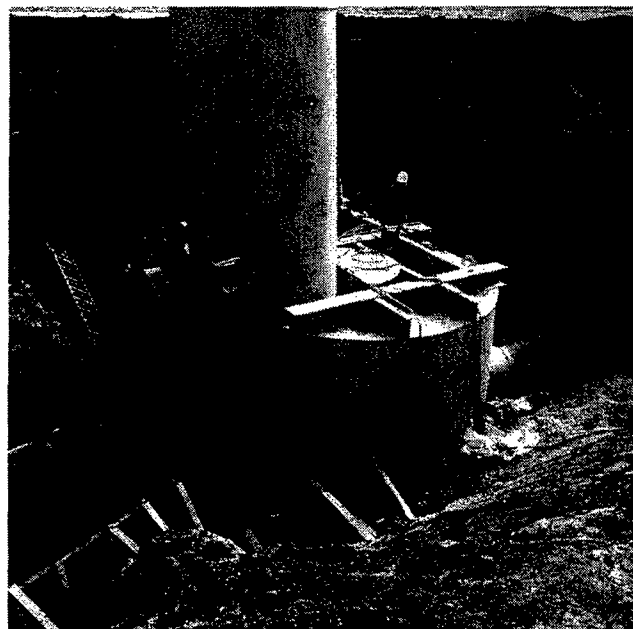
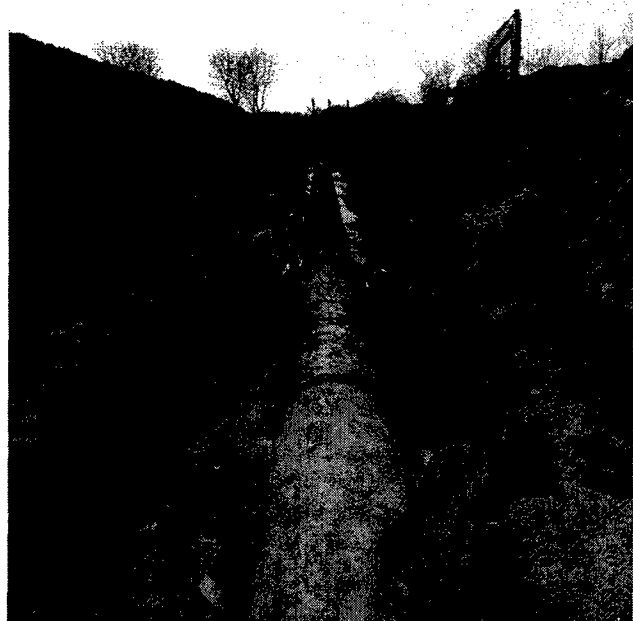


Figure 2. Top: light pipe installation. Bottom: Underground equipment enclosure, fondly referred to as the "peanut".

The cooling systems in the Recycler operate in the frequency bands of 0.5-4 GHz. Coax cable with a 7/8-inch diameter would provide 20-60 dB insertion loss and phase dispersion of hundreds of degrees, both unacceptable. Even the best cable has a propagation velocity of 88% c, requiring a longer chord than a light link.

A civil construction project is currently underway to bury a 24-inch diameter steel pipe between the ten and twenty sectors of the Main Injector/Recycler complex. (Figure 2) There are a total of four cooling systems that will have their signals transmitted through this pipe. The large pipe size was chosen to minimize civil construction tolerances based on a trade off in material versus labor costs. At the ends of pipe, underground enclosures are buried just outside the minimum shielding requirements for the Main Injector, hence allowing unlimited occupancy. Beneficial occupancy of the light link enclosures is expected by April 1999. Initial light link tests will begin shortly there after. Commissioning of Recycler stochastic cooling is expected for later in the summer of 1999.

Due to the longer length of the Recycler light link, the laser beam will experience more beam dispersion. It is expected that the beam diameter will increase to near 8 centimeters. This coupled with a long baseline will add to the position sensitivity of the system. Bench experiments have shown that the laser beam can be focused to a full width of 100 microns utilizing the twenty-power telescope. Due to the large size of the photo detector (200x200 microns), it is hoped that position sensitivity will not be a problem.

## 3 ACCUMULATOR PERFORMANCE

A complete core vertical cooling system was installed in the Accumulator ring in July of 1997 before the long site shutdown to finalize Main Injector installation. This system was installed in parallel to the original cable based cooling system so that a side by side comparison could be made. Figure 3 shows the amplitude and phase transfer functions for the two systems under identical beam conditions. As can be seen from the cable based system, there is a high frequency degradation in signal to noise ratio because of the gain slope losses. The light link with its flat response shows improved signal to noise at the high frequency end of the band. The remnant gain slope present in both responses is due to bandwidth limitations of the system pickups and kickers. Figure 4 depicts the difference in signal suppression between the cable and light link system. A customized equalizer has been designed to remove the gain slope and will be installed in the near future. Both core transverse-cooling systems will be upgraded to light links for the startup of the Accumulator ring.

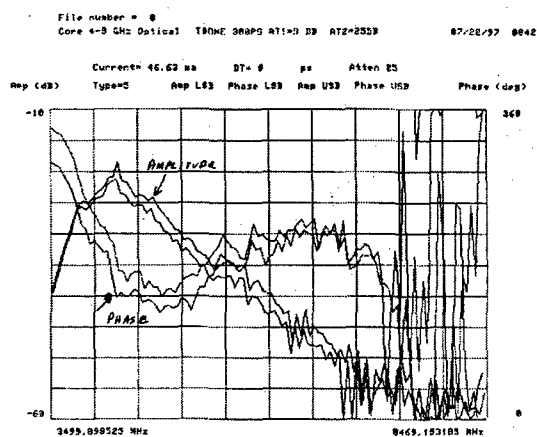
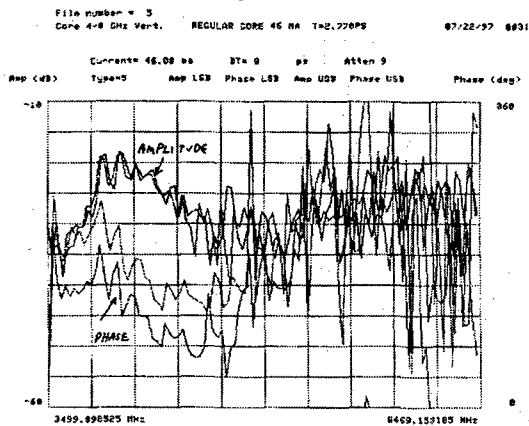


Figure 3. Accumulator beam transfer functions. Top: original cable transmission across ring. Bottom: optical link transmission across ring. Taken under identical conditions. Scale: 5 dB and 36 degrees per division. Frequency sweep: 3.5-8.5 GHz

#### 4 ACKNOWLEDGEMENTS

The work to create the light links has been possible by the efforts of the Beams and FESS Divisions of Fermilab. The civil construction is critical to system performance. The diligence of the Antiproton Source Stochastic Cooling group made the Accumulator test possible.

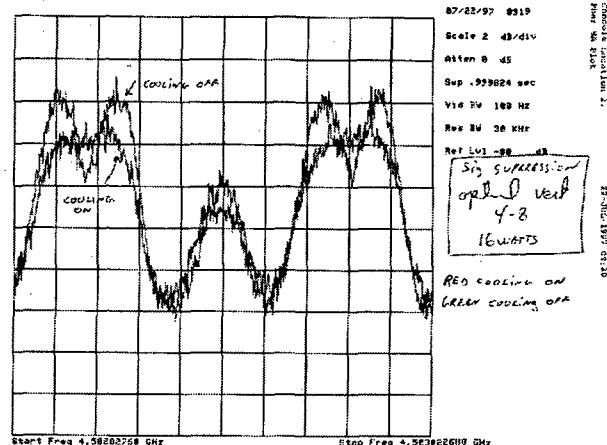
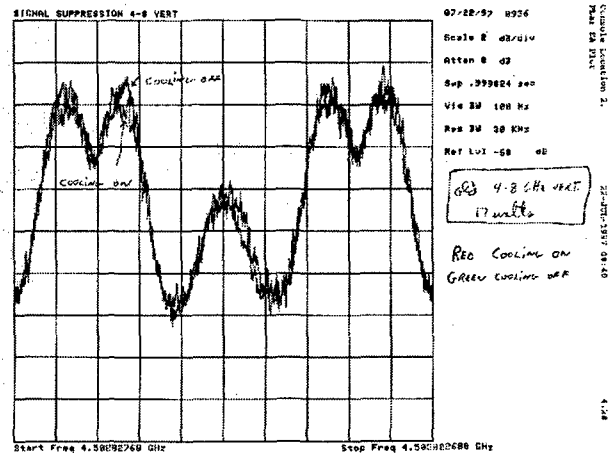


Figure 4. Signal Suppression measurements on Accumulator Beam. Top: Original cable transmission. Bottom: Optical link transmission. Red closed loop, Green open loop. Taken under identical conditions. Scale: 2 dB/div, Span 100 kHz at 4.5 GHz

#### 5 REFERENCES

- [1] Electro-Optical Technology Applied to Accelerator Beam Measurement and Control, Ralph J. Pasquinelli, IEEE Nuclear Science, May 1993, Washington D.C.
- [2] Fiber Optic Links for Instrumentation, Ralph J. Pasquinelli, Conference Proceedings of the Accelerator Instrumentation Workshop, October 1990
- [3] Optical Notch Filters for Fermilab Debuncher Betatron Stochastic Cooling, Ralph J. Pasquinelli et. al., IEEE Nuclear Science, March 1989
- [4] Hamamatsu Corporation, Ultrafast InGaAs MSM Photodetectors G7096 series, July 1997.
- [5] Recycler Ring Technical Design Report; Gerry Jackson, editor, Fermilab internal report TM-1991, 1996.

# RF COGGING IN THE FNAL BOOSTER ACCELERATOR

W.A.Pellico, Robert C.Webber, Fermi National Accelerator Laboratory<sup>1</sup>, Batavia, IL 60510

## Abstract

The Fermilab Booster operates at a Radio Frequency (RF) harmonic number of 84 with beam in all buckets. One or two bunches of beam are systematically lost in the 8 GeV extraction process as beam is swept across a magnetic septum during the extraction kicker rise time. The prompt radiation and component activation resulting from this localized high energy beam loss become serious concerns as Booster beam throughput must be increased more than tenfold to meet the requirements of RUN II, NUMI, and MiniBooNE experiments. Synchronizing a gap in the beam to the firing of the extraction kickers, a relatively easy and standard practice in many machines, can eliminate the problem. This seemingly simple operation is greatly complicated in the Booster by the need to synchronize extraction to beam already circulating in the Main Injector. Coupled with the inflexibility of the Booster resonant magnetic cycle, cycle to cycle variations, and constraints inherent in the accelerator physics, that requirement forces active control of the gap's azimuthal position throughout the acceleration process as the revolution frequency sweeps rapidly. Until recently, the complexities of actually implementing and demonstrating this process in the Booster had not been worked out. This paper describes a successful demonstration of gap cogging in the Booster.

## 1. INTRODUCTION

The Booster accelerates protons from 400MeV to 8GeV for injection into the Main Injector accelerator. The Main Injector, seven times the Booster circumference, has numerous operating modes requiring 1 to 7 batches of Booster beam per cycle. The method of synchronous transfer between the Booster and the Main Ring was historically done by extracting Booster beam upon receipt of a marker signal corresponding to the desired Main Ring bucket [1]. The extraction pulse was tuned by changing the marker delay in units of RF cycles. The risetime of the extraction kicker is approximately twice the Booster bunch spacing, resulting in 8GeV Booster beam loss. A solution to the loss would be to put a gap in Booster beam at the injection energy and then cog the gap to be synchronous with the desired Main Injector bucket marker at extraction. An analysis of Booster's acceleration process is needed to understand some of the difficulties in accomplishing a gap synchronous transfer.

## 2. TYPICAL BOOSTER CYCLE

Injected beam is adiabatically captured in Booster using a RF paraphasing process that takes approximately 600 us. Acceleration phase and position feedback is turned on after the beam is bunched. The Booster's time dependent radial position curve, radial gain curve, a frequency curve, and associated high level curves are triggered by clock events delivered by a 10Mhz clock distribution system. The Booster magnets are powered as part of a 15 Hz resonant circuit. The beam momentum will therefore ideally be a sinusoidal function of time:

$$p(t) = p_i + 0.5(p_f - p_i)(1 - \cos(30\pi t))$$

where  $p_i$  is the Booster injection momentum and  $p_f$  is the final Booster momentum

The magnet circuit is driven at one-fourth the power line frequency, not identically 15 Hz. The clock system has feedback to track the line frequency for slow variations. However, the clock and magnet current exhibit pulse to pulse timing variations due, at least in part, to changes in power line frequency drift that occurs on a short time scale. At about 18ms in the cycle the Booster beam goes through transition. At the end of the acceleration cycle, approximately 3 ms prior to extraction, position feedback is shut off and phase lock between Booster and Main Injector is enabled. Hardware design requires the phase lock on time to be set to the time when Booster RF is 8 kHz below Main Injector RF. The acceleration frequency changes rapidly early in the cycle with very little change occurring after transition. The synchrotron frequency also changes rapidly early in the cycle, goes to zero at transition, then levels off at about 2.5Khz for the remainder of the cycle. Booster's revolution period changes from 2.22us to 1.69us in 33ms. During the Booster cycle, the Main Injector rests at a fixed injection frequency of 52.811 MHz; its revolution marker period is fixed at seven times 1.69us. Figure 1 shows some useful RF curves plotted versus time in the Booster cycle.

## 3. MEASUREMENT SYSTEM LAYOUT

A measurement system was assembled to track the location of the Booster beam gap relative to the MI revolution marker throughout the Booster cycle. The measurement consists of counting the number of Booster RF cycles between each MI marker (occurring about every 10 usec) and the first Booster gap marker to follow. The measurement system was able to be tested online with

<sup>1</sup> Operated by the University Research Association, under contract with the U.S. Department of Energy.

actual beam signals or to be run off-line in a more controlled environment. The test setup adapted spare operational low level hardware to minimize the initial engineering setup time [2]. The system consists of a VXI crate with a Direct Digital Synthesizer (DDS), a

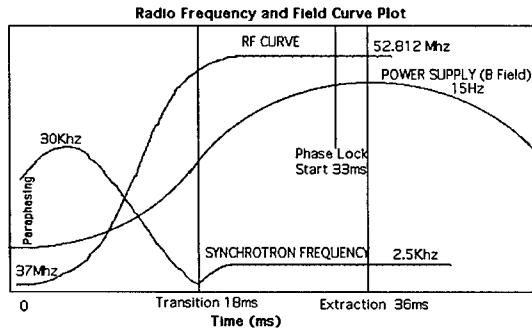


**Figure 1: Booster RF and magnet field curves for a typical cycle.**

Digital Synthesizer Processor (DSP), a programmable VLSI chip located on the DSP VXI card, and a personnel computer (PC). The DDS generates simulated beam RF when running off-line. The DSP reads and processes data and writes it to shared memory and to one of three on-board DACs. The programmable VLSI acts as a counter, buffer, and timer interface for the test setup. The PC provides a user interface for the necessary online control and a platform for off-line analysis. The interface between the PC and DSP was done using the VXI based CPU.

#### 4. DESIRED BUCKET VERSE MAIN INJECTOR

In a typical Booster cycle the Booster gap marker wraps past the MI revolution marker many times [3]. The rate of wrap is greatest in the beginning of the cycle and slows as the RF frequency difference between the two machines diminishes. The initial offset between the MI marker and Booster gap marker can be made to be zero by starting the gap marker synchronously with the MI marker. The RF count measured throughout the cycle will be in the range of 0 to 84. The wrap in RF counts is the result of mixing two different frequencies, which will result in a sinusoidal term corresponding to the signal's frequency difference. Figure 2 shows a typical measurement data set during a Booster cycle. The plot size does not allow one to see the initial bucket offset or step size.

The DSP software can be set up to recognize the fact that the error count need not be greater than 42 (half a Booster turn) and give a count plot that wraps at 42 buckets.

Figure 2 has 3000 data points that were generated by the VLSI counter. Each data point, in units of Booster RF cycles, is obtained by starting the counter on a MI

marker and stopping it on the first Booster Gap marker to follow. The DSP is given an interrupt after each count to let it know there is new data to be read. The VXI CPU is used to collect the data from shared memory to be used for off-line analysis. The majority of phase wrap that occurs is expected and does not change pulse to pulse. A small fraction of the phase wrap is due to cycle to cycle

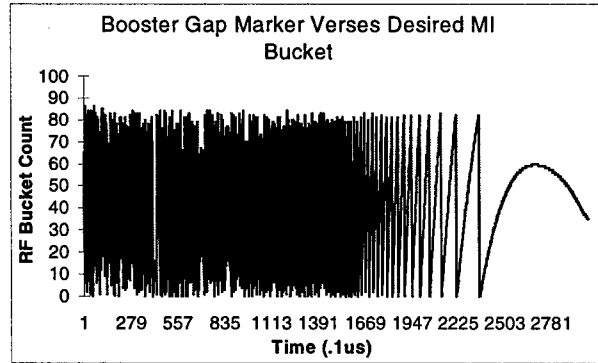


**Figure 2: Plot of the RF bucket count between the MI revolution marker and the Booster Gap marker.**

variations. The cycle dependent RF count difference can be filtered out of the bucket wrap error by defining a nominal cycle.

The result of comparing a nominal cycle to other Booster cycles is a slowly varying error count that is more easily managed. Figure 3 below shows a typical comparison between a nominal cycle and another Booster cycle. The DSP can also be made to integrate the error count. A comparison between the nominal cycle and one that is allowed to integrate the error will show the difference in the total number of revolutions. The variations in Booster

#### RF Count Error (Using Nominal Cycle)

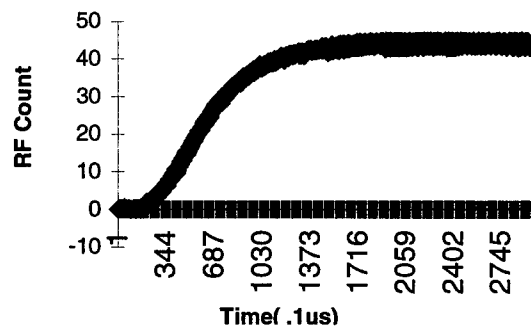


**Figure 3: A typical cycle RF count slip when a nominal cycle count is subtracted.**

cycles can be traced to several factors. The largest variance appears to come from the previously mentioned variation between timing of Booster triggers and the magnetic field cycle. When the radial position is held fixed, a bend field out of synch with the frequency curve will necessitate a frequency correction. Another contributor of pulse to pulse variations is incoming beam momentum fluctuations.

## 5. GAP BUCKET CONTROL

The Booster gap needs to be created early in the cycle in order to guarantee enough time to cog the worst case 42 buckets. Booster's large  $\eta$  before transition allows the radial position to have a greater lever arm in controlling the cogging during that portion of the cycle. A one-millimeter radial position offset from injection to the end of the cycle will result in a 55 bucket offset from that of a nominal cycle. That same one-millimeter position offset beginning at transition, about half way through the cycle, will result in only a 5 bucket offset at the end of the cycle. Clearly the control process needs to start shortly after injection.

With the gap created early in the cycle, there is the problem of integrating the cogging feedback with the required low level feedback systems. The different systems may fight, making the overall feedback unstable. The radial position feedback attempts to force the radial position to track a programmed curve. The cogging feedback may well require a different position offset. In the cogging test, the cogging error signal was used to modify the programmed radial position curve, but clipped in amplitude to limit resulting position excursions. The DSP controls the cogging error gain and correctly handles the sign flip required at transition.

The resulting system proved able to cog Booster beam to  $\pm 3$  RF cycles of the desired target (see Figure 4.) Initially, large position swings from overly aggressive cogging sometimes resulted in beam loss. A solution was to make the DSP smarter, calculating a predicted final bucket offset from a few milliseconds of observed bucket error at the start of the cycle. The prediction relied upon the fact that once the cycle begins the relative frequency curve/Booster momentum offset can be determined. This offset will manifest itself in terms of a bucket slip rate. (As mentioned

earlier, measurements have shown that the initial mismatch between the Booster's momentum cycle and frequency curve timing will be the major contributor to the final bucket offset.) This bucket prediction alleviated some over correction and allowed for most of the correction to be done early in the cycle. The DSP was also set up to have different gains before and after transition. The reason for different gains was to give flexibility and control the amount of position correction after transition. Other work is in progress to define an improved cogging prediction and control algorithm [4].

## 6. CONCLUSION

The ability to cog beam in a rapidly cycling machine with a large frequency swing has proven to be a difficult task. The successful outcome was made possible by using a system that could quickly gather and perform the necessary mathematical computations. The DSP software allows for flexibility in data collection and error calculation. This proved important since the required functions seemed to need to change during each step of the cogging development process. The software now does all the number crunching for the feed forward prediction, gain control, and data I/O. The VLSI hardware puts out a count, the number of Booster RF cycles between the MI revolution marker and the first Booster gap marker it sees, which is detected by the DSP. The DSP will then collect enough points to make a prediction of the gap and MI revolution marker's final separation. The error will translate into a position correction, which has both amplitude and time constraints. The ability to control both the horizontal position amplitude and duration will allow greater operational tuning.

A possible upgrade to the prediction code will be to incorporate the predicted error into the creation of the gap. This will alleviate the need to make any large initial corrections. The trade off between smaller positional corrections and creating a gap later in the cycle needs further analysis.

## 7. REFERENCES

- [1] R. J. Ducar, et al., "FNAL Booster Intensity, Extraction, and Synchronization Control for Collider Operation", IEEE Catalog No. 87CH2387-9, Proceedings of the 1987 IEEE Particle Accelerator Conference, Washington, D.C., March 1987, pp.1937-1939.
- [2] Robert C. Webber, "Fermilab Booster Low Level RF System -206 Upgrades", IEEE Catalog No. 95CH35943, Proceedings of the 1995 particle Accelerator Conference, Dallas, TX, May 1995.
- [2] The SSC Low Energy Booster, H. Ulrich Wienands, IEEE Press, 1997, New York, NY, pp.192-206 (contribution of L.K. Mestha).
- [4] David A. Herrup, "Cogging in the Fermilab Booster", paper TUA11, this conference.

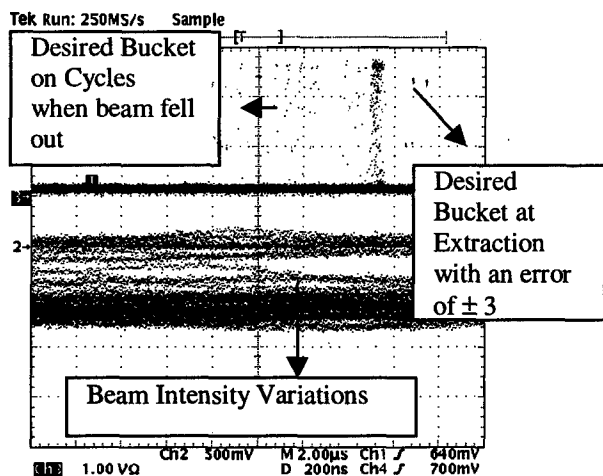


Figure 4: The cogged Booster Gap at extraction showing a small error. The top trace is the marker at extraction time on a 200ns/division time scale.

## THE RHIC BEAM ABORT KICKER SYSTEM\*

H. Hahn,<sup>†</sup> A. Dunbar, C. I. Pai, R. T. Sanders, N. Tsoupas,  
J. E. Tuozzolo, BNL, Upton, NY

### Abstract

The energy stored in the RHIC beam is about 200 kJ per ring at design energy and intensity. To prevent quenching of the superconducting magnets or material damage, the beam will be safely disposed of by an internal beam abort system, which includes the kicker magnets, the pulsed power supplies, and the dump absorber. Disposal of heavy ions, such as gold, imposes design constraints more severe than those for proton beams of equal intensity. In order to minimize the thermal shock in the carbon-fiber dump block, the bunches must be laterally dispersed. The nominal horizontal beam deflection angle is required to vary from  $\sim 1.7$  to  $2.5$  mrad, which is obtained from five  $1.22$  m long kicker modules operating at a magnetic field of  $\sim 3.5$  T. The kickers are constructed as window frame magnets with an  $50.8$  by  $76.2$  mm aperture and are operated in the ring vacuum. The pulsed power supplies run at  $33$  kV and deliver the  $12.8$   $\mu$ s long pulse. The peak current required is  $\sim 21$  kA and the 50% modulation is generated by means of a pulse forming network with non-uniform characteristic impedance.

### 1 INTRODUCTION

The Relativistic Heavy Ion Collider, RHIC, is a machine with two superconducting magnet rings capable of accelerating and storing particles at energies from  $10$  to  $100$  GeV/u in each beam. There are nominally  $60$  beam bunches with a total stored energy of  $\sim 200$  kJ at top energy and design intensity of  $10^9$  ions in the case of gold. This energy is large enough to quench the superconducting magnets or cause material damage if lost in an uncontrolled manner but it is small enough to be disposed of in an economical internal dump.

The stored beam energy can be disposed of within the constraints of the lattice without damage to the machine equipment or operation, provided that certain precautions are taken. Disposal of gold beams imposes more severe constraints on the dump block design than protons due to the large,  $Z^2$  dependent,  $dE/dx$  and short interaction length of the Au ions. This problem is handled by adopting at the dump entry a special carbon-carbon absorber material having extremely high thermal shock resistance.<sup>[1]</sup> The absorber is located in the beam vacuum, but properly pumped. Minimizing the thermally induced stress is achieved by lateral dispersion of the beam on the face of the C-C block.

The beam abort systems are located in the  $34$ -m long warm straight sections of the outer rings down stream of the  $10$  o'clock intersection point. At this location, the lattice properties favor horizontal deflection. In addition to the dump absorber proper, the beam abort system includes the kicker magnet and the pulsed power supply subsystems. The principle requirements and design features of the kicker magnets and the pulsed power supplies are presented in this paper.

### 2 DESIGN REQUIREMENTS

The kick strength is determined by the transverse dimensions of the CC block and the distance between kicker and dump face. The C-C block is  $0.5$  m long with a cross section of  $58 \times 58$  mm. Its distance from the nominal closed orbit is  $19$  mm. In order to fully use the C-C block, and given the limited distance of  $23.7$  m between kicker center to dump face, the deflection angle of a single ion can cover the range from  $0.82$  to  $3.22$  mrad. The deflection is provided by  $5$  separate kickers; allowing for malfunction of one unit and to accommodate a  $\sim 7\pi$  mm.mrad (unnormalized) dump aperture, the beam center is scanned over the range from  $1.68$  to  $2.52$  mrad, thereby spreading ions laterally over  $\sim 42$  mm.

One kicker unit is  $1.22$  m long and has an aperture of  $50.8$ -mm horizontal  $\times$   $76.2$ -mm vertical. Deflecting the beam at full energy of  $100$  GeV/u by  $2.52/5$  mrad is achieved with a magnetic field of  $0.35$  T, corresponding to a current of  $21$  kA. The pulsed power unit generates the current pulses with a voltage of  $33$  kV.

The beam structure imposes several basic design constraints on the abort system. The rotation time of the bunches is  $12.8$   $\mu$ s which determines the length of the deflecting pulse. The spacing of bunches is  $0.213$   $\mu$ s and the total bunch length is expected to be  $\leq 16$  ns under normal operating conditions. Thus, allowing for a gap in the beam created by  $4$  missing bunches, the rise time of the deflecting kick must be  $< 1$   $\mu$ s. Spreading of the beam over the C-C block could be achieved by a wiggler; a more economical solution is obtained by adopting a pulse forming network with non uniform characteristic impedance.

\* Work performed under the auspices of the U. S. Dept. of Energy.

<sup>†</sup> E-mail: hahn@bnl.gov



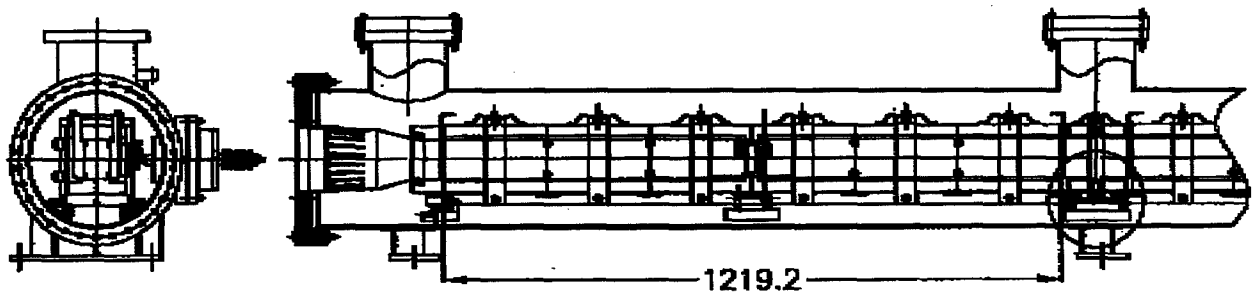


Fig. 1. Abort kicker vessel (in mm).

### 3 KICKER MAGNETS

The series of five kicker magnets is mounted in one common vacuum vessel. A partial side view and its cross section with the magnets installed are shown in Fig. 1. Also shown are the shields to reduce the coupling impedance of the device. The vessel with the magnets is part of the ring vacuum, the required vacuum levels being maintained by six sputter ion pumps placed atop the structure. To achieve the required vacuum, the entire unit is bakeable to 250 °C.

The kicker is constructed as a window frame magnet employing Ceramics Magnetics CMD 5005 ferrite blocks as shown in Fig. 2. The magnetic field in the return path is kept below 0.32 T. Finite element analysis has been performed showing a field uniformity of better than 5% over the full aperture of the magnet in spite of a local saturated spot. The mechanical construction of the magnets is straight forward, with the exception of the busbar. Arcing problems in a model were eliminated in the final units by using a highly polished stainless steel bus bar. The bus bar is electrically isolated from the vacuum vessel and connected to the pulser via the feedthrough, specially developed for this application and shown in Fig. 3.

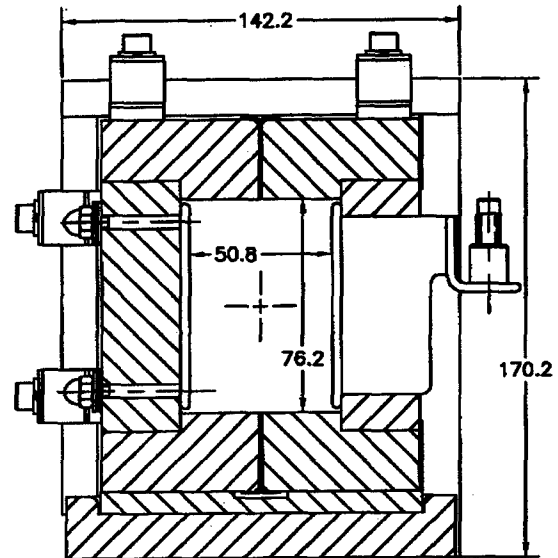


Fig. 2. Abort kicker cross section (in mm).

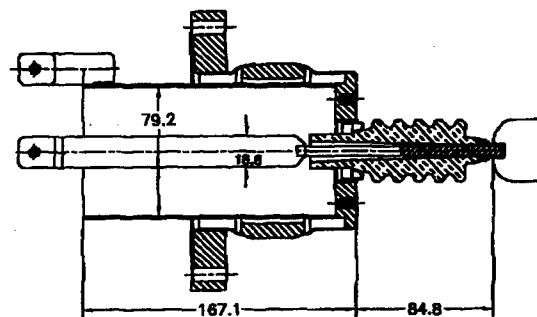


Fig. 3. Feedthrough by ISI (in mm).

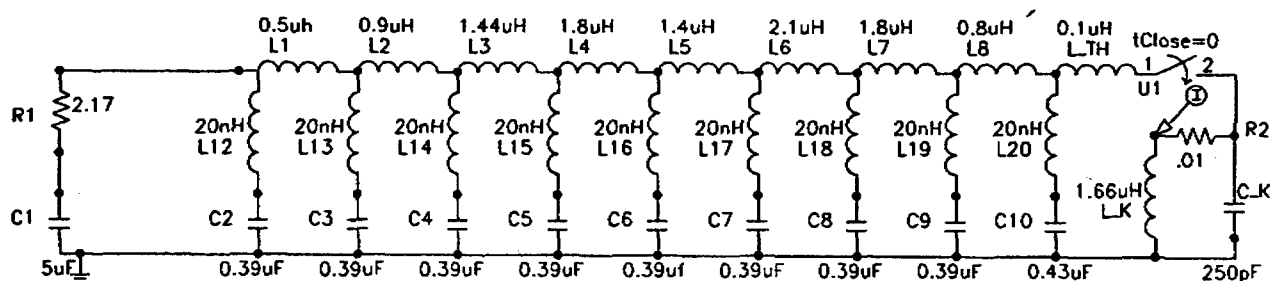


Fig. 4. Pulse forming network.

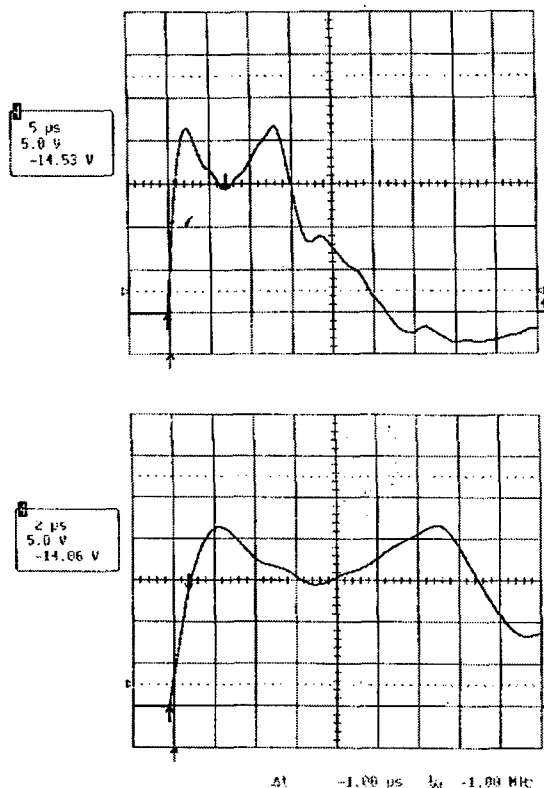


Fig. 5. Abort kicker current pulse shape at 33 kV (5 kA per unit).

## 4 PULSED POWER SUPPLY

A separate power modulator powers each abort kicker magnet. The main components of the modulator are the Pulse Forming Network, the deuterium thyatron EEV CX1575C to hold off voltage, the DC power supply, and the trigger circuitry. The ceramic 4.5-in. diameter hollow anode tube was selected in view of its reverse current capabilities and is operated in air. The measured inductance of the kicker magnet with feedthrough is 1.67  $\mu$ H. In order to achieve the 1  $\mu$ s rise time, a PFN impedance of  $\sim 2 \Omega$  is required, which brings the voltage into the 30 - 40 kV range.

Dispersing the beam on the dump block is achieved by modulating the current during the pulse between 14 and 21 kA at top energy. This is accomplished by using a PFN in

which the impedance of the network is mismatched and tapered from one end to the other (Fig. 4). The observed current pulse at 33 kV is shown in Fig. 5. Although relatively conventional in its design, pre-fire problems plagued the units. Holding the voltage during the 10-hour store time was finally demonstrated after careful conditioning of the thyatron and proper choice of the trigger circuitry. The latter design was complicated by the broad operating range from RHIC injection energy to storage energy or  $\sim 3$  to 33 kV.

## 5 ACKNOWLEDGEMENTS

The conceptual design of the beam abort system was finalized by Michael Harrison and the preliminary design of the pulsed power supply was done by Eric Forsyth and Chris Pappas. It is with pleasure to acknowledge consultations on the pre-fire problem with Ron Sheldrake (EEV), Ron Navrocky and Joe Sheehan (NSNLS), Laurent Ducimetiere (CERN), Chris Jensen (FNAL), and our colleagues from the AGS and RHIC.

## 6 REFERENCES

- [1] A. J. Stevens, *Conceptual Design of the RHIC Dump Core*, Report AD/RHIC/RD-94 (BNL 1995).

# THE COUPLING IMPEDANCE OF A TOROIDAL BEAM TUBE WITH CIRCULAR CROSS SECTION\*

H. Hahn,<sup>†</sup> BNL, Upton, NY

## Abstract

In this paper, the longitudinal coupling impedance of a toroidal beam tube with circular cross section is derived in the frequency domain using the toroidal coordinate system. Exact, although coupled, differential equations for the azimuthal field components are obtained. An approximate solution, valid in the limit of small curvature, is then derived. Assuming extreme relativistic energies and a beam tube with perfectly conducting walls, one finds a closed-form expression for the purely reactive coupling impedance which at low mode numbers is dependent on the tube geometry but which at very large mode numbers approaches the free space impedance.

## 1 INTRODUCTION

In contrast to the incoherent synchrotron radiation, the coherent radiation has been so far of limited practical importance but could become important for machines with very short bunches. In any case, the study of the interaction of a circular beam with its environment, here described by the coupling impedance, is a topic of considerable theoretical interest and has been addressed by many accelerator physicists, most recently in the paper by Murphy et al.<sup>[1]</sup> or in the book by Zotter and Kheifets,<sup>[2]</sup> where references to many relevant studies can be found. The complete expression for the coupling impedance due to coherent synchrotron radiation in *free space* is found in ref. 1; from this follow the Bonch-Osmolovski/Faltens/Laslett asymptotic approximation valid at mode numbers  $n \ll n_c$  as well as the asymptotic approximation valid when  $n \gg n_c$ , the latter given by

$$Z_n \approx Z_0 \gamma \left[ \frac{\sqrt{\pi}}{4} \left( \frac{3}{2} \frac{n}{n_c} \right)^{1/2} e^{-n/n_c} + j \frac{4}{9} \frac{n_c}{n} \right]$$

with the critical mode number  $n_c = (3/2) \gamma^3$  and the free space impedance  $Z_0 = \mu_0 c$  ( $= 1$  in natural units used in this paper). Note that at very large  $n$ , the real part decreases exponentially and the free space coupling impedance becomes predominately inductive.

In accelerators/colliders the beam is enclosed in a beam tube of dimensions small compared to the bending radius. The coherent radiation by beam bunches of finite length has a spectrum mainly with wavelengths longer than the dimensions of the bunch and thus comparable to

the transverse dimensions of the beam tube. Hence the presence of the walls, in this paper assumed perfectly conducting, changes the field configuration and leads to radiation shielding. The shielding effect has been analyzed for the simple geometries of a beam centered between parallel plates<sup>[1], [2]</sup> and in a toroidal tube with rectangular<sup>[3]</sup> or circular cross section.<sup>[4]</sup> The results show that the shielding effect is most pronounced at low mode numbers for which asymptotic approximations exist in closed form. The situation at large mode numbers is less clear, in particular with respect to the reactive part, since no closed form approximation seems to be known. Attempting to fill this gap, in this paper the general solution for a beam in a toroidal beam tube with circular cross section is derived using a perturbation method valid in the case of small curvature. From this solution, valid at all mode numbers, an approximate expression in closed form for the case of  $n \gg \gamma R/b$  is derived, which shows that the free space impedance is approached. Although the analysis is based on a specific beam tube the solution, the result is believed to be representative for any fully shielded geometry.

## 2 MAXWELL'S EQUATIONS IN TOROIDAL COORDINATES

The study of a toroidal beam tube with circular cross section suggests the use of the toroidal coordinate system ( $u, p, \theta$ ) even though the vector wave equation is not separable.<sup>[5]</sup> Toroidal coordinates are defined in terms of circular cylinder coordinates ( $\rho, \theta, z$ ) by

$$\rho = \frac{R \sinh u}{\cosh u - \cos p}; \quad z = \frac{R \sin p}{\cosh u - \cos p}$$

and have the metric coefficients

$$h_\theta = \frac{R \sinh u}{\cosh u - \cos p} \equiv R g_\theta$$

$$h_p = -h_u = \frac{R}{\cosh u - \cos p} \equiv R g$$

where  $R$  is the curvature radius of the beam orbit. The minus sign for  $h_u$  is required to make  $E_u$  point in the same direction as  $E_p$  when  $p = 0$ .

Assuming a time harmonic current density,  $i_\theta$ , one can write the field vectors as  $\mathbf{F} = (F_u, F_p, jF_\theta) \exp j(n\theta - \omega t)$  with  $\omega = \nu n/R$ . Maxwell's equations now take

\* Work performed under the auspices of the U.S. Dept. of Energy.

<sup>†</sup> E-mail hahn@bnl.gov

the form

$$\begin{aligned}\frac{\partial}{g\partial p} g_{\theta} E_{\theta} + nE_p + vng_{\theta} H_u &= 0 \\ \frac{\partial}{g\partial u} g_{\theta} E_{\theta} - nE_u + vng_{\theta} H_p &= 0 \\ \frac{\partial}{g\partial u} gE_p + \frac{\partial}{g\partial p} gE_u + vngH_{\theta} &= 0 \\ \frac{\partial}{g\partial p} g_{\theta} H_{\theta} + nH_p - vng_{\theta} E_u &= 0 \\ \frac{\partial}{g\partial u} g_{\theta} H_{\theta} - nH_u - vng_{\theta} E_p &= 0 \\ \frac{\partial}{g\partial u} gH_p + \frac{\partial}{g\partial p} gH_u - vngE_{\theta} &= i_{\theta}\end{aligned}$$

In the current free region, this set of 6 equations can be reduced to two coupled equations by introducing complex transverse fields,  $E_T = E_u + iE_p$  and  $H_T = H_u + iH_p$  and the differential operators

$$D \equiv \frac{\partial}{\partial u} + i \frac{\partial}{\partial p}; D^* \equiv \frac{\partial}{\partial u} - i \frac{\partial}{\partial p}$$

leading to

$$\begin{aligned}\text{Re } Dg_{\theta} D^* g_{\theta} E_{\theta} - n^2(1-v^2)g^2 E_{\theta} \\ - vng \text{Re } Dig(g_{\theta}^2 - 1)H_T = 0\end{aligned}$$

and

$$\begin{aligned}\text{Re } Dg_{\theta} D^* g_{\theta} H_{\theta} - n^2(1-v^2)g^2 H_{\theta} \\ + vng \text{Re } Dig(g_{\theta}^2 - 1)E_T = 0\end{aligned}$$

together with the expressions for the transverse components, of which only  $H_p$  is needed:

$$n(1-v^2g_{\theta}^2)H_p = -\frac{\partial}{g\partial p} g_{\theta} H_{\theta} + vng_{\theta} \frac{\partial}{g\partial u} g_{\theta} E_{\theta}$$

### 3 PERTURBATIVE SOLUTION

For small curvature, i.e. beam tube radius divided by beam orbit radius,  $b/R \ll 1$ , one has  $u \sim \infty$ , and thus  $\cosh u \sim \sinh u \sim \exp(u)/2$ , resulting in  $g_{\theta} \sim 1$  which implies almost decoupled equations for the azimuthal components. The weak coupling can be conveniently handled by a perturbation method, in which the metric coefficients are asymptotically approximated by

$$g \sim \frac{2}{e^u - 2\eta \cos p}; g_{\theta} \sim \frac{e^u}{e^u - 2\eta \cos p}$$

with  $\eta = 1$  the perturbation parameter. In order to simplify the solution, a change of the radial coordinate is indicated from  $u$  to  $x = 2(n/\gamma)e^{-u}$  with the filamentary beam at  $x = 0$ . The beam tube radius and the wall boundary locus can now be approximated by  $x_b = (n/\gamma)(b/R)$  since the resulting off-center beam position is a second order effect.

The differential operator becomes in the new coordinate system

$$D \equiv -x \frac{\partial}{\partial x} + i \frac{\partial}{\partial p}$$

The solution takes a simple and transparent form by restricting the present study to the representative case of a filamentary beam thereby neglecting the space charge effect which decreases with  $\gamma^2$ . The azimuthal current density for a current  $I = 2\pi$  is given by  $i_{\theta} = \delta(x-0)$  (the time harmonic factor is suppressed) and one can write the associated "TM<sub>01</sub>"-like perturbative solution as follows

$$\begin{aligned}E_{\theta} = E_{\theta 0}(x) + \eta E_{\theta 1}(x) \cos p + \\ + \eta^2 (E_{\theta 20}(x) + E_{\theta 2p}(x) \cos 2p) + K\end{aligned}$$

$$H_{\theta} = \eta H_{\theta 1}(x) \sin p + K$$

$$H_p = H_{p0}(x) + \eta H_{p1}(x) \cos p + K$$

Note that the longitudinal coupling impedance is determined from  $E_{\theta 20}$  only and the  $E_{\theta 2p}$  term is not required.

*Zeroth order solution.* In zeroth order, the fields due to a filamentary beam are those of the TM<sub>01</sub> mode in a straight beam tube, with the azimuthal component a solution of  $L_0(E_{\theta 0}) = 0$  and the boundary condition  $E_{\theta 0}(x_b) = 0$  where  $L_m$  represents the modified Bessel function differential equation,

$$L_m(y) \equiv x^2 \frac{d^2 y}{dx^2} + x \frac{dy}{dx} - (x^2 + m^2)y$$

The following expressions are required in finding the first order solution,

$$E_{\theta 0} = \frac{n}{v\gamma^2 R} [K_0(x) - I_0(x)K_{0b}/I_{0b}] \equiv \frac{n}{v\gamma^2 R} C(x)$$

$$H_{p0} = \frac{n}{\gamma R} [K_1(x) + I_1(x)K_{0b}/I_{0b}] \equiv \frac{n}{\gamma R} C'(x)$$

with the shorthand notation  $I_{0b} = I_0(x_b)$  and  $K_{0b} = K_0(x_b)$ .

*First Order Solution.* The first order field components are obtained from Bessel's equation with forcing term,

$$L_1(E_{\theta 1}) = -3 \frac{\gamma x^2}{n} E'_{\theta 0} + 2 \frac{v\gamma^2 x^2}{n} (2H_{p0} + xH'_{p0})$$

$$L_1(H_{\theta 1}) = 2 \frac{v\gamma^3 x^2}{n} E'_{\theta 0}$$

where the prime denotes differentiation with respect to the argument. Together with the boundary conditions  $E_{\theta 1}(x_b) = 0$  and  $H'_{\theta 1}(x_b) = 0$ , one finds after some manipulations

$$E_{\theta 1} = \frac{1}{2v\gamma R} \left\{ (1-\gamma^2) \frac{x_b}{I_{0b}I_{1b}} I_1(x) + (1+2\gamma^2)x C(x) - (1-\gamma^2)x^2 C'(x) \right\}$$

$$H_{\theta 1} = \frac{\gamma}{R} \left\{ \frac{x_b}{I_{0b}(x_b I_{0b} - I_{1b})} I_1(x) + x C(x) \right\}$$

The transverse field component required for the second order solution is found from

$$H_{p1} = -v\gamma \left( \frac{1}{vx} H_{\theta 1} + E'_{\theta 1} \right)$$

$$-\frac{v\gamma^2}{n} (E_{\theta 0} - xE'_{\theta 0}) - 2\frac{v\gamma^4 x}{n} E'_{\theta 0}$$

*Second order solution.* The second order solution is obtained from the Bessel function differential equation with forcing term,

$$L_0(E_{\theta 20}) = -\frac{3\gamma x}{2n} (E_{\theta 1} + xE'_{\theta 1})$$

$$-\frac{3\gamma^2 x^2}{2n^2} (2E_{\theta 0} + xE'_{\theta 0})$$

$$+\frac{v\gamma^2 x^2}{n} (2H_{p1} + xH'_{p1})$$

$$+\frac{1}{2} \frac{v\gamma^3 x^3}{n^2} (7H_{p0} + xH'_{p0})$$

together with the boundary condition  $E_{\theta 20}(x_b) = 0$ . The solution is somewhat lengthy, but can readily be handled with the aid of a computer program such as MACSYMA. Only the second order azimuthal electric field component contributes to the curvature induced coupling impedance; its expression is

$$E_{\theta 20}(0) = \frac{n}{24vR} \left\{ \frac{b^2}{R^2} \frac{1}{I_{0b}^2 I_{1b} (I_{0b} - I_{1b})} \right.$$

$$\left[ \gamma^2 (10I_{1b}^2 + 5I_{0b}I_{1b} - 3I_{0b}^2) \right.$$

$$- 6(I_{1b}^2 + 2I_{0b}I_{1b} - I_{0b}^2)$$

$$- \frac{1}{\gamma^2} (4I_{1b}^2 - 7I_{0b}I_{1b} + 3I_{0b}^2) \left. \right]$$

$$- \frac{5 - 24\gamma^2 + 16\gamma^4}{n^2} \frac{I_{0b}^2 - 1}{I_{0b}^2} \left. \right\}$$

#### 4 THE COUPLING IMPEDANCE

The curvature-induced coupling impedance is obtained from the azimuthal electric field component by the integral

$$Z_n = -\frac{R}{I} \int_0^{2\pi} E_{\theta} e^{jn\theta} d\theta$$

With the use in this paper of the particular current strength,  $I = 2\pi$ , the general expression for the coupling impedance becomes simply  $Z_n = -j E_{\theta 20}(0)$ . Numerical results can be readily obtained for all mode numbers, provided that double-precision Bessel function routines are used. (As example, results for a RHIC-like machine with  $\gamma=100$  and  $b/R = 2 \times 10^{-4}$  are shown in Fig. 1.)

Approximate expressions valid at very low and very large mode numbers follow from the general expression:

$$\frac{Z_n}{n} \sim -j \frac{Z_0}{4v} \frac{b^2}{R^2} \left( 1 - \frac{7}{8} n^2 \frac{b^2}{R^2} \right); (n < 3\gamma R/b)$$

$$\frac{Z_n}{n} \sim j \frac{Z_0}{vn^2} \left( \frac{2}{3} \gamma^4 - \gamma^2 + \frac{5}{24} \right); (n > 3\gamma R/b)$$

$$\sim j \frac{4}{9} \gamma Z_0 \frac{n_c}{n^2}$$

thereby providing the mathematical prove, that at sufficiently large mode numbers the coupling impedance of a circular machine approaches the free space value, a fact previously suggested, but only proven for a circular beam between parallel plates. Although the present result was derived for a beam tube with circular cross section, it is expected to be valid for any beam tube geometry.

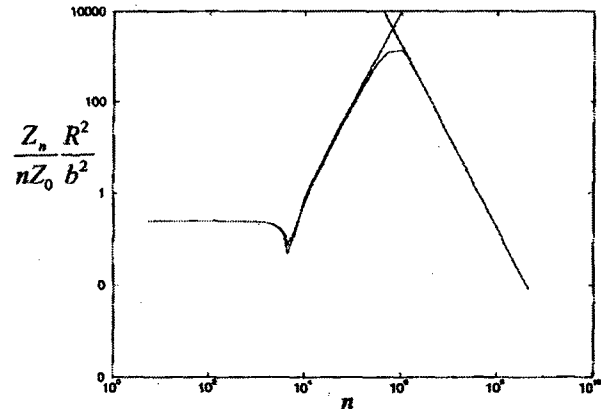


Fig. 1: Exact results and asymptotic approximation for curvature-induced coupling impedance.

#### 5 REFERENCES

- [1] J. B. Murphy, S. Krinsky, and R. L. Gluckstern, *Particle Accelerators*, **57**, pp. 9-64 (1997).
- [2] B.W. Zotter and S. A. Kheifets, "Impedances and Wakes in High-Energy Particle Accelerators, (World Scientific Publishing, Singapore, 1998) p.283.
- [3] H. Hahn, S. Tepikian, and G. Dome, *Particle Accelerators*, **49**, 163 (1995).
- [4] H. Hahn, *Particle Accelerators*, **51**, 181 (1995), *Proc. 1995 PAC*, **5** 2952.
- [5] B. Zotter, Report CERN/ISR-TH/77-56 (1977).

# A STUDY ON MICROWAVE INSTABILITY INDUCED RADIATION\*

J.B. Murphy<sup>#</sup> & J.M. Wang, NSLS/BNL, Upton, NY 11973

## Abstract

It has been shown in the context of a solvable model that the microwave instability can be described in terms of "coherent states" [1]. Building on this model, we first show that the simplicity of the model arises from the fact that the key integral-differential equation can be reduced to the Karhunen-Loeve equation of the theory of stochastic processes. We present results on the correlation functions of the electric field. In particular, for the second order correlation function, we show that a relation akin to the Hanbury Brown-Twiss correlation holds for the coherent states of the microwave-instability induced radiation. We define an entropy-like quantity and we introduce a Wigner distribution function representation.

## 1 INTRODUCTION

Recently a new theory of the microwave instability in an electron storage ring was proposed [1]. An analytic solution for the electron distribution function and the electric field was obtained for the model of a bunched electron beam interacting with the model impedance,

$$Z_n = \begin{cases} \bar{Z} & \text{if } n_0 - b \leq n \leq n_0 + b \\ 0 & \text{otherwise} \end{cases}, \quad (1)$$

with  $n > 0$  and  $\bar{U} \equiv -in_0 \bar{Z}$ . The instability in the presence of this impedance can be characterized in terms of a complete set of "periodic, localized coherent states",

$$\sqrt{2\pi(2b+1)}\Gamma_\alpha(\phi) \equiv \sum_{m=-b}^b e^{im(\phi-\phi_\alpha)} = \frac{\sin\left[(2b+1)\left(\frac{\phi-\phi_\alpha}{2}\right)\right]}{\sin\left[\frac{\phi-\phi_\alpha}{2}\right]}.$$

$\Gamma_\alpha(\phi)$  is localized near  $\phi_\alpha \equiv 2\pi\alpha/(2b+1)$ ,  $\alpha = 0, \pm 1, \pm 2, \dots, \pm b$  with a width in  $\phi$  given by the wavelength,  $\Delta\phi = \ell_w \equiv (2b+1)^{-1}$  and a frequency width of  $\Delta n = (2b+1)$ . The  $\Gamma_\alpha(\phi)$  span the space  $M_b$  of periodic functions that are bandlimited to  $-b \leq n \leq b$ , they are orthonormal on  $[-\pi, \pi]$  and they are complete on  $M_b$ ,

$$\sum_{\alpha=-b}^b \Gamma_\alpha(\phi) \Gamma_\alpha(\phi') = \frac{\sqrt{(2b+1)}}{2\pi} \Gamma_0(\phi - \phi'). \quad (3)$$

The  $\Gamma_\alpha(\phi)$  are simply the basis functions for a periodic version of the classic Shannon sampling theorem [2-3].

## 2 INITIAL CONDITIONS: SHOT NOISE

The initial electron beam consisting of  $N$  particles is

\* Work supported by USDoE under contract DE-AC02-98CH10886  
# Email: jbm@bnl.gov

assumed to be mono-energetic and the electron distribution function in  $\phi$  is given as,

$$F(\phi, t=0) = \frac{1}{N} \sum_{j=1}^N \delta(\phi - \phi_j), \quad (4)$$

where the individual electrons positions are assumed to be independent and randomly distributed with a weight function  $\rho(\phi)$ , so-called "shot noise". The average line density is obtained as an ensemble average,

$$\langle F(\phi, 0) \rangle \equiv \int F(\phi_1, \dots, \phi_N) \rho(\phi_1) \dots \rho(\phi_N) d\phi_1 \dots d\phi_N = \rho(\phi). \quad (5)$$

Provided that the electron bunch length,  $\sigma \gg 2\pi/b \approx \ell_w$ ,  $\rho(\phi)$  is well approximated by its projection into the space  $M_b$ , i.e., an expansion in the bandlimited coherent states.

## 3 APPLICATION OF COHERENT STATES

In [1] the Vlasov-Maxwell equations for the microwave instability were reduced to a Fredholm integral equation for the perturbed electron distribution function  $I(\phi, t)$ ,

$$\ddot{I}(\phi, t) = \kappa \rho(\phi) \int_{-\pi}^{\pi} \Gamma_0(\phi - \phi') [e^{in_0(\phi - \phi')} \bar{U} + \text{c.c.}] I(\phi', t) d\phi' \quad (6)$$

where  $\kappa \equiv e\omega_0^2 \alpha I_{av} / E_0$ ,  $I_{av} \equiv eN\omega_0 / 2\pi$  and initial condition  $\dot{I}(\phi, 0) = 0$ . We define some simplifying notation,

$$I(\phi, t) \equiv e^{in_0\phi} J(\phi, t) + e^{-in_0\phi} J^*(\phi, t) + \ddot{I}(\phi, t), \quad (7)$$

where  $J(\phi, t) \in M_b$  is a bandlimited function and  $\ddot{I}(\phi, t)$  represents that portion of  $I(\phi, t) \notin e^{\pm in_0\phi} \otimes M_b$ . Because  $J(\phi, t) \in M_b$  it can be expanded as follows,

$$J(\phi, t) = \sum_{\alpha} J_{\alpha}(t) \Gamma_{\alpha}(\phi), \quad (8)$$

Using the properties of the  $\Gamma_{\alpha}(\phi)$ , equation (6) can be split into a pair of coupled equations for  $J(\phi, t)$  and  $\ddot{I}(\phi, t)$ ,

$$\ddot{J}(\phi, t) = \kappa \bar{U} \int_{-\pi}^{\pi} \Gamma_0(\phi - \phi') \rho(\phi') J(\phi', t) d\phi', \quad (9a)$$

$$\ddot{I}(\phi, t) = \kappa \sum_{\alpha} [\rho(\phi) - \rho(\phi_{\alpha})] \Gamma_{\alpha}(\phi) [\bar{U} e^{in_0\phi} J_{\alpha}(t) + \text{c.c.}]. \quad (9b)$$

We call (9a) the "self consistent closed loop equation" and we call (9b) the "mode coupling equation". Note that (9b) is coupled to (9a), but (9a) is self-contained and can be analyzed alone. We will not consider the mode coupling equation any further here.

## 4 SELF-CONSISTENT LOOP EQUATION

Substituting in (9a) the coherent state expansions of  $J(\phi, t)$ ,  $\rho(\phi)$  and  $\Gamma_0(\phi - \phi')$  and simplifying yields,

$$\ddot{J}_\alpha(t) = \kappa \bar{U} \rho_\alpha J_\alpha(t). \quad (10)$$

Assuming  $J_\alpha(t) = J_\alpha(0)e^{-i\Omega_\alpha t}$ , where  $\Omega_\alpha$  is termed the coherent frequency yields the dispersion relation,

$$\Omega_\alpha^2 = -\kappa \bar{U} \rho_\alpha = i n_0 \kappa \bar{Z} \rho_\alpha. \quad (11)$$

The coherent states  $\Gamma_\alpha(\phi)$  are eigenfunctions of (9a) with a pair of eigenvalues,  $\Omega_\alpha^\pm = \sqrt{\pm i n_0 \kappa \bar{Z} \rho_\alpha}$ . To satisfy  $\dot{J}(\phi, 0) = 0$ , the eigensolutions are combined as follows,

$$J(\phi, t) = \sum_{\alpha=-b}^b J_\alpha(0) \cos \Omega_\alpha t \Gamma_\alpha(\phi). \quad (12)$$

The physical interpretation is that the spectrum of the initial shot noise within the bandwidth of the impedance is modulated ( $\text{Re} \Omega_\alpha$ ) and amplified ( $\text{Im} \Omega_\alpha$ ) with a growth rate that depends on the local peak current in the electron beam  $\rho_\alpha$ .

### 5 1<sup>st</sup> ORDER CORRELATION FUNCTION

The first order correlation function of the bandlimited portion of the current density at two different azimuths  $\phi$  and  $\phi'$  at time  $t$  is defined as an ensemble average,

$$G^{(1)}(\phi, \phi', t) \equiv \langle J(\phi, t) J^*(\phi', t) \rangle \\ = \sum_{\alpha, \beta=-b}^b \langle J_\alpha(0) J_\beta^*(0) \rangle \cos[\Omega_\alpha t] \cos[\Omega_\beta^* t] \Gamma_\alpha(\phi) \Gamma_\beta^*(\phi'). \quad (13)$$

To proceed we must relate the correlation function at  $t = 0$  to the initial electron distribution function. We define the "centered particle distribution function",  $f(\phi, 0) \equiv F(\phi, 0) - \rho(\phi)$ , this is convenient since  $\langle J(\phi, 0) \rangle = 0$ . It is straightforward to show that,

$$\langle f(\phi, 0) f(\phi', 0) \rangle = \frac{1}{N} \rho(\phi) \delta(\phi - \phi') - \frac{1}{N} \rho(\phi) \rho(\phi'). \quad (14)$$

It has been shown in [1] that provided that  $\lambda \ll \ell_w < \sigma$ , the second term in the RHS of equation (14) will not be amplified during the instability and it can be ignored. From above we obtain that,

$$\langle J_\alpha(0) J_\beta^*(0) \rangle = \frac{(eN\omega_0)^2}{N} \rho_\alpha \delta_{\alpha\beta}. \quad (15)$$

The coefficients in the coherent state expansion of  $J(\phi, t)$  are uncorrelated. It is this explicit diagonalization of  $G^{(1)}(\phi, \phi', t)$  that makes the coherent states so useful.

Combining the above results, the first order correlation function can be written in a diagonalized form,

$$G^{(1)}(\phi, \phi', t) = \frac{(eN\omega_0)^2}{N} \sum_{\alpha=-b}^b \rho_\alpha \cos^2 \Omega_\alpha t \Gamma_\alpha(\phi) \Gamma_\alpha^*(\phi'). \quad (16)$$

This correlation bears a striking resemblance to the mutual coherence function in statistical optics [4]. If there were only one coherent state present, the system could be called "completely coherent"; when several states are present, the system is "partially coherent". In the present problem, for sufficiently long times in the presence of the instability, the coherent state that is centered at the peak

of the initial density distribution, will dominate and the system evolves toward "complete coherence".

### 6 KARHUNEN-LOÈVE EXPANSION

The correlation function in equation (16), along with the coherent states  $\Gamma_\alpha(\phi)$ , can be used to write an integral eigenvalue equation as follows,

$$\frac{(Ne\omega_0)^2 \rho_\alpha}{N} \Gamma_\alpha(\phi) = \frac{(Ne\omega_0)^2}{N} \int_{-\pi}^{\pi} d\phi' \Gamma_\alpha(\phi') \sum_{\beta} \rho_\beta \Gamma_\beta(\phi) \Gamma_\beta^*(\phi') \\ = \int_{-\pi}^{\pi} d\phi' \Gamma_\alpha(\phi') \langle J(\phi, 0) J^*(\phi', 0) \rangle \quad (17)$$

where  $\Gamma_\alpha(\phi)$  is the eigenfunction and  $(Ne\omega_0)^2 \rho_\alpha / N$  is the eigenvalue. This is precisely the form of the integral eigenvalue equation that is the centerpiece of the Karhunen-Loève expansion for stochastic processes [4]. If equation (10) is multiplied by  $\Gamma_\alpha(\phi)$  and summed over  $\alpha$ , equation (17) can be used to write the evolution equation for  $J(\phi, t)$  as,

$$\ddot{J}(\phi, t) = \kappa \bar{U} \sum_{\alpha=-b}^b \rho_\alpha \Gamma_\alpha(\phi) \Gamma_\alpha^*(\phi') J(\phi', t) d\phi' \\ = \frac{N}{(eN\omega_0)^2} \kappa \bar{U} \int_{-\pi}^{\pi} \langle J(\phi, 0) J^*(\phi', 0) \rangle J(\phi', t) d\phi' \quad (18)$$

In this case the time dependence complicates the expression but the underlying form is again the integral eigenvalue equation of the Karhunen-Loève expansion where the kernel is simply a symmetric correlation function expanded in terms of the eigenvalues and eigenfunctions [4].

### 7 WIGNER DISTRIBUTION FUNCTION

The Wigner distribution function can be introduced to yield a quasi-probability density in both the angular position  $\phi$  and its Fourier conjugate  $n$  [5-6]. For a stochastic process the Wigner distribution function is defined in terms of the first order correlation function [6],

$$W(\phi, n, t) \equiv \int_{-\pi}^{\pi} G^{(1)}\left(\phi + \frac{\xi}{2}, \phi - \frac{\xi}{2}, t\right) e^{-in\xi} d\xi. \quad (19)$$

Substituting equation (16), the Wigner function can be written as a sum over the coherent modes,

$$W(\phi, n, t) = \sum_{\alpha=-b}^b \rho_\alpha |\cos(\Omega_\alpha t)|^2 W_\alpha(\phi, n), \quad (20)$$

where

$$W_\alpha(\phi, n) = \int_{-\pi}^{\pi} \Gamma_\alpha\left(\phi + \frac{\xi}{2}\right) \Gamma_\alpha^*\left(\phi - \frac{\xi}{2}\right) e^{-in\xi} d\xi. \quad (21)$$

A routine procedure leads to the result,

$$W_\alpha(\phi, n) = \frac{\left[ \sin[(2b-2|n|+1)(\phi-\phi_\alpha)] + \frac{4}{\pi} \sum_{k=0}^{b-1} \frac{(-1)^{k-n}(1+2k)}{(1+2k)^2 - 4n^2} \sin[(b-k)\pi(\phi-\phi_\alpha)] \right]}{(2b+1) \sin(\phi-\phi_\alpha)}$$

for  $-b \leq n \leq b$  and  $W_\alpha(\phi, n) = 0$  otherwise. For the special case of a coasting beam, where all the eigenvalues are the same, all the summations in equation (22) can be done and the Wigner distribution function takes a particularly simple form,

$$W(\phi, n, t) = \begin{cases} \frac{1}{2\pi} |\cos(\Omega t)|^2, & -b \leq n \leq b \\ 0, & n \text{ otherwise} \end{cases} \quad (23)$$

From the Wigner distribution function we can obtain the marginal distribution functions,

$$\Phi(\phi, t) \equiv \sum_{n=-b}^b W(\phi, n, t) = 2\pi \sum_{\alpha=-b}^b \rho_\alpha |\cos \Omega_\alpha t|^2 \Gamma_\alpha^2(\phi), \quad (24a)$$

$$\Psi(n, t) \equiv \int_{-\pi}^{\pi} W(\phi, n, t) d\phi = \frac{2\pi}{2b+1} \sum_{\alpha=-b}^b \rho_\alpha |\cos \Omega_\alpha t|^2. \quad (24b)$$

## 8 RADIATION POWER

In [1] it was shown that  $G^{(1)}(\phi, \phi', t)$  can be used to obtain the power in the electric field as follows,

$$\langle P(\phi, t) \rangle = \hat{R} \frac{(eN\omega_0)^2}{N} \sum_{\alpha=-b}^b \rho_\alpha \cos^2 \Omega_\alpha t \Gamma_\alpha(\phi) \Gamma_\alpha(\phi). \quad (25)$$

If we integrate (25) over all  $\phi$  we find that the total power is the sum over the coherent states, the intensity of each state depends on the initial shot noise,  $\rho_\alpha$ , and the growth rate of the instability,  $\text{Im} \Omega_\alpha$ ,

$$\langle P(t) \rangle \equiv \sum_{\alpha=-b}^b P_\alpha(t) = \hat{R} \frac{(eN\omega_0)^2}{N} \sum_{\alpha=-b}^b \rho_\alpha |\cos[\Omega_\alpha t]|^2 \quad (26)$$

We can also define the power as a function of harmonic number in terms of one of the marginal distributions of the Wigner distribution function,

$$\begin{aligned} \langle P(n, t) \rangle &= \hat{R} \frac{(eN\omega_0)^2}{N} \frac{1}{(2b+1)} \sum_{\alpha=-b}^b \rho_\alpha |\cos[\Omega_\alpha t]|^2 \\ &= \hat{R} \frac{(eN\omega_0)^2}{N} \frac{\Psi(n, t)}{2\pi} \end{aligned} \quad (27)$$

for  $-b \leq n \leq b$  and zero otherwise. The fact that  $\langle P(n, t) \rangle$  is independent of "n" is due to the fact that Z has been assumed to be constant. If the expression in (27) is summed over "n" we again obtain the result (26) for the total power.

## 9 ENTROPY

Paralleling the analysis for coherent light we can define an entropy [7],

$$H(t) \equiv - \sum_{\alpha} \Theta_{\alpha}(t) \log \Theta_{\alpha}(t) \quad (28)$$

where

$$\Theta_{\alpha}(t) \equiv \rho_{\alpha} |\cos[\Omega_{\alpha} t]|^2 / \sum_{\alpha} \rho_{\alpha} |\cos \Omega_{\alpha} t|^2, \quad (29)$$

$\Theta_{\alpha}(t)$  is the relative probability that a given coherent mode is excited. It is straightforward to prove that  $H_{\min}(0) = 0$  when  $\Theta_{\alpha}(0) = 1$ ,  $\Theta_{\beta}(0) = 0$ ,  $\alpha \neq \beta$ , &

$H_{\max}(0) = \log(2b+1)$  when  $\rho_{\alpha} = [2\pi(2b+1)]^{-1/2}$  for all  $\alpha$ . Since the entropy is the logarithm of the number of coherent modes excited on the beam it is also a measure of "coherence", lower entropy implies greater coherence. For a Gaussian electron beam, where many modes are initially excited; the entropy will decrease toward zero with time as the mode with the largest growth rate dominates.

## 10 2<sup>nd</sup> ORDER CORRELATION FUNCTION

The second order correlation function is defined as,

$$G^{(2)}(\phi, \phi', \phi'', \phi''', t) \equiv \langle J(\phi, t) J^*(\phi', t) J(\phi'', t) J^*(\phi''', t) \rangle. \quad (30)$$

After considerable manipulation it can be shown that the second order correlation function can be written in solely in terms of the first order correlation function,

$$G^{(2)}(\phi, \phi', \phi'', \phi''', t) = [G^{(1)}(\phi, \phi', t) G^{(1)}(\phi'', \phi''', t) + G^{(1)}(\phi, \phi'', t) G^{(1)}(\phi', \phi''', t)] \quad (31)$$

Using this key result we can derive a Hanbury-Brown Twiss-like relation [4,8] between the power in individual coherent states,

$$\frac{\langle P_{\alpha}(t) P_{\beta}(t) \rangle}{\langle P_{\alpha}(t) \rangle \langle P_{\beta}(t) \rangle} = 1 + \delta_{\alpha\beta}. \quad (32)$$

This implies there is an enhanced correlation of light in a particular coherent state, a characteristic of so-called "chaotic light". However there is no such correlation between two different coherent states.

It can be shown that the total radiation power satisfies,

$$\frac{\langle P(t)^2 \rangle}{\langle P(t) \rangle^2} = 1 + \frac{\sum \langle P_{\alpha}(t) \rangle^2}{\langle P(t) \rangle^2}. \quad (33)$$

For the specific case of a "flat electron beam" of bunch length  $\ell_b = 2\pi \frac{2a+1}{2b+1}$  equation (33) simplifies to,

$$\frac{\langle P(t)^2 \rangle}{\langle P(t) \rangle^2} = 1 + \frac{1}{2a+1} \quad (34).$$

## 11 REFERENCES

- [1] J.M. Wang, Phys. Rev. E, p. 69 (1998).
- [2] C.E. Shannon and W. Weaver, "Mathematical Theory of Communication", University of Illinois Press (1963).
- [3] L. Brillouin, "Science & Information Theory", Academic (1962).
- [4] J.W. Goodman, "Statistical Optics", Wiley (1985).
- [5] E. Wigner, Phys. Rev. 40, p. 749 (1932).
- [6] M.J. Bastiaans, JOSA A, Vol. 3, p. 1227 (1986).
- [7] H. Gamo, Progress In Optics, Vol. 3, p. 189 (1964).
- [8] H.R. Brown & R.Q. Twiss, Nature, 178, p. 481 (1956).



# FEEDBACK DESIGN METHOD REVIEW AND COMPARISON \*

E. Onillon, BNL, Upton, NY

## Abstract

Different methods for feedback designs are compared. These includes classical Proportional Integral Derivative (P. I. D.), state variable based methods like pole placement, Linear Quadratic Regulator (L. Q. R.),  $H_\infty$  and  $\mu$ -analysis. These methods are then applied for the design and analysis of the RHIC phase and radial loop, yielding a performance, stability and robustness comparison.

## 1 INTRODUCTION

In the last two decades, new developments in control theory have been made, particularly in the field of state space based techniques like  $H_2$  or  $H_\infty$ . The RHIC phase and radial loop have been designed using an  $H_2$  approach (L. Q. R.), the state variables being beam phase, radius and the integral of the radius error. Studies, based on an  $H_\infty$  approach, have been performed for a new design approach for those loops.

## 2 DESCRIPTION OF THE SYSTEM

The main variables used to describe the system are [1]:  $\phi$  the instantaneous phase deviation of the bunch from the synchronous phase,  $\delta R$  the variations of the beam radius and  $\delta\omega_{rf}$  the RF frequency deviation,  $b$  a scaling factor). The cavity transfer function is assumed to be the identity

These variables are related by the two following transfer functions (Fig. 1) [1]:

$$\begin{aligned} \phi &= B_\phi \delta\omega_{rf} \\ \delta R &= B_R \delta\omega_{rf} \end{aligned} \quad \text{with } B_\phi = \frac{s}{s^2 + \omega_s^2}$$

and  $B_R = \frac{b}{s^2 + \omega_s^2}$ :

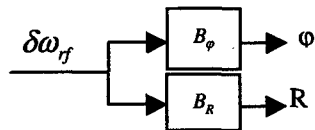


Figure 1: Block diagram

The system represented in Fig. 1 can be described using

two state variables:

$$\begin{cases} \dot{x}_1 = \dot{x}_2 = \phi \\ \dot{x}_2 = \frac{R}{b} = \frac{1}{s^2 + \omega_s^2} \delta\omega_{rf} \end{cases}$$

A third one,  $x_3 = \int (R - R_{steer}) dt$ , is introduced to force the radius to follow its reference  $R_{steer}$ . These state variables, which are all observed, lead to the state space representation:

$$\begin{pmatrix} \dot{x}_1 \\ \dot{x}_2 \\ \dot{x}_3 \end{pmatrix} = \begin{pmatrix} 0 & -\omega_s^2 & 0 \\ 1 & 0 & 0 \\ 0 & b & 0 \end{pmatrix} \begin{pmatrix} x_1 \\ x_2 \\ x_3 \end{pmatrix} + \begin{pmatrix} 1 \\ 0 \\ 0 \end{pmatrix} \delta\omega_{rf} + \begin{pmatrix} 0 \\ 0 \\ -1 \end{pmatrix} R_{steer} \quad (\text{eq 1})$$

## 3 $H_\infty$ AND MIXED SENSITIVITY APPROACH

### 3.1 Sensitivity Functions and Loop Shaping

If we consider the following block diagram [2] where  $K(s)$  is a feedback controller and  $G(s)$  the transfer matrix of the system,

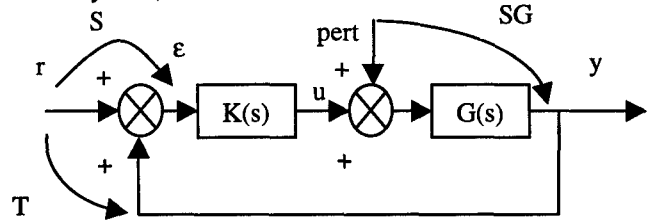


Figure 2: Sensitivity Function diagram

the transfer matrices relating the reference to the error  $\epsilon$  and to the output  $y$  are respectively

$$S(s) = (I + G(s)K(s))^{-1} \text{ and}$$

$$T(s) = (I + G(s)K(s))^{-1} G(s)K(s) = I - S(s)$$

$S(s)$  and  $T(s)$  are known respectively as the sensitivity function and the complementary sensitivity function.

From that diagram, one can see that

- a good reference tracking and a good rejection of the perturbation  $\text{pert}$  are obtained when  $S$  and  $SG$  are small
- the command effort is small when  $KS$  is small
- a good noise rejection is obtained when  $T$  is small

The gain of a transfer matrix, at a given frequency  $\omega$ , will be characterized by its upper  $\bar{\sigma}$  and lower  $\underline{\sigma}$  singular values.

A transfer matrix  $G$  will be characterised by its  $H_\infty$  norm defined as its biggest singular value:

$$\|G\|_\infty := \sup_{\omega} \bar{\sigma}(G(j\omega)).$$

To design a feedback matrix  $K$  that matches the performance and robustness criteria, one will try to minimize  $S$  at low frequency ( $S$  behaves like the identity at high frequencies), and  $T$  at high frequency ( $T$  behaves like the identity at low frequencies), by choosing two

\* Work performed under the auspices of the U.S. Department of Energy

weight matrices  $W_1$  and  $W_3$  that correspond to the shape of  $S$  and  $T$  or the open loop  $KG$ .

$\bar{\sigma}(S(j\omega)) \leq |W_1^{-1}(j\omega)|$  and  $\bar{\sigma}(T(j\omega)) \leq |W_3^{-1}(j\omega)|$ . These two requirements are combined into a single infinity norm specification of the form  $\|T_{y_1 u_1}\|_{\infty} \leq 1$  where by

definition  $T_{y_1 u_1} = \begin{bmatrix} W_1 S \\ W_3 T \end{bmatrix}$ , leading to the augmented plant:

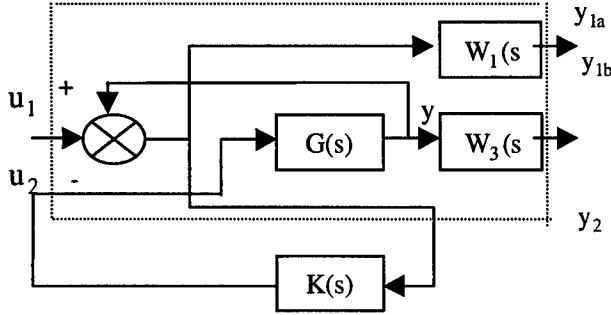


Figure 3: Augmented plant

### 3.2 Case of the phase and radial loop

$W_1^{-1}$  was chosen to be:

$$\begin{bmatrix} \frac{s^2 + 2.10^3 s + 1.410^6}{s^2 + 1.910^3 s + 10^6} & 0 & 0 \\ 0 & \frac{10^2 s^2 + 810^4 s + 110^8}{s^2 + 2.310^3 s + 310^6} & 0 \\ 0 & 0 & \frac{10^2 s^2 + 810^4 s + 110^8}{s^2 + 2.310^3 s + 310^6} \end{bmatrix}$$

and

$$W_3^{-1} = \begin{bmatrix} 8/(s+100) & 0 & 0 \\ 0 & 3010^6/s^2 & 0 \\ 0 & 0 & 10^2(s+9.310^3)/s^2 \end{bmatrix}.$$

The system having a resonance at  $\omega_s$ , a bilinear transform has been performed to avoid a pole zero cancellation. A circle, which should contain the open loop poles, is defined [3]. The following results have been obtained:

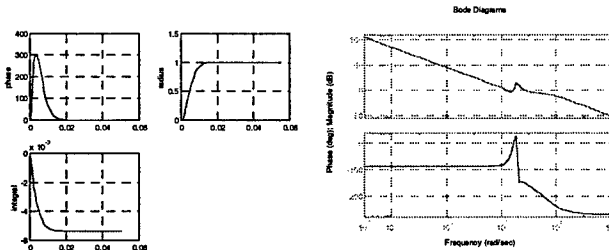


Figure 4: Step response and open loop Bode plot

The system settles in 10 ms. The phase and gain margins are respectively: 38 degrees and 9 dB.

The closed loop system is now:

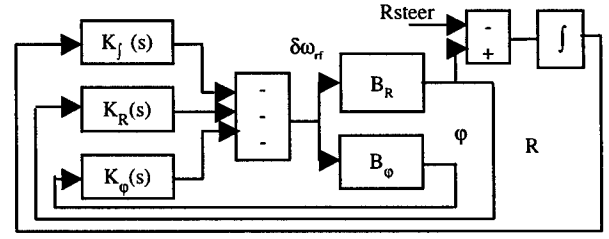


Figure 5: Closed loop system

$K_R(s)$ ,  $K_\phi$ ,  $K_f$  are the three feedback transfer functions:

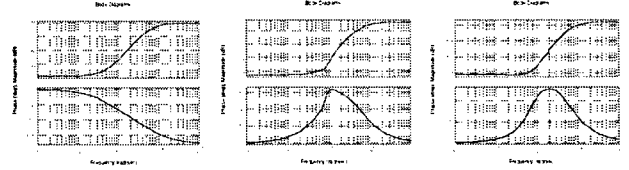


Figure 6: Controller Bode plot

### 3.3 Robustness and $\mu$ analysis

One advantage of the previous approach is the ability to take into consideration the uncertainties on parameters or neglected dynamics. In the case of the phase and radial loop, the synchrotron frequency varies during

acceleration:  $\omega_s = \bar{\omega}_s \left(1 + \frac{\omega_0}{\bar{\omega}_s} \delta\right)$  which can be represented as follows:

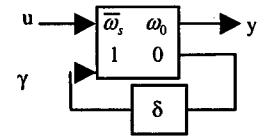


Figure 7:  $\omega_s$  representation

The phase radial system, with no integral action, can now be represented as follows:

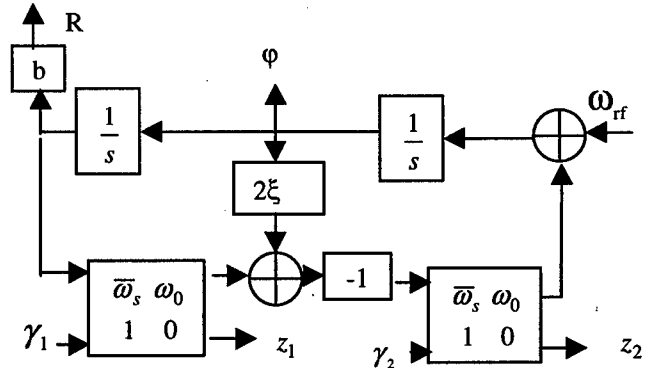


Figure 8: System representation

With  $\Delta = \begin{bmatrix} \delta_1 & 0 \\ 0 & \delta_2 \end{bmatrix}$ ,  $\delta_1 \in \mathfrak{R}$ ,  $\delta_2 \in \mathfrak{R}$  and  $K$  the

$H_\infty$  controller, one gets the generic  $M-\Delta$  block diagram:

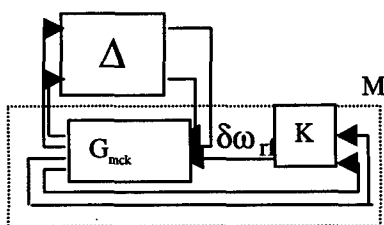


Figure 9:  $M \Delta$  bloc diagram

The robustness is a measure of the size of the perturbation  $\Delta$  that will make the system unstable. It requires the structured singular value  $\mu$  of  $M$  with respect to the uncertainty  $\Delta$ . The stability margin is defined as

$$\frac{1}{\max_{\omega} \mu_{\Delta}(M(j\omega))} \text{ where}$$

$\mu_{\Delta}(M) := \frac{1}{\min(\overline{\sigma}(\Delta) : \det(I - M\Delta) = 0)}$ . The following  $\mu$  plot was obtained, where  $\max(\mu) = 0.9$  or  $\delta_{\max} = 1.11$

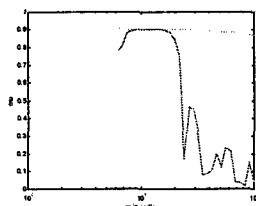


Figure 10:  $\mu$  plot ( $\mu$  as a function of  $\omega$  in rad/s)

## 4 LOR APPROACH

Using the state variable representation defined in Eq 1, we can determine a Linear Quadratic Regulator (LQR), with the following quadratic performance index:

$$J = \frac{1}{2} \int_0^{+\infty} (X^T Q X + \omega_{ff}^T R \omega_{ff}) dt, \quad X \text{ being the state}$$

vector,  $Q$  minimising the deviation in states and  $R$  the input energy [3]. The  $Q$  and  $R$  matrices are chosen by the designer to obtain the desired system dynamic.

With  $Q = \begin{pmatrix} 600 & 0 & 0 \\ 0 & 100 & 0 \\ 0 & 0 & 10^6 \end{pmatrix}$  and  $R = 10^{-6}$ , one gets the

following step radius response and open loop Bode plot:

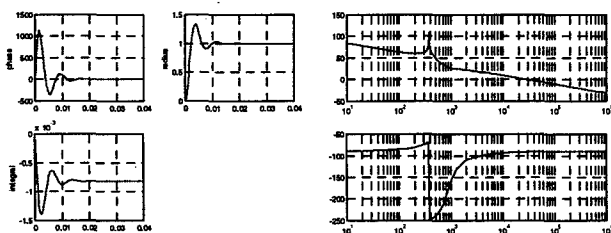



**Figure 11: Step response and open loop Bode plot**

This system settles also in 10 ms. The phase and gain margins are respectively: 90 degrees and infinity (propriety of LQR). The closed loop system is the same as in Fig.5 except that  $K_R, K_\omega, K_f$  are just gains.

## 5 CLASSICAL APPROACH

The phase and radial loop are two cascaded loops, the loop controllers being just classical filters.

With  $K_{\varphi}(s) = 132 \left( 1 + \frac{1}{2.2 \cdot 10^{-3} s} + 5.5 \cdot 10^{-4} s \right)$  (PID) and

$K_R(s) = 510^3 \frac{510^3}{s + 510^3}$  the following radius step response was obtained:
 

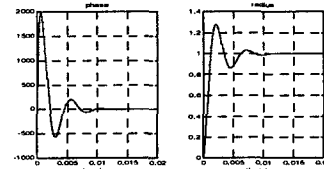


**Figure 12: Step response  
(1 phase, 2 radius)**

The system of Fig. 13 settles in 15 ms:

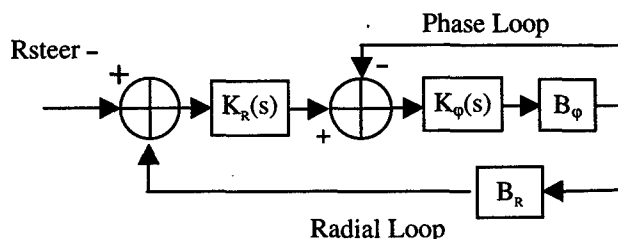


**Figure 13: Closed loop system**

## 6 CONCLUSION

The  $H_\infty$  approach allows us to design a controller, by either shaping the open loop response or by defining a certain set of uncertainties and perturbations. Its realization will require the synthesis of three transfer functions. A robust analysis is then easy to perform.

The LQR approach will lead to a very simple realization: three gains and good stability margins. If the system is well known, it can lead to the programming of the feedback gains by switching to pole placement [4].

The traditional approach allows the decoupling between the phase and radial loop but the design of the controllers is more empirical.

## 7 REFERENCES

- [1] RF Beam Control System for the AGS Booster, J. M. Brennan, BNL – 52438 Formal Report.
- [2] Essentials of Robust Control, Kemin Zhou, Prentice Hall.
- [3] R. Y. Chiang, M. G. Safonov, Design of an  $H_\infty$  Controller for a Lightly Damped System using a Bilinear Pole Shifting Transform, American Contr. Conf, May 90.
- [4] The New BNL AGS Phase, Radial and Synchronization Loops, E. Onillon, J.M. Brennan, EPAC 1996.

# OBSERVATIONS OF A LONGITUDINAL COUPLED BUNCH INSTABILITY IN CESR<sup>†</sup>

M.G. Billing\*, S. Belomestnykh, Laboratory of Nuclear Studies,  
Cornell University, Ithaca, NY 14853

## Abstract

During the last several years of operating with trains of bunches, a longitudinal dipole coupled bunch instability has been observed at the Cornell Electron Storage Ring (CESR). Without the use of multibunch longitudinal feedback this instability would limit the total stored current in the two beams during High Energy Physics (HEP) operation. This paper gives an updated report on observations of this instability, its strength, its dependence on bunch spacing within the trains, its relationship to changes made in the RF accelerating system and results of simulations using the observed mode spectra of the RF cavities.

## 1 INTRODUCTION

Since February of 1995 during HEP, CESR has operated with angle crossing collisions of two beams (electrons and positrons) with 9 nearly equally spaced trains of 2 to 4 bunches per train.[1] The spacing between lead bunches in the trains is either 280 ns or 294 ns and the bunch spacing within the train occurs in multiples of 14 ns with a maximum train length of 56 ns. When the longitudinal feedback is not employed for beam stabilization and at currents above 200 mA in a single beam or 300 mA in two beams, a dipole longitudinal coupled bunch instability may occur.

As reported earlier[2] a number of effects are associated with the instability which may be observed with either positrons, electrons or both beams. The instability threshold is defined as the current at which the amplitude of the synchrotron sidebands in a beam position monitor's spectrum begin to grow rapidly in amplitude vs. current. This effect is often a 6 dB increase in amplitude for a few percent change in current. The dipole oscillations of the bunches appear to self-limit above the instability threshold, but the amplitude of the oscillation grows as current increases until at a higher current quadrupole coupled bunch oscillations are observed both in the frequency spectrum and recently in the bunch shape oscillations observed by a streak camera.[3] Over long times the instability threshold currents can vary by as much as 10-15% with no intentional change in operating conditions. The onset of the instability is a function of the number of bunches within the trains and of the spacing of the bunches within the train. Horizontal displacement of the beam within the 500 MHz normal conducting RF (NRF) accelerating cavities alone or changing the cavity temperature make small, but repeatable, differences in the threshold current. These cavities also have higher order modes with damping times longer than the spacing

between trains. From these observations it is concluded that the impedance of the NRF cavities plays a significant role in the instability.

During operations a longitudinal bunch by bunch feedback system and a narrowband feedback system (which stabilizes the lower synchrotron sideband of the first rotation harmonic) are in routine use.[4] The wideband longitudinal feedback system drives a stripline kicker and stabilizes the coupled bunch instability which can manifest itself as different synchrotron sidebands becoming unstable depending on the pattern of bunches filled. The narrowband feedback uses the NRF cavities as a kicker and is important at the highest currents to stabilize the coupled bunch mode of oscillation which is destabilized by the detuning of the NRF cavities needed to compensate beam loading. The feedback systems provide sufficient damping to store a total current in the two beams well in excess of the 550 mA HEP operating levels.

## 2 RECENT OBSERVATIONS

The systematic replacement of NRF cavities with superconducting RF (SRF) cavities[5] during the last two years has made it possible to examine the effect of the NRF cavities on the beam's stability. At the time the longitudinal instability was first observed there were four 5 cell NRF cavities installed in CESR. In October of 1997 two NRF cavities were removed and an SRF single cell cavity and a fifth 5 cell NRF cavity were installed. In November of 1998 this fifth NRF cavity was removed and a second SRF cavity was installed.

Before and after these changes to the accelerator's impedance, the instability thresholds for positrons alone in positron injection conditions and for both electrons and positrons in electron injection conditions were measured with the longitudinal feedback system off for a number of the different bunch spacings with 9 trains. Positron injection conditions maintain a flat injection orbit while the electron injection conditions use electrostatically separated orbits for the counter-rotating beams. Figure 1 shows the results of these threshold measurements. Note that in the data for 4 NRF cavities there are bunch patterns that have much higher thresholds than for the other patterns of bunches. Presumably for these bunch spacings there were modes in the cavities which were destructively interfering. As the NRF cavities were exchanged with SRF cavities there is not as large a variation in the thresholds for different bunch patterns. Since the impedance of the single cell SRF cavities is much lower than the five cell NRF cavities and the higher order modes of the SRF cavities have much lower Q's, one would generally expect the instability would weaken and the thresholds should increase. Although this trend is visible for some patterns, it is not at all dramatic even in these cases.

<sup>†</sup> Work supported by the National Science Foundation.

\* Email address: MGB@CESR10.LNS.CORNELL.EDU

### 3 RF SYSTEM MEASUREMENTS AND SIMULATIONS

During the last two years measurements of the properties of the modes of the NRF cavities were made using single 5 mA bunches of positrons. Each of the NRF cavity cells has a field probe installed and, since only one of

these is used for field regulation, the signals from the remaining probes could be observed with a spectrum analyzer. These signals contain a line spectrum at the rotation frequency of CESR and their spectral envelopes give the RF spectrum of the cavity times the coupling for the probes. Spectral data was acquired at times corresponding approximately to the times when the threshold measurements were made.

The spectral data was analyzed to find peaks which were greater than 6 dB above the surroundings and these were fit to a resonance plus a linear baseline. Modes computed by both URMELT and SUPERFISH were used to guide the identification of the different spectral peaks by frequency. Spectral peaks from all the cells in one NRF cavity were compared to select the best fits for each passband member. Then under the assumptions that each passband member could be identified with a particular cell and each would have the same R/Q as a single cell, the ratio of the fitted maximum spectral amplitudes divided by the fitted Q's were compared for peaks in a neighborhood of the passband. Since this ratio is proportional to the R/Q times the coupling coefficient of the probe, the same mode in different cells will have nearly the same ratio. Lastly the peaks for which this ratio changed when the beam was displaced in the cavities were identified as dipole (or higher) modes. From this analysis a set of TM<sub>0</sub> passband members for each of the NRF cavities were identified as having the fitted frequencies and Q's and the R/Q's computed by URMELT.

The results for each of the NRF cavities was used as an input to the program MBI[6] which computes the growth rate of the most unstable eigen mode at 10 mA per bunch for the different possible bunch spacings. The greatest growth rate for each of the time periods of April 97, November 97 and November 98 was  $15.4 \text{ sec}^{-1} \text{ mA}^{-1}$ ,  $15.2 \text{ sec}^{-1} \text{ mA}^{-1}$  and  $8.6 \text{ sec}^{-1} \text{ mA}^{-1}$ , respectively. (These growth rates are comparable to the  $14 \text{ sec}^{-1} \text{ mA}^{-1}$  damping rate of the feedback system.) If the natural damping of the beam is the same for all bunch patterns, the instability growth rate and the threshold current will be inversely proportional to each other. For each time period the growth rate for each of the patterns of bunches was divided by the maximum growth rate to give the relative growth rate; likewise the inverse of the threshold current may be scaled by the lowest threshold current for a given time period. The relative growth rates and relative inverse of the threshold currents are plotted for each time period in figure 2 for each pattern. If the NRF cavity impedance dominates the longitudinal dynamics then these two plots should correspond. As is seen in figure 2, the calculations and measurements for April 97 are generally in good agreement, but measurements at later times with fewer NRF cavities in CESR show poorer agreement. It is likely that as the cavities are exchanged, the impedance of the rest of CESR becomes comparable to the impedance of the cavities thereby altering the threshold currents. A second result which points toward this hypothesis is that the calculated maximum growth rates decrease by almost a factor of two from the first to the last measurements, but the threshold currents increase by much less than this in

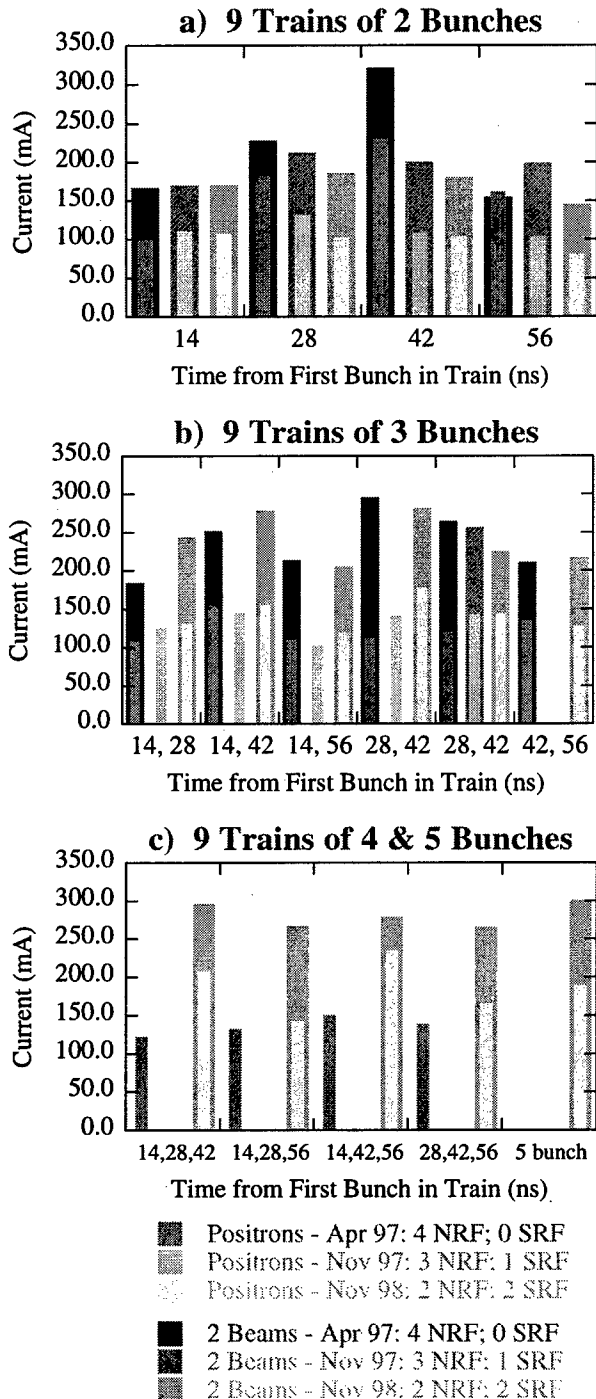


Figure 1. Highest measured instability threshold currents with beam feedback off for different patterns of bunches and different numbers of NRF and SRF cavities in CESR.

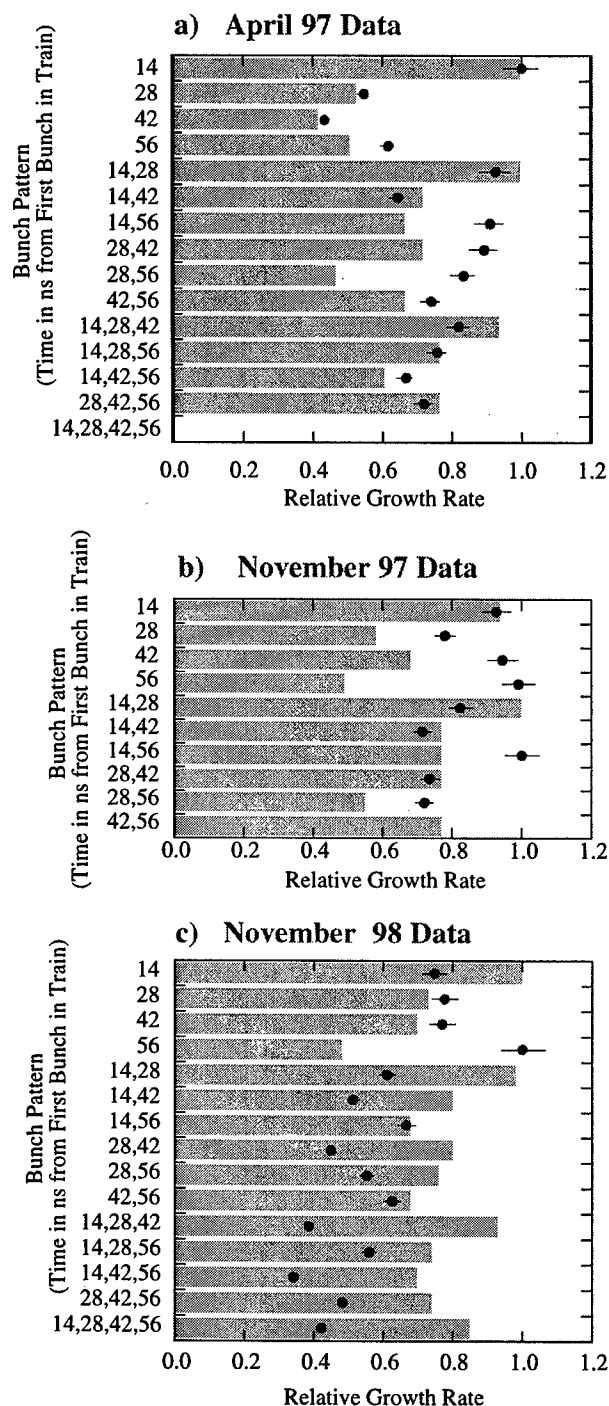


Figure 2. Calculated growth rates for positrons alone relative to the maximum calculated growth rate and the inverse of the corresponding threshold current relative to the lowest threshold current for each time period vs. bunch pattern for 9 trains of 2, 3, 4 and 5 bunches. The bars represent the MBI calculation and the round data points are the inverse of the measured threshold currents for the same pattern. The bunch patterns are expressed as times of subsequent bunches (in ns) relative the leading bunch in the train.

general. Lastly the higher mode loss parameter  $k$  for 2 NRF cavities is comparable to the loss parameter for the remaining structures for CESR so it is not surprising that impedance of the rest of the ring would begin to become important in determining the longitudinal dynamics. Calculations by MBI suggest that the instability growth rates for April 97 are dominated by a TM0 passband near 2.7 GHz (just below the beam pipe cutoff.)

## 4 CONCLUSIONS

The longitudinal coupled bunch instability with trains of bunches in CESR has been observed for the last 4 years. The present longitudinal feedback system has sufficient strength to permit storing much higher currents in CESR than are needed for operations. The NRF cavities have had a major effect on the instability thresholds when the 4 original 5 cell structures were operating in CESR. As the SRF cavities have begun to replace the NRF cavities, the instability thresholds have not in general grown as rapidly as would be expected if the NRF cavities were the only impedance in CESR which contributed to the instability. In March of 1999 the last two 5 cell NRF cavities have been removed and a third SRF cavity installed. Measurements of the instability thresholds will be undertaken once beam is again stored in CESR.

## 5 ACKNOWLEDGMENTS

We would like to thank our colleagues at CESR for help with the measurements performed for this paper, especially G. Codner, R. Meller J. Sikora, and S. Temnykh for important measurements and discussions.

## 6 REFERENCES

- [1] S.B. Peck, et al, CESR Performance and Upgrade Status, these proceedings.
- [2] M. Billing, Observation of a Longitudinal Coupled Bunch Instability with Trains of Bunches in CESR, Proc. of 1997 Part. Acc. Conf., pp. 2317-2319.
- [3] R. Holtzapple, et al, Streak Camera Measurements of the Longitudinal Distribution with Multiple Bunches in CESR, these proceedings.
- [4] J. Sikora, et al, Longitudinal Feedback at CESR, these proceedings.
- [5] S. Belomestnykh, et al, Commissioning of the Superconducting RF Cavities for the CESR Luminosity Upgrade, these proceedings.
- [6] M.M.Karliner, et al, Longitudinal Stability of Colliding Beams in e-e+ Storage Rings with the Account of Beam Coupling with the Environment, Proc. of the Third Advanced ICFA Workshop on Beam-Beam Effects in Circular Colliders, pp. 131-134, Novosibirsk, 1989.

# LONGITUDINAL FEEDBACK AT CESR\*

J.Sikora<sup>&</sup>, M.Billing, G.Codner, R.Meller, C.Strohman, Cornell University, Ithaca, NY 14853  
T.Pelaia QLI, Newark, DE

## Abstract

Total stored electron and positron beam currents at the Cornell Electron Storage Ring (CESR) have been limited by the presence of a dipole multibunch longitudinal instability having a threshold at approximately 250mA of total current. A longitudinal feedback system has been under constant development, test, operation and upgrade over the past several years. The result has been an increase in the High Energy Physics (HEP) operating current to over 500mA total. This paper describes the overall design of the present system, using a horizontal stripline kicker to produce combined horizontal and longitudinal bunch by bunch beam stabilization. Some details on specific subsystems, including: receiver design, individual bunch phase DC offset correction, digital signal filtering, and the RF modulator will be given, as well as an outline of plans for further development.

## 1 INTRODUCTION

The CESR Storage Ring has been colliding short trains of electrons and positrons since 1995. Each beam consists of 9 trains of up to 5 bunches, with a minimum bunch spacing of 14ns. The spacing between bunch trains is either 280 or 294ns in a quasi-uniform pattern over the 2.56 $\mu$ s revolution period. The positron and electron beams circulate in the same beampipe, separated by pretzeled orbits, and collide in a single interaction region.

In April 1996, during HEP operation with nine trains of two bunches, a longitudinal instability appeared when total currents were above 250mA. Although the instability threshold current depended somewhat upon bunch spacing[1], RF cavity parameters, orbit and other variables, active feedback was required in order to make significant increases above 250mA total.

## 2 SYSTEM OVERVIEW

A block diagram of the present longitudinal feedback system is given in Fig. 1. A Beam Position Monitor (BPM) signal is filtered and phase detected using the same 500MHz reference that is used by the CESR RF system. The result is amplified and sent to a Digital Signal Processor (DSP) which samples and filters the data from each bunch. The DSP output is converted back to an analog signal that is further processed and amplified. In the present system, a horizontal kick at a point of

dispersion is used to produce a longitudinal impulse [2]. The error signals from the longitudinal and horizontal feedback systems are combined to yield a single horizontal output kick for each bunch.

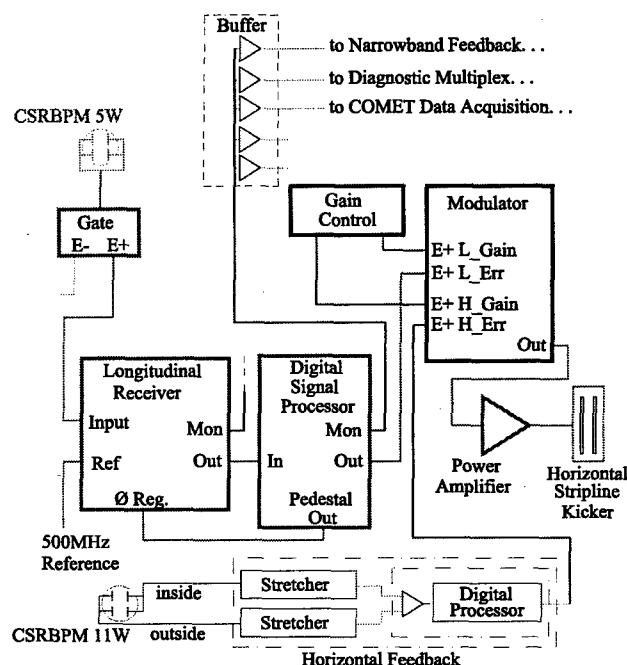


Figure 1: Block diagram of the combined horizontal and longitudinal feedback systems (positron channel shown).

## 3 SYSTEM DESIGN

Given the maximum output voltage provided by an amplifier, the maximum loop gain of the system will be limited by signal to noise ratio, beam transients, or DC offsets. The signal to noise ratio fixes the gain at which receiver noise begins to saturate the output amplifier. Further increasing the low-level gain only increases the proportion of the noise-saturated signal, resulting in little or no increase in system gain. The presence of beam transients (primarily of the zero mode) can produce an error signal exceeding the system's dynamic range and make the system insensitive to small higher frequency mode oscillations. DC phase offsets, e.g. due to beam loading with unequal bunch currents, will saturate the system unless they are properly nulled. The following subsections describe the feedback system in more detail, and outline how system gain was maximized.

\* Work supported by the National Science Foundation.

<sup>&</sup> jps@lns62.lns.cornell.edu

### 3.1 Pickup, Filters and Gating

The signals from four capacitive buttons are combined in order to minimize the sensitivity of the detector to transverse motion, which can be much larger than the longitudinal transient produced during injection. The button signals are first combined in pairs using 100Ω striplines to a 50Ω tee. The signals from the two tees are then combined in a terminated tee and the result sent to the feedback electronics using heliax cable. At typical operating currents in the region of 5 to 10mA per bunch ( $.5$  to  $1.0 \times 10^{11}$  Particles), the beam signal at the input to the feedback electronics is a bipolar pulse with a peak voltage of roughly 16V. After filtering, using a lowpass 0.6ns quasi-gaussian filter<sup>1</sup>, the signal is about 5V peak.

Since both beams are counter-rotating in a single pipe, the positron and electron bunch signals are present in the same cable. The positron and electron signals are demultiplexed using a GaAs switch to allow processing by separate hardware. The maximum filtered signal level that can be handled by the GaAs switch is roughly +20dBm (1dB compression point), which requires that the button signal be attenuated by 16dB.

In addition to minimizing sensitivity to transverse motion, the signal combination scheme gives a minimum of reflections over a very wide bandwidth. This is crucial, since reflections will appear at an arbitrary phase. After phase detection, signal amplifiers could saturate on these unwanted variations rather than on the error signal itself.

### 3.2 Longitudinal Receiver

In the longitudinal receiver the phase of the bunch signal is mixed with a 500MHz reference signal (the same reference used by the CESR RF cavities). The reference signal is routed through a voltage controlled phase shifter controlled by the sum of an offset voltage, a regulation voltage, and an external modulation signal. The offset voltage can be adjusted via the control system computer to bring the phase shifter control voltage into regulation.

The phase regulation error signal comes from the DSP pedestal output (see section 3.3), which is the sampled phase offset of each bunch. The phase regulation loop has a bandwidth of <10 kHz, so it regulates on the average of the pedestal signal from all of the bunches, and therefore on the average bunch phase. The phase error signal is low pass filtered, amplified, and sent to the input of the DSP.

The maximum signal voltage that can appear at the input to the mixer without causing receiver distortion is +23dBm, roughly coinciding with the maximum signal handling capability of the GaAs switch in the previous gating stage. The sensitivity of the present receiver is about 280mrad/volt, with a maximum output of  $\pm 1$ Vpp. The noise output of the receiver is about 10mV (sigma) at 5mA/bunch or about 2.8mrad. However, the measured phase noise of the 500MHz reference is much larger than

this, 12mrad[3]. Presumably,  $1/f$  noise from the reference is being filtered by the receiver's phase regulation loop.

### 3.3 Digital Signal Processor

The digital signal processors reside in a VME crate, one VME board for the electrons and another for positrons. An analog gain of 15 is applied to longitudinal receiver output before being digitized by a 10 bit ADC at 71.4MHz (the maximum practical bunch frequency used in CESR). There are two separate paths for the digitized data: the pedestal correction circuit and the digital filter.

The pedestal correction circuit integrates phase error data from each bunch with a time constant of 8 turns, and passes this data to a DAC and the input opamp, subtracting the result from the incoming signal bunch by bunch. In this way the average signal seen by the ADC will regulate around zero for each bunch. DC phase errors due to the beamloading of uneven bunch currents (e.g. during injection) can easily approach 20mrad. At our present gain settings, the ADC will saturate at about 9mrad, while system gain saturates at 1mrad (amplifier limit). Nulling the DC bunch phase errors increases the gain that can be applied before the error signal is digitized.

The digital filter is constructed of two FIFO memories and two programmable logic devices (PLDs). It contains 183 bandpass and lowpass filters (for 183 bunches/turn). Filter frequencies can be adjusted with a resolution of 0.1kHz near the 20kHz synchrotron sidebands, and the bandpass filter Qs can be adjusted from 3 to about 200 (6 is used in operation). Registers allow the control of the filter parameters via the control system computer and the VME crate microprocessor. Digital filtering reduces the noise on individual bunch signals by about 20dB, allowing a corresponding increase in loop gain. Analog and digital versions of the output signal are available.

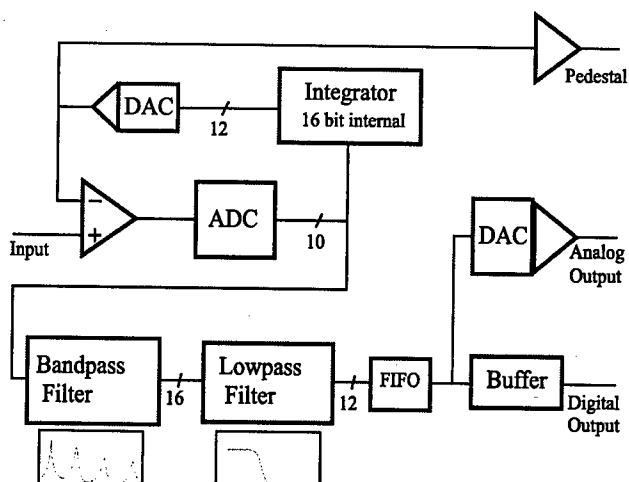


Figure 2: Block Diagram of DSP showing the signal path of each bunch. The output can be delayed up to 16 turns.

<sup>1</sup> Picosecond Pulse Labs. Box 44, Boulder, CO 80306.



### 3.4 Analog Modulator and Amplifiers

The analog error signals from four feedback channels: e+ and e-, horizontal and longitudinal, are scaled and summed to form a combined horizontal-longitudinal correction kick. Electron and positron signals are time multiplexed. A GaAs switch under the control of the CESR timing system alternately selects positive and negative versions of this combined error signal. This produces a 14ns long bipolar pulse whose amplitude is proportional to the error signal. A limiting signal amplifier ensures that the power amplifier will not be saturated.

The delta output of a 180° hybrid splitter converts a single amplifier output into differential signals that are then applied to the inside and outside plates of a shorted stripline kicker. An advantage of this scheme is a considerable cancellation of beam induced voltages seen by the amplifier [4].

## 4 SYSTEM PERFORMANCE AND FUTURE PLANS

Amplifier power limited the maximum output voltage to 200V peak. Applied to the horizontal stripline, this results (through dispersion) in a longitudinal output kick of 140V/turn. Given this amplifier output, damping rates of 200sec<sup>-1</sup> were obtained without digital filtering. Gain could not be increased further since the 1σ receiver noise voltage was at the level corresponding to maximum amplifier output. Once digital filtering of each bunch signal was applied, the reduced noise allowed gain to be increased tenfold, with damping rates now measured at about 2000sec<sup>-1</sup> (14sec<sup>-1</sup>mA<sup>-1</sup>). This increase in gain gives a corresponding decrease in the linear dynamic range of the system, but we have not yet observed this to be a limitation on the amount of current that can be stored. HEP total currents are now in excess of 500mA total. Table 1. compares the phase error that produces system saturation (on amplifier maximum voltage) with the errors observed in operation. This points out the necessity of nulling the DC phase offsets.

Measurements indicate that the dominant longitudinal excitation during injection is of the zero mode, at a level that is well beyond system saturation at the peak of the transient (see Fig. 4). Since the zero-mode is Robinson stabilized, we may filter this lowest sideband from the error spectrum, so that it will not interfere with the damping of other modes.

Further improvements in performance are being explored. The wire-wrapped prototype DSP boards, are being replaced with printed circuit boards with some additional diagnostic features and a zero mode filter. A digital amplifier, with a peak output voltage of 1kV is under test [5], and an RF cavity kicker is being developed similar to that at DAΦNE.

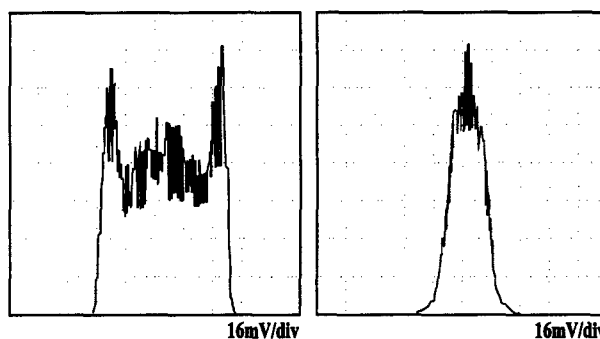


Figure 3: Voltage Histograms of the modulator output showing limiting on receiver noise (left), and the noise reduction after being filtered by the DSP (right). System gain is also four times higher with the DSP installed.

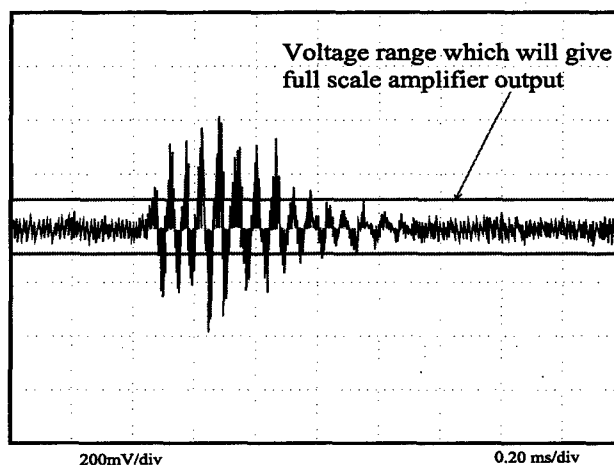


Figure 4: DSP output monitor during an injection transient. System saturation occurs at 100mV or less.

Table 1: Phase errors in the CESR feedback system

Conditions	Phase at 500MHz
System saturation (output amplifier)	1.0 mrad
Receiver output noise sigma	2.8
DSP filtered output noise sigma	0.2
ADC saturation	9.0
Injection transient peak	3.0
DC phases between bunches (max)	20.0

## 5 REFERENCES

- [1] M.G. Billing, *et al*, Observations of a Longitudinal Coupled Bunch Instability in CESR, these proceedings.
- [2] D. Sagan, M. Billing, Cornell LNS note CBN 96-06 (1996).
- [3] K. Ormond, *et al*, Cornell LNS note CON 96-16 (1996).
- [4] J.T. Rogers, *et al*, Proc. 1995 Particle Accelerator Conf.
- [5] G. Codner, *et al*, CESR Feedback System Using a Constant Amplitude Pulser, Proceedings of the 8<sup>th</sup> Beam Instrumentation Workshop, pp. 552-59.

# ON THE SYMMETRY OF THE IMPEDANCE\*

S. Heifets,<sup>†</sup>, B Zotter, CERN

## Abstract

The reciprocity theorem is used to prove the symmetry of the longitudinal impedance of an accelerating structure with respect to exchange of the coordinates of the leading and trailing particles.

## 1 INTRODUCTION

The longitudinal impedance  $Z(\omega, r_t, r_l)$  is a Fourier component of the longitudinal wake field generated by a leading particle with transverse offset  $r_l$  and experienced by the trailing particle with offset  $r_t$  lagging behind the leading particle at the distance  $s$ .

Current of a relativistic particle moving in  $\pm z$ -direction with transverse offset  $r_l = (x_l, y_l)$  has only longitudinal component  $j^\pm(r, r_t, t) = \pm e \delta(r - r_l) \delta(s \mp ct)$ .

We use Fourier harmonics defined as  $j(t) = \int j(\omega) e^{-i\omega t} d\omega / 2\pi$ . Fourier harmonics of the current are

$$j^\pm(r, r_l) = \pm \delta(x - x_l) \delta(y - y_l) e^{\pm i\omega s/c}. \quad (1)$$

The leading particle moving in an accelerator structure and having charge  $e$  may excite in the structure the longitudinal electric field  $E_\omega(r, s, r_l)$ . The longitudinal impedance is defined as integral

$$Z^\pm(\omega, r_t, r_l) = \pm \frac{1}{e} \int ds E_\omega^\pm(r_t, s, r_l) e^{\mp i\omega s/c}, \quad (2)$$

for the beam propagating in  $\pm z$  directions, respectively.

We want to prove that impedance is symmetric in respect with exchange of the transverse coordinates of the leading and trailing particles,

$$Z^+(\omega, r_t, r_l) = Z^+(\omega, r_l, r_t). \quad (3)$$

For a particular case of the resistive wall impedance of a straight pipe, the symmetry was noticed before[1] from the explicit form of the longitudinal impedance. We try to prove the theorem for an arbitrary structure but with mirror symmetry in respect with  $z \rightarrow -z$ . The proof is based on the reciprocity theorem and symmetry of EM fields generated by particles in a symmetric structure.

## 2 SYMMETRY OF THE LONGITUDINAL IMPEDANCE

The reciprocity theorem relates EM fields  $(E(r, r_t), H(r, r_t))$  and  $(E(r, r_l), H(r, r_l))$  driven by two arbitrary currents  $j(r, r_t)$  and  $j(r, r_l)$  correspondingly.

\* Work supported by Department of Energy contract DE-AC03-76SF00515.

<sup>†</sup> Email: heifets@slac.stanford.edu

The reciprocity can be deduced directly from Maxwell equations[2] which give the following identity:

$$\text{div}\{E(r, r_t) \times H(r, r_l) - E(r, r_l) \times H(r, r_t)\} = \quad (4)$$

$$Z_0[j(r, r_t)E(r, r_l) - j(r, r_l)E(r, r_t)] \quad (5)$$

Cross here means vector product.

Integral taken over the left-hand-side over the volume of a beam pipe can be transformed in the surface integral. On the metallic walls of the beam pipe, the tangential components of electric fields are related to the tangential components of the magnetic fields  $E = \zeta H \times n$ , where  $n$  is unit vector perpendicular to the wall,  $\zeta = (1 - i)(\omega\delta/2c)$  is surface impedance, and  $\delta(-\omega) = -i\delta(\omega)$  is skin depth.

The surface integral over beam pipe with ideal conductivity ( $\zeta \rightarrow 0$ ) is zero.

For a surface with finite conductivity, the surface integral

$$\int dV \text{div}(E_t \times H_l) = \int dS n \cdot (E_t \times H_l) \quad (6)$$

$$= \zeta \int dS (H_t \times n) \cdot (H_l \times n) \quad (7)$$

is symmetric with respect to indexes  $t, l$ . Hence, the surface integral over the left-hand-side of Eq. (4) is zero for the finite conductivity as well.

Consider now the surface integrals over the surfaces closing the beam pipe volume at  $s \rightarrow \pm\infty$  in the plane perpendicular to the  $z$ -axis. In the case of finite conductivity of the walls, the integrals are zero because radiated fields are absorbed in the walls. For ideal walls the integral

$$\int_{\infty} dS \{E(r, r_t) \times H(r, r_l) - E(r, r_l) \times H(r, r_t)\} \quad (8)$$

is the difference of two integrals

$$\int_{\infty} dS [E_x(r, r_l) H_y(r, r_t) - E_x(r, r_t) H_y(r, r_l)] \quad (9)$$

$$- \int_{\infty} dS [E_y(r, r_l) H_x(r, r_t) - E_y(r, r_t) H_x(r, r_l)]. \quad (10)$$

We can assume that the beam pipes at infinity are straight pipes and express transverse components of the fields in the TM waves in terms of the longitudinal components:

$$E_x = \frac{iq}{\kappa^2} \frac{\partial E_z}{\partial x}, E_y = \frac{iq}{\kappa^2} \frac{\partial E_z}{\partial y}, \quad (11)$$

$$H_x = -\frac{ik}{\kappa^2} \frac{\partial E_z}{\partial y}, H_y = \frac{ik}{\kappa^2} \frac{\partial E_z}{\partial x}. \quad (12)$$

Here  $q$  is propagating constant,  $(\omega/c)^2 = q^2 + \kappa^2$ .

It is easy to see that both integrals are zero. Cancellation of the surface integrals for the TE waves can be seen in the same way.

Interference between TM and TE modes depends on position of the flanges because, for a given frequency, these modes have different propagating constants. Therefore, the interference term can be put to zero by proper choice of the flanges location.

Hence, integration of Eq. (4) gives

$$\int dV [j(r, s, r_t) E(r, s, r_l) - j(r, s, r_l) E(r, s, r_t)] = 0. \quad (13)$$

This is correct for arbitrary currents. For the currents  $j(r, r_l)$  propagating in  $z$ -direction, and  $j(r, r_t, s)$  in  $-z$  direction  $j(r, s, r_t) = -\delta(r - r_t) e^{-i\omega s/c}$ , Eq. (9) gives

$$-\int ds E_{\omega}^{+}(r_t, s, r_l) e^{-i\omega s/c} = \int ds E_{\omega}^{-}(r_l, s, r_t) e^{i\omega s/c}. \quad (14)$$

Expressions in this equation are the same as those in definition of impedance. Hence,

$$Z^{+}(r_t, r_l, \omega) = Z^{-}(r_l, r_t, \omega). \quad (15)$$

Now we have to relate impedances  $Z^{-}$  and  $Z^{+}$ .

To do this, let us compare solutions  $E^{\pm}(r, s, r_0)$  of the wave equation driven by currents

$$j^{\pm}(r, r_0) = \pm \delta(r - r_0) e^{\pm i\omega s/c}, \quad (16)$$

with the same transverse offsets but moving in opposite direction along the  $z$ -axis. The boundary conditions on the beam pipe are the same in both cases but two solutions  $E^{\pm}(r, s, r_0)$  have different asymptotics. For  $z$ -components, for example,

$$E^{+}(s) \rightarrow D(\omega) e^{iq_{\omega} s}, \quad s \rightarrow \infty, \quad (17)$$

$$E^{+}(s) \rightarrow A(\omega) e^{iq_{\omega} s} + B(\omega) e^{-iq_{\omega} s}, \quad s \rightarrow -\infty \quad (18)$$

and

$$E^{-}(s) \rightarrow -[A(\omega) e^{-iq_{\omega} s} + B(\omega) e^{iq_{\omega} s}], \quad s \rightarrow \infty \quad (19)$$

$$E^{-}(s) \rightarrow -D(\omega) e^{-iq_{\omega} s}, \quad s \rightarrow -\infty. \quad (20)$$

Hence, wave equations, boundary conditions and asymptotics are the same for the fields  $E^{+}(s)$  and  $E^{-}(-s)$ . Therefore,  $z$ -components are related:

$$E^{-}(r, s, r_0) = -E^{+}(r, -s, r_0). \quad (21)$$

Using this result and the definition of  $Z^{-}$  Eq. (2), we obtain

$$Z^{-}(r_l, r_t, \omega) = - \int ds E_{\omega}^{-}(r_l, s, r_t) e^{i\omega s/c}, \quad (22)$$

or

$$Z^{-}(r_l, r_t, \omega) = \int ds E_{\omega}^{+}(r_l, -s, r_t) e^{i\omega s/c}. \quad (23)$$

Expression in the right-hand-side after change of the sign of integrand  $s$  coincide with  $Z^{+}$ , See Eq. (2). Hence, for a mirror symmetric structure, we get

$$Z^{-}(r_l, r_t, \omega) = Z^{+}(r_l, r_t, \omega). \quad (24)$$

and Eq. (11) gives finally

$$Z^{+}(r_t, r_l, \omega) = Z^{+}(r_l, r_t, \omega). \quad (25)$$

The symmetry means that beam-pipe radii at  $\infty$  are equal. The self-field of the beam has only transverse components and does not contribute to the right-hand side.

This conclude the proof.

## 2.1 References

## 3 REFERENCES

- [1] A. Piwinsky, "Impedances in lossy elliptical vacuum chambers", DESY 94-068, April 1994
- [2] L.D. Landau, E.M. Lifshitz, "Electrodynamics of Continuous Media", \$69, Nauka, 1957

# DESIGN CONSIDERATIONS FOR THE ELETTRA TRANSVERSE MULTI-BUNCH FEEDBACK

R. Bressanutti\*, D. Bulfone<sup>#</sup>, S. D'Orlando\*, A. Fabris, M. Ferianis, C. Gamba, M. Lonza, M. Svandrlik, L. Tosi, R. Ursic<sup>+</sup>, Sincrotrone Trieste, SS 14-Km 163.5, 34012 Basovizza, Trieste, Italy

## Abstract

The ELETTRA Transverse Multi-Bunch Feedback consists of a wide-band bunch-by-bunch system where the positions of the 432 bunches, separated by 2 ns, are individually sampled and corrected. Digital electronics is used for processing data. After a description of the system parameters and architecture, the status of the project is presented.

## 1 INTRODUCTION

The electromagnetic fields associated with the very high intensity electron beam accumulated in third generation synchrotron light sources can generate Coupled Bunch Instabilities (CBI) through the interaction with the vacuum chamber (resistive wall effect) and/or cavity Higher Order Modes (HOMs). Multi-bunch instabilities degrade the quality of the beam (e.g. increased beam emittance, energy spread) and can lead to beam loss. At ELETTRA, multi-bunch instabilities are presently dealt with by shifting HOM frequencies by acting on the cavity temperatures and/or HOM shifters [1]. In view of future operation of the facility at higher currents, a feedback system to damp transverse multi-bunch instabilities is under development. The project is being developed in collaboration with the Swiss Light Source.

## 2 SYSTEM PARAMETERS

The main feedback parameters are shown in table 1. The system is designed to operate with beam currents and energies up to 400 mA and 2.5 GeV respectively. The lowest operating frequency corresponds to the first betatron sideband in the baseband signal spectrum (0-250 MHz). The RF power/plane is the typical maximum power available from a couple of commercial amplifiers featuring the required bandwidth. The kicker shunt impedance refers to that of a 30 cm long cylindrical stripline type kicker, which has been preliminarily designed.

\* Email: daniela.bulfone@elettra.trieste.it

<sup>+</sup> Instrumentation Technologies, Slovenia

\* Hosted by Sincrotrone Trieste for the thesis work

Table 1: ELETTRA Transverse Multi-Bunch Feedback parameters

PARAMETER	VALUE
Beam Current, $I_b$	400 mA
Beam Energy, $E_b$	2.5 GeV <sup>♣</sup>
Number of bunches	432
Bunch spacing	2 ns
Lowest Frequencies ( $q_x=0.3$ , $q_y=0.2$ )	0.34, 0.23 MHz
Highest Frequency	250 MHz
$\beta_x, \beta_y$ @ BPM	5.2, 8.9 m
$\beta_x, \beta_y$ @ kicker	6.5, 7.5 m
Max. $Z_{RW}$ , min $\tau_{RW}$	0.5 MOhm/m, 4 ms
Max. $Z_{HOM}$ , min $\tau_{HOM}$	11.2 MOhm/m, 0.12 ms
Amplifier Power, $P_K$	300 W/plane
Kicker Shunt Impedance, $R_K$ @ DC, 250 MHz	16.5, 6.5 kOhm

<sup>♣</sup> In view of future ELETTRA upgrades [2]

## 3 THE TRANSVERSE MULTI-BUNCH FEEDBACK SYSTEM

The ELETTRA Transverse Multi-Bunch Feedback (TMBF) consists of a wide-band bunch-by-bunch system where the positions of the bunches are individually sampled and corrected. The block diagram of the TMBF for one of the two transverse planes is shown in figure 1. Wide-band signals from a standard Beam Position Monitor (BPM) pick-up are combined into a "hybrid network" producing x, y, and I signals. These are entered into a "RF front-end" which demodulates the inputs to baseband.

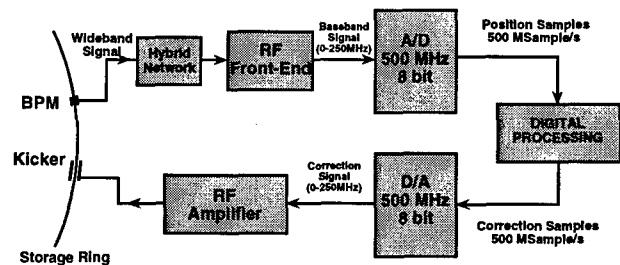


Figure 1: Block diagram of the Transverse Multi-Bunch Feedbacksystem

Baseband bunch-by-bunch position information is sampled by a fast 8 bit 500 Msample/s analog-to-digital converter (ADC) and the amplitude of the corrective kick

is calculated using digital processing electronics. The correction values are transmitted to an 8 bit 500 Msample/s digital-to-analog converter (DAC), amplified by a RF Power Amplifier and applied to the beam by a kicker.

#### 4 THE RF FRONT-END

The standard ELETTRA BPM pick-up has four buttons symmetrically positioned around a diamond shaped vacuum chamber. The location of the buttons is such that it yields the same position sensitivity on both the x and y planes.

The processing of the four pick-up signals takes place in two geographically separated modules (figure 2). The first module is a hybrid network that resides in the tunnel, close to the pick-up. The purpose of this module is to deliver two signals proportional to the x and y positions scaled by the bunch current and a signal proportional to the beam current. We use commercially available hybrid blocks to perform sum and difference operations on the four button signals. Three low loss cables connect the hybrid network with the RF front-end that resides in the service area.

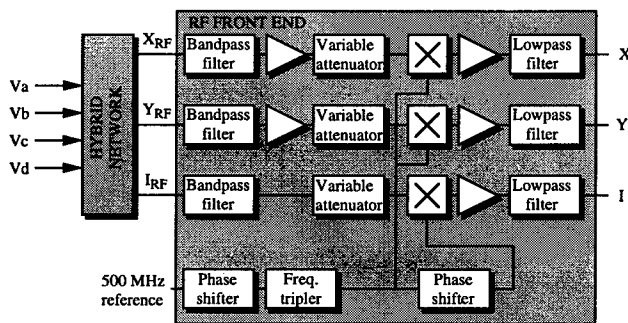


Figure 2: RF front-end block diagram

The RF front-end module operates at a 1.5 GHz carrier frequency, which is the third harmonic of the RF. The purpose of the RF front-end is to convert the input 1.5 GHz signals to baseband. The x (y) input signal gets first processed by a bandpass filter followed by a fixed gain low noise amplifier. A gain control in excess of 20 dB is accomplished by a variable attenuator downstream the amplifier. The x (y) signal then enters a mixer that shifts the frequency spectrum from 1.5 GHz to baseband. A processing chain consisting of an amplifier, a low pass filter and a second amplifier eventually follows. The beam current signal is processed in a similar way with the exception that it does not have an amplifier following the input bandpass filter since the signal range is much higher than that in the x and y chains. A 500 MHz RF signal is used as a reference to generate the 1.5 GHz signal through a tripler. Two phase shifters allow independent control of the x and y chains on one side and the beam current chain on the other.

A prototype hybrid network and RF front-end have been developed and installed on the machine. In order to improve the input dynamic range of the feedback, a scheme is being integrated in the RF front-end to partially reject the DC closed orbit and revolution harmonic components of the input x and y signals.

#### 5 THE DIGITAL PROCESSING ELECTRONICS

In order to damp the oscillations of a bunch, the correcting kick signal must be shifted by  $\pi/2$  betatron phase with respect to the position signal of the same bunch in the kicker. In our scheme the kick value is determined by detecting the bunch position signal at the BPM and by shifting its phase through a digital filter in the processing block. As filters can be programmed to provide any phase, the BPM and the kicker can reside at any position in the ring.

In the bunch-by-bunch approach the feedback uses only the position information from a particular bunch to calculate the corrections for that bunch. It is therefore possible to split the required processing power among several computing units, where each of them is in charge of a number of bunches.

A block diagram of the ADC, Digital Processing and DAC blocks is shown in figure 3. A modular upgradable design based on the VME standard has been adopted, where the main components are interfaced through standard high-speed communication paths. The 500 Mbyte/s data flux is de-multiplexed in the ADC Board on six Front Panel Data Ports [3] (FPDP). Each FPDP is connected to a Digital Signal Processor (DSP) board where data is de-multiplexed again towards up to four DSPs.

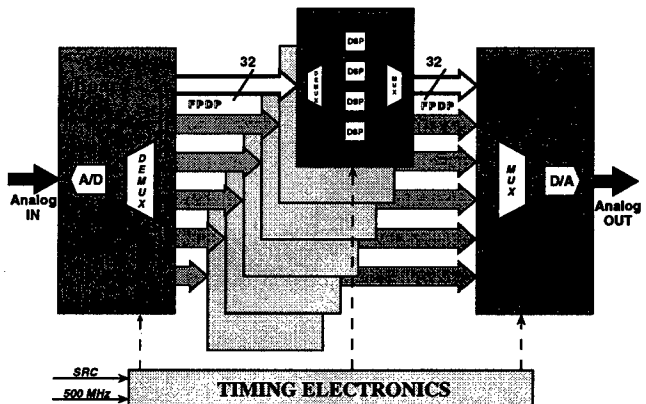


Figure 3: Block diagram of the digital processing electronics.

The calculated correction kick values are eventually transmitted to the DAC board following a symmetric multiplexing mechanism. The whole process is synchronized with the Storage Ring Clock (SRC) and the 500 MHz main RF signal through the Timing Electronics.

The digital programmable approach for the processing block provides a very high level of flexibility, as different processing algorithms can be run on the DSPs. In parallel to this, a number of beam diagnostic tasks (e.g. tune measurement, growth/damping time measurements, oscillation mode detection) will also be available.

The TI-TMS320C60 DSP has been adopted. The processing algorithms have been run on a DSP simulator and on an evaluation board equipped with the real processor to check processing time and capabilities.

An extensive use of commercial off-the-shelf (COTS) boards has been considered for the digital electronics (ADC, DAC and DSP boards) to reduce development times.

## 6 SIMULATIONS AND FILTER STUDIES

A simulator has been developed to preliminary study the effects of the TMBF on the machine. It consists of a tracking program written in "C" which comprehends the machine components, the cavity HOMs and the natural damping. This program has been integrated in Matlab [4], where the processing algorithms are implemented and the simulation results are analyzed.

Processing algorithms mainly consist of Finite Impulse Response (FIR) and Infinite Impulse Response (IIR) digital filters [5]: the filtering is applied individually to each bunch. Several filter types have been evaluated: the most simple one is a 3-tap FIR filter which provides DC rejection and appropriate gain and phase at the betatron frequency. Figure 4 is an example of a simulated beam mode damped by the feedback running such a filter.

Although a 3-tap FIR filter includes all the basic required functions of a TMBF, other important features can be added when designing a more complicated filter.

The sensitivity of the feedback to tune changes leads to degradation of the performance or even to the non-controllability of the instabilities. Special 5-tap FIR filters with appropriate frequency response can be designed in order to keep the same damping capability in case of tune shift.

Optimum control theory can also be applied to the multi-bunch feedback problem. Simulations show the same closed-loop damping behaviour with less RF power delivered when LQR (Linear Quadratic Regulator) controllers are used.

Errors in the position samples, due to conversion quantization and noise, affect the residual oscillation amplitude. The adoption of IIR band-pass digital filters centered at the betatron frequency can sensibly reduce the noise and thus lower the resolution limit.

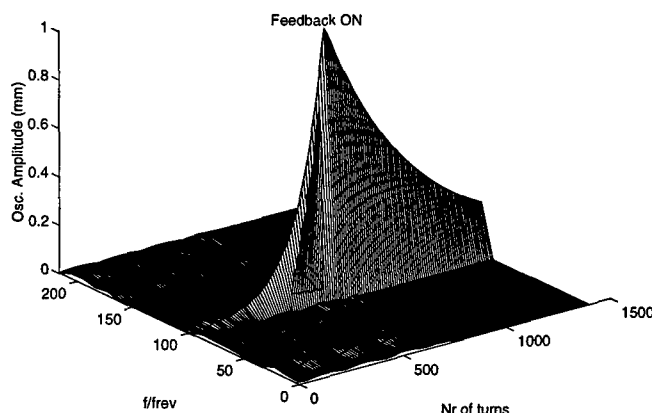


Figure 4: Simulated beam mode damped by the TMBF running a 3-tap FIR filter

## 7 CONCLUSIONS

A wide band bunch-by-bunch TMBF system is under development at ELETTRA.

A prototype RF front-end module has been installed.

Digital processing electronics, which relies on COTS components, provides a high level of flexibility and integrates different beam diagnostics tools. The adopted modular architecture allows to use the same digital processing hardware on different machines and/or for longitudinal multi-bunch feedback systems.

In the frame of an active collaboration, the kicker development is being undertaken by the Swiss Light Source.

The first system tests are foreseen for the end of '99.

## 8 ACKNOWLEDGEMENTS

The authors would like to thank M. Serio (INFN-Frascati), J. Fox (SLAC) and their respective teams, W. Barry and G. Stover (LBL), V. Schlott and M. Dehler (SLS), for the stimulating discussions on multi-bunch feedback systems; M. Bossi, R. De Monte and G. Mian for their technical skill.

## 9 REFERENCES

- [1] M. Svandrlik et al., 'Improvements in Curing Coupled Bunch Instabilities at ELETTRA by Mode Shifting after the Installation of the Adjustable Higher Order Mode Frequency Shifter (HOMFS)', Proc. Particle Accelerator Conference, Vancouver, May 1997.
- [2] C.J. Bocchetta et al., 'ELETTRA Status and Development Plans' these Proceedings.
- [3] 'FPDP Specification', VITA 17-199x Rev. 1.1, October 1995.
- [4] 'Matlab User's Guide', The MathWorks, Inc. 24 Prime Park Way, Natick, Mass. 01760-1500, 1994.
- [5] A. V. Oppenheim and R. W. Schaffer: 'Digital Signal Processing', Prentice Hall, 1975.

# HOM CHARACTERISATION OF THE ANKA RF CAVITIES FOR COUPLED BUNCH INSTABILITY CALCULATIONS

P. Craievich, A. Fabris, C. Pasotti, M. Svandrlík, SINCROTRONE TRIESTE, Trieste, Italy

## Abstract

The Higher Order Modes (HOM) spectrum of the first RF cavity of the ANKA storage ring has been fully characterised. Possible beam-cavity interactions leading to unstable longitudinal and transverse coupled bunch oscillations have been then analysed as a function of the cavity temperatures. Proper temperature settings are computed in view of the commissioning start of ANKA, scheduled for the end of 1999.

## 1 INTRODUCTION

The ANKA storage ring cavities are of the Elettra-type. Some improvements have been introduced on the cooling circuit, to improve its efficiency [1]. Coupled Bunch Instabilities will be cured following the same approach than in ELETTRA, that is using the mode shifting technique by cavity temperature tuning and with the additional degree of freedom of the HOM Frequency Shifter. This requires full characterisation of the HOM spectrum to identify any possible beam-cavity interactions. As foreseen by the time schedule, by the end of February one out of four ANKA cavities was fully characterised and tested at the ELETTRA laboratory (cavity ANKA\_1), while a second one was under test (cavity ANKA\_2). The cavity characterisation follows a standard procedure which foresees the measurement of the fundamental cavity mode parameters included in the acceptance test protocol, like frequency, quality factor and R/Q, and the identification of the HOM. HOM measurements include frequency, quality factor and, for longitudinal modes, the R/Q. Transverse dipole modes are identified with field measurements. Field measurements have been performed with the cavity at atmospheric pressure, under nitrogen flux to prevent cavity surface pollution. The frequency and the quality factor are measured with the cavity under vacuum.

## 2 THE LONGITUDINAL MODES

The resonance frequency of the longitudinal modes up to the cut off frequency of the cavity beam pipes has been computed with MAFIA 4.0. The real value of the mode frequency is found for each cavity by identifying the electric field along the beam path for those peaks resonating close to the computed value. After mode identification the R/Q has been measured with the perturbation method, that is by measuring the frequency shift caused by a bead moving along the beam path. The measurement set-up is the same already used to

characterise ELETTRA cavities [2]. The loaded value of the quality factors are measured with the Network Analyser HP 8510B in transmission mode. The unloaded values are then computed by taking into account the coupling coefficients  $\beta$  of the Input Power Coupler and of the RF signal pick-ups mounted on the cavity.

### 2.1 R/Q and Q of the accelerating mode

Particular care has been dedicated to the evaluation of the shunt impedance of the accelerating mode L0 which defines the cavity acceleration efficiency. The perturbing bead for the L0 mode is a stainless steel calibrated needle [2]. The frequency shift measured along the beam axis for this mode is shown in fig. 1a. To eliminate the noise that occurs at the tails of the measurement, where the frequency shifts introduced by the bead can be compared to the measurement error, the noisy data are interpolated with a polynomial curve of order 3. Figure 1b shows the interpolated curve after the fit. The R/Q and Q values measured on the first two ANKA cavities are listed in table 1.

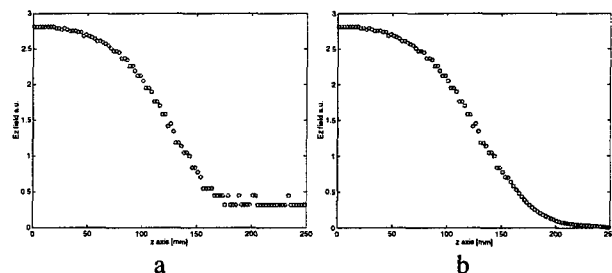


Fig. 1: L<sub>0</sub> Electric field on half cell: measured (a) and interpolated data (b).

Table 1: R/Q and Q measured values of the longitudinal accelerating mode (Transit time factor 0.700)

Cavity	R/Q ( $\Omega$ )	Q	Rsh (M $\Omega$ )
ANKA_1	174.2	39000	3.33
ANKA_2	174.5	41200	3.52

The Q factor could be improved in the second cavity after a modification in the fabrication procedure, avoiding the diffusion of the filler material on the inner cavity surface during the brazing process [3].

### 2.2 R/Q and Q of the HOM longitudinal modes

The comparison of the computed on-axis electric field profile with the measured one allows safe identification of each HOM. The measurement of the electric field becomes

critical for modes resonating close to the cut-off frequency of the beam ports, like mode L9. In this case the field begins to penetrate into the beam tubes. To perform the measurement a 300 mm tube, diameter 100 mm, is then connected to the beam port. This reproduces fairly well in the laboratory the situation on the machine where there are bellows and connection tubes on each side of the cavity. In figure 2, the computed field (solid line) can be compared with the measured one (dotted line).

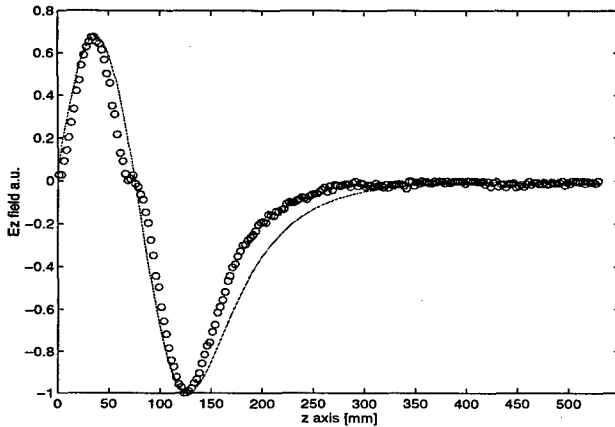


Figure 2: Measured electric field on half cavity length for the L9 mode (dotted line), compared with the computed field (solid line).

The parameters of the nine longitudinal modes below cut-off as measured on cavity ANKA\_1 are listed in table 2 along with the computed ones. The computed R/Q of mode L8 (frequency 2088 MHz) is close to zero, resulting in an impedance below the threshold to excite coupled bunch oscillations; in fact it is not possible to measure it.

Table 2: Cavity ANKA\_1 longitudinal modes

mode	fr, MHz	R/Q, $\Omega$	R/Q, $\Omega$	Q	Q	R <sub>sh</sub> , k $\Omega$
	measured	comp.	meas.	computed	measured	measured
L1	947.0	29.3	27.6	46900	36200	1000
L2	1056.3	0.7	1.0	66600	48400	48
L3	1421.6	5.0	5.1	57800	44400	226
L4	1511.4	4.8	4.2	63500	46000	193
L5	1604.6	9.8	9.8	79100	44800	439
L6	1875.6	0.4	0.5	59000	39400	20
L7	1947.8	1.6	1.6	83600	67900	109
L8	n.m.	0.0	n.m.	63400	n.m.	n.m.
L9	2126.7	7.8	7.8	53700	32400	253

Cavity ANKA\_2 characterisation is not yet completed. Table 3 shows the data for the two modes with the highest shunt impedance, L1 and L5.

Table 3: Selection of measured data, cavity ANKA\_2

mode	fr, MHz	R/Q, $\Omega$	Q	R <sub>sh</sub> , k $\Omega$
L1	947.3	26.7	37500	1001
L5	1605.6	10.3	48200	496

### 3 DIPOLE MODES

The first nine dipole modes resonate below the cut off frequency of the beam pipe and are therefore trapped into the cavity. If their frequency overlaps exactly a line of the beam spectrum, their transverse impedance can excite transverse coupled bunch instabilities in ANKA [4]. However, using the mode shifting technique in Elettra, only modes D2, D3 and D5 interacted sometime in the past with the beam. To identify the dipole modes we start from the MAFIA frequency list and select the dipole modes using the perturbation method. In fact we look for modes with electric and magnetic field on the beam axis, while sextupole modes have zero field on the axis. This is particularly important to identify the mode D3 which resonating frequency is very close to that of mode S1. Due to the asymmetries in the cavity geometry, each dipole mode generates two polarisations, which we call *a* and *b*, resonating at slightly different frequencies. Only one polarization could be measured for modes D5 and D8. Table 4 lists the measured value of the resonance frequencies and quality factors, while (R/Q)' is given by MAFIA.

Table 4: Cavity ANKA\_1 dipole modes

Mode	fr, MHz	(R/Q)', $\Omega$	Q	R <sub>⊥</sub> , M $\Omega$ /m
D1a	743.73	4.7	35500	2.6
D1b	743.94			
D2a	746.39	15.8	36400	9.0
D2b	746.71			
D3a	1112.48	13.0	33200	10.1
D3b	1112.65			
D4a	1220.33	0.1	78400	0.2
D4b	1220.79			
D5	1244.80	4.5	24000	2.8
D6a	1304.89	0.3	15000	0.1
D6b	1305.07			
D7a	1557.29	0.0	7600	0.0
D7b	1557.74			
D8	1631.28	2.4	22000	1.8
D9a	1716.08	1.6	18100	1.0
D9b	1716.32			

### 4 COUPLED BUNCH INSTABILITIES

The use of Elettra-type cavity, with a cooling system layout similar to the Elettra-one, will allow to cure Coupled Bunch Instabilities (CBI) in ANKA by mode shifting, as successfully experienced at ELETTRA. It has already been demonstrated in [4] that both for longitudinal and transverse oscillations a proper setting of the temperature of the cavities can guarantee stable machine operation for ANKA at 2.5 GeV, up to 400 mA of stored beam. The situation can be more critical at lower energies, particularly at the injection energy of 500 MeV, where transverse effects could disturb the machine operability. To avoid this it will probably be necessary to excite a longitudinal mode on purpose to increase the



thresholds for the transverse ones, as it is done in ELETTRA. The calculations presented in [4] were performed on random generated frequencies, starting from the statistical spread of HOM frequencies observed in the existing Elettra-type cavities. Now we want to verify on the first real cavity for the ANKA storage ring that stable intervals are actually available and to give a first indication of what will be the temperature settings for that cavity.

Table 5: ANKA Storage Ring parameters

Parameter	Design Value
Energy, E/e	2.5 GeV
Momentum Compaction, $\alpha$	$8.1 \cdot 10^{-3}$
Beam Current, $I_b$	400 mA
RF frequency, $f_{RF}$	499.652 MHz
Revolution frequency, $f_0$	2.7155 MHz
Harmonic number, h	184
Long. Rad. Damp. Time, $\tau_L$	1.45 ms
Hor. Rad. Damp. Time, $\tau_x$	3.08 ms
Ver. Rad. Damp. Time, $\tau_y$	2.96 ms

The growth rates of the longitudinal Coupled Bunch (CB) modes have been computed as a function of temperature for cavity ANKA\_1, following the usual approach [5]. The cavity data are those listed in table 2 and the ANKA machine parameters are shown in table 5. The result for a stored beam of 400 mA (184 equally filled and spaced bunches) at 2.5 GeV, is shown in figure 3. Growth rates above the radiation damping rate, leading therefore to unstable coupled bunch oscillations, are computed for CB number 165 between 41 °C and 44 °C (interacting with cavity mode L7); for CBN 46 between 56 °C and 60 °C (cavity mode L9); for CBN 155 between 56 °C and 60 °C (cavity mode L3). Two stability windows are present between 45 °C and 55 °C and between 62 °C and 69 °C.

The calculation for the transverse horizontal case shows a significant excitation for CBN 86 between 40 ° and 47 °C (figure 4). The machine is slightly less sensitive to vertical CB oscillation, due to the lower value of the betatron function at the cavity location, which is less than half the horizontal value [4]. In the vertical case CBN 91 is predicted to be unstable from 43 ° to 47 °C (figure 5).

Overlapping the three pictures we see that, for cavity ANKA\_1, temperature settings between 47 °C and 54 °C or between 62 °C and 69 °C should avoid any excitation of coupled bunch oscillations in ANKA.

## 5 CONCLUSION

Stable operating conditions are predicted for cavity ANKA\_1 on the base of the measured HOM data. They will be confirmed after checking the HOM spectrum after in situ installation of the cavity.

All other ANKA Storage Ring cavities will be characterised in the same way and the complete prediction of stable operating intervals will be available.

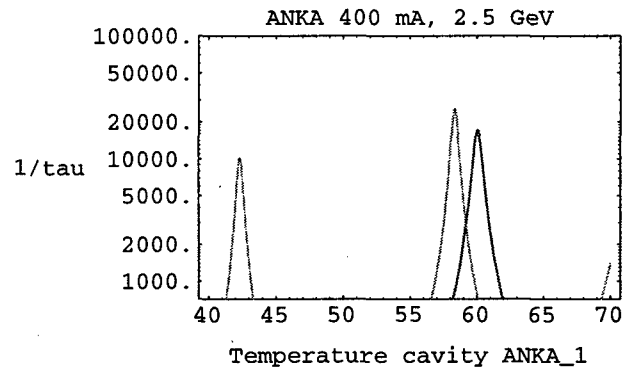


Fig. 3: Longitudinal CB growth rates vs. temperature

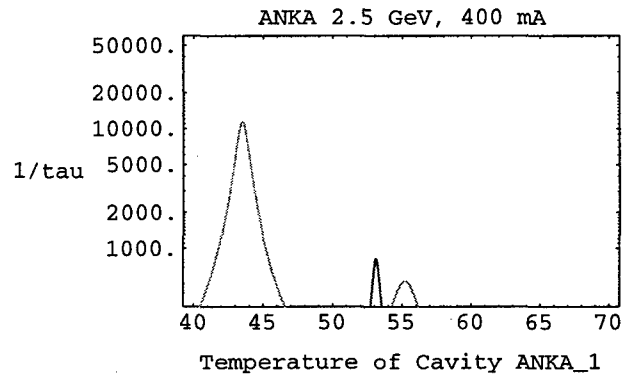


Fig. 4: Transv. horizontal growth rates vs. temperature

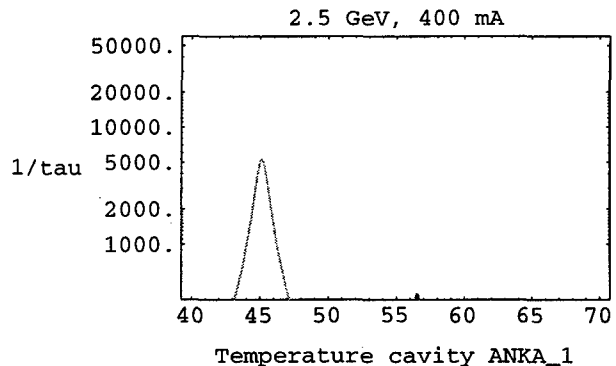


Fig. 5: Transv. vertical growth rates vs. temperature

## 6 REFERENCES

- [1] M. Svandrlik et al., "The Anka RF Cavities", in *Proceedings of the 1998 EPAC*, Stockholm, pp. 1817-1819.
- [2] C. Pasotti et al., "Field Measurement of the ELETTRA Cavity HOM", in *Proceedings of the 1998 EPAC*, Stockholm, pp. 1802-1804.
- [3] F. Pérez et al., "Status of the RF System for the ANKA Storage Ring", these proceedings.
- [4] M. Svandrlik et al., "CBI Calculations for the ANKA Storage Ring", in *Proceedings of the 1998 EPAC*, Stockholm, pp. 1011-1013.
- [5] M. Svandrlik et al., "The Cure of MBI in Elettra", *Proc. of PAC 95*, Dallas, May 95, pp. 2762-2764.

# EFFECTS OF THE HARMONIC SEXTUPOLE ON TRANSVERSE MULTIBUNCH INSTABILITIES AT ELETTRA

L. Tosi\* and E. Karantzoulis, Sincrotrone Trieste, Trieste, Italy

## Abstract

The results of measurements on the ELETTRA storage ring which show a strong dependence of the excitation of transverse multibunch instabilities on the settings of the harmonic sextupole are presented. A strong correlation with the coefficients involved in the non-linear tune shifts with amplitude induced by the sextupole has been observed.

## 1 INTRODUCTION

In order to achieve an emittance of 7.0 nm rad at 2.0 GeV, the lattice of ELETTRA was designed to be a double bend achromat of the expanded Chasman Green type with strong focussing quadrupoles. The resulting fairly large natural chromaticities are compensated by two sextupole families in the dispersive arcs. In addition, a family of harmonic sextupoles has been introduced in the dispersion free straight sections, in order to enlarge the dynamic aperture and thus compensate to a large extent the non-linear effects of the chromatic ones.

In general, non-linear elements produce a distortion of the phase space distribution of the particles, accompanied by a non-linear tune shift with amplitude, so that two particles with different amplitudes will oscillate with different tunes. For sextupoles, the tune shifts with amplitude appear as higher order effects and are obtainable by applying perturbation theory to the Hamiltonian describing the dynamics in the action and angle variables [1]. For the purpose of this paper, only the tune shifts with amplitude due to second order effects of the sextupoles will be considered. These may be expressed according to :

$$\begin{aligned}\Delta\nu_x &= C_{11} 2J_x + C_{12} 2J_y \\ \Delta\nu_y &= C_{12} 2J_x + C_{22} 2J_y\end{aligned}$$

where the subscripts x and y denote the horizontal and vertical planes respectively,  $\Delta\nu_u$  are the non-linear tune shifts,  $J_u$  the perturbed action variables and  $C_{11}$ ,  $C_{12}$ ,  $C_{22}$  are coefficients which depend on the sextupole strengths, on the beta functions at their locations and on the relative phase advances between them [1,2]. Figure 1 shows the theoretical behaviour of the three coefficients as functions of the harmonic sextupole settings (nominal value is 46 A).

It has been observed in ELETTRA that the harmonic sextupole S1 plays an essential role in the dynamics when

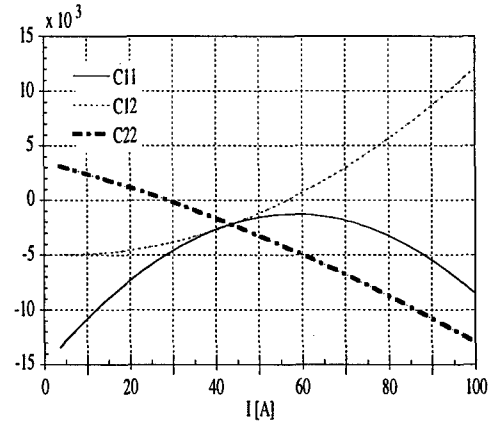


Figure 1: Theoretical behaviour of the three coefficients  $C_{11}$ ,  $C_{12}$  and  $C_{22}$  as functions of the harmonic sextupole settings.

the beam is being affected by coherent transverse multibunch instabilities, to the extent that they can even be totally sup-pressed for appropriate settings of the sextupole [3]. Many measurements were performed and they all indicate a strong correlation with the behaviour of the coefficients  $C_{11}$  and  $C_{22}$ . This paper presents the main results of the observations, of the measurements performed and of preliminary simulations.

## 2 MEASUREMENTS

Modes driven by the four rf cavities in ELETTRA are controlled by setting the temperatures of the cavities [4]. Most of the measurements were made in the presence of horizontal coupled bunch modes (HCBM), in that it was found quite difficult to excite vertical cavity driven modes in the range of temperatures at which the rf cavities routinely operate. In particular, the behaviour of HCBM 318 with the harmonic sextupole settings, driven by the cavity HOM T3 [5], was investigated, as well as that of HCBM 414-417 the origin of which is still a matter of investigation. Since the horizontal instabilities are rather strong, with visibly large oscillations observed on the synchrotron light beam profile monitor, measurements concentrated on correlating the behaviour of the modes with  $C_{11}$ .

Figure 2 compares  $C_{11}$  with the amplitude of HCBM 318 as a function of the current setting of the harmonic sextupole. The mode could be totally suppressed by setting the sextu-pole below 28 A or above 90 A. The same parabolic beha viour as  $C_{11}$  was found for the excita-

\* Email: tosi@elettra.trieste.it

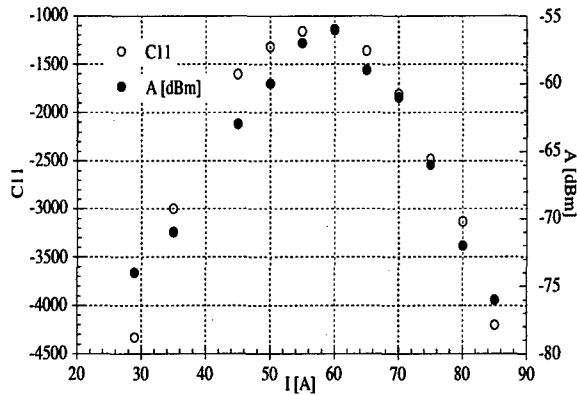


Figure 2: Comparison of the amplitude of HCBM 318 with  $C_{11}$  as functions of the harmonic sextupole settings

tion levels of HCBM 414, although in this case the two current values of the sextupole for which the mode was totally suppressed were found to be different. While the peak of the excitation level of the modes was always found to be at the setting of 60 A, investigations revealed that the two boundary current values of the sextupole at which the modes can be suppressed depend on the beam current, on the modes excited, on the filling pattern and on the presence or less of longitudinal instabilities. It was noticed that the stronger the mode, the higher the filling percentage and the lower the longitudinal excitations were, the wider was the range of the sextupole settings for which the modes were excited. This namely translates into requiring higher absolute values for  $C_{11}$  in order to achieve the suppression of the horizontal modes. While the dependence on the beam current and on the particular mode excited reflects the 'strength' of the driving force, the one on the filling pattern and on the presence or not of longitudinal modes is thought to be due to how 'well' the driving force manages to couple to the beam's modes. The coupling efficiency of a transverse driving force may be diminished by a gap within the bunch train, by the different arrival times of the bunches and possibly also on the density of the bunches.

It has to be strongly underlined that even in the total absence of longitudinal modes, confirmed by measurements of the full longitudinal spectrum, it was found that the amplitudes of the excited transverse modes follow the same trend of  $C_{11}$  with the harmonic sextupole settings, excluding thus any interference of longitudinal modes in the mechanism by which the sextupole may be influencing the dynamics. This was a particularly important point to confirm, also because the cavities are located in the dispersive arc. Furthermore, it was found, by measuring full longitudinal spectra as a function of the harmonic sextupole settings, that the excitation level of any longitudinal instabilities did not depend on the sextupole.

The major beam parameters, such as tunes, closed orbit, dispersion and chromaticities were measured as a function of the harmonic sextupole settings. No significant changes were noticed in these quantities, with the exception of the horizontal chromaticity, which for the measurement of figure 2 was found to vary from 0.1 for the setting of  $I = 28$  A to 1.6 for  $I = 90$  A (both currents are values for which the mode was suppressed). This effect is not expected to be the major cause for the suppression of the mode. In fact, no change in the excitation level of the mode was noticed when the horizontal chromaticity was set to 1.6, by using the chromaticity correcting sextupoles. Since the value of  $C_{11}$  also depends on the settings of the chromaticity correcting sextupoles, investigations were carried out in order to confirm the leading role of  $C_{11}$  in the phenomenon against that of the horizontal chromaticity. The results revealed that the suppression of excited modes using the chromaticity correcting sextupoles required horizontal chromaticities which could be even greater than 7 times the one measured when the suppression was achieved using the harmonic sextupole. The values of  $C_{11}$  instead in the two situations of suppression of the modes were computed to be almost identical.

Low frequencies in the spectrum (below 100 Hz) have also been observed, associated with the presence of the transverse modes. Whereas in some situations there appears a well defined peak at low frequency, in others the whole background noise level increases by 1-2 orders of magnitude. Whenever well defined low frequencies were noticed, measurements on the spectrum analyzer in zero span mode of the unstable sideband showed periodicities corresponding to the peaks measured in the low frequency spectrum range. Detailed investigations in a narrow frequency range around the unstable sideband with an appropriate sweeping time showed a fine structure indicating that the sideband was moving with the measured low frequency. It is believed that in this scenario the mode is shifting along the impedance experiencing different real and imaginary parts of it, until it eventually goes out of its frequency range of influence. The beam then loses coherence and is damped until the coherence builds up again. Increasing the absolute value of  $C_{11}$  by lowering the sextupole current changed the dynamics and the unstable sideband presented only a frequency spread. It has been found that the settings of the harmonic sextupole influence the values of the low frequencies. Figure 3 shows the dependence of the low frequencies both on the harmonic sextupole settings and on the beam current for a fixed setting of the sextupole of 60 A. The low frequencies fit extremely well to a second order polynomial as a function of the sextupole, presenting a maximum where the absolute value of  $C_{11}$  is minimum.

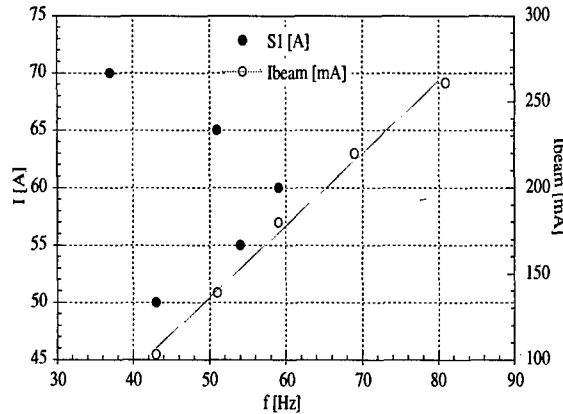


Figure 3: Low frequencies associated to transverse instabilities as functions of the harmonic sextupole settings and of beam current for a fixed setting ( $I = 60$  A)

Another measurement that was considered necessary was to confirm that effectively the horizontal tune shift with amplitude  $\Delta\nu_x$  follows the same behaviour as  $C_{11}$ . For this purpose, the horizontal tune spread of a 1 mA beam in single bunch mode was measured as a function of the sextupole settings, by exciting the beam with a constant amplitude using the spectrum analyser of the tune measurement system. A good agreement was found.

Table 1: Amplitudes of vertical modes vs. harmonic sextupole settings

Setting [A]	VCBM 167 [dB]	VCBM 246 [dB]	VCBM 344 [dB]	VCBM 422 [dB]
30	16.7	16.3	17.0	37.3
36	18.6	10.8	11.0	38.7
91	6.1	-	-	25.4

Only recently, it was possible to find temperature settings of the cavities which would give rise to vertical modes. Assuming the same hypothesis as for the horizontal plane, some preliminary studies have been made on the dependence of the vertically excited modes on  $C_{22}$ . As it can be seen in figure 1,  $C_{22}$  presents very low values, in the range of settings for the harmonic sextupole between 20 and 40 A, becoming fairly large for settings above 60 A. Thus, if the hypothesis that the coefficients in the tune shift with amplitude is the leading mechanism by which excitation levels of the instabilities depend on the harmonic sextupole, one would expect an enhancement of the vertical modes for lower settings of the sextupole and suppression for higher ones. Table 1 illustrates the amplitudes of the modes as function of the settings. In particular, during the measurement, it was noticed that trying to set the harmonic sextupole to 27 A ( $C_{22} = 0$  for 26 A), the vertical instability grew stronger with an evident vertical beam size blow up on the synchrotron light beam profile monitor and subsequent loss of 100 mA of beam current.

### 3 CONCLUSIONS

All measurements which have been performed indicate that there is a strong correlation between the levels of excitation of transverse coupled bunch instabilities and the coefficients involved in the non-linear tune shift with amplitude induced by sextupoles. Theoretical investigations with simulations of the cavity transverse HOMs are being undertaken in parallel on both the effect of the harmonic sextupole on the internal distributions of amplitudes within a bunch and its effect on the dynamics when the bunches are considered as macroparticles. Particular attention is being paid on the non-linear tune shift with amplitude, which has a straightforward dependence on the coefficients  $C_{11}$  and  $C_{22}$ . One of the hypothesis which is being considered for the phenomenon is that of an induced tune spread among the macroparticles. A tracking program, used also for the design of the transverse feedback system[6], which takes into account sextupoles, HOMs in the cavities and the radiation damping, has been developed. The first preliminary results in the horizontal plane yield a confirmation of the dependence of the excited modes on the harmonic sextupole settings. Amplitudes of particles are found to grow until a certain final level, around which the amplitudes of the particles then perform oscillations. Both the final level and the amplitudes of the oscillations performed once the latter is reached are found to increase as the harmonic sextupole is set to give smaller absolute values of  $C_{11}$ , indicating effectively that the mode becomes more excited when  $C_{11}$  is smaller in absolute value, as observed in the measurements.

### 4 REFERENCES

- [1] R. Nagaoka et al, "Nonlinear dynamics with sextupoles in low-emittance light source storage rings", Nuclear Instruments and Methods in Physics Research A302 (1991) 9-26
- [2] Y. Ng, Fermilab Report TM-1281 (1984)
- [3] E. Karantzoulis et al, "Collective Effects at Elettra", EPAC Conference Proceedings, Stockholm, 1998
- [4] M. Svandrlik et al., "The Cure of Multibunch Instabilities in Elettra", PAC Conference Proceedings, Dallas, 1995
- [5] M. Svandrlik et al., "Simulations and Measurements of Higher Order Modes of the Elettra RF Cavities in View of Coupled Bunch Instability Compensation by Temperature Variation", EPAC Conference Proceedings, Stiges, 1996
- [6] D. Bulfone et al., "Design Considerations for the Elettra Transverse Multibunch Feedback", this conference

# FAST CLOSED ORBIT CONTROL IN THE SLS STORAGE RING

M. Böge, M. Dehler, T. Schilcher, V. Schlott, R. Ursic, Paul Scherrer Institute, Switzerland

## Abstract

Concepts for a fast orbit feedback in the SLS storage ring are presented. The Singular Value Decomposition (SVD) based orbit correction scheme is supposed to fight orbit oscillations up to 100 Hz stabilizing the orbit to 1/10th of the beam sigma at the locations of the insertion devices. For an emittance ratio of 1%, this corresponds to 1  $\mu\text{m}$  tolerance in the vertical plane. In order to achieve this high accuracy strong restrictions are imposed on the residual noise of the beam position monitoring and the correction system. Theoretical estimates for the feedback gain are made using a simplified feedback model. The proposed layout of the feedback electronics based on the SLS digital BPM system [1] is also described.

## 1 ORBIT STABILITY

The initial orbit stability is determined by three factors:

- The ground motion spectrum
- The girder response
- The orbit response

Measurements of the ground motion spectrum [3] indicate that the amplitudes are well below 100 nm except for a 27 Hz/300 nm peak which however could not be reproduced in recent measurements [4]. Assuming a girder response factor of ten for certain eigenmodes the maximum excursion of the elements on the girder is determined to be 3  $\mu\text{m}$ . Taking into account simulation results for the corresponding orbit response orbit excursions of the electron beam with rms values of up to 15  $\mu\text{m}$  [2] at the location of the experiments are expected for the vertical plane. This corresponds to 150% of the vertical beam sigma for an emittance coupling of 1% (It should be noted that this coupling factor is somehow arbitrary in the sense that much smaller coupling ratios are achievable utilizing a proper coupling compensation of the lattice [2]). This worst case estimate shows that it is necessary to introduce a fast orbit feedback system which attenuates the oscillations to the desired limit.

In this paper a concept for such a feedback system is presented. It is followed by a description of the actual implementation at the SLS storage ring. Requirements on corrector granularity and BPM noise are defined. Simulations will then show that a fast orbit feedback is capable of attenuating the residual oscillations such that the requirements of the experiments are fulfilled.

## 2 FAST ORBIT FEEDBACK

In general an orbit feedback detects the orbit oscillations induced by incoming ground waves using the beam position monitors around the ring. A lattice dependent well known correlation between monitors and corrector magnets is then used to fight the oscillation (see subsection "Theoretical Concepts"). No information on amplitude, frequency and phase of the distortion is needed for the correction. If the noise source would be exactly known a feed forward would be much more appropriate and much easier to implement. There are two different approaches to implement a feedback. Firstly it could be tried to minimize orbit variations at each experiment individually involving only correctors around the insertion device. This would have the main disadvantage that non locality of the correction would lead to a crosstalk between the local feedbacks which could be extremely difficult to control. A much better alternative represents a global orbit feedback which tries to minimize the orbit variations at all experiments at the same time. Following this approach a global orbit feedback will be adopted at SLS.

### 2.1 Theoretical Concepts

The correlation between correctors and monitors for the linear optics is established by superimposing the monitor reading pattern for every single corrector. The horizontal and vertical plane are treated independently assuming a small betatron coupling. The coefficients of the two resulting correlation matrices also called response matrices can be derived analytically from the machine model or from orbit measurements in the real machine. In the SLS storage ring these matrices have a dimension of 72x72 corresponding to the 72 correctors per plane built into sextupoles and 72 monitors adjacent to the corresponding sextupoles. To turn this into a correction algorithm it is necessary to invert the matrices in order to get the corrector pattern as a function of a given monitor pattern. If the correlation matrix is a quadratic  $n \times n$  matrix and has  $n$  independent eigenvectors this is easy to accomplish and one gets a unique solution for the problem. In reality the number of correctors and monitors can be reduced due to monitor failures and magnet saturations in such a way that the matrix is no longer quadratic and the solution is no longer unique.

A very flexible way to handle these scenarios offers the SVD algorithm [5]. This numerically very robust method minimizes the rms orbit and the rms orbit kick at the same time if the number of correctors is larger than the number of monitors while the rms orbit is minimized in the reverse case. Figure 1 depicts the 72x72 correlation matrix for the vertical plane as derived from the machine model.

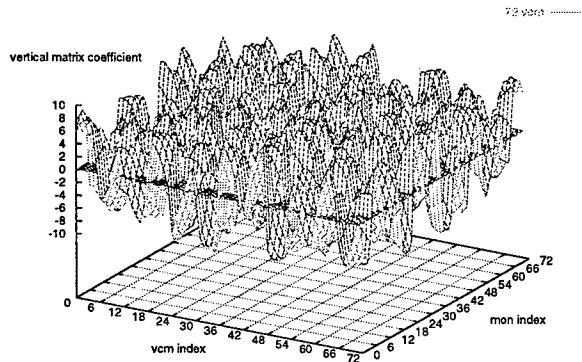


Figure 1: Response matrix for the vertical plane.

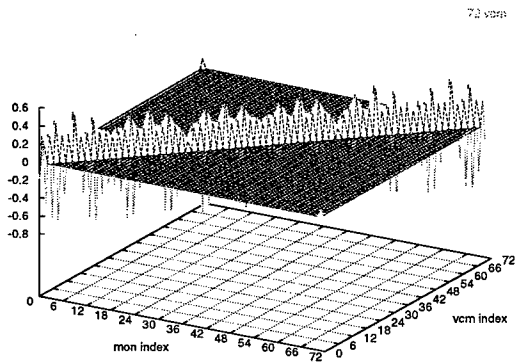


Figure 2: Inverse of the response matrix shown in Figure 1 for the vertical plane.

It should be noted that the coefficients of the matrix are highly correlated. As a result the inverse matrix in Figure 2 has the property that only the diagonal and their adjacent coefficients have significant values. In spite of the fact that the matrix contains the global correlation information of all correctors and monitors the nonzero coefficients gather around the diagonal of the matrix. Thus given a corrector only adjacent monitors determine its value.

This is also true under the condition that the number of correctors used for the orbit correction is reduced. Figure 3 illustrates this for the first row of the nonquadratic “inverse” matrix which corresponds to the first vertical corrector. Successively the total number of vertical correctors (“vcm”s) is reduced from 72 to 48 and 36 (every third/second corrector is disabled). For the latter case 12 adjacent coefficients are necessary to determine the value of the corrector instead of 3 in the 72 “vcm” case. The same statement holds for the removal of certain ineffective corrector combinations by zeroing the corresponding small weighting factors calculated by SVD. This has a direct influence on the implementation of the feedback.

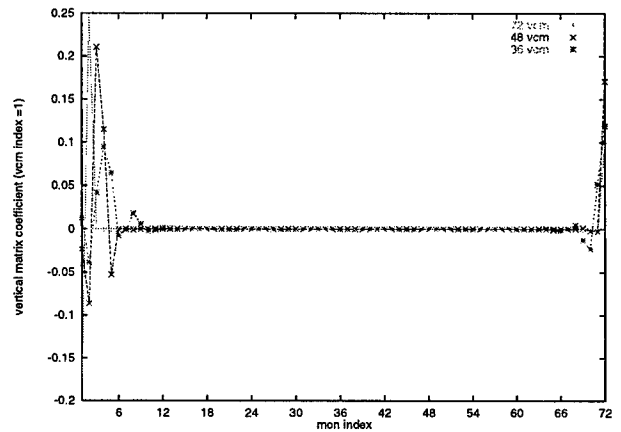


Figure 3: First row of the “inverse” of the response matrix for 72 monitors and 72, 48 and 36 vertical correctors (“vcm”s).

## 2.2 Implementation

The SLS storage ring is partitioned in 12 sectors containing 6 monitors and 6 correctors per plane. Figure 4 illustrates the partitioning of the inverse response matrix. Corresponding submatrices are distributed to the sectors in order to determine their corrector settings based on their monitor readings. Obviously there must be the possibility to get monitor and matrix information from the adjacent sectors to cover correctors close to the edges of a sector. This can be implemented by means of dedicated links between adjacent sectors. The result is a “leap frog” link structure around the machine (see Figure 4).

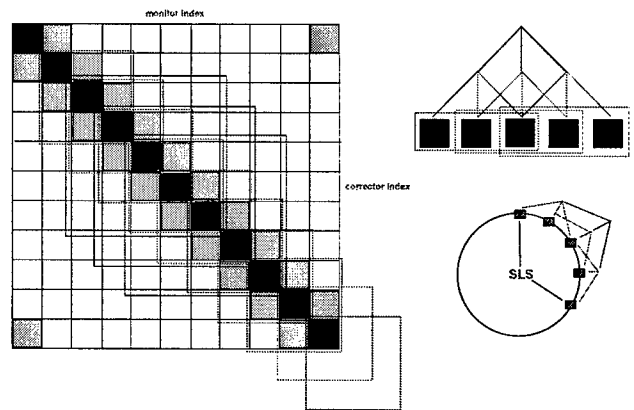


Figure 4: Schematic view of the inverse of the response matrix partitioned into 12 sectors (black boxes) containing 6 monitors and 6 correctors each. The principle layout of the proposed “leap frog” link structure between sectors is shown on the right side.

Figure 5 shows a schematic view of the implementation of the feedback. A central unit named “SVD Engine” performs the SVD based response matrix inversion and distributes the submatrices. All subsequent matrix operations are then performed in parallel by the individual sectors.



# FIRST BEAM COLLISION IN THE KEKB

Y. Funakoshi\*, K. Akai, N. Akasaka, A. Enomoto, J. Flanagan, H. Fukuma, K. Furukawa, S. Hiramatsu, K. Hosoyama, N. Huan, T. Ieiri, N. Iida, T. Kamitani, S. Kato, M. Kikuchi, E. Kikutani, H. Koiso, M. Masuzawa, S. Michizono, T. Mimashi, T. Nakamura, Y. Ogawa, K. Ohmi, Y. Ohnishi, S. Ohsawa, N. Ohuchi, K. Oide, D. Pestrikov, K. Satoh, M. Suetake, Y. Suetsugu, T. Suwada, M. Tawada, M. Tejima, M. Tobiyama, N. Yamamoto, M. Yoshida, S. Yoshimoto, KEK, 1-1 Oho, Tsukuba, Ibaraki 305-0801 Japan

## Abstract

The first beam collision study was done in the KEKB double ring collider. Beam collision conditions were found by searching beam-beam deflection curves in a trial-and-error method. From these curves, beam sizes at IP and a luminosity was estimated.

## 1 INTRODUCTION

Unlike single ring colliders, special cares are needed to bring two beams into collision in double ring colliders like the KEKB. Generally speaking, there are several methods to detect beam collision. Among those methods, we have been made use of a beam-beam deflection technique, pioneered at the SLC[1], for this purpose. In this report, results of the first beam collision study are described where the beam-beam deflection method has been successfully applied to the KEKB collider to find beam collision conditions.

## 2 PROCEDURE OF FINDING BEAM COLLISION CONDITIONS

To establish a beam collision condition, we have to tune beams both in longitudinal and in transverse directions. As for the longitudinal direction, relative timing of the two beams have to be adjusted so that the two beams collide at the nominal collision point. As for the transverse direction, beam positions of the two beams at IP have to coincide with each other. In addition to this, beam crossing angles should be removed to ensure a stable beam collision. A vertical crossing angle is generally important. On the other hand, a horizontal crossing angle is usually less harmful and we have intentionally introduced a horizontal crossing angle of  $\pm 11 \text{ mrad}$  to simplify an IR design. In this beam study, however, we did not care the crossing angles and committed ourselves to the beam offset at IP.

### 2.1 Bassetti-Erskine formula

In analyzing data of the beam-beam deflection, we used the Bassetti-Erskine formula[2] which gives 2-dimensional beam-beam kick. This means that we ignored bunch length effects of the beam-beam interaction. With the rigid Gaussian model, the coherent beam-beam kick is given by the

following expression.

$$\begin{aligned} \Delta y' + i\Delta x' &= -\frac{N_* r_e}{\gamma} \sqrt{\frac{2\pi}{\Sigma_x^2 - \Sigma_y^2}} \left\{ w\left(\frac{x + iy}{\sqrt{2(\Sigma_x^2 - \Sigma_y^2)}}\right) \right. \\ &\quad \left. - \exp\left(-\frac{x^2}{2\Sigma_x^2} - \frac{y^2}{2\Sigma_y^2}\right) w\left(\frac{\frac{\Sigma_y}{\Sigma_x}x + i\frac{\Sigma_x}{\Sigma_y}y}{\sqrt{2(\Sigma_x^2 - \Sigma_y^2)}}\right) \right\}, \end{aligned}$$

where

$$\begin{aligned} \Sigma_x &= \sqrt{\sigma_x^2 + \sigma_{x*}^2}, \\ \Sigma_y &= \sqrt{\sigma_y^2 + \sigma_{y*}^2}, \end{aligned}$$

and

$$w(z) = e^{-z^2} \left[ 1 + \frac{2i}{\sqrt{\pi}} \int_0^z e^{\xi^2} d\xi \right]$$

is the complex error function. Here,  $x$  and  $y$  denote offsets of the horizontal and the vertical directions, respectively.  $r_e$  denotes the classical radius of the electron. Asterisks in subscripts mean that the values belong to the counter-rotating beam. When we can assume that there is an offset only in the vertical direction, the beam-beam dipole kick is expressed as:

$$\begin{aligned} \Delta y' &= -\frac{N_* r_e}{\gamma} \sqrt{\frac{2\pi}{\Sigma_x^2 - \Sigma_y^2}} \exp\left(\frac{y^2}{2(\Sigma_x^2 - \Sigma_y^2)}\right) \\ &\quad \times \left\{ \text{Erf}\left(\frac{\frac{\Sigma_x}{\Sigma_y}y}{\sqrt{2(\Sigma_x^2 - \Sigma_y^2)}}\right) - \text{Erf}\left(\frac{y}{\sqrt{2(\Sigma_x^2 - \Sigma_y^2)}}\right) \right\} \end{aligned} \quad (1)$$

When there is an offset only in the horizontal direction, the beam-beam dipole kick is expressed as:

$$\begin{aligned} i\Delta x' &= -\frac{N_* r_e}{\gamma} \sqrt{\frac{2\pi}{\Sigma_x^2 - \Sigma_y^2}} \exp\left(-\frac{x^2}{2(\Sigma_x^2 - \Sigma_y^2)}\right) \\ &\quad \times \left\{ \text{Erf}\left(\frac{-i\frac{\Sigma_y}{\Sigma_x}x}{\sqrt{2(\Sigma_x^2 - \Sigma_y^2)}}\right) - \text{Erf}\left(\frac{-ix}{\sqrt{2(\Sigma_x^2 - \Sigma_y^2)}}\right) \right\} \end{aligned} \quad (2)$$

where

$$\text{Erf}(x) = \frac{2}{\sqrt{\pi}} \int_0^x e^{-t^2} dt$$

\* Email: yoshihiro.funakoshi@kek.jp



is the error function.

## 2.2 Longitudinal

The collision point can be shifted by changing relative beam timing between LER (low energy ring) and HER (high energy ring). We adjusted an RF phase of LER so that relative timing of an LER bunch and an HER bunch at the BPM's agrees with a design value. Beam timing was observed by monitoring signals from a BPM nearest to IP with an oscilloscope. The BPMs are located at positions where it can detect timing of both beams.

## 2.3 Horizontal

We observed a horizontal beam-beam deflection with scanning horizontal orbit offsets at IP. The scan was done by changing the RF phase of LER by making use of a design horizontal crossing angle of  $\pm 11 \text{ mrad}$ .

The beam-beam deflection was detected by measuring orbit change at BPM's beside quadrupole magnets named "QC2" where betatron phase advances from IP are almost  $\pi/2$ . A beam-beam kick is obtained from the following expression.

$$\Delta x' = \frac{\Delta x_{QC2R}}{\sqrt{\beta_x^* \beta_{xQC2R}}} + \frac{\Delta x_{QC2L}}{\sqrt{\beta_x^* \beta_{xQC2L}}}$$

Here,  $L$  and  $R$  denote the left side and right side viewed from the ring center, respectively. As shown in the formula, we took sum of these two BPM's to cancel out an effect of orbit drifts. A horizontal orbit offset at IP found from the scan was removed by making an orbit bump.

## 2.4 Vertical

A vertical collision condition was searched by scanning a size of an orbit bump made in one of the rings. Beam-Beam deflection was detected by measuring orbit change at BPM's beside quadrupole magnets named "QCS" where betatron phase advances from IP are almost  $\pi/2$ . A beam-beam kick is obtained from the following expression.

$$\Delta y' = \frac{\Delta y_{QCSR}}{\sqrt{\beta_y^* \beta_{yQCSR}}} + \frac{\Delta y_{QCSL}}{\sqrt{\beta_y^* \beta_{yQCSL}}}$$

To avoid an effect of orbit drift, we took sum of these two BPM's. The scan was continued until we obtained a deflection pattern which characterizes a beam-beam kick.

# 3 RESULTS OF COLLISION STUDY

## 3.1 Longitudinal

Beam collision timing was observed by monitoring signals from one of the electrodes of the BPM closest to IP under the condition that a single bunch is stored in each ring. First, RF buckets of the bunches was adjusted so that the bunches collide roughly at the nominal collision point. And

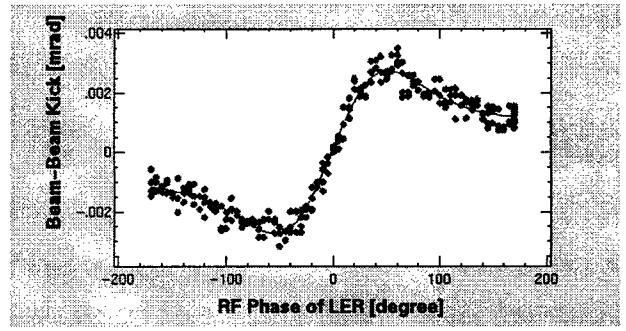


Figure 1: Horizontal Beam-beam scan with large vertical offset.

then, beam collision timing was adjusted finely by changing an RF phase of LER. An amount of phase adjustment was 7 degree in this study. Since resolution of the timing measurement was around  $10 \sim 20 \text{ psec}$ , an error of the tuning was considered to be less than 3mm ( $10 \text{ psec}$ ).

## 3.2 Horizontal

The collision study has been done twice. One was done in a single bunch mode and the other was with multibunch beams. Thereinafter in this report, we will only mention about the multibunch beam collision study most recently performed. Typical machine parameters relevant to the present study are summarized in Table 1. Figure 1 shows a typical result of the horizontal (RF phase) scan. In this case, there remained a relatively large vertical offset. The deflection curve was fitted by formula (2) to find a horizontal offset. To remove the horizontal offset, a horizontal orbit bump was made in LER. This process was repeated several times until the center of the curve coincides with the nominal RF phase ( $-7$  degree in the present case). This iteration was needed since the beam-beam kick itself makes some orbit changes and we did not take this effect into account.

After removing the vertical offset (see below), the horizontal scan was done again. Figure 2 shows a result. Again the deflection curve was fitted by formula (2). From the fit, a horizontal beam size was estimated as shown in Table 1. We should note that the estimated value include some error, since we have not yet estimated the effect of the orbit change due to the beam-beam kick.

## 3.3 Vertical

After the horizontal beam offset was removed, a vertical beam-beam scan was done to search for an optimum collision condition by scanning a size of an orbit bump made in HER. A result of the search is shown in Fig. 3. As is seen in the figure, a relatively large offset of 0.73mm was observed. The vertical beam size was estimated by a fit using formula (1). Again we should note that the estimated beam size includes some error from the beam-beam kick itself.

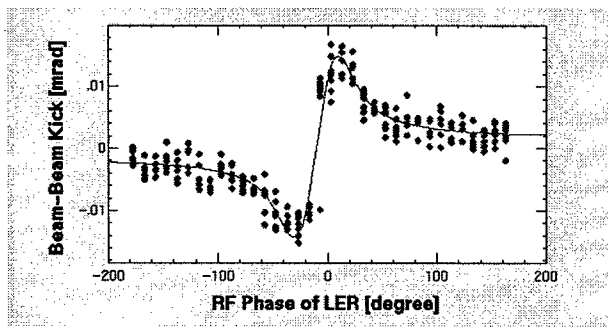


Figure 2: Horizontal Beam-beam scan without vertical offset.

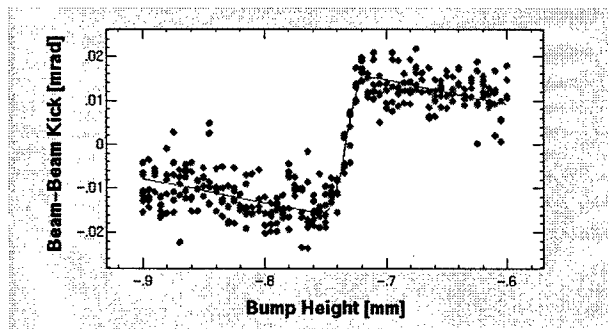


Figure 3: Vertical Beam-beam deflection.

### 3.4 Luminosity

From the horizontal and vertical beam sizes estimated from the deflection data, a luminosity was estimated to be around  $1.7 \times 10^{31}$  with an assumption that the two beam collide head-on. After removing the orbit offsets in both horizontal and vertical directions, a physics detector (BEAST) took data. Although beam collision was confirmed by events taken with EFC (Extremely Forward Calorimeter) in the BEAST detector, we could not make quantitative comparison due to a low event rate.

Table 1: Machine parameters used in the study

	HER	LER	
$\beta_x^*/\beta_y^*$	1/0.01		$m$
Beam current	13	65	$mA$
Number of bunches	200	200	
Beam size ( $\Sigma_x/\Sigma_y$ )	278/5.6		$\mu m$
Lifetime	40	200	$min.$
Estimated luminosity	$1.7 \times 10^{31}$		$/cm^2/sec$

## 4 SUMMARY AND FUTURE PLAN

A fine tuning on a collision timing was done by measuring a time difference of two beams. An error of the tuning was considered to be less than 3mm (10psec). A horizontal orbit offset at IP was measured by scanning an RF phase

of LER. An offset was removed by making an orbit bump in LER. A vertical beam-beam scan was done by scanning a size of an orbit bump made at IP in HER. A relatively large vertical offset of 0.73 mm was observed. From the beam-beam deflection curves, beam sizes at IP and a luminosity were estimated. The first multibunch beam collision was done on 25th March with an estimated luminosity of  $1.7 \times 10^{31} cm^{-2} s^{-1}$ . We will do more precise analysis on the beam-beam deflection including a self-consistent orbit change due to a beam-beam effect.

The next step of the study is to keep the beam collision condition once found. For this purpose, we are preparing a special orbit feedback system also based on the beam-beam deflection technique.

## 5 REFERENCES

- [1] P. Bambade and R. Erickson, SLAC-PUB-3979 (1986).
- [2] M. Bassetti and R. Erickson, CERN-ISR-TH/80-06 (1980).

# MEASUREMENT OF LONGITUDINAL INSTABILITY THRESHOLD IN THE PF-AR

Takao Ieiri and Takashi Obina

KEK, 1-1 Oho, Tsukuba-shi, Ibaraki, 305-0801 Japan

## Abstract

A single bunch longitudinal instability was experimentally investigated in the PF-AR under the condition that the number of cavity-cell which greatly contributed to longitudinal impedance was changed. The bunch length was measured as a function of the bunch current. Hysteresis phenomena in bunch lengthening process were discovered in the former condition of fully installed cavities. The present condition of reduced cavity-cells to 3/4 indicated an abrupt increase of the bunch length together with the energy spread at a bunch current. The instability threshold current was measured as a function of the bunch length. Measured results are consistent with Oide's criterion.

## 1 INTRODUCTION

A single bunch longitudinal instability is discussed with potential-well distortion [1] and microwave or turbulent instability [2] in electron storage rings. The Haïssinski equation gives an exact solution to the bunch-shape deformation if the wake potential is determined. As the beam current increases, turbulent instability may be excited above a threshold. Turbulent instability causes bunch lengthening together with energy spreading, which has been almost explained by the Boussard criterion [3]. However, the Boussard criterion is only useful for long bunch length or an inductive wake. Oide and Yokoya [4] and D'yachkov and Baartman [5] independently investigated the longitudinal instability using simple wakefields models. It is important to study an instability for actual wakefields in storage rings.

Former experiments [6,7] showed that hysteretic behavior was observed in bunch lengthening process, where the PF-AR had fully installed 88 cavity-cells. The hysteresis disappeared when the number of the cavity-cell reduced to 44 without changing other components. It was pointed out that the hysteresis was caused by a composite wake produced by the cavity and bellows. Now the PF-AR has 66 cells and it is interesting to investigate how the bunch length behaves. This note experimentally evaluates the threshold of a longitudinal instability when the impedance was changed.

## 2 PF-AR

The PF-AR is a storage ring of 377 m in circumference. There are four long straight sections, each with a length of approximately 20 m. Two straight lines, east and west parts, are prepared for rf cavities.

Alternating periodic structure (APS) cavities with multi-cells [8] were installed to raise the beam energy from 2.5 GeV to 6.5 GeV. Each APS cavity has 11 accelerating cells. The PF-AR usually runs with a single bunch operation. The main parameters at the energy of 2.5 GeV are listed in Table I.

The impedance of the PF-AR is dominated by the APS cavities and non-shielded bellows. The wake potential of the cavity showed a resistive type for bunch length of 1.5 cm. On the other hand, the wake of 130 bellows with 12 convolutions was inductive. Thus a bunch is affected by the two different types of wakes. The number of the cavities was historically changed according to required beam energy. When the AR was used as an injector for the TRISTAN main ring, the number of the cavity-cells was 88. Now the number is 66.

Table I : Main parameters of the PF-AR.

E	Beam Energy	2.5GeV
$f_{rf}$	Accelerating Frequency	508.58MHz
h	Harmonic Number	640
$V_c$	Accelerating Cavity Voltage	0.5 - 4.0 MV
$f_s$	Synchrotron Frequency	10 - 36 kHz
$\alpha_p$	Momentum Compaction	0.0129
$\sigma_{e0}$	Natural Energy Spread	$4.4 \times 10^{-4}$
$\tau_d$	Longitudinal Damping Time	21.6 ms
$\sigma_{z0}$	Natural rms Bunch Length	0.8 - 3.0 cm

## 3 MEASUREMENT

The bunch length was measured both from the beam spectrum and by a streak camera. A streak camera took a bunch profile and measured its FWHM(full width half maximum). An rms bunch length was obtained in real time from the spectrum. The bunch length was measured as a function of the bunch current at constant cavity voltage,  $V_c = 1.5$  MV. Figure 1 shows rms bunch length as a function of the bunch current. The bunch length gradually increases as the bunch current increases, where the natural bunch length is 1.3 cm. When the bunch current reaches 8.0 mA, the bunch length abruptly increases from 2.0 cm to 2.8 cm. Next, the bunch length was measured as a function of cavity voltage starting at bunch current of 8.7 mA. The bunch length was 2.9 cm at  $V_c = 1.5$  MV and suddenly decreased to 1.9 cm when the

$V_c$  reached 1.7 MV. The bunch length has two values around  $V_c=1.65$  MV as shown in Fig. 2. The bunch length went and came back between two separate values there. Though a hysteresis observed in the previous condition [6,7] disappeared, the flip-flop phenomenon was observed instead.

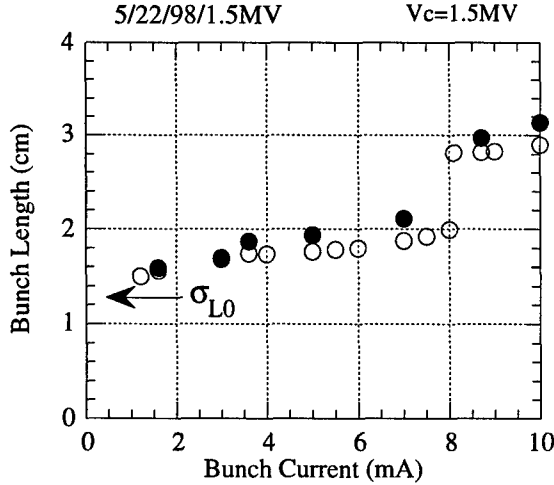


Figure 1: Bunch length vs bunch current. Dots are by streak and circles are from the spectrum.

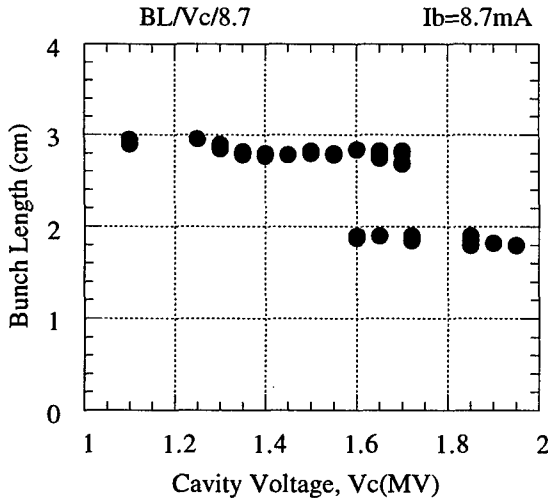


Figure 2: Bunch length as a function of cavity voltage.

A change of the beam energy spread was estimated from the quantum lifetime. The quantum lifetime is given by the ratio between the energy acceptance formed by the cavity voltage and the energy spread. However, the cavity voltage is affected by other effects. The net accelerating voltage  $V_a$  should compensate the energy loss; the radiation energy loss of  $V_{rad}=0.15$  MeV and higher-order-mode (HOM) loss. The energy loss per turn is given by

$$V_a = V_c \cos \phi = V_{rad} + kT_r I_b, \quad (1)$$

where  $\phi$  is the synchronous phase angle,  $k$  is the loss parameter depending on the bunch length and  $T_r$  is the revolution time. The loss parameter of the PF-AR is

estimated to be 25 V/pC at the bunch length of 2.0 cm. The loss parameter is mainly caused by the APS cavity. Moreover, the cavity voltage should ensure a phase stability condition due to beam loading in a cavity. A stored maximum current is expressed by

$$I_{bm} = \frac{2V_c \sin \phi}{\sin 2(\phi - \alpha)} \frac{1}{\left(\frac{R}{Q}\right)Q_L}. \quad (2)$$

Here,  $\alpha$  is the tuning offset angle,  $R$  the shunt resistance and  $Q_L$  the loaded Q value of a cavity. From eq.(1) and eq.(2), the cavity voltage is increased to be proportional to square root of the beam current under constant energy loss. A calculated voltage is shown in Fig. 3 including the HOM loss. The HOM loss was estimated from the ABCI code [9] based on measured bunch length data. A plateau in the voltage seen above 8 mA in Fig. 3 is due to an abrupt increase of the bunch length. A measurement was carried out by slowly reducing the cavity voltage while keeping a bunch in a bucket. The beam lifetime was above 60 minutes if an instability did not take place. As the cavity voltage gradually lowered, the lifetime slowly decreased. When the voltage reached  $V_c=0.72$  MV at bunch current of 5.0 mA, the lifetime suddenly reduced to less than 1 minute and a beam was lost. The minimum cavity voltage with which a beam was lost was measured as a function of the bunch current as shown in Fig. 3. The measured voltage approximately agrees with the calculated one below 7 mA. However, the measurement requires 30 % higher voltage than the calculated value. This extra voltage should be caused by an increase of the energy spread. The increase of the energy spread corresponds to an abrupt increase of the bunch length.

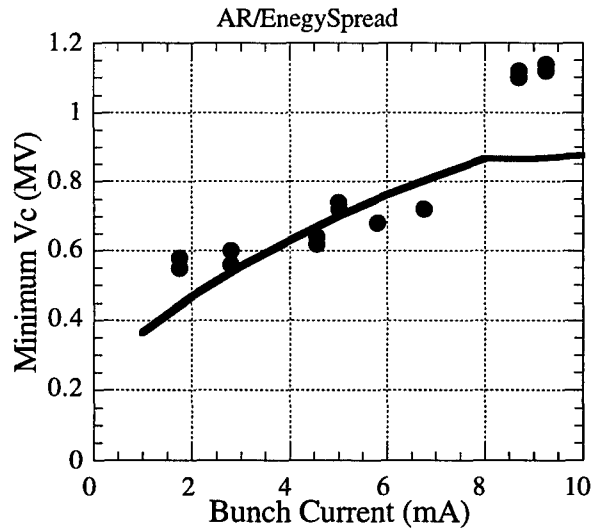


Figure 3: Measured minimum cavity voltage determined from the beam lifetime as a function of the bunch current. The solid line shows estimated voltage including HOM effects.

## 4 DISCUSSION

A threshold current for the longitudinal instability is clearly characterized by an abrupt increase of the bunch length and of the energy spread. The threshold current is plotted as a function of the bunch length as shown in Fig. 4 together with calculated values obtained using a code [4]. The measured current decreases from 8.5 mA to 7.1 mA though the bunch length increases from 1.8 cm to 2.5 cm. The calculated threshold current takes a minimum around the bunch length of 2.0 cm. Though they have a disparity of about 30%, they are consistent with each other.

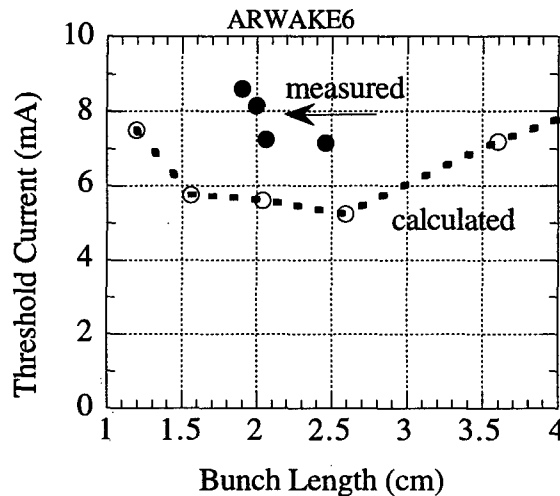


Figure 4: Threshold current as a function of the bunch length. Dots are measured and circles calculated. The bunch length is a value just before an instability.

On the other hand, Oide *et al.* indicated that the threshold current has a minimum in a region that the normalized resonant frequency  $\omega_0 \sigma_z / c$  is around 0.7, where  $\omega_0$  is the resonant frequency of a model impedance [4]. The region is dominated by a resistive wake. The impedance of the PF-AR also shows a resistive wake produced by the multi-cell cavity. Figure 5 indicates that the threshold current as a function of the number of cavity-cell under the same synchrotron tune. The number of cavity-cell represents an intensity of a resistive wake. The experimental result suggests that the threshold decreases linearly as the resistive wake increases. From a theoretical aspect, Oide derived a simple stability condition [10] which represents

$$kL \geq \frac{2}{9} kRq_0. \quad (3)$$

Here,  $k$  is a beam intensity,  $L$  represents a pure-inductive wake,  $R$  represents a pure-resistive wake and  $q_0$  an equilibrium position of a bunch. The stability condition suggests that an inductive wake raises threshold current but a resistive part strengthens an instability. The experimental result is consistent with the stability condition. In conclusion, the longitudinal instability threshold current of the PF-AR characterized by a resistive wake behaves in different variations than those observed in many other storage rings, which has been already predicted by Oide *et al.* except the hysteresis and the flip-flop phenomena.

The authors thank Prof. Z.Y.Guo of IHEP for promoting the energy spread measurement and Prof. K.Oide for encouragements of this work.

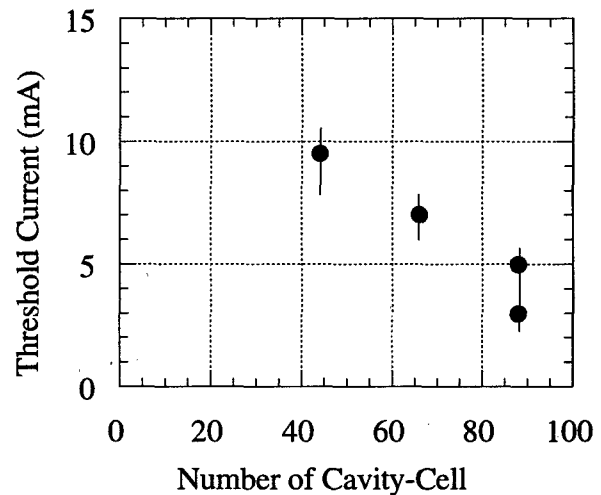


Figure 5: Threshold current as a function of the number of cavity-cell under the same synchrotron tune of 0.021.

## 5 REFERENCES

- [1] J. Hajssinski, Nuovo Cimento 18B No.1, (1973)72.
- [2] J.M.Wang and C.Pellegrini, Proc. of the 11th Int. Conf. on High-Energy Accelerator, CERN (1980)554.
- [3] D. Boussard, LAB II / RF / Int. /75-2 (1975).
- [4] K. Oide and K. Yokoya, KEK Prepr. 90-10 (1990).
- [5] M. D'yachkov and R. Baartman, Proc. 4th European Particle Accelerator Conf., London, (1994)1075.
- [6] T. Ieiri, Nucl. Instrum. Methods A 329 (1993)371.
- [7] T. Ieiri, Jpn. J. Appl. Phys. 36 (1997)6965.
- [8] T. Higo *et al.*, Proc. 5th Symp. Accelerator Science and Technology, Tsukuba, (1984)114.
- [9] Y. H. Chin, LBL-35258 UC-414 (1994).
- [10] K. Oide, Particle Accelerator 51 (1995) 43.

# COMMISSIONING OF KEKB BUNCH FEEDBACK SYSTEMS

M. Tobiyama and E. Kikutani, KEK, Tsukuba, Japan

## Abstract

Commissioning of KEKB started at the end of the last year. In the early stages of the commissioning, we observed transverse instabilities in both rings and started tuning of the bunch feedback systems. Even though the tuning is now at the initial stage, the feedback systems are contributing to an increase of the maximum storable currents in the KEKB rings. Feedback-related systems, tune meters and bunch-current monitors, are also working well.

## 1 INTRODUCTION

KEKB, an asymmetric electron-positron collider facility at KEK, is now in the first stage of commissioning. It consists of an 8 GeV electron ring (HER) and a 3.5 GeV positron ring (LER), both fed by a common injector-linac feeds beams. About 5000 bunches/ring will be stored and the total current will amount to 1.1 A and 2.6 A, respectively. As a part of this complex facility, bunch-by-bunch feedback systems have begun operation. Each of the feedback systems consists of (1) wide-band position detection systems, (2) high-speed digital signal processing systems with large-scale memories, and (3) wide-band kickers fed by high-power amplifiers. At the same time, betatron tune meters and bunch current monitors, which share some components with the feedback systems, have also begun operation. With the requirement that the systems be able to handle 5120 bunches/ring at a bunch frequency of 509MHz, the design of these systems is very challenging. For example, all parts of the systems have a bandwidth of half the bunch frequency, 255 MHz. The final design of the feedback systems is described in reference[1]. In this paper, we describe the initial experiences with these systems in the commissioning of the KEKB rings.

## 2 OUTLINE OF THE KEKB FEEDBACK SYSTEMS

For both the transverse and longitudinal planes, the feedback monitors use specially designed button electrodes and the 2GHz (4 $\times$  the rf frequency) component of the signal is used to detect the bunch position. Figure 1 is a photo of the monitor chamber installed in the LER.

For the transverse feedback, two sets of button electrodes are installed in two points in each ring. The signal from these electrodes needs to be combined appropriately to make the feedback signal.

A common digital signal processing board is used in the transverse- and longitudinal-plane feedback systems. It can work up to 500MHz bunch-frequency owing to specially fabricated high-speed de-multiplexers (FDMUX) and

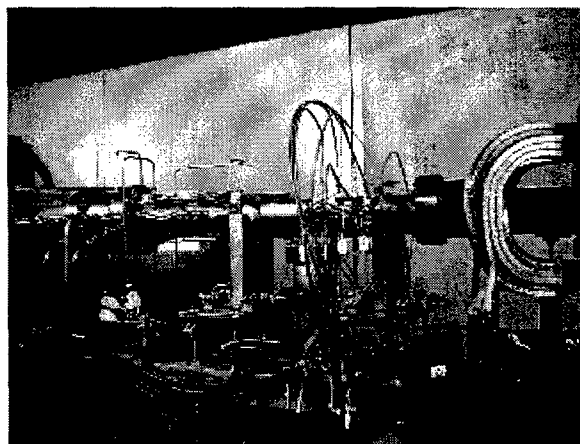


Figure 1: Feedback monitor chamber in the LER. Specially designed button pickup are used in this monitor system.

multiplexers (FMUX)[2]. The board works as a two tap filter[3], which is powerful for the longitudinal feedback, and a simple digital delay.

For the transverse kicker we use two types of stripline kicker: one is wide-band with a length of 40cm and the other is narrow-band with a length of 1.2m. Each electrode of the kicker is fed by a 250-Watts amplifier.

The longitudinal kicker is a low-Q cavity, which has originally been developed at FRASCATI for DA-NE[4], and we modified it to fit our parameters. As the longitudinal instability is expected to be the least serious in the HER, only 2 sets of the longitudinal kickers are installed in the LER. The photo in Fig. 2 shows these kickers.

The technology employed in the bunch feedback systems has wide a variety of applications. The most straightforward application is transverse tune measurement. The transverse kicker with the amplifiers kicks the beam and, we measure beam's proper oscillation frequency, i.e., the tune, from the response to this kick.

Another system which can be understood as a byproduct of our feedback systems is the memory board. The digital processing board of the feedback systems is modified to realize a kind of a transient digitizer. It utilizes the same mother board and the same input part (A-to-D converter) as the signal processing board. But the output part is removed and the storage size, which was 2MBytes for the processing board, is increased to 20MBytes.

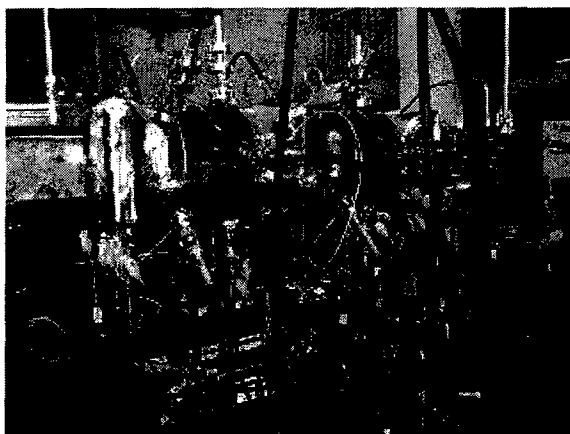


Figure 2: Two longitudinal kickers installed in the LER. Each kicker has four input ports and four output ports. The Q-value of the kicker lowered to about 5.

### 3 PRESENT STATUS OF THE MACHINE COMMISSIONING

We started the commissioning[5] of the HER at the beginning of December 1998 and the LER at the beginning of this year. Since then, the storable currents of the rings increased rapidly. At present (middle of March 1999), the highest stored currents are 240 mA and 370 mA for the HER and the LER, respectively. The minimum bunch spacing is 10 ns (HER) / 4 ns (LER).

In both rings we observe transverse instabilities, though we find some difference between them. In order to suppress them we started to operate the transverse feedback systems. On the other hand, up to present time, we have not observed longitudinal instability and we have not started to operate the longitudinal feedback system.

### 4 THE FIRST EXPERIENCE WITH THE TRANSVERSE FEEDBACK SYSTEMS

#### 4.1 Hardware configuration

At present, we are operating the transverse feedback systems not with the final configuration but with some simplified one.

The signal process system is working as a simple digital delay, not as the two-tap filter, because the two-tap filter approach is complicated when the optics parameter is not completely known to us. When the optics become well under the control, we might be able to operate it with the two-tap filter mode.

Out of two sets of the kickers, we started to operate the feedback system only with the wide-band systems, which cover the frequency range of 100 kHz to 250 MHz. By this simplification, we are free from the complexity coming from unwanted effects in the overlapped band. However, this system is less powerful for lower-mode dominant instabilities such as the resistive wall instability.

#### 4.2 Performance with the present hardware

In order to check the performance of the feedback systems, we compared the frequency spectra of the signal from a pickup, with the feedback on and off. When the feedback is off, a large peak ( $> 40$  dB higher than the noise level) was observed at the tune-frequency, as shown in the left photo in Fig. 3, while with the feedback on, this peak has disappeared (comparable with the noise level), as shown in the right photo. This phenomenon is more or less common to the both rings and the both planes (horizontal/vertical).

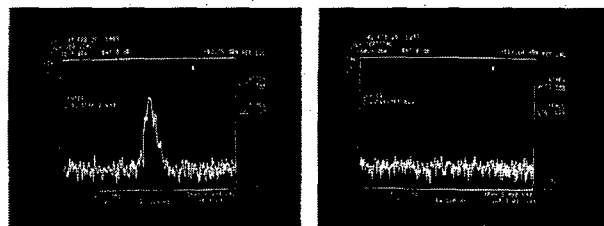


Figure 3: Frequency spectra of the signal from a pickup of the HER (vertical). The center frequency was adjusted to the frequency corresponding to the tune. In the left photo a peak is found, which showed us the instability occurred. On the other hand, in the right photo, we found no peak at this frequency.

In addition, when the feedback system was turned off with stored current higher than 250 mA in the HER, non-negligible fraction of the stored beam was lost and the beam current was decreased to about 60% of the original one. In this case the fill pattern, i.e., bunch-current distribution, got irregular. Particularly, particles in buckets close to the tail of a train have more chance to be lost, in a bunch-train operation.

We can estimate the damping time of the feedback systems from the several parameters, sensitivity of the monitor, gain of the power amplifiers (gain 53 dB, maximum power 250 Watts), shunt impedance of the kicker (order of  $10k\Omega$ ), and losses in cables etc. and betatron function at the monitor and the kicker ( $10m \gg 25m$ ). Estimated damping times (at present stage) are summarized below:

	horizontal	vertical
HER	1.2 ms	2 ms
LER	1.3 ms	1.8 ms

More precise estimation of the damping time with actual measurements will be done in near future as explained later. Shorter damping times will be realized by tuning the power balances in the systems.

#### 4.3 A problem to be solved

At present, the KEKB rings are suffering from unwanted drift of closed orbit, particularly in the vertical plane. The

stationary change of the beam position is seriously harmful for the feedback systems, since it wastes the dynamic range of the A-to-D converter whose resolution is 8-bit. In order to use this dynamic range effectively, we must subtract the DC component from the detected signal. A simple high-pass filter approach does not work well, because output of the filter depends not only on the DC-component but also on the bunch-filling pattern, which is essentially the duty factor of the pulses corresponding to the beam positions.

We are planning to introduce a DC-canceling circuit which detect "real" DC-component with a relatively high-speed sample/hold circuit. This circuit is now under tuning and will be included in our systems, in near future.

## 5 RELATED SYSTEMS

We have started to operate two feedback-related systems, the tune meters and the bunch current monitors. At present, the tune-measurement systems are operated with the narrow (lower band) amplifier/kicker systems. The signal source for the kicker is a spectrum analyzer equipped with a tracking generator. The kicking frequency is swept around 2-GHz, and this signal is down-converted to the base-band of the tune, roughly from 5kHz to 500 kHz. Figure 4 schematically explains the tune measurement system.

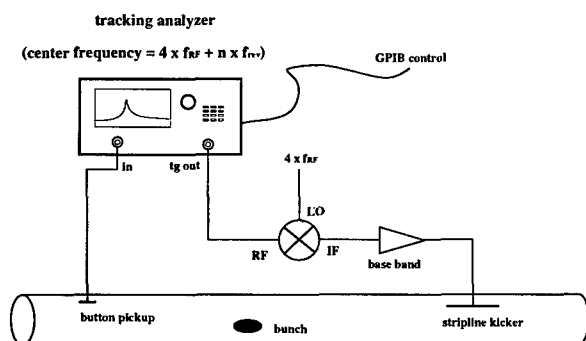


Figure 4: Blockdiagram of the tune measurement system. Relatively higher frequency components, about 4 times of the RF frequency, is used for this system. This choice enable us to increase the S/N ratio in the measurement.

We are operating the bunch current monitor consisting of a front-end detector circuit, which is essentially the same as the longitudinal position detector, and the memory board with a fast-read-out interface. Blockdiagram of the system is shown in Fig. 5.

The bunch-current is measured every 20ms (i.e. 50 Hz), and obtained bunch-current distribution is transferred to the injector linac to be used by the bucket selection system of the KEKB rings[6]. Simultaneously, the bunch-current distribution is graphed out in a display in the main control room.

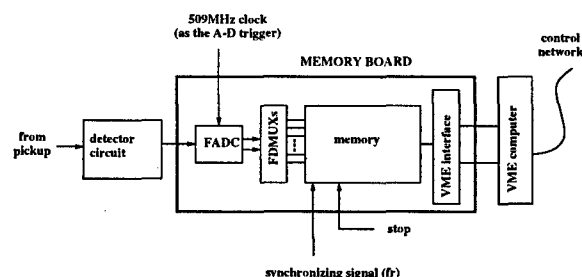


Figure 5: Blockdiagram of the bunch-current monitor. Output of the bunch-current detector circuit is A-to-D converted (509MHz sampling rate) and stored in the memory board. The contents of the memory is read-out via the VME bus.

## 6 PLANS IN NEAR FUTURE

The following items are our targets which should be realized in near future.

- † As we mentioned, we are using only wide-band kickers (the short kickers) fed by the wide-band amplifiers. In the next step, we must employ the lowest-band long kickers, which should be effective to suppress the instability caused by the resistive wall impedance.
- † The next theme is an operation of the large-size memory board which can store 20MBytes of data, that corresponds to 4096 turns of 5120 bunches. This is a very powerful beam-diagnostic device for the investigation of the instabilities observed in the rings. It is also useful for measuring the damping time of the feedback systems, by catching the beam behavior just before/after the feedback system ON and OFF.
- † The third theme is the operation of the longitudinal feedback system, particularly the study of the longitudinal kicker. As described first, we have not observed the longitudinal instability. However, the surveying the performance of the longitudinal system is a very important study-issue for us.

## 7 ACKNOWLEDGMENTS

The authors are grateful to the commissioning group of KEKB for their operation of the machines during our study. They thank also Dr. Y. Ohnishi for his efforts to develop the operator interface for the feedback and the related systems.

## 8 REFERENCES

- [1] M. Tobiyama *et al.*, Proceedings of APAC98 p. 540 .
- [2] E. Kikutani *et al.*, Proceedings of EPAC96, p. 1893.
- [3] Y. Minagawa *et al.*, Nucle. Instr. Meth. A416, 193 (1998).
- [4] R. Boni *et al.*, Part. Accel. 52, 95 (1996).
- [5] K. Oide, these proceedings.
- [6] E. Kikutani *et al.*, Proceedings of APAC98, p 525.



# The Eddy-current-induced Head-tail Instability at the KEK-PS

T. Toyama, D. Arakawa, S. Igarashi, J. Kishiro, E. Nakamura and K. Takayama

High Energy Accelerator Research Organization (KEK)

1-1 Oho, Tsukuba, Ibaraki 305 Japan

## Abstract

The head-tail instability of the 12 GeV PS at KEK, has been confirmed by extensive experiments. It turns out that the eddy-current-induced sextupole fields in the rectangular-shaped vacuum pipe in the main bending magnets played a crucial role in the head-tail instability during acceleration. The eddy current effect was verified by field measurement and chromaticity measurement in a way of different field-rampings. The coupling impedances of the present injection kickers and new fast-extraction (FX) kickers, the dominant impedance sources, have been examined on the test bench. The growth rate is calculated.

## 1 INTRODUCTION

The head-tail instability limited the beam intensity of the 12 GeV PS at KEK[1]. The eddy-current-induced sextupole field in the vacuum pipe in the main bending magnets forces the horizontal chromaticity into shifting from negative to positive value during acceleration. Then longitudinal modes  $\ell = 0, 1$  and  $2$  become unstable. Especially the mode  $\ell = 0$  is fatal.

The chromaticity change is proportional to  $(dB/dt)/B$  if it comes from eddy current. In the KEK-PS MR  $dB/dt$  saturates at 2.3 T/s, while  $B$  increases as the beam is accelerated. Therefore the chromaticity change is larger for lower energy. That is why the instability occurs just after acceleration start.

Organization of the present paper is as follows. First, the eddy current in the vacuum pipes in the bending magnets is manifested to be a main source that causes the positive chromaticity. Second, the result of impedance measurement of injection and FX kickers is given. The observed growth rate before and after the installation of the FX kickers are briefly described.

## 2 EDDY-CURRENT-INDUCED SEXTUPOLE FIELD

The sextupole fields induced by the eddy current proportional to  $dB/dt$  is considered to cause a change in the chromaticity. Its size was measured for two different  $dB/dt$  patterns. One is  $dB/dt = 2.3[T/s] \times t/(100[ms])$  for  $0 < t < 100$  ms, i.e. 100 ms smoothing pattern. The other is  $dB/dt = 2.3[T/s] \times t/(200[ms])$  for  $0 < t < 200$  ms, i.e. 200 ms smoothing pattern. The calculated and measured chromaticities during a beginning part of acceleration are plotted in Fig.1 and Fig.2, respectively. Solid line and dashed line in Fig.1 indicate the case of the 100 ms and 200 ms smoothing pattern, respectively. Filled circles and

open circles in Fig.2 indicate the case of the 100 ms and the 200 ms smoothing pattern, respectively. Global feature in the measured temporal variation of  $\xi_x$  is qualitatively and quantitatively similar to the calculated one except an unknown  $\xi_x$  shift of 1-2, which has been observed for these years.

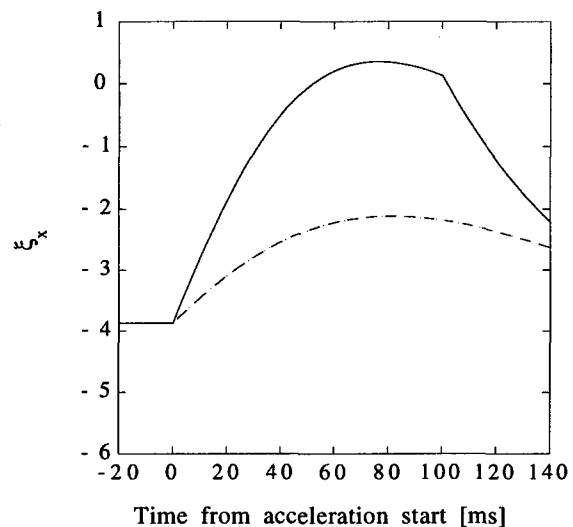


Figure 1: Calculated horizontal chromaticity

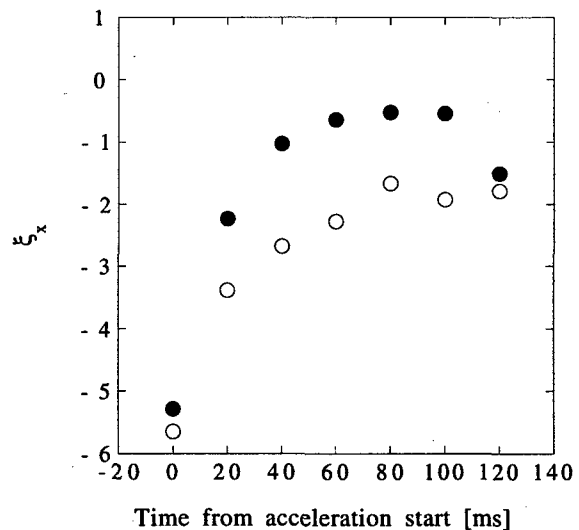


Figure 2: Measured horizontal chromaticity

The eddy-current-induced sextupole field component was directly measured in a case with/without a model pipe

of SUS316L in the monitor bending magnet connected with main bending magnets in series. "Gaussmeter"(LakeShore 460) consisting of Hall probes and processing units was employed for the measurement. Two Hall probes were placed almost at the center in the longitudinal direction of the magnet. One probe locating at a fixed position was used as a reference. The output voltage excursion of the other probe from the reference signal is recorded by using time domain data acquisition of a 16-bit FFT analyzer (ADVANTEST R9211C SERVO ANALYZER). The signal was averaged over a few tens of field pattern cycles. It was essential to use a difference signal of two probes to maximize the ADC signal-to-noise-ratio and to cancel an undesirable long-term field variation. The frequency band width of the measurement system was sufficient for our purpose.

The difference between the measured fields *with* and *without* the vacuum pipe is taken. In Fig. 3 a field variation along the horizontal axis at the timing of 100 ms from the beginning of acceleration is indicated by open circles. The field variation at the center is set to be zero for convenience.

It is in good agreement with the calculations using three analytic formulae: a two-parallel-plate approximation (dashed line) [2], a numerical integration with a realistic shape (solid line) [3]. A 2D simulation by the boundary element method for eddy-current-induced fields also gives a consistent result[4].

Consequently, the change in the chromaticity is attributed to the eddy-current-induced sextupole fields.

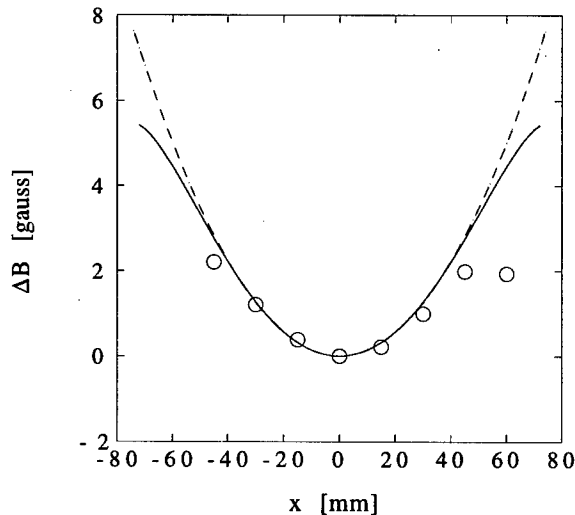


Figure 3: Field variation due to eddy current in the vacuum pipe

### 3 KICKER IMPEDANCES

The growth rate measurement has suggested that the main sources of the coupling impedances are kickers and resistive wall[1]. It was urgent to evaluate the coupling impedance of newly installed FX kickers[5] for long-baseline neutrino oscillation experiment.

To evaluate the kicker coupling impedance, both of theoretical and experimental approach have been employed. The real part of the transverse coupling impedances of the injection and FX kickers were calculated by using the standard theory of travelling wave kickers[6],

- C-type

$$\text{Re}[Z_T] \approx \frac{c}{\omega} \frac{Z_0}{4b^2} \eta,$$

- "Twin c-type"[5]

$$\text{Re}[Z_T] \approx \frac{c}{\omega} \frac{Z_0}{b^2} \eta,$$

where  $c$  is the velocity of light,  $Z_0$  the characteristic impedance of the kicker,  $\omega$  the angular frequency,  $b$  the gap width and  $\eta$  the factor depending on the cable connection and termination of the kicker.

The measurement was performed using a copper wire of 1 mm in diameter. At first  $S_{21}$  in "S" matrix was measured with a network analyzer (hp8753E) by displacing the wire in the horizontal direction. The  $S_{21}$  component was translated to the  $Z_T$  by using the formula for distributed impedance[7].

The results are plotted in Fig.4 for the injection kicker and in Fig.5 for seven FX kickers. In the figures dots indicate the measured value and solid line the calculated one. Due to the limitation of the experimental setup, the terminations of the kickers are not same as to the practical setup. In the present measurement, the matched loads were connected with the injection kicker at both ends. The FX kicker is connected with a matched load at one end and short-circuited at the other end. The disagreement between the calculated and measured  $\text{Re}[Z_T]$  for both type of kickers may come from incomplete error correction or ferrite loss which were not included in the calculations. They are subjects to be solved in future.

The additional impedance newly introduced by the seven FX kickers seems to be much larger than that of the five injection kickers for the frequency range of our interest.

In addition, the longitudinal impedance measurement of the FX kickers embedded in the large rectangular chamber implied sharp resonances in a few hundred MHz region as shown by the dashed line in Fig.6. It is potentially dangerous for the microwave instability serious at transition crossing[8]. It seems to be caused by the gaps between kicker modules. Then the gaps between kickers were filled up by the short copper pipes of the similar inner size. It reduced the impedance peak height by a factor of two to four as indicated by the solid line in Fig.6.

### 4 CONCLUSION

The growth rate which is calculated by introducing the coupling impedances of the resistive wall and kickers into Sacherer's formula[9] should become to be large after installing the FX kickers. The growth rate measurements

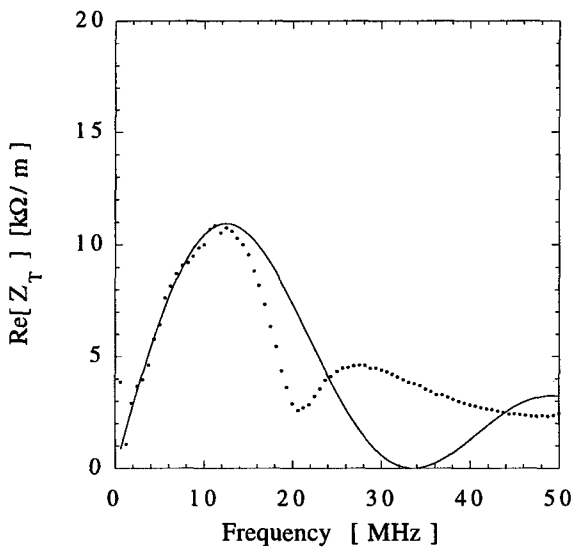


Figure 4: Coupling impedance of one injection kicker

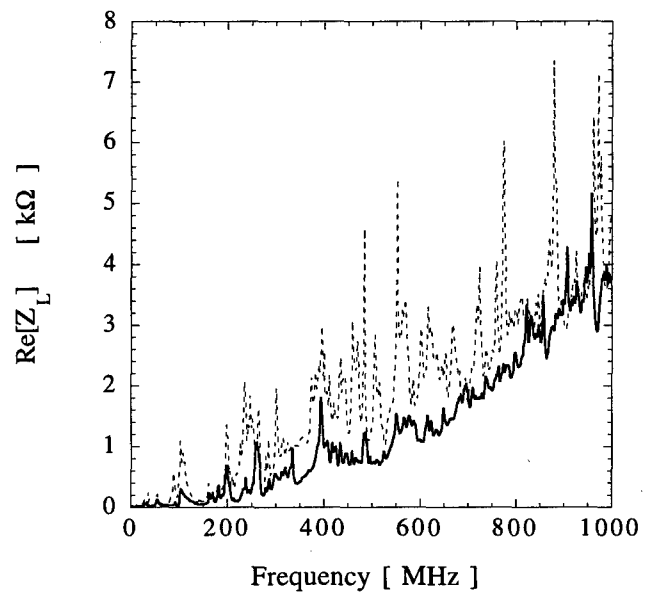


Figure 6: Coupling impedance of seven FX kickers

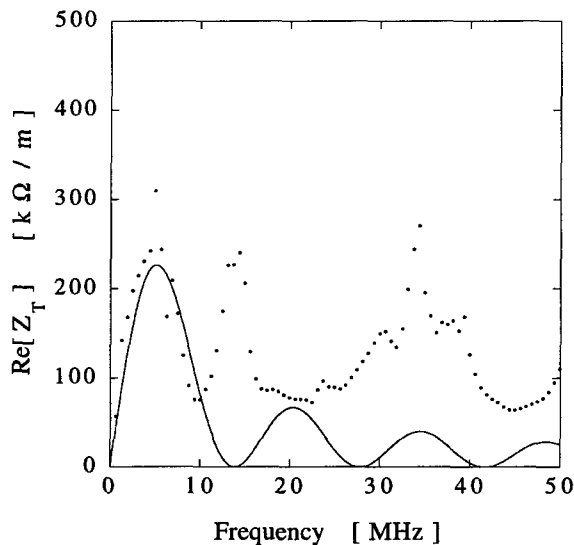


Figure 5: Coupling impedance of seven FX kickers

have been performed during a commissioning run for the long-baseline neutrino oscillation experiment. The growth rate has increased by about a factor of two after installing the FX kickers under certain conditions. Although this can be reproduced by the calculation, a full agreement in the overall behaviour has not been achieved yet.

Octupole magnets have been re-located with four-fold symmetry so as to minimize a dynamic aperture reduction. Landau damping effect with the octupoles was crucial for the operation after installing the FX kickers not only during acceleration but also during the injection flat bottom.

## 5 ACKNOWLEDGEMENTS

M. Shirakata assisted us in the experiment with a beam. Y. Kanai and Y. Shimosaki contributed to field measurement. F. Caspers gave useful comments on the coupling impedance measurement. M. Uota assisted in measuring the coupling impedance. W. Chou called our attention to the work of S. Y. Lee. M. Kumada suggested chromaticity measurement with different  $dB/dt$ 's and readily accepted our request to use his gaussmeter.

## 6 REFERENCES

- [1] T. Toyama, D. Arakawa, S. Igarashi, J. Kishiro, K. Koba and K. Takayama, Proc. of the 1997 Part. Accel. Conf. (1997) 1599. T. Toyama, D. Arakawa, S. Igarashi, J. Kishiro and K. Takayama, Proc. of the first Asian Part. Accel. Conf. (1998) 471.
- [2] D. A. Edwards and M. J. Syphers, "An Introduction to the Physics of High Energy Accelerators", John Wiley & Sons, Inc., 1993.
- [3] S.Y. Lee, Nucl. Instrum. Methods A300 (1991) 151.
- [4] T. Toyama, to be published.
- [5] T. Kawakubo, S. Murasugi, E. Nakamura and S. Tazawa, Proc. of the first Asian Part. Accel. Conf. (1998) 582.
- [6] H. Hahn and A. Ratti, AD/RHIC/RD-111, 1997.
- [7] L.S. Walling, D.E. McMurry, D.V. Neuffer and H.A. Thiessen, N.I.M. A281 (1989) 433.
- [8] K. Takayama, D. Arakawa, J. Kishiro, K. Koba and M. Yoshii, Phys. Rev. Lett. 78 (1997) 871. K. Takayama, D. Arakawa, J. Kishiro, K. Koba, T. Toyama and M. Yoshii, Proc. of the 1997 Part. Accel. Conf. (1997) 1548.
- [9] A. Chao, "Physics of collective beam instabilities in high energy accelerators", John Wiley & Sons, Inc., 1993 and the references there in.

## BESSY II FEEDBACK SYSTEMS \*

S. Khan <sup>†</sup>, T. Knuth, BESSY, Berlin, Germany

### Abstract

The present status of feedback systems to counteract unwanted beam motion and coupled-bunch beam instabilities in the BESSY II storage ring is reviewed.

### 1 INTRODUCTION

BESSY II [1] is a high-brilliance synchrotron radiation source in Berlin/Adlershof. The first beam was stored in April 1998, regular user shifts started in January 1999.

Several effects tend to reduce the brilliance of the synchrotron radiation delivered to the users:

- Unwanted motion of the closed orbit e.g. from ground vibration or from power supply ripple may increase the effective beam emittance seen by the experimenter.
- Longitudinal coupled-bunch oscillations caused by higher-order modes (HOMs) of the rf cavities may limit the beam current, deteriorate undulator spectra, and increase the beam size in dispersive regions.
- Transverse coupled-bunch instabilities from HOMs and due to the resistive-wall effect may also limit the beam current and increase the effective emittance.

Plans to counteract these effects by feedback systems are reviewed in this paper. For each project, the layout of the system and its expected performance are described, and the present status is reported.

### 2 LOCAL ORBIT FEEDBACK SYSTEM

Slow orbit drifts ( $<1$  Hz) can be handled by the global orbit correction system of the storage ring using corrector coils integrated in the sextupole and dipole magnets. To counteract orbit motion in the 1-100 Hz regime on the  $1\text{ }\mu\text{m}$  level, the rate of sampling and correcting the beam should be of the order of 1 kHz, and dedicated computer hardware and magnets are required. As a prototype, a local feedback system with a closed bump enclosing an undulator (U-49) will be installed and tested in summer 1999. For a review of local and global correction schemes see e.g. [2].

As outlined previously [3, 4], the feedback system uses 4 window frame magnets, each equipped with horizontal and vertical coils on a yoke of granulated iron. Their design is a compromise between low inductance, low eddy currents, space requirements and sufficient kick strength. Excited by bipolar 20V/20A power supplies of 1 kHz bandwidth, each corrector magnet produces a maximum kick of 0.9 mrad horizontally and 0.7 mrad vertically (at a beam energy of

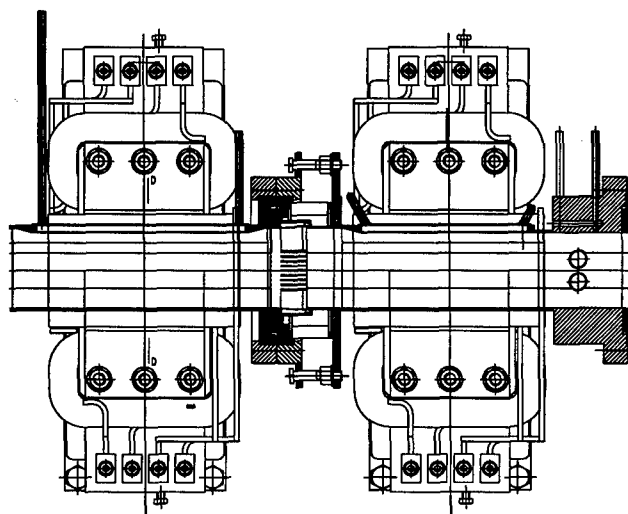


Figure 1: Vacuum chamber and corrector magnets to be installed on either end of the undulator chamber. The drawing shows the upstream end (beam from left to right).

1.7 GeV). The distance between the magnets, 255 mm from center to center, defines the dynamic range for displacing the beam to be  $\pm 0.23$  mm horizontally and  $\pm 0.18$  mm vertically.

Figure 1 shows the magnets and the vacuum chamber to be installed on either side of the undulator. The chamber is tapered from an octagonal cross section ( $65 \times 35$  mm) to the elliptical profile ( $60 \times 16$  mm) of the adjacent undulator chamber, and a bellow is placed between the two magnets. Beam position monitors (BPMs) on both sides of the undulator yield the electron beam position and angle within the closed bump.

In addition to the electron beam position, the information from photon BPMs is available. By rejecting photoelectrons below a tunable threshold, the background radiation from the adjacent dipoles can be suppressed [5].

The hardware (vacuum chamber, magnets, power supplies) has been delivered and awaits installation in the next suitable shutdown period. Software development is underway. Tests performed using Motorola MVME-162 CPUs under VxWorks were satisfactory. However, to allow for more flexibility, the use of VME-based DSPs is considered, while a VME master CPU would establish the communication with the BESSY II control system.

\* This work is funded by the Bundesministerium für Bildung, Wissenschaft, Forschung und Technologie and by the Land Berlin.

<sup>†</sup> Email: khan@bii.bessy.de

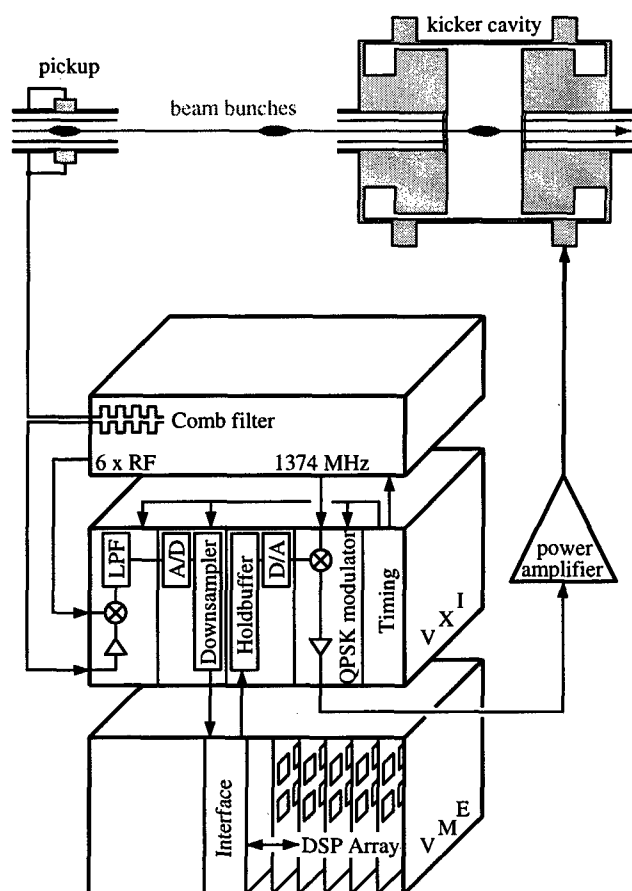


Figure 2: Layout of the longitudinal feedback system

### 3 LONGITUDINAL BUNCH-BY-BUNCH FEEDBACK SYSTEM

The BESSY II storage ring is operated using four DORIS-type pillbox cavities with a rich HOM spectrum. Damping antennas have been added to suppress the most prominent HOMs [6], and tuning the HOM positions by controlling the cavity temperature is in preparation. Furthermore, the design of Landau cavities to further suppress coupled-bunch instabilities and to increase the bunch length is underway. In addition to these measures, a longitudinal feedback system (LFB) will be installed in summer 1999.

The LFB electronics developed for the ALS (Berkeley), PEP-II (Stanford) and DAΦNE (Frascati) [7, 8] will be used in combination with a kicker cavity designed for DAΦNE [9] and modified for a bunch frequency of 500 MHz [10]. For details on the kicker cavity see [11].

Figure 2 shows the LFB schematically. The bunch signal from a pickup passes a comb filter to produce a 3 GHz signal for phase detection. The moment signal (phase-charge) is digitized at a rate of 500 MHz, downsampled and distributed to an array of DSPs, where a correction signal is computed. The D/A-converted correction signal QPSK-modulates a carrier at 1374 MHz (11/4 times the rf fre-

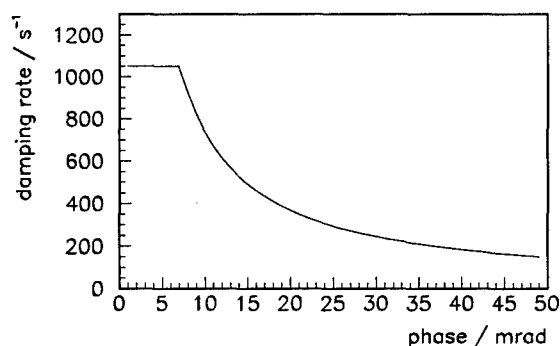


Figure 3: Long. damping rate versus phase deviation.

quency). A simulation demonstrates the beneficial effect of this particular modulation scheme [13].

The longitudinal damping rate can be expressed as [12]

$$\frac{1}{\tau} = \frac{f_{rf} \alpha}{2 \nu_s E / e} \cdot G, \quad (1)$$

where  $f_{rf}$  is the rf frequency,  $\alpha$  is the momentum compaction factor,  $\nu_s$  is the synchrotron tune, and  $E$  is the beam energy. The feedback gain i.e. the kick voltage per unit phase deviation  $G = \Delta U / \Delta \phi$  is limited by the phase resolution and by the maximum amplifier power  $P = 220$  W via  $\Delta U \leq \sqrt{2 R_s P}$ , where  $R_s = 960 \Omega$  is the kicker shunt impedance. Assuming 50% power loss and saturation of the amplifier at  $\Delta \phi = 7$  mrad as an example, the maximum damping rate is about  $1000 \text{ s}^{-1}$ , as shown in figure 3. If necessary, the damping rate can be improved by adding rf power, by using more kickers, or – subject to operational experience – by increasing the gain.

The LFB electronics is currently being tested at SLAC, Stanford. The kicker cavity as well as the amplifier and other commercially available components have been delivered.

### 4 TRANSVERSE BUNCH-BY-BUNCH FEEDBACK SYSTEM

Apart from the transverse impedance of HOMs, the resistive-wall impedance can be quite significant for a synchrotron light source with narrow undulator chambers. For BESSY II, transverse growth rates of the order of  $10^3 \text{ s}^{-1}$  were estimated [14].

The transverse feedback system (TFB) for BESSY II is modelled after the analog system developed for the ALS [15]. Figure 4 shows a block diagram of the TFB, where signals from two sets of button-type pickups approximately  $90^\circ$  apart in betatron phase are used. The moment signals (displacement-charge) are detected at 3 GHz, differenced, mixed down to baseband, and combined in proper proportion. For offset rejection, the correction signals from subsequent revolutions are subtracted. The resulting kicks are provided by stripline kickers driven by 150 W power amplifiers. A  $180^\circ$  power splitter is used to drive opposite

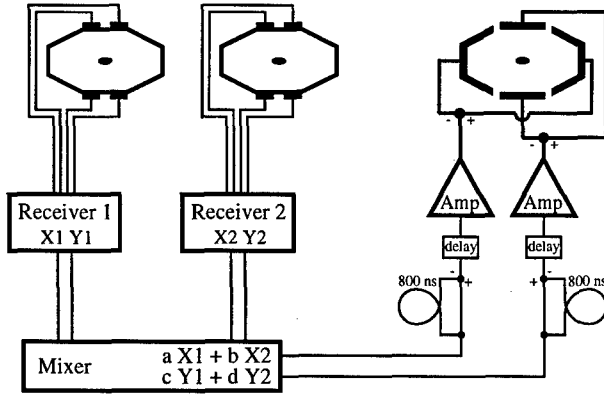


Figure 4: Block diagram of the transverse feedback system.

electrodes. Alternatively, the full power could be applied to a single electrode. The kicker geometry and performance is described in [11].

The damping rate of the TFB can be written as

$$\frac{1}{\tau} = \frac{f_0 \sqrt{\beta_1 \beta_2}}{2 E/e} \cdot G, \quad (2)$$

where  $\beta_1$  and  $\beta_2$  are the beta functions at the pickup and at the kicker position, respectively, and  $G = \Delta U / \Delta y$  is the feedback gain i.e. the kick voltage per unit displacement.

With a 150 W amplifier connected to each pair of electrodes and assuming 50% power loss, the vertical damping rate is shown in figure 5 at both ends of the relevant frequency range. In this example, the amplifier saturates at  $\Delta y = 1$  mm, leading to a maximum vertical damping rate of  $5300 \text{ s}^{-1}$  at low frequency, dropping to  $3500 \text{ s}^{-1}$  at 250 MHz. Due to the smaller shunt impedance in the horizontal plane (where the resistive-wall effect is irrelevant), the horizontal damping rates are  $\sim 0.7$  times smaller.

The design of the kicker has been finalized, and its installation is scheduled for fall 1999. Power amplifiers have been purchased. The two receivers have been completed, the mixing chassis and the digital interface to the control system are underway.

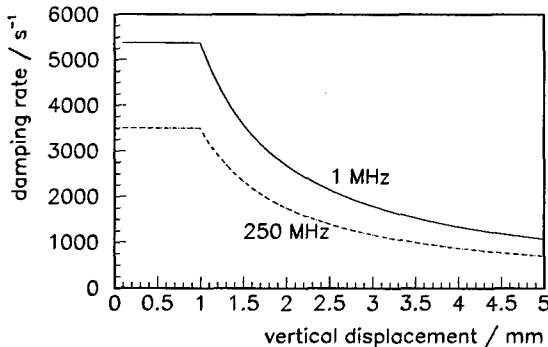


Figure 5: Transverse damping rate versus displacement.

## 5 ACKNOWLEDGEMENTS

The contributions of J. D. Gilpatrick (LANL, Los Alamos) to the local orbit feedback system are gratefully acknowledged. As for the bunch-by-bunch systems, valuable information and help was provided by W. Barry, J. Byrd, J. Corlett, G. Stover (ALS, Berkeley), J. Fox, H. Hindi, S. Prabhakar, D. Teytelman (SLAC, Stanford), A. Gallo, F. Marcellini, M. Serio and M. Zobov (INFN, Frascati).

## 6 REFERENCES

- [1] R. Bakker for the BESSY II Project Team: 'Status and Commissioning Results of BESSY II', this conference.
- [2] J. N. Galayda, Y. Chung, R. O. Hettel: in 'Synchrotron Radiation Sources - a Primer', ed. H. Winick (World Scientific 1994), p.344, and references therein.
- [3] J. D. Gilpatrick, S. Khan, D. Krämer: 'A State-Variable Approach to the BESSY II Local Beam-Position-Feedback System', Proc. of the 5th Europ. Part. Acc. Conf., Sitges (1996), p.1902.
- [4] S. Khan, D. Krämer, J. D. Gilpatrick: 'Layout and Time-domain Simulation of a Local Beam Position Feedback System for BESSY II', Proc. of the 5th Europ. Part. Acc. Conf., Sitges (1996), p.1839.
- [5] K. Holldack et al.: 'Suppression of Dipole Background from Position Signals of Photon BPMs', BESSY Jahresbericht 1995, 497.
- [6] N. Lehnart, H. Petersen: 'Ferrit-Dämpfungsantennen gegen parasitäre Cavity-Modes in den DORIS-Hohlraumresonatoren', DESY Techn. Notiz H2-77/12 (1977).
- [7] D. Teytelman et al.: 'Operation and Performance of the PEP-II Prototype Longitudinal Damping System at the ALS', Proc. of the 1995 Part. Acc. Conf., Dallas (1995), p.2420.
- [8] S. Prabhakar et al.: 'Commissioning Experience from PEP-II HER Longitudinal Feedback', Proc. Beam Instrumentation Workshop, Stanford, AIP 451 (1998), p.529.
- [9] R. Boni et al.: 'A Waveguide Overloaded Cavity as Longitudinal Kicker for the DAΦNE Bunch-by-Bunch Feedback System', Part. Acc. Vol.52 (1996), p.95.
- [10] A. Gallo et al.: 'Adaption of the DAΦNE Longitudinal Kicker Geometry to the Needs of the BESSY-II Synchrotron Light Source', DAΦNE Technical Note RF-21 (1998).
- [11] T. Knuth, S. Khan: 'Longitudinal and Transverse Feedback Kickers for the BESSY II Storage Ring', this conference.
- [12] M. Bassetti et al.: 'DAΦNE Longitudinal Feedback', Proc. of the 3rd Europ. Part. Acc., Berlin (1992), p.807.
- [13] S. Khan: 'Simulation of Longitudinal Coupled-Bunch Instabilities in BESSY II', Proc. of the 6th Europ. Part. Acc. Conf., Stockholm (1998), p.966.
- [14] S. Khan: 'Simulation of Transverse Coupled-Bunch Instabilities', Proc. of the Part. Acc. Conf., Dallas (1995), p.3019.
- [15] W. Barry et al.: 'Transverse Coupled-Bunch Feedback in the Advanced Light Source (ALS)', Proc. of the 4th Europ. Part. Acc. Conf., London (1994), p.122.

# LONGITUDINAL AND TRANSVERSE FEEDBACK KICKERS FOR THE BESSY II STORAGE RING\*

S. Khan, T. Knuth<sup>†</sup>, BESSY, Berlin, Germany

A. Gallo, F. Marcellini, B. Sparato, M. Zobov, INFN, Frascati, Italy

## Abstract

This paper presents an overview of the bunch-by-bunch feedback kickers designed for the BESSY II storage ring. Simulation results for the longitudinal kicker cavity and for the transverse stripline kicker are discussed.

## 1 INTRODUCTION

Bunch-by-bunch feedback systems are required to cure multibunch beam instabilities at high currents in the BESSY II storage ring [1]. The present status of the longitudinal feedback system (LFB) and the transverse feedback system (TFB) is reported in [2]. As longitudinal correcting element, a waveguide-overloaded cavity was favored over a drift-tube structure. The kicker cavity designed for DAΦNE [3] was modified to meet the requirements for BESSY II. A shunt impedance of 960 Ω and effective damping of higher-order modes (HOMs) has been achieved. For the TFB, stripline electrodes will be used. The stripline pairs for each transverse plane will be combined in one structure.

This paper describes the design issues and focusses on simulation results for both kickers using the computer codes MAFIA [4], POISSON [5] and HFSS [6]. The parameters used in the simulations are given in Table 1.

Table 1: Simulation parameters for BESSY II.

$f_{rf}$	rf frequency	499.65 MHz
$n$	harmonic number	400
$E$	beam energy	1.7 GeV
$I$	assumed beam current	400 mA
$P$	total rf power (LFB)	220 W
	total rf power (TFB)	$2 \times 150$ W

## 2 LONGITUDINAL KICKER

### 2.1 Geometry and Performance

The LFB kicker is based on a pillbox cavity design as shown in Fig. 1. In order to achieve the desired bandwidth of [7]

$$f_{bw} = 0.53 f_{rf} = 265 \text{ MHz}, \quad (1)$$

eight waveguides are attached to provide suitable damping. Four waveguides are used as power inputs, the four other waveguides are connected to loads.

\* This work is funded by the Bundesministerium für Bildung, Wissenschaft, Forschung und Technologie and by the Land Berlin

<sup>†</sup> Email: knuth@bii.bessy.de

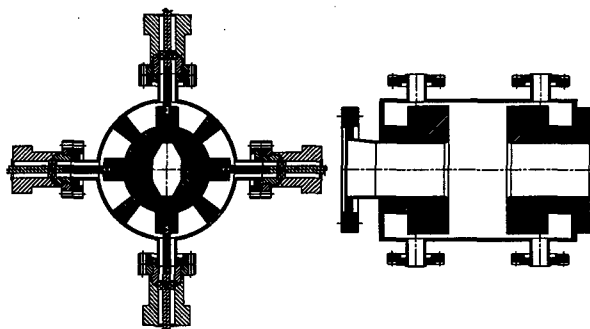


Figure 1: Longitudinal kicker structure.

MAFIA calculations yield an optimum  $R/Q$ -value of 87 Ω at a cavity length of  $l=72$  mm. The center frequency has to fulfill the condition [8]

$$f_c = (p \pm 0.25) f_{rf} \quad (2)$$

where  $p$  is a positive integer. In order not to deviate too much from the original design, a center frequency of 1374 MHz (i.e.  $2.75 f_{rf}$ ) was chosen, leading to a theoretical pillbox radius of 83 mm. Extensive simulations were performed using the 3D-code HFSS in order to check the HOM content of the structure, to obtain the required  $Q$ -value of 5.2, and to optimize the transition from the coaxial feedthrough to the waveguide. Fig. 2 shows 1/8th of the kicker structure. The reflected power up to the cut-off frequency does not exceed 6%. The port-to-port frequency response is shown in Fig. 3. With a center frequency of 1380 MHz and a bandwidth of 270 MHz, a  $Q$ -value of 5.1 is obtained.

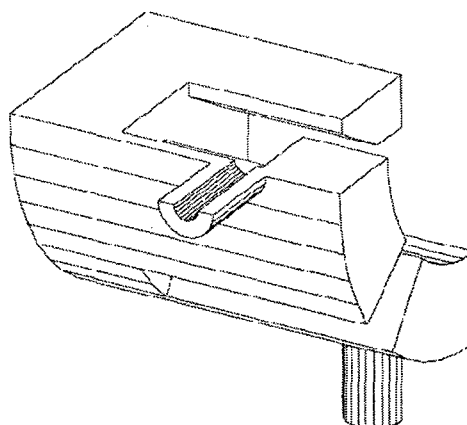


Figure 2: HFSS model as 1/8th of the whole structure.

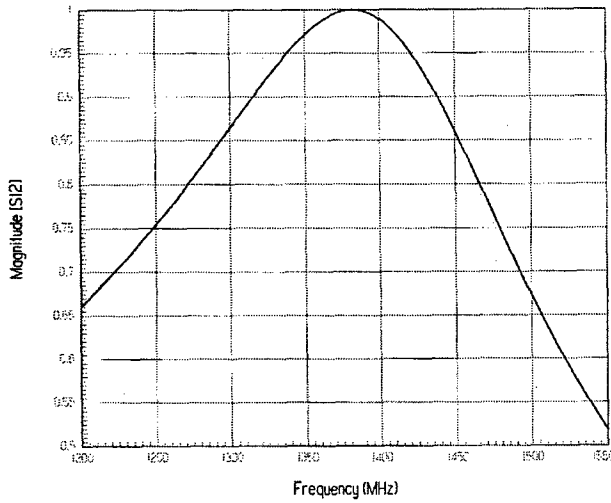


Figure 3: Frequency response of the fundamental mode.

For a given input power  $P$ , the simulation yields an electric field amplitude  $E_z(z)$  and phase  $\Theta_z(z)$  on the cavity axis, from which the accelerating voltage

$$V_{\text{acc}} = \int_{-l/2}^{l/2} E_z(z) \exp(i[2\pi f_c z/c - \theta_z(z)]) dz \quad (3)$$

is obtained. The resulting shunt impedance, given by

$$R_s = \frac{|V_{\text{acc}}|^2}{2P}, \quad (4)$$

is 1100  $\Omega$ . An independent method to obtain  $R_s$  by simulating a wire along the beam axis yields a slightly lower value of 960  $\Omega$ . Table 2 summarizes the kicker parameters.

Table 2: Longitudinal kicker parameters.

pillbox length	72 mm
length including waveguides	260 mm
overall length	310 mm
pillbox radius	82 mm
number of waveguides	8
center frequency	1380 MHz
bandwidth	270 MHz
Shunt impedance	960 $\Omega$

## 2.2 HOM Characterization

Monopole and dipole HOMs were selected using 2D MAFIA calculations, and their center frequencies were verified by 3D runs. In the vicinity of these frequencies, HFSS runs were performed to obtain the  $Q$ -values and shunt impedances listed in table 3 and table 4. The power generated by the monopole modes was computed up to the cut-off frequency of 5.2 GHz, where each mode contributes a power of

$$P_G = \sum_i \frac{1}{2} \text{Re}[R_c(\omega_i)] I_i^2 \quad (5)$$

with  $I_i$  representing the beam spectrum and  $R_c$  the coupling impedance, which turned out to be twice the shunt impedance. Table 5 lists the total power contribution of the fundamental mode and the total power of all HOMs for beam currents of 200 mA and 400 mA in 320 buckets. Since the cavity is a non-directional device, about half of the generated power is seen by the amplifier i.e. 130 W at 400 mA. A circulator for protection is not immediately needed, since the amplifier is capable of absorbing up to 100% of its output value (220 W).

Table 3: Monopole modes of the kicker cavity.

Mode	$f_{\text{MAFIA-3D}}$ [MHz]	$R_s/Q$ [ $\Omega$ ]	$f_{\text{HFSS}}$ [MHz]	$Q$	$R_s$ [ $\Omega$ ]
0	1405.8	86.9	1382	5.2	887
1	2518.5	13.9	2250	7.1	99
2	3231.1	2.6	3257	65	169
3	3872.5	13.6	3849	149	2026
4	4379.7	2.6	4195	32	83

Table 4: Dipole modes of the kicker cavity.

Mode	$f_{\text{MAFIA-3D}}$ [MHz]	$R_s^\perp/Q$ [ $\Omega$ ]	$f_{\text{HFSS}}$ [MHz]	$Q$	$R_s^\perp$ [ $\Omega$ ]
1	2190.5 2082.8	4.32	2176 2062	15 18	64.8 77.8
2	2279.7 2108.0	0.07	2257 2085	30 97	2.1 6.8
3	2968.4	3.3	3019	18	59.4

Table 5: Total beam induced power with 320 buckets filled.

$I$	$P_{\text{fund.}}$ [W]	$P_{\Sigma\text{HOM}}$ [W]	$P_G$ [W]
200 mA	35.5	29.9	65.4
400 mA	142.0	119.5	261.5

## 3 TRANSVERSE KICKER

### 3.1 Geometry and Performance

For the transverse kicker, a stripline geometry will be employed. The horizontal ( $x$ ) and vertical ( $y$ ) electrodes are combined in a single structure to minimize space requirements and to obtain a moderate loss factor. Each pair of electrodes is driven in differential mode using a 180° power divider connected to a 150 W linear amplifier.

Fig. 4 shows the model of the kicker for MAFIA calculations. C-shaped electrodes for the  $x$ -plane and flat electrodes for the  $y$ -plane match the octagonal shape of the adjacent vacuum chamber without tapering, leaving only a 5 mm wide gap in longitudinal direction. The electrode length of 300 mm maximizes the shunt impedance. To improve radiative heat dissipation, the outside surface is increased by adding cooling vanes. Using the 2D code POISSON, the electrodes and the surrounding chamber were shaped to meet the line impedance requirement of  $R_L = 50 \Omega$ . A model was built and TDR (time domain



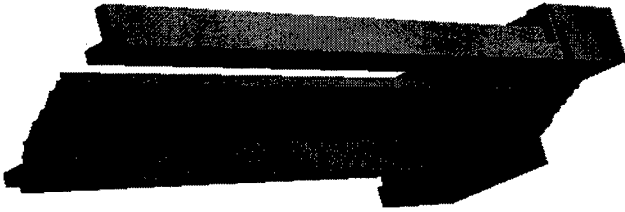


Figure 4: MAFIA model of the transverse kicker (1/8th of the full structure).

reflectometry) measurements were performed to verify the line impedance of the electrodes, which agrees well with the calculations, and to minimize reflections at the transition to the coaxial feedthroughs. The different geometry of the electrodes in  $x$  and  $y$  leads to a different transverse shunt impedance  $R_s^\perp$  [9]

$$R_s^\perp = 2R_L \left( g_{x,y} \frac{2}{kh} \right)^2 \sin^2 \theta, \quad (6)$$

where  $g_{x,y}$  is the respective geometric coverage factor,  $k$  is the wavenumber,  $l$  is the electrode length,  $h$  is the distance between opposite electrodes and  $\theta = kl$ . Fig.5 shows the frequency dependence of the shunt impedance in both planes.

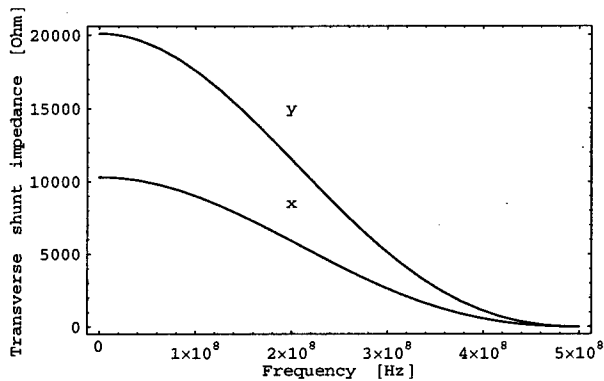


Figure 5: Shunt impedance of the transverse stripline kicker.

A higher vertical shunt impedance is preferred because of the larger vertical resistive wall impedance of a flat vacuum chamber. Over the entire mode spectrum (DC to 250 MHz), the kick voltage exceeds 1.7 kV vertically and 1.2 kV horizontally.

### 3.2 HOMs and Power Losses

HOMs found by performing MAFIA calculations in the frequency domain are trapped behind the electrodes and couple only weakly to the beam. Even though HFSS calculations show that most of the HOM power dissipates through the feedthroughs, at least one damping loop will be installed to further damp the the strongest modes.

Ohmic losses from the image currents passing the electrodes were calculated for a beam current of 400 mA. A

total power loss of 5 W for stainless steel (specific resistivity  $\rho_{St} = 0.71 \cdot 10^{-6} \Omega m$ ) and 0.8 W for copper electrodes ( $\rho_{Cu} = 0.017 \cdot 10^{-6} \Omega m$ ) was obtained. On the other hand, using the Stefan-Boltzmann law and the emission coefficients for steel ( $\epsilon_{St} = 0.29$ ) and copper ( $\epsilon_{Cu} = 0.03$ ) electrode temperatures of  $T_{St} = 80^\circ C$  and  $T_{Cu} = 105^\circ C$  were found. In order to decrease the electrode temperature, the possibility of blackening the electrode surfaces is being considered.

Table 6: Transverse kicker parameters.

line impedance	50 $\Omega$
length of kicker structure	310 mm
overall length	600 mm
(incl. bellow and pumping port)	
electrode separation ( $x, y$ )	65 mm, 35 mm
Coverage factor ( $x, y$ )	1.1, 0.83
Kick voltage at DC ( $x, y$ )	1.7 kV, 2.4 kV
Kick voltage at 250 MHz ( $x, y$ )	1.2 kV, 1.7 kV

## 4 ACKNOWLEDGMENTS

The authors from BESSY would like to thank the members of the DAΦNE rf group (INFN, Frascati) for their guidance in redesigning the kicker cavity. Valuable information for the layout of the transverse kicker was provided by W. Barry and J. Corlett (LBNL, Berkeley).

## 5 REFERENCES

- [1] R. Bakker for the BESSY team: 'Status and Commissioning Results of BESSY II', this conference.
- [2] S. Khan, T. Knuth: 'BESSY II Feedback Systems', this conference.
- [3] R. Boni et al.: 'A Waveguide Overloaded Cavity as Longitudinal Kicker for the DAΦNE Bunch-by-Bunch Feedback System', Part. Acc. Vol.52 (1996), p.95.
- [4] 'MAFIA User's Guide', CST, Darmstadt.
- [5] J. H. Billen: 'The Superfish Manual', Los Alamos LA-UR-96-1834.
- [6] Hewlett-Packard Co.: 'HFSS, the High Frequency Structure Simulator HP85180A™'.
- [7] A. Gallo et al.: 'Efficiency of the Broadband Rf Cavity Longitudinal Kicker in DAΦNE', internal note.
- [8] M. Bassetti et al.: 'DAΦNE Longitudinal Feedback', Proceedings of the 3rd Europ. Part. Acc. Conference (1992), p.807.
- [9] D. Goldberg, G. Lambertson: 'Dynamic Devices: A Primer on Pickups and Kickers', AIP Conf. Proc. No. 249 (1992), p. 537.

# UTILITY OPTIMIZATION FOR THE BEAM ORBIT STABILITY AT SRRC

H. M. Cheng<sup>#</sup>, C. R. Chen, Z. D. Tsai, and J. R. Chen<sup>\*</sup>

Synchrotron Radiation Research Center, Taiwan, R.O.C.

also at <sup>\*</sup>Department of Nuclear Science, National Tsing-Hua University, Taiwan, R.O.C.

## Abstract

At the Taiwan Light Source (TLS), the stability of the electron beam orbit is sensitive to the utility conditions. The beam position showed strong correlation with the temperature while the tunnel temperature variation was more than 0.4°C. In this work, the coolant temperature and the air temperature in the storage ring tunnel were tuned to test the sensitivity of the electron beam orbit. The temperature difference of the devices in the TLS might be as high as 10°C between the system shutdown and operation. These temperature variations affected the beam stability through some specific routes. Some modeling technique was also applied to identify the correlation factors among the beam position and the utility conditions.

## 1 INTRODUCTION

In 1997, Keller et al. [1] studied the correlation between the beam orbit stability and the utility conditions for the Advanced Light Source (ALS). At TLS, a series of experiments were also conducted [2]. From the daily observation of the beam status at TLS, the beam orbit is sensitive to the utility conditions. Although an orbit-feedback system is being implemented at TLS, the requirement for a stable utility system should never be ignored. It is easy to imagine that the positions of beam position monitors, which used for orbit feedback, would follow the tiny thermal distortions.

To study the propagation routes caused by the utility perturbation, experiments have been setup. In this work, the experiments concentrated on thermal effects from the temperature varying devices. In the second section, a simulation model and the results for optimizing the control parameters of the utilities is mentioned. Instead of using linear modeling approach, a fuzzy modeling technique was applied to acquire the beam-position/utility-system model. In the third section, the optimization for deionized water (DIW) temperature setting is described.

## 2 UTILITY SYSTEM AND MODELING

The TLS utility consists of three major systems: the water system, the air conditioning system, and the electricity system. In this work, only the studies on the temperature varying systems are mentioned.

### 2.1 Temperature Varying Devices

The devices that might cause thermal variations are the cooling water system and the air-conditioning system. The cooling water system consists of three subsystems: the chilled water system (CHW), the cooling tower water system (CTW), and the de-ionized water system (DIW). The de-ionized water system consists of three loops. The DIW system-1 (Cu) supplies the coolant to the major devices, such as the RF systems, the magnets, and the power supplies. The DIW system-2 (Al) is used for the vacuum beam ducts. The DIW system-3 (Beamline) supplies to the photon-beamline devices.

The air-conditioning system of the storage ring includes five major air-handling units supplying to the storage ring, the laboratory, and the experimental area. In addition, the air-conditioning system also supplies to the core area devices, at where the RF transmitters, magnet power supplies, vacuum controllers, and other associated instruments are located. Table 1 lists the current set points and the varying temperature range of the TLS utility systems.

Table 1: Operation temperature of the TLS utility system.

System	CHW	CTW	DIW(Cu)	DIW(Al)	A/C
Set Point	7.0°C	30.0°C	23.5°C	25.0°C	24.5°C
Range	±0.2°C	~ ±0.5°C	±0.2°C	±0.2°C	±0.1°C

### 2.2 Monitoring Systems

The beam orbit was monitored by the electron beam position monitors (EBPM, ≈5μm resolution) and the photon beam position monitors (PBPM, with resolution <0.5μm). The temperature sensors at the coolant loop and in the ring tunnel monitored the utility performance. Most part of the utility system is using temperature sensors with 0.1°C sensitivity and part with 0.03°C sensitivity.

### 2.3 System Modeling

Figure 1 shows the possible transferring routes to the electron beam and photon beam perturbation from utility systems. The effects among the subsystems are cascades. In this work, the system modeling approach was studied for optimizing the utility status.

Based on the propagation routes, a mathematical model was established to calculate the orbit for a given set of

<sup>#</sup> Email: hmcheng@srcc.gov.tw

operating parameters. The simulation code representing the TLS storage ring was written in MATLAB.

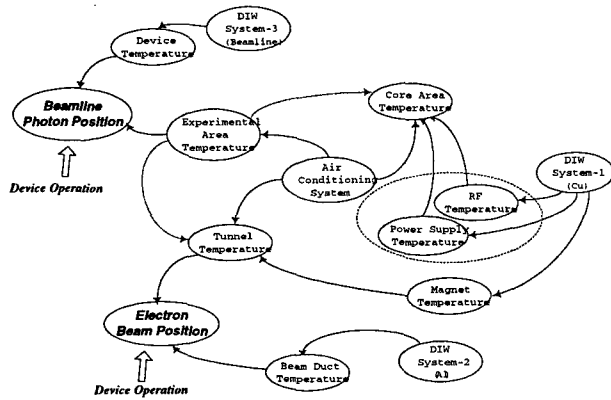


Figure 1: The propagation routes from the utility variation to the variations of electron- and photon-beam position.

The mathematical model of a linear time-invariant (LTI) system was described as:

$$\text{state equation: } \frac{d\mathbf{X}_{\text{Status}}}{dt} = \mathbf{A}\mathbf{X}_{\text{Status}} + \mathbf{B}\mathbf{U}_{\text{Util}} + \mathbf{F}\mathbf{w}, \text{ and } (1)$$

$$\text{output equation: } \mathbf{Y}_{\text{BPS}} = \mathbf{D}\mathbf{X}_{\text{Status}} + \mathbf{E}\mathbf{U}_{\text{Util}} + \mathbf{H}\mathbf{w}, (2)$$

where  $\mathbf{Y}_{\text{BPS}}$  is the beam position,  $\mathbf{X}_{\text{Status}}$  is the temperature status vector at the storage ring,  $\mathbf{U}_{\text{Util}}$  is the set points vector of the utility systems,  $\mathbf{w}$  is the disturbance vector, and  $\mathbf{A}$ ,  $\mathbf{B}$ ,  $\mathbf{D}$ ,  $\mathbf{E}$ ,  $\mathbf{F}$  and  $\mathbf{H}$  are the coefficient matrices with constant elements. For an LTI system  $\mathbf{w}$  is always a null vector. In real life, the disturbance term always contains the nonlinearity of system fluctuation, invalid measurement, or the external unpredictable signals. In this work, the output is the EBPM results along the y-axis. The elements chosen in the input vector are the ambient temperatures around the kicker and the RF cavity in the tunnel, the outlet temperature of the DIW system-1 (Cu) and system-2 (Al), and the temperature of the quadrupole magnet cable. The input data are shown in Figure 2a.

As a LTI system, the ARMAV [3] modeling approach was proposed. The standard deviation  $\sigma$  of the calculating error (the difference between the measured and the calculated results) is about  $18\mu\text{m}$  (Table 2).

To predict the effect caused by the nonlinear term, the fuzzy modeling approach proposed by M. Sugeno [4] was applied to build the simulation model in this work. Assuming that the beam position in the storage ring is only affected by the utility conditions, the data points shall locate in the  $s+1$  dimensional space  $(\mathbf{X}^{(i)}, y^{(i)})$ , where  $\mathbf{X}^{(i)} = (x_1^{(i)}, x_2^{(i)}, \dots, x_s^{(i)})$ ,  $x_j^{(i)}$  denotes the  $j$ -th (sensor index) input's at the  $i$ -th (time) point, and  $y^{(i)}$  is the output's (beam position) coordinate of the  $i$ -th point. In the simulation result, the inputs are the same as the LTI modeling approach. The standard deviation of the calculation error is about  $8\mu\text{m}$ .

The nonlinear simulation procedure was applied to observe the performance of the generated model. Figure 2b illustrates the simulation results of Sugeno's fuzzy

model. In Table 2, the performance of the LTI model and the Sugeno's fuzzy model is compared.

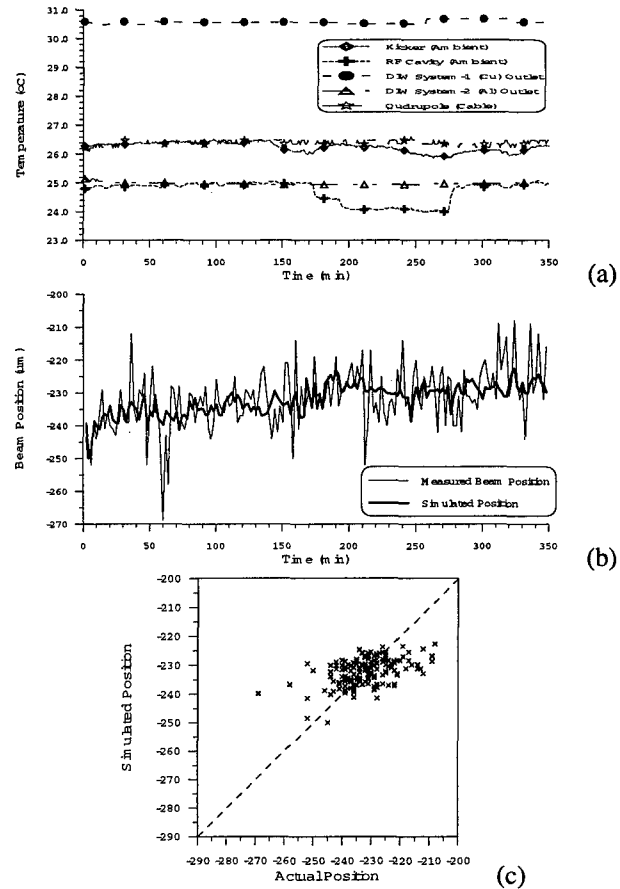


Figure 2: (a) Measured temperature inputs; (b) measured beam position and the simulation results of the fuzzy model; and (c) the statistics between the measured and simulated beam position.

In this simulation, the trend of the simulation results meet quite good with the measured data (Figure 2b). However, some parts of the simulation output do not meet the result (for example, the discrepancies at  $t \approx 60, 120-150, 210-240, 260-280, 320$ , etc.). For improving, the model could be modified by two approaches. The first method is to divide the whole process into several different modes (e.g. transient mode, steady state mode, high/low current, etc.). The other method is to include more modeling parameters, such as mechanical vibration and electricity fluctuations.

Table 2: Standard deviation comparison of calculating error between ARMAV and Sugeno's fuzzy model.

	Linear (ARMAV)	Nonlinear (Sugeno)
$\sigma$	$\sim 18\mu\text{m}$	$\sim 8\mu\text{m}$

In Figure 2c, the comparison of the results shows the performance of the model. As stated in Table 2, the standard deviation of the error is  $\sim 8\mu\text{m}$ .

### 3 TEMPERATURE SETTING OPTIMIZATION

A series of experiment was conducted to test the relationships between the beam orbit variation and the utility parameters. The experimental results showed that some of the orbit oscillations were correlated to the temperature variation while the variation was larger than  $0.4^{\circ}\text{C}$ .

At TLS, the utility capacity might saturate because of improper settings. The saturation conditions of the utility system were mainly determined by the DIW system-1. When the temperature set point of DIW system-1 is below  $25.0^{\circ}\text{C}$ , the air-conditioning system is capable to keep the air temperature variation within  $\pm 0.2^{\circ}\text{C}$ , and the beam orbit drift is therefore improved. If the set point falls beyond this range, some air-conditioning subsystems saturate. For example, if the set point is  $25.0^{\circ}\text{C}$ , the AHU duty factor is 100% and saturates. Table 3 lists the relationship between the AHU duty factor and the temperature set point of DIW system-1.

Two major methods were adopted to stabilize the beam position in order to keep the utility systems unsaturated and to achieve an optimized balance. The first one was to optimize the set points for individual subsystems. Figure 4 shows the correlation between the beam drift in one shift and the DIW system-1 set point. It shows that the lower the DIW temperature is, the smaller the air temperature variation will be, and thus the smaller beam orbit variation occurs.

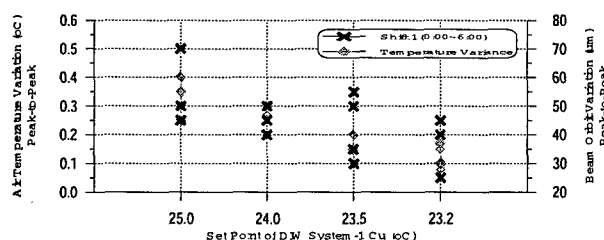


Figure 4: Relationship among the beam orbit variation, the air temperature, and the copper DIW temperature.

The second method was to improve the temperature shock in the air-conditioned area covered by two different AHUs. This kind of shock might be caused by an asynchronous control command or signal feedback. By following independent responses, sudden changes might occur between two separated AHUs. Instead of controlling the temperature of the storage ring with individual feedback, all the controllers in the ring follow the average temperature readout for feedback signal.

Table 3: Relationship between the DIW system-1 set points and the AHU duty factors.

DIW set point( $^{\circ}\text{C}$ )	25.0	24.0	23.5	23.2	23.0
Duty Factor	Saturated	~80%	~50%	~25%	Saturated

### 4 DISCUSSION AND CONCLUSION

Currently, the air temperature in the storage ring tunnel was held within  $\pm 0.1^{\circ}\text{C}$ , and the cooling water system could also hold the outlet temperature within  $\pm 0.2^{\circ}\text{C}$ . The source capacity of both air-handling units and the DIW system achieved a balance without saturation. After the improvements, the beam orbit variation was controlled to be less than  $\pm 15\mu\text{m}$ .

Though a modeling tool has been developed to correlate the beam position and the utility system, some ambiguities need to be resolved. Three major factors are to be considered for the improvement. The first factor is inhomogeneous air temperature in the storage ring tunnel. The second factor is the injection process between two shifts. The third, probably the most important factor, is the insufficient input parameters.

To solve these problems, some projects are underway. The injection energy is to be increased from 1.3GeV to 1.5GeV (so that no ramping process during injection) in order to overcome the transient phenomenon after injection. A series of experiments are being conducted to analyze the inhomogeneous environment so that the parameters for temperature control system can be better tuned. Some environmental factors, such as the mechanical vibration, the decreasing beam current, and the electricity perturbations, etc., will be added to make the model more complete. The improvement on modeling will help the optimization of the utility set points.

### 6 ACKNOWLEDGEMENT

The authors would like to thank to their colleagues in the utility group of TLS for their assistance. Thanks are also to the TLS operators for their engagement and help in all phases of the investigations.

### 7 REFERENCES

- [1]R. Keller, and H. Nishimura, "Orbit Stability of the ALS Storage Ring," Vancouver (1997).
- [2]J.R. Chen, H.M. Cheng, C.R. Chen, Z.D. Tsai, G.Y. Hsiun, and T.F. Lin, "The Correlation between Beam Orbit Stability and the Utilities at SRRC", Stockholm (1998).
- [3]S.M. Pandit, and S.M. Wu, Time Series and System Analysis with Applications, John Wiley (1983).
- [4]M. Sugeno, and T. Tanaka, "A Fuzzy Logic Based Approach to Qualitative Modeling", IEEE Trans. Fuzzy Systems, vol. 1, no. 1, pp.7-31, 1993.
- [5]W.H. Hsieh, and C.C. Cheng, "A New Approach to Complex Systems Modeling via Fuzzy Crystallization Algorithm and Its Application to Precision Insertion Operation", Kaohsiung (1995).

# INTEGRATED SOFTWARE ENVIRONMENT OF LONGITUDINAL FEEDBACK SYSTEM FOR TLS

C. H. Kuo\*, W. K. Lau, M. S. Yeh, K. H. Hu, K. T. Hsu

Synchrotron Radiation Research Center

No.1 R&D Road VI, Hsinchu Science-Based Industrial Park, Hsinchu 30077, Taiwan, R. O. C.

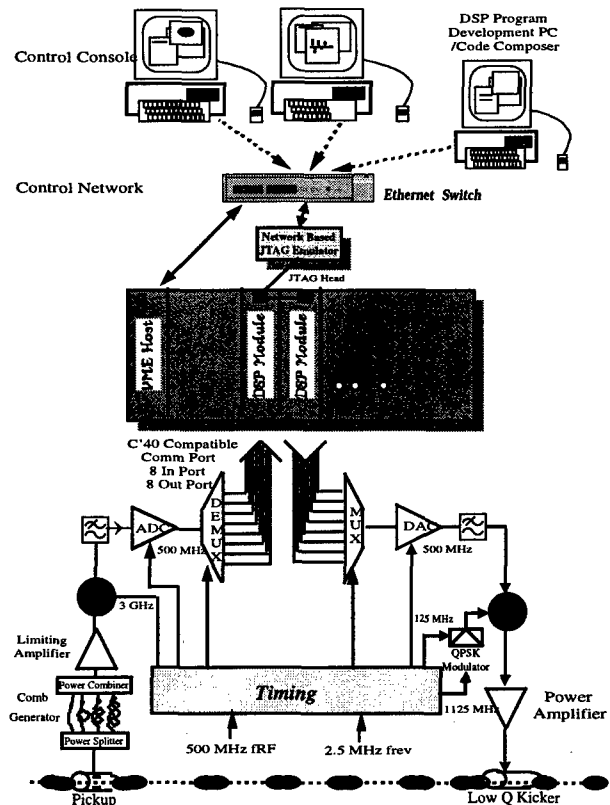
## Abstract

A DSP based longitudinal multi-bunch feedback system is being developed in SRRC. The software structure of feedback consist of a digital signal processors array to execute feedback algorithm and to provide raw data for beam diagnostic purposes. In order to develop, commission and operate this system efficiently, an integrated software environment has been developed. In such environment, we have major software components including, (1) feedback control algorithm on DSP, (2) DSP developing environment is on PC, (3) diagnostics toolkits is on PC and embedded computer, (4) operator interface on PC and workstation. The feedback control loop is a combined with digital filter and controller. DSP developing environment includes a code composer running on PC as well as a remote Ethernet based JTAG emulator to debug program. The system will equip diagnostic toolkits to acquire and analyse data. The associated hardware and software are commercial products that may help to reduce the system development time. The design features and performance of such will be reported

## 1 INTRODUCTION

A digital longitudinal damper is being developed in SRRC to stabilise the longitudinal coupled-bunch instabilities observed in the TLS storage ring [1]. It is a bunch by bunch feedback system designed for 200 bunches at 2 ns bunch interval. The longitudinal feedback ( LFB ) system in SRRC consists of five parts. The front-end RF electronic system, data input and output system, data processing and low-Q kicker. The Commercial Off-the-Shelf (COTS) extensive product solutions are used in DSP to reduce development times. Designs of the bunch phase detection circuit, the digital electronics and the 1125 MHz wide-band RF system for correction of phase errors have been tested with the beam. The core of the digital electronics is a DSP array that utility DSP modules performing parallel processing at a data throughput of 500 Mbytes/sec. This COTS products take off the expense and risk of in-house development, A prototype operating at one eighth of the data rate of the final system is under construct to evaluate the system design.

Figure 1: System diagram



## 2 LFB SYSTEM ARCHITECTURE

The data processing is divided to two major parts. One is data communication, other is digital signal processing and development system. The data transportation is by the C'40 compatible communication ports of digital processing unit. There are eight input ports and eight output ports in this system. The digital processing unit is consists of VME hosts, DSP modules and JTAG emulator.

### 2.1 LFB electronics

The longitudinal feedback ( LFB ) system in SRRC is separated to five parts. The ADC/DEMUX and DAC/MUX circuits with peak data transfer rate of 500 Mbytes/s. The ADC/DEMUX board digitises the discrete phase error signal for search bunches at 500 MHz and

\* Email: longmild@src.gov.tw

distributes to the processors that have slower clock rate for signal filtering. By using the DAC/MUX board, the filtered signals from the processors are then combined in correct sequence and converted into a single analog signal (the correction signal). The signal is amplified up to 200 Watts, and the RF power amplifier is used to drive the longitudinal kicker that in turn kicks individual bunches every 2 nanoseconds. The RF system consists of the 3 GHz prompt bunch phase detection unit, and the 1.0-1.25GHz broad band drive chain is used to drive kicker [2,3].

## 2.2 Data throughput considerations

The front-end electronics sample the data in 500 Mbytes/sec. Decimate factor is 18 in present system configuration. Another decimation factor is possible. Bunch oscillation is sampled at one turn, the following consecution 17 turns data is omitted. The communication ports, use in the LFB system as a unidirection communication interface to bunch oscillation detector and kicker system. A communication port sends or reads each of the stored words in its FIFO on a byte-to-byte basis. The separated input and output COMM port support 20 Mbytes per second. The transfer time is 1.4 us in each twenty-five bunch. Performance of communication port is satisfied with the requirement of LFB system.

## 2.2 DSP modules

There are two kinds of DSP modules. One is TMS320C4x, another is TMS320C6x. In prototype test, TMS320C4x are used. The TMS320C4x can deliver up to 30 MIPS/60 MFLOPS performance with a maximum I/O bandwidth of 384M bytes/s. However, data type in LFB system is byte oriented, floating point features in 'C40 is useless. High MIPS integer DSP is preferred for LFB application. The TMS320C6x is upgraded processor in LFB system. There is 1600 MIPS and 200 MHz (5 ns instruction cycle time) in C6x. Advanced Velocity VLIW architecture that enables sustained throughput of up to eight instructions in parallel. New development paradigm is based on software, not hardware. C6x DSPs use RISC-like instructions, which facilitate mapping to multiple functional units for additional scheduling flexibility. It is very efficient for LFB system on filtering operation, especially.

# 3 SOFTWARE ENVIRONMENT

## 3.1 DSP software development environment

This development system is an Ethernet based JTAG emulator. It is able to remote control by local computer

with window user interface in windows95/NT operation system. It supports to multi-processor download and develops DSP program in the same time. The code composer is a system development tool that supports an integrated development environment (IDE) for C4x and C6x. This environment allows DSP code designer to edit, build, manage products, debug and profile from a single application. In addition, the IDE lets user compile in the background as well as analyze signals graphically (including Eye Diagnostic, Constellation Diagnostic, FFT Waterfall, Image display etc.), perform file I/O, debug multiprocessors, and customise a C-interpretative scripting language in the IDE.

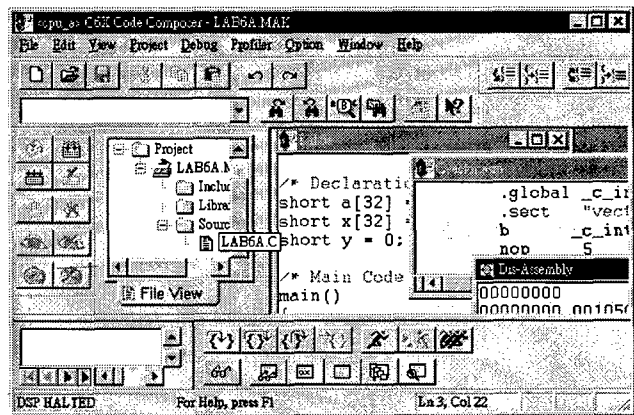


Figure 2: Development tool.

## 3.2 Feedback software

All tasks of feedback software are optimal for communication and filtering. This task can't be swapped when processor is accessing from COMM port memory. The phase shift, and band-pass filter tasks are embedded in DSP module. In the meantime, it receive filter control and feedback status control from host. The DSP modules include of multiprocessors to process input data, to kick system.

## 3.3 Host

The tasks of host are embedded in VME controller, are connected with console computer to support to feedback remote control, filter coefficient update, status reports and data analysis. The relationship tasks are shown in figure 3. The setting service handles filter and status control. General reading handles raw data store.

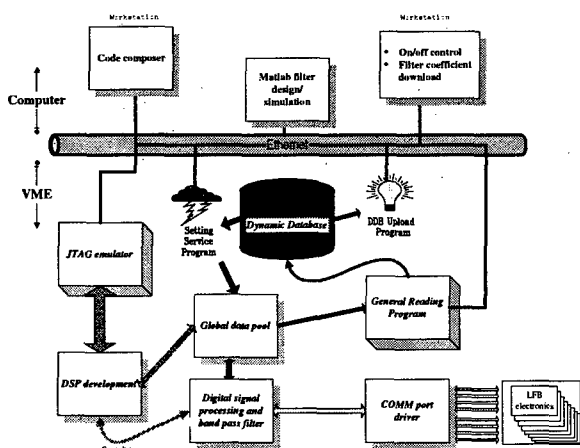


Figure 3: Relationship between software components

### 3.4 System management

There are many tasks in host that is necessary to be managed, for diagnostic request. These tasks include of download filter coefficient, on/off control, and save raw data. For example, feedback is necessary to be stopped when host is updating filter coefficient. and then re-turn on feedback. Status control task has lower priority than filter control.

### 3.5 Console software

There are several tools in console except for development tool, such as, filter simulation and raw data on line display. An integrated MATLAB simulation tool is applied in console. To support to various conditions in commission, adjust phase and centre frequency of band-pass filter on online that is efficient. The 200 samples will equally distribute via eight C'40 COMM ports to DSP modules. Every COMM port handles twenty-five bunches data. Current design use synchronous data transfer scheme, i. e. All data is collected, and then is blocked filtering [3]. The cycle time of output via out component is 7.2 us, 25 bunches data is parted to 28 bytes, and transfer to DSP module via COMM port. The data transfer time is about 2 us. Peak data throughput is about 10 Mbytes/sec per COMM port.

## 5 CURRENT STATUS AND FUTURE WORKS

The preliminary test has suppressed longitudinal oscillation successfully. The analog input of LFB electronics has been connected with COMM port of processors. This testing is a single bunch longitudinal oscillation that is suppressed by the feedback loop and RF cavity [5]. The oscillation frequency is destroyed when feedback is turned on. The band-pass filter will be improved to infinite impulse response filter. There is narrower bandwidth than FIR filter in the same tap. The parts of LFB electronics are still in implementation stage.

The analog input electronics have been finished testing. The processors are successfully connected with this board. The analog output electronics is designing now. The data transformation is by JTAG port now. The process will be paused when data is sending with JTAG port. The software for the control in the longitudinal feedback system has been developed with COTS product.

In the future, Feedback software will be developed continuously software and to aid commission of the system.

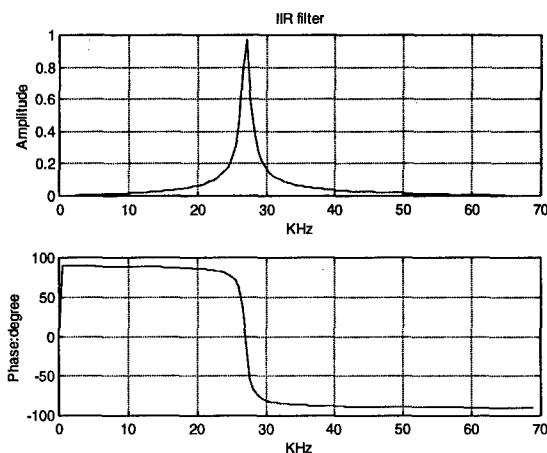


Figure 4: IIR filter simulation.

## 6 REFERENCE

- [1] W. K. Lau et al: Study of Longitudinal Coupled-Bunch Instabilities in the SRRC Storage Ring, Proceedings of 1997 IEEE Particle Accelerator Conference, Vancouver, 1997.
- [2] W. K. Lau, S. J. Lin, M. S. Yeh, L. H. Chang, T. T. Yang, K. T. Hsu, M. H. Wang, C. C. Kuo: Development Of A Digital Longitudinal Damper For The TLS Storage Ring, Proceedings of 1997 IEEE Particle Accelerator Conference, Vancouver, 1997.
- [3] M. S. Yeh, K. T. Hsu, C. H. Kuo, W. K. Lau, J. F. Lee, S. J. Lin: High Speed Digital Processing Electronics for the TLS Longitudinal Feedback System in this proceeding.
- [4] J. G. Proakis and D. G. Manolakis, Introduction To Digital Signal Processing, Macillan 1988.
- [5] W. K. Lau, L. H. Chang, K. T. Hsu, C. H. Kuo, J. A. Li, M. S. J. Lin, T. T. Yang, M. S. Yeh: Progress of the TLS Longitudinal Feedback System and Associated Beam Longitudinal-Dynamics Studies, in this proceeding.

# LOCAL FEEDBACK APPLICATION IN TLS

C. H. Kuo<sup>\*</sup>, K. H. Hu, K. T. Hsu

Synchrotron Radiation Research Center

No.1 R&D Road VI, Hsinchu Science-Based Industrial Park, Hsinchu 30077, Taiwan, R. O. C.

## Abstract

The various orbit perturbations are enhanced after many insertion devices are installed in the storage ring of TLS. These sources will interfere to system performance. The local orbit feedback system is used to suppress miscellaneous local orbit perturbation. The feedback system consists of sensor and feedback control loop. The sensors are electron beam position monitor (BPM) and photon monitor of elliptical polarization undulator (EPU). The feedback control loop architecture share same hardware with global orbit feedback. The VME-based crates interconnected with high performance daisy-chained global reflective memory networks are used to share position data with DSP. The result is shown in this report.

## 1 INTRODUCTION

Taiwan Light Source (TLS) in Synchrotron Radiation Research Center (SRRC) is one of the third-generation synchrotron light sources, which are characterised by low emittance of the charged particle beams and high brightness of photon beams radiated from insertion devices. These insertion devices are useful for the brightness and spectrum of beam, but are also make some influences for the electron orbit and the lattice of storage ring. Any vibrations and orbit drift that lead to distortions in the closed orbit will result in a larger effective emittance. Together with the brightness reduction, unwanted beam motion that causes the incident light position and angle to vary can degrade the experimental advantages of synchrotron. Cancel these negative local bump are main purpose for the local orbit feedback of development [1]

## 2 SYSTEM STRUCTURE

### 2.1 Hardware structure

The hardware configuration of local feedback (LOFB) system is shown in figure 1. The photon BPM reading systems are combined in photon BPM node. This node includes a PowerPC 604e/200 MHz CPU board, reflective memory with PMC, VME bus and A/D interface cards. The PBPM signals are connected to current amplifier

inputs and then outputs are connected to the front-end of PBPM node interface card. The PMC or VME bus is between reflective memory and CPU board that support wide bandwidth transfer rate. The configuration of feedback system is presently distributed in two VME crates. The orbit readings are by multi-channels 16 bit high precision A/D cards. Sampling rate of system is 1 KHz now. The inputs and outputs interfaces are all 16 bit high precision cards to support exactly corrector control [2].

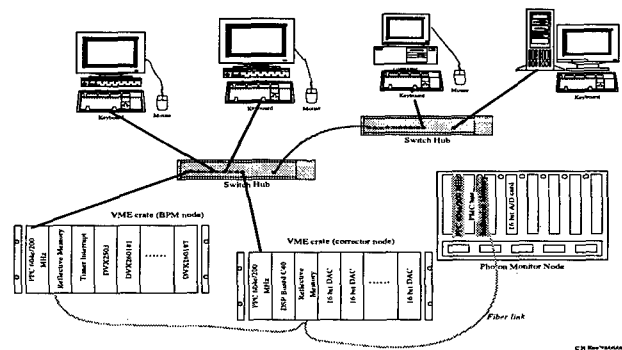


Figure 1: Hardware diagram for orbit feedback.

There are two orbit feedback systems in this control loop. One is local feedback, and other is global feedback. Integrating these two feedback loops for better co-operation, bandwidth of 10 - 100 Hz is necessary to suppress vibration and power supply ripple related beam motion, etc. These feedback systems are integrated with the existed control system. BPMs data and correctors readback are updated into control system dynamic database in the period of 100 msec. Local feedback system is bounded on I/O as well as computation. It is important to arrange the real time task and to arbitrate computer bus properly in order to optimise system performance.

### 2.2 Software structure

A local feedback system has been developed to suppress orbit disturbances caused by low-frequency drift and insertion devices. First, a local bump of four magnets ratio is measured by taking beam position monitor (BPM)

<sup>\*</sup> Email: longmild@srcc.gov.tw



reading in outside of bump when the corrector are individually perturbed. The feedback controller is based on PID algorithm [3]. Infinite impulse response digital filtering (IIR) [4] techniques were used to removed noise of electron beam position reading, to compensate eddy current effect of vacuum chamber, and to increase bandwidth of local feedback loop.

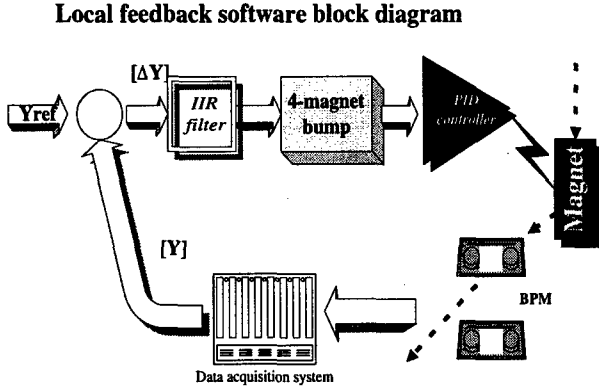


Figure 2: Software diagram for orbit feedback

### 3 LOCAL BUMP

#### 3.1 Four-magnets local bump

The four-magnets are combined by two independent three-magnet bumps a and b. Let  $\theta_1, \theta_2, \theta_3$ , and  $\theta_4$  be the kick strength on four corrector, then we have

$$\theta = \begin{bmatrix} \theta_1 \\ \theta_2 \\ \theta_3 \\ \theta_4 \end{bmatrix} = \begin{bmatrix} k_{a1} & 0 \\ k_{a2} & k_{b2} \\ k_{a3} & k_{b3} \\ 0 & k_{b4} \end{bmatrix} \cdot \begin{bmatrix} \theta_a \\ \theta_b \end{bmatrix} = K \cdot \begin{bmatrix} \theta_a \\ \theta_b \end{bmatrix} \quad (1)$$

$$\begin{bmatrix} \theta_a \\ \theta_b \end{bmatrix} = R^{-1} \cdot \begin{bmatrix} y_a \\ y_b \end{bmatrix} \quad (2)$$

where  $R$  is local response matrix. The local response matrix is a linear response matrix that is measured by taking photon monitor or beam position monitor (BPM) reading when the magnet are kicked one by one.  $K$  is bump ratio. The local bump coefficient is consisted of inverse local response and bump ratio. That is a four by two matrix.

#### 3.2 DECOUPLING

For independently control two four-magnets bump, decoupling procedure is necessary. To avoid two-detectors inference each other in feedback loop. The coefficient of bump a and bump b is transferred to

$$k'_a = k_a - \frac{R_{12}}{R_{22}} \cdot k_b \quad (3)$$

$$k'_b = k_b - \frac{R_{21}}{R_{11}} \cdot k_a \quad (4)$$

where  $R$  is response matrix,  $k$  is bump coefficient.

An idea de-coupled bump only affect one position detector. There is a little difference between photon monitor and BPM for detector of feedback loop inside bump. If the bump is decoupled by BPM, equation 3 and 4 is satisfied to this transformation. If the bump is decoupled by photon monitor, equation 3 and 4 must be modified to angular bump. So, original equation is transferred to

$$k''_a = k'_a + c_a k_b \quad (5)$$

$$k''_b = k'_b + c_b k_a \quad (6)$$

where  $c$  are constant.

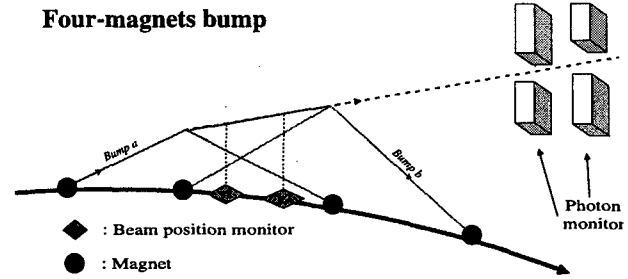


Figure 3: Four-magnets bump.

### 4 APPLICATION

In this report, local feedback is applied in EPU section. There are perturbation sources in other location of ring, but the photon monitor is stable in beam-line. The BPM of outside bump is shown in figure 4.1. There are two detectors in the inside bump. One is R1BPM9Y that is BPM, other is BL05PBPM1V that is photon monitor. Their behaviours are shown in figure 4.2 and 4.3. Two-photon monitor's status in feedback loop is shown in figure 5.1 and 5.2 when beam is unstable. The unstable beam is shown in figure 5.3.

### 5 CONCLUSION

In the future, the local feedback system will be merged in beam-line with electron BPMs and photon monitors. An extended feedback bandwidth in local feedback system is necessary to suppress various perturbations. The BPM and photon monitors readings are contaminated by ripple noise. Advance signal processing and filtering technique is applied in LFB that will help to the performance of system.

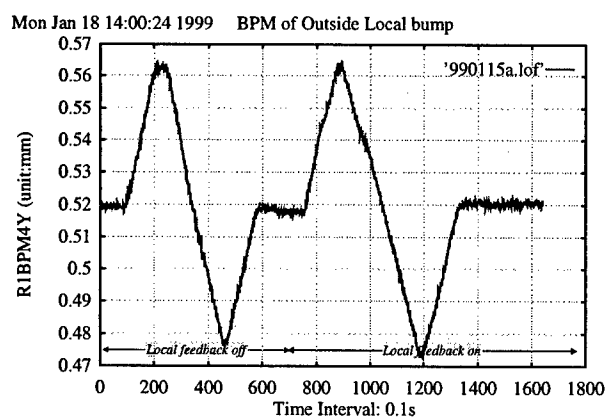


Figure 4.1: BPM out of local bump.

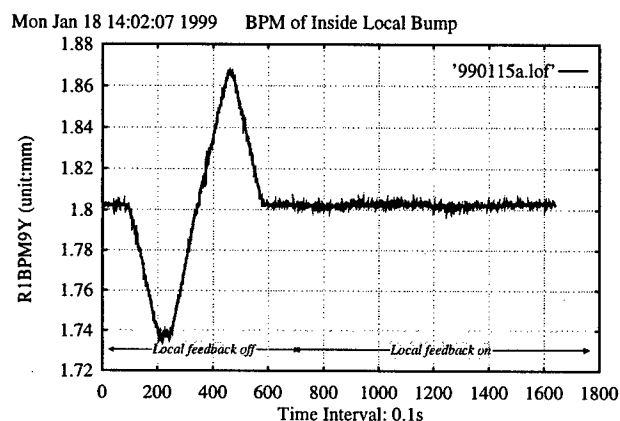


Figure 4.2: BPM in feedback loop.

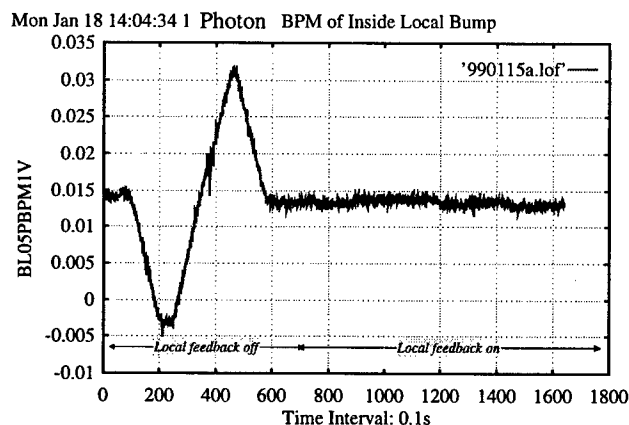


Figure 4.3: Photon monitor in feedback loop.

## 6 REFERENCES

- [1] E. Plouviez, F. Uberto, A Fast Local Feedback System to Correct The Beam Position Deviation in The ESRF Storage Ring, Proceedings of 1996 IEEE Particle Accelerator Conference, Barcelona, 1996.
- [2] C. H. Kuo, J. R. Chen, G. Y. Hsiung, K. T. Hsu, T. F. Lin: Development of Local Orbit Feedback for Taiwan Light Source, Proceedings of 1998 IEEE Particle Accelerator Conference, Stockholm, 1998
- [3] B. C. Kuo: Automatic Control Systems, Prentice Hall, p.691, 1995
- [4] J. G. Proakis and D. G. Manolakis, Introduction to Digital Signal Processing, Macmillan 1988.

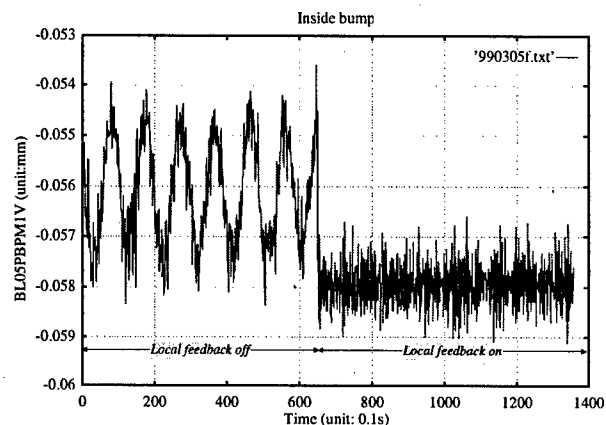


Figure 5.1: Photon Monitor in feedback loop.

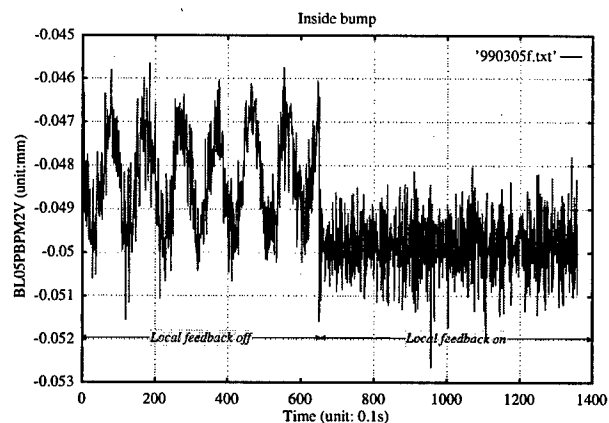


Figure 5.2: Photon Monitor in feedback loop.

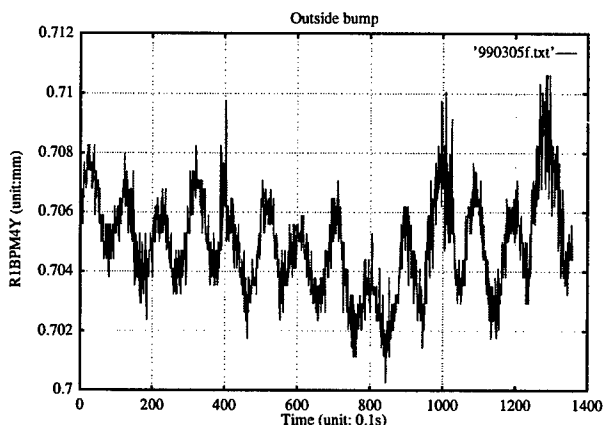


Figure 5.3: BPM out of feedback loop.

## PROGRESS OF THE LONGITUDINAL FEEDBACK SYSTEM AND ASSOCIATED BEAM OBSERVATIONS IN TLS

W. K. Lau, L. H. Chang, P. J. Chou, K. T. Hsu, C. H. Kuo, M. H. Wang, T. T. Yang, M. S. Yeh,  
SRRC, Hsinchu, Taiwan

### Abstract

A digital feedback control system against longitudinal coupled-bunch instability is being developed for the Taiwan Light Source (TLS). This system is designed to stabilize bunch-phase oscillation of each of the 200 electron bunches in the TLS storage ring, and it operates at a bunch crossing frequency of 500 MHz. Two innovative aspects of this system are (1) the special design of the digital signal processing (DSP) electronics, which run at a peak data rate of 500 Mbytes per second, and (2) the compact broadband longitudinal kicker for bunch-phase correction. Recent progress of this work and preliminary results of associated observations of beam longitudinal-dynamics will also be reported.

### 1 INTRODUCTION

Longitudinal coupled-bunch instability (LCBI) that occurred in the TLS storage ring electron beam is believed to be driven by cavity high order modes (HOMs). Since LCBI is the main obstacle in preserving the natural emittance at higher beam current. They broaden the spectra of undulators and which cause slow fluctuations of the photon beam intensity. A digital feedback control system is designed to stabilize dipole-mode LCBI in a bunch-by-bunch manner. Design of such system has been discussed elsewhere [1]. However, specific constraints have to be considered when such system is designed to operate in the TLS storage ring. First, maximum longitudinal dimension is limited to 230 mm (including the transitions from round to elliptical beam pipes) which is relatively short in comparison with other kicker structure design. Second, the expectations from the users require that the system have to be operational within a short period. In order to reduce system development time, commercially available embedded DSP modules were chosen as the core of signal processing electronics - a DSP array performs parallel digital signal filtering. A unique signal conversion plus data-transfer unit was developed as the interface between the fast changing analog signals and the DSP array (in which DSP chips run at a slower processing rate). A compact longitudinal kicker with 250 MHz bandwidth (FWHM) operates at a center frequency of 1125 MHz to provide energy kicks to the bunches. This structure is equipped with magnetic loops which permit rf power to be coupled out from the structure (through high power, coaxial, rf feedthroughs) in order to "de-Q" the acceleration mode for wide-bandwidth and to damp high-order modes. Also, rf power

can be coupled into the kicker through symmetrically placed ports for kicker voltage enhancement. This paper reports the progress of the development of such system. During the construction stage, longitudinal dynamics has been observed by using part of the system. For examples, the bunch phase detector is used to measure synchrotron tunes via beam transfer function measurements in the single bunch mode. A preliminary observation of bunch phase oscillations induced by zero-LCBI mode.

### 2 SUMMARY OF RECENT PROGRESS

#### 2.1 Installation of the Longitudinal Kicker

The longitudinal kicker described above has recently been installed into the storage ring (Figure 1). It has been used to kick the beam with voltage modulation on the reference signal that drive the 200 watts power amplifier. The power of synchrotron sideband has increased by more than 10 dB when full power was applied to the kicker. Beam signal picked-up from one of the magnetic loop of the kicker is used to estimate the kicker shunt impedance and bandwidth. At very low beam current, the observed signal power at 1 GHz is measured. The deduced shunt impedance is quite close to its predicted value that is about 100 Ohms. The strength of the picked-up beam signal is maximized within a bandwidth of about 250 MHz as expected.

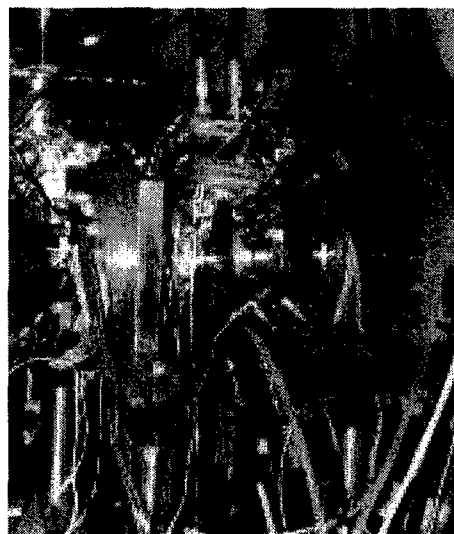


Figure 1: The longitudinal kicker installed in the TLS storage ring

## 2.2 The Bunch Phase Detector and the Wide-band RF System

The bunch phase detector and the 1.0-1.25 GHz rf system has been built and tested. The detector has been used for beam observation (see Section 3), physically meaningful results has been obtained.

The correction signal from the DAC is used to modulate the 1 GHz carrier signal (locked to the ring master clock) that drive the power amplifier. A double side-band carrier suppressed (DSB-CS) modulator is made for this purpose during initial beam test. A QPSK modulated 1.125 GHz locked source is being built to replace the 1 GHz carrier when it is needed. Now, the system is equipped with a 200 Watts power amplifier with instantaneous bandwidth from 1.0-2.0 GHz.

## 2.3 Signal Processing Electronics

Signal processing electronics is perhaps the most time consuming part in developing the feedback system. Since the 60 MHz C44 DSP chips is chosen as the signal processing element, digitized signal is transfer to the DSP modules via communication ports (modules with even faster DSP chips are now under evaluation). The ADC/DEMUX unit has been built to digitize the analog bunch phase signal into 8 bits data and are distributed to the DSP chips [2]. The DAC/MUX unit is equipped with hold buffer circuitry that holds the digital filter output for eighteen turns. Simulation shows that the system gain is significantly increased with this hold buffer capability [3]. Full speed system can only be possible until the DAC/MUX unit is completed.

## 2.4 Feedback with Main Cavity as Kicker

Single bunch experiment can be performed to test subsystem and parts online in this intermediate stage.

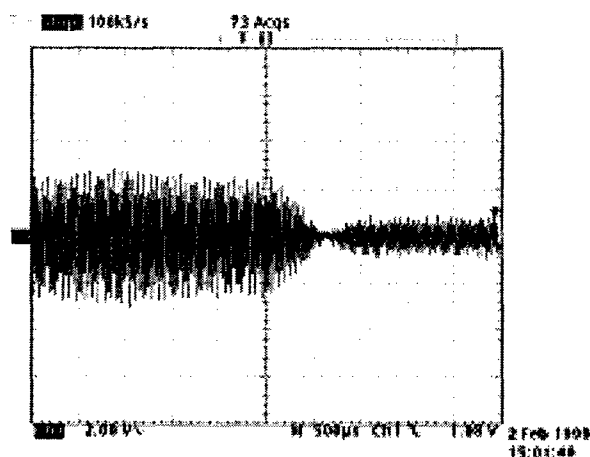


Figure 2: Result of feedback with main cavity as kicker. Showing phase oscillation of a bunch is damped

Figure 2 shows the amplitude of the phase oscillation of a bunch is damped to a small value within a few synchrotron oscillation cycles.

The TLS rf system consists of two independent rf stations. We used one of the cavity as a kicker to drive bunch phase oscillations and with the other one in the feedback loop to damp the oscillation (the compact longitudinal kicker is not available during the experiment). In this experiment, a 4-tap FIR filter is used. However, further optimization in controller design is required. We are now working on single bunch experiment with the installed longitudinal kicker.

## 3 PRELIMINARY OBSERVATIONS OF LONGITUDINAL BEAM DYNAMICS

Since the bunch phase detector, ADC/DEMUX unit and DSP modules are partially installed, some observations on beam longitudinal dynamics are now become possible.

### 3.1 Tune Measurement

Longitudinal beam transfer function can be measured by injecting phase modulation to the main cavity voltage and bunch phase oscillation is detected by the system bunch phase detector. From this measurement, synchrotron tune as a function of gap voltage can be found. It shows good agreement between theoretical and measured data.

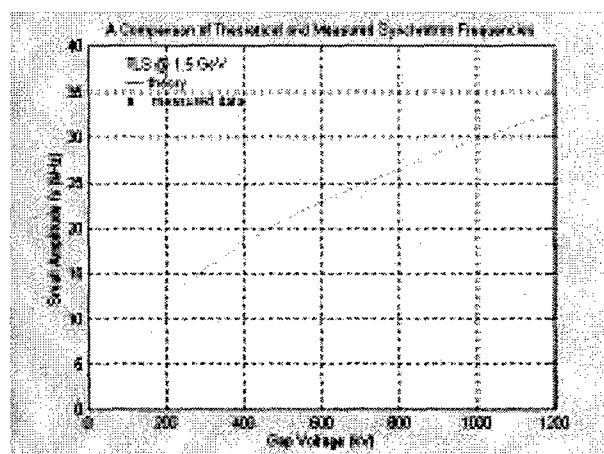


Figure 3: Measured synchrotron tune versus gap voltage in TLS

### 3.2 Observation of a Zero-mode LCBI

Zero-mode LCBI is excited in purpose by de-tuning the main cavities, phase error signals of each bunches are detected and digitized and distributed to the DSP modules by the ADC/DEMUX unit. Data representing 25 equally spaced bunches are collected by one of the DSP.

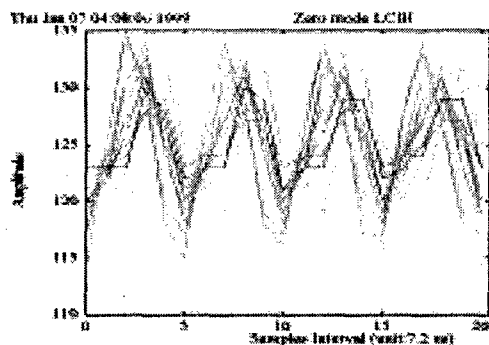


Figure 4: The measured coherent phase oscillation of the bunches is a characteristic of zero-mode LCBI

#### 4 DISCUSSIONS

Recent progress of developing a digital longitudinal feedback is reported. The system is partially installed. Beam observation has been made to verify subsystem performance. Since we have a major modification that a hold buffer circuit is included into the DAC/MUX unit, the schedule may be delayed for a few of months. The full speed system test will be performed in near future.

#### 5 REFERENCES

- [1] W. K. Lau et al., "Development of a Digital Longitudinal Damper for the TLS Storage Ring" Proceedings of the Particle Accelerator Conference 1997.
- [2] M. S. Yeh et al., "High Speed Digital Signal Processing Electronics for the TLS Longitudinal Feedback System" these proceedings.
- [3] W. K. Lau et al., "Analysis of the TLS Longitudinal Feedback System" these proceedings.

# HIGH SPEED DIGITAL SIGNAL PROCESSING ELECTRONICS FOR THE TLS LONGITUDINAL FEEDBACK SYSTEM

M. S. Yeh, K. T. Hsu, C. H. Kuo, W. K. Lau, J. F. Lee, H. J. Tsai, SRRC, Hsinchu, Taiwan

## Abstract

A high-speed digital signal processing system is being built for feedback control of bunch phase in the TLS storage ring. It consists of (1) an analog-to-digital converter plus demultiplexer (ADC/DEMUX) unit (2) a digital filters (DIFI) array and (3) a digital-to-analog converter plus multiplexer (DAC/MUX) unit. The ADC/DEMUX unit has a fast ADC that digitizes the discrete signal of bunch phases. The data are then down-sampled and distributed to the slower DSP chips in the DIFI array via communication ports. The DIFI array performs digital filtering such that phase error of each bunch is extracted. In the DAC/MUX, processed data from DIFI array are collected and organized in a proper sequence (there is a buffer that hold the output data for number of turns if higher loop gain is required). This stream of data is then converted back to analog signal for bunch phase correction. Design and construction issues of this system are reported.

## 1 INTRODUCTION

A bunch-by-bunch longitudinal feedback system based on parallel digital signal processing techniques is being built for TLS storage ring. One of the technological challenges is to implement a high-speed digital signal processing system at a peak data processing rate of 500 MB/s. It performs simple but fast digital filtering for extraction of phase error information from each of the 200 bunches. With these data, an adequate correction signal is constructed for feedback. This system consists of three parts. They are the ADC/DEMUX unit, the DIFI array and the DAC/MUX unit. The ADC/DEMUX unit has a 500 MHz 8-bits ADC that digitizes the discrete signal of bunch phases. The data are then down-sampled by a factor of 18 and distributed via communication ports to 60 MHz C44 processors that run at a lower speed. The DIFI array performs simple but fast digital filtering (e.g.  $n$ -taps FIR filters) such that phase errors of each bunch are extracted. In the DAC/MUX, processed data from DIFI array are collected and organized at right sequence. This stream of data is then converted back to analog signal by a 12 bits fast DAC for bunch phase correction. Section 2 describes the ADC/DEMUX unit that has been built and tested successfully. Section 4 describes the evaluation test of using C44 as processing elements in the DIFI array. It has been discussed that whether one should include hold buffers in the DAC/MUX unit. Section 3 describes a modified version of DAC/MUX having hold-buffers for loop gain enhancement. A summary of recent

progress and possibility of using processing elements other than DSP chips are discussed in the last section.

## 2 THE ADC/DEMUX UNIT

This ADC/DEMUX unit digitizes, down-samples and distributes the discrete signal of bunch phases. Recently, this unit has already been fabricated and tested (Figure 1). Some preliminary beam observations have been performed with it [1].

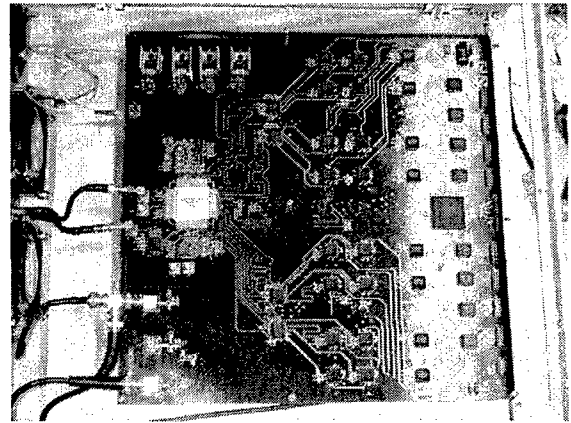


Figure 1: The ADC/DEMUX unit has been built and tested successfully

### 2.1 Fast ADC

The ADC we employed is the 500 Msp/s 8-bits MAX101A produced by MAXIM. It has two 250 MHz ECL signal outputs that are 180° out of phase.

### 2.2 Demultiplexer

Each channel of the 250 MHz ECL output from MAX101A is then demultiplexed into four channels by using the MC100E445 serial to parallel converter. To each channel, data rate is therefore slowed down by a factor of four (i.e. 62.5 Mbytes/s). To keep the demultiplexed ECL signal from each channels in synchronous with each other. Propagation delays have to be carefully controlled during circuit board layout. Data in ECL logic are converted into TTL logic before they are stored in first-in-first (FIFO) memories.

### 2.3 Down-Sampling and Interface Control

Down sampling and data transfer from FIFO memories to the C44 processors via communication ports are control by a single CPLD chip which is programmed in house. It takes the advantage of in-system-programmability that

control logic may change from time to time during prototyping. For example, down-sampling factor can easily be changed without changing the layout of the circuit. Note that the down sampling factor was set at 18.

## 2.4 Circuit Board Layout and Fabrications

The work of PCB layout is complicated by the mixed signals running at high speed require impedance control, skew control and avoid cross talks between signals. There are the four signal layers and eight power/ground layers so that interference between layers can be avoided.

## 3 THE DAC/MUX UNIT

The multiplexer in the DAC/MUX unit receives data from the C44 processors (also via communication ports) that represent filtered phase errors and reorganize in a proper sequence. And they are converted back to analog signal by a fast DAC and send to the modulator of the 1.0-1.25 GHz rf system. Hold buffers are also implemented to allow repeated kicks for higher loop gain. Figure 2 shows a functional block diagram of this unit. PCB layout of this unit is in progress.

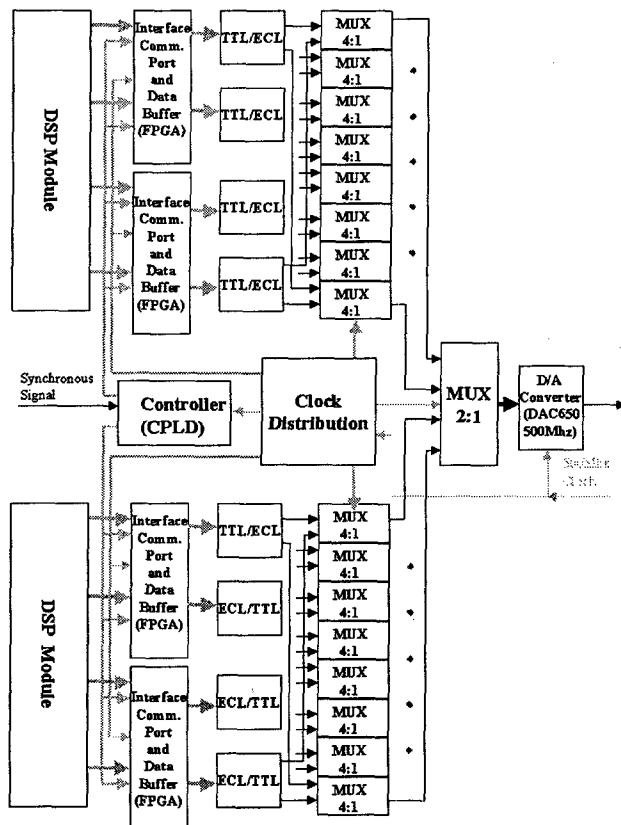


Figure 2: Functional Block Diagram of the DAC/MUX Unit

## 3.1 Fast DAC

The fast 12 bits DAC we used is the Burr-Brown DAC650 running at 500 MHz (only 8 bits are used). A prototype PCB was made to test the performance of this chip. The result is quite satisfactory.

## 3.2 Multiplexer

Multiplexer is just the reverse of the demultiplexer in the ADC/DEMUX unit.

## 3.3 Hold Buffer and Interface Control

According to the results from feedback loop simulation [2]. It is desirable to have data buffers that allow repeated kicks for many turns. Data buffer have been implemented by field programmable gate array (FPGA). Again, interface between C44 processors and data buffer in multiplexer is controlled by CPLD.

## 4 THE DIFI ARRAY

The DIFI array is a system of VME DSP modules and each module has a number of DSP chips. The number of chips modules and number of chips per modules depend on the type of processors and commercial DSP modules we choose as long as the communication ports are provided for data transfer. The possible candidates of processors are chips of the TI C4X and C6X series. We reported here the evaluation test we have done with the C44 processors. The C6201 processor is another possibility and is under studied. The software structure of the system consist of a algorithm for DIFI and to provide raw data for beam diagnostic purposes and is reported elsewhere [3].

### 4.1 Evaluation Test with C44 Processor

Using C44 processors in the DIFI array is being tested. Data transfer between individual C44 and external circuits via communication ports are satisfactory. The processing speed per modules depends on both the hardware and software architecture of the module. Global on-board memory is essential.

### 4.2 Possibility of using the C6201Processor

Rapid development in DSP technology provides a wide range in processor selection. Modules with high speed C6201 fixed point processor are now commercially available. The use of these processors in the system allows a sophisticated controller design for better feedback loop performance. Possibility of the option is under consideration.

## 5 DISCUSSION

The unique design of the ADC/DEMUX and DAC/MUX units provides flexibility in choosing commercially available DSP modules provided that the communication ports exist. This capability is ideal for system upgrade to a more sophisticated controller design. The ADC/DEMUX unit has been built and tested. DAC/MUX unit is being built and will be tested in the near future. Possibility of using FPGA as processing elements is in the list of further studies.

## 6 REFERENCES

- [1] W. K. Lau et al, "Progress of the Longitudinal Feedback System and Associated Beam Observations in TLS", these proceedings.
- [2] W. K. Lau et al., "Analysis of the TLS Longitudinal Feedback System" these proceedings
- [3] C. H. Kuo et al., " Integrated Software Environment of Longitudinal Feedback System for TLS" these proceedings.



# ANALYSIS OF THE TLS LONGITUDINAL FEEDBACK SYSTEM

W. K. Lau, C. H. Kuo, SRRC, Hsinchu, Taiwan

## Abstract

Effectiveness of the TLS longitudinal feedback system to damp bunch phase oscillations has been studied under various operation conditions. Maximum kick voltage that is available for bunch phase correction is limited by power amplifier saturation. Operation of the feedback system in the linear and nonlinear regions of power amplifier have been simulated. In case of power amplifier saturation, the damping time is proportional to the initial oscillation amplitude. Oscillation amplitude decrease linearly before the power amplifier reaches its linear regime. The effects of hold buffer in the DAC/MUX unit and time delay of the feedback loop will also be discussed.

## 1 INTRODUCTION

The longitudinal feedback system is designed [1,2] to control beam dipole-mode longitudinal coupled-bunch instability (LCBI) in the TLS storage ring. It is believed that LCBI is driven by higher order modes of the main rf cavities. Since the growth rates of LCBI depend on cavity temperatures, tuner positions (in TLS, each cavity has an extra tuner for shifting higher order modes [3]) and beam filling patterns etc. It is not an easy task to predict exactly behavior of LCBI and put it into a realistic simulation model. In growth rate calculations, a worst case scenario is usually used. The methodology we employed to study the behavior and limitations of the feedback system operation is to treat such system ideally as independent feedback loops for each of the bunches, damping time can be found by applying an impulse excitation to the bunch. The feedback loop is considered to be effective against LCBI instability if the total damping time is shorter than the growth time of that instability. However, as mentioned above, the exact growth times of LCBI are difficult to predict. Therefore, the goal of this work is to design a digital controller which maximize damping rate. Further, the maximum available voltage to kick the beam is limited by amplifier power and kicker impedance. The feedback system is very likely to be operated in a nonlinear regime that the rf power amplifier is saturated. It is important to know how the system behaves in these circumstances. It has been discussed whether we should include a hold buffer circuitry into the DAC/MUX unit [4] to get enough loop gain. On the other hand, it is obvious that the effect of signal delay is not negligible. We reported here the works we have done in simulating the cases as described above. Section 2 describes the simulation model we are using. Section 3 summarized the results in various circumstances. Finally, the expected

operational performance of the system is discussed in Section 4.

## 2 SYSTEM MODEL

Since the TLS longitudinal feedback is a bunch-by-bunch system, we can treat it as a system that consists of independent bunch phase control loops. The following figure depicted the system model we used in computer simulation.

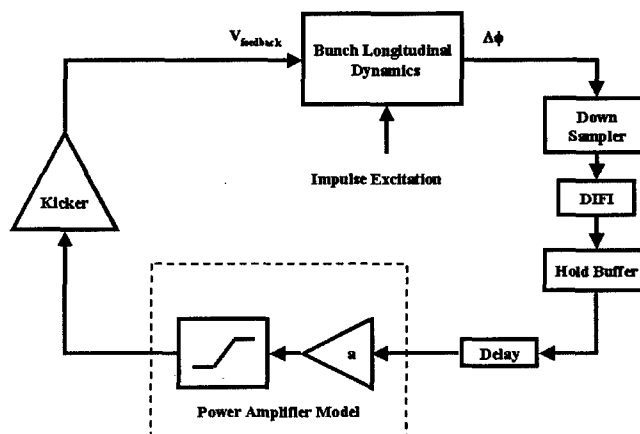


Figure 1: Longitudinal Feedback System Model used in Computer Simulation

The "bunch longitudinal dynamics" block is a tracking routine that calculates the bunch phase relative to the reference phase with feedback voltage and impulse voltage energy kick as input. In the case of TLS, input to the digital filter (DIFI) is down-sampled by 18. In this study, we tried a 5-taps FIR filter that provides a pass band around synchrotron frequency and adequate phase shift by choosing the coefficients. The filtered signal is then hold for 18 turns by the hold buffer circuit. The time needed for digital signal processing and signal synchronization require that the output from hold buffer is delayed by 18 (or its multiples) turns. However, a delay of 18 turns is used throughout the study except in the case where the effect of time delay is being studied. In order to simulate the power amplifier, the input signal is amplified by a constant gain of "a" and clipped off at a certain limit. The output power of the amplifier is converted into E-field via the longitudinal kicker. Obviously, we neglected things that may be very important such as quantization error sampled signal due to the 8-bits fast analog-to-digital converter, response of kicker and mixer noise etc. Relevant parameters of the TLS longitudinal feedback system at 1.5 GeV are recalled in Table 1 for reference.

Table 1: Relevant Parameters of the TLS Longitudinal Feedback System

Beam energy	1.5 GeV
RF frequency	500 MHz
Revolution frequency	2.5 MHz
Maximum bunch number	200
Synchrotron tune	0.0106
Radiation damping time	4.9 msec
Maximum kicker voltage	200 volts
Down sampling factor	18
Number of FIR filter taps	5

### 3 RESULTS OF COMPUTER SIMULATIONS

The computer code was written in MATLAB language and was run on a WIN98 platform. The simulation results are summarized as follows:

#### 3.1 Beam Response without Feedback

Without feedback, the response of a bunch is calculated at 1.5 GeV. The initial energy offset is arbitrarily chosen a small but nonzero value of  $1e-6$  and the bunch phase was set at synchronous phase. An impulse kick was applied at the 2000<sup>th</sup> turn. The response of the bunch to impulse kick obtained from the calculation in the first 18000 turns is shown in Figure 2. The damping time is 4.90 msec or 12,250 turns. This is the natural damping time for longitudinal motion at 1.5 GeV with the lattice that is used for user operation [5].

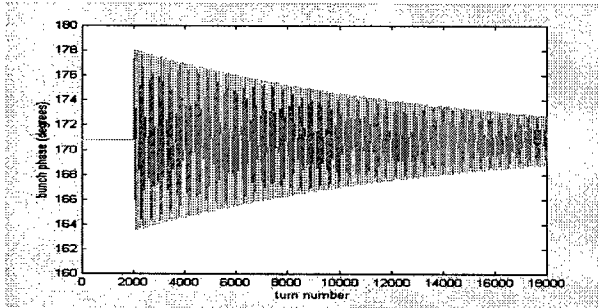


Figure 2: Damping of bunch phase oscillation due to synchrotron radiation loss

#### 3.2 Feedback in the Linear Regime

By limiting the loop gain "a" within a certain value, the power amplifier is not saturated. With the same initial condition as in the case discussed above, bunch phase oscillation is damped at a faster rate than the case without feedback as expected. Figure 3 shows the response of the beam with feedback system operated in linear regime at a gain of 8. Coefficients of the FIR filter and the initial phase of the feedback voltage are optimized for fastest damping. The total damping time is 3.34 msec or 8,357 turns.

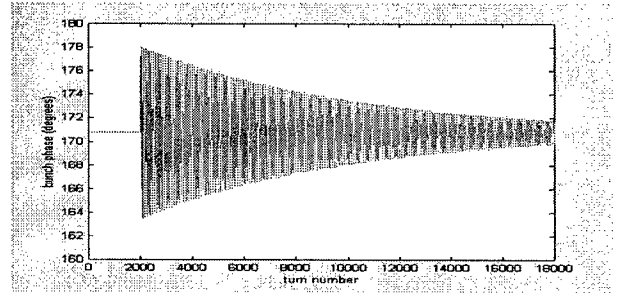


Figure 3: Damping of bunch phase oscillation with feedback system operated in the linear regime

In this specific case, the feedback loop is not strong enough for significant damping. Note also that damping time is independent of the strength of the impulse kick or initial amplitude in the linear region at a given loop gain.

#### 3.3 Power Amplifier Saturation

As long as the feedback loop is kept stable, damping time can be further reduced by cranking up the loop gain. However, increase of gain is limited by power amplifier saturation. In our case, the maximum kick voltage is limited to 200 volts. Figure 4 shows an example with loop gain of 1000, the bunch phase oscillation is damped at constant rate until its amplitude is small enough that the power amplifier is operated in its linear regime. Figure 5 shows the variation of amplitude of kicker voltage in this case.

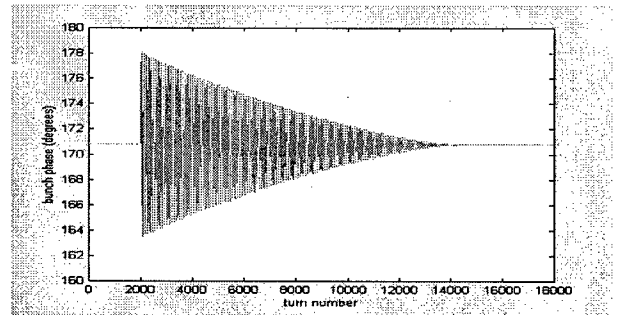


Figure 4: Damping of bunch phase oscillation in case of power amplifier saturation

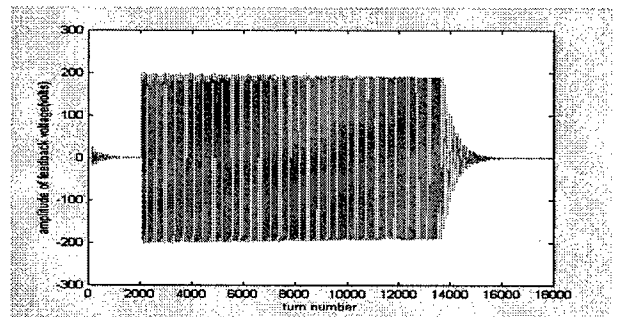


Figure 5: The corresponding amplitude of kick voltage in case of loop gain is 1000

Damping time of the oscillation in these nonlinear operation conditions is hard to define. However, we technically defined the time required to reach an acceptable small value energy deviation. We think that our criteria should be set at  $1e-4$ . Besides loop gain, we found also that this damping time proportional to initial amplitude of the impulse kick (Figure 6).

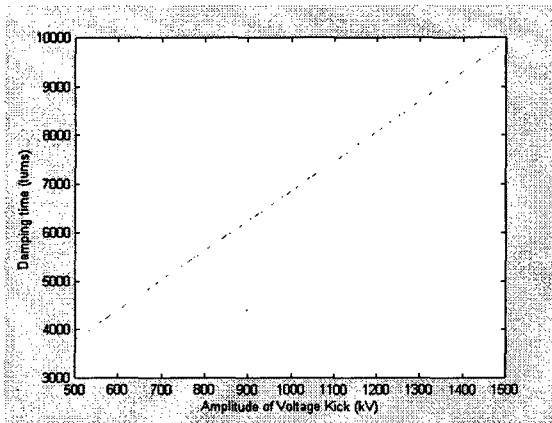


Figure 6: Damping time versus impulse kick strength at loop gain "a" equals 1000

### 3.4 Effect of Hold Buffer and Time Delay

In the simulations as discussed above, the DIFI output holds for 18 turns. However, without hold buffer, the loop gain is reduced significantly and the damping is much weaker. Therefore, a hold buffer circuitry is implemented in the DAC/MUX unit that the hold time is adjustable. A time delay of one down-sampled period (18 turns) has been set in the above simulations. Longer time delay has the advantage that more time is available for the DSP chips for calculation. The effect of more time delay (two or three periods) has also been tested. For longer delay, the phase of correction signal has been changed. One has to readjust both the phase shift of the DIFI or the initial phase of the feedback voltage to retain best performance. However, the ability of the feedback loop to damp the oscillation is weaker for a longer delay.

## 4 DISCUSSIONS

A computer code is developed to simulation the longitudinal feedback system behavior. The nonlinear characteristics of the TLS longitudinal feedback have been studied. In these simulations, quantization error resulted from analog-to-digital converter and individual device response are not included. Effects of hold buffer and time delay on system gain is also studied. We found that it is advantageous to add hold buffer circuit into DAC/MUX unit for higher loop gain. A time delay of one down sampled period is acceptable. The effect of increasing the delay time to damping rate can not be compensated by adjusting DIFI phase shift and initial phase of kick voltage. In the saturation region, the total

damping time versus impulse kick strength at a given loop gain is obtained. It is linearly proportional to the kick voltage. Further studies will include effects of individual response of components, new controller design etc.

## 5 REFERENCES

- [1] W. K. Lau et al., "Development of a Digital Longitudinal Damper for the TLS Storage Ring" Proceedings of Particle Accelerator Conference 1997.
- [2] W. K. Lau et al., "Progress of the Longitudinal Feedback System and Associated Beam Observations in TLS", these proceedings.
- [3] Ch. Wang et al., "Stabilization of the Spectral Intensity Fluctuations with the Higher Order Mode Frequency Tuners" Proceedings of Particle Accelerator Conference 1997.
- [4] M. S. Yeh et al., "High Speed Digital Signal Processing Electronics for the TLS Longitudinal Feedback System" these proceedings.
- [5] M. H. Wang, private discussion.

# A FAST GLOBAL BEAM POSITION FEEDBACK SYSTEM FOR SUPER-ACO\*

L. Cassinari<sup>#</sup>, J. Darpentigny, J.-N. Maymon, A. Nadji, D. Pédeau  
LURE, Université Paris-Sud, Bât. 209A, BP 34, 91898 Orsay Cedex, France

## Abstract

A fast global feedback system has been installed on Super-ACO in order to improve beam stability. The feedback uses all the 16 BPMs of the machine and 8 correctors in each plane. Two different correction algorithms have been tested, an harmonic based method and a direct inversion of the response matrix using SVD technique. The fast corrections are computed by 8 DSPs connected by a fast digital data link in order to achieve a correction bandwidth exceeding 100 Hz. Each DSP acquires the data for both planes of 2 BPMs and computes the output correction for 2 correctors. In this paper, we present the current status of the implementation of the system. We give the results on the efficiency of the orbit correction and the improvements on the photon beam stability.

## 1. INTRODUCTION

Among other recent developments on the Super-ACO storage ring, improvement in the orbit stability constitutes a major goal. The starting point of this work was the characterization of the beam position instability [1]. The orbit drift during operational runs has been measured several times at each BPM, and analysed. The spectrum analysis of the beam motion has also been measured at each BPM, and on a photon beam line, revealing several peaks in the horizontal plane, about from 10 to 30 Hz.

In this paper, we will present the analysis of the beam motion, the implementation and the operation of the global feedback system, as well as the home developed acquisition and computation boards, based on DSP.

## 2. SYSTEM OVERVIEW

The system uses all the 16 BPMs of the machine, and 8 correctors in each plane to correct the orbit at a 16 kHz rate, in order to achieve the correction bandwidth from DC to 100 Hz, both in horizontal and vertical plane. Figure 1 shows the layout of the global feedback system.

The BPMs consist of four-button monitors placed between the quadrupoles of each doublet, at each side of the 8 straight sections.

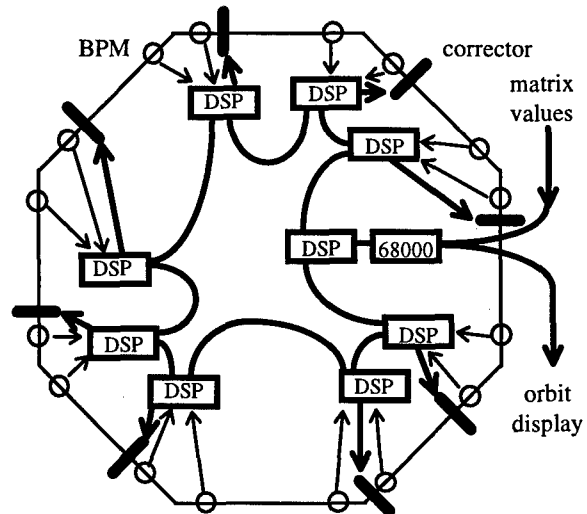


Fig. 1. Layout of the global feedback system.

### 2.1. Beam Position Measurement

The peak detector originally installed at the beginning of Super-ACO has been replaced 2 years ago by 16 BPM signal processors (one for each BPM) developed by BERGOZ Precision Beam Instrumentation. They consist of a four channel multiplexer, a heterodyne receiver with frequency synthesiser of the local oscillator, phase locked synchronous detector and low noise preamplifier with automatic gain control [2]. For Super-ACO, the processors use the 2nd RF harmonic of the picked-up signals (i.e. 199.756 MHz). The sampling frequency has been set to 33 kHz by external clock, in order to avoid any aliasing problem related with synchrotron oscillations.

Each processor delivers X and Z quasi-continuous output signals which allow to analyse the beam motion noise up to several hundreds of Hz. The achieved resolution is of  $0.5 \mu\text{m}/\text{Hz}$  over the full operating range, from 0.5 to 500 mA.

### 2.2. Digital Signal Processing

The digital processing system is home developed. Eight DSP boards acquire the X and Z signals from the 16 BPM processors (2 stations per DSP). They include two 16 bit MAX195 ADC, a four-channel MAX536 DAC, HDMP-1014/1012 low cost, high speed serial transmitter/receiver ; the DSP is an ADSP2115.

\* Work supported by CNRS, CEA and MENESR

# Email : cassinari@lure.u-psud.fr

The 8 DSP boards are linked via fast high rate serial links and form a ring controlled by a DSP master board.

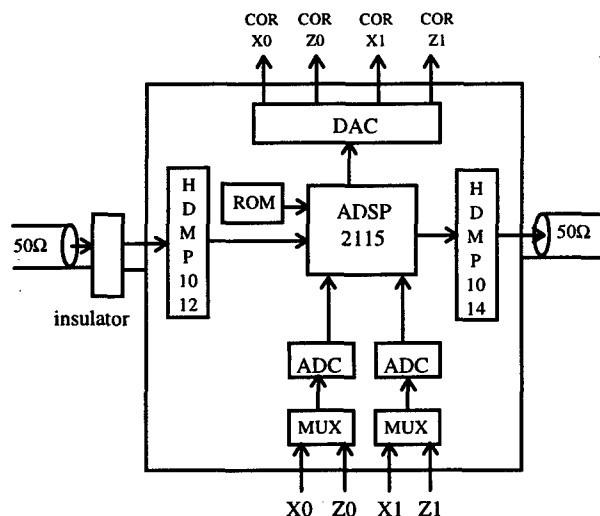


Fig. 2. DSP board.

The master controls the transmission cycle and ensures external communications. It delivers the orbit measurement to the general operating system. Its messages to the ring include the reference orbit, the coefficients of the matrix used for correction, and the status of the feedback (on/off, valid/non-valid).

During each cycle, each DSP board gets all the updated orbit data all along the ring, in order to calculate the correction needed for each corrector.

Each DSP board gets back the data it has delivered, and checks the conformity with the message sent ; in case of problem, the cycle is ignored (no change in the output). It takes 60  $\mu$ s to complete the whole acquisition, transmission, checking and calculation cycle for the 32 data (16 X and 16 Z). Data concerning the reference orbit and matrix coefficient are permanently transmitted by the master, at a rate of 4 values per cycle (it takes 136 cycles to ensure the full updating of all the data).

### 2.3. Orbit Corrections

The correction kicks are produced by 8 coils in each transverse plane. These coils are mounted in the quadrupole magnets, in addition to the dipolar correctors used to correct the orbit at the beginning of every run. They are powered by current-controlled wideband power amplifiers.

## 3. BEAM TESTS

### 3.1. Beam Behaviour without Feedback

The orbit stability is affected by 2 main parameters : long term drifts and low frequency fluctuations.

In Super-ACO, drifts occurring with usual beam intensity decay can be as large as 500  $\mu$ m in the

horizontal plane and 100  $\mu$ m in the vertical plane (with respective rms values of 300 and 50  $\mu$ m) [3].

In one case, it has been possible to show that thermal distortion of the vacuum chamber pushing the quadrupole magnet, was responsible of a large amount of the horizontal drifts [4]. This problem has been cured, yielding to a reduction of drift excursions, but most of the origins of these drifts are still unknown.

Currently, an automatic correction in the horizontal plane is applied every 3 min, in order to keep orbit drifts inside a max tolerance of 100  $\mu$ m.

Noise spectrum of position measurement shows a different look in horizontal and vertical plane (see Fig. 3). While in the vertical plane, the only noticeable noise line is due to the 50 Hz, in the horizontal, vibrations in the 10 to 30 Hz zone represent a large contribution ; these vibrations correspond to the girder mechanical eigenmodes.

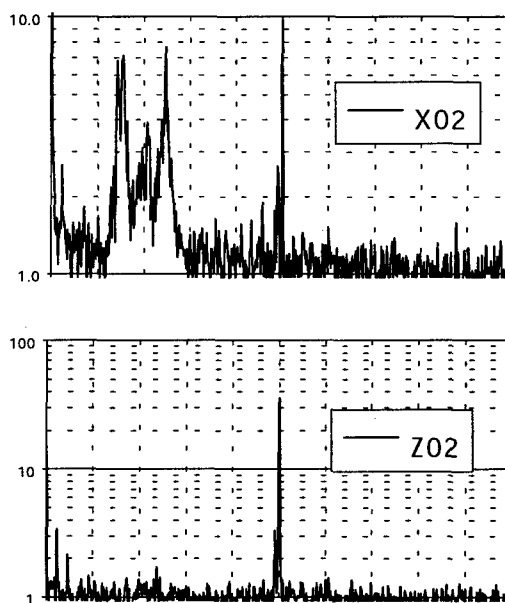


Fig. 3. Typical X and Z motion spectrum (vert. scale :  $\mu$ m rms ; horiz. scale : 0 to 100 Hz).

### 3.2. Frequency Response

The efficiency of the feedback loop has been measured in both planes by comparing the effect of a steering magnet (not included in the loop) with the feedback ON and OFF (see Fig. 4).

In the 2 bunch operating mode, the feedback bandwidth is of about 40 Hz in the horizontal plane, and of about 150 Hz in the vertical plane. The difference between the 2 planes is not due to differences in the electronics, but only to the efficiency of the steerers, probably because of the eddy currents in the non isotropic vacuum chamber. Nevertheless, the achieved bandwidth in the horizontal plane ought to be large enough to cure the 10 to 30 Hz zone vibrations.

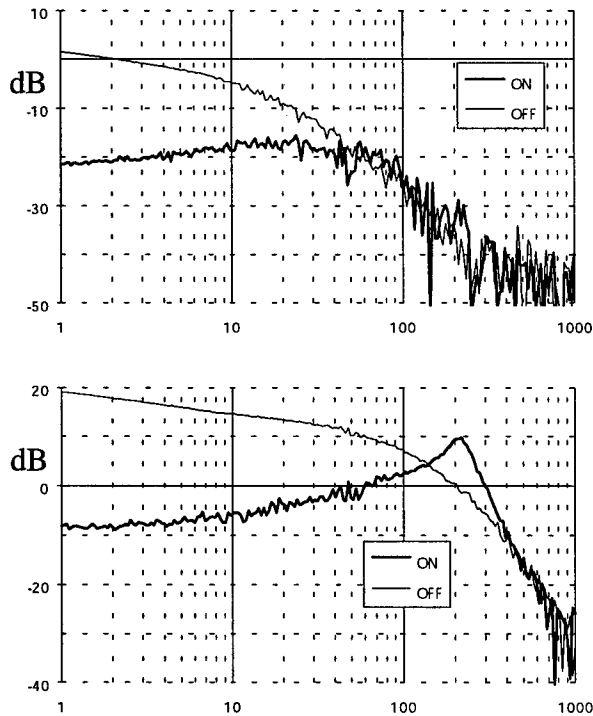
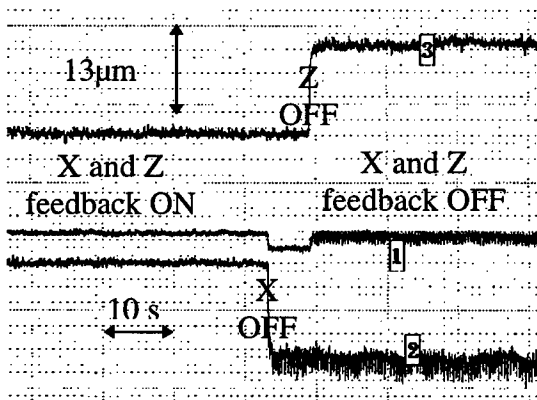


Fig. 4. Feedback bandwidth in the 2 bunch mode.  
(Upper : horizontal ; lower : vertical).

### 3.3. Effects on the Beam Motion

In the 2 bunch mode, the effect of the feedback is clearly visible on the beam position, both on drifts and on low frequency fluctuations. The later effect is particularly obvious when the beam transport from the linac is powered (in that case, without feedback, one can observe periodic fluctuations at 2.35 Hz on the beam position, in both planes, which are not explained at the moment).

The effect is also clear on the photon beam monitor installed in the SB3 photon beamline.



[1] Photon detector SB3 ; [2] BPM X30 ; [3] BPM Z30.  
Fig. 5. Position record, feedback ON/OFF.

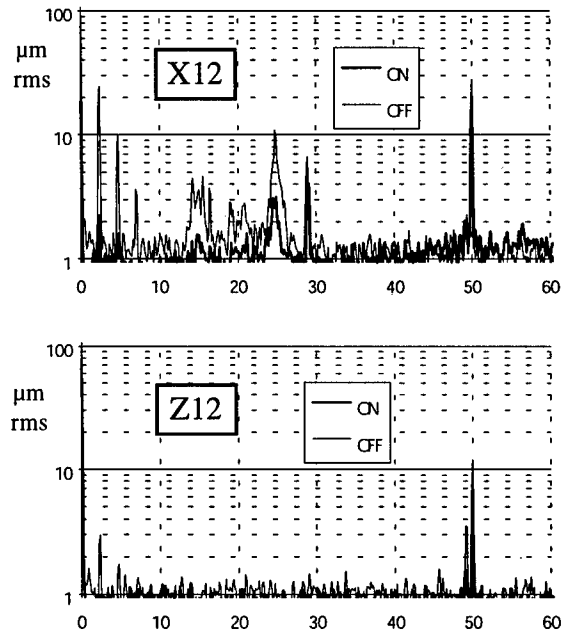


Fig. 6. Spectrum of the beam position signal at station 12  
(upper : horizontal ; lower : vertical)  
feedback ON and OFF.

Most of our tests have been performed in the 2 bunch mode, while only preliminary tests have been carried out in the 24 bunch mode. The first results show that the feedback efficiency is dramatically reduced in the vertical plane with the harmonic matrix usually used in the 2 bunch mode. The SVD matrix seems to be more efficient, but we need to go on with further tests before we are ready to use the feedback for users sessions in the different operating modes.

## 4. CONCLUSION

A fast global beam position feedback system has been implemented and tested on Super-ACO. The achieved bandwidth is 40 Hz in the horizontal plane and 150 Hz in the vertical, yielding to a reduction by a factor 10 in the low frequency region. Additional tests are being carried out in order to have the feedback operational during users sessions.

## 5. ACKNOWLEDGMENTS

It is a pleasure to thank all the members of the operation staff of Super-ACO for their collaboration.

## 6. REFERENCES

- [1] L. Cassinari, NI/97-08.
- [2] K. B. Unser, BIW 96, "New Generation Electronics Applied to Beam Position Monitors".
- [3] J.-F. Lamarre, Super-ACO/97-06.
- [4] J.-F. Lamarre, Super-ACO/98-09.

# Fast Feedback Systems for Orbit Correction in the TESLA Linear Collider

R.-D. Kohaupt, I. Reyzl\*, DESY, Notkestr. 85, 22 607 Hamburg, Germany

## Abstract

In the TESLA Linear Collider feedback systems will provide an orbit correction within the bunch train. To limit the reduction in the targeted luminosity of  $3.1 \cdot 10^{34} \text{ cm}^{-2} \text{ s}^{-1}$  due to beam separations to less than a few percent, the collisions have to be vertically stabilized within a fraction of the beam spot size of 5 nm. One system, located in the beam delivery system (BDS), is used to correct vertical bunch offsets generated upstream in the main linear accelerator and BDS. The second at the interaction point (IP) brings the two beams into collision using the beam-beam deflection method. Both digital feedback systems provide a correction on a bunch-to-bunch basis. Their design is based on classical proportional-integral control (PI-control). This paper describes the feedback system designs. Results of simulations are presented.

## 1 INTRODUCTION

TESLA 500 is a conceptual design study of a future  $e^+e^-$  linear collider using superconducting Nb accelerating structures operating at 1.3 GHz with a gradient of 25 MV/m. TESLA is going to operate at a center of mass energy of 500 GeV targeting a nominal luminosity of  $3.1 \cdot 10^{34} \text{ cm}^{-2} \text{ s}^{-1}$  produced by head-on collision [1]. Reaching this goal requires beam spot sizes at the IP of  $\sigma_x^* = 553 \text{ nm}$  horizontally and  $\sigma_y^* = 5 \text{ nm}$  vertically. Each bunch train consists of 2820 bunches spaced by 337 ns. The pulse repetition rate is 5 Hz.

Due to the large vertical disruption parameter  $D_y = 33$  the luminosity is very sensitive to beam separations and crossing angles in the vertical plane, Fig.1. Limiting the maximum luminosity loss per bunch crossing to 10%, two bunches have to interact within a separation of  $5 \text{ \AA} = 0.1 \sigma_y^*$  and with a crossing angle smaller than  $1.23 \mu\text{rad} = 0.1 \sigma_y^*$ ;  $\sigma_y^*$  denotes the natural divergence at the IP. Sources of undesired beam separations and crossing angles are e.g. Lorentz force detuning, wakefield effects and quadrupole movements or mechanical vibrations. The displacement of the two opposing final doublet magnets is a major concern, since a stationary final doublet displacement of  $5 \text{ nm} = 1 \sigma_y^*$  will half the luminosity. Simulations assuming large contributions of human produced noise to the ground motion spectrum predict a  $1 \sigma_y^*$  beam separation within 1 ms [3], which is roughly the bunch train length. From pulse to pulse the expected separation is at least  $8 \sigma_y^*$ .

\*Email: ingrid.reyzl@desy.de

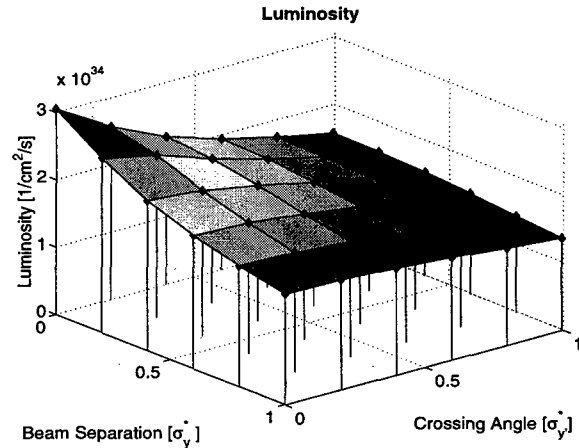


Figure 1: Luminosity as a function of beam separation and crossing angle. Data of surface plot are results of the program GUINEA PIG [6]

The size and the time scale of the vertical beam separation emphasize the necessity of a feedback system providing an intra-bunch train stabilization of the beam interaction at the IP. Due to the large bunch spacing of 337 ns a very beneficial orbit stabilization from one bunch to the next but one becomes feasible. In order to control the other beam phase a further feedback system will remove bunch offsets in the BDS within the bunch train. In this paper we describe the designs of these two digital feedback system using classical PI-control and present simulation results.

## 2 FEEDBACK SYSTEM IN THE BDS

The digital feedback system with a working frequency of 3 MHz is located in the  $30^\circ$  FODO-lattice of the tuning and diagnostic section in the BDS [2]. It provides a correction of bunch offsets in position and angle within the bunch train requiring a minimal feedback configuration of two beam position monitors (BPM) and two correctors. In order to correct offsets, bunch position measurements are taken with a resolution below  $1 \mu\text{m}$  [4] and transferred to a PI-controller determining the requested correction kicks. These kicks are then provided upstream by two correctors made up of fast kickers with a maximum kick of  $0.12 \mu\text{rad}$  and a rise time of 35 ns [7]. Since the processing time of BPM electronics incl. analog to digital conversion (ADC), of the controller and digital to analog conversion of its output signal, of amplifier and kicker and in addition the signal

transmission time in the cables exceeds the bunch spacing of 337 ns, a correction from one bunch to the second following bunch becomes feasible. The controller design ensures a reduction of a stationary bunch offset by two order of magnitudes after the 8<sup>th</sup> bunch. Offsets below 157 kHz are damped with 15 dB per decade.

After correction the beam trajectory can be distorted by displacement of magnets located in the final focus system. Quadrupole offsets will mainly lead to beam separations, since quadrupoles of large beta function are in phase with the final doublet. Beam separations created here will be then removed by the feedback system located at the IP.

### 3 FEEDBACK SYSTEM AT THE IP

In order to avoid serious luminosity loss a feedback system (working frequency 3 MHz) will stabilize the beam collision. It has to detect beam separations below the nanometer range, to steer the beams into collision, to complete the correction within a time which is much shorter than the bunch train length and to sustain the collision within a fraction of the vertical beam spot size. The design goal is a correction limiting the maximum luminosity loss to 10 %.

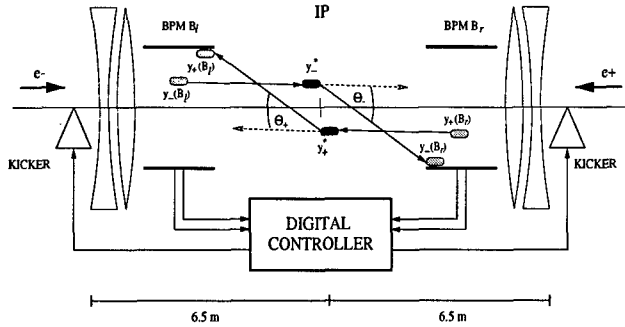


Figure 2: Scheme of the digital feedback system at the IP.

#### 3.1 Feedback Loop

The feedback loop is characterized by four steps: detection of bunch separation, estimation of bunch separation, determination of correction kick by PI-controller and orbit correction of subsequent bunches by using fast kickers.

**Detection of Bunch Separation** The actual separation  $\Delta y^*$  between two bunches is given by

$$\Delta y^* := y_-^* - y_+^* \quad (1)$$

with  $y_-^*$  and  $y_+^*$  the  $e^-$  and  $e^+$  bunch positions at the IP.

Bunch separations become detectable by the beam-beam deflection caused by the attraction of the opposite charged bunches [5]. The experienced kick results in measurable position shifts of the outgoing bunches, Fig. 2. From the beam position measurements of the incoming and outgoing bunch of both beams at the two opposing final doublets the size and the sign of the bunch separation can be ascertained. We assume the  $e^-$  bunch reaches the interaction

region from the left, the  $e^+$  bunch from the right side. The trajectory of the  $e^-$  ( $e^+$ ) bunch between the left and the right BPM  $B_l$  and  $B_r$  is completely defined by its position  $y_-^*$  ( $y_+^*$ ) and angle  $y_-'^*$  ( $y_+'^*$ ) at the IP, the drift space  $L = 3$  m between IP and BPMs together with the experienced beam-beam deflections  $\theta_-$  ( $\theta_+$ , assumed to be  $-\theta_-$ ). Including measurement errors  $v$  and BPM misalignments  $\delta$  the measurement of the incoming  $e^-$  bunch at BPM  $B_l$  is

$$m_-(B_l) = y_-^* - L y_-'^* + v_-(B_l) - \delta(B_l) \quad (2)$$

and of the outgoing  $e^-$  bunch at BPM  $B_r$

$$m_-(B_r) = y_-^* + L(y_-'^* + \theta(\Delta y^*)) + v_-(B_r) - \delta(B_r). \quad (3)$$

The measurements  $m_+(B_r)$  of the incoming  $e^+$  bunch at the right BPM  $B_r$  and  $m_+(B_l)$  of outgoing  $e^+$  bunch at the left BPM  $B_l$  are defined accordingly. The combination of these four position measurements results in the starting equation for the orbit correction:

$$M = 2 \Delta y^* + 2 L \theta(\Delta y^*) + V, \quad \text{with} \quad (4)$$

$$M := m_-(B_l) - m_+(B_l) + m_-(B_r) - m_+(B_r),$$

$$V := v_-(B_l) - v_+(B_l) + v_-(B_r) - v_+(B_r).$$

Note, since only difference measurements are involved, the control does not depend on BPM misalignments  $\delta(B_{l,r})$ .

**Estimation of Bunch Separation** Knowledge about the beam-beam deflection allows to find a suitable model needed by the controller to extract  $\Delta y^*$  from the BPM measurements. To receive an estimate  $\Delta y_{FB}^*$  of the bunch

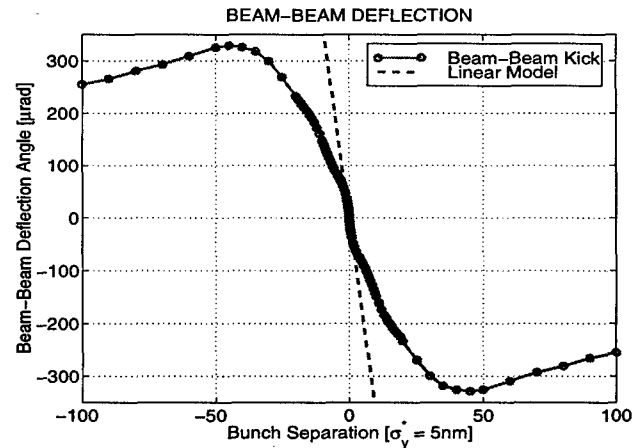


Figure 3: Beam-beam deflection angle  $\theta$  vs. bunch separation; data are results of the program GUINEA PIG [6].

separation the beam-beam kick  $\theta$  is substituted in Equ. 4 by its linear approximation  $\theta^{FB}$ , both plotted in Fig. 3:

$$\theta^{FB}(\Delta y^*) = -37.27 \frac{\Delta y^*}{\sigma_y^*} \quad [\mu\text{rad}]. \quad (5)$$

The slope of this linear approximation presents an essential value of the feedback loop: it determines how accurately the controller will determine a bunch separation in



the nanometer range and by how much large separations will be underestimated. For example with the given linear model a bunch separation of  $100 \sigma_y^*$  is interpreted as  $7 \sigma_y^*$ . The effect of this model error on the control is shown in 3.2.

**Determination and Provision of Correction** The determination of the correction kick  $u$  by the digital controller is based on the estimate bunch separations  $\Delta y_{FB}^*$ . Implementing a PI-controller results in the control law

$$u(k) = -K_P \Delta y_{FB}^*(k) - K_I \sum_{j=0}^{k-1} \Delta y_{FB}^*(j) \quad (6)$$

where  $k$  indicates the number of interaction (time step).  $K_P$  and  $K_I$  denote the gain of the proportional and integral controller. Their values define the feedback loop response.

Two kickers [7] with a rise time of 35 ns are placed on both sides of the IP, one meter upstream to the final doublet. They allow the coverage of a control range of  $\pm 100 \sigma_y^*$ . The overall processing time of the feedback loop and the signal transmission time in a 50 m long cable insert a correction delay of two sample period.

### 3.2 RESULTS

Even so the linear model  $\theta^{FB}$  used by the feedback system deviates severely from the non-linear beam-beam kick for large separations, large stationary offsets are successfully rejected. A constant beam separation of  $100 \sigma_y^*$  is reduced by 3 orders of magnitude already after 80 bunch interactions, emphasizing the robustness of the feedback system to model errors, Fig. 4. During correction the actual ver-

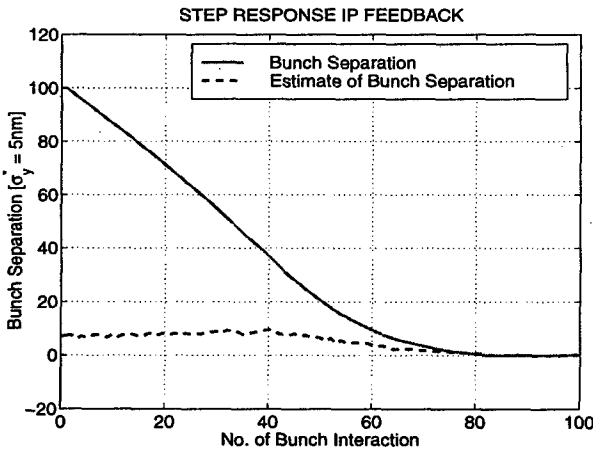


Figure 4: Response to a stationary  $100 \sigma_y^*$  beam separation.

tical separation is continuously underestimated. However, the feedback loop steers subsequent bunches in the right direction decreasing stepwise the occurring offset.

More realistic simulations include the bunch offsets at the linac exit. At the IP we further assume an rms BPM resolution of  $5 \mu\text{m}$  (add. noise), quantization errors caused

by ADC, a 10% jitter of the beam-beam deflection angle due to bunch charge jitter (mult. noise) and kicker errors of 0.1% (mult. noise). Without the use of a feedback sys-

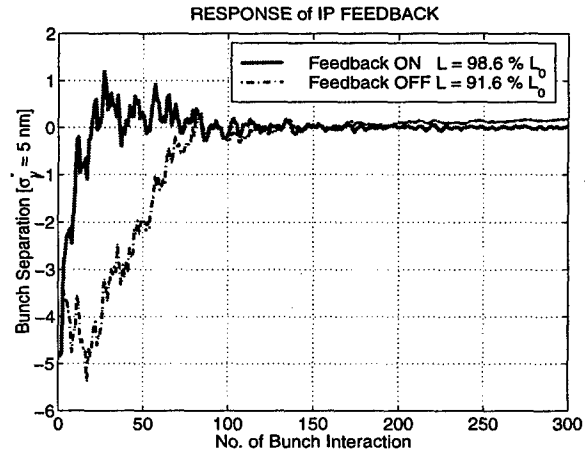


Figure 5: Response to beam separation including noise from the linac.

tem the luminosity is lowered by 8.4%, whereas an active stabilization of the beam-interaction by a feedback system allows to achieve 98.6% of the nominal luminosity denoted by  $L_0$ , Fig. 5.

Assuming an additional stationary beam separation of  $50 \sigma_y^*$  and  $100 \sigma_y^*$  caused by the displacement of the two final doublets, a luminosity of 95.6%  $L_0$  and 91.8%  $L_0$ , respectively, becomes feasible. Limiting the maximum luminosity loss by 10%, the use of the IP-feedback system thus relaxes the rms displacement tolerance of pulse-to-pulse jitter of the final doublet magnets to 200 nm.

### 4 ACKNOWLEDGMENTS

It is a pleasure for us to thank our colleagues at DESY.

### 5 REFERENCES

- [1] R. Brinkmann, *High Luminosity with TESLA 500*, DESY, TESLA 97-13, 1997
- [2] I. Reyzl, *Feasibility Study of Feedback Systems for Orbit Correction in the TESLA, Linear Collider*, Shaker Verlag, Aachen, 1999
- [3] R. Brinkmann, G. Materlik, J. Rossbach, A. Wagner, *Conceptual Design of a 500 GeV  $e^+e^-$  Linear Collider with Integrated X-ray Laser Facility*, DESY 1997-048, 1997
- [4] R. Lorenz, *Cavity Beam Position Monitors*, AIP Conference Proceedings 451, p. 53-73, 1999
- [5] P. Bambade, R. Erickson, *Beam-Beam Deflection as an Interaction Point Diagnostic for the SLC*, SLAC-PUB 3979, 1986
- [6] D. Schulte, *Study of Electromagnetic and Hadronic Background in the Interaction Region of the TESLA Collider*, TESLA 97-08, 1997
- [7] J. Rümmler, *Feedback Kickers in the DESY Rings*, IEEE Conference Proc. of the EPAC 94, London, England, 1994

# ERROR ANALYSIS OF A NEW COD CORRECTION METHOD UNITING GLOBAL AND LOCAL ORBIT FEEDBACKS

Y. Kamiya, N. Nakamura, M. Satoh<sup>#</sup>,

Synchrotron Radiation Laboratory, Institute for Solid State Physics, The University of Tokyo,  
3-2-1 Midori-cho, Tanashi, Tokyo 188-8501, Japan

## Abstract

A new COD correction method suitable for orbit feedback was already proposed[1]. This is the eigenvector method with constraints, which can have both functions of global and local COD corrections. In this paper, we will present the effects of errors in beam position monitor(BPM) reading and steering magnet setting on the orbit correction. We will show analytical expressions of these errors. In addition, we will show results of computer simulations for the VSX light source[2], a VUV and soft X-ray high-brilliance synchrotron radiation source being planned at the University of Tokyo, and compare them with the analytical results.

## 1 INTRODUCTION

Photon beam positions or closed orbits in synchrotron radiation sources are usually stabilized by global and/or local feedbacks. The global feedback efficiently corrects COD around the whole ring with the harmonic method, the least squares method or the eigenvector method, while the local orbit feedback tightly fix the beam position at a photon source point by the local orbit bump method. However, the two feedbacks may interfere with each other and deteriorate the orbit stability when they are operated at the same time. We proposed a new correction method, the eigenvector method with constraints, which can have both functions of global and local COD corrections. Furthermore, the computer simulations were already carried out in only cases without any errors[1]. Since the orbit correction suffers the effect of errors in BPM reading and steering magnet setting, it is practical to examine the effects of such errors on COD corrections. In this paper, several such error effects are discussed and computer simulations are carried out.

## 2 ERROR ANALYSIS

### 2.1 A New COD Correction Method

In this sub-section, a new COD correction method is reviewed. The measured COD at BPMs, the kick angle strengths of the steering magnets and the response matrix are denoted by  $\vec{y}$ ,  $\vec{\theta}$  and  $R$  respectively. Here, the

numbers of BPMs and steering magnets used in the correction are  $M$  and  $N$ , and  $R$  is a  $M \times N$  matrix. The residual vector of COD is defined by

$$\vec{\Delta} \equiv R\vec{\theta} + \vec{y}. \quad (1)$$

A new COD correction method is the eigenvector method with constraints. Here, the constraint conditions are given by

$$\vec{C}_i^T \cdot \vec{\theta} + z_i = 0 \quad (i = 1, \dots, N_c), \quad (2)$$

where  $N_c$  means the number of constraint conditions, and the superscript "T" stands for the transposed matrix.

We minimize the norm of  $\vec{\Delta}$  in Eq.(1) under the constraint conditions Eq.(2) using Lagrange's method of indeterminate multipliers. After the straightforward calculations, the kick angle strengths of steering magnets using a new COD correction method are obtained by

$$\vec{\theta} = B\vec{y} - D\vec{z}, \quad (3)$$

where  $A = R^T R$ ,  $P = C^T A^{-1} C$ ,

$$B = (-A^{-1} + A^{-1} C P^{-1} C^T A^{-1}) R^T, \quad (4)$$

$$D = A^{-1} C P^{-1}, \quad (5)$$

and the superscript "-1" stands for the inverse matrix. The inverse matrix  $A^{-1}$  in Eq.(4) can be expressed by the  $N_v$  eigenvectors and eigenvalues used for the COD correction as follows,

$$A^{-1} = \sum_{i=1}^{N_v} \frac{\vec{v}_i \vec{v}_i^T}{\lambda_i}, \quad (6)$$

where  $\vec{v}_i$  and  $\lambda_i$  are the  $i$ -th eigenvector and eigenvalue of the real symmetric matrix  $A$ , respectively.

If  $z_i$  in Eq.(2) is taken as the beam position observed at an arbitrarily selected BPM and  $C$  as the corresponding part of the response matrix  $R$ , the beam position can be fixed at zero.

### 2.2 Errors in BPM Reading

In this sub-section, we consider the effects of BPM errors. In order to simplify the discussion, first of all we examine separately the following 2 cases.

(i) In case of  $\vec{z} = 0$  and  $\vec{y} \neq 0$ .

<sup>#</sup> Email: sato@issp.u-tokyo.ac.jp

In this case, Eq.(3) is replaced by  $\vec{\theta} = B\vec{y}$ . Here,  $\delta\vec{y}$  is BPM errors and  $\delta\vec{\theta}$  is steering setting errors caused by  $\delta\vec{y}$ . If COD errors caused by BPM errors are denoted by  $\delta\vec{c}$ , we can obtain,

$$\delta\vec{\theta} = B\delta\vec{y}, \quad (7)$$

$$\delta\vec{c} = R\delta\vec{\theta}. \quad (8)$$

When BPM reading errors have a gaussian distribution with the standard deviation  $\sigma_{\text{BPM}}$ , it can be expressed using Eqs.(7) and (8) as follow,

$$\langle \delta\vec{c}^T \cdot \delta\vec{c} \rangle = \text{Tr}(B^T R^T R B) \cdot \sigma_{\text{BPM}}^2, \quad (9)$$

where the symbol " $\langle \rangle$ " and "Tr" mean the average and the trace of a matrix respectively. If the number of used eigenvalues and BPMs are denoted by  $N_V$  and  $N_{\text{BPM}}$  respectively, Eq.(9) can be represented by

$$\langle \delta\vec{c}^T \cdot \delta\vec{c} \rangle = (N_V - N_C) \cdot \sigma_{\text{BPM}}^2 \quad (10)$$

or

$$\overline{\sigma_{\text{COD}}^2} = \frac{N_V - N_C}{N_{\text{BPM}}} \cdot \sigma_{\text{BPM}}^2, \quad (11)$$

where the symbol " $\bar{\phantom{x}}$ " stands for the mean value.

Eq.(11) shows that the greater number of eigenvalues is used for correction, the  $\sigma_{\text{COD}}$  caused by BPM errors become worse. The factor  $(N_V - N_C)$  in Eq.(11) can be interpreted as the effective number of eigenvalue used for the COD correction.

(ii) In case of  $\vec{y} = 0$  and  $\vec{z} \neq 0$ .

In this case, since Eq.(3) is represented by  $\vec{\theta} = -B\vec{y}$ , we can express

$$\delta\vec{\theta} = -D\delta\vec{z}. \quad (12)$$

If the errors of  $z_i$  have a gaussian distribution with the standard deviation  $\sigma_z$ , it can be expressed using Eqs.(12) and (8) as follows,

$$\langle \delta\vec{c}^T \cdot \delta\vec{c} \rangle = \text{Tr}(D^T R^T R D) \cdot \sigma_z^2, \quad (13)$$

or

$$\overline{\sigma_{\text{COD}}^2} = \frac{\text{Tr}(P^{-1})}{N_{\text{BPM}}} \cdot \sigma_z^2. \quad (14)$$

Eq.(14) shows that the mean variance of COD varies in inverse proportion to the number of used BPMs and are proportional to the variance of  $z$ .

In practical,  $\vec{y}$  and  $\vec{z}$  are non-zeros because these are considered as beam position at BPMs. If the correlation between beam positions at different BPMs does not exist and  $z$  is taken as the beam position, a variance of COD errors can be expressed by the summation of (i) and (ii) as follows,

$$\overline{\sigma_{\text{COD}}^2} = \frac{N_V - N_C + \text{Tr}(P^{-1})}{N_{\text{BPM}}} \cdot \sigma_{\text{BPM}}^2. \quad (15)$$

### 2.3 Errors in Steering Magnet Setting

In this sub-section, we consider the effects of errors in steering magnet setting. Since the effects of errors do not depend on a COD correction scheme, the error effects in this case are completely same as that of an eigenvector method. If only the steering errors are taken into account, we can obtain

$$\delta\vec{c}^T \cdot \delta\vec{c} = \delta\vec{\theta}^T R^T R \delta\vec{\theta}. \quad (16)$$

In the same manner as sub-section 2.2, Eq.(16) can be rewritten by

$$\langle \delta\vec{c}^T \cdot \delta\vec{c} \rangle = \text{Tr}(R^T R) \cdot \sigma_s^2, \quad (17)$$

or

$$\overline{\sigma_{\text{COD}}^2} = \frac{1}{N_{\text{BPM}}} \left( \sum_i^{\text{all}} \lambda_i \right) \cdot \sigma_s^2, \quad (18)$$

where  $\sigma_s$  is the standard deviation of steering magnet

steering errors, and  $\sum_i^{\text{all}}$  means the summation of all  $\lambda_i$ , which are non-zeros.

Eq.(18) shows that the effects of errors in steering magnet setting do not depend on the number of eigenvalues used for the COD correction and the mean variance of COD varies in inverse proportion to the number of used BPMs.

## 3 RESULTS OF SIMULATION

The VSX project aims at constructing third-generation synchrotron light source in the Kashiwa campus of Tokyo University. The 2GeV VSX ring is 388m in circumference. 14 insertion devices will be installed there. 128 BPMs and 112 steering magnets will be used for beam orbit feedback.

A computer simulation for the new COD correction method with BPM or steering errors has been carried out for the VSX ring. The constraints adopted here are that the positions at BPMs on the downstream sides of 14 insertion devices are zeros i.e. the number of the constraints is 14. Figure 1 shows a typical COD before correction. Here, we assumed that the alignment error of quadrupole magnet has a gaussian distribution with the standard deviation 50[μm]. Figure 2 shows a COD after correction without any errors. Here, the symbol "♦" stands for a beam position at the BPM selected as constraint and all of them are fixed at zeros.

Figure 3 and 4 show the rms ratio of CODs before and after correction with BPM reading errors and steering magnet setting errors respectively.

Figure 3 shows that the greater number of eigenvalues is used for correction, the CODs after correction become

worse. In the sub-section 2, the correlation between beam positions at different BPMs is not taken into account. However, the result of this simulation gives good agreement with Eq.(15) as the analytical formulae qualitatively.

As shown in figure 4, the rms ratio of CODs before and after correction with steering magnet setting errors does not depend on the number of used eigenvalues for correction. This result gives good agreement with Eq.(18) as the analytical expression.

#### 4 CONCLUSIONS

The effects of errors in BPM reading and steering magnet setting were analyzed, and the computer simulations were carried out using a new COD correction method. The results of these computer simulations give good agreement with the analytical expressions. According to the effects of BPM errors, a suitable number of used eigenvalues should be selected in the practical orbit feedback systems, otherwise the performance of the correction become worse.

The effects of errors in response matrix elements, the error analysis taken account of the correlation between beam positions at different BPMs and a computer simulation for the repeated correction are discussed elsewhere.

#### 5 REFERENCES

- [1] M. Satoh, N. Nakamura and Y. Kamiya, "A New COD Correction Method for Orbit Feedback", Proceedings of the 6th European Particle Accelerator Conference, Stockholm, p.1723, 1998.
- [2] See, for instance, Y. Kamiya et al., "A Future Project of VUV and Soft X-ray High-Brilliant Light Source in Japan", Proceedings of European Particle Accelerator Conference, London, p.639, 1994.

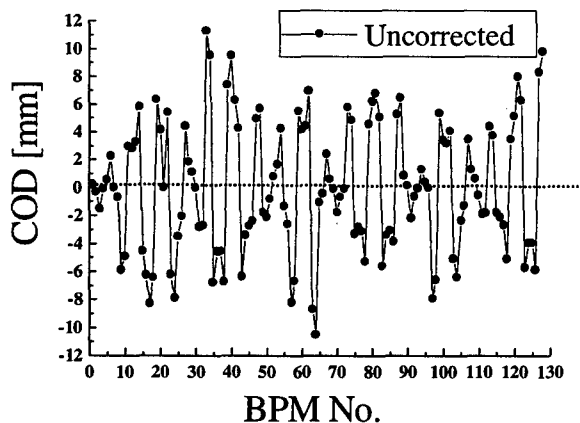


Figure 1: A typical horizontal COD without correction around the whole ring for the VSX ring.

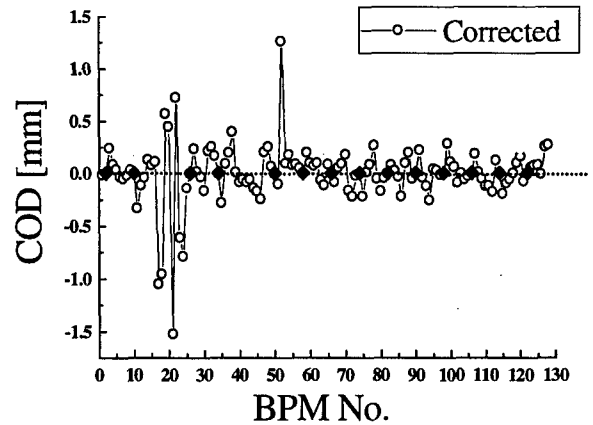


Figure 2: A horizontal COD after one turn correction using a new COD correction method.

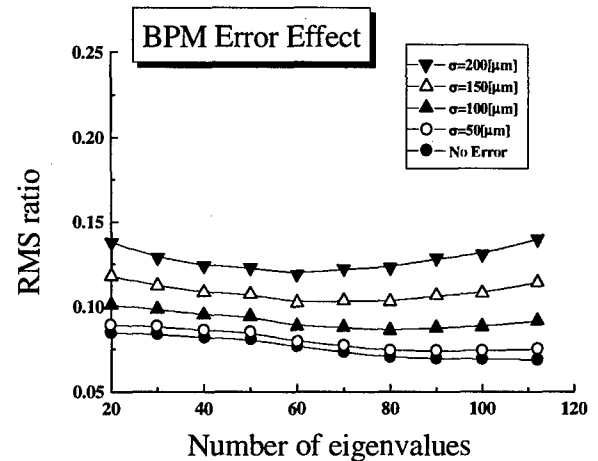


Figure 3: Rms ratio of horizontal CODs before and after correction with BPM reading errors. Here,  $\sigma$  means  $\sigma_{\text{BPM}}$ .

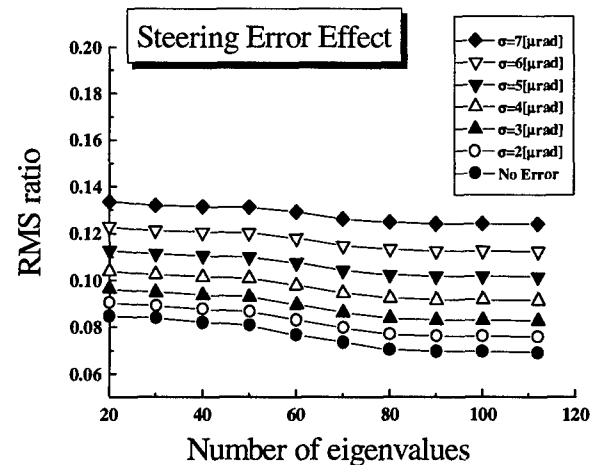


Figure 4: Rms ratio of horizontal CODs before and after correction with steering magnet setting errors. Here,  $\sigma$  means  $\sigma_s$ .

# BEAM CURRENT LIMITATIONS IN THE JEFFERSON LAB FEL: SIMULATIONS AND ANALYSIS OF PROPOSED BEAM BREAKUP EXPERIMENTS\*

I. E. Campisi, D. Douglas, C. Hovater, G. A. Krafft, L. Merminga<sup>#</sup>, B. C. Yunn,  
Thomas Jefferson National Accelerator Facility, Newport News, VA

## Abstract

A series of beam experiments is being planned in the Jefferson Lab FEL driver accelerator in order to study multi-pass beam breakup instabilities in the machine and to test the predictions of the numerical code TDBBU. The tests are extensions of previously performed or proposed experiments, and will be considerably more sensitive with the present configuration. The experiments will include: a) observing the onset of instabilities by lowering the threshold current through manipulation of the beam energy, phase advance, and beam transfer matrices; b) measurements of beam transfer functions in the recirculating mode; and c) measurements of the single pass beam transfer functions to obtain direct measurements of the transverse shunt impedance of cavity modes with strong coupling to the beam. Simulations of the different experiments and studies of the sensitivities to the accelerator and beam parameters are presented.

## 1 INTRODUCTION

The Jefferson Lab Free-Electron Laser's driver accelerator is a 42 MeV recirculated superconducting linac, presently being operated in the energy-recovery mode for production of IR radiation [1].

The beam stability against multipass beam breakup in the FEL is predicated upon the appropriate damping of higher-order modes in the superconducting cavities and on the installed optics and path lengths.

Recent measurements of the dominant dipole modes' external Q's and frequencies [2] have been used to perform computer simulations using the code TDBBU [3], [4]. The results of those simulations have indicated that threshold currents of a few tens of mA should be expected, only a few times larger than 5 mA, the nominal operating current of the machine.

In this paper we describe briefly the results of the simulations performed on the beam breakup simulations performed on the FEL driver and then discuss a number of planned experiments which are designed to both establish a solid experimental counterpart to the numerical simulations and to more carefully determine the limits which the FEL might encounter in the future

operation [5]. The investigations of the validity of the numerical simulations offer, in addition, a reliable baseline for the use of TDBBU in the design of the future CEBAF Energy Upgrade [6], [7]. In addition, these experimental activities are important for the qualification and the testing of the HOM performance of the Upgrade Cryomodule cavities. This will allow us to detect potentially trapped modes and this information can be utilized for the final design of the cryomodules before the full production is under way.

## 2 BACKGROUND

### 2.1 HOM measurements

The 5-cell, 1.497 GHz Nb superconducting cavities in the FEL cryomodule can have HOM excitations up to hundreds of GHz, the inverse time length of the submillimeter long bunch. The dominant dipole bands  $TE_{111}$  and  $TM_{110}$  occur between 1.720 GHz and 2.125 GHz. The damping of modes above 1.9 GHz is effected via the HOM coupling waveguides, which can extract both polarizations of the dipoles.

Below 1.9 GHz the only possible coupling can occur through the fundamental power coupler. The first four doublets of the  $TE_{111}$  passband fall in this category. The data taken on the HOM's show that the two polarizations of these modes possess very different external Q's, indicating poor coupling of one of the polarizations, possibly due to self-polarizing effects of the coupler itself. Some of the lightly damped modes have external Q's as high as  $4 \times 10^7$ .

### 2.2 Simulations

The measurements of HOM's prompted us to study more in detail the possible thresholds for transverse instabilities. From these simulations it appears that the presently configured FEL may become unstable at around 28 mA. Given the uncertainties of the simulations and of the unknown sensitivities to optics and transfer matrix variations, the safety factor of five seemed too small to safely extend operations past the design value and to comfortably prepare for upgrades of both the FEL and CEBAF with HOM's Q's in the  $10^7$  range.

The closeness of the predicted instability and of the operating current presents itself as an extraordinary opportunity to study the detailed physics of the instability

\*Supported by US DOE Contract No. DE-AC05-84ER40150.

<sup>#</sup> Email: merminga@jlab.org

and to establish once and for all the accuracy of the predictions of the TDBBU simulations.

The ability to do so can translate into the possibility of tailoring specific cavity characteristics and HOM damping requirements to the specific application with a degree of reliability impossible till now.

The availability of TDBBU as a tested tool will translate into a more efficient design of the Upgrade Cryomodule cavities for the CEBAF Energy Upgrade and of future FEL upgrades.

### 3 PROPOSED EXPERIMENTS

We propose to perform three experiments. In the first experiment we will attempt to induce BBU instabilities in the FEL driver in the energy recovery mode by lowering the beam energy, and varying the phase advance and transfer matrix elements  $M_{12}/M_{34}$  in the recirculation arcs.

Figure 1 shows the clear convergence of the vertical beam offset versus bunch number, as predicted by TDBBU with the nominal recirculator optics at 5 mA.

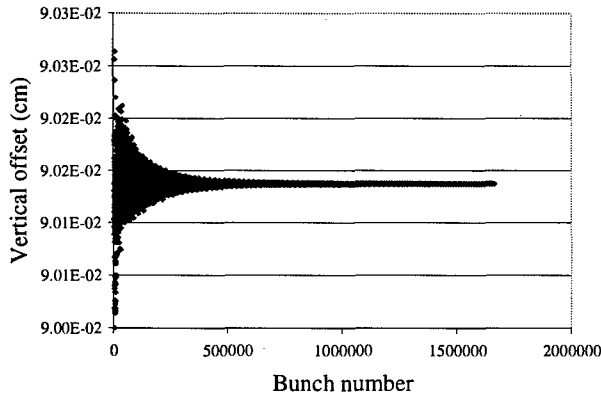


Figure 1: BBU simulations at 5 mA with nominal optics.

Figures 2 and 3 show simulations for a modified recirculator optics with vertical beta function at the reinjection point into the cryomodule increased by a factor of a hundred from nominal to  $\beta_y=500$  m, and the phase advance from the exit of the cryomodule back to the reinjection point into the cryomodule set equal to exactly a quarter integer. With this modified optics the new threshold current is somewhere between 4 and 5 mA with a clear divergence at 5 mA (Figure 3) that is within the capability of the present FEL gun.

Additional sensitivity can be obtained by lowering the beam energy. Operational experience indicates that the accelerator configuration is flexible enough to allow for ample energy changes. We expect that this experiment will be performed in the near future.

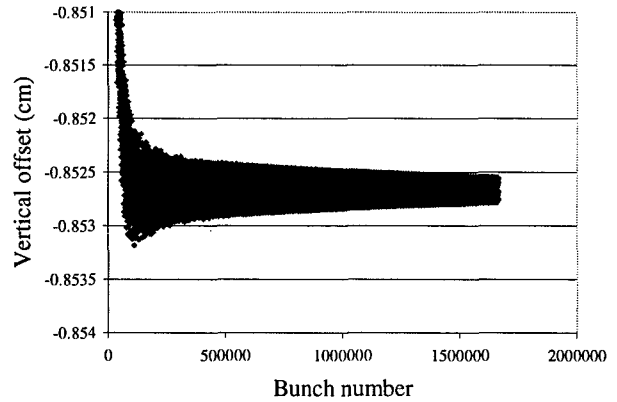


Figure 2: BBU simulations at 4 mA with modified optics.

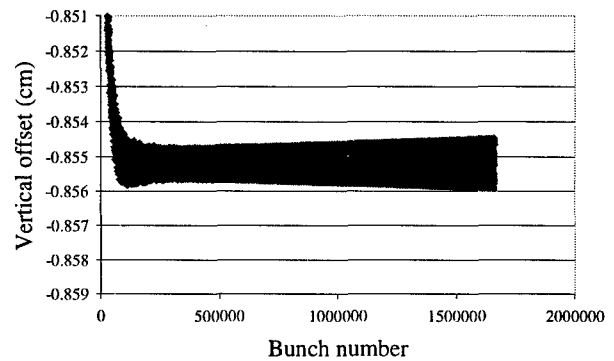


Figure 3: BBU simulations at 5 mA with modified optics.

In the second experiment we plan to measure the beam transfer functions in the recirculating mode. These measurements can be performed at currents considerably lower than the threshold current, yet lead to clear indirect estimates of the instability threshold in the event that the first experiment would not yield a direct observation of the onset of instability.

These measurements require modulation of the current moment  $I\Delta x$  (or  $\Delta y$ ) at the HOM frequencies or sub-harmonics.

The modulation can be achieved in several different ways. We plan to employ four separate techniques, to achieve independent confirmation of the threshold estimates.

In the first method, which employs modulation of beam displacement at constant current [8], the basic RF measurements consist in using a broadband RF kicker, which in our case is a stripline BPM already installed in the accelerator, to excite the beam. The detection of the modulation can either be done with one of the SRF cavities' field probe, or by a dedicated broadband pickup BPM. The optimal location for maximum signal of the kicker BPM is in the 10 MeV injection line, near an existing BPM.

The second method consists in injecting RF power at selected HOM frequencies in an unpowered cavity with an

external 300 W broadband generator and exciting a  $TE_{111}$  mode around 1.9 GHz., as described by Lyneis [9]. The third method uses beam current modulation at static displacement and the fourth requires tuning of the relevant HOM frequencies of an unpowered cavity to match a resonance condition with the bunch repetition frequency [10], [11], [12].

As a third experiment, we plan to measure the single-pass transfer functions of the present 5-cell cavities, and in the future of the 7-cell CEBAF Upgrade cavities and of strings of cavities, to obtain direct measurements of the shunt impedance of transverse HOM's. These measurements will be implemented on an unpowered two-cavity cryomodule placed in the return line of the FEL at first, possibly followed by tests on a half cryomodule. The measurements on this four-cavity module will also allow us to uncover long range trapped modes in the cavity string.

The proposed experiments will be carried out with a minimal disruption to the present configuration of the FEL accelerator and to its schedule.

The first experiment requires no hardware installation. Only dedicated time is required to perform studies of new optics and beam dynamics outside the canonical configuration.

The third experiment requires the installation of the cavity (-ies) under study in the accelerator beam line. It will require a drastic reconfiguration of the accelerator hardware. The detailed design of this activity is under way.

#### 4 CONCLUSIONS

The FEL accelerator at Jefferson Lab presents itself as an unparalleled instrument to perform tests to establish the beam stability limitation in multi-pass BBU. These tests will not only shed light on the ultimate performance of the FEL itself, but will also determine the high-current limitations of the 1.5 GHz superconducting cavity technology for these types of applications. The proposed studies will also assess the accuracy of the numerical codes used to estimate BBU in recirculated electron linacs and to determine the HOM damping requirements for the CEBAF Energy Upgrade cavities.

#### 5 ACKNOWLEDGMENTS

We would like to thank C. Bohn, G. Neil, M. Piller, S. Benson, L. R. Doolittle, J. R. Delayen, J. J. Bisognano, and J. C. Denard for useful discussions.

#### 6 REFERENCES

- [1] C. Bohn et al., "Performance of the Accelerator Driver of Jefferson Laboratory's Free-Electron Laser", these proceedings.
- [2] I. E. Campisi and L. Merminga, "Higher-Order-Mode Spectra in the FEL cavities", JLab TN 98-011, March 1998.
- [3] L. Merminga and I. E. Campisi, "Beam Breakup Simulations in the Jefferson Lab Free-Electron Laser", JLab Technical Note TN 98-031, August, 1998.
- [4] L. Merminga, I. E. Campisi, "Higher-Order-Modes and Beam Breakup Simulations in the Jefferson Lab FEL recirculating Linac", Proceedings of the XIX Linac conference, Chicago, Illinois, August 1998.
- [5] Minutes of FEL Upgrade Brainstorming Meeting, Jefferson Lab, October 22-23, 1998.
- [6] J. R. Delayen, "Development of an Upgrade of the CEBAF Acceleration System", Proceedings of the XIX Linac conference, Chicago, Illinois, August 1998.
- [7] I. E. Campisi, J. R. Delayen, L. R. Doolittle, P. Kneisel, J. Mammoser, L. Phillips "Superconducting Cavity Development for the CEBAF Upgrade", these proceedings.
- [8] N. S. R. Sereno, "Experimental Studies of Multipass Beam Breakup and Energy recovery Using the CEBAF Injector Linac", PhD. D. Thesis, U. of Illinois, 1994.
- [9] C. M. Lyneis, R. E. Rand, H. A. Schwettman, A. M. Vetter, "Standing Wave Model of Regenerative Beam Breakup in Recirculating Electron Accelerators", Nucl. Instr. and Meth., 204 (1983), 269-284.
- [10] S. Fartoukh, "A New Method to Detect the High Impedance Dipole Modes of TESLA Cavities", Note CEA/DAPNIA/SEA-98-18, Saclay, 1998.
- [11] S. Fartoukh, "RF Steering Experiments on TTF", Note CEA/DAPNIA/SEA-98-02, Saclay, 1998.
- [12] S. Fartoukh, "Multi-bunch Experiments on TTF", Note CEA/DAPNIA/SEA-98-04, Saclay, 1998.

## BEAM BREAKUP SIMULATIONS FOR THE JEFFERSON LAB FEL UPGRADE\*

I. E. Campisi, D. Douglas, L. Merminga<sup>#</sup>, B. C. Yunn

Thomas Jefferson National Accelerator Facility, Newport News, VA

### Abstract

As the Jefferson Lab Free Electron Laser steadily approaches its goal of producing 1 kW of IR radiation at 5 mA of beam current at 42 MeV, plans are being considered for possible upgrade scenarios, which will extend the IR power output and allow generation of UV radiation.

The upgrade scenario presently considered will bring the beam current to 10 mA and increase the energy to values close to 200 MeV. These parameters will most likely be realized in a machine configuration with a single recirculation loop for energy recovery and a linac consisting of three IRFEL-type cryomodules.

Measurements of frequencies and external Q's of the first two HOM passbands in the eight IRFEL cavities revealed anomalous high-Q resonances which could lead to transverse BBU instabilities at currents close to the operating current of the machine. In this paper we use the simulation code TDBBU to study the BBU behavior of the FEL upgrade and estimate its threshold current under nominal settings. Furthermore we study its dependencies on small variations of machine parameters, such as the path length of the recirculator and the frequency of selected HOMs, around their nominal points.

### 1 INTRODUCTION

The Jefferson Lab Free Electron Laser is currently configured as a recirculating machine capable of producing 1 kW of IR radiation at 5 mA of beam current at 42 MeV. Its most recent record has been 710 W of 4.8  $\mu$ m radiation produced by 3.6 mA of beam current at 38.5 MeV [1], [2]. As the FEL is starting to operate as a user facility, plans are being considered for upgrade scenarios, which will extend the IR power output and allow generation of UV radiation [3].

The most likely upgrade scenario will bring the beam current up to 10 mA and increase the energy to values close to 200 MeV, thereby allowing production of greater than 10 kW in the IR wavelengths between 1 to 2  $\mu$ m, as well as production of approximately 1 kW in the UV wavelengths, between 250 and 350 nm.

According to the present thinking [3], the above parameters are to be realized in a machine configuration very much similar to the IRFEL, with a single recirculation loop for energy recovery, and a linac consisting of three slightly modified, CEBAF type 2 K

cryomodules containing eight 5-cell superconducting rf (srf) cavities operating in the  $TM_{010}$   $\pi$  mode at 1497 MHz.

Measurements of the frequencies and external Q's of the first two higher order mode (HOM) passbands in the eight srf cavities of the IRFEL cryomodule revealed anomalous high-Q resonances [4] which could lead to beam instabilities at currents close to the operating current of the machine. These results motivated detailed simulations of the beam breakup (BBU) behavior of the IRFEL. The analysis indicated that a few modes are responsible for the relatively low value of 28 mA of the threshold current.

As the operating current of the FEL upgrade is planned to be raised to 10 mA, it is essential that we understand the BBU behavior of this machine and its sensitivities to machine parameters, and that we ensure that the final design has a BBU threshold current with a comfortable margin from the operating current.

In this paper we first present a brief description of the FEL upgrade machine configuration and the results of the HOM measurements and simulations done on the IRFEL. We then describe the BBU simulations we performed for the FEL upgrade, starting first with a short description of the simulation code, TDBBU [5], the assumptions and the results.

### 2 A POSSIBLE FEL UPGRADE CONFIGURATION

Figure 1 shows a possible configuration for the FEL upgrade. As in the IRFEL, the injector produces and accelerates electrons to 10 MeV. For modeling purposes the linac is assumed to consist of three cryomodules capable of delivering energy gains of 55, 60 and 55 MV, for a final beam energy of 180 MeV. After lasing the beam will be transported to the linac for energy recovery, to a final energy of 10 MeV. The design current of 10 mA can be reached in three different combinations of charge per bunch and bunch repetition frequency: 37.425 MHz at roughly 250 pC per bunch, 74.85 MHz at roughly 120 pC per bunch and 149.7 MHz at roughly 60 pC per bunch.

One of the goals of this study is to assess whether a preferred combination of charge per bunch and bunch repetition frequency exists from the point of view of BBU instabilities.

\*Supported by US DOE Contract No. DE-AC05-84ER40150.

<sup>#</sup> Email: merminga@jlab.org



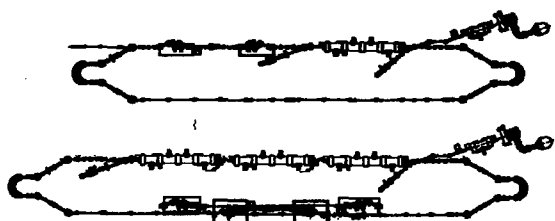


Figure 1: Top: Present FEL configuration. Bottom: Proposed FEL Upgrade configuration.

## 2.1 Lattice

The recirculator delivers beam to a set of wigglers (IR and UV) with the phase space configured properly for lasing, then transports spent beam from the wigglers back to the linac for deceleration to the injection energy.

Of interest in this context is the implementation of transverse and longitudinal matching in the recirculator. As it will be based on the Bates-like transport system design used in the Jefferson Lab IRFEL project [6], full six dimensional phase space matching of the recirculated beam will be available. At present, the linac beam envelopes will be reflectively symmetric about the recirculator, with average (peak) beam envelope functions of 10 (20) m amplitude and nearly a full betatron wavelength phase advance in either transverse plane during both acceleration and energy recovery. The total recirculation path length will nominally be  $(n+1/2) \cdot (RF \text{ wavelength})$ , with the integral part being chosen to minimize instability effects as dictated by work in progress. At present, the recirculator is expected to have integer betatron phase advance. This, coupled with the linac phase advance, will insure that the beam will have no positional offset during energy recovery at any linac location where there was imposed an impedance-driven impulse during acceleration. This design choice will thereby maximize thresholds for impedance-driven instabilities. As in the IRFEL, available beamline matching modules (including quadrupole telescopes for transverse matching and magnetic bunch length compressors/decompressors for longitudinal matching) will allow operation variation of this condition to provide opportunity to study impedance driven effects [7].

## 2.2 Linac Cavities

The accelerating-decelerating linac consists of three IRFEL cryomodules, each one containing eight 5-cell cavities. The HOMs are extracted by two mutually orthogonal waveguides, with a frequency cutoff of 1900 MHz, terminated in loads thermally anchored at 50 K. Modes at frequencies below 1.9 GHz can only be extracted via the fundamental power coupler (FPC). Four out of five dipole modes of the  $TE_{111}$  passband fall into this category, and their external  $Q$ 's can be lowered only if

some component of their fields is aligned with the FPC. In the case of strong polarization, orthogonal modes could exhibit large values of  $Q_{ext}$ .

The  $TE_{111}$  and  $TM_{110}$  passbands frequencies and  $Q$ 's were systematically measured for all eight cavities in the IRFEL linac. Several modes exhibited high  $Q$ 's, with the highest  $Q$ 's associated with the vertical polarization of the  $TE_{111} \pi/5$  mode [8], [9].

Although this mode was observed to have the highest  $Q_{ext}$ , it was actually the  $4\pi/5$  mode which contributed more to possible beam instabilities because of its substantially higher transverse impedance. Six out of eight cavities showed that the vertically polarized  $TE_{111} 4\pi/5$  mode has a  $Q$  high enough to generate a shunt impedance of  $1-3 \times 10^{10}$ , two orders of magnitude larger than what originally was measured by Amato [10].

As the only data available to date are from the IRFEL cavities, the simulations described below assume that the three cryomodules are identical, consisting of cavities whose HOM characteristics are identical to the IRFEL cavities. Clearly these studies are only preliminary and will have to be repeated when either data from the second and third cryomodule become available, or with statistically distributed frequencies and  $Q$ 's among the 24 cavities.

## 3 BEAM BREAKUP SIMULATIONS

### 3.1 Method

The BBU simulations were performed using the code TDBBU. In it, every bunch is characterized by a phase space vector which gets updated according to the fundamental equations of dynamics, as deflecting modes in each cavity impart kicks in the horizontal and vertical directions.

In the FEL upgrade simulations, a 10 MeV beam is injected into the linac, interacts with the HOM fields of each cavity, gets transported around the recirculation path and enters the linac again,  $180^\circ$  out of phase for energy recovery. As the decelerated beam traverses the RF cavities, it interacts with the HOM fields of the cavities again, and, as the beam energy becomes smaller, the transverse deflections imparted to the beam have a stronger effect.

Each cavity in TDBBU is described by a 0.25 m drift delivering an energy gain equal to half the nominal energy gain per cavity, followed by the "HOM-kick" section for the particular cavity and this is followed by another 0.25 m drift delivering another half of the nominal energy gain.

The "HOM-kick" section includes all five  $TE_{111}$  and five  $TM_{110}$  horizontal and vertical modes. Each mode is characterized by its  $Q$  value, frequency, and transverse shunt impedance, as given by Amato scaled by the frequency of the mode.

The total path length of the recirculator is 715.5 RF wavelengths and the transport matrix elements are calculated using DIMAD.

### 3.2 Results

The threshold current for the system at the nominal design point was determined to be about 75 mA. This result is independent of the bunch repetition frequency. The limiting modes affect the stability in the vertical plane. In the horizontal plane no instability is observed at these current values, since the relevant modes are polarized in such a way that those aligned with the horizontal axis are well damped by the FPC.

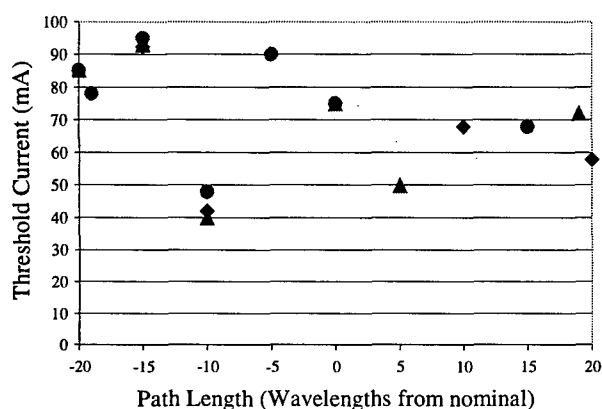


Figure 2: Dependence of  $I_{th}$  on recirculator pathlength

To understand the sensitivity of the BBU threshold current on some of the design parameters, simulations were performed for a system with recirculation path length which differs from nominal by  $\pm 20$  rf wavelengths. Figure 2 shows a graph of threshold current vs. recirculation path length. A minimum threshold of 40 mA is possible, indicating increased sensitivity to the setup of the recirculator.

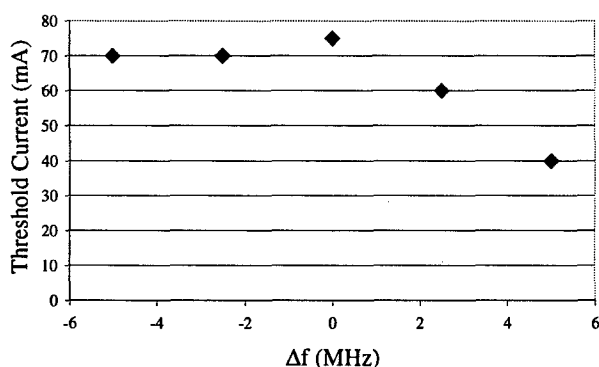


Figure 3: Dependence of  $I_{th}$  on the frequency of the  $4\pi/5$   $TE_{111}$  mode.

Finally the sensitivity of the threshold current on the frequency of the HOMs was studied. The frequency of the  $TE_{111}$   $4\pi/5$  mode, which is the mode most responsible for the value of the threshold current, was varied by  $\pm 5$  MHz,

in all 24 cavities, and the new threshold current was determined. Threshold currents as low as 40 mA are possible as shown in Figure 3. Although this case can be considered as a worst case scenario, the resulting large variations of the threshold current are a sufficient motivation for further understanding.

## 4 CONCLUSIONS

Preliminary BBU simulations performed on the present version of Jefferson Lab's FEL upgrade driver accelerator show that a threshold current of about 75 mA is possible. Small variations in machine parameters such as the path length of the recirculator, and the frequency of the HOM most responsible for the threshold current, can result in much reduced threshold currents, possibly dangerously close to the operating current. Measurements of HOM frequencies and Q's should be done as soon as the other two cryomodules become available. Given realistic HOM parameters, a thorough study of the BBU is essential with fixed parameters, before an engineering design starts.

A machine design with a BBU threshold current that is a factor of 3-4 higher than the operating current could be acceptable, under certain conditions. One of them has to be the unconditional confidence in the simulation tools that only benchmarking against experimental data can provide [7].

## 5 REFERENCES

- 1 C. Bohn, et al., "Performance of the Accelerator Driver of Jefferson Laboratory's Free-Electron Laser", these proceedings.
- 2 S. V. Benson, "High Average Power Free-Electron Lasers", these proceedings.
- 3 Minutes of FEL Upgrade Brainstorming Meeting, Jefferson Lab, October 22-23, 1998.
- 4 L. Merminga, I. E. Campisi, "Higher-Order-Modes and Beam Breakup Simulations in the Jefferson Lab FEL Recirculating Linac", Proceedings of the Linac Conference, Chicago, IL, August 1998.
- 5 TDBBU was written by G. A. Krafft at Jefferson Lab.
- 6 D. Douglas, "Lattice Design for a High-Power Infrared FEL", Proceedings of the 1997 IEEE Particle Accelerator Conference, Vancouver, BC, May 1997.
- 7 I. E. Campisi et al. "Beam Current Limitations in the Jefferson Lab FEL: Simulations and Analysis of Proposed Beam Breakup Experiments", these proceedings.
- 8 I. E. Campisi and L. Merminga, "Higher-Order Mode Spectra in the FEL Cavities", JLab TN 98-011, 1998.
- 9 L. Merminga and I. E. Campisi, "Beam Breakup Simulations in the Jefferson Lab Free Electron Laser", JLab TN 98-031, August 1998.
- 10 J. Amato, "Summary of HOM Measurements to Date", Cornell LNS Tech Note SRF-831002, 1983.

# HIGH-PRECISION BEAM-BASED RF PHASE STABILIZATION AT JEFFERSON LAB\*

V. A. Lebedev, J. Musson, and M. G. Tiefenback<sup>†</sup>,  
Thomas Jefferson National Accelerator Facility, Newport News, VA

## Abstract

A non-invasive monitor has been implemented for the relative phase of the beam and the accelerating RF of each of the two CW superconducting linacs at TJNAF. Its noise level and resolution are below  $0.1^\circ$  at beam currents as low as 2 microamperes, and it been successfully tested for use in feedback correction for the overall RF accelerating phase of each linac. The 70 MHz frequency reference in each linac is phase modulated by approximately  $\pm 0.05^\circ$  at different frequencies (383 and 397 Hz). A single analog beam position signal from a dispersive region is used to monitor the resulting micron-level position modulation via off-the-shelf lock-in amplifiers, which also supply the modulation signals. The off-crest phase is proportional to the first harmonic coefficient of the energy modulation. This technique can be applied as well to pulsed machines and to systems for which the beam-to-RF relative phase may be non-zero. Other applications are discussed.

## 1 INTRODUCTION

CEBAF is a superconducting CW recirculating electron accelerator, one design goal of which was to achieve the very low RMS energy spread of  $2.5 \times 10^{-5}$ . Achieving this requires both a short electron bunch and an RF accelerating system with low phase noise. Past and future Master Oscillator (MO) system sources meet the requirements[1], but phase drifts in the MO distribution have required attention since early commissioning activities. Improved thermal regulation of the distribution lines has reduced the intrinsic drifts to within  $\pm 2^\circ$ , and software feedback loops and manual readjustments have provided adequate phase control to date. However, the continuous phase monitoring provided by this system will help in maintaining the design energy spread goal by providing the information needed for immediate correction of the residual drifts.

## 2 PHASE SENSITIVITY

Changes in beam energy are monitored through the beam position monitor (BPM) system in dispersive regions, and a feedback system for energy correction has recently been provided[2] at the experimental hall transport lines (point of delivery monitoring and correction). Stabilizing beam energy at one point in the system, however, does not stabilize the energy spread, and under certain conditions may

not sufficiently stabilize the beam energy for other acceleration passes. The energy spread depends upon many factors, including the bunch length, the overall coherence of the linac accelerating systems (periodically adjusted to correct for local hardware drifts), and the overall vector phase of the linac with respect to the various recirculating beams.

This system is intended to improve monitoring and correction of the overall phase of the linac. We have adapted the signal processing hardware used in the Hall B nanoampere BPM system[3] to measure the global phase of each linac with respect to the beam with better than  $0.1^\circ$  resolution. The technique involves phase modulation of each linac at the  $0.05^\circ$  level, contributing at the  $3 \times 10^{-6}$  level to the overall RMS energy spread.

### 2.1 Induced Energy Spread

The energy gain from an RF system, initially at some phase  $\psi$  with respect to crest, by a perturbation  $\delta$  at an angular frequency  $\omega$ , is of the form

$$\cos(\psi + \delta \sin(\omega t)).$$

In addition to a slight level shift, there are first and second harmonic contributions to the energy of the beam approximately given by

$$\delta \sin(\psi) \sin(\omega t) + \frac{\delta^2}{4} \cos(\psi) \cos(2\omega t).$$

The  $\sin(\omega t)$  term provides the detection capability used here. It is possible that the  $\cos(2\omega t)$  term may be usable as a "system on and working" flag. In the CEBAF system, each linac provides about half of the beam energy. For a modulation amplitude of  $\pm 0.05^\circ$  at an off-crest phase of  $0.5^\circ$ , these two terms provide RMS additions to the energy spread of  $2.5 \times 10^{-6}$  at the fundamental harmonic and  $1.3 \times 10^{-7}$  at the second harmonic.

## 3 SYSTEM LAYOUT

The detection system is presently installed in the "spreader" (region for vertical separation of the multiple beam passes) at the end of the South Linac (see Fig. 1. The dispersion at the BPM used for detection is 1.4 m, so that a  $2.5 \times 10^{-6}$  RMS energy (momentum) modulation results in an RMS beam position modulation of 3.5 microns. This location was chosen because a single BPM here allows monitoring of both linacs for all beam delivery configurations. Adding BPM pick-ups for recirculated beam is an option discussed below.

\* Work supported by the U.S. Department of Energy under contract number DE-AC05-84ER40150.

<sup>†</sup> Email: tiefen@jlab.org

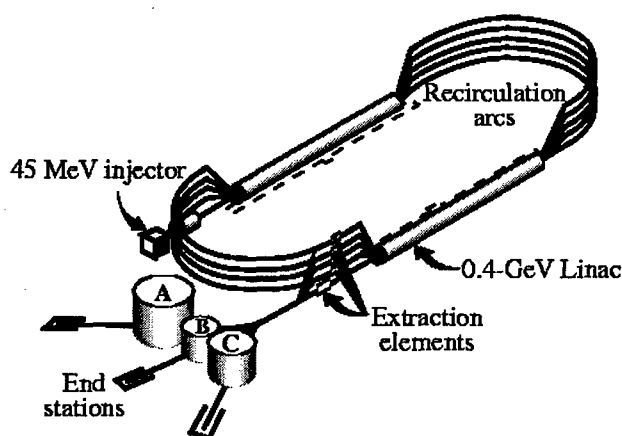


Figure 1: Physical layout of CEBAF beam lines. The BPM used for signal detection is near the foreground end of the right-hand linac.

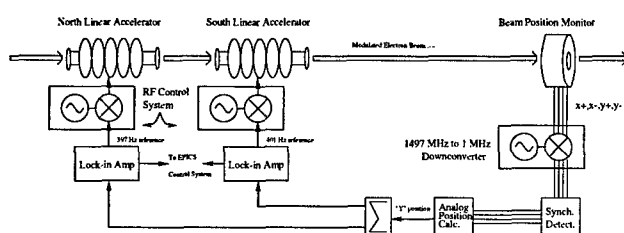


Figure 2: Layout of Master Oscillator Modulation system at CEBAF. Each linac uses one lock-in amplifier for a phase modulation reference and to detect the position modulation resulting from the energy modulation. A single BPM serves to detect the beam position for both systems.

### 3.1 Phase Modulation Subsystem

The overall MO Modulation system is shown in Fig. 2. It consists of commercial, off-the-shelf, lock-in amplifiers (model 7220 from EG&G), a phase modulation system, and a beam position monitor (BPM) pick-up. The lock-in units both provide the phase modulation source and detect the resulting beam energy modulation,

In each linac, the RF systems use 1427 MHz and 70 MHz signals supplied by the MO system to control the cavities at 1497 MHz. The 70 MHz signal is phase modulated at different frequencies in each linac. The modulation frequencies are 383 Hz for the North (first) Linac and 397 Hz for the South Linac. These frequencies ( $\pm 7$  Hz from the 13th harmonic of 30 Hz) were chosen for their low background noise and for isolation from the experimentally sensitive 30 Hz frequency at which the sign of beam spin polarization is changed. The phase modulators were carefully adjusted to give zero amplitude modulation of the 70 MHz signal at the fundamental phase modulation frequency. Any such amplitude modulation would couple directly into gradient modulation of each linac, interfering with the phase detection.

### 3.2 Sensor and Calibration

The BPM used for detection is of the "4-channel" type, with independent amplifier and demodulation channels for each of the four pickups. Each of these four signals is continuously available (low-pass filtered to 50 kHz). The standard BPM system digitizes these signals at 60 Hz, numerically processing them to provide laboratory frame vertical and horizontal beam positions. The pick-ups in the CEBAF accelerator are rotated  $45^\circ$  about the beam axis away from horizontal and vertical to avoid photo-emission interference from synchrotron radiation. The analog signal can be used to detect very small position modulations by using an analog processing circuit to generate laboratory frame analog beam position signals. For convenience, the analog signal processor both provides lab frame outputs and normalizes the signal against the beam current, providing a sensitivity of 750 mV/mm. The vertical position output is used by the two GPIB-interfaced lock-in amplifiers, the reference from each of which supplies the phase modulation reference for one linac.

The overall system sensitivity to changes in the linac RF phase was measured so that  $1^\circ$  of indicated phase error would correspond to the same shift of the global phase control for each linac. The measured system sensitivities were 9000  $\mu\text{V}/\text{deg}$  for the North Linac and 6430  $\mu\text{V}/\text{deg}$  for the South Linac. This correlates well with the expected sensitivities. Sideband power levels measured on the 70 MHz signal of the linacs at the relevant phase modulation frequency at -62 dBc for the North Linac and -67 dBc for the South Linac, correspond to  $0.07^\circ$  and  $0.05^\circ$  of phase modulation. From the measured sensitivity of the analog bpm signal, the known beam line dispersion, and knowing that the energy gain of each linac is about 47% of the total beam energy for the first pass beam (in addition to the injector energy), the expected system sensitivity should be 7400  $\mu\text{V}/\text{deg}$  for the North Linac and 5300  $\mu\text{V}/\text{deg}$  for the South Linac. These values are listed in Table 1.

Table 1: System Sensitivity( $\mu\text{V}/\text{deg}$ ), estimated vs. measured

Linac	Estimate	Measured
North Linac	7400	9000
South Linac	5300	6400

## 4 PERFORMANCE

The system as presently configured can only be used with continuous beam, although this is an artificial limitation caused by the analog signal processing. The current normalization provided in the analog bpm processing circuit induces too much noise when the beam current is lower than about 2  $\mu\text{A}$ . Although the zero current periods between beam macropulses during pulsed mode operation could be handled by gating the signals to the lock-ins, it

might be better to extend the operating range to lower current by doing the current normalization after the lock-in signal extraction. This would have the added benefit of providing a useful signal for pulsed beam, although the integration period might have to be increased significantly to improve the signal-to-noise for this case.

A plot of the measured phase errors over a thirty minute period for the two linacs is shown in Fig. 3. The coherent portion of the signals in the two linacs is very possibly due to a modulation of the beam phase from the injector, but the roughly 20 minute oscillation of the South Linac phase with respect to that of the North Linac is probably due to residual thermal regulation effects in the MO distribution line for the South Linac. The noisy portion of the traces at the far left resulted from a short period of pulsed beam. Shifts of  $0.1^\circ$  in the global phase set point for each linac can readily be detected when CW beam is present.

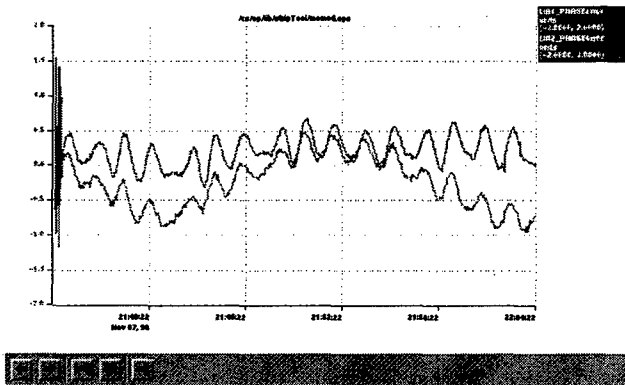


Figure 3: Thirty minute data stream from MO Modulation system for both linacs. The upper trace is the North Linac, and the lower trace is the South Linac. The vertical scale is  $\pm 2^\circ$ . See text for discussion.

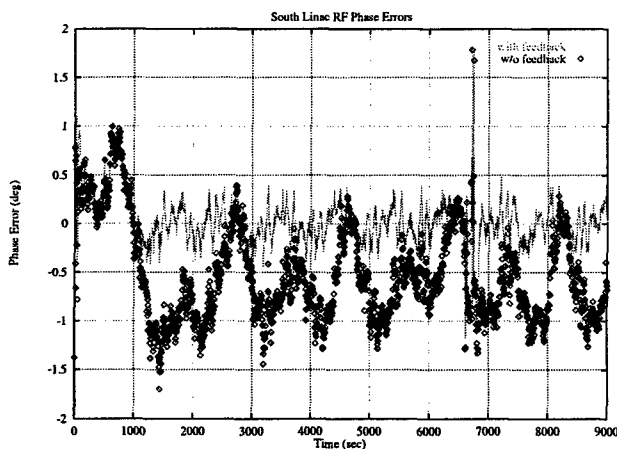


Figure 4: A 2.5 hr data sample for the measured South Linac RF phase with feedback enabled. The upper trace is the actual measured phase error signal, while the lower trace has the feedback correction added back to recover the uncorrected phase drift. See the text for discussion.

The result of our first efforts at using this monitor as a feedback signal are shown in Fig. 4 for the South Linac. The phase correction is done in software by simple dead-band limiting ( $\pm 0.3^\circ$ ), with corrections applied in discrete  $0.1^\circ$  steps at intervals of one second. The data shown were taken at five-second intervals. The lower trace is the measured phase error offset by the cumulative shift of the linac phase setpoint, while the upper trace is the feedback-limited actual phase error. The two traces are the same for the first 1000 seconds after beam is restored (near the left-hand side of the plot) until the feedback software is enabled.

The EG&G 7220 amplifiers are typically configured to average over a 1 second period. Improvements in resolution are possible with longer integration periods, but not clearly beneficial in this application. The empirical noise floor for beam measurements at low beam currents is consistent with detection of RMS beam motion at the  $0.5 \mu\text{m}$  level.

## 5 CONCLUSION AND FUTURE APPLICATIONS

The present system monitors the relative phase of the beam and the RF in each linac for only the first acceleration pass. It provides data suitable for use by a feedback system which will maintain the RF of each linac on crest in each linac to within a few tenths of a degree. Similar detectors in the transport lines for the experimental halls would allow for point of delivery cresting of the multipass RF for each linac. Adding additional detector systems in the recirculation arcs (peak dispersion 2.5 m) would allow for differential phase monitoring for recirculated beam. This would provide a sensitive monitor for the variations in the recirculation path length for CW beam, something we are presently able to measure only with short beam pulses. Such readily available digital information would be useful in automating the path length correction procedures.

Another application of interest is in monitoring the phase of one eight-cavity cryomodule in the injector. This section of the RF system is presently configured  $10^\circ$  off-crest to provide a coherent energy spread along the electron bunch. The bunch is then magnetically compressed in the injection chicane as the beam from the injector is joined with the recirculating electrons before passing through the main linacs.

## 6 REFERENCES

- [1] A Low-Cost, NIST-Traceable, High Performance Dielectric Resonant Master Oscillator for the Thomas Jefferson National Accelerator Facility, Larry Doolittle, *et al.*, these proceedings
- [2] Fast Digital Feedback System for Energy and Beam Position Stabilization, V. A. Lebedev, R. Dickson, these proceedings
- [3] 1 nA Beam Position Monitoring System, Rok Ursic, *et al.*, Proc. of the 1997 Part. Acc. Conf., Vancouver, B. C., Canada, 12-16 May, 1997.

# TECHNIQUE FOR FORMING AN RF SAMPLE SIGNAL FOR ACCELERATING FIELD FEEDBACK STABILIZATION IN TRAVELING WAVE LINACS\*

A. M. Vetter<sup>#</sup>, Boeing Phantom Works, Seattle, WA

## Abstract

Feedback loop techniques have been employed for decades in the stabilization of linac RF systems. Systems using these techniques require an input signal which represents the accelerating fields which are to be stabilized. Early implementations have taken a sample of the klystron output power as the source for this signal, thus enabling stabilization of fluctuations in the level and phase of klystron output due to variations in the high voltage pulse, droop in the driver amplifier gain, etc. However, fluctuations produced by beam loading, thermal drift of the linac section, and other effects which occur downstream from the sample point cannot be sensed or corrected using this approach.

A technique for combining samples of the input and output power from all of the traveling wave sections driven by a given klystron, enabling the system to respond to perturbations introduced at points throughout the RF system, has been developed. This approach is extended to both constant impedance and tapered section types. Described here are the laws which relate the phases and levels of the sample signals which are to be presented to the summing circuit to form the input to the stabilization loop.

## 1 BACKGROUND

The first visible FEL at the Boeing Physical Sciences Research Center was driven by an L band linac consisting of six traveling wave sections, each powered by a pulsed klystron stabilized by a feedback loop operating on a klystron output sample. The system worked well enough (after a settling period of 10-20  $\mu$ s) to stabilize the output power level to better than 1% and phase to better than 1° for the duration of the 100- $\mu$ s macropulse. The perturbations corrected by the feedback loop were chiefly due to klystron high voltage ripple (principally due to residual PFN unflatness) and droop in the klystron driver amplifier output. With this simple scheme, operators succeeded in achieving lasing in the FEL, but found the accelerator drifted out of tune frequently, probably because of inadequate temperature stabilization of the linac sections.

Present plans for a second generation visible FEL based on pulsed linac technology call for increasing macropulse repetition rate from 2 Hz to 30 Hz,

macropulse length from 100 to 200  $\mu$ s, and macropulse average beam current from 10 mA to 100 mA. The first two items, constituting a 30-fold RF duty factor increase to 0.6%, will drive much greater thermal drifts in both the modulator output and the linac section cell tuning over minute time scales as PFN coils, pulse transformer, and linac sections heat up. The increased beam loading will cause a ~5% linac energy droop (relative to low tune-up beam currents). These greatly enhanced perturbing effects could render the FEL virtually inoperable at its design output power unless the RF stabilization system is capable of stabilizing the accelerating voltage rather than solely the klystron output.

## 2 APPROACH

The 1.3 GHz RF systems of the upgraded linac typically contain two traveling wave linac sections powered by a single klystron. Given that our traveling wave sections incorporate no provision for sampling internal RF fields, the best approximation to the total complex accelerating voltage  $V_{system}$  applied to the beam (by all the cells of both the sections of a given RF system) which can be determined by available measurements is an appropriately weighted average of phase-adjusted coupler cell accelerating voltages  $V_b$ ,  $V_c$ ,  $V_e$ , and  $V_f$  (subscripts refer to points labeled in Fig. 1) which can be deduced from samples of the RF waves entering the input couplers and leaving the output couplers. That is,

$$V_{system} = D_b V_b + e^{i\Phi_{bc}} D_c V_c + e^{i\Phi_{be}} (D_e V_e + e^{i\Phi_{ef}} D_f V_f), \quad (1)$$

where the  $D$ 's are the weighting coefficients (determined as described below) and  $\Phi_{xy}$  represents the phase elapsed during the time required for beam electrons to move from point x to point y. This average reflects the effects of beam loading along both real and imaginary axes, thermal drift in phase length of the sections, etc.

As noted above, the coupler cell voltages are determined from the sample signal voltages  $V_1 \dots V_4$ , which are added in the power combiner. These sample signals must be correctly related in phase and signal level if their sum is to be proportional to  $V_{system}$ . The remainder of this paper describes how the weighting coefficients are determined and gives the relative phase and level relationships which must be obtained between sample signals for our upgraded FEL linac.

\*Work supported by USA/SSDC under Contract DASG-60-97-C-0105.

<sup>#</sup>Email: arthur.m.vetter@boeing.com

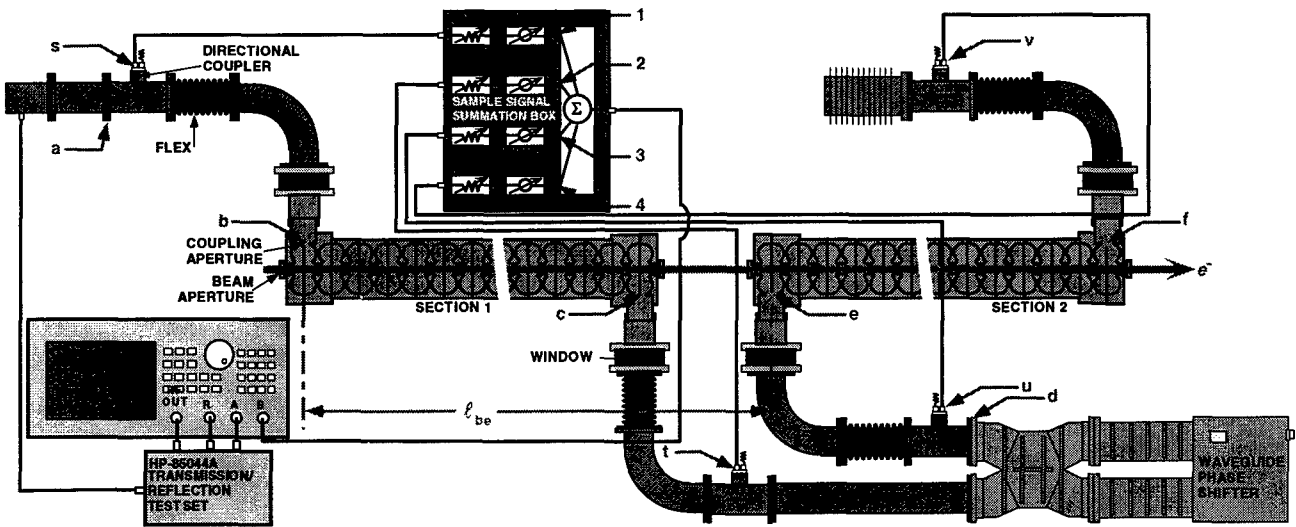


Figure 1: Representative configuration of the chief RF system components and network analyzer for measuring relative sample signals and adjusting summation box attenuators and phase shifters. Points of reference in the text are labeled with red arrows. Network analyzer is connected to the linac network in place of the klystron at point a.

### 3 DETERMINING WEIGHTS

To determine the best choice for the weighting factors  $D_b, D_c, \dots$ , a simple spread sheet model of the accelerating voltage in a typical traveling wave section of the proposed linac has been developed. Vector accelerating fields are computed for each cell, given the power entering from the upstream cell, local shunt impedance, and group velocity, after subtracting power transferred to the beam and applying a specified cell phase advance error  $\phi_{err}$ . The vector addition of the 18 cell voltage phasors of a second generation section described previously [1]

$$V_{true} = \sum_{i=1}^{18} V_i$$

is shown in Fig. 2 (solid lines) for five choices of phase advance error. For comparison, two linear combinations of the first and last cell voltage phasors are also shown: (1) the "unweighted" average of the first and last cell voltages multiplied by the number of cells; i.e.

$$V_{unwt} = 18 \left( \frac{V_1 + V_{18}}{2} \right) = 9 (V_1 + V_{18}),$$

shown as dotted lines, and (2) the weighted average

$$V_{wt} = D_1 V_1 + D_{18} V_{18},$$

shown as dashed lines, where weights  $D_1 = 8.26$  and  $D_{18} = 9.86$  are chosen so that

$$\lim_{\phi_{err} \rightarrow 0} V_{wt} = \lim_{\phi_{err} \rightarrow 0} V_{true}.$$

The first linear combination, while an improvement over the historical approach (which essentially delivers a result extending along the real axis to the red cross at

15.8 units regardless of  $\phi_{err}$ ) tracks the true section voltage rather imperfectly, giving a net phase error even at very low  $\phi_{err}$  and giving a significant amplitude error at larger  $\phi_{err}$ .

The second linear combination's weights are chosen so that it gives the correct value at a (low)  $\phi_{err}$  of  $0.1^\circ/\text{cell}$ . The dashed lines in Fig. 2 show that this approach corrects the phase error fairly well even for higher  $\phi_{err}$ , although the amplitude error remains for larger values of phase advance error.

The next question is how well this linear combination performs when there is beam loading. For the case  $\phi_{err} = 0$  (i.e., phase advance per cell is exactly the nominal  $135^\circ$ ), the effect of beam loading has been modeled with an input power of 10 MW for beam currents from zero to

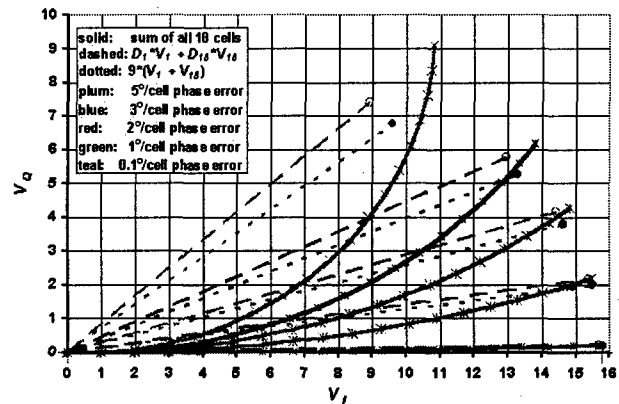


Figure 2:  $V_{true}$  (solid lines),  $V_{unwt}$  (dotted lines), and  $V_{wt}$  (dashed lines) in the 18-cell constant impedance linac section, with phase advance error as a parameter.

Table 1. FEL linac section parameters impacting relative sample signal strength. Total section attenuation  $A_{sec}$  is measured. Values of  $v_g/c$  and  $R/Q_o$  are computed [2]. Values of  $D$  are determined using spread sheet model described above. Note: L band RF systems of this linac are numbered 3 through 6.

Section Type Designation	Location(s)*	No. cells	$A_{sec}$ (dB)	End	bore (in)	$v_g/c$	$R/Q_o$ ( $\Omega$ )	$R_{cell}$ (M $\Omega$ )	$D$
HAP/MOPA	4U, 4D, 5D, 6U, 6D	18	2.6	IN	2.2	.0036	84.5	.1106	8.24
				OUT	2.2	.0036	84.5	.1106	9.88
HAP Prototype	3D	25	2.2	IN	2.92	.0167	62.8	.0177	21.10
				OUT	2.18	.0035	84.7	.1140	7.63
Original FEL Oscillator	5U	35	4.3	IN	2.51	.0074	75.2	.0479	22.42
				OUT	2.07	.0026	87.7	.1590	14.49

\*Numeral indicates RF system. A/B designates upstream/downstream in beam line order.

0.5 A. Even at beam currents up to 5 times nominal for the upgraded linac, resulting in a 24% droop in accelerating voltage, the relative amplitude error in the weighted average never exceeds 1.4%, and is less than 0.25% at the 0.1-A nominal beam current, within the acceptable range.

The numerical values found for the  $D$ 's are specific to the section modeled; i.e., the values must be recomputed if structure parameters such as number of cells and impedance profile change. Results for the three section types used in the new linac are listed in Table 1.

#### 4 CONDITIONS ON SAMPLE SIGNALS

Eq. 1 being established as the expression of the physical quantity which we seek to control, with  $D$  coefficients in that equation determined as described above, it remains to write down the phase and amplitude relations which must be maintained between the sample signals presented to the power combiner in order for the combined signal to be proportional to  $V_{system}$ . The phase and level of each sample signal are measured in turn with the other sample lines disconnected, using the test configuration shown in Fig. 1. It can be shown [3] that, provided the linac sections and waveguide phase shifter are correctly tuned to preserve beam synchronicity with the RF wave, **all the sample signal paths must have the same phase length from point a in Fig. 1 to the summing junction.**

It can further be shown that the sample signal strengths must be related by

$$\frac{P_2}{P_1} = A_{sec1} \frac{R_c}{R_b} \left( \frac{D_c}{D_b} \right)^2, \quad (2)$$

$$\frac{P_3}{P_1} = A_{sec1} \frac{R_c}{R_b} \left( \frac{D_c}{D_b} \right)^2, \text{ and} \quad (3)$$

$$\frac{P_4}{P_1} = A_{sec1} A_{sec2} \frac{R_c}{R_b} \left( \frac{D_c}{D_b} \right)^2, \quad (4)$$

where  $A_{sec1}$  and  $A_{sec2}$  are the power attenuation in the first and second sections respectively, and  $R_{b,f} = \frac{2\phi}{v_g/c} \left( \frac{R_c}{Q_o} \right)$ ,

where  $\phi = 3\pi/4$  and where  $(R/Q_o)$  and  $(v_g/c)$  are the local section parameters at the appropriate end cells (Table 1).

Using the linac section parameter values shown in Table 1 in Eqs. 2-4, the relative levels can be found for each of the four L band RF systems in the upgraded linac. The results each system appear in Table 2. Note that System 3 has only one section which operates as an accelerator section, and that in System 5 the sections appear in reverse order on the beam line so that Section 5D is the first section in the RF circuit.

Table 2: Relative levels of sample signals required for summed output to be proportional to system accelerating voltage.

RF System	3	4	5	6
$P_2/P_1$ (dB)	-1.9	-1.1	-1.1	-1.1
$P_3/P_1$ (dB)		-2.6	+2.4	-2.6
$P_4/P_1$ (dB)		-3.7	-0.4	-3.7

#### 5 REFERENCES

- [1] A.M. Vetter, et al., "First Operation of the HAP/MOPA Traveling Wave Structure at Boeing FEL", Proc. 1997 Particle Accelerator Conference, Vancouver BC, May 12-16, 1997, p. 2950 (1998).
- [2] A.M. Vetter, "Performance Expectations for Original HAP Linac Sections", Boeing Free Electron Laser Program report FEL/AT97-001, March, 1997.
- [3] A.M. Vetter, "Optimally Weighted Sample Signal Combination for Traveling Wave Linac Section Pairs", Boeing Free Electron Laser Program report FEL/AT99-003, March, 1999.



# RESONANT BEHAVIOUR OF HEAD TAIL MODES

K. Cornelis

CERN, Switzerland

## Abstract

Bunched beams in synchrotrons suffer from synchro-betatron resonances. They are produced by the coupling of the longitudinal motion into the transverse plane via dispersion and/or off-centre orbits in the accelerating cavities. These resonances are incoherent. The wake fields from bunches on central orbits, provoke head tail modes, which at a certain intensity will lead to the mode coupling instability. Besides head-tail modes, these wake fields create also new resonant conditions for coherent motion. In LEP, these coherent resonances, which are also present for central orbits, start to dominate the beam behaviour as of a certain bunch current and the mode coupling instability limit can only be reached for well defined betatron tunes

## 1 INTRODUCTION

In LEP the intensity is normally limited by the transfer mode coupling instability (TMCI). The threshold for this instability increases proportional with  $Q_s$  (synchrotron tune). When more RF power became available for the LEP2 stage, higher  $Q_s$  values could be used at injection. It was found that for  $Q_s$  values above 0.15 the TMCI threshold could not be reached anymore (fig 1), and the intensity limit became very strongly dependent on the tune, suggesting a limitation due to synchro-betatron resonances. Incoherent synchro-betatron resonances could be observed in LEP [1], but they were never considered to be a big problem since there is enough comfortable tune space left and the resonances due to the Sundelin effect (which is intensity depending) were found to be rather weak. On the other hand, coherent resonances could be observed. For an intensity higher than 0.4 mA per bunch head tail modes become visible in the tune spectra and they show clearly a resonant behaviour [2],[3]. In order to understand the resonant behaviour of this modes, and their relationship to the "normal" synchro-betatron resonances calculations were performed using a two particle head-tail model. Such a model was already successfully used in order to explain the effect of the beam-beam interaction on head tail modes in LEP [4]. The two particle head tail model describes very well the behaviour of the dipole and quadrupole modes and, since the bunches in LEP are very short (1 to 2 cm at injection), higher modes can be ignored.

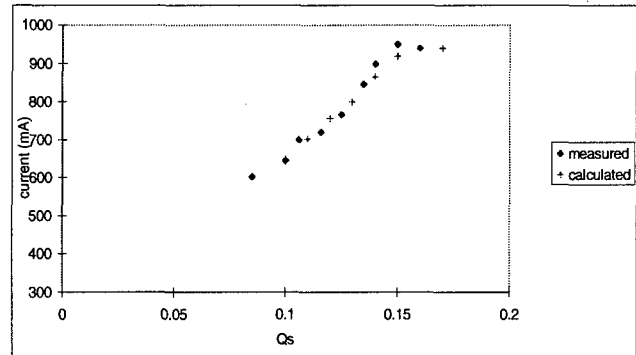


Fig 1 : The TMCI threshold can normally be increased by increasing  $Q_s$ . At a certain  $Q_s$  value however, coherent synchro-betatron resonances take over and limit the current to a value lower than the TMCI. In 1996 there was no gain for the LEP bunch current when pushing  $Q_s$  above 0.15. The limit was then 0.95 mA/bunch. In 1998 this limit was increased to 1.05 mA/bunch by reducing the impedance (taking out copper cavities).

## 2 THE CALCULATION

The transverse coordinates of the two macro particles are represented by  $x$  and  $y$ . The equation of motion can be written as the equations of two coupled oscillators and an external oscillator describing the synchro betatron coupling :

$$x'' + \omega^2 x = k_1 x + g(t) y + \delta \sin \omega_s t$$

$$y'' + \omega^2 y = k_1 y + g(-t) x - \delta \sin \omega_s t$$

With :

$\omega$  : unperturbed betatron tune

$k_1$  : describes the wake field from head on head or tail on tail

$\delta \sin(\omega_s t)$  : describes coupling from synchrotron motion

The coupling coefficient  $g(t)$  describes the wake field from head on tail. It describes the fact that the wake field can only be "felt" when the particle is behind the other one and it can be represented as a square pulsed function with  $\omega_s$  (the synchrotron frequency), as fundamental frequency. This block function can be developed in a

fourier series of odd multiples of  $\omega_s$ . For our calculation we will at first take only the fundamental mode into account.

$$g(t) = \frac{g_0}{2} + \frac{2}{\pi} g_0 \sum_{n=0}^{\infty} \frac{1}{(2n+1)} \sin((2n+1)\omega_s t)$$

putting :  $S = x + y$  and  $D = x - y$

$$w_1^2 = \omega^2 - k_1 - g/2$$

$$w_2^2 = \omega^2 - k_1 + g/2$$

$$k = g/\pi$$

( $k_1, g_0$  and  $k$  are proportional to the bunch current) and keeping only the first harmonic of  $g(t)$  one gets :

$$S'' + w_1^2 S - 2k \sin(\omega_s t) D$$

$$D'' + w_2^2 D - 2k \sin(\omega_s t) S + 2\delta \sin(\omega_s t)$$

The variable  $S$  describes the centre of mass motion of the two particles (dipole mode) and the variable  $D$  describes the beam size (quadrupole mode). On a normal pick-up only the centre of mass motion is visible.

The fourier transform of the two equations looks like :

$$\tilde{S}(\Omega) \frac{ik\tilde{D}(\Omega + \omega_s) - ik\tilde{D}(\Omega - \omega_s)}{w_1^2 - \Omega^2}$$

$$\tilde{D}(\Omega) \frac{ik\tilde{S}(\Omega - \omega_s) - ik\tilde{S}(\Omega + \omega_s)}{w_2^2 - \Omega^2} + 2\delta\tilde{Y}(\Omega)$$

The system can be described as two resonators ( $S$  and  $D$ ) with frequencies  $w_1$  and  $w_2$ . The two resonators are coupled through a frequency shifter ( $\pm \omega_s$ ) and the gain of the coupling is proportional to  $k$  i.e. the bunch intensity (fig 2). The external driving term from the synchro betatron resonance is coupled to the  $D$  resonator, because it has opposite phase for head and tail. In order to calculate the eigenfrequencies one can inject white noise in the system e.g. at the entrance of  $S$  and calculate how it evolves following the arrows. The  $S$  modes represent the motion of the centre of mass and hence are visible on a normal pick up. The  $D$  modes represent the quadrupole mode and are invisible.

What has been left out in the formula for simplicity is the coupling to the systematic integer resonance which acts on the  $S$  resonator since it has the same phase for both particles. This coupling leads to the same conclusions as the synchro-betatron coupling.

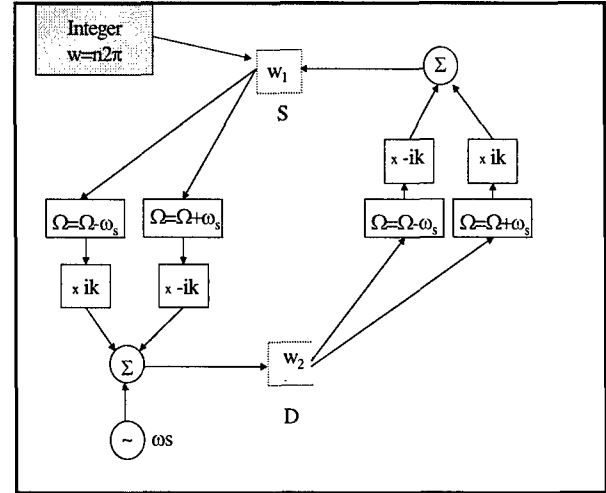


Fig 2 : Schematic representation of the two coupled oscillators  $S$  and  $D$ .

Only by looking at fig 2 one can draw some very interesting conclusions :

- $w_1$  and  $w_2$  are changing with intensity in a different way . Once  $w_1$  comes close to  $w_2 + \omega_s$  the system starts to become unstable. This is the so called transfer mode coupling instability.
- The  $\omega_s$  which injected at the  $D$  resonator gets shifted by  $+\omega_s$  when it gets to the  $S$  resonator and the shifted again when going to, the  $D$ . This has two consequences :
  - 1) Even if the  $Q_s$  oscillator is linear i.e. has no higher harmonics, the system will see higher harmonics of  $Q_s$ .
  - 2) The  $S$  oscillator sees only the even multiples of  $Q_s$ , the  $D$  oscillator sees the odd harmonics of  $Q_s$
- The systematic integer resonance is injected at the  $S$  resonator since it has the same phase for head and tail. The consequences are exactly the same as for the synchro-betatron coupling.
- **VERY IMPORTANT :** even in the absence of synchro-betatron coupling in the classical way (Sundelin or dispersion in cavities), the  $Q_s$  harmonics will still be present. They are injected in the system from the systematic integer resonance which is frequency shifted by  $\pm n\omega_s$ ,  $n$  being even for the  $S$  resonator and odd for the  $D$  oscillator.
- Any frequency in  $S$  that comes close to  $w_2 + \omega_s$  will lead to a resonance.
- Any frequency in  $D$  that comes close to  $w_1 + \omega_s$  will lead to a resonance.
- The feedback from  $S$  to  $D$  is proportional to  $k$  (impedance  $\times$  intensity), so the resonances become stronger for higher intensities.

### 3 RESULTS

Fig 3 and 4 show the calculated spectrum of S and D modes. In order to avoid singularities, a damping term ( $i\lambda S'$  and  $i\lambda D'$ ) was added to the equation of motion,  $\lambda$  being the damping constant at injection in LEP. The S modes can be compared to the measured spectrum in fig 5.

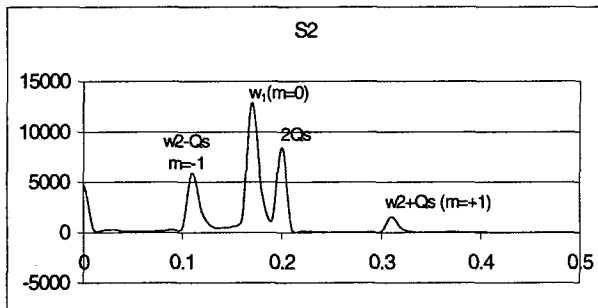


Fig 3 : calculated S-modes (visible modes)

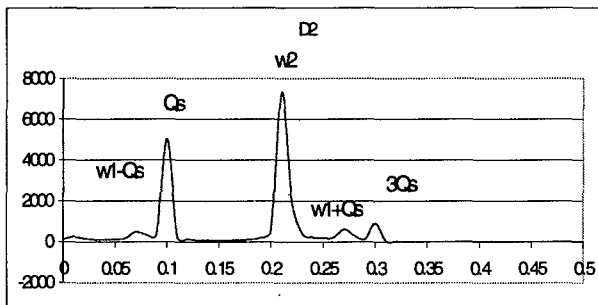


Fig 4 : calculated D modes (invisible)

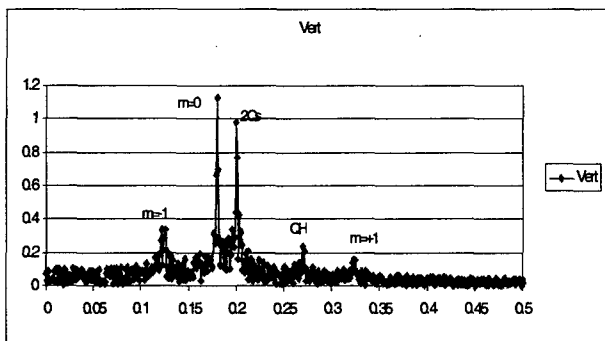


Fig 5 : measured vertical spectrum in LEP. Ibunch=0.5 mA.

In fig 6 the growth rate of the individual particle S and D modes combined as a function of the unperturbed tune ( $I=0.5$  mA). The dark lines are de visible modes, the faint lines are the invisible modes. The horizontal lines correspond to the multiples of  $Q_s$  ( $Q_s=0.15$ ). Resonances occur when lines of the same colour cross. In fig 7, the

same calculation was done for a bunch current of 0.8mA. The resonances start to become so strong that not much stable tune space is left.

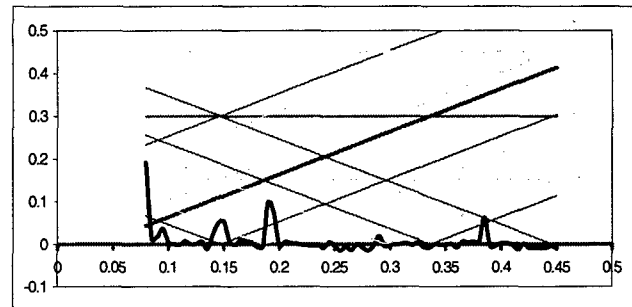


Fig 6

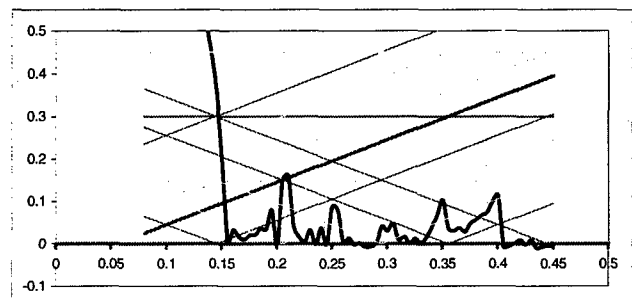


Fig 7 :Growth rate / damping for an intensity of 0.8 mA per bunch and a  $Q_s$  of 0.15.

### 4 REFERENCES

- [1] P. Collier, K. Cornelis, A. Hofmann, S. Myers, H. Schmickler, *Experimental observations of Synchro-Betatron resonances*, proceedings EPAC London, 1994.
- [2] K. Cornelis, *Observations in LEP on coherent Synchro-betatron Resonances*, Proceedings of the ICFA workshop, Madeira, 1993
- [3] K. Cornelis, M. Meddahi, H. Schmickler, *Resonant behavior of head tail modes*, SL-MD note 145, CERN, 1994.
- [4] K. Cornelis, Guangxiao Li, *Calculation of TMC Threshold in the precence of Beam-Beam Force*, proceedings EPAC London, 1994.

# TRANSVERSE INSTABILITIES IN THE ESRF STORAGE RING: SIMULATION, EXPERIMENTAL RESULTS AND IMPEDANCE MODELLING

R. Nagaoka, J.L. Revol, P. Kernel, ESRF, Grenoble, France  
G. Besnier, University of Rennes, Rennes, France

## Abstract

Transverse coherent single bunch motions are studied theoretically and experimentally for the ESRF machine. Starting from the mode-merging instability observed at low chromaticities, the head-tail mode frequencies and current thresholds are measured systematically in the vertical plane as functions of chromaticity, beam current, RF voltage and optics. Measurement of damping and growth rates of the dipolar mode is also attempted as a function of chromaticity to characterise the machine impedance empirically. Theoretical analysis is made in parallel to investigate the dynamics and to fit the model impedance to best reproduce the observations. Two numerical methods are employed: the multi-particle tracking and solution of an extended Sacherer's equation with the program MOSES. It is found that the machine impedance can be well represented by a simple BBR (Broad Band Resonator) impedance, the parameters of which are quasi uniquely determined from the fit of the mode-merging instability. It is experimentally shown that the low gap vacuum chamber sections contribute largely to the machine impedance. The resultant model is found to describe the observed thresholds at higher chromaticities as well, the dynamics of which is analysed to consist of higher-order head-tail instabilities.

## 1 INTRODUCTION

Associated with increasing low gap insertion device vacuum chambers in the ring, the encountered reduction of the threshold current of the transverse instabilities has been compensated at the ESRF by the use of large positive chromaticities, which, however, generally induce adverse effects of reducing the dynamic acceptances. To improve the machine performance, theoretical and experimental studies have been initiated [1]. The primary objective of the theoretical studies is to understand the dynamics occurring at high currents. As the dynamics is determined by the way the beam mode spectra interact with the machine impedance, the modelling of the impedance becomes one of the central issues. Numerical tools are employed and developed in both the time domain (multi-particle tracking) and the frequency domain (the program MOSES), in which a BBR (Broad Band Resonator) impedance is taken as the starting point. Experiments are made to survey systematically the coherent transverse motions in **various regimes** to provide inputs for the theoretical analysis, with a

particular effort to measure the damping and growth rate of the dipolar mode to empirically **characterise the ESRF storage ring impedance**.

## 2 MODE-MERGING REGIME

At low chromaticities  $|\xi_V| = |(\Delta Q_V/Q_V)/(\Delta p/p)| < 0.2$ , in accordance with theory the single bunch stability is largely limited by the merging of 0 and -1 vertical head-tail modes, whose threshold current is measured around 0.8 mA (Fig. 1).

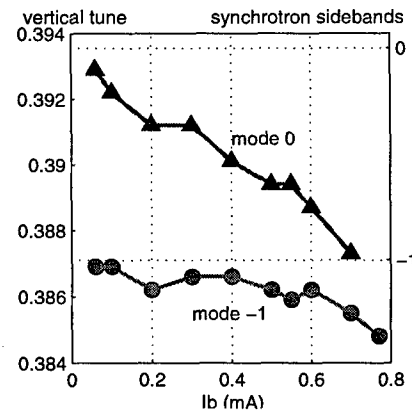
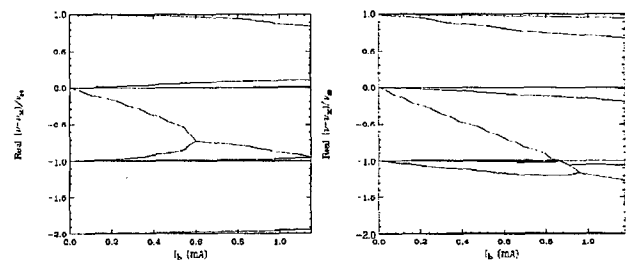


Figure 1: Observed mode-merging instability.



Figures 2: Fit with the BBR parameters. ( $f_R$  GHz,  $R_T$  MΩ/m,  $Q$ ) = (5, 8, 1) left and (22, 5, 1) right.  $\beta = 2.7$  m.

In the model of a Gaussian beam interacting with a BBR impedance, the tracking and MOSES give identical results for the mode coupling (the bunch lengthening included as a function of beam current). Fitting the observed merging with the BBR parameters leads to

$$f_R = 22 \text{ GHz}, R_T \beta = 13.5 \text{ M}\Omega \text{ and } Q = 1. \quad (1)$$

While the resonant frequency  $f_R$  is found to influence the merging frequency, the product of the shunt impedance  $R_T$

and the beta function  $\beta$  affects the threshold current. The BBR parameters are thus quasi uniquely determined from the fit. An observation that -1 mode is also slightly defocused requires  $f_R$  to be 22 GHz instead of e.g. 5 GHz (Figs. 2). The implication of the fitted BBR impedance shall be discussed further below.

### 3 DYNAMICS AT HIGHER CHROMATICITIES

With chromaticities slightly above that of the mode-merging, the beam becomes unstable at a certain current and stabilises again as the current is increased, without any merging of the modes. Several of such unstable points may be observed before reaching saturation. The measured coherent tunes indicate that higher-order modes -1, -2, ... are excited one after the other. Instead of mode-merging instabilities among higher-order modes that might be expected to take place, the observations therefore match with the classical picture of the head-tail instabilities [2]: With a shift of chromaticity, modes that overlap with a large real part of the impedance in the negative frequency region are unstable, while those that have passed this region are stabilised by the impedance in the positive frequency region. The fact that both the observations and the analysis indicate less detuning of the modes as the chromaticity is increased, is also in favour of this interpretation, as it results in weaker interactions among themselves.

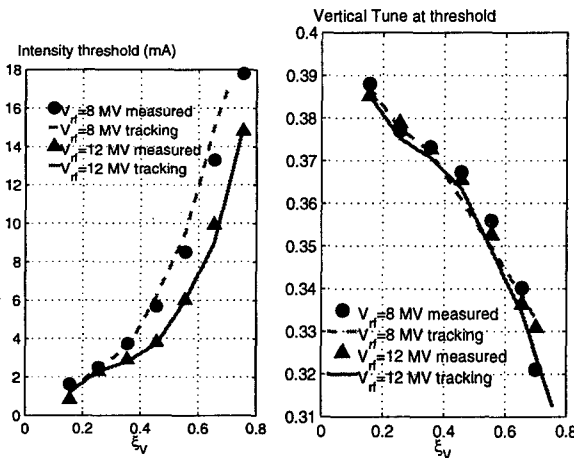


Figure 3: (Left) Measured threshold current versus chromaticity.

Figure 4: (Right) Measured coherent tunes at threshold versus chromaticity. Curves are the theoretical calculation using the BBR impedance of Eq. 1.

To see if the observed trend continues over larger chromaticities, mappings of the current  $I_{th}$  and the coherent tune  $(Q_V)_{th}$  at threshold versus chromaticity  $\xi_V$ , were constructed for two RF voltages  $V_{RF}$ 's (Figs. 3 and 4). The expected fast non-linear rise of  $I_{th}$  with  $\xi_V$  is observed until the stability is limited by optical reasons. A large increase of  $I_{th}$  is also noticed as the bunch is lengthened via  $V_{RF}$ . Whereas, the relation between  $(Q_V)_{th}$

and  $\xi_V$  (Fig. 4) exhibits two noteworthy features: i) a large excursion of  $(Q_V)_{th}$  across  $\xi_V$  that amounts to excitation of head-tail modes higher than  $|m|=10$ ; ii) accordance of the curves of  $(Q_V)_{th}$  for two different  $V_{RF}$ 's (in contrast to the variation of  $I_{th}$ ), which is supposed to be non-accidental.

It becomes a key issue to verify if the observed instability thresholds at high chromaticities can be described with the assumption of successive head-tail instabilities using the obtained BBR parameters. As reproduction of  $I_{th}$  requires the knowledge of damping forces, we focused on the relation between  $(Q_V)_{th}$  and  $\xi_V$ . The computations were made in three ways; a semi-analytical, MOSES and tracking. In the first two methods, the mode with the largest growth rate was searched by taking the measured  $I_{th}$  for a given  $\xi_V$ , and its mode frequency was identified as  $(Q_V)_{th}$ . Whereas with the tracking,  $I_{th}$  and  $(Q_V)_{th}$  were fully computed. Although the radiation damping time had to be shortened, it managed to reproduce the entire  $I_{th}$  versus  $\xi_V$ . In view of the Landau damping that exists in reality, the overall agreement is considered as meaningful. Note that all methods include the bunch lengthening by taking the measured data. All three approaches produced similar results, which agree well with the measured points (Fig. 4).

The agreement implies that the unstable modes interact with the negative resistance of the BBR impedance peaked at -22 GHz and not with the resistive wall impedance at low frequencies.

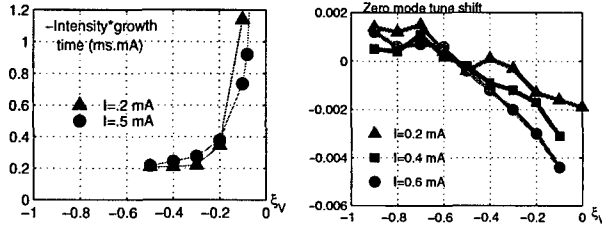
### 4 IMPEDANCE MODELLING

The fact that no resistive wall impedance is required at low frequencies appears to be contradicting to the continuously limited vertical stability with increasing low gap chambers as well as with the observation of resistive wall instabilities in the multibunch operation. Further studies have been made experimentally and theoretically to assess the obtained model.

#### 4.1 Dipole mode frequency measurement

Attempts were made to measure the damping and growth rates of the dipolar mode versus chromaticity to characterise the real part of the impedance. Details are given in Ref. 3. With  $\xi_V > 0$ , damping times were measured by fitting the peaks of the chromatically modulated amplitude decaying exponentially in time. Growth rates were measured with  $\xi_V < 0$ , thanks to the sufficiently large tune spread with amplitude to store beam as well as to the time gated transverse feedback to suppress the initial amplitude. However, the chromatic frequency could only go down to about -15 GHz due to the loss of beam signal. The monotonous decrease of the measured growth time as  $|\xi_V|$  is increased is in favour of the high resonant frequency of 22 GHz of the BBR impedance (Fig. 5 left). Furthermore, a preliminary

measurement of the dipolar frequency versus negative chromaticities for different beam currents shows convergence of the curves at around the expected position (Fig. 5 right).



Figures 5: Measured growth times (left) and the frequency shifts (right) of the dipolar mode versus negative chromaticity.

#### 4.2 Effect of low gap chamber sections

To explore the impact of the low gap vacuum vessels, the measurement of  $I_{th}$  versus  $\xi_V$  was repeated with an optics that increases the vertical  $\beta$  function by nearly a factor of 4 at every two straight sections without affecting much the rest of the optics (the low gap chambers are installed in the straight sections). The observed drastic reduction of  $I_{th}$  by a factor of 2 to even larger values at high currents (Fig. 6) confirms a large contribution of the low gap sections to the impedance.

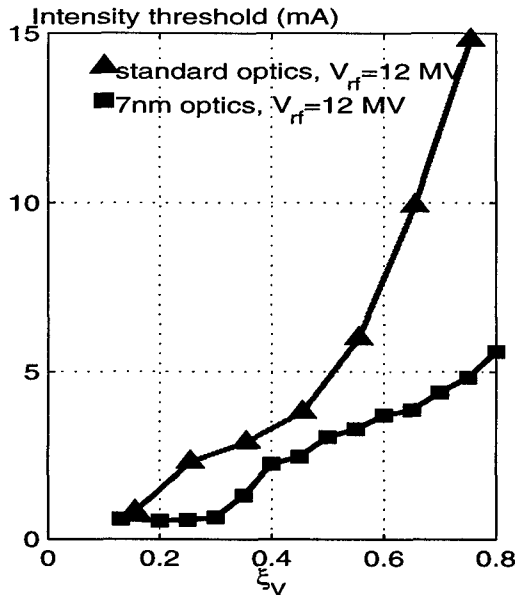


Figure 6: Current threshold  $I_{th}$  versus  $\xi_V$  measured in an increased  $\beta$  optics as compared to those of the standard optics.

#### 4.3 Resistive wall effects

Even though the real part of the resistive wall impedance may not be seen by the beam due to its odd function nature, the same may not be true for the imaginary part.

The effect of the resistive wall impedance was investigated in the mode-merging regime where its influence could be relatively important. The impedance of the existing low gap chambers was evaluated with the expression,

$$Z_{LR.W.}(\omega) = \frac{2R}{\epsilon_0 b^3} \left[ \sqrt{\frac{\kappa\omega}{2\epsilon_0}} (1-j) + j \frac{\omega^2 b}{2c} \right]^{-1} \quad (2)$$

derived by solving the Maxwell equation without the long range approximation (symbols have their usual meanings). Unlike the standard formula, the corresponding wake function converges correctly to zero in the  $t=0$  limit. With these functions, MOSES and tracking computations were made to estimate the dipolar detuning. Taking the beta value at the centre of the low gap vessels, the resistive wall explains at most 10% of the observed detuning.

A systematic evaluation of the various vacuum chamber impedances in the ring is to be made and compared with that empirically obtained. One such study has already been made evaluating the tapers of the low gap chambers in an approximate way with TBCI [4]. The mostly inductive nature found, along with the experimental evidence, leads one to assume that the tapers are largely responsible for the imaginary part of the obtained BBR impedance. The contribution of the resistive wall to the BBR is to be investigated in more detail.

### 5 CONCLUSION

A simple BBR impedance with the resonant frequency  $f_R$  at 22 GHz, the product of the shunt impedance  $R_T$  and the beta function  $\beta$  of 13.5 M $\Omega$  and  $Q$  equal to 1, fitted from the mode-merging instability, appears to give a good overall description of the observed vertical instabilities. The dynamics at high currents is analysed to consist of high order head-tail instabilities extending beyond  $|m|=10$ . The measured growth times and the detuning of the dipolar mode are basically consistent with  $f_R > 20$  GHz. A large contribution of the low gap chambers to the machine impedance was experimentally demonstrated.

### ACKNOWLEDGEMENT

The authors would like to thank N. Michel and E. Plouviez for their help in the experimental set-ups.

### 6 REFERENCES

- [1] J. Jacob, P. Kernel, R. Nagaoka, J.-L. Revol, A. Ropert, G. Besnier, "Experimental and Theoretical Studies of Transverse Single Bunch Instabilities at the ESRF", EPAC'98, Stockholm, 1998, p.999.
- [2] F.J. Sacherer, "Transverse Bunched Beam Instability - Theory", Proc. 9th Int. Conf. on High Energy Accelerators, Stanford 1974, p.347.
- [3] P. Kernel, J.-L. Revol, R. Nagaoka, G. Besnier, "Analysis of the Head Tail Damping and Growth Time for the Estimation of the ESRF Machine Impedance", this conference.
- [4] T. Günzel, "Estimation of the Impedance of ID-chambers", ESRF Machine Technical Note, 9-97/Theory, 1997.

# ANALYSIS OF THE HEAD TAIL DAMPING AND GROWTH TIME FOR THE ESTIMATION OF THE ESRF MACHINE IMPEDANCE

P. Kernel, J.-L. Revol, R. Nagaoka, ESRF, Grenoble, France  
G. Besnier, University of Rennes, France

## Abstract

A theoretical and experimental characterisation of transverse damping mechanisms was initiated within the framework of the single bunch transverse instability studies. An attempt is made to estimate the machine impedance through the measurement of the head tail damping time as a function of the chromaticity. The presence of strong sextupole fields used for chromaticity compensation however induces large momentum and amplitude dependent tune shifts. A systematic study of the different damping mechanisms was therefore performed in order to quantify the different contributions, which for the ESRF storage ring are in the same range. Numerical simulations and record of the beam response to a kick were performed. The transverse signal decay after the excitation was observed on the tune monitor system used in zero span mode. The tune amplitude dependence which depends on the kick amplitude is discussed first. Then the modulation induced by chromaticity overcompensation which could blind the observation is described. The measurement of the head tail damping and growing time, under precise operating conditions, with positive and negative chromaticity, is presented. Finally, a model for the machine impedance is discussed.

## 1 INTRODUCTION

The optimisation of the machine operation and the understanding of the feedback system efficiency for future operation are the ultimate purpose of the transverse motion study at the ESRF. The modelling of the storage ring transverse impedance is a key point for the study of single bunch instability limitations. For this purpose, a campaign of measurements has been performed, their interpretation is under progress [1,2]. The head tail damping time and the growth rate of the transverse signal resulting from the interaction of the beam modes with the machine impedance are accessible physical quantities. These data are complementary in order to cross-check the impedance model resulting from measurements of mode merging observed at low current [2] and threshold curve associated to higher order head-tail instability [1] for the high current regime. Head tail damping time extraction from the measurement requires a methodical approach, which is part of this paper. The characterisation and the description of the different mechanisms occurring at ESRF, the measurement methods and data are presented. The results (in vertical plane)

are compared to the tracking simulation in order to discuss the impedance model for single bunch.

## 2 DIFFERENT MECHANISMS REVIEW

The damping time measurement presents many difficulties in practice due to the fact that different other damping mechanisms can occur at the same time and spoil the observed signal.

### 2.1 Transverse Radiation Damping

Radiation damping mechanism presents a characteristic and constant decay time of 7 ms for the ESRF storage ring. This value is long enough not to perturb the head tail measurements.

### 2.2 Chromatic Modulation

After a transverse kick excitation, the frequency mixing of the individual particles oscillations, at slightly different betatron frequencies depending on the chromaticity  $\xi = (dQ/Q)/(dp/p)$ , results in a modulation of the transverse signal of period  $T_s$ , the synchrotron period [Fig.1.a and 1.b,  $T_s = 0.5$  ms]. The peak widths, which only depend on the chromaticity, narrow when the chromaticity increases. To avoid confusing the chromatic modulation with the head-tail damping, the head tail damping decay should be much **longer** than  $T_s$ . In that case, from the amplitude of a few peaks, the **envelope** of the modulated signal can be extracted.

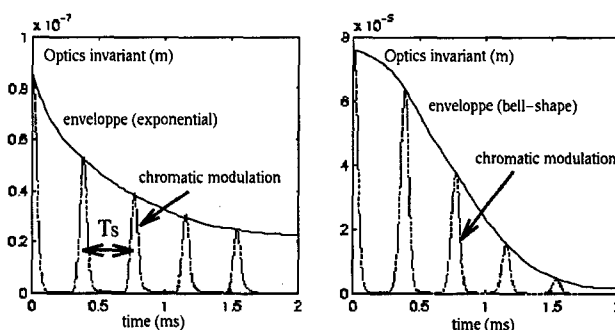


Fig 1.a (left) Modulated head tail damping (simul.)  
Fig 1.b (right) Modulated tune spread damping (simul.)

### 2.3 Amplitude-Dependant Tune Spread Damping

If the transverse kick is too large, additional tune spread is induced within the bunch by the non-linearity coming from the strong sextupoles fields. The corresponding damping signal resulting from this mechanism presents a bell-shape decay (Fig.1.b). The strength of the tune

spread damping, which is independent of the beam current, increases with the kick amplitude, Fig.2. For the head tail damping time measurement, the kick should be chosen small to keep the tune spread damping time long enough to be negligible (in the order of a few ms).

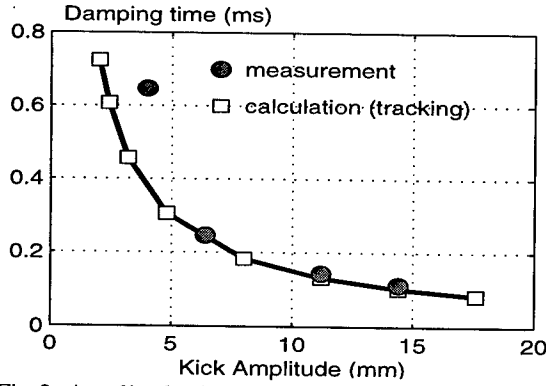


Fig 2: Amplitude-dependant tune spread damping time

### 2.4 Head Tail Damping and Growing time.

For Hermitian modes that are not interacting in a mode-coupling regime, the head tail characteristic time for a mode  $m$  is given by the formula (cf. [2]):

$$\tau_m = \frac{2^{2m} m!}{(2m-1)!!} \frac{\sigma_\tau}{I} \frac{4\sqrt{\pi} E/e}{\beta} \frac{\sum_p h_m(\omega_p - \omega_\xi)}{\sum_p \text{Re}(Z(\omega)) h_m(\omega_p - \omega_\xi)} \quad (1)$$

with  $\omega_p = \omega_\beta + m\omega_\alpha + p\omega_0$ .

The mode spectrum  $h_m(\omega_p - \omega_\xi)$ , is shifted in frequency by  $\omega_\xi = \omega_0 Q_\beta \xi / \alpha$ , proportional to the chromaticity. The measurement of the head tail **damping** or **growing** time  $\tau_m$  versus chromaticity, is characteristic of the interaction of the mode spectrum with the real part of the transverse impedance  $Z(\omega)$ . For the head tail mechanism, the transverse pick-up signal is exponential (fig.1a). The damping time  $\tau_m$  should be inversely proportional to the peak current  $I/\sigma_\tau$ , and to the optical beta function  $\beta$ . These parameters can be mastered during the experiments. The bunch length which also defines the width of the mode spectrum  $h_m(\omega_p - \omega_\xi)$ , should be long in order to scan the impedance in more detail.

## 3 HEAD TAIL DAMPING TIME ( $\xi > 0$ )

### 3.1 Measurement Methods

At **positive** chromaticities, the head tail damping time has been scanned versus  $\xi$ , in both vertical and horizontal planes, much below the current threshold. The transverse excitation is produced by a kick of the injection kicker for the horizontal plane, or by the gated tune monitor shaker for the vertical plane. The particle distribution resulting from the kick is equivalent to a low frequency shaker mode, and its corresponding envelope spectrum for Gaussian beam is (different of the spectrum of the Hermitian modes assumed in Eq.1 when  $m \neq 0$ ):

$$h_m(\omega - \omega_\xi) = \exp\left[-\frac{1}{2}\left((\omega - \omega_\xi)^2 + (\omega_{sh} - \omega_\xi)^2\right)\sigma_\tau^2\right] \times I_m\left[(\omega - \omega_\xi)(\omega_{sh} - \omega_\xi)\sigma_\tau^2\right] \quad (2)$$

where  $I_m$  is the modified Bessel's function of the 1<sup>st</sup> kind and  $\omega_{sh} \approx 0$  is the shaker frequency, which is null for a kick. Kicked and shaken modes present exactly the same spectrum.

Synchronously with a kick, the transverse signal decay is measured with a spectrum analyser used in the zero span mode adjusted to the betatron frequency. This method improved by averaging was efficient for the detection of very low response defined by the following operating conditions:

- **Low intensity per bunch**, necessary for a head tail damping to be longer than  $T_s = 0.5$  ms, to be able to extract the envelope from the chromatic modulation.

- **Small transverse kick** to avoid the tune spread damping. The absence of tune spread can be checked by the linear dependence with current.

- **Increased average intensity**, in some cases, to keep the transverse signal out of the noise level, (few bunch modes, with low single bunch intensity).

On Fig.3b, the expected shape of the head tail damping time **after a kick** has been computed with a tracking code, using a BBR model for the transverse vertical impedance with  $f_i = 22$  GHz,  $Q = 1$ ,  $R \times \beta = 13.5$  M $\Omega$ .

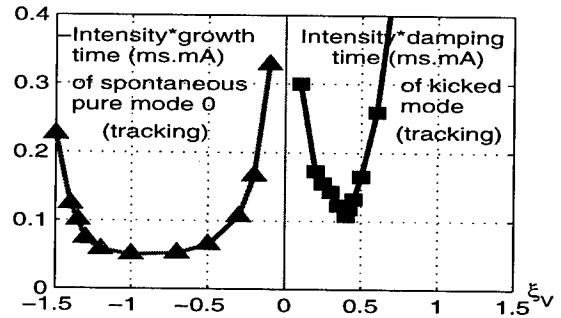


Fig3a(left) Head tail growth time simul. (mode 0)

Fig3b(right) Head tail damp. time simul. after a kick

### 3.2 Results

According to theory, the damping time should **increase** when  $\xi$  is close to 0, because of the cancellation due to the anti-symmetric real part of  $Z(p)$ ; and **increase** at large  $\xi$ , due to the decreasing of impedance. The curve should present a minimum at the resonant frequency of the BBR model. These curves (Fig.4 right, vert. plane) do not present the expected shape and no proportionality with the current, which is a hint to say that the observed damping time was not a pure head tail phenomena. This discrepancy with the theory might come from a measurement problem. Despite the efforts employed to avoid all the perturbing phenomena and to extract the pure head tail damping mechanism, it seems that another mechanism has polluted the measurement. The obtained results should be clarified by further theoretical studies.



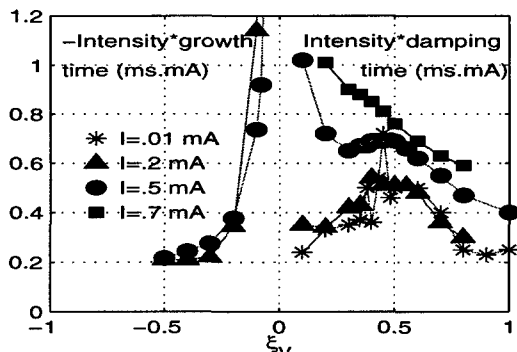


Fig 4: Measured head tail growth and damping times

## 4 HEAD TAIL GROWING TIME ( $\xi < 0$ )

### 4.1 Measurement Methods

Growth rate measurement of the strongly unstable mode 0 has been realised in the **negative** chromaticity regime. In that case the spectrum, which is not distorted by any kick, is purely **Gaussian**. As the mode grows, the amplitude-dependent tune spread filamentates the beam and leads to a destruction of the initial mode coherence. A saw-tooth motion with a period in the range of millisecond may be observed at this stage (Fig.5), which is supposed to be due to the vanishing of the head-tail growth for a filamented beam. The radiation damping then concentrates the particles to the initial state. The strong tune spread damping would be a characteristic effect of the ESRF optics. It allows storing beam above head-tail threshold. For the measurement, the beam is stabilised with the transverse **feedback** system, which send the vertical transverse signal to the shaker, with proper gain and phase. At a given time, the feedback is suppressed for a few milliseconds and the transverse signal is analysed synchronously. (Fig.5 and 6)

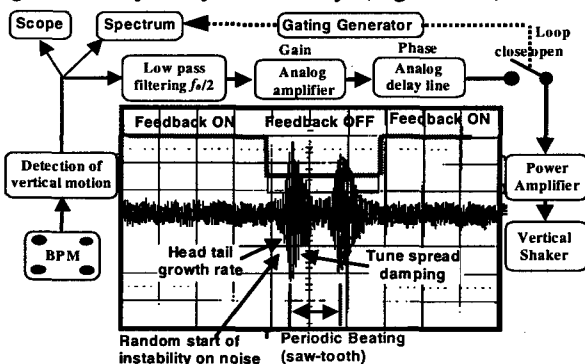


Fig 5: Measurement set-up at negative chromaticities

This method allows to go up to  $\xi = -0.5$ , but at larger negative vertical chromaticities, the feedback becomes inefficient. Due to the large mode spectrum shift by  $\omega_\xi$ , the measurement system which works at low frequency cannot pick-up the mode signal when  $\xi$  is too far from 0.

## 4.2 Results

The growing time which monotonously decreases up to  $\xi = -0.5$ , is in agreement with the 22 GHz BBR impedance model given by other modelling methods [1] (Fig.4 left). Nevertheless, the limitation of the measurement at  $\xi = -0.5$  (corresponding to -13 GHz) does not allow to measure the turning point where the growing time should increase again. According to the theoretical curve, the turning point should be located at  $\xi = -0.8$  (Fig.3.a). With a scaling of the parameter  $R$ , the measurement confirms that the 22 GHz BBR is a reasonable model for the ESRF storage ring impedance. A possibility to measure the turning point could be to lengthen the spectrum by shortening the bunch. For a given  $\xi$ , this will increase the spectrum amplitude at zero frequency and improve the efficiency of the detected signal and of the feedback.

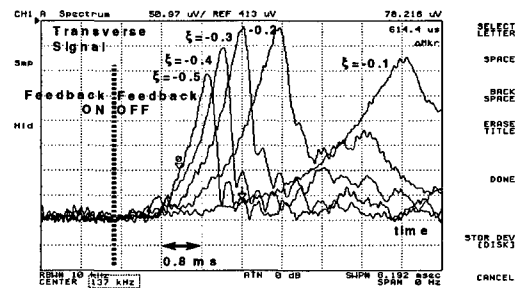


Fig 6: Growth rate as a function of the chromaticity

## 5 CONCLUSION

The different damping mechanisms at ESRF have been investigated and observed. The measurement of the head tail damping time cannot be interpreted but further theoretical studies will be done to understand the observation. The measurement of the growth time was successful and is compatible with BBR impedance model. Attempts are in progress to understand the imaginary part of the impedance by measuring the mode 0 detuning versus  $\xi$ , in the negative chromaticity regime.

## 6 ACKNOWLEDGEMENTS

The authors would like to thank E. Plouviez for his support for measurements and diagnostics, and N. Michel for the feedback development.

## 7 REFERENCES

- [1] R. Nagaoka, J.-L. Revol, P. Kernel and G. Besnier, "Transverse Instabilities in the ESRF Storage Ring: Simulation, Experimental Results and Impedance Modelling", PAC'99, New-York, 1999.
- [2] J. Jacob, P. Kernel, R. Nagaoka, J.-L. Revol, A. Ropert, G. Besnier, "Experimental and Theoretical Studies of Transverse Single Bunch Instabilities at the ESRF", EPAC'98, Stockholm, 1998.
- [3] F.J. Sacherer, "Transverse Bunched-Beam Instabilities", CERN/PS/BR 76-21, Geneva, 1976.

# AN INTEGRABLE OPTICS LENS FOR THE PSR AND SNS\*

V.Danilov, J.Galambos, D.Jeon, J.Holmes, D.Olsen, ORNL SNS Project, Oak Ridge, TN  
D.Fitzgerald, R.Macek, M.Plum, LANL LANSCE, Los Alamos, NM

## Abstract

This is a study to increase the threshold of the Los Alamos LANSCE Proton Storage Ring (PSR) to the electron-proton (e-p) instability. The approach is to use a solenoid lens system to increase the Landau damping and betatron tune spread, without producing betatron resonances or energy spread that would necessitate increased aperture. This study rests upon the concept of integrable optics, which is a branch of Hamiltonian dynamics that determines how to modify dynamic systems to obtain integrable Hamiltonians having regular phase space maps and no chaos. For such cases, the particle trajectories, when integrated as functions of time and initial conditions, follow invariant surfaces. In essence, the maps are similar to linear maps with the addition of a betatron tune spread; however, the magnetic fields required to obtain such maps are complicated.

## 1 INTRODUCTION

Prior to the recent upgrade program, the average beam current in the PSR was limited to 70μA, at 20Hz and  $2 \times 10^{13}$  protons/pulse. At this intensity, the threshold for the PSR e-p instability limits further current [1]. The PSR e-p instability limits the performance of the LANSCE facility and provides a fundamental uncertainty and risk to the performance of a new spallation neutron source such as the SNS Project.

One of the potential explanations of this instability is the large electron charge in the vacuum chamber, produced by multipactoring and other effects. It has been found [1] that increasing the betatron tune spread using octupoles increases the instability threshold. In particular, increasing the betatron tune spread by about 0.01 could increase the threshold by about a factor of three. Unfortunately, octupoles excite nonlinear resonances that lead to an uncontrolled beam loss. Even so, this is an important result because it shows that modifying the magnetic fields to increase the tune spread can raise the instability threshold. Increasing the energy spread can also increase the tune spread in the PSR; however, this is not a viable solution because of the limited horizontal aperture. We propose to use a special nonlinear element to increase the betatron tune spread without introducing nonlinear resonances. We call such a system "integrable", though in general, phase space from integrable systems can contain resonances.

## 2 INTEGRABLE OPTICS

One particularly simple class of integrable optics applies to axially symmetric magnetic fields. Under certain conditions, solenoid lenses can be used to construct these integrable maps for circular rings. To apply this to the PSR, the lattice must meet two conditions: (1) the solenoid lenses must be installed in a straight section at a location with  $\beta_x = \beta_y$ , so that a beam with equal emittances is round; and (2) the fractional tunes of the ring in both planes, without the solenoids, must be either 0.25 or 0.75. Once these conditions are satisfied the angular momentum,  $M = x \cdot p_y - y \cdot p_x$ , an integral of the motion, will be conserved by the axial symmetry of the system.  $M$  will also be conserved in the linear storage ring structure.

There is an additional invariant of motion, which is conserved for all values of the angular momentum whenever the nonlinear kick is axially symmetric and the change in radial momentum  $p_r$  is given by  $\Delta p_r = -b \cdot r / (1 + a \cdot r^2)$ , where  $a$  and  $b$  are free parameters [2]. Throughout, the normalised variables,  $x_n = x / \sqrt{\beta_x}$ ,  $y_n = y / \sqrt{\beta_y}$ , are used along with the same normalization for radial variables. If the linear transfer matrices for one turn around the ring for both horizontal and vertical normalised variables are given by

$\begin{pmatrix} 0 & 1 \\ -1 & 0 \end{pmatrix}$ , then, the invariant after the above lens is:

$$I(r_n, p_r) = (a \cdot r_n^2 + 1) \cdot (r_n + p_r)^2 + b \cdot r_n \cdot (r_n + p_r) + (r_n^2 + M^2 / r_n^2). \quad (1)$$

Figure 1 plots the invariant surfaces given by Eq. 1. In order to model the PSR with an aperture of about 5 cm, the x coordinate unit scale in Fig. 1 is 10 cm. For this calculation the angular momentum is equal to zero and the coefficients in scaled units are  $a = -0.40$  and  $b = 1.17$ . The reference orbit betatron fractional tune for both planes is 0.35 with the solenoid present.

The stable motion is bounded by two separatrices, which occur at the points:

$$\left( \sqrt{\frac{(b-2)}{2a}}, \sqrt{\frac{(b-2)}{2a}} \right) \text{ and } \left( \sqrt{\frac{(b-2)}{2a}}, -\sqrt{\frac{(b-2)}{2a}} \right). \quad (2)$$

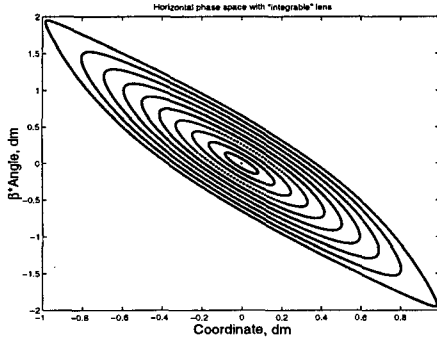


Fig. 1 Phase space motion in the integrable cell. The contours represent motion with initial conditions from the closed orbit up to the limit of the dynamic aperture.

These two points are critical points of the Eq.1 invariant and define the region of stable phase space. If, for example, the beam occupies half the aperture, then the tune spread is found numerically to be 0.006 and is close to what is required. This increase in tune spread is produced without exciting any betatron resonances. If we take into account only the octupole term, the formula for tune spread is:  $\Delta\nu = 3/(8 \cdot 2 \cdot \pi) \cdot b \cdot a \cdot \varepsilon_0 = 6 \cdot 10^{-3}$  for emittance  $\varepsilon_0 \approx 20 \cdot 10^{-6} \text{ m} \cdot \text{rad}$ .

We must form the lenses using an axially symmetric magnetic structure in order to preserve angular momentum invariance. All the fields in such a system can be calculated from a single function  $H(s)$ , the longitudinal magnetic field on the axis of the lens, which corresponds to the reference orbit. The longitudinal magnetic field in all space is then [3]:

$$H(s, r) = \sum_{n=0}^{\infty} \frac{(-1)^n}{(n!)^2} \cdot H^{(2n)}(s) \cdot (r/2)^{2n}, \quad (3)$$

where  $r$  is the radius from the axis,  $s$  is the longitudinal coordinate, and the superscript  $(2n)$  denotes the  $2n$ -th derivative of  $H(s)$  with respect to the coordinate  $s$ . Calculation of nonlinear kicks through third order from such a lens was made in [4]. Here the exact expressions for the nonlinear kick will be used.

The radial and azimuthal motion of a particle can be described by the two simple equations:

$$r'' - r \cdot \theta' \cdot (\theta' + e \cdot H_s / p) = 0, \quad \theta' = \theta_0 \cdot r_0^2 / r^2 - e \cdot \Phi / (2\pi r^2), \quad (4)$$

where the derivatives are taken on the longitudinal coordinate, and  $\theta, \theta_0$  are the azimuthal and initial azimuthal angle of the particle, and the same notation is used for the radius  $r$ . The symbol  $\Phi$  stands for the magnetic flux and is equal to  $\Phi = 2\pi \int_0^r H_s \cdot r' dr'$ ,

where  $H_s$  is taken from Eq. 3. Finally, Eqs. 4 can be combined to yield:

$$r'' - r \cdot \theta_0 \cdot r_0^2 / r^2 = \frac{e}{p} \cdot \theta_0 \cdot r_0^2 / r^2 \left( \frac{\Phi(r)}{\pi^2} - H_s(r) \right) + \frac{e^2}{(2\pi)^2 r^3} \cdot (\Phi(r)^2 - \Phi(r) \cdot \Phi(r)'_r \cdot r). \quad (5)$$

The force term on the L.H.S. of Eq. 5 is just the centripetal force, which always appears in cylindrical coordinates. The first term on the R.H.S. is a linear function of the longitudinal field derivatives, and its integral is zero because the function at the ends is zero. Consequently, only the last term of the R.H.S. is of interest, and is denoted by:

$$K(r, s) = \frac{e^2}{p^2} \left( -\frac{1}{4} (H^{(0)})^2 \cdot r + \frac{1}{8} H^{(0)} \cdot H^{(2)} \cdot r^3 - \frac{1}{128} H^{(0)} \cdot H^{(4)} \cdot r^5 + \frac{3}{256} (H^{(2)})^2 \cdot r^5 + \left( \frac{1}{4608} H^{(0)} \cdot H^{(6)} + \frac{1}{768} H^{(2)} \cdot H^{(4)} \right) \cdot r^7 \dots \right)$$

where  $H^{(n)}$  is the  $n$ -th derivative of the longitudinal field on the axis.

The radial kick can be obtained by integrating  $K(r, s)$  over  $s$ , regarding the radius  $r$  as a constant. The integration yields, where we ignore the centripetal force and consider only the kick from the magnetic field:

$$\Delta r' = \frac{e^2}{p^2} \left( -\frac{r}{4} \int_{-\infty}^{\infty} (H^{(0)})^2 ds - \frac{r^3}{8} \int_{-\infty}^{\infty} (H^{(1)})^2 ds - \frac{5 \cdot r^5}{256} \int_{-\infty}^{\infty} (H^{(2)})^2 ds - \frac{7 \cdot r^7}{4608} \int_{-\infty}^{\infty} (H^{(3)})^2 ds \dots \right) \quad (6)$$

## 2.1 Physics Design of Axially Symmetric Integrable Lens from Solenoids

Now let us construct the integrable lens from one-wire coils. The magnetic field from a one-wire coil on the symmetry axis is:

$$H [\text{Tesla}] = 2\pi \cdot 10^{-7} I [\text{Amp}] \cdot R^2 / (R^2 + s^2)^{3/2}, \quad (7)$$

where  $R$  is the radius of the coil,  $I$  is the current, and  $s$  is the longitudinal coordinate with respect to the coil. It has found numerically that two coils with the same longitudinal coordinate dependence can be utilised to produce the needed nonlinear lens with very good accuracy. A ninth order Taylor expansion of the kick on the radial coordinate found relative coil radii of  $R$  and

$1.5R$ , and relative currents of  $I$  and  $-0.65I$ , respectively. Fig. 2 shows a schematic view of this lens.

Now let us write the parameters of this lens in terms of the inner radius  $R$  and current  $I$ . The radial angle change is:

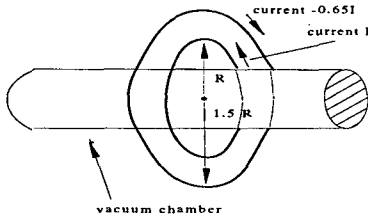


Figure 2: Schematic view of nonlinear lens

$$\Delta r' = \frac{R^2 \cdot 0.1}{r_L^2} \left( -0.73 \frac{r}{R} - 0.64 \frac{r^3}{R^3} - 0.6 \frac{r^5}{R^5} - 0.55 \frac{r^7}{R^7} - 0.5 \frac{r^9}{R^9} \right),$$

where  $r_L(m)$  is the Larmour radius corresponding to the maximum magnetic field at the axis. The ratio of all successive pairs of coefficients is nearly constant, and is equal to  $0.90 \pm 0.02$ . This provides the value of  $a$  for the kick:  $a = -0.9 \cdot \beta / R^2$ . The coefficient  $b$  for the same kick is  $0.073 \cdot R \cdot \beta / r_L^2$ .

To obtain a linear shift from this lens the coefficient  $b$ , as shown in Fig. 1, must be 1.17. Substituting the parameter values  $R = 0.05m$ ,  $\beta = 10m$  appropriate to the PSR, we obtain  $r_L = 0.2m$ ,  $D \approx 5cm$  for the Larmour radius and dynamic aperture, respectively, and the coil current is:

$$I(A) = \frac{v}{c} \cdot E(GeV) \cdot R(m) / 0.6\pi \cdot 10^{-7} \cdot r_L(m) \approx 2 \cdot 10^6 A.$$

Clearly such a solenoid with normal conducting cu coils would require many turns. When many turns are used with a reasonable current density it is impossible to design a coil producing the correct end field shape to serve as an axially symmetric integrable-optics lens.

A superconducting variation of this idea may be more feasible. Consider a 10-coil variant with an optimal coil aspect ratio found by numerical optimisation. The current in the coil is taken to be 600 kA. Additionally, the inclusion of iron provides a 65% increase in the cubic nonlinearity compared to the case with no iron. Figure 3 shows the coil configuration used to model the impact of the iron inserts on the field as calculated with Poisson. Contours of constant field level are also shown. The iron encompasses all the coils and extends up to 13 cm from the axis, the white contour delineates the positive current area (600 kA) and the black contours delineate the negative current (-600 kA)

area. The fields and current density can be achieved with NbTi cable. A more detailed description of the calculations can be found in Ref. [5]. The betatron tune spread for this case is 0.004, which is close that needed. A more expensive superconducting variant could use lower temperatures and higher fields to permit operation at up to 14 T, which would provide a tune spread four times higher. Another variant is a pulsed lens with the magnetic field up to 20 Tesla.

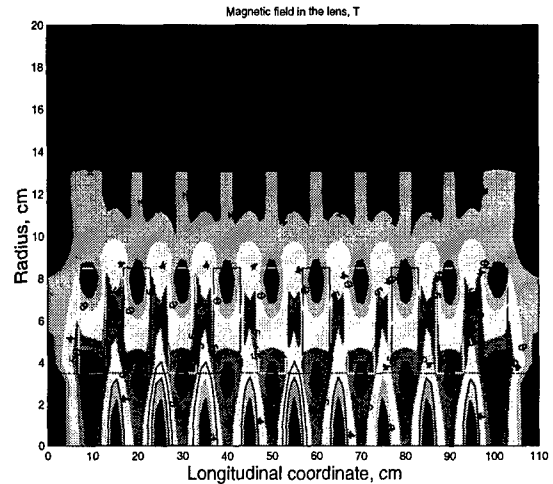


Fig. 3. Magnetic field in superconducting solenoid

## 5 CONCLUSIONS

The use of a solenoid lens to increase the betatron tune spread, and hence Landau damping and the threshold of the LANSCE PSR instability has been studied. Such a lens could increase the threshold without producing betatron resonances or energy spread that would require increased aperture. It is found that such a lens could be fabricated, but the required field shape and intensity would require the use of superconducting cable.

## 6 ACKNOWLEDGMENT

\*Research on the Spallation Neutron Source is sponsored by the Division of Materials Science, U.S. Department of Energy, under contract number DE-AC05-96OR22464 with Lockheed Martin Energy Research Corporation for Oak Ridge National Laboratory.

## 6 REFERENCES

- [1] D. Neuffer, et al., *Particle Accelerators* **23**, 133-148 (1988).
- [2] V. Danilov, E. Perevedentsev in *PAC 97*, 1997
- [3] V.V. Batygin, I.N. Toptygin, in *Problems in Electrodynamics*, ed. By D. ter Haar (Academic Press, London, 1978), p.279.
- [4] V. Danilov et al. "Dynamic Aperture Limitations in Storage Rings Due to Solenoids", EPAC 1990, Nice, France
- [5] V. Danilov et al. "Proposal for Solenoid Lens Experiment at PSR", SNS Tech Memo, March, 1999

## A STUDY ON THE POSSIBILITY TO INCREASE THE PSR E-P INSTABILITY THRESHOLD\*

V.Danilov, J.Galambos, D.Jeon, J.Holmes, D.Olsen, ORNL SNS Project, Oak Ridge, TN

D.Fitzgerald, R.Macek, M.Plum, LANL LANSCE, Los Alamos, NM

J.Griffin, A.Burov, FNAL, Batavia, IL

### Abstract

The Proton Storage Ring (PSR) has a fast intensity-limiting instability, which may result from an electron cloud interaction with the circulating proton beam leading to a transverse mode coupling instability. Multipacting may also be very important. A PSR beam experiment is proposed with an available 150-350 MHz RF cavity. This cavity would produce a high frequency longitudinal density ripple on the proton bunch which could reduce the e-p instability by two mechanisms: (1) a ~350 MHz ripple could clear electrons by creating an unstable parametric resonance between the electrons and protons, and (2) a ~150 MHz ripple could reduce multipacting by reducing the electron energy at the vacuum chamber.

### 1 INTRODUCTION

The LANL PSR has a fast instability that limits the proton beam intensity. A probable explanation of this instability is that there exists a large electron density in the vacuum chamber resulting in an electron interaction with the proton beam leading to a transverse mode coupling instability between the circulating protons and oscillating electrons trapped in the proton potential well. Multipacting can drastically increase the electron density, increasing the instability. A high frequency longitudinal density ripple on the proton bunch could reduce this instability by two mechanisms.

(1) The first mechanism is clearest for a coasting beam. Electrons could accumulate during beam injection in the proton potential well, and after reaching some threshold density, could generate unstable coupled oscillations between themselves and the proton beam. In this case the lighter electrons gain large amplitudes and strike the vacuum chamber wall, producing an avalanche of secondary emission SEM electrons, resulting in the instability. A high frequency, ~350 MHz, variable frequency cavity could continuously clear electrons by creating a longitudinal bunch ripple. The frequency of the cavity could be adjusted to produce an unstable parametric resonance between this longitudinal bunch ripple frequency and electron oscillation frequency.

(2) The second mechanism is applicable to bunched beams. It reduces multipacting occurring on the bunch tail, which has decreasing longitudinal density. For the case of a constant longitudinal density, electrons with zero initial kinetic energy at the vacuum chamber wall

oscillate across the vacuum chamber gap through the circulating beam with zero energy gain. If the longitudinal bunch density is decreasing the electrons gain energy. It is speculated that a multipacting avalanche can build on the trailing edge of the proton bunch if the energy gain of the electrons is above 50 eV (for aluminium vacuum chamber). Instability measurements [1] show large proton beam oscillations on the bunch tail. This is evidence in favour of the multipactor effect. A lower frequency ~150 MHz cavity could reduce multipacting on the trailing edge of the beam bunch by reducing the kinetic energy gain of the electrons as they traverse the proton beam tail.

Combining both effects could facilitate removal of electrons from the beam vicinity without producing a secondary emission avalanche. A PSR beam experiment is being considered, with an available RF cavity to investigate these effects.

### 2 PARAMETRIC RESONANCE

Consider a coasting beam with a constant transverse density and a sinusoidal longitudinal density. The equation of motion for electron oscillations in the resulting potential well is the Mathieu equation:

$$y'' + (a - 2q \cdot \cos(2t))y = 0, \quad (1)$$

where  $t$  is time in period units of the high-frequency RF cavity divided by  $\pi$ ,  $q$  is the half amplitude of the proton beam longitudinal density variation, and  $a$  is the squared electron tune wrt the half frequency of the RF cavity. The electron oscillation frequency is about 50 times the revolution frequency for the PSR.

It is evident that Eq. 1 has stable and unstable parameter zones. The widest unstable resonance exists when  $a=1$  and in the region of  $a = 1.0 \pm 0.1$ , the parameter  $q$  must be 0.05 to provide unstable electron motion. It is the equivalent of a  $\pm 5\%$  tune spread in the electron oscillation frequency. Since  $q$  is 0.05 for unstable motion, the peak-to-peak amplitude of the density variation must be 0.2. The high-frequency RF should have twice the electron frequency. For the PSR  $\sqrt{a} \approx 50\Omega$ ,  $\Omega_{RF} = 100\Omega$ , and  $\Omega$  is the 2.8-MHz revolution frequency.

For a bunched beam the electron stability issues are less transparent; however, the longitudinal density

modulation would help make the electron motion unstable. Figure 1 shows the half trace modulus of the electron motion stability matrix versus intensity for their small oscillations in the proton beam potential. The RF cavity frequency is twice the electron maximum frequency for  $4 \times 10^{13}$  protons per bunch and the longitudinal ripple relative amplitude is 25%. For bunch intensities greater than  $3 \times 10^{13}$  protons, the electrons can not be trapped in the proton potential. It is important to appreciate that a longitudinal density modulation could cause an energy increase in the electrons at the vacuum chamber wall and multipacting could occur.

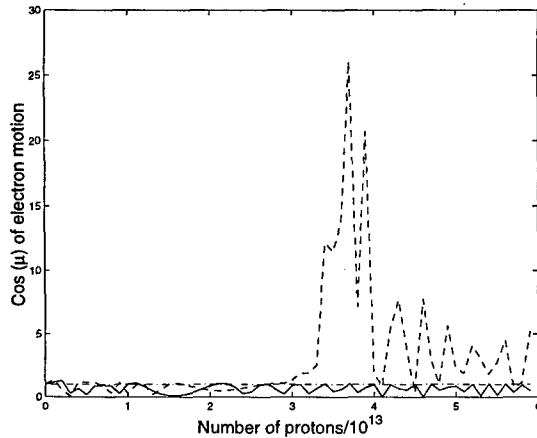


Fig. 1 Half trace modulus of electron stability matrix for electron motion versus number of protons per bunch. The dash-dot line shows the boundary of unstable motion, the solid line is a Gaussian distribution, and the dashed line is the same Gaussian with a 25% sinusoidal ripple.

### 3 REDUCTION OF MULTIPACTING

To investigate the effect of secondary emission from multipacting, a code was created that calculates 1D electron trajectories, starting from the vacuum chamber wall. After hitting the wall secondary emission electrons are produced depending on the primary initial energy. The secondary electrons oscillate with zero momentum in the proton potential since their initial energies are small in comparison with the average single-pass energy gain in the proton potential, about 100 eV. The formula for secondary emission yields from Ref. [2] was used for AI, assuming the primary electrons are normal to the surface. The peak yield is at about 400 eV.

The final result is presented as the SEM coefficient which is the natural logarithm of the average number of electrons, produced by one electron. Assuming an initial electron population of the order of 0.1% of the proton intensity, then for the total compensation of the proton charge by electrons during a single turn, the SEM needs to be about seven. That is, this initial 0.1% electron population can produce about 1000 times more electrons,

$\ln(1000) = 6.9$ , in a single turn which is enough for the instability to occur.

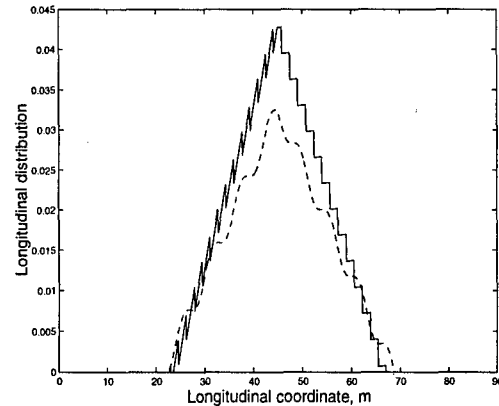


Fig. 2 Two bunch distributions used for multipacting.

Figure 2 shows two proton bunch distributions that were used to calculate secondary emission from multipacting. The upper distribution is triangular with an additional saw-tooth ripple. This is the most ideal distribution to eliminate multipacting. The lower distribution is a triangular distribution with a sinusoidal ripple. Both cases have ripple to make the biggest area with zero slopes, approaching a step function, to minimise multipacting. Figure 3 shows the SEM coefficient versus ripple amplitude with the ripple starting point at the center of the proton bunch and the end at the end of the bunch. The ripple unit is the ratio of the ripple height over the main distribution height. The dashed line presents this coefficient for the saw tooth distribution with the ripple frequency of 40 MHz. One can see that the SEM coefficient dips below zero for some optimum ripple which means that the vacuum chamber absorbs the electrons. The solid line shows this coefficient for a sinusoidal 200 MHz ripple. It has a minimum for a ripple of about 0.03. For this minimum the SEM coefficient is 2.5 times lower than without ripple.

The numerical calculations indicate that with optimum sinusoidal the bunch intensity could be increased by about 100% and produce the same amount of electrons per turn as with no ripple. For the saw tooth optimum ripple, the electron cloud is absent for all intensities due to the large reduction of the electron energy gain during a single turn. If the bunch longitudinal tail consists of flat regions separated by a small number of density jumps, as shown as the dotted line in Fig. 2, the average energy of electrons is close to zero after oscillating through the proton bunch. Hence the number of SEM electrons is close to zero. This is valid only for ripple frequencies less than the electron oscillation frequency, since for high frequency ripple the effect averages to zero. For a high frequency sinusoidal distribution the results for an arbitrary frequency are very similar to solid line in Fig. 3. The SEM coefficient has a minimum for some ripple and

then grows with increasing ripple magnitude, so the RF cavity voltage needs to be controlled.

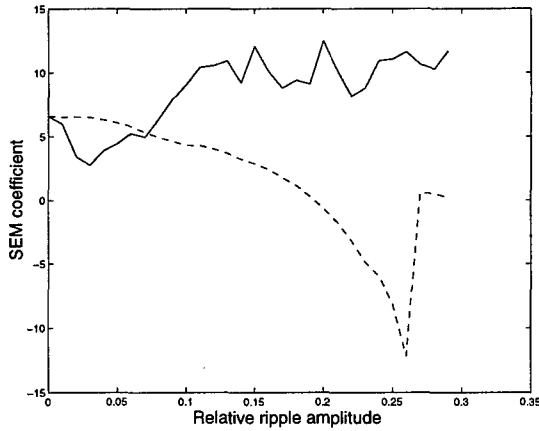


Fig. 3 The SEM coefficient versus amplitude for saw tooth (dashed line) and sinusoidal (solid line) ripples.

#### 4 REQUIRED CAVITY

The longitudinal ripple can be produced with an appropriate RF voltage and frequency. The voltage can be either applied externally or generated passively by the beam. First consider an external voltage. Assume the proton longitudinal distribution in  $\Delta E$  and  $\phi$  space has the form [3]:

$$f(\Delta E, \phi) \propto \exp\left(-\left((\Delta E)^2 + \frac{2v^2 E_s eV}{\eta\omega_{RF} \tau c^2} \cos(\phi)\right) / 2\sigma^2\right) \quad (4)$$

where  $v$  is the proton velocity,  $E$  is the proton energy,  $V$  and  $\omega$  are the RF voltage and frequency,  $\eta$  is the frequency slip factor,  $\tau$  is the revolution period,  $\phi$  is the synchrotron phase, and  $\sigma$  is the rms energy spread. Without space charge, the amplitude  $h$  of the density variation is the difference of Eq. 4 integrated over all energies  $\Delta E$  for the angles  $\phi$  equal to zero and  $\pi/2$ , divided by the  $\Delta E$  integrated distribution at  $\phi=\pi/2$ :

$$h = \exp\left(\frac{v^2 E_s eV}{\eta\omega_{RF} \tau c^2 \sigma^2}\right) - 1 \quad (5)$$

For a 10% amplitude modulation in the PSR,  $h = 0.1$ , and the needed RF voltage is about 40 kV, where the initial relative rms energy spread was taken equal to  $10^{-3}$  and  $\omega_{RF} = 280$  MHz.

Figure 4 shows that it is also possible to create a ripple at the end of injection using a passive cavity with the appropriate resonant frequency and shunt impedance. The code ORBIT [4] was used for this simulation, injecting  $3 \times 10^{13}$  protons, using parameters near an existing FNAL cavity. In particular, a 159-MHz passive RF cavity was assumed with a shunt impedance of 40 k $\Omega$  and  $Q = 100$ . One can see flat areas with zero slopes at both bunch sides. The relative ripple amplitude is about 5%. This case is applicable to the solid line of Fig. 3

which indicates that this cavity could help to reduce multipacting and increase the e-p instability threshold. This cavity does not affect the electron stability in the proton potential well since its frequency is far from twice the electron oscillation frequency. The ideal cavity system would be two or three harmonic combinations, one of which is close to twice the electron frequency in order to eliminate both multipacting and electron accumulation.

The ripple appearance in Fig. 4 is related to a slow longitudinal instability. This follows from the dependence of the ripple on the shunt impedance. For example, if one uses 60 k $\Omega$  for the shunt impedance, the simulated ripple would be about 50% and many protons would be lost. Consequently the RF cavity shunt impedance must be adjustable to operate close to the instability threshold.

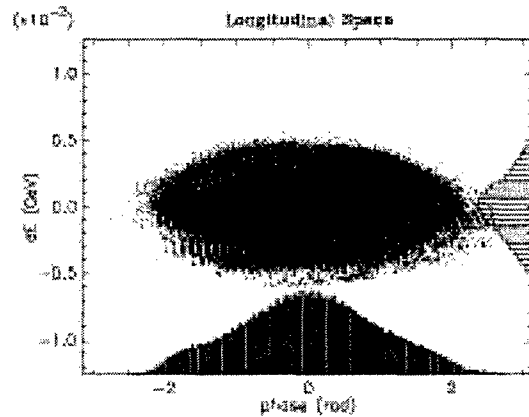


Fig. 4 Calculated PSR longitudinal distribution at the end of injection for  $3 \times 10^{13}$  protons with a 159-MHz passive,  $Q = 100$ , shunt impedance = 40 k $\Omega$ , cavity.

\*Research sponsored by the DOE, under contract no. DE-AC05-96OR22464 with LMER Corp. for ORNL.

#### 5 REFERENCES

- [1] M.Plum, PSR Buncher Workshop, LANL, Jan 1999.
- [2] F.Zimmerman, SLAC-PUB-7664 (1997).
- [3] D. A. Edwards, M. J. Syphers, in *An Introduction to the Physics of High Energy Accelerators*, edited by M. Month (J. Wiley & Sons, Inc., New York, 1993), p 37.
- [4] J.Galambos, *et al.*, "ORBIT", these proceedings.

# TRANSVERSE BEAM MOTION ON THE SECOND AXIS OF THE DUAL AXIS RADIOGRAPHIC HYDRODYNAMIC TEST FACILITY\*

Yu-Juan Chen<sup>†</sup>, George J. Caporaso, Arthur C. Paul, LLNL, Livermore, CA  
William M. Fawley, LBNL, Berkeley, CA

## Abstract

The accelerator on the second-axis of the Dual-Axis Radiographic Hydrodynamic Test (DARHT-II) facility [1] will generate a 20 MeV, 2-4 kA, 2  $\mu$ s long electron beam with an energy variation  $\leq \pm 0.5\%$ . Four short current pulses with various lengths will be selected out of this 2  $\mu$ s long current pulse and delivered to an x-ray converter target. The DARHT-II radiographic resolution requires these electron pulses to be focused to sub-millimeter spots on Bremsstrahlung targets with peak-to-peak transverse beam motion less than a few hundred microns. We have modeled the transverse beam motion, including the beam breakup instability, corkscrew motion [2, 3], transverse resistive wall instability [4] and beam induced transverse deflection in the kicker system, from the DARHT-II injector exit to the x-ray converter target. Simulations show that the transverse motion at the x-ray converters satisfies the DARHT-II radiographic requirements.

## 1 INTRODUCTION

To identify the test object's edges precisely, the DARHT-II beam needs to be focused to a sub-millimeter spot on the x-ray converter through its entire pulse. Transverse beam motion, which increases the time integrated spot size, is one of principle limitations in achieving the spot size requirement. The main sources of transverse motion in the accelerator are injector noise, misalignments and energy variations. These sources lead to the beam breakup instability (BBU) and corkscrew motion. The leading sources in the downstream beamline are beam induced transverse deflection in the kicker system and the head and tail of beam motion due to the switching of the kicker pulser. The DARHT-II accelerator will deliver a 2  $\mu$ s long, 2-4 kA electron beam. The long duration and the high current make the transverse resistive wall instability a possible concern for the transverse beam motion.

We have modeled the transverse motion of a 2-4 kA beam from the exit of the DARHT-II injector to the x-ray converter to ensure that the DARHT-II facility meets design goals. The DARHT-II injector delivers a 400 ns rise time current pulse, and the accelerator gap voltage has a 200 ns rise time. There are concerns that the 400 ns long beam head would be lost in the accelerator and cause gas desorption from the wall. A beam head cleanup zone after the first 8-cell block is being proposed. Various accelerator configurations without the beam head cleanup zone are simulated. However, the current rise time sharpener effect of the beam head cleanup is included.

\* The work was performed under the auspices of the U.S. Department of Energy by LLNL under contract W-7405-ENG-48, and by LBNL under contract AC03-76SF00098

<sup>†</sup>Email: yjchen@llnl.gov

Three simulation codes are used for the modeling: BREAKUP for transport in the accelerator, TRANSPORT to determine transformation matrices of the downstream beamline components, and KICKER to transport the BREAKUP outputs to the x-ray converter through a kicker system. Section 2 shows that corkscrew motion can be controlled by using the corkscrew tuning V algorithm, and the BBU and the rise time sharpener effect of the cleanup zone do not change the DARHT-II performance. We will discuss the transverse resistive wall instability in Section 3. In section 4, we will present our modeling of the transverse beam motion in the kicker system and the final beam motion at the converter target. A summary will be given in Section 5.

## 2 BEAM MOTION IN THE ACCELERATOR

### 2.1 Accelerator Configuration and Cell Impedance

The DARHT-II accelerator consists of eleven 8-cell blocks [1, 5]. Three cell configurations, which differ in the insulator geometry and bore size, have been designed [6]. Four cell combinations were used in the simulations: 88 initial cells, 88 standard cells, 8 injector cells with 80 standard cells, and again 8 injector cells with 80 standard cells. Except the fourth one, all combinations have one intercell magnet within each intercell. All the solenoids are wrapped with steering/correction coils. The magnetic tune focuses the 8 cm radius electron beam at the injector exit rapidly to a 5 mm - 1 cm radius without adversely affecting the current distribution and losing beam head in the first block. The small beam radius is then maintained through the rest of the accelerator. The pertinent cell characteristics for BBU calculations are listed in Table 1. For the configurations consisting of 8 injector cells and 80 standard cells, only three dominant modes (171 MHz, 200 MHz and 635 MHz) are modeled in the simulations. We expect the simulation results with the discrete, dominant modes to be similar to that with a continuous BBU spectrum [7].

Table 1: Impedances of different cell configurations

Design	Freq. (MHz)	Z/Q ( $\Omega$ )	Q
Initial Cell (25.4 cm ID)	262	34.9	2.0
	580	1.1	7.2
	672	3.9	6.9
Standard Cell (25.4 cm ID)	200	37.57	1.9
	635	7.28	3.8
Injector Cell (35.6 cm ID)	171	25.41	2.0
	443	4.3	4.2



## 2.2 Beam Breakup Instability

The convective BBU instability arises from the beam interacting with the accelerating cells' dipole TM modes. For a current pulse with a long rise time, the BBU instability driven by the shock excitation of misalignment starts to grow at the beam head and may not propagate into the main body of the pulse before the beam leaves the accelerator. Therefore, the BBU instability driven by misalignment is generally not a threat to a long rise time DARHT-II pulse. However, to minimize the beam head loss to the wall, the head cleanup zone between the first two blocks sharpens the current rise time to 50 ns with or without a current precursor depend on the cleanup zone's configuration [8]. The fourth accelerator configuration is used to model the beam head cleanup's current rise time sharpening effect on BBU. Two cases are studied. In the first case, the current pulse's rise time is 45 ns through the entire accelerator. In the second case, the current pulse has a 140 ns rise time initially and is shortened to 45 ns between the first two blocks (the potential cleanup zone), and a 800 A current precursor is added at 50 ns before the head of the current flattop. A injector noise is also included in the simulations since the BBU driven by injector noise would appear throughout the pulse length and causes concerns.

## 2.3 Corkscrew and Tuning Strategy

Corkscrew motion driven by the focusing elements' chromatic aberration and the machine's misalignment is a differential oscillation of the beam centroid between the leading and trailing portions of a beam pulse. The simulations use the DARHT-I accelerator's alignment specification: 1.95 mrad of random 3- $\sigma$  magnetic tilt and 0.45 mm of random 3- $\sigma$  magnet offset. Without corrective measures, this specification would produce a corkscrew amplitude of several millimeters at the accelerator exit. The simulated beam pulse has an energy variation of  $\pm 0.5\%$ . Large injector offset ( $\sim 1$  mm) and tilt ( $\sim 1$  mrad) introduced by the dipole field in the DARHT-II injector configuration is also modeled. Let  $R$  be the averaged centroid radial displacement over the flattop portion of the current pulse, and  $A$  be the averaged corkscrew amplitude. The tuning-V steering algorithm, which has demonstrated an order of magnitude reduction in corkscrew on the ETA-II accelerator [3, 9] and the Flash X-ray Radiography accelerator (FXR) [10], is used to minimize a figure of merit  $W$ , where  $W = R^2 + A^2$ . The available steering field for each steering coil is limited to 5 Gauss in the simulations, and only 1-4 pairs of steering coils per beam position monitor (BPM) are used to steer the beam.

## 2.4 BREAKUP Results

Several observations can be made from the simulations. First, the beam head electrons with energy less than 10 MeV are lost early in the accelerator due to large corkscrew motion and BBU. At the accelerator exit, the BBU on a 2 kA beam body is insignificant compared with the corkscrew amplitude even if there is a 170–200 MHz, 100  $\mu$ m injector noise imposed on the initial beam centroid as shown in Figs. 1(a), (b) and (c). A similar

observation can be made for a 4 kA with a 10 mm injector noise. For a 2 kA beam with 45 ns rise time, the projected beam centroid on the x-y plane for the flattop portion of a beam (a) without and (b, c) with steering are presented in Fig. 1. Figures 1(b) and (c) show that the corkscrew amplitudes are  $\sim 0.3$  mm with the tuning-V steering regardless whether there is a current precursor. The BBU caused by the shock excitation of misalignment extends only a short distance into the flattop of a 4 kA pulse and does not appear in the flattop of a 2 kA pulse for both current rise time sharpening cases. The tuning-V steering reduces the corkscrew amplitude by an order of magnitude even though a large injector offset and tilt are present. Though the steering reduces the beam offset at the BPM by making the beam centroid cross the axis, the reduction of the beam displacement between the BPMS is less than a factor of two. Hence, the BBU amplitude stays almost unchanged regardless of steering. The average beam offset in the accelerator is about 2–3 mm which is much less than beam pipe radius. Emittance growth due to the nonlinear image forces is expected to be small.

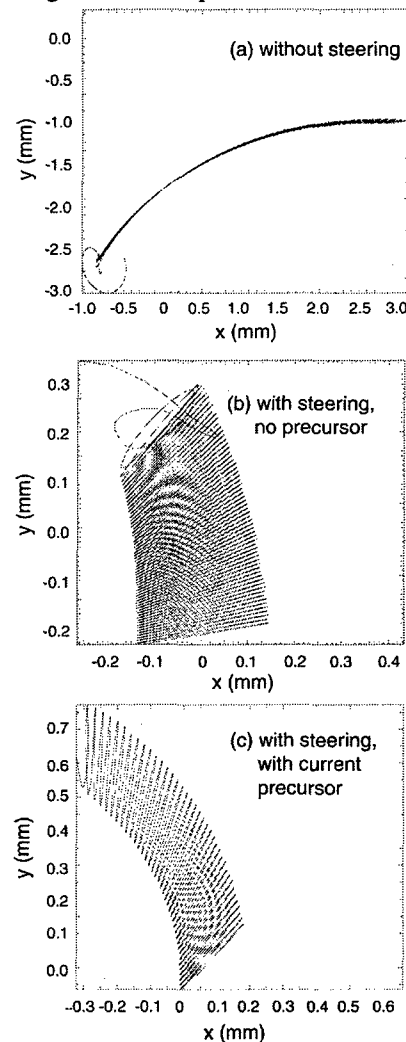


Fig. 1 The projected beam centroids on the x-y plane for the flattop portion of a 2 kA beam shows corkscrew amplitude is (a)  $\sim 2$  mm without steering and (b, c)  $\sim 0.3$  mm with the tuning-V steering.

### 3 TRANSVERSE RESISTIVE WALL INSTABILITY

The transverse resistive wall instability arises from the head-to-tail growth of the non-cancellation forces of the surface charges and the surface currents created by an offset beam in the conducting pipe. Providing a continuous focusing channel with a large pipe aperture is an effective way to minimize the instability growth. Generally, the instability growth for a few hundred nanosecond long beam is insignificant. The transverse resistive wall instability may be a concern for the 2  $\mu$ s long, 2-4 kA beam while it travels in the drift regions between the injector and the kicker septum. However, we find that the instability is not an issue in the proposed beam head cleanup zone ( $\sim$  a 2 m drift space) with a 25.4 cm diameter stainless steel pipe since the characteristic growth length is 6.4 m for a 2 kA beam and 4.5 m for a 4 kA. In the downstream (with two  $\sim$ 3 m long drift regions) with a 16 cm diameter stainless steel pipe, the characteristic growth length is also 6.4 m for a 2 kA beam and 4.5 m for a 4 kA. We have included the transverse resistive wall instability in the modeling (see the next section).

### 4 BEAM MOTION IN DOWNSTREAM TRANSPORT LINE

The transverse centroid is modeled by using the system simulation code Extend. The centroid motion as a function of time at the accelerator exit as taken from BREAKUP is used as input into the Extend simulation. There is a detailed model of the kicker, its pulser system and transit time isolation cable system including dispersion due to skin effect. There is also a model of the quadrupole lens which acts as a septum magnet [11] and a model for the split beam pipe which treats the impedance of the pipe as due to a single high Q mode. The transport from the accelerator output to the input of the kicker is computed by using a 6 x 6 matrix, obtained from the TRANSPORT code, for this section of beamline. Similarly, another matrix, extracted from the TRANSPORT code, is used to represent the transport line from the output of the septum pipe to the focal plane (on the target) of the final lens. The simulation incorporates a model of a rise time sharpening aperture at the output of the split beam pipe. The beam profile is assumed to be a Gaussian and there is an aperture of radius 2 cm. This aperture is able to sharpen up the rise time of the selected pulse.

A typical resultant centroid motion at the target and transmitted current are shown in figure 2. The current pulse selected by the kicker system has a 8 ns rise/fall time. The maximum beam displacement (occurring at the rising part of the pulse) within the FWHM is  $\sim$  0.35 mm which is about a half of the beam radius on the target. On the flattop portion of the beam, the displacement (the high frequency BBU oscillations) is less than 100  $\mu$ m. Even if the pulse width is very short, the averaged beam displacement weighted by the beam current is about 100

$\mu$ m which is reasonably small compared with the required beam radius, 0.65 mm FWHM.

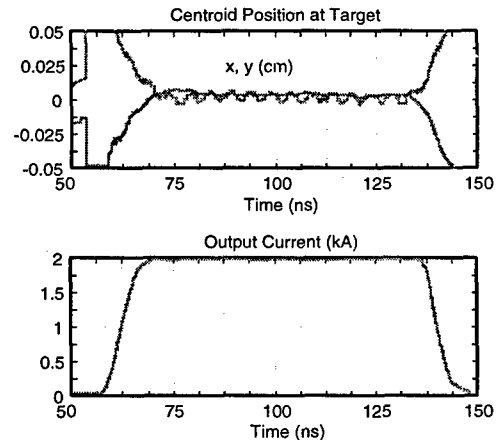


Fig 2. Extend simulation output showing the centroid motion on the x-ray target of a section selected out of the accelerator output pulse and the associated transmitted current arriving at the target.

### 5 SUMMARY

We have modeled the transverse motion of a 2-4 kA beam from the exit of the DARHT-II injector to the x-ray converter. The simulation model includes the beam breakup instability, corkscrew motion, the transverse resistive wall instability, the kicker induced transverse kick, the head and tail's beam motion due to the switching of the kicker pulser. The model also includes the rise time sharpening effect of the beam head cleanup scheme and the small output aperture of the septum. Simulations show that the transverse motion on the x-ray converter target should meet the DARHT-II radiographic requirements.

### 6 REFERENCES

- [1] M. J. Burns, et al., "DARHT Accelerators Update and plans for Initial Operation", proceedings of this conference.
- [2] Y.-J. Chen, "Corkscrew Modes in Linear Accelerators", Nucl. Instr. and Meth. A **292** (1990) p.455-464.
- [3] Y.-J. Chen, "Control of Transverse motion Caused by Chromatic Aberration and Misalignments in Linear Accelerators", Nucl. Instr. and Meth. A **398** (1997) p.139-146.
- [4] G. J. Caporaso, W. A. Barletta, and V. K. Neil, "Transverse Resistive Wall Instability of a Relativistic Electron Beam", Particle Accel. (1980) pp.71-79.
- [5] H. Rutkowski, et al., "A Long Pulse LINAC for the Second Phase of DARHT", proceedings of this conference.
- [6] T. L. Houck, et al., "Physics Design of the DARHT 2nd Axis Accelerator Cell," proceedings of LINAC98, Chicago, 1998.
- [7] W. M. Fawley, Y.-J. Chen and T. L. Houck, "Beam Breakup Calculations for the Second Axis of the DARHT", proceedings of this conference.
- [8] T. Houghes and A. C. Paul, Private communications.
- [9] J. Weir, et al., "Improved ETA-II Accelerator Performance", proceedings of this conference.
- [10] R. Scarpetti, Private conversation.
- [11] A. C. Paul, et al., "The Beamline for the Second Axis of the Dual Axis Radiographic Hydrodynamic Test Facility", proceedings of this conference.

# OPERATIONAL EXPERIENCE WITH THE PEP-II TRANSVERSE COUPLED-BUNCH FEEDBACK SYSTEMS\*

W. Barry, J. Byrd, J. N. Corlett, D. Li, LBNL Center for Beam Physics, Berkeley, CA,  
J. Fox, M. Minty, S. Prabhaker, D. Teytelman, SLAC, Stanford, CA.

## Abstract

Operational experience with the PEP-II high energy ring (HER) and low energy ring (LER) transverse coupled-bunch feedback systems is discussed. In particular, some key performance data including beam transfer function, mode spectrum, and some growth rate observations are presented. In general, growth rates much greater than expected have been observed in the HER. LER growth rates have not been measured but are thought to be lower than those of the HER based on lower feedback gains required for LER beam stabilization. Some results from experiments using the longitudinal feedback system electronics in conjunction with the transverse feedback system to study the HER instabilities are presented.

## 1 INTRODUCTION

The PEP-II B-Factory [1] is a high-luminosity, asymmetric electron-positron collider consisting of a 9 GeV, 1.0 A high-energy electron storage ring (HER), and a 3.1 GeV, 2.14 A low-energy positron storage ring (LER). Because of the high average beam currents in both rings, active feedback systems [2] are used to suppress the growth of transverse coupled-bunch instabilities.

During the past year, PEP-II has completed several very successful commissioning periods, the most recent being the Jan/Feb 1999 run during which both rings achieved substantial currents ( $>500$  mA HER and  $>1100$  mA LER) and significant luminosity ( $5 \times 10^{32}$ ) was obtained [3]. At these high currents, the transverse feedback systems played a critical role in beam containment and stabilization.

In general, the HER has been observed to be less stable than the LER. Typical HER transverse instability thresholds are on the order of ten milliamps while LER thresholds are in the 100 mA area. Feedback gains required to stabilize the two beams roughly reflect the order of magnitude difference in thresholds. Growth rates four-to-ten times greater than expected for the HER have been measured [2]. LER growth rates have not been measured but will be during the next run. Experience thus far with the LER points towards transverse growth rates more in line with predicted rates (table 1). Many

experiments and a great deal of data has been taken to try to determine the origin of the HER instabilities. Work towards a conclusion in this area is ongoing and will be published at a future date.

## 2 PARAMETER AND SYSTEM REVIEW

A brief list of accelerator and transverse feedback system design parameters appears in Table 1. Nominally, PEP-II operates with every other bucket filled (238 MHz bunch rate). This sets the minimum bandwidth for the feedback system at 119 MHz. However, the electronics has been designed to have a bandwidth of 250 MHz to allow for possible operation with every bucket filled. The kickers cover DC-119 MHz for maximum shunt impedance in the every-other-bucket operating mode. They can be replaced with 238 MHz versions if an every-bucket fill becomes a likely operating mode. The feedback systems are designed to provide a damping rate that is approximately three times greater than the growth rate of the fastest expected (vertical resistive wall) coupled-bunch mode.

Table 1: Accelerator / feedback design parameters.

Parameter	Description	HER / LER Value
E	Beam energy	9.0 / 3.1 GeV
$f_{rf}$	RF frequency	476 MHz
—	Bucket space	2.1 ns
—	Bunch space	4.2 ns
$I_{av}$	Average current	1.0 / 2.14 A
$f_0$	Orbit frequency	136.3 kHz
$v_v$	Vertical tune	23.64 / 34.64
$v_h$	Horizontal tune	24.57 / 36.57
$\alpha_v$	Vertical R-wall growth rate (calc)	0.26 / 1.09 $ms^{-1}$
$\alpha_h$	Horizontal R-wall growth rate (calc)	0.18 / 0.71 $ms^{-1}$
$\alpha_f$	Feedback design damping rate	3.2 $ms^{-1}$
Required feedback bandpass		13.6 kHz-119 MHz
Feedback electronic bandpass		10 kHz-250 MHz
Kicker bandpass		DC - 119 MHz

The feedback system diagram is shown in figure 1. Beam moment signals ( $I\Delta x$ ) from two sets of pickups are detected with microwave receivers at  $3f_{rf}$ . After down-conversion to baseband, the signals are proportionately summed to produce a correction signal that is 90 degrees

\*Supported by the US Department of Energy under contract numbers DE-AC03-76SF00098 (LBNL) and AC03-76SF00515 (SLAC).

out of phase with beam position at the kickers. A digital delay provides the pickup-to-kicker timing and the kicker electrodes are individually driven differentially with 120 W class-A power amplifiers. Other system features include a provision for single-bunch kickout, predigitization orbit-offset-rejection electronics, and fast switches to gate the feedback on/off for grow damp measurements with the longitudinal feedback system front-end.

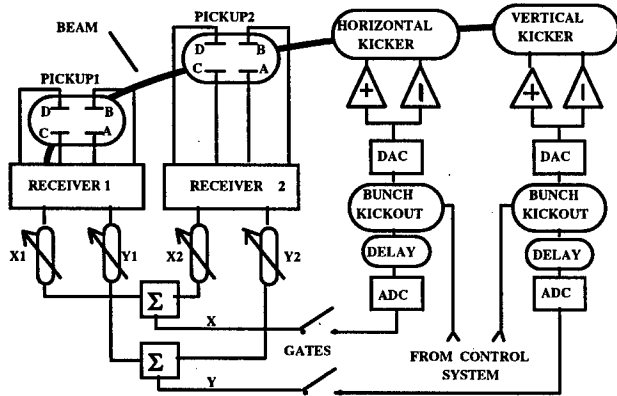


Figure 1: Transverse feedback system.

## 2 LER OPERATION

Commissioning of the LER began in July, 1998. Experience gained with the HER feedback system made the LER system commissioning a simple and straight forward task. The system was quickly timed using the simple technique described in reference [2]. For rough phasing, the signs of the signals from each of the two pickups were simply set for stability without measuring transfer phase. The system performed well in this rough configuration and was subsequently left alone to make way for other commissioning tasks.

At the beginning of the Jan/Feb 99 run, the LER system was properly phased using a network analyzer in anticipation of going to higher currents. An example vertical transfer function for the properly tuned system appears in figure 2. In this configuration, the system stabilized the beam to the highest currents to date, >1100 mA.

Because of the early success, only limited time was allotted to LER coupled-bunch mode studies. Despite the limited experimental time, some important stability observations were made for the LER. In particular, the beam was found to be less stable in the horizontal plane. This is contrary to theory which indicates that the strongest expected source of instability is the vertical resistive wall impedance. The threshold for horizontal instability is in the 100 mA region. The vertical threshold was not measured but appears to be much higher. The effect of horizontal feedback on the LER beam at 100 mA is shown over the first ten orbit harmonics in figures 3 and

4. In general, the strongest unstable modes appeared at frequencies below 3 or 4 MHz indicating horizontal resistive wall as a possible source. More detailed measurements for the LER including modal growth rates are planned for the next run beginning May 99.

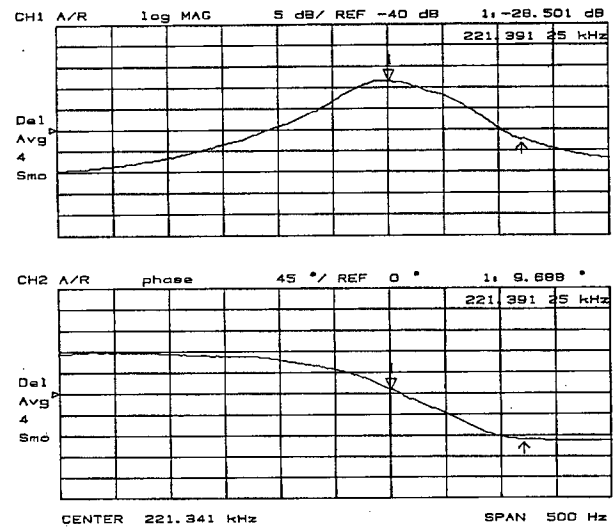


Figure 2: Transfer function of lower vertical sideband of second orbit harmonic (LER).

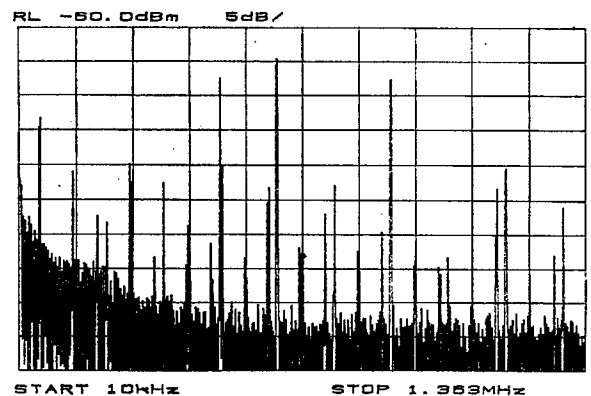


Figure 3: Spectrum of horizontal sidebands about first ten orbit harmonics, feedback off (LER, 100 mA).

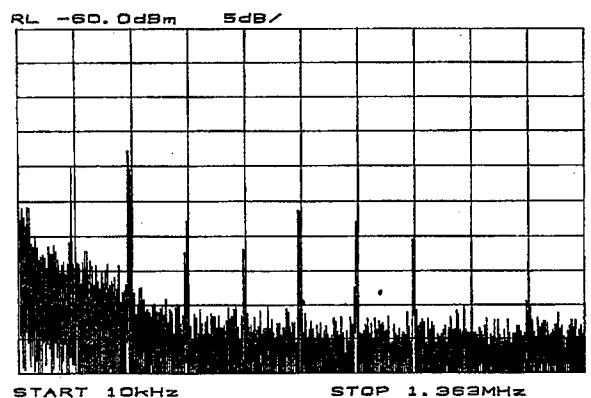


Figure 4: LER spectrum about first ten orbit harmonics with horizontal feedback on, 100 mA.

### 3 HER OPERATION

During the past several commissioning periods, efforts have been focused on finding the source of the fast HER instabilities [4,5]. Some brief comments on measurement techniques and initial observations are discussed here.

The measurement technique uses one of the longitudinal feedback systems to gate the transverse feedback system off and on with broadband GaAs FET T-section switches allowing beam motion to grow then damp. Bunch-by-bunch transverse motion from the transverse receivers during the grow/damp is recorded and processed with the longitudinal feedback system front-end and DSP farm. With off-line analysis, modal growth/damping rates, closed-loop feedback system behavior, and beam impedance information can be obtained.

An example measurement using this technique for the horizontal plane of the HER is shown in figures 5 and 6 for a 290 bunch, 40 mA beam. Figure 5 shows bunch-by-bunch growth and damping as a function of time. Using Fourier transform techniques, the modal structure of the beam vs. time can be obtained as shown in figure 6. In this case, two low-frequency modes are clearly present. Also note that the growth is non-exponential and that for one mode, the beam decays with feedback to a steady state level. Although not measured here, the growth rates are known to be large and amplitude dependent with the fastest rates occurring for small amplitudes. Thus one explanation for the residual level is that the mode grows to an amplitude (with decreasing growth rate) to where it is marginally controlled by the feedback system gain.

One consequence of extremely high growth rates is that correspondingly high feedback gains are required to stabilize the beam. At these high gains, the system is extremely sensitive to residual orbit-offset signal saturation effects. Efforts to reduce residual orbit-offset signal levels even further are presently underway.

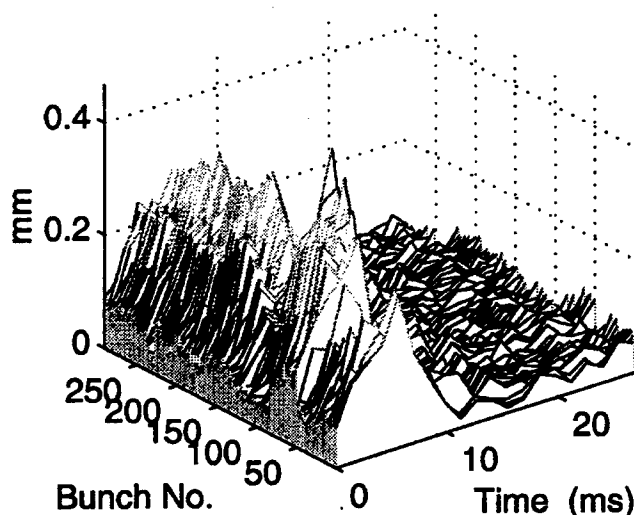


Figure 5: HER horizontal time domain bunch-by-bunch oscillation envelopes,  $I_{av} = 40$  mA, 290 bunches.

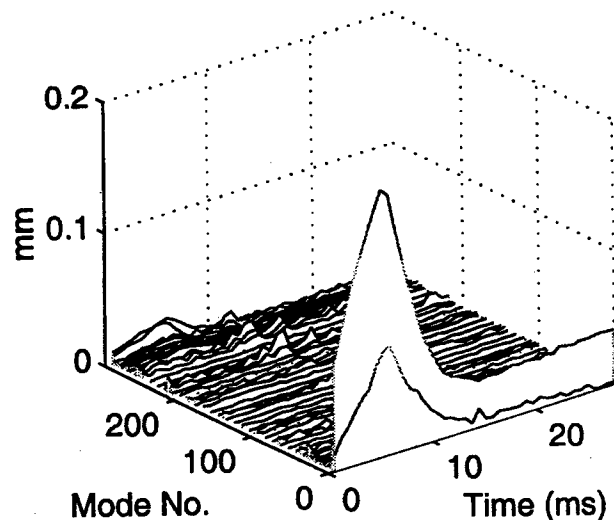


Figure 6: HER time evolution of horizontal modes,  $I_{av} = 40$  mA, 290 bunches.

### 4 CONCLUSION

Both the HER and LER transverse coupled-bunch feedback systems are operational and in use for controlling instabilities in both rings. Observations thus far indicate that the LER is generally well behaved with unstable modes easily controlled by the feedback system. Instabilities in the HER, although basically controlled by the feedback system, are more severe with growth rates much greater than expected. During the next run, HER stability studies will continue, growth rates in the LER will be measured, orbit offset rejection will be improved, and the single-bunch knockout feature for both systems will be tested.

### 5 REFERENCES

- [1] "PEP-II Conceptual Design Report", LBL-PUB-5379, SLAC-418, CALT-68-1869, UCRL-ID-114055, UC-IIRPA-93-01, June, 1993.
- [2] W. Barry, et al, "Initial Commissioning Results From the PEP-II Transverse Coupled-Bunch Feedback Systems", Proceedings of the 1998 European Particle Accelerator Conference, Stockholm, Sweden, June 1998.
- [3] J. Seeman, "Commissioning Results of B-Factories", These Proceedings
- [4] D. Teytelman, et al, "Transverse Multibunch Instability Diagnostics via Downsampled Transient Techniques", These Proceedings.
- [5] S. Prabhaker, et al, "Measurement of a Fast Vertical Instability in the PEP-II HER", SLAC PEP-II-AP-Note-99-04, 1998.

# Beam Breakup Calculations for the Second Axis of DARHT\*

W. M. Fawley<sup>†</sup>, LBNL, Berkeley, CA

Y.-J. Chen and T. L. Houck, LLNL, Livermore, CA

## Abstract

The accelerator for the second axis of the Dual Axis Radiographic Hydrodynamic Test (DARHT) facility will produce a 4-kA, 20-MeV, 2- $\mu$ s output electron beam with a design goal of less than  $1000 \pi$  mm-mrad normalized transverse emittance and less than 0.5-mm beam centroid motion. In order to meet this goal, the beam transport must have excellent optics and the beam breakup instability (BBU) must be limited in growth. Using a number of simulation codes such as AMOS and BREAKUP, we have modeled the transverse impedances of the DARHT-II accelerator cells and the electron beam response to different transverse excitations such as injector RF noise, magnetic dipole fields arising from the 90-degree bend between the cathode stalk and insulator column, and downstream solenoid alignment errors. The very low  $Q$  ( $\sim 2$ ) predicted for the most important TM dipole modes has prompted us to extend the BREAKUP code to be able to use the dipole wakefields calculated by AMOS in addition to the most usual discrete frequency BBU mode model. We present results for the predicted BBU growth and the empirical sensitivity to various machine parameters.

## 1 INTRODUCTION

As part of the Science-based Stockpile Stewardship Program (SBSS), a high current (2-4 kA), relativistic (20 MeV), electron beam accelerator for the second axis of DARHT is being designed and constructed over the next few years. A great deal of attention is being paid to generating a high brightness beam out of the injector and to preserving the low normalized emittance ( $\epsilon_N \leq 1000 \pi$  mm-mrad) through the accelerator. Achieving this goal requires excellent transport optics and control of the beam breakup instability (BBU). Since BBU arises from dipole cavity modes in the induction cell gap regions excited by an offset beam, we are optimizing geometry of this region and determining the best positions for ferrite absorbers to reduce the BBU mode  $Q$ 's as much as possible while still maintaining adequate safety margins for electric field stresses. Previous papers (e.g. [1]) have discussed these issues in the context of radiographic machines such as FXR and DARHT giving specific examples of gap and ferrite damper geometry. An accompanying paper [2] discusses growth of "corkscrew" transverse beam offsets from the convolution of temporal beam energy variations with solenoid misalignments.

\* Work supported by the U.S. Department of Energy under Contracts No. DE-AC03-76SF00098 (LBNL), and W-7405-ENG-48 (LLNL).

<sup>†</sup> Email: fawley@lbl.gov

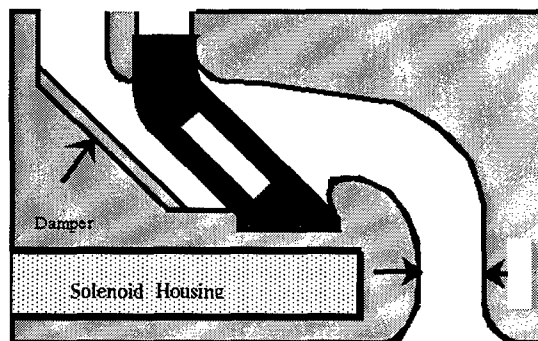


Figure 1: General gap and insulator geometry for the "standard" DARHT-2 accelerating cell.

AMOS code [3] calculations for the current design for the DARHT-2 "standard" 10-inch diameter cells, which comprise the last 80 of the total 88 accelerator cells, show quite low values for both the impedance and  $Q$  ( $\approx 2$ ) for the most important dipole modes. These low values have raised a minor concern that the usual way of using a small number (typically 2) of discrete, damped modes in the LLNL BREAKUP code for calculating beam BBU response and overall gain might be giving too optimistic a result. Moreover, the long duration ( $\approx 2 \mu$ s) of the DARHT-2 pulse and the expected "shock" offset in the risetime portion of the pulse from dipole magnetic fields from the 90-degree bend between the cathode stalk and insulator column makes it important to calculate accurately BBU convection from the beam head back into the main body. Consequently, we extended the BREAKUP code to use dipole wake potentials input directly in the time domain from the AMOS code and calculated overall BBU growth in DARHT-2 cells arising from various initial excitations.

## 2 AMOS-CALCULATED WAKE POTENTIALS

Fig. 1 presents the rough geometry of a standard DARHT-2 cell. The gap width is 2.54 cm while the gap voltage is nominally 193 kV. A Mycalex insulator separates the oil-filled Metglas and transmission line from the high vacuum ( $\leq 10^{-7}$  T) beam pipe region. One or more damping ferrites will be used in the upstream side of the insulator.

The AMOS code calculates the wakefields left behind by an ultrarelativistic test charge propagating by an accelerating gap. Given the high degree of damping in the DARHT-2 accelerating cell, the wake potential near a gap remains large for only a few ns after passage of the test particle. Nonetheless, we recorded the wake for 100 ns with a reso-

lution of a 3.3 ps which, for purposes of BBU calculations in the BREAKUP code, was then averaged down to 65 ps, equivalent to a Nyquist frequency of about 7.5 GHz. The strongest dipole modes lie at approximately 190 and 630 MHz and should be well-resolved at 65 ps resolution. In Fig. 2 we plot the wake potential both on a linear scale out to 25 ns (upper plot) and on a semilogarithmic scale out to the full 100 ns of the AMOS calculation. In the first 10 or so ns one can see the two aforementioned BBU modes interfering and rapidly ( $\tau_{damp} \approx 2.7$  ns) dropping in amplitude. At times greater than about 15 ns, there is a weakly damped ( $\tau_{damp} \approx 32$  ns), very low amplitude, high frequency wake extending out to the full 100 ns. The plot of  $Z_{\perp}(\Omega)$  indicates that this is a mode centered around 1300 MHz, just below cutoff of the  $TM_{01}$  mode at 1.44 GHz. An examination of the phase of the transverse impedance versus  $\omega$  shows that the two primary modes have similar values of  $\approx +1$  radian.

### 3 COMPARISON OF BBU GROWTH ALGORITHM RESULTS

The BREAKUP code has been recently upgraded to utilize various Fortran90 features both to improve its maintainability and to permit more flexible memory management. With these changes, we were able to extend its capabilities to exploit the direct wakefield potentials produced by the AMOS code as opposed to the more usual method of expressing the transverse wake impedance as a sum of discrete modes. In order to examine how well the discrete mode approach was predicting BBU growth in the DARHT-2, we compared total growth at the end of the  $\sim 50$ -m transport lattice for a number of different excitations at the injector exit. These cases included: (a) "shock" excitation due to a uniform 100- $\mu$ m transverse offset convolved with a very short (10 ns) current risetime as might be produced by beam-head "cleanup region" tentatively being considered (b) a time-varying beam offset produced by a 3-G dipole bend field in the A-K gap with a more moderate 40-ns risetime for the injector current and energy (c) a transverse oscillation at 90 MHz (as is predicted for a dipole RF mode in the injector column vacuum tank) of 100- $\mu$ m amplitude together with a rapid 10-ns risetime for the current and energy (d) the sum of transverse oscillations at 190 and 630 MHz (the strongest dipole BBU modes in the standard DARHT-2 cells), both initially excited at 50- $\mu$ m amplitude (e) a 100- $\mu$ m amplitude 170 MHz excitation, corresponding to the strongest BBU mode in the first 8 so-called injector cells (14-inch diameter) of DARHT-2.

Each of these cases was run twice with the BREAKUP code, first employing the wakefield formulation and second employing the discrete mode approximation. In the latter case, the  $Z_{\perp}$ 's for the two modes were 337 and 306  $\Omega$ /m and the  $Q$ 's 2 and 4, respectively, to which was added a zero-frequency displacement mode impedance of 95  $\Omega$ /m. The beam parameters were 4-kA current, 3.2-MV injector energy, 88 identical gaps which accelerate the beam to a

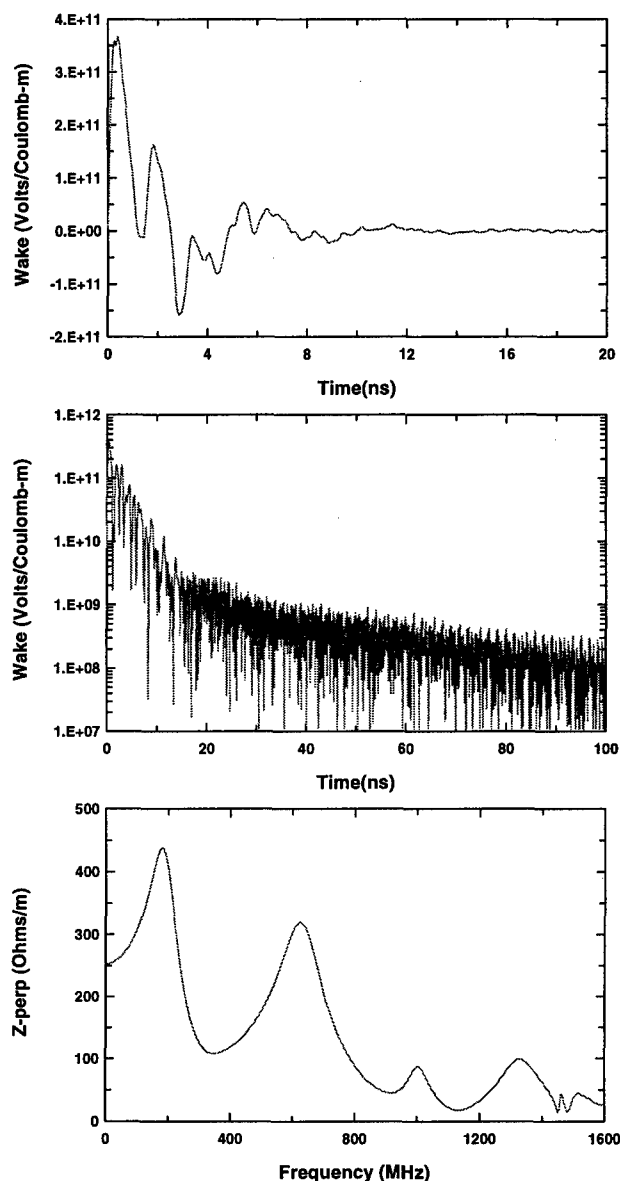


Figure 2: Dipole wake potential versus time and transverse impedance  $Z_{\perp}(\Omega)$  calculated by the AMOS code for a "standard" 10-inch diameter DARHT-2 accelerating cell.

final 20-MV energy, and magnetic field tune which ramps nearly linearly from 0.25 to 2.0 kG over the full lattice. No solenoid tilts or time-varying gap voltages (apart from a 5-ns Gaussian rise and fall time) were used in these runs.

Table 1 displays a sample of some of the resultant comparison. For most of the cases, both the peak final offset versus time (which generally occurs just past the end of the current rise time) and an average over the time corresponding to the current flat top are given, both determined at the end of the transport lattice. One sees that the full temporal wake formulation and the discrete mode formulation give quite similar results, seldom differing by more than 50% even though the accumulated BBU growth in case (d) exceeds 30. Consequently, we believe the predictions concerning overall BBU growth in the DARHT-2 accelerator

**Table 1.** Final BBU Amplitudes (mm) from different initial excitations

Excitation Type $\Rightarrow$	(a) Shock		(b) 3G Bend		(c) 90 MHz Inj.		(d) 190 + 630 MHz	(e) 170 MHz
	peak	average	peak	average	peak	average	average	average
WAKEFIELD	0.29	0.035	0.24	0.025	0.45	0.09	0.68	0.48
DISCRETE MOD E	0.27	0.029	0.58	0.042	0.29	0.08	0.51	0.88

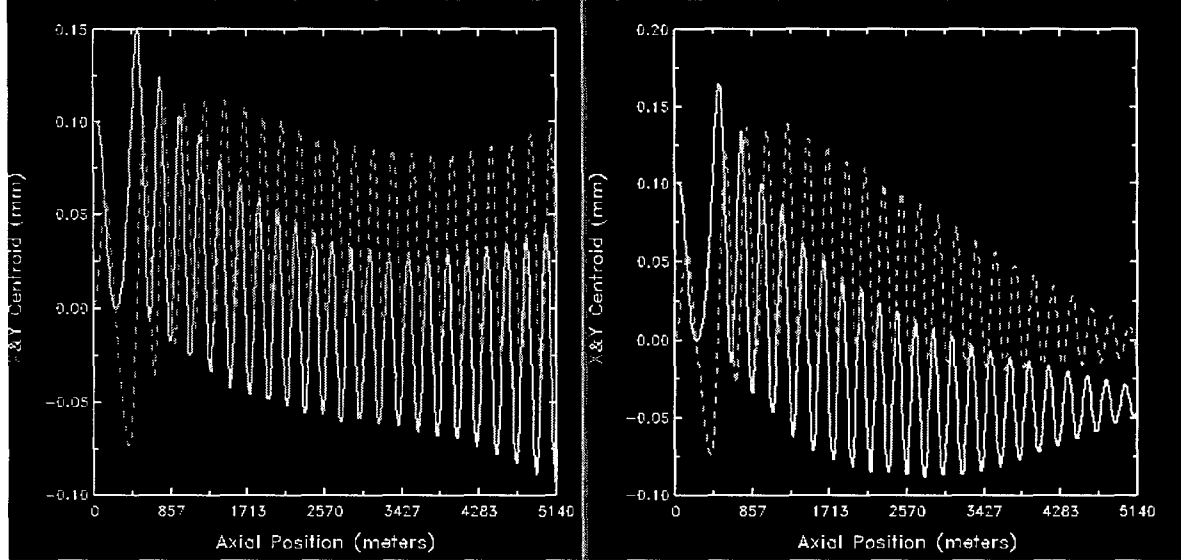


Figure 3:  $x$  and  $y$  centroid positions versus  $z$  at  $t=40$  ns for “shock”-excited BBU as computed by the BREAKUP code. The left plot is from a run utilizing the temporal wakefield potential, whereas the right used a discrete mode formulation.

made previously with the BREAKUP code, including those in the low  $Q$  regime, are reasonably accurate.

Nonetheless, there are differences in the detailed results between use of the two formulations. Fig. 3 plots the  $x(z)$  and  $y(z)$  centroids at  $t = 40$  ns for the case (a) (shock excitation) described above, 30 ns beyond the position at which the current flat top begins. In the left plot (temporal wake formulation), there is some initial damping of the centroid oscillations (as would be expected from the rapidly increasing solenoidal field in the first 10 meters of the lattice) but then they begin to grow to a final peak-to-peak amplitude of about  $150\mu\text{m}$ . In contrast, the discrete mode formulation run shows continued adiabatic damping throughout the full 50 m. The underlying cause of this difference is likely associated with a somewhat faster convective velocity for the instability and details of the low frequency ( $\leq 150$  MHz) instability spectrum not modeled exactly in phase and amplitude by the discrete mode formulation. For the specific case of DARHT-2 in which the pulse length is extremely long compared with the net convection of BBU, these differences will be important only in the first few per cent of the pulse.

#### 4 CONCLUSION

We have extended the BREAKUP code to use the full temporal dipole wake potentials produced by the AMOS code and investigated the sensitivity of DARHT-2 BBU growth

predictions to use of this model as compared with the more usual discrete mode formulation. Despite the predicted low  $Q$ 's of the current DARHT-2 accelerator cell design, we find that over a fairly broad range of initial transverse excitations, the two formulations give similar overall results. While there are differences in the details, these appear to arise mainly in the front portion of the pulse where the beam current and/or energy vary rapidly with time. Hence, unless the main body of the pulse is extremely short in duration or there are numerous BBU modes whose very low  $Q$ 's cause significant overlap in the frequency domain, we believe the discrete mode formulation is reasonably accurate for BBU growth prediction.

#### 5 REFERENCES

- [1] C.C. Shang *et al.*, “BBU Design of Linear Induction Accelerator Cells for Radiography Application”, *Proc. 1997 Particle Accel. Conf.*, **IEEE 97CH36137**, p. 2633, 1998.
- [2] Y.-J. Chen, G.J. Caporaso, A.C. Paul, W.M. Fawley, “Transverse Beam Motion on the Second Axis of the Dual Axis Radiographic Hydrodynamic Test Facility”, Paper TUA54, these proceedings.
- [3] J.F. DeFord, G.D. Craig, R. McLeod, “The AMOS Code”, *Proc. 1989 Particle Accel. Conf.*, **IEEE 89CH2669-0**, p. 1181, 1989.



# Enhanced functionality and Performance of the Longitudinal Damping System at the ALS\* using a New VXI Based Processing System

G.D. Stover<sup>\*</sup>, LBNL, Berkeley, CA J. Fox, D. Teytelman, A. Young, SLAC, Palo Alto, CA

## Abstract

The ALS longitudinal feedback electronics, designed and developed at the Stanford Linear Accelerator center (SLAC), has been operating very reliably at the ALS for over four years [1]. Recently a new VXI based implementation of the entire RF and timing electronics has been built, tested, and will soon replace an earlier prototype installation. The components designed are contained in three VXI packages along with a VXI controlled system oscillator chassis. The new system contains a number of functional enhancements that most notably include: enhanced timing control, internal temperature monitoring of all VXI modules, simulated beam signal generation, automatic locking of the phase detector servo loop, and the monitoring and alarm of critical RF signal levels. The details of the design and implementation of the VXI modules along with performance characteristics are presented below.

## 1 INTRODUCTION

The longitudinal multi-bunch feedback (LFB) system currently in operation at the Advanced Light Source (ALS) was a "first version" demonstration unit designed as part of a multi-lab collaboration for use at the ALS, PEP-II, and DAΦNE machines. Since the commissioning of the ALS damping system a number of VXI based modules especially for the RF and timing sections have been designed and constructed for the PEP-II [2] machine to enhance operational reliability and equipment problem analysis. Early versions of these modules have been constructed and debugged for the ALS system and are now ready for installation.

## 2 OVERVIEW OF LFB SYSTEM

The LFB system was designed to suppress longitudinal coupled bunch instabilities in the PEP-II and ALS electron storage rings. The basic scheme is a bunch-by-bunch feedback system that measures the instantaneous phase error of each bunch with respect to the average bunch synchronous phase. The system then applies a delayed longitudinal correction voltage to each

identical bunch through a low Q multiple gap drift tube kicker structure [3].

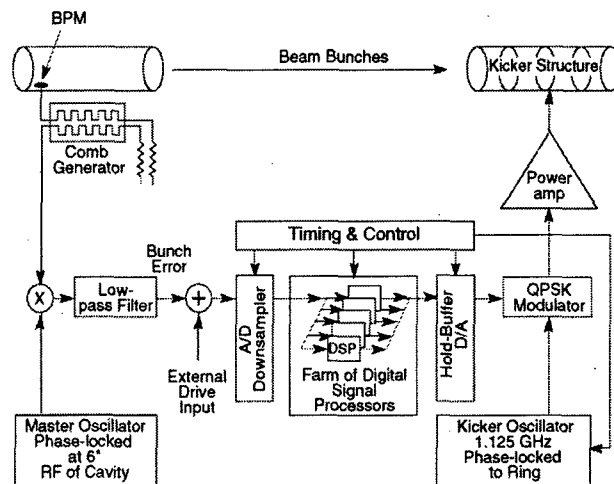


Figure 1 Block Diagram of the Longitudinal Feedback System

As shown in fig 1 the longitudinal beam bunch phase motion (error signal) is initially detected through a precisely balanced four button beam position monitor (BPM) at the 6th harmonic (3.0 GHz) of the ALS cavity RF. A passive "comb type" band pass filter with a 4 cycle 'tone burst' response creates a precisely defined bunch phase error signal and reduces the inter-bunch phase motion crosstalk. The  $6 \times \text{RF}$  (3.0 GHz) 'front-end' phase detector down-converts the beam signal to a base band (DC to 500 MHz) which contains all the coupled-bunch modes of beam motion. The resultant signal is digitised at 500 MHz, downsampled (by a factor of 24 for the ALS), tagged, and packed for serial transmission to the digital signal processor (DSP) array in the 'down sampler' module [4][5]. The low frequency of the coupled bunch instabilities ( $< 20$  kHz) allows for a distributed array of 40 DSP's (4 per DSP module) to apply a tailored 6 tap FIR algorithm to each and every bunch. The resultant digital correction words are repacked and serially transmitted to a high speed (500 MHz) circular memory in the 'hold buffer' module. The converted analog output signal amplitude modulates (AM) a quadrature phase shift keyed (QPSK) carrier generated by the 'back-end' module. The QPSK carrier signal centred at 1.125 GHz ( $9/4^{\text{th}}$  of ALS RF) was chosen to accommodate the electrodynamic dimensions of the kicker structure and commercially available power amplifiers. Reference signals for the front and back end modules are generated

\*Work was supported by the Office of Science, Office of Basic Energy Sciences, Materials Sciences Division, of the U.S. Department of Energy, under Contract No. DE-AC03-76SF00098.

\*Email: gdstover@lbl.gov

in the System Oscillator chassis. Timing signals for the digital cards are generated in the timing module [6].

The RF, timing, and high speed digital modules have been packaged in RF tight VXI modules and adhere to the VXI standard interface. The DSP modules are packaged in a VME format. All electronic systems are directly controlled through a VXWorks real time operating system that is linked to an extensive EPICS graphical interface [7].

### 3 RF AND TIMING SYSTEM

#### 3.1 Front End Module:

The front-end VXI module as shown in fig. 2 contains a phase detector, low frequency DC phase servo loop, an RMS beam motion detector and appropriate signal monitor points. The phase detector baseband output is bandpass limited ( $< 500$  MHz) to further reduce inter-bunch phase motion crosstalk. A signal splitter provides a feedback signal to a series pair of SLAC designed phase shifters that are connected to form a phase servo loop. The loop corrects for slow DC drifts in the average synchronous bunch phase and compensates for any thermal drifts in the front-end electronics. The beam motion detector provides a signal to the EPICS panel display that mimics the synchronous phase motion of the beam. Additionally an amplitude level can also be chosen to trigger a visual alarm. These two features provide a machine operator with a clear 'loss of lock' indication without the need to tie up an expensive monitoring oscilloscope. A useful software enhancement that is made possible through the new 'front end' hardware is the inclusion of an auto zeroing routine for the phase servo loop.

For normal machine set-up or occasionally after an RF cavity trip the 'front end' phase servo loop will have to be opened and re-locked. The process is simple and can be accomplished automatically (auto zero and lock) from the EPICS panel, or manually from the front panel of the VXI module in the equipment rack.

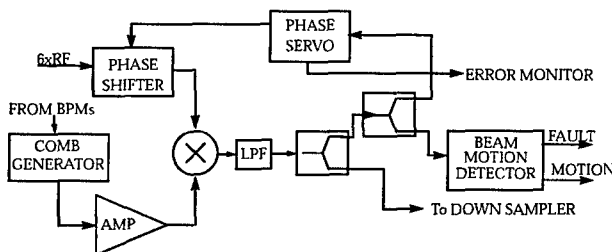


Figure 2. Block Diagram of Front-end module.

#### 3.2 Back End Module:

The back-end VXI module as shown in fig. 3 contains a QPSK modulator, amplitude modulator, RMS kick

output detector, QPSK test mode circuits, and appropriate signal monitor points.

The QPSK modulator impresses a 90 deg. phase shift every 2 NS on the 1.125 GHz ( $9/4^{\text{th}} \cdot \text{RF}$ ) carrier signal for the kicker electrode. The phase of the carrier is synchronised to provide the proper accelerating/decelerating voltage to the specific bunch within the kicker electrode gap.

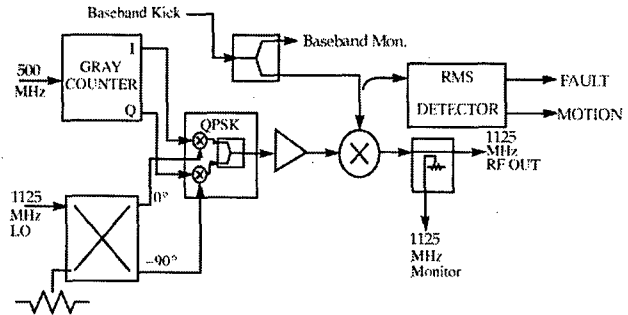


Figure 3 Block diagram of Back-end module

The in-line AM modulator, driven by the DSP generated baseband kick signal for each bunch, determines the amplitude and polarity of the correction voltage to be applied to the bunch within the electrode gaps.

The RMS kick output detector provides a signal to an EPICS panel display that is proportional to the kick amplitude required to damp the bunch train. This signal is a key system indicator that can confirm the loss of feedback lock, mode zero instabilities in the cavity, or back-end timing misalignment and again obviates the need of an external monitoring oscilloscope.

The QPSK test mode circuit can force the modulator to halt at one of four (0,90,180,270 deg.) selected phases. This feature provides a direct test of the QPSK modulator and provides a single tone test of AM modulator and the following amplifier chain.

#### 3.3 System Oscillator chassis and Breakout panel:

The System oscillator (SO) chassis generates the 3.0 GHz ( $6 \cdot \text{RF}$ ) mixing and 1.125 GHz ( $9/4 \cdot \text{RF}$ ) carrier signals for the Front and Back-end modules, houses the front-end comb filter, generates a simulated beam signal, provides real time monitoring and alarm functions of critical signals, and contains all the appropriate monitor points for expeditious hardware checkouts. The S.O. electronics is contained in a 19"x83/4"x24" rack mounted chassis that is connected to the EPICS/VXWorks software through a VXI interface card located in the chassis.

All the S.O. signals are derived from a 125 MHz square wave that is phase locked to the 500 MHz ALS master oscillator and divided by four in the Timing module. The 3.0 GHz ( $6 \cdot \text{RF}$ ) signal for the front-end phase detector is generated twice using two different techniques: the first

uses a Magnum Microwave (TLS22-06) x24 multiplier and phase locked loop (PLL) and the second uses a Herotek (GC125-188) step recovery diode whose rich spectral output is filtered by a 3.0 GHz band pass filter. Both methods produce spectrally clean and linear sine waves. The x 24 PLL output is a ready spare and a source for external mixer experiments. The 1.125 GHz carrier and the systems test 'fake beam' signal are also generated using the step diode recovery technique.

The 'fake beam' signal is a 3.0 GHz carrier modulated by the approximate synchrotron frequency (12 kHz) of the ALS and then is passed through an identical auxiliary comb filter. The resultant signal is a spectrally accurate reproduction of a longitudinally unstable beam with random coupled bunch motion. At the choice of the operator this signal can be switched to the input port of the front-end module thus providing a true calibration signal for the entire electronics chain from the front-end module to the power amplifier driving the kicker electrodes. This simple test along with alarm monitoring will allow technical personnel to quickly determine whether the electronics or the machine is at fault. System checkout is further enhanced by extensive front panel monitor points and the inclusion of a signal 'breakout panel' that collects all the signal monitor points from the other three modules into one 19" rack panel directly above the S.O chassis.

### 3.4 Timing module:

The timing module generates the fiducial (bucket zero trigger) for the down sampler module, the 500 MHz clock for both high speed digital modules, the 125 MHz source signal for the S.O. chassis, the re-synchronising pulse for the QPSK modulator, and complete temperature monitoring and alarm control for all the VXI modules and the S.O. chassis.

The temperature monitoring is a hardware only function that will automatically turn off the AC power to the VXI chassis if any of the sensors exceed pre-set limits. This feature is very crucial in preventing the burn-out of scarce and expensive high-speed memory chips in the downsampler and holdbuffer VXI modules.

## 4 RESULTS

The oscilloscope waveforms displayed in Figure 4 demonstrate the function of the Front-end RMS motion detector circuitry. The bottom waveform (trace 4) is an AM modulated sine wave injected into the Front-end module phase detector that mimics a slowly growing 'all mode' synchrotron bunch motion. Please note: The 27 ms periodic structure impressed on trace 4 is an artefact of the digital oscilloscope. The output of the RMS motion detector (trace 2) effectively tracks the growing synchrotron motion. At a pre-defined threshold set through the EPICS panel a comparator is tripped (trace 1). The comparator output which sends an alarm to the

EPICS panel can also be used to trigger the DSP farm to record a growing or runaway beam instability.

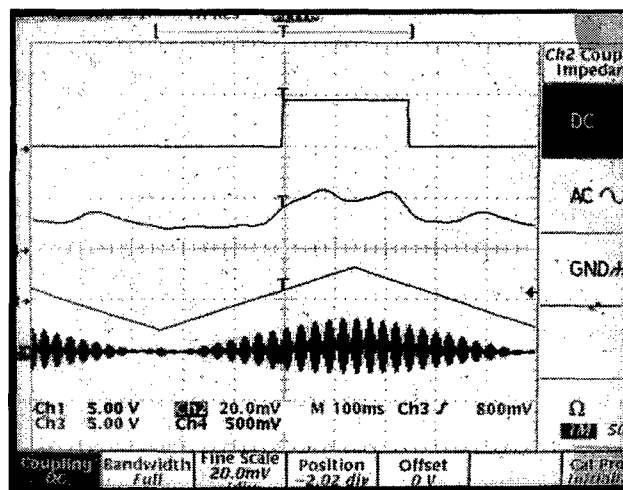


Figure 4. Hardware simulation of all mode beam instabilities (4), RMS motion detector output (2), comparator output (1), modulation envelope (3)

## 5 ACKNOWLEDGEMENTS

The author wishes to extend his great appreciation to M. Monroy, W. Byrne, and the ALS operators for their very expert help. To A. Geyer and A. Kruser respectively for their help in the coordination and construction of the Timing and Back-end modules and S. O. chassis. W. Ross of SLAC who designed the Timing module and provided invaluable information concerning the general operation of the digital systems. Also D. Anderson and B. Cordova-Grimaldi of SLAC are recognized for their technical support of all aspects of the Front-end module construction.

## 6 REFERENCES

- [1] D. Teytelman et. al, "Operation and Performance of the PEP-II Prototype Longitudinal Damping System at the ALS, Proc. PAC95, Dallas, pp 2420-2422.
- [2] A. Young et. al, "BXI Based Multibunch Detector and QPS Modulator for the PEP-II/ALS/DAONE Longitudinal Feedback System", Proc. PAC97, Vancouver, pp 2368-2370.
- [3] J. Corlett, et al., "Longitudinal and Transverse Feedback Kickers for the ALS", Proc. EPAC 94, pp. 1625-1627, London.
- [4] E. Kikutani, et. al., "Recent Progress in Development of Bunch Feedback System for KEKB", Proc. PAC 95, Dallas, pp. 2726-2728.
- [5] G. Oxoby, et al, "Bunch by Bunch Longitudinal Feedback System for PEP-II," Proc. EPAC 94, pp. 1616-1618, London.
- [6] W. Ross, "PEP-II Longitudinal Feedback System Timing Board Functional Specification", SLAC Internal Document, 5/97.
- [7] R. Claus, et al., "Software Architecture of the Longitudinal Feedback System for PEP-II, ALS and DAONE", Proc. PAC 95, Dallas, pp. 2660-2662.

# A CURE FOR THE ENERGY SPREAD INCREASING RELATED BUNCH LENGTHENING IN ELECTRON STORAGE RINGS

J. Gao, LAL, B.P. 34, F-91898 Orsay cedex, France

## Abstract

Having revealed the cause of the energy spread increasing and the corresponding bunch lengthening in electron storage rings in ref. 1, in this paper, we will propose a cure for the suppression of these collective effects. It is suggested to install an active rf cavity in the ring with the working rf wavelength about four to five times the rms bunch length. The limitation about this cure is also discussed. Finally, in the postscript, we will give an empirical bunch lengthening equation and compare the analytical results with some experimental results.

## 1 INTRODUCTION

In modern electron colliders, such as B and Tau-C Factories, short bunch lengths are required in order to get high luminosities. In practice, the bunch length will suffer from two kinds of lengthening effects. The first one is due to the potential well distortion and the second is due to the so-called collective random excitation (CRE) revealed in ref. 1. According to ref. 1 one has two equations for the energy spread increasing ( $R_\epsilon = \sigma_\epsilon/\sigma_{\epsilon 0}$ ) and the bunch lengthening ( $R_z = \sigma_z/\sigma_{z0}$ )

$$R_\epsilon^2 = 1 + \frac{C(R_{av}RI_b\mathcal{K}_{||,0}^{\text{tot}})^2}{\gamma^7 R_z^{2.42}} \quad (1)$$

$$R_z^2 = 1 + \frac{C_{PWD}I_b}{R_z^{1.5}} + \frac{C(R_{av}RI_b\mathcal{K}_{||,0}^{\text{tot}})^2}{\gamma^7 R_z^{2.42}} \quad (2)$$

where

$$C = \frac{576\pi^2\epsilon_0}{55\sqrt{3}\hbar c^3} \quad (3)$$

$\epsilon_0$  is the permittivity in vacuum,  $\hbar$  is Planck constant,  $c$  is the velocity of light,  $I_b = eN_e c/2\pi R_{av}$ ,  $R_{av}$  is the average radius of the ring,  $R$  is the bending radius,  $\mathcal{K}_{||,0}^{\text{tot}}$  is the total longitudinal loss factor at the zero current bunch length,  $C_{PWD}$  represents potential well distortion effect,  $N_e$  is the electron number in a bunch, and  $\gamma$  is the normalized particle energy.

In this paper we will investigate the possibility to suppress the CRE induced bunch energy spread increasing and the corresponding bunch lengthening.

## 2 CURE: INTRODUCING AN ACTIVE RF CAVITY IN THE RING

A bunch of  $N_e$  particles inside will have a definite short range wake potential profile corresponding to its charge distribution. What should be stressed is that for a given bunch current even the longitudinal position of each electron inside the bunch is a random variable, the collective

wake potential profile remains stable. As shown in ref. 1, after each turn an electron will get a net kick on its energy by

$$\Delta E_i = \mathcal{U}_w \sin(\Omega_s t - \phi_i) \quad (4)$$

where  $\phi_i$  is a random variable,  $\Omega_s$  is the angular synchrotron oscillation frequency, and  $\mathcal{U}_w = e^2 N_e \mathcal{K}_{||}^{\text{tot}}(\sigma_z)$  is the average single particle energy loss due to short range wakefield per turn. It is these random energy fluctuations which are responsible for the bunch energy spread increasing. The idea to suppress these kicks is to create an artificial counteract kicks  $-eV_0 \sin(\Omega_s t - \phi_i)$ . Since it is known that an electron will get maximum positive kicks at the very head and the tail of the bunch, and the maximum negative kick near the middle of the bunch as shown in Fig. 1a, one can use a standing wave rf cavity with the wavelength of the working mode (with rf input power) about four to five times the rms bunch length. The phase relation of this mode with respect to the passing bunch should be arranged as follows: The head and the tail gets the maximum energy reduction by  $-eV_0$  each turn and the middle of the bunch gets the maximum energy gain  $eV_0$  per turn as shown in Fig. 1b (in a practical point of view, the phase shift should be adjustable to adapt different shape of wake potentials). Obviously, to cancel the collective random kicks one has to choose  $V_0 = \mathcal{U}_w/e$  which is the peak voltage gain of an electron passing through the cavity. The required rf input power can be easily obtained by

$$P_0 = V_0^2/R_{sh} \quad (5)$$

where  $R_{sh}$  is the shunt impedance of the standing wave rf cavity. Once this is done, eqs. 1 and 2 will be changed to

$$R_\epsilon^2 \approx 1 \quad (6)$$

$$R_z^2 \approx 1 + \frac{C_{PWD}^* I_b}{R_z^{1.5}} \quad (7)$$

where  $|C_{PWD}^*| > |C_{PWD}|$  due to the additional impedance contribution from the rf cavity. Till now the CRE induced energy spreading increasing and the related bunch lengthening effects have been suppressed.

As a natural rule one has to pay for what he gains, and this time it is the transverse instability.

## 3 LIMITATION COMING FROM THE TRANSVERSE INSTABILITY

Here, we will make a quick review of the single bunch transverse instability in electron storage rings. The threshold bunch current for the transverse instability derived in

ref. 2 is expressed as:

$$I_{b,gao}^{th} = \frac{4f_y\sigma_{e0}\mathbf{R}_\epsilon|\xi_{c,y}|}{e < \beta_{y,c} > \mathcal{K}_\perp^{tot}(\sigma_z)} \quad (8)$$

where  $\nu_y$  is the vertical betatron oscillation tune, respectively,  $< \beta_{y,c} >$  is the average beta function in the rf cavity region,  $\xi_{c,y}$  is the chromaticity in the vertical plane (usually positive to control the head-tail instability), and  $\mathcal{K}_\perp^{tot}(\sigma_z)$  is the total transverse loss factor over one turn. This threshold current indicates the disappearance of Landau damping. On the other hand, the usually used Zotter's formula coming from the mode coupling theory gives

$$I_{b,zotter}^{th} = \frac{Ff_sE_0}{e < \beta_{y,c} > \mathcal{K}_\perp^{tot}(\sigma_z)} \quad (9)$$

where  $F$  is variable depending on bunch length,  $f_s$  is the synchrotron oscillation frequency, and  $E_0$  is the particle energy. To compare eq. 8 with eq. 9 one can write eq. 8 in a similar form as eq. 9

$$I_{b,gao}^{th} = \frac{F'f_sE_0}{e < \beta_{y,c} > \mathcal{K}_\perp^{tot}(\sigma_z)} \quad (10)$$

with

$$F' = 4\mathbf{R}_\epsilon|\xi_{c,y}|\frac{\nu_y\sigma_{e0}}{\nu_sE_0} \quad (11)$$

where  $\nu_s$  is the synchrotron oscillation tune. Apparently, if  $F' < F$ ,  $I_{b,gao}^{th} < I_{b,zotter}^{th}$  and this situation can always be realized experimentally by reducing  $|\xi_{c,y}|$ . If, however, eq. 9 and eq. 10 describe the same physical process, one finds the explicit expression of  $F$  ( $F = F'$ ).

The impact of the longitudinal motion on that of the transverse one can be perceived by finding  $\mathbf{R}_\epsilon$  and  $\sigma_z$  in eq. 8. Obviously, better longitudinal bunch properties (smaller energy spread and shorter bunch length) result in lower transverse instability threshold current.

## 4 DISCUSSION

Recent experiments on super-ACO [4] show that by using negative momentum compaction factor  $\alpha$  one can get shorter bunch length, and unfortunately, larger energy spread compared with positive  $\alpha$  case. This result is easily understood by looking at eqs. 1 and 2. With negative  $\alpha$ ,  $C_{PWD}$  becomes negative, and in consequence, one gets smaller  $\mathbf{R}_z$  and larger  $\mathbf{R}_\epsilon$ . Now, if one uses the additional active rf cavity proposed in section 2, eqs. 1 and 2 are reduced to eqs. 6 and 7. Obviously,  $\mathbf{R}_z$  and  $\mathbf{R}_\epsilon$  are decoupled from each other, and hopefully, one can get at the same time smaller energy spread and shorter bunch length. As far as the rf cavity design is concerned, one should manage to avoid the cavity beam pipe being excessively small. The detailed discussion on the cavity design will be made after the cure principle shown in this paper be justified by the numerical simulations.

## 5 CONCLUSION

An additional active rf cavity is proposed to be installed in the ring to suppress the collective random excitation induced energy spread increasing and the corresponding bunch lengthening. The wavelength of the working mode should be four to five times the rms bunch length. One should be cautious to the transverse instability since smaller energy spread and shorter bunch length will result in lower transverse instability threshold current. It could be interesting to use this technique together with negative momentum compaction factor to obtain short bunch with small energy spread.

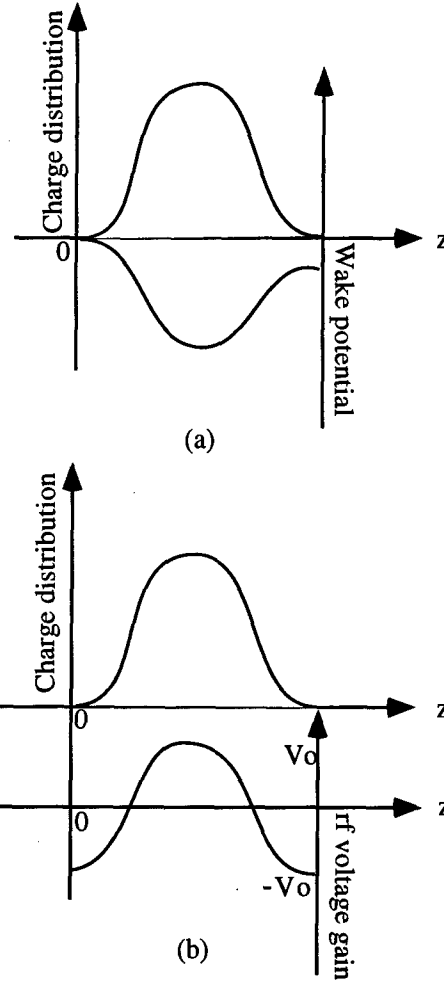


Figure 1: (a) Schematic showing of the bunch charge distribution and the short range wake potential. (b) Schematic showing of the rf voltage gain with respect to the particle position within the bunch.

## 6 POSTSCRIPT

Here, exceptionally, we add a section of "postscript" where an empirical bunch lengthening equation is given as:

$$\mathbf{R}_z^2 = 1 + \frac{\sqrt{2}C_{av}R\mathcal{K}_{||,0}^{tot}I_b}{\gamma^{3.5}\mathbf{R}_z^{1.21}} + \frac{C(R_{av}RI_b\mathcal{K}_{||,0}^{tot})^2}{\gamma^7\mathbf{R}_z^{2.42}} \quad (12)$$

An interesting property of this formula is that  $\mathcal{K}_{||,0}^{\text{tot}}$  plays a unique dominating role. The reason for my calling this equation as empirical is because the second term on the right side of eq. 12 is not derived on a theoretical base. In Figs. 2 to 6 we make the comparison between the analytical and the experimental results of different machines. More detailed explications and comparison results can be found in ref. 5

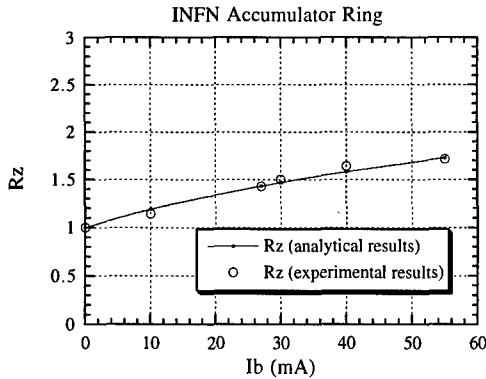


Figure 2: Comparison between INFN ( $R = 1.15$  m and  $R_{av} = 5$  m) experimental results and the analytical results at 510 MeV with  $\sigma_{z0} = 3.57$  cm and  $\mathcal{K}_{||,0}^{\text{tot}} = 0.39$  V/pC.

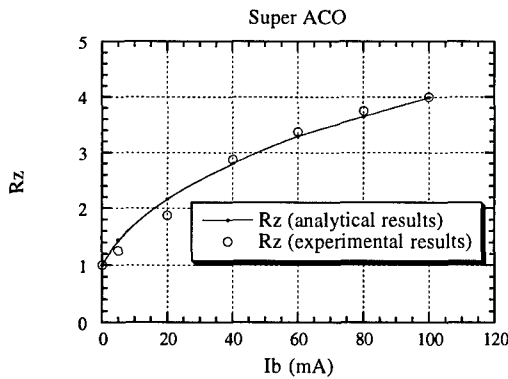


Figure 3: Comparison between Super-ACO ( $R = 1.7$  m and  $R_{av} = 11.5$  m) experimental results and the analytical results at 800 MeV with  $\sigma_{z0} = 2.4$  cm and  $\mathcal{K}_{||,0}^{\text{tot}} = 3.1$  V/pC.

## 7 REFERENCES

- [1] J. Gao, "Bunch lengthening and energy spread increasing in electron storage rings", *Nucl. Instr. and Methods*, A418 (1998), p. 332.
- [2] J. Gao, "Theory of single bunch transverse collective instabilities in electron storage rings", *Nucl. Instr. and Methods*, A416 (1998), p. 186.
- [3] B. Zotter, LEP note 363 (1982).
- [4] A. Nadji, P. Brunelle, G. Flynn, M.-P. Level, M. Sommer, H. Zyngier, "Experiments with low and negative momentum compaction factor with super-ACO", Proceedings of EPAC96, Barcelona, Spain, 1996.
- [5] J. Gao, "An empirical equation for bunch lengthening in electron storage rings", to be published.

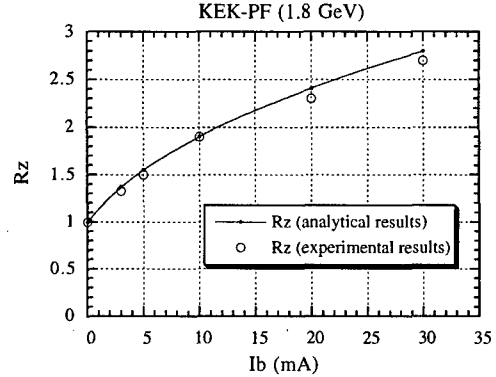


Figure 4: Comparison between KEK-PF ( $R = 8.66$  m and  $R_{av} = 29.8$  m) experimental results and the analytical results at 1.8 GeV with  $\sigma_{z0} = 1.47$  cm and  $\mathcal{K}_{||,0}^{\text{tot}} = 5.4$  V/pC.

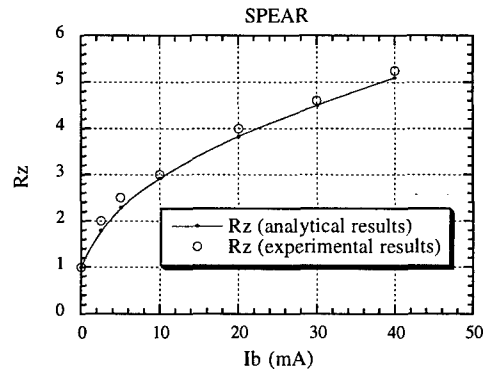


Figure 5: Comparison between SPEAR ( $R = 12.7$  m and  $R_{av} = 37.3$  m) experimental results and the analytical results at 1.5 GeV with  $\sigma_{z0} = 1$  cm and  $\mathcal{K}_{||,0}^{\text{tot}} = 5.2$  V/pC.

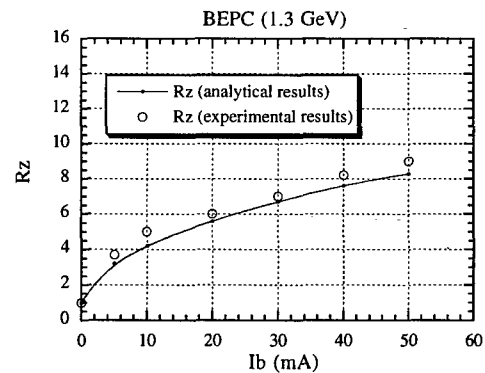


Figure 6: Comparison between BEPC (1.3 GeV) ( $R = 10.345$  m and  $R_{av} = 38.2$  m) experimental results and the analytical results at 1.3 GeV with  $\sigma_{z0} = 1$  cm and  $\mathcal{K}_{||,0}^{\text{tot}} = 9.6$  V/pC.

# A SAW TOOTH INSTABILITY MODEL IN STORAGE RINGS

M. Migliorati\*, L. Palumbo, University of Rome - Dip. Energetica, Italy  
G. Dattoli, L. Mezi, ENEA, Dip. Innovazione, Frascati, Rome, Italy

## Abstract

The time evolution of the energy spread above the microwave instability threshold in a storage ring is described by means of two coupled non linear differential equations. The results are in agreement with a time domain simulation code. The model equations are combined to those accounting for the storage ring Free Electron Laser dynamics, in order to study the interplay between the FEL and the storage ring instability dynamics.

## 1 INTRODUCTION

The microwave instability produces an increase of energy spread and a consequent anomalous bunch lengthening, and limits the performances of storage rings. It has been the subject of several investigations [1, 2, 3, 4], and the problem has been studied by exploiting the linearized Vlasov equation, which describes the time evolution of the single bunch distribution function in the phase space. The threshold of the instability depends on the wake fields and on the current intensity. Above the threshold the linear theory can not explain the time evolution of the distribution function. The increase of the bunch phase space dimensions may provide the conditions for a new equilibrium configuration. It may happens, however, that the equilibrium is never reached, and the energy spread oscillates in time with a pattern similar to relaxation type oscillations, as shown in Fig. 1. Such a behavior is known as saw tooth instability [4], and it occurs in storage rings characterized by intense beam currents.

An appropriate analysis of the saw tooth instability, requires the inclusion of non linear terms in the Vlasov equation. The problem has been afforded in ref. [5], where it is shown that the time evolution of the distribution function may have different patterns, including relaxation type oscillations.

In this paper, analyzing the results of appropriate numerical simulations, we study the conditions for the onset, growth and relaxation of the saw tooth oscillations for a pure inductive impedance. The analysis points out the mechanisms responsible for the saw tooth behavior: the growth of the instability is produced by non linear wakes, it is counteracted by the Landau damping, and it is finally damped by the radiation process. We describe these effects through some quantities averaged over the bunch distribution, giving a model employing two coupled non linear equations which reproduce the relaxation oscillations of the instability in a fairly satisfactory way. We employ numerical simulations to show that a Free Electron Laser (FEL),

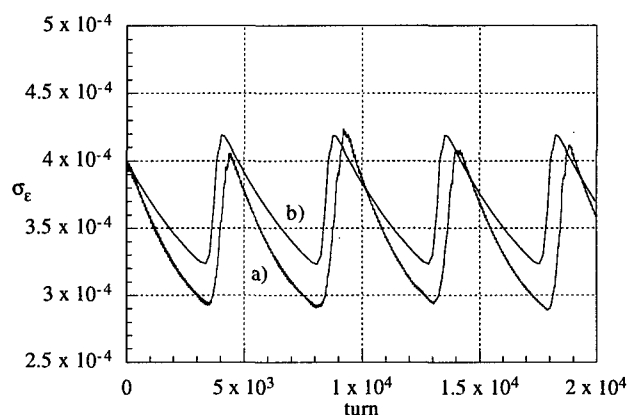


Figure 1: Energy spread vs number of turns: a) simulations, b) model equations.

used either as an amplifier or an oscillator, may be an efficient tool to damp the saw tooth instability. The physical interpretation of the simulation results has also suggested the way to extend the model equations by including the effects of the FEL in the oscillator mode. This approach provides a clear picture of the FEL-storage ring mutual feedback, and clarifies the mechanism of the instability inhibition.

## 2 SAW TOOTH INSTABILITY

For the study of the saw tooth instability, we use a time domain simulation code, which includes the effects of the self induced wake fields. The simulations, using a pure inductive impedance and employing  $3 \times 10^5$  macroparticles, show a clear saw tooth behavior (Fig. 1, a) line) above the microwave threshold. The evolution of the phase space distribution gives further insight for a better understanding of the mechanisms responsible for the growth of the energy spread and of its damping. In fact, referring to Fig. 1, when the energy spread is close to one minimum, the phase space distribution shows a perturbation, superimposed to the stationary distribution, which suggests the existence of a coherent microstructure (microbunching) inside the bunch [6]. This microbunching increases the energy spread producing a turbulent distribution. In some regions the particles, due to the wake fields non linearities, experience larger oscillation amplitudes, and the distribution endures a filamentation process. The phase space evolution is then characterized by a reduction of the local density due to the particle diffusion which tends to decrease the microbunching efficiency so that, the natural radiation and Landau dampings are able to counteract the

\* Email: migliorati@axrma.uniroma1.it

phase space anomalous growth, until the initial configuration is restored.

The microbunching mechanism producing the microwave instability has been discussed in ref. [7], where it is considered the responsible for coherent radiation emission observed in operating storage rings affected by strong microwave instability, an effect similar to the Free Electron Laser dynamics.

The analysis of the simulations clarifies also the contribution of the damping mechanisms: the radiation process is the main responsible for the saw tooth behavior, while the Landau damping is important in counteracting the instability. In fact, by running simulations with a very long radiation damping time, the saw tooth pattern disappears, the bunch distribution remaining stable with an energy spread slightly larger than the maximum obtained from Fig. 1.

### 3 DYNAMICAL MODEL

To model the saw tooth behavior, we start by considering the coasting beam case, for which the linear theory predicts an instability caused by a growth of a perturbation produced by the wake fields, and an opposed damping deriving from a spread in the oscillation frequencies (Landau damping) [1]. The extension of the theory to the bunched beam case is known as Boussard criterion [8].

If we suppose that the energy spread  $\sigma_\epsilon$  is a quadratic combination of the natural ( $\sigma_{\epsilon n}$ ) and instability induced ( $\sigma_i$ ) parts, that is

$$\sigma_\epsilon = (\sigma_{\epsilon n}^2 + \sigma_i^2)^{\frac{1}{2}} = \sigma_{\epsilon n} (1 + \sigma_r^2)^{\frac{1}{2}} \quad (1)$$

and consider a Gaussian bunch distribution with a Lorentz spectrum of the oscillation frequencies, then the growth rate of the instability induced by the wake fields can be written as [6]

$$\frac{n}{T_0} \sqrt{\frac{(2\pi)^{3/2} I_0 \nu_s |Z/n|}{(E_0/e) \sigma_{\epsilon n}}} \frac{1}{(1 + \sigma_r^2)^{\frac{1}{4}}} = \frac{A}{(1 + \sigma_r^2)^{\frac{1}{4}}} \quad (2)$$

and the Landau term as

$$\frac{n}{T_0} 2\pi \alpha_c \sigma_{\epsilon n} (1 + \sigma_r^2)^{\frac{1}{2}} = B (1 + \sigma_r^2)^{\frac{1}{2}} \quad (3)$$

where  $n$  is an harmonic of the revolution frequency,  $\alpha_c$  the momentum compaction,  $T_0$  the revolution period,  $I_0$  the average beam current,  $Z/n$  the broad band impedance at the  $n^{\text{th}}$  harmonic of the revolution frequency,  $E_0$  the beam energy.

We derive now differential equations, governing the time evolution of the energy spread and of the saw tooth growth rate, without entering into the details of the phase space dynamics. We denote the growth rate of the instability by  $\alpha$  and relate such a quantity with the induced energy spread  $\sigma_r$ , according to the obvious relation

$$\frac{1}{\sigma_r^2} \frac{d\sigma_r^2}{dt} = \left( \alpha - \frac{2}{\tau_s} \right) \quad (4)$$

where  $\tau_s$  is the longitudinal damping time.

To explain the saw tooth behavior, we assume that  $\alpha$  is a time dependent function. Physical observations suggest that the equation should include the Boussard criterion stationary solution, thus yielding a dependence of the energy spread on the current as  $I_0^{1/3}$ . The equation should also be capable of reproducing relaxation type oscillations. From these considerations, we make the ansatz that  $\alpha$  satisfies an equation of the type

$$\frac{1}{\alpha} \frac{d\alpha}{dt} = \frac{c_1 A}{(1 + \sigma_r^2)^{\frac{1}{4}}} - c_2 B (1 + \sigma_r^2)^{\frac{1}{2}} \quad (5)$$

which contains, on the right hand side, the two opposite terms (2) and (3), accounting respectively for the wake fields instability and the Landau damping,  $c_1$  and  $c_2$  being constant parameters.

Eqs. (4) and (5) provide our model equations. They give stationary solutions with  $\sigma_\epsilon = \sigma_{\epsilon n}$  in any situation for which  $c_1 A < c_2 B$ . The case  $c_1 A = c_2 B$  is exactly the Boussard criterion which is therefore satisfied.

The above equations rely on simple assumptions. For example, in case of the  $A$  parameter, the actual bunch shape is distorted by the potential well and is not Gaussian. Furthermore a local density perturbation may be responsible for the microwave instability [7]. This is the reason we introduced the factor  $c_1$  in eq. (5).

For what concern the  $B$  parameter, and then the introduction of the factor  $c_2$ , the major approximations are in the linear relationship assumed between the spectrum width producing Landau damping and the energy spread  $\sigma_\epsilon$ , and the assumption of a Lorentz spectrum. Actually the oscillation frequency spectrum depends on the bunch distribution and on the non linearities of the wake fields.

To verify the model, we first estimate the constants  $c_1$  and  $c_2$  by comparing the simulations and the solution of Eqs. (4) and (5) under the condition of stability, that is for  $c_1 A < c_2 B$ , getting, as best fit,  $c_1 = 0.35$  and  $c_2 = 2.1$ . Then, with the same factors  $c_1$  and  $c_2$ , we analyze the case of instability. The resulting time behavior of the energy spread, given by Eqs. (4) and (5), is shown in Fig. 1 (the b) line), which shows a good agreement with the simulation results. If we increase the damping time  $\tau_s$  and eventually it tends to infinity, the saw tooth behavior disappears, thus giving a stationary energy spread which depends on the initial conditions and on the coefficients  $c_1 A$  and  $c_2 B$ , that is on the intensity of both the instability and Landau damping. In this case, from eq. (5), we get that the energy spread has a dependence on the current of the kind  $I_0^{1/3}$ .



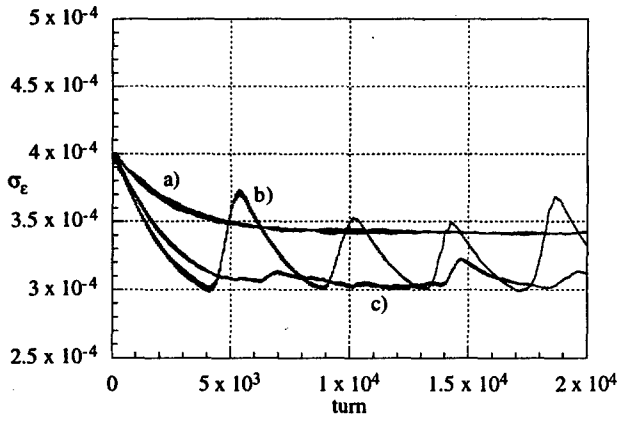


Figure 2: Energy spread vs number of turns with the FEL amplifier for different FEL intensities.

#### 4 FEL CONTRIBUTION

We have investigated the effect of the FEL on the storage ring saw tooth instability. The FEL induced energy spread and associated bunch lengthening decrease the peak current and the wake field intensity, thus shifting the instability threshold to higher levels. The parameter which can be used to control the instability is the intensity of the laser field itself. In Fig. 2 we have considered a storage ring FEL amplifier. When the laser intensity is sufficiently large (the a) curve), the FEL interaction destroys completely the saw tooth instability pattern, the beam energy spread is essentially that induced by the FEL. For lower intensity the saw tooth oscillation amplitudes are reduced (the b) curve), for intermediate intensity (the c) curve) it is possible to switch off the instability without inducing any energy spread.

A similar analysis has been performed with the FEL in the oscillator mode. In this case, the extension of the model to include the FEL dynamics can be useful to provide an explanation of the complex phenomenology of the interplay between the FEL and the storage ring by means of simple but physically pregnant and transparent formulae. By recalling that the FEL induced energy spread, proportional to the laser power, combines quadratically to the natural one [9], eq. (4) is modified in

$$\frac{d\sigma_r^2}{dt} = \alpha\sigma_r^2 - \frac{2}{\tau_s}(\sigma_r^2 - x_0) \quad (6)$$

where  $x_0$  is linked to the intracavity power and satisfies the differential equation

$$\frac{1}{x_0} \frac{dx_0}{dt} = \frac{.85g_0}{T_0} \left[ \frac{1}{\sqrt{1 + \sigma_r^2 + 1.7\mu_e(0)^2(1 + \sigma_r^2)^{3/2}}} - \frac{\eta}{.85g_0} \right] \quad (7)$$

where  $g_0$  is the FEL small signal gain coefficient,  $\mu_e(0) = 4N\sigma_{en}$  with  $N$  being the number of undulator periods,

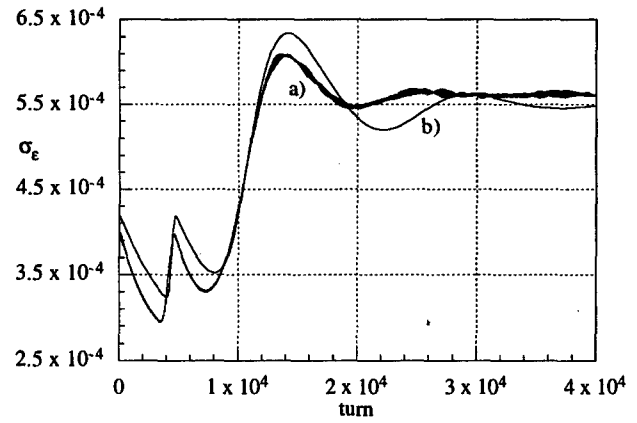


Figure 3: Energy spread vs number of turns with the FEL oscillator.

and  $\eta$  represents the cavity losses. The results of the coupled equations in presence of the FEL oscillator show that the saw tooth instability is critical to the ratio between the losses and the gain. If this ratio is relatively small, the intracavity power grows and induces a large energy spread which overcomes the saw tooth instability. Then the growth rate  $\alpha$  is suddenly brought to zero and the total energy spread tends to a stable behavior. When the ratio increases, the onset of the laser takes longer time to establish. In Fig. 3 we show a preliminary comparison between the results of the model (the b) line) and the more time consuming numerical simulations (the a) line). The agreement is fairly satisfactory, and further investigations are in progress.

#### 5 REFERENCES

- [1] A. W. Chao, *Physics of Collective Beam Instabilities in High Energy Accelerators*, Wiley-Interscience, New York (1993).
- [2] K. Oide, and K. Yokoya, KEK Report 90-10, KEK, Tsukuba, Japan (1990).
- [3] K. L. F. Bane, and K. Oide, in *Proc. IEEE Particle Accelerator Conference*, Washington, (1994).
- [4] M. D'yachkov, Ph.D. thesis, University of British Columbia, (1995).
- [5] G. V. Stupakov, *et al.*, Physical Review E **55**, 5976 (1997).
- [6] G. Dattoli, *et al.*, in *Proc. of 16th ICFA Workshop on Nonlinear and Collective Phenomena in Beam Physics*, Arcidosso, Italy, (1998).
- [7] J. M. Wang, Physical Review E **58**, 984 (1998).
- [8] D. Boussard, Technical Report No. LABII/RF/Int./75-2, CERN, Geneva, (1975).
- [9] G. Dattoli, *et al.*, NIM A **393**, (1997).

# NONLINEAR DAMPING OF INJECTION OSCILLATIONS

V. M. Zhabitsky

Joint Institute for Nuclear Research, 141980 Dubna, Moscow region, Russia

## Abstract

The theory of a transverse feedback system with a nonlinear regime of injection oscillations damping in circular accelerators and colliders is described. For this feedback loop the dependence between the kick value in the deflector and the beam deviation at the pick-up location is a nonlinear function. The beam dynamic nonlinear equation of the transverse coherent motion for deviation from the closed orbit has been solved using the approximation procedure based on the Krylov-Bogoliubov method for nonlinear differential equations. Approximate expressions for damping time and beam oscillation amplitude are analysed for different nonlinear transfer functions.

## 1 INTRODUCTION

Transverse feedback systems (TFS) are used in synchrotrons to damp the coherent transverse beam oscillations. In these systems (see Fig.1) the kicker (DK) corrects the beam angle according to the beam deviation from the closed orbit in the pick-up (PU) location at every turn. TFS have been widely used to suppress resistive wall instability and to provide a beam oscillation amplitude decrease after injection.

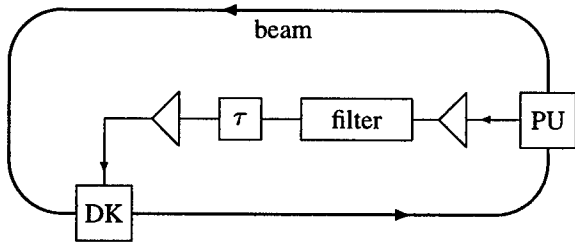


Figure 1: Layout of a transverse feedback system

Most TFS use electronics for signal processing in the feedback loop in order to obtain different dependences  $f(x)$  between the beam deviation  $x[n, s_K]$  in PU and the kick  $\Delta x'[n, s_K]$  in DK at the  $n$ -th turn:

$$\sqrt{\beta_P \beta_K} \Delta x'[n, s_K] = g f(x[n, s_P]). \quad (1)$$

Here  $\beta_P$  and  $\beta_K$  are the transverse betatron amplitude functions in the PU and DK locations;  $g$  is the gain of the feedback loop. Usually power amplifiers with a linear characteristic are employed. Hence, a transfer function  $f(x)$  of this feedback loop is a linear one (see Fig.2, dashed line).

However, many TFS use digital electronics in the feedback loop (for example, filters and delays). Their transfer functions have a quasi-linear step character. Sometimes the regime with limitation of a power for amplifiers is employed for large amplitudes of beam oscillations. On the SPS at CERN, the "bang-bang" regime was realized to increase the efficiency of TFS [1]. Its transfer function consists of a linear part for small amplitude oscillations and a high fixed level gain for large oscillations (see Fig.2, solid line). Thus, the transfer functions  $f(x)$  of these TFS are nonlinear.

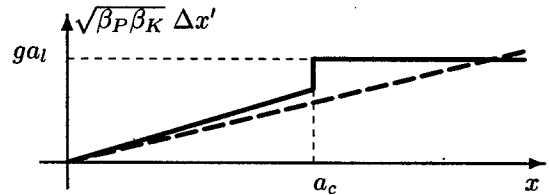


Figure 2: Dependence of the kick  $\Delta x'$  on the beam deviation  $x$  for the linear (dashed line) and "bang-bang" (solid line) transfer functions.

The so-called "logical regime" was described in [2]. Its transfer function is a step function with two jumps. This nonlinear regime was tested on the SPS at CERN [3]. The fast damping of initial oscillations was observed.

These experiments initiated some theoretical studies. A numerical simulation was used in [2] to estimate the damping time. It has been found that the amplitude of oscillations decreases linearly in time for some regimes.

The analytical approach for nonlinear damping was developed in [4]. It is shown that the transverse coherent motion for the particle deviation from the closed orbit, when instability is neglected, is fully described by the difference equation of the second order:

$$\begin{aligned} x[n+2, s_P] - 2x[n+1, s_P] \cos \mu + x[n, s_P] \\ = \sqrt{\beta_P \beta_K} \Delta x'[n+1, s_K] \sin(\mu - \eta) \\ + \sqrt{\beta_P \beta_K} \Delta x'[n, s_K] \sin \eta, \end{aligned} \quad (2)$$

where  $\mu = 2\pi Q$  is a betatron phase advance per revolution in the transverse plane,  $Q$  is the number of unperturbed betatron oscillations per revolution, and  $\eta$  is the betatron phase advance from PU to DK.

To solve equation (2), the approximation procedure based on the Krylov-Bogoliubov method [5] for nonlinear

differential equations was used in [4, 6]. These approximation approaches for nonlinear damping are generalized below. Damping time and asymptotic behaviour of the beam oscillation amplitude are analysed for different parameters of the nonlinear transfer function. All results are obtained for feedback description when instability is neglected.

## 2 THEORY

### 2.1 Basic Equation

In order to simplify final expressions, it will be supposed further that the phase advance  $\eta$  from the PU to the DK is equal to an odd number of  $\pi/2$  radians. So,  $|\sin \eta| = 1$  and the best damping is realised for TFS with the linear transfer function. Substituting for  $\Delta x'$  from (1) into (2) in this case yields

$$\begin{aligned} x[n+2, s_P] - 2x[n+1, s_P] \cos \mu + x[n, s_P] \\ = g f(x[n, s_P]) - g f(x[n+1, s_P]) \cos \mu. \end{aligned} \quad (3)$$

Equation (3) is a basic equation for studying beam dynamics with a nonlinear transfer function for a feedback loop. This equation is good for numerical calculations and convenient for analytical work.

### 2.2 Solution (First Approximation)

The gain  $g$  in (3) for feedback realized is a small value. Normally,  $g \approx 0.01$  for instability damper systems and  $g \approx 0.1$  for damping of injection errors. Since  $g$  is small, equation (3) is weakly nonlinear, and a number of perturbation methods is available to determine an approximate solution of this equation. It was demonstrated in [4, 6] that the Krylov-Bogoliubov method [5] can be used for solving the weakly nonlinear equation (3). This approach is used and generalized below.

When  $g = 0$ , the solution of (3) can be written as

$$\begin{aligned} x[n, s_P] &= a \cos(\mu n + \phi) = a \cos \psi_n, \\ \psi_n &= \mu n + \phi, \end{aligned} \quad (4)$$

where  $a$  and  $\phi$  are constants. When  $g \neq 0$ , the solution of (3) can still be expressed in form (4), provided that  $a$  and  $\phi$  are considered to be functions of  $n$  rather than constants. In accordance with the Krylov-Bogoliubov method, the solution of (3) can be written as a series of the form

$$x[n, s_P] = a_n \cos \psi_n + \sum_{m=1}^{\infty} g^m \xi_m(a_n, \psi_n), \quad (5)$$

where  $\xi_i$  is unknown functions of full amplitude  $a_n$  and periodical functions of  $\psi_n$ . Functions  $\xi_i$  are small corrections of the main harmonic  $a_n \cos \psi_n$ . The order of these corrections is given by small parameter  $g$ . The amplitude and phase are the functions of  $a_n$ . Hence, for their derivatives we can write:

$$\frac{da_n}{dn} = g A_1(a_n) + g^2 A_2(a_n) + \dots, \quad (6)$$

$$\frac{d\psi_n}{dn} = \mu + g \Phi_1(a_n) + g^2 \Phi_2(a_n) + \dots \quad (7)$$

Functions  $\xi_m$  as the periodical functions of  $\psi_n$  can be expanded into the Fourier series:

$$\begin{aligned} \xi_m(a_n, \psi_n) &= \nu_{m0}(a_n) \\ &+ \sum_{k=2}^{\infty} [\nu_{mk}(a_n) \cos k\psi_n + \gamma_{mk}(a_n) \sin k\psi_n], \end{aligned}$$

where  $\nu_{m1} = \gamma_{m1} = 0$ , because amplitude  $a_n$  is the full amplitude of the main (first) harmonic of oscillations.

For the left-hand side of (3) we expand all values into the Taylor series taking into account (6) and (7). The first approximation of these expansions is:

$$\begin{aligned} l.h.s. &\simeq g A_1(a_n) [\cos(\psi_n + 2\mu) - \cos \psi_n] \\ &+ g \Phi_1(a_n) a_n [\sin \psi_n - \sin(\psi_n + 2\mu)] \\ &+ g \xi_1(a_n, \psi_{n+2}) - 2g \cos \mu \xi_1(a_n, \psi_{n+1}) \\ &+ g \xi_1(a_n, \psi_n). \end{aligned} \quad (8)$$

For the first level of approximation, the right-hand side of (3) is determined by a zero level of approximation. Substituting for  $x$  from (5) into (3) yields

$$\begin{aligned} r.h.s. &= g f(a_n \cos \psi_n) \\ &- g f(a_n \cos(\psi_n + \mu)) \cos \mu. \end{aligned} \quad (9)$$

Equating coefficients of Fourier series in (8) and in (9) yields for main harmonic:

$$\frac{da_n}{dn} = -\frac{g}{2\pi} \int_0^{2\pi} f(a_n \cos \psi_n) \cos \psi_n d\psi_n; \quad (10)$$

$$\frac{d\psi_n}{dn} = \mu + \frac{g}{2\pi a_n} \int_0^{2\pi} f(a_n \cos \psi_n) \sin \psi_n d\psi_n. \quad (11)$$

Equation (10) yields the amplitude damping rate per turn. The phase dependence on  $n$  for the beam transverse oscillations is determined by equation (11).

It is clear from (8) and (9) that the third and higher harmonics of oscillations can be excited. It depends on the transfer function. This typical effect for nonlinear systems is not discussed in this paper because of pages limitation.

## 3 RESULTS

### 3.1 Linear Transfer Function

For TFS with a linear transfer function we have  $f(x) = x$ , where  $x = a_n \cos \psi_n$  at zero level of approximation. Taking into account (5), (10) and (11), we obtain the following solution:

$$x[n, s_P] \simeq a_0 \exp\left(-\frac{g}{2} n\right) \cos \psi_n; \quad (12)$$

$$\psi_n = \mu n + \phi_0. \quad (13)$$

where  $a_0$  and  $\phi_0$  are constants depending on initial conditions. This solution coincides with the well known result (see, for example, [7]).

### 3.2 Transfer Function with Linear and Cubic Terms

Performing the integration in (10) for the transfer function with linear and cubic terms

$$g f(x) = gx + gg_3 x^3, \quad (14)$$

we obtain:

$$a_n = \frac{a_0 \exp(-gn/2)}{\sqrt{1 - (3g_3 a_0^2/4)(\exp(-gn) - 1)}}. \quad (15)$$

Performing the integration in (11), we obtain the expression for the phase of oscillations that coincides with formula (13). Thus, at the first level of approximation, the frequency is not affected by the damping, while the amplitude decreases in accordance with dependence (15). Formula (15) coincides with the well known result for the amplitude solution of Rayleigh's equation

$$\ddot{x} + \omega_0^2 x = \epsilon(\dot{x} - \lambda \dot{x}^3).$$

Other results concerning damping parameters for TFS with this transfer function are discussed in [4].

### 3.3 Coulomb Damping

In this case the transfer function is

$$g f(x) = \begin{cases} ga_l & \text{when } x_n > 0; \\ -ga_l & \text{when } x_n < 0. \end{cases} \quad (16)$$

Performing the integration in (10) and (11), we obtain formula (13) for the phase of oscillation and the following dependence on  $n$  for the amplitude:

$$a_n = a_0 - \frac{2}{\pi} ga_l n. \quad (17)$$

Thus, to this level of approximation, the amplitude decreases linearly with time. Formula (17) for amplitude dependence coincides with the well known result for amplitude solution of Coulomb damping nonlinear differential equation

$$\ddot{x} + \omega_0^2 x = \begin{cases} -g\lambda & \text{when } x > 0; \\ g\lambda & \text{when } x < 0, \end{cases}$$

where  $\lambda = \text{const.}$

### 3.4 "Bang-Bang" Damping

For TFS with a "bang-bang" transfer function we have (see Fig.2):

$$g f(x) = \begin{cases} gx_n & \text{when } -a_c \leq x_n \leq a_c; \\ ga_l & \text{when } x_n > a_c; \\ -ga_l & \text{when } x_n < -a_c. \end{cases} \quad (18)$$

Therefore, from (10) we have for  $a_n < a_c$

$$\frac{da_n}{dn} \simeq -\frac{g}{2} a_n, \quad (19)$$

and for  $a_n > a_c$

$$\frac{da_n}{dn} \simeq -\frac{g}{2\pi} \left( (4a_l - 2a_c) \sqrt{1 - \left(\frac{a_c}{a_n}\right)^2} + \left( \pi - 2 \arccos \left( \frac{a_c}{a_n} \right) \right) a_n \right). \quad (20)$$

For the phase of oscillations we get formula (13). Hence, to the first level of approximation, the frequency is not affected by the damping, while the amplitude decreases in accordance with dependence (20) or (19).

For  $a_n \gg a_c$  we have from (20)

$$a_n \simeq a_0 - \frac{2}{\pi} ga_l n. \quad (21)$$

Thus, to this level of approximation, large initial amplitudes decrease linearly with time. This formula (21) for amplitude dependence coincides with the result for amplitude solution of Coulomb damping (17). The linear amplitude decreasing with time was also obtained in [2] where a numerical simulation was used to estimate the damping time. Other results for the "bang-bang" regime are shown in [6].

## 4 CONCLUSION

The approaches demonstrated in [4, 6] have been developed and generalized in this paper for studying TFS with various nonlinear transfer functions. It gives analytical approximate solutions to calculate the damping time and other parameters of the particle motion.

## 5 REFERENCES

- [1] X. Altuna et al. *CERN Note SPS/ABM/RB/nb1*, Geneva, 1987.
- [2] I. N. Ivanov and V. A. Melnikov. Nonlinear damping of coherent oscillations of a beam in hadron cyclic accelerators and colliders. *Nuclear Instruments and Methods in Physics Research, A* 391(1):52-55, 1997.
- [3] W. Höfle, I. N. Ivanov, R. Louwerse, and V. A. Melnikov. Suggestion to increase the transverse damper efficiency. *Particle Accelerators*, 58(1-4):281-286, 1997.
- [4] V. M. Zhabitsky. Theory of a transverse feedback system with a nonlinear transfer function. In *EPAC98. Proceedings of the Sixth European Particle Accelerator Conference, Stockholm, 22-26 June 1998*, pages 1380-1382. IOP Publishing, Bristol and Philadelphia, 1998.
- [5] N. M. Krylov and N. N. Bogoliubov. *Introduction to Nonlinear Mechanics*. Princeton University, 1947.
- [6] V. M. Zhabitsky. Damping parameters of a transverse feedback system with a "bang-bang" transfer function. In *HEACC'98. XVII International Conference on High Energy Accelerators. Dubna, 7-12 September 1998*. JINR, E9-99-26, pages 391-393.
- [7] V. M. Zhabitsky. Transverse feedback system with a digital filter. *Nuclear Instruments and Methods in Physics Research, A* 391(1):96-99, 1997.

# CALCULATION OF THE LHC-KICKER BEAM IMPEDANCE\*

Glen R. Lambertson  
Lawrence Berkeley National Laboratory  
Berkeley, California 94720

## Abstract

Longitudinal and transverse beam impedances are calculated for the injection kickers designed for use in the CERN large hadron collider. These combine the contributions of a ceramic beam tube with conducting stripes and a traveling-wave kicker magnet. The results show peak impedances of 1300 ohm longitudinal and 8 MΩ/m transverse for four units per ring.

## 1 INTRODUCTION

The design for the LHC calls for four injection-kicker units for each beam[1], each unit is a c-magnet with an alumina beam tube, shown schematically in Fig. 1. Thirty conducting stripes are applied inside the beam tube (See Table 1); each of these connects to the continuing metal tube through R-C networks. The impedances  $Z_L$  of this liner and  $Z_M$  of the magnets are combined in parallel to give the total impedance  $Z_B$ .<sup>a</sup>

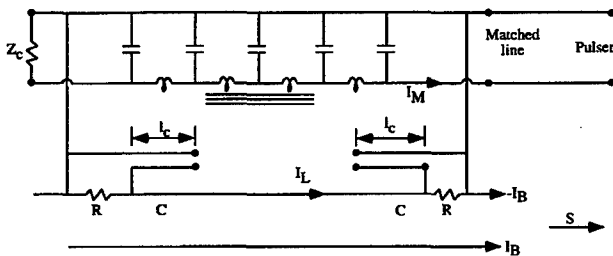


Figure 1: Schematic of circuits in kicker magnet with liner.  $I_B$  is the beam current.

## 2 LINER LONGITUDINAL IMPEDANCE

A metallized outer sleeve on the ceramic tube overlaps the inner stripes by about 0.28 m to provide 600 pF capacitance. Calculated as an open-ended transmission line this capacitor's impedance is  $\left[jC \frac{v_c}{\ell_c} \tan \frac{\omega \ell_c}{v_c}\right]^{-1}$ . The stripes on the ceramic contribute a small inductance; this has been calculated to be only 6.5 pico-henry. Combining the liner's components, the liner impedance becomes

Table 1: Liner Parameters

Tube inner radius	b	21 mm
Ceramic well thickness		4 mm
Relative dielectric constant	$\epsilon_r$	9
Number of stripes	N	30
Length of stripe	$\ell_s$	3540 mm
Width of stripe	w	4 mm
Space between stripes	a/2	4 mm
Capacitance (30 stripes, one end)	C	600 pF
Length of capacitor line	$\ell_c$	280 mm
Phase velocity along capacitor	$v_c$	$\sim 0.385 c$
Resistance (5000/30)	R	169 ohm

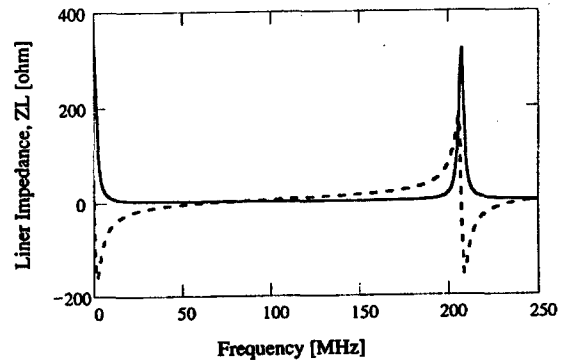


Figure 2: Impedance of the liner. Solid —  $Re Z_L$  [ohm]. Dashed —  $Im Z_L$  [ohm].

$$Z_L = \frac{2}{\frac{1}{R} + j \frac{C v_c}{\ell_c} \tan \frac{\omega \ell_c}{v_c}} + j \frac{\omega \mu_0 \ell_s}{2\pi N} \frac{\epsilon_r - 1}{\epsilon_r + 1} \left( \csc \frac{\pi w}{2a} \right) \quad (1)$$

which is plotted in Fig. 2. We see at intervals of 206 MHz the impedance maxima that occur when the capacitor length is multiples of one-half wavelength.

## 3 IMPEDANCE FROM THE MAGNET

The portion of the beam current that is not shielded by the liner current  $I_L$  induces voltages in the magnet. This current  $I_M = I_B + I_L$  couples to the magnet in two ways, (1)

\* Work supported by the U.S. Dept of Energy under Contract No. DE-AC03-76SF00098.

<sup>a</sup>More details of these calculations are given in Ref. [2]

Table 2: Magnet Parameters

Length	$\ell$	2657 mm
Aperture gap	$g$	54 mm
Aperture width	$d$	54 mm
Winding inductance per unit length ( $=\mu_o$ )	$L'$	$1.25 \times 10^{-6}$ Hy/m
Winding line-impedance	$Z_c$	5 ohm
Phase velocity ( $Z_c/L'$ )	$v$	$4 \times 10^6$ m/sec
Drive line delay (example)	$\tau$	0.233 $\mu$ sec

magnetic images in the yoke and conductors and (2) currents induced in the winding. Parameters of the magnet are given in Table 2 and the geometry of its square aperture in Fig. 3.

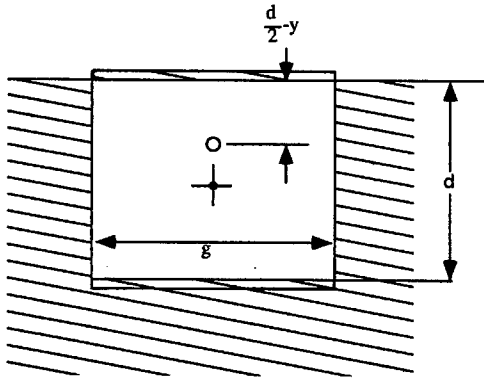


Figure 3: Aperture of the magnet bounded by winding conductors at  $Y = \pm d/2$ . Current  $I_M$  is shown at distance  $y$  from the center.

Coupling to the yoke has been calculated by summing the fields of image currents in the ferrite and in the conductor surfaces. This gives an inductance of  $0.317 L' \ell$ .

To calculate the mutual coupling to the winding one must consider in detail the propagation of induced currents in the winding and reflection or absorption at the ends of the winding circuit [2][3]. The drive line is assumed to be open at the pulser; the other end is impedance-matched by terminator  $Z_c$ . In an increment of length  $ds$ , the mutual inductance between beam and winding is

$$M' ds = \mu_o \frac{\frac{d}{2} - y}{g} ds \quad (2)$$

Currents induced by this coupling propagate away from  $ds$  at velocity  $v$ . Integrating over the winding length we obtain the directly-induced current

$$I = -I_M \frac{v L'}{2 Z_c} \left(1 - \frac{2y}{d}\right) \left(1 - e^{-\frac{k\ell}{2}} \cos ks\right) \quad (3)$$

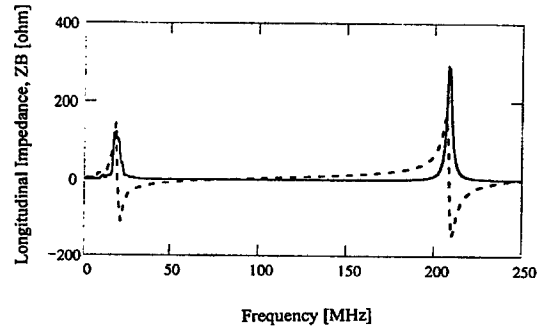
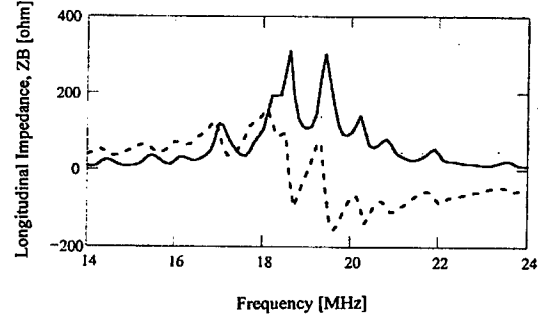


Figure 4: Total longitudinal impedance. Solid —  $Re Z_B$  [ohm]. Dashed —  $Im Z_B$  [ohm].

where  $k = \omega/v$ . This is then reflected at the pulser and the resultant net current induces at the beam positron  $y$  (Fig. 3) the voltage (Here  $\theta = \frac{k\ell}{2}$ )

$$V = \frac{I_m Z_c}{2} \left(1 - \frac{2y}{d}\right)^2 \left[ j\theta - e^{-j\theta} j \sin \theta + e^{-j2(\omega\tau+\theta)} \sin^2 \theta \right] \quad (4)$$

Adding to this the voltage from the yoke we get from the magnet the impedance at aperture center

$$Z_M = \frac{Z_L}{2} [0.268 j\theta + e^{-j\theta} j \sin \theta - e^{-j2(\omega\tau+\theta)} \sin^2 \theta] \quad (5)$$

The total impedance is now the parallel combination of Eq. 1 and Eq. 4 plotted in Fig. 4. In addition to the capacitor resonances at 206 MHz intervals, we see here at 19 MHz a resonance between the liner's capacitance and the magnet's inductance. These peaks are limited to 330 ohm by the series resistors of the liner.

#### 4 TRANSVERSE IMPEDANCES

Because the liner is azimuthally symmetric about the beam centerline, its transverse impedance is given in terms of  $Z_L$  from Eq. 1 as

$$Z_{Lt} = \frac{2c}{\omega b^2} Z_L \quad (6)$$

Images in the yoke and conductors give zero impedance in the direction  $y$  parallel to the pole faces.

In the  $x$ -direction, images sum to give

$$Z_{Mx} = 0.019 j \frac{\mu_0 c \ell}{g^2} \quad (7)$$

In Eq. 3 we have shown the  $y$ -dependence of the winding contribution to  $Z_{||}$ . The Panofsky-Wenzel theorem allows us to calculate  $Z_y$  from  $Z_{||}$  as

$$Z_y = \frac{c}{\omega} \frac{\partial}{\partial y} \frac{\Delta Z_{||}}{\Delta y} \quad (8)$$

This is

$$Z_{My} = \frac{c}{\omega} \frac{2}{d^2} Z_c \left[ -j\theta + j e^{-j\theta} \sin\theta - e^{-j2(\omega\tau+\theta)} \sin^2\theta \right]$$

Combining contributions to the transverse impedances, the totals are shown in Figs. 5 and 6. The  $2M\Omega/m$  peak in  $Z_x$  that appears at 40 MHz is a resonance between liner and magnet.  $Z_y$  is strongest at low frequency where at orbital frequency, 11.2 kHz, it is  $169 - j 3.40 \times 10^3$  ohm/m.

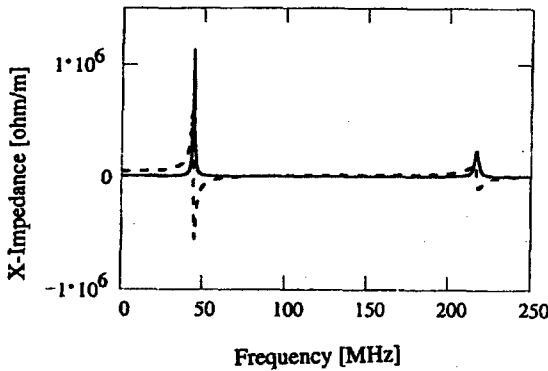


Figure 5: Total horizontal impedance. Solid —  $ReZ_x$ . Dashed —  $ImZ_x$ .

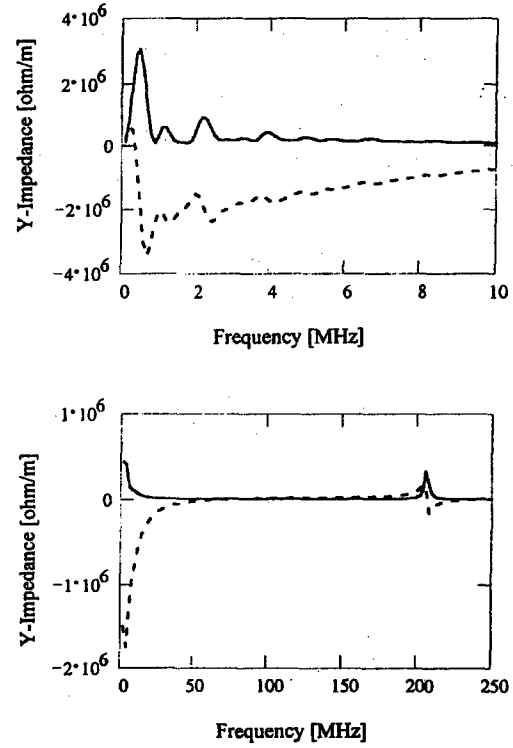


Figure 6: Total vertical impedance. Solid —  $ReZ_y$ . Dashed —  $ImZ_y$ .

## 5 REFERENCES

- [1] L. Ducimetière, U. Jansson, G. H. Schröder, E. B. Vossenberg, M. J. Barnes, G. D. Wait, "Design of the Injection Kicker Magnet System for CERN's 14 TeV Proton Collider LHC," 10th IEEE Pulsed Power Conference, Albuquerque, NM, July 10 - 13, 1995.
- [2] G. R. Lambertson, "LHC Kicker Beam-Impedance Calculation," LBNL-42838, CBP Note-283, October 1998.
- [3] W. R. Smythe, Static and Dynamic Electricity, McGraw Hill, New York, 1939, p. 89.

# THE FUTURE OF THE SPS INJECTION CHANNEL

J. Bonthond, L. Ducimetière, G.H. Schröder, J. Uythoven<sup>\*</sup>, G. Vossenberg  
CERN, SL Division, Geneva, Switzerland  
Q. Han, IHEP, Beijing, China

## Abstract

The SPS accelerator will be used as injector for the LHC [1] and has to be adapted to the LHC requirements. The tight specification on beam blow-up in the SPS requires a reduction of the magnetic field ripple of the SPS injection kicker magnets to less than  $\pm 0.5\%$ . The bunch spacing of the LHC ion beam requires a reduction of the kicker magnets' rise time from 145 ns to less than 115 ns. To obtain the shorter rise time the existing kicker magnets have to be reduced in length and the characteristic impedance has to be increased. The resulting loss in magnetic field has to be compensated by the installation of additional magnets.

Results of studies on the required kicker strengths and physical apertures for the different types of beam and corresponding operational modes are shown. Changes to the Pulse Forming Network (PFN) and the option of using Pulse Forming Lines (PFL) are presented. Results of first magnet measurements are shown.

## 1 SYSTEM REQUIREMENTS

In the LHC era four different types of beam will be injected into the SPS. For their injection the MKP kicker magnets in the LSS1 area will be used and a modification of the present system is necessary to fulfil the future needs [2]. Table 1 shows the kicker system requirements for the different types of beam. The most stringent kicker rise time requirement comes from the LHC type ion beam injection. As the PS bunch structure has to be conserved in the SPS, the kicker rise time has to be reduced from the present 145 ns (2 - 98 % rise time) to less than 115 ns (0 - 100 % rise time). The total deflection strength required is determined by the relatively high injection energy of the LHC type proton beam. On top of this, the ripple of the

magnetic field has to be reduced for both the LHC proton beam and the LHC ion beam. The present ripple is not critical and is around  $\pm 1\%$ . For the LHC beams the ripple will have to be less than  $\pm 0.5\%$ .

## 2 SYSTEM LAYOUT

To obtain the shorter rise time of the kicker pulse the magnets will be increased in impedance, from  $12.5\ \Omega$  to  $16.67\ \Omega$ , and the number of cells will be decreased, from 22 to 17 cells. Both changes decrease the kicker strength and additional magnets have to be added to continue to work with HV values below 50 kV.

The new system layout is shown in figure 1. It shows an additional fourth kicker tank with two magnets placed between the present second and third tank. The magnets in this tank and in the first two tanks have the increased impedance of  $16.67\ \Omega$  and a reduced length. Because of the reduced magnet length 5 magnets instead of 4 can be placed in each of the first two existing tanks.

In the new layout the magnets in the first three tanks will be used for ion injection and will have the required fast rise time. The four magnets in the last kicker tank, which are at the moment already of a different type, will have an unchanged impedance and length. However, changes have to be made to the magnet and the PFN to meet the specification on the ripple and rise time for the LHC-type proton beam.

Figure 1 also shows a Pulse Forming Line (PFL) in parallel with the PFN (indicated with pulser  $0.5\ \mu\text{s}$ ). As it is uncertain that the specifications on rise time and ripple can be met by using a PFN, it might be necessary to use PFLs for the LHC ion beam injection. Because the required pulse length for this beam is only 500 ns, a PFL cable length of about 60 m will be sufficient.

Table 1: The different types of beam to be injected with their kicker magnet requirements.

Beam	Injection Energy	Kicker Rise time	Kicker Flat top	Kicker Fall time	Kicker Ripple
LHC protons	26 GeV/c	< 220 ns	2.1 $\mu\text{s}$	No restriction	< $\pm 0.5\%$
Fixed target protons	14 GeV/c	< 1.0 $\mu\text{s}$	10.5 $\mu\text{s}$	1.0 $\mu\text{s}$	< $\pm 1.0\%$
LHC ions	12.9 GeV/c	< 115 ns	0.5 $\mu\text{s}$	No restriction	< $\pm 0.5\%$
Fixed target ions	12.9 GeV/c	< 1.0 $\mu\text{s}$	2.0 $\mu\text{s}$	3.8 $\mu\text{s}$	< $\pm 1.0\%$

<sup>\*</sup> E-mail: jan.uythoven@cern.ch



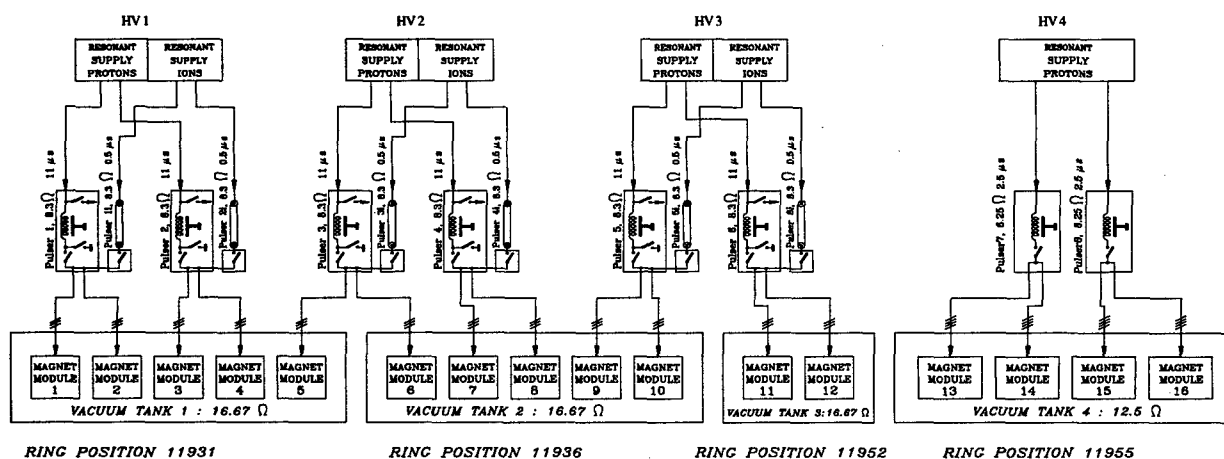


Figure 1: New kicker system layout.

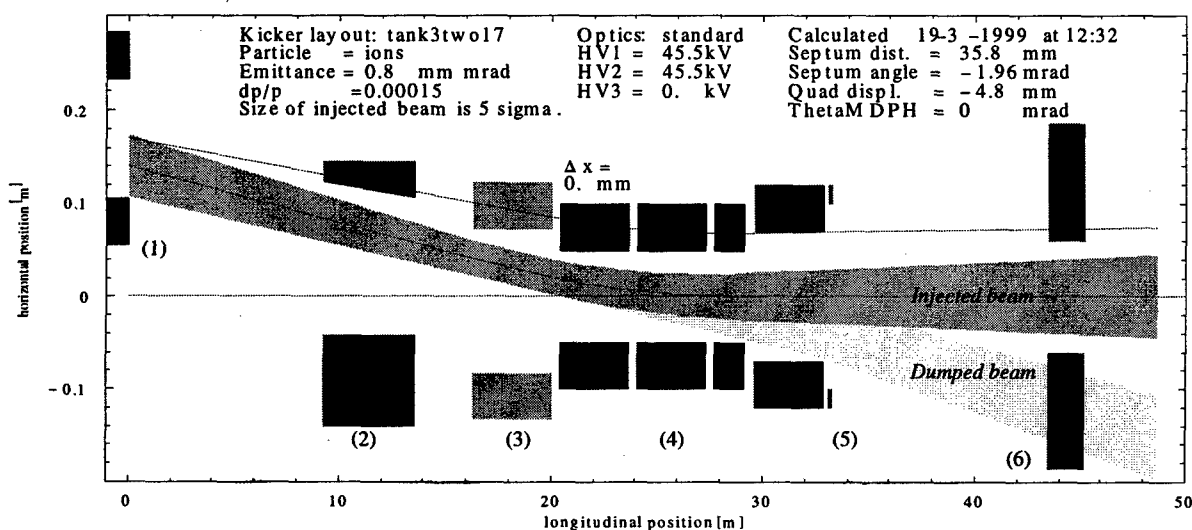


Figure 2: Model of injection of the fixed target ion beam for the horizontal plane. This is the type of beam with the smallest physical aperture in the kicker area, but still more than  $5\sigma$ . The numbers in the figure correspond to the following elements: (1) Injection septum magnet; (2) High-energy beam dump; (3) Quadrupole magnet; (4) Kicker magnet vacuum tanks; (5) Dump magnet for the injected beam; (6) Beam dump for the injected beam.

## 2 PHYSICAL APERTURES AND REQUIRED KICKER STRENGTH

A computer model of the injection system has been made. The model is used to calculate the required kicker strengths and to examine the physical apertures available in the kicker region for the old and for the new system layout.

To calculate the beam size, the standard values for the emittance and energy spread are taken [3], together with the standard optical functions of the transfer line [4].

An overview of the physical apertures and the required kicker strengths for the different types of beam is given in table 2. The voltages HV1 to HV4 correspond to the charging voltages, also indicated in figure 1.

From table 2 it can be concluded that with the new layout all required kicker voltages are below 50 kV which is within the capabilities of the present hardware. The physical aperture is ample for the future LHC beams. For the future fixed target beams the physical aperture is slightly reduced for the new system relative to the present situation, but is still well over  $5\sigma$ . The smallest physical apertures occur for the fixed target ion beam, see also figure 2.

In the vertical plane the physical aperture is just below  $5\sigma$  and is limited by the high energy dump. This is also the case for the present system.

## 3 MAGNET DEVELOPMENT

Low voltage measurements on the first modified short magnet have been performed. The magnet was equipped

with 47  $\Omega$  resistors in parallel with the cell inductance, to damp the field oscillations. Standard low voltage coaxial cables were used as a PFL. The rise time of the low power switch was adjusted to be 45 ns. The results of the measurements are shown in figure 3. The rise time of the pulse is just within the specification, but the field ripple is slightly too large (about 1.3 % and 1.0 % required). At the moment the surface of the high voltage plates is further reduced by 4 % to increase the actual magnet impedance from 16.03  $\Omega$  to 16.33  $\Omega$  (the PFN/PFL and magnet impedance are designed to be slightly below the transmission line impedance). Simulations have shown that this should bring the field ripple within specification.

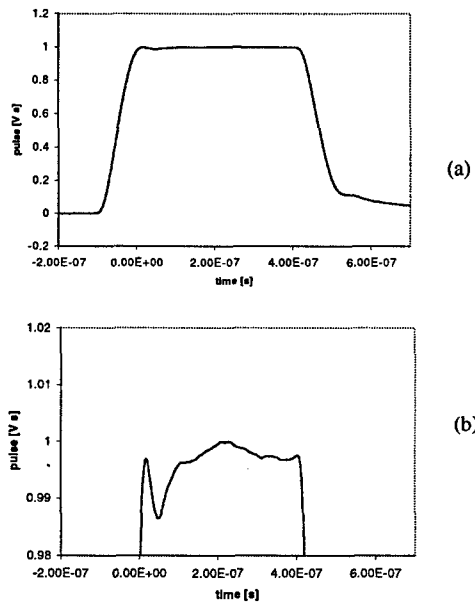


Figure 3: Measured pulse of a modified kicker magnet (a). The lower graph shows the field ripple in more detail (b).

### 3 GENERATOR DEVELOPMENT

The modified PFN used for the longer kicker pulses will be equipped with a 3.5 m long coil. Having a single coil which spans many capacitors should reduce the pulse ripple and improve stability. It has been verified that for a test coil with a diameter of 70 mm and a length of 1.5 m the PFN impedance increases from 6.25  $\Omega$  to about 8.2  $\Omega$ . New PFN front cells are being manufactured.

An existing thyatron switch is being modified with 'speed-up cells' to obtain the required fast switching characteristics. The cells will be adapted to the PFL cable, transmission cable and modified magnet.

### 5 CONCLUSIONS

The LHC-type ion beam that will be injected in the SPS requires an injection kicker rise time of less than 115 ns. On top of this, both LHC type beams require a field ripple of less than  $\pm 0.5$  %. To fulfil the rise time condition two third of the present magnets will have to be shortened and have their impedance increased. The loss in kick strength

will be compensated by the installation of an additional four magnets. Two of those magnets will be installed in an additional vacuum tank, the other two can be added to the present first two tanks.

As it is not certain that the required kicker magnet rise time can be obtained with PFNs, the option to use a Pulse Forming Line instead of a PFN is being studied simultaneously.

In the new set-up all required kicker voltages for the different types of beam are calculated to be below 50 kV. The physical apertures are sufficient, with a  $5\sigma + 3.5$  mm being the smallest aperture, calculated for the dumped fixed target ion beam.

Low voltage measurements of the modified magnet have shown that the required kicker pulse rise time can be obtained with a switch rise time of about 45 ns. The measured field ripple is presently too large, but should be within the specifications after a slight increase of the magnet impedance.

Table 2: Calculated charging HV values and physical apertures in the horizontal plane for the different beams.

Beam	Layout	Operational HV values		Smallest physical aperture
		HV1 to HV3 [kV]	HV4 [kV]	
Fixed target protons	Present layout	26.1	-	5.0 $\sigma$ + 8.3 mm
Fixed target ions	Present layout	24.2	-	5.0 $\sigma$ + 7.9 mm
LHC protons	New layout	48.4	48.4	5.0 $\sigma$ + 14.1 mm
Fixed target protons,	New layout	49.2	0	5.0 $\sigma$ + 4.4 mm (dump side)
LHC ions	New layout	45.5	0	5.0 $\sigma$ + 16.5 mm (dump side)
Fixed target ions	New layout	45.5	0	5.0 $\sigma$ + 3.5 mm (dump side)

### REFERENCES

- [1] L.Evans, "LHC accelerator physics issues and technology challenges", these proceedings.
- [2] L.Ducimetière, G. Schröder, J. Uythoven, E.Vossenber, "Upgrading of the SPS injection kicker system for the LHC requirements", EPAC'98, Stockholm, June 1998, also CERN SL-98-050 BT.
- [3] J.Uythoven, "The new SPS injection channel", Proceedings of the workshop on LEP-SPS performance, Chamonix 1999, CERN-SL-99-007 DI.
- [4] G.Arduini, M.Giovannozzi, K.Hanke, J.-Y.Hémery, M.Martini, "MAD and BeamOptics description of the TT2/TT10 Transfer Lines Part I: Optics without Emittance Exchange Insertion", CERN SL-98-040 OP.

# IMPACT OF THE LHC BEAM ABORT KICKER PREFIRE ON HIGH LUMINOSITY INSERTION AND CMS DETECTOR PERFORMANCE\*

A. I. Drozhdin, N. V. Mokhov<sup>†</sup>, FNAL, Batavia, IL  
M. Huhtinen, CERN, Geneva, Switzerland

## Abstract

The effect of possible accidental beam loss in LHC on the IP5 insertion elements and CMS detector is studied via realistic Monte Carlo simulations. Such beam loss could be the consequence of an unsynchronized abort or – in worst case – an accidental prefire of one of the abort kicker modules. Simulations with the STRUCT code show that this beam losses would take place in the IP5 inner and outer triplets. MARS simulations of the hadronic and electromagnetic cascades induced in such an event indicate severe heating of the inner triplet quadrupoles. In order to protect the IP5 elements, two methods are proposed: a set of shadow collimators in the outer triplet and a prefired module compensation using a special module charged with an opposite voltage (antikicker). The remnants of the accidental beam loss entering the experimental hall have been used as input for FLUKA simulations in the CMS detector. It is shown that it is vital to take measures to reliably protect the expensive CMS tracker components.

## 1 INTRODUCTION

At nominal operation parameters each of the 7 TeV circulating beams of the LHC contains approximately 334 MJ of energy[1], which is enough to cause severe damage to the expensive machine and detector equipment. It must be dealt with by a reliable abort system which uses fast extraction to divert the beam to an external graphite absorber at the end of a normal fill or in case of a detected anomaly in beam behaviour. The LHC abort kicker system consists of 14 pulsed magnets having a rise time of about  $3\mu\text{s}$ . Normally this system is triggered during the  $3\mu\text{s}$  abort gap in the circulating beam. An accidental prefire of one of the abort kicker modules induces coherent oscillations of the circulating bunches. As a result, the beam may not reach the absorber, being lost instead on the machine limiting apertures. With the abort system at IP6, the high-luminosity insertion at IP5 is the first limiting aperture for the counterclockwise beam, where about 10% of the misbehaved beam is lost. The detailed analysis of such a phenomenon and possible protective measures has been performed in [2, 3] for the SSC. Without protection, accidental beam loss consequences in LHC would range from superconducting magnet quenches, to overheating of some components or even total destruction of some units through their explosion. In this paper, the problem is studied—as in[4]—

via realistic Monte Carlo simulations with the STRUCT[5], MARS[6] and FLUKA[7] codes.

## 2 FAST ACCIDENTAL BEAM LOSS

### 2.1 Parameters and Assumptions

The simulations were done for a  $\pm 150\mu\text{rad}$  horizontal crossing angle, which is chosen for IP5. Calculations verified that a horizontal crossing is the favourable choice, since a vertical crossing would result in significantly higher accidental beam loss level. Only the worst case is investigated: closed orbit deviation in the Q2B is 4 mm, mechanical error is 0.6 mm and alignment accuracy is 1 mm. These are simulated by a bump with  $\Delta x_{\text{max}} = \Delta y_{\text{max}} = 5.6\text{ mm}$  in the inner quadrupole triplet in the horizontal and vertical planes. Every bunch is affected by the abort kicker with a gradually increased strength. The counterclockwise beam direction is studied. It turns out that for the injection optics, all losses would take place at the beam cleaning insertions only.

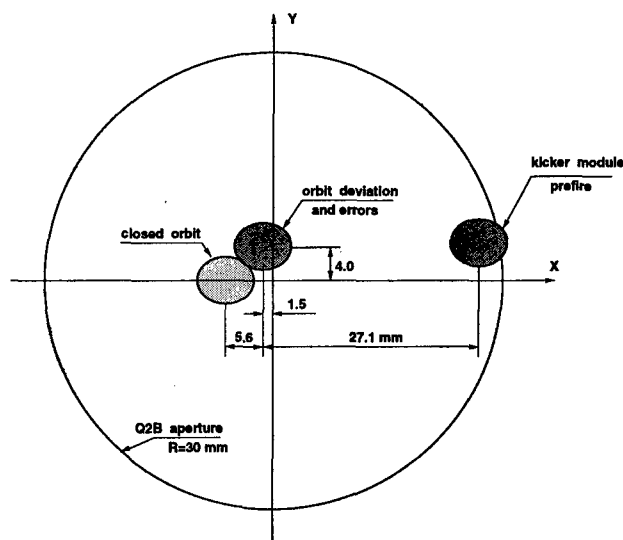


Figure 1: Beam positions in the Q2B quadrupole at the kicker module prefire with a horizontal crossing at IP5.

### 2.2 Kicker Module Prefire

The assumption is that one of the abort kicker modules accidentally prefires. A prefired kicker module induces coherent oscillations of the beam with an amplitude equal to  $21\sigma$  of the beam at collisions. Starting from 80% of the kicker strength, the disturbed protons hit the aperture of the IP5 elements, if the kicker module prefires at col-

\* Work supported by the Universities Research Association, Inc., under contract DE-AC02-76CH00300 with the U. S. Department of Energy.

<sup>†</sup> Email: mokhov@fnal.gov

lisions. The disturbed and undisturbed beam positions in the Q2B quadrupole are shown in Fig. 1. The beam is lost at the first limiting aperture—Q2B.R5 quadrupole—where  $\beta$ -function reaches its maximum. One module kick and  $3\sigma$  beam size for the counterclockwise direction are shown in Fig. 2 for the collision optics. Energy deposition density in the Q2B.R5 quadrupole coil reaches several kJ/g with the peak temperature rise exceeding the melting point.

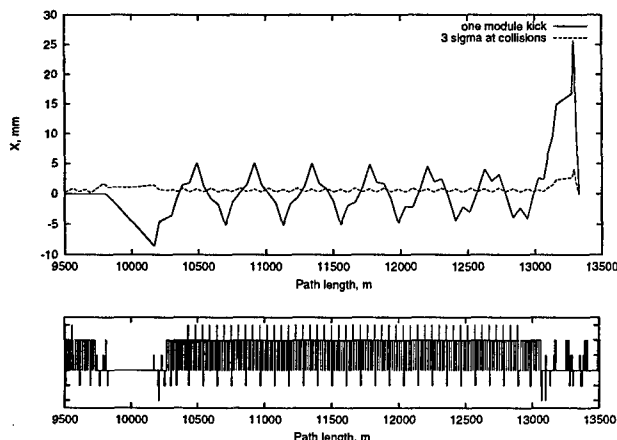


Figure 2: 1-module kick and a  $3\sigma$  beam size at collisions.

### 2.3 Unsynchronized Abort

An unsynchronized abort could be the consequence of a control system or timing failure but it could also result from an immediate firing of the rest of the kicker modules in an attempt to cure a kicker prefire. At an unsynchronized abort, the kicker front does not necessarily come into the longitudinal abort gap. This causes coherent oscillations of some bunches and corresponding beam loss until the kicker reaches the needed strength. Calculated beam losses are presented in Fig. 3. Peak energy deposition in the low- $\beta$  quadrupoles are lowered by about a factor of 300 compared to the prefire case. The irradiation pulse duration is  $0.26 \mu\text{s}$ .

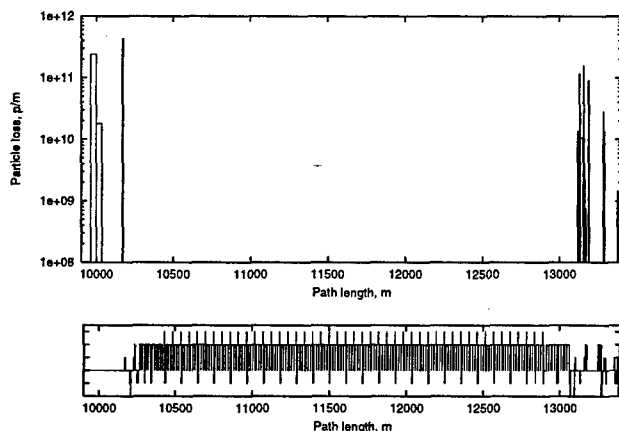


Figure 3: Beam loss at unsynchronized abort at collisions.

## 3 SHADOW COLLIMATORS

A possible way to protect the collider and detector components is a set of shadow collimators in IP6 or in the IP5 matching quadrupole triplet. The first location is attractive because it allows in principle to intercept most of the losses in the warm IP6 section downstream of the abort system. It assumes very tight movable jaws which have to follow the beam over the cycle. The system efficiency, jaw survivability and design have to be studied yet.

In this paper, detailed simulations have been performed for stationary collimators in the IP5 outer triplet (Fig. 4). At the top energy with low- $\beta$  optics the beam can be efficiently intercepted by these shadows. The first shadow is positioned at  $21\sigma_{\text{collis}} = 10.3\sigma_{\text{inject}} = 10 \text{ mm}$  from the beam orbit (11.8 mm from the beam pipe center). Second and third collimators are used to protect magnets from secondary particles emitted from the first shadow. The collimator configuration, materials and dimensions have been carefully optimized to provide reliable protection of the inner triplet and to ensure collimator survivability. Combined with an unsynchronized abort, such a system reduces peak energy deposition in the IP5 inner triplet quadrupoles by almost six orders of magnitude compared to the disastrous case of a 1-module prefire.

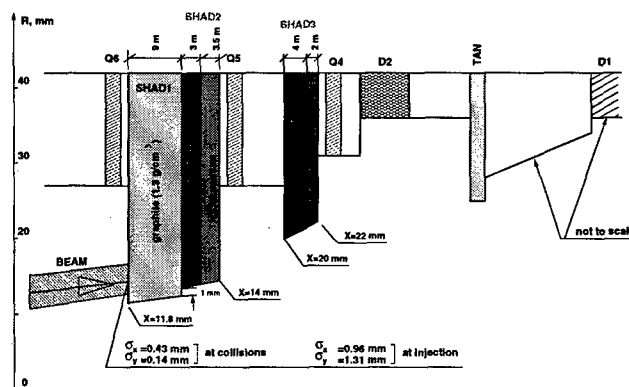


Figure 4: Shadow collimators in the IP5 outer triplet.

The IP5 shadow system alone, gives a factor of 300-1000 reduction in peak energy deposition in the low- $\beta$  quadrupoles. Instantaneous peak temperature rise for all the considered cases is shown in Fig. 5 and 5 for the inner and outer triplet elements. Horizontal position of the first shadow collimator depends on the accelerator tune, closed orbit displacement at the shadow location and beam crossing scenario. This shadow at the specific horizontal position (determined by tune) protects the elements of the IP5 insertion at any accelerator tune in the range of  $\nu = Q_0 \pm 2$ .

## 4 ANTIKICKER

Another way proposed in [2, 3] is to compensate the prefired module by an additional module charged with an opposite voltage (antikicker). The antikicker should be fired with a delay less than  $1 \mu\text{s}$  after the kicker prefire to eliminate

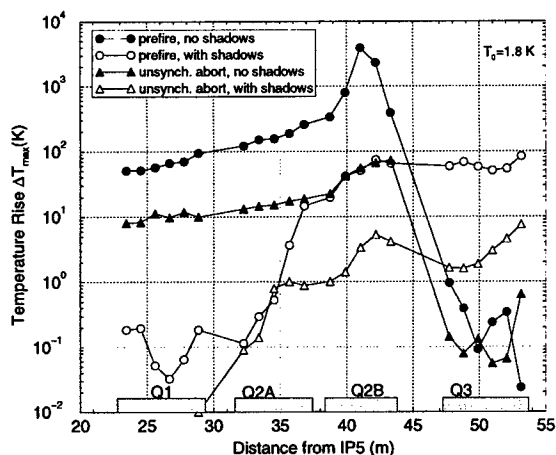


Figure 5: Peak temperature rise in the IP5 inner triplet superconducting coils.

losses in the IP5. After this, the beam can be safely aborted using the abort gap. This method seems to be rather attractive because it does not depend on the accelerator tune, closed orbit deviation, beam crossing scenario, and protects the entire accelerator from losses at kicker prefire.

## 5 DETECTOR PERFORMANCE

Our simulations show that even the most severe accidental beam loss (prefire) is equivalent less than 50 hours of normal operation. Thus no significant contribution from beam accidents is expected to integral damage of detectors. The main worry seems to be, however, that large instantaneous ionization over all the detector volume could cause irreversible damage by creating breakdown in some components. For the worst case (prefire), we observe a dose rate of 20 MGy/s at the inner pixels ( $R=4.3$  cm) which is 9 orders of magnitude above the normal conditions. At the MSGC ( $R=75$  cm), which are likely to be the most sensitive

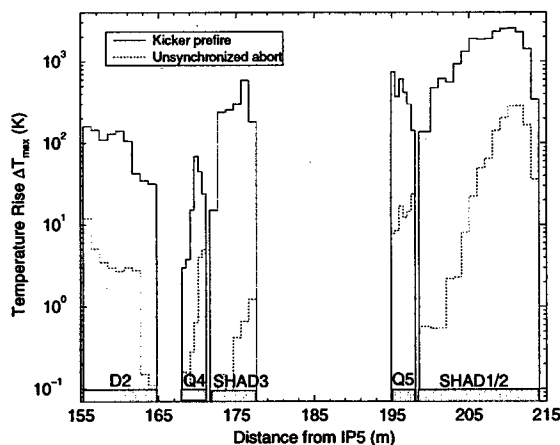


Figure 6: Peak temperature rise in the IP5 outer triplet.

detectors with respect to such accidents, the corresponding worst case dose rate is 6 kGy/s which still is more than 7 orders of magnitude above nominal. Although, the unsynchronized abort significantly decreases the total dose, it lowers the dose rate during the pulse by less than a factor of 2. The shadow collimators reduce the dose rate at the inner pixels by a factor of  $10^4$ , but by only a factor of 40 at the MSGC detectors. This 'best protected' dose of 150 Gy/s at the MSGC is still a factor of  $10^6$  above nominal conditions and there is a fear that it could have severe consequences on the rather sensitive detectors. This observation has the more general implication that any fast losses close to IP5 could lead to extremely high dose rates in the detectors. While all possible measures to mitigate such losses close to IP5 should be taken, detectors still should be prepared to survive fast pulses with several orders of magnitudes higher particle rates than in nominal conditions.

## 6 CONCLUSION

Abort kicker prefire, which happened twice at Tevatron over a 20 month collider run and which would be disastrous at LHC parameters, should be suppressed by the more modern LHC beam abort system. Unsynchronized abort in combination with the shadow collimators in IP5 or IP6 are sufficient to protect the LHC machine against irreversible consequences of the fast beam loss. The proposed antikicker scheme looks rather attractive, but even with this system, the shadow collimators should be installed as a last line of defense. A major concern might be that the dose and particle rates (but not integrated values) in experiments are very high in all cases where a fast beam loss takes place in the interaction region, no matter if on magnets or protective elements.

## 7 REFERENCES

- [1] "The LHC Conceptual Design", CERN/AC/95-05(LHC) (1995), P. Lefèvre and T. Pettersson, editors.
- [2] A. Drozhdin et al., *Proc. 1993 IEEE Particle Accelerator Conference*, Washington, May 17-20, 1993, pp. 3772-3774; SSCL-Preprint-329 (1993).
- [3] A. Drozhdin, N. Mokhov and B. Parker, SSCL-Preprint-556 (1994).
- [4] A.I. Drozhdin, M. Huhtinen and N.V. Mokhov, *Nucl. Instr. and Methods*, **A381**, pp. 531-544 (1996).
- [5] I. Baishev, A. Drozhdin and N. Mokhov, "STRUCT Program User's Reference Manual", SSCL-MAN-0034 (1994).
- [6] N. V. Mokhov, Fermilab-FN-628 (1995); N. V. Mokhov et al., *Fermilab-Conf-98/379* (1998); LANL Report LA-UR-98-5716 (1998); *nucl-th/9812038 v2 16 Dec 1998*; <http://www-ap.fnl.gov/MARS/>.
- [7] P. A. Aarnio et al., CERN TIS-RP/168 (1986) and CERN TIS-RP/190 (1987)  
A. Fassò et al., *Proc. SATIF*, Arlington, Texas, April 28-29, 1994. NEA/OECD doc. p. 287 (1995).

# ON POSSIBLE USE OF BENT CRYSTAL TO IMPROVE TEVATRON BEAM SCRAPING \*

V. M. Biryukov<sup>†</sup>, Institute for High Energy Physics, Protvino, Russia  
A. I. Drozhdin, N. V. Mokhov, FNAL, Batavia, IL

## Abstract

A possibility to improve the Tevatron beam halo scraping using a bent channeling crystal instead of a thin scattering primary collimator is studied. To evaluate the efficiency of the system, realistic simulations have been performed using the CATCH and STRUCT Monte Carlo codes. It is shown that the scraping efficiency can be increased and the accelerator-related backgrounds in the CDF and DØ collider detectors can be reduced by about one order of magnitude. Results on scraping efficiency versus thickness of amorphous layer of the crystal, crystal alignment and its length are presented.

## 1 INTRODUCTION

Bent-crystal technique is well established for extracting high energy beams from accelerators. It was successfully applied at up to 900 GeV[1], and simulations were able to predict the results correctly. Recent experiments at IHEP Protvino[2] have demonstrated that 50-70% of the beam can be extracted using a thin (3-5 mm) Si channeling crystal with bending of 0.5-1.5 mrad. It would be promising to apply this technique for a beam halo scraping at high energy colliders[3, 4]. A bent crystal, serving as a primary element, should bend halo particles onto a secondary collimator. A demonstration experiment of this kind was recently performed at IHEP[2] where a factor of 2 reduction in the accelerator background was obtained with a bent crystal.

## 2 BEAM LOSS AND BACKGROUNDS

The current approach to the Tevatron Run II collimation system is described in detail in[5]. Below we show how a silicon bent crystal can improve the Tevatron collimation system efficiency. Two cases are compared for a 900 GeV proton beam:

- the Run II collimation system with only one of three primary collimators—(D17h) horizontal—used. It intercepts large-amplitude protons and protons with positive  $\Delta p$ ;
- the same collimation scheme, but a silicon bent crystal is used instead of D17h.

In reality, two additional primary collimators (bent crystals) should be used at D17v and D49h locations for vertical amplitude and off-momentum scraping. Therefore, results presented here represent about 30% of total losses in the machine.

\* Work supported by the U. S. Department of Energy under contract No. DE-AC02-76CH03000

<sup>†</sup> Email: biryukov@mx.ihep.su

The studies[6] have shown that the accelerator related background in the DØ and CDF collider detectors is originated from beam halo loss in the inner triplet region. In addition to the optically small aperture at  $\beta_{max}$  location, the aperture restrictions in this area are the DØ forward detector's Roman pots placed at  $8\sigma$  and the BØ Roman pots placed at  $10\sigma$  at the entrance and exit of the beam separators. Beam losses in BØ and DØ depend strongly on the secondary collimator offset with respect to the primary collimators. Each of the Roman pot detectors at DØ consists of four  $2 \times 2$  cm<sup>2</sup> plates (two horizontal and two vertical placed on the both sides of the beam). Each of the CDF Roman pots consists of twelve units: three DØ type sets with 12 cm between them, which results in higher total hit rates at CDF[7]. The CDF detectors are made of a silicon wafer, about 400  $\mu$ m thick, on which a thin 50  $\mu$ m layer of diamond is deposited. Each DØ detector is a box that includes a scintillation fiber detector with a total length of 37.7 mm along the beam. The vacuum windows are composed of a 50  $\mu$ m stainless steel foil in order to reduce multiple Coulomb scattering.

## 3 USING BENT CRYSTAL

A silicon (110) crystal bent at an angle of 0.1-0.3 mrad is placed upstream of the D17 secondary collimator instead of the original thin scattering tungsten target[5, 7] in the same position. Crystal channeling is simulated as described in[8]. Particle tracking in the lattice is done with the STRUCT code[9] with updated MARS physics[10]. A non-channeling amorphous layer on the crystal surface due to its irregularity at a micron level is taken into account as a silicon target upstream of the crystal as shown in Fig. 1.

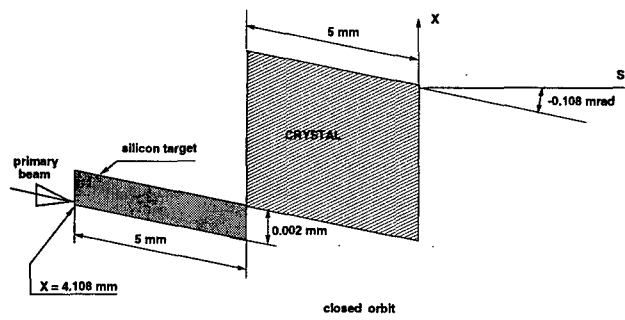


Figure 1: Amorphous layer and crystal layout at D17 used in simulations.

A number of protons passed through the Roman pots upstream of the DØ and CDF main detectors with a 5 mm

thick tungsten target at D17 as a primary collimator and with a crystal instead is presented in Table 1. A crystal angle with respect to the beam is  $-0.108$  mrad, and its length is 5 mm. In both cases, a nuclear interaction rate in the primary element itself is also shown as a measure of irradiation of the downstream superconducting components at D17. One can see that the use of the crystal can reduce background in the detectors by about one order of magnitude and decrease the machine irradiation by a factor of four.

Table 1: Halo hit rates at the DØ and CDF Roman pots and nuclear interaction rates  $N$  in target and crystal (in  $10^4 p/s$ )

	with target	with crystal		
		amorphous layer thickness		
		10 $\mu m$	5 $\mu m$	2 $\mu m$
DØ	11.5	1.35	1.60	1.15
CDF	43.6	5.40	3.20	3.43
$N$	270	82.4	70.6	50.3

Extracted and scattered beam densities at the entrance and exit of the crystal with a  $5\mu m$  amorphous layer is presented in Fig. 2-3. Several groups of particles are clearly seen. They represent protons which come to the crystal on the 8-th, 13-th, 18-th, 20-th, 32-nd, 37-th and 51-st turn after interaction with the amorphous layer.

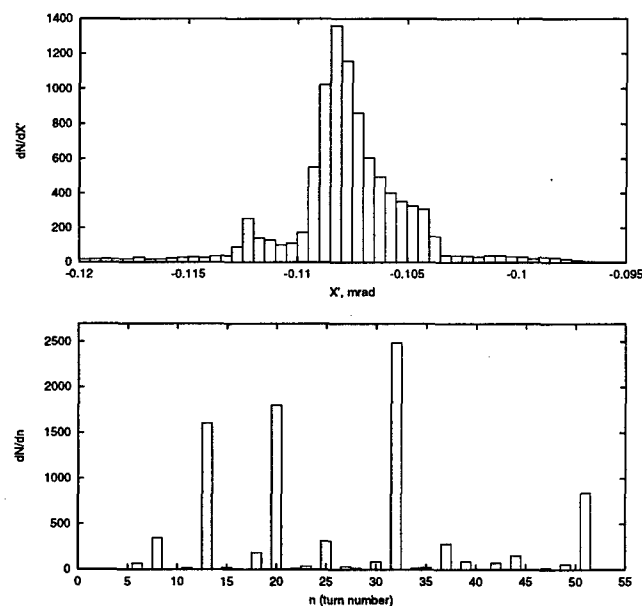


Figure 2: Proton angular distribution on the crystal (top) and distribution of the number of turns for protons to be captured after scattering in the amorphous layer (bottom).

The crystal critical angle is  $\pm 5 \mu rad$ , therefore the efficiency depends strongly on the crystal alignment. With the alignment of  $-(104 - 111) \mu rad$  the large amplitude protons are captured by the crystal over the next 32 turns after the first scattering. For poorer alignment it takes longer time for

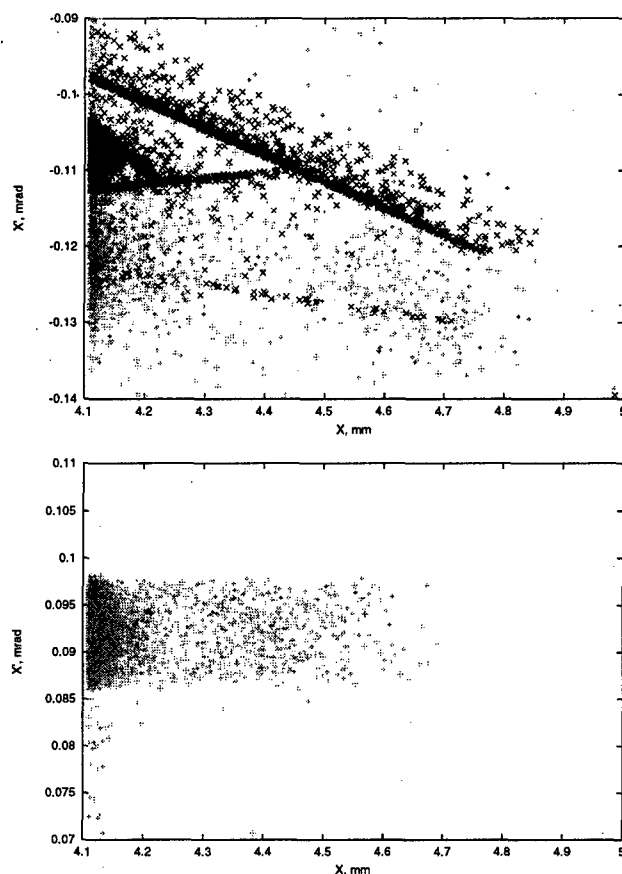


Figure 3: Horizontal phase space on the crystal entrance (top) and exit (bottom). The top plot also shows (gray) uncaptured protons at the crystal exit.

the scattered protons to get into the critical region, which increases background in the detectors as shown in Fig. 4 for a 5 mm crystal with a  $2\mu m$  amorphous layer. Angular distribution of protons after scattering on the amorphous layer depends on the crystal length. Shorter crystal would give smaller particle divergence, which should improve the system efficiency. In reality, a combined effect of scattering, channeling and tracking in the lattice could smear such a simple dependence as shown in Fig. 5 for a crystal with a  $2\mu m$  amorphous layer. A shorter crystal indeed is better for the CDF Roman pots if its length  $< 5$  mm, but for longer

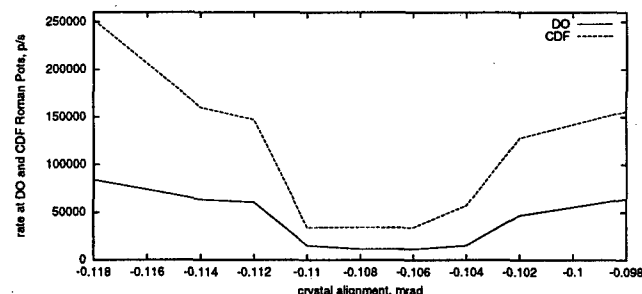


Figure 4: Hit rates on the DØ and CDF Roman pots versus crystal alignment.

crystals and for the DØ detectors the results obtained are almost independent of length.

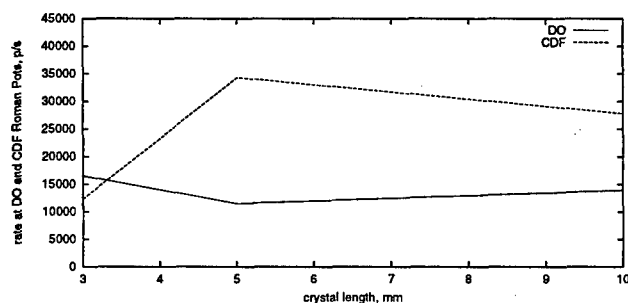


Figure 5: Hit rates on the DØ and CDF Roman pots versus crystal length.

Overall beam loss distribution along the Tevatron lattice is shown in Fig. 6 for the two studied cases with a 5 mm thick tungsten target and a 5 mm thick silicon bent crystal as the D17 primary scatterer at  $5\sigma$ . The secondary collimators are installed at  $6\sigma$ . Beam loss on the primary element itself is not shown. One sees that not only beam loss is lower at the collider detectors at BØ and DØ, but the entire machine becomes cleaner if the bent crystal is used.

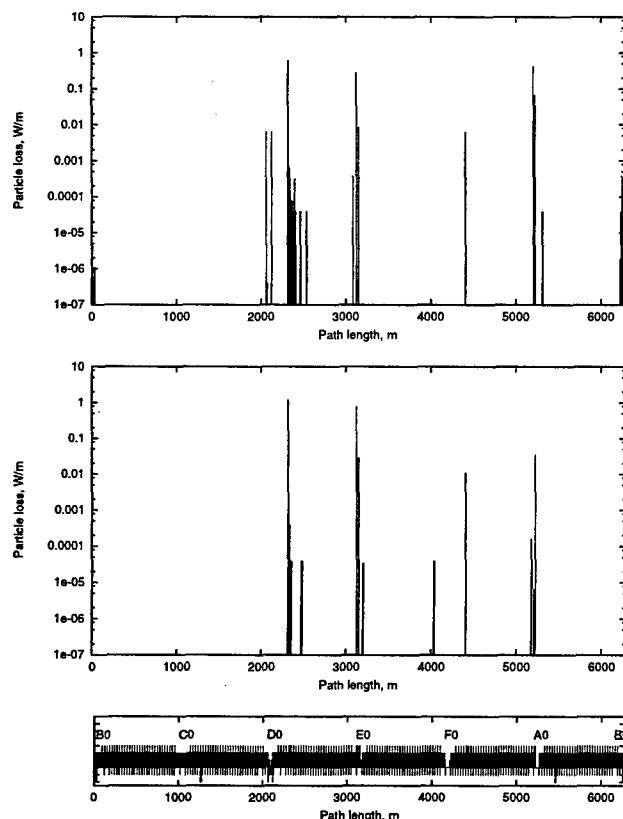


Figure 6: Beam loss distribution in the Tevatron with a 5 mm thick tungsten target (top) and a 5 mm thick silicon bent crystal (bottom) as a primary scatterer at D17.

## 4 CONCLUSIONS

The studies performed show that a replacement of the amorphous tungsten target as a primary collimator in the Tevatron beam collimation system with a 5 mm thick silicon bent crystal would reduce by about one order of magnitude the accelerator-related backgrounds in the CDF and DØ detectors and decrease beam losses in the superconducting magnets of the D sector by a factor of four.

## 5 REFERENCES

- [1] C. T. Murphy and R. Carrigan, p.157 in Proceed. of "Near Beam Physics" Symp., Fermilab (1997)
- [2] A. G. Afonin, V. M. Biryukov, Yu. A. Chesnokov, et al., "New Projects of Crystal Extraction at IHEP 70 GeV Accelerator", these Proceedings.
- [3] M. Maslov, N. Mokhov, I. Yazynin, "The SSC Beam Scraper System", SSCL-484 (1991).
- [4] V. Biryukov, p.179 in Proceed. of "Near Beam Physics" Symp., Fermilab (1997).
- [5] M. D. Church, A. I. Drozhdin, B. J. Kramper, A. Legan, N. V. Mokhov, R.E. Reilly, "Tevatron Run-II Beam Collimation System", these Proceedings.
- [6] J. M. Butler, D. S. Denisov, H. T. Diehl, A. I. Drozhdin, N. V. Mokhov, D. R. Wood, "Reduction of Tevatron and Main Ring Induced Backgrounds in the DØ Detector", Fermilab-FN-629 (1995).
- [7] A. I. Drozhdin and N. V. Mokhov, "Detector-Accelerator Interface Studies at the Tevatron", Fermilab-Conf-98/105 (1998).
- [8] V. M. Biryukov, Yu. A. Chesnokov and V. I. Kotov, "Crystal Channeling and its Application at High Energy Accelerators", Berlin: Springer (1997)
- [9] I. Baishev, A. Drozhdin, and N. Mokhov, "STRUCT Program User's Reference Manual", SSCL-MAN-0034 (1994).
- [10] N. V. Mokhov, "The MARS Code System User Guide, Version 13(95)", Fermilab-FN-628 (1995); N. V. Mokhov et al., Fermilab-Conf-98/379 (1998); LANL Report LA-UR-98-5716 (1998); *nucl-th/9812038 v2 16 Dec 1998*; <http://www-ap.fnal.gov/MARS/>.



# OPTIMIZATION OF THE PARAMETERS IN THE RHIC SINGLE CRYSTAL HEAVY ION COLLIMATION

V.M. Biryukov, Y.A. Chesnokov, V.I. Kotov, IHEP, Protvino, Russia  
D. Trbojevic, A. Stevens, BNL, Upton, NY

## Abstract

In the framework of the project to design and test a collimation system prototype using bent channeling crystal for cleaning of the RHIC heavy ion beam halo, we have studied the optimal length and bending angle of a silicon (110) single crystal proposed to be a primary element situated upstream of the traditional heavy amorphous collimator. Besides the matters of the channeling and collimation efficiency, we also looked into the impact the crystal may have on the non-channeled particles that go on circulating in the ring, so as to reduce the momentum offset of the particles scattered of the crystal.

## 1 INTRODUCTION

The project of a collimation system using bent channeling crystal for cleaning of the RHIC heavy ion beam halo has been described in some detail in Ref.[1] where we refer for the basic ideas and results, and more technical information. In order to optimize the crystal collimation scheme for RHIC, we have studied the influence of the silicon (110) single crystal parameters (length, bending angle, curvature gradient) on the efficiency of bending of the beam of fully ionized Au ions. The beam distribution at the entrance of the crystal was presented by the sample of 19258 fully stripped gold ions generated as described in our previous article [1].

We have also postulated that at the entrance to the crystal all the particles have the same momenta, corresponding to the Lorentz factor of 108.40, in order to evaluate then the momentum distribution in the beam downstream of the crystal.

In our first study [1] the crystal length of 10 mm and the bending angle of 1 mrad were used, as it was a practical choice corresponding to the state of art on that date. It was concluded that the bending angle can be reduced substantially. In the mean time, the IHEP Protvino experimental practice has shown that shorter crystals of high quality can be produced and they behave in perfect agreement with theory [2].

## 2 TRACKING IN CRYSTAL

With the above said arrangements, we have performed tracking of the 19258 particles through various crystals by means of CATCH code [3]. Typical distribution of the particles downstream of the crystal consists of a sharp peak

of the particles channeled through the full crystal length and bent the full angle, some particles unbent but scattered of the crystal, few particles bent partial angle between the bent and unbent peaks, and few particles nuclear interacted in the crystal. Fig. 1 represents gold ion distribution in the horizontal phase space at the downstream edge of the crystal.

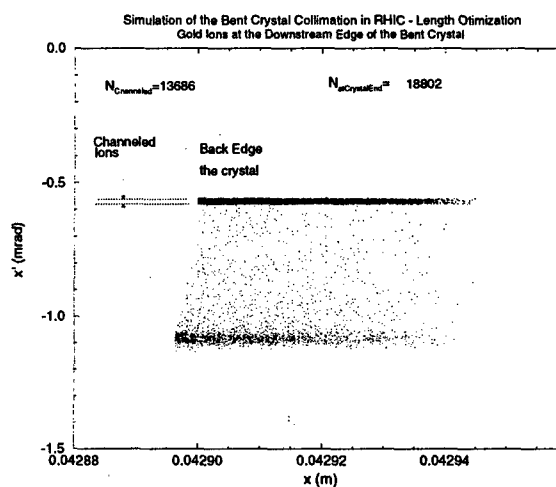


Figure 1: Gold ion distribution in the horizontal phase space at the downstream edge of the 5-mm long crystal.

Having studied such distributions for the crystals with different length but the same bending angle of 0.5 mrad, we plot in Fig. 2 how many particles were bent at least 0.1 mrad (this includes the particles channeled part of the crystal length as they are steered through the angles that might be sufficient for interception by the downstream collimator). One can see that, from standpoint of physics alone, one can reduce the crystal length to nearly 2 mm without seriously affecting the efficiency of bending of the above-defined sample of particles.

Further we studied how the efficiency of the 5-mm long crystal would depend on the bending angle in the range of about 0.2-1.0 mrad. There was hardly any dependence up to at least 1 mrad, so this gives us the freedom to adjust the bending angle to what seems appropriate for collimation purpose in RHIC.

One objective on the agenda was to find if we could benefit in the efficiency from a variable curvature of the crystal (in the above simulations the curvature was constant). The motive is that, whereas in the extraction mode one has to deliver the bent beam to a single direction, in the collimation mode it is sufficient to deliver the bent beam to a range of directions, say from 0.3 to 1.0 mrad in our case, as the particles are absorbed anyway (it might be even useful

\* Work performed under the auspices of the U.S. Department of Energy.

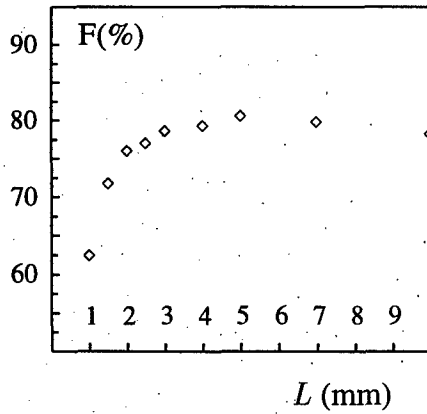


Figure 2: Single-pass bending efficiency vs crystal length; for 0.5 mrad bending angle.

to spread the irradiation load over the collimator). In the simulation we have tried variable curvature of the 5-mm crystal, with the curvature peak being factor of 2, 4, 8, and 16 of the average. However, the fraction of the particles bent at the angles greater than 0.1 mrad has not changed significantly as compared to the above studies, so we don't mention this option further on.

Table 1 summarizes comparative characteristics of the beam interaction with two crystals, 5 mm long and 10 mm long. The total number of the gold ions incident on the crystals was  $N_{particles}$ . The number of particles which interacted with the crystal nuclei was  $N_{Lostparticles}$ . The  $N_{channeled}$  represents the number of particles channeled through the full length of the crystal and hence bent the full angle, and  $E_{ff}$  is their fraction to the total.

Table 1: The results of beam interaction with two Si(110) crystals.

Crystal-1 cm	Crystal 0.5 cm
19258	19258
962	456
12532	13686
17289	18628
467	174
65.1%	71.1%

The momentum distribution has substantially improved with shorter crystals as compared to the earlier study [1]. The  $N_{inbucket}$  and  $N_{outoffbucket}$  in Table 1 show the corresponding number of the particles from the momentum distribution downstream of the crystal. Figure 3 shows phase space of the gold ions at the end of the 5-mm long crystal, where on the x coordinate is shown as  $dp/p$  dependent. Taking into account also the practical considerations and experience obtained with crystals at IHEP Protvino, we can conclude that 5-mm long crystal seems well suited for the job of Au beam bending at the angle of the order of 0.5 mrad in a single passage. Several crystals of this size have

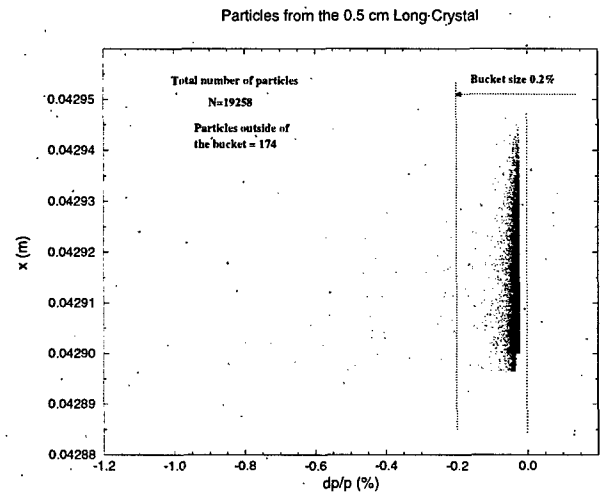


Figure 3: Phase space of the gold ions at the end of the 5-mm long crystal.

been already produced and tested at Protvino [2].

One option for the future simulation studies may sound interesting. Fig. 2 shows that from physics considerations we can reduce the crystal length to order of 1-2 mm, if it appears convenient technically. Such crystal would make a rather little disturbance to the circulating beam, thus allowing potentially many passages of the circulating particles through the bent crystal and enhancing the overall efficiency of bending. To benefit from this mode, such a crystal should have also a sufficient transversal size (possibly greater than the longitudinal size). Studies on feasibility of such crystal deflectors are in progress.

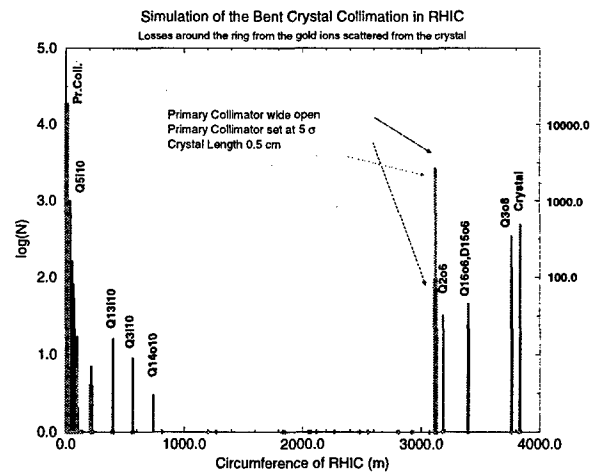


Figure 4: Losses around the RHIC rings

### 3 COLLIMATION SIMULATION IN RHIC

The gold ions tracked through the crystal have been transported through the RHIC ring using the tracking program

TEAPOT [4], with accelerator setting as described in Ref. [1]. Fig. 4 shows the losses around the RHIC rings from the particles scattered of the primary and secondary collimators and the losses from the particles deflected by the crystal. Two extreme cases are presented when the primary collimator downstream of the crystal is wide open and when it is set at  $5\sigma_x$ , the same horizontal distance as a front edge of the crystal.

#### 4 CONCLUSIONS

An improvement in the momentum distribution of the ions passed through the crystal and a reduction of lost particles around the ring have been achieved by optimizing the crystal length. Another result is the freedom we have in choosing the angle of bending, which can be left about 0.5 mrad, or be chosen from consideration of collimation physics, or be just varied in the course of experimentation at RHIC.

#### 5 REFERENCES

- [1] D. Trbojevic et al., in EPAC Proceedings (Stockholm, 1998) and references therein
- [2] A.G.Afonin et al., Phys. Lett. **B 435** (1998), 240
- [3] Valery Biryukov, "Crystal Channeling Simulation - CATCH 1.4 User's Guide", SL/Note 93-74(AP), CERN, 1993.
- [4] L.Schachinger and R.Talman, "A Thin Element Accelerator Program for Optics and Tracking", SSC Central Design Group, Internal Report SSC-52 (1985).

# ON POSSIBILITY OF CRYSTAL EXTRACTION AND COLLIMATION AT 0.1-1 GeV

V. M. Biryukov

*Institute for High Energy Physics, Protvino, Russia*

## Abstract

Bent crystal situated in a circulating beam can serve for efficient slow extraction or active collimation of the beams. This technique, well established at 10-1000 GeV, could be efficient also at the energies as low as 0.1-10 GeV according to the computer simulations presented in this paper. Applications might include halo scraping in the Spallation Neutron Source or slow extraction from synchrotrons.

## 1 INTRODUCTION

Bent crystals are successfully applied at IHEP Protvino[1] for slow extraction of 70 GeV protons. This technique is well explored in a broad energy range 14-900 GeV [2], and some projects for halo scraping with crystals at RHIC and Tevatron are in progress[3, 4]. It would be interesting to study the feasibility of this technique also at essentially lower energies, where it may assist in scraping beam halos e.g. at the Spallation Neutron Source, or assist in slow extraction from multi-hundred MeV proton or light ion accelerators[5]. In the present contribution we study only physical aspects of the job, i.e. how much of the beam can be steered at how much angle.

Bent crystal channeling was first demonstrated at a few GeV in Dubna, 1979, and its physics first studied at 1 to 12 GeV at Petersburg, Dubna and CERN. Crystal-based extraction from accelerator was also first demonstrated at 4-8 GeV in Dubna in 1984. So the 1-10 GeV domain is well familiar to bent crystals.

## 2 CRYSTAL COLLIMATION AT THE SNS

The Spallation Neutron Source will require an efficient halo collimation of the protons accumulated in 1 GeV ring. The general idea of the crystal-assisted collimation is that a crystal, serving as a primary element, gives the incident halo particles a bend of e.g. a few mrad so as to provide a big impact parameter at some secondary element. Then the bent particles are absorbed with a higher probability there, and so the backscattering is much less a problem. A radical solution might even be an extraction of bent particles to some external dump.

"Single-pass scraping". A straightforward option would be to bend particles in a single pass through the bent crystal, at an angle of the order of 10 mrad. The protons with 1 GeV kinetic energy can move through Silicon in

the channeled states over 1-1.5 mm. The bending radius  $R$  must be greater than critical one ( $R_c=0.25$  cm here); we take  $R=10$  cm as an example for our simulation. Figure 1 shows the angular distribution downstream of the bent crystal 1 mm long. In this simulation first we assumed that proton divergence at the incidence on the crystal was much narrower than the acceptance of the Si(110) crystal planes  $2\theta_c=0.25$  mrad. About 77% of the particles have exit angles greater than 1 mrad, and 30% of the total are bent at the full bending angle, 10 mrad. Further example in Figure 1 repeats the simulation for the incident beam with divergence of 0.2 mrad. In that case 70% of the particles are bent more than 1 mrad, and 22% of the total are bent at 10 mrad.

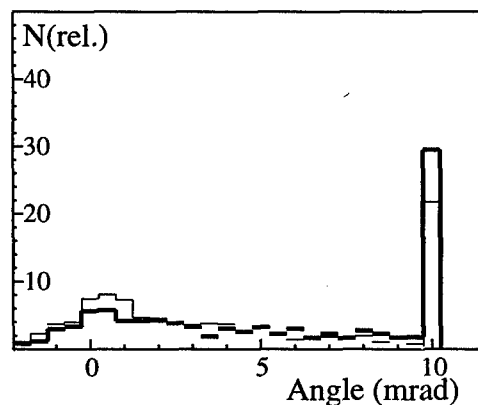


Figure 1: Angular distribution of 1 GeV protons downstream of the silicon crystal bent 10 mrad. For the parallel incident beam (thick line), and for the beam incident with divergence of 0.2 mrad (thin line).

Actual bending angles and the particle distribution downstream of a bent crystal can be designed as required to match some particular design of a cleaning system. The examples shown are for illustrative purpose only.

"Multi-pass scraping". Rather interesting would be the option where halo particles can encounter the crystal several times (multiturn, multipass 'extraction'), while circulating in the ring, which increases the extraction efficiency substantially. This option is feasible if the crystal is short enough along the beam, to reduce particle losses and scattering when it encounters the crystal, thus retaining the scattered particles in circulation.

In this option, several bending angles were tried from a fraction of mrad up to 5 mrad. Upon first encounter with a crystal, particles were allowed to circulate in the SNS

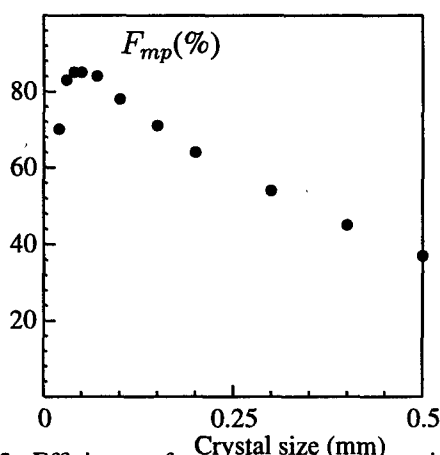


Figure 2: Efficiency of crystal multipass scraping for the 1 GeV particles that were not channeled on the first encounter, as a function of the crystal size along the beam.

ring (linear transfer matrix was used with  $\nu_{x,y}=5.82/5.80$  and beta tentatively chosen as 10 m) and have further encounters with crystal or aperture (in that case the particle was removed). The aperture limitation was imposed on the particle's angle at the crystal location: if its absolute value was greater than 0.5 (but less than 0.9) of the crystal bending angle, that particle was removed (considered lost at a collimator edge), so we counted only channeled particles that were steered at the proper angle.

The efficiency (the number of particles bent the full angle) was roughly independent of the chosen bending angle in the range studied, up to 5 mrad, and totalled typically 85-90% of the beam incident on the crystal. The unchanneled 10-15% of the particles reach the collimator edge (the aperture) and can be handled by more traditional "amorphous" collimation.

Figure 2 shows the probability with which the particles unchanneled in the first encounter with crystal (bent 3 mrad) are channeled on later encounters. If the crystal is as short along the beam as order of 50  $\mu\text{m}$ , this probability is very high, so even the particles multiply scattered in the crystal at first incidence can be efficiently channeled on later turns and steered away. Due to multiple encounters, the initial divergence of particles at the crystal becomes not so critical and can be about the scattering angle along the crystal length. Crystal efficiency in multi-pass mode is defined mainly by the interplay of channeling and scattering processes in multiple encounters with a short crystal. The overall energy loss in multiple encounters with crystal is within the nominal energy spread of the SNS beam,  $\Delta E/E < 4 \times 10^{-3}$  (rms).

For a typical particle, it takes 5 to 10 encounters with a crystal on average before the particle is channeled and extracted. This corresponds to order of 100 turns from the moment of the first encounter with a crystal to the moment of the particle extraction from circulation in the ring.

Further simulation involving realistic description of the SNS machine and beam parameters will be necessary for

realistic evaluation of a crystal-assisted scraping.

### 3 SLOW EXTRACTION FROM MULTI-HUNDRED MEV MACHINES

The above-considered multipass channeling may be well suited for efficient slow extraction from medium-energy synchrotrons [5]. The analytical theory[6] expects that as the beam energy lowers from multi-GeV to 0.1-1 GeV, one could reduce by a big factor the crystal size. Tiny crystal size may permit a huge multiplicity of particle encounters with the crystal, and hence a very high overall efficiency of crystal channeling.

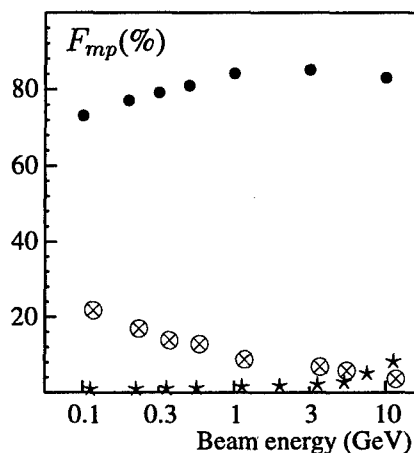


Figure 3: Efficiency (●) of crystal-assisted slow extraction, and beam lost in nuclear interactions in crystal (\*) and on the aperture (⊗), as functions of beam kinetic energy.

However, simulations (Figure 3) show that, although the loss for nuclear interaction in thin crystal at lower energy becomes insignificant, the extraction efficiency is limited by another factor - multiple scattering to the aperture (set in these simulations at 0.8 times the bending angle). This factor is dominating with decreasing energy, Figure 3. Nonetheless, the efficiency of crystal-assisted extraction is still 75-80% at a few hundred MeV. In these simulations we assumed the bending angle of 2 mrad at any energy, and described particle revolutions in the ring by linear matrices with parameters chosen from the Indiana University CIS [7] - just for illustrative purpose, despite the very broad energy range considered. The crystal size was scaled linearly with energy as suggested by the physics. Besides the two kinds of beam loss shown in the picture, nuclear interactions in the crystal (\*) and multiple scattering to the aperture (⊗), there was a dechanneling loss, 7-8% of the beam total in the cases considered, due to the particles channeled only part of the crystal and respectively bent just part of the 2 mrad. The dechanneled particles are then lost somewhere on the machine apertures, similarly to multiply scattered particles.

The divergence of the extracted beam in the horizontal plane (plane of bending) is as small as  $\pm 0.15 \text{ mrad} \times (pv)^{-1/2}$  (full width, where  $pv$  is beam momentum

times velocity in GeV) and defined by crystal properties only. In vertical plane, the scattering in the encounters with crystal contributes (about 1 mrad at 250 MeV), to be added quadratically to the initial divergence. The experience in crystal extraction also shows that this method may have other benefits such as flat time structure of the extracted beam.

## 4 CONCLUSIONS

Efficient systems for slow extraction and halo scraping at 0.1-10 GeV accelerators and storage rings can be designed on the base of bent crystals. Beam particles can be steered at the angles of several mrad with efficiencies of 70-90%.

## 5 ACKNOWLEDGEMENTS

I am very much indebted to Jie Wei, Wu-Tsung Weng, Dejan Trbojevic, and Walter Scandale for useful discussions and support.

## 6 REFERENCES

- [1] A.G.Afonin, V.M.Biryukov, Y.A.Chesnokov, et al. "New Projects of Crystal Extraction at IHEP 70 GeV Accelerator", these Proceedings.
- [2] V.M. Biryukov, Yu.A. Chesnokov and V.I. Kotov "Crystal Channeling and its Application at High Energy Accelerators" (Berlin: Springer, 1997)
- [3] D.Trbojevic, A.Stevens, V.M.Biryukov, Y.A.Chesnokov, V.I.Kotov. "Optimization of the Parameters in the RHIC Single Crystal Heavy Ion Collimation", these Proceedings.
- [4] A.I.Drozhdin, N.V.Mokhov, V.M.Biryukov. "On Possible Use of Bent Crystal to Improve Tevatron Beam Scraping", these Proceedings.
- [5] Walter Scandale, private communication.
- [6] V.M.Biryukov. "Analytical theory of multipass crystal extraction", EPAC Proceedings (Stockholm, 1998), p.2091.
- [7] X.Kang, K.Fung, S.Y.Lee, and G.P.Berg. "Slow extraction method for the Cooler Injector Synchrotron", EPAC Proceedings (Stockholm, 1998), and G.P.Berg, private communication.
- [8] This and other papers on the subject of beam steering by crystal channeling can be found at <http://beam.ihep.su/~biryukov>.

## DESIGN OF THE MAIN INJECTOR EXTRACTION BEAMLINES\*

D. E. Johnson†

Fermi National Accelerator Laboratory P.O. Box 500, Batavia, IL 60510

### Abstract

The Main Injector (MI) supports the Tevatron Fixed Target and Proton-Antiproton Collider modes of operation as well as providing 120 GeV/c resonantly extracted beam for the Main Injector Fixed Target Program. A set of beam transport lines, called A1 and P1, from the Main Injector converge on the injection point of the Tevatron, with the A1 being used to transport 150 GeV/c antiprotons (pbars) to the Tevatron. P1 is used to transport 150 GeV/c protons to the Tevatron, 120 GeV/c protons to the pbar target, and eventually 120 GeV/c resonantly extracted protons to the existing Fixed Target areas. In addition, the P1 line will be used to transport 8.9 GeV/c pbars from the Source back to the MI and recycled 150 GeV/c pbars at the end of Collider stores. In order to accomplish the second and third function, the P1 beamline is continued beyond the Tevatron injection point in a section of the decommissioned Main Ring, called the P2 beamline. This transports the protons to a magnetic switch used to select either the modified transport line, used for targeting protons for pbar production, or the transport line which connects to the existing Fixed Target beamlines. The design of these beamlines will be discussed.

### 1 BEAMLINE LAYOUT

The MI is 2-fold symmetric about the center point (Q605) of the long straight section which contains the RF and instrumentation. This straight is parallel to and offset from the Tevatron injection straight section by 11.31 meters. The MI is 2.133 meters below the Tevatron and the P2 line (which is comprised of a remnant section of the decommissioned Main Ring) is 0.646 m above the Tevatron. Figure 1 shows a cartoon of the plan and elevation of the P1 and A1 beamline layout wrt the MI, Tevatron, and the P2 beamline. The MI extraction straight sections for protons and pbars are located symmetrically about Q605 in the MI and the injection point (TEV60) in the Tevatron injection straight section. The horizontal angle between the MI extraction and Tevatron injection straight sections is 305.8 mr. The total length of each beamline is 260 m.

Each line includes three 2.8 m vertical bending Lambertsons and a 3.3 m vertical c-magnet for extraction; fifteen 6 m dipoles (recycled from the decommissioned Main Ring, MR); four vertical bending c-magnets, and

four vertically bending Lambertsons used for injection. The focussing is provided by: sixteen quadrupoles where seven are 2.1 m recycled quads from MR (Q3-Q9), seven new 3 m quads (Q1, Q2, Q10-Q14) and two new 1.5 m quads (Q12B and Q13B). Both the A1 and P1 dipoles and quads are powered by the same set of power supplies and are alternately energized through a load transfer switch. Eight horizontal and seven vertical BPM's along with six multiwire profile monitors are used to monitor the orbit and optical properties of the beam. Ion chamber loss monitors are located on Lambertsons, c-magnets and each quadrupole. Horizontal (vertical) trim dipoles are located at each focussing (de-focussing) quadrupole for orbit correction and control.

### 2 OPTICAL DESIGN

#### a. Extraction lattice

Each extraction straight is a dispersion free FODO lattice made up of three MI half cells, with a half-cell length of 17.288 m and a  $\beta_{\max}$  of 60 m. Figure 2 shows the elements and lattice functions of the P1 extraction straight section starting at the beginning of the two cell dispersion suppressor. Extraction of protons and pbars is initiated by a pair of horizontal extraction kickers ( $s=55$  m) located at the proton (or pbar) upstream end of the straight  $90^\circ$  in phase of a set of three vertically bending Lambertsons ( $s=85$  m) and a c-magnet ( $s=98$  m). The P1 extraction kicker is designed for multiple energies and pulse lengths to accommodate the various functions of the P1 beamline while the A1 extraction kicker is a single energy /pulse length kicker. A pair of electrostatic septa ( $s=63$  m) used for resonant extraction is located just downstream of the P1 kickers, filling the straight. The beam enters the first quad ( $s=100$  m) of the transport line at an elevation of 218 mm above the MI centerline at an upward angle of 28.5 mr.

#### b. Tevatron Injection

Half of the 52 m Tevatron F0 straight section, bounded by a doublet, is used for injection with the remaining half used for RF cavities. The lattice functions of the Tevatron injection straight section are anti-symmetric with non-zero horizontal

\* Work supported by the U.S. Department of Energy under contract No. DE-AC02-76CHO3000

† Email: [dej@fnal.gov](mailto:dej@fnal.gov)

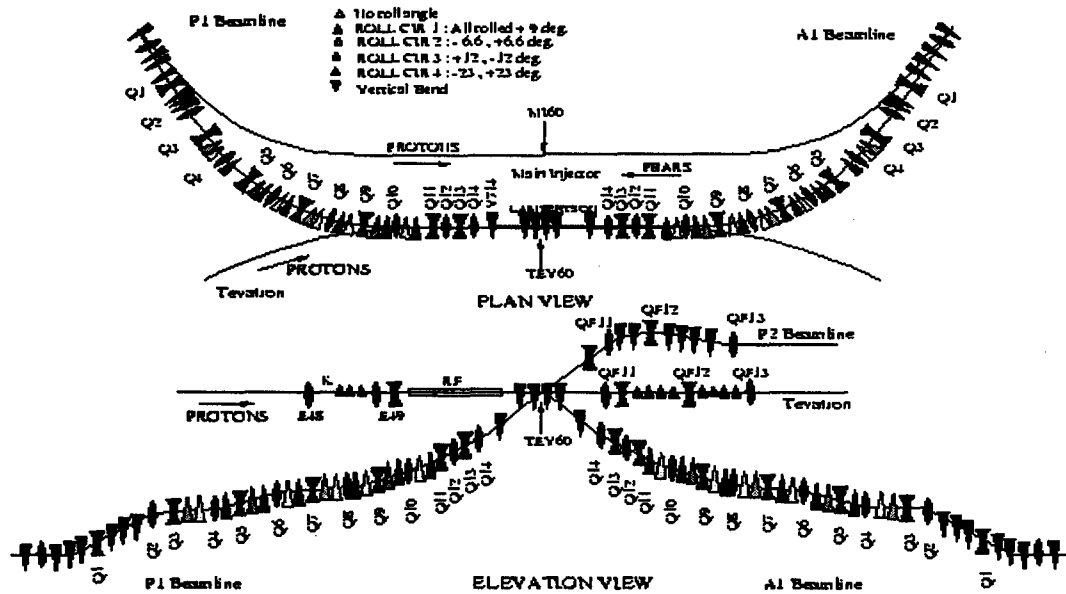


Figure 1. Plan and elevation of the P1, A1, and P2 beamlines in relation to the Main Injector and the Tevatron. The drawing is not to scale. The Main Injector and Tevatron magnets are not shown on the plan view for clarity.

dispersion, as shown in Fig. 3. Here the proton direction is from left to right. This requires two different optical

the 24 mr vertical injection angle. The horizontal position and angle of the injected beam at the Lambertsons are removed by proton kicker, at F17, ( $s=1258$  m) and pbar kicker, at E48, ( $s=988$  m).

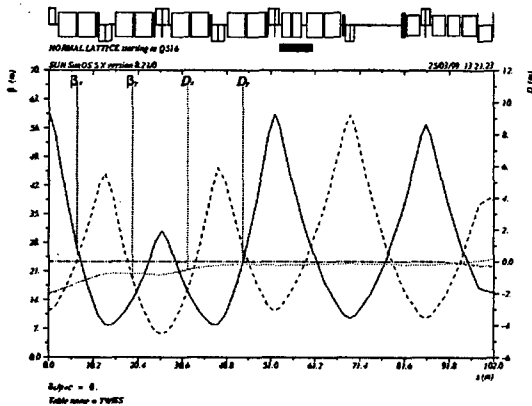


Figure 2. Main Injector Extraction straight section. The extraction kickers underlined in center of plot. The first quad in the beamline, Q1, is at  $s=100$  m.

solutions for the proton (via P1) and pbar (via A1) injection. Both protons and pbars approach the Tevatron from below. The 4 injection Lambertsons ( $s=1058$  m) remove

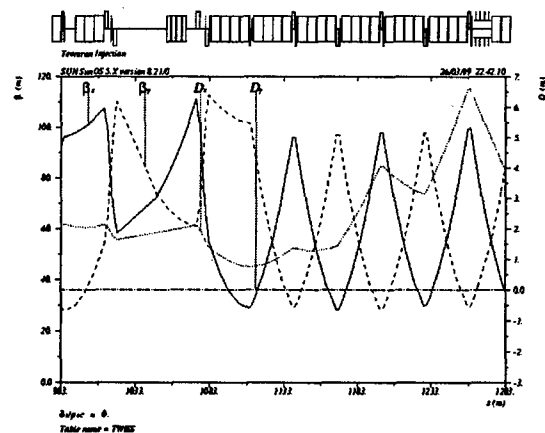


Figure 3. Tevatron injection lattice.

### c. Transport Lines

The program TRANSPORT [1] was used to layout the central trajectory of the beamline. All of the di



poles are powered by two horizontal and two vertical supplies. Fifteen of the horizontal dipoles are arranged on a single circuit. The second dipole after Q3 (fig. 1) is powered independently, and has a reversed polarity. The two vertical supplies control the vertical c-magnets at the beginning and end of the line. The fifteen dipoles are additionally arranged in four families of rolled dipoles to provide vertical trajectory and dispersion control.

The correction of central trajectory errors due to quadrupole alignment errors, dipole roll errors, and dipole field errors was simulated with random misalignments ( $\theta_x = \theta_y = 0.25$  mm and  $\theta_{roll} = 0.5$  mr) and field errors of  $\Delta B/B = 0.25\%$ . The installed corrector strengths of 0.72 kG-m and 0.52 kG-m are 20% stronger than required for correction.

The transport section both the P1 and A1 beamlines consist of 10 quads which make up four  $90^\circ$  FODO cells in each plane. The half-cell length and quad focal length was chosen to replicate the amplitude functions in the MI. The first two quads in the transport line are on independent power supplies to aid in matching from the MI into the FODO lattice. Quads 3 through 9 are all powered on a single quad bus (QCELL). Additionally, the last quad, Q10, in the FODO lattice is individually powered to aid in matching. Figures 4 and 5 show the lattice functions for the P1 and A1 beamlines starting at Q1 and matching into the Tevatron in the proton and pbar directions, respectively.

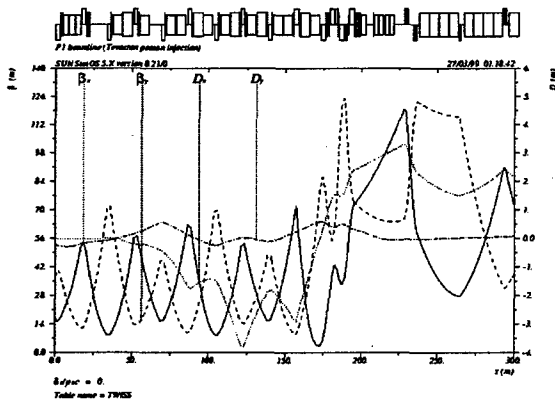


Figure 4. Lattice functions for the P1 beamline match into the Tevatron.

The matching section at the Tevatron end of the beamline contains four quads. These, along with QCELL, are used to match  $\beta_x$ ,  $\beta_y$ ,  $\alpha_x$ , and  $\alpha_y$  into either the Tevatron or P2 beamline, each with a different optical solution. For matching into P2, used at both 8.9 GeV and 120 GeV/c, the lattice functions in both x and y are set to a waist. Both TRANSPORT and MAD [2] were used for matching

The vertical dispersion generated by the extraction Lambertsons is almost canceled by the injection Lambertsons. To complete the cancellation and aid in meeting the tight geometrical tolerances, four families of rolled dipoles are used. The first family, R1, consists of two pairs of dipoles separated by  $180^\circ$

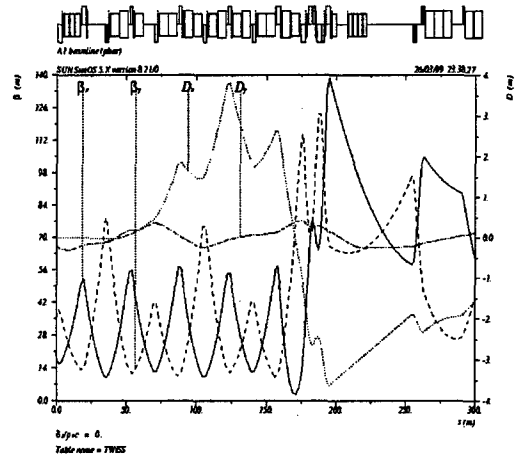


Figure 5. Lattice functions for the A1 beamline matched into the Tevatron.

and each pair separated by  $90^\circ$ . All four dipoles are rolled 157 mr counter clockwise to produce the majority of the vertical elevation needed at the injection Lambertsons (1.5 m), with negligible effect on the vertical dispersion. The other three families, R1 (116 mr), R2 (210 mr), and R3 (410 mr) are used in pairs with opposite rolls for controlling  $\eta_y$  and  $\eta_y'$ . The residual coupling generated by these rolls is small, it can be removed by rolling the last four quads in the FODO lattice.

### 3 REFERENCES

- [1] K. L. Brown et al., "TRANSPORT, A Computer Program for Designing Charged Particle Beam Transport Systems", SLAC-91, Rev. 2, SLAC, 1977.
- [2] H Grote, F.C. Iselin, "The MAD Program", CERN/SL/90-13 (AP).

# STATUS OF RESONANT EXTRACTION FROM THE FERMILAB MAIN INJECTOR\*

C.D. Moore\*, J. Firebaugh, P. Lucas, P. Prieto  
FNAL, Batavia, IL

## Abstract

One of the major advantages of the Fermilab Main Injector is that it will allow a vigorous program of fixed target physics to proceed independently from collider operations. Thus the commissioning goals for this new accelerator include a demonstration of resonant extraction. For purposes of this demonstration the extracted beam will be sent to the antiproton target station where the measured beam sizes will be used to help design beamlines for the 120 GeV fixed target programs. In order to achieve this goal an experiment has been performed to measure stopband parameters. An outline of the hardware and software to be used for extraction is described with an emphasis on upgrades to the system. Utilization of modern microprocessor technology and real-time software techniques will greatly simplify the regulation of extraction to obtain a smooth spill. The present state of extraction studies is given and the short term goals are explained.

## 1 INTRODUCTION

Extraction from the Main Injector takes place by bringing the beam into a half integer resonance thereby inducing the amplitude of betatron oscillations to increase until the particles are deflected by an electrostatic septum located at the MI32 region of the Main Injector [1]. The kick supplied by this electrostatic septum causes the particles to enter into the deflection region of two other electrostatic septa located at MI52. The kick supplied by these septa allows particles about to be extracted to move sufficiently far away from the circulating beam that a thicker magnetic septum may be used to eject the beam from the machine.

The extraction process begins by raising the normal horizontal machine tune from 26.42 toward 26.5. Because of tune spread, the number of particles with a tune in the half integer stop band can be controlled. There is enough octupole component from the main quadrupoles to provide the zero-th harmonic amplitude dependent tune shift needed for extraction although we have a set of independent zero-th harmonic octupoles to increase the efficiency of extraction. The stopband width is enlarged by a time varying set of 53rd harmonic quadrupoles, and the

smoothness of the spill is modulated by moving the tune with a microprocessor system called QXR (Quad eXtraction Regulator). The extraction system design is based on the Tevatron beam extraction system [2].

## 2 EXTRACTION SYSTEM COMPONENTS

The different components of the extraction system are described.

### 2.1 Extraction Magnets

There are 16 quadrupoles arranged into two orthogonal families (sine and cosine) with a strength of .255 kg-m/m per amp to give control of the 53<sup>rd</sup> harmonic.

There are 54 correction octupoles arranged to give a 0-th component octupole of strength 28 kg-m/m<sup>3</sup> per amp.

There are two .2 $\Omega$ , 1 mH air-core magnets used by the QXR system each with a strength of .092 kg-m/m per amp.

### 2.3 QXR Hardware

The QXR air-core quadrupoles are driven by a current regulated power supply controlled by a VME-based microprocessor. Common mode and differential mode ripple current due to the dipole magnet power supplies is expected to be 20 mA at 360 Hz and 720 Hz. To attenuate ripple of these frequencies by 20 dB the magnets were designed around ceramic beam tubes, which permits the B field to have frequency components in the 3 kHz range. Background tasks running between extraction cycles (~ 2 seconds) are used for computations, communications and downloading parameters.

A MVME 2300 POWER PC CPU board residing in a VME-64 crate regulates the extraction process responding to accelerator timing events marking the beginning and end of flattop through a Fermilab designed interrupt handling board (VUCD). A 16 bit A/D digitizes the output of the 53 MHz resonant RF spill detector that measures the extracted beam. Circulating beam intensity is measured by a toroid in the machine, digitized and encoded onto a machine-wide communication system (MDAT). The processor responds to clock events through a board that decodes events. Communications between the processor and the current regulated power supply is done through a dedicated fiber optics link at 5760 Hz.

### 2.4 QXR Software

A finite state machine (FSM) which changes states driven by clock events and software timers controls QXR

\*Work supported by the Universities Research Association, Inc., under contract DE-AC02-76CH00300 with the U. S. Department of Energy.

\* Email: cmoore@fnal.gov

software. A 5760 Hz interrupt drives the FSM and is used to derive 2880 and 720 Hz timers which activate extraction and noise rejection regulation tasks which have highest priority. Background tasks running between extraction cycles (~ 2 seconds) are used for computations, communications and downloading parameters.

The extraction process is divided into two independent regulation loops. The loop in figure 1 maintains constant the rate at which the beam leaves the machine by comparing the amount of circulating beam against a calculated reference. Its loop bandwidth ranges from DC to 30 Hz (nominally). The regulation process utilizes a feedback loop operating in real time at 720 Hz during extraction; however the error signal is also stored during the spill and processed between spill cycles.

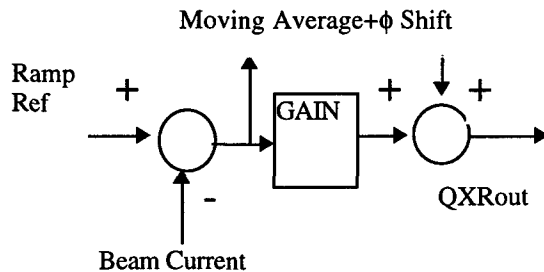


Figure 1: Representation of QXR beam extraction fast feedback and feedforward regulation components.

Error signals, which repeat from cycle-to-cycle, are averaged and weighted, then applied to the next cycle during spill. The averaged data is added to the present QXR output with a phase advance correction, compensating for unwanted signals that repeat from cycle to cycle and have a fixed phase.

Frequencies present in the spill between 30 Hz and kHz are bucked out using a separate regulation loop based on an adaptive noise compensation scheme. Sixty Hz and its harmonics comprise the majority of the unwanted frequencies modulating the spill. Therefore an adaptive rejection loop shown in figure 2 was designed to primarily attenuate these frequencies.

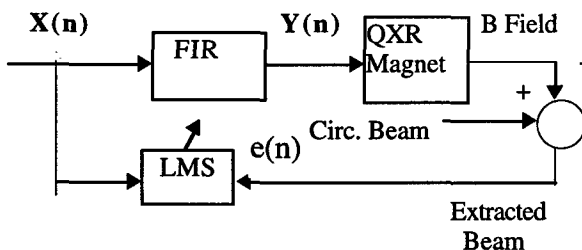


Figure 2: X(n) represents 60 Hz and its harmonics generated by a line locked software generator. It is used by the Least Mean Squares and FIR filter sections as reference signals. Y(n) drives the air core magnets that attenuate the unwanted line frequencies in the extracted beam.

The finite impulse response filter (FIR) is defined by

$$y_n = \sum_{i=0}^{L-1} w_i(n) x_{n-i} \quad (1)$$

and the filter coefficients are computed during the adaptation process by the Least Mean Squares (LMS) algorithm using the method of steepest decent.

$$w(n+1) = w(n) + 2\mu x(n) e$$

The coefficient  $\mu$  is a convergence factor. Since extraction and spill smoothing are non-stationary processes, an adaptive approach to noise attenuation may prove to be more robust than the approach taken in the TeV QXR.

## 2.5 Electrostatic Septa

There is one 10-foot long electrostatic septum with 2 mil diameter tungsten-rhenium wires at location MI-32 and two 10-foot septa with 4 mil wires at location MI-52. At 80 kV/cm they each will give a 68-microradian kick to a 120 GeV/c beam.

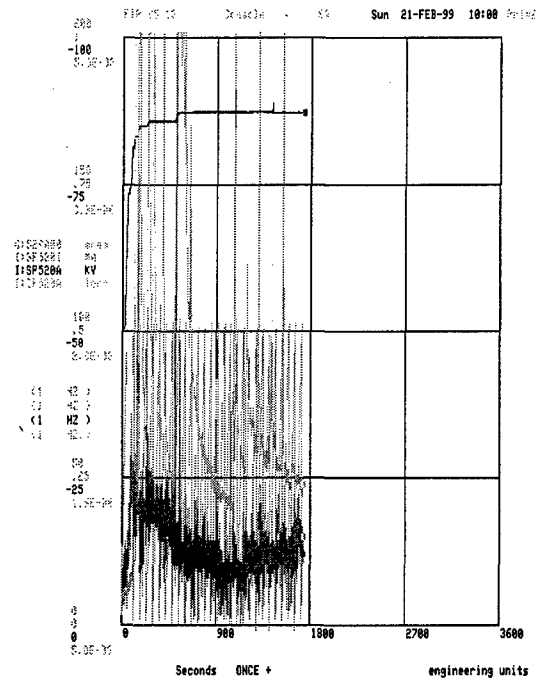


Figure 3. Conditioning the MI-52 septa

Figure 3 shows the start of conditioning the septa in order to prepare them for use. The graph shows the first half hour during which the voltage was raised to 88 kV. The lower traces show the effect of sparking on the vacuum and the current drawn from the supply.



## BEAM SWEEPING SYSTEM

F.M. Bieniosek<sup>†</sup>, O. Kurnaev<sup>†</sup>, A. Cherepakhin<sup>†</sup>, J. Bielicki  
*Fermi National Accelerator Laboratory\*, Batavia, IL 60510*

J. Dinkel

*Creative Designs, Inc., Oak Brook, IL 60523*

### Abstract

The sweeping system deflects high-energy proton and antiproton beams in a single-turn rotating-field magnet that combines deflection in both planes into a single unit. The magnet current has a peak amplitude of 10 kA and the sweep time is 1.6  $\mu$ s. At the Fermilab Antiproton Source increasing proton beam intensities incident on the antiproton production target threaten to damage the target. The purpose of the sweep magnet is to spread the hot spot on the target with a sweep radius of up to 0.5 mm, greatly reducing the peak energy deposition.

### 1 INTRODUCTION

At Fermilab, antiprotons are collected from the interaction of a 120-GeV proton beam with a solid nickel target. The efficiency of collecting antiprotons from the target rises as the size of the proton beam spot on the target is reduced. However at the same time the peak energy deposition on target rises. Under Main Injector conditions ( $5 \times 10^{12}$  protons in a 1.6- $\mu$ s pulse with a repetition rate of 1.5 seconds), the spot size will have to be increased to at least 0.25 mm to keep peak energy deposition near current levels. To bring the density of energy deposition with a 0.1-mm spot size down to currently-existing levels, a system to sweep the beam spot on the target [1] has been under development. Larger sweep radii will be required if proposed upgrades for the Main Injector [2], e.g., "slip stacking", result in increases in proton intensity.

Figure 1 shows a layout of the target station. Two upstream sweep magnets will be installed at the end of the 120-GeV proton beamline (after quadrupole magnet PQ9B). This location is the focal point of the proton lithium lens[3]. Antiprotons created in the target are collected by a lithium lens, and deflected by the pulsed magnet into the AP2 beam line for collection in the Debuncher. A single downstream sweep magnet will redirect the 8 GeV antiprotons parallel to the AP2 beamline.

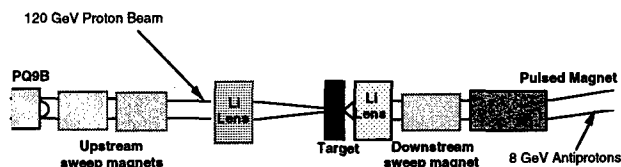


Figure 1. Major components in the target station. The three sweep magnets are identical.

### 2 SWEEP MAGNET

The beam sweeping system traces a 0.33 to 0.5-mm-radius circular pattern on the target over the 1.6- $\mu$ s proton beam pulse. The magnets have a 2-phase, 4-conductor winding excited by two power supplies that deliver balanced 625 kHz sinusoidal current waveforms in quadrature to generate a 625-kHz rotating dipole field[1]. The magnetic field due to two pairs of current-carrying conductors oriented 90° apart is rotating on axis if the current in the two pairs of conductors is  $I_0 \cos(\omega t)$  and  $I_0 \sin(\omega t)$ . If the conductors are twisted such that the axial current integrated over the length of the magnet has the distribution  $I_0 \sin(\omega t - \theta)$ , the line integral of the field along the beam path is uniform and rotating.

The average deflecting field required for a 0.5-mm sweep radius is 1.26 kG on the downstream sweep magnet, which is 56 cm long. Because of the twist in the conductors, the peak field on axis must be a factor  $4/\pi$  times larger than the average field, or 1.60 kG. The ratio of the magnet current to the local magnetic field on axis, calculated by POISSON for a straight conductor, is 6.1 A/Gauss. Thus to provide the desired field, the peak current required from the power supply is 9.8 kA, and the peak inductive voltage drop across the magnet is 7.7 kV (peak voltage to ground 3.85 kV) for a magnet inductance of 0.2  $\mu$ H.

A cross sectional view of the sweep magnet is shown in Figure 2. The clear bore of the magnet is 28.5 mm. The region of antiproton flux that is collected downstream has a diameter of 22 mm. The conductors are hollow 6.35-mm diameter aluminum tubes. Hollow aluminum tubes were chosen to minimize the beam-induced heating of the conductors, and to allow the passage of cooling air through the center of the conductors. A ceramic tube provides electrical insulation between the conductor assembly and the magnetic cores. No vacuum wall is required, because the beam is transported through air

\*Operated by the Universities Research Association Inc., under contract with the U.S. Department of Energy.

<sup>†</sup>Present address: LBNL, Berkeley, CA 94720, email [fmbieniosek@lbl.gov](mailto:fmbieniosek@lbl.gov)

<sup>†</sup>On leave IHEP, Protvino, Russia

from upstream of the target to downstream of the pulsed magnet. Molybdenum Permalloy Powder (MPP) cores were chosen for the magnet yoke. The core material has relatively low losses, and adequate inorganic insulation. A magnet assembled with powder cores has the advantages of ease of construction, and the relatively high thermal conductivity and Curie temperature of this material. The fairly small thermal stresses are contained by press-fitting the cores in a water-cooled nickel housing. Estimated beam thermal power is 54 Watts per core at  $1 \times 10^{13}$  protons per pulse, or a total power of 1944 Watts for all 36 cores.

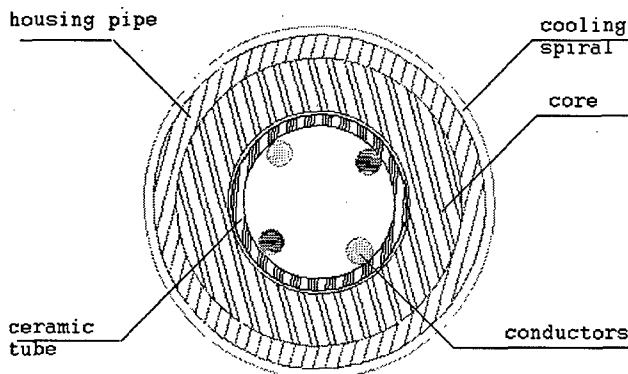


Figure 2. Sweep magnet cross section.

A longitudinal view of the magnet is shown in Figure 3. The current leads are located in the midplane of the magnet. The conductors are grounded at the end ring by the end flange on both sides of the magnet. Four ceramic bushings are used to support the current leads and insulate them from the magnet body. Silver-coated beryllium copper finger stock is attached between thin copper rings and copper spacers. The copper spacers are located between each two pairs of cores. The fingerstock serves as a slide guide and stress relief for the insulating ceramic tube, and provides a thermal conductive path for removal of beam-induced heating from the tube and current conductors.

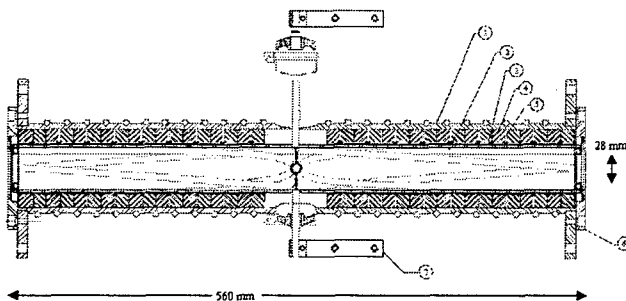


Figure 3. Longitudinal cross section of rotating field magnet. 1 - housing pipe, 2 - twisted conductors, 3 - ceramic pipe, 4 - MPP core, 5 - spacer, 6 - end flange, 7 - current lead

Magnetic measurements of the sweep magnet were performed with stretched wires. Ribbon cable was used to pick up the  $dB/dt$  signal along the whole magnet length and then was integrated to obtain a signal proportional to magnetic flux through the measurement loop. The signal amplitude was as expected. The line-integrated field distribution was uniform within  $\pm 1\%$  over a 20-mm horizontal window for three planes at 0 and  $\pm 7$ mm vertical offset from center.

### 3 POWER SUPPLY

Power will be supplied through coaxial cables over a distance of approximately 10 m into the target vault, and (for downstream magnet) by 2.5 m of strip line through steel shield modules to the magnets at the bottom of the target vault. A simplified circuit diagram is depicted in Figure 4. The solid-state power supply is based on a two-stage compression circuit with saturating reactors. Pulse compression facilitates transfer of the current pulse to the ringing circuit in a high-radiation environment. An SCR switch is used for resonant charging of the first stage capacitor C1 using the leakage reactance of a 1:10 step-up transformer.

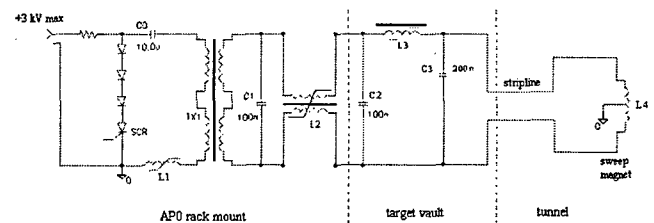


Figure 4. Simplified schematic diagram of power supply.

Energy storage capacitor C0 is initially charged up to 3 kV by the DC high voltage supply. The energy is transferred to the first compression stage capacitor C1 via the step-up transformer by closing the thyristor switch SCR. The small saturating choke  $L_1$  protects the SCR by limiting the initial  $dI/dt$  of the thyristor switch to 100 A/ $\mu$ s for the first microsecond after turnon. To limit the reverse current of the thyristor, which has a relatively long recovery time, a stack of fast recovery diodes is connected in series. When the first saturating reactor  $L_2$  becomes conductive the energy from C1 transfers to the second stage capacitor C2. The second stage is located about 10 m away in a high radiation area and is connected to the first stage by a pair of coaxial cables (RG 220/U). Saturation of  $L_3$  initiates the discharge of C2 into the ringing circuit  $L_4$ , C3. Capacitor C3 is connected to the sweep magnet (inductance  $L_4$ ) via the strip line.

The first stage switching reactor  $L_2$  is wound on four 2.3 mV-sec/turn Magnetic Metals Square-50 (25  $\mu$ m) nickel-iron tape cores. The winding is split into two equal halves. Each half has 8 turns. The circuit between the step-up transformer and the reactor is balanced, with peak voltages of  $\pm 15$  kV. When the reactor saturates, the voltages on the two terminals of C1 approach 15 kV, and

the voltage on one of the two output terminals approaches 30 kV. The other terminal remains at ground potential until the second reactor saturates. A DC bias current of up to 5 A is provided for both reactors L2 and L3.

The second stage reactor is wound on three 3.0 mV-sec/turn Allied-Signal 2605-SC Metglas cores, annealed and cowound with 3- $\mu$ m mylar insulation. The reactor L3 has 4 turns. With these windings, the volt-seconds capability of the cores is 150 mV-sec for the first stage, and 36 mV-sec for the second stage. Inductive voltage per lamination in the first stage is about 0.6 V, and in the second stage about 2.2 V. Nickel-iron tape cores were chosen for the first stage because of their very square B-H loop; relatively large packing factor, acceptable losses and adequate insulation. Metglas cores were chosen for the second stage because of their small losses and good insulation properties of the mylar film.

Measurements of the losses in energy transfer were made at 2.9 kV. The initial energy stored on capacitor C0 was 42 J. Energy delivered to capacitor C1 was 35 J. Of the 7 J loss in this energy transfer the losses were distributed 4 J to the SCR switch and 3 J to the balance of the circuit. Energy transferred from C1 to C2 was 31.5 J. The losses were dominated by resistive losses in the windings. Switching losses in the cores, determined from the B-H loops, are small, 0.3 J in the first stage, and 0.5 J in the second stage. Energy transferred to the ringing circuit was 22 J.

The least efficient part of the circuit is the final transfer from capacitor C2 to the ringing circuit L4, C3. When the reactor L3 saturates, a single current pulse passes to the ringing circuit. It is relatively inefficient for two reasons. First, it is necessary to prevent saturating the reactor a second time, and passing a second reverse current pulse that effectively extracts energy from the magnet circuit. The necessary voltage reversal is naturally accomplished if the ratio of capacitor C3 to capacitor C2 is at least 2. This reflected voltage also provides a reset pulse to the reactors, ensuring highly stable operation even with no reverse bias current.

Second, some current flows in the inductance of the sweep magnet, L4, before the energy transfer is completed. For typical saturated inductance of the output switch, about 0.5  $\mu$ H, the efficiency of final energy transfer is about 80%.

The power supply was built and tested for 7 million pulses at 3 kV (full charge). At 3 kV charge, the output current amplitude is 11.6 kA. Oscilloscope pictures of voltages and currents under typical operation are shown in Figures 5 and 6. Power supply jitter does not exceed  $\pm 2$  ns, while slow drift is about 20 ns. Installation of the complete system is expected in the year 2000.

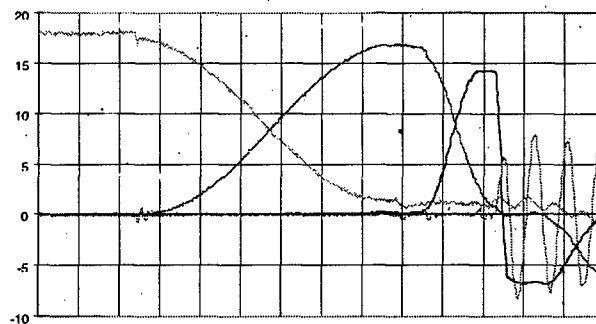


Figure 5. Scope picture of voltages in compression stages. Initial voltage = 1.8 kV. Vertical scale = 5 kV/div, horizontal scale = 2  $\mu$ s/div. Green - first charging capacitor  $\times 10$ . Red - first compression stage capacitor. Blue - second compression stage capacitor. Pink - ringing circuit (magnet) voltage.

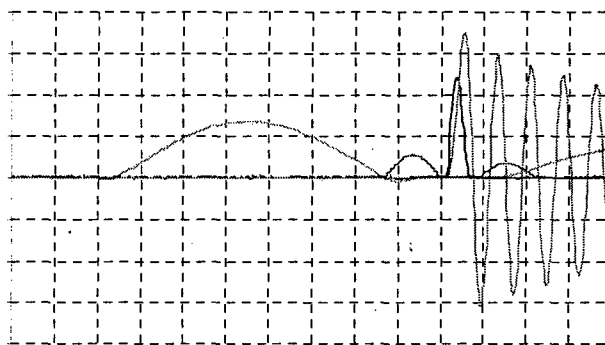


Figure 6. Scope picture of currents in compression stages of power supply. Peak magnet current is 7 kA, corresponding to 2.2 kV charge. Vertical scale = 2 kA/div, horizontal scale = 2  $\mu$ s/div. Green - SCR current. Red - first compression stage. Blue - second compression stage. Pink - ringing circuit (magnet) current.

## 5 REFERENCES

- [1]. F. M. Bieniosek, O. Kurnaev, A. Cherepakhin, J. Dinkel, Proc. 1997 Particle Accelerator Conference, paper 8P10.
- [2] P.P. Bagley, et. al., Summary of the TeV33 Working Group, in 1996 Snowmass Conf.
- [3] F. M. Bieniosek and K. Anderson, Lithium Lens for Focusing Protons on Target in the Fermilab Antiproton Source, Proc. Particle Accelerator Conf, Washington, 1993.

## LER INJECTION LINE B2/B4 STUDY

R.H. Iverson, F.-J. Decker, D. Schultz, C. Spencer, J. Turner, U. Wienands, SLAC\*

### Abstract

During the Pep-II LER commissioning run in July 1998 the beam profile in the tune up dump profile monitor just before LER injection showed an anomalous parabolic shape. The sextupole component of the field of bend magnets B2 and B4 in the beginning of the south injection tunnel (SIT) was thought to be the cause of this. An off-line model of the B2/B4 bend magnet field was created using DIMAD. Results of particle tracking simulated in dimad were compared with on-line lattice diagnostic data and observations of the beam profile on the tune up dump screen.

### I. INTRODUCTION

We carried out beam-based lattice diagnostics for the entire injection line to discover the cause of the parabolic beam profile on the tune-up dump screen just before the LER injection point (Fig. 1). The data revealed a possible optical error in the B2/B4 region. Grid scan data taken at the entry to B4 shows a sextupole component to the field that the beam sees (Fig. 2). Originally, B2/B4 was a single magnet designed to bend the 14 GeV Pep-I beams through a fairly shallow arc. Now B2/B4 is split into two separate C-magnets which bend the 3.11 GeV Pep-II beam through a much larger arc. (Fig. 3). The difference in sagitta for the new configuration requires an 11 mm shift in the horizontal alignment. After re-alignment, the optical error revealed by grid scan data is greatly reduced. However, the swoosh shaped beam profile persisted even after re-alignment.

\*Work supported by Department of Energy contract DE-AC03-76SF00515.



Figure 1: Dump screen profile.

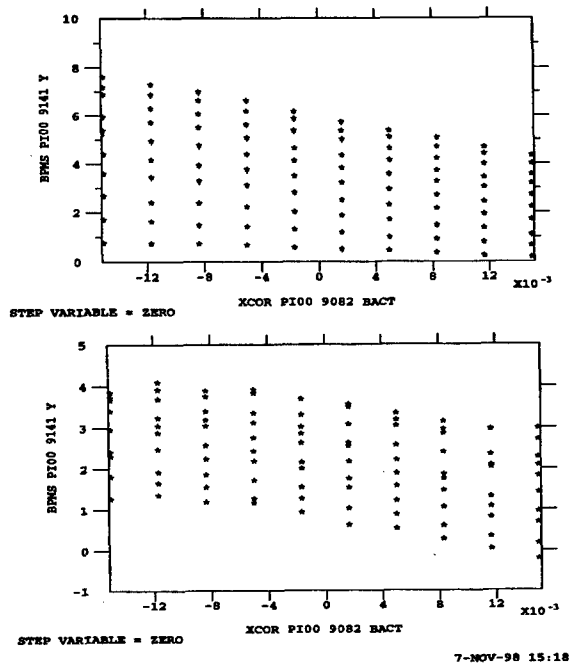


Figure 2: Grid scan data before and after re-alignment of B2 and B4.

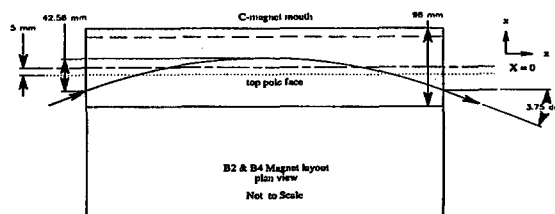


Figure 3: Beam trajectory through B4.



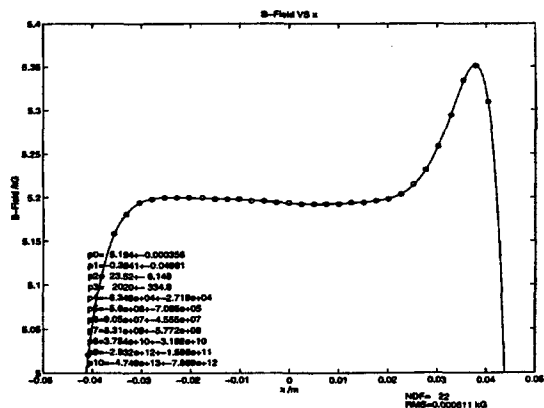


Figure 4: Measured field of B4.

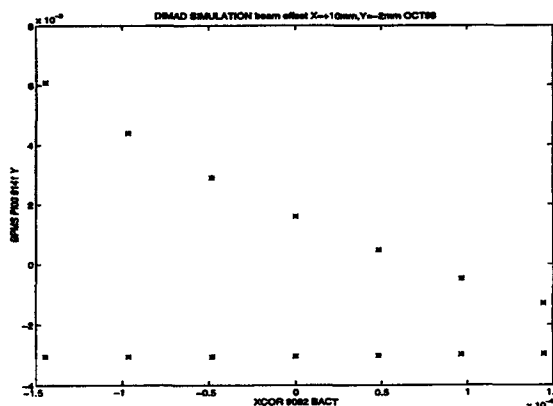


Figure 6: DIMAD simulation of grid scan.

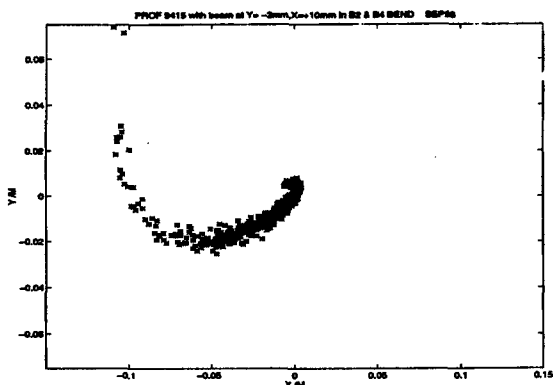
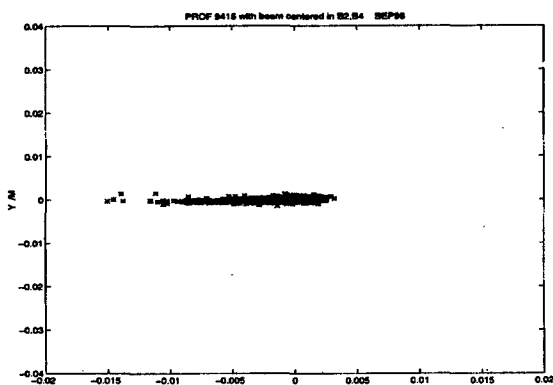


Figure 5: DIMAD simulation of beam profile with nominal B2&B4 (top) and with measured field and offset included (bottom).

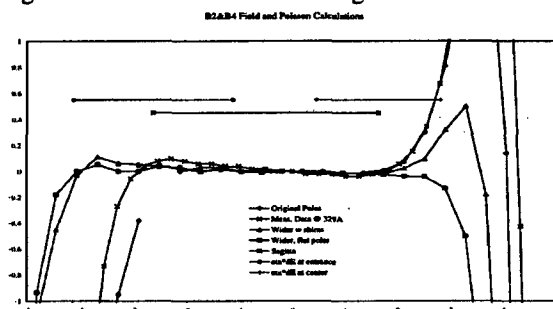


Figure 7: Poisson simulation of B4 field with different shims and pole tip extensions.

## II. POSSIBLE EXPLANATION

The swoosh could be caused by the small size of the good field region of the B4 bend magnet. (Fig. 4). The dispersion at the entry to B4 is 2 meters which creates a full width beam size of 30 mm in the horizontal plane. The beam path through this bend follows quite a large arc. So that a large portion of the bend's width is traversed (Fig. 8).

Off-line DIMAD-based model simulations show what the nominal beam profile should look like (Fig. 5 top). When measured B4 field and offset are included, the predicted beam shape and grid scan pattern correspond well with observation (Fig. 5 bottom, Fig. 6).

The effect of a dispersion error at the linac extraction point was calculated and proved to be much smaller than the effect from the anomalous field of B4.

### III. PROPOSED FIX

Calculations based on Poisson show that the B4 field could be much improved by the addition of shims and pole-tip extensions. (Fig. 7). The B4 magnet will be modified before the Pep-II start-up in May 1999.

In addition, the beam size in regions of high dispersion can be reduced by minimizing energy spread. Decreasing the compressor klystron voltage in the South Ring To Linac (SRTL) line should help to reduce the energy spread [1].

### IV. CONCLUSION

The correction of the B4 bend field with shims combined with reduced energy spread should produce a beam shape at the entry to the LER which has a much more normal elliptical shape. This should allow the capture efficiency for the LER to come up the 100% level that is the norm for the HER.

#### Acknowledgments

T. Fieguth, W. Colocho, R. Atkins, H. Smith, and S. DeBarger contributed much to this effort with many helpful discussions.

#### References

[1] F.J. Decker, R.H. Iverson, H. Smith, M.S. Zelazny, S. LAC, *The SLAC Linac During the Pep-II Era*, in these proceedings.

# PARTIAL BEAM EXTRACTION SCHEME OF NEGATIVE HYDROGEN ION\*

H. E. Ahn<sup>†</sup>, Y. S. Cho, and B. H. Choi

Korea Atomic Energy Research Institute, P.O. Box 105, Yusong, Taejeon, Korea 305-600

## Abstract

A new scheme for beam extraction is presented to partially extract a negative hydrogen ion beam at 260 MeV from the main linac where both protons and negative hydrogen ions are accelerated up to 1 GeV. The negative hydrogen ions are extracted by a stripper magnet and the un-extracted ions are returned to the linac. The main feature of this extractor is its ability to regulate the intensity of the extracted beam with the stripper magnet. This extraction scheme will be utilized for the KOMAC (Korea Multi-purpose Accelerator Complex) linear accelerator of 1 GeV cw proton ( $H^+$ )/negative-hydrogen ( $H^-$ ) beams with an intensity of 20 mA.

## 1 INTRODUCTION

Korea Atomic Energy Research Institute (KAERI) is proposing to develop a 20 MW (1 GeV and 20 mA) cw  $H^+/H^-$  linear accelerator (Fig. 1) under the KOMAC [1] (Korea Multi-purpose Accelerator Complex) project. The KOMAC linac will accelerate both  $H^+$  and  $H^-$  up to 1 GeV while partially extracting  $H^-$  at 100 and 260 MeV. Since the accelerator is to be utilized multi-purposely, regulating the beam intensity is a crucial requirement for the beam extraction system. The extraction method developed in this study is to use a stripper magnet for magnet stripping [2] which removes the weakly bound electron from  $H^-$ . The 260 MeV  $H^-$  beam extractor design is the main objective of this study, where the beam can be used for deep-sited tumor therapy.

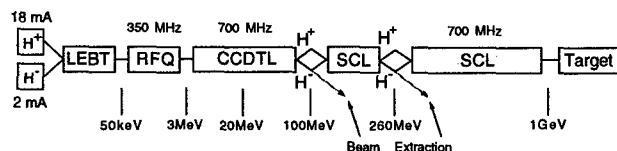


Figure 1: Schematic layout of the KOMAC linac.

## 2 MAGNET DESIGN

Since we need to extract  $H^-$  at the desired intensity, a new stripper magnet is needed. The design requirements for the stripper magnet are (1) minimizing the emittance growth of the extracted beam, (2) minimizing the centroid-shift of the extracted beam in angle, (3) decoupling the  $H^-$  bending from the stripping process, and (4) maximizing the angle between the extracted beam direction and the un-extracted  $H^-$  beam direction. The first requirement is very important

since there is an emittance limit for a given vacuum pipe dimension. The second requirement is due to the fact that if the  $H^-$  beam is extracted at a different horizontal angle for a given intensity, the downstream beamline has to transport all the extracted beams with different centroid angles. The third requirement is also important since the un-extracted  $H^-$  beam must be returned to the main linac. The last requirement is important because the beamline element for the extracted beam must be placed as close as possible for focusing. Fig. 2 shows the design of the stripper magnet using POISSON [3]. The stripper magnet consists of super-

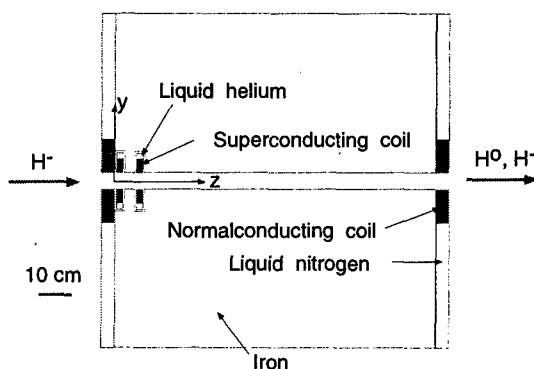


Figure 2: Stripper Magnet

conducting and normalconducting coils. When  $H^-$  travels through this stripper, it first encounters the field generated by the superconducting coils. If the field is higher than the threshold field ( $\approx 0.97$  T), then it has a significant probability for losing an electron and becoming an  $H^0$ . By varying the current in the superconducting coil, the intensity of the extracted beam can be regulated as shown in Fig. 3. The

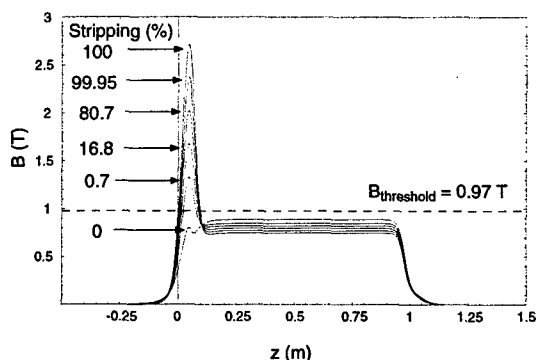


Figure 3: Stripper magnetic field at the mid-plane ( $y = 0$ ).

cross-sectional area of the coil is  $2 \text{ cm} \times 4 \text{ cm}$  and the current density changes from 0 to  $165 \text{ A/mm}^2$ . The magnet gap is 5 cm. The stripping region is less than 7 cm along the beam direction, and the angle between the extracted

\* Work supported by the Korea Ministry of Science and Technology.

<sup>†</sup> Email: heahn@nanum.kaeri.re.kr

beam centroid and the initial beam direction is about 30 mr. The surviving  $H^-$  must be returned to the linac, and initially the normalconducting current is adjusted so that  $\int B dl / B_\rho$  is fixed at  $20^\circ$ , where  $B$  is the vertical field and  $B_\rho (= 2.487 \text{ T}\cdot\text{m})$  is the beam rigidity. The cross-section of the coil is  $4 \text{ cm} \times 10 \text{ cm}$  and the maximum current density is  $4.4 \text{ A/mm}^2$ .

### 3 SIMULATION

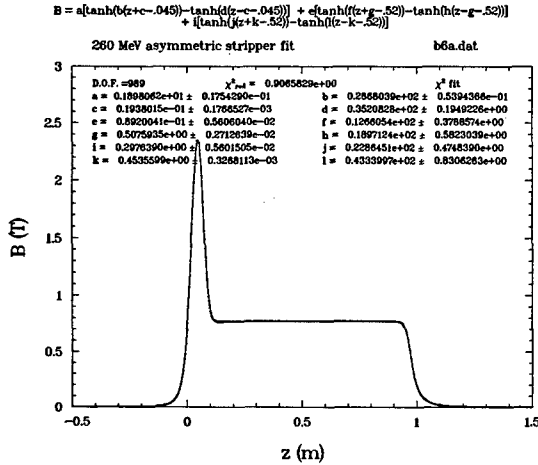


Figure 4: Mid-plane  $B_y$  field fitting.

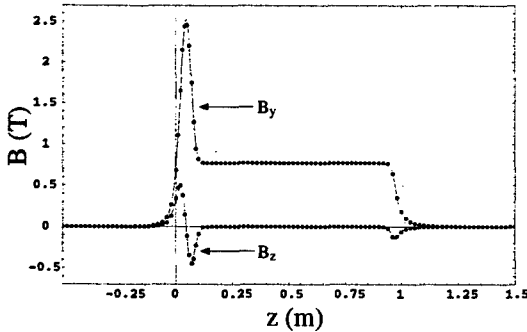


Figure 5: Off-mid-plane field at  $y = 1 \text{ cm}$ .

After the POISSON run is finished with given currents in the superconducting and normalconducting coils, the field

at the mid-plane is fitted with a sum of six tanh functions. Fig. 4 shows that the field is described analytically with a fitting function of 12 parameters. The off-mid-plane field which interacts with  $H^-$  sitting at some distance from the mid-plane could be computed from the mid-plane field as

$$\begin{aligned} B_y(y, z) &= \text{Re}[B_y(0, z + iy)], \\ B_z(y, z) &= \text{Im}[B_y(0, z + iy)], \end{aligned} \quad (1)$$

and Fig. 5 shows the field data (solid circle) which is obtained from POISSON at a vertical distance of 1 cm from the mid-plane. The field (solid curve) computed from the mid-plane field matches well with the data points. Tracking  $H^-$  through the stripper magnet is done by solving a first order differential equation. The DIVPAG subroutine from IMSL MATH/LIBRARY was used to obtain results with an accumulated error of  $10^{-10}$ . The stripping process is also simulated using the life time given in the reference [2].

### 4 BEAM EXTRACTOR DESIGN

The beam extractor design is shown in Fig. 6. It consists of a stripper magnet, 5 dipoles (BM), 12 quadrupoles (QM), and 4 steering magnets (SM). The dipole bends the

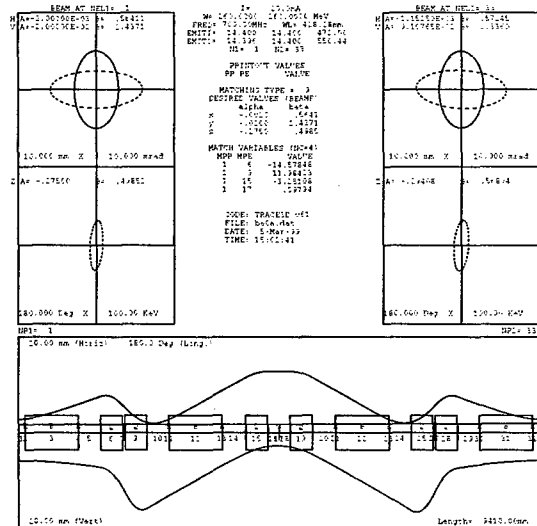


Figure 7:  $H^+$  beamline setup (TRACE 3-D[4]).

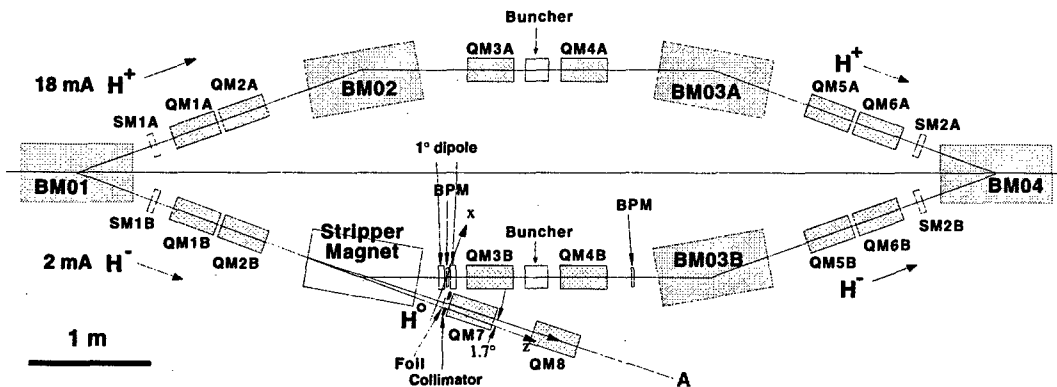


Figure 6: 260 MeV  $H^-$  beam extractor layout.

$H^-$  (or  $H^+$ ) beam by  $20^\circ$  with 0.904 T magnetic field. The effective length is 96 cm. Initially, a beam ( $H^+$  and  $H^-$ ) enters the beam extractor and encounters a dipole BM01 which separates  $H^+$  and  $H^-$  by  $40^\circ$ . The subsequent six quadrupoles (QM1A to QM6A) are placed between dipoles so that the outgoing beam exactly matches the incoming beam shown in Fig. 7 for the  $H^+$  beam. The effective length of each quadrupole is 40 cm and the maximum field gradient is less than 15 T/m. The settings of the quadrupoles in the  $H^-$  line are opposite to those in the  $H^+$  line. The beam intensity depends upon the field from the superconducting coil. Fig. 8 shows the horizontal phase-space plots for the extracted  $H^0$  beams ((b) and (d)) and the un-extracted  $H^-$  beams ((a) and (c)). The (a)

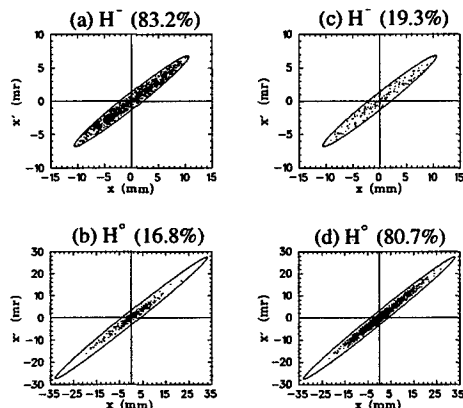


Figure 8: Horizontal phase-space plots for  $H^-$  and  $H^0$  beams.

and (b) plots are the case which 16.8% of the  $H^-$  beam is extracted, and the (c) and (d) plots are for 80.7% of the  $H^-$  beam. The emittance of the initial beam is  $14.4 \pi$  mm-mr. All the extracted beams with 0 to 100% can be enclosed with a large ellipse shown in (b) and (d) plots. The emittance of the large ellipse is  $110 \pi$  mm-mr which is about a factor of eight larger than the initial beam. There is no emittance growth for the un-extracted  $H^-$  beam shown in (a) and (c) plots. The surviving  $H^-$  beam is bent by the stripper magnet where the bending angle is fixed at  $20^\circ$ . Fig. 9(a) shows the horizontal angle of  $H^-$  as a function of a longitudinal position. The stripper with high  $H^-$  extraction tends to bend  $H^-$  to a large angle initially. This effect provides the horizontal position difference for different stripper settings (Fig. 9(b)). This problem can be fixed by placing two  $1^\circ$  dipoles downstream of the stripper magnet, with a beam position monitor (BPM) between the dipoles for a diagnostic tool. For the 0% stripping case, the stripper bends  $H^-$  by  $20^\circ$  while bending less for the high intensity  $H^-$  stripping. Figs. 9(c) and (d) shows that the maximum angle difference is about  $2^\circ$  for two extreme beams at the center of the BPM. The maximum path difference is 3 mm. The remaining  $2^\circ$  or lesser angle is provided by two  $1^\circ$  dipoles and the alignment of the beam will be achieved by utilizing the BPM between two  $1^\circ$  dipoles and the second BPM placed upstream of BM03B. The  $H^-$  beam is then bent by BM03B and returns to the

main linac by BM04 for further acceleration. The extracted  $H^0$  beam drifts toward the foil located downstream of the stripper magnet and becomes  $H^+$ . The quadrupole doublet (QM7 and QM8) transports the beam at the position labeled 'A' (Fig. 6) with the  $\pm 1$  cm beam size and  $\pm 10.5$  mr divergence. For proton therapy, the emittance growth is not disadvantageous because a lead plate is usually used to spread a pencil beam laterally.

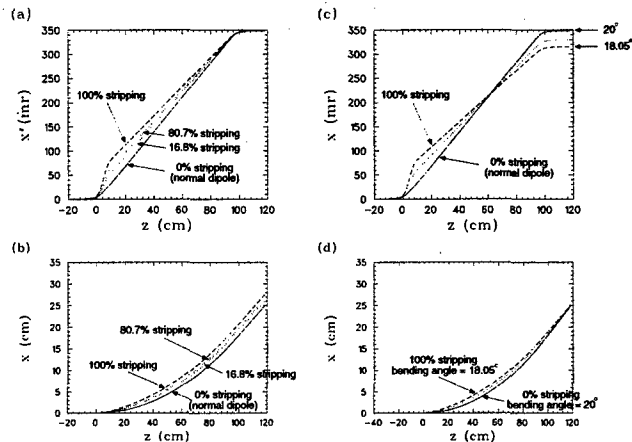


Figure 9: Tracking of un-extracted  $H^-$  beam.

## 5 SUMMARY

This paper discussed a feasibility of 260 MeV  $H^-$  beam extractor using a stripper magnet. It is shown that a desired intensity from 0 to 100% of  $H^-$  beam could be extracted and all the extracted beams from 0 to 100% could be enclosed with a large ellipse which represents a factor of eight emittance growth. The un-extracted  $H^-$  beam is returned to the main linac with no emittance growth.

## 6 ACKNOWLEDGMENT

The author<sup>†</sup> would like to thank David Barlow at LANL for helping in stripper magnet design.

## 7 REFERENCES

- [1] C.K. Park, H.E. Ahn, B.H. Choi, T.Y. Eom, Y.S. Cho, J.M. Han, J.H. Lee, W.S. Park, S.S. Kang, W.S. Song, T.Y. Song, Y.K. Kim, C.K. Hwang, J.H. Chang, S.Y. Suh, M.H. Yang, and J.K. Chung, "The KOMAC Project: Accelerator and Transmutation Project in Korea," Proceedings of the first Asian Particle Accelerator Conference (APAC98), Tsukuba, Japan, March 23-27, 1998.
- [2] Andrew J. Jason, Daniel W. Hudgings, and Olin B. van Dyck, "Neutralization of  $H^-$  Beams by Magnetic Stripping," IEEE Nucl. Sci., NS-28, 2704 (1981).
- [3] J. H. Billen and L. M. Young, "POISSON SUPERFISH," Los Alamos National Laboratory report LA-UR-96-1834 (revision April 22, 1997).
- [4] K.R. Crandall and D.P. Rusthioi, "TRACE 3-D Documentation", Third edition, Los Alamos National Laboratory Report LA-UR-97-886(May 1997).

# MICRO & MINI-BUNCHING OF THE SLOW EXTERNAL BEAM AT THE AGS\*

JW Glenn\*, M Brennan, KA Brown BNL, D Majka YALE, A Mincer NYU

## Abstract

The AGS's prime function when RHIC comes on line will be as a heavy ion injector, free time will exist for unique operation that can be tailored and dedicated to users. Many of the next generation of experiments require RF time structure in the spill as it is extracted to time events or assure no background during decay times. Two methods have been developed to meet these needs. Micro-bunching where the beam is forced between empty buckets producing bursts at arbitrary integer harmonics of rotation period[1], and mini-bunching where the beam is kept bunched to provide high extinction between bursts [2]. With an RF dipole the period may be increased to three times the rotation period of the beam. Further modelling and test results with beam will be presented. At high beam currents above transition, tight clusters of beam form causing severe random spike structure in the spill. Forcing the beam between empty buckets before extraction breaks up these clusters with minimal modulation of the spill at the RF frequency. Results of spill structure and loss reduction will be given.

## 1 INTRODUCTION

There are two approved future experiments that use bunched extraction from the AGS. One measuring the branching ratio of Klong to pi-zero and neutrinos needs a 250 pico-Sec burst every 300 nano-Sec. This will be accomplished using micro-bunching[1] where the debunched coasting is forced between empty longitudinal buckets by slowly reducing the main magnet field across the flat top. The extraction third integer transverse resonance is set-up at a momentum matching the RF bucket, thus the beam is extracted in short bursts at the phase where the longitudinal motion carries it to the resonance (Fig 1). Variations of this process have been modelled and measured showing that bunching can be maintained without beam loss, extraction losses can be reduced and the beam can be smoothed without major bunching. Also micro-bunching provides the possibility of fast control of the beam delivery rate. The other experiment measures the branching ratio of direct conversion of muons to electrons. Here it is vital to eliminate the possibility of any protons delivered to the pion production target during the time the muons are decaying. The process here is mini-bunching[2] where beam is kept within buckets and the bunch is slowly

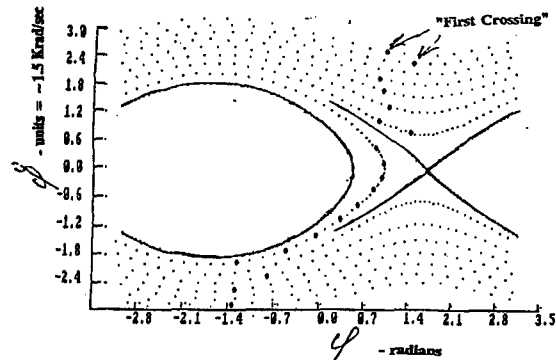


Fig 1 Particle Trajectory Near Empty Buckets.

deaccelerated to the extraction resonance. Those particles at the edge of the bunch are extracted while the space between bunches is swept of particles at the resonance turn on and thus is without beam. The option of extracting a burst every three turns has been partially tested with a kicker.

## 2 FOUR DIMENSIONAL MODELLING.

Previous modelling of micro-bunching[1] was done with separate transverse and longitudinal models. The results were then folded together. The possibility of error here prompted an effort to combine the two models and run particles in a four dimensional space of transverse X & X' and longitudinal phi & phi dot. The predicted bunch widths are similar to those previously predicted. A plot of bunch width verses the offset of the resonance momentum in units of phi dot is shown in Fig 2

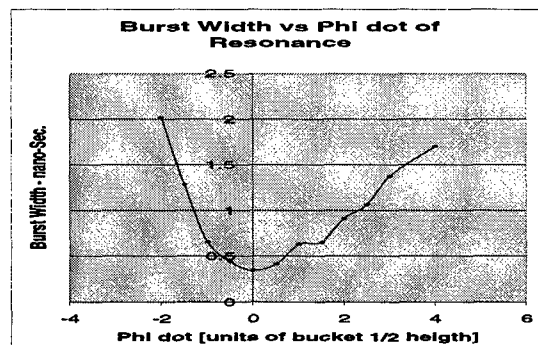


Fig 2. Burst Width as Function of Momentum.

### 2.1 Increased Losses during Micro-bunching

Initial modelling of micro-bunching indicated an increase in the number of low transverse emittance particles that would be retrapped in the stable region of phase space as the particle moves through the resonance. This has not

\*Work supported in part by US Dept of Energy

\* Email: glenn@bnldag.bnl.gov

been seen in any tests of micro-bunching even at full AGS intensities of 60 TP/cycle. Further modelling using a more realistic distribution of particles (gaussian in radius) show fewer retrapped particles as there are fewer small amplitude particles than previously estimated. Combining both transverse and longitudinal motions together show that when the resonance is before the central momentum of the RF bucket (the centre of the bucket is offset below the resonance momentum), particles spend more time near the resonance momentum than if there in no RF on. Consider particle that follows a trajectory in longitudinal phase space that approaches the unstable fixed point; it nearly stops at this point which is the lowest  $\phi$  dot (highest momentum if above transition) of the trajectory. If the transverse resonance is at this momentum, the particle spends a lot of time on resonance. As Fig. 2 shows, there is some increase in bunch width.

### 3 BUNCHING FACTOR.

The results of increased RF voltage on the bunching factor was checked. At 100 kV per turn a bunching factor (rms width divided by period of RF voltage) of 100 was measured. These tests were done during a Heavy Ion run using a gold beam. Instead of using the 93 MHz VHF system normally used for micro-bunching, the 4 MHz acceleration system was used. After beam was accelerated to flattop, voltage was turned down, the frequency lowered to place the buckets near the resonance with a ramp to match reducing field, then turned back on. The beam was then spiralled through the gaps between buckets. The time that a gold ion passed a counter compared to a zero crossing of the RF was recorded for each ion and a time distribution obtained and extraction efficiency noted. Runs were made for various RF voltages from 50 to 300 Volts per turn. The bunching factor for 50 kV was 86 and for 100 kV it was 118. (Time distribution of the beam for 100 kV is shown in Fig. 3.)

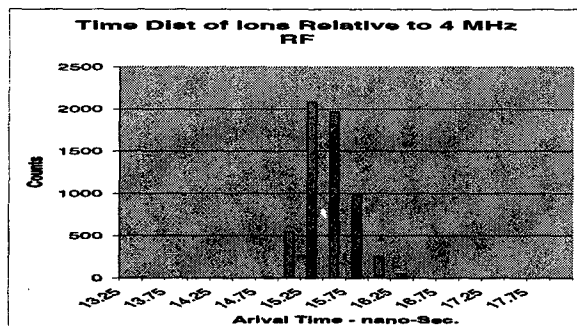


Fig 3. Burst Width for 100 kV of RF Voltage

These factors are consistent with root voltage scaling of previous measurements with the 93 MHz cavity. Unfortunately it was latter found for the higher voltages, the zero crossing detector saturated so timing was lost. Extraction efficiency did not drop noticeably at higher voltages in these tests indicating no increase in losses.

### 4 SPILL STRUCTURE REDUCTION

The AGS was plagued this year with random structure on the spill[3]. Total beam loss including extraction, beam splitting and transport was reduced with the VHF on line. Careful placement of the VHF buckets between the stored beam and the resonance reduces the micro-bunch structure in the extracted beam. It was also noted that the beam that was not extracted was trapped within the "empty" buckets and carried to the end of flat top as shown in the blowup of Fig 4 from Ref. 3 (Fig. 5). This may be a new loss mechanism associated with micro-bunching. An advantage of this mode of loss is that this beam may be easily dumped into a beam catcher and does not spread around the accelerator.

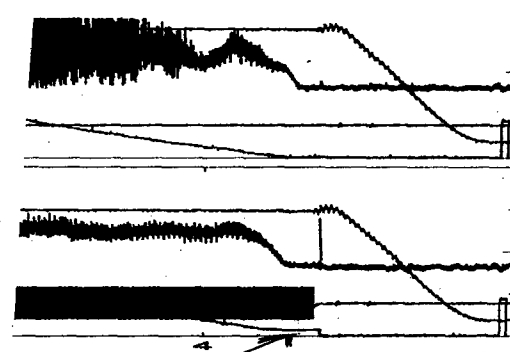


Fig 4. Beam Current (arrow) Recaptured in Homogenising Buckets.

### 5 SPILL MODULATION

In the process of setting up the VHF cavity for homogenising the beam before extraction, it was discovered that modulating the frequency of the RF strongly modulates the spill. The gain and phase response of the frequency modulation for various frequencies was measured with all slow loops closed. We measured the response of the spill to square wave modulation to estimate the dead delay of the system. A fast detector was made using the signal from an experimenters 50-100 MHz counter into a 100 nano-Sec diode isolated integrator. The data was "eyeball fitted" assuming minimum phase response with a dead delay. The results are plotted in Fig. 5.

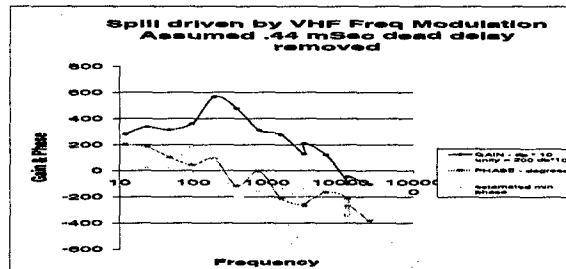


Fig 5. Gain and Phase Response of Spill to VHF Frequency Modulation.

. The dead delay that best fits the data is only 0.4 milli-Seconds which is consistent with the estimated value. The spill responds to many kilo hertz of modulation.

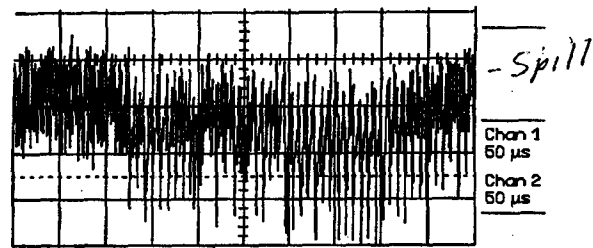
## 6 MINI-BUNCHING EXTENSION MEASUREMENT

We measured the cleanliness of the quiet periods between beam bursts using a separated Kaon beam looking at a production target in the Slow Beam. This was a short test run at a new extraction energy of 7 GeV. One run showed 5 counts in the counter for a (corrected) count of 60 million during the burst for an extinction of  $1.2 \times 10^8$ .

## 7 BEAM BURST EVERY THREE TURNS.

We did a quick check of the modelled prediction that spill structure of one third of the rotation period would be produced by introducing horizontal coherent motion during the resonant process. As no RF dipole exists for horizontal motion the tune kicker was used to create a short burst of coherent motion. The resultant spill

structure was recorded using the fast detector used for spill modulation studies. The rotation period of the AGS is 2.7uSec and the periodicity of the bursts is 8 uSec as shown on Fig. 6.



## 7 REFERENCES

- [1] MICRO-BUNCHING THE AGS SLOW EXTERNAL BEAM JW Glenn, M Brennan, L Littenberg, J Rose, C Woody, A Zoltzman BNL P Bergbusch, TRIUMF and Dick Mjka, YALE Session 9w005 PAC97
- [2] MINI-BUNCHING THE AGS SLOW EXTERNAL BEAM JW Glenn, L Ahrens, T Hayes BNL, R Lee UC-Irvine Session 9w004 PAC97
- [3] AGS RESONANT EXTRACTION WITH HIGH INTENSITH BEAMS L Ahrens, K Brown, JW Glenn, T Roser, N Tsoupas, W VanAsselt, AGS Dept, BNL Session THP140 these proceedings to be published



# **RHIC INJECTION KICKER POWER SUPPLY SYSTEM CONTROL, INTEGRATION AND COMMISSION\***

W. Zhang, R. Sanders, W. Fisher, and L. Hoff

AGS Department, Brookhaven National Laboratory, Upton, NY 11973-5000

## **Abstract**

The RHIC Yellow ring Fast Injection Kicker Power Supply System was successfully commissioned in January 1997 as part of the Sextant Test. Construction of an identical system for the Blue ring has been completed and will be commissioned during the 1999 RHIC start-up. Each of these Injection Kicker systems consists of four subsystems and a control system center. The four subsystems are located on a floating high voltage deck inside a protective caged room because of the unusual grounding of the structure. The kicker power supplies and auxiliary equipment jump to potentials as high as 10 kV during each pulse and must be inaccessible during operation. The RHIC Injection Kicker Power Supply System Control, Integration and Commissioning results are presented in this paper.

## **1 INTRODUCTION**

The RHIC injection kicker system modulators, including four Blumleins, auxiliary power supplies and controls, are secured inside a safety cage. The Blumleins are mounted on insulated stands and the high voltage power supplies, auxiliary power supplies and controls are located on an isolated floating deck. The deck equipment is powered through a set of six high voltage isolation transformers. The communication and control to the system are via fiber optic cables.

The design of the RHIC injection fast kicker power supply control architecture was driven by recent successful experience with the AGS G10 fast extraction kicker system. Also, concerns about maintaining a high level of kicker noise immunity for the computer control system made it necessary to use of optical fiber isolation for remote control to local control interfaces in both the AGS and Booster fast extraction kickers. The RHIC injection fast kicker power supply system also has the additional need to isolate the control system from the high voltage pulses present at the floating deck. The system is designed to allow full local control as well as remote computerised control functions.

The upper level remote controls are VME based systems. It includes an Allen-Bradley PLC 5/V40B for remote command and status readback interface, A V102 timing delay generator for power supply timing signals, and a VME waveform generator for power supply voltage reference and charging waveform readback.

Two 50 kV rated ALE 802L power supplies serve as charging supplies for each of two kicker systems, both having four modulators. The operating voltage is limited to 34 kV by the power supply voltage limiting function, and by the interface reference voltage clamping circuit, to protect magnet. The voltage charging of the Blumlein pulse forming line(PFL), is limited to less than 20 millisecond to avoid the PFL arcing. A backup trigger is required to discharge the PFL during the beam gap, in the event of the occurrence of an extra charging cycle.

## **2 SUBSYSTEM DESCRIPTION**

### **2.1 Command Control and Status Monitoring**

The Allen-Bradley PLC based command control and status-monitoring system uses Data Highway Plus network architecture. It consists of a PanelView 1400E industrial control terminal and a VME based PLC for a remote control interface. Both are located in control racks outside the high voltage cage area. An Allen-Bradley PLC 5 series processor is mounted in a control rack on the high voltage floating deck. The PanelView terminal is used for local command control and status monitoring. The VME PLC processor and PanelView terminal communicate to the floating deck PLC processor through a pair of Allen-Bradley PLC Fiber-Optic converter modules. This PLC network has been fully tested and experienced no communication interruptions due to use of fiber-optic communication or network structure.

The PLC ladder logic program is based on an AGS standardized kicker power supply format. The VME PLC is shared with other RHIC injection line power supply equipment. It communicates to the injection line equipment through Remote I/O network, and to the injection kicker system through DH+ network.

### **2.2 Charging Reference and Readback**

The high voltage power supply command reference signal is generated at the VME waveform generator. Its complementary unit "16-bit serial data link" performs analog to digital and digital to analog conversions. It communicates to kicker power supply interface unit with analog signals.

The fiber optic power supply interface pair I & II, as shown in Figure 1, were designed to interface with ALE 402 and 802 series power supplies. Their function is to

\* Work performed under the auspices of the U.S. Department of Energy

prevent the kicker and beam noise that might possibly be carried back from accelerator ring by high voltage cables, from interfering with other systems, especially the remote control equipment. The analog reference signal and charging waveform signal are converted by voltage to frequency converters that communicate through a fiber optic transmitter/receiver pair. They are converted back to analog signals by frequency to voltage converter units. The charging command signal is determined by "Start Charge" and "Stop Charge" triggers which, in turn, enable and inhibit the high voltage power supply output circuit. Its complementary bit controls a trigger delay generator and prohibits it from pulsing during high voltage power supply charging cycle. This reduces the chance of high voltage power supply converter damage and thyatron lock up. A local reference control function is included in both ends of the interface pair to allow local testing which is independent of the remote control network.

### 2.3 Timing and Trigger

The RF synchronised discharge trigger is distributed to the AGS extraction fast kickers and the RHIC injection fast kicker system via fiber links. Two DG535 pulse delay generators are used in each kicker system. An RF synchronised trigger initiates the first delay generator, which, in turn, triggers the second unit. The high current output pulses of the first delay generator drives a solid state high voltage pulse generator that drives the grid 1 of the CX1168-C thyatron. A second delay generator output pulse drives four "Hard Tube Trigger Generators", which deliver 5kV trigger pulses to the bias grid of the thyatron.

It was found during the 1997 Sextant test, that the commercial XD-7430/RD-7430 fiber optic transmitter/receiver pair was affected by local noise. It will be replaced by transmitter/receiver circuits designed at the AGS. Also, during the Sextant Test, the RF trigger was linked through the fiber optic transmitter/receiver channel of the backup trigger of the power supply interface units. The output pulse time jitter of the solid-state trigger generator and the hard tube trigger generator are within sub-nanosecond range similar to the scope rating. We control the fine delay adjustment of the delay generators via its GPIB interface.

### 2.4 Signal Monitoring

The terminating resistor current and thyatron current are monitored by fast four-channel digital scopes. Their waveform data will be retrieved via GPIB upon request.

### 2.5 Grounding Structure and Other Issues

The grounding structure of the RHIC injection kicker system is different from AGS kicker systems. It uses a separate ground in the RHIC ring. The Blumlein PFL

outer conductors are joined with the floating deck and associated equipment racks electrically. During pulsing they rise as high as 10kV. This configuration has introduced noise spikes through the local ground. This noise is especially noticeable when the four PFLs are pulsed in a non-synchronised.

The kicker magnets are driven by two 50 ohm lines in parallel and have a resistive termination. The load resistor value was reduced from 25 ohm to 20 ohm in order to mismatch the load thus lowering the magnet voltage and raising the current, [4, 5]. In this case, the reversed voltage and current imposed to thyatron might have to be considered carefully because that CX-1168C is not rated for reversed conduction. This reversing voltage and current might cause thyatron cathode arcing at high voltage, and affect auxiliary circuits. During the RHIC Sextant Test, all thyatron and electronic equipment had survived the PFL arcing, reverse voltage, grounding loop noise, etc. We will have to learn from future operations the reliability and survivability of the thyatrons as well as other equipment.

## 3 CONCLUSIONS

The RHIC injection kicker systems used as many AGS standard designs as possible. This was done to expedite construction, assembly and installation, as well as reduce the number of stocked operational spares.

The RHIC yellow ring fast injection kicker system was brought into operation in a few hours after completion of the system installation and check out. The performance of its kickers and controls was satisfactory as indicated in papers [1], [2], [3] and [6].

During the RHIC Dry Run, we tested the Yellow ring injection kicker system with local and remote control functions. The Blue ring injection kicker system has just been powered and is being checked out at this stage.

## 4 REFERENCES

- [1] S. Peggs, "RHIC Status", Proceeding IEEE 1997 Particle Accelerator Conference, pp. 56-60.
- [2] J. Wei, et. Al., "RHIC Sextant Test - Physics and Performance", Proceeding IEEE 1997 Particle Accelerator Conference, pp. 69-71.
- [3] F. Pilat, et. Al., "RHIC Sextant Test: Accelerator Systems and Performance", Proceeding IEEE 1997 Particle Accelerator Conference, pp. 98-100.
- [4] H. Hahn and A. Ratti, "Equivalent circuit Analysis of the RHIC Injection Kicker", Proceeding IEEE 1997 Particle Accelerator Conference, pp. 216-218.
- [5] H. Hahn and A. Ratti, "The Coupling Impedance of the RHIC Injection Kicker System", Proceeding IEEE 1997 Particle Accelerator Conference, pp. 1706-1708.
- [6] H. Hahn and A. Ratti, "The RHIC Injection Kicker", Proceeding IEEE 1997 Particle Accelerator Conference, pp. 213-215.

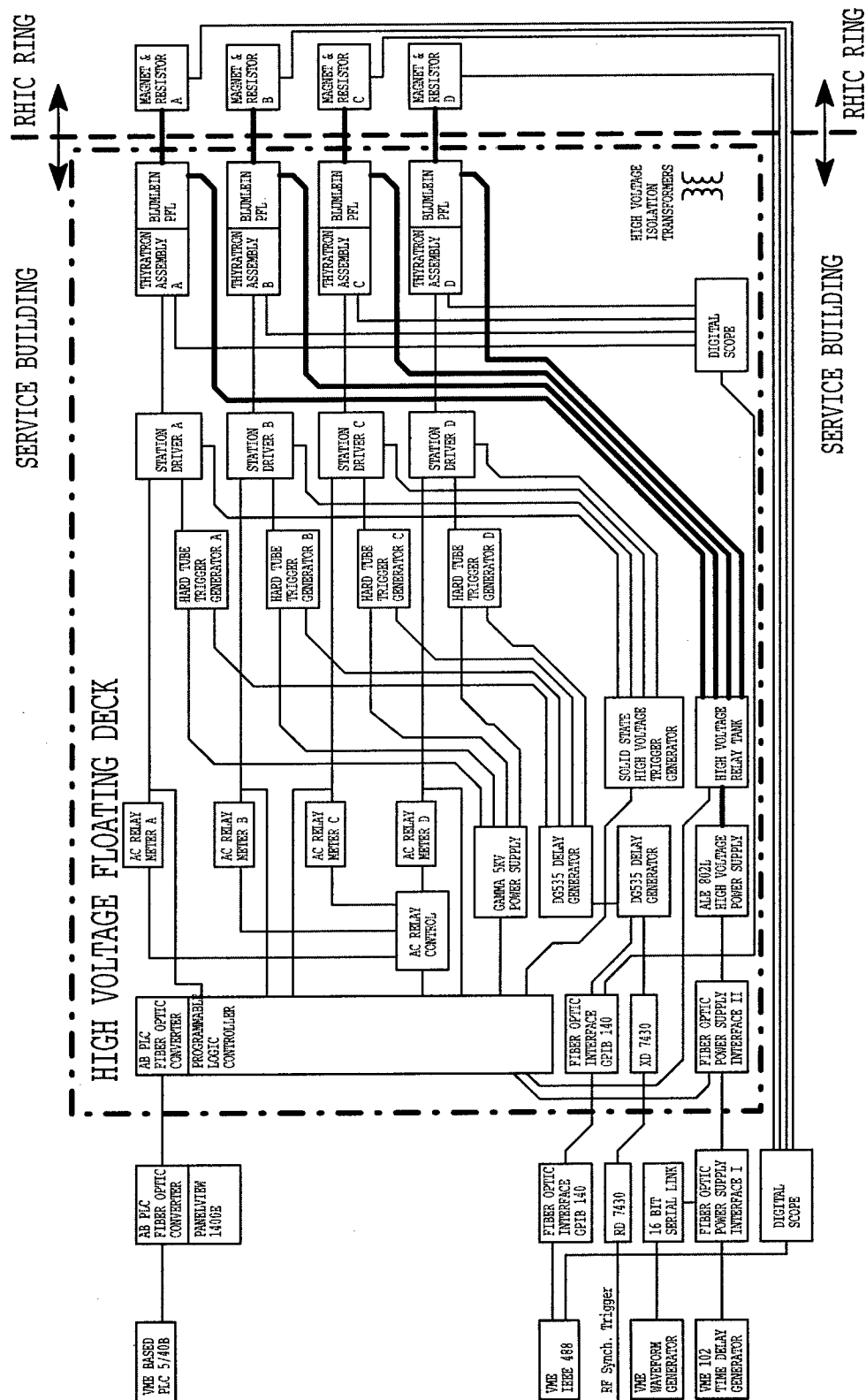


Figure 1. The simplified RHIC injection fast kicker control and auxiliary system block diagram.

## AN OVERVIEW OF THE FAST INJECTION-EXTRACTION KICKER SYSTEMS OF THE BROOKHAVEN AGS-BOOSTER COMPLEX\*

W. Zhang, R. Sanders, A. Soukas and J. Tuozzolo

AGS Department, Brookhaven National Laboratory, Upton, NY 11973-5000

### *Abstract*

The expansion of the Brookhaven accelerator facilities, and the on-going efforts to raise the AGS beam intensity, have been a driving force for the addition of new kickers and the upgrading of older ones to meet this challenge. All kicker power supply systems are running above their design specifications to provide wider operating ranges. The newly upgraded Booster fast extraction kicker power supply was commissioned in September 1997. Its compact high voltage modulator structure offers a pulse length almost three times longer than the preceding package within the confines of the same physical space. The AGS A5 injection kicker and the AGS G10 extraction kickers are also discussed. In order to expedite design, assembly, and commissioning, and to facilitate interchangeability, standardized modules have been adopted where possible. This paper gives an overview of the AGS and Booster fast injection and extraction kicker systems including their parameters, structure and status.

### 1 THE AGS FAST KICKER SYSTEMS OVERVIEW

Through a decade of research and development effort, we have built up a series of fast kicker power supply systems to serve the AGS accelerator complex. A unique feature of these fast kicker systems is that they are all lumped magnet type. The main advantage is the cost savings in materials and manpower. The budgets of the AGS kicker systems are typically a small fraction of the comparable transmission line type kicker systems. The reliability of our fast kicker power supply systems have been very high, especially when we take into account that all injection/extraction fast kicker modulators are located inside of the AGS and Booster rings and have been subjected to a high level of radiation over many years. However, continually increasing intensities of the particle beams, and in turn radiation levels, has made the maintenance of the high voltage modulators difficult. Hence, consideration is being given to the development of future fast kicker systems that are transmission line type, minimizing the amount of equipment in the accelerator ring enclosure.

The AGS Department has undertaken, under restrained budget conditions, an expansion of its high energy/nuclear energy facilities. Thus, most of our electronic equipment has been designed with strong considerations to economy while trying not to sacrifice performance. We try, whenever possible, to use low-cost components and make effective use of innovative industrial developments in the integration of our kicker systems. In some cases we have spurred on these industrial developments to enhance our technical advances.

### 2 SYSTEMS SUMMARY

The AGS accelerator complex has a number of injection and extraction kickers. With the consideration of building systems in the most expeditious manner, interchangeability of equipment and components, and similarity of operation, standardization is stressed. The Pulsed Power Group and other AGS systems groups all use Allen-Bradley Programmable Logic Controller (PLC) based systems for control of command and status in new and upgraded equipment. Stanford Research DG535 delay generators are used to time, synchronize and trigger charging power supplies and high level thyatron trigger pulse generators. Finally, standard in-house designs are used for auxiliary power supplies and thyatron trigger pulse generators. The high voltage charging power supplies are usually located in the nearby ring service buildings. The charging cable feeds into the ring use a commercially available 3-conductor, 15 kV, ac cable and terminations.

Reliability, simplification, costs, compatibility with other systems, and safety is paramount factors in all new system designs. Because the AGS accelerators are synchronized to the power line, unregulated power supplies are used in trigger circuits and thyatron auxiliary power supplies without the risk of unwanted jitter. Where possible, reconstituted mica dielectric instead of oil filled capacitors are used in high radiation areas. High voltage circuitry is high potential tested to levels as high as twice the anticipated operating level where possible. Careful system grounding (star configuration) is used for both safety and noise reduction (as much as 20db lower than previous systems).

\* Work performed under the auspices of the U.S. Department of Energy

The magnets of the existing AGS kickers are single turn lumped inductance type ferrite magnet. They are inside of vacuum chambers. The beam image current related phenomena have been observed on all kicker power supply systems.

## 2.1 The Upgraded AGS Booster Extraction Fast Kicker System

The Booster fast extraction kicker is located in the F3 section of the accelerator. It consists of four full aperture picture frame lumped ferrite magnets with their adjacent modulators, and remotely located power supplies, controls, timing and other system equipment.

This system underwent a major upgrade in 1997. System specifications were changed. Kicker strength was raised a few percent for protons. The PFN was modified to provide a pulse length of at least 1800 Ns for a full-turn extraction capability for heavy ions. The previous maximum pulse length was 800 Ns.

A simplified schematic diagram is shown in Figure 1.

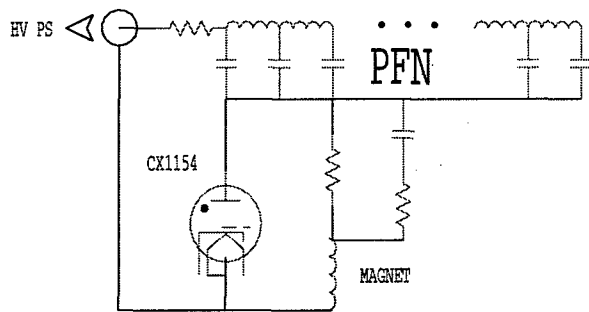


Figure 1. The Booster Extraction Fast Kicker

The equipment changes were extensive but the available space in the accelerator was limited to the mechanical package outline of the previous modulators. Because of volume constraints, it was necessary to simplify the circuits and to select components with tighter margins. The need for a higher stored energy would have required a larger volume for the PFN. The previous PFN capacitors were rated 50 kV with 100% reversal. The new capacitors were rated 40 kV with 50% reversal thus giving a comparable volume for a longer pulse length.

In anticipation of future dust build-up and moisture, high voltage surfaces were properly rounded and smooth. Careful thought was given to component placement, creepage length and spacing. Each modulator was hi-potted to 60 kV before installation. The design operating voltage was 28.6 kV. The floating common deck was hi-potted to 50 kV because of transient voltages.

These PFN's are now operating successfully above their design specifications. The PFN voltage has been raised to 35 kV and the magnet current has increased accordingly. It should be noted that with seven pulses per

AGS cycle, they are operating at 200% of their original power rating. Table 1 lists the system parameters.

Table 1: Booster F3 Extraction Fast Kicker Parameters

	Proton	Heavy Ion
Rigidity	<b>(9.5 T-m)</b>	7.7 T-m
Deflection Angle	5.0 mrad	3.8 mrad
Magnetic Field Strength	<b>(206 Gauss)</b>	127.44 Gauss
Pulse Current	<b>(1095 A)</b>	683 A
Pulse Rise Time (3% - 97%)	≤ 140 nS	≤ 140 nS
Pulse Flat Top	<b>(2250 nS)</b>	<b>(2250 nS)</b>
Flat top Ripple	≤ ± 3 %	≤ ± 2 %
PFN Voltage	28.30 kV <b>(35 kV)</b>	20.49 kV
Maximum Number of Pulses per AGS Cycle (2.0 second or longer)	<b>(7)</b>	5
Pulse Repetition Rate inside Burst	≤ 7.5 Hz	≤ 7.5 Hz

Bold letter parameters indicate actual operating values.

## 2.2 The AGS Injection Fast Kicker System

The AGS injection fast kicker is located at the A5 section of the ring. It consists of three full aperture picture frame lumped magnets and their associated PFN modulators, similar to the aforementioned F3 system. It features an innovative tail-biting circuit design, which has proved to be successful and reliable. This systems has been operating for almost eight years.

In 1995, the modulator circuit was modified. The original design used a double ended thyatron, which was replaced by a single ended type. The unidirectional conducting property of single ended thyatron blocks reverse current reflection from the PFN and inductive load. This current is forced to flow through a tail-biting circuit that is parallel with the magnet. This circuit has helped to improve injection stability. Table 2 summarises the system parameters.

Table 2: AGS A5 Injection Fast Kicker Parameters

	Proton	Heavy Ion
Rigidity	<b>(8.1 T-m)</b>	<b>(8.1 T-m)</b>
Deflection Angle	2.85 mrad	2.85 mrad
Magnetic Field Strength	<b>(242 Gauss)</b>	<b>(242 Gauss)</b>
Pulse Current	<b>(1100 A)</b>	<b>(1100 A)</b>
Pulse Rise Time (3% - 97%)	≤ 140 nS	≤ 160 nS
Pulse Flat Top Length	360 nS	> 1100 nS

Pulse Fall Time	(~ 140 nS)	~ 500 nS
Flat top Ripple	$\leq \pm 3 \%$	$\leq \pm 2 \%$
PFN Voltage	<b>(32.5 kV)</b>	<b>(32.5 kV)</b>
Maximum Number of Pulses per AGS Cycle	<b>(7)</b>	5
Pulse Repetition Rate inside Burst	$\leq 7.5 \text{ Hz}$	$\leq 7.5 \text{ Hz}$

Bold letter parameters indicate actual operating values.

Figure 2 is a simplified schematic diagram of the AGS injection fast kicker modulator.

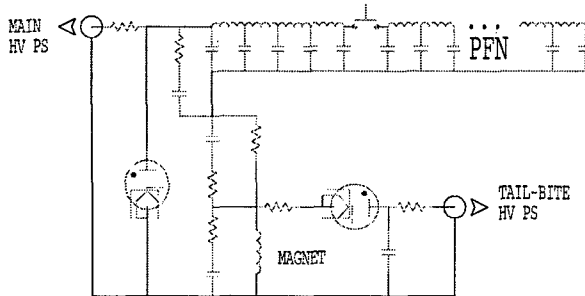


Figure 2. The AGS Injection Fast Kicker

### 2.3 The AGS Extraction Fast Kicker System

The G10 fast extraction kicker was another recent addition to the AGS. It was installed in 1995 and has been running successfully. It serves the AGS fast extract beam (FEB) program, the g-2 experiment and RHIC. These kickers allow extraction of a series of individual beam bunches (the number depends on the AGS harmonic number) at the peak of the magnet cycle. FEB differs from slow extracted beam (SEB) which smears the bunches and extracts it more slowly.

The system concept is similar to others in that it uses a multiple of magnets and modulators. It uses small aperture C-type ferrite magnets. As with the other kickers, each magnet is driven by a separate modulator.

Table 3 is a tabulation of the system parameters. Figure 3 is a simplified schematic diagram.

Table 3: AGS G10 Extraction Fast Kicker Parameters

	<b>RHIC</b>	<b>G-2</b>
Extraction Momentum	30 GeV	(24 – 30) GeV
Deflection Angle	2.0 mrad	2.0 mrad
Magnetic Field Strength	830 Gauss <b>(955 Gauss)</b>	830 Gauss <b>(955 Gauss)</b>
Pulse Current	1650 A <b>(1900A)</b>	1650 A <b>(1900A)</b>
Pulse Waveform	Half Sine	Half Sine
Pulse Rise Time	$\leq 180 \text{ nS}$	$\leq 180 \text{ nS}$

Pulse Flat Top	$\geq 20 \text{ nS}$ <b>(40nS)</b>	$\geq 40 \text{ nS}$ <b>(&gt;100nS)</b>
Flat top Ripple	$\leq \pm 1 \%$	$\leq \pm 5 \%$
Stability and Reproducibility	1 % <b>(<math>\pm 0.12 \%</math>)</b>	1 % <b>(<math>\pm 0.12 \%</math>)</b>
Pulse Base Width	380 nS	380 nS
Capacitor Voltage	28.7 kV <b>(35 kV)</b>	28.7 kV <b>(35 kV)</b>
Max. Number of Pulses per AGS Cycle	12	12
Pulse Repetition Rate inside Burst	$\leq 30 \text{ Hz}$	$\leq 30 \text{ Hz}$

Bold letter parameters indicate actual operating values..

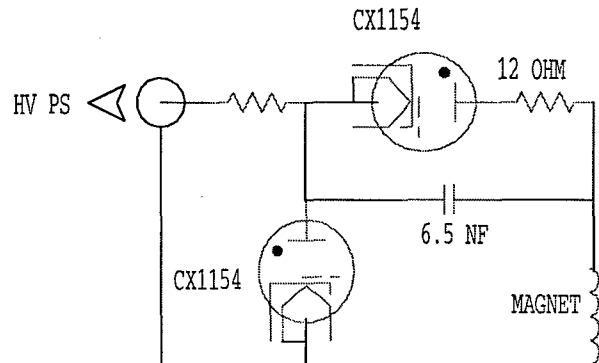


Figure 3. The AGS G10 Extraction Fast Kicker

## 3 ACKNOWLEDGEMENTS

We would like to thank Mr. J. Addressi, Mr. P. Benjamin, Mr. C. Eld, Mr. K. Hartmann, Mr. S. Perlstein, Mr. D. Warburton, and Mr. R. Zapasek of pulsed power group for their technical support.

## 4 REFERENCES

- [1] M. Tanaka, Y.Y. Lee, "The AGS-Booster Complex for g-2 experiment and RHIC injection", Proceeding, IEEE Particle Accelerator Conference, 1993.
- [2] W. Zhang, J. Bunicii, A.V. Soukas, S. Y. Zhang, "The Booster to AGS Beam Transfer Fast Kicker Systems", Conference Record, IEEE 20th Power Modulator Symposium, 1992.
- [3] W. Zhang, J. Bunicii, W.W. Frey, A.V. Soukas, S. Y. Zhang, "The Booster-to-AGS Beam Transfer Fast Kicker Modulators", Proceeding, IEEE Particle Accelerator Conference, 1991.
- [4] M. Tanaka, Y.Y. Lee, "The AGS new fast extraction system for g-2 experiment and RHIC injection", Proceeding, IEEE Particle Accelerator Conference, 1991.
- [5] W. Zhang, W.W. Frey, A.V. Soukas, S. Y. Zhang, J. Bunicii, "Test Modulator of AGS Injection Fast Kicker", Conference Record, IEEE 19th Power Modulator Symposium, 1990.

# THE BOOSTER APPLICATION FACILITY (BAF) BEAM TRANSPORT LINE OF THE BNL-AGS BOOSTER\*

N. Tsoupas<sup>♣</sup>, K.A. Brown, J. R. Cullen, Y.Y. Lee, A. J. Mc Nerney, P.H. Pile, T. Roser,  
A. Soukas, and J.E. Tuozzolo  
Brookhaven National Laboratory, Upton, NY 11973 USA

## Abstract

An experimental facility<sup>1</sup>, to irradiate materials with energetic ion beams, has been proposed to be built at the Brookhaven National Laboratory. The BAF facility will mainly consist of the AGS-Booster slow extraction, of a beam transport line, and a target room. The beam transport line will transport the slow extracted beam of the AGS-Booster to the target location for the irradiation of various materials and specimens. A variety of ion beams like (p, <sup>28</sup>Si, <sup>56</sup>Fe, <sup>63</sup>Cu, <sup>197</sup>Au) in the energy range of 0.04 to 3.07 GeV/nucleon will be transported by the BAF line which is designed to provide variable beam spot sizes on the BAF target with sizes varying from 2.0 cm to 20.0 cm in diameter. The beam spot sizes will include 95% of the beam intensity with the beam distributed normally (Gaussian) on the target area. It is also possible by introducing magnetic octupoles at specified locations along the beam transport line, to modify the distribution on the BAF target and provide well confined beams with rectangular cross section and with uniform distribution on the target[1].

## 1 INTRODUCTION

The function of the AGS Booster synchrotron is to accelerate a variety of ion species (protons to Au) to a maximum rigidity of  $B\rho=7.5$  T.m for protons to 17.5 T.m for Au ions and then inject the accelerated bunches into the AGS synchrotron which further accelerates the beam bunches to a rigidity of  $B\rho=100$  T.m (proton momentum equivalent  $p=29.9$  GeV/c). Subsequently the accelerated beam will be injected into the Relativistic Heavy Ion Collider (RHIC) which will accelerate and store the bunches to the desired energy for the beam-beam experiments. Since the storage cycle in the RHIC synchrotron may last many hours, all the pre-accelerators will be available during this time to provide high energy beams to other facilities at BNL. The proposed BAF facility shown in Figure 1 is one which will operate during the storage cycle of RHIC synchrotron. The construction of the BAF facility is scheduled for completion commissioning and operation by the year 2001.

\* Work supported by the U.S. Department of Energy  
♣ email tsoupas@bnl.gov

<sup>1</sup> In this document, this facility will be referred to as the Booster Applications Facility (BAF).

## 2 THE (BAF) BEAM TRANSPORT LINE

The BAF beam transport line will consist of a set of magnetic elements (Dipoles, Quadrupoles, Octupoles, and orbit correction Dipoles) to be placed in the BAF tunnel (Fig.1). These elements will transport the slow extracted ion beam[2] from the AGS-Booster and focus it on the BAF target, which will be located 100 m downstream from the slow-beam extraction point of the AGS Booster.

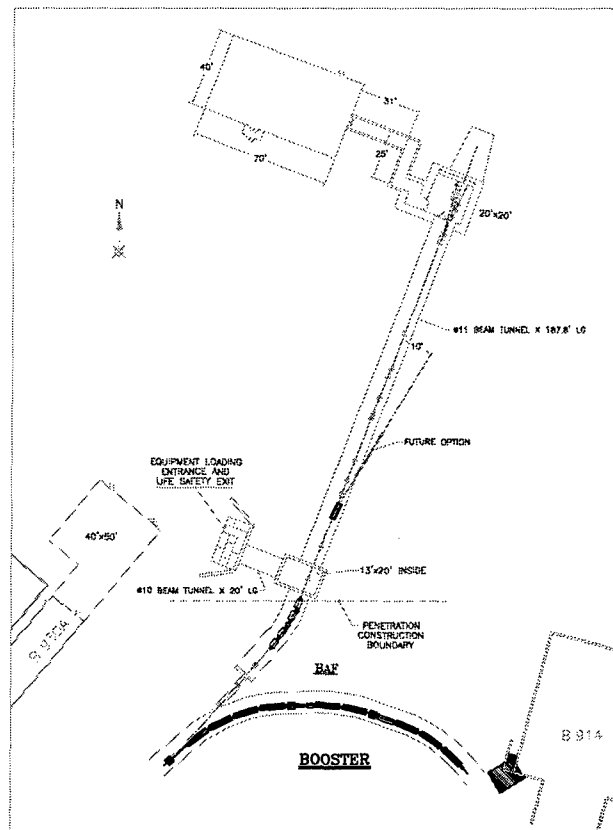


Figure 1: A schematic diagram of the BAF facility with a section of the AGS Booster shown at the bottom of the figure.

The following magnetic elements are used in the beam transport optics of the BAF transport line in the sequence they appear in the line.

A septum magnet, three quadrupoles, two dipoles ( $5^\circ$  bend each), a quadrupole, two dipoles ( $5^\circ$  bend each), five quadrupoles, an octupole two quadrupoles, an octupole and two quadrupoles. In total there will be five dipoles thirteen quadrupoles and two octupoles. All quads are 40 cm long and have an aperture of 10 cm except the last quadrupole which is 50 cm long and has an aperture of 15 cm. Each of the octupoles is 50 cm long with an aperture of 10 cm. The septum dipole is 2.3 m long with a gap of 2.1 cm. Each of the  $5^\circ$  dipoles is 1.25 m long with a gap of 8.3 cm.

### 3 THE BEAM OPTICS OF (BAF)

The beam optics of the BAF transport line has been designed to satisfy the following constraints:

- Transport ion beams with maximum rigidity<sup>2</sup>  
 $B\rho=13$  Tm.
- Transport ion beams with maximum emittances of  $\epsilon_x=3\pi(\text{mm})(\text{mrad})$  and  $\epsilon_y=15\pi(\text{mm})(\text{mrad})$  in the horizontal and vertical plane respectively<sup>3</sup>.
- Generate variable beam sizes at the target, with low and upper limits of 2 cm to 20 cm in diameter. These beam spot sizes will include 95% of the beam.
- The beam parameters at two locations along the beam line will satisfy certain conditions[1]. These conditions will allow the insertion of octupole magnetic elements which, when turned on, will provide beam spots with rectangular cross section at the target. The beam will be well confined and uniformly distributed over these rectangular areas.

The beam parameters at the beginning of the BAF transport line (see TABLE I) were calculated by modeling the Booster synchrotron[2] using the MAD[3] computer code. In this model the slow extracted beam process was simulated by introducing sextupoles in the Booster lattice, which generated a third order resonance in the beam.

Table I: Beam Parameters at Entrance of BAF

	$\beta[\text{m}]$	$\alpha$	$\eta[\text{m}]$	$\eta'$
Hor(x)	10.0	1.87	30.0	-3.4
Ver(y)	4.4	-0.67	0.0	0.0

<sup>2</sup> A stripping foil located at the entrance of the BAF line will reduce the rigidity of many charged ions species.

<sup>3</sup> The low value of the horizontal emittance is a result of the slow beam extraction process and includes the increase of the emittance when the beam goes through a stripping foil located at the beginning of the BAF transport line, in front of the septum magnet.

The transport system of the BAF transport line, which satisfies the conditions (a) to (d) above, was designed by using the computer codes MAD[3] or TRANSPORT[4]. A particular horizontal/vertical beam envelope along the BAF transport line is shown in Fig. 2. This beam envelope contains 95% of the beam intensity, corresponds to the emittances and beam parameters shown in Table I and a beam momentum spread  $\delta p/p = \pm 0.05\%$ . The beam envelope shown in Fig. 2 corresponds to the lowest momentum that will be extracted from the Booster and thus represents the maximum beam envelope that the BAF line will transport.

The beam spot size on the target can be varied, within the low and upper limits mentioned above(c), by tuning the strength of the last two quadrupoles of the BAF line.

### 4 THIRD ORDER OPTICS

The first order optics of the BAF transport line, discussed in the previous section, has been designed to allow the placement of two octupoles O1 and O2 (see Fig. 2.) at specified locations along the transport line. The beam parameters, at these locations, as calculated from the first order beam optics must satisfy certain conditions[1] for the octupoles to create the desired rectangular and uniform beam spot on the target.

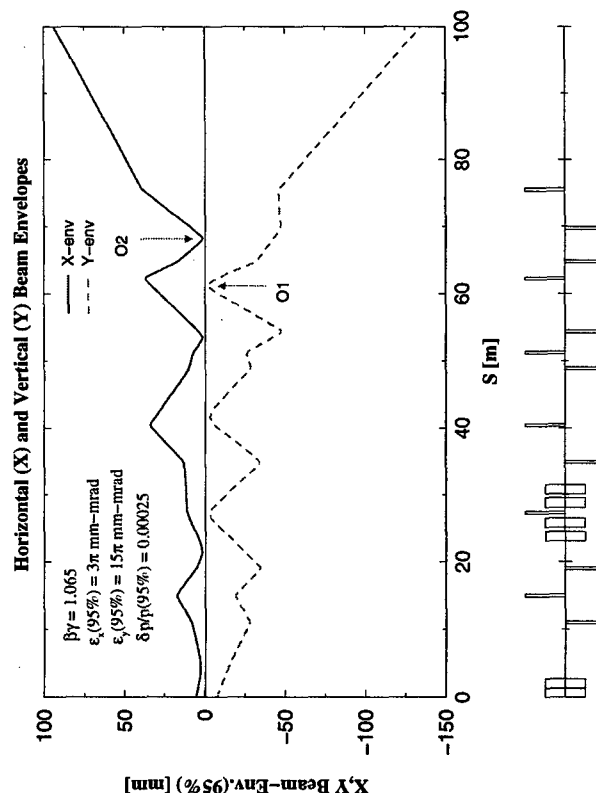


Figure 2: Horizontal and vertical half beam envelopes as calculated using first order beam optics. The beam envelopes contains 95% of the beam



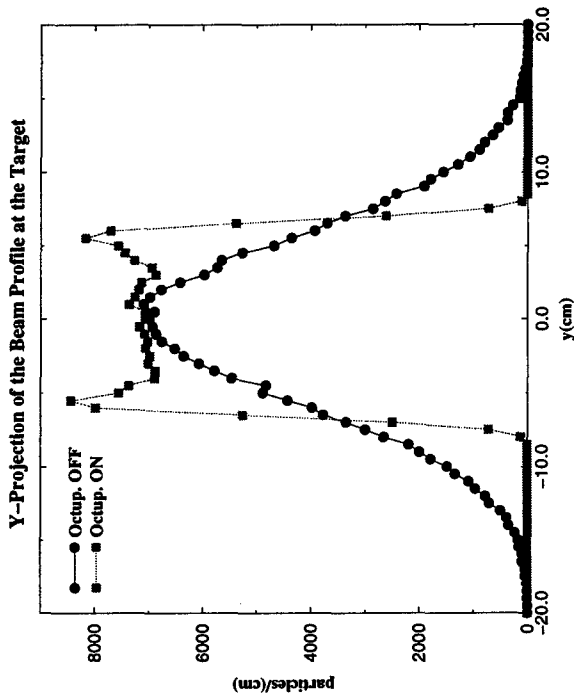


Figure 3a: Horizontal projection of the beam profile on target with the octupole "off" and "on".

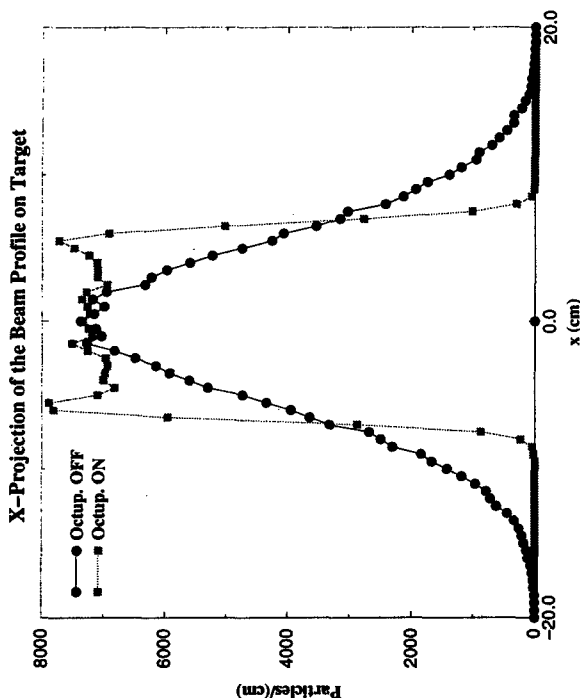


Figure 3b: Vertical projection of the beam profile on target with the octupole "off" and "on".

The third order calculations[1] are required to include the effect of the octupoles on the beam and therefore predict the beam size and its uniformity at the target. For a particular strength of each of the octupoles and the last two quadrupoles, a rectangular beam profile is generated at the target. Within this rectangle all beam intensity is confined and distributed rather uniformly over the target. By varying the strength of the above four elements, any rectangular beam spot within the dimensions of  $5\text{cm} < x < 20\text{cm}$  and  $5\text{cm} < y < 20\text{cm}$  can be generated.

A projection of the horizontal and vertical beam profiles at the target location is shown in Fig. 3a and 3b respectively. Each figure shows the beam profile with the octupoles "off" and the octupoles "on" for comparison purposes.

## 5 REMARKS

A new beam optics for the BAF transport line is being investigated[5] to replace the one presented above. This new beam optics will utilize fewer quadrupoles and dipoles with larger apertures but will retain all the beam requirements discussed earlier.

In the slow extraction process, the beam momentum may vary by 1% during the cycle of the Booster main magnet, with the beam of lower momentum to be extracted at the end of the extraction cycle. This variation of the beam momentum during the extraction cycle of the Booster can be the cause of beam-spot movement at the BAF target.

This beam-spot movement on target can be eliminated by either ramping down the strength of both, the septum magnet and the  $20^\circ$  dipole or by making achromatic the section of the beam line starting from the septum and finishing at the exit of the  $20^\circ$  bend.

## 6 REFERENCES

- [1] N. Tsoupas, M. S. Zucker, T. E. Ward, and C. L. Snead "Uniform Particle Beam Distributions Produced by Octupole Focusing" Nuclear Science and Engineering 126, 71-79 (1997)
- [2] K. Brown et. al. "Design of a Resonant Extraction System for the AGS Booster" These Proceedings.
- [3] Hans Grote, and F. Christoph Iselin "The MAD Program" CERN/SL/90-13(AP)
- [4] D.C. Carey, K.L. Brown, and F. Rothacker "Third-Order Transport Computer Program for Designing Charged Particle Beam Transport System" SLAC-R-95-462
- [5] P. File, BNL Private communication

# Design of a Resonant Extraction System for the AGS Booster \*

K. Brown<sup>†</sup>, J. Cullen, J.W. Glenn, Y.Y. Lee, A. McNerney, J. Niederer, T. Roser, A. Soukas, J. Tuozzolo, N. Tsoupas, AGS Dept., BNL, Upton, NY

## Abstract

The Booster Application Facility (BAF) will employ heavy ion beams of many different ion species and at beam energies ranging from 0.04 to 3.07 GeV/nucleon. Resonant extraction is required in order to deliver a continuous stream of particles. In this report we describe the beam requirements and the system design. The basic design is a third integer resonant extraction process which employs a single thin magnetic septum and a thick septum ejector magnet. The expected extraction efficiency is about 85 %, based on the thin septum thickness and the predicted step size of the resonant beam at the septum. This is more than sufficient for the low intensity low energy heavy ion beams needed for the BAF. In this report we will present a detailed discussion of the design of the various elements and a discussion of the detailed modeling of resonant extraction from the AGS Booster. The extraction process was modeled using a BNL version of MAD which allowed us to interactively observe detailed particle tracking of the process. This was a key tool to have in hand which permitted us to pose and answer various questions in a very short period of time.

## 1 INTRODUCTION

The AGS Booster has operated since 1991 as an injector of protons and heavy ions into the AGS. The operating parameters are summarized in table 1. The design of the resonant extraction system from the Booster for BAF requires some rearrangement of existing apparatus in the Booster. In the Booster D6 straight section (2.6 m in length), we will be removing the Booster Beam dump and a wall current monitor. These will be relocated in the Booster B6 straight section. The D6 straight section will then contain a new thick septum magnet, a stripping foil and flag (for beam profiles) mechanism. In addition we will modify the quarter cell vacuum chambers. In the D3 straight section we will remove the current beam dump kicker magnet (which will not be relocated), move an ionization profile monitor instrument to the upstream end of the section, and install a new thin septum magnet. The D4 half cell will be modified for a larger aperture quadrupole vacuum chamber. In addition four horizontal sextupoles will have new power supplies so that they may be used to create a sextupole resonance, as well as track the normal chromaticity system. Finally, the existing backleg windings in the Booster Dipole magnets

D1, D2, D7 and D8 will be connected to provide local orbit bump control at D3 and D6. The D3 thin septum magnet will be movable over a small range, to allow maximizing the extraction efficiency for a given resonance step size.

Table 1: AGS Booster Parameters

Parameter	Value
Circumference	201.78 (1/4 AGS) m
Ave. Radius	32.114 m
Magnetic Bend R	13.75099 m
Lattice Type	Separated Function, FODO
No. Superperiods	6
No. of Cells	24
Betatron Tunes, X, Y	4.82, 4.83
Vacuum Chamber	70 x 152 mm Dipoles 152 mm (circular) Quads
Max. Rigidity	17 Tm
Injection Rigidity	2.2 Tm (200 MeV protons) 0.9 Tm (1 MeV/nuc Au(32+))
Acceleration Rate	8.9 T/s up to 7.5 Tm (7.5 Hz) 1 T/s up to 17 Tm (0.7 Hz)

The maximum kinetic energy of the extracted beams corresponds to the maximum Booster rigidity of 17 Tm for the heavier ions, which are fully stripped at the stripping foil located at the entrance of the D6 septum magnet, and 13 Tm for lighter ions. The maximum rigidity of the BAF transport line is 13 Tm. Lower energies are possible at lower intensity. Intensities as low as  $10^6$  ions per pulse will be available to experimenters through collimation just after the D6 septum magnet. Table 1 summarizes the operating parameters for Booster BAF operation.

Table 2: SEB Operating Parameters for Typical Ions

Ion	Charge in Booster	K.E. Range (GeV/nuc.)	Est. Inten. [ $10^9$ Ions/pulse]
p	1	0.73...3.07	100
28 Si	14	0.09...1.23	4
56 Fe	21	0.10...1.10	0.4
63 Cu	22	0.10...1.04	1
197 Au	32	0.04...0.30	2

## 2 BOOSTER RESONANT EXTRACTION

The main challenge in our design is to have a flexible extraction system, capable of extracting ions uniformly for a duration of several hundred to one thousand milliseconds, without significant impact on the existing subsys-

\* Work supported by the U.S. Department of Energy.

<sup>†</sup> Email: kbrown@bnl.gov

tems, including the single turn fast extraction system for beam transfer to the AGS.

The Booster consists of six superperiods and each superperiod has two long open or missing dipole straight sections. The machine will be modified in order to place the extraction magnet at D6. This permits the construction of the experimental area in one of the few available spaces outside the Booster.

Slow extraction is achieved by the controlled excitation of a non-linear betatron third integer resonance. A slow spill is controlled by steering the beam slowly so that particles with different momenta move progressively onto the resonance. Third integer resonant extraction has been used at the AGS for many years for the high energy and heavy ion physics programs, as well as for the radiobiology program. The AGS system is efficient and reliable with a typical extraction efficiency over 96 %. [1, 2]

The Booster extraction system will make use of the horizontal third integer resonance at the tune of  $Q_h = 13/3$ . This tune is significantly lower than the nominal Booster tune, as shown in table 1. This is required because the Booster tune quadrupoles do not have enough strength to maintain the horizontal betatron tune at the value of  $14/3$  at the highest energies. To reach even  $13/3$  at 12 Tm a new power supply for the tune quadrupoles is needed. The required crossing of the half integer resonance at  $Q_h = 9/2$  during acceleration is accomplished easily with the fast slew rate available from the tune quadrupole systems, which has been experimentally verified. [3]

A third integer resonance is excited by the  $13^{th}$  harmonic of two sextupole pairs located at C8, F8, B4, and E4. We plan to utilize four of the existing 24 horizontal lattice sextupoles as drive sextupoles. The maximum field of the existing sextupoles is sufficient for their use as drive sextupoles. At the resonance, a stable triangular region of the horizontal phase space is defined within three linear separatrices and the area and orientation of this region can be controlled by the drive sextupoles. In the vicinity of the resonance there is a small range of tunes over which the separatrix degenerates into three narrow legs which have a phase advance of  $2/3 \pi$  radians with respect to each other. A particle leaving the stable area within the separatrix moves out along one of these legs as it spirals out of the machine. This particle will move from one leg to the next every turn, each revolution stepping further out along the separatrix legs. (see figure 1).

The extraction efficiency depends on the thickness of the first septum as compared to the growth of the resonant betatron amplitude in the final few turns before extraction. So the first septum is made as thin as possible and is aligned precisely so that the maximum growth per turn can be obtained for the available aperture and for the given beam emittance. The step size of a particle at the septum depends on its momentum, betatron amplitude and its proximity to the resonant tune value as well as the drive sextupole strength.

The thin septum is located in the D3 straight section of

the Booster. The phase advance to the D6 thick septum is about 71 degrees. An angular kick from the thin septum translates into a large displacement at D6. This can be seen more clearly in figures 1 and 2, which show the phase space separatrices and the extracted beam trajectories at the thin septum and the thick septum.

The thin septum has an effective thickness of 0.76 mm and maximum kick of 3 mrad, for a length of 1 m. The thick septum has an effective thickness of 15.2 mm, is operated in a dc mode, and gives a kick of 155 mrad, for a length of 2.5 m. The drive sextupoles have a maximum normalized strength of  $K_s = B_2 \cdot L / B\rho = 0.29 m^{-2}$  where  $L = 0.1 m$ .

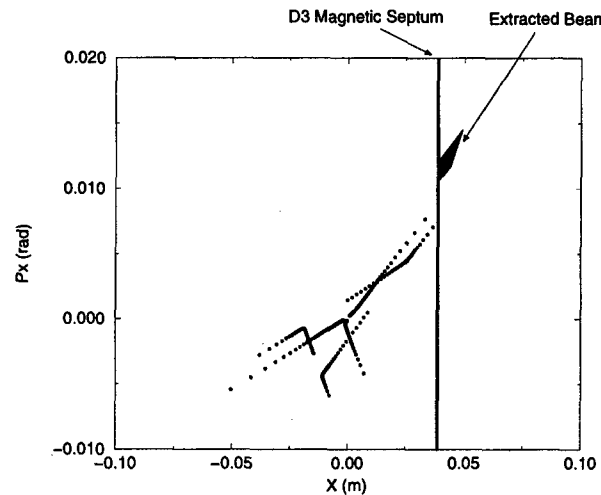


Figure 1: Simulation of resonant beam at the D3 thin septum

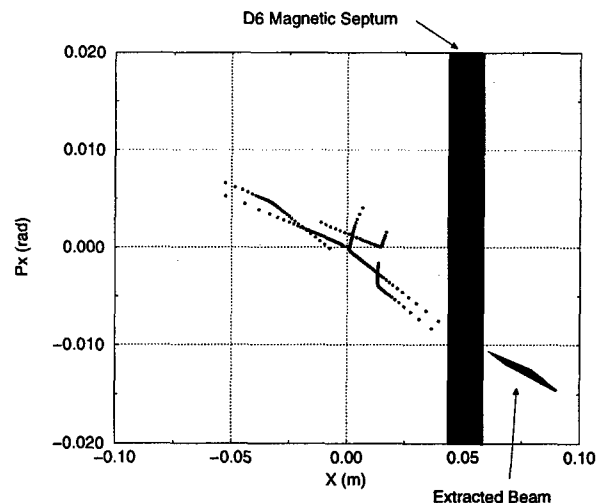


Figure 2: Simulation of resonant beam at the D6 thick septum

Figure 1 shows the phase space growth at the thin magnetic septum with the four drive sextupoles energized. The tune is set to  $Q_h = 13/3$  for the particle on the closed orbit, and slightly higher for the particle with emittance of  $15 \pi$  mm-mrad. The two pairs of sextupoles are powered with opposite sign at a strength of  $0.25 m^{-2}$ . The spiral pitch is

slightly over 4.0 mm, which would give an extraction efficiency of 85 %. Figure 2 similarly shows the phase space at D6, the location of the thick septum. These simulations were done using a BNL version of MAD, which incorporates interactive graphics. Using the single particle tracking facilities and the interactive graphics we were able to very quickly study and test different extraction schemes.

### 3 PARTICLE DISTRIBUTIONS

The experimenters that will be using the BAF facilities require highly uniform beam distributions over a 10 cm diameter beam. In order to accomplish this the beam line will incorporate octupole magnets to create a rectangular distribution at the target.[4] In order to model the behavior of the octupoles we needed to clearly understand the phase space of the extracted beam.

The vertical emittance of the extracted beam is unchanged by the extraction process. To first order, the horizontal emittance is zero, as the phase space area of the extracted beam is completely determined by the momentum spread. A significant amount of dispersion is generated by the extraction process. The extracted beam passes through a stripping foil before entering the D6 thick septum magnet. The thickness of this foil can be adjusted to not only completely strip the ions, but also to provide a large enough horizontal emittance to allow for a uniform spot at the target area. From simulations we determined the beam parameters as shown in table 3. The horizontal emittance is given as  $3 \pi$  mm mrad, which would require a 0.08 mm thick copper stripping foil for a 1 GeV/nucleon Fe beam.

Table 3: Extracted Beam Characteristics

	Horizontal	Vertical
Emittance	$3 \pi$ mm mrad	$15 \pi$ mm mrad
Beta	10.0 m	4.4 m
Alpha	1.87	-0.67
$D_x$	30 m	0 m
$D'_x$	-3.4	0.0

To further understand the behavior of the beam down the BAF line, we performed simulations of 100000 particles, to study beam losses and the uniformity of the beam on target. To do tracking simulations with large numbers of particles is not easily done with a modeling program such as MAD, so we developed a simple program to track many particles, in order to provide a set of input particles for the beam line simulations, and to get a picture of the beam distributions of the beam entering the septum magnets. Figure 3 shows the beam distributions of the extracted beam in the D3 and D6 septums, before any stripping foils. Even before any stripping the beam distributions appear to be Gaussian, even though initially the distribution is rectangular. This is an important result, since the octupoles are most effective at creating a uniform beam distribution when the input beam is Gaussian. [4]

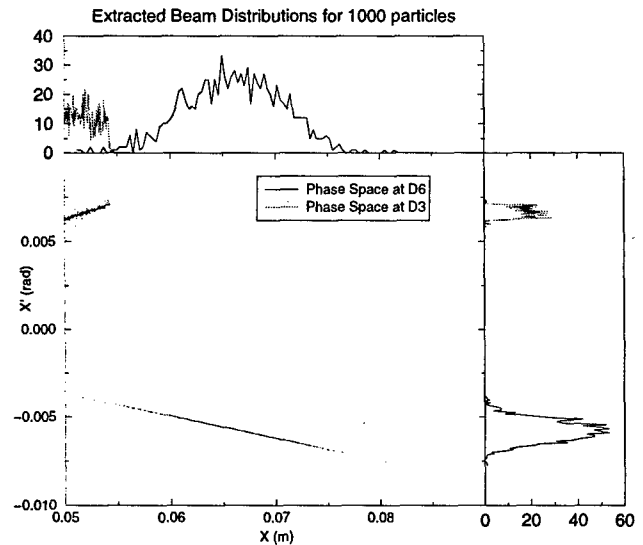


Figure 3: Beam Distributions of Extracted Beam

### 4 SPILL STRUCTURE

To achieve a constant stable output beam intensity, sophisticated control systems are needed in combination with low-ripple power supplies for the main magnets and the extraction magnets. A closed-loop servo will be required which is gated on at the beginning of the flat-top. A measurement of the beam spill is compared to a reference signal and generates a correction output signal that controls the Booster main magnet current on flat-top and the low frequency part of the spill (to create a constant current beam). The high frequency control is achieved by reducing the ripple of the power supplies. We are also looking into a high frequency feedback to the tune quadrupoles, which has been used successfully at CERN and BNL. In addition we could incorporate a high frequency RF cavity to smooth out 60 Hz harmonics, again a technique that has been successfully used at both CERN and BNL.

### 5 STATUS

As of the time of this meeting the BAF project has been approved and is funded by the National Aeronautics and Space Administration. Construction has not yet begun, primarily due to the operations schedule for the Booster and AGS, but will begin this summer. The first commissioning of the facility will occur in mid-2001.

### 6 REFERENCES

- [1] H. Weisberg and J.W. Glenn, "Exploitation of Nonlinear Growth of Betatron Oscillations to Obtain Efficient Slow Extraction at the AGS", Nucl. Inst. & Methods 169, 319(1980).
- [2] L.Ahrens et al, "AGS Resonant Extraction with High Intensity Beams", THP140 in these proceedings.
- [3] AGS Internal studies report.
- [4] N.Tsoupas et al, "The Booster Applications Facility (BAF) Beam Transfer Line of BNL-AGS Booster", these proceedings.

# THE MUON SOURCE WITH SMALL PHASE-SPACE PRODUCED FROM THE COMPRESSED TARGET FOR MUON-MUON COLLIDER

Hiroshi Takahashi and Jun Zhang

Brookhaven National Laboratory, Upton, NY 11973

## Abstract

For the muon-muon collider, we proposed using a target compressed by high intensity laser or heavy-ions irradiation, to collect the pions produced in very small phase-space and then to cool them by another high intensity laser in the PAC 97. Although the pions are produced initially with small phase space, they will be spread transversely in a short time because of their large transverse momentum; consequently a broad high-intensity laser irradiation is needed to collect and accelerate them, and thus the process is not economical. To keep the transverse dimension small, a high solenoidal magnetic field is needed. This field can be created using circularly polarized laser irradiation to the target's surface. A magnetic field of mega-tesla order of magnetic field can be created by the laser intensity of  $10^{15}$  watt/cm<sup>2</sup>, using approach developed Eliser; the Larmor radius of the produced pions becomes less than 0.01 mm, and they can be accelerated by another laser irradiation while in this confined state. Since the target is compressed at not a high temperature, the energy required for this compression is much smaller than the inertial confinement fusion-device, and the higher density reduces the target's mass. This approach is more effective than the one used in the RF field for producing cold muons. This approach also can be applied for anti-baryon production.

## 1. INTRODUCTION

To achieve a luminosity of  $10^{35}$  cm<sup>-2</sup>s<sup>-1</sup> for a 2 + 2 Tev muon-muon collider machine as well as a luminosity of  $10^{33}$  cm<sup>-2</sup>s<sup>-1</sup> for a 250+250 GeV collider [1], it is necessary to produce and collect a large number of muons. The basic method presently used starts with a proton beam impinging on a thick target (one to two interaction lengths), followed by a long solenoid which results mainly from the decay of pions. Since a substantially large amount of the energy is deposited to the small target, heat removal from it is one of most important problems in designing the target to efficiently collect pions. The energy needed, and the cost of collecting the secondary beam using the high solenoid magnetic field and RF cavity is very high. To reduce the energy cost of producing and collecting the muons which result from the decay of the pions, the approach of using a highly compressed target[2], which is practiced in inertial fusion, is promising.

A  $10^{18}$  watt/cm<sup>2</sup> laser beam-power can create an electric field of  $10^9$  V/cm by using inverse cherenkov radiation[3]. An extensive study is underway on the acceleration of electrons using a laser, such as a plasma acceleration, two beat wave-beams acceleration using a strong laser intensity[4,5]. By modulating a high intensity laser, we might control the secondary particles produced by a high-power accelerator in a similar way as laser acceleration.

By using the RF cavity, the secondary particles produced are confined with a high magnetic field of a few tens Tesla, and the phase rotation cavity is located far from the target area; the secondary beam is elongated during its travel from the point of generation to this cavity, and long cavity is required which has low frequency RF.

When secondary particles are created from a small sized target of high density, the particles are small in size and can be controlled directly just after their creation by a strong laser field. The cavity is not needed.

## 2 COMPRESSED TARGET

In an inertial-confinements fusion experiment, a high density of 600 times that of the density of liquid hydrogen was achieved by compressing the target with 15 KJ pulsed-laser irradiation [6,7]. When a target is compressed to 1000 times its original density, and high-energy protons impinge on it, then pions are produced at a 1000 times higher density.

When the size of the original uncompressed target is 1cm-1cm-10 cm, by compressing the target 1000 times, the size of the compressed target in to which the protons are injected becomes 0.001cm-0.001cm-0.01cm =  $10^{-8}$  cc. Further, the total number of Pb atoms in the compressed target is  $(0.3 \cdot 10^{23} \cdot 10^{-8} = 0.3 \cdot 10^{15}) \cdot 10^3 = 0.3 \cdot 10^{18}$ ; if we assume that Pb atoms in the compressed state have 100 ev potential energy, then the total potential energy of the compressed target is  $3 \cdot 10^{19}$  eV /  $(6 \cdot 10^{18}$  eV / J) = 5 Joules. If it is further assumed that 1000 times the driving energy is required to achieve this compressed state, then the total driving energy to compress this target is 5K joule.

According to hydrodynamic simulations [8] for laser-driven implosions, a DT solid layer of 0.250 mm thickness for  $2.250 \text{ mm} < r < 2.5 \text{ mm}$  contained in a polyethylene shell of 0.045 mm thick can be compressed

by a 600g/cc, with a radius from 0.06 to 0.1 mm after a 35.5 nsec layer irradiation. This high density can be maintained for about 2 n sec.

The passing time of 30 GeV protons with a beam length of 100 cm is shortened to  $100\text{cm}/3 \cdot 10^{10}(\text{cm/sec})/30 = 0.11$  n sec; this time is far shorter than the above compressing time of 2 n sec.

### 3 PION PRODUCTIONS

To produce the pions, the heavy nuclei, such as Pb, are more effective than light nuclei, but to compress these high-Z materials a higher energy is required. When a light nuclei target, such as Be, is compressed to 1000 times its normal density, the radiation length is shortened by factor 1000, but the probability of proton collisions is reduced about a 10 fold smaller factor for Be target with the same size radius; thus 90% of the incident protons pass through without colliding with the target. To increase the probability of collision, the cylindrical geometry target should be compressed by employing a Z-pinch-type inertial fusion method, instead of spherical geometrical compression.

To use the uncollided protons, tandem targets which are equivalent to a cylindrical target geometry can be used, or the protons can be recirculated adding accelerating energy. The latter option needs a more complicated engineering design, so it is more practical to use a cylindrical target with longer axial length. The production rate of pions from the light nuclei is smaller than that from heavy nuclei because of the smaller numbers of intra-nuclear cascade processes that occur in the nuclear collisions. Although the light-nuclei target reduces the production probability per one injecting proton compared with the heavy nuclei target, the use of the light nuclei target with long axial length might be more practical than using a heavy nuclei target. These alternatives should be studied by the nuclear-cascade code and by simulating compression processes, not only laser or heavy-ion compression or z-pinch machines.

The compressed target is impinged upon by the high-energy protons with an energy above 30GeV, and focused into radius of 0.06mm. When the primary proton number in one pulse is  $10^{13}$  then the density of protons becomes  $10^{14}$  P/cc. By focusing the beam, the problem of charge space can be resolved.

By employing a compressed target and a proton beam, secondary particles are produced with a high luminosity. However, the secondary particles have a high transverse momentum; thus, they will quickly be spread, and so large RF powers are required to focus and control the secondary beam, similar to the case of using an uncompressed target.

### 4 SOLENOIDAL MAGNETIC FIELD CREATED BY CIRCULAR POLARIZED BEAM

To confine the secondary particles in a small cylindrical space, a solenoidal magnetic field is needed. By imposing a high-intensity solenoidal Bz magnetic field to the secondary beam just after its production, its transverse dimension can be kept small. Elizer [9] suggested that a mega-gauss magnetic solenoidal field can be generated using a circularly polarized laser light (CPLL).

The generation of the Bz field by CPLL is formulated as

$$B(\text{Gauss}) = 2 \cdot 10^4 \cdot [I_M \cdot 10^{14} \text{W} \cdot \text{cm}^{-2}] \cdot [\lambda / \mu\text{m}]^2 \cdot [n / 10^{21} \text{cm}^{-3}], \quad (1)$$

where B is the magnetic field,  $\lambda$  is the laser wave-length, I is the laser intensity, and n is the plasma density.

Using a  $\lambda = 10$  micron wave-length laser with a high intensity of  $10^{16} \text{W/cm}^2$  to  $n = 10^{20}$  plasma density, a magnetic field of 200MG can be produced. The  $\lambda$  radius of pions and muons with 100MeV transverse kinetic energy in this high magnetic field is 0.003cm. By irradiating the target just after their production with this high-intensity laser of  $10^{16} \text{W/cm}^2$  in a radius of 0.006cm, the pions and muons can be confined in a cylinder with a 0.006cm radius. The total laser power to create this field is  $10^{14}$  Watt, and if we confine the beam for 30 n sec, we need to have 30 KJ of laser energy.

As shown in Eq.1, the laser power required to create a high magnetic field is proportional to cubic power of the wave-length of laser, and inversely proportional to plasma's, electron-density. The use of a longer wave-length laser is beneficial, but the plasma's electron density affects the penetration of the laser into the target plasma frequency also becomes high and then a laser with a frequency less than this plasma frequency not can penetrate; hence, a circularly polarized laser not can create a high current and a high solenoidal field. A high frequency laser can penetrate more deeply into plasma, so that a high Bz field can be created; however the laser power then required to generate a high Bz field is proportional to the cube of the laser's frequency, and so the laser power needed becomes prohibitively high for practical purposes.

In this paper, we did not optimize our study for designing target compression nor for the use of the high intensity laser for controlling the secondary particles; we simply analyzed the orders of magnitude of the required laser energy. This value is much smaller than the conventional RF field. In further analyses, we need to simulate compression ( laser, heavy ions, Z-pinch type), and laser-plasma interactions, as well as making nuclear-cascade calculations.

To compress the target material initially requires a large amount of energy for driving devices, such as a laser, light- and heavy-ions drivers, the substantial expense of energy required for controlling the secondary particles can be saved in this approach. The reduction of the emittance confers a tremendously high cost-benefit advantage.

This approach of using the laser is especially useful for collecting the anti-protons which cannot use ionization cooling because of its annihilation of anti-protons.

The technology of accelerating a charged beam by laser is still in its infancy, but this technology also should be applied to target technology.

To compress the target material, we can employ a high-z pinch device instead of irradiation by laser, light- and heavy-ions. This suggested approach to compression is much simpler than the others.

## 5. ACKNOWLEDGMENT

The authors would like to express their thanks to Drs. R.Palmer, A.N.Skrinsky, F.E.Mills J.Gallardo, S. Eliezer, C.Yamanaka, H.Takabe, This work was performed under the auspices of the U.S. Department of Energy under Contract No. DE-AC02-76CH00016.

## 6. REFERENCES

1. R.Palmar et al. "Muon Collider Design " BNL-62949(1996), "Muon Collider" 9th advanced ICFA, Beam Dynamics and Technology Issue for Mu-Mu collider, Beam Dynamics Workshop. Oct. 1995, AIP Conf. 372, p.3. Montauk, NY, 1995 Edited by J. Gallardo.
2. H. Takahashi, Y.An, X.Chen, M. Nomura " Optimization of the Target for Muon Colliders" Proc. of the 1997 particle Accelerator conference (PAC-97), p.402 Vancouver ,B.C., Canada 12-16, May 1997.
3. A. Fisher, J.Gallardo, J. Sandweiss, A. Van Steenbergen , " Inverse Free- Electron Laser Accelerator P.299. AIP Conference Proceeding 279 Advanced accelerator concepts Port Jefferson, NY 1992. Editor J. S. Wurtelle.
4. T. Tajima and J.M.Dawson Phys. Rev. Lett. 43 , 267 (1979)
5. T. Katsouleas " Summary of the working group on Plasma Accelerator' P371, C.M. Tang "Report of the working group on Far Field Accelerators, p. 259,
6. C. Yamanaka " Advances in inertial Confinement Fusion" OR3.1, ICENES'89, Karlsruhe, 1989.
7. H.Azechi et al 1991, Laser and Particle beams 9, 193, 1991.
8. H. Takabe " Hydrodynamic Simulation Code for Laser Driven Implosion" Private communication, oct, 97.
9. E.Kolka, S.Eliezer, Y.Paiss, "Miniature Magnetic Bottle confined by circularly polarized laser light " Laser and Particle Beams (1995) 13, 83-93.

# Injection of Gold Ions in the AGS Booster with Linear Coupling\*

C. Gardner, L. Ahrens, T. Roser, K. Zeno, BNL, Upton, NY 11973, USA

## Abstract

Linear Coupling, introduced by skew quadrupoles, has been used for several years to enhance the multi-turn injection efficiency of gold and other heavy ions in the AGS Booster. In this paper we describe our latest measurements of the injection process and compare with models.

## 1 INTRODUCTION

An important consideration in our effort to meet the intensity requirements for the Relativistic Heavy Ion Collider (RHIC) has been the efficiency of the multi-turn injection of heavy ions in the AGS Booster. A number of years ago we introduced linear coupling (using existing skew quadrupoles) into our injection scheme [1] and found, as others have [2], that one can significantly enhance the injection efficiency. The principle parameters of the scheme are the tunes, the skew quadrupole current, and the position and angle of the injection bump. In the past we have simply tuned these parameters on the basis of intensity using models of the injection process as a general guide. However, recently we developed a non-destructive way to observe the turn-by-turn evolution of the injected beam and this has paved the way for more detailed tuning and analysis of the injection parameters. We report here the results of our efforts and what we hope to accomplish for the upcoming commissioning of RHIC.

Heavy ion beams are injected into the Booster by means of an electrostatic inflector and a programable injection bump. The injection bump initially places the closed orbit near the septum at the exit of the inflector. As beam is injected and begins to circulate, the orbit must be moved away to keep the circulating beam from hitting the septum. The incoming beam is therefore deposited into a series of *phase space layers* surrounding the orbit as the bump collapses. The process continues until the orbit is so far from the septum that any additional beam injected will be outside the acceptance of the machine.

The number of turns that can be injected into a given layer will depend on the tunes and the coupling introduced by the skew quadrupoles. By judicious choice of these parameters, one can maximize the time that the circulating beam stays clear of the septum. Of course, the introduction of coupling has a price; it increases the size of the vertical envelope of the beam. This means that in the dipoles of the Booster lattice, where the vertical beta function is large and the vertical aperture is small, one can start to lose beam if too much coupling is introduced. Finding the optimum settings for the tunes and the skew quadrupole current

therefore requires keeping track of the vertical beam envelope in the dipoles as well as the horizontal envelope at the septum.

We assume that the beam distribution emerging from the inflector is contained in a four-dimensional *beam ellipsoid* with an emittance small compared to the machine acceptance. At any point in the machine, the horizontal and vertical oscillation envelopes of the *center* of the ellipsoid are given by

$$|X| \leq \sqrt{d^2 \beta_1 \epsilon_1} + \sqrt{\beta_{x2} \epsilon_2} \quad (1)$$

and

$$|Y| \leq \sqrt{\beta_{y1} \epsilon_1} + \sqrt{d^2 \beta_2 \epsilon_2} \quad (2)$$

where

$$\beta_{x2} = \beta_2 W_{22}^2 + 2\alpha_2 W_{22} W_{12} + \gamma_2 W_{12}^2, \quad (3)$$

$$\beta_{y1} = \beta_1 W_{11}^2 - 2\alpha_1 W_{11} W_{12} + \gamma_1 W_{12}^2. \quad (4)$$

The parameters  $\alpha_1$ ,  $\beta_1$ ,  $\gamma_1$ ,  $\alpha_2$ ,  $\beta_2$ ,  $\gamma_2$ ,  $W_{11}$ ,  $W_{12}$ ,  $W_{21}$ ,  $W_{22}$ , and  $d$  are determined by the one-turn transfer matrix at the given point and can be obtained from the MAD code [3].  $\epsilon_1$  and  $\epsilon_2$  are the Courant-Snyder Invariants associated with the two normal-modes of oscillation of the beam ellipsoid center about the closed orbit.

The extent of the beam ellipsoid with respect to its center is defined by a four-by-four symmetric positive-definite matrix,  $\mathbf{E}$ , which we assume is matched to the lattice. The maximum possible horizontal and vertical excursions of a beam particle with respect to the center of the ellipsoid are then given by

$$|U - X| \leq \sqrt{\epsilon_b E_{11}}, \quad |V - Y| \leq \sqrt{\epsilon_b E_{33}} \quad (5)$$

where  $E_{11}$  and  $E_{33}$  are matrix elements of  $\mathbf{E}$  and  $\epsilon_b$  is the beam ellipsoid emittance. (Here  $U$  and  $V$  are the horizontal and vertical coordinates of a beam particle with respect to the closed orbit.) The beam envelope at a given point in the ring is then defined by the equations

$$|U| \leq \sqrt{d^2 \beta_1 \epsilon_1} + \sqrt{\beta_{x2} \epsilon_2} + \sqrt{\epsilon_b E_{11}} \quad (6)$$

and

$$|V| \leq \sqrt{\beta_{y1} \epsilon_1} + \sqrt{d^2 \beta_2 \epsilon_2} + \sqrt{\epsilon_b E_{33}}. \quad (7)$$

## 2 TURN-BY-TURN MEASUREMENTS

The horizontal and vertical positions (with respect to the closed orbit) of the beam ellipsoid center at a given point on the  $n$ th turn around the machine are given by

$$X_n = A_1 \cos(n\psi_1 + \phi_1) + A_2 \cos(n\psi_2 + \phi_2) \quad (8)$$

\* Work supported by the U.S. Department of Energy.



and

$$Y_n = B_1 \cos(n\psi_1 + \eta_1) + B_2 \cos(n\psi_2 + \eta_2) \quad (9)$$

where  $\psi_1 = 2\pi Q_1$  and  $\psi_2 = 2\pi Q_2$ . Here we see that the motion in each plane is the superposition of two modes of oscillation, and the tunes ( $Q_1, Q_2$ ), amplitudes ( $A_1, A_2, B_1, B_2$ ) and phases ( $\phi_1, \phi_2, \eta_1, \eta_2$ ) are the 10 parameters that characterize the oscillations. These parameters are not all independent; the amplitudes and phases are each functions of only 4 independent parameters, the initial positions and angles  $X_0, X'_0, Y_0, Y'_0$  of the beam ellipsoid center. Including the tunes, there are therefore only 6 independent parameters and these ultimately are what one wants to obtain from turn-by-turn measurements.

To observe the turn-by-turn evolution of the beam position, it is necessary to chop the beam so that a short pulse corresponding to each turn can be seen on PUE's (PickUp Electrodes) in the Booster ring. The chopper is located in the transport line upstream of the Booster, and consists of two parallel plates with one plate above and the other below the midplane of the beamline. The upper and lower plates are connected respectively to pulsed and DC high-voltage power supplies, and the beam is deflected vertically by applying voltages to the plates. In the past, the chopper has been set up so that only a half-turn pulse of beam is transmitted down the beamline and injected into the Booster; the turn-by-turn evolution of the half-turn can then be observed on the PUE's in the ring. In this mode of operation, beam is transmitted down the line only when the upper plate is pulsed with a voltage which just cancels a DC bias voltage applied to the lower plate. Putting only a half-turn pulse (some 7.5  $\mu$ s) down the line is, of course, destructive to the Physics programs; they require the full long pulse from the ion source (typically 500–1000  $\mu$ s) which corresponds to several tens of turns around the ring. However, the chopper also can be set up so that all of the long pulse is transmitted except for a half-turn portion which may be selected from any part of the long pulse. In this mode, no bias voltage is applied to the lower plate and beam is transmitted down the line except when a deflecting pulse is applied to the upper plate. The deflecting pulse produces a half-turn gap or "hole" in the long pulse that is essentially invisible to the Physics programs and at the same time provides a turn-by-turn signal on the PUE's. We have found that the turn-by-turn evolution of this "hole" is essentially the same as that of a half-turn pulse of beam by itself. This mode of operation allowed us to make several turn-by-turn measurements of the injected beam without interrupting the Physics program.

A computer program called "PIP" [4] collects and analyzes oscilloscope traces of the turn-by-turn signals obtained from a given PUE in the Booster ring. The program first obtains the position of the injected beam versus turn at the PUE; a Discrete Fourier Transform of the data then gives the normal-mode tunes and initial phases associated with the coupled betatron oscillations. Using these as starting values, the horizontal or vertical function

(8–9) is fitted to the data. From the fitted parameters and the lattice parameters at the PUE and at the inflector exit, the program then calculates the initial positions and angles of the beam at injection. Figure 1 shows typical position-versus-turn data along with the fitted curve; the FFT of the data is shown in Figure 2. Here the normal-mode tunes are  $Q_1 = 4.699(1)$ ,  $Q_2 = 4.801(1)$ . With these tunes the injected beam returns to its initial position every 10 turns; hence, a maximum of 10 turns can be injected into a phase-space layer before the bumped orbit must be moved away from the septum. Figures 3 and 4 are the corresponding figures for another set of data. Here the normal-mode tunes are  $Q_1 = 4.736(1)$ ,  $Q_2 = 4.803(1)$  and the injected beam returns to its initial position every 15 turns.

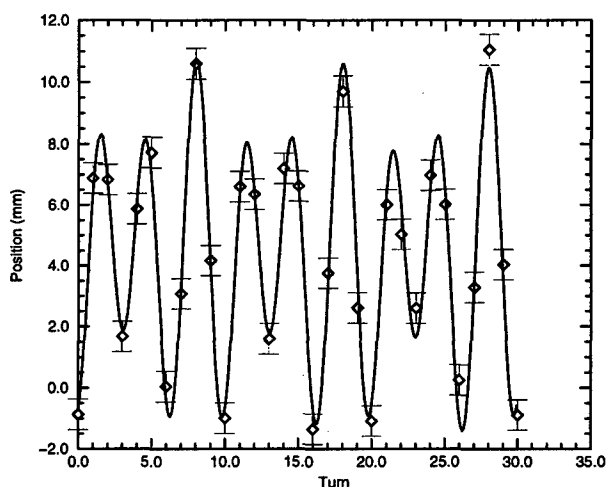


Figure 1: Position-vs-Turn Data and Fitted Curve.

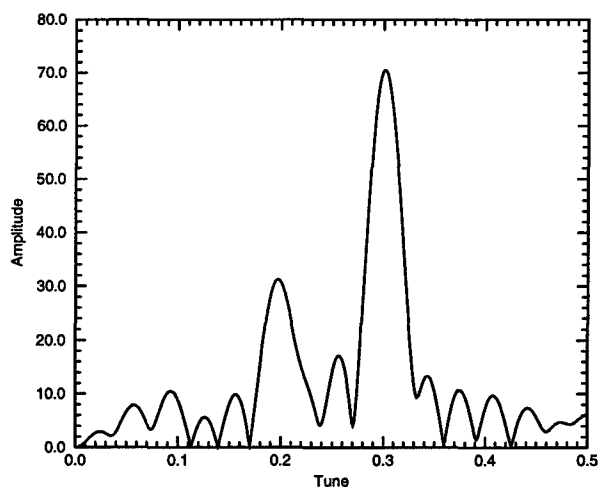


Figure 2: FFT of Position-vs-Turn Data.

### 3 INJECTION SETUP

The turn-by-turn measurements provide a useful tool for setting up various coupled injection schemes. Although

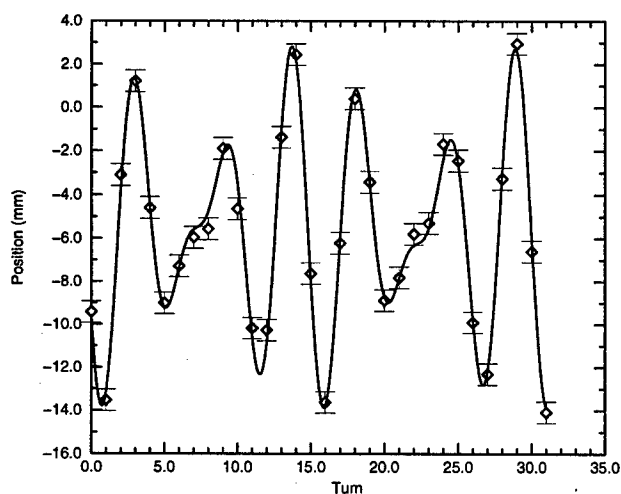


Figure 3: Position-vs-Turn Data and Fitted Curve.

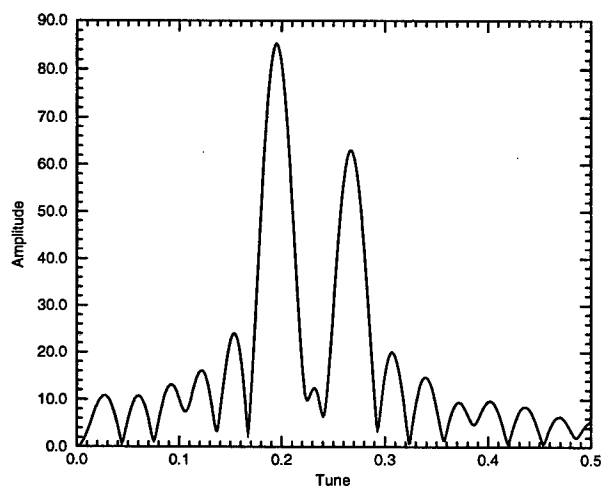


Figure 4: FFT of Position-vs-Turn Data.

not yet implemented in practice, one can proceed in the following way. A given scheme is defined by the settings of the unperturbed (i.e. uncoupled) horizontal and vertical tunes,  $Q_x$  and  $Q_y$ , and the skew quadrupole current,  $I$ . These determine the normal-mode tunes,  $Q_1$  and  $Q_2$ , and the amount of coupling between the two planes. Using the MAD code to obtain the necessary parameters, equations (6–7) then give the maximum horizontal and vertical extent of the beam at the septum and at the vertical beta maximums in the Booster. This allows one to determine how far the orbit has to be moved to keep the beam from hitting the septum. It also tells us when the vertical envelope becomes too large in the Booster dipoles. We define  $X_M$  to be the maximum horizontal excursion of the beam ellipsoid center on its passes by the septum at the inflector exit;  $X_M + \sqrt{\epsilon_b E_{11}}$  must not exceed 45 mm in order for the injected beam to be inside the Booster acceptance once the injection bump has collapsed completely. Similarly, we define  $Y_M$  to be the maximum vertical excursion of the ellipsoid center at the vertical beta maxi-

mums in the Booster;  $Y_M + \sqrt{\epsilon_b E_{33}}$  must not exceed 33 mm. (We assume that the closed orbit is centered in the dipoles.) Assuming the incoming beam has an emittance of  $1\pi$  mm milliradian in both planes, one finds that for a 10-turn scheme similar to that of Figure 1, three layers of 10 turns can be injected before the vertical beam envelope becomes too large in the Booster dipoles. For a 15-turn scheme similar to that of Figure 3, one can inject two layers of 15 turns before the vertical envelope becomes too large. To put beam into additional layers, one must reduce the coupling so that the vertical envelope does not increase any further. One way to do this is to move the uncoupled tunes further apart. (In practice one can change the tunes faster than the skew quadrupole current.) For the 15-turn scheme, a shift of the vertical tune reduces the coupling and allows two more layers to be injected with 9 and 19 turns respectively. In principle, a total of 62 turns can then be injected; the relevant parameters are summarized in Table 1. Here the normal-mode tunes are  $Q_1 = 4 + 11/15 = 4.733$ ,  $Q_2 = 4 + 12/15 = 4.800$ , and the required skew quadrupole current is 3.7 Amps.  $X_b$  and  $X'_b$  are the horizontal position and angle of the bumped orbit at the inflector exit; the units are mm and milliradians. In practice we have not yet injected this many turns. Anec-

Table 1: Coupled Injection Scheme

$Q_x = 4.7767, Q_y = 4.7567$					
Layer	$X_b$	$X'_b$	Turns	$X_M$	$Y_M$
1	41.81	6.58	4	10.00	10.32
2	34.19	5.38	15	17.61	18.19
3	26.58	4.18	15	25.23	26.05
$Q_x = 4.7767, Q_y = 4.7000$					
4	18.96	2.97	9	32.85	22.89
5	11.34	1.78	19	40.47	28.20

dotal evidence suggests that the stripping foil in the beam-line upstream of the Booster may significantly increase the beam emittance, so that the number assumed above may be too small. Nevertheless, we believe that our measurement technique and an injection scheme similar to the one above will prove useful during the upcoming commissioning of RHIC.

## 4 REFERENCES

- [1] T. Roser, "Multi-turn Injection with Coupling", AGS/AD/Tech. Note No. 354, November 7, 1991.
- [2] K. Schindl and P. Van der Stok, IEEE Transactions on Nuclear Science, Vol. NS-24, No. 3, June 1977, pp. 1390–1392.
- [3] H. Grote and F. C. Iselin, "The MAD Program Version 8.4 User's Reference Manual", CERN/SL/90-13 (AP), 27 August 1991.
- [4] C. J. Gardner, "Turn-by-Turn Analysis of Proton and Gold Beams at Injection in the AGS Booster", Proceedings of the 1999 Particle Accelerator Conference.

# Operational Experiences with the BESSY II Injection System \*

O. Dressler, J. Feikes<sup>#</sup>, BESSY, Berlin

## Abstract

The performance during commissioning and reliability of the BESSY II injection system, delivered by Sincrotrone Trieste, is reviewed.

## 1 INTRODUCTION

During the successful commissioning of the BESSY II storage ring [1] the high reliability and stability of performance of the BESSY II injection system was a major support. The BESSY II injection system was constructed by Sincrotrone Trieste [2] by modifying their own injection system according to the different requirements of BESSY II as beam energy and available space.

As the BESSY II storage ring should be capable to operate with an energy as high as 1.9 GeV, actually routine operation is at 1.7 GeV, the requirements concerning the deflection angles were based on that energy.

The system was built up in Berlin at the end of year 1997 and all relevant parameters were measured during the acceptance tests in Trieste and Berlin. Actually the injection system proved its reliable function at three different storage ring energies, 0.9 GeV, 1.7 GeV and 1.9 GeV. Some specific observation which showed up in the routine operation of the system are reported.

## 2 DESCRIPTION OF THE SYSTEM

As the system is very similar to that of Sincrotrone Trieste described elsewhere [2], no technical details are mentioned here. The BESSY pre-accelerators are located inside the main ring, so that the injection channel connects them to the storage ring from inside. The injection consists of four identical kicker magnets, grouped symmetrically around the injection point and two septum magnets built into the same septum tank Fig. 1. The septa are operating at a mean pressure of some  $10^{-9}$  mbar in order to avoid electrical discharges.

The kicker pulser are mounted directly in front of the magnets at the outer side of the girder in order to keep the cable connections as short as possible.

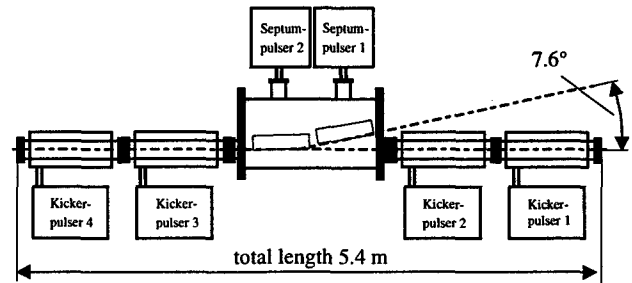


Figure 1: Layout of the Injection System

The kicker pulses have a total length of about 6.5  $\mu$ sec, Fig. 2, which has to be compared to a revolution time of about 800 nsec. The correct polarity of each kicker allow them to form a symmetric orbit bump.

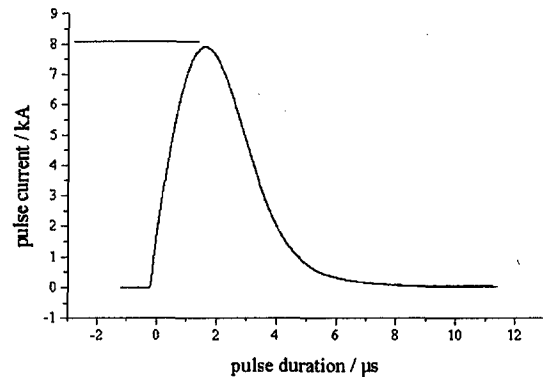


Figure 2: Kicker pulse at recharging voltage of 15 kV

As the betafunctor is the same at all the kicker positions ( $\beta_x=16$  m) the kicker bump is powered symmetrically allowing to move the beam 22 mm at 1.9 GeV towards the septum sheet which is located 24 mm away from the beam pipe center. The main parameters of kicker and septa are shown in Table 1.

Table 1: Main Parameters of Injection Subsystems

Parameters	Kicker	Septa
peak current pulse (nominal)	8.4 kA	9.1 kA
recharging voltage (typical)	15 kV	1.4 kV
current puls legh (typical)	6.5 $\mu$ s	50 $\mu$ s
peak magnetic field (nominal)	0.24 T	0.76 T
deflection angle at 1.9 GeV	21 mrad	133 mrad

\*Work supported by the Bundesministerium für Wissenschaft, Forschung und Technologie and by the Land Berlin

<sup>#</sup> Email: dressler@bii.bessy.de, feikes@bii.bessy.de

During the first function tests of the kicker magnets electrical flashovers between the lower half of the kicker support and the girder structure were noticed.

But these are passive electrical elements which should be on the same ground level. The concept was changed and a star like grounding connection of the kicker supports together with the pulser cages was realized, Fig. 3. Since then flashovers between cages were no longer observed.

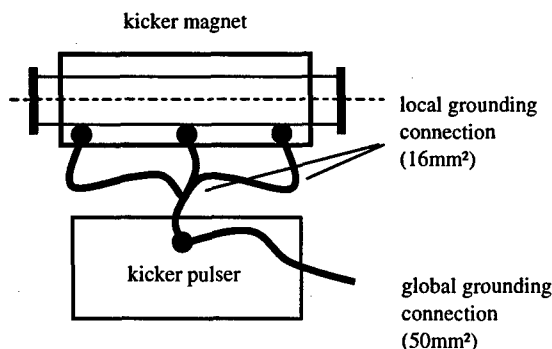


Figure 3: Star like grounding concept

### 3 UNIFORMITY OF KICKER PULSES

During the commissioning period uniformity and time stability of the four kicker pulses were monitored. Beam losses due to a misfire of one of the four kickers were never observed. Careful analysis of the pulse form of all four kickers show slight differences between them in the order of some percent relative to the peak amplitudes.

The accuracy of these pulse measurement is determined by the resolution and precision (approximately 0.5 %) of the oscilloscope (Tektronix TDS754 A). As an example in Fig. 4 two curves show the difference of two corresponding kicker pulses, kicker4-kicker3 and kicker1-kicker2, working equally at a charging voltage of 15 kV, giving a peak current of 7.8 kA.

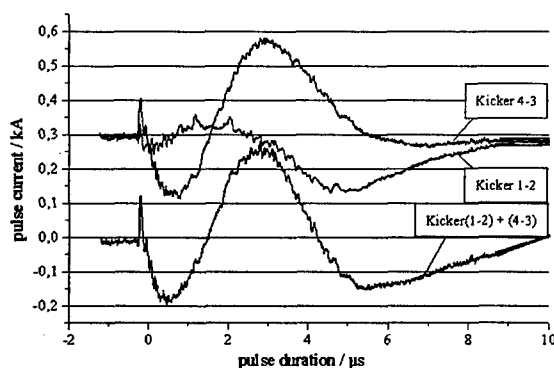


Figure 4: Differences of acquired current pulses

The difference of all four kicker pulses, with the sign according to their polarity, is also shown. The relative timings between the pulses are adjusted in such a way,

that the difference pulse has an amplitude as low as possible. This is the same strategy an operator would use to adjust the single kicker timings in the machine. The lower graph in Fig 4 shows that the spurious pulses resulting from the uncompensated action of all kickers is about 3 % of the total kicker bump amplitude.

The reasons for the differences in the acquired pulse forms are the slightly different values of the electrical network components. Indeed measurements of capacity, inductance and resistance of the main components show slight variations which are still inside the tolerance band given by the manufacturer, but which are sufficiently large to explain the measured deviation from uniformity [3].

### 4 INJECTION EFFICIENCY

The question arises if the differences in the pulse form might cause a reduction of injection efficiency. To answer this we measured the influence of not well adjusted single kicker amplitudes on the injection rate. First we confirmed that the kicker bump seen by the closed orbit is well closed. Then the amplitude of only one of the four kickers was detuned and the injection efficiency as a function of the detuning was measured.

Fig. 5 shows that a detuning of the individual kicker strength equivalent to 2-3 % gives an optimum injection rate (according the calibration of the injection line beam current monitor the rate then was near to 100 %).

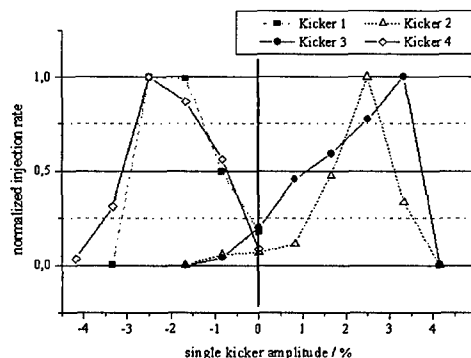


Figure 5: Normalized injection rate vs. detuning of single kicker amplitude

The optimal detuning of each of the kicker tends to reflect the beam always away from the septum sheet. The magnitude of the remaining excitation caused by the non-uniformity of the kicker pulses is of the same order as that of the detuned injection bump at best injection rate. The conclusion is, that the non-closure of the injection bump caused by differing pulse forms can be properly and stably compensated by a readjustment of one of the four kicker amplitudes.

It is surprising that for amplitudes of the injection kicker bump between 6 kV to 15 kV (at 1.7 GeV) corresponding to a bump height between 8 mm to 21 mm we get full injection efficiency.

On the other hand the injection is very sensitive to the single kicker timing. Fig. 6 shows the injection efficiency as function of the detuning of a single kicker timing.

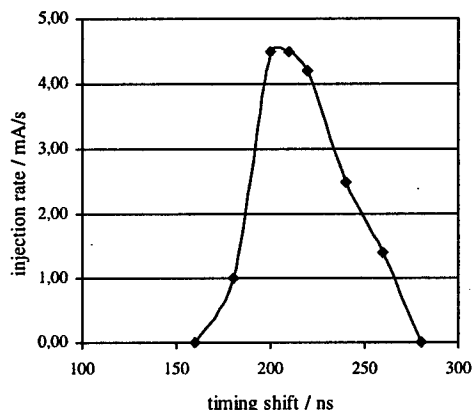


Figure 6: Injection vs. shift of single kicker timing

At detunings of 40 nsec the injection rate breaks down drastically. This can not be recovered by readjustment of the kicker amplitudes.

## 5 SUMMARY

Although the kicker pulses differ slightly to the other, it is shown, that the beam excitation generated by an equally powered kicker bump affects the injection rate. This can be compensated by the readjustment of a single kicker amplitude. That allows a stable injection at a high efficiency, but the injection is sensitive to shifts of the single kicker timing.

## 6 REFERENCES

- [1] Renè Bakker et al., Status and Commissioning-Results of BESSY II, this conference
- [2] M. Giannini et al., Design, Construction and Installation of the Elettra Injection System, Proceedings of the EPAC 1994, p. 2352
- [3] O. Dressler, Commissioning of Storage Ring Injection of BESSY II, BESSY internal report,

# MEASUREMENT AND OPTIMISATION OF THE PS-SPS TRANSFER LINE OPTICS

G. Arduini, M. Giovannozzi, K. Hanke\*, D. Manglunki, M. Martini, G. Métral  
CERN, 1211 Geneva 23, Switzerland

## Abstract

The beam optics of the PS-SPS transfer line at CERN has been studied and optimised for a variety of beams. Betatron and dispersion matching has been performed for the fixed-target proton and ion beams, as well as for the future LHC proton beam. The techniques applied to the measurement of the optical parameters in the transfer line are discussed and experimental results are presented.

## 1 INTRODUCTION

The TT2/TT10 beam line is used to transfer from PS to SPS protons and lead ions for fixed-target physics, protons to simulate the future LHC-type beam and positrons for LEP. In recent years, there has been a renewed interest in the optics of this transfer line for two main reasons.

Firstly, the tight emittance budget for the LHC beam. The maximum allowed emittance blow-up in the transfer from PS extraction to SPS extraction is 17 % and only a small fraction of this is assigned to mismatch at injection. Since this beam has a small emittance and a large momentum spread [1], dispersion mismatch is a major concern.

Secondly, high-intensity proton and lead ion beams are required by the physics community, therefore minimum emittance blow-up is needed to minimise beam losses and thus increase the beam intensity delivered to the experiments.

For these reasons, a measurement campaign was undertaken during the 1998 physics run to define and improve the model of the TT2/TT10 transfer line [2, 3] and to measure the optical parameters  $\alpha, \beta$ , the dispersion  $D$  and its derivative  $D'$  so that improved optics could be computed and tested in operation.

## 2 DEFINITION AND MEASUREMENT OF INJECTION BLOW-UP FACTORS

The Twiss parameters at any point in a transfer line depend not only on the settings of the magnets but also on the values of  $\alpha$  and  $\beta$  at the beginning of the line. Therefore their knowledge is mandatory to carry out optics calculations.

The initial values of  $\alpha$  and  $\beta$  can be obtained by measuring the optical parameters at a given location and then by back-propagating them to the entry point of the line. The optical parameters can be obtained by measuring the beam profile at three different locations in the line, using e.g. secondary emission monitors (SEMs) (three of them

are installed in TT2 and three in TT10) or optical transition radiation (OTR) monitors (three of such monitors are installed in TT10). Under the hypothesis that the transfer matrices between the three monitors are known as well as the value of  $D$  at the three monitor locations<sup>1</sup>, the beam emittance,  $\alpha$  and  $\beta$  can be computed [5].

To evaluate the blow-up due to the mismatch of the Twiss parameters  $\alpha, \beta$  at injection the *geometrical blow-up*  $G_b$  and the *blow-up after filamentation*  $H$  are defined [5].  $G_b$  is the ratio between the area of the circle having the major axis of the mismatched ellipse as diameter and the area of the circle representing the matched beam.  $H$  provides the emittance blow-up once the dilution due filamentation is taken into account, namely:

$$G_b = H + \sqrt{H^2 - 1}, \quad (1)$$

$$H = \frac{1}{2} \left[ \frac{\beta_0}{\beta_m} + \left( \alpha_0 - \alpha_m \frac{\beta_0}{\beta_m} \right)^2 \frac{\beta_m}{\beta_0} + \frac{\beta_m}{\beta_0} \right]. \quad (2)$$

In Eq. (2),  $\alpha_m, \beta_m$  stand for the measured Twiss parameters while  $\alpha_0, \beta_0$  are the nominal Twiss parameters. The blow-up after filamentation, which is the relevant quantity, is always smaller than the geometrical blow-up.

The measurement of the dispersion is performed by varying the momentum of the beam extracted from PS in steps and by recording the transverse displacement at each available beam position monitor (BPM) in TT2/TT10 and in the SPS first-turn (see Fig. 1) considered as a continuation of the transfer line. The momentum offset  $\Delta p$  with

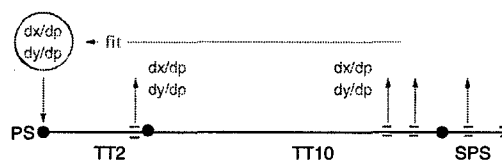


Figure 1: Schematic representation of the dispersion measurement

respect to the reference momentum  $p$  is calculated by measuring the change in radial position  $\Delta R$  of the beam in its first turn according to

$$\frac{\Delta p}{p} = \frac{\Delta R}{\alpha_p}, \quad (3)$$

provided the momentum compaction factor  $\alpha_p$  of the SPS machine is known. The beam displacement measurements

<sup>1</sup>This last condition can be dropped, provided more profiles are measured, see [4].

\* Email: Klaus.Hanke@cern.ch

as a function of the momentum offset are fitted to a straight line for each BPM and the slope  $dx/dp$  is obtained. A three-parameter  $((dx/dp)_m, (dx'/dp)_m, \delta)$  least-squares fit of the calculated  $(dx/dp)_i$  to the function

$$C_i \left( \frac{dx}{dp} \right)_m + S_i \left( \frac{dx'}{dp} \right)_m + \xi_i \delta \quad (4)$$

is performed in the horizontal plane while in the vertical plane  $\delta = 1$  is assumed.  $C_i, S_i, \xi_i$  are the elements of the  $3 \times 3$  transfer matrix [5] from the measurement point  $m$  to the  $i$ -th beam position monitor and  $\delta$  is a calibration factor to correct for possible scaling errors in the measurement of the momentum offset. The value of the parameter  $\delta$  obtained from the fit of the data in the horizontal plane is used to correct the momentum offsets considered for the data relative to the vertical plane. As a result of the fit,

$$D_m^{fit} = \frac{(dx/dp)_m^{fit}}{\delta^{fit}} \quad D_m'^{fit} = \frac{(dx'/dp)_m^{fit}}{\delta^{fit}} \quad (5)$$

at any point in the line if the transfer matrix from the measurement point to any BPM is known. The presented method takes advantage of the large number of BPMs in the SPS ring (108 per plane) and provides an immediate picture of the mismatch with respect to the dispersion in the ring but it requires beams with small emittance and small momentum spread.

In the presence of dispersion mismatch, the beam will blow-up. These effects can be quantified by means of the *geometrical blow-up*  $G_d$  and the *blow-up after filamentation*  $J$  [6]

$$G_d = 2J - 1, \quad (6)$$

$$J = 1 + \frac{\Delta D^2 + (\Delta D' \beta_0 + \Delta D \alpha_0)^2}{2 \varepsilon_{r.m.s.} \beta_0} \left( \frac{\Delta p}{p} \right)_{r.m.s.}^2 \quad (7)$$

where  $(\Delta p/p)_{r.m.s.}$  and  $\varepsilon_{r.m.s.}$  are the r.m.s. momentum spread and r.m.s. emittance,  $\alpha_0, \beta_0$  are the nominal Twiss parameters and  $\Delta D$  ( $\Delta D'$ ) is the difference between theoretical and measured dispersion (dispersion derivative).

We stress that to derive the expression for  $G_b, H, G_d, J$  one assumes to have filled ellipses and no linear coupling.

### 3 EXPERIMENTAL RESULTS

For the different beam types (26 GeV/c fast extracted proton beam, 14 GeV/c continuous transfer proton beam and fast extracted lead ion beam) the same measurement procedure has been applied. Firstly  $D$  has been measured in TT2/TT10, then the Twiss parameters have been deduced using the SEMs in TT2 and TT10. Finally, the optical parameters at the entry point of the transfer line have been obtained by tracking back the values at the SEM locations. The knowledge of the model and of the initial optical parameters has allowed the computation of new optics for the transfer line with reduced blow-up.

#### 3.1 The 26 GeV/c fast extracted beam

The 26 GeV/c fast extracted proton beam is the so-called LHC beam. The detailed beam parameters can be found in [7]. The measured values of  $D_H$  in TT2/TT10 and

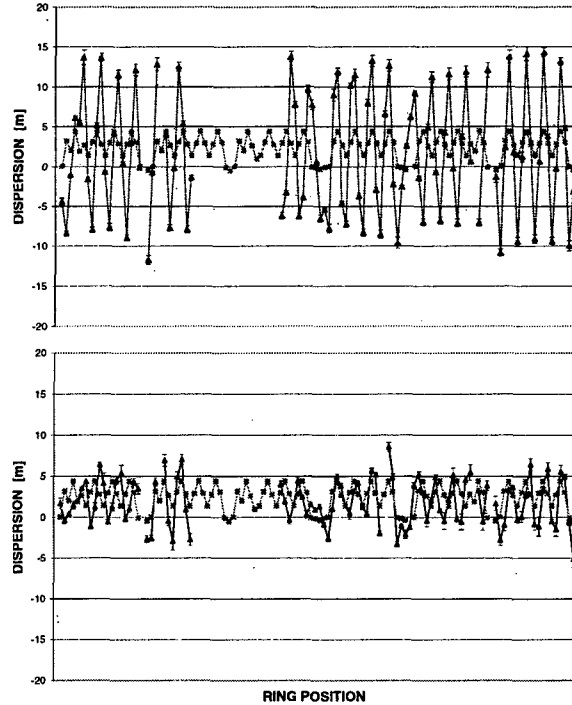


Figure 2: Measured (darker triangles) and theoretical (squares) horizontal dispersion in the SPS ring before (upper) and after (lower) matching the injection line

the SPS for the initial optics (upper) and the matched one (lower) are shown in Fig. 2. The overall reduction of  $D_H$  is clearly visible. The values of the mismatch factors after filamentation for the old and new optics are listed in Table 1. The improvement is remarkable, even though the blow-up

	Old optics	New optics
$H$ (H-plane)	1.1	1.0
$H$ (V-plane)	1.3	1.0
$J$ (H-plane)	11.6	1.7
$J$ (V-plane)	1.0	1.0

Table 1: Measured filamented betatron and dispersion blow-up factors for old and new optics

due to  $D_H$  is far from the nominal value imposed by the real LHC emittance budget. Further studies are needed to improve this situation.

#### 3.2 The 14 GeV/c continuous transfer beam

The control of the mismatch for the high intensity (about  $3 \times 10^{13}$  ppp) 14 GeV/c proton beam for fixed target physics is mandatory in order to reduce beam losses and thus increase the intensity delivered to the targets. For this beam the TT2/TT10 line is set-up with an emittance exchange

section to match the beam envelope with the physical aperture of the SPS.

A new optics tested in operation (see [8]) allowed the reduction of the injection losses by a factor two and the increase of the transmission efficiency by 2 %, reaching a value of 92 %. Furthermore, the improved knowledge of the optical parameters allowed the elimination of a long-lasting discrepancy between the emittance values measured in TT2 and TT10. In Fig. 3 the beam emittance measured in TT2 and TT10 as a function of time during the physics run is shown. The better agreement is correlated with the use of the measured optical parameter in the emittance measurement program.

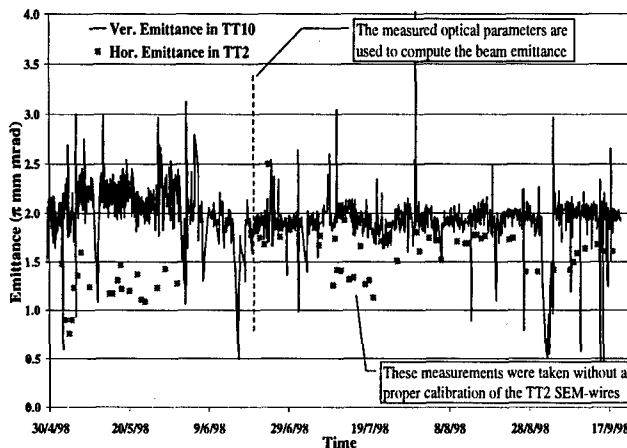


Figure 3: Comparison between the emittance value measured using monitors in TT2 and in TT10 during the 1998 run at 14 GeV/c. The good trend due to the use of the measured optical parameters is visible

### 3.3 The lead ion beam

As a result of the betatron matching of the transfer line, the transmission through the SPS went up from 75 % to 88 % and the beam intensity delivered to the targets increased accordingly [9]. In Fig. 4 the average number of lead ions is shown: the sudden increase in the intensity is due to the new optics in TT2/TT10.

## 4 CONCLUSIONS

The study described in this paper will continue during the 1999 run with particular attention to: precise measurement of the beam energy and adjustment of its control value accordingly, extension of the error analysis to all measurement stages, measurement of the dependence of mismatch on extraction conditions (energy, extraction trajectory), on-line measurement of optical parameters and matching correction [10].

## 5 ACKNOWLEDGEMENTS

The support of the PS and SPS operation teams is acknowledged.

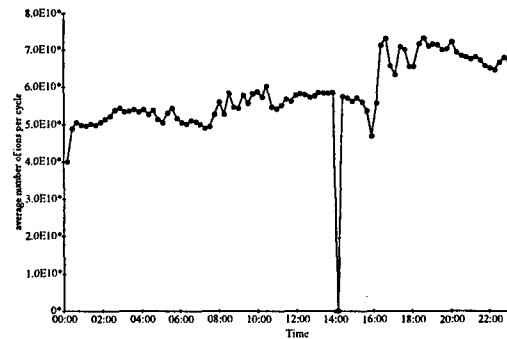


Figure 4: Average number of lead ions per cycle over 24 hours. The step function in efficiency is due to the matched optics in TT2/TT10.

## 6 REFERENCES

- [1] P. Collier (ed.), "The SPS as Injector for LHC, Conceptual Design", *CERN SL (DI) 97-07* (1997).
- [2] G. Arduini, M. Giovannozzi, K. Hanke, J.-Y. Hémerly, M. Martini, "MAD and BeamOptics Description of the TT2/TT10 Transfer Line - Part I: Optics without Emittance Exchange Insertion", *CERN PS Note (CA) 98-014* and *CERN SL Note (OP) 98-040* (1998).
- [3] G. Arduini, M. Giovannozzi, K. Hanke, J.-Y. Hémerly, "Study of the TT2/TT10 Transfer Line Optics via Transfer Matrix Measurement", *CERN PS Note (CA) 98-020* and *CERN SL-MD Note 98-058* (1998).
- [4] G. Arduini, M. Giovannozzi, D. Manglunki, M. Martini, "Measurement of the optical parameters of a transfer line using multi-profile analysis", *CERN PS (CA) 98-032* (1998).
- [5] P. J. Bryant, K. Johnsen, "The principles of circular accelerators and storage rings", (Cambridge University Press, Cambridge, 1993).
- [6] D. A. Edwards, M. J. Syphers, "An introduction to the physics of high energy accelerators", (John Wiley & Sons, New York, 1993).
- [7] G. Arduini, G. Crockford, C. Despas, M. Giovannozzi, K. Hanke, D. Manglunki, M. Martini, G. Métral, C. Niquille, "Betatron and dispersion matching of the TT2/TT10 transfer line for the 26 GeV/c fast extraction", *CERN PS Note (CA) 99-07* and *CERN SL Note 99-003 MD* (1999).
- [8] G. Arduini, G. Crockford, M. Giovannozzi, K. Hanke, D. Manglunki, M. Martini, G. Métral, C. Niquille, "TT2/TT10 transfer line studies for the 14 GeV/c continuous transfer", *CERN PS Note (CA) 99-08* and *CERN SL Note 99-013 MD* (1999).
- [9] G. Arduini, G. Crockford, C. Despas, M. Giovannozzi, K. Hanke, D. Manglunki, M. Martini, G. Métral, C. Niquille, "Betatron and dispersion matching of the TT2/TT10 transfer line for the fixed target lead ion beam", *CERN PS Note (CA) 99-09* and *CERN SL Note 99-018 MD* (1999).
- [10] G. Arduini, K. Hanke, "Tuning Knobs for the PS-SPS Transfer Line", these proceedings, (1999).



# TUNING KNOBS FOR THE PS-SPS TRANSFER LINE

G. Arduini, K. Hanke\*, CERN, Geneva, Switzerland

## Abstract

Transverse emittance preservation will be an important issue for the LHC injector chain. Minimization of the blow-up at injection by tuning independently the Twiss parameters ( $\alpha$ ,  $\beta$ ), the dispersion  $D$  and the dispersion derivative  $D'$  is therefore mandatory. The optics of the transfer line between the PS and SPS machines was modeled and matched using the program package MAD. Tuning knobs were developed using a singular value decomposition (SVD) algorithm. Coupled to the measurement of the Twiss parameters at a given point downstream of the correction elements they provide a fast correction algorithm for the betatron mismatch.

## 1 INTRODUCTION

The PS and SPS machines are part of the CERN injector chain for LHC. In the tight transverse emittance budget for the LHC beam a maximum of 17 % blow-up is allocated for the transfer from PS extraction to SPS extraction [1] and only a small fraction of it is assigned to injection mismatch. The injection line must be therefore very accurately matched to the optics parameters of the PS at the extraction point and of the SPS at injection.

The transfer line optics was modeled using the program package MAD [2]. The geometry of the model was verified versus the official CERN survey data, while the correct magnetic behaviour was verified in a series of measurements. Based on the model, the line was successfully rematched [3] (and references therein). For the matched optics no blow-up due to mismatch could be detected except for the component due to dispersion in the horizontal plane. The residual mismatch is due both to the unavoidable discrepancy between model and reality and to the uncertainty in the measurement of the initial optical parameters. An on-line measurement of the optics parameters at the injection point together with 'knobs' allowing to tune  $\alpha$ ,  $\beta$ ,  $D$ ,  $D'$  orthogonally is therefore very important.

## 2 CORRECTION MECHANISM

The developed tuning knobs are based on the inversion of the matrix  $\left(\frac{\partial \Delta_i}{\partial K_j}\right)$  ( $i, j = 1, \dots, 8$ ), where  $\Delta_i = (\alpha_{H(V)}, \beta_{H(V)}, D_{H(V)}, D'_{H(V)})$  and  $K_j$  is the strength of the  $j^{th}$  matching quadrupole [4]. As a first attempt only the eight independent quadrupoles of the matching section controlled from the SPS control room have been considered for simplicity reasons.

Frequently, as in our case, the coefficient matrix for a given

optics will be either singular or numerically close to singular. Singular value decomposition (SVD) algorithms provide a tool to diagnose a matrix and to solve the resulting system of equations even for ill-conditioned matrices [5]. An ill-conditioned matrix implies the onset of non-orthogonality in the variation of the optics parameters as well as a reduced efficiency of the knob for the tuning of some of the optical injection parameters. This could be confirmed with an extensive test of the knob by means of MAD simulations: the variations of the quadrupole strengths calculated with the reconditioned inverse matrix for a given optics parameter trim were introduced in the optical model and the resulting modification of the optics parameter at injection was simulated. This showed in particular that the knob was not effective for the trim of  $\beta_H$ .

## 3 EXPERIMENTAL RESULTS

The tuning tool was tested with beam, using the SPS mismatch monitor [6]. This system is based on a turn-by-turn measurement of the beam size with an OTR screen and a fast CCD camera. Oscillation of the beam size indicates betatron or dispersion mismatch at injection into the SPS. In the assumption that no dispersion mismatch is present (or at least is known), a measurement of  $\alpha$  and  $\beta$  (and of the emittance of the beam) can be performed by measuring the beam profile at three successive turns in the SPS. The Twiss parameters can then be obtained in the same way as from a multi-grid measurement in a transfer line [7]. Since the measurement of the Twiss parameters can be performed much faster than a precise measurement of the dispersion<sup>1</sup>, it was decided to detune the horizontal and vertical  $\beta$ -functions and to measure Twiss parameters and mismatch factor using the SPS mismatch monitor. Starting from a matched setting, the  $\beta$ -functions were detuned by  $\pm 10\%$  and  $\pm 20\%$ . Figure 1 shows the desired change of the horizontal  $\beta$ -function (dashed line), the result obtained from the simulations above discussed and the measured values. As previously mentioned, already in the simulation the expected variation is not achieved. Only the points for  $\Delta\beta = 0$ ,  $-10$  m and  $-20$  m could be measured due to a technical problem. For the initial setting ( $\Delta\beta = 0$ ), the measured value lies already below the theoretical one. This means that the line is not perfectly matched as can be observed also in Figure 2 showing the horizontal geometrical blow-up factor (calculated from the obtained Twiss parameters) as a function of the change of  $\beta_H$  for the same measurement. The above data are consistent with

<sup>1</sup>A faster but, for the moment, less precise measurement of the horizontal dispersion can be performed by measuring at least 5 consecutive profiles [8].

\*Email: klaus.hanke@cern.ch

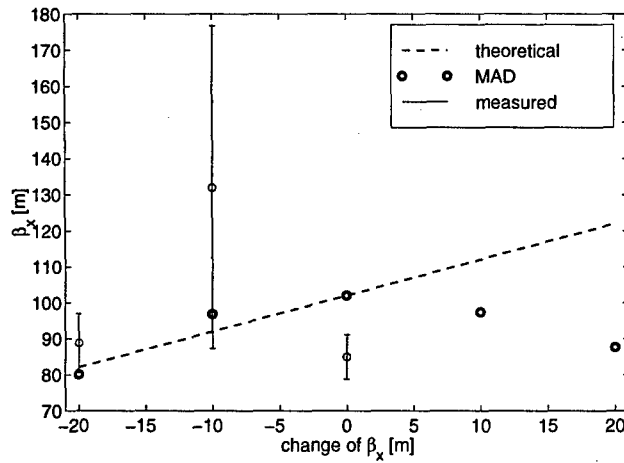


Figure 1: Horizontal  $\beta$ -function at the injection point as a function of the variation applied using the tuning knob. Starting from a matched optics ( $\Delta\beta = 0$ ), the  $\beta$ -function is detuned by  $\pm 10$  m and  $\pm 20$  m. The expected, simulated and measured behaviour of the  $\beta$ -function is shown.

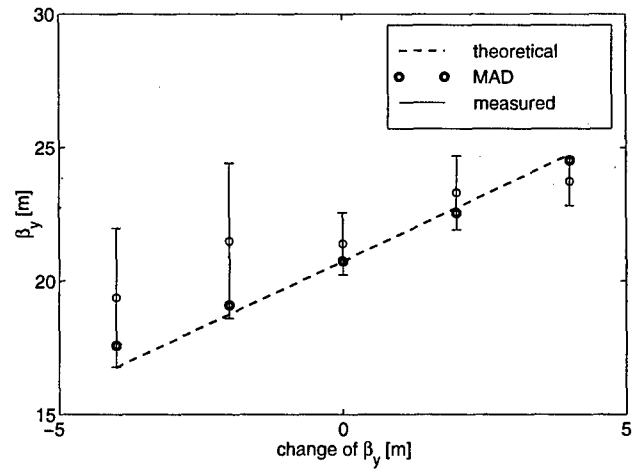


Figure 3: Vertical  $\beta$ -function at the injection point as a function of the variation applied using the tuning knob. Starting from a matched optics ( $\Delta\beta = 0$ ), the  $\beta$ -function is detuned by  $\pm 2$  m and  $\pm 4$  m. The expected, simulated and measured behaviour of the  $\beta$ -function is shown.

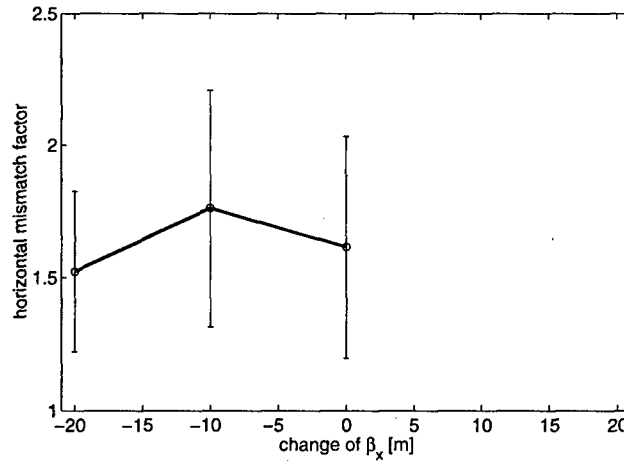


Figure 2: Measured horizontal mismatch factor as a function of the variation applied using the tuning knob.

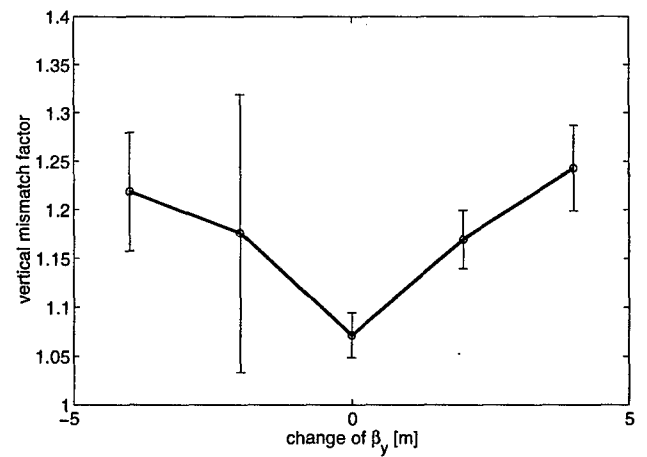


Figure 4: Measured vertical mismatch factor as a function of the variation applied using the tuning knob.

the horizontal geometrical blow-up of 1.3 obtained from a multi-grid measurement in the line for the matched conditions. Figure 5 shows the horizontal  $\alpha$  for the same measurement. Since the knob is orthogonal, it is supposed to stay constant. The significant statistical errors in the measurement can be explained partly by some fluctuations in the beam characteristics provided by the injectors but also by the residual dispersion mismatch present in the matched optics. This constitutes a source of 'background' for the Twiss parameter measurement. The inefficiency of the knob for  $\beta_H$  adjustment, the small number of points available and the large errors make a conclusion impossible for the measurement in the horizontal plane. The same mea-

surement was done in the vertical plane. All five settings could be measured, virtually no dispersion mismatch was present for the matched optics and the stability of the beam characteristics was excellent. Figure 3 shows theoretical, simulated and measured values of  $\beta_V$  for five different settings of the tuning knob. All data agree within the statistical error. From the same measurement, the vertical geometrical blow-up factor was computed. The result is shown in Fig. 4. For the matched optics ( $\Delta\beta = 0$ ), a vertical geometrical blow-up factor of 1.1 is found, which is in agreement with the result obtained from a multi-grid measurement in the line [3]. Detuning the  $\beta$ -function at the injection point in both directions leads to an increase of the mismatch fac-

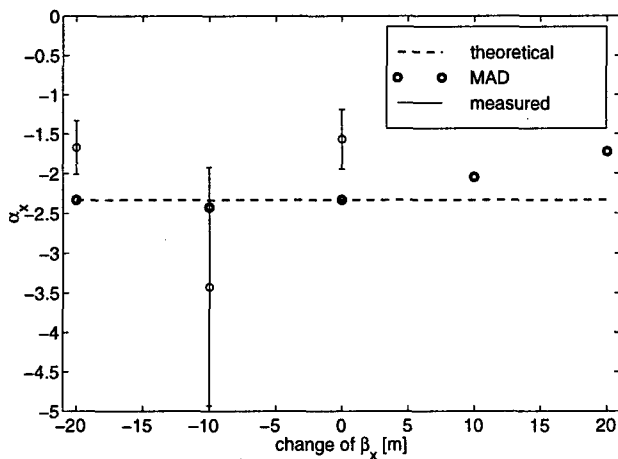


Figure 5: Measured horizontal  $\alpha$  for the same measurement as shown in Figs 1 and 2.

tor as expected. Figure 6 shows the vertical  $\alpha$  for the same measurement. It stays constant within the errors, which means that the tuning knob acts only on the  $\beta$ -function as specified.

For both measurements in the horizontal and vertical plane, also the beam parameters in the other plane were observed. They were found to be unaffected as specified. For details see Ref. [4].

#### 4 CONCLUSIONS AND OUTLOOK

An analytical approach was used to develop a tool for selective orthogonal tuning of the optics parameters in the PS-SPS transfer line. Eight independent quadrupole strengths are used as free parameters to tune eight beam parameters. A coefficient matrix which contains the variation of the Twiss parameters as a function of eight quadrupole strength parameters was generated based on a MAD simulation of the line. It was reconditioned and inverted using a singular value decomposition algorithm. The resulting system of equations can be solved and yields the change of quadrupole strength required to obtain a given change of any of the parameters  $\alpha, \beta, D, D'$  at injections while the others remain unchanged. A first measurement with beam, carried out during the 1998 SPS run, allowed to confirm that for the horizontal and vertical  $\beta$ -functions.

It is planned to continue the development and test of the measurement and tuning devices during 1999 and to provide the following enhancements:

- to consider a different set of quadrupoles to get effective variation of all the optics parameters at injection;
- to minimise the source of errors in the measurement by reducing the dispersion mismatch in the horizontal plane for the matched optics;
- to extend the measurement of the effect of the knob not only to all the Twiss parameters but also to the dispersion

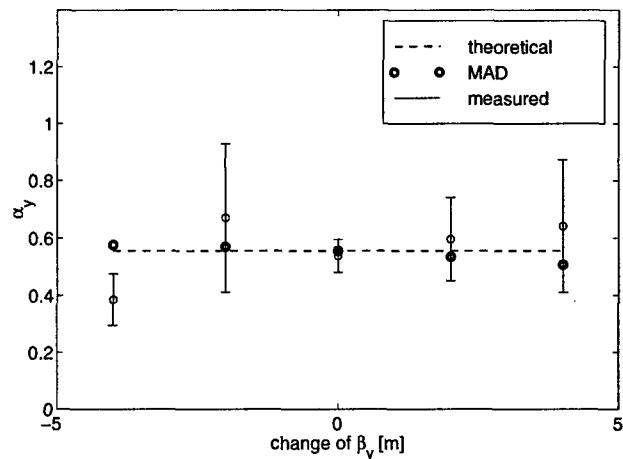


Figure 6: Measured vertical  $\alpha$  for the same measurement as shown in Figs 3 and 4.

and its derivative.

#### 5 ACKNOWLEDGEMENTS

The authors would like to thank R. W. Assmann and P. Raimondi for fruitful discussions, R. Jung and his team for the setting-up of the mismatch monitor in the SPS, M. Giovannozzi and D. Manglunki for the setting-up and monitoring of the beam used for the measurement.

#### 6 REFERENCES

- [1] P. Collier (ed.), *The SPS as Injector for LHC, Conceptual Design*, CERN-SL-97-07 DI (1997).
- [2] H. Grote, F. C. Iselin, *The MAD Program, User's Reference Manual*, CERN-SL-90-13 AP (1990).
- [3] G. Arduini, M. Giovannozzi, K. Hanke, D. Maglunki, M. Martini, G. Métral, *Measurement and Optimisation of the PS-SPS Transfer Line Optics*, these proceedings.
- [4] G. Arduini, K. Hanke, *Tuning Knobs for the TT2/TT10 Transfer Line*, in preparation.
- [5] B. P. Flannery, W. H. Press, S. A. Teukolsky, W. T. Vetterling, *Numerical Recipes in Fortran, The Art of Scientific Computing*, 2<sup>nd</sup> edition, Cambridge University Press (1986).
- [6] C. Bovet, R. Jung, *A New Diagnostic for Betatron Phase Space Matching at Injection into a Circular Accelerator*, LHC project report 3, rev. (1996).
- [7] P. J. Bryant, K. Johnsen, *The Principles of Circular Accelerators and Storage Rings*, Cambridge University Press, Cambridge (1993).
- [8] G. Arduini, M. Giovannozzi, D. Manglunki, M. Martini, *Measurement of the Optical Parameters of a Transfer Line using Multi-profile Analysis*, CERN PS-Note-98-032 (CA) (1998).

# STUDY OF SPACE CHARGE COMPENSATED LEBT FOR ESS \*

A. Lakatos, J. Pozimski, O. Meusel, A. Jakob, H. Klein

Institut für Angewandte Physik, Universität Frankfurt, 60054 Frankfurt, Germany

## Abstract

To fulfil the requirements of ESS on beam transmission and emittance growth a detailed knowledge of the physics of beam formation as well as the interaction of the  $H^-$  with the residual gas is substantial. Space charge compensated beam transport using solenoids for ion optics is in favour for the Low Energy Beam Transport (LEBT) between ion source and the first RFQ. Space charge compensation reduces the electrical self fields and beam radii and therefore emittance growth due to aberrations and redistribution. Transport of  $H^-$  near the ion source is negatively influenced by the dipole fields required for beam extraction and  $e^-$ -dumping and the high gas pressure. The destruction of the rotational symmetry together with the space charge forces causes emittance growth and particle losses within the extraction system. High residual gas pressure near the extractor together with the high cross section for stripping will influence the transmission as well as space charge compensation. Therefore a detailed knowledge of the interaction of the residual gas with the beam and the influence of the external fields on the distribution of the compensation particles is necessary to reduce particle losses and emittance growth. Preliminary experiments using positive hydrogen ions for reference already show the influence of dipole fields on beam emittance. First measurements with  $H^-$  confirm these results. Additional information on the interactions of the residual gas with the beam ions have been gained from the measurements using the momentum and energy analyser.

## 1 INTRODUCTION

The production and low energy transport of high current negative ion beams is a key issue for future high current accelerators (i. g. spallation sources like ESS [1] (generalised perveance  $K=0.0035$ ) and SNS [2]). The extraction and transport of these beams have intrinsic difficulties different from positive ion beams. Different extraction and ion beam transporting schemes are under discussion [3,4], each have various positive and negative aspects.

A compact caesium free [5]  $H^-$  volume source delivering a low energy high perveance beam ( $H^-$ , 6.5 keV, 2.3 mA,  $K=0.0034$ ) has been built to study the fundamental physics of beam transport [6,7].

To improve the  $H^-$  to  $e^-$  ratio magnetic filterfields (i. g.

dipoles) are used [8]. These filter fields in conjunction with dipole fields for electron dumping impede exact beam extraction simulations by destruction of the rotational symmetry. This destruction on the other hand can cause together with the influence of the dipole fields on the plasma sheath emittance growth within the extraction system, this has been proven for positive ions.

## 2 EXPERIMENTAL SET UP

A schematic drawing of our source is shown in Fig. 1. The source can be divided into three parts: the plasma generator (left), the extraction system (centre) and the dumping system (right). The plasma generator is equipped with a solenoid and a filter magnet on the front end. The filter magnet, an electrical dipole magnet, is installed near the plasma electrode.

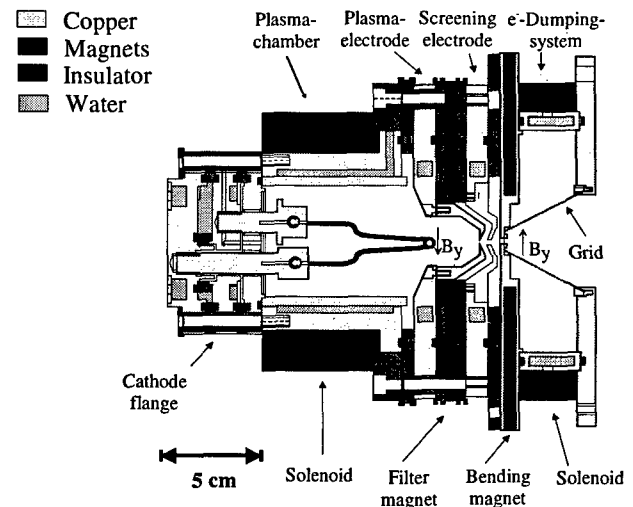


Figure 1: Schematic drawing of the ion source.

The magnetic field of the bending magnet deflects the simultaneously extracted electrons into the dumping system. To reduce the magnetic field strength at the outlet aperture and therefrom the influence on beam emittance, the filter magnet and the bending magnet of the dumping system have opposite polarity. To study the fundamental behaviour of the ion source for different parameters of the plasma generator a test bench was installed. A schematic drawing of the test bench is shown in Fig. 2. Multiple beam diagnostic elements like a magnetic and electrostatic spectrometer, an emittance measurement device, a residual gas ion energy spectrometer (RGI) and Faraday cups are available along the beam path.

\* Work supported by BMBF under contract no. 06 OF 841

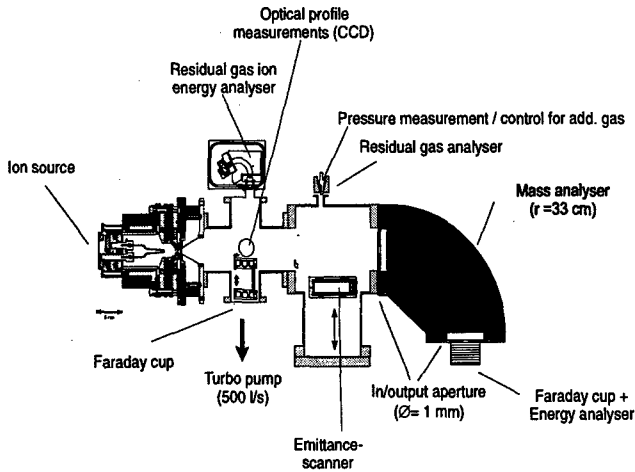


Figure 2: Schematic drawing of the experimental set up of the test bench for the H-source.

The radial density profile of the extracted beam can be measured by a CCD-Camera using the incident light emitted by collisions of the beam ions with the residual gas atoms. The measurements can be performed at different residual gas pressures.

### 3 REFERENCE MEASUREMENTS WITHOUT MAG. DIPOL FIELDS

Magnetic filter field are used near the extraction system of the ion source to generate negative ions. These fields influence the beam extraction and can be a source of emittance growth. Additionally they influence the current density delivered by the source. On the other hand theory of ion extraction shows that the extracted emittance for a given extraction system varies with the extracted beam current [9]. To distinguish these two effects on the beam emittance it was necessary to make the beam emittance insensitive to current variation by optimisation of the triode extraction system for wide range of current fluctuation [6]. This was done by carefully designing the extractor geometry by the use of numerical simulations[10].

To proof the results of the simulation and to have reference data we measured the emittance as function of the ion current in absence of the magnetic dipole fields. This is only possible for positive ions, because filter fields are essential for generation of negative ions. Fig. 3 shows the measured function  $\epsilon = f(I)$  of the extraction system without dipole fields in the range of interest for the measurements with dipole fields (see. Fig. 5, next chapter). The ion current was varied by increasing the arc current of our source. All other source parameter have been kept constant.

The emittance was measured 38 cm behind the outlet aperture. The generalised perveance in this measurement varied between  $K=0.0011$  and  $K=0.003$ .

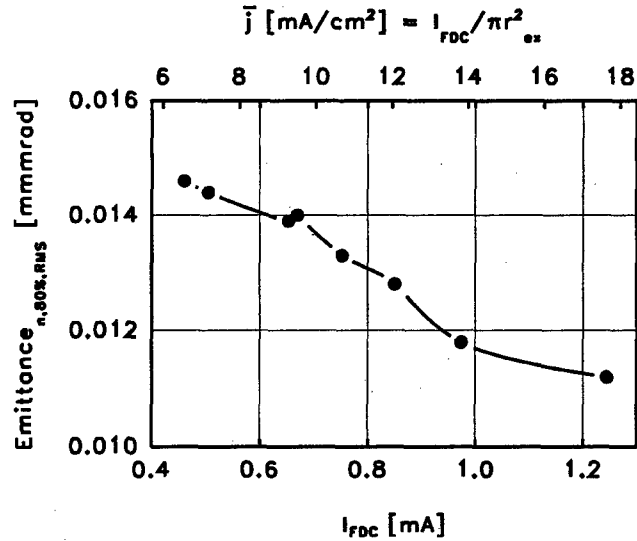


Figure 3: Measured emittance as function of the beam current for positive ions (extraction voltage 6 keV, radius of extraction hole  $r_{ex} = 1.5$  mm, see also fig. 4).

The emittance decreases with increasing the extractable current. The absolute change of the emittance is app.  $\epsilon_{0.80\%, RMS} = 0.003 \pi \text{ mmrad}$  (40 %) induced by a current variation of 300%. Therefore an emittance growth larger than 0.003 can be interpreted as influence of the magnetic dipole fields.

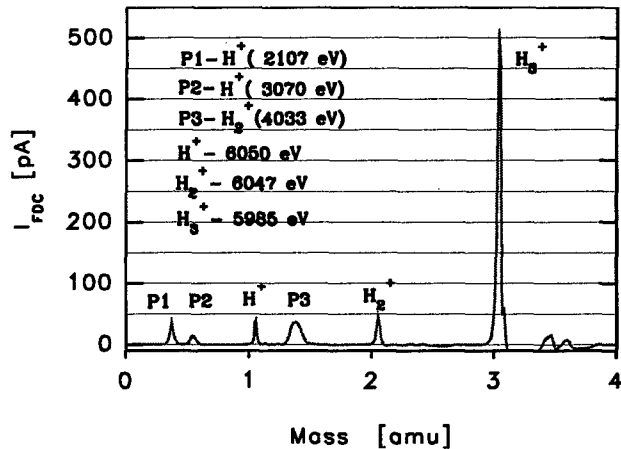


Figure 4: Result of the energy and mass spectrum of the extracted beam (6 keV).

Fig4. shows the result of the energy and mass spectrum of the extracted beam. The main fraction of the positive ion peak was  $H^+$ . Minor changes of the  $H^+$  and  $H_2^+$  fraction have been measured with filter fields. The ion energy of the peaks P1, P2 and P3 indicate that the ions are produced by interaction of  $H^+$  with residual gas atoms in the extraction area. Their energy is determined by the momentum exchange at interaction. Further work to understand these results in more detail are planned.

#### 4 $\epsilon$ -MEASUREMENTS WITH MAGNETIC DIPOL FIELDS

Second we measured the emittance as function of the fields of the bending and filter magnet (Fig.5). At the location of the plasma sheath the magnet is excited to about 20 G per 1 A. The negative current on the axis means an opposite polarity to the filter magnet. The current extracted from the source was in the range of Fig.3 (0.4 mA – 1.2 mA). Thus all emittance growth larger than 0.003 can be interpreted as influence of the magnetic dipole fields. Without the help of the bending magnet some of the emittance was deflected partial out of the range of the emittance scanner. The grid is built by the measurements points, the coloured area corresponding to truncated emittances.

One can see an drastic emittance growth for exclusive use of the filter field. One can reduce this emittance growth (up to 500 %), which is an factor 10 higher than the influence of the extraction system (Fig.3) contracting the influence of the filter by using the bending dipole magnet in opposite polarity. To understand the little influence of the bending magnet on beam emittance further experiments are planned. At present it seems helpful to reduce the emittance growth due to the necessary filter fields by use of the bending magnets. This measurements will be repeated with negative ions.

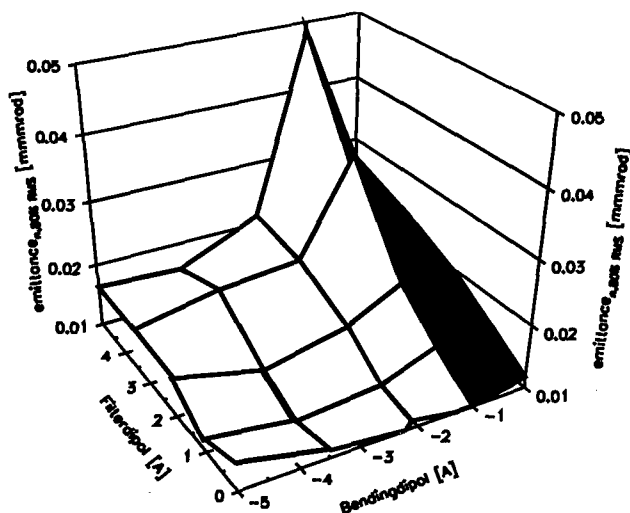


Figure 5: Influence of the dipole magnets on the measured emittance (negative current =opposite polarity)

#### 5 OUTLOOK

After finishing the measurements on the test bench the source will be incorporated into the existing LEBT which is capable with the ESS scenario. The details of the beam line layout are shown in Fig. 6.

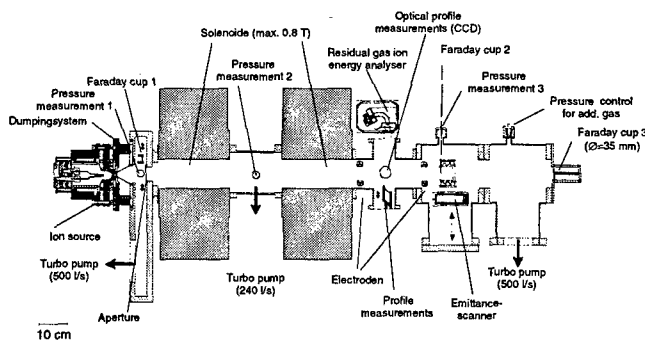


Figure 6: Schematic drawing of the experimental set up of the Frankfurt LEBT line.

First measurements to test the diagnostics (CCD, RGI) have already been performed using a beam of positive hydrogen ions with comparable beam parameters delivered by a different source. The extraction voltage was 6.6 kV, the ion current 3 mA measured after transport through the LEBT section ( $K=0.0042$ ).

The experiments will start with a DC H<sup>+</sup> beam to study the influence of the external parameters (filter fields, solenoids, residual gas pressure, voltage on decompensation electrodes, source noise) on emittance and transmission. For a next step the set up is already prepared for pulsed mode operation.

#### 6 REFERENCES

- [1] H. Klein et. al., "The ESS Technical Study", ESS-96-53-M, November 1996
- [2] B.R. Appleton, J.B. Ball and J.R. Alonso , "The National Spallation Neutron Source", EPAC'96, Sitges, June 1996. p. 575
- [3] J. W. Staples et al. , "All Electrostatic Split LEBT Test Results", LINAC'96, Geneva, August 1996. p. 157
- [4] J. Pozimski, P.Groß, R. Dölling, K. Reidelbach and H.Klein, "LEBT-Design Studies for ESS", Proc. of ESS-PM4, October 1995, Weinfelden, PSI-Proc. 95-02
- [5] Ehlers, K. N. Leung et. al., "Increasing the efficiency of a multicusp ion source", Rev. Sci. Instr. 53(2), 1982, p. 1429
- [6] A. Lakatos, J. Pozimski, A. Jakob, K. Klein, Proc. of EPAC 98, Stockholm, June 22-26, 1998, p.1400
- [7] A. Lakatos, J. Pozimski, A. Jakob, K. Klein, Proc. of LINAC 98, Chicago, August 23-28, 1998, TU4056
- [8] Ehlers, K. N. Leung et. al., "Effect of a magnetic filter on hydrogen ion species in a multicusp ion source", Rev. Sci. Instr. 52(2), 1981, p. 1452
- [9] R. G. Wilson, G. R. Brewer, Ion Beams, John Wiley & Sons, New York, London, Sydney, Toronto(1973)
- [10] R. Becker, W. B.Herrmansfeldt, Proc. of the 4<sup>th</sup> International Conference on Ion Source, Bensheim, Germany (1991)

# FORMATION OF BREMSSTRAHLUNG FLOW WITH SMALL DIVERGENCE AT LINAC OUTPUT FOR PLANET SURFACE SOUNDING WITH INTERPLANETARY SPACE STATIONS

B. Bogdanovitch<sup>1</sup>, V. Kudinov, S. Minaev, A. Nesterovitch,  
Yu. Pomazan, MEPhI, Moscow, Russia.

## Abstract

The task of atmosphere structure or planet surface definition from interplanetary space stations can be decided both with use of hydrogen neutral atoms beams [1], and flows of brake radiation. One case depth of an analysed layer is much higher in view of greater penetrating ability of quanta in comparison with neutral particles. The brake radiation is used by search of minerals with the definition from interplanetary space stations accelerators help. Till now space geophysics development restrained by radiation large angular divergence, caused target significant thickness at the accelerator. In works [2-3] the research results of various ways of electron flows radiation formation, driven on a cyclic or spiral orbit were stated. The opportunity of a radiation intensity increase due to electron multifold passage of the thin target under condition at the electron flow adiabatic cooling was experimentally confirmed.

The main difference of these modes was the maximum energy and minimum radiation flow divergence restriction caused by realising design specificity. The research results of system intended for electron beams with energy up to several hundreds MeV and angular divergence (1-10) mrad are described in the paper given.

## 1 THE BREMSSTRAHLUNG FLOW FORMATION SCHEME

The device scheme realising an proposed method in the specified parameters region, is shown in a Fig. 1.

To avoid attenuation of radiation in a target and to increase an electron beam use efficiency, it is proposed to set a sequence of thin targets (foils) in periodic magnetic system (PMS) with a vertical rejecting magnetic field with changing direction (the "wiggler" type system). If to place thin targets in each second interval between magnets, i.e. in points with maximal on value and identical on sign by an beam trajectory angular deviation, the radiation from each previous targets within the limits of some angular divergence will pass all next foils, and the beam incidence direction on each target can be made identical. Hence, in such system the effect of generated radiation attenuation in a thick target will be excluded with remaining of separate radiation vectors parallelism.

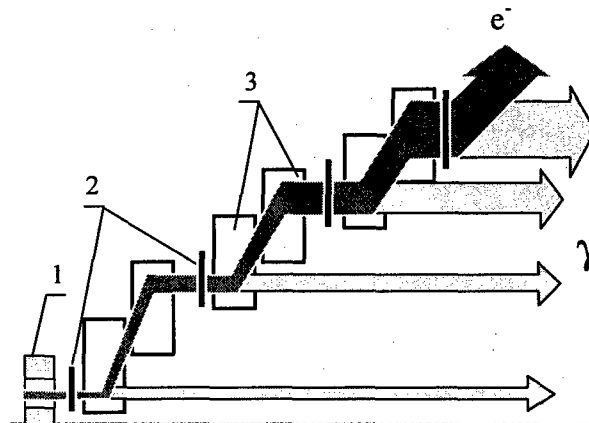


Figure 1: The bremsstrahlung flow formation scheme (1 - electron accelerator; 2 - foils; 3 - magnets)

The single target thickness defines as well radiation angular divergence. With passage of an electron beam through substance the electron angular disorder stochastically grows, so beam cross temperature and, accordingly, it's emittance are increasing. It is obvious, that thus bremsstrahlung photons, produced in the target depth, also have a wider angular spectrum. Thus, if a subject of interest is the energy irradiated within a small cone angle, it is possible to tell, that the beam use efficiency on a thick target decreases not only due to attenuation in deep layers, but also because of the electron angular disorder increase.

The PMS with thin targets proposed can partially compensate this effect. The beam angular disorder is increased by jump after each target passing. If in PMS it was possible to provide effective simultaneous beam focusing in both cross directions (vertical and horizontal), on each site between the previous and subsequent targets it would be possible to reduce a little a beam angular divergence in comparison to equivalent uniform thick target. Certainly, thus it is impossible to prevent or to reduce beam cross emittance growth due to stochastic processes of dispersion in substance. It is possible to hope only for some reduction of angular divergence by the cross sizes increase. So with the successfully chosen PMS with thin targets parameters the electron beam can have smaller angular divergence, but more large cross sizes in comparison to a thick target.

<sup>1</sup>E-mail: bogdan@uni.mephi.ru

## 2 BREMSSTRAHLUNG PHOTONS OUTPUT FROM THE TARGET

The expression for bremsstrahlung radiation angular distribution from thick targets can be received by taking into account repeated dissipate electron distribution on the target depth. Lawson, Lanzl and Hanson used for it distribution Moliere in the form:  $\exp(-E_0^2\theta^2/ct)$ . A constant  $c$  chose so that distribution width was same, that exact expression. The repeated dissipate electron distribution convolution and bremsstrahlung radiation angular distribution for an indefinitely thin target, integrated by complete thickness, gives the following expression for bremsstrahlung radiation angular distribution from a target thickness  $t$ :

$$F(\theta, E_0) = F_1(\theta, E_0) + F_2(\theta, E_0)$$

$$F_1(\theta, E_0) = \frac{0.85\theta_1^2 \left( -Ei \left( -\frac{E_0\theta^2}{ct + \theta_1^2} \right) + Ei \left( -\frac{E_0^2\theta^2}{\theta_1^2} \right) \right)}{0.85\theta_1^2 \ln \left( 1 + \frac{ct}{\theta_1^2} \right) + 0.15\theta_2^2 \ln \left( 1 + \frac{ct}{\theta_2^2} \right)}$$

$$F_2(\theta, E_0) = \frac{0.85\theta_2^2 \left( -Ei \left( -\frac{E_0\theta^2}{ct + \theta_2^2} \right) + Ei \left( -\frac{E_0^2\theta^2}{\theta_2^2} \right) \right)}{0.85\theta_1^2 \ln \left( 1 + \frac{ct}{\theta_1^2} \right) + 0.15\theta_2^2 \ln \left( 1 + \frac{ct}{\theta_2^2} \right)}$$

Where:  $\theta_1^2 = 0.533 \text{ rad}^2$ ,  $\theta_2^2 = 2.85 \text{ rad}^2$ ,  $E_0$  - electron energy,  $t$  - a target thickness in  $\text{g/cm}^2$ , expressed further through radiating length  $X_0$  for aluminium, copper and tungsten through factors 24.3, 13.0 and 6.8, accordingly. The constant  $c$  is defined for these three elements as  $(\pi/180)^2 2.8 \cdot 10^4$ ,  $(\pi/180)^2 6.12 \cdot 10^4$ ,  $(\pi/180)^2 1.23 \cdot 10^5$ .

The integrate indicated function in the large importance field is tabulated, and in the small importance field has a kind:

$$E_i = \sum_{m=1}^{100} \frac{(-1)^{m+1} x^m}{m! m} - \ln(x) - 0.5772$$

## 3 CHOICE OF MAGNETIC SYSTEM PARAMETERS

Having limited general length of 6 m, the eight targets variant is considered in the present paper. On which target is lost 10% of beam energy, so the energy in PMS changes from 200 up to 90 MeV. The magnetic field induction in the beginning PMS is chosen close to a limit of electrotechnical steel saturation and equals to 2 T. To keep the beam incidence angular on a target by an energy reduction all magnets are chosen identical on length, and magnetic field induction in the gap are chosen accordingly decreasing. It enables to increase gap height with inevitable growth of beam sizes owing to dispersion on targets. The magnet lengths were choosed proceeding of beam focusing conditions, and in the given variant make 250 mm with an interval 100 mm. The value of induction and gradients on system length were selected by a consecutive approximate method by the account results proceeding from beam behaviour and beam cross sizes.

Previously chosen magnetic system parameters are submitted in Table 1.

Table 1: Parameters of periodic magnetic system

Cell number	1	2	3	4	5	6	7	8	9	10	11	12	13	14	15
Induction, T	-2	2	-1.8	1.8	-1.58	1.58	-1.4	1.4	-1.26	1.26	-1.14	1.14	-1.04	1.04	1
Gradient, T/m	1	1	0.9	0.9	0.8	0.8	0.7	0.7	0.6	0.6	0.5	0.5	0.5	0.5	0.5

## 4 TARGET RADIATION CHARACTERISTICS CALCULATED RESULTS

The calculated results of bremsstrahlung energy integrated angular distribution from all targets PMS, which parameters are given in the table (8 copper targets, initial electron energy 200 MeV, energy loss in each of targets make 10 %), are submitted on Fig.2. The normalised distribution function value  $W(\theta)$  for axial-symmetric beam shows, what part of energy is radiated inside of cone with uncover angle  $\theta$ . As in this case

conditions of movement in horizontal and vertical planes are various, the separate functions  $W_x(\theta)$  and  $W_y(\theta)$  are used. Ones describes angular distribution in sectors of an elliptic cone located near to axes  $OX$  and  $OY$ , accordingly. The size  $W_0(\theta)$  is designed for an ideal hypothetical case when the strictly parallel electron beam falls on each target and is, in essence, unattainable top limit of radiation focusing with the given targets system. Opposite, the function  $W_i(\theta)$  shows angular distribution from targets in magnetic field absence and, accordingly, beam focusing (total thick target). As it is possible to see from a Fig.2, half of energy from a thick target (stroke-



dotted curve) is radiated inside of an angle about 2.5 degrees, whereas in an ideal case of parallel beam (dotted curve) this size makes by few more than 0.5 degrees. The functions of distribution in horizontal and vertical planes (continuous curves), designed for the given system, not strongly differ and lay closer to ideal curve.

Half of bremsstrahlung energy in both planes is made in this case in limits about 1 degree. Thus, on distance from system, it is essential greater, than its length, is possible to expect increase of bremsstrahlung flow density in 6-7 times in comparison with a uniform target of equal total thickness.

## 5 THE CONCLUSION

The basic result of the paper given is the physical substantiation of bremsstrahlung density increasing (focusing) method in periodic magnetic system with thin targets, development of account methods of the electron dynamic, radiation characteristics and computer programs. The submitted results are not optimum and can be improved by a more careful choice of the PMS parameters, sizes distributions of an induction and gradients.

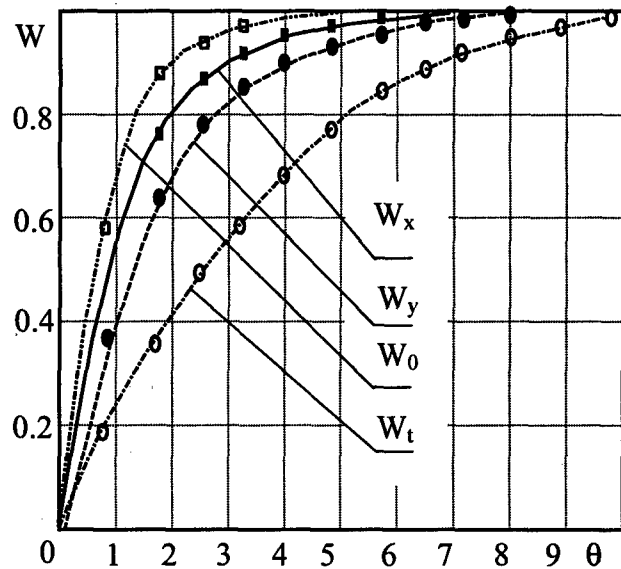


Figure 2 : Integrated angular distribution functions of bremsstrahlung energy from all targets in periodic magnetic system

## 6 REFERENCES

- [1] B. Bogdanovitch, A. Nesterovitch, et al. "A Space Accelerator Station for Planet Substance Analysis." EPAC-98 (6-th Europ. Part. Accel. Conf.), Stockholm, 22-26 June, 1998, Abstracts, p. 37.
- [2] B. Bogdanovitch, A. Nesterovitch, et al. "X-ray Radiation Intensity Increasing by means of a Discrete Target in a Magnetic Field. " EPAC-98 (6-th Europ. Part. Accel. Conf.), Stockholm, 22-26 June, 1998, Abstracts, p. 37.
- [3] B. Bogdanovitch, A. Nesterovitch, et al. " Bremsstrahlung Intensity and Average Energy Increase, it's Divergence Reduction in the Target of New Type. " Bull. Of American Phys. Soc., Vol. 42, № 3 (1997), p. 1388.

# SLOW BEAM EXTRACTION AT KSR WITH COMBINATION OF THIRD ORDER RESONANCE AND RFKO\*

A.Noda<sup>†</sup>, T. Shirai, H. Tonguu, T. Sugimura, Y. Iwashita, A. Morita and M. Inoue  
Nuclear Science Research Facility, Institute for Chemical Research, Kyoto University  
Gokanoshō, Uji-city, Kyoto 611-0011, Japan

## Abstract

Slow extraction system for 100 MeV electron at KSR utilizing third order resonance and RFKO is designed using the same straight section for beam injection. COD control system with use of a steering magnet together with correction coils in three dipole magnets enable coexistence of such injection and extraction channel.

of the 100 MeV electron beam from  $2 \times 10^{-5}$  to  $\sim 90\%$  has been constructed[1]. The output beam from the s-band linac operated with the pulse duration of 100 ns is to be injected into the KSR ring[2]. Its repetition rate is reduced to 1 Hz from the former design of 10Hz in order to reduce the X-ray radiation due to beam losses at the beam injection and the extraction processes.

The beam injection is performed with use of a

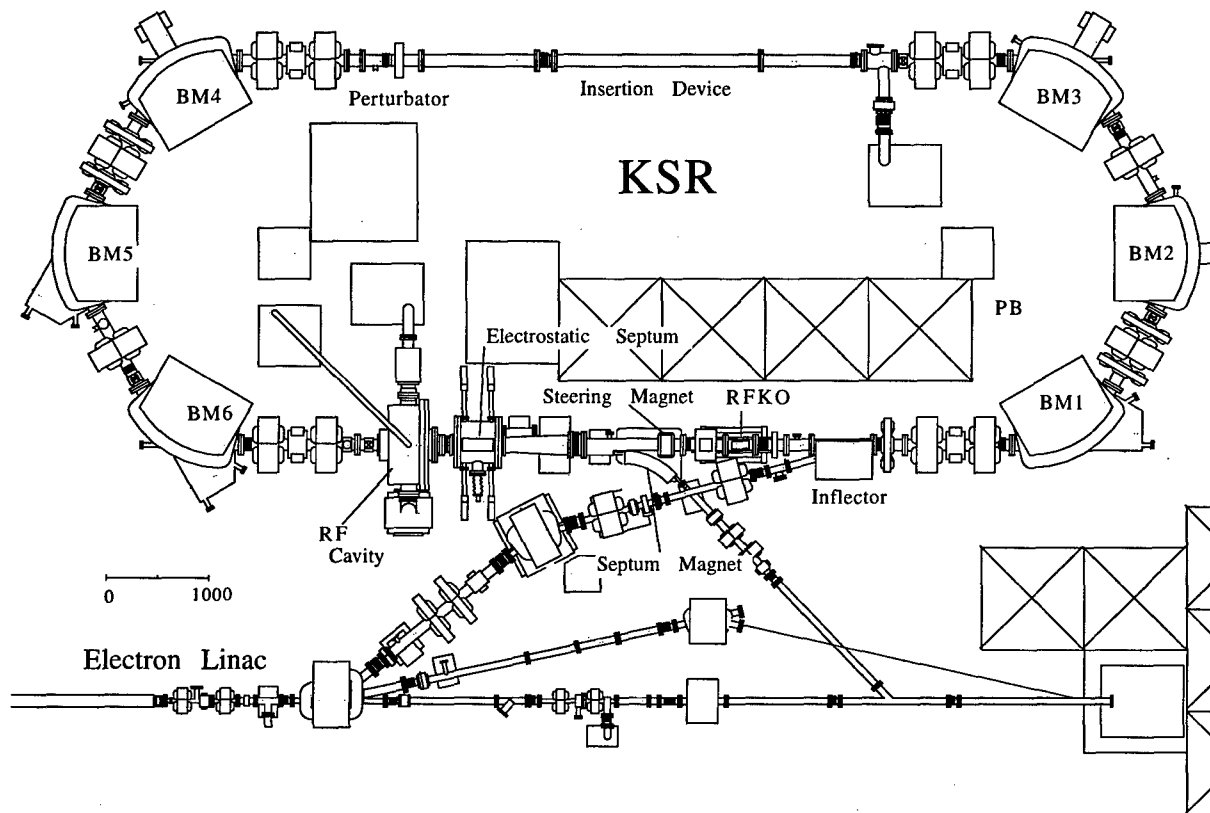


Figure 1: Layout of the injection and extraction system of KSR.

## 1 INTRODUCTION

At Institute for Chemical Research, Kyoto University, an electron stretcher ring which stretches the duty factor

\*Work supported in part by Grant-in-Aid for Scientific Research from Ministry of Education, Science Sports and Culture.

<sup>†</sup> Email: noda@kyticr.kuicr.kyoto-u.ac.jp

perturbator. For the present case, the slow beam extraction channel composed of an electrostatic septum and a septum magnet is located at the same straight section as the inflector for beam injection as shown in Fig. 1 in order to guide the extracted beam to the same beam dump as the output beam of the injector linac[3].

For slow beam extraction, it is essential to make the aperture minimum at the entrance of the first septum, which is the electrostatic septum (ESS) for the present

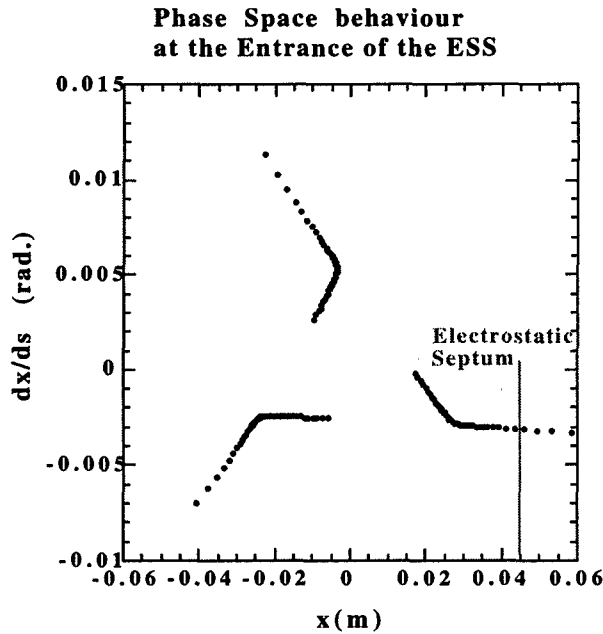


Figure 2: Phase space behavior at the entrance of the first septum.

case. It is important to compromise the beam injection and extraction to be made at the same straight section. In the present paper, the closed orbit control for this purpose is described together with the basic scheme of slow extraction.

## 2 BASIC SCHEME OF STRETCHER OPERATION OF KSR

The output beam from the linac is injected into the KSR through the inflector with use of the perturbator located just half circumference away from the inflector[1]. From the condition that the radiation shielding of the accelerator room is concrete wall 1 m in thickness, it is required to restrict the beam loss during injection and extraction processes below a certain amount. From this consideration, the repetition rate is reduced from 10 Hz to 1 Hz. In order to realize the duty factor  $\sim 90\%$ , beam extraction should be performed slowly enough. For

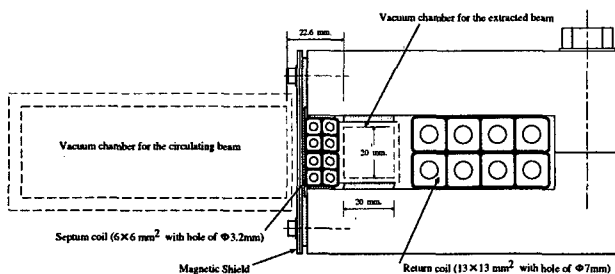


Figure 3: Cross-sectional view of the septum magnet.

heavy ions, slow beam extraction with duration about 1.5 sec has been successfully performed and the damping time of 100 MeV electron at KSR is estimated at 3.4 sec and 1.6 sec for horizontal and vertical directions, respectively. So the similar beam spill is considered to be possible for 100 MeV electron beam.

The horizontal betatron tune is adjusted at 2.364 in order to make the adequate size of the triangular separatrix with existence of sextupole field as a resonance exciter for the third order resonance,  $3\nu_H = 7$ . The injected beam circulates the ring stably at first and then application of an transverse RF electric field which resonates with the horizontal betatron oscillation (RFKO), its betatron-oscillation amplitude becomes larger and after reaching the separatrix, its motion becomes unstable and comes out along the outgoing separatrix as shown in Fig.2. The beam which deviates more than 45 mm from the central orbit of the KSR is deflected outwards by the electrostatic septum, the septum of which is 0.1 mm in thickness, locates at the position of 45 mm. The extracted beam is then guided to the septum magnet located  $\sim 1.2$  m downstream from the exit of the ESS. The extracted beam is further deflected as large as  $45^\circ$  by the magnetic field of  $\sim 5$  kG. In Fig. 3, the cross-sectional view of the septum magnet is shown.

## 3 CLOSED ORBIT CONTROL FOR INJECTION AND EXTRACTION

The central position of the injection beam from the linac is set at 41 mm from the central orbit of the KSR. The inflector is a magnetic one and the septum thickness is 5 mm and the minimum distance of the inflector septum from the KSR central orbit becomes as small as 31 mm at the exit of the inflector. In order to cope with this situation, we consider the closed orbit control. The required condition to be satisfied for such control is summarized as follows,

- (1) the aperture minimum should be realized at the entrance of the electrostatic septum,
- (2) the beam injected through the inflector, the center of which is 41 mm apart from the ring central orbit, should avoid the extraction septum and circulates until it is enlarged in amplitude by application of horizontal transverse RF electric field(RFKO voltage).

In order to satisfy the first condition, it is required to kick the beam toward inside of the ring between the electrostatic septum and the inflector as shown in Fig. 4.

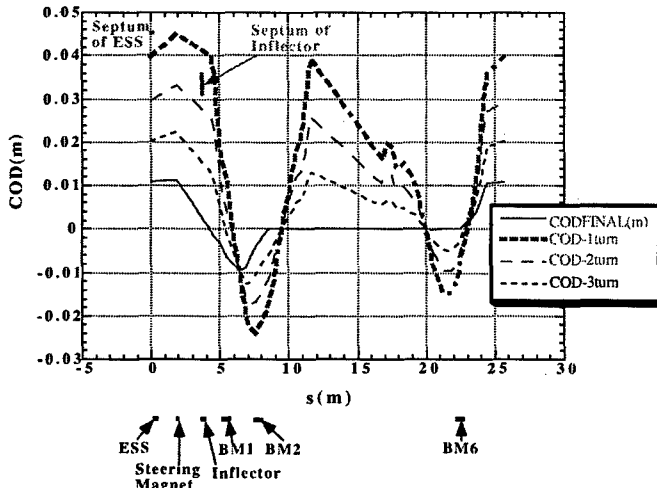


Figure 4: Closed orbit distortions during injection and after injection.

For this purpose, a steering magnet, which deflects the beam in horizontal direction, is to be utilized. With such a kick, however, it is anticipated that the closed orbit distortion will spread out to the whole circumference. Correction coils wound in three dipole magnets are also to be utilized as shown in Fig. 4 in order to localize the closed orbit distortion in the region between BM6 and BM2. The closed orbit distortion at the position  $s$ ,  $x_{\text{COD}}(s)$ , caused by the kick,  $\psi_i$  made by the steering magnet or the correction coils in the dipole magnets can be written as,

$$x_{\text{COD}}(s) = \frac{\sqrt{\beta(s)\beta(s')}}{2 \sin \pi \nu} \cos \left\{ \nu \pi - \left| \mu(s) - \mu(s') \right| \right\} \psi_i$$

where  $\beta(s)$  and  $\mu(s)$  represent beta-function and betatron-oscillation phase at the azimuthal position,  $s$ , respectively and  $\nu$  is the number of betatron oscillations per turn. Imposing the condition that superposed COD should vanish at the outside of the region between BM6 and BM2, we have obtained the closed orbit distortion as is shown in Fig.4 by the solid line. From the figure, it is known that the distance from the central orbit to the septum of the ESS is  $\sim 34$  mm, while that of the inflector septum is 29 mm, which seems not to satisfy the first condition above mentioned. The beam increased in betatron oscillation amplitude, however, always comes out along the outgoing separatrix. The beam which pass just inside the septum of the ESS has phase space coordinate of (0.045 m, -3 mrad) and comes inside of the aperture almost 10 mm during passage of the drift space between the ESS and the inflector. Thus the minimum aperture is realized at the entrance of the ESS.

The closed orbit displacement made by the excitation of the perturbator is superposed on the effect of the orbit distortion by correction coils and the steering magnet at the injection process. In Fig. 4 such superimposed

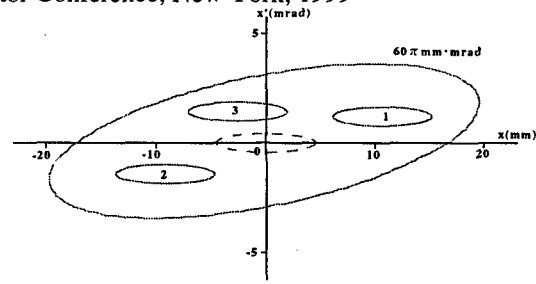


Figure 5: Phase space plot at the position of the exit of the inflector.

closed orbit distortions are shown. The beam from the injector linac comes into the KSR ring 41 mm apart from the ring center orbit at the inflector position. If the COD is displaced as shown in Fig.4 by bold broken line (COD-1turn), the beam is injected to the center of the transverse phase space as is indicated by a dashed ellipse. For this case, the beam with the amplitude  $\pm 4$  mm is just on the closed orbit and comes to the dashed line (COD-2turn) after 1 turn and collide with the inflector septum which exists in the region between 31 and 36 mm as indicated in the figure. So as to avoid this situation, the beam is injected as is indicated in Fig.5 by making COD of  $\sim 30$  mm at the inflector position then the beam rotates in the phase space as is indicated in Fig.5. Thus the beam comes into inner part of the KSR aperture after 1 turn and collision with the inflector septum can be avoided.

## ACKNOWLEDGEMENTS

The authors would like to present their sincere thanks to continuous support from HIMAC accelerator group leaded by Drs. S. Yamada and K. Noda. They are also grateful for Mr. I. Kazama for his cooperation during the present work. This work is supported by Grant-in-Aid for Scientific Research from Ministry of Education, Science, Sports and Culture under contact No. of 09304042.

## REFERENCES

- [1] A. Noda et al., "Electron Storage and Stretcher Ring, KSR", Proc. of the 5th European Particle Accelerator Conf, Barcelona, Spain (1996) pp451-453.
- [2] T. Shirai et al., "First Beam Circulation Test of an Electron Storage/Stretcher Ring, KSR", contribution to this conference.
- [3] A. Noda et al., "KSR as a pulse stretcher", Proc. of the Particle Accelerator Conf., Vancouver, Canada (1997) pp339-341.
- [4] A. Noda et al., "Design of an Electron Storage Ring for Synchrotron Radiation", Proc. of the 3rd European Particle Accelerator Conf. Berlin, Germany (1992) pp645-647.

# THE SNS RING TO TARGET BEAM TRANSPORT LINE

D. Raparia, J. Alessi, Y.Y. Lee, and W.T. Weng

AGS Department, Brookhaven National Laboratory, Upton, NY 11973.

## Abstract

The Ring to Target Beam Transport (RTBT) line connects the Spallation Neutron Source (SNS) accumulator ring to the target, with the required footprint for the accelerator complex. This line also provides four sets of beta collimators to clean any beam halo. This 160 meter long transport line consists of eleven 90 degree FODO cells, beam extraction and a beam spreader system, in addition to a ring extraction dump line.

## 1 INTRODUCTION

In the 1 MW SNS [1], the Ring to Target Beam Transport line (RTBT) connects the 1 GeV accumulator ring [2] to the target. A major requirement of all parts of this accelerator is to have low uncontrolled beam losses ( $\leq 1$  nA/m), to allow hands on maintenance. The RTBT is equipped with four sets of beam halo scrapers, and the ratio of aperture to rms beam size is kept greater than 3.5 up until the beam spreader section. Fig. 1 shows the RTBT line.

The beam requirements at the target are given in Table 1. Table 2 gives the Twiss parameters at the beginning of the extraction kicker magnet and at the target.

Table 1 Beam requirements at the target.

Beam width	200 mm
Beam height	70 mm
Time average current density, over beam footprint	$\leq 0.091$ A/m <sup>2</sup>
Beam power within target and outside nominal footprint	< 5%
Peak time-average beam current density, over 1 cm <sup>2</sup>	$\leq 0.182$ A/m <sup>2</sup>
Peak 1-pulse density, over 1 cm <sup>2</sup>	1.89 $10^{16}$ protons/m <sup>2</sup>

Table 2 Twiss Parameters at the Entrance and Exit of the RTBT for a 1 MW beam.

Twiss parameters	Entrance	Exit	Units
$\alpha_x$	0.00	-2.1	
$\beta_x$	4.15	17.4	mm/mrad
$\epsilon_x(\text{unnor.}, 100\%)$	120	120.0	$\pi$ mm mrad
$\alpha_y$	0.00	0.7	
$\beta_y$	1.97	4.2	mm/mrad
$\epsilon_y(\text{unnor.}, 100\%)$	120	120.0	$\pi$ mm mrad

## 2 FUNCTIONS OF THE RTBT LINE

The RTBT uses a FODO lattice up to the beam spreading section. The 90°/cell phase advance and length of 11.6 m/cell matches very closely the ring lattice. The line has following elements: (a) extraction, (b) beam dump, (c) halo collimation, (d) beam spreader, and (e) diagnostics. The first four functions have essentially been decoupled in the RTBT. The extraction system starts in the ring with a kicker magnet and continues through four cells in the RTBT. Following the extraction system, the beam can be dumped straight through a 15.5° dipole magnet. After this 15.5° bend, two cells are used for the halo collimation. Following another 4 cells of transport, the last five quadrupoles in the line are used for final beam spreading to produce the beam size required at the target. Every other two quadrupoles in the RTBT are followed by small dipole corrector magnets for steering of the beam in the quadrupole focusing plane. To reduce the probability of uncontrolled beam losses and define the beam size precisely on the target, RTBT is equipped with four transverse beam halo scrapers and several types of diagnostic devices. Table 3 shows the magnet requirements for the RTBT.

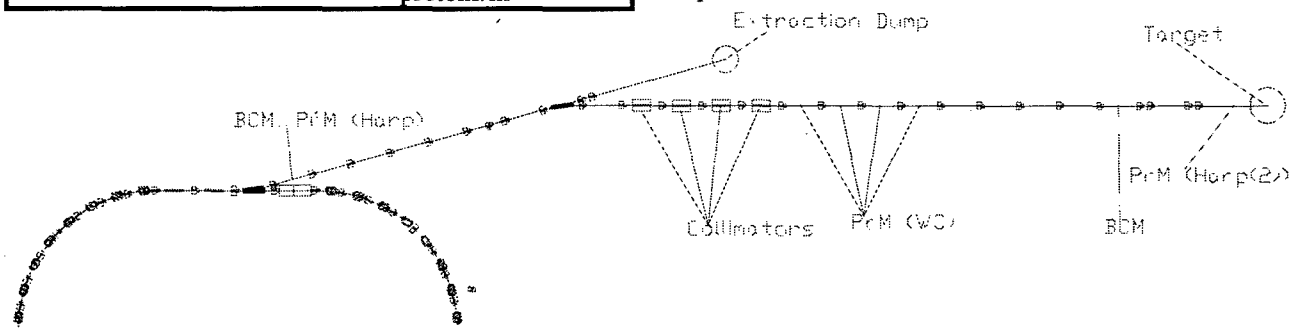


Fig 1. Layout and diagnostics location of the RTBT.

Table 3 Magnet requirement for the RTBT

Type	Number	Field (T)	Aperture (cm)	Length (m)
<b>Dipoles</b>				
15.5°	1	0.71	17 x 45	3.1
Correctors	12	0.02	20 x 20	0.3
Correctors	5	0.02	36 x 36	0.3
Corrector	1	0.13	20 x 45	1.4
<b>Quadrupoles</b>				
QH/QV	23	3.4 T/m	20 $\phi$	0.5
Spreader	5	3.0 T/m	36 $\phi$	0.8

(V)

Fig. 2 shows the amplitude functions ( $\beta_x$ ,  $\beta_y$ ) and the dispersion function ( $\eta$ ) along the RTBT. This line is designed such that it can accommodate the beam current required for the upgrade to 2 MW.

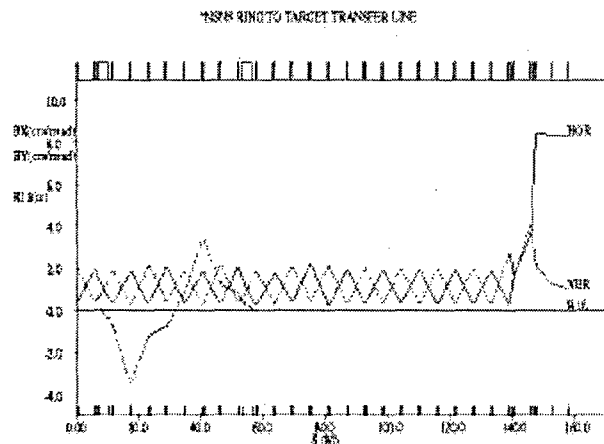
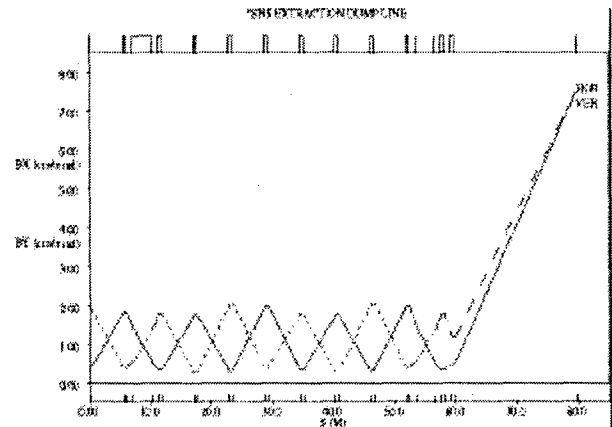


Fig 2. The amplitude function ( $\beta_x, \beta_y$ ) and the dispersion function ( $\eta$ ) along the RTBT.

### Extraction

The extraction of the beam is done in a single turn with full aperture at a pulse repetition frequency of 60 Hz. The extraction system consists of a full-aperture kicker and a Lambertson magnet septum and dipole magnet. The kick will be in the vertical direction. The Lambertson septum magnet (90° phase advance from kicker) will receive the vertically kicked beam and will provide large deflection (15.5°) to enable ejection horizontally from the accumulator ring. A dipole, which is 360° phase advance away from the Lambertson magnet, bends the beam horizontally in the opposite

direction by 15.5°, making the extraction system achromatic. At end of extraction the horizontal dispersion and its derivative are zero (see figure 2). A magnet to bend the beam vertically downward by 32.3 mrad (opposite direction to the kicker magnet) is located about 9.3 meter away from the kicker magnet, providing a  $\approx 30$  cm difference vertically between the ring and the target planes.



### Extraction dump

Following the extraction section, the beam dump is in a line straight through the 15.5° dipole magnet. This dump can handle up to 200 kW beam power and will be used for accumulator tuning purposes. This line is 28 m long and the optics of this line is shown in Fig. 3.

Fig 3. TRANSPORT output showing beam optics to the ring extraction dump.

### Beam spreader

The beam spreader consists of five quadrupoles near the end of the RTBT. These five 32 cm diameter aperture quadrupoles provide the desired beam size at the target, as given in Table 1. Due to thermal considerations of the target, the beam current density on target must remain below the limits shown in the table. This requirement results in a non-Gaussian beam distribution in space (with rms emittance of  $36 \pi$  mm mrad). The required current density distribution can be obtained using the injection painting scheme described elsewhere [3]. Fig. 4 shows the current density distribution at the target using such a scheme. Scattering effects of a 4 mm thick inconel window, 2 meters from the target, were included.

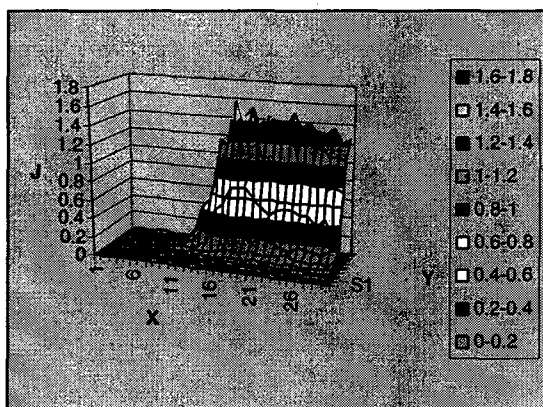


Fig 4. Current density distribution at the target in units of  $10 \text{ A/m}^2$ . Only one quadrant of the beam foot print is shown.

### Diagnostics

There must be enough diagnostic devices in the RTBT line to determine beam quality and beam losses in the line, as well as to determine the beam profile as close as possible to the target. There is one beam loss monitor per quadrupoles and one per dipole, with 17 units left for additional (still to be determined) critical locations. Horizontal and vertical beam position monitors are located near every other pair of quadrupoles. Current toroids will allow continuous monitoring of beam current near the beginning and end of the transport line. Using profiles from four crawling-wire profile monitors located between four consecutive quadrupole magnets in the line, one will be able to infer the beam emittance in the line. These units will have 4 wires, taking profile measurements in four projections -  $0^\circ$  (horizontal),  $30^\circ$ ,  $60^\circ$ , and  $90^\circ$  (vertical). From these projections, we will use an algebraic reconstruction technique[4], to get a detailed 2-dimensional density distribution of the beam. Finally, there will be one harp located near the ring extraction and a pair of harps  $\sim 2 \text{ m}$  in front of the target. The lifetime of the harps should not be a problem, since the current density at the RTBT harps will be lower than in the HEBT line, and the power deposited in the wires will be less than that in harps used in the BNL Booster injection line. Since the harp in front of the target is important for guaranteeing beam flatness, there will be two units for redundancy. An excursion from the target requirements given in Table 1, as inferred by the harp measurements, will trigger a fast beam inhibit. A list of the diagnostic devices is given in Table 4, and the locations are shown in Fig. 1.

Table 4 Diagnostic devices in the RTBT

Device	Number
Beam loss Monitor (BLM)	50
Beam Current Monitor (BCM)	2
Beam Position Monitor (BPM)	16
HARP(PrM)	3
Crawling Wire Scanner (PrM(WS))	4

### Beam collimation

To scrape any beam halo produced in the ring, there are four collimators in the RTBT line. These collimators are located just after the last  $15.5^\circ$  bend in the line spread over two cells defining full emittance ellipse, and each is designed to handle up to 1 kW of beam power[5]. There is a three meter long collimator just before the target window to prevent beam from hitting outside of the target area.

### 3 REFERENCES

- [1] B. Appleton, "The NSNS Project", Proc. 1997 Particle Accelerator Conference, p. 20.
- [2] W. T. Weng, *et al.*, "Accumulator Ring Design for the NSNS Project", Proc. 1997 Particle Accelerator Conference, p. 970.
- [3] J. Beebe-Wang and Y.Y. Lee, "Transverse Phase Space Painting for SNS Accumulator Ring Injection", these proceedings.
- [4] D. Raparia, *et al.*, "The Algebraic Reconstruction Technique", Proc. 1997 Particle Accelerator Conference, p. 2023.
- [5] H. Ludwig, *et al.*, "Collimator Design for the NSNS Accumulator Ring", to be published in ANS Winter Conf., Albuquerque, New Mexico, Nov. 1997.

# CESR IV PROPOSED TRANSFER LINE DESIGN\*

Z. Greenwald, D.L. Rubin

Laboratory of Nuclear Studies, Cornell University, Ithaca, NY 14853

## Abstract

CESR IV is a proposed dual-bore colliding beam accelerator for B-meson production. It has been designed to be built on the top of the injection synchrotron ring so as to co-exist with the present CESR III ring [1]. In this paper we will describe the design of the CESR IV transfer line. This transfer line splits from the existing transfer line and guides the beam, extracted from the synchrotron, 43 cm vertically and then injects horizontally into the new ring. The trajectory, taking into account the available space, was determined by horizontal and vertical bending magnets and drift lines. The quadrupoles were optimized to match the TWISS parameters at the input and the output of the transfer line to those of the synchrotron and the new CESR IV ring respectively.

## 1 INTRODUCTION

In the CESR IV design [1], the present storage ring and the new one - which will be on top of the synchrotron, will share the synchrotron ring as injector. When designing the new transfer line for CESR IV the following requirements should be considered:

- It will share the input point (coming from the synchrotron) with that of the existing transfer line [2] and will split after *QT02*.
- It will have the same beam pipe radius of 1.27 cm as that of the present transfer line.
- The beam should be guided up to the level of CESR IV, which is 0.43 m above the synchrotron, and then curved back connecting tangentially to CESR IV.
- TWISS parameters at the input of the transfer line should match those of the synchrotron at S133 and the TWISS parameters at the output of the transfer line should match those of CESR IV at Q051.
- Vertical dispersion should be minimized which requires small bending angles in the vertical direction.
- The new transfer line should fit together with the present one in the available space.

## 2 TRANSFER LINE DESIGN

CESR IV transfer line will share the present transfer line up to *QT02* and then will split off with an angle of 9°. The splitting dipole will be located in the drift line *F146* (2.4 m). *BEND 1* of the existing transfer line will have to be moved slightly or be modified to accommodate the new beam pipe.

The trajectory is constructed by Horizontal and Vertical bending magnets and tangential drift lines. See *Figure 5*. The bending magnets angles and their desired fields are summarized in Table 1.

Table 1: Summary of the bending magnets needed for CESR IV transfer line

Bending magnet	Length (m)	Bending angle	Magnetic field (Tesla)	Total current (KA-t)
HSWT	1.53	9.04	1.821	18.41
V100	1.53	-2.54	0.512	5.176
V300	1.53	2.54	0.512	5.176
HB10	1.53	8.37	1.686	1.704
HB20	1.53	4.34	0.874	8.835
dc septum	1.65	-1.36	0.254	2.569
p. septum	1.50	-2.24	0.461	4.668

At the input of the transfer line the TWISS parameters are set identical to those of the synchrotron ring at S133, while the TWISS parameters at the output of the transfer line are matched to those of CESR IV at Q051 by varying both the strength and longitudinal position of the quadrupoles. This match of the optics is done by using the optimization program *DIMAT* [4] with the constraints that the quadrupoles strength be less than  $0.6 m^{-2}$  and  $\beta$  less than 80 m. The variations of the TWISS parameters along the transfer line are seen in *Figures 1 – 4* with the corresponding quadrupole strengths in Table 2. Note, the strength and location of *QT01* and *QT02* which are shared by the two transfer lines were set for the present CESR and have not been changed.

Table 2: Quadrupoles strengths optimized to match input to CESR IV

Quadrupole	Length (m)	Optimized strength
Q306	0.8	0.5837
Q100	0.8	-0.3584
Q200	0.8	-0.2538
Q304	0.8	0.4926
Q300	0.8	-0.1680
Q303	0.8	0.0721
Q305	0.8	-0.2423

\* Work supported by NSF.



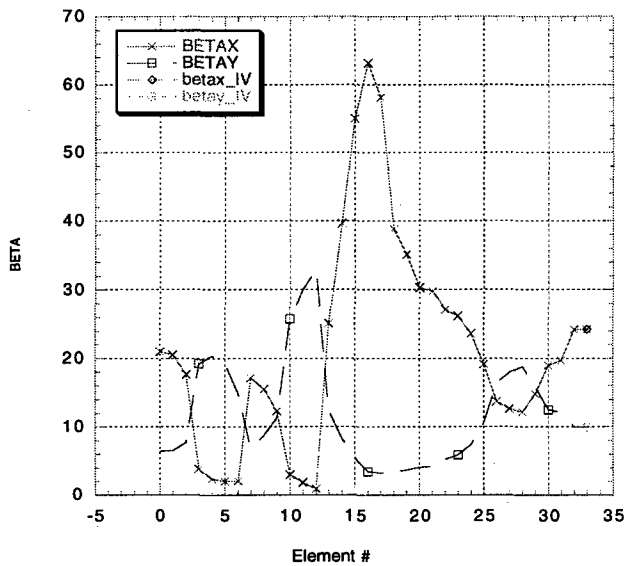


Figure 1: Variations of  $\beta$  along CESR IV transfer line. The vertical section is constructed by elements 10 – 18

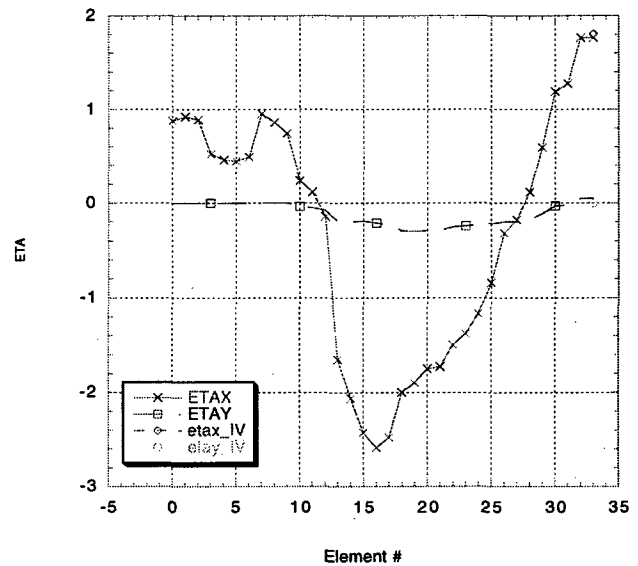


Figure 3: Variations of  $\eta$  along CESR IV transfer line. The vertical section is constructed by elements 10 – 18

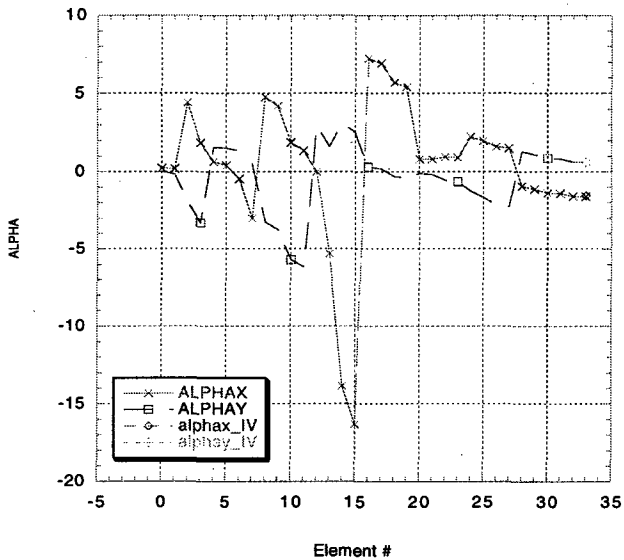


Figure 2: Variations of  $\alpha$  along CESR IV transfer line. The vertical section is constructed by elements 10 – 18

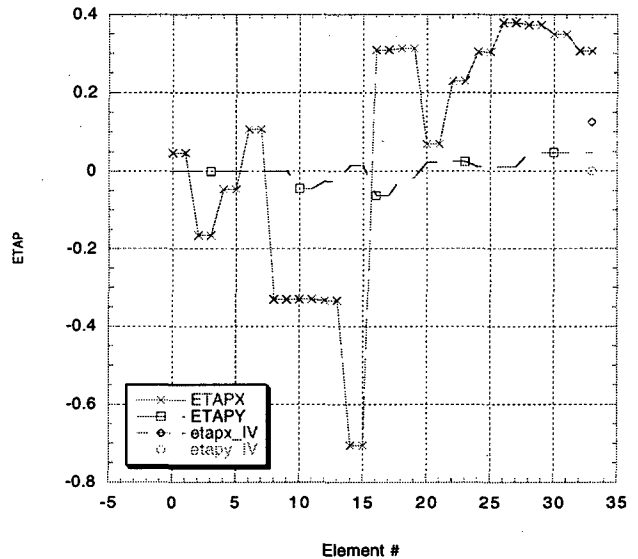


Figure 4: Variations of  $\eta'$  along CESR IV transfer line. The vertical section is constructed by elements 10 – 18

### 3 CONCLUSION

The total length of the transfer line will be 35.765 m. The obtained TWISS parameters at the output of the transfer line match those of CESR IV well except those of  $\eta'$ . Diagnostic components have not been included yet.

### 4 ACKNOWLEDGMENT

I would like to thank Scott Chapman for supplying the the survey measurements of the synchrotron and the present transfer line.

### 5 REFERENCES

- [1] G. Dugan, A. Mikhailichenko, J. Rogers, D. Rubin, "Dual Aperture Luminosity Colider at Cornell University," PAC 1997.
- [2] J. T. Seeman, "Injection Process of the Cornell electron Storage Ring CESR," thesis 1979.
- [3] S. Chapman, "Survey Measurements of the Synchrotron-private communication".
- [4] R. V. Servranckx, K.L. Brown, "DIMAT", SLAC report 270 UC-28 (A) 1984.

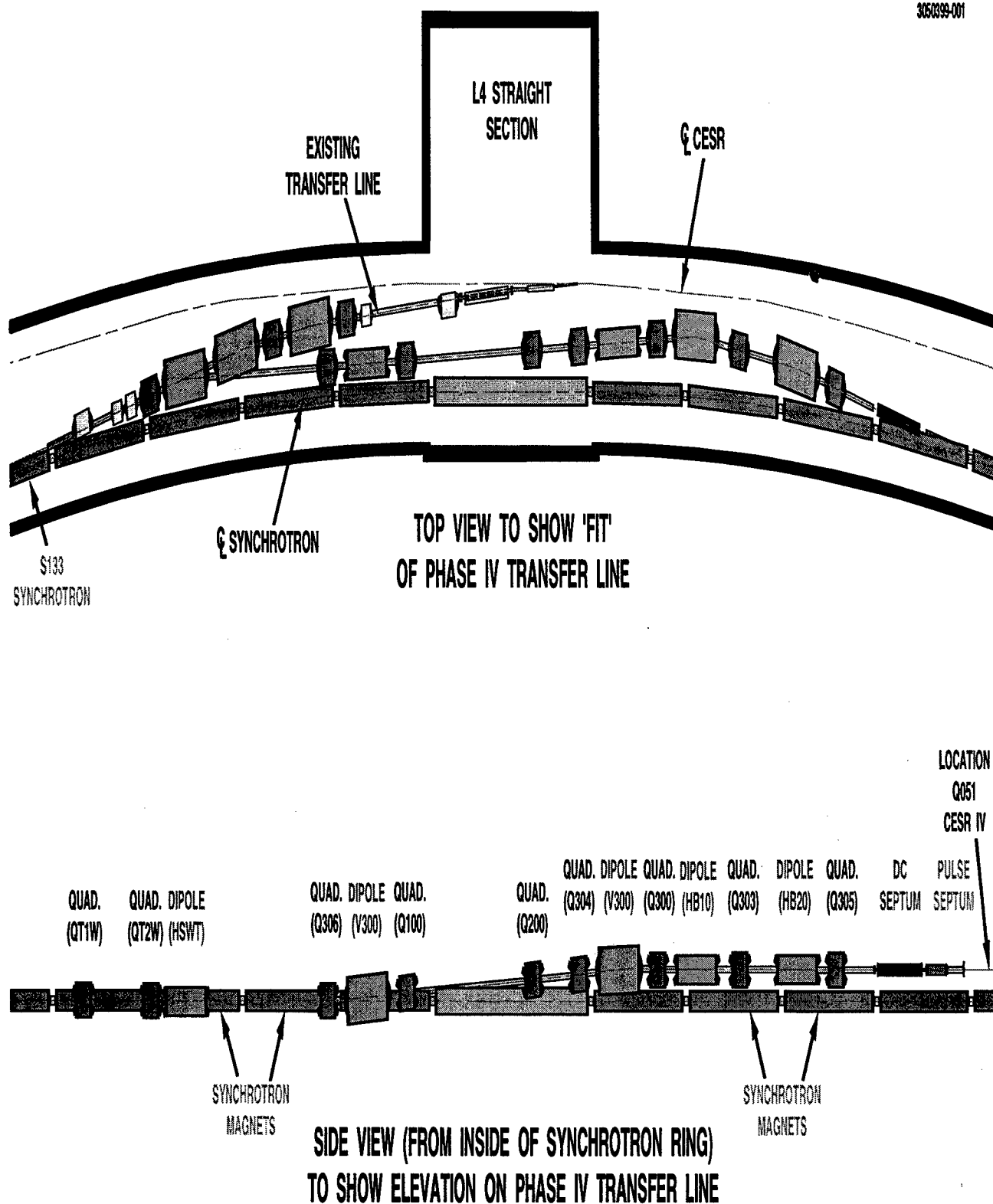


Figure 5: Top and side views of the proposed transfer line for CESR IV.

## BEAM-TARGET INTERACTION EXPERIMENTS FOR BREMSSTRAHLUNG CONVERTER APPLICATIONS\*

S. Sampayan, R. Buckles<sup>+</sup>, G. Caporaso, Y-J Chen, C. Crist<sup>++</sup>, S. Falabella, T. Houck, M. Krogh<sup>+++</sup>, J. McCarrick, R. Richardson, D. Sanders, J. Weir, and G. Westenskow  
Lawrence Livermore National Laboratory, Livermore, California 94550 USA

### Abstract

For multi-pulse radiography facilities, we are investigating the possible adverse effects of (1) backstreaming ion emission from the Bremsstrahlung converter target and (2) the interaction of the resultant plasma with the electron beam during subsequent pulses. These effects would primarily manifest themselves in a static focusing system as a rapidly varying x-ray spot. To study these effects, we are conducting beam-target interaction experiments on the ETA-II accelerator (a 6.0 MeV, 2.5 kA, 70 ns FWHM pulsed, electron accelerator) by measuring spot dynamics and characterizing the resultant plasma for various configurations. Thus far, our experiments show that the first effect is not strongly present when the beam initially interacts with the target. Electron beam pulses delivered to the target after formation of a plasma are strongly affected, however. We have also performed initial experiments to determine the effect of the beam propagating through the plasma. This data shows that the head of the beam is relatively robust, but that backstreaming ions from the plasma can still manifest itself as a dynamic focus toward the tail of the beam. We report on the details of our experimental work to study these effects.

### 1 INTRODUCTION

We are presently working on Linear Induction Accelerator (LIA) based radiography projects under the US Department of Energy (DOE). These projects, known as the Dual Axis Radiography Hydrotest Facility II (DARHT II) and the Advanced Hydrotest Facility (AHF), are an element of this Country's strategy of science based stockpile stewardship (SBSS). The DARHT II is presently being built at Los Alamos National Laboratory and it is planned that AHF will be built at the Nevada Test Site. The DARHT II machine is a multi-pulse, single-axis flash radiography machine. The AHF machine is envisioned as a multi-pulse, multi-axis flash radiography machine designed for full 3d imaging. These

machines are being designed to be capable of taking a sequence of closely spaced radiographic images so as to produce a time sequenced image of the test object.

DARHT II uses a kicker system to provide a sequence of 4 pulses over a 2  $\mu$ s window. On AHF, the process of producing these radiographic images consists of generating a 10-15 shot burst of 200 ns electron beam pulses at a 1 MHz repetition rate. These pulses are further chopped into a series of 50 ns sub-pulses and are redirected through a series of magnets to converter targets at each axis. The electron beam impacting the converter target generates an intense x-ray cone which produces a radiographic image on a fast detector array.

The converter target consists of an 0.5-1 mm thick tantalum or tungsten foil. The electron beam is focused to <1 mm and allowed to impinge on this target to create the x-ray pulse. Two effects are of concern. As the electron beam interacts with the target surface, a plasma promptly develops. As the beam electrons create a strong space charge field in front of the target, ions can be extracted and accelerated in a direction opposite to the electron beam propagation. These ions partially neutralize the beam space charge and defocusing of the beam results.

The second effect results from the direct interaction of the electron beam with the target plasma on subsequent pulses. Such an interaction, depending on the interaction length and plasma density, may have an adverse effect on the beam propagation and the resultant spot on the converter target.

Our on-going experimental program at LLNL is to study the interaction of the electron beam with the x-ray converter target. In these experiments, we focus on the dynamics of the spot behavior measuring x-ray spot blur across an edge (so called "roll-bar" technique), and 2-d imaging with a gated, multiframe, pinhole camera. Further, we are characterizing the properties of the plume by using various plasma diagnostic techniques.

### 2 EXPERIMENTAL

We described our experimental set-up and preliminary experiments in a previous paper [1]. Additional diagnostics that we are implementing are shown schematically in Figure 1. Among those additional diagnostics are interferometer systems and a Laser Induced Fluorescence system (LIF). The interferometer

\* Work performed under the auspices of the U. S. Department of Energy by LLNL under contract W-7405-ENG-48.

+ Bechtel-Nevada, Livermore, CA

++ Sandia National Laboratories, Albuquerque, NM

+++ AlliedSignal, FM&T, Kansas City, MO

systems allow observation of the spatial extent, expansion velocity, and density of the target plasma. The LIF system, which consists of a tunable pulsed dye laser system and gated spectrometer allows: (1) measurement of the desorption delay time of neutrals from the target, and (2) measurement of the neutral density as a function of time. The tunable laser is used to excite a particular species of interest at a defined location and time; the spectrometer is used to record the subsequent transition to a lower energy state.

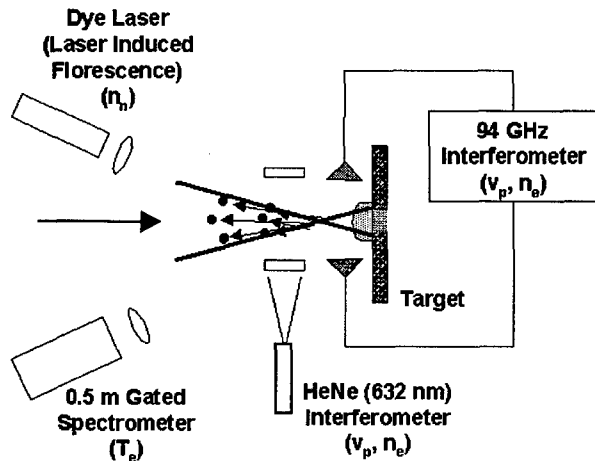


Figure 1: Modified target experiment layout. Neutral diagnostics are being added to system.

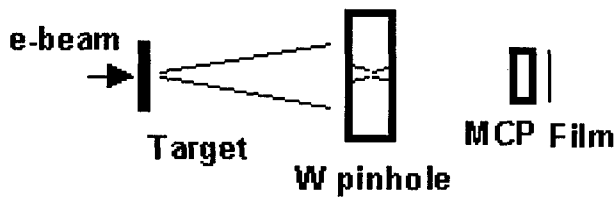


Figure 2: Single channel of the x-ray pinhole framing camera. System consists of six such channels to allow a full 2-d, time resolved observation of the x-ray spot.

As the principal objective of our experiment is to observe the dynamic behavior of the x-ray spot, we have implemented a method of direct observation of the x-ray spot. This device consists of tungsten pin-holes imaged onto an x-ray photocathode and amplified with a gated micro-channel plate (Fig. 2). The camera we are using creates 6 sequentially gated images so as to produce a 6 frame movie of the hard x-rays produced from the target interaction during the 70 ns (FWHM) beam pulse. Calculations show optimum sensitivity of the camera to be from 1-2 MeV with a 20% decrease at 5 MeV (Fig. 3).

Additional diagnostics (not shown) include imaging instruments consisting of gated, image intensified cameras for observation of Optical Transition Radiation (OTR) from the target surface and ion diagnostics consisting of multiple Faraday cups to observe plasma velocities and to obtain estimates of the plasma density. And an alternate method to measure the x-ray spot: the so called "roll-bar" technique. This technique infers spot size from the blur across a hard edge.

To simulate the effect of a high repetition rate multipulse, we have implemented an 0.8J Nd:YAG laser focused on the target. The laser beam can be directed to the target and timed to produce a plasma of sufficient density so as to simulate target debris as would encountered in a multipulse electron beam system.

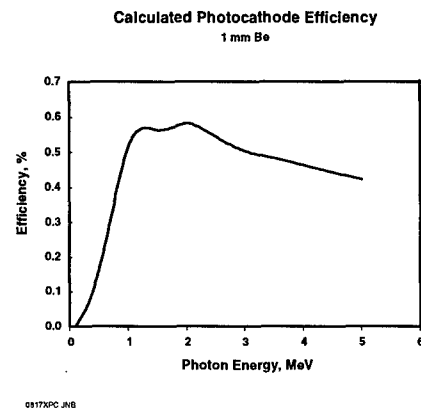


Figure 3: Pinhole framing camera photocathode response.

### 3 RESULTS AND DISCUSSION

Figure 4 shows a representative sample of images from the x-ray pinhole camera. Gate time of each image is approximately 6 ns and spacing between images is 7-10 ns. Time position relative to the beam current pulse is shown in Fig. 5.

Images taken with the beam at normal incidence show an almost constant spot diameter. An intensity profile through the center of each image shows a 1 mm spot diameter (FWHM) for this beam current of 1.4 kA. We observe similar results from this current up to the maximum ETA-II operational current of approximately 2.0 kA. These data show an almost constant spot radius with a variation of approximately 25%. Additionally, in this data, we do not observe evidence of backstreaming ions with the Faraday cups.

We performed electron beam/laser induced plasma experiments. To perform this set of experiments, we pulsed the Nd:YAG laser just prior to beam time. This laser pulse generated a prompt plasma and the electron beam from ETA-II was used as a probe pulse to determine e-beam/plasma interaction effects. Typical data from the final frame of the x-ray pinhole framing

camera is shown in Fig. 6a. A plot of the spot diameter dynamics shows an almost constant beam diameter throughout the pulse with a prompt expansion at the end of the pulse (dotted line, Fig. 7). This laser induced dynamic spot is accompanied by a very prompt positive signature in the upstream Faraday cups (i.e., indicating ions) within 30 ns following the end of the beam pulse.

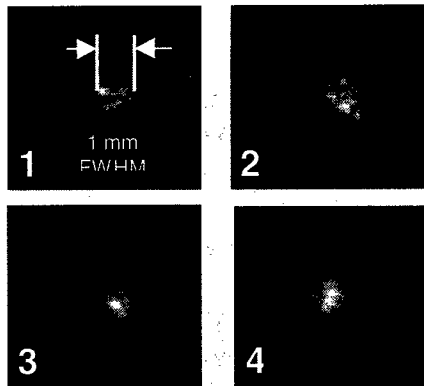


Figure 4: Time resolved sequence of x-ray spot images.

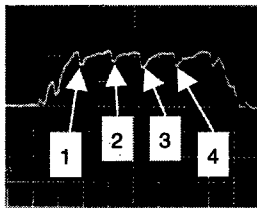


Figure 5: Timing fiducials superimposed on the beam current trace taken at the target. Numbers correspond to frame numbers above.

In order to ascertain the primary mechanism of this laser induced dynamic spot (which we presumed to result from backstreaming light ions due to surface contaminants), we attempted to clean the target surface with a laser prepulse. This laser prepulse was applied approximately 100  $\mu$ s prior to the laser pulse used to induce the simulated target plasma. We find that the spot dynamics can be minimized (Figs. 6b and solid line, Fig. 7) with this prepulse.

Initial experiments to determine beam propagation effects through a plasma (without a cleaning prepulse) were done by triggering the laser a fixed time prior to the e-beam. This delay allowed the laser induced plasma plume to expand. From the measured speed from the Faraday cups and integration of the signal, we are able to infer an average plasma density and beam/plasma interaction length for a given delay. For a typical data set and a delay of 100 ns prior to beam time, we infer

densities of about  $5 \times 10^{18} \text{ cm}^{-3}$ . We performed measurements with various delay times and observe that the head of the beam (i.e., first 20 ns) can propagate through the target plasma with minimal effects for 1.5-3.0 cm. However, we observe defocusing toward the tail of the beam presumably due to backstreaming ions.

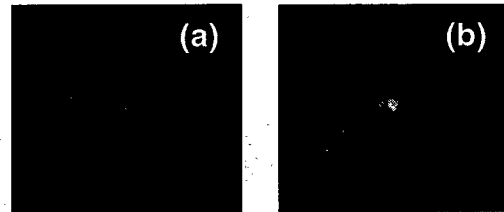


Figure 6: Final frame showing late time expansion of the x-ray spot (a) without and (b) with a laser cleaning prepulse.

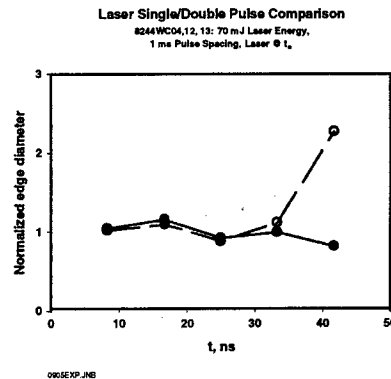


Figure 7: X-ray spot expansion generated by a laser induced plasma (dotted line) and effect of a cleaning target surface with a laser prepulse 100  $\mu$ s prior to normal laser pulse.

## 4 SUMMARY

We described our ongoing experiments to determine the interaction effects of an electron beam and Bremsstrahlung converter target used for multipulse radiography. Ion backstreaming and plasma interaction effects have been defined as two of the most predominant mechanisms which could degrade the focal spot on the target. We were unable to observe the first effect. The second effect can be observed in the beam head after traversing 1.5-3.0 cm through the plasma.

## 5 REFERENCES

- [1] S. E. Sampayan, et. al. "Experimental Investigation of Beam Optics Issues at the Bremsstrahlung Converters for Radiographic Applications", in *Proc. 1998 Linear Accelerator Conf.*

# CHARACTERISTICS OF HELIUM ION BEAMS FROM MULTICUSP SOURCE AND STUDY OF BEAM TRANSPORT\*

M. Sasao<sup>a</sup>, M. Nishiura, NIFS-509-5292, Japan

S. K. Guharay, U. of Maryland, MD20742

T. Kuroda, M. Hamabe, Chubu U. 480, Japan

H. J. Ramos U. of the Philippines-1101, M. Wada, Doshisha U., 610-0321, Japan,.

## Abstract

A test stand with a multicusp type  $\text{He}^+$  ion source and an electrostatic transport system was built for the study of beam characteristics at relatively low energy,  $E < 10$  keV, and beam transport in a space-charge dominated region with  $\beta (=v/c) < 0.0025$ . The measured normalized beam emittance (90%) of the  $\text{He}^+$  beam extracted from a compact multicusp source is about  $0.08 \pi$  mm-mrad for the emission current density of about  $5\text{--}15$  mA/cm<sup>2</sup> at  $6\text{--}9$  kV. An electrostatic quadrupole transport system (ESQ) is designed for this beam. Preliminary experimental results show that the ESQ has a potential to transport a beam without any significant emittance growth over a length of about 50 cm.

## 1 INTRODUCTION

With the goal to generate a high energy (1.7 MeV)  $\text{He}^0$  beam probe for a burning plasma experiment[1], we have been developing an intense  $\text{He}^-$  ion beam [2]. A  $\text{He}^-$  beam can only be produced effectively from  $\text{He}^+$  via a two step electron capture process in an alkali metal gas cell, such as Li, Na, Mg, K, Rb, or Cs. Because the optimum energy for these processes was reported to be around 6 keV [3], the essential point of the development is extraction of an intense  $\text{He}^+$  beam at relatively low energy.

Another key issue is the transport of a high perveance beam, with a good focusing property onto an aperture of the charge exchange cell. The aperture should be small enough to minimize the alkali vapor leakage. In

transporting a high perveance beam, the charge neutralization due to background gas pressure usually prevents the beam expansion. We cannot use this method in our experiment. The ionization cross section of  $\text{He}^+$  is very low in this region ( $2 \times 10^{-18}$  cm<sup>2</sup>). At higher gas pressure, the collisional charge exchange process of  $\text{He}^+$  with the residual helium gas results into a ground state  $\text{He}^0$ . This cross section is  $5 \times 10^{-16}$  cm<sup>2</sup>. A long-life,  $10\text{--}300$   $\mu\text{s}$ ,  $\text{He}^-$  ( $^4\text{P}_j$ ) is produced only through its metastable state. Therefore, in order to avoid any beam loss and produce  $\text{He}^-$  effectively, a low gas pressure,  $\ll 10^{-2}$  Torr, should be maintained. One of the solutions of this problem is to employ an efficient transport system using electrostatic lenses[4-7]. In the present paper, an experimental study of a low energy  $\text{He}^+$  beam characteristics, the design of the transport system for it, and its initial results are described.

## 2 EXPERIMENTAL ARRANGEMENT

A schematic diagram of the test stand with a  $\text{He}^+$  ion source and an electrostatic transport is shown in Fig. 1. A helium plasma is generated by two hair-pin type of tungsten filaments (0.4 mm-diameter) in an 8.5 cm-diameter and 10 cm-long compact multicusp ion source, which can be operated either in a pulsed mode or in a DC mode with discharge current up to 15 A. An  $\text{He}^+$  beam is extracted from a set of three electrodes of 6 mm-diameter. The ion source itself is biased at acceleration voltage,  $V_{\text{acc}}$ , and the second electrode is negatively biased ( $-V_{\text{dec}}$ ), and the beam is accelerated to  $V_{\text{acc}} + V_{\text{dec}}$  in the first extraction gap. The third electrode is grounded, and the beam is decelerated by  $V_{\text{dec}}$  so that the final beam energy is  $eV_{\text{acc}}$ .

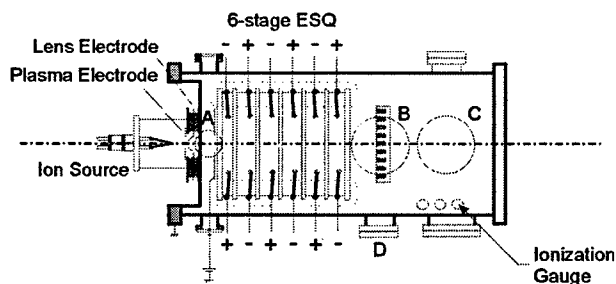


Figure 1: Schematic View of Experimental Arrangement

\*Work supported in part by Japanese Society of Promotion of Science, grant # 10480110.

One of the authors (S. K. Guharay) thankfully acknowledges Prof. M. Reiser for introducing the idea of ESQ transport and for many valuable discussions. Dr. C.K. Allen's work for developing the K-V code is also acknowledged.

#Email: sasao@nifs.ac.jp

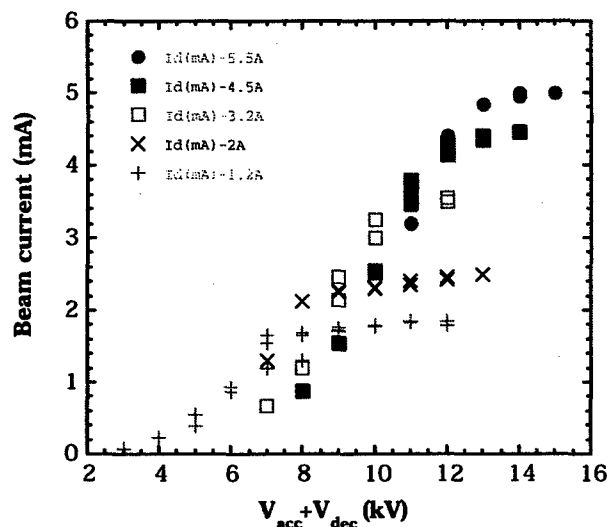


Figure 2 The extraction voltage ( $V_{acc} + V_{dec}$ ) dependence of the  $\text{He}^+$  beam current measured by the large Faraday cup (with a 36 mm-diam.) at 15 cm down stream.

The electrostatic transport system, developed at Maryland, is composed of six ESQ lenses. The geometrical parameters are given in Table 2 of the previous work[7]

There are several diagnostic ports, and the diagnostic tools developed are: a large Faraday cup for total beam current measurement, a Faraday cup array for beam profile measurements, and three types of emittance gauge. The large Faraday cup was specially designed to measure full beam currents, avoiding spurious contributions due to co-moving electrons and any secondary electrons. It has an entrance aperture diameter of 36mm, a pair of magnets, and a caterpillar shaped electron collector.

Two emittance gauges are slit-and-multi-electrode type; one of which has insulators between electrodes, and the other has a structure so that no dead layer exists between them. The third one is a pepper-pot type gauge[8]. Detail description of them and comparison will be reported elsewhere.

### 3 BEAM EXTRACTION CHARACTERISTICS

The  $\text{He}^+$  beam characterization was performed without the transport system. Fig. 2 shows the extraction voltage ( $V_{acc} + V_{dec}$ ) dependence of the  $\text{He}^+$  beam current measured by the large Faraday cup at 15 cm down stream from the exit of the source. Here the discharge current was varied so that the

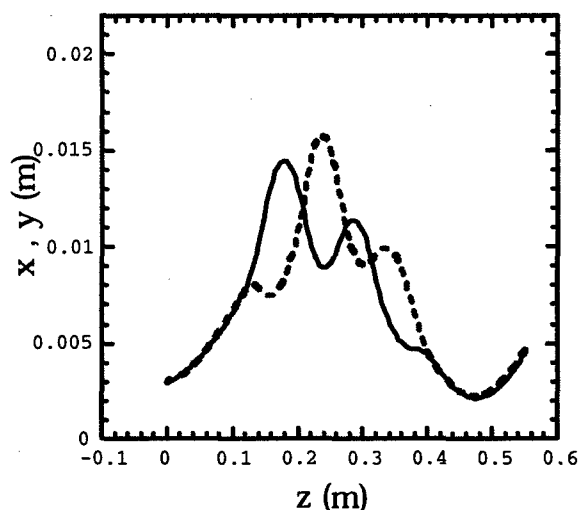


Figure 3 The beam envelope in x and y direction in the ESQ, where z is the direction of the propagation, for a case of 1mA, 8kV beam with  $r = 3$  mm,  $r' = 10$  mrad. The lower graph shows the voltage applied on the lenses.

space charge limited region and that limited by the source emission can be clarified. Extensive studies of the source property in higher power region will be reported elsewhere. The beam profiles measured at various z locations show that the beam is strongly diverging.

The normalized beam emittance (90%) of the  $\text{He}^+$  beam extracted from the source is measured by the slit-and-multi-electrode emittance gauge, and it is about  $0.08 \pi$  mm-mrad at the current density of about 5-15 mA/cm<sup>2</sup> at 6 - 9 kV. The pepper pot measurement gives the value of about  $0.075 \pi$  mm-mrad.

## 4 BEAM TRANSPORT STUDIES

### 4.1 ESQ design

In order to transport such a diverging high-perveance beam, and to focus it onto the entrance of the charge exchange cell, an efficient low-energy beam transport system [7] has been considered. The original design was made for the transport of 30 mA, 35kV  $\text{H}^+$  beam for the SSC injector. The present beam, 1-5 mA, 6-10 kV  $\text{He}^+$ , however, has higher perveance  $K \approx 0.004 - 0.02$ . A set of lens parameters, which can transport over about 50 cm, has been found after a wide range of parameter survey using a simulation code solving the K-V envelope equations [6]. Fig. 3 shows the beam envelope in x and y directions in the ESQ, for a case of 1mA, 8kV beam with the initial beam radius, r, of 3 mm, and the initial beam divergence,  $r'$ , of 10mrad.

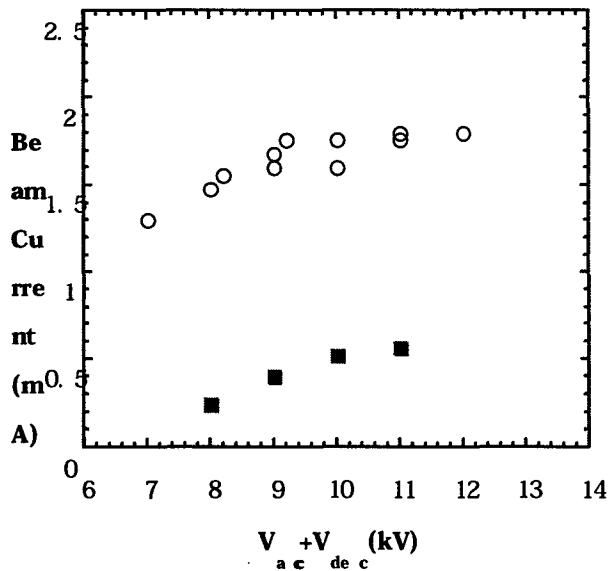


Figure 4 The  $\text{He}^+$  beam current measured at about 10 cm down stream from the exit of the ESQ. The circles are with ESQ excitation, and squares are without ESQ. The beam energy is 8 keV.

#### 4.2 Experimental results with ESQ

Preliminary experiment has been carried out to examine the ESQ performance and to characterize the beam after the transportation. The twenty four electrodes are biased by using twelve independent power supplies. The voltages are set at the optimum values determined by the simulation calculation. In the Fig. 4 are shown the total beam current measured by the large Faraday cup at about 10 cm down stream from the exit of the ESQ: with ESQ excitation (circles), and without excitation (squares). The 70% of the whole beam from the source are detected at the 60 cm downstream. Considering the beam loss between the source and the entrance of the ESQ, the results in Fig. 4 show that the most of the beam is successfully transported by ESQ.

The focusing property was examined by the Faraday cup array. Figure 5 shows one example of the 8kV, 2mA beam profile measured at about 60 cm down stream, for the case ESQ excited (solid line) and that without ESQ excitation (dashed line). Although this position does not correspond to the beam waist as shown in Fig. 3, we can expect that the charge exchange cell can be set well apart from the ESQ, with 100% beam throughput.

The emittance was also measured at 10 cm down stream from the exit of ESQ, for a 2mA, 8 keV beam. The one dimensional normalized emittance was about  $0.11 \pi$  mm-mrad. Considering the  $\pm 15\%$  ambiguity of the emittance evaluation, the emittance growth in the ESQ transport system seems to be low.

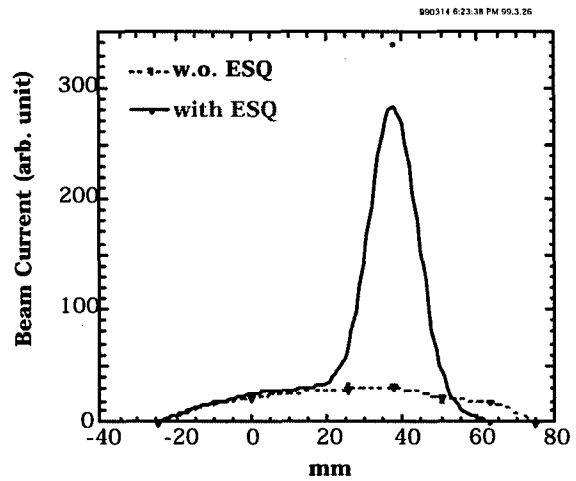


Figure 5 The beam profile measured at about 60 cm down stream, for the case ESQ excited (solid line) and that without excitation (dashed line). The beam energy is 8 keV, and the initial beam current 2 mA.

In conclusion, the present experimental results indicate that the ESQ has a potential to transport a  $\text{He}^+$  beam without any beam loss, and without any significant emittance growth over a length of about 50-cm, and to focus it on to a charge exchange cell well apart from the source.

## 5 REFERENCES

- [1] D.E.Post et al., Fusion Technology 1 (1978), 355  
M.Sasao et al., Fusion Technology 10 (1986), 236
- [2] M.Sasao et al., Rev. Sci. Instrum. 69-2 (1998) 974
- [3] R.J. Girnius et al., Nucl. Instrum. Methods, 137 (1976) 373.
- [4] Theory and Design of Charged Particle Beams, M. Reiser (Wiley, N.Y.) 1994.
- [5] S. K. Guharay, C. K. Allen, and M. Resier, in "High-brightness beams for Advanced Accelerator Applications" edited by W.W. Destler and S. K. Guharay, AIP Conf. Proc. No 253, 1992, pp 67-76.
- [6] C.K. Allen, S.K. Guharay, and M. Reiser, Proc. 1995 Particle Accelerator Conference, Dallas, Texas (IEEE, New York, 1996), p. 2324.
- [7] S.K.Guharay et al., Nucl. Instrum. Methods A339 (1994) 429.
- [8] S.K.Guharay et al., Rev. Sci. Instrum. 67 (1996) 2534.



# A DEVELOPMENT OF AUTOMATIC TUNING FOR HIGH ENERGY BEAMLINES AT HIMAC

M. Torikoshi, K. Noda, E. Takada, H. Tsubuku<sup>1</sup>, S. Kai<sup>1</sup>, T. Katsumata<sup>1</sup>  
 National Institute of Radiological Sciences, 4-9-1 Anagawa, Inage, Chiba 263, Japan  
<sup>1</sup>Accelerator Engineering Corporation, 2-13-1 Konakadai, Inage, Chiba 263, Japan

## Abstract

A beamline tuning system based on automatic procedure for steering a beam with observing the beam position has been under development for the transport of high energy beams at HIMAC. A daily beamline tuning for radiotherapy and for most biological experiments is carried out to precisely transport the beam to beam delivery devices. This system replays the daily procedure automatically. A beam is steered using steering magnets in accordance with the deviation of beam positions from intended beam positions. How much the beam positions shift due to adjusting a steering magnet is determined by the beam optics design. Therefore, if correlation between deflection angles at the steering magnets and variations in the beam position measured by wire-grids are known, the deflection angles can be calculated by solving linear simultaneous equations. The correlation was measured and compared with those calculated. Most of them are in good agreement. At present, the beamline tuning for delivering beams to the biological experiment room is finished in about 10 minutes automatically.

## 1 INTRODUCTION

A heavy ion medical accelerator, HIMAC, has been providing carbon beams for cancer radiotherapy since June of 1994[1]. The beams extracted from synchrotron rings are transported to three treatment rooms, a biological experiment room and a physics-general experiment hall through high energy beam transport lines (HEBT). The beamline is changed from one to another by only exciting or deexciting switching magnets without tuning the beamlines to change the treatment room in less than 5 minutes. The beamlines are tuned only a few times a day, when the accelerated beam energy or the accelerated ion is changed. The beamline tuning for the radiotherapy and most biological experiments is done in fixed forms, but the beam position, a centroid of a beam profile, should be finally positioned on a central axis of a beam delivery system within in a precision of  $\pm 2.5$  mm [2]. At present, two operators are engaged in the operation of the HEBT beamline tuning for the radiotherapy. We want, however, one operator to tune the beamline efficiently. Especially, since the HIMAC has two synchrotron rings, the HEBT beamlines are divided into two systems, a horizontal beamline system (LBT) and a vertical beamline system (UBT) [3]. Each system is operated independently. If we

have, therefore, an automatic beam tuning system, only one operator can tune two beamlines of both systems, respectively, at the same time. In this paper, we report our automatic tuning system which is under development for the HEBT system.

## 2 PRINCIPLE OF THE AUTOMATIC TUNING

In everyday's beamline tuning for the radiotherapy and for most of the biology experiments, we basically steer the beam using steering magnets and sometimes bending magnets with monitoring the beam positions using wire-grids. The goal of the beamline tuning is to position the beam on the designed points in the beam delivery devices. The points are defined by two wire-grids, one is located upstream of the isocenter of a treatment room or the biology experiment room, and another is in front of the entrance of the room. The beam profile is not necessary to be adjusted insofar as the profile is approximately round shape in the rooms where horizontal and vertical components of the  $\beta$  function were designed to be a same value. Therefore, quadrupole magnets are usually excited in designed strengths.

The principle of the beamline tuning is to steer the beam with the steering magnets and move it to a required position at each wire-grid as shown in Fig. 1. Insofar as a

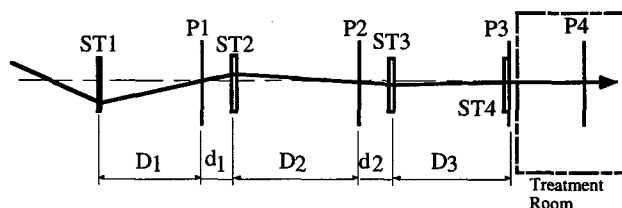


Figure 1: A typical configuration of steering magnets and wire-grids for observation of beam positions. ST's and P's mean steering magnets and wire-grids, respectively.

condition,  $d/D < 1$ , is satisfied, incident angles of the beam with respect to a required path converge, where  $D$  is a distance between a steering magnet and a downstream wire-grid, and  $d$  is a distance between a wire-grid and a next steering magnet. If we know how much the beam position varies at a wire-grid for changing the excitation current of a steering magnet, we can calculate the excitation current of a steering magnet in order to move the beam to a required position at the wire-grid. Once beam optical design has been fixed, the variation in

a beam position at an arbitrary wire-grid with respect to the variation in a deflection angle at an arbitrary steering magnet upstream of the wire-grid is calculated using transfer matrix equation as the following,

$$\begin{pmatrix} u \\ u' \end{pmatrix} = \begin{pmatrix} M_{11} & M_{12} \\ M_{21} & M_{22} \end{pmatrix} \begin{pmatrix} u_0 \\ u'_0 \end{pmatrix}$$

where  $u_0$  and  $u'_0$  are a beam position and a slope of the beam's trajectory at a steering magnet, respectively. The  $u$  and  $u'$  are a position and a slope at a wire-grid, respectively. When the beam is deflected by a steering magnet in different strengths without altering the beam position, we can observe beam positions  $u_A$  and  $u_B$  at a downstream wire-grid, which are corresponding to the strengths A and B of a steering magnet. They are described as follows,

$$u_A = M_{11}u_0 + M_{12}u'_{A0}$$

$$u_B = M_{11}u_0 + M_{12}u'_{B0}$$

Subtracting the second equation from the first, the ratio of the variation in the beam position to the variation in the deflection angle is derived as follow,

$$\alpha = (u_A - u_B) / (u'_{A0} - u'_{B0}) = M_{12} \quad (1)$$

where  $\alpha$  is the ratio in the unit of mm/mrad. Assuming a linear relation between the deflection angle and the excitation current, the  $\alpha$  can be converted to the ratio of the position to the excitation current with respect to a certain magnetic rigidity of the beam, which we call it  $\eta$ . Then, if we know the differences between the initial beam positions and the required positions, we can calculate the current variations of steering magnet by solving the following matrix equation inversely,

$$\begin{pmatrix} \Delta u_1 \\ - \\ - \\ \Delta u_n \end{pmatrix} = \begin{pmatrix} \eta_{11} & 0 & 0 & 0 \\ - & - & - & - \\ - & - & - & - \\ \eta_{n1} & - & - & \eta_{nn} \end{pmatrix} \begin{pmatrix} \Delta I_1 \\ - \\ - \\ \Delta I_n \end{pmatrix} \quad (2)$$

where  $\eta_{ij}$  is the ratio of the position variation of an  $i$ -th wire-grid to the current variation of a  $j$ -th steering magnet.  $\eta_{ij}=0$  for  $i < j$ . A  $\Delta I_j$  is the current variation to be solved and a  $\Delta u_i$  is the deviation of the beam position from the required beam position at the  $i$ -th wire-grid. A case of  $i=j$  indicates a relation between a steering magnet and the nearest wire-grid which is immediately downstream from the steering magnet, such as the relation of ST1 and P1 shown in the figure 1. As shown in the equation (1), the  $\alpha$  is equal to the transfer matrix element  $M_{12}$  which is described as follows:

$$M_{12} = \sqrt{\beta_{ST}\beta_{WG}} \sin \Psi_{ST-WG}$$

where  $\beta_{WG}$  and  $\beta_{ST}$  are values of a  $\beta$  function at the wire-grid and the steering magnet, respectively, and the  $\Psi_{ST-WG}$  is a phase advance from the steering magnet to the wire-grid. So the  $\alpha$ 's can be calculated. In our tuning system, however, the measured values are used.

The last steering magnets (ST4 in the figure) is only about 20 cm away from the wire-grid (P4) which is in front of the room. Therefore, if the beam is in the center of the wire-grid, the beam can be aligned to the required path in the room by only steering the beam with the last steering magnets with a negligibly small change in the beam position at the wire-grid.

### 3 PERFORMANCE OF THE AUTOMATIC TUNING SYSTEM

At present, the automatic tuning process is divided into three parts. Fig. 2 shows the configuration of steering magnets and wire-grids of the vertical beamlines with omitting quadrupole magnets in order to simplify.

The first part is to align a beam with a path of the HEBT beamline which is defined by the first two wire-grids with help of steerers of a synchrotron extraction

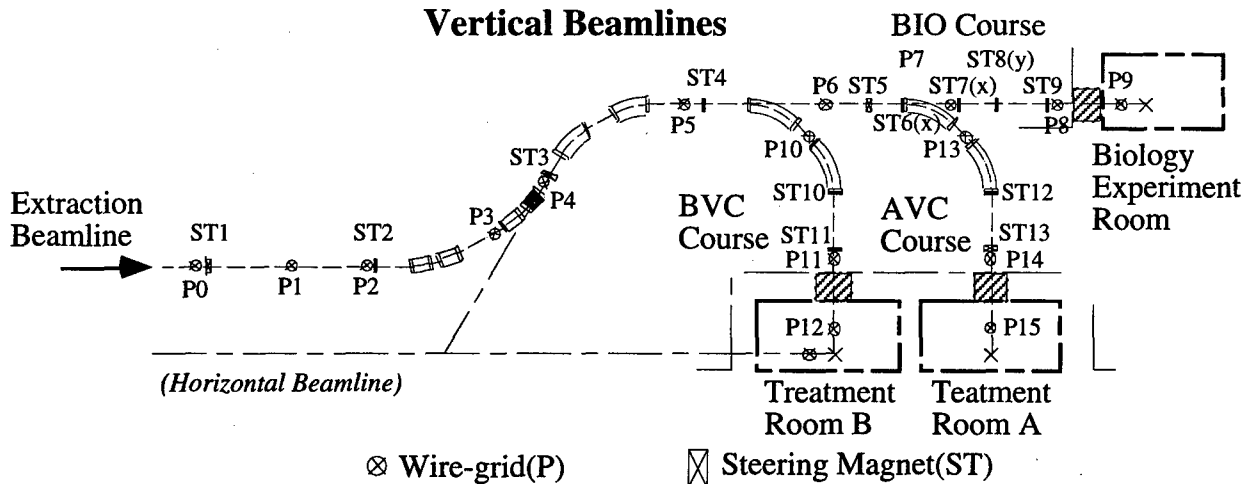


Figure 2: The configuration of steering magnets, wire-grids and bending magnets in vertical beamlines of the high energy beam transport system at the HIMAC. ST and P mean a steering magnet and a wire-grid, respectively.

beamline. In this part, the beam is adjusted to be positioned on the centers of the two wire-grids, P1 and P2, using steerers of the extraction beamline as well as the first pair of the steering magnets, ST1. But each beamline is controlled by the different computer one another, and the HEBT's computer cannot directly control the steerers of the extraction beamline. The HEBT's computer adjusts the excitation currents of the ST1, but it only informs us how much change the excitation currents of the steerers of the extraction beamline in order to adjust the beam position in the centers of the wire-grids P1 and P2. Therefore, this part is said to be a computer aided tuning rather than the automatic tuning.

The second part is to automatically transport the beam to the entrance of the treatment room or the biology experiment room. In this part, the wire-grids and the steering magnets which are located along the beamline downstream of the P2 are in use. In a case of BIO course, the beam positions at the wire-grids of P3 ~ P8 are measured first. In this process, the  $\Delta u$ 's are immediately obtained. Then the  $\Delta I$ 's are derived by inversely solving the equation (2). We can arbitrarily select which wire-grids or steering magnets are in use, and how many times this part is repeated. One of  $15^\circ$  deflection bending magnets can be also involved to steer the beam vertically as an auxiliary steerer. We can also set values as parameters for the position in which the beam should go and for the tolerance of positioning the beam around the required position at each wire-grid. In most cases,  $\pm 0.5$  mm is set as the tolerance. When the repetition number is set to be more than one time, this part is repeated until the beam position coincides with the required position within the assigned tolerance at every wire-grid. If it has not completed within the repetition times, the computer informs the operators it by indicating "TIME OUT". The

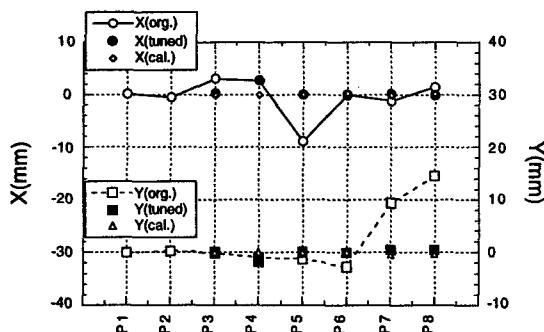


Figure 3: Results of automatic tuning BIO course which transfer beams to the biology experiment room for a carbon beam of 290 MeV. The abscissa is indicating the wire-grids. The open circles and squares show the beam position before the tuning. The black circles and squares show those after the tuning of the second part. Every beam position is on the center of the wire-grid within  $\pm 0.5$  mm except at the wire-grid P4 which is out of use in the tuning.

wire-grid P4 and the steering magnet ST6 are usually out of use. The former is mainly used for tuning the beamline which joints the vertical beamline and the horizontal beamline. The steering magnet ST6(x) is only manually used, when the horizontal tuning is out of range of the steering magnet ST5. The vertical deflection steering magnets ST8(y), which should be paired with ST7(x) near the wire-grid P7, separates from the ST7(x), because of too tight space near the P7. But the configuration of them still satisfies the condition for the convergence mentioned above. A result of the automatic tuning for the BIO course is shown in Fig. 3, which has been done in 10 minutes.

The final part is to steer the beam using the pair of the most downstream steering magnet and to position the beam on the center of the wire-grid located in the treatment room or the biology experiment room. Taking the BIO course as an example again, the beam has been adjusted to be in the center of the wire-grid P8 in the second part. Since the pair of the most downstream steering magnets ST9 are very close to the wire-grid P9, both of the locations can be regarded as being same. Only moving the beam position to the center of the wire-grid P9 by using the steering magnets ST9, the beam should be aligned on the required path of the irradiation devices for the biology experiments or the treatment, which is defined by the P8 and P9.

## 4 SUMMARY

These scenarios of the automatic tuning the other beamlines for the treatments, such as AVC course, are same. The first and second parts are well used, for especially tuning the BIO course which has the longest beamline. This system transports the beams to the treatment rooms and biology experiment room with sufficiently good precision for the radiotherapy and the biology experiments, while the operator does not need a special knowledge of the beam transportation. The beam transportation for the most treatments is done in fixed forms, so the automatic tuning system is easily applicable and very convenient.

## REFERENCES

- [1] S. Yamada: 'Commissioning and performance of the HIMAC medical accelerator', Proc. of the 1995 IEEE PAC, Vol.1 pp.5.
- [2] T. Kanai, et al.: 'HIMAC beam delivery system - physical characteristics-', Proc. of XXI PTCOG Meeting, Chiba, 1994, HIMAC Rep. 008, 1994, pp.26.
- [3] M. Torikoshi, et al.: 'Control system of a high energy beam transport system of HIMAC', Proc. of the 10th Symp. on Accelerator Science and Technology, Hitachi Naka, 1995, pp. 306.

# THE PROBLEM OF RADIOACTIVE PARTICLE BEAMS TRANSPORTATION AND THE EXPERIMENTAL REALIZATION OF THE PHENOMENON OF SUPPRESSED GAMMA-DECAY OF RADIOACTIVE NUCLEI

Vladimir I. Vysotskii

Kiev Shevchenko University, Radiophysical Faculty  
Vladimirskaya St. 64, Kiev, Ukraine, 252033; e-mail viv@vhome.kiev.ua

Vladimir P. Bugrov, Alla A. Kornilova, Sergei I. Reiman  
Moscow State University, 119899, Moscow, Russia

## 1. INTRODUCTION AND THEORETICAL MODEL

The problem of acceleration and long-distance transportation of high-radioactive beams and short-life-time radioactive nucleus beams is interesting for future beam and nuclear technologies. The method of short-life-time radioactive nuclei and high-radioactive beams spontaneous decay braking and suppression at long distance transportation and acceleration is the most optimal solution of this problem. The paper discusses the successful experiments on controlling the probability of spontaneous gamma-decay and life-time of radioactive and excited nuclei of several isotopes..

It is well known that in free space (without adjacent material bodies) the radiative life-time  $\tau$  of an excited nucleus is constant and equals

$$\tau = 3 \hbar / c^3 / 4 \omega_{\alpha}^3 |d_{eg}(\omega_{\alpha})|^2 \quad (1)$$

The total life-time of this excited nucleus  $\tau_{tot} = \tau / (1 + \alpha)$  in free space is constant too. Here  $d_{eg}$  is the matrix element of nucleus dipole momentum,  $\alpha$  is the coefficient of internal electron conversion for nuclear transition  $E_e \rightarrow E_g = 0$  with frequency  $\omega_{\alpha} = (E_e - E_g) / \hbar$ .

We have created the theory of resonant screen influence on the gamma-decay probability and life-time of excited and radioactive nuclei<sup>1,2,3</sup>. The phenomenon of nuclear decay controlling is a result of interaction of the nucleus with zero-energy electromagnetic modes, which in turn interact with the screen. It was shown that the result of action of resonant ( $\omega_{h0} \approx \omega_{\alpha}$ ) screen on the excited nucleus is the change of radiative and total life-times

$$\tau \rightarrow \tau^* \equiv \tau / \text{Re}[(1 - 2i\tau\Delta\omega_0)/(1 + iG/2 - \Delta\Omega_r)^4], \quad (2)$$

$$\tau_{tot} \rightarrow \tau_{tot}^* \equiv \tau_{tot}(\alpha + 1) / \{ \alpha + \text{Re}[(1 - 2i\tau\Delta\omega_0)/(1 + iG/2 - \Delta\Omega_r)^4] \} =$$

$$\tau / \{ \alpha + \text{Re}[(1 - 2i\tau\Delta\omega_0)/(1 + iG/2 - \Delta\Omega_r)^4] \}, \quad (3)$$

Here

$$G \approx 2fN\pi^2 |d_{eg}(\omega_{\alpha})|^2 / 3\tau_{tot}^* \hbar v_0 [(\omega_{h0} - \omega_{\alpha})^2 + (1/2\tau_{tot}^*)^2],$$

$$\Delta\Omega_r \approx 2fN\pi |D_{eg}(\omega_{h0})|^2 / 3 \hbar v_0 [(\omega_{h0} - \omega_{\alpha})^2 + (1/2\tau_{tot}^*)^2] \equiv (\omega_{h0} - \omega_{\alpha}) G \tau_{tot}^* / \pi,$$

$D_{eg}$  is a matrix element of screen atom dipole momentum,  $v_0$  is a volume of electromagnetic mode quantization,  $f$  is the Mossbauer parameter,

$$\Delta\omega_0 = \hat{P} \int_0^{\infty} 2\omega_{\alpha}^3 |d_{eg}(\omega_{\alpha})|^2 d\omega_{\alpha} / 3\pi c^3 (\omega_{\alpha} - \omega_{\alpha})$$

— radiative shift of excited level energy of the nucleus,

$$G = 2N\pi^2 |d_{eg}(\omega_{h0})|^2 / 3\tau_{atot} \hbar v_0 [(\omega_{h0} - \omega_{\alpha})^2 + (1/2\tau_{atot})^2];$$

$$\Delta\Omega_r = (\omega_{h0} - \omega_{\alpha}) G \tau_{atot} / \pi.$$

For  $|G|, |\Delta\Omega_r| \ll 1$  we have

$$\tau_{tot}^* = \tau / [\alpha + 1 - 8f\tau\Delta\omega_0 N\pi^2 c^3 / (\alpha + 1) v_0 \omega_{h0}^3] =$$

$$\tau / [(\alpha + 1 - (1 - \tau/\tau^*) f\Delta\Theta/4\pi)], \quad (4)$$

$$\tau^* = \tau / [1 - f\tau\Delta\omega_0 N\pi^2 c^3 / (\alpha + 1) v_0 \omega_{h0}^3]. \quad (5)$$

For the case of nonresonant ( $\omega_{h0} \neq \omega_{\alpha}$ ) screen

$$\tau_{tot}^* = \tau / [\alpha + (1 - \Delta\Omega_{nr})^4]; \quad (6)$$

$$\Delta\Omega_{nr} = 2\pi \sum_s N_s |D_{eg}(\omega_{ns})|^2 (\omega_{ns} - \omega_{\alpha}) / 3 \hbar v_{0s} [(\omega_{ns} - \omega_{\alpha})^2 + (2\tau_{tot}^*)^2] \quad (7)$$

It was shown that resonant screen effect in all cases appears to be more significant than for the nonresonant one. For the same relation  $N/V_0$  the influence of the resonant screen upon life-times  $\tau_{tot}^*, \tau^*$  of excited nucleus is by several orders more effective than the influence of the nonresonant screen.

Two experiments on controlling of the nuclei decay and changing  $\tau_{tot}^*, \tau^*$  were performed based on our theory.

## 2. THE EXPERIMENTAL STUDY OF THE PHENOMENON OF CONTROLLING TIME-LIFE OF SPONTANEOUS DECAY OF EXCITED NUCLEI BY MOSSBAUER SPECTRUM INVESTIGATION

The aim of the first experiment was to measure the changing (decreasing at  $\omega_{h0} = \omega_{\alpha}$ ) of the spectral width of Mossbauer radiation  $\Gamma \equiv 1/\tau_{tot} \rightarrow \Gamma^* \equiv 1/\tau_{tot}^*$ , (as a result of

changing life-times  $\tau_{\text{tot}}^*$  and  $\tau^*$ ) during action of resonant screen. The layouts of the experiments are presented on Fig.1.

The anticipated change in radiative and total widths of gamma-spectrum increases with the decrease of life-time  $\tau$ . In order to reduce the influence of technical fluctuations the Mossbauer isotope  $\text{Sn}^{119\text{m}}$  with short total  $\tau_{\text{tot}} = 1,85 \cdot 10^{-8}$  s and radiative  $\tau = 1,2 \cdot 10^{-7}$  s life-times was used. The experimental installation was mounted on the double layer of acoustic isolation.

The excited  $\text{Sn}^{119\text{m}}$  isotope (chemical compound  $\text{CaSn}^{119\text{m}}\text{O}_3$ ) with activity of 5 mCi and  $\alpha=5,5$  was used as a source 1 of Mossbauer radiation with the energy of quanta  $E_\gamma = 23,8$  KeV. This source had a radiation spectrum in the form of a single line of nearly natural width.

The resonant absorber 2 had a form of disk with diameter  $D \approx 3$  cm, made of stable  $\text{Sn}^{119}$  isotope (average surface density  $\sigma_m \approx 1,4$  mg/cm<sup>2</sup>  $\approx 6 \cdot 10^{18}$  atoms  $\text{Sn}^{119}$  per cm<sup>2</sup>, chemical compound  $\text{Sn}^{119}\text{O}_2$ ). This absorber (screen) had a spectrum of absorption with almost natural width.

The lead diaphragm 3 with diameter  $D_1 \approx D$  was fixed at distance  $L = 3$  cm from source. The diaphragm had a hole with diameter  $D_0 = 1$  cm and length  $L_0 = 2,5$  cm. Behind the diaphragm there was a resonant detector 4 (a compound  $\text{CaSn}^{119}\text{O}_3$  was used as this detector) and a system for changing the Doppler velocity of detector 4.

The measurements with gamma-beam (traveling from source through resonant absorber and hole of the diaphragm to resonant detector) were performed in two regimes.

In the first regime the resonant absorber 2 was fixed in position a) near source 1 (at distance  $l_1 \approx 0,2$  cm). The finite quantizing volume  $V_0$  in this regime existed only for those electromagnetic modes which were localized in solid angle between source and the diaphragm. The volume of each of these modes corresponded to the value  $V_0 \approx \pi \lambda L^2/3$  of space between two cones with common apex on the excited nucleus that cut a single Fresnel zone with area  $S_0 \approx \pi \lambda L$  on the diaphragm surface. Only for

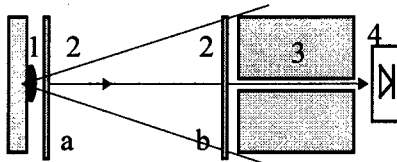


Fig 1

these modes  $\tau_{\text{tot}}^* \neq \tau_{\text{tot}}$ ,  $\tau^* \neq \tau$ .

For other space directions and for other space mode orientations we have  $V_0 \rightarrow \infty$ . In accordance with (4) and (5) in these cases of modes unlimited in space we have  $\tau_{\text{tot}}^* = \tau_{\text{tot}}$ ,  $\tau^* = \tau$ .

In the second regime the resonant absorber 2 was fixed at distance  $l_2 \approx 3$  cm from source in position b) near the diaphragm 3 ( $l_2 \approx L$ ).

The relation  $N/V_0$  was different in these two regimes.

For the first regime

$$(N/V_0)_a \approx 3\sigma_m l_1^2/L^3 \approx 2,7 \cdot 10^{16} \text{ cm}^{-3}$$

and

$$\Delta\Theta_a \approx 2\pi\{1-1/[1+(D_1/2L)^2]^{1/2}\} \approx 0,4\pi.$$

For the second regime

$$(N/V_0)_b \approx 3\sigma_m/l_2 \approx 6 \cdot 10^{18} \text{ cm}^{-3}$$

and

$$\Delta\Theta_b \approx 2\pi\{1-1/[1+(D/2L)^2]^{1/2}\} \approx \Delta\Theta_a \approx 0,4\pi.$$

In the regimes (a) and (b) the total widths  $\Gamma_{(a,b)}^* = \Gamma_{s(a,b)}^* + \Gamma_d + \Delta\Gamma$  of gamma-spectrums included both the sum of source ( $\Gamma_{s(a,b)}^*$ ) and resonant detector ( $\Gamma_d$ ) resonant-line widths, and the broadening  $\Delta\Gamma$  (as a result of resonant absorption) in absorber 2.

In order to verify the stability of gamma-line position and width the measurement of gamma-spectrum was performed in the system of source 1 — hole of diaphragm 3 — resonant detector 4 without the resonant absorber 2. The resulting value

$\Gamma_s + \Gamma_d = \Gamma_{s0} + \Delta\Gamma_{s0} + \Gamma_{d0} + \Delta\Gamma_{d0} \approx (0,809 \pm 0,002)$  mm/s (in Doppler velocity units  $c\Gamma/\omega_a$ ) for this case demonstrates that the nonradiative broadening  $\Delta\Gamma_{s0} \approx \Delta\Gamma_{d0} \approx 0,081$  mm/s in the source and detector is small in relation to natural widths  $\Gamma_{s0} = \Gamma_{d0} = 1/\tau_{\text{tot}} \approx 0,323$  mm/s. It follows from these results that there are no sources of technical nonstability and systematic errors in the experimental installation.

For the regime (a) we have

$$\Gamma_{s0} \rightarrow \Gamma_{s0(a)}^* \equiv 1/\tau_{\text{tot}(a)}^*, \Gamma_{s(a)}^* \rightarrow \Gamma_{s0(a)}^* + \Delta\Gamma_{s0}.$$

As a result for this regime we have the following expression for the total width of gamma-spectrum

$$\Gamma_{(a)}^* = 1/\tau_{\text{tot}(a)}^* + \Delta\Gamma_{s0} + \Gamma_{d0} + \Delta\Gamma_{d0} + \Delta\Gamma. \quad (8)$$

For the regime (b) with presence of the resonant absorber 2 near the diaphragm we have the similar result for the total width of gamma-spectrum

$$\Gamma_{(b)}^* = 1/\tau_{\text{tot}(b)}^* + \Delta\Gamma_{s0} + \Gamma_{d0} + \Delta\Gamma_{d0} + \Delta\Gamma. \quad (9)$$

Then (using the results of theoretical calculation (8), (9) for  $\Gamma_{(a)}^*$  and  $\Gamma_{(b)}^*$  and equations (3) - (5)) we find the expressions that describe the changing of total and radiative (for controlled Mossbauer part) life-times

$$1/\tau_{\text{tot}(b)}^* - 1/\tau_{\text{tot}(a)}^* = \Gamma_{(b)}^* - \Gamma_{(a)}^*, \quad (10)$$

$$1/\tau_{\text{eff}(b)}^* - 1/\tau_{\text{eff}(a)}^* = (\Gamma_{(b)}^* - \Gamma_{(a)}^*) [4\pi(1+\alpha)/f\Delta\Theta] \quad (11)$$

At small change of life-time  $|\tau_{\text{tot}(a)}^* - \tau_{\text{tot}(b)}^*| \ll \tau_{\text{tot}}$  we have

$$(\tau_{\text{tot}(a)}^* - \tau_{\text{tot}(b)}^*)/\tau_{\text{tot}} \approx (\Gamma_{(b)}^* - \Gamma_{(a)}^*)\tau_{\text{tot}}, \quad (10a)$$

$$\tau/\tau_{\text{eff}(b)}^* - \tau/\tau_{\text{eff}(a)}^* = (\Gamma_{(b)}^* - \Gamma_{(a)}^*)\tau_{\text{tot}} [4\pi(1+\alpha)/f\Delta\Theta] \quad (11a)$$

Using the expression (4) and the results of measuring

$\tau_{\text{tot}(a,b)}^*$  we can calculate the radiative shift

$$\Delta\omega_0 \approx \{(\tau_{\text{tot}(a)}^* - \tau_{\text{tot}(b)}^*)/\tau_{\text{tot}}\}(\alpha+1)^2 \omega_{n0}^3 / \{2\pi\pi^3 [\Delta\Theta_a (N/V_0)_a - \Delta\Theta_b (N/V_0)_b]\}. \quad (12)$$

Each measurement of  $\Gamma_{(a)}^*$  and  $\Gamma_{(b)}^*$  in both cases lasted  $\Delta t = 0,5$  hour. The average values measured were

$$\Gamma_{(a)}^* = (1,167 \pm 0,003) \text{ mm/s and}$$

$$\Gamma_{(b)}^* = (1,184 \pm 0,003) \text{ mm/s with corresponding changes of total life-time of } \text{Sn}^{119\text{m}}$$

$$\{\tau_{\text{tot}(a)}^* - \tau_{\text{tot}(b)}^*\}/\tau_{\text{tot}} = (0,63 \pm 0,12) \cdot 10^{-2}$$

and life-time for controlled Mossbauer component of  $\text{Sn}^{119\text{m}}$  gamma-radiation

$$\{\tau/\tau_{\text{eff}(b)} - \tau/\tau_{\text{eff}(a)}\} = (0,82 \pm 0,16).$$

Using the result of measuring  $(\tau_{\text{tot}(a)}^* - \tau_{\text{tot}(b)}^*)/\tau_{\text{tot}}^*$  and the general expression (12) we for the first time have obtained the magnitude and sign of radiative shift (radiation correction) of excited nucleus  $\text{Sn}^{119\text{m}}$  level

$$\Delta\omega_0 \approx - (2,9 \pm 0,55) \cdot 10^{14} \text{ s}^{-1}.$$

The measures taken to improve the reliability of measurements in the "frequency-response" regime allow to connect with a high degree of certainty the experimental results with theoretically predicted controlled charge of nucleus gamma-decay probability and life-time and not with false factors.

### 3. THE EXPERIMENTAL STUDY OF THE PHENOMENON OF CONTROLLED SPONTANEOUS GAMMA-DECAY OF RADIOACTIVE NUCLEI BY INVESTIGATION OF INTENSITY OF GAMMA-RADIATION

The aim of the second experiment was to measure the changing of total intensity  $J_\gamma \rightarrow J_\gamma^*$  of resonant nuclei radiation (as a result of changing life-times  $\tau \rightarrow \tau^*$ ) in the direction  $(4\pi - \Delta\Omega)$  not blocked by the resonant screen 2. Equation for population  $n_e^*$  of excited nuclei has a form

$$\frac{dn_e^*}{dt} = \sum_{i>e} n_i/\tau_{i2} - n_e^* \Delta\Omega f/4\pi\tau^* - n_e^* (1-f)/\tau - n_e^* f(1 - \Delta\Omega/4\pi)/\tau - n_e^* \alpha/\tau. \quad (13)$$

Here  $\Delta\Omega$  is a solid angle blocked by the absorber. In equilibrium state the relation of population of excited nuclei  $n_2^*$  for  $\Delta\Omega \neq 0$  (with selective absorption) to population of excited nuclei  $n_2$  for  $\Delta\Omega = 0$  (without selective absorption) has a form

$$n_2^*/n_2 = 1/[1 - f \Delta\Omega(1 - \tau_2/\tau_2^*)/4\pi(1 + \alpha)]. \quad (14)$$

Intensity  $J_\gamma^* \sim n_1^*$  of resonant radiation (Mossbauer's probability  $f$ ) in not blocked direction increase and

$$J_\gamma^*/J_\gamma = n_e^*/n_e = 1/[1 - f(1 - \tau/\tau^*) \Delta\Omega/4\pi(1 + \alpha)]. \quad (15)$$

The layout of the experiment is presented on Fig.2.

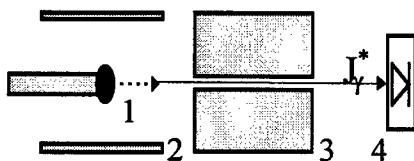


Fig 2

A excited  $\text{Co}^{57}(\text{Fe}^{57*})$  isotope source 1 of spontaneous radiation ( $\tau \approx 10^{-6} \text{ s}$ ,  $\tau_{\text{tot}} = \tau/W \approx 10^{-7} \text{ s}$ ,  $\hbar\omega = 14,4 \text{ KeV}$ ) with activity of 10 mCi in a chromium matrix was used as a source of Mossbauer radiation. This source has a spectrum in the form of single line of natural width.

The source was put in the center or near the diaphragm-oriented edge of the resonant screen 2, having a form of cylinder made of stable  $\text{Fe}^{57}$  isotope. The source is fixed in the Plexiglas disc and put in the center ( $l=2,5 \text{ cm}$ ) or near the edge ( $l=1 \text{ cm}$ ) of the resonant absorber 2, having a form of cylinder with diameter  $D = 2 \text{ cm}$  and length  $L = 5 \text{ cm}$ , made of  $\text{Fe}^{57}$  isotope (200 mg) in stainless

steel (100 mg). The thickness of absorber was  $7 \text{ mg/cm}^2$ . The lead diaphragm 3 has a hole with diameter  $D_0 = 1 \text{ cm}$  and length  $L_0 = 2,5 \text{ cm}$ . Behind the diaphragm there was amplitude detector 4 -  $\text{NaJ(Tl)}$  crystal with width  $10^{-2} \text{ cm}$  and photo-electronic multiplier.

The signal processing system picked out the part of amplitude specter close to the gamma-line with  $E_\gamma = 14,4 \text{ KeV}$ .

For the first time in this experiment we have discovered the change of radiative transition life-time  $\tau^*$  by 40-100% and total life-time  $\tau_{\text{tot}}^*$  (including non-resonant radiation with probability  $1-f$  and non-radiative channel of decay with probability  $W$ ) by 0.6-2%.

### 4. CONCLUSION

By optimization of decay controlling system parameters (using the nuclei without the electron conversion decay channel  $\alpha \rightarrow 0$ , the resonance absorbers with a maximum solid angle screening  $\Delta\Omega \rightarrow 4\pi$ , with maximum weight part of the gamma-radiative resonance channel  $f \rightarrow 1$ ) it is possible to achieve significantly higher influence upon the spontaneous decay characteristics and, respectively, sharp increase of total life-time  $\tau_{\text{tot}}^* \gg \tau_{\text{tot}}$ .

Among other conclusions, the obtained results in fact prove the existence of a peculiar macroscopic "distance effect" predicted above, namely the dependence of the effectiveness of quantum spontaneous decay process of the excited nuclei on macroscopically remote position of a resonant absorbing screen (unlike, for example, Kazimir's effect manifesting itself only at microscopic distances).

In conclusion we would like to note that the effect of influence upon the spontaneous radiation characteristics of excited (radioactive) nuclei may manifest itself not only for Mossbauer nuclei and transitions but also for other excited states and nucleus types provided the existence for them of an obviously expressed resonance absorption. By this method of spontaneous decay braking and suppression of short-life-time radioactive nuclei and high-radioactive beams it is possible long distance transportation and acceleration of radioactive beam.

### 5. REFERENCES

1. V.I. Vysotskii, R.N.Kuzmin On change of characteristics of spontaneous radiation at reformation of electromagnetic vacuum, *Soviet Phys - J.T.P. Letter*, **10**, 300 (1984)
2. V.I. Vysotskii, V.P. Bugrov, A.A.Kornilova, R.N.Kuzmin, S.I Reiman, "The problem of gamma-laser and controlling of Mossbauer nuclei decay (theory and practica)", *Hyperfine Interactions*, **107**, 277 (1997)
3. V.I. Vysotskii, "The problem of controlled spontaneous nuclear gamma-decay: theory of controlled excited and radioactive nuclei gamma-decay,". *Phys. Rev. C*, **58**, 337 (1998)

# THE PROGRESS OF DEVELOPMENT OF FOUR KICKERS' BUMP SYSTEM FOR INJECTION IN HLS RING

X.Q. Wang<sup>#</sup>, Y.J. Pei, L. Shang, L. Wang, K.J. Fan, H.L. Xu, D.M. Jiang

Y.B. Leng, G.C. Wang, X.Y. He, F. Zhao, J.G. Zhang

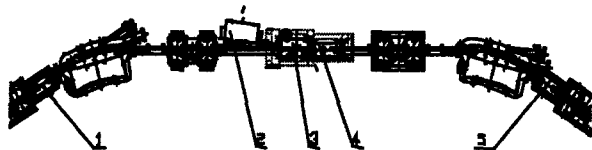
NSRL, USTC, P.O. Box. 6022, Hefei, Anhui 230029, China

## Abstract

There are three kicker magnets to manipulate local bump orbit in Hefei storage ring, which could satisfy basically the commissioning and operations of General Purpose Light Source (GPLS) mode. In the Phase Two Project of HLS, four kicker magnets will be employed and installed in one straight section to form a ladder-shaped bump orbit. So the parameters of bump orbit are independent of the ring lattice. The new system also satisfies the multicycle and multiturn injection of High Brightness Light Source (HBLS) mode and other modes, and it expected to run stably for a long time. This paper presents the development of the new bump orbit system.

## 1 INTRODUCTION

A multicycle and multiturn injection scheme is adopted to accumulate beam in HLS ring<sup>1</sup>. The injection system consists of three kicker magnets, one pulse septum magnet, one DC septum magnet and their power supplies<sup>2</sup>. The pulse septum magnet which is made of steel sheet and copper current strip with  $\text{Al}_2\text{O}_3$  powder coating runs well for ten years, and its steel sheets have some absorption capacity after baking<sup>3</sup>. The air-core of kicker magnet in the vacuum pipe produces pulse field. The pulse formation circuit uses a spark gap switch to generate a half sinewave current pulse with attenuation which can satisfy the commissioning and operation of the GPLS mode<sup>4-6</sup>. Fig.1 shows the distribution of the magnets and vacuum chambers. Fig.2 shows local bump orbits corresponding separately to the GPLS with emittance of  $133 \text{ nm} \cdot \text{rad}$  and the HBLS-1 of  $27 \text{ nm} \cdot \text{rad}$ .



1,4,5: kicker; 2: DC septum; 3: pulse septum.

Fig.1 Layout of the injection system of the HLS ring

There are four quadrupole magnets and two bending magnets within the bump orbit of three kicker magnets. So the parameters of kicker magnets are decided by local Twiss functions and phase shifts. Such bump orbit system

couldn't satisfy injection<sup>2,7,8</sup> of HBLS-2 mode of  $13 \text{ nm} \cdot \text{rad}$ . The two kickers (first and fifth in fig.1) occupy installation space suitable for two sextupole magnets, it's a disadvantage and decreases the dynamic aperture.

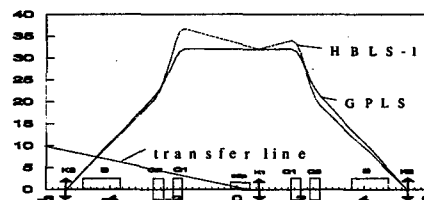


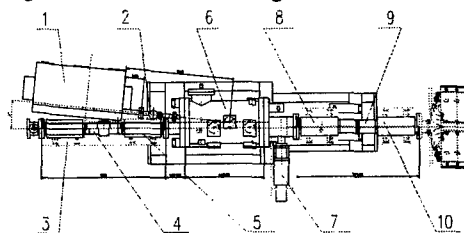
Fig.2 Scheme of bump orbits and the layout of the inj. sys.

In order to form a reasonable bump orbit, HBLS-1 requires the middle kicker to deflect beam with a small angle. However, it is too difficult for the pulse power supply with spark-gap switches to generate such a small pulse current with little time jitter, furthermore, the lifetime of switch is too short and needs maintenance frequently.

In the new injection system, four kicker magnets will be installed in one straight section, and thyratrons will be used as switch, which can decrease the time jitter to less than 10ns. Two sextupole magnets will be added at the place which were now occupied by two kickers, this will increase the dynamic aperture.

## 2 NEW OVERALL ARRANGEMENT

The HLS straight section for injection is only 3 meters long, it's quite difficult to install four kickers in such a short extent. Installation method and injection tracking<sup>8</sup> have been carefully studied. The overall arrangement of the new bump orbit system is shown in fig.3. Fig.4 shows the redesigned distribution of ring.



1: DC septum; 2, 7: beam monitor; 3, 5, 8, 10: kicker; 6: pulse septum; 4, 9: ceramic vacuum.

Fig.3 Plane distribution of magnets and scheme of bump orbit in the inj. sys. with centralizing overall arrangement.

<sup>#</sup> Email: wangxaqi@ustc.edu.cn

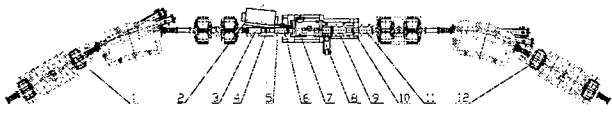


Fig.4 New plane distribution diagram of the area involved in injection system reconstruction of HLS ring.

### 3 PREFABRICATED STUDY

Some key techniques have been studied and solved since 1993.

#### 3.1 Kicker magnets

Kickers with 270mm long are divided into two types in cross section<sup>11</sup>. A pair of kickers (shown in fig.3) are installed upstream the pulse septum, the others are installed downstream. Fig.5 shows the cross section of a kind of yoke which size is  $92 \times 36 \text{ mm}^2$ , the other is  $108 \times 36 \text{ mm}^2$ . The material of yoke is MnZn ferrite which has a wide frequency spectrum<sup>12</sup>. A prototype kicker magnet with the ferrite yoke has been assembled to study the properties of the ferrite and the distribution of magnetic field. Fig.6 shows relationship between the magnetic field and the excited current ( $B/I$ ), the measured maximum magnetic field is about 2.9 kilo gauss which far exceed the need of injection. The  $B/I$  curve (signed by black dots in fig.6) is approximately linear quite conform the calculated result

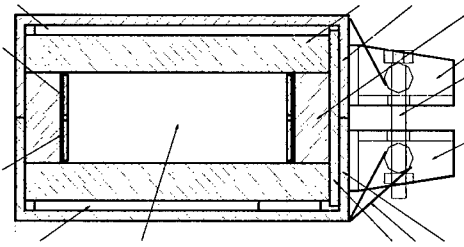


Fig.5 Cutaway view of kicker measured & calculated

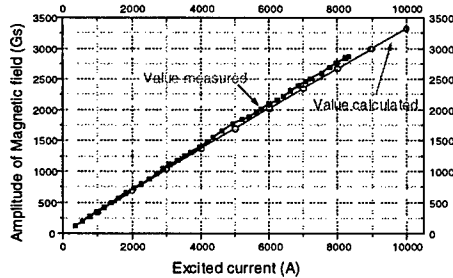
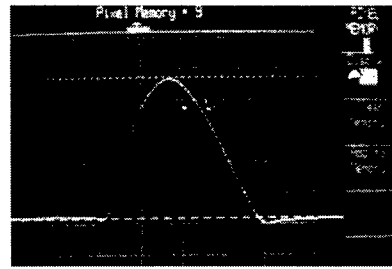


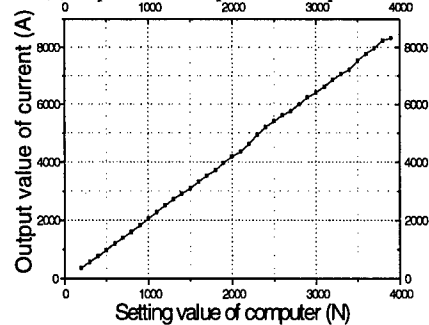
Fig.6  $B_p/I_p$  Curves measured & calculated

#### 3.2 Pulse power supply

Two pulse power supplies are employed to drive kickers separately, one is for K1 and K2, the other is for K3 and K4, this can decrease the timing jitter among kickers. Thyatron, EEV CX1174, is used as main switch, which has a good property with timing jitter less than 5ns and the stability up to 0.1%<sup>14,15</sup>. A prototype pulse power supply has been constructed, some new techniques have been adopted to improve its performance<sup>14,15</sup>.



(a) A photo of output current pulse.



(b) The pertinence of output current & control number.

Fig.7 The prototype of pulse power supply of kicker magnet.

#### 3.3 Ceramic vacuum chamber

The ceramic chambers are both 971mm long (No.3 and No.9 in fig.3), their inner aperture are  $80 \times 24 \text{ mm}^2$  and  $96 \times 24 \text{ mm}^2$  respectively, the cross section is racetrack. They are key hardware and are being prefabricated now. Physical analysis indicates<sup>16</sup> that coatings with suitable metal material in inner surface with proper thickness can meet requirements of vacuum impedance and pulse magnetic penetrability. The losing impedance measurement system, based on HP instruments and HPVEE software, is set up<sup>17</sup>. The techniques related to fabrication of ceramic chamber are studied.

#### 3.4 Magnetic field measurement

Surveying the electromagnetic characteristic of the yoke, adjusting the waveform of kickers' field and measuring the distribution of magnetic field, will be done soon. Automatic measurement system of micro second magnetic field has been set up. Magnetic field distribution of prototype kicker<sup>18</sup> was obtained. The measurement data (see in fig.6 and fig.7) indicates that it is feasible using this kind of ferrite material to meet the requirement of injection.

### 4 CONSTRUCTION DESIGN

Since June of 1997, the project came into the phase of construction. Some contracts have been signed. All the non-standard measurement facilities are being constructed. Parts of them have already finished by the end of 1998. Four vacuum chambers with DC clearing electrodes and close orbit monitors will be installed in the ring. These new increased electrodes will improve symmetry of the ring lattice<sup>19</sup> and restrain ion trapping instability<sup>20</sup>.



## REFERENCE

- [1] Y J Pei, Multiturn injection, Reported in particle dynamic symp. (Huangshan, China), 1981.
- [2] X Q Wang et al., Proce. of Hefei ICSRL (Hefei, China), 1989, p.192.
- [3] Y J Pei et al., Nucl. Instr. and Meth. in Phys. Res. A **398** (1997) 368.
- [4] X Q Wang et al., Proc. of 1st Taiwan Straits Symp. on SR, 1993, p.32.
- [5] X Q Wang et al., Jour. of China Univ. of S. & T., **23**(2) (1993) 151.
- [6] X Q Wang, Jour. of China Univ. of S. & T. **24**(4) (1994) 536.
- [7] X Q Wang et al., 6th China-Japan joint symp. on acc. for nucl. S. and Their Appl., 1996, p.300.
- [8] L Shang et al., Nucl. Instr. & Meth. In Phys. Res. **406**(2) (1998) 177.
- [9] A Q Zhou et al., Proc. of the 6th parti. acc. phys. symp. (Zhangjiajie, China), 1997, p.105.
- [10] Saewoong Oh, Proc. of Hefei ICSRL (Hefei, China), 1989, p.111.
- [11] L Wang et al., Proc. of the 6th parti. acc. phys. symp., 1997, p.156.
- [12] L Wang et al., Proc. of the 2nd national symp. on acc. tech. (Ningbo, China), 1998, p.430.
- [13] K J Fan et al., Proc. of the 6th particle acc. phys. symp. (Zhangjiajie, China), 1997, p.167.
- [14] L Shang et al., Jour. of China Univ. of S. & T. **28**(2) (1998) 172.
- [15] L Shang et al., High Power Laser and Particle Beams **29** (1) (1998) 103.
- [16] L Shang et al., Proc. of the 2nd national symp. on acc. tech. (Ningbo, China), 1998, p.561.
- [17] Y B Leng et al., Proc. of the 2nd national symp. on acc. tech. (Ningbo, China), 1998, p.299.
- [18] K J Fan et al., Necl. Techniques, **21**(3) (1998) 167.
- [19] X Q Wang et al., High Energy Phys. & Nucl. Phys. **22**(8) (1998) 755.
- [20] X Q Wang et al., Jour. of China Univ. of S. & T. **28**(2) (1998) 168.

# THE K500-to-K1200 COUPLING LINE FOR THE COUPLED CYCLOTRON FACILITY AT THE NSCL\*

X. Wu, H. Blosser, D. Johnson, F. Marti, R.C. York

National Superconducting Cyclotron Laboratory

Michigan State University

East Lansing, MI 48824

## Abstract

An upgrade now in progress at the National Superconducting Cyclotron Laboratory (NSCL) facility will couple two existing superconducting cyclotrons. This will provide significant beam intensity gains for all ions and for heavier ions, also increased energy. These gains will greatly enhance the performance of the NSCL facility, particularly for nuclear studies with radioactive beams and nuclear reaction physics. A significant element of this upgrade is the K500-to-K1200 coupling line used to transport beam between the two cyclotrons. Beyond satisfying the geometric constraints of beam transport, the system must match the six-dimensional phase space obtained from the K500 to that required for injection into the K1200. The transported beams range from low energy, heavy ions like  $^{238}\text{U}^{28+}$  at 6.9 MeV/u to high energy, light ions like  $^{16}\text{O}^{3+}$  at 16.7 MeV/u. Tracking studies have been done to simulate the required matching conditions and performance of the coupling line. The result of these studies, including required magnets and beam diagnostics are presented in this paper.

## 1 INTRODUCTION

The coupled cyclotron facility at the NSCL will consist of an ECR-ion-source-injected K500 cyclotron followed by a K500-to-K1200 coupling line, and then by radial, charge-stripping injection into the K1200 cyclotron for final acceleration to 100-200 MeV/nucleon [1]. The basic requirement for the K500-to K1200 coupling line is to transport the required ion beams between two cyclotrons and match the six-dimensional phase space to ensure efficient injection into the K1200 cyclotron. A wide range of ion beams is required to support the proposed nuclear physics research program. Table 1 shows a selected beam list for the K500-to-K1200 coupling line. For this analysis, the beam emittance from the K500 cyclotron was assumed to be  $5 \pi \text{ mm-mrad}$  (unnormalized) with a momentum spread  $\Delta p/p$  of 0.2%. The required ion beams for the K500-to-K1200 coupling line will have a maximum beam momentum  $P/Q$  of 1.0 GeV/c and a charge/mass ratio  $Q/A < 0.2$ .

Table 1: Beam List for the K500-to-K1200 Coupling Line

ION	A	Q	Energy (MeV/u)
O	16	3	16.7
Ar	40	7	15.3
Kr	84	14	14.0
Xe	129	21	12.9
U	238	28	6.9

## 2 COUPLING LINE MATCHING CONDITIONS

The matching conditions for the coupling were obtained by simulating the K500 beam extraction and the K1200 beam injection process.

The K500 beam extraction simulation was done using magnetic field measurements both in the acceleration and extraction regions [2]. The ion beams were tracked using code CYCLONE from the spiral inflector at the center, through the central region electrodes, accelerating region and K500 extraction system to the beginning of the coupling line. The modified K500 extraction system consists of 2 electrostatic deflectors and 7 focusing bars. In addition, a new combined function magnet was implemented to provide additional deflection and focusing. The design philosophy was to maintain the beam envelope within the available aperture and to minimize the divergence of the beam at the exit of the cyclotron. To obtain this objective not all bars are active for each test beam. The resultant K500 extracted beam parameters for 3 typical beams at the matching point are given in Table 2.

The K1200 injection simulation [3] was done by backward tracking of particle trajectories from the stripping foil inside K1200 (at a radius of  $\sim 33 \text{ cm}$ ) through the Dee gap and injection channel of the yoke towards the end of the coupling line. A new combined-function magnet inside the injection channel is required to provide both beam deflection and focus. The resultant K1200 injected beam parameters for the same 3 beams at the end of the coupling line are given in Table 3.

\*Work supported by NSF contract number PHY-952884.

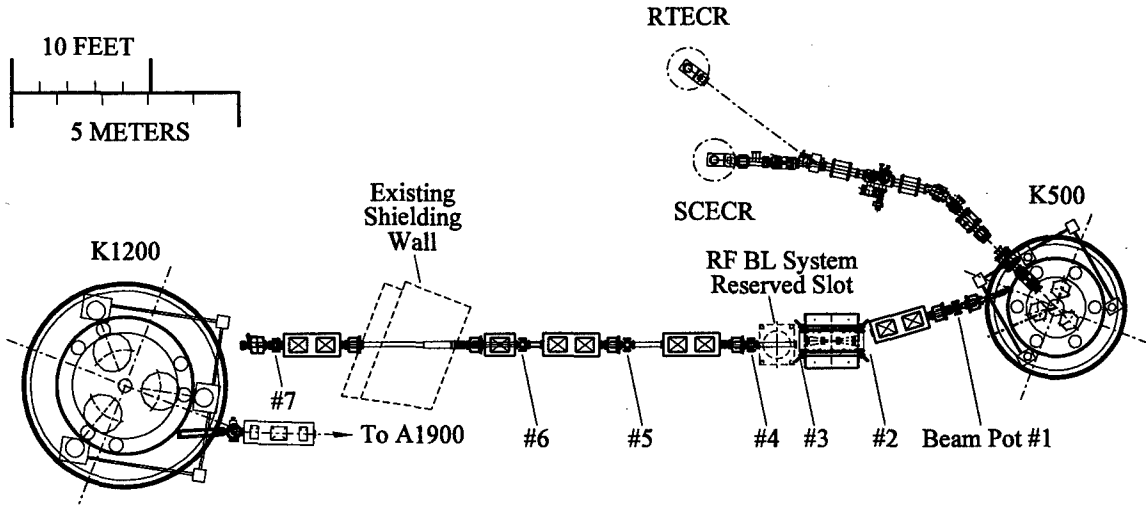


Figure 1. Layout of the proposed K500-to-K1200 coupling line.

Table 2: K500 Extracted Beam Parameters.

Beam Parameter	$^{16}\text{O}^{3+}$	$^{40}\text{Ar}^{6+}$	$^{238}\text{U}^{21+}$
$\beta_x$ (m)	4.723	2.999	3.663
$\alpha_x$	-2.517	-2.442	-2.588
$\beta_y$ (m)	0.918	1.135	0.482
$\alpha_y$	0.429	0.494	0.052
$\eta_x$ (m)	4.488	5.563	5.327
$\eta_x'$	1.440	1.809	2.784

Table 3: K1200 Injected Beam Parameters.

Beam Parameter	$^{16}\text{O}^{3+}$	$^{40}\text{Ar}^{6+}$	$^{238}\text{U}^{21+}$
$\beta_x$ (m)	121.274	86.946	49.251
$\alpha_x$	-30.195	-34.733	-21.839
$\beta_y$ (m)	3.990	5.794	12.846
$\alpha_y$	2.012	3.233	7.838
$\eta_x$ (m)	5.770	5.050	4.440
$\eta_x'$	1.720	2.279	2.279

### 3 K500-TO-K1200 COUPLING LINE

Figure 1 shows the configuration of the planned, K500-to-K1200 coupling line. The lattice uses a single  $16^\circ$  dipole, a quadrupole singlet, and four quadrupole doublets to transport the beam from K500 to K1200 while satisfying the required matching conditions. All of these magnets will be obtained from the decommissioned A1200 fragment separator. The dipole has a full gap of 5.0 cm. The quadrupoles have an

effective length of 0.4 m and a radial aperture of 6.5 cm. The maximum quadrupole field gradient available is about 35 T/m. A slot has also been reserved for a RF system for possible future control of the bunch length between the two cyclotrons.

The resultant coupling line  $\beta$  functions for the 3 beams covering the operating diagram are shown in Figure 2, 3 and 4, respectively with the dispersion functions shown in Figure 5. Due to the varied matching conditions required for different beams, the tuning of the coupling line changes significantly. Beam simulations were done to check whether the coupling line could match K1200 beam conditions if the K500 beam conditions varied from 50% to 200% of the original value. The results were very satisfactory. In addition, as shown in Figure 5, the coupling line was designed to achieve  $\eta=0$  at the same position for all beams where a 4-jaw collimator will be placed to clean up the phase space from the K500.

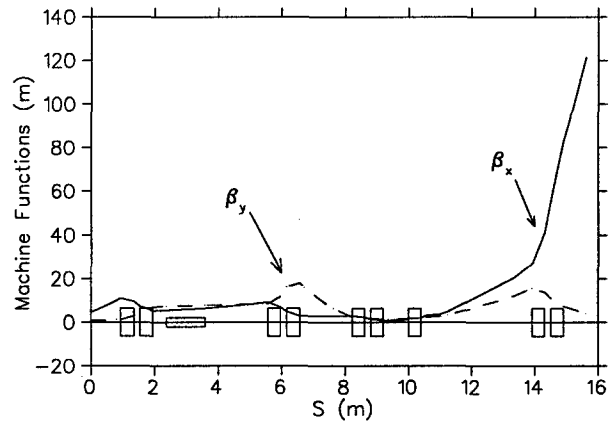


Figure 2. Lattice functions for  $^{16}\text{O}^{3+}$  beam

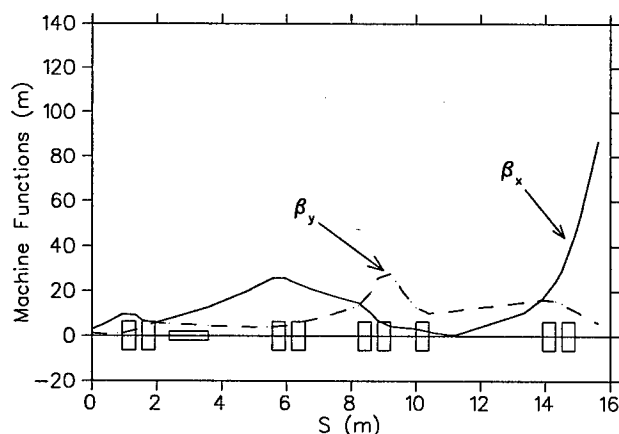
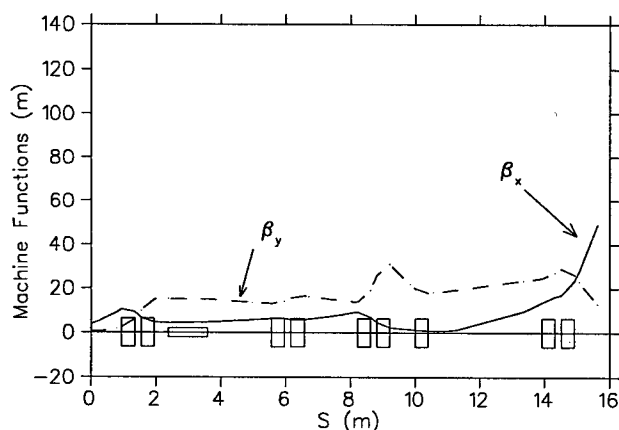
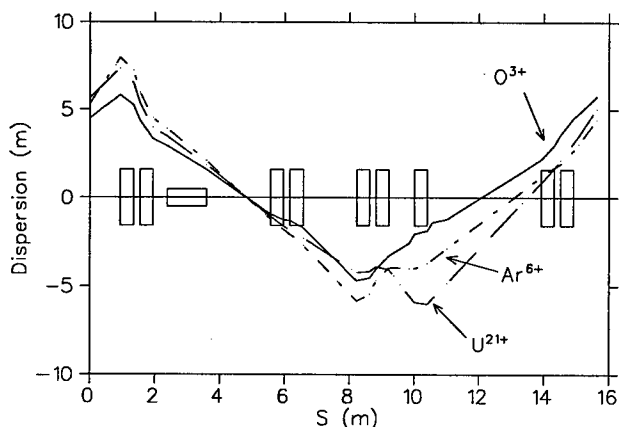

 Figure 3. Lattice functions for  $^{40}\text{Ar}^{6+}$  beam.

 Figure 4. Lattice functions for  $^{238}\text{U}^{21+}$  beam.


Figure 5. Dispersion functions for all 3 beams.

The beam envelopes for all 3 beams with an emittance of  $5.0 \pi \text{ mm-mrad}$  and a momentum spread  $\Delta p/p$  of 0.2% are shown in Figure 6, and the maximum required quadrupole gradients are listed in Table 4. The beam envelopes are well within in the aperture limits and the field gradient requirements can easily be achieved.

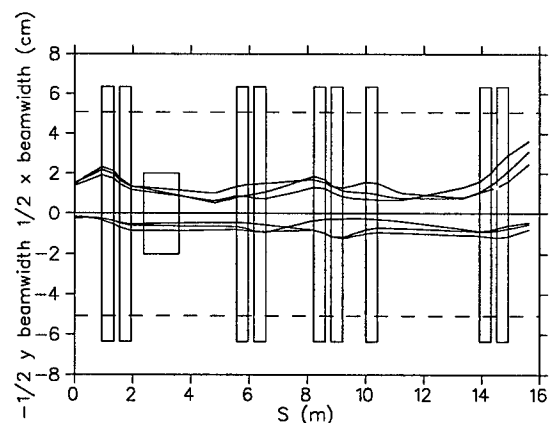


Figure 6. Beam envelopes for all 3 beams.

Table 4: Required Coupling Line Quadrupole Gradient.

Quadrupole	Quadrupole Gradient (T/m)		
	$^{16}\text{O}^{3+}$	$^{40}\text{Ar}^{6+}$	$^{238}\text{U}^{21+}$
QK5F1	7.19	7.03	7.47
QK5F2	-4.50	-5.19	-6.18
QK12F1	9.19	-1.02	6.81
QK12F2	-7.87	0.71	-4.60
QK12F3	6.63	6.38	-0.31
QK12F4	-4.87	-5.92	-1.86
QK12F5	1.51	1.44	5.03
QK12F6	-2.00	-0.82	2.54
QK12F7	-0.28	-1.86	-5.10

## 4 BEAM DIAGNOSTICS

The K500-to-K1200 coupling line tuning depends closely on the K500 beam conditions. The determination of beam emittance, phase space parameters, beam energy and energy spread from the K500 is very important for proper K1200 stripping injection. As shown in Figure 1, the coupling line will have 7 beam diagnostic areas. Faraday cups and phosphor screens will be used to monitor the beam intensity and profile, and two non-intercepting bunch length probes at the entrance and the exit will be used to monitor beam bunch length. Beam phase space parameters will be determined with slits and a phosphor screen. In addition, we are evaluating the use of PPAC or MCP detectors for beam phase space as well as beam energy and energy spread measurements.

## 5 REFERENCES

- [1] R. C. York et al., "Proposed Upgrade of the NSCL", IEEE Particle Accelerator Conference, Dallas, TX, p. 345, (1998).
- [2] F. Marti et al., "Modifications to K500 focusing bars", December 1998, MSU, NSCL-CCP-19-1998.
- [3] D. A. Johnson et al., "Survey of injected beam parameters at the K1200 cyclotron", August 1995, NSCL-CCP6-1995.

# EFFICIENCY ESTIMATION OF BEAM EXTRACTION BY THE SCATTERING TARGET

I.I.Degtyarev, I.A.Yazynin, SRC Institute for High Energy Physics, Protvino, Russia

E-mail: yazynin@mx.ihep.su

## Abstract

The possibility of using the scattering targets for forming and extraction beam in the modern circular accelerators is considered in paper. Is shown that the minimum losses of particles will be by use of targets from heavy elements such as tungsten. The optimum sizes of a target, its displacement from septum and frequency of the betatron oscillations are determined.

The analytical and numerical accounts show, that at a beam extraction of energy 70 GeV from U70 and 600 GeV from U600 is possible to reach efficiency ~70% and ~90% accordingly.

## 1 Introduction

The use of amorphous target as a scatter of charged particles is widely applied in circular accelerators (IHEP, JINR, DESY, FNAL, CERN) [1,2] for the forming a beam, localization of losses and beam extraction. A main problem arising at the designing of such systems is the decrease of inevitable losses of particles on the scattering target, on the septum or deflector partition, on the collimators and vacuum chambers.

With increase of beam energy the efficiency of considered extraction beam systems because of reducing of root-mean-square magnitude of angular scattering of particles on the target  $\sigma \sim 1/\gamma$  considerably may decrease. With increase of beam intensity and with use of superconductor magnetic elements the solution of localization problem of the inevitable losses becomes complicated. There is a probability of the overheating and destruction the target and significant radiation of the neighboring magnetic equipment and the problem of using possibility such systems is put.

In work the choice and account of optimum parameters of the scattering target from the viewpoint of losses minimization is considered. The advantage of use the targets from heavy elements such as tungsten are proved. The numerical simulation of beam extraction from the UNK and U70 is made.

## 2 The beam extraction of charged particles on the amorphous target

The layout of the beam extraction system with use of the amorphous target is shown on Fig.1. The beam by the bump - magnet is guided to the target which executed as a slice standing across a beam. At the interaction with substance atoms the particle in main due to the multiple Coulomb scattering change the amplitude of betatron oscillations and such have a possibility through some turns

in the accelerator to hit in the septum - magnet clearance and to send in the extraction channel.

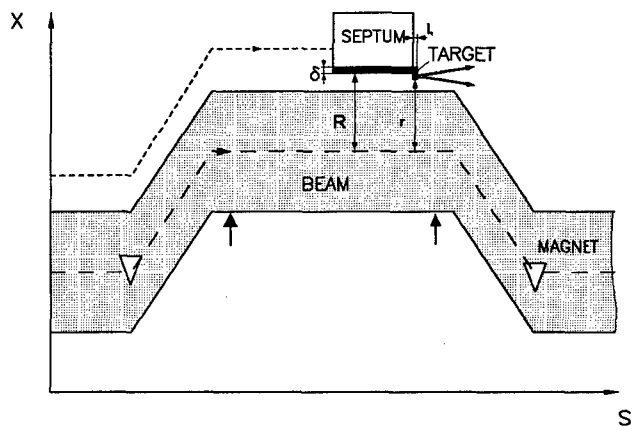


Fig.1: The extraction system layout.

At the extraction the particles are lost on the target due to the nuclear interactions  $\eta_t$ , some hit on the septum partition  $\eta_s$ , and the part of protons scattered on the large angles hits on the equipment standing on a beam course behind the target  $\eta_a$ . That is the total magnitude of losses can be defined  $\eta = \eta_t + \eta_s + \eta_a$ . The extraction efficiency depends on the beam parameters, structure, substance of the target, its sizes and position, effective thickness of the septum. Determination of conditions, at which the losses will be minimum, is the purpose of the given work.

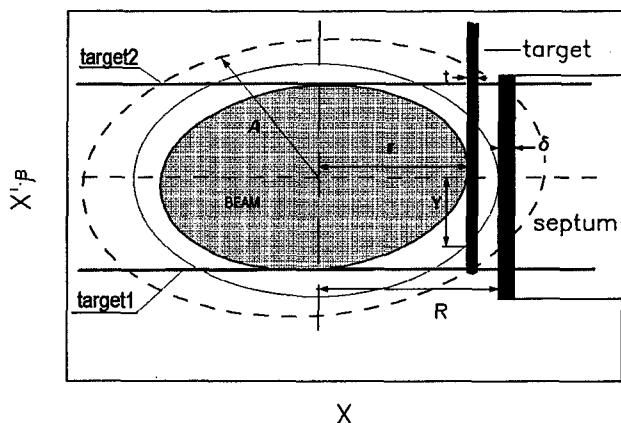


Fig.2: The extraction phase space.

At the extraction of a beam on the scattering target we have a diffusion process of amplitude growth the beam particles with boundary conditions. At the magnitude of amplitude  $A > R$  the particles can hit on the septum. For the target, which has small transversal size  $t$ , the average passages of the particle through it can be estimated:

$\bar{N} = 1 + k \left( \frac{y}{D} \right)^m$ . Where  $y = \sqrt{R^2 - r^2}$  is the coordinate of the such point (Fig.2), that if particle is farther than it,

it hit on the septum in main, and  $r = r_t \sqrt{\beta_s / \beta_t}$ ,  $r_t$  - distance of the target edge from the beam axis,  $D = \sigma \beta$ ,  $\sigma$  and  $D$  are the r.m.s. magnitude of scattering on the target on angle and coordinate accordingly,  $\beta = \sqrt{\beta_t \beta_s}$ ,  $\beta_t, \beta_s$  is the amplitude functions in the location of the target and septum. Magnitude of scattering on the amorphous target:

$$\sigma = \frac{13.6 \sqrt{l_t / L_r} \cdot [1 + 0.038 \cdot \ln(l_t / L_r)]}{E_0 \gamma \sqrt{1 - \gamma^{-2}}} [\text{mpad}],$$

where  $L_r$  is the radiation length,  $E_0$  is the rest energy of the particle in a GeV,  $\gamma$  is the relativistic parameter. In case of use the targets for extraction of the relativistic protons:  $\gamma \gg 1$  and  $D \approx \frac{14\beta}{\gamma} \sqrt{\frac{l_t}{L_r}}$ . Then the losses of

particles on the target due to the nuclear interactions will be defined:  $\eta_t = 1 - e^{-N l_t / L_n} \approx N \frac{l_t}{L_n} = \frac{l_t}{L_n} [1 + k(\frac{\gamma}{D})^m]$ , (1) where  $l_t$  is the target thickness on the beam, and  $L_n$  is the nuclear length.

At the account of the extraction with use of the scattering target it is necessary to consider losses  $\eta_a$  of particles deflected by the target on the large angles and lost on the collimators and other elements of the accelerator. The magnitude of such losses can be estimated by the probability formula of the accidental process:

$$\eta_a \approx (1 - \eta_t) \cdot \int_A \frac{e^{-x^2/2D^2}}{\sqrt{2\pi D}} dx, \quad (2)$$

where, as it is visible from Fig.2,  $A^2 = A_m^2 - R^2$ . For U70 the bounding aperture makes  $A_m \sim 30$  mm ( $\beta \approx 25$  m). Then  $A/D \gg 1$  and the magnitude of this losses will be little (Fig.5 (•)). Such losses some increased due to nuclear elastic interaction of particles with the target.

The magnitude of losses on the septum can be defined from the probability of hit the particles on the septum partition. Generally amount of lost particles on the septum depends on what place on the extraction phase space the particles scattered on the positive and negative angles hit in. The most simple case for definition of losses on the septum will when a phase shift of betatron oscillations in the extraction plane between the target and septum equals  $\pi/2 + \pi n$  and the betatron frequency  $Q = m/4$ , where  $n$  and  $m$  is integers. Then the image of particles scattered by the target on the phase space of septum location will intercross its partition under right angle (Fig.2, target1,2). The particles not hit on the septum again will dissipate on the target and the process of the extraction will proceed. As have shown analytical and numerical calculations (fig.6) the losses close to minimum in these conditions.

The losses on the septum partition can be defined from the coordinate density of scattered particles hit on a septum. In case of little sizes of a beam when  $R \ll D$  it is possible to consider distribution of particles on the septum how Gaussian with r.m.s. =  $D$  and on the thin parti-

tion of septum ( $\delta \ll D$ ) the losses will make  $\eta_s = \frac{\delta}{\sqrt{2\pi D}}$

and the value of total losses:

$$\eta \approx \eta_t + \eta_s \approx \frac{l_t}{L_n} + \frac{2\delta}{\sqrt{2\pi D}}. \quad (3)$$

That is have received a rather simple losses function depending only from one variable - target thickness and its optimum size can be found from the equation  $d\eta/dl_t = 0$ . Solving which is gained:

$$l_t \approx \sqrt[3]{\frac{\delta^2 \gamma^2}{2\pi 14^2 \beta^2} L_r L_n^2}, \quad \eta_{t0} \approx \sqrt[3]{\frac{\delta^2 \gamma^2}{2\pi 14^2 \beta^2} \frac{L_r}{L_n}}, \quad (4)$$

$$\eta_{s0} = 2\eta_{t0} \quad u \quad \eta_{\min 0} \approx 3\eta_{t0}.$$

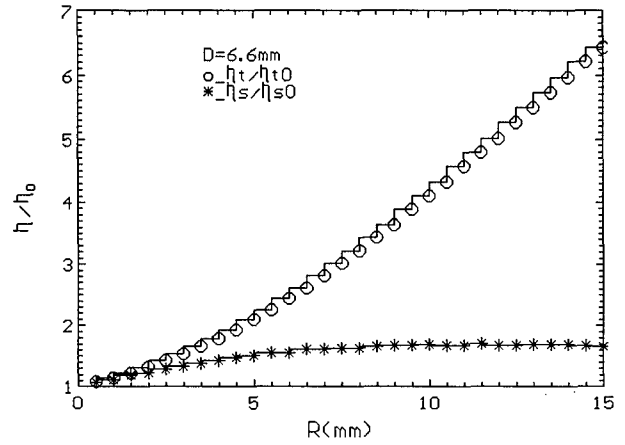


Fig.3: Dependence of relative losses versus the septum displacement from the equilibrium orbit.

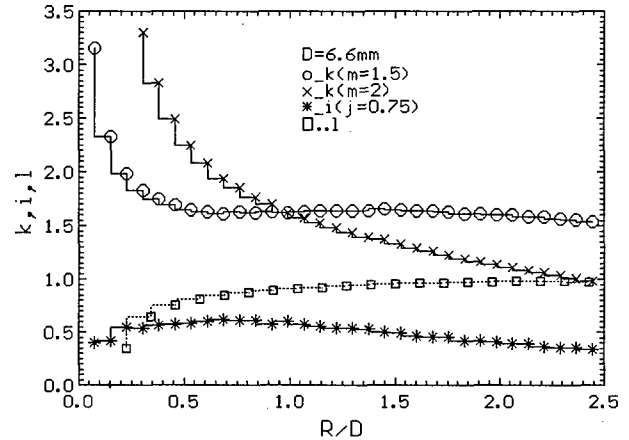


Fig.4: Dependence of approximation coefficients versus the septum displacement.

With consideration of concrete beam sizes the losses on the target and septum partition will increase (Fig.3), but the optimum target thickness (Fig.5) can be kept above-stated and then the losses will be defined:

$$\eta \approx \eta_{t0} [1 + k(\frac{R}{D})^m] + \eta_{s0} [1 + i(\frac{R}{D})^j] = \eta_{t0} [3 + k(\frac{R}{D})^m + 2i(\frac{R}{D})^j]. \quad (5)$$

For viewed forming and extraction systems the value  $D$  at which will be minimum losses lies in field  $0.5 < R/D < 2.5$  and with precision in some percents the functions of

losses on the target and septum approximate by the coefficients  $k = 1.7$ ,  $m = 1.5$  and  $i = 0.6$ ,  $j = 0.75$ . At the large size of beam  $R/D > 3$  the coefficients accept reference values of a diffusion process  $k=1$ ,  $m=2$  (fig.4 (x)). And at the finally we may done estimation of losses for all extracted beam  $\eta \approx \eta_{10}(3+l \cdot R/D)$ , where  $l \sim 1$  (Fig.4 ( )) and  $R$  is the beam size. From the losses dependencies it is visible, that in this case the total losses decrease with approaching septum to the beam and will be minimum at the  $r = R$ .

With consider that beam size  $r \approx \sqrt{\varepsilon \cdot \beta / \gamma}$ , where  $\varepsilon$  is invariant emittance, the value  $\frac{R}{D} = 0.23 \cdot \sqrt[3]{\frac{\varepsilon}{\delta}} \cdot \sqrt[3]{\frac{L_r}{L_n}} \cdot \sqrt[3]{\frac{\gamma}{\beta}}$ . That

is at increasing energy of particles the influence of the beam size on the losses slowly raising.

In table 1 the significances of radiation and nuclear lengths for different substances are indicated, from which it is visible, that the least ratio  $L_r/L_n$  have the substances with large nuclear number. So the total losses in the extraction system using as the scattering target W will be in  $\sim 3$  times less than with the target from Be.

Table 1:

	Be	C	Al	Fe	Cu	W
$L_r$ , mm	353	188	89	17.6	14.3	3.5
$L_n$ , mm	407	400	394	168	151	96
$L_r/L_n$	0.87	0.45	0.24	0.10	0.095	0.036

Table 2:

	$\gamma$	$\beta$	$r$	$\sigma$	$l_t$	$\eta_0$	$\eta_1$	$\eta_{si}$
		m	mm	mm	mm	%	%	%
U70	70	25	6	1	6	19	25	26
U600	600	380	10	0.2	1.4	5	9	9

In the Fig.5 are shown the dependencies of losses versus target thickness obtained by computer simulation. Optimum thickness of the tungsten target and appropriate efficiency for U70 and U600 designed analytically and obtained by computer simulation are represented in table 2.

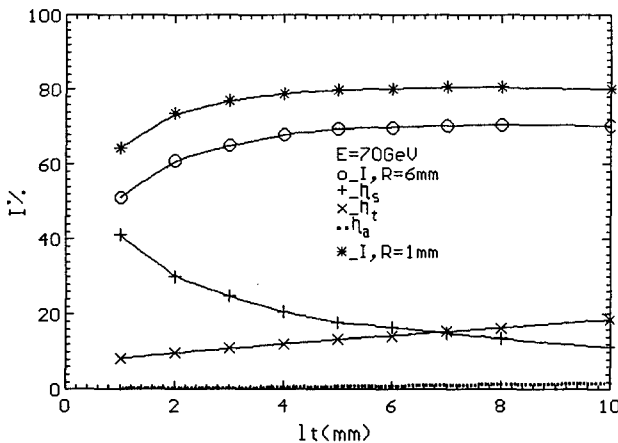


Fig.5: Dependence of losses versus the target thickness.

The total magnitudes of losses defined analytically from (3) and numerically with consider Gaussian beam density from (5) are shown with indexes (0) and (1) accordingly.

For the optimum target and septum location on the azimuth and choice the betatron frequencies are necessary to consider on the phase space how particles scattered by the target on positive and negative angles  $\eta = \eta_{s+} + \eta_{s-}$  hit

on the septum partition. In Fig.6 are indicated the dependence of the extraction efficiency versus of betatron oscillations frequency in U70 at the use of the tungsten target with the thickness  $l_t = 6$  mm, obtained in computer simulation by the program "SCRAPER" [3]. Near to resonance lines  $Q_r = m/3$ , where  $m$  is integer, the reducing of the extraction efficiency is observed.

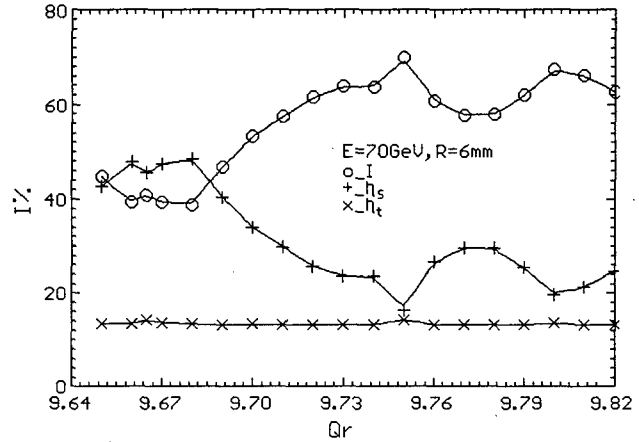


Fig.6: Dependence of the extraction efficiency and losses versus the betatron frequency.

### 3 Conclusions

From the table and expressions of losses it is visible, that the losses of particles at the extraction on the scattering target will increase with magnification of energy and reduce with magnification of  $\beta$ -function and diminution of a septum partition thickness. In modern developed circle accelerators as UNK, CERN for the extraction of particles the special insertions with large magnitudes  $\beta$ -functions  $\sim 1000$  m are provided. The modern electrostatic deflectors have a thickness up to 0.1 mm (that is effective thickness  $\delta \sim 0.2$  mm). Then the minimum losses if extracted all beam ( $\varepsilon = 2 \cdot 10^{-4}$  m-rad) with the use of tungsten target for crude estimation will be  $\eta \sim 5E^{3/4}$ , where  $E$  is the energy of particles in TeV. That is for energy 3 TeV, as in UNK project, when we will use such extraction is possible to receive extraction efficiency  $\sim 90\%$ , and at the energies 8 TeV  $\sim 75\%$ . That is such method of extraction can be considered as alternate for the solution of some problems at the high energies on modern circle accelerators. In particular in the collider mode the extraction on the amorphous target can be used as additional, cutting the halo beam for parallel experiment. At the appropriate construction the target can scatter significant intensity of the beam  $\sim 5 \cdot 10^{12}$  particles in the second 1/4.

### References:

1. A.V.Maksimov, "Slow extraction from the U70 at the scattering on the inner targets", Preprint IHEP 94-38, Protvino, 1994.
2. Ch.Steinbach "Slow extraction by target scattering", CERN/MPS/CO 70-7, 1970.
3. I.I.Degtyarev, et al., "Beam losses simulation in accelerators with extended version of the RTS&T code." HEACC 98, Dubna, 1998.
4. I.I.Degtyarev, A.E.Lokhovitskii, Yu.S.Fedotov, I.A.Yazynin, "Substance choice of the scraper system elements", PAC 1997.

# HELIUM GAS EVACUATION IN SUPERCONDUCTING RFQ STRUCTURE

A. Lombardi, G. Bisoffi, F. Chiurlotto, E. Tovo, A.M. Porcellato, L. Badan,  
INFN-LNL via Romea 4, I35020 Legnaro (PD), Italy,

L. Taffarello, INFN Padova, via Marzolo 8, Padova (PD), Italy

G. Navarro, M. Antonello, M. Masi

Università di Padova, Dipartimento di Ingegneria Meccanica, via Venezia 1, Padova, Italy

## Abstract

The PIAVE injector for the Legnaro Accelerator complex is an accelerating machine made of superconducting resonators. One of them, the superconducting RFQ, needs to be cooled by the helium bath on the whole outer surfaces. In particular the region of the electrode tips and the lower vertical electrode are interested to RF power dissipation and can be a trapped volume of liquid. During the operation the liquid evaporates and the produced gas needs to be evacuated, in order to cool the structure properly. The problem of gas production and evacuation from a trapped volume of liquid helium has been studied and solved. Studies of the possible evacuation systems and of the experimental apparatus are presented.

## 1 Scope of the test

The superconducting RFQ (Radio Frequency Quadrupole) structures [1], made of niobium sheets formed and eb-welded, are cooled by the direct contact with the liquid helium bath. Figure 1 shows the longitudinal section of the test cryostat. The outer tank, the thermal shield operated at liquid nitrogen, the liquid helium reservoir and the SRFQ vertical electrodes can be seen.

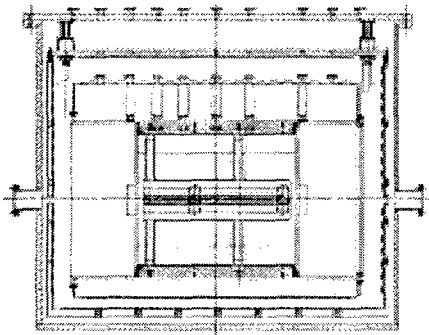


Figure 1: The SRFQ structure inside the test cryostat.

The RF power on the wall of the resonator is dissipated inside the liquid helium bath through the evaporation of the liquid with a gas production rate of:  $1\text{ W} \Leftrightarrow 1\text{ m}^3/\text{h}$ .

The SRFQ electrodes are hollowed and they are filled by liquid helium. The geometrical disposition of the vertical electrodes allows the trapping of the helium gas evaporated by the RF power dissipation on the bottom electrode.

The scope of the experiment is to verify if the natural draining due to the hydrostatic pressure of the liquid

helium itself through a siphon ending over the liquid helium level and controlled by a needle valve is sufficient to keep the trapped volume filled by liquid. We want to avoid the use of a forced flow of liquid helium because of the sensitivity of the resonator to the mechanical noise.

The experiment was performed using a model of the trapped volume made with an upside-down cylinder isolated by the liquid helium. The thermal insulation of the apparatus is made with a chamber around the cylinder simulating the electrode (fig. 2). The inter-space is evacuated to simulate the inner part of the SRFQ resonator. The RF power was simulated by means of a resistor placed inside the trapped volume.

## 2 Theoretical description

The possibility of draining the gas helium from the SRFQ electrode is subject to the value of the liquid height above the trapped volume and to the pressure heads of the draining system.

The draining is realised via a standard tube of some mm diameter going from the lower electrode to the top of the liquid helium reservoir. The tube will run outside the liquid helium reservoir to avoid condensation of the cold vapour.

The present analysis is devoted to estimate the pressure heads of the elements of the experimental apparatus (figure 2) so as to verify the pressure drop of the needle valve which is the only home made element.

The methodology, indicated for standard pipes [2, 3], can be used to calculate the pressure losses into pipes with small diameter, considering a relative roughness large than in the normal pipe, because there is a scale effect. The evaporation rate for the liquid helium in standard condition is 1.4 l/h per dissipated watt.

During the standard operation the RF power dissipation foreseen for the SRFQ, in the area interested by the gas trapping problem, is of the order of 2 W and exceptionally it produces a rate flow equivalent to 4 W.

The calculation presented here are related to the experiment where the maximum power dissipated inside the test volume was 2.5 W

The pressure heads are defined as localised pressure drops and distributed ones.

The localised losses,  $h_l$ , are calculated at the mouthpiece of the pipe, at the bow elements, at the section contraction of the pipe, at the outlet of the pipe and at the valve, whereas the distributed ones are defined in relation with the length and the diameter of the pipe.



The pressure losses due to the inlet sections as well as for the element contraction are calculated by the following equation:

$$h_i = Q_g / C_i (K_c) \quad (1),$$

with  $Q_g$  the volumetric rate flow and  $C_i$  the loss coefficient for the localised losses described in reference [4]. Using figure 2 in the ref. [4] we fixed the loss coefficient  $K_c$  equal to 0.622 for the inlet to the 12 mm pipe and 0.605 for the transition to the 3 mm pipe. For the successive transition from 3 mm to 2 mm pipe section we used  $K_c = 0.42$ .

An equation similar to (1) is used for the computation of the pressure drop in the bow elements. The diagram of figure 3 in [5] defines the loss coefficient  $K_b$  as a function of the bending angle of the bow element. In the reference the value of the Reynolds number ( $Re$ ) is fixed equal to  $10^6$  and in this calculation it has been used a correction factor when the value of  $Re$  is different. The pressure drop at the outlet section of the pipe is still calculated using an equation similar to (1), fixing equal to 1 the value of the loss coefficient.

The distributed losses in the pipe are defined by the following equation:

$$h_d = f \cdot \frac{L}{D_b} \cdot \frac{8 \cdot Q_g^2}{g \cdot \pi^2 \cdot D_b^4} \quad (2),$$

with  $L$  is the tube length,  $D_b$  the tube diameter and the friction factor  $f$  is calculated using the Hagen-Poiseuille law for laminar flow.

In the turbulent flow Jain's law is applicable for Reynolds number less than  $10^8$  and  $f$  follows the relation:

$$f = \frac{0.25}{\left[ \log_{10} \left( \frac{5.74}{Re^{0.9}} + \frac{e}{3.7} \right) \right]^2} \quad (3).$$

The friction loss is defined in relation to the equivalent relative roughness  $e$ .

In the experimental apparatus we decided to have two different tube diameters in two sections, 3 and 2 mm respectively. This is done so as to operate the needle valve in a convenient opening range for all the operation conditions. The pipe length  $L$  is the sum of all the pipe straight sections.

If  $\Delta p_a$  is the total pressure drop, it is possible to compute the pressure drop  $\Delta p_v$  that the valve causes to obtain the equilibrium with the static head  $z_{st}$  of liquid helium.

$$\Delta p_v = \rho_l \cdot g \cdot z_{st} - \rho_g \cdot g \cdot (z_E - z_B) - \Delta p_a \quad (4).$$

Here  $(z_E - z_B)$  is the elevation difference of the gas helium between the inlet section of the pipe (B) and the position of the valve (E),  $\rho_l$  and  $\rho_g$  are the liquid and gas densities respectively.

Defined the valve type, it is possible to plot the parametric curve to define the loss coefficient for various fully and partially open valve. Therefore it is possible to obtain also a working range for the values of pressure head in the valve in relation with the gas flow rate when

the valve opening passes from fully open to closed. The values of the physical quantities of the helium and the results of the numerical simulation of the pressure head are shown in table 1. The reasonable valve pressure drop shows that the pipe diameters with 2 and 3 mm are suitable to obtain the draining of the small gas helium rates from the trapped volume.

Dissipated power (W)	Gas flow rate (mm <sup>3</sup> /s)	$\Delta p_a$ (Pa)	$\Delta p_v$ (Pa)
0.1	292	1.2	536.2
0.54	1576	26.3	488.5
1.1	3210	104.7	394.7
1.5	4377	190.4	273.4
2.1	6127	367.6	37.4
2.3	6711	438.6	188.3
2.5	7295	515.8	124.6
$\rho_l = 125 \text{ kg/m}^3$		$\rho_g = 17 \text{ kg/m}^3$	
$\mu_g = 1.3 \cdot 10^{-6} \text{ kg/(m}\cdot\text{s)}$		$e = 0.0075$	
$z_E - z_B = 500 \text{ mm}$		$z_{st} = 375 \text{ mm} + \text{liquid helium hydrostatic height}$	

Table 1. Theoretical estimations of the needle valve pressure heads.

We can cope with the eventual dissipation of a higher RF power using a 4 mm draining pipe.

### 3 The experimental apparatus

Before using the siphon draining system inside a complex structure such as the SRFQ resonators test cryostat, which needs long cooling down and warm up periods, we decided to construct a model (figure 2).

It consists in an upside down cylinder included into a vacuum jacket and suspended to the top flange of a dewar.

In figure 2 one can see: the top flange; the radiation shields; the liquid helium level meter; the gas draining system and the needle valve.

Inside the trapped volume there are four temperature sensors, one resistor for the power dissipation and a liquid helium level meter.

The draining tube, which ends with the valve above the liquid level, is thermally isolated by the liquid helium bath being inside a vacuum jacket.

In order to be able to warm up the liquid which might fill up the draining tube, a second resistor is placed inside the vacuum jacket (particular number 4).

The experiments consisted in powering the resistor inside the trapped volume with a known current and finding the proper opening of the needle valve that reaches the equilibrium between the gas production and the gas draining.

The experiments were done with different liquid helium level above the inlet of the draining tube. This was done to simulate the different operational conditions of the real resonator inside its cryostat. The various liquid heights are in table 2.

The liquid helium level inside the trapped volume was measured using the properly calibrated temperature sensors and a level meter.

The aim of the tests was to check if the system is able to deal with the power dissipation of the order of 2.5 W, which is the maximum power foreseen for the lower electrode of the SRFQ (figure 1).

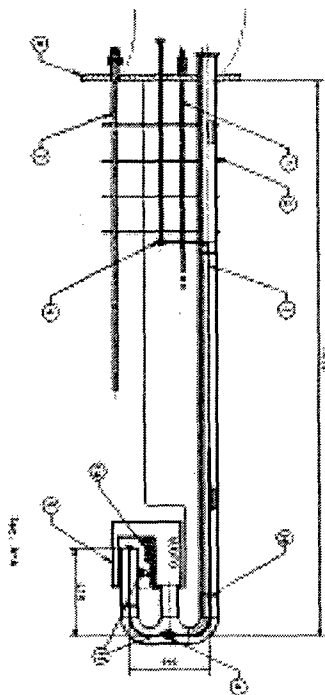


Figure 2: The experimental apparatus.

The experimental procedure adopted for the tests was to insert the apparatus inside a dewar and cool it down to liquid helium temperature. Once the trapped volume was filled with liquid helium the needle valve was closed and the resistor was powered with a known input power. The gas filled the volume and the liquid level underneath the upside-down cylinder was controlled with the level meter and with calibrated temperature sensors.

The second operation was to open the needle valve to a fix opening and see if the gas was drained properly and in a stable flux in equilibrium with the gas production due to the power dissipation.

During the tests the liquid level inside the whole dewar was controlled with a second level meter in order to check the hydrostatic pressure to compare with the calculation.

The open questions were:

Does we need a pumping system to drain the gas or is the hydrostatic pressure of the liquid helium enough? Is the size of the draining tube correct? Can the draining system be recovered if some liquid flows inside the draining tube, avoiding bubbling and mechanical noise? Are the theoretical assumptions on the pressure losses correct?

#### 4 Experimental results

The experimental results are summarised in table 2.

The draining system worked properly and the draining tube did not show a severe problem with its filling up with liquid helium. In effect the tube was not filled with liquid even when the liquid helium level overcame the tube inlet. This is connected with the level of the insulation vacuum. During the first test the vacuum was in the  $10^{-4}$  mbar range and we did not have problem with liquid into the tube; during the successive tests the vacuum deteriorated and we had to power the second resistor to evaporate the liquid inside the draining tube. Once the liquid is removed the system worked properly again.

Dissipated Power (W)	Valve opening at equilibrium (%)	Liquid helium (mm)
.1	18.5	159
.54	18.5	141
1.1	27.1	128
1.5	47	99
2.1	100	51
2.3	100	232
2.5	No equil.	243
2.1	77	328

Table 2: Experimental results.

#### 5 Conclusions

The experimental results show that it is possible to drain the trapped gas produced in an upside-down container using the hydrostatic pressure.

We will insert the system inside the SRFQ resonator using, for this application up to few watts of dissipation, a 3 mm diameter tube and a proper needle valve operated at room temperature.

The thermal load to keep the draining tube empty will be provided by the irradiation to the liquid nitrogen shield because the tube will run outside the liquid helium reservoir.

#### 6 Acknowledgements

We acknowledge very much the mechanical support given by Enzo Bissiato concerning the realisation of the needle valve.

#### 7 References

- [1] A. Pisent et al. *The new LNL injector PIAVE, based on a superconducting RFQ* Proc. of the European Particle Accelerator Conf., Stockholm, Sweden, 1998, Institute of Physics Publishing Bristol and Philadelphia, pp758-760 1998
- [2] Schlichting, H., *Boundary-Layer Theory*, McGraw-Hill, Seventh Edition, New York, 1979.
- [3] Ghetti, A., *Idraulica*, Libreria Cortina, Second Edition, Padova, 1991.
- [4] Haghighi, K., Bralts, V.F., and Segerling, L.J., "Finite Element Formulation of Tee and Bend Components in Hydraulic Pipe Network Analysis", Transactions of the ASAE 31(6): 1750-1758, 1988.
- [5] Haghighi, K., Bralts, V.F., Mohtar, R., and Segerling, L.J., "Modeling Expansion/Contraction, Valve and Booster Pump in Hydraulic Pipe Network Analysis: A Finite Element Approach", Transactions of the ASAE 32(6): 1945-1953, 1989.

# ENGINEERING ANALYSIS OF THE APT CRYOMODULES\*

B.M. Campbell, K.C.D. Chan, M.J. Fagan #,  
R.A. Valicenti, and J.A. Waynert, LANL

## Abstract

The superconducting radio frequency (SRF) part of the Accelerator Production of Tritium (APT) linac will accelerate a 100-mA proton beam from 217 MeV to 1700 MeV. Since SRF cavities can accept protons over a wide velocity range, cavities with only two different betas are required; however, three different length cryomodules are required. A modular design was adopted that will reduce the engineering and design effort to produce these cryomodules. A final design of the APT Engineering Development and Demonstration (ED&D) cryomodule for a two-cavity  $\beta=0.64$  cryomodule has been completed, and a single cryomodule will be fabricated by industry next year. The cavities will be cooled in a 2.15-K superfluid helium bath similar to the Continuous Electron Beam Accelerator (CEBAF) system. What sets the APT cryomodules apart is the high radio frequency (RF) power that must be delivered to the cavities. The RF losses in the cavities and power couplers place a large heat load on the central helium liquifier. Minimizing these loads required extensive iterations of the power coupler cooling schemes and thermal shield. A spoke support arrangement was developed to keep the beam centerline fixed and to minimize forces acting on the helium vessel/cavity during cool down. Laminar flow through the cryomodule during clean room assembly dictated the use of a vacuum vessel with large top and bottom openings. Analyses were performed to ensure structural integrity under vacuum loading, while also minimizing vessel deflections which could impact beam centerline positioning.

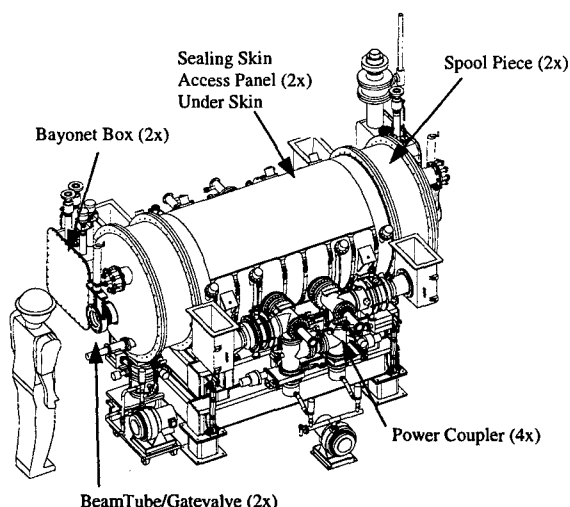


Figure 1:  $\beta=0.64$  two cavity ED&D cryomodule

\* Work supported by US Department of Energy  
# E-Mail: fagan@lanl.gov

The structural/thermal analysis used to optimize the cryomodule design will be presented in this paper.

## 1 INTRODUCTION

A cryomodule containing two  $\beta=0.64$  cavities ( $\beta$ =particle velocity/speed of light) is being designed at Los Alamos as part of the Engineering Development and Demonstration (ED&D) program. The other types of cryomodules will be designed by General Atomics, one type for three  $\beta=0.64$  cavities and another type for four  $\beta=0.82$  cavities. A modular approach was adopted that will reduce the total engineering and design effort required to produce these cryomodules. Detailed descriptions for the cryomodule designs have been published [1]. The  $\beta=0.64$  ED&D cryomodule is pictured in Figures 1 and 2. The length is 3.3 m, width is 3 m, diameter is 1 m, and the weight is 3000 kg.

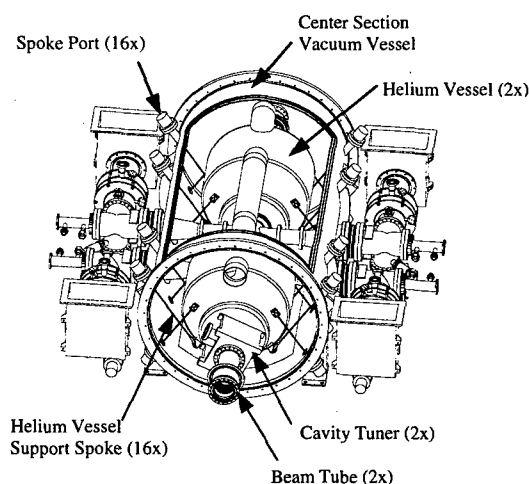


Figure 2: Center section without shields

## 2 VACUUM TANK

### 2.1 Vacuum Tank Description

The  $\beta=0.64$  cryomodule vacuum tank is a cylinder which is composed of a center section, spool pieces, and two domed ends, as shown in Figure 1. The center section has two large openings, 120 degrees on the top and 90 degrees on the bottom, to improve access to the interior of the tank for installation of the helium vessels, beam piping, and shields, as shown in Figure 2. The access openings also allow for laminar air flow in the clean room. Once installation of internal parts is complete, access panels are placed over the openings, and a sealing

skin is placed over the panels. An o-ring surrounding the openings creates a vacuum-tight seal with the sealing skin. The design was adopted from the CERN-LEP cryomodule.

## 2.2 Vacuum Tank Analysis

The vacuum tank components were analyzed for stress and buckling. The center section analysis is more involved, based upon the unusual geometry, as well as the fact that it must perform other functions. These functions include supporting the helium vessels (via spokes mounted on the tank wall) and allowing an interface to the power couplers. The access panels and skins carry the pressure load and create a seal, respectively. The panels carry the pressure load by transmitting hoop stress and longitudinal stress throughout the cylinder, as if it were a continuous cylinder without interruption. The buckling strength of the center section was also analyzed. Hoop stress and longitudinal stress are carried across the panel to center section interface due to the fact that these stresses are compressive. Bending stress cannot be carried across the center section to panel interface. This interface flexibility reduces the buckling strength of the center section under vacuum. The center section/panel/skin geometry was analyzed for buckling in several different ways using both hand calculations and finite element (COSMOS) analyses. The minimum factor of safety obtained was 3, while much higher factors were obtained for other cases.

## 3 HELIUM VESSEL SUPPORT

### 3.1 Helium Vessel Support Arrangement

The helium vessel is supported from the vacuum tank center section with spokes. There are four spokes at each end of a helium vessel, placed in a radial arrangement to restrain the helium vessel in the radial direction, as shown in Figure 3. The cavities are aligned at room temperature and it is very desirable that this alignment not change after cooldown and thermal equilibrium is reached. In addition to maintaining alignment, the spokes were arranged to minimize loads and stresses in the spokes and helium vessels, and to minimize heat leak to the liquid helium. Two key geometrical features were incorporated into the spoke design that maintain cavity alignment. First, all of the spoke angles to vertical were maintained identical. This ensures that the forces in the vertical direction balance as spoke forces increase during cooldown, as the result of thermal shrinkage strain. The differing spoke lengths have the same thermal shrinkage strain, and will thus have the same stress and force. Accordingly, the beam centerline will not move because of a force imbalance in the vertical direction. Second, a 90 degree angle is maintained between the spoke, and an imaginary radial line which connects the spoke

attachment point on the helium vessel to the beam centerline, as shown in Figure 3. Under the premise that the beam centerline remains motionless during cooldown, all points on the helium vessel migrate towards the beam centerline during cooldown. With the 90 degree angle maintained, the helium vessel shrinkage has no effect on spoke force, since the cold end of the spoke translates towards the beam centerline, neither lengthening nor shortening the spoke. There is then no effect on spoke

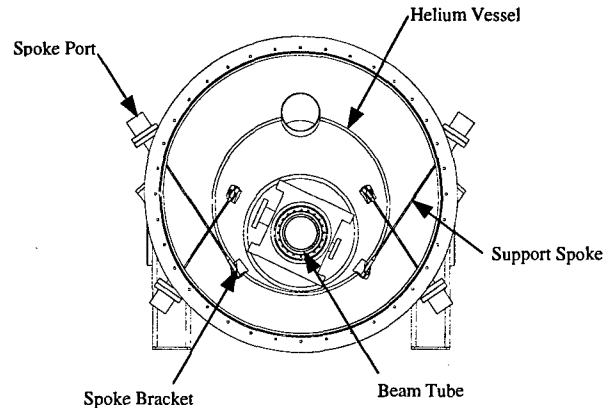


Figure 3: Support spoke arrangement

force from helium vessel shrinkage during cooldown. Analysis of the thermally-induced displacements showed that this arrangement maintains cavity alignment after thermal equilibrium has been reached.

The spokes were placed at an angle to vertical which provides sufficient load carrying capability in both the vertical and horizontal directions. The spokes are 0.25 inches in diameter and will be made of Nitronic stainless steel. Belleville springs will be placed at the warm ends of the spokes to absorb a portion of the thermal shrinkage of the spokes, as shown in Figure 4. Three disc springs will be stacked in series at the warm end of the upper spokes, while two disc springs will be stacked in series at the warm end of the lower spokes. The springs will be

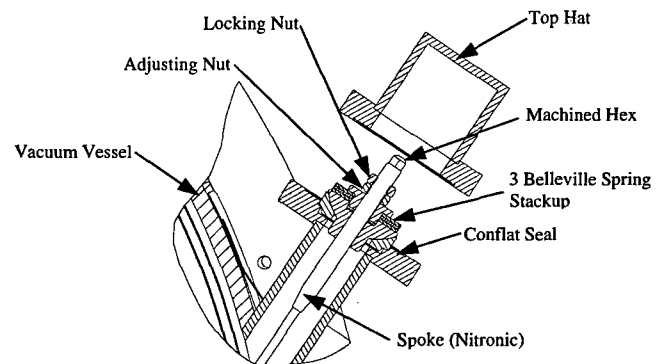


Figure 4: Belleville spring detail

made of either 17/7 PH or 17/4 PH stainless steel. Upon room temperature alignment of the helium vessel, all spring sets will be partially compressed. At operating temperatures, springs are fully compressed and the spoke system is "solid." The results are summarized in Table 1.

Table 1: Spoke Forces & Stresses

	Room Temp		Operating Temp	
With Springs	450 lb	9170 psi	2250 lb	46 kpsi
Without Springs	450 lb	9170 psi	4060 lb	83 kpsi

## 4 POWER COUPLER THERMAL ANALYSIS

The cryomodule heat loads to the low-temperature helium coolant are dominated by the RF loads in the superconducting niobium cavities. In the  $\beta=0.64$  cryomodule, the cavity heat loads account for over 50% of the total room temperature refrigeration input power. Some of the other contributors to the heat loads are the power couplers, thermal shield, tuner levers, support structure, beamtube, valves, bayonets, and instrumentation. After the cavities, the next biggest contributor to the heat load is the power coupler.

The thermal analysis of the power coupler naturally divides into separate consideration of the inner and outer conductors. Generally, the inner conductor analysis focuses on demonstrating adequate thermal stability against the RF losses from both traveling and standing waves, with some margin added. The outer conductor represents a thermal short connecting room temperature to the 2-K cavity-cooling system. Thermal intercepts are used to remove outer conductor heat loads at temperatures between room temperature and 2 K. Thus, the outer conductor thermal analysis is aimed at minimizing the room-temperature refrigeration input power necessary to offset the heat loads at lower temperatures. The thermal intercepts must be chosen consistent with the refrigerator and cryomodule design.

A 200-node, axisymmetric model using the finite difference approximation was made to describe the inner and outer conductors. The model includes gray body; diffuse, infra-red radiation exchange; conduction through stainless steel, copper, and niobium; RF heating (traveling or standing wave power distributions); and forced convection cooling of the inner and outer conductors. Detailed results for the inner and outer conductor have been published [2]. The inner conductor is found to be adequately cooled for both traveling and standing waves by using 300-K helium at 1.2 atmospheres pressure flowing at 3 g/s through a 3-mm annular space, between a stainless-steel sleeve within the copper inner conductor.

The outer conductor cooling approaches considered both distributed counter-flow and localized thermal intercepts. The selected cooling scheme was the result of an

extensive trade-study which considered: integration of the power coupler cooling into the cryomodule; impact on the cryo-plant and distribution system; room temperature refrigeration input power; and manufacturability, maintainability, and reliability issues. The selected configuration is a double-point thermal intercept in which the low temperature thermal intercept inlet fluid is 4.6 K, 12 bar helium. After exiting the low temperature intercept, the supercritical helium is used to intercept heat loads from the beam tube, thermal shield, and structural supports, and then circulated through the power coupler high-temperature intercept. The fluid is then returned to the cryo-plant at about 30 K.

## 5 STATUS

A final design review is scheduled for April of this year for the  $\beta=0.64$  ED&D cryomodule. Detailed drawings are being prepared to send to vendors for bids in mid-July, with fabrication of the two cavity  $\beta=0.64$  ED&D cryomodule scheduled for the Fall of 1999.

## 6 REFERENCES

- [1] B.M. Campell et al., "Engineering Design of the APT Cryomodules," Proceedings of LINAC98, Chicago, Aug 24-28, 1998
- [2] J.A. Waynert et al., "A Thermal Analysis and Optimization of the APT 210 kW Power Coupler," Proceedings of LINAC98, Chicago, Aug 24-28, 1998

# UPDATE OF THE LHC ARC CRYOSTAT SYSTEMS LAYOUT AND INTEGRATION

J-C. Brunet, P. Cruikshank, R. Ostojic, A. Poncet<sup>\*</sup>, P. Proudlock, P. Rohmig, L. Tavian,  
B. Skoczen, CERN, Geneva, Switzerland

## Abstract

Since the LHC Conceptual Design report's publication in October 1995 [1], and subsequent evolutions [2], the LHC Arc Cryostat System has undergone recently a number of significant changes, dictated by the natural evolution of the project.

Most noteworthy are the recent decisions to route the large number of auxiliary circuits feeding the arc corrector magnets in a separate tube placed inside the cryostat with connections to the magnets every half-cell.

Further decisions concern simplification of the baseline vacuum and cryogenic sectorization, the finalization of the design of the arc cryogenic modules and the layout of the arc electrical distribution feedboxes.

The most recent features of the highly intricate cryogenics, magnetic, vacuum and electrical distribution systems of the LHC are presented.

## 1 INTRODUCTION

The Large Hadron Collider (LHC) to be installed in the LEP tunnel at CERN will produce two proton beams of 7 TeV energy for head on collisions in 4 points around the circumference. The machine is subdivided in 8 octants, each one comprising a standard arc layout composed of 54 optical half-cells, flanked on each side by dispersion suppressors and experimental and machine insertions (injection, dump, cleaning, RF, etc.). The standard arc and dispersion suppressors are housed in a common cryostat of diameter 914-mm (36"), together with some adjacent insertion devices, depending on the octant. The cryostat length of an octant varies between 2.7 km and 3 km, and is bounded at each extremity by electrical current feedboxes.

With the passage from version 5.0 to the current baseline version 6.0 of the optics, additional families of independently powered magnets have been added in the dispersion suppressors and matching sections, leading to a large increase of the number of electrical circuits integrated into the arc cryostat. The cryogenic distribution line (QRL) housing various headers servicing the main stream of cryomagnets runs parallel to the arc cryostat, and is fed at the 4 even points of the machine from cryoplants installed at ground and underground levels. The basic cooling segments fed from cryogenic service

modules connected to the QRL installed every cell are: a half-cell (beam screens, magnet support posts) and a cell (magnet string helium filling, cooling at 1.9 K, and discharge).

## 2 ARC CRYOSTATS LAYOUTS

A schematic of the arc cryostat between octants 1 & 2 is given in Figure 1. Other arcs differ slightly in length and composition, depending on the octant.

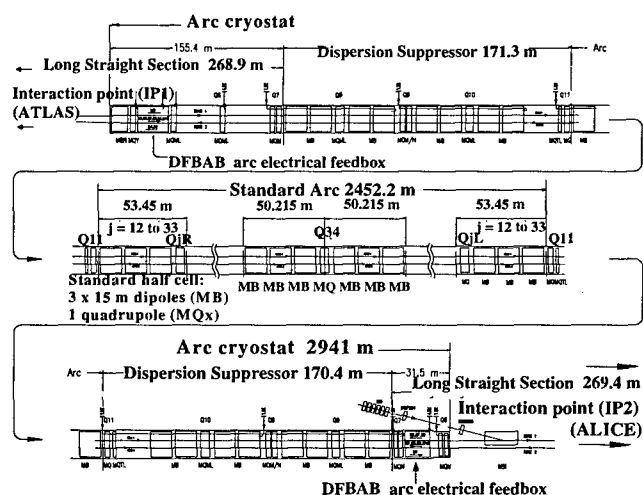


Figure 1: Layout of the Arc Cryostat between Octants 1 & 2 – Optics V6.0.

The basic repetitive magnetic segment of the arc is the half-cell of 53.4-m length providing 45° phase advance for the beams [5]. It is composed of 3 two-in-one 9 T (ultimate) dipoles of 15-m length, a two-in-one quadrupole and various sets of correcting magnets. The Short Straight Section (SSS) housing the quadrupole, sextupole, octupole, dipole orbit correctors, and beam position monitors is flanked every cell by a cryogenic service module housing service piping for quench discharge into the cryogenic service line (QRL), phase separation for 1.9 K heat exchanger cooling, etc. The core of the arc cryostat system is the regular arc, composed of 46 standard half-cells (2452.2 m), flanked by the dispersion suppressors (170 m). It is linked to the QRL every cell (107 m), which provides cooling at pressurized superfluid helium temperature of 1.9 K. The left and right extremities include matching section quadrupoles, beam separation dipoles, and the electrical distribution

<sup>\*</sup> Email: alain.poncet@cern.ch

feedboxes. Some of these assemblies operate at 4.5 K in saturated helium, provided by the QRL.

## 2.1 Arc magnetic systems

The main lattice is made up of FODO cells and the two rings are connected in series. Each of the eight arcs of the machine is separately powered. There are 154 twin-aperture main dipoles connected in series per arc and when powered to their ultimate current of 13 kA have a stored energy of 1.33 GJ. The focussing and defocussing functions are separated and also require 13 kA.

The dispersion suppressors at the extremities of the arcs have individually powered quadrupoles of the same type as in the matching sections of the experimental insertions. They require 6 kA and each aperture is individually fed giving up to 12 circuits.

Spool piece correctors are associated with every main dipole, and correct their higher order multipoles errors. At the moment, correction of b3, b4 and b5 is foreseen. The correctors are connected in series for each type and aperture giving a total of 6 circuits. However, spare positions have been left in one of the two types of dipole in the case that additional correctors are required.

The Short Straight Sections (SSS) contain a series of lattice corrector magnets requiring 600 A. There are families of lattice sextupoles, octupoles, trim quadrupoles, skew quadrupoles and skew sextupoles. In all there are typically between 16 and 32 circuits fed from each end of the arcs.

## 2.2 Arc electrical distribution

The circuits associated with the main dipoles (dipole plus spool pieces), as well as the two quadrupole circuits are fed through the cold masses of all magnets. Bus bars are installed in slots in the cold masses. The dipoles use 2 bus bars of 7.4 mm<sup>2</sup> NbTi with 300 mm<sup>2</sup> of copper stabilizer. Cold diodes are connected across each dipole magnet and energy is extracted, in case of a quench, at an initial rate of 125 A/second. The quadrupoles use 4 bus bars of 7.4 mm<sup>2</sup> NbTi with 180 mm<sup>2</sup> of copper. Again by-pass diodes are used and the initial discharge rate is 320 A/second. The dipole corrector magnets use 20 monolithic rectangular conductors with a cross section of 3 mm<sup>2</sup> and a copper to superconducting ratio of 9:1.

The individually powered quadrupoles and the array of corrector circuits associated with the SSS need to by-pass the dipoles and a link is provided along the 53 meters of the half-cell. For the 600 A circuits a flexible multi-wire cable is used containing 36 superconducting wires with a diameter of 1.6 mm and a ratio Cu/SC ratio of 9.5:1. The outer diameter of the complete cable is 15.5 mm. A similar cable is used for the 6 kA circuits containing 18 conductors and having an external diameter of 23 mm. These need to be installed in a tube containing helium running from one SSS to another. The number and type

of cable varies around the machine according to the local needs.

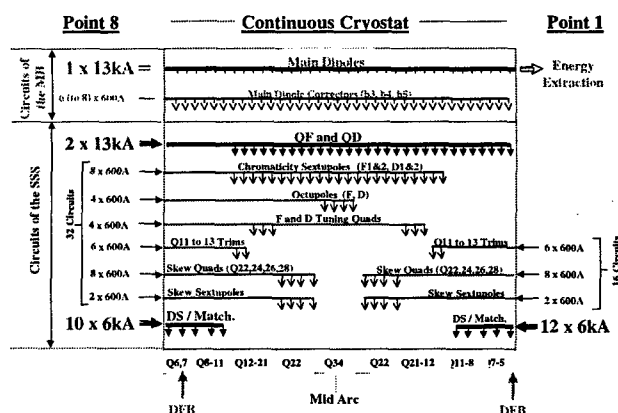


Figure 2: Electrical superconducting circuits feeding the arc cryostat superconducting magnets. The SSS 600 A circuits are routed in the external auxiliary bus bar tube.

## 2.3 Arc cryostat design

The string of superconducting magnets operates in a static 1.9 K superfluid helium bath pressurized at 1.3 bar absolute [3]. The heat load budget to 1.9 K is composed of static heat losses through cryostat components (radiation, conduction through support posts, vacuum barriers, etc.) and dynamic loads resulting from resistive heating in splices between cables, beam losses into the 1.9 K bath, synchrotron radiation and RF image current power deposited on the beam screen at 5-20 K. To minimize the static heat load to the 1.9 K level an all-welded aluminum thermal shield operating at 60 K is installed. The thermal shield is covered by 30 layers of multi-layers insulation (MLI) pre-fabricated blankets to reduce thermal radiation load. The option of an actively cooled shield operating at the sufficient cooling power installed, and of its additional complication.

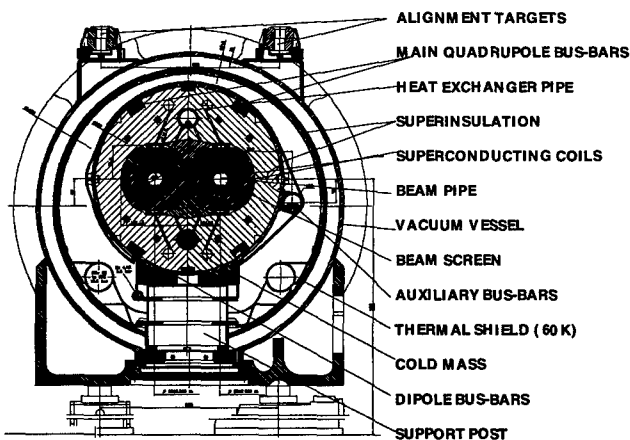


Figure 3: 2D cross-section of the arc cryostat, through one dipole.

The cold mass is simply wrapped with 10 layers of MLI, to reduce conductive heat losses in case of degraded vacuum.

This MLI covers the auxiliary bus bar tube, thermalized to the cold mass via metallic supports.

The transverse dimensions of magnet cold masses with its shield have been minimized to fit in an insulating vacuum tank of diameter 914 mm (36" standard pipe dimension), see Figure 3.

The 15-m long cryodipole external supporting system has been improved to obtain higher positioning precision. It is composed of three high-precision jacks distributed over the length of the dipole, at the longitudinal position of the internal supports (cold posts).

Figure 4 shows the integration of the various arc cryostat systems in a zone of interconnection between magnets, cryogenic service module and transverse connection to the QRL.

The routing of superconducting cables feeding the lattice correctors installed in the SSS (octupoles, sextupoles, skew quadrupoles, etc.) is done via a 50 mm O.D. tube, thermalized to cold masses via metallic supports, connected each half-cell to the corresponding magnetic elements. Thermal contraction during cool down is taken care of by flexible hoses located at each interconnect. The continuous 53.5-m cable unit lengths will be inserted after installation of the cryomagnets in the machine. This solution, compared to previous designs where routing was done inside the cold masses, permits a large reduction of passive electrical interconnections, and yields flexibility, simplifications and reduction in costs.

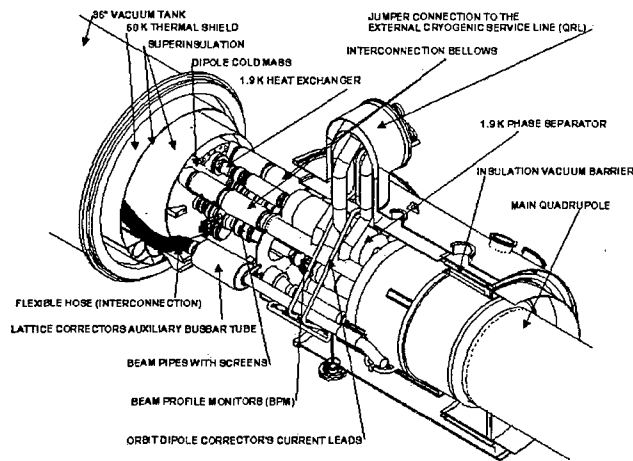


Figure 4: Interconnection of cryogenic, electrical, vacuum and magnetic systems between a lattice quadrupole and a dipole.

## 2.4 Sectorization of sub-systems

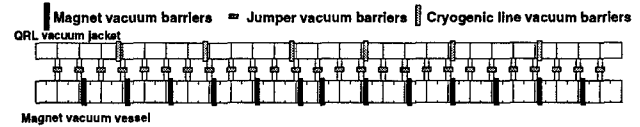
To limit commissioning times (e.g. leak search), some intervention times for repair (e.g. defective protection diode) [8], and to limit risks in case of catastrophic vacuum and/or cryogenic failure (e.g. release of cold helium in the tunnel), the 2.7-km arc cryostat cryogenic and insulation vacuum systems are sectorized every 2 cells (214 m) [4, 6]. A previous option for full sectorization in 4 subsectors of the arc cryostat included

beam vacuum cold valves, permitting replacement of faulty magnets without having to warm-up a full sector. This option has been abandoned in view of its operational complexity [7].

Sectorization is done by means of hydraulic dams-or plugs-installed around bus bars in interconnects, and vacuum barriers in the corresponding SSS.

## LHC ARC - CRYOGENIC AND VACUUM BASELINE DESIGN

### Vacuum sectorization:



### Cold-mass sectorization:

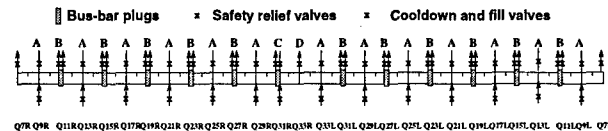


Figure 5: Sectorization of the insulation vacuum systems and cold masses in the LHC arc cryostat.

The arc cryostat has a cold mass of more than 5000 tons. One cryoplat at the corresponding even point will be able to cool down and warm-up such a mass via the QRL in about 24 days. For some interventions for repair such as replacement of defective diodes or instrumentation feedthroughs, this sectorization will allow to cool down/warm-up only small stretches of the arc cryostat (6 cells) in only about 8 days.

## 3 ACKNOWLEDGEMENTS

A large design, development and testing effort is being pursued to integrate all LHC intricate systems in the LHC arc cryostat, and credit goes to the whole of the LHC project staff.

## 4 REFERENCES

- [1] The Large Hadron Collider, conceptual design, CERN/AC/95-05 (LHC) (<http://www.cern.ch/CERN/LHC/YellowBook95/LHC95/LHC95.html>)
- [2] L. Tavani et al, A simplified cryogenic Distribution Scheme for the LHC, ICEC/ICMC'97, Portland, USA, August 97 (LHC Project Report 143 - <http://preprints.cern.ch/cgi-bin/setlink?base=preprint&categ=cerm&id=LHC-PROJECT-REPORT-143>)
- [3] Ph. Lebrun, Superfluid Helium Cryogenics for the LHC, ICEC 15, 1994, CERN AT/94-18 (LHC Note 274)
- [4] O. Gröbner, The LHC Vacuum System, PAC, Vancouver, 1997 (LHC Project Report 181 - <http://preprints.cern.ch/cgi-bin/setlink?base=preprint&categ=cerm&id=LHC-PROJECT-REPORT-181>)
- [5] J-C. Brunet et al, Mechanical Design and Layout of the LHC Standard Half-Cell, PAC, Vancouver, 1997 (LHC Project Report 111 - <http://preprints.cern.ch/cgi-bin/setlink?base=preprint&categ=cerm&id=LHC-PROJECT-REPORT-111>)
- [6] Cryogenic and Vacuum Sectorization of the LHC Arcs, M. Bona et Al, LHC Project Report 60 (<http://preprints.cern.ch/cgi-bin/setlink?base=preprint&categ=cerm&id=LHC-PROJECT-REPORT-60>)
- [7] A. Poncet, T. Wikberg, Summary Report of the Workshop on LHC Arc Sectorization, LHC Project Note 127, 1998 (<http://preprints.cern.ch/cgi-bin/setlink?base=lhcnot&categ=Note&id=project-note-127>)
- [8] M. Chorowski et al, Preliminary risk analysis of the LHC cryogenic system, LHC Project Note 177, 1999 (<http://preprints.cern.ch/cgi-bin/setlink?base=lhcnot&categ=Note&id=project-note-177>)



## TESTING OF VACUUM SYSTEM FOR APT/LEDA RFQ \*

S. Shen<sup>+</sup>, D. Behne, J. Berg, T. DaCosta, M. Harper, K. Kishiyama  
Lawrence Livermore National Laboratory, Livermore, CA

and

R. Valdiviez, F. Spinos, D. Schrage  
Los Alamos National Laboratory, Los Alamos, NM

### Abstract

We have designed, built and operated two vacuum systems for the RFQ (Radio Frequency Quadrupole) in the APT/LEDA (Accelerator Production of Tritium/Low Energy Demonstration Accelerator) linac: a cryopump system for the RFQ cavity and a non-evaporable getter (NEG) pump system for the RF window system. They were designed to provide very high hydrogen pump speed ( $>2 \times 10^4$  L/s) and sorption capacity. Both systems underwent performance tests in mock assembly before the installation. This paper presents the mock test results of both vacuum systems. It also discusses the preliminary test results from the commissioning of the APT/LEDA RFQ.

### 1 INTRODUCTION

The APT/LEDA RFQ consists of four resonantly coupled two-meter segments and 12 RF windows connected via ridged waveguides to 3 sections of the RFQ [1]. The over-riding requirement for the APT/LEDA RFQ vacuum pumping system is that it be capable of pumping the combined gas load from the lost proton beam, gas streaming from the LEBT (Low Energy Beam Transport), and out-gassing from the surfaces of both the RFQ cavity and the RF window system. The total air-based gas load from the cavity will be on the order of  $7.2 \times 10^{-4}$  Torr-liters/sec, and  $8 \times 10^{-5}$  Torr-liters/sec are expected from each RF window. The main gas to be pumped will be hydrogen and the system must be able to pump hydrogen on a continual basis. Vacuum pumps are to be completely oil-free (both high-vac and roughing) and a single pump type must pump all other species of gas ( $O_2$ ,  $N_2$  and any outgassed mixture). For the RFQ cavity, redundancy must be provided in the pumping and gauging systems to ensure that the minimal "operating vacuum level" of  $1 \times 10^{-6}$  Torr is maintained despite pump failures in the system. All pumps and gauges must be replaceable without bringing the RFQ cavity up to atmospheric pressure.

\* Work performed under the auspices of the US Department of Energy by Lawrence Livermore National Laboratory under Contract W-7405-ENG-48

<sup>+</sup> Email: shen2@llnl.gov

### 2 SYSTEM DESCRIPTIONS

For the RFQ cavity, there are 36 vacuum pumping ports connected to 3 distributed manifolds. Five Ebara ICP200 cryopumps are used to handle all the gas loads [1][2]. For the high power RF windows which also required very high hydrogen pump speed, non-evaporable getter (NEG) cartridges were selected. This is mainly because they are relatively small in size and lightweight. The SAES CapaciTorr B1300 NEG cartridge pump that utilizes the sintered ST185 blades, can provide hydrogen-pumping speeds of more than 1000 L/s for each RF window. Both cryopumping and NEG systems are built with automatic pumping and regeneration systems. As reported earlier [3], hydrogen pump speed and capacity measurements were carried out for both types of pumps. From these component tests, we have verified the manufacturer's specifications and thus validated the major design parameters

### 3 MOCK SYSTEM TESTS

Since LEDA is a demonstration facility for APT, beam availability must be high to prove that APT production goals can be met, it was important to ensure the performance of the vacuum system would support the operational requirements for LEDA. Therefore, in addition to the pump verification tests, we also have carried out mock assembly system tests for both cavity and window systems before the shipment. These tests turned out to be extremely useful in developing procedures for installation and system commissioning tests.

#### 3.1 Mock Cavity Testing

A mock cavity was fabricated to simulate the cavity conductance and the volume. As depicted in Fig. 1, the whole cavity vacuum system was then assembled and connected to the mock cavity at LLNL. A series of performance tests were carried out; the results were satisfactory and can be summarized in Table 1.

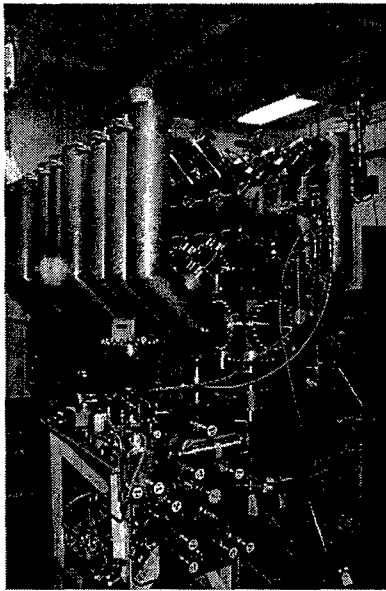


Figure 1: RFQ Mock Cavity Vacuum Assembly

Table 1: Results of Mock Cavity Vacuum Tests

Test	Results
Pumpdown	From atmosphere to $10^{-6}$ Torr in 30 minutes
Instrumentation & Control	Gauges calibrated and all control functions verified.
Base Pressure	$10^{-8}$ Torr (> 50 hrs)
Transient Gas Pulse	Time constant ~ 5 sec.
Abnormal Condition Tests	Measured pressures with simulated gas loads agreed with calculation. Measured pressures with one and two pumps off agreed with calculation.

The results of the "Abnormal Condition Tests" listed in Table 1 are also illustrated in Fig. 2 for Segment A. A direct comparison with the calculation results shown in Fig. 3, indicates that measurement results are in good agreement with the design analysis. (The Sequence of Events are described in Table 2.)

Table 2: Sequence of Abnormal Condition Tests

Time Interval Fig. 2 (min)	Time Interval Fig. 3 (sec)	Descriptions
0-7	0-5	Base pressure
7-14	5-10	With simulated gas loads
14-23	10-15	With one pump off
23-40	15-25	With two pumps off

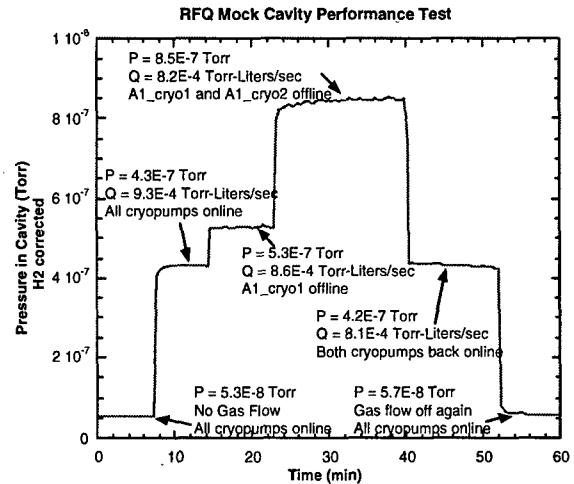


Figure 2: Measured Vacuum in Mock Cavity Assembly

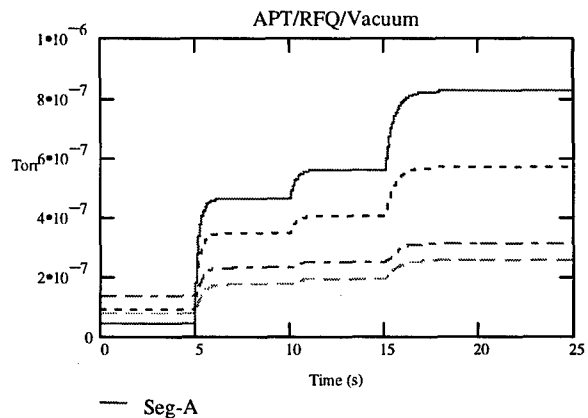


Figure 3: Analytical Results for Comparison

### 3.2 Mock Window Testing

A mock window cavity (see Fig. 4) simulating the RFQ cavity was used to assemble all four arms of one section of the RF window vacuum system. The purpose of this assembly was to conduct integrated tests on the RF window vacuum control system. In the stand-alone mode, the control system consisted of a Modicon PLC and a PC running Labview. Once installed and commissioned on the actual RFQ, the PC was replaced by an interface to EPICs.

All the valves, pumps and instrumentation on the mock cavity used the actual cables that were to be used on the real RFQ. In this way, both the hardware and PLC software of the control system were validated on the

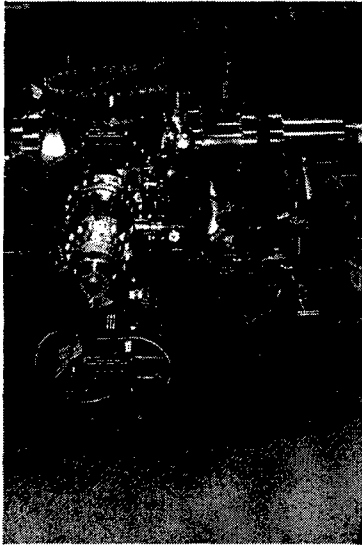


Figure 4: Mock RF Window Vacuum Assembly

mock cavity. It was also used to develop the interlocks and controls for the safe operation of the high temperature regeneration of the NEG pumps. The mock cavity provided an easy and safe method to completely test the entire vacuum system before delivery. The cost of testing with the mock cavity was necessary to guarantee the system will be fully operational immediately after installation was completed

#### 4 COMMISSIONING TESTS

The high RF power conditioning of the RFQ began when the first klystron had been connected to the RFQ via 4 window and waveguide sets. The base pressure in the RFQ cavity and window/waveguide sets prior to the start of conditioning was in the  $1 \times 10^{-7}$  to  $5 \times 10^{-7}$  Torr range. First, RF power at approximately the 1 kW level was introduced into the waveguides and RFQ cavity, producing a vacuum level of approximately  $3 \times 10^{-6}$  Torr in the waveguides. For purposes of reconditioning the RF windows, a vacuum level of  $5 \times 10^{-6}$  Torr was set as the limiting pressure. Pressure in the RFQ cavity remained at about  $5 \times 10^{-7}$  Torr. Within the first 2 hours of high RF power conditioning, the power level was increased to 3 kW while the waveguide pressure remained at approximately  $5 \times 10^{-6}$  Torr. During the next 10 hours of high RF power conditioning the power level was increased to 71 kW with waveguide pressures remaining in the  $3 \times 10^{-6}$  Torr range. Once the RF power was increased over the 10 kW range, some multipactoring bands were encountered in the RF window/waveguide sets. These multipactoring regions required steady RF power level operation for various amounts of time in order to break through them. Even with occasional multipactoring having occurred, the operating RF power level that was attained in the first 12 hours is significant.

At approximately the 50 kW RF power level the RFQ cavity began to be excited. At power levels of 50 kW and higher, the RFQ cavity and waveguides were alternating as to which would dictate the operating power level in order to remain below the pressure set point of  $5 \times 10^{-6}$  Torr. After a conditioning period of approximately 40 operating hours, a power level of 950 kW was reached. Subsequently, another set of 4 RF windows and waveguides was connected to the RFQ. However, this new set was not connected to a klystron immediately. The initial conditioning of these window/waveguide sets was carried out by operating the first klystron and reflecting power into and out of the 4 new window/waveguide sets via the RFQ cavity. The behavior of this new set of windows and waveguides during the initial conditioning was about the same as with the first set of windows and waveguides.

The second klystron was connected to the RFQ via the 4 new sets of windows and waveguides. Power levels in the 900 kW range were used to condition primarily the RFQ cavity. The limiting pressure in the cavity was lowered to  $2 \times 10^{-6}$  Torr. The cavity was conditioned to the 1.2 MW power level. Once this conditioning level was reached, the base pressure in the RFQ cavity and window/waveguide sets was about  $2 \times 10^{-8}$  Torr with no RF power being conducted. RF power in the 1.0 MW range could be fed into the RFQ with pressures stabilizing in the  $1 \times 10^{-7}$  Torr range in both the cavity and waveguides.

The vacuum levels attained during high RF power operation provide further verification that the RFQ cavity and RF window vacuum systems will meet the operational requirements for proton beam operation of 6.7 MeV at 100 mA.

#### 5 CONCLUSIONS

The APT/LEDA RFQ vacuum system performed successfully in the mock assembly as well as in the commissioning tests. The test results presented in this paper validated the design of the vacuum system. It is also demonstrated that the vacuum system is capable of providing comfortable vacuum levels for conditioning the high power RF windows.

#### 6 REFERENCES

1. D. Schrage, et al, "CW RFQ Fabrication and Engineering," LINAC98, (1998)
2. S. Shen, et al, "APT/LEDA RFQ Vacuum System" Proceedings of the 1997 Particle Accelerator Conference, Vancouver, (1997)
3. K. Kishiyama, et al, "Testing of Vacuum Pumps for APT/LEDA RFQ," LINAC98, (1998)

## DESIGN AND DEVELOPMENT OF THE VACUUM SYSTEMS FOR THE APT PROJECT ED&D CRYOMODULE\*

G. Hansen, K. Kishiyama, S. Shen, P. V. Shoaff<sup>#</sup>, LLNL, Livermore, CA

### Abstract

The mechanical design for both the insulating vacuum system and the cavity vacuum system of the APT ED&D Cryomodule is summarized. The pre-cooldown pressure limits for the insulating vacuum and the cavity vacuum are  $10^{-3}$  Torr and  $10^{-6}$  Torr, respectively. In addition, the cold cavity operating pressure limits are  $10^{-6}$  Torr for the insulating system and  $10^{-8}$  Torr for the cavity system. The designs of these systems utilize both turbomolecular pumps and the cold surfaces of the superconducting Nb cavities to arrive at and maintain their operating vacuum pressures. A synopsis of the analysis undertaken to predict the vacuum system performance is also presented.

### 1 INTRODUCTION

The Accelerator Production of Tritium (APT) Project Engineering Design and Development (ED&D) Cryomodule consists of a cryostat with all accelerator components and auxiliary systems installed. The vacuum system for the Cryomodule is composed of two distinct subsystems. The first subsystem, the insulating vacuum system, is responsible for evacuating the insulating chamber of the external cryostat. The other subsystem, the cavity vacuum system, evacuates the RF coupler, beam tube, and Nb cavity assemblies.

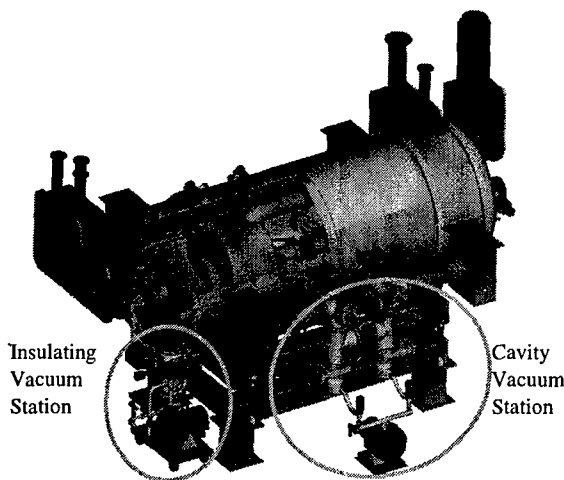


Figure 1: Final Design Layout for the Insulating and Cavity Vacuum Systems

\*Work supported by the US Department of Energy under Contract W-7405-Eng-48.

<sup>#</sup> Email: shoaff1@llnl.gov

Figure 1 shows the layout for the final design of both the insulating vacuum system station and the cavity vacuum system stations. The insulating vacuum system is composed of a single portable turbo pump station attached to a cryostat endcap. The cavity vacuum system includes two pump stations on either side of the Cryomodule. Each station contains two turbo pumps, which are permanently attached to RF power coupler ports.

### 2 DESIGN CONCEPTS

#### 2.1 System Requirements

The cryostat chamber pumped by the insulating vacuum system must be evacuated in order to minimize convective heat transfer to the He vessels surrounding the Nb beam cavities. The turbo pump of the insulating vacuum system is required to bring the chamber pressure level to  $10^{-3}$  Torr prior to cryogen transfer. As the Nb cavities are cooled to 2 K, the He vessel surfaces will cryopump the insulating space and maintain it below the prescribed operating pressure of  $1 \times 10^{-6}$  Torr.

The two Nb cavity assemblies and their respective power couplers share a common ultra-clean vacuum system. The turbo pumps are required to initially evacuate the cavity and power coupler to  $1 \times 10^{-6}$  Torr. Upon cooldown the cavity surfaces, in conjunction with the continuously running turbo pumps, should bring the pressure below the required  $10^{-7}$  Torr at the RF windows and  $10^{-8}$  Torr in the Nb cavities. All pumps for both systems are required to be oil-free [1].

#### 2.2 Insulating Vacuum System Station

The insulating vacuum system station consists of a Varian Turbo V-700HT pump. The turbomolecular pump provides a pumping speed of 680 L/s for  $N_2$ . It is backed by a Varian DS610 Dry Scroll pump. The roughing pump provides a pumping speed of 585 L/min, for an ultimate total pressure of  $< 7.5 \times 10^{-3}$  Torr, and operates hydrocarbon free.

As seen in Figure 2, the access port will be connected to the vacuum system through an 8" MDC C-Loc Gate Valve. The gauge ports on the access stem allow for mounting of both a convectron and a Granville-Phillips Stabil-Ion gauge. In addition, the roughing pump can be directly connected to one of these ports in order to bypass the turbo pump during system roughdown. This will minimize the risk of contaminants being sucked through the turbo pump during the viscous flow phase of the initial pump down.

The turbo pump will be connected to the gate valve through a stainless steel spool connected to a flexible bellows assembly with 10" stainless conflat flanges. A Residual Gas Analyzer can be attached to a 2.75" conflat on a 1.5" diameter access stem provided on the spool. Also, to accommodate gas analysis, a manual valve is provided in the foreline of the turbo pump to throttle down the pump speed. As called for by the program design requirements, the insulating vacuum system can be fully detached from the cryomodule at the gate valve and transported on the cart provided.

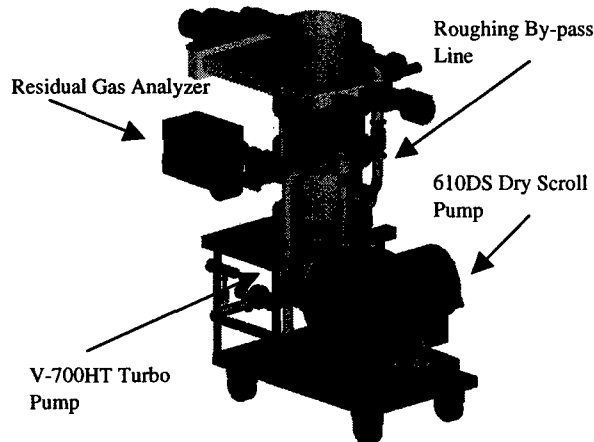


Figure 2: Details of the Insulating Vacuum System Station

### 2.3 Cavity Vacuum System Station

There will be two cavity vacuum stations and each will consist of two Varian Turbo V-300HT pumps backed by a single Varian 610DS Dry Scroll pump. Every turbo pump will provide a pumping speed of 280 L/s for  $N_2$  to give a total system turbo speed of 1120 L/s. The roughing pumps are again hydrocarbon free and provide 585 L/min pumping speed per station and an ultimate total pressure of  $< 7.5 \times 10^{-7}$  Torr.

As seen in Figure 3, the pump stations will be hard mounted to the 6" power coupler vacuum access ports with 8" conflat flanges and run continuously throughout Cryomodule operation in order to maintain the vacuum level at the RF windows and reduce the system gas load. Each of the vacuum access stems will host a 1.5" diameter gauge port ending in a 2.75" conflat flange. The roughing pumps will be floor mounted and attached to the hanging turbo pumps on each station via a 1.5" flexible stainless tube. Since the cavity system will be clean and free of contaminants, no bypass of the turbo pump will be necessary and the cavity system will be roughed directly through the foreline.

The goal post configuration mounts each turbo pump vertically through a 6" MDC C-Loc gate valve to a 6" stainless Tee attached to the power coupler vacuum access port. Each Tee hosts an additional 2 3/4" conflat

gauge port. All connections are made with 8" conflat flanges. The Tees are then vacuum coupled across a 6" bellows with rotatable 8" conflat flanges. The addition of a vacuum coupling tube connecting the adjacent turbo pumps of a cavity vacuum station prevents the isolation of any RF window from a turbo pumping source in the event of a single pump shutdown. This helps to reduce the risk of a RF window failure.

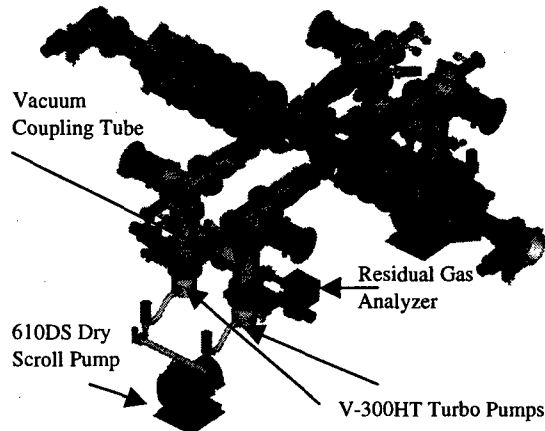


Figure 3: Detail of Cavity Vacuum Station with Cavity System Removed from the Cryostat

A Granville-Phillips Stabil-Ion gauge will be attached to each of the gauge ports on the power coupler vacuum access stem. Two convectron gauges will be placed at either side of the cryostat on the 6" Tee gauge ports opposite and diagonal from each other. The third Tee gauge port will accommodate an RGA and the fourth Tee gauge port will host the gas purge system. This purge system will provide clean filtered inert gas to pressurize the cavity volume.

For both the insulating and cavity vacuum system designs, all the high-vacuum valves are electro-pneumatic actuated and sealed using Viton O-Rings with a leak-rate at the body and valve seat of  $< 1 \times 10^{-7}$  Torr-Liters/sec. Finally, all plumbing will consist of 304 stainless steel tubing, bellows, and off-the-shelf fittings, whenever possible. Additional design details are found in [2].

### 2.4 Cryomodule Vacuum Control Systems

As per design requirements, the design of the Cryomodule systems incorporates a control system that can either operate as a stand-alone system or interface with the supervisory control system, EPICS. The vacuum control system will have interlocks to close the high-vacuum valves in the event of a high-vacuum pump failure or other vacuum system problem. In the event of a vacuum system malfunction, interlocks will also be available to the cryogenic controls to shutdown the cryogenic refrigeration. In the event of a power failure, the vacuum system will shutdown, i.e. the high-vacuum pumps will stop and valves will close. When power is restored, the

control system will restart, but the vacuum system will require a manual restart of the pumps and opening of any valves.

### 3 ANALYSIS

The APT ED&D Cryomodule Vacuum System performance has been analyzed numerically both during the initial pump down and nominal operation.

#### 3.1 Initial Pump Down

The first analysis stage examines the initial pump down from 760 Torr of both the cavity and insulating vacuum systems. It is assumed that the RF power is off and the Nb cavities are at room temperature. Additionally, the pressure dependence of the mechanical pump speeds and the time dependence of the surface outgassing loads are taken into account.

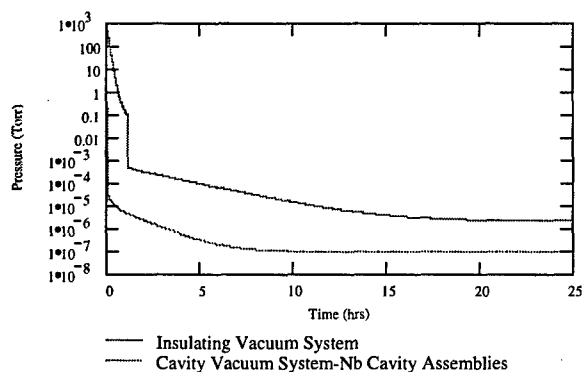


Figure 4: Initial Pump Down Curves for Both Cavity and Insulating System

Figure 4 illustrates the performance of both the cavity and insulating vacuum systems during the initial pump down stage. The analysis predicts that the insulating system will reach its warm cavity design requirement within 13 hours and the cavity system will reach its analogous requirement within 4 hours. Additionally, both of their base pressures are below the pressure limits required for RGA analysis.

#### 3.2 Cavity Specific Analysis during Nominal Operation

The second analysis stage occurs during nominal operation when there is full RF power transfer and the Nb cavities are held at a constant 2 K. During this stage, the temperature profile of the cavity system is assumed constant, full cryopumping exists, and the gas loads are adjusted by temperature and RF power transfer effects. The RF power effects are approximated using empirical results obtained by LANL during testing of the APT RFQ windows [3].

Applying these conditions, the analysis shows that, within seconds, the minimum base pressures obtained in the Nb cavity assemblies are well below their operational requirements, however, the base pressures in the RF window volumes are estimated to be  $1.07 \times 10^{-7}$  Torr. Thus, the current design is at the operational limit. A plot of the pressure vs. time curve is seen in Figure 5.

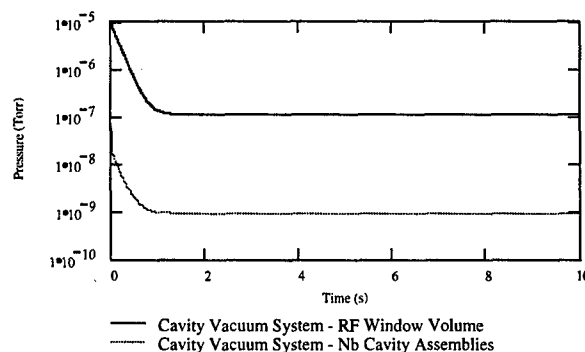


Figure 5: Pump Down Curves from  $10^{-5}$  Torr for the RF Window Volumes and the Nb Cavity Assemblies under Nominal Operating Conditions

The final design analysis also included an examination of several sets of failure scenarios including turbo pump shutdowns and RF window failures. The analysis parameters and more detailed results of the Cryomodule vacuum system, including the various failure scenarios can be found in [2], [4].

### 4 CONCLUSION

The designed system presented in this paper is consistent with the requirements of the APT ED&D Cryomodule. It is a robust, reliable, and redundant system capable of providing the required vacuum level for the APT ED&D Cryomodule with comfortable margins. A review of the final design for the ED&D Cryomodule will be scheduled in the near future and held at Los Alamos National Laboratory.

### 5 REFERENCES

- [1] B. Campbell, "Preliminary Design Requirements of the ED&D Cryomodule for the Accelerator Production of Tritium," LANL, (1997)
- [2] P. Shoaff, et al., "APT/ED&D Cryomodule Vacuum Pumping System, Final Design Report," LLNL/APT 99002, (1999)
- [3] P. Shoaff, et al., "RF Window Vacuum Quality Report," LLNL-APT-98-006, (1998)
- [4] P. Shoaff, et al., "Analysis of the Cavity Vacuum System Response to an RF Window Failure," LLNL-APT-98-007, (1998)

## BEAM VACUUM INTERCONNECTS FOR THE LHC COLD ARCS

R.Veness<sup>\*</sup>, J-C. Brunet, O.Grobner, P. Lepeule, C.Reymermier, G. Schneider, B. Skoczen, CERN  
V.Kleimenov<sup>\*</sup>, I.Nikitine<sup>#</sup>, IHEP Protvino

### Abstract

Cold arcs of the LHC will consist of twin aperture dipole, quadrupole and corrector magnets in cryostats, operating at 1.9 K. Beam vacuum chambers, along with all connecting elements require flexible 'interconnects' between adjacent cryostats to allow for thermal and mechanical offsets foreseen during machine operation and alignment. In addition, the beam vacuum chambers contain perforated beam screens to intercept beam induced heat loads at an intermediate temperature. These must also be connected with low impedance RF bridges in the interconnect zones.

The design of the beam vacuum interconnect is described in this paper. Features include a novel RF bridge design to maximise lateral flexibility during cryostat alignment and so-called 'nested' bellows to minimise the required length of the assembly.

### 1 INTRODUCTION

The Large Hadron Collider (LHC) is a 7 TeV proton-proton collider under construction at CERN, planned for start-up in 2005. Each of the 8 arcs of the machine will consist of repeating half-cells comprising three twin aperture dipole magnets, each 15.2 m long and a 6 m long 'short straight section' (SSS) containing lattice quadrupole and corrector magnets. Each arc is a continuous 2.5 km long cryostat operating at 1.9 K.

All of the links between these magnets required for electrical power, cryogenics and beam vacuum (the subject of this article) must be connected at room temperature before the cryostat can be closed and cooled down. Thus, all these 'interconnects' must allow for the thermal contraction of the magnet cold masses. Due to the time and cost involved, the magnets will be warmed-up as seldom as possible. This means that the interconnects must have the flexibility to allow for re-alignments of the machine when cold or warm.

The beam vacuum system is described in detail elsewhere [1], however, a particular requirement for the LHC will be for a beam screen [2] inside the vacuum chambers to intercept beam induced heat loads at an intermediate temperature. These beam screens must also be connected with low impedance RF bridges between magnets.

### 2 DESIGN REQUIREMENTS

Design offsets required for the beam vacuum interconnect can be divided into those expected during normal operation of the machine, transient offsets during machine cool-down and warm-up and 'exceptional' values due to possible faults, e.g. in the cryogenic system. The totals comprise mechanical tolerances, alignment tolerances and ground movements between alignment periods in addition to thermal expansion and contraction. For longitudinal offsets this sum is made arithmetically as the causes are principally thermal expansions. However, the lateral offsets are due to alignment and assembly tolerances, so the decision has been taken to assume a normal distribution of random errors and to calculate the offset for 3 standard deviations.

Following a review of similar RF bridge designs, in particular those for LEP [3], KEKB [4] and the SSC [5], a minimum contact force of 35g per finger under all operation conditions was specified. An upper value for the contact force of 70g was imposed on the sliding contact to avoid the possibility of particulate generation. Beam screens are cooled by supercritical helium flowing in two cooling tubes welded to each screen. Since the heat loads in the two beam apertures are not the same, the tubes must be swapped over between beam lines at each interconnect zone.

The envelope available for the interconnect is restricted in all directions. The length is limited to 480 mm between dipole magnets to minimise the loss of magnetic length around the machine. The radial space available for bellows and welding equipment is also limited by the other interconnect lines. In addition the beam screen must be passed through the 50 mm cold bore, which prevents the pre-mounting of equipment on one end.

The interconnects on either side of the SSS have additional requirements. On one side a pumping port is required on the beam lines. On the other side, the inter-magnet zone contains a beam position monitor on each aperture.

### 3 GENERAL DESCRIPTION

The layout of a dipole-dipole beam vacuum interconnect is shown in figure 1 with the main features labelled. Each interconnect zone contains two such beam lines in

<sup>\*</sup> Email: raymond.veness@cern.ch

<sup>#</sup> Scientific Associate at CERN

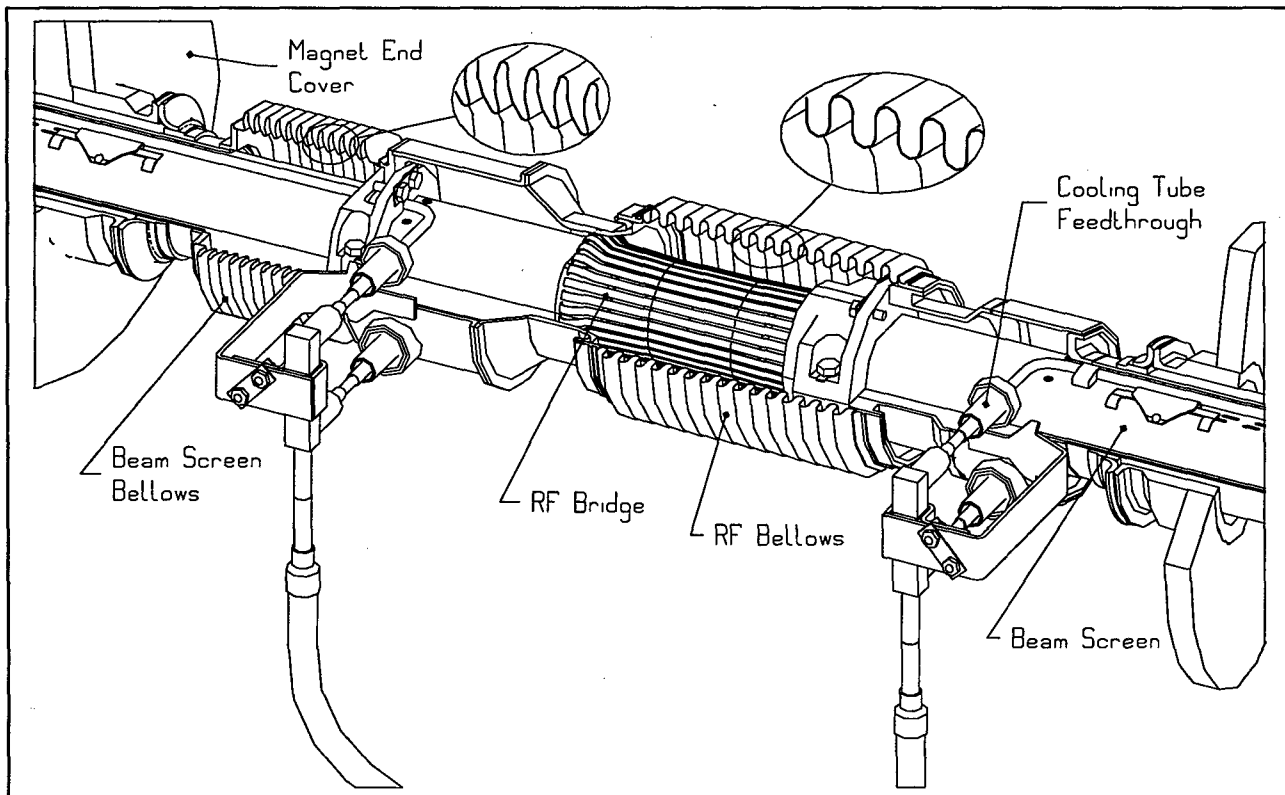


Figure 1: View of one Dipole-Dipole Beam Vacuum Interconnect.

parallel. A line contains two bellows; an 'RF bellows' around the RF bridge which allows for the thermal contraction and lateral offset of the magnet cold masses and a 'beam screen bellows' which absorbs differential thermal expansion between beam screen and magnet cold mass during thermal transients, preventing damage to the cooling tube feedthroughs. The required offsets of these elements both for normal machine operation (including thermal cycles) and for exceptional conditions (including re-alignment) are given in table 1. The 'tolerances' column contains static mechanical and alignment values.

Table 1: Design Offsets of the Interconnect Flexible Elements in mm

	Transverse (All designs)	Longitudinal (Dipole-Dipole)	Longitudinal (SSS-Dipole)	Longitudinal (Dipole-SSS)	Longitudinal Tolerances
<b>Beam Screen Bellows</b>					
Normal	0	34	8	34	8
Exceptional	0.5	75	29	75	8
<b>RF-Bellows: Normal</b>	2	52	36	34	12
Exceptional	4	62	38	57	12
<b>RF-bridges: Normal</b>	2	52	36	34	12
Exceptional	4	62	38	57	12

Each line has four feedthroughs for the helium cooling tube cross-overs. There are fixed mechanical links between both ends of the beam screens and the interconnect to prevent stressing of these feedthroughs. As explained in section 2, the SSS interconnects have some additional requirements. However, the same principals, and a majority of common components are used in all three designs.

Details of the other principal components are given in the following sections.

#### 4 RF BRIDGE DESIGN

The RF bridge design concept was developed to avoid the high shear stress in contact fingers associated with the large lateral offsets required to re-align the machine when warm. The solution adopted was to provide a clearance, rather than a contact when warm and to use a change in the chamber wall diameter to apply the contact finger force only when the magnets are cold. This principle is shown in figure 2.

One RF bridge form was developed for all interconnects, fulfilling the 'normal' offset requirements of table 1 with a force per finger as defined in section 2. It was also designed so as not to plastify when under the 'exceptional' offsets from table 1.

Both beam screen ends have a transition from their standard 'racetrack' section to a circular section for the RF bridge. The profile of the fingers was optimised to minimise the variation of contact force over a range of offsets and to avoid buckling during magnet warm-up.



The baseline material for the fingers is 0.2 mm CuBe2 sheet which is electro-etched, formed and plated with 30  $\mu$ m of silver. It is then rolled to shape and electron beam welded to a copper retaining ring.

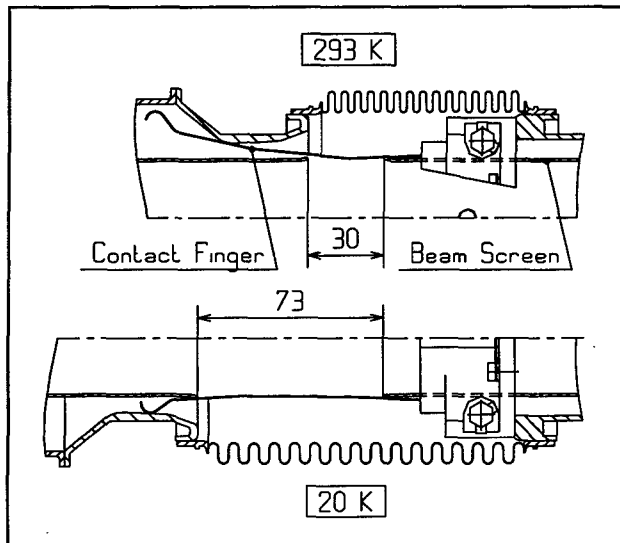


Figure 2: Section Through One Interconnect Line, Showing the RF bridge with the Beam Line at 293 K (Installed Position) and 20 K (Operating Position).

## 5 BELLOWS DESIGN

The minimised space in the interconnection zone imposes strong limitations on the length of both bellows units. The RF bellows is a hydroformed U-type profile, with offsets as described in table 1. The size and axial stiffness were optimised for mechanical stability (buckling) and fatigue (thermo-mechanical cycles). The optimisation procedure is mainly based on the EJMA standards [6], extended to low temperature applications [7].

For the beam screen bellows a very compact 'nested bellows' has been designed for this application to compensate for the large transient axial offsets which occur during cool-down and warm-up (see table 1). The bellows profile, which has a large local curvature of the convolutions, has been analysed for local buckling, global mechanical stability and low cycle fatigue. Although this unit gives little lateral flexibility, it can accept 10-15 % more stroke for a given unit length than a U-type bellows. The alternative would be to use edge-welded bellows, however, this would imply more than 30 km of additional weld length in the 1.9 K system. A more detailed description of the bellows design is given in [8].

## 6 MANUFACTURE AND ASSEMBLY

The LHC will require a total of 3292 beam vacuum interconnect assemblies (1232 cryodipoles and 410 SSSs each with two apertures) which will be manufactured in European industry. All components except bellows and RF bridges will be manufactured in 316LN stainless steel. This grade has been chosen to ensure a fully austenitic

structure at the operating temperatures, even after welding.

In order to maximise the reliability of the beam vacuum system, all sub-components will be manufactured without welds. Welds between components will be made by automated orbital TIG welding without the use of filler metal. The only exception will possibly be in the capillary exits, where laser welding is being considered to avoid the possibility of over-penetration into the capillaries containing high-pressure helium.

The design has been optimised to maximise the pre-assembly of the connections, either in a clean workshop or magnet assembly environment. Mechanical fixed points and RF bridges will be screwed in place inside the beam vacuum and held by tab washers. This leaves only the welds connecting the adjacent magnets, i.e. the RF bellows ends and cooling line cross-overs, to be performed in the tunnel. A number of intermediate quality controls and leak checks can therefore be performed to minimise the risk of interference to the very tight LHC installation schedule.

## 7 WORK IN PROGRESS

Manufacture of a pre-series of beam vacuum interconnects is under way. These will be installed in the LHC prototype string, consisting of 6 dipoles and 2 SSS's during 1999. This will allow a thorough testing of assembly and operation under cryogenic conditions. Extensive RF tests are under way to show that the bridge conforms to requirements.

## 8 ACKNOWLEDGEMENTS

The authors would like to thank F. Caspers, D. Chauville, G. Favre, H. Kos and F. Ruggiero for helpful discussions and their significant contributions to the design.

## 9 REFERENCES

- [1] O.Grobner. The LHC Vacuum System. PAC 97, Vancouver, May 1997
- [2] P.Cruikshank et.al. Mechanical Design of the LHC Beamscreen. PAC 97, Vancouver, May 1997.
- [3] Specification for the Standard Bellows Assemblies of the LEP Main-Ring Vacuum system. CERN/I-1318/LEP. February 1985.
- [4] K.Kanazawa, Y.Suetsugu. Development of a Bellows Assembly with RF-Shield for KEKB. EPAC 96, Sitges, June 1996.
- [5] Design Report on the SSCL Prototype Synchrotron Radiation Liner System. SSCL note SSCL-SR-1224, September 1993.
- [6] Standards of the Expansion Joint Manufacturers Association Inc., 6<sup>th</sup> Edition 1993, Tarrytown, New York 10591. USA.
- [7] B.Skoczen. Preliminary Optimum Design of the Expansion Joints for the LHC Dipole-Dipole Interconnects. CERN LHC Project Note 34, 1996
- [8] B.Skoczen et.al. Development and Optimisation of Nested Bellows for the LHC Beam Line interconnection. CERN LHC/CRI Report 1-1998

## COATINGS FOR THE APS RF CAVITY TUNERS FOR THE REDUCTION OF SECONDARY ELECTRONS \*

G. Harris, Q. Ma, D. R. Walters<sup>#</sup>

Argonne National Laboratory, Advanced Photon Source  
9700 South Cass Avenue, Argonne, Illinois 60439 USA

### Abstract

Thin film coatings are used to reduce the generation of secondary electrons at the ends of the Advanced Photon Source (APS) rf cavity tuners because these electrons result in increased temperatures on the tuner. To improve the film properties over the existing evaporated titanium film, a magnetron-sputtered film of titanium nitride has been developed that is both harder and adheres more strongly than the past evaporated film. This paper describes the process for creating this new coating.

### 1 INTRODUCTION

The Advanced Photon Source (APS) is a facility for material science research. It provides users with a source of X-rays at an energy of 7 GeV. The main positron beam is contained within the storage ring that is two-thirds of a mile in circumference. The storage ring is divided into 40 sectors with isolation valves between each sector. Sixteen rf cavities are used to maintain the electron beam energy in the APS storage ring at 7 GeV. In each cavity there is a tuner piston, as seen in Fig. 1, that can be extended or retracted to match the cavity's resonance to the required frequency.

### 2 RF TUNERS

The rf cavity tuner is a copper piston that, when moved, changes the volume of the cavity; this in turn changes the resonance of the cavity. From the electrical field point of view this method of tuning is lossy, and with the high field gradients, many aspects of the design need to be optimized to keep the tuner temperatures under control [1]. The problem of electron heating of the tuner in the annulus between it and the tuner sleeve can be severe if the surfaces of the piston are not correctly prepared. In the annulus, electrons coming from the high electrical field of the cavity strike the copper of the piston and produce secondary electrons. These in turn bounce around and again strike the piston, producing more secondary electrons. Every strike of electrons heats the tuner more, so if the surface can be modified not to produce secondary electrons, the temperature of the tuner will be reduced. This paper reports on a thin film coating

that reduces the secondary electrons produced on the surface of the copper piston and aids in the control of the tuner temperature.

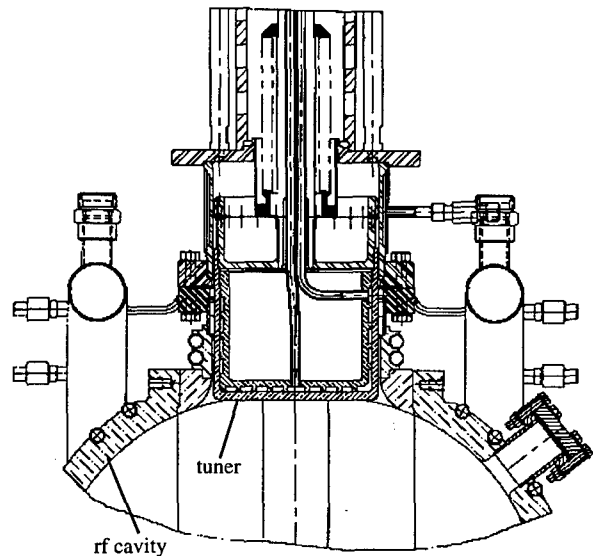


Figure 1: Rf cavity with tuner

### 3 TITANIUM NITRIDE COATING

#### 3.1 Coating System Description

The coating system used at the APS is pictured in Fig. 2. It consists of a main bell jar, into which the tuner is loaded, on top of a base plate where the pump and the sputtering gun are also mounted. The tuner is placed on a turntable so that it can be rotated in front of the sputtering gun while the thin film coating is being applied. The turntable has the added characteristic of being electrically isolated from the system. The turntable and tuner can then have a biasing voltage applied to it to alter the properties of the thin film. This became important while developing of the coating process because it directly altered the surface of the tuner during the coating process.

The magnetron sputtering gun used in this system is a 1.5 inch  $\times$  8 inch linear type gun that is mounted 6 inches from the tuner. The power for the gun comes from a 2.5-kW DC power supply connected to an Advanced Energy Sparc-le™ unit. The Sparc-le™ unit adds a 20-kHz AC signal to the main power that helps in the coating of

\* Work supported by the U.S. Department of Energy, Office of Basic Energy Sciences, under Contract No. W-31-109-ENG-38.

<sup>#</sup> Email: drw@aps.anl.gov

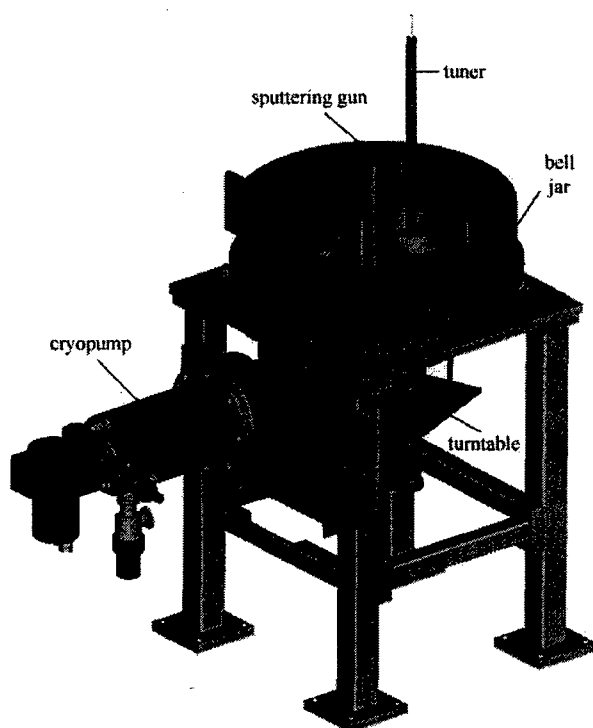


Figure 2: Coating system

insulating films. To apply voltage to the tuner, a 5-kW DC power supply is configured so that the voltage range of the bias supply was adjustable between 0 and 1,000 volts.

The gas inlet system is made up of two MKS Model 1179A mass flow controllers: one for argon, 200 standard cubic centimeters per minute (sccm), and one for nitrogen, 20 sccm. On each line there is a high efficiency gas filter as well as a gas purifier to remove gaseous contaminants. The total system pressure is measured using a capacitance diaphragm gauge. A 2-Torr head was chosen so that readings in the milliTorrrange would be repeatable and reliable.

The vacuum system is comprised of a 9 cfm dry pump for roughing and a cryopump as the main high vacuum pump. The cryopump was throttled by a VAT Series 64 valve to obtain the desired process pressure independently of gas flow into the system.

### 3.2 Titanium Nitride Process

Reactive sputtering is a process where the nitrogen and titanium are brought to the tuner surface and a stoichiometric compound of titanium nitride forms on it [2]. The sputtering gun is the source of titanium for the coating. However, the nitrogen,  $N_2$ , is a nearly inert gas and must be changed to atomic nitrogen in order to form titanium nitride.

In most cases the sputtering gun's glow discharge is energetic enough to break the  $N_2$  bonds to produce  $N^+$  ions. This did not work in our case because the distance the ions had to travel before striking the surface of the tuner was sufficient for the nitrogen to reform into  $N_2$ . At

the process pressure of 20 milliTorrr the resulting mean free path is 2.5 mm. With a distance between the gun and tuner of 60 mean-free-path lengths, it is highly unlikely that the atomic nitrogen will get from the gun to the tuner surface. Over time, what was found to work was a secondary glow discharge on the tuner that would locally dissociate nitrogen so that titanium nitride could form on the tuner surface. Applying a high voltage on the tuner made the glow, which cracked the nitrogen. The energy of the glow is high enough that the nitrogen's bonds are broken right over the surface that is being coated. In this way the atomic nitrogen only needs to travel a few millimeters before it hits the tuner surface.

The completeness of the nitrogen dissociation was judged by the color of the film. A bright gold color was considered an indication that the film composition was approximately correct. Other means were also employed to more fully qualify the film. The surface science technique of using Auger signatures was used to make the final determination of the quality of the film composition. A series of tests confirmed that the best film was produced with the tuner at 700 VDC.

The other set-up parameters for the film are: gun wattage of 400 watts, bias voltage of 700 VAC, argon flow rate of 50 sccm, system pressure of 20 milliTorrr, and a nitrogen gas flow rate of 0.8 sccm.

### 3.3 Characteristics of Thin Film

The new film being developed needed to be an improvement over the evaporated film that had been made in the past. The evaporated film suffered from poor adhesion, brittleness, low strength, and was easily scratched. The goal of the new film was to use a method that would solve the adhesion problem and increase the film strength and hardness. Those last two characteristics could be solved by controlling the composition of the coating to a higher degree than was done in the past.

The film that resulted from the set-up described in the previous section greatly improves upon the earlier film. The process of sputtering while biasing the tuner immediately improved the adhesion. The final film process produces a film that adheres so well it cannot be pulled off with scotch tape and is so hard that a knife with a steel blade can hardly scratch it.

To verify the composition of the coating, a comparison was performed between a known sample of titanium nitride and a sample from this machine. There is a very high correlation between the two samples, as seen in Fig. 3. The upper peaks show the known sample and the lower peaks are from our process using 0.8 sccm of  $N_2$ . The coating itself was gold in color with a shiny finish. We will be testing its secondary electron yield in the future, but reports [3] concerning its performance show that the  $\sigma$ , yield, is less than 0.4 for TiN and  $\sigma \approx 1.0$  for titanium. This is an improvement over copper, which has a  $\sigma$  of 1.3 [4].

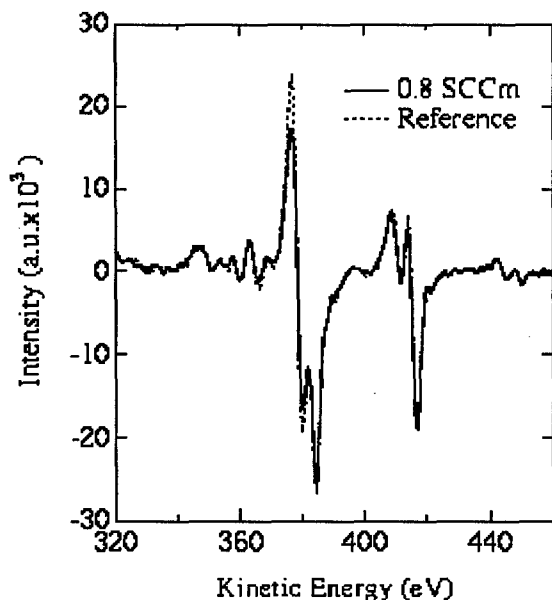


Figure 3: Auger comparison of reference and 0.8 sccm TiN film

#### 4 CONCLUSIONS

The coating produced by the process described here is a great improvement over the old process. The new coating is very robust and does not suffer from handling damage as the old one did. With the improved adherence there is no flaking of the film as there once was. Overall, the new process provides a better film that, when installed into the rf cavity, behaves closer to its theoretical capabilities.

#### 5 ACKNOWLEDGMENTS

The authors would like to thank Cathy Eyberger for her help in compiling and editing this paper. We have had the guidance of Joseph Gagliano and John Noonan (ANL) in the details of the design of the system. The process development was greatly aided by suggestions from Mark Bernick of Angstrom Sciences.

#### 6 REFERENCES

- [1] J. Jones, D. Bromberek, Y. Kang, R. Kustom, L. Morrison, R. Piech, E. Rotela, S. Sharma, I.C. Sheng, Proceedings of the 1997 Particle Accelerator Conference, Vancouver, B.C., pp. 29-29 (1997).
- [2] W.D. Sproul, P.J. Rudnik, and M.E. Graham, "The Effect of  $N_2$  Partial Pressure, Deposition Rate and Substrate Bias Potential on the Hardness and Texture of Reactively Sputtered TiN Coatings," Surface and Coatings Technology, 39/40, p. 355 (1989).
- [3] M. A. Lewis, D. A. Glocker, J. Jorne, "Measurement of Secondary Electron Emission in Reactive Sputtering of Aluminum and Titanium Nitride," J. Vac. Sci. Technol. A 7(3), p. 1019, May/June 1989.
- [4] CRC Handbook of Chemistry and Physics, 64<sup>th</sup> Edition. Ed Robert Weast. Boca Raton: CRC Press, 1983.

# DESIGN OF THE SNS ACCUMULATOR RING VACUUM SYSTEMS\*

H.C. Hseuh\*, C.J. Liaw, M. Mapes, BNL, Upton, NY 11973

## Abstract

Brookhaven is undertaking the design, construction and commissioning of the accumulator ring and the beam transport lines for the 1-GeV Spallation Neutron Source. The operating pressure of the accumulator ring vacuum system will be  $10^{-9}$  Torr and is needed to minimize the beam-residual gas ionization. The vacuum requirement, the layout of the ring vacuum system, and the design of the vacuum chambers, vacuum pumps and other hardware are presented here.

## 1 INTRODUCTION

The goal of the Spallation Neutron Source (SNS)[1] is to provide a short pulse ( $\sim 0.5 \mu\text{s}$ ) of proton beam with an average beam power of 1 MW to a neutron generating target. This is to be achieved by a 1-GeV linac and accumulator ring operated at 60Hz with  $1 \times 10^{14}$  protons per pulse. To improve reliability and to allow hands-on maintenance, the radiation level caused by uncontrolled particle loss in the ring during one msec period must be less than  $10^4$  per pulse. There are several vacuum related beam loss mechanisms, which are nuclear scattering, multi-Coulomb scattering and residual gas ionization.

The nuclear scattering cross sections,  $\sigma_n$ , are proportional to the geometrical cross section of the target nucleus and are  $\sim 4 \times 10^{-25} \text{ cm}^2$ ,  $\sim 3 \times 10^{-25}$  and  $\sim 4 \times 10^{-26} \text{ cm}^2$  for CO,  $\text{H}_2\text{O}$  and  $\text{H}_2$  respectively. These gasses are the most common residual gasses in a clean ultrahigh vacuum system. The beam loss due to nuclear scattering is given by  $\Delta I / I = \int \beta C \sigma_n N dt$  with  $N$  being the residual gas density in the vacuum system. At the designed pressure of  $1 \times 10^{-9}$  Torr,  $N$  will be  $6 \times 10^{-7} \text{ atoms/cm}^3$ . The resultant  $\Delta I / I$  will be  $< 10^{-9}$  over one msec.

The multi-Coulomb scattering causes growth of the RMS beam size. The fraction of the increase in beam size can be calculated by [2]  $\Delta \sigma_y / \sigma_y = \int k \beta_y N / (p^2 \epsilon) dt$ , with  $\sigma_y$  the transverse beam dimension,  $k = 1.085 \times 10^{-23} (\text{GeV}/c)^2 \text{ m}^3 \text{ sec}^{-1}$ ,  $\beta_y$  the betatron amplitude ( $< 20\text{m}$ ),  $p$  the momentum ( $= 1.696 \text{ GeV}/c$ ) and  $\epsilon$  the transverse emittance ( $< 240 \text{ mm mrad}$ ). The fraction of beam growth over one millisecond will be  $< 10^{-8}$  at the design pressure of  $1 \times 10^{-9}$  Torr.

The  $e$ - $p$  instability can limit the achievable intensity [3] when excessive electrons are generated and trapped.

Therefore, the production of electrons due to beam-residual gas ionization must be minimized. The ionization cross sections  $\sigma_i$  of the 1 GeV protons on residual gas molecules can be calculated using Bethe formula [4]:

$$\sigma_i = 4\pi \left( \frac{h}{m_e c} \right)^2 \left( M^2 \left[ \frac{1}{\beta^2} \ln \frac{\beta^2}{1 - \beta^2} - 1 \right] + \frac{C}{\beta^2} \right)$$

with  $4\pi(h/m_e c)^2 = 1.87 \times 10^{-20} \text{ cm}^2$ , and  $M^2$  and  $C$  the experimentally determined coefficients for different molecules. With a residual gas composition of 40%  $\text{H}_2$ , 40%  $\text{H}_2\text{O}$  and 20% CO in the accumulator ring, the average  $\sigma_i$  for 1 GeV proton ( $\beta = 0.875$ ) will be  $\sim 6 \times 10^{-19} \text{ cm}^2$ . At the designed vacuum of  $1 \times 10^{-9}$  Torr, the rate of electron production is given by:

$$\frac{dn_e}{dt} = \beta N \sigma_i n(t)$$

with  $n(t)$  being the instantaneous number of protons in the ring. Integration and averaging of the above equation over a one-millisecond cycle gives  $\sim 3 \times 10^4$  electrons per proton which is negligible [3] in comparison with the production of the electrons from other mechanisms.

## 2 RING VACUUM LAYOUT

The accumulator ring, with a circumference of 220 m has four arc regions and four long straight regions (a four-fold symmetric lattice). The vacuum system is divided into eight vacuum sectors, four arc vacuum sectors and four straight vacuum sectors, isolated with all-metal pneumatic gate valves. The arc vacuum sectors are  $\sim 32 \text{ m}$  long, consisting of eight half-cell vacuum chambers which are 4 meters long. The straight vacuum sectors are  $\sim 23 \text{ m}$  long, consisting of four quarter-cell chambers as well as special chambers for injection, collimation, RF, instrumentation and extraction.

Metals and ceramics are used exclusively in the construction of the vacuum system since they are UHV compatible and radiation resistant. No elastomer or organic materials are allowed. Stainless steel, which has excellent mechanical/vacuum properties and is easy to use during fabrication, has been selected as the material for the half-cell and quarter-cell chambers. Conflat-type flanges and seals will be used to join the chambers together. In several locations with potentially high background radiation, such as the injection, extraction and collimator regions, quick-disconnect type flanges and seals will be used, which will minimize the radiation exposure during machine maintenance periods. All chambers will be chemically cleaned and assembled in a

\*Work performed under the auspices of the U.S. Department of Energy

\* Email: hseuh@bnl.gov

clean environment to minimize contamination.

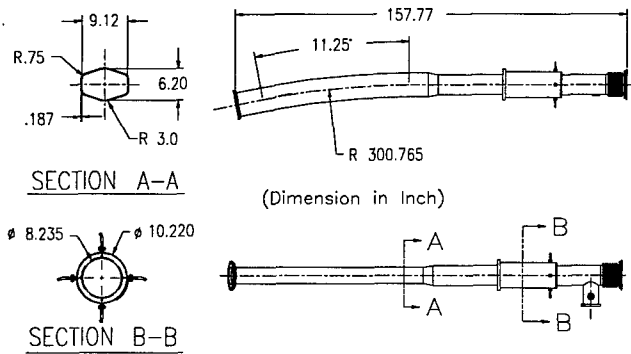


Fig.1 Design of Arc Halfcell Chamber

## 2.1 Half-cell Chambers

Fig. 1 shows a standard arc half-cell chamber. The two-meter long dipole chamber will have an elliptical inside cross section of 23cm (H) by 16cm (V), providing ample aperture for future upgrade to 2 MW. The chamber will be curved with a bending angle of 11.25 degrees and fabricated from 300 series stainless steel. The top and bottom halves of the dipole chamber will be formed by rolling stainless steel sheets on a curved die. The two halves will then be TIG welded together along the mid plane. To minimize the deflection and to assure the structural stability of the chamber under vacuum load, the wall thickness of the dipole sections will be ~ 5 mm. Results of the stress, deformation and buckling analysis, using ANSYS code, are given in Fig.2.

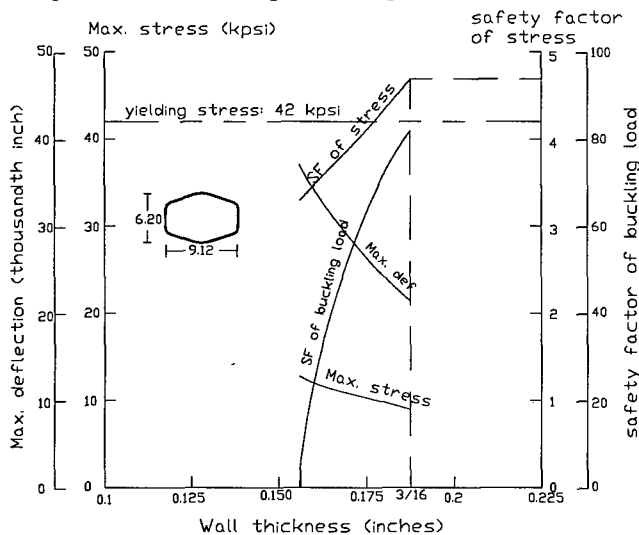


Fig.2: Structural Analysis of SNS Dipole Chamber

With the selected wall thickness and a safety factor of 4.5, the maximum deflection of the chamber is ~ 0.5mm. The safety factor for the buckling is ~ 90. To reduce wall impedance, there will be a tapered transition from the dipole chamber to the round quadrupole pipe. The quadrupole pipe has an I.D. of 19 cm and will be seamless stainless steel tubing. The remainder of the half-cell chamber consists of a beam position monitor (BPM), a

pump port and a bellows. The stripline-type BPM is ~ 0.5m long and is to be precisely aligned with respect to the quadrupole magnet.

To minimize distortion, the BPM housing will be copper brazed to a rigid connecting flange which is then TIG welded to the quadrupole pipe. The quadrupole-BPM section will then be joined to the dipole section with an automated welder on a precision fixture. The short pump section contains the bellows and the pump port and will be tapered to match the elliptical cross section of the adjacent dipole chamber. To minimize the radiation induced stress corrosion, the thin wall bellows will be fabricated from Inconel. The pump port which has a 203mm Conflat flange will be screened with >80% transparency for evacuation. Side ports with 70mm Conflat flanges will be provided above the pump port for other vacuum hardware such as vacuum gauges, residual gas analyzers and roughing valves. The pump section and the end Conflat flanges will be TIG welded to the dipole/quadrupole chamber. The completed half-cell chambers will be wrapped with a thin layer of Kapton insulation before installation into the 'opened' magnets.

## 2.2 The Straight Section Chambers

Each straight vacuum sector will have four quarter-cell chambers and the special chambers housing collimators, RF cavities and injection and extraction equipment. The quarter-cell chamber consists of a quadrupole pipe, BPM, pump port, bellows and flanges and will be made of stainless steel. The fabrication of the quarter-cell chambers will be similar to that of the half-cell chambers.

## 3 VACUUM PERFORMANCE

The eight ring vacuum sectors will be isolated with all-metal gate valves. Vacuum sensors (i.e., vacuum gauge and ion pump readings) upstream and downstream of the gate valves will interlock the valves protecting the ring from catastrophic vacuum failures. The valves also allow repair and modification of components without venting other regions to ambient air. Turbomolecular pump stations backed by dry mechanical pumps will be used to pump down the vacuum sectors and allow the high vacuum pumps to be conditioned and activated. The high linear conductance provided by the large aperture of the half-cell and quarter-cell chambers makes distributed pumping unnecessary. Lumped pumps will be used. One sputter ion pump of ~ 200//sec will be installed on each chamber. In addition, titanium sublimation pumps of ~ 500//sec each, which are housed inside the sputter ion pump, will be used to compliment the sputter ion pumps. The net pumping speed at the pump port will exceed 500 //sec.

The thoroughly cleaned stainless steel chambers will have an outgassing rate of ~  $1 \times 10^{-11}$  Torr./sec.cm<sup>2</sup>, a few

days after pump down from atmosphere. The pressure inside the chambers can be calculated by:

$$P(x) = Q \left( \frac{L}{S} + \frac{L^2 - x^2}{2C'} \right)$$

with  $Q$  being the outgassing per linear length ( $\sim 1 \times 10^9$  Torr./sec.cm),  $2L$  the distance between pumps ( $2L = 400$  cm in the arc sectors),  $2S$  the pumping speed at the neck of the pump ( $2S = 500$  l/s),  $C'$  the linear conductance of the chamber ( $\sim 3 \times 10^5$  l.cm/sec for  $H_2$ ,  $\sim 1 \times 10^5$  l.cm/sec for  $H_2O$  and  $\sim 8 \times 10^4$  l.cm/sec for  $CO$ ), and  $x$  the distance to the nearby pump ( $x = 0$  at the pump and  $x = L$  halfway between the pumps). The pressure distribution in the half-cell chamber with no beam is shown in Fig. 3. The average pressure will be  $\sim 7 \times 10^{-10}$  Torr.

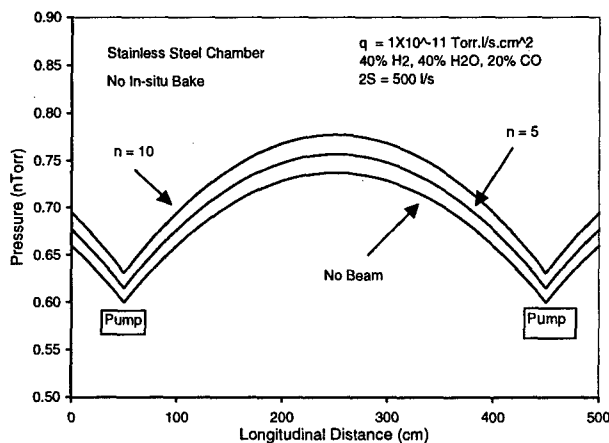


Fig. 3. Pressure in Ring Arc Sectors without beam and with beam using different ion desorption coefficients

With beam present, protons will ionize the residual gas molecules. These new ions, repelled by the beam-wall potential, will bombard the chamber wall and desorb molecules. Each ion with  $\sim$  keV energy [5] will desorb  $\sim$  5 molecules from the unbaked stainless steel surface [6]. The equilibrium pressure in the chamber with the beam will then be given by [7]:

$$P(I, x) = \frac{Q}{C'W^2} \left[ \frac{\cos Wx}{\cos WL - \frac{WC'}{S} \sin WL} - 1 \right]$$

where  $W^2 = I \sigma_i \eta / C'$ ,  $I$  being the average proton intensity over the 16-millisecond cycles, and  $\eta$  being the average number of molecules desorbed from the chamber wall by an incident ion. The pressure distribution inside the half-cell chambers is plotted for  $\eta = 5$  and  $\eta = 10$  in Fig. 3. Due to the large linear conductance of the chambers and the high pumping speed available, the pressure increase due to ion desorption is less than 10% even for  $\eta = 10$ . No pressure bump instability is expected. The pumping requirement in the four straight regions will be modeled with the detailed design of these regions. The designed vacuum will be achieved by positioning several large pumps adjacent to the high outgassing components such as the extraction kickers.

#### 4 VACUUM INSTRUMENTATION

Two sets of pirani and cold cathode gauges (CCGs) will be installed in each vacuum sector, covering the pressure range from 1000 Torr down to  $10^{-3}$  Torr, and from  $10^{-3}$  Torr to  $10^{-10}$  Torr, respectively. The sputter ion pumps will be powered by 5KV controllers, which are capable of reading current down to sub microampere levels. The pump current, proportional to pressure, will give a more detailed pressure profile around the ring. All gauges, residual gas analyzers, controllers and power supplies are commercially available. Due to the radiation level in the tunnel, all electronics including controllers and power supplies will be located in the ring support building. All controllers will have remote capabilities in addition to front panel switches. They will communicate with the vacuum programmable logic controllers (PLCs) through RS-485 type serial links for remote monitoring and control. The PLCs with PC-based LabView type application software will provide the interlock logic and on-line menu for the operation of the gate valves. An ethernet-type link will connect the PLC to the main control console for monitoring, logging and control of the vacuum devices. In addition, hardwired interlocks will connect the PLCs to the beam permit chassis and abort the beam in the event of a vacuum fault.

#### 5 SUMMARY

There are unique features in the design of the SNS accumulator ring vacuum system. To avoid the e-p instability due to beam-residual gas ionization, ultrahigh vacuum of  $1 \times 10^{-9}$  Torr is required. This will be achieved by using UHV compatible materials, processes, and providing sufficient pumping from the combination of sputter ion pumps and titanium sublimation pumps. To minimize radiation exposure during maintenance periods, large quick-disconnect flanges will be used. All vacuum instruments will be capable of remote operation.

#### 6 REFERENCES

- [1] W.T. Weng, 'Accumulator Ring Design for SNS Project', PAC'97, Vancouver, May, 1997.
- [2] G. Guignard, CERN 77-10, p33, June 1977.
- [3] Ruggiero, A.G. and Blaskiewicz, M., BNL/SNS Tech. Note #8, January, 1997.
- [4] Baconnier, Y., Proc. CERN Accel. School, CERN 85-19, pp267-300, Nov. 1985.
- [5] Hseuh, H.C., BNL/SNS Tech. Note #15, February, 1997.
- [6] R. Calder and A.G. Mathewson, Vacuum, 29, 53(1979).
- [7] Fischer, E. and Zankel, K., CERN-ISR-VA/73-52, Nov. 1973.

# RHIC VACUUM INSTRUMENTATION AND CONTROL SYSTEM\*

R.C. Lee, D. Pate, L. A. Smart<sup>†</sup>, D. Weiss, D. Zigrosser, RHIC Project, BNL, Upton, NY

## Abstract

The Relativistic Heavy Ion Collider (RHIC) Project is a nuclear physics research accelerator at Brookhaven National Laboratory (BNL) with beam circulation scheduled for May 1999. To achieve the necessary beam lifetime, the vacuum in the two concentric rings must be constantly monitored to isolate problem vacuum regions. One function of the RHIC vacuum instrumentation and control (I&C) system is to operate sector valves with inputs from several hundred gauges and pumps distributed around the 3.8 km circumference of the accelerator rings. The architecture and implementation of the RHIC vacuum I&C system from the pumps and gauges to the remote user interfaces are described.

## 1 RHIC VACUUM SYSTEMS

There are three distinct vacuum systems in RHIC proper (see Fig. 1). The insulating cryostat vacuum houses the helium-cooled superconducting magnets. The cold beam tube vacuum passes through the center of the magnets. The warm beam tube vacuum, which connects magnet strings, makes up roughly 16% of the RHIC beam line.

Ions from the linear accelerator or Tandem Van de Graaff are accelerated by the Alternating Gradient Synchrotron/Booster, and injected into one of the two RHIC rings. RHIC has six equidistant sites for beam collision detection.

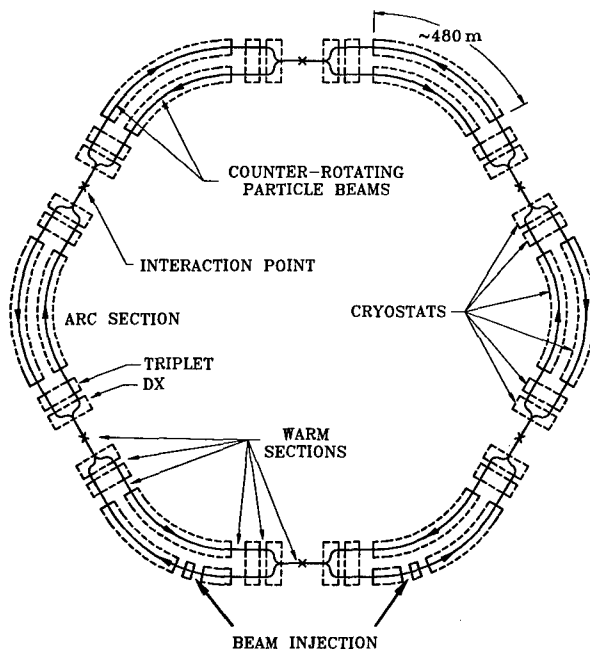


Figure 1: The RHIC layout

### 1.1 Insulating Cryostat Vacuum System

The insulating vacuum must be kept below  $10^{-5}$  Torr to minimize heat transfer to the 4.2 K superconducting magnet cold mass. From earlier test measurements, the cryostat total pressure falls into the low  $10^{-7}$  Torr range[1]. The cold mass of the superconducting magnets pumps all but the lightest gases, so turbomolecular pumps (TMPs) with mechanical backing pumps are employed. Inverted magnetron cold cathode gauges (CCGs) and convection-enhanced Pirani gauges are used to monitor the cryostat pressure. Partial pressure analyzers (PPAs) are used to sample the gas composition of the cryostat and beam vacuum environments and can give an indication of helium leaks from magnet vessels or air leaks in the cryostat after cool-down.

### 1.2 Warm Bore Vacuum System

For the ten-hour-plus beam lifetime, the average ambient (or warm) beam vacuum must be below  $5 \times 10^{-10}$  Torr. A warm sector is the warm bore between two sector valves. Sector valves are all-metal gate valves used to isolate the warm beam tube vacuum from adjacent warm sectors or from the cold beam tube. Ion pumps are installed in the warm beam vacuum sectors. Each ion pump has two pockets into which titanium sublimation pump (TSP) cartridges are installed. There are fifty-two distinct warm sectors in RHIC proper. The number of ion pumps in each sector depends on the gas load of various chambers. Prior to installation, warm bore gauges are baked and leak checked on their instrument trees.

### 1.3 Cold Bore Vacuum System

The average cold beam vacuum must be less than  $1 \times 10^{-11}$  Torr. The cold beam tube or cold bore, is passively pumped by the cold tube walls and charcoal-filled sorption pumps that are installed at  $\sim 30$  m intervals. The cold bore temperature is  $\sim 4.5$  K and the sorption pump temperature is less than 10 K. The pressure in the cold bore is monitored by gauges that are also  $\sim 30$  m apart. Small americium alpha sources are installed inside the cold bore CCG tubes to help start the gauge discharge at very low pressures [2]. This modification allows a single type of gauge to be used for all of the ring vacuum systems.

\* Work performed under the auspices of the U.S. Energy Department.

<sup>†</sup> Email: lsmart@bnl.gov



## 2 THE VACUUM I&C SYSTEM

The heart of the vacuum I&C system is a peer-to-peer network of programmable logic controllers (PLCs). The control of vacuum devices is divided geographically among eight PLCs. The PLCs take care of the safe operation of the vacuum system, and are the link between the intelligent gauge and pump controllers and the controls system front-end computers (FECs). Data from the FECs is transmitted to remote Console-Level Computers (CLCs) where applications are available to display and log vacuum system parameters. A bottom-up description of the system follows.

### 2.1 The Instrumentation

There are over one thousand gauges and ion pumps in the RHIC vacuum systems. Although all interface with the controls system, only two thirds control ~125 sector valves. Controllers for gauge and ion pumps whose pressures directly affect the operation of valves are located in one of eight service buildings in racks adjacent to the vacuum PLC. Cables are run from gauges and pumps in the RHIC tunnel to the service building several hundred feet away (see Fig 2). A normally open set point relay is associated with each gauge. When the gauge pressure is below the selected set point level, the relay contact is closed indicating good vacuum. The rest of the gauge controllers are installed in the accelerator tunnel; one is incorporated in each TMP station. The PPAs have the electronic control unit directly mounted on the sensor. All TMPs and PPAs are located in the tunnel.

### 2.2 The PLC

Each PLC chassis comprises one processor module, one or two communication coprocessors with serial expander modules, and several input and output (I/O) modules.

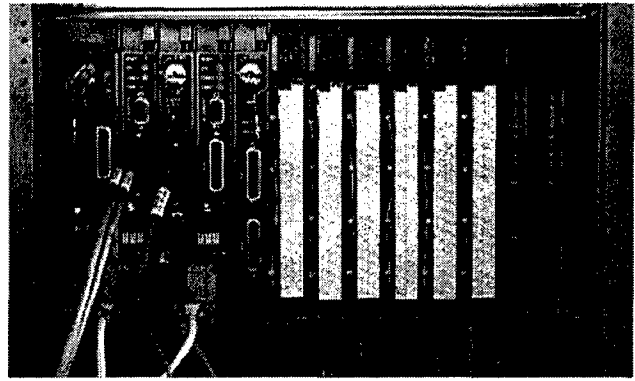


Figure 2: A typical PLC chassis

Data is transferred between PLCs on a high-speed Data Highway Plus™ serial communication networks [3]. Each coprocessor with serial expander has six serial communication ports assigned to five types of vacuum devices: gauge controllers, ion pump controllers, TMPs, PPAs, and TSPs. The I/O modules have either 32 inputs or outputs, with control voltages ranging from 10 to 30 Vdc.

Ladder logic programs reside in the PLC processor module. The ladder programs control the valve solenoids based on user inputs and the input module signals from gauges, pumps, and valves. Each sector valve has open and closed limit switches wired to the PLC inputs and a solenoid that is wired to the PLC output module. A valve can be opened only if the vacuum level satisfies gauge set points on both sides of the valve. Valves are closed by the PLC under a number of conditions, such as when the vacuum is bad or multiple controllers fail.

### 2.3 The Beam Permit Link

Beam can only be introduced into a RHIC ring if accelerator system safety precautions are met. One of these measures, the vacuum system beam permit link (BPL), provides a positive indication that all sector valves for a

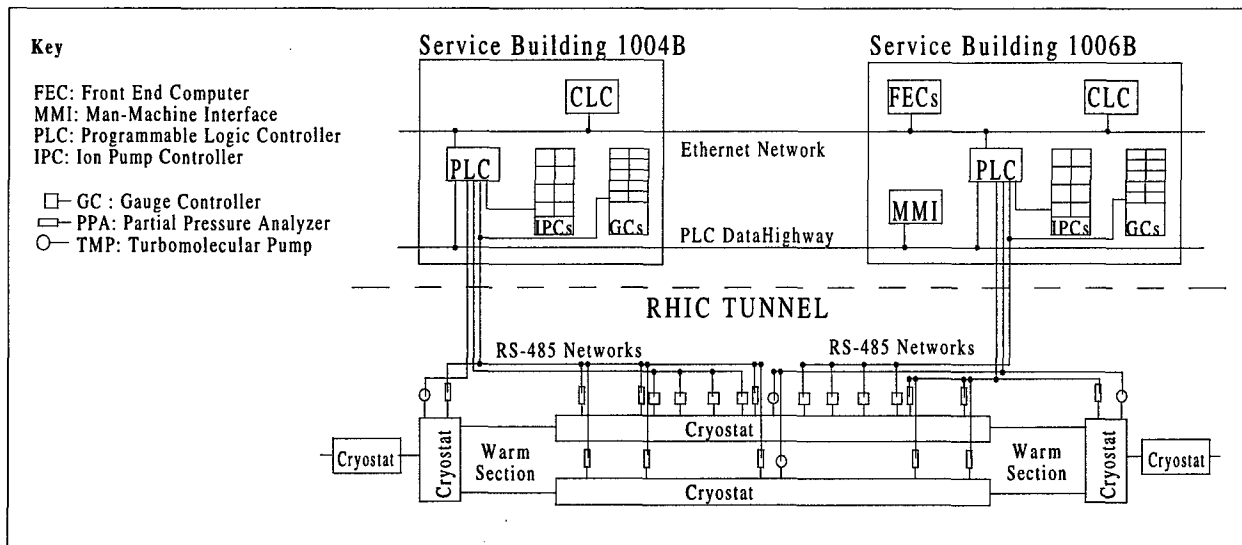


Figure 3: System architecture for one sixth of RHIC.

given ring are open. There are permit signals for both rings at each vacuum system PLC. If a single valve closes, or the limit switches do not indicate that the valve is open, then the beam permit is removed. The BPL will also inhibit beam if there is a failure of the PLC or its power source.

Two of three pressure readings must rise above the set points to close a sector valve, causing the PLC to remove the BPL. A single high pressure reading will not trip the BPL. To minimize the chance of removing the beam permit during short power outages, the PLC and associated power supplies are backed by an uninterruptible power supply.

## 2.4 Remote Monitoring and Control

In addition to protecting the ring from injecting beam with valves closed, the I&C system must provide remote control of devices.

C-language programs in the PLC coprocessor poll gauge controllers, ion pump controllers, TMP stations and PPAs on five networks (the gauge controllers are divided on two networks due to the number of devices). Distinct networks are needed because each device has a unique command structure or protocol. For example, the gauge controllers and TMP stations reply in ASCII characters, the ion pumps talk back in hexadecimal codes, and the PPAs use a 9-bit protocol that manipulates the parity bit. The coprocessor software receives the data in many formats and re-packages it for the controls system FECs.

The coprocessor has an Ethernet port through which data is uploaded to the control section FEC. Since all data transfer between the FEC and the vacuum system occurs through the coprocessor, the data in the PLC processor memory must be copied to coprocessor memory for FEC retrieval. Similarly, commands from the FEC are routed through the coprocessor to the PLC.

## 2.5 The Front-End Computer

There are four FECs for the RHIC vacuum devices. The FECs are VME based processors with up to 32 Mbytes of memory. All data from the vacuum system to the Controls System, including PLC I/O status, is routed through the PLC coprocessor Ethernet port. That data is exchanged at a rate of 10Mb/s.

## 2.6 The Console-Level Computer

The CLCs are UNIX workstations that run applications to display and log the FEC. One application, Parameter Editing Tool, is a general-purpose program developed at BNL for viewing and modifying RHIC control system parameters. Users can see gauge pressures, ion pump current, and the status of valves or TMP stations in spreadsheet format. The user can also send commands to manipulate sector valves, change PPA parameters, turn ion pumps on/off, or control TMP stations valves and

pumps. Other applications perform data logging and archiving tasks. The CLC and FEC exchange data at a rate of 100 Mb/s over the Ethernet network.

## 2.7 The Man-Machine Interface

A back-door provision for the control and monitoring of the vacuum devices was built into the system in the event that the FEC or Ethernet link fails. There is another user interface called the MMI (man-machine interface) that is independent of the controls system computers. The MMI is an industrial computer with software that interfaces directly with all PLCs on the DataHighway network. This allows control all RHIC vacuum sector valves from a limited number of locations (presently two) should the FECs or CLCs become unavailable. All gauge relay contact and valve limit switch data is displayed in a graphic format, so that the state of the vacuum system can be determined at a glance. The MMI currently does not have the capability to display remote serial data, but it does provide an alternate means of determining the status of the entire vacuum system's readiness for beam.

# 3 CURRENT STATUS

To date, over 85% of gauge controllers, ion pump controllers, and TMPs are reporting device readings to the controls system. Pressure readings from 250+ gauge controllers throughout the vacuum system are being monitored. Over ninety percent of the ion pumps are operational with most warm sectors at high vacuum. PPAs are also on-line, reporting partial pressure readings in a few warm regions. All cold bore beam tubes are under rough vacuum in preparation for the cool-down of the magnet strings. All PLC processors and co-processors are programmed and operational. Controls system data logging and plotting software is also operational. The BPL signals from the PLCs are wired to the controls system inputs in preparation for accelerated beam in May.

# 4 ACKNOWLEDGEMENTS

The authors would like to credit Robert Burns for the design of the vacuum instrumentation and control system architecture. We also thank the Vacuum System Section staff for the years of effort that went into assembling and installing the system, and for making it work.

# 5 REFERENCES

- [1] H.C Hseuh, et al., Proc. 14<sup>th</sup> Int'l Vac. Congress, Birmingham UK, Sept. 1998.
- [2] K.M. Welch, et al, J. Vac. Sci. Technol A 14(3), May/Jun 1996.
- [3] DataHighway is a trademark of Rockwell Automation (Allen-Bradley brand).

# A METHOD FOR GOLD COATING EXPERIMENTAL DETECTOR BEAMPIPES\*

S. Henderson<sup>†</sup>, S. Roberts, Cornell University, Ithaca, NY

## Abstract

A thin metallic coating is required on the inside of central detector beryllium beampipes at high-current  $e^+e^-$  colliders in order to suppress detector backgrounds that arise from scattered synchrotron radiation. As part of two CESR/CLEO upgrades, three beryllium beampipes have been coated with gold using a magnetron sputtering technique. The apparatus will be described as well as the factors that influence the adhesion and uniformity of the resulting films. Finally, we discuss the characterization methods of the resulting films.

## 1 INTRODUCTION

High luminosity  $e^+e^-$  colliders require that unprecedented beam currents be brought into collision, while the high-energy experimental requirements demand that beam-induced detector backgrounds be minimized. Such beam-generated detector backgrounds arise from interaction of beam particles with residual gas in the vacuum chamber (beam-gas interactions) and from synchrotron radiation (SR) generated in nearby magnetic elements which scatters into the detector. Careful interaction region design [1] provides shielding of the detector for lost beam particles and shielding of the central detector beampipe from synchrotron radiation by careful placement of apertures. Even with apertures placed to eliminate direct SR that would otherwise strike the beampipe directly, the *scattered* radiation from these apertures is great enough that further suppression is required. A common method for further suppressing the scattered SR flux which is in use at the Cornell Electron Storage Ring (CESR), PEP-II, KEK-B and elsewhere is to apply a thin metallic coating to the inner surface of the collider detector beampipe (which is generally made of beryllium). Since the scattered SR flux strikes the beampipe at very shallow angles, very thin metallic layers provide adequate suppression of the scattered SR flux entering the detector.

As part of two recent upgrades to CESR and the CLEO detector [2, 3], we have developed a technique for coating the inside of small-radius ( $r \approx 2$  cm) beryllium beampipes with gold. For the CESR Phase II upgrade, a  $10 \mu\text{m}$  gold coating was required, and for the upcoming CESR Phase III upgrade, a  $5 \mu\text{m}$  layer is required. Both CLEO detector beampipes are double-walled, actively cooled Be beampipes manufactured by Brush Wellman-Electrofusion [4, 3]. The inner radius and length of the as-coated beampipe assemblies were 1.9 cm, 43 cm (Phase II) and

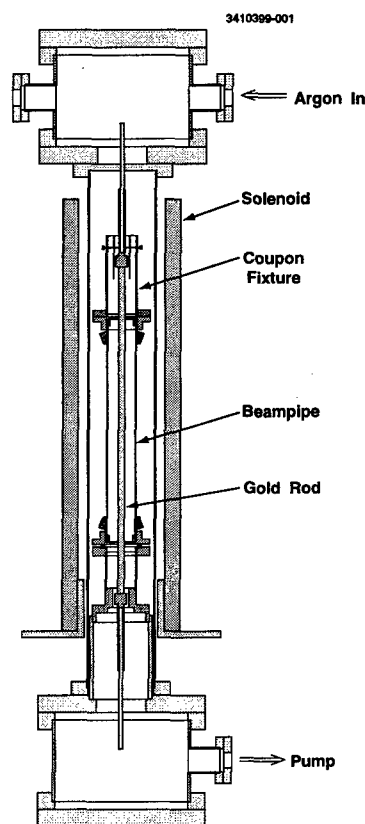


Figure 1: Beampipe coating apparatus

2.1 cm, 36.5 cm (Phase III), respectively. We describe the deposition technique, the coating "recipe" and the characterization of the resulting thin films.

## 2 COATING METHOD AND APPARATUS

We use a cylindrical magnetron sputtering technique [5] for application of the gold coating. Due to the small radius of the beampipes, DC-diode sputtering without magnetic field was not practicable, since high sputtering gas pressures would be required ( $\sim 300$  mTorr) to sustain a discharge. Sputtering at such high pressures results in very slow deposition rates and in films with undesirable surface structure. As a result, we sputtered in the presence of an axial magnetic field, which allows a discharge to be maintained at much smaller sputtering gas pressures; acceptable deposition rates result because of the enhanced ionization by secondary electrons as they travel in cycloidal, rather than straight-line, paths.

The coating apparatus which was recently used for the CESR Phase III/CLEO-III Be beampipe is shown in Figure 1. The Be beampipe is mounted to a stand which is elec-

\* Work supported by the National Science Foundation.

<sup>†</sup> Email: sdh9@cornell.edu

trically isolated from the chamber by ceramic standoffs. Atop the beampipe is mounted a small chamber to hold witness coupons which are coated along with the beampipe for quality control purposes. A water-cooled gold rod is mounted axially in the beampipe. This rod consists of a 1 mm thick layer of gold clad on 1/4 inch stainless steel tubing. Water cooling of the cathode is essential as very high power densities are reached at the surface due to ion-bombardment.

The beampipe and gold rod assembly sits inside an ultra-high vacuum system with large chambers on top and bottom for instrumentation, feedthroughs, and access. High-voltage water feedthroughs provide voltage and cooling water to the gold rod. The axial magnetic field is provided by a solenoid placed external to the vacuum system. The system is pumped with a 500 l/s turbo pump. Chamber pressure is monitored with a Granville-Phillips Stabil-Ion<sup>TM</sup> hot filament gauge. Argon (UHP 99.999%) is introduced at the top of the chamber and is pumped at the bottom of the chamber, ensuring flow through the pipe. A commercial magnetron gun power supply is used for sputtering. An electrical connection to the beampipe is brought via a feedthrough outside the vacuum chamber. For back-sputtering of the beampipe (see below), high-voltage leads on the beampipe and gold rod are reversed. A thermocouple monitors the temperature of the witness coupon chamber during processing.

### 3 COATING RECIPE AND SPUTTERING PARAMETERS

The sputtering conditions and coating recipe were chosen to maximize the adhesion of the deposited film and to assure its longitudinal uniformity. Each will be discussed in turn.

#### 3.1 Factors affecting adhesion

As is the case with any thin-film deposition, cleanliness of the substrate, cathode and vacuum system is the single most important factor in achieving an adherent film. Standard ultra-high vacuum handling techniques were followed for all components entering the vacuum chamber. All fixtures were acid etched prior to initial introduction into the vacuum system. Subsequent handling of fixtures was followed by scrubbing in soap and water, ultrasonic cleaning in Liquinox, and rinsing in isopropanol.

We found that cleanliness alone was not sufficient for acceptable adhesion of gold on beryllium or stainless steel. Three additional steps were required. First, prior to deposition, the Be beampipe was back-sputtered. That is, the beampipe itself was sputtered in order to remove surface contaminants. In addition to cleaning the surface, back-sputtering may also help to remove the BeO layer. Secondly, we found that a thin layer of Cr (~150 nm) deposited on the Be substrate prior to gold deposition improved the adhesion. This technique of using a Cr interlayer is com-

mon in the semiconductor industry [6] and is thought to improve adhesion by bonding to the oxide layer [7]. Finally, after gold deposition the beampipe is vacuum baked at 300°C for 1 hour. This relatively low temperature bake is thought to promote diffusion at the Au-Be interface and thus improve adhesion [8, 9, 7].

In addition we found that proper Ar flow was essential for achieving adherent films. Argon was introduced at one end of the system and made to flow preferentially through the beampipe in order to supply fresh Ar to the discharge. Argon was pumped through the other end of the chamber always at the maximum possible throughput allowed by the turbo pumping system.

#### 3.2 Factors affecting uniformity

We found three factors which strongly influenced the resulting gold thickness uniformity: 1) solenoid length, 2) magnetron operating point, and 3) cathode uniformity. The reduced magnetic field at the end of the solenoid produces a weaker discharge at the ends. We used a solenoid 66 cm in length whereas the beampipes were ~40 cm in length. Care was taken to center the beampipe in the middle of the solenoid.

The operating region of the apparatus in magnetron mode is shown in Figure 2. For a given Argon gas pressure there is a minimum magnetic field required to sustain a plasma discharge. This minimum field is that which provides sufficient ionization by secondary electrons to just make up for losses, and is approximately given by the field for which secondary electron trajectories just miss the beampipe wall, thus making full cycloidal orbits in the system. In addition, there is a maximum magnetic field above which the discharge is extinguished. This is approximately the magnetic field for which the secondary electron path-length is shorter than the mean-free-path and hence secondary electrons are recaptured at the cathode surface. We found that the choice of operating point affects the resulting uniformity.

We chose to operate the magnetron at  $P_{Ar} = 4$  mTorr and  $B = 250$  G. This is sufficiently well removed from the extinguish lines of Figure 2 so that we achieve sputtering along the whole length of the rod despite the small drop in magnetic field at the ends due to finite solenoid length. For gold sputtering, we typically operated at 150 W (750 V, 0.2 A), which provided a deposition rate of ~3  $\mu\text{m/hr}$ .

Finally, we found that longitudinal nonuniformity of the cathode can deform the plasma discharge and produce longitudinally non-uniform coatings. We found that the plasma discharge was enhanced in regions where the cathode was of smaller radius. Nonuniformity in cathode radius of only ~5% is significant and can produce non-uniform deposition profiles (see below).

### 4 COATING PROCEDURE

The step-by-step coating procedure is as follows. The magnetron supply power, magnetic field, and flowing Ar gas

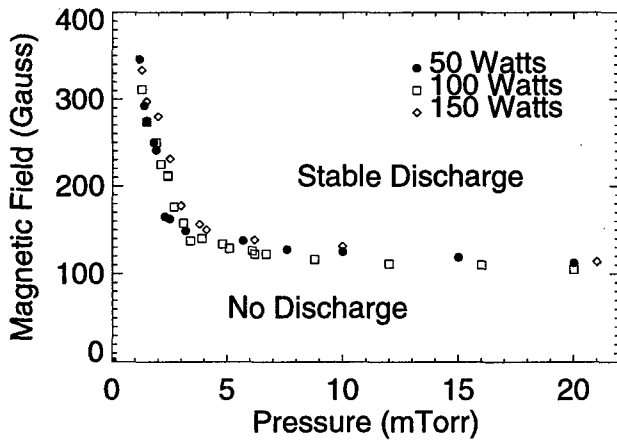


Figure 2: Magnetron operating region. Above the points a discharge is self-sustained. Below the points the discharge extinguishes.

pressure are noted.

1. Clean all fixture parts by scrubbing with abrasive pad and soap. Place in ultrasonic bath with Liquinox. Rinse in isopropanol and blow dry with  $N_2$ .
2. Assemble fixtures, Be beampipe and Cr rod. Place in vacuum system. Pump down.
3. Backsputter Be beampipe: 100 W (250 V) for 15 minutes, 275 mTorr Ar,  $B = 0$ .
4. Apply 150 nm Cr: 100 W (600 V) for 9 minutes, 4.0 mTorr Ar,  $B = 250$  G.
5. Open vacuum system when cool, replace Cr with Au rod, reinstall in vacuum system and pump down.
6. Backsputter Be beampipe: 100 W (250 V) for 15 minutes, 275 mTorr Ar,  $B = 0$ .
7. Apply 5  $\mu m$  Au: 150 W (750 V) for 90 minutes, 4.0 mTorr Ar,  $B = 250$  G.
8. Remove assembly from vacuum system when cool.
9. Bake in vacuum furnace at 300°C for 1 hour.

## 5 RESULTS

Throughout the development of the coating procedure, coupons of Be and Stainless Steel were coated for various sputtering conditions. Two adhesion tests were found to be the most useful. The first is the simple "scotch-tape test" in which adhesive tape is attached to the film and pulled quickly in an attempt to remove the film. The second more demanding test requires scribing a grid of finely spaced cuts through the film down to the substrate (typically a 4x4 grid with cuts spaced  $\sim 1$  mm apart). This portion of the coupon was then subjected to the tape test. Generally, if a

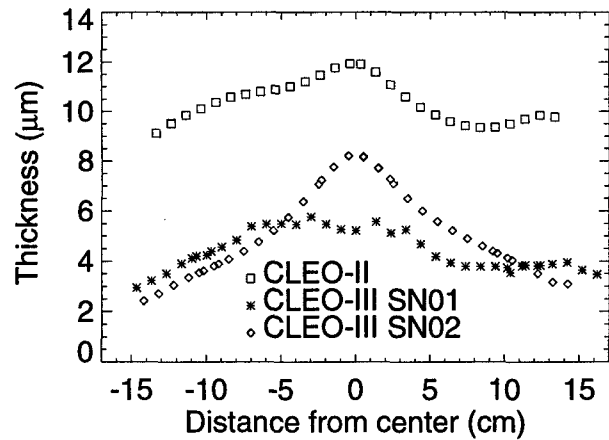


Figure 3: Gold thickness uniformity results for three Be beampipes measured by x-ray absorption.

film passed this test, it could not be removed by any other means. The principal function of the witness coupons which were coated with the beampipe was to subject them to these adhesion tests. No tests were performed on the Be beampipe itself in order to maintain UHV cleanliness.

The various factors which affect thickness uniformity described above were discovered in the development stage through repeated test coupon runs. The thickness was determined by weighing coupons before and after coating.

The thickness uniformity of the coated Be beampipes was measured by a simple x-ray absorption method performed at the Cornell High-Energy Synchrotron Source (CHESS). The attenuation of an x-ray beam with energy just below the gold  $L_{III}$  edge was measured as a function of the longitudinal position on the beampipe. The thickness profiles for the three coated Be beampipes is shown in Figure 3. Uniformity is good for two pipes, but the third is thicker in the middle due to a non-uniform gold cathode, as described above. It should be mentioned that the detector tracking volume is within  $\pm 6$  cm, so it is this thickness which is most important.

## 6 REFERENCES

- [1] S. Henderson, Proc. Second Workshop on Backgrounds at the Machine Detector Interface, World Scientific (1998) 6.
- [2] S. Henderson, Proc. 1997 Part. Acc. Conf., 291.
- [3] S. Henderson, et. al., these proceedings.
- [4] S. Henderson, Proc. 8th Mtg. DPF (1994) 1480.
- [5] J.A. Thornton and A. S. Penfold, "Cylindrical Magnetron Sputtering", in *Thin Film Processes*, ed. J.L. Vossen and W. Kern, Academic Press, New York, 1978.
- [6] V. Malina et. al., Semi. Sci. Tech. 3 (1988) 1015.
- [7] B.N. Chapman, J. Vac. Sci. Tech. 11 (1974) 106.
- [8] P. Madakson, J. Appl. Phys. 70 (1991) 1380.
- [9] M. Nayak et. al., J. Mat. Sci. Lett. 12 (1993) 119.

# CONCEPTUAL DESIGN OF A VACUUM SYSTEM FOR A COMPACT, HIGH LUMINOSITY CESR UPGRADE\*

Kern W. Ormond<sup>†</sup>, Joseph T. Rogers, Laboratory of Nuclear Studies, Cornell University

## Abstract

A conceptual design study for a vacuum system for a possible compact high luminosity upgrade to CESR is presented. The vacuum chamber consists of an elliptical cross-section beam chamber connected to a pumping chamber by holes recessed in several channels in the beam chamber wall. Recessing the hole provides a decrease in the impedance of the beam chamber while still providing protection to the pumping chamber from RF fields generated by the beam. The beam chamber has a very compact cross-section compatible with two-in-one quadrupole magnets and inexpensive compact dipole magnets [1,2]. Pumping will be provided by a combination of non-evaporable getter (NEG) and ion pumps. Calculations were carried out of the impedance and loss factor of the chamber as well as transmission of RF field power through the slots and the conductance of the pumping slots. We have also calculated the linear synchrotron radiation power density and the pressure profile and beam-gas life time for this chamber and pump configuration. We consider the time between necessary NEG pump reactivations and the total capacity of the pumps.

## 1 INTRODUCTION

The vacuum system for a very high luminosity  $e^+e^-$  collider must be capable of handling a large synchrotron radiation heat load, maintaining a low pressure, and must be very smooth to keep the coupling impedance at a level where the beam remains stable. We present a conceptual design of a vacuum system for a high luminosity CESR upgrade using two-in-one quadrupole magnets. The goal of this upgrade is to achieve a luminosity of  $3 \times 10^{34} \text{ cm}^{-2} \text{ s}^{-1}$  through a combination of a high beam current (3.06 A/beam), low  $\beta_y$  at the interaction point (7 mm), and a correspondingly short bunch length. To store the necessary number of bunches, independent vacuum chambers are needed for the two beams. To minimize the size and cost of the storage rings, the dipole magnets are shared between the two rings, and two-in-one quadrupole, sextupole, and steering magnets are used [1,2].

\*Work supported by the National Science Foundation.

<sup>†</sup>Email: kwo1@cornell.edu.

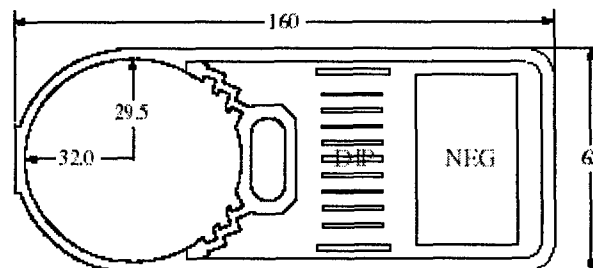


Figure 1: Cross section of the proposed vacuum system design. All dimensions are in millimeters.

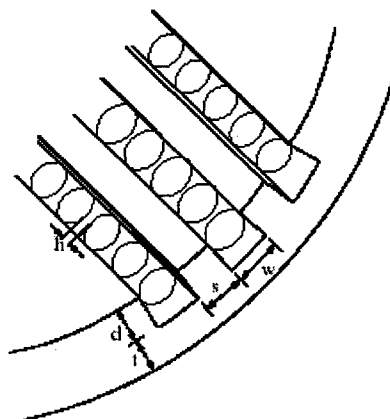


Figure 2: Detail of recessed slots in proposed chamber design.

## 2 CHAMBER DESIGN

The chamber design for the upgrade consists of a copper beam chamber of elliptical cross-section connected to a pumping chamber through holes recessed in long channels in the chamber walls. Figures 1 and 2 show the proposed vacuum system geometry. The parameters we arrived at for our chamber design are shown in Table 1.

Table 1: Vacuum chamber parameters(Refer to Fig. 2)

Parameter		Value
Channel width	$w$	3.5 mm
Channel depth	$d$	2.5 mm
Channel spacing	$s$	2 mm
Number of channels		6

Hole radius	$a$	1.75 mm
Hole depth	$t$	2.5 mm
Hole spacing	$h$	1 mm
Total pumping holes per ring	$N_h$	$10^6$

### 2.1 Impedance

The inductive part of the impedance of a single hole in a vacuum chamber is given by [3]

$$\text{Im } Z(\omega) = -\frac{Z_0 \omega \tilde{e}_v^2}{2c} (\psi - \chi), \quad (1)$$

where  $Z_0 = 120\pi \Omega$  is the impedance of free space,  $\tilde{e}_v$  is the normalized electrostatic field produced at the hole location by a line charge on the chamber axis, and  $\chi$  and  $\psi$  are the electric and magnetic polarizabilities of the hole. For a circular beam pipe of radius  $b$ , the normalized electric field  $\tilde{e}_v = 1/(2\pi b)$ . The real part of the impedance is given by

$$\text{Re } Z(\omega) = \frac{Z_0 \omega^4 \tilde{e}_v^2}{12\pi c^4} (\psi^2 + \chi^2). \quad (2)$$

The power per unit length of the beam chamber dissipated due to beam fields scattered by the holes is

$$P' = \frac{N_h f_{rev} q_b^2}{S_b} K \quad (3)$$

Where  $N_h$  is the total number of holes,  $S_b$  is the bunch spacing,  $f_{rev}$  is the revolution frequency and  $q_b$  is the bunch charge. The loss factor per hole,  $K$ , is given by

$$K = \frac{1}{\pi} \int_0^{\tilde{\sigma}} d\omega \text{Re } Z(\omega) \exp\left[-\left(\frac{\omega\sigma}{c}\right)^2\right], \quad (4)$$

where  $\sigma$  is the bunch length.

If the pumping holes are recessed in channels on the walls of the chamber, the normalized field,  $\tilde{e}_v$ , can be reduced by a large factor and thus the impedance would also be reduced [4]. For the current design parameters, the normalized electric field was calculated using POISSON [5]. The electric field at the recessed holes is a factor of 7.5 less than at the wall of the chamber. This gives a factor of 56 reduction in the impedance of the holes.

For the current ring design with recessed holes the loss factor per hole for 7 mm bunches is  $K = 4.6 \times 10^{-9} \text{ V pC}^{-1}$  which corresponds to a power loss of  $P' = 0.68 \text{ W m}^{-1}$ . The total inductive impedance  $\text{Im}(Z/n)$  from  $10^6$  recessed holes is  $-2.7 \times 10^{-3} \Omega$ , which is a negligible fraction of the expected total impedance of the storage ring.

### 2.2 RF Fields

One of the main reasons for using recessed holes rather than just a few long slots in the chamber is to prevent direct transmission of TE fields generated by the beam into the pumps. The direct beam fields are produced by scattered fields from the holes as calculated above for the loss factor. The power that is directly transmitted to the pumping chamber can be calculated similarly with the inclusion of a factor depending on the cutoff frequency of the holes. The power per unit length transmitted is given by

$$P' = \frac{N_h f_{rev} q_b^2}{S_b} K_r \quad (5)$$

as above in Eq. 3, but where  $K_r$  includes factors for the cutoff frequency and depth of the holes. For bunch lengths longer than the hole diameter, a long wavelength approximation can be used,

$$K_r = \exp\left(-\frac{2t\omega_c}{c}\right) K, \quad (6)$$

where  $\omega_c$  is the cutoff frequency of the pumping holes,  $t$  is the depth of the holes, and  $K$  is the loss factor from before. For the parameters given earlier with 7 mm bunches, the power radiated through the holes is  $P' = 0.78 \text{ mW m}^{-1}$ .

### 2.3 Conductance

The size of the holes was limited primarily by the loss factor and RF fields. We calculated the conductance of the holes to determine how many rows of holes would be needed for adequate pumping speed. The conductance of the channels with recessed holes was calculated using MOLFLOW [6]. For the current design parameters the conductance was calculated to be  $135 \text{ l s}^{-1} \text{ m}^{-1}$  per channel or  $810 \text{ l s}^{-1} \text{ m}^{-1}$  for six channels.

## 3 PUMP DESIGN

The vacuum pumps for the upgrade need to maintain a low chamber pressure when pumping the large gas load due to the increased current in the ring while also being as compact as possible keeping with the compactness of the rest of the design. We settled on a design where the primary pumping will come from distributed non-evaporable getter (NEG) pumps with distributed and lumped ion pumps to supplement for non-getterable gases.

For the NEG pumps, we plan to use standard St707 getter wafer modules from SAES Getters, Inc. These should provide us with the necessary pumping speed in a compact volume. Based on our calculations of the expected gas load, they should need to be reactivated about once a week through heating of the getter strip.

For the distributed ion (DIP) pumps, we plan on using a plate type pump with only a single row of cells. Table 2 lists parameters for a possible ion pump design. Based on empirical ion pump design formulae [7], we expect a pumping speed of around  $85 \text{ l s}^{-1} \text{ m}^{-1}$  for our design which should provide us with more than adequate pumping for methane and other non-getterable gases.

Table 2:DIP parameters.

Parameter	Value
Magnetic field strength	2.0 kG
Anode voltage	5000 V
Cell diameter	15 mm
Cell height	39 mm
Anode-cathode gap distance	5.5 mm

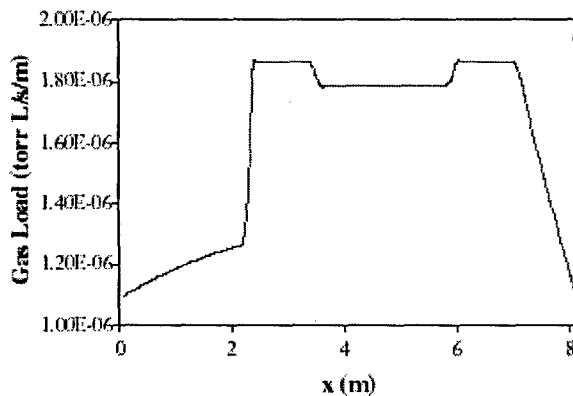


Figure 3: Gas load profile in a half cell of the storage ring arcs.

Figures 3 and 4 show the gas load and pressure profiles in a single half-cell in the storage ring arcs. The regions from 0 to 3.45 m and 3.55 to 7 m are within or near the dipole magnets and contain pumping holes and distributed pumps. The region between 7 and 8.1 m is within or near the quadrupole, sextupole, and steering magnets and does not contain pumping holes. This region is pumped by conduction through the beam pipe. The conductance through the beam pipe is  $32.8 \text{ l s}^{-1} \text{ m}^{-1}$ . A single  $100 \text{ l s}^{-1}$  lumped sputter ion pump at 7.1 m is used to maintain high vacuum when the dipole magnets are turned off. The pressure profile was calculated using a program based on a finite element method [8]. Our program includes in the calculation the conductance of the beampipe and pumping holes as well as allowing for different pumping speeds for NEG and ion pumps and the presence of non-getterable gases. For these calculations we used a DIP pump speed of  $85 \text{ l s}^{-1} \text{ m}^{-1}$  and a NEG pump speed of  $1000 \text{ l s}^{-1} \text{ m}^{-1}$  was assumed. The photodesorption coefficients used for our calculations are listed in Table 3 [9]. Also listed in Table 3 are the

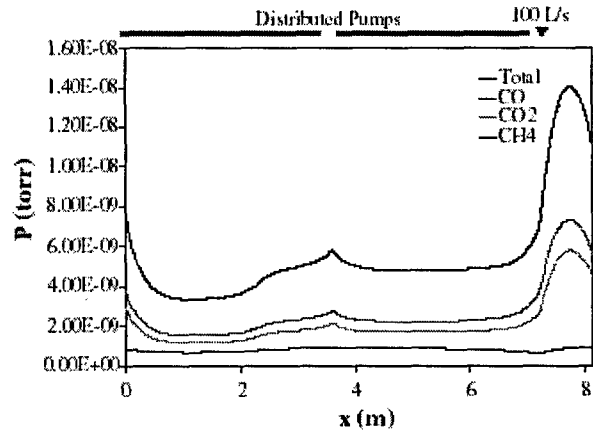


Figure 4: Pressure profile in a half cell of the storage ring arcs.

Table 3: Photodesorption coefficients, partial pressures, and beam-gas lifetimes for different gas species.

Gas	Photodesorption Coefficient (mol./photon)	Average Pressure (nTorr)	Beam-Gas Lifetime (hours)
CO	$1.5 \times 10^{-6}$	2.7	11.3
CO <sub>2</sub>	$1.0 \times 10^{-6}$	2.1	9.1
CH <sub>4</sub>	$1.0 \times 10^{-7}$	0.8	82
Total		5.6	4.7

results of our calculations for the average pressures and beam-gas lifetimes for the primary gas species we expect. A large pressure bump exists within the unpumped region, but the average total pressure is 5.6 nTorr giving a beam-gas lifetime of 4.7 hours.

## 4 CONCLUSION & FUTURE PLANS

We have developed a conceptual design of a vacuum system that meets our needs for compactness, low impedance, and low pressure. We are currently in the process of constructing prototype pumps for testing in the near future.

## 5 REFERENCES

- [1] A. Mikhailichenko and D. Rubin, Proc. of the 5th European Particle Accelerator Conference (EPAC96), Sitges, Spain (1996) 433.
- [2] D. Rubin, G. Dugan, A. Mikhailichenko, J. Rogers, Proc. of the 1997 Particle Accelerator Conference (PAC97), Vancouver, BC, Canada (1997) 318.
- [3] S.S. Kurennoy and Y.H. Chin, Part. Accel. **52**, 201 (1996).
- [4] T. Weiland, Part. Accel. **51**, 53 (1995).
- [5] Los Alamos Accelerator Code Group, "The POISSON/SUPERFISH Group of Codes", LANL report LA-UR-87-115 (1987).
- [6] R. Kersevan, "MOLFLOW User's Guide", Sincrotrone Trieste Technical Report, ST/M-91/17 (1991).
- [7] Y. Suetsugu and M. Nakagawa, Vacuum **42**, 761 (1991).
- [8] Y. Li, Cornell LNS Report CBN 97-7 (1997).
- [9] C.L. Foerster, et. al., BNL report BNL-48367, 1992.



# BEAM-GAS LIFETIME IN A LOW EMITTANCE, MEDIUM-ENERGY STORAGE RING\*

S. M. Chung, C. D. Park, S. H. Gu, and M. Kwon

Pohang Accelerator Laboratory, Pohang University of Science and Technology,

Pohang, Kyungbuk 790-784, Korea

## Abstract

In order to understand the beam-lifetime limiting process in a medium-energy machine like the 2 GeV Pohang Light Source, the beam-gas scattering effects have been measured by using helium gas and the effects of the transverse aperture height on the lifetime have also been examined by using a beam scraper. It is found that for a medium to large gap vacuum chamber the lifetime is mainly limited by Touschek effect at the machine operating pressure, low  $10^{-9}$  Torr. For a very small gap undulator, however, the beam-gas scattering makes substantial contribution to the beam lifetime even at  $\sim 1 \times 10^{-9}$  Torr because of Coulomb scattering.

## 1 INTRODUCTION

The Pohang Light Source (PLS) of the Pohang Accelerator Laboratory is a low emittance third generation synchrotron radiation source with a nominal electron beam energy of 2 GeV. The storage ring vacuum system of the PLS has been designed to maintain the average pressure of 1 nTorr over the 280 m circumference with a circulating current of 400 mA to enable beam lifetimes longer than 10 hours.

The performance of the vacuum system is measured primarily in terms of beam lifetime, and achieving a long lifetime is a key issue for the third generation light sources. In PLS, the lifetime of 100-mA beam in the early stage of the commissioning was less than 50 minutes due to a poor vacuum. However, gradual decrease in pressure due to synchrotron radiation cleaning of the vacuum chamber resulted in continuous improvement in lifetime. To date a total beam dose of 1600 Ampere-hour has been accumulated and beam lifetimes in excess of 20 hours with 170 mA of stored beam are regularly obtained.

As in the case of high-energy machines, probably scattering of beam electrons on residual gas molecules is the most important physical process determining the beam lifetime.[1] Furthermore, the narrow gap undulators foreseen in the straight sections make the machine particularly sensitive to beam-gas scattering.

However, due to the intrinsic small emittance coupling ( $< 1\%$ ), the lifetime may also be limited by pressure independent intra-beam scattering (Touschek effect)[2], which is proportional to the electron density in the bunch. Moreover, increasing the electron density to increase

beam current results in enhancing the intra-beam scattering rate and reducing Touschek lifetime. After all, unlike low or high energy machines, the lifetime limiting factor which will prevail in a medium energy machine like the 2 GeV PLS depends on the competition between the intra-beam and beam-gas scattering. The question of which of the two scattering effects dominates the lifetime in the specific pressure then remains open.

In order to help resolve these difficulties, the beam-gas lifetimes were measured by using helium in the pressure range from  $\sim 5 \times 10^{-9}$  to  $\sim 3 \times 10^{-7}$  Torr. The effect of the accommodation of a small-gap undulator on the lifetime was also examined. The implications of the results of the lifetime measurements will be discussed in terms of the lifetime limiting process in PLS storage ring.

## 2 EXPERIMENTS

Inert gas helium was used for the present work to control the chamber pressure. By introducing helium gas into the storage ring with sputter ion pumps (SIPs) switched off, we can make the pressure uniform all over the circumference, whereas other active gases are continuously pumped by non-evaporable getters. Then the beam-gas lifetime can be easily measured and calculated using the uniform and monitored pressure with average beta function.

Besides its vacuum characteristics, the light mass of helium makes sure that helium gas is cleared by the long bunch gap. And the beam-gas scattering effect for helium is close to that for the residual gas at the operating pressures of a storage ring. Note that the ratio of the total scattering cross section or the beam lifetime for helium, to that for the residual gas measured during the machine operation (90%  $H_2$ , 2%  $CH_4$ , 1%  $H_2O$ , 6%  $CO$  and 1%  $CO_2$ ) is  $\sim 2.2$ . Therefore we can simulate the beam-gas lifetime as close as the real situation.

The beam lifetimes were measured with/without a medium-gap undulator. The base pressure was  $\sim 5 \times 10^{-10}$  Torr without beam and was  $\sim (1-4) \times 10^{-9}$  Torr during measurements, depending on the beam current and also on the SIPs on and/or off. The electron beam was stored to a value, which is lower than the threshold current of the strong collective instabilities induced by the high order mode of the RF cavities. Helium gas was admitted step by step into the storage ring with increasing pressures and the helium pressure was stabilised in few minutes. Finally, the

beam-gas lifetimes for the small gap undulators were simulated using a beam scraper. Since insertion devices for the third generation light sources generally varies with the vertical gap, we measured the lifetime with a vertical-beam scraper only.

### 3 RESULTS AND DISCUSSION

The measured beam lifetimes,  $\tau_{He}$  (Fig. 1(●)), for the PLS storage ring having a medium gap undulator is shown in Fig. 1. The corresponding acceptance limiting half-aperture is 6 mm (vertical). The calculated beam-gas (Fig. 1(Δ)), Touschek (Fig. 1(+)) and total lifetimes (Fig. 1, solid line) are also shown for comparison. It is clear from the figure that the measured lifetime for helium depends linearly on the pressure at high helium pressures,  $\geq 1 \times 10^{-7}$  Torr (Fig. 1(c)), indicating that the beam-gas scattering effect dominates the total lifetime.

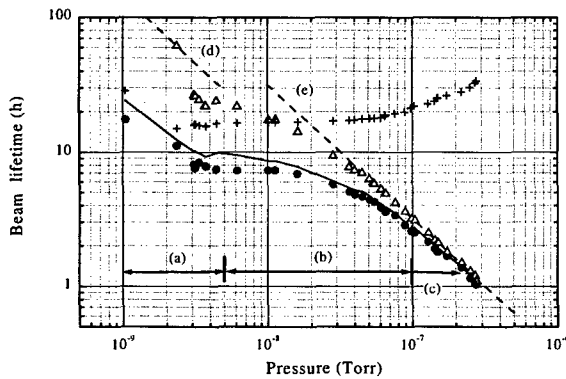


Figure 1: Measured (●) and calculated lifetimes. The initial stored current was 167 mA in 250 bunches.

In the helium pressure range from  $\sim 5 \times 10^{-9}$  to  $\sim 1 \times 10^{-7}$  Torr (Fig. 1(b)), it can be stated that the beam-gas scattering effect competes with Touschek effect. At a point in this pressure range, both effects make equal contribution to the total lifetime for the Touschek lifetime changes greatly according to the number of electrons per bunch and the machine coupling while the beam-gas lifetime is constant at a given pressure.

Below the pressure of  $\sim 5 \times 10^{-9}$  Torr (Fig. 1(a)), we could not measure the lifetime with helium. As the SIPs were switched off, the pressure went up to  $\sim 3.5 \times 10^{-9}$  Torr. And the lifetime was reduced immediately by  $\sim 25\%$  according to the pressure change. The result directly reflects the importance of the beam-gas scattering effect in the low  $10^{-9}$  Torr range. Nevertheless, we can find from the figure that Touschek effect mainly limits the lifetime in low  $10^{-9}$  Torr.

In the meantime, the measured lifetimes in the high-pressure ranges ( $\geq 5 \times 10^{-8}$  Torr) where the helium content was at least  $\geq 97\%$  closely followed the predicted values, meaning that a good knowledge of the machine

parameters had been made. With the agreement of the measured and calculated beam lifetimes for helium, the beam-gas lifetimes were studied analytically based on the equations and the residual gas described in section 2.

The calculations show that with large transverse apertures, Bremsstrahlung ( $\tau_b \approx 409$  [nTorr·hr]) is dominant beam-gas interaction for the PLS as in most other machines. As the vertical gap is decreased, the Coulomb scattering becomes important. Both the Coulomb and Bremsstrahlung lifetime are comparable at a gap half-height of 8–9 mm. With a medium gap undulator (6 mm), the beam-gas lifetime ( $\tau_{gas}$ ) for the PLS storage ring is  $P \cdot \tau \approx 145$  [nTorr·hr] (Fig. 1(d)). In this regard, if we directly compare  $\tau_{gas}$  with  $\tau_{He}$  (Fig. 1(e)), the pressure at which the beam-gas scattering effect dominates may corresponds to  $\sim 5 \times 10^{-8}$  Torr. And from  $\sim 5 \times 10^{-9}$  Torr to  $\sim 5 \times 10^{-8}$  Torr, both effect may competes and finally Touschek effect dominates the lifetime below middle  $10^{-9}$  Torr.

On the other hand, for a very small gap undulator to be installed in straight sections, the Coulomb scattering effect will be significant. Since undulators become narrower and narrower, the beam lifetimes were examined with a vertical-beam scraper to see the beam-gas scattering effect in low  $10^{-9}$  Torr in detail. Figure 2 gives the beam-gas lifetimes measured as a function of the vertical aperture height at two different operating pressures of  $5 \times 10^{-10}$  Torr and  $1 \times 10^{-9}$  Torr. The beam current of  $\sim 5$  mA was stored in 350 bunches to minimise Touschek effect. The calculated beam lifetimes using the measured residual gas and the machine parameters are also shown in Fig. 2. Discrepancies between the measure and calculated lifetimes reflect the non-uniform pressure distributions, which makes it difficult to fit the measured data to calculated ones.

It can be found that the contribution of the beam-gas scattering effect to the total lifetime is small for a medium gap undulator, 5–6 mm. (Note that the Touschek lifetime ( $\tau_c$ ) ranges from a few hours to  $\sim 30$  hours). However, for the aperture half-height of, around 3–4 mm the beam-gas scattering may compete with the Touschek effect even at low  $10^{-9}$  Torr because of Coulomb scattering which varies with the transverse aperture size while Bremsstrahlung keeps constant at a given pressure. The lifetime can be further reduced due to small vertical gap of the insertion devices since the  $\tau_c$  depends indirectly on the transverse aperture because of the reduced momentum aperture of the storage ring. Thus the beam-gas scattering effect for a very small gap undulator will be critical factor to make decisions to keep the best machine performance. The measurement also shows that the beam-gas lifetime of the 2-GeV PLS storage ring will be within the shaded area in Fig. 2, depending on the pressure and the vertical gap of the insertion devices.

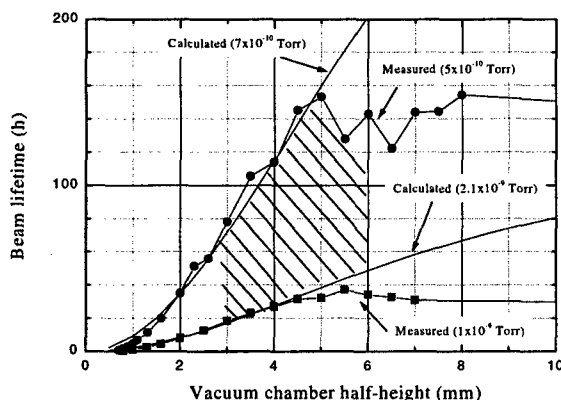


Figure 3. Measured beam-gas lifetimes using a vertical scraper. The solid lines are fitted to the measured data by varying pressure.

In order to compensate for the degradation in the machine performance because of small vertical gap, various methods have been studied in many storage rings regardless of their energy. For example, the longer beam lifetime can be achieved by increasing the momentum acceptance of the storage ring, by manipulating bunch dimensions, by minimising beta function in the insertion straight region, and by using the so-called "In-Vacuum Undulator". [4-5]

A simple method to increase the lifetime is to decrease Touschek effect by reducing the current density in bunches. But in general the brightness must be compromised with the lifetime. Increasing the beam energy to an available amount can be a possible way to increase the beam lifetime without degradation of beam quality. For example, about 30% increment in beam lifetime with 2.4 GeV already achieved for the PLS (Note that Coulomb and Touschek lifetimes are proportional to  $E^2$  and  $E^3$ , respectively). However we may lose the low energy photons to some extent.

From the vacuum point of view, the lower pressure can compensate for the reduction in lifetime. As high as ~50% increment in lifetime can be achieved by reducing the pressure from  $\sim 2 \times 10^{-9}$  down to low  $10^{-10}$  Torr as shown in Fig. 3. Since the insertion devices being installed in the straight sections may occupy  $1/4 \sim 1/5$  of the circumference of the ring, the pressure reduction can be done in part by reducing the pressure inside the insertion device vacuum chambers.

In summary, we measured the beam-gas lifetime using helium gas and the vertical scraper in order to understand the beam-lifetime limiting process in a medium energy machine like the 2 GeV PLS. It is found that for a medium to large gap vacuum chamber, the beam-gas scattering determines the beam lifetime at high pressures,  $> 5 \times 10^{-8}$  Torr. And the pressure independent Touschek effect

mainly limits the lifetime and the contribution of the beam-gas lifetime to the total lifetime is small at the machine operation pressure of low  $10^{-9}$  Torr. However, for a very narrow-gap undulator, Coulomb scattering may compete with the Touschek effect even at  $\sim 1 \times 10^{-9}$  Torr indicating that the vacuum is still an important factor that determines the lifetime in a medium-energy, third generation light source.

## 4 REFERENCES

\* Work supported by MOST and POSCO fund.

- [1] J. Le Duff, Nucl. Instr. And Meth. A239, 83 (1985)
- [2] Y. Miyahara and H. Nishimura, IEEE Trans. Nucl. Sci. NS-32, 3821 (1985).
- [3] W. Decking, et al, Presented at the Sixth European Particle Accelerator conference EPAC98, Stockholm, 1998.
- [4] C. J. Bocchetta, et al, Presented at the Particle Accelerator conference PAC97, Vancouver, 1997.
- [5] Annick Ropert, Presented at the Sixth European Particle Accelerator conference EPAC98, Stockholm, 1998.

# LAYOUT OF THE ABSORBERS FOR THE SYNCHROTRON LIGHT SOURCE ANKA

S.Hermle, D.Einfeld, E.Huttel

Forschungszentrum Karlsruhe, ANKA, P.O. 3640, 76021 Karlsruhe, Germany  
G. Heidenreich, Paul Scherrer Institut, 5232 Villigen, Switzerland

## Abstract

The 2.5 GeV Synchrotron Light Source ANKA is now under construction at the Research Center in Karlsruhe. For a designed current of 400 mA, a power of 250 kW is radiated by the circulating e-beam in the 16 dipole magnets. 90% of the synchrotron radiation (SR) is absorbed by the 32 crotch absorbers in the dipole and the adjacent ante chamber, the remaining 10 % by distributed absorbers in the straight chambers. The power per length is up to 50 W/mm for the crotch and 2 W/mm for the distributed absorbers. A special design was needed for the crotch absorbers due to the limited space. The final design is optimized for reduced thermal stress in order to increase the number of maximum possible cycles. The temperature distribution and the stresses were calculated with the finite element program ANSYS[1]. The maximum temperature is 270 °C, the maximum strain 0.13%. The achieved strain will be small enough in order to sustain more than  $10^4$  cycles, the expected lifetime of the absorbers. The SR entering the beam lines (15 mrad) will be absorbed either by one moveable absorber before the first valve or by the movable radiation protection shutter close to the shielding wall. The power per length is 13 W/mm, respectively 7 W/mm.

## 1 INTRODUCTION

The total power radiated by a Synchrotron Radiation

Source from the bending magnets is given by [2]:

$$P[\text{kW}] = 88.6 E[\text{GeV}]^4 I[\text{A}] / r[\text{m}]$$

For the design parameter of ANKA : E: 2.5 GeV, I: 0.4 A and r: 5.559 m the radiated power is:  $P = 250 \text{ kW}$ .

The vertical power distribution has a FWHM of 0.7 mm at a distance of 1 m from the source point [3].

In Fig.1 the absorbers of the dipole vacuum chambers and the adjacent sextupole section are shown. The maximum power loads and temperatures of the different absorbers are summarised in Table 1.

90% of the synchrotron radiation will be absorbed by crotch absorbers ((1) in Fig.1) in the ante chambers of the dipole and the adjacent quadrupole / sextupole chamber. The first crotch absorber covers the radiation from  $0^\circ$  to  $11^\circ$  of a dipole, corresponding to a heat load of 8 kW, the second crotch absorber the radiation up to  $21^\circ$ . The power per length at the crotch absorbers increases from 20 close to the flange to 50 W/mm at the top due to the different distance from the source point.

10 % of the synchrotron power will be absorbed by distributed absorbers ((2,3) in Fig.1) which are part of the outer side of the vacuum chamber in the straight vacuum chambers. The inner side of the distributed absorber of the first vacuum chamber behind the dipole ((2) in Fig.1) has a copper plating in order to distribute the higher heat

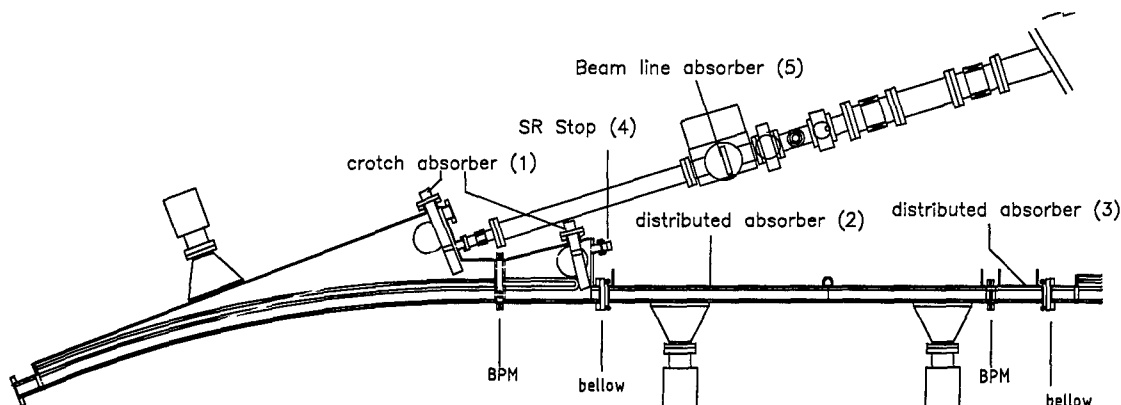


Figure 1: Distribution and lay out of the absorbers at the Synchrotron Radiation Source ANKA.

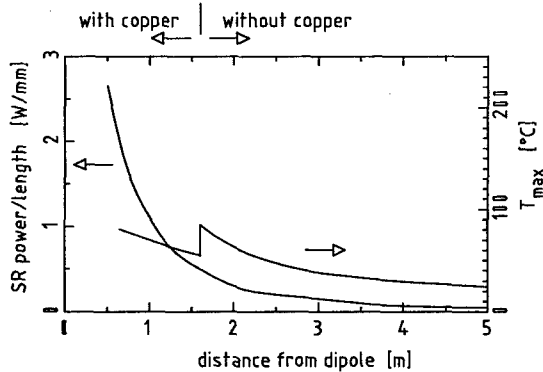


Figure 2: Power and temperature distribution of the distributed absorbers.

load. The power per length decreases as a function of the distance from the source point from 2 W/mm for the copper plated and 0.4 W/mm for the stainless steel type. The power and temperature distribution is given in Fig. 2.

The SR entering the beam lines (15 mrad) will be absorbed either by a moveable absorber ((5) in Fig.1) before the first valve or by the movable radiation protection shutter close to the shielding wall. The power density is 13 W/mm, respectively 7 W/mm. Parts of the SR exit ports where a front end is not installed are equipped with a cooled end flange ((4) in Fig.1). It's power per length is 44 W/mm.

## 2 THE CROTCH ABSORBERS

In Fig. 4 the design of the lumped absorber is shown. Due to the inner height of the vacuum chamber of 32 mm the vertical size of the absorber is limited to 31 mm. Cooling is done by four 9 mm pin holes with a 6 x 0.5 mm tube for the incoming water. A wire is wound around the inner tube in order to enhance the heat transfer. A thermal conductivity of 380 W/Km for copper and a heat transfer coefficient of 12 kW/Km<sup>2</sup> for 3 m/s water velocity was used for the calculations. The temperature distribution for the highest load are also given in Fig. 4. The maximum temperature is 270°C. The highest temperature at the cooling canal is 120°C. The temperature of the water

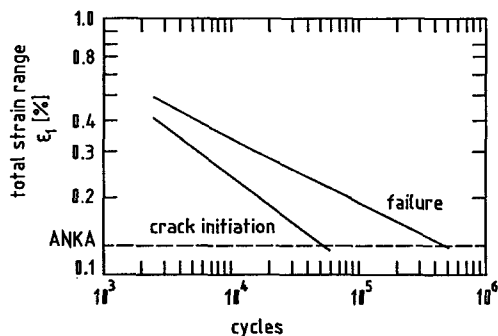


Figure 3: Fatigue behavior of OFHC copper as a function of strain and cycles.

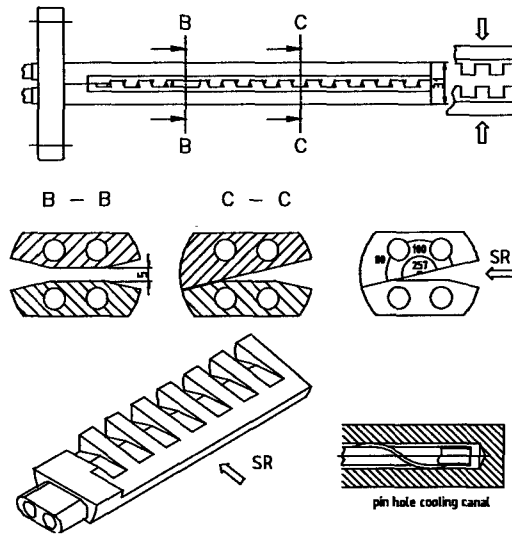


Figure 4: Final design of the crotch absorber.

should be kept below boiling point. But since the inlet water is pressurised (about 3 bar at the top of the absorber) the boiling temperature is above 100 °C (10°C per bar).

Parts at higher temperature ( $T_m$ ) tend to expand by a strain  $\epsilon = \alpha (T_m - T_b)$  which is hindered by the bulk of the material which is at the lower bulk temperature ( $T_b$ ).  $\alpha$  is the thermal expansion coefficient (For copper  $\alpha = 1.7 \cdot 10^{-5}$  1/K.)

The cyclic temperature changes and the corresponding strains lead to fatigue of the material which can lead to failure. Fig. 3 shows the failure of OFHC copper as a function of the cycles and strain [4]. Since more than 10 000 cycles should be guaranteed the strain should be less than 0.2 %.

In order to reduce the strain, the absorber is split into two halves with a comb like structure each with two cooling canals. The comb structure of the upper and the lower part fit together with 0.1 mm separation. Due to an angle between the synchrotron radiation and the normal of the absorber no radiation can pass the absorber. Since the synchrotron radiation now hits alternating small sections of the upper or lower part of the absorber which are slightly separated, the hot sections can expand slightly and thus the maximum stress is reduced from 0.27 to 0.13 %.

## 3 DISTRIBUTED ABSORBER

The cross sections of the straight vacuum chamber are shown in Fig. 5. The synchrotron radiation hits the vacuum chamber which is water cooled from the outside. But since the vacuum chamber is generally built from stainless steel having a low thermal conductivity of 16 W/Km the wall temperature would become too high close to the dipole magnet. Thus the inner side of the vacuum chamber of the section which is close to the magnet is plated by 3 mm copper, which will distribute the heat load before it is transferred through 1 mm stainless steel to the

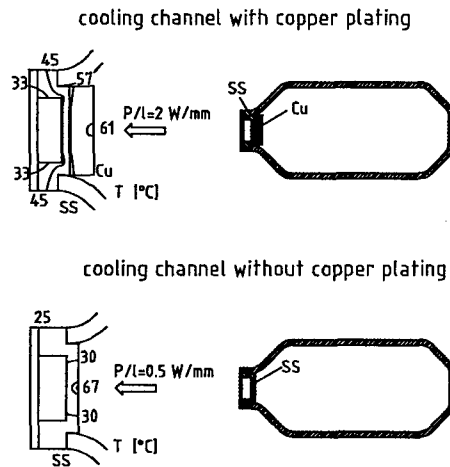


Figure 5: Distributed absorber and their temperature distribution.

cooling water. Fig.5 also shows maximum temperature profiles for both types of distributed absorbers. The copper plating of the stainless steel was done by explosion bonding. Each copper stainless steel compound was controlled with ultra sonic for proper bonding. Compounds with improper bonding areas larger than 0.5 mm have been excluded.

#### 4 FRONT END ABSORBER

Each synchrotron beam line is equipped with an all metal gate valve and a moveable absorber in front of it in order to protect the closed valve. Since this absorber has a distance of 2.5 m from the source point the power density is smaller compared to the absorbers in the dipole. Thus a copper plate with a copper tube brazed in it is sufficient as an absorber. The design is shown in Fig.6 together with the temperature distribution.

Parts of the SR beam ports which are not yet equipped with a front end are closed with a cooled end flange. This consists of conical block made of OFHC

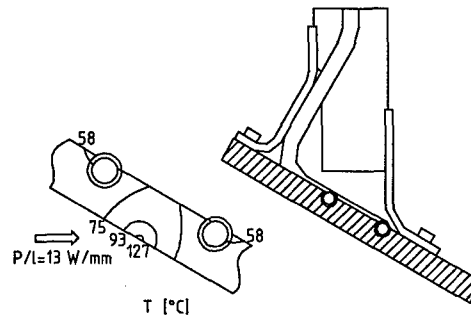


Figure 6: Absorber in the Frontends.

copper with a spiral cooling canal on it. The design and the temperature distribution are shown in Fig. 7.

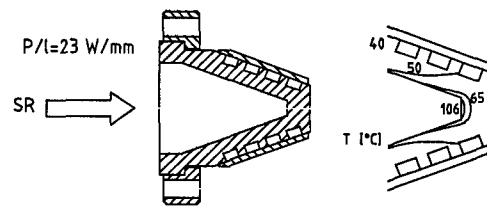


Figure 7: Design and temperature distribution of the cooled end flange.

#### 5 REFERENCES

- [1] ANSYS, Swanson Analysis Systems, Inc.
- [2] H.Wiedemann: Particle Accelerator Physics I, Springer Verlag.
- [3] H.Wiedemann: Particle Accelerator Physics II, Springer Verlag.
- [4] K.C.Liu and C.M.Loring, Jour.Nucl.Mat.122(1984)783

**Table 1:** Power and Temperature of the different absorbers, dps refers to a dipole followed by a sextupole section, dqs for a dipole followed by a quadrupole doublet.

absorber	Angle [°]	D source [m]	P [kW]	P/l [W/mm]	P/a [W/mm <sup>2</sup> ]	v <sub>water</sub> [m/s]	Flow <sub>w</sub> [l/min]	T <sub>max</sub> [°C]	T <sub>bulk</sub> [°C]
1 crotch dps	10.5	2.1 - 1.1	7.5	20 - 40	7 - 24	3	16	190	80
2 crotch dps	10	1.7 - 0.8	6.5	25 - 50	10 - 50	3	16	270	120
Distr. copper	1.6	0.9 - 2.8	1.3	2 - 0.2	7 - 0.2	2	3	60	40
1. crotch dpq	11.5	2.1 - 0.9	8.5	20 - 40	7 - 32	3	16	220	100
2. crotch dpq	8.5	1.7 - 0.9	5.9	23 - 40	9 - 32	3	16	220	100
Distr. copper	0.7	1.1 - 1.8	.6	1.5 - 0.5	4 - 0.9	2	3	60	40
Distr. steel	1	1.8 - 8	.6	0.4	0.8 - 0.01	2	3	70	40
Front end 1	1	3	.8	13	10	2	3	130	70
Front end 2	1	6	.8	7	4	2	3	110	50
flange	1	1.7	.8	23	44	2	3	170	80

# OVERVIEW OF THE SPEAR3 VACUUM SYSTEM\*

N. R. Kurita, R. M. Boyce, E. F. Daly, B. D. Scott, T. A. Trautwein

Stanford Synchrotron Radiation Laboratory, Stanford University, Stanford, CA 94309 USA

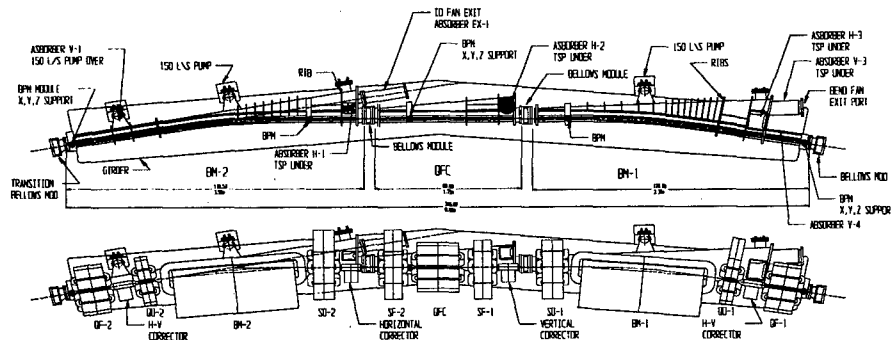


Figure 1: Standard Girder Layout

## Abstract

The conceptual design of the vacuum system for the upgrade project of SPEAR3 is reviewed. The majority of the vacuum system components, except for insertion devices, will be replaced with components capable of 500 mA operation at 3 GeV. General requirements and overall layout of the vacuum system are discussed. Diagnostic chambers and speciality components are briefly discussed.

## 1 INTRODUCTION

SPEAR3 is a 3 GeV and 500 mA synchrotron light source. The magnet lattice was modified to an 18 nm-rad double-bend achromat (DBA)[1]. The SPEAR3 ring is a racetrack oval 243m in circumference, consisting of two arcs and two 6m long straights. Each arc contains two 11m matching girder chambers adjacent to the long straights and seven 9m standard magnet girders joined by six 3m straight sections. New vacuum chambers will be constructed except for the Insertion Device (ID) chambers. The standard girder layout is shown in figure 1.

## 2 GENERAL REQUIREMENTS

SPEAR3 incorporates an antechamber design with discrete pumping and crotch absorbers. The vacuum chambers are designed to reach 500 mA at 3GeV and initial operation goals for FY 2002 is to achieve 200 mA. To reach 500 mA, ID chambers and beamline front ends will need to be upgraded. The desired lifetime during 500 mA operation is 40 hours.

The beam-stay-clear (BSC) envelope is defined for the entire vacuum system, excluding insertion devices, by the largest beam aperture in the ring. This occurs at the injection area and is modeled as an ellipse 30 mm high by 80 mm wide.[2] The interlock system trip level for high current operation will be set at  $\pm 1$ mm and a vertical emittance near 50 nm<sup>2</sup>/rad. The trip level for the horizontal closed orbit shifts is set at  $\pm 5$ mm. The interlock trip levels ensure that a mis-steered beam would not result in synchrotron radiation striking the vacuum chamber above or below the slot. The trip levels accommodate

alignment and manufacturing tolerances of the vacuum chambers and the magnets, as well as, deflection of the chambers and BPM accuracy. [2] The orbit shifts used for the design of the chamber are,

- Horizontal:  $\pm 10$  mm with 1.34 mrad angular offset,
- Vertical:  $\pm 6$  mm with 0.8 mrad angular offset.

### 2.1 Steady State and Transient Thermal Loads

During normal operation, the thermal loads due to resistive wall losses in SS are estimated to be 0.005 W/cm<sup>2</sup> and create less than a 10°C rise in the chamber. HOM losses are negligible. Axial cooling tubes with minimal flow removes this small amount of power.

During off-axis operation, the largest source of thermal loading is from ID SR impinging on the chamber walls, with a heat flux of  $\sim 140$  W/mm<sup>2</sup> from beamline 6. The secondary source is SR emitted from the dipoles, approximately 20% of the maximum ID power. No practical amount of water cooling close to the strike can protect the chamber. At full power, the time-to-melt for Cu (MP = 1085°C) exceeds 500 ms and the time-to-melt for SS (MP = 1397°C) is less than 100 ms.

### 2.2 Masks and Absorbers

The primary function of the discrete masks and absorbers is to shadow the chamber from dipole radiation. A distinction is made between absorbers and masks; absorbers are located in crotch areas between exit beamlines, masks are not.

Mask or Absorber	Ave. Fan Ht (mm)	Power (kW)	Heat Flux (W/mm <sup>2</sup> )
Mask V-1	1.56	0.42	5.7
Mask V-2	2.42	0.53	2.4
Absorber H-1	0.48	4.76	21.5
Absorber H-2	0.94	3.92	5.5
Mask V-3	1.95	0.56	3.7
Absorber H-3	0.56	8.11	15.4
Mask V-4	0.43	1.95	19.3

Table 1: Absorber & Mask Heat Fluxes

\* Work supported by the U.S. Department of Energy under contract number DE-AC03-768F00515

Three of the four masks are located along the outside of the chamber to intercept SR power. The total power incident on these three is only 500W. The surface that intercepts the power is a sheath of GlidCop™ brazed to a Cu cooling tube. The planar face on the sheath is oriented vertically and sloped at 30° to grazing.

The fourth mask, V-4, located behind absorber H-3, protects the downstream bellows module and chamber wall. The lineal heat flux on this GlidCop™ 7.5°-to-grazing surface is 83 W/cm.

The absorbers have crenulated surfaces that spreads out the intercepted power and are sloped at 10°-to-grazing relative to the horizontal plane. Water cooling is provided on the backside of the incident surface.

The exit aperture from the ring for all ID beamlines is 18 mrad. Three of the ID fans are nearly as wide as the aperture, and therefore are more likely to strike the masks or absorbers during horizontal mis-steering. The masks and absorbers cannot withstand these large power densities. An additional mask, EX-1, is installed in these locations and defines the 18 mrad aperture for these specific beamlines. It is designed with a shallow angle-to-grazing to reduce the heat flux to acceptable levels.

The exit aperture for all insertion device beamlines is 18 mrad. The SR fan for three beamlines (4, 7 and 9) are nearly as wide as the aperture and are more likely to strike the masks and absorbers for small amounts of mis-steering. The power densities are about X times larger if ID power is intercepted on the V-1 mask. The power density on H-1 is X times greater, again unacceptable. The approach for exit ports is to have the mask and absorber define a 22 mrad aperture, and then add an additional shallow angle surface beyond the exit port to then define the 18 mrad aperture.

### 3 GIRDER CHAMBER DESIGN

The vacuum chamber cross section is a 34 mm high by 84 mm wide octagon with a 12 mm tall slot, see figure x. This cross section allows a minimum of ±2 mm between both the magnets and the prescribed BSC. The 2mm clearance accommodates manufacturing and alignment tolerances, as well as the deflection of the chamber due to vacuum loading. The height of the slot is the most critical dimension of the vacuum chamber profile.

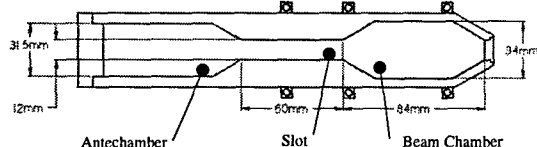


Figure 2: Typical Beam Cross Section, Copper Design.

Presently, two different designs are being pursued. One design is a Cu-coated, formed SS chamber similar to the ANKA and BESSY designs. The other is a machined Cu chamber incorporating PEP-II experience. Copper chambers will increase the passively safe dipole current of the machine from 20 mA for SS to >500 mA, increase the thermal response time

to more than 500 ms and decrease resistive wall losses. The driving factors for material choice are cost and manufacturing risk.

#### 3.1 Stainless Steel Chamber

**Material Properties:** SS has excellent vacuum properties, high mechanical strength, and is easy to weld. Rib placement is challenging but, they are necessary to keep the deflections of the chamber low especially at the slot. Since the deflections of the chamber are kept to a minimum the stresses due to vacuum loading are negligible. Optimization of rib geometry in ANSYS shows a 0.3mm deflection can be achieved at the slot.

**Eddy Currents:** Orbit feedback is required for SPEAR3 to stabilize the beam orbit to less than 5  $\mu\text{m}$  [2]. Four corrector magnets on each girder are modulated as part of the orbit feedback scheme. Modulation of corrector elements in the lattice can create eddy currents within the vacuum chamber walls, inducing bucking fields that reduce the amplitude and shift the phase of the correction field. Primarily, the vertically modulated fields that provide horizontal beam correction are affected. SS has low electrical conductivity, thus circulating eddy currents are minimal. Initial calculations using MAFIA show acceptable field amplitudes for a 3mm SS chamber with 1mm of Cu plating. The calculations indicate that Cu compensating plates are required at the corrector locations to counteract the asymmetry created by the Cu coating on the slot.

**Collective Effects:** Resistive wall losses are high for a SS chamber. Beam instability calculations show that with a chromaticity of 0.1 the beam is stable up to 274 mA. Therefore transverse feedback is not needed for initial commissioning, but may be necessary to achieve 500 mA.

**Manufacturing:** The manufacturing process of the SS chambers is similar to ANKA and BESSY chambers. The chamber is formed from 3 mm SS into two halves, fired at 900 C to reduce hydrogen and to stress relieve, cleaned for UHV and EB welded. After final assembly of absorbers and pumps the chamber will be baked at 200 C.

A Cu layer 1mm thick is thermally sprayed onto the SS chamber to increase the passively safe operating current for dipole power to 50 mA and to enable the brazing of Cu cooling tubes. Metallurgy and brazing tests are being performed on the sprayed Cu. Also, to increase the passively safe operating current for insertion device power and thermal response time, a Cu insert was designed in the BM-2 chamber. The insert is machined from explosion bonded Cu/SS transition material and EB welded into the chamber. With this addition the stainless chamber performs like a Cu chamber for ID power only.

#### 3.2 Copper Chamber

**Material Properties:** Copper has excellent thermal properties that enable a more robust design when considering safe operating current and transient thermal response. The vacuum performance of Cu is nearly identical to SS for both thermal outgassing rates and photon stimulated desorption (PSD). The



mechanical properties are more than adequate to achieve acceptable slot deflections and react vacuum loads as well as other loading conditions due to assembly.

**Eddy Currents:** Induced eddy currents can be significant in Cu due to its high electrical conductivity. By inserting a high resistance material in the loop, the effective circulating eddy current is reduced. MAFIA analysis has verified this approach. CuproNickel™ has an electrical conductivity about  $1/20^{\text{th}}$  of Cu and can be welded reliably to Cu. The design requires that all other conductive parts such as cooling tubes must not bridge the eddy current break.

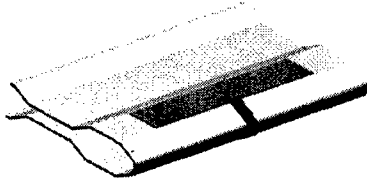


Figure 3: Chamber with CuNi Eddy Current Break

**Collective Effects:** Resistive wall losses for Cu are reduced by a factor of seven compared to SS, and potentially eliminate the need for a transverse feedback system. [3]

**Manufacturing, Assembly and Processing:** Copper chamber construction is divided into three major portions: machining of mating, mirror-image halves, and ancillary ports and flange preps, EB welding and assembly, and vacuum processing.

The upper and lower halves of each of the girder chambers are machined from single pieces of OFE Cu plate. For the quantities required in SPEAR3, this approach falls within existing budgetary constraints.

After EB welding the chamber is required leak tight to  $2 \times 10^{-10}$  std cc/sec using Helium gas. The option for glow-discharge processing the beam passage with a 5%Oxygen/95%Argon gas mixture prior to bake-out is being considered to help reduce overall PSD rates. The chambers are then placed in vacuum ovens and processed at 200C until outgassing rates and partial pressures are below acceptable limits.

#### 4 STRAIGHT SECTION CHAMBERS

The straight sections contain the ID, diagnostic and injection chambers, and RF cavities. SPEAR3 requires that the existing standard cell lengths and ID beam alignments be preserved. Also, all existing ID chambers will be kept, although they are only designed for 200 mA. New masking is required for 500 mA operation.

Physics requirements dictate that the straight sections also maintain the BSC described previously. The same internal octagonal profile will be used for all new straight section chambers. Smooth transitions (1:5) are made between existing ID's where space permits.

Straight sections with no special chambers require two masks that intercept less than 10 W/cm of SR power. Two refurbished ion pumps are mounted near the masks and additional pump ports may be added for future upgrades.

Straight section drift chambers are machined from copper and subsequently EB welded. Cu-to-SS adapters are used to weld on conflat flanges. Rectangular cooling tubes are welded directly to the chamber. This design allows a passively safe operating current well above 500 mA.

**Injection Kicker:** The injection kicker, based on the proven DELTA design, consists of 2 conductors separated by four axial slots. The conductors produce an inductive loop and are connected to ground by metal bands. The design is electrically symmetric with two inputs for current pulses of opposite polarity. The slotted kicker pipe is 0.4 m long and is housed in a vacuum tank. The metal bands maintain the cross section, reducing impedance. Cooling channels inside of vacuum are required to cool a SR strike of 6.2 W/cm.

**Transverse Kickers:** Two Cu plates formed into partial ellipses are connected by Inconel flex supports to four 50Ω ceramic feedthrus that are welded to an elliptical vacuum chamber. Flex supports allow for the differential thermal expansion between the plates and the chamber.

The vertical kicker requires a 5 mm offset to shadow a direct SR strike, the horizontal does not. The primary mode of heat transfer is through radiation, because there is no significant conductive path to the vacuum chamber and internal cooling tubes could alter the performance of the kicker. A Cu-oxide using an arc deposition process developed at LBL for PEP-II is being investigated to blacken the electrodes.

**Synchrotron Light Monitor (SLM):** The SLM images visible and near ultraviolet light and is located in the 4.5m matching straight section. The longer straight allows the primary mirror to be further away from its SR source, reducing the power density. The x-rays are concentrated in the vertical midplane of the radiation pattern, while the visible and UV light have much larger vertical opening angles and do not produce a significant amount of power. A thin mask intercepts the high power x-ray light and reduces thermal distortion of the primary mirror. The primary mirror is designed to withstand the compressive thermal stresses from an off-axis hit.

#### 5 BELLOWS MODULE

The bellows module bridges the gap between the chambers and allows for thermal expansion, alignment, manufacturing tolerances and installation of the vacuum chambers. It also serves to isolate and stabilize the BPM's. SPEAR3 will use the double finger mechanism successfully developed at SLAC for PEP-II. It may be necessary to employ a mask to prevent the module from being destroyed by an off-axis SR strike.

#### 6 REFERENCES

- [1] Y. Nosochkov and J. Corbett, Dynamic Aperture Studies for SPEAR3 SLAC-PUB-7965, October 1998.
- [2] SPEAR3 Conceptual Design Report, July 14, 1998.
- [3] C. Limborg, J. Sebek, "Collective Effects in SPEAR3", US PAC99 Conference Proceedings, New York, New York.

# VACUUM SYSTEM FOR THE ACCELERATING STRUCTURE OF THE IFUSP MICROTRON

J. Takahashi, M. N. Martins\*, L. Portante, R. da R. Lima, Laboratório do Acelerador Linear  
Instituto de Física da Universidade de São Paulo, CP 66318, 05315-970 São Paulo, SP, Brazil  
F. T. Degasperi, Faculdade de Tecnologia de São Paulo, FATEC-SP

## Abstract

This paper describes the vacuum system adopted for the accelerating structures of the IFUSP Microtron accelerator. The structure uses the Los Alamos side-coupled cavities and presents a vacuum port at each coupling cavity. We describe the vacuum system, the advantages of the adopted configuration, some construction details and calculations on the expected performance.

## 1 INTRODUCTION

The Laboratório do Acelerador Linear do Instituto de Física da Universidade de São Paulo (LAL-IFUSP) finished the construction of a  $\beta = 1$  continuous wave

accelerating structure [1] for the IFUSP microtron [2], which presented excellent properties [3]. The structure is a 1.04-m long standing wave, side coupled (SCS) design, with 17 accelerating cavities and 16 coupling cavities.

One of the main advantages of the side-coupled accelerating structure, as compared to other structure designs, is the possibility of pumping each of the coupling cavities. This is an important feature, for it allows a quick pumping of the degassing produced by RF heating or sparking in the structure. Our structure presents 16 coupling cavities, each of them connected by a tube with a conductance of 12 l/s. Figure 1 shows a schematic drawing of the structure, with dimensions and details of the cavities.

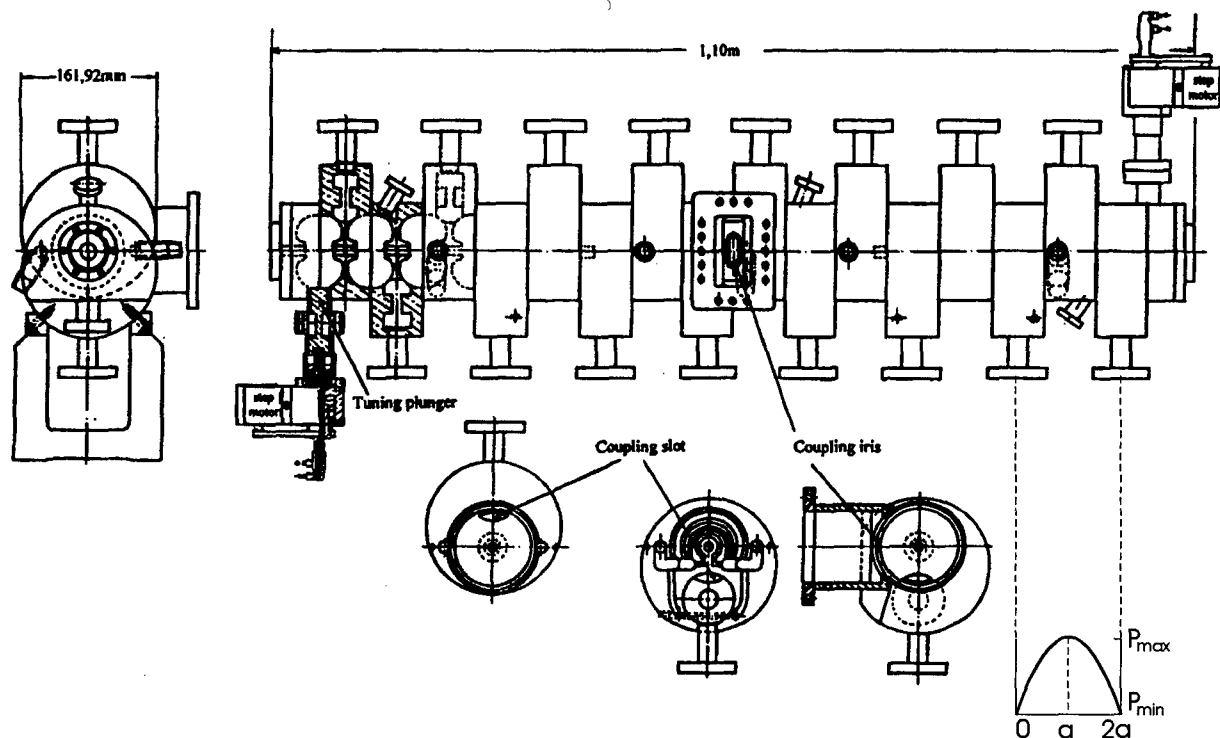


Figure 1: Schematic drawing of the structure, with detail showing the pressure along the length of a "module" (see text).

\* E-mail: martins@if.usp.br

To ease the mechanical design of the vacuum system we decided to use only the ports facing downwards, as shown in Fig. 2, which presents a side view of the structure and the manifold.

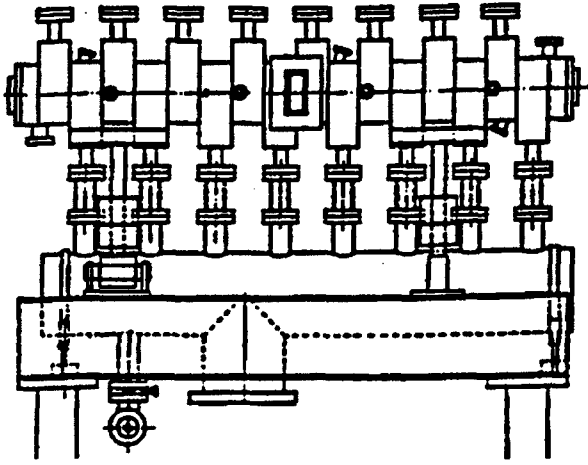


Figure 2: Side view of the structure, showing the coupling with the manifold.

## 2 MODELING

There are two basic options on how to pump the 8 vacuum ports: with 8 vacuum pumps of about 40 l/s pumping speed, or with a manifold connecting the 8 ports to a single 300 l/s vacuum pump. Figure 3 shows a schematic drawing of the manifold used.

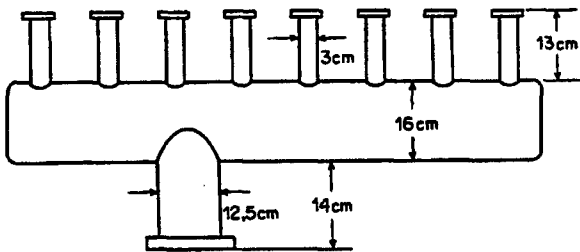


Figure 3: Schematic drawing of the manifold.

A simplified model was used to evaluate the effective pumping speed of the system and also the steady state pressure along the length of the structure. We divided the structure in 8 modules composed of one half of a coupling cavity, two full accelerating cavities, one coupling cavity (facing down) and another one half of a coupling cavity, as depicted in Fig. 1. We then proceeded to evaluate the conductance and the degassing of the main parts of this module. Beginning with the conductance, to pump the gas in the furthestmost volume, the coupling cavity facing up, it has to go through the accelerating cavity, down to the coupling cavity facing down, to the exit tube, to the connecting tube of the manifold, the manifold itself and finally to the pump. In the evaluation of the pressure profile along the structure, we need the effective pumping speed at the accelerating

cavity, because that is where the electric field is most intense.

The effective pumping speed can then be written as

$$\frac{1}{S_{eff}} = \frac{1}{C_T} + \frac{1}{S_p} \quad (1)$$

where  $S_{eff}$  is the effective pumping speed at the accelerating cavity,  $S_p$  is the pumping speed of the vacuum pump and  $C_T$  is the total conductance of the system.  $C_T$  can be calculated by

$$\frac{1}{C_T} = \frac{1}{C_w} + \frac{1}{C_{CC}} + \frac{1}{C_{ET}} + \frac{1}{C_{CT}} + \frac{1}{C_M} + \frac{1}{C_{PT}} \quad (2)$$

where  $C_w$  is the conductance of the window between the coupling and accelerating cavities (approximated by an ellipse shape),  $C_{CC}$  the conductance of the coupling cavity,  $C_{ET}$  the conductance of the exit tube,  $C_{CT}$  the conductance of the connecting tube (between the exit tube and the manifold),  $C_M$  the conductance of the manifold, and  $C_{PT}$  the conductance of the tube that connects the manifold to the vacuum pump. We consider the gas to be  $N_2$ , at 298 K and molecular flow. Several simplifications were done, mainly in the geometry of the cavities, which are very complex.

$C_w$  was calculated considering the window to be elliptical, with major and minor axes equal to 2.4 cm and 1.6 cm, respectively. Then  $C_w = 36$  l/s. The coupling cavity was approximated by two curved tubes of rectangular cross section, forming a shape close to a toroid, resulting in  $C_{CC} = 94$  l/s. The exit and connecting tubes present the most restricted conductance of the whole system, being narrow (2- and 3-cm in diameter, respectively) and long (5.4- and 20.6-cm long, respectively), resulting in  $C_{ET} = 12$  l/s and  $C_{CT} = 11$  l/s. The conductance of the manifold will depend on the port which is being pumped. We calculated the two extreme cases (850 and 1300 l/s) and used the average,  $C_M = 1075$  l/s. The pumping tube of the manifold presents  $C_{PT} = 780$  l/s (which includes the whole distance from the manifold to the ion pump). Then, using Eq. (2), the total conductance of the system is  $C_T = 4.7$  l/s. Substituting this value in Eq. (1) and considering  $S_p = 300$  l/s, we obtain for the effective pumping speed on each module, at the entrance of the accelerating cavity,  $S_{eff} = 4.6$  l/s.

If, instead of the manifold, eight 40 l/s pumps were used, connected at each port by 100-cm long and 7.5-cm in diameter tubes, the effective pumping speed at the accelerating cavity would be 4.9 l/s. The difference is less than 7 %. So the effective pumping speed with the manifold and a 300 l/s pump, is equivalent to eight 40 l/s pumps, but the manifold solution costs about 30 % of the other.

To determine the pressure distribution along the structure, we must calculate the degassing of the cavities and the local effective pumping speed. In our simple model, we consider the pumping volume to be that of one accelerating cell plus one half of the volume of the coupling cell and exit tube (closed) facing upwards. This corresponds, in the structure depicted schematically in Fig. 1, to the portion between points  $O$  and  $a$ . The accelerating cavity presents a degassing surface of approximately  $190 \text{ cm}^2$ , while the coupling cell plus exit tube add up to  $180 \text{ cm}^2$ . Since we are considering just one half of this last surface, the total degassing surface will be  $280 \text{ cm}^2$ . Since the window between the coupling and accelerating cavities presents the lowest conductance, to simplify the calculation we will model the system by a cylindrical cavity with internal surface of  $280 \text{ cm}^2$  over a length  $a$ , and conductance of  $36 \text{ l/s}$ , with pumping ports separated by a distance  $2a$  ( $a = 6 \text{ cm}$ ). This model presents a quadratic solution that can be written as

$$p(x) = \frac{-q}{c}x^2 + \frac{2qa}{c}x + \frac{qa}{S_{\text{eff}}}, \text{ for } 0 \leq x \leq 2a \quad (3)$$

Where  $p(x)$  is the pressure at the point  $x$  along the structure,  $q$  is the degassing per unit length, and  $c$  is the specific conductance. For our specific conditions, we find  $p(0) = 3.7 \times 10^{-8} \text{ Torr}$  and  $p(a) = 3.9 \times 10^{-8} \text{ Torr}$ .

### 3 CONCLUSIONS

The adopted configuration worked well. The final pressure at the manifold should be better than  $3 \times 10^{-8} \text{ Torr}$ . The manifold option presents a performance very close to the one using 8 individual pumps, with a cost about 70 % lower. The difference of about 10 % between the maxima and minima of the pressure distribution along the structure is acceptable and supports the decision to close the vacuum ports facing up.

### 4 ACKNOWLEDGMENTS

This work was supported by FAPESP (Fundação de Amparo à Pesquisa do Estado de São Paulo), and CNPq (Conselho Nacional de Desenvolvimento Científico e Tecnológico).

### 5 REFERENCES

- [1] L.M. Young and J.M. Potter, "CW side coupled linac for the Los Alamos-NBS racetrack microtron", Los Alamos National Laboratory Report, LA-9324-C, 1982.
- [2] J. Takahashi *et al.*, "The IFUSP racetrack microtron", in Proceedings of the 3<sup>rd</sup> European Particle Accelerator Conference, edited by HHenke and P. J. Genaz, Editions Frontières, France, 1992. Vol. 1, p. 429-431.

- [3] J. Takahashi *et al.*, "Plunger frequency control of the side coupled accelerating structure for the IFUSP microtron", in Proceedings of the 1997 Particle Accelerator Conference, <http://www.trimf.ca/pac97/papers/pdf/4p038.pdf>.

# THE VACUUM CHAMBERS FOR THE VUV SASE FEL AT THE TESLA TEST FACILITY (TTF FEL) AT DESY\*

U. Hahn, J. Pflüger, M. Rüter

Hamburger Synchrotronstrahlungslabor HASYLAB at Deutsches Elektronen-Synchrotron DESY  
Notkestrasse 85, 22603 Hamburg, Germany

P. K. Den Hartog, M. Erdmann, E. M. Trakhtenberg<sup>†</sup>, G. Wiemerslage, and S. Xu

Advanced Photon Source, Argonne National Laboratory, Argonne, IL 60439

## Abstract

A vacuum chamber for the VUV SASE FEL undulators at the TESLA Test Facility (TTF) was designed, a prototype was built and tested, and seven complete chambers were manufactured. The chambers use the aluminum extrusion technology developed for the insertion device vacuum chambers of the Advanced Photon Source. Each chamber is 4.5 m long with a beam aperture of 9.5 mm and an external thickness of 11.5 mm. Three of the chambers include ports for integral beam position monitors (10 horizontal and vertical pairs) inserted into the chambers, and all of the chambers include grooves for mounting correction coils. Bimetallic flanges (stainless steel to aluminum) are welded to the ends of the chamber for connection to the beamline. Special processing was performed to meet the stringent vacuum and particle-free requirements of the TTF.

## 1 INTRODUCTION

At DESY, a VUV free-electron laser (FEL) based on the principle of self-amplified spontaneous emission (SASE) is under construction [1] to make use of the unique electron beam properties of the TESLA Test Facility (TTF). The FEL will be built in two phases [2]. Phase one, with a FEL operating down to 42 nm, is under construction. The major component for the generation of the FEL photon beam is the undulator, which will consist of three 4.5-m-long modules separated by 0.3-m-long beam diagnostic sections. The undulators are permanent magnet structures with a fixed gap of 12 mm. The electron beam must be kept small over the entire undulator length by an added sequence of focusing and defocusing quadrupoles (FODO lattice) [3]. Additionally, electron beam position monitoring and steering in the undulator gap is needed to achieve a sufficient ( $< 12 \mu\text{m}$ ) overlap [4] between the particle beam and the photon beam. Three 4.5-m-long

vacuum chambers with an open aperture of 9.5 mm guide the electron beam through the undulator sections. The simple vacuum pipe becomes rather complicated by the addition of 40 electrodes for the beam position monitors required for each chamber and the related 36 correction coils. A special alignment system for the flat, flexible chamber is also needed. Because the chamber tube must reach a specific outgassing rate  $< 1 \cdot 10^{-11} \text{ mbar} \cdot \text{l/sec} \cdot \text{cm}^2$ , the cleaning and assembly of the chamber was made inside a clean room better than class 100 [5].

## 2 VACUUM CHAMBER DESIGN

There are several design criteria for the undulator vacuum chamber:

- The undulator gap size is 12 mm.
- The chamber has to permit beam position measurement and steering in the gap.
- The chamber has to be vertically and horizontally aligned within 0.1 mm.
- Low electrical resistance and small micro-roughness of the inner beam pipe are needed to minimize resistive wall wake field effects on the beam.

Therefore, the vacuum chamber for the DESY FEL un-

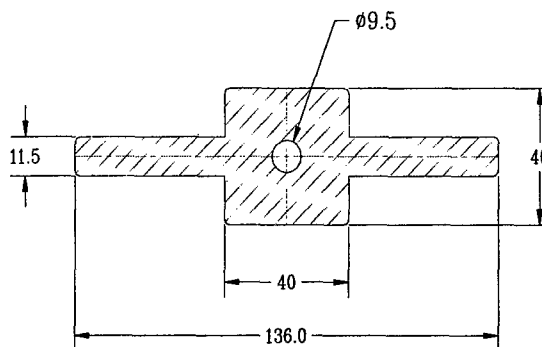


Figure 1: Cross section of the aluminum extrusion for the FEL vacuum chamber.

\*Supported in part by the U.S. Dept. of Energy, BES-Materials Sciences, under Contract No. W-31-109-Eng-38.

<sup>†</sup>Email: emil@aps.anl.gov

dulators is a flat, long structure with the base dimensions of 11.5 mm x 128 mm x 4500 mm. The central aperture for the beam has a diameter of 9.5 mm. Aluminum was the first choice as chamber material because of the low electrical resistance and because extrusion profiles specifically tailored for this application could be obtained. The previous Advanced Photon Source (APS) experience

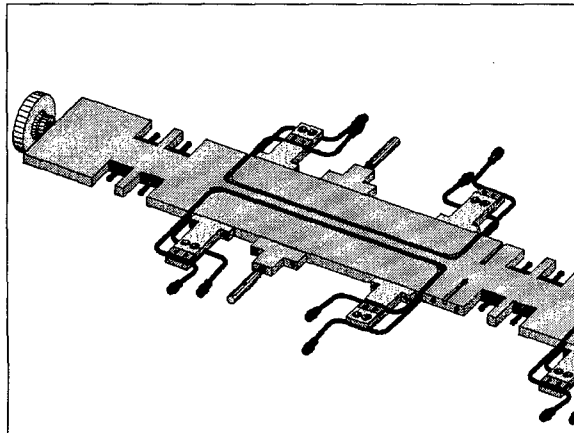


Figure 2: General layout of the undulator vacuum chamber, with pickup monitors, correction coils, and chamber support.

with the design of aluminium vacuum chambers for insertion devices was extremely helpful [6].

Considerable care was exercised to maintain the flatness of this intrinsically nonrigid structure and to ensure the precision of the location of the central aperture as required for precise measurements with the beam position monitors (BPMs). A special extrusion of aluminium alloy 6063-T5 was prepared for these chambers. The cross section chosen is shown in Fig. 1. The cross design adds rigidity to the extrusion and helps to decrease twist and bow. Machining of this alloy progresses readily, so the additional stock did not add unduly to the fabrication cost and schedule. Additionally, the material at the ends was used effectively to form the welding joints to bimetallic ConFlat flanges. The general layout of the chamber is

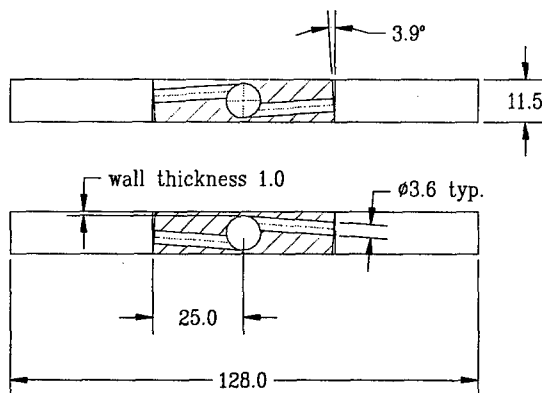


Figure 3: Cross section of the vacuum chamber at the position of the button BPM

shown in Fig. 2. Before machining, the flatness of the extrusion was further improved by bending with a hydraulic press. As a result, we were able to achieve a vertical wall

thickness precision of  $1.0 \pm 0.1$  mm. The thickness was checked by slicing and then measuring a short prototype extrusion. Production chambers were checked ultrasonically in the vertical direction.

The inclusion of integral BPMs, which would fit within the 12-mm undulator pole gap, along the chamber was a major challenge in the design and manufacturing. Two types of BPMs were developed: a button-type pickup monitor [7] for two chambers and a wave guide monitor that couples to the rf of the beam via small rectangular slots for a third chamber. The cross sections at

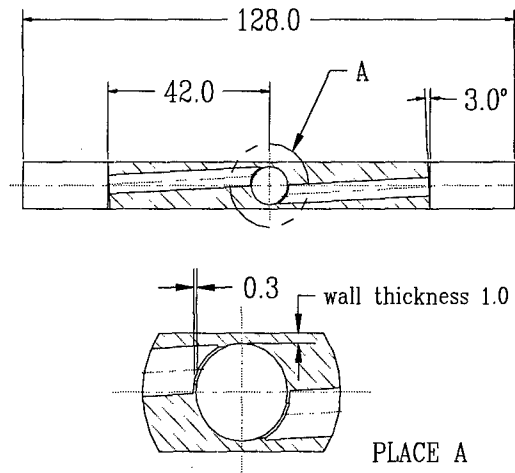


Figure 4: Cross section of the vacuum chamber at the position of the waveguide BPM.

the locations of these devices in the vacuum chamber are shown in Fig. 3 and Fig. 4, correspondingly. The complicated structure of the waveguide monitors was machined using EDM. Small prototype chambers of both monitor types were successfully tested. Each vacuum chamber has ten sections designated for BPMs, and each section consists of four BPMs. The remaining four chambers were fabricated without provision for BPMs. The final decision on the BPM type for these chambers is contingent on the results of beam tests.

Custom thin metal seals [8] were used to make the electrical feedthroughs of the BPM vacuum tight. The seals were manufactured especially for the purpose of the monitor sealing. The hardness of the chamber material is about B60 (Rockwell). This is sufficient to work with the silver-plated copper seals.

Each vacuum chamber has 36 grooves on the top and side for installation of the correction coils. Additional grooves for thermocouples to control the chamber temperature are located between BPM areas. Precise fi-

ducial holes in each BPM section will be used for alignment of the vacuum chamber in the undulator gap.

It was realized that the surface finish of the aperture would be very important because small beam emittance, high beam peak currents, and very short beam pulses are expected [1]. Rough surfaces can cause wake field effects that are deleterious to the beam quality. On the other hand, small burrs on the button BPM holes could be a source of arcing related to the very high field strength induced by the beam pulse. Therefore, the surface quality was carefully checked after the extrusion was fabricated. An additional electrochemical polishing of the aperture was performed on the pick-up monitor chambers after machining the BPM holes. A sample was measured with a stylus profiler. Before polishing, the RMS inner surface roughness was  $\sim 1.6 \mu\text{m}$  along the extrusion direction. After polishing, the RMS roughness was improved to  $\sim 0.8 \mu\text{m}$ . Optical measurements show that the roughness transverse to the extrusion direction is about two times larger than along the extrusion, but surface smoothness in this direction is less important.

One of the main objectives of the assembly process for the FEL vacuum chambers was to preserve the cleanliness of the superconducting cavities of the TTF. This means that the chambers should be vacuum clean and dust free according to the class 100 clean room specification. After manufacturing, the vacuum chambers were cleaned in a 2% solution of Ridoline 18 and then rinsed in purified DI water which was filtered to  $25 \mu\text{m}$ . The chambers finally were dried with high purity and particle free ( $1\text{-}\mu\text{m}$  filtered) dry nitrogen in a class 100 clean room. The procedure was continuously controlled by a particle counter. The final assembly of the chambers was performed in a class 100 clean room as well. During the assembly and subsequently during each pumping cycle, a strict venting procedure will be used to prevent contamination of the TTF.

### 3 CONCLUSION

The extruded aluminum vacuum chamber technology developed for the Advanced Photon Source has been successfully applied to a new and challenging application, the vacuum chambers for the TTF FEL. Seven vacuum chambers have been fully machined, cleaned, tested, and shipped to DESY. First beam tests are scheduled for early summer of 1999.

### 4 ACKNOWLEDGMENTS

The authors are grateful to John Noonan for the fruitful technical discussions. We also thank the technicians of the XFD and ASD divisions at Argonne and Günther Marquart of DESY for a great job, helping to finish this work on time and to achieve the design goals.

### 5 REFERENCES

- [1] J. Roßbach, Nucl. Instrum. and Methods A 375, 269 (1996)
- [2] J. Feldhaus and B. Sonntag, Synch. Rad. News 11, 1, 14 (1998)
- [3] Yu. M. Nikitina and J. Pflüger, Nucl. Instrum. and Methods A 375, 325 (1996)
- [4] B. Faatz, J. Pflüger, and Yu. M. Nikitina, Nucl. Instrum. and Methods A 393, 380 (1997)
- [5] D. Edwards, D. Hubert, A. Matheisen, H. P. Wedekind, H. Weise, and K. Zapfe-Düren, "Proposed Cleaning Procedures for the Vacuum Components for the TESLA Test Facility," TESLA report 15 (1997)
- [6] P. Den Hartog, E. Trakhtenberg, G. Wiemerslage et al., "Advanced Photon Source Experience with Vacuum Chamber for Insertion Devices," PAC 97, Vancouver, Canada, 12-16 May 1997.
- [7] R. Lorenz, T. Kamps, U. Hahn, and M. Wendt, "Beam Position Monitors inside the FEL - Undulator at the TTF Linac," PAC 97, Vancouver, Canada, 12-16 May 1997
- [8] VATSEAL, VAT Vakuumventile AG, Schweiz

# VACUUM SIMULATION OF RF CAVITIES TO OPTIMIZE PUMP CONFIGURATIONS \*

S. Shen, L. S. Tung<sup>#</sup>, LLNL, Livermore, CA

## Abstract

The pressure history in the components of an rf linac has been modeled using *Mathematica*. [1] Specifically the Cavity Coupled Drift Tube Linac (CCDTL) and Cavity Coupled Linac (CCL) sections of the Accelerator Production of Tritium (APT) plant [2] have been modeled in order to predict the optimal pump configuration over the 224 meter length. The pressure history in up to 43 sub-volumes within three representative modules (about three meters long) is analyzed in detail. Included in our model are time-dependent outgassing rates and pressure-dependent pump speeds. With this information, we solve for the pressure history during roughing and with turbo and ion pumps. The number and size of each pump is optimized to achieve the desired pressure with minimal costs.

## 1 APT DESCRIPTION

A high-energy proton beam is accelerated by a series of rf cavities that have 11 different types of geometries or modules. The entire length of the 11 modules that encompass the CCDTL and CCL configurations is 224 m. Over this length there are 341 (individually numbered) segments that are composed of from 1 to 7 rf cavity cells. Because the rf cavities and magnets surround the beam tube, the beam tube must be evacuated via pumping connected to the coupling cavities. Within each module, each cavity geometry is unique because of its dependence on the proton beam energy.

## 2 VACUUM REQUIREMENTS

The requirement for the CCDTL/CCL vacuum system is to provide sufficient pumping to overcome the surface outgassing of vacuum facing components and the rf window in order to maintain a beam tube pressure that is below  $10^{-6}$  Torr. The system must be designed for plant operation, which implies continuous operation with minimal downtime. In addition if one ion pump fails per manifold, the remaining ion pump must keep the beam line below the operating pressure. The cavity components are composed of brazed OFE copper. The manifold, pumping ports, and beam tube are composed of electropolished 316 stainless steel.

\* Work performed under the auspices of the U. S. Department of Energy by the Lawrence Livermore National Laboratory under contract number W-7405-ENG-48.

<sup>#</sup> Email: lstung@llnl.gov

## 2 VACUUM MODEL

### 2.1 Overview

The numerical model described here is for the vacuum system for a six-cavity section that represents the first module in the CCDTL. In actuality, the geometry of each cavity is unique because of its dependence on the proton beam energy. However in our model, the six cavities have the same size as the actual first cavity. This has the smallest geometry and so provides a conservative description without having to include the details for all the cavities.

We built two numerical models: first to study the effect of manifold size on the pumping configuration and second to take the first model with the optimized configuration and install an rf window system to determine its pumping needs. A layout of evacuated components for the first model is shown in Fig. 1. In the second model, the rf window and its pumping system are modeled as *half* a system and are placed after the 6<sup>th</sup> cavity along a mirror symmetry line. In this way our 6-cavity model with the rf window system represents a 12-cavity section with one manifold.

Figure 1 shows how the evacuated space is divided into sub-volumes and interconnecting conductances for the first model (without the rf window). Note that there are two ion pumps and one turbo pump shown for six cavities. However, as will be discussed shortly, the optimized configuration requires only two ion pumps and one turbo pump for 12 cavities. Consequently the pump speeds in the six-cavity model is exactly half of the actual pump speed. Two "half-speed" ion pumps are used so that we can shutoff one pump to study the pressure gradient along the beam tube. (A 12-cavity model will be written in the near future with only "whole pumps".)

### 2.2 Method

Pressure history is studied by solving the coupled the energy balance between all the sub-volumes. (The routine is written with *Mathematica* [1] and runs on a 266 MHz Power Mac G3. The entire run requires at most 70 sec.) For each sub-volume, the following energy balance equation is solved simultaneously for all 43 volumes for each time during pumpdown.

$$V_i dp_i / dt = \Sigma Q_{i-in} - \Sigma Q_{i-out} \quad (1)$$

where  $i$  is the index for the  $i$ th sub-volume,  
 $V$  is the volume (liters);

$dp/dt$  is the rate of change in pressure (Torr/sec);



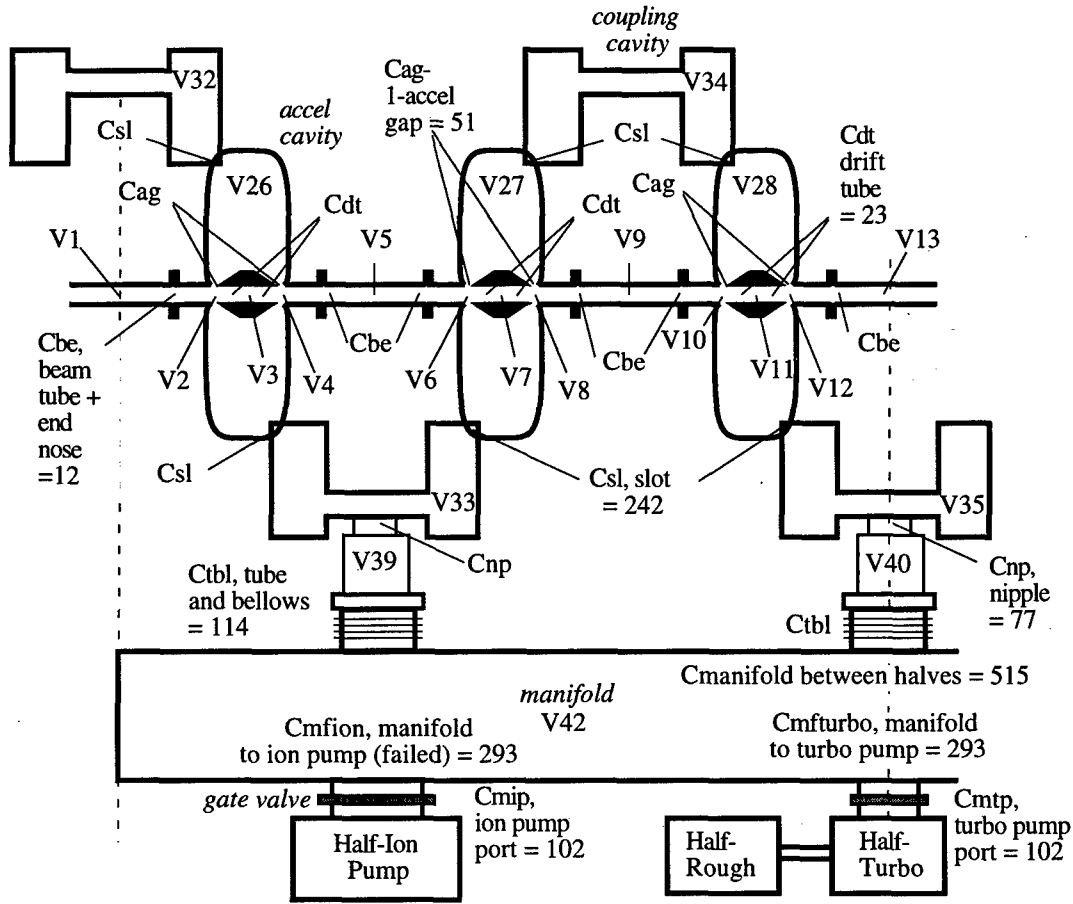


Figure 1: Evacuated space for the first six cavities of the APT/CCDTL as divided into sub-volumes and conductances. Only the left half of the layout is shown. The right half is symmetric to the left. Sub-volumes are labeled numerically and indicated with a "V". Conductances are labeled with the actual conductance values in lit/sec. Note that between each sub-volume is a conductance.

$\Sigma Q_{i-in}$  is the sum of time-dependent outgassing or leaking into  $V_i$  (Torr-lit/sec);  
 and  $\Sigma Q_{i-out}$  is sum of energy removed from  $V_i$  via conduction,  $Q_{i-out} = C_{i-j}(p_i - p_j)$  (2)  
 and  $C_{i-j}$  is the conductance (lit/sec) between sub-volumes;  
 and/or via pumping,  $Q_{i-out} = S(p_i) p_i$  (3)  
 and  $S(p_i)$  is the pressure-dependent pumping speed (lit/sec).

This set of equations is solved four times: 1) with the roughing pump down to 0.05 Torr; 2) with the turbo pump down to  $4 \times 10^{-7}$  Torr; 3) with the ion pumps down to below  $2 \times 10^{-7}$  Torr; and 4) with one ion pump off for 50 seconds. The roughing pump pressure is initially at 720 Torr. The final pressure at the end of each pumping phase is then saved to be the initial pressure for the next pumping phase.

### 3 DETAILED RESULTS

#### 3.1 Final characteristics

Aside from geometry, surface outgassing is the strongest factor to determine pumping needs. For our time-dependent model, we combined the early outgassing rates of stainless steel from Roth [3] with long term rates after ten hours. The long term rates are dependent on the final material preparation and handling. We derived a numerical fit that describes this time-dependence of outgassing:

$$R [\text{Torr-lit/sec/cm}^2] = 2.4 \times 10^{-8} \exp(-2.2 \times 10^{-3} t) + 7.2 \times 10^{-8} \exp(-1.7 \times 10^{-3} t) + B, \quad (3)$$

where  $B = 1 \times 10^{-10}$ , the outgassing rate after ten hours and  $t$  is time in seconds.

For a ten-fold in increase in  $R$ , we found that the base pressure followed linearly.

A summary of the total area, volumes, and outgassing is provided in Table 1. Also given is the final optimized pumping configuration. Following this table, Fig. 2 shows the pumping history. When one ion pump fails,

our model shows that the beam tube pressure above the failed pump nearly doubles within 50 seconds.

Table 1: Summary of geometry, optimized pumping configuration, and final pressures

Pumping System for 12 Cavities	
One 6" diameter manifold	
One 300 lit/min roughing pump	
One 70 lit/sec turbo pump	
Two 55 lit/sec ion pumps (for redundancy)	
Three gate valves (one for each turbo and ion pump)	
<b>Detailed system parameters for a 12-cavity section (including manifold and pumping ports but no rf window)</b>	
Total copper surface area = 42,582 cm <sup>2</sup>	
Total stainless steel surface area = 16,920 cm <sup>2</sup>	
Total volume = 137 lit	
Total surface outgassing = 5.9 x 10 <sup>-6</sup> Torr-lit/sec	
Beam tube pressure during normal ion pump operation = 1.4 x 10 <sup>-7</sup> Torr	
Beam tube pressure with one ion pump failed = 2.5 x 10 <sup>-7</sup> Torr	

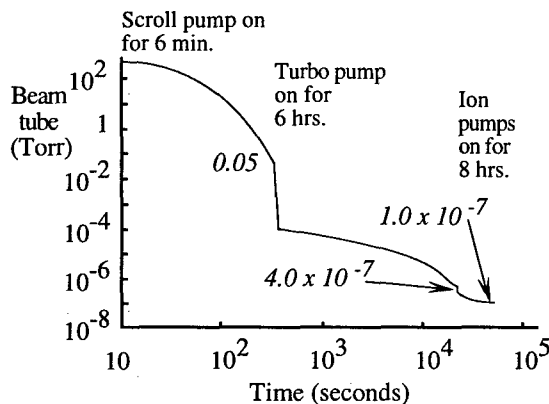


Figure 2: Pressure history of optimized pumping of 12 cavities for the first module of the APT/CCDTL

### 3.2 Component Optimization

The vacuum components that we optimized were manifold diameter and length, bellows size (between the lower coupling cavities and manifold), and pump number and size.

The largest contribution to optimization was the manifold. Use of a manifold allows the use of fewer larger pumps. For the same total pumping speed, one can look at prices in the vender catalogs and conclude that for the same total pumping speed, fewer larger pumps cost substantially less than more smaller pumps. In our case of ion pump failure, if the manifold diameter is too small, the reduction in manifold conductance reduces pumping of

the beam tube above the failed pump. If the manifold diameter is too large, the additional outgassing increases the beam tube pressure. Thus our simulation determined that a 6" or 8" diameter allows the most cost effective pumping configuration. In addition, because the manifold is attached from above and the accelerator is supported on box beams that are spaced 18" apart, then a 6" or smaller manifold is much easier to install. Thus we chose a 6" diameter manifold.

Pump sizes were chosen so that the smallest pump size available from vendors evacuated the beam tube to below  $2 \times 10^{-7}$  Torr. Thus with the failure of one ion pump the beam tube pressure would be less than  $4 \times 10^{-7}$  Torr. In this way we have a considerable design margin in case the surface outgassing exceeds  $10^{-10}$  Torr-lit/sec/cm<sup>2</sup>.

A second study included an rf window assembly (with its own pump) at the location of sub-volume 38. Based on preliminary outgassing data for the rf window, the assumed rate was  $2.7 \times 10^{-5}$  Torr-lit/sec.[4] We ran the code for a range of window pumping speeds and looked at beam tube and rf window pressures. Maintaining a pressure of at least  $1 \times 10^{-7}$  Torr in the rf window volume was an operational requirement. To accomplish this required that the rf window pumping speed be at least 275 lit/sec. Because of the small space and weight restrictions, a NEG (non-evaporable getter) pump was chosen for this job. With no window pumping, the rf window pressure reached  $7 \times 10^{-5}$  Torr. Based on available NEG pump designs, we conservatively chose a pump size of 500 lit/sec.

## 4 EXTRAPOLATION TO PLANT

We also analyzed two other representative modules – one in the CCDTL section and the third in the CCL section. The optimized configuration for each section modeled is then linearly extrapolated to the entire 341 segments to characterize the pumping needs for the plant.

## 5 REFERENCES

- [1] *Mathematica* version 3.0 by Wolfram.
- [2] R. L. Wood et al., "Status of Engineering Development of CCDTL for Accelerator Production of Tritium," Proc. LINAC98, Chicago.
- [3] Roth, A., 1996, Vacuum Technology, (North Holland, Amsterdam) 190.
- [4] APT/LEDA RFQ RF Window Pumping System, Sept. 24, 1997.

# THE COMPARISON OF VACUUM PERFORMANCE IN THE UNDULATOR CHAMBERS INSTALLED AT THE TAIWAN LIGHT SOURCE

S. H. Chang<sup>a</sup>, J. R. Chen<sup>a,b</sup>, K. M. Hsiao<sup>a</sup>, G. Y. Hsiung<sup>a</sup>, S. N. Hsu<sup>a</sup>, Y. J. Hsu<sup>a,1</sup>, T. F. Lin<sup>a</sup>,  
T. S. Ueng<sup>a</sup>, W. H. Wei<sup>a</sup>,

<sup>a</sup>SRRC, No.1 R&D Road VI, Hsinchu Science-Based Industrial Park, Hsinchu 30077, Taiwan

<sup>b</sup>Department of Nuclear Science, National Tsing-Hua University, Hsinchu 30077, Taiwan

## Abstract:

The U5, EPU, U9 undualtor chambers have been installed at Taiwan Light Source (TLS) since 1997. One sheet of non-evaporable getter was inserted into each of the undulator chamber. The basic designs in these undulator chambers are almost the same except the length and the geometry of pumping systems. The comparison of vacuum performance in these undulator chambers will be described.

## 1. INTRODUCTION

Several insertion devices (ID) have been built in the straight sections at Taiwan Light Source (TLS) to obtain coherent and high brightness photons. A W20 wiggler and a U5 undulator were installed in February of 1995 and March of 1997, respectively [1]. A U9 and an EPU5.6 undulator are to be installed in the April of 1999. Prior to the installation of insertion devices, U9 and EPU5.6, the ID chambers for these undulators have been installed during several previous shutdown periods. The comparison of vacuum performance in these undulator chambers, the effective pumping speed and the impact to the beam lifetime, etc., are described in this article.

## 2. VACUUM SYSTEM

The chamber designs in the undulator chambers, U5, EPU5.6 and U9 are similar [2]. The specifications for these insertion devices and chambers are shown in Table 1. The plane view and the cross section view of this type chamber are shown in Figs. 1(A) and 1(B), respectively. The inner cross section for the electron beam channel is an elliptical shape with 13 mm vertical height and 80 mm horizontal width. A pumping channel of 16 mm in height and 46 mm in width for assembling the NEG strips is located on other side. In the pumping configuration, the U5 and EPU5.6 have the same geometry. In addition to the NEG strip of ID chambers, a combination of two sets of 350 l/s NEG pumps and 400 l/s sputter ion pumps which were located at the upstream and the downstream

is used to evacuate the whole system. Owing to the limited space in the straight section, the two sets of NEG pumps and sputter ion pumps were withdrawn in the U9 system. The configuration of vacuum systems for U5, EPU5.6 and U9 are shown in Fig. 2.

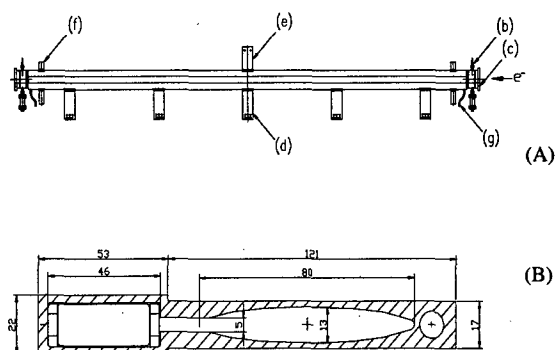


Fig.1. (A) Plane view and (B) cross section view of the undulator chamber. In Fig. 1(A), names of the indicated parts are (a) aluminum pipe, (b) taper piece and current feedthrough for NEG, (c) aluminum conflat flange, (d) and (e) supporting pads, (f) pad for limiting switch contact, and (g) water cooling pipe.

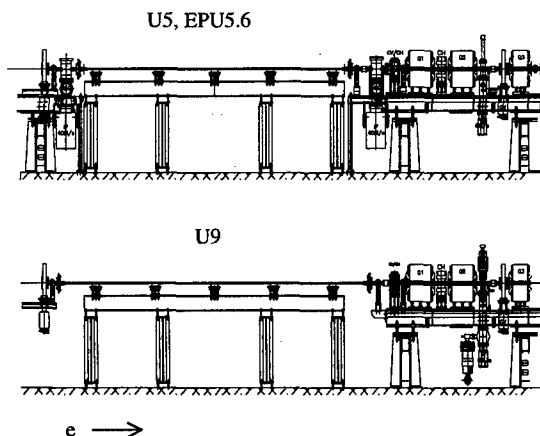


Fig. 2. The configuration of vacuum systems for U5, EPU5.6 (top) and U9 (bottom) respectively.

<sup>1</sup> Email: yjhsu@.src.gov.tw

Table. 1 The specification of insertion devices and vacuum chambers.

Straight Section	R2	R3	R6
Insertion Device	EPU5.6	U5	U9
Period Length ( $\lambda_u$ )	5.6cm	5.0cm	9.0cm
No. of Poles (N)	66	76	48
Minimum Gap	18mm		
Undulator Chamber	B type		
Chamber Length	4.16m	4.16m	4.76m
Outside Vertical Height	17mm		
Inner Cross Section for Electron Orbit	13mm×80mm(H×W)		
Chamber Material	A6063T5 aluminum alloy		
Fabrication	Extrusion		
Flatness on Outside	< ±0.2mm		
Distributed Pumping Inside ID Chamber	Non-Evaporabl Getter (st707)		
Dimension of NEG (L×W)	3.54m×3cm	3.54m×3cm	4.14m×3cm
Installation Date	1997/03	1997/03	1998/06

### 3. DISCUSSION

The static pressures after installation and baking of the ID chambers are about ~0.3, ~0.2, and ~0.9 nTorr for U5, EPU5.6, and U9 respectively. In this article, the vacuum performance of U5 and U9 is compared only because the vacuum systems of U5 and EPU5.6 have the same configuration. Owing to the same dimension in the cross section and the similar length, the estimated conductance (~0.56 l/s for U5, ~0.6 l/s for U9) and the pump speed of NEG strip (390 l/s for U5, 455 l/s for U9) in the ID chambers is similar [2]. We thought the ratio of pressure in the center regime of U5 and U9 system is nearly one by this similar effective pumping speed. The additional pumping speed of 750 l/s of sputter ion pump and NEG pump at both of the upstream and the downstream regime in the U5 system could further lower the pressure at the regime far away from the center of ID chambers. This effect was more obvious in the pressure rise by the photon stimulated desorption during initial commissioning.

Figure.3 shows the normalized pressure rise versus the accumulated beam dose after the installation of these undulator chambers. The pressure rise (measured by an upstream gauge) was about ~50 nTorr/mA for U9 system, but about ~2 nTorr/mA for U5 and EPU5.6 system at the beginning. For the high pressure rise in U9 system, the reactivation process (450°C, 30 min) of NEG strip was proceeded after an accumulated beam dose up to 10 Ah. The slightly steep slope of pressure rise after 10 Ah for U9 system was attributed to this reactivation process. The ratio of the pressure rise in U9 and U5 system was about ~25 at the beginning and gradually decreased to 10 at the final. When an accumulated beam dose up to 200 Ah, the values of pressure rise in these ID chambers were decreased by three orders of magnitude. The beam self-cleaning effects in the above ID chambers are the same as the previously installed W20 wiggler chamber [1]. The ratio of pressure rise in U9 and U5 is dominated by the division of the outgassing rate and the effective pumping speed, i.e.,

$$R = P_{U9} / P_{U5} = (Q_{U9} / S_{U9}) / (Q_{U5} / S_{U5})$$

where Q is the outgassing rate of the chamber, and S is the effective pumping speed, the ratio of the pressure value R is estimated to 2. This estimated value is much smaller than the value of 25 at the beginning and the value of 10 at the final. We thought several factors were contributed to the phenomena: (1) limited diffusion rate of NEG strips when large amount of photon stimulated desorption was occurred, (2) the shortage of the pumping speed at the upstream and downstream region in U9 system.

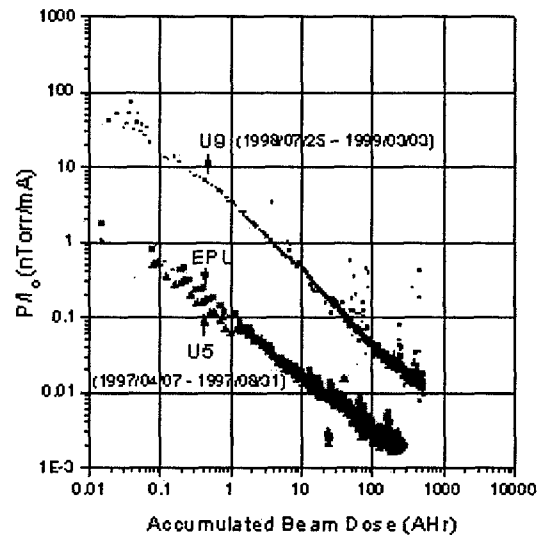


Fig. 3. The normalized pressure rise versus the accumulated beam dose in the upstream regime of U5, EPU5.6 and U9.

Figure. 4 shows the product of the electron-beam current and the lifetime versus the accumulated beam dose. The similar behavior of beam lifetime versus accumulated beam dose in this two systems was observed. A beam lifetime of 5 h at a beam current of 200 mA was achieved after an accumulated beam dose of 10 Ah for these two systems. However, the impact of the high pressure rise due to U9 ID chamber on the electron beam lifetime was small. For achieving better performance, the upgrade plan of U9 ID chamber will be proceeded in the future.

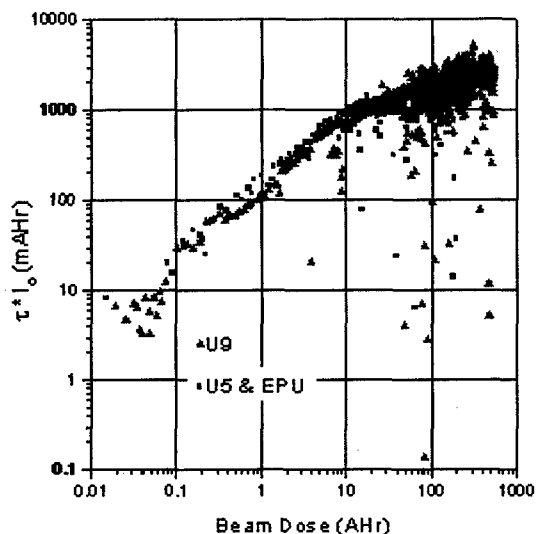


Fig. 4. The product of the beam current ( $I_0$ ) and beam lifetime ( $\tau$ ) vs the accumulated beam dose.

#### 4. SUMMARY

The chamber design, vacuum configuration and commissioning results of U5, EPU5.6 and U9 ID system are described in this article. The normalized pressure rise per mA in U9 system was one order magnitude higher than U5 and EPU5.6 system due to the shortage of the pumping speed at the upstream and downstream regime. However, the reduction of the electron beam lifetime was negligible due to this pressure rise.

#### 5. ACKNOWLEDGMENTS

The authors would like to thank their colleagues in the SRRC for their invaluable contribution to this work.

#### 6. REFERENCES

- 1.D. J. Wang, J. R. Chen, G. Y. Hsiung, J. G. Shyy, J. R. Huang, S. N. Hsu, K. M. Hsiao, and Y. C. Liu, J. Vac. Sci. Technol. A14, 2624 (1996).
- 2.G. Y. Hsiung, D. J. Wang, J. G. Shyy, S. N. Hsu, K. M. Hsiao, M. C. Lin, and J. R. Chen, J. Vac. Sci. Technol. A15, 2624 (1997).

## MODULAR COMPONENT POSITIONING ALONG THE BEAMLINE AXIS\*

Kevin J. Beczek, Dean R. Walters, Jack M. Jagger

Advanced Photon Source, Argonne National Laboratory, Argonne IL 60439 USA

### Abstract

In general, mechanical systems for particle accelerators are designed to remain stationary after they have been aligned. At the Advanced Photon Source (APS), a new device has been developed for the low-energy undulator test line (LEUTL), an experimental free-electron laser, that allows the components to be easily installed, removed, or exchanged without additional survey or alignment. A pair of high-precision linear guide rails fastened to a welded aluminum box beam provides the structure for this versatile and innovative method. The precision of this system exceeds  $\pm 380 \mu\text{m}$  along the beam axis and transverse to the beam. Design details and analysis are described as well as the present capabilities and those planned for the future.

### 1 INTRODUCTION

The concept of a modular and dynamic support structure grew out of the need to run experiments with components that could be rearranged or substituted as quickly and efficiently as possible, so as not to be inhibited by an excessively long construction phase. Although several alternatives presented themselves, it was decided that a rail and carriage system, aligned parallel to the beamline, would give the desired repeatability of transposition at the lowest cost, within the time required to fabricate it.

### 2 DESIGN, ANALYSIS, AND FABRICATION

#### 2.1 Structural Design Criteria

Based upon the authors' experience with beamline construction, it was decided that the precision of the system needed to be within a  $380\text{-}\mu\text{m}$  radius from the beam centerline along the entire length of the rails. It soon became apparent that in order for the mounted devices to be able to meet the intended goal, the underlying supports would have to perform just as well. In other words, the precision had to be built in from the ground up. From this evolved a design with rails fastened to a box-beam-shaped stiffening girder. The girder would also need to be made of nonferrous materials to minimize any residual magnetic effects to the electromagnets sitting on top of it. Contrary to popular notion, however, yield strength under a static load alone as a design criteria

would not suffice. Rather, the criteria focused primarily on the rigidity of the beam and secondly on a sufficiently high natural frequency, i.e., a frequency greater than 20 Hz.

Deflection and vibration of beams has traditionally been based on classic mechanics theory. Applicable equations used in structural design can be readily found in publications by authorities such as Timoshenko [1] and Harris [2].

#### 2.2 Finite Element Analysis

However, in recent years the use of finite element analysis software has made the typically iterative design process much more accurate and efficient. More to the point, the Pro/Engineer Mechanica [3] finite element program has been applied to a three-dimensional solid model of the girder to both improve the accuracy beyond the classic equations and give a better idea of the stress distribution and frequency response of a proposed geometry. Using this method, the girder design was optimized in a much shorter time than was previously possible.

The information from the analysis can be presented in several ways including contour map, color fringe plot, Cartesian coordinate graph, and animation. One of the more meaningful forms of display, particularly for stress distributions (Von Mises; i.e., distortion energy [4]) is the fringe plot as shown in Figure 1. This displays the response of the girder to a combination load of 4.448 kN (1000 lbs) and its own weight at the iteration of 3.260 kN (733 lbs). Constraints were placed upon the beam, e.g., simulating flat surfaces 30.5 cm (12 in) from each end and bolting it down as opposed to simply having it

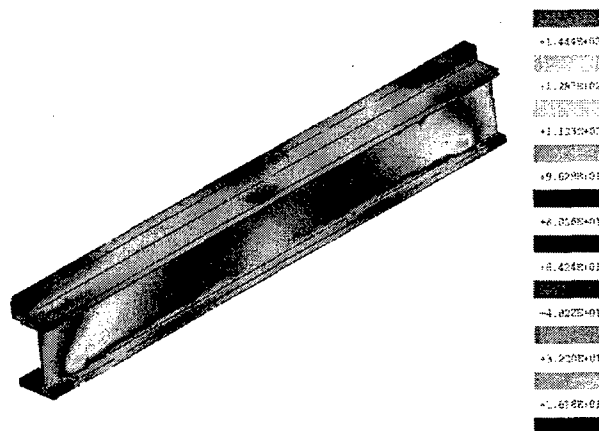


Figure 1: Girder distortion energy (color fringe plot)

\* Work supported by the U.S. Department of Energy, Office of Basic Energy Sciences, under Contract No. W-31-109-ENG-38.

Notice that the author has taken advantage of symmetry and analyses only half of the girder, cutting it lengthwise. (If the applied load and center of mass were exactly centered along the span, it would be possible to further simplify this by cutting the said section in half again.) Similar studies were undertaken to examine the deflection of the beam. Extensive nodal analysis of the beam and support structure is planned to continue in the future. Results are shown in Table 1.

Table 1: FEA modeled girder characteristics

Maximum Deflection with 4.448 kN (1000 lbs) load centered at midpoint of length	0.0178 mm (0.0007 in)
First Harmonic (x-y plane)	In progress
Total Weight	3.260 kN (733 lbs)
Length	3 m (118.1 in)
Material	6061-T6 aluminum

### 2.3 Fabrication

In an attempt to reduce costs and hasten the lead time, "off the shelf" items were used wherever possible. For example, the girder web uses the widest production aluminum c-channels available [5]. Prior to building the full-scale version, two 1.02-m-long prototypes of identical cross section were made. These were used to test the new carriage designs and to serve as staging platforms for installation on the large girder. Both large and small girders were intermittently (stitch) welded to minimize distortion. After welding they were vibration stress relieved, then the top and bottom surfaces were finish machined with a flycutter to within 0.381mm flatness over the entire length. The carriage securing block of the girder was then machined to the same level of repeatability along the entire length. This feature allows carriages to be fastened securely to the girder in a manner similar to a conventional milling machine. Mating holes for the guide rails and securing block were drilled and tapped with threaded inserts screwed in place [6,7,8].

### 2.4 Girder Adjustment and Base

The precise fabrication of the girder would be meaningless if there was no capability to adjust it when surveyed during installation. Consequently, the girder was bolted atop an adjustment mechanism that had been used successfully in the past at the APS. Two A36 structural steel plates became the "bed" for the girder and attachment points for two pairs of 1¼-inch 4140 fine-threaded steel rods. These rods were then screwed into mating thrust bearings of heat-treated 420 stainless steel and coated with Dicronite (WS2 lamellar tungsten disulfide) [9] to ensure a highly lubricious surface. Opposing swivel-head clamps allow this assembly to move in the horizontal plane, and the rod and bearing allow it to move in the vertical direction. The entire

mechanism rests on two industrial-grade and substantially gusseted machine tables also made from A36 structural steel and purchased from a local vender.

### 2.5 Rail and Bearing Selection

Perhaps one of the most crucial aspects of this design was the use of THK brand model GSR rails and linear bearings. In addition to having a low friction coefficient and an extremely high load capacity (approximately 0.003 and 25.9 kN each, respectively [10]), the bearings can be installed or removed from the side of the mating guide rail (see Fig. 2). Notice that one bearing individually does not completely envelop the guide rail, yet when assembled in a mirror configuration, provides ample resistance to transverse loads, making the bearings and the objects upon them highly stable.

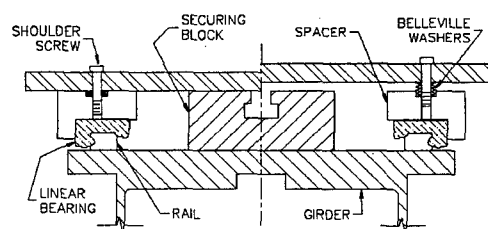


Figure 2: Cross-section of type "B" carriage (simplified for clarity)

### 2.6 Carriage Design and Mechanics

Straddling the securing block are several carriages, upon which the desired piece of beamline equipment rests; i.e., quadrupole magnets, corrector magnets, etc. Two types of carriages have been developed, each meeting the following design criteria: They must be removable from the bearings, and they must be able to be repeatedly raised and lowered onto the securing block to within a 380-µm radius from the beam axis. However, each carriage differs with respect to precision and simplicity of the mechanism. The type "A" carriage uses a plate translating along the length of a set of dowel pins. A stack of Belleville springs with sufficient lifting force to raise the intended weight is inserted on the pins. When the plate is clear of the surface of the block, the carriage rests completely on the THK bearings and is then free to travel the length of the guide rail as far as the operator desires, or until it comes in contact with another carriage. A set of bolts flanking the pins allow the plate to lower onto the securing block, compressing the springs in the process. Once the plate has made contact with the machined surface of the securing block, it can be fastened down with a diamond-shaped rotary T-nut. The type "B" carriage, while operating on the same physical principle, uses fewer parts, with shoulder screws and coaxial Belleville springs replacing the dowel pin and bolts.

### 3 INHERENT VERSITILITY

This support structure was designed from the start with the capability of being modified to suit the researcher's needs in the future. Installation of a mechanical or electromechanical transmission to move the components along the rails is certainly possible. Moreover, with the addition of a feedback device, the components might be controllable via computer to allow dynamic positioning or perhaps self-positioning. The entire structure can certainly be disassembled and rearranged to accommodate all of the aforementioned modifications.

### 4 SUMMARY

A modular method of positioning components along the beamline axis has been presented. A typical completed assembly is shown in Fig. 3. Although this is certainly not the only design that would meet our requirements, it is an innovative step forward in accelerator component support systems.

### 5 ACKNOWLEDGEMENTS

The author wishes to thank John Noonan for his constant support, Frank DePaola and the many skilled tradesmen and technicians, especially Leonard Morrison, Bruce Hoster, Aaron Lopez, Mark Martens and Ron Kmak.

Also, kudos to Ms. Catherine Eyberger for her patience in editing this paper. Finally and most importantly, thanks to LEUTL chief engineer Dean Walters for his mentoring and seemingly tireless energy in helping make this project a success.

### 6 REFERENCES

- [1] J. M. Gere and S. P. Timoshenko, *Mechanics of Materials*, second edition PWS Publishers, MA (1984).
- [2] C. M. Harris and C. M. Crede, *Shock and Vibration Handbook Vol. 1 Basic Theory*, McGraw Hill, NY (1961).
- [3] Pro/Engineer and Mechanica are registered trademarks of Parametric Technology Inc. Waltham, MA USA.
- [4] G. E. Dieter, *Mechanical Metallurgy*, third edition McGraw Hill, NY (1986).
- [5] *Engineering Data for Aluminum Structures*, third edition, the Aluminum Association, NY (1975).
- [6] R. T. Reese, F. Cericola, T. L. Ernest, "Small Threaded Connections - Recommendations for Design and Testing," Report SAND91-1047, Sandia National Laboratories (1992).
- [7] "Analysis of Pretensioned Bolted Joints Subject to Tensile Forces," Report ESDU-85021, Document ID 19890069141 N (89N71514), NASA Technical Reports (1985).
- [8] A. W. Brisbane, "The Evaluation of Some Threaded Inserts," Report AD-A085070, Document ID 19800020217 N (80N28718), NASA Technical Reports (1979).
- [9] Diconite is a registered trademark of Lubrication Sciences Inc. San Jose, CA USA
- [10] *Linear Motion Systems Handbook No. 200*, THK America, Schaumburg IL.

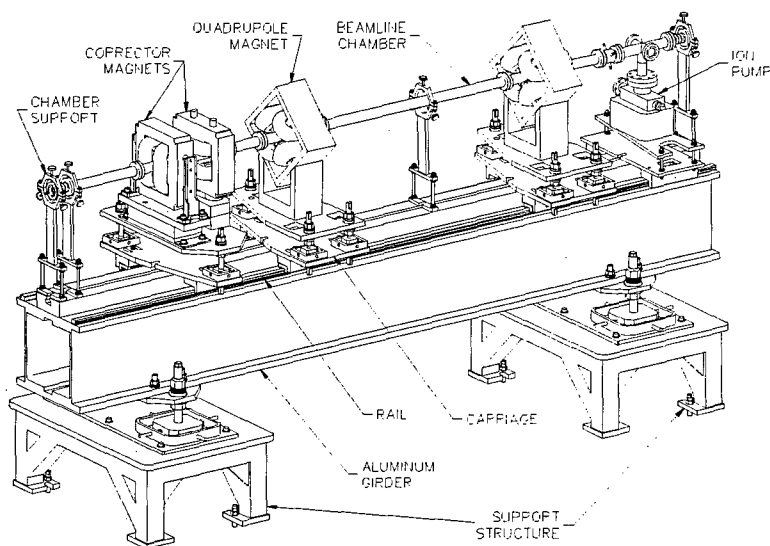


Figure 3: Beamline modular component station



# ALIGNMENT TECHNIQUES FOR THE HIGH CURRENT AIRIX ACCELERATOR

C. Bonnafond, D. Villate

CEA / CESTA BP n°2 33114 LE BARP - FRANCE

## Abstract

AIRIX is a linear induction accelerator which will produce by the end of 1999, a 20 MeV, 3.5 kA, 60 ns electron beam for X-Ray Radiographic applications. The high performance required for the French Radiographic Hydrotest Facility is connected to the beam quality and thus to the accelerator alignment. To minimize corkscrew motion and emittance increase of the beam, mechanical and magnetic alignments have been performed to assemble and align the accelerator cells by using capacitive detectors such as HLS (Hydrostatic Levelling System) and WPS (Wire positioning System). In order to perform magnetic alignment, the stretched wire technique has been developed for an automatic magnetic characterization of the cells. In this paper we will present and discuss the different alignment techniques but also the first results obtained

## 1 INTRODUCTION

The AIRIX induction LINAC will produce in Summer 1999, a 3.5kA, 20MeV, 60ns electron beam for flash X-ray radiography applications. This accelerator consists of 64 induction cells with a solenoidal focusing magnet and X, Y dipole steering magnets in order to perform the beam transport. The cells are assembled in blocks of 4 cells to obtain 16 blocks. The first 4 blocks were tested [1] at the beginning of 1999. The high beam quality requires low emittance increase ( $<10\%$ ) and energy spread ( $<1\%$ ). To achieve such performance, we must take care of the mechanical and magnetical alignments to minimize the chromatic effects. The goal is to enclose all the cell magnetic axes in a  $250\mu\text{m}$  diameter cylinder with an angle spread less than  $500\mu\text{rad}$ .

The solenoidal magnet is equipped with homogenizer rings, mechanically centered in the solenoid, to minimize the field errors. The cell magnetic axis is thus referenced to the mechanical one with a high accuracy ( $B_r/B_z < 8 \cdot 10^{-4}$ ). So these two axes are considered as the same in the alignment procedure.

In this paper we will present the mechanical technique to align the cells and the blocks on the accelerator axis. The magnetic characterization of the cells and the results obtained with the first 8 cell-blocks will be developed

## 2 MECHANICAL ALIGNMENT

### 2.1 Cell block assembling

The cells are first assembled with locating pins on a standard mounting bench SMB to obtain a block of 4 cells [2]. This bench is equipped with two standard references. The cells are aligned and assembled with an error less than  $30\mu\text{m}$  by using a laser and a moving CCD detector along the cell centerline. This accuracy includes the laser and the block positioning. In order to perform high accuracy block alignment all along the accelerator and control their position between two hydro-shots without breaking the vacuum, we define an external reference, outside the blocks, by means of HLS (Hydrostatic Levelling System), WPS (Wire Positioning System) capacitive detectors and an inclinometer. These detectors define respectively the vertical, the horizontal and angular positions of the block. These positions are recorded on a block-data file with an accuracy of  $10\mu\text{m}$  due to thermal effects.

### 2.2 Block alignment on the accelerator

This procedure can be characterized by the following steps: -calibration of the standard accelerator references on the SMB;

-alignment of these references with a theodolite on the accelerator axis. This axis is defined by the centered normal injector cathod;

- alignment of the blocks with respect of these references by using its block data file.

The positioning error and the measurement sensitivity of the blocks are less than  $10\mu\text{m}$  and  $1\mu\text{m}$  respectively.

A LabView program has been developed in order to control and follow the alignment continuously. The overall mechanical alignment accuracy is estimated at  $50\mu\text{m}$ .

## 3 CHARACTERIZATION OF THE SOLENOIDAL MAGNETS

The aim is to characterize for each block, the offset and the tilt misalignments of the cell solenoid magnets with respect to the block axis by using the stretched wire alignment technique [3] and cancel the tilt one with the steering magnets. The block axis is defined by the entrance and exit center block.

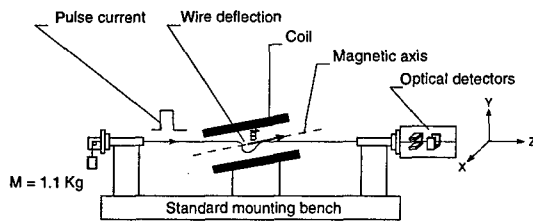


Figure 1: stretched wire technique

### 3.1 Principle

A wire is centered on the solenoid mechanical axis. If this axis is different from the magnetic one, transverse magnetic fields occur. The method (Fig. 1) consists in sending a short pulse of current and observing the motion induced in the wire due to Lorentz force. In order to measure the wire deformations in the two transverse X and Y directions, two optical detectors are placed close to the wire. The typical flaws measured are an offset and/or tilt of the solenoid magnetic axis with respect of the wire which materialize the solenoid mechanical axis. The two types of flaws (Fig 2) are so different that they can easily be distinguished.

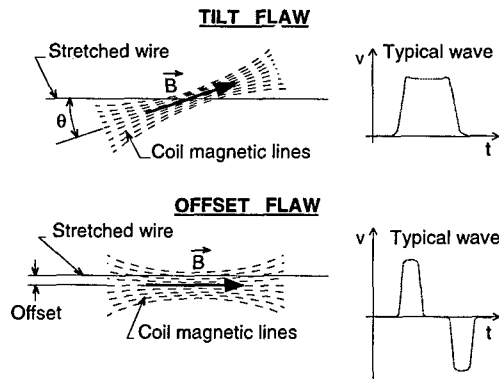


Figure 2: typical flaws

### 3.2 Procedures

The following steps for the 4 cells of each block must be achieved:

- center the wire on the block axis and then on a cell axis by taking into account the sag deformation of the wire;
- calibrate the optical detectors in a linear region;
- record the base line (deformations due to the external magnetic fields) by injecting a pulse current in the wire without a current in the solenoid. In order to eliminate the noise, we must average over several shots;
- measure the solenoid flaws with the base line subtraction, by injecting the pulse current in the wire with a current in the solenoid and average over several shots for the noise subtraction;

- calibrate the tilt and the offset flaws by moving the wire in the X and Y directions to obtain the desired flaws;
- apply X and Y dipole steering magnets in order to cancel the tilt signals produced by the cell solenoid magnet.

An automatic procedure with LabView has been developed to test the 16 blocks.

### 3.3 Experimental set-up

These measurements are made for each block on the SMB bench. We used a 125  $\mu\text{m}$  diameter Cu(98)/Be(2) wire. This wire is tensioned by a 1100 g weight and centered at the two block ends by means of two polarized straight edges precisely located by locating pins. The positioning procedure consists in moving the wire until it makes an electrical contact with these polarized edges. These edges are made of a polished surface with a gold layer coating to increase the contact which is performed when a sinusoidal current is established. In order to avoid a stick effect between the wire and the edges, we used a 5V sinusoidal polarization. To align the wire in the two X, Y transverse directions, two isolated edges are required. By making a succession of 10 measurements, a standard deviation value less than 5  $\mu\text{m}$  is obtained. To take into account the sag deformation of the wire, we finally move the wire in the middle of the cell solenoid.

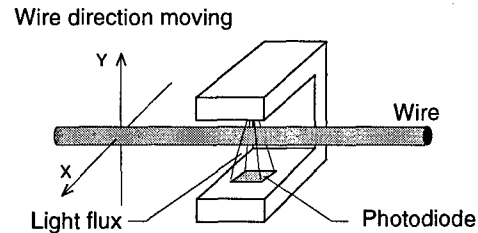


Figure 3: an optical detector

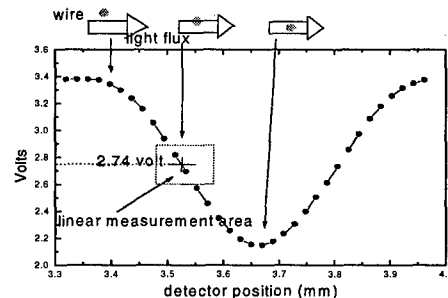


Figure 4: experimental detector calibration

The wire deflection is created by injecting a 5A, 300  $\mu\text{s}$  pulse current. This deflection is determined by measuring its time-varying obstruction of the light beam (Fig. 3) which is generated and detected by a pair of orthogonal, small, cheap, optical detectors (Hamamatsu P3784).

This detector is calibrated in a region of linear response (Fig. 4) by moving it in the two transverse X and Y directions by means of micrometers.

The signal of the detector is amplified with a gain of 100 and recorded on a AT-MIO-16E-2 DAQ National Instruments board sampling at 500kS/s with 12-bit resolution. The sensitivity of the detector/amplifier circuit is about 800mV/ $\mu\text{m}$  of wire deflection. The electronic noise, around 5mV, is very low compared to the noise generated by the structure's vibrations which can reach 1V. The eigen resonant frequency of the wire is 43Hz. To decrease the vibration noise level under 50mV, air cushions are placed under the SMB with an eigen resonant frequency of 2Hz. We also average over 20 measurements to cancel the statistical noise. The dead time between two pulses must be long enough (around 5s) to put the wire in quiet situation after all the damped reflected waves.

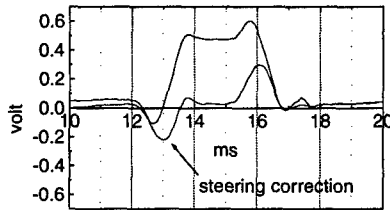


Figure 5: measured X flaws with and without steering correction

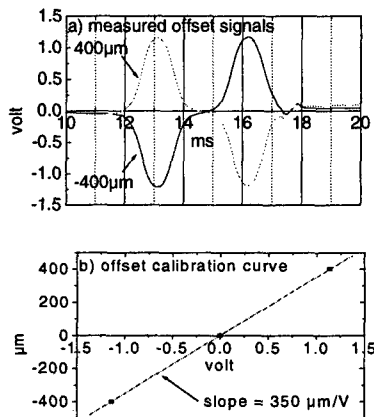


Figure 6a,b: experimental offset calibration

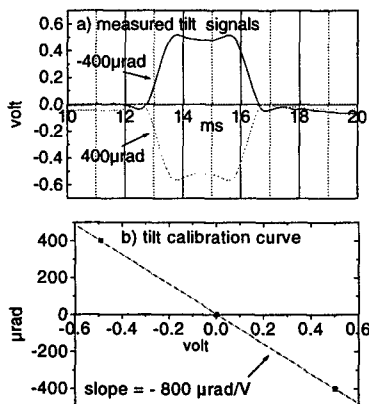


Figure 7a,b: experimental tilt calibration

### 3.4 Results

Measurements have been performed with a 5A, 300 $\mu\text{s}$  pulsed current in the wire and a 220A current in the solenoid magnet. In figure 5 we present a typical measurement of a cell magnetic flaw and the signal in the horizontal X direction with a 0.15A steering correction to cancel the magnetic tilt misalignment. The calibration of the tilt and offset is performed by moving the wire at various values to obtain the calibration curves by means of automatic micrometers. Figures 6, 7 show the offset and the tilt calibration curves with their measured signals. For an signal amplitude equal to 1 volt, we obtain an equivalent magnetic tilt and offset values of 800 $\mu\text{rad}$  and 350 $\mu\text{m}$  respectively. The sensitivity is around 50mV which corresponds to 40  $\mu\text{rad}$  and 17  $\mu\text{m}$ . The accuracy is estimated at 45  $\mu\text{m}$  and 130 $\mu\text{rad}$ . In table 1 we present the results for the 32 first accelerator cells without steering corrections.

	Mean value	RMS	max.
Offset <sub>x,y</sub> ( $\mu\text{m}$ )	30	45	90
tilt <sub>x,y</sub> ( $\mu\text{rad}$ )	700	400	1600

Table 1

By using steering corrections, the final tilt flaws are less than 130 $\mu\text{rad}$ . The steering currents are typically less than 0.5A for 220A solenoid magnet current, which correspond to a 1600 G magnetic field. A scale law has been established to adjust the steering current whatever the solenoidal current is. With the first 32 cells, the corresponding factor between the measured magnetic tilt and the steering current is  $(0.5 \pm 0.05) \text{ mA}/\mu\text{rad}$ .

## 3 CONCLUSIONS

The high quality beam requested for the AIRIX accelerator, leads us to use severe alignment specifications. We have demonstrated that the mechanical and the stretched wire techniques with steering corrections are adapted to align accelerator cells within the specifications. However, these techniques need to take care of mechanical tolerances and assembly of the cells as well as to use solenoid magnet with homogenizing ring to produce acceptable field errors. Thanks to automatic procedures, we have increased the measured accuracy.

## 4 REFERENCES

- [1]: E. Merle and al « Status of the AIRIX Accelerator » to be published in PAC'99 at New-York (USA)
- [2]: C.Bonafond, E. Merle and al « Status of AIRIX alignment and high current electron beam diagnostics » EPAC96, Sitges (Barcelona), 10-14 Juin 1996
- [3]: R.W. Warren and C.J. Elliot « A new system for wiggler fabrication and tuning ». Proceeding Adriatico Res. Conf. (28-38) R. Bonifacio, L. Fonda, C. Pellegrini (Word Scientific Singapore 1988), Trieste, Italy, June 1987.

# STUDY ON THE DETERMINATION OF REFERENCE CLOSED ORBIT OF THE STORAGE RING IN POHANG LIGHT SOURCE\*

A. H. Maeng<sup>#</sup>, K. W. Kim, T. Y. Lee, S. C. Lee, and J. S. Bak

Pohang Accelerator Laboratory, POSTECH, Pohang 790-784, Korea

## Abstract

We have studied the methods for the determination of reference closed orbit of the storage ring in PLS using magnet misalignment data. The reference closed orbit was determined by (1) a smoothing analysis using a low-pass filter method, and (2) a MAD (methodical accelerator design) simulation using the real parameters such as magnet misalignment data. Based on the estimated reference closed orbit, the relative positional errors of the storage ring magnets were evaluated. The results of case studies on the comparison of the smoothing analysis and the MAD simulation are described in this presentation.

## 1. INTRODUCTION

Since the control networks in the Pohang Light Source (PLS) storage ring tunnel were established in June 1993, we have monitored the networks periodically. The PLS storage ring tunnel was deformed unequally in vertical direction about 3 mm (peak-to-peak) a year. The range of the maximum deviation of storage ring magnets was extended to  $\pm 3$  mm from the ideal beam path [1]. Therefore, we have studied the methods such as smoothing analysis and MAD simulation for the determination of reference closed orbit using magnet misalignment data. The relative positional errors of magnets were estimated from the reference closed orbit. The estimated relative positional errors from 1996 to 1998 are summarized as follows: while the absolute positional tolerance, which was defined as the maximum deviation of magnets from the ideal beam path, showed  $\pm 3$  mm, the magnets were placed within the relative positional tolerance of 0.15 mm (rms) [2]. As a result, we decided that the period of magnet realignment of the PLS storage ring should be about two years [3].

## 2. TUNNEL DEFORMATION

The first survey of the PLS control networks was done in June 1993, and tunnel deformations in lateral and vertical directions have been monitored at every six months. The control networks consist of an ENET which controls elevations and a TNET which controls horizontal locations. Conventional survey instruments such as

theodolites (E2, T3000) and mekometer (ME5000) were used for the direction and distance survey, respectively. For the elevation survey, N3 Level and NEDO invar staff were used. The absolute error ellipses of TNET survey were in the range of 0.2 mm. The accuracy of ENET survey was about 0.07 mm ( $1\sigma$  value). This estimation was obtained by a GEONET program, which was developed at SLAC.

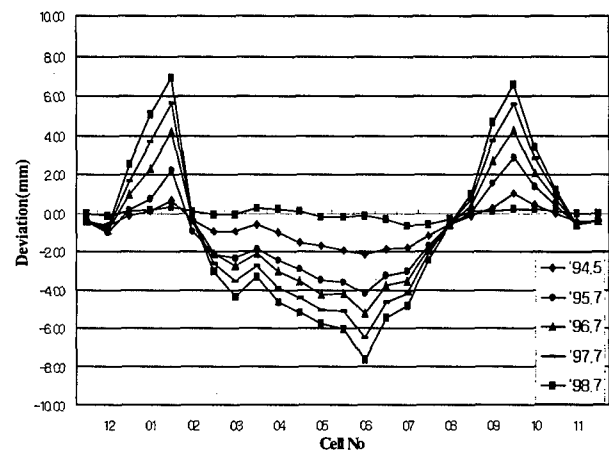


Figure 1: PLS storage ring settlement surveys.

As shown in Fig. 1, the storage ring tunnel was deformed in the vertical direction unevenly about 3.0 mm (peak to peak) per year. The lateral deformation, which is not shown in this graph, was within the range of  $\pm 1.0$  mm.

## 3. REFERENCE CLOSED ORBIT USING A SMOOTHING ANALYSIS

The tunnel deformation, which is discussed in the above, coincided with the storage ring deformation as a whole. We needed to apply a proper method for the estimation of the relative positional errors that could eliminate systematic errors due to the tunnel deformation. Studying a few smoothing analysis methods using deformation data of the storage ring surveyed in August 1995, we chose a smoothing analysis using a low-pass filter method. The smoothing analysis is a process of

\*Work supported by MOST and POSCO fund

<sup>#</sup>Email: mah@postech.ac.kr

determining the reference closed orbit of the storage ring which is close to the actual electron beam path [4].

Table 1: Results of the smoothing analysis for the PLS storage ring deformation in July 1996.

Freq. (MHz)	Relative Positional Errors (1 $\sigma$ ;mm)		Number of Outliers		Remarks
	Lat	Ver	Lat	Ver	
0	0.456	1.087	81	113	
1	0.300	0.742	51	92	
2	0.250	0.538	40	91	
3	0.217	0.294	32	59	
4	0.171	0.199	7	21	
5	0.153	0.162	6	9	
6	<b>0.136</b>	<b>0.130</b>	<b>2</b>	<b>3</b>	<b><math>\leq 0.15\text{mm}</math></b>
7	0.130	0.127	2	2	
8	0.126	0.115	2	1	
9	0.125	0.104	2	1	
10	0.125	0.089	2	0	

The deformations of the storage ring from the ideal beam path were 0.5 mm and 1.1 mm in the lateral and vertical directions, respectively in 1996. The relative positional errors and the number of outliers decreased as the filtered frequency increased as listed in Table 1.

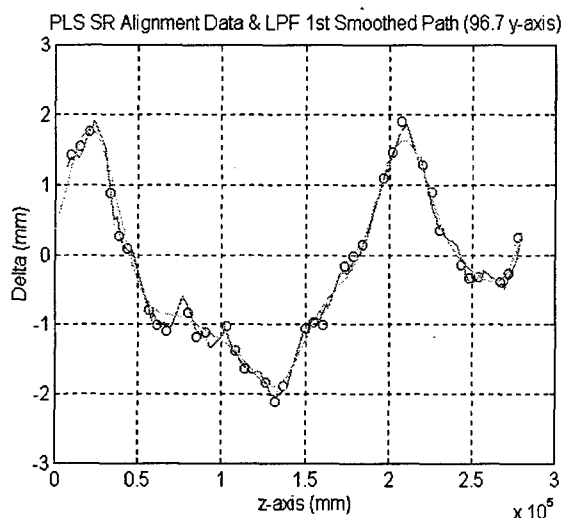


Figure 2: Vertical displacements of all storage ring magnets in 1996 (by smoothing analysis).

When the filtered frequency was 6 MHz, the errors became smaller than the positional tolerance of 0.15 mm and there were only a few outliers. Considering these results, we estimated that the relative positional errors of magnets were 0.14 mm (rms) in the transverse direction and 0.13 mm (rms) in the vertical direction. The result of smoothing analysis is shown in the Fig. 2 for the vertical direction. The estimated reference closed orbit deviates from the ideal position by  $\pm 2$  mm. However, we could have left the storage ring without the adjustment

of magnets by considering the following facts. First, the storage ring was in normal operation, second, the relative positional errors were within the tolerance of 0.15 mm, and third, the deviations from the reference closed orbit were within 2  $\sigma$  range ( $\pm 0.3$  mm) except for 2 or 3 magnets. The issue of the magnet adjustment was discussed with beam physicists. The maximum deviation from the ideal closed orbit was required to be kept within  $\pm 3$  mm range. Based on this requirement, we estimated the positional errors of storage ring magnets in July 1997 by the smoothing analysis. The relative positional errors of magnets were 0.13 mm (rms) and 0.10 mm (rms) in transverse and vertical direction, respectively.

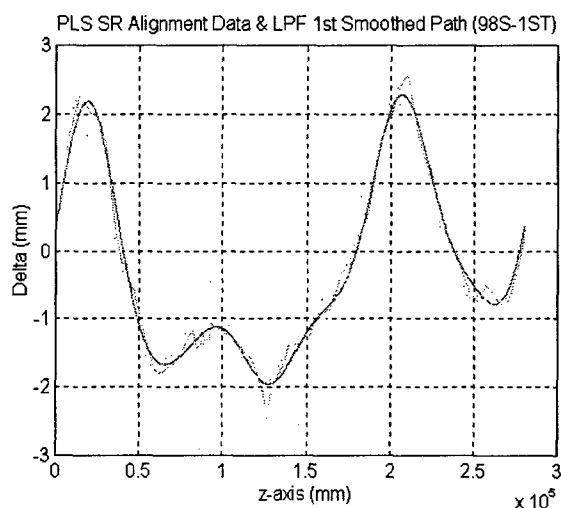


Figure 3: Vertical displacements of all storage ring magnets in 1998 (by smoothing analysis).

The results of the storage ring deformation and the reference closed orbit by the smoothing analysis in July 1998 are shown in Fig. 3. At the 6 MHz of filtered frequency, the relative positional errors of magnets were 0.12 mm (rms) transversely and 0.13 mm (rms) vertically and there was no outlier. It is shown that all magnets were placed within the expected maximum deviation range of  $\pm 2.5$  mm from the ideal beam path, and the quadrupole magnets were placed within 2  $\sigma$  range ( $\pm 0.3$  mm).

#### 4. REFERENCE CLOSED ORBIT USING A MAD SIMULATION

The reference closed orbit can be determined by a MAD (methodical accelerator design) simulation using real parameters. The most significant parameter that has an effect on the determination of closed orbit is as follows: quadrupole misalignment ( $\Delta x, \Delta y$ ), bending magnet field error ( $\Delta B/B$ ), and bending magnet rotation error with respect to the beam axis ( $\Delta\phi$ ) [5]. We simulated the reference closed orbit using quadrupole misalignment data, bending magnet rotation error. The analytical

formulas for reference closed orbit are given by:

$$x_{rms} = \frac{\sqrt{\beta_x}}{2\sqrt{2} \sin \pi \nu_x} [\theta_B^2 (\frac{\Delta B}{B})^2 \sum_i \beta_{xi} + (\Delta x)^2 \sum_i (kl)_i^2 \beta_{xi}]^{1/2}$$

$$y_{rms} = \frac{\sqrt{\beta_y}}{2\sqrt{2} \sin \pi \nu_y} [\theta_B^2 (\Delta \phi)^2 \sum_i \beta_{yi} + (\Delta y)^2 \sum_i (kl)_i^2 \beta_{yi}]^{1/2}$$

The result obtained by MAD simulation is shown in Fig. 4. The figure shows the displacements of all magnets from the ideal beam path and the estimated reference closed orbit in July 1996. The relative positional errors of magnets were 0.13 mm (rms) and 0.10 mm (rms) in transverse and vertical direction, respectively.

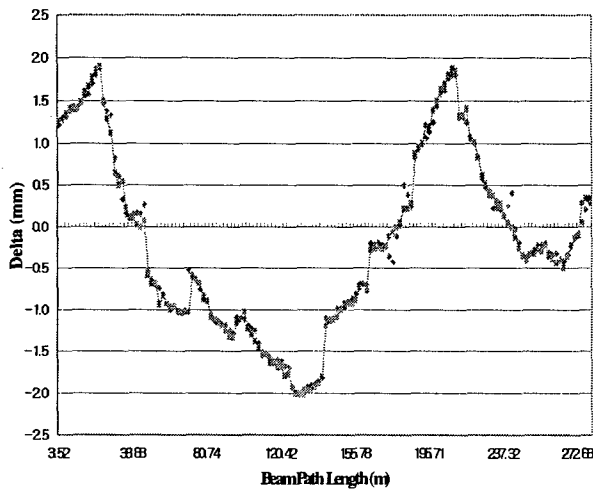


Figure 4: Magnets vertical displacements and closed orbit in 1996 (by MAD simulation).

Fig. 5 shows the displacements of the magnets measured in 1998 and the deviations of magnets from the estimated reference closed orbit in the vertical direction. The relative positional errors of magnets were 0.11 mm (rms) transversely and 0.12 mm (rms) vertically. All magnets were placed within the allowable positional tolerance of 0.15 mm (rms).

As a result, the relative positional errors estimated from the two different reference closed orbits, one was determined from the smoothing analysis and the other was from the MAD simulation, coincided with each other within the range of tolerance.

## 5. CONCLUSION

Settlement of the PLS storage ring tunnel results in the machine deformation of 3 mm (peak to peak) a year in vertical direction. By employing the smoothing analysis by the low-pass filter method, we could get the reference closed orbit in the form of a smoothed curve. And we determined the reference closed orbit by the MAD

simulation using the real parameters such as magnet misalignment data. The estimation of the relative positional errors based on the reference closed orbits was carried out.

The results of closed orbit studied using deformation data of the storage ring from 1996 to 1998 showed that the relative positional errors estimated from the two different reference closed orbits coincided with each other within the range of tolerance. The absolute positional tolerance of magnets could be extended to  $\pm 3$  mm and the deviation of magnets from the reference closed orbit extended to  $2\sigma$  range ( $\pm 0.3$  mm), because the storage ring operated normally and the relative positional error of magnets was within 0.15 mm (rms).

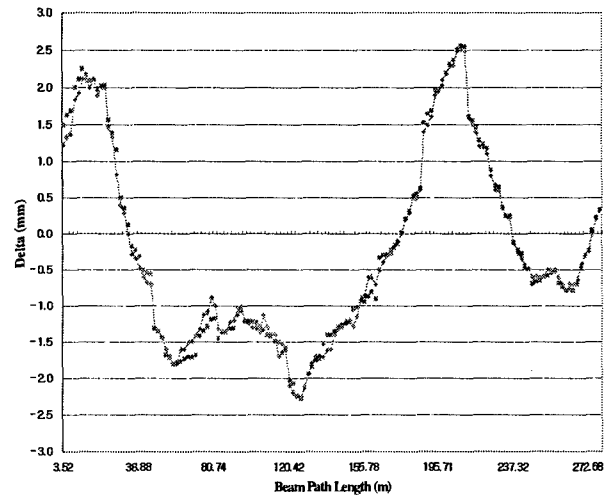


Figure 5: Magnets vertical displacements and closed orbit in 1998 (by MAD simulation).

## 6. REFERENCES

- [1] A. H. Maeng, K. W. Seo and S. C. Lee, "Survey and Alignment of Pohang Light Source", Proceedings of the 4th International Workshop on Accelerator Alignment, Tsukuba, Japan, Nov. 1995.
- [2] S. C. Lee, A. H. Maeng and K. W. Seo, "Measurement of Deformation and Smoothing Method for Pohang Light Source", Proceedings of the 5th International Workshop on Accelerator Alignment, ANL/FNAL, USA, Oct. 1997.
- [3] S. C. Lee, A. H. Maeng, K. W. Seo, J. S. Bak and I. S. Ko, "Determination of Magnet Realignment Period based on Smoothing Analysis", Proceedings of the APAC Meeting, KEK, Japan, Mar. 1998.
- [4] J. G. Yoon and S. C. Lee, "Smoothing Analysis of PLS Storage Ring Magnet Alignment", Proceedings of the 4th International Workshop on Accelerator Alignment, Tsukuba, Japan, Nov. 1995.
- [5] The MAD Program (Methodical Accelerator Design) ver 7.2, User's Reference Manual

# GROUND MOTION MEASUREMENTS FOR FERMILAB FUTURE COLLIDER PROJECTS

B. Baklakov, T. Bolshakov, A. Chuprya, A. Erokhin, P. Lebedev, V. Parkhomchuk, Sh. Singatulin, BINP, Novosibirsk, Russia; and J. Lach, V. Shiltsev, FNAL, Batavia, IL, USA

## Abstract

This article presents results of wide-band seismic measurements at the Fermilab site, namely, in the tunnel of the Tevatron and on the surface nearby, and in two deep tunnels in the Illinois dolomite, thought to be a possible geological environment of the Fermilab future accelerators.

## 1 MEASUREMENTS

There are several future collider projects under consideration at Fermilab, including muon collider, linear collider and Very Large Hadron Collider (VLHC). Ground motion is of concern for all of the projects, although due to different effects [1]. That was major reason for seismic studies at the Fermilab site and in the Illinois dolomite tunnels which we carried out in 1997. Our seismic instrumentation included eight modified geophone of SM3-KV type (frequency range from 0.07 to 120 Hz) two tri-axial STS-2 seismometers (0.005-15 Hz), and two Wiloxon-731A piezoaccelerometers (10-400 Hz).

**Measurements at Fermilab** Vibration measurements in the Tevatron tunnel have been done at Sector F11 (not far from the Tevatron RF station and the E4R building) and Sector F21 some 300 m apart. The computer was located on the surface in the F0 building. Seven SM3-KV probes (four vertical and three horizontal) and two vertical piezoaccelerometers were used. Two seismic stations were placed at a distance 296 m apart. Station 1 digitized the signals from one vertical and one horizontal SM3-KV probes on the floor of the tunnel at F21, and from vertically oriented piezoaccelerometer and vertical and horizontal SM3-KV geophones on the Tevatron quadrupole magnet. Station 2 digitized the signals from four SM3-KV geophones (vertical and horizontal on the quadrupole magnet at F11 and vertical and horizontal on the tunnel floor nearby), one piezoaccelerometer placed on the same magnet, and additionally from a beam position monitor (BPM) and a beam loss monitor (BLM). Recording vibration signals in the Tevatron tunnel over several days, we observed little day-night variation of the maximum tunnel floor motion amplitude. Cultural noise dominates in vibrations of the magnet and the tunnel floor. At frequencies above 1 Hz it is due to the technical equipment (water and helium pipes, power cables, magnets themselves, etc.) At frequencies around 1 Hz and lower the main contribution is possibly due to strong mechanical distortions of the magnets during the Main Ring acceleration cycle (about 3 s) and the Tevatron acceleration cycle (about 60 s in fixed target operation).

The closed orbit distortions are caused by the displacements of all magnetic elements along the circumference of Tevatron. We detected strong coherence between the magnet and beam vibrations. It means that there is a common source of vibration along the whole accelerator ring. For example, several remarkable peaks in the orbit-magnet coherence occur at 4.6 Hz, 9.2 Hz, 13.8 Hz, etc., at the Fermilab site specific frequencies caused by Central Helium Liquefier plant operation.

**Measurements in deep tunnels** Specific locations for possible Fermilab Future Colliders have not yet been chosen. There is also no definite requirement to be located within the FNAL site. For the purposes of radiation safety and tunnel stability, deep tunnels in the Illinois dolomite layer are alternative. This several hundreds feet thick layer is considered as moderately hard and stable. We studied seismic vibrations at two points of the Illinois dolomite layer. The first is a 250 ft deep mine (Conco Mine - Western Stone Co., North Aurora, IL; about 500ft above sea level) located about 5 miles North-West of Fermilab. The second location is a 300 ft deep tunnel of the Metropolitan Water Reclamation District of Greater Chicago (MWRDGC) about 30 miles East of the Fermilab in the Chicago suburb of Hodgkins, IL. It is near (<0.5 mile) from an active interstate highway I-55, and very close to a stone quarry. The tunnel was constructed as a part of the Tunnel and Reservoir Project (TARP) of the MWRDGC.

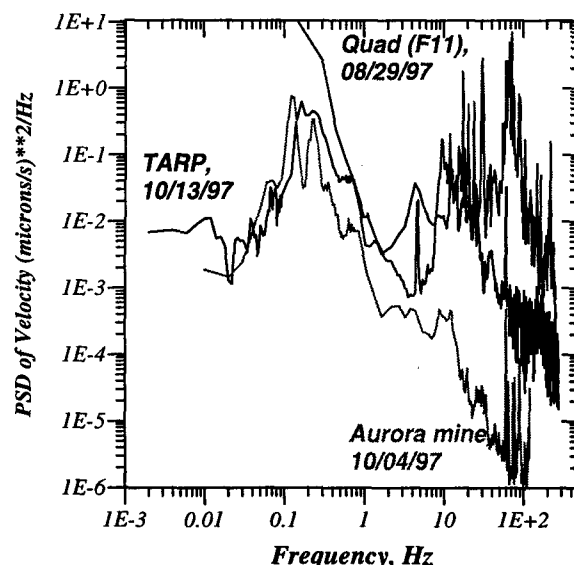


Figure 1: Spectra of ground motion in Aurora mine, TARP tunnel, and the Tevatron magnet vibrations

Power spectral densities of the ground velocities  $S_v(f)$  measured in the Aurora mine, in the TARP shaft are presented in Fig.1 in comparison with the Tevatron quadrupole magnet vibration PSD. These spectra cover five decades of frequency band from 0.005 Hz to 280 Hz and are obtained with different probes and with different sampling rates (besides different places and different times). For example, the TARP curve (solid line) consists of spectrum measured by the STS-2 vertical probe (from 0.005 Hz to 0.1 Hz), by the SM3-KV geophone (from 0.1 Hz to 120 Hz) and by the Wiloxon piezo-probe (from 120 to 280 Hz). The Aurora data (dashed line) show no vibration spectrum above 120 Hz – the motion is too small to be detected by the piezoaccelerometers.

One can see that the Aurora mine is the quietest place of the three. Some technologically related peaks are seen in the “Aurora” PSD only at 60-120 Hz range. We believe that it is due to lighting transformers in the tunnel. Below 0.5 Hz the spectral density in Aurora mine and in the TARP tunnel are about the same, and are mainly due to microseismic waves. Above 2 Hz, the TARP PSD is 20-800 times the Aurora mine PSD. Noisier environment on the surface and more technological equipment in the tunnel itself are probable reasons for two very broad peaks in the TARP spectrum at 5 Hz and around 25 Hz, respectively (as damping decrement of the ground grow with frequency). Finally, the Tevatron quadrupole spectrum consists of many peaks (4.6Hz, 9.2Hz, 20Hz, 60Hz, etc.) and is much noisier (as we discussed above - due to the Tevatron equipment) than the others above 10 Hz. All three spectra show “a microseismic peak” near 0.2 Hz. Usually, the rms amplitude of the tunnel motion is less than a micron everywhere, but occasionally we observed ground motion amplitude is of the order of 10-25 microns, like during Oct.14, 1997 M6.8 Chile earthquake. These waves with periods of 20-80 sec were well correlated over maximum distances of our studies (about 80 m).

Fig.2 shows real and imaginary parts of the correlation spectrum  $C_{x_1 x_2}(f)$  of signals from two vertical SM3-KV geophones placed 75 m apart in the TARP shaft. Each of the curves is an average over 200 measurements that gives an estimate of the statistical error of about 0.1. The first remarkable feature of the data is that at frequencies below 100 Hz the real part is much larger than the imaginary one. The latter is almost zero below 10 Hz, while the real part performs some damped oscillations with the frequency increase. Such a behavior is close to prediction of the model in which the vibration sources are uniformly and continuously distributed over ground surface and generate waves at all frequencies without any phase correlation, see e.g. [4]. Under these assumptions the correlation spectrum between signals detected in two points  $L$  meters apart is equal to  $ReC(f) = J_0(2\pi Lf/v(f))$ ,  $ImC(f) = 0$ , where  $v(f)$  is the wave propagation velocity and  $J_0(x)$  is zeroth order Bessel function. In Fig.2 we present the fitting curves with parameters  $L = 75\text{m}$  and  $v(f)[\text{m/s}] = 3800 - 4 \cdot f[\text{Hz}]$ .

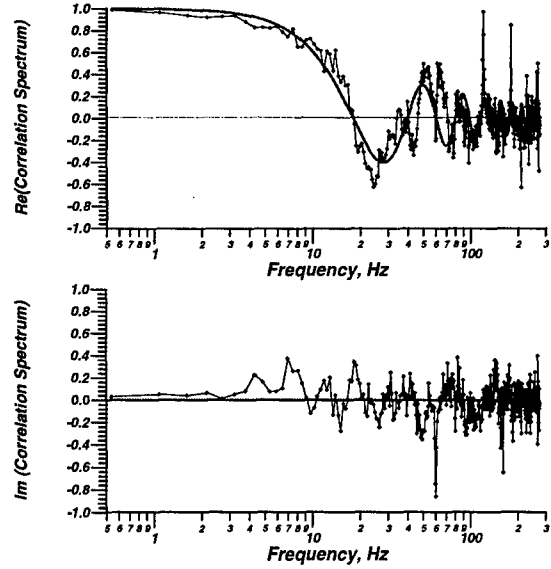


Figure 2: Real and Imaginary parts of correlation spectra measured in the TARP shaft at distance of 75m between probes and fit accordingly to random source model.

## 2 DISCUSSION AND PLANS

Integration of the PSDs accordingly to

$$\sigma_x(f) = \int_f^\infty S_x(f) df = \int_f^\infty S_v(f) \frac{df}{(2\pi f)^2}, \quad (1)$$

(here  $S_v(f)$  is the PSD of velocity,  $S_x(f) = S_v(f)/\omega^2$  is the PSD of displacement) gives us the rms amplitudes of vibrations. Fig.3 presents integrated vibration amplitudes in the Aurora mine and on top of the Tevatron quadrupole. One can see that the amplitudes in the deep tunnels are about  $0.3 \mu\text{m}$  at frequencies  $\sim 0.5$  Hz and below, while above 100 Hz they are less than  $0.1 \text{ nm} = 10^{-4} \mu\text{m}$ . Motion of the quadrupole is several times larger. Other curves are for the tolerances: for the X-band linear collider it is the ground motion which causes 1.5% luminosity degradation accordingly to Ref.[4]. We would like to emphasize, that the tolerances for other than X-band LCs can be much less stringent if larger bunch spacing allows to implement bunch-by-bunch trajectory correction feedback system. The muon collider requirement is presented by the rms amplitude of focusing magnets that leads to beams separation of about 10% of the rms beam size at the interaction point. The VLHC tolerance consists of two parts [2]: at frequencies below 10 Hz the curve shows the vibration amplitude that causes the beam orbit vibration amplitude about 10% of the rms beam size. Above 90 Hz the line corresponds to requirement on the rms transverse emittance growth less than  $0.1 \pi \text{ mm-mrad/5 hours}$  without (solid line) and with feedback system to damp excited betatron oscillations (dashed line, feedback allows to ease the ground motion tolerances some 10 times or more depending on the beam tunespread). One can see that the Aurora mine amplitudes are below all the tolerances, although close to the VLHC ones around 90-120 Hz. In contrast, vibrations of the Tevatron quadrupole are potentially very dangerous for



all three machines at frequencies below 20-60 Hz (orders of magnitude excess), and several times above the VLHC requirement above 70 Hz.

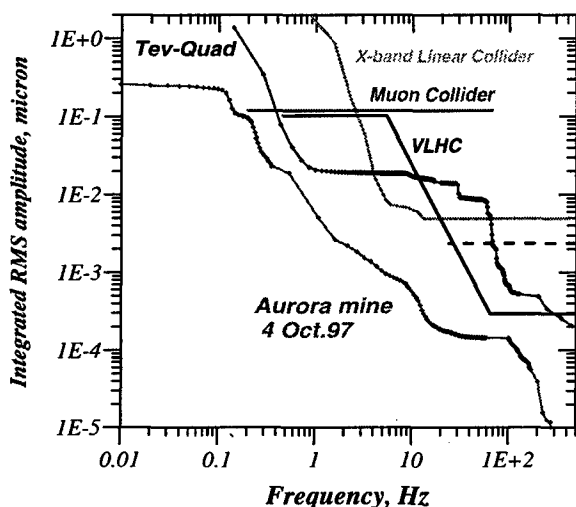


Figure 3: Comparison of the measured ground and quadrupole vibration amplitudes with tolerances for the muon collider, X-band linear collider and the VLHC.

We have to note that, in general, accelerators are relatively 'noisy' sites because of their technical noises. We compare our data with previous measurements at accelerator facilities in Fig.4. It presents the PSDs of ground velocity  $S_v(f) = S_x(f)(2\pi f)^2$  measured in the Aurora mine (marked as FNAL) and in the tunnels of the SLAC(SLAC)[4], HERA [5], KEK[6], LEP(CERN)[7], and so-called "New Low Noise Model" [8] – a minimum of geophysical observations worldwide. One can see that the PSDs measured at accelerators are well above the "low-noise" spectrum. At the same time, vibrations in HERA, which is located under populated area in city of Hamburg, are somewhat larger than in the other tunnels.

Main conclusions of our studies are:

1. Ground vibration have been measured at the FNAL site and in deep tunnels outside in wide frequency band from few hundredths of a Hz to several hundreds Hz. We have observed that vibrations above 1 Hz are well affected by cultural noise which vary significantly in time and also strongly depend on location and the depth, while below 1 Hz main contribution to the ground motion comes from natural sources and performs slow temporal variations.

2. Comparison of on-surface and underground sites have shown that levels of vibrations are typically smaller in deep tunnels. Effects due to on-surface noise sources are less seen in the deep tunnels, though visible. Amplitudes of horizontal and vertical vibrations are approximately the same.

3. The maximum amplitudes are observed for the motion of the Tevatron quadrupole magnets when the Tevatron and the Main Ring accelerators were operating. It was somewhat larger than the motion of the tunnel floor nearby. Careful engineering of mechanical supports, of vacuum, power and cooling systems should be an important part of

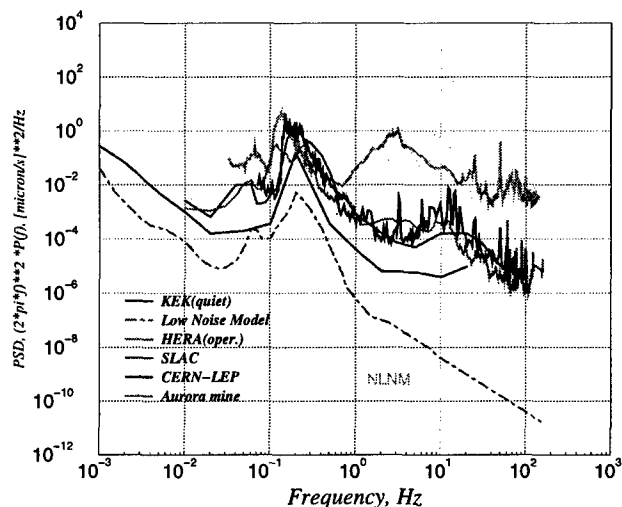


Figure 4: Ground motion spectra at different accelerator sites and the USGS New Low-Noise Model.

R&D efforts to decrease the level of vibrations in any other future collider.

4. In deep tunnels in the Illinois dolomite (Aurora mine, the TARP shaft) we observed vibrations below the tolerances for all the collider projects, while the Main Ring tunnel is not quiet enough for future colliders, especially for the VLHC.

5. Investigations of a spatial characteristics of the fast ground motion have shown that above 1-4 Hz the correlation significantly drops at dozens of meters of the distance between points.

Our future plans include measurements of a very slow ground motion (time scale from minutes to a year) in the Tevatron tunnel and in deep tunnels in the Illinois dolomite with use of a hydrostatic leveling system. Experimental data on long term tunnel stability are needed to design orbit correction and alignment systems of future colliders.

Seismic studies presented above would not have been done without help of many people from FNAL, BINP, ANL, SLAC, MWRDGC, Conco Co.. We are indebted to all of them.

### 3 REFERENCES

- [1] V.Shiltsev, *Proc. EPAC'96*, Barcelona(1996), 32.
- [2] V. Shiltsev, Preprint FNAL-TM-1987(1996).
- [3] B.Baklakov, *et. al*, *Phys. Rev. ST Accel. Beams*, 1, 031001 (1998).
- [4] Appendix C of NLC ZDR, Report SLAC-R-0485 (1996).
- [5] V.Shiltsev, *et.al*, *Proc. PAC'95*, Dallas(1995) 2078, 3424.
- [6] S.Takeda, M.Yoshioka, KEK-Preprint 95-209 (1996).
- [7] V.Jouravlev, *et.al*, CERN-SL/93-53, CLIC-Note-217 (1993).
- [8] J.Peterson, USGS Open-File Report 93-322, Albuquerque, NM (1993).

# ALIGNMENT OF THE VISA UNDULATOR\*

R. Ruland, D. Arnett, G. Bowden, R. Carr, B. Dix, B. Fuss, C. Le Cocq, Z. Wolf, SLAC, Stanford, CA  
J. Aspenleiter, G. Rakowsky, J. Skaritka, BNL, Upton, NY  
P. Duffy, M. Libkind, LLNL, Livermore, CA

## Abstract

The Visible-Infrared SASE Amplifier (VISA) undulator [1] consists of four 99cm long segments. Each undulator segment is set up on a pulsed-wire bench, to characterize the magnetic properties and to locate the magnetic axis of the FODO array [2]. Subsequently, the location of the magnetic axis, as defined by the wire, is referenced to tooling balls on each magnet segment by means of a straightness interferometer. After installation in the vacuum chamber, the four magnet segments are aligned with respect to themselves and globally to the beam line reference laser. A specially designed alignment fixture is used to mount one straightness interferometer each in the horizontal and vertical plane of the beam. The goal of these procedures is to keep the combined rms trajectory error, due to magnetic and alignment errors, to 50 $\mu$ m.

## 1 INTRODUCTION

The four-meter long undulator consisting of four 99cm long segments is supported on a strongback. The undulator system needs to be aligned to 50 $\mu$ m so that maximum Self-Amplified Spontaneous Emission (SASE) gain can be attained. Each magnet must be aligned with respect to each other and, at the same time, with respect to the global beam line coordinate system. In addition, the beam of a laser (Reference Laser Beam - RLB) defines the global position of the undulator's centerline in the beam line coordinate system.

The extremely tight alignment tolerance precludes the application of traditional high precision optical alignment methods, including laser tracker based procedures. However, because of the straight-line geometry and the relatively short length, interferometric straightness measurement techniques can be used. A standard HP straightness interferometer in "long distance" mode (0.5m - 30m) will provide a straightness resolution of 0.8 $\mu$ m with 5 $\mu$ m accuracy over the length of the undulator, and a straightness measurement range of  $\pm 1.5$ mm. This method is one dimensional, i.e. horizontal and vertical positioning will be accomplished using two independent straightness interferometer systems.

The final alignment residuals should be less than 50 $\mu$ m. However, the total alignment tolerance also includes the fiducialization error, which in itself consists of two contributions. The first part is related to the precision with which the true magnetic centerline can be

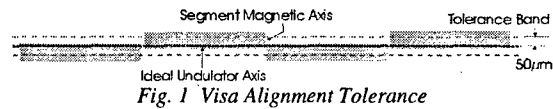


Fig. 1 VISA Alignment Tolerance

determined. The second on how the centerline can be transferred onto mechanical fiducials. Each undulator has an error budget as shown in the following table.

Table 1: Alignment Error Budget	[ $\mu$ m]
Magnetic Centerline Determination	20
Transfer onto Fiducials	23
Reference Undulators to RLB	29
Positioning	28
Total (added in quadrature)	51

## 2 ALIGNMENT CONCEPT

### 2.1 Fiducialization (Magnetic Measurements)

The first step in fiducialization of the undulator magnets involves determining the magnetic centerline yielding a wire that is physically positioned along the magnetic centerline of the undulator [3].

Next the wire position is measured with respect to the Wire Finder's (WF) reference tooling ball. One WF is positioned on each the upstream and downstream sides of an undulator segment to detect the wire position in the horizontal orientation only. To avoid wire sag effects that would bias the vertical measurements, the vertical positioning will be accomplished by rolling the undulator segment by 90° creating another horizontal measurement. Now with the WF tooling balls positioned relative to the magnetic centerline, a straightness interferometer setup can be used to measure the undulator tooling balls relative to the WF tooling balls. These steps are all repeated with the undulator segment rolled each time by 90°. After correcting for the non-parallelity effect between the wire and the interferometer axes, adding the fiducialization values of the two tooling balls in both the horizontal and vertical plane should equal the spatial distance between the respective two tooling balls. This value is compared against a previous measurement on a high accuracy Coordinate Measurement Machine (CMM).

### 2.2 Installation Alignment

Conventional alignment methods will be used to for mechanical installation achieving about 200 $\mu$ m accuracy.

### 2.3 Fine Alignment

#### Positioning the Alignment Jig

The absolute distance between the Laser Finder (LF) tooling ball and the Straightness Interferometer (SI) reference line is unknown, all SI measurements are only relative. Theoretically, the SI reference line must be

\*Work supported by the United States Department of Energy, Office of Basic Energy Sciences under contract No. DE-AC03-76SF00515.

precisely parallel to the RLB in order to avoid applying corrections to each undulator tooling ball measurement.

Using the same constant length offset bar for the "A" and "B" measurements, parallelity is achieved when  $A1 + A2$  equals  $B1 + B2$ . However, tests have shown that it is difficult and time-consuming to achieve this condition. On the other hand, a parallelity of about 0.5 mm can be achieved quickly by adjusting the pointing of the interferometer laser. Therefore, the effects of the remaining skewness of the straightness interferometer axis with respect to the LF line will be taken out numerically by applying a similarity transformation.

#### Detect RLB Position with Laser Finders-Reference to SI

A kinematic mount will be installed on both the upstream and downstream sides of the undulator assembly (fig. 2). This is necessary, since only one Laser Finder will be used to detect the RLB in order to avoid systematic errors. First, the LF is set into the downstream mount, and the RLB position is measured with respect to the horizontal and vertical tooling balls of the LF. Second, these tooling balls are referenced against the respective SIs integrated into the alignment jig. Last, these two steps are repeated for the upstream LF position.

#### Measure Positions of Undulator Segments With SI

It should be stressed again that the SI is only a relative alignment tool. The capability to position the undulators to an absolute position is only gained through the absolute calibration of the LF. The absolute calibration of the LF yields a metric measurement of the horizontal and vertical projected distances between the RLB and the LF tooling balls in the horizontal and vertical planes, respectively. The subsequent SI measurements let us relate the unknown undulator segment fiducial positions to the known LF positions. To create an accurate snap shot of an undulator segment's position, the horizontal and vertical SI readings are taken simultaneously.

#### Position Undulators

Before the position correction values can be calculated, the SI readings need to be corrected for the non-parallelity of the RLB and SI coordinate systems. A similarity transformation (fig. 3) is used to compute the corrected SI readings. The basic similarity transformation can be written as:

$$\begin{pmatrix} x \\ y \end{pmatrix} = \begin{pmatrix} t_x \\ t_y \end{pmatrix} + \begin{pmatrix} \cos \theta & \sin \theta \\ -\sin \theta & \cos \theta \end{pmatrix} \begin{pmatrix} u \\ v \end{pmatrix}$$

The three unknowns:  $t_x$ ,  $t_y$ ,  $\theta$  can be determined by substituting the coordinates of two points known in both systems into a set of four equations. Because the coordinate systems are almost parallel, only approximations for  $x$  and  $u$  are required. Subsequently, the solution of the

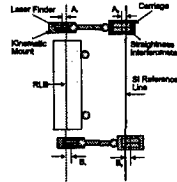


Fig. 2 Alignment jig

equation yields the unknown offset value of an undulator fiducial from the RLB axis. This offset reduced by the fiducial's fiducialization value (FV) gives the position adjustment value ( $\Delta P$ ). The undulator's position is then adjusted under the control of the SI.

#### Quality Control

After all adjustments are applied, the undulator fiducial positions are recorded. Due to the geometry and construction of the supports, a slight coupling between the adjustment axes is to be expected. This might require iterating the last two steps.

$$\Delta P_i = RLB + \overline{SI}_{RLB} - FV_i - \overline{SI}_i$$

### 3 IMPLEMENTATION

#### 3.1 Fiducials

Fiducials are measured independently and considered as such for both horizontal and vertical coordinates. The single dimensionality does not, however, represent a limitation. To obtain micron type results, great care must be taken to avoid any kind of first order errors. Hence, in high precision industrial metrology, measurements are always taken in the principal plane, i.e. horizontal measurements are carried out in the horizontal plane and vertical measurements in the vertical plane, respectively. Consequently, the undulator is designed to have the horizontal fiducials on the side and the vertical fiducials on the top. For redundancy reasons tooling balls are also placed on the opposing sides (fig. 4).

#### 3.2 Straightness Measurements

The SI is not much different from a typical distance measurement interferometer. The Michelson interferometer is replaced by a Wollaston prism and the retro reflector by a straightness reflector. To measure straightness, however, the reflector is held fixed, and the

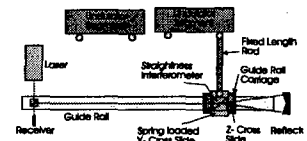


Fig. 4 Interferometer

Wollaston prism moves along the to be measured object. Since the interferometer counts fringes, the beam signal must never be interrupted, e.g. due to a deviation of the prism from the beam or by blocking off the beam transport, since this would cause the interferometer to loose count. To prevent a possible deviation of the prism from the beam path and to also maintain maximum measurement range to both sides, i.e.

to keep the prism centered on the beam, the prism is usually mounted to a carriage riding on a precision guide rail. Because the rail moves the prism parallel to the measurement object, an interface between the prism and the fiducials is needed such as a constant distance rod. Whenever the prism is near a fiducial, the rod is inserted between the prism and the fiducial. To facilitate the insertion and to provide constant measurement conditions,

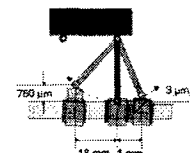


Fig. 5 Arcing

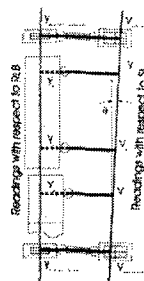


Fig. 3 SI Position

the prism is mounted on a spring loaded cross slide (fig. 4). This implementation does not provide any indication when the rod is truly perpendicular to the measurement interferometer beam. Fortunately, this is not a new and unique problem being typical to optical tooling measurements. To overcome this, the rod is arced while the scale is read. At the smallest value, the scale is perpendicular to the line of sight. Scale arcing can be implemented in this set up by moving the prism in the Z direction while watching the SI read-out (fig. 5). A motor driven stage is added between the carriage and the X cross slide and moved by hand near the measurement point. Then the Z stage drive is engaged, which moves the prism across the unknown measurement point. A computer interfaced to the drive readout and the interferometer readout records coordinate pairs (z, x) over this distance. Subsequently, a simple circle fit not only solves for the true measurement point and thus for the shortest distance, but also improves the significance of the solution by fitting many readings.

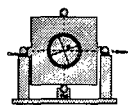


Fig. 6 Quad.

### 3.3 RLB Laser Finder

A laser beam cannot be picked up accurately by standard alignment instrumentation. A tool needs to be developed which references an optical beam to mechanical fiducials.

#### Detector fixture design

The proposed Laser Finder (LF) consists of a frame, which carries four tooling balls in the same geometry and dimensions as they are mounted to the end of an undulator. A quadrant detector is mounted to the center of the frame within a few hundred microns (fig. 6) giving the beam position in its own coordinate system.

Two distinct methods are employed to detect the laser position. The first works on the principle of a slit that allows the laser light to pass through. Thus, even if the laser cross section is not uniform in intensity, the slit is immune to this since only a profile of the laser light that passes through the slit is used to determine the beam position. This method will not be able to average out atmospheric effects or other effects due to vibrations. The other method is based on using the quadrant detector by summing the laser intensity readings on each of the two halves of the sensitive surface and then comparing the two. The arrangement is automatically rotated 90° to measure the other dimension. Tooling ball and detector coordinate systems need to be related via a calibration.

#### Detector fixture calibration

The positions of the four tooling balls are first measured accurately on a coordinate measurement machine. Then the frame is set up on the same calibration stand as the WF (fig. 6). An X, Y reading of the beam spot is taken. Rolling the frame 180° allows a second reading. The depiction in fig. 7 combines the geometric relationship from both readings. A simple vector algebra operation will produce the unknown calibration offsets with D being the laser beam

$$\bar{D} = \frac{1}{2}(\bar{A}_1 + \bar{A}_2)$$

$$\bar{C} = \frac{1}{2}(\bar{A}_2 - \bar{A}_1)$$

position vector and C being the electrical center position vector, both expressed in a Cartesian coordinate system with its datum located with respect to the symmetry axes of the two horizontal tooling balls. This procedure does not solve for the rotation between the tooling ball coordinate system and the quadrant detector system.



Fig. 7 Relating Readings

While the procedure could be expanded to include this, it is believed not to be required as long as the quadrant detector is carefully aligned with respect to the tooling balls.

### 3.4 Finding the Wire

#### Wire finder design

The wire position on either side of an undulator segment is measured with WFs. The position measurement is carried out in one plane at a time with one device on either side of the undulator. A laser avoids wire contact. This consists of a laser emitter mounted so that the emerging beam will pass through a slit across the wire to a receiver on the other side (fig. 8). After measuring the intensity of the signal received, a computation based on the signal profile will provide an accurate determination of the wire position. A mechanical WF is also used which touches both sides of the wire to determine its position. Assuming the wire has an ideal round profile, the average of both measurements gives the wire position in the WF's "arbitrary" coordinate system.



Fig. 8 Laser finder on calibration fixture

#### Wire finder calibration

Next, the wire position measurements need to be related to the tooling balls on the WF frame. Since the device measures only in one dimension the wire measurement is made a second time with the fixture yawed by 180°. A calibration mount is required to retain the position (analogous to fig. 7). The kinematic mount can be realized by a combination of the standard cone, V-groove, and flat mounts. The distance between the tooling balls needs to be measured accurately.

#### Reference wire finder fiducials to undulator fiducials

Lastly, the WF tooling ball positions are referenced to the tooling balls on the undulator following the procedure already described in chapter 2.1.

## 4 CONCLUSION

Alignment will begin in April/May of 1999 and the first beam is expected in June.

## 5 REFERENCES

- [1] R. Carr et al.: The VISA Free Electron Laser
- [2] G. Rakowsky et al., Measurement and Optimization of the VISA Undulator
- [3] G. Rakowsky, *ibid.*

# AN OGIVE SHAPED CARBON-CARBON COMPOSITE BEAM STOP\*

R. T. Acharya, D. W. Doll, K. Redler, T. Van Hagan, General Atomics, San Diego, CA

## Abstract

An ogive shaped carbon-carbon composite (CCC) beam-stop has been designed to replace the original nickel ogive beam stop for the Low Energy Development Accelerator (LEDA) of the APT (Accelerator Production of Tritium) project. The nickel beamstop has been used for initial testing of the 6.7 MeV, 100 mA cw proton beam from the APT RFQ (Radio Frequency Quadrupole). Because of activation concerns, another beam stop is needed for future tests on the first module of the Coupled-Cavity Drift-Tube Linac (CCDTL), which will increase proton beam energy to 10.4 MeV. The CCC ogive has been integrated into the nickel structure as a direct replacement. The design and fabrication of the CCC ogive beamstop is presented with a review of the original nickel ogive design.

## 1 BACKGROUND

Beamstops have been designed to accommodate each level of LEDA [1] testing as part of the APT program [2]. The injector was tested cw through a low energy RFQ to 1.2 MeV into an ogive shaped copper target [3]. A second beamstop was designed and built for testing the RFQ to 6.7 MeV and 100 mA [3]. Unlike the first ogive, which operated below the threshold of neutron production, this target was made from nickel in order to minimize the neutrons per proton (n/p) ratio while being structurally compatible with the vacuum and cooling water requirements. As successive segments of the CCDTL are added to the RFQ raising the proton energy, the n/p and activation products become too high to permit the required access flexibility during commissioning. A low n/p ratio is necessary in the target and the surrounding structural materials need to have short half-life activation products.

A carbon target satisfies the low n/p ratio and low activation criteria best [4]. However, it is unsuitable as a primary vacuum barrier and is not compatible with traditional metal seals and flanges. Nickel activates from neutrons but these activation products have a short half-life. An optimum solution to the problem is a carbon lining bonded directly to the inside of an ogive shaped nickel backing that replaces the existing beamstop. This provides a carbon target for the protons and a nickel vacuum barrier to seal the vacuum from the water coolant. This paper addresses the design of such a beamstop configured to upgrade the LEDA installation to 10 MeV operation.

\* Work supported by the Department of Energy contract No. DE-AC04-96AL89607

## 2 DESCRIPTION

The cartridge containing the CCC target replaces the one originally installed for 6.7 MeV operation. In all external features, including hydrophones for boiling detection, it is the same as its predecessor. The cartridge housing made from nickel, is 3.2 m long by 0.23 m in diameter; the target contained in it is ogive shaped with a close fitting shroud that directs cooling water from the aft end over the outer surface through a 4 mm gap (Figure 1). The water exits the gap at the forward end where the beam enters, turns 180 degrees, then returns to the aft end where it exits to the cooling-cart. This cooling-cart was designed initially to be upgraded to 10.4 MeV operation (1 MW) and will remain unchanged.

The ogive is made from a special CCC, 2.5 mm thick, on which a 2.5 mm thick layer of nickel is electro-deposited. The CCC thickness is set by the 0.76 mm range of a 10 MeV proton in 1.65 g/cm<sup>3</sup> carbon and stress considerations. The nickel layer is subsequently (electroform) joined to a nickel flange at the beam opening and to a wheel-and-spokes shaped support at the pointed end. The CCC utilizes polyacrylonitrile (PAN) fibers in mat form with the fibers running axially and circumferentially. The multiple layers (approximately 11) have their joints overlapping out of phase and are bound together through their thickness with cross stitches (tufting) comprising about 3% of the fiber volume. This provides the required strength in the transverse direction.

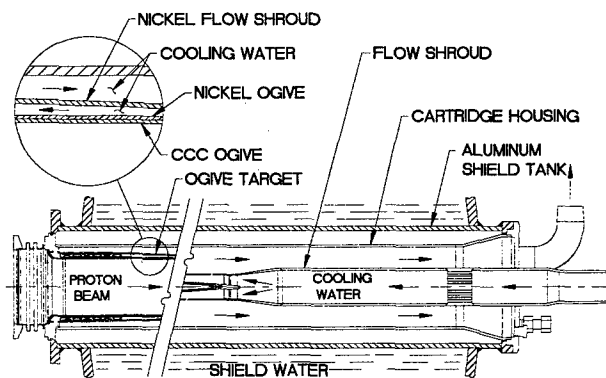


Figure 1: Cross section of beamstop cartridge showing CCC ogive target

## 3 MATERIALS SELECTION

Materials of construction were selected on the basis of nuclear, thermal, and mechanical properties. A tensile test was run to confirm the CCC-to-nickel bond strength.

### 3.1 Nuclear Considerations

One of the key considerations in the choice of materials is radiation exposure to linac operating personnel. This radiation exposure has two components. The first component is from the prompt neutrons and gammas produced in the stopping material. Prompt radiation is of little importance since the area is clear of personnel during accelerator operation. The second component of the radiation exposure is from gammas emitted by the activated materials. This includes the concentric layers that make up the cartridge and inner liner of the shield tank. The radiation dose from these components affects personnel access to areas near the beamstop immediately after the beam shut-down. Minimizing neutron production minimizes both components of radiation exposure (Fig. 1).

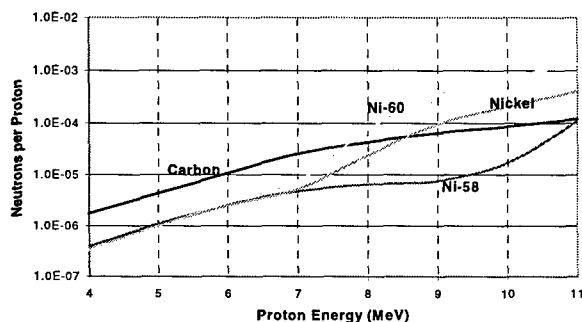


Figure 1: n/p ratio as function of proton energy

A carbon target [5] with nickel structures satisfies both the need to minimize neutron production and inventory of long half-life activation products. Stainless steel (SS), used for the original cartridge housing, was rejected for the replacement because the Fe-59 and Cr-51 produced by neutrons (Table 1) have relatively long half-lives and emit high energy gammas when they decay.

Table 1: Neutron Activation Products from Beamstop Materials

Isotope	Half-life	$\gamma$ Energy (MeV)
C-12	-----	-----
Ni-65	2.52 h	1.46
Cu-64	12.8 h	1.34
Cr-51	27.7 d	0.321
Fe-59	44.51 d	1.099, 1.291
Na-24	14.96 h	1.37, 2.75

C-12 (99%) produces no neutrons at proton energies below 19.6 MeV; below this threshold, C-13 (1%) produces neutrons in a  $^{13}\text{C}+p \Rightarrow ^{13}\text{N}+n$  reaction. Nickel becomes Ni-65 with a 2.52-h half-life. Although the gamma energy associated with this decay is high, its half-life is short. The dose rate near the beamstop will be low after a one to two day cool-down period. The aluminum shield tank inner liner activates to produce Na-24, which decays with the emission of very high-energy gammas. It will reach equilibrium levels within 2

to 3 days of continuous beamstop operation. Supplemental shielding will be needed if unlimited access to the areas near the beamstop is necessary soon after the beam is turned off.

### 3.2 Bond Strength Test

Six 25 mm diameter by 3 mm thick CCC disks with 0.5 mm of electroformed nickel on one side were tensile tested to determine the adhesion strength of the coating-to-substrate bond. Testing was based upon ASTM Specification No. C 633 - 79. While the tests demonstrated that the electroformed nickel coating is well adhered to the CCC substrate, the actual strengths of the bonds for the test specimens could not be determined directly. This was because the CCC was not tufted, which resulted in low transverse tensile strength. With tufting, a transverse tensile strength of 20 Pa (3000 psi) could be expected. Consequently, five of the six test specimens failed in the CCC near the uncoated face at 3.5 to 5 MPa (510 to 730 psi). The sixth specimen failed at 6.2 MPa (895 psi) in the adhesive under at the interface between the nickel coating and the steel test fixture. From these data, it was shown that the bond strength withstood the highest applied stress, 6.2 MPa.

Remnant pieces of the coated CCC panel were also examined by scanning electron microscopy (SEM) to characterize the coated CCC material. SEM and energy dispersive X-ray (EDX) examinations showed that the coating was essentially pure nickel with slight traces of carbon and oxygen. An EDX examination of the CCC near the nickel coating showed traces of oxygen, silicon, sulfur and nickel. SEM photographs (Fig. 2) show a pore-free coating that is well attached or bonded to the CCC substrate. A few traces of the nickel coating material and impurities from the electroforming process can be observed to a depth of approximately 1.2 mm into the CCC. This is still beyond the range of the 10 MeV protons.

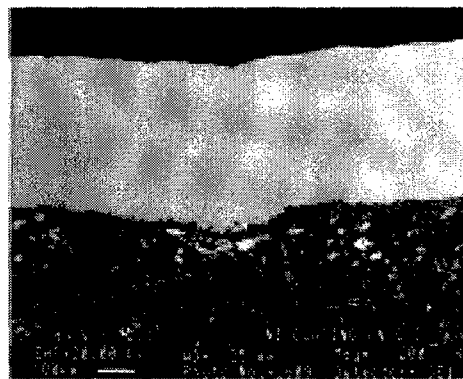


Figure 2: SEM image of the nickel/CCC interface

## 4 THERMAL AND STRESS ANALYSES

The principal concern with a CCC/nickel lamination is the large difference in thermal expansion of the two materials. The nickel is electroformed at room

temperature, leaving no residual stress. However, the thermal and mechanical properties in the CCC vary depending on the choice of carbon fibers and curing temperature. Curing at a high temperature (2500°C) results in an increase in the transverse thermal conductivity and in-plane tensile modulus. This correspondingly causes a reduction in the in-plane (fiber) CCC strength; curing at a lower temperature (1200°C) maintains the in-plane tensile strength but results in a lower in-plane tensile modulus and transverse thermal conductivity.

Two cases were analyzed. The first case used the properties of T-300, a PAN-based carbon fiber CCC cured at 1200°C. The second case used the properties of K321, a pitch-based carbon fiber CCC cured at 2500°C. The thermal and mechanical properties of both materials show that graphitization of the composite increases the thermal conductivity by a factor of 14 in the in-plane direction and by a factor of 2 in the transverse direction. However, the in-plane strength decreases by a factor of 1.8, and the tensile modulus increases by a factor of 1.5. This made it necessary to determine whether the benefits of increased thermal conductivity (i.e., decrease in temperature gradient through the thickness and a lower surface temperature) were enough to offset the increase in modulus (i.e., higher stress caused by the deformation due to the expanding nickel) and the decrease in transverse tensile strength.

An axisymmetric ANSYS model was created as a thin slice through the thickness of the ogive at the location of the peak heat flux, 68.6 cm from the entrance of the beamstop. The peak heat flux is 264 W/cm<sup>2</sup> applied to the inner surface of the model. The cooled outer surface has a heat transfer coefficient of 2.97 W/cm<sup>2</sup>-K and a fluid bulk temperature of 26.6°C. The slice is free to expand radially. In the axial direction, the rear surface is constrained not to move, and all the nodes on the opposing surface are constrained to move equally.

The results for both types of CCC are shown in Table 2. The stress in the T-300 CCC is lower than in K321 due to the lower modulus of elasticity of T-300 indicating that it is more compliant to the expanding nickel. Similarly, the Von Mises stress in the nickel is lower with the T-300.

With the T-300 PAN CCC selected, it was necessary to optimize its thickness as well as that of the nickel. By limiting the overall ogive thickness to 5.08 mm, varying the interface and analyzing the resulting stress, an optimum was derived. The results show that as the thickness of the nickel increases, the stresses in both the nickel and the CCC increase indicating that the nickel should be as thin as possible. However, in order to prevent the ogive from buckling due to the external hydraulic pressure from the coolant 0.55 MPa (80 psi), the nickel thickness was set at 2.5 mm to assure that it acts alone in withstanding the pressure. The minimum thickness of the nickel ogive to withstand 3 times the

external pressure is 2.41 mm, a reasonable margin of safety. The transverse tensile stress in the CCC is at a maximum in this allowed region for the nickel. However, it is still well below the minimum ultimate for the CCC or the interface bond strength.

Table 2: Calculated stress for T-300 CCC and K321 CCC Ogives bonded to nickel outer surface.

	T-300, PAN	K321, Pitch
T beam wall (°C)	544	411
T interface (°C)	214	214
T water wall (°C)	109	109
S radial (psi)	645	898
S axial (psi)	21500	29000
S hoop (psi)	20800	28000
Transverse S <sub>ult</sub> (psi)	3000	3000
In-Plane S <sub>ult</sub> (psi)	54200	30200

## 5 CONCLUSIONS

A beamstop has been designed to accommodate the upgrade of the LEDA from RFQ operation at 6.7 MeV to 10 MeV CCDTL operation. It utilizes an ogive shaped carbon-carbon composite liner intimately bonded to a nickel backing to satisfy the thermal and mechanical requirements while minimizing the inventory of activated materials. The uncertainty in the transverse tensile strength remains a concern. The margin of safety is small, and the properties are tied to the densification and curing, a somewhat art-driven proprietary process. This too can be said of the electroforming process that forms the nickel over the carbon. Demonstration of this technology will enable similar beamstop designs to be developed.

## 6 ACKNOWLEDGEMENTS

The authors wish to thank Dr. J. D. Schneider and his associates at LANL for their encouragement in pursuing this technology. We thank Albany Technowave, Inc., Refractory Composites, Inc., and American Galvano, Inc. for their CCC and electroforming expertise.

## 7 REFERENCES

- [1] H. V. Smith, Jr., J. D. Schneider, "Status Update on the Low Energy Demonstration Accelerator (LEDA)", XIX International Linac Conference, August 23-28, 1998, Chicago, Illinois
- [2] G. Lawrence, "High-Power Proton Linac for APT; Status of Design and Development", (LEDA), XIX International Linac Conference, August 23-28, 1998, Chicago, Illinois
- [3] T. Van Hagan, et al., "Design of an Ogive-Shaped Beamstop", proceedings, XIX International Linac Conference, August 23-28, 1998, Chicago, Illinois
- [4] D. Doll, et al., "Low to high Energy Beamstops for APT", XIX International Linac Conference, August 23-28, 1998, Chicago, Illinois
- [5] E. A. Burrill, "Direct Nucleon Accelerators," Engineering Compendium on Radiation Shielding, Vol. III, Shield Design and Engineering, 1970

# A ROOM TEMPERATURE TEST BED FOR EVALUATING 700-MHz RF WINDOWS AND POWER COUPLERS FOR THE SUPERCONDUCTING CAVITIES OF THE APT LINAC\*

J. Gioia<sup>#</sup>, General Atomics, San Diego, CA

K. Cummings, C. Gautier, T. Hargenrater, W. B. Haynes, F. L. Krawczyk, M. Madrid, W. Roybal, B. Rusnak, E. N. Schmierer, B. Smith, R. Zimmerman, Los Alamos National Lab

K. Kishiyama, S. Shen, Lawrence Livermore National Lab

H. Safa, CEA, Saclay, Gif-Sur-Yvette, France

## Abstract

Superconducting radio frequency (SCRF) cavities are used in the high-energy portion of the Accelerator Production of Tritium (APT) linac to accelerate the beam to approximately 1700 MeV. To accelerate the 100 mA proton beam and to maintain the field levels in the cavity, up to 420 kW of CW (continuous wave) 700-MHz rf power needs to be delivered to the cavity. This is done using two rf window and power coupler assemblies that can each transmit 210 kW. To evaluate developing window-coupler designs, a Room Temperature Test Bed (RTTB) has been built that utilizes a room-temperature copper coupling cavity for mating two power couplers together. Several parameters are being tested such as: (1) power coupler matching, (2) maximum power handling, (3) rf losses in the power coupler, (4) SCRF window/power coupler matching, and (5) power coupler/cavity coupling adjustability. The RTTB is also meant to be a conditioning stand for window-coupler assemblies that will go on cryomodules [1]. The design features of the coupling cavity, test stand & layout, vacuum system & controls, data acquisition, rf controls and contamination control will be discussed.

## 1 INTRODUCTION

To evaluate the high power transmission capabilities of the APT power coupler, a Room Temperature Test Bed (RTTB) has been built. Two couplers in transmission through a copper coupling cavity will be tested simultaneously. One power coupler [2] is used to feed the power (more than 500 kW) to the cavity, while the second coupler will act to remove the rf power and direct it to a 1 MW waste load. Coaxial rf windows [3] interface the power couplers to WR-1500 waveguide.

The coupling cavity is necessary to test the couplers as-built configuration. The tip geometry (a disk slightly larger than the coaxial center conductor of the coupler) does not permit a direct coupler-to-coupler transmission test. The use of a normal conducting (rather than a superconducting) cavity is highly desirable since it reduces the complexity of the test and it separates pure rf-issues of the design from those closely related to the aspects of operation in a cryogenic environment. Finally,

the turnaround time for re-testing after adjustments or swapping of components is reduced from about a week for a superconducting test to just several hours for a room temperature test.

## 2 COPPER CAVITY DESIGN

The rf design for this configuration is aimed at maximizing  $Q_0$ , minimizing  $Q_{ext}$  (good coupling and lowered cavity fields) and maintaining a short accelerating gap for field-emitted electrons. Low cavity fields and accelerating voltages may significantly reduce or even remove shielding requirements for the high power operation of the test stand. After a trade-off study regarding the criteria mentioned above, we opted for a pillbox cavity operated in a TM010 mode with couplers attached to the two end-walls. The cavity resonates at 707.6 MHz without the couplers present. The couplers, intruding into the cavity by 14 mm, lower this frequency to the nominal 700 MHz accelerator operating frequency. Table 1 gives a number of parameters for the copper test-cavity. All field and power levels are quoted for the nominal 210 kW operation power level.

To allow for proper tuning of the cavity without the power couplers, the sensitivity of the frequency with inner diameter of the cavity was calculated (with MAFIA 2D) for resonance without the couplers. The frequency was measured between iterations of machining the inner diameter until convergence on the desired frequency. The end plates were then brazed to the cylinder. The final resonant frequency after brazing was measured and agrees with the simulations.

The power deposited in the cavity was calculated with a  $Q_{ext}$  of 31 to be 450 W. The cooling system was designed for 7500 W deposited in the cylindrical region. This was to allow for a factor of safety and flexibility in cavity temperature as cavity temperature may be used for 'fine tuning' of cavity during operation. To remove the heat from the cavity, channels were machined in the cylinder prior to final braze and tuning. Two Plenums at each end, 0.75 in. x 0.25 in., distribute and collect the cooling water, and 20,  $\varnothing$  0.25 in. holes run the length of

\*Work supported by DOE contract: DE-AC04-96AL89607

#Email: [gioiaj@gat.com](mailto:gioiaj@gat.com)



the cavity parallel to its axis. A water temperature increase of 3 °C was calculated for a flow rate of 11.8 gpm for a maximum cavity temperature,  $T_{\max}$ , rise of 15 °C. Coolant entrance and exit paths are at opposite sides of the cavity to balance the pressure drop through all the cooling passages to achieve a uniform flow. Channel sizes were a balance between fabricability and flexibility in  $T_{\max}$  of the cavity.

The cavity was made of OFE ASTM F68-93 Cu, with 28% Cu – 72% Ag 0.002 in. foil braze alloy used for the Cu-Cu joints, and 50% Cu – 50% Au alloy for the SST-Cu joints. See Figure 1. Final overall internal dimensions of the cavity are  $\varnothing$  328 mm and 250 mm in length.

Table 1: Pillbox Cavity Parameters

parameter	value	comment
$f_o$	707.6 MHz	measured with no couplers in
$f_{oc}$	700 MHz	couplers present
length	328 mm	measured
diameter	250 mm	measured
$Q_o$	33500	----
$R/Q$	122 Ohm	----
$P_{cav}$	450 W	total rf power deposited into cavity wall
$P_{cav}$	0.4 W/cm <sup>2</sup>	maximum power density on cavity wall
voltage	0.05 MV	V across cavity gap
$E_{peak}$	0.35 MV/m	peak electric field (at coupler tip)
$Q_{ext}$	31	----

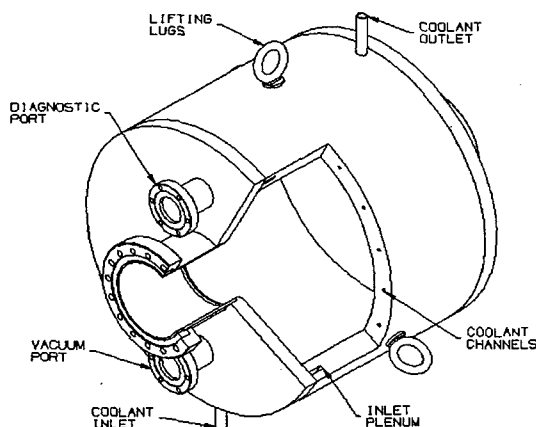


Figure 1: Pillbox Resonant Cavity View

### 3 RTTB STAND & LAYOUT

The RTTB stand was designed to accomplish several functions. See Figure 2. First, several power coupler and vacuum window assemblies will be transported from the clean room to the building where the stand is located for testing. The stand had to be able to support the components in a transfer by forklift between buildings (cavity, 250 lbs., power coupler, 150 lbs., and vacuum window assembly, 120 lbs. each). This meant that flexure of the table had to be a minimum. To assist and protect equipment during this transfer process, forklift fork guides were provided. The top of the table is a detachable aluminium mill plate, which allows flexibility for design changes later. The second attribute was to allow for a clean environment to connect assemblies to the copper cavity and for doing coupling adjustments with the power coupler tip. This requirement led to the need for a canopy that could support two ~800 cfm HEPA units, Lexant™ windows, and sufficient lighting to create a clean air, laminar flow environment for these tasks. The canopy is detachable and will also support individual components if assembly requires rigging equipment with the canopy in place. The third attribute was modularity. Adjustable feet, self contained electrical power and Instrumentation & Control distribution system, and isolation from other support equipment allows this.

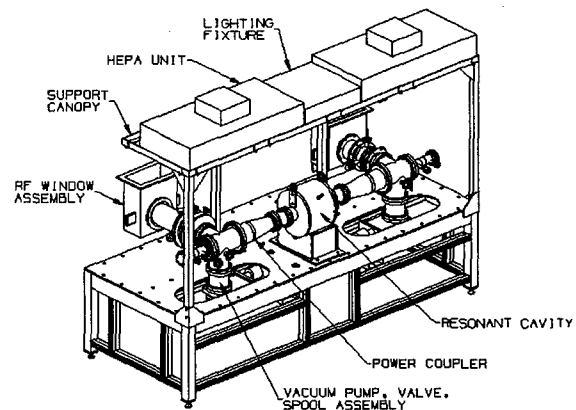


Figure 2: RTTB Test Stand

### 4 VACUUM SYSTEM & CONTROLS

The RTTB vacuum system has a Varian 300 l/sec turbomolecular pump for each of the two rf window/power coupler assemblies. There is also one Varian 70 l/sec turbomolecular pump on the copper cavity. The pumps were sized based on a vacuum model of the RTTB that was developed using MathCad™ and will provide enough pumping to meet the required operating pressure of  $1 \times 10^{-7}$  Torr. Each turbo has an electro-pneumatically actuated gate valve to isolate it from the vacuum system. Each turbo also has an electro-pneumatically actuated foreline valve and one Varian 300

l/min dry scroll pump that backs all three turbomolecular pumps.

A Modicon Programmable Logic Controller (PLC) was used to control the pumps and valves. The PLC also provides the interlocks that will prevent rf operation if the vacuum, power coupler air flow, cavity water flow or cavity temperature conditions are not met. LabView™ will be used to communicate with the PLC and will provide a graphical user interface that will be very intuitive and easy for an operator to use.

Each rf window/power coupler assembly has a Granville-Phillips Stabil-ion gauge™ and Convectron™ gauge to measure pressure. There is also a Stabil-ion gauge™ on the cavity and a Convectron™ gauge on the foreline. The process control functions on the Stabil-ion gauge™ controller are used to provide set-points to the PLC for vacuum interlocks.

There is a residual gas analyzer (RGA) mounted on the cavity that has LabView™ drivers provided by the vendor. By using LabView™ to acquire the total pressure, partial pressure, rf power, temperature of the cavity, power couplers and rf windows there will be a very good understanding of the vacuum system performance under operating conditions. The LabView™/PLC control system was successfully used on the LEDA RFQ and rf window vacuum systems [4]. It has proved to be reliable and easy to maintain. It is also a very flexible system that will allow the RTTB vacuum system to be easily reconfigured if necessary for future experiments.

## 5 DATA ACQUISITION

Data acquisition is handled by LabView™, running on a Power Macintosh™. A National Instruments SCXI™ rack contains modules for digitizing RTDs and thermocouples. Fifty RTDs are used on the exterior surfaces of the rf windows, power couplers and copper cavity. Eight thermocouples are used inside the power coupler inner conductors at various points of interest.

The LabView™ program also reads incident, reflected and transmitted rf power via a GPIB™ interface connected to two Hewlett-Packard 438A power meters. Vacuum data is recorded by SCXI™ digitization of three 0-10 volt analog voltages provided by the model 360 Granville-Phillips Stabil-ion gauge™ controllers. In addition, the Power Macintosh™ interfaces with an Allen-Bradley PLC which monitors critical waveguide and rf window locations for arcs by way of 7 fiber-optic links and arc detector units.

The data taking repetition rate is user selectable. For an extended duration test (weeks) data collection can be intentionally slowed down providing a reasonable data file size for all collected data. All the experimental data is stored on the Power Macintosh™ hard drive using a spreadsheet format. Ultimate data archiving is achieved by transferring these files to a ZIP drive.

## 6 RF KLYSTRON CONTROLS

The klystron transmitter, which can provide up to 1 MW of rf power at 700 MHz to the RTTB, is located more than 100 feet from the test bed on a second story mezzanine. For ease of operation, a remote control method was implemented at the RTTB location to allow all rf control functions without leaving the test area. A SUN Workstation™ (running the LANL EPICS control system) communicates over a serial coaxial "data highway" to an Allen-Bradley PLC at the klystron transmitter station. With this in place, all klystron functions are controlled while maintaining control over the experimental area.

There are two main klystron shutdown features, which are hardwired: (a) loss of cooling water to the 1 MW rf waste load. This will inhibit klystron operation by shutting down the high voltage to the tube and (b) occurrence of arcs at the seven monitored locations. This fault will remove the klystron drive for 100 milliseconds.

## 7 CONTAMINATION CONTROL

Contamination control is achieved by mounting two self-driven HEPA filters each providing ~800 cfm of nearly laminar flow, 0.3 micron filtered air over the power coupler/window surfaces. Support structures for the components consist of Teflon guided rails that allow flexibility in design and minimize particulate production during component change out.

## 8 CONCLUSION

The RTTB test stand is ready for testing SCRF power couplers and SCRF 700 MHz window assemblies. The new SCRF clean room is completed and will facilitate cleaning both power coupler and window assemblies before installation onto the test stand. Although testing is planned for mid-April, we're confident this configuration will be a valuable testing tool to evaluate power coupler and rf window designs. This test stand design may also be used for conditioning of assemblies prior to installation in the APT plant.

## 9 REFERENCES

- [1] R. Bourque, *et al*, "The APT Cryomodule: Present Status and Potential Future Plans", PAC99, NY, NY, 1999.
- [2] E. N. Schmierer, *et al*, "Development of the SCRF Power Coupler for the APT Accelerator", PAC99, NY, NY, 1999.
- [3] Personal communication with K. Cummings, *et al*, at LANL, 1998.
- [4] K. Kishiyama, *et al*, "Testing of Vacuum Pumps for APT/LEDA RFQ," LINAC '98, Chicago, IL, 1998.

# MEANDER-LINE CURRENT STRUCTURE FOR SNS FAST BEAM CHOPPER\*

S.S. Kurennoy, J.F. Power, and D.L. Schrage, LANL, Los Alamos, NM 87545, USA

## Abstract

A new current structure for the fast traveling-wave 2.5-MeV beam chopper for the Spallation Neutron Source (SNS) project has been proposed recently [1]. It is based on the meander-folded straight or notched stripline with separators. Detailed electromagnetic modeling with MAFIA has been used to optimize the structure design and parameters. The time-domain 3-D MAFIA simulations predict the structure rise and fall times around 1 ns. A notched meander line with a dielectric substrate has been developed to accommodate both electromagnetic and mechanical requirements.

## 1 INTRODUCTION

The SNS is a next-generation pulsed spallation neutron source designed to deliver 1 MW of beam power on the target at 60 Hz in its initial stage [2]. The SNS design stipulates a 1-GeV linear H<sup>+</sup> accelerator and an accumulator ring. The SNS storage ring accumulates the linac beam during a few hundred turns (a macropulse, about 1 ms) using H<sup>+</sup> injection through a carbon foil. The beam injected into the ring is stacked into a single long bunch, and the linac macropulse must be chopped at near the ring revolution frequency, 1.188 MHz, to provide a gap required for the kicker rise time during a single-turn ring extraction. The final clean beam chopping in the linac is to be done by a fast chopper in the Medium Energy Beam Transport (MEBT) line. For more detail on the chopper function and requirements, see [3].

The MEBT transports 28 mA of peak beam current from a 2.5-MeV 402.5-MHz RFQ to a drift-tube linac. A 0.5-m space is allocated for the chopper that deflects the beam into a beam stop during the 35% beam-off time. The updated chopper parameters are listed in Table 1.

Table 1: MEBT Chopper Specifications

Parameter	Value	Comment
Beam energy	2.5 MeV	$\beta=0.073$
Length	$\leq 0.5$ m	shorter is better
Gap	$\geq 15$ mm	adjustable
Pulser voltage	$\pm 1500$ V	2 FETs in series
Deflection angle	18 mrad	90 % effective field
Chopping period	841 ns	
Duty factor	35 %	65 % beam on
Rise / fall time	$< 2.4$ ns	4.8 ns as initial goal

\*Work supported by the U.S. Department of Energy.

Based on the results of MAFIA simulations [1] and [4], the chopper current structure consisting of a meander-folded notched stripline with separators was chosen as the one providing the best rise and fall times, in the 1-ns range. However, a mechanical design and manufacturing of a thin (0.25 mm) metal notched strip with some kind of supporting dielectric pins are rather complicated. To find a compromise satisfying both electromagnetic and mechanical requirements, we have studied a few variants of the notched meander line with a dielectric support. Fortunately, materials with a low dielectric constant and low losses in a wide frequency range, up to 10 GHz, and good mechanical properties are available from industry (see Sect. 2). After a series of MAFIA simulations, we have arrived to a new current-structure design which provides about the same electromagnetic performance as the previous one [1],[4], but is much better mechanically.

## 2 MATERIAL CHOICE

To keep the structure design close to the original one, which guarantees good electrical properties, we needed materials with a low dielectric constant and low losses. Materials for high-frequency applications like printed-circuit boards are available from industry, e.g., from the Rogers Corp. They usually also come with deposited copper layers that fit quite well our goal: the required meander pattern can be chemically etched with a high precision. The properties of some Rogers' glass microfiber reinforced PTFE composites are listed in Table 2.

Table 2: Some Properties of RT/duroids®

Property	RT/5880	RT/6002	RO3003
Diel. constant	2.20 $\pm$ 0.02	2.94 $\pm$ 0.04	3.0
Loss tangent @ 10 GHz	0.0009	0.0012	0.0013
Resistivity, $10^{10}$ $\Omega$ m	20.0	1.0	10.0
Density, g/cm <sup>3</sup>	2.2	2.1	2.1
Thermal exp., $10^{-6}/K$ X/Y/Z	31/48/237	16/16/24	24/17/17

Our first choice was RT/5880 as having the lowest dielectric constant. However, due to its thermal expansion anisotropy the samples we received had a significant bow, which makes difficult its processing within the required tolerances. The two other materials in Table 2 are more isotropic, but RO3003 was unavailable with a desired copper layer thickness. It left us with RT/6002.

### 3 NEW CURRENT STRUCTURE

The current structure design should provide the proper wave phase velocity along the beam path ( $\beta=0.073$ ) while keeping the characteristic impedance of the line equal to  $50\ \Omega$ . The rise and fall times of the deflecting field (due to the current structure itself) has to be in the 1-ns range. In addition, the structure should be mechanically stable and reasonably easy to manufacture. These requirements lead us to the design illustrated by Figs. 1-3. Figure 1 shows a piece of the full-length 3-D MAFIA model used to calculate and optimize the structure parameters. The notched meander line (see Fig. 2) is supported by a T-shaped dielectric support that goes all along the stripline length (Fig. 3). The T-support will be carved from a continuous dielectric plate, as well as wide side supports, see Fig. 3. The structure will be clamped by bolts near its sides to the metal ground plate. The grounded metal separators protrude through the narrow cuts in the dielectric plate.

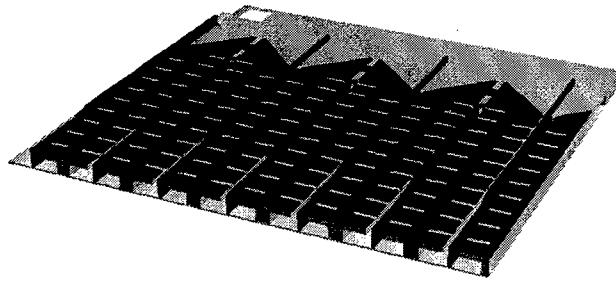


Figure 1: A small part of the 3-D model of the meander structure with dielectric supports: notched metal meander strip (dark-blue) with dielectric supports (green), metal separators (red) are connected to the ground plate (light-blue). Yellow pin in the corner is a clamping bolt.

Table 3 lists some relevant dimensions of the meander-line structure. The metal thickness in the strip is 0.25 mm. The separators are flush with the meander line near the beam path and rise 0.75 mm higher to the sides.

Table 3: Structure Dimensions

Parameter	Value
Length along the beam path	50 cm
Meander width, $b$	98 mm
Notched-strip width, $w$	8 mm
Strip-to-strip gap width, $g$	2 mm
Width of dielectric plate	130 mm
Thickness of dielectric, $h$	2.5 mm
T-support top	8 x 0.75 mm
T-support leg	2 x 1.75 mm
Notch spacing period	4 mm
Notch depth / width	3 mm / 1 mm

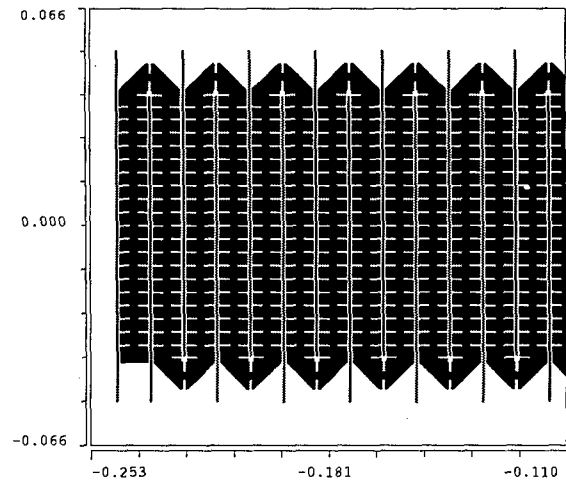


Figure 2: A part of the meander structure (about  $1/4$  of the total length) in the plane of the notched stripline, at  $z=h$ . Dimensions are in meters.

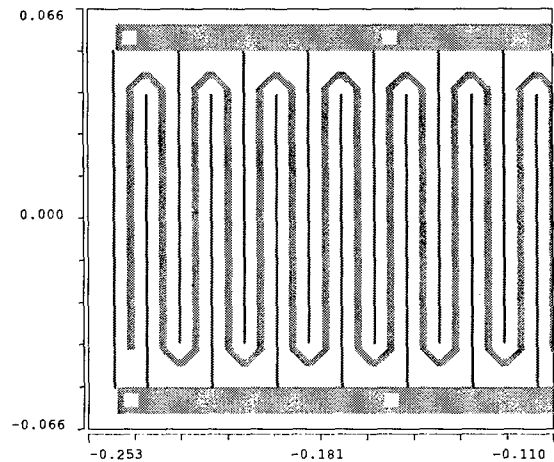


Figure 3: Same as Fig. 2, cut in the middle plane between the stripline and the ground, at  $z=h/2$ .

The notches provide some additional inductance, see [4], and the dielectric presence increases the capacitance  $C'$  per unit length of the line. From 3-D time domain MAFIA simulations the phase velocity  $v_{ph} = 1/(L'C')^{1/2}$  of the TEM wave along the stripline was found to be  $0.68c$ . The line characteristic impedance  $Z_c = (L'/C')^{1/2}$  was adjusted to be  $50\ \Omega$  by a proper choice of the dielectric thickness and the T-support shape. For  $Z_c$  calculation we first apply 2-D and 3-D electrostatic solvers to obtain an average  $C'$ , then derive  $Z_c$  as  $1/(v_{ph}C')$ . Finally, the pulse phase velocity along the beam path was adjusted to match the beam velocity  $0.073c$  by changing the meander width. To avoid pulse reflections from the meander bends, we adjust depth of the additional notches on the bends. All MAFIA simulations have been performed on a Sun Ultra 60 360-MHz workstation. For a detailed full-length 3-D model (about 3.5 million mesh points) a typical time-domain run with T3 takes about 30 hours of CPU time.

## 4 SIMULATION RESULTS

To model the chopper field pulse, we assume that a generator produces an idealized voltage pulse with smooth 2-ns rise and fall and a flat top of 5 ns at 1500 V. This voltage is fed into the meander stripline, and the produced fields are calculated with the MAFIA T3 module, see [4] for details. In Fig. 4 the deflecting electric field near the beam path is shown as a function of time  $t$  for three different locations  $x$  along the structure. Three snapshots of the field profile are presented in Fig. 5.

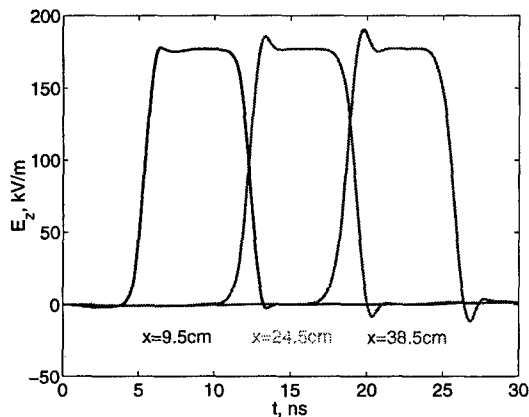


Figure 4: Deflecting field versus time in 3 different points on the beam path in the chopper.

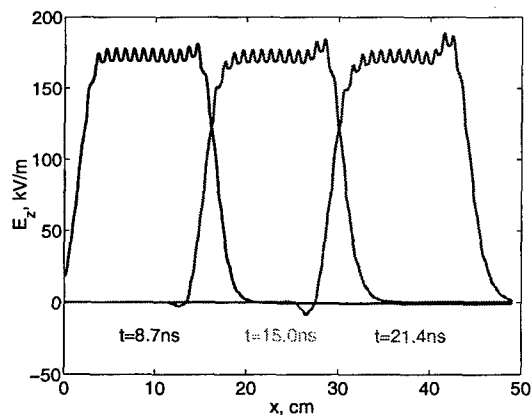


Figure 5: Snapshots of the deflecting field in the chopper.

As the pulse propagates along the chopper, its shape is slightly distorted by developing some overshoots. However, both the pulse front and end do not exceed 2.5 ns – the bunch-to-bunch temporal separation, – so that the meander structure contributes only a little to the initial 2-ns voltage fronts. Similar calculations with sharp voltage fronts show the structure rise and fall times around 1 ns. Obviously, for 4-ns voltage fronts the pulse distortion by the current structure will be smaller than in Figs. 4-5.

Figure 6 shows the deflecting field in the beam plane: a horizontal cut in the middle plane between two current structures with opposite voltages, at 7.5 mm from both of

them. The same part of the structure as in Figs. 2-3 is shown. Small variations of the field along the beam path (center line of Fig. 6, at  $y=0$ ) are due to field differences above the strip middles and above the grounded separators, compare the wiggles on the pulse tops in Fig. 5.

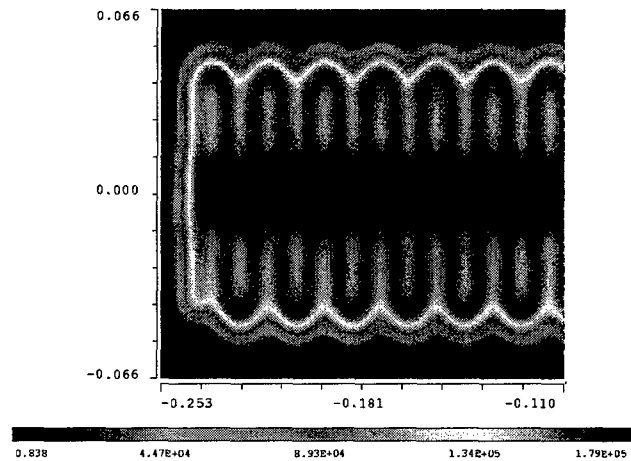


Figure 6: Contour plot of the chopper deflecting field.

An ideal flat capacitor with 3-kV voltage across 15-mm gap would have the electric field 200 kV/m. As one can see from Figs. 4-6, the calculated field at the pulse top is near 180 kV/m, which means the structure efficiency is close to 90%. One should mention that our simulations include all details of the mechanical design. In particular, we have not seen any influence on the deflecting field when dielectric clamping bolts were replaced by metal ones, or when a finite metal conductivity and/or dielectric resistivity were introduced.

## 5 SUMMARY

A new design of the current structure for the SNS fast chopper has been developed. Being based on the notched meander stripline that was developed earlier [1,3-4], it includes now a special dielectric substrate, which makes the structure mechanically stronger and easier to manufacture. The structure rise and fall times remain in the 1-ns range. A full-length prototype manufacturing is in progress, and its electrical measurements are expected soon.

## 6 REFERENCES

- [1] S.S. Kurennoy et al., In Proceed. PAC, Vancouver, Canada, 1997, p.3731; S.S. Kurennoy and J.F. Power, in Proceed. LINAC98, Chicago, 1998.
- [2] NSNS Collaboration, "NSNS Conceptual Design Report", NSNS-CDR-2/V1, Oak Ridge, TN (1997); also available at URL: <http://www.ornl.gov/~nsns/nsns.html>
- [3] S.S. Kurennoy, "Beam Chopper System for SNS", Report LA-CP-98-156, Los Alamos (1998).
- [4] S.S. Kurennoy, In Proceed. ICAP98, Monterey, CA, 1998; Report LA-UR-98-5344, Los Alamos (1998).

# A METHOD FOR COOLING RF WAVEGUIDES ON APT\*

M. McCarthy and H. Yip<sup>#</sup>, General Atomics, San Diego, CA

D. Rees and W. Roybal, LANL, Los Alamos, NM

J. Anderegg and S. Satpute, Burns & Roe, Aiken, SC

D. McGuire and L. Toole, Westinghouse Savannah River Co., Aiken, SC

## Abstract

The Accelerator Production of Tritium (APT) project will require up to 244 1-MW klystrons to provide radio frequency (RF) power for acceleration of a 100-mA proton beam. A major source of heat in the klystron gallery and the accelerator tunnel will be the RF waveguides, which conduct the RF power from the klystrons to the linac. Each waveguide is estimated to dissipate 11 kW of heat in the gallery and 17.5 kW in the tunnel. Base-case design called for conditioned-air cooling (to 104°F) of the tunnel space, with waveguide cooling by forced external convection. For more uniform and efficient waveguide cooling, several other techniques have been investigated, including water-cooling, cooling by nitrogen purging, and direct cooling of the waveguides by using them as air conditioning "ducts." Models were created simulating the last technique. This paper will report on measurements to be made on the Low Energy Demonstration Accelerator (LEDA) at the Los Alamos National Laboratory (LANL) based on these models.

## 1 INTRODUCTION

The klystrons in the gallery output 1-MW of 700 MHz RF power. The WR-1500 (15" x 7.5") rectangular, aluminum waveguide carries this power to ports on the linac. Because of the surface resistivity inside the aluminum waveguide, RF-induced currents generate heat. Calculations show that this frequency and magnitude of RF power through this size waveguide will generate 122 watts per linear foot. The surface resistivity of the waveguide rarely matches the ideal resistivity of the material. From empirical evidence, the actual power deposited in the guide is estimated to be about 250 watts per linear foot.

Experimental measurements at LANL's LEDA facility have shown the equilibrium temperature of an exposed waveguide is about 150°F for 6061 aluminum and 175°F for 5052 aluminum. In the klystron gallery, the temperature of the exposed waveguide must stay below 140°F for safety and technical reasons such as loss of efficiency, decrease in standoff voltage, and waveguide thermal expansion. Cooling the waveguide with internal air is an attractive alternative to water-cooling. The moving air inside the waveguide cools internal waveguide

structures such as gas barriers and windows and can sweep away ions after an arc. Maintaining a positive pressure in the waveguide prevents the influx of contaminants. In addition, air exhausted from the waveguide may be used to cool the klystron garage, solenoids, dry loads, and planar windows.

## 2 THEORY

Under steady-state conditions, the heat generated in the waveguide wall is equal to the sum of heat transferred to the ambient air and to the heating, ventilation, and air conditioning (HVAC) air flowing inside the waveguide. A heat balance on a differential section of the waveguide wall yields the following equation for the surface:

$$P_{WG}dx = h_i(T_w - T_f)l dx + h_o(T_w - T_a)l dx + h_r(T_w - T_a)l dx$$

or

$$T_w = \frac{P_{WG} + (h_i + h_o + h_r)l}{(h_i + h_o + h_r)l} \quad (1)$$

where:

$h_i$  = heat transfer coefficient for internal waveguide surface, BTU/hr-ft<sup>2</sup>-°F

$h_o$  = heat transfer coefficient for external waveguide surface, BTU/hr-ft<sup>2</sup>-°F

$h_r$  = radiation heat transfer coefficient, BTU/hr-ft<sup>2</sup>-°F

$P_{WG}$  = power loss in waveguide walls per length, W/ft

$l$  = perimeter of waveguide cross-section, ft

$T_w$  = waveguide surface temperature, °F

$T_a$  = ambient air temperature, °F

$T_f$  = temperature of HVAC air inside the waveguide, °F

A heat balance on the HVAC air flowing inside the waveguide for the same differential section yields the following equation:

$$mC_p \frac{dT_f}{dx} = h_i l (T_w - T_f) \quad (2)$$

where:

$m$  = mass flow rate of HVAC air, lb/hr

$C_p$  = heat capacity of HVAC air, BTU/lb-°F

These two equations were solved simultaneously to determine the required HVAC airflow rate to cool the waveguide surface to an acceptable temperature. Figure 1 shows the predicted waveguide surface temperature and

\* Work supported by DOE under contract DE-AC04-96AL89607

<sup>#</sup> E-mail: harry.yip@gat.com

HVAC temperature as a function of waveguide length. The calculation was done for an airflow rate of 1,000 cfm at 60°F, a waveguide power loss factor of 250 W/ft, an internal surface heat transfer coefficient from Dittus-Boelter equation, and a weighted-average external surface transfer coefficient from correlations for vertical and horizontal flat plates. The calculation shows that the surface temperature is below 140°F at the exit of a 32-ft long waveguide. Therefore, it is feasible to cool the waveguide with HVAC air.

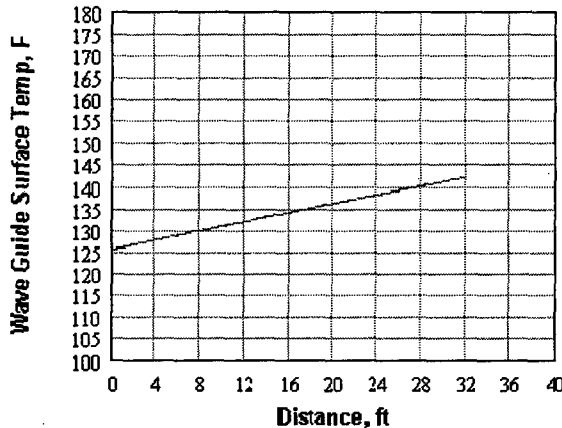


Figure 1: Predicted waveguide surface temperature

### 3 EXPERIMENTAL CONFIGURATION

The above calculations used approximate values for the power loss factor and heat transfer coefficients. An experimental program to determine these parameters is being carried out so that an accurate trade study may be conducted. Figure 2 shows the experimental configuration.

The device for determining the power loss factor is a water calorimeter, which consists of a 5-ft section of an actual waveguide wrapped with a 48-in. long water jacket. The jacket's annular gap is about 3/8-in. and it is subdivided into 6-in. wide flow channels so that water flows in a spiral pattern in the jacket. Water enters the jacket at one end through a manifold and exits at the other end. To prevent eddy air currents inside the waveguide, Teflon sheets are installed at the flanges before and after the test section. The external surface of the water jacket is insulated with a fiber blanket to minimize the free convection loss.

As the beam is conveyed through the guide, the water absorbs the heat due to power deposited in the walls. The amount of heat transferred is calculated from the measured water flow rate and temperature rise. The heat transferred divided by the waveguide water jacket length gives the power loss factor per unit length. The heat flux in W/ft<sup>2</sup> is obtained by dividing the heat transferred by the total surface area.

The apparatus for determining the internal convection heat transfer coefficients consists of from one to several 12-ft straight sections of waveguide with external

insulation and two tees, one upstream and one downstream, for air inlet and outlet. The High Frequency Structural Simulation (HFSS) computer code was used to ensure no RF leakage for the air inlet and outlet boxes. Teflon sheets are used to block air convection between the test section and upstream and downstream waveguide sections.

Filtered air from a portable air conditioner or from a blower will be used for the experiments. By measuring the airflow rate, and the inlet and outlet air temperatures and relative humidity, the amount of heat transferred from the waveguide walls to the air can be calculated. The heat transfer coefficient is then calculated from the measured waveguide wall temperature and the surface area of the guide.

The apparatus for determining the external surface natural heat transfer coefficient is the same as that for the internal heat transfer coefficient except the thermal insulation is removed.

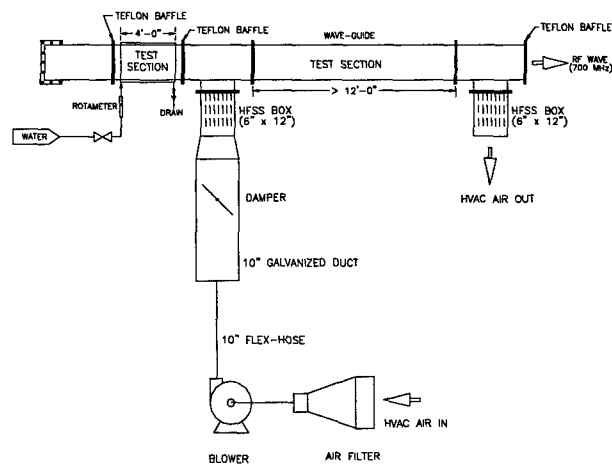


Figure 2: Experimental configuration

### 4 EXPERIMENTAL PROCEDURES

Waveguide power loss factor experiments will be performed for the following parameters:

- Water flow rate: 0.2 gpm and 0.5 gpm
- Wave frequency: 700 MHz
- Waveguide: 15" x 7.5" rigid aluminum
- Power output: 1 MW, 0.5 MW, 0.25 MW

The internal heat transfer coefficient experiments will be performed for the following parameters:

- Airflow rate: 500 to 1500 cfm, in 250 cfm increments
- Air inlet temp.: 55°F & 65°F (room temperature)
- Wave frequency: 700 MHz
- Power output: 1 MW

For each experiment, the airflow rate is adjusted to the desired rate. When steady state is reached, the inlet and outlet air dry-bulb and wet-bulb temperatures, waveguide surface temperature at various locations, and ambient temperatures are recorded.

The heat transfer coefficient is calculated from a heat balance for each experiment. The coefficient, along with the physical properties of air, are then used to calculate the Nusselt, Reynolds, and Prandtl numbers. The Nusselt number is plotted against  $Re^a Pr^b$  to obtain a correlation for predicting the heat transfer coefficient.

The external heat transfer experiments will be performed for all combinations of the following parameters:

- Airflow rate: 0, and 500 to 1500 cfm in 250 cfm increments
- Air inlet temp.: 55°F
- Wave frequency: 700 MHz
- Power output: 1 MW

The experimentally-determined coefficient is the combined coefficient for natural convection and radiation.

## 5 ANTICIPATED RESULTS

Figure 3 shows the CCDTL Section 1 waveguide layout. The waveguide is subdivided within three areas: klystron gallery, under-borm conduit, and the tunnel. The total length of waveguide in the gallery is about 44-ft. The total length of the conduit is also 44-ft of which 12-ft is exposed and 32-ft is in a concrete conduit. In the tunnel, the waveguide splits twice in the low-energy linac section. The total length is approximately 6.9-ft for the first splitter and 13.8-ft for the second splitter. Whenever there is a split, the RF power loss factor also is reduced by half.

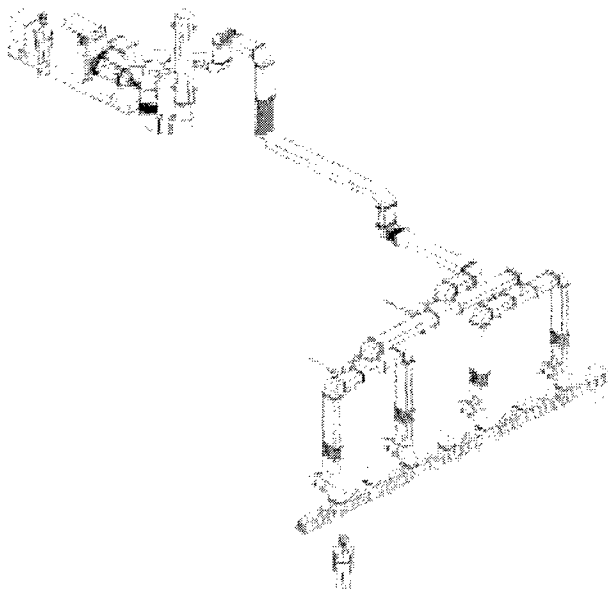


Figure 3: CCDTL Section 1 waveguide layout

Figure 4 shows the maximum waveguide surface temperature as a function of HVAC airflow. Table 1 shows predicted airflows required to maintain the coupled cavity drift tube linac (CCDTL) Section 1 waveguide below the 130°F maximum temperature.

## 6 CONCLUSIONS AND RECOMMENDATIONS

Test component design for the experimental set-up is currently in progress. The test results, when available, will be used to refine the heat transfer model used for the performance prediction.

Other techniques for cooling or reducing the heat produced by the waveguide include:

- Copper plate the waveguide inside surface to reduce the resistivity.
- Paint the outside surface of the waveguide with black high emissivity paint to enhance heat transfer by radiation.
- Increase the cross-sectional area of the guide.
- Air cool the outside of the guide by directing HVAC air on the guide.
- Water cool the outside of the guide with aluminum water channels brazed to the guide.

A trade study will compare the various techniques suggested in this paper. Life cycle costs, including capital equipment and operating and maintenance considerations, will be calculated and weighed against the perceived benefits of each approach. The final selection for cooling the RF waveguides on APT will emerge from the trade study as the lowest life cycle cost alternative that will meet the required availability and reliability criteria.

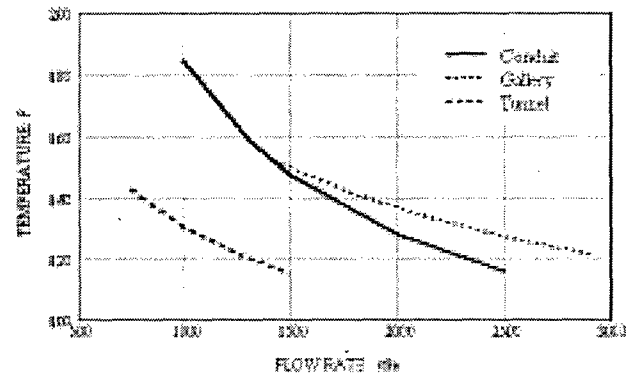


Figure 4: Maximum waveguide temperatures decrease with increasing airflow rate

Table 1: Predicted airflows to maintain CCDTL Section 1 waveguide temperatures below 130°F

	Gallery	Conduit	Tunnel
Heat Removed, W	10,975	11,000	6,400
Airflow, cfm	2,250	1,950	1,000
Ambient Temp., °F	90	104	104
Inlet Air Temp., °F	57	57	57
Outlet Air Temp., °F	74	81	79

## 7 ACKNOWLEDGEMENTS

The authors would like to thank S.C. Yung, P. Davidson, T. Rosetta, and S. Wojtowicz for their design, performance predictions, and editorial contributions.



# TEST RESULTS ON THE FIRST 13 kA PROTOTYPE HTS LEADS FOR THE LHC

A. Ballarino<sup>\*</sup>, L. Serio, CERN, Geneva, Switzerland

## Abstract

Prototypes of 13 kA HTS current leads for the Large Hadron Collider (LHC) have been specified by CERN and produced by several manufacturers. The specification defines the required thermo-electric performance and the geometric limitations imposed by the LHC infrastructure. A report is given of the results obtained from extensive tests on these leads.

## 1 INTRODUCTION

Following encouraging test results on High Temperature Superconducting (HTS) samples [1] and theoretical studies [2], a technical specification has been issued by CERN for the design and fabrication of 13 kA HTS prototype leads. Several companies have been selected for the manufacture of pairs of leads of different design. Different types of HTS materials (YBCO 123, BSCCO 2212, BSCCO 2223) have been proposed, both in bulk (MCP cylinders, MT bars) and in metal-stabilised form (PIT tapes, AFM and DIP bars). This report presents the test results of the first prototypes delivered to CERN.

## 2 TEST SET UP

A cryostat has been built at CERN to test the thermo-electric performance of the prototype leads [3]. The helium flow (20 K, 1.3 bar), needed for the cooling of the resistive heat exchanger, is obtained by mixing of room temperature helium gas and gas vaporised from the 4.5 K liquid helium bath. The cold end of the HTS dips into 4.5 K saturated liquid helium. The vapour generated by the lead at 4.5 K cools the HTS element prior being released into the cryostat environment.

The leads are tested in pairs, with a low-temperature superconducting short at the cold end. The instrumentation (temperature probes and voltage taps) is installed on the leads by the companies according to the CERN specification. Voltages, temperatures and current are recorded by a data acquisition system built with LabVIEW<sup>®</sup>. The same system is used for the control of the power converter and for the simulation of the exponential decay of the current. The cryogenic parameters are controlled by an industrial PLC with an operator interface based on PCVUE32<sup>®</sup>.

Signals interlocked to the power supply are the voltage across the resistive heat exchanger, the voltage across the superconducting circuit and the liquid helium level.

<sup>\*</sup> Email: amalia.ballarino@cern.ch

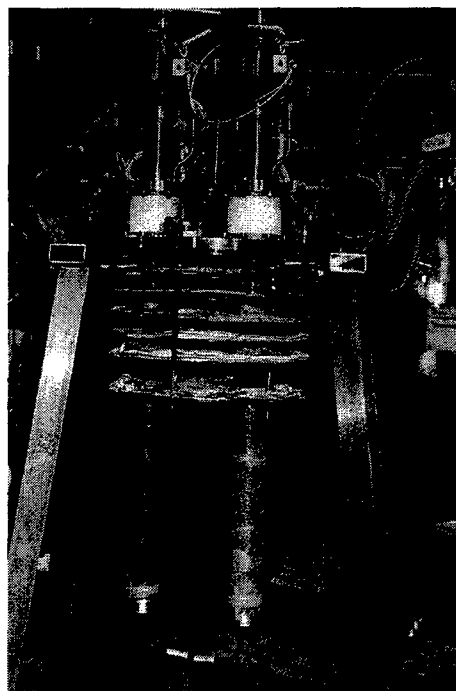


Figure 1: pair of 13 kA prototype leads on the test stand

## 3 TEST RESULTS

Measurements have been performed in stand-by ( $I=0$  A) and in nominal operation ( $I=13$  kA).

The leads are optimised for operating at 13 kA with the minimum 20 K helium flow ( $\dot{m}$ ) which maintains the warm end of the superconductor at temperatures ( $T_x$ ) below 50 K. The flow is controlled by a warm valve at the outlet of the resistive heat exchanger. The temperature is read via a platinum sensor located inside the warm end cap of the HTS element. In stand-by operation, the flow is reduced and  $T_x$  is kept equal to the value in nominal operation. The temperature at the warm end of the lead is maintained at about 290 K by a heater, thermostatically controlled, included at the warm terminal of the resistive heat exchanger.

The specified values defining the thermo-electric performance of the leads have been previously presented [4], [5].

Measurements have been performed in transient operation in order to study the lead behaviour in case of:

- loss of the 20 K helium flow cooling the resistive part of the lead;
- resistive transition of the superconducting part of the lead.

For the first test in operating conditions ( $I=13$  kA,  $T_x \leq 50$  K), the valve supplying the 20 K helium flow to the leads is closed and, within 5 seconds from the detection of the coolant loss, the current is made to decay exponentially with a time constant of 120 seconds. During the discharge, the temperature at the warm end of the HTS element must stay below its critical value.

For the second test, the temperature at the warm end of the superconductor is brought to its critical value by increasing, at nominal current, the inlet temperature of the gas cooling the resistive heat exchanger. The resistive heat exchanger is over cooled and the voltage drop is kept equal to about the value in nominal operation. The quench detection signal is the voltage drop across the HTS element. When it reaches the critical value, indicating a resistive transition of the superconductor, the current is made to decay exponentially with a time constant of 120 seconds. The current is by-passed in a metallic shunt, included in the HTS element to protect the superconductor. The resulting ohmic heating must not damage or modify the properties of any part of the lead.

### 3.1 BSCCO 2223 Ag/Au tapes

The first pair of 13 kA prototype leads were supplied by Fuji Electric. The resistive part consists of a CIC copper heat exchanger, while the HTS element is made with BSCCO 2223 Ag/Au tapes produced by Sumitomo [6].

At zero current, the leads were operated with the mass flow required to maintain the warm end of the superconductor at 30 K and 40 K, which is equal for both leads and corresponds to respectively 0.32 g/s and 0.27 g/s. The heat conducted by the HTS element into the liquid helium ( $Q$ ) is 0.5 W, for  $T_x=30$  K, and 0.64 W, for  $T_x=40$  K.

The current was increased from 0 to 13 kA with a maximum ramp rate of 50 A/s. At 13 kA, the steady state mass flow required to cool the resistive heat exchanger between 40 K and 300 K corresponds to 1.12 g/s for lead A and 0.97 g/s for lead B. The measured pressure drop is 16 mbar for lead A and 19 mbar for lead B. The voltage drop across the resistive heat exchanger ( $U$ ) is 99.5 mV for lead A and 84 mV for lead B.

At nominal current, each lead dissipates 0.715 W into the liquid helium. This value corresponds to the sum of the heat conduction plus the Joule dissipation at 4.5 K due to the contact resistance ( $R_c$ ) between the high temperature superconductor and the cold end cap. The contact resistance at 40 K between the warm end cap and the high temperature superconductor ( $R_{\mu}$ ) is about 1.15 n $\Omega$ .

Both leads were able to withstand the test of coolant loss without suffering damage. During the transient,  $T_x$  has increased from 40 K to 60 K.

To perform the quench test of the HTS material, the quench detection voltage was increased in steps of 1 mV from 1 to 5 mV. For voltages below 5 mV, the voltage across the high temperature superconductor decreases as soon as the quench is detected and the current starts to decay: the resistive zone does not propagate and the material recovers the superconducting state. For a quench detection voltage of 5 mV, corresponding to a temperature ( $T_Q$ ) of about 86 K, the resistive zone propagates and the voltage increases up to a peak ( $U_Q$ ) of 0.1 V for lead A and 0.11 V for lead B. The maximum temperature measured on the HTS during the transition is about 110 K. The total energy deposition corresponds to about 0.13 MJ.

In Fig. 2 is represented the time dependence of the voltage across the HTS element and of the current during the resistive transition of the superconductor.

The two leads presented a comparable behaviour. The critical temperature remained the same throughout the exercise. After the quench tests, the leads have shown no deterioration in their properties.

The results of the measurements on the leads are summarised in Table 1.

The leads withstood the electrical insulation test performed by applying 3.5 kV between the current carrying part and the ground, in helium gas atmosphere (300 K, 1.3 bar). The leakage current measured is less than 3.5  $\mu$ A, corresponding to an insulation resistance of better than 1 G $\Omega$ .

Table 1: Measurements on Fuji prototype leads

	LEAD A	LEAD B
	I=0 A	I=0 A
$T_x$ (K)	40	40
$m$ (g/s)	0.27 $\pm$ 0.01	0.27 $\pm$ 0.01
$\Delta p$ (mbar)	2.5 $\pm$ 1	2.5 $\pm$ 1
$Q$ (W)	0.64 $\pm$ 0.04	0.64 $\pm$ 0.04
	I=13 kA	I=13 kA
$T_x$ (K)	40	40
$m$ (g/s)	1.12 $\pm$ 0.01	0.98 $\pm$ 0.01
$\Delta p$ (mbar)	16 $\pm$ 1	19 $\pm$ 1
$U$ (V)	0.099	0.084
$R_{\mu}$ (n $\Omega$ )	1.15	1.15
$R_c$ (n $\Omega$ )	0.5	0.7
$Q$ (W)	0.715 $\pm$ 0.04	0.715 $\pm$ 0.04
$T_Q$ (K)	86.9	86.3
$U_Q$ (V)	0.1	0.11

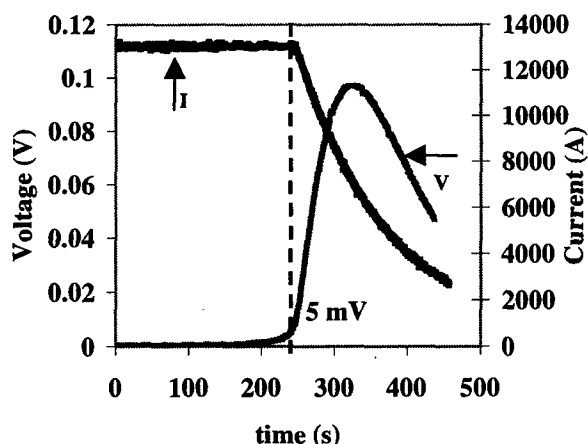


Figure 2: resistive transition on 13 kA Fuji HTS leads

### 3.2 BSCCO 2212 DIP bars

A pair of 13 kA prototype leads has been supplied by Oxford Instruments. The HTS section consists of bars made up of dip coated BSCCO 2212 produced by OST.

At zero current, the leads operated with a flow of about 0.19 g/s. The temperature at the warm end of the superconductor is about 30 K. The heat conduction into the liquid helium corresponds to about 1.1 W/lead.

The measurements with current have been performed at 10 kA: at higher current rates, a high contact resistance, on the resistive heat exchanger of one lead, was spoiling the thermal performance. At 10 kA each lead requires about 0.79 g/s of 20 K helium flow when Tx is equal to 48 K, and about 1.2 g/s when Tx is equal to 40 K. The measured heat conducted into the liquid helium, when Tx is 40 K, is about 1.82 W/lead.

The leads could withstand the coolant loss test according to specification.

Quench measurements have been performed by increasing the quench detection voltage on the HTS element from 1 to 50 mV in steps of 5 mV. In all the tests, the voltage decreases as soon as a quench is detected and the current starts to decay. At 50 mV, the temperature at the warm end of the superconductor is 90 K. The maximum temperature measured is 94.7 K. No propagation of the resistive length has been measured.

The results of the tests are promising. Measurements up to 13 kA will be performed after repair of the resistive joint.

### 3.3 BSCCO 2223 AFM bars

A pair of 13 kA prototype leads has been supplied by Enel in collaboration with Cryogenic Ltd. The resistive heat exchanger consists of brass tubes. The HTS element is an assembly of Ag/Au AFM bars produced by Enel [7]. The results of the measurements are presented in Table 2.

The leads could withstand the coolant loss tests. During the transient, Tx has increased from 40 K to about 60 K. Quench measurements are in progress.

Table 2: Preliminary measurements on Enel/Cryogenic prototype leads

	LEAD A	LEAD B
	I=0 A	I=0 A
T <sub>x</sub> (K)	40	40
m (g/s)	0.27	0.27
Δp (mbar)	<1	<1
Q (W)	~1.62	~1.62
	I=13 kA	I=13 kA
T <sub>x</sub> (K)	40	40
m (g/s)	~0.97	~1
Δp (mbar)	3	3
U (V)	0.082	0.082
R <sub>H</sub> (nΩ)	7.7	9
R <sub>C</sub> (nΩ)	2	2
Q (W)	~1.68	~1.68

## 4 CONCLUSION

Three pairs of 13 kA HTS prototype leads have been tested at CERN. The measurements have shown that the cryogenic and electrical requirements within the stringent geometrical limitations defined in the technical specification are achievable on prototype leads. In particular, the heat load into the liquid helium at nominal current can be reduced by a factor up to 19 with respect to conventional self-cooled leads. Other prototypes will be tested at CERN over the next few months.

## 5 REFERENCES

- [1] M. Teng, A. Ballarino, R. Herzog, A. Ijspeert, C. Timlin, S. Harrison, K. Smith, "Evaluation of HTS Samples for 12.5 kA Current Leads", Applied Superconductivity 1997, vol 2, pp 1203-6, (1997)
- [2] A. Ballarino, "Discendenti di corrente realizzati con materiale superconduttore ad alta temperatura critica per l'alimentazione dei magneti del Large Hadron Collider", PhD Thesis, Politecnico di Torino, Torino, (1997)
- [3] A. Ballarino, A. Bezaguet, P. Gomes, L. Metral, L. Serio, A. Suraci, "A Low Heat Inleak cryogenic Station for testing HTS Current Leads for the Large Hadron Collider", paper to be presented at CEC-ICMC '99, Montreal, Canada, (1999)
- [4] A. Ballarino, "High Temperature Superconducting Current Leads for the Large Hadron Collider", ASC '98, Palm Desert, California, (1998)
- [5] T. Taylor, "HTS Current Leads for the LHC", ASC '98, Palm Desert, California, (1998)
- [6] T. Uede, Y. Yasukawa et al, paper to be presented at CEC-ICMC '99, Montreal, Canada, (1999)
- [7] L. Martini, F. Curcio, E. Marelli, V. Ottoboni, 1.5 kA-Class Multilayered Bi-2223/Ag Conductors: DC and AC Characterization, ICEC 16, Japan, (1996)

## RF SCREENING BY THIN RESISTIVE LAYERS

F. Caspers, G. Dôme, C. Gonzalez, E. Jensen\*, E. Keil,  
M. Morvillo, F. Ruggiero, G. Schröder, B. Zotter, CERN, Geneva, Switzerland  
and M. D'Yachkov TRIUMF, 4004 Wesbrook Mall, Vancouver, B.C., Canada V6T 2A3

### Abstract

We discuss the results of recent impedance measurements for an LHC dump kicker prototype, performed at CERN using the coaxial wire method. The kicker design includes a vacuum barrier consisting of a ceramic chamber internally coated with a thin metallic layer having good electric contact with the external beam pipe. For the bench test the coated ceramic tube was replaced by a kapton foil with a  $0.2\ \mu\text{m}$  copper layer having the same DC resistance of  $0.7\ \Omega$ . The measurements show that this resistive coating provides a very effective RF screening down to frequencies below 1 MHz, where the skin depth is two orders of magnitude larger than the layer thickness and one could expect full penetration of the electromagnetic fields. We also present simulation results and analytic considerations in agreement with the measurements, showing that the return currents almost entirely flow through the copper layer down to frequencies where the reactive impedance of the kicker elements located behind it becomes comparable to the layer resistance. Finally we discuss the relevance of such coaxial wire measurements to the RF shielding by thin metallic layers in the presence of a highly relativistic proton beam.

### 1 INTRODUCTION AND SUMMARY

The question of how the RF impedance of thin metal films is to be computed and measured in practical situations may have a significant impact on the design of metallized ceramic chambers for kicker magnets or metal screens in the experimental beam pipes. These are examples of structures of finite length, while analytic results on electromagnetic penetration are available only for infinitely long structures (see for example [1, 2]).

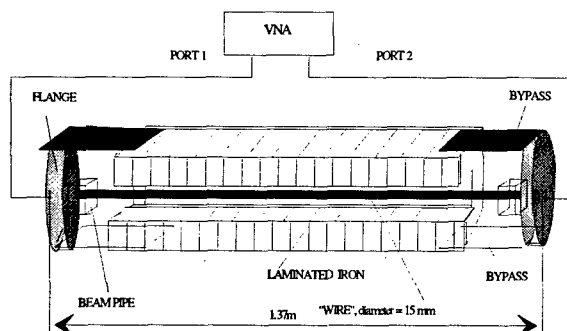


Figure 1: Longitudinal cross section of an LHC dump kicker with flanges and measurement setup.

\* Email: Erk.Jensen@cern.ch

The coating resistance of ceramic chambers for kicker magnets should be low for good RF screening, but not too low to avoid eddy currents that would prevent kicker field penetration. In the LHC dump kicker, a good compromise is obtained with a DC resistance per square  $R_{\square} = 0.1\ \Omega_{\square}$ , corresponding to a  $4.2\ \mu\text{m}$  Ti layer or to a  $0.2\ \mu\text{m}$  Cu layer. The skin depth  $\delta$  in copper at 1 MHz is about  $60\ \mu\text{m}$  and one may expect penetration at frequencies below 100 GHz. However, the effective skin depth  $d_{\text{eff}} = \delta^2/D$  at 1 MHz for a  $0.2\ \mu\text{m}$  copper coating on a ceramic tube with thickness  $D = 3\ \text{mm}$  is only  $1.2\ \mu\text{m}$  according to Ref. [2] and RF shielding is expected above 6 MHz. A  $0.1\ \text{mm}$  thick kapton foil was used in the kicker impedance measurements discussed in Sec. 2, instead of the ceramic tube, and the effective skin depth at 1 MHz should then be about  $36\ \mu\text{m}$ . For a  $0.2\ \mu\text{m}$  copper layer one would therefore expect RF shielding only at frequencies above 200 MHz, while the measurements show a clear shielding effect already above 1 MHz.

The coaxial wire measurements have been successfully simulated using the program HFSS. Modelling the kicker by a cylindrical cavity having a thin screen of radius  $a = 50\ \text{mm}$  and sheet resistance  $R_{\square} = 0.2\ \Omega_{\square}$ , the electric field created in the cavity by a sinusoidal signal at 5 MHz on the inner conductor is attenuated by a factor 1000 compared to the case without resistive screen. This confirms that the shielding effect does not require any dielectric. Several independent current sources with proper phase shifts have been used to model a beam, rather than an inner conductor; the results are virtually the same.

The same cylindrical structure used for the simulations with HFSS has been investigated analytically using field matching of the unknown longitudinal electric field  $E_z(r = a)$ . This yields an integral equation containing a dimensionless parameter  $\zeta = Z_0/R_{\square}$ , where  $Z_0$  is the free space impedance. When  $\zeta$  is large the screening is good. However field penetration is enhanced near resonant frequencies corresponding to coaxial cavity modes and may become significant if  $\zeta$  is smaller than their quality factors. For a  $0.2\ \mu\text{m}$  copper layer  $\zeta \approx 4400$ . When the cavity length tends to infinity there is no shielding.

### 2 MEASUREMENTS

The coaxial wire method is a convenient bench method for the simulation of charged particle beams. For longitudinal impedance measurements, the test bench setup (see Fig. 1) consists of a single conductor ("wire") in the centre of the vacuum chamber, at the position of and replacing the beam.

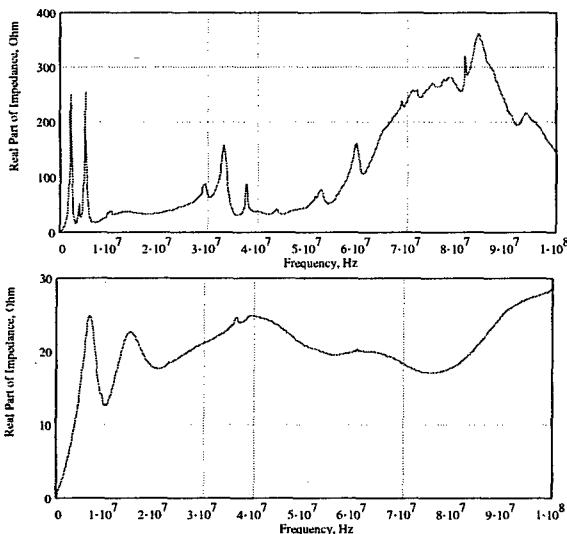


Figure 2: Real part of the impedance when the kicker body is either disconnected (top) or connected with four copper foils (bottom) to the supports of the RF connectors.

Figure 2 shows the effect of an external bypass, consisting of four 0.3 mm thick copper foils connecting the flanges to the aluminum case which surrounded the magnets, in the absence of the resistive layer.

The fact that the impedance doesn't change if we move/connect the kicker magnets, as shown in Fig. 3, indicates that the metallized kapton foil (and therefore the metallized ceramic pipe with similar surface resistance) is very effective in shielding the kicker magnets from the electromagnetic fields produced by the LHC bunches. In Fig. 4 we compare the transmission coefficients measured in presence of the resistive layer with and without external bypass. The effect of the bypass on the transmission coefficient can be seen only at very low frequencies: the maximum difference is observed at 0.1 MHz and is equivalent to 0.05  $\Omega$ . The difference becomes negligible above 1 MHz.

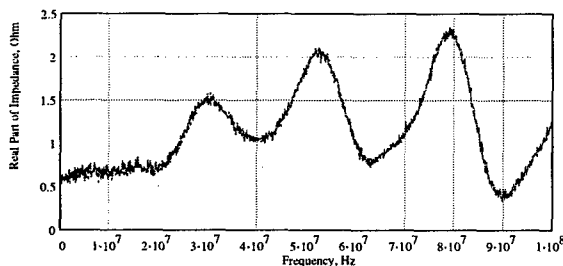


Figure 3: Real part of the impedance measured with the resistive layer for kicker magnets either closed or open (the two curves are indistinguishable). The resistive layer reduces the impedance significantly (compare to Fig. 2).

### 3 NUMERIC SIMULATIONS

An idealized, empty cavity-like object was used instead of kicker magnets with complicated geometry. The resistive layer, of radius  $a$  and length  $g$  as shown in Fig. 5, was assumed to have zero thickness and could thus be charac-

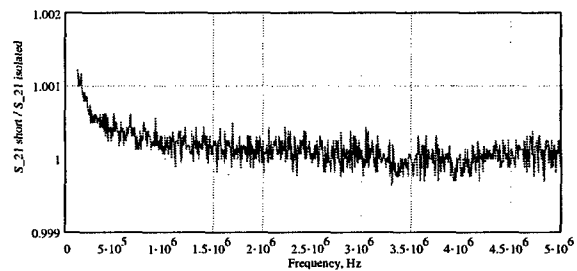


Figure 4: Ratio of the transmission coefficients  $S_{21}$  measured in presence of the resistive layer with and without external bypass.

terized by its sheet resistance  $R_{\square}$  and by the total resistance  $R = R_{\square}g/2\pi a$ . This was easily modelled with the program HFSS (High-Frequency Structure Simulation) by Ansoft [3], that was adopted for the calculation.

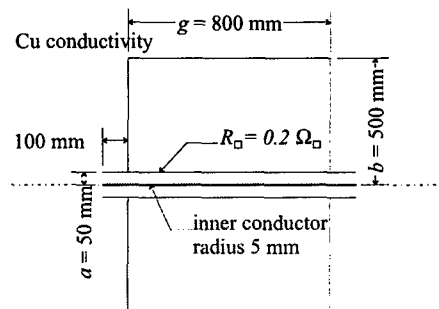


Figure 5: Pillbox cavity with cylindrical symmetry and resistive layer used in the simulations.

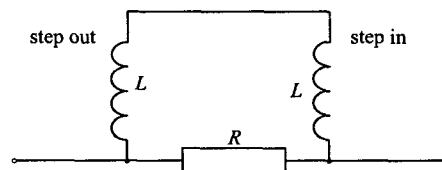


Figure 6: Equivalent circuit for the setup of Fig. 5.

In the cavity-like geometry which we considered, we find the simplified equivalent circuit shown in Fig. 6 to be valid for frequencies of up to 100 MHz, i.e. as long as the length can be considered short compared to the wavelength. As shown in Figs. 7 and 8, at 100 MHz the electric field is diminished outside of the layer by a factor of at least 100. A stronger attenuation is found at lower frequencies, down to a few MHz. At 100 kHz the electric field is still shielded, but the magnetic field starts penetrating. Each step in the beam chamber radius can be represented by a concentrated inductance  $L$ , the resistive layer by a resistor of in our case  $R = 0.5 \Omega$ . Note that the latter is proportional to the length. Any possible kicker impedance  $Z$  will appear in parallel to the resistor. Hence, the value of  $R$  gives an easy worst case estimate for the impedance of the considered section, as shown in Fig. 9. An inductance  $L = 100$  nH, associated with the geometric step of a typical kicker tank, corresponds to an impedance of about  $6 \Omega$  at 10 MHz. For a metallic layer with typical specific

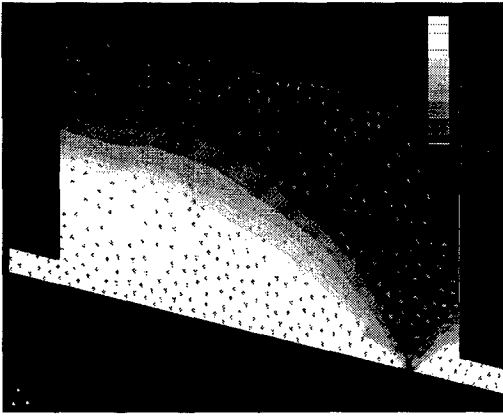


Figure 7: Electric field at 100 MHz, without the resistive layer. The arrows indicate the directions, the shading the intensity of the field, in arbitrary units. At this frequency, more than a quarter wavelength fits into the structure - note the electric field node at the right.

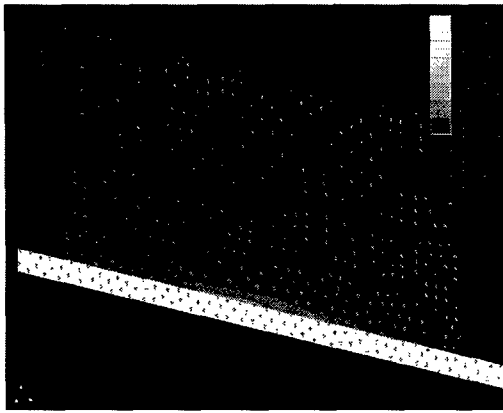


Figure 8: Electric field at 100 MHz, with the resistive layer. The same units as in Fig 7 were used, but for the shading the sensitivity was increased by a factor 100. Note the change of the electric field direction at the layer.

resistance of  $1 \Omega/\text{m}$ , the asymptotic regime where the image currents flow in the outer conductor and the resistive layer provides no shielding requires lengths of the order of several meters.

The wire does not only carry a current which is similar to that of a charged particle beam, but it is also a conductor. Consequently, it can be argued that the coaxial wire method makes a systematic error which may not be small in all cases. In HFSS, it is possible to excite the structure with ideal current sources (with infinite inner resistance) which resemble the ultrarelativistic beam much more. We distributed 16 short current sources along the axis of the structure. Their currents were equal but adjusted to have a phase advance from one to the next equivalent to a phase velocity of  $c$ , i.e.,  $\Delta\phi = (\omega/c) \Delta z$ . The results of the simulation with current sources and those with an inner conductor are virtually identical outside of the resistive layer. They differ only in the vicinity of the axis.

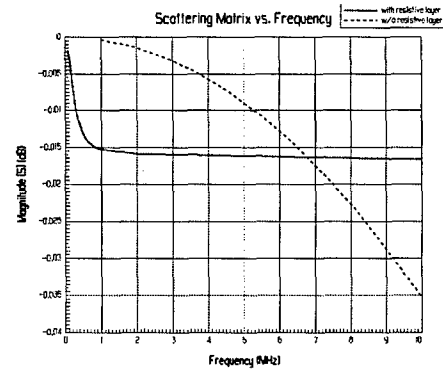


Figure 9: Transmission coefficient  $\log |S_{21}|$ , from 70 kHz to 10 MHz, with resistive layer (solid line) and without (dashed line). The impedance predicted by the equivalent circuit model of  $R = 0.5 \Omega$  corresponds to a transmission loss of  $-0.016 \text{ dB}$  and agrees well with these simulation results above 1 MHz.

#### 4 ANALYTIC CONSIDERATIONS

A charged particle travels on the axis of the cavity shown in Fig. 5 with a Lorentz factor  $\gamma = 1/\sqrt{1-\beta^2}$  corresponding to the velocity  $\beta = v/c$ . We want to compute in frequency domain the electromagnetic fields induced by the charge in the cavity; these fields can be computed once the longitudinal electric field  $E_z$  is known in the gap  $g$  at  $r = a$ . It can be shown that  $E_z(r = a)$  is determined by a Fredholm integral equation of the second kind. The kernel of the integral equation is built up from two parts: a pipe kernel, which involves the cut-off frequencies of the  $E_{0n}$  modes of the beam pipe, and a cavity kernel, which involves the resonant frequencies of the coaxial cavity corresponding to the boundary condition  $E_z = 0$  at  $r = a + d$ , where  $d \ll \delta$  is the layer thickness. For the resistive layer being an effective screen, it must carry almost all of the image current which flows along the beam pipe, which means that  $\zeta E_z(r = a)$  must be as large as possible (here  $\zeta = Z_0/R_\square$ ). Without solving the Fredholm integral equation, what seems to be a formidable task, it can be seen that this will happen when  $\zeta$  is large enough and the cavity kernel is small enough. Since this part of the kernel has poles at the resonant frequencies of the coaxial cavity, this means that these frequencies are not screened by the resistive layer. Since the integral over the kernel is taken along the gap  $g$ , the product  $(\omega/c)g$  must not be too large. When  $(\omega/c)g \rightarrow \infty$ , it can be shown that  $E_z(r = a)$  contains a factor  $1/\beta^2\gamma^2$  which makes  $E_z(r = a)$  much too small to provide any screening.

#### 5 REFERENCES

- [1] B. Zotter, 'Longitudinal instabilities of charged particle beams inside cylindrical walls of finite thickness', Part. Acc. **1**, 311-326 (1970).
- [2] A. Piwinski, 'Penetration of the field of a bunched beam through a ceramic vacuum chamber with metallic coating', IEEE Trans. Nucl. Sci. **24**, 1364-1366 (1977).
- [3] World-wide web page <http://www.ansoft.com/>

# CONSTRUCTION AND MEASUREMENT TECHNIQUES FOR THE APS LEUTL PROJECT RF BEAM POSITION MONITORS\*

Anthony J. Gorski,<sup>#</sup> Robert M. Lill, Accelerator Systems Division, Advanced Photon Source, Argonne National Laboratory, 9700 South Cass Avenue, Argonne, IL 60439 U.S.A.

## Abstract

The design, construction, and assembly procedure of 24 rf beam position monitors used in the Advanced Photon Source low-energy undulator test line and linear accelerator (linac) are described. Beam stability as well as beam positioning capabilities are essential to the LEUTL project. A design objective of the LEUTL facility is to achieve better than 1- $\mu$ m resolution. The highest care was used in the mechanical fabrication and assembly of the BPM units. The latest experimental results using these BPMs will be presented.

## 1 INTRODUCTION

The Advanced Photon Source (APS) low-energy undulator test line (LEUTL) was designed to test prototype undulators and to develop the technology necessary for a fourth-generation synchrotron light source [1]. The LEUTL beam position monitor (BPM) system employs both 4-mm buttons and S-band stripline BPM detectors as shown in Fig. 1 and schematically in Fig. 2. The total length of the stripline assembly is 83 mm, the electrode length is 28 mm, and the inner electrode diameter is 35 mm, the same as the linac vacuum chamber ID. The metal electrodes form 50-ohm transmission lines between each of the four blades and the vacuum chamber housing. The downstream end of the

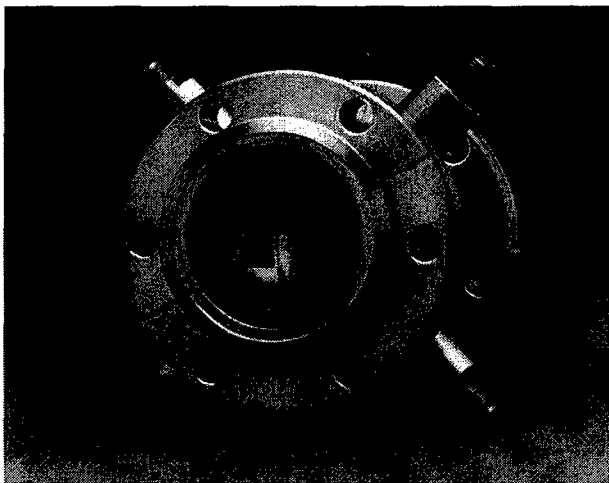


Figure 1: The LEUTL shorted S-band quarter-wave four-plate stripline BPM

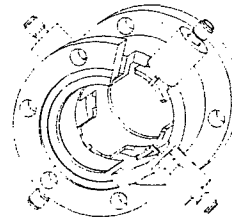


Figure 2: Cut away 3D drawing of LEUTL-BPM showing internal structure

transmission line is electrically shorted, which also provides mechanical strength and rigidity to support the stripline pickup. This technique of supporting the stripline results in a TEM wave velocity induced on the stripline that is approximately equal to the beam velocity.

The receiver topology used is a monopulse amplitude to phase (AM/PM) technique for measuring the beam position in the x and y axes and a logarithmic amplifier channel for measuring the beam intensity. The striplines are installed with the blades rotated 45 degrees from axis to operate in the monopulse system. The stripline output signals are conditioned by the down converter monopulse comparator (DCMC). The DCMC provides signal filtering and down converts the 2856-MHz position information to 351 MHz. It also generates horizontal and vertical difference and sum signals through a 180-degree hybrid rat race network.

## 2 DESIGN

The LEUTL BPM stripline was designed to operate at 2856 MHz and is similar to that implemented for the APS linac [2]. The design was optimized using standard design equations [3] and then empirically refined. The design goal was to enhance port isolation, reduce reflections, and increase BPM stripline production yields. The impedance of the stripline was optimized to 50 ohms to match that of the SMA feedthrough. Figure 2 illustrates the internal structure and Fig. 3 shows how the output of the stripline is connected via a short tantalum ribbon to the molybdenum feedthrough connector. This technique minimizes the electrical mismatch that is typically encountered when transitioning from the stripline to the feedthrough. The ribbon also acts as a strain relief for any forces acting on the ceramic vacuum seal.

\* Work supported by the U.S. Department of Energy, Office of Basic Energy Sciences, under contract number W-31-109-ENG-38.

#Email: gorski@aps.anl.gov

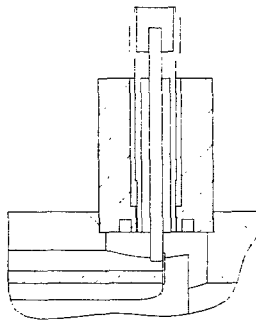


Figure 3: Cross-sectional view showing attachment of the SMA feedthrough center conductor to the internal blade by means of a thin tantalum ribbon

The length of the stripline, 28 mm, was optimized for maximum isolation at 2856 MHz between ports. This is also the electrical length, which offers the maximum amplitude and zero crossing phase at 2856 MHz. This was approximately 7% longer than the theoretical quarter wavelength of 26 mm. The inductive mismatch at the transition area shown in Fig. 3 could account for this difference.

### 3 COMPONENTS AND FABRICATION

The 50-ohm feedthrough used was a Kamen Instrument model 853872. The material of the outer body is 316 stainless steel and the center conductor is TZM molybdenum per ASTM B365. The vacuum seal insulator material is  $\text{Al}_2\text{O}_3$ -strengthened borosilicate with 130,000-psi compression strength. The feedthrough is specified with an operating temperature range of  $-269^\circ$  to  $300^\circ$  Celsius and a hermeticity of  $< 1 \times 10^{-11}$  cc He/s.

Previous experience with assembling these types of BPMs resulted in a high failure rate of feedthrough during the welding process. The major cause of the failure is believed to be caused by the differential linear expansion of the stripline and the molybdenum center conductor, which were welded directly together. In the new design a short piece of tantalum ribbon sheet is used to bridge the stripline and molybdenum center conductor as shown in Fig. 3.

The fabrication of the BPM starts with standard stock 316 stainless steel. The four quarter-wave plates on the electrode port are cut by a traveling wire-type EDM machine. This cutting process used a brass wire for an initial cut, then a smoothing cut followed by an acid washing of the finished part to remove any brass from the stainless steel surface. Since the EDM process does not involve mechanical energy, the hardness or the strength of the workpiece is not affected by the removal rate.

The traveling wire EDM procedure is also used to cut the 0.064-inch TZM molybdenum center conductor to the required length. The conductor is held by the free end such that no stress is applied to the insulator/outer body vacuum seal. Finally, tantalum strips are cut to length for the feedthrough to quarter-wave plate connection.

### 4 ASSEMBLY PROCESS

The assembly process starts with cleaned stainless steel components and chemically etched feedthrough center conductors, and tantalum strips. At this stage, all parts are handled with proper gloves, and etched parts are kept in closed vials. Since the etched parts are e-beam brazed within 12 to 24 hours after etching, a dry nitrogen atmosphere is not necessary.

First the feedthroughs are e-beam welded to the connector and vacuum leak tested. The next step is the e-beam silver wetting of the feedthrough conductor by means of thin silver foil. Then the brazing operation couples the tantalum strip to the molybdenum conductor, and the completed units are stored until final assembly.

The two halves of the body unit are TIG welded together, and the four completed connector columns are aligned and TIG welded to the body of the conductor piece. It is necessary for the columns to be perpendicular to the conductor surface and aligned such that the final e-beam brazing to the face of the electrode plate can be made. After a final vacuum leak check, the conventional welding of the two rotatable flanges completes the assembly.

### 5 MEASURED PERFORMANCE

The stripline was measured using the HP 8510C network analyzer with the time domain reflectometer (TDR) option. Using the TDR in the low pass mode, stripline mismatches can be located and characterized. The stripline return loss was measured using a gating technique that electrically eliminates all other reflections. The gate is a time filter in which specific mismatches such as the short at the end of the line can be filtered out of the measurement. Measuring only the stripline, a 20-dB return loss at 2856 MHz was realized.

The electrical length of the stripline was optimized to 28 mm to improve port isolation. The isolation between ports measures typically about 60 dB at 2856 MHz (see Fig. 4), which is about a 25-dB improvement over the original design.

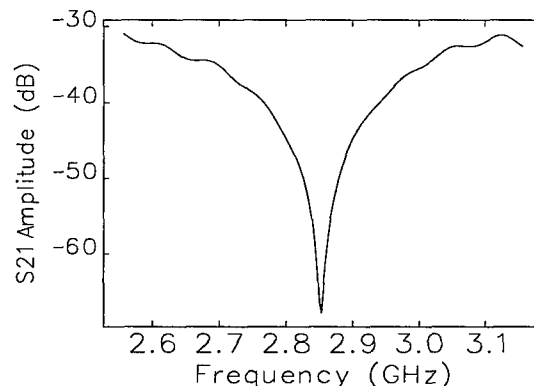


Figure 4: Measured port isolation



The stripline and BPM electronics were tested on the bench using a wire stretched through the stripline vacuum chamber. The vacuum chamber was mounted on an adjustable two-axis precision micrometer table that was used to simulate beam position motion. An rf isolator was implemented at the input of the chamber to properly match the source, masking the input VSWR of the chamber transition. The results indicate a linear range of operation of about  $\pm 10$  mm from the center of the chamber, as shown in Fig. 5. The horizontal position data measured coincide approximately with the calculated values shown in Fig. 5. The deviation from the theoretical response is shown in Fig. 6. The measured vertical response results are similar.

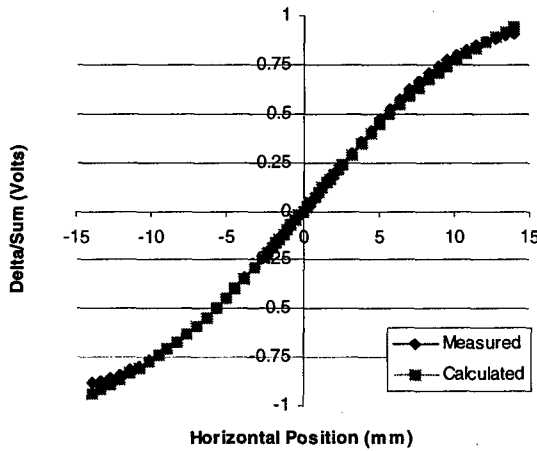


Figure 5: Delta/sum vs. horizontal position wire test data

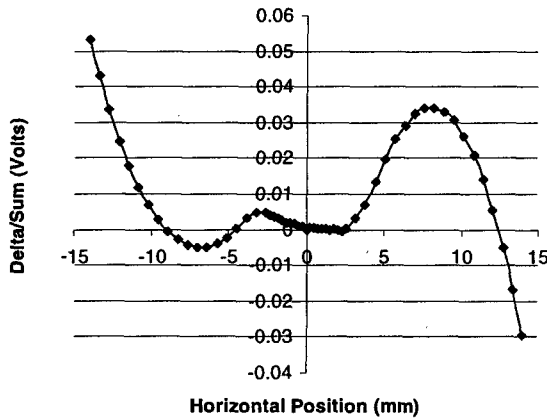


Figure 6: Deviation from expected response

The LEUTL BPM system must provide high-resolution beam position at rated operating beam currents. The AM/PM phase detector has a linear voltage vs. phase output with a sensitivity of 90 degrees/volt. The AM/PM transfer function can be described as follows:

$$E_{\text{out}} = \frac{4}{\pi} \tan^{-1} \frac{\Delta}{\Sigma} \quad (1)$$

where  $E_{\text{out}}$  is the receiver output.

It is desirable to operate the BPM system such that the maximum receiver input (+10 dBm) is realized in order to maximize beam position resolution. The output noise of the receiver can be described as follows [3, 4]:

$$\left( \frac{\Delta}{\Sigma} \right)_{\text{sensitivity}} = 1 \text{ volt} / 90 \text{ degrees}, \quad (2)$$

$$\Delta\theta_{\text{phase jitter}} = 1/\sqrt{\text{SNR}} \text{ rads}, \quad (3)$$

$$\text{Receiver Output Noise} = \text{Phase Jitter} \times \left( \frac{\Delta}{\Sigma} \right)_{\text{sensitivity}}, \quad (4)$$

$$\text{Resolution limit} \cong \frac{b}{2\sqrt{2}} \sqrt{\frac{P_n}{P_s}}, \quad (5)$$

where  $b$  is half aperture,  $P_s$  is the signal power on a single electrode, and  $P_n$  is the noise power.

The thermal noise power (kTB) for the 20-MHz bandwidth is -91 dBm. Since there are two channels (delta and sum), the noise is incoherent and will add in quadrature for a total equivalent noise of -88 dBm. The receiver input is +10 dBm at rated beam current, yielding a signal-to-noise ratio (SNR) of 98 dB. This corresponds to a resolution limit of about 1  $\mu\text{m}$  for a 34.8-mm-diameter aperture.

## 6 CONCLUSION

The assembly of 24 rf beam position monitors has been successfully accomplished with a yield of 100%. The preliminary bench test results have been encouraging and further tests are ongoing. Operational and commissioning data will be obtained as the LEUTL facility becomes operational in the next few months.

## 7 ACKNOWLEDGEMENTS

The authors would like to acknowledge Glenn Decker, Raymond Fuja, and Dean Walters for many helpful discussions. Chuck Gold and Robert Keane provided valuable electrical measurement and assembly expertise. The mechanical advice of Frank DePaola and William Totter proved to be most useful. And finally, the e-beam expertise of Robert Sommer and Robin Reiersen, and etching assistance of Richard Lee made it all look simple.

## 8 REFERENCES

- [1] S. Milton, J. Galayda, E. Gluskin, "The Advanced Photon Source Low-Energy Undulator Test Line," 1997 Particle Accelerator Conference, Vancouver, BC, Canada, IEEE (1998), pp. 877-879.
- [2] R. Fuja, Y. Chung, "The APS Linac Beam Position Detectors and Electronics," 4<sup>th</sup> Accelerator Instrumentation Workshop, LBL, Berkeley, CA, 1992, pp. 248-255.
- [3] R. Shafer, "Beam Position Monitoring," AIP Conference Proceedings 212, Accelerator Instrumentation, Upton, N.Y., 1989, pp. 26-58.
- [4] Watkins Johnson, "Monopulse Receiver Technical Proposal," WJ-253199, Vol. I, 1992.

# IMPROVED TEMPERATURE REGULATION AND CORROSION PROTECTION OF APS LINAC RF COMPONENTS\*

M. White, R. Dortwegt, S. Pasky

Argonne National Laboratory, Argonne, Illinois, USA 60439

## Abstract

Water from individual closed-loop deionized (DI) water systems is used to regulate the temperature of high-power rf components at the Advanced Photon Source (APS) S-Band linac. The rf components are made of oxygen-free high-conductivity copper and respond quickly to temperature, resulting in changes in the beam energy when the temperature is poorly regulated. Temperature regulation better than  $\pm 0.1^\circ\text{F}$  is required to achieve good energy stability. Improvements in the closed-loop water systems have enabled us to achieve a regulation of  $\pm 0.05^\circ\text{F}$  over long periods. In the long term, depletion of copper from the water circuits is a very real and serious concern, thus steps are being taken to reduce corrosion. Temperature regulation philosophy and equipment are discussed and numerical results are presented. Steps to decrease copper corrosion are also discussed.

## 1 INTRODUCTION

The APS linear accelerator [1] rf system includes SLED cavity assemblies and accelerating structures that require temperature stability of  $\pm 0.1^\circ\text{F}$  or better. The required stability is achieved using linac closed-loop (LCL) water systems that provide constant temperature water to the SLEDs, accelerating structures, waveguide, loads, and to the rf reference and drive line.

Each LCL has an optimum temperature in the range of 105-116°F that maximizes beam energy [2]. Absolute knowledge of the temperature is not essential, but long-term stability is, especially since the linac is now being modified to become an FEL driver.

Corrosion and erosion of copper are other issues related to use of DI water in copper systems. Possible equipment failure can occur as a result of leaks and/or blockages.

## 2 TEMPERATURE REGULATION

A schematic of an LCL system is depicted in Fig. 1 and includes the APS primary (APS-PS) and klystron gallery secondary (KGSS) DI process water systems through which heat is ultimately rejected. There are five LCLs, all with identical hardware components. Three LCLs provide total flows of 80 gpm and the other two provide 25 and 40 gpm.

LCL components include an end-suction centrifugal pump, a shell-and-tube heat exchanger (HX), a 12-kW electric heater, and a 3-way mixing valve to regulate the temperature. The heater provides energy input to the system on cold startup so the setpoint value is reached in

a reasonable time. It also matches steady-state energy input with heat rejection capacity, since the temperature control valve and HX capacities are more than adequate to remove heat from rf input and frictional flow loss.

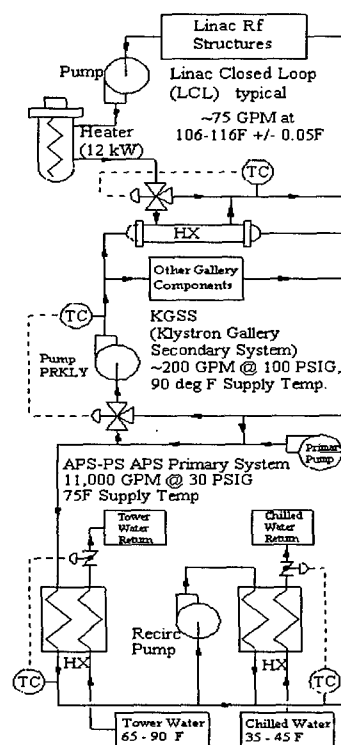


Figure 1: Overview of the heat-rejection system, including the LCL, KGSS, and APS-PS.

All LCLs are cooled by water circulated by the KGSS pump. KGSS water temperature is controlled at 90°F by a 3-way mixing valve. Water from the primary system at 75°F is admitted to the recirculating KGSS. APS-PS water is cooled using cooling-tower water, but chilled water is used when the tower water is too warm.

The original linac water system provided long-term temperature stability no better than  $\pm 0.5^\circ\text{F}$ . Intervention was required after large power transients or equipment upsets. Performance was limited by the thermal sensor resolution and the  $\pm 1.0^\circ\text{F}$  variation of the KGSS coolant temperature. The sensors were installed in thermowells, resulting in slow response times. Upgrades were staged.

First, a 30-gallon holding tank was installed on the coolant inlet side of the HX, thus averaging out the fluctuations. A similar tank was installed on the linac side of the HX to increase capacitance. Mixing valve actuators were replaced by Worcester units. These upgrades

\* Work supported by the U.S. Department of Energy, Office of Basic Energy Sciences, under Contract No. W-31-109-ENG-38.

reduced the temperature fluctuations to  $\pm 0.15^\circ\text{F}$ .

Changes in the output control signal were slow to affect the sensor due to the long distance between the KGSS RTD and the mixing valve, and because the KGSS RTD was installed in a thermowell. The RTD was replaced by a direct-immersion RTD and was relocated immediately downstream of the pump. This permitted improved tuning of the secondary loop with PI control. The control algorithm (Johnson Metasys with "tune override" that imposes "stronger" PID parameters when the temperature error deviates by more than a set amount) was removed, and traditional PI tuning was implemented. These modifications resulted in KGSS stability on the order of  $\pm 0.1$  to  $0.2^\circ\text{F}$  and LCL stability of  $\pm 0.1^\circ\text{F}$ .

Valve tuning is a critical element in system control and tuning the 3-way mixing valves in the LCLs (controlled by Johnson Controls LCP controllers) was not routine. The Johnson LCP has no specific "tune override" feature, but its response to temperature disturbances did not seem "classical." As a test, a Watlow 965FDO controller was substituted for one of the Johnson LCP controllers for a short time, during which it was observed that valve tuning in the classic closed-loop manner was possible [3]. Based on these results, it was decided to search for a high-resolution, stand-alone temperature controller that could be tuned to the required tolerance.

An error-correcting feedback control system can only take action after the error is detected. Temperature changes had to be recorded on a significantly smaller level than the acceptable tolerance. The Johnson Controls LCP was able to discern changes only as small as  $0.06^\circ\text{F}$ . Thus, 60% of the available tolerance had already been expended before control action was initiated.

The Honeywell Progeny, whose A/D converter can resolve changes less than  $0.01^\circ\text{F}$  when scaled across the  $40^\circ\text{F}$  range of the applicable transmitter, was chosen as the stand-alone controller. Using this controller, steady-state temperature was controllable to within  $\pm 0.05^\circ\text{F}$ .

Coolant flow through the LCL HXs was reduced so that the control valves passed 65-75% of the load-side flow through the HXs, since regulation sensitivity improves if a larger flow is heated or cooled. As the coolant flow was reduced below 2 or 3 gpm, however, the HX demanded 100% of the load flow yet process temperature continued to climb. At such a reduced flow, the coolant transitioned from turbulent to laminar flow resulting in a loss of overall heat transfer coefficient. The HX surface area was reduced by 50% by rotating one endcap of the 4-pass shell-and-tube unit by  $90^\circ$  so coolant passes through only half of the tubes.

Coolant flow rate in each LCL is regulated at a fixed, heat-load-dependant value of 7-10 gpm by Griswold flow control cartridges. The flow rate is varied until the 3-way control valve on the linac (load) side is 65-75% open at 100% load. The output of the electric heaters is set at a constant value to fix the heat load.

All control units were replaced by Allen-Bradley PLC-

5/20 processors with 1771-N4BS analog I/O modules. Temperature changes on the order of  $0.003^\circ\text{F}$  can now be discerned. Previously, system noise levels alone were  $0.015^\circ\text{F}$  higher than the applicable system resolution.

Other benefits of the Allen-Bradley processors include the ability to tune valves with response characteristics that permit LCL startup from a cold condition to a steady operating temperature without supervision. Use of Allen-Bradley PLCs permits communication between the LCL water stations and the APS control room. The LCLs can now be operated remotely in "real time" via the EPICS [4] control system. The LCLs now consist of:

- 1) 3-way Durco ball-type control valves to divert water through or around the HX as required for stable temperature regulation.
- 2) Worcester series 75 electric control valve actuators with AF-17 positioners with a resolution of 0.5%.
- 3) Electric heaters to provide fixed heat input rates; rates between 0% and 100% are chosen at setup.
- 4) 3-wire, direct immersion, 4-s time constant, Minco S603PD8 RTDs.
- 5) Analog temperature transmitters scaled in the range  $85\text{--}125^\circ\text{F}$  (Minco TT676PD1QG).
- 6) Allen-Bradley PLC-5/20s with P/N 1771-NB4S high-resolution analog I/O cards for PID temperature control (the D feature is not used).

Use of a 3-way diverter valve in the load stream rather than a throttling valve in the coolant stream is especially important. An order of magnitude faster temperature response is obtained with the diverter valve since the final temperature is a result of mixing, and flow ratio changes are immediate upon valve movement. Throttling of the coolant flow results in relatively slower response, since the entire mass of the load stream and the mass of the HX surfaces must change temperature.

### 3 CORROSION MITIGATION

Operating experience with deionized water systems at APS and DESY demonstrates that dissolved oxygen (DO) concentrations  $\geq 20$  ppb result in unacceptably high copper corrosion rates. The corrosion is manifested as insoluble particles of  $\text{CuO}$  and  $\text{Cu}_2\text{O}$  that agglomerate in the system after removal from the parent surface. Filtration to levels as low as  $0.5\text{ }\mu\text{m}$  is useful, but build-up of copper oxides is regularly found in system components when DO levels are elevated. Components that regulate flow become clogged where significant pressure reduction occurs. Components subject to clogging are orifices, valves, self-regulating flow-control valves ("Griswolds"), and pressure regulators that have orifices very small compared to their inlets and outlets. Agglomeration also occurs on pump impellers.

In a closed-loop system with a low rate of oxygen ingress and without facilities to remove DO, corrosion can occur at a rate greater than the influx of new oxygen. This results in a significant reduction of DO in the

system. Unfortunately, the reduction occurs at the expense of components that should be protected from corrosion but are in fact consumed.

The LCLs are pseudo-closed-loop systems. The water flows in a closed loop; however, there is a constant leakage of oxygen through the open-top expansion tanks. A reliable DO monitor, the Orbisphere Laboratories model 3660 with accuracy  $\pm 1\%$  or  $\pm 1$  ppb, whichever is greater, was installed in the closed loop. We saw that DO in the loop tended toward its saturated value of around 4000 ppb when the oxygen scavenger was removed.

In December 1998, 2.5 l of oxygen-scavenging resin (type 1 strong base anion in sulfite form) was installed in each LCL upstream of the mixed-bed resin of the "slipstream" that is used for continuous polishing of the closed loop. The slipstream is installed in the loop as indicated in Fig. 2. Flow through the resins is in parallel with linac components. The open top expansion tank and fill tube at the pump suction are also indicated in Fig. 2.

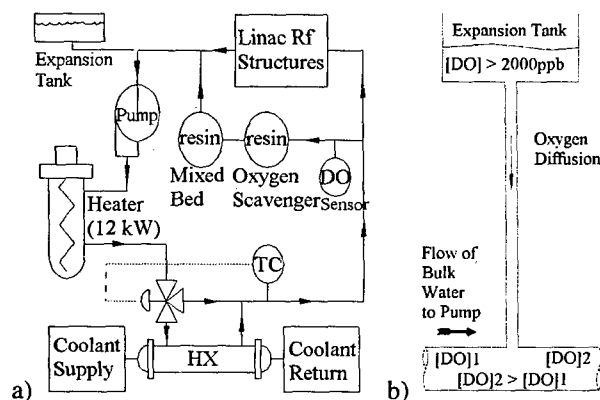


Figure 2: a) Detail of an LCL showing location of polishing resins and the DO sensor; b) Oxygen diffusion mechanism from expansion tank to bulk water flow.

With a water flow of 3.5 gpm through the resins, the DO content was reduced to 30 ppb. It fell to 24 ppb after the slipstream flow was increased to 7.5 gpm. DO data taken over an 11-day period are shown in Fig. 3.

We expected that use of oxygen-scavenging resin in a closed loop would reduce DO levels below 5 ppb, yet this was not observed. The anticipated, but yet unproved, explanation of this phenomenon is the influx of oxygen through the open-top tank. In another APS system, water residing in a stagnant portion of piping and contaminated with oxygen was a source of DO to the bulk flow of "oxygen-free" water flowing past the stagnant portion. Fig. 2b illustrates a similar situation in the LCL. As oxygen-free water flows by the line to the expansion tank, oxygen diffuses from the stagnant water to the flowing bulk. Removing oxygen in this manner is time consuming and inefficient. In other APS systems, lines were installed to flush the stagnant piping sections and clean the water.

The open top expansion tanks in the LCLs are clearly a source of diffusing oxygen to the closed loop. Plans are in

place to isolate the expansion tanks from the closed loops and provide oxygen-free makeup from a separate source.

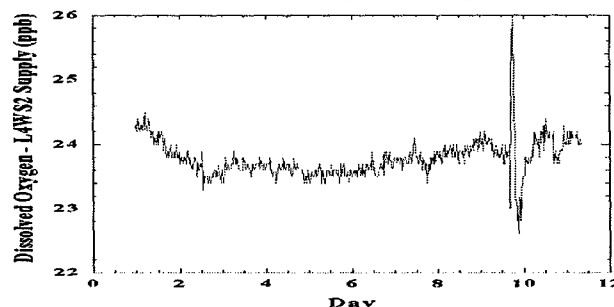


Figure 3: Dissolved oxygen [ppb] over an 11-day period in one LCL with oxygen-scavenging resin.

## 4 CONCLUSIONS

Temperature regulation of high-power rf components to within  $\pm 0.05^\circ\text{F}$  has been achieved at the APS linac. The system responds quickly to changes in rf power load and maintains long-term temperature stability. The water system and the techniques to optimize the temperature are described more completely in [5]. Efforts to reduce copper corrosion by reducing the DO content of the water are well underway. Radiation and friction can also lead to erosion and corrosion and will be studied in our systems.

## 5 ACKNOWLEDGMENTS

The authors would like to acknowledge R. Damm for leading efforts to improve system performance; E. Swetin for installing holding tanks, downsizing HXs, and assisting with KGSS tuning; C. Putnam and H. DeLeon for implementing the PLCs; N. Arnold and M. Kramer for implementing network communication; R. Kneebone and W. Matz for implementing changes prior to 1996; D. Haid for graphics advice; and C. Eyberger and K. Jaje for editorial assistance. We are also very grateful to our colleagues at DESY who made us aware of their data [6] in time to learn the causes of copper loss and begin efforts to mitigate DI-water-related copper loss in the APS linac long before failures occur.

## 6 REFERENCES

- [1] M. White et al., "Construction, Commissioning and Operational Experience of the Advanced Photon Source (APS) Linear Accelerator," Proc. of the XVIII Intl. Linear Accelerator Conf., pp. 315-319 (1996).
- [2] R. Dortwegt, S. Pasky, M. White, "Improved Temperature Regulation of APS Linac Rf Components," Proc. of the XIX Intl. Linac Conf., Chicago, IL, USA, 23-28 August 1998, pp. 1001-1003.
- [3] P. W. Murrill, "Fundamentals of Process Control Theory," 2nd Ed., Instrument Society of America, pp. 126-129 (1991).
- [4] W. P. McDowell et al., "Status and Design of the Advanced Photon Source Control System," Proc. of the 1993 Particle Accelerator Conference, Washington, DC, May 1993, pp. 1960-1962 (1993).
- [5] R. Dortwegt, S. Pasky, M. White, "Temperature Regulation of the APS Linac High-Power Rf Components," APS-LS Note, to be publ.
- [6] H. Poggensee, "Korrosionsursachen und Korrosionsverhinderung in Kupferkuehlleitungen im LINACII," DESY M-93-04, June 93.

# BENT SOLENOIDS FOR SPECTROMETERS AND EMITTANCE EXCHANGE SECTIONS

J. Norem<sup>†</sup>, Argonne National Laboratory, Argonne IL, 60439 USA

## Abstract

Bent solenoids can be used to transport of low energy beams as they provide both confinement and dispersion of particle orbits. Solenoids are being considered both as emittance exchange sections and spectrometers in the muon cooling system as part of the study of the muon collider. We present the results of a study of bent solenoids which considers the design of coupling sections between bent solenoids to straight solenoids, drift compensation fields, aberrations, and factors relating to the construction, such as field ripple, stored energy, coil forces and field errors.

## 1 INTRODUCTION

While the optics of beams in straight solenoids is well understood in accelerator physics[1], and the behavior of charged particles in toroidal geometries is also well understood in plasma physics[2], the optics of beams which traverse both bent and straight sections have not had significant applications in either field, are not simple or symmetric, and are not particularly well understood[3]. Beams in bent solenoids are subject to drifts perpendicular to the bend plane. The geometry is shown in Fig. 1.

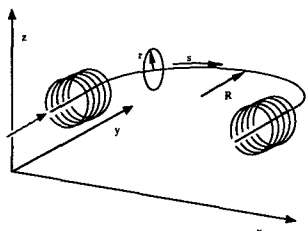


Figure 1, A bend without coupling sections.

In a straight solenoid the magnetic field is homogeneous, while in a bend the field is distributed according to  $1/R$ , this means that there is a transition region where the field is difficult to parametrize and should be calculated numerically see Figure 2.

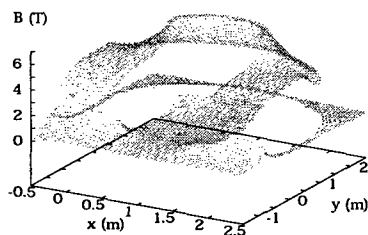


Figure 2, The field in a bent solenoid

As a result this complexity there are a large number of variables associated with the design of a solenoidal bend. In addition to the nominal field on axis, bend radius, coil radius and bend length, there is the choice of field to compensate perpendicular drifts, the bending algorithm used to couple the bend to the straight section, and the algorithm used to compare the field in the bent and straight sections.

## 2 BEND BASICS

A particle passing through the magnet system described in Figures 1 and 2 will be mismatched to the bend and execute an orbit like that shown in figure 3, where the centrifugal momentum drives the particle to larger radii, produces an upward drift and excites Larmor oscillations at the end of the bend.

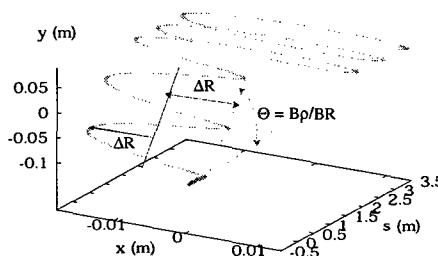


Figure 3, particle orbits in bent solenoids, where  $x$  and  $y$  are perpendicular to the particle motion.

The vertical drift is described by the relations

$$\mathbf{v}_c = \frac{\gamma m_0 v_{\parallel}^2}{q B^2} \frac{\mathbf{R} \times \mathbf{B}}{R^2}$$

$$\mathbf{v}_{\nabla B} = \pm \frac{1}{2} v_{\perp} r_L \frac{\mathbf{B} \times \nabla B}{B^2}$$

$$\mathbf{v}_{drift} = \mathbf{v}_c + \mathbf{v}_{\nabla B} = \frac{\gamma m_0}{q} \frac{\mathbf{R} \times \mathbf{B}}{B^2 R^2} (v_{\parallel}^2 + 0.5 v_{\perp}^2)$$

$$\theta_{drift} = B\rho / B_{\parallel} R - B_{\perp} / B_{\parallel}$$

$$\Delta R = (B\rho)_{drift} / B = (B\rho)^2 / B^2 R$$

where Larmor length is  $L = 2\pi B\rho / B$ , and  $B\rho$  is the magnetic rigidity.

### 2.1 Compensating Fields

The vertical drift can be eliminated with a compensating field  $B_{\perp}$  which provides a negative slope of the magnetic

<sup>†</sup> norem@hep.anl.gov

field lines so that  $\theta_{drift} = B\rho/B_{||}R - B_{\perp}/B_{||} = 0$ . Thus a single momentum can be confined to a plane, while other momenta will be subject to the same momentum dependence, giving a dispersion

$$D = \theta_{drift} s = \int B\rho/B_{||}R ds \sim \Theta B\rho/B.$$

The vertical field can be applied either with an external coil set or by tipping the coils. An advantage of tipping the coils is that the vertical field component can be tailored to the local bend radius. The coils would be tipped as shown in figure 4

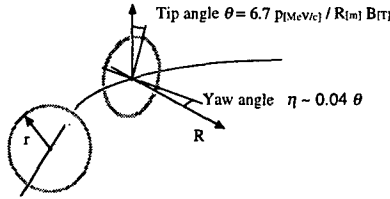


Figure 4, Tipping and turning coils.

### 3 COUPLING SECTIONS

It is possible to minimize the mismatch where straight meets bend by using a variety of coupling sections. The mismatch can be caused by two effects: 1) the orbit cannot adjust smoothly to the position of the equilibrium orbit as it goes through the bend, and, 2) the magnetic field lines are displaced from what would be the particle orbit by  $1/R$  (or other) effects. Both of these effects can be minimized using a good coil design.

#### 3.1 Adiabatic Bends

If the mismatch that causes the oscillations in Figure 3 is spread out over many Larmor lengths and phases, the transverse oscillations will be canceled, unfortunately at the cost of a long solenoid.

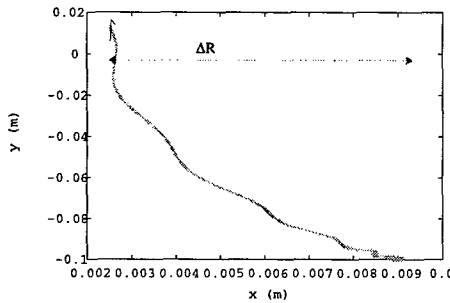


Figure 5, A two dimensional projection of the motion of a particle in an adiabatic coupler.

#### 2.2 $L = n \lambda_L$

If the overall bend length is adjusted to be equal to an even number of Larmor oscillations, the particle can exit from the bend at the point of the cusp (see figure 3) where it has no momentum perpendicular to the direction of motion. This method had two problems: 1) the length of the magnet is fixed and, 2) effects due to coil size can

complicate the effective length of the bend section. Nevertheless, for small dispersion systems this solution can be very useful.

#### 2.3 $L = \lambda_L/2$ Coupler

While the mismatch produced at discontinuities is generally a problem, it is possible to use the mismatch constructively to create a half Larmor oscillation of the correct size and length to couple into a bend of arbitrary radius. This can be done by designing a coupling section with half the bend radius of the primary bend and a length equal to  $L = \lambda_L/2$ . The coupling section then brings the particle to what would be its equilibrium offset  $\Delta R$  in the bend without residual perpendicular momentum (fig.6). The use of this technique is complicated by coil radius effects which can complicate evaluating the section length, causing mismatch at the ends of the sections.

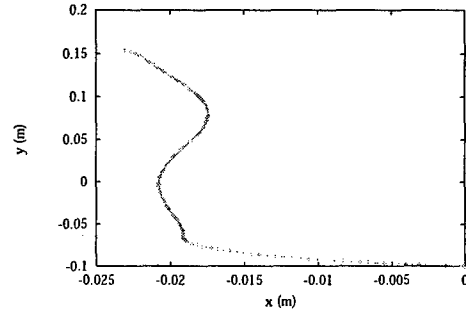


Figure 6. A particle orbit in a  $L = \lambda_L/2$  coupler, showing mismatch at the end of the section.

#### 2.4 Short Smooth Couplers

An extension of the  $L = \lambda_L/2$  coupler is to use a smoothed curve which has the advantages that discontinuities in both  $d\Theta/ds$  and its derivatives are avoided. The expression used by Fernow and Palmer[4],

$$\frac{d\Theta}{ds} = 0.5 \left\{ \cot\left(\frac{s-s_1}{\sigma}\right) - \cot\left(\frac{s-s_2}{\sigma}\right) \right\},$$

where the length over which the transition is made  $\sigma = \lambda_L/2$  seems to be optimum, consistent with the arguments presented in Sections 3.1 and 3.3, see Figure 7.

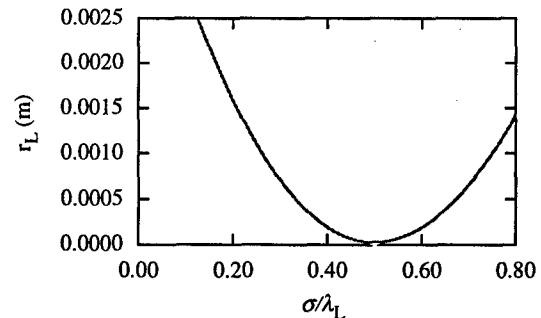


Figure 7, Mismatch produced as a function of short, smooth coupler length.

## 4 ABERRATIONS

In addition to the time slewing due to the longer path traveled by particles on the outside of a bend, there are a number of aberrations which complicate the optics.

### 4.1 $x'$ $y'$ Dependence

Particles with momentum perpendicular to the beam will drift vertically due to grad  $B$  drift. This can be eliminated with equal numbers of bends of opposite direction, but in most cases with  $x' < 0.3$  the drift is small, comparable to a  $\delta p/p \sim 2\%$ . This is shown in Figure X

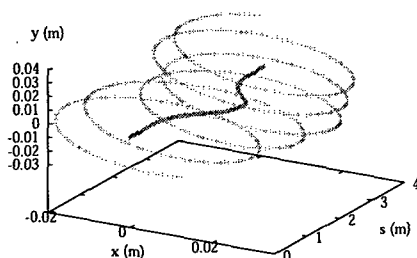


Figure X, Grad B drift for orbits with  $p_{\perp} = 0$ .

### 4.2 Shears

Even if all translation of the central orbit is canceled using a good coil design the orbits off center are subject to a shear. This shear is a result of mismatches between the ideal compensation field and that provided by physical coils. The effects of this shear are shown in Fig Y, and the shear can be eliminated by equal right and left bend angles.

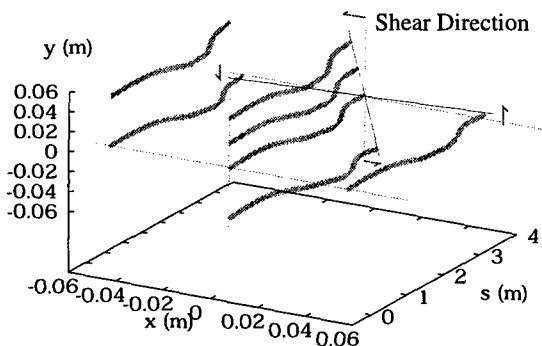
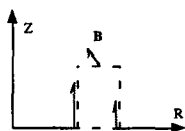


Figure Y, Shears in large beams over a bend.

The sum of horizontal and vertical components of the shear should be constant because the perpendicular field components that cause it are determined by Amperes law, integrating around the path shown at right. The relative amplitude of horizontal and vertical shear can be altered by



altering the geometry of the coils causing the compensating field.

### 4.3 Coil Geometry Effects

The coil geometry interacts strongly with the optics, as shown in figure Z below, which looks at an orbit for two different coil radii.

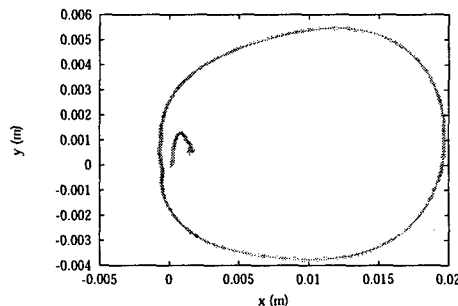


Figure Z, Orbits for coil radii  $r = 0.3$  and  $0.03$ .

The sensitivity to coil and geometry parameters emphasizes the importance of using an accurate representation of the problem. The calculations in this paper were done using GPT [5], which calculates fields from coils and tracks the particles through the fields, thus avoiding approximations or simplifications which can completely change the nature of the problem.

## 5 CONCLUSIONS

This paper outlines the effects encountered when using both bent and straight solenoidal sections. Emittance growth can be produced by mismatches, however it is possible to minimize the effects of these by optimizing the coupling section and compensating field geometries. It seems important to track particles from coil geometries since the effects produced can seem nonintuitive.

## REFERENCES

- [1] S. Humphries, Charged Particle Beams, Wiley, (New York) 1990
- [2] F. F. Chen, Introduction to Plasma Physics, Plenum, (New York), 1974
- [3] J. Norem, Submitted to Physica Review Special Topics/ Accelerators and Beams, 1998
- [4] R. Fernow, *ICOOL: a simulation code for the ionization cooling of muon beams*, this conference
- [5] Pulsar Physics, De Bongerd, NL-3762, X A Soest, The Netherlands (1998)

# HTS POWER LEAD TEST RESULTS\*

G. Citver, S. Feher<sup>†</sup>, P.J. Limon, D. Orris, T. Peterson, C. Sylvester,  
M.A. Tartaglia, J.C. Tompkins, FNAL, Batavia, IL

## Abstract

R&D High Temperature Superconductor (HTS) power leads were developed and built for Fermilab by American Superconductor Corporation and Intermagnetics General Corporation. Each company provided one pair of 5kA HTS current leads, and these have been successfully tested at Fermilab. This paper summarizes the test results.

## 1 INTRODUCTION

Conventional power leads carry electric current from room temperature to the superconducting magnets in the Tevatron at Fermi National Accelerator Laboratory. Over 50 pair of leads carry up to 6000 amps of current and result in substantial heat loads for the cryogenic system. Reducing the total heat load to the liquid helium temperature level would allow either savings in operational costs or make more refrigeration available for lower temperature and higher energy operation of the Tevatron. Using a combined liquid nitrogen and liquid helium cooled power lead design, one can reduce the heat load to LHe by a factor of ten. A proposal to replace most of the conventional power leads at Fermilab with more efficient HTS leads is under consideration. As a first step toward realizing this plan, American Superconductor Corporation and Intermagnetics General Corporation each developed and built a pair of 5000A HTS current leads. These leads went through extensive tests at Fermilab.

## 2 TEST APPARATUS

The HTS power lead testing equipment is located in the Magnet Test Facility (MTF) at Fermilab. The mechanical system consists of a liquid nitrogen shielded helium cryostat with a baffle system that includes an 80 K intercept, and the instrumentation necessary to monitor mass flow rates, measure and regulate system pressures and liquid level, and record system temperatures. The 20 inch diameter by 42 inch long helium vessel is sized to accommodate power lead pairs, which are spaced on a 4 inch center-to-center distance, and are up to 30 inches long. The leads are mounted on a plate that is separate from the main vessel cover plate. This feature allows for power lead removal without complete disassembly of the vessel cover plate. The remaining top surface area of the vessel accommodates fill and vent lines, valves, liquid level sensors, and other instrumentation.

To thermally separate the main dewar volume from the volume immediately around the power leads, the leads are housed inside a glass/epoxy tube that extends from the

cover plate to several inches below the minimum liquid helium level in the main dewar. To further thermally isolate the two volumes, the power lead pair and glass tube assembly is mounted inside a vacuum jacketed sleeve, that extends to the depth of the liquid nitrogen cooled intercept. Anticipating differences in pressure due to the different thermal environment in each, the system provides for independent or simultaneous venting of the two volumes. A backpressure regulator, sensitive to 1/8 inch of H<sub>2</sub>O pressure changes was installed to help maintain a constant pressure in the main bath, while pressure changes may be occurring inside the glass/epoxy tube.

The mass flow meters and rotameters used in the system were carefully calibrated and sized to operate effectively over the range of flows required. A simplified mechanical system schematic is shown in the online overview, Figure 1.

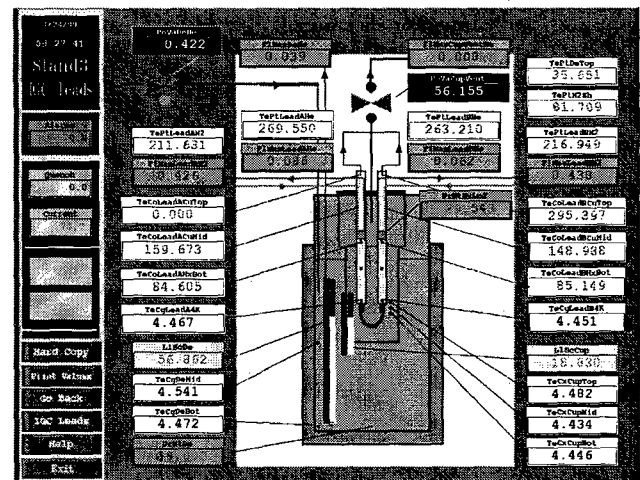


Figure 1: Schematic overview of the HTS test setup.

The HTS data acquisition (DAQ), and the quench detection and management systems used in this test are adapted and extended from those systems developed at MTF to conduct tests on superconducting R&D magnets [3]. Temperature and voltage measurements from the DAQ scans are monitored by a new software quench detection system [4] that triggers the quench management system to protect the leads from (relatively slow) quenches. An independent hardware backup system protects against ground faults as well as fast resistive voltage growth across the leads. A quench is detected when one of the analog signals or software process variables exceeds a (configurable) threshold, or when a scan malfunctions. When triggered, the management system initiates fast quench data logging, and slow power supply ramp down.

\* Work supported by the U.S. Department of Energy.

<sup>†</sup> Email: feher@fnal.gov



The quench thresholds were set low, for any temperature rise of 5K above the zero-current baseline temperature profile, or HTS (Copper) voltage (imbalance) greater than one(32) millivolt(s). Temperature and voltage process variables were monitored and logged by two independent scan systems, which used complementary instrumentation schemes. The carefully wired and isolated sensors delivered typical noise levels of less than 1K for temperatures, and less than 3  $\mu$ V for voltage taps at 5000A.

### 3 THE LEADS

American Superconductor Corporation (ASC) and Inter-magnetics General Corporation (IGC) developed and built HTS leads following the Fermilab lead specification (see Table 1). Both companies utilized Ag-alloyed sheathed BSCCO-2223 (powder-in-tube) multifilamentary high temperature superconducting tapes between 4K and 80K cooled with helium liquid and vapor. The upper section (80K-300K) of the lead was made from copper cooled with liquid and gaseous nitrogen and helium vapor. The vendors instrumented these R&D leads with RTD temperature sensors and voltage taps across HTS and copper sections.

Table 1: Lead specifications and requirements

Gas cooled power lead operating between 300 - 4.3K
Maximum operating current 5000A
Case leak rate to vacuum $< 2 \times 10^{-8}$ atm cc/sec
Low helium consumption
Thermal intercepts at 80K
Voltage standoff to ground or other lead $> 2000$ V
Magnetic field environment $< 100$ gauss
Radiation environment $\sim 1$ -5 Rad/hour
Electric current decay time constant = 12 second
Cool down rate from 80k to 4.3K within 60 sec
Robustness, withstand thermal cycles

### 4 TEST HISTORY

#### 4.1 ASC Lead

The first version of the ASC lead was tested in December, 1997. At recommended helium and nitrogen flow rates, neither section of the lead exhibited stable operation. At 3500A DC operation the voltage across the HTS section rose slowly and exceeded the 1mV threshold limit specified by the vendor. Voltage across the copper section also rose and showed no sign of reaching a stable value. The HTS section of the lead was re-built and was then successfully tested in August, 1998, reaching 5000A stable operation. In October 1998 the lead was tested again, however a leak developed between the helium and nitrogen flow passages making it impossible to continue the test. In the following discussion, we only refer to the second version of the ASC lead [2] and the August, 1998, ASC test results.

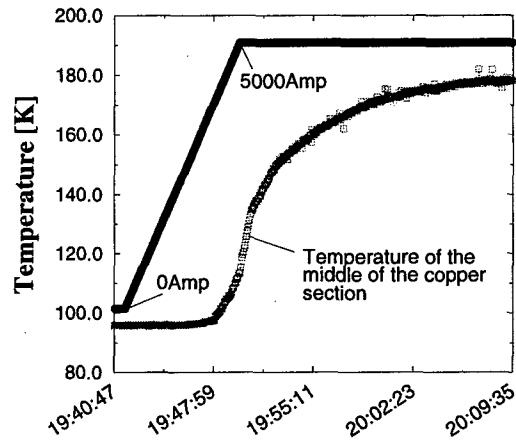


Figure 2: Temperature rise of the middle of the copper section due to 0 to 5000A current ramp.

#### 4.2 IGC Lead

The IGC lead was first tested in March-April, 1998. Unreliable lead temperature sensors made the test difficult and required in-situ calibration. The lead was able to conduct 5000A steadily. In May, 1998, the lead was tested again. In an attempt to quench the HTS section, the current was raised to 7500A. At this current the low temperature superconductor (LTS) cable attached to the bottom of the lead burned out. The lead was repaired with a better transition to the LTS cable. Several successful tests to 5000A have been performed since then.

### 5 TEST RESULTS

The primary goal of the tests was to verify whether the leads met all the requirements and specifications. First, nominal cooling conditions were established, then the current was ramped up to 5000A. All the lead temperatures and voltages at both sections (copper and HTS) of the lead remained unchanged after equilibrium was reached, indicating steady-state operation. The next test verified that stable operation can be achieved by ramping the current up and down at 350A/sec between 0 and 5000A. Both temperature and voltage values were stable but not constant; temperature showed periodic behaviour correlated with current, as one would expect.

Extensive thermal studies on the copper section, including temperature profiles as a function of nitrogen flow rates and transient effects due to sudden change of the current or nitrogen flow rate, were performed on the IGC lead and the results were compared with calculations [1]. A fast response to transients was found. In Figure 2, the temperature rise of the middle of the copper section as a function of time after ramping the current up to 5000A is plotted. It took 15-20 minutes to reach stable operation.

We also measured the minimum liquid nitrogen flow rates required to keep the upper part of the HTS section at

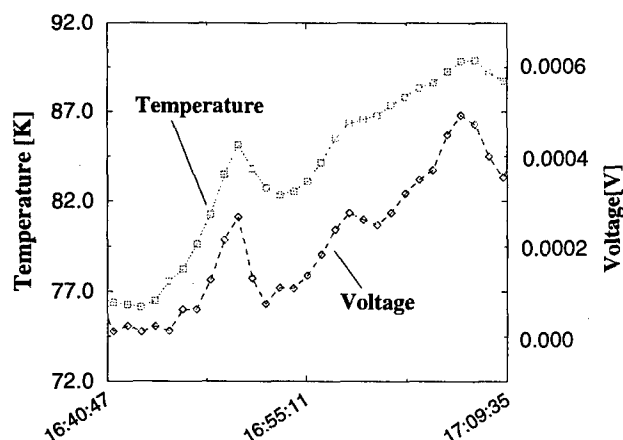


Figure 3: Voltage of the HTS section and temperature at the top of the HTS section are plotted as a function of time.

80K (see Table 2). All of the measured values show good agreement with calculations [1]. Both current leads were able to operate with no helium flow through the lead. The current flag temperature was kept close to 300K by using a water heater-chiller attached to the flag. There was no need to regulate the coolant flow rate as a function of current; no freezing at the top of the lead was observed even at 0A applied current and nominal coolant flow rates.

Table 2: Minimum liquid nitrogen mass flow rates at nominal liquid helium mass flow rates (IGC lead).

Vendor recommended (g/sec)	measured (g/sec)	Applied current (Ampere)
0.30	0.24	0
0.83	0.53	5000

Voltages across the HTS section, across the HTS-copper joints, and across the HTS-LTS joints were measured. Both IGC and ASC had low joint resistances (ASC: 80-100n $\Omega$ , IGC: 12 n $\Omega$ ) and low voltages ( $\sim 25\mu\text{V}$ ) across the HTS section at 5000A and nominal coolant flow rates.

A quench performance study of the IGC lead was carried out at 5000A DC: the voltages across the entire HTS section were monitored as the temperature of the upper part of the HTS section was increased, by varying the nitrogen flow rate. The voltage-based quench detection threshold was set to 1mV. The voltage change was highly correlated with the temperature change (see Figure 3). There was no sign of any instability even if the HTS was forced to operate in current sharing mode. The temperature at the middle of the copper section also rose and stabilized around 300K. It seems that protection of the copper section of the lead would be sufficient for protection of the entire lead, since loss of cooling would be seen in the copper section first. It was hard to do further quantitative analysis of the HTS section since the temperature values were not accurate.

The IGC lead went through several thermal cycles (see Table 3) and was then power tested successfully. There was no performance degradation observed.

Table 3: Thermal cycles.

HTS upper section from 300K to 80K and HTS lower section from 300K to 4K	x5
HTS upper section from 300K to 80K and HTS lower section from 300K to 80K	x22
HTS upper section from 200-300K to 80K and HTS lower section from 50-150K to 4K	x8

The heat leak to the cold (4K) end of the lead was estimated by measuring the evaporation rate through the lead while keeping the helium liquid level constant and high enough to reach the bottom of the current lead. The LTS part of the lead was completely immersed in liquid helium. The liquid level was controlled by adjusting the outgoing helium gas flow rate through the lead. Due to background effects we were able to estimate only the upper limit of the heat load. ASC and IGC helium boil-off rates were less than or equal to 0.045 g/sec and 0.050 g/sec, respectively.

## 6 CONCLUSIONS

Two pairs of HTS current leads (from ASC and IGC) were successfully tested at Fermilab. Stable steady-state operation was observed at nominal cooling conditions and at nominal 5000A current. The transient effect recovery time in the copper section of the IGC lead was fast ( $\sim 15$  min). Low joint resistances (ASC: 80-100n $\Omega$ , IGC: 12 n $\Omega$ ) and low voltages ( $\sim 25\mu\text{V}$ ) across the HTS section were measured at nominal current and cooling conditions. There was no sign of any instability even if the HTS was forced to operate in current sharing mode. There was no performance degradation observed due to thermal cycles. The upper limit on the heat leak to the helium bath was estimated (ASC: less than 0.045 g/sec; IGC: less than 0.050 g/sec).

## 7 REFERENCES

- [1] G. Citver, E. Barzi, A. Burov, S. Feher, P.J. Limon, T. Peterson, "Steady State and Transient Current Lead Analysis", ASC'98, Palm Desert, CA (1998).
- [2] A.J. Rodenbush, D. Aized and B.B. Gamble, "Conduction and Vapor Cooled HTS Power Lead for Large Scale Applications", ASC'98, Palm Desert, CA (1998).
- [3] M.Lamm, *et al.*, "A New Facility to Test Superconducting Accelerator Magnets", PAC'97, p 3395, Vancouver B.C. Canada, (1997).
- [4] J.Nogiec, *et al.*, "Architecture of HTS Leads Software Protection System", PAC'99, New York, NY, (1999) contribution to this conference.

# MICROBIOLOGICALLY INFLUENCED CORROSION IN THE FERMILAB MAIN INJECTOR MAGNET LOW CONDUCTIVITY WATER SYSTEM\*

P. G. Hurh<sup>#</sup>, N. Kubantseva, M. P. May, FNAL, Batavia, IL

## Abstract

In mid-November of 1997, numerous pinhole leaks in the new 304L stainless steel header piping of the Main Injector Magnet Low Conductivity Water System (MI LCW) were discovered. Metallurgical and biological analysis of the extensive corrosion damage in the welded areas of the piping revealed that microbiological organisms played a key role in the corrosion process. The resulting massive repair efforts included microbe eradication (through chemical biocides), damage assessment (through biological and metallurgical analysis, radiography, and internal remote video inspection), pipe cleaning (through custom designed mechanical cleaning devices), weld repair (through weld overlay), and microbiological control during system start-up (through ultra-violet radiation and heat treatments). Multiple contributing factors leading to the corrosion problems were identified, including poor welding practice (inadequate technical specifications and inspection), improperly treated fill water, and insufficient water flow for extended periods of time (several months) prior to system use. Lessons learned from these experiences will be of extreme importance to the design of similar cooling systems in the future.

## 1 INTRODUCTION

The MI LCW System consists of 6 above ground pumping stations distributed around the MI ring supplying cooling water to the bus of all magnets in the tunnel (650+ magnets). Only the stainless steel header piping was affected by the corrosion problems.

All of the piping components are 304L stainless steel welded with 308L filler metal. The majority of piping is seam welded 6-inch nominal pipe size, schedule 10 pipe with larger piping in the pumping stations. The system has approximately 5,400 welded joints. Total water volume for the system is approximately 66,000 gallons.

Each pumping station includes a large heat exchanger (also 304L) and a de-ionizing (DI) and filtering circuit. All 6 pumping stations are connected through the tunnel via the 6-inch headers. One pumping station (MI-60) includes a fill station and a 3,000-gallon reservoir tank. The design operating pressure of the system is 150 psi.

In mid-November of 1997, evidence of a severe corrosion problem in the MI Magnet LCW System was observed. Leaks in the new stainless steel header system became apparent during start-up operations, some months after hydrostatic pressure testing. Engineering consultants immediately diagnosed the problem as Microbiologically Influenced Corrosion (MIC). This paper is an abbreviation of a report which describes the repair efforts, identifies some of the causes of the MIC problem, and makes some recommendations for prevention of MIC in the future [1].

## 2 DETECTION & STABILIZATION

The first sector of the MI Magnet LCW System was filled with chlorinated well water on May 29, 1997, for the purposes of hydrostatic testing of the completed piping. Each remaining sector was then filled by "pushing" the test water from the first sector with new well water. In this manner the entire system was filled and pressure tested over a period of 6 months. Between fills, the water was allowed to remain static in the tested piping.

When circulation pumps were started in November, several pinhole-sized leaks were discovered on the weld joints of the LCW piping. Although the vast majority of leaks were observed on welds, several leaks were also found as far as one inch from the nearest weld joint. In a few days, the number of leaks multiplied to almost 400. From visual inspections of the leaks and bacteria tests conducted on water samples (high levels of aerobic/low nutrient bacteria and trace levels of sulfate reducing and iron-related bacteria were found), expert consultants suggested the cause of the leaks was MIC.

### 2.1 MIC Description

Microbiologically Influenced Corrosion is a phenomenon whereby corrosion of a surface is induced and/or accelerated by the presence of microbiological organisms. One description of the MIC mechanism to failure is as follows: A thick biofilm (layer of live bacteria) develops on a susceptible metal surface. The microorganisms develop colonies and form nodules (biomasses containing microbiological/corrosion by-products and deposits). These formations can trap ions and occlude the metal surfaces directly beneath them from oxygen dissolved in the water. Thus the nodules can create localized physical and chemical gradients at the metal surface, which initiate corrosion cells (such as a differential aeration cell). The electrochemical process dissolves metal beneath the biomass and a localized pit is formed [2].

\*Work supported in part by the U.S. Department of Energy under contract No. DE-AC02-76CH3000.

<sup>#</sup> Email: hurh@fnal.gov

The MIC corrosion process is very similar to crevice corrosion. In crevice corrosion, corrosion is often initiated by the creation of an oxygen or ion concentration cell. Stagnant water in a crevice cannot supply oxygen to maintain a passive oxide layer in the crevice. As oxygen is consumed in the crevice by the corrosion reaction, the water in the crevice becomes depleted of oxygen while oxygen is still available in the water at the mouth of the crevice. This creates a differential aeration cell accelerating the corrosion further. Corrosion rates for MIC can be greater than that for crevice corrosion because of the smothering coverage of the large biomass. Also, byproducts of some bacteria growth are acidic, accelerating the localized pitting even further. Some case histories report through-wall pitting of stainless steel pipes in a few months. One of these reported an effective corrosion rate of 0.055 inch per month for a 308 stainless steel weld [3].

## 2.2 Stabilization and Damage Assessment

After preliminary confirmation of MIC, biocides (glutaraldehyde and quaternary ammonium compounds) were added to control the bacteria growth. The system was drained and then dried using high-speed blower fans.

Each accessible weld in the entire system was labeled. Damage assessment was performed through two methods, radiographic examination and internal visual inspection.

10% (208) of the accessible welds were radiographed. Of these, 61% showed flaws that could be associated with MIC (deep pitting or tunneling). Most of the welds also showed flaws suggesting poor welding practice (incomplete fusion/penetration, etc.)

Internal visual inspection of the piping was accomplished using custom designed and fabricated remotely operated video camera devices. The most useful design utilized a radio controlled gimbal mount to aim the camera in both yaw and pitch. Using this device, operators were able to videotape all accessible welds in the system.



Figure 1: Typical corrosion site on MI LCW pipe weld.

The internal visual inspection revealed that almost every weld in the piping exhibited signs of advanced corrosion. Most welds had orange colored streaks flaring

out from tack welds that had not been consumed by the final weld pass. A majority of welds had a build up of corrosion byproduct (and MIC nodules) in several places on each weld. Some of the nodules were crumbled and/or knocked off by the passage of the camera device. The worst damage was usually at the bottom of the pipe.

## 3 RECOVERY EFFORTS

While the MIC situation was stabilized, research and development explored recovery options. Weld repair and pipe-cleaning techniques were researched and compared.

### 3.1 Weld Repair

Repair techniques considered ranged from cutting out and replacing bad welds to patching bad welds with epoxy/fiberglass wraps. Repair options were tested and compared in categories such as longevity, serviceability, ease of application, and cost. Our comparison led us to choose a combination of repair methods to apply to welds in various locations and in various conditions.

The most widely used repair method was to remove the crown of the old, defective weld and then overlay with a new weld (316L stainless steel filler material). In this manner, the existing weld metal was re-fused and a new crown layer was added. In addition, the entire weld area was exposed to high temperature during welding which helped sterilize any remnant bacteria.

Detailed technical specifications were written for each of the weld repair methods. These specifications and the results from metallurgical evaluations of the test repairs were reviewed positively by welding engineers and metallurgists. In addition, stringent procedures for welder qualification and quality control were implemented to ensure consistent quality throughout the weld repairs.

On March 2, 1998, welders and pipe fitters arrived on site. The workers attended meetings to learn the weld repair techniques and review specifications. Field testing of welders was begun immediately, and the first weld repairs were made on March 3, 1998.

As weld repairs progressed, inspection of the work was performed and results recorded in a weld database. Technicians trained by Fermilab's Weld Shop, performed visual examinations of each weld and weld repair within one day after they were made. In addition, suspect welds were visually examined internally using the remote video devices. As sectors of piping were completed, 5% radiography and 100% pneumatic bubble tests were performed to ensure quality.

### 3.2 Pipe Cleaning

Although the addition of biocides and draining/drying of the pipes presumably halted the MIC process, complete mitigation required the removal of the entire MIC habitat. Deposits in the pipe, in the form of nodules and tubercles, were tenaciously adhered to the pipe walls and could not be removed by water circulation alone. These deposits, besides harboring bacteria, could have been sites for future

infestations. Thus, removal of as much MIC deposit as possible was considered necessary to leave a passivated stainless steel surface that would resist future corrosion.

Initially consultants suggested using a 20% nitric and 4% hydrofluoric acid combination to remove the deposits and heat tint completely. Treatment using such a harsh etchant in large volumes created safety and health concerns along with schedule and cost concerns. Therefore, mechanical cleaning methods were developed using custom devices that were inexpensive and effective.

These devices all utilized spinning sets of abrasive pads (silicon carbide) driven by air motors. One device consisted of a spinning abrasive disk and an air motor mounted on spring-loaded wheels. This device was designed to be pulled through the pipes and buff the entire pipe inner surface including welds. A more sophisticated device design utilized a digital video camera to allow the operator to locate the cleaning pads on the dirty welds.

These devices eliminated all discoloration, both from heat tint and MIC deposits, on the pipe inner surface. In order to ensure that our techniques were adequate to protect against future corrosion, a microbiologist and a metallurgist reviewed the mechanical cleaning method and approved of its use.

After completing repairs, the piping was filled sector by sector with filtered and UV treated water and then hydrostatic pressure tested (225-psi). Pressure testing found several leaks (17 out of about 4000 weld repairs). These leaks were repaired and re-tested successfully.

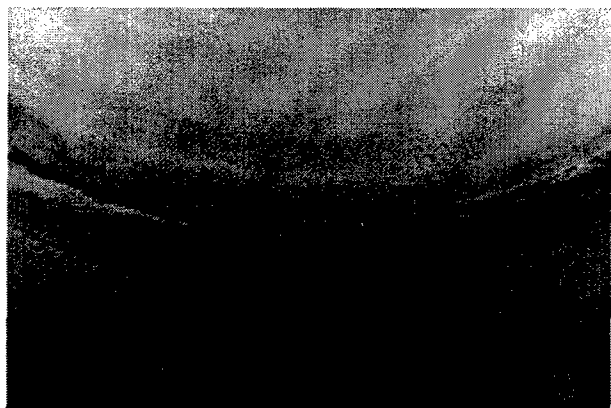


Figure 2: Mechanically cleaned SS pipe weld.

#### 4 CAUSES & RECOMMENDATIONS

Observations made during damage assessment suggest two direct causes of our MIC problem. One is simply the fact that low quality water was allowed to stand in sections of the piping system for extended periods of time. This allowed thick biofilms and nodules to grow on the pipe interior since insufficient water velocity was present to shear away the biofilms as they formed. The other is the poor corrosion resistance of the piping welded areas that existed due to improper welding practices during initial installation. Excessive heat, incomplete penetration and fusion and high heat input, among other defects,

encouraged localized corrosion and played a large role in the susceptibility of the welds to MIC attack.

Both direct causes stem from one root cause, the lack of awareness of MIC dangers. The original piping designers, fabricators, and operators were unaware of the problems that MIC can cause in piping systems. Specifying corrosion resistant materials and final water quality will not ensure corrosion prevention or abatement. Start-up, lay-up, and maintenance operations must also be addressed.

Preventative measures which help a piping system resist MIC can be employed. These include chemical treatment, heat treatment, ultra-violet radiation, de-ionization and filtering, and maintaining fluid velocity [4]. In the case of the MI LCW System, we initially heat treated our piping system to 135 degrees F in an attempt to sterilize the system. Then new water added to the system was sterilized using commercially available UV disinfection units. De-ionization and filtering was begun immediately after filling to maintain ultra-pure water. Procedural constraints were implemented limiting low flow conditions to a maximum of 5 days. Finally, monitoring of the system is achieved using custom designed MIC coupons which act as an early warning system of future MIC attack.

Our experiences have shown that corrosion, especially MIC, should be addressed early in the design process. Besides obvious issues such as material selection and water quality, the water system designer should consider compatibility with heat treatment and biocides during the design process. Welding technical specifications should describe acceptable welding practice in detail plus fully explain mandatory inspection requirements. Start-up and lay-up guidelines and/or procedures should be written and enforced with corrosion problems in mind.

#### 5 ACKNOWLEDGEMENTS

Although it is not possible to thank everyone here, we would like to acknowledge the following Fermilab personnel: B. Autro, M. Ball, D. Capista, H. Casebolt, R. Ducar, R. Farritor, J. Finks, B. Fritz, C. Gattuso A. Germain, B. Hanna, R. Hiller, B. Hoffman, S. Holmes, T. Johnson, F. Juravic, P. Martin, P. Mazur, G. Pewitt, D. Plant, J. Roberts, J. Satti, T. Schmitz, B. Slazyk, B. Smith, I. Stauersboll, L. Vonasch, and K. Williams.

#### 6 REFERENCES

- [1] Hurh, P. G., "Microbiologically Influenced Corrosion in the MI Magnet LCW System; Case History and Final Recommendations", MI Technical Note #0254, FNAL, Batavia, IL, (1999)
- [2] Borenstein, S.W., Microbiologically Influenced Corrosion Handbook, Woodhead Publishing, Cambridge, p. 4, (1994).
- [3] Chung, Y., Mantle, H.J., Lasko, G.E., 'Selective Attack in Microbiologically Influenced Corrosion of UNS S30800 and S32100 Welds', Corrosion/95, 13-1, NACE, Houston, TX, (1995).
- [4] Husted G.R., 'Sanitization: A Comparison of Different Sanitants Used in Microelectronics High-Purity Water Systems', Ultrapure Water, Jan, (1998).

# ARCHITECTURE OF HTS LEADS SOFTWARE PROTECTION SYSTEM

J.M.Nogiec\*, S.Feher, D.F.Orris, J.Sim, M.Tartaglia,  
Fermi National Accelerator Laboratory\*, Batavia, Illinois 60510

## Abstract

A software system to detect quenches in high temperature superconducting (HTS) power leads has been developed as a part of the Fermilab HTS R&D program. The system has been successfully applied to protect leads during several tests of various types of HTS leads.

The software architecture of the configurable quench detection system and capabilities of the quench management system are described. All major system components are presented along with the solutions to their communication and distribution problems. In addition, failure protection aspects of the design are discussed. Graphical user interfaces used to monitor the quench protection system are also presented.

## 1 INTRODUCTION

High temperature superconducting leads have been considered at Fermilab as a cost-effective replacement of traditional power leads. Thus, a new system has been built to test and study performance of these leads. This system is based on the Distributed Monitoring and Control System (DMCS) developed at Fermilab.

The DMCS [1][2] provides a framework for constructing data acquisition, monitoring and control systems, and has been previously successfully applied to control cold tests of superconducting accelerator magnets [3], and studies of future accelerator magnets (Pipetron project [4]).

The DMCS is a decentralised, configurable, multi-platform system with open architecture. Core components of this system include (see Figure 1):

- A memory resident Real-Time Data Base (RTDB) supporting triggers, caching, and locking mechanisms, and providing transparent access to local and remote objects
- A scan system that supports a uniform, common approach to data archiving, data acquisition, control, and on-line processing through various scan types
- A distributed synchronisation and communication mechanism based on a software bus approach, that enables synchronisation between active system components such as scans and servers

- A configuration subsystem with Data Base Definition Language describing system configurations
- Unified user interfaces that enable monitoring of the system under control (trends, numerical values, overviews), and status of the communication and scan subsystems
- Off-line data analysis tools.

The state of the process under control is monitored and altered through manipulations done on a set of process variables (PVs). Some PVs reflect directly measured process parameters, whereas others contain control variables used to regulate the process. Still other PVs may contain system control parameters, internal system variables, statistics, long-term trends, etc.

The scan system links the RTDB with the process under control by uniformly accessing devices and pseudo-devices and passing data to and from the RTDB. In addition to the already mentioned PVs, RTDB also contains all system configuration data.

The core system components are supplemented by specialised subsystems, such as the power supply control system [5], to form the full-featured operating environment.

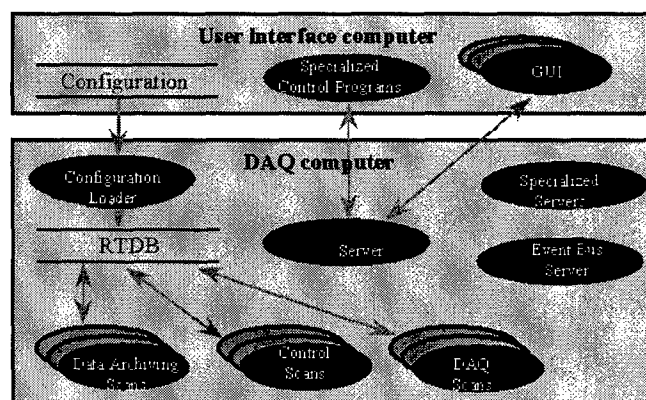


Figure 1: Overview of DMCS

## 2 REQUIREMENTS

The moderate quench development speeds in high temperature superconductors, measured in seconds, allow for software-based quench protection systems. Despite the fact that the system does not have hard real-time requirements, it still has to be deterministic. The protection system should also be highly reliable to

\*Operated by the Universities Research Association under contract with the U.S. Department of Energy

\* Email: nogiec@fnal.gov





## 4 INTERACTIONS IN QUENCH PROTECTION SYSTEM

Components of the software quench protection system interact by sending and receiving events. The interactions which take place upon detection of a quench are shown using a collaboration diagram (Figure 5).

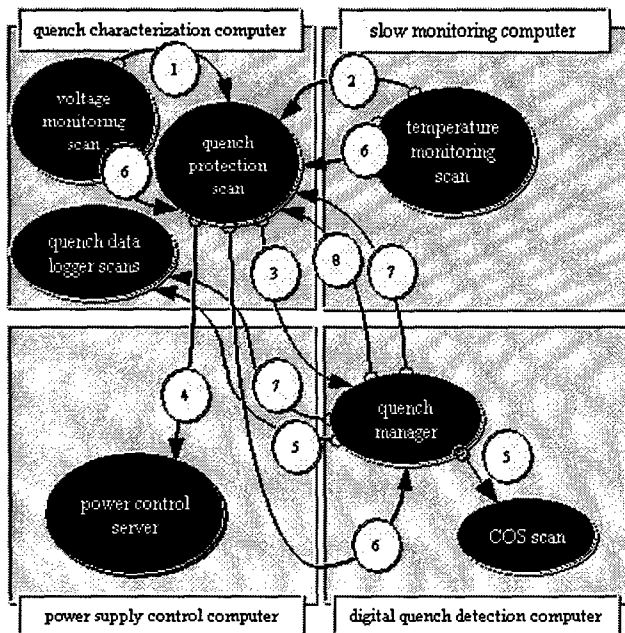


Figure 5: Quench system interaction diagram

Upon detection of a quench by one of the monitoring scans (temperature or voltage), an appropriate event is sent to the *software quench manager* (1,2). The *software quench manager* informs the central *quench manager* about the quench detected by the software quench protection system (3) and sends a request to the *power supply server* to ramp the current down (4). Afterwards, fast *data logging scans* are triggered to latch and save quench data (5).

If a quench is detected first by the hardware detection system the *software quench manager* is informed about it by the *quench manager* (8).

Quench status is reset by the *quench manager* in response to the user request sent from the quench manager user interface (7) which restarts the whole quench system and allows for ramping current in the leads.

The components vital to quench protection periodically exchange heartbeat events to detect any malfunctions of the system (6).

## 5 SYSTEM FEATURES

The required high reliability of the system has been achieved through the distribution of system components, independent voltage and temperature monitoring, implementation of heartbeat signals, and usage of a backup hardware quench detection system.

Determinism of the quench protection system, important in the case of a software system, has been guaranteed by using a real-time operating system as a system run-time environment.

The software quench protection system can be easily re-configured and adapted to accommodate various HTS leads. Among others, the number and location of sensors can be modified, new quench detection scans can be added, and thresholds used to determine presence of a quench in the leads can be modified.

## 6 CONCLUSIONS

The moderate quench development speeds in HTS leads make it possible to rely on software systems for quench protection. Software-based systems can offer potentially high flexibility and configurability in comparison with purely hardware-based systems.

The required high reliability can be achieved through duplication and distribution of system components and deployment of a backup hardware solution.

Relying on a common framework makes integration of the quench system with the rest of the monitoring and control system seamless.

Basing the implementation of the quench system on a configurable and open system makes this system extensible and allows for:

- modification of quench detection methods or algorithms;
- introduction of other quench protection mechanisms;
- modification of quench characterisation elements; and,
- modification of the interactions between system components.

## 6 REFERENCES

- [1] J.M.Nogiec, E.Desavouret, D.Orris, J.Pachnik, S.Sharonov, J.Sim, J.C.Tompkins, and K.Trombly-Freytag, "A Distributed Monitoring and Control System", PAC97, Vancouver, (1997)
- [2] J.M.Nogiec, E.Desavouret, J.Pachnik, S.Sharonov, and J.Sim, "An Open Distributed Monitoring and Control System", CHEP97, Berlin, (1997)
- [3] M.J.Lamm, J.DiMarco, E.Desavouret, S.Feher, J.D.Garvey, C.Hess, P.J.Limon, J.M.Nogiec, D.F.Orris, J.Pachnik, T.Peterson, S.Sharonov, J.B.Strait, C.Sylvester, J.W.Sim, M.Tartaglia, J.C.Tompkins, and A.V.Zlobin, "A New Facility to Test Superconducting Accelerator Magnets", PAC97, Vancouver, (1997)
- [4] G.W.Foster, P.O.Mazur, T.Peterson, C.D.Sylvester, and P.Schlabach, "Design and Operation of an Experimental Double-C Transmission Line Magnet", PAC97, Vancouver, (1997)
- [5] S.Sharonov, J.M.Nogiec, "An Embedded Power Supply Controller", Pac97, Vancouver, (1997)
- [6] D.F. Orris, S. Feher, M.J. Lamm, J. Nogiec, S. Sharonov, M. Tartaglia, and J. Tompkins, "Digital Quench Detection System for Superconducting Magnets", PAC99, New York, (1999)



# LASER PULSE HEATING\*

Xintian E. Lin

Stanford Linear Accelerator Center, Stanford University, Stanford, CA 94309

## Abstract

Recently, interest has developed in pulsed heating effects on a copper surface[1]. Pulsed heating is one of the limits on the gradient of a structure based linac. The heat generated by an intense RF pulse on the metal surface can result in hundreds of degrees of temperature rise at 1 GeV/m. After a certain number of cycles, the metal may crack due to thermal fatigue and the surface properties may deteriorate. In this article, we describe an experiment to use a high power laser to study the pulsed temperature rise on a metal surface.

## 1 INTRODUCTION

Laser induced damage in optical materials is a discipline in its own right. Many publications have tried to address the issue from theoretical and experimental point of view for more than 30 years[2]. However most of them concerns single or a few shots damage threshold. Thomas etc[3] has measured up to 100 shots. The damage criteria is usually a quantitative visual inspection under microscope. For a few ns and longer pulse, the threshold corresponds roughly to single shot melting of the surface. For accelerator applications, we are interested in the thermal fatigue threshold on the order of a billion shots with temperature measurement on the surface. To bypass the requirement of high power, high repetition rate microwave source, we describe an alternative experiment using a laser to test pulsed temperature rise on a copper surface.

In the geometric setting illustrated in Fig. 1, the temper-

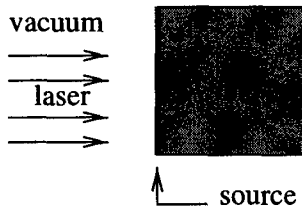


Figure 1: Surface heating.

ature rise resulting from a surface heat source induced by a laser, for example, is given by

$$T(t_p) - T_0 = \int_0^{t_p} \frac{F_d(t') dt'}{\sqrt{\pi K \rho C_v (t_p - t')}}, \quad (1)$$

where  $K$ ,  $\rho$  and  $C_v$  are the thermal conductivity, density and heat capacity respectively. The initial temperature is

denoted by  $T_0$ . If we assume that  $F_d(t)$ , the power flux deposited into the material, is a square pulse in time, then

$$T(t_p) - T_0 = F_d \frac{2\sqrt{t_p}}{\sqrt{\pi K \rho C_v}}. \quad (2)$$

The temperature rises as one half power of the pulse length, a generic character of heat diffusion.

In the case of a Gaussian pulse profile, the maximum temperature rise on the surface becomes

$$T_{max} - T_0 = 0.783 \frac{F}{t_p} \frac{2\sqrt{t_p}}{\sqrt{\pi K \rho C_v}}, \quad (3)$$

where  $F$  is the fluence deposited into the copper, and  $t_p$  is the FWHM of the pulse. Compared to a square pulse with fluence  $F$  and pulse length  $t_p$ , the lower temperature rise of Gaussian pulse is a result of the lower peak power and the spread of energy.

When the temperature rise  $T$  is high, the dependence of material property on temperature needs to be considered, thus Eq. 1 becomes[1]

$$\begin{aligned} T(t_p) - T_0 &= \int_{-\infty}^{t_p} \frac{F_d(t', T(t')) dt'}{\sqrt{\pi K(T(t')) \rho C_v(T(t')) (t_p - t')}} \\ &= \int_{-\infty}^{t_p} \frac{f(t', T(t')) dt'}{\sqrt{t_p - t'}}. \end{aligned} \quad (4)$$

Because of the singularity at  $t' = t_p$ , the integral may be evaluated as[4]

$$T(t_n) - T_0 = \sum_{j=-\infty}^{n-1} 2(\sqrt{t_n} - \sqrt{t_j}) f(t_j, T(t_j)). \quad (5)$$

If one were to scale time  $t$  by a factor  $\beta$ , i.e.  $\hat{t} \rightarrow \beta t$  and flux by  $\sqrt{\beta}$ , i.e.  $\hat{F}_d \rightarrow F_d/\sqrt{\beta}$ , then from Eq. 4,

$$\hat{T}(\beta t) - T_0 = T(t) - T_0 \quad (6)$$

regardless of the temperature dependence of the material property. Thus to get the same temperature rise,  $F/\sqrt{t_p}$  needs to be constant.

## 2 LASER ABSORPTANCE IN METAL

Shining a laser with wavelength  $\lambda$  perpendicularly onto a copper surface, the reflection coefficient can be expressed as

$$r = \frac{n-1}{n+1}, \quad (7)$$

where the refractive index  $n = \sqrt{\epsilon}$ . The Drude model is quite adequate in infrared[5]. It gives

$$\epsilon = 1 - \frac{\omega_p^2}{\omega^2 + i\omega\omega_r}. \quad (8)$$

\* Work supported by U.S. Department of Energy, contract DE-AC03-76SF00515

The plasma frequency  $\omega_p^2 = n_e e^2 / m \epsilon_0$ , and the collision frequency  $\omega_\tau = n_e e^2 / m \sigma(T)$ . The electron density  $n_e$  inside copper is roughly  $8.4 \times 10^{22} / \text{cm}^3$ . Notice that electric conductivity  $\sigma$  is temperature dependent. From energy conservation, the flux into copper has the form

$$F_d = (1 - |r|^2) I_0, \quad (9)$$

where  $I_0$  is the laser irradiance. In the frequency region  $\omega_\tau \ll \omega \ll \omega_p$ , i.e.  $0.11 \mu\text{m} \ll \lambda \ll 46 \mu\text{m}$ , the Drude model gives

$$F_d \approx \frac{2\omega_\tau}{\omega_p} I_0. \quad (10)$$

The absorptance is wavelength independent. So the following experiment may be carried out at other wavelengths with about the same temperature rise.

When laser wavelength approaches  $1 \mu\text{m}$ , other contribution becomes important[8], and analysis becomes more involved.

### 3 EXPERIMENT

The experiment, illustrated in Fig. 2, utilizes high energy laser pulses to heat up the sample surface repeatedly and uses interference between the reflected pulse and original pulse to monitor the surface temperature. Mirror 1 and 2

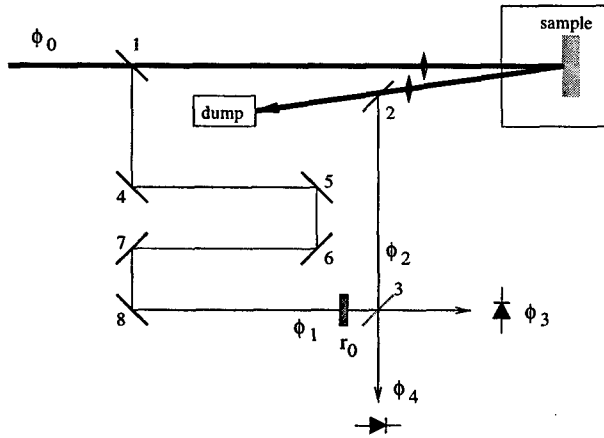


Figure 2: Laser pulse heating experiment.

are beam splitters and mirror 3 is a combiner such that the wave functions  $\phi$ 's are given by

$$\left. \begin{aligned} \phi_1 &= \alpha \phi_0 \\ \phi_2 &= r \alpha \phi_0 \\ \phi_3 &= \frac{1}{\sqrt{2}} (r_0 \phi_1 - \phi_2) = \alpha \phi_0 \frac{r_0 - r}{\sqrt{2}} \\ \phi_4 &= \frac{1}{\sqrt{2}} (r_0 \phi_1 + \phi_2) = \alpha \phi_0 \frac{r_0 + r}{\sqrt{2}} \end{aligned} \right\} \quad (11)$$

where we have assumed the splitting factor  $\alpha \ll 1$ . A phase shifter/attenuator  $r_0$  is inserted in  $\phi_1$  to insure null reading of  $\phi_3$  at low power.

At  $10.6 \mu\text{m}$  wavelength,  $|r|$  is very close to 1. Therefore,  $\phi_4$  is a good measure of the pulse energy and  $\phi_3$  is a measure of energy loss to the surface, and thus gives the surface temperature through the  $\sigma(T)$  dependence.

The temperature dependence of the copper properties  $K$  and  $\sigma$  are tabulated in [6], and a polynomial fit is used to interpolate to other temperatures. The heat capacity  $C_v$  of copper is given in [7].

Taking  $\lambda = 10.6 \mu\text{m}$ , a square pulse with  $t_p = 16 \text{ ns}$  and  $I_0 = 1.5 \text{ GW/cm}^2$  for example, the pulsed temperature rise is as high as  $991^\circ \text{C}$ . The surface temperature, plotted in Fig. 3, has an initial value of  $300 \text{ K}$ . The solid

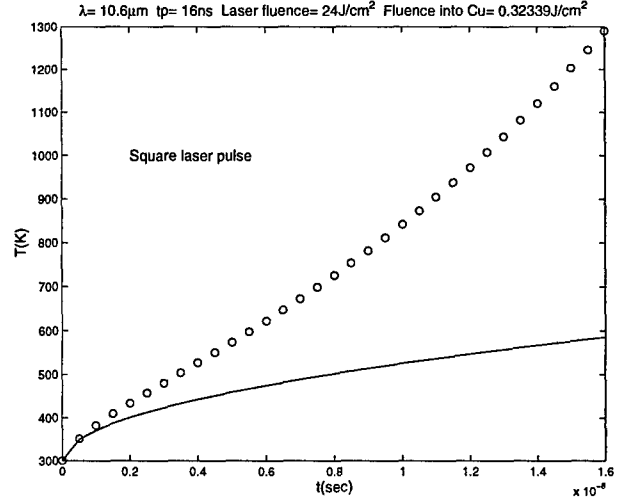


Figure 3: Pulsed temperature rise. The solid curve is estimation from Eq. 2 and circles are from Eq. 4.

curve is calculated from Eq. 2. The circles, with temperature dependence of the material property included (Eq. 4), depart significantly from Eq. 2 at higher temperatures. The faster temperature growth is primarily due to higher electric resistivity at higher temperature. The heat capacity and thermal conductivity, on the other hand, change less than 20% in this temperature range.

In the case of a comparable Gaussian pulse, the maximum temperature rise, illustrated in Fig. 4, is about  $556^\circ \text{C}$ , 44% lower than the square pulse case. The rest of the discussions all concern Gaussian pulses.

The temperature rise  $T_{max}$  and diode outputs  $\int |\phi_3|^2 dt$ ,  $\int |\phi_4|^2 dt$  are plotted in Fig. 5 and 6 as a function of laser fluence. The maximum temperature rise  $T_{max}$ , plotted against the signal  $s = \int |\phi_3|^2 dt / \int |\phi_4|^2 dt$ , is illustrated in Fig. 7. A least square fit given by

$$s = 6.83 \times 10^{-7} \left( 1 - 2.31 \frac{T_{max}}{300} + 1.273 \left( \frac{T_{max}}{300} \right)^2 \right) \quad (12)$$

is also plotted. It is the basis of surface temperature monitoring.

### 4 CONCLUSION

This experiment can be carried out using  $10.6 \mu\text{m}$   $\text{CO}_2$  laser with  $2.4 \text{ mJ}$  in  $16 \text{ ns}$  pulse running at  $1 \text{ kHz}$ . The laser needs to be focused to a  $100 \mu\text{m}$  spot to deliver  $24 \text{ J/cm}^2$  fluence. It is then able to test surface temperature rise up to  $556^\circ \text{C}$  reaching  $10^9$  pulses in 2 weeks. To see a 100 degree

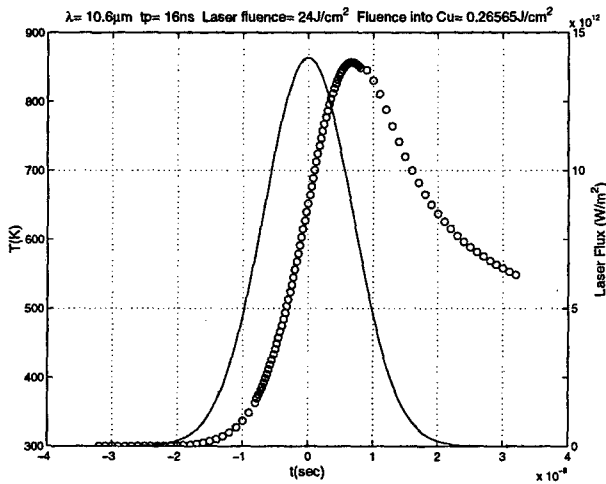


Figure 4: Pulsed temperature rise for a Gaussian laser pulse. The solid line represents the laser irradiance, and the surface temperature is drawn in circles.

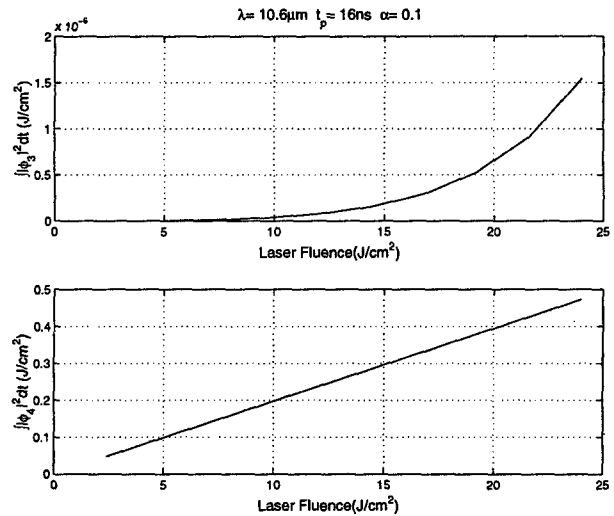


Figure 6: The integrated diode signals as a function of laser fluence.

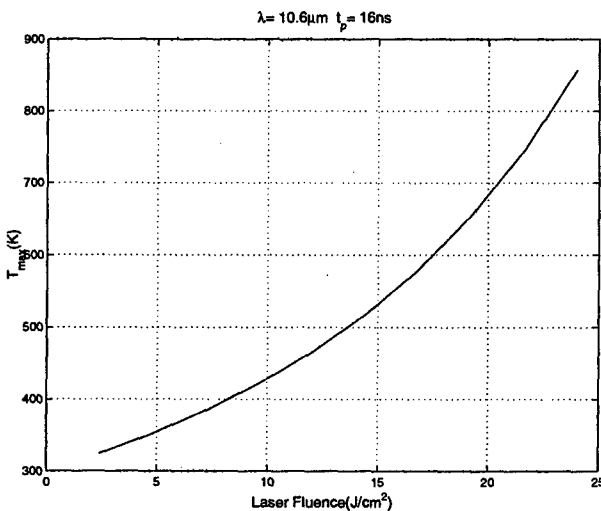


Figure 5: Maximum pulsed temperature rise.

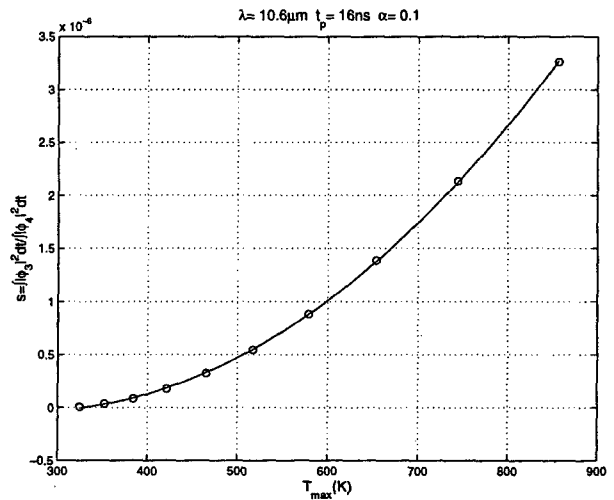


Figure 7: The signal  $s = \int |\phi_3|^2 dt / \int |\phi_4|^2 dt$  plotted as a function of the maximum surface temperature rise  $T_{max}$ . The circles are the result of Eq. 4 and 11. The solid line is a quadratic least square fit.

temperature rise, a 2 nJ diode detector running at 1 Hz rate suffices. The drift in diode reading is an indicator of the surface degradation. The same experiment, carried out at other wavelengths, 1  $\mu\text{m}$  or 100  $\mu\text{m}$  for example, are also desirable to check the frequency dependence. The laser fluence requirement is about the same. The spot size may need to be increased to alleviate focusing requirement at the longer wavelength. The data analysis is more involved at shorter wavelength because the interband contribution to absorptance is significant[8].

## 5 REFERENCES

- [1] D. Pritzkau, *et al.* "Experimental study of pulsed heating of electromagnetic cavities", 1997 IEEE PAC, Vancouver, Canada, 12-16 May 1997.
- [2] Laser Induced Damage in Optical Materials, NIST and SPIE publications. 1969-

- [3] S.J. Thomas, R.F. Harrison and J.F. Figueira. "Observations of the morphology of laser-induced damage in copper mirrors", *Appl. Phys. Lett.* **40**, 200(1982).
- [4] P. Linz, "Analytical and Numerical Methods for Volterra Equations", 1985, Eq.(8.15)
- [5] CRC handbook of Laser Science and Technology Volume IV, Boca Raton, Fla. 1986.
- [6] David R. Lide, "Handbook of Chemistry and Physics" 77th edition. 1997 p12-40, p12-174.
- [7] G. T. Furukawa and T. B. Douglas, "American Institute of Physics Handbook", 3rd edition. p4-113
- [8] M. Sparks and E. Loh, Jr., "Temperature dependence of absorptance in laser damage of metallic mirrors: I. Melting", *J. Opt. Soc.Am.*, Vol 69, 1979, 847-858.

# PLANAR WAVEGUIDE HYBRIDS FOR VERY HIGH POWER RF\*

C.D. Nantista<sup>‡</sup>, W.R. Fowkes, N.M. Kroll<sup>#</sup>, and S.G. Tantawi<sup>+</sup>  
Stanford Linear Accelerator Center, Stanford, CA

## Abstract

Two basic designs have been developed for waveguide hybrids, or 3-dB couplers, capable of handling hundreds of megawatts at X-band. Coupling is provided by one or two connecting waveguides with h-plane junctions and matching elements. In the former case, the connecting waveguide supports two modes. Small apertures and field-enhancing e-bends are avoided to reduce the risk of rf breakdown. The h-plane symmetry also allows the use of over-moded rectangular waveguide in which the height has been increased to reduce field amplitudes without affecting the scattering matrix. The theory and designs are presented, along with the results of prototype tests of functionality and power-handling capability. Such a device is integral to the rf pulse compression or power distribution system [2] of the Next Linear Collider (NLC) [1] for combining, splitting, and directing power. This work was motivated by the observation of rf breakdown at power levels above 200 MW in conventional and modified magic-T's.

## 1 INTRODUCTION

The design of the Next Linear Collider (NLC) [1] includes plans for powering the high-gradient accelerator structures of the main linacs with 11.424 GHz X-band klystrons through a pulse compression or power distribution system [2]. In such a system pulsed rf will need to be combined, split, or directed at peak power levels reaching 600 MW. A basic component required is a waveguide hybrid, or 3-dB directional coupler, capable of handling very high power levels. Prototype rf systems have employed conventional, matched magic T's in WR90 (0.9"x0.4") waveguide. As power levels were increased, these proved inadequate and a modified design was developed, in which the matching post in the waveguide junction was replaced with a thick fin. While simulations showed this design to have lower field strengths, its reliability proved to still be inadequate. These magic T's exhibited frequent rf breakdown at power levels above 200 MW, which inspection showed to occur primarily at the mouth of the e-bend [3].

With this motivation, we have subsequently developed two novel planar hybrid designs capable of reliably handling hundreds of megawatts of peak power at X-band (11.424 GHz). These each consist of four rectangular waveguide ports, which operate in the TE<sub>10</sub> mode, connected through four or two h-plane T-junctions, yielding, respectively, a two-rung ladder or an "H" geometry. In the latter case, the single connecting waveguide carries two modes. Figure 1 illustrates the two design geometries.

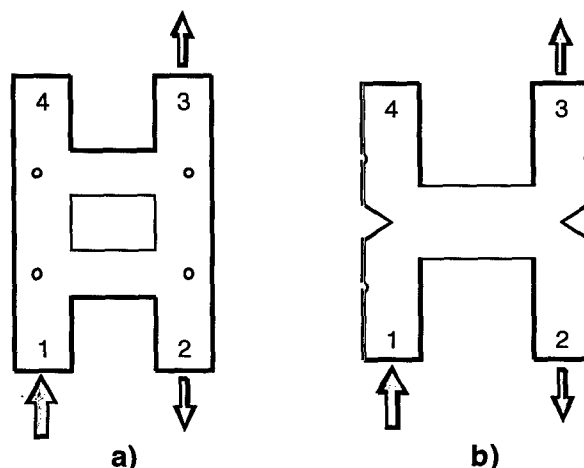


Figure 1: Schematic of the h-planar geometries of the a) two-rung ladder and b) "H" hybrid designs. Power-flow arrows indicate output ports for the indicated input port.

Small apertures, slots, and field-enhancing e-bends are avoided to reduce the risk of rf breakdown. Matching features maintain the translational symmetry of these cross-sections. Electric fields terminate only on the flat top and bottom surfaces. This h-plane symmetry also allows the use of over-moded rectangular waveguide in which the height has been increased to reduce field amplitudes without affecting the scattering matrix. Both are quadrature hybrids (i.e. the coupled port fields are 90° out of phase), and directly opposite port pairs are isolated. That is, the scattering matrices, with properly chosen, symmetric reference planes and the indicated port numbering, are of the form

$$S = \frac{1}{\sqrt{2}} \begin{bmatrix} 0 & 1 & -i & 0 \\ 1 & 0 & 0 & -i \\ -i & 0 & 0 & 1 \\ 0 & -i & 1 & 0 \end{bmatrix}$$

\* Work supported by the U.S. Department of Energy under contract DE-AC03-76SF00515 and grant DE-FG03-93ER40695.

<sup>‡</sup> Email: nantista@slac.stanford.edu

<sup>#</sup> Also University of California, San Diego, La Jolla, CA 92093.

<sup>+</sup> Also with the Communications and Electronics Department, Cairo University, Giza, Egypt.

## 2 TWO-RUNG LADDER HYBRID

The two-rung ladder hybrid is basically a realization in rectangular waveguide of R.H. Dicke's coaxial-line synthesis of a biplanar magic T [4], or of a modified microstrip branch-line hybrid. In transmission line theory, this device requires the distances between all adjacent junctions to be  $(n/2 \text{ plus})$  one quarter wavelength and the two connecting lines to have a characteristic admittance that is  $\sqrt{2}$  times that of the main lines. The resulting circuit can be shown to yield the desired scattering matrix.

In waveguide, whose width is not small compared to a wavelength, the two-dimensional geometry necessitates matching elements in the T-junctions to adjust the complex impedances. A mode matching code was used to determine the radius and placement of a post that would yield a three-port junction with the desired scattering matrix, from which the hybrid ring circuit could then be constructed. The fields were expanded in cylindrical harmonics about the post in the junction region and in normal modes in the rectangular port regions. The full hybrid design was verified with the finite-element field solver HFSS. The peak field amplitude was found to be 44.1 MV/m at 300 MW with a waveguide height of 0.900 inch.

## 3 "H" HYBRID

The "H" hybrid can be viewed as a variation of the above with the two connecting waveguides collapsed into one in which two modes are utilized. Thus, in a transmission line picture, the requirement of two connecting lines is not circumvented. The coupling mechanism is actually the same as that of the Riblet short-slot coupler [5], although this geometry provides separated ports and no sharp-edged wall interruptions.

The connecting guide is wide enough that both the  $TE_{10}$  and the  $TE_{20}$  modes can propagate, and these are excited with comparable amplitudes by the fields of a single port. They are excited with a relative phase such that their fields add constructively on the side nearest the input port and destructively on the other side. If they were to slip in phase by  $\pi$  radians, the  $TE_{10}$  wave would enhance the opposite lobe of the  $TE_{20}$  wave, sending the power out the farthest port. To get a 3-dB split, therefore, the total phase lengths for these two modes through the connecting guide must differ by an odd multiple of  $\pi/2$ .

The T-junctions in this design have been matched by shaping the walls with blunt, triangular protrusions at the symmetry plane, rather than with free-standing posts. The result is essentially a side-wall coupler with the common wall removed and two back-to-back mitred  $90^\circ$  bends at either end. The connecting guide must be narrower than twice the standard guide width in order to keep the  $TE_{30}$  mode cut off. Simple mitred bends used in a preliminary design therefore led to narrow ports (half the connecting

guide width). To accommodate standard-width ports and avoid the added length of width tapers, a small vertical ridge was placed in each port to match into an effective asymmetric mitred bend. The  $TE_{20}$  mode is thus matched independently at each junction. The width and length of the connecting guide are adjusted to simultaneously meet the above phase length difference requirement and cause the small  $TE_{10}$  mismatch at the two junctions to cancel. HFSS was used extensively in the design process to calculate scattering matrices. The peak field of the final design was found from simulation to be 39.5 MV/m at 300 MW with a waveguide height of 0.900 inch.

## 4 TESTS

A copper high-power vacuum-flanged prototype of each of these hybrids has been built and tested. They were both made over-moded, the two-rung ladder in 0.9 inch square guide and the "H" in double-height (0.9"x0.8") guide. This necessitated height tapers at the ports for compatibility with our test setup and other WR90-based components. The top and bottom were tapered symmetrically with one-inch long half-cosine tapers. An HP 8510C Network Analyzer was used to measure the scattering matrix parameters in the vicinity of the design frequency. The results over a 500 MHz span are presented in Figure 2.

The measured insertion losses, when corrected for the predicted loss of the flange adaptors used and WR90 curved h-bends built onto two ports of the "H" hybrid to accommodate a particular installation, give  $\sim 1.5\%$  for the two-rung ladder hybrid and  $\sim 0.9\%$  for the "H" hybrid. We define this loss as  $1 - (|S_{21}|^2 + |S_{31}|^2)$ . It is dominated by ohmic loss. For the two-rung ladder, the reflected signal and isolation at 11.424 GHz were both about -26 dB, accounting together for 0.49% misdirected power. For the "H" they were -33 dB and -37 dB, respectively, accounting for 0.07% misdirected power. The measured coupling at 11.424 GHz, corrected for loss (i.e.  $10 \log[|S_{31}|^2 / (|S_{21}|^2 + |S_{31}|^2)]$ ), was -3.19 dB for the former hybrid and -2.96 dB for the latter (the ideal being -3.01 dB). Finally, Figure 2 shows the "H" hybrid to have a significantly broader bandwidth, as one would expect from the more compact geometry.

The hybrids were later high-power tested in the pulse compression system of the Accelerator Structure Test Area (ASTA) [3], where they were processed with pulsed rf to peak power levels exceeding 400 MW in 150 ns pulses and performed successfully without breakdown problems or excessive X-ray production.

## 5 CONCLUSIONS

In response to the problem of rf breakdown in multi-hundred-megawatt X-band rf systems being developed for a next generation linear collider, we have conceived and

produced two new types of rectangular waveguide hybrid, with relatively open interiors and completely two-dimensional designs, perpendicular to the electric field lines. The latter feature makes their circuit properties independent of height, allowing for their construction in over-height waveguide to reduce fields. Prototypes of both designs performed similarly and quite well. The "H"-shaped hybrid has the advantage of broader bandwidth and is more compact. HFSS simulation suggests that it has peak fields lower by about 11% for a given power flow and waveguide height. The absence of free-standing matching elements may also be an advantage with regard to cooling.

One goal in our component development program is to limit surface fields at anticipated power levels to values below 40 MV/m in order to avoid rf breakdown problems. For a power flow of 300 MW in one port, both hybrid designs meet or approach this goal in square guide (0.9"x0.9"). By contrast, our original and modified magic T's had peak fields of approximately 80 MV/m and 63 MV/m, respectively, at this power level and could not be made over-moded in height.

For testing and for their intended use, we required standard, single moded ports on our prototypes, for which the peak field at 300 MW is 49 MV/m. Smooth height tapers were incorporated at the ports to bring the peak fields in the interior of these devices, where standing waves cause some enhancement, below the peak port field. With reference planes taken just inside these tapers, the hybrids proper are thus over-moded. To take full

advantage of these hybrid designs, one would not normally use single-moded ports, but remain over-moded, perhaps matching into a  $TE_{11}$  mode in circular waveguide.

To comfortably handle 600 MW, the hybrid height would have to be increased to 1.75 inches. In such waveguide, taper design becomes non-trivial because the  $TE_{12}$  mode can propagate. Mode conversion due to mechanical imperfections also becomes more of a concern as a device becomes more over-moded. It may therefore be preferable to use a configuration which incorporates two hybrids to further increase power-handling capacity.

## 6 REFERENCES

- [1] The NLC Design Group, Zeroth-Order Design Report for the Next Linear Collider, LBNL-PUB 5424, SLAC Report 474, and UCRL-ID 124161, May 1996.
- [2] S.G. Tantawi *et al.*, "A Multi-Moded RF Delay Line Distribution System (MDLDS) for the Next Linear Collider," to be published in Physical Review-Special Topics.
- [3] A.E. Vlieks *et al.*, "High Power RF Component Testing for the NLC," presented at the 19th International Linear Accelerator Conference (LINAC 98) Chicago, IL, August 23-28, 1998.
- [4] Montgomery, Dicke, and Purcell, Principles of Microwave Circuits, Radiation Lab. Series, 1948, p. 451.
- [5] Henry J. Riblet, "The Short-Slot Hybrid Junction," Proceedings of the I.R.E., February 1952, p. 180.

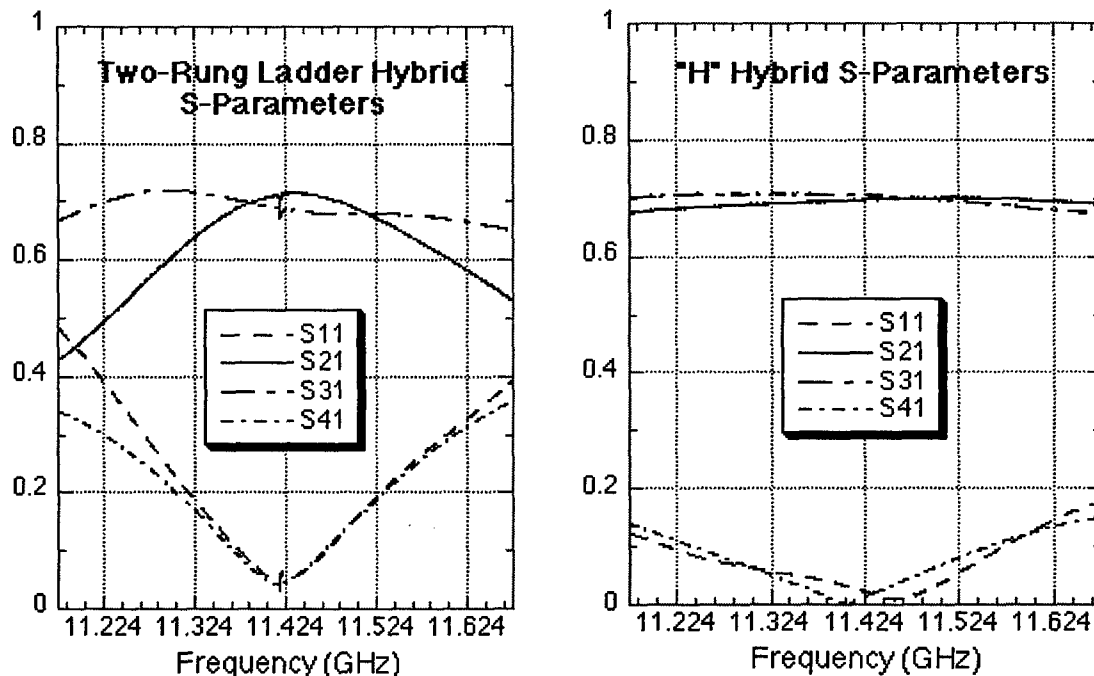


Figure 2: Scattering matrix elements for our two hybrid prototypes measured over a frequency range of 500 MHz centered on the design frequency of 11.424 GHz.

# RF COMPONENTS USING OVER-MODED RECTANGULAR WAVEGUIDES FOR THE NEXT LINEAR COLLIDER MULTI-MODED DELAY LINE RF DISTRIBUTION SYSTEM\*

S. G. Tantawi<sup>†‡</sup>, N. M. Kroll, And K. Fant, SLAC, Stanford, CA

## Abstract

We present the design and analysis for a set of smooth transitions from rectangular to circular waveguide that preserves their common reflection symmetries. The S-matrix of the transition connects modes of the same symmetry class, and for a sufficiently adiabatic transition preserves their TE (or TM) character. It is then also non-reflecting and, in the absence of degeneracy, its modal connections are one to one and order preserving. This property enables us to carry out all of the RF manipulations in the more easily handled over-moded rectangular waveguide.

## 1 INTRODUCTION

The Multi-moded Delay Line Distribution System (MDLDS) was suggested as an alternative for rf pulse compression for the Next Linear Collider (NLC)[1-2]. MDLDS propagates several modes in a single circular highly over-moded waveguide. This system uses a set of complicated over moded rf components. Most of these components manipulate several modes at the same time.

Manipulation of several modes in a single component is easier in rectangular waveguides. To take advantage of this, we present several rf tapers which maps the modes in circular waveguides into modes in rectangular guides.

Three types of tapers are presented:

1. A taper from circular waveguide to a square waveguide. The circular guide diameter is such that all modes with cut-off frequency above that of the  $TE_{01}$  do not propagate.
2. A taper from circular waveguide to a square waveguide with the circular waveguide diameter is such that all modes with cut-off frequency above that of the  $TE_{12}$  do not propagate.
3. A taper from circular waveguide to a rectangular guide. The circular guide diameter is such that all modes with cut-off frequency above that of the  $TE_{01}$  do not propagate.

## 2 SIMULATION TECHNIQUE

We assumed that all these tapers will be built using wire Electron Discharge Machining (EDM). When tapering from one shape, e.g. a circle, to another shape, e.g., a square, the length of the taper  $l$  and the connecting points between the two shapes uniquely define the taper. In cylindrical coordinates a shape  $i$  placed with cylindrical symmetry around the  $z$ -axis can be described by a relation  $r_i(\phi)$ , which gives the radius as a function of the angle  $\phi$ . The taper between two shapes  $r_1(\phi)$ , and  $r_2(\phi)$  is then given by

$$r(\phi, z) = r_1(\phi) + \frac{r_2(\phi) - r_1(\phi)}{l} z. \quad (1)$$

This taper is compatible with the process of wire EDM when the two heads of the machine are moving synchronously with the same angular speed. More complicated tapers are described by a set of tapers, each have the form of Eq.(1) and cascaded together.

All simulations were performed using HFSS [3]. The shapes  $r_i(\phi)$  were plotted using a finite number of points (72 points) using Visual Basic Application (VBA) in AutoCAD [4]. The shapes were then imported into HFSS, and the interpolation described in Eq. (1) was done using the *connect* function, to generate the solid model. This process was used to design all the tapers described in this work. All tapers were optimized around 11.424 GHz.

## 3 TAPER DESIGNS

### 3.1 Type 1: $TE_{01}$ Circular to Square Taper

In this taper the circular waveguide diameter is chosen such that all modes, that have a cut-off frequency above that of the  $TE_{01}$  mode do not propagate. The square waveguide is just large enough to allow both  $TE_{20}$  and  $TE_{02}$ . However, it does not allow the propagation of  $TE_{22}$  and  $TM_{22}$  modes. Because of reflection symmetries, only the two degenerate modes,  $TE_{20}$  and  $TE_{02}$ , in the rectangular guide are exited when the incident mode in the circular guide is  $TE_{01}$ . The design process for this taper is simply done by increasing the length until the reflection coefficient for the  $TE_{01}$  mode in the circular guide is small enough. Fig. 1 shows the taper design and Fig.2 shows the  $TE_{01}$  mode reflection coefficient for this design. Because of degeneracy the combination between the two modes in the square waveguide could be regarded as one single

\*This work is supported by Department of Energy Contract DE-AC03-76SF00515.

†Email: tantawi@slac.stanford.edu

‡Also with the Communications and Electronics Department, Cairo University, Giza, Egypt.

mode. When exciting the circular guide with the  $TE_{12}$  mode, again, it couples to the two modes  $TE_{02}$  and  $TE_{20}$ . However, the phase between them is a 180-degree different from the previous case, i.e., when they are excited because of the  $TE_{01}$  mode in the circular guide. Again this combination could be regarded as a different single mode in the square guide.

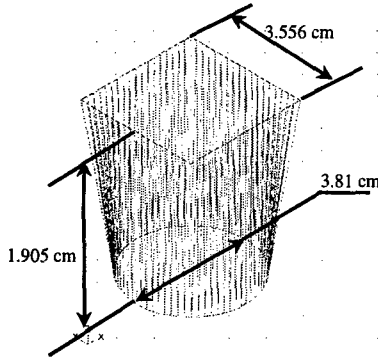


Fig. 1 Type 1 taper design

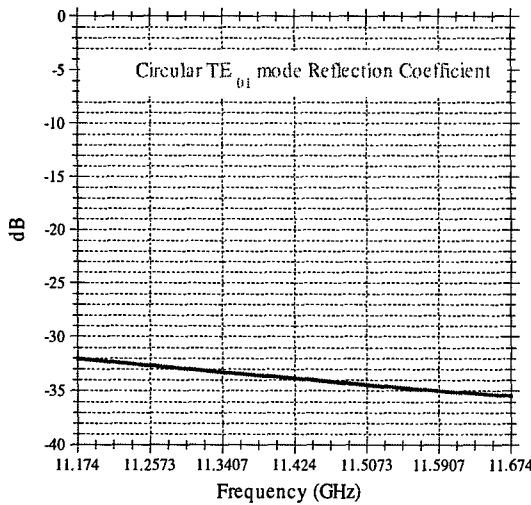


Fig. 2. Simulated results of the type 1 taper design.

### 3.2 Type 2: $TE_{01}$ and $TE_{12}$ Circular to Square Taper.

The circular waveguides used in the long delay lines of the MDLDS uses three different modes. These modes are the  $TE_{01}$ , and the two polarizations of the  $TE_{12}$  mode [1]. In tapers of this type, the diameter of the circular waveguide is increased to 5.08 cm to support the  $TE_{12}$  mode. Correspondingly, the width of the square waveguide was increased to 4.491 cm to support the  $TE_{30}$  and the  $TE_{03}$  modes. At this width the square waveguide supports both the  $TE_{22}$  and the  $TM_{22}$  modes. These modes have the same reflection symmetries as the  $TE_{01}$  mode in circular waveguide and the  $TE_{02}$  and  $TE_{20}$  in rectangular waveguide. The design process of this taper was simply

increasing the length until the coupling from the circular  $TE_{01}$  mode to the square  $TE_{22}$  and  $TM_{22}$  is small enough.

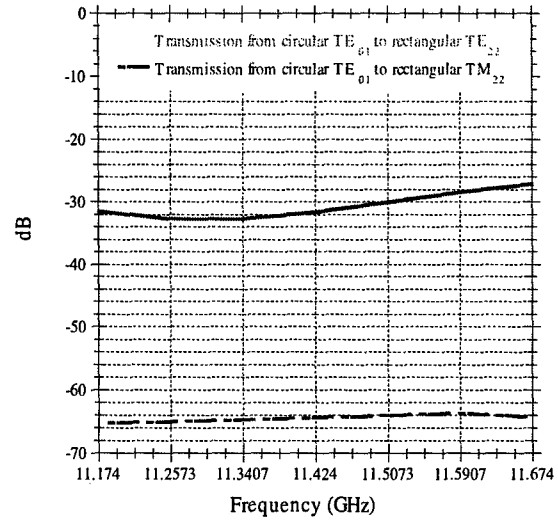


Fig. 3 coupling of the  $TE_{01}$  in the circular guide to spurious modes in the square guide. At the design length for Type 2 taper.

The length required is 10.16 cm. Fig. 3 shows the coupling of the  $TE_{01}$  in the circular guide to unwanted modes in the square guide. At this length the coupling between modes in the circular guide to modes in the square guide is one to one with a transmission coefficient that is better than  $-0.017$  dB over a 0.5 GHz bandwidth around 11.424 GHz. The modes connect to each other according to the following table:

Circular Guide modes	Square Guide Modes
TE11 (Polarization #1)	TE10
TE11(Polarization #2)	TE01
TM01	TM11
TE21 (Polarization #1)	TE20 and TE02 (In Phase)
TE21 (Polarization #2)	TE11
TE01	TE20 and TE02 (out of Phase by 180 degrees)
TM11 (Polarization#1)	TM12
TM11 (Polarization#2)	TM21
TE31 (Polarization #1)	TE12
TE31 (Polarization #2)	TE21
TM21 (Polarization #1)	TM22
TM21 (Polarization#2)	TM13 and TM13 (In phase)
TE41 (Polarization#1)	TE22
TE41 (Polarization#2)	TE31 and TE13
TE12(Polarization#1)	TE30
TE12(Polarization#1)	TE03
TM02	TM31 and TM13 (out of phase by 180 degrees)



### 3.3 Type 3: $TE_{01}$ Circular to $TE_{02}$ Rectangular Taper.

In several applications one would want to convert the  $TE_{01}$  mode in the circular guide to a single polarization of the  $TE_{02}$  in the square guide. Modifying the square waveguide to a rectangular waveguide to break the degeneracy between the  $TE_{02}$  and  $TE_{20}$  modes could do this. However, in this case, the length of the taper required to achieve an adiabatic transition to a single mode in the rectangular guide is excessive (approximately 17.78 cm). Instead, we construct this taper from three sections as shown in Fig 4.

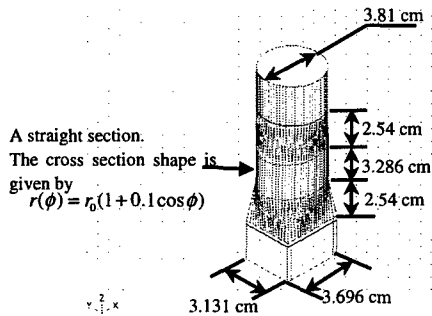


Fig. 4. The design of a  $TE_{01}$  Circular to  $TE_{02}$  Rectangular Taper.

The middle section is a cylinder with the following shape

$$r_2(\phi) = r_0(1 + 0.1 \cos 2\phi); \quad (2)$$

where  $r_0$  is the radius of the circular guide. The dimensions of the rectangular guide is chosen such that the rectangular cross section satisfies the following equation

$$r_3(\phi) = r_0(1 + 0.1 \cos \phi + \sum_{i=2}^{\infty} \alpha_i \cos 2i\phi); \quad (3)$$

where the coefficients  $\alpha_i$  are chosen to produce a rectangular shape.

The taper from the circle to the intermediate shape scatters the  $TE_{01}$  mode into two modes  $M_1$  and  $M_2$  in the intermediate section. Also the taper between the rectangular waveguide to the intermediate shape scatters the rectangular mode  $TE_{02}$  into  $M_1$  and  $M_2$ . The lengths of both tapers are adjusted such that the magnitude of the coefficients of the scattered modes  $M_1$  and  $M_2$  are the same from both sides. Since  $M_1$  and  $M_2$  propagate with different phase velocities in the intermediate section, the length of that section could be adjusted so that the circular  $TE_{01}$  mode get completely converted into the rectangular  $TE_{02}$  mode.

Fig. 5 shows the simulated performance of that taper. The coupling to the cross-polarized mode is below 20dB. Further refinement of the design could be made to reduce this level further.

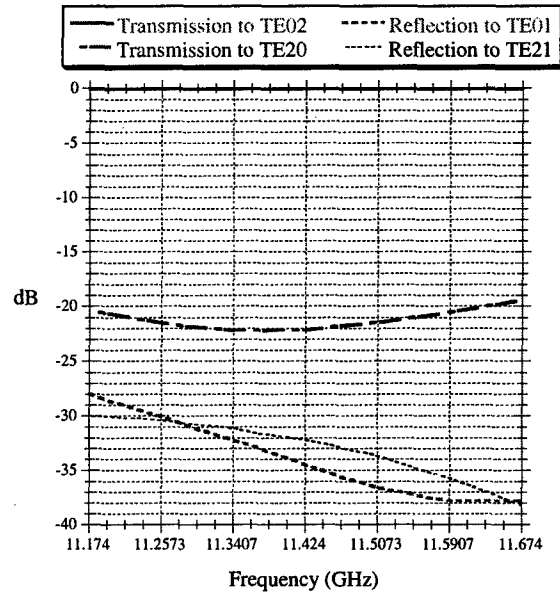


Fig. 5 Simulated performance of type 3 taper

## 4 CONCLUSION

We presented a set of smooth transitions from rectangular to circular waveguide. These transition maps modes from circular guides into modes in rectangular guides with one to one model connection. We showed that these tapers could be quite compact and efficient. These tapers could be used in a variety of applications for designing over-moded microwave components. All rf manipulations could be made in the more easily handled rectangular waveguide, while tapering back and forth to circular waveguide.

## 5 ACKNOWLEDGMENT

The authors wish to thank Z. D. Farkas, P.B. Wilson, R. M. Miller and R. D. Ruth for many useful discussions.

## 6 REFERENCES

- [1] The NLC Design Group "Zeroth-Order Design Report for the Next Linear Collider," SLAC-Report-474, May 1996.
- [2] S.G. Tantawi, et al. "A Multi-Moded RF Delay Line Distribution System for the Next Linear Collider," to be published in the proc. of the Eighth Workshop on Advanced Accelerator Concepts, Baltimore, MD, USA 6-11 Jul 1998.
- [3] "HP High-Frequency Structure Simulator," HP EEsof, Hewlett Packard.
- [4] AutoCAD, Copyright 1982-1998, Autodesk, Inc.

# A SAMPLED MASTER OSCILLATOR FOR THE PEP-II B FACTORY\*

R. C. Tighe<sup>#</sup>, SLAC, Stanford, CA

## Abstract

A sampled phase-locked loop synchronizes the PEP-II B Factory rings to their SLAC Linac injector. The injection of both electrons and positrons into the separate rings and into their proper RF buckets requires phase shifting the linac RF with respect to the PEP rings. One of every three machine cycles provides the PEP ring an undisturbed reference while the other two thirds of the time the reference is unusable due to the injection scheme. The ring RF must be tunable about its nominal frequency for machine physics use. A sampled phase-locked loop handles the task of synchronizing the PEP-II RF to the linac while maintaining good phase noise. The input reference is sampled at 120 Hz and provides a ring RF signal with less than  $0.1^\circ$  of rms phase jitter at 476 MHz.

## 1 REQUIREMENTS

The PEP-II master oscillator provides the RF reference for the RF system [1], the beam feedback systems, tune monitor, and other timing needs. The design criterion for the tolerance on phase noise was the collision point offset.

During commissioning a tighter tolerance was found to be imposed by the longitudinal feedback; so the performance specification has been driven by that.

Ring RF with low phase jitter must be derived from the SLAC Linac drive signal which contains fiducials and an interferometer signal. The task is complicated by the injection scheme which shifts the phase of the linac drive signal according to the target ring and bucket of the injection bunch. The phase reference is left undisturbed for 2.8 ms of every 8.3 ms for locking the ring RF to the injection linac.

In addition to the phase shifting mentioned above, double-height, single-cycle fiducials are broadcast every 2.8 ms for machine timing use. A linac interferometer signal is superimposed on the RF for phase length stabilization. There is a 500  $\mu$ s period when the bunch is in the linac when the interferometer and fiducial are not present in order to provide unmodulated RF for the linac klystrons. It is during one of every three of these periods that the PEP-II master oscillator samples the linac RF for phase locking.

The master oscillator must provide frequency tunability, smooth unlocking for tuning, and smooth locking for maintaining beam.

## 2 ARCHITECTURE

The PEP-II Master Oscillator resides in the region 8 control room of the PEP-II ring. It takes linac RF as its input and produces RF fanned out for use by the RF, feedback, and timing systems, see figure 1. The designation of master oscillator is perhaps a misnomer as it actually slaves off of the linac RF.

The system consists of two second-order phase-locked loops (PLLs). The sampling first loop creates a 59.5 MHz clock with a voltage controlled crystal oscillator (VCXO). This 59.5 MHz serves as the reference for the continuous second loop which controls a voltage-controlled surface acoustic wave oscillator (SAW) running at 476 MHz. The close-in phase noise of the crystal, even after multiplication is better than the SAW oscillator's phase noise at lower frequencies.

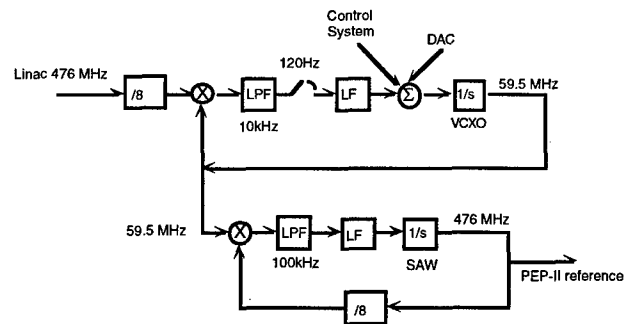


Figure 1. System Block Diagram

Most PLLs are continuous-time, closed-loop feedback systems. The nature of the PEP-II reference dictates a sampled feedback system. A low sample rate (120 Hz) restricts the available gain in the loop in order to maintain stability. The loop bandwidth must be less than the Nyquist frequency of 60 Hz. The ability to track the reference is therefore compromised. Fortunately the reference is fixed and thus only the lowest frequency behavior must be matched. The challenge is to lock with such low bandwidth and produce clean RF for the rings.

### 2.1 The Use of Two Loops

The loop gain in the first PLL is defined by three gain terms and the loop filter chosen. The required tuning range for machine physics and the sample rate define a frequency by which the open loop gain must be reduced to unity for stability of the sampled loop. In order to provide  $\pm 10$  kHz of tuning range, the VCO selected has 60 ppm tuning sensitivity which defines the gain,  $K_{vco}$  (see figure 2). The digital phase/frequency detector has a gain of

\*Work supported by DOE contract DE-AC03-76SF00515

<sup>#</sup> Email: rtighe@slac.stanford.edu

0.302V/rad. The divider ratio in the feedback is settable within a range specified by the phase-locked loop chip chosen [2]. Using the notation of e.g. [3], the loop filter is designed to provide a lead-lag effect that provides phase margin to the loop.

The tuning range and sample rate require attenuation in the loop in order to maintain stability. A better method to preserve signal-to-noise quality is for the first loop to produce an intermediate frequency which is multiplied by a second phase-locked loop. In this way, no analog attenuation, excessive component values or divider ratios (which bring about additional noise) are used. The key is to produce a low phase noise intermediate frequency which is multiplied, along with the phase noise, to 476 MHz by the second loop. The sample and hold operation introduces a 30° phase lag at 10 Hz, so in order to achieve adequate phase margin the loop bandwidth must be kept low.

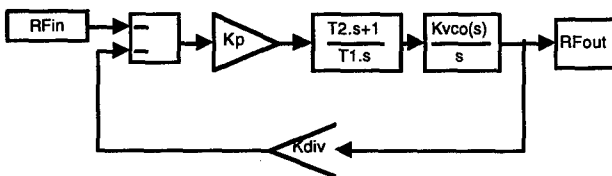


Figure 2. PLL Block Diagram

In a sampled system an antialiasing filter is used to prevent out of band information aliasing into the feedback loop. In this case the lowest bandwidth lowpass, antialiasing filter that can be used is one whose rise time must be short compared to the time span between the phase-shifted reference and the non-shifted reference to the loop. A low pass filter with 35  $\mu$ s rise time is used. The rise time of a proper antialiasing filter would be nearly 6 ms and would integrate unusable reference signals along with the desired portion of the reference.

## 2.2 Phase Noise Apportionment

Three distinct phase noise regions contribute to the output spectrum. The first loop tracks the reference phase noise up to the extent of its bandwidth, defining the close-in phase noise of the master oscillator. The second loop tracks the first oscillator's phase noise through the second loop's bandwidth. Finally, above the second loop's bandwidth the noise is due to the final oscillator's phase noise. The SAW oscillator has a fairly low bandwidth for modulation and therefore the second loop's bandwidth is lower than would be desired from examining the optimum bandwidth based on where the first and second oscillator's phase noises cross.

The low bandwidth of the first loop means that extra care must be taken to prevent noise from reaching the first oscillator since above 60 Hz there is no disturbance rejection. Any noise imparted on the low frequencies of the first loop are dutifully reproduced by the second loop. The DC power supplies are placed in a separate chassis

from the PLL circuitry for this reason. Fans for cooling are in this second chassis as well.

A signal isolation problem with the layout of the circuitry in the original design led to excess phase noise on the ring RF. A small amount of the phase-shifted reference was picked up on the clean intermediate frequency which was reproduced on the output of the second PLL. This was fixed by separating the PLL functions onto two circuit boards.

A second improvement was to use a higher frequency crystal allowing for a smaller multiplication factor leading to lower overall phase noise. The noise floor of the crystal outside the first loop's bandwidth is multiplied by the second loop within that loop's bandwidth.

## 2.3 Additional Features

The ring RF must be capable of running unlocked from the linac reference to vary the frequency of the rings for machine physics. The locking and unlocking procedure must be sufficiently smooth so that beam is not lost. To enable unlocking, the system has a DAC which provides the nominal voltage to the first VCO in order to produce the correct 476 MHz. The phase-locked loop provides correction about this DC value. An additional DAC is provided to allow the control system to drive the VCO in the unlocked state.

The three clocks in the system (linac reference and two VCOs) are all monitored. Should any clock fail, the loop will unlock and a flag is set in the PEP-II control system. A lock indicator is provided for the first loop. Analog signals like the first loop's raw phase error, the first loop's sampled and held phase error, and the second VCO's tuning voltage are also monitored in the control system.

# 3 PERFORMANCE

## 3.1 Jitter Analysis

A phase noise spurious sideband of low modulation index produces phase jitter according to:

$$\phi_{\text{rms}}^2 = 2\mathcal{L}(f) \quad (1)$$

where  $\mathcal{L}(f)$  is the single-sideband phase noise to carrier ratio per Hz, usually presented logarithmically in dBc/Hz [4].

The largest spur is the one at the phase shift rate which is -90 dBc/Hz. This produces only 0.0036° of phase jitter. The phase-shifted linac reference leaks onto the reference to the second PLL and leads to this spur.

It is the integrated phase noise spectral density that leads to the bulk of the phase jitter. The relation for finding the rms phase jitter for a given single-sideband spectral density is:

$$\phi_{rms}^2 = \int_{f1}^{f2} 2 \mathcal{L}(f) df \quad (2)$$

where  $f1$  and  $f2$  are the starting and ending frequencies of interest, respectively.

Presently, the phase noise spectral density is  $< -100$  dBc/Hz at 300 Hz and is lower at higher frequencies as shown in figure 3. The integration of the spectrum leads to  $0.075^\circ$  rms phase jitter on the RF. At 476 MHz this is 0.44 ps of timing jitter. The noise floor of the spectrum analyzer is comparable to the spectrum observed when measuring the master oscillator output. The calculation is therefore a worst case value. As the PEP-II bunch length is 1 cm or  $5.7^\circ$ , the rms jitter equates to about 1.3% of the bunch length.

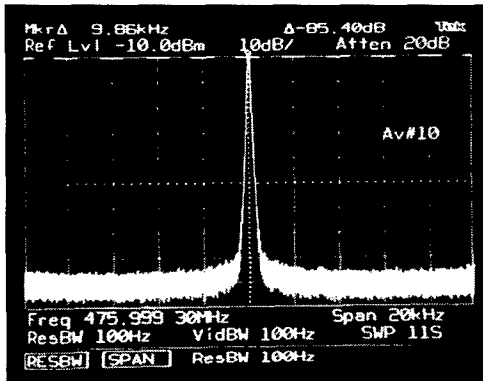


Figure 3. PEP-II RF Spectrum

The spectral density of the 59.5 MHz output is difficult to measure directly because the spectrum analyzer noise floor is higher than that of the 59.5 MHz signal. This is confirmed by noting that the 476 MHz measurement has essentially the same characteristics at the higher frequency, when it is expected to be degraded by  $20 \cdot \log(N)$ , where  $N$  is 8 leading to a degradation of 18 dB. The two measured spectra are comparable, for example, at a 1 kHz offset, confirming that spectrum analyzer limitations are being observed. The spectrum is better than that of its reference since the reference is produced by multiplying a 8.5 MHz crystal to 476 MHz. The specification for the present SLAC linac crystal is  $-135$  dBc/Hz at 1 kHz which when multiplied by 56 adds 35 dB. An imminent upgrade of the SLAC linac crystal should bring about an improvement to the PEP-II spectrum at low frequencies in the bandwidth of the first loop.

### 3.2 Jitter on the Beam

The rms beam motion is the integration of the product of the spectral density in Eq. 2 and the absolute value of the beam phase transfer function as shown in Eq. 3. and plotted in figure 4,

$$\phi_{rms}^2 = \int_{f1}^{f2} 2 \left| \frac{\omega_s^2}{(j2\pi f)^2 + \frac{j2\pi f \omega_s}{Q} + \omega_s^2} \right| \mathcal{L}(f) df \quad (3)$$

where  $\omega_s$  is the synchrotron frequency,  $Q$  is  $\tau \cdot \omega_s / 2$ , where  $\tau$  is the radiation damping time [5].

Using this calculation with the phase noise density and the beam phase transfer function indicates that the synchrotron resonance has a slight amplification effect on the phase noise transmitted to the beam.

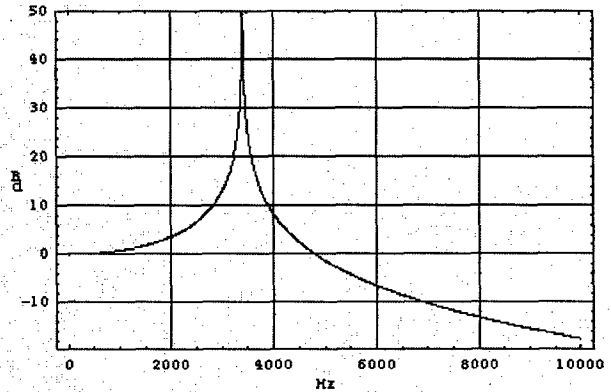


Figure 4. RF Phase to Beam Phase Response

Integrating the expression in equation (3) for the two PEP-II beams leads to  $0.099^\circ$  rms jitter for the LER and  $0.107^\circ$  for the HER.

Measurements in PEP-II before the modifications described here (circuit separation, higher frequency VCXO) indicated longitudinal beam motion of less than  $0.3^\circ$  in each ring. Before improvements to the layout, when the effects of the phase shifting were felt, motion was more than a degree. It is believed that the two modifications should bring about further improvement to the levels arrived at in this paper.

## 4 CONCLUSION

Using two phase-locked loops in succession, the PEP-II Master Oscillator provides a low jitter RF source for the RF, timing, and feedback systems.

## 5 REFERENCES

- [1] P. L. Corredoura, "Architecture and Performance of the PEP-II Low-Level RF System", these proceedings.
- [2] Qualcomm Q3236 Phase-locked Loop Frequency Synthesizer, Qualcomm Incorporated, San Diego, California 92121.
- [3] VCO Designer's Handbook, VCO-97-1, Mini-Circuits, Brooklyn, NY 11235
- [4] Hewlett Packard Product Note 11729C-2, "Phase Noise Characterization of Microwave Oscillators, Frequency Discrimination Method"
- [5] J.M. Byrd, "Effects of Phase Noise in Heavily Beam Loaded Storage Rings", these proceedings.

# COMMISSIONING AND PERFORMANCE OF LOW IMPEDANCE ELECTROSTATIC SEPARATORS FOR HIGH LUMINOSITY AT CESR<sup>\*</sup>

J.J. Welch G.W. Codner W. Lou<sup>†</sup> Cornell University, Ithaca NY

## 1 INTRODUCTION

Electrostatic separators have been used extensively for a number of years in colliding beam storage rings because of their ability to generate closed orbits displacements which are of opposite sign depending on the charge of the stored beams, [1], [2], [3], [4] As higher beam currents became more in demand, it was realized that separators could provide a means of multiplying the maximum beam current without needing to build a second ring to avoid unwanted collisions that additional bunches would make [5]. Much higher beam currents have resulted and have in turn placed new demands on the separator performance. To this end four new horizontal separators were designed and installed in CESR at Cornell in the fall of 1995. As of the end of 1998 they have operated with beams of up to 300 mA per beam. Next year they will be required to work at 500 mA per beam. This paper reviews their performance, especially under high current conditions.

## 2 DESCRIPTION

At CESR six electrostatic separators generate closed-orbit displacements 'pretzels', which weave back and forth around the ring. These pretzels allow the electrons and positrons to simultaneously be stored in the same vacuum chamber without destructive unwanted collisions. The lobes of the pretzel and the distribution of the bunches in the beams are carefully designed to give good separation at the numerous bunch crossing points. Four of the six separators are horizontal separators and these are the subject of this paper. The two vertical separators will not be discussed further.

The four horizontal separators are all identical<sup>1</sup> and consist of 3 m long high voltage (HV) electrodes parallel to the beam. See Figure 1. Operating voltages of  $\pm 85$  kV are applied to the electrodes to produce a uniform horizontal electric field of approximately 2 MV/m.

The design of the separators attempted to minimize the interaction of the beam induced electromagnetic fields as well as improving the high voltage behavior. Extra 'ground electrodes' which are not needed to make the electric field, serve to confine the beam induced fields to the beam axis. These have been shown to reduce the overall loss factor by about one half. Also the ends of the vacuum chamber are

continuously tapered and the ground electrodes smoothly joined to the ends with good rf contacts. These features gave another reduction in loss factor by about one half.

Another design issue was to limit the photoelectron current generated when synchrotron radiation (SR) strikes either the negative electrode or a part of the chamber at ground potential but with a negative electric field at the surface. Previous experience had shown that the photocurrent are usually much larger than the high voltage field emission currents, and present technical demands for the power supply and electrode cooling.

## 3 PERFORMANCE

Overall the separators have been one of most reliable systems in the accelerator. Performance issues are dominated by the effects of RF power produced by the beams and photoelectron current.

### 3.1 Beam RF Resonances

A typical bunch length in CESR is 1.8 cm and is much smaller than structures inside separators. So there are a multitude of possible resonances which may effectively couple to the beam. If nothing were done to damp these resonances, RF fields would rapidly build up until RF breakdown occurs, and indeed damage from such arcing has been observed [7]. Intense resonant fields have another deleterious effect in that they can degrade beam stability. Fortunately the vast majority of the resonances couple to the electrodes and the high voltage cables. In the CESR separators beam induced RF fields are propagated along the electrodes and HV cables to high power absorbers about 2 m from the vacuum feedthrough. away, where the RF power is dissipated as heat.

The electrodes and HV cables form a transmission line structure and will therefore propagate all frequencies as TEM waves. However, not all resonances are necessarily effectively damped. Because of various unavoidable impedance mis-matches between the cables, terminations, feedthroughs and electrode structure, standing waves can form on the high voltage cable. If a standing wave happens to have a current node at the location of the high power assembly, then the absorber would be ineffective and a high RF field level can result. This situation has occurred on at least two times at CESR. In the first occasion high RF currents built up and melted the connector between the HV cable and the separator. In the second case high RF voltage

<sup>\*</sup> Supported by the National Science Foundation

<sup>†</sup> Formally of Cornell, now at ADC Telecommunications, CT

<sup>1</sup> One separator has an additional external resistor for faster bleed-down

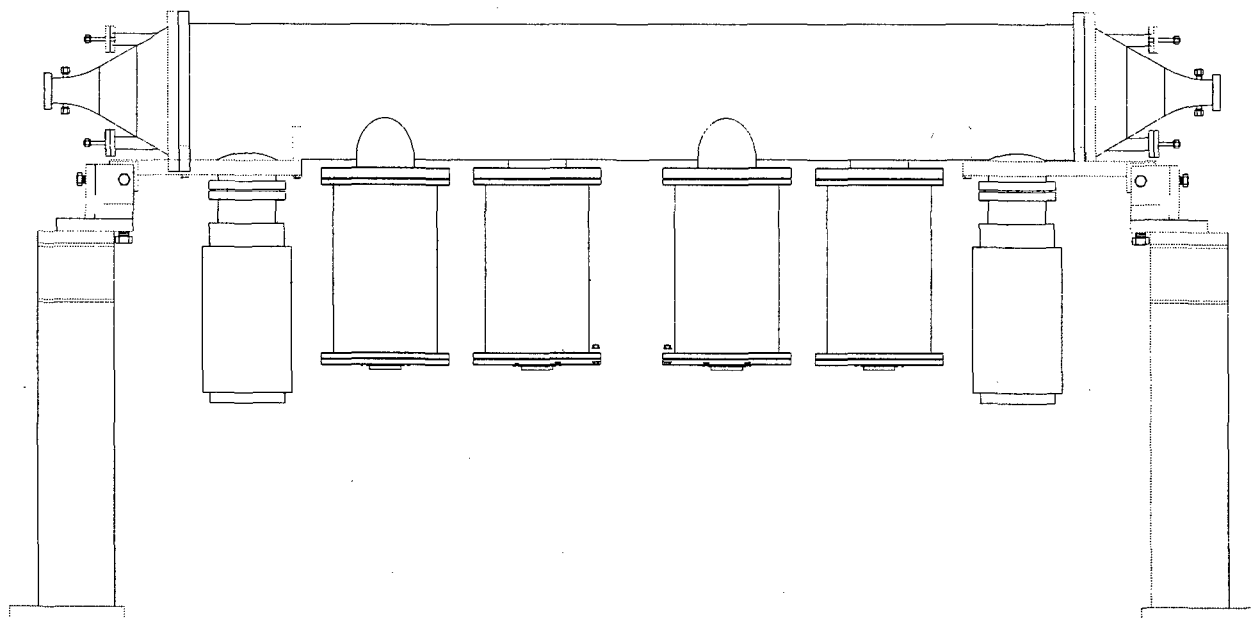


Figure 1: Low impedance electrostatic separator at CESR.

built up and caused repeated failures (HV tracking) across the HV connector about 3 m from the separator. In both cases, the problem was eliminated by changing the length of the cables, basically by trial and error, until one was found which didn't have the unfortunate phase at the absorber assembly.

### 3.2 Loss Factor Measurement

The "loss factor" is defined as the average electromagnetic energy (mainly RF) left behind by a bunch divided by the bunch charge squared. It is measured using calorimetry. The RF absorbers are cooled by essentially boiling in a bath of liquid freon (TF-113). Freon is also circulated in a closed loop to cool the electrodes and feedthroughs, and the heat is removed via a heat exchanger. The difference between the input and output temperature at the heat exchanger together with the flow rate is used to estimate the total heat being taken up by the freon system. Assuming all beam RF power is ultimately absorbed in the freon, loss factors  $k$  were calculated and given in Table 1. These measurements indicate the overall loss factor is low, as expected from impedance measurements on mock-ups [6].

A significant amount of power generated by photocurrents driven by the high voltage power supplies causes some overestimate of the loss factor. On the other hand, there is also some cooling of the body of the separator by tunnel air which is not accounted for in this calculation and would tend to underestimate the loss factor. Limits on the overestimation of loss factor can be determined from measured HV power supply currents and voltages. Photoelectrons striking the positive electrodes ultimately transfer their energy to the freon cooling. The photoelectron kinetic energy at impact will either be equal to the electrode volt-

Table 1: Beam RF loss factors  $k$  averaged over one day with typical currents of 190 mA/beam 36 bunches. Also given is the calculated beam RF power at higher current levels. The average daily power during the measurement in the 45W separator was 800 W.

Name	$k[V/pC]$	Power [W]	Power [W]
		300 mA	500 mA
8E	0.11	1918	3196
45E	0.13	1837	3061
45W	0.14	2439	4065
8W	0.11	2281	3802
Ave.	0.124	2119	3531

age or double it, depending on whether it originates at a grounded surface or on the negative electrode. For the 45W separator this works out to a range of between 120 W and 240 W, amounting to 15-30% of the total power.

### 3.3 Synchrotron Radiation and Photoelectron Current

Because synchrotron radiation cuts a swath in the horizontal plane, the electrodes for the horizontal separators are made in two pieces with the midplane missing. See Figure 2. A small bridge connects the upper and lower halves and is masked by apertures at the end of the separators, so direct synchrotron radiation cannot strike the electrodes. Nevertheless a strong photoelectron current is observed, so the photoelectrons must be generated by scattered radiation. The scattered SR photons come from two sources: scattered photons from the SR absorbers built into the sep-



Figure 2: The electrode structure of the CESR separators.

Table 2: Coefficients which determine the high voltage power supply photocurrent from the electron and positron currents in the machine. The definition of the terms is  $I_{ps} = \alpha I_{positron} + \beta I_{electron}$

Separator	$\alpha+$	$\beta+$	$\alpha-$	$\beta-$
8E	0.0018	0.0012	0.0028	0.0006
45E	0.0074	0.0059	0.0018	0.0004
45W	0.0074	0.0007	0.0142	0.0022
8W	0.0009	0.0024	0.0000	0.0000

arators, and SR scattered photons from adjacent vacuum chambers. It appears that the latter dominates at CESR.

Interpretation of power supply current as photocurrent is straightforward. The power supply current is almost independent of voltage above a few kV. It is quite linearly proportional to beam current. In most cases it is much larger the field emission current. The photocurrents depend somewhat on the closed orbit and the photoemission coefficients are not constant in time. However, these effects are at the 50% level or less. The linearity with beam current is diagnostic and was used to determine coefficients of photocurrent versus beam current given in Table 2. The data was based on one day of high current running. With no beam the current drawn is about 0.03 mA on each supply.

### 3.4 Spark rate

Low spark rate is critical to efficient operation of the storage ring. In the past high spark rates have been obtained episodically; that is they come in groups. In some cases sparks have been attributed to failing cables or connectors, but in most cases the cause was either a vacuum arc, or an arc on the power supply side of the spark detector whose cause was undetermined. During the first two years of operation the spark rate was much higher, typically 1 spark per day per separator. After new high voltage power supplies were installed the rate dropped dramatically. It is not clear

why this occurred but a prime suspect is that control electronics (which were replaced with the new supplies) may have been turning off the supplies unnecessarily. There does not seem to be any general correlation with beam current though occasionally it was observed in the past. At the present time the spark rate is practically negligible. In the past three months of operation there was only one recorded spark that caused significant beam loss.

### 3.5 Other Operational Issues

A few miscellaneous issues are discussed in this section. Not long after the separators were installed, the Clean Air Act was revised to include many new procedures and restriction on freon usage because it is an ozone depleter. We chose to keep Freon 113 as the primary coolant/dielectric fluid, as no other alternate could perform as well in the RF absorbers. It was necessary to rebuild the plumbing systems to make them 'hard sealed' and preserve the existing freon supplies. Since then, freon loss rates have been negligible and the freon has served well. Radiation damage to a HV power supply occurred several times at one location, until it was understood what was happening. Voltage slewing rate when dropping voltage has been of concern. Most power supplies have a high photocurrent drain load on the power supplies and as a result bleed down rapidly. One separator is apparently well shielded from SR and required an external resistor shunting about 1 mA for good bleed down times.

## 4 REFERENCES

- [1] D.L. Rubin, *CESR Status and Plans*, (PAC95), vol. 1, pp 481f, CBN 95-8 <http://www.lns.cornell.edu/public/CBN>
- [2] W. Kalbreier, N. Garrel, R. Guinard, R.L. Keizer, K.H. Kissler, *Layout, Design, and Construction of the Electrostatic Separator System of the LEP  $e^+e^-$  Collider*, Proc. EPAC, vol 2, June 1988, or CERN SPS/88-20 (ABT)
- [3] T. Shintake, Y. Suetsugu, K. Mori, M. Sato, T. Higo, *Design and Construction of Electrostatic Separators for TRISTAN Main Ring*, KEK Report 88-17, March 1989 A.
- [4] B. Goddard, *Separator Performance with Bunch Trains and Pretzel*, Proc. 6th LEP Performance Workshop, Chamonix, (1996)
- [5] R.M. Littauer, B.D. Mcdaniel, D. Morse and D.H. Rice, "Proposed Multibunch Operation Of Cest," IN \*BATAVIA 1983, PROCEEDINGS, HIGH ENERGY ACCELERATORS\*, 161-163. .
- [6] J.J. Welch, Z.X. Xu, *Low Loss Parameter for New CESR Electrostatic Separators*, Proc IEEE Particle Accelerator Conference, May 1991, vol 3., pp 1851f.
- [7] J.J. Welch, *High Voltage Sparking in a Decommissioned CESR Horizontal Separator*, CBN 94-7, <http://www.lns.cornell.edu/public/CBN/1994>
- [8] Personal communication.

# PROTON BEAM VERIFICATION USING RF POWER MEASUREMENT DATA FOR A CW RADIO FREQUENCY QUADRUPOLE LINAC\*

G.O. Bolme, L.D. Hansborough, T.W. Hardek, D.J. Hodgkins, D.R. Keffeler, J.D. Sherman,  
H.V. Smith, R.R. Stevens, L.M. Young, T.J. Zaugg, LANL, Los Alamos, NM  
A.H. Arvin, A.S. Bolt, M.C. Richards, Savannah River Site, Aiken, SC  
P.P. Balleyguier, CEA-Bruyeres le Chatel, France  
J.H. Kamperschroer, GA, San Diego, CA

## Abstract

A cw radio frequency quadrupole (RFQ) LINAC section and klystron based rf system was obtained from the Chalk River Laboratories and was recommissioned at LANL to conduct demonstration proton beam experiments in support of a spallation neutron source driver for tritium production. A variation of the Low Energy Demonstration Accelerator (LEDA) proton injector, modified to operate at 50 keV, was mated to the RFQ and was operated to support the high current (up to 100 mA), proton beam advance studies for the Accelerator Production of Tritium (APT) program. Detailed measurements and calibrations of the RFQ at both low and high power provided the corroborating data to other available beam measurements for verification of the accelerator design.

## 1 INTRODUCTION

The Chalk River Injector Test Stand (CRITS) was the LANL designation given to a proton accelerator designed, built, and originally commissioned at the Chalk River Laboratories (CRL) in Canada [1]. The CRITS accelerator apparatus includes a 1.25 MeV RFQ accelerator structure and a prototype klystron-based rf system for powering the RFQ. An earlier independent study at LANL, utilizing the RFQ, focussed on the high-power operation of the rf structure [2].

The LEDA program has the objective of developing a high-current, cw injector and the initial rf accelerating structures for APT. The LEDA injector is comprised of the proton ion source and a Low Energy Beam Transport (LEBT) section to the RFQ. A 75 kV cw proton ion source was developed for LEDA and has produced a proton beam with measured current and emittance meeting program requirements. A state-of-the-art LEBT was designed and built to match the ion source beam to the LEDA RFQ [3].

The functionality of an injector is best confirmed by injecting its beam into an RFQ. The availability of the CRITS RFQ provided the opportunity for an initial shakedown of the LEDA injector prior to installing the injector as a LEDA subsystem. The modification of the ion source to 50 kV and adaptation of the LEBT exit

section to the CRITS RFQ made the LEDA injector/CRITS RFQ configuration a realistic testbed for this injector development. Furthermore, this configuration also supported RFQ experiments to evaluate the system modeling codes and to learn the details of cw RFQ operations. Figure 1 shows the full beamline used in this project.

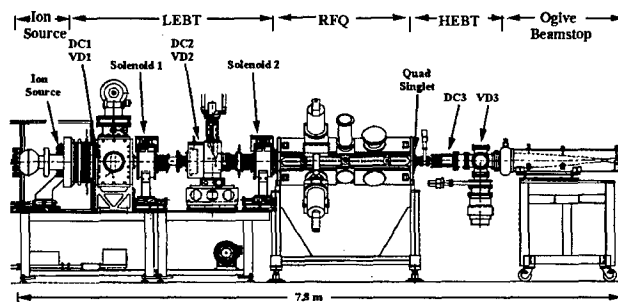


Figure 1: The LEDA Injector/CRITS RFQ beamline.

In order to meet the project objectives, the RFQ specific studies focussed on verifying the RFQ field configuration, successfully operating the RFQ at high power, verifying the accelerating fields in the RFQ, and accelerating the proton beam from the modified LEDA injector.

## 2 RFQ FIELD DISTRIBUTIONS

Although the Q and resonant frequency of the RFQ were close to the expected values following shipment of the RFQ from CRL, the verification of the modeling codes mandated that the field distribution in the structure be confirmed. A perturbation measurement of the cavity fields was made by inserting a probe through the various vacuum pumping holes in each of the quadrants, and the dipole field contributions to the quadrupole fields were calculated from these measurements. The uncorrected dipole fields across quadrants 1 and 3 (dipole 1) were measured to be up to 14% of the quadrupole field and up to 8% across quadrants 2 and 4 (dipole 2). The dipole field distribution along the RFQ length indicated that the vane coupling rings near the ends held the distribution close to the desired quadrupole configuration, thus, dipole field reduction at the center should achieve an acceptable field pattern in the RFQ. Adjustment of movable tuners in quadrants 2 and 4 and modification of the fixed tuner in quadrant 3 corrected the field distribution to less than 4%

\*Work supported by the US Department of Energy.



dipole contribution. This was considered acceptable for the beam studies. Figures 2 and 3 display the corrected and uncorrected dipole contributions for dipoles 1 and 2 respectively.

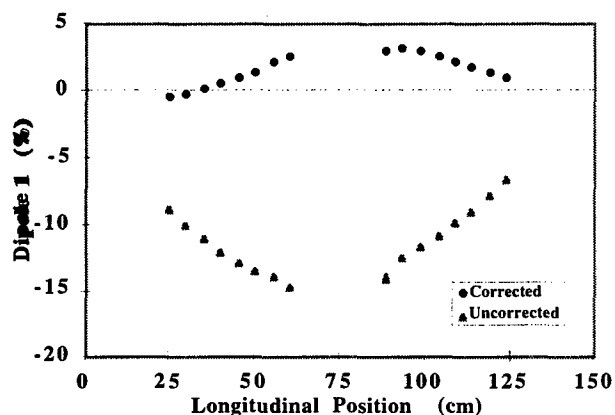


Figure 2: Dipole 1 Contribution to the quadrupole field distribution.

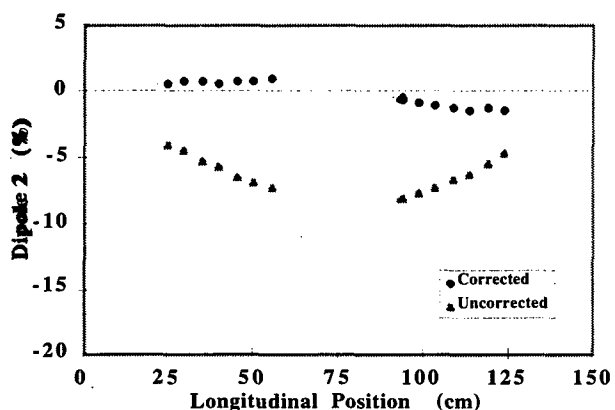


Figure 3: Dipole 2 Contribution to the quadrupole field distribution.

### 3 CALIBRATIONS

Accurate predictions of the acceleration and focusing fields require consistent measurements of the RFQ response to rf power. The RFQ driveline coupling and Q were measured using a Hewlett Packard 8753 Network Analyzer. The driveline coupling was verified from subsequent high power measurements. The Q was measured using reflected power, transmitted bandwidth, and transmitted delta phase techniques as shown in Figures 4, 5, and 6. The close agreement in Q measurements is shown in Table 1.

Table 1: Measured RFQ Q values

Measurement	Loaded Q	Unloaded Q
Reflected Power		6780
Transmitted Bandwidth	2650	6760
Transmitted Delta Phase	2640	6720

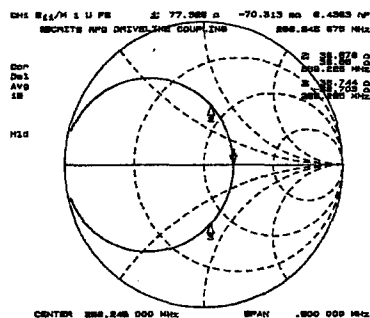


Figure 4: Reflected power Q measurement.

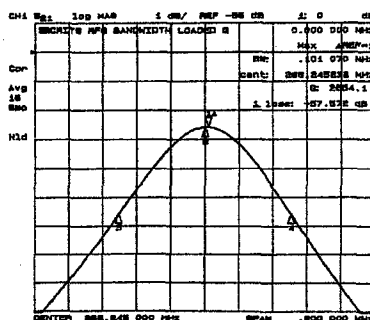


Figure 5: Transmitted bandwidth Q measurement.

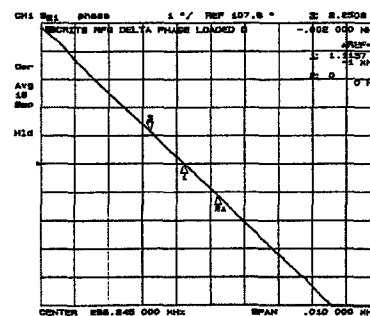


Figure 6: Transmitted delta phase Q measurement.

The calibrations of the field sampling loops were also completed using a Hewlett Packard 8753 Network Analyzer, and the rf signals from these loops at high power were monitored using power meters and oscilloscope measurements of the unrectified rf signals. Again, the measurement of forward, reflected, and RFQ cavity powers by Hewlett Packard 438A power meters and a Tektronix 2465A oscilloscope provided redundancy in the high-power measurements.

### 4 HIGH-POWER FIELD LEVEL VERIFICATION

The RFQ was conditioned to high power based on the SUPERFISH prediction of the design power level. High-power measurements of the actual field level were made using the x-ray endpoint method [4], a technique pioneered

by accelerator scientists at CRL. Measurements made throughout the duration of the proton beam studies verified that the peak intervane gap voltage tracked the measured power levels according to the expected square root dependency, and comparisons of the power meter to the oscilloscope measurements confirm an estimated  $\pm 5\%$  accuracy to the power measurements. Furthermore, the field levels were measured to be the same when the proton beam was being accelerated by the RFQ. Figure 7 displays the gap voltage data and the curve used to project the peak intervane gap voltage as a function of the measured power.

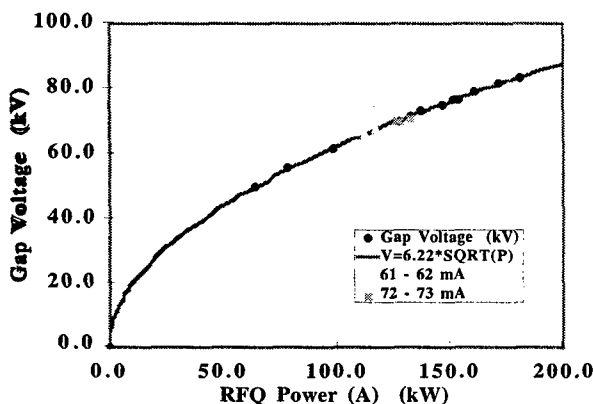


Figure 7: Peak intervane gap voltage as a function of RFQ cavity power.

## 5 PROTON BEAM MEASUREMENTS

The proton beam studies with the RFQ proceeded cautiously by increasing current only as the injector match to the RFQ could be confirmed by the beam transmission. The desired field level for the RFQ was set from the x-ray endpoint measurement, but a measurement of beam transmission as a function of the RFQ cavity power was also used to confirm the expected behavior. As expected, a knee in the transmission curve was observed below the design field level.

As a separate check for accelerated beam, the incident power difference and beam stop calorimetry were compared to the expected beam power under the assumption that the entire proton beam was accelerated. Although this assumption is known to be false, this calculation does allow us to compare the beam transmission data with the two beam power measurements using the same units. These data are shown in Figure 8. The rf incident power difference and calorimetry measurements of the beam as a function of RFQ cavity power show a discrepancy in absolute calibrations, but the knee in the curve for both measurements agree. The disagreement in predicted beam powers by the two diagnostic methods is probably due to the identified errors in the rf power measurements and errors in beam stop calorimetry. The lower RFQ cavity power correlated with the knee for beam transmission

compared with the other power measurements indicates that beam is transmitted even though it is not accelerated.

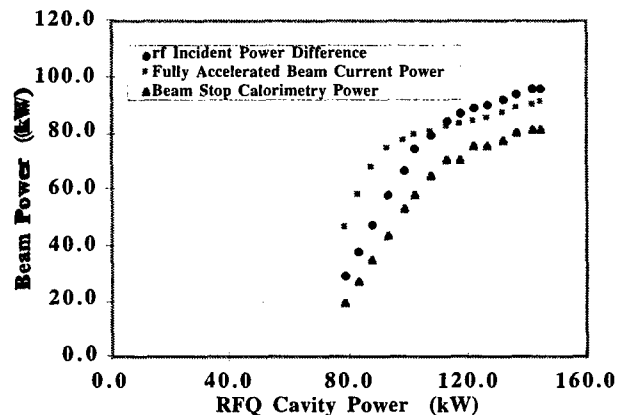


Figure 8: Peak intervane gap voltage as a function of RFQ cavity power.

## 6 SUMMARY

The CRITS RFQ proved to be an excellent test device for checking out all components of the injector. By optimizing the current through the RFQ, all injector systems demonstrated that they could operate across the required parameter space. The procedures developed during the CRITS RFQ beam operations have expedited the commissioning of LEDA. The successful transmission of beam currents with good agreement to the simulations [5] also provides confidence in the codes as we proceed into future projects.

## 7 ACKNOWLEDGMENTS

With the conclusion of the RFQ studies using the CRITS RFQ, we would like to thank and express our gratitude to the personnel at Chalk River Laboratories who designed, fabricated, assembled, and commissioned this accelerator section under the RFQ1 program. The technical progress made in our programs is a result of their groundbreaking efforts and the follow-on studies done with the equipment developed at their laboratory.

## 8 REFERENCES

- [1] J.Y. Sheikh, *et al.*, "Operation of a High-Power CW Klystrone with the RFQ1 Facility", Proc. 1993 Particle Accel. Conf., IEEE 93CH3279-7, p. 1175.
- [2] G.O. Bolme, *et al.*, "High-Power RF Operations Studies with the CRITS RFQ", Proc. 1995 Particle Accel. Conf., IEEE 95CH35843, p. 923.
- [3] J. Sherman, *et al.*, Rev. Sci. Instrum. **69** (1998) 1003-1008.
- [4] G.O. Bolme, *et al.*, "Measurement of RF Accelerator Cavity Field Levels at High Power from X-ray Emissions" in Proceedings of the 1990 Linear Accelerator Conference, LA-12004-C, 219 (1990).
- [5] H.V. Smith, *et al.*, "Comparison of Beam Simulations with Measurements for a 1.25-MeV, CW RFQ" in Proceedings of the 1998 Linear Accelerator Conference.

# SPARKING RATE STUDIES AND SPARK BREAKDOWN PROTECTION STUDIES WITH A CW RADIO FREQUENCY QUADRUPOLE LINAC\*

G.O. Bolme, J.R. Carathers, L.D. Hansborough, T.W. Hardek, D.J. Hodgkins, D.R. Keffeler, J.D. Sherman, H.V. Smith, R.R. Stevens, L.M. Young, T.J. Zaugg, LANL, Los Alamos, NM  
P.P. Balleyguier, CEA-Bruyeres le Chatel, France  
A.H. Arvin, A.S. Bolt, M.C. Richards, Savannah River Site, Aiken, SC  
J.H. Kamperschroer, GA, San Diego, CA

## Abstract

A high-current, cw linear accelerator has been proposed as a spallation neutron source driver for tritium production. Key features of this accelerator are high current (100 mA), low emittance-growth beam propagation, cw operation, high efficiency, and minimal downtime. A 268 MHz, cw radio frequency quadrupole (RFQ) LINAC section and klystron based rf system was obtained from the Chalk River Laboratories and was recommissioned at LANL to support systems development and advanced studies in support of cw, proton accelerators. System protections were previously installed to preclude damage to the RFQ at the large stored energies, high field levels, and intense powers sustained under cw operation. An rf power blanking system has proven effective in quenching the damaging, sustained arcs following structure sparkdowns. A detailed study of the sparking rate and the rf blanking parameters has demonstrated that a cw RFQ can be maintained under almost continuous operation with minimal interruptions from spark induced transients or shutdowns.

## 1 INTRODUCTION

The Chalk River Injector Test Stand (CRITS) was the LANL designation given to a proton accelerator designed, built, and originally commissioned at the Chalk River Laboratories (CRL) in Canada under the RFQ1 program [1]. The rf structure for this accelerator, shown in Figure 1, is a 1.25 MeV, 268 MHz RFQ LINAC designed to operate at 1.75 times the Kilpatrick field level. During commissioning of the rf structure, it was discovered that sparks inside the vacuum region of the RFQ system developed into arcs which were sustained by the cw power. These sustained arcs sputtered the copper in the driveline resulting in damage to the vacuum window. It was learned at CRL that providing a momentary power interruption quenched the arc and protected the system from damage.

In cooperation with the CRL commissioning team, an rf blanking module was developed at LANL which

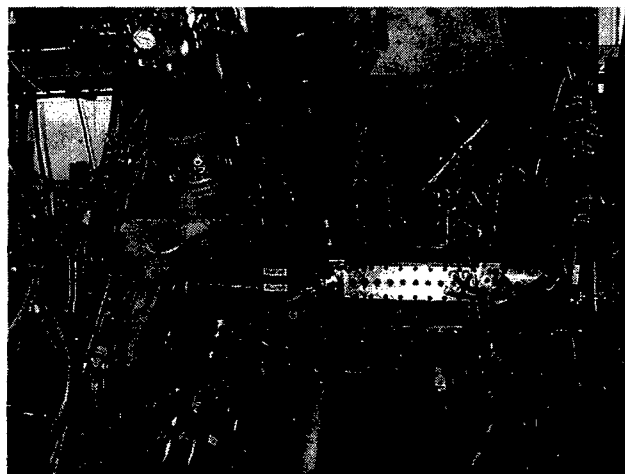


Figure 1: The CRITS RFQ accelerating structure.

interrupted power upon the detection of high VSWR (reflected power) and provided a ramped turn-on after system recovery. This module provided the necessary rf structure protections to facilitate the commissioning of the accelerator at CRL.

In 1983, the accelerator and supporting systems were shipped from CRL and reassembled at LANL to support accelerator technology development programs. During the following years, the CRITS related programs have supported high-power rf operations studies [2], injector development studies [3], cw proton beam studies [4,5,6,7], and this study of sparking rates and spark breakdown protection.

## 2 THE RF BLANKING MODULE

The rf blanking module not only provided the system protection from sustained arcs but also provided the logical signal for the counting of sparkdown rates. Key features of this module were the detection of the high VSWR, a response feature providing a brief rf OFF period, and a ramped restoration of rf power to minimize repeat sparks. Through the use of this module, power could be restored to the RFQ within 100  $\mu$ sec, a desirable feature for high-intensity cw accelerators dependent upon uninterrupted operation for rf structure stability and other

\*Work supported by the US Department of Energy.

target related considerations. Because this module protected against system damage, a key design requirement was a no-deadtime response, allowing it to protect against repetitive sparks.

During the evaluation of this module at CRL, it was determined that the optimal configuration blanked the analog amplitude setpoint rather than attenuating the rf signal between the low-level rf amplifier and the intermediate drive amplifier. The blanking function was then integrated into an amplitude setpoint control within the module for overall control of the low-level rf drive.

An RFQ cavity spark is identified by an increase in reflected power as shown in Figure 2. Figure 3 displays the setpoint response and the subsequent ramped demand signal for rf turn-on. Figures 4 and 5 show the response of the forward power and cavity field signals respectively. The gradual power increase following the sparkdown reduces reflected power, and the cavity field rises more slowly than the forward power due to the cavity fill time. As a result, the field response following a spark is gentler allowing additional cavity recovery time.

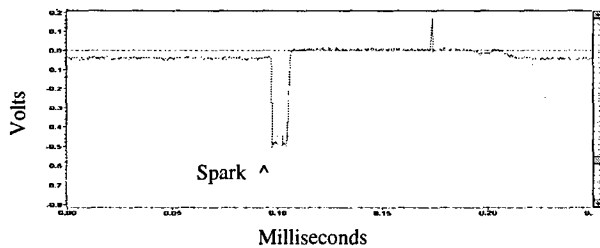


Figure 2: Rectified rf reflected power signal (negative signal) during a sparkdown.

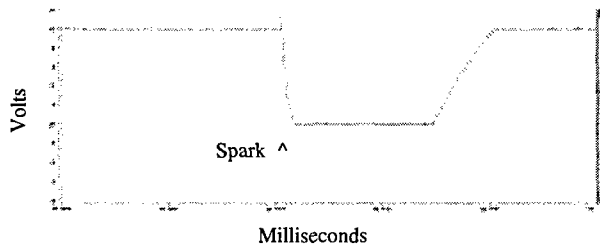


Figure 3: Setpoint signal during a sparkdown.

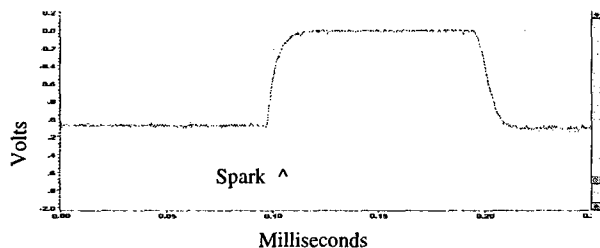


Figure 4: Rectified rf forward power signal (negative signal) during a sparkdown.

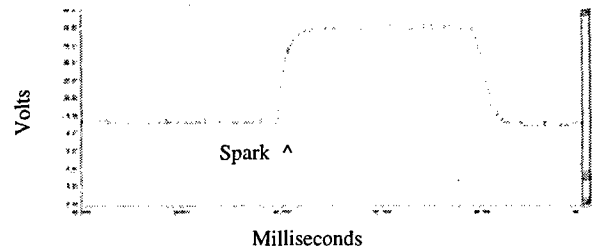


Figure 5: Rectified RFQ cavity signal (negative signal) during a sparkdown.

### 3 SPARK RATE ANALYSIS

During the CRITS RFQ operation, the total number of sparks was systematically measured and stored each second. At one minute intervals, the raw number of sparks as well as the number of seconds with at least one spark (spark-seconds) was stored. In fact, this last information is more relevant since spark avalanches do not bias it. Corresponding with the spark rates, the forward, reflected, and cavity rf power levels were also recorded along with the residual vacuum pressure. Figure 6 displays a representative data set.

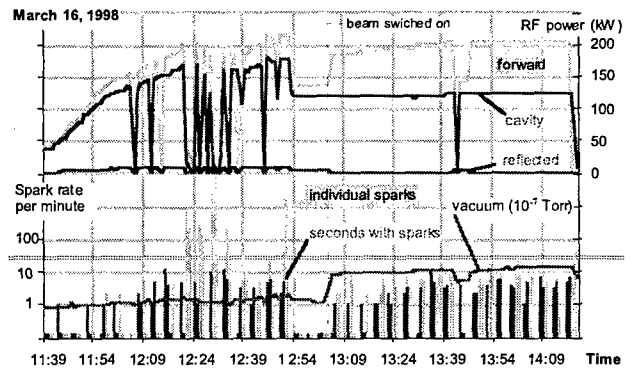


Figure 6: Example of archived rf power operations.

Long data, sets of continuous operation (between 22 and 163 minutes) have been extracted for count rate analysis - 34 runs without beam and 24 with beam. For each run, the average rate of spark-seconds was computed. As some runs yielded no sparks at all, one spark has been added arbitrarily to each data point in order to be able to plot the zero-spark points on a log scale (Figure 7).

Without beam, the rate is typically 0.3 spark-seconds per minute at the design field (77.4 kV intervane voltage), i.e. the average time between two bunches of sparks is two minutes. The slope shows that a 0.22 Kilpatrick decrement in the electric field lowers the sparking tendency by an order of magnitude.

During beam operations, the RFQ was run about 10% below the design field because of a peak rf power limitation. The rate jumped to 3.0 per minute, independent of the beam current (20 to 80 mA) and the field (1.5 to 1.7 Kilpatrick tested). This is about 6 times more than without beam at 1.75 Kilpatrick. It was established that the spark rate has some influence on vacuum, but there is no evidence of any reciprocal effect.

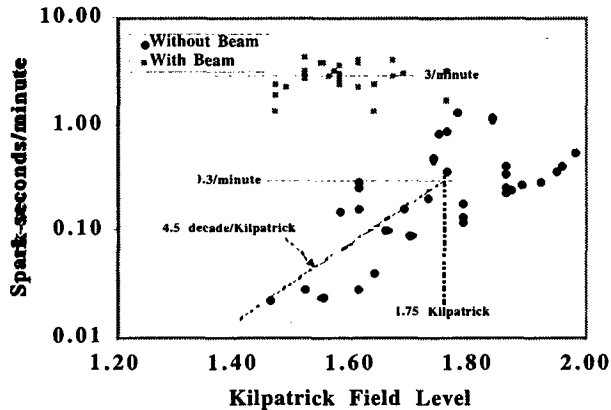


Figure 7: Spark rates during long runs.

#### 4 BLANKING PARAMETER STUDY

Since the interruption of rf power was essential for extinguishing arcs which could damage the RFQ, it was of interest to determine whether the blanking parameters, rf-off duration and rf turn-on ramp time, would have any effect on the sparking rate. Throughout the high-power studies and the proton beam operations, the blanking module adequately protected the RFQ with blanking module settings resulting in an rf-off time of 64  $\mu$ sec and a turn-on ramping time of 29  $\mu$ sec. After the beam studies were complete, a test program was commenced to evaluate the effects of these parameters.

The test sequence involved conditioning the RFQ at the beginning of each day at 1.75 Kilpatrick until stable operation was sustained for at least 15 minutes. A single parameter, blanking width or turn-on ramp, was changed and the spark rates measured for run times of 30 minutes or greater. These measurements were taken throughout the day at different parameter settings; and, at the end of each testing day, another measurement was made at the nominal settings. The blanking parameters were adjusted from settings near the fill time of the cavity up to several times that of the nominal settings. The spark rates and spark-second rates for the blanking width parameter study are shown in Figures 8 and 9, respectively.

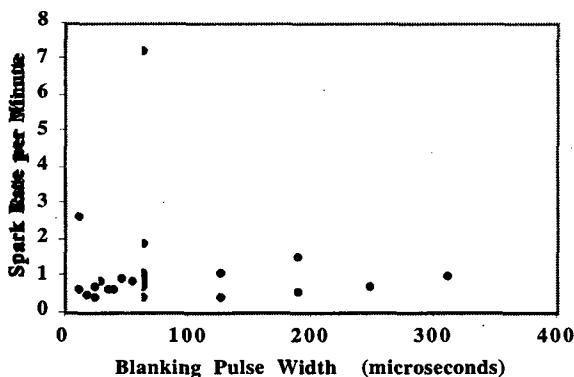


Figure 8: Spark rates as a function of blanking width.

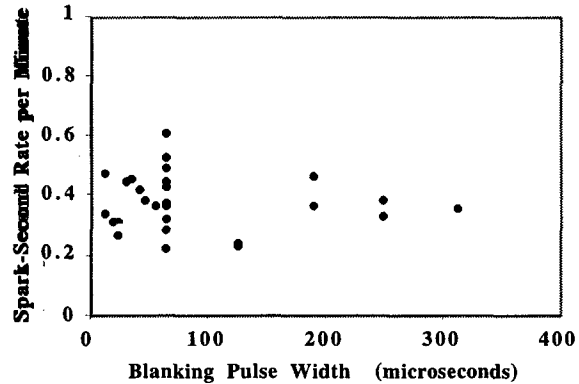


Figure 9: Spark-second rates as a function of blanking width.

Although the rates vary from measurement to measurement, there was no systematic variation observed across a large span of blanking width times. The same was observed from those measurements in which the turn-on ramping time was varied. From this study, we have concluded that it is essential only to interrupt the rf power to extinguish the arc, and varying the blanking time parameters does not reduce the sparking for the RFQ.

#### 5 ACKNOWLEDGMENTS

We would like to thank the personnel of the Chalk River Laboratories who developed the understanding and concepts of operation necessary to protect rf structures under cw, high-power operation. Their initial studies in the operation of this RFQ has been the groundwork for our present cw accelerator program at LANL.

#### 6 REFERENCES

- [1] J.Y. Sheikh, *et al.*, "Operation of a High-Power CW Klystron with the RFQ1 Facility", Proc. 1993 Particle Accel. Conf., IEEE 93CH3279-7, p. 1175.
- [2] G.O. Bolme, *et al.*, "High-Power RF Operations Studies with the CRITS RFQ", Proc. 1995 Particle Accel. Conf., IEEE 95CH35843, p. 923.
- [3] J. Sherman, *et al.*, Rev. Sci. Instrum. **69** (1998) 1003-1008.
- [4] H.V. Smith, *et al.*, "Comparison of Beam Simulations with Measurements for a 1.25-MeV, CW RFQ" in Proceedings of the 1998 Linear Accelerator Conference.
- [5] G.O. Bolme, *et al.*, "Proton Beam Studies with a 1.25 MeV, cw\_Radio Frequency Quadrupole LINAC" in Proceedings of the 1998 Linear Accelerator Conference.
- [6] G.O. Bolme, *et al.*, "Proton Beam Verification Using RF Power Measurement Data for a cw\_Radio Frequency Quadrupole LINAC" these Conference Proceedings.
- [7] J.D. Sherman, *et al.*, "Half-Power Test of a cw Proton Injector Using a 1.25 MeV RFQ" these Conference Proceedings.

# THE UPGRADE OF SRRC BOOSTER EXTRACTION SYSTEM

J. P. Chiou, J. S. Chen, C. S. Fann, C. H. Ho, K. T. Hsu, S. Y. Hsu, C. S. Hwang,  
K. K. Lin<sup>\*</sup>, J. T. Sheu, T. S. Ueng, SRRC, Hsinchu, TAIWAN

## Abstract

It is planned to upgrade the SRRC booster from 1.3 GeV to 1.5 GeV for full energy injection into the storage ring before the end of 1999. Based on the technical specification and operation experience, it is concluded that some of the subsystem components need to be rebuilt, such as the magnet power supply systems and beam extraction elements. A review of the power supply system will be reported elsewhere. In this report, the brief review of the beam extraction process is given according to the 1.5 GeV parameters. The test result of a modified kicker magnet is presented.

## 1 INTRODUCTION

The SRRC booster had been operated as a full energy injector to the 1.3 GeV storage ring since 1992 [1,2]. Beam energy ramping to the 1.5 GeV in the storage ring was implemented in 1996 due to the increasing user's demand [3]. The limited capability of power supplies prevented booster from carrying out the 1.5 GeV full energy injection. During the refilling of storage ring beam current, a routine process of energy ramping down (1.5 to 1.3 GeV), beam current accumulation, ramping up (1.3 to 1.5 GeV) was performed. The observed deficiency occurred with this process, in comparison with the full energy injection operating at 1.3 GeV, is described as follows. First, it takes typically 20 minutes for every refilling process. Second, the storage ring tunnel temperature was observed to become stable one hour after the completion of refilling process. It is due to the different power loading of components activated at 1.3 or 1.5 GeV. Third, it takes longer time for beam line elements to reach thermal equilibrium due to different refilling time in comparison with the case of full energy injection. Moreover, this accelerator configuration cannot provide the capability of performing top-up mode injection at 1.5 GeV. Consequently, a full energy injection at 1.5 GeV is considered and is planned to implement in this year. Aside from the mentioned booster power supply limitation, the pulsed extraction system (bumpers, septum, and kicker) was also reviewed and decided to be modified. Fixtures of the septum coil need to be enforced in order to avoid insulation breakdown due to mechanical damage. Concerning kicker magnet, we modify this window frame ferrite, one-turn coil magnet into two-turn coil magnet, to reduce the amount of work and cost. The existing kicker power

supply is similar to that built in MAX [4] and will be preserved. In this report, we describe briefly the examination of extraction mechanism and the test result of the modified version of kicker magnet.

## 2 EXTRACTION PROCESS

### 2.1 Description

The SRRC booster is fast cycling at 10 Hz. Electron beam injected at 50 MeV is ramped up to 1.3 GeV in 50 ms for extraction. As the accelerated beam approaches the extraction energy, three bumper magnets, with 2 ms half sine base width, are energized to produce a local orbit bump. This slow local orbit bump moves the beam orbit close to the extraction septum with largest amplitude at 1 ms, which corresponds to a duration of about 4000 turns after starting the extraction process. Then, the single turn extraction process is triggered by firing extraction kicker. Caution is made to properly trigger the extraction kicker so that the gap of bunch train, generated at the injection process, is utilized for the response duration of extraction kicker field. Thus, the extraction efficiency is optimized. When the kicker is triggered, an extra kick is added onto the horizontal deflection strength and deflects the electron beam to the other side of the septum magnet. The electron beam is then travelling along a 10 degrees bend trajectory and is injected into the transport line.

### 2.2 Beam Parameters at Extraction of 1.5 GeV

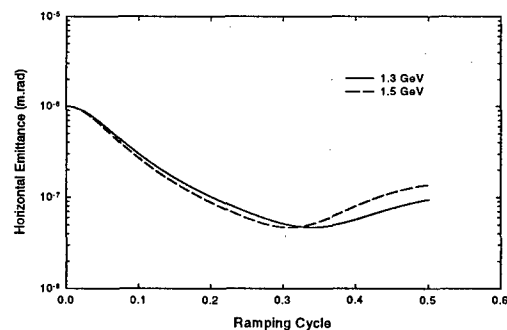


Figure 1: Calculated emittance variation of electron beam during ramping for both 1.3 and 1.5 GeV cases.

As shown in figure 1, the calculated result shows a larger beam emittance at extraction for 1.5 GeV than that for 1.3 GeV. For the beam clearance consideration, the extraction bump amplitude at the septum location shall be adjusted

<sup>\*</sup> Email: kklin@src.gov.tw

accordingly. The cross sectional view of the stored, bumped, and kicked beam at the septum location in  $x$ - $p_x$  plane is depicted in figure 2 for illustration purpose.

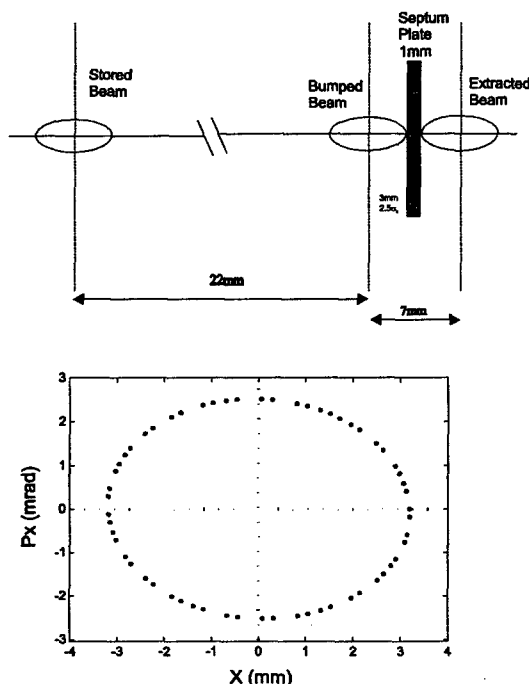


Figure 2: Tracking result on the  $x$ - $p_x$  plane of the extracted beam at 1.5 GeV. On top of the figure is the cross sectional view of the relative location of stored, bumped, and extracted beam at the septum entrance.

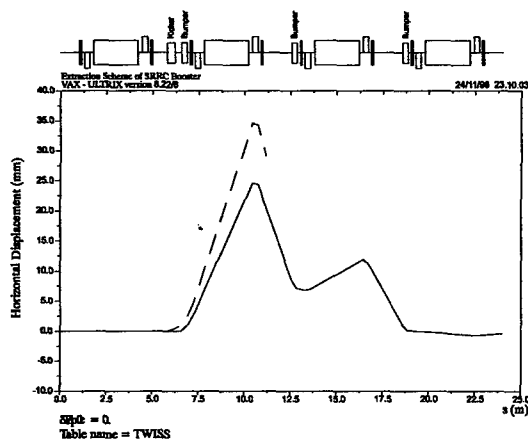


Figure 3: Trajectories of the electron beam centerline, bumped beam, and extracted beam after the ignition of extraction kicker. The figure shows two consecutive lattice cells in the extraction section.

Ellipses of tracking result shown in the figure cover the beam area of  $2.5 \sigma_x$ . In order to fulfill the criterion, the beam extraction process needs to be properly tuned. The calculated beam centerline, beam trajectory with local bump, and extracted beam trajectory, together with the schematic layout of the corresponding extraction elements at 1.5 GeV, are shown in figure 3.

Considering the designed lattice for extraction at 1.5 GeV, the kicker strength will require 30% increment over the present 1.3 GeV case. This requirement is beyond the operating margin of the present unit. Therefore the extraction kicker system need to be modified. Among several possible options, it is chosen to modify kicker coil into two-turn unit in order to ease the amount of work.

### 3 THE MODIFIED KICKER UNIT AND TEST RESULTS

A modified two-turn coil with ferrite block was put into place instead of the present one-turn coil for testing purpose. The schematic layout of the testing unit is shown in figure 4. Figure 4a and 4b give the modified test unit of

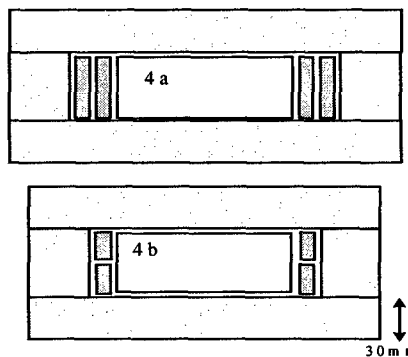


Figure 4: Window frame ferrite and coil arrangements of the (a) test unit of two-turn coil; and (b) two-turn coil of fabricating version.

different coil arrangement driven by the present power supply unit. The test unit of Fig. 4a type was assembled and tested in conjunction with daily operation at 1.3 GeV for a short period of time. The result was encouraging. Figure 5 gives the comparison of the operation data between the original one-turn coil and the modified unit.

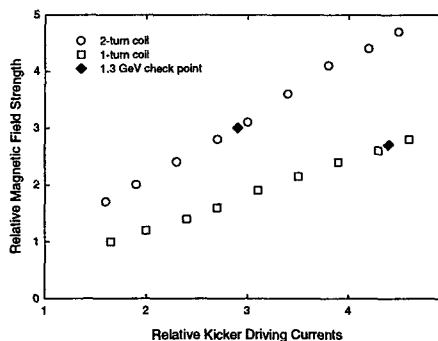


Figure 5: Comparison of the required kicker driving currents of one-turn coil and two-turns coil using the same existing power supply unit. Two check points working separately at daily operation of 1.3 GeV electron beam extraction are also indicated in the figure.

It shows that the driving current of the two-turn coil kicker could be largely reduced. According to the working points indicated in Fig. 5, this two-turn coil arrangement is capable of operation for 1.5 GeV beam extraction.

In order to ease the engineering work and reduce the inductance of the kicker magnet, the two-turn coil was further modified and shown in Fig. 4b. The calculated result of Fig. 4b arrangement is shown in figure 6 [5]. It shows that the field strength distribution and its horizontal uniformity is better than 0.3% over  $\pm 15$  mm range which is larger than the region of interest. Therefore we have chosen the Fig. 4b arrangement and it is under fabrication. The calculated result of field strength uniformity of Fig. 4b is shown in figure 6.

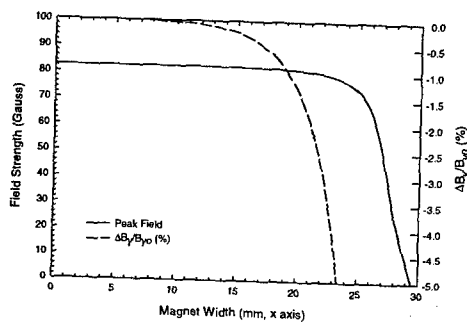


Figure 6: The kicker field strength in the region of interest is obtained using POISSON for two-dimensional calculation.

## 4 SUMMARY

In order to meet the requirement of operating SRRC booster at 1.5 GeV, engineering criterions for extraction process were reviewed in this report. The results suggest that the upgrade of SRRC extraction kicker is necessary. Among several alternatives, modifying one-turn coil into two-turn coil and preserving the existing power supply unit is chosen. The test result shows that the modified unit gives a satisfactory performance during daily operation at 1.3 GeV. This test unit also provides comfortable margin while operating at 1.5 GeV.

## 5 REFERENCES

- [1] J. Modeer, "1.3 GeV electron synchrotron", Proceeding of PAC93, p.2034, Washington, D.C., May 17-20, 1993.
- [2] K. K. Lin, K. T. Hsu, T. S. Ueng, J. P. Chiou, J. I. Hwang, Y. C. Liu, J. Modeer, "Performance of SRRC 1.3 GeV electron booster synchrotron", Nucl. Inst. and Meth. in Phys. Res. A, 361(1995)1.
- [3] G. H. Luo, P. Chang, K. T. Hsu, J. Chen, C. C. Kuo, Y. K. Lin, R. C. Sah, Y. C. Liu, "The 1.5 GeV operation parameters and performance at SRRC", Proceeding of PAC97, p.853.
- [4] L. J. Lindgren, A. Sandell, M. Eriksson, "Fast kicker magnet system", Nucl. Instr. and Meth. 214(1983)179.
- [5] POISSON/SUPERFISH reference manual, LA-UR-87-126, Los Alamos Accelerator Code Group, MS H829, LANL, Los Alamos, NM 87545, U. S. A.



# HOMS EFFECTS IN THE BEPC DC SEPARATOR

J.P. Dai, X.D. Chai, Z.T. Zhao, IHEP, Beijing, China

## Abstract

During the operation of BEPC, the cable isolation layer near the high voltage connector of the DC separator is often melted, which is probably caused by the HOMs power. This paper presents the measurement results of the HOMs shunt impedance, the calculation of the power dissipated in the separator and through the connector, and the analysis of the HOMs effects.

## 1 INTRODUCTION

The Beijing Electron-Positron Collider (BEPC) is a high energy accelerator for high energy physics and synchrotron radiation (SR) application in China. In the storage ring there are four direct current (DC) separators used to separate the electron and positron beams during the injection. BEPC usually operates in two modes: collision mode and dedicated mode for SR users. During the operation, the cable isolation layer near the high voltage connector of the DC separator is often melted, which is probably caused by the HOMs power. In order to analyse the power quantitatively and absorb it more effectively, we measured the longitudinal R/Q and Q value of the HOMs, and calculated the HOMs power dissipated in the separator and the connector.

## 2 MEASUREMENT OF THE HOMS

The DC separator is something like a coaxial-cavity, shown in Figure 1.

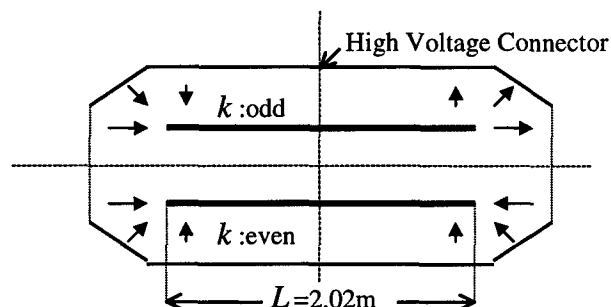


Figure 1. The schematic diagram of the DC separator

The main modes excited by the beam are TEM ones, and their resonant frequencies are:

$$f_m \approx m \cdot \frac{c}{2L} \quad (1)$$

where  $m = 1, 2, 3, 4, 5, \dots$ ,  $c$  is the speed of the light,  $L$  is the length of the inner plate of the separator.

From the characteristics of TEM modes, we know[1]:

- If  $m$  is odd, the longitudinal component of the electric field is of the same direction, and the field is weak in the middle of the separator where the high voltage cable is connected to the separator. These are shown in the up side of Figure 1.
- If  $m$  is even, the longitudinal component of the electric field is of the opposite direction, and the field is strong in the middle, shown in the low side of Figure 1.

Substituting  $L=2.02m$  into equation (1), the resonant frequencies of the HOMs may be got. For example, if  $m = 1$ , then  $f_1=74.3MHz$ . This agrees roughly with the measurement value,  $f_1=71.7MHz$ . To other  $m$ , the comparison result is the same. Figure 2 shows the transparent spectrum of the modes. (Those whose frequencies are higher than 750MHz are omitted, since their shunt impedance is very small)

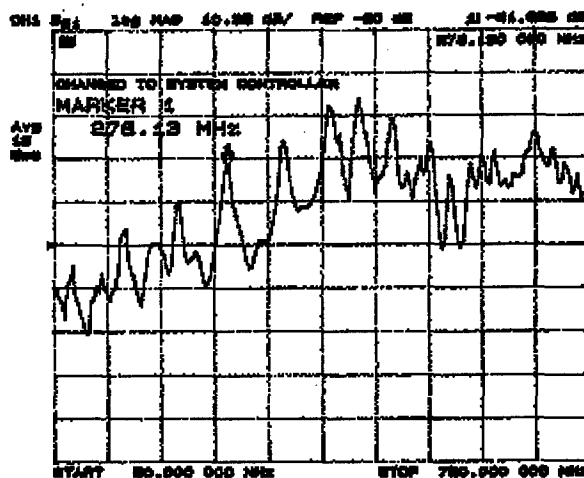


Figure 2 The transparent spectrum of the HOM modes

The longitudinal shunt impedance of the HOMs is measured using the perturbation method. The main instrument of the measuring system is a HP573C network analyser, controlled by a PC computer. The perturbing object is like a cage, made of some metallic needles glued to the plastic foils at the two ends. The factor of the cage is scaled from a standard cavity. Table 1 shows the measurement results.

\* Email: daijp@bepc4.ihep.ac.cn

Table 1 HOMs parameters of the DC separator

$m$	$f_m$ (MHz)	$R_m / Q_m$ ( $\Omega$ )	$Q_0$	$Q_L$	$Q_L^*$
1	71.73	10.5	2280	2220	2163
2	144.86	6.5	2980	745	426
3	214.74	1.9	3700	3660	3621
4	281.03	8.1	3238	160	82
5	354.51	0.9	3630	3586	3543
6	428.18	6.7	2925	95	48
7	490.57	2.7	2640	2625	2610
8	552.5	30.4	175	60	30
9	623.51	22.5	970	956	942

\* The operating separator is connected with two high voltage cables. We measured the loaded Q merit ( $Q_L$ ) of the separator with only one cable, and calculated  $Q_L$  of the separator with two cables.

From table 1 we find that the cables affect the Q value of the even mode seriously. The reason is the peak of the field of the even mode locates in the middle where the cables are connected

### 3 CALCULATION OF HOMS POWER

Using the cavity impedance and beam spectrum to characterise the interaction between the cavity and the beam in storage rings, a general equation to calculate the HOMs power in the cavity excited by the beam was developed[2]. As a special case, when the storage ring is filled symmetrically with particle bunches, the equation can be simplified[3]. In this paper, we use a computer to simulate the voltage induced in the DC separator by the beams and calculate the HOMs power.

#### 3.1 Model of the code

B Gaussian bunches are assumed to be distributed unsymmetrically in storage ring. From the shortest time interval between two bunches in the beam one can find an integer N, the smallest harmonic number of buckets. The buckets are fractionally filled by B bunches, each bunch has the same particle distribution form but could have different number of particles, which is controlled by the normalised filling factor  $\alpha_n$ ,  $n = 0, 1, 2, \dots, N-1$ ,  $\alpha_k$  can get the value from zero to one according to the particle numbers in the  $n$  bunch.  $\alpha_n = 0$  when the bucket  $n$  is empty;  $\alpha_n = 1$  when the bucket has the most particles, whose charge is  $q$ .

Ignoring the longitudinal oscillation of the bunch and supposing that  $J$  turns later after the bunch is injected into the ring, the voltage ( $V_m(t)$ ) of the mode at  $\omega_m$  induced by the beam is saturated and does not change with the turn any more, then:

$$V_m(t) = qH_m \cdot \left\{ \sum_{j=1}^{J-1} \sum_{n=1}^N \alpha_n e^{-\frac{\omega_m T_{nj}}{Q_m}} \cdot e^{j\omega_m T_{nj}} + \sum_{n=1}^K \alpha_n e^{-\frac{\omega_m (t-t_n)}{Q_m}} \cdot e^{j\omega_m (t-t_n)} \right\} \quad (2)$$

where

$$H_m = \frac{\omega_m R_m}{Q_m} \cdot e^{-\frac{(\omega_m \sigma_l)^2}{2}} \quad (3)$$

$\omega_m$ ,  $R_m$  and  $Q_m$  are the angle frequency, longitudinal impedance and the loaded Q merit of the mode.  $\sigma_l$  is the bunch length. And,

$$T_{nj} = t - t_n + (J - j)T_0 \quad (4)$$

$t_n$  is the time of the bunch  $n$  traverse the centre of the cavity at turn  $j$ ,  $T_0$  is the bunch revolution time in the ring. The bunch  $K$  is determined by  $t - t_K \geq 0$ .

Equation (2) is suitable to the case of single beam. If there are two beams in the ring, we need to consider the voltage induced by the other beam. According to the charge of the beams and the field pattern of the mode, we may get the voltage induced by the two beams similarly[2].

With the given voltage is calculated, the power of the mode at  $\omega_m$  is:

$$P_m = \frac{1}{2T_0} \int_0^{T_0} \frac{|V_m(t)|^2}{R_m} dt \quad (5)$$

The total HOMs power  $P_{total}$  is:

$$P_{total} = \sum_{m=1}^M P_m \quad (6)$$

where  $M$  is the number of the HOMs.

#### 3.2 Comparison with analytical result

If the storage ring is filled symmetrically with Gaussian bunches of charge  $q$ , the HOM power  $P_m$  of the mode at  $\omega_m$  is [3][4]:

$$P_m = \frac{1}{2T_b} \int_0^{T_b} \frac{|V_m(t)|^2}{R_m} dt = \frac{1}{T_b} \cdot K_m \cdot q^2 \cdot F(\tau, \delta) \quad (7)$$

where

$$F(\tau, \delta) = \frac{(1 - \exp(-\tau))(1 + \exp(-\tau))}{1 - 2 \cos \delta \exp(-\tau) + \exp(-2\tau)} \quad (8)$$

$$\tau = \omega_m T_b / (2Q_m) \quad (9)$$

$$\delta = \omega_m T_b \quad (10)$$

$T_b$  is the time interval between two bunches,  $K_m$  is the loss parameter of the mode at  $\omega_m$ ,

$$K_m = \frac{1}{2} \omega_m \left( \frac{R_m}{Q_m} \right) \cdot \exp(-(\omega_m \sigma_l)^2) \quad (11)$$

Assume BEPC operates in single bunch mode, and the particle number of the bunch is  $3.75 \times 10^{11}$ , the bunch length is  $\sigma_l = 8.5$  cm. For the mode at  $\omega_m = 2\pi \times 552.5 = 3471.9$  MHz, substitute  $Q_m = 30$  and  $R_m / Q_m = 30.5 \Omega$  into equation (7), we get the power  $P_m = 95$  W. The power calculated by the code is  $P_m = 100$  W, agrees well with the analytical result.

### 3.3 HOMs power of the BEPC DC separator

As we know, BEPC usually operates in two modes. By their typical parameters, the code may tell us the HOMs power of the DC separator, shown in table 2.

Table 2 The HOMs power of the DC separator

Operating Modes	Collision Mode	SR Mode I	SR Mode II
Beam Energy $E$ (GeV)	1.548	2.2	2.2
Cavity Voltage $V_c$ (MV)	1.0	0.65	0.6
Bunch Number $B$	1	1	60
Bunch Length $\sigma_l$ (cm)**	4.73	8.29	-4.0
Beam Current $I_b$ (mA)	50	75	110
Even Mode Power $P_e$ (KW)	0.056	0.191	0.004
Odd Mode Power $P_o$ (KW)	0.023	0.095	0.001

\*\*

a) In single bunch case,  $\sigma_l$  is given by the scaling law of BEPC bunch length

$$\sigma_l = 0.404 \times \left( \frac{I_b (mA) \alpha_p}{E (GeV) v_s^2} \right)^{\frac{1}{2.80}} \quad (12)$$

where  $I_b$  is the current of the single bunch,  $\alpha_p$  is momentum compression factor,  $v_s$  is the longitudinal tune.

b) In multi-bunch case, since the bunches have different charges,  $\sigma_l$  is an average value.

From table 1, we know that the power of the odd mode dissipates mainly in the separator itself, while the power of the even modes dissipates mainly in the high voltage cable and the connector which will cause the isolation layer to melt.

### 3.4 Analysis of the result

Since there are some differences between the operating separator and the measured one, and the measurement errors are unavoidable, we need to consider the error between the calculated power dissipated in the measured separator and the actual one in the operating separator. By changing the parameters: the frequency, the Q merit and  $R_m / Q_m$  in the code, we find that:

- To the odd modes, the power error caused by the frequency error may be very large. For example, to the mode  $m = 7$ , if the frequency is  $f_7 = 491.37$  MHz instead of  $f_7 = 490.57$  MHz, then the power will be 58W (in the mode SR I), not 4W. However, to the even modes, which we are interested in, is very small because of the very low Q merit.
- The power error caused by the Q merit error is small
- The power is almost proportional to  $R_m / Q_m$ , so the power error will not be very large since the measured  $R_m / Q_m$  is not very large.

## 4 ACKNOWLEDGEMENT

We would like to express our great appreciation to our colleagues: Y.D. Hao, Z.Y. HAO and S.P. Li for their help in the measurement of the separator.

## 5 REFERENCES

- [1] F. Zhou, "Research of impedance theory and its application", Doctor Thesis, IHEP, (1997)
- [2] Z.T. Zhao, "The HOMs power generated by unequally spaced and populated bunches in storage ring", High Energy Physics and Nuclear Physics, (to be published)
- [3] Haebl E., "RF design -higher order modes", Lecture Note in Physics No.425, W.Beiglbock, et al, Eds, Springer-Verlag, Berlin Heidelberg, (1992)
- [4] Wilson P., "High energy electron linacs: application to storage ring RF systems and linac collider", SLAC-PUB-2884, (Feb. 1982)

# THERMOSTABILIZATION SYSTEM OF VEPP-5 PREINJECTOR

K.V.Gubin, V.D.Hambikov, A.G.Igolkin, P.V.Martyshekin  
BINP, Novosibirsk, Russia

## 1 HEATING EFFECTS AND ENERGY SPREAD IN A BEAM

The temperature conditions changes of an accelerating structure influence on its RF characteristics. This fact leads to the change in the beam average energy as well the supplementary energy spread in structure.

Let's consider ultrarelativistic charged particles in the field of running RF wave with phase velocity  $\beta_{ph} = 1 + \Delta\beta_{ph}$ . For the simplicity we shall assume that there is no group effects in the beam and no interaction between the beam and the accelerating structure.

If we assume that  $\Delta\beta_{ph} L/\lambda \ll 1$  where  $L$  – the length of the structure,  $\lambda$  – the length of the RF wave,

then the energy, gained by the particle in the accelerating structure will be

$$\Delta E = -\frac{A\omega\Delta\beta_{ph}}{c} \left( \sin\left(\phi_0 - \frac{\omega\Delta\beta_{ph}L}{c}\right) - \sin\phi_0 \right), \quad (1)$$

where  $A$  – energy gradient of the structure,  $\omega$  – operation frequency and  $\phi_0$  – initial RF phase of particle.

For a beam of the phase length  $2\phi$  the part of heating effects in the beam energy spread can be estimated as

$$\delta = \frac{E_{0min} - E_{min}}{E_{0max}} = \frac{\omega}{2c} \Delta\beta_{ph} L \sin\phi \quad (2)$$

where  $E_{0min}$  and  $E_{0max}$  – minimum ( $\phi_0 = \phi$ ) and maximum ( $\phi_0 = 0$ ) energy gain when  $\Delta\beta = 0$ ,  $E_{min}$  – minimum energy gain when  $\Delta\beta \neq 0$ .

Relation between the change of resonant frequency and the phase velocity of RF wave can be written as: [2]

$$\frac{\Delta\beta_{ph}}{\beta_{ph}} = \frac{\beta_{ph}}{\beta_{gr}} \frac{\Delta\omega}{\omega} = \frac{\beta_{ph}}{\beta_{gr}} \alpha \Delta T_{av}, \quad (3)$$

here  $\alpha$  – the temperature expansion ratio of copper,  $\Delta T_{av}$  – the value of average temperature changing

Equation (2) together with (3) determines the maximum acceptable change of an average temperature of the accelerating structure with a certain energy spread limit, caused by heating:

$$\Delta T_{av} = \frac{\lambda}{L} \frac{\beta_{gr}}{\pi\alpha\beta_{ph}h\sin\phi} \delta \quad (4)$$

For the linear distribution of temperature along the structure maximum acceptable temperature gradient  $\Delta T$  will be

$$\Delta T = 6 \frac{\lambda}{L} \frac{\beta_{gr}}{\pi\alpha\beta_{ph}h\sin\phi} \delta \quad (5)$$

For the accelerating structure of VEPP-5 preinjector prototype parameter  $\beta_{gr}/\beta_{ph}$  is equal to  $2 \cdot 10^{-2}$ . Taking the value of acceptable energy spread of 0.5% for a beam of RF-phase length about  $20^\circ$ , we obtain that the system of thermostabilization should ensure the average temperature of the accelerating structure with the precision of  $\pm 0.1^\circ C$  and the temperature gradient along the structure not more than  $1.2^\circ C$

## 2 TEMPERATURE CONDITIONS OF ACCELERATING STRUCTURE

Accelerator section (fig. 1) is a cylindrical disk-loaded waveguide, placed inside the stainless steel coat for better rigidity. Inner surface of the coat and outer surface of structure form the channel with a ring-shaped section of water cooling system. The main parameters of section are listed in table 1. Present construction of the section determines the method of thermostabilization: to stabilize of the temperature and the cooling water flow.

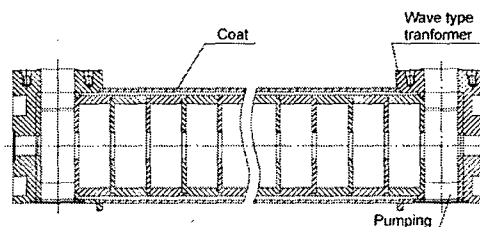


Figure 1: Accelerator section.

When the structure is filled with RF field, the part of energy transforms into heat in the skin-layer on the inner surface. The heating of skin-layer can be estimated, using nonstationary equation of thermal conductivity  $\Delta T \simeq (P\delta)/(\alpha S)$  where  $P$  – pulse power of heating,  $\delta$  – depth of skin-layer,  $\alpha$  – thermal conductivity of copper,  $S$  – square of inner surface of accelerating structure.

Assuming  $P=100$  MW,  $\delta = 1 \cdot 10^{-6}$  m,  $S = 2m^2$ , we obtain that by the end of RF-pulse the heating of skin-layer will be about  $0.13^\circ C$ . Taking into account that without

Table 1: Main parameters of accelerator section.

Length	280 m
Inner diameter of structure	84 mm
Outer diameter of structure	100 mm
Inner diameter of coat	108 mm
Outer diameter of coat	112 mm
Resonance frequency	2856 MHz
Repetition rate	50 Hz
RF pulse duration	0.5 $\mu$ sec
Heating per one pulse	up to 80 J

cooling the heating would be about  $20^\circ\text{C}$ , we suggest that even for the single pulse duration, and for the time of several milliseconds between pulses as well, all the heat will be distributed uniformly along the radius of accelerating structure.

Present estimations illustrate, that the distribution of temperature along the radius of accelerating structure and pulse nature of heating can be neglected. Thus, we can analyse one dimensional model with quasistationary heating: long and thin rod of copper (accelerating structure) with nonuniform heating along it, placed into cylindrical coat. In the ring channel formed by outer surface of structure and inner surface of coat, the cooling water is circulated. Thermal contact with air and heat currents from butt-ends supposed to be equal to zero.

So, we should solve the system of three nonstationary equations of thermal conductivity with common border conditions of third kind. Analytical solving of such system in general case is rather complicated. Due to this fact, numerical simulation, based on final differences method, was realised. This model was experimentally tested on the prototype of accelerator section and thermostabilization system of VEPP-5 preinjector.

In the experiment the temperature of cooling water at the section entrance was changing and the cooling water flow was constant. The dependence of the input and output water temperature and its flow on the time was measured and expected value of this dependences was numerically simulated with the same parameters. Several series of measurements were done. In fig. 2, 3 expected and measured data are shown. The difference between it doesn't exceed 2%.

Thus we can calculate the temperature distribution in structure and water along the axis of section in any moment of time with any input parameters such as flow and temperature of the water and RF power in the section.

To determine the section sensitivity to the disturbance of input water temperature, the following model was tested: temperature disturbance was put over the steady-state of section without RF power. ( $T_{as}(x, t) =$

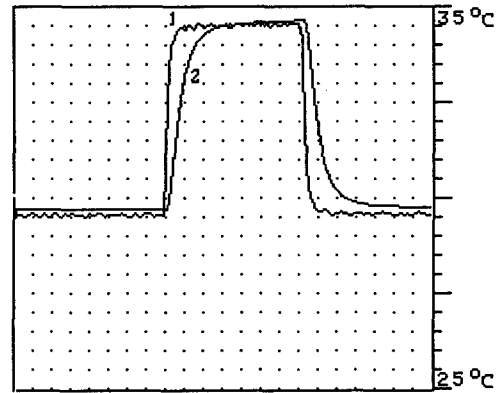


Figure 2: Experimental correlation between temperature of input (1) and output(2) cooling water and time. The scale of horizontal axis – 60 seconds per point. Water flow 0.27 lps

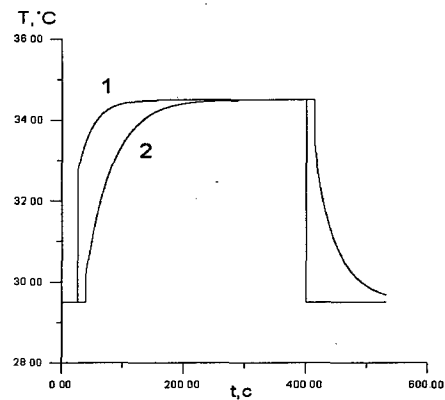


Figure 3: Numerically simulated correlation between temperature of input (1) and output(2) cooling water and time.

$$T_c(x, t) = T_w(x, t) = 0$$

$$T_w(0, t) = \begin{cases} 0, & t < 0 \\ T_{dist}, & 0 < t < \tau \\ 0, & t > \tau \end{cases}$$

where  $T_{as}$  - temperature of accelerating structure,  $T_w$  - temperature of water,  $T_c$  - temperature of coat,  $T_{dist}$  - value of disturbance.

The results of simulation are shown in fig. 4 As one can see, with the present geometry of section (table 1) and the flow of water in the certain bounds the following correlation is observed:

$$T_{dist} \tau Q \leq 2 [l \cdot ^\circ\text{C}] \quad (6)$$

Corellation (6) determines the quality of thermostabilization of water at the entrance of the section.

Next problem: how does the steady-state condition of section sense the change of water flow and RF power.

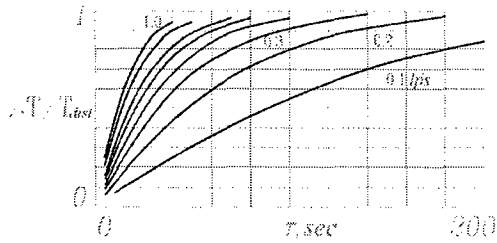


Figure 4: Corellation between maximal deviation of average accelerating structure temperature, relating to amplitude of disturbance, and the duration of temperature disturbance of cooling water at the entrans of section.

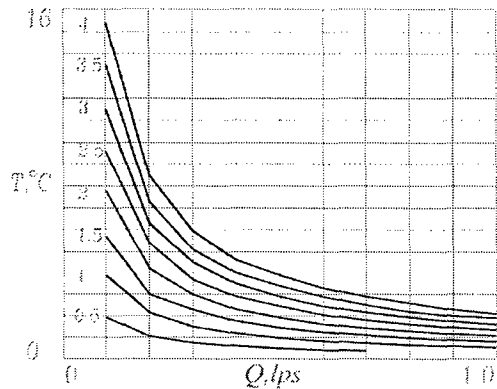


Figure 5: Correlation between the average accelerating structure temperature and the flow of cooling water at different power of heating.

Simulations were done for RF power range from 500 Wt to 4000 Wt and the flow range from 0.1 lps to 1.0 lps. The main results are:

- over the whole range of RF-power the temperature gradient along the section is not significant and with a flow over 0.2 lps doesn't exceed  $0.6^{\circ}\text{C}$ ,
- knowing the heating power we can select the flow for each section in order to compensate the tolerance of RF parameters of different sections with the help of calculated corellation between the average temperature of section and the flow of water (fig. 5), mentioned correlation is following.

$$QT/P \approx 0.5 [^{\circ}\text{C}/\text{kJ}] \quad (7)$$

It allows to determine the section sensitivity to disturbances of heating and water flow.

### 3 TECHNICAL REALIZATION AND PRESENT STATUS

Technically the system of thermostabilization supposed to be performed by two-contour water scheme (fig. 6). All elements to be stabilized are connected in parallel to

the inner closed water contour. Stabilization of temperature is realized as a controlled heating of input water by the heating unit, individual for each element. Dumping of heat surplus is produced by the heat exchanger.

This construction allows to stabilize the cooling water flow through the elements, to decrease the power consumption, to change the individual heating conditions for each element of accelerator to compensate the tolerance in RF parameters during the adjusting process.

Main characteristics of the system are shown in table 2. At the present time the assembly of water contours is in progress. The heating unit that consists of heater, controlled power supply, flow meter, thermistors and control device, has been completely designed, tested on preinjector prototype and now is in serial production.

Table 2: Main parameters of thermostabilization system.

Number of elemets/branches	20
Flow of water per branch	0.5..1.0 lps
Total flow	15..20 lps
Operating temperature of elements	$40 \pm 3^{\circ}\text{C}$
Precision of temperature stabilization	$0.1..0.2^{\circ}\text{C}$
Peak power consumption	300 kWt
Nominal power consumption	50..100 kWt
Capacity of water in the system	$10 \text{ m}^3$

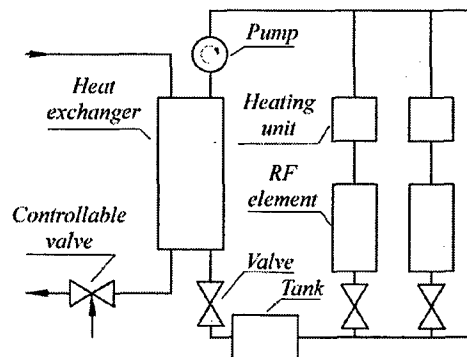


Figure 6: Construction of two-contour system of thermostabilization.

### 4 REFERENCES

- [1] A.V.Alexandrov and others. Test of prototype of preinjector for VEPP-5. Preprint INP 97-64, Novosibirsk, 1997.
- [2] O.A.Waldner and others. Disk-loaded waveguides references guide. Moscow, Atomizdat, 1977. (in Russian).
- [3] S.S.Kutateladze. Heat transfer and hydrodynamical resistance. Moscow, Energoatomizdat, 1990. (in Russian).

## DEVELOPMENT OF A 50 KW CW L-BAND RECTANGULAR WINDOW FOR JEFFERSON LAB FEL CRYOMODULE\*

V. Nguyen<sup>#</sup>, H.L. Phillips, and J. Preble,

Thomas Jefferson National Accelerator Facility, Newport News, VA

### Abstract

A 50 kW CW L-Band Rectangular Ceramic Window has been developed for the Jefferson Lab FEL quarter cryomodule. RF properties of the windows were optimized using high-frequency simulation codes and S-parameter measurements confirmed the predicted broad band matching properties of the structure. Metallized AL 995 alumina ceramic was brazed to a thin copper eyelet and the eyelet to a copper plated stainless steel flange. Losses in the metallization were removed efficiently by a water cooling circuit. High power tests in a resonant ring showed that the ceramic temperature rise was very low at 50 kW CW level.

### 1 INTRODUCTION

The Jefferson Lab FEL injector uses a pair of superconducting cavities inside a quarter cryomodule. The RF waveguide assembly of each cavity consists of a warm RF window, a warm to cold vacuum waveguide and a cold RF window. Each of the two cavities needs 35 kW of RF CW power (including microphonic headroom) to accelerate a 5 mA beam to a total of 10 MeV. The polyethylene warm window used in CEBAF cannot handle that amount of power. Originally, a few warm windows were fabricated using the cold ceramic window's design [1] by replacing the niobium flange by a copper plated stainless steel flange. High power tests in a resonant ring showed that they failed at 20-25 kW CW power levels, due to thermally-induced stress cracking of the glass-free pure alumina ceramic. Infrared temperature measurements showed that the temperature rise at the center of the ceramic window was abnormally high, contrary to expectation. This material had exhibited the lowest loss at 2 K, but became very lossy at 300 K. It is a transparent polycrystalline alumina which is fired in hydrogen instead of air during manufacture. A partial reduction of the alumina produced an RF loss at 300 K but not at 2 K. Air firing restores the ceramic at 300 K to a state of low RF loss. When the lossy ceramics were replaced by a low loss alumina, the temperature rise at the center of the ceramic was much lower than that at the edge. Losses in the metallization therefore become dominant.

We took advantage of this opportunity to reduce thermal gradients and the ensuing stress by absorbing the heat where it is produced. This is accomplished by incorporating water cooling within the flexible braze transition between the ceramic window and the surrounding metal flange, such that the braze metallization is directly cooled by the water through a thin copper layer. In this configuration, the power level at which thermally-induced stress cracks can occur is limited by thermal gradients in the ceramic. These are produced by a non-zero thermal heat transfer coefficient between water and copper, and dielectric losses in the ceramic. The new design will provide higher transmitted power levels than the existing design, and consequently a better margin of safety for the Jefferson Lab FEL.

### 2 RF DESIGN

The voltage standing wave ratio (VSWR) should be a minimum, less than 1.10:1 at the nominal design frequency of 1.5 GHz and should be less than 1.50:1 at frequencies up to 2.2 GHz. Minimum VSWR at 1.5 GHz is achieved by providing a protruding iris in the frame from each side of the waveguide wall. This iris will produce a reflection which is opposite in phase to the unavoidable reflection from the ceramic. By choosing the proper iris size and thickness the reflections can be made to nearly cancel at the design frequency thereby producing a minimum in VSWR at that frequency.

The minimum will be either broad or narrow depending on the thickness of the window and size of the iris. If the window reflection is small and therefore the canceling reflection from the iris is also small, then the minimum will be broad.

The ceramic reflection is kept small by making that portion of the ceramic protruding into the waveguide as thin as possible. The edges of the ceramic, which are thicker for reasons of strength and providing a substantial boundary to braze to, are recessed into the waveguide walls. Fig. 1 shows the basic design of the window.

The ceramic is ground to a desired shape which varies in thickness, being 0.050" at the mid-section and 0.250" at the edges. The ceramic is thin enough to keep the VSWR low from 1.3 GHz to 2.2 GHz and thick enough to withstand a pressure differential of approximately three atmospheres. The ceramic is a polycrystalline high purity alumina (WESGO AL995) having a dielectric constant of about 9.3 at 1.5 GHz. The ceramic is placed at the center of a thin wall copper eyelet 0.9" in length. The length of the thin wall copper eyelet is chosen long enough to allow

\* Work supported by the U.S. Department of Energy under contract DE-AC05-84-ER40150.

<sup>#</sup> Email: [nguyen@jlab.org](mailto:nguyen@jlab.org)

flexibility between the ceramic and the stainless steel flange.

The thickness at mid-section of the ceramic and the length of the eyelet have been optimized using HFSS [2]. The window is inserted between two 5.292" x 0.986" rectangular waveguides.

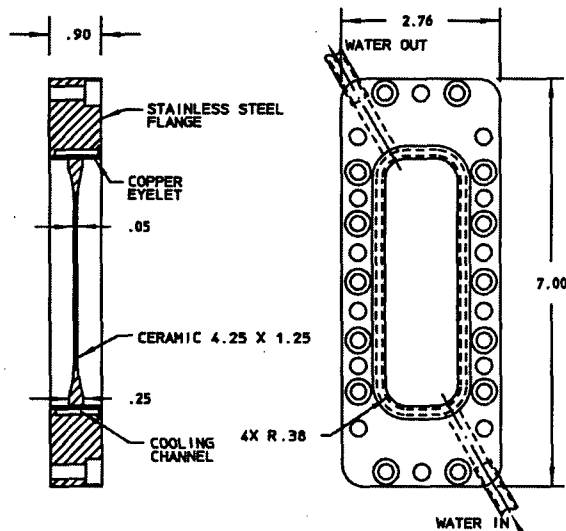


Figure 1. Basic design of the window

The calculated VSWR of the window between 1.3 GHz and 2.2 GHz is given in Fig. 4 (dotted line). When using a dielectric constant of 9.3, the minimum is at 1.48 GHz and the VSWR at the operating frequency of 1.497 GHz is less than 1.02:1. Choosing a dielectric constant lower than 9.3 would shift the minimum to higher frequencies.

### 3 WINDOW FABRICATION

Fig. 2 shows the main elements of the window: the ceramic, the thin wall copper eyelet and the copper plated stainless steel flange. The ceramic was ground from AL-995 material and metallized with a conventional tungsten-manganese process. The ceramic was first brazed to the copper eyelet using 50-50 copper-gold alloy. This assembly is then brazed to the copper plated stainless steel flange using copper-silver eutectic alloy. After brazing and leak checking, the ceramic window is coated with 35 of chrome oxide on the vacuum side to prevent multipactoring.

Fig. 3 shows the completed window with cooling tube as seen from the klystron side.

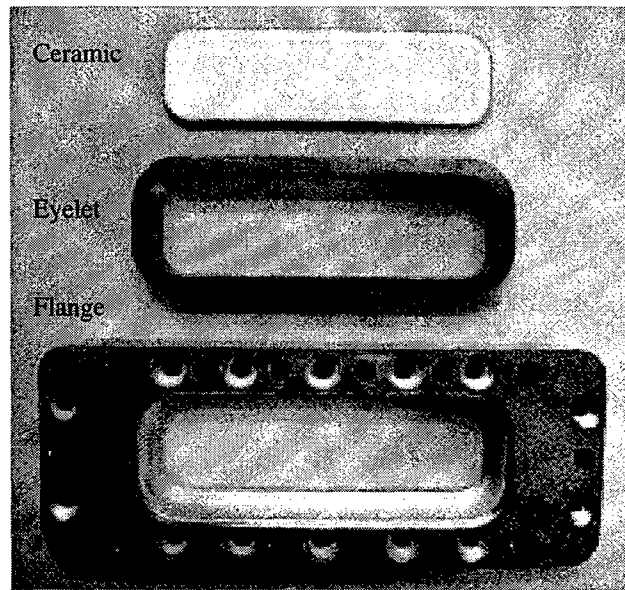


Figure 2. Main elements of the window

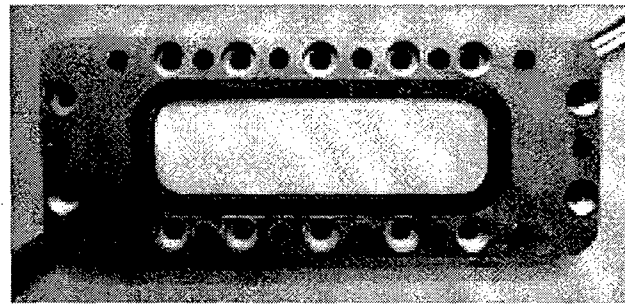


Figure 3. Completed window

### 4 LOW POWER TESTS

The window was measured using a vector network analyzer. The analyzer was calibrated in 5.292" x 0.986" waveguide using the Thru-Reflect-Line (TRL) method. The measured and calculated VSWRs as a function of frequency are shown in Fig. 4.

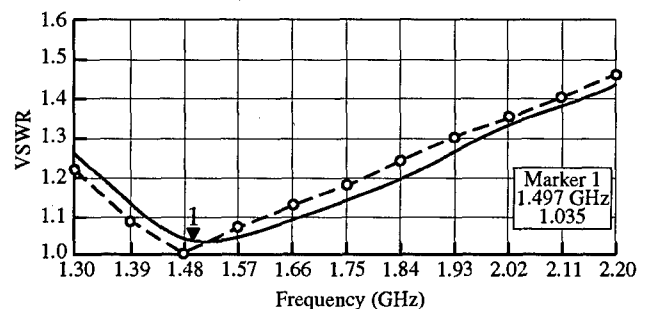


Figure 4. VSWR vs Frequency. Comparing measured data (solid line) to HFSS calculation (dotted line)

The actual measured VSWR confirmed quite well the calculated values.



## 5 HIGH POWER TESTS

The window was first tested in a resonant ring [3] with air on the two sides to evaluate its thermal performance. RF power up to 53 kW was applied to the window while the ceramic temperature was monitored by an infrared-thermometer. For a window cooled with 34°C Low Conductivity Water (LCW), the temperature rise of the window ceramic is shown on Fig. 5. At 53 kW, the temperature rise was only 7.2°C. On the other hand, when the window was not cooled with LCW, the temperature rise above room temperature increased to 36°C.

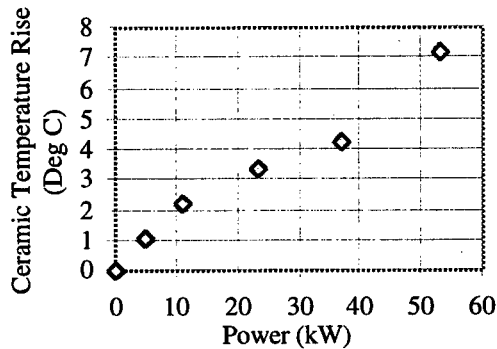


Figure 5. Ceramic temperature rise vs power

The window was examined after testing. No visible damage was observed, and it remained leak tight.

High power testing of the windows under vacuum is carried out using a test setup which uses two windows back-to-back with a vacuum region in between. This test setup is evacuated with a 160 l/s ion pump and is equipped with a pressure gauge, an electron probe and an arc detector. An infrared-thermometer is used to record the temperature of the window ceramic from the air side. The window test setup is also equipped with an interlock system which shuts off automatically the RF power if there are any sustained light longer than 100  $\mu$ s and/or any increase in the pressure between the two windows beyond  $3 \times 10^{-7}$  Torr.

Fig. 6 shows the layout of the high power test setup. RF power was fed by a 35 kW klystron. The output side was terminated with a matched load. Prior to applying high CW power, the windows were conditioned up to a peak power of 35 kW with a pulse width of 5  $\mu$ s and a repetition rate of 100 Hz. During the conditioning, sudden gas bursts and electron currents were observed. After conditioning, CW power up to 35 kW could be applied quickly to the windows without any sign of electron activity. The temperature rise above LCW temperature (33°C) of the window 2 was 5.7°C at 31 kW.

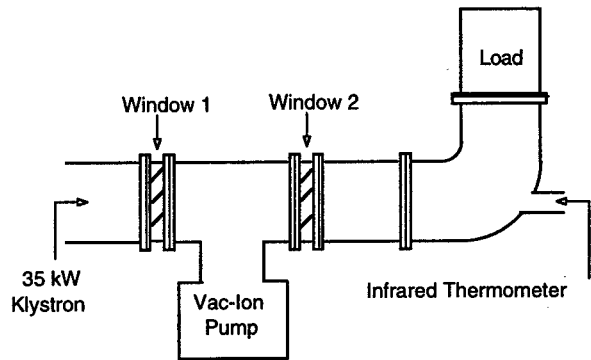


Figure 6. High power test setup

## 6 CONCLUSIONS

A window has been designed and fabricated which meets fully the design goals. Both low and high power tests of the window have been performed. As temperature rise of the window was very low at 50 kW, it should be possible to use the window at power higher than 100 kW, which is required to increase the beam current of the FEL injector beyond 5 mA.

## 7 ACKNOWLEDGMENTS

The authors gratefully acknowledge valuable discussion of window issues and help from Michael Neubauer and Heinz Schwarz of SLAC. We are indebted to Robert Weikle of UVA for his expertise and help on RF measurement. We also wish to thank Genfa Wu, the technical staff of the Cryomodule Group for their assistance, John Brawley for electron beam welding and Tom Elliott for brazing. The efforts of Danny Machie, Jaynie Martz and Sherry Thomas in preparing this publication are very much appreciated.

## 8 REFERENCES

- [1] H.L. Phillips and T.S. Elliott, U.S Patent 5610567, Mar. 11, 1997
- [2] Ansoft HFSS, by Ansoft Corporation, <http://www.ansoft.com>, commercially licensed software
- [3] V. Nguyen-Tuong and L. Phillips, "Resonant Ring and RF Window Testing", Jefferson Lab TN #95-022

## AN R.F. INPUT COUPLER SYSTEM FOR THE CEBAF ENERGY UPGRADE CRYOMODULE \*

J. R. Delaysen, L.R. Doolittle, T. Hiatt, J. Hogan, J. Mammosser, L. Phillips<sup>#</sup>, J. Preble,  
W.J. Schneider, G. Wu, Jefferson Lab, Newport News, VA

### Abstract

Long term plans for CEBAF at Jefferson Lab call for achieving 12 GeV in the middle of the next decade and 24 GeV after 2010. Thus an upgraded cryomodule to more than double the present voltage is under development. A new waveguide coupler system has been designed and prototypes are currently being developed. This coupler, unlike the original, has a nominal  $Q_{ext}$  of  $2.1 \times 10^7$ , reduced sensitivity of  $Q_{ext}$  to mechanical deformation, reduced field asymmetry within the beam envelope, freedom from window arcing with a single window at 300 K, and is capable of transmitting 6 kW CW both traveling wave and in full reflection.

### 1 INTRODUCTION

The CEBAF upgrade baseline design calls for 1500 MHz, 7-cell cavities operating at 12.1 MV/m with a circulating current up to 400  $\mu$ A. [1] To minimize cost, our goal is only a modest increase of the RF power available to each cavity from 5.5 to 6 kW. This puts stringent constraints on the maximum amount of detuning (static and dynamic) and on coupling system  $Q_{ext}$  accuracy. Figure 1 shows the of RF power required as a function of  $Q_{ext}$  at the gradient of 12.5 MV/m, detuning of 25 Hz and for circulating currents of 0, 200, and 400  $\mu$ A. The optimal  $Q_{ext}$  is  $2.1 \times 10^7$  with an acceptable range of  $1.5$  to  $3 \times 10^7$ .

Both coaxial and waveguide couplers were explored. The waveguide concept was retained for its simplicity and flexibility at 1500 MHz. Unlike the present design, however, the fundamental power coupling (FPC) and

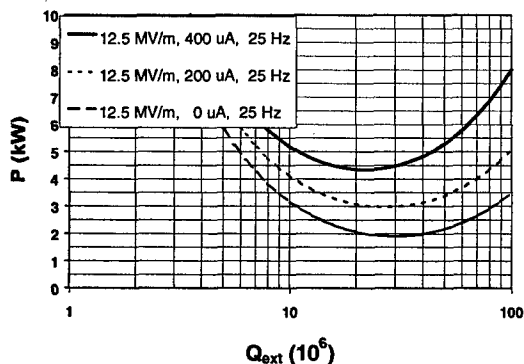


Figure 1

\*Supported by U.S. DOE contract DE-AC05-84-ER40150

\*Email: phillips@jLab.org

higher order mode (HOM) extraction functions are completely separate. This produces a coupler design that, unlike the present one, is free of transverse beam kick, and allows a cryostat design with all the power couplers on the same side.

### 2 THE CAVITY-COUPLER SYSTEM

The nominal cavity gradient is 12.5 MV/m with a beam current of 400  $\mu$ A. A shorted waveguide intercepting the beam pipe couples RF power to the evanescent  $TM_{010}$  mode of a 7-cell cavity (Figure 2). A copper-plated stainless steel waveguide provides a thermal transition between the cavity at 2 K and the outer cryostat envelope at 300 K. The cavity vacuum extends to a single rectangular waveguide window at 300 K.

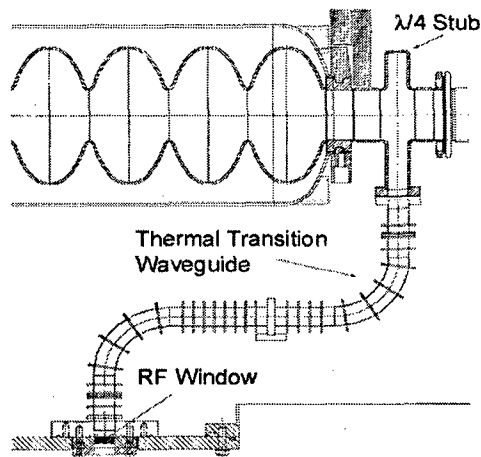


Figure 2

The new beam line configuration reflects several changes. With no gatevalves or bellows between cavities, cavity length increased from five to seven cells. This requires both lateral and radial flexibility in the waveguide thermal transition to allow for thermal differential contraction between the cavity string and the outer vacuum envelope, the accumulated cavity motion arising from cavity tuner operation, and manufacturing tolerances. The longitudinal motion of the string of eight cavities will be fixed at the center of the cryomodule requiring a displacement at each end amounting to 1.3 cm. This motion is provided by three short waveguide bellows appropriately placed.

The cavities' flexible waveguides and warm windows are attached in the clean room, with the entire cavity

string then permanently evacuated for all subsequent cryomodule assembly. As shown, each waveguide has two 90° elbows. This accomplishes two purposes: reduction of radial penetration ports from eight to four, and avoidance of window charging leading to "arc" trips by removing the ceramic window from the cavity fields' radiation flux. Currently 40% of CEBAF cavities are limited in gradient by field-emission-induced "arcing." Tests have shown that moving the RF window from a direct line-of-sight view of the high field region of the cavity can eliminate field-emission-induced window "arcs." The need to offset the window to prevent "arcing" and the need for longitudinal motion were factors favoring the simplicity of a waveguide coupler over a coaxial design.

### 3 BEAM LINE COUPLER

The cavity-coupling factor was chosen to be  $2.1 \times 10^7$  (Figure 1). A  $\lambda/4$  stub waveguide coupler intersecting the beam pipe couples the  $TE_{01}$  waveguide mode to the evanescent  $TM_{01}$  cavity mode. The waveguide-coupler-to-cavity separation was selected to achieve the desired coupling. The Cornell/CEBAF cavity currently used has a  $\lambda/2$  stub waveguide coupler and was originally designed for storage ring applications. The  $\lambda/2$  stub coupler provided a  $Q_{ext}$  of  $3 \times 10^5$  and was located up against the iris of an end cell. Coupling to the fundamental can occur with the stub length slightly less than  $\lambda/2$ , while  $TE_{111}$  cavity modes in the 1.7 to 1.9 GHz range, which are beyond cut-off of the waveguide HOM couplers, are even more strongly damped. This feature is not relevant for the energy upgrade cavity, which will have coaxial HOM dampers. Furthermore, there are several disadvantages to the  $\lambda/2$  coupler over the  $\lambda/4$  coupler. Locating the beam line close to the null in the standing wave pattern makes the coupler  $Q_{ext}$  quite sensitive to small shifts in this pattern due to manufacturing tolerances and subsequent waveguide deformations. This becomes even more acute for the higher fundamental rejection required for  $Q_{ext}$  of  $2.1 \times 10^7$  as opposed to  $3 \times 10^5$ . Another drawback is the field asymmetry across the beam pipe giving rise to a "coupler kick"

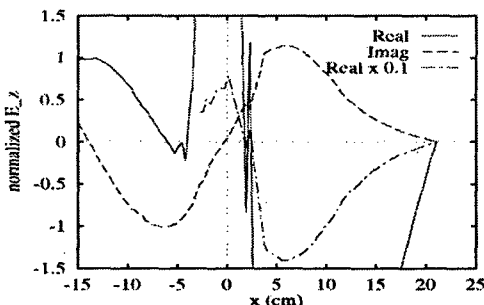


Figure 3: Electric fields in the centerline of  $\lambda/2$  stub-on-stub PC used by the Cornell/JLab cavity system [2]

In CEBAF this effect was reduced by alternating the longitudinal coupler orientation in a pattern averaging the net kick to an acceptable level. [2], [3]

We have chosen the  $\lambda/4$  stub waveguide coupler for the 7-cell energy upgrade cavity. (Figure 4 show the electric field along the FPC waveguide centered on the beam line for this configuration. [2] In addition to eliminating the "coupler kick," the reduced coupler fields will contribute negligible heat to the coupler body outside the helium envelope.

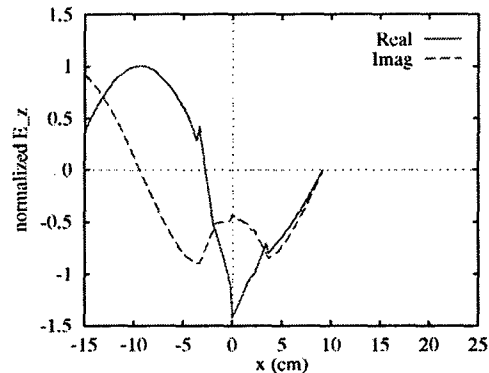


Figure 4: Electric fields in the centerline of  $\lambda/4$  stub FPC proposed for the CEBAF energy upgrade cryomodule. [2]

The sensitivity of  $Q_{ext}$  of the FPC to mechanical deformation and variations in manufacturing tolerances has also been reduced significantly. We have used this insensitivity by allowing the FPC waveguide to take up cavity misalignment and axial beam line displacement without significant change in the cavity coupling factor. The  $Q_{ext}$  variation with axial deformation (i.e., reducing or increasing the height of the FPC waveguide at the beam pipe) is 6%/mm for small displacements. For angular displacements of the beam pipe away from the beamline, rotating about the center of the FPC waveguide, the  $Q_{ext}$  variation is 0.15%/mrad. Consequently, the beamline between cavities is entirely niobium with no bellows. Some flexibility has also been included in the niobium flanges joining cavities. These two flexible elements are used to absorb all misalignment in the beamline.

### 4 WAVEGUIDE THERMAL TRANSITION

A copper-plated stainless steel waveguide provides the required thermal isolation between an RF window at 300 K and the cavity waveguide coupler flange at 2 K, with a thermal intercept at 50 K. The FPC refrigeration load at 2 K is the sum of thermal conduction and RF dissipation from the waveguide between 2 K and 50 K, and is minimized, for a given waveguide structure, with respect to waveguide length.

The RF fields averaged circumferentially over a slice of waveguide perpendicular to the direction of propagation is shown in Figure 5 for normal operating conditions and in Figure 6 for the worst case condition.[4]

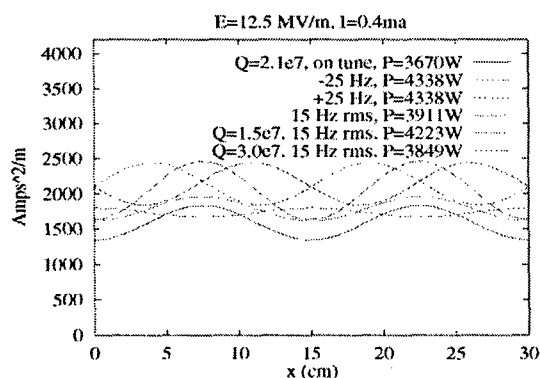


Figure 5: Typical currents on waveguide walls [4]

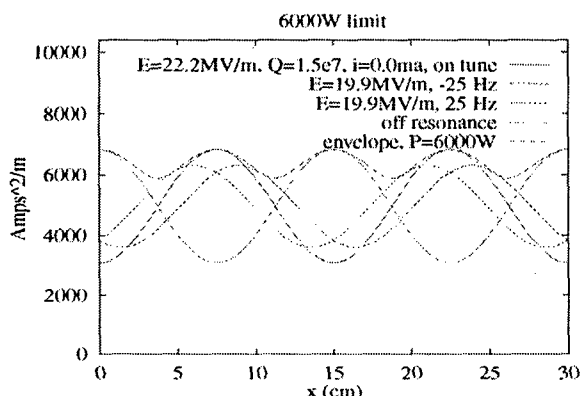


Figure 6: Worse case current on waveguide walls [4]

In balancing RF dissipation against heat conduction down the guide, a broad minimum in 2 K heat load as a function of waveguide length is seen (Figure 7).

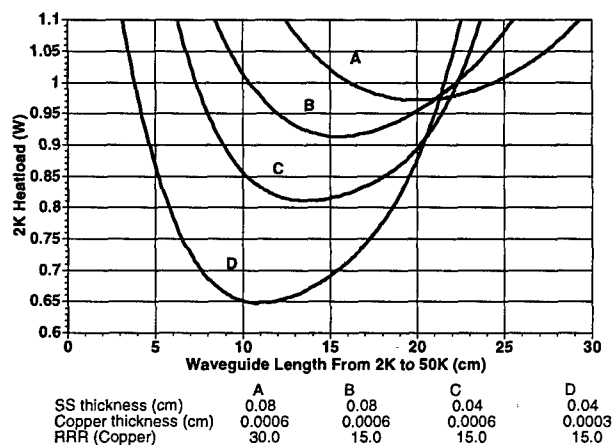


Figure 7

When operated at a minimum, the highest temperature along the waveguide will be at the high temperature end of the guide. Under worst case conditions the same waveguide will reach a peak temperature somewhere along the guide significantly higher than the end of the guide. The potential for sudden gas migration in such an excursion possibly inducing waveguide discharge will be studied with prototype components in a horizontal test

cryostat later this year. Details of the copper plating will also be studied.

The heat load at 2 K will be less than 1 W under normal operating conditions. The minimum length-optimized heat load will depend on the total thermal conductance of the stainless steel waveguide walls and of the copper plating in addition to the RF loss in the copper. Although the surface impedance of the copper is predominantly in the anomalous limit between 2 K and 50 K, the residual resistivity ratio (RRR) and thickness of the copper layer have a significant influence, and must be chosen to balance performance risk against overly conservative manufacturing tolerances. [5]

## 5 RF WINDOW

Each coupler contains one RF window at 300 K. The window is a thin metal-ceramic waveguide window using a rectangular copper-gasketed knife-edge seal on the cavity vacuum side. A variety of similar windows have been developed at JLab having RF power handling capabilities in excess of the CEBAF energy upgrade requirements. The VSWR is less than 1.1 to 1 through the use of compensating irises built into the window.

## 6 SUMMARY

A fundamental power coupler prototype has been designed for the CEBAF Energy Upgrade Cryomodule having several advantages over the existing design; most notably, the elimination of window arcs and unwanted beam steering from "coupler kicks". Prototype fabrication has begun and testing is scheduled later this year.

## ACKNOWLEDGEMENTS

The authors wish to thank the staff of the Accelerator Development group and in particular the support of Sherry Thomas, Carolyn Camp, and Kelly Hanifan in the preparation of this work.

## REFERENCES

- [1] J. R. Delayen, "Upgrade of the CEBAF Acceleration System", these Proceedings.
- [2] L. R. Doolittle, "Strategies for Waveguide Coupling for SRF Cavities", Proceedings of Linac98, Chicago, IL.
- [3] R. C. York, C. Reece, "RF Steering in the CEBAF CW Superconducting Linac", Proceedings of the 1987 Particle Accelerator Conference, Washington, D.C.
- [4] L. R. Doolittle, "Waveguide Surface Currents", Jefferson Lab Technote.
- [5] L. Phillips, G. Wu, JLab Technote to be published, "Material Properties and Thermal Transitions in RF Power Couplers".

# ACCELERATOR RELIABILITY DATABASE

Christopher M. Piaszczyk  
Advanced Energy Systems, Inc.  
Bethpage, NY 11714

## Abstract

Accelerator beam trips have been identified as a significant issue in the development of high power accelerator driven systems envisioned for transmutation of waste, energy amplifiers, etc. where the accelerator must work in conjunction with a subcritical reactor. In order to enable the design of these systems with the high reliability required, a reliability database is being assembled. This paper provides preliminary results which may be of use in conceptual design considerations.

## 1 INTRODUCTION

The idea of the database effort originated with the International Fusion Materials Irradiation Facility (IFMIF) accelerator reliability analyses in 1995 when it was realized that information available at the time to support these analyses was very limited [1]. A reliability survey of operating accelerator facilities has been started in the summer of 1997. Data was collected from literature, personal communications via phone and email with staff members and site visits at a number of accelerator facilities, including: ISIS, CERN, DESY, LANSCE, TJNAF, Fermilab, etc. While the completion of the accelerator reliability database is still far ahead, the LANSCE data set was analyzed in early 1998 and the details of this effort are described in [2,3,4]. In [5], the data was analyzed as a random process. Here, we present additional results believed to be of potential utility in Accelerator Driven System (ADS) system planning. Since the subcritical reactor in ADS is very sensitive to beam trips, it is important to know the distributions of the beam trip down times and the times between down time events. Although these statistics will be different for each specific design, the scale of the LANSCE linac is believed to be

representative of a linac for ADS (it is noted, however, that the Proton Storage Ring is included here).

## 2 DATA

Table I summarizes the statistics for all the data points available, which consist of cycles 71 through 76 from 7/10/96 to 7/27/97 (some data had to be censored: primarily to eliminate a number of overlapping down time events, but it should be noted that the sampling of data at one minute intervals represents another censoring mechanism). Each cycle is a separate campaign separated from the others by a built-in production stop for maintenance. Additional maintenance budget is included in the schedule and exercised during each cycle as listed.

Detailed data is provided in the figures on the next page. Figure 1 shows the cumulative number of down time events as a function of calendar time. Figure 2 shows the same data as a function of the cumulative uptime. Figure 3 shows the histogram of the Times Between Events (TBE) and Figure 4 shows the histogram of the Down Times (DT). Since the DT histogram is highly skewed to the left, Figure 5 shows the DT histogram with an expanded horizontal axis to show more details. This distribution is typical of the down times. Most of the down times are very short (75% below 15 min.), but there are usually a few outliers (here, 58h 54 min. due to a magnet power supply).

Figure 6 illustrates an attempted fit of the TBE's with an exponential distribution. Clearly, the fit is not so good. However, a Weibull distribution with characteristic life of 6 hours and shape factor of 0.67, shown in Figure 7 fits the data remarkably well. When plotted on the log-linear paper in Figure 8, one can see that the Weibull fit slightly underpredicts the probability of the short TBE's but it is still very satisfactory.

Table I. LANSCE Summary of Operational Data

Cycle#	71	72	73	74	75	76	Total
Run Start Time	7/10/96 8:00	8/30/96 2:10	10/29/96 20:00	3/7/97 8:00	4/23/97 8:00	6/18/97 8:00	
Run End Time	8/24/96 8:00	10/21/96 7:00	11/28/96 20:00	4/21/97 8:00	5/16/97 8:00	7/27/97 8:00	
Calendar Time (h:min)	1080:00	1252:50	720:00	1080:00	1296:00	936:00	6364:50
Built in Stops (h:min)	115:07	191:00	66:00	84:11	38:50	44:41	539:49
Cum Uptime (h:min)	811:14	1042:23	626:47	952:01	1129:33	825:54	5387:52
Cum Downtime (h:min)	153:39	19:27	27:13	43:48	127:37	65:25	437:09
Availability	0.84	0.98	0.96	0.96	0.90	0.93	0.93
Total Number of Down Time Events	135	140	75	97	175	109	731
Mean Time Between Events (h:min)	5:56	7:14	8:16	9:48	6:21	6:44	7:23
Mean Down Time (h:min)	1:08	0:08	0:21	0:27	0:43	0:36	0:34

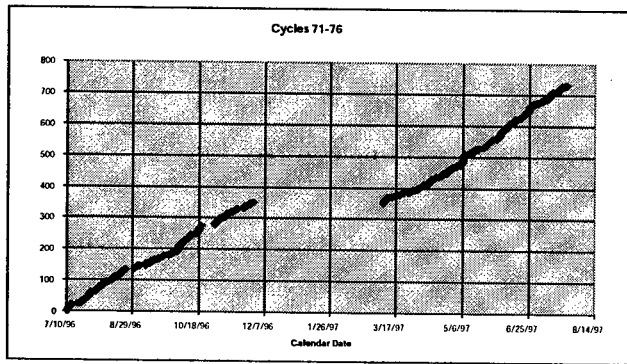


Figure 1. Cumulative Number of Down Time Events vs. Calendar Time

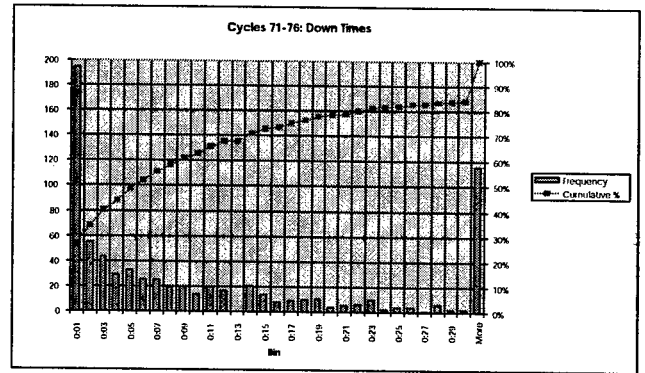


Figure 5. Histogram of Down Times (Expanded)

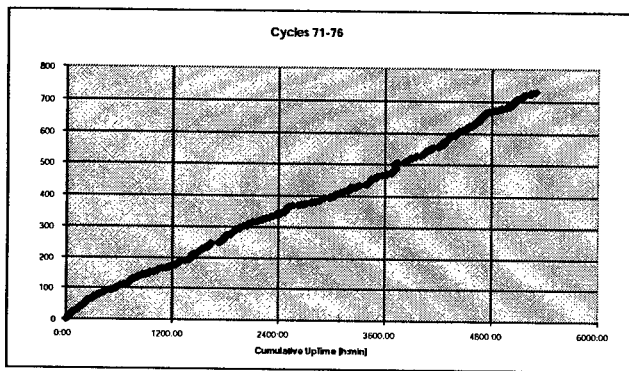


Figure 2. Cumulative Number of Down Time Events vs. Cumulative Uptime

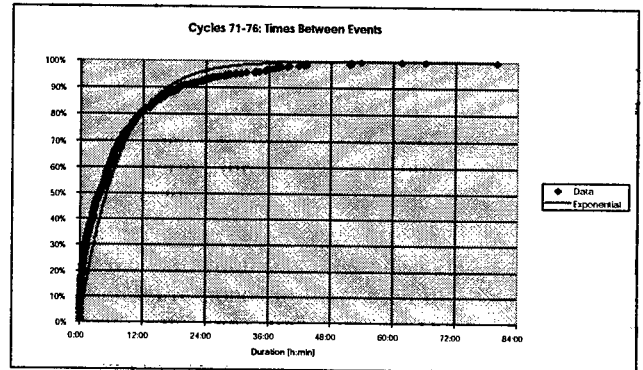


Figure 6. Exponential Fit of Times Between Events Data

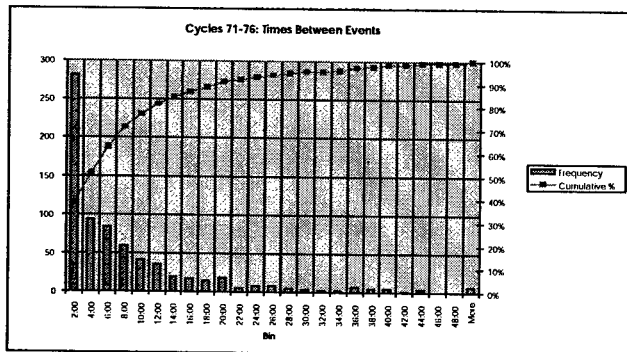


Figure 3. Histogram of Times Between Events

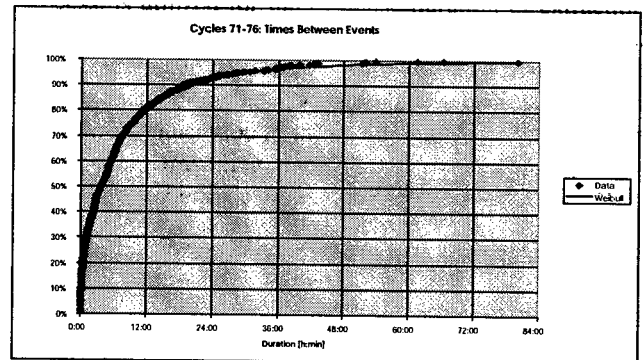


Figure 7. Weibull Fit of Times Between Events Data

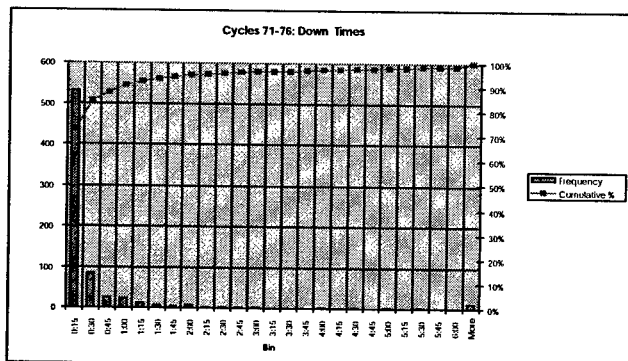


Figure 4. Histogram of Down Times

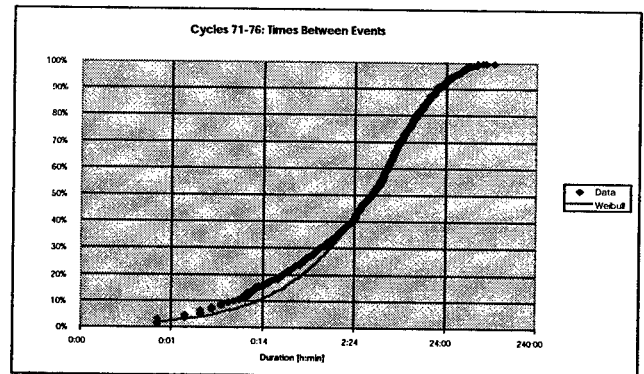


Figure 8. Weibull Fit of Times Between Events Data (Expanded)

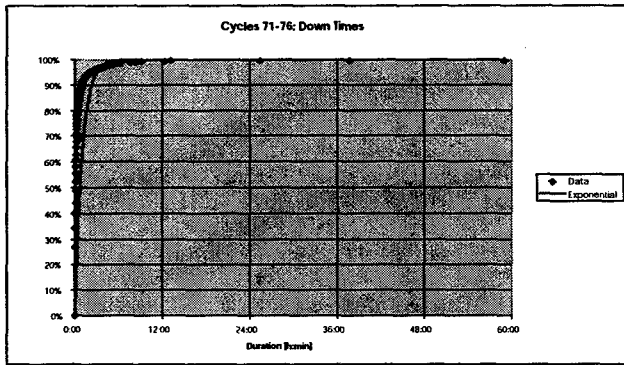


Figure 9. Exponential Fit of Down Times Data

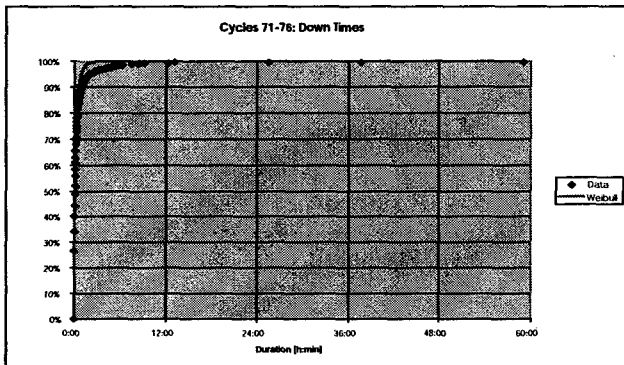


Figure 10. Weibull Fit of Down Times Data

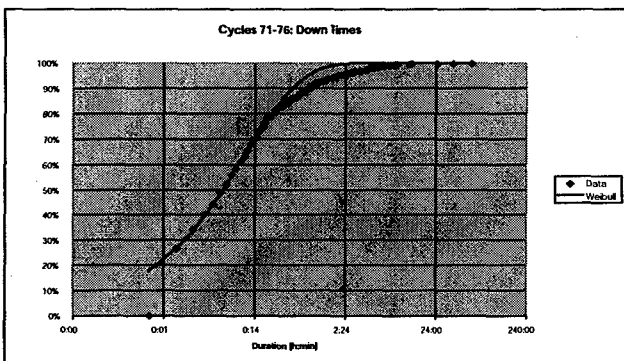


Figure 11. Weibull Fit of Down Times Data (Expanded)

The DT's cannot be fitted so easily. Figure 9 shows an unsuccessful fit of the DT data with an exponential distribution. A Weibull curve with characteristic life of 11 minutes and shape factor 0.7 shown in Figure 10 fits the data very well in the short duration range. This can be seen more clearly in Figure 11 with the horizontal axis stretched out via the log scale. Figure 11 shows also that this Weibull distribution overshoots the data in the range of the long down times. However, 75% of the data falls below 15 min.

### 3.0 CONCLUSIONS

The capability to predict the reliability characteristics of the linac driver in the future ADS system is important for

many reasons. Primarily, the beam trips will be a significant neutron flux driver in the subcritical reactor. In addition, prediction of beam trip probabilities is needed for maintenance scheduling, advance spare parts procurement, and general reliability and availability design. While each particular design will require a separate reliability analysis, the data presented in this paper may be useful for preliminary planning. For the long term, the first step in assuring a satisfactory reliability performance of complex repairable systems such as accelerator facilities will have to be a thorough analysis of all existing operations data.

### REFERENCES

- [1] C. M. Piaszczyk and M. Rennich, "Reliability Analysis of the IFMIF", AccApp '98, 2nd Topical Meeting on Nuclear Applications of Accelerator Technology, September 20-23, 1998, Gatlinburg, TN
- [2] M. Eriksson, C. M. Piaszczyk, "Reliability Assessment of the LANSCE Accelerator System", AccApp '98, 2nd Topical Meeting on Nuclear Applications of Accelerator Technology, September 20-23, 1998, Gatlinburg, TN
- [3] C. M. Piaszczyk, "Operational Experience at Existing Accelerator Facilities", NEA Workshop on Utilization and Reliability of High Power Accelerators, Mito, Japan, October 1998
- [4] C. M. Piaszczyk and M. Rennich, "Reliability Survey of Accelerator Facilities", Maintenance and Reliability Conference Proceedings, May 12-14, 1998, Knoxville, Tennessee
- [5] C. M. Piaszczyk, "Understanding Accelerator Reliability", Linac '98, August, 1998, Chicago, Illinois

## MAGNETIC FIELD DISTRIBUTION MEASUREMENT BY VIBRATING WIRE STRAIN GAUGE

Arutunian S.G., Dobrovolski N.M., Egiazarian S.L.,  
Mailian M.R., Sinenko I.G., Sinjavski A.V., Vasiniuk I.E.

Yerevan Physics Institute 375036, Br. Alikhanian St. 2, Yerevan, Armenia

### Abstract

Development of a simple and cheap device for measurement of magnetic field spatial distribution is an urgent problem [1-3]. In this paper we propose the method of magnetic field spatial distribution definition by magnetic interaction measurement of probes from known materials. The developed system for such gravimetric measurement of magnetic field gradients partially solves this problem.

### PRELIMINARY NOTES

The force of interaction  $\vec{F}$  between a small sample of magnetic moment  $\vec{M}$  with an external magnetic field of strength  $\vec{H}(\vec{r})$  is defined by expression

$$\vec{F} = \text{grad}(\vec{M}\vec{H}). \quad (1)$$

We are mainly interested in two cases: when the magnetic moment is entirely induced and is determined by the magnetic permeability  $\mu$  of the sample's material and, the second, when the magnetic moment is independent of the external field.

In the first case one has to take into account the proportionality of magnetic moment to the internal field  $\vec{H}_i$  of the sample, which in its turn, is determined by the external magnetic field, magnetic susceptibility and sample's geometric form. For sample located in an axially symmetric magnetic field the interaction force is defined as follows [1]:

$$F_z = \frac{\mu - 1}{8\pi(1 + D(\mu - 1))} V \frac{\partial H_z^2}{\partial z}, \quad (2)$$

where  $D$  is demagnetisation factor determined by the sample's geometry.

The force of interaction of a permanent magnet of magnetic moment  $M_z$  with an external field  $H_z$  is determined by the expression:

$$F_z = M_z \frac{\partial H}{\partial z}. \quad (3)$$

When studying samarium-cobalt magnets in the fields of the order of Earth's magnetic field one also can ignore the induced magnetisation.

The scanning of a probe along the  $z$  axis gives an information about the spatial distribution of the interaction force, which restores the gradient of the magnetic field.

### EXPERIMENTAL SETUP

#### Wire Strain Gauge

A specially developed Wire Strain Gauge (WSG) was used to measure the force of interaction between the sample and magnetic field. String magnetometer [2] with some improvements was taken as a prototype. In particular, by special means the lower end of the string with load was fixed in horizontal plane. As strings were used tungsten or beryl bronze wires of diameter 100  $\mu\text{m}$ .

The magnetic system was made on the basis of samarium-cobalt permanent magnets.

An electromechanical generator excites the string oscillations due to the interaction of alternating current through the string with the magnetic field in the magnet gap. A system of forced automatic regulation keeps a stable current in the string.

Mentioned measures allowed to improve the level of relative sensitivity of WSG down to  $10^{-5}$  at the load  $\leq 3\text{N}$ . Since the magnetometric measurements are done by slow rate scanning, it was necessary to provide long time stability at the level  $10^{-5}$ . A special method of fixation of the string's lower end practically excludes wire's drawing out of clips. Pickup's thermostabilisation allowed to achieve long-time stability during many hours.

Fig. 1 shows a typical behaviour of pickup readings at permanent load 2.25N during more than 64 hours. The temperature of the base was stabilised, with accuracy  $0.1^\circ\text{C}$ . From Fig. 1 one can see that mean square deviation was  $6.65 \cdot 10^{-6}$ . This value is



more promoted than that of known pickups based on measuring of vibrating wire frequency. E.g. in [5]

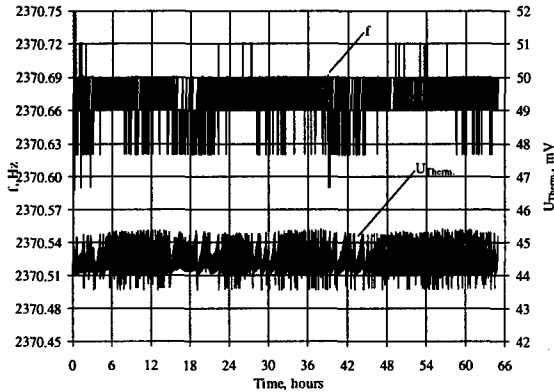


Fig. 1

string pressure pickups of resolution  $10^{-4}$  from measurements interval are presented. String pressure pickups are used in oceanology investigations, and due to some improvement (pickup's thermostabilisation, string's preliminary ageing etc.) the error was lowered to the value  $\pm 1 + 2 \cdot 10^{-4}$  ( $\pm 4 \cdot 10^{-5}$  is needed) [6]. The string pickups for measurement of tension in steel and concrete of the firm GeoKon have resolution  $\pm 3 \cdot 10^{-5}$  [7].

#### Probes

Rings from soft magnetic steel, permalloy as well as of samarium-cobalt permanent magnets were used as probes. Usage of ferromagnetic probes in strong magnetic fields entails some difficulties caused by nonhomogenous and non-linear dependence between magnetisation of probes' material and the external field. Since the measurements were done in weak magnetic fields, we had ignored this nonhomogeneity.

### EXPERIMENTAL RESULTS

Experiments were done on two types of magnets: composite solenoid with symmetry axis along the  $z$  axis and Helmholtz coils system designed to compensate Earth's magnetic field (coils lay in horizontal plane). Each gravimetric measurement was a representation of interaction force between the probe and magnetic field under scanning of  $z$  axis. Currents in solenoids and coils were selected to have such a value that the measured values lay in operating range of WSG with optimal range of sensitivity. In case of composite solenoid this current was  $I=200\text{mA}$ , for Helmholtz coils  $I=3.1\text{A}$ . Since

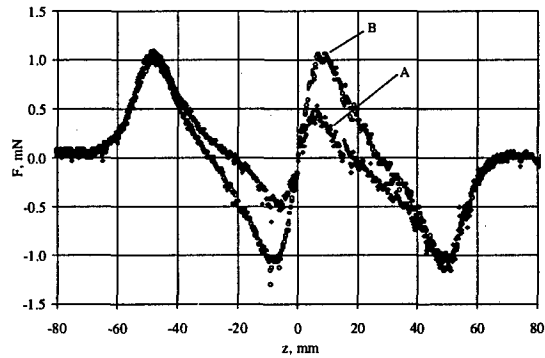


Fig. 2

both systems consist of two separated coils, the measurements were done for parallel and antiparallel currents. Fig. 2 represents the primary experimental results for composite solenoid for parallel (curve A) and antiparallel (B) currents respectively.

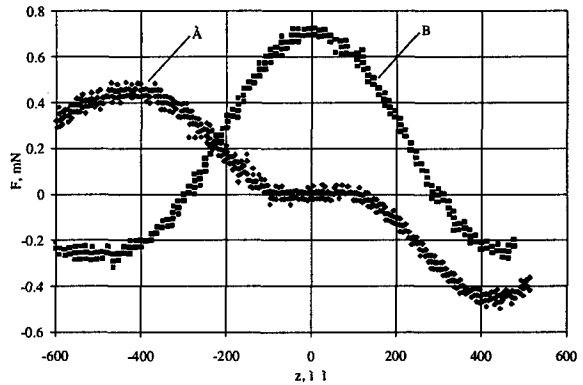


Fig. 3

Vertical axis represents the interaction force in mN. The scanning speed was  $0.113\text{mm/sec}$ . A steel-3 ring with inner diameter  $3\text{mm}$ , external diameter  $13\text{mm}$  and thickness  $6.4\text{mm}$  was used as a probe. Signals at going in and out of the solenoid were coincide in satisfactory level (null signals with switched off currents are omitted). The width of experimental track is about  $0.1\text{mN}$  and is greater than the resolution of string tension pickup and is mainly caused by swinging of rather big probe in the narrow hole of coils during the scanning. Division of  $F$  by the factor  $(\mu - I)V/8\pi(I + D(\mu - I))$  gives dependence of the value  $\partial H_z^2/\partial z$  on  $z$ . In its turn the last function allows to restore the function  $H_z(z)$  along the axis of solenoid.

Fig. 3 represents similar gravimetric measurements for Helmholtz coils system (A corresponds to parallel currents, B - to antiparallel ones). Samarium-cobalt magnets were used as

probes. Here the track width was about 0.04mN. This is less than that in previous case, since the probes relative sizes were much more less than coils diameter. Presented curves define the Helmholtz coils system magnetic field gradient up to a constant.

## PROCESSING OF EXPERIMENTAL RESULTS

Obtained experimental results were processed to define the magnetic field gradients. To find it actually one have to find the factor  $(\mu - I)V/8\pi(I + D(\mu - I))$  for probes with magnetic susceptibility  $\mu$  or magnetic moment  $M_z$  for probes from permanent magnet. In principle, one can estimate these parameters using the tabulated values of known materials in use, however, since these factors depend on the samples' shape, finding of these parameters using special calibrating measurements by Hall detectors seemed preferable. Note that measurements done near the experimental points of field's gradient are sufficient.

There are two way to compare the gravimetric measurements with Hall detectors ones: integrate gravimetric curves or differentiate Hall's detectors' ones. Taking into account that during each period of measurement the current trough coils was switched off, the numerical differentiation is preferable, because it uses information of local sections of experimental curves.

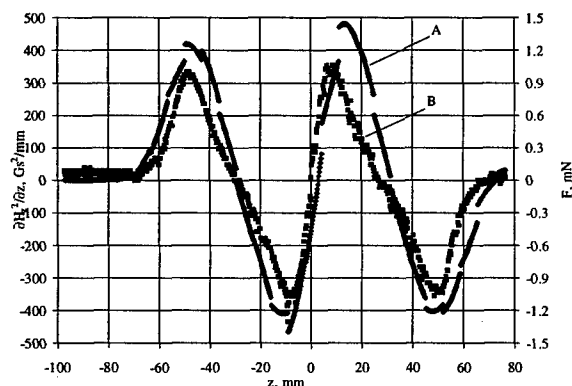


Fig. 4

To calibrate measurements of composite solenoid the experimental results for antiparallel currents were used. Calculation of gradient of magnetic field square using experimental points for composite solenoid was done by numerical approximation of seven groups of currents switching on. Results were compared with gravimetric measurements and are presented in Fig. 4. Such a comparison gives a coefficient of proportionality between gradient of

magnetic field square and interaction force equal to 445.48 (Gs<sup>2</sup>/cm)/mN with correlation factor 87%.

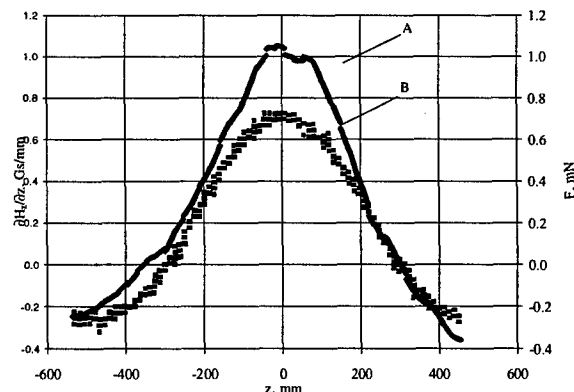


Fig. 5

Similar calculations of the field gradient for the Helmholtz coils system using Hall detector measurements are presented in Fig. 5. In this case comparison with the gravimetric measurements defines the probes magnetic moment of the order of 1.35 (Gs/cm)/mN with correlation factor 95%.

## CONCLUSION

This work was aimed to develop and construct a complete system of measurements, although the measurements were done on demonstration samples. Varying of temperature both to the high and low temperatures are possible and will essentially broaden unit's possibilities.

Combination of these method with other measurements of magnetic field characteristics gives a possibility to fulfil sufficiently simple and precise definition of magnetic parameters.

This work was carried out by support of firm HTM Reetz (Berlin), and authors are thankful to Dr. R.Reetz. Authors also thank V.Gavalian and A.Aleksanian for their help.

## REFERENCES

1. Methods of Experimental Physics, v.1, Classical Methods, - Ed. by I.Estormann, Acad.Press, 1959, N7, p. 537
2. El'tsev Ju. F., Zakosarenko V.M., Tsebro V.I., String Magnetometer, Trudy FIAN, v. 150, M, 1984.
3. A. Harvey, Proc. Magnet measurement and alignment CERN Accelerator School, Ed. S. Turner (Switzerland, 16-20 March 1992), CERN 92-05, p. 228-239.
4. Tamm I.U. Basics of Theory of Electricity. - M, Nauka, 1976.
5. Asch G. Les Capteurs en Instrumentation Industrielle, v. 1, 2. Dunod, 1991.
6. Kovchin I.S. Autonomous Oceanographic means of Measurement.. - L, Gidrometeoizdat, 1991.
7. Geokon incorporated.- <http://www.geokon.com/products>.

## A NEW WINDOW COATING SYSTEM AND A NEW WINDOW FOR THE ALS\*

C.C. Lo<sup>\*\*</sup>, J. Julian, K. Baptiste and B. Taylor<sup>\*\*\*</sup>

Advanced Light Source  
Lawrence Berkeley National Laboratory  
1 Cyclotron Road,  
Berkeley, California USA 94720

### Abstract

A new window coating system has been developed to coat a newly designed window for the Storage Ring RF System in the Advanced Light Source(ALS). A bell jar large enough to accommodate the 15cm (OD) x 50cm (L) tubular ceramic window is used for a vacuum chamber. Methodical procedures are employed to ensure the chamber is free of contaminants before any coating is carried out. A single filament is used to coat the new tubular window, however other shapes of filaments could be used for coating other windows if necessary. Details of the coating system and window construction as well as the performance of the coating system and the new windows will be presented.

### 1 INTRODUCTION

In the ALS Booster and Storage ring the RF cavities operate at ultra high vacuum (UHV) and require ceramic windows to serve as barriers between UHV and atmospheric pressure. These windows enable the cavity to be isolated and at the same time allows Radio Frequency (RF) signals to be transmitted from the wave guide to the cavity. Since these windows are installed at the window coupling ports of the cavities they must be able to withstand the high electric field of the cavity, have low RF power dissipation and present a low secondary electron emission coefficient to reduce multipactoring that usually leads to catastrophic break downs. The last item dictates that the ceramic window be coated with materials which would provide a small secondary electron emission coefficient. Another very important function of the coating is to drain the charge on the ceramic away before it is charged to a flash over potential. Therefore it is imperative that the two ends of the ceramic tube be metalized around the perimeter at the ends and 1mm into the inner wall so that the coating can make connection to ground through them.

### 2 THE COATING SYSTEM

Fig. 1 is a diagram showing the details of the coating system. The bell jar has a diameter of 48cm and a height of 76cm. The total height of the tubular window including flanges measures 53.2cm. The titanium filament runs straight through from the top to the

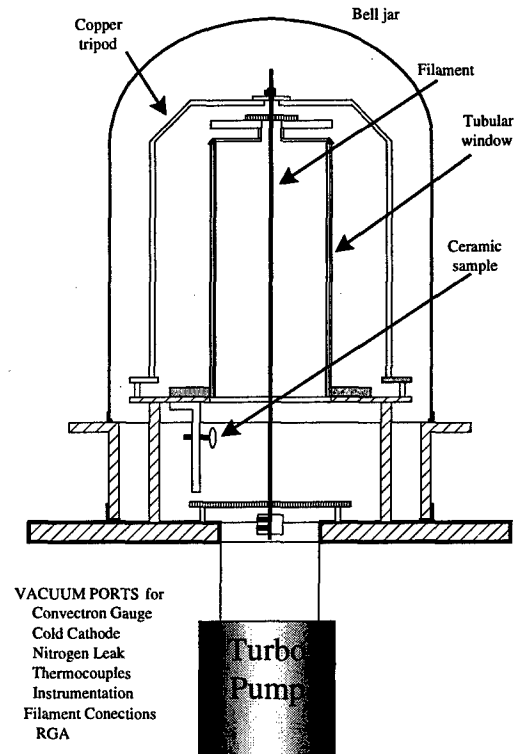


Fig. 1 Coating System

bottom of entire length of the window and beyond. It is important to have the window's inside surface facing a uniformly heated portion of the filament as much as possible to obtain a uniform coating. Power is delivered to the top connection of the filament via a tripod supporting structure. The lower part of the filament is weighted down to keep the filament straight through out the coating cycle. A turbo pump is used in series with a dry scroll pump to evacuate the bell jar chamber. A residual gas analyzer (RGA) is used to look at the evacuated chamber for any unusually high residuals before starting the coating process. After many discussions with others<sup>1,2,3</sup> who have done this process before we decided to coat the ceramic window with a coat of approximately 10 to 20 Angstrom (1-2nm)<sup>4</sup> of Titanium Nitride (TiN). The filament operates on 0 to 30V AC power.

### 3 THE WINDOW

On going effort for aperture window development has been in progress for at least 30 years, pursuing a course from DESY to Daresbury to LBNL. The Daresbury Laboratory S.R.S. developed a series of ceramic windows that can handle a maximum of 45kW cw RF power into the unloaded cavity. Power was limited by ceramic charging effects resulting in non destructive flashover on the atmospheric side of the window.

The ALS requires two cavity windows rated at 70kW cw input each and a total input power with beam of 250kW. A new window was designed in which the ceramic disc was replaced by a ceramic tube with a metal top cap that can be fitted to the waveguide upper wall. Typically a disc window could provide a coupling factor up to 5. Without a ceramic disc loading the cavity port, the tubular window has a lower coupling factor. By adding loading vanes at the bottom flanges as in Fig. 3, the cut off frequency of the aperture was lowered to the benefit of the coupling factor attainable, both for the input power and exit HOM frequencies. Typically a coupling factor of 3 can be achieved with the loading vanes. Figure 2 is a diagram of the ceramic tubular window that has a length of 50cm and an internal diameter of 14cm. The thickness of the ceramic tube is 0.5cm. The bottom flange is made out of oxygen free copper with water cooling chamber and is brazed to the ceramic tube. It also has a stainless steel knife-edge that provides UHV seal to the cavity connecting flange. The top flange construction incorporates a flexible diaphragm to accommodate thermal expansion and alignment problems. The two loading vanes for obtaining higher coupling factor are integral parts of the bottom flange.

### 4 THE COATING PROCESS

The tubular ceramic RF window is given a thorough cleaning of the through and blind holes to remove all lubrication products by cleaning with acetone, isopropyl alcohol, and finally ethyl alcohol. The whole window is UHV cleaned in the plating shop, and then mounted in the vacuum coating system. Temperature probes are installed at the top, middle, and bottom of the ceramic for monitoring of the bake-out and coating temperature. A titanium filament wire, 2.0mm diameter of 99.7% purity, is installed through the center of the tubular window. A vertical filament wire is used twice before being replaced, and the lower ring filament wire is being used only once because of mounting difficulties, sagging, and becoming very brittle after a single run. This lower ring filament is used to coat the lower part of the ceramic tube in the older version of the window only. The new windows do not need this extra coating process. Verification targets are installed to verify the thickness of the TiN coating of every run. The vacuum coating system base, spool, and bell jar are wiped down with ethyl alcohol

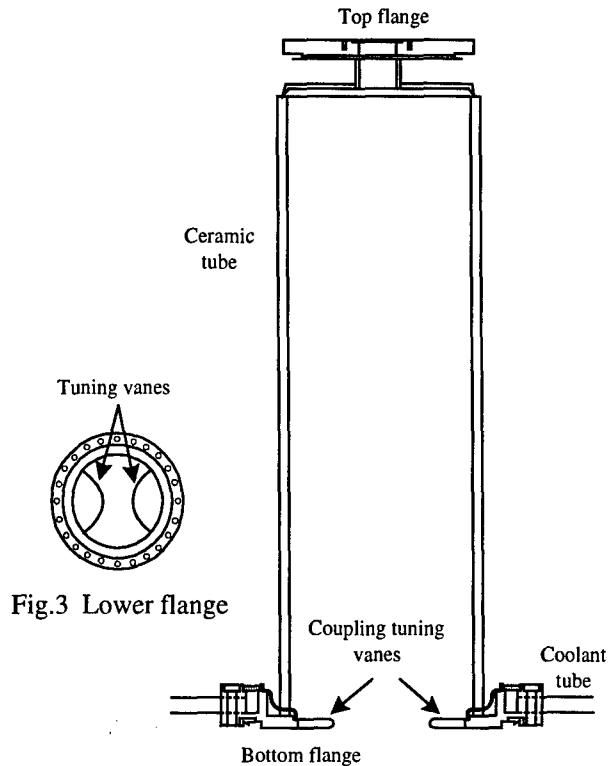


Fig. 2 RF Window

and the vacuum system is closed up for pumping. A Varian 600DS-scroll vacuum pump with a turbo-V 300HT pump is used to pump down the chamber. Four 250W IR lamps, a base plate heater that can provide a maximum temperature of 70°C and the Ti filament running between 10A to 13A are used to bake out the vacuum chamber. This low temperature bake will last for a period of 3 to 5 days or until the vacuum pressure is in the low  $10^{-7}$  Torr range or better. An RGA scan is taken to check for water, petroleum products, etc. before coating.

Two hours before the coating run, the cold trap is filled and the nitrogen lines are purged for twenty minutes from a full Dewar flask. Next, the vacuum chamber is purged with dry nitrogen at a pressure of 3 to 8 x  $10^{-4}$  Torr via the .01 micron particle filter through the leak valve for period of ten to twenty minutes. This nitrogen purge is repeated for a total of up to four times. The optical pyrometer and Infrared thermometer are mounted on fixed supports and aligned using an illumination lamp. The two units are used to monitor the filament wire at the base of the window. Ten minutes before coating, the IR lamps and the base heater are secured, and the nitrogen leak is set for 5 x  $10^{-5}$  Torr. At the start of the coating run, the timing clock is started and the filament is brought up to 30A. After fifteen seconds, the filament current is adjusted for a filament temperature of 1050°C. The optical pyrometer temperature is used as the reference for the coating process. The infrared thermometer is used as a backup because of its limited focal size on the wire that has a tendency to change if moved. Throughout the coating process, the filament voltage

and the nitrogen leak are adjusted repeatedly to maintain the prescribed coating parameters. All readings are logged every ten minutes. At the completion of the 2-hour coating run, the temperature of the ceramic window will have risen from 60°C to 114°C. The filament current is reduced to 10A for a period of one hour for cool down, and the nitrogen pressure in the bell jar is increase to  $5 \times 10^{-4}$ . At the end of one hour, the filament is turned off, bell jar isolation valve is closed, vacuum pumps secured, and then the bell jar is back filled with nitrogen pressure to  $1 \times 10^{-1}$  Torr.

## 5 WINDOW PERFORMANCE

We have used the coating system to coat four tubular windows. The coatings on all four windows were successful. Of the four windows two were new ones made for us by EEV of England, and the other two were reclaimed units from a different vendor. The two reclaimed windows came with some unmanageable physical flaws and hence can only be used at lower power levels and are serving as emergency backup units. We experienced an unusually high operating temperature in one of the two new windows since conditioning and the temperature has not come down as yet. The cause of the high operating temperature is not entirely clear at this time however it could be due to the fact that this window was rejected by the factory due to a vacuum leak and subsequently was not handled or cleaned as a new window. The vacuum leak, however, was circumvented in LBNL after many iterations of solution. The plan is to remove this window at a convenient time, have it cleaned, alumina bead blasted and re-coat. Despite its higher than normal operating temperature (above 100°C) this

window is free of voltage breakdowns. The fourth window operates without any problem and both new windows were conditioned up to full power within a relatively short time (a few hours).

## 6 CONCLUSION

Our new coating system performs very well. The recipe we have developed for coating this type of windows is quite effective and the performance of the coating is consistent. We are still in the process of acquiring a few more good windows for ALS.

## 7 REFERENCES

1. Rich Callen, Private communication.  
SLAC
2. Karen Cummings, Private communication.  
LANL
3. K. Primdahl, R. Kustom, J. Maj  
"Reduction of Multipactor in RF Ceramic Windows Using a Simple Titanium-Vapor Deposition System", IEEE PAC Proceedings, May 1-5, 1995, pp 1687-1689.
4. Y. Saito, "Breakdown Phenomena in Vacuum", KEK. Linear Accelerator Conference Proceedings (1992)

\*Work supported by the Director, Office of Energy Research, Office of Basic Energy Science, Materials Science Division, of the U.S. Department of Energy under Contract No. DE-AC03-76F00098

\*\* cclo@lbl.gov

\*\*\* Retired

# 100 MW ACTIVE X-BAND PULSE COMPRESSOR\*

A. L. Vikharev<sup>1</sup>, A. M. Gorbachev<sup>1</sup>, O. A. Ivanov<sup>1</sup>, V. A. Isaev<sup>1</sup>,  
S. V. Kusikov<sup>1</sup>, L. Kolysko<sup>1</sup>, A. G. Litvak<sup>1</sup>, M. I. Petelin<sup>1</sup>,  
J. L. Hirshfield<sup>2, 3</sup>, O.A. Nezhevenko<sup>3</sup> and S. H. Gold<sup>4</sup>

<sup>1</sup>Institute of Applied Physics, Nizhny Novgorod, Russia

<sup>2</sup>Physics Department, Yale University, New Haven, Connecticut 06520-1820

<sup>3</sup>Omega-P, Inc., 345 Whitney Av., New Haven, Connecticut 06511

<sup>4</sup>Plasma Physics Division, Naval Research Laboratory, SW, Washington, DC 20375-5346

## 1 INTRODUCTION

It is widely accepted that microwave pulse compressors are required to achieve the high power and short pulse lengths for high-gradient linear accelerators. Compressors are categorized within two main classes: passive (e.g., SLAC Energy development-SLED) [1,2] and active [3]. Active compressors have great potential for application with linear accelerators. The current Omega-P/IAP program is to develop and study the operation of a novel active microwave compressor that utilizes an oversized waveguide and electrically controlled Bragg reflectors. An active pulse compressor has been developed that is able to provide output pulses of at least 100 MW power with pulse duration of 100 ns at X band, and with a power gain of 12-15. The compressor is being evaluated using 1-1.5  $\mu$ sec pulses from the Omega-P/NRL 11.424 GHz magnicon being operated at NRL. This paper describes design of the

compressor and the magnicon-compressor microwave circuit, and gives first experimental results from low-power tests.

## 2 DESIGN OF ACTIVE BRAGG COMPRESSOR (ABC)

In the framework of the Project for realization of a Microwave Active Bragg Compressor (ABC) with its output power of at least 100 MW, we manufactured an ABC prototype. This is an evacuated version made of copper. The compressor design is distinguished from prior active compressors in that microwave energy is stored in a resonator operating in the "breakdown-proof"  $TE_{01n}$  mode, with  $n \gg 1$ . The testing of prototype designs of such a compressor using  $\sim 100$  kW-level microwaves ( $f = 9.4$  GHz) showed that a compressor of this design is able to provide power gains up to 20.

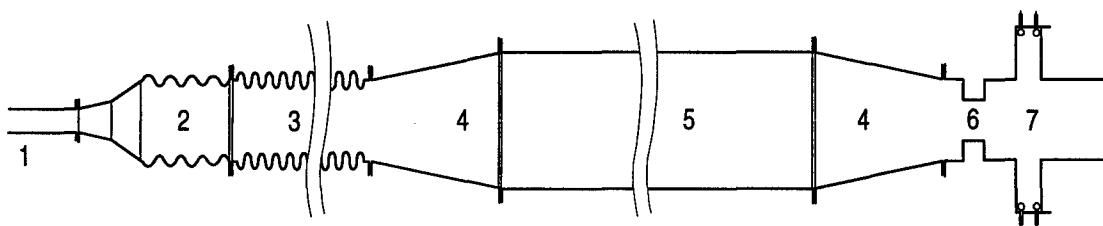


**Fig.1.** Schematic diagram of the Active Bragg Compressor operating in the  $TE_{01}$  mode: 1 - input waveguide, 2 -  $TE_{01}$ -mode converter, 3 - input Bragg reflector, 4 - smooth tapered transition, 5 - storage cavity, 6 - over-critical narrowing of the waveguide, 7 - output reflector with electrically controlled gas discharge switches.

The scheme of the compressor is shown in Fig.1. The compressor consists of mode converters ( $TE_{01} \rightarrow TE_{11}^0$ ,  $TE_{11}^0 \rightarrow TE_{01}$ ) connected with smooth tapered transitions and a resonator formed by a Bragg reflector, a

section of a cylindrical waveguide and an output reflector. The central part of the resonator is a section of an over-sized 1m long waveguide 80 mm in diameter which is equipped with a tapered 400 mm long transition to a narrower waveguide. The diameter of the latter waveguide was 55 mm, and the  $TE_{01}$  mode is the only propagating mode of all the axially symmetric ones.

\* Supported by the U. S. Department of Energy, Division of High Energy Physics.

The output reflector consists of the active and passive sections. The active section is based on a step-wise widening of a circular waveguide. This stepped widening section comprises a cylindrical  $TE_{311}$  mode resonator containing a quartz ring-shaped gas-discharge tube. The discharge tube is used to switch in about 10 nsec from the regime of energy storage to the regime of energy extraction. The diameter of the wider waveguide is 140 mm, and it can excite high order axially symmetric modes. The passive section is a waveguide section with a narrowing beyond cutoff. This combined output reflector makes it possible to reduce the intensity of the electric field in the region of the gas-discharge tubes in the active section. By changing dimensions of the cutoff waveguide narrowing in the passive reflector section, one can change the transmission coefficient and, thus, control the amplitude and duration of the compressed pulse. ABC is evacuated via three pumping ports. The compressor was tested for vacuum. It was evacuated up to the pressure  $10^{-6}$  Torr.

#### Specified characteristics of the $TE_{01}$ mode compressor

Input pulse duration	2.1 $\mu$ s
Output pulse duration	100 ns
Power amplification	17
Compression efficiency	60%
Inherent Q-factor of the whole resonator	150000
Specified load Q-factor provided by the input Bragg-type reflector with power reflection coefficient 98.5%.	56000

### 3 LOW POWER TEST MEASUREMENTS

The compressor was tuned in two stages. Initially the output reflector was adjusted in such a way as to provide a match of the maximum non-transmission and in the operating frequency of the compressor. Then, by changing the length of the cylindrical waveguide, the resonator was tuned precisely to the frequency of  $f_0 = 11.424$  GHz at the minimum of the compressor-reflected signal. When a high-voltage pulse was fed in, the microwave power stored in the resonator was discharged from the resonator in the  $TE_{01}$  operating mode.

The efficiency of pulse compression was optimized by changing the length of the step-wise widening of the waveguide. The measurements were performed when the

resonator was excited in the CW regime. A characteristic oscillogram of the compressed pulse is shown in Fig. 2. The compression coefficient was determined by the ratio of the peak power of the compressed pulse,  $P_p$  to the power  $P_0$  at the compressor input. The compression coefficients obtained in the experiment amounted to  $k = 11-12$  at a half-width pulse duration of  $\tau_p = 45-55$  ns.

Based on the experimental data, compressor efficiency in the pulse excitation regime was found. According to [4] energy accumulation in the resonator is described by the following expression:

$$W(t) = W_0[1 - \exp(-t/2\tau)]^2$$

where  $W_0 = (4\beta/(1+\beta))P_0\tau$  is the energy accumulated in the resonator in the stationary state,  $\beta = Q_0/Q_e$  is the coefficient of resonator coupling with the input aperture,  $Q_0$  and  $Q_e$  are the inherent Q-factor of the resonator and Q-factor of the coupling,  $\tau = Q_L/\omega$  is characteristic time of excitation of the loaded resonator with  $Q_L = Q_0Q_e/(Q_0 + Q_e)$ . Total efficiency of pulse compression in the compressor,  $\eta$ , is determined by expression

$$\eta = \eta_1\eta_2$$

where  $\eta_1 = W_p/W_0$  is the efficiency of transmission of the accumulated power to the load,  $W_p = \int P_p(t) dt$  is energy in the compressed pulse,  $\eta_2 = W(t)/W_i$  is efficiency of power accumulation in the resonator, and  $W_i = P_0t$  is energy at the compressor input at time moment  $t$ . The value of  $\tau$  required for efficiency determination was found by measuring the loaded Q-factor of the resonator. According to these measurements  $Q_L = 2.3 \cdot 10^4$  and  $\tau = 300$  ns. The value of  $\beta$  determined in the experiment was 2.2.

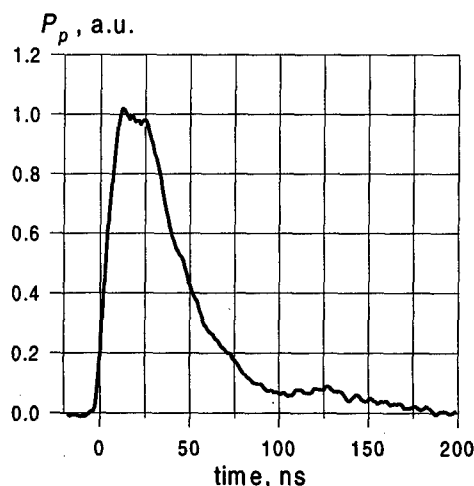
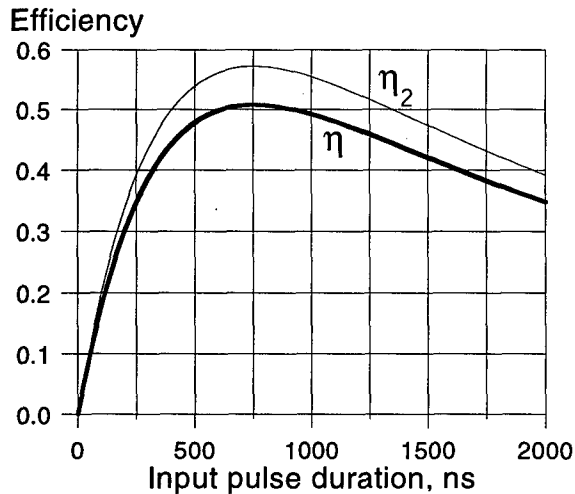


Fig.2 Envelope of compressed microwave pulse.

Efficiency of pulse compression calculated from the experimental data for cases of resonator fed with pulses of different duration is shown in Fig. 3. The same figure shows the curve for efficiency of power accumulation (upper curve) in the resonator. It is seen from the figure that when pumping pulses with a duration of 1  $\mu$ s are used, the total compression efficiency will be 50%. This efficiency proved to be somewhat lower than the value of

efficiency of power accumulation  $\eta_2$ , because of energy losses in the Bragg reflector. These losses can be eliminated by using the scheme of compressor excitation by means of a 3-db coupler with a common power input-output element.

#### 4 REFERENCES



**Fig.3** Total efficiency ( $\eta$ ) and energy storage efficiency( $\eta_2$ ) vs input pulse duration.

- [1] Z.D. Farkas et al., " SLED: A Method of Doubling SLAC's Energy," Proc.9<sup>th</sup> Conf. On High Energy Accelerators, 1974, SLAC-PUB-1453,p.576.
- [2] Z.D. Farkas , " Binary peak power multiplier and its application to linear accelerator design ".- 1985, SLAC-PUB-3694.
- [3] M.I. Petelin, A.L. Vikharev and J.L. Hirshfield, " Pulse compressor based on electrically switched Bragg reflectors," Advanced Accelerator Concepts, 7<sup>th</sup> Workshop-Lake Tahoe, CA,1996. AIP Conf. Proc. **398**, 822 (1997)
- [4] R.A.Alvarez, Some properties of microwave resonant cavities relevant to pulse-compression power amplification, Rev. Sci. Instrum., 1986, v.57, No10, pp.2481-2488



## Author Index

- Abe, Hiroshi 2015, 2749  
 Aberle, Oliver 949  
 Abo-Bakr, Michael 2385  
 Acharya, R. 1393  
 Adachi, Toshikazu 2271, 3348, 3752  
 Adamenko, Stanislav V. 3269, 3271  
 Adams, D.J. 2199  
 Adderley, P. 1991  
 Adolphsen, Christopher D. 253, 777, 3411, 3423, 3477  
 Afonin, A.G. 53  
 Agafonov, Alexey V. 1731, 1734  
 Agematsu, Takashi 2259  
 Ahle, Larry 1937, 3248  
 Ahn, Hyo-Eun 875, 1255  
 Ahrens, Leif A. 614, 1276, 1746, 2063, 2286, 2918, 3291, 3294  
 Akagi, Hirofumi 3749  
 Akai, Kazunori 440, 1132, 2731  
 Akaoka, Nobuo 3546  
 Akasaka, Nobumasa 1132, 2238, 2731, 3411  
 Akemoto, Mitsuo 3414  
 Akiyama, Atsuyoshi 343, 3158  
 Akre, Ronald A. 2846  
 Alai Tafti, A. 2722  
 Alba, Rosa 2578  
 Aleksandrov, A. 237, 3321  
 Aleksandrov, Aleksander V. 78, 2948  
 Aleksandrov, Vladimir S. 3501  
 Alekseev, Nicolay N. 1479  
 Aleshaev, Alexander N. 750  
 Alessi, James G. 106, 614, 1297, 1902, 1964, 3300  
 Alexahin, Yuri 1527  
 Alford, Owen J. 2590, 3251  
 Alimov, Andrey S. 2301, 2555  
 Alonso, Jose 574  
 Alton, Gerald D. 1878, 1881  
 Alton, William J. 845  
 Altuna, Xavier 2617  
 Amano, Daizo 2403, 2689  
 Amatuni, Andrey Ts. 3657, 3660  
 Ambrosio, G. 174  
 Ames, Friedhelm 1955  
 Andereg, Jim 1402  
 Anders, W. 197, 2385  
 Anderson, David E. 3390  
 Anderson, Edwin B. 1686  
 Anderson, James L. 571  
 Anderson, Oscar 1908, 1937  
 Anderson, Scott 217, 2006, 2039, 2042, 2045  
 Andersson, Ake 2945  
 Andreev, N. 174, 3194, 3197  
 Andreev, Nikolai 154  
 Andreev, V.A. 2256  
 Andrianov, Serge N. 1866, 2701  
 Anerella, Michael D. 185, 3161, 3170  
 Anferov, Vladimir A. 392  
 Anguelov, Vladimir 2289  
 Anthouard, Philippe 3260  
 Antoine, Claire 919  
 Antonello, M. 1324  
 Antonsen Jr., Thomas M. 360  
 Aoki, Yasushi 2018, 2036  
 Apel, Ruediger 812, 818  
 Arakawa, Dai 1141, 1653, 1821  
 Arakawa, Kazuo 2259  
 Araki, Sakae 343  
 Arapov, L. 237  
 Arcan, T. 174, 3197  
 Archambault, L. 325, 3705  
 Arduini, Gianluigi 1282, 1285, 2617, 2996  
 Argan, Andrea 1599  
 Arimatea, Claudio 2617  
 Arkan, T. 3194  
 Arkan, Tug T. 3242  
 Arnett, Don 1390  
 Arnold, Ned D. 2024  
 Aronson, A. 548  
 Artoos, Kurt 154  
 Arutunian, Suren G. 1468, 2105, 3657  
 Arvin, Adrian H. 1444, 1447, 1929, 1946  
 Arvin, Andy 349  
 Asaka, Takao 2015, 2749, 3507  
 Asano, K. 777, 3417, 3423  
 Asaoka, Seiji 667, 670  
 Aspenleiter, Jeffrey 1390, 2698  
 Assadi, Saeed 711, 720, 1082, 1085, 2719  
 Assmann, Ralph 330, 2996, 2999, 3002  
 Aston, David 2990  
 Atencio, Samuel J. 965  
 Aune, Bernard 432  
 Autin, Bruno 3071  
 Autrey, Daryl 3248  
 Avilov, Alexandr M. 2549  
 Ayers, James J. 1961  
 Baartman, Richard A. 128, 3534, 3537  
 Babayan, Ruben A. 2424  
 Baboi, N. 922  
 Babzien, Marcus 2024, 2158, 2471, 2480, 3722  
 Bach, H. 2427  
 Backe, H. 165  
 Badan, L. 1324  
 Badea, V. 3767  
 Bae, Young-Soon 3525  
 Bai, Mei 387, 471, 2725, 3336  
 Bailey, Roger 2617, 2996  
 Bak, J. S. 1384  
 Bak, Peter A. 2167  
 Bakker, Rene J. 197, 726, 2078, 2379, 2382  
 Baklakov, Boris 1387  
 Balakin, Vladimir 461  
 Balbekov, Valeri I. 315, 3062, 3146  
 Baldis, Hector A. 2000  
 Ball, M. 498, 1545, 1548  
 Ball, Millicent J. 3245  
 Ballarino, Amalia 1405  
 Balleyguier, Pascal P. 1444, 1447, 1946  
 Baltadoros, D. 1037  
 Bane, Karl F. 3432, 3486  
 Bane, Karl L.F. 1725, 1728, 2822, 3423, 3453, 3474, 3477  
 Bangerter, Roger O. 3215  
 Banks, Thomas I. 1686  
 Banna, S. 3600, 3606, 3609  
 Bannon, M. 3767  
 Baptiste, Ken 1471, 3131  
 Baranauskas, V. 2811  
 Barber, D. P. 2635  
 Bardy, Jacques 3260  
 Barklow, Timothy L. 307, 3489  
 Barlow, D. 3576  
 Barnard, John J. 1761, 1803, 1830, 3248  
 Barnes, C. 321  
 Barnes, Michael J. 1509, 3378  
 Barnes, Peter D. 2590  
 Barnes, Phil 980  
 Barnett, Ian 3743  
 Barone Tonghi, L. 2578  
 Barov, N. 2027  
 Barr, Dean S. 2214, 2241  
 Barraza, Juan 2090  
 Barry, Walter C. 636, 1207  
 Barsotti, E.L. 2146, 2211  
 Bartolini, R. 1557  
 Barzi, E. 174, 3330  
 Bassalleck, B. 471  
 Batchelor, Kenneth 75  
 Batsikh, Gennady I. 2564  
 Battle, Chris 2936  
 Batygin, Yuri K. 1737, 1740  
 Bauda, B. 197  
 Bauer, P. 3194  
 Baumann, C. A. 2659  
 Bayanov, Boris F. 3086  
 Bazhan, Anatoli 461  
 Bazzani, Armando 1773  
 Bechstedt, Ulf 1701, 2292  
 Bechtold, Alexander 530  
 Beck, David 1937, 2849  
 Beck, U. 206  
 Becker, R. 1899  
 Becker, T. 197  
 Becker, Ulrich 2951  
 Beczek, Kevin J. 1378  
 Beebe, E. 1902  
 Beebe-Wang, Joanne J. 1743, 2843, 3143, 3185  
 Beetham, C. Gary 765  
 Behne, Dan 1333  
 Beinhauer, Wolfgang 1647  
 Bellavia, S. 1902  
 Bellomo, Giovanni 1776  
 Bellomo, Paul 206, 3429  
 Belomestnykh, Sergey A. 272, 980, 1112  
 Belousov, Ilja V. 750  
 Belov, Victor P. 3086  
 Ben-Zvi, Ilan 75, 2018, 2158, 2471, 2480, 2552, 3495, 3722  
 Benabed, Karim 2990  
 Benjamin, John 2277  
 Benjegerdes, R. 3233  
 Benson, S.V. 212, 2456  
 Bent, Bruce 931  
 Berg, Georg P. A. 2519  
 Berg, J. Scott 3152  
 Berg, Jeff 1333  
 Berg, William J. 2024, 2134  
 Berger, Christoph 2172  
 Bergstrom, Paul M. 1827  
 Bernal, Santiago 234, 1749, 1758, 1970, 2102, 3372  
 Bernard, Michel 922  
 Bertolini, Louis R. 2477, 3251  
 Besnier, Gilbert 1192, 1195  
 Besson, Jean-Claude 1569, 2686

- Bharadwaj, Vinod K. 3429, 3447, 3450  
 Bhat, Chandra M. 114, 717, 3155  
 Bhatia, Tarlochan S. 3585  
 Biagini, Maria E. 1536  
 Biallas, George 2456, 3306, 3312  
 Bibber, Karl V. 2480  
 Bickley, Matthew H. 732, 735, 741  
 Biedron, Sandra G. 2024, 2471, 2483, 2486, 2945  
 Bieler, Michael 554  
 Bielicki, J. 1249  
 Bieniosek, F. M. 1249, 1937  
 Bienvenu, Gerard 913  
 Billen, James H. 3570, 3585  
 Billen, Ronald 2617  
 Billing, Michael G. 410, 1112, 1115, 2975, 2978, 3221, 3501  
 Birke, Thomas 197, 726, 2382  
 Birx, D. 3257  
 Biryukov, Valery M. 53, 1234, 1237, 1240, 3050  
 Biscari, Caterina 131, 1536  
 Bish, P. 3233  
 Bishofberger, Kip 2006  
 Bisoffi, Giovanni 1324  
 Blank, M. 1016  
 Blas, Alfred 143  
 Blasche, K. 527, 1704, 1788  
 Blaskiewicz, Michael M. 109, 614, 857, 1611, 2280, 3185  
 Blazhevich, Sergey V. 2584  
 Blind, B. 611, 3582  
 Blinov, Boris B. 392  
 Bliss, Neil 2656  
 Blokland, Wim 1085, 2211  
 Blondel, Alain 2999  
 Blosser, H. 1318  
 Bluem, Hans 3570  
 Blum, Eric B. 2304  
 Bocchetta, Carlo J. 2060, 2313  
 Boege, Michael 1129, 1542, 2430  
 Boehnke, Michael 851  
 Bogacz, S. Alex 738, 2897  
 Bogart, S. Locke 603  
 Bogdanovitch, Boris Yu. 1291, 1932, 2570, 2573  
 Boggia, Antonio 1905  
 Bogomolov, Guenrikh. D. 592  
 Bohl, Thomas 2617  
 Bohlen, Heinz P. 445  
 Bohn, Courtlandt L. 2450, 2456  
 Bohne, D. 2513  
 Boine-Frankenheim, B. 1788  
 Boine-Frankenheim, O. 1785  
 Boisvert, Veronique 2217  
 Boivinnet, Raynald 3260  
 Bollen, Georg 1955  
 Bolme, Gerald O. 1444, 1447, 1946  
 Bolotin, Igor M. 1482  
 Bolshakov, Timophei 1387  
 Bolt, A. Scott 349, 1444, 1447, 1929, 1946  
 Bonati, R. 3767  
 Bondarev, Boris I. 1764, 2808  
 Bongardt, Klaus 1767  
 Bongers, Henning 3516  
 Boni, Roberto 866  
 Bonnafond, Christophe 1381, 3260  
 Bonthond, J. 1228  
 Booch, Rex 1506  
 Bopp, Markus 795  
 Borak, Thomas 2990  
 Borburgh, Jan C. 2283  
 Bordry, Frederick 3203, 3740  
 Boriskin, V.N. 753  
 Borland, Michael D. 200, 1587, 1644, 1979, 2319, 2939  
 Borne, Jean-Luc 919  
 Borodich, Andrei, I. 1869, 1872  
 Borovina, Dan L. 786, 2772  
 Borunov, Ivan E. 750  
 Bosch, Robert A. 2388, 2394, 2397, 2659  
 Boscolo, Ilario 1982, 1985  
 Boscolo, M. 1536  
 Bossart, R. 250  
 Bossier, Jacques 465  
 Bossert, R. 3194, 3197  
 Botman, J.I.M. 759, 1539, 2825, 2864, 3266  
 Bottura, Luca 154, 3179  
 Boucham, Abdel 2990  
 Bourdon, Jean-Claude 2012  
 Bourque, Robert F. 2954  
 Boussard, Daniel 946, 949  
 Bousson, Sebastien 919  
 Boutigny, D. 2990  
 Bovet, Claude 465  
 Bowden, Gordon B. 206, 824, 1390, 3423, 3426  
 Bower, Gary 307  
 Bowles, Edward 3755  
 Bowling, Bruce A. 732  
 Bowman, Jim 1333  
 Boyce, Richard M. 206, 1363  
 Boyd, John K. 3513  
 Brabson, B. 1548  
 Bracco, Roberto 2680  
 Bradley III, Joseph T. 1010  
 Bradshaw, David J. 2656  
 Braeutigam, Werner 957, 959, 3549  
 Brandt, Daniel 304, 3005  
 Brandt, J. 3194, 3197  
 Braun, Hans H. 250, 3402  
 Brautti, Giulio 1905  
 Breese, Mark 53  
 Breidenbach, Martin 3384  
 Brennan, Joseph M. 614, 857, 1746, 2280  
 Brennan, Michale 1258  
 Bressanutti, Raffaele 1120  
 Bricault, P. 100, 450, 3540  
 Briggs, R. 3257  
 Brinkmann, Reinhard 16  
 Bromberek, David J. 3095  
 Brooksby, Craig A. 625  
 Brouet, Michel 562  
 Brovko, Oleg I. 2262  
 Browman, Andrew A. 518, 998, 2790, 3582  
 Brown, Bruce C. 714, 717, 3315, 3318  
 Brown, C.N. 3324  
 Brown, Kevin A. 614, 1258, 1267, 1270, 2123, 2722, 2725, 2728, 2918, 3291  
 Brown, Terence F. 3381  
 Brown, Winthrop J. 81, 833  
 Bruenger, W.H. 2575  
 Bruhwiler, David L. 369  
 Brumwell, Franklin R. 2274  
 Brunelle, Pascale 1569, 2686  
 Brunet, Jean-Claude 1330, 1339  
 Bruning, Oliver 40, 2629  
 Bruno, Donald 3734  
 Bruns, Warner 2767  
 Bryan, David A. 732, 735  
 Bryant, Phil 2957  
 Buckles, Robert 1303  
 Budnick, J. 1545, 1548  
 Buerkmann, K. 197  
 Buerkmann, Klaus 2385  
 Bugrov, Vladimir P. 1312  
 Bulfone, Daniele 1120  
 Bullard, D. 3309  
 Bullard, Donald 3306  
 Bultman, Nathan K. 3591, 3594  
 Bulyak, Eugene V. 1770, 3122, 3269, 3271  
 Bunce, G. 471  
 Burgess, Edward L. 617, 3257  
 Burke, D.L. 3423  
 Burke, Jason 1952  
 Burkhardt, Helmut 2996, 3011  
 Burla, Paolo A. 762  
 Burn, Kenneth W. 2531  
 Burns, Michael J. 617  
 Burov, Alexey V. 521, 1088, 1201, 1608, 1707, 1710  
 Bushuev, Alexander A. 2033  
 Busse-Grawitz, Max Erick 986  
 Butenko, Andrey V. 2262  
 Buth, Gernot 2424  
 Butterworth, Andy 2996  
 Buxton, W. 2128  
 Bychenkov, Valery Yu. 3716  
 Byer, Robert L. 321  
 Byers, B. 2990  
 Bylinsky, Yuri V. 450, 893  
 Byrd, John M. 382, 495, 1207, 1806, 2370, 3131  
 Cai, Y. 296  
 Calabretta, Luciano 2578, 3288  
 Calame, J. 1016  
 Calatroni, Sergio 949  
 Callin, Richard S. 783  
 Cameron, Peter R. 2114, 2117, 2146, 2250, 3185  
 Campbell, B. 965  
 Campbell, Billy M. 971, 1327, 2954  
 Campbell, Lora P. 3722  
 Campbell, Richard 1515  
 Campisi, Isidoro E. 937, 1177, 1180, 2456  
 Cao, Jianshe 2140  
 Capista, David P. 714  
 Caporaso, George J. 617, 622, 625, 1204, 1303, 1824, 1827, 3254, 3381  
 Carathers, Jeremy R. 1447  
 Carlier, Etienne 1509  
 Carlson, Charles 2277  
 Carlsten, Bruce E. 477, 617  
 Carneiro, Jean-Paul 992, 2027  
 Carr, G. Lawrence 134  
 Carr, Roger 1390, 2477, 2698  
 Carrigan, R.A. 2027  
 Carron, Georges 250  
 Carter, Anthony 3101  
 Carwardine, John A. 2093  
 Cary, John R. 369, 377, 2784  
 Casas-Cubillos, Juan 3203  
 Casey, Jeffrey A. 568, 1491  
 Caspers, Fritz 1408, 2629  
 Caspi, Shlomo 174, 2793, 3194, 3197, 3233, 3236  
 Cassel, Richard L. 1494, 1500, 3429  
 Cassinari, Lodovico 1168, 1569  
 Castellano, Michele 1985, 2193, 2196, 2695  
 Castillo, Vincent 490  
 Castle, Mike 1040, 1046  
 Castro, Maurizio 97  
 Castro, Pedro 456  
 Catani, Luciano 1985, 2196  
 Catravas, Palmyra 325, 330, 2111, 3705  
 Caussyn, D.D. 1548  
 Celata, Christine M. 1716, 1803, 1830

- Celona, Luigi 97, 2578  
 Cerny III, Joseph 533  
 Chae, Yong-Chul 1644, 2486  
 Chai, Jongseo 2265, 3137  
 Chai, Xuedong 1453  
 Champion, Mark S. 992, 2027  
 Chan, C. F. 1937  
 Chan, K.C.D. 1327, 2954, 3582  
 Chan, Kwok-Chi D. 965, 968, 971  
 Chang, Cheng-Hsiang 2671  
 Chang, H.P. 2409  
 Chang, J. H. 2593  
 Chang, Lung Hai 1159  
 Chang, Peace 2837  
 Chang, S. S. 2009  
 Chang, S.S. 679, 2205, 2501  
 Chang, Shi-Hong 1375  
 Chang, Suk S. 2418  
 Channell, Paul J. 1629  
 Chao, Yu-Chiu 738  
 Chapelle, Sonja 3758  
 Chapman-Hatchett, Arthur 2202, 2223  
 Chargin, Anthony (Tony) K. 2590  
 Charrier, Jean-Pierre 432, 919  
 Chattopadhyay, Swapn 330, 2370  
 Chavanne, Joel 2662, 2665  
 Cheever, Dan 3101  
 Chel, Stéphane 916  
 Chen Y.-J. 617  
 Chen, C.S. 682, 685, 2412  
 Chen, Chien-Rong 1150  
 Chen, Chipping 1875, 2752  
 Chen, H.H. 2671  
 Chen, J. 682, 2021  
 Chen, J.R. 1605, 2409, 2415  
 Chen, J.S. 682, 1450  
 Chen, Jenny 685, 2069, 2072, 2412, 2671  
 Chen, Jie 741, 747  
 Chen, June-Rong 1150, 1375  
 Chen, Longkang 2184  
 Chen, Pisin 224, 330, 3648  
 Chen, Senyu 209  
 Chen, Szu-Yuan 3666, 3716  
 Chen, W. 3345  
 Chen, Y. J. 1824  
 Chen, Yu Ju (Judy) 617, 622, 2235, 3254, 3381  
 Chen, Yu-Juan 1204, 1210, 1303, 1827, 3254, 3257, 3513  
 Chen, Zukun 3591, 3594  
 Cheng, Daniel W. 1911, 1914, 1958, 1961  
 Cheng, Hung-Ming 1150  
 Cheng, W.H. 382  
 Chepegin, V.N. 53  
 Chepurinov, Alexander S. 2584  
 Cherbak, Ernest E. 1019  
 Cherenshchikov, S. A. 1973, 1976  
 Cherepakhin, A. 1249  
 Cherix, Jacques 418  
 Cherniakin, Alexander D. 3086  
 Chernin, David P. 360  
 Cherwinka, Jeffrey J. 3221  
 Chesnokov, Yury A. 53, 1237  
 Chesworth, Andrew A. 2433  
 Chiaveri, Enrico 946, 949  
 Chichili, Deepak R. 174, 3194, 3197, 3242  
 Chin, Y.H. 1058  
 Chin, Paul 234, 1970, 2102, 3369, 3372  
 Chin, Yongho 633, 3414  
 Chines, Franco 97  
 Chiou, J.P. 1450, 2009  
 Chishiro, Etsuji 3546  
 Chitose, Norihisa 2602  
 Chiurlotto, F. 1324  
 Cho, M.H. 2593  
 Cho, Yong-Sub 875, 1255, 3525  
 Chohan, Vinod 2202  
 Choi, B. H. 206  
 Choi, Byung-Ho 875, 1255, 3525  
 Choi, J. 1016  
 Choi, Jae-Young 2205, 2501, 2593  
 Choi, Jinhyuk 2418  
 Chojnacki, Eric 845, 980, 2635  
 Chong, Henry 2370, 2498  
 Chou, Ping-Jung 1159, 2415, 2837  
 Chou, W. 565, 3285  
 Chow, Ken P. 171, 3233, 3236  
 Christiansen, David W. 3573  
 Christina, Vincent 780, 3306  
 Chu, C.M. 392, 1545, 1548, 2286  
 Chu, Chunjie 1940  
 Chu, W. 2537  
 Chung, Kie-Hyung 2558, 2561  
 Chung, Sukmin 1357  
 Chupyr, Andrei 1387  
 Church, Michael D. 56  
 Church, Roy A. 1013  
 Cianchi, Alessandro 2193, 2196  
 Ciavola, Giovanni 97, 2578  
 Cimabue, Anthony G. 965  
 Cinabro, David 3221  
 Citver, G. 1420  
 Clark, George S. 3378  
 Clark, J. 1991  
 Clark, John C. 3513  
 Clark, Robert E. 2746  
 Clark, William L. 965  
 Clarke, James A. 2433, 2653, 2656  
 Clauser, Tarcisio 1779  
 Claverie, Joseph 2686  
 Clayton, Christopher E. 330, 2006, 3651, 3654, 3708  
 Clendenin, James E. 1988, 3384, 3447, 3450  
 Clifft, Ben E. 524  
 Cline, D. B. 2552, 3639, 3722  
 Codner, Gerald W. 1115, 1441, 3221, 3224  
 Cola, Mark J. 962  
 Colby, E. 321  
 Cole, M. 780  
 Cole, Michael D. 3570  
 Colestock, Patrick L. 114, 2027, 2181, 3155  
 Collier, Michael 3594  
 Collier, Paul 2617, 2996  
 Collins, Ian R. 2629  
 Collins, J.C. 673, 1548  
 Comins, J.D. 3257  
 Comunian, Michele 1773  
 Conde, Manoel E. 2030, 3621  
 Conkling Jr., Charles R. 699  
 Connolly, Roger C. 2114, 2117, 2250  
 Cooke, Simon J. 360  
 Coosemans, W. 250  
 Corbett, Jeff 206, 2355, 2358, 2364  
 Corlett, John N. 296, 800, 896, 1207, 3149, 3429  
 Corlier, Muriel 2686  
 Cornacchia, Max 267, 2480  
 Cornelis, Karel 1189, 2617, 2996  
 Cornelius, W. D. 1884, 1887  
 Cornuelle, J. 3423  
 Corredoura, Paul L. 435, 800, 3429  
 Corsini, Roberto 250, 3396  
 Corstens, J.M. 2864  
 Counsell, Joseph 1025  
 Coupal, David 2990  
 Cours, Alexander 1022  
 Cousin, J.M. 1569  
 Coutrakon, George 11  
 Cozzolino, John 185, 3230  
 Craddock, Michael 2620, 2623  
 Craievich, P. 1123  
 Craig, George D. 1830, 3248  
 Crandall, K.R. 611, 3582  
 Crandell, D.A. 392  
 Crawford, A.C. 521  
 Crawford, Curtis 237, 3321  
 Crisp, J. L. 2164  
 Crisp, Jim 2146, 2211  
 Crist, Charles 1303  
 Crockford, Guy 2617  
 Crosbie, Edwin A. 1587, 2325  
 Cruikshank, Paul 1330, 3203  
 Ctcherbakov, Anatoliy M. 1482  
 Cullen, J.R. 1267, 1270  
 Cummings, Karen A. 881, 1396  
 Cundiff, Tim 2090  
 Cupola, J. 2117  
 Cuttone, Giacomo 2578  
 Czarnaski, Mark 360  
 d'Amico, Tommaso E. 250, 1638, 2202, 3399  
 D'Olando, Stefano 1120  
 D'Ottavio, Theodore W. 693  
 D'Yachkov, Mikhail 128, 1408  
 DaCosta, Tony 1333  
 Dahlerup-Petersen, Knud 3200, 3203  
 Dai, Jianping 1453  
 Dalesio, Leo R. 349, 652, 655  
 Daly, E. T. 206, 1363  
 Dambach, S. 165  
 Danared, Håkan 1698  
 Danby, Gordon T. 3185, 3333  
 Danilov, Vyacheslav V. 109, 641, 1198, 1201, 1608, 1710, 3140, 3143, 3303, 3728  
 Danly, B. 1016  
 Danowski, G. 3767  
 Darpentigny, Jacques 1168, 1569  
 Date, Schin 2346  
 Dattoli, Giuseppe 1219  
 Datz, Sheldon 1671  
 Davidson, Ronald C. 1518, 1623, 1626, 1629, 1875  
 Davis, Brent 1506  
 Davis, Jerry L. 1001  
 Davis, Roger 557  
 Day, T. 1991  
 de Hoon, Michiel J.L. 1803, 1830  
 de Loos, Marieke 2462, 3266  
 De Monte, R. 2253  
 De Ryck, C. 3212  
 De Santis, Stefano 2075, 2873  
 De Wit, F.F. 759  
 Debeling A. 3248  
 Debiak, Ted, W. 587  
 Debus, J. 2513  
 Decker, Franz-Josef 307, 330, 771, 774, 1252, 1728, 2846, 2987, 3384, 3648  
 Decker, Glenn A. 2051, 2093, 3092  
 Decking, Winfried 1581  
 Decyk, V. K. 3672  
 Degasper, Francisco T. 1366  
 Degtyarev, I.I. 1321  
 DeHart, Terrance E. 2668

- Dehler, Micha 1129, 2087  
 Dehning, Bernd 2999  
 Dejus, Roger J. 2486, 2489, 2492  
 Dekin, W. D. 2590  
 Delahaye, J.P. 250  
 DeLamare, Jeffery E. 1494  
 Delayen, Jean R. 925, 928, 934, 937, 940, 955, 1462, 3498  
 Dell'Orco, D. 206, 2355  
 Den Hartog, P.K. 1369, 2483, 2489  
 Deng, Jianjun 3263  
 Denker, A. 3519  
 Denz, Reiner 3200  
 Derbenev, Yaroslav S. 392  
 Derenchuk, V. 1548  
 Derrick, M. 2635  
 Deruyter, H. 590, 3423  
 Deryuga, Vyacheslav A. 2546, 2549  
 DeSantis, Stefano 382  
 Desforges, Bernard 2617  
 Desmons, Michel 916  
 Despas, Claude 2617  
 Despe, Oscar 3773  
 DeStaebler, Herbert 2990  
 Detweiler, Gerald 2468  
 DeVan, W.R. 355  
 Devin, André 3260  
 Devmal, S. 2990  
 DeVries, Jan 162  
 Dewa, Hideki 3690, 3702  
 Dey, Joseph E. 869  
 Di Bartolo, Gaetano 2578  
 Diaczenko, Nick 2936  
 Dias, Joao M. 3725  
 Dickson, R. 646  
 Dietderich, D.R. 171, 3233, 3236  
 Diete, W. 957  
 Dietrich, J., 2054  
 Dietrich, Jürgen 1701, 2292  
 Dikansky, Nikolay S. 78, 2167, 2948  
 Dimaggio, S. 325  
 DiMaggio, S. 3705  
 DiMarco, Joseph 3194, 3197, 3318, 3327  
 Ding, Bainan 3263  
 Ding, X. 2504  
 Ding, X. 2003, 2021, 2039, 2042, 2045  
 Ding, Xiaodong 2006  
 Dinkel, J. 1249  
 Dittmann, B. 197  
 Diviacco, Bruno 2680  
 Divin, Yuri Y. 2178  
 Diwan, Milind V. 3023  
 Dix, Brendon 1390  
 Dobbing, Gavin S. 2433, 2653  
 Dobrovolski, Nikolaj M. 1468, 2105  
 Dohlus, Martin 1650  
 Dolgashev, Valery 2822  
 Doll, D.W. 1393  
 Dombisky, M. 100  
 Dome, George 1408  
 Domer, Gregory A. 649  
 Donald, Martin H. 296, 1584  
 Dong, Xiaoli 1596  
 Donohue, John T. 1797, 3387  
 Dooling, Jeffrey C. 2274  
 Doolittle, Lawrence R. 768, 928, 934, 937, 940, 1462  
 Doose, Charles L. 2024, 2093  
 Dormiani, M. 206  
 Dortwegt, Robert J. 1414, 2024  
 Doskow, J. 471  
 Doss, J. Daniel 426  
 Douglas, David 1177, 1180, 2456, 3306, 3312  
 Douryan, Adnan 2471  
 Dovbnya, A. 3122  
 Doyle, Stephen 2424  
 Doyuran, Adnan 2480, 2942  
 Drago, Alessandro 131, 636  
 Dragt, Alex J. 1551, 1593, 2761  
 Drees, K. Angelika 2117  
 Dressler, Olaf 1279  
 Drivotin, Oleg I. 1857  
 Drozhdin, Alexandr I. 56, 1231, 1234, 2614, 3050  
 Drury, Michael 931  
 Ducimetière, Laurent 1228, 1509  
 Duda, Brian J. 3669  
 Duerr, Volker 2385  
 Duffau, Michael J. 2096  
 Duffy, Patrick 1390, 2477  
 Dugan, Gerald F. 48, 2057, 2632, 3221, 3224  
 Duke, Jonathan P. 2208  
 Dunbar, Ann 1100  
 Dunham, B. 1991  
 Dupaquier, Andre 3740  
 Dur, V. 197  
 Durkin, Alexander P. 1764, 2808  
 Dutto, Gerardo 106, 893  
 Dykes, Michael D. 1025, 2096  
 Eardley, Matthew 1943  
 East, G. 1548  
 Ecklund, Stan D. 296, 3450  
 Economou, A. 1037  
 Edamenko, N. S. 1866  
 Edgell, Dana 1043, 1890  
 Edwards, Helen T. 992, 2027  
 Egawa, Kazumi 3351, 3354, 3357  
 Egiastian, Suren L. 1468  
 Ehrlich, Richard 980  
 Eichhorn, Ralf 2951  
 Eichner, John 1512  
 Eickhoff, Hartmut 527, 1704, 2513  
 Eilerts, S. 471  
 Einfeld, Dieter 806, 809, 1360, 2424, 2427, 3375  
 Eisert, D. E. 2659  
 El-Shazly, M.N. 1896  
 Elbakian, Sergey S. 3657, 3663  
 Elioff, T. 206  
 Elleaume, Pascal 2662, 2665, 3119  
 Elliott, T. 780  
 Elliott, Tim 2936  
 Ellis, Gretchen G. 965  
 Ellison, M. 1548  
 Elmer, John 777  
 Elzhov, Artem V. 3393  
 Emamian, Mark 221, 2468  
 Emery, Louis 200, 401, 1644, 2137, 2319, 2939  
 Emhofer, Stephan 3516  
 Emma, Paul 3429, 3438, 3447, 3456  
 Emmerling, M. 1788  
 Endo, Akira 2018, 2036, 2552  
 Endo, M. 600  
 Engels, Oliver 3519  
 Enomoto, A. 1132, 2731  
 Eppley, Kenneth R. 2778  
 Erdmann, M. 1369, 2489  
 Erickson, John L. 3594  
 Eriksson, L. 3462  
 Eriksson, Mikael 2945  
 Ermakov, Dimitry I. 2555  
 Erokhin, Alexander 1387  
 Esarey, E. 330, 2111  
 Esarey, Eric 325, 3696, 3699  
 Escallier, John 3161  
 Eschenko, Viktor N. 3086  
 Esin, Sergei K. 3561  
 Etzkorn, Franz-Josef 851  
 Evans, I. 206  
 Evans, Jr., Kenneth 352, 744  
 Evans, Lyndon R. 21  
 Evans, R. 2456  
 Eyl, Patrick 3260  
 Eylon, Shmuel 1934, 3248, 3390  
 Eyssa, Y. 3227  
 Ezura, Eiji 413, 440  
 Faatz, B. 2486  
 Fabris, Alessandro 809, 1120, 1123  
 Fagan, M.J. 1327  
 Fahmie, Michael P. 756  
 Falabella, Steve 1303  
 Falkenstern, F. 2078  
 Fallmann, W. 2575  
 Faltens, Andris 1503, 1830, 1937, 2849, 2852, 3215, 3339  
 Fan, Kuanjun 1315, 1596  
 Fan, Mingwu 1940  
 Fan, T.C. 2671  
 Fang, J.M. 3627  
 Fang, Lei 2125  
 Fang, Shouxian 1695  
 Fang, Shuyao 890  
 Fang, Si 3761  
 Fang, Zhigao 2125  
 Fann, C.S. 1450  
 Fant, Karen 1435  
 Farkas, Zoltan David 771, 774, 3423  
 Farrell, J. Paul 75  
 Fartoukh, Stéphane 922  
 Farvacque, Laurent 3119  
 Faugier, Andre 2617, 2996  
 Faulbaum, D. 197  
 Fawley, William M. 1204, 1210, 1934, 3254, 3257  
 Fedorov, Vacheslav 1479, 1485  
 Fedorov, Vladimir M. 1734  
 Fedorova, Antonina 1614, 1617, 1620, 2900, 2903, 2906, 2909, 2912  
 Fedotov, Alexei V. 606, 1752, 1755  
 Fedotov, M. G. 2167  
 Fedotov, Yu.S. 53  
 Feher, Sandor 1420, 1426, 3191, 3194, 3197  
 Feigenbaum, Irv 2277  
 Feikes, Joerg 197, 1279, 2376  
 Feldl, Erich 928, 934  
 Fellenz, Brian 2146, 2211  
 Feng, Z.Q. 3345  
 Ferianis, Mario 1120  
 Fernow, Richard C. 3020, 3032  
 Ferracin, Paolo 3206  
 Ferrari, Antoin 2617  
 Ferrario, Massimo 1985, 1997, 2734  
 Fessenden, Tom 2235  
 Fieguth, Theodore 296, 2990  
 Field, R. Clive 296, 307  
 Fields, D. 471  
 Figueira, Goncalo 3725  
 Figueroa, Terry L. 1929  
 Filhol, Jean-Marc 2331, 2334, 3119  
 Filippas, A. V. 1037  
 Finkelstein, Ken D. 2217  
 Finley, David A. 3728

- Finocchiaro, Paolo 2578  
 Fiorito, Ralph B. 487, 3722  
 Firebaugh, J. 1246  
 Firjahn-Andersch, Arne 530  
 Fisch, Nathaniel J. 3675  
 Fischer, Claude 465  
 Fischer, Wolfram 702, 1261, 2716, 2725, 2921  
 Fisher, Alan S. 296  
 Fisher, M. V. 2659  
 Fitch, Michael J. 2027, 2181  
 Fitze, Hansruedi 418, 795  
 Fitzgerald, Daniel H. 518, 1198, 1201  
 Fitzgerald, Jim 2211  
 Flanagan, John W. 1132, 2120, 2731  
 Flechtner, D. 3600, 3606  
 Fliflet, Arne W. 1049  
 Flippo, Kirk 3716  
 Floersch, D. 652  
 Floersch, Richard H. 649  
 Flora, R. H. 714  
 Flottman, K. 3450  
 Flynn, G. 1533, 1569  
 Fong, Ken 450, 890  
 Foose, R. 590  
 Forest, Etienne 404  
 Foster, G. William 182, 3324, 3327, 3330  
 Fouaidy, Mohammed 913, 919  
 Fournier, P. 103  
 Fowkes, W.B. 3423  
 Fowkes, William R. 783, 1432, 3426  
 Fox, John D. 131, 636, 1207, 1213  
 Franchetti, Giuliano 1782, 1785  
 Franco, Jose G.S. 2421  
 Franczak, B. 527, 1704  
 Franks, R. Mark 800, 803  
 Franzcak, B. 1788  
 Franzke, B. 527, 1704  
 Freedman, Stuart J. 1952  
 Frei, Hans 418, 795  
 Fresquez, M.G. 426  
 Freund, Henry P. 2486  
 Friedman, Alex 1830, 2758, 3248  
 Friedsam, Horst 2051, 2635  
 Friesel, Dennis L. 498, 1548  
 Frigola, Pedro 217, 2480  
 Frisch, Josef C. 253, 3447, 3450  
 Fritz, A. 3248  
 Frommberger, Frank 3098  
 Fromowitz, Daniel B. 1632  
 Fuerst, Joel D. 992, 2027  
 Fugita, H. 3110  
 Fujieda, Miho 413, 798, 857, 860, 863, 1007, 1653, 2271, 2280  
 Fujikawa, Brian 1952  
 Fujioka, M. 3348  
 Fujiwara, Chikara 842  
 Fukuda, Mitsuhiro 2259  
 Fukuda, Shigeki 3414  
 Fukui, Yasuo 3032  
 Fukuma, H. 633, 1132, 2731  
 Funahashi, Y. 777, 3423  
 Funahashi, Yoshisato 2731, 3417  
 Funakoshi, Yoshihiro 1132, 2108  
 Fung, K.M. 1545, 1548, 2286  
 Funk, L.W. 3582  
 Furman, Miguel A. 1674, 1791, 1794  
 Furst, Mitchell L. 2388  
 Furukawa, Kazuro 1132, 2238, 2731  
 Furuya, Takaaki 440  
 Fuss, Brian 1390  
 Futami, Y. 600  
 Gaedke, Rudolph 2936  
 Gahl, John M. 786, 2772  
 Gai, Wei 2030, 3618, 3621  
 Gaillard, Michel 2012  
 Gaiser, H. 3552  
 Galambos, John D. 109, 1198, 1201, 3140, 3143, 3303  
 Galayda, John N. 2024, 2471  
 Galdi, Vincenzo 2882  
 Galimberti, Andrea 2060  
 Gallardo, Juan C. 3032, 3722  
 Gallo, Alessandro 131, 866, 1147  
 Galstjan, Eugene A. 1477  
 Galvin, J. 2537  
 Gamba, Claudio 1120  
 Gambitta, A. 2060  
 Gammino, Santo 97, 2578  
 Ganetis, George L. 3161, 3170, 3734  
 Gao, Jie 1216, 1809, 1812, 1815, 3017  
 Gardelle, Jacques 1797, 3387  
 Gardner, Christopher J. 614, 1276, 2063, 3182, 3185  
 Gardner, K. 2918  
 Garnett, Robert 518  
 Garren, A. 206  
 Garren, Alper A. 2364, 2439, 3050, 3065, 3068, 3152  
 Garven, M. 1016  
 Garvey, Terrence 916, 2012  
 Gassner, D. M. 2123  
 Gassot, Huimin 919  
 Gaudreau, Marcel P.J. 568, 1491  
 Gautier, Cort 977, 1396  
 Gavrilov, Nikolay M. 1932  
 Gebel, Ralf 2292  
 Gebre-Amlak, K. 3681  
 Geer, S. 3062  
 Geitz, Marc 2172, 2175, 2178, 2507  
 Geld, T. 2990  
 Gelfand, Norman M. 1677, 2861  
 Geller, Joseph M. 2247  
 Geng, Rong-Li 429, 980, 983  
 Gentzlinger, Robert C. 962, 965, 968  
 Georgsson, Mattias 2945  
 Gericke, W. 197  
 Ghebremedhin, Abiel 11  
 Ghigo, Andrea 131, 1536  
 Ghiorso, William 2849  
 Ghosh, Arup K. 185, 3161, 3188, 3197, 3230  
 Ghosh, Subhendu 952  
 Giachino, Rossano 2617  
 Giannessi, L. 1985  
 Gibbins, Peter E. 1025  
 Gies, Albert 2424  
 Gillespie, George H. 1551, 2805  
 Gilpatrick, John D. 2152, 2214, 2241, 3528, 3582  
 Ginzburg, Naum S. 1055  
 Gioia, Jack G. 977, 1396, 2954  
 Giovannozzi, M. 1282  
 Girault, F. 1569  
 Gladkikh, P. 3122  
 Glass, Henry D. 3318  
 Glazov, Alim A. 2262  
 Glenn, Joseph W. 614, 702, 1258, 1270, 1746, 2918, 3291  
 Glover, Ernie 2370, 2498  
 Gluckstern, Robert L. 606, 1752, 1755, 2876  
 Gluskin, Efim 2489  
 Godefroy, Jean-Marie 2686  
 Godlove, Terry F. 234, 1758, 1970, 3369  
 Godot, J.C. 250  
 Goeppner, George A. 2024  
 Goergen, R. 2078  
 Goerz, D. 625  
 Goethe, J.W. 3516  
 Gold, Saul 1512  
 Gold, Steven H. 1049, 1474  
 Goldberg, J. D. 1043  
 Goldenberg, Constantin A. 1055  
 Golkowski, Cz. 3600, 3603  
 Gomez-Costa, Jose Louis 3200  
 Gonzalez, Carlota 474, 1408  
 Goodenough, C. 2990  
 Goodzeit, Carl L. 3245  
 Gorbachev, A.M. 1474  
 Gorchenko, V.M. 2256  
 Gordon, Daniel 3684  
 Gorev, V. V. 3711  
 Gorski, Anthony J. 1411, 2635, 3342  
 Goto, Akira 2268  
 Goto, Y. 471  
 Gottschalk, Stephen C. 2668, 2674, 2677, 3722  
 Gouard, P. 1797  
 Gough, Richard A. 884, 1911, 1914, 1917, 1920, 1952, 1958  
 Gourlay, S. A. 171, 3236  
 Govorov, A.I. 2256  
 Graef, Hans-Dieter 2951  
 Grafstrom, Per 1671  
 Granatstein, Victor 1040, 1046  
 Graves, Bill 2471  
 Graves, Rossie M. 2388  
 Graves, Williams S. 1949  
 Green, Michael A. (LBL) 2439, 3149, 3227  
 Green, Michael A. (SRC) 2391, 2659  
 Greenler, Lee 2388  
 Greenwald, Shlomo 3221  
 Greenwald, Zipora 1300, 3221  
 Greer, James B. 1961  
 Gregoire, Guillaume 103  
 Grelick, A. 2024  
 Greninger, Paul 878, 3570, 3573  
 Griep, B. 957  
 Grieser, Manfred 1955, 3543  
 Griesmayer, Erich 2957  
 Griffin, James E. 1201, 3152  
 Griffiths, Stephen A. 2960  
 Grigorev, Yu. 2927, 3122  
 Grimm, Terry L. 3719  
 Grippo, A. 2229  
 Grishin, Vladislav K. 2581, 2584, 2587  
 Grishui, V.N. 392  
 Grobner, Oswald 1339  
 Groening, L. 527, 1704  
 Gromov, Roman G. 78, 750  
 Gross, Dan 2936  
 Grossberg, Phyllis 338  
 Grote, David P. 1761, 1830, 1833, 1937, 2758, 3248  
 Grobner, Oswald 2629  
 Gu, Shaoting 3716  
 Gu, Sunhee 1357  
 Gubin, Konstantin V. 750, 1456, 2167  
 Guerra, Al 3306  
 Guharay, S.K. 234, 1306  
 Guidi, Vincenzo 2948  
 Guiducci, Susanna 277, 1536  
 Guignard, Gilbert F. 250, 1635, 1638, 3399  
 Guler, Hulya 3026

- Guo, Fanqing 533  
Guo, Zhiyuan 633  
Gupta, Ramesh C. 171, 185, 3161, 3176, 3236, 3239  
Gurd, David P. 355, 3528  
Guthrie, Arthur 3594  
Guy, F.W. 3531  
Göettert, Jost 2424  
Ha, Jangho 2265, 3137  
Haagenstad, Harvey 965  
Haber, Irving 234, 1749, 1758, 1830, 1970  
Haberer, Th. 2513  
Habib, Salman 366, 1845  
Habs, Dietrich 3516  
Haebel, Ernst 946, 949  
Hacuser, Juergen 3519  
Hafizi, Bahman 3687, 3693  
Haga, Kaiichi 2310  
Hagedoom, H.L. 1539, 2825  
Hagedorn, Dieter 3200  
Hagel, Johannes 250, 1635  
Hagelstein, Michael 2424  
Hagenbuck, F. 165  
Hagedstedt, Andre 2424  
Hahn, Alan A. 468, 1085, 2066, 2164  
Hahn, Harald 1100, 1103  
Hahn, Robert von 1955  
Hahn, Ulrich 1369  
Hairapetian, G. 3708  
Halaxa, Ernie 1937, 3248  
Halbach, K. 2301  
Haldemann, Paul 234, 1970  
Hama, Hiroyuki 592  
Hambikov, Valeriy D. 1456  
Hamilton, Andrew 2388  
Hamilton, B. 498, 1545, 1548  
Hammen, A.F.J. 759, 2825, 2864  
Hammon, Duncan L. 965  
Hammonds, J.P. 355  
Han, Bum-Soo 3525  
Han, D. H. 1079  
Han, Jang-Min 875, 3525  
Han, Qian 1228  
Han, Y.J. 3345, 3504  
Hanaki, Hirofumi 2015, 2749, 3507  
Hancock, Steven 143, 2226  
Hanke, K. 2178  
Hanke, Klaus 1282, 1285, 2617  
Hanks, Roy L. 625  
Hanna, S. 3423  
Hanna, Samy M. 2516  
Hannaford, R. 3233  
Hanni, Raymond 949  
Hansborough, Lash D. 1444, 1447, 1929, 1946  
Hansen, Gene 1336  
Hansen, Jan 562  
Hansen, Robert 1049  
Hansknecht, J. 1991  
Hanuska, S. 2635  
Harada, Hisashi 848  
Harada, Kentaro 2436  
Harano, Hideki 2605  
Hardek, Thomas W. 1444, 1447, 1946  
Hardekopf, Robert A. 3597  
Harding, David J. 3318  
Hardy, L. 2331, 2334  
Hargenrater, Thomas 1396  
Harkay, Katherine C. 123, 1641, 1644  
Harnden, W. 171, 3233  
Harper, Mark 1333  
Harrington, Margye P. 349, 1929  
Harriott, Lloyd 595  
Harris, Guy 1342  
Harris, Neville 2656  
Harrison, Michael A. 6, 3176, 3230  
Hartemann, Frederic V. 2000, 2003  
Hartill, Don 980, 2975, 2978  
Hartman, N. 3149  
Hartmann, H. 696  
Hartmann, P. 1991  
Hartouni, Edward P. 2590  
Hartung, Walter H. 992, 2027  
Harvey, A. 3576, 3579  
Harwood, Leigh 3306, 3309  
Hasan, A. 2990  
Hasegawa, Kazuo 3546  
Hasegawa, N. 3690  
Haserorth, Helmut 103  
Hashimoto, Yoshinori 860  
Hassanein, A. 3062  
Haustein, Peter 533  
Hawkey, Timothy P. 568, 1491  
Hawkins, Alonzo 1037, 1515  
Hayano, H. 1994  
Hayano, Hitoshi 256, 2143  
Hayano, Hiyooshi 3432  
Hayashi, K. 3330  
Hayashi, Y. 3600, 3606  
Haynes, W. Brian 965, 977, 1396  
Hayoshi, N. 471  
He, P. 2552, 3639, 3722  
He, Xiaoye 1315  
Heese, Richard H. 2304  
Heidenreich, G. 1360  
Heifets, Samuel 1118, 1665  
Heimann, Philip 2370, 2498  
Helm, D. 259  
Hemker, Roy G. 330, 3672  
Hemmer, Michael 37  
Henchel, Bill 2936  
Henderson L. 296  
Henderson, Stuart D. 410, 1351, 2217, 3221  
Henderson, Tom 803  
Hendrickson, Linda J. 307, 338, 3456  
Henestroza, Enrique 1934, 1937, 2849, 2852, 3390  
Henke, Heino 812, 815, 818, 1034  
Henn, Kurt 1701, 2292  
Henrist, Bernard 2629  
Herbeaux, Christian 2686  
Hermle, Stefan 1360, 2424  
Hernandez, Kenneth 803  
Heron, Mark T. 661  
Herr, Werner F. 304, 3005  
Herrmann, J. 2915  
Herrmannsfeldt, William 1937  
Herrup, David A. 1091  
Hershcovitch, Ady I. 584, 1902  
Hertel, N. 2427  
Hess, Mark 2752  
Hettel, R. 206  
Hezel, T. 165  
Hiatt, Thomas 1462, 3306, 3309  
Hickman, Bradley C. 625  
Hidaka, S. 1821  
Hig 3423  
Higashi, Yasuo 777, 3417, 3423  
Higley, H. 3233  
Higo, Toshiyasu 777, 3417, 3420, 3435, 3468, 3477  
Hilaire, Alain 40  
Hildreth, Mike 2999  
Hill, Barrey W. 1551, 2805  
Hill, Ed 2936  
Hill, Jeremy M. 2480  
Hill, M.E. 3612  
Hill, Marc E. 545  
Hill, R. 2456  
Hilleret, Noel 2629  
Himmel, Thomas M. 293, 296, 338  
Hinson, William M. 3212  
Hiramatsu, Shigenori 492, 633, 1132, 2120, 2731  
Hiramoto, Kazuo 2528, 3366  
Hirata, Kohji 1689  
Hiraya, A. 2689  
Hirose, Tachishige 256, 2552  
Hirota, Jun'ichi 3366  
Hirshfield, Jay L. 1049, 1052, 1474, 3627, 3630  
Hitomi, Nobuteru 777, 3417  
Ho, C.H. 1450, 2000, 2009  
Ho, Darwin D.-M. 1827  
Hoag, Harry 777, 3423  
Hoberg, H. G. 197  
Hockman, Jeffrey N. 2590  
Hodgkins, David J. 349, 1444, 1447, 1946  
Hodgkinson, Cheryl L. 2656  
Hoellering, Frank 3519  
Hoeltermann, H. 1899  
Hoff, Lawrence T. 693, 1261  
Hoff, Matthew D. 884, 1958, 1961  
Hoffman, J.R. 3651  
Hoffmann, Markus 3098  
Hoffstaetter, George H. 407  
Hofmann, A. 296  
Hofmann, Ingo 137, 1782, 1785, 1788  
Hogan, Bart 1046  
Hogan, G. E. 579  
Hogan, J. 1462, 1991  
Hogan, John 934  
Hogan, M. 217  
Hogan, Mark J. 330, 1997, 2111  
Holden, Travis 2006  
Holder, David J. 2433  
Holmes, Clifford 2235  
Holmes, Jeffrey A. 109, 1198, 1201, 3140, 3143, 3303  
Holmes, Stephen D. 43  
Holstein, Friedrich 2424  
Holtkamp, Norbert 896, 3062, 3149  
Holtzapfel, Robert L. 410, 2057, 2972, 2975, 2978  
Homeyer, H. 3519  
Homeyer, William G. 2954  
Homma, T. 600  
Homscheidt, M. 165  
Honda, Tohru 2310  
Horan, Douglas 1019, 1022  
Hori, H. 3507  
Hori, Toshitada 2298, 2400, 2403, 3702  
Horioka, Kazuhiko 3690  
Horny, M.J. 2000, 2009  
Hosaka, Masahito 592  
Hosokai, Tomonao 3690, 3702  
Hosoyama, Kenji 440, 1132, 2731  
Houck, Timothy L. 1210, 1303, 2755, 3257, 3390  
Hourican, Michael D. 2283  
Hovater, Curt 768, 1177  
Howell, Joseph W. 3095  
Hower, Nelson L. 221, 2099, 2468  
Hoyer, Egon H. 162

- Hseuh, Hsiao-Chaun 557, 1345  
Hsi, W.C. 1548, 2286  
Hsiao, Ko-Ming 1375  
Hsiung, Gao-Yu 1375, 1605  
Hsu, Ian C. 2220  
Hsu, Kuo Tung 682, 685, 1153, 1156, 1159, 1162, 1450, 1605, 2009, 2069, 2072, 2220, 2409, 2412, 2671, 2837  
Hsu, S.Y. 1450, 2009, 2072  
Hsu, Shen-Nung 1375  
Hsu, Yao-Jane 1375  
Hu, Hongliang 1596  
Hu, Kuo Hwa 2412  
Hu, Kwo Hwa 682, 1153, 1156, 2069, 2072  
Hu, Shouming 1596  
Huan, N. 1132  
Huang, H. 471, 1548, 2128  
Huang, Hong 633  
Huang, Jung-Yun 1076, 2131, 2418  
Huang, M.H. 2671  
Huang, N. 2731  
Huang, Nan 2963  
Huang, Yen-Chieh 321  
Huang, Zhirong 262, 1644, 2495  
Hubbard, E. 3576, 3579  
Hubbard, Richard F. 3687, 3693  
Huelsmann, Peter 3405  
Hughes, Thomas P. 2746  
Hughey, Lanny R. 2388  
Huhtinen, Mika 1231  
Humpert, Michael 806  
Humphries Jr., Stanley 2737, 2772, 2778  
Hundzinger, Denis 3743  
Hunt, W. A. 676  
Hunter, W. Ted 3576, 3594  
Hurh, Patrick G. 1423  
Husmann, Dirk 3098  
Hutchins, S. 250  
Huttel, Erhard 1360, 2424  
Hwang, C.S. 1450, 2671  
Hwang, J.Y. 2000, 2009  
Iazzourene, Fatma 2707  
Ichihara, Masahiro 3546  
Iciri, Takao 1132, 1135, 2731  
Igarashi, Susumu 1141  
Igolkin, Aleksandr G. 1456  
Iida, Naoko 1132, 2108, 2731  
Iino, Youshuke 842  
Ikegami, Kiyoshi 1653  
Ikegami, Masanori 62, 1818, 1821, 3546  
Ikezawa, Mikihiro 2187  
Ilg, Thomas 3594  
Imai, K. 471  
Ingalls, William B. 1917, 1923  
Inoue, Makoto 1294, 2528, 3110  
Irwin, John 259, 363, 3423, 3453, 3480  
Isaev, V.A. 1474  
Ishchanov, Boris S. 2584  
Ishi, Kimihiro 2187  
Ishi, Sadahiro 2271  
Ishi, Yoshihi 1653  
Ishibori, Ikuo 2259  
Ishihara, M. 471  
Ishkhanov, Boris S. 2555  
Issinsky, Igor B. 2262, 2289  
Ito, Takashi 3546  
Ivanov, Alexander P. 3501  
Ivanov, G. M. 1973, 1976  
Ivanov, O.A. 1474  
Ivanov, Yu.M. 53  
Ivers, J.D. 3600, 3603, 3606  
Iverson, R. 2111  
Iverson, Richard H. 330, 1252, 2987, 3648  
Iwasaki, H. 492  
Iwashita, Y. 2280  
Iwashita, Yasuhisa 3110  
Iwashita, Yoshihisa 857, 1294, 2528, 3645  
Izawa, Masaaki 633, 904  
Jablonka, Marcel 922  
Jackson, Alan 2641  
Jackson, G.P. 3324  
Jackson, John W. 3185, 3333  
Jackson, Leslie T. 3257  
Jacob, Jorn 1647  
Jacobs, Kenneth D. 3101  
Jaekel, Markus 2424  
Jaeschke, E. 197  
Jagger, Jack M. 1378, 1979, 2635  
Jaggi, Andreas 2087  
Jahnel, Lucia 2421  
Jain, Animesh 185, 3161, 3170, 3173, 3176, 3179, 3188, 3336  
Jaitly, Ray 1010  
Jakob, Ansgar 1288, 1836  
Jander, Donald R. 2668  
Janssen, Dietmar 2033  
Jansson, Andreas 2223, 2226  
Jeanneret, Jean-Bernard 40, 2620, 2623  
Jensen, C. 2164  
Jensen, Erk 250, 1408  
Jeon, D. 1545  
Jeon, Dong-o 109, 1198, 1201, 3140, 3143, 3303  
Jeong, S. C. 1893  
Jeram, B. 658  
Jericha, Erwin 2957  
Jett, Nelson D. 649  
Jia, Qika 2406  
Jiang, Daoman 1315  
Jin, Yuming 2184, 2406  
Job, P.K. 2090  
Jobe, R. Keith 253, 3411, 3429, 3447, 3453  
Johnson, D. 1318  
Johnson, David 518  
Johnson, David E. 714, 717, 1243, 2647  
Johnson, Erik D. 584, 2471, 2480  
Johnson, Kenneth F. 1929, 3528  
Johnson, Mark 2936  
Johnson, Marty 2468  
Johnson, Neil G. 3764  
Johnstone, Carol J. 1677, 3050, 3065, 3068, 3071, 3152  
Johnstone, John A. 1082  
Joly, Jean-marc 922  
Jones, Frederick W. 128, 2933  
Jones, Justin 2051, 3095  
Jones, Kevin H. 518, 3528  
Jones, Roger M. 777, 3423, 3468, 3471, 3474, 3477  
Jones, W.P. 1548, 2519  
Jongewaard, Erik N. 783  
Jonker, Michel 2617, 2996  
Joosten, Rainer 533  
Jordan, Kevin 2229, 2456  
Joshi, Chad 931  
Joshi, Chan 330, 2006, 3651, 3654, 3684, 3705, 3708  
Jowett, John M. 1680  
Judkins, J. 206  
Juillard, Michel 432  
Julian, James 1471, 3131  
Julian, R.A. 2394  
Jung, Roland 465  
Jungmann, K. 1488  
Junquera, Tomas 919  
Juras, M. 658  
Kabel, Andreas 1650, 2507  
Kabeya, Zenzaburo 842  
Kadantsev, S. 106  
Kaganovich, Dmitri 3693  
Kageya, Tsuneo 392  
Kahn, S. 185  
Kahn, Stephen A. 3023, 3026  
Kai, Satoru 1309  
Kaiser, Hartwig 2385  
Kaiser, K.-H. 165, 2915  
Kaji, M. 343  
Kako, Eiji 432  
Kalinichenko, Alexandr I. 2546  
Kaltchev, Dobrin 2620, 2623  
Kamada, Susumu 256, 2155, 3432  
Kaminsky, Alexander A. 1055, 3393  
Kaminsky, Alim K. 1055, 3393  
Kamitani, T. 1132, 2731  
Kamitsubo, Hiromichi 188  
Kamiya, Yukihide 904, 1174, 2436, 3363  
Kamperschroer, James H. 1444, 1447, 1929, 1946, 2214  
Kamps, T. 2075  
Kamykowski, Edward 587  
Kanai, T. 600  
Kanai, Y. 1653  
Kanai, Yasumori 3348  
Kanaya, Noriichi 664, 667, 670  
Kanazawa, Mitsutaka 413, 600, 798, 863, 2271  
Kando, Masaki 3690, 3702  
Kaneda, T. 592  
Kang, H.S. 2205, 2501, 2593  
Kang, X. 1545  
Kang, Yoon W. 168, 3092  
Kaplan, Dannie M. 3032  
Kaplan, Roger 980  
Karabarbounis, A. 1037  
Karantzoulis, Emanuel 1126, 2316  
Karasuk, V. 3086  
Karlner, Marlen M. 2033  
Karn, Jeff 3306, 3309, 3312  
Karnaukhov, I.M. 2930, 3122  
Karyotakis, Yannis 2990  
Kashikhin, Vladimir 174, 182, 3327  
Kashiwagi, Shigeru 256, 2143, 3432  
Kaspar, Klaus 3552  
Kasuga, Toshio 633, 2310  
Katane, Mamoru 2528  
Katayama, Takeshi 404, 1719, 1722, 1737, 3164  
Kato, S. 1132, 2731  
Katoh, Masahiro 664, 2307  
Katoh, Tadahiko 343  
Katonak, David J. 974  
Katsouleas, Thomas C. 330, 3651, 3654, 3672, 3708, 3713  
Katsumata, Tadasu 1309  
Katsumura, Yosuke 2602  
Kawachi, K. 600  
Kawamoto, Takashi 343, 2108  
Kaye, Robert A. 524  
Kazacha, Vladimir I. 3393  
Kazakov, S. 1058  
Kazakov, Serguei 3414  
Kazanskiy, Lev N. 1477  
Kazarinov, Nikolai Yu. 3501

- Kazimi, R. 1991  
 Keane, John 1028  
 Kedzie, Mark 524, 955  
 Keesee, Marie 747  
 Keffeler, David R. 1444, 1447  
 Kehne, David M. 234, 1970  
 Keil, Eberhard 1408  
 Keil, J. 2054, 3098  
 Keller, L. 2990  
 Keller, Roderich 87, 884, 1911, 1914, 1917, 1923, 1926, 1943, 1958  
 Kelley, John P. 965  
 Kelly, Eugene 185, 3161  
 Kempkes, Michael A. 568, 1491  
 Kenda, K. 658  
 Kennedy, K. 206  
 Kennedy, Kurt D. 884  
 Kenney, S. 3227  
 Kerby, J. 3194, 3197  
 Kernel, Philippe 1192, 1195  
 Kerner, Thomas M. 696, 699  
 Kerstiens, Debora M. 349, 652, 655, 1929, 1946  
 Kesselman, Martin 2250  
 Kester, Oliver 3516  
 Kewisch, Jorg 705, 708  
 Kezerashvili, Guram Ya. 2232  
 Khachatryan, Arsen G. 3663  
 Khan, Sameen A. 2817, 3280  
 Khan, Shaikat 197, 1144, 1147, 2831  
 Khodyachikh, A. 3122  
 Khodzhibagiyani, Gamlet G. 2262  
 Khomenko, S. 103  
 Kiang, L.L. 1545  
 Kikuchi, Mitsuo 1132, 2108, 2731  
 Kikutani, Eiji 633, 1132, 1138, 2731  
 Kikuzawa, Nobuhiro 2459  
 Kim, Eun-San 3053, 3056  
 Kim, G.N. 2593  
 Kim, Han-Sung 2558, 2561  
 Kim, Jin-Soo 1043, 1890  
 Kim, Jong-Won 2268  
 Kim, K.R. 3504  
 Kim, Kwang W. 1384  
 Kim, Kwang-Je 2495  
 Kim, Mun-Gyung 2418  
 Kim, Sang-Ho 2558, 2561  
 Kim, Y.C. 3504  
 Kim, Yong-Hwan 2558, 2561  
 Kim, Young-Hwan 2558, 2561  
 Kim, Yujung 1076, 1079  
 Kim, Yuseok 3137  
 Kimura, Wayne D. 487, 3722  
 Kincaid, Brian 162  
 Kindermann, Hans-Peter 946  
 King, Bruce J. 318, 3035, 3038, 3041  
 King, Quentin 762, 3743  
 Kinkad, Allen K. 1049  
 Kinoshita, Kenichi 2605  
 Kinsho, Michikazu 3128, 3546  
 Kirbie, Hugh C. 625  
 Kirichenko, A.E. 2256  
 Kirk, Harold G. 896, 3029, 3032, 3149  
 Kishek, Rami A. 234, 1656, 1749, 1758, 1761, 1830, 1970, 3274, 3369, 3372  
 Kishiro, Jun'ich 1141  
 Kishiyama, Keith 1333, 1336, 1396  
 Kitabayashi, Teruyuki 343  
 Kitagawa, A. 600  
 Kitazawa, Yasuji 592  
 Klaffky, Roger 2304  
 Klaisner, L. 206  
 Kleev, Andrey I. 592  
 Kleimenov, Victor 1339  
 Klein, Horst 1288, 1836, 3405  
 Klein, John 551  
 Kleinod, M. 1899  
 Klenov, V. 106  
 Klette, Hallgeir 562  
 Klingmann, Jeffrey 777  
 Knapp, Edward A. 2301, 2555  
 Kneisel, Peter 937, 943  
 Kniegl, Gregor 3740  
 Knobloch, Jens 980  
 Knoch, Herbert 2424  
 Knudsen, Helge 1671  
 Knuth, Thomas 197, 1144, 1147  
 Ko, In-Soo 1076, 1079, 2131, 2593, 3525  
 Ko, Kwok 2822, 3423, 3480  
 Koba, Kiyomi 1653, 2271  
 Kobayashi, T. 3507  
 Kobayashi, Yukinori 633, 2436, 3113, 3363  
 Koehler, G. 800  
 Koepke, Karl P. 992, 2027  
 Koeth, Tim 995  
 Koganeya, M. 3330  
 Kohaupt, Rolf Dieter 1171  
 Koiso, H. 1132, 2731  
 Koizumi, Nozomi 343  
 Kolbe, J. 197  
 Kolysko, A.L. 1474  
 Komada, Ichitaka 343  
 Kondo, Shuji 3690, 3702  
 Kondo, Yasuhiro 2187  
 Kondrashev, S. 103  
 Kondratenko, Anatoly 2289  
 Konecny, Richard 2030, 3618, 3621  
 Kononenko, S. 3122  
 Konstantinov, Sergey G. 2033  
 Koontz, Roland 1512  
 Korabelnikov, Maxim B. 2167  
 Korenev, Igor L. 1764  
 Kornilova, Alla A. 1312  
 Korolev, Aleksey 2567  
 Koroliov, Alexander N. 2570  
 Koscielniak, Shane R. 143, 1839  
 Koseki, Shoichiro 3770  
 Koseki, Tadashi 592, 2436, 3363  
 Koseki, Takashi 904  
 Kostas, Chris 360  
 Kostial, Stephan 2740, 2951  
 Kostin, Denis V. 910, 2301  
 Kotaki, Hideyuki 3690, 3702  
 Kotov, V.I. 53, 1237  
 Kotseroglou, T. 3432, 3447  
 Kotseroglou, Theofilos 3450  
 Koupsidis, J. 2385  
 Kourbanis, Ioanis 2840  
 Koutchouk, Jean-Pierre 372  
 Koutin, S.V. 392  
 Kovalenko, Alexander D. 2256, 2289  
 Kowalski, Ludwik 490  
 Koyama-Itou, H. 600  
 Kozanecki, W. 2990  
 Kozanecki, Withold 296  
 Kozawa, Takahiro 2018, 2596  
 Koziol, Heribert 465  
 Kozyrev, Evgeny V. 1049  
 Kponou, A. 1902  
 Kraemer, Dieter 197, 2379  
 Krawczyk, George 3761  
 Krafft, Geoffrey A. 1177, 2229, 2448, 2456  
 Kraft, G. 2513  
 Krakauer, D. 2635  
 Kramer, Stephen L. 134, 140  
 Krasnopolsky, Vsevolod A. 1479  
 Krasnykh, Anatoly 1512  
 Kraus, David E. 490  
 Krause, Herbert F. 1671  
 Kravchuk, Leonid V. 2799, 3282, 3561  
 Krawczyk, Frank L. 965, 977, 1396, 3588  
 Kreischer, Kenneth E. 81  
 Krejcik, Patrick 296, 3429, 3447, 3450  
 Kresnin, Yuri A. 2546  
 Krienen, Frank 3134  
 Krietenstein, Bernd 3552  
 Krinsky, Samuel 2304, 2471  
 Krisch, Alan D. 392  
 Krishnagopal, Srinivas 1674  
 Krishnan, Mohan 3666  
 Kriznar, I. 658  
 Kroc, T. 521  
 Krogh, Michael L. 1303, 2611  
 Kroll, Norman M. 777, 830, 1432, 1435, 3423, 3468, 3471, 3474, 3477, 3612  
 Kruchkov, Jaroslav G. 2033  
 Kruessel, Alois 2424, 3375  
 Krylov, Stanislav Y. 1479, 1485, 2567  
 Krämer, D. 2078  
 Kubantseva, Natalia 1423  
 Kube, G. 165  
 Kubo, Hiroshi 3770  
 Kubo, Kiyoshi 256, 2143, 3432, 3435  
 Kubo, Ta. 3158  
 Kubota, Chikashi 1653  
 Kuchnir, Moyses 992, 2027  
 Kudinov, Valery V. 1291  
 Kudo, Hirofumi 3363  
 Kudo, Kikuo 343  
 Kugler, Hartmut 103  
 Kuhler, S. 197  
 Kulikov, Artem V. 3447, 3450  
 Kulikov, I.I. 2256  
 Kumada, Masayuki 600, 2510  
 Kumagai, Keiko 2337, 2343, 2346  
 Kumagai, Noritaka 188, 2337, 2340, 2343, 2346, 2349, 2352  
 Kuner, B. 197  
 Kuno, Kazuo 3363  
 Kuo, C.C. 2409, 2412, 2837  
 Kuo, Chang Hor 685, 1153, 1156, 1159, 1162, 1165, 2069, 2409, 2412  
 Kurennoy, Sergey S. 1399, 2867, 3588  
 Kurita, Nadine R. 206, 1363  
 Kurnae, O. 1249  
 Kuroda, Ryunosuke 2298  
 Kuroda, T. 1306  
 Kurokawa, S. 633  
 Kurz, Stefan 2796  
 Kusano, Joichi 3128, 3546  
 Kusche, Karl P. 2552, 3722  
 Kushin, Victor V. 3564  
 Kusikov, S.V. 1474  
 Kuske, Bettina 197, 2379, 2382  
 Kuske, Peter 197, 2078, 2379, 2385  
 Kustom, Robert L. 168, 518, 998  
 Kuszynski, J. 2078  
 Kuzay, Tuncer M. 2090  
 Kuzminski, Joze 965  
 Kuzminski, Jozef 968, 2954  
 Kuznetsov, G. 237, 1902



- Kuznetsov, Yu. 106  
 Kvasha, Adolf I. 893, 3561  
 Kwan, Joe 1937, 1943, 2537  
 Kwan, Thomas J.T. 617, 1842  
 Kwiatkowski, K. 471  
 Kwon, Hyeok-Jung 2558, 2561  
 Kwon, Myeun 899, 902, 1076, 1079, 1357  
 Kwon, Sung-il 1064, 1067, 1070  
 Kwon, Y. K. 1893  
 Kühnel, K.U. 3516  
 Lach, Joseph 1387  
 Laclare, Jean-Louis 1533  
 Ladrán, A. S. 2590  
 Lager, Darrel L. 3513  
 Lakatos, Andreas 1288, 1836  
 Lalot, Michel 922  
 Lamanna, Giuseppe V. 2948, 3522  
 Lamarre, J.F. 1569  
 Lambertson, Glen R. 1225  
 Lambiase, Robert F. 3734  
 Lamm, Michael J. 3191, 3194, 3197  
 Lamont, Michael 304, 2996, 3008  
 Landahl, Eric C. 2000, 2003  
 Lange, M. 2424  
 Lange, R. 197  
 Lange, Ralph 2382  
 Lanting, T. 2990  
 Lanza, Richard C. 584  
 Lapi, Roman M. 2170  
 LaPointe, Mike A. 3627  
 Lapostolle, Pierre 1860  
 Lapshin, V. 3122  
 Larbalestier, David C. 177  
 Larimer, Ruth-Mary 533  
 Larrieu, Christopher A. 741, 747  
 Larsen, Ray 636  
 Larsen, Richard C. 490  
 Latypov, Tomas A. 1485, 2567  
 Lau, Wai Keung 1153, 1159, 1162, 1165, 2000, 2837  
 Laurent, Jean-Michel 2629  
 Lauth, W. 165  
 LaVeigne, Joseph 134  
 Laverty, Michael 890  
 Lawrence, George P. 3567, 3582  
 Lawson, Wesley 1040, 1046  
 Lawton, Don 234  
 Laxdal, Robert E. 893, 3534, 3537  
 Lazarus, Donald M. 490  
 Laziev, Eduard M. 3393  
 Le Duff, Joel 913, 2012  
 Le Sage, G.P. 2480  
 Lebedev, Pavel 1387  
 Lebedev, Valeri A. 646, 738, 1183, 2897  
 Leblanc, G. 206  
 LeBlanc, Greg 2945  
 LeBon, Douglas J. 3758  
 Lebrun, Paul 3032, 3062  
 LeCocq, C. 1390  
 Lee, Y. Y. 1267  
 Lee, Bryan S. 625  
 Lee, Chun Sik 1893  
 Lee, Edward P. 1830, 3254  
 Lee, Hyeyoung 3137  
 Lee, J.C. 1602, 1605, 2837  
 Lee, J.W. 679  
 Lee, Jan Fung 1162  
 Lee, Jinhyung 2784  
 Lee, Kang-ok 2558, 2561  
 Lee, P. B. 1716  
 Lee, Peter J. 177  
 Lee, Roger C. 557, 1348, 2146  
 Lee, S. 3672  
 Lee, S.H. 682  
 Lee, S.Y. 109, 392, 1545, 1548, 1854, 2286  
 Lee, Seung 330  
 Lee, Seung C. 1384  
 Lee, T. 2021  
 Lee, Tae-Yeon 679, 1384, 2131, 2418  
 Lee, W. Wei-Li 1623, 1626  
 Lee, Yong Y. 1297, 1488, 1743, 3182, 3185, 3300  
 Lee, Yvette 2540, 2575  
 Leemans, Wim P. 325, 330, 2111, 3696, 3699, 3705  
 Lefebvre, Daniel 2686  
 Lefevre, Thibaud 1797, 3387  
 Legan, Al. 56  
 Lehrach, A. 1578  
 Lehrach, Andreas 1701, 2292  
 Lei, Ge 747  
 Leissner, Boris 2172  
 Leitner, Matthaeus A. 1911, 1914, 1958  
 Lekston, J.M. 3387  
 Len L. K. 70  
 Leng, Yongbin 1315, 2125  
 Lenkszus, Frank R. 333, 2093  
 Leon, Asunción 2531, 2534  
 Lepercq, Pierre 916  
 Lepeule, Patrick 1339  
 Lesjak, B. 658  
 Lesrel, Jean 919  
 Lessner, Eliane S. 1644, 1967, 2325  
 Letchford, Alan P. 1767, 2208  
 Lettry, J. 92  
 Leung, Ka-Ngo 1911, 1914, 1917, 1920, 1923, 1943, 1958, 2540, 2575  
 Leunissen, Leonardus H.A. 1557, 1683  
 Level, Marie-Paule 1533  
 Levush, Baruch 360, 1016  
 Levy, C.D. Philip 106, 1964  
 Lewellen, John W. 1979, 2024, 2134, 2483  
 Lewis, B. 471  
 Lewis, S.A. 355  
 Li, C.D. 2671  
 Li, Derun 382, 800, 896, 907, 1207, 1548, 3149  
 Li, Guangyong 2125  
 Li, Jingyi 2048  
 Li, Nanyang 3339  
 Li, Rui 118, 2456  
 Li, Shaopeng 633  
 Li, Weimin 2406  
 Li, Yongjun 2406  
 Li, Yulin 3221  
 Li, Yun 234, 1656, 1758, 1970, 2102, 3369  
 Li, Zenghai 2822, 3423, 3447, 3468, 3480, 3483, 3486  
 Liaw, Chong-Jer 1345, 3300  
 Libkind, Marcus A. 1390, 2477, 2590  
 Lidia, Steven M. 1797, 1800, 2698, 2870, 3387, 3390  
 Liebermann, Holger 530  
 Lietzke, A. 171, 3233  
 Likhachev, Sergey P. 2587  
 Liljeby, Leif 1955  
 Lill, Robert M. 1411  
 Lima, Roberto R. 1366  
 Limberg, Torsten 1650  
 Limborg, Cecile G. 206, 2361, 3104, 3107  
 Limon, Peter J. 174, 1420, 2644, 3194, 3197  
 Lin, F.Y. 2671  
 Lin, Ke Kang 682, 1450, 2009, 2409, 2412, 2415  
 Lin, Tsai-Fu 1375  
 Lin, Xintian E. 75, 1429, 3612  
 Lindgren, Lars-Johan 2945  
 Lindroos, Mats 143, 2226  
 Linnekar, T. 2617  
 Lira, Antonio C. 3125  
 Lisi, Nicola 103  
 Lisitsyn, A. 461  
 Littauer, Raphael M. 410, 2057  
 Litvak, A.G. 1474  
 Litvinenko, Vladimir N. 221, 2099, 2468  
 Liu, Chen-Yao 3776  
 Liu, Dekang 633, 2140  
 Liu, G. 2337  
 Liu, Guangjun 2125  
 Liu, H.C. 2671  
 Liu, James 3450  
 Liu, Jinhong 2048  
 Liu, Kuo-Bin 3776  
 Liu, Lin 2421, 2891, 2894, 3125  
 Liu, Y. 2552, 3639, 3722  
 Liu, Yuan 1878, 1881  
 Liu, Zuping 2048, 2406  
 Lo, C.C. 1471, 3131  
 Lobo, Ricardo P.S.M. 134  
 Lockey, R. 1902  
 Loew, G.A. 3423  
 Loewen, Roderick J. 3420, 3423, 3426, 3480  
 Logan, B. Grant 3248  
 Logatchov, Pavel V. 78, 237, 2167, 2948  
 Loh, M. 3708  
 Lohrmann, Erich 554  
 Lombardi, Alessandra M. 103, 1860  
 Lombardi, Augusto 1324, 3522  
 Lonza, Marco 1120  
 Lopes, Nelson 3725  
 Lorenz, Ronald 2075  
 Lorenzon, Wolfgang 392  
 Loschner, H. 2575  
 Losito, Roberto 946, 949  
 Lou, G.H. 2220  
 Lou, Weiran 1441, 3221, 3224  
 Loulergue, Alexandre 1530  
 Low, Raymond 1920  
 Lozowski, B. 471  
 Lu, Chang-guo 3026  
 Lu, Ping 2184  
 Lucas, Peter W. 1246, 2614  
 Luccio, Alfredo U. 1578, 3143  
 Ludewig, Hans 548, 3185  
 Ludewigt, B. 2537  
 Luft, P. A. 1914  
 Luhmann, Jr., Neville C. 2000  
 Luiten, O.J. 3266  
 Lujan, Richard E. 977  
 Lumpkin, Alex H. 1644, 2134, 2137, 2161  
 Lund, Steven M. 1785, 1788, 3248, 3381  
 Lundah, Eric W. 3480  
 Lunev, Pavel 461  
 Luo, Xiaonan 2963  
 Luo, Xuefang 1596  
 Luo, Yun 633  
 Luong, Michel 250, 821  
 Lyles, John T. M. 998, 1001  
 Lynch, Don 2244  
 Lynch, Michael T. 453, 1061  
 Lyneis, Claude M. 533, 1952  
 Lyons, Mike B. 962  
 Lysenko, Walter P. 3528

- Ma, Li 633, 2140  
 Ma, Qing 1342  
 Macek, Robert J. 518, 1198, 1201  
 MacGill, R.A. 3149  
 MacGill, Robert 884  
 Machida, Shinji 62, 1653, 1818, 1821, 2271  
 Machie, D. 1991  
 MacKay, William W. 693, 702  
 MacLachlan, J. 521, 1707  
 MacLaren, Stephan A. 1937, 2849, 2852  
 Madden, Robert P. 2388  
 Madrid, Mike 1396  
 Maeng, AeHee 1384  
 Maerki, Max 418  
 Maezawa, Hideki 667, 670  
 Magerski, Andy W. 3573  
 Magne, Christian 922  
 Magumo, Benjamin 490  
 Mahler, G. 2128  
 Maier, Rudolf 851, 1701, 2292  
 Mailian, M.R. 1468, 2105, 3657  
 Majka, Richard 1258  
 Makarov, A. 3327  
 Makarov, K. 103  
 Makdisi, Y. 471  
 Makhnenko, L. A. 1973, 1976  
 Makita, Yo 848  
 Mako, Frederick M 70  
 Maksimchuk, Anatoly 3666, 3716  
 Malamud, E. 3330  
 Malchow, Russell 2990  
 Malitsky, Nikolay 2713, 3185  
 Malone, Robert G. 2158, 2471, 2942  
 Mamaev, Gennady L. 1479, 1482, 1485, 2564, 2567  
 Mamaev, Sergey L. 1479, 1482, 1485, 2567  
 Mamaev, Yuri A. 1988  
 Mammosser, John 925, 934, 937, 955, 1462  
 Manglunki, D. 1282  
 Mangra, Danny 1967, 1979  
 Manni, Mario 2277  
 Mant, Geoff 3248  
 Manwaring, Wm. 498, 673  
 Manzo, Mario P. 965  
 Mao, Stan 3429  
 Mapes, M. 1345  
 Marcellini, Fabio 131, 866, 1147  
 Marchand, Patrick 986, 989  
 Marcouille, Olivier 2686  
 Marhauser, Frank 3405  
 Marini, J. 919  
 Markiewicz, Thomas W. 307, 3462, 3489  
 Markovich, G. M. 2024  
 Marks, Steve 162, 3429  
 Marl, Ron 2656  
 Marlats, Jean-Louis 2686  
 Marletta, Salvo 97  
 Marneris, Ioannis 2543, 3767  
 Marone, Andrew 3161, 3170  
 Marque, Sébastien 946, 949  
 Marriner, John 641, 1707, 2638  
 Marsh, Kenneth A. 330, 2006, 3651, 3705  
 Marshall, Thomas C. 3627  
 Marteau, Fabrice 2686  
 Marti, F. 1318  
 Martin, D. 206  
 Martin, Edward 3309  
 Martin, K. S. 714  
 Martin, Michael C. 495  
 Martin, Philip S. 31, 1082, 3318  
 Martin, Siegfried A. 959, 3549  
 Martinez, D. 2214  
 Martinez, Derwin G. 2241  
 Martinez, Felix A. 965  
 Martinez, Horace J. 965  
 Martini, M. 1282  
 Martins, Marcos N. 1366  
 Martlew, Brian G. 661  
 Martono, Hendy 1551, 2805  
 Martyshkin, Pavel V. 1456, 2170  
 Marusic, A. 2128  
 Marutsuka, Katumi 3360  
 Maruyama, T. 3447  
 Maruyama, Takahashi 3450  
 Maruyama, Takashi 1988  
 Marx, Michaela 2385  
 Masahiro, Kaji 343  
 Masaki, Mitsuhiro 2346  
 Masi, M. 1324  
 Masullo, Maria R. 1599  
 Masunov, E. 2855, 2858  
 Masuzawa, Mika 1132, 2731, 3351, 3354, 3357  
 Matheisen, A. 2033  
 Matheson, John 2999  
 Mathis, Yves-Laurent 2424  
 Matoba, Suguru 2271  
 Matsufuji, N. 600  
 Matsumoto, Hiroshi 536, 842, 3411  
 Matsumoto, Shuji 3414  
 Mattison, Thomas 2990  
 Matuk, Charles 1920  
 May, Michael P. 1423  
 May, T.E. 2394  
 Maymon, Jean-Noel 1168  
 Mazaheri, G. 296  
 Mazur, Peter O. 182, 3318, 3330  
 Mazzitelli, Giovanni 1536  
 McAllister, Brian 3101  
 McCashan, M.S. 182  
 McCandless, Brian 3480  
 McCarrick, James F. 1303, 1827, 2755  
 McCarthy, Michael P. 1061, 1402  
 McChesney, David D. 3179, 3188  
 McClellan, Jonathan T. 965  
 McCormick, Douglas J. 253, 307, 1994, 3411, 3453, 3477  
 McDaniel, Boyce 410  
 McDonald, Kirk T. 310, 3026  
 McGehee, Peregrine M. 652, 3528  
 McGehee, Robert 688  
 McGinnis, David 59, 854, 1713  
 McGuire, David 1402  
 McIntosh, Peter A. 1025  
 McInturff, Alfred D. 171, 3197, 3233, 3236  
 McIntyre, Gary T. 3336  
 McIntyre, Peter 2936  
 McKee, B.D. 3429, 3447  
 McKemey, Adrian 2990  
 McKinney, W. 495  
 McMahan, Margaret A. 533  
 McMichael, Gerald E. 2274  
 McNerney, A.J. 1267, 1270  
 Mead, William C. 2790  
 Meadow, B. 2990  
 Meads, Phillip, F. 3549  
 Meddahi, Malika 304, 2996, 3005  
 Meier, Wayne R. 1503  
 Meilunas, Ray 2599  
 Meinke, Rainer B. 3212, 3215, 3245  
 Mele, K. 658  
 Melissinos, Adrian C. 2027, 2181  
 Meller, Robert E. 1115  
 Melnychuk, Stephan T. 587, 2599  
 Mendonca, Jose T. 3725  
 Menefee, Tina 3306  
 Menegat, Al 824, 3420  
 Menna, Mariano 2578  
 Menshov, Alexander A. 893  
 Menzel, Jan 2178  
 Meot, Francois 2445  
 Merl, Robert 2093  
 Merle, Eric 3260  
 Meringa, Lia 768, 1177, 1180, 2456  
 Merrill, Frank 518  
 Merte, Rolf 815, 818  
 Mertens, Volker 40  
 Meseck, Atoosa 554  
 Meth, Marvin 3336  
 Metral, G. 1282  
 Meurdesoif, Y. 3387  
 Meusel, Oliver 1288, 1836  
 Mexner, Wolfgang 2424  
 Meyer, Christophe 103  
 Meyer, Dirk 1917  
 Meyer, Earl 1946  
 Meyer, H.O. 471  
 Meyer, Ross K. 3594  
 Meyer-ter-Vehn, Jürgen 3675  
 Mezi, Luca 1219  
 Mi, J.-L. 1488  
 Michaut, Jean 2686  
 Michelato, P. 2027  
 Michizono, Shin-ichiro 1132, 2731, 3414  
 Michnoff, Robert J. 693, 2114, 2247  
 Michta, Richard J. 2081  
 Middendorf, Mark E. 2274  
 Miera, D.A. 426  
 Miertusova, Jana 2316  
 Migliorati, M. 131  
 Migliorati, Mauro 1219  
 Mikawa, Katsuhiko 3360  
 Mikhailichenko, Alexander A. 2814, 3218, 3633, 3636  
 Mikhailov, Vladimir A. 2256, 2262, 2289  
 Miki, Miyako 2596  
 Mikkelsen, Ulrik 1671  
 Milardi, Catia 1536  
 Milharcic, T. 658  
 Millage, Kyle K. 3429, 3447, 3450  
 Miller, J.R. 3227  
 Miller, Roger H. 777, 3423, 3426, 3468, 3471, 3474, 3477, 3480, 3483, 3486  
 Millich, Antonio 250, 1863  
 Millo, Daniele 2680  
 Millos, Gabriel 171, 3236  
 Mills, Frederick E. 3152  
 Milton, Bruce 587  
 Milton, Stephen V. 1644, 1979, 2024, 2134, 2325, 2483, 2486  
 Mimashi, T. 1132, 2731  
 Minaev, Sergey A. 1291, 3552  
 Minaev, Serguei 3555  
 Mincer, Allen 1258  
 Minehara, Eisuke J. 2459, 3546  
 Minohara, S. 600  
 Minty, Michiko G. 256, 296, 307, 338, 771, 800, 1207, 2846, 3384, 3432  
 Mirabal, J.S. 426  
 Mirochnik, E. 2567  
 Mirzozan, Alexandr N. 3561

- Mischenko, Aleksandr V. 2564  
Mishin, Andrey V. 590  
Mishnev, V. M. 2167  
Mishra, C. Shekhar 31, 2641, 2644, 2647, 2719, 3318  
Mistry, Nariman B. 3221  
Mitchell, John C. 965  
Mitchell, Russell R. 965  
Mitra, Amiya K. 450, 839, 893  
Mitsubishi, Toshiyuki 492, 2120, 2143, 2307  
Mitsumoto, Toshinori 2268  
Mitsunobu, Shinji 440  
Miyade, Hiroki 2403  
Miyahara, N. 600  
Miyahara, Tsuneaki 2155  
Mizumoto, Motoharu 513, 3128, 3546  
Mizuno, Akihiko 2015, 2749, 3507  
Mizuno, Hajime 3414  
Mizutani, Yasuhiro 2596  
Moallem, M. 2099  
Mocheshchnikov, N.I. 2924  
Mochihashi, Akira 1821  
Moeller, Soeren Pape 2295, 2427  
Mohos, I., 2054  
Moir, David C. 617, 1842  
Moir, Ralph W. 1503  
Mokhov, Nikolai V. 56, 1231, 1234, 2525, 2614, 3041, 3047, 3050, 3074  
Molodkin, V. 3122  
Molodozhentsev, Alexander 2522  
Molvik, Arthur W. 1503, 3248  
Monard, H. 2012  
Monchinsky, V.A. 2256  
Mondelli, Alfred A. 360  
Montag, Christoph 1566  
Montoya, Debbie I. 965  
Montoya, Dennis R. 965  
Moog, Elizabeth R. 2483, 2489  
Moore, Christopher I. 3687, 3693  
Moore, Craig D. 1246, 2614  
Moore, D. 652  
Moore, John M. 1551, 2805  
Moore, T. L. 2590  
Morcombe, Peter H. 221, 688  
Moretti, Alfred 896, 3032, 3149, 3152  
Morgan, Gerry H. 185, 3161, 3170  
Mori, Warren B. 330, 3669, 3672, 3684  
Mori, Yoshiharu 106, 413, 565, 798, 857, 860, 863, 1007, 1653, 1821, 1964, 2271, 2280, 3348, 3770  
Morita, Akio 1294, 2528  
Morpurgo, Giulio 2996  
Morrison, L. 171, 3233  
Morrison, M. 171, 3233  
Morse, W.M. 1488  
Mortazavi, Payman 1028  
Morvillo, Michele 1408, 2629  
Moser, Herbert O. 165, 2424  
Moser, S. Scott 3041  
Mosnier, Alban 628, 1533, 1662, 2834  
Moss, Andrew J. 1025  
Moss, James D. 965  
Mostacci, Andrea 2873  
Mouillet, Marc 3260  
Mouton, Bernard 2012  
Muchnoi, Nikolay Yu. 2232  
Mueller, Roland M. 726, 2078, 2379, 2382, 2385  
Mugge, Marshall 777  
Muggli, Patrick 330, 2006, 3651, 3654, 3708  
Mugnai, G. 2999  
Mukherjee, Sam K. 1911, 1914  
Mukugi, Ken 3546  
Mulholland, Gregory A. 1988, 3447, 3450  
Mullacraane, I. D. 2656  
Muller, Anke-Susanne 2885, 3011  
Muller, Ralph 197  
Mulvaney, J. Michael 568, 1491  
Muneyoshi, T. 2689  
Munoz, Marc 1542  
Munro, Morrison H. 3429, 3447  
Munson, D.V. 3257  
Murakami, T. 600  
Muramatsu, M. 600  
Muramatsu, Ryosaku 413, 798, 860, 863, 1007, 2271  
Murata, Hirohiko 2403  
Muratore, Joseph F. 185, 3161, 3170  
Murokh, Alex 217, 2006, 2480  
Muroya, Yusa 2602  
Murphy, James B. 134, 140, 1106  
Musameci, Pietro 2480  
Mussion, John 768, 1183  
Muto, Masayuki 565, 3348, 3770  
Myakishev, Dmitry G. 2775  
Myers, Stephen 299  
Myskin, O. 2033  
Mytsykov, A. 3122  
Nadji, Amor 1168, 1533, 1569  
Nagai, Ryoji 2459  
Nagaitsev, Sergei 521, 1088, 1707  
Nagaoka, Ryutaro 1192, 1195, 3119  
Nagayama, Takahisa 848  
Nahon, Laurent 2686  
Naito, Takashi 256, 343, 1994, 2143, 2155, 3432  
Naitoh, Takashi 492  
Nakajima, Kazuhisa 2510, 3690, 3702  
Nakajima, Mitsuo 3690  
Nakajima, Tsukasa 3360  
Nakamura, Eiji 1141  
Nakamura, M. 471  
Nakamura, Norio 1174, 2436, 3363  
Nakamura, Shinsuke 3098  
Nakamura, T. 1132, 2731, 3158  
Nakamura, Takeshi 2346  
Nakamura, Tatsuro 343  
Nakamura, Yoshiteru 2259  
Nakanishi, T. 3098  
Nakayama, Hitoshi 413, 798, 1007  
Nam, S.H. 2205, 2501, 3504  
Namito, Yoshihito 3450  
Namkung, W. 2593  
Nantista, Christopher D. 1432  
Napoly, Olivier 922  
Nara, Takayuki 2259  
Narang, R. 3708  
Nasonov, Nikolay N. 2584, 2587  
Nassiri, Alireza 1073, 1979, 2024, 2483  
Nath, Subrata 611, 1929, 3528, 3582  
Nation, J.A. 3600, 3603, 3606, 3609  
Naumann, Olaf 1647  
Navarro, G. 1324  
Nawrath, Guenther 554  
Nawrocky, Roman J. 2081  
Neil, G. R. 2456  
Nelson, Eric M. 360, 2778  
Nelson, Scott D. 1824, 2235  
Nelson, W. Ralph 253, 2990, 3450  
Nemoshkalenko, V. 3122  
Nesterovitch, Alexandre V. 1291, 1932, 2573  
Neuffer, David V. 3062, 3080, 3083, 3152  
Neugebauer, F. 2764  
Neuman, Charles P. 1949  
Neurath, R. 2611  
Nevada, Bechtel 1506  
Newman, Ernest W. 971  
Newsham, D. 2003, 2021  
Nezhevenko, Oleg A. 1049, 1052, 1474, 3492  
Ng, Cho-Kuen 206, 800, 3423, 3426  
Ng, King Y. 872, 1545, 1548, 1854, 3077  
Nghiem, Phi 1533  
Nguyen, Dinh C. 217, 2480  
Nguyen, K. 1016  
Nguyen, Minh N. 1494, 1497  
Nguyen, Viet 780, 928, 931, 934, 1459  
Niederer, James A. 1270, 1578, 2722  
Nief, J.-Y. 2990  
Niell, Fred M. 237, 1004  
Nielsen, B.R. 2427  
Niki, Kazuaki 3770  
Nikiforov, Alexej A. 750  
Nikitine, Iouri 1339  
Ninomiya, Shiro 1821  
Niquille, C. 2617  
Nishi, Masatsugu 2528  
Nishimori, Nobuyuki 2459  
Nishimura, Hiroshi 203, 234  
Nishiura, M. 1306  
Nobrega, A. 3194, 3197  
Noda, Akira 857, 1294, 2280, 2528, 3110  
Noda, Fumiaki 3128, 3546  
Noda, Koji 413, 600, 798, 863, 1309, 1821, 2271  
Noda, Takashi 2352  
Nogiec, Jerzy M. 1426, 3191  
Noguchi, Shuichi 432  
Nordberg, Emery 980, 3221  
Norem, J. 1417, 2635, 3062  
Norman, Eric B. 533  
Normann, L. 2617  
North, William 1037, 1515  
Norum, W. Eric 3764  
Nosochkov, Yuri 206, 2355, 2358, 2364, 3465  
Novikov, Gleb A. 2301  
Novikov, Vladimir N. 3716  
Novikova, Tat'ana A. 2581  
Novitski, I. 3194, 3197  
Novokhatski, Alexander 2743, 2879  
Nuhn, H. D. 2486  
Nurushev, S. 471  
Nusinovich, G. 1040  
Nyman, M. 3257  
O'Hara, James F. 2214  
O'Neil, James 533  
O'Shea, Patrick G. 234, 1949  
Oakeley, Owen 221, 2099  
Oakley, Owen 2468  
Obina, Takashi 1135, 2310  
Oerter, Brian R. 699  
Ogata, Atsushi 3713  
Ogawa, Y. 2731  
Ogawa, Yujiro 1132, 2984  
Ogitsu, T. 174, 3158, 3194  
Oguri, Hidetomo 3546  
Oguri, Yoshiyuki 3525  
Oh, Saewoong 2265, 3137  
Ohkuma, Haruo 2337, 2340, 2343, 2346, 2349, 2352  
Ohmi, Kazuhito 633, 1132, 2731, 3113  
Ohmori, Chihito 413, 798, 857, 860, 863, 1007, 1653, 2271, 2280  
Ohnishi, Y. 1132, 2731, 2981

- Ohnuma, S. 2590  
 Ohsawa, S. 2731  
 Ohsawa, Satoshi 1132, 2238  
 Ohshima, Takashi 2346  
 Ohtomo, Kiyotaka 1722  
 Ohuchi, N. 1132, 2731, 3158  
 Oide, Katsunobu 288, 1132, 2238, 2731, 3432  
 Oishi, Masaya 2352  
 Okada, Yasuhiro 2018, 2036  
 Okamura, M. 3161  
 Okamura, Masahiro 106, 471, 1964, 3164  
 Oki, Toshiyuki 1821  
 Okita, Shunsuke 2605  
 Okugi, Toshiyuki 256, 2143, 2155, 3432  
 Okumura, Susumu 2259  
 Oliveira e Silva, Luis 3725  
 Olsen, David K. 109, 1198, 1201, 3140, 3143, 3303  
 Omori, Tsunehiko 2552  
 Onda, Takashi 842  
 Ongaro, Carla 2531, 2534  
 Onillon, Emmanuel 1109  
 Ono, Masaaki 432  
 Op de Beeck, W.J. 3212  
 Opanasenko, Anatoly N. 1976  
 Oragiri, Jun-ichi 343  
 Oren, Will 3309  
 Orlandi, Gianluca 2193, 2196  
 Ormond, Kern W. 1354  
 Orris, Darryl F. 1420, 1426, 3191, 3194, 3197, 3318  
 Orsini, Fabienne 2834  
 Ostiguy, Jean-Francois 2710  
 Ostojic, R. 1330, 2921  
 Ostrikov, Sergey V. 1932  
 Ostroumov, Petr N. 103, 893, 3282, 3561  
 Otboev, Alexey 1524  
 Ott, Klaus 197, 2385, 2608  
 Otting, Donnie 803  
 Ouchi, Nobuo 3546  
 Overett, Trevor 1061, 3755  
 Ovsyannikov, Alexander D. 2808  
 Ovsyannikov, Dmitri A. 1857  
 Owen, Hywel L. 2433  
 Oyaizu, M. 1893  
 Ozaki, K. 592  
 Ozaki, T. 3158  
 Ozelis, J.P. 174, 3194, 3197  
 Pabst, Michael 1767  
 Padamsee, Hasan S. 429, 980, 983  
 Pagni, Carlo 1776, 2027  
 Pagano, Oreste 3209  
 Pai, Chien-Ih 1100, 1488  
 Pakter, Renato 1875, 2752  
 Palmer, Dennis T. 545, 1997, 3612  
 Palmer, Robert B. 3023, 3032, 3062, 3149, 3152  
 Palmieri, Vincenzo 541, 943  
 Palumbo, Luigi 1219, 1599, 2873  
 Pantell, R. H. 3722  
 Panvier, Roger 916  
 Paolicelli, Guido 2060  
 Paolucci, Giorgio 2060  
 Papaleo, R. 2578  
 Papanicolas, N. 1037  
 Papaphilippou, Yannis 1554, 1557, 1560  
 Pappas, Chris 1494, 1500, 3429  
 Pappas, G.C. 1488  
 Paramonov, Valentin V. 893, 2799  
 Pardo, R. C. 1890  
 Parietti, L. 3591  
 Park, Chongdo 1357  
 Park, E.S. 2418  
 Park, H. J. 899  
 Park, I. S. 899, 902  
 Park, S. 206, 2367  
 Park, Seong Hee 221, 2468  
 Parker, Brett L. 3336  
 Parkhomchuk, Vasily V. 1387, 1704  
 Parodi, Renzo 913  
 Parsa, Zohreh 2820, 3044  
 Pasky, Stanley J. 1414, 2024  
 Pasotti, Cristina 809, 1123  
 Pasquinelli, Ralph J. 1094  
 Pastnak, J. W. 2590  
 Pate, David 557, 1348  
 Paterson, J.M. 3423  
 Patterson, Janet L. 2468  
 Paul, Arthur C. 1204, 3251, 3254, 3513  
 Pavlovic, M. 2513  
 Pavlovskii, V. V. 2178  
 Payet, Jacques 1530  
 Pearce, P. 250  
 Pearson, Chris 777, 3423, 3426  
 Pearsons, R. 3579  
 Peaupardin, Philippe 2686  
 Peck, Stuart B. 285, 980  
 Pedeau, Dominique 1168  
 Pedersen, Flemming 143, 474  
 Pedrozzi, Marco 81  
 Peggs, Stephen G. 705, 1572, 3176, 3179, 3336  
 Pei, A. 1545  
 Pei, X. 1548  
 Pei, Yuanji 1315, 1596  
 Peikert, Martin 815  
 Peiniger, M. 957, 3510  
 Pekeler, M. 245, 2033  
 Pelaia, Thomas A. 1115  
 Pellegrin, Eric 2424  
 Pellegrini, Claudio 217, 2006, 2021, 2045, 2480, 2504, 3708  
 Pellico, William A. 1097  
 Pelzer, Wolfgang 3519  
 Penn, Gregg 3059  
 Peraire, Serge 40  
 Perelstein, Elkuno A. 3393, 3501  
 Perera, Lalith 3221  
 Perevedentsev, Eugene 1521, 1524  
 Perez, Francisco 806, 809, 2424  
 Perko, M. 658  
 Pershing, D. 1016  
 Peskov, Nikolay Yu. 1055  
 Pestrikov, D. 1132, 2731  
 Petelin, M.I. 1474  
 Peternel, M. 658  
 Peters, Craig 3257  
 Peterson, Edward 551  
 Peterson, T. 1420, 3194, 3197  
 Petillo, John J. 360, 2737, 2778  
 Petit, Annie 2686  
 Petitpas, Patrick 2990  
 Petracca, Stefania 1689, 2882  
 Petrak, Sibylle 2990  
 Petree, Mark 2990  
 Petrichenkov, Michael V. 3086  
 Petrossian, Marzik L. 3657  
 Petrov, Viktor M. 2033  
 Pett, John G. 762, 3743  
 Petukhov, Vladimir P. 2584  
 Pfeffer, Howie 3761  
 Pflüger, Joachim 157, 1369  
 Phelps, R.A. 392  
 Phillips, H.L. 1459  
 Phillips, Lawrence 780, 934, 937, 1462  
 Phinney, Nan 307, 338, 3384, 3447, 3456  
 Piasczyk, Christopher 1465  
 Pichoff, Nicolas 1860, 3277  
 Pickard, D. 1943  
 Pico, Randolph E. 2590  
 Picon, Jean-Claude 3260  
 Pieck, M. 652  
 Piekarz, Henryk 182, 3330  
 Piel, C. 3510  
 Pierini, Paolo 1776  
 Pierret, Olivier 3260  
 Pikin, A. 1902  
 Pilat, Fulvia 37, 2716, 2728, 3179  
 Pile, P.H. 1267  
 Pile, Geoffery 1022  
 Pilipenko, Yuri 2289  
 Pillai, Chandra 518  
 Piller, C. 955  
 Pinayev, Igor V. 221, 2468  
 Pincosy, Philip A. 1827  
 Pinto, Innocenzo 2882  
 Piot, Philip 2229, 2456  
 Pipersky, Paul 162  
 Piquemal, Alain C. 1851  
 Pirkel, Werner 103  
 Pirozhenko, A. 2567  
 Pirozhenko, Vitaly M. 2564  
 Pisent, Andrea 1773, 3522  
 Pitts, Cliff 3342  
 Pivarc, J. 1896  
 Pivarc, J., Jr. 1896  
 Pivi, Mauro 2629  
 Placidi, Massimo 296, 2999  
 Plate, David 162, 803  
 Platise, U. 658  
 Plawski, Eugeniusz 3408  
 Plesko, M. 658, 2424, 2424  
 Plettner, Tomas 321  
 Plotnikov, Sergey V. 3564  
 Plum, Michael A. 518, 1198, 1201  
 Podlech, Holger 1955, 3543  
 Podlevskii, Vitaly V. 2802  
 Podobedov, Boris 146, 1665, 2978  
 Poelker, B.M. 1991  
 Pogorelsky, Igor V. 2471, 2552, 3722  
 Poirier, Roger L. 450, 839, 893, 3540  
 Pollet, Patrick 2087  
 Polozov, S. 2858  
 Pomazan, Yu. V. 1291  
 Poncet, A. 1330  
 Pont, Montse 2424, 3375  
 Poole, Brian R. 1824, 3381  
 Poole, Michael W. 2433, 2656  
 Pope, Rodd 777  
 Popov, Gennadiy F. 2546, 2549  
 Poppe, Uli 2178  
 Porcellato, A.M. 1324  
 Portante, Luciano 1366  
 Portmann, Gregory, J. 2373  
 Potier, J.P. 250  
 Potukuchi, Prakash N. 952  
 Poutchkov, Sergey N. 1479, 1482, 1485, 2567  
 Powell, James 533  
 Power, John F. 1399, 2214, 2241  
 Power, John G. 1967, 2024, 2030, 3621  
 Pozimski, Jürgen 1288, 1836  
 Prabhakar, Shayam 131, 636

- Prabhaker, Shyam 1207  
 Pradal, Franco 2316  
 Praestegaard, L. 2427  
 Prange, H. 197  
 Prasuhn, Dieter 1701, 2292  
 Preble, Joseph P. 780, 931, 934, 1459, 1462, 2456  
 Prebys, Eric J. 3026  
 Preger, Miro A. 131, 1536  
 Prelec, K. 1902  
 Prestemon, S. 3227  
 Price, J.S. 1991  
 Prichard, Benjamin A. 1917, 1923  
 Prieto, Peter S. 1246  
 Pritzkau, David P. 824  
 Prodell, Albert 185, 3161, 3170  
 Pronin, Oleg D. 3561  
 Prono, Daniel S. 617  
 Proudlock, Paul I. 1330, 3200, 3203, 3746  
 Pruessner, Marcel 234  
 Przeklasa, Roy 1010  
 Przewos, B. 471  
 Puitsin, Vadim I. 37, 702, 1575, 2716, 2921  
 Puggli, P. 3705  
 Pugh, M. J. 2656  
 Pukhov, Alexander 3675  
 Puntus, Vladimir A. 3561  
 Pusterla, Modesto 3280  
 Péerez, José 2531  
 Qian, Zubao 872  
 Qiang, Ji 137, 366, 1845  
 Qin, Hong 1623, 1626, 1629  
 Qin, Qing 633  
 Qinggui, Lai 3263  
 Quigley, Peter 980  
 Quimby, David C. 2668, 2674, 2677, 3722  
 Quintana, Bobby 349  
 Quintana, Stephen W. 965  
 Rabedeau, T. 206  
 Radecke, F. 197  
 Radeka, Veljko 2114  
 Rago, C. E. 3447  
 Raia, Guido 2578  
 Raimondi, Pantaleo 307, 338, 2996, 3384  
 Raino, Antonio 1905  
 Rakowsky, George 1390, 2471, 2477, 2698  
 Ramamoorthy, Susila 690  
 Ramanathan, Mohan 2051  
 Rambo, Peter W. 1827  
 Ramos, H.J. 1306  
 Ramsell, Christopher T. 3719  
 Raparia, Deepak 1297, 1743, 1964, 3185  
 Rasson, J. 800  
 Rathjen, Eric 2424  
 Rathke, J. 780  
 Rathke, John 551  
 Ratner, Lary G. 392  
 Ratschow, S. 2915  
 Ratti, Alessandro 884, 1961  
 Ratzinger, Ulrich 1788, 1955, 3552, 3555  
 Raubenheimer, Tor O. 240, 250, 253, 338, 800, 3423, 3429, 3438, 3441, 3444, 3447, 3453, 3456, 3462, 3465, 3474, 3483, 3486, 3489  
 Rauch, Helmut 2957  
 Ravello Alberto 2936  
 Reass, William A. 426, 453  
 Redin, Sergei I. 3167  
 Redler, K. 1393  
 Reece, C.E. 940  
 Reed, C. 3062  
 Reed, C.A. 1881  
 Rees, Daniel E. 786, 881, 1010, 1061, 1402, 2772, 3528  
 Regan, Amy H. 1061, 1064, 1067, 1070, 3528, 3582  
 Reginato, Louis L. 2537, 3257  
 Regler, Meinhard 2957  
 Reiche, S. 2486  
 Reichel, I. 296  
 Reid, Ron J. 2656  
 Reijonen, Jani 1943  
 Reilly, John 980  
 Reilly, Robert E. 56  
 Reiman, Sergei I. 1312  
 Reiser, Martin 234, 1040, 1046, 1656, 1659, 1749, 1758, 1970, 2102, 3274, 3369, 3372  
 Reitze, David H. 134  
 Rendon, Armando M. 965  
 Rensfelt, K.G. 1955  
 Repnow, Roland 1955, 3543  
 Revol, Jean-Luc 1192, 1195  
 Reymermier, Christian 1339  
 Reyzi, Ingrid 1171  
 Riabko, A. 1548  
 Ribes, Jean-Bernard 765  
 Rice, David H. 410, 2217, 2972, 3221  
 Rice, John A. 3242  
 Richards, Mitchell C. 349, 655, 1444, 1447, 1929, 1946  
 Richardson, Roger A. 1303, 2149  
 Riche, A.J. 250, 1863  
 Richied, Donald, E. 2954  
 Richter, Achim 2740, 2951  
 Richter, D. 197  
 Riddone, Germana 3203  
 Ries, T. 3540  
 Rieul, B. 1569  
 Rifkin, Jeff 777, 3423  
 Rifuggiato, Danilo 2578, 3288  
 Rimmer, Robert A. 800, 803, 896, 907, 3131, 3429  
 Rindfleisch, Ulrich 851  
 Ringwall, A. 3462  
 Rinkel, Tomas 392  
 Rinolfi, I. 250  
 Ristau, U. 2424, 2427  
 Ritchie, Gary 2852, 3339  
 Rizawa, Takahito 1722  
 Roberts, L. 1488  
 Roberts, Scott E. 1351, 3221  
 Robin, David 203, 1581  
 Robin, G. 2617  
 Robinson, Kern E. 2668, 2674, 2677, 3722  
 Robinson, Theodore G. 702  
 Robl, Phil 2388  
 Rodarte, Henry J. 3573  
 Rode, Claus 3309  
 Rodenas, Jose 2534  
 Rodier, Jacques 2012  
 Rodriguez-Mateos, Felix 154, 3200, 3203  
 Roerich, V. 103  
 Rogers, G. C. 2659  
 Rogers, Joseph T. 1354, 1686  
 Rohmig, P. 1330  
 Rokni, Sayed 253, 330, 3429  
 Romanov, G.V. 2799, 3561  
 Romanov, S.V. 2256  
 Roncarolo, Frederico 2999  
 Root, Larry 3534  
 Roper, R. 3540  
 Ropert, Annick 2328  
 Rosenberg, Richard A. 1641  
 Rosenzweig, James B. 217, 2003, 2006, 2021, 2027, 2039, 2042, 2045, 2480, 2504, 3624, 3708  
 Roser, Thomas 26, 614, 857, 1267, 1270, 1276, 1578, 1746, 1964, 2128, 2280, 2725, 3291, 3336  
 Roshal, A. 2858  
 Ross, Marc C. 253, 307, 800, 1994, 3411, 3429, 3432, 3447, 3453, 3477  
 Rossmanith, R. 165, 2424, 2427  
 Rotela, E. 2635  
 Rothmund, Karsten 2787  
 Rothman, Jeffrey L. 2081  
 Roudskoy, I. 103  
 Rovelli, Alberto 482, 2578  
 Rowe, Michael 533  
 Roy, Ghislain 2617, 2996  
 Roybal, William 1396, 1402  
 Roódenas, José 2531  
 Rubin, David L. 285, 410, 980, 1300, 3221  
 Rudiger, H. 197  
 Rudolph, Klaus 3516  
 Rudychev, Vladimir G. 2549  
 Ruegg, Roman 587  
 Rueter, M. 1369  
 Ruggiero, Alessandro G. 2590, 3731  
 Ruggiero, Francesco 1408, 2626, 2629  
 Ruland, Robert 1390, 2698  
 Rule, Donald W. 487, 3722  
 Rullier, Jean-Luc 1797, 3387  
 Rusnak, Brian 965, 974, 977, 1396  
 Russell, Steven J. 477  
 Russenschuck, Stephan 154, 2796  
 Ruth, Ronald D. 250, 262, 423, 777, 3423, 3468, 3480  
 Rutkowski, Henry L. 617, 3257  
 Rutt, P.M. 1991  
 Ryan, K. 1991  
 Ryan, W. 2114, 2117  
 Rybalchenko, G.V. 2689  
 Rybaryk, Lawrence J. 881, 3528, 3582  
 Ryne, Robert D. 137, 366, 611, 1845  
 Rödel, Volker 946  
 Saban, Roberto 3203  
 Sabbi, Gianluca 3179, 3194, 3197  
 Sabjan, R. 658  
 Sachleben, W. 928  
 Saeki, Akinori 2596  
 Saeki, Hiroshi 2352  
 Saethre, Robert B. 625  
 Saewert G. 237  
 Safa, Henri 432, 919, 1396  
 Safranek, James 206, 1584, 2244, 2304, 2364, 3101  
 Sagan, David C. 410, 2966, 2969  
 Sah, R.C. 2409, 2415  
 Saito, Kenji 432  
 Sajaev, Vadim V. 2471, 2942  
 Saka, K. 592  
 Sakai, Fumio 2036, 2298, 3702  
 Sakai, I. 2271  
 Sakai, Y. 592  
 Sakaki, Horonao 3507  
 Sakanaka, Shogo 904, 2310  
 Sala-Ferrari, Paola 40  
 Salakhutdinov, A.S. 2555  
 Salazar, Gilbert A. 655  
 Sampayan, Stephen E. 617, 1303, 2611  
 Sampson, William B. 185, 3230  
 Sandberg, J. 3767  
 Sander, Oscar R. 518, 1917, 1923

- Sanders, David M. 1303, 2611  
 Sanders, Ralph T. 1100, 1261, 1264, 1488, 3336  
 Sandner, Wolfgang 2033  
 Sandweiss, J. 3722  
 Sangster, T. Craig 1937, 3248  
 Sannibale, Fernando 131, 1536  
 Santucci, James K. 237, 2027  
 Sapp, W. 590  
 Sarkisov, Gennady S. 3716  
 Sasao, M. 1306  
 Sassowsky, Manfred 3378  
 Sato, H. 3098  
 Sato, Hikaru 392, 2650, 3360, 3749, 3752  
 Sato, Shigeru 664  
 Sato, Yasuo 413, 600, 633, 798, 857, 860, 863, 1007, 2271, 2280  
 Satogata, Todd J. 693, 705, 2722, 2728  
 Satoh, Kotaro 1132, 2084, 2108, 2731  
 Satoh, Masanori 1174  
 Satov, Y. 103  
 Satpute, Sharad 1402  
 Sattarov, Dior 2936  
 Savchenko, A.N. 753  
 Sawada, Junichi 3546  
 Sawamura, Masaru 2459  
 Sazonov, Michael N. 3501  
 Scandale, Walter 53, 3206, 3209  
 Scanlan, Ronald M. 171, 3194, 3197, 3233, 3236  
 Schachter, L. 3600, 3603, 3606, 3609  
 Schaffner, Sally K. 729  
 Scheer, Michael 2385  
 Scheidenberger, Christoph 1671  
 Schempp, Alwin 530, 1955, 3516, 3519  
 Schep, T.J. 1539  
 Schieler, H. 658, 2424  
 Schilcher, Thomas 1129  
 Schill, J. 75  
 Schlabach, Phillip 3194, 3197, 3327  
 Schlarb, Holger 2879  
 Schleuter, Ross 3429  
 Schlicher, Thomas 2087  
 Schlitt, Bernhard 3555  
 Schlott, Volker 1129, 2087  
 Schlueter, Ross 162  
 Schmalzle, Jesse D. 3170  
 Schmickler, Hermann 465  
 Schmidt, C.W. 521  
 Schmidt, Frank 1557, 1560, 1563  
 Schmidt, Gerald 2172, 2175, 2507  
 Schmidt, Rüdiger 3200, 3203  
 Schmierer, Eric N. 977, 1396  
 Schmolke, Michael 1034  
 Schmor, Paul W. 100, 106, 508  
 Schmueser, Peter 2172, 2175, 2178  
 Schnase, Alexander 851, 1701, 2292  
 Schneegans, T. 197  
 Schneider, Gerhard 1339  
 Schneider, Herbert 1701  
 Schneider, J. David 503, 1946, 3528  
 Schneider, Th. 165  
 Schneider, William J. 934, 1462, 1991  
 Schnuriger, Jean-Claude 103  
 Schoenlein, Robert 2370, 2498  
 Schoessow, Paul 1967, 2030, 3621, 3624  
 Scholfield, George 1010  
 Schonauer, Horst O. 2933, 2957  
 Schonberg, R.G. 590  
 Schrage, Dale L. 965, 1333, 1399  
 Schreiber, Siegfried 84, 922  
 Schröder, Gerhard H. 1228, 1408, 1509  
 Schuch, Reinhold H. 1671  
 Schuett, Petra 2951  
 Schug, Gebhard 3549  
 Schulte, Daniel 250, 259, 1668, 1863, 3441  
 Schultheiss, Carl M. 3737  
 Schultheiss, Thomas 780, 3306  
 Schultz, David C. 1252, 3447, 3450  
 Schultz, Sheldon 830  
 Schulze, Martin E. 3528, 3576, 3579, 3582, 3758  
 Schwalm, Dirk 1955, 3543  
 Schwandt, Peter 392  
 Schwartz, Charles 1073  
 Schwartzkopf, S. 545  
 Schwarz, Heinz 206, 800, 3429  
 Scorzato, Carlos 2421  
 Scott, Benjamin 206, 1363  
 Scott, Mike 1010  
 Scott, Paul K. 1911, 1926  
 Scrivens, Richard 103  
 Sears, James 980  
 Sebek, James J. 206, 2361, 3104, 3107  
 Sedlyarov, Igor K. 2033  
 Sedykh, Sergey N. 1055, 3393  
 Seeman, John T. 1, 296  
 Seidel, Mike 34, 554  
 Seidl, Peter 1937, 2849, 2852  
 Selchow, Nicholas 2235  
 Seleznev, Igor B. 2567  
 Sellyey, W. C. 2152, 2214  
 Semenov, P.A. 392  
 Semertzidis, Yannis K. 490, 1488  
 Sen, T. 1677, 2635  
 Senichev, Yurij V. 2442, 3549  
 Senioukov, Victor A. 2570  
 Senti, M. 3212  
 Seon, Dong K. 2131  
 Serafini, Luca 1997, 2039, 2734  
 Sereno, Nicholas S. 1587, 1644, 2322  
 Sergeev, Anatoly P. 1055, 3393  
 Serio, Luigi 1405, 3203  
 Serio, Mario 131, 636, 1536  
 Serov, Valeri L. 3561  
 Sertore, D. 2027  
 Servranckx, Roger 2620  
 Sery, Andrey 237, 3321, 3728  
 Sessler, Andrew M. 1716, 3053, 3056  
 Setzer, Stefan 2951  
 Shabunov, Alexey V. 2262  
 Shadwick, Bradley A. 1716, 2888  
 Shafer, Robert E. 3758  
 Shang, Clifford C. 3251  
 Shang, Lei 1315, 1596  
 Shank, Charles 2370  
 Shapiro, Michael A. 81, 833, 836  
 Shapiro, Stephen 2990  
 Sharamentov, S.I. 3561  
 Sharapa, Anatoly 237  
 Sharkov, B. 103  
 Sharma, Sushil K. 2635, 3095, 3342  
 Sharonov, S. 3191  
 Sharp, William M. 1830, 1833, 3248  
 Shasharina, Svetlana G. 369, 377  
 Shatilov, Dmitry 1536  
 Shchepounov, V. 3288  
 Shcherbakov, A. 3122  
 Shea, Thomas J. 2114, 2117, 2146, 2250  
 Sheehan, J. 3495  
 Sheffield, Richard L. 217  
 Shemyakin, Alexander 237, 521  
 Shen, Stewart S. 1333, 1336, 1372, 1396  
 Shepard, Kenneth W. 524, 952, 955  
 Sheppard, John C. 3429, 3447, 3450, 3486  
 Sherman, Joseph D. 349, 655, 1444, 1447, 1929, 1946, 3528  
 Sheu, Jeng-Tzong 1450, 3776  
 Shevchenko, Oleg A. 2492  
 Sheynin, S. 3576, 3579  
 Shibata, Yukio 2187  
 Shibuya, S. 1653  
 Shibuya, Takashi 3363  
 Shiltsev, Vladimir 237, 641, 1387, 1608, 1692, 2638, 3321, 3728  
 Shimbo, M. 600  
 Shinn, M. 2456  
 Shinoe, Kenji 3363  
 Shintake, Tsumoru 3411  
 Shinto, Katsuhiko 1653  
 Shioya, Tatsuro 2683  
 Shirai, Toshiyuki 1294, 2528, 3110  
 Shirakabe, Y. 565  
 Shirakata, Masashi 3360  
 Shirasawa, K. 2689  
 Shirotov, V. V. 2178  
 Shishido, Toshio 432  
 Shiyankov, Sergei V. 2948  
 Shoaee, Hamid 338  
 Shoaff, Phillip V. 1336  
 Shpak, A. 3122  
 Shu, Deming 2051, 2090  
 Shumakov, Igor V. 1764  
 Shuman, Derek 3339  
 Shumshurov, A. 103  
 Shurter, Robert B. 2214, 2241  
 Shvedunov, Vasilij I. 910, 2301, 2555, 2584, 2915  
 Shvets, Gennady 3675  
 Sibley, Coles 3101  
 Sidorov, Aleksey 1479, 1485  
 Sidorov, Guennady 2522  
 Sieber, Thomas 3516  
 Siedling, Rolf 2172  
 Siegel, Norbert 154  
 Siemann, Robert H. 146, 321, 330, 545, 824, 3612, 3648  
 Siemko, Andrzej 154  
 Sigg, Peter K. 418  
 Siggins, T. 2456  
 Sikora, John P. 1115  
 Sikora, Robert E. 2114, 2117  
 Silbar, Richard R. 2790  
 Silvestri, M. 2578  
 Silvestrov, Gregory I. 3062, 3086, 3089  
 Sim, James W. 1426, 3318  
 Simmering, D. 197  
 Simon, Rolf 2424  
 Simonov, Karlo G. 2567, 2570  
 Simos, Nikolaos 548  
 Simrock, Stefan 922  
 Sinclair, Charles K. 65, 1991  
 Sinenko, Irina G. 1468, 2105  
 Singatulin, Shavkat 1387  
 Singh, Om 2051, 2093, 2244  
 Sinjavski, A.V. 1468  
 Sivers, Dennis W. 392  
 Skarbo, Boris 237, 3321  
 Skarita, John 2552  
 Skaritka, John 1390, 2471, 2477, 2480, 3722  
 Skarpass, Knut VIII 3384  
 Skocic, Ante 2951  
 Skoczen, Blazej 1339

- Skowbo, D. 590  
 Skozen, Blazej 1330  
 Skrinsky, Alexander N. 3089  
 Slater, James 11  
 Slaton, Timothy 3411, 3477  
 Sloan, T. 498, 1545, 1548  
 Smart, Loralie A. 557, 1348  
 Smedley, John 75, 75  
 Smirnov, Alexei V. 3615  
 Smith, Brian G. 977, 1396  
 Smith, David R. 830  
 Smith, Frank M. 965, 968  
 Smith, G. 2128, 2286  
 Smith, H. Vernon 1444, 1447, 1929, 3528  
 Smith, Howard 2987  
 Smith, John D. 355, 690, 2713  
 Smith, Jr., H. Vernon 1946  
 Smith, Kevin 2280  
 Smith, Kevin S. 614, 857, 2725  
 Smith, Peter D. 2954, 3573  
 Smith, Robert J. 2096  
 Smith, Susan L. 2433  
 Smith, Terry L. 3755, 3758  
 Smith, Todd I. 321  
 Smithwick, J. 3233  
 Smolej, M. 658  
 Smolyakov, M. N. 2692  
 Smolyakov, N.V. 2689  
 Snell, Charles M. 1842  
 Snodgrass, N. Leon 3594  
 Snyder, Arthur 2990  
 Sobenin, Nicolay P. 910, 2301  
 Soga, F. 600  
 Soika, Rainer 2936  
 Sokoloff, M. 2990  
 Solheim, Larry 1515  
 Solomon, Lorraine 2244, 2471, 2698  
 Solyak, Nikolay 461  
 Solyga, Steffen 1034  
 Someya, Hirohiko 3348, 3752  
 Sommer, M. 1569, 2686  
 Song, Jinhua 2229  
 Song, Joshua J. 168, 789, 3092  
 Sonnemann, Florian 154, 2999, 3200  
 Sonnendruker, Eric 1830, 2758  
 Soukas, A. 1264, 1267, 1270, 3767  
 Sourkont, Konstantin V. 392  
 Soutome, Kouichi 2337, 2340, 2343, 2346, 2349, 2352  
 Souza, R. J. 2590  
 Spalek, George 3573  
 Spataro, Bruno 1147, 2873  
 Spataro, Charles 3333  
 Spence, William 1043  
 Spencer, Cherrill M. 1252, 3429, 3447  
 Spencer, James E. 321  
 Spentzouris, Linda K. 114, 2027, 3155  
 Spentzouris, Panagiotis 3062, 3083  
 Sperisen, Franz 392  
 Spiller, P. 1785, 1788  
 Spinos, Frank 1333  
 Spitz, Richard 857, 2280  
 Sprangle, Phillip A. 3687, 3693  
 Spyropoulos, Basile 2543  
 Sredniawski, Joseph 587  
 Srinivasan-Rao, Triveni 75, 490  
 Staats, Joachim 2740  
 Stagno, Vincenzo 1779  
 Stanford, G. 100, 3540  
 Staples, John W. 884, 1958, 1961  
 Starling, W.J. 3531  
 Starostenko, Alexander A. 2167  
 Stassen, Rolf 1701, 2292  
 Steck, M. 527, 1704  
 Stedinger, M. 2978  
 Stefani, Giovanni 2060  
 Steier, Christoph 3098  
 Steigerwald, M. 1991  
 Steinhauer, Loren C. 3722  
 Steinhof, A. 165  
 Steininger, Ralph 2424  
 Stella, A. 131  
 Stelzer, James E. 1923  
 Stengl, G. 2575  
 Stepanov, A. 103  
 Stepanov, Anatoli A. 3561  
 Stepanov, Sergey S. 1932, 2573  
 Stephani, Dmitri 2114  
 Steski, Dannie B. 2277  
 Stettler, Mathew W. 349, 652, 1946, 2214, 2241  
 Stevens, Alan F. 1013  
 Stevens, Alan J. 1237  
 Stevens, Jr., Ralph R. 1444, 1447, 1917, 1923, 1929, 1946  
 Stiliaris, E. 1037  
 Stirbet, Mircea 946  
 Stockhorst, Hans 851, 1701, 2292  
 Stoner, J. M. 2590  
 Stout, Daniel S. 3597  
 Stover, Greg D. 636, 1213  
 Strait, J. 2921, 3194, 3197  
 Strasburg, Sean 1518  
 Stratienco, Vladimir A. 3269, 3271  
 Street, Richard W. 3755  
 Streun, Andreas 1542, 2430  
 Striganov, Sergei I. 2614  
 Stroman, Charles R. 1115  
 Stronisch, U. 197  
 Strubin, Pierre M. 346, 562  
 Stupakov, Gennady V. 382, 3444, 3453, 3474  
 Subashiev, Arsen V. 1988  
 Suberlucq G. 250  
 Suda, M. 600  
 Suemine, Shouji 2596  
 Sueno, Takeshi 3360  
 Suetake, M. 1132, 2731  
 Suetsugu, Y. 633, 1132, 2731  
 Sugahara, Jun 2187, 2602  
 Sugimoto, Masayoshi 2459  
 Sugimura, Takashi 1294, 3110  
 Suk, H. 1659  
 Suk, Hyoyong 2006, 3708  
 Sukhanova, Asiya K. 2262  
 Sukhina, Boris 237, 3321  
 Suller, Victor P. 2433  
 Sullivan, Kevin 3306, 3309  
 Sullivan, Michael K. 296, 2990  
 Summers, Don 3149, 3152  
 Sun, Baogen 2048, 2184, 2406  
 Sun, Ding 854  
 Sun, H. 913  
 Sun, Yong 3480  
 Sutton, Terry D. 3597  
 Suwada, T. 1132  
 Suwada, Tsuyoshi 2108, 2238, 2731  
 Suzuki, Shinsuke 2015, 2749, 3507  
 Suzuki, Shoji 664  
 Suzuki, Toshikazu 777, 3417  
 Suzuki, Yasuaki 2352  
 Svandrik, Michele 809, 1120, 1123  
 Sveshnikov, B.N. 2256  
 Swenson, Donald A. 3531  
 Swent, Richard L. 321  
 Swift, Gary 221, 2099, 2468  
 Sylvester, C. 1420  
 Sylvester, C. 3194  
 Syphers, Michael J. 1578, 2128, 2632  
 Syphers, Mike 2641  
 Syratcev, I. 250  
 Tadokoro, Masahiro 2528, 3366  
 Taffarello, L. 1324  
 Tafti, A. Alai 2728  
 Tagawa, Seiichi 2018, 2596  
 Tajima, Tsuyoshi 440  
 Takada, Ei-ichi 600, 1309  
 Takado, Hiroshi 3546  
 Takagi, Akira 413, 565, 798, 860, 863, 1007, 1653  
 Takagi, Makoto 343  
 Takahashi, Hiroshi 1273  
 Takahashi, Jiro 1366  
 Takahashi, Takeshi 904  
 Takaki, Hiroyuki 592, 2436, 3363  
 Takanaka, Masao 1719  
 Takano, M. 256, 3432  
 Takano, Siro 2346  
 Takao, Masaru 2337, 2340, 2343, 2346, 2349, 2352  
 Takata, Koji 3414, 3417  
 Takatomi, Toshikazu 777, 3417  
 Takayama, Ken 1141  
 Takayama, T. 592  
 Takayama, Takeshi 2403, 2689  
 Takayama, Yasuhiro 256, 2155  
 Takeda, Harunori 3585  
 Takeda, Osamu 3546  
 Takeda, S. 3447  
 Takeichi, N. 592  
 Takeuchi, Takeshi 106, 1964  
 Takiyama, Youichi 3363  
 Tallerico, Paul J. 426, 453  
 Talman, Richard 410, 2713  
 Tamura, Hiroyuki 2259  
 Tamura, Kazuhiro 2346  
 Tanabe, J. 206, 2355  
 Tanabe, Toshiya 1722  
 Tanaka, Hitoshi 2337, 2340, 2343, 2346, 2349, 2352  
 Tang, Ch. 2769  
 Taniguchi, Yoshiki 1007  
 Taniuchi, Tsutomu 2015, 2749, 3507  
 Taniuchi, Yukiko 2352  
 Tanke, E. 1860  
 Tanner, David B. 134  
 Tantawi, S.G. 3423  
 Tantawi, Sami G. 423, 783, 1432, 1435  
 Tao, Xiaoping 2125  
 Tarakanov, Vladimir P. 1734  
 Tarasov, Sergej G. 2799  
 Tartaglia, Michael A. 1420, 1426, 3191, 3194, 3197  
 Tassotto, Gianni 2211  
 Tatanov, V.I. 753  
 Tavares, Pedro F. 2421, 2894, 3125  
 Tavian, L. 1330  
 Tawada, M. 1132, 2731  
 Taylor, Brian 1471  
 Taylor, C. 3233  
 Tazzari, Sergio 2313  
 Tazzioli, Franco 1985, 2734

- Tecchio, Luigi B. 2948, 3558  
 Tecker, Frank A. 711, 720, 1082, 2719  
 Tejima, M. 1132, 2731  
 Telegin, Yu. 3122  
 Telfer, S. 2021  
 Temkin, Richard J. 81, 833, 836  
 Temnykh, Alexander B. 410, 3221  
 Tenenbaum, Peter G. 253, 338, 3453, 3456, 3459, 3462  
 Teng, Lee C. 2635  
 Tenishev, Vladimir 103  
 Tenyakov, Igor E. 1479, 1485, 2567  
 Tepes, Frank 3306  
 Tepikian, Steven 37, 1575, 2114, 2728  
 Terechkine, Iouri 174, 3242  
 Terekhov, V.I. 53  
 Terunuma, Nobuhiro 2143, 3432  
 Teter, Dave F. 962  
 Teytelman, Dmitry 131, 636, 1207, 1213  
 Theuws, W.H.C. 759, 2825  
 Thibus, Jan 530  
 Thieberger, Peter 548, 2277  
 Thiery, Yves 2012  
 Thikim, M. 2659  
 Thivent, Michel U. 2283  
 Thomae, Rainer 1917, 1920, 1943  
 Thomas, Catherine 913  
 Thomas, Manfred 1028  
 Thomas, Richard A. 3170, 3188  
 Thompson, K. 3465  
 Thompson, Kathleen A. 259, 307, 3423, 3489  
 Thompson, Kenneth 1979, 2635  
 Thompson, Pat 185, 3176  
 Thorndahl, L. 250  
 Thorson, I. 100  
 Thuot, Michael E. 349, 1929, 1946  
 Tichonchuk, Vladimir T. 3716  
 Tiefenback, Michael G. 1183  
 Tighe, Richard C. 800, 1438, 3429  
 Tilley, K. 2199  
 Timm, Martin 2879  
 Ting, Antonio C. 3687, 3693  
 Tisserand, Vincent 2990  
 Tiunov, M. 1902  
 Tkacik, G. 658  
 Tobiyama, Makoto 633, 1132, 1138, 2731  
 Toda, Makoto 413, 1007  
 Todd, Robert 557  
 Todesco, Ezio 3206, 3209  
 Todosow, M. 548  
 Toelle, Raimund 2292  
 Toge, Nobukazu 777, 2143, 3414, 3417, 3432  
 Tohyama, I. 592  
 Tojyo, E. 1893  
 Toki, Walter 2990  
 Tokumoto, Shuichi 3414  
 Tollestrup, Alvin V. 3032, 3062  
 Tolmachev, Nikolay G. 3269, 3271  
 Tolstun, Nickolay 603  
 Tominaka, Toshiharu 3164  
 Tomisawa, Tetsuo 3546  
 Tommasini, Davide 154  
 Tompkins, John C. 174, 3191, 3194, 3197, 3318  
 Tonguu, Hiromu 1294, 3110  
 Tonutti, Manfred 2172, 2178  
 Tooker, Joseph F. 1061, 2954, 3567  
 Toole, Loren 1402, 2772  
 Torikoshi, Masami 600, 1309  
 Toriyama, Minoru 3770  
 Torrence, Eric 2999  
 Tosi, Lidia 1120, 1126, 2316  
 Tosin, Giancarlo 3125  
 Tovo, E. 1324  
 Towne, Nathan A. 1028, 1031, 2828  
 Toyama, Takeshi 1141, 1653, 1821, 3098  
 Trakhtenberg, Emil 1369, 2489  
 Trautwein, T. Ann 206, 1363  
 Travier, Christian 916  
 Travish, Gil 2024, 2045, 2483  
 Trbojevic, Dejan 37, 1237, 2117, 3176, 3336  
 Tremaine, Aaron 217, 2006, 2021, 2480  
 Tremblay, Kelly 3306, 3312  
 Treps 2990  
 Tribendis, Alexey G. 2033  
 Trines, D. 245  
 Trines, R.M.G.M. 1539  
 Trofimov, A.V. 2704  
 Trofimov, Nikolai 346  
 Troha, Anthony L. 2000  
 Tromba, G. 2316  
 Trombly-Freytag, Kelley 3318  
 Tron, Alexander 2190  
 Tron, Wolfgang 986  
 Tropea, Paola 3206  
 Trower, W. Peter 910, 2301, 2555  
 Troyanov, E. 53  
 True, Richard 1049  
 Trujillo, Marcos C. 965  
 Trzeciak, Walter S. 2388, 2391, 2659  
 Tsai, H.J. 1162, 2409  
 Tsai, Y.L. 2000, 2009  
 Tsai, Zone-Da 1150  
 Tsang, Thomas 490  
 Tsarenkov, A.P. 2256  
 Tsoupas, Nicholas 702, 1100, 1267, 1270, 1578, 2114, 2117, 2722, 2725, 2918, 3182, 3185, 3291  
 Tsubuku, Hideo 1309  
 Tsuchidate, Hiroyuki 848  
 Tsuchiya, Kimichika 2683, 3158  
 Tsukamoto, K. 633  
 Tsukishima, Chihiro 848  
 Tsunemi, Akira 2036, 2552  
 Tsung, F. S. 3672  
 Tsutsui, Hiroshi 1058, 3414  
 Tuckmantel, Joachim 949  
 Tung, Louann S. 1372  
 Tuozzolo, Joseph E. 1100, 1264, 1267, 1270, 3300  
 Tupikov, Vitaliy S. 2167  
 Turner, James 256, 774, 1252, 3432, 3450  
 Turner, William C. 1674, 3149  
 Tölle, Reimund 1701  
 Ueda, Toru 2187, 2602, 2605  
 Ueng, Tzong-Shyan 1375, 1450, 2069, 2072, 2412  
 Ueno, Ryuichi 2271  
 Uesaka, Mitsuru 2187, 2602, 2605  
 Uesugi, Tomonori 62, 413, 798, 860, 863, 1007, 1653, 1818, 1821, 2271  
 Umezawa, K. 2271  
 Umezawa, Masumi 2528, 3366  
 Umstadter, Donald 3666  
 Urabe, Osamu 2602  
 Urakabe, E. 600  
 Urakawa, Junji 256, 2143, 2155, 2552, 3432  
 Urbanus, W.H. 2462  
 Urita, K.K. 471  
 Ursic, Rok 1120, 1129, 2087, 2253  
 Usack, Victor 490  
 Usher, Tracy 307, 3384  
 Uythoven, Jan 1228, 2996, 2999  
 Uzat, H. W. 450  
 Uzunoglou, N. 1037  
 v. Drachenfels, Wolther 3098  
 Vaccaro, Vittorio G. 1599  
 Vahsen, Sven E. 3026  
 Vaillancourt, Kurt W. 3423, 3480  
 Valdiviez, Robert 1333  
 Valentini, Marco 250, 3402  
 Valentino, Vincenzo 1905  
 Valero, Saby 1860  
 Valicenti, Raymond A. 971, 1327  
 Valla, Arthur S. 2668  
 van Asselt, Willem K. 1746  
 van Bibber, Karl A. 777, 3447, 3450  
 van der Geer, Bas 2462, 3266  
 van der Wiel, M.J. 3266  
 van Duppen, Piet 1955  
 Van Eijndhoven, S.J.L. 1539  
 Van Ginneken, Andy 2525, 3074, 3080  
 Van Hagan, T. 1393  
 Van Rienen, U. 2764, 2787  
 van Steenberg, Arie 3722  
 Van Vaerenbergh, Pierre 2662, 2665  
 van Zeijts, Johannes 705, 732, 2146, 2722, 2725, 2728  
 VanAsselt, W. 614, 3291  
 VanBrocklin, Henry 533  
 Vane, C. Randy 1671  
 Vanecek, David L. 3390  
 Vanenkov, Iouri 154  
 Varela-Rodriguez, F. 103  
 Variale, Vincenzo 1779, 1905  
 Vascotto, Alessandro 2316  
 Vasilishin, Bogdan V. 2256, 2262  
 Vasiniuk, Ivan E. 1468, 2105  
 Vasserman, Isaac B. 2471, 2489  
 Vasyuchenko, Alexandr V. 3561  
 Vella, Michael C. 3257  
 Veness, Raymond J. 1339  
 Vengrov, R. M. 3561  
 Venturini, Marco 234, 1590, 1593, 1752, 1758, 1970, 3274, 3369, 3372  
 Ver Planck, Peter 1491  
 Verbeke, Jerome M. 1926, 2540  
 Verdier, Andre 304, 398, 1557, 1563, 2623, 3005  
 Verdu, Gumersindo 2534  
 Verhoeven, A.G.A. 2462  
 Vermare, C. 3387  
 Vernon, W. 2021  
 VerPlanck, Peter 568  
 Verstovsek, I. 658  
 Verzilov, Viktor A. 2193, 2196  
 Veshcherevich, Vadim 980  
 Vest, Robert E. 2388  
 Veteran, J. 2686  
 Vetter, Arthur M. 1186  
 Vetter, Paul 1952  
 Vier, David C. 830, 3612  
 Vignola, Gaetano 131, 866, 1536  
 Vikharev, A.L. 1474  
 Vilakazi, Zebulon Z. 1671  
 Villate, Denis 1381  
 Vinciguerra, Domenico 2578  
 Vinogradov, N. 2855  
 Vinogradov, Stanislav V. 1764  
 Vinokurov, Nikolai A. 2492  
 Virostek, Steve 884  
 Vlieks, Arnold E. 3420, 3423, 3447  
 Voevodin, M.A. 2256



- Vogel, Greg 2211  
 Vogel, Hans 957, 2033, 3510  
 Vogel, Vladimir 461  
 Vogt, S. 197  
 Voigt, Siegfried 806, 809, 2424  
 Volfbeyn, Paul 325, 330, 3696, 3705  
 Volk, J.T. 182, 3324  
 Volkov, Igor A. 1872  
 Volkov, O. Y. 2178  
 Volkov, V.I. 2256  
 Volkov, Vladimir N. 2033  
 vom Stein, Peter 957, 2033, 3510  
 von Hahn, R. 3543  
 von Hartrott, M. 197  
 von Holtey, Georg 3008  
 von Przewoski, Barbara 392  
 Vondrasek, R. 1890  
 Vorobiev, Leonid G. 234, 2781, 3116  
 Vos, Lucien 304, 465  
 Voss, Gustav A. 2385  
 Vossenbergh, Eugene B. 1228, 1509  
 Vsevolozhskaya, Tatiana A. 3062, 3086, 3089  
 Vujic, Jasmina 2540  
 Vysotskii, Vladimir I. 1312, 3642  
 Wada, M. 1306  
 Wagner, Stephen 2990  
 Wahl, Dan 2388  
 Wait, Gary D. 1509  
 Wake, M. 174, 3330  
 Walbridge, Dana G.C. 3318  
 Walcher, Th 165  
 Waldron, William L. 3257  
 Walker, J. 548  
 Walker, R. 182, 2456  
 Walker, Richard P. 2313, 2680  
 Wallen, Erik 2945  
 Walters, Dean R. 1342, 1378  
 Walther, R. 2424  
 Walz, Dieter R. 253, 330, 2111, 3453  
 Wan, Weishi 395, 1677, 2465, 3065, 3068, 3152  
 Wan, Xiang 81  
 Wanderer, Peter J. 185, 3161, 3170, 3173, 3176, 3230  
 Wang, C.J. 682, 685  
 Wang, Ch. 2409, 2671  
 Wang, Changbiao 1052, 3630  
 Wang, Chunxi 363  
 Wang, D. X. 934  
 Wang, Fuhua 3101  
 Wang, Guicheng 1315, 1596, 2048, 2125, 2184  
 Wang, Huacen 3263  
 Wang, J.G. 1659, 1970  
 Wang, J.M. 1106  
 Wang, J.Q. 1058  
 Wang, J.W. 3423, 3468  
 Wang, Jian-Guang 234, 1656, 2102, 3369, 3372  
 Wang, Jihong 2125  
 Wang, Jiuqing 633, 3414  
 Wang, Ju 3773  
 Wang, Junhua 2048, 2184  
 Wang, Juwen 777, 3420, 3426, 3477, 3480  
 Wang, Lanfa 633  
 Wang, Li-Fang 3381  
 Wang, Lin 1315, 1596, 2140  
 Wang, M.H. 1159, 1602, 1605, 2837  
 Wang, P. 3600, 3603, 3606, 3609  
 Wang, Ping 221, 2099  
 Wang, S. 330, 1695, 3705  
 Wang, S.T. 3227  
 Wang, Sho Qin 3651  
 Wang, Shuhong 633  
 Wang, Shumei 2140  
 Wang, Tai-Sen F. 1623, 1848, 2876  
 Wang, X. 2018  
 Wang, X.J. 229, 2024, 3495, 3627  
 Wang, Xiangqi 1315, 1596  
 Wang, Xijie 2158, 2471, 2480, 2942  
 Wang, Yi-Ming 1064, 1067, 1070  
 Wangler, Thomas P. 611, 1061, 1848, 3582  
 Warburton, D. 1488  
 Warner, A. 521  
 Warren, David S. 349, 655  
 Warsop, C.M. 2199  
 Washio, Masakazu 2018, 2298, 2552  
 Watanabe, Kowashi 2352  
 Watanabe, Takahiro 2187, 2602, 2605  
 Watanabe, Tamaki 1653  
 Watanabe, Yuichi 777, 3417  
 Watson, Scott A. 617  
 Waynert, J.A. 977, 1327  
 Webber, Robert C. 1097  
 Weber, Robert 3740  
 Weggel, Robert J. 3041, 3047  
 Wei, Jie 548, 1575, 1743, 2713, 2921, 3176, 3179, 3182, 3185  
 Wei, Wen-His 1375  
 Weihreter, Ernst 197, 2385  
 Weijers, S.R. 759  
 Weiland, Thomas 2740, 2743, 2879, 2951  
 Weindl, A. 658  
 Weinrich, U. 2331, 2334  
 Weir, John T. 622, 1303, 3513  
 Weise, Hans 922, 2507  
 Weiss, Daniel 557, 1348  
 Weiss, M. 759  
 Weisse, Eberhard 40  
 Welch, James J. 1441, 3221, 3224  
 Welsch, C. 3516  
 Welz, J. 100  
 Wen, Long 3263  
 Weng, Wu-Tsung W. 1297, 3185  
 Wenninger, Joerg 2885, 2996, 2999, 3011, 3014  
 Werin, Sverker 2945  
 Wermelskirchen, C. 206  
 Westenskow, Glen A. 617, 1303, 3251, 3254, 3387, 3390  
 Westphal, T. 197  
 White, Jeff 2217  
 White, Karen S. 729, 732, 735  
 White, Marion M. 1414, 1967  
 Whittum, David H. 330, 2111, 3612  
 Wiedemann, Helmut 206, 321  
 Wiemerslage, G. 1369  
 Wienands, Hans-Ulrich 296, 1252, 2993  
 Wieting, James 1923  
 Wight, Geoff. W. 106  
 Wilcox, Marc 1926  
 Wilde, Stephen 1920  
 Wildman, David W. 237, 869, 2840  
 Will, Ingo 2033  
 Wille, K. 206  
 Willeke, Ferdinand 407, 554  
 Willen, Erich 185, 3161, 3173  
 Williams, C. 1881  
 Williams, David J. 2223  
 Williams, Malcom D. 1911, 1914, 1917, 1920, 1923, 1943, 1958, 2540, 2575  
 Williams, Neville W. 2063, 2128, 2286  
 Williams, Robert A. 2790  
 Williams, Ronald L. 3681  
 Wilson, Ian 250, 821  
 Wilson, J. H. 2590  
 Wilson, P. 2003  
 Wilson, Perry B. 423, 3423  
 Wind, D. 2936  
 Wines, Robin 3309  
 Winick, Herman 2385  
 Winkler, Martin 2578  
 Winkler, T. 527, 1704  
 Winschuh, Erich 530  
 Winter, W. R. 2659  
 Wiseman, Mark 934, 3309  
 Wisnivesky, Daniel 792  
 Wissmann, Mark 768  
 Witherspoon, R. 545  
 Witherspoon, Sue D. 732  
 Witkover, Richard L. 2128, 2247, 2250  
 Wolcott, Chip 1037, 1515  
 Wolf, Z. 1390  
 Wolff, Dan 3761  
 Wolfley, Rick 3306  
 Wollnik, Hermann 2578  
 Wolski, Andrzej 2433  
 Wong, Seung 1043, 1890  
 Wong, Tom 3618  
 Wong, Victor K. 392  
 Woodle, Martin 1028, 2471  
 Woodley, Mark D. 256, 307, 3384, 3429, 3432, 3447, 3456  
 Woods, Mike 3465  
 Woodworth, Lee 2114  
 Wright, R. 652  
 Wright, Robert 3342  
 Wrulich, Albin F. 192  
 Wu, G. 714, 717, 1462  
 Wu, Guozhong 2602  
 Wu, Lydia K. 1926, 2540  
 Wu, Xiaoyu 1318, 3116  
 Wu, Ying 221, 688, 2099, 2468  
 Wu, Yingzhi 282  
 Wuensch, Walter 250, 821, 827, 3387  
 Wuestefeld, Godehard 197, 2376, 2385  
 Wurtele, Jonathan S. 1716, 2888, 3053, 3056, 3059  
 Wutte, Daniela 533, 1952  
 Wyss, Carlo 149, 3203  
 Xavier, Jr., Ademir L. 2891  
 Xiao, Meiqin 404  
 Xie, Ming 3678  
 Xie, Zu Qui 533, 1952  
 Xu, Hongjie 209  
 Xu, Hongliang 1315  
 Xu, Jingwei 633  
 Xu, S. 1369  
 Xu, X.J. 533  
 Xu, Z. 3600  
 Xue, K. 2140  
 Yadav, S. 174, 3194, 3197  
 Yakimenko, Vitaly 461, 2158, 2471, 2552, 2942, 3495, 3722  
 Yakovlev, Vyacheslav P. 1049, 2775, 3492  
 Yamada, Hironari 592  
 Yamada, R. 174  
 Yamada, S. 600, 2271  
 Yamaguchi, Seiya 1058, 3414  
 Yamamoto, Masanobu 413, 798, 860, 863, 1007, 1653  
 Yamamoto, N. 2731  
 Yamamoto, Nobor 1132  
 Yamamoto, Noboru 343

- Yamamoto, Tamotsu 2596  
 Yamamoto, Y. 492, 2271  
 Yamashita, H. 600  
 Yamauchi, Toshihiko 2459  
 Yamazaki, Junichiro 592  
 Yamazaki, Yoshishige 513  
 Yan, Yiton T. 363  
 Yanagida, Kenichi 2015, 2749, 3507  
 Yanaoka, Eiichi 3348  
 Yang, Bingxin 1644, 2024, 2134, 2137, 2161  
 Yang, J. S. 902  
 Yang, Jinfeng 2018, 2036, 2298, 3702  
 Yang, Ming-Jen 711, 720, 723, 1082, 1085, 2719  
 Yang, Tz Te 1159, 2000  
 Yang, W. Y. 2265  
 Yano, Yasushige 2268  
 Yao, Chenggui 1596  
 Yarba, V. 174  
 Yashin, Yuri P. 1988  
 Yazynin, Igor A. 1321  
 Ye, Kairong 633  
 Yeh, Meng Shu 1153, 1159, 1162, 2000  
 Yen, Boris 1506  
 Yeremian, A. D. 1994  
 Yin, B. G. 3345  
 Yin, Yan 2048  
 Yip, Harry H. 1402  
 Yokoi, Takeichiro 1653  
 Yokomizo, Hideaki 3128, 3507, 3546  
 Yokota, Watalu 2259  
 Yokoya, Kaoru 633, 1725, 3435  
 Yoon, Byung-Ju 3525  
 Yoon, J. C. 679  
 Yoon, Moohyun 2265, 3137  
 York, Richard C. 234, 1318, 2781, 3116, 3719  
 Yorozu, Masafumi 2018, 2036  
 Yosh 2731  
 Yoshida, H. 2689  
 Yoshida, Katsuhisa 848, 848  
 Yoshida, Mitsuhiro 3158, 3411  
 Yoshida, Susumu 343  
 Yoshida, Yoichi 2596  
 Yoshida, Youichi 2018  
 Yoshii, Jean 3654  
 Yoshii, Kenji 343  
 Yoshii, Koji 2187, 2602, 2605  
 Yoshii, Masahito 413, 798, 857, 860, 863, 1007, 1653, 2280  
 Yoshii, Masato 2271  
 Yoshikawa, H. 3507  
 Yotam, R. 206  
 Young, Andrew 131, 636, 1213  
 Young, Anthony 162  
 Young, Lloyd M. 881, 1444, 1447, 1929, 1946, 3528, 3570, 3582  
 Yourd, Roland 884  
 Youssof, S. S. 392  
 Yovchev, I. 1040, 1046  
 Yu, D. 2042  
 Yu, David 815, 2003, 2021  
 Yu, H. 2140  
 Yu, Li Hua 2471, 2474, 2942  
 Yu, Simon S. 1800, 1934, 2746, 3257, 3390  
 Yudin, Ivan P. 2704  
 Yun, V. 3372  
 Yunn, Byung C. 1177, 1180, 2453, 2456  
 Zachariadou, Katerina 2990  
 Zadorozhny, Vladimir 2820  
 Zagar, K. 658  
 Zagel, James R. 468, 2164, 2211  
 Zahir, Nastaran 1926, 2540  
 Zalateu, M. 2680  
 Zaltsman, Alexander 857, 2280  
 Zalyubovskiy, Ilya I. 2549  
 Zangrando, Dino 2680  
 Zanini, Alba 2531  
 Zapasek, R. 1488  
 Zaplatine, Evguenii N. 887, 959, 3549  
 Zaugg, Thomas J. 349, 655, 1444, 1447, 1923, 1929, 1946  
 Zavialov, V. 592  
 Zeitlin, Michael 1614, 1617, 1620, 2900, 2903, 2906, 2909, 2912  
 Zelazny, Michael S. 2987  
 Zelenski, Anatoli N. 106, 1964  
 Zelinsky, A. Yu. 2924, 2927, 2930, 3122  
 Zeng, J. 2003, 2021  
 Zeno, Keith L. 1276  
 Zhabitsky, Vyacheslav M. 1222  
 Zhang, Chuang 633, 1695  
 Zhang, F. Q. 3348, 3752  
 Zhang, Jinguo 1315  
 Zhang, Jun 1273  
 Zhang, Kaizhi 3263  
 Zhang, Min 2769  
 Zhang, S. Y. 614, 3185, 3294, 3297  
 Zhang, T-B. 3627  
 Zhang, T. 1881  
 Zhang, Tiejue 1940  
 Zhang, Wenwei 234, 1970, 3263, 3372  
 Zhang, Wu 1261, 1264, 2406  
 Zhang, Xiaolong 2629  
 Zhao, Feng 1315, 2125  
 Zhao, G. Y. 3345  
 Zhao, Yongxiang 3149  
 Zhao, Zheng 2140  
 Zhao, Zhentang 209, 1453  
 Zhogeev, Pavel 461  
 Zholents, Alexander A. 1794, 2370, 2465, 2498  
 Zhou, Anqi 2406  
 Zhou, Feng 633, 2963  
 Zigler, Arie 3687, 3693  
 Ziggrosser, Douglas 557, 1348  
 Zimmerman, Robert 1396  
 Zimmermann, F. 1560, 2626  
 Zimmermann, Frank 206, 256, 307, 382, 1728, 3432  
 Zimmermann, Holger 530  
 Zinchenko, Alexander 1692  
 Ziomek, Chris D. 1064, 1070  
 Zisman, Michael S. 293, 296  
 Zlobin, Alexander V. 174, 3194, 3197  
 Zbov, Mikhail 131, 1147, 1536  
 Zolecki, Robert A. 2274  
 Zolfaghari, Abbi 1037, 1515  
 Zolotarev, Max S. 2111, 2370, 2498  
 Zorko, B. 658  
 Zotter, Bruno 1118, 1408  
 Zou, Peng 3618  
 Zou, Yong 3263  
 Zou, Yun 234, 1659, 1970, 2102, 3369  
 Zoubets, V. 106  
 Zubovsky, Victor P. 1932  
 Zumdick, John F. 2668  
 Zuo, K. 206  
 Zvonaryova, O. 2927



# 1999 PARTICLE ACCELERATOR CONFERENCE

Brookhaven National Laboratory, Bldg. 911B, P.O.Box 5000, Upton, New York USA 11973-5000 <http://pac99.bnl.gov/>

AT THE NEW YORK MARRIOTT MARQUIS

MARCH 29 - APRIL 2, 1999

#### Conference Chairman

W.T. Weng, BNL  
Telephone: 516-344-2135  
Fax: 516-344-5954  
E-mail: [weng@bnl.gov](mailto:weng@bnl.gov)

#### Program Chairman

I. Ben-Zvi, BNL  
Telephone: 516-344-5143  
Fax: 516-344-3029  
E-mail: [ilan@bnl.gov](mailto:ilan@bnl.gov)

#### Organizing Committee

M. Allen, SLAC (NPSS)  
J. Ball, ORNL  
W. Barletta, LBNL  
I. Ben-Zvi, BNL  
Y. Cho, ANL  
L. Costrell, NIST  
M. K. Craddock, UBC & Triumf  
W.K. Dawson, TRIUMF (IEEE)  
D. Finley, FNAL  
D. Friesel, IUCF  
D. Hartill, Cornell U.  
C. Joshi, UCLA  
M. Kihara, KEK (APAC)  
S. Krinsky, BNL  
C. Leemann, TJNAF  
J. Peoples, FNAL (DPB)  
M. Reiser, U. Maryland  
B. Ripin, APS  
C. Roberson, ONR  
S. Schriber, LANL  
R. Siemann, SLAC  
D. Sutter, DOE  
S. Tazzari, U. Roma & INFN-LNF (EPAC)  
W.T. Weng, BNL, Chairman  
G. Westenkow, LLNL  
R. York, NSCL

#### Conference Secretary

M. Campbell, BNL  
Telephone: 516-344-5458  
Fax: 516-344-5954  
E-mail: [pac99@bnl.gov](mailto:pac99@bnl.gov)

#### Local Committee, BNL

J. Becker, Treasurer  
H. Kirk, Coordinator, Poster & Exhibits  
J. Laurie, Printing  
E. Lowenstein, BNL Tour  
P. Lucas, Publishing (FNAL)  
A. Luccio, Editor  
W. MacKay, Editor  
C. Ronick, Hotel Coordinator  
J. Smith, Electronic Publishing  
P. Yamin, Social & Spouse Activities

The  
American  
Physical  
Society



BROOKHAVEN NATIONAL LABORATORY  
BROOKHAVEN SCIENCE ASSOCIATES

February 23, 2000

DTIC

8725 John J Kingman Road

Ste. 0944

Ft. Belvoir, VA 22060-6218

Dear Sir,

The 1999 Particle Accelerator Conference (PAC'99) took place on March 29 - April 2, 1999 at the New York Marriott Marquis. We had approximately 1,195 registrants, 76 invited speakers and 1,528 abstracts covering all aspects of accelerator science, technology and applications. Among the registrants, approximately 2/3 were from the United States, 1/3 from abroad - truly an international conference in its scope and participation. Concurrent with the conference, there were 40 industrial firms participating in the exhibition.

The proceedings of PAC'99 were published and distributed in November 1999. Total published papers are 1,223 which are published in a 5 volume set with the total pages numbering 3,779.

The total amount of the ONR grant of \$10,000.00 was all used in the support of the expense of junior staff, graduate students, and scientists from the developing nations and former Soviet Union.

As requested form SF298 is enclosed, and shipped separately is one set of the PAC '99 proceedings.

I would like to express my sincere thanks to ONR for its support to PAC'99 which is a very effective vehicle for the development and communication in the accelerator profession.

Sincerely yours,

Wu-Tsung Weng  
Chair, PAC'99

attachment: Form SF298

cc: K. Galuchie, IEEE  
Grant Administrator - ONR

WTW:mc

A373870 Vol 5

A 373874 Vol 1 / A373873 Vol 2 / A373872 Vol 3 / A373871 Vol 4

